รายงานวิจัยฉบับสมบูรณ์

(เล่มที่ 1 ของจำนวน 3 เล่ม)

โครงการ
งานวิจัยขั้นสูงทางการไหลสองสถานะและการเพิ่มความสามารถในการถ่ายเทความร้อน

โดย

ศ. ดร. สมชาย วงศ์วิเศษ

ภาควิชาวิศวกรรมเครื่องกล คณะวิศวกรรมศาสตร์

มหาวิทยาลัยเทคโนโลยีพระจอมเกล้าธนบุรี

วันที่ 31 มีนาคม 2557

สัญญาเลขที่ DPG5380003
รายงานวิจัยฉบับสมบูรณ์

โครงการ
งานวิจัยขั้นสูงทางการไหลสองสถานะและการเพิ่มความสามารถในการถ่ายเทความร้อน

โดย

ศ. ดร. สมชาย วงศ์วิเศษ
ภาควิชาวิศวกรรมเครื่องกล คณะวิศวกรรมศาสตร์
มหาวิทยาลัยเทคโนโลยีพระจอมเกล้าธนบุรี

สนับสนุนโดย

สำนักงานกองทุนสนับสนุนการวิจัย (สกว.)
สำนักงานคณะกรรมการการอุดมศึกษา (สกอ.)
มหาวิทยาลัยเทคโนโลยีพระจอมเกล้าธนบุรี

(ความเห็นในรายงานนี้เป็นของผู้วิจัย สกอ.และ สกว. ไม่จำเป็นต้องเห็นด้วยเสมอไป)

กิตติกรรมประกาศ

โครงการ “งานวิจัยขั้นสูงทางการไหลสองสถานะและการเพิ่มความสามารถในการถ่ายเทความร้อน” นี้ได้รับการสนับสนุนด้านเงินทุน จาก 3 สถาบัน ได้แก่ สำนักงานคณะกรรมการการอุดมศึกษา (สกอ.) สำนักงานกองทุนสนับสนุนการวิจัย (สกว.) และ มหาวิทยาลัยเทคโนโลยีพระจอมเกล้าธนบุรี ภายใต้ชื่อ “ทุนศาสตราจารย์วิจัยดีเด่น”

จากการได้รับทุนสนับสนุนดังกล่าวทำให้ผู้วิจัยสามารถทำงานวิจัยได้อย่างต่อเนื่องเป็นเวลา 4 ปี ผู้วิจัยพึงพอใจกับผลงานที่ได้มาเป็นอย่างมาก โดยสามารถแบ่งผลงานได้เป็น 5 ประเด็น ได้แก่

1. การสร้างองค์ความรู้ใหม่ในเรื่องของการเพิ่มประสิทธิภาพของอุปกรณ์แลกเปลี่ยนความร้อน: งานวิจัยนี้ทำให้ผู้วิจัยมีความรู้ที่ละเอียดลึกซึ้ง และสามารถมองโจทย์ที่ประชาคมวิจัยหรืออุตสาหกรรมต้องการคำตอบ ทำให้รู้ State of the art ของ งานวิจัยในสาขานี้

2. การตีพิมพ์ผลงานการค้นคิดใหม่: สามารถตีพิมพ์ ในวารสารระดับนานาชาติที่มีคุณภาพ (126 บทความ) ยื่นจด สิทธิบัตร (7 ผลงาน) และลิขสิทธิ์ (3 ผลงาน) Book chapter (3 chapters) นอกจากนั้น ผู้ทำวิจัยยังได้เขียนหนังสือ “กลศาสตร์ของไหล” หนังสือเล่มนี้สามารถใช้ประกอบการเรียนการสอนในวิชากลศาสตร์ของไหลสำหรับนิสิต นักศึกษาวิศวกรรมศาสตร์ หรือผู้ที่สนใจทั่วไป หนังสือประกอบด้วย 14 บท ผู้เขียนได้รวมผลงานที่ได้ จากงานวิจัยของตัวเองใส่เข้าไว้ในหนังสือ ซึ่งจะทำให้นักศึกษาหรือผู้อ่านได้เข้าใจเนื้อหาอย่างถ่องแท้ มีพื้นฐานที่ดีสามารถนำไปประยุกต์ใช้หรือนำความรู้ไปต่อยอดในงานวิจัยต่อไป

3. การสร้างคนที่มีความรู้ความสามารถ: จากโครงการนี้ ผู้วิจัยสามารถผลิตดุษฎีบัณฑิต ได้ 5 คน มหาบัณฑิต 9 คน และเป็นพี่เลี้ยงให้อาจารย์ทั้งในมหาวิทยาลัยของตัวเอง และมหาวิทยาลัยอื่นๆทั้งในประเทศและต่างประเทศ

4. การช่วยเหลือเชิงสาธารณะ: จากผลงานวิจัยที่ปรากฏต่อสาธารณะทำให้ผู้วิจัยได้เข้าไปมีส่วนช่วยเหลือประชาคมวิจัยต่างๆเช่นได้รับการแต่งตั้งเป็น Editor ของวารสาร Experimental Thermal and Fluid Science (Elsevier) ซึ่งเป็นวารสารระดับนานาชาติที่มีชื่อเสียง เป็นการทำชื่อเสียงให้กับประเทศชาติในอีกมิติหนึ่ง นอกจากนั้นผลงานตีพิมพ์หลายชิ้นยังได้รับการอ้างอิงจำนวนมาก (The most cited papers) จนได้รับจดหมายแสดงการให้กำลังใจจาก Thomson Reuters

5. การช่วยเหลือภาคอุตสาหกรรม: ผู้วิจัยได้ช่วยเหลือให้คำแนะนำ เพื่อเพิ่มคุณภาพของผลิตภัณฑ์ให้กับภาคอุตสาหกรรม หลายแห่ง ตัวอย่างหนึ่งได้แก่การ ช่วยเหลือบริษัท ไทย-เยอรมัน โปรดักส์ จำกัด (มหาชน) จนผลงานวิจัยมีส่วนช่วยให้ บริษัทฯ ได้รับรางวัลเกียรติยศจากรัฐสภา เมื่อวันที่ 2 ก.ย. 2556

ท้ายที่สุด ผู้เขียนขอขอบคุณ สำนักงานคณะกรรมการการอุดมศึกษา (สกอ.) สำนักงานกองทุนสนับสนุนการวิจัย (สกว.) และ มหาวิทยาลัยเทคโนโลยีพระจอมเกล้าธนบุรี ที่ให้ความช่วยเหลือเรื่องเงินทุน อธิการบดี และผู้บริหารของมหาวิทยาลัยเทคโนโลยีพระจอมเกล้าธนบุรี สมาชิกทุกคนใน FUTURE Lab เพื่อนอาจารย์ ในภาควิชาวิศวกรรมเครื่องกล คณะวิศวกรรมศาสตร์ ที่ให้ความช่วยเหลือด้วยดีอย่างไม่มีที่ติ

สมชาย วงศ์วิเศษ
ภาควิชา วิศวกรรมเครื่องกล คณะวิศวกรรมศาสตร์
มหาวิทยาลัยเทคโนโลยีพระจอมเกล้าธนบุรี

รหัสโครงการ: DPG5380003

ชื่อโครงการ: งานวิจัยขั้นสูงทางการไหลสองสถานะและการเพิ่มความสามารถในการถ่ายเทความร้อน

หัวหน้าโครงการ: ศาสตราจารย์ ดร. สมชาย วงศ์วิเศษ
ภาควิชาวิศวกรรมเครื่องกล คณะวิศวกรรมศาสตร์
มหาวิทยาลัยเทคโนโลยีพระจอมเกล้าธนบุรี

E-mail Address: somchai.won@kmutt.ac.th

ระยะเวลาโครงการ: 1 เม.ย. 2553 ถึง 31 มี.ค. 2557

1. บทคัดย่อ

กลุ่มวิจัยได้นำศาสตร์ของ การถ่ายเทความร้อนและมวล กลศาสตร์ของไหล การไหลสองเฟส และเธอร์โมไดนามิกส์ มาประยุกต์ เพื่อพัฒนาอุปกรณ์แลกเปลี่ยนความร้อนให้มีสมรรถนะสูงขึ้น ทำให้ได้ผลิตภัณฑ์ที่ประหยัดพลังงานและรักษาสิ่งแวดล้อม ความรู้ใหม่ต่างๆที่ได้จากงานวิจัยพื้นฐานเหล่านี้สามารถนำไปประยุกต์ใช้ในการออกแบบอุปกรณ์แลกเปลี่ยนความร้อนให้มีสมรรถนะสูงขึ้นได้ ซึ่งเป็นประโยชน์ต่ออุตสาหกรรมโดยตรง

โดยปกติกระบวนการแลกเปลี่ยนความร้อนระหว่างของไหลสองชนิดที่มีอุณหภูมิแตกต่างกันสามารถทำได้โดยใช้อุปกรณ์ที่เรียกว่า อุปกรณ์แลกเปลี่ยนความร้อน ถ้าอุปกรณ์แลกเปลี่ยนความร้อนถูกออกแบบมาอย่างเหมาะสม การถ่ายเทความร้อนก็จะเป็นไปอย่างมีประสิทธิภาพ การเพิ่มการถ่ายเทความร้อน ถือเป็นสิ่งหนึ่งที่จะช่วยเพิ่มสมรรถนะของอุปกรณ์แลกเปลี่ยนความร้อน ซึ่งก็เท่ากับเป็นการประหยัดพลังงานหรือเป็นการใช้พลังงานอย่างคุ้มค่า

ตัวอย่างหนึ่งของงานวิจัยคือ การเพิ่มประสิทธิภาพและลดการใช้พลังงานในระบบการทำความเย็นและการปรับอากาศ โดยทำงานวิจัยลงลึกตั้งแต่งานวิจัยพื้นฐาน เข้าสู่งานวิจัยประยุกต์ จนถึงการจดสิทธิบัตร ผลลัพธ์จากงานวิจัย อยู่ในรูปของการตีพิมพ์เผยแพร่ต่อสาธารณชนทั้งระดับชาติและระดับนานาชาติ โดยผลงานวิจัยได้ถูกนำไปอ้างอิงจำนวนมากเพื่อต่อยอดงานวิจัยหรือถูกนำไปใช้งาน ซึ่งหมายถึงเป็นการทำประโยชน์ให้สังคมโดยส่วนรวม และสร้างชื่อเสียงให้กับประเทศชาติ และเนื่องจากประเทศไทยอยู่ในเขตร้อนชื้น การทำความเย็นและการปรับอากาศถือเป็นสิ่งจำเป็นในชีวิตประจำวัน ประกอบกับประเทศไทยเป็นฐานการผลิตเครื่องปรับอากาศเพื่อการส่งออกระดับต้นๆของโลก ดังนั้นงานวิจัยและพัฒนาในเรื่องเหล่านี้จึงมีประโยชน์อย่างยิ่งต่อประเทศชาติ

2. Abstract

The research interests include two-phase flow, heat transfer enhancement and thermal system design. Generally, the process of heat exchange between two kinds of fluids of different temperatures can be accomplished with equipment called a heat exchanger. A well-designed heat

exchanger can transfer heat effectively. Heat transfer enhancement can increase the performance of a heat exchanger through the saving or cost-effective use of energy.

Since Thailand is situated in a tropical zone, air conditioners and refrigerators are considered necessary appliances in Thai daily life. Additionally, Thailand has become an important production base for air conditioner and refrigerator manufactoring, as well as a top exporter of these products to the world market. Therefore, research and development, as well as the preparation of specialists in this field is necessary.

The research team have applied the sciences of heat and mass transfer, fluid mechanics, and thermodynamics in developing higher-performance heat exchangers, the main focus being on increasing the efficiency and reducing the power consumption of air conditioners and refrigerators. The new body of knowledge gained from this basic research can be applied in designing high-performance equipment that is directly useful in the industry.

3. Executive Summary

Gas-liquid two-phase flow is one of four types of two-phase flows. It occurs commonly in both the power and the process industries and in ordinary life. Gas-liquid flows are the most complex. They combine the characteristics of the compressibility of gas and a deformable interface. Gas-liquid flow occurs in a wide variety of equipment, for example, in all condenser and evaporator of refrigeration and air conditioning system and in petroleum pipelines which carry a mixture of gas and oil. In fact, the majority of the real heat-mass transfer problems in the industries is related with changes of phase during boiling and condensation.

Boiling and condensation under the conditions of free or forced convection is an extreamly important subject that confronts engineers in the process industries. The design and analysis of refrigeration and air conditioning system, distillators, water-tube and fire-tube boiliers, process industry reboilers and condensers, surface condensers, automotive industries, pressurized water reactors in nuclear power plants, heat pumps and various kinds of heat exchanger and many other equipment in chemical and power plant are examples which are based on the knowledge of the two-phase flow and heat-mass transfer characteristics occurring during the changes of phase.

In general, the heat and mass transfer rate and the pressure drop in a considered system are the usual design parameters of interest. It is very meaningful to know the phenomena which occurs. This is because it may impose some limitation in the performance of the system, for example, a change in hydrodynamic or heat transfer characteristics. In boiling and condensation, the flow and heat transfer characteristics are very closely related and the coupling is much closer than in single-phase flows.

The exchange rates of heat, mass and momentum, pressure drop, holdup and system stability causes variations in the amount and distribution of each phase and topology of the flow. The subject of the heat transfer enhancement has been developed generally for the purpose of heat exchange applications. It is also not possible to understand the two-phase flow phenomena without a clear understanding of the flow patterns encountered.

The ability to predict the type of flow accurately is necessary before the relevant calculation techniques will be developed. The external and internal extended surfaces in forms of, for example, longitudinal or radial fins are also alternative ways to enhance the heat transfer rate between the surface and the adjacent fluid. However, while the heat transfer rate is augmented, the flow characteristic is changed and the resistance resulted from extended surface becomes higher. This is still big room to discuss and go further into detail.

The main objective of this project is to study experimentally and theoretically the two-phase gas-liquid flow characteristics and its relations with the heat-mass transfer mechanism and to enhance the heat transfer rate by considering in the view of the fluids and equipment. All these fundamental works will be concentrated on the improvement of the performance of the refrigeration and air-conditioning system.

The project is divided into various relevant related sub-projects as follows;

-Micro-Channel Heat Exchanger used for Refrigeration and Air Conditioning

-Heat and Mass Transfer Characteristics of Fin-and-Tube Evaporators used in Air conditioning system

-Saturated Pool Boiling Characteristics of New Alternative Fluorine-Based Refrigerants

-Pool Boiling Characteristics of New Alternative Refrigerants “Nano-Fluids”

-Hydrocarbon Mixtures to Replace Refrigerants used in an Automotive Air Conditioning System

-Heat Transfer, Pressure Drop and Effect of Flow Direction of Working Fluids Flowing Through a Plate Heat Exchanger Simulated as Evaporator and Condenser

-Characteristics of Refrigerant HFC-134a Flowing Through Micro-Scale Short Tube Orifices

-Vertical Upward Gas-Liquid Flow in Sinusoidal Wavy Channels

-Heat Transfer and Pressure Drop Characteristics of Refrigerant HFC-134a During Evaporation and Condensation in Annulus Coil Evaporator and Condenser

-Two-Phase Flow Patterns, Void Fraction and Pressure Drop in a Narrow Concentric Annuli

-Performance of a Vapor Compression Refrigeration Cycle Using a Two-Phase Ejector as an Expansion Device

-Experimental and Theoretical Investigations of Two-Phase Flow in Micro-Channels

-Effects of Electrohydrodynamics on the In-Tube Condensation and Boiling Heat Transfer – Enhancement of a New Alternative Refrigerant in Smooth and Micro-Fin Tubes

-Two-Phase Flow Patterns and Pressure Drop in a Small Circular Tube Vertical Bend used in Refrigeration and Air conditioning

-Forced Convective Heat Transfer Characteristic of New Alternative Refrigerants “Nano-fluid”

-Selection Charts for Fluorine-Based Capillary Tubes Used in Refrigerator and Air-Conditioner

-Effect of Geometric Parameters on the Air-Side Performance of Crimped Finned Tube Condenser used in the Air-Conditioning System

-Heat Transfer Performance of a Helically Coiled Heat Exchanger

-Performance of New Alternative Refrigerants Flowing Through Non-Adiabatic Capillary Tubes Used as An Expansion Device in Refrigeration and Air Conditioning System

-Combined Refrigeration and Solar Energy Systems

4. เนื้อหางานวิจัย

การมุ่งสู่การพัฒนาเครื่องปรับอากาศและอุปกรณ์ทำความเย็นให้มีสมรรถนะสูงขึ้น คณะวิจัย ได้ศึกษาวิธีพัฒนา คอนเดนเซอร์ และ อีวาโปเรเตอร์ ซึ่งถือเป็นอุปกรณ์แลกเปลี่ยนความร้อนที่อยู่ในวงจรการปรับอากาศและการทำความเย็น ให้สามารถแลกเปลี่ยนความร้อนระหว่าง สารทำความเย็นกับอากาศได้ดียิ่งขึ้น การศึกษาสามารถทำทั้งจากการทดลองและจากการสร้างแบบจำลองทางคณิตศาสตร์ ตัวอย่างของงานวิจัยได้แก่ การออกแบบอุปกรณ์แลกเปลี่ยนความร้อนแบบใหม่ๆซึ่งอาจเป็นแนวทางในการนำไปประยุกต์ใช้ต่อไปในอนาคต การศึกษาถึงผลของ รูปร่างของครีบที่ใช้ในการถ่ายเทความร้อน ความหนาของครีบ ระยะห่างระหว่างครีบ วัสดุที่ใช้ ลักษณะการวางท่อ ต่อสมรรถนะทางการถ่ายเทความร้อน และการลดลงของความดันของอากาศขณะไหลผ่านอุปกรณ์แลกเปลี่ยนความร้อน ทั้งที่ภาวะที่ผิวท่อด้านนอกของคอนเดนเซอร์มีสภาพแห้ง และที่ภาวะที่ผิวท่ออีวาโปเรเตอร์เปียกด้วยน้ำที่เกิดจากการควบแน่น

คณะวิจัยยังศึกษาในส่วนอุปกรณ์ระเหยซึ่งถือเป็นอุปกรณ์ที่สำคัญอีกตัวหนึ่งในวงจรการปรับอากาศและทำความเย็น ได้แก่ การนำอีเจ็กเตอร์ และ การนำท่อคาปิลลารีทั้งแบบแอเดียแบติก และ แบบนอนแอเดียแบติก มาใช้เป็นอุปกรณ์ระเหย โดยสามารถพัฒนาแบบจำลองทางคณิตศาสตร์เพื่อจำลองการไหลของสารทำความเย็นในท่อคาปิลลารี ซึ่งมีการไหลสองเฟสเป็นกลไกสำคัญ แบบจำลองดังกล่าวสามารถนำไปใช้ในการออกแบบหาขนาดท่อคาปิลลารีที่เหมาะสมที่ใช้กับสารทำความเย็นประเภทต่างๆ ที่ทำงานที่ภาวะต่างๆตามแต่กำหนด และเพื่อให้สะดวกต่อการใช้งานในภาคสนาม กลุ่มวิจัยได้พัฒนาแผนภูมิ เพื่อใช้เลือกขนาดท่อคาปิลลารี ที่เหมาะสมกับสารทำความเย็นและภาวะการใช้งานจริง

ในส่วนของสารทำงานในวงจรการปรับอากาศและการทำความเย็นซึ่งเราเรียกว่าสารทำความเย็น และคณะวิจัย ได้ศึกษาลักษณะเฉพาะในการไหลของสารทำความเย็นทางเลือกใหม่ทั้งจากการทดลองและจากการพัฒนาแบบจำลองทางคณิตศาสตร์ ทั้งในด้านการถ่ายเทความร้อนและด้านกลศาสตร์ของไหลในขณะที่สารทำความเย็นระเหย และควบแน่นภายในท่อเรียบและท่อที่ผิวภายในไม่เรียบ โดยศึกษาทั้ง

กับสารทำความเย็นบริสุทธ์และกับสารทำความเย็นที่มีน้ำมันหล่อลื่นผสมซึ่งตรงกับสภาพการใช้งานจริง ผลลัพธ์จากการศึกษาทางด้านการถ่ายเทความร้อนจะอยู่ในรูปของสัมประสิทธิ์การถ่ายเทความร้อน สำหรับในเชิงกลศาสตร์ของไหลจะเสนอผลในรูปของ รูปแบบการไหลสองเฟสซึ่งเป็นไปได้หลากหลายรูปแบบการไหล แฟกเตอร์ความเสียดทาน และ ความดันลด สหสัมพันธ์ที่พัฒนาได้ทั้งสัมประสิทธิ์การถ่ายเทความร้อนและแฟกเตอร์ความเสียดทาน สามารถนำไปใช้ในการออกแบบอีวาโปเรเตอร์ และคอนเดนเซอร์ ได้โดยตรง นอกจากนั้นแบบจำลองทางคณิตศาสตร์ที่พัฒนาขึ้นมาสามารถนำไปเป็นแนวทางและใช้ดัดแปลงเพื่อการออกแบบอุปกรณ์แลกเปลี่ยนความร้อนที่มีลักษณะแตกต่างออกไปได้

นอกจากการศึกษาคุณสมบัติของสารทำความเย็นขณะไหลและเปลี่ยนสถานะแล้ว คณะนักวิจัยยังสามารถพัฒนาอุปกรณ์การทดลองเพื่อศึกษาการเดือดของสารทำความเย็นประเภทต่าง ๆขณะไม่มีการไหล โดยมุ่งพัฒนา เส้นโค้งการเดือด ข้อมูลดังกล่าวจะทำให้เข้าใจถึงกลไกการเดือดของสารทำความเย็นชนิดต่าง ๆ ซึ่งจะมีประโยชน์ในการออกแบบอุปกรณ์แลกเปลี่ยนความร้อนที่จะนำสารทำความเย็นนั้น ๆไปใช้ นอกจากสารทำความเย็นปกติแล้ว คณะวิจัย ได้พยายามศึกษา คุณสมบัติของสารทำความเย็นทางเลือกใหม่ที่น่าจะมีศักยภาพ อาทิ ไฮโดรคาร์บอน หรือ ของไหลนาโน ซึ่งคาดหมายว่าจะเป็นของไหลชนิดใหม่ที่มีศักยภาพในการเพิ่มการถ่ายเทความร้อนของอุปกรณ์แลกเปลี่ยนความร้อน

งานวิจัยเกือบทั้งหมดดำเนินการด้วยตัวเองภายในประเทศ ผลลัพธ์จากงานวิจัยในเรื่องที่กล่าวมาอยู่ในรูปของการตีพิมพ์เผยแพร่ต่อสาธารณะชนทั้งระดับชาติและระดับนานาชาติ โดยผลงานวิจัยได้ถูกนำไปอ้างอิงจำนวนมากเพื่อการต่อยอดงานวิจัยหรือถูกนำไปใช้งาน ซึ่งหมายถึง เป็นการทำประโยชน์ให้สังคมโดยส่วนรวม และสร้างชื่อเสียงให้กับประเทศชาติเป็นอย่างยิ่ง และเนื่องจากประเทศไทยอยู่ในเขตร้อนและชื้น การทำความเย็นและการปรับอากาศ ถือเป็นสิ่งจำเป็นในชีวิตประจำวัน ประกอบกับประเทศไทยเป็นฐานการผลิตเครื่องปรับอากาศเพื่อการส่งออกเป็นอันดับต้น ๆของโลก งานวิจัยและพัฒนา ในเรื่องเหล่านี้จะมีประโยชน์อย่างยิ่งต่อประเทศชาติ

5. Output ที่ได้จากโครงการ

5.1 ผลงานการตีพิมพ์ในวารสารระดับนานาชาติ (สามารถดู reprint ได้ในภาคผนวก ก)

1. Saisorn S, Wongwises S. (2010) The effects of channel diameter on flow pattern, void fraction and pressure drop of two-phase air-water flow in circular micro-channels *Experimental Thermal and Fluid Sciences*, 34(4) : 454-462.

2. Laohalertdecha S, Kaw-on, J., Wongwises S., (2010) The effect of the electrohydrodynamic technique on the two-phase flow pressure drop of R-134a during evaporation inside horizontal smooth and micro-fin tubes, *Heat Transfer Engineering* 31 (2): 108-118.

3. Pirompugd W, Wang CC, Wongwises S., (2010) Correlation for wet surface ratio of fin-and – tube heat exchanger, *International Journal of Heat and Mass Transfer* 53(1-3): 568-573.

4. Daungthongsuk, W., Wongwises, S., (2010) An experimental study on the heat transfer Performance and pressure drop of TiO_2-water nanofluids flowing under turbulent flow regime, *International Journal of Heat and Mass Transfer* 53(1-3): 334-344.

5. Chen, Wongwises, Yang, Wang, (2010) Two-Phase Flow Across Small Sudden Expensions and Contractions, *Heat Transfer Engineering.* 31 (4):298-309.

6. Godson Asirvatham , B.Raja, D. Mohan Lal and S. Wongwises, (2010) Enhancement of Heat Transfer using Nanofluids- An Overview, *Renewable and Sustainable Energy Reviews* 14 (2): 629-641.

7. Liu, Y.C., Wongwises, S., Wang, C.C., (2010) Air-side performance of fin and tube heat exchangers in dehumidifying conditions-Data with larger diameter, *International Journal of Heat and Mass Transfer* 53(7-8) : 1603-1608.

8. Daungthongsuk, W., Wongwises, S., (2010) Comparison of the effects of measured and computed thermophysical properties of nanofluids on heat transfer performances, *Experimental Thermal and Fluid Science* 34 (5): 616-624.

9. Laohalertdecha S, Wongwises S. (2010) The effects of corrugation pitch on the condensation heat transfer coefficient and pressure drop of R-134a inside horizontal corrugated tubes, International Journal of Heat and Mass Transfer 53(13-14): 2924-2931.

10. Dalkilic, A.S., Agra, O., Teke, I., Wongwises, S., (2010) Comparison of frictional pressure drop models during annular flow condensation of R600a in a horizontal tube at low mass flux and of R134a in a vertical tube at high mass flux, International Journal of Heat and Mass Transfer,53 (9-10): 2052-2064.

11. Nilpueng, K., Wongwises, S., (2010) Flow mechanisms of HFC-410A inside short tube orifices during flashing process, International Journal of Heat and Mass Transfer 53 (17-18) 3449-3459.

12. Saisorn, S., Kaew-on, J., Wongwises, S., (2010) Flow pattern and heat transfer characteristics of R-134a refrigerant during flow boiling in a horizontal circular mini-channel, International Journal of Heat and Mass Transfer, 53 (19-20): 4023-4038..

13. Dalkilic, A.S., Wongwises, S., (2010) An investigation of a model of the flow pattern transition mechanism in relation to the identification of annular flow of R134a in a vertical tube using various void fraction models and flow regime maps, *Experimental Thermal and Fluid Science* 34 (6): 692-705.

14. Dalkilic, A.S., Laohalertdecha, S., Wongwises, S., (2010) New experimental approach on the determination of condensation heat transfer coefficient using frictional pressure drop and void fraction models in a vertical tube,Energy Conversion and Management 51 (12): 2535-2547.

15. Dalkilic, A.S., Wongwises, S., (2010) Validation of void fraction models and correlations using a flow pattern transition mechanism model in relation to the identification of annular vertical downflow in-tube condensation of R134a, International Communications in Heat and Mass Transfer 37 (7): 827-834

16. Chingulpitak, S., Wongwises, S., (2010) Two-phase flow model of refrigerants flowing through helically coiled capillary tubes, Applied Thermal Engineering 30 (14-15) 1927-1936.

17. Suriyawong, A., Wongwises, S. (2010) Nucleate pool boiling heat transfer characteristics of TiO_2- water nanofluids at very low concentrations, Experimental Thermal and Fluid Science 34 (8) 992-999.

18. Nilpueng, K., Wongwises, S. (2010) Two-phase gas–liquid flow characteristics inside a plate heat exchanger, Experimental Thermal and Fluid Science 34: 1217-1229.

19. Godson Asirvatham, D. Mohan Lal and S. Wongwises (2010) Experimental measurement of temperature-dependent thermal conductivity and viscosity of silver-water nanofluids, Nanoscale and Microscale Thermophysical Engineering 14 (3) 152-173.

20 . Borwornsethanan, S., Wongwises, S.,(2010) Assessment of Useful Life of Lubricants Using Analytical Hierarchy Process (AHP) and Vector Projection Approach (VPA), *American Journal of Engineering and Applied Science* 32 (2) 470-475.

21. Kanokjaruvijit K, Thaworn-ngamyingsakul, C., Wongwises S. (2010) Numerical investigation of an axisymmetric laminar jet impinging on a uniform heat flux dimpled surface using finite element method, *Journal of Mechanical Science and Technology* 24 (9) 1809-1818.

22. Godson Asirvatham, L., Mohan Lal, D., Wongwises, S., (2010) Experimental Investigation on the Thermal Conductivity and Viscosity of Silver-Deionized Water Nanofluid, *Experimental Heat Transfer* 23 (4) 317-332.

23. Chingulpitak, S., Wongwises, S., (2010) Effects of Coil Diameter and Pitch on the Flow Characteristics of Alternative Refrigerants Flowing Through Adiabatic Helical Capillary Tubes, *International Communications in Heat and Mass Transfer* 37 (9): 1305-1311.

24. Naphon, P., Wongwises, S. (2010) Investigation on the jet liquid impingment heat transfer for the central processing unit of personal computers, *International Communications in Heat and Mass Transfer* 37 (7): 822-826.

25. Dalkilic, A.S., Wongwises, S. (2010) A performance comparison of vapour compression refrigeration system using various alternative refrigerants, *International Communications in Heat and Mass Transfer* 37 (9): 1340-1349.

26. Kundu, B., Mondal, P.K., Datta, S.P., Wongwises, S. (2010) Operating design conditions of a solar-powered vapor absorption cooling system with an absorber plate having different profiles: An analytical study, *International Communications in Heat and Mass Transfer* 37 (9): 1238-1245.

27. Laohalertdecha S, Wongwises S. (2011) An experimental study into the evaporation heat transfer and flow characteristics of R134a refrigerant flowing through corrugated tubes, *International Journal of Refrigeration* 34 (1):280-291.

28. Balcilar, M., Dalkilic, A.S., Wongwises, S., (2011), Artificial neural network (ANN) techniques for the determination of condensation heat transfer characteristics during downward annular flow of R134a inside a vertical smooth tube, *International Communications in Heat and Mass Transfer* 38 (1): 75-84.

29. Aroonrat K., Wongwises, S., (2011) Evaporation heat transfer and friction characteristics of R-134a flowing downward in a vertical corrugated tube, *Experimental Thermal and Fluid Science* 35 (1): 20-28.

30. Dalkilic, A.S., Wongwises, S. (2011) Experimental study on the modeling of condensation heat transfer coefficients in high mass flux region of refrigerant HFC-134a inside the vertical smooth tube in annular flow regime, *Heat Transfer Engineering* 32 (1): 33-44.
31. Dalkilic, A.S., Teke, I., Wongwises, S., (2011) Experimental Analysis for the Determination of the Convective Heat Transfer Coefficient by Measuring Pressure Drop Directly During Annular Condensation Flow of R134a in a Vertical Smooth Tube, *International Journal of Heat and Mass Transfer* 54 :1008-1014.

32. Kaew-On, J., Sakamatapan, K., Wongwises, S. (2011) Flow Boiling Heat Transfer of R-134a in a Multiport Minichannel Heat Exchangers, *Experimental Thermal and Fluid Science* 35: 364-374.

33. Nilpueng, K, Wongwises, S., (2011) Choked flow mechanism of HFC-134a flowing through ahort-tube orifices, *Experimental Thermal and Fluids Science.* 35:347-354.

34. Demir, H., Dalkilic, A.S., Kürekci, N.A., Duangthongsuk, W., Wongwises, S., (2011) Numerical investigation on the single phase forced convection heat transfer characteristics of TiO2 nanofluids in a double-tube counter flow heat exchanger *International Communications in Heat and Mass Transfer* 38:218-228.

35. Saisorn, S., Wongwises, S. (2011),Two-phase air-water flow in micro-channels: An inspection of viscosity models for pressure drop prediction, *International Communications in Heat and Mass Transfer* 38: 212-217.

36. Chingulpitak, S., Wongwises, S., (2011) A Comparison of Flow Characteristics of Refrigerants Flowing Through Adiabatic Straight and Helical Capillary Tubes, *International Communications in Heat and Mass Transfer* 38: 398-404.

37. Pongsoi, P., Pikulkajorn, S., Wang, C.C., Wongwises, S., (2011) Effect of fin pitches on the air-side performance of crimped spiral fin-and-tube heat exchangers with a multipass parallel and counter cross-flow configuration, *International Journal of Heat and Mass Transfer* 54:2234-2240.

38. Laohalertdecha S, Wongwises S. (2011) Condensation heat transfer and flow characteristics of R-134a flowing through corrugated tubes, *International Journal of Heat and Mass Transfer* 54: 2673-2682.

39. Wongwises, S., Laohalertdecha, S., Kaew-on, J., Duangthongsuk, W., Aroonrat, K., Sakamatapan, K., (2011) Evaporation heat transfer and flow characteristics of R-134a flowing through internally grooved tubes, *Heat and Mass Transfer* 47 (6): 629-640.

40. Aschariyaphotha N., Wongwises P., Humphries UW, Wongwises S., (2011) Study of storm due to Typhoon Linda 1997 in the Gulf of Thailand using a three dimensional ocean model. *Applied Mathematics and Computation* 217 (21): 8640-8654.

41. Saisorn, S., Kaew-On, J. Wongwises, S., (2011) Two-phase flow of R-134a refrigerant during flow boiling through a horizontal circular mini-channel, *Experimental Thermal and Fluid Science* 35 (2011): 887-895.

42. Ebrahimnia-Bajestan, E., Niazmand, H., Duangthongsuk, W., Renksizbulut, M., Wongwises, S., (2011) Numerical Investigation of Effective Parameters in Convective Heat Transfer of Nanofluids Flowing under a Laminar Flow Regime, *International Journal of Heat and Mass Transfer* 54 (19-20): 4376-4388.

43. Nilpueng, K., Wongwises,S. (2011) Performance characteristics of HFC-134a and HFC-410A refrigeration system using a short-tube orifice as the expansion device, *Heat and Mass Transfer* 47 (10) (2011): 1219-1227.

44. Dalkilic, A.S., Balcilar, M., Bolat, B., Wongwises, S. (2011) Investigation of empirical correlations on the determination of condensation heat transfer characteristics during downward annular flow of R134a inside a vertical smooth tube using computational numerical methods, *Journal of Mechanical Science and Technology* 25 (10): 2683-2701.

45. Godson, L., Raja.,B., D.M. Lal., Wongwises, S. (2011) Convective Heat Transfer Applications in Nanofluids and Development of Correlations, *Particuology* 9 (6): 626-631.

46. Laohalertdecha, S., Dalkilic, A.S., Wongwises, S. (2011) Correlations for evaporation heat transfer coefficient and two-phase friction factor for R-134a flowing through horizontal corrugated tubes, *International Communications in Heat and Mass Transfer,* 38 (10): 1406-1413.

47. Naphon, P., Wongwises, S. (2011) Experimental study of jet nanofluids impingement system for cooling computer processing unit, *Journal of Electronics Cooling and Thermal Control* 1: 38-44.

48. Kaewnai, S., Wongwises, S. (2011) Improvement of the Runner Design of Francis Turbine using CFD *American Journal of Engineering and Applied Science* 4(4):540-547.

49. Kaew-On, J., Sakamatapan, K., Wongwises, S. (2012) Flow boiling pressure drop of R134a in the counter flow multiport minichannel heat exchangers, *Experimental Thermal and Fluid* Science 36 (1): 107-117.

50. Nilpueng, K., Wongwises, S. (2012) Review on the Experimental Studies of Refrigerant Flow Mechanisms inside Short-Tube Orifices, *International Journal of Refrigeration* 35 (1): 27-35.

51. Dalkilic, A.S., Kürekci, N.A., Wongwises, S. (2012) Effect of void fraction and friction factor models on the prediction of pressure drop of R134a during downward condensation in a vertical tube. *Heat and Mass Transfer* 48 (1): 123-139.

52. Saha, S., Celata, G. Wongwises, S. (2012) Selected papers on advances in heat transfer, *Heat Transfer Engineering* 33 (4-5): 281-283.

53. Dalkilic, A.S., Teke, I., Wongwises, S. (2012) Heat transfer enhancement during downward laminar flow condensation of R134a in vertical smooth and micro-fin tubes, *Journal of Thermal Science and Technology* 32(1):19-31.

54. Pongsoi, P. Wongwises, S. (2012) Experimental study on the air-side performance of a multipass parallel and counter cross-flow L-footed spiral fin-and-tube heat exchanger, *Heat Transfer Engineering* 33 (15)1251-1263.

55. Pongsoi, P., Pikulkajorn, S., Wang, C.C., Wongwises, S., (2012) Effect of number of tube rows on the air-side performance of crimped spiral fin-and-tube heat exchanger with a multipass parallel and counter cross-flow configuration, *International Journal of Heat and Mass Transfer* 55 (4): 1403-1411.

56. Vahid Etminan-Farooji, Ehsan Ebrahimnia-Bajestan, Hamid Niazmand, Somchai Wongwises (2012) Unconfined laminar nanofluid flow and heat transfer around a square cylinder, *International Journal of Heat and Mass Transfer* 55 (5-6): 1475-1485.

57. Kundu, B., Wongwises, S., (2012) A decomposition analysis on convecting-radiating rectangular plate fins for variable thermal conductivity and heat transfer coefficient, *Journal of the Franklin Institute* 349 (3): 966-984.

58. Daungthongsuk, W., Wongwises, S., (2012) A dispersion model for predicting the heat transfer performance of TiO2 Water nanofluids under a laminar flow regime, *International Journal of Heat and Transfer* 55 (11-12): 3138-3146.

59. Duangthongsuk, W., Dalkilic, A.S., Wongwises, S. (2012) Convective heat transfer of Al_2O_3-water nanofluids in a microchannel heat sink, *Current Nanoscience* 8(3):317-322.

60. Nilpueng, K., Wongwises, S., (2012) A review of numerical modelling studies on short-tube orifices performance with application to air-conditioning, *International Journal of Refrigeration* 35 (4):740-749.

61. Aschariyaphotha, N., Wongwises, S. (2012) Simulations of Seasonal Current Circulations and Its Variabilities Forced by Runoff from Freshwater in the Gulf of Thailand, *The Arabian Journal for Science and Engineering* 37:1389-1404.

62. Kaewon J., Wongwises, S. (2012) New proposed two-phase multiplier and evaporation heat transfer coefficient correlations for R134a flowing at low mass flux in a multiport minichannel, *International Communications in Heat and Mass Transfer* 39 (6):853-860.

63. Balcilar, M., Dalkilic, A.S., Agra, O., Atayilmaz, S.O., Wongwises, S. (2012) A Correlation Development for predicting the Pressure Drop of various refrigerants during Condensation and Evaporation in Horizontal Smooth and Micro-fin Tubes, *International Communications in Heat and Mass Transfer* 39(7):937-944.

64. Naphon, P., Wongwises, S., Wiriyasart, S. (2012) On the thermal cooling of central processing unit of the PCs with vapor chamber *International Communications in Heat and Mass Transfer* 39 :1165-1168.

65. Yiamsawas, T., Wongwises, S. (2012) Measurement of the thermal conductivity of Titania and Alumina nanofluids, *Thermochimica Acta* 545 : 48-56.

66. Pongsoi, P., Pikulkajorn, S., Wongwises, S. (2012) Effect of fin pitches on the optimum heat transfer performance of crimped spiral fin-and-tube heat exchangers, *International Journal of Heat and Mass Transfer*, 55:6555-6566.

67. Dalkilic, A.S., Kaya, N., Tabatabei, M., Yıldız, O., Yavuz, B., Daungthongsuk, W., Wongwises, S. (2012) Forced convective heat transfer of nanofluids - A review of the recent Literature, *Current Nanoscience* 8: 949-969.

68. Yiamsawasd, T., Dalkilic, A.S., Wongwises, S. (2012) Measurement of Specific Heat of Nanofluids, *Current Nanoscience* 8: 939-944.

69. Balcilar, M., Dalkilic, A.S., Suriyawong, A., Yiamsawas, T., Wongwises, S. (2012) Investigation of pool boiling of nanofluids using artificial neural networks and correlation development techniques, *International Communications in Heat and Mass Transfer* 39 (3): 424-431.

70. Saisorn, S., Wongwises, S. (2012) A critical review of recent investigations on heat transfer in flow boiling micro-channels, *Frontier in Heat and Mass Transfer* 3-013006.

71. Saisorn, S., Wongwises, S. (2012) A critical review of recent investigations on two-phase pressure drop in flow boiling micro-channels, *Frontier in Heat and Mass Transfer* 3-013007.

72. Kaew-On, J., Chingulpitak, S., Wongwises, S. (2012) Experimental investigation of R134a flowing through adiabatic helically coiled capillary tubes, *International Journal of Air conditioning and Refrigeration* 20(1):1250001.

73. Godson, L., Raja, B., Mohan Lal, D. (2012) Wongwises, S., Convective Heat Transfer Characteristics of Silver-Water Nanofluid Under Laminar and Turbulent Flow Conditions, *The ASME Journal of Thermal Science and Engineering Applications,* Vol. 4: 031001.

74. Suriyawong, A., Dalkilic, A.S., Wongwises, S. (2012) Nucleate pool boiling heat transfer correlation for TiO_2-water nanofluids, *Journal of ASTM International* 9(5)(Paper ID JAI104409).

75. Laohalertdecha, S., Dalkilic, A.S., Wongwises, S. (2012) A Critical Review on the Heat-transfer Performance and Pressure-drop Characteristics of Various Enhanced Tubes, *International Journal of Air Conditioning and Refrigeration* 20 (4): 1230003.

76. Chingulpitak, S., Kaew-On, J., Wongwises,S. (2012) Numerical and Experimental Investigation of the Flow Characteristics of R134a Flowing Through Adiabatic Helical Capillary Tubes *International Journal of Air Conditioning and Refrigeration* 20(4): 1250019.

77. Phoolphundh, S., Hathaisamit, K., Wongwises, S. (2013) Performance of Two-stage Upflow Anaerobic Sludge Blanket (UASB) Reactor Treating Wastewater from Latex-Processing
Factory, *Journal of Environmental Engineering*. 139: 141-146.

78. Naphon, P., Wongwises, S., Wiriyasart, S. (2013) Application of two-phase vapor chamber technique for hard disk drive cooling of PCs, *International Communications in Heat and Mass Transfer* 40 : 32-35.

79. Mahian, O., Mahmud, S., Wongwises, S. (2013) Entropy Generation Between Two Rotating Cylinders in the Presence of Magnetohydrodynamic Flow using Nanofluids, *Journal of Thermophysics and Heat Transfer* 27: 161-169.

80. Aroonrat, K., Dalkilic, A.S., Wongwises, S. (2013) Experimental study on evaporative heat transfer and pressure drop of R-134a flowing downward through vertical corrugated tubes with different corrugation pitches, *Experimental Heat Transfer* 26 : 41-63.

81. Mahian, O.,Oztop, H.F., Pop, I, Mahmud, S., Wongwises, S., (2013) Design of a vertical annulus with MHD flowing using entropy generation analysis, Thermal Science 17 (4): 1013-1022.

82. Mahian, O., Oztop, H., Pop, I., Sahin, A.Z., Wongwises, S. (2013) Estimation of operational costs due to entropy generation in a vertical annulus, *International Journal of Exergy* 13(4): 472-486.

83. Wongwises, S., Ghajar, A.J., Chau, K.W., Valladares, G. O., Kundu, B., Dalkilic, A.S., Lazarus, G.A., Two-phase flow and heat transfer enhancement, *Advances in Mechanical Engineering,* 2013 Article ID 256839.

84. Mahian, O., Kianifar, A., Kalogirou, S., Pop, I., Wongwises, S. (2013) A Review of the Applications of Nanofluids in Solar Energy, *International Journal of Heat and Mass Transfer* 57: 582-594.

85. Duangthongsuk, W., Wongwises, S. (2013) An Experimental Investigation into the Heat Transfer and Pressure Drop Characteristics of a Circular Tube Fitted with Rotating Turbine-Type Swirl Generators, *Experimental Thermal and Fluid Science* 45:8-15.

86. Nilpueng, K., Wongwises, S. (2013) Numerical simulation of refrigerants flowing through short-tube orifices during flashing process, *HVAC&R* 19: 159-174.

87. Kayaci, N., Balcilar, M., Tabetebai, M., Celen, A., Yıldız, O., Dalkilic, A.S., Wongwises, S. (2013)Determination of the Single-Phase Forced Convection Heat Transfer Characteristics of TiO_2 Nanofluids Flowing in Smooth and Micro-Fin Tubes by Means of CFD and ANN Analyses *Current Nanoscience* 9: 61-80.

88. Duangthongsuk, W, Yiamsawas, T., Dalkilic, A.S.,Wongwises, S. (2013) Pool-Boiling Heat Transfer Characteristics of Al_2O_3–Water Nanofluids on a Horizontal Cylindrical Heating Surface *Current Nanoscience* 9: 56-60.

89. Aroonrat, K., Jumpholkul, C., Leelaprachakul, R., Dalkilic, A.S., Mahian, O., Wongwises, S.,Heat transfer and single-phase flow in internally grooved tubes *International Communications in Heat and Mass Transfer* 42 : 62-68.

90. Saisorn, S., Kaewon, J., Wongwises, S. (2013) An Experimental Investigation of Flow Boiling Heat Transfer of R134a in horizontal and Vertical Mini-channels, *Experimental Thermal and Fluid Science* 46:232-244.

91. Pongsoi, P., Promoppatum, P., Pikulkajorn, S., Wongwises, S. (2013) Effect of fin pitches on the Air side performance of L-footed spiral fin and tube heat exchangers, *International Journal of Heat and Mass Transfer*, 59: 75-82.

92. Asirvatham, L.G., Nimmagadda, R., Wongwises, S. (2013) Heat transfer performace of screen wick heat pipes using silver-water nonofluid, *International Journal of Heat and Mass Transfer* 60:201-209.

93. Dalkilic, A.S., Kürekci, N.A., Kincay, O., Wongwises, S. (2013) Fundamental basis and application of cold room project design: a turkish case study, *Arabian Journal for Science and Engineering* 38(5): 1115-1130.

94. Mahian, O., Oztop, H., Pop, I., Mahmud, S., Wongwises, S., (2013) Entropy generation between two vertical cylinders in the presence of MHD flow subjected to constant wall temperature, *International Communications in Heat and Mass Transfer* 44: 87-92.

95. Dalkilic, A.S., Kundu, B., Wongwises, S. (2013) An experimental investigation on the Reynolds analogy applied to annular condensation laminar flow of R134a in a vertical tube, *Arabian Journal for Science and Engineering* 38: 1493-1507.

96. Jongpradist, P., Rojbunsongsri, R., Kamnerdtong, T., Wongwises, S. (2013) Parametric study and optimization of a food can corrugation design, *Journal of Mechanical Science and Technology* 27: 2043-2052.

97. Pirompugd, W., Wongwises, S. (2013) Partially Wet Fin Efficiency for the Longitudinal Fins of Rectangular,Triangular, Concave Parabolic, and Convex Parabolic Profiles, *Journal of Franklin Institute* 350: 1424-1442.

98. Pongsoi, P., Wongwises, S. (2013) A review on nuclear power plant scenario in Thailand, *Renewable and Sustainable Energy Reviews* 24: 586-592.

99. Celen, A., Dalkilic, A.S., Wongwises, S. (2013) Experimental analysis of the single phase pressure drop characteristics of smooth and microfin tubes, *International Communications in Heat and Mass Transfer* 46: 58-66.

100. Pirompugd W, Wongwises S. (2013) Efficiencies for partially wetted spine fins: uniform cross section, conical, concave parabolic, and convex parabolic spines, *ASME Journal of Heat Transfer* 135:081903-1.

101. Sakamatapan, K., Kaewon, J.,Dalkilic, A.S., Mahian, O., Wongwises, S. (2013) Condensation heat transfer Characteristics of R-134a flowing inside the multiport minichannels, *International Journal of Heat and Mass Transfer* 64: 976-985.

102. Mahian ,O., Pop,I., Sahin,A.Z., Oztop,H., Wongwises, S. (2013) Irreversibility Analysis of a Vertical Annulus Using TiO_2/ Water Nanofluid with MHD Flow Effects, *International Journal of Heat and Mass Transfer* 64 :671-679.

103. Duangthongsuk, W., Wongwises, S.(2013) Comparison of the heat transfer performance and friction characteristics between fixed and rotating turbine-type swirl generators fitted in a small circular tube *Experimental Thermal and Fluid Science* 50:222-228.

104. Mahian, O., Kianifar A., Kleinstreuer, C., Al-Nimr, M., Pop, I., Sahin, A., Wongwises, S. (2013) A review of entropy generation in nanofluid flow, *International Journal of Heat and Mass Transfer* 65:514-532.

105. Nitiapiruk, P., Mahian, O., Dalkilic, A.S., Wongwises, S. (2013) Performance characteristics of a microchannel heat sink using TiO_2/water nanofluid and different thermophysical models, *International Communications in Heat and Mass Transfer* 47:98-104.

106. Matin, H., Mahian, O., Wongwises, S. (2013) Nanofluids flow between two rotating cylinders: Effects of thermophoresis and Brownian motion,*Journal of Thermophysics and Heat Transfer* 27(4): 748-755.

107. Asirvatham, L.G., Nimmagadda, R. (2013) Wongwises, S. Operational limitations of heat pipes with silver-water nanofluids, *ASME Journal of Heat Transfer* 135:111011-1-111011-9.

108. Yiamsawas, T., Kaewnai, S., Mahian, O., Dalkilic, A.S., Wongwises, S. (2013) Experimental studies on the viscosity of TiO_2 and Al_2O_3 nanoparticles suspended in a mixture of ethylene glycol and water for high temperature applications, *Applied Energy* 11: 40-45.

109. Balcilar, M., Aroonrat, K., Dalkilic, A.S., Wongwises, S. (2013) A numerical correlation development study for the determination of Nusselt numbers during two-phase flow of R134a inside smooth and corrugated tubes, *International Communications in Heat and Mass Transfer* 48: 141-148.

110. Mahian, O., Kianifar A., Wongwises, S. (2013) Dispersion of ZnO nanoparticles in a mixture of Ethylene Glycol-Water, Exploration of temperature-dependent density, and sensitivity analysis, *Journal of Cluster Science* 24:1103-1114.

111. Balcilar, M., Aroonrat, K., Dalkilic, A.S., Wongwises, S. (2013) A generalized numerical correlation study for the determination of pressure drop during condensation and boiling of R134a inside smooth and corrugated tubes, *International Communications in Heat and Mass Transfer* 49: 78-85.

112. Yiamsawas, T., Dalkilic, A.S., Omid, Mahian, Wongwises, S. (2013) Measurement and correlation of the viscosity of water-based Al2O3 and TiO2 nanofluids in high temperatures and comparisons with literature report, *Journal of Dispersion Science and Technology* 34: 1697-1703.

113. Kaewnai, S., Wongwises, S. (2013) Analysis of Flow through a Double-acting Impeller with a Straight Radial Blades Using CFD, *International Journal of Applied Research in mechanical Engineering* 3 (1):37-43.

114. Chingulpitak, S., Wongwises, S. (2014) Critical Review of the Current Status of Wind Energy in Thailand, *Renewable and Sustainable Energy Review* 31 : 312-318.

115. Dalkilic, A.S., Omid, M., Wongwises, S. (2014) Selection of the most suitable refrigerant for a shell and tube condenser, *Heat and Mass Transfer* 50: 183-197.

116. Balcilar, M., Dalkilic, A.S., Aroonrat, K., Wongwises, S. (2014) Neural network based analyses for the determination of evaporation heat transfer characteristics during

downward flow of R134a inside a vertical smooth and corrugated tube, *Arabian Journal for Science and Engineering*, 39: 1271-1290.

117. Laohalertdecha, S., Aroonrat, K., Dalkilic, A.S., Mahian, O., Wongwises, S. (2014) Prediction of heat transfer coefficients and friction factors for evaporation of R-134a flowing inside corrugated tubes, *Heat and Mass Transfer* 50: 469-482.

118. Esfe, M.H., Saedodin, S., Mahian, O., Wongwises, S.(2014) Heat transfer characteristics and pressure drop of COOH-functionalized DWCNTs/water nanofluid in turbulent flow at low concentrations, *International Journal of Heat and Mass Transfer* 73: 186-194.

119. Heris, S.Z., Mahian, O., Wongwises, S. (2014) A comparative experimental study on the natural convection heat transfer of the different metal oxide nanopowders suspended in turbine oil inside an inclined cavity, *International Journal of Heat and Mass Transfer* 73:231-238.

120. Celen, A., Kayaci, N., Cebi, A., Demir, H., Dalkilic, A.S., Sonmex, A.C.,Wongwises, S., (2014) Numerical investigation for the calculation of TiO2-water nanofluids pressure drop in plain and enhanced pipes, *International Communications in Heat and Mass Transfer* 53:98-108.

121. Balcilar, M., Dalkilic, A.S., Sonmex, A.C., Wongwises, S. (2014) Classification of in-tube boiling R134a data belonging to the smooth and corrugated tubes, *International Communications in Heat and Mass Transfer* 53:185-194.

122. Saisorn, S., Kuaseng, P., Wongwises, S. (2014) Heat transfer characteristics of gas-liquid flow in horizontal rectangular micro-channels, *Experimental Thermal and Fluid Science* 55: 54-61.

123. Esfe, M.H., Saedodin, S., Mahian, O., Wongwises, S., Thermal Conductivity of Al_2O_3/water nanofluids: measurement, correlation, sensitivity analysis, and comparisons with literature reports, *Journal of Thermal Analysis and Calorimetry* (in press).

124. Rashidi, I., Mahian, O., Lorenzini, G., Biserni, C., Wongwises, S., Natural Convection of Al_2O_3/water nanofluid in a square cavity: Effects of heterogeneous heating, *International Journal of Heat and Mass Transfer* (in press).

125. Sakamatapan, K., Wongwises, S., Pressure drop during condensation of R134a flowing inside a multiport minichannel, *International Journal of Heat and Mass Transfer* (in press)

126. Srisomba, R., Wongwises, S., Measurement of Void Fraction of R-134a Flowing Through Horizontal Tube, *International Communications in Heat and Mass Transfer* (accepted)

5.2 ผลงานการตีพิมพ์ในการประชุมระดับนานาชาติ

1. Dalkilic, A.S., Wongwises, S., A heat transfer model for co-current downward laminar film condensation of R134a in a vertical micro-fin tube during annular flow regime, the Eleventh UK National Heat Transfer Conference, September 6-8, Queen Mary University of London, UK.

2. Kaew-On, J., Nilpueng, K., Chingulpitak, S., Wongwises, S., An experimental study of the flow phenomena of R134a flowing through a capillary tube, FEDSM-ICNMM2010-30953: Proceedings of the 8th International Conference on Nano-channel, Micro-channel and Mini-channel, August 1-5, 2010, Montreal, Canada.

3. Saisorn, S., Kaew-On, J., Wongwises, S., Flow Boiling Heat Transfer Characteristics of R-134a in Horizontal and Vertical Mini-channels, Proceedings of the 8th International Conference on Nano-channel, Micro-channel and Mini-channel, August 1-5, 2010, Montreal, Canada.

4. Duangthongsuk, W., Wongwises, S., A Comparison on the Heat Transfer and Flow Characteristics of TiO2-Water Nanofluids Having Two Different Chemical Agents FEDSM-ICNMM2010-31020: Proceedings of the 8th International Conference on Nano-channel, Micro-channel and Mini-channel, August 1-5, 2010. Montreal, Canada.

5. Balcilar, M., Dalkilic, S.,Wongwises, S., Determination of condensation heat transfer characteristics of R134a by means of artificial intelligence method, *Proceedings of the 2010 ASME International Mechanical Engineering Congress and Exposition*, November 12-18, 2010, Vancouver, British Columbia, Canada.

6. Dalkilic, A.S., Laohalertdecha, S., Wongwises, S., Comparison of condensation frictional pressure drop models and correlations during annular flow of R134a inside a vertical tube, Thermal and Environmental Issues in Energy Systems, ASME-ATI-UTI, May 16-19, 2010, Italy.

7. Dalkilic, A.S., Wongwises, S., Experimental study on the flow regime identification in the case of co-current condensation of R134a in a vertical smooth tube, International Heat Transfer Conference, ASME, August 8-13, 2010, USA.

8. Demir, H., Dalkilic, A.S., Kurekci, N.A., Kelesoglu, B., Wongwises, S., A numerical investigation of nanofluids forced convection flow in a horizontal smooth tube, International Heat Transfer Conference, ASME, August 8-13, 2010, USA.

9. Dalkilic, A.S., Wongwises, S., Comparison of various alternative refrigerants for vapour compression refrigeration systems, accepted draft paper, ASME/JSME 8th Thermal Engineering Joint Conference, March 13-17, 2011, Honolulu, Hawaii, USA.

10. Nilpueng, K., Wongwises, S., Flashing flow mechanisms of HFC-134a and HFC-410A through short tube orifice, ASME/JSME 8th Thermal Engineering Joint Conference, March 13-17, 2011, Honolulu, Hawaii, USA.

11. Bolat, B., Balcilar, M., Dalkilic, A.S., Wongwises, S., Optimization of the relationship between the two-phase friction factor and Reynolds equivalent number model by means of genetic algorithm, ASME/JSME 8th Thermal Engineering Joint Conference, March 13-17, 2011, Honolulu, Hawaii, USA.

12.Laohalertdecha, S. Wongwises, S., Effect of pitch and depth on the condensation heat transfer of R-134a flowing through corrugated tubes, ASME/JSME 8th Thermal Engineering Joint Conference, March 13-17, 2011, Honolulu, Hawaii, USA.

13.Nilpueng, K., Wongwises, S., Two-phase flow characteristics refrigerant flowing through short-tube orifices, Proceedings of International Conference on Air-Conditioning & Refrigeration, July 6-8, 2011, Yongpyong Resort, Gangwon-Do, Korea.

5.3 การจดสิทธิบัตร (สามารถดู เอกสาร ได้ในภาคผนวก ข)

1 อุปกรณ์แลกเปลี่ยนความร้อนแบบท่อขดเป็นวง
(สิทธิบัตรเลขที่ 31282)

2 กรรมวิธีการเลือกขนาดท่อคาปิลลารีเพื่อใช้ในระบบทำความเย็นที่ใช้สารทำความเย็น R404A, R407B, R407C, R410A, R410B, R502A, R507A โดยใช้แผนภาพ
(คำขอรับสิทธิบัตรเลขที่ 0901004855)

3 วิธีการหาขนาดออริฟิซท่อสั้นที่ใช้เป็นอุปกรณ์ขยายในระบบปรับอากาศ
(คำขอรับสิทธิบัตรเลขที่ 1001001785)

4 แผนภาพสำหรับการเลือกขนาดออริฟิซท่อสั้นเพื่อใช้เป็นอุกรณ์ขยายในระบบปรับอากาศที่ใช้สารทำความเย็น R134a, R407C, R410A
(คำขอรับสิทธิบัตรเลขที่ 1001001909)

5 แผนภาพสำหรับการเลือกขนาดท่อคาปิลลารีแบบขดเพื่อใช้ในระบบทำความเย็นสำหรับสารทำความเย็น R134a, R404A.R407B, R407C, R410A
(คำขอรับสิทธิบัตรเลขที่ 11010000167)

6 อุปกรณ์เพิ่มสมรรถนะการถ่ายเทความร้อนชนิดกังหันแบบหมุนได้ภายในท่อ
(คำขอรับสิทธิบัตรเลขที่ 1101003266)

7 ท่อเพิ่มสมรรถนะการถ่ายเทความร้อนแบบร่องเกลียว
(คำขอรับสิทธิบัตรเลขที่ 1101003634)

8 อุปกรณ์เพิ่มสมรรถนะการถ่ายเทความร้อนชนิดกังหันหมุนเองได้เหนือพื้นผิวของการเดือด
(คำขอรับสิทธิบัตรเลขที่ 1201000625)

5.4 การจดลิขสิทธิ์ (สามารถดู เอกสาร ได้ในภาคผนวก ค)

1. โปรแกรมสำหรับหาขนาดท่อคาปิลลารีแบบแอไดเอบาติก
   (คำขอแจ้งข้อมูลลิขสิทธิ์เลขที่ ลข 98447 ทะเบียนข้อมูลเลขที่ ว1.1755)
2. โปรแกรมการออกแบบคอนเดนเซอร์แบบท่อติดครีบที่ระบายความร้อนด้วยอากาศ
   (คำขอแจ้งข้อมูลลิขสิทธิ์เลขที่ ลข 189622 ทะเบียนข้อมูลเลขที่ ว1.2873)
3 โปรแกรมคำนวณอัตราการไหลของสารทำความเย็นที่ไหลผ่านออริฟิซท่อสั้น
   (คำขอแจ้งข้อมูลลิขสิทธิ์เลขที่ ลข 287701 ทะเบียนข้อมูลเลขที่ ว1.4613)

5.5 <u>หนังสือ</u>(สามารถดู เอกสาร ได้ในภาคผนวก ง)

กลศาสตร์ของไหล เล่ม 1 (อยู่ในขั้นตอนการจัดพิมพ์ที่ สำนักพิมพ์แห่งจุฬาลงกรณ์มหาวิทยาลัย)

5.6 <u>Book chapters</u> (สามารถดู เอกสาร ได้ในภาคผนวก จ)

- A.S. Dalkilic, S., Wongwises, Two-Phase Heat Transfer Coefficients of R134a Condensation in vertical Downward Flow at High Mass Flux, in: A. Belmiloudi and D. Barbin (Eds.),Heat Transfer, InTech, Vienna, 2011, pp. 15-32 (ISBN 978-953-307-226-5).
- B. Kundu, S. Wongwises, Optimum Fin Profile under Dry and Wet Surface Conditions, in: A. Belmiloudi and D. Barbin (Eds.), Heat Transfer, InTech, Vienna, 2011 pp. 3-32 (ISBN 978-953-307-550-1) .
- A.S. Dalkilic, S., Wongwises, Condensation Heat Transfer in Smooth and Enhanced Geometrics: A Review of the Recent Literature, in: D. Alda and D. Ciarlo (Eds.), Refrigeration Systems, Design Technologies and Developments, Nova, New York, 2012, pp. 113-154 (ISBN 978-1-62417-229-8).

5.7 การนำผลงานไปใช้ประโยชน์

<u>เชิงวิชาการ</u>

- นักศึกษาระดับปริญญาเอกจบการศึกษา 5 คน คือ นายวีระพันธ์ ด้วงทองสุก นายศิระ สายศร นายกิตติ นิลผึ้ง นายสุริยัน เลาหเลิศเดชา และ นายจตุพร แก้วอ่อน
- นักศึกษาระดับปริญญาโทจบการศึกษา 9 คน คือ นายอดิเรก สุริยะวงศ์ นายปริญญา พงสร้อย นายคณิต อรุณรัตน์ นายศักรินทร์ ชินกุลพิทักษ์ นายทแกล้ว เยี่ยมสวัสดิ์ นายรวมศักดิ์ บุญศรี นายภูเบศร์ เที่ยงธรรม นายกิตติพงษ์ ศักดิ์อมตพันธ์ และ นางสาวปานสุนี สุวรรณกำเนิด

- เป็นพี่เลี้ยงให้นักศึกษาต่างชาติ 5 คน ได้แก่ Dr. Godson Asirvatham Lazarus Dr. Ahmet Selim Dalkilic, Dr. Balarum Kundu Mr. Omid Mahianและ Mr. Ehsan Ebrahimnia Bajestan
- เป็นพี่เลี้ยงให้อาจารย์มหาวิทยาลัยเทคโนโลยีพระจอมเกล้าธนบุรี และมหาวิทยาลัยอื่นๆ จำนวนมาก

<u>เชิงสาธารณะ</u> (สามารถดู เอกสาร ได้ในภาคผนวก ฉ)

- เป็น Reviewer พิจารณาโครงการที่เสนอขอทุนวิจัยต่างๆของ สกว.
- เป็นกรรมการบัญญัติคำศัพท์ทางวิศวกรรมเครื่องกลของราชบัณฑิตยสถาน
- เป็นกรรมการพิจารณาผลงานเพื่อเข้าสู่ตำแหน่งทางวิชาการให้มหาวิทยาลัยต่างๆ
- เป็น Reviewer พิจารณาบทความให้กับวารสารระดับชาติและระดับนานาชาติ
- เป็นวิทยากรให้องค์กร และ มหาวิทยาลัยต่างๆในเรื่องที่เกี่ยวกับงานวิจัย
- เป็น Editor ของวารสารระดับนานาชาติ Experimental Thermal and Fluid Science (Elsevier Publisher)
- เป็น Lead Guest Editor ของวารสารระดับนานาชาติ Advances in Mechanical Engineering ใน special issue เรือง “Two-Phase Flow and Heat Transfer Enhancement”.
- เป็น Guest Editor ของวารสารระดับนานาชาติ Heat Transfer Engineering (special issue)(Taylor and Francis Publisher)
- ได้รับการประกาศจาก Thomson Reuters ว่ามีบทความต่อไปนี้เป็น a highly-cited article “Trisaksri V, Wongwises S. (2009) Nucleate Pool Boiling Heat Transfer TiO_2-R141b nanofluids, *International Journal of Heat and Mass Transfer* 52 (5-6): 1582-1588.”
- ได้รับการประกาศจากวารสาร Heat and Mass Transfer ว่ามีบทความต่อไปนี้เป็น the popular paper “Srisawas, K., Wongwises S. (2009) Heat transfer characteristics of a new helically coiled crimped spiral finned tube heat exchanger, *Heat Mass Transfer* 45 (4):381-391.”
- ได้รับการประกาศจากวารสาร Experimental Thermal and Fluid Science ว่ามีบทความต่อไปนี้เป็น the most cited article “Daungthongsuk, W., Wongwises, S. (2009) Measurement of temperature-dependent thermal conductivity and viscosity of TiO_2-water nanofluids, *Experimental Thermal and Fluid Science* 33 (4): 706-714.”
(โปรดดูเอกสารในภาคผนวก ฉ)

<u>เชิงพาณิชย์</u> (สามารถดู เอกสาร ได้ในภาคผนวก ช)

ช่วยเหลือให้คำแนะนำ เพื่อเพิ่มคุณภาพของผลิตภัณฑ์ ให้กับภาคอุตสาหกรรม ได้แก่
บริษัท ไซโจเดนกิ อินเตอร์เนชันแนล จำกัด

บริษัท ซี แอร์คอน เทค จำกัด

บริษัท สมชายอินดัสตรี จำกัด

บริษัท ไทย-เยอรมัน โปรดักส์ จำกัด (มหาชน)

โดยเฉพาะอย่างยิ่งได้ให้ความช่วยเหลือบริษัท ไทย-เยอรมัน โปรดักส์ จำกัด (มหาชน) จนกระทั่งผลงานวิจัยมีส่วนช่วยให้ บริษัทฯ ได้รับรางวัลเกียรติยศจากรัฐสภา เมื่อวันที่ 2 ก.ย. 2556 (โปรดดูเอกสารในภาคผนวก ช)

(ศ. ดร. สมชาย วงศ์วิเศษ)

หัวหน้าโครงการ

ภาคผนวก ก.

ผลงานที่ตีพิมพ์ในวารสารระดับนานาชาติ

This article was downloaded by: *[Uppsala University Library]*
On: *20 October 2009*
Access details: *Access Details: [subscription number 786945523]*
Publisher *Taylor & Francis*
Informa Ltd Registered in England and Wales Registered Number: 1072954 Registered office: Mortimer House, 37-41 Mortimer Street, London W1T 3JH, UK

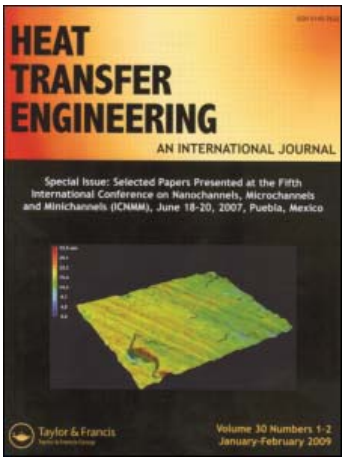

Heat Transfer Engineering
Publication details, including instructions for authors and subscription information:
http://www.informaworld.com/smpp/title~content=t713723051

The Effect of the Electrohydrodynamic on the Two-Phase Flow Pressure Drop of R-134a during Evaporation inside Horizontal Smooth and Micro-Fin Tubes

Suriyan Laohalertdecha [a]; Jatuporn Kaew-On [ab]; Somchai Wongwises [a]
[a] Fluid Mechanics, Thermal Engineering and Multiphase Flow Research Laboratory (FUTURE), Department of Mechanical Engineering, King Mongkut's University of Technology Thonburi, Bangkok, Thailand [b] Department of Physics, Faculty of Science, Thaksin University, Papayom, Phattalung, Thailand

Online Publication Date: 01 January 2010

To cite this Article Laohalertdecha, Suriyan, Kaew-On, Jatuporn and Wongwises, Somchai(2010)'The Effect of the Electrohydrodynamic on the Two-Phase Flow Pressure Drop of R-134a during Evaporation inside Horizontal Smooth and Micro-Fin Tubes',Heat Transfer Engineering,31:2,108 — 118

To link to this Article: DOI: 10.1080/01457630903285369

URL: http://dx.doi.org/10.1080/01457630903285369

PLEASE SCROLL DOWN FOR ARTICLE

Full terms and conditions of use: http://www.informaworld.com/terms-and-conditions-of-access.pdf

This article may be used for research, teaching and private study purposes. Any substantial or systematic reproduction, re-distribution, re-selling, loan or sub-licensing, systematic supply or distribution in any form to anyone is expressly forbidden.

The publisher does not give any warranty express or implied or make any representation that the contents will be complete or accurate or up to date. The accuracy of any instructions, formulae and drug doses should be independently verified with primary sources. The publisher shall not be liable for any loss, actions, claims, proceedings, demand or costs or damages whatsoever or howsoever caused arising directly or indirectly in connection with or arising out of the use of this material.

Heat Transfer Engineering, 31(2):108–118, 2010
Copyright © Taylor and Francis Group, LLC
ISSN: 0145-7632 print / 1521-0537 online
DOI: 10.1080/01457630903285369

Taylor & Francis
Taylor & Francis Group

The Effect of the Electrohydrodynamic on the Two-Phase Flow Pressure Drop of R-134a during Evaporation inside Horizontal Smooth and Micro-Fin Tubes

Downloaded By: [Uppsala University Library] At: 08:02 20 October 2009

SURIYAN LAOHALERTDECHA,[1] JATUPORN KAEW-ON,[1,2] and SOMCHAI WONGWISES[1]

[1]Fluid Mechanics, Thermal Engineering and Multiphase Flow Research Laboratory (FUTURE), Department of Mechanical Engineering, King Mongkut's University of Technology Thonburi, Bangkok, Thailand
[2]Department of Physics, Faculty of Science, Thaksin University, Papayom, Phattalung, Thailand

This article concerns the pressure drop caused by using the electrohydrodynamic (EHD) technique during evaporation of pure R-134a inside smooth and micro-fin tubes. The test section is a counter-flow concentric tube-in-tube heat exchanger where R-134a flows inside the inner tube and hot water flows in the annulus. A smooth tube and micro-fin tube having an inner diameter of 8.12 mm and 8.92 mm, respectively, are used as an inner tube. The length of the inner tube is 2.50 m. The outer tube is a smooth copper tube having an inner diameter of 21.2 mm. The electrode, which is a cylindrical stainless steel wire having diameter of 1.47 mm, is placed in the center of the inner tube. The electrical field is established by connecting a DC high voltage power supply of 2.5 kV to the electrode while the inner tube is grounded. Experiments are conducted at saturation temperatures of 10–20°C, mass fluxes of 200–600 kg/m^{2}s, and heat fluxes of 10–20 kW/m^2. The experimental results indicate that the application of EHD introduces a small pressure drop penalty. New correlations for the pressure drop are proposed for practical applications.

INTRODUCTION

Normally, heat transfer enhancement techniques can be divided into two groups: namely passive techniques and active techniques. The passive techniques require special surface geometries, such as rough surface or extended surface. The active techniques require external forces, such as fluid vibration, surface vibration, and an electrical field. An electrohydrodynamic (EHD) technique is one of the types of active techniques, which can be achieved by the interaction between the electrical field and the flow of dielectric fluid medium. This interaction creates additional fluid motion which leads to a higher heat transfer coefficient. The electrical body force density acting on the fluid element of dielectric fluid in the presence of an electrical field can be expressed as:

$$f_e = qE - \frac{1}{2}E^2\nabla\varepsilon + \frac{1}{2}\nabla\left[E^2\rho\left(\frac{\partial\varepsilon}{\partial\rho}\right)_T\right] \qquad (1)$$

The three terms on the right side of Eq. (1) represent the electrophoretic, dielectrophoretic, and electrostrictive components of the force, respectively. The first term represents the force acting on the free charges in the presence of an electrical field, called Coulomb force. The second term is a consequence of inhomogeneous or spatial change in the permittivity of the dielectric fluid due to non-uniform electrical fields, temperature

The present study was supported financially by the Joint Graduate School of Energy and Environment (JGSEE) and the Thailand Research Fund (TRF) whose guidance and assistance are gratefully acknowledged.

Address correspondence to Professor Somchai Wongwises, King Mongkut's University of Technology Thonburi, 126 Pracha-utid Road, Bangmod, Toongkru, Bangkok 10140, Thailand. E-mail: somchai.won@kmutt.ac.th

Table 1 Refrigerants, electrode and tube configurations studied by various researchers

Source	Refrigerant	Test section	Electrode geometry	Experimental condition	Supplied energy to the test section
Singh et al. [1]	R-123	Smooth stainless steel tube ID = 9.4 mm Length = 1220 mm	Cylindrical stainless steel electrode having diameter of 3 mm	T_{sat} = 27.52°C EHD = 0, 10 kV q'' = 5, 10, 20 kW/m^2 G = 50–400 kg/m^{2}s Inlet quality = 0–0.5	Hot water
Singh et al. [2]	R-134a	Smooth stainless steel tube ID = 9.4 mm Length = 1220 mm	Cylindrical stainless steel electrode having diameter of 3 mm	T_{sat} = 20.15°C EHD = 0, 10 kV q'' = 5, 10, 20 kW/m^2 G = 50–400 kg/m^{2}s Inlet quality = 0–0.5	Hot water
Salehi et al. [3]	R-404A	Micro-fin copper tube ID = 11.78 mm OD = 12.7 mm Length = 304.8 mm	Cylindrical stainless steel wire having diameter of 0.46 mm Helical electrode ID = 8.92 mm, OD = 9.84 mm	T_{sat} = 20.15°C EHD = 0–3 kV q'' = 5, 10 kW/m^2 G = 50–200 kg/m^{2}s Average quality = 0–0.8	Electric heater
Salehi et al. [4]	R-134a	1. Smooth copper tube ID = 9.5 mm OD = 11.56 mm Length = 114.3 mm 2. Corrugated copper tube with helical angle of 18 with height of ridge of 0.25 mm	Cylindrical rod	Re =500, 1000 EHD = 0–3 kV q'' = 25 kW/m^2 Inlet quality = 0–0.6	Electric heater
Bryan and Seyed-Yagoobi [5]	R-134a	Smooth copper tube ID = 14.1 mm OD = 15.9 mm Length = 100, 200, 300, 500 mm (connecting in series)	Cylindrical brass rod electrode having diameter of 1.6 mm	T_{sat} = 4.9–25.1°C EHD = 0, 5, 15 kV G = 99.9–300.7 kg/m^{2}s Inlet quality = 0–0.8	Hot water
Cotton et al. [6]	R-134a	Smooth stainless steel tube ID = 10.92 mm OD = 12.7 mm Length = 1800 mm	Cylindrical stainless steel electrode having diameter of 3.175 mm	T_{sat} = 24°C EHD = 0–8 kV q'' = 10, 20 kW/m^2 G = 100–500 kg/m^{2}s Inlet quality = 0–0.6	Hot water

Downloaded By: [Uppsala University Library] At: 08:02 20 October 2009

gradients, and phase differences. The third term is caused by inhomogeneous electrical field strength and the variation in dielectric constant with temperature and density.

Heat transfer enhancement during evaporation using EHD has been published in the literature. Some of the works were performed by Singh et al. ([1, 2]), Salehi et al. [3, 4], Bryan and Seyed-Yagoobi [5] and Cotton et al. [6] as shown in Table 1.

It can be noted that the mass fluxes of the reported test tubes are almost all below 300 kg/s.m^2. As a consequence, the objective of this study is to study the pressure drop penalty from the use of electrohydrodynamic technique during evaporation of R-134a flowing in a horizontal smooth tube and micro-fin tube at high mass flux conditions.

EXPERIMENTAL APPARATUS

The experimental apparatus can be divided into two parts: the refrigeration test unit and the direct current (DC) high voltage power supply unit. A schematic diagram of the test apparatus is shown in Figure 1. This experimental apparatus was designed to measure the heat transfer coefficient and pressure drop of pure R-134a over the length of the test tube.

The test loop consists of a test section, refrigerant loop, heating water flow loops, sub-cooling loop, and the relevant instrumentation. For the refrigerant circulation loop, liquid refrigerant is pumped by a magnetic gear pump which is regulated by an inverter. The refrigerant flows in series through a filter/dryer, a sight glass tube, and enters the test section. The inlet quality before entering the test section is controlled by the pre-heater. The pre-heater is a spiral counter flow heat exchanger that supplies energy to control inlet quality of the refrigerant. The refrigerant leaving the test section is then condensed and sub-cooled by the chilling loop that removes heat load receiving from the pre-heater and, returns from the two-phase refrigerant to a sub-cooled state and later collects in a receiver and eventually returns to the refrigerant pump to complete the cycle.

The test section as shown in Figure 2 is a horizontal counter-flow double tube heat exchanger. The length of the heat exchanger is 2.5 m. Refrigerant temperature and the tube

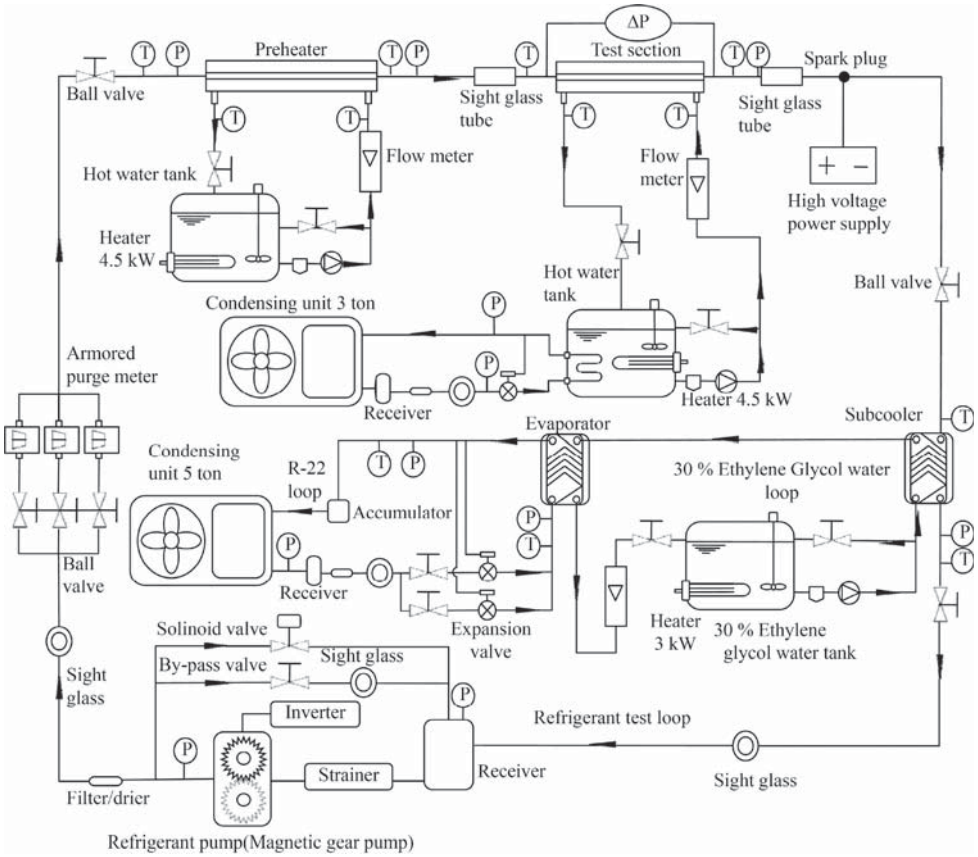

Figure 1 Schematic diagram of experimental apparatus.

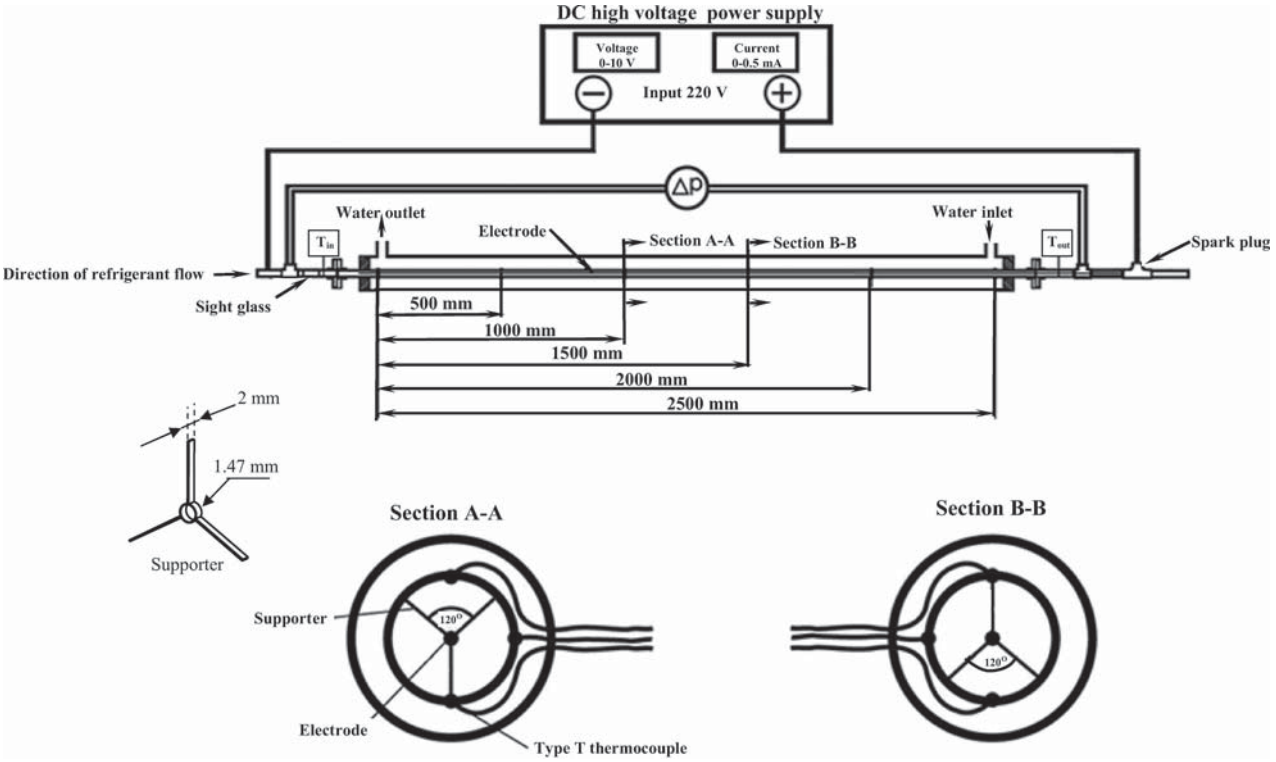

Figure 2 Schematic diagram of test section.

Downloaded By: [Uppsala University Library] At: 08:02 20 October 2009

Downloaded By: [Uppsala University Library] At: 08:02 20 October 2009

Table 2 Smooth tube and micro-fin tube dimensions

Parameter	Smooth tube	Micro-fin tube
Outside diameter, D_o (mm)	9.52	9.52
Bottom thickness, t (mm)	0.7	0.3
Wwetted perimeter (mm)	25.5	43.2
Maximum inner diameter, D_i (mm)	8.12	8.92
Hydraulic diameter, D_h (mm)	8.12	5.43
Cross sectional area, A_c (mm^2)	51.78	61.31
Number of fins, n	—	60
Spiral angle, β (degrees)	—	18
Fin height, e_f (mm)	—	0.2
Fin pitch, p (mm)	—	0.47
Bottom width (mm)	—	0.27
Apex angle, γ (degrees)	—	52.45
Fin tip diameter, D_t (mm)	—	8.52

wall temperatures in the test section are measured by T-type thermocouples. A total of eighteen thermocouples are soldered at the top, bottom and side at six points along the tube. All the temperature measuring devices are well calibrated in a controlled temperature bath using standard precision mercury glass thermometers. The uncertainty of the temperature measurements after considering the data acquisition system is ± 0.1°C. All static pressure taps are mounted in the tube wall. The refrigerant flow meter is a variable area type. The flow meter is specially calibrated in the range of 0–8.3 × 10^{-3} m^3/min for R-134a by the manufacturer. The differential pressure transducer and pressure gauges are calibrated against a primary standard, the dead weight tester. A stainless steel cylindrical electrode, 1.47 mm in diameter, is used in all experiments. The cylindrical electrode is supported in the center of the test section by electrically insulating spacers (Teflon type material) at intervals of 250 mm. The electrode is attached to the spacers by using a special epoxy-resin. Since the electric field is applied to the test section by a DC high voltage power supply, the electrode attached to a modified automotive spark plug serves as the charged electrode and the heat transfer surface as the receiving electrode.

The dimensions of the smooth and micro-fin tubes are shown in Table 2. The cross-section of micro-fin tube is shown in

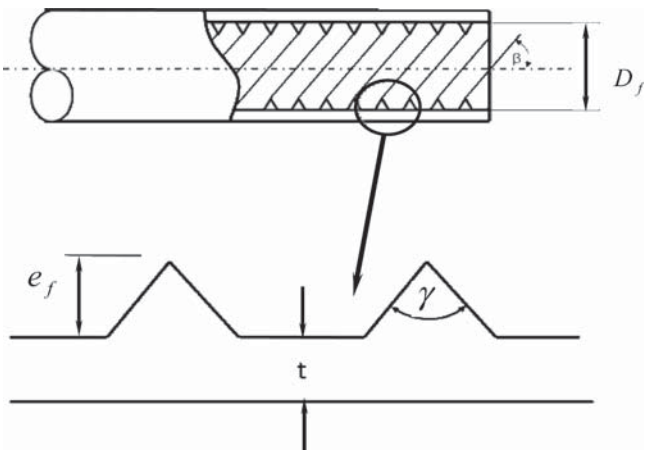

Figure 3 The cross-section of micro-fin tube.

Table 3 Experimental uncertainty

Parameter	Uncertainty
Temperature, T (°C)	±0.1°C
Pressure drop, ΔP(kPa)	±0.075 kPa
Mass flow rate of refrigerant, $\dot{m}_{ref}$	±2% Full scale
Mass flow rate of water, $\dot{m}_w$	±5% Full scale
Heat transfer rate at test section, $\dot{Q}_{TS}$	±11%
Heat transfer rate at pre-heater, $\dot{Q}_{ph}$	±8%
Heat transfer coefficient, h_{avg}	±12%
Inlet quality, x_{in}	±8%

Figure 3. The inlet water temperature is controlled by a thermostat. A differential pressure transducer and thermocouples are installed at the test section to measure the pressure drop and temperature across the test section respectively. The length between the pressure taps is 3 m.

It is necessary to realize that the maximum voltage before starting the electrical breakdown in the test section must be known and should not be exceeded during any steady-state condition. Before the two-phase experiment was performed, the heat balance between refrigerant-side and water-side of the single-phase experiment was conducted. The uncertainties of the heat balance were within 8% and 5% for the pre-heater and the test section, respectively. The uncertainties of the measured quantities and calculated parameters are shown in Table 3.

DATA REDUCTION

The data reduction of the measured results can be summarized as follows:

The inlet vapor quality of the test section ($x_{TS,in}$)

$$x_{TS,in} = \frac{i_{TS,in} - i_{f@T_{TS,in}}}{i_{fg@T_{TS,in}}} \tag{2}$$

where i_f is the enthalpy of the saturated liquid based on the temperature of the test section inlet, i_{fg} is the enthalpy of vaporization based on the temperature of the test section inlet, $i_{TS,in}$ is the refrigerant enthalpy at the test section inlet and is given by:

$$i_{TS,in} = i_{ph,in} + \frac{\dot{Q}_{ph}}{\dot{m}_{ref}} \tag{3}$$

where $i_{ph,in}$ is the inlet enthalpy of the liquid refrigerant before entering the pre-heater, $\dot{m}_{ref}$ is the mass flow rate of the refrigerant and $\dot{Q}_{ph}$ is the heat transfer rate in the pre-heater:

$$\dot{Q}_{ph} = \dot{m}_{w,ph} c_{p,w} (T_{w,in} - T_{w,out})_{ph} \tag{4}$$

where $\dot{m}_{w,ph}$ is the mass flow rate of water entering the pre-heater.

The outlet vapor quality of the test section ($x_{TS,out}$)

$$x_{TS,out} = \frac{i_{\mathrm{TS,out}} - i_{f@T_{\mathrm{TS,out}}}}{i_{fg@T_{\mathrm{TS,out}}}} \tag{5}$$

where $i_{TS,out}$ is the refrigerant enthalpy at the test section outlet, i_f is the enthalpy of the saturated liquid based on the temperature of the test section outlet, and i_{fg} is the enthalpy of vaporization. As a consequence, the outlet enthalpy of the refrigerant flow is calculated as:

$$i_{TS,out} = i_{TS,in} + \frac{\dot{Q}_{TS}}{\dot{m}_{ref}} \tag{6}$$

where the heat transfer rate in the test section is obtained from:

$$\dot{Q}_{TS} = \dot{m}_{w,TS} c_{p,w} (T_{w,in} - T_{w,out})_{TS} \tag{7}$$

where $\dot{m}_{w,TS}$ is the mass flow rate of the water entering the test section.

The average heat transfer coefficient (h_{avg})

$$h_{avg} = \frac{\dot{Q}_{TS}}{A_{inside}(T_{avg,wall} - T_{avg,sat})} \tag{8}$$

where h_{avg} is the average heat transfer coefficient, $\dot{Q}_{TS}$ is the heat transfer rate in the test section, $T_{avg,wall}$ is the average temperature of the wall, $T_{avg,sat}$ is the average temperature of the refrigerant at the test section inlet, and outlet.

$$T_{avg,sat} = \frac{T_{in,sat} + T_{out,sat}}{2} \tag{9}$$

A_{inside} is the inside surface area of the test section:

$$A_{inside} = \pi D_f L \tag{10}$$

where D_f is the inside diameter of the test tube. L is the length of the test tube. The inside diameter of the micro-fin tube is defined as the outer diameter of the micro-fin tube minus twice the minimum wall thickness.

RESULTS AND DISCUSSION

In general, the EHD technique can provide enhancement of heat transfer. However, the heat transfer enhancement should be considered together with pressure drop penalty. In the present study, the effects of electrode, supporter, mass fluxes, saturation temperatures, heat fluxes, and applied voltage of 2.5 kV on the pressure drop during evaporation of R-134a inside smooth and micro-fin tubes are experimentally investigated. The test conditions were selected to cover as much as possible of the range of inlet quality. The pressure drop is the sum of a frictional pressure drop and a momentum pressure drop. The pressure drop per unit length is obtained by dividing the measured pressure drop by the length between pressure taps. In our apparatus, the length between pressure taps is 3 m, while the length of the heat exchanger is 2.5 m.

There are two phenomena that are usually encountered inside EHD-enhanced smooth and micro-fin tubes [7]. The first is the liquid-extraction phenomenon. When a coaxial cylindrical electrode is used with a smooth tube, the highest electrical field is at the electrode surface due to its small radius of curvature

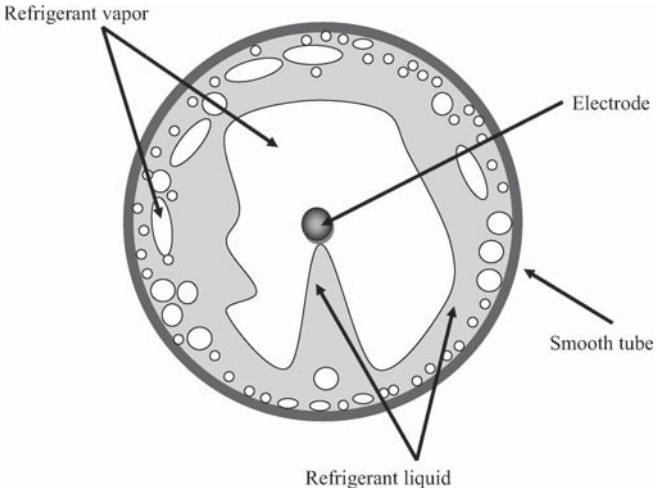

Figure 4 Liquid-extraction phenomenon [7].

since the liquid surface extends into the gas toward the electrode as shown in Figure 4. The second is the electro-convection phenomenon. When a coaxial cylindrical electrode is used with a micro-fin tube, the highest electrical field is at the tip of the fin due to its small radius of curvature (sharp) since the liquid interface is pulled toward the tip of the fin, as shown in Figure 5. Both liquid-extraction and electro-convection phenomena generate a secondary fluid motion inside the tube leading to increase in heat transfer and pressure drop.

Figures 6 and 7 show the comparisons of the measured pressure drop inside smooth and micro-fin tubes for the absence of an electrode, the presence of an uncharged electrode (0 kV), and the presence of a charged electrode (2.5 kV). The test conditions are performed at the saturation temperature (T_{sat}) of 20°C, heat flux (q") of 10 kW/m^2, and mass flux (G) of 400 kg/m^{2}s. The measured pressure drop in the absence of an electrode is obtained by Wongsa-ngam et al. [8]. These figures also show that the pressure drops obtained from both tubes increase with increasing inlet quality. At the same quality, the pressure drop obtained with the presence of an uncharged electrode (0 kV) is higher than that with the absence of an electrode up to

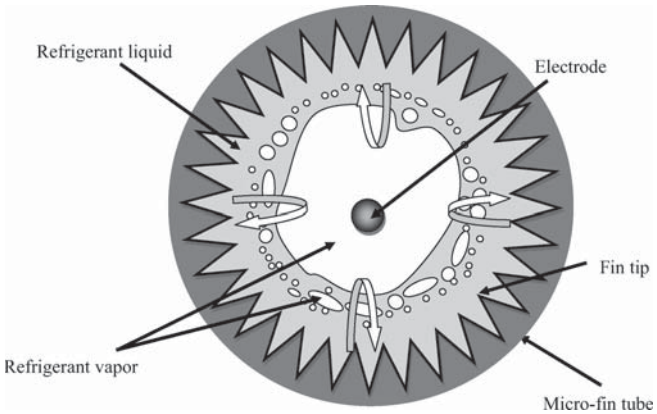

Figure 5 Electro-convection phenomenon [7].

Downloaded By: [Uppsala University Library] At: 08:02 20 October 2009

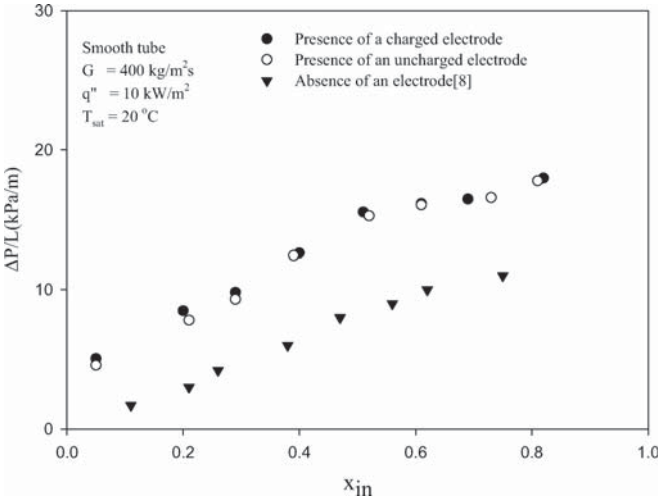

Figure 6 Pressure drop versus inlet quality for smooth tube at $T_{sat} = 20°C$, $G = 400$ kg/m^{2}s and $q'' = 10$ kW/m^2.

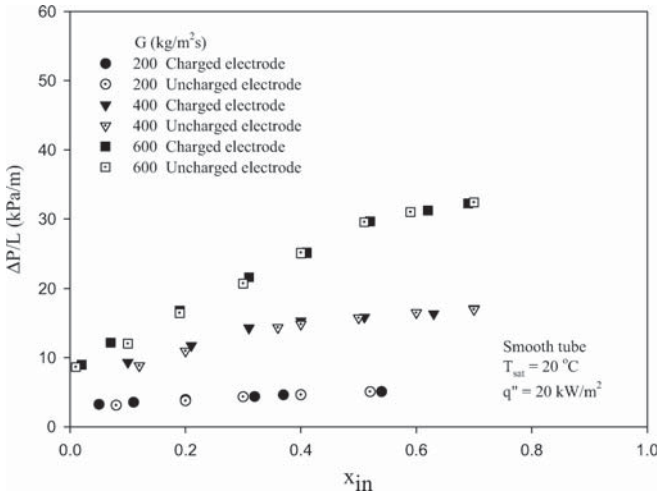

Figure 8 The effect of mass flux on the pressure drop for smooth tube at $T_{sat} = 20°C$ and $q'' = 20$ kW/m^2.

Downloaded By: [Uppsala University Library] At: 08:02 20 October 2009

100% for smooth tube and 80% for micro-fin tube. This is because the supporter and electrode obstruct the fluid flow. The pressure drop obtained with the presence of a charged electrode is slightly higher than that with the presence of an uncharged electrode at the same inlet quality because of the instabilities at the liquid-vapor interface resulting from the molecules of refrigerant disturbed by the EHD force.

Figures 8 and 9 show the variation of the measured pressure drop with inlet quality of pure R-134a during evaporation in the smooth and micro-fin tubes for the presence of an uncharged electrode (0 kV) and for the presence of a charged electrode (2.5 kV) at a saturation temperature of 20°C and heat flux of 20 kW/m^2 for different mass fluxes of 200, 400, and 600 kg/m^2 s. These figures show that the measured pressure drops obtained from the presence of an uncharged electrode (0 kV) and the presence of a charged electrode (2.5 kV) increase with increasing inlet quality. As expected, at the same quality the pressure drops for the presence of an uncharged electrode (0 kV) and the presence of a charged electrode (2.5 kV) obtained from higher mass flux are always higher than at lower mass fluxes across the range of the inlet quality. However, the effect of the mass flux on the pressure drop can be clearly seen at higher inlet quality, i.e., the pressure drop is much higher for a higher mass flux than that for a lower mass flux. The application of EHD seems to be negligible for almost all pressure drops obtained from the broadest range of inlet quality.

Figures 10 and 11 show the variation of the measured evaporation pressure drop with inlet quality in the smooth and micro-fin tubes for the presence of an uncharged electrode (0 kV) and the presence of a charged electrode (2.5 kV) at a mass flux of 400 kg/m^2 s and saturation temperature of 20°C for different heat fluxes of 10, 15 and 20 kW/m^2. These figures also show that

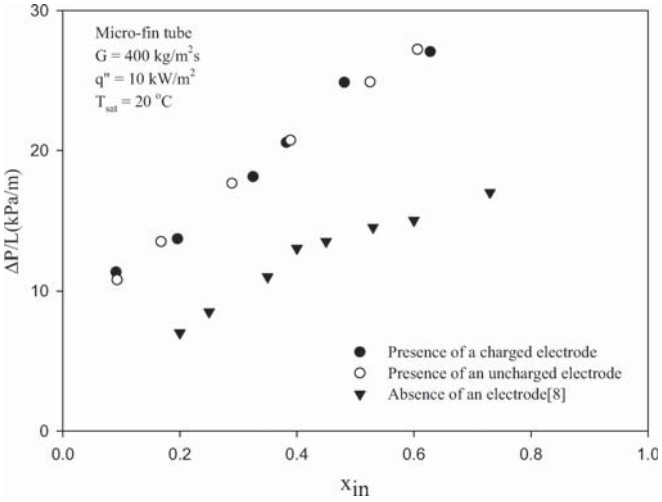

Figure 7 Pressure drop versus inlet quality for micro-fin tube at $T_{sat} = 20°C$, $G = 400$ kg/m^{2}s and $q'' = 10$ kW/m^2.

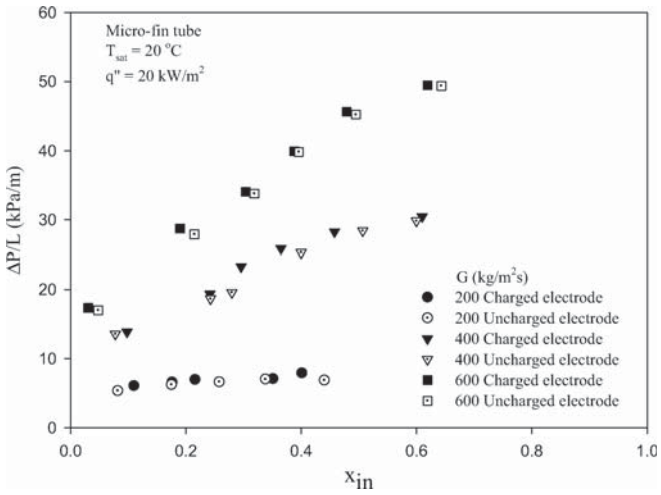

Figure 9 The effect of mass flux on the pressure drop for micro-fin tube at $T_{sat} = 20°C$ and $q'' = 20$ kW/m^2.

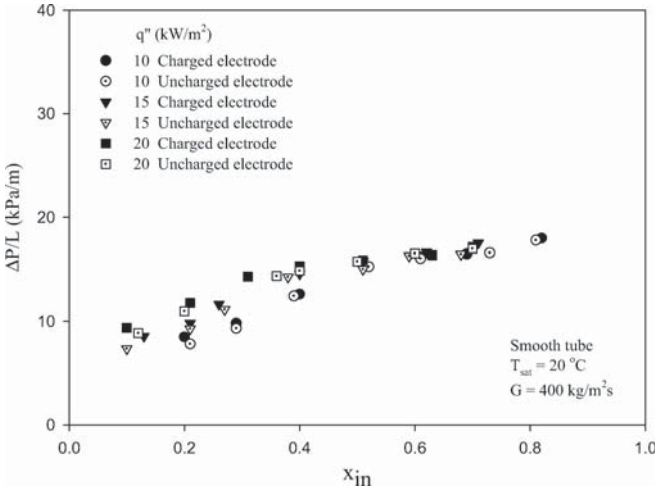

Figure 10 The effect of heat flux on the pressure drop for smoth tube at $T_{sat} = 20°C$ and $G = 400$ kg/m^{2}s.

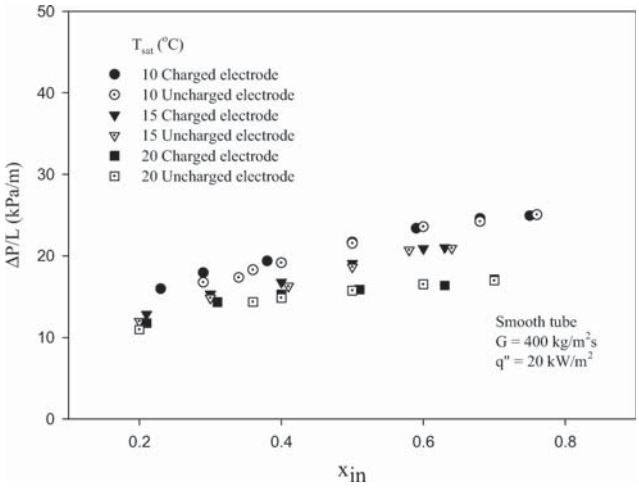

Figure 12 The effect saturation temperature on the pressure drop for smooth tube at $T_{sat} = 20°C$ and $G = 400$ kg/m^{2}s.

the pressure drops for both smooth and micro-fin tubes with the presence of an uncharged electrode (0 kV) and the presence of a charged electrode (2.5 kV) increase with increasing inlet quality. It can be seen that pressure drop increases with increasing heat flux. This is because more vapor bubbles are created at higher heat flux. This phenomenon promotes more agitation in the fluid flow, leading to the increase in pressure drop. Application of EHD voltage of 2.5 kV also has a slight effect on the pressure drop in a wide range of inlet qualities.

Figures 12 and 13 show the variation of the measured evaporation pressure drop with inlet quality in the smooth and micro-fin tubes for the presence of an uncharged electrode (0 kV) and the presence of a charged electrode (2.5 kV) at a mass flux of 400 kg/m^2 s, heat flux of 20 kW/m^2 and different saturation temperatures of 10, 15 and 20°C. These figures also show that the pressure drops increase slightly with increasing inlet quality. As expected, the pressure drop at lower saturation temperatures is higher than those at higher saturation temperatures at an equivalent inlet quality. The effect of the saturation temperature on the pressure drop is clear at higher inlet quality. The pressure drop is higher for a lower saturation temperature than that for a higher saturation temperature, and this is caused by the decrease in the mixture viscosity. The application of an EHD voltage of 2.5 kV for smooth and micro-fin tubes slightly increases the pressure drop at all saturation temperatures.

Figures 14 and 15 show the comparisons of the average measured evaporation heat transfer coefficient obtained from the smooth tube with that obtained from the micro-fin tube at a mass flux of 400 kg/m^2 s, a heat flux of 20 kW/m^2, and saturation temperatures of 20°C for the presence of an uncharged electrode and a charged electrode, respectively. It can be clearly seen that the heat transfer coefficient increases with increasing inlet quality. Both in the presence of uncharged electrode and charged electrode, the heat transfer coefficient obtained from

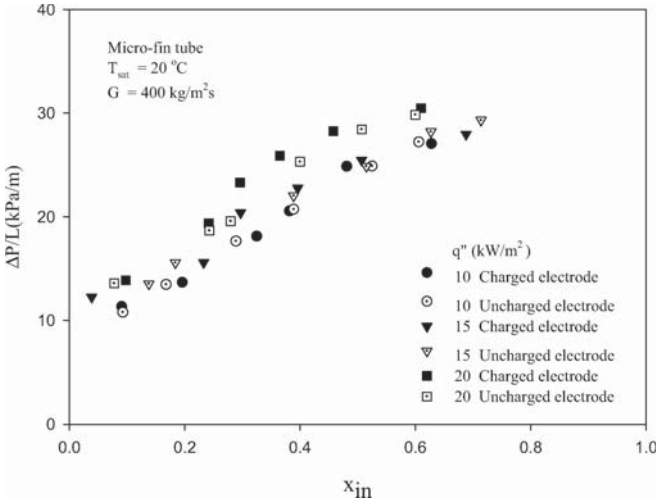

Figure 11 The effect of heat flux on the pressure drop for micro-fin tube at $T_{sat} = 20°C$ and $G = 400$ kg/m^{2}s.

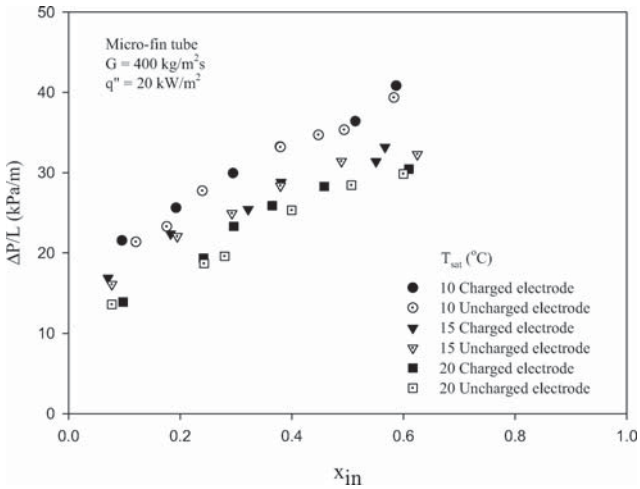

Figure 13 The effect saturation temperature on the pressure drop for micro-fin tube at $T_{sat} = 20°C$ and $G = 400$ kg/m^{2}s.

Downloaded By: [Uppsala University Library] At: 08:02 20 October 2009

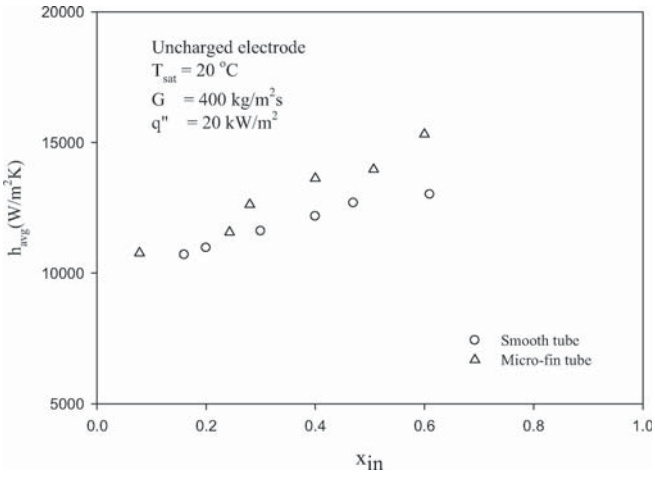

Figure 14 Heat transfer coefficient versus inlet quality for the presence of an uncharged electrode at $T_{sat} = 20°C$, $G = 400$ kg/m^{2}s, and $q'' = 20$ kW/m^2.

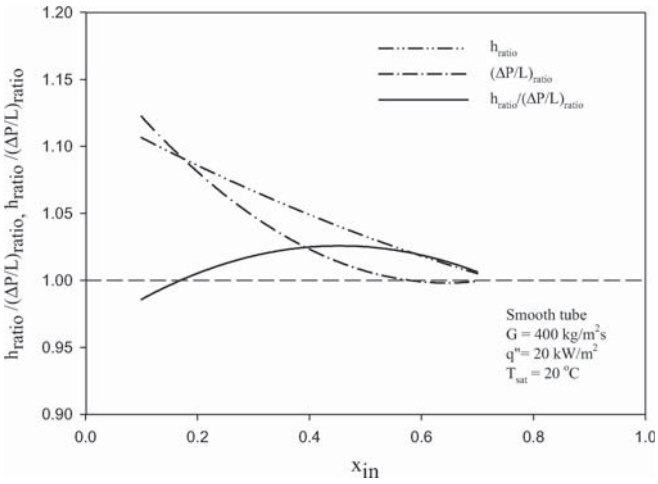

Figure 16 The heat transfer ratio and the pressure drop ratio versus inlet quality for smooth tube at $T_{sat} = 20°C$, $G = 400$ kg/m^{2}s, and $q'' = 20$ kW/m^2.

the microfin tube are higher than that obtained from the smooth tube at the same inlet quality.

In the case of a smooth tube, with the presence of charged electrode, due to liquid extraction phenomenon, the liquid-vapor interface becomes unstable. This causes the average heat transfer coefficient to be higher than in the case of uncharged electrode. In the case of micro-fin tube, due to electro-convection phenomenon, the liquid interface was pulled toward the tip of the fin causing the increase of heat transfer coefficient.

Figures 16 and 17 show the heat transfer coefficient ratio (h_{ratio}), pressure drop ratio $(\Delta P/L)_{ratio}$ and enhancement factor $((h_{ratio})/(\Delta P/L)_{ratio})$ with inlet quality at a saturation temperature of 20°C, heat flux of 20 kW/m^2 and mass flux of 400 kg/m^2 s in smooth and micro-fin tubes, respectively. The heat transfer coefficient ratio (h_{ratio}) is defined by $h_{avg,e}/h_{avg,o}$, where $h_{avg,e}$ is the heat transfer coefficient with the presence of a charged electrode (2.5 kV) and $h_{avg,o}$ is the heat transfer coefficient with the presence of an uncharged electrode (base case, 0 kV). The pressure drop ratio ($(\Delta P/L)_{ratio}$) is defined by $[(\Delta P/L)_e/(\Delta P/L)_o]$, where $(\Delta P/L)_e$ is the pressure drop with the presence of a charged electrode (2.5 kV) and $(\Delta P/L)_o$ is the pressure drop with the presence of an uncharged electrode (base case, 0 kV). From these figures it can be seen that heat transfer coefficient ratio and pressure drop ratio are decreased with an increase in inlet quality. The heat transfer coefficient ratios are all higher than the pressure drop ratio. The enhancement ratios $(h_{ratio}/(\Delta P/L)_{ratio})$ are almost always higher than 1 in the whole range of the tested inlet quality. It can be explained that the slight pressure drop penalty is compensated by the heat transfer augmentation.

Correlation for Predicting Pressure Drop

The two-phase friction pressure gradient (dp_F/dz) of smooth and micro-fin tubes may be expressed in term of two-phase

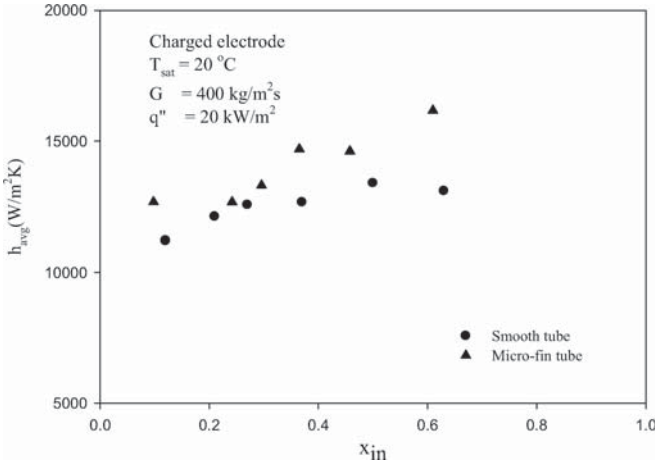

Figure 15 Heat transfer coefficient versus inlet quality for the presence of a charged electrode at $T_{sat} = 20°C$, $G = 400$ kg/m^{2}s, and $q'' = 20$ kW/m^2.

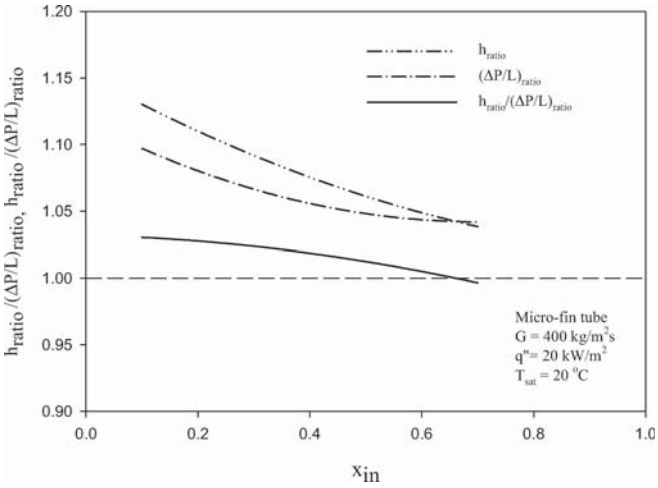

Figure 17 The heat transfer ratio and the pressure drop ratio versus inlet quality for micro-fin tube $T_{sat} = 20°C$, $G = 400$ kg/m^{2}s, and $q'' = 20$ kW/m^2.

Downloaded By: [Uppsala University Library] At: 08:02 20 October 2009

multiplier ϕ_l^2 defined as follow:

$$\phi_l^2 = \left(\frac{dp_F}{dz}\right) / \left(\frac{dp_F}{dz}\right)_l \tag{11}$$

Martinelli parameter (X) is given by:

$$X = \sqrt{\frac{(dp_F/dz)_l}{(dp_F/dz)\,v}} \tag{12}$$

where $(dp_F/dz)_l$ and $(dp_F/dz)_v$ are the single-phase liquid and vapor pressure gradients (kPa/m) calculated by using the actual phase flow as follows:

$$(dp_F/dz)_l = \frac{2f_l G^2(1-x)^2}{D\rho_l} \tag{13}$$

and

$$(dp_F/dz)_v = \frac{2f_v G^2 x^2}{D\rho_v} \tag{14}$$

where f_l is the single phase liquid friction factor calculated from:

$$4f_l = 1.325\left[\ln\left(\frac{e/D}{3.7} + \frac{5.74}{\mathrm{Re}_l^{0.9}}\right)\right]^{-2} \tag{15}$$

And

$$\mathrm{Re}_l = \frac{GD(1-x)}{\mu_l} \tag{16}$$

where f_v is the single phase vapor friction factor calculated from:

$$4f_v = 1.325\left[\ln\left(\frac{e/D}{3.7} + \frac{5.74}{\mathrm{Re}_v^{0.9}}\right)\right]^{-2} \tag{17}$$

And

$$\mathrm{Re}_v = \frac{GDx}{\mu_v} \tag{18}$$

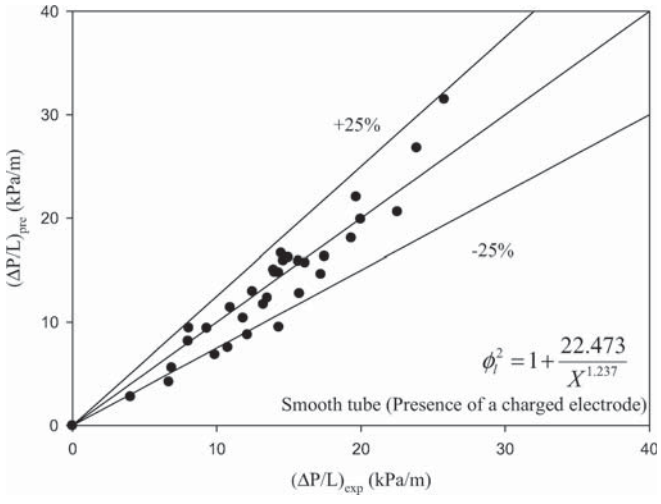

Figure 18 Predicted pressure drop versus the measured pressure drop.

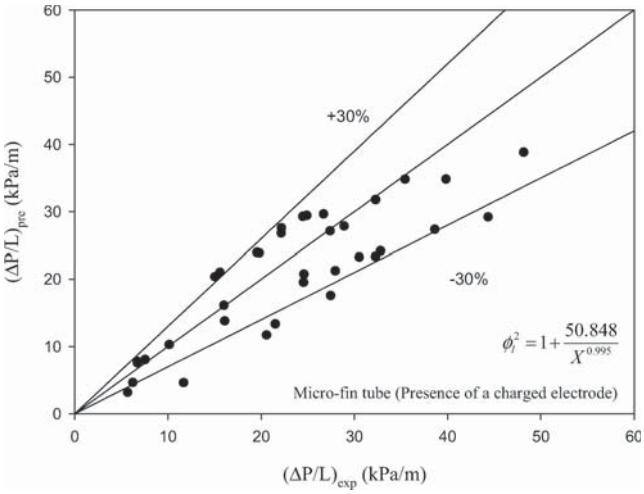

Figure 19 Predicted pressure drop versus the measured pressure drop.

For micro-fin tube the relative roughness (e/D) in Eqs. (15) and (17) are replaced by the equation: Cavalini and Zecchin [9]:

$$e/D = 0.18(e_f/D_t)/(0.1 + \cos\beta) \tag{19}$$

where e_f is the fin height. D_t is the fin tip diameter. β is the spiral angle.

For smooth tube, empirical correlation shown in Eq. (20) is developed based on the presence of a charged electrode. It is created by fitting the Martinelli parameter (X) against a two-phase multiplier.

The presence of a charged electrode the two-phase multiplier is:

$$\phi_l^2 = 1 + \frac{22.473}{X^{1.237}} \tag{20}$$

The correlation is also plotted in Figure 18. It can be explained that the present correlation can predict the pressure drop within a deviation of ±25%.

For micro-fin tube, the empirical correlation shown in Eq. (21) is developed based on the presence of a charged electrode. It is created by fitting the Martinelli parameter (X) against a two-phase multiplier.

The presence of a charged electrode the two-phase multiplier is:

$$\phi_l^2 = 1 + \frac{50.848}{X^{0.995}} \tag{21}$$

The correlation is also plotted in Figure 19. It can be explained that the present correlation can predict the pressure drop within a deviation of ±30%.

CONCLUSIONS

The present article reports the pressure drop penalty from the application of EHD force on evaporation heat transfer enhancement of R-134a in horizontal smooth and micro-fin tubes. The pressure drop obtained from the presence of an uncharged

Downloaded By: [Uppsala University Library] At: 08:02 20 October 2009

electrode (0 kV) is higher than that from the absence of an electrode, up to 100% for smooth tube and 80% for micro-fin tube. Pressure drop results from both smooth and micro-fin tubes indicate that the application of an EHD voltage of 2.5 kV slightly increases the pressure drop across the range of tested conditions. The enhancement ratio is almost always higher than 1. The present correlation can predict the pressure drop within a deviation of ±25% for smooth tube and ±30% for micro-fin tube, respectively.

NOMENCLATURE

A_{inside}	inside surface area of test section (m^2)
A_c	cross section area (m^2)
c_p	specific heat at constant pressure (J/kg-K)
D_h	hydraulic diameter (m)
D_o	outside tube diameter (m)
D_f	inside tube diameter (m)
e_f	fin height (m)
E	electric field strength (V/m)
f_e	EHD force density (N/m^3)
G	mass flux (kg/m^2s)
h	heat transfer coefficient (W/m^2 K)
i	enthalpy (J/kg)
L	tube length (m)
$\dot{m}$	mass flow rate (kg/s)
n	number of fin
p	fin pitch (m)
P	pressure (Pa)
$\dot{Q}$	heat transfer rate (W)
q''	heat flux (W/m^2)
q	electric charge density (C/m^3)
T	temperature (°C)
u	velocity (m/s)
x	quality
X	Martinelli parameter
ϕ_l^2	two-phase multiplier

Greek Symbols

β	spiral angle (degree)
γ	apex angle (degree)
ε	electric permittivity (F/m)
ε_o	electric permittivity of free space (8.854×10^{-12}) (F/m)
ρ	density (kg/m^3)

Subscripts

avg	average
e	presence of an uncharged electrode
exp	experiment
f	saturated liquid
fg	difference in property between saturated liquid and vapor
in	inlet
l	liquid
o	presence of a charged electrode
out	outlet
ph	pre-heater
pre	prediction
ref	refrigerant
sat	saturation
TS	test section
V	vapor
w	water
wall	wall

REFERENCES

[1] Singh, A., Dessiatoun, S., Ohadi, M. M., Salehi, M., and Chu, W., In-tube Boiling Heat Transfer Enhancement of R-123 using the EHD technique. *ASHRAE Transactions: Symposia*, pp. 818–825, 1994.

[2] Singh, A., Dessiatoun, S., Ohadi, M. M., Salehi, M., and Chu W., In-tube Boiling Enhancement of R-134a Utilizing the Electric Field Effect, *ASME/JSME Thermal Engineering Conference*, vol. 2, pp. 215–223, 1995.

[3] Salehi, M., Ohadi, M. M., and Dessiatoun, S., The Applicability of the EHD Technique for Convective Boiling of Refrigerant Blends—Experiments with R-404A, *ASHRAE Transactions: Symposia,* pp. 839–844, 1996.

[4] Salehi, M., Ohadi, M. M., and Dessiatoun, S., EHD Enhanced Convective Boiling of R-134a in Grooved Channels—Application to Subcompact Heat Exchangers, *Journal of Heat Transfer*, vol. 119, pp. 805–809, 1997.

[5] Bryan, J. E., and Seyed-Yagoobi, J., Elecrohydrodynamically Enhanced Convective Boiling: Relationship between Electrohydrodynamic Pressure and Momentum Flux Rate, *Transaction of the ASME*, vol. 122, pp. 266–277, 2000.

[6] Cotton, J., Robinson, A. J., Shoukri, M., and Chang, J. S., A Two-Phase Flow Pattern Map for Annular Channels under a DC Applied Voltage and the Application to Electrohydrodynamic Convective Boiling Analysis, *International Journal of Heat and Mass Transfer*, vol. 48, pp. 5563–5579, 2005.

[7] Singh, A., Ohadi, M. M., and Dessiatoun, S., EHD Enhancement of In-tube Condensation Heat Transfer of Alternate Refrigerant R-134a in Smooth and Microfin Tubes, *ASHRAE Transactions: Symposia*, pp. 813–823, 1997.

[8] Wongsa-ngam, J., Nualboonrueng, T., and Wongwises, S., Performance of Smooth and Micro-fin Tubes in High mass Flux Region of R-134a during Evaporation, *Heat and Mass Transfer*, vol. 40, pp. 425–435, 2004.

[9] Cavallini, A., and Zecchin, R., A Dimensionless Correlation for Heat Transfer Coefficient in Forced Convection Condensation, *International Journal of Heat and Mass Transfer conference*, pp. 193–200, 1974.

Downloaded By: [Uppsala University Library] At: 08:02 20 October 2009

Suriyan Laohalertdecha is currently a Ph.D. student at the Joint Graduate School of Energy and Environment, King Mongkut's University of Technology Thonburi, Bangmod, Thailand. He received his Master's degree in energy technology from the same department in 2005. He also received his B.Eng. degree from the Department of Mechanical Engineering at the same university in 2002. Currently, his research works concern heat transfer enhancement.

Jatuporn Kaewon is currently a Ph.D. student at the Joint Graduate School of Energy and Environment, King Mongkut's University of Technology Thonburi, Bangmod, Thailand. He received his Master's degree in energy technology from the same department in 2003. He also received his B.Eng. degree from the Department of Mechanical Engineering at the same university in 1999. He is also currently a lecturer at Thaksin University.

Somchai Wongwises is a Professor of Mechanical Engineering at King Mongkut's University of Technology Thonburi, Bangmod, Thailand. He received his Doktor-Ingenieur (Dr.-Ing.) in mechanical engineering from the University of Hannover, Germany, in 1994. His research interests include two-phase flow, heat transfer enhancement, and thermal system design. Professor Wongwises is the head of the Fluid Mechanics, Thermal Engineering and Multiphase Flow Research Lab.

Downloaded By: [Uppsala University Library] At: 08:02 20 October 2009

International Journal of Heat and Mass Transfer 53 (2010) 568–573

Contents lists available at ScienceDirect

International Journal of Heat and Mass Transfer

journal homepage: www.elsevier.com/locate/ijhmt

Technical Note

Correlations for wet surface ratio of fin-and-tube heat exchangers

Worachest Pirompugd [a,*], Chi-Chuan Wang [b], Somchai Wongwises [c]

[a] Department of Mechanical Engineering, Faculty of Engineering, Burapha University, Saensook, Muang, Chonburi 20131, Thailand
[b] Energy and Environment Research Laboratories, Industrial Technology Research Institute, Hsinchu 310, Taiwan, ROC
[c] Fluid Mechanics, Thermal Engineering and Multiphase Flow Research Lab. (FUTURE), Department of Mechanical Engineering, King Mongkut's University of Technology Thonburi, Bangmod, Bangkok 10140, Thailand

ARTICLE INFO

Article history:
Received 10 September 2008
Received in revised form 21 August 2009
Accepted 21 August 2009
Available online 7 October 2009

Keywords:
Dehumidifying condition
Finite Circular Fin Method
Heat and mass transfer characteristics
Partially wet surface
Fin-and-tube heat exchanger

ABSTRACT

Correlations are proposed for the wet surface ratio of a fin-and-tube heat exchanger with plain and wavy fin geometry under dehumidifying conditions. The 'Finite Circular Fin Method' (FCFM) is used for data reduction. It is found that the percentage of wet surface area increases with increasing fin spacing or number of tube rows and decreasing Reynolds number. Despite the addition of tube rows or reduced fin spacing the effective surface area is increased, and its influence on a partially wet surface is apparently the opposite. This is because adding tube rows will provide a more effective temperature drop in air flow than adding fins, Moreover, the heat and mass transfer characteristics of j_h and j_m increase with an increase in the area of wet surface. Correlations for prediction of the percentage of wet surface area are proposed. These correlations can describe 83.81% of the area of wet surface to within ±10%.

© 2009 Elsevier Ltd. All rights reserved.

1. Introduction

Fin-and-tube heat exchangers are widely-used heat transfer devices in association with applications like refrigeration and air-conditioning systems. They can be applicable to both condensers and evaporators. For a typical evaporator, the outside surface temperature of the heat exchanger is generally below the dew point temperature, and therefore condensation of water vapour takes place around the outside surfaces. As a result, simultaneous heat and mass transfer occurs and it becomes even more complicated as the condensate may interact with the air flow, yet may result in full or partial condensation along the surface. In this regard, detailed simulation of the performance of the heat exchanger is rather difficult.

The heat and mass transfer characteristics of fin-and-tube heat exchangers have been studied by many researchers (McQuiston [1,2], Beecheer and Fagan [3], Yan and Sheen [4], Mirth and Ramadhyani [5,6], Wang et al. [7–13], Pirompugd et al. [14–19]). The published data were mainly focused, however, on sensible heat transfer characteristics rather than on mass transfer characteristics. Moreover, in a typical operation some outside surface temperature is higher than the dew point temperature while the other surface is lower than the dew point temperature, indicating a partially wet surface. There were even limited studies dealing with the heat and mass transfer characteristics of fin-and-tube heat exchangers under partially wet surface conditions. Pirompugd et al. [16,17] presented the fully wet and fully dry tiny circular fin method for evaluation of heat and mass transfer characteristics under fully wet and partially wet surface conditions. Xia and Jacobi [20] formulated the logarithmic-mean temperature difference (LMTD) and logarithmic-mean enthalpy difference (LMED) methods for fully dry, fully wet, partially wet and frosted surface conditions. Pirompugd et al. [18,19] developed a new mathematical reduction method, the 'Finite Circular Fin Method (FCFM)' for fin-and-tube heat exchangers under fully dry, fully wet and partially wet surface conditions. The FCFM is capable of dividing a fin-and-tube heat exchanger into many tiny segments through which the detailed surface conditions (fully dry, fully wet, or partially wet) are taken into account. In this study, the objective is to investigate the effect of a partially wet surface on the heat and mass transfer characteristics of the plain and wavy fin-and-tube heat exchanger based on the FCFM methodology.

2. Experimentation

The experimental apparatus can be found in Pirompugd et al. [18,19]. A total of fifteen plain fin-and-tube heat exchangers and eighteen wavy fin-and-tube heat exchangers with various geometric parameters are tested in this study. The details of test samples are shown in Tables 1 and 2. The test conditions approximate those encountered with typical fan-coils and evaporators of air-conditioning applications.

* Corresponding author. Tel.: +66 818048996.
E-mail address: worapiro@yahoo.com (W. Pirompugd).

0017-9310/$ - see front matter © 2009 Elsevier Ltd. All rights reserved.
doi:10.1016/j.ijheatmasstransfer.2009.09.025

Nomenclature

A_o	total surface area, m^2	P_d	wave height, m
A_{wet}	outside surface area of wet portion, m^2	P_l	longitudinal tube pitch, m
D_c	collar diameter, m	P_t	transverse tube pitch, m
F_p	fin pitch, m	Re_{Dc}	moist air-side Reynolds number based on the collar diameter
j_h	Colburn heat transfer group or Chilton-Colburn j-factor for the heat transfer	RH_{in}	inlet relative humidity
j_m	Colburn mass transfer group or Chilton-Colburn j-factor for the mass transfer	S_p	fin spacing, m
N	number of tube row	t	fin thickness, m
		X_f	projected fin length, m

Table 1
Geometric dimensions of the sample plain fin-and-tube heat exchangers.

No.	F_p (mm)	t (mm)	D_c (mm)	P_t (mm)	P_l (mm)	N
1	1.19	0.115	8.51	25.4	19.1	1
2	1.75	0.120	10.34	25.4	22.0	1
3	1.23	0.115	8.51	25.4	19.1	2
4	1.23	0.115	7.53	21.0	12.7	2
5	1.23	0.115	10.23	25.4	19.1	2
6	1.82	0.130	10.23	25.4	22.0	2
7	1.23	0.115	10.23	25.4	19.1	4
8	1.23	0.115	7.53	21.0	12.7	4
9	1.55	0.115	10.23	25.4	19.1	4
10	1.60	0.115	8.51	25.4	19.1	4
11	2.03	0.130	10.23	25.4	22.0	4
12	2.31	0.115	10.23	25.4	19.1	4
13	1.85	0.130	10.23	25.4	22.0	6
14	2.21	0.130	10.23	25.4	22.0	6
15	3.16	0.130	10.23	25.4	22.0	6

The test conditions of the inlet-air are as follows:

Dry-bulb temperature of the air	27 ± 0.5 °C
Inlet relative humidity for the incoming air	50% and 90%
Inlet-air velocity	From 0.3 to 4.5 m/s
Inlet-water temperature	7 ± 0.5 °C
Water velocity inside the tube	1.5–1.7 m/s

3. Data reduction

In the present study, the 'Finite Circular Fin Method (FCFM)' published in our previous literature (Pirompugd et al. [18,19]) is used for calculating the heat and mass transfer characteristics of a fin-and-tube heat exchanger. The heat exchanger is divided into many tiny segments by number of tube rows, number of tube passes per row and number of fins. The surface conditions of each tiny segment can be fully wet, partially wet, or fully dry. If the surface is fully wet, the fin tip temperature is lower than the dew point temperature of moist air. Both sensible and latent heat transfers take place along this tiny segment. For the second case, where partially wet conditions prevail, in which the outside tube (including collar) temperature is lower than the dew point temperature, part of the fin temperature is higher than the dew point temperature. The last case is the fully dry condition, in which the outside tube (including collar) temperature is higher than the dew point temperature, yet only sensible heat transfer occurs on the whole area of this tiny segment. In this study, FCFM is used to explain the heat and mass transfer characteristics of fin-and-tube heat exchangers. The reduced results of the heat and mass transfer characteristics are presented in terms of dimensionless groups of j_h and j_m, respectively.

4. Results and discussion

In practice it is very interesting to examine the wet/dry surface distribution pertaining to influences such as inlet conditions and flow conditions. The partially dry condition becomes even more conspicuous when the inlet humidity is reduced. Fig. 1 shows the percentage of wet surface area for all the test samples with an inlet relative humidity of 50%. As seen from the figure, at a very low Reynolds number (<1000), the partially dry surface is hardly seen, yet

Table 2
Geometric dimensions of the sample wavy fin-and-tube heat exchangers.

No.	F_p (mm)	t (mm)	D_c (mm)	P_t (mm)	P_l (mm)	P_d (mm)	X_f (mm)	N
1	1.60	0.12	10.38	25.4	19.05	1.18	4.7625	1
2	1.64	0.12	8.62	25.4	19.05	1.58	4.7625	1
3	2.82	0.12	10.38	25.4	19.05	1.18	4.7625	1
4	2.92	0.12	8.62	25.4	19.05	1.58	4.7625	1
5	3.54	0.12	8.62	25.4	19.05	1.58	4.7625	1
6	3.63	0.12	8.62	25.4	25.40	1.68	6.3500	1
7	1.69	0.12	8.62	25.4	19.05	1.18	4.7625	2
8	1.71	0.12	8.62	25.4	19.05	1.58	4.7625	2
9	3.12	0.12	8.62	25.4	19.05	1.58	4.7625	2
10	3.17	0.12	8.62	25.4	19.05	1.18	4.7625	2
11	1.64	0.12	8.62	25.4	19.05	1.58	4.7625	4
12	1.70	0.12	8.62	25.4	19.05	1.18	4.7625	4
13	3.07	0.12	8.62	25.4	19.05	1.58	4.7625	4
14	3.14	0.12	8.62	25.4	19.05	1.18	4.7625	4
15	1.57	0.12	10.38	25.4	19.05	1.18	4.7625	6
16	1.65	0.12	8.62	25.4	19.05	1.58	4.7625	6
17	2.82	0.12	10.38	25.4	19.05	1.18	4.7625	6
18	3.06	0.12	8.62	25.4	19.05	1.58	4.7625	6

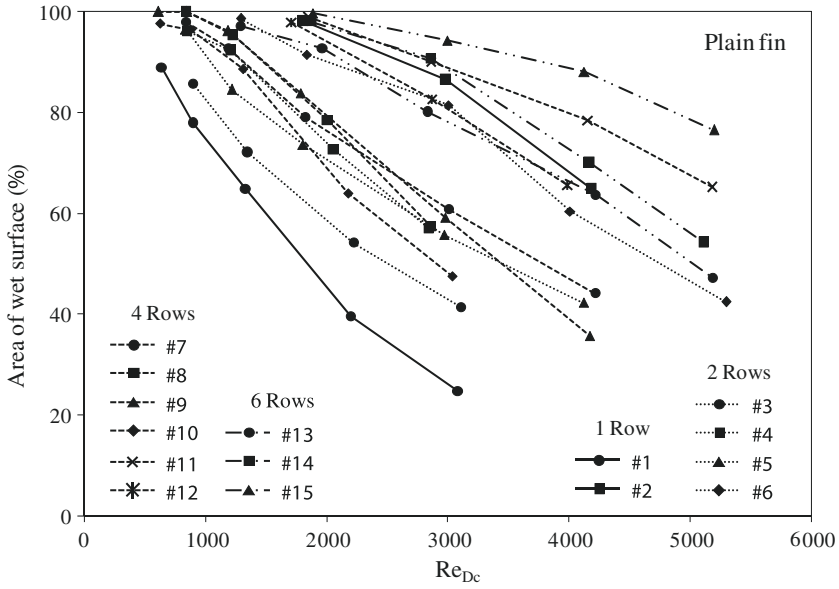

Fig. 1. Area of wet surface percentage plotted against Reynolds number.

the percentage of wet surface area drops with the rise of the Reynolds number. This is because a higher Reynolds number results in higher heat transfer coefficient, thereby leading to a smaller temperature difference and corresponding to a higher surface temperature. In this context, the temperature of part of the fin surface may exceed that of the dew point temperature and become partially dry. This phenomenon becomes more evident when the number of tube rows is reduced or when the fin spacing is reduced. Again, one of the reasons may be attributed to the heat transfer coefficient. The heat transfer coefficient usually decreases with the number of tube rows (Wang et al. [8]). This may not, however, be the main cause. As air flows into the heat exchanger under dehumidifying conditions, the temperature of the air flow decreases along the air flow direction, resulting in a rise of relative humidity as the number of tube rows rises. In essence, the surface can become wet more easily. Moreover, one can see that the percentage of the wet surface area is increased with the increase of the fin spacing. In the beginning, with more fins being added (smaller fin spacing), it is expected that the temperature of air flow will drop and should exhibit the same results as obtained when tube rows are added. The results, however, are the opposite of what we originally expected. Although extra tube rows and extra

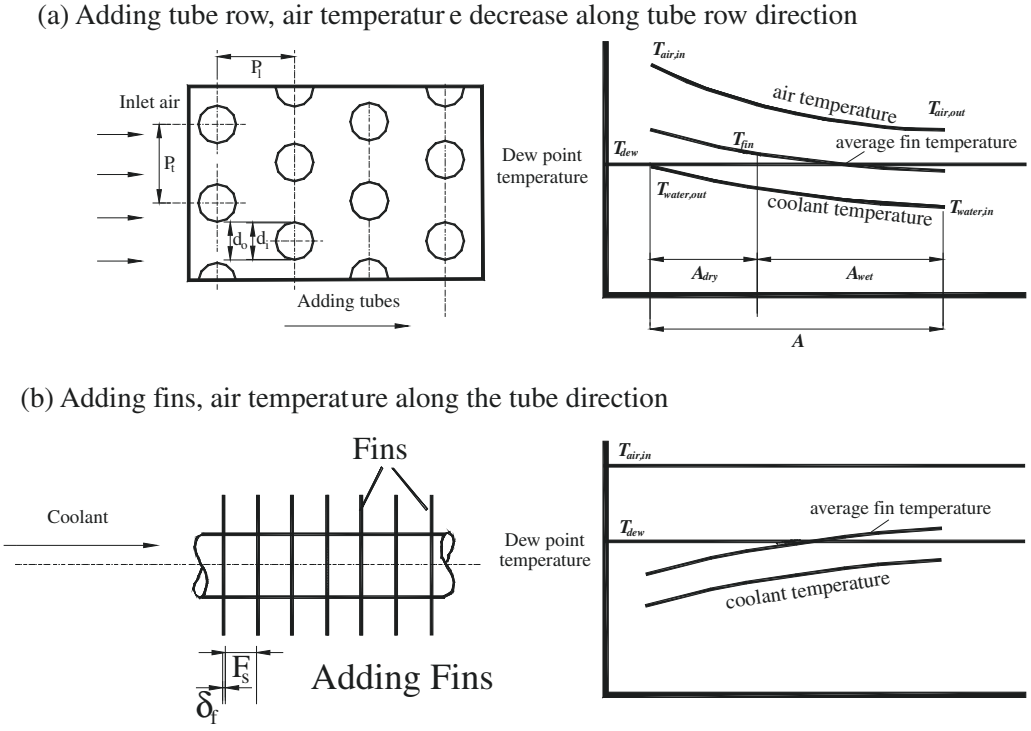

Fig. 2. A schematic showing the difference in adding surface amid adding tube rows and reducing fin spacing.

fins act similarly in increasing surface temperature, they are not the same in fact. The following schematic shows the difference between adding rows and adding fins. Note that the coolant flows into the heat exchangers parallel to each row, so adding rows may effectively reduce the air temperature along the flow direction, as seen in Fig. 2(a). In the meantime, the coolant in the tube is rising with further reduction in fin spacing (adding fins). As shown in Fig. 2(b), the inlet-air temperature remains unchanged by the addition of fins despite the average air temperature being slightly reduced. It becomes less evident for air flow temperature to fall below the dew point temperature. Accordingly, adding surface by reducing fin spacing reveals less partially wet conditions compared with adding tube rows. In fact, adding tubes is more like 'mixed flow', whereas adding fins produces a more 'unmixed' flow situation.

The heat and mass transfer characteristics are presented in the dimensionless terms of j_h and j_m, respectively. In Fig. 3a and b, the transfer characteristic of j_h and j_m increases with an increase of wet surface. In the present study, the percentage of the wet portion depends on the moist air velocity. Raising the air velocity means that the convective heat and mass transfer coefficient will be increased but the percentage of the wet portion dwindles considerably, indicating a drop in the heat and mass transfer characteristic of j_h and j_m. Moreover, it can be seen that the j_h and j_m drop with an increase of the fin spacing. This phenomenon can be described from the flow field within the fin passage. In the numerical simulation (Torikoshi et al. [21]), the entire flow region can be kept laminar and steady and the vortex forming behind the tube can be suppressed for the tight fin. The cross-stream width of the vortex region behind the tube will take place when the fin spacing increases. Then,

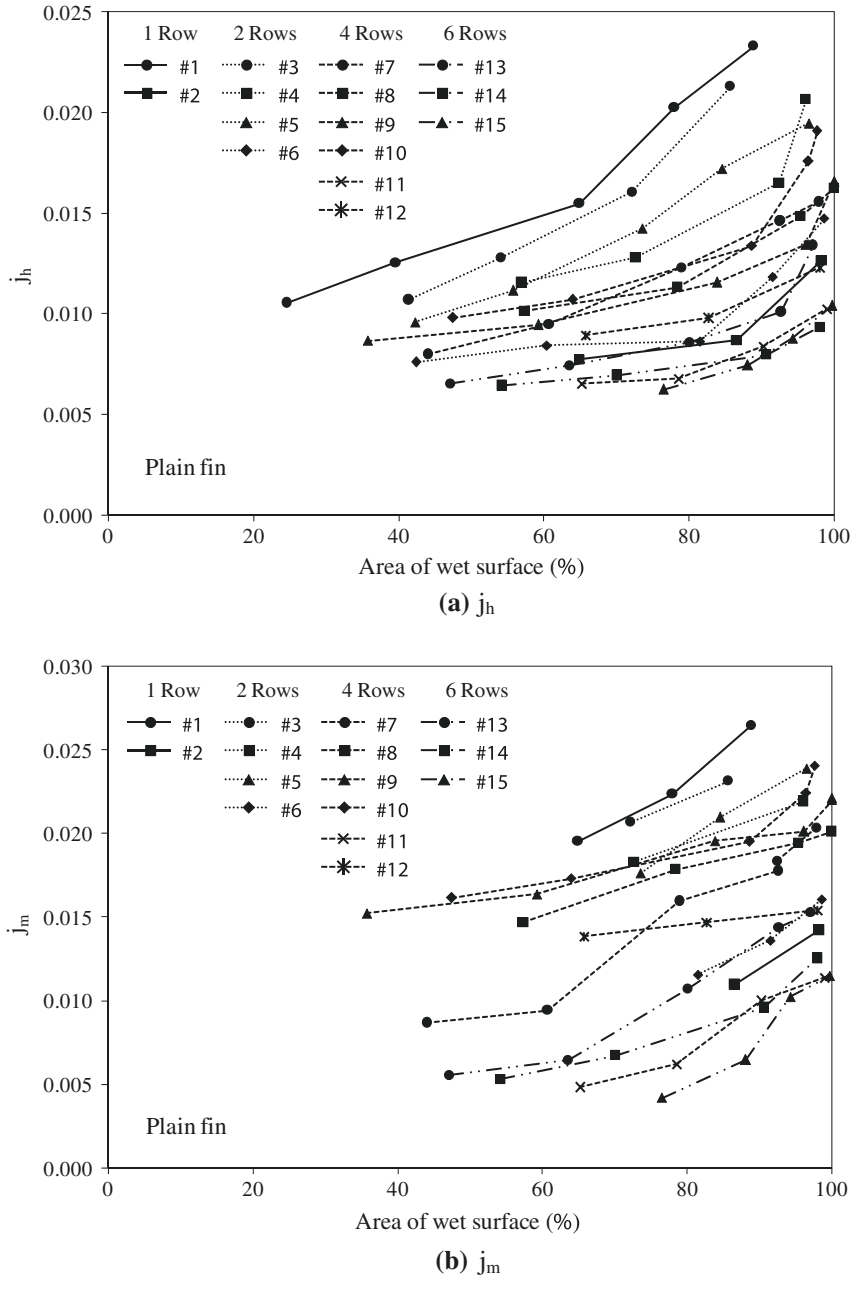

(a) j_h

(b) j_m

Fig. 3. j_h and j_m plotted against area of wet surface.

Table 3
Coefficients for the correlations.

Type	N	a_1	a_2	a_3	a_4	b_1	b_2	b_3	b_4
Plain	1	0	0	374.2	79.1	0	0	0.0115	−0.0020
	2	−391,566.8	173,756.3	−24,895.6	1272.9	−3.7345	1.6463	−0.2373	0.0109
	4	101,167.3	−49,475.7	7893.4	−281.7	−0.7475	0.3840	−0.0629	0.0030
	6	0	−5827.6	2608.3	−143.7	0	0.0084	−0.0031	0.0001
Wavy	1	0	0	−3.0062	187.3	0	0	0.0012	−0.0008
	2	0	0	−1497.3	406.8	0	0	−0.0395	0.0070
	4	0	10,363.9	−5247.6	709.7	0	−0.0786	0.0413	−0.0050
	6	−24,596.9	19,730.9	−5083.2	501.7	0.1308	−0.1024	0.0259	−0.0021

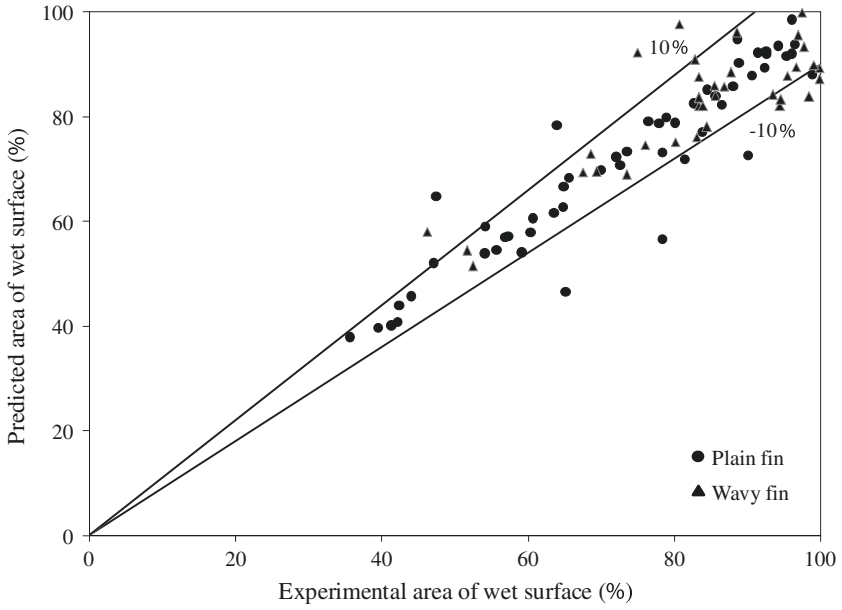

Fig. 4. Comparison of the area of wet surface between those obtained from the correlation and those obtained from experiment.

the j_h and j_m decrease with the increase in fin spacing for one-row configuration, indicating a detectable influence of fin spacing. The effect of fin spacing on j_h can be negligible when the number of tube rows is increased. This is because with the increasing number of tube rows the subsequent row can block the condensate blow-off phenomenon from the preceding row.

Using a multiple linear regression technique in a range of experimental data ($300 < Re_{Dc} < 5500$, $RH_{in} \approx 50\%$), we present the appropriate correlations of the percentage area of wet surface based on the present data as follows:

$$\frac{A_{wet}}{A_o} = \left(a_1\left(\frac{S_p}{D_c}\right)^3 + a_2\left(\frac{S_p}{D_c}\right)^2 + a_3\frac{S_p}{D_c} + a_4\right) \times e^{\left(\left(b_1\left(\frac{S_p}{D_c}\right)^3 + b_2\left(\frac{S_p}{D_c}\right)^2 + b_3\frac{S_p}{D_c} + b_4\right)Re_{D_C}\right)} \quad (1)$$

The coefficients for the equation are shown in Table 3. Detailed comparisons of the proposed correlations against the experimental data are shown in Fig. 4. It is found that the correlations can describe 83.81% of the area of the wet surface within 10%.

5. Conclusions

This study explored the partially wet characteristics of fin-and-tube heat exchangers with the help of the FCFM reduction method. A total of fifteen plain fin-and-tube heat exchangers and eighteen wavy fin-and-tube heat exchangers were tested and compared. On the basis of previous discussions, the following conclusions were drawn:

1. The percentage of wet surface area increases with the increase of the Reynolds number or fin spacing or the number of tube rows. Whether tube rows are added or fin spacing is reduced, the effective surface area is increased, and its influence on partially wet surfaces is apparently the converse. This is because adding tube rows will provide more effective temperature drop of air flow than the addition of fins.
2. The heat and mass transfer characteristic of j_h and j_m increases with an increase in the area of wet surface.
3. Correlations applicable to the present fin-and-tube heat exchangers are proposed. These correlations can describe 83.81% of the area of wet surface within ±10%.

Acknowledgments

The authors are indebted to the Thailand Research Fund (TRF), Commission on Higher Education of Thailand (CHE), Support Fund for Research and Development (No. 22/2552) from Faculty of Engineering, Burapha University, and the Energy R&D foundation funding from the Bureau of Energy of the Ministry of Economic Affairs, Taiwan, for supporting this study.

References

[1] F.C. McQuiston, Heat mass and momentum transfer data for five plate-fin tube transfer surface, ASHRAE Trans. 1 84 (1978) 266–293.
[2] F.C. McQuiston, Correlation of heat, mass and momentum transport coefficients for plate-fin-tube heat transfer surfaces with staggered tubes, ASHRAE Trans. 1 84 (1978) 294–309.
[3] D.T. Beecher, T.J. Fagan, Effects of fin pattern on the air-side heat transfer coefficient in plate finned-tube heat exchanger, ASHRAE Trans. 93 (2) (1987) 1961–1984.
[4] W.M. Yan, P.J. Sheen, Heat transfer and friction characteristics of fin-and-tube heat exchangers, Int. J. Heat Mass Transfer 43 (2000) 1651–1659.
[5] D.R. Mirth, S. Ramadhyani, Prediction of cooling-coils performance under condensing conditions, Int. J. Heat Fluid Flow 14 (4) (1993) 391–400.
[6] D.R. Mirth, S. Ramadhyani, Correlations for predicting the air-side Nusselt numbers and friction factors in chilled-water cooling coils, Exp. Heat Transfer 7 (1994) 143–162.
[7] C.C. Wang, W.L. Fu, C.T. Chang, Heat transfer and friction characteristics of typical wavy fin-and-tube heat exchangers, Exp. Therm. Fluid Sci. 14 (2) (1997) 174–186.
[8] C.C. Wang, Y.C. Hsieh, Y.T. Lin, Performance of plate finned tube heat exchangers under dehumidifying conditions, J. Heat Transfer 119 (1997) 109–117.
[9] C.C. Wang, Y.M. Tsi, D.C. Lu, Comprehensive study of convex-louver and wavy fin-and-tube heat exchangers, AIAA J. Thermophys. 12 (3) (1998) 423–430.
[10] C.C. Wang, Y.T. Lin, C.J. Lee, Investigation of wavy fin-and-tube heat exchangers: a contribution to data bank, Exp. Heat transfer 12 (1999) 73–89.
[11] C.C. Wang, K.U. Chi, Heat transfer and friction characteristics of plain fin-and-tube heat exchangers: part I: new experimental data, Int. J. Heat Mass Transfer 43 (2000) 2681–2691.
[12] C.C. Wang, Y.M. Hwang, Y.T. Lin, Empirical correlations for heat transfer and flow friction characteristics of herringbone wavy fin-and-tube heat exchangers, Int. J. Refrig. 25 (2002) 673–680.
[13] C.C. Wang, J. Lo, Y.T. Lin, C.S. Wei, Flow visualization of annular and delta winglet vortex generators in fin-and-tube heat exchanger application, Int. J. Heat Mass Transfer 45 (2002) 3803–3815.
[14] W. Pirompugd, S. Wongwises, C.C. Wang, A tube-by-tube reduction method for simultaneous heat and mass transfer characteristics for plain fin-and-tube heat exchangers in dehumidifying conditions, Heat Mass Transfer 41 (8) (2005) 756–765.
[15] W. Pirompugd, S. Wongwises, C.C. Wang, Simultaneous heat and mass transfer characteristics for wavy fin-and-tube heat exchangers under dehumidifying conditions, Int. J. Heat Mass Transfer 49 (3–4) (2006) 132–143.
[16] W. Pirompugd, C.C. Wang, S. Wongwises, A fully wet and fully dry tiny circular fin method for heat and mass transfer characteristics for plain fin-and-tube heat exchangers under dehumidifying conditions, J. Heat Transfer 129 (9) (2007) 1256–1267.
[17] W. Pirompugd, C.C. Wang, S. Wongwises, Heat and mass transfer characteristics for finned tube heat exchangers with humidification, J. Thermophys. Heat Transfer 21 (2) (2007) 361–371.
[18] W. Pirompugd, C.C. Wang, S. Wongwises, Finite circular fin method for heat and mass transfer characteristics for plain fin-and-tube heat exchangers under fully and partially wet surface conditions, Int. J. Heat Mass Transfer 50 (3–4) (2007) 552–565.
[19] W. Pirompugd, C.C. Wang, S. Wongwises, Finite circular fin method for wavy fin-and-tube heat exchangers under fully and partially wet surface conditions, Int. J. Heat Mass Transfer 51 (15–16) (2008) 4002–4017.
[20] Y. Xia, A.M. Jacobi, Air-side data interpretation and performance analysis for heat exchangers with simultaneous heat and mass transfer: Wet and frosted surfaces, Int. J. Heat and Mass Transfer 48 (2005) 5089–5102.
[21] K. Torikoshi, G. Xi, Y. Nakazawa, H. Asano, Flow and heat transfer performance of a plate-fin and tube heat Exchanger (1st report: effect of fin pitch), Tenth International Heat Transfer Conference, 1994, paper 9-HE-16, 1994, pp. 411–416.

International Journal of Heat and Mass Transfer 53 (2010) 334–344

Contents lists available at ScienceDirect

International Journal of Heat and Mass Transfer

journal homepage: www.elsevier.com/locate/ijhmt

An experimental study on the heat transfer performance and pressure drop of TiO_2-water nanofluids flowing under a turbulent flow regime

Weerapun Duangthongsuk, Somchai Wongwises *

Fluid Mechanics, Thermal Engineering and Multiphase Flow Research Laboratory (FUTURE), Department of Mechanical Engineering, King Mongkut's University of Technology Thonburi, Bangmod, Bangkok 10140, Thailand

ARTICLE INFO

Article history:
Received 9 February 2009
Received in revised form 21 August 2009
Accepted 21 August 2009
Available online 6 October 2009

Keywords:
Nanofluid
Heat transfer coefficient
Friction factor
Particle concentration

ABSTRACT

Nanofluid is a new class of heat transfer fluids engineered by dispersing metallic or non-metallic nanoparticles with a typical size of less than 100 nm in the conventional heat transfer fluids. Their use remarkably augments the heat transfer potential of the base liquids. This article presents the heat transfer coefficient and friction factor of the TiO_2-water nanofluids flowing in a horizontal double tube counter-flow heat exchanger under turbulent flow conditions, experimentally. TiO_2 nanoparticles with diameters of 21 nm dispersed in water with volume concentrations of 0.2–2 vol.% are used as the test fluid. The results show that the heat transfer coefficient of nanofluid is higher than that of the base liquid and increased with increasing the Reynolds number and particle concentrations. The heat transfer coefficient of nanofluids was approximately 26% greater than that of pure vol.%, and the results also show that the heat transfer coefficient of the nanofluids at a volume concentration of 2.0 vol.% was approximately 14% lower than that of base fluids for given conditions. For the pressure drop, the results show that the pressure drop of nanofluids was slightly higher than the base fluid and increases with increasing the volume concentrations. Finally, the new correlations were proposed for predicting the Nusselt number and friction factor of the nanofluids, especially.

© 2009 Elsevier Ltd. All rights reserved.

1. Introduction

Conventional heat transfer fluids such as oil, water and ethylene glycol are widely used in many industries, including power generation, chemical processes, heating and cooling processes, transportation, microelectronics and other micro-sized applications. In general, the heat transfer performance of these fluids is restricted by their poor thermal properties compared to those of most solids. This is the important reason why the development of heat transfer devices is retarded. Based on industrial needs, the enhancement techniques meet an astronomical increase in heat flux and high degree of compactness of the heat transfer equipment. So, a search for high efficiency heat transfer fluid is a challenging task for today. In recent years, many researchers have attempted to develop special classes of heat transfer fluids for augmentation of their heat transfer properties. An innovative method is to suspend small solid particles in the common fluid to form fluid slurries. Different types of solid particles, such as metallic, non-metallic and polymeric can be added into fluids. In the early studies, however, use of suspended particles of millimetre or even micrometre-size demonstrated unusually high thermal enhancement, but some extreme problems are also experienced, such as poor stability of the suspension, clogging of flow channels, eroding of pipelines and increase in pressure drop in practical applications. Although the solutions show better thermal performance compared to common heat transfer fluids, they are still not suitable for use as heat transfer fluids in practical applications, especially for the mini and/or micro-channel or even electronic cooling equipment.

A decade ago, with the rapid development of modern nanotechnology, particles of nanometre-size (normally less than 100 nm) are used instead of micrometre-size for dispersing in base liquids, and they are called nanofluids. This term was first suggested by Choi [1] in 1995, and it has since gained in popularity. Compared with millimetre or micrometre sized particle suspensions, a number of researchers have reported that nanofluids have shown a number of potential advantages, such as better long-term stability, little penalty in pressure drop, and can have significantly greater thermal conductivity. As a result, many researchers have investigated the heat transfer performance and flow characteristics of various nanofluids with different nanoparticles and base fluid materials. Several following existing published articles which associate with the use of nanofluids are described in the following sections.

Pak and Cho [2] investigated experimentally the heat transfer performance of γ-Al_2O_3 and TiO_2 nanoparticles dispersed in water flowing in a horizontal circular tube with a constant heat flux

* Corresponding author. Tel.: +662 470 9115; fax: +662 470 9111.
E-mail address: somchai.won@kmutt.ac.th (S. Wongwises).

0017-9310/$ - see front matter © 2009 Elsevier Ltd. All rights reserved.
doi:10.1016/j.ijheatmasstransfer.2009.09.024

Nomenclature

C_p	specific heat, J/kg K
d	nanoparticle diameter, m
D	tube diameter, m
f	friction factor
h	heat transfer coefficient, W/m^2 K
k	thermal conductivity, W/m K
L	length of the test tube, m
$\dot{m}$	mass flow rate, kg/s
Nu	Nusselt number
ΔP	Pressure drop, Pa
Pe	Peclet number
Pr	Prandtl number
q	heat flux, W/m^2
Q	heat transfer rate, W
Re	Reynolds number
T	temperature, °C
u	mean velocity, m/s
$\dot{V}$	volume flow rate, m^3/s

Greek symbols

ϕ	volume fraction
ε	tube roughness
ρ	density, kg/m^3
α	thermal diffusivity
μ	viscosity, kg/ms

Subscripts

ave	average
f	fluid
h	heating fluid
in	inlet
m	mean
out	outlet
p	particles
nf	nanofluid
w	water
wall	tube wall

under turbulent flow conditions. The results showed that the Nusselt number of nanofluids increased with increasing Reynolds number and the volume concentration. However, they still found that the convective heat transfer coefficient of the nanofluids with 3 vol.% nanoparticles was 12% lower than that of pure water at a given condition. Finally, a new heat transfer correlation for predicting the convective heat transfer coefficient of nanofluids in a turbulent flow regime was proposed.

Li and Xuan [3] and Xuan and Li [4] studied experimentally the convective heat transfer and flow features for Cu-water nanofluids flowing through a straight tube under laminar and turbulent flow regimes with a constant heat flux. The experimental results showed that addition of nanoparticles into the base liquid remarkably enhanced the heat transfer performance of the base liquid. Moreover, the friction factor of nanofluids coincided well with that of the water. They also proposed new convective heat transfer correlations for calculating the heat transfer coefficients of the nanofluid for both laminar and turbulent flow conditions.

Tsai et al. [5] studied experimentally gold-DI water nanofluids flowing in a conventional heat pipe. The experimental results illustrated that use of the nanofluids led to a significant reduction in the thermal resistance of the heat pipe when compared with DI water at given concentrations.

Wen and Ding [6] investigated the convective heat transfer coefficient of Al_2O_3-DI water flowing through a copper tube under a constant heat flux for a laminar flow regime and placed emphasis on the entrance region in particular. Their results showed that the local heat transfer coefficient increased with increasing the Reynolds number as well as the volume concentration of nanofluids.

Yang et al. [7] investigated the convective heat transfer coefficient of graphite nanoparticles dispersed in two liquids flowing in a horizontal tube heat exchanger under laminar flow conditions. Their results showed that the heat transfer coefficient increased with the Reynolds number and the particle volume concentration. Furthermore, two graphite nanoparticle sources at the same particle loading gave different values of heat transfer coefficient. Finally, they proposed a new heat transfer correlation to predict the heat transfer coefficient of nanofluids under laminar flow conditions.

Ding et al. [8] reported on an experiment in which the local heat transfer coefficient of CNT-distilled water nanofluids flowing through a tube under a laminar flow regime. They found that the local heat transfer coefficient of CNT nanofluids is much greater than that of pure water, and the enhancement depends on the flow conditions, CNT concentration and the PH value. However, they reported that the effect of pH value is smallest compared with other parameters. They also suggest that the aspect ratio should be associated with the high enhancement of heat transfer performance of CNTs based nanofluids [9].

Heris et al. [10,11] studied experimentally the heat transfer performance of Al_2O_3-water and CuO-water nanofluids flowing in an annular concentric tube under constant wall temperature boundary condition for a laminar flow regime. The results indicated that the heat transfer coefficient increased with an increasing Peclet number as well as particle volume concentration, and CuO-water nanofluids showed smaller heat transfer enhancement than Al_2O_3-water nanofluid.

He et al. [12] investigated the heat transfer performance and flow characteristic of TiO_2-distilled water nanofluids flowing through a vertical pipe in an upward direction under a constant heat flux in both a laminar and a turbulent flow regime. Their results indicated that the local heat transfer coefficient increased with increasing nanoparticle concentration in both laminar and turbulent flow regimes at a given Reynolds number and particle size. Moreover, the results showed that the pressure drop of the nanofluids was very close to that of the base fluid.

Nguyen et al. [13] reported on an experiment in which the heat transfer coefficient of Al_2O_3 nanoparticles was dispersed in water flowing through a liquid cooling system of microprocessors under turbulent flow condition. They found that the nanofluid gave a higher heat transfer coefficient than the base liquid. Moreover, the results also showed that the nanofluid with a 36 nm particle diameter gave higher heat transfer coefficient than the nanofluid with a 47 nm particle diameter.

Ko et al. [14] investigated the pressure drop and viscosity of carbon nanotubes dispersed in distilled water flowing through a horizontal tube and also reported the effect of the CNT concentrations and preparation methods on the viscosity of nanofluids. Their results showed that the nanofluids prepared by acid treatment (TCNT) have much smaller viscosity than the ones made with surfactant (PCNT). Under laminar flow conditions, the friction factor of the PCNT nanofluids is much higher than that of the TCNT nanofluids. Moreover, both nanofluids show larger friction factors than the base fluid. In contrast, under turbulent flow conditions, the friction factor of both nanofluids becomes similar to that of the base fluids as the flow rate increases.

Chein and Chuang [15] reported experimentally on microchannel heat sink (MCHS) performance using CuO-water nanofluids as coolants.

The thermal and physical properties of nanofluids were calculated using the following equations: the Brinkman equation [16] for viscosity, the Xuan and Roetzel equation [17] for specific heat, and the Hamilton and Crosser model [18] for thermal conductivity. The results showed that the presence of nanoparticles creates greater energy absorption than pure water at a low flow rate and that there is no contribution from heat absorption when the flow rate is high.

Duangthongsuk and Wongwises [19,20] investigated the effect of thermophysical properties models on prediction of the heat transfer coefficient and also reported the heat transfer performance and friction characteristics of nanofluid, respectively. The 0.2 vol.% TiO_2 naoparticles are used to disperse in the water. The results showed that the various thermophysical models have no significant effect on the predicted values of Nusselt number of the nanofluid. The results also indicated that the heat transfer coefficient of nanofluid is slightly greater than that of water by approximately 6–11% and use of nanofluid has little penalty in pressure drop.

However, the previous work of the authors did not examine the effect of the particle concentrations on heat transfer and pressure drop of nanofluids. The authors used the existing thermophysical property model to calculate the thermal conductivity and viscosity of nanofluids, which may have caused a small error in the results. In vies of that consequence, this article is aimed at reporting the effect of particle concentration on the heat transfer performance and pressure drop of nanofluids experimentally. Moreover, the thermal conductivity and viscosity of nanofluids are measured. Finally, new heat transfer and friction factor correlations of nanofluids are proposed.

2. Sample preparation

The term 'nanofluid', meaning a two-phase mixture usually consists of nanoparticles dispersed in common liquids. In order to prepare the nanofluids by dispersing the nanoparticles in a base fluid, proper mixing, and stabilisation of the particles is required. There are three effective methods used to attain stability of suspension against sedimentation of nanoparticles, and these are summarised as follows: (1) control of ph value of the suspensions, (2) addition of surface activators or surfactants, (3) use of ultrasonic vibration. All of these techniques aim at changing the surface properties of suspended nanoparticles and suppressing formation of the cluster of particles, in order to obtain stable suspensions. In the present study, nanofluids provided by a commercial source (DEGUSSA, VP Disp. W740×) are used. This mixture is composed of TiO_2 nanoparticles with average diameter of 21 nm, dispersed in water. The original particle concentration was 40 wt%. In order to produce other required particle volume fractions, dilution with water followed by a stirring action was effected. Moreover, an ultrasonic vibrator was used to sonicate the solution continuously for approximately 2 h in order to break down agglomeration of the nanoparticles. The desired volume concentrations used in this study are 0.2%, 0.6%, 1.0%, 1.5% and 2.0%, with pH values of 7.5, 7.1, 7.0, 6.8 and 6.5, respectively. From the pH values, it can be seen that the solution chemistry of nanofluids is nearly neutral in nature. A transmission electron microscope (TEM) was used to approximate the size of the primary nanoparticles. As shown in Fig. 1, it is clear that the primary shape of nanoparticles is approximately spherical, with an average diameter of approximately 21 nm.

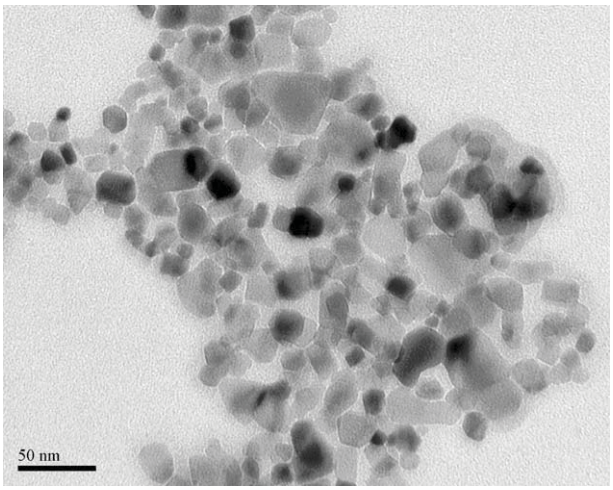

Fig. 1. TEM image of dispersed TiO_2 nanoparticles in water.

3. Experimental apparatus

3.1. Convective heat transfer coefficient and pressure drop of nanofluids

The experimental apparatus used in this study is shown schematically in Fig. 2a. It mainly consists of a test section, two receiver tanks, a magnetic gear pump, a hot water pump, a cooler tank, a hot water tank and a collection tank. The test section is a 1.5 m long counter-flow horizontal double tube heat exchanger with nanofluid flowing inside the tube while hot water flows in the annular. The inner tube is made from smooth copper tubing with a 9.53 mm outer diameter and an 8.13 mm inner diameter, while the outer tube is made from PVC tubing and has a 33.9 mm outer diameter and 27.8 mm inner diameter. The test section is thermally isolated from its upstream and downstream sections by plastic tubes in order to reduce heat loss along the axial direction. The differential pressure transmitter and T-type thermocouple are mounted at both ends of the test section to measure pressure drop and the bulk temperature of the nanofluid, respectively. Thermocouples are mounted at different longitudinal positions on the inner tube surface of the wall, each with three thermocouples equally space around the tube circumference. The inlet and exit temperatures of hot water are measured using T-type thermocouples which are inserted directly into the flow. The receiver tanks of 60 L capacity are made from stainless steel to store the nanofluid and hot water leaving from the test section. The cooler tank with a 4.2 kW cooling capacity and a thermostat is used to keep the nanofluid temperature constant. Similar to the cooler tank, a 3 kW electric heater with a thermostat was installed to keep the temperature of the hot water constant. The nanofluid flow rate is controlled by adjusting the rotation speed of the magnetic gear pump. The hot water flow rate is measured by a rotameter whereas the nanofluids flow rate is evaluated by the time taken for a given volume of nanofluid to be discharged.

In the present study, the differential pressure transmitter was calibrated using an air operated dead weight tester. The uncertainty of the pressure measurement is ±0.030 kPa. Then, a portable programmable calibrator having a maximum precision of 0.1 °C was used to calibrate all of the T-type thermocouples. Furthermore, the nanofluid flow rates were determined by electronic balance. The uncertainty of the electronic balance is ±0.0006 kg. Therefore, the uncertainty of the measured heat transfer coefficient is approximately 5%.

During the test run, wall temperatures of the test section, mass flow rates of the hot water and nanofluids, the pressure difference in the nanofluid, the inlet and exit temperatures of the hot water and nanofluids were recorded.

3.2. Measurement of the thermal conductivity and viscosity of nanofluid

The thermal conductivity and viscosity of the nanofluids are important thermophysical properties. In order to apply the nanofluids

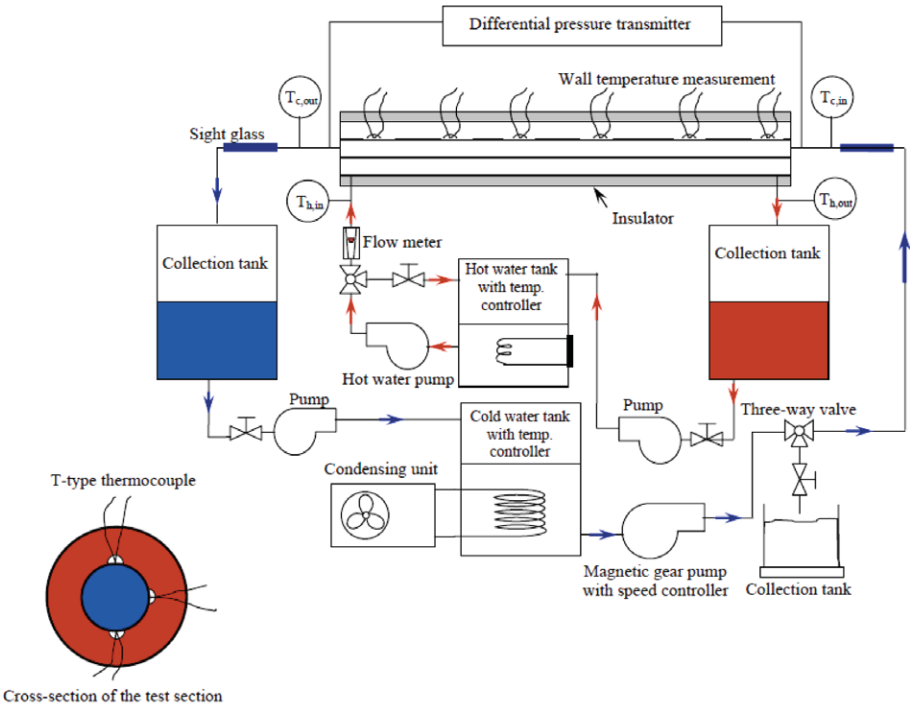

(a) Convective heat transfer coefficient and pressure drop

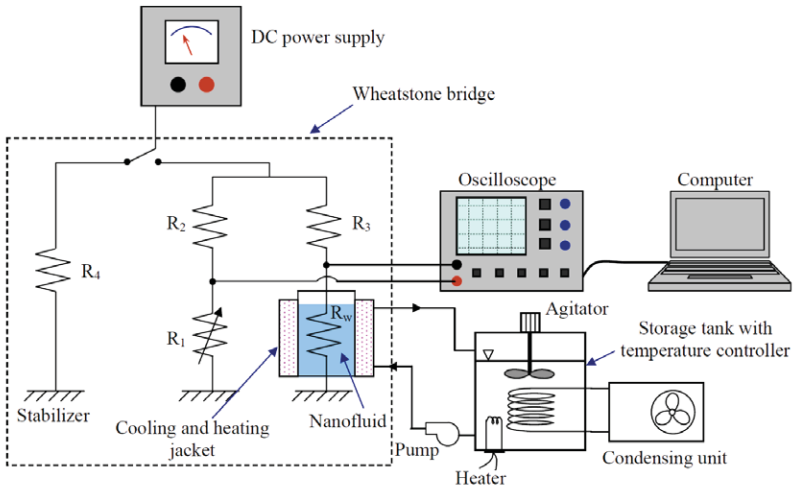

(b) Transient hot-wire apparatus

Fig. 2. Schematic diagram of the experimental apparatus.

for the practical application, the exact value of thermal conductivity and viscosity of nanofluids are needed. In the case of thermal conductivity, the transient hot-wire technique is used to measure the thermal conductivity of nanofluids. The experimental system of the transient hot-wire method is shown schematically in Fig. 2b. The main parts consist of the Wheatstone bridge, and cooling and heating jacket. In the Wheatstone bridge circuit, R_w is the resistance of the platinum wire (named hot-wire), R_1 is a potentiometer, and R_2 and R_3 are resistors. The main reasons for choosing the platinum wire as a hot-wire cell is due to its well-known relationship between temperature and resistance through a wide temperature range. The resistance–temperature coefficient of the platinum wire is 0.0039092/°C [21]. The platinum wire of 76.2 μm and length of 200 mm coated with teflon produced by OMEGA was used as a hot-wire cell. The wire length to diameter ratio of the wire is approximately 2625 for minimisation of loss due to heat conduction at both ends of the wire. A nanofluid polypropylene container of 700 mL volume, 50 mm inner diameter and 350 mm length was used as the container which is sufficiently large to be considered infinite compared with the diameter of the wire. The storage tank with temperature controller was used to keep the temperature of water constant and circulate to the cooling and heating jacket by a pump in order to keep the nanofluid temperature at the desired value. The thermal conductivity of nanofluids with various volume fractions (0.2%. 0.6%, 1.0%, 1.5% and 2.0%,) were measured at temperatures of 15 °C, 25 °C and 35 °C, respectively. Finally, the thermal conductivity of the nanofluids is calculated from:

$$k = \frac{q}{4\pi(T_2 - T_1)} \ln\left(\frac{t_2}{t_1}\right) \quad (1)$$

where k is the thermal conductivity, q is the applied electric power per unit length of the wire, and $T_2 - T_1$ is the temperature rise of the

wire between time t_1 and t_2. Then, the measured thermal conductivity of nanofluids is compared with those obtained from the well-known correlations, which are defined as follows:

One well-known formula for computing the thermal conductivity of nanofluid is the Hamilton and Crosser [18] model (H–C model), which is expressed in the following form:

$$k_{nf} = \left[\frac{k_p + (n-1)k_w - (n-1)\phi(k_w - k_p)}{k_p + (n-1)k_w + \phi(k_w - k_p)}\right]k_w \quad (2)$$

$$n = 3/\psi \quad (3)$$

In which, n is the empirical shape factor and Ψ is the sphericity, defined as the ratio of the surface area of a sphere (of the same volume as the given particle) to the surface area of the particle. The sphericity is 1 and 0.5 for the spherical and cylindrical shapes, respectively. Moreover, k_{nf} is the thermal conductivity of the nanofluid, k_p is the thermal conductivity of the nanoparticles, and k_w is the thermal conductivity of the base fluid.

The thermal conductivity of the nanofluids is calculated from the Wasp [22] model, which is defined as follows:

$$k_{nf} = \left[\frac{k_p + 2k_m - 2\phi(k_w - k_p)}{k_p + 2k_w + \phi(k_w - k_p)}\right]k_w \quad (4)$$

For spherical particles, the results given by the Wasp model coincide with those of the Hamilton and Crosser model.

An alternative formula for calculating the thermal conductivity was introduced by Yu and Choi [23], which is expressed in the following form:

$$k_{nf} = \left[\frac{k_p + 2k_w + 2(k_p - k_w)(1+\beta)^3\phi}{k_p + 2k_w - (k_p - k_w)(1+\beta)^3\phi}\right]k_w \quad (5)$$

where β is the ratio of the nanolayer thickness to the original particle radius. Normally $\beta = 0.1$ is used to calculate the thermal conductivity of the nanofluid.

Murshed et al. [24] introduced the Bruggeman model [25] for calculating the thermal conductivity of nanofluids, which is expressed as follows:

$$k_{nf} = \frac{1}{4}[(3\phi - 1)k_p + (2 - 3\phi)k_w] + \frac{k_w}{4}\sqrt{\Delta} \quad (6)$$

$$\Delta = \left[(3\phi-1)^2(k_p/k_w)^2 + (2-3\phi)^2 + 2(2 + 9\phi - 9\phi^2)(k_p/k_w)\right] \quad (7)$$

Finally, Timofeeva et al. [26] introduced the effective medium theory for computing thermal conductivity of nanofluids, which is defined as follows:

$$k_{nf} = [1 + 3\phi]k_w \quad (8)$$

In the case of viscosity measurement, the viscosity of nanofluids was measured by using the rotational rheometer (Gemini 200HR Nano, Ultra low viscosity) manufactured by Malvern-Bohlin Instruments. The measurement conditions are the same as those of the thermal conductivity measurement. Moreover, the measured data are compared with those obtained from the well-known correlations, which are summarised as follows:

Brinkman [16] suggested the equation for calculating the viscosity of the suspension, which is defined as follows:

$$\mu_{nf} = \frac{1}{(1-\phi)^{2.5}}\mu_w \quad (9)$$

Drew and Passman [27] suggested the well-known Einstein's equation for calculating viscosity, which is applicable to spherical particles in volume fractions less than 5.0 vol.%, and is defined as follows:

$$\mu_{nf} = (1 + 2.5\phi)\mu_w \quad (10)$$

Batchelor [28] introduced a correlation for calculating the viscosity of nanofluids with spherical shape nanoparticles, which is defined as:

$$\mu_{nf} = (1 + 2.5\phi + 6.2\phi^2)\mu_w \quad (11)$$

Furthermore, Wang et al. [29] proposed a model to predict the viscosity of nanofluids which is expressed as:

$$\mu_{nf} = (1 + 7.3\phi + 123\phi^2)\mu_w \quad (12)$$

where φ is the volume concentration, μ_{nf} is the viscosity of the nanofluid and μ_w is the viscosity of the base fluid.

4. Data reduction

In the present study, the TiO_2 nanoparticles dispersed in water with volume concentrations of 0.2%, 0.6%, 1.0%, 1.5% and 2.0% were used to investigate the convective heat transfer coefficient and pressure drop of the nanofluids. Thus, the heat transfer coefficient and pressure drop of nanofluids can be calculated from the following equations.

The heat transfer rate from the heating fluid is calculated from:

$$Q_w = \dot{m}_w Cp_w (T_{in} - T_{out})_w \quad (13)$$

where Q_w is the heat transfer rate of the hot water and $\dot{m}_w$ is the mass flow rate of the hot water.

The heat transfer rate into the nanofluid is defined as:

$$Q_{nf} = \dot{m}_{nf} Cp_{nf} (T_{out} - T_{in})_{nf} \quad (14)$$

where Q_{nf} is the heat transfer rate of the nanofluid and $\dot{m}_{nf}$ is the mass flow rate of the nanofluid.

The average heat transfer rate is defined as follows:

$$Q_{ave} = \frac{Q_w + Q_{nf}}{2} \quad (15)$$

where Q_{ave} is the average heat transfer rate between the hot water and the nanofluid.

In this study, the energy differences between nanofluid and heating fluid are approximately 3%.

The experimental heat transfer coefficient and Nusselt number of the nanofluid are computed from the following equation:

$$h_{nf} = \frac{q_{ave}}{T_{wall} - T_{nf}} \quad (16)$$

$$Nu_{nf} = \frac{h_{nf} D}{k_{nf}} \quad (17)$$

where h_{nf} is the heat transfer coefficient of the nanofluid, q_{ave} is the average heat flux between the hot water and the nanofluid, T_{wall} is the average temperature of the wall, T_{nf} is the bulk temperature of the nanofluid, Nu_{nf} is the Nusselt number of the nanofluid, D is the inner diameter of the test tube, and k_{nf} is the thermal conductivity of the nanofluid.

Similarly to the heat transfer coefficient, the friction factor of the nanofluid is calculated from:

$$f_{nf} = \frac{2D\Delta P_{nf} L}{u_m^2 L \rho_{nf}} \quad (18)$$

where f_{nf} is the friction factor of the nanofluid, ΔP_{nf} is the measured pressure drop of the nanofluid, L is the length of the tube, D is the diameter of the tube, ρ_{nf} is the density of the nanofluid, and u_m is the mean velocity of the nanofluid.

The density and specific heat of the nanofluids presented in the above equation are calculated by use of the Pak and Cho [2] correlations, which are defined as follows:

$$\rho_{nf} = \phi\rho_p + (1 - \phi)\rho_w \quad (19)$$

and

$$Cp_{nf} = \phi Cp_p + (1-\phi)Cp_w \quad (20)$$

where Cp_{nf} is the specific heat of the nanofluid, Cp_p is the specific heat of the nanoparticles and Cp_w is the specific heat of the base fluid.

The properties of the nanofluid shown in the above equations are evaluated from water and nanoparticles at average bulk temperature.

5. Results and discussion

5.1. The thermal conductivity of nanofluids

In order to validate the transient hot-wire system, the thermal conductivity of water was measured at temperatures of 15 °C, 25 °C and 35 °C. Then, the measured data of water were compared with the reference data presented in the standard textbook [30]. As shown in Fig. 3, the results show that the measured data gave reasonable agreement with the reference data. Furthermore, the results also show that the uncertainty of the thermal conductivity measurement is approximately 2.5%. Fig. 4 shows the thermal conductivity of TiO_2-water nanofluids as a function of temperature and particle volume concentration. The results indicated that the thermal conductivity of nanofluids substantially increases with increasing particle volume concentration as well as nanofluid temperature. Fig. 5 shows a comparison of measured values of thermal conductivity of nanofluids with the calculated values from well-known correlations. The results show that the measured thermal conductivity of the nanofluids is significantly greater than the computed value of the H–C model, Wasp model, Bruggeman model, and the effective medium theory. However, the results showed that the measured values are closer to the calculated values of the Yu and Choi equation than of the other equations.

5.2. The viscosity of nanofluids

In compliance with the thermal conductivity measurement, the viscosity of pure water was first measured for validating the experimental apparatus. The measurement conditions are the same as those of the thermal conductivity measurement. Then, the reference data presented in the standard textbook [31] were used to compare with the measured data. Fig. 6 shows the comparison of viscosity between the measured data and the reference data for water. The results show a good correspondence between the measured data and the reference data, and the uncertainty of the viscosities measurement is approximately 3.5%. As shown in Fig. 7, the results show that the viscosity of nanofluids increases with increasing particle volume concentration and also increases with decreasing nanofluid temperature. Fig. 8 shows a comparison of measured values with the predicted values from well-known correlations. The results show that the measured data of nanofluids are much larger than those of predicted values by use of the Einstein equation, Brinkman equation and Batchelor equation. However, the results also show that the measured values are rather consistent with the calculated values by using the Wang et al. equation.

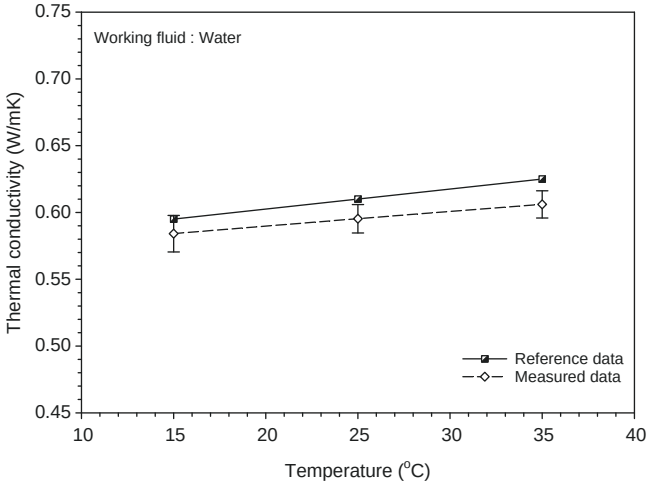

Fig. 3. Comparison of the thermal conductivity between measured data and standard data.

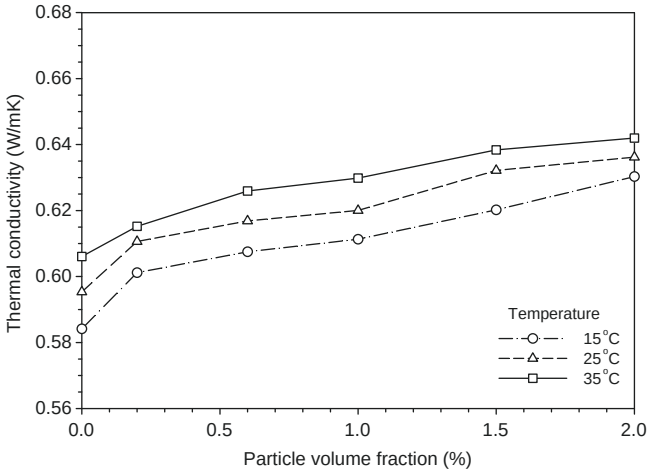

Fig. 4. Thermal conductivity of TiO_2-water nanofluids as function of temperature and volume fraction.

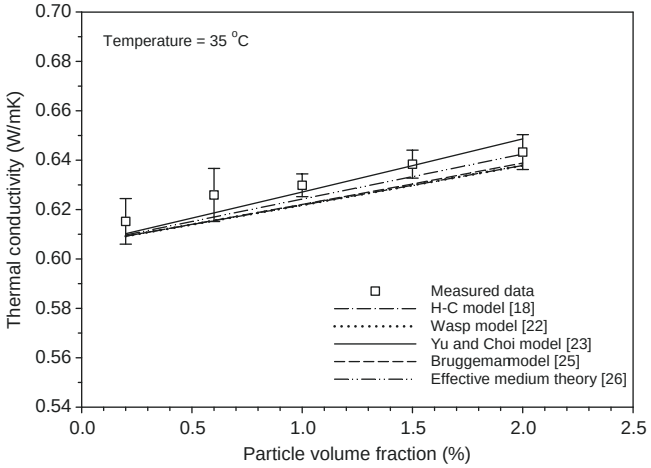

Fig. 5. Comparison of the thermal conductivity between measured data and calculated value from the other correlations.

5.3. Convective heat transfer of nanofluid

In the present study, TiO_2 nanoparticles dispersed in water for 0.2%, 0.6%, 1.0%, 1.5% and 2.0% by volume are used to investigate the heat transfer performance and the pressure drop characteristics of the nanofluid. The test conditions used in this study are summarised as follows: (1) the Reynolds number of the nanofluid varies in the approximate range of 3000–18,000, (2) the temperature of the nanofluid is 15 °C, 20 °C and 25 °C, (3) the mass flow

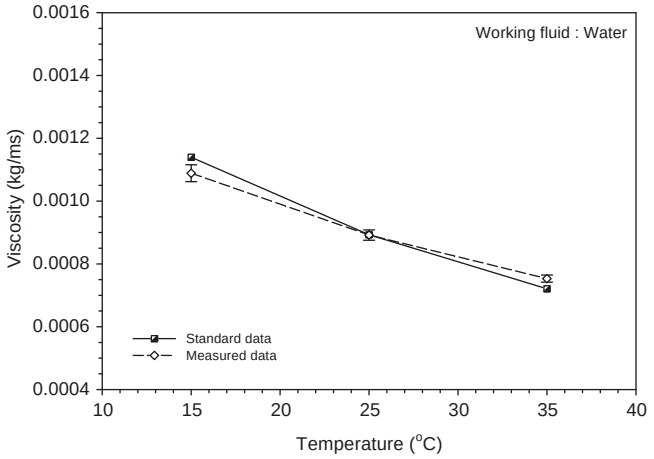

Fig. 6. Comparison of the viscosity between measured data and reference data.

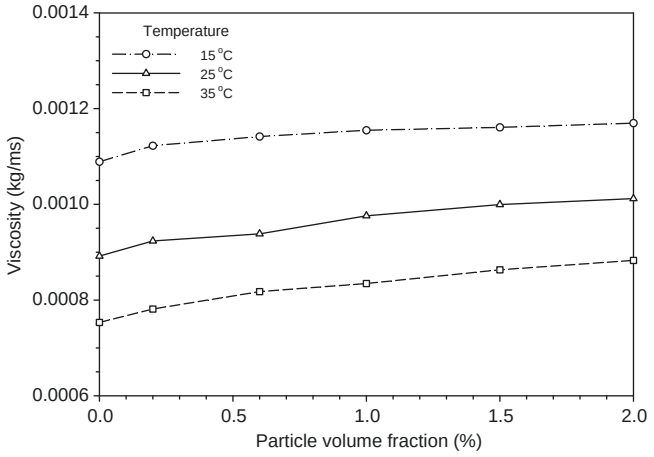

Fig. 7. Viscosity of TiO_2-water nanofluids as a function of temperature and volume fraction.

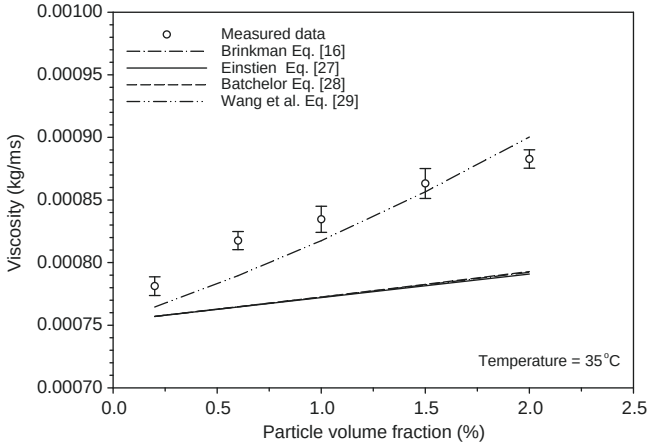

Fig. 8. Comparison of the viscosity between measured data and calculated value from the other correlations.

rates of hot water is 3 LPM and 4.5 LPM, and (4) the temperature of the hot water is 35 °C and 45 °C.

Before evaluating the heat transfer performance of the nanofluids, the pure water is used as the working fluid for estimating the reliability and accuracy of the experimental system. The results of the experimental Nusselt number are compared with those obtained from the Gnielinski equation [32], which is defined as follows:

$$Nu = \frac{(f/8)(Re - 1000)Pr}{1 + 12.7(f/8)^{0.5}(Pr^{2/3} - 1)} \tag{21}$$

where Nu is the Nusselt number, Re is the Reynolds number, Pr is the Prandtl number and f is the friction factor.

The friction factor can be calculated from the Colebrook equation [33] as follows:

$$\frac{1}{\sqrt{f}} = -2.0\log\left(\frac{\varepsilon/D}{3.7} + \frac{2.51}{Re\sqrt{f}}\right) \tag{22}$$

where ε is the roughness of the test tube.

Moreover, the existing correlations for calculating the Nusselt number for nanofluids were used for comparison with the experimental results. Up to now, there are only two correlations for predicting the heat transfer performance of nanofluids flowing in the turbulent flow regime, namely the Pak and Cho [2] and Xuan and Li [4] correlations, which are defined as follows:

The Pak and Cho correlation is defined as:

$$Nu_{nf} = 0.021 Re_{nf}^{0.8} Pr_{nf}^{0.5} \tag{23}$$

The Xuan and Li correlation is defined as:

$$Nu_{nf} = 0.0059\left(1.0 + 7.6286\phi^{0.6886} Pe_d^{0.001}\right) Re_{nf}^{0.9238} Pr_{nf}^{0.4} \tag{24}$$

The Reynolds number of the nanofluid is expressed as:

$$Re_{nf} = \frac{\rho_{nf} u_m D}{\mu_{nf}} \tag{25}$$

The Prandtl number and Peclet number of the nanofluid can be calculated from the following equation:

$$Pr_{nf} = \frac{\mu_{nf} Cp_{nf}}{k_{nf}} \tag{26}$$

$$Pe_{nf} = \frac{u_m d_p}{\alpha_{nf}} \tag{27}$$

where d_p is the diameter of the nanoparticles.

In order to calculate the Peclet number, the thermal diffusivity of the nanofluid (α_{nf}) is defined as:

$$\alpha_{nf} = \frac{k_{nf}}{\rho_{nf} Cp_{nf}} \tag{28}$$

As shown in Fig. 9, the measured Nusselt number coincided well with the calculated values for pure water.

As shown in Fig. 10, the heat transfer coefficient and the Nusselt number of the nanofluids are higher than those of the base liquid, and they increase with increasing the Reynolds number as well as the particle volume concentration for the volume concentration $\leqslant$1.0 vol.%. At 1.0 vol.%, the enhancement range between 20% and 32% is observed. However, the heat transfer coefficient for particle concentration of 1.5 vol.% is smaller than that for the volume concentration of 1.0 vol.%, but still larger than for the base liquid. It was also found that the heat transfer coefficient of nanofluid at volume fraction of 2.0 vol.% was approximately 14% **s**maller than that of pure water when compared under the same conditions. This behaviour may be due to the fact that the nanoparticles presented in the base liquid increase the thermal conductivity and the viscosity of the base liquid at the same time, and increase with increasing the particle concentrations. The increasing of the thermal conductivity leads to an increase in the heat transfer performance, whereas the increasing of the viscosity of the fluid leads to an increase in the boundary layer thickness, which results in a decrease in the heat transfer performance. As a result, for the volume

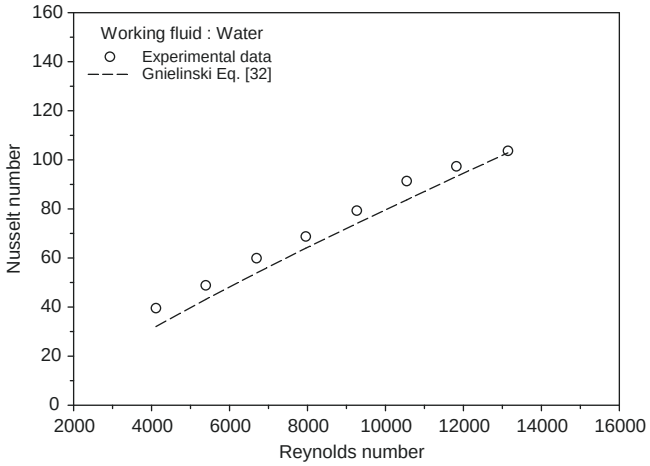

Fig. 9. Comparison between measured heat transfer coefficient and that calculated from Gnielinski equation [32].

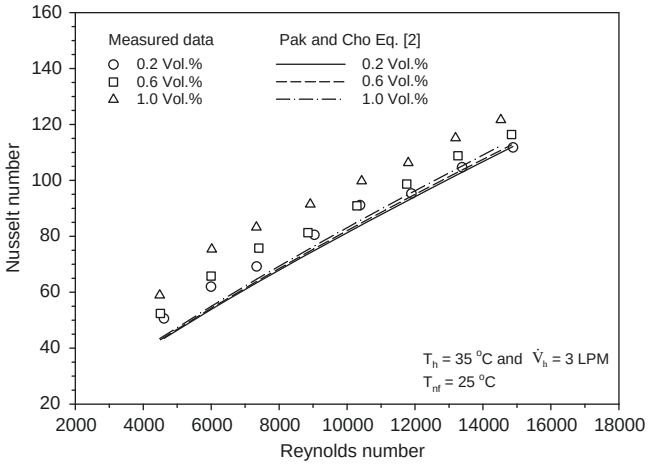

Fig. 11. Comparison of Nusselt number between the measured data and calculated values from nanofluid correlations.

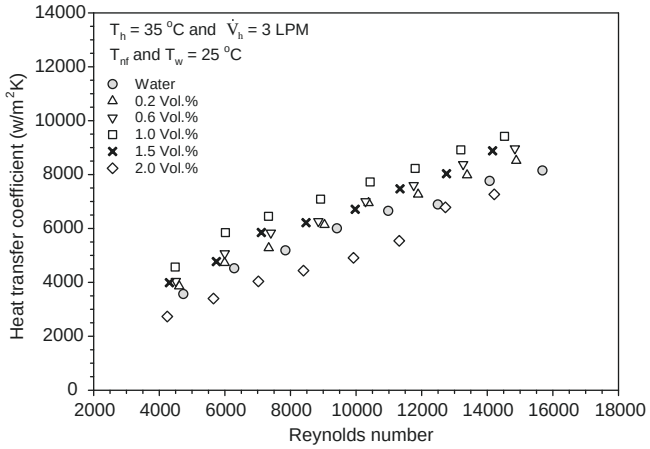

(a) Heat transfer coefficient

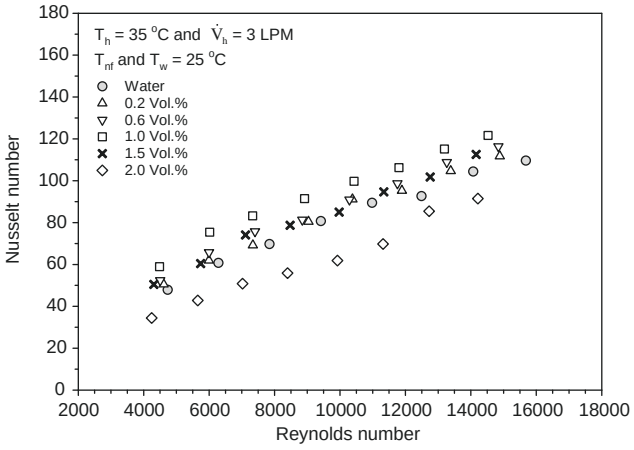

(b) Nusselt number

Fig. 10. Experimental heat transfer coefficient and Nusselt number for water and TiO_2-water nanofluids versus Reynolds number at various volume concentration.

concentration $\leqslant$1.0 vol.%, the effect of thermal enhancement may overcome the effect of the increasing of the viscosity. On the other hand, for the volume concentration of more than 1.0 vol.%, the effect of the viscosity increase may overcome the effect of thermal conductivity enhancement, which leads to a decrease in the heat transfer performance of the nanofluids. Moreover, in our opinion, the nanoparticles at higher volume concentration may become combined together, which caused the size became bigger and leads to a decrease in the heat transfer performance. According to this study, the present results are found to be different from those obtained from other researchers. For example, Xuan and Li [4] investigated experimentally the convective heat transfer and flow characteristics for Cu-water nanofluids. They found that the Nusselt number of the nanofluid is increased more than 39% for the particle volume fraction of 2.0 vol.%. He et al. [12] determined experimentally the heat transfer and flow behaviour of TiO_2-distilled water nanofluids in both laminar and turbulent flow condition. The results showed that the convective heat transfer coefficient increased more than 40% for a volume fraction of 1.1 vol.%. Nguyen et al. [13] experimentally investigated the heat transfer behaviour of Al_2O_3-water nanofluid flowing under a turbulent flow regime inside an electronic cooling system. They found that the heat transfer coefficient of nanofluids for particle volume concentration of 6.8 vol.% is greater than the base fluid by approximately 40%. However, Pak and Cho [2] experimentally studied heat transfer performance of γ-Al_2O_3 and TiO_2 nanoparticle dispersed in water flowing in a horizontal circular tube. Their results showed that the Nusselt number of nanofluids increased with an increase in the Reynolds number as well as the volume fraction. Moreover, their results still showed that the heat transfer coefficient of the nanofluids for a volume concentration of 3 vol.% was 12% lower than that of pure water under the same conditions. As mentioned above, it is difficult to explain this difference in behaviour. It may be caused by several factors, such as particle source, particle size, particle shape, particle preparation, and even solution chemistry (e.g. pH value). Therefore, more experimental works are needed in order to address the exact heat transfer behaviour of nanofluids for applying them in practical applications.

From the previous work of the authors [20], the results indicated that the Pak and Cho [2] equation can be used to predict the heat transfer performance of TiO_2-water nanofluid with a volume concentration of 0.2% and give an agreement that compares with the experimental results. At the same time, the Xuan and Li [4] correlation gives a significantly lower heat transfer coefficient compared with the measured data and the Pak and Cho correlation. However, in this study, Fig. 11 shows that Pak and Cho [2] correlation fails to predict the Nusselt number of nanofluids for volume concentrations of 0.6% and 1.0%. This may be caused by the effect of the particle concentrations, which was not considered in their correlation, and by different configuration of the test section. Thus,

a new heat transfer correlation which gives better accuracy for predicting the heat transfer performance of the nanofluids may still be required. This is an important subject for the present study.

In general, Nusselt numbers of nanofluids may be related with the parameters as follows:

$$Nu_{nf} = f(Re_{nf}, Pr_{nf}, \phi) \tag{29}$$

Considering the above mentioned, the equation for predicting the heat transfer performance of nanofluid was formed and is proposed in the following form:

$$Nu_{nf} = 0.074 Re_{nf}^{0.707} Pr_{nf}^{0.385} \phi^{0.074} \tag{30}$$

The above equation is obtained by curve fitting all the experimental data for the nanofluids. Comparisons of the experimental Nusselt number with those calculated by the proposed correlation are shown in Fig. 12. The results show good correspondence between the experimental values and the calculated values by the above equation. It is clearly seen that the majority of the data falls within ±10% of the proposed equation. The authors would like to introduce that this equation can be used for predicting the heat transfer coefficient of nanofluids with a volume concentration of $\leqslant$1.0% and a Reynolds number range between 3000 and 18,000. Moreover, it is very important to note that this equation is only established with respect to the data for TiO_2-water nanofluids.

5.4. Pressure drop of nanofluid

In order to apply the nanofluids for practical application, in addition to the heat transfer performance of the nanofluids it is necessary to study their flow features. In this study, nanofluid with 0.2, 0.6, 1.0, 1.5 and 2.0 vol.% suspended nanoparticles are used in the pressure drop test under the turbulent flow condition. Similar to the convective heat transfer coefficient of nanofluids, pure water is used as the working fluid in order to estimate the reliability and accuracy of the measured pressure.

As shown in Fig. 13, the measured friction factor agrees well with those of calculated values for pure water.

As shown in Fig. 14, the results show that the pressure drop and friction factor of the nanofluids increase with increasing Reynolds number and that there is a small increase with increasing particle concentrations. This means that using the nanofluids at higher particle volume fraction may create a small penalty in pressure drop. Moreover, although the Colebrook equation can fairly predict the pressure drop of nanofluids as shown in Fig. 14a, a new correlation

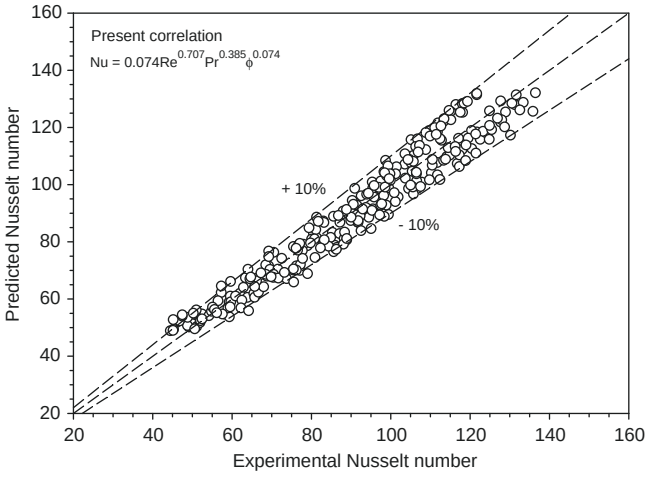

Fig. 12. Comparison of the Nusselt number of nanofluids between predicted values by presented correlation and experimental data.

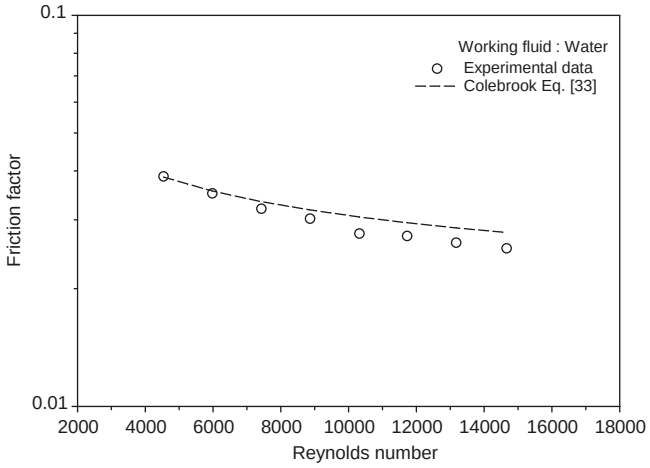

Fig. 13. Comparison between measured friction factor and that calculated from Colebrook equation [33].

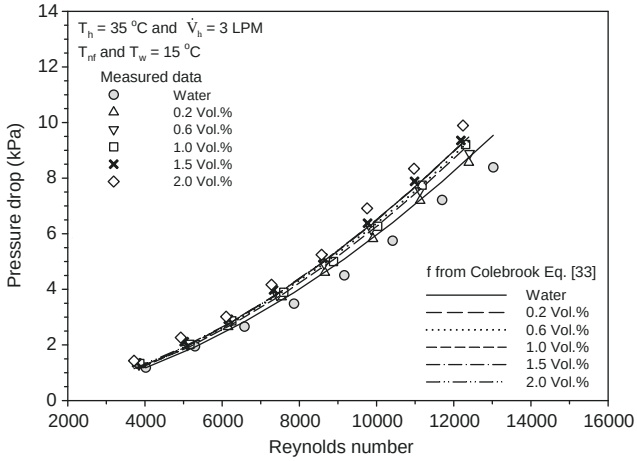

Fig. 14. Comparison of pressure drop and friction factor obtained from water and that from the TiO_2-water nanofluids at different volume fraction.

which gives better accuracy and that is easy to use for calculating the friction factor of nanofluids is still needed. Similar to the heat transfer correlation, a new equation for predicting the friction factor of nanofluids is proposed in the following form:

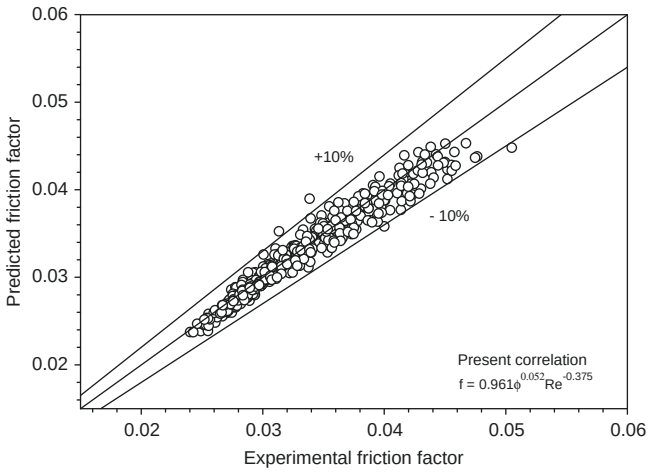

Fig. 15. Proposed pressure drop versus experimental pressure drop.

$$f_{nf} = 0.961\phi^{0.052}Re^{-0.375} \quad (31)$$

As shown in Fig. 15, the results show that the present correlation gave reasonably good agreement with the experimental data. This equation can be used to compute the friction factor of nanofluids with particle volume concentrations range between 0% and 2.0%.

6. Conclusions

The convective heat transfer performance and flow characteristic of TiO_2-water nanofluid flowing in a horizontal double tube counter-flow heat exchanger was experimentally investigated. Experiments were carried out under turbulent flow conditions. The effect of particle concentrations and the Reynolds number on the heat transfer performance and flow behaviour of nanofluids are determined. Important conclusions have been obtained and are summarised as follows:

- Dispersion of the nanoparticles into the base liquid increases the thermal conductivity and viscosity of the nanofluids, and this augmentation increases with increasing particle concentrations.
- At a particle volume concentration of $\leqslant$1.0 vol.%, the use of TiO_2-water nanofluid gives significantly higher heat transfer coefficients than those of the base fluid. For example, at the 1.0 vol.%, the heat transfer coefficient of nanofluids was approximately 26% greater than that of pure water. However, at the particle concentration of 2.0 vol.%, it was found that the heat transfer coefficient of nanofluids was roughly 14% smaller than that of pure water for the given conditions.
- The pressure drop of nanofluids increases with increasing Reynolds number and there is a small increase with increasing particle volume concentrations. This is caused by increase in the viscosity of nanofluids, and it means that nanofluids incur little penalty in pressure drop.
- The results showed that the Pak and Cho [2] correlation can predict the heat transfer coefficient of nanofluids and gives results that corresponded well only with the experimental results for the volume concentration of 0.2%. However, for the volume concentrations of 0.6% and 1.0%, the Pak and Cho equation fails to predict the heat transfer performance of the nanofluids.
- New heat transfer and friction factor correlations for predicting the Nusselt number and friction factor of TiO_2-water nanofluids are proposed in the form of $Nu = 0.074Re^{0.707}Pr^{0.385}\phi^{0.074}$, and $f = 0.961\phi^{0.052}Re^{-0.375}$, respectively. The majority of the data falls within ±10% of the proposed equation. These equations are valid in the range of Reynolds number between 3000 and 18,000 and particle volume concentrations in the range of 0 and 1.0 vol.% for Nusselt number and 0 and 2.0 vol.% for friction factor.

Acknowledgments

The authors would like to express their appreciation to the Thailand Research Fund (TRF) for providing financial support for this study. The authors also wish to thank DEGUSSA AG, Germany for the valuable donation of the nanoparticles used in the present study.

References

[1] S.U.S. Choi, Enhancing thermal conductivity of fluids with nanoparticle, ASME FED 231 (1995) 99.
[2] B.C. Pak, Y. I Cho, Hydrodynamic and heat transfer study of dispersed fluids with submicron metallic oxide particles, Exp. Heat Transfer 11 (1998) 151.
[3] Q. Li, Y. Xuan, Convective heat transfer and Flow characteristics of Cu-water nanofluid, Sci. China E 45 (2002) 408.
[4] Y. Xuan, Q. Li, Investigation on convective heat transfer and flow features of nanofluids, ASME J. Heat Transfer 125 (2003) 151.
[5] C.Y. Tsai, H.T. Chien, P.P. Ding, B. Chan, T.Y. Luh, P.H. Chen, Effect of structural character of gold nanoparticles in nanofluid on heat pipe thermal performance, Mater. Lett. 58 (2004) 1461.
[6] D. Wen, Y. Ding, Experimental investigation into convective heat transfer of nanofluids at the entrance region under laminar flow conditions, Int. J. Heat Mass Transfer 47 (2004) 5181.
[7] Y. Yang, Z.G. Zhang, E.A. Grulke, W.B. Anderson, G. Wu, Heat transfer properties of nanoparticle-in-fluid dispersions (nanofluids) in laminar flow, Int. J. Heat Mass Transfer 48 (6) (2005).
[8] Y. Ding, H. Alias, D. Wen, R.A. Williams, Heat transfer of aqueous suspensions of carbon nanotubes (CNT nanofluids), Int. J. Heat Mass Transfer 49 (1–2) (2005) 240.
[9] X.Q. Wang, A.S. Mujumdar, Heat transfer characteristics of nanofluids: a review, Int. J. Therm. Sci. 46 (2007) 1.
[10] S.Z. Heris, S.G. Etemad, M.N. Esfahany, Experimental investigation of oxide nanofluids laminar flow convective heat transfer, Int. Commun. Heat Mass Transfer 33 (2006) 529.
[11] S.Z. Heris, M.N. Esfahany, S.G. Etemad, Experimental investigation of convective heat transfer of Al2O3/water nanofluid in circular tube, Int. J. Heat Fluids Flow 28 (2) (2007) 203.
[12] Y. He, Y. Jin, H. Chen, Y. Ding, D. Cang, H. Lu, Heat transfer and flow behavior of aqueous suspensions of TiO_2 nanoparticles (nanofluids) flowing upward through a vertical pipe, Int. J. Heat Mass Transfer 50 (2007) 2272.
[13] C.T. Nguyen, G. Roy, C. Gauthier, N. Galanis, Heat transfer enhancement using Al_2O_3-water nanofluid for electronic liquid cooling system, Appl. Therm. Eng. 28 (2007) 1501.
[14] G.H. Ko, K. Ho, K. Lee, D.S. Kim, C. Kim, Y. Sohn, M. Choi, An experimental study on the pressure drop of nanofluids containing carbon nanotubes in the horizontal tube, Int. J. Heat Mass Transfer 50 (2007) 4749.
[15] R. Chein, J. Chuang, Experimental microchannel heat sink performance studies using nanofluids, Int. J. Therm. Sci. 46 (1) (2007) 57.
[16] H.C. Brinkman, The viscosity of concentrated suspensions and solution, J. Chem. Phys. 20 (1952) 571.
[17] Y. Xuan, W. Roetzel, Conceptions for heat transfer correlation of nanofluids, Int. J. Heat Mass Transfer 43 (2000) 3701.
[18] R.L. Hamilton, O.K. Crosser, Thermal conductivity of heterogeneous two-component systems, I&EC Fund. 1 (3) (1962) 187.
[19] W. Duangthongsuk, S. Wongwises, Effect of thermophysical properties models on the prediction of the convective heat transfer coefficient for low concentration nanofluid, Int. Comm. Heat Mass Transfer 35 (2008) 1320.
[20] W. Duangthongsuk, S. Wongwises, Heat transfer enhancement and pressure drop characteristics of TiO_2-water nanofluid in a double-tube counter flow heat exchanger, Int. J. Heat Mass Transfer 52 (2009) 2059.
[21] J.P. Bentley, Temperature sensor characteristics and measurement system design, J. Phy. E: Sci. Instrum. 17 (1984) 430.
[22] F.J. Wasp, Solid–liquid slurry pipeline transportation, Trans. Tech, Berlin, 1977.
[23] W. Yu, S.U.S. Choi, The role of interfacial layers in the enhanced thermal conductivity of nanofluids: a renovated Maxwell model, J. Nanoparticle Res. 5 (2003) 167.
[24] S.M.S. Murshed, K.C. Leong, C. Yang, Enhanced thermal conductivity of TiO_2-water based nanofluids, Int. J. Therm. Sci. 44 (2005) 367.
[25] D.A.G. Bruggeman, Berechnung verschiedener physikalischer konstanten von heterogenen substanzen, I. Dielektrizitatskonstanten und Leitfahigkeiten der Mischkorper aus Isotropen Substanzen, Annalen der Physik 14 (1935) 636.
[26] E.V. Timofeeva, A.N. Gavrilov, J.M. McCloskey, Y.V. Tolmachev, Thermal conductivity and particle agglomeration in alumina nanofluids: experiment and theory, Phy. Rev. 76 (2007) 061203.

[27] D.A. Drew, S.L. Passman, Theory of Multi-Component Fluids, Springer, Berlin, 1999.
[28] G.K. Batchelor, The effect of Brownian motion on the bulk stress in a suspension of spherical particles, J. Fluid Mech. 83 (1) (1977) 97.
[29] X. Wang, X. Xu, S.U.S. Choi, Thermal conductivity of nanoparticles-fluid mixture, J. Thermophys. Heat Transfer 13 (4) (1999) 474.
[30] F.P. Incropera, D.P. DeWitt, Fundamentals of Heat and Mass Transfer, Springer, 1996.
[31] R.W. Fox, A.T. McDonald, P.J. Pritchard, Introduction to Fluid Mechanics, John Wiley & Sons, 2004.
[32] V. Gnielinski, New equations for heat and mass transfer in turbulent pipe and channel flow, Int. Chem. Eng. 16 (1976) 359.
[33] C.F. Colebrook, Turbulent flow in pipes, with particular reference to the transition between the smooth and rough pipe laws, J. Inst. Civ. Eng. Lond. 11 (1939) 133.

Renewable and Sustainable Energy Reviews 14 (2010) 629–641

Contents lists available at ScienceDirect

Renewable and Sustainable Energy Reviews

journal homepage: www.elsevier.com/locate/rser

Enhancement of heat transfer using nanofluids—An overview

Lazarus Godson [a,*], B. Raja [b,1], D. Mohan Lal [a], S. Wongwises [c]

[a] Refrigeration & Air-Conditioning Division, Department of Mechanical Engineering., College of Engineering, Anna University, Chennai 600 025, Tamil Nadu, India
[b] Indian Institute of Information Technology, Design & Manufacturing-Kancheepuram Indian Institute of Technology-Madras, Chennai 600 036, Tamil Nadu, India
[c] Fluid Mechanics, Thermal Engineering and Multiphase Flow (FUTURE), Dept. of Mechanical Engineering, King Mongkut's University of Technology Thonburi, Bangmod, Bangkok 10140, Thailand

ARTICLE INFO

Article history:
Received 26 June 2009
Accepted 6 September 2009

Keywords:
Nanofluid
Convective heat transfer
Laminar flow
Turbulent flow
Nanoparticles
Dispersion
Thermal conductivity

ABSTRACT

A colloidal mixture of nano-sized particles in a base fluid, called nanofluids, tremendously enhances the heat transfer characteristics of the original fluid, and is ideally suited for practical applications due to its marvelous characteristics. This article addresses the unique features of nanofluids, such as enhancement of heat transfer, improvement in thermal conductivity, increase in surface volume ratio, Brownian motion, thermophoresis, etc. In addition, the article summarizes the recent research in experimental and theoretical studies on forced and free convective heat transfer in nanofluids, their thermo-physical properties and their applications, and identifies the challenges and opportunities for future research.
© 2009 Elsevier Ltd. All rights reserved.

Contents

1. Introduction . . . 630
2. Nanofluids . . . 630
3. Enhancement of thermal conductivity . . . 631
   3.1. Dispersion of the suspended particles . . . 631
   3.2. Intensification of turbulence . . . 631
   3.3. Brownian motion . . . 631
   3.4. Thermophoresis . . . 631
   3.5. Diffusiophoresis . . . 631
4. Experimental investigation . . . 632
   4.1. Forced convection heat transfer experiments with nanofluids . . . 632
      4.1.1. Experiments with metal oxide nanoparticles . . . 632
      4.1.2. Experiments with pure metal nanoparticles . . . 633
      4.1.3. Inferences from forced convection heat transfer experimental studies . . . 633
   4.2. Natural convection heat transfer experiments with nanofluids . . . 633
      4.2.1. Inferences from natural convection heat transfer experimental studies . . . 634
   4.3. Boiling heat transfer experiments with nanofluids . . . 634
      4.3.1. Inferences from boiling heat transfer experimental studies . . . 635
5. Mathematical modeling . . . 635
   5.1. Theoretical investigations for convective heat transfer of nanofluids . . . 635
   5.2. Inferences from theoretical studies with nanofluids . . . 637
6. Applications . . . 638
   6.1. Micro-channels . . . 638
   6.2. Heat pipes . . . 638

* Corresponding author. Tel.: +91 99944 55741; fax: +91 44 22203261.
E-mail addresses: godasir@yahoo.co.in (L. Godson), rajab@iiitdm.ac.in (B. Raja), mohanlal@annauniv.edu (D. Mohan Lal), somchai.won@kmutt.ac.th (S. Wongwises).
[1] Tel.: +91 44 22578556; fax: +91 44 22574691.

1364-0321/$ – see front matter © 2009 Elsevier Ltd. All rights reserved.
doi:10.1016/j.rser.2009.10.004

7. Outlook and future challenges . . . 638
8. Conclusion . . . 639
Acknowledgements . . . 639
References . . . 639

Nomenclature

A	cross-sectional area (m^2)
C_p	specific heat (J/kg K)
D	tube diameter (m)
h	heat transfer coefficient (W/m^2 K)
k	thermal conductivity (W/m K)
m	mass flow rate (kg/s)
Nu	Nusselt number
Pr	Prandtl number
q''	heat flux (W/m^2)
Re	Reynolds number
T	temperature (°C)

Greek symbols

β	thermal dispersion coefficient (N/m^2 K)
φ	volume fraction
ρ	density (kg/m^3)
μ	dynamic viscosity (kg/m s)
γ	particle size (nm)

Subscript

f	bulk fluid
nf	nanofluid
w	tube wall
x	axial distance
bf	base fluid
i	inner wall
o	outer wall

Abbreviation

CHF	critical heat flux
CNT	carbon nano tube
HTC	heat transfer coefficient

1. Introduction

Ever since the adverse effect of green house gases was discovered, leading to the Kyoto Protocol [1], the search for methods and technological advancement to mitigate the impact of global warming on Planet Earth became a pressing need for the research and industrial communities. The Protocol had exhorted both the developed and developing countries to show intense curiosity with a sense of participation, to find definitive ways to tackle the issue. Subsequent meetings which were held in many countries had called for a gentle decline in the production of green house gases. Even as scientists subscribed to a number of methods to tackle the carbon footprints, the global energy need and inefficient thermal-fluid systems always increased the green house gases.

A reduction in energy consumption is possible by enhancing the performance of heat exchange systems. Heat transfer is one of the most important processes in industrial and consumer products and it is worth addressing its influence over carbon footprints. For instance, the present telecommunication demand for enhanced functionality in circuit boards, results in high process density circuit boards. In such cases, the company spends more than 50% of the total electricity on the thermal management of electronic cooling systems [2]. Further, one of the most influential regulations is the 65 Dba noise limit in a central office environment compared to the 85 Dba in data centers and thus, typical air-cooling methods are unsuitable for these conditions [3]. The dozens of methods such as Fin-Foam Heat Sink, Minichannels, Microchannels, Novel interface materials, Dielectric mist cooling, Forced convective boiling, etc. and their combinations are limited to heat removal of up to 1000 W/cm^2. Some of the electronic systems like ultra-high heat flux optical devices, high-powered X-rays and lasers demand as high as 2000 W/cm^2 of heat removal [4]. Similarly, the growth of Heating Ventilation and Air-Conditioning (HVAC) and chemical processing equipment had adversely increased the carbon footprints. The paradigm shift in their design with respect to heat transfer will both simultaneously reduce the size of the heat exchangers and the energy consumption. In many industrial applications, the conventional heat transfer fluids are refrigerants, water, engine oil, ethylene glycol, etc. Even though an improvement in energy efficiency is possible from the topological and configuration points of view, much more is needed from the perspective of the heat transfer fluid. Further, enhancement in heat transfer is always in demand, as the operational speed of these devices depends on the cooling rate. New technology and advanced fluids with greater potential to improve the flow and thermal characteristics are two options to enhance the heat transfer rate and the present article deals with the latter option. One such latest advancement in heat transfer fluids, is an engineered colloidal mixture of the base fluids and nano-sized metallic particles (1–100 nm). The earlier versions of colloidal fluids such as micro-fluid substances tend to sediment and cause erosion in the moving component. However, nanofluids are claimed to be a non-agglomerated mono-dispersed particles in the base fluids, which proved to be enhancing the heat transfer more than 50% in real-time applications even when the volume ratio of the nanoparticle to base fluid is less than 0.3% [5]. As the need for more efficient heat transfer systems increases, researchers have introduced various heat transfer enhancement techniques since the middle of the 1950s. The exponential increase in the number of research articles dedicated to this subject thus far shows a noticeable growth and the importance of heat transfer enhancement technology. Some recent review articles [6–10] have covered a variety of methods for the enhancement of heat transfer. Investigation in convective heat transfer characteristics has been carried out in recent times. In this paper, the various articles related to the mechanism of nanofluid heat transfer, thermo-physical properties and pioneering experiments related to convective and boiling heat transfer of nanofluids are discussed. This article presents the recent research in natural, forced and two-phase convective heat transfer in nanofluids and its applications, and identifies the challenges and opportunities for future research.

2. Nanofluids

Enhancement of convective heat transfer and thermal conductivity of liquids was earlier made possible by mixing micron-sized particles with a base fluid (Maxwell paper) [11]. However, rapid sedimentation, erosion, clogging and high-pressure drop caused by these particles has kept the technology far from practical

use. A very small amount of nanoparticles, when dispersed uniformly and suspended stably in base fluids, can provide impressive improvements in the thermal properties of base fluids. Nanofluids, which are a colloidal mixture of nanoparticles (1–100 nm) and a base liquid (nanoparticle fluid suspensions) is the term first coined by Choi in the year 1995 [12] at the Argonne National Laboratory to describe the new class of nanotechnology based heat transfer fluids that exhibit thermal properties superior to those of their base fluids or conventional particle fluid suspensions.

The phases in the colloid are distinguishable and interact through weak surface molecular forces, preferably without any chemical reaction. Compared to micron-sized particles, nanoparticles are engineered to have larger relative surface areas, less particle momentum, high mobility, better suspension stability than micron-sized particles and importantly increase the thermal conductivity of the mixture. This makes the nanofluids a promising working medium as coolants, lubricants, hydraulic fluids and metal cutting fluids. Further, a negligible pressure drop and mechanical abrasion makes researchers subscribe to nanofluids for the development of the next generation miniaturized heat exchangers.

Based on their application, nanoparticles have been made of various materials [13–27] such as oxide ceramics, nitride ceramics, carbide ceramics, metals, semiconductors, carbon nanotubes and composite materials such as alloyed nanoparticles Al70Cu30 or nanoparticle core–polymer shell composites. In addition to nonmetallic, metallic, and other materials for nanoparticles, completely new materials and structures have been used, such as materials "doped" with molecules in their solid–liquid. The goal of nanofluids is to achieve the best possible thermal properties at the least possible volume fraction ($\varphi < 1\%$) in the base fluids. Thus, the suspension of nearly non-agglomerated or mono-dispersed nanoparticles in liquids is the key to significant enhancement in the heat transfer. In addition, Xuan and Li [28] suggested ultrasonic vibration of nanofluids and addition of surfactants to enhance the suspension.

3. Enhancement of thermal conductivity

A substantial increase in liquid thermal conductivity, liquid viscosity, and heat transfer coefficient, are the unique features of nanofluids. It is well known that at room temperature, metals in solid phase have higher thermal conductivities than those of fluids [29]. For example, the thermal conductivity of copper at room temperature is about 700 times greater than that of water and about 3000 times greater than that of engine oil. The thermal conductivity of metallic liquids is much greater than that of nonmetallic liquids. Thus, fluids containing suspended metal particles are expected to manifest enhanced thermal conductivities relative to pure fluids [30]. Masuda et al. [31] dispersed oxide nanoparticles (γ-Al_2O_3 and TiO_2 with $\varphi = 4.3\%$) particles in liquid and showed the increase in the thermal conductivity to be 32 and 11%, respectively. Grimm [32] dispersed aluminum particles ($\gamma = 80$–$1\ \mu m$) into a fluid and claimed a 100% increase in the thermal conductivity of the fluid for $\varphi = 0.5$–10%. Choi and Eastman [33] showed that the thermal conductivity of Cu–water and CNT–water nanofluids was higher compared to that of their base liquids. Eastmann et al. [34] showed that Cu–ethylene glycol (nanoparticles coated with thioglycolic acid) with $\varphi = 0.3\%$ gave a 40% increase in thermal conductivity. Recently, an attempt at the Indira Gandhi Centre for Atomic Research (IGCAR) was made, to align magnetic nanoparticles (Fe_3O_4 coated with Oelic acid) in a base fluid (hexadecane) in a linear chain using a magnetic field, which was applied to increase the thermal conductivity by 300% [35]. Further, it was proved that the thermal properties are tunable for magnetically polarizable nanofluids that consist of a colloidal suspension of magnetite nanoparticles. Moreover, the effective thermal conductivity depends also on other mechanisms of particle motion; the commonly explained physics are as follows.

3.1. Dispersion of the suspended particles

Dispersion is a system in which particles are dispersed in a continuous phase of a different composition. Surface-active substances (surfactants) can increase the kinetic stability of emulsions greatly so that, once formed, the emulsion does not change significantly over years of storage. Some of the surfactants are thiols [36], oleic acid [37,38], laurate salts, etc. Pak and Cho [39], Xuan and Li [28] and others claimed that the abnormal increase in thermal conductivity is due to uniform dispersion of the nanoparticles.

3.2. Intensification of turbulence

Even though thermal conductivity (k_{th}) is a function of primary variables such as thermodynamic pressure and temperature, in a turbulent flow the effective thermal conductivity ($k_{th} + k_{turb}$) due to the effects of turbulent eddies is many times higher than the actual value of k_{th}. Similarly in nanofluids, such intensification is believed to be possible due to the addition of nanoparticles. Xuan and Li [28]. However, Buongiorno [40] has claimed that due to the particle size, the effects of both dispersion and turbulence are negligible and not sufficient to explain the enhancement of thermal conductivity in nanofluids.

3.3. Brownian motion

It is a seemingly random movement of particles suspended in a liquid or gas and the motion is due to collisions with base fluid molecules, which makes the particles undergo random-walk motion. Thus, the Brownian motion intensifies with an increase in temperature as per the kinetic theory of particles. Keblinski et al. [41] and Koo and Kleinstreuer [42] have suggested that the potential mechanism for enhancement of thermal conductivity is the transfer of energy due to the collision of higher temperature particles with lower ones. The effectiveness of the Brownian motion decreases with an increase in the bulk viscosity.

3.4. Thermophoresis

Thermophoresis or the Sorét effect is a phenomenon observed when a mixture of two or more types of motile particles (particles able to move) is subjected to the force of a temperature gradient. The phenomenon is most significant in a natural convection process, where the flow is driven by buoyancy and temperature. The particles travel in the direction of decreasing temperature and the process of heat transfer increases with a decrease in the bulk density.

3.5. Diffusiophoresis

Diffusiophoresis (also called as Osmo-phoresis) occurs when there is a migration of particles from a lower concentration zone to a higher concentration one. However, this is not a favorable condition since the nanofluids may lose their non-agglomeration characteristics. Thus, the resulting fluid will result in a discrete spread in the particle density. Buongiorno [40] has stressed that the Brownian motion, thermophoresis and diffusiophoresis are significant in the absence of turbulent eddies.

The thermal conductivity enhancement ratio is defined as the ratio of the thermal conductivity of the nanofluid to that of the base fluid and this ratio depends on the material, size and shape of the

particle, volume concentration and the operating temperature itself. The influence of type of material on thermal conductivity enhancement has no effect for relatively low thermal conductivity particles and positive enhancement with higher thermal conductivity particles. For instance, the enhancement of thermal conductivity using metal particles is higher that the metal oxide particles. However, it is difficult to create metal particle nanofluids without particles oxidizing during the production process. A major obstacle for metal-particle nanofluids is eliminating the oxidation process during production and later during usage. Particle coating is one technique that has received some attention to solve this problem.

The smaller in particle size higher will be the enhancement. Since the surface to volume ratio will be higher for small diameter particles which results in uniform distribution of particles gives and the best enhancement. The most commonly used geometric shape of the particles is spherical and cylindrical. The cylindrical particles show an increase in thermal conductivity enhancement due to a mesh formed by the elongated particles that conducts heat through the fluid. This indicates the elongated particles are superior to spherical for thermal conductivity. The thermal conductivity enhancement increases with increased particle volume concentration. Metal oxide particle volume concentrations below φ = 4–5% produces an enhancement level up to about 30% is typical and metal particles with less than $\varphi < 1.5\%$ gives an enhancement up to 40%. The thermal conductivity of nanoparticles is more temperature sensitive than that of the base fluid. Consequently, the thermal conductivity enhancement of nanofluids is also rather temperature sensitive and a strong dependence of nanofluid thermal conductivity is due to the random motion of nanoparticles.

The physics of the above explained mechanisms is important and to be considered while studying the enhancement of thermal conductivity and the convective heat transfer of nano-sized colloidal mixture; the mechanisms are studied experimentally and theoretically by researchers and the summary of these investigations, findings and suggestions are presented in the following sections.

4. Experimental investigation

Enhancement in heat transfer was tried earlier also, with the help of suspended micro-particles. Ahuja [43,44] conducted experiments on the enhancement of heat transport in the laminar flow of water with micro-sized polystyrene suspension. The results showed a significant enhancement in the Nusselt number and heat exchanger effectiveness compared to that of a single phase liquid. Hetsroni and Rozenblit [45] investigated the thermal interaction between liquid and solid mixtures consisting of water and polystyrene particles in a turbulent flow. Interestingly, polystyrene has very low thermal conductivity close to only 0.08 W/m K. Still, the turbulence intensification and particle rotation effect are to be reasoned for an enhancement of heat transfer. The penalty in pumping power, clogging, agglomeration, sedimentation and erosion are some of the adverse effects of micro-particles. However, this issue has been eliminated with the use of stable nano-sized particulate colloids, and this has paved the way for researchers to further investigate the enhancement of convective heat transfer.

4.1. Forced convection heat transfer experiments with nanofluids

4.1.1. Experiments with metal oxide nanoparticles

Nanoparticles made from metal oxides, metals, nanotubes and graphite are widely investigated in base fluids such as water, ethylene glycol, acetone, etc. Some of the important experiments in macro, mini channels, heat pipes, etc. commonly used in many industrial heat transfer applications are discussed in the following sections.

Lee and Choi [46] used a nanofluid as a coolant in a microchannel heat exchanger and compared the enhanced cooling rates with those of conventional water-cooled and liquid-nitrogen cooled micro-channel. The intensification of turbulence or eddy, suppression of the boundary layer, dispersion of the suspended particles, besides the augmentation of thermal conductivity and the heat capacity of the fluid were suggested to be the possible reasons for heat transfer enhancement. Eastman et al. [47] conducted tests to assess the thermal performance of CuO–water with φ = 0.9% under turbulent flow conditions and the heat transfer coefficient was higher by 15% than that of pure water. Pak and Cho [39] presented an experimental investigation of the convective turbulent heat transfer characteristics of nanofluids (γAl_2O_3–water and TiO_2–water) with φ = 1–3%. The Nusselt number for the nanofluids increased with an increasing volume concentration and Reynolds number. Wen and Ding [48] assessed the convective heat transfer of nanofluids in the entrance region under laminar flow conditions. Aqueous based nanofluids containing γ-Al_2O_3 nanoparticles (γ = 27–56 nm; φ = 0.6–1.6%) with sodium dodecyl benzene sulfonate (SDBS) as the dispersant, were tested under a constant heat flux boundary condition. For nanofluids containing φ = 1.6%, the local heat transfer coefficient in the entrance region was found to be 41% higher than that of the base fluid at the same flow rate. It was observed that the enhancement is particularly significant in the entrance region, and decreases with axial distance. Particle migration was reasoned for the enhancement. Heris et al. [49] examined and proved the enhancement of in-tube laminar flow heat transfer of nanofluids (water–CuO and water–Al_2O_3) in a constant wall temperature boundary condition. Similarly, Esfahany et al. [50] presented an investigation of the laminar flow convective heat transfer of Al_2O_3–water under constant wall temperature with φ = 0.2–2.5% for Reynolds number varying between 700 and 2050. The Nusselt number for the nanofluid was found to be greater than that of the base fluid; and the heat transfer coefficient increased with an increase in particle concentration. The ratio of the measured heat transfer coefficients increases with the Peclet number as well as nanoparticle concentrations. Lai et al. [51] studied the flow behavior of nanofluids (Al_2O_3–DI water; γ = 20 nm) in a millimeter-sized stainless steel test tube, subjected to constant wall heat flux and a low Reynolds number (Re < 270). The maximum Nusselt number enhancement of the nanofluid of 8% at φ = 1% was recorded. Jung et al. [52] conducted convective heat transfer experiments for a nanofluid (Al_2O_3–water) in a rectangular micro-channel (50 μm × 50 μm) under laminar flow conditions. The convective heat transfer coefficient increased by more than 32% for φ = 1.8% in base fluids. The Nusselt number increased with an increasing Reynolds number in the laminar flow regime (5 < Re < 300) and a new convective heat transfer correlation for nanofluids in Microchannels was also proposed. Williams et al. [53] investigated the turbulent convective heat transfer behavior of alumina (Al_2O_3–water and ZrO_2–water). The convective heat transfer and pressure loss behavior of nanofluids under a fully developed turbulent flow, matched the correlations of a single-phase flow. Duangthongsuk and Wongwises [54] showed an enhancement of heat transfer at a lower concentration of TiO_2–water (φ = 0.2%) and claimed that the convective heat transfer coefficient also depends on the experimental measurement system and calibration. Jang and Choi [55] showed an enhancement of the convective heat transfer coefficient of nanofluids (Al_2O_3–water with φ = 0.3%) up to 8%. Duangthongsuk and Wongwises [56] reported an experimental study on the forced convective heat transfer under varied heat flux boundary conditions and pressure drop characteristics of a

nanofluid consisting of water and 0.2 vol.% TiO_2 nanoparticles of 21 nm diameter flowing in a horizontal double-tube counter flow heat exchanger under turbulent flow conditions. The results showed that the convective heat transfer coefficient of nanofluid is slightly higher than that of the base liquid by about 6–11%. The heat transfer coefficient of the nanofluid increases with an increase in the mass flow rate of the hot water and nanofluid. It was seen that the Gnielinski equation failed to predict the heat transfer coefficient of the nanofluid. Finally, it was also observed that the use of the oxide nanofluid has a little penalty in pressure drop.

4.1.2. Experiments with pure metal nanoparticles

Xuan and Li [57] experimentally studied the single phase heat transfer of the Cu–water nanofluid in tubes in the turbulent flow regime (Reynolds number between 10,000 and 25,000) with $\varphi = 0.3$–2.0% and proposed a heat transfer correlation. The convective heat transfer coefficient increased remarkably with the volume-fraction and with the flow velocity, with a negligible penalty in pumping power. Xuan and Li [58] measured the convective heat transfer of the Cu–water nanofluid in a small-hydraulic-diameter flat tube under laminar flow conditions. The Nusselt number of the nanofluid with $\varphi = 2\%$ increased by more than 39% compared with that of pure water. Zhou [59] investigated the enhancement of the single phase heat transfer of Cu–acetone particles with average particle sizes in the $\gamma = 80$–100 nm range and concentrations ranging from 0.0 to 4.0 g/l. Xuan et al. [60] investigated Cu–water (deionised) with $\gamma = 26$ nm and $\varphi = 0.5$–2%. The Nusselt number increased proportionately with the Reynolds number, and for the same Reynolds number the ratio of Nusselt number of Cu–water to water varied from 1.06 to 1.39 when the volume fraction of copper nanoparticles increased from 0.5 to 2.0%.

Faulkner et al. [61] investigated the convective heat transfer of a CNT–water nanofluid in a micro-channel, with a hydraulic diameter of 355 μm, a Reynolds number between 2 and 17 and $\varphi = 1.1$, 2.2 and 4.4%. The results showed an enhanced heat transfer coefficient of CNT–water at highest concentration. Yang et al. [62] investigated the convective heat transfer of graphite nanoparticles dispersed in liquid in laminar flow in a horizontal tube heat exchanger, and reported that at 2 wt% the heat transfer coefficient of the nanofluids increased, compared with that of the base fluid; at 2.5 wt% the heat transfer coefficient 22 and 15% was higher than that of pure fluid at 50 and 70 °C respectively. Ding et al. [63] tested multi-walled carbon nanotubes (MCNT with $\varphi = 0.1$–1.0% with 0.5 wt% in aqueous solution) in a horizontal tube, and obtained a maximum enhancement of heat transfer (350%) at a Reynolds number of 800. Particle re-arrangement, shear induced thermal conduction, reduction of thermal boundary layer due to the presence of nanoparticles and high aspect ratio of CNTs were reasoned for the enhancement. Yulong et al. [64] experimentally analyzed forced convective heat transfer using aqueous and ethylene glycol-based spherical titania, and aqueous-based titanate nanotubes, carbon nanotubes and nano-diamond nanofluids. For aqueous-based titania, carbon and titanate nanotube nanofluids, the convective heat transfer coefficient enhancement exceeded, by a large margin. The competing effects of particle migration on the thermal boundary layer thickness and the effective thermal conductivity were suggested to be responsible for the heat transfer enhancement.

4.1.3. Inferences from forced convection heat transfer experimental studies

The observed results from the prior work done on the convective heat transfer performance of nanofluids clearly shows, that the suspended particles outstandingly increase the heat transfer performance of the base-fluid; and the nanofluids have higher heat transfer coefficients than those of the base-fluids at the same Reynolds number. High aspect ratio nanoparticles such as carbon nanotubes resulted in greater enhancement in thermal conductivity and the heat transfer coefficient, compared to spherical and low aspect ratio nanoparticles. It has been shown in many references that the heat transfer behavior of nanofluids and the application of nanofluids for heat transfer enhancement, are influenced by the effective thermo-physical properties of nanofluids and many other factors such as particle size, shape and distribution; Brownian motion, particle–fluid interaction and particle migration also have an important influence on the heat transfer performance of nanofluids. However, because of the lack of agreement between the experimental results reported by various groups, most of the studies lack physical explanation for their observed results. All the convective studies have been performed with oxide particles, Future convective studies must be performed with metallic nanoparticles with different geometries and concentrations to consider heat transfer enhancement in laminar, transition and turbulence regions. Besides, the experimental data available for convective heat transfer are limited and insufficient to exactly predict the trend for heat transfer enhancement. Maiga et al. [65] reported that, with regard to the nanofluid thermal properties, the actual amount of experimental data available in the literature remains surprisingly small, and it is obvious that more works in this area will be published in the near future. Therefore, further research on the convective heat transfer of nanofluids is needed. Table 1 shows the summary of published experimental investigations of the convective heat transfer performance of various nanofluids.

4.2. Natural convection heat transfer experiments with nanofluids

Putra et al. [66] presented a study of the natural convection of nanofluids (Al_2O_3–water, CuO–water with $\varphi = 1$–4%) using a horizontal cylinder test section with one end heated and the other cooled. The time to reach the steady state was much lesser even at relatively high particle concentrations, due to the non-agglomerative and mono-dispersive nature of the nanofluids. The heat transfer coefficient was found to be higher at the hot wall than at the cold wall. The natural convective heat transfer is higher for the CuO–water than the Al_2O_3–water nanofluid. Wen and Ding [67] conducted experiments on nanofluids (TiO_2–water with $\varphi = 0$–1%) using two horizontally positioned aluminum discs separated by a 10 mm gap filled with nanofluid. The lower disc was heated at the bottom surface and the upper surface was open to the atmosphere. The temperature rose smoothly without any initial temperature oscillations as compared to micro-sized particles. The time to reach the steady state was also shorter and the heating surface temperature was found to increase with nanoparticle concentrations. The temperature difference between the walls increased with the volume fraction and reached 2.3 K for a $\varphi = 0.57\%$ compared to 1.5 K for pure liquid. Hwang et al. [68] theoretically presented the effects of the volume fraction, the size of nanofluids (Al_2O_3–water), and the average temperature of nanofluids on natural convective heat transfer characteristics in a rectangular cavity heated from the bottom. The results were validated with Touloukian et al. [69]. The results showed that as the volume fraction the of nanoparticles increased, the size of the nanoparticles decreased, the average temperature of nanofluids increased and the ratio of the heat transfer coefficient of nanofluids to that of base fluid decreased. Polidori et al. [70] investigated the natural convection heat transfer of Newtonian nanofluids in a laminar flow region with γ-Al_2O_3–water nanofluids whose Newtonian behavior was experimentally confirmed for $\varphi < 4\%$. The experimental investigations showed that the addition of nanoparticles deteriorated the heat transfer characteristics in the natural convective heat transfer region, whereas, the theoretical models predicted otherwise.

Table 1
Summary of experimental investigations in convective heat transfer of nanofluids.

Author	Base fluid	Particle material	Particle size	Volume fraction (vol.%)	Dimension	Flow regime, Re	Results and remarks
Pak and Cho. [39]	Water	$\gamma A1_2O_3$ TiO_2	13 nm 27 nm	1–3 1–3	ID: 1.066 cm Length: 480 cm S.S. tube	$Re = 10^4$–10^5 (turbulent flow)	Nu increased with increase in φ and Re
Eastman et al. [47]	Water	CuO	<100 nm	0.9	–	(Turbulent flow conditions)	HTC increased by >15% compared with pure water.
Wen and Ding [48]	Water	$\gamma A1_2O_3$	26–56 nm	0.6, 1, 1.6	ID: 4.5 mm Length: 970 mm Copper tube	Re = 500–2100 (laminar flow)	For φ = 1.6%, the HTC is 41% higher than the base fluid
Heris et al. [49]	Water	$A1_2O_3$ CuO	20 nm 50–60 nm	0.2–3.0 0.2–3.0	ID: 6 mm Copper tube	Re = 650–2050 (laminar flow)	HTC was high when φ increases for $A1_2O_3$, Nu is high
Esfahany etal. [50]	Water	γAl_2O_3	20 nm	0.2, 0.5, 1, 1.5, 2, 2.5	ID: 6 mm Length: 1 m Copper tube	Re = 700–2050 (laminar flow)	HTC ratio increases with φ and 22% increase with Pe
Lai et al. [51]	Water	$A1_2O_3$	20 nm	0–1%	ID: 1 mm S.S. tube	Re < 270	Nu enhancement of 8% for φ = 1%. $A1_2O_3$ nanofluid at Re = 270
Jung et al. [52]	Water	$A1_2O_3$	l0 nm	0.5–1.8%	Rectangular microchannel (50 μm × 50 μm)	5 < Re < 300	Conv. HTC increased by 32% for φ = 1.8%. Nu increases with Re
Williams et al. [53]	Water	ZrO_2	46 nm 60 nm	0.9–3.6 0.2–0.9	OD: 1.27 cm Thick. = 1.65 mm S.S. tube	9000 < Re < 63,000 (turbulent flow)	Considerable heat transfer enhancement is observed
Xuan and Li [57]	Water	Cu	<100 nm	0.3, 0.5, 0.8, 1, 1.2, 1.5, 2	ID: 10 mm Length: 800 mm Brass tube	Re = 10,000–25,000 (turbulent flow)	Conv. HTC increases with increase in φ and flow velocity
Xuan and Li [58]	Water	Cu	26 nm	0.5, 1, 1.5, 2	Hydraulic diameter = 1.29 mm	Re = 200–2000 (Laminar flow)	Nu of nanofluid with φ = 2% is 39% more than pure water
Zhou [59]	Acetone	Cu	80–100 nm	0.0–4.0 g/1	ID: 16 mm Length: 200 mm Copper tube	–	Conv. HTC increases with addition of Cu nanoparticles
Xuan and Li [60]	Water	Cu	26 nm	0.5, 1, 1.5, 2	ID: 10 mm Length: 800 mm Brass tube	Re = 1000–4000 (laminar and turbulent flow)	Nu ratio varied from 1.06 to 1.39 when φ increases from 0.5 to 2%
Faulkner et al. [61]	Water	CNT	<100 nm	1.1, 2.2, 4.4	Hydraulic diameter = 355 μm	Re = 2–17 (laminar flow)	HTC was found to be high at higher concentrations
Yang et al. [62]	Oil	Graphite	20–40 nm	0.7–1.0	ID: 4.57 mm Smooth tube	Re = 5 < 110 (laminar flow)	HTC was 22% higher at 50 °C and 15% higher at 70 °C for 2.5 wt%.
Ding et al. [63]	Water	MWCNT	100 nm	0.1–1.0 wt%	ID: 4.5 mm Length: 970 mm Copper tube	Re = 800–1200 (laminar flow)	350% enhancement was found for 0.5 wt% at Re = 800
Yulong et al. [64]	Ethylene glycol	TiO_2 CNT	–	–	–	–	Conv. HTC increases with φ and Re

4.2.1. Inferences from natural convection heat transfer experimental studies

Based on the limited experimental studies and contradictory results found in natural convective heat transfer of nanofluids, a firm conclusion cannot be drawn. However, the heat transfer enhancement of nanofluids in natural convective conditions needs further experimental and theoretical investigations, to exactly predict the behavior of nanofluids. Many factors such as particle size, shape and distribution, and the particle–fluid interactions should also be considered as significant parameters in the heat transfer performance of nanofluids in natural convective heat transfer.

4.3. Boiling heat transfer experiments with nanofluids

Boiling is an effective method of heat removal used in a variety of phase change heat exchanger like boilers, evaporators, etc. When the boiling occurs under a quiescent fluid condition, it is referred to as nucleate boiling and under a forced-flow condition; it is referred as forced convective boiling or convective vaporization. The former depends of the microstructure and the active nucleation cites (pits and crevices, Collier and Thome, [71] of the heat surface and heat flux. Whereas, the latter depend on tube dimension and mass flow rate. The nucleate boiling and its onset depends wall superheat, surface characteristics, presence of dissolved gas, the number of nucleation sites and frequency, and the bubble growth rates. Critical heat flux in pool boiling is peak heat flux under which a boiling surface can sustain nucleate boiling. Reaching the CHF causes a transition from nucleate boiling regime to film boiling regime, which undesirable and causes temperature of the heated surface to reach the melting point. Therefore, an enhanced CHF provides increase in the safety margin of the thermal system and to design compact and efficient cooling systems for electronic devices, nuclear and chemical reactors, air conditioning, etc. Further, the invention of nanofluid has paved way for investigation on improvising the heat transfer in a phase change process. The boiling heat transfer characteristics are broadly investigated with respect to enhancement, critical heat flux and hysteresis. For instance, Chang and You [72] applied micro-porous coat to increase the number of active sites and enhanced the nucleate boiling heat transfer in a plain copper/FC-72 tube by 330% and increased CHF by 100%.

Pool boiling heat transfer using nanofluids has been a subject of many investigations and incoherent results have been reported in literature regarding the same. In the past, experiments were conducted in nucleate pool boiling with varying parameters such as particle size, concentration, surface roughness, etc. and the results showing heat transfer enhancement, deterioration and negligible effect were reported [73,74]. It has been found that deterioration in heat transfer coefficient is mainly observed at higher particle concentrations (4–16% by weight) and enhance-

ments mainly at lower particle concentrations (0.32–1.25% by weight). Moreover, the relative size of the particle with respect to the surface roughness of the heating surface seems to play an important role in understanding the boiling behavior.

Yang and Maa [75] performed pool boiling experiments with Al_2O_3–water (γ = 50, 300 nm, 1 μm) and found that pool boiling performance is greatly improved for φ = 0.1–0.5% in nucleate pool boiling regime. However, micron sized particle suspensions are known to cause problems of erosion and clogging. Das et al. [76] who investigated nucleate pool boiling characteristics of Al_2O_3–water (γ = 20–50 nm; φ = 4–16%) using cartridge heater and found that the nanoparticles sediment on the heater at higher concentration, and deteriorating the boiling performance.

Das et al. [77] showed that pool boiling of nanofluids on narrow horizontal tubes (4 and 6.5 mm diameter. It was found that at this range of narrow tubes the deterioration rate boiling performance with nanofluids is less compared to large industrial tubes, which make it less inclined to local overheating in convective applications because of the relatively small size of the tube.

Bang and Chang [78,79] studied pool-boiling characteristics of Al_2O_3–water nanofluids with (φ = 4–16%) concentration at high heat flux condition. It was observed that the boiling characteristics of nanofluids deteriorated with high concentration similar to Das et al. [76] but the rate of heat transfer was different due to the difference in geometrical features of the heaters in the two studies.

Wen and Ding [80] studied pool boiling heat transfer using spherical Al_2O_3–water (γ = 10–50 nm). The results were quite different from the earlier studies. It was observed that the pure water results matched with the Rohsenow correlation and the heat transfer with nanofluids showed an enhancement in heat flux at the same wall super heat and this enhancement increased with particle volume fraction. It was also observed 40% increase in heat transfer coefficient between nanofluids and pure water. Also, the enhancement was with just 1.25 wt% of particles, which is about 0.3% by volume. Hence, the study concluded saying that this increase is much more than the measured value of thermal conductivity enhancement and hence the boiling enhancement cannot be explained by conductivity enhancement alone.

You et al. [81] performed experiments with alumina-water nanofluids of very small solid particle concentrations (0.0001–0.005% by weight) on a 10 mm square heater in sub-atmospheric conditions and found no significant change in nucleate pool boiling. Vasallo et al. [82] conducted experiments with SiO_2–water nanofluids (γ = 15–50 nm; φ = 2%) on a NiCr wire heater and found no significant change in the boiling performance at low and medium heat fluxes. But at heat fluxes near to CHF of water, it was observed that there is boiling deterioration for the 50 nm nanofluid. Similar increase in CHF is observed in many references (You et al. [81]; Bang and Chang [78,79]; Kim et al. [83,84]; Milanova et al. [85] Jackson et al. [86]).

Witharana [87] carried out experiments using Au–water nanofluids of very low solid particle concentrations (0.001% by weight) on plate heater. An enhancement of 11–21% in heat transfer coefficient was found. With increasing particle concentration the percentage enhancement in heat transfer coefficient also increased.

Nguyen et al. [88] showed enhancement of boiling heat transfer using Al_2O_3–nanofluids (γ = 47 nm) under atmospheric pressure, at various particle concentrations. The critical heat flux had considerably decreased with the augmentation of particle concentrations. For distilled water, the value of CHF was 1192 kW/m^2 which was quite close to that predicted by using the modified Zuber formula. The corresponding values for nanofluids of 0.5, 1 and 2% concentration were 744, 690, and 422 kW/m^2. Thus, the decrease of maximum heat flux was nearly 65% for 2% nanofluid as compared to distilled water.

Jung et al. [89] measured nucleate boiling heat transfer data of eight halocarbon refrigerants and made a specific correlation for halocarbon refrigerants based on the observed data. Test results showed that nucleate boiling HTCs of these halocarbon refrigerants were increased with the addition of CNTs. Especially, heat transfer was enhanced up to 36.6% at low heat flux. As the heat flux increased, the heat transfer enhancement with CNTs decreased. The developed correlation agreed best with these halocarbon refrigerants.

Tu et al. [90] carried out pool boiling experiments using Al_2O_3–water nanofluids on a 26 mm × 40 mm rectangular surface at the atmospheric pressure and an enhancement of heat transfer of 64% was recorded. Zhou [91] investigated experimentally the heat transfer characteristics of Cu–acetone based nanofluids with and without acoustic cavitation and showed that the copper nanoparticles and acoustic cavitation had significant influence on heat transfer in the fluid. The addition of nanoparticles did not affect the dependence of the heat transfer on acoustic cavitation and fluid sub-cooling. In an acoustic field, the boiling heat transfer of nanofluids was enhanced and the boiling hysteresis disappeared.

Park and Jung [92] conducted a study on nucleate boiling heat transfer coefficients of R123 and R134a, on a 152.0 mm long horizontal plain tube of 19.0 mm outside diameter with and without 1.0 vol.% of carbon nanotubes. The addition of CNTs resulted in heat transfer enhancement at low heat flux was up to 36.6%. Further, unlike conventional nanoparticles, no fouling was observed on the surface with CNTs.

Park and Jung [93] investigated pool boiling of CNT-R22 and CNT–water (φ = 1.0%) of CNTs and showed that CNTs increase boiling heat transfer coefficients of these fluids up to 28.7%. With increasing heat flux, however, the enhancement was suppressed due to vigorous bubble generation. Penetration into the thermal boundary layer by CNTs to generate more bubbles at the surface seemed to be the key element in the improvement of nucleate boiling heat transfer associated with the use of CNTs.

4.3.1. *Inferences from boiling heat transfer experimental studies*

The observations based on the studies of boiling heat transfer of nanofluids shows that the boiling performance is inversely proportional to nanoparticle concentration. However, Wen and Ding [80] have reported a trend contradictory to this. As far as the effect of nanoparticles on the boiling heat transfer performance is concerned, conflicting results were observed from these limited data. The inconsistencies indicate that the understanding of the thermal behavior of nanofluids related to the boiling heat transfer is still poor. The pool boiling is affected by the surface properties such as surface roughness, surface wettability, and surface contamination. In the reviewed studies, only the surface roughness is the most often considered parameter. Also no study on boiling of metallic nanofluids or flow boiling of nanofluids is available. Further, detailed investigations are necessary to understand the phenomena of boiling of nanofluids and the influence on the above factors.

5. Mathematical modeling

5.1. *Theoretical investigations for convective heat transfer of nanofluids*

The mixture of nanoparticles and base fluid is a multiphase problem and thus, could be approximated as either a homogeneous fluid or heterogeneous mixture. In the case of a homogeneous approach, because of the size of the nanoparticles, it has been suggested that these particles may easily be fluidized and consequently, can be considered to behave more like a single phase fluid. Further, by assuming a negligible motion slip between

the particles and the thermal equilibrium conditions, the nanofluid could be considered as a conventional single-phase fluid with averaged physical properties of individual phases [39,94]. However, because the effective properties of the nanofluids are not known precisely, the numerical predictions of this approach are not in good agreement with the experimental results. Choi et al. [95] first adopted a homogeneous model and used the conventional heat transport equations for pure fluids, such as the Dittus–Boelter correlation, to the nanofluids. In the case of a heterogeneous approach (two-phase), factors such as gravity, friction between the phases, Brownian diffusion, sedimentation, and dispersion are included in the flow model. The two-phase approach provides the possibility of understanding the functions of both the fluid phase and the solid particles in the heat transfer process, and provides a field description of both the phases.

Xuan and Roetzel [96] proposed a two-phase thermal dispersion model and assumed that the convective heat transfer enhancement in nanofluids comes from two factors, (i) higher thermal conductivity, and (ii) the thermal dispersion of the nanoparticles. In this approach, the effect of the nanoparticle/base fluid relative velocity and temperature are treated as a perturbation of the energy equation. The thermal dispersion coefficient was introduced to describe the heat transfer enhancement. Khanafer et al. [97] investigated the heat transfer enhancement in a two-dimensional enclosure utilizing the nanofluid. The effective thermal conductivity was taken as the sum of the mixture thermal conductivity evaluated from the conventional theory and a dispersion thermal conductivity. It was observed that in any of the numerical studies in convection, the effect of temperature on thermal conductivity was not considered. However, the effect of temperature on the thermal conductivity of nanofluids was proved significant from studies made by Das et al. [98].

Buongiorno [99] developed an alternative model that eliminates the shortcomings of the homogeneous and dispersion models. The homogeneous flow models are in conflict with the experimental observation and the pure-fluid correlations underpredict the heat transfer coefficient. In this model, a detailed analysis of convective transport with seven slip conditions between particles and fluid were considered, for explaining the enhancement of heat transfer with nanofluids. In these mechanisms the Brownian diffusion and thermophoresis were the two most important nanoparticles/base fluid slip mechanisms. Convective heat transfer enhancement was obtained with a decrease in viscosity and consequent thinning of the laminar sub-layer. It was observed that the radial distribution of the particle concentration (more concentration at the core than the walls) brought about by thermophoresis make the temperature profile flatten, thus giving a higher heat transfer coefficient and finally, a new correlation was developed to predict the enhanced heat transfer coefficient of nanofluids.

Behzadmehr et al. [100] applied a two-phase mixture model to study the heat transfer of nanofluids (Cu–water; $\varphi = 1\%$) for forced turbulent convection in a uniformly heated tube. The Nusselt number increased by more than 15%, was proportional to the Reynolds number and resulted in a more uniform velocity profile. The frictional coefficient decreased as the Reynolds number increased when compared with that of pure fluid. Finally, increasing particle concentration caused the Nusselt number to increase and thus, the convective heat transfer coefficient.

Maïga et al. [101] modeled the forced convection flow of a nanofluid (γAl_2O_3 with water and ethylene glycol) in a straight tube of circular cross-section. A single-phase flow was assumed to derive the governing equations to calculate the heat transfer enhancement by the nanofluids in the laminar flow as well as the turbulent flow regime, with nanofluid concentrations ranging from 0 to 10%. For laminar flow, the results indicated an increase in the heat transfer rate, particularly at the walls, with the augmentation of φ (for $\varphi = 10\%$, the product ρc_p and thermal conductivity, k increased by $\sim$18 and $\sim$33%, respectively). The heat transfer coefficient ratio h_r also increases with particle loading and particularly at the tube end (by nearly 60%). Further, averaged heat transfer enhancement was clearly more pronounced for the γAl_2O_3–ethylene glycol than for the γAl_2O_3–water nanofluid for $\varphi > 3\%$ (identical otherwise). The wall shear stress was found to increase considerably with the particle volume fraction and along the tube length. For the turbulent flow regime, the heat transfer coefficient increased steeply for a very short distance from the inlet section. The properties h_r and τ_r varied in a similar manner as in the previous case.

Roy et al. [102] modeled the hydrodynamic and thermal fields of a γAl_2O_3–water nanofluid ($\varphi = 1$–10%) in a radial laminar flow cooling system. Considerable increases in the wall shear stress were predicted on account of the increase in the fluid viscosity (a maximum of 2.5-fold increase for $\varphi = 5\%$). Overall, the study indicated that considerable heat transfer enhancement was possible and a maximum increase of twice the value of the base fluid in the case of $\varphi = 10\%$. Ding and Wen [103] modeled the effects of particle migration in pressure driven laminar flows of nanofluids and predicted the particle concentration and velocity field of nanofluids; in the transverse plane of the pipe by taking into account the effects of the shear induced and viscosity gradient induced particle vibrations as well as self-diffusion due to the Brownian motion. Two approaches were used, one was based on mass conservation law for the dispersed phase and the other on the momentum balance of the particle phase. The results indicate that the Peclet number increased rapidly with increasing particle size and Reynolds number. The Brownian motion had a significant effect on the particle migration of nanofluids and became important at Peclet numbers less than 10. At the limit of zero Peclet number, the particle concentration is uniform. Further, the smaller the particle size, the more uniform the distribution of particles in the transverse plane. The existence of an optimal particle size at which the thermal conductivity was enhanced with little penalty due to pressure drop is suggested.

Palm et al. [104] numerically investigated the enhanced heat transfer capabilities of Al_2O_3–water ($\gamma = 38$ nm; $\varphi = 1$–4%) in a radial laminar flow cooling system and used temperature-dependant nanofluid properties. The experimental results obtained using the single-phase approach indicated that property fluctuations are noticed near the injection inlet. Lower viscosities at higher temperature, decrease in wall shear stress for increase in wall heat flux and greater wall heat transfer rates were shown when compared to predictions using constant properties.

Kim et al. [105] theoretically investigated the Thermo-diffusion (Soret effect) and diffusion thermo (Dufour effect) effects on convective instabilities in binary nanofluids (the base-fluid is a binary mixture). Data from silver and copper nanofluids studies were used in this investigation, which showed that the particles caused a unique convective motion in binary nanofluids. The heat transfer enhancement by the Soret effect in binary nanofluids is more significant than that in mono-nanofluids. Further, the heat transfer coefficient of silver nanofluids was higher than that of copper, owing to the higher thermal conductivity of silver. Studies predicted that the Soret and Dufour diffusions make the nanofluids unstable and this was more profound for denser nanofluids. Further, the convective motion in nanofluids sets easily in both the effects as the concentration increased.

Mansour et al. [106] investigated the effect of the Hamilton–Crosser model and the Modified Maxwell model, to predict nanofluid (γAl_2O_3–water; $\varphi = 1$–10%) physical properties, on their thermal and hydrodynamic performance for both fully developed laminar and turbulent forced convection in a tube with uniform

Table 2
Existing convective heat transfer correlations for nanofluids.

Reference	Correlation
Pak and Cho [39]	$Nu = 0.021\,Re^{0.8}Pr^{0.5}$
Xuan and Li [57]	$Nu = 0.4328(1.0 + 11.285\varphi^{0.754}Pe_p^{0.218})Re_{nf}^{0.333}Pr_{nf}^{0.4}$ for laminar flow $Nu = 0.0059(1.0 + 7.6286\varphi^{0.6886}Pe_p^{0.001})Re_{nf}^{0.9238}$ for turbulent flow
Maiga et al. [65]	$Nu = 0.86\,Re^{0.55}Pr^{0.5}$ for constant wall heat flux $Nu = 0.86\,Re^{0.35}Pr^{0.36}$ for constant temperature
Buongiorno [40,99]	$Nu_b = \frac{(f/8)(Re-1000)Pr}{1+\delta_\nu^+\sqrt{(f/8)(Pr_\nu^{2/3}-1)}}$
Maïga et al. [118]	$Nu = 0.085\,Re^{0.71}Pr^{0.35}$ for fully developed (fd) turbulent flow

heat flux at the wall. Two models gave substantially different results for thermal conductivity, specific heat and viscosity, and the differences were more profound for higher particle loading. The expressions failed to account for the size disparity between the nanoparticles. The two models revealed in very different predictions and it was not possible to ascertain which was accurate. The study illustrated that the operational conditions or the design parameters varied significantly with the thermo-physical properties of the nanofluid.

Prakash and Giannelis [107] calculated the thermal conductivity of nanofluids (Al_2O_3–water and ethylene glycol) using temperature and concentration dependent viscosity relations. The temperature profile was obtained using the Gaussian fit to the available experimental data. The micro-convection of the alumina nanoparticle ($\gamma < 100$ nm) was included through the Reynolds and Prandtl numbers. The model was further improved by explicitly incorporating the thermal conductivity of the nano-layer surrounding the nanoparticles. The results indicated that the thermal conductivity ratio depends on both the temperature variation in viscosity and the Brownian motion. However, the thermal conductivity was more sensitive to the Reynolds number than to the Prandtl number. As a result, there is net enhancement in thermal conductivity as the temperature was increased. Studies showed that a cylindrical-shaped particle leads to much higher thermal transport than a spherical-shaped particle.

Li and Peterson [108] simulated the mixing effect of the base fluid with nanoparticles caused by the Brownian motion; they modeled and compared it with the existing experimental data available in the literature. The mixing effect predicted a significant influence on the effective thermal conductivity of nanofluids.

5.2. Inferences from theoretical studies with nanofluids

The observations based on the reviewed literature for theoretical studies in the convective heat transfer of nanofluids clearly shows, that the models developed by the various researchers have been satisfactory only under very stringent conditions. However, a generalized theoretical model should be developed by considering all the factors such as inertia, thermophoresis, Brownion motion, and gravity which influences the heat transfer characteristics and the behavior of nanofluids under convective heat transfer conditions. The correlations based on the experimental data for finding the Nusselt number of nanofluids

Table 3
Summary of theoretical investigations in convective heat transfer of nanofluids.

Author	Theoretical investigations	Approach	Results and remarks
Xuan and Li [28]	Theoretical heat transfer characteristics of transformer oil–Cu and water–Cu nanofluids	Single phase fluid approach	The heat transfer coefficient improved dramatically with decrease in particle size and not only due to thermal conductivity increase
Xuan and Roetzel [96]	Heat transfer of nanofluids	1. Single phase fluid approach 2. Dispersion model approach	Suspended particles increase the thermal conductivity. Chaotic movement of ultrafine particles and the thermal dispersion accelerates the energy exchange process
Buongiorno [40,99]	Convective transport in nanofluids	Two-component non-homogeneous equilibrium model	Brownian diffusion and thermophoresis are the two most important nanoparticles/basefluid slip mechanisms
Behzadmehr et al. [100]	Turbulent forced convection flow in a uniformly heated tube	Two phase mixture model	HTC increases with φ and Re. Higher Re resulted more uniform velocity profile
Maiga et al. [101]	Forced convection flow of nanofluid (water/Al_2O_3 and ethylene glycol/Al_2O_3) in a circular tube	Single phase fluid approach	60% enhancement in HTC was found and turbulent flow enhancement increases with Re
Roy et al. [102]	Hydrodynamic and thermal flow fields of water/Al_2O_3 nanofluid in a radial laminar flow cooling system		Two fold increase in heat transfer coefficient was observed along with wall shear stress and particle concentration
Ding and Wen [103]	Effects of particle migration in laminar flows of nanofluids	Mass conservation laws and momentum balance	Shear induced migration, viscosity gradient migration and self-diffusion. Highly non-uniform thermal conductivity profile obtained
Palm et al. [104]	Heat transfer capabilities and temperature-dependant properties of nanofluids in radial flow cooling systems	Single phase fluid approach	Temperature dependent properties lead to greater heat transfer performance with the decrease in wall shear stresses
Kim et al. [105]	Thermo diffusion (Soret effect), diffusion thermo (Dufour effect) effects in binary nanofluids	One fluid model	As the Soret and Dufour effects and φ increases the convective motion sets in easily
Mansour et al. [106]	Thermal and hydrodynamic performance for both laminar and turbulent forced convection in a tube with uniform heat flux at the wall	Single phase fluid approach	Both the models predicted increased HTC with particle concentration
Prakash and Giannelis [107]	Thermal conductivity of Al_2O_3 nanofluids using temperature and concentration dependent viscosity		Dependence of the thermal conductivity on the size of the nanoparticle, temperature viscosity and particle concentration
Maïga et al. [118]	Forced convection flow of nanofluid (water/Al_2O_3 and ethylene glycol/Al_2O_3) in a circular tube and radial channel between a pair of parallel coaxial discs	Single phase fluid approach	HTC increased by 63 and 45%. Increased heat transfer and dynamic viscosity resulted in increased wall shear stress with partial loading

from laminar to turbulent regions reported in the published literature are presented in Tables 2 and 3 gives a summary of the various theoretical investigations in the convective heat transfer of nanofluids.

6. Applications

6.1. Micro-channels

The micro-channel heat sink (MCHS) has the capability to dissipate large amounts of heat from a small area with a very high heat transfer coefficient and less fluid inventory. Using nanofluids as a coolant in the MCHS could further improve its performance. Chein and Huang [109] analyzed the performance of the MCHS (silicon channel of 100 μm × 300 μm dimension) using a Cu–water nanofluid with φ = 0.3–2%. The Nusselt number increased significantly with an increase in Re and φ. The maximum reduction in thermal resistance as compared to pure water was found to be 15% at φ = 2% and power = 3 W. The additional reduction in R_{th} is clearly due to thermal dispersion. With regard to pressure drop, no significant differences existed between the nanofluid and water flows.

Jang and Choi [110] numerically investigated the cooling performance of a silicon micro-channel heat sink under forced convective flow with nanofluid (Cu–water; γ = 6 nm and diamond–water; γ = 2 nm particle size) for φ = 1%. The nanofluids reduced the thermal resistance of the heat sink and enhanced the cooling performance by 10 and 4%, respectively. Further, the potential of employing a micro-channel heat sink with nanofluid to remove ultra high heat flux as much as 1350 W/cm^2 when the difference between the junction temperature and inlet coolant temperature is 80°C, was demonstrated.

Chein and Chuang [111] used a nanofluid (CuO–water, φ = 0.204, 0.256, 0.294 and 0.4%) with 80 nm long and 20 nm wide particles. The energy absorbed by the nanofluid was greater than that absorbed by water and was found to increase with the increase in particle volume fraction. A large temperature difference between the MCHS inlet and outlet was obtained at a low flow rate. Thermal resistance was found to reduce with an increase in the flow rate. Although the nanofluids had higher viscosity, only a marginal increase (around 5%) in the pressure drop across the MCHS was reported.

Koo and Kleinstreuer [112] simulated and analyzed the conduction-convection heat transfer of nanofluid (CuO–water and ethylene glycol, γ = 20 nm) in a micro-channel (300 μm × 50 μm). The new model incorporated static and Brownian heat transfer, and hence the thermal conductivity and dynamic viscosity were suggested to be $k_{eff} = k_{static} + k_{Brownian}$ and $\mu_{eff} = \mu_{static} + \mu_{Brownian}$. The Nusselt number for ethylene glycol based nanofluids was always higher than for water based ones, due to stronger thermal flow development effects. Moreover, the viscous dissipation effect was found to affect only ethylene glycol based nanofluids and was more important for flows through very narrow channels.

Nguyen et al. [113] investigated the heat transfer enhancement of Al_2O_3–water (γ = 36 and 47 nm) in the cooling systems of microprocessors and electronic components. The inclusion of nanoparticles in distilled water produced a considerable enhancement convective heat transfer coefficient (around 40% for φ = 6.8%) and a clear decrease of the heated component temperature was recorded. In addition, smaller nanoparticles were found to produce greater enhancement in the heat transfer coefficient.

6.2. Heat pipes

Chien et al. [114] studied heat transfer in a disk-shaped miniature heat pipe (DMHP) using nanofluid (Au–DI water; φ = 18, 37 and 55%; γ = 17 nm). The average decrease of 40% in thermal resistance was achieved as compared to that of pure DI water. Tsai et al. [115] studied a heat pipe using the Au–DI water nanofluid (γ = 8–43.7 nm) and a 37% lower thermal resistance was achieved (at γ = 21.3 nm) when compared to that of DI–water. Smaller nanoparticles have greater reduction in thermal resistance in conditions of equal aggregation. A major reduction in thermal resistance is from the evaporator section to the adiabatic section (a maximum of 56% reduction), which is attributed to the bombardment of vapor bubbles by the nanoparticles.

Kang et al. [116] investigated heat transfer in a grooved heat pipe using Ag–water and Ag–DI water (γ = 10–35 nm) with particle concentrations ranging from 1 to 100 mg/l. The results indicated that after adding a small amount of silver nanoparticles in pure water, the heat pipe wall temperature became lower than that of pipes filled only with pure water. As more nanoparticles became dispersed in the working fluid, the heat pipe wall temperature increase became smaller. The maximum reduction in thermal resistance of a heat pipe containing γ = 10 nm was 52% lower, while that containing γ = 35 nm was 81% lower than that of DI–water. The enhancement of heat pipe performance was attributed to the increase in effective liquid conductance that flattens the temperature of the fluid.

Ma et al. [117] studied the nanofluid (diamond–water; φ = 1%) behavior in an oscillating heat pipe (OHP) and thus developed an ultrahigh performance cooling device, called the nanofluid oscillating heat pipe in which when the input power was increased to the highest value, the temperature difference between the evaporator and the condenser for the nanofluid OHP was less than that for the OHP with only pure water.

7. Outlook and future challenges

Many interesting properties of nanofluids have been reported in the review. In the previous studies, thermal conductivity has received the maximum attention, but many researchers have recently initiated studies on other heat transfer properties. The use of nanofluids in a wide variety of applications appears promising. But the development of the field is hindered by (i) lack of agreement of results obtained by different researchers; (ii) poor characterization of suspensions; (iii) lack of theoretical understanding of the mechanisms responsible for changes in properties. Therefore, this article concludes by outlining several important issues that should receive greater attention in the near future. Experimental studies in the convective heat transfer of nanofluids are needed. Many issues, such as thermal conductivity, the Brownian motion of particles, particle migration, and thermophysical property change with temperature, must be carefully considered with convective heat transfer in nanofluids. Though, all the convective studies have been performed with oxide particles in high concentrations, (for example Pak and Cho [39] used 10 vol.% of Al2O3 which increased the viscosity and pumping power of the fluid), it is interesting to know the energy transport in low-concentration (<1 vol.%) nanofluids with metallic particles, since the thermal conductivity of pure metallic nanoparticles is more than 100 times higher than that of the oxide nanoparticles. Future convective studies must be performed with metallic nanoparticles with different geometries and concentrations to consider heat transfer enhancement in laminar, transition and turbulence regions. The use of nanofluids in heat pipes has shown enhancement in performance and considerable reduction in thermal resistance. However, recent studies indicate particle aggregation and deposition in micro-channel heat sinks. Further study is required in these areas to identify the reasons for and the effects of particle deposition. Finally, there appears to be hardly any research in the use of nanofluids as refrigerants. Nanoparticle-refrigerant dispersions in two-phase heat transfer applications can be studied

to explore the possibility of improving the heat transfer characteristics of evaporators and condensers used in refrigeration and air-conditioning appliances. Applied research in nanofluids which will define their future in the field of heat transfer is expected to grow at a faster pace in the near future.

8. Conclusion

The present review is a comprehensive outlook on the research progress made in the convective heat transfer characteristics of nanofluids. The salient feature that can be drawn from the reviewed literature is that nanofluids are a new class of heat transfer fluids and show greater promise for use in cooling and related technologies. From the observed results it is clearly seen, that nanofluids have greater potential for heat transfer enhancement and are highly suited to application in practical heat transfer processes. This offers an opportunity for engineers to develop highly compact and effective heat transfer equipment. Several published articles show that the heat transfer coefficient of nanofluids is much higher than that of the common-base fluid and gives little or no penalty in pressure drop. The main reason for the heat transfer enhancement of nanofluids is that the suspended nanoparticles increase the thermal conductivity of the fluids, and the chaotic movement of ultrafine particles increases fluctuation and turbulence of the fluids, which accelerates the energy exchange process. Convective heat transfer is enhanced by increasing the particle concentration and the Reynolds number. Besides, the experimental data available for convective heat transfer in laminar, transition and turbulence regions are limited and insufficient to exactly predict the trend for heat transfer enhancement. Furthermore, only very few correlations are available to exactly predict the heat transfer performance of nanofluids, and correlations which include the effect of volume fraction, particle shape and particle size are nil to-date. Therefore, further research on convective heat transfer of nanofluids, and more theoretical and experimental research works are needed in order to clearly understand and accurately predict their hydrodynamic and thermal characteristics. The trends reported in literature on nucleate boiling of nanofluids are conflicting and the results are contradicting. The authors have tried to arrive at a common reasoning for the seemingly conflicting results. Also no study on boiling of metallic nanofluids or flow boiling of nanofluids is available. Further work is required to determine the effect of surface wettability on pool boiling of nanofluids in the nucleate boiling regime especially for the low concentration metallic nanoparticles.

Generally, many researchers indicated that nanofluids behave like pure fluids because the suspended particles are ultrafine. However, at present, no formulated advanced theory exists to explain the behavior of nanofluids by considering them as multi-component materials. Greater enhancement was observed when nanofluids were used in heat pipes and in micro-channel heat sinks, as well as other applications. Further, theoretical and experimental research investigations are needed to comprehensively understand the heat transfer mechanism in nanofluids for evolving new energy efficient heat transfer fluids specific to applications.

Acknowledgements

The authors would like to thank Prof. Jacopo Buongiorno, Ph.D., Massachusetts Institute of Technology, Cambridge, MA, for rendering a helpful review and constructive suggestions during the preparation of the above research article.

References

[1] Kyoto Protocol to the United Nations framework convention on climate change; 1992.
[2] Yang J, Chan K-t, Wu X, Energy savings with energy-efficient HVAC systems in commercial buildings of Hong Kong, ICEBO2006, Shenzhen, China, (7):5–2.
[3] Thermal Management, Technical report, Alcatel-Lucent Technologies, Ireland.
[4] Das SK, Choi SUS, Yu W, Pradeep T. Nanofluids—science and technology. Wiley-Interscience; 2008.
[5] Hwang YJ, Ahn YC, Shin HS, Lee CG, Kim GT, Park HS, Lee JK. Investigation on characteristics of thermal conductivity enhancement of nanofluids. Current Applied Physics 2006;6:1068–71.
[6] Eastman JA, Phillpot SR, Choi SUS, Keblinski P. Thermal transport in nanofluids. AR Reviews. In Advance. Annual Review of Materials Research 2004;34:219–46.
[7] Keblinski P, Eastman JA, Cahill DG. Nanofluids for thermal transport. Review Feature Materials Today June, 2005.
[8] Daungthongsuk W, Wongwises S. A critical review of convective heat transfer of nanofluids. Renewable Sustainable Energy Reviews 2007;11(5):797–817.
[9] Wang XQ, Mujumdar AS. Heat transfer characteristics of nanofluids: a review. International Journal of Thermal Science 2007;46(1):1–19.
[10] Yu W, France DM, Choi SUS, Routbort JL. Review and assessment of nanofluid technology for transportation and other applications. Argonne National Laboratory; 2007. p. 1–78.
[11] Maxwell JC. Treatise on electricity and magnetism. Oxford: Clarendon Press; 1873.
[12] Choi SUS. Enhancing thermal conductivity of fluids with nanoparticles, in Developments and Applications of Non-Newtonian Flows. ASME FED 231/MD 1995;66:99–103.
[13] Dreizin EL. Metal-based reactive nanomaterials. Progress in Energy and Combustion Science 2009;35(2):141–67.
[14] Joseph Lik Hang Chau, Chih Chun Kao. Microwave plasma synthesis of TiN and ZrN nanopowders. Materials Letters 2007;61(7):1583–7.
[15] Hayashi C, Oda M. Research and applications of nano-particles in Japan. Journal of Aero solid Science 1998;29:757–60.
[16] Granqvist CG, Buhrman RA. Ultrafine metal particles. Journal of Applied Physics 1976;47:2200.
[17] Gleiter H. Nanocrystalline materials, Program. Material Science 1989;33:223–315.
[18] Neikov OD. Nanopowders, handbook of non-ferrous metal powders; 2009. p. 80–101.
[19] Fissan HJ, Schoonman J. Vapor-phase synthesis and processing of nanoparticle materials (nano): a European Science Foundation (ESF) program. Journal of Aero solid Science 1998;29:755–7.
[20] Akoh H, Tsukasaki Y, Yatsuya S, Tasaki A. Magnetic properties of ferromagnetic ultrafine particles prepared by a vacuum evaporation on running oil substrate. Journal of Crystal Growth 1978;4:495–500.
[21] Biercuk BJ, Llaguno MC, Radosavljevic M, Hyun JK, Johnson AT. Carbon nanotube composites for thermal management. Applied Physics Letters 2002;80:2767–72.
[22] Ju S, Li ZY. Theory of thermal conductance in carbon nanotube composites. Applied Physics Letters 2006;353:194–7.
[23] Yao N, Wang ZL, editors. Handbook of microscopy for nanotechnology. Boston: Kluwer Academic Publishers; 2005.
[24] Daniel MC, Astruc D. Gold nanoparticles: assembly, supramolecular chemistry, quantum-size-related properties, and applications toward biology, catalysis, and nanotechnology. Chemical Reviews 2004;104:293–346.
[25] Trindade T, O'Brien P, Pickett NL. Nanocrystalline semiconductors: synthesis, properties, and perspectives. Chemical Materials 2001;13:3843–58.
[26] Rajamathi M, Seshadri R. Oxide and chalcogenide nanoparticles from hydrothermal/solvothermal reactions. Current Opinion Solid State Material Science 2002;6:337–45.
[27] Hulteen JC, Martin CR. In: Fendler JH, editor. Nanoparticles and nanostructured films: preparation, characterization and applications. New York: Wiley; 1998.
[28] Xuan Y, Li Q. Heat transfer enhancement of nanofluids. International Journal of Heat and Fluid Flow 2000;21:58–64.
[29] Bejan A, Kraus AD. Heat transfer handbook. John Wiley and Sons Inc.; 2003.
[30] Choi SUS. Nanofluid technology: current status and future research, Korea-U.S. Technical Conference on Strategic Technologies, Vienna, VA, US; 1998.
[31] Masuda H, Ebata A, Teramae K, Hishinuma N. Alteration of thermal conductivity and viscosity of liquid by dispersing ultra-fine particles (dispersion of γ-Al_2O_3, SiO_2 and TiO_2 ultra-fine particles). Netsu Bussei (Japan) 1993;4(4):227–33.
[32] Grimm A. Powdered aluminum-containing heat transfer fluids. German Patent DE 4131516 A1 (1993).
[33] Choi SUS, Eastman JA, U.S. Patent 6,221,275 (April 2001).
[34] Eastman JA, Choi SUS, Li S, Yu W, Thomson LJ. Anomalously increased effective thermal conductivities of ethylene glycol based nanofluids containing copper nanoparticles. Applied Physics Letters 2001;78:718–20.
[35] Philip J, Laskar JM, Raj B. Magnetic field induced extinction of light in a suspension of Fe_3O_4 nanoparticles. Applied Physics Letters 2008;92.
[36] Bhat S, Maitra U. Facially amphiphilic thiol capped gold and silver nanoparticles. Journal of Chemical Sciences 2008;120(6):507–13.
[37] Frimpong RA, Hilt JZ. Poly (n-isopropylacrylamide)-based hydrogel coatings on magnetite nanoparticles via atom transfer radical polymerization. Nanotechnology 2008;(17), doi:10.1088/0957-4484/19/17/175101.
[38] Jean NC, Tan CP, Yaakob CMB, Misni M. α-Tocopherol nanodispersions: preparation, characterization and stability evaluation. Journal of Food Engineering 2008;89:204–9.

[39] Pak BC, Cho IY. Hydrodynamic and heat transfer study of dispersed fluids with sub-micron metallic oxide particles. Experimental Heat Transfer 1998;11: 151–70.
[40] Buongiorno J. Convective transport in nanofluids. Journal of Heat Transfer ASME 2006.
[41] Keblinski P, Phillpot SR, Choi SUS, Eastman JA. Mechanisms of heat flow in suspensions of nano-sized particles (nanofluids). International Journal of Heat and Mass Transfer 2002;45:855–63.
[42] Koo J, Kleinstreuer C. Impact analysis of nanoparticle motion mechanisms on the thermal conductivity of nanofluids. International Communication on Heat and Mass Transfer 2005;32(9):1111–8.
[43] Ahuja AS. Augmentation of heat transport in Laminar flow of polystyrene suspensions. I. Experiments and results. Journal of Applied Physics 1975;46 (83):408–3416.
[44] Ahuja AS. Thermal design of heat exchanger employing Laminar flow of particle suspensions. International Journal of Heat and Mass Transfer 1982;25(5):725–8.
[45] Hetsroni G, Rozenblit R. Heat transfer to a liquid–solid mixture in a flume. International Journal of Multiphase flow 2005;20(4):671–89.
[46] Lee S, Choi SUS. Application of metallic nanoparticle suspensions in advanced cooling systems. Recent advances in solid/structures and applications of metallic materials, PVP vol. 342/MD-vol 72. New York: ASME; 1996. p. 227–234.
[47] Eastman JA, Choi SUS, Li S, Soyez G, Thompson LJ, DiMelfi RJ. Novel thermal properties of nanostructure materials. Material Science Forum 1999;312:629–34.
[48] Wen D, Ding Y. Experimental investigation into convective heat transfer of nanofluids at the entrance region under laminar flow conditions. International Journal of Heat and Mass Transfer 2004;47:5181–8.
[49] Heris SZ, Etemad SGh, Nasr Esfahany M. Experimental investigation of oxide nanofluids laminar flow convective heat transfer. International Communications in Heat and Mass Transfer 2006;33(4):529–35.
[50] Heris Z, Esfahany MN, Etemad SGh. Experimental investigation of convective heat transfer of Al_2O_3/water nanofluid in circular tube. International Journal of Heat and Fluid Flow 2007;28(2):203–10.
[51] Lai WY, Duculescu B, Phelan PE, Prasher RS. Convective heat transfer with nanofluids in a single 1.02-mm tube. In: Proceedings of ASME International Mechanical Engineering Congress and Exposition (IMECE 2006); 2006.
[52] Jung J-Y, Oh HS, Kwak HY. Forced convective heat transfer of nanofluids in microchannels. In: Proceeding of ASME International Mechanical Engineering Congress and Exposition (IMECE 2006); 2006.
[53] Williams W, Buongiorno J, Hu L-W. Experimental investigation of turbulent convective heat transfer and pressure loss of alumina/water and zirconia/water nanoparticle colloids (nanofluids) in horizontal tubes. ASME Journal of Heat Transfer 2008;130:1–6.
[54] Duangthongsuk W, Wongwises S. Effect of thermo-physical properties models on the prediction of the convective heat transfer coefficient for low concentration nanofluid. International Communications in Heat and Mass Transfer 2008;35(10):1320–6.
[55] Jang SP, Choi SUS. Role of Brownian motion in the enhanced thermal conductivity of nanofluids. Applied Physics Letters 2004;84:4316–8.
[56] Duangthongsuk W, Wongwises S. Heat transfer enhancement and pressure drop characteristics of TiO_2–water nanofluid in a double-tube counter flow heat exchanger. International Journal of Heat and Mass Transfer 2009;52(7–8):2059–67.
[57] Xuan Y, Li Q. Investigation on convective heat transfer and flow features of nanofluids. Journal of Heat Transfer 2003;125:151–5.
[58] Xuan Y, Li Q. Flow and heat transfer performances of nanofluids inside small hydraulic diameter flat tube. Journal of Engineering Thermophysics 2004;25(2):305–7.
[59] Zhou DW. Heat transfer enhancement of copper nanofluid with acoustic cavitation. Int Journal of Heat and Mass Transfer 2004;47:3109–17.
[60] Li Q, Xuan Y, Jiang J, Xu JW. Experimental investigation on flow and convective heat transfer feature of a nanofluid for aerospace thermal management. Journal of Astronautics 2005;26:391–4.
[61] Faulkner D, Rector DR, Davison JJ, Shekarriz R. Enhanced heat transfer through the use of nanofluids in forced convection. In: Proceedings of ASME Heat Transfer Div; 2004. p. 219–24.
[62] Yang Y, Zhang ZG, Grulke EA, Anderson WB, Wu G. Heat transfer properties of nanoparticles-in-fluid dispersions (nanofluids) in laminar flow. International Journal of Heat and Mass Transfer 2005;48:1107–16.
[63] Ding Y, Alias H, Wen D, Williams RA. Heat transfer of aqueous suspensions of carbon nanotubes (CNT nanofluids). International Journal of Heat and Mass Transfer 2006;49:240–50.
[64] Ding Y, Chen H, He Y, Lapkin A, Yeganeh M, Siller L, Butenko YV. Forced convective heat transfer of nanofluids. Advanced Powder Technology 2007;18(6):813–24.
[65] Maiga SEB, Palm SJ, Nguyen CT, Roy G, Galanis N. Heat transfer enhancements by using nanofluids in forced convection flows. International Journal of Heat and Fluid Flow 2005;26:530–46.
[66] Putra N, Roetzel W, Das SK. Natural convection of nano-fluids. International Journal of Heat and Mass Transfer 2003;39:775–84.
[67] Wen D, Ding Y. Formulation of nanofluids for natural convective heat transfer applications. International Journal of Heat and Fluid Flow 2005; 26:855–64.
[68] Hwang KS, Lee J-H, Jang SP. Buoyancy-driven heat transfer of water-based Al_2O_3 nanofluids in a rectangular cavity. International Journal of Heat and Mass Transfer 2007;50(19):4003–10.
[69] Touloukian YS, Powell RW, Ho CY, Klemens PG. Thermo-physical properties of materials, vol. 2. New York: Plenum Press; 1970.
[70] Polidori G, Fohanno S, Nguyen CT. A note on heat transfer modeling of Newtonian nanofluids in laminar free convection. International Journal of Thermal Science 2007;46(8):739–44.
[71] Collier J, Thome JR. Boiling and condensation. Oxford University press; 1994.
[72] Chang JY, You SM. Enhanced boiling heat transfer from microporous surfaces: effects of a coating composition and method. International Journal of Heat and Mass Transfer 1997;40:4449–60.
[73] Trisaksri V, Wongwises S. Critical review of heat transfer characteristics of nanofluids. Renewable and Sustainable Energy Reviews 2007;11(3):512–23.
[74] Trisaksri V, Wongwises S. Nucleate pool boiling heat transfer of an alternative refrigerant with nanoparticle suspension. International Journal of Heat and Mass Transfer 2009;52(5–6):1582–8.
[75] Yang YM, Maa JR. Boiling of suspension of solid particles in water. International Journal of Heat and Mass Transfer 1984;27:145–7.
[76] Das SK, Putra N, Roetzel W. Pool boiling characterization of nano-fluids. International Journal of Heat and Mass Transfer 2003;46:851–62.
[77] Das SK, Putra N, Roetzel W. Pool boiling nano-fluids on horizontal narrow tubes. International Journal of Multiphase Flow 2003;29:1237–47.
[78] Bang IC, Chang SH. Boiling heat transfer performance and phenomena of Al_2O_3–water nano-fluids from a plain surface in a pool. International Journal of Heat and Mass Transfer 2005;48:2407–19.
[79] Bang IC, Chang SH. Direct observation of a liquid film under a vapor environment in a pool boiling using a nanofluid. Applied Physics Letters 2005;86(13): 134107-1–7.
[80] Wen D, Ding Y. Experimental investigation into the pool boiling heat transfer of aqueous based alumina nanofluids. Journal of Nanoparticle Research 2005;7:265–74.
[81] You SM, Kim JH, Kim KM. Effect of nanoparticles on critical heat flux of water in pool boiling of heat transfer. Applied Physics Letters 2003;83(16):3374–6.
[82] Vassallo P, Kumar R, D'Amico S. Pool boiling heat transfer experiments in silica-water nano-fluids. International Journal of Heat and Mass Transfer 2004;47(2):407–11.
[83] Kim H, Kim J, Kim M. Experimental study on CHF characteristics of water–TiO_2 nano-fluids. Nuclear Engineering and Technology 2006;38(1).
[84] Kim SJ, Bang IC, Buongiorno J, Hu LW. Surface wettability change during pool boiling of nanofluids and its effect on critical heat flux. International Journal of Heat and Mass Transfer 2007;50:4105–16.
[85] Milanova D, Kumar R, Kuchibhatla S, Seal S. Heat transfer behavior of oxide nanoparticles in pool boiling experiment. In: Proceedings of 4th International Conference on Nanochannels, Microchannels and Minichannels; 2006.
[86] Jackson JE, Borgmeyer BV, Wilson CA, Cheng P, Bryan JE. Characteristics of nucleate boiling with gold nanoparticles in water. In: Proceedings of IMECE 2006; 2006.
[87] Witharana S. Boiling of refrigerants on enhanced surfaces and boiling of nanofluids. Ph.D. thesis. Royal Institute of Technology, Stockholm, Sweden; 2003.
[88] Nguyen CT, Galanis N, Roy G, Divoux S, Gilbert D. Pool boiling characteristics of water-alumina nanofluids 2006, doi:10.1615/IHTC13.p8.20.
[89] Jung D, Kim Y, Ko Y, Song K. Nucleate boiling heat transfer coefficients of pure halogenated refrigerants. International Journal of Refrigeration 2003;26: 240–8.
[90] Tu JP, Dinh N, Theofanous T. An experimental study of nanofluid boiling heat transfer. In: Proceedings of 6th International Symposium on Heat Transfer; 2004.
[91] Zhou DW. Heat transfer enhancement of copper nanofluid with acoustic cavitation. International Journal of Heat and Mass Transfer 2004;47:3109–17.
[92] Park K-J, Jung D. Boiling heat transfer enhancement with carbon nanotubes for refrigerants used in building air-conditioning. Energy and Buildings 2007;39(9):1061–4.
[93] Park K-J, Jung D. Enhancement of nucleate boiling heat transfer using carbon nanotubes. International Journal of Heat and Mass Transfer 2007;50(21): 4499–502.
[94] Landau LD, Lifshitz EM. Electrodynamics of continuous media, translated by Sykes JB, Bell JS, Oxford: Pergamon Press; 1960.
[95] Choi S, Zhang Z, Yu W, Lockwood F, Grulke E. Anomalously thermal conductivity enhancement of in nanotube suspensions. Applied Physics Letters 2001;79(14):2252–4.
[96] Xuan Y, Roetzel W. Conceptions for heat transfer correlation of nanofluids. International Journal of Heat and Mass Transfer 2000;43:3701–7.
[97] Khanafer K, Vafai K, Lightstone M. Buoyancy-driven heat transfer enhancement in a two-dimensional enclosure utilizing nanofluids. International Journal of Heat and Mass Transfer 2003;46:3639–53.
[98] Das SK, Choi SUS, Patel HE. Heat transfer in nanofluids—a review. Heat Transfer Engineering 2006;27(10):3–19.
[99] Buongiorno J. Convective heat transfer enhancement in nanofluids. Heat and Mass Transfer Conference, January, 2006, HMT-2006-C335.
[100] Behzadmehr A, Saffar-Avval M, Galanis N. Prediction of turbulent forced convection of a nanofluid in a tube with uniform heat flux using two phase approach. International Journal of Heat and Fluid Flow 2007;28(2): 211–9.

[101] Maiga SEB, Nguyen CT, Galanis N, Roy G. Heat transfer behaviors of nanofluids in a uniformly heated tube. Superlattices and Microstructures 2003.
[102] Roy G, Nguyen CT, Lajoie PR. Numerical investigation of laminar flow and heat transfer in a radial flow cooling system with the use of nanofluids. Superlattices and Microstructures 2003.
[103] Ding Y, Wen D. Particle migration in a flow of nanoparticles suspensions. Powder Technology 2005;149:84–92.
[104] Palm SJ, Roy G, Nguyen CT. Heat transfer enhancement with the use of nanofluids in radial flow cooling systems considering temperature-dependent properties. Applied Thermal Engineering 2006;26(17–18):2209–18.
[105] Kim J, Kang YT, Choi CK. Soret and Dufour effects on convective instabilities in binary nanofluids for absorption application. International Journal of Refrigeration 2007;30(2):323–8.
[106] Mansour RB, Galanis N, Nguyen CT. Effect of uncertainties in physical properties on forced convection heat transfer with nanofluids. Applied Thermal Engineering 2007;27(1):240–9.
[107] Prakash M, Giannelis EP. Mechanism of heat transfer in nanofluids. Journal of Computer-Aided Materials Design. doi:10.1007/s10820-006-9025-x.
[108] Li CH, Peterson GP. Mixing effect on the enhancement of the effective thermal conductivity of nanoparticle suspensions (nanofluids). International Journal of Heat and Mass Transfer 2007;23(May). doi: 10.1016/j.ijheatmasstransfer.2007.03.015.
[109] Chein R, Huang G. Analysis of microchannel heat sink performance using nanofluids. Applied Thermal Engineering 2005;25:3104–14.
[110] Jang SP, Choi SUS. Cooling performance of a microchannel heat sink with nanofluids. Applied Thermal Engineering 2005;26:2457–63.
[111] Chein R, Chuang J. Experimental microchannel heat sink performance studies using nanofluids. International Journal of Thermal Science 2006.
[112] Koo J, Kleinstreuer C. Laminar nanofluid flow in micro heat-sinks. International Journal of Heat and Mass Transfer 2005;48:2652–61.
[113] Nguyen CT, Roy G, Gauthier C, Galanis N. Heat transfer enhancement using Al_2O_3–water nanofluid for an electronic liquid cooling system. Applied Thermal Engineering 2007;27(8):1501–6.
[114] Chien H-T, Tsai C-I, Chen P-H, Chen P-Y. Improvement on thermal performance of a disk shaped miniature heat pipe with nanofluid. IEEE ICEPTD; 2003. p. 381–391.
[115] Tsai CY, Chien HT, Ding PP, Chan B, Luh TY, Chen PH. Effect of structural character of gold nanoparticles in nanofluid on heat pipe thermal performance. Materials Letters 2004;58:1461–5.
[116] Kang SW, Wei WC, Tsai SH, Yang SY. Experimental investigation of silver nano-fluid on heat pipe thermal performance. Applied Thermal Engineering 2006;26:2377–82.
[117] Ma HB, Choi SUS, Tirumala M. Effect of nanofluid on the heat transport capability in an oscillating heat pipe. Applied Physics Letters 2006;88:116–43.
[118] Sidi el Bécaye Maïga, Nguyen CT, Galanis N, Roy G, Maré T, Coqueux M. Heat transfer enhancement in turbulent tube flow using Al_2O_3 nanoparticle suspension. International Journal of numerical methods for heat and fluid flow 2006;16(3):275–92.

International Journal of Heat and Mass Transfer 53 (2010) 1603–1608

Contents lists available at ScienceDirect

International Journal of Heat and Mass Transfer

journal homepage: www.elsevier.com/locate/ijhmt

Technical Note

Airside performance of fin-and-tube heat exchangers in dehumidifying conditions – Data with larger diameter

Young-Chang Liu [a], Somchai Wongwises [b], Wen-Jeng Chang [c], Chi-Chuan Wang [a,d,*]

[a] Energy and Environment Research Laboratories, Industrial Technology Research Institute, Hsinchu 310, Taiwan
[b] Fluid Mechanics, Thermal Engineering and Multiphase Flow Research Lab. (FUTURE), Department of Mechanical Engineering, King Mongkut's University of Technology Thonburi, Bangmod, Bangkok 10140, Thailand
[c] Department of Mechanical and Computer Aided Engineering Feng Chia University, Taichung, Taiwan
[d] Department of Mechanical Engineering, National Chiao Tung University, Hsinchu 300, Taiwan

ARTICLE INFO

Article history:
Received 22 September 2009
Received in revised form 15 November 2009
Accepted 15 November 2009
Available online 13 January 2010

Keywords:
Fin-and-tube heat exchanger
Plain fin
Dehumidification

ABSTRACT

This study presents the airside performance of the fin-and-tube heat exchangers having plain fin geometry with a larger diameter tube (D_c = 15.88 mm) under dehumidifying condition. A total of nine samples of heat exchangers subject to change of the number of tube row and fin pitch are made and tested. It is found that the effect of fin pitch on the sensible j factor is, in general, diminished with the rise of tube row. However, there is a unique characteristic of fin pitch at a shallow tube row, the heat transfer performance is first increased at a wider pitch but a further increase of fin pitch lead to a falloff of heat transfer performance due to interactions amid flow development and bypass flow. The influence of tube row on the airside performance is rather small for both heat transfer and frictional characteristics at a fin pitch of 2.1 mm and when the Reynolds number is less than 4000. A slight deviation of this effect is encountered when fin pitch is increased to 2.54 mm or 3.1 mm due to condensate adhered phenomena.

© 2009 Elsevier Ltd. All rights reserved.

1. Introduction

Fin-and-tube heat exchangers are widely-used heat transfer devices in applications like refrigeration and air conditioning systems. Its easier manufacturing, simpler construction, lower cost, and relatively easy in maintenance makes it one of the most commonly used heat exchangers. They can be applicable to both heating and cooling. Once the cooling process takes place below dew point temperature, condensate forms on the surface and result in a complex heat and mass transfer interactions. The heat transfer characteristics of fin-and-tube heat exchangers under this dehumidifying conditions had been studied by many researchers (e.g. McQuiston [1,2], Beecheer and Fagan [3], Yan and Sheen [4], Mirth and Ramadhyani [5,6], Wang et al. [7], Pirompugd et al. [8,9]). The published literatures offer considerable test results of plain fin data in wet condition.

However, the foregoing tests were conducted for typical heat exchangers of small air-conditioners where nominal tube diameters of 9.52, 7.94 or 7 mm were generally employed. In typical applications like fan-coil or ventilator, exploitation of larger diameter like 15.88 mm is also very common. Unfortunately, there is very limited performance data of the fin-and-tube heat exchanger with larger diameter tube in the open literature and is virtually no data available in dehumidifying conditions. Hence, the objective of the present study is to provide relevant performance data to the database.

2. Experimental setup

The schematic diagram of the experimental air circuit assembly is shown in Fig. 1. It consists of a closed-loop wind tunnel in which air is circulated by a variable speed centrifugal fan (7.46 kW, 10 HP). The air duct is made of galvanized sheet steel and has an 850 mm × 550 mm cross-section. The dry-bulb and wet-bulb temperatures of the inlet-air are controlled by an air-ventilator that can provide a cooling capacity of up to 21.12 kW (6RT). The air flow-rate measurement station is an outlet chamber set up with multiple nozzles. This setup is based on the ASHRAE 41.2 standard [10]. A differential pressure transducer is used to measure the pressure difference across the nozzles. The air temperatures at the inlet and exit zones across the sample heat exchangers are measured by two psychrometric boxes based on the ASHRAE 41.1 standard [11].

The working medium for the tube side is cold water. A thermostatically controlled reservoir provides cold water at selected temperatures. The temperature differences on the water side are measured by two pre-calibrated RTDs. The water volumetric flow

* Corresponding author. Address: Energy and Environment Research Laboratories, Industrial Technology Research Institute, Hsinchu 310, Taiwan. Tel.: +886 3 5916294; fax: +886 3 5820250.
E-mail address: ccwang@itri.org.tw (C.-C. Wang).

0017-9310/$ - see front matter © 2009 Elsevier Ltd. All rights reserved.
doi:10.1016/j.ijheatmasstransfer.2009.12.015

Nomenclature

A_c	minimum flow area, m^2
A_f	fin surface area, m^2
$A_{p,i}$	inside surface area of tubes, m^2
A_o	total surface area, m^2
b'_p	slope of the air saturation curved between the outside and inside tube wall temperature, J kg^{-1} K^{-1}
b'_r	slope of the air saturation curved between the mean water temperature and the inside wall temperature, J kg^{-1} K^{-1}
$b'_{w,f}$	slope of the air saturation curved at the mean water film temperature of fin surface, J kg^{-1} K^{-1}
$b'_{w,p}$	slope of the air saturation curved at the mean water film temperature of tube surface, J kg^{-1} K^{-1}
$C_{p,a}$	moist air specific heat at constant pressure, J kg^{-1} K^{-1}
D_c	collar diameter, m
D_h	hydraulic diameter, m
f	Fanning friction factor
F_p	fin pitch, m
G_c	maximum mass flux at minimum flow area, kg m^{-2} s^{-1}
$h_{c,o}$	sensible heat transfer coefficient, W m^{-2} K^{-1}
h_i	inside heat transfer coefficient, W m^{-2} K^{-1}
j	Colburn j factor
k_p	thermal conductivity of tube, W m^{-1} K^{-1}
L	streamwise duct length, m
N	number of tube row
P_l	longitudinal tube pitch, m
P_t	transverse tube pitch, m
Pr	Prandtl number of air
ΔP	pressure drop, Pa
$\dot{Q}_a$	air side heat transfer rate, W
$\dot{Q}_{avg}$	average heat transfer rate, W
$\dot{Q}_r$	water side heat transfer rate, W
Re_{Dc}	air side Reynolds number based on the collar diameter
Re_{Dh}	Reynolds number based on hydraulic diameter
RH_{in}	inlet relative humidity
$U_{o,w}$	wet surface overall heat transfer coefficient, based on enthalpy difference, kg m^{-2} s^{-1}
x_p	wall thickness, m
x^+	inverse Graetz number
σ	contraction ratio
$\eta_{f,wet}$	fully wet fin efficiency
ρ	air density, kg m^{-3}
δ_f	fin thickness, m

rate is measured by a magnetic flow meter with a ±0.001 L/s precision. All the temperature measuring probes are resistance temperature devices (Pt100), with a calibrated accuracy of 0.05 °C. In the experiments, only the data that satisfy the ASHRAE 33-78 [12] requirements (namely, the energy balance condition, $|\dot{Q}_r - \dot{Q}_a|/\dot{Q}_{avg}$, is less than 0.05, where $\dot{Q}_r$ is the water-side heat transfer rate for and $\dot{Q}_a$ air-side heat transfer rate) are considered in the final analysis. Detailed geometry used for the present plain fin-and-tube heat exchangers is tabulated in Table 1. The test fin-and-tube heat exchangers are tension wrapped having a "L" type fin collar. The test conditions of the inlet-air are as follow:

Dry-bulb temperature of the air	27 ± 0.5 °C
Inlet relative humidity for the incoming air	50% and 80%
Inlet-air velocity	From 1 to 4 m/s
Inlet-water temperature	7 ± 0.5 °C
Water velocity inside the tube	1.5–1.7 m/s

The test conditions approximate those encountered with typical fan-coils and evaporators of air-conditioning applications. Uncertainties reported in the present investigation, following the single-sample analysis proposed by Moffat [13]. The maximum uncertainty occurred at the smallest frontal velocity and is less than ±4.7% for reduction of the sensible heat transfer coefficient whereas it is within ±6% for the frictional reduction.

3. Data reduction

Basically, the present reduction method is analogous to Threlkeld's approach [14]. Details of the reduction process can be found from the previous studies by Wang et al. [7]. Notice that the Threlkeld method is an enthalpy-based reduction method. A brief description of the reduction of heat and mass transfer is given as follows:

The overall heat transfer coefficient is related to the individual heat transfer resistance (Myers, [15]) as follows;

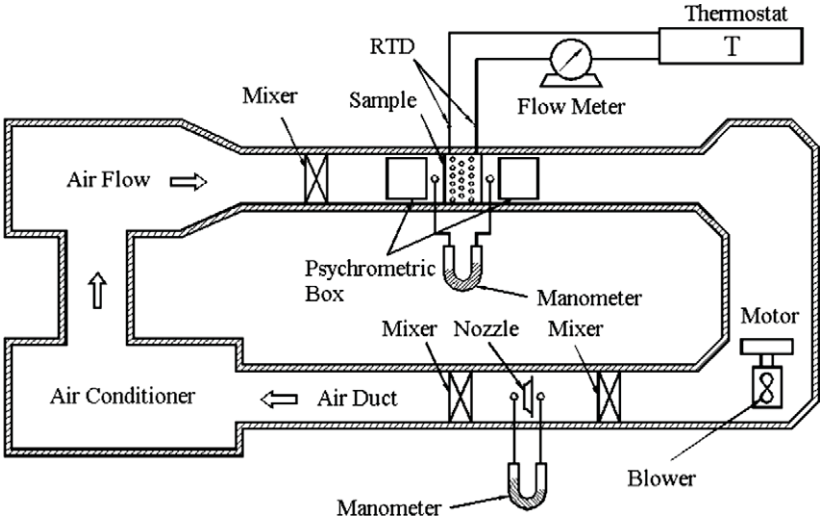

Fig. 1. Schematic of the test apparatus.

Table 1
Detailed geometric parameters of the test samples.

No.	Fin type	F_p (mm)	δ_f (mm)	D_c (mm)	P_t (mm)	P_l (mm)	N, row
1	Plain	2.12	0.12	16.68	38.1	33	2
2	Plain	2.54	0.12	16.68	38.1	33	2
3	Plain	3.17	0.12	16.68	38.1	33	2
4	Plain	2.06	0.12	16.68	38.1	33	4
5	Plain	2.54	0.12	16.68	38.1	33	4
6	Plain	3.13	0.12	16.68	38.1	33	4
7	Plain	2.12	0.12	16.68	38.1	33	8
8	Plain	2.54	0.12	16.68	38.1	33	8
9	Plain	3.17	0.12	16.68	38.1	33	8

$$\frac{1}{U_{o,w}} = \frac{b'_r A_o}{h_i A_{p,i}} + \frac{b'_p x_p A_o}{k_p A_{p,m}} + \frac{1}{h_{o,w}\left(\frac{A_{p,o}}{b'_{w,p} A_o} + \frac{A_f \eta_{f,wet}}{b'_{w,m} A_o}\right)} \tag{1}$$

where

$$h_{o,w} = \frac{1}{\frac{C_{p,a}}{b'_{w,m} h_{c,o}}} \tag{2}$$

The tube-side heat transfer coefficient, h_i, is evaluated from the Gnielinski correlation. The four quantities ($b'_{w,m}$, $b'_{w,p}$, b'_p, and b'_r) in Eq. (1) involving enthalpy–temperature ratios must be evaluated in

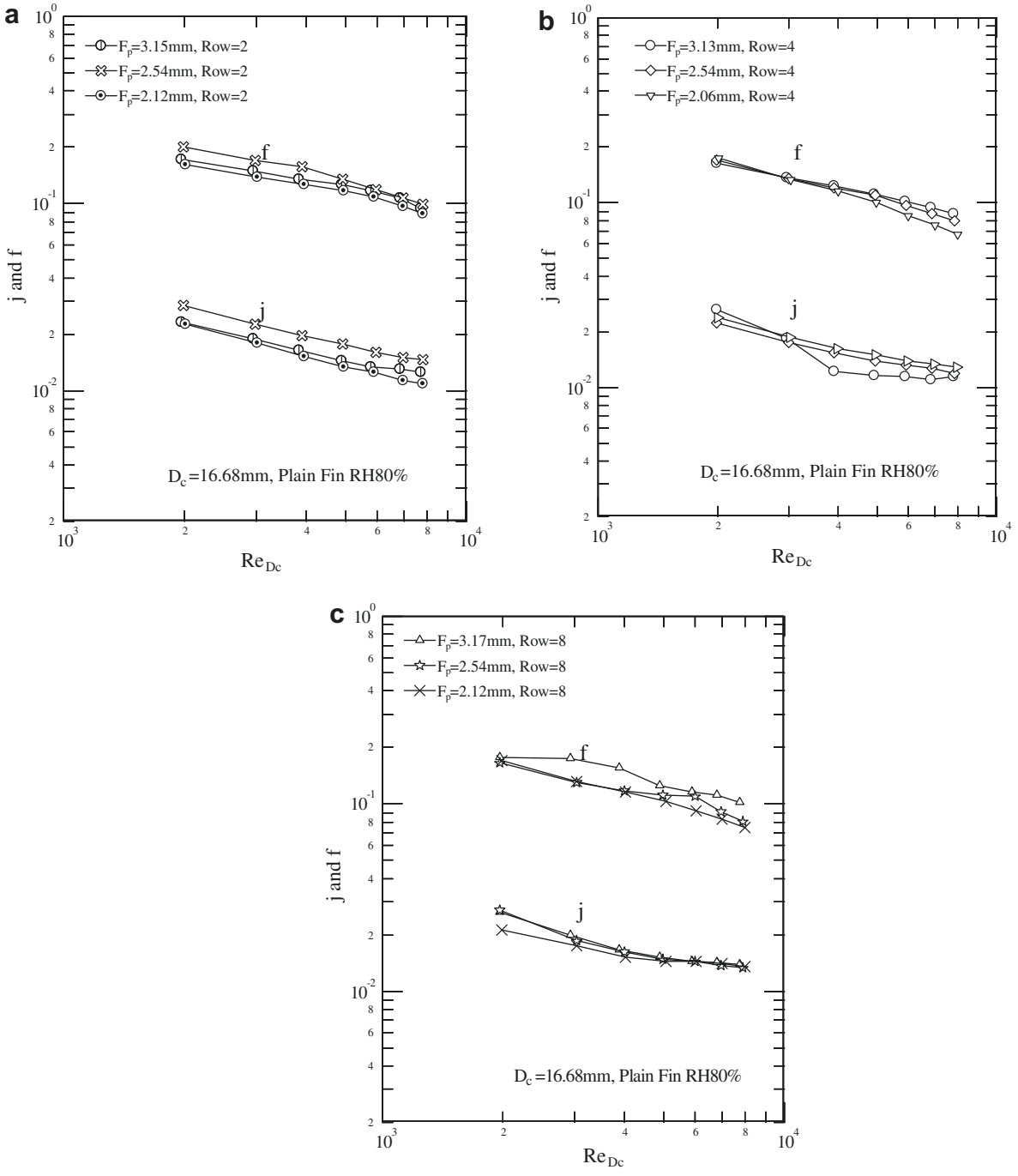

Fig. 2. Effect of fin pitch on heat transfer and friction characteristics (a) $N = 2$; (b) $N = 4$ and (c) $N = 8$ (RH = 80%).

advance. A detailed evaluation of these four terms can be found from Wang et al. [7]. The heat transfer performance is in terms of the Colburn j factor, i.e,

$$j = \frac{h_{c,o}}{G_c C_{p,a}} \mathrm{Pr}^{2/3} \tag{3}$$

The reduction of the friction factor of the heat exchanger is evaluated from the pressure drop equation proposed by Kays and London [16] as

$$f = \frac{A_c}{A_o}\frac{\rho_i}{\rho_m}\left[\frac{2\rho_i \Delta P}{G_c^2} - (1+\sigma^2)\left(\frac{\rho_i}{\rho_o} - 1\right)\right] \tag{4}$$

Related explanation and calculation of the terminology can be seen from Wang et al. [7].

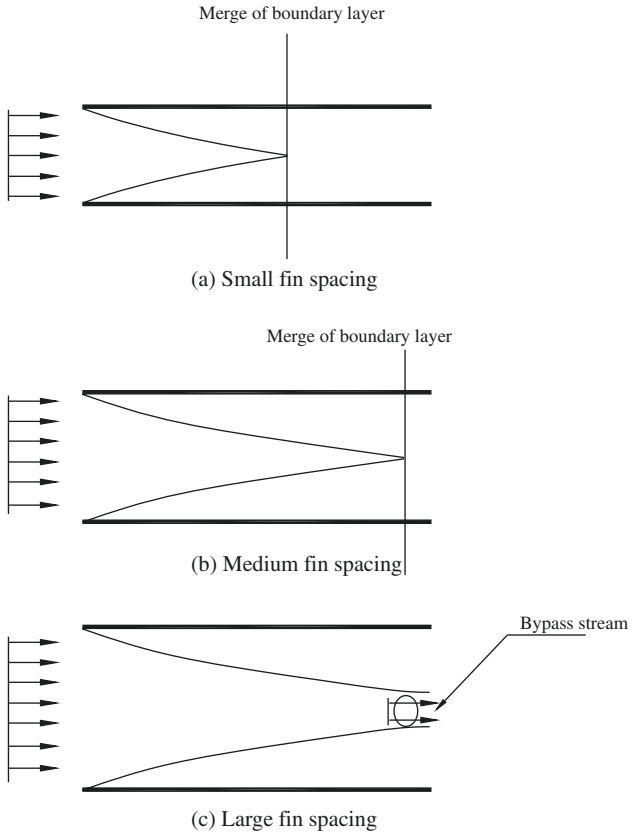

Fig. 3. Schematic of flow development alongside the fin channel: (a) small fin spacing, (b) medium fin spacing and (c) large fin spacing.

4. Results and discussion

A typical result concerning the effect of fin pitch on the airside performance for RH = 80% is schematically shown in Fig. 2. The corresponding tube rows are 2, 4, and 8, respectively. As expected, the friction factors and the sensible j factors decrease with increase of the Reynolds number. The effect of fin pitch on the sensible j factor is, in general, diminished with the rise of tube row. This is because more tube rows provide significantly mixing, thereby leading to a hardly detectable difference of j factor as the row number is increased to 8. However, there is a unique feature of the j factor for $N = 2$. The j factor shows appreciable increase when the fin pitch is increased from 2.12 mm to 2.54 mm, and a further rise to $F_p = 3.15$ mm yields a detectable drop of heat transfer performance. In fact it falls back to that of $F_p = 2.12$ mm. The special phenomenon is actually related to the developing characteristics of thermal and flow field. For further illustration of this phenomenon, one can examine the corresponding reciprocal of the inverse Graetz number x^+, which is defined as

$$x^+ = \frac{L/D_h}{\mathrm{Re}_{D_h}\mathrm{Pr}} \tag{5}$$

where L is the streamwise duct length and Pr is the Prandtl number. The flow may be considered to be fully developed when $x^+ > 0.1$ [17]. In general, the heat transfer performance within the heat exchanger is quite complex for it related to the interactions amid tubes and fins. For a shallow row number like $N = 2$, the effect of tube row is comparatively small, hence one can check the associated influence of development of flow field within channels. A close examination of the present test samples of $N = 2$ using Eq. (5) indicates that the contribution of development and fully developed region are quite corresponding. In this regard, one can realize the whole picture about the heat transfer performance subject to change of fin spacing as schematically shown in Fig. 3. For a smaller fin pitch as shown in Fig. 3(a), the flow develops along the

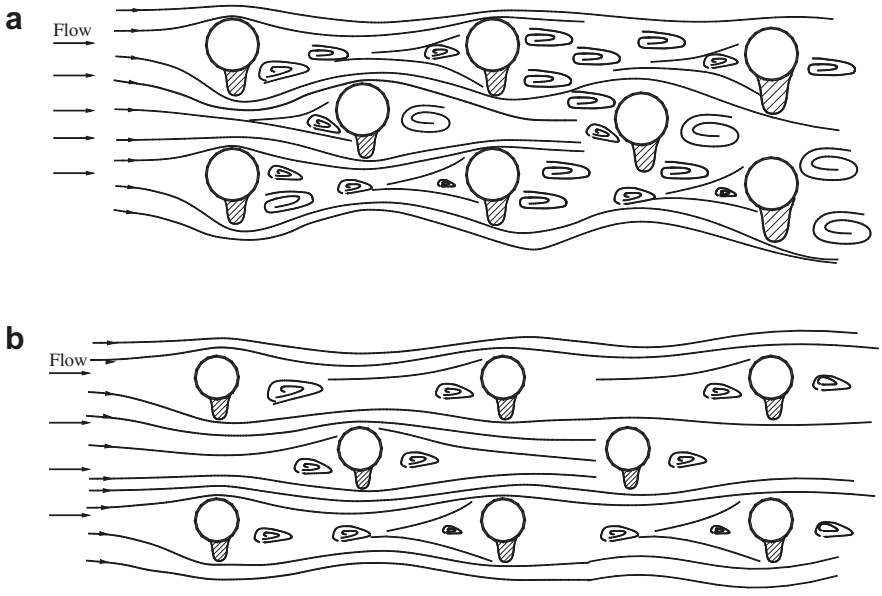

Fig. 4. Schematic of secondary flow subject to vapor shear (a) large fin spacing and (b) small fin spacing.

channel and merge accordingly somewhere alongside the channel, resulting in a comparatively low heat transfer performance. A further increase of fin spacing as seen in Fig. 3(b) will delay the conglomeration of boundary layer and increase the development length which gives rise to an increase of heat transfer performance. In the meantime, there will be no merge of boundary layer with a further increase of fin spacing as seen in Fig. 3(c). The nascent sign would suggest that the heat transfer performance will continue to rise since there is no boundary layer conglomeration. However, as clearly seen in Fig. 3(c), a bypass flow stream at the center region will offset the heat transfer gain from the development. In this sense, the heat transfer performance reveals a fallback when the fin spacing is sufficient large. However, it must be emphasized that this is applicable for shallow tube row where mixing caused by tubes is not so intensive.

In the meantime, the corresponding influence of fin pitch on the friction factor shows a slight scattering despite the variation is not so prominent. However, one can still see a marginal increase of friction factor for $N = 8$. The results are not in line with those in dry condition. For heat exchangers under completely dry operation, Rich [18] concluded that the friction factors were essentially independent of the number of tube row. The recent experimental data having larger diameter tube by Liu et al. [19] also support this finding. It is likely that the slight rise of friction factor with the fin pitch is associated with the condensate drainage. For a better understanding about the influence of condensate, Fig. 4(a) presents a cartoon to demonstrate how the friction factor may be slightly increased at a larger row number and a wider fin pitch. With a larger fin pitch, the effective vapor shear inside the fin spacing is comparatively small, the condensate is therefore easier to accumulate and

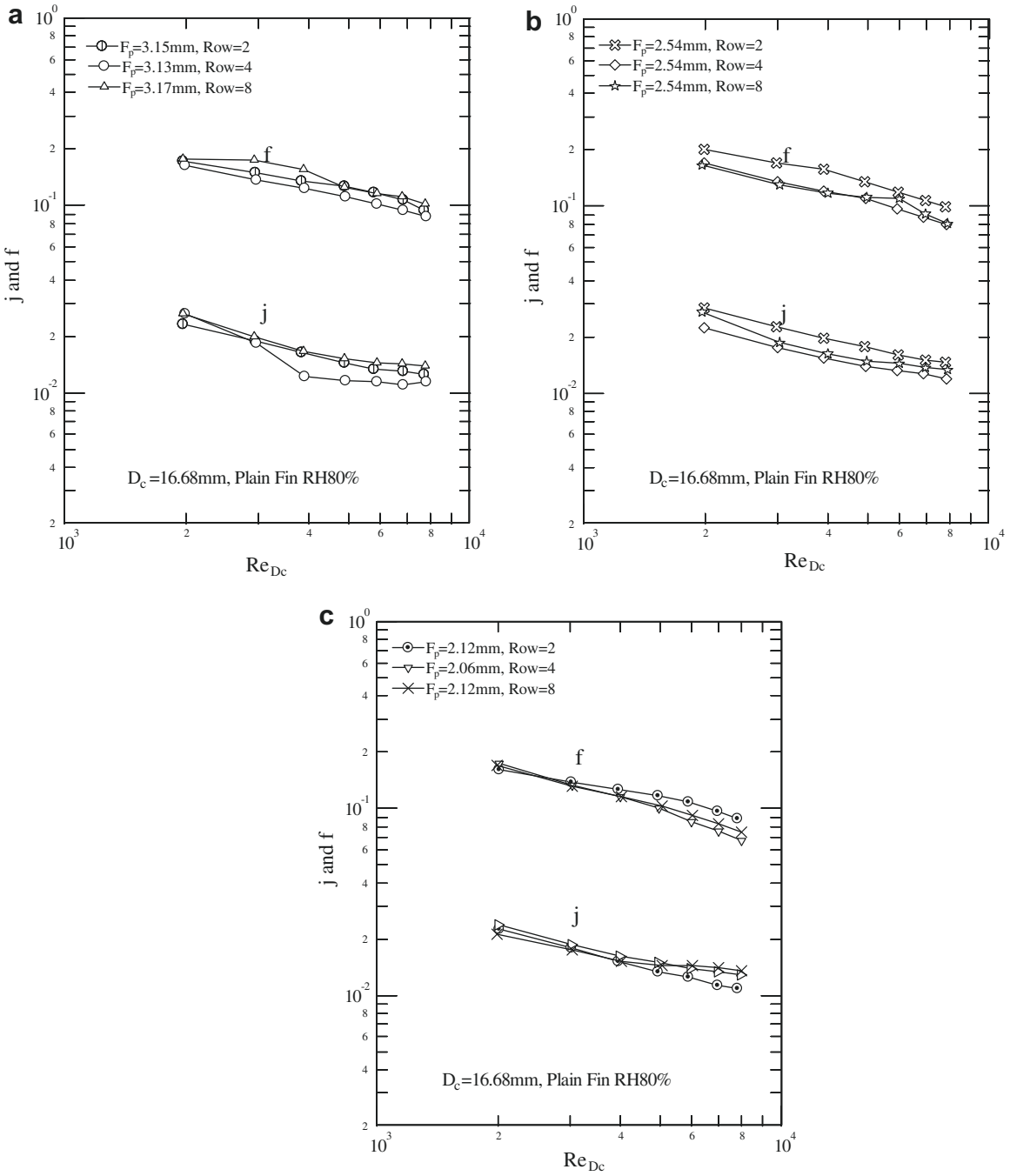

Fig. 5. Effect of the number of tube row on the heat transfer and friction characteristics: (a) $F_p = 2.1$ mm, (b) $F_p = 2.54$ mm and (c) $F_p = 3.15$ mm.

hang upon the surface. As a result, it is prone to having a higher frictional characteristic, yet the phenomenon may become more pronounced as the number of tube row is increased. On the other hand, the effect of vapor shear is reinforced at a smaller fin pitch and the condensate is easier to be removed from the surface. As a consequence, lower frictional performance is shown in Fig. 4(b) as the effect of secondary flow is reduced. Notice that condensate drainage within fin-and-tube heat exchanger is a very complex phenomenon for it interacts with both fin and tube surfaces.

Results regarding to the influence of the number of tube row on the airside performance are shown in Fig. 5. In general, the influence of tube row becomes less conceived when the fin pitch is reduced to 2.1 mm. As can be seen from Fig. 5(a), for a Reynolds number less than 4000, there is hardly any effect of the number of tube row on both heat transfer and frictional performance. By contrast, the sensible heat transfer j factors decrease with the rise of tube row when the Reynolds number is increased further. This is associated with the condensate blow off. The condensate is easier to adhere to the fin surface when the Reynolds number is low, resulting in a less influence of tube row. In the meantime, the adhered condensate may be blown off the fin surfaces when vapor shear is increased. Conversely, this phenomenon is not so significantly seen when the fin spacing is increased. This is because large condensate is prone to suspending between fins whereas smaller condensate just rolls alongside the fin, leading to this inconsistency.

5. Conclusion

This study presents the airside performance of the fin-and-tube heat exchangers having plain fin geometry with a larger diameter tube (D_c = 15.88 mm) under dehumidifying conditions. A total of nine samples of heat exchangers subject to change of the number of tube row and fin pitch are made and tested. Tests are conducted in a wind tunnel at controlled environment. Major conclusions of this study are summarized as follows:

(1) The effect of fin pitch on the sensible j factor is, in general, diminished with the rise of tube row. However, there is a distinct feature of the heat transfer performance occurring at a shallow row number (N = 2). The heat transfer performance is first increased when the fin pitch is increased from 2.12 mm to 2.54 mm, followed by a conceivable falloff if the fin pitch is increased to 3.15 mm. This unique characteristic is associated with the interaction between flow field development and bypass flow.
(2) The effect of fin pitch on the friction factor is somehow slightly scattering. There is a slight increase in friction factor for a tube row of eight. This is especially observable when the fin pitch is large. It is found that this phenomenon is related to condensate retention.
(3) The influence of tube row on the airside performance is rather small for both heat transfer and frictional characteristics. However, there is a slight deviation of this effect when fin pitch is increased to 2.54 mm or 3.1 mm. This is due to the condensate blown off phenomenon.

Acknowledgments

The authors would like to express gratitude for the Energy R&D foundation funding from the Bureau of Energy of the Ministry of Economic, Taiwan, Thailand Research Fund (TRF) and King Mongkut's University of Technology Thonburi for supporting the research.

References

[1] F.C. McQuiston, Heat mass and momentum transfer data for five plate-fin tube transfer surface, ASHRAE Trans. Part 1 84 (1978) 266–293.
[2] F.C. McQuiston, Correlation of heat, mass and momentum transport coefficients for plate-fin-tube heat transfer surfaces with staggered tubes, ASHRAE Trans. Part 1 84 (1978) 294–309.
[3] D.T. Beecher, T.J. Fagan, Effects of fin pattern on the air-side heat transfer coefficient in plate finned-tube heat exchanger, ASHRAE Trans. 93 (2) (1987) 1961–1984.
[4] W.M. Yan, P.J. Sheen, Heat transfer and friction characteristics of fin-and-tube heat exchangers, Int. J. Heat Mass Transfer 43 (2000) 1651–1659.
[5] D.R. Mirth, S. Ramadhyani, Prediction of cooling-coils performance under condensing conditions, Int. J. Heat Fluid Flow 14 (4) (1993) 391–400.
[6] D.R. Mirth, S. Ramadhyani, Correlations for predicting the air-side Nusselt numbers and friction factors in chilled-water cooling coils, Exp. Heat Transfer 7 (1994) 143–162.
[7] C.C. Wang, Y.C. Hsieh, Y.T. Lin, Performance of plate finned tube heat exchangers under dehumidifying conditions, J. Heat Transfer 119 (1997) 109–117.
[8] W. Pirompugd, S. Wongwises, C.C. Wang, A tube-by-tube reduction method for simultaneous heat and mass transfer characteristics for plain fin-and-tube heat exchangers in dehumidifying conditions, Heat Mass Transfer 41 (8) (2005) 756–765.
[9] W. Pirompugd, C.C. Wang, S. Wongwises, A fully wet and fully dry tiny circular fin method for heat and mass transfer characteristics for plain fin-and-tube heat exchangers under dehumidifying conditions, J. Heat Transfer 129 (9) (2007) 1256–1267.
[10] ASHRAE Standard 41.2-1987, Standard methods for laboratory air-flow measurement, American Society of Heating, Refrigerating and Air-Conditioning Engineers, Inc., Atlanta GA, 1987.
[11] ASHRAE Standard 41.1-1986, Standard method for temperature measurement, American Society of Heating, Refrigerating and Air-Conditioning Engineers, Inc., Atlanta, GA, 1986.
[12] ASHRAE Standard 33-78, Method of testing forced circulation air cooling and air heating coils, American Society of Heating, Refrigerating and Air-Conditioning Engineers, Inc., Atlanta, GA, 1978.
[13] R.J. Moffat, Describing the uncertainties in experimental results, Exp. Thermal Fluid Sci. 1 (1987) 3–17.
[14] J.L. Threlkeld, Thermal Environmental Engineering, Prentice-Hall, Inc., New-York, 1970.
[15] R.J. Myers, The Effect of Dehumidification on the Air-Side Heat Transfer Coefficient for a Finned-Tube Coil, M.S. Thesis, University of Minnesota, Minneapolis, 1967.
[16] W.M. Kays, A.L. London, Compact Heat Exchanger, third ed., McGraw-Hill, New York, 1984. A.L.
[17] J.E. Sergent, A. Krum, Thermal Management Handbook for Electronic Assemblies, McGraw-Hill, New York, 1998.
[18] D.G. Rich, The effect of the number of tube rows on heat transfer performance of smooth plate fin-and-tube heat exchanger, ASHRAE Trans. 81 (1) (1975) 307–317.
[19] Y.C. Liu, R. Hu, R.B.C. Yang, I.Y. Chen, I.Y.C.C. Wang, Sensible airside performance of fin-and-tube heat exchangers – data with larger diameter tube, ASHRAE Trans. 114 (1) (2008) 379–386.

This article was downloaded by: *[2007-2008-2009 National Chiao Tung University]*
On: *24 December 2009*
Access details: *Access Details: [subscription number 907850282]*
Publisher *Taylor & Francis*
Informa Ltd Registered in England and Wales Registered Number: 1072954 Registered office: Mortimer House, 37-41 Mortimer Street, London W1T 3JH, UK

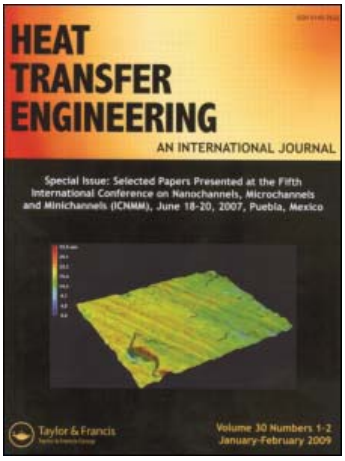

Heat Transfer Engineering

Publication details, including instructions for authors and subscription information:
http://www.informaworld.com/smpp/title~content=t713723051

Two-Phase Flow Across Small Sudden Expansions and Contractions

Ing Young Chen [a]; Somchai Wongwises [b]; Bing-Chwen Yang [c]; Chi-Chuan Wang [cd]
[a] Mechanical Engineering Department, National Yunlin University of Science and Technology, Yunlin, Taiwan [b] Department of Mechanical Engineering, King Mongkut's University of Technology Thonburi, Bangmod, Thailand [c] Energy & Environment Research Laboratories, Industrial Technology Research Institute, Hsinchu, Taiwan [d] Department of Mechanical Engineering, National Chiao Tung University, Hsinchu, Taiwan

Online publication date: 13 November 2009

To cite this Article Chen, Ing Young, Wongwises, Somchai, Yang, Bing-Chwen and Wang, Chi-Chuan(2010) 'Two-Phase Flow Across Small Sudden Expansions and Contractions', Heat Transfer Engineering, 31: 4, 298 — 309
To link to this Article: DOI: 10.1080/01457630903312056
URL: http://dx.doi.org/10.1080/01457630903312056

PLEASE SCROLL DOWN FOR ARTICLE

Full terms and conditions of use: http://www.informaworld.com/terms-and-conditions-of-access.pdf

This article may be used for research, teaching and private study purposes. Any substantial or systematic reproduction, re-distribution, re-selling, loan or sub-licensing, systematic supply or distribution in any form to anyone is expressly forbidden.

The publisher does not give any warranty express or implied or make any representation that the contents will be complete or accurate or up to date. The accuracy of any instructions, formulae and drug doses should be independently verified with primary sources. The publisher shall not be liable for any loss, actions, claims, proceedings, demand or costs or damages whatsoever or howsoever caused arising directly or indirectly in connection with or arising out of the use of this material.

Heat Transfer Engineering, 31(4):298–309, 2010
Copyright © Taylor and Francis Group, LLC
ISSN: 0145-7632 print / 1521-0537 online
DOI: 10.1080/01457630903312056

Taylor & Francis
Taylor & Francis Group

Two-Phase Flow Across Small Sudden Expansions and Contractions

ING YOUNG CHEN,[1] SOMCHAI WONGWISES,[2] BING-CHWEN YANG,[3] and CHI-CHUAN WANG[3,4]

[1]Mechanical Engineering Department, National Yunlin University of Science and Technology, Yunlin, Taiwan
[2]Department of Mechanical Engineering, King Mongkut's University of Technology Thonburi, Bangmod, Thailand
[3]Energy & Environment Research Laboratories, Industrial Technology Research Institute, Hsinchu, Taiwan
[4]Department of Mechanical Engineering, National Chiao Tung University, Hsinchu, Taiwan

Downloaded By: [2007-2008-2009 National Chiao Tung University] At: 05:18 24 December 2009

Two-phase flow approaching singularities such as abrupt expansions and sudden contractions is widely encountered in typical industrial and heat exchanging devices. There have been some studies concerning this subject but they mostly are applicable for larger channels. In this study, the first attempt is made to review the existing efforts concerning two-phase flow across sudden expansions/contractions and to examine the applicability of the existing correlations with respect to the recent data in small channels. The second part of this study presents some newly measured pressure drops and observed flow patterns pertaining to some special flow phenomena by expansion/contraction. For an abrupt expansion, it is found that the existing correlations all fail to provide a reasonably predictive capability against the newly collected data. Furthermore, a unique flow pattern called "liquid jet-like flow pattern" occurs at a very low quality region of total mass flux of 100 $kg{\cdot}m^{-2}{\cdot}s^{-1}$, and it raises a setback phenomenon of pressure drop. By contrast, an appreciable increase of pressure difference is seen when the liquid jet-like flow pattern is completely gone. A similar conclusion is drawn for the data of contractions. For the correlations/predictive models, the homogeneous model gives satisfactory prediction for conventional macro-channels but fails to do so when the channels become smaller. This is especially pronounced for a small-diameter tube with a Bond number being less than 1, in which the effect of surface tension dominates.

INTRODUCTION

In recent years, utilization of mini- and micro-channels has become quite attractive in heat exchanging devices. However, the length of the mini-/micro-channel is normally shorter than that in a macro-channel to eliminate the accompanied high pressure loss. This eventually leads to another problem of accurate estimation of the total pressure drop in the mini/micro system. Flow of two-phase mixtures across sudden expansions and contractions is relevant in many applications, including heat-exchanging equipment and connection pipelines. As the two-phase mixture flows through the sudden area changes, the flow might form a separation region at a sharp corner and cause an irreversible pressure loss. For the macro system, this loss is usually regarded as a minor loss, but its role becomes more and more crucial as the channel size gets smaller and shorter. Accurate methods for predicting the pressure drop in such systems are therefore important. This is particularly true for modern cooling systems where numerous channels or micro-channels are exploited to distribute the working fluid. There have been some developed correlations applicable to the pressure loss for the conventional tubes; however, very few investigations have been reported for this abrupt pressure change with respect to mini-channels (Abdelall et al. [1], Chen et al. [2, 3]). Applicability of the existing correlations/models to this area is quite ambiguous. It is therefore essential to examine the corresponding applicability.

The authors acknowledge the financial support provided by the Energy Bureau and Department of Industrial Technology both from the Ministry of Economic Affairs. The last author acknowledges a visiting professorship for his short stay in King Mongkut's University of Technology Thonburi, during the period of writing this article in Thailand.

Address correspondence to Dr. Chi-Chuan Wang, Senior Lead Researcher, D100 EEL/ITRI, Bldg. 64, 195-6, Sec. 4, Chung Hsing Rd., Chutung, Hsinchu, Taiwan, 310. E-mail: ccwang@itri.org.tw

LITERATURE REVIEW

For single-phase flow, by combining with the pressure balance equation, the static pressure difference subject to the

Downloaded By: [2007-2008-2009 National Chiao Tung University] At: 05:18 24 December 2009

sudden expansion is related to the kinetic energy of the flow:

$$\frac{\Delta P_e}{\frac{G^2}{2\rho}} = -2\sigma_A(1-\sigma_A) \tag{1}$$

where the mass flux density (G) and velocity (u) are calculated based on the smaller cross-sectional area of the inlet tube. The negative sign indicates a pressure recovery whose value varies from zero to a maximum of 0.5 at $\sigma_A = 0.5$. Analogously, the pressure loss subject to sudden contraction is normally in terms of the contraction loss coefficient (K) and multiplication of kinetic energy of the flow:

$$\frac{\Delta P_c}{\frac{G^2}{2\rho}} = K \tag{2}$$

where σ_A is the passage cross-sectional area ratio and $0 < \sigma_A < 1$, and total mass flux (G) and velocity (u) are calculated based on the smaller cross-sectional area of the outlet tube. The value of K is related to the Reynolds number and contraction ratio, and it is close to 0.5 and 1.0 with a very small cross-sectional area ratio ($\sigma_A < 0.05$) (Kays and London [4]).

For single-phase flow through the contraction, Chisholm [5] combined the static pressure drop to the vena contracta (ΔP_{iv}) and the pressure recovery downstream of the vena contracta (ΔP_{vc}) to give the total static pressure drop at the contraction (ΔP_c):

$$\Delta P_{iv} = \left(\frac{G^2}{2\rho_L}\right)\left[(\sigma_A C_C)^{-2} - 1\right] \tag{3}$$

$$\Delta P_{VC} = \frac{\left(\frac{G}{\sigma_A}\right)^2}{\rho_L}\left[C_c^{-1} - 1\right] \tag{4}$$

$$\Delta P_C = \Delta P_{iv} - \Delta P_{vc} = \left(\frac{G^2}{2\rho_L}\right)\left[\frac{1}{(\sigma_A C_C)^2} - 1 - \frac{2\left(C_C^{-1}-1\right)}{\sigma_A^2}\right] \tag{5}$$

By comparing Eq. (2) with Eq. (5), the contraction loss coefficient can be found as:

$$K = \frac{1}{(\sigma_A C_C)^2} - 1 - \frac{2\left(C_C^{-1}-1\right)}{\sigma_A^2} \tag{6}$$

The contraction coefficient C_C correlated by Chisholm [5] is given as follows:

$$C_C = \frac{1}{[0.639(1-\sigma_A)^{0.5}+1]} \tag{7}$$

Another contraction coefficient C_C proposed by Geiger [6] is:

$$C_C = 1 - \frac{(1-\sigma_A)}{[2.08(1-\sigma_A)+0.5371]} \tag{8}$$

Two-Phase Pressure Change Across Sudden Expansion

For the two-phase pressure change across sudden expansion, Romie [7] derived the following expression for sudden enlargement:

$$\Delta P_e = \frac{-G^2\sigma_A(1-\sigma_A)}{\rho_L}\left[\begin{array}{l}\left(\frac{(1-x)^2}{(1-\alpha_{in})} + \frac{(\rho_L/\rho_G)x^2}{\alpha_{in}}\right) - \\ \sigma_A\left(\frac{(1-x)^2}{(1-\alpha_{\exp})} + \frac{(\rho_L/\rho_G)x^2}{\alpha_{\exp}}\right)\end{array}\right] \tag{9}$$

where the subscript "in" denotes upstream of expansion whereas "exp" represents downstream of expansion. If the void fraction remains unchanged, Eq. (9) becomes

$$\Delta P_e = \frac{-G^2\sigma_A(1-\sigma_A)}{\rho_L}\left[\frac{(1-x)^2}{(1-\alpha)} + \frac{(\rho_L/\rho_G)x^2}{\alpha}\right] \tag{10}$$

Richardson [8] simplified the energy balance model and assumed that the pressure recovery is proportional to the kinetic energies of the phases, yielding:

$$\Delta P_e = -0.5G^2\left(1-\sigma_A^2\right)\left[\frac{\sigma_A\left(1-x^2\right)}{\rho_L(1-\alpha)}\right] \tag{11}$$

Assuming that a heterogeneous flow and a loss of dynamic pressure head takes place in the liquid phase, Lottes [9] derived:

$$\Delta P_e = \frac{-G^2\sigma_A(1-\sigma_A)}{\rho_L(1-\alpha)^2} \tag{12}$$

By considering the pressure rise in a sudden expansion with irreversible flow induced in a rough tube, Chisholm and Sutherland [10] also developed a heterogeneous model based on the momentum balance:

$$\Delta P_e = -G^2\sigma_A(1-\sigma_A)(1-x)^2 \times \left[\frac{\left(1+C_h/X_{CH}+1/X_{CH}^2\right)}{\rho_L}\right] \tag{13}$$

where

$$X_{CH} = \left(\frac{\rho_G}{\rho_L}\right)^{0.5}\frac{(1-x)}{x} \tag{14}$$

$$C_h = \left\{1 + 0.5\left[1-\left(\frac{\rho_G}{\rho_L}\right)\right]^{0.5}\right\}\left\{\left(\frac{\rho_L}{\rho_G}\right)^{0.5} + \left(\frac{\rho_G}{\rho_L}\right)^{0.5}\right\} \tag{15}$$

The model of Chisholm and Sutherland [10] was compared with the bubbly flow data ($\alpha < 0.35$) for an air–water mixture. Although their predictions remain reasonably good, their model slightly underestimated the data (Attou et al. [11]).

Downloaded By: [2007-2008-2009 National Chiao Tung University] At: 05:18 24 December 2009

Based on some test data, Wadle [12] proposed a formula to describe the pressure recovery in an abrupt diffuser. The model includes an artificial constant K in connection with different working fluids ($K = 0.667$ for steam-water, $K = 0.83$ for air–water):

$$\Delta P_e = -\left(1-\sigma_A^2\right)\frac{1}{2}G^2K\left[\frac{(1-x)^2}{\rho_L}+\frac{x^2}{\rho_G}\right] \tag{16}$$

From the mechanical energy equation without friction dissipation, Collier and Thome [13] derived the following expression:

$$\Delta P_e = \frac{-G^2\left(1-\sigma_A^2\right)}{2\left(\frac{x}{\rho_G}+\frac{1-x}{\rho_L}\right)}\left[\frac{(1-x)^3}{(1-\alpha)^2\rho_L^2}+\frac{x^3}{\alpha^2\rho_G^2}\right] \tag{17}$$

For estimation of the void fraction α, a very simple correlation was recently proposed by Kawahara et al. [14] as

$$\alpha = \frac{0.03\beta^{0.5}}{\left(1-0.97\beta^{0.5}\right)} \tag{18}$$

where β is the gas volumetric flow ratio, given as $\beta = j_G/(j_G + j_L)$, j_L is the superficial liquid velocity, and j_G is the superficial gas velocity. For homogeneous flow, Eq. (10) becomes:

$$\Delta P_e = -G^2\sigma_A(1-\sigma_A)\left[\frac{(1-x)}{\rho_L}+\frac{x}{\rho_G}\right] \tag{19}$$

Since the gas phase and liquid phase have different velocities, particularly for a large density difference between the gas and liquid phases, more realistic models and additional parameters are needed for the pressure recovery calculation.

Based on an annular-mist flow model accompanied with mass and momentum balance, Schmidt and Friedel [15] proposed a rather complex formula:

$$\Delta P_e = \frac{G^2\left[\frac{\sigma_A}{\rho_{eff}}-\frac{\sigma_A^2}{\rho_{eff}}-f_e\rho_{eff}\left(\frac{x}{\rho_G\alpha}-\frac{(1-x)}{\rho_L(1-\alpha)}\right)\left(1-\sqrt{\sigma_A}\right)^2\right]}{1-\Gamma_e(1-\sigma_A)} \tag{20}$$

where

$$\frac{1}{\rho_{eff}} = \frac{x^2}{\rho_G\alpha}+\frac{(1-x)^2}{\rho_L(1-\alpha)}+\frac{\alpha_E\rho_L(1-\alpha)}{1-\alpha_E} \times\left[\frac{x}{\rho_G\alpha}-\frac{1-x}{\rho_L(1-\alpha)}\right]^2 \tag{21}$$

$$\alpha = 1-\frac{2(1-x)^2}{1-2x+\sqrt{1+4x(1-x)\left(\frac{\rho_L}{\rho_G}-1\right)}} \tag{22}$$

$$\alpha_E = \frac{1}{S}\left[1-\frac{1-x}{1-x(1-0.05We^{0.27}\mathrm{Re}^{0.05})}\right] \tag{23}$$

$$S = \frac{x}{1-x}\frac{(1-\alpha)}{\alpha}\frac{\rho_L}{\rho_G} \tag{24}$$

$$We = G^2x^2\frac{d}{\rho_G\sigma}\frac{(\rho_L-\rho_G)}{\rho_G} \tag{25}$$

$$\mathrm{Re} = \frac{G(1-x)d}{\mu_L} \tag{26}$$

$$\Gamma_e = 1-\sigma_A^{0.25} \tag{27}$$

$$f_e = 4.9\times10^{-3}x^2(1-x)^2\left(\frac{\mu_L}{\mu_G}\right)^{0.7} \tag{28}$$

By applying the momentum balance within the boundary of the conical jet for an incompressible and adiabatic flow, Attou and Bolle [16] obtained a correlation for the two-phase flow pressure recovery from a sudden expansion.

$$\Delta P_e = -\sigma_A(1-\sigma_A)\theta_\sigma^r G^2\Phi + \frac{\left(1-\theta_\sigma^r\right)\sigma_A(1-\sigma_A)G^2}{\rho_L} \tag{29}$$

where $\Phi = x^2/(\alpha\rho_G) + (1-x)^2/[(1-\alpha)\rho_L]$, $\theta_\sigma = 3/[1+\sigma_A^{0.5}+\sigma_A]$, and r is a correction factor related to the physical properties of the mixture. For a gas quality $x = 0$, Eq. (29) can be reduced to $\Delta P_e = -\sigma_A(1-\sigma_A)G^2/\rho_L$. The best fitting to the correction factor is $r = 1$ for a steam–water mixture and $r = -1.4$ for an air–water mixture. The predictive ability of Eq. (29) associated with the air–water and steam–water data is around 23.4% or less (mean deviation). The correlation is particularly good for small mass velocities, but it is inapplicable to high quality flows.

More recently, Abdelall et al. [1] investigated air–water pressure drops caused by abrupt flow area expansions in two small tubes. The tube diameters were 1.6 and 0.84 mm, respectively. Their measured two-phase pressure difference indicated the occurrence of significant velocity slip. Assuming an ideal annular flow regime in accordance with minimum kinetic energy of the flowing mixture (slip ratio $S = (\rho_L/\rho_G)^{1/3}$) leads to a reasonable agreement between the data and the predictions. However, in practice the slip ratio is actually varying along the flow path. The pressure drop across the sudden expansion (ΔP_e) is the difference between the reversible pressure change (ΔP_{eR}) and the irreversible pressure changes (ΔP_{eI}), i.e., $\Delta P_e = \Delta P_{eR} - \Delta P_{eI}$. For an incompressible and adiabatic flow,

$$\Delta P_{eR} = \frac{-0.5\rho_h G^2\left(1-\sigma_A^2\right)}{\rho''^2} \tag{30}$$

$$\Delta P_{eI} = 0.5\rho_L G^2\left[\frac{2\rho_L\sigma_A(\sigma_A-1)}{\rho'}-\frac{\rho_h\rho_L(\sigma_A-1)}{\rho''^2}\right] \tag{31}$$

Where

$$\rho_h = \left[\frac{x}{\rho_G}+\frac{(1-x)}{\rho_L}\right]^{-1} \tag{32}$$

$$\rho' = \left[\frac{(1-x^2)}{\{\rho_L (1-\alpha)\}} + \frac{x^2}{(\rho_G \alpha)} \right]^{-1} \quad (33)$$

$$\rho'' = \left[\frac{(1-x)^3}{\rho_L^2 (1-\alpha)^2} + \frac{x^3}{(\rho_G^2 \alpha^2)} \right]^{-1/2} \quad (34)$$

To apply Eqs. (30) and (31), an empirical relation between α and x is needed. The predictions of the Abdelall et al. slip flow model [1] are only slightly higher than the experimental data, but the simplified momentum balance model, Eq. (8), by Collier and Thome [13] significantly overpredicts the data.

Two-Phase Pressure Change Across Sudden Contraction

Geiger [6] measured pressure drops for steam–water mixtures flowing through sudden contraction with area ratios (σ_A) of 0.398, 0.253, and 0.144. His data were compared with the homogeneous model, momentum equation, and mechanical energy equation across the contractions. The homogeneous model gave the best predictions of the data.

McGee [17] had also measured the steam–water mixtures flowing through sudden contraction using the same test rig as Geiger [6], but with different test sections and conditions (σ_A = 0.608, 0.546). The predictions by homogeneous model when compared with his test data are quite satisfactory. The predictions by the momentum and mechanical energy equations were much lower than the test data. This deviation is believed to be due to the assumption of no mechanical energy loss for the acceleration of the fluids at the downstream of the contraction.

For two-phase flow, the frictional pressure drop due to contraction can be estimated using a homogeneous flow model as recommended by Collier and Thome [13]:

$$\Delta P_c = \left(\frac{G^2}{2\rho_L} \right) \left[\left(C_C^{-1} - 1 \right)^2 + \left(1 - \sigma_A^2 \right) \right] \left[1 + x \left(\frac{\rho_L}{\rho_G} - 1 \right) \right] \quad (35)$$

The mass flux G is calculated based on the cross-sectional area of the outlet tube with smaller cross-sectional area.

Chisholm [5] also used his contraction loss coefficient K, Eq. (5), in association with the homogeneous model, i.e.,

$$\Delta P_c = \left(\frac{G^2}{2\rho_L} \right) \left[\frac{1}{(\sigma_A C_C)^2} - 1 - \frac{2\left(C_C^{-1} - 1 \right)}{\sigma_A^2} \right] \times \left[1 + x \left(\frac{\rho_L}{\rho_G} - 1 \right) \right] \quad (36)$$

Furthermore, Chisholm [5] introduced a constant B coefficient for flow through a discrete interval in evaluating the contraction loss:

$$\Delta P_c = \Delta P_{cL} \left[1 + \left(\frac{\rho_L}{\rho_G} - 1 \right) \left(Bx(1-x) + x^2 \right) \right] \quad (37)$$

$$B = \frac{\left\{ \frac{1}{K_O} \left(\frac{1}{(\sigma_A C_C)^2} - 1 \right) - \frac{2}{(K_O C_C \sigma_A^2)} + \frac{2}{(\sigma_A^2 K_O^{0.28})} \right\}}{\frac{1}{(\sigma_A C_C)^2} - 1 - \frac{2}{(C_C \sigma_A^2)} + \frac{2}{\sigma_A^2}} \quad (38)$$

where ΔP_{cL} is the contraction pressure drop for total flow assumed liquid across the same sudden contraction as shown in Eq. (5), contraction coefficient C_C is given in Eq. (7), and K_O is given as

$$K_o = \begin{cases} \left(1 + x \left(\frac{\rho_L}{\rho_G} - 1 \right) \right)^{0.5} & \text{for} \quad X > 1 \\ \left(\frac{\rho_L}{\rho_G} \right)^{0.25} & \text{for} \quad X \le 1 \end{cases} \quad (39)$$

where X is the Martinelli parameter.

Based on the momentum and mass transfer balance, Schmidt and Friedel [18]developed a new pressure drop model for sudden contraction that incorporates all of the relevant boundary conditions. In this model all the relevant physical parameters were also included in their sudden expansion paper [15]. In addition, the influence of liquid entrainment (α_E) in the gas stream is included, along with relevant parameters like area ratio (σ_A), mass flux (G), gas quality (x), mean void fraction (α), surface tension (σ), the viscosity and density of the gas and liquid phases (μ_G, μ_L, ρ_G, ρ_L), and slip ratio (S), to calculate the effective two-phase density (ρ_{eff}). Their test sections incorporated inlet tube diameters in the range of 44.2–72.2 mm and with outlet tubes in the range of 17.2–44.2 mm. The model predicts several experimental data sets with different physical properties. The comparison of the model and test results is fair, with 80% of the data sets being predicted within ±30%. For incompressible and adiabatic flow, the equation for pressure drop across a sudden contraction is given as:

$$\Delta p_c = \frac{G^2 \left[\frac{1}{\rho_{eff}} - \frac{\sigma_A}{\rho_{eff}} + f_{con} \rho_{eff} \left(\frac{x}{\rho_G \alpha} - \frac{1-x}{\rho_L (1-\alpha)} \right)^2 (1 - \sigma_A^{1/2})^2 \right]}{1 + \Gamma_{con} \left(\frac{1}{\sigma_A} - 1 \right)} \quad (40)$$

where f_{con} is the total fiction factor for the contraction, α is the void fraction, ρ_{eff} is the effective density, Γ_{con} is the base pressure coefficient for the contraction, Re is the Reynolds number, and *We* is the Weber number; ρ_{eff}, α, α_E, S, We, and Re are given in Eqs. (19)–(24) and

$$\Gamma_{con} = 0.77 \sigma_A \left(1 - \sigma_A^{0.306} \right) \quad (41)$$

$$f_{con} = 5.2 \times 10^{-3} x^{0.1} (1-x) \left(\sigma_A \frac{\mu_L}{\mu_G} \right)^{0.8} \quad (42)$$

Abdelall et al. [1] investigated air–water pressure drops caused by abrupt flow area expansion and contraction in a very small test section. The larger and small tube diameters were 1.6 and 0.84 mm, respectively. Assuming incompressible gas and liquid phases, and assuming x and α remained constant across

Downloaded By: [2007-2008-2009 National Chiao Tung University] At: 05:18 24 December 2009

the sudden contraction, the pressure drop across the sudden contraction was derived as

$$\Delta P_c = G^2 \left\{ \frac{\rho_h \left(\frac{1}{C_C^2} - \sigma_A^2 \right)}{2\rho''^2} + \frac{(1 - C_C)}{\rho'} \right\} \tag{43}$$

where ρ_h, ρ' *and* ρ'' are given in Eqs. (32)–(34).

The contraction coefficient C_C, Eq. (7), given by Geiger [6], is utilized in the Abdelall et al. correlation, as in Eq. (43). The two-phase flow pressure change across the sudden contraction data was found significantly lower than the predictions of the homogeneous model. It may be attributed to the significant velocity slip at the vicinity of the flow area change. As a consequence, Abdelall et al. reappraised the suitability of homogeneous flow and concluded that the slip ratio model may be more relevant to accelerating two-phase flow (Moody [19]). Using the Zivi [20] model with the assumption of an ideal annular flow regime, the slip ratio becomes:

$$S = \frac{u_G}{u_L} = \frac{(1 - \alpha)\,\rho_L x}{[(1 - x)\rho_G \alpha]} = \left(\frac{\rho_L}{\rho_G} \right)^{\frac{1}{3}} \tag{44}$$

where u_G and u_L are the actual gas and liquid velocities of gas and liquid phases, respectively. The void fraction (α) is calculated from Eq. (44) by using gas quality and gas and liquid densities. Subsequently Eq. (43) is combined with the slip flow model to give a relatively close agreement with Abdelall et al.'s experimental data. An attempt was also made to correlate the two-phase pressure change data at the contraction point in terms of the Martinelli parameter (X), yielding

$$X = \left(\frac{u_L}{u_G} \right)^{0.1} \left(\frac{1}{x} - 1 \right)^{0.9} \left(\frac{\rho_G}{\rho_L} \right)^{0.5} \tag{45}$$

$$\frac{\Phi_{cL}}{X} = 120\,(X\mathrm{Re}_L)^{-0.7} \tag{46}$$

where $\Phi_{cL} = \Delta P_c / \Delta P_{cL}$ is the two-phase multiplier with all liquid flow through the contraction, and ΔP_{cL} is the pressure drop assuming total flow to be liquid flow. Re_L is the Reynolds number in the smaller tube (considering total flow to be liquid). Thus, the two-phase pressure change at the sudden contraction can be predicted by

$$\Delta P_c = \Delta P_{cL} X \left[120\,(X\mathrm{Re}_L)^{-0.7} \right] \tag{47}$$

From the foregoing review of the two-phase pressure change across the sudden contraction, most of the investigations are related to the abrupt area change for the upstream and downstream having round tube configuration and the tube sizes are generally above 10 mm. However, it should be mentioned that configuration variation across singularity (e.g., from rectangular to round) is very common in practice. Hence the first objective of this study is to provide new test data regarding to this influence. Further, it will be shown in subsequent comparisons that most of the proposed correlations/models are only applicable to their own database. In addition, a flow visualization experiment is also carried out to link with certain special pressure drop phenomenon.

EXPERIMENTAL SETUP

The test rig shown in Figure 1 is designed to conduct tests with air–water mixtures. Air is supplied from an air compressor and then stored in a compressed-air storage tank. Air flows through a pressure reducer and, depending on the mass flux range, is measured by three Aalborg mass flow meters for different ranges of flow rates with measurement uncertainty ranging from 0.5 to 2%. The water flow loop consists of a variable-speed gear pump that delivers water, and the water volumetric flow rate is detected by a magnetic flow meter with 0.001 L/s resolution. A self-made Y-shape mixer having a spring insert that provides good mixing amid air and water is placed ahead of the test section. An extra calming test section with a length of 300 mm after the mixer is used before the mixture goes into the test section. The gas quality is calculated from the measured air flow rate and water flow rate, namely,

$$x = \frac{\dot{m}_G}{\dot{m}_G + \dot{m}_L}$$

The total mass flux (G) of air and water flow rate evaluated at the entrance of rectangular test section range from 100 to 700 $\mathrm{kg \cdot m^{-2} \cdot s^{-1}}$ with gas quality (x) varying from 0.001 to 0.8. The corresponding uncertainties for x are within ±4.3%. The inlet temperatures of air and water are near 25°C. The pressure drops of the air–water mixtures are measured by three Yokogawa EJ110 differential pressure transducers having an adjustable span of 1300 to 13,000 Pa. Resolution of this pressure differential transducer is 0.3% of the measurements. The drilled holes of the pressure taps are perpendicular to the test sections with a diameter of 0.5 mm. Pressure measurements are made at nine locations along the inlet tube and along the rectangular channel as shown in Figure 1. For validation of the present test setup, measurements of the single-phase pressure drops for air and water alone are in terms of friction factors to compare with the friction factor equations for laminar and turbulent flows in rectangular channels. The results are in line with the known correlations having a deviation within ±5%. Leaving the test section, the air–water mixture is separated by an open water tank in which the air is vented and the water is recirculated. The air and water temperatures are measured by resistance temperature device (Pt100Ω) having a calibrated accuracy of 0.1 K (calibrated by Hewlett-Packard quartz thermometer probe with quartz thermometer, models 18111A and 2804A). Observations of flow patterns are obtained from images produced by a high-speed camera of Redlake Motionscope PCI 8000s. The maximum camera shutter speed is 1/8000 s. The high-speed camera can be placed at any position along the rectangular channels or at the side view of the abrupt change of flow area.

Downloaded By: [2007-2008-2009 National Chiao Tung University] At: 05:18 24 December 2009

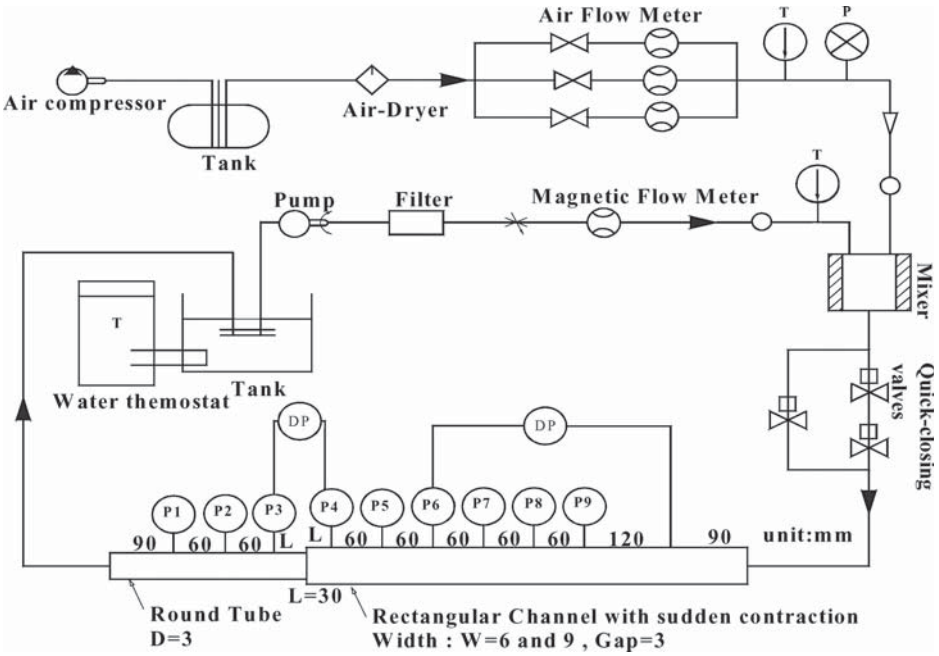

Figure 1 Schematic of test rig and test section.

The test sections are made of transparent acrylic resin, so that the flow pattern and flow structure at the vicinity of the abrupt cross-sectional area change can be visualized. For the expansion test sections, the test sections have the dimensions of gap $(G) \times$ width $(W) = 3 \times 6$ mm and 3×9 mm, and thus the corresponding aspect ratio $A = g/W = 0.333$–ß0.50. These test sections are also arranged in horizontal longitudinal (HL, the wide side is vertical) and the intersection between the rectangular and round tube is well fabricated to avoid any irregularity. The area ratio for the abrupt flow area change (σ_A) is in the range of $0.26 \sim 0.39$. The schematic and the dimensions of the test sections are also shown in Figure 1.

Figure 2a shows a typical change of static pressure along the axis for flow across the expansion. Due to the deceleration of the flow in the transitional region, the static pressure initially increases at the expansion area. After the pressure reaches the maximum, the pressure gradient merges with the downstream pressure gradient line. The pressure change at the sudden expansion is defined as the pressure difference for upstream and downstream fully developed pressure gradient lines extended to the expansion position, i.e., ΔP_{exp}, as shown in Figure 2a. Similarly, Figure 2b represents the variation of static pressure along the flow direction across singularity (for expansion and contraction). When flow approaches the contraction, due to the acceleration of the flow in the transitional region, the static pressure initially decreases to the contraction area. After the pressure reaches the minimum, the pressure increases to a downstream point and then merges with the downstream fully developed pressure gradient line. The pressure change at the sudden contraction is defined as the pressure difference at the interception of singularity evaluated using the fully developed pressure

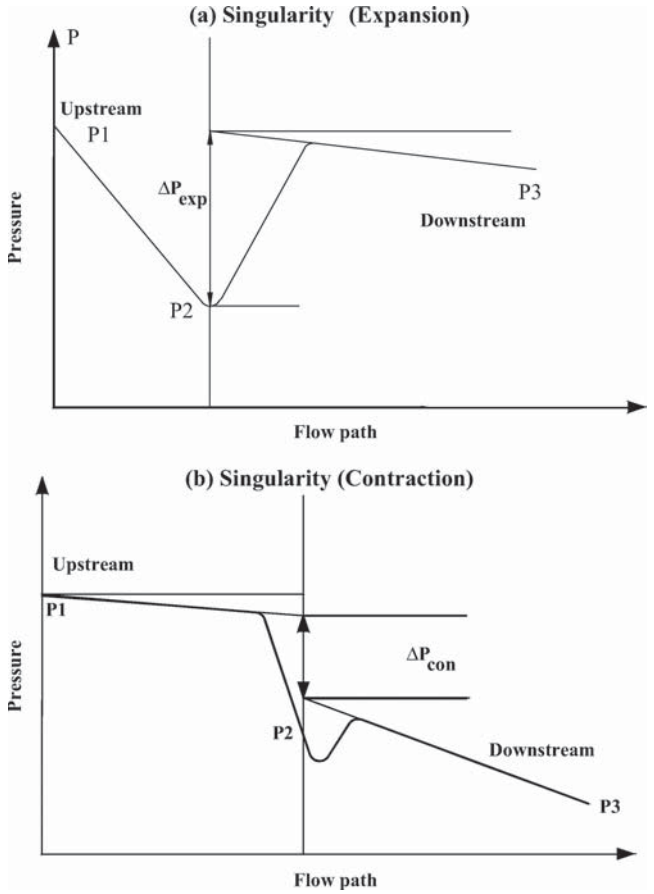

Figure 2 Definition of pressure drop subject to the influence of (a) sudden enlargement and (b) abrupt contraction.

Downloaded By: [2007-2008-2009 National Chiao Tung University] At: 05:18 24 December 2009

gradients from upstream and downstream, respectively, i.e., ΔP_{con}, as shown in Figure 2b.

Some previous investigations used a single pressure differential transducer to measure the difference across the sudden contraction. This kind of measurement cannot actually reflect the pressure loss and pressure recovery across the abrupt area change. In this study, several pressure transducers are utilized for measuring the local pressures in the upstream and downstream parts of the test sections as shown in Figure 1. The measured axial pressures versus the pressure tap positions are plotted in a figure to setup the fully developed pressure gradient lines in the upstream and downstream for further obtaining the corresponding pressure change at the sudden contraction/expansion.

Downloaded By: [2007-2008-2009 National Chiao Tung University] At: 05:18 24 December 2009

RESULTS AND DISCUSSION

Results for Expansion

The corresponding measured pressure drops subject to the sudden enlargement is shown in Figure 3. In general, the pressure drops increase with the rise of vapor quality. However, a notable drop of pressure difference is seen for $G = 100$ kg·m^{-2}·s^{-1} near a vapor quality of 0.01. A similar phenomenon was also reported by Schmidt and Friedel [15]. They also found that the pressure difference occurs at the very low quality region (∼0.005–0.02, depending on the mass flux) and argued that this phenomenon is not due to experimental errors but is associated with the flow pattern changes. For better understanding about this unique phenomenon, one can examine the variation of the corresponding flow pattern. Photographs that are representative of the observed flow patterns for 9 × mm and 6 × mm rectangular channels with a mass flux density of 100 kg·m^{-2}·s^{-1} and vapor qualities ranging from 0.001 to 0.5 are displayed in Figure 4 to show the flow progress in the presence of abrupt enlargement. As seen in Figure 4, for $G = 100$ kg·m^{-2}·s^{-1} at $x = 0.001$ flowing into the 9 × mm enlarged section, the original flow pattern before flowing across the sudden enlargement is elongated bubbly flow, which turns into slug flow after the abrupt area change. This is due to the considerable increase of cross-sectional area, leading to a decline of velocity and to aggregation of elongated bubble.

Note that the original liquid flow gathers at the bottom due to gravity. Hence, as the vapor quality is increased further, the entering flow contains sufficient momentum to become a jet-like (Figure 4c, $x = 0.01$) pattern. However, the liquid jet front heads towards the bottom section since its accompanied liquid momentum is unable to sustain itself against the gravity. For a further increase of vapor quality (Figure 4d, $x = 0.05$), the liquid jet spreads more evenly around the periphery pertaining to the higher momentum. The liquid jet-like flow pattern is similar to the quasi-free-jet pattern observed by Attou et al. [11]. The confined free-jet pattern appears to be conical with a small opening angle. With a further increase of vapor quality, the

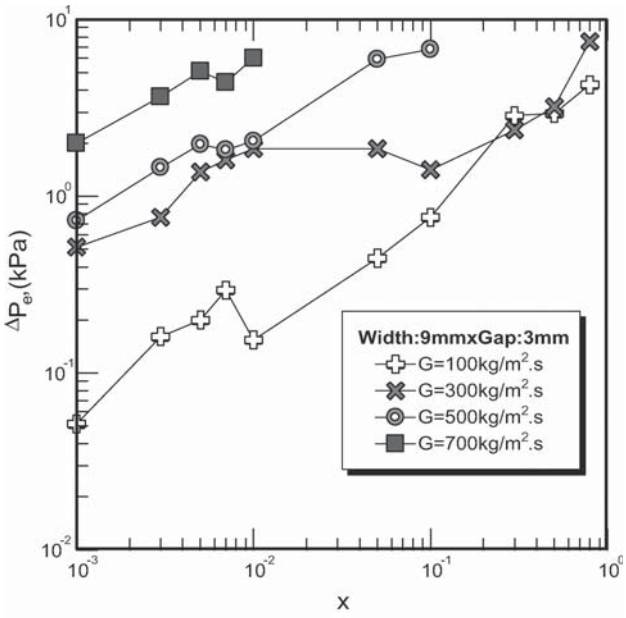

(a) Width: 9 mm x Gap: 3 mm

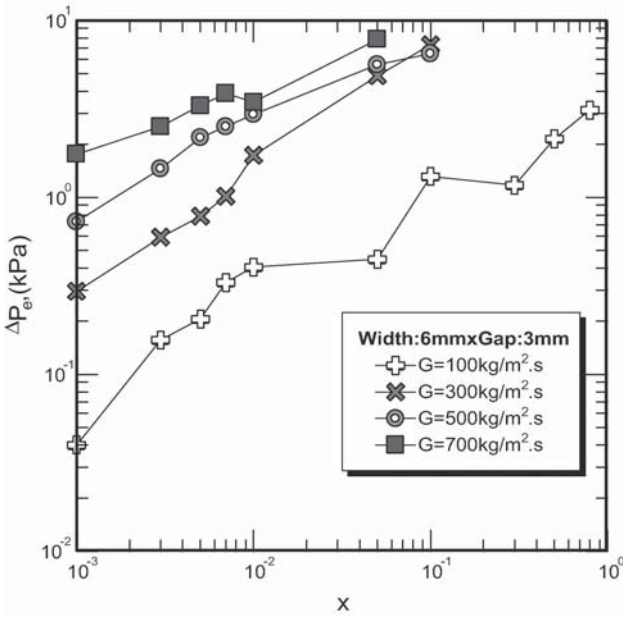

(b) Width: 6 mm x Gap: 3 mm

Figure 3 Measured pressure changes as a function of mass flux and gas quality.

inherited momentum can easily break up the liquid into droplets and a quite uniformly spread film around the whole rectangular section. The flow pattern is thus an annular flow pattern (e.g., Figure 4f, $x = 0.5$). The unique "liquid jet-like" flow pattern persists at the entrance of the 9 × mm test section. This flow pattern, however, is not seen for the 6 × mm test section as seen from Figures 4g–l. However, by comparing the foregoing observed flow patterns, one can see the unusual phenomenon

Downloaded By: [2007-2008-2009 National Chiao Tung University] At: 05:18 24 December 2009

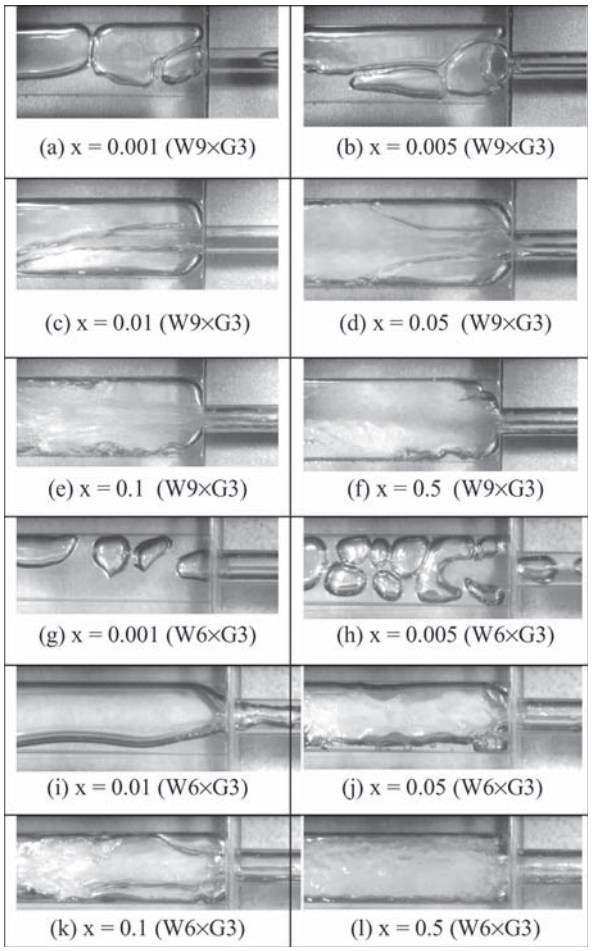

Figure 4 Progress of flow pattern for sudden enlargement vs. quality at $G = 100\ \mathrm{kg{\cdot}m^{-2}{\cdot}s^{-1}}$.

is actually related to the liquid jet-like flow pattern. When the liquid jet flows across the sudden enlargement, part of its momentum is conserved and the gas flow is alongside the liquid jet. In this regard, the corresponding expansion pressure change decreases.

In fact, some of the measured pressure difference data of this study also reveal a flat or slightly leveled-off phenomenon versus vapor quality (e.g., $G = 300\ \mathrm{kg{\cdot}m^{-2}{\cdot}s^{-1}}$). A close examination of the data suggests that this region is also related to the "liquid jet-like" flow pattern. The observations suggest that a conceivable reduction of the pressure difference is encountered when liquid jet-like flow pattern prevails, yet a flattening or leveling off of the pressure difference is seen when the liquid jet-like flow is less pronounced. By contrast, one can find an appreciable increase of pressure difference when the liquid jet-like flow pattern is completely gone. Apparently the confinement effect of this test section is the main cause for the disappearance of this flow pattern. Note that the distance from the brim of the small diameter tube at the intersection of the abrupt enlargement to the upper or lower surface of the rectangular tube for the 9 × 3 mm tube is two times larger than that of the 6 × 3 mm tube. Hence, the liquid flowing out of the smaller diameter tube touches the adjacent walls comparatively easily, thereby eliminating the "liquid jet-like" flow pattern accordingly. In addition, the size of air bubbles of the 6 × 3 mm tube (Figure 4g) is much smaller than that of the 9 × 3 mm tube at $x = 0.001$ (Figure 4a).

For a higher mass flux of 300 $\mathrm{kg{\cdot}m^{-2}{\cdot}s^{-1}}$, progress of flow pattern change is somewhat similar to that at $G = 100\ \mathrm{kg{\cdot}m^{-2}{\cdot}s^{-1}}$ except that the development of flow pattern moves toward a lower quality region. However, the liquid jet-like flow pattern is rather unclear at higher gas quality in both test sections. Therefore, the leveling-off phenomenon of the expansion pressure loss is almost unseen.

The measured pressure differences subject to abrupt enlargement are compared with the foregoing models/correlations described in the literature review. In total, nine models and correlations were used for comparison; detailed comparisons indicated that none of the models/correlations can predict the present test results with an acceptable accuracy. There are several possible causes for this significant departure. The first one is attributable to the evaluation of void fraction. Note that most of the models/correlations require information on a void fraction, except for the homogeneous model, the Chisholm and Sutherland [10] correlation, and the Wadle correlation [12]. This eventually involves suitable selection of the correlation of void fraction. In this study, the void fraction correlation being used is identical to those suggested in previous researchers. However, one still sees a tremendous digression from these comparison charts. The second cause of this deviation is related to the geometric difference. The previous geometries are mostly at a much larger scale, except those by Abdelall et al. [1]. Furthermore, previous studies are generally applicable for round/round sudden enlargement, while the present experiments are conducted for round/rectangular transformation. The best predictive abilities for the previous models are those by Wadle [12] with a mean deviation around 200%. The deviation is calculated as $\frac{1}{N}(\sum_{1}^{N}\frac{|\Delta P_{PRED}-\Delta P_{EXP}|}{\Delta P_{EXP}}) \times 100\%$, where N is the number of total data points. The results imply that further efforts should be made for seeking a better correlation.

Results for Contraction

Figure 5 shows the measured two-phase pressure drops subject to the sudden contraction for the 6 × 3 mm and 9 × 3 mm channels, respectively; each test section has 40 data points. In general, the contraction pressure drops increase with the quality and mass flux. However, a noticeable drop of the pressure loss is encountered at a low mass quality region ($x < 0.1$). This phenomenon was also observed by Schmidt and Friedel [18] for their air–water data at $G = 1000\ \mathrm{kg{\cdot}m^{-2}{\cdot}s^{-1}}$, where a local peak of pressure drop versus vapor quality is seen at a low mass flow quality. This phenomenon was characterized as a change of flow pattern in the inlet pipe or outlet pipe. In this study, a notable pressure drop is seen for $G = 100\ \mathrm{kg{\cdot}m^{-2}{\cdot}s^{-1}}$ and a gas quality

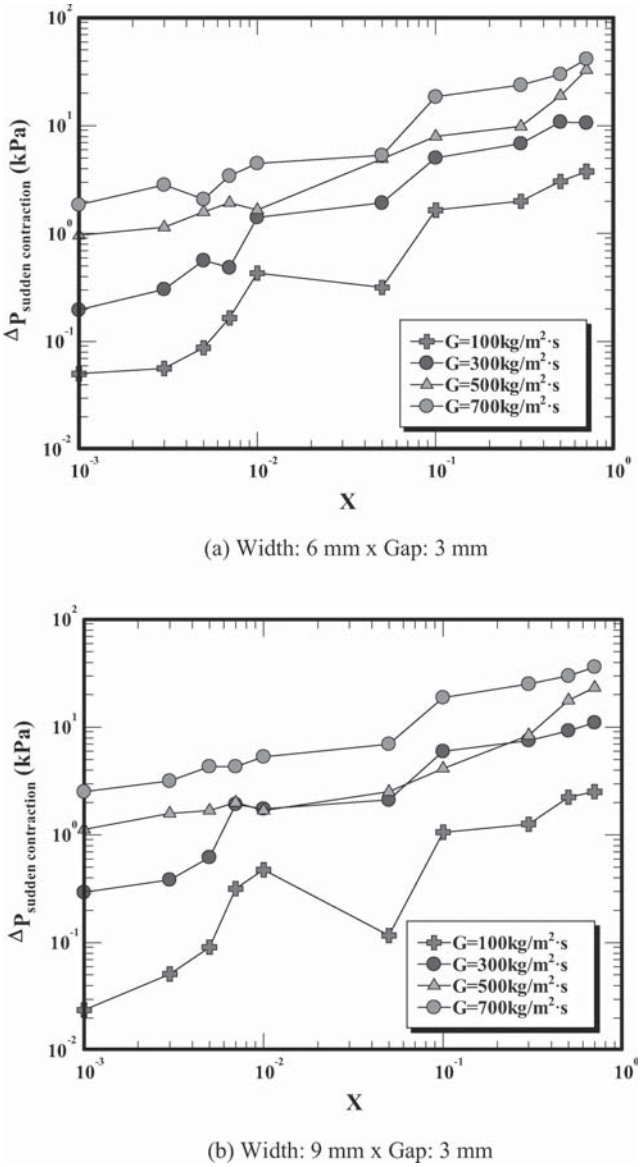

Figure 5 Measured pressure change as a function of mass flux and quality for (a) 6 mm × 3 mm and (b) 9 mm × 3 mm channel.

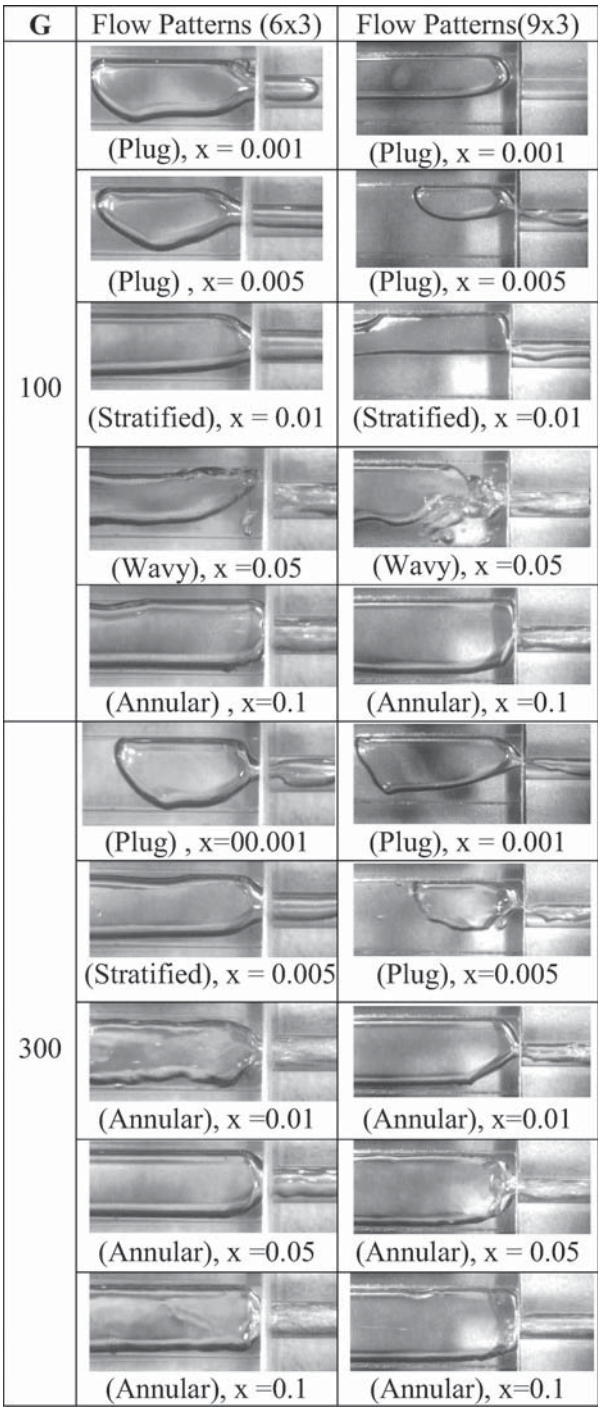

Figure 6 Progress of flow pattern vs. quality across the sudden contractions for $G = 100$ and 300 kg·m^{-2}·s^{-1}.

of 0.05 as shown in Figure 5. For further understanding about the phenomenon, one can see the progress of the flow pattern subject to the influence of contraction from Figure 6. As shown in the figure, for a mass flux of 100 kg·m^{-2}·s^{-1} at a low quality less than 0.01, one can see that the intermittent flow pattern prevails before and after the contraction. Although the stratified flow might persist after the contraction, one can see that the vena contracta is clearly absent. Note that the mentioned vena contracta is slightly different from that in single-phase flow. For single-phase flow, the vena contracta represents the point in a fluid stream where the diameter of the jet stream is the least, such as in the case of a stream issuing out of a nozzle. Here the observed vena contracta denotes the gas stream surrounded by liquid with the smallest diameter of gas core.

With the rise of vapor quality ($x = 0.01$–0.1), the vena contracta is observable for the major flow pattern after the contraction turn into an annular flow pattern. As delineated by Collier and Thome [13], the presence of the vena contracta effectively converted the accelerated and pressure energy into kinetic energy with little or no frictional dissipation from upstream. This

Downloaded By: [2007-2008-2009 National Chiao Tung University] At: 05:18 24 December 2009

Downloaded By: [2007-2008-2009 National Chiao Tung University] At: 05:18 24 December 2009

will certainly offset the irreversible pressure loss caused by the singularity. Beyond the vena contracta position, the conditions are similar to those of sudden enlargement through which considerable frictional dissipation occurs. In essence, the considerable deflection of the contraction pressure drop is associated with the transition of forming the vena contracta. For a larger mass flux like $G = 300\ \mathrm{kg{\cdot}m^{-2}{\cdot}s^{-1}}$, the vena contracta is still seen even at a very low quality range of 0.001–0.005. However, the rising frictional contribution with mass flux will counteract the occurrence of vena contracta, thereby leading to a comparatively small influence of vena contracta on the pressure drop. In addition, formation of vena contracta also shifts toward a smaller gas quality, giving rise to an early deflection of pressure drop at a lower gas quality. However, it should be mentioned that this phenomenon becomes less and less pronounced when the mass flux is increased. This is because the increasing frictional performance counterbalances the effect of the vena contracta.

To test the validity of the foregoing described models/correlations from the existing literatures, the measured two-phase pressure drop data subject to abrupt contraction in two test sections are compared with the previously described homogeneous model (Collier and Thome [13]), and correlations of Chisholm [5], Schmidt and Friedel [18], and Abdelall et al. [1]. The detailed comparisons and relevant mean deviations for the models/correlations give fair predictions of the present data, but none of them can accurately predict the entire database. Note that most of the existing data were conducted for the geometry from round/rectangular to round/rectangular configuration, while the present test section is from rectangular to round tube configuration. The average mean deviations of the relevant predictions are 49.15%, 54.12%, 50.8%, 64.5%, and 74.8% by the homogeneous model (Eq. 35), Chisholm homogeneous model (Eq. 36), Chisholm correlation (Eq. 37), Schmidt and Friedel correlation (Eq. 40), and Abdelall et al. correlation (Eq. 43), respectively. Also, the Abdelall et al. simplified correlation (Eq. 43) gave a mean deviation of more than 100%. The homogeneous model gives better predictive ability than the others, which had also been indicated by Geiger [6] and McGee [17]. For homogeneous predictions, the data with higher pressure drop give a good agreement with the predictions. Note that the flow patterns for these data with good predictions are actually annular flow. However, the data for all slug and stratified flows, where buoyancy force plays a significant role, are greatly over the predictions.

There are some pressure drop data for two-phase flow across sudden contractions available from the literature, as mentioned earlier. For comparison purposes, the present data and some available data along with some databases (Geiger [6]; McGee [17]; Schmidt and Friedel [18]; Abdellal et al. [1]) are compared with the relevant correlations and models. In general, the homogeneous predictions give a very good agreement with the two data sets reported by Geiger [6] and McGee [17], with corresponding mean deviations of 19.93% and 16.81%, respectively. The mean deviations for the data of Schmidt and Friedel [18] and the present data are 43.46% and 49.15%, respectively. Nevertheless, the homogeneous model significantly overpredicted the data of Abdelall et al. [1] with 468.79% mean deviation, which was also previously reported by these authors. The possible cause for this large deviation is associated with the micro-tubes (with one inner diameter of 1.60 mm and the other of 0.84 mm) being tested. For these micro-tubes, influence caused by surface tension takes control. For obtaining a better predictive ability, one should also take into account the influence of surface tension force (Tripplet et al. [21]). The balance of buoyancy and surface tension force can be represented by the Bond number (Bo) as:

$$Bo = \frac{g(\rho_L - \rho_G)(D/2)^2}{\sigma} \tag{48}$$

When the value of Bo is near or less than 1.0, the stratified flow pattern is not able to exist in most of the two-phase flow conditions. Chen et al. [2] had utilized the Bond number (Bo) to count for the force balance between buoyancy and surface tension in development of the two-phase frictional pressure drop correlation in small tubes. From the foregoing comparison, it is found that the homogeneous model gives good predictive ability but fails to predict the Abdelall et al. microchannel data. By examining the corresponding Bond number for these five databases, it is found that the departure of the predictive ability of homogeneous model is strongly related to the Bond number. In that regard, it is suggested that the influence of Bond number should be included in future development of the correlation.

CONCLUSIONS

Two-phase flow approaching singularities such as abrupt expansion and sudden contraction is widely encountered in typical industrial and heat-exchanging devices. For conventional channels where the flow path may be comparatively long, the associated pressure drops relative to the total pressure drops may be small and are often neglected. However, with smaller and smaller channels being introduced (such as mini- or microchannels) to the real world, one can no longer ignore their influence, and the need for more accurate estimation of the expansion/contraction loss becomes evident. There have been some studies concerning this subject but mostly applicable for larger channels. The major effort of this study is to review the existing efforts concerning two-phase flow across sudden expansions/contractions and to examine the applicability of the existing correlations with respect to the recent data in small channels. The second part of this study is to present some newly measured pressure drops and observed flow patterns pertaining to influence of expansion/contraction. For an abrupt expansion, it is found that the existing correlations all fail to provide a reasonably predictive capability versus the newly collected data. Furthermore, a unique flow pattern called a "liquid jet-like flow pattern" occurs at a very low quality region of $G = 100\ \mathrm{kg{\cdot}m^{-2}{\cdot}s^{-1}}$, and it raises a setback phenomenon of

pressure drop. By contrast, an appreciable increase of pressure difference is seen when the liquid jet-like flow pattern is completely gone. Similar conclusion is drawn to the data of contractions. For the correlations/predictive models, the homogeneous model gives satisfactory prediction for conventional macrochannels but fails to do so when the channels become smaller. This is especially pronounced for a small-diameter tube with a Bond number being less than 1, in which the effect of surface tension dominates. It is also found that most existing correlations can only predict their own database, and extrapolation of their correlations outside their test range is questionable. Hence, it is suggested that the Bond number should be introduced to modify the existing homogeneous model.

Downloaded By: [2007-2008-2009 National Chiao Tung University] At: 05:18 24 December 2009

NOMENCLATURE

A	aspect ratio, gap/width, $0 \leq A \leq 1$
C_h	Chisholm's factor, defined in Eq. (15)
Bo	Bond number, defined in Eq. (48)
C_C	contraction coefficient
d	internal diameter of circular tube, m
D_h	hydraulic diameter, m
f	friction factor
f_{con}	total fiction factor for the contraction
g	rectangular channel gap, mm
G	total mass flux, $kg \cdot m^{-2} \cdot s^{-1}$
j_L	superficial liquid velocity, $m \cdot s^{-1}$
j_G	superficial gas velocity, $m \cdot s^{-1}$
K	loss coefficient
$\dot{m}$	mass flow rate, $kg \cdot s^{-1}$
P	pressure, Pa
ΔP_c	pressure change across the sudden contraction, Pa
ΔP_{cL}	pressure drop across the sudden contraction for total flow assumed liquid, Pa
ΔP_{iv}	static pressure drop to the vena contracta, Pa
ΔP_{vc}	pressure recovery downstream of the vena contracta, Pa
ΔP_e	pressure change across the sudden expansion, Pa
ΔP_{eI}	irreversible pressure changes across the sudden expansion, Pa
ΔP_{eR}	reversible pressure changes across the sudden expansion, Pa
dP/dz	frictional pressure gradient, $Pa \cdot m^{-1}$
Re	Reynolds number, $\rho ud/\mu$
S	slip ratio
u	mean axial velocity in the small tube, $m \cdot s^{-1}$
x	gas quality
W	rectangular channel width, mm
We	Weber number
Γ_{con}	base pressure coefficient for the contraction
X	Martinelli parameter
X_{CH}	correlation parameter for Chisholm and Sutherland [10]; see Eq. (14)

Greek Symbols

σ	surface tension, $N \cdot m^{-1}$
σ_A	flow cross-sectional area contraction ratio
α	mean void fraction
α_E	mean volumetric liquid entrained in the gas flow
μ	viscosity, $N \cdot s \cdot m^{-2}$
Φ_{cL}	two-phase multiplier with all liquid flow through the contraction
β	gas volumetric flow ratio, $=j_G/(j_G + j_L)$
ρ	density, $kg \cdot m^{-3}$
ρ'	fictitious mixture density defined in Eq. (33), $kg \cdot m^{-3}$
ρ''	fictitious mixture density defined in Eq. (34), $kg \cdot m^{-3}$
ρ_{eff}	effective density defined in Eq. (21), $kg \cdot m^{-3}$

Subscripts

con	contraction
EXP	experiments
G	gas-phase
h	homogeneous
L	liquid-phase
PRED	values for correlation or model predictions

REFERENCES

[1] Abdelall, E. F., Hahm, G., Ghiaasiaan, S. M., Abdel-Khalik, S. I., Jeter, S. S., Yoda, M., and Sadowski, D. L., Pressure Drop Caused by Abrupt Flow Area Changes in Small Channels, *Experimental Thermal & Fluid Science*, vol. 29, pp. 425–434, 2005.

[2] Chen, I. Y., Yang, K. Y., and Wang, C. C., An Empirical Correlation for Two-Phase Frictional Performance in Small Diameter Tubes, *International Journal of of Heat and Mass Transfer*, vol. 45, pp. 3667–3671, 2002.

[3] Chen, I. Y., Liu, C. C., Chien, K. H., and Wang, C. C., Two-phase Flow Characteristics Across Sudden Expansion in Small Rectangular Channel, *Experimental Thermal & Fluid Science*, vol. 32, pp. 696–706, 2007.

[4] Kays, W. M., and London, A. L., *Compact Heat Exchangers,* 3rd ed., McGraw-Hill, New York, p. 112, 1984.

[5] Chisholm, D., *Two-Phase Flow in Pipelines and Heat Exchangers,* George Godwin, London, pp. 175–192, 1983.

[6] Geiger, G. E., *Sudden Contraction Losses in Single and Two-Phase Flow*, Ph.D. Thesis, University of Pittsburgh, Pittsburgh, PA, 1964.

[7] Romie, F., Private communication to P. Lottes (see Lottes [9]).

[8] Richardson, B., *Some Problems in Horizontal Two-Phase*, *Two-Component Flow*, Report ANL-5949, 1958.

[9] Lottes, P. A., Expansion Losses in Two-Phase Flow, *Nuclear Science and Engineering*, vol. 9, pp. 26–31, 1961.

[10] Chisholm, D., and Sutherland, L. A., Prediction of Pressure Gradients in Pipeline System During Two-Phase Flow, *Proc. Institute of Mechanical Engineers*, vol. 184, pt. 3C, pp. 24–32, 1969.

[11] Attou, A., Giot, M., and Seynhaeve, M., Modeling of Steady Two-Phase Bubbly Flow Through a Sudden Enlargement, *International Journal of Heat and Mass Transfer*, vol. 40, pp. 3375–3383, 1997.
[12] Wadle, M., A New Formula for the Pressure Recovery in an Abrupt Diffuser, *International Journal of Multiphase Flow*, vol. 15, pp. 241–256, 1989.
[13] Collier, J. G., and Thome, J. R., *Convective Boiling and Condensation*, 3rd ed., Oxford, New York, pp. 109–111, 1994.
[14] Kawahara, A. A., Chung, P. M. Y., and Kawaji, M., Investigation of Two-Phase Flow Pattern, Void Fraction and Pressure Drop in a Microchannel, *International Journal of Heat and Mass Transfer*, vol. 28, pp. 1411–1435, 2002.
[15] Schmidt, J., and Friedel, L., Two-Phase Flow Pressure Change Across Sudden Expansions in Duct Areas, *Chemical Engineering Communications*, vol. 141–142, pp. 175–190, 1995.
[16] Attou, A., and Bolle, L., A New Correlation for the Two-phase Pressure Recovery Downstream From a Sudden Enlargement, *Chemical Engineering Technology*, vol. 20, pp. 419–423, 1997.
[17] McGee, J. W., *Two-Phase Flow Through Abrupt Expansions and Contractions*, Ph.D. Thesis, University of North Carolina at Raleigh, 1996.
[18] Schmidt, J., and Friedel, L., Two-Phase Flow Pressure Drop Across Sudden Contractions in Duct Areas, *International Journal of Multiphase Flow*, vol. 23, pp. 283–299, 1997.
[19] Moody, F. J., Maximum Flow Rate of a Single Component, Two-Phase Mixture, *ASME Journal of Heat Transfer*, vol. 86, pp. 134–142, 1965.
[20] Zivi, S. M., Estimation of Steady State Void Fraction by Means of Minimum Entropy Production, *Journal of Heat Transfer*, vol. 86, pp. 247–252, 1964.
[21] Tripplet, K. A., Ghiasiaan, S. M., Abdel-Khlik, S. L., LeMouel, A., and McCord, B. N., Gas–Liquid Two-Phase Flow in Microchannels, Part II: Void Fraction and Pressure Drop, *International Journal of Multiphase Flow*, vol. 25, pp. 395–410, 1999.

Ing Youn Chen is a professor at mechanical engineering of National Yunlin University of Science and Technology, Taiwan. He received his B.S. in mechanical engineering from National Taiwan University in 1971, and received his M.S. in 1979 and Ph.D. in 1984 in mechanical engineering from the University Wisconsin–Milwaukee. He joined Sundstrand and McDonell Douglas space companies from 1985 to 1989 and from 1989 to 1994, respectively. In this period, he was involved in the analysis and testing of two-phase thermal control system for the international space station. Currently, he conducts teaching and research in two-phase flow and heat transfer areas. He is also a reviewer for several international journals.

Somchai Wongwises is a professor in the Department of Mechanical Engineering at King Mongkut's University of Technology Thonburi, Bangmod, Thailand. He received his Doktor Ingenieur (Dr.-Ing.) in mechanical engineering from the University of Hannover, Hannover, Germany, in 1994. His research interests include two-phase flow, heat transfer enhancement, and thermal system design. He is the head of the Fluid Mechanics, Thermal Engineering, and Two-Phase Flow Research Laboratory.

Bing-Chwen Yang is a senior researcher in the Energy & Environment Research Laboratory, Industrial Technology Research Institute (ITRI), Hsinchu, Taiwan. He received his M.S. from the Department of Mechanical Engineering at the University of South Carolina in 1988 and his Ph.D. from the Department of Mechanical Engineering at Pennsylvania State University in 1992. He joined ITRI in 1992. His research areas include heat transfer, two-phase systems, micro cooling systems, and air-conditioning technology. He is the division head of the Residential & Commercial Energy Saving Technology Division in EEL, ITRI. He is also a committee member of ASHRAE technology committee 8.6 for cooling towers.

Chi-Chuan Wang is a senior lead researcher in the Energy & Environment Research Laboratory, Industrial Technology Research Institute (ITRI), Hsinchu, Taiwan. He received his B.S., M.S., and Ph.D. all in mechanical engineering from National Chiao-Tung University, Hsinchu, Taiwan during 1978–1989. He joined ITRI in 1989. His research areas include enhanced heat transfer, multiphase systems, micro-scale heat transfer, and heat pump technology. He is also a regional editor of the *Journal of Enhanced Heat Transfer* and an associate editor of *Heat Transfer Engineering*.

Downloaded By: [2007-2008-2009 National Chiao Tung University] At: 05:18 24 December 2009

International Journal of Heat and Mass Transfer 53 (2010) 2052–2064

Contents lists available at ScienceDirect

International Journal of Heat and Mass Transfer

journal homepage: www.elsevier.com/locate/ijhmt

Comparison of frictional pressure drop models during annular flow condensation of R600a in a horizontal tube at low mass flux and of R134a in a vertical tube at high mass flux

A.S. Dalkilic [a,*], O. Agra [a], I. Teke [a], S. Wongwises [b,*]

[a] Heat and Thermodynamics Division, Department of Mechanical Engineering, Yildiz Technical University, Yildiz, Besiktas, Istanbul 34349, Turkey
[b] Fluid Mechanics, Thermal Engineering and Multiphase Flow Research Lab. (FUTURE), Department of Mechanical Engineering, King Mongkut's University of Technology Thonburi, Bangmod, Bangkok 10140, Thailand

ARTICLE INFO

Article history:
Received 28 May 2009
Received in revised form 13 December 2009
Accepted 13 December 2009
Available online 27 January 2010

Keywords:
Condensation
Pressure drop
Horizontal flow
Downward flow
R600a
R134a

ABSTRACT

This study compares well-known two-phase pressure drop models with the experimental results of a condensation pressure drop of (i) R600a in a 1 m long horizontal smooth copper tube with an inner diameter of 4 mm, outer diameter of 6 mm and (ii) R134a in a 0.5 m vertical smooth copper tube with an inner diameter of 8.1 mm and outer diameter of 9.52 mm. Different vapour qualities (0.45–0.9 for R600a and 0.7–0.95 for R134a), various mass fluxes (75–115 kg m^{-2} s^{-1} for R600a and 300–400 for R134a kg m^{-2} s^{-1}) and different condensing temperatures (30–43 °C for R600a and 40–50 °C for R134a) were tested under annular flow conditions. The quality of the refrigerant in the test section was calculated considering the temperature and pressure obtained from the experiment. The pressure drop across the test section was directly measured with a differential pressure transducer. The most agreeable correlations of various available options were then identified according to the results of analysis during annular flow regime.

© 2009 Elsevier Ltd. All rights reserved.

1. Introduction

The two-phase flow occurs when the two phases, separated from each other by a distinct interface, flow simultaneously. Gas–liquid flows can be observed in many industrial applications such as oil–gas flow in oil pipelines, steam–water flow in nuclear reactors, steam flows in heat pipes and vapour–liquid flow of refrigerants in cooling and air-conditioning applications. This study is concerned with an annular flow regime for the liquid and vapour flow of R600a and R134a in horizontal and vertical tubes respectively.

The actual technologies of nuclear reactors, the aerospace industry, microelectronics, cooling systems, refrigeration, the automotive industry, process industry etc. are characterised by a disposition towards using packages of large power conversion or heat transfer in small volumes. There has been a recent fast development of better, more effective, heat exchangers together with a demand for more compact systems, higher energy efficiency and lower material costs. Heat exchangers are devices that are commonly used to transfer heat between two or more fluids at different temperatures. They are used in a wide variety of applications, e.g. refrigeration and air conditioning systems, power engineering and other thermal processing plants.

One of the major contributors to the depletion of the ozone layer are the hydrochlorofluorocarbon refrigerants used in the refrigeration and air conditioning industries. More compact equipment with higher system operating efficiency for air conditioning has been investigated following changes in efficiency standards. Refrigerant mixtures with enhanced surfaces have been developed as an alternative solution to replace hydrochlorofluorocarbon refrigerants. Accurate methods for the determination of the thermal and fluid-dynamic behaviour of new refrigerants need to be researched in order to improve the efficiency of heat exchangers.

The use of natural refrigerants such as hydrocarbons is one of the possible solutions to avoid the use of CFCs, HCFCs and HFCs. In spite of the prohibition due to safety concerns placed on the use of flammable hydrocarbon refrigerants a few decades ago for normal refrigeration and air conditioning applications, some of the flammable refrigerants have, nevertheless, been used in certain applications according to Kruse [1] and Jung et al. [2]. Recently, isobutene (R600a), propane (R290) and propylene (R1270) have been used for such heat transfer applications as are found in refrigerators, freezers, and heat pumps. Besides this, R429A and R432A including dim ethyl ether (DME, RE170), have been proposed as alternatives to R134a and R22. Unfortunately, some of the new

* Corresponding authors. Tel.: +90 2123832819; fax: +90 2122616659 (A.S. Dalkilic), Tel.: +66 24709115; fax: +66 24709111 (S. Wongwises).
E-mail addresses: dalkilic@yildiz.edu.tr (A.S. Dalkilic), somchai.won@kmutt.ac.th (S. Wongwises).

0017-9310/$ - see front matter © 2009 Elsevier Ltd. All rights reserved.
doi:10.1016/j.ijheatmasstransfer.2009.12.051

Nomenclature

Bo	Bond number
c_p	specific heat, J kg^{-1} K^{-1}
d	internal tube diameter, m
f	friction factor
Fr	Froude number
G	mass flux, kg m^{-2} s^{-1}
g	gravitational acceleration, m s^{-2}
i	enthalpy, J kg^{-1}
i_{fg}	latent heat of condensation, J kg^{-1}
j	superficial velocity
L	length of test tube, m
m	mass flow rate, kg s^{-1}
N_{coff}	confinement number
P	pressure, N m^{-2}
Re	Reynolds number
S	slip ratio
Q	heat transfer rate, W
We	Weber number
x	average vapor quality
X	Lockhart and Martinelli parameter
z	axial coordinate, m
ΔP	pressure drop, Pa
ΔT_{sat}	$T_{sat} - T_{wi}$, °C

Greek symbols

α	void fraction
ϕ	two-phase multiplier
ψ	surface tension parameter
ε	height of roughness
Ω	modifier to the Friedel correlation
σ	surface tension, N m^{-1}
ρ	density, kg m^{-3}
μ	dynamic viscosity, kg m^{-1} s^{-1}

Subscripts

avg	average
evap	evaporator
exp	experimental
F	frictional term
G	gravitational term
g	gas/vapor
go	gas only
i	inlet
int	interfacial
l	liquid
lo	liquid only
M	momentum term
o	outlet
ph	preheater
ref	refrigerant
sat	saturation
t	test section
TP	two-phase
TS	test section
w	water
wi	inner wall

alternative refrigerants have additional problems such as extensive heat transfer degradation during condensation due to the zeotropic characteristics of the refrigerant. For that reason, there is still room for research on alternative refrigerants such as R600a, R744 and R407C.

Annular flow conditions along the tube length include convective condensation which occurs for many applications inside tubes. Annular two-phase flow is one of the most important flow regimes, and is characterised by a phase interface separating a thin liquid film from the gas flow in the core region. Two-phase annular flow occurs widely in film heating and cooling processes, particularly in power generation, and especially in nuclear reactors. This flow regime has received the most attention, both analytically and experimentally, because of its practical importance and the relative ease with which analytic treatment may be applied. In addition to this, condensate distribution inside the tube wall is almost symmetric, and there is high velocity vapour flow in the core during annular flow.

The two-phase pressure drop is a significant design parameter in many engineering applications such as the chemical process industry, the nuclear industry, the petroleum industry, refrigeration and air conditioning applications and space applications. There have been a number of investigations into this subject in the literature due to its importance. The frictional, acceleration, and gravitational components form the two-phase total pressure drop in tubes. Determination of void fraction is necessary for computing the acceleration and gravitational components and, in a similar way, determination of whether either the two-phase friction factor or the two-phase frictional multiplier is also necessary for computing the frictional component of pressure drop.

The Lockhart and Martinelli [3], Chisholm [4] and Friedel [5,6] correlations are generally used for the determination of pressure drop in conventional channels. Some modifications to account for specific geometry or flow conditions are made in these correlations. In spite of their large deviations from the data for small channels in the condensation process, they have still been used as the basis for many recent correlations.

Condensation phenomena inside horizontal tubes represent an important issue in the chemical process and power industries. Shell side condensation is rarely preferred to tube side condensation when the coolant is air or a process gas, or when the condensing refrigerant is at high pressure, dirty or corrosive. For tube side condensers, the horizontal orientation is most commonly applied.

Lee et al. [7,8] examined the condensing heat transfer coefficients and pressure drop of hydrocarbons (R-290, R-600a, R-1270) in the evaporator and condenser, and compared them with those of R22. A tube diameter of 12.7 mm was used for this experiment. As a result of the experimental study it was determined that the condensing heat transfer coefficients and pressure drop of the hydrocarbons in both cases were higher than those of R22 under similar test conditions.

In a study performed by Wen et al. [9] the condensing heat transfer coefficients and pressure drop of the R290, R600 and R290/R600 refrigerants during their condensation inside a serpentine with a 2.46 mm diameter were examined and compared with those for the R134a refrigerant. As a result of these experiments it was determined that the condensing heat transfer coefficients of the hydrocarbons are higher than those of the R134a refrigerant under the same conditions.

Condensation inside vertical tubes usually occurs in nuclear reactors. In the design of passive containment cooling systems (PCCS), the presence of non-condensable gases inside condensed steam is an important technical problem. These kinds of condensers have vertical stainless steel tubes, almost 50 mm in diameter, immersed in a tank of water under atmospheric pressure conditions outside the containment.

Goodykoontz and Dorsch [10] investigated the local condensation heat transfer coefficients and pressure distribution of R113 for the mass fluxes of 21–455 kg m^{-2} s^{-1} in a 7.4–15.9 mm i.d. vertical tube. Kim and No [11] developed a turbulent film condensation model including pressure drop for high pressure steam in a 46 mm i.d. vertical tube. Ma et al. [12] studied the two-phase friction factors of downward flow of R113 for the mass fluxes of 400–800 kg m^{-2} s^{-1} in 20.8 mm i.d. smooth and micro-fin tubes.

To the best of the authors' knowledge, apart from the authors' previous publications [13–28], there has been insufficient work dealing with the heat transfer characteristics during downward condensation in small diameter tubes, and, moreover, no work on condensation of new generation refrigerant R600a inside horizontal tubes. Although some information is currently available on the frictional pressure drop in annular flow, room still remains for further discussion of whether it gives reliable predictions of frictional pressure drop in the high mass flux region of R134a inside vertical tubes and in the low mass flux region of the alternative, environmentally friendly refrigerant R600a inside horizontal tubes. Moreover, there are plenty of experimental and theoretical studies in the literature on the condensation of refrigerants in horizontal smooth tubes but their working fluids are mainly ozone depleting substances such as CFCs and HCFCs. It should also be noted that the reported mass fluxes, heat fluxes, condensation pressures and dimensions of the test tubes do not include studied parameters. Therefore, the main aim of this study was to extend the existing pressure drop data for R134a and R600a according to the specific experimental conditions respectively tested. The results obtained from analysis of the various experimental data at different saturation temperatures, mass fluxes and vapour qualities were used to determine the best predictive models.

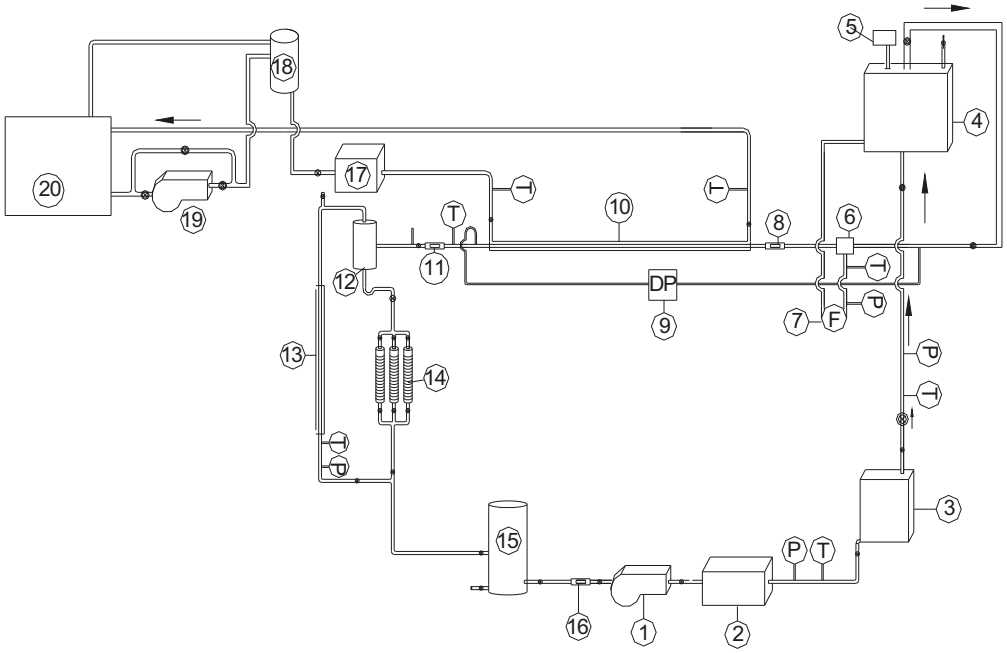

1- Refrigerant Pump 2- Filter 3- Primary heater 4- Evaporater 5- Level gauge 6- Liquid-gas mixture chamber 7- Flow meter 8- Sight glass 9- Differancial Pressure Transmitter 10- Test section 11- Sight glass 12- Liquid/Gas Seperator 13- Air-cooled condenser 14- Scaled vessels 15- R600a Reserve Tank 16- Sight glass 17- Flow meter 18- R134a reserve tank 19- Cooling water reserve tank 20- Water pump

Fig. 1. Schematic diagram of experimental apparatus for the condensation of R600a. [21].

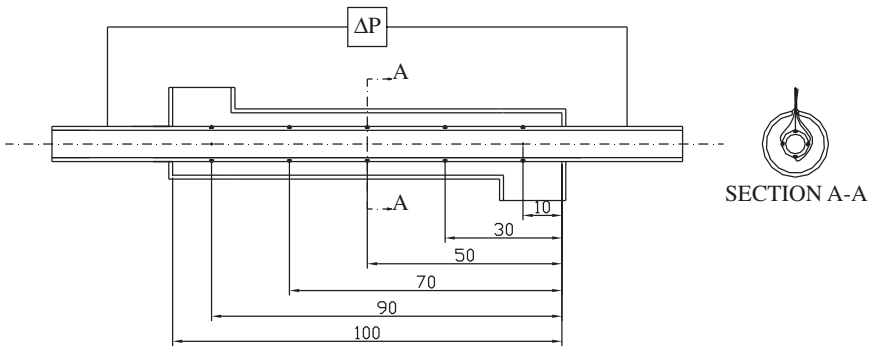

Fig. 2. Schematic diagram of test section for the condensation of R600a [22].

2. Experimental apparatus and procedure

2.1. Experimental apparatus for the condensation of R600a inside a horizontal tube

The experimental apparatus prepared for this study which is illustrated in schematic form in Fig. 1, comprised three major units, namely: the refrigerant cycle, the cooling water cycle and a data collection unit made up of 20 components. Since R600a exhibits combustible and explosive characteristics when mixed with air, special care was taken to ensure that the experiment apparatus was of ex-proof quality. The refrigerant was transferred to the test area using an ex-proof Lewa Ecodos diaphragm pump with a precisely adjustable stroke and flow rate. To identify the flow rate of the refrigerant, a coriolis-type flow meter with a measuring range of 0–250 kg h^{-1} capable of measuring with a precision of ±0.10% was employed. To ensure that the refrigerant pumped to the test tube had the desired vapour quality at the inlet of the test tube, an evaporator (4) was installed in the system. A schematic illustration of this evaporator has been given in the author's previous publications [21,22].

The lower part of the evaporator yields saturated fluid and the upper part yields saturated steam. Different vapour qualities needed to be obtained for the purposes of the experimental study and this is achieved as the steam leaving the evaporator passes through the specially designed mixing chamber (6). Here it amalgamates with the liquid surface at a determined rate to form an annular flow with no droplets. Annular flow is obtained in the mixing chamber. The liquid–steam mixture in annular form passes through a specially designed 10-cm sight glass of the same diameter as a test tube (Fig. 2). To keep the heat loss minimised in the sight glasses mounted on the inlet and outlet of the test tube (8, 11), the glasses were coated with acetate and insulated by means of the air layer between.

The test area is comprised of two concentric circular tubes. The inner one is of copper and the outer one has a Plexiglas construction. The copper tube used as the test tube (10) has an outer diameter of 6 mm and inner diameter of 4 mm, and the Plexiglas tube has an inner diameter of 16 mm. To determine the pressure drop occurring on the inlet and outlet of the test area, a differential pressure transmitter (9) calibrated at a measuring range of 0–500 mm-wg with a precision of ±0.075% was installed in the apparatus. A T-type thermocouple with a diameter of 0.3 mm was installed on the test tube to measure the surface temperature. Large, u-type grooves were slotted onto the walls of the tested copper tube, and thermocouples were mounted in horizontal form and attached to the tube to prevent wing effect. In the experimental study, the $(T_{sat} - T_{wi})$ difference was measured directly with a gauge developed on the data collection unit as illustrated in the author's previous publications [21,22]. The refrigerant leaving the test area reaches a liquid/vapour separator (12) where the liquid and vapour content of the refrigerant is separated. The refrigerant flows to the pressure-resistant graduated cups (14) to determine the quantity of the condensate. On the other hand, its vapour is driven to the air-cooled condenser (13) installed in the apparatus, condenses there and is then transferred to the receiver in liquid form. To bring the cooling water received from a container to the desired temperature, it is first heated and then accumulated in constant the water that will be transferred to the test area at constant temperature from getting impacted by vibrations due to the pump, it is accumulated in another reservoir (18) fitted close to the test area. From this reservoir, the cooling water flows to the test area under its own static pressure. After the cooling water leaves this reservoir at constant flow rate it passes through a turbine-type Honsberg flow meter with a capacity of 2–10 l h^{-1} to reach the test area. The temperature of the cooling water is measured by means of RTDs fitted on the inlet and outlet of the test area. The flow of the cooling water and the refrigerant in the test area is designed in a counter flow pattern to ensure an almost constant $(T_{sat} - T_{wi})$ temperature difference along the tube. In the cooling cycle when the refrigerant was circulating, pressures were measured by means of Bourdon Haenni-type pressure transmitters with a measuring

Table 1
Uncertainty of experimental parameters.

Condensation of R600a inside horizontal tube		Condensation of R134a inside vertical tube	
Parameters	Uncertainty	Parameters	Uncertainty
T_{sat} (°C)	0.069	T_{sat} (°C)	0.19
x_i	±1.11–2.16%	x_i	±6.96–8.24%
ΔT_{sat} (K)	±0.07	ΔT_{sat} (K)	±0.191
$(T_{w,o} - T_{w,i})_t$ (K)	±0.02	$(T_{w,o} - T_{w,i})_t$ (K)	±0.045
$(T_{w,i} - T_{w,o})_{evap}$ (K)	±0.011	$(T_{w,i} - T_{w,o})_{evap}$ (K)	±0.13
m_{ref} (g s^{-1})	±0.019	m_{ref} (g s^{-1})	±0.023
$m_{w,t}$ (g s^{-1})	±0.281	$m_{w,t}$ (g s^{-1})	±0.35
$m_{w,evap}$ (g s^{-1})	–	$m_{w,evap}$ (g s^{-1})	±0.38
q_t (kW m^{-2})	±2.1–3.3%	q_t (kW m^{-2})	±6.55-8.93%
q_{evap} (kW m^{-2})	±3.78–4.9%	q_{evap} (kW m^{-2})	±12–14.81%
ΔP_t (kPa)	±0.123	ΔP_t (kPa)	±0.13

Table 2
Operating conditions of the study.

Refrigerant	HFC-134a	HC-600a
Test tube material, inner diameter d, length L	Copper, ϕ8.1 mm, 500 mm	Copper, ϕ4 mm, 1000 mm
Range of condensing pressure, P_{sat} (bar)	10–12	4–5.73
Range of condensing temperature, T_{sat} (°C)	40–50	30–43
Range of mass flux, G (kg m^{-2} s^{-1})	300–400	75–115
Range of liquid Reynolds number, Re_l	628.74–4630.31	208.33–1571.42
Range of vapour Reynolds number, Re_g	139990–237243	21375–48875
Range of Lockhart–Martinelli number, X	0.015–0.12	0126–0.89
Range of average vapour quality, x	0.7–0.95	0.45–0.9

Table 3
Frictional pressure drop models and correlations.

Number	Frictional pressure drop model/correlation	Model/correlation
1 Experimental frictional pressure drop [15]	$(\Delta P)_G = g(\alpha\rho_g + (1-\alpha)\rho_l)L \quad \alpha = \frac{1}{1+\left(\frac{1-x}{x}\right)\left(\frac{\rho_g}{\rho_l}\right)S} \quad S = \left(1 - x + x\frac{\rho_l}{\rho_g}\right)^{1/2}$	
	$\left(\frac{dP}{dz}\right)_M = -G^2\frac{d}{dz}\left[\frac{x^2}{\rho_g\alpha} + \frac{(1-x)^2}{\rho_1(1-\alpha)}\right] \left(\frac{dP}{dz}\right)_F = \left(\frac{dP}{dz}\right)_{\text{Exp}} - \left(\frac{dP}{dz}\right)_G - \left(\frac{dP}{dz}\right)_M$	
2 Lockhart and Martinelli [3]	$X = \left[\frac{(dP/dz)_l}{(dP/dz)_g}\right]^{1/2} \quad \phi_l^2 = 1 + \frac{C}{X} + \frac{1}{X^2} \quad \left(\frac{dP}{dz}\right)_l = \frac{f_l G^2(1-x)^2}{2d\rho_l} \quad \left(\frac{dP}{dz}\right)_g = \frac{f_g G^2 x^2}{2d\rho_g}$	
	$\text{Re}_l = \frac{Gd(1-x)}{\mu_l} \quad f_l = \frac{64}{\text{Re}}\,(\text{laminar}) \quad f_l = \frac{0.316}{(\text{Re}_l^{0.25})}\,(\text{turbulent}) \quad \text{Re}_g = \frac{Gdx}{\mu_g}$	
	$f_g = \frac{0.184}{\text{Re}_g^{0.2}}\,(\text{turbulent}) \quad \left(\frac{\Delta P}{L}\right)_F = \phi_l^2\left(\frac{dP}{dz}\right)_l$	
	C: 20 / 12 / 10 / 5 — Liquid: Turbulent / Laminar / Turbulent / Laminar — Vapor: Turbulent / Turbulent / Laminar / Laminar	
3 Chisholm [4]	$Y = \sqrt{\frac{(dP/dz)_{go}}{(dP/dz)_{lo}}} \quad \left(\frac{dP}{dz}\right)_{lo} = \frac{f_{lo}G^2}{2d\rho_l} \quad \left(\frac{dP}{dz}\right)_{go} = \frac{f_{go}G^2}{2d\rho_g}$	
	$\phi_{lo}^2 = 1 + (Y^2-1)[Bx^{(2-n)/2}(1-x)^{(2-n)/2} + x^{(2-n)}] \quad n = \begin{cases} \text{Re}_{lo} \le 2100 \\ \text{Re}_{lo} > 2100 \end{cases}$	
	$f = 8\left[\left(\frac{8}{\text{Re}}\right)^{12} + \left\{\left[2.457\ln\left(\frac{1}{\left(\frac{7}{\text{Re}}\right)^{0.9} + 0.27\varepsilon/d}\right)\right]^{16} + \left(\frac{37530}{\text{Re}}\right)^{16}\right\}^{-1.5}\right]^{1/12}$	
	$B = \begin{cases} 55/\sqrt{G} \\ 520/\left(Y\sqrt{G}\right) \\ 15000/\left(Y^2\sqrt{G}\right) \end{cases} \text{ for } \begin{matrix} 0 < Y < 9.5 \\ 9.5 < Y < 28 \\ 28 < Y \end{matrix} \quad \left(\frac{\Delta P}{L}\right)_F = \phi_{lo}^2\left(\frac{dP}{dz}\right)_{lo}$	
4 Friedel et al. [5–6]	$E = (1-x)^2 + x^2\frac{\rho_l f_{go}}{\rho_g f_{lo}} \quad F = x^{0.78}(1-x)^{0.24} \quad H = \left(\frac{\rho_l}{\rho_g}\right)^{0.91}\left(\frac{\mu_g}{\mu_l}\right)^{0.19}\left(1 - \frac{\mu_g}{\mu_l}\right) \quad We = \frac{G^2 d}{\rho_{TP}\sigma}$	
	$\rho_{TP} = \left(\frac{x}{\rho_g} + \frac{1-x}{\rho_l}\right)^{-1} \quad Fr = \frac{G^2}{gd\rho_{TP}^2} \quad \phi_{lo}^2 = E + \frac{3.24FH}{Fr^{0.045}We^{0.035}} \quad \left(\frac{\Delta P}{L}\right)_F = \phi_{lo}^2\left(\frac{dP}{dz}\right)_{lo}$	
5 Chen et al. [33]	$\Omega = \begin{cases} \frac{0.0333\text{Re}_{lo}^{0.45}}{\text{Re}_g^{0.09}(1+0.4\exp(-Bo))} & Bo < 2.5 \\ \frac{We^{0.2}}{(2.5+0.06Bo)} & Bo \ge 2.5 \end{cases} \quad We = \frac{G^2 d}{\sigma\rho_{TP}} \quad Bo = g(\rho_l - \rho_g)\left(\frac{(d/2)^2}{\sigma}\right) \frac{dP}{dz} = \left(\frac{dP}{dz}\right)_{\text{Friedel}}\Omega$	
6 Cavallini et al. [34–35]	$E = (1-x)^2 + x^2\frac{\rho_l f_{go}}{\rho_g f_{lo}} \quad F = x^{0.6978} \quad H = \left(\frac{\rho_l}{\rho_g}\right)^{0.3278}\left(\frac{\mu_g}{\mu_l}\right)^{-1.181}\left(1 - \frac{\mu_g}{\mu_l}\right)^{3.477} \quad We = \frac{G^2 d}{\sigma\rho_{avg}}$	
	$\phi_{lo}^2 = E + \frac{1.262FH}{We^{0.1458}} \quad \left(\frac{\Delta P}{L}\right)_F = \phi_{lo}^2\left(\frac{dP}{dz}\right)_{lo}$	
7 Garimella et al. [36–37]	$\alpha = \left[1 + \left(\frac{1-x}{x}\right)^{0.74}\left(\frac{\rho_v}{\rho_l}\right)^{0.65}\left(\frac{\mu_l}{\mu_g}\right)^{0.13}\right]^{-1} \quad \text{Re}_l = \frac{Gd(1-x)}{\mu_l(1+\sqrt{\alpha})} \quad \text{Re}_g = \frac{Gdx}{\mu_g\sqrt{\alpha}} \quad f = \frac{64}{\text{Re}}\,(\text{laminar})$	
	$\psi = \frac{j_l\mu_l}{\sigma} \quad f = \frac{0.316}{\text{Re}^{0.25}}\,(\text{turbulent}) \left(\frac{dP}{dz}\right)_l = \frac{f_l G^2(1-x)^2}{2d\rho_l} \quad \left(\frac{dP}{dz}\right)_g = \frac{f_g G^2 x^2}{2d\rho_g}$	
	$X = \left[\frac{(dP/dz)_l}{(dP/dz)_g}\right]^{1/2} \quad j_l = \frac{G(1-x)}{\rho_l(1-\alpha)} \quad \frac{f_{\text{int}}}{f_l} = Ax^a\text{Re}_l^b\psi^c \quad \text{Re}_l < 2100\ A = 1.308\times10^{-3}$	
	$a = 0.4273\ b = 0.9295\ c = -0.1211 \quad \frac{\Delta P}{L} = \frac{1}{2}f_{\text{int}}\frac{G^2x^2}{\rho_g 2^{2.5}}\frac{1}{d}$	
8 Mishima and Hibiki [38]	$\phi_l^2 = 1 + \frac{C}{X} + \frac{1}{X^2} \quad C = 21(1 - e^{-0.319d}) \quad \left(\frac{\Delta P}{L}\right)_F = \phi_l^2\left(\frac{dP}{dz}\right)_l$	
	X should be calculated from Lockhart and Martinelli [3].	
9 Wang et al. [39]	$G > 200\ \text{kg m}^{-2}\text{s}^{-1} C = 4.56610^{-6}X^{0.128}\text{Re}_{lo}^{0.938}\left(\frac{\rho_l}{\rho_g}\right)^{-2.15}\left(\frac{\mu_l}{\mu_g}\right)^{5.1} \quad \text{Re}_{lo} = \frac{Gd}{\mu_l}\left(\frac{\Delta P}{L}\right)_F = \phi_l^2\left(\frac{dP}{dz}\right)_l$	
	$G < 200\ \text{kg m}^{-2}\text{s}^{-1}\phi_g^2 = 1 + 9.4X^{0.62} + 0.564X^{2.45} \left(\frac{\Delta P}{L}\right)_F = \phi_g^2\left(\frac{dP}{dz}\right)_g \phi_l^2 = 1 + \frac{C}{X} + \frac{1}{X^2}$	
	$(dP/dz)_l$ and $(dP/dz)_g$ should be calculated from Lockhart and Martinelli [3].	
10 Wilson et al. [40]	$\phi_{lo}^2 = 12.82Xtt^{-1.47}(1-x)^{1.8} \quad X_{tt} = \left(\frac{(1-x)}{x}\right)^{0.9}\left(\frac{\rho_g}{\rho_l}\right)^{0.5}\left(\frac{\mu_l}{\mu_g}\right)^{0.1} \quad \left(\frac{\Delta P}{L}\right)_F = \phi_{lo}^2\left(\frac{dP}{dz}\right)_{lo}$	
11 Souza et al. [41]	$\phi_l^2 = 1.376 + C_1 X_{tt}^{-C_2} \ Fr_l < 0.7 \begin{cases} C_1 = 4.172 + 5.48\ Fr_l \\ C_2 = 1.773 - 0.169Fr_l \end{cases} Fr_l \ge 0.7\ C_1 = 7.242$	
	$C_2 = 1.655\ Fr_l = \frac{G}{\rho_l\sqrt{gd}}\left(\frac{dP}{dz}\right)_l = \frac{f_l G^2(1-x)^2}{2d\rho_l}\frac{1}{\sqrt{f_l}} = -2\log\left(\frac{(\varepsilon/d)}{3.7} + \frac{2.51}{\text{Re}_l\sqrt{f_l}}\right)$	
	$\text{Re}_l = \frac{Gd(1-x)}{\mu_l}\left(\frac{\Delta P}{L}\right)_F = \phi_l^2\left(\frac{dP}{dz}\right)_l$	
12 Tran et al. [42]	$\phi_l^2 = 1 + (4.3Y^2 - 1)\ N_{conf}x^{0.875} + x^{1.75} N_{conf} = \frac{\left[\frac{\sigma}{g(\rho_l - \rho_g)}\right]^{1/2}}{d} \left(\frac{\Delta P}{L}\right)_F = \phi_{lo}^2\left(\frac{dP}{dz}\right)_{lo}$	
	$(dP/dz)_{lo}$ should be calculated from Chisholm [4].	
13 Lee and Lee [43]	$\phi_l^2 = 1 + \frac{C}{X} + \frac{1}{X^2} \ C = A\lambda^q\psi^r\text{Re}_{lo}^s \ \lambda = \frac{\mu_l^2}{\rho_l\sigma d} \ \psi = \frac{\mu_l j}{\sigma} \ \left(\frac{\Delta P}{L}\right)_F = \phi_l^2\ \left(\frac{dP}{dz}\right)_l$	

Liquid	Vapor	A	q	R	s	X Range	Re_{lo} range
Laminar	Laminar	6.833×10^{-8}	−1.317	0.719	0.557	0.776–14.176	175–1480
Laminar	Turbulent	6.185×10^{-2}	0	0	0.726	0.303–1.426	293–1506
Turbulent	Laminar	3.627	0	0	0.174	3.276–79.415	2606–17642
Turbulent	Turbulent	0.408	0	0	0.451	1.309—14.781	2675–17757

range of 0–10 bars and precision of ±0.2%. Temperatures were measured by means of RTDs.

2.2. Experimental apparatus for the condensation of R134a inside a vertical tube

Detailed descriptions of the experimental apparatus for studying condensation of R134a inside a vertical tube can be found in the authors' previous publications.

3. Data reduction

The data reduction of the measured results can be analysed as follows:

3.1. The inlet vapor quality of the test section ($x_{TS,i}$)

$$x_{TS,i} = \frac{i_{TS,i} - i_{l@T_{TS,i}}}{i_{fg@T_{TS,i}}} \quad (1)$$

Table 4
Main parameters of models and correlations.

Model number	Main parameters of equations																						
	μ_l	μ_g	ρ_l	ρ_g	ρ_{TP}	σ	x	d	G	α	S	j	ψ	f_l	f_g	f	Re	Re_l	Re_g	Re_{lo}	Re_{go}	Bo	X	We	Fr
1			x	x			x		x	x	x														
2			x	x				x	x					x	x			x	x				x		
3			x	x			x	x	x							x				x	x				
4	x	x	x	x	x	x		x																x	x
5			x	x	x	x		x	x								x					x		x	
6	x	x	x	x	x	x	x	x	x															x	
7	x	x	x	x		x	x	x	x			x				x		x	x				x		
8	x	x	x	x			x																x		
9	x	x	x	x			x		x											x			x		
10	x	x	x	x			x																x		
11	x		x				x	x	x					x				x							x
12			x	x		x	x	x								x									
13	x	x	x	x		x	x	x				x	x							x			x		

Table 5
Deviations of models according to the operating conditions during condensation tests of R134a.

R134a	Model/Correlation number and deviation (%)														
T_{sat}(°C)	P_{sat} (bar)	G (kg m^{-2} s^{-1})	x_{avg}	2	3	4	5	6	7	8	9	10	11	12	13
40	10	300	0.9	39.16	44.22	20.66	8.01	−12.59	33.41	−92.18	39.14	29.52	44.84	91.58	–
40	10	300	0.8	41.77	43.48	24.38	13.29	0.53	34.65	−64.62	40.75	9.75	−21.21	91.24	–
40	10	300	0.75	15.51	37.74	26.66	17.45	10.32	35.24	−48.64	30.40	−11.27	−48.65	90.00	–
40	10	300	0.7	3.82	33.54	26.01	17.88	12.14	34.26	−28.64	21.32	−20.31	−50.08	89.08	–
50	12	300	0.9	33.61	39.92	13.71	6.05	−12.86	25.56	−102.40	35.61	15.08	19.48	88.87	–
50	12	300	0.8	24.75	28.72	3.00	−4.64	−18.96	14.04	−107.55	26.72	−21.16	−78.16	86.88	–
50	12	300	0.75	−26.26	18.14	4.14	−0.79	−6.93	12.13	−68.99	5.31	−56.91	−97.61	84.83	–
50	12	300	0.7	−44.75	8.44	−2.79	−7.23	−12.36	−57.79	−74.63	−8.00	−75.99	−124.35	82.97	–
40	10	400	0.95	42.67	53.27	33.92	14.28	9.40	45.51	−28.29	46.42	39.99	37.71	92.91	–
40	10	400	0.9	39.16	50.06	33.05	14.09	14.77	42.91	−112.63	43.42	17.78	−47.16	92.07	–
40	10	400	0.85	25.02	46.64	32.84	14.86	18.25	41.71	−38.37	29.63	3.59	−31.55	91.20	–
40	10	400	0.8	15.81	43.36	32.58	15.58	20.48	6.11	−27.31	20.01	−6.24	−43.74	90.37	–
50	12	400	0.95	34.51	40.48	14.77	−4.49	−8.47	27.94	−105.63	32.60	15.97	−2.73	88.89	–
50	12	400	0.9	28.64	43.45	22.27	5.55	7.24	32.23	−159.57	36.79	2.19	−85.81	89.30	–
50	12	400	0.85	8.74	40.20	23.08	7.67	13.01	31.28	−51.55	20.12	−15.32	−56.16	88.50	–
50	12	400	0.8	−3.07	36.42	23.12	8.85	16.28	−29.97	−43.25	9.22	−27.70	−77.67	87.58	–

Table 6
Deviations of models according to the operating conditions during condensation tests of R600a.

R600a	Model/correlation number and deviation (%)														
T_{sat} (°C)	P_{sat} (bar)	G (kg m^{-2}s^{-1})	x_{avg}	2	3	4	5	6	7	8	9	10	11	12	13
30	4	85	0.9	−13.15	16.18	−63.44	33.68	–	−78.45	22.26	−61.24	–	–	77.73	–
30	4	85	0.8	−24.72	5.04	−75.91	28.60	–	−86.69	16.88	−71.78	–	–	73.58	–
30	4	85	0.75	−30.96	−4.61	−78.68	27.19	–	−80.64	16.34	−70.82	–	–	69.03	–
30	4	85	0.7	−39	−15.11	−84.47	23.91	–	−83.02	13.17	−75.06	–	–	64.94	–
30	4	75	0.9	−2.21	27.48	−57.20	38.78	–	30.27	29.32	−25.63	–	–	80.27	–
30	4	75	0.8	−13.10	16.45	−64.77	35.12	–	29.58	25.64	−30.63	–	–	75.71	–
30	4	75	0.75	−22.36	5.28	−71.92	31.78	–	30.01	22.70	−32.73	–	–	70.99	–
30	4	75	0.6	−27.21	−6.80	−71.65	30.70	–	36.47	23.79	−23.39	–	–	65.04	–
43	5.73	115	0.85	−32.15	1.33	−49.56	26.94	–	8.98	10.19	−59.07	–	–	73.99	–
43	5.73	115	0.7	−76.56	−44.79	−81.53	9.71	–	−5.98	−11.27	−90.22	–	–	57.77	–
43	5.73	115	0.65	−112.89	−87.01	−109.83	−5.89	–	−17.80	−29.28	−112.70	–	–	42.95	–
43	5.73	115	0.55	−147.17	−129.39	−138.16	−21.67	–	−27.32	−45.93	−129.53	–	–	27.48	–
43	5.73	95	0.85	−9.49	22.09	−34.80	39.13	–	27.19	26.80	−29.22	–	–	77.94	–
43	5.73	95	0.7	−33.86	−5.39	−49.68	31.27	–	25.55	17.96	−36.66	–	–	66.93	–
43	5.73	95	0.6	−49.13	−26.20	−60.73	24.89	–	25.51	12.26	−37.26	–	–	58.50	–
43	5.73	95	0.45	−69.40	−54.37	−80.71	13.74	–	24.80	3.72	−36.88	–	–	46.82	–

where $i_{l@T_{TS,i}}$ is the enthalpy of the saturated liquid based on the temperature of the test section inlet, $i_{fg@T_{TS,i}}$ is the enthalpy of vaporization based on the temperature of the test section inlet, and $i_{TS,i}$ is the refrigerant enthalpy at the test section inlet, given by:

$$i_{TS,i} = i_{ph,i} + \frac{Q_{ph}}{m_{ref}} \tag{2}$$

where $i_{ph,i}$ is the inlet enthalpy of the liquid refrigerant before entering the pre-heater, m_{ref} is the mass flow rate of the refrigerant, and Q_{ph} is the heat transfer rate in the pre-heater:

$$Q_{ph} = m_{w,ph} c_{p,w} (T_{w,i} - T_{w,o})_{ph} \tag{3}$$

where $m_{w,ph}$ is the mass flow rate of the water entering the preheater, $c_{p,w}$ is the specific heat of water, and $(T_{w,i} - T_{w,o})_{ph}$ is the temperature difference between inlet and outlet positions of the preheater.

3.2. The outlet vapor quality of the test section ($x_{TS,o}$)

$$x_{TS,o} = \frac{i_{TS,o} - i_{l@T_{TS,o}}}{i_{fg@T_{TS,o}}} \tag{4}$$

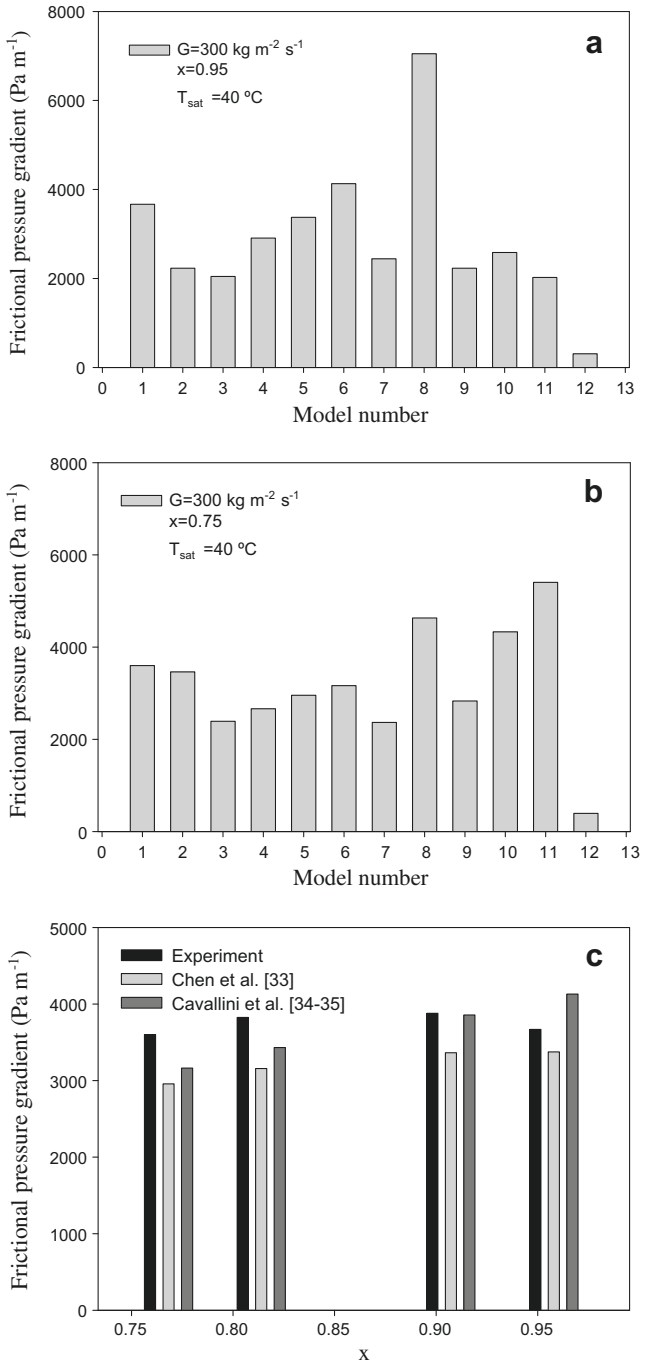

Fig. 3. Comparison of frictional pressure drop correlations at different vapour qualities of R134a for the mass flux of 300 kg m^{-2} s^{-1} and condensation temperature of 40 °C inside vertical tube.

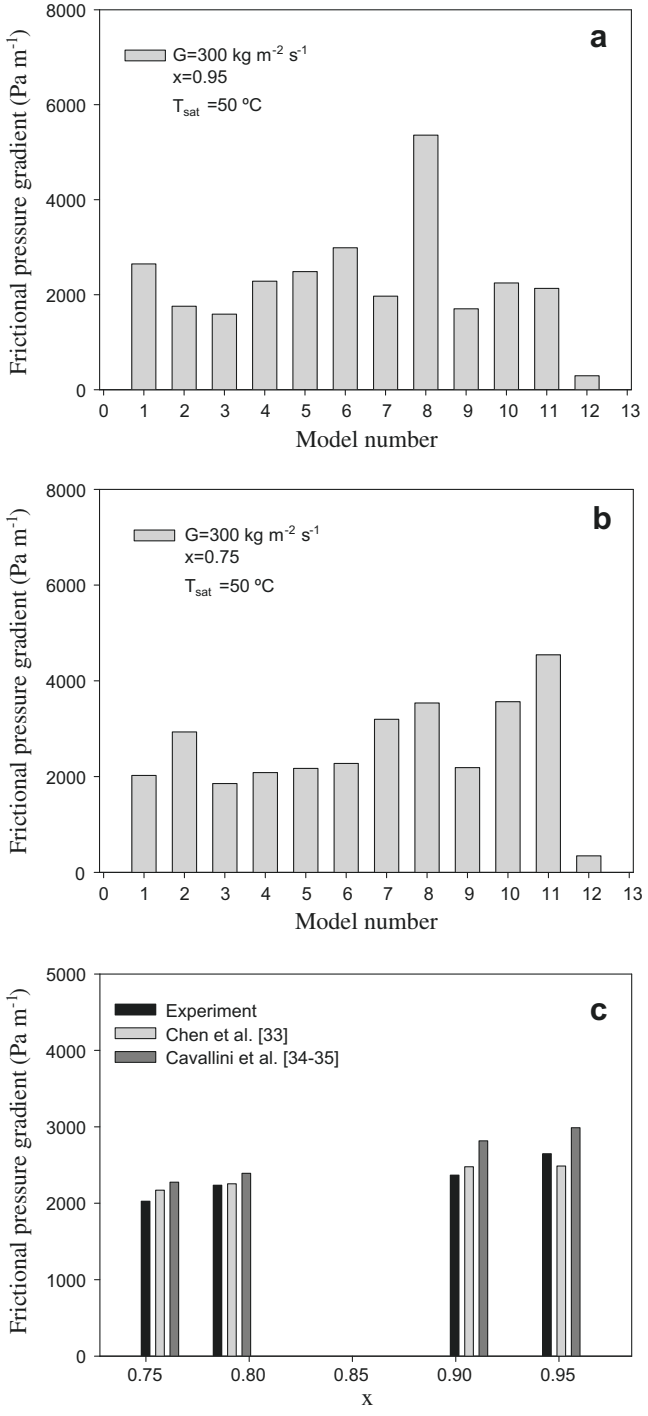

Fig. 4. Comparison of frictional pressure drop correlations at different vapour qualities of R134a for the mass flux of 300 kg m^{-2} s^{-1} and condensation temperature of 50 °C inside vertical tube.

where $i_{TS,o}$ is the refrigerant enthalpy at the test section outlet, $i_{l@T_{TS,o}}$ is the enthalpy of the saturated liquid based on the temperature of the test section outlet, and $i_{fg@T_{TS,o}}$ is the enthalpy of vaporization. The outlet enthalpy of the refrigerant flow is calculated from

$$i_{TS,o} = i_{TS,i} - \frac{Q_{TS}}{m_{ref}} \tag{5}$$

where the heat transfer rate, Q_{TS}, in the test section is obtained from:

$$Q_{TS} = m_{w,TS} c_{p,w} (T_{w,o} - T_{w,i})_{TS} \tag{6}$$

where $m_{w,TS}$ is the mass flow rate of the water entering the test section, and $(T_{w,o} - T_{w,i})_{TS}$ is the temperature difference between water at the outlet and inlet positions.

3.3. Uncertainties

The maximum uncertainties are shown in Table 1. The largest uncertainties occurred in the low mass flux region. The uncertainties of the experimental frictional pressure drop were around ±0.123 in the horizontal tube for R600a, ±0.13 in the vertical tube for R134a. The procedures of Kline & McClintock [29] were used for the calculation of all uncertainties. Operating conditions of the study are given in Table 2.

4. Results and discussion

The following paragraphs present a summary of the operating conditions of the models and correlations, and these are presented in Table 3. The main variables of them are shown in Table 4 and deviations of them according to the experimental frictional pressure drop are shown in Tables 5 and 6. A comparison of experimental frictional condensation pressure drop against predicting models using relevant annular flow of measured data during downward condensation of R134a at high mass flux in a vertical smooth tube, and condensation of R600a at low mass flux in a horizontal smooth tube over a range of experimental conditions is shown in Figs. 3–10.

Based on Hewitt and Robertson's [30] flow pattern map for the vertical tube and Tandon et al.'s [31] flow pattern map for the horizontal tube, the data shown in all figures was collected in an annular flow regime and also checked by sight glass at the inlet and outlet of the test section. In order to obtain annular flow conditions at various high and low mass fluxes, a specific vapour quality range is kept at approximately between 0.7–0.95 in the 0.5 m long test tube for R134a, and at between 0.45–0.9 in the 1 m long test tube for R600a. In the present study various pressure drop models and correlations are used to show the similarity of annular flow correlations which are independent of tube orientation (horizontal or vertical). Chen et al. [32] also mentioned this similarity in their article.

Frictional pressure drop can be determined using the Lockhart and Martinelli method [3] which expresses the division of viscous drag to vapour kinetic energy in horizontal and vertical tubes. This method was developed for adiabatic flow of air-benzene, kerosene and for water inside 1.5–26 mm tubes. Chisholm [4] developed a two-phase multiplier based on Lockhart and Martinelli parameters [3] using steam in a tube. It is used for vertical and horizontal tubes in the literature. Friedel [5,6] proposed a two-phase multiplier considering surface tension effects with 25000 data points during adiabatic flow through the vertical and horizontal channels with hydraulic diameters of more than 1 mm. Moreover, the proportion of vapour dynamic viscosity to liquid dynamic viscosity was below 1000 in his study. Chen et al. [33] accounted for the effects of surface tension and mass flux including Bond and Weber numbers in their model. They condensed R410A at 5–15 °C in several horizontal tubes ranging from 3.17 to 9 mm in diameter for the mass fluxes of 50–600 kg m^{-2} s^{-1}. They also coupled air–water at room temperature in several horizontal tubes ranging from between 1.02 and 7.02 mm in diameter for the mass fluxes of 50–3000 kg m^{-2} s^{-1}. Cavallini et al. [34,35] modified Friedel's [5,6] correlation to develop an annular flow model during the condensation of R22, R134a, R125, R32, R236ea, R407C, R410A in a 8 mm i.d. horizontal tube for the mass fluxes of 100–750 kg m^{-2} s^{-1} at saturation tempera-

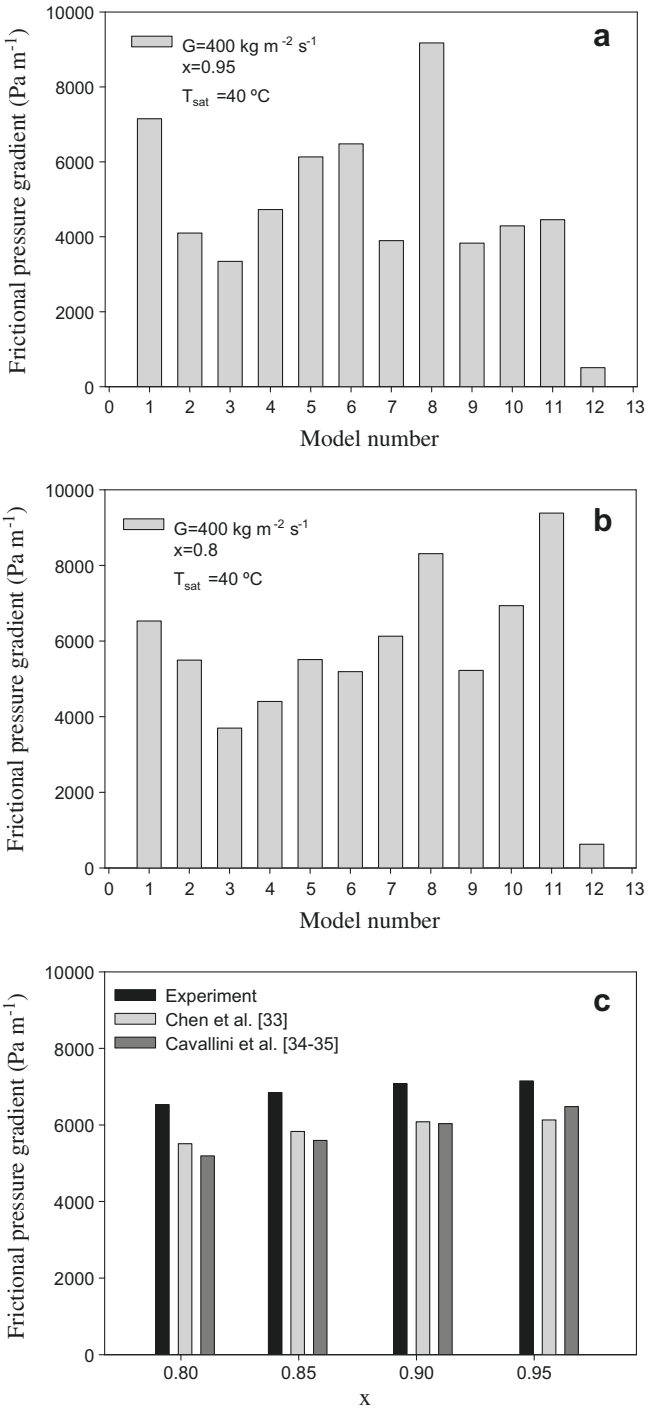

Fig. 5. Comparison of frictional pressure drop correlations at different vapour qualities of R134a for the mass flux of 400 kg m^{-2} s^{-1} and condensation temperature of 40 °C inside vertical tube.

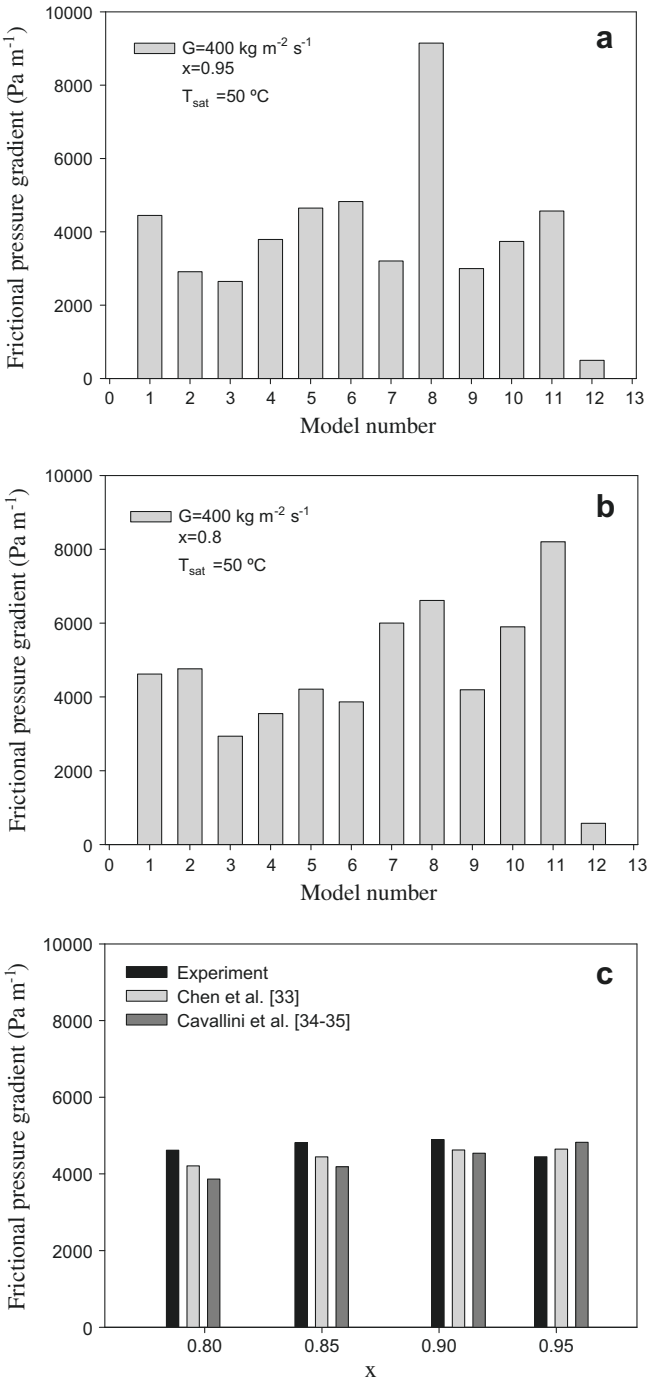

Fig. 6. Comparison of frictional pressure drop correlations at different vapour qualities of R134a for the mass flux of 400 kg m^{-2} s^{-1} and condensation temperature of 50 °C inside vertical tube.

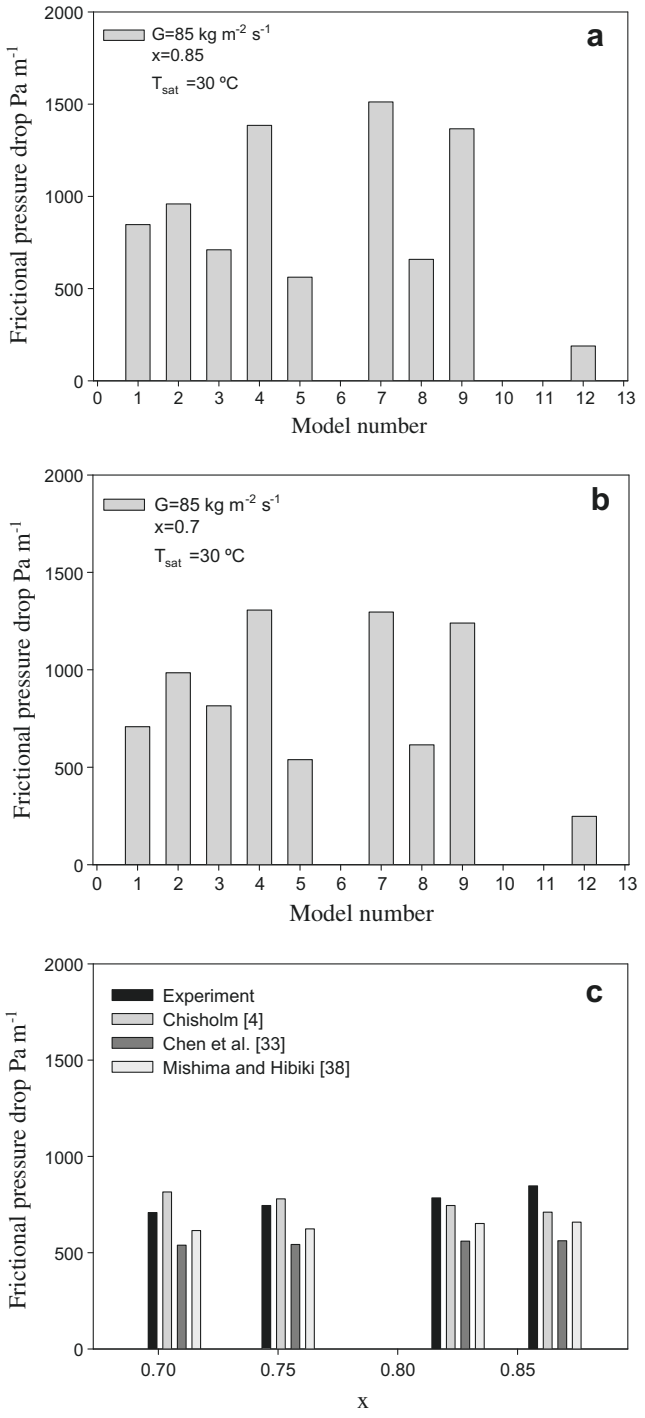

Fig. 7. Comparison of frictional pressure drop correlations at different vapour qualities of R600a for the mass flux of 85 kg m^{-2} s^{-1} and condensation temperature of 30 °C inside horizontal tube.

tures between 30–50 °C. As a result of the study, a model for predicting condensing heat transfer coefficient was developed by means of frictional pressure drop. Garimella et al. [36,37] developed a flow regime based model for intermittent and annular/mist/disperse flow regimes regarding the condensation of R134a in 0.5–4.91 mm i.d. horizontal tubes at the condensing temperature of 52 °C for mass fluxes of between 150–750 kg m^{-2} s^{-1}. Mishima et al. [38] investigated two-phase upward flow of air–water in 1–4 mm i.d. vertical tubes. Their model has limitations when it comes to accounting for the superficial velocities of vapour and liquid of phases. Wang et al. [39] studied the two-phase flow pattern of R22, R134a and R407C in a 6.5 mm i.d. horizontal tube for the mass fluxes of 50–700 kg m^{-2} s^{-1} at the condensing temperatures of 2.6–20 °C. Wilson et al. [40] condensed R134a and R410A in several 1.84–7.79 mm in diameter, horizontal, flattened, round, smooth, axial and helical micro-fin tubes for mass fluxes of between 75–400 kg m^{-2} s^{-1} at saturation temperatures of 35 °C. Souza et al. [41] showed the effect of oil in R12 and R134a on the pressure drop in a horizontal flattened tube with a hydraulic diameter of 10.9 mm for the mass fluxes of 200–600 kg m^{-2} s^{-1}. Tran et al. [42] boiled R134a, R12 and R113 in

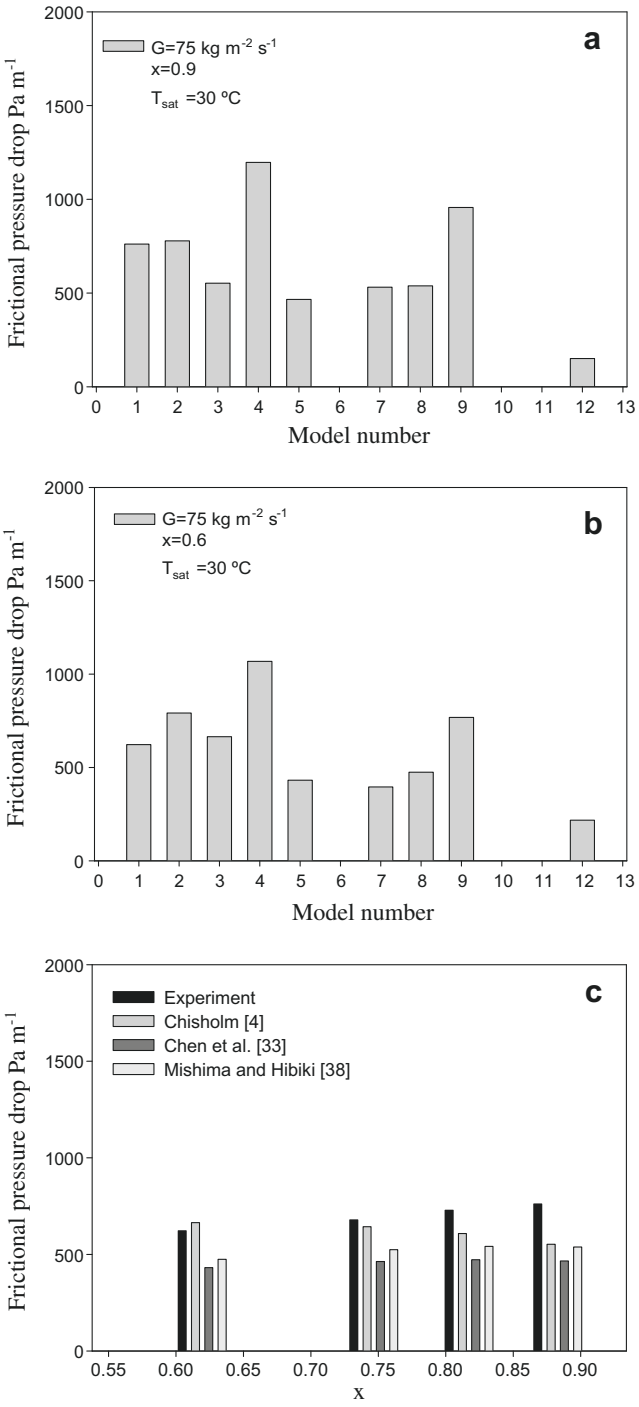

Fig. 8. Comparison of frictional pressure drop correlations at different vapour qualities of R600a for the mass flux of 75 kg m^{-2} s^{-1} and condensation temperature of 30 °C inside horizontal tube.

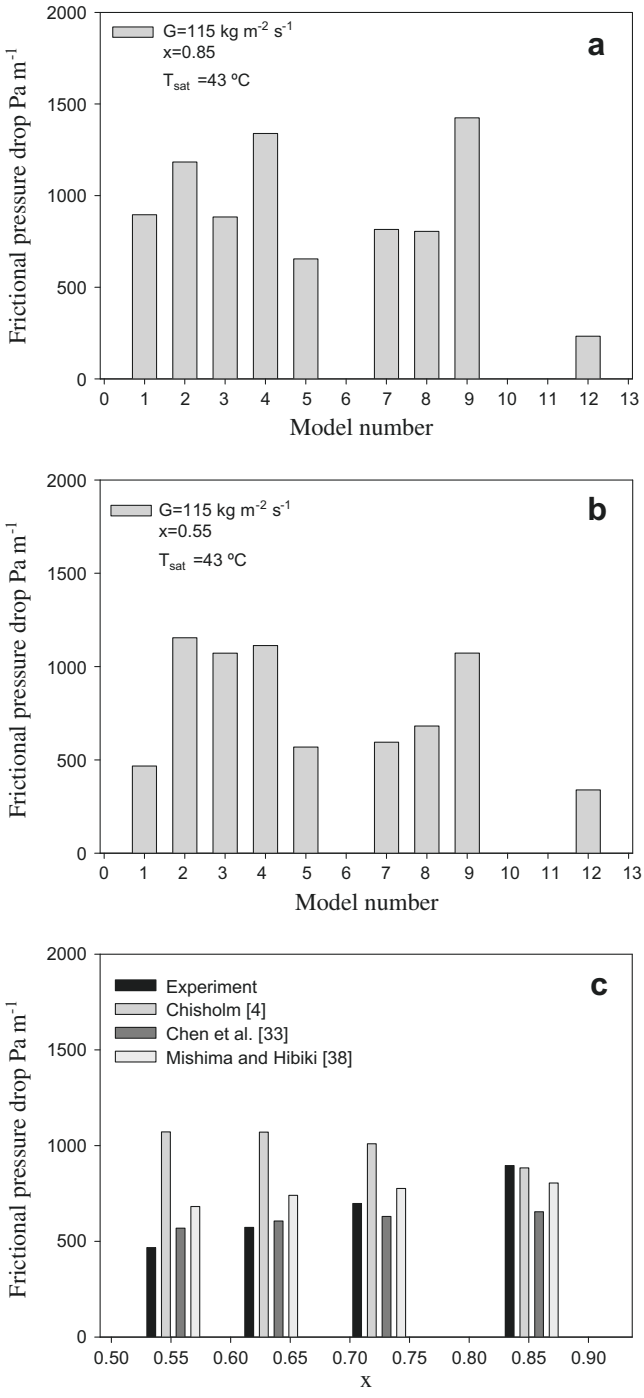

Fig. 9. Comparison of frictional pressure drop correlations at different vapour qualities of R600a for the mass flux of 115 kg m^{-2} s^{-1} and condensation temperature of 43 °C inside horizontal tube.

small diameter horizontal circular (2.4, 2.46, 2.92 mm) and rectangular tubes (4.06 × 1.7 mm) at boiling pressures between 138–836 kPa and for mass fluxes of between 33–832 kg m^{-2} s^{-1}. They proposed a pressure drop correlation modifying Chisholm [4]'s correlation to consider surface tension effects. Lee and Lee [43] studied the air–water couple to develop a two-phase multiplier for small hydraulic diameter (0.4 × 20 mm, 1.2 × 20 mm, 4 × 20 mm) rectangular horizontal channels. Their model has limitations with the Reynolds number and Lockhart and Martinelli [3] parameter.

The experimental frictional pressure drop shown in Table 3 and defined as model number 1 is calculated by means of the extraction of the gravitational component and of the component due to momentum change from the total measured pressure drop regarding condensing fluid of R134a in a vertical tube. It should be noted that the gravitational term of total measured pressure drop is neglected for the condensation of R600a in the horizontal tube. The experimental frictional pressure drop value is assumed to be the comparative value in all the figures and in Tables 5 and 6. The importance of void fraction models used for the determination of gravitational and momentum terms of pressure drop has been

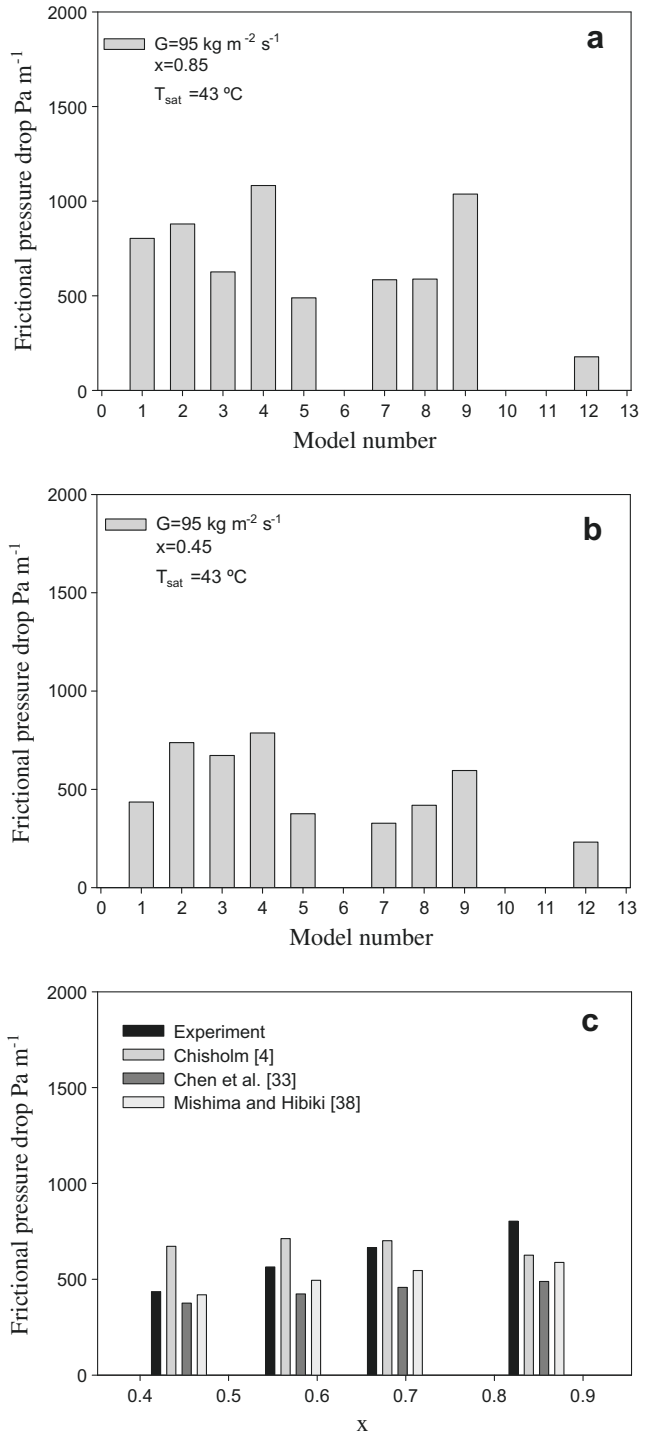

Fig. 10. Comparison of frictional pressure drop correlations at different vapour qualities of R600a for the mass flux of 95 kg m^{-2} s^{-1} and condensation temperature of 43 °C inside horizontal tube.

examined in great detail in the author's previous studies [13,16,17].

The main parameters of frictional pressure drop models and correlations mentioned in this study are shown in Table 4. They are necessary for the validation of experimental results characterising the flow and accurate predictions for untested conditions. Single phase–two phase pressure drop gradients (liquid only/vapour only), friction factors (liquid only/vapour only), Reynolds numbers, Bond numbers, Weber numbers, Froude numbers and Lockhart and Martinelli parameters were used as the main variables in the models and correlations given in Table 3. Reynolds number gives a measure of the ratio of inertial forces to viscous forces characterising different flow regimes such as laminar or turbulent flow. Bond number expresses the ratio of body forces to surface tension forces; low Bond numbers indicate surface tension domination of the system. Weber number is defined as a measure of the relative significance of the fluid's inertia compared to its surface tension. It is useful in analysing thin film flows where there is an interface between two different fluids, and the formation of droplets and bubbles. The Froude number is used to compare inertial and gravitational forces. The Lockhart and Martinelli parameter is used in internal two-phase flow calculations expressing the liquid fraction of a flowing fluid. Other important parameters belong to fluid and geometric parameters such as mass flux, vapour quality, surface tension, density, dynamic viscosity in the frictional models and correlations.

The data on the effects of heat flux, mass flux and condensation temperature on the pressure drop are discussed in the authors previous publications [13,15,18] in detail. As can be seen from the figures, pressure drop decreases with decreasing mass flux and increases with increasing vapour quality for the same condensing temperature as expected. In addition to this, calculating from the figures frictional pressure drop values at high condensing temperatures are lower than those at a low condensing temperature for the same mass flux. Therefore, the different pressure drop characteristics should be accounted for in the comparison of the heat transfer performance of fluids in spite of the same condensing temperature and mass velocity due to far different operating pressures.

In Figs. 3–6, experimental condensation frictional pressure drop data for R134a inside a vertical tube are plotted against the various models and correlations shown in Table 3 according to the condensation temperatures of 40 and 50 °C for the mass fluxes of 300 and 400 kg m^{-2} s^{-1}.

It is found that all data belong to the comparison of Cavallini et al.[34,35] and Chen et al.'s [33] correlations with the experimental frictional pressure drop fall within ±20% for all the mass fluxes and condensing temperatures of R134a. These correlations were the most predictive correlations according to the various experimental conditions in Table 5. The model of Cavallini et al. [34,35] and Chen et al.'s [33] operating conditions explained above seems similar to that of our study except for tube orientation. Moreover, Chen et al. [33] used the Bond number in their model and this is especially significant at high vapour qualities. In addition to this, the majority of the data calculated by the Lockhart and Martinelli [3], Friedel [5], Wang et al [39] and the Wilson et al. [40] correlations all fall within ±30%. On the other hand, the Lee and Lee [43] correlation is found to be incompatible with the experimental data due to the inappropriate operating conditions and lack of flow parameters in the equations. Nevertheless, the Garimella et al. [37], the Mishima et al. [38], the Souza et al. [41] and the Tran et al. [42] correlations also have poor agreement with the experimental data. Deviations of all models and correlations for the condensation of R134a inside vertical tube according to the different experimental conditions can be clearly seen in Table 5.

In Figs. 7–10 the experimental condensation frictional pressure drop data of R600a inside horizontal tube are plotted against the various models and correlations shown in Table 3 according to the condensation temperatures of 30 and 43 °C for the mass fluxes of 75, 85, 95 and 115 kg m^{-2} s^{-1}.

The majority of the data belonging to the comparison of frictional pressure drops for the Chisholm [4], Chen et al. [33] and Mishima and Hibiki [38]correlations fall within ±30% for the all mass fluxes and condensing temperatures of R600a. These correlations were the most predictive correlations according to the various experimental conditions in Table 6. Mishima and Hibiki [38]

developed Chisholm's [4] correlation for small diameter tubes and the Chen et al. [33] correlation emphasises the importance of surface tension force which should be taken into account as compared to gravitational force for two-phase flow in small diameter tubes in low mass flux regions due to low vapour shear forces. On the other hand, the Cavallini et al. [34,35], Lee and Lee [43], Wilson et al. [40] and Souza et al. [41] correlations are found to be incompatible with the experimental data due to their inappropriate operating conditions and the lack of flow parameters in the equations. Nevertheless, the Lockhart and Martinelli [3], Friedel et al. [5,6], Garimella et al. [37], Tran et al [42] and Wang et. al. [39] correlations have poor agreement with the experimental data. Deviations of all models and correlations for the condensation of R600a inside a horizontal tube according to the different experimental conditions can be clearly seen from Table 5.

In addition to these explanations, the pressure drop per length shown in Figs. 3–10 is obtained from dividing the measured pressure drop by the length between pressure taps. In our apparatus, the length between pressure taps is 0.7 m for the vertical tube, 1.5 m for the horizontal tube.

5. Conclusion

The aim of this investigation was to compare frictional pressure drop values obtained from various pressure drop models at high mass flux during downward annular flow condensation of R134a in a vertical, smooth, 8.1 mm i.d. copper tube, and at low mass flux during annular flow condensation of R600a in a horizontal, smooth, 4 mm i.d. copper tube.

In this study, accurate and repeatable condensation pressure drop data were taken and their applicability to the various pressure drop models under different operating conditions was examined. This study performed tests for the validation of models with different operating conditions. Moreover, there is little research on the parameters used in this study described in the current literature. The content of this study is expected to fill this gap in the literature.

Chisholm's void fraction correlation [4] is used to calculate the gravitational and momentum pressure drop. Frictional pressure drop is obtained from measured total pressure drop data. The model by Cavallini et al. [34,35] and Chen et al. [33] valid for the annular flow regime can determine condensation frictional pressure drop values fairly well for R134a. On the other hand, only Chen et al. [33]'s correlation from this couple can predict the data well for the new hydrocarbon R600a. It can be seen that, due to its incompatible operating conditions as explained above, Lee and Lee's model [41] disappears in Figs. 3–6 and Table 5 for the condensation of R134a inside vertical tube and Cavallini et al. [34,35], Lee and Lee [43], Wilson et al. [40] and Souza et al.'s [41] models disappear in Figs. 7–10 and Table 6 for the condensation of R600a inside a horizontal tube due to their values which are extremely higher than others.

According to the analysis in this paper, it is shown that annular flow models are independent of tube orientation provided that annular flow regime exists along the tube length and that they are capable of predicting condensation pressure drop inside the tested tubes.

Acknowledgements

The present study was financially supported by Yildiz Technical University (YTU) and King Mongkut's University of Technology Thonburi (KMUTT). The first author thank KMUTT for providing him with a Post-doctoral fellowship, while the fourth author acknowledge the financial support provided by the Thailand Research Fund.

References

[1] H. Kruse, The state of the art of the hydrocarbon technology in household refrigeration, in: Proceedings of the International Conference on Ozone Protection Technologies, Washington, DC, 1996, pp. 179–188.
[2] D. Jung, C. Kim, K. Song, B. Park, Testing of propane/isobutene mixture in domestic refrigerators, Int. J. Refrig. 23 (2000) 517–527.
[3] R.W. Lockhart, R.C. Martinelli, Proposed correlation of data for isothermal two-phase, two-component flow in pipes, Chem. Eng. Prog. 45 (1949) 39–48.
[4] D. Chisholm, Pressure gradients due to friction during the flow of evaporating two-phase mixtures in smooth tubes and channels, Int. J. Heat Mass Transfer 16 (1973) 347–358.
[5] L. Friedel, Improved friction pressure drop correlation for horizontal and vertical two-phase pipe flow, Eur. Two-phase Flow Group Meeting Pap. E2 18 (1979) 485–492.
[6] L. Friedel, Pressure drop during gas/vapor–liquid flow in pipes, Int. J. Chem. Eng. 20 (1980) 352–367.
[7] Ho-Saeng Lee, Jung-In Yoon, Jae-Dol Kim, P.K. Bansal, Condensing heat transfer and pressure drop characteristics of hydrocarbon refrigerants, Int. J. Heat Mass Transfer 46 (2006) 1922–1927.
[8] Ho-Saeng Lee, Jung-In Yoon, Jae-Dol Kim, P.K. Bansal, Characteristics of condensing and evaporating heat transfer using hydrocarbon refrigerants, Appl. Therm. Eng. 26 (2006) 1054–1062.
[9] Mao-Yu Wen, Ching-Yen Ho, Jome-Ming Hsieh, Condensation heat transfer and pressure drop characteristics of R-290 (propane), R600(butane), and a mixture of R290/R600 in the serpentine small-tube bank, Appl. Therm. Eng. 26 (2006) 2045–2053.
[10] J.H. Goodykoontz, R.G. Dorsch, Local heat transfer and pressure distributions for Freon-113 condensing in downward flow in a vertical tube, NASA TN D-3952, 1967.
[11] S.J. Kim, H.C. No, Turbulent film condensation of high pressure steam in a vertical tube, Int. J. Heat Mass Transfer 43 (2000) 4031–4042.
[12] X. Ma, A. Briggs, J.W. Rose, Heat transfer and pressure drop characteristics for condensation of R113 in a vertical micro-finned tube with wire insert, Int. Commun. Heat Mass Transfer 31 (2004) 619–627.
[13] A.S. Dalkilic, S. Laohalertdecha, S. Wongwises, Effect of void fraction models on the two-phase friction factor of R134a during condensation in vertical downward flow in a smooth tube, Int. Commun. Heat Mass Transfer 35 (2008) 921–927.
[14] A.S. Dalkilic, S. Yildiz, S. Wongwises, Experimental investigation of convective heat transfer coefficient during downward laminar flow condensation of R134a in a vertical smooth tube, Int. J. Heat Mass Transfer 52 (2009) 142–150.
[15] A.S. Dalkilic, S. Laohalertdecha, S. Wongwises, Two-phase friction factor in vertical downward flow in high mass flux region of refrigerant HFC-134a during condensation, Int. Commun. Heat Mass Transfer 35 (2008) 1147–1152.
[16] A.S. Dalkilic, S. Laohalertdecha, S. Wongwises, Effect of void fraction models on the film thickness of R134a during downward condensation in a vertical smooth tube, Int. Commun. Heat Mass Transfer 36 (2009) 172–179.
[17] A.S. Dalkilic, S. Laohalertdecha, S. Wongwises, A comparison of the void fraction correlations of R134a during condensation in vertical downward laminar flow in a smooth and microfin tube, in: Proceedings of the First International Conference on Micro/Nanoscale Heat Transfer, ASME, January 06–09, Taiwan, 2008.
[18] A.S. Dalkilic, S. Laohalertdecha, S. Wongwises, Two-phase friction factor obtained from various void fraction models of R-134a during condensation in vertical downward flow at high mass flux, in: Proceedings of the first International Conference on Heat Transfer, ASME, August 10–14, USA, 2008.
[19] A.S. Dalkilic, S. Wongwises, Intensive literature review of condensation inside smooth and enhanced tubes, Int. J. Heat Mass Transfer 52 (2009) 3409–3426.
[20] A.S. Dalkilic, Investigation of the Convective Heat Transfer Coefficient During Condensation in Vertical Tubes, Ph.D. Thesis, Yildiz Technical University, İstanbul, Turkey, 2007.
[21] O. Agra, I. Teke, Experimental investigation of condensation of hydrocarbon refrigerants (R600a) in a horizontal smooth tube, Int. Commun. Heat Mass Transfer 35 (2008) 1165–1171.
[22] O. Agra, Condensation of Refrigerants in a Horizontal Tube in Annular Flow Regime, Ph.D. Thesis, Yildiz Technical University, Istanbul, Turkey, 2007.
[23] A.S. Dalkilic, S. Laohalertdecha, S. Wongwises, Experimental investigation on heat transfer coefficient of R134a during condensation in vertical downward flow at high mass flux in a smooth tube, Int. Commun. Heat Mass Transfer 36 (2009) 1036–1043.
[24] A.S. Dalkilic, S. Laohalertdecha, S. Wongwises, Experimental investigation on the condensation heat transfer and pressure drop characteristics of R134a at high mass flux conditions during annular flow regime inside a vertical smooth tube, Summer Heat Transfer Conference, ASME, July 19–23, USA, 2009.
[25] A.S. Dalkilic, O. Agra, Experimental apparatus for the determination of condensation heat transfer coefficient for R134a and R600a flowing inside vertical and horizontal tubes, Summer Heat Transfer Conference, ASME, July 19–23, USA, 2009.
[26] A.S. Dalkilic, S. Laohalertdecha, S. Wongwises, Experimental research on the similarity of annular flow models and correlations for the condensation of R134a at high mass flux inside vertical and horizontal tubes, International

Mechanical Engineering Congress and Exposition, ASME, November 13–19, USA, 2009.
[27] A.S. Dalkilic, S. Wongwises, A heat transfer model for co-current downward laminar film condensation of R134a in a vertical micro-fin tube during annular flow regime, Eleventh UK National Heat Transfer Conference, September 6–8, Queen Mary University of London, UK, 2009.
[28] H. Demir, O. Agra, S.O. Atayilmaz, Generalized neural network model of alternative refrigerant (R600a) inside a smooth tube, Int. Commun. Heat Mass Transfer 36 (2009) 744–749.
[29] S.J. Kline, F.A. McClintock, Describing uncertainties in single sample experiments, Mech. Eng. (1953).
[30] G.F. Hewitt, D.N. Robertson, Studies of two-phase flow patterns by simultaneous x-ray and flash photography, Rept AERE-M2159, UKAEA, Harwell, 1969.
[31] T.N. Tandon, H.K. Varma, C.P. Gupta, Heat transfer during forced convection condensation inside horizontal tube, Int. J. Refrig. 18 (1995) 210–214.
[32] S.L. Chen, F.M. Gerner, C.L. Tien, General film condensation correlations, Exp. Heat Transfer 1 (1987) 93–107.
[33] I.Y. Chen, K.S. Yang, Y.J. Chang, C.C. Wang, Two-phase pressure drop of air–water and R-410a in small horizontal tubes, Int. J. Multiph. Flow 27 (2001) 1293–1299.
[34] A. Cavallini, G. Censi, D. Del Col, L. Doretti, G.A. Longo, L. Rossetto, Experimental investigation on condensation heat transfer and pressure drop of new HFC refrigerants (R134a, R125, R32, R410A, R236ea) in a horizontal smooth tube, Int. J. Refrig. 24 (2007) 73–87.
[35] A. Cavallini, G. Censi, D. Del Col, L. Doretti, G.A. Longo, L. Rossetto, Condensation of halogenated refrigerants inside smooth tubes, HVAC R. Res. 8 (2002) 429–451.
[36] S. Garimella, Condensation flow mechanisms, pressure drop and heat transfer in microchannels, in: S. Kakac, L.L. Vasiliev, Y. Bayazitoglu, Y. Yener (Eds.), Microscale Heat Transfer-Fundamental and Applications, Kluwer Academic Publishers, The Netherlands, 2005.
[37] S. Garimella, A. Agarwal, J.D. Killion, Condensation pressure drop in circular microchannels, Heat Transfer Eng. 26 (2005) 1–8.
[38] K. Mishima, T. Hibiki, Some characteristics of air–water two-phase flow in small diameter vertical tubes, Int. J. Multiph. Flow 22 (1996) 703–712.
[39] C.C. Wang, C.S. Chiang, D.C. Lu, Visual observation of two-phase flow pattern of R-22, R-134a, and R-407C in a 6.5-mm smooth tube, Exp. Ther. Fluid Sci. 15 (1997) 395–405.
[40] M.J. Wilson, T.A. Newell, J.C. Chato, C.A. Infante Ferreira, Refrigerant charge, pressure drop, and condensation heat transfer in flattened tubes, Int. J. Refrig. 26 (2003) 442–451.
[41] D.A.L. Souza, M.D.M. Pimenta, Prediction of pressure drop during horizontal two-phase flow of pure and mixed refrigerants, in: Proceedings of the 1995 ASME/JSME Fluids Engineering and Laser Anemometry Conference and Exhibition, August 13–18, Hilton Head, SC, ASME, NewYork, NY, 1995, pp. 161–171.
[42] T.N. Tran, M.C. Chyu, M.W. Wambsganss, D.M. France, Two-phase pressure drop of refrigerants during flow boiling in small channels: an experimental investigation and correlation development, Int. J. Multiph. Flow 26 (2000) 1739–1754.
[43] H.J. Lee, S.Y. Lee, Pressure drop correlations for two-phase flow within horizontal rectangular channels with small heights, Int. J. Multiph. Flow 27 (2001) 783–796.

Experimental Thermal and Fluid Science 34 (2010) 454–462

Contents lists available at ScienceDirect

Experimental Thermal and Fluid Science

journal homepage: www.elsevier.com/locate/etfs

The effects of channel diameter on flow pattern, void fraction and pressure drop of two-phase air–water flow in circular micro-channels

Sira Saisorn [a], Somchai Wongwises [b,*]

[a] Energy Division, The Joint Graduate School of Energy and Environment (JGSEE), King Mongkut's University of Technology Thonburi, Bangmod, Bangkok 10140, Thailand
[b] Fluid Mechanics, Thermal Engineering and Multiphase Flow Research Lab. (FUTURE), Department of Mechanical Engineering, King Mongkut's University of Technology Thonburi, Bangmod, Bangkok 10140, Thailand

ARTICLE INFO

Article history:
Received 17 November 2008
Received in revised form 17 February 2009
Accepted 17 February 2009

Keywords:
Two-phase flow
Micro-channel
Flow pattern
Void fraction
Pressure drop

ABSTRACT

Two-phase air–water flow characteristics are experimentally investigated in horizontal circular micro-channels. Test sections are made of fused silica. The experiments are conducted based on three different inner diameters of 0.53, 0.22 and 0.15 mm with the corresponding lengths of 320, 120 and 104 mm, respectively. The test runs are done at superficial velocities of gas and liquid ranging between 0.37–42.36 and 0.005–3.04 m/s, respectively. The flow visualisation is facilitated by systems mainly including stereozoom microscope and high-speed camera. The flow regime maps developed from the observed flow patterns are presented. The void fractions are determined based on image analysis. New correlation for two-phase frictional multiplier is also proposed for practical applications.

© 2009 Published by Elsevier Inc.

1. Introduction

Two-phase flow in micro-channel flow passages has been studied over the years. The clarifications of micro-scale effects on two-phase flow and heat transfer characteristics have become more necessary due to the rapid development of microstructure devices used for several engineering applications including medical devices, high heat-flux compact heat exchangers, and cooling systems of various types of equipment such as high performance micro-electronics, supercomputers, high-powered lasers.

In addition to the attractive phenomena caused by the significant role of surface effects, this emerging field enables us to develop powerful miniature devices for operation in a domain which seemed to be unfeasible in the past. However, it is obvious that a comprehensive understanding of the trends and parameters dominating flow behavior in mini- and micro-channels is still lacking. Thus, fundamental heat transfer and flow characteristics problems encountered in the development and processing of micro-electronic-mechanical-systems (MEMS) have become a significant challenge in the design and control of these micro-systems. Because of the requirement for new solutions to dissipate heat and maintain uniform temperature distributions in modern devices, a clear understanding of the major mechanisms affecting micro-scale heat transfer is essential for optimum design and process control of micro-systems.

Two-phase flow and heat transfer characteristics in small channels such as micro-channels and mini-channels are likely to be strongly dependent on surface tension effects in addition to viscosity and inertia forces, resulting in significant differences in two-phase flow phenomena between ordinarily sized channels and small channels. Several investigators have proposed criteria to address the definition of a micro-channel. The proposed channel classifications are often based on different parameters. For instance, arbitrary channel classifications based on the hydraulic diameter D_h have been proposed. Recently, Mehendale et al. [1] employed the hydraulic diameter as an important parameter for defining heat exchangers and Kandlikar [2] proposed criteria for small flow channels used in engineering applications.

In the past decade, there have been a relatively small amount of publications available for both mini-channels and micro-channels compared to those for ordinarily sized channels.

Triplett et al. [3,4] studied adiabatic two-phase air-deionized water (DI water) flow characteristics in micro-channels with hydraulic diameter ranging from 1.1 to 1.5 mm. The flow patterns observed were bubbly, slug, churn, slug–annular and annular. The measured void fraction and two-phase pressure drop in the relevant flow regimes were also investigated. The void fraction data were obtained, based on the image analysis.

Serizawa et al. [5] investigated the visualization of the two-phase flow pattern in circular micro-channels. The flowing mixture

* Corresponding author. Tel.: +66 2 470 9115; fax: +66 2 470 9111.
E-mail address: somchai.won@kmutt.ac.th (S. Wongwises).

0894-1777/$ - see front matter © 2009 Published by Elsevier Inc.
doi:10.1016/j.expthermflusci.2009.02.006

of air and water in channels of 20, 25 and 100 μm in diameter and that of steam and water in a channel of 50 μm in diameter were conducted experimentally. Two-phase flow patterns obtained from both air–water and steam-water flows were quite similar and their detailed structures were described. The study confirmed that the surface wettability had a significant effect on the two-phase flow patterns in very small channels.

Chung and Kawaji [6] performed an experiment in order to distinguish two-phase flow characteristics in micro-channels from those in mini-channels. Four different circular diameters ranging from 50 to 526 μm were employed to examine a scaling effect on nitrogen–DI water two-phase flow. The results including the flow patterns, void fraction and two-phase pressure drop were analyzed.

The applicability of several widely used viscosity models to the pressure drop prediction of air–water flow through a 0.53 mm diameter channel was examined by Saisorn and Wongwises [7]. The other relevant models for the two-phase flow pressure drop prediction in micro-channels were also examined by Kawahara et al. [8], Chung and Kawaji [6], Saisorn and Wongwises [9,10], and Triplett et al. [4].

Although some information is currently available on flow pattern, void fraction, and pressure drop in micro-channels, there still remains room for further research.

The aim of this paper is to compare the two-phase air–water flow characteristics in different size micro-channels. The results are compared based on flow pattern, void fraction and two-phase frictional pressure drop.

2. Experimental apparatus and procedure

The experiments were carried out using the apparatus along with the instruments as shown in Figs. 1 and 2. The corresponding details are described as follows. Fig. 1 illustrates a schematic diagram of the test facility. Air, nitrogen gas, water and de-ionized water are used as working fluids in the system. Instead of a conventional pump, which may contribute to pulsation and fluid contamination, either air or nitrogen gas and the liquid-filled tank are combined and operated as a pneumatic pump to supply a constant flow rate of liquid through test section. The mixing chambers as shown in Fig. 2 are designed to introduce the air–water mixture smoothly along the channel. The mixture flows freely from the channel outlet where atmospheric pressure is realized. The gas flow rates were able to be measured by four sets of rotameters within the range of 5–50 sccm, 0.05–0.5, 0.2–2.0, 1–10 SCFH, respectively. For liquid flow rate measurements, an electronic balance (320 ± 0.001 g) was used to measure the weight of the liquid flowing freely from the outlet over a time. The test sections used in this work are fused silica tubes with inner diameters of 0.53 mm (320 mm length), 0.22 mm (120 mm length) and 0.15 mm (104 mm length). The single-phase and two-phase pressure drops across the test section were determined by two pressure transduc-

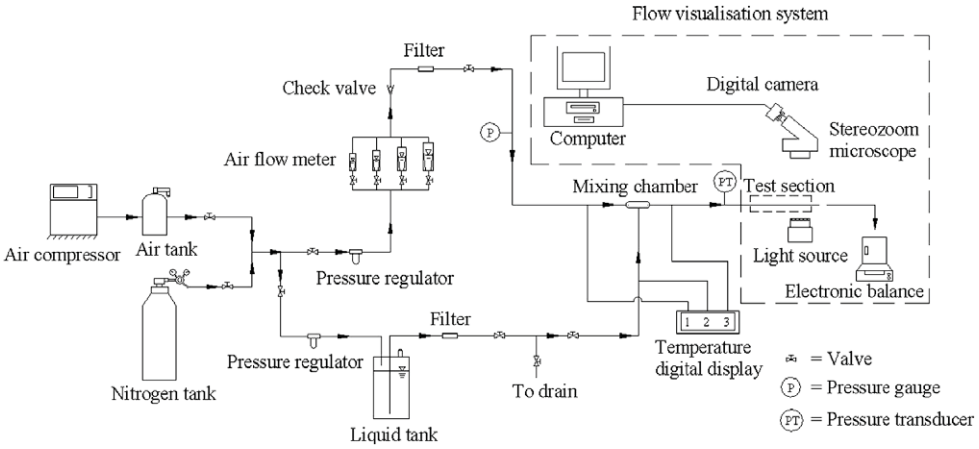

Fig. 1. Experimental apparatus.

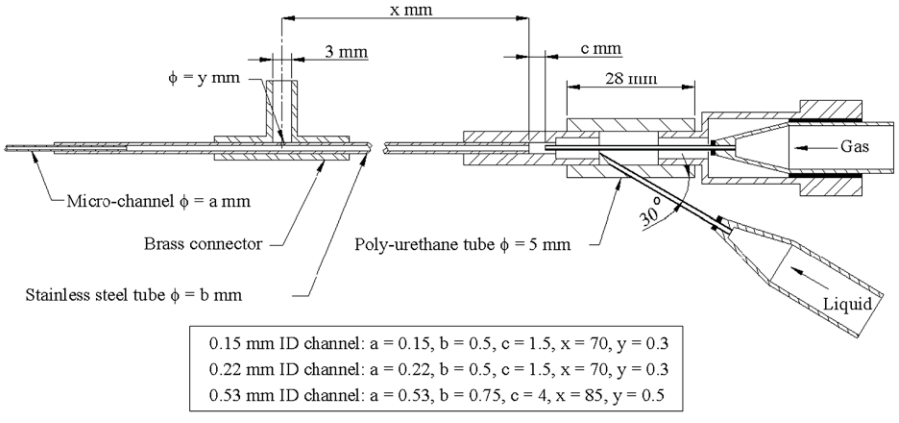

Fig. 2. Mixing chamber.

ers installed at the channel inlet. The low range pressure transducer was calibrated from 0 to 250 kPa with a ±0.5 kPa accuracy and the high range one was calibrated from 0 to 1000 kPa with a ±2 kPa accuracy. Type T thermocouples were used to measure fluid temperatures. The degree of uncertainty of the temperature measurements was ±0.1 °C.

The detailed formation of each flow pattern is registered by precise stereozoom microscope (Nikon SMZ-1) having a continuous zoom ranging between 0.7× and 3.0×, including 20× eyepieces mounted together with a camera system (Fujifilm FinePix S7000) having shutter speeds of 1/15 to 1/10,000 s and a frame rate of 30 frames per second. According to the above system, a magnified image of up to 60 times can be obtained. In this study, however, the magnification is adjusted so that the appropriate view field (L/D = 10) is obtained. The region near the channel outlet is always selected as the viewing window available for the captured image. An adjustable light source consisting of 150 watt halogen lamp and dimmer is placed under the test section to provide illumination for the flow visualization. The lighting condition can be refined by placing the frosted glass between the light source and the test section.

The single-phase flow experiments with different fluids were the first to be performed. Following this, the two-phase flow experiments were conducted at various gas and liquid flow rates. In this work, the gas flow rate was increased by small increments, while the liquid flow rate was kept constant at a pre-selected value. The system was allowed to approach steady conditions before the fluid flow rates, flow patterns and pressure drops were recorded. Visual observation shows that different flow patterns may occur with gas–liquid co-current flow in a horizontal microchannel. The main systems composing of stereozoom microscope and high-speed camera are located above the test section to facilitate the flow visualisation. The image analysis was carried out to estimate the void fraction based on the scale provided by micrometer.

3. Results and discussion

3.1. Flow pattern

A camera used in this work is Fujifilm FinePix S7000 by which the flow in the test section can be photographed with shutter speeds of 1/15–1/10,000 s. For video system, the recording speed or frame rate of the camera is 30 frames per second. In the present work, two groups of images, including a number of images extracted from the video files and a set of photographed images shot by the camera, are analysed for flow regime identification.

For a given experimental condition, the first step for the analysis is to open a video file to see the fluids flowing through the test section. With the image processing software, around 300 images are extracted from the video file to conduct the flow regime identification. The identification process for the channels with diameters of 0.53 and 0.22 mm is done based on the flow pattern which is mostly observed under a given flow condition. In the case of a 0.15 mm diameter channel, the process is done according to grouping method associated with the appearance of flow patterns.

The image analysis is used for void fraction estimation and thus, high quality of images is needed for the process. As a consequence of this requirement, the other group of the photographs (around 50–70 images for each flow condition) shot by the camera are analysed for void fraction and are selected to illustrate the flow structure as presented in Fig. 3.

Fig. 3 shows typical photographs of various flow patterns obtained from the test sections. Based on different channels, the flow patterns are observed as follows.

3.1.1. 0.53 mm diameter channel

Four different flow patterns covering slug flow, throat-annular flow, churn flow and annular–rivulet flow are observed.

Slug flow, which occurs at a relatively low air velocity, is characterized by elongated bubble flowing in the axial direction.

Throat-annular flow is considered as a unique flow pattern in micro-channels because this flow pattern has never been observed in the ordinarily sized channels under normal gravity conditions.

Churn flow is characterized by a disruption near the bubble tail of the slug flow pattern.

Annular–rivulet flow corresponds to the situation that both annular flow and rivulet flow appear interchangeably as discussed in Saisorn and Wongwises [9].

3.1.2. 0.22 mm diameter channel

Based on a 0.22 mm diameter channel, the observed flow patterns include throat-annular flow, annular flow and annular–rivulet flow. It should be noted that annular flow is characterized by the stable flowing of the water film on the tube wall and continuous air in the tube core whereas annular–rivulet flow concerns with the simultaneous appearance of both annular flow and rivulet flow. The rivulet flow is a flow pattern characterized by the flowing of a river-like water stream on the tube surface.

3.1.3. 0.15 mm diameter channel

There are four different flow patterns observed in a 0.15 mm diameter channel. These flow patterns are liquid-alone flow, throat-annular flow, serpentine-like gas core flow, which is characterized by small ripple on the gas–liquid interface, and annular flow. It is important to note that such four flow patterns tend to appear alternately with time even at a given flow condition. This unstable appearance was also reported by Serizawa et al. [5], Kawahara et al. [8] and Wu and Cheng [11]. The flow regimes for the 0.15 mm circular micro-channel can be defined according to the appearance of the flow patterns as follows.

(a) In the region of low gas flow rates, an alternating flow mode consisting of liquid-alone flow, annular flow, and either or both of throat-annular flow and serpentine-like gas core flow is observed. A new flow pattern referred to as liquid/unstable annular alternating flow (LUAAF) is represented to describe these flow characteristics.
(b) A flow mode represented by liquid/annular alternating flow (LAAF) pertains to the alternating appearance of liquid-alone flow and annular flow (AF). This flow mode occurs in the region of high liquid flow rates.
(c) In the region of high gas flow rates, the flow is quite stable and only annular flow is observed.

3.2. Flow regime map

Parameters used in the presentation of flow pattern data are the phase superficial velocities. The superficial velocities of gas (j_G) and liquid (j_L) refer to the situation where the designated phase flows alone in the channel. The present flow pattern transition maps pertaining to two-phase air–water flow in horizontal circular microchannels with diameters of 0.53, 0.22 and 0.15 mm are shown in Fig. 4. The lines along with the flow pattern names indicated on the figure refer to the transition boundaries corresponding to different channels. An interesting point, which can be seen from the comparison, is that the variation of channel diameter tends to have no significant effects on the vicinity relating to the gas core flow with deformed interface. The throat-annular flow regime based on both channels with diameters of 0.53 and 0.22 mm corresponds well with LUAAF regime obtained from a 0.15 mm diameter

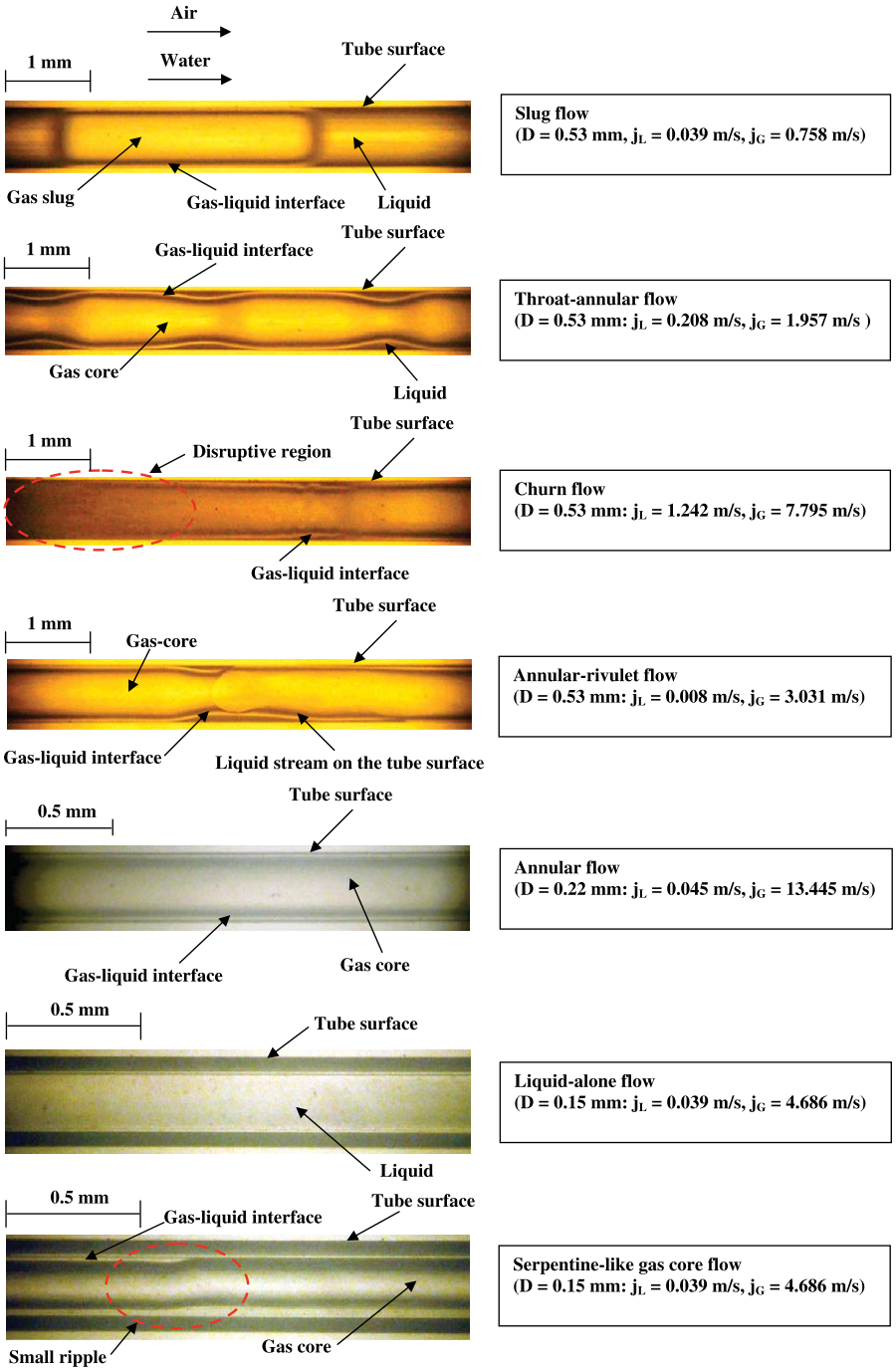

Fig. 3. Photographs of two-phase flow patterns.

channel. However, in this region, generally observed in only small channels, the interfacial waves appearing in the gas core flow patterns become thin as the channel diameter is decreased. The cause for this is due to the dominant role of surface tension on the gas–liquid interface.

The present flow pattern maps are also compared with the transition lines by Garimella et al. [12] and Revellin and Thome [13] who conducted the experiments with the phase change of refrigerant R134a in micro-channels.

The criteria for intermittent flow to wavy flow (or annular flow) transition was proposed by Garimella et al. [12] as follows:

$$x \leqslant \frac{a}{G+b} \tag{1}$$

where x denotes mass quality, G represents mass velocity and a and b are given by

$$a = 69.5673 + 22.595e^{0.2586d} \tag{2}$$

$$b = -59.9899 + 176.8137e^{0.3826d} \tag{3}$$

where d stands for tube diameter in mm. The data points which follow these criteria are considered to be located on the intermittent flow regime and the others refer to either annular regime or wavy regime. Figs. 5–7 show the comparisons of the present data with the transition criteria by Garimella et al. [12]. For a 0.53 mm diameter channel illustrated in Fig. 5, all flow pattern data, including slug flow, throat-annular flow, churn flow and annular–rivulet flow, lie

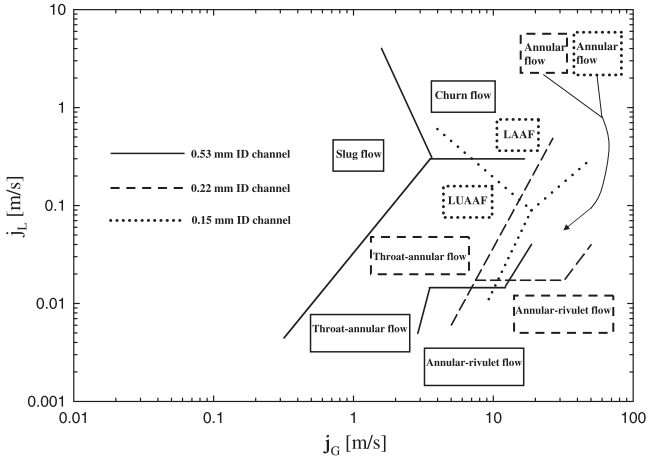

Fig. 4. Comparison of flow pattern maps.

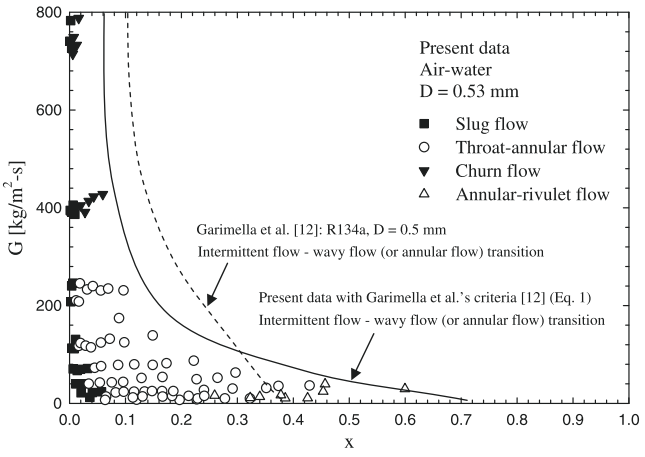

Fig. 5. Comparison of the flow patterns for a 0.53 mm diameter channel with the transition criteria by Garimella et al. [12].

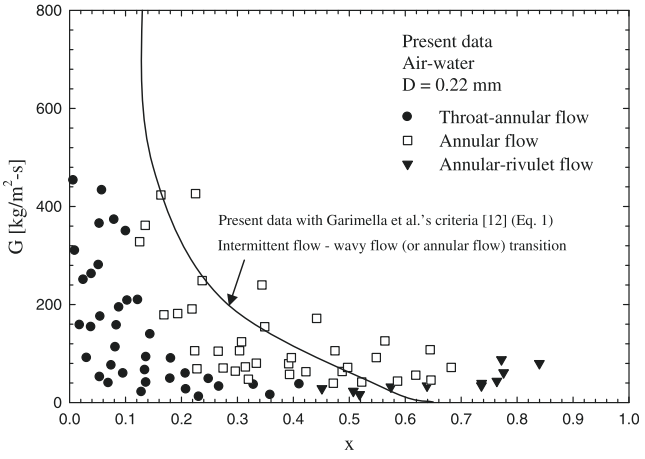

Fig. 6. Comparison of the flow patterns for a 0.22 mm diameter channel with the transition criteria by Garimella et al. [12].

in the intermittent flow regime and agree with the transition line by Garimella et al. [12]. Also, such transition criteria seem to be in fair agreement with the present data for the other two channels as shown in Figs. 6 and 7.

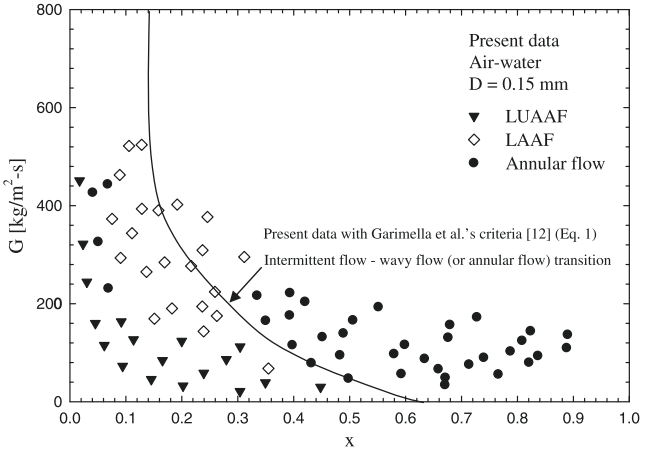

Fig. 7. Comparison of the flow patterns for a 0.15 mm diameter channel with the transition criteria by Garimella et al. [12].

The present data for the channel with the diameter of 0.53 mm is compared with the transition lines by Revellin and Thome [13] for flow boiling of R134a in a 0.51 mm diameter channel, in Fig. 8. The dash lines along with the flow pattern names indicated on the figure stand for the present transition boundaries whereas the solid lines and the names refer to the transition boundaries proposed by Revellin and Thome [13]. The comparison shows that bubbly flow, bubbly/slug flow, slug flow and slug/semi-annular flow obtained from Revellin and Thome [13] are located in the vicinity of slug flow regime of the present study. Their semi-annular flow regime, which corresponds to gas core flow with deformed interface, is found to agree well with our throat-annular flow pattern. In the region of high gas flow rates, our annular–rivulet flow is established, which is in relative agreement with their annular flow.

3.3. Void fraction

Void fraction is also one of the most important parameters used to evaluate the gravitational and accelerational terms in the total pressure drop of two-phase gas–liquid flow in various channels. Different methods available for void fraction estimation have been used by previous researchers.

Conventional methods such as a constant electric current method generally used to measure void fraction in ordinarily sized

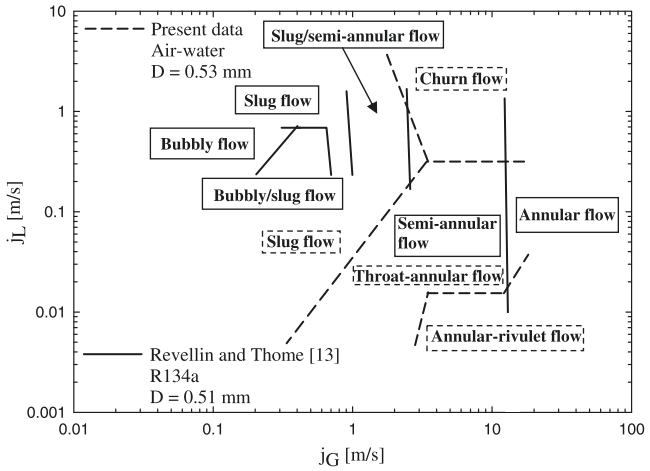

Fig. 8. Comparison of the present transition lines for a 0.53 mm diameter channel with the lines of Revellin and Thome [13].

channels were carried out by Kariyasaki et al. [14] to obtain void fractions in channels with three different diameters of 1, 2.4, and 4.9 mm. In a method based on quick-closing valves, Wongwises and Pipathattakul [15] measured void fraction in an inclined narrow annular channel with a hydraulic diameter of 4.5 mm.

For channels with hydraulic diameters of less than around 1 mm, it may be convenient to estimate volumetric void fraction by image analysis.

As previously mentioned, there are two sources of images which are obtained from flow visualisation. For a given flow condition, the first group of the images refers to approximately 300 images extracted from the video file and the other group stands for around 50–70 photographed images shot by the camera. The flow pattern identification is conducted based on both groups whereas the latter group, which corresponds to the images photographed with high shutter speed, is available for void fraction estimation.

In the present work, the void fraction is the average value estimated from about 50–70 photographed images. The image analysis is considered by assuming symmetrical volumes, covering spherical and ellipsoidal segments as well as cylinders, formed by gas–liquid interface. The volumetric void fraction was determined, based on the micrometer scale with an accuracy of ±0.05 mm and the effect of the curvature radius of the tube, which is firstly introduced by Kawahara et al. [8], is taken into account for the estimation. The uncertainty is around ±13% for the channels with diameters of 0.53 and 0.22 mm, and around ±39% for the 0.15 mm diameter channel.

The void fraction data obtained from a 0.53 mm diameter channel were found to agree well with the linear relationship of Eq. (4) which corresponds to the homogeneous flow model.

$$\alpha = \beta. \tag{4}$$

The Armand-type correlation of Eq. (5) recommended for small channel [6] was found to represent well the data for a 0.22 mm diameter channel.

$$\alpha = 0.833\beta. \tag{5}$$

For the two-phase flow in a channel having a diameter of 0.15 mm, the measured void fractions were found to be no longer linear relationship. Instead, the data were correlated well by the empirical form of Eq. (6) which is proposed by Kawahara et al. [8]. The non-linear relationship is mainly attributed to the highly frequent appearance of the gas core flow patterns which are inherent flow with large slip ratios. In addition, Kwak et al. [16] reported that void fraction data, obtained based on two-phase air–DI water flow through a fractal-like branching flow network, showed the non-linear relationship as well.

$$\alpha = \frac{C_1\beta^{0.5}}{1 - C_2\beta^{0.5}}. \tag{6}$$

In Eqs. (4)–(6), α represents volumetric void fraction, β represents volumetric quality, C_1 and C_2 are obtained based on the experimental data and are equal to 0.036 and 0.945, respectively.

According to the above discussion, Fig. 9 illustrates the measured results along with the data obtained from previous researchers.

3.4. Two-phase frictional pressure drop

Prior to obtaining data for the frictional pressure drop and two-phase multiplier, measurements of the total pressure drop are taken under various different conditions. In this work, the total pressure drop of a two-phase flow in each horizontal channel is composed of three terms: frictional pressure drop, accelerational

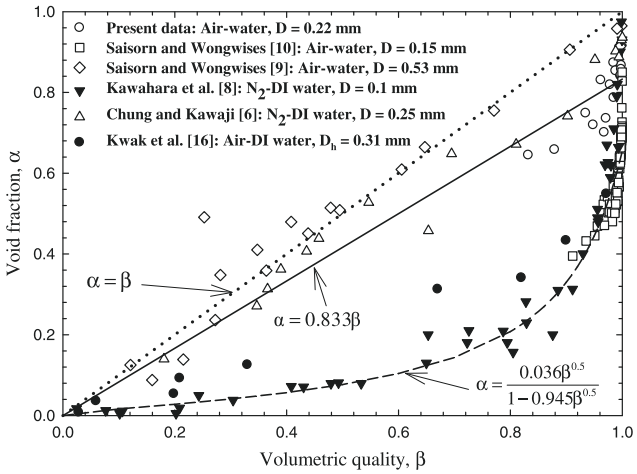

Fig. 9. Void fraction data for different channels.

pressure drop and pressure drop due to sudden contraction. According to the recent publication reported by Abdelall et al. [17], they reported that their data concerned with the air–water two-phase pressure drop in the circular micro-channel having abrupt flow area section agree very well with the slip model rather than with the homogeneous model. Therefore, it is important to note that the pressure drop due to sudden contraction should be carefully evaluated and a comprehensive review of the relevant calculations can be seen in Saisorn and Wongwises [10]. For the largest channel with a diameter of 0.53 mm, very small differences of up to 2% were indicated when the predictions obtained from the Abdelall et al.'s correlation [17] were compared with those from the homogeneous model. Nevertheless, for the other smaller channels, the sudden contraction pressure drops based on the Abdelall et al.'s correlation [17] were up to 98% lower than those calculated using the homogeneous flow model. Such considerable differences obtained from the other smaller channels are mainly due to the relatively high slip ratio as indicated in Fig. 9.

Finally, the two-phase frictional pressure drop in this study is determined by subtracting the accelerational term and sudden contraction term from the total pressure drop. For the sudden contraction term, the homogeneous flow model can be applicable in a 0.53 mm diameter channel whereas the Abdelall et al.'s correlation [17] is used for calculating in the other smaller channels. Fig. 10 shows frictional pressure drop data for different size channels. As

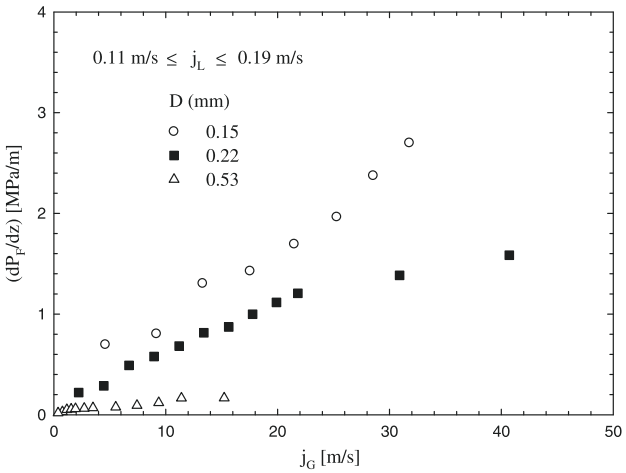

Fig. 10. Frictional pressure drop data for different channels.

expected, reducing the channel diameter increases the frictional pressure drop.

3.4.1. Two-phase frictional multiplier

The two-phase frictional multiplier for a smooth circular tube can be proposed in the form of the Lockhart–Martinelli correlation as follows:

$$\phi_L^2 = 1 + \frac{C}{\chi} + \frac{1}{\chi^2}, \tag{7}$$

where ϕ_L^2 represents two-phase frictional multiplier, χ represents Lockhart–Martinelli parameter. The constant C in the equation is the parameter which indicates the two-phase flow condition. The value of this parameter proposed by Chisholm [18] varies from 5 to 20 depending on the flow condition of the gas and liquid. For instance, the constant $C = 20$ when the gas and liquid flow is in the turbulent region and $C = 5$ if the two-phase flow is in the laminar region, which corresponds to the present study.

Mishima and Hibiki [19] proposed a correlation for the value of C as a function of the channel diameter and thus, the relationship between ϕ_L^2 and χ is given by

$$\phi_L^2 = 1 + \frac{21(1 - e^{-319D_h})}{\chi} + \frac{1}{\chi^2} \tag{8}$$

where D_h stands for hydraulic diameter.

Recently, English and Kandlikar [20] proposed a correlation which was modified, based on the Mishima and Hibiki's correlation [19] as shown in Eq. (9).

$$\phi_L^2 = 1 + \frac{C(1 - e^{-319D_h})}{\chi} + \frac{1}{\chi^2} \tag{9}$$

where the value of C depends on the flow condition and is similar to that proposed by Chisholm [18]. For the present data, the two-phase flow is in the laminar region and hence C = 5 is recommended for the calculation.

It is found from Figs. 11–13 that mass flux plays the most important role on the frictional multiplier data dealing with a 0.53 mm diameter channel but the dominating effect decreases thereafter with decreasing the channel diameter. The reason for this may be due to a level of the interaction between gas and liquid phases. According to Eq. (7), the level of the interaction corresponding to momentum coupling between the two phases can be implicitly represented by C parameter relating to the experimental data. Fig. 14 shows the data of C parameter obtained from different channels. It is found that the C parameter decreases with decreasing channel diameter. Additionally, the trend is similar way as that reported by Fujita et al. [21] and Lee and Lee [22].

In addition to mass flux, Figs. 15–17 illustrate that the orderly distribution of the data shows the dependence of flow pattern on the frictional multiplier.

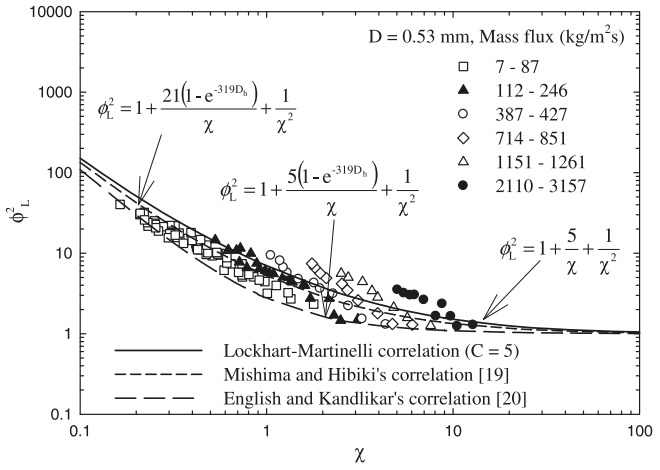

Fig. 11. Two-phase frictional multiplier data with various mass flux values for a 0.53 mm diameter channel.

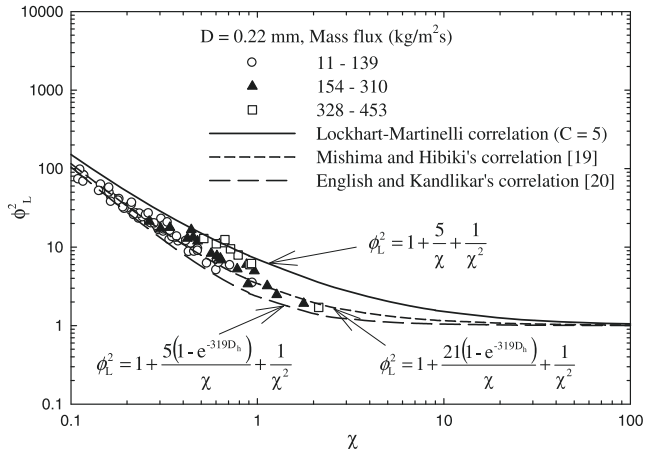

Fig. 12. Two-phase frictional multiplier data with various mass flux values for a 0.22 mm diameter channel.

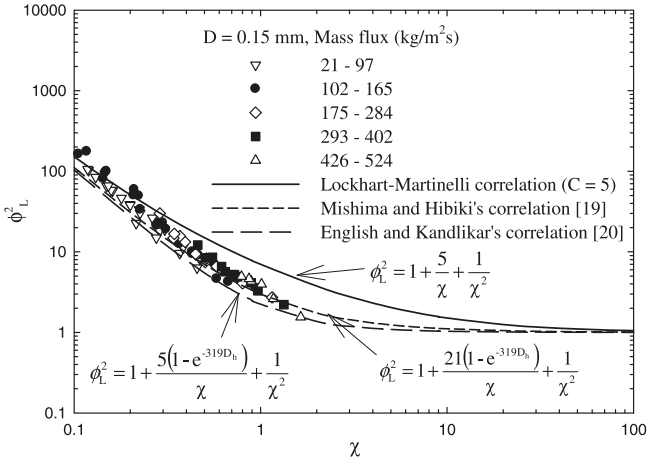

Fig. 13. Two-phase frictional multiplier data with various mass flux values for a 0.15 mm diameter channel.

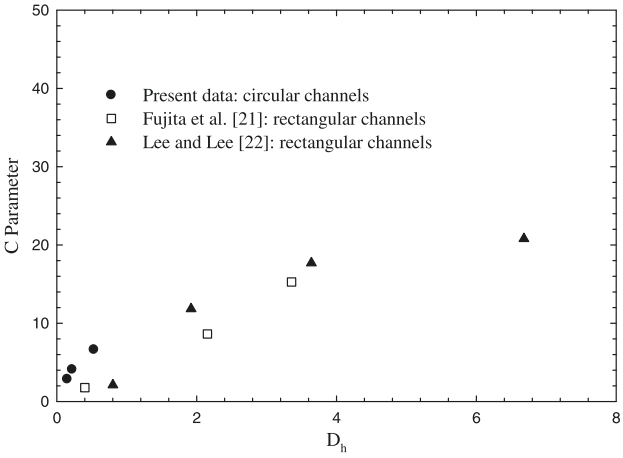

Fig. 14. C parameter versus channel diameter.

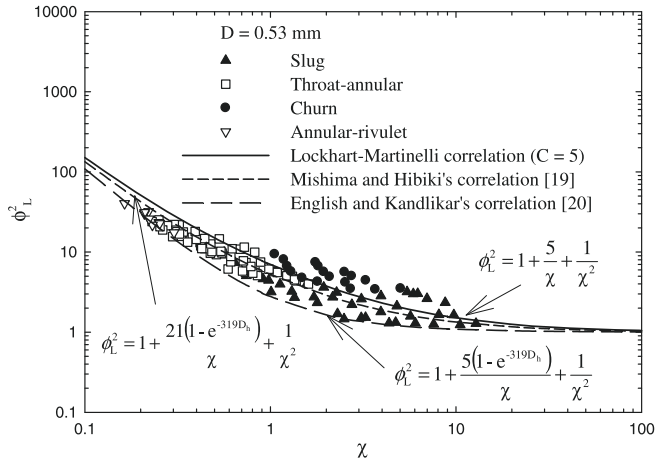

Fig. 15. Two-phase frictional multiplier data with various flow patterns for a 0.53 mm diameter channel.

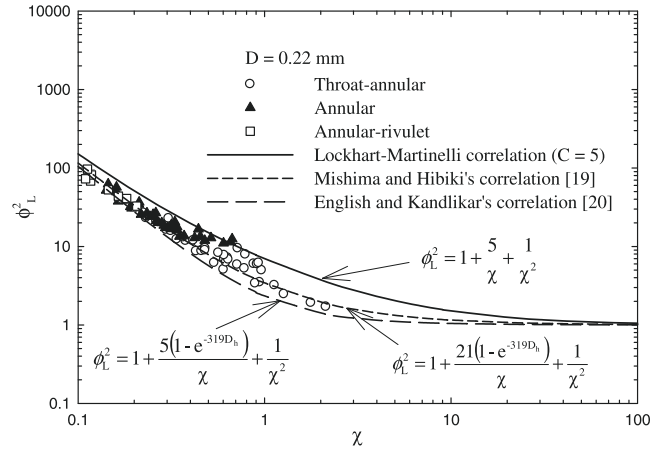

Fig. 16. Two-phase frictional multiplier data with various flow patterns for a 0.22 mm diameter channel.

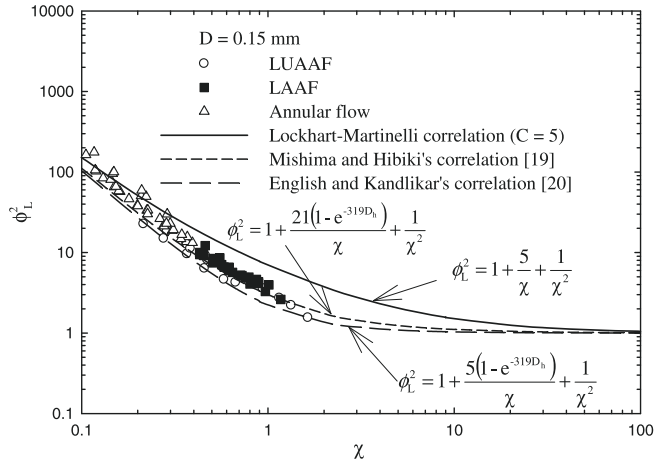

Fig. 17. Two-phase frictional multiplier data with various flow patterns for a 0.15 mm diameter channel.

Concerned with the comparisons between the pressure drop correlations and the measured data, it is found that the Lockhart–Martinelli correlation with $C = 5$ seems to be able to fairly predict the results only obtained from the largest channel whereas the Mishima and Hibiki's correlation [19] tends to be predictable for all three channels. The correlation proposed by English and Kandlikar [20] shows good agreement with the data in the range of very low mass flux values.

The pressure drop data are also compared with the correlation, working for refrigerants under certain condition, which is proposed by Muller-Steinhagen and Heck [23]. The correlation is given by the following equation:

$$\left(\frac{dP_F}{dz}\right)_{TP} = \left\{\left(\frac{dP_F}{dz}\right)_{LO} + 2x\left[\left(\frac{dP_F}{dz}\right)_{GO} - \left(\frac{dP_F}{dz}\right)_{LO}\right]\right\}(1-x)^{1/3} + \left(\frac{dP_F}{dz}\right)_{GO} x^3 \quad (10)$$

where $(dP_F/dz)_{TP}$ is two-phase frictional pressure gradient, $(dP_F/dz)_{LO}$ represents frictional pressure gradient for the total flow having liquid properties and $(dP_F/dz)_{GO}$ denotes frictional pressure gradient for the total flow having gas properties. Fig. 18 shows all present data compared with the predictions by Muller-Steinhagen and Heck [23]. The comparison shows that 60% of the present data fall within ±25% of the prediction by Muller-Steinhagen and Heck [23]. According to this comparison, the mean absolute error is around 0.13 MPa/m and the mean relative error is around 24%.

Although the pressure drop correlations presented by Mishima and Hibiki [19] and English and Kandlikar [20] were proposed at micro-scale, they do not take into account the mass velocity, viscous and surface tension effects which have significant influence on the two-phase flow in micro-channel. In this study, thus, the correlation for C parameter, proposed by Lee and Lee [22], which is developed based on two-phase air–water flow through horizontal rectangular channels with hydraulic diameter ranging from 0.78 to 6.67 mm is modified here to determine the value of C for the present test sections.

Based on all experimental data, a new correlation which takes into account the major effects dominating in the two-phase flow through micro-channel is expressed by

$$C = 7.599 \times 10^{-3} \lambda^{-0.631} \psi^{0.005} Re_{LO}^{-0.008} \quad (11)$$

where Re_{LO} represents the all-liquid Reynolds number as given below.

$$Re_{LO} = \frac{GD}{\mu_L} \quad (12)$$

where G is mass velocity and μ_L denotes liquid viscosity. λ and ψ are dimensionless parameters, introduced by Suo and Griffith [24], which are defined as

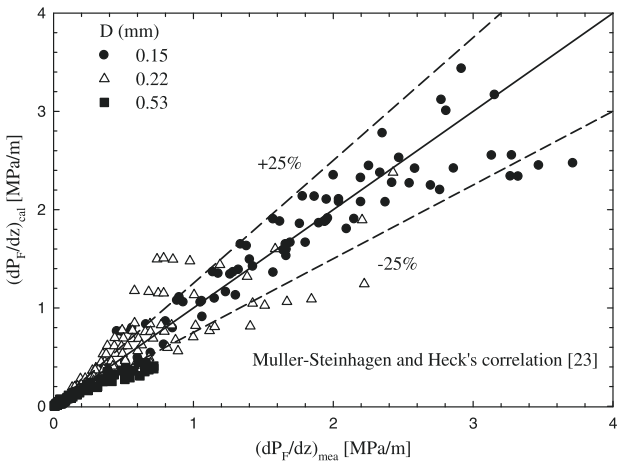

Fig. 18. Comparison of the experimental data with predictions by Muller-Steinhagen and Heck [23].

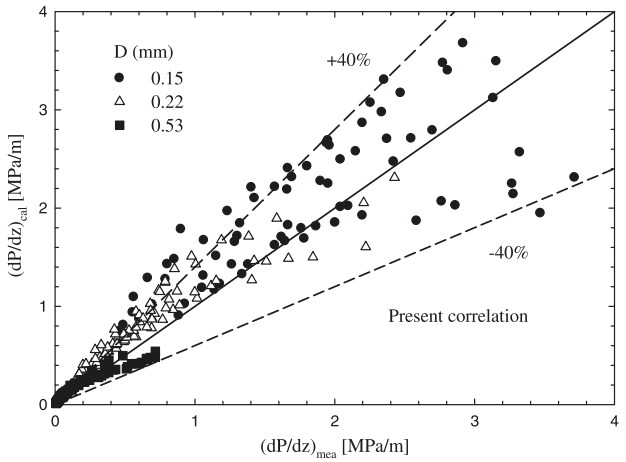

Fig. 19. Prediction of the frictional pressure drop.

$$\lambda = \frac{\mu_L^2}{\rho_L \sigma D} \tag{13}$$

$$\psi = \frac{\mu_L j}{\sigma} \tag{14}$$

where σ, ρ_L and j stand for surface tension, liquid density and total superficial velocity, respectively.

Fig. 19 shows the two-phase frictional pressure gradient obtained from measurement, $(dP/dz)_{mea}$ plotted against the two-phase frictional pressure gradient obtained from prediction, $(dP/dz)_{pre}$. Based on 285 data points, the mean absolute error is 0.2 MPa/m and the mean relative error is 47.98%, and around 52 percent of the data fall within ±40% of the proposed correlations.

The present correlation is obtained based on the channels with diameters of 0.53, 0.22 and 0.15 mm. The constant and all exponents are obtained from the data regression analysis. A notable point for the present correlation is addressed as follow. The exponent for all-liquid Reynolds number is very small, indicating that the C parameter is not strongly dependent on the mass velocity, especially in relatively small diameters. This point is also evident by Figs. 11–13.

4. Conclusion

Two-phase air–water flow is carried out in channels with diameters of 0.15, 0.22 and 0.53 mm which are made of fused silica. The gas superficial velocity and liquid superficial velocity are varied in a range of 0.37–42.36 m/s and 0.005–3.04 m/s, respectively. Seven different flow patterns including slug flow, throat-annular flow, churn flow, annular–rivulet flow, annular flow, liquid-alone flow and serpentine-like gas core flow are observed from the present test sections. The relationships dealing with void fraction are obtained, based on the measured data. The trend of the void fraction in a 0.15 mm diameter channel is no longer linear relationship. The two-phase pressure drop data indicate that mass flux and flow regime have a detectable effect on the two-phase frictional multiplier. A new correlation taking into account the major effects in two-phase flow through circular micro-channels is developed from the present data.

Acknowledgements

The authors would like to express their appreciation to the Thailand Research Fund (TRF) and the Joint Graduate School of Energy and Environment (JGSEE) for providing financial support for this study.

References

[1] S.S. Mehendale, A.M. Jacobi, R.K. Ahah, Fluid flow and heat transfer at micro- and meso-scales with application to heat exchanger design, Appl. Mech. Rev. 53 (2000) 175–193.
[2] S.G. Kandlikar, Fundamental issues related to flow boiling in mini-channels and micro-channels, Exp. Therm. Fluid Sci. 26 (2002) 389–407.
[3] K.A. Triplett, S.M. Ghiaasiaan, S.I. Abdel-Khalik, D.L. Sadowski, Gas–liquid two-phase flow in microchannels Part I: two-phase flow patterns, Int. J. Multiphase Flow 25 (1999) 377–394.
[4] K.A. Triplett, S.M. Ghiaasiaan, S.I. Abdel-Khalik, A. LeMouel, B.N. McCord, Gas–liquid two-phase flow in microchannels Part II: void fraction and pressure drop, Int. J. Multiphase Flow 25 (1999) 395–410.
[5] A. Serizawa, Z. Feng, Z. Kawara, Two-phase flow in micro-channels, Exp. Therm. Fluid Sci. 26 (2002) 703–714.
[6] P.M.-Y. Chung, M. Kawaji, The effect of channel diameter on adiabatic two-phase flow characteristics in microchannels, Int. J. Multiphase Flow 30 (2004) 735–761.
[7] S. Saisorn, S. Wongwises, An inspection of viscosity model for homogeneous two-phase flow pressure drop prediction in a horizontal circular micro-channel, Int. Commun. Heat Mass Transfer 35 (2008) 833–838.
[8] A. Kawahara, P.M.-Y. Chung, M. Kawaji, Investigation of two-phase flow pattern, void fraction and pressure drop in a microchannel, Int. J. Multiphase Flow 28 (2002) 1411–1435.
[9] S. Saisorn, S. Wongwises, Flow pattern, void fraction and pressure drop of two-phase air–water flow in a horizontal circular micro-channel, Exp. Therm. Fluid Sci. 32 (2008) 748–760.
[10] S. Saisorn, S. Wongwises, An experimental investigation of two-phase air–water flow through a horizontal circular micro-channel, Exp. Therm. Fluid Sci. 33 (2009) 306–315.
[11] H.Y. Wu, P. Cheng, Liquid/two-phase/vapor alternating flow during boiling in microchannels at high heat flux, Int. Commun. Heat Mass Transfer 30 (2003) 295–302.
[12] S. Garimella, J.D. Killion, J.W. Coleman, An experimentally validated model for two-phase pressure drop in the intermittent flow regime for circular microchannels, J. Fluid Eng. 124 (2002) 205–214.
[13] R. Revellin, J.R. Thome, A new type of diabatic flow pattern map for boiling heat transfer in microchannels, J. Micromech. Microeng. 17 (2007) 788–796.
[14] A. Kariyasaki, T. Fukano, A. Ousaka, M. Kagawa, Characteristics of time-varying void fraction in isothermal air–water co-current flow in horizontal capillary tube, Trans. JSME 57 (1991) 4036–4043.
[15] S. Wongwises, M. Pipathattakul, Flow pattern, pressure drop and void fraction of two-phase gas–liquid flow in an inclined narrow annular channel, Exp. Therm. Fluid Sci. 30 (2006) 345–354.
[16] Y. Kwak, D. Pence, J. Liburdy, V. Narayanan, Gas–liquid flows in a fractal-like branching flow network, in: Engineering Conference International Heat Transfer and Fluid Flow in Microscale III, Whistler, BC, Canada, September 21–26, 2008.
[17] F.F. Abdelall, G. Hahn, S.M. Ghiaasiaan, S.I. Abdel-Khalik, S.S. Jeter, M. Yoda, D.L. Sadowski, Pressure drop caused by abrupt flow area changes in small channels, Exp. Therm. Fluid Sci. 29 (2005) 425–434.
[18] D. Chisholm, A theoretical basis for the Lockhart–Martinelli correlation for two-phase flow, Int. J. Heat Mass Transfer 10 (1967) 1767–1778.
[19] K. Mishima, T. Hibiki, Some characteristics of air–water two-phase flow in small diameter vertical tubes, Int. J. Multiphase Flow 22 (1996) 703–712.
[20] N.J. English, S.G. Kandlikar, An experimental investigation into the effect of surfactants on air–water two-phase flow in minichannels, Heat Transfer Eng. 27 (2006) 99–109.
[21] H. Fujita, T. Ohara, M. Hirota, H. Furuta, Gas-liquid flows in flat channels with small channel clearance, in: Proceedings of the Second International Conference on Multiphase Flow'95, Kyoto, Japan, IA3-37-IA3-44, 1995.
[22] H.J. Lee, S.Y. Lee, Pressure drop correlations for two-phase flow within horizontal rectangular channels with small heights, Int. J. Multiphase Flow 27 (2001) 783–796.
[23] H. Muller-Steinhagen, K. Heck, A simple friction pressure drop correlation for two-phase flow in pipes, Chem. Eng. Process. 20 (1986) 297–308.
[24] M. Suo, P. Griffith, Two-phase flow in capillary tubes, Trans. ASME J. Heat Transfer (1964) 576–582.

Experimental Thermal and Fluid Science 34 (2010) 616–624

Contents lists available at ScienceDirect

Experimental Thermal and Fluid Science

journal homepage: www.elsevier.com/locate/etfs

Comparison of the effects of measured and computed thermophysical properties of nanofluids on heat transfer performance

Weerapun Duangthongsuk [a,b], Somchai Wongwises [b,*]

[a] Department of Mechanical Engineering, South-East Asia University, Bangkok, Thailand
[b] Fluid Mechanics, Thermal Engineering and Multiphase Flow Research Laboratory (FUTURE), Department of Mechanical Engineering, King Mongkut's University of Technology Thonburi, Bangmod, Bangkok 10140, Thailand

ARTICLE INFO

Article history:
Received 22 April 2009
Received in revised form 31 October 2009
Accepted 2 November 2009

Keywords:
Thermophysical property
Heat transfer performance
Nanofluid
Particle volume concentration

ABSTRACT

This article reports a comparison of the differences between using measured and computed thermophysical properties to describe the heat transfer performance of TiO_2–water nanofluids. In this study, TiO_2 nanoparticles with average diameters of 21 nm and a particle volume fraction of 0.2–1 vol.% are used. The thermal conductivity and viscosity of nanofluids were measured by using transient hot-wire apparatus and a Bohlin rotational rheometer, respectively. The well-known correlations for calculating the thermal conductivity and viscosity of nanofluids were used for describing the Nusselt number of nanofluids and compared with the results from the measured data. The results show that use of the models of thermophysical properties for calculating the Nusselt number of nanofluids gave similar results to use of the measured data. Where there is a lack of measured data on thermophysical properties, the most appropriate models for computing the thermal conductivity and viscosity of the nanofluids are the models of Yu and Choi and Wang et al., respectively.

© 2009 Elsevier Inc. All rights reserved.

1. Introduction

Nanofluids are innovative heat transfer fluids engineered by dispersing metallic or non-metallic nanoparticles with typical sizes of less than 100 nm in conventional heat transfer fluids. This term was coined by Choi [1] in 1995, and has since gained popularity. Normally, common heat transfer fluids such as oil, water, and ethylene glycol are used as the heat transfer fluid, and they are widely used in many industries in power generation, chemical processes, heating and cooling processes, transportation, microelectronics, and other micro-sized applications. However, these fluids have poor heat transfer properties compared with those of most solids, and this is the primary hindrance to the development of heat transfer equipment. The key idea is to disperse small solid particles in common base liquids in order to enhance their heat transfer properties. In recent years, with the rapid development in the field of nanotechnology, particles that are nanometer sized (normally less than 100 nm), instead of micrometer sized are dispersed in conventional base liquids in order to avoid problem of abrasion of the flow channel. Many researchers demonstrated that nanofluids have created various potential advantages, such as better long-term stability, and little penalty in term of drop in pressure, and can have drastically greater thermal conductivity compared with millimeter or even micrometer sized particle suspensions. Although nanofluids have significant potential for use in advanced thermal applications, they remain in the early stages of development. A decade ago, a number of researchers reported the heat transfer and flow characteristics of the different nanofluids. Moreover, Trisaksri and Wongwises [2], Duangthongsuk and Wongwises [3] and Wang and Mujumdar [4] reviewed the literature on the general heat transfer characteristics of nanofluids, especially. In our opinion, however, before starting to determine the heat transfer performance of nanofluids, it is first necessary to know about their thermophysical properties, especially thermal conductivity and viscosity. Many researchers have used well-known correlations for predicting the thermophysical properties of nanofluids and many researchers have measured these properties. Their works have been both theoretical and experimental. The sample investigations which have reported the heat transfer of nanofluids are summarized below.

Pak and Cho [5] evaluated the heat transfer performance of γ-Al_2O_3 and TiO_2 nanoparticles dispersed in water flowing in a horizontal circular tube under a turbulent flow regime experimentally. The experimental results of Masuda et al. [6] were used to obtain the relative thermal conductivity of nanofluids, while the viscosity of nanofluids was measured using a Brookfield viscometer. The results indicated that the Nusselt number of nanofluids increased with increases in the Reynolds number as well as the increases in the particle concentration. Moreover, their results also showed

* Corresponding author. Tel.: +662 470 9115; fax: +662 470 9111.
E-mail address: somchai.won@kmutt.ac.th (S. Wongwises).

0894-1777/$ - see front matter © 2009 Elsevier Inc. All rights reserved.
doi:10.1016/j.expthermflusci.2009.11.012

Nomenclature

Cp	specific heat, J/kg K
D	tube diameter, m
f	friction factor
h	heat transfer coefficient, W/m^2 K
k	thermal conductivity, W/m K
$\dot{m}$	mass flow rate, kg/s
Nu	Nusselt number
Pr	Prandtl number
q	heat flux, W/m^2
Q	heat transfer rate, W
Re	Reynolds number
T	temperature, °C

Greek symbols

ϕ	particle volume fraction
ε	tube roughness
ρ	density, kg/m^3
μ	viscosity, kg/m s

Subscripts

ave	average
f	fluid
h	heating fluid
in	inlet
out	outlet
p	particles
nf	nanofluid
w	water
wall	tube wall

that the heat transfer coefficient of the nanofluids with a particle volume fraction of 3% was around 12% smaller than that of pure water in the same condition. Finally, a novel heat transfer equation for computing the Nusselt number of nanofluids was proposed.

Li and Xuan [7] and Xuan and Li [8] reported experimentally the heat transfer performance and flow characteristics of Cu–DI water nanofluids flowing through a straight tube under laminar and turbulent flow conditions. The thermal conductivity and viscosity of nanofluids were measured. The results indicated that the heat transfer coefficient of nanofluids was remarkably higher than that of water and the friction factor of nanofluids coincided well with that of the water. Furthermore, new convective heat transfer correlations were proposed to calculate the heat transfer coefficients of the nanofluids for both laminar and turbulent flow conditions.

Wen and Ding [9] investigated the convective heat transfer coefficient of Al_2O_3–DI water flowing through a copper tube under a laminar flow regime experimentally. A KD2 thermal property meter was used to measure the thermal conductivity of nanofluids at 22 °C. The Einstein equation was used for calculating the viscosity of nanofluids. The experimental results indicated that the local heat transfer coefficient increased with increases in the Reynolds number as well as increases in the particle volume concentration. Moreover, the results also showed that the Shah correlation for laminar flow and the Dittus–Boelter equation for turbulent flow failed to predict the Nusselt number of nanofluids.

Ali et al. [10] studied the heat and mass transfer between air and falling film with ultrafine Cu nanoparticles in a cross flow configuration numerically. The thermophysical properties of nanofluids were calculated from the following existing formulas: the Hamilton and Crosser model (H–C model) [11] for thermal conductivity and the Brinkman equation [12] for viscosity. The results indicated that the dehumidification and cooling process increased under the following conditions: a low air Reynolds number, a high Cu particle volume fraction, increases in the height and length of the channel, and decreases in the channel width.

Roy et al. [13] investigated the heat transfer and wall shear stress of radial laminar flow in a cooling system of water–γ-Al_2O_3 nanofluids compared with water, glycol, and oil, numerically. The H–C model was used to compute the thermal conductivity and the equation of Wang et al. [14] was used to calculate the viscosity of nanofluids. Their results showed that the heat transfer rate and wall shear stress were higher with increases in the particle concentration as well as increases in the Reynolds number.

Ali and Vafai [15] reported numerical formulations to determine the effects of the inclination angle of parallel-and-counter-flow on heat and mass transfer between air and falling desiccant film, with suspended Cu nanoparticles. The H–C model was used to calculate the thermal conductivity whereas the Brinkman equation was used to compute the viscosity of nanofluids. The results indicated that the dehumidification and cooling process of air and the regeneration process of the liquid desiccant were enhanced by an increasing inclination angle for both parallel-and-counter flow channels.

Yang et al. [16] studied the heat transfer performance of graphite nanoparticles dispersed in two liquids flowing in a horizontal tube heat exchanger under laminar flow regimes. The thermal conductivity and viscosity of nanofluids were measured using a transient hot-wire apparatus and a capillary viscometer, respectively. The experimental results indicated that the heat transfer coefficient increased with increases in the Reynolds number and in the particle volume concentration. Two graphite nanoparticle sources at equal particle concentrations gave different values of the heat transfer coefficients. The results also showed that the calculated values of the Nusselt number using Li and Xuan's correlation [7] gave a higher value than the measured data did. Finally, a new heat transfer correlation for predicting the Nusselt number of nanofluids under laminar flow conditions was proposed by modifying the Seider–Tate equation (1936).

Ding et al. [17] investigated the local heat transfer coefficient of CNT-distilled water nanofluids flowing through a horizontal tube under a laminar flow regime, experimentally. A KD2 thermal property meter and a Bohlin CVO rheometer were used to measure the thermal conductivity and viscosity of nanofluids, respectively. The results showed that the local heat transfer coefficient of CNT nanofluids is much higher than that of pure water. This enhancement depends on the flow conditions, CNT concentration, and the pH value. However, they indicated that the effect of pH value is smallest compared with other parameters. Heris et al. [18,19] reported an experimental study of the heat transfer performance of Al_2O_3–water and CuO–water nanofluids flowing in an annular concentric tube under a laminar flow regime. The Einstein equation was used to calculate the viscosity of nanofluids whereas the H–C model and Yu and Choi [20] model were used to compute the thermal conductivity of nanofluids. The experimental results showed that the heat transfer coefficient increased with an increasing Peclet number and particle volume concentration. Moreover, their results also indicated that CuO–water nanofluids showed smaller heat transfer enhancement than Al_2O_3–water nanofluids.

He et al. [21] studied experimentally the heat transfer performance and pressure drop characteristic of TiO_2–distilled water nanofluids flowing through a vertical pipe in an upward direction

in both the laminar and turbulent flow regimes. A KD2 thermal property meter and a Bohlin CVO rheometer were used to measure the thermal conductivity and viscosity of nanofluids, respectively. The experimental results showed that the local heat transfer coefficient increased with an increasing concentration of nanoparticles in both the laminar and turbulent flow regimes at a given Reynolds number and particle size. The results also showed that the pressure drop of the nanofluids was very close to that of the base fluid.

Nguyen et al. [22] studied the heat transfer coefficient of Al_2O_3–water nanofluids flowing through an electronic liquid cooling system under turbulent flow conditions, experimentally. The Chon et al. equation [23] was used to calculate the thermal conductivity of nanofluids. The results showed that the Nusselt number of the nanofluids was much higher than that of the base liquid. Moreover, their results also indicated that the nanofluid with a 36 nm particle diameter gave a higher heat transfer coefficient than the nanofluid which was 47 nm in size.

Ko et al. [24] reported an experimental study of the pressure drop of carbon nanotubes dispersed in distilled water flowing through a horizontal tube. An AR2000 viscometer (TA Instruments) was used to measure the viscosity of nanofluids. The results showed that the nanofluids prepared by the acid treatment (TCNT) had much smaller viscosities than those made with surfactant (PCNT). Moreover, both nanofluids showed larger friction factors than the base fluids did.

Chein and Chuang [25] studied experimentally the heat transfer performance of a microchannel heat sink (MCHS) using CuO–water nanofluids as coolants. The thermal conductivity of nanofluids was calculated using the H–C model while the Brinkman equation was used to compute the viscosity. The results indicated that the presence of nanoparticles creates greater energy absorption than pure water at a low flow rate and there is no contribution from heat absorption when the flow rate is high.

Duangthongsuk and Wongwises [26] reported experimentally the heat transfer performance and pressure drop characteristics of TiO_2–water nanofluid flowing in a horizontal double tube counter flow heat exchanger. The Yu and Choi model was used to calculate the thermal conductivity of the nanofluids while the Einstein equation was used to compute the viscosity of the nanofluids. The results showed that the heat transfer coefficient of 0.2 vol.% nanofluid is slightly larger than that of water by about 6–11%. Moreover, the results also showed that use of nanofluid has a small penalty in terms of pressure drop.

Santra et al. [27] investigated the heat transfer behaviour of Cu–water nanofluids flowing through two isothermally heated parallel plates, numerically. The thermal conductivity and viscosity of nanofluids were calculated using the Patel et al. [28] equation and Brinkman equation, respectively. Their results showed that the local Nusselt number of nanofluids is larger than that of base fluid and increases with increases in the Reynolds number as well as with increases in the particle volume fraction.

Moreover, the other aspect of heat transfer performance of nanofluids such as pool boiling heat transfer is shown in the published article of Trisaksri and Wongwises [29].

As mentioned above, it is evident that some researchers measured the thermophysical properties of nanofluids and used them to evaluate the heat transfer performance and flow characteristics. However, some researchers used existing well-known equations to calculate the thermophysical properties of nanofluids. Many researchers (for example [5,9,14,21,30–32]) reported that the thermophysical properties model underestimated the viscosity and thermal conductivity of nanofluids. Mansour et al. [33] and Duangthongsuk and Wongwises [34] reported the effect of the thermophysical properties on the calculation of the heat transfer performance of nanofluid; however, they did not consider the discrepancy between use of the measured values and use of the calculated values of thermophysical properties to describe the Nusselt number of nanofluids. So far, this article has aimed to report the difference between the use of measured values and the use of calculated values of themophysical properties, which affects the Nusselt number of nanofluids.

2. Sample preparation

In the present study, nanofluids provided by a commercial source (DEGUSSA, VP Disp. W740×) are used as working fluid. This mixture is composed of TiO_2 nanoparticles with an average diameter of 21 nm dispersed in water. The original particle concentration was 40 wt.%. In order to produce other required particle volume fractions, dilution with water followed by a stirring action was effected. Moreover, an ultrasonic vibrator was used to sonicate the solution continuously for about 2 h in order to break down agglomeration of the nanoparticles. The desired volume concentrations used in this study were 0.2%, 0.6%, and 1.0% with pH values of 7.5, 7.1, and 7.0, respectively. From the pH values, it can be seen that the solution chemistry of nanofluids is nearly neutral in nature. A transmission electron microscope (TEM) was used to approximate the size of the primary nanoparticles. As shown in Fig. 1, it is clear that the primary size of nanoparticles is approximately spherical with an average diameter of around 21 nm.

3. Experimental apparatus

The experimental system used in the present study is shown schematically in Fig. 2. It mainly consists of a test section, two receiver tanks, a magnetic gear pump, a hot water pump, a cooler tank, a hot water tank, and a collection tank. The test section is a 1.5 m long counter-flow horizontal double tube heat exchanger with nanofluid flowing inside the tube while hot water flows in the annular. The inner tube is made from smooth copper tubing with a 9.53 mm outer diameter and a 0.7 mm thickness while the outer tube is made from PVC tubing and has a 33.9 mm outer diameter and 3 mm thickness. The test section is thermally isolated from its upstream and downstream sections by plastic tubes in order to reduce the heat loss along the axial direction. The differential pressure transmitter and T-type thermocouple are mounted at both ends of the test section to measure the pressure drop and the bulk temperature of the nanofluid, respectively. Thermocouples are mounted at different longitudinal positions on the inner

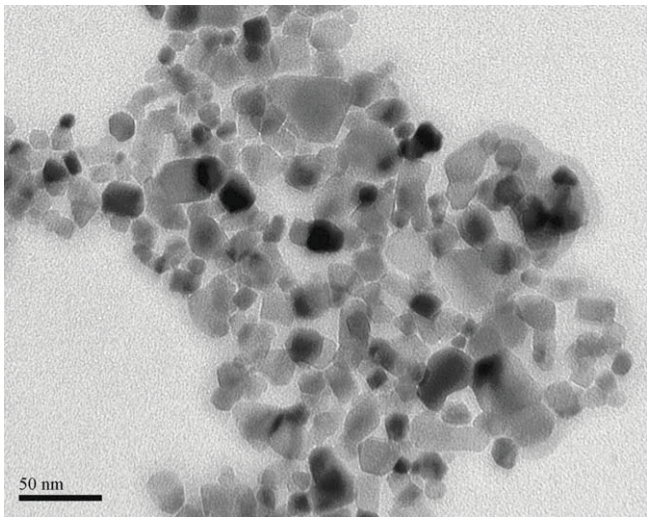

Fig. 1. TEM image of dispersed TiO_2 nanoparticles in water.

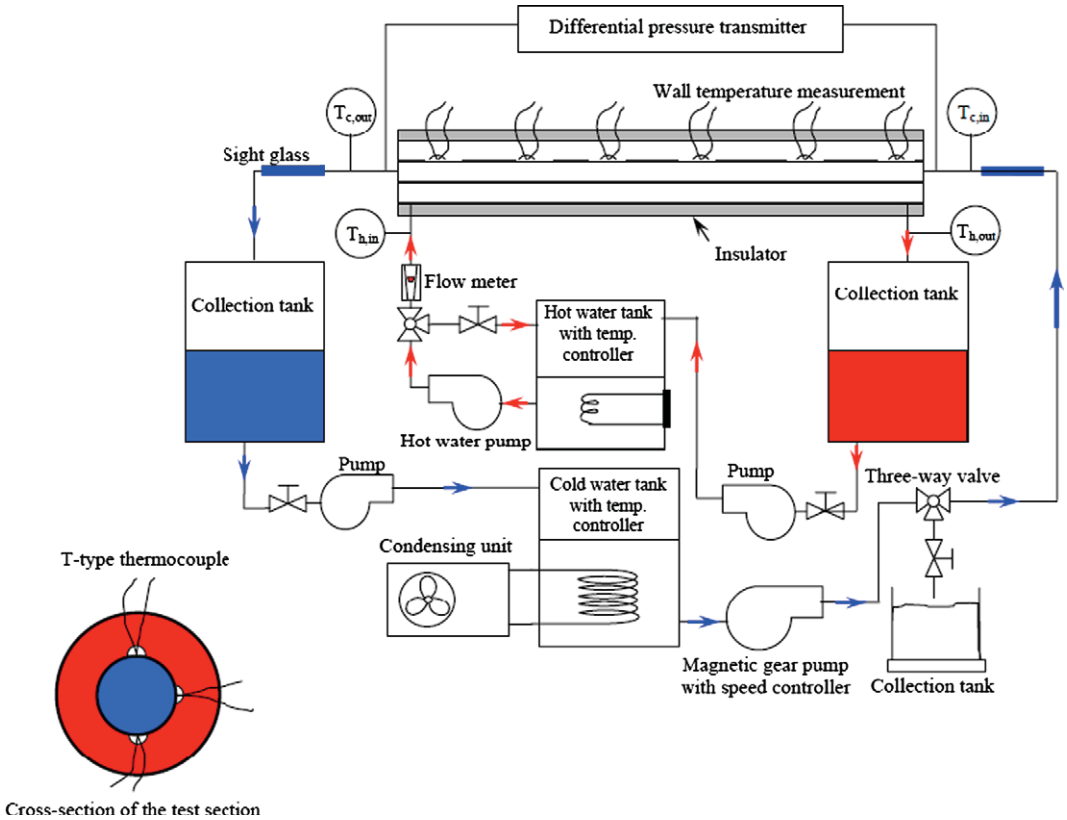

Fig. 2. Schematic diagram of the experimental apparatus.

tube surface of the wall, each with three thermocouples equally spaced around the tube circumference. The inlet and exit temperatures of hot water are measured using T-type thermocouples which are inserted into the flow directly. The receiver tanks of 60 L are made from stainless steel to store the nanofluid and hot water leaving from the test section. The cooler tank with a 4.2 kW cooling capacity and a thermostat is used to keep the nanofluid temperature constant. Similar to the cooler tank, a 3 kW electric heater with a thermostat was installed to keep the temperature of the hot water constant. The nanofluid flow rate was controlled by adjusting the rotation speed of the magnetic gear pump. The hot water flow rate was measured by a rotameter while the nanofluid flow rate was evaluated directly from the time taken for the exact mass of nanofluid to be discharged. For each speed of the pump, five measurements were done. The average of all data was used in the present study.

A portable programmable calibrator was used to calibrate all T-type thermocouples with a maximum precision of 0.1 °C. The nanofluid mass flow rates were determined by electronic balance. The uncertainty of the electronic balance was ±0.0006 kg. Maximum uncertainty of the nanofluid mass flow rate was evaluated as 2.2%. This uncertainty was taken into account to calculation of the uncertainty of the Nusselt number.

Moreover, the uncertainty of the hot water mass flow rate is ±7% (full scale). As mentioned above, it can be evidently seen that the uncertainty of the measured Nusselt number depends on the temperature measurement, and nanofluid and hot water flow rate measurement. The uncertainty of the measured Nusselt number was evaluated from the Root Mean Sum Square Method and found as 5%.

During the test run, wall temperatures of the test section, mass flow rates of the hot water and nanofluids, and the inlet and exit temperatures of the hot water and nanofluids were measured.

This study is a continuation of the authors' previous work. The details of the measurement of the thermal conductivity and viscosity of nanofluids, including the effect of temperature on these properties are presented in our previous article [35].

4. Data reduction

In this study, TiO_2–water nanofluids with particle volume concentrations of 0.2%, 0.6%, and 1.0% are used to evaluate the heat transfer performance of nanofluids. Thus, the Nusselt number of nanofluids can be computed from the following equation.

The heat transfer rate from the heating fluid is calculated from:

$$Q_w = \dot{m}_w Cp_w (T_{in} - T_{out})_w \tag{1}$$

where Q_w is the heat transfer rate of the hot water and $\dot{m}_w$ is the mass flow rate of the hot water.

The heat transfer rate into the nanofluid is computed from:

$$Q_{nf} = \dot{m}_{nf} Cp_{nf} (T_{out} - T_{in})_{nf} \tag{2}$$

where Q_{nf} is the heat transfer rate of the nanofluid and $\dot{m}_{nf}$ is the mass flow rate of the nanofluid.

The average heat transfer rate is defined as follows:

$$Q_{ave} = \frac{Q_w + Q_{nf}}{2} \tag{3}$$

where Q_{ave} is the average heat transfer rate between the hot water and the nanofluid.

In the experiments, only the data that satisfy the energy balance conditions ($|Q_w - Q_{nf}|/Q_{ave}$ are less than 3%), are considered in the analysis.

Finally, the Nusselt numbers of the nanofluid are computed from the following equations.

$$h_{nf} = \frac{q_{ave}}{T_{wall} - T_{nf}} \tag{4}$$

$$\mathrm{Nu}_{nf} = \frac{h_{nf} D}{k_{nf}} \tag{5}$$

where h_{nf} is the heat transfer coefficient of the nanofluid, q_{ave} is the average heat flux between the hot water and the nanofluid, T_{wall} is the average temperature of the wall, T_{nf} is the bulk temperature of the nanofluid, Nu_{nf} is the Nusselt number of the nanofluid, D is the inner diameter of the test tube and k_{nf} is the thermal conductivity of the nanofluid.

5. Thermophysical properties of nanofluid

The well-known correlations for calculating the thermophysical properties of the nanofluid which are often cited by a number of researchers are expressed as follows:

5.1. Thermal conductivity

One well-known equation for computing the thermal conductivity of nanofluid is the Hamilton and Crosser [11] model, which is expressed in the following form:

$$k_{nf} = \left[\frac{k_p + (n-1)k_w - (n-1)\phi(k_w - k_p)}{k_p + (n-1)k_w + \phi(k_w - k_p)}\right] k_w \tag{6}$$

$$n = 3/\psi \tag{7}$$

where n is the empirical shape factor and ψ is the sphericity, defined as the ratio of the surface area of a sphere (with the same volume as the given particle) to the surface area of the particle. The sphericity is 1 and 0.5 for the spherical and cylindrical shapes, respectively. Moreover, ϕ is the volume concentration, k_{nf} is the thermal conductivity of the nanofluid, k_p is the thermal conductivity of the nanoparticles and k_w is the thermal conductivity of the base fluid.

Moreover, the thermal conductivity of the nanofluids is calculated from Yu and Choi [20], which is expressed in the following form

$$k_{nf} = \left[\frac{k_p + 2k_w + 2(k_p - k_w)(1+\beta)^3\phi}{k_p + 2k_w - (k_p - k_w)(1+\beta)^3\phi}\right] k_w \tag{8}$$

An alternative formula for calculating the thermal conductivity was introduced by the Wasp [36] model, which is defined as follows:

$$k_{nf} = \left[\frac{k_p + 2k_w - 2\phi(k_w - k_p)}{k_p + 2k_w + \phi(k_w - k_p)}\right] k_w \tag{9}$$

where β is the ratio of the nanolayer thickness to the original particle radius. Normally $\beta = 0.1$ is used to calculate the thermal conductivity of the nanofluid. For spherical particles, the results given by the Wasp model coincide with those of the H–C model.

Murshed et al. [37] introduced the Bruggeman model [38] for calculating the thermal conductivity of nanofluids which is expressed as follows:

$$k_{nf} = \frac{1}{4}[(3\phi - 1)k_p + (2 - 3\phi)k_w] + \frac{k_w}{4}\sqrt{\Delta} \tag{10}$$

$$\Delta = \left[(3\phi - 1)^2(k_p/k_w)^2 + (2 - 3\phi)^2 + 2(2 + 9\phi - 9\phi^2)(k_p/k_w)\right] \tag{11}$$

Finally, Timofeeva et al. [39] introduced the effective medium theory for computing the thermal conductivity of nanofluids, which is defined as follows:

$$k_{nf} = [1 + 3\phi]k_w \tag{12}$$

5.2. Viscosity

Brinkman [12] suggested an equation to calculate the viscosity of the suspension, which is defined as follows:

$$\mu_{nf} = \frac{1}{(1-\phi)^{2.5}}\mu_w \tag{13}$$

In addition, Wang et al. [14] proposed a model to predict the viscosity of nanofluids which is expressed as:

$$\mu_{nf} = (1 + 7.3\phi + 123\phi^2)\mu_w \tag{14}$$

Drew and Passman [40] suggested the well-known Einstein's equation for calculating viscosity, which is applicable to spherical particles in volume fractions less than 5.0 vol.% and is defined as follows:

$$\mu_{nf} = (1 + 2.5\phi)\mu_w \tag{15}$$

Furthermore, Batchelor [41] introduced a correlation for calculating the viscosity of nanofluids with spherical shape nanoparticles which is defined as:

$$\mu_{nf} = (1 + 2.5\phi + 6.2\phi^2)\mu_w \tag{16}$$

where μ_{nf} is the viscosity of the nanofluid and μ_w is the viscosity of the base fluid.

5.3. Density and specific heat

The density and specific heat of the nanofluids are calculated by use of the Pak and Cho [5] correlations, which are defined as follows:

$$\rho_{nf} = \phi\rho_p + (1-\phi)\rho_w \tag{17}$$

and

$$Cp_{nf} = \phi Cp_p + (1-\phi)Cp_w \tag{18}$$

An alternative equation to compute the specific heat of the nanofluids was suggested by Xuan and Roetzel's equation [42], which is defined as

$$(\rho Cp)_{nf} = \phi(\rho Cp)_p + (1-\phi)(\rho Cp)_w \tag{19}$$

where Cp_{nf} is the specific heat of the nanofluid, Cp_p is the specific heat of the nanoparticles, and Cp_w is the specific heat of the base fluid.

Up to now, there are several models proposed for calculating the relevant properties. However, only a few correlations have been favorably accepted and often cited by a number of researchers.

For thermal conductivity of nanofluids, the models used in the present study are very famous. These models were developed based on theoretical investigation and always used and cited by many researchers. These models can be used to estimate the thermal conductivity of nanofluids. .

Similarly, the viscosity of nanofluids can be calculated using different existing formulas obtained for two-phase mixtures. The first well-known equation is the Einstein's equation. This relation has been found to be valid for particle concentration less than 2 vol.%. Then, this equation was extended to a more generalized form by Brinkman [12]. Moreover, one more well-known relation for calculating the viscosity of nanofluid was proposed by Bachelor [41], in 1977. The effect of Brownian motion of particles in a statistically homogeneous suspension was taken into account in this

model and this model was often cited by a number of researchers as well as Wang et al. [14] equation.

For the specific heat of the nanofluid, up to now, there are only two well-known models to calculate the specific heat of nanofluids which are Pak and Cho model [5] and Xuan and Roetzel model [42], respectively. The first model is based on the volume fraction whereas the second model is based on heat capacity concept. Both models are often cited by a number of researchers for calculating the specific heat of nanofluid.

As aforementioned, it is clearly seen that the correlations used in this study are based on the results published in open literature and often used and cited by many outstanding researchers. That is the reason for choosing these models to calculate the thermophysical properties of nanofluids for comparing with the experimental data.

The properties of the nanofluid shown in the above equations are calculated from water and nanoparticles at average bulk temperature.

6. Results and discussion

The measurement results of the thermal conductivity and viscosity of the nanofluids were expressed in a previous paper by the author [35]. In respect of the heat transfer performance, TiO_2 nanoparticles dispersed in water at 0.2%, 0.6%, and 1.0% by volume

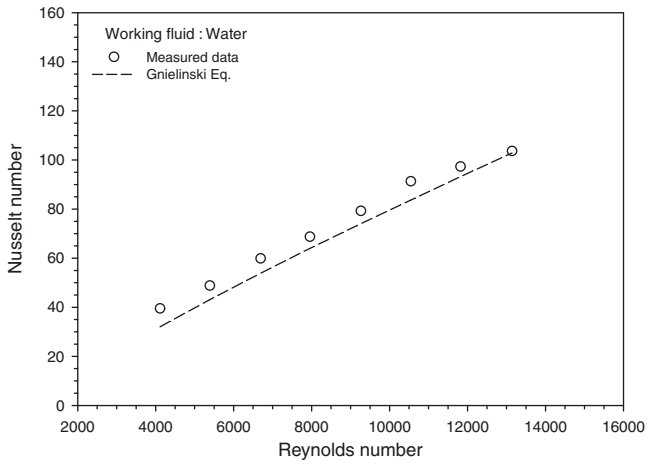

Fig. 3. Comparison between measured heat transfer coefficient and that calculated from Gnielinski equation [39].

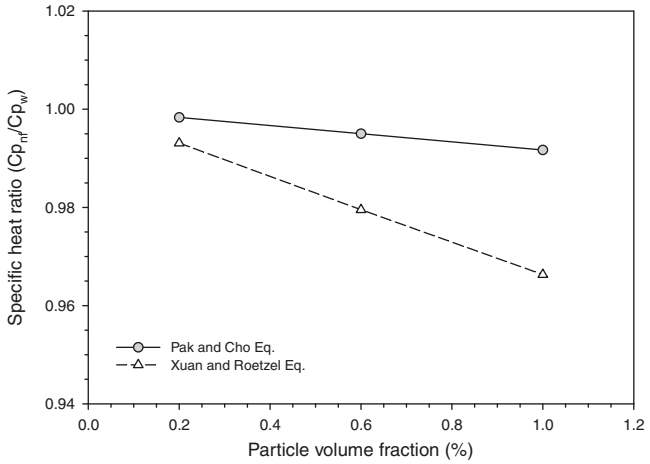

Fig. 4. Comparison of the specific heat equations of nanofluid as a function of particle volume fraction.

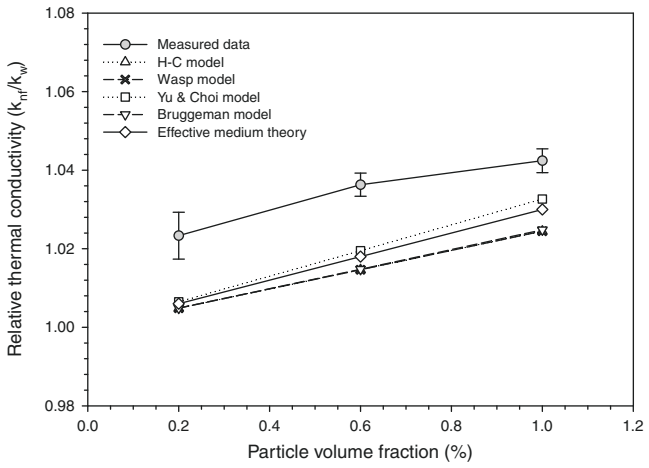

Fig. 5. Comparison of the relative thermal conductivity of nanofluids between measured data and the well-known correlations.

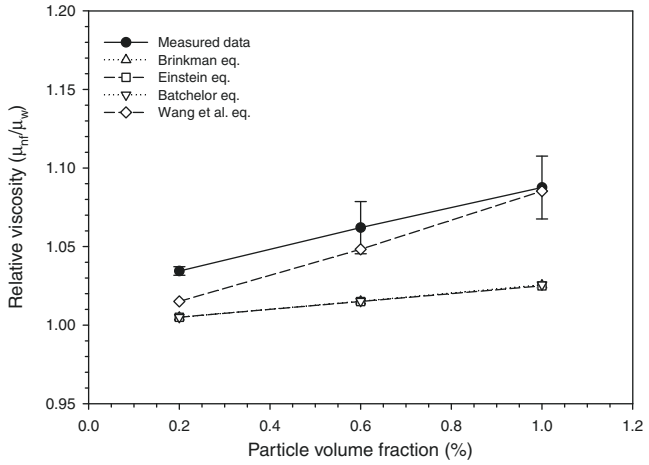

Fig. 6. Comparison of the relative viscosity of nanofluid between measured data and the well-known correlations.

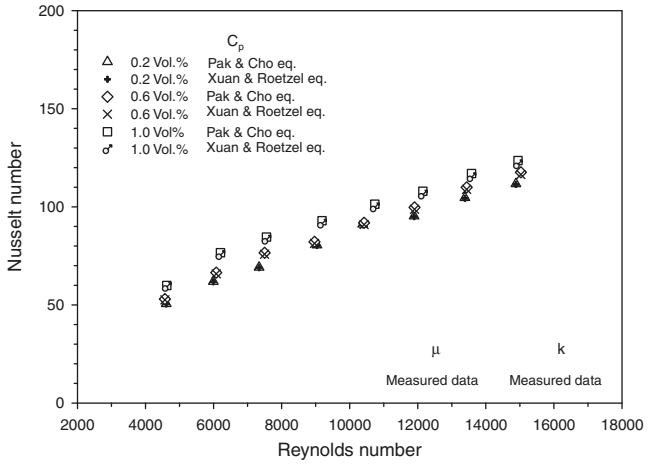

Fig. 7. Effect of the specific heat equations on the prediction of the Nusselt number of nanofluids.

are used to investigate the Nusselt number of the nanofluid. However, before measuring the Nusselt number of the nanofluids, the pure water is used as the test fluid to estimate the reliability and accuracy of the experimental system. The results of the experimental Nusselt number are compared with those obtained from the Gnielinski equation [43], which is defined as follows:

$$\mathrm{Nu} = \frac{(f/8)(\mathrm{Re} - 1000)\mathrm{Pr}}{1 + 12.7(f/8)^{0.5}(\mathrm{Pr}^{2/3} - 1)} \tag{20}$$

where Nu is the Nusselt number, Re is the Reynolds number, Pr is the Prandtl number and f is the friction factor.

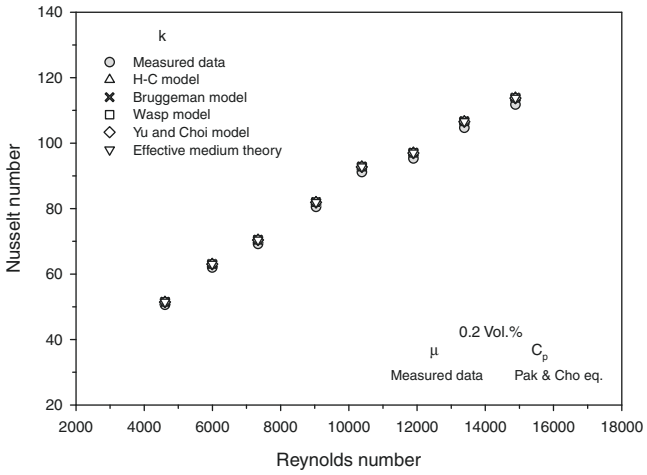

(a) at 0.2 vol.%

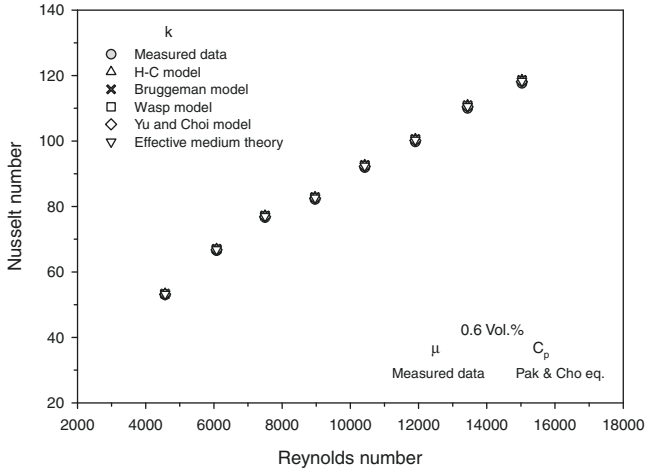

(b) at 0.6 vol.%

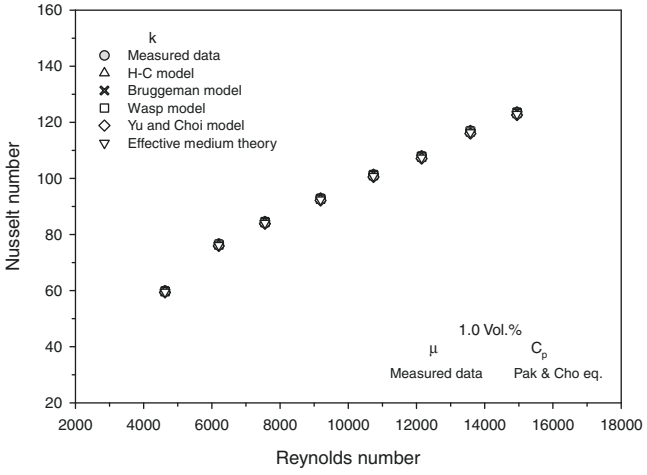

(c) at 1.0 vol.%

Fig. 8. Effect of the thermal conductivity value of nanofluid on the prediction of the Nusselt number of nanofluids.

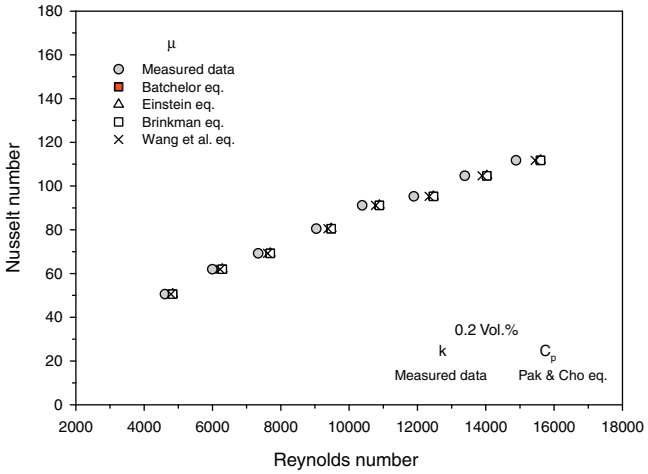

(a) at 0.2 vol.%

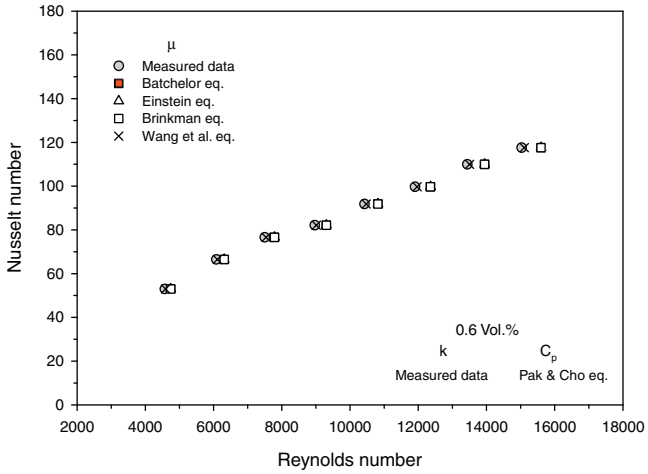

(b) at 0.6 vol.%

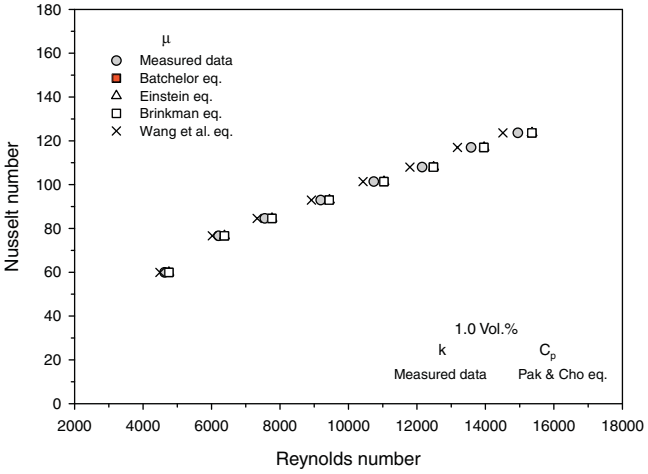

(c) at 1.0 vol.%

Fig. 9. Effect of the viscosity value of nanofluid on the describing of the Nusselt number of nanofluids.

The friction factor can be calculated from Colebrook's equation [44] as follows:

$$\frac{1}{\sqrt{f}} = -2.0\log\left(\frac{\varepsilon/D}{3.7} + \frac{2.51}{\mathrm{Re}\sqrt{f}}\right) \quad (21)$$

where ε is the roughness of the test tube.

As shown in Fig. 3, the measured Nusselt number coincided well with the calculated values for pure water.

Fig. 4 shows the specific heat ratio (Cp_{nf}/Cp_w) as a function of the particle volume concentrations. The figure shows that the two different specific heat equations give significantly different values of the specific heat ratio. Similarly, Figs. 5 and 6 show the variation between relative thermal conductivity (k_{nf}/k_w) and viscosity (μ_{nf}/μ_w) of nanofluids as a function of the particle volume concentrations, respectively. As shown in Fig. 5, it is clearly seen that all of the well-known correlations for computing the thermal conductivity of nanofluids give results that are remarkably lower than those given by the measured data. The results showed that the Yu and Choi equation gives results closest to the measured data in comparison to the H–C model, Wasp model, Bruggeman model, and even effective medium theory. Similar to the thermal conductivity, Fig. 6 shows that the Wang et al. equation for calculating the viscosity of nanofluids give results closest to the measured data in comparison to the Brinkman equation, Einstein equation, and Batchelor equation.

As mentioned above, it is evident that the various models and the measured data give difference results for evaluating the thermophysical properties of nanofluids. The following figures illustrate how big the difference is between the use of the measured data and use of the various models to describe the heat transfer performance of the nanofluids.

Fig. 7 shows that the Nusselt number increases with increases in the Reynolds number as well as in the particle volume concentrations. The results also indicated that the specific heat models have no significant effect on the prediction of the Nusselt number. Fig. 8a–c shows the effect of the thermal conductivity value on the calculation of the Nusselt number of nanofluids for particle volume concentrations of 0.2%, 0.6%, and 1.0%, respectively. The results showed that the different values of thermal conductivity give similar results for evaluating the Nusselt number of nanofluids. Similarly to the effect of the thermal conductivity, Fig. 9a–c shows the effect of the viscosity value on the description of the Nusselt number of nanofluid. The results indicated that the different values of viscosity give similar results in evaluating the Nusselt number of the nanofluids. However, the results also showed that use of the viscosity model to describe the Nusselt number of nanofluids gives different values compared with use of the measured data, by about 2–3%. In addition, the calculated values from the Wang et al. equation are closer to the results of the measured data than to the calculated values using the other correlations.

Since the models for determining various properties of nanofluids were developed from theoretical basis, it may be expected that the effect of model predictions on the results for the use of another nanofluids should give the same results.

7. Conclusions

The discrepancies between use of the measured data and use of the well-known correlations of the thermal conductivity and viscosity of nanofluid to describe the Nusselt numbers of nanofluids were investigated. TiO_2–water nanofluids with particle volume concentrations of 0.2%, 0.6%, and 1.0% flowing under turbulent flow conditions were tested. The results showed that all of the well-known correlations underestimate the thermal conductivity and viscosity of nanofluids compared with the measured data. Moreover, the different models gave different results. However, the use of the thermophysical models for calculation of the Nusselt number of nanofluids gave differences of a few percentage points when compared with the measured data. Due to lack of measured data on the thermophysical properties of the nanofluids, the use of the Yu and Choi model for thermal conductivity and the Wang et al. equation for viscosity to describe the Nusselt number of the nanofluids gave good agreement with the use of the measured data. Finally, measurement of the thermophysical properties of nanofluids is an important way to address the transport behaviour of nanofluids.

Acknowledgments

The authors would like to express their appreciation to the Thailand Research Fund (TRF) for providing financial support for this study. The authors also wish to thank DEGUSSA AG, Germany for the valuable donation of the nanoparticles used in the present study.

References

[1] S.U.S. Choi, Enhancing thermal conductivity of fluids with nanoparticle, ASME Fluids Engineering Division (FED) 231 (1995) 99-105.
[2] V. Trisaksri, S. Wongwises, Critical review of heat transfer characteristics of the nanofluids, Renewable and Sustainable Energy Reviews 11 (3) (2007) 512–523.
[3] W. Duangthongsuk, S. Wongwises, A critical review of convective heat transfer of nanofluids, Renewable and Sustainable Energy Reviews 11 (2007) 797–817.
[4] X.Q. Wang, A.S. Mujumdar, Heat transfer characteristics of nanofluids: a review, International Journal of Thermal Sciences 46 (2007) 1–19.
[5] B.C. Pak, Y.I. Cho, Hydrodynamic and heat transfer study of dispersed fluids with submicron metallic oxide particles, Experimental Heat Transfer 11 (1998) 151–170.
[6] H. Masuda, A. Ebata, K. Teramae, N. Hishinuma, Alteration of thermal conductivity and viscosity of liquid by dispersing ultra-fine particles (dispersion of Al_2O_3, SiO_2 and TiO_2 ultra-fine particles), Netsu Bussei (Japan) 7 (4) (1993) 227–233.
[7] Q. Li, Y. Xuan, Convective heat transfer and flow characteristics of Cu–water nanofluid, Science in China E 45 (2002) 408–416.
[8] Y. Xuan, Q. Li, Investigation on convective heat transfer and flow features of nanofluids, ASME Transactions, Journal of Heat Transfer 125 (2003) 151–155.
[9] D. Wen, Y. Ding, Experimental investigation into convective heat transfer of nanofluids at the entrance region under laminar flow conditions, International Journal of Heat Mass Transfer 47 (2004) 5181–5188.
[10] A. Ali, K. Vafai, A.R.A. Khaled, Analysis of heat and mass transfer between air and falling film in a cross flow configuration, International Journal of Heat Mass Transfer 47 (2004) 743–755.
[11] R.L. Hamilton, O.K. Crosser, Thermal conductivity of heterogeneous two-component systems, Industrial & Engineering Chemistry Fundamentals 1 (3) (1962) 187–191.
[12] H.C. Brinkman, The viscosity of concentrated suspensions and solution, Journal of Chemical Physics 20 (1952) 571–581.
[13] G. Roy, C.T. Nguyen, P.R. Lajoie, Numerical investigation of laminar flow and heat transfer in a radial flow cooling system with the use of nanofluids, Superlattices and Microstructures 35 (2004) 497–511.
[14] X. Wang, X. Xu, S.U.S. Choi, Thermal conductivity of nanoparticles–fluid mixture, Journal of Thermophysics Heat Transfer 13 (4) (1999) 474–480.
[15] A. Ali, K. Vafai, An Investigation of heat and mass transfer between air and desiccant film in an inclined parallel and counter flow channels, International Journal of Heat Mass Transfer 47 (2004) 1745–1760.
[16] Y. Yang, Z.G. Zhang, E.A. Grulke, W.B. Anderson, G. Wu, Heat transfer properties of nanoparticle-in-fluid dispersions (nanofluids) in laminar flow, International Journal Heat Mass Transfer 48 (6) (2005) 1107–1116.
[17] Y. Ding, H. Alias, D. Wen, R.A. Williams, Heat transfer of aqueous suspensions of carbon nanotubes (CNT nanofluids), International Journal Heat Mass Transfer 49 (1–2) (2005) 240–250.
[18] S.Z. Heris, S.G. Etemad, M.N. Esfahany, Experimental investigation of oxide nanofluids laminar flow convective heat transfer, International Communication in Heat and Mass Transfer 33 (2006) 529–535.
[19] S.Z. Heris, M.N. Esfahany, S.G. Etemad, Experimental investigation of convective heat transfer of Al_2O_3/water nanofluid in circular tube, International Journal of Heat Fluids Flow 28 (2) (2007) 203–210.
[20] W. Yu, S.U.S. Choi, The role of interfacial layers in the enhanced thermal conductivity of nanofluids: a renovated Maxwell model, Journal of Nanoparticle Research 5 (2003) 167–171.
[21] Y. He, Y. Jin, H. Chen, Y. Ding, D. Cang, H. Lu, Heat transfer and flow behavior of aqueous suspensions of TiO_2 nanoparticles (nanofluids) flowing upward through a vertical pipe, International Journal Heat Mass Transfer 50 (2007) 2272–2281.

[22] C.T. Nguyen, G. Roy, C. Gauthier, N. Galanis, Heat transfer enhancement using Al_2O_3–water nanofluid for electronic liquid cooling system, Applied Thermal Engineering 28 (2007) 1501–1506.
[23] C.H. Chon, K.D. Kihm, S.P. Lee, S.U.S. Choi, Empirical correlation finding the role of temperature and particle size for nanofluid (Al_2O_3) thermal conductivity enhancement, Applied Physics Letters 87 (15) (2005) 153107–153110.
[24] G.H. Ko, K. Ho, K. Lee, D.S. Kim, C. Kim, Y. Sohn, M. Choi, An experimental study on the pressure drop of nanofluids containing carbon nanotubes in the horizontal tube, International Journal Heat Mass Transfer 50 (2007) 4749–4753.
[25] R. Chein, J. Chuang, Experimental microchannel heat sink performance studies using nanofluids, International Journal of Thermal Sciences 46 (1) (2007) 57–66.
[26] W. Duangthongsuk, S. Wongwises, Heat transfer enhancement and pressure drop characteristics of TiO_2–water nanofluid in a double-tube counter flow heat exchanger, International Journal of Heat Mass Transfer 52 (2009) 2059–2067.
[27] A.K. Santra, S. Sen, N. Chakraborty, Study of heat transfer due to laminar flow of copper–water nanofluid through two isothermally heated parallel plates, International Journal of Thermal Sciences 48 (2009) 391–400.
[28] H.E. Patel, T. Pradeep, T. Sundararajan, A. Dasgupta, N. Dasgupta, S.K. Das, A micro-convection model for thermal conductivity of nanofluid, Pramana Journal of Physics 65 (2005) 863–869.
[29] V. Trisaksri, S. Wongwises, Nucleate pool boiling heat transfer of TiO_2-R141b nanofluids, International Journal of Heat Mass Transfer 52 (2009) 1582–1588.
[30] S. Lee, S.U.S. Choi, S. Li, J.A. Eastman, Measuring thermal conductivity of fluids containing oxide nanoparticles, Journal of Heat Transfer 121 (1999) 280–289.
[31] B.X. Wang, L.P. Zhou, X.F. Peng, A fractal model for predicting the effective thermal conductivity of liquid with suspension of nanoparticles, International Journal of Heat Mass Transfer 46 (2003) 2665–2672.
[32] J. Koo, C. Kleinstreuer, A new thermal conductivity model for nanofluids, Journal of Nanoparticle Research 6 (2004) 577–588.
[33] R.D. Mansour, N. Galanis, C.T. Nguyen, Effect of uncertainties in physical properties on forced convection heat transfer with nanofluids, Applied Thermal Engineering 27 (1) (2007) 240–249.
[34] W. Duangthongsuk, S. Wongwises, Effect of thermophysical properties models on the prediction of the convective heat transfer coefficient for low concentration nanofluid, International Communication in Heat and Mass Transfer 35 (2008) 1320–1326.
[35] W. Duangthongsuk, S. Wongwises, Measurement of temperature-dependent thermal conductivity and viscosity of TiO_2–water nanofluids, Experimental Thermal and Fluid Science 33 (2009) 706–714.
[36] F.J. Wasp, Solid–Liquid Slurry Pipeline Transportation, Trans Tech, Berlin, 1977.
[37] S.M.S. Murshed, K.C. Leong, C. Yang, Enhanced thermal conductivity of TiO_2–water based nanofluids, International Journal of Thermal Sciences 44 (2005) 367–373.
[38] D.A.G. Bruggeman, Berechnung verschiedener physikalischer konstanten von heterogenen substanzen. I. Dielektrizitatskonstanten und Leitfahigkeiten der Mischkorper aus Isotropen Substanzen, Annalen der Physik 14 (1935) 636–679.
[39] E.V. Timofeeva, A.N. Gavrilov, J.M. McCloskey, Y.V. Tolmachev, Thermal conductivity and particle agglomeration in alumina nanofluids: experiment and theory, Physical Review 76 (2007) 061203.
[40] D.A. Drew, S.L. Passman, Theory of Multi Component Fluids, Springer, Berlin, 1999.
[41] G.K. Batchelor, The effect of Brownian motion on the bulk stress in a suspension of spherical particles, Journal of Fluid Mechanics 83 (1) (1977) 97–117.
[42] Y. Xuan, W. Roetzel, Conceptions for heat transfer correlation of nanofluids, International Journal of Heat Mass Transfer 43 (2000) 3701–3707.
[43] V. Gnielinski, New equations for heat and mass transfer in turbulent pipe and channel flow, International Chemical Engineering 16 (1976) 359–368.
[44] C.F. Colebrook, Turbulent flow in pipes with particular reference to the transition between the smooth and rough pipe laws, Journal of the Institution of Civil Engineers, London 11 (1939) 133–156.

International Journal of Heat and Mass Transfer 53 (2010) 2924–2931

Contents lists available at ScienceDirect

International Journal of Heat and Mass Transfer

journal homepage: www.elsevier.com/locate/ijhmt

The effects of corrugation pitch on the condensation heat transfer coefficient and pressure drop of R-134a inside horizontal corrugated tube

Suriyan Laohalertdecha [a,b], Somchai Wongwises [b,*]

[a] The Joint Graduate School of Energy and Environment (JGSEE), King Mongkut's University of Technology Thonburi, Bangmod, Bangkok 10140, Thailand
[b] Fluid Mechanics, Thermal Engineering and Multiphase Flow Research Lab. (FUTURE), Department of Mechanical Engineering, King Mongkut's University of Technology Thonburi, Bangmod, Bangkok 10140, Thailand

ARTICLE INFO

Article history:
Received 15 April 2009
Received in revised form 10 December 2009
Accepted 10 December 2009
Available online 1 March 2010

Keywords:
Condensation
Heat transfer coefficient
Pressure drop
Smooth tube
Corrugated tube

ABSTRACT

The heat transfer coefficient and pressure drop of R-134a inside a horizontal smooth tube and corrugated tubes are experimentally investigated. The test section is a 2.0 m long counter-flow concentric double tube heat exchanger with refrigerant flowing in the inner tube and cooling water flowing in the annulus. A smooth tube and corrugated tubes having inner diameters of 8.7 mm are used as an inner tube. The corrugation pitches are 5.08, 6.35, and 8.46 mm, respectively. The corrugation depth of all corrugated tubes is fixed at 1.5 mm. The outer tube is made from smooth copper tube having an inner diameter of 21.2 mm. The test runs are performed at the saturation temperatures of 40, 45, and 50 °C, heat fluxes of 5 and 10 kW/m^2, and mass fluxes ranging from 200 to 700 kg/m^2 s. The results obtained from the corrugated tubes are compared with that of the smooth tube. It is found that the corrugation pitches have a significant effect on the heat transfer coefficient and pressure drop augmentations.

© 2010 Published by Elsevier Ltd.

1. Introduction

Heat exchangers can be improved by using various enhancement techniques. In general, enhancement techniques can be divided into two groups: namely active and passive techniques. The active technique requires external forces such as an electric field or acoustic or surface vibration, whereas the passive technique requires special surface geometries such as a rough surface, extended surface, or fluid additives. Both active and passive techniques were used by several researchers over a century ago to increase the heat transfer rate in heat exchangers [1].

Micro-fin tubes have been successfully implemented in the air-conditioning and refrigeration industries for effectively tube-side performance. This success is because of their ability to significantly improve the heat transfer coefficient [2–5] with only a moderate increase of the friction penalty.

The corrugated tube is a kind of tube having corrugation on the surface that is expected to increase the heat transfer coefficient with a very small increase of the friction penalty, by mixing the fluid boundary layers and also by limiting the growth of fluid boundary layers close to the heat transfer surfaces. Corrugated tubes are sometimes chosen in the design of industrial shell-and-tube heat exchangers. The size of these heat exchangers can be reduced considerably by using corrugated tubes instead of smooth tubes. Heat transfer enhancement using corrugated tubes has been studied by several researchers as shown in Table 1. The heat transfer and flow characteristics of working fluid in enhanced tubes have been studied by a number of researchers, and some examples of the most productive studies are described below.

Dong et al. [6] studied the turbulent friction and heat transfer characteristics of four spirally corrugated tubes with various geometrical parameters. Their results indicated that the spirally corrugated ribs have an effect on the enhancement of heat transfer but not as large as the effect on the increases in friction.

Barba et al. [7] presented the experimental results of heat transfer and pressure drop in corrugated tube, which is used in the chemical and food industries for single-phase flow at moderate Reynolds numbers of $100 < Re < 800$. The working fluid used in their study is ethylene glycol, which is a highly viscous Newtonian fluid. The inside Nusselt number in the corrugated tube is improved very significantly in comparison to those in the smooth wall, while the friction factor increases up to a factor of 2.45–1.83. Based on the experimental data, Nusselt number and friction factor correlations are proposed for the periodically fully developed region.

Rainieri and Pagliarini [8] studied the thermal performances of corrugated tubes in order to increase convective heat transfer. Axial symmetrical and helical corrugated tubes with different pitch values were considered. The tests were conducted at Reynolds numbers ranging between 90 and 800. The results showed that the helical corrugation induces significant swirl components.

* Corresponding author. Tel.: +662 470 9115; fax: +662 470 9111.
E-mail address: somchai.won@kmutt.ac.th (S. Wongwises).

0017-9310/$ - see front matter © 2010 Published by Elsevier Ltd.
doi:10.1016/j.ijheatmasstransfer.2010.01.037

Nomenclature

A	surface area of the test section (m^2)
c_p	specific heat at constant pressure (J/kg K)
D	diameter (m)
e	corrugation depth (mm)
G	mass flux (kg/m^2 s)
h	heat transfer coefficient (W/m^2 K)
i	enthalpy (J/kg)
k	thermal conductivity (W/m K)
L	length of the test tube (m)
$LMTD$	logarithmic mean temperature difference
m	mass flow rate (kg/s)
Nu	Nusselt number
p	corrugation pitch (mm)
Pr	Prandtl number
Q	heat transfer rate (W)
Re	Reynolds number
q''	heat flux (W/m^2)
T	temperature (°C)
x	average quality
X	Martinelli parameter

Greek letters

α	void fraction
β	helix angle (deg)
ε	relative roughness (m)
ρ	density (kg/m^3)
ϕ_l^2	two-phase multiplier
μ	dynamic viscosity (Pa s)
ΔP	pressure drop (Pa/m)

Subscripts

a	acceleration
avg	average
f	friction factor
in	inlet
i	inside
l	liquid
out	outlet
o	outside
ph	pre-heater
ref	refrigerant
sat	saturation
TS	test section
v	vapor
w	water
$wall$	tube wall

Among all these previous studies, the most productive studies have continually been performed by Zimparov [9]. Extended performance evaluation criteria for enhanced heat transfer surfaces at constant wall temperature were studied. Zimparov [10] presented heat transfer and isothermal friction pressure drop results of two three-start and two single-start spirally corrugated tubes combined with five twisted tape inserts with different relative pitches. The friction factors and inside heat transfer coefficients obtained from these tubes were higher than those obtained from the smooth tube. Moreover, Zimparov [11,12] applied a simple mathematical model for predicting the friction factors and heat transfer coefficients in a spirally corrugated configuration combined with a twisted tape insert flowing in the turbulent flow regime. The calculated friction factors and heat transfer coefficients were compared with the experimental data. The results showed that the agreement between predicted and experimental data is fairly good.

Vicente et al. [13,14] experimentally studied the mixed convection heat transfer and isothermal pressure drop in corrugated tubes for laminar, transition, and turbulent flow regions. At a high Rayleigh number, the Nusselt number obtained from these tubes is 30% higher than that obtained from the smooth tube. The friction factors of the corrugated tube were between 5% and 25% higher than those of the smooth tube.

Naphon et al. [15] studied the heat transfer and pressure drop characteristics of water flowing in horizontal double pipes with helical ribs. Nine test sections with different characteristic parameters were tested, namely helical rib height to diameter h/d = 0.12, 0.15, and 0.19 and helical rib pitch to diameter p/d = 1.05, 0.78, and 0.63. It was found that the helical ribs have a significant effect on the heat transfer and pressure drop augmentations. Both the proposed correlations for the heat transfer coefficient and friction factor give good agreement with the present data to within 15%.

Targanski and Cieslinski [16] studied the evaporation for the pure R407C and R407C/oil mixtures in two smooth tubes and two enhanced tubes, experimentally. The advantages of the micro-fin tube and corrugated tube were quantified and discussed. Test runs were performed as follows: inlet and outlet vapor quality were set at 0 and 0.7, respectively, and mass flux density ranged from 250 to 500 kg/m^2 s. The experiments were conducted at an average saturation temperature of 0 °C. It was found that the corrugated tube and micro-fin tube had a significant effect on the heat transfer coefficient and pressure drop augmentations.

Bilen et al. [17] experimentally investigated the heat transfer and friction characteristics of an air flow in different grooved tubes under turbulent flow regime. Reynolds numbers ranging from 10,000 to 38,000 were tested. The circular, trapezoidal, and rectan-

Table 1
Experimental investigation on the corrugated tube with various working fluid and tube configurations.

Sources	D (mm)	e/D	p/D	β (deg)	Phase
Dong et al. [6]	16.04–22.82	0.0243–0.0398	0.438–0.623	78.8–82.1	Single phase
Barba et al. [7]	14.5	0.103	0.793	45	Single phase
Rainieri and Pagliarini [8]	14	0.107	1.143–4.571	–	Single phase
Zimparov [9]	13.68–13.73	0.0407–0.0569	4.7–15.3	67.4–68	Single phase
Zimparov [10]	13.39–13.65	0.0371–0.0441	2.4–7.7	79.3–82.2	Single phase
Zimparov [11]	12.44–13.90	0.0224–0.0569	7.45–21.17	67.4–90	Single phase
Zimparov [12]	12.44–13.90	0.0224–0.0569	7.45–21.17	67.4–90	Single phase
Vicente et al. [13]	18	0.0239–0.0572	0.608–1.229	68–80	Single phase
Vicente et al. [14]	18	0.0239–0.0572	0.608–1.229	68–80	Single phase
Naphon et al. [15]	8.1	0.12–0.19	0.63–1.05	45	Single phase
Targanski and Cieslinski [16]	8.8	0.0511	0.681	77.75	Two phase
Bilen et al. [17]	36	0.0833	0.333–0.416	90	Single phase

gular grooves were used as the test section. The tube's length-to-diameter ratio was 33. The maximum heat transfer enhancements were up to 63% for the circular groove, 58% for the trapezoidal groove, and 47% for the rectangular groove in comparison with the smooth tube at the given Reynolds number.

In the above literature review, a number of researchers mainly focused on the effects of the corrugation on the heat transfer coefficient and pressure drop of single-phase flows in corrugated tubes. Moreover, although many papers have been published on two-phase flow, only one of these papers concerned the evaporation of refrigerants inside corrugated tube; this was carried out by Targanski and Cieslinski [16]. It can also be noted that most of the works were conducted by employing tubes having inside diameters greater than 10 mm, the data obtained from tubes having inside diameters less than 10 mm are relatively small. As a consequence, the objective of this work is to study the heat transfer coefficient and pressure drop during condensation of R-134a inside horizontal corrugated tubes having inside diameters of 8.7 mm.

2. Experimental apparatus

A schematic diagram of the test apparatus is shown in Fig. 1. The experimental apparatus was designed to determine the heat transfer coefficient and pressure drop of pure R-134a over the length of the test tube. The test loop consists of a test section, refrigeration loop, cooling water flow loops, subcooling loop, and the relevant instrumentation. The objective of the water loop before the test section is to provide controlled inlet quality. The second water loop located in the test section can provide controlled heat output from the test section. The subcooling loop is used to prevent any two-phase flow condition of the refrigerant occurring before it enters the refrigerant pump.

For the refrigeration circulating loop, liquid refrigerant is discharged by a gear pump regulated by an inverter. The refrigerant passes in series through a filter/dryer, sight glass tube, flow meter, and pre-heater and enters the test section. The inlet quality before entering the test section is controlled by the pre-heater. The pre-heater is a spiral counter-flow heat exchanger that supplies energy to provide a controlled inlet quality for vaporization of the refrigerant. Leaving the test section, the refrigerant is then condensed and subcooled by the chilling loop that removes the heat input from the pre-heater and test section, returns from the two-phase refrigerant to a subcooled state, collects later in a receiver, and eventually returns to the refrigerant pump to complete the cycle.

The test section is a horizontal counter-flow double tube heat exchanger. The length of the heat exchanger is 2.0 m. The detailed dimensions of the heat exchanger and the location of the thermocouples can be seen in Fig. 2. Fig. 3 shows a drawing of a helically corrugated tube and nomenclature to describe the geometry. The dimensions of the test section are shown in Table 2.

The inlet temperature of the water is controlled by a thermostat. A differential pressure transducer and thermocouples are installed in the test section to measure the pressure drop and temperature across the test section. The length between pressure taps is 2.5 m. The system pressure of the refrigerant flow is mainly controlled by a low temperature thermostat.

Refrigerant temperature and the tube wall temperatures in the test section are measured by T type thermocouples. A total of 15 thermocouples are soldered at the top, bottom, and side at five points along the tube as shown in Fig. 2. All the temperature measuring devices are well calibrated in a controlled temperature bath using standard precision mercury glass thermometers. The uncertainty of the temperature measurements after considering the data acquisition system is ±0.1 °C. All static pressure taps are mounted

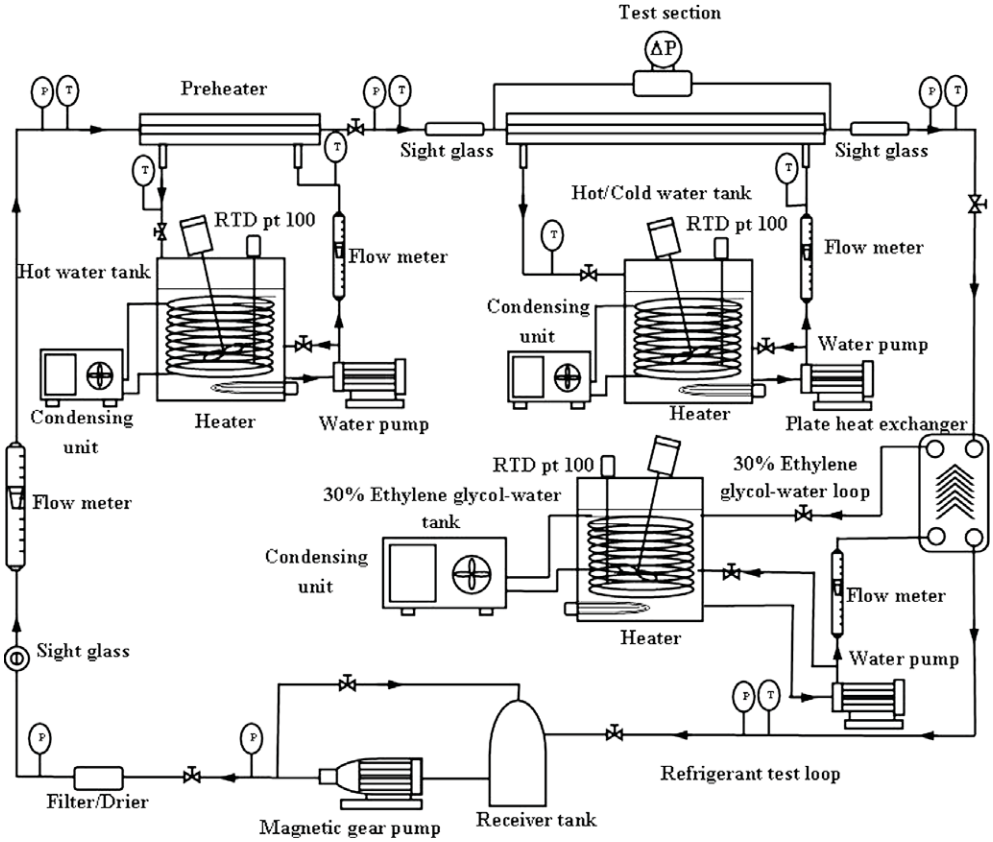

Fig. 1. Schematic diagram of experimental apparatus.

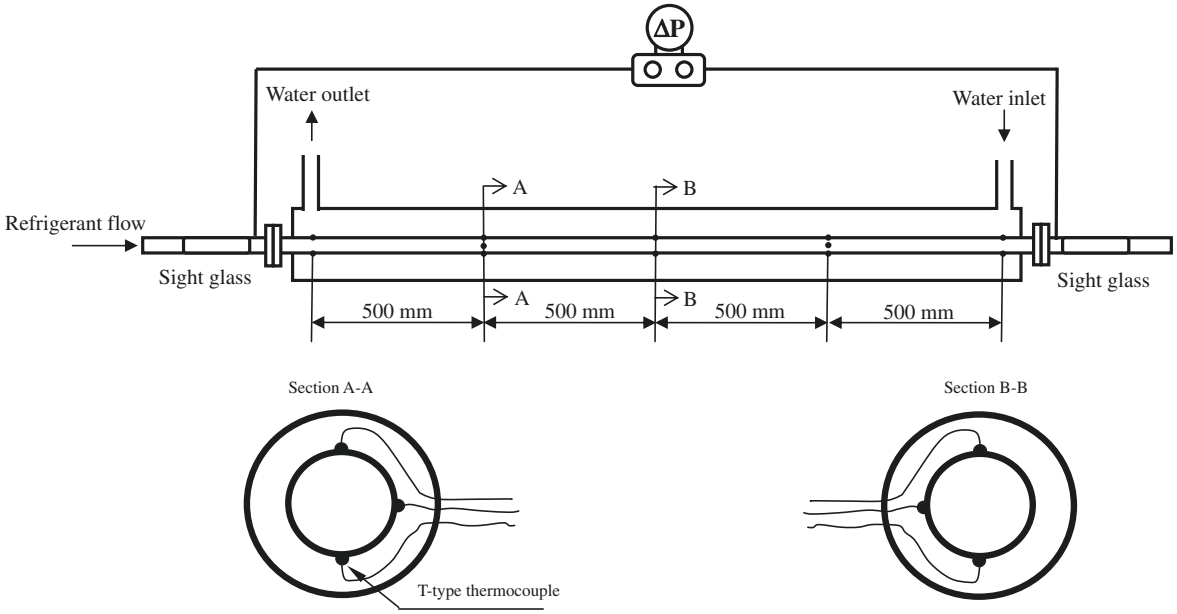

Fig. 2. Schematic diagram of the test section.

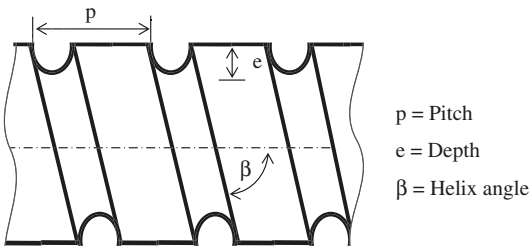

Fig. 3. Drawing of a helically corrugated tube.

in the tube wall. The refrigerant flow meter is a variable area type. The flow meter is specially calibrated in the range of 0.2–3.4 LPM for R-134a by the manufacturer. Also, the differential pressure transducer is calibrated by the manufacturer.

Experiments were conducted with various flow rates of refrigerant, vapor qualities of refrigerant entering the test section, heat fluxes, and temperatures of refrigerant condensing in the test section. In the experiments, the refrigerant flow rate in the test section was controlled by adjusting the speed of the magnetic gear pump. To vary the vapor qualities at the inlet of the test section, the heating water flow rate and the cooling water flow rate were varied by small increments while the refrigerant flow rate was kept constant. The cold water in the test section was circulated by centrifugal pump to remove heat from the refrigerant to the water. During each experiment, the heat transferred from the test section was kept at a desired value. This might be obtained by simultaneously adjusting and controlling the temperature and flow rate of the cold water entering the test section. The system was allowed to approach the steady state before any data were recorded. After stabilization, temperatures on the tube wall, refrigerant temperatures at the locations mentioned above, inlet and outlet temperatures of the heating water and cooling water, and flow rates of heating water, cooling water, and refrigerant were recorded. The pressure drop was measured by a pressure transducer installed between the inlet and outlet of the test section. It was possible to carry out the experiments by increasing the refrigerant flow rate while the saturation temperature in the test section was kept constant. The accuracies of the direct measurements and the uncertainties, which are calculated from the root mean sum square method, are shown in Table 3.

3. Data reduction

The data reduction of the measured results can be summarized as follows:

3.1. The vapor quality at the test section inlet ($x_{TS,in}$)

$$x_{TS,in} = \frac{i_{TS,in} - i_{f@T_{TS,in}}}{i_{fg@T_{TS,in}}} \quad (1)$$

where $i_{f@T_{TS,in}}$ is the enthalpy of the saturated liquid based on the temperature of the test section inlet, $i_{fg@T_{TS,in}}$ is the enthalpy of

Table 2
The dimensions of the test section.

Parameter	Smooth tube	Corrugated tube		
Depth, e (mm)	–	1.5	1.5	1.5
Pitch, p (mm)	–	5.08	6.35	8.46
Helix angle, β (deg)	–	79.47	76.56	74.20
Outside diameter, D_o (mm)	9.52	9.52	9.52	9.52
Inside diameter, D_i (mm)	8.7	8.7	8.7	8.7
Inside tube area, A_i (mm^2)	54,663	82,789	76,773	72,045
Length of the test tube, L (mm)	2000	2000	2000	2000

Table 3
Uncertainties of measured quantities and calculated parameters.

Parameter	Uncertainty
Temperature, T (°C)	±0.1
Pressure drop, ΔP (kPa)	±0.075%
Mass flow rate of refrigerant, m_{ref}	±2% full scale
Mass flow rate of water, m_w	±5% full scale
Heat transfer rate at test section, Q_{TS}	±12.9%
Heat transfer rate at pre-heater, Q_{ph}	±8.5%
Condensation heat transfer coefficient, h	±18.8%
Average quality, x	±5.2%

vaporization based on the temperature of the test section inlet, and $i_{TS,in}$ is the refrigerant enthalpy at the test section inlet given by

$$i_{TS,in} = i_{ph,in} + \frac{Q_{ph}}{m_{ref}} \tag{2}$$

where $i_{ph,in}$ is the inlet enthalpy of the liquid refrigerant before entering the pre-heater, m_{ref} is the mass flow rate of the refrigerant, and Q_{ph} is the heat transfer rate in the pre-heater:

$$Q_{ph} = m_{w,ph} c_{p,w} (T_{w,in} - T_{w,out})_{ph} \tag{3}$$

where $m_{w,ph}$ is the mass flow rate of water entering the pre-heater.

3.2. The vapor quality at the test section outlet ($x_{TS,out}$)

$$x_{TS,out} = \frac{i_{TS,out} - i_{f@T_{TS,out}}}{i_{fg@T_{TS,out}}} \tag{4}$$

where $i_{TS,out}$ is the refrigerant enthalpy at the test section outlet, $i_{f@T_{TS,out}}$ is the enthalpy of the saturated liquid based on the temperature of the test section outlet, and $i_{fg@T_{TS,out}}$ is the enthalpy of vaporization based on the temperature of the test section outlet. As a consequence, the outlet enthalpy of the refrigerant flow is calculated as

$$i_{TS,out} = i_{TS,in} - \frac{Q_{TS}}{m_{ref}} \tag{5}$$

where Q_{TS} is the heat transfer rate in the test section is obtained from

$$Q_{TS} = m_{w,TS} c_{p,w} (T_{w,out} - T_{w,in})_{TS}. \tag{6}$$

where $m_{w,TS}$ is the mass flow rate of the water entering the test section.

3.3. The heat transfer coefficient (h)

$$h = \frac{1}{\left(\frac{1}{U_i}\right) - \left(\frac{1}{2k}\right) D_i \ln\left(\frac{D_o}{D_i}\right) - \left(\frac{D_i}{D_o}\right)\left(\frac{1}{h_o}\right)} \tag{7}$$

where U_i is the overall heat transfer coefficient, k is the thermal conductivity of tube material, and h_o is the outside heat transfer coefficient.

$$U_i = \frac{Q_{TS}}{A_i (LMTD)} \tag{8}$$

where A_i is the inside tube surface and $LMTD$ is the logarithmic mean temperature difference.

$$LMTD = \frac{\Delta T_1 - \Delta T_2}{\ln\left(\frac{\Delta T_1}{\Delta T_2}\right)} \tag{9}$$

$$\Delta T_1 = T_{ref,in} - T_{w,out} \tag{10}$$

$$\Delta T_2 = T_{ref,out} - T_{w,in} \tag{11}$$

where $T_{w,in}$ and $T_{w,out}$ denote the inlet and outlet temperatures of the water on the annulus. $T_{ref,in}$ and $T_{ref,out}$ are the inlet and outlet refrigerant temperatures.

Average outside heat transfer coefficient is calculated as

$$h_o A_o = \frac{Q_{TS}}{T_{wall,avg} - T_{w,avg}} \tag{12}$$

where A_o is the outside test tube surface, $T_{wall,avg}$ is the average wall temperature, and $T_{w,avg}$ is the average cooling water temperature flowing inside annulus.

3.4. The frictional pressure drop (ΔP_f)

The total pressure drop, ΔP_{total}, is expressed as the sum of the two different components, as follows:

$$\Delta P_{\text{total}} = \Delta P_f + \Delta P_a \tag{13}$$

The two terms on the right-hand side represent the frictional pressure drop (ΔP_f) and accelerational pressure drop (ΔP_a). The accelerational pressure drop, ΔP_a, was proposed by Tran [18]:

$$\Delta P_a = G^2 \left(\left(\frac{x_{out}^2}{\rho_v \alpha_{out}} + \frac{(1-x_{out})^2}{\rho_l (1-\alpha_{out})} \right) - \left(\frac{x_{in}^2}{\rho_v \alpha_{in}} + \frac{(1-x_{in})^2}{\rho_l (1-\alpha_{in})} \right) \right) \tag{14}$$

where α is the void fraction and is presented by Zivi's correlation [19] as follows:

$$\alpha = \left(1 + \frac{(1-x)}{x} \left(\frac{\rho_v}{\rho_l} \right)^{\frac{2}{3}} \right)^{-1} \tag{15}$$

The frictional pressure drop, ΔP_f, can be obtained by subtracting the accelerational pressure drop from the total measured pressure drop.

4. Results and discussion

In the present study, the effects of corrugation pitch on the condensation heat transfer coefficient and pressure drop of R-134a inside horizontal corrugated tubes are experimentally investigated. Before measuring the two-phase heat transfer and pressure drop, a single-phase heat transfer test is first conducted to check the energy balance in the test section. The results indicate that the energy balance between the cold water and the refrigerant is within 10% for all runs. This ensures that the heat loss from the test section is rather small and the test section is appropriate for the measurement.

To check the suitability of the above experimental system for the present measurement, the single-phase liquid R-134a heat transfer data are measured first and compared with the well known correlations from the Dittus–Boelter [20] equation and the Gnielinski [21] equation, which are defined as follows.

The Dittus–Boelter equation is defined as

$$Nu = \frac{hD}{k} = 0.023 Re^{0.8} \mathrm{Pr}^{0.4} \tag{16}$$

An alternative formula for calculating the Nu was introduced by the Gnielinski equation, which is defined as

$$Nu = 0.012 (Re^{0.87} - 280) \mathrm{Pr}^{0.4} \tag{17}$$

The friction factor data were compared with the well known correlation from the Haaland equation [22] and the Blasius equation, which are defined as follows.

The Haaland equation is defined as

$$\frac{1}{\sqrt{f}} = -1.8 \log \left[\left(\frac{6.9}{Re} + \left(\frac{\frac{\varepsilon}{D}}{3.7} \right)^{1.11} \right) \right] \tag{18}$$

The Blasius equation is presented in the following form:

$$f = \frac{0.316}{Re^{\frac{1}{4}}} \tag{19}$$

As shown in Figs. 4 and 5, an agreement between the experimental results and the calculated values for single-phase liquid R-134a can be seen.

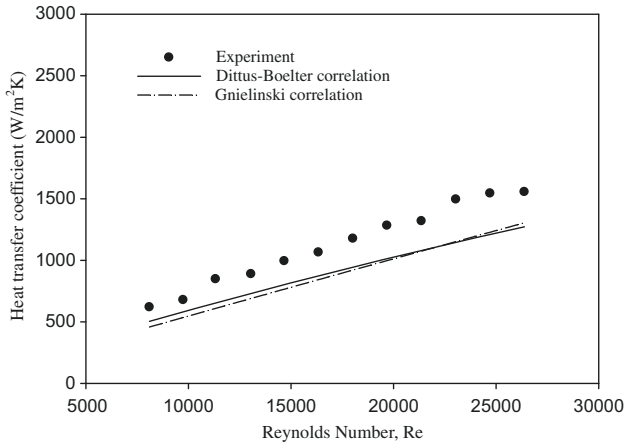

Fig. 4. Comparison of the present data for the single-phase liquid R-134a heat transfer coefficients obtained from the present study with those obtained from Dittus–Boelter and Gnielinski correlations.

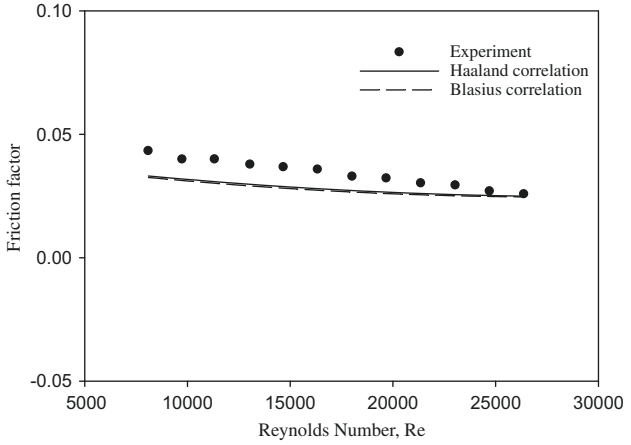

Fig. 5. Comparison of the present data for the single-phase liquid R-134a friction factor obtained from the present study with those obtained from Haaland and Blasius correlations.

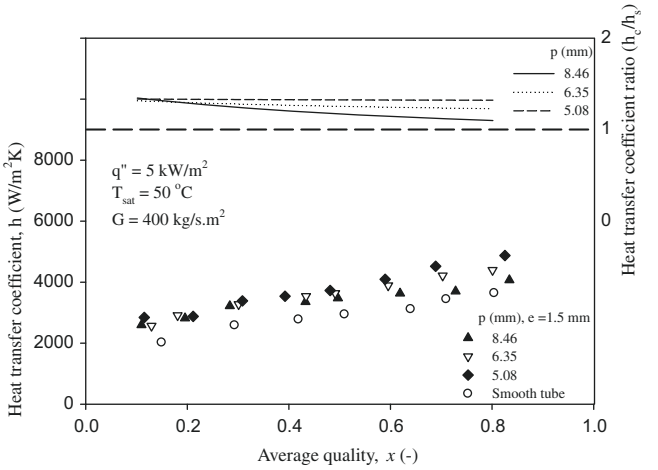

Fig. 6. Heat transfer coefficient versus average quality at T_{sat} = 50 °C, G = 400 kg/m^2 s and q'' = 5 kW/m^2.

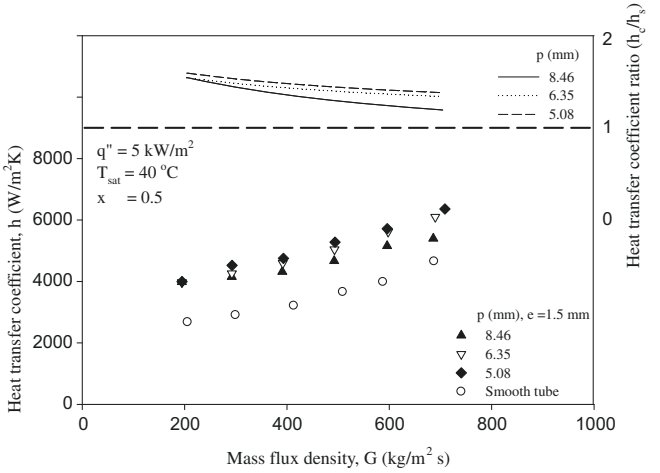

Fig. 7. Heat transfer coefficient versus mass flux at T_{sat} = 40 °C, q'' = 5 kW/m^2, and x = 0.5.

4.1. Heat transfer coefficient

Fig. 6 demonstrates the variation of the average condensation heat transfer coefficient with average quality in the smooth and corrugated tubes at a mass flux of 400 kg/m^2 s, heat flux of 5 kW/m^2, and saturation temperatures of 50 °C, respectively. During the condensation, the liquid film thickness gradually increases and the thermal resistance is therefore increased, resulting in a decrease in the heat transfer rate. A smaller liquid film thickness together with higher vapor velocity at the vapor–liquid interface results in an increase in the heat transfer coefficient when the average quality is higher. The results reveal that the average heat transfer coefficient increases with increasing average quality.

At the same average quality, the average condensation heat transfer coefficient in the smooth tube is lower than that in corrugated tubes across the range of the average quality. This is because the corrugated tube has a significant effect on mixing of the condensate film at the tube wall and increasing the turbulent flow.

The effect of the corrugation pitch on the heat transfer coefficient can be seen: the heat transfer coefficient tends to increase as the corrugation pitch decreases. This is because the lower corrugation pitch promotes turbulence of the refrigerant flow and mixing of the condensate film. These agitations are mainly due to corrugation of the surface. The ratio of the convective heat transfer coefficient of the corrugated tube to that of the smooth tube varies from 1.1 to 1.5 under the same average quality. This means that the corrugated tubes had a heat transfer coefficient approximately 10–50% higher than that of the smooth tube.

Fig. 7 displays the variation of the heat transfer coefficient with mass flux in smooth and corrugated tubes at a heat flux of 5 kW/m^2, saturation temperature of 40 °C, and average quality of 0.5. The figure shows that the average heat transfer coefficient increases with increasing mass flux. The heat transfer coefficient obtained from the smooth tube is relatively low when compared with that obtained from corrugated tubes. The reason for this is similar to the explanation concerning the corrugation pitch mentioned above. However, the maximum heat transfer coefficient ratio of the corrugated tube is up to 50% higher than that of the smooth tube. It is obtained at the lowest mass flux of 200 kg/m^2 s, saturation temperature of 40 °C, and heat flux of 5 kW/m^2.

4.2. Comparison of experimental data with existing correlations for heat transfer coefficient

Fig. 8 shows a comparison of the experimental data for smooth tube with the existing correlations proposed by Aker et al. [23], Traviss et al. [24], Cavallini and Zechin [25], Chen et al. [26], Dob-

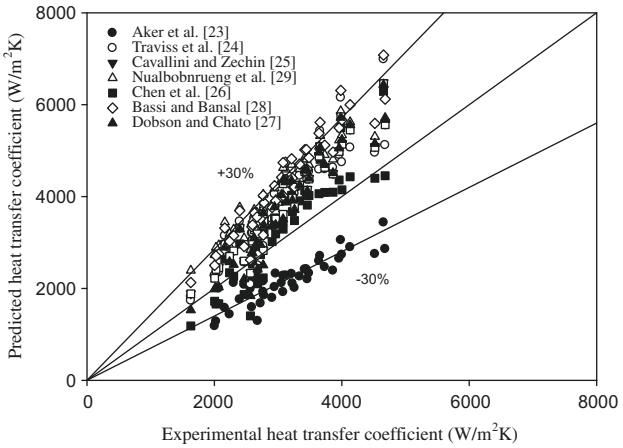

Fig. 8. Comparison of present R-134a heat transfer coefficient data with existing correlation.

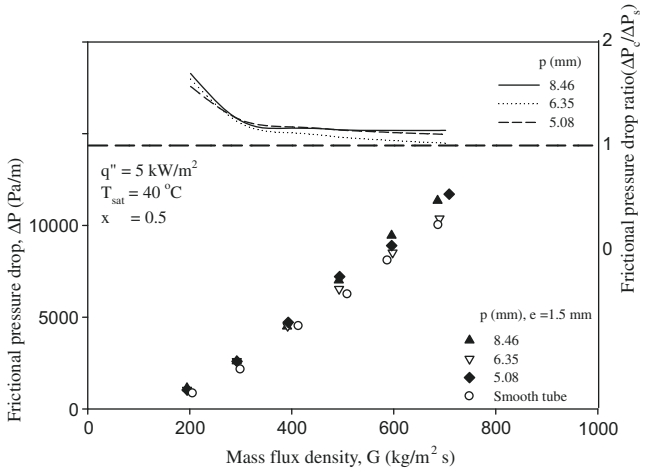

Fig. 10. Pressure drop versus mass flux at T_{sat} = 40 °C, q'' = 5 kW/m^2 and x = 0.5.

son and Chato [27], Bassi and Bansal [28], and Nualboonrueng et al. [29] for smooth tubes. Almost all the correlations give agreement with the present data to be within 30%.

4.3. Pressure drop

Fig. 9 shows the variation in the frictional pressure drop with average quality. The frictional pressure drop can be obtained by subtracting the accelerational pressure drop from the total measured pressure drop. The pressure drops are obtained by dividing the measured pressure drop by the length between pressure taps. In our apparatus, the length between pressure taps is 2.5 m while the length of the heat exchanger is 2 m. These figures show that for smooth and corrugated tubes, the frictional pressure drop increases with increasing average quality. The frictional pressure drop obtained from the corrugated tube is significantly higher than that obtained from the smooth tube. This is due to (1) drag forces exerted on the flow field by the corrugation, (2) flow blockage due to area reduction, (3) turbulence augmentation, and (4) rotational flow produced by the corrugation depth (Vicente et al., [13,14]. The ratio of the frictional pressure drop of the corrugated tube to that of the smooth tube varies from 1.0 to 1.7 under the same average quality. This means that the corrugated tubes had a frictional pressure drop approximately 0–70% higher than that of the smooth tube.

Fig. 10 displays the variation of the frictional pressure drop with mass flux in smooth and corrugated tubes at a heat flux of 5 kW/m^2, saturation temperature of 40 °C, and average quality of 0.5. The figure illustrates that the frictional pressure drop increases with increasing mass flux. Compared with the smooth tube, the frictional pressure drop obtained from the corrugated tube is relatively high. However, the maximum frictional pressure drop ratio of the corrugated tube is up to 70% higher than that of the smooth tube. It is obtained at the lowest mass flux of 200 kg/m^2 s, saturation temperature of 40 °C, and heat flux of 5 kW/m^2.

4.4. Comparison of experimental data with existing correlations for pressure drop

The two-phase frictional multiplier for the smooth tube can be calculated by using the Lockhart–Martinelli correlation as follows:

$$\phi_l^2 = 1 + \frac{C}{X} + \frac{1}{X^2} \tag{20}$$

The constant C in the above equation is the parameter which indicates the two-phase flow condition. The value of this parameter proposed by Chisholm [30] varies from 5 to 20 depending on the flow condition of the vapor and liquid. For instance, the constant

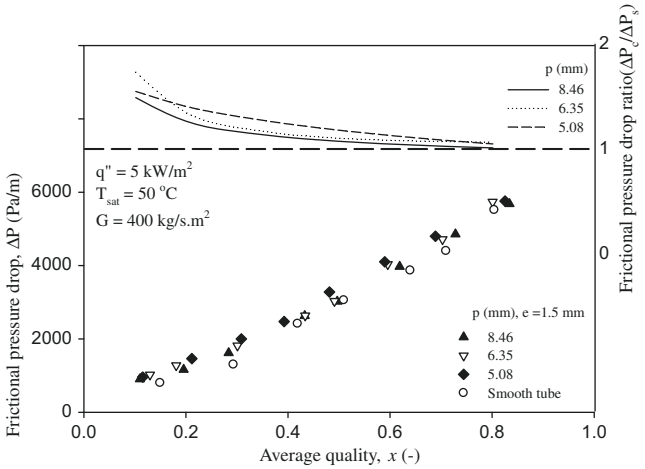

Fig. 9. Pressure drop versus average quality at T_{sat} = 50 °C, G = 400 kg/m^2 s and q'' = 5 kW/m^2.

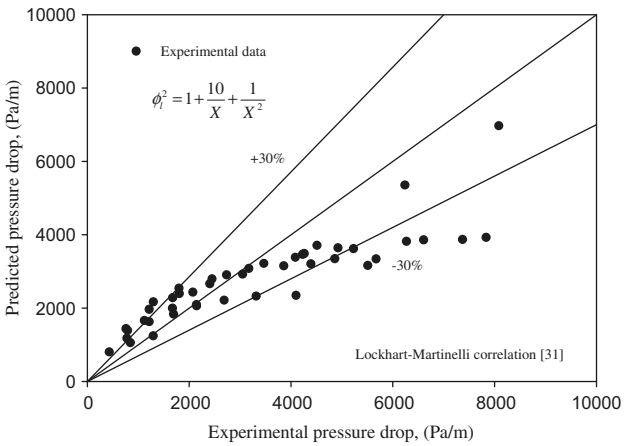

Fig. 11. Comparison of present R-134a pressure drop data for smooth tube with existing correlation.

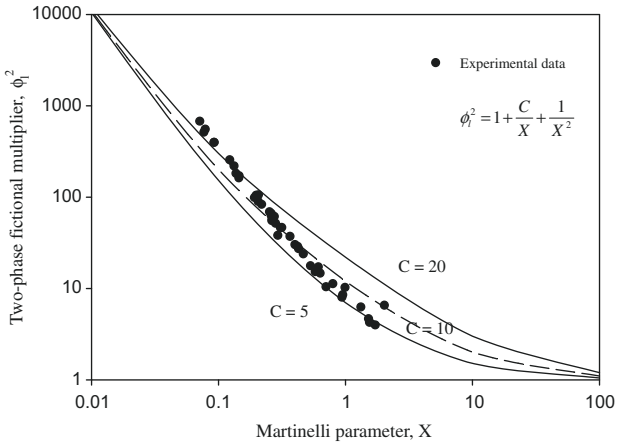

Fig. 12. The two-phase frictional multiplier versus Martinelli parameter.

$C = 20$ when the vapor and liquid flow is in the turbulent region and $C = 5$ when the two-phase flow is in the laminar region. Fig. 11 displays the frictional pressure drop for the smooth tube and shows the comparison of the experimental data with the existing correlation proposed by Lockhart and Martinelli [31] by using $C = 10$. The results showed that this correlation gives good agreement with the present data to be within 30%. The relationships of the two-phase multiplier with the Martinelli parameter are plotted in Fig. 12. As shown in this figure, almost all the measured data are in the region between $C = 5$ and $C = 20$.

5. Conclusion

The effects of corrugation pitch on the condensation heat transfer coefficient and pressure drop of R-134a inside horizontal corrugated tubes are experimentally investigated. A smooth tube and corrugated tubes having inner diameters of 8.7 mm are used as the inner tube. The corrugation pitches are 5.08, 6.35, and 8.46 mm. The corrugation depth of all corrugated tubes is fixed as 1.5 mm. The test runs are performed at saturation temperatures of 40–50 °C, heat fluxes of 5 and 10 kW/m^2, and mass fluxes ranging from 200 to 700 kg/m^2 s. The experimental results show that the average heat transfer coefficient and pressure drop increase with increasing mass flux as well as average quality. In addition, the results obtained from the corrugated tubes are compared with those obtained from the smooth tube. It is found that the corrugation pitches have a significant effect on the heat transfer coefficient and pressure drop augmentations. The maximum heat transfer coefficient ratio and frictional pressure drop ratio of the corrugated tube are up to 50% and 70% higher than those of the smooth tube, respectively.

Acknowledgments

The present study was supported by the Joint Graduate School of Energy and Environment, King Mongkut's University of Technology Thonburi, Office of the Higher Education Commission and the Thailand Research Fund, whose guidance and assistance are gratefully acknowledged.

References

[1] A. Bejan, A.D. Kraus, Heat Transfer Handbook, Wiley, New Jersey, 2003. pp. 1029–1130.
[2] L.M. Schlager, M.P. Pate, A.E. Bergles, Evaporation and condensation heat transfer and pressure drop in horizontal, 12.7-mm micro-fin tubes with refrigerant 22, J. Heat Transfer 112 (1989) 1041–1047.
[3] V. Shinohara, M. Tobe, Development of an improved thermofin tube, Hitachi Cable Rev. 4 (1985) 47–50.
[4] C.S. Kuo, C.C. Wang, In-tube evaporation of HCFC-22 in a 9.52 mm micro-fin/smooth tube, Int. J Heat Mass Transfer 39 (1996) 2559–2569.
[5] Y. Kim, K. Seo, J.T. Chung, Evaporation heat transfer characteristics of R-410A in 7 and 9.52 mm smooth/micro-fin tubes, Int. J. Refrig. 25 (2002) 716–730.
[6] Y. Dong, L. Huixiong, C. Tingkuan, Pressure drop, heat transfer and performance of single-phase turbulent flow in spirally corrugated tubes, Exp. Therm. Fluid Sci. 24 (2001) 131–138.
[7] A. Barba, S. Rainieri, M. Spiga, Heat transfer enhancement in a corrugated tube, Int. Commun. Heat Mass Transfer 29 (2002) 313–322.
[8] S. Rainieri, G. Pagliarini, Convective heat transfer to temperature dependent property fluids in the entry region of corrugated tubes, Int. J. Heat Mass Transfer 45 (2002) 4525–4536.
[9] V. Zimparov, Enhancement of heat transfer by a combination of three-start spirally corrugated tubes with a twisted tape, Int. J. Heat Mass Transfer 44 (2001) 551–574.
[10] V. Zimparov, Enhancement of heat transfer by a combination of a single-start spirally corrugated tubes with a twisted tape, Exp. Therm. Fluid Sci. 25 (2002) 535–546.
[11] V. Zimparov, Prediction of friction factors and heat transfer coefficients for turbulent flow in corrugated tubes combined with twisted tape inserts. Part 1: friction factors, Int. J. Heat Mass Transfer 47 (2004) 589–599.
[12] V. Zimparov, Prediction of friction factors and heat transfer coefficients for turbulent flow in corrugated tubes combined with twisted tape inserts. Part 2: heat transfer coefficients, Int. J. Heat Mass Transfer 47 (2004) 385–393.
[13] P.G. Vicente, A. Garcia, A. Viedma, Experimental investigation on heat transfer and friction factor characteristics of spirally corrugated tubes in turbulent flow at different Prandtl number, Int. J. Heat Mass Transfer 47 (2004) 671–681.
[14] P.G. Vicente, A. Garcia, A. Viedma, Mixed convection heat transfer and isothermal pressure drop in corrugated tubes for laminar and transition flow, Int. Commun. Heat Mass Transfer 31 (2004) 651–662.
[15] P. Naphon, M. Nuchjapo, J. Kurujareon, Tube side heat transfer coefficient and friction factor characteristics of horizontal tubes with helical rib, Energy Convers. Manag. 47 (2006) 3031–3044.
[16] T. Targanski, J.T. Cieslinski, Evaporation of R407C/oil mixtures inside corrugated and micro-fin tubes, Appl. Therm. Eng. 27 (2007) 2226–2232.
[17] K. Bilen, M. Cetin, H. Gul, T. Balta, The investigation of groove geometry effect on heat transfer for internally grooved tubes, Appl. Therm. Eng. 29 (2009) 753–761.
[18] T.N. Tran, Pressure drop and heat transfer study of two-phase flow in small channels, Ph.D. Dissertation, Texas Tech University, Texas, 1998.
[19] S.M. Zivi, Estimation of steady-state steam void-fraction by mean of the principle of minimum entropy production, Trans. ASME J. Heat Transfer 86 (1964) 247–252.
[20] F.W. Dittus, L.M.K. Boelter, Heat transfer in automobile radiators of the tubular tube, Pub. Eng. 2 (1930) 443.
[21] V. Gnielinski, New equations for heat and mass transfer in turbulent pipe and channel flow, Int. Chem. Eng. 16 (1976) 359–368.
[22] S.E. Haaland, Simple and explicit formulas for the friction factor in turbulent pipe flow, J. Fluids Eng. (1983) 89–90.
[23] W.W. Aker, H.A. Beans, O.K. Crosser, Condensation heat transfer within horizontal tubes, Chem. Eng. Prog. Symp. 55 (1959) 171–176.
[24] D.P. Traviss, W.M. Rohsenow, A.B. Baron, Forced-convection condensation inside tubes: a heat transfer equation for condenser design, ASHRAE Trans. 79 (1973) 157–165.
[25] A. Cavallini, R. Zechin, A dimensionless correlation for heat transfer coefficient in forced-convection condensation, in: Proceedings of the Fifth International Heat Transfer Conference, Japan, vol. 3, 1974, pp. 309–313.
[26] S.L. Chen, F.M. Gerner, C.L. Tien, General film condensation correlation, Exp. Heat Transfer 1 (1987) 93–107.
[27] M.K. Dobson, T.J. Chato, Condensation in smooth horizontal tubes, J. Heat Transfer 120 (1998) 193–213.
[28] R. Bassi, P.K. Bansal, In-tube condensation of mixture of R134a and ester oil: empirical correlations, Int. J. Refrig. 26 (2003) 402–409.
[29] T. Naulboonrueng, J. Kaew-on, S. Wongwises, Two-phase condensation heat transfer coefficients of HFC-134a at high mass flux in smooth and micro-fin tubes, Int. Commun. Heat Mass Transfer 30 (2003) 577–590.
[30] D. Chisholm, Pressure gradients due to friction during the flow of evaporating two-phase mixtures in smooth tubes and channels, Int. J. Heat Mass Transfer 16 (1973) 347–358.
[31] R.W. Lockhart, R.C. Martinelli, Proposed correlation of data for isothermal, two-phase two-component flow in pipes, Chem. Eng. Prog. 45 (1949) 39–48.

Experimental Thermal and Fluid Science 34 (2010) 692–705

Contents lists available at ScienceDirect

Experimental Thermal and Fluid Science

journal homepage: www.elsevier.com/locate/etfs

An investigation of a model of the flow pattern transition mechanism in relation to the identification of annular flow of R134a in a vertical tube using various void fraction models and flow regime maps

A.S. Dalkilic [a,*], S. Wongwises [b,*]

[a] Heat and Thermodynamics Division, Department of Mechanical Engineering, Yildiz Technical University, Yildiz, Besiktas, Istanbul 34349, Turkey
[b] Fluid Mechanics, Thermal Engineering and Multiphase Flow Research Lab. (FUTURE), Department of Mechanical Engineering, King Mongkut's University of Technology Thonburi, Bangmod, Bangkok 10140, Thailand

ARTICLE INFO

Article history:
Received 19 August 2009
Received in revised form 4 December 2009
Accepted 28 December 2009

Keywords:
Condensation
Flow regime map
Vertical down flow
R134a
Phase change

ABSTRACT

In the present study, new experimental data are presented for literature on the prediction of film thickness and identification of flow regime during the co-current downward condensation in a vertical smooth copper tube having an inner diameter of 8.1 mm and a length of 500 mm. R134a and water are used as working fluids in the tube side and annular side of a double tube heat exchanger, respectively. Condensation experiments are done at mass fluxes of 300 and 515 kg m^{-2} s^{-1}. The condensing temperatures are between 40 and 50 °C; heat fluxes are between 12.65 and 66.61 kW m^{-2}. The average experimental heat transfer coefficient of the refrigerant HFC-134a is calculated by applying an energy balance based on the energy transferred from the test section. A mathematical model by Barnea et al. based on the momentum balance of liquid and vapor phases is used to determine the condensation film thickness of R134a. The comparative film thickness values are determined indirectly using relevant measured data together with various void fraction models and correlations reported in the open literature. The effects of heat flux, mass flux, and condensation temperature on the film thickness and condensation heat transfer coefficient are also discussed for the laminar and turbulent flow conditions. There is a good agreement between the film thickness results obtained from the theoretical model and those obtained from six of 35 void fraction models in the high mass flux region of R134a. In spite of their different valid conditions, six well-known flow regime maps from the literature are found to be predictive for the annular flow conditions in the test tube in spite of their different operating conditions.

© 2010 Elsevier Inc. All rights reserved.

1. Introduction

In spite of a large number of flow pattern identification studies of horizontal and upward flow, few investigators have examined flow regime maps for downward flow.

The orientation and interaction of the liquid and vapor phases inside the tubes are among the most significant characteristics of two-phase flow. These phenomena are related to flow regime and flow pattern. A specific kind of geometric distribution of the phases is called a flow pattern or flow regime. The interfacial area of the phases is affected by geometry, and thus mass, momentum, and energy exchange between phases have come to play important roles in the design. Different flow patterns may occur depending on the tube position, the geometry of the tube, flow rates, superficial velocities, and physical properties such as density, viscosity, and surface tension of the two phases. Generally, flow patterns are observed by visual inspection and include bubble flow, slug flow, churn flow, wispy-annular flow, and annular flow for vertical flow, and bubble flow, plug flow, stratified flow, wavy flow, slug flow, and annular flow for horizontal flow. However, Hubbard and Dukler [1] classified the flow patterns as separated flow patterns (stratified flow, annular flow), intermittent flow patterns (elongated bubble flow, slug/plug flow, churn/froth flow), and dispersed flow patterns (bubble flow, dispersed bubble flow).

Two-phase annular flow occurs widely in film heating and cooling processes, particularly in power generation and especially in nuclear reactors. This flow regime has received the most attention, both analytically and experimentally, because of its practical importance and the relative ease with which analytical treatment may be applied. Annular two-phase flow is characterized by a phase interface separating a thin liquid film from the gas flow in the core region. In addition to this, condensate distribution inside the tube wall is almost symmetric and there is high velocity vapor

* Corresponding authors. Tel.: +90 212 3832819; fax: +90 212 2616659 (A.S. Dalkilic), tel.: +66 2 470 9115; fax: +66 2 470 9111 (S. Wongwises).
E-mail addresses: dalkilic@yildiz.edu.tr (A.S. Dalkilic), somchai.won@kmutt.ac.th (S. Wongwises).

0894-1777/$ - see front matter © 2010 Elsevier Inc. All rights reserved.
doi:10.1016/j.expthermflusci.2009.12.011

Nomenclature

A	inside surface area, m^{-2}
C	coefficient for the friction factor
c_p	specific heat, J kg^{-1} K^{-1}
d	internal tube diameter, m
f	friction factor
F_r	Froude rate parameter
G	mass flux, kg m^{-2} s^{-1}
g	gravitational constant, m s^{-2}
h	heat transfer coefficient, W m^{-2} K^{-1}
i	enthalpy, J kg^{-1}
i_{fg}	latent heat of condensation, J kg^{-1}
j	superficial velocity in Hewitt and Robertson's map
K	coefficient in Smith correlation
L	length of test tube, m
m	mass flow rate, kg s^{-1}
Re	Reynolds number
S	perimeter over which the stress acts, m
s	slip ratio
T	temperature, °C
Q	heat transfer rate, W
u	velocity, m s^{-1}
x	mean vapor quality
X	Lockhart–Martinelli parameter
We	Weber number
ΔT	vapor side temperature difference, $T_{sat} - T_{wi}$, °C

Greek symbols

σ	surface tension, N m^{-1}
ρ	density, kg m^{-3}
λ	property parameter of Baker flow regime map
ψ	property parameter of Baker flow regime map
μ	dynamic viscosity, kg m^{-1} s^{-1}
δ	film thickness, m
$\overline{\delta}$	dimensionless form of film thickness
α	void fraction
τ	shear stress, N m^{-2}
v	kinematic viscosity, m^2 s^{-1}

Subscripts

a	air
cond	condensate
corr	correlation
exp	measured
g	gas/vapor
H	homogen
i	inlet
int	interfacial
l	liquid
mdl	model
o	outlet
ph	preheater
ref	refrigerant
s	superficial for one phase flow alone in the pipe
sat	saturation
T	total
TS	test section
w	water
wi	inner wall

Exponentials

n	exponent in Eq. (20)
m	exponent in Eq. (21)

flow in the core during annular flow. In this flow regime, it is generally true that due to the breakup of the disturbance wave, part of the liquid phase is entrained as droplets into the gas core. It is also accepted that mass, momentum, and energy transfers are strongly affected by entrainment of the droplets to the gas core.

Two-dimensional flow pattern maps are used to determine flow patterns depicting flow regime transition boundaries. It is usually preferred that their coordinates have dimensional values such as superficial velocities and mass fluxes instead of dimensionless variables such as Weber number. Flow regime maps can be categorized into two groups: experimental flow pattern maps and mechanistic flow pattern maps. The first is obtained from a large number of experimental data and limited by its experimental parameters such as fluid properties, tube diameter, and mass flux. The second is built up from examination of various transition mechanisms using fundamental equations and its range for different experimental conditions is wider than the first one due to having incorporated system parameters. The most widely recommended flow pattern maps for vertical tubes are those of Barnea et al. [2], Fair [3], Hewitt and Robertson [4], Chen et al. [5], Zhao and Bi [6], and for horizontal tubes, those of Baker [7], Mandhane et al. [8], Thome [9], El Hajal et al. [10], Coleman and Garimella [11,12], Kattan et al. [13], Taitel and Dukler [14], Weisman et al. [15], Breber et al. [16], Soliman [17], Tandon et al. [18], and Mederic et al. [19].

Void fraction is an important parameter and is always used to determine the flow pattern transition, heat transfer coefficient, and two-phase pressure drop and is defined as the cross-sectional area occupied by the vapor in relation to the area of the flow channel. Two-phase separated flow is commonly analyzed using the slip flow model. In this model, it is assumed that the separated phases have different uniform velocities. By contrast, the homogeneous model is defined as an ideal case, as it assumes a homogeneous mixture providing uniform velocities for both phases, and for that reason it is the simplest method of determination of the void fraction.

In the technical literature, numerous studies have been carried out on the modeling of the void fraction and can be divided into several groups: general void fraction models and correlations [20–25]), K_H parameter-based void fraction models and correlations [26–28], flow regime-based void fraction models and correlations [29–31], Lockhart and Martinelli parameter-based void fraction models and correlations [32–40], and slip ratio void fraction models and correlations [10,41–52]. A brief and comprehensive overview of these works is presented in the authors' previous publications [53,56,59,60].

This paper provides a comprehensive review of the published literature on flow regime maps in relation to a flow transition model having a relationship between the film thickness and void fraction models and correlations. The experiments include a wide range of high mass fluxes with different saturation temperatures as they relate to 380 data points of R134a belonging to the condensation heat transfer database of FUTURE Lab in KMUTT. Apart from the authors' previous publications [53–65], few studies exist in the literature for the investigation of heat transfer characteristics in a small diameter vertical tube during co-current down flow condensation, and besides this, there is no study with the experimental parameters of this work and its content in the open literature. In this study, determination of the condensation film thickness is presented by means of the model of Barnea et al. [2] and verified by relating the void fraction models and correlations. In addition to this, the changes

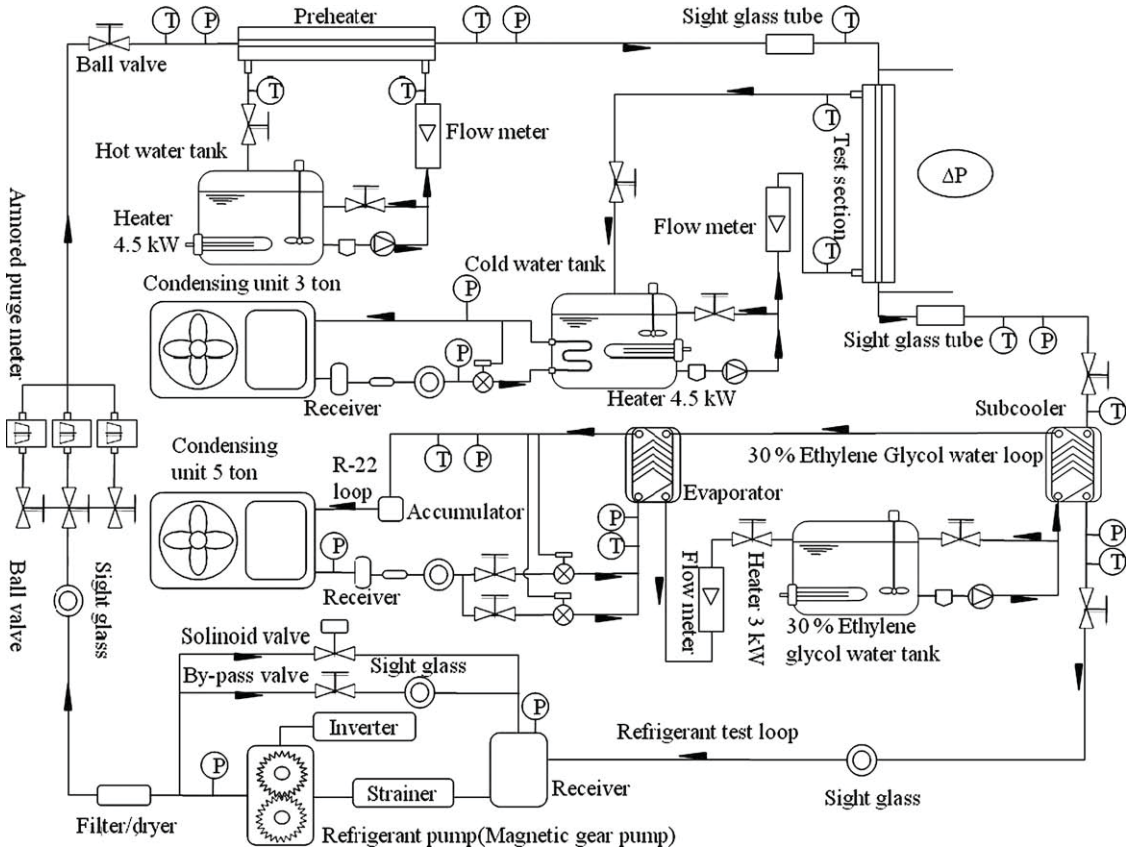

Fig. 1. Schematic diagram of experimental apparatus.

in the heat transfer coefficient, vapor quality and condensation temperature difference between the tube wall and refrigerant with film thickness and verification of the void fraction values obtained from the flow transition model are investigated. Moreover, flow regime identification is performed using various flow pattern maps valid for horizontal and vertical tubes to show the independence of the annular flow regime from tube orientation [58,66].

2. Experimental apparatus and method

A schematic diagram of the test apparatus is shown in Fig. 1. The refrigerant loop consists of a pre-heating loop, test section, cooling loop and chilling loop. The refrigerant is circulated by a gear pump controlled by an inverter. The refrigerant flows in series through a filter/dryer, a sight glass tube, a refrigerant flow meter and a preheater and enters the test section. A spiral counter-flow double tube heat exchanger is designed to supply heat to control the inlet quality of the refrigerant before entering the test section. After exiting the test section, the chilling loop condenses and subcools the refrigerant and removes the heat input from the pre-heater and test section, and ejects it into the surroundings. After leaving the chilling loop, the refrigerant changes from the two-phase refrigerant to a sub-cooled state. Eventually, the refrigerant returns to the refrigerant pump to complete the cycle.

The test section, well insulated with a proper material to minimize the heat loss, is a vertical counter-flow tube-in-tube heat exchanger with refrigerant flowing downward (co-current liquid and vapor of R134a's down flow) in the inner tube and cooling water

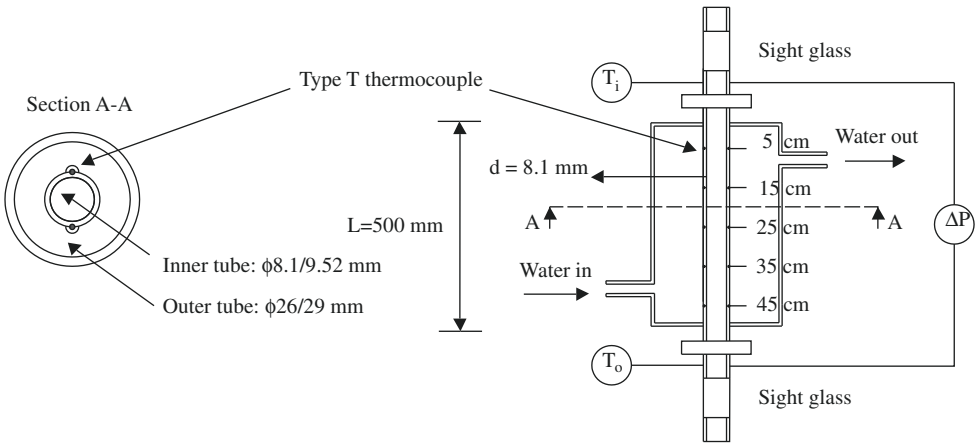

Fig. 2. Schematic diagram of test section.

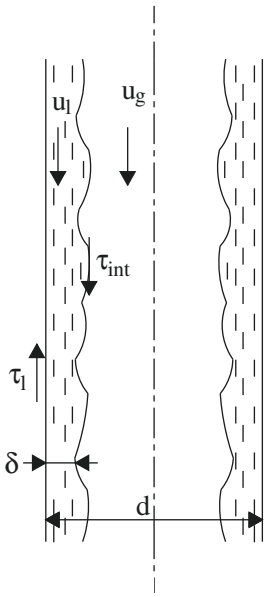

Fig. 3. System model for analysis of annular downward vertical flow.

Table 1
Coefficients of the Eqs. (20) and (21) according to flow types.

Flow types	Laminar flow	Turbulent flow
Coefficients		
n	1	0.2
m	1	0.2
C_l	16	0.046
C_g	16	0.046

flowing upward in the annulus. The inner and outer tubes are made from smooth vertical copper having inner diameters of 8.1 and 26 mm, respectively. The length of the heat exchanger is 0.5 m. Fig. 2 shows the detailed dimensions of the heat exchanger and the location of the thermocouples.

T-type thermocouples are used to measure refrigerant temperature and the tube wall temperatures in the test section. A total of ten thermocouples are located on the sidewall at five points along the test tube. A thermostat is used to control the inlet temperature of the water. All the temperature measuring devices are calibrated in a controlled temperature bath using standard precision mercury glass thermometers. The uncertainty of the temperature measurements is ±0.1 °C. All static pressure taps are mounted on the tube wall. The refrigerant flow meter is a variable area type. The flow meter was calibrated in the range of 0–2.2 gal min^{-1} for HFC-134a by the manufacturer. Pressure drop is measured by a differential pressure transducer installed between the inlet and outlet of the test section. The length between pressure taps is 0.7 m. A low temperature thermostat is used to control the system pressure of the refrigerant flow. The differential pressure transducer and pressure gauges are calibrated against a primary standard, the dead weight tester. All signals from thermocouples and pressure transducers are recorded by a data logger. Tests are performed in the steady state.

3. Data reduction and experimental uncertainty

The data reduction of the measured results can be analyzed as follows:

3.1. The inlet vapor quality of the test section ($x_{TS,i}$)

$$x_{TS,i} = \frac{i_{TS,i} - i_{l@T_{TS,i}}}{i_{fg@T_{TS,i}}} \tag{1}$$

where $i_{l@T_{TS,i}}$ is the enthalpy of the saturated liquid based on the inlet temperature of the test section, $i_{fg@T_{TS,i}}$ is the enthalpy of vapor-

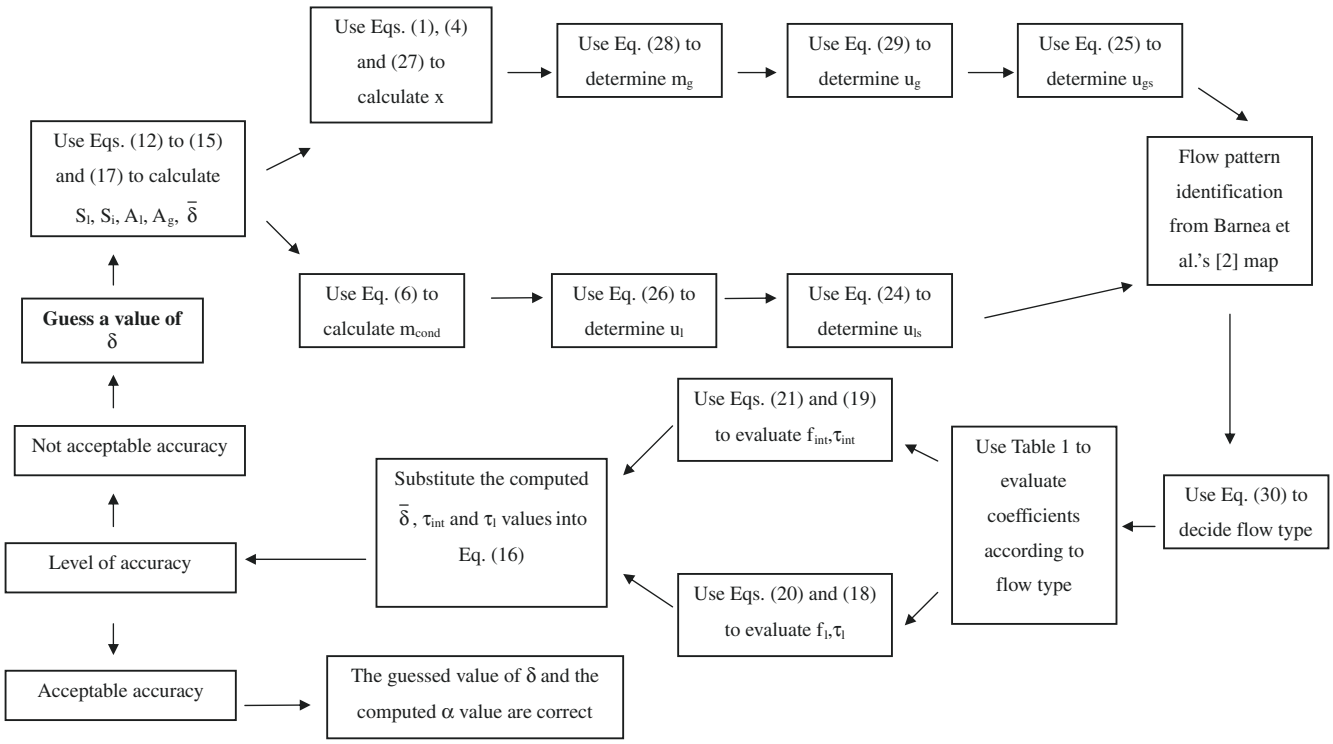

Fig. 4. Flow chart of iteration process.

ization based on the inlet temperature of the test section, $i_{TS,i}$ is the refrigerant enthalpy at the test section inlet and is given by:

$$i_{TS,i} = i_{ph,i} + \frac{Q_{ph}}{m_{ref}} \tag{2}$$

where $i_{ph,i}$ is the inlet enthalpy of the liquid refrigerant before entering the pre-heater, m_{ref} is the mass flow rate of the refrigerant, and Q_{ph} is the heat transfer rate in the pre-heater:

$$Q_{ph} = m_{w,ph} c_{p,w} (T_{w,i} - T_{w,o})_{ph} \tag{3}$$

where $m_{w,ph}$ is the mass flow rate of the water entering the pre-heater, $c_{p,w}$ is the specific heat of water, $(T_{w,i} - T_{w,o})_{ph}$ is the temperature difference between inlet and outlet positions of the preheater.

3.2. The outlet vapor quality of the test section ($x_{TS,o}$)

$$x_{TS,o} = \frac{i_{TS,o} - i_{l@T_{TS,o}}}{i_{fg@T_{TS,o}}} \tag{4}$$

where $i_{TS,o}$ is the refrigerant enthalpy at the test section outlet, $i_{l@T_{TS,o}}$ is the enthalpy of the saturated liquid based on the outlet temperature of the test section, and $i_{fg@T_{TS,o}}$ is the enthalpy of vaporization. The outlet enthalpy of the refrigerant flow is calculated as follows:

$$i_{TS,o} = i_{TS,i} - \frac{Q_{TS}}{m_{ref}} \tag{5}$$

where the heat transfer rate, Q_{TS}, in the test section is obtained from:

$$Q_{TS} = m_{w,TS} c_{p,w} (T_{w,o} - T_{w,i})_{TS} \tag{6}$$

where $m_{w,TS}$ is the mass flow rate of the water entering the test section, and $(T_{w,o} - T_{w,i})_{TS}$ is temperature difference between outlet and inlet position of the test section.

3.3. The average heat transfer coefficient

$$h_{exp} = \frac{Q_{TS}}{A_{wi}(T_{ref,sat} - T_{wi})} \tag{7}$$

where h_{exp} is the experimental average heat transfer coefficient, Q_{TS} is the heat transfer rate in the test section, T_{wi} is the average temperature of the inner wall, $T_{ref,sat}$ is the average saturation temperature of the refrigerant at the test section inlet and outlet, and A_{wi} is the inside surface area of the test section:

$$A_{wi} = \pi d L \tag{8}$$

where d is the inside diameter of the test tube. L is the length of the test tube.

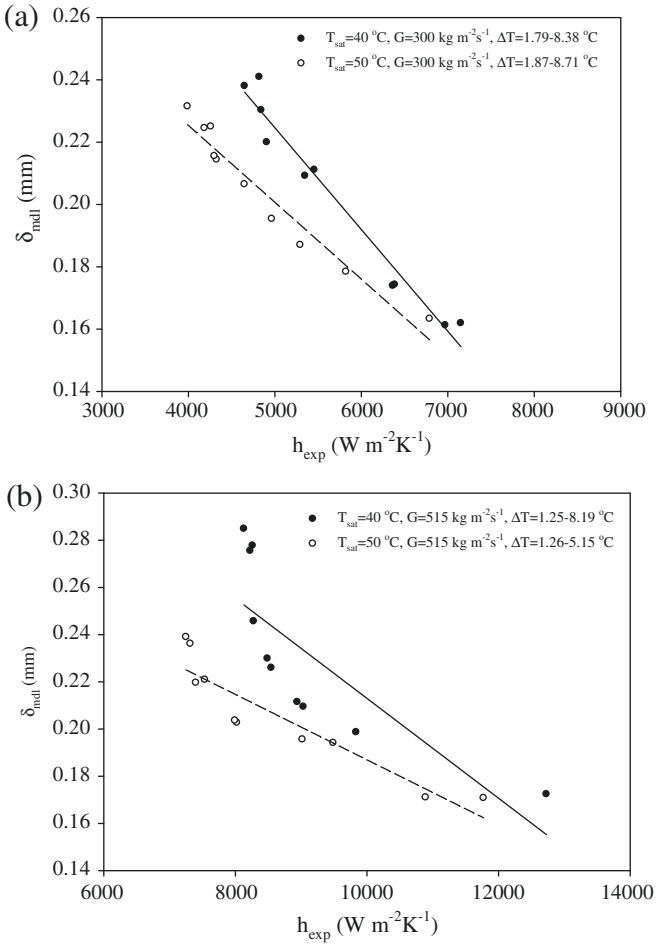

Fig. 5. Comparison of film thickness obtained from model regarding heat transfer coefficient at different condensation temperatures and ΔT_{sat} for the mass fluxes of 300 kg m^{-2} s^{-1} (a) and 515 kg m^{-2} s^{-1} (b) for the laminar flow data.

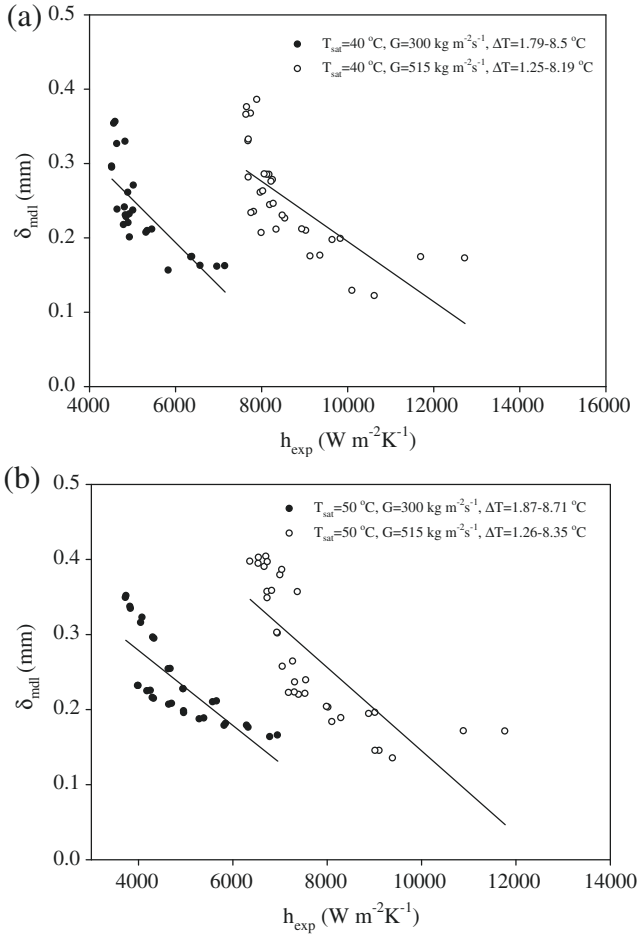

Fig. 6. Comparison of film thickness obtained from model regarding heat transfer coefficient at different condensation temperatures and ΔT_{sat} for the mass fluxes of 300 kg m^{-2} s^{-1} (a) and 515 kg m^{-2} s^{-1} (b) for the laminar flow data.

3.4. Uncertainties

The uncertainties of the Nusselt number and condensation heat transfer coefficient in the test tube varied from ±7.64% to ±10.71%. It should be noted that similar ranges of uncertainty with minimum and maximum values exist in the literature. The procedures of Kline and McClintock [67] were used for the calculation of all uncertainties. Various uncertainty values of the study can be seen from authors' previous works [54,61,63].

3.5. Calculation procedure for the annular flow model

The steady-state physical model of downward annular flow condensation of R134a in a vertical tube is shown in Fig. 3. Details of the development of the relationship among the film thickness and the flow parameters and flow pattern transition mechanisms can be seen in Barnea et al. [2].

Momentum balances of liquid and vapor phases can be defined respectively as follows:

$$-A_l\left(\frac{dP}{dx}\right)-\tau_l S_l+\tau_{int}S_i+\rho_l A_l g=0 \tag{9}$$

$$-A_g\left(\frac{dP}{dx}\right)-\tau_{int}S_i+\rho_g A_g g=0 \tag{10}$$

Eqs. (9) and (10) can be rearranged, equating pressure drop as:

$$\tau_{int}S_i\left(\frac{1}{A_l}+\frac{1}{A_g}\right)+g(\rho_l-\rho_g)-\tau_l\frac{S_l}{A_l}=0 \tag{11}$$

Flow cross-sectional areas and perimeters over which the stress acts are expressed respectively as:

$$S_l=\pi d \tag{12}$$

$$S_i=\pi(d-2\delta) \tag{13}$$

$$A_l=\pi(d\delta-\delta^2) \tag{14}$$

$$A_g=\pi\left(\frac{d}{2}-\delta\right)^2 \tag{15}$$

Eq. (16) can be obtained from the substitution of Eqs. (12)–(15) into Eq. (11)

$$\frac{\tau_{int}}{d(\overline{\delta}-\overline{\delta}^2)(1-2\overline{\delta})}+g(\rho_l-\rho_g)-\frac{\tau_l}{d(\overline{\delta}-\overline{\delta}^2)}=0 \tag{16}$$

where the dimensionless form of film thickness is determined as:

$$\overline{\delta}=\frac{\delta}{d} \tag{17}$$

Liquid shear stress and interfacial shear stress are calculated respectively as follows:

$$\tau_l=f_l\frac{\rho_l u_l^2}{2} \tag{18}$$

$$\tau_{int}=f_i\frac{\rho_g(u_g-u_l)^2}{2} \tag{19}$$

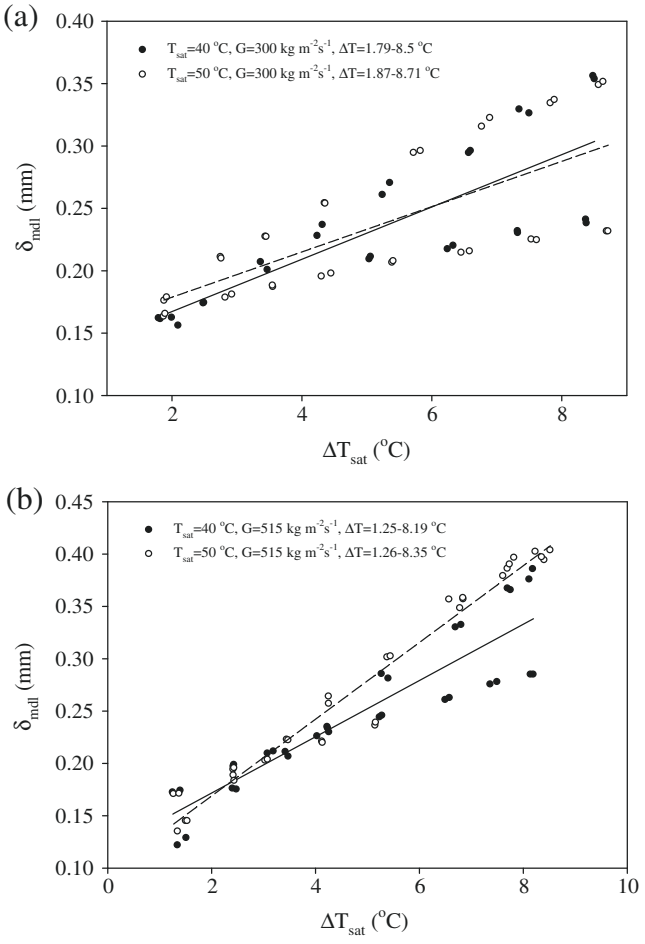

Fig. 7. Comparison of film thickness obtained from model regarding ΔT_{sat} at different condensation temperatures for the mass fluxes of 300 kg m^{-2} s^{-1} (a) and 515 kg m^{-2} s^{-1} (b) for the laminar and turbulent flow data.

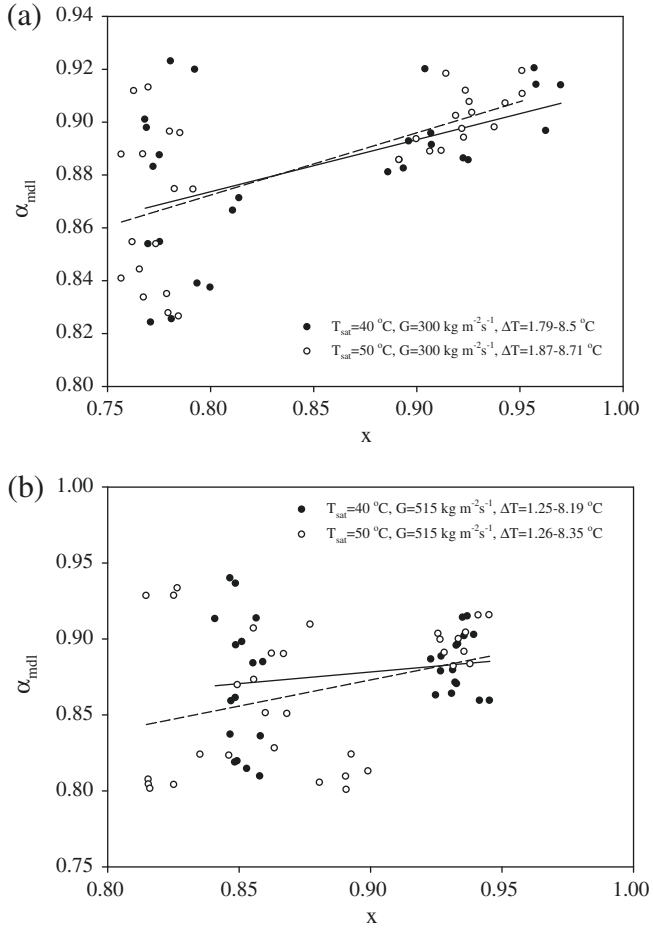

Fig. 8. Comparison of film thickness obtained from model regarding vapor quality at different condensation temperatures and ΔT_{sat} for the mass fluxes of 300 kg m^{-2} s^{-1} (a) and 515 kg m^{-2} s^{-1} (b) for the laminar and turbulent flow data.

where the liquid and interfacial friction factor are evaluated respectively as:

$$f_l = C_l\left(\frac{d_l u_l}{\nu_l}\right)^{-n} \tag{20}$$

$$f_{int} \cong f_g = C_g\left(\frac{d_g u_g}{\nu_g}\right)^{-m} \tag{21}$$

where

$$d_l = \frac{4A_l}{S_l} = 4d(\bar{\delta} - \bar{\delta}^2) \tag{22}$$

$$d_g = \frac{4A_g}{S_g} = (1 - 2\bar{\delta})d \tag{23}$$

$$u_l = \frac{u_{ls}}{4(\bar{\delta} - \bar{\delta}^2)} \tag{24}$$

$$u_g = \frac{4u_{gs}}{1 - 4\bar{\delta} + 4\bar{\delta}^2} \tag{25}$$

It should be noted that the coefficients of Eqs. (20) and (21) can be obtained from Table 1 using Eq. (30).

Condensate flow rate can be obtained from Eq. (6), and thus condensate velocity is determined from Eq. (26) as:

$$m_{cond} = \rho_l A_l u_l \tag{26}$$

Vapor flow rate is obtained from Eq. (27), and thus vapor velocity is determined as follows:

$$x = \frac{x_{TS,i} + x_{TS,o}}{2} \tag{27}$$

$$m_g = x m_T \tag{28}$$

$$m_g = \rho_g A_g u_g \tag{29}$$

Liquid Reynolds number can be determined to decide if flow is laminar or turbulent as:

$$\mathrm{Re}_l = \frac{Gd(1-x)}{\mu_l}\begin{cases} < 2300 & \text{laminar} \\ > 2300 & \text{turbulent} \end{cases} \tag{30}$$

The void fraction value from the model is estimated using an estimated film thickness value shown in Fig. 4, assuming $\delta \ll d$ as follows:

$$\alpha = \frac{A_g}{A} = \left(1 - \frac{\delta}{r}\right)^2 = 1 - \frac{4\delta}{d} \tag{31}$$

The film thickness, void fraction, and interfacial shear can be determined using an iterative technique for specified mass flux, vapor quality, condensation pressure, and thermo physical properties. After estimating a value for film thickness, Eqs. (12), (13), (14), (15), and (17) should be used to evaluate the dimensionless film thickness value, flow areas, and perimeters of phases. By means of Eqs. (1), (4), and (27), desired vapor quality can be calculated. Using Eqs. (28), (29), and (25), mass flux, velocity, and the superficial form of vapor are determined respectively and at the

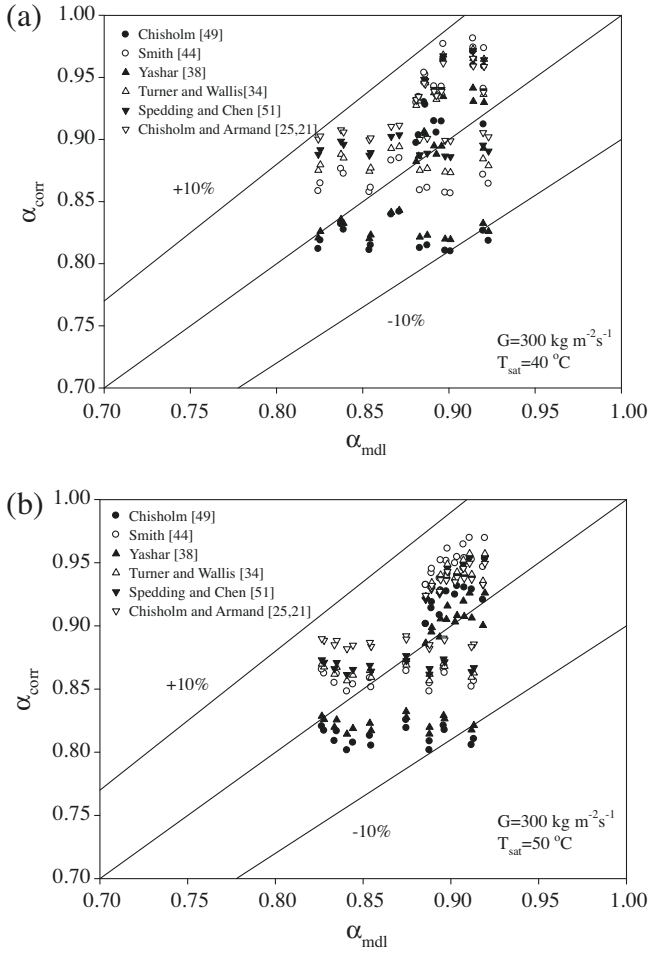

Fig. 9. Comparisons between the model and calculated void fraction values for the mass flux of 300 kg m^{-2} s^{-1} at the condensing temperatures of 40 °C (a) and 50 °C (b) using laminar and turbulent flow data.

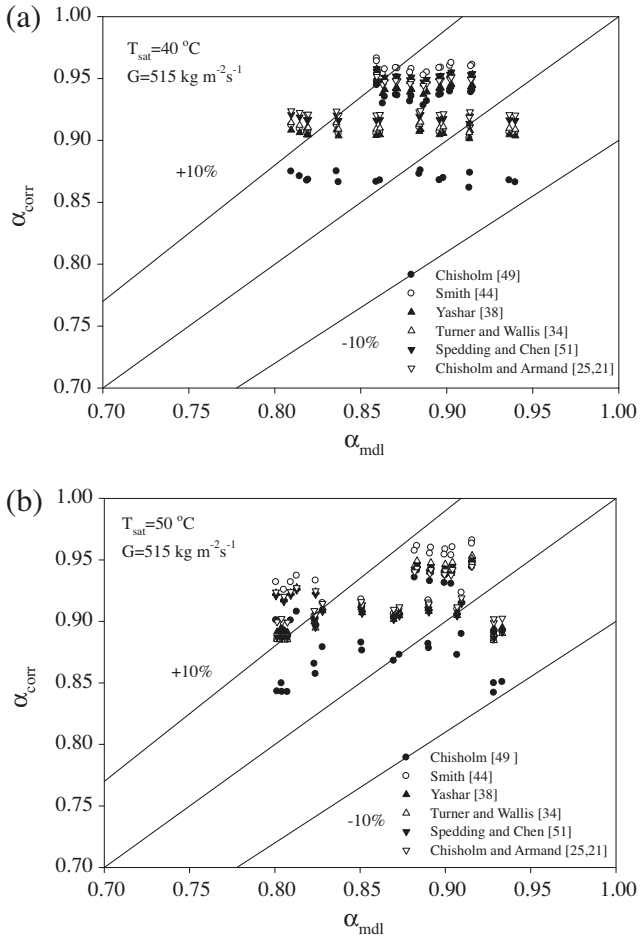

Fig. 10. Comparisons between the model and calculated void fraction values for the mass flux of 515 kg m^{-2} s^{-1} at the condensing temperatures of 40 °C (a) and 50 °C (b) using laminar and turbulent flow data.

Table 2
Agreed void fraction models and correlations.

Void fraction model/correlation	Model/correlation
Chisholm and Armand model [25,21]	$\alpha = \frac{1}{\alpha_H + (1-\alpha_H)^{0.5}}\alpha_H \quad \alpha_H = \frac{1}{1+\left(\frac{1-x}{x}\right)\left(\frac{\rho_g}{\rho_l}\right)s} \quad s = 1$
Turner and Wallis two-cylinder model [34]	$\frac{1-\alpha}{\alpha} = A\left(\frac{1-x}{x}\right)^p \left(\frac{\rho_g}{\rho_l}\right)^q \left(\frac{\mu_l}{\mu_g}\right)^r$

Correlation or model	A	p	q	r
Homogeneous	1	1	1	0
Zivi	1	1	0.67	0
Turner-Wallis	1	0.72	0.4	0.08
Lockhart-Martinelli	0.28	0.64	0.36	0.07
Thom	1	1	0.89	0.18
Baroczy	1	0.74	0.65	0.13

Yashar correlation [38]	$\alpha = (1 + F_t^{-1} + X)^{-0.321} \quad F_t = \left(\frac{x^3 G^2}{\rho_g^2 g d(1-x)}\right)^{0.5} \quad X = \left(\frac{1-x}{x}\right)^{0.9}\left(\frac{\rho_g}{\rho_l}\right)^{0.5}\left(\frac{\mu_l}{\mu_g}\right)^{0.1}$
Smith model [43]	$\alpha = \left\{1 + \left(\frac{\rho_g}{\rho_l}\right)K\left(\frac{1}{x}-1\right) + \left(\frac{\rho_g}{\rho_l}\right)(1-K)\left(\frac{1}{x}-1\right)\left[\frac{\left(\frac{\rho_l}{\rho_g}\right)+K\left(\frac{1}{x}-1\right)}{1+K\left(\frac{1}{x}-1\right)}\right]\right\}^{-1} \quad K = 0.4$
Chisholm correlation [48]	$\alpha = \frac{1}{1+\left(\frac{1-x}{x}\right)\left(\frac{\rho_g}{\rho_l}\right)s} \quad s = \left(1 - x + \frac{x\rho_l}{\rho_g}\right)^{1/2}$
Spedding and Chen correlation [51]	$\alpha = \left(1 + 2.22\left(\frac{1-x}{x}\right)^{0.65}\left(\frac{\rho_g}{\rho_l}\right)^{0.65}\right)^{-1}$

same time condensation rate, velocity, and the superficial velocity of the liquid phase are calculated using Eqs. (6), (26), and (24) respectively. It should be noted that having the superficial vapor and liquid velocities, flow identification of data can be performed from the flow pattern map of Barnea et al. [2]. After deciding the flow type using Eq. (30) and selecting coefficients from Table 1, interfacial and liquid friction factors and shear stresses can be obtained from Eqs. (21), (20), (19), and (18) respectively. The estimated dimensionless film thickness value and calculated interfacial and liquid shear values are substituted into Eq. (16). These values are updated and the film thickness value is repeatedly estimated until convergence. If the level of accuracy is acceptable, the values of estimated film thickness and void fraction value calculated by Eq. (31) are correct. This procedure can also be seen in Fig. 4.

In addition to the above explanations, the variables below are used in the calculations of flow pattern maps in the paper as follows:

Superficial momentum fluxes of the liquid and gas phases can be determined respectively for the calculations of Hewitt and Roberts' flow pattern map [4] as follows:

$$\rho_l j_l^2 = \frac{[G(1-x)]^2}{\rho_l} \tag{32}$$

$$\rho_g j_g^2 = \frac{[Gx]^2}{\rho_g} \tag{33}$$

The property parameters of Baker's flow regime map [7] and the liquid and vapor phases of mass flux are defined respectively as follows:

$$\lambda = \left[\frac{\rho_g}{\rho_a}\frac{\rho_l}{\rho_w}\right]^{1/2} \tag{34}$$

$$\psi = \left(\frac{\sigma_w}{\sigma}\right)\left[\left(\frac{\mu_l}{\mu_w}\right)\left(\frac{\rho_w}{\rho_l}\right)^2\right]^{1/2} \tag{35}$$

$$G_l = G(1-x) \tag{36}$$

$$G_g = Gx \tag{37}$$

The Weber number in the flow regime map of Chen et al. [5] can be determined as follows:

$$We = \left[\frac{\rho d u^2}{\sigma}\right] \tag{38}$$

It should be noted that u_{ls} obtained from Eq. (24) and u_{gs} obtained from Eq. (25) can used as velocity term in Eq. (38).

4. Results and discussion

The present study is performed to study the relationship between void fraction models and the annular flow model of Barnea et al. [2] and to investigate the well-known flow pattern maps to verify the annular flow conditions of experimental data for the downward two-phase flow of R134a in a vertical round tube with an inner diameter of 8.1 mm. Pure HFC-134a was used in the experiments. The effect of the temperature difference between the saturated temperature of the vapor and the inlet wall temperature of the tube (ΔT_{sat}), mass flux, vapor quality, and condensation temperature on the heat transfer coefficients and void fraction are shown in Figs. 5–8. It should be noted that R134a was entering the test section as pure saturated vapor in the figures

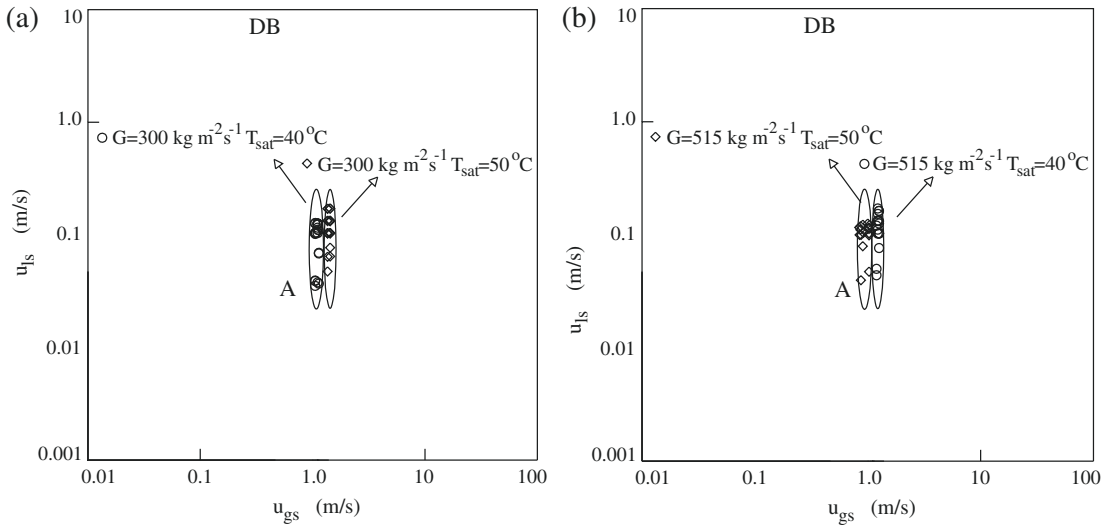

Fig. 11. Flow pattern identification of the experimental data by means of Barnea et al. [2] flow regime map for the mass fluxes of 300 kg m^{-2} s^{-1} (a) and 515 kg m^{-2} s^{-1} (b) at the condensing temperatures of 40–50 °C.

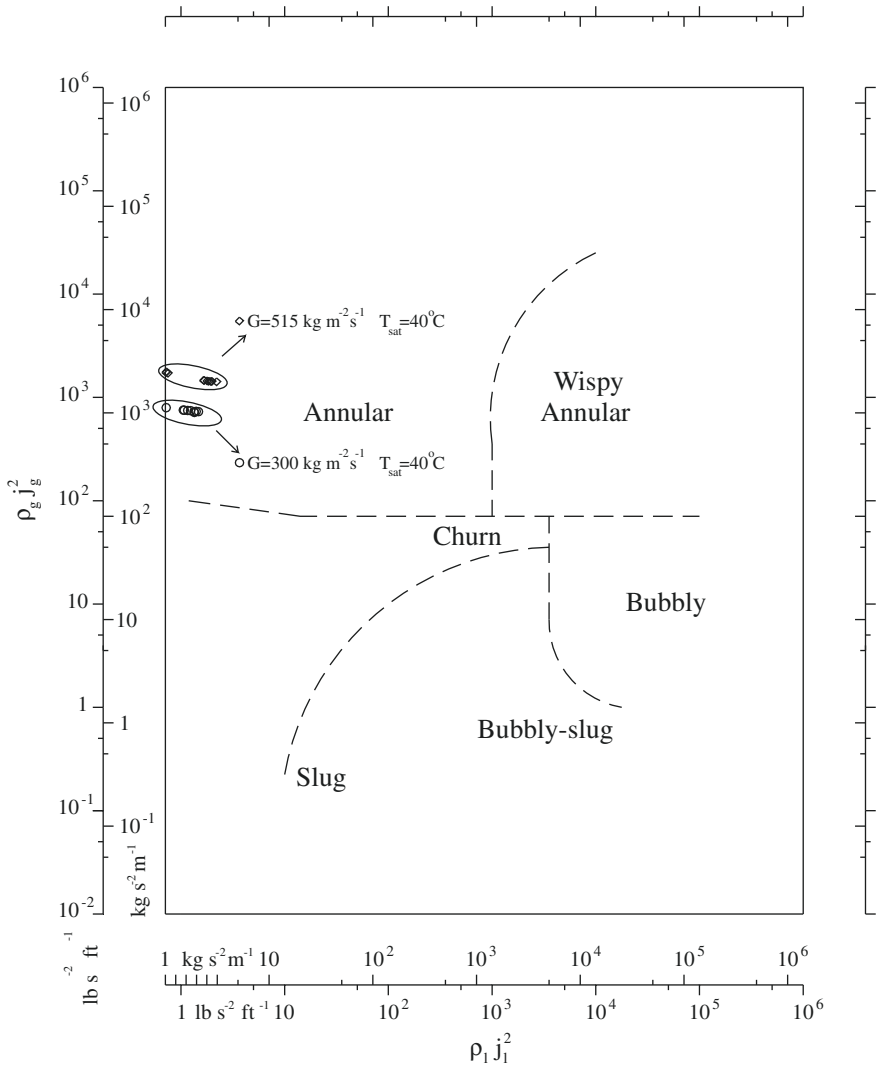

Fig. 12. Flow pattern identification of the experimental data by means of Hewitt and Robertson [4] flow regime map for the mass fluxes of 300–515 kg m^{-2} s^{-1} at the condensing temperature of 40 °C.

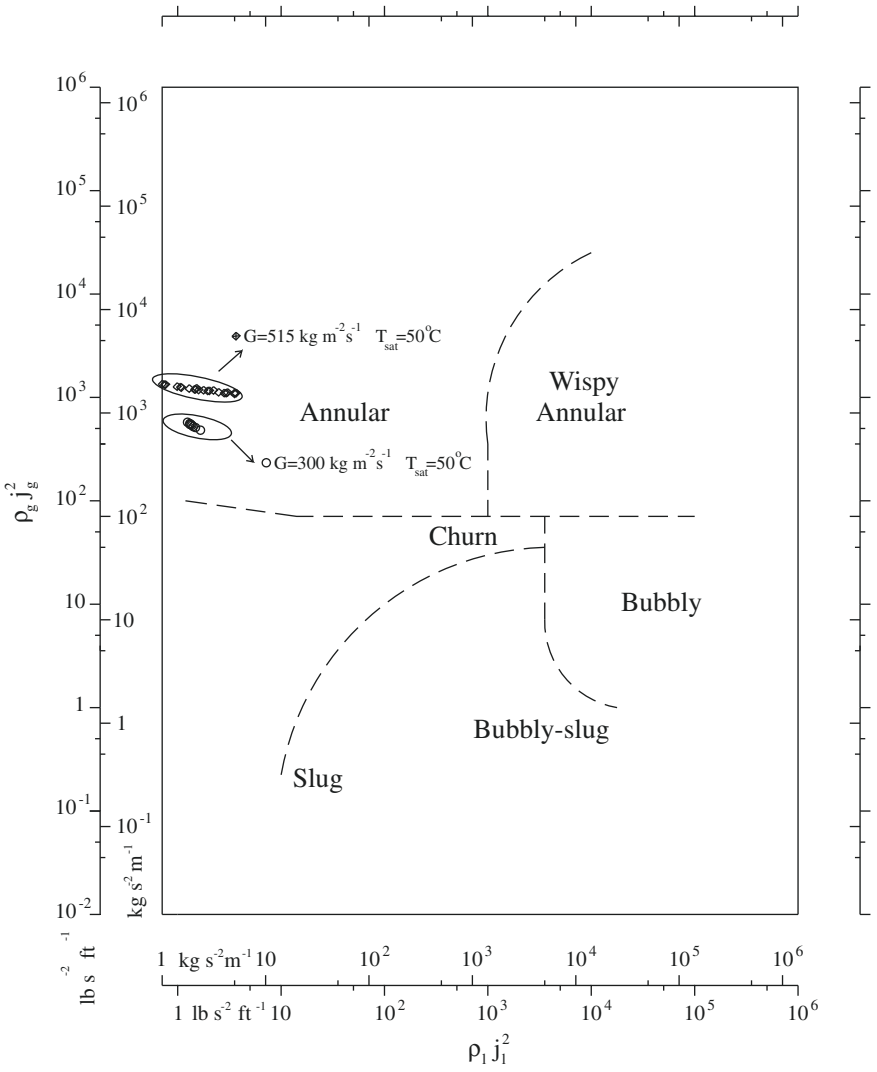

Fig. 13. Flow pattern identification of the experimental data by means of Hewitt and Robertson [4] flow regime map for the mass fluxes of 300–515 kg m^{-2} s^{-1} at the condensing temperature of 50 °C.

of laminar flow. Discussion of the results will be given in turn as follows:

Fig. 5 shows the relationship between the mean film thickness obtained from the model of Barnea et al. (Eq. (17)) and the experimental heat transfer coefficient (Eq. (7)) for the condensation temperatures of 40–50 °C at the mass fluxes of 300 kg m^2 s^{-1} (a) and 515 kg m^{-2} s^{-1} (b) for laminar flow data (Eq. (30)) in a vertical smooth tube. It can be seen that film thickness decreases with increasing heat transfer coefficient; in other words, film thickness decreases with decreases in ΔT_{sat} for similar test conditions. The increase in heat flux in relation to ΔT_{sat} in Eq. (7) increases the condensation rate. In other words, the film thickness on the tube wall increases due to the constant latent heat of condensation for a specific saturation temperature of condensation. It can also be seen that low condensation temperature conditions (40 °C) give larger condensation heat transfer coefficients than high condensation temperature conditions (50 °C) at the same condensing temperature differences for a constant film thickness value. Low condensation pressures, in other words, high temperature differences and alteration of physical properties at low pressure, cause higher local heat transfer coefficients than high condensation pressure.

Fig. 6 shows the same relationship as Fig. 5 for the mass fluxes of 300–515 kg m^{-2} s^{-1}. The effect of the mass flux on the condensation heat transfer coefficient with the condensation temperatures of 40 °C (a) and 50 °C (b) can be seen for the same mass flux in this figure. It can be clearly seen that heat transfer coefficients increase with increasing mass fluxes for a constant film thickness value. This is due to the increase in vapor velocity of R134a.

Fig. 7 shows the relationship between the mean film thickness obtained from the model of Barnea (Eq. (17)) and ΔT_{sat} in the test tube for the mass fluxes of 300 kg m^{-2} s^{-1} (a) and 515 kg m^{-2} s^{-1} (b) and condensing temperatures of 40–50 °C. Trend lines of data indicate that the average film thickness increases with increases in ΔT_{sat} for similar test conditions as explained in the above paragraphs. Verification of the reliability of the calculated film thickness from the model is checked using different condensing temperatures.

Fig. 8 shows the relationship between the void fraction obtained from the model of Barnea et al. (Eq. (31)) and vapor quality in the test tube for the mass fluxes of 300 kg m^{-2} s^{-1} (a) and 515 kg m^{-2} s^{-1} (b) and condensing temperatures of 40–50 °C. Comparison of the void fraction at higher and lower average vapor qualities and smaller liquid film thickness together with higher vapor velocity at the vapor–liquid interface shows an increase in the void fraction when the average quality is higher. Trend lines of data are in accordance with this basic knowledge of in-tube condensation.

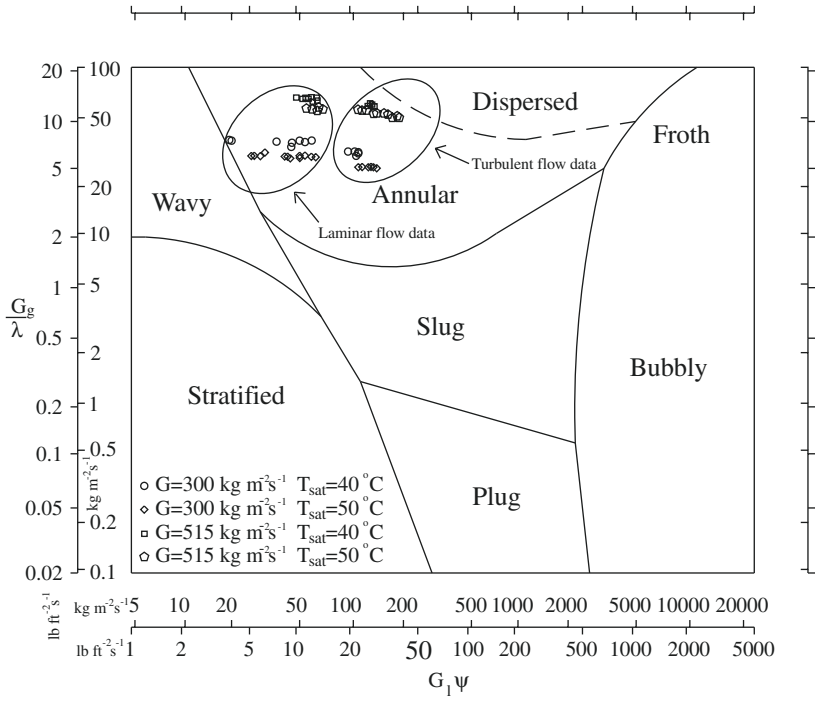

Fig. 14. Flow pattern identification of the experimental data by means of Baker [7] flow regime map for the mass fluxes of 300–515 kg m^{-2} s^{-1} at the condensing temperatures of 40–50 °C.

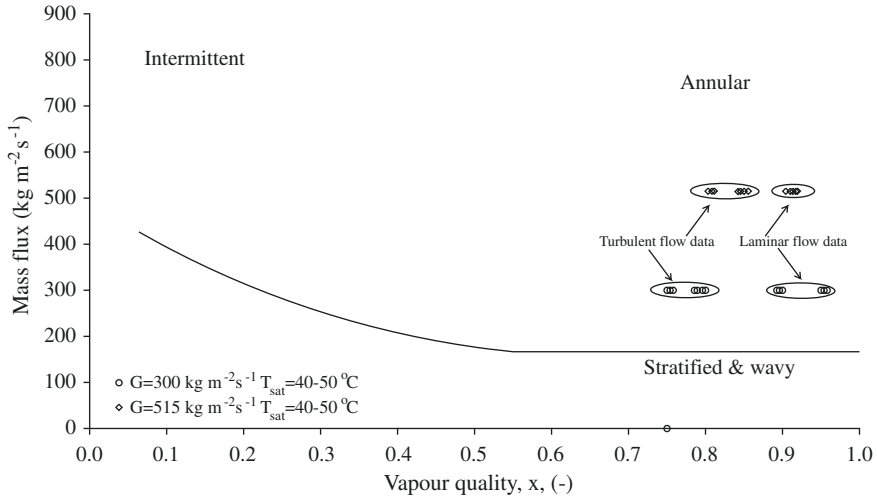

Fig. 15. Flow pattern identification of the experimental data by means of Thome [9] flow regime map for the mass fluxes of 300–515 kg m^{-2} s^{-1} at the condensing temperatures of 40–50 °C.

In Figs. 9 and 10, comparison of the void fraction obtained from the model of Barnea et al. (Eq. (31)) with the most predictive void fraction and correlations shown in Table 2 are presented with a 10% deviation line for the minimum mass flux of 300 kg m^{-2} s^{-1} (Fig. 9) and maximum mass flux of 515 kg m^{-2} s^{-1} (Fig. 10) according to the condensation temperatures of 40 °C (Figs. 9a and 10a) and 50 °C (Figs. 9b and 10b). It is clearly seen from the figures that the void fraction models and correlations of Turner and Wallis [34] and Spedding and Chen [51] have the best predictability of experimental data among 35 void fraction models and correlations given in the authors' previous publications [53,56,59,60]. In addition to this, the majority of the data calculated by the void fraction models of Chisholm and Armand [25,21], Yashar et al. [38], Smith [43], and Chisholm [48] and correlations fall within ±10% and has a good agreement with experimental data.

In Figs. 11–17, well-known flow pattern maps valid for horizontal and vertical tube orientations are presented with the plotted experimental data of the current study. These flow pattern maps are used to show the similarity of annular flow conditions which are independent of tube orientation (horizontal or vertical). Chen et al. [66] also mentioned this similarity in their article. In addition to this, the data shown in these figures were checked by sight glass at the inlet and outlet of the test section. Verification of visual control of the flow regime in the test tube is done using these flow pattern maps in the literature. The flow regime map of Barnea et al. [2] is shown in Fig. 11 for the mass fluxes of 300 kg m^{-2} s^{-1} (a) and

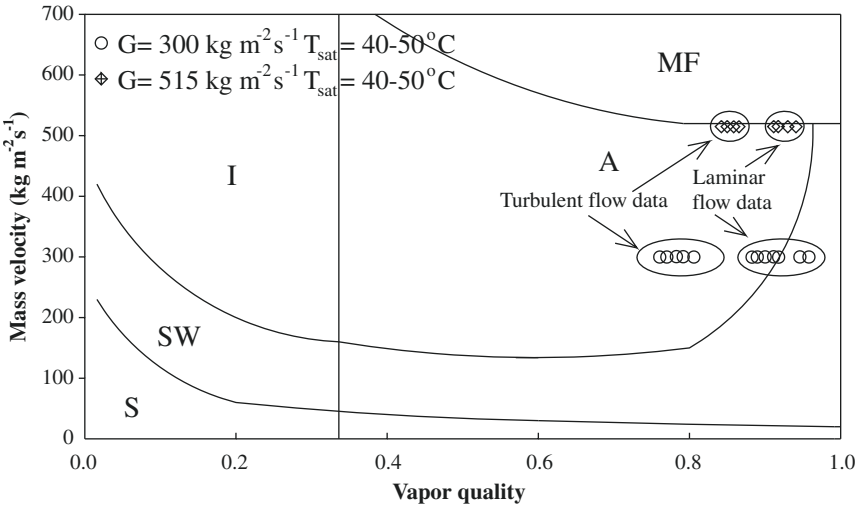

Fig. 16. Flow pattern identification of the experimental data by means of Kattan et al. [13] flow regime map for the mass fluxes of 300–515 kg m^{-2} s^{-1} at the condensing temperatures of 40–50 °C.

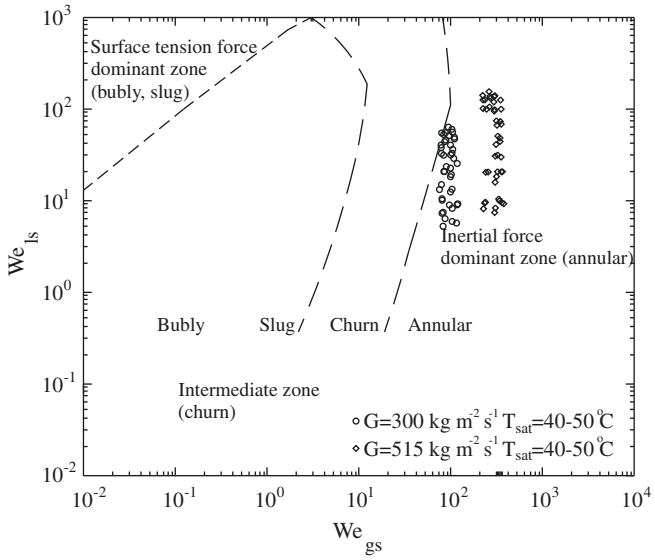

Fig. 17. Flow pattern identification of the experimental data by means of Chen et al. [5] flow regime map for the mass fluxes of 300–515 kg m^{-2} s^{-1} at the condensing temperatures of 40–50 °C.

515 kg m^{-2} s^{-1} (b) at the condensing temperatures of 40 and 50 °C respectively. It is developed for the downward condensation of air–water at the condensing pressure of 0.1 MPa inside 2.5–51 cm i.d. vertical tubes. The results from the analysis using the annular flow model of Barnea et al. [2] were plotted on their map using u_{ls} and u_{gs}, obtained from Eqs. (24) and (25) respectively, as coordinates. The plotted data are in the annular flow area on the map. It shows the accuracy of calculations and visual observation of flow regime by means of sight glasses. Hewitt and Robertson's flow regime map [4] is shown in Figs. 12 and 13 for the mass fluxes of 300–515 kg m^{-2} s^{-1} at the condensing temperatures of 40 °C (Fig. 12) and 50 °C (Fig. 13) separately. It is obtained for the downward condensation of air–water at low pressure and **water-steam at high pressure inside 1–3 cm i.d. vertical tube. Baker's flow regime map [7] is shown in Fig. 14 for the mass fluxes of 300–515 kg m^{-2} s^{-1} at the condensing temperatures of 40–50 °C. It is produced from other researchers' data including condensation of air–water and natural gas oil in horizontal tubes. Thome's flow regime map [9] is shown in Fig. 13 for the mass fluxes of 300–515 kg m^{-2} s^{-1} at the condensing temperatures of 40–50 °C. It is prepared by means of several different experimental conditions belonging to boiling and evaporation for 0.9–10 mm i.d. horizontal tubes up to 64 bars. The flow regime map of Kattan et al. [13] is shown in Fig. 16 for the mass fluxes of 300–515 kg m^{-2} s^{-1} at the condensing temperatures of 40–50 °C. It is the reference flow regime map of Thome [9] and is based on boiling experiments. The flow regime map of Chen et al. [5] is shown in Fig. 17 for the mass fluxes of 300–515 kg m^{-2} s^{-1} at the condensing temperatures of 40–50 °C; these experiments were done for the boiling of R134a at 6–14 bars during vertical upward flow in 1.1–4.26 mm i.d. tubes. It can be clearly seen from these figures that all the data were collected in the annular flow regime sections of these figures.

A large number of graphics could be generated from the output of the calculations; however, due to repetition of similar characteristics of trend lines in figures, only typical results are shown for limited data. It should also be noted that detailed information on the explanations above and some additional figures with different experimental parameters related to this study can be seen in the authors' previous publications [53–65].

5. Conclusion

Co-current downward condensation heat transfer of R134a was experimentally investigated in a 8.1 mm i.d. vertical smooth tube. Accurate and repeatable heat transfer data during annular flow are obtained. There are few researches on the parameters and content of such cases in the literature. For this reason, the results of this study are expected to fill a gap in the literature. The validation process of the investigated annular flow model and correlation development was accomplished by using a large number of data points in each case. The following results were obtained:

A study on the theoretical model of the flow regime transition mechanism of Barnea et al. [2] was performed using experimental data in an algorithm to determine accurate film thickness and void fraction values under the various test conditions. The effects of various relevant parameters such as condensing temperature, condensation temperature difference, vapor quality, and mass flux on the film thickness and void fraction are discussed and investigated in detail. In order to verify the results of calculations, the data obtained from various void fraction correlations were compared. The void fraction models and correlations of Turner and Wallis

[34], Spedding and Chen [51], Chisholm and Armand [25,21], Yashar et al. [38], Smith [43], and Chisholm [48] are found to be in good agreement with the void fraction values obtained from the model of Barnea et al. [2] in the ±10% error band.

According to the flow regime identification analysis in the paper, the flow pattern maps of Barnea et al. [2], Hewitt and Robertson [4], Baker [7], Thome [9], Kattan et al. [9], and Chen et al. [5] are capable of predicting the annular flow regime conditions checked by sight glasses in the experimental apparatus.

Acknowledgements

The authors are indebted to the Department of Mechanical Engineering, King Mongkut's University of Technology Thonburi (KMUTT) and the Thailand Research Fund for supporting this study. Especially, the first author wishes to thank KMUTT for providing him with a Post-doctoral fellowship.

References

[1] M.G. Hubbard, A.E. Dukler, The characterization of flow regimes for horizontal twophase flow, in: Proceedings of the Heat Transfer and Fluid Mechanics Institute, Stanford University Press, 1966.
[2] D. Barnea, O. Shoham, Y. Taitel, Flow pattern transition for vertical downward two phase flow, Chemical Engineering Science 37 (1982) 741–744.
[3] J.R. Fair, What you need to know to design thermosyphon reboilers, Petroleum Refiner 39 (2) (1960) 105.
[4] G.F. Hewitt, D.N. Robertson, Studies of Two-Phase Flow Patterns by Simultaneous X-ray and Flash Photography, Rept. AERE-M2159, UKAEA, Harwell, 1969.
[5] L. Chen, Y.S. Tian, T.G. Karayiannis, The effect of tube diameter on vertical two-phase flow regimes in small tubes, International Journal of Heat and Mass Transfer 49 (2006) 4220–4230.
[6] T.S. Zhao, Q.C. Bi, Co-current air–water two-phase flow patterns in vertical triangular microchannels, International Journal of Multiphase Flow 27 (2001) 765–782.
[7] O. Baker, Design of pipe lines for simultaneous flow of oil and gas, Oil and Gas Journal 26 (1954) 185–195.
[8] J.M. Mandhane, G.A. Gregory, K. Aziz, A flow pattern map for gas–liquid flow in horizontal pipes, International Journal Multiphase Flow 1 (1974) 537–553.
[9] J.R. Thome, Update on advances in flow pattern based two-phase heat transfer models, International Journal of Heat and Mass Transfer 29 (2005) 341–349.
[10] J. El Hajal, J.R. Thome, A. Cavallini, Condensation in horizontal tubes, part 1: two-phase flow pattern map, International Journal of Heat and Mass Transfer 46 (2003) 3349–3363.
[11] J.W. Coleman, S. Garimella, Characterization of two-phase flow patterns in small diameter round and rectangular tubes, International Journal of Heat and Mass Transfer 42 (1999) 2869–2881.
[12] J.W. Coleman, S. Garimella, Two-phase flow regimes in round, square and rectangular tubes during condensation of refrigerant R134a, International Journal of Heat and Mass Transfer 26 (2003) 117–128.
[13] N. Kattan, J.R. Thome, D. Favrat, Flow boiling in horizontal tubes. Part 1: development of a diabatic two-phase flow pattern map, Journal of Heat Transfer 120 (1998) 140–147.
[14] Y. Taitel, A.E. Dukler, A model for prediction flow regime transitions in horizontal and near horizontal gas–liquid flow, AIChE Journal 22 (1976) 47–55.
[15] J. Weisman, D. Duncan, J. Gibson, T. Crawford, Effects of fluid properties and pipe diameter on two-phase flow patterns in horizontal lines, International Journal Multiphase Flow 5 (1979) 437–462.
[16] G. Breber, J.W. Palen, J. Taborek, Prediction of horizontal tube-side condensation of pure components using flow regime criteria, Journal of Heat Transfer 102 (1980) 471–476.
[17] H.M. Soliman, On the annular-to-wavy flow pattern transition during condensation inside horizontal tubes, Canadian Journal of Chemical Engineering 60 (1982) 475–481.
[18] T.N. Tandon, H.K. Varma, C.P. Gupta, A new flow regime map for condensation inside horizontal tubes, Journal of Heat Transfer 104 (1982) 763–768.
[19] B. Mederic, P. Lavieille, M. Miscevic, Heat transfer analysis according to condensation flow structures in a minichannel, Experimental Thermal and Fluid Science 30 (2006) 785–793.
[20] R.H. Huq, J.L. Loth, Analytical two-phase flow void fraction prediction method, Journal of Thermo Physics 6 (1992) 139–144.
[21] A.A. Armand, The resistance during the movement of a two-phase system in horizontal pipes, Izvestiya Vsesoyuznogo Teplotekhnicheskogo Instituta 1 (1946) 16–23.
[22] D. Chisholm, A.D.K. Laird, Two phase flow in rough tubes, Transactions of ASME 80 (1958) 276–286.
[23] D. Steiner, Heat transfer to boiling saturated liquids, VDI-Warmeatlas (VDI Heat Atlas), in: Verein Deutscher Ingenieure (Ed.), VDI-Gessellschaft Verfahrenstechnik und Chemie-ingenieurwesen (GCV), Translator: J.W. Fullarton, Dusseldorf, 1993.
[24] T. Harms, D. Eckart, A. Groll, J. Braun, A void fraction model for annular flow in horizontal tubes, International Journal of Heat and Mass Transfer 46 (2003) 4051–4057.
[25] D. Chisholm, Two Phase Flow in Pipelines and Heat Exchangers, George Godwin in Association with The Institution of Chemical Engineers, London, 1983.
[26] A.A. Armand, G.G. Treschev, The resistance during the movement of a two-phase system in horizontal pipes, Izvestiya Vsesoyuznogo Teplotekhnicheskogo Instituta 1 (1946) 16–23.
[27] S.G. Bankoff, A variable density single-fluid model for two-phase flow with particular reference to steam–water flow, Transactions ASME Journal of Heat Transfer 82 (1960) 265–272.
[28] V. Czop, D. Barbier, S. Dong, Pressure drop, void fraction and shear stress measurements in adiabatic two-phase flow in coiled tube, Nuclear Engineering Design 149 (1994) 323–333.
[29] T.N. Tandon, H.K. Varma, C.P. Gupta, A void fraction model for annular two-phase flow, International Journal of Heat and Mass Transfer 28 (1985) 191–198.
[30] D. Graham, J.C. Chato, T.A. Newell, Heat transfer and pressure drop during condensation of refrigerant 134a in an axially grooved tube, International Journal of Heat and Mass Transfer 42 (1999) 1935–1944.
[31] G.A. Hughmark, Holdup in gas–liquid flow, Chemical Engineering Progress 58 (1962) 62–65.
[32] P.J. Hamersma, J. Hart, A pressure drop correlation for gas/liquid pipe flow with a small liquid holdup, Chemical Engineering Science 42 (1987) 1187–1196.
[33] R.W. Lockhart, R.C. Martinelli, Proposed correlation of data for isothermal two-phase, two-component flow in pipes, Chemical Engineering Progress 45 (1949) 39–48.
[34] J.M. Turner, G.B. Wallis, The Separate-Cylinders Model of Two-Phase Flow, Paper No. NYO-3114-6. Thayer's School Eng., Dartmouth College, Hanover, NH, USA, 1965.
[35] G.B. Wallis, One-Dimensional Two-Phase Flow, McGraw-Hill, 1965. pp. 51–54.
[36] P. Domanski, D. Didion, Computer modeling of the vapor compression cycle with constant flow area expansion device, Building Science Series, National Bureau of Standards of USA, 1983.
[37] M.J. Wilson, T.A. Newell, J.C. Chato, C.A. Infante Ferreira, Refrigerant charge, pressure drop and condensation heat transfer in flattened tubes, International Journal of Refrigeration 26 (2003) 442–451.
[38] D.A. Yashar, T.A. Newell, J.C. Chato, Experimental Investigation of Void Fraction During Horizontal Flow in Smaller Diameter Refrigeration Applications, ACRC TR-141, Air Conditioning and Refrigeration Center, University of Illinois, Urbana–Champaign, IL, 1998.
[39] A. Premoli, D. Francesco, A. Prima, An empirical correlation for evaluating two-phase mixture density under adiabatic conditions, in: European Two-Phase Flow Group Meeting, Milan, Italy, 1970.
[40] A. Kawahara, M. Kawaji, P.M.Y. Chung, M. Sadatomi, K. Okayama, Effects of channel diameter and liquid properties on void fraction in adiabatic two-phase flow through microchannels, Heat Transfer Engineering 26 (2005) 13–19.
[41] S.M. Zivi, Estimation of steady-state steam void-fraction by means of the principle of minimum entropy production, Transactions ASME Journal of Heat Transfer Series C 86 (1975) 247–252.
[42] G. Rigot, Fluid capacity of an evaporator in direct expansion, Plomberie 328 (1973) 133–144.
[43] S.L. Smith, Void fractions in two-phase flow: a correlation based upon an equal velocity head model, Proceedings of the Institution of Mechanical Engineers 36 (1969) 647–664.
[44] S. Levy, Steam slip theoretical prediction from momentum model, Transactions ASME Journal of Heat Transfer Series C 82 (1960) 113–124.
[45] H. Fauske, Critical two-phase, steam–water flows, in: Proceedings of the 1961 Heat Transfer and Fluid Mechanics Institute, Stanford University Press, Stanford, CA, pp. 79–89.
[46] J.R.S. Thom, Prediction of pressure drop during forced circulation boiling of water, International Journal of Heat and Mass Transfer 7 (1964) 709–724.
[47] C.J. Baroczy, Correlation of liquid fraction in two-phase flow with application to liquid metals, Chemical Engineering Progress Symposium Series 61 (1965) 179–191.
[48] D. Chisholm, Pressure gradients due to friction during the flow of evaporating two-phase mixtures in smooth tubes and channels, International Journal of Heat and Mass Transfer 16 (1973) 347–358.
[49] N. Madsen, A void fraction correlation for vertical and horizontal bulk-boiling of water, AIChE Journal 21 (1975) 607–608.
[50] F.W. Ahrens, Heat pump modeling, simulation and design, in: Proceedings of the NATO Advanced Study Institute on Heat Pump Fundamentals, Espinho, Spain, 1980.
[51] P.L. Spedding, J.J. Chen, Holdup in two phase flow, International Journal of Multiphase Flow 10 (1984) 307–339.
[52] J.J.J. Chen, A further examination of void-fraction in annular two-phase flow, International Journal of Heat Mass Transfer 29 (1986) 1760–1763.
[53] A.S. Dalkilic, S. Laohalertdecha, S. Wongwises, Effect of void fraction models on the two-phase friction factor of R134a during condensation in vertical downward flow in a smooth tube, International Communications in Heat and Mass Transfer 35 (2008) 921–927.
[54] A.S. Dalkilic, S. Yildiz, S. Wongwises, Experimental investigation of convective heat transfer coefficient during downward laminar flow condensation of

R134a in a vertical smooth tube, International Journal of Heat and Mass Transfer 52 (2009) 142–150.
[55] A.S. Dalkilic, S. Laohalertdecha, S. Wongwises, Two-phase friction factor in vertical downward flow in high mass flux region of refrigerant HFC-134a during condensation, International Communications in Heat and Mass Transfer 35 (2008) 1147–1152.
[56] A.S. Dalkilic, S. Laohalertdecha, S. Wongwises, Effect of void fraction models on the film thickness of R134a during downward condensation in a vertical smooth tube, International Communications in Heat and Mass Transfer 36 (2009) 172–179.
[57] A.S. Dalkilic, S. Wongwises, Intensive literature review of condensation inside smooth and enhanced tubes, International Heat and Mass Transfer 52 (2009) 3409–3426.
[58] A.S. Dalkilic, S. Laohalertdecha, S. Wongwises, Experimental investigation on heat transfer coefficient of R134a during condensation in vertical downward flow at high mass flux in a smooth tube, International Communications in Heat and Mass Transfer 36 (2009) 1036–1043.
[59] A.S. Dalkilic, S. Laohalertdecha, S. Wongwises, A comparison of the void fraction correlations of R134a during condensation in vertical downward laminar flow in a smooth and micro-fin tube, in: Proceedings of the 1st International Conference on Micro/Nanoscale Heat Transfer, January 06–09, ASME, Taiwan, 2008.
[60] A.S. Dalkilic, S. Laohalertdecha, S. Wongwises, Two-phase friction factor obtained from various void fraction models of R-134a during condensation in vertical downward flow at high mass flux, in: Proceedings of the 1st International Conference on Heat Transfer, August 10–14, ASME, USA, 2008.
[61] A.S. Dalkilic, S. Laohalertdecha, S. Wongwises, Experimental investigation on the condensation heat transfer and pressure drop characteristics of R134a at high mass flux conditions during annular flow regime inside a vertical smooth tube, in: Summer Heat Transfer Conference, July 19–23, ASME, USA, 2009.
[62] A.S. Dalkilic, O. Agra, Experimental apparatus for the determination of condensation heat transfer coefficient for R134a and R600a flowing inside vertical and horizontal tubes, in: Summer Heat Transfer Conference, July 19–23, ASME, USA, 2009.
[63] A.S. Dalkilic, S. Laohalertdecha, S. Wongwises, Experimental research on the similarity of annular flow models and correlations for the condensation of R134a at high mass flux inside vertical and horizontal tubes, in: International Mechanical Engineering Congress and Exposition, November 13–19, ASME, USA, 2009.
[64] A.S. Dalkilic, S. Wongwises, A heat transfer model for co-current downward laminar film condensation of R134a in a vertical micro-fin tube during annular flow regime, in: Eleventh UK National Heat Transfer Conference, September 6–8, Queen Mary University of London, 2009.
[65] A.S. Dalkilic, O. Agra, I. Teke, S. Wongwises, Comparison of frictional pressure drop models during annular flow condensation of R600a in a horizontal tube at low mass flux and of R134a in a vertical tube at high mass flux, International Journal of Heat and Mass Transfer, in press, doi:10.1016/j.ijheatmasstransfer.2009.12.051.
[66] S.L. Chen, F.M. Gerner, C.L. Tien, General film condensation correlations, Experimental Heat Transfer 1 (1987) 93–107.
[67] S.J. Kline, F.A. McClintock, Describing uncertainties in single sample experiments, Mechanical Engineering (1953) 3–8.

International Journal of Heat and Mass Transfer 53 (2010) 3449–3459

Contents lists available at ScienceDirect

International Journal of Heat and Mass Transfer

journal homepage: www.elsevier.com/locate/ijhmt

Flow mechanisms of HFC-410A inside short-tube orifices during flashing process

Kitti Nilpueng, Somchai Wongwises *

Fluid Mechanics, Thermal Engineering and Multiphase Flow Research Lab (FUTURE), Department of Mechanical Engineering, King Mongkut's University of Technology Thonburi, Bangmod, Bangkok 10140, Thailand

ARTICLE INFO

Article history:
Received 4 January 2010
Received in revised form 26 February 2010
Accepted 26 February 2010
Available online 3 May 2010

Keywords:
Expansion device
Short-tube orifice
Temperature distribution
Metastable flow
Choked flow

ABSTRACT

New experimental data of HFC-410A flow mechanisms, including pressure and temperature distributions, flow pattern, and mass flow rate inside a short-tube orifice are studied. Different short-tube orifice lengths of 10 mm, 15 mm, and 20 mm, with short-tube orifice diameters ranging from 0.849 to 1.096 mm were manufactured for this experiment. The test runs are done at upstream pressures ranging from 2100 to 2600 kPa, and with a degree of subcooling between 4 and 12 °C. The results show that the refrigerant flow mechanisms in the entrance region and inside a short-tube orifice agree with incompressible flow theory, but the refrigerant flow mechanisms in the exit region are similar to choked flow in a theoretical compressible flow. The temperature distribution inside a short-tube orifice is directly related to the pressure distribution. The mass flow rate is directly proportional to the upstream pressure and degree of subcooling, whereas it is strongly affected by the short-tube diameter. The downstream pressure has insignificant effects on the mass flow rate and pressure distribution inside a short-tube orifice. However, the downstream pressure has a slight effect on the temperature distribution inside a short-tube orifice.

© 2010 Elsevier Ltd. All rights reserved.

1. Introduction

In recent years, hydrofluorocarbon (HFC) refrigerants and HFC refrigerant mixtures have been developed for use as alternatives to chlorofluorocarbon (CFC) and hydrochlorofluorocarbon (HCFC) refrigerants which are applied in refrigeration and air-conditioning systems, because the chlorine molecules from these refrigerants destroy the earth's ozone layer. Although the change of refrigerant properties will help to protect the environment, it may lead to a change in system performance. Therefore, in order to obtain the proper system performance with the new HFC refrigerants, performance data are required for each component.

An expansion device is another basic component of a refrigeration system. The main purpose of the expansion device is to reduce the pressure of the refrigerant from the condenser pressure to the evaporator pressure and to regulate the mass flow rate of refrigerant flowing from the condenser to the evaporator at a rate equal to the evaporation rate in the evaporator. During the flow of liquid refrigerant through the expansion device, the pressure decreases rapidly below the saturation pressure and the refrigerant is changed from a subcooled liquid or saturated liquid to a liquid–vapour mixture. This behaviour is defined as a flashing process. The short-tube orifice is one type of expansion device popularly used in residential and automotive air-conditioning systems. The advantages of a short-tube orifice are its simplicity, low initial cost, high reliability, and ease of maintenance. To obtain appropriate operation and performance of refrigeration systems using short-tube orifices as expansion devices, the flow of refrigerant should be choked flow. Under choked flow conditions, the flow of refrigerant through the short-tube orifice corresponds to the critical flow rate, which is the maximum flow rate that can be attained by reducing the downstream pressure under given upstream conditions. Consequently, an understanding of the flow mechanisms of the refrigerant through a short-tube orifice under choked flow conditions is very important for the proper design of the system.

During past decades, the performance characteristics of short-tube orifices have been studied by a number of researchers. Recent studies associated with flow patterns, pressure and temperature distributions and mass flow rate under choked flow conditions inside the short-tube orifice are outlined in the following paragraphs.

1.1. Flow pattern

For two-phase flow studies, it is not possible to understand flow phenomena without a clear understanding of the flow patterns, as these influence the two-phase pressure drop, holdup, system stability, and exchange rate of momentum, heat, and mass during the phase-change heat transfer process. Therefore, identification of the flow pattern inside the channel is very useful for developing suitable calculation techniques. Investigations of refrigerant flow pattern inside short-tube orifices have been published by some researchers.

* Corresponding author. Tel.: +662 470 9115; fax: +662 470 9111.
E-mail address: somchai.won@kmutt.ac.th (S. Wongwises).

0017-9310/$ - see front matter © 2010 Elsevier Ltd. All rights reserved.
doi:10.1016/j.ijheatmasstransfer.2010.04.005

Pasqua [1] studied the characteristics of subcooled and saturated liquid CFC-12 flow inside glass short tubes. For subcooled liquids entering short tubes, he found that the liquid flashed inside the short tube when the downstream pressure was near or below the saturation pressure. The fluid inside the short tube was described as a metastable inner core of liquid surrounded by a two-phase annular ring. The diameter of the metastable liquid core decreased as the fluid proceeded to the tube exit. Aaron and Domanski [2] observed the flow pattern of subcooled liquid HCFC-22 at the inlet and outlet of short tubes with $5 < L/D < 20$. They stated that the microscopic bubbles suspended in the liquid covered the short-tube outlet in a homogeneous form over several inches when the downstream pressure was close to saturation pressure. Kim [3] investigated experimentally the flow pattern of two-phase and subcooled liquid HCFC-22 and HFC-134a through short-tube orifices with a length to diameter ratio ranging between 7 and 20. The results showed that the liquid refrigerant did not flash in the inlet region although the pressure was lower than the saturation pressure. The flashing point moved to the outlet section of the short-tube when increasing the degree of subcooling. Nilpueng and Wongwises [4] investigated experimentally the two-phase flow pattern of HFC-134a through short-tube orifices. The results showed that flow patterns could be divided into two types: metastable liquid flow, and two-phase flow. In the metastable liquid flow region, the liquid refrigerant which looked like a cone shape flowed in the central core of the tube while a two-phase flow which had many tiny bubbles mixed in the liquid refrigerant surrounded the liquid refrigerant. In the two-phase flow region, there were many tiny bubbles mixed with the liquid refrigerant.

1.2. Pressure and temperature distribution

The pressure and temperature distributions of refrigerant inside a short-tube are some of the most important parameters required for the selection of the proper short-tube size for given operating conditions and capacity. However, it is found that the pressure and temperature distributions have been studied and published by only a few previous researchers.

The pressure distribution of HCFC-22 inside a short-tube orifice was measured by Aaron and Domanski [2]. In their experiment, six pressure taps which were bored to 0.08 mm were located along a short-tube orifice. The results indicated that a large variation of pressure appeared at the inlet and outlet of the short-tube orifice. The pressure tended to recover and slightly decrease inside the tube after the refrigerant flowed through the inlet section. Kim [3] studied the pressure profile of HCFC-22 and HFC-134a through a short-tube orifice. He reported that the pressure was lower than the saturation pressure when the flow of refrigerant passed through the inlet section. The pressure profile along the short-tube was increased as the degree of subcooling was increased. Liu et al. [5] investigated the pressure profile of R744 flow through short-tube orifices. They described that the rapid change of velocity and abrupt inlet loss of fluid were the cause of a large pressure drop at the inlet while the large pressure drop at the outlet was produced by the great expansion of refrigerant. The average pressure inside the short-tube increased when the upstream pressure was increased. The pressure and temperature distributions of HFC-134a inside a short-tube orifice were studied by Nilpueng and Wongwises [4] and Nilpueng and Wongwises [6]. The results indicated that the pressure greatly decreased at the inlet, then slightly increased and steadily decreased inside the tube. They concluded that the refrigerant in the short-tube orifice exists under non-equilibrium thermodynamic conditions.

1.3. Mass flow rate

In order to achieve an appropriate operation and performance of refrigeration systems, it is very important to quantify the maximum flow rate through a short-tube orifice. Consequently, the mass flow rate of refrigerant inside a short-tube orifice under choked flow conditions was investigated by several researchers.

Mei [7] investigated the flow of subcooled liquid HCFC-22 through short-tubes with $7.5 < L/D < 11.9$. He reported that first-stage choking occurred at a degree of subcooling of 22.2 °C. However, there was no indication of second-stage choking in the normal heat pump operating range. The effects of upstream subcooling, upstream pressure, downstream pressure, tube length, tube diameter, entrance chamfering, and exit chamfering on the flow rate of HCFC-22 through a short-tube were examined by Aaron and Domanski [2], Kim[3], and Kim and O'Neal [8]. Their results showed that the mass flow rate depends on upstream pressure and upstream subcooling, but that it is insensitive to downstream pressure due to approximate choking. Aaron and Domanski [2] recommended that the L/D ratio should be greater than 5 in order to achieve choked flow. The mass flow rate of HFC-134a along a short-tube was reported by Kim [3], Singh et al. [9], Tu et al. [10] and Nilpueng and Wongwises [6]. Their results showed that the short-tube orifice diameter has a significant effect on the increase in flow rate. In addition, Nilpueng and Wongwises [6] recorded that the choked flow phenomenon disappeared inside a short-tube orifice when L/D was less than 2.91. Payne and O'Neal [11] studied the flow rate of HFC-407C through short-tube orifices with diameters of 1.09–1.94 mm. They found that the addition of oil to the refrigerant increased the mass flow rate by more than 12% for two-phase flow entering the short tube; but, it had little effect on mass flow rate at a high degree of subcooling. Liu et al. [5] studied the flow of R744 through short-tube orifices. Short tubes with lengths between 8.02 and 25.42 mm and diameters between 0.83 and 1.53 mm were tested. The results showed that choked flow existed under a wide range of operating conditions. Kim et al. [12] investigated the mass flow rate of HFC-410A through short-tube orifices at upstream pressures approaching the critical point. They found that the decrease of mass flow rate with a reduction of subcooling became more significant when upstream pressure increased beyond 3.604 kPa, due to a higher density change.

As described above, it can be clearly seen that previous published papers have reported the flow mechanisms of CFC and HCFC refrigerants through short-tube orifices. But, the studies on HFC refrigerants and HFC refrigerant mixtures inside short-tube orifices have been investigated by only a few previous research works; especially, HFC-410A which is favourably used to replace HCFC-22 in domestic air conditioners and heat pumps. The main purpose of the present paper is to study the HFC-410A refrigerant flow mechanisms inside short-tube orifices, including pressure and temperature distributions, flow pattern, mass flow rate, metastable flow, and choked flow. The effects of the relevant parameters, i.e., upstream pressure, downstream pressure, degree of subcooling, short-tube diameter, and short-tube length on flow pattern, mass flow rate, and pressure distribution that have never been observed before are also investigated.

2. Experimental apparatus

The experimental apparatus described in Nilpueng and Wongwises [4] was used in the present study. A schematic diagram of the test facility is provided in Fig. 1. The system consists of three main loops: the refrigerant loop, the hot water loop and the cold water loop. The refrigerant loop consists of the main refrigeration system components: compressor, condenser, short-tube orifice (test

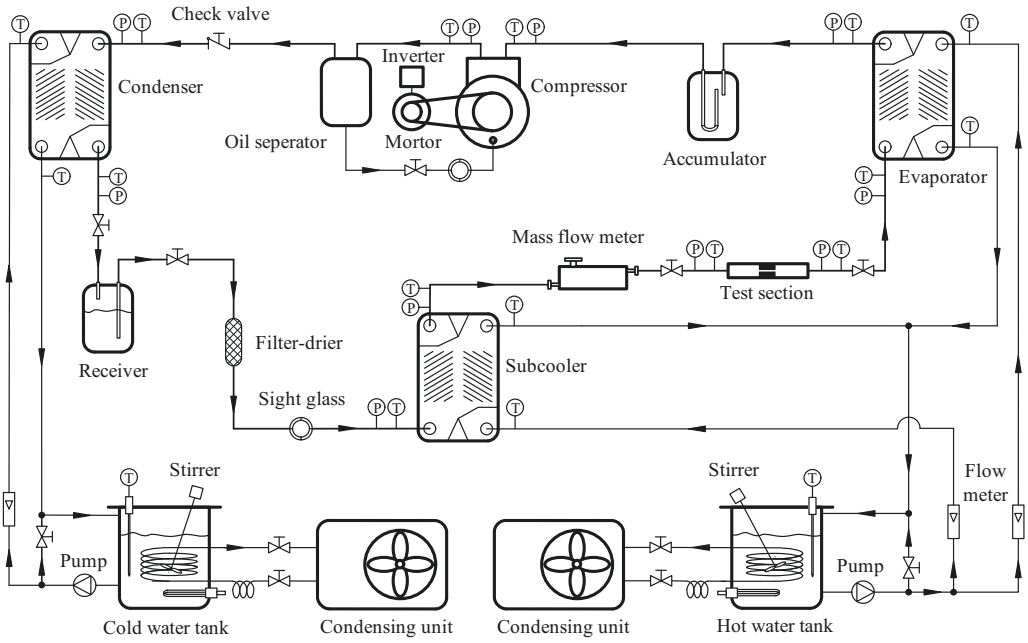

Fig. 1. Schematic diagram of experimental apparatus.

section), evaporator, and other accessory parts: oil separator, liquid receiver, filter/drier, sight glass, sub-cooler and accumulator. A commercial HFC-410A is used as the working fluid. A two-cylinder single stage reciprocating compressor, driven by an electric motor, is used to discharge the refrigerant. The speed of the motor is varied so as to provide a wide range of mass flow rates by means of an inverter. A helical oil separator is used to minimize the effect of lubricating oil on refrigerant flow through short-tube orifices. The efficiency of oil separation is approximately 99%. Compact plate heat exchangers are used as condenser, evaporator and subcooler.

In this experiment, the hot water loop and cold water loop are used for transferring heat to evaporator and from condenser, respectively. An electric heater and a separated refrigeration system are installed in the water tank so as to control the water temperature. The hot water is supplied from a hot water tank by the circulating pump and passes through the flow meter and evaporator. The downstream pressure of the test section is controlled by adjusting the temperature and the flow rate of hot water. The condenser rejects heat to the water coming from a cold water tank. The upstream pressure of the test section is regulated by adjusting the temperature of the cold water. The degree of subcooling of the refrigerant entering the test section is adjusted by varying the flow rate of water to the sub-cooler. The test runs are chosen to cover a wide range of working conditions of an air-conditioner and heat pump. The upstream pressures are set at 2100, 2250, 2400 and 2600 kPa, while downstream pressures are varied between 1000 and 1250 kPa. The degree of subcooling is varied from 4 to 12 °C.

There are two groups of short-tube orifices used in the experiment. The first group consists of the specially designed glass short-tube orifices, which permit visual observation of the flow patterns of refrigerant inside the tubes. The other group is made of brass and is used to study the temperature and pressure distributions. Table 1 lists the short-tube orifices used in this study. A specially designed short-tube orifice is used to observe the flow behaviour of refrigerant inside the tube (Fig. 2). It consists of glass short-tube orifices, a glass tube, acrylic tube, brass connector, copper tube, rubber o-ring and attachment set. Glass short-tube orifices were manufactured from glass capillary tube so as to allow

Table 1
Dimension of the short-tube orifices.

Short tube	Diameter (mm)	Length (mm)
1	0.851	10
2	0.849	15
3	0.869	20
4	0.961	10
5	0.961	15
6	0.935	20
7	1.096	10
8	1.085	15
9	1.091	20

the visualization of refrigerant flow inside short-tube orifices. The glass short-tube orifice and the glass tube are fitted into the acrylic tube. The brass connectors are used to link the copper tube with the glass tube. The rubber o-rings are inserted between the glass short-tube orifice, glass tube, and brass connector in order to prevent leakage of refrigerant. The glass short-tube orifice is supported by the attachment set to resist high pressure. The flow pattern of refrigerant inside the short-tube orifice is registered by a digital camera (Sumsung Digimax V3) with shutter speed of 1/2000 s, mounted together with a 20× magnification lens.

Fig. 3 shows a schematic diagram of the short-tube orifice for pressure and temperature distribution measurements. Six pressure and temperature taps are drilled at 0.2 mm diameter along the orifices using a wire cutting machine. Two pressure and temperature taps are drilled to 0.5 mm before and after the short-tube orifice. The thermocouples are installed into a 2 mm diameter hole without disturbance in the flow field and fixed with special glue applied to the outside of the short-tube orifice. The thermocouples are insulated with a 6.4 mm thick Aeroflex standard sheet to reduce the effect of heat transfer on measurement errors.

A microscope (Olympus BX51) is used to measure the diameter of the short-tube orifice. The length of the short-tube orifice is measured with a digital calliper. The accuracies of diameter and length measurements are ±0.001 mm and ±0.01 mm, respectively. The pressure distribution inside the short-tube orifice was detected by pressure transducers calibrated from 0 to 30 bar with

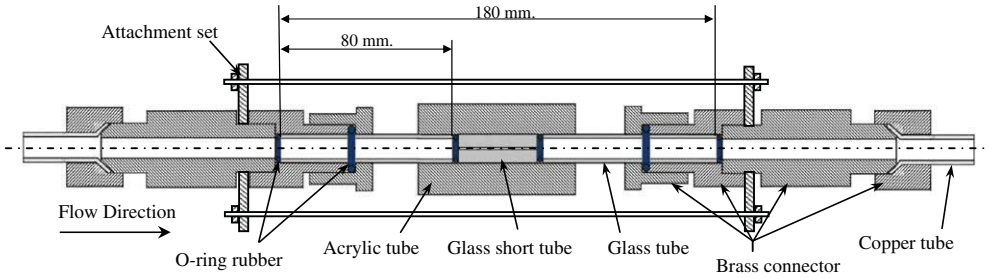

Fig. 2. Schematic diagram of test section for visual observation.

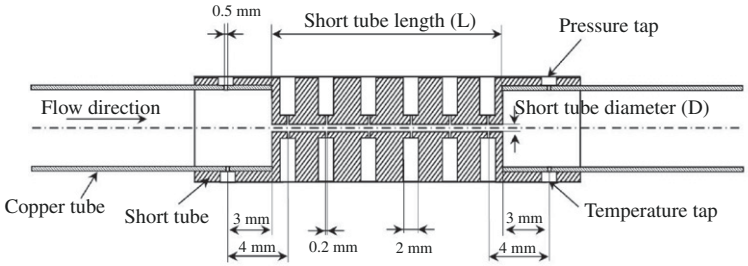

Fig. 3. Schematic diagram of test section for measuring pressure and temperature distribution.

±20 mbar accuracy. T-type thermocouples were used to measure fluid temperature. The uncertainty of the temperature measurement was ±0.1 °C. The differential transducer had an accuracy of ±0.1% of its calibrated span. The flow rate of refrigerant through the short-tube orifice was measured by a Coriolis mass flow meter (ABB FCM2000) with an accuracy of ±0.25%.

3. Results and discussion

This study presents the flow mechanisms of HFC-410A, including pressure distribution, temperature distribution, flow pattern, metastable flow, choked flow and mass flow rate, inside a short-tube orifice during a flashing process. The effects of operating conditions and short-tube orifice dimensions on the flow mechanisms are also explained.

3.1. Pressure and temperature distributions

One of the purposes of the refrigerant expansion device is to reduce the refrigerant pressure from the condenser pressure to the evaporator pressure, which also results in a temperature drop. Therefore, knowledge of the pressure and temperature distributions inside short-tube orifices is important for the proper design and selection of short-tube orifices.

The pressure and temperature distributions of HFC-410A along a short-tube orifice are shown in Fig. 4. It is found from the figure that the pressure and temperature greatly decrease in the entrance region, slightly increase over a short length and gradually decrease thereafter inside the short-tube orifice, and rapidly decrease in the exit region. In addition, it can be seen that the temperature distribution inside the short-tube orifice is directly related to the pressure distribution. This is because the refrigerant pressure is lower than the saturation pressure corresponding to upstream pressure after the flow of refrigerant passes the entrance plane. This means that the liquid refrigerant changes into a liquid–vapour mixture and the temperature varies directly with pressure.

The large pressure drop in the entrance region can occur because the refrigerant flow area is constricted into *vena contracta*. Therefore, the upstream pressure is suddenly converted into kinetic energy and becomes the minimum pressure in the *vena contracta*. Moreover, it is also found that a pressure loss is produced due to an inertial effect and wall shear stress in the entrance region. The results from this study show that the minimum pressure appears about 1 mm from the entrance plane. The cause of the pressure rise and pressure decrease inside the short-tube can be explained by the slight increase of flow area in the entrance region and shear stress between refrigerant and tube wall inside the short-tube orifice, respectively. Considering the pressure variation in the exit region, this implies that the flow behaviour of the refrigerant does not conform to incompressible fluid flow theory, but is similar to the compressible flow through a converging nozzle when the velocity in the exit plane reaches sonic speed. Under these conditions, the pressure reduces discontinuously from the exit plane to the downstream pressure value.

The effect of upstream pressure on the pressure and temperature distributions of refrigerant inside a short-tube orifice is shown in Fig. 5. It can be clearly seen from this figure that the average pressure and temperature inside the short-tube orifice increase as the upstream pressure is boosted. This is because the refrigerant velocity is increased when the pressure difference between upstream and downstream pressure is increased. Therefore, the pressure loss due to sudden contraction and wall friction is augmented. The reason for the temperature variation inside the short-tube orifice is similar to that described above. However, it is observed that the increase of upstream pressure causes a slight decrease of downstream temperature even though the downstream pressure is unchanged.

Fig. 6 shows the pressure and temperature distributions along a short-tube orifice at different degrees of subcooling. The augmentation of the degree of subcooling leads to an increase of the pressure drop in the entrance region while the average pressure and temperature inside the short-tube orifice are lowered. It is also found that the downstream temperature is slightly decreased when the degree of subcooling is increased. This is due to the fact

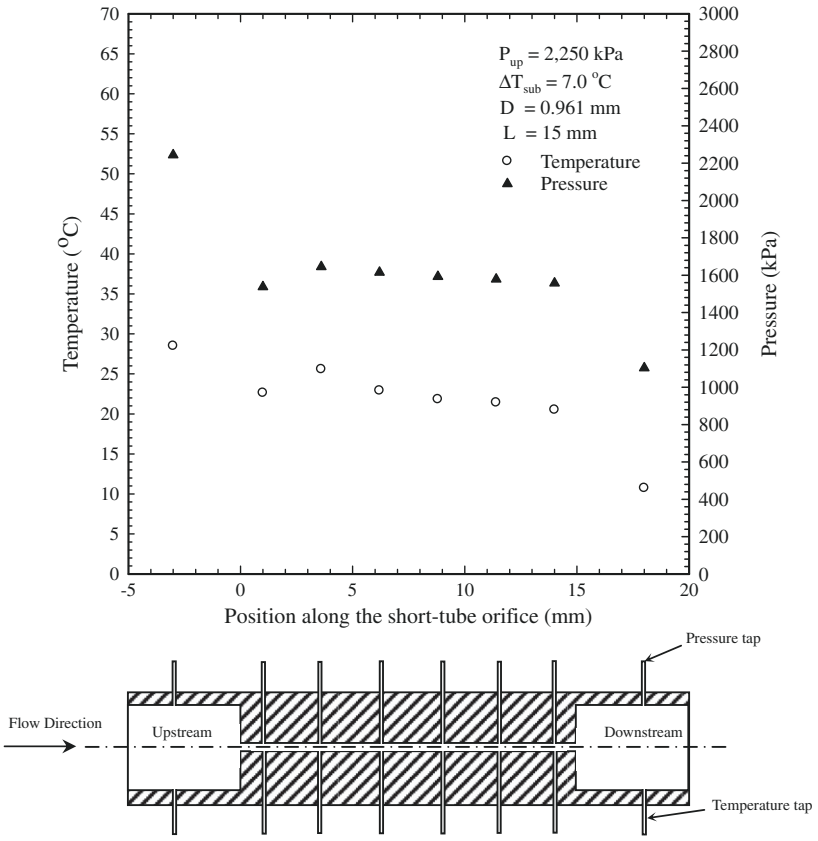

Fig. 4. Pressure and temperature distribution of HFC-410A inside a short-tube orifice.

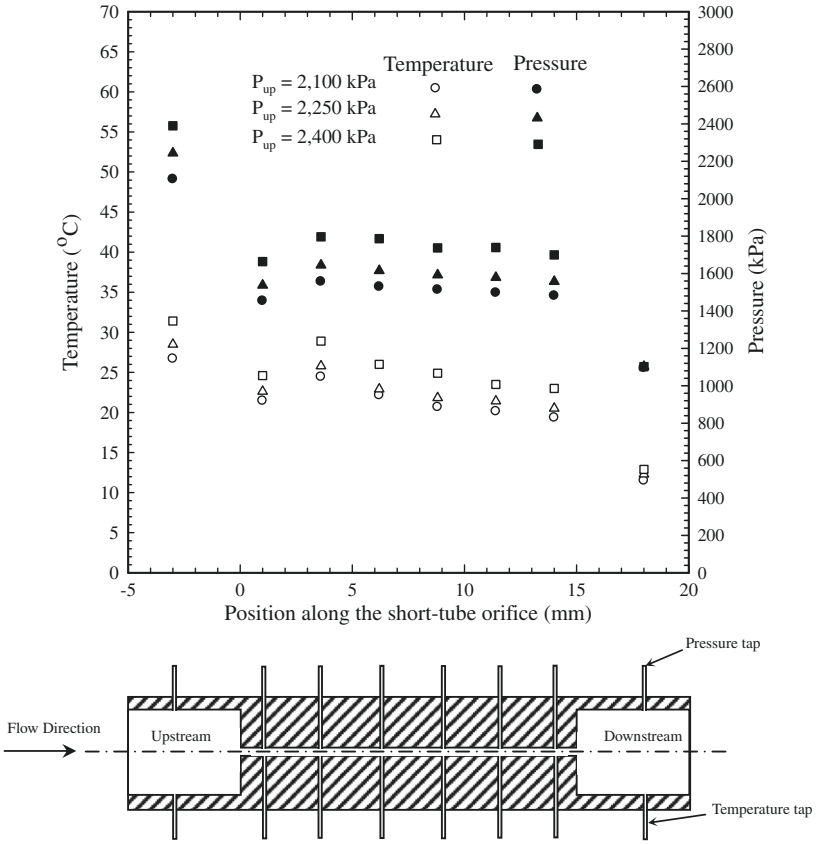

Fig. 5. Effect of upstream pressure on the pressure and temperature distribution at $D = 0.961$ mm, $L = 15$ mm, $\Delta T_{sub} = 7.8–8.5$ °C and $P_{down} = 1100$ kPa.

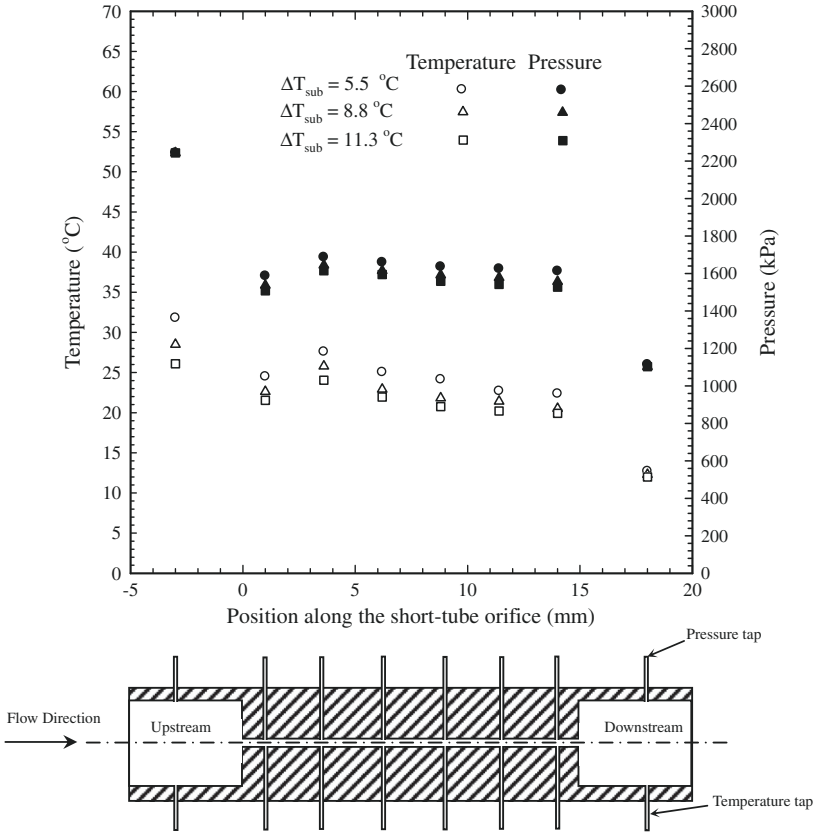

Fig. 6. Effect of degree of subcooling on the pressure and temperature distribution at D = 0.961 mm, L = 15 mm, P_{up} = 2250 kPa and P_{down} = 1100 kPa.

that the increase of the degree of subcooling leads to increases in the density and mass flow rate of refrigerant which result in an increase of pressure loss inside the short-tube orifice.

Considering the pressure and temperature distributions inside the short-tube orifice shown in Fig. 7, it is found that the long length of the short-tube orifice results in increases of recovery pressure and average pressure in the short-tube orifice; however it also leads to a slight decrease of downstream temperature. As mentioned above, it can be noted that the downstream temperature is slightly decreased by increasing the degree of subcooling and the length of the short-tube orifice, but increased by increasing the upstream pressure.

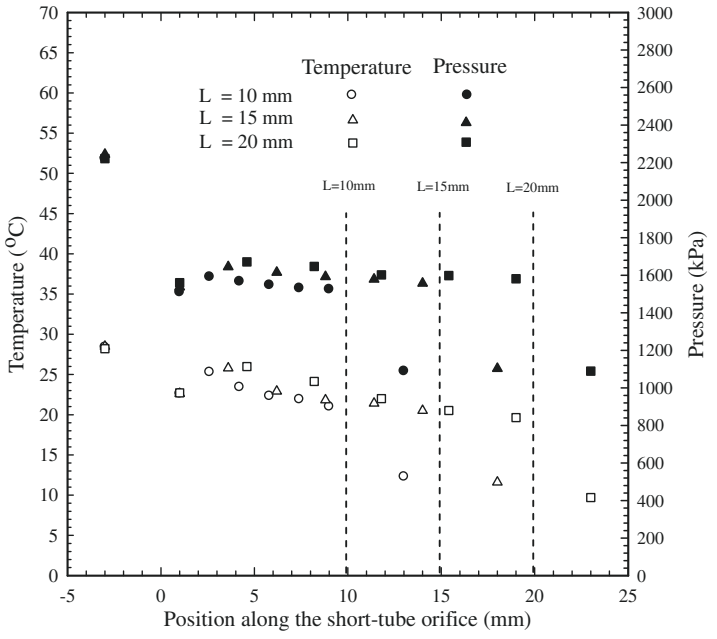

Fig. 7. Effect of short-tube orifice length on the pressure and temperature distribution at D = 0.961 mm, ΔT_{sub} = 7.8–8.5 °C, P_{up} = 2250 kPa and P_{down} = 1100 kPa.

3.2. Metastable flow phenomenon

Metastable flow is the flow phenomenon which occurs during the transition from liquid to vapour state according to a flashing process in the expansion device. In this section, the existence of metastable flow in the short-tube orifice is described.

In order to verify the existence of metastable flow, the relationship between pressure distribution and flow pattern inside the short-tube orifice is presented in Fig. 8. In the photograph of the flow pattern in the figure, the flow of liquid refrigerant is displayed by the bright (white) region, whereas the two-phase refrigerant flow is displayed by the dark (black) region. The increase of darkness level in the dark region represents the high level of quality. As shown in Fig. 8(a), it is found that the conical liquid refrigerant appears in a core of the tube while the other area is covered by the two-phase refrigerant, which consists of tiny bubbles mixed with liquid refrigerant and is similar to a mist. In addition, it is found that the darkness level in the dark region increases along the tube length, especially in the exit plane of the short-tube orifice.

As shown in Fig. 8(b), when the flow of refrigerant passes the entrance region, the measured pressure along the short-tube orifice is lower than the saturation pressure in response to the measured temperature. The result indicates that the refrigerant is in a superheated vapour state after it passes the entrance plane. That is, the subcooled liquid refrigerant ought to be evaporated at 1 mm from the entrance plane. However, after consideration of the flow pattern in Fig. 8(a), it is found that the refrigerant at the core of tube remains in the liquid state. This means that the vaporization of refrig-

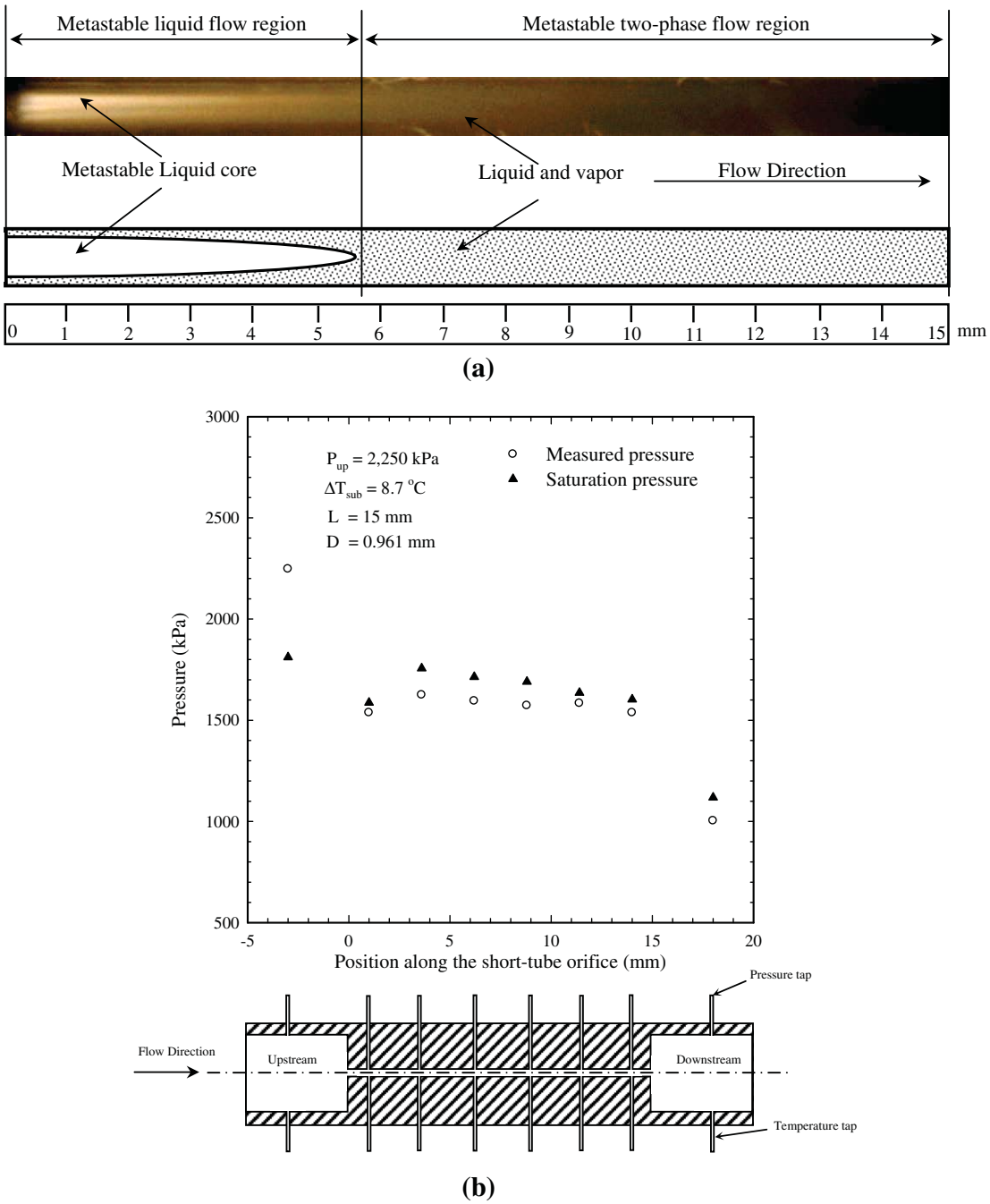

Fig. 8. Flow behaviour of HFC-410A along a short-tube orifice: (a) flow pattern and (b) pressure and temperature distribution.

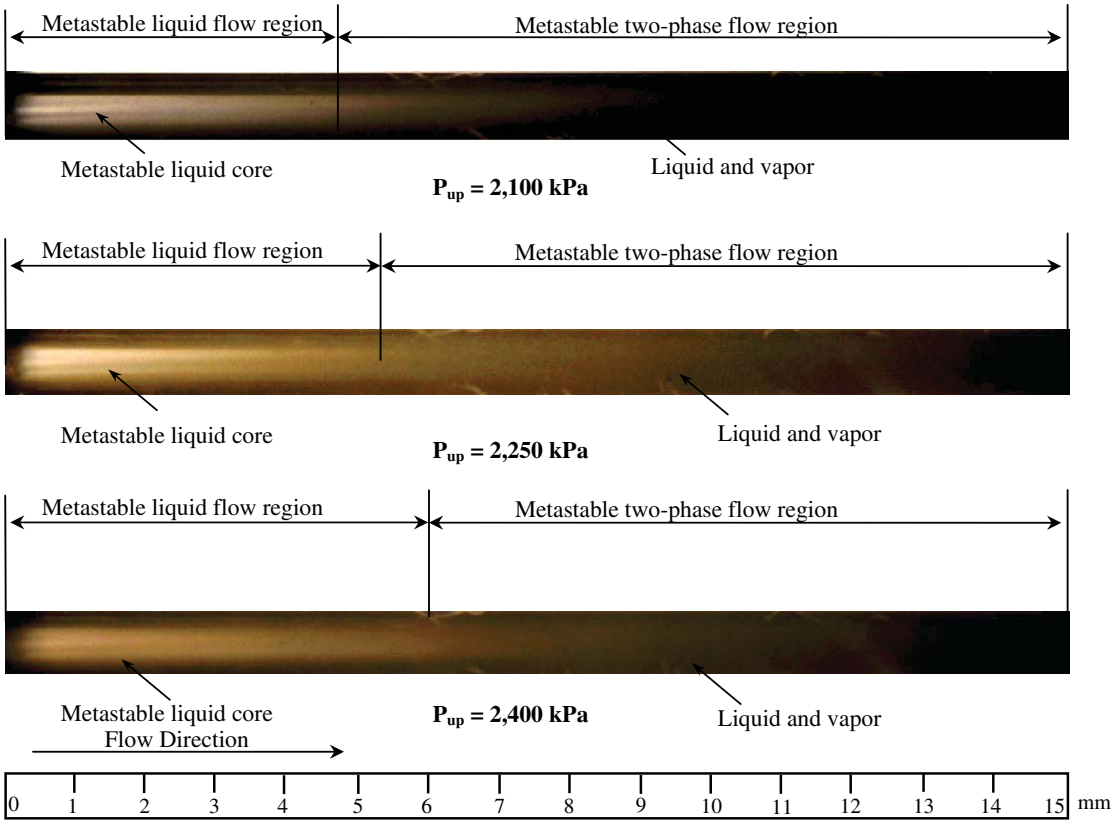

Fig. 9. Effect of upstream pressure on the flow pattern inside a short-tube orifice at $D = 0.961$ mm, $L = 15$ mm, $\Delta T_{sub} = 7.8–8.5$ °C and $P_{down} = 1100$ kPa.

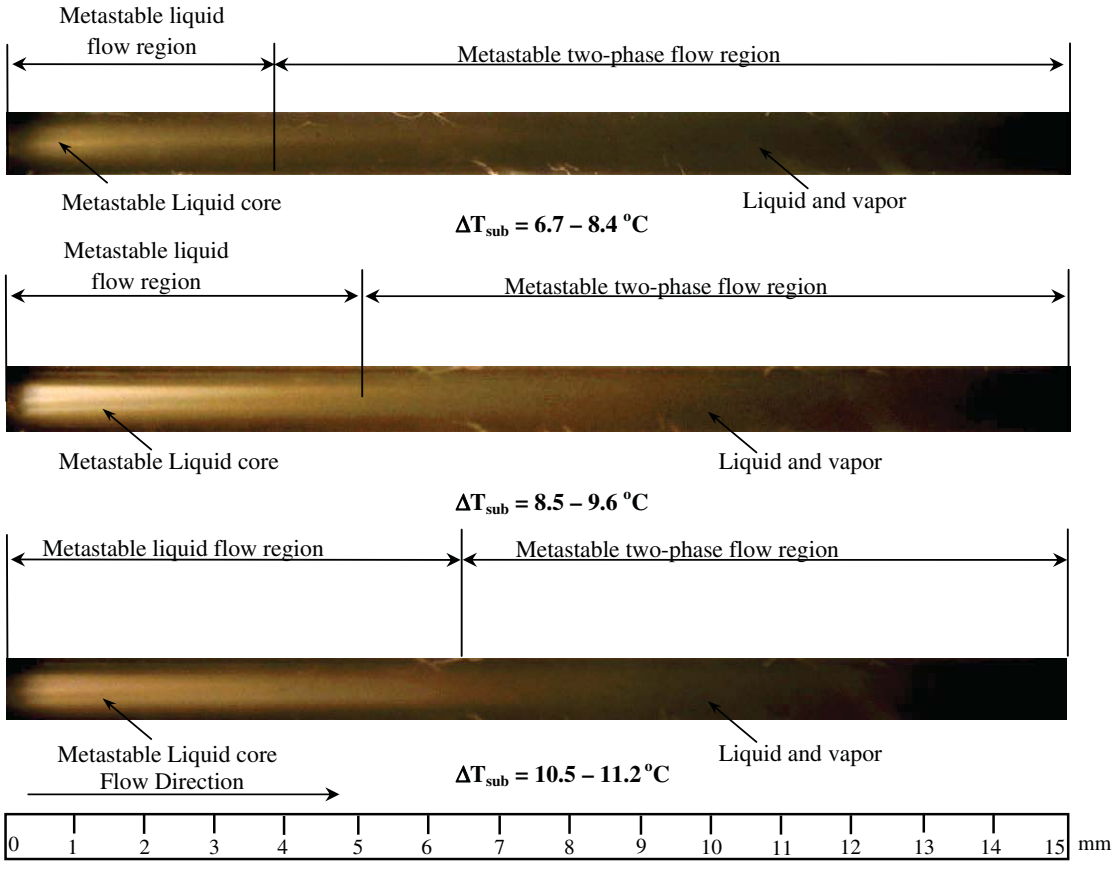

Fig. 10. Effect of degree of subcooling on the flow pattern inside a short-tube orifice at $D = 0.961$ mm, $L = 15$ mm, $P_{up} = 2250$ kPa and $P_{down} = 1100$ kPa.

erant is delayed and the flow of refrigerant inside the short-tube orifice exists under non-equilibrium thermodynamic conditions. Therefore, this flow region is called metastable liquid flow. On the other hand, when the entire flow area of the tube is covered by two-phase liquid–vapour refrigerant, it is called metastable two-phase flow. In order to identify the extent of the metastable liquid flow region, the image was magnified for clearness and the variations in the colour level of liquid refrigerant at the central core of the tube were observed by eye. The end point of metastable liquid flow length is the point where the dark region completely covers the flow area. The average length of metastable liquid flow represented in this paper is obtained from several repetitions.

Figs. 9 and 10 show the flow pattern of refrigerant inside the short-tube orifice which is changed by the upstream pressure and degree of subcooling, respectively. It is discovered that the length of the metastable liquid flow region is extended by increasing the upstream pressure and degree of subcooling. The reason for this is that the difference between upstream pressure and saturation pressure is increased as upstream pressure and degree of subcooling are increased. This means that the inception of flashing is delayed when the upstream pressure and degree of subcooling are increased.

3.3. Mass flow rate

Another purpose of the expansion device is to regulate the mass flow rate of refrigerant flowing from the condenser to the evaporator. In this section, the effects of operating conditions and short-

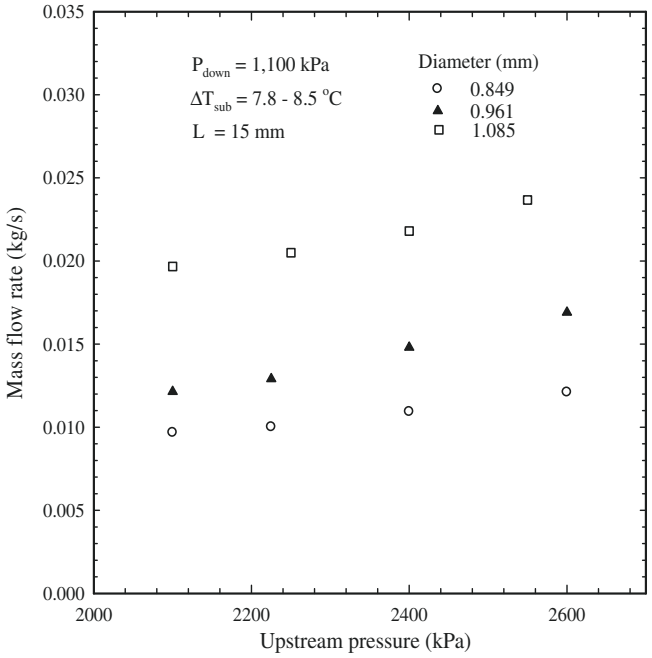

Fig. 11. Effect of upstream pressure on mass flow rate.

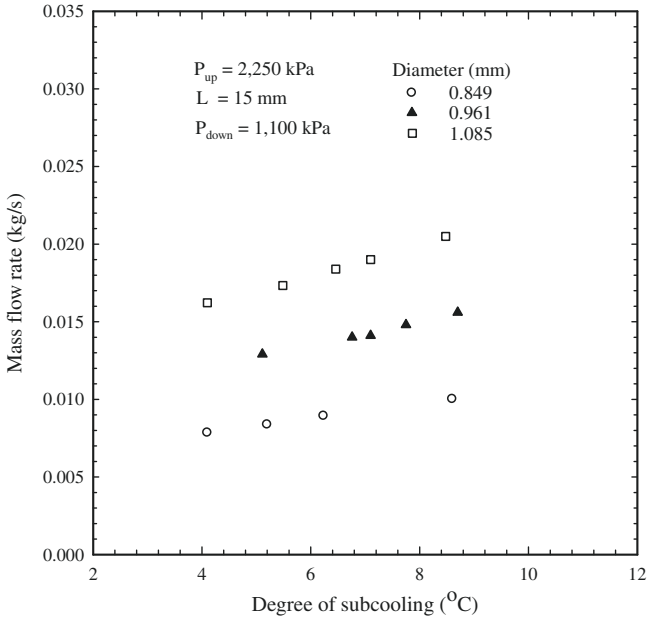

Fig. 12. Effect of degree of subcooling on mass flow rate.

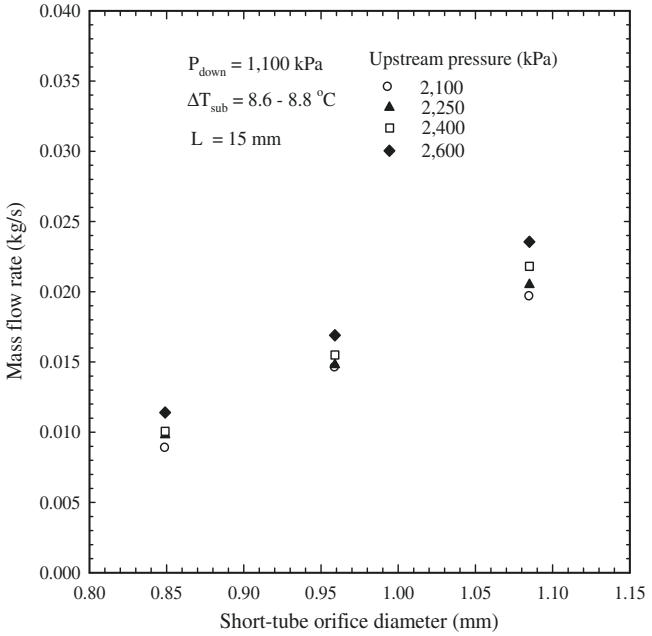

Fig. 13. Effect of short-tube orifice diameter on mass flow rate.

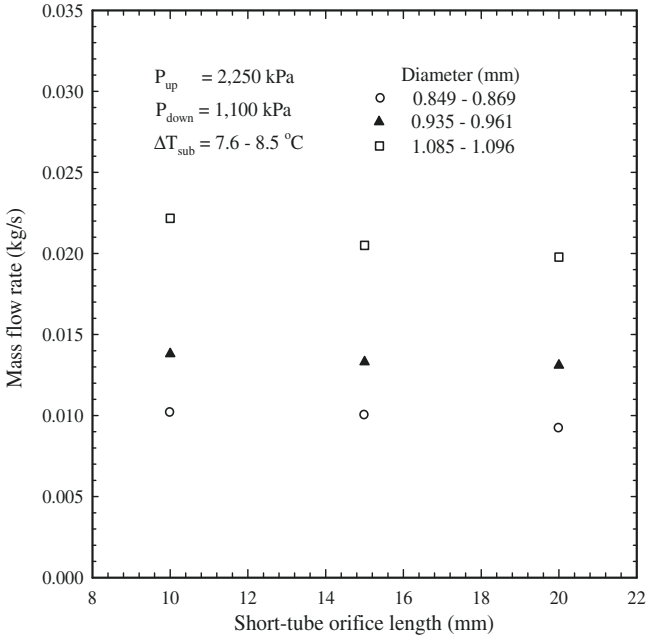

Fig. 14. Effect of short-tube orifice length on mass flow rate.

tube orifice dimensions on the mass flow rate of HFC-410A through short-tube orifices are described.

As shown in Fig. 11, it can be seen that the mass flow rate is increased when the upstream pressure is increased. In addition, it is found that the tendency in the data is dependent on short-tube diameter. That is, the data tendency is lifted when the upstream pressure is increased. The reason for this is that the refrigerant velocity is increased as the upstream pressure is increased, which is responsible for the increase in mass flow rate.

Fig. 12 shows the effect of the degree of subcooling on mass flow rate. The results show that increasing the degree of subcooling produces an increase in mass flow rate. However, it is discovered

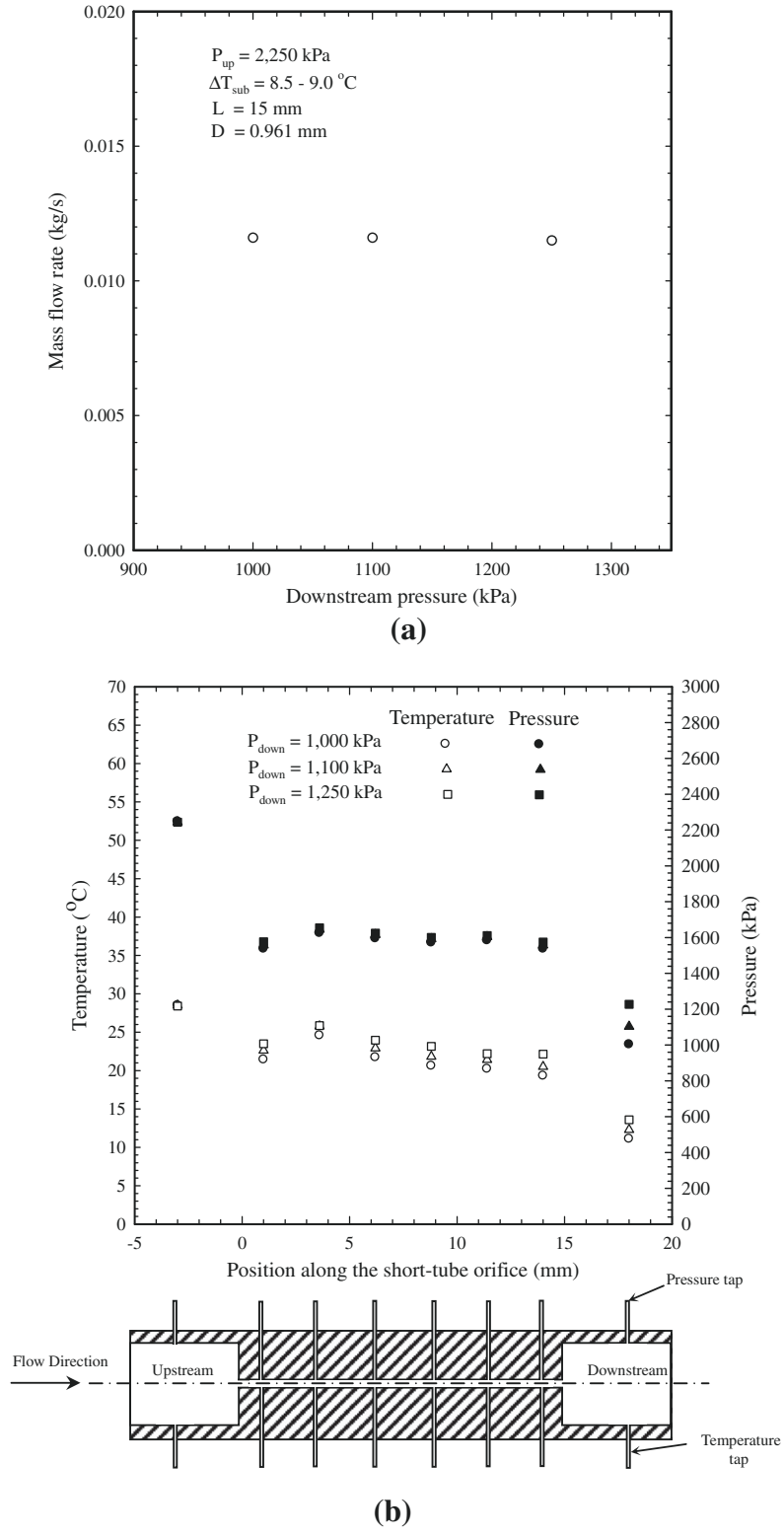

Fig. 15. Effect of downstream pressure on the flow mechanism of HFC-410A inside a short-tube orifice: (a) mass flow rate and (b) pressure and temperature distribution.

that the mass flow rate is related to short-tube diameter. This means that an increase of the short-tube diameter tends to lift the data tendency. This is due to the fact that the refrigerant density is increased as the degree of subcooling is increased. This impact causes the mass flow rate to be increased.

As shown in Fig. 13, the mass flow rate increases greatly as the short-tube orifice diameter is increased. The flow rate is found to change by an average of 173 kg/h/mm. This is because the cross-sectional area is expanded when the short-tube orifice diameter is increased.

The relationship between mass flow rate and short-tube orifice length is shown in Fig. 14. It can be seen that the mass flow rate decreases slightly when the shot-tube length is increased. The average variation of mass flow rate is 0.252 kg/h/mm. This is because the frictional pressure drop is increased when the shot-tube length is increased, which leads to a reduction of the flow rate.

3.4. Choked flow phenomenon

Choked flow is a limiting condition which occurs inside the short-tube orifice when the velocity of refrigerant reaches sonic velocity. Under this condition, the mass flow rate of refrigerant is restricted, although the downstream pressure is decreased. Therefore, this phenomenon is necessary for the flow of HFC-410A inside the short-tube orifice. In this section, the verification of choked flow inside the short-tube orifice is presented.

Considering the effect of downstream pressure on the mass flow rate, pressure distribution, and temperature distribution of HFC-410A in Fig. 15, it can be clearly seen that the mass flow rate and pressure distribution inside the short-tube orifice are nearly constant while the downstream pressure is decreased. Therefore, it can be confirmed that the flow of HFC-410A is choked inside the short-tube orifice. However, it is found that the temperature distribution inside the short-tube orifice is diminished by decreasing the downstream pressure. This flow behaviour is consistent with the results of past researches [4,6]. The results from this study indicate that choked flow appears over the entire range of experimental conditions.

4. Conclusion

This paper presents new experimental data of HFC-410A flow mechanisms, including the pressure distribution, temperature distribution, flow pattern, choked flow phenomenon, metastable flow and mass flow rate inside a short-tube orifice. The influences of upstream pressure, downstream pressure, degree of subcooling, and short-tube orifice length on the flow mechanisms are discussed. The following conclusions can be drawn from this study:

1. The flow pattern with which the liquid refrigerant flows in a conical form at the core of the tube, surrounded by tiny bubbles mixed in the liquid refrigerant, has been discovered inside short-tube orifices.
2. The pressure and temperature of refrigerant decrease rapidly in the entrance and exit regions. However, the pressure and temperature of the refrigerant increase only slightly over a short length and gradually decrease thereafter inside the short-tube orifice.
3. The mass flow rate increases in proportion when the upstream pressure and degree of subcooling are increased, but it is greatly increased by increasing the short-tube diameter.
4. The mass flow rate and pressure distribution inside a short-tube orifice are nearly constant as the downstream pressure is varied. However, the temperature distribution of the refrigerant inside a short-tube orifice is slightly decreased when the downstream pressure is decreased.

Acknowledgements

The authors would like to express their appreciation to the Thailand Research Fund (TRF) and the Office of Higher Education Commission for providing financial support for this study. The authors also wish to thank Mr. Chiatta Supawarasuwat of C-Aircon Tech Company for the valuable donation of the short-tube orifices used in the present study.

References

[1] P.F. Pasqua, Metastable flow of Freon-12, Refrig. Eng. 61 (1953) 1084–1088.
[2] A.A. Aaron, P.A. Domanski, Experimentation analysis and correlation of refrigerant-22 flow through short tube restrictors, ASHRAE Trans. 96 (1990) 29–742.
[3] Y. Kim, Two-phase flow of HFC134a and HCFC22 through short tube orifices, Ph.D. thesis, Texas A&M University, USA, 1993.
[4] K. Nilpueng, S. Wongwises, Experimental investigation of two-phase flow characteristics of HFC-134a through short-tube orifices, Int. J. Refrig. 32 (2009) 854–864.
[5] J.P. Liu, Y.M. Niu, J.P. Chen, Z.J. Chen, X. Feng, Experimental and correlation of R744 two-phase flow through short tubes, Exp. Therm. Fluid Sci. 28 (2004) 565–573.
[6] K. Nilpueng, S. Wongwises, Flow pattern, mass flow rate, pressure distribution, and temperature distribution of two-phase flow of HFC-134a inside short-tube orifices, Int. J. Refrig. 32 (2009) 1864–1875.
[7] V.C. Mei, Short tube refrigerant flow restrictors, ASHRAE Trans. 88 (1982) 157–169.
[8] Y.C. Kim, D.L. O'Neal, Refrigerant flow through flexible short tube orifices, HVAC Res. 8 (2002) 179–190.
[9] G.M. Singh, P.S. Hrnjak, C.W. Bullard, Flow of refrigerant R134a through orifice tubes, Int. J. HVAC Res. 7 (2001) 245–262.
[10] X. Tu, P.S. Hrnjak, C.W. Bullard, Refrigerant 134a liquid flow through micro-scale short tube orifices with/without phase change, Exp. Therm. Fluid Sci. 30 (2006) 253–262.
[11] W.V. Payne, D.L. O'Neal, Mass flow characteristics of R407C through short-tube orifices, ASHRAE Trans. 104 (1998) 197–209.
[12] Y. Kim, V. Payne, J. Choi, P. Domanski, Mass flow of R410A through short tube working near the critical point, Int. J. Refrig. 28 (2005) 547–553.

International Journal of Heat and Mass Transfer 53 (2010) 4023–4038

Contents lists available at ScienceDirect

International Journal of Heat and Mass Transfer

journal homepage: www.elsevier.com/locate/ijhmt

Flow pattern and heat transfer characteristics of R-134a refrigerant during flow boiling in a horizontal circular mini-channel

Sira Saisorn [a,c], Jatuporn Kaew-On [b,c], Somchai Wongwises [c,*]

[a] King Mongkut's Institute of Technology Ladkrabang Chumphon Campus, Chumphon 86160, Thailand
[b] Department of Physics, Faculty of Science, Thaksin University, Phattalung, Thailand
[c] Fluid Mechanics, Thermal Engineering and Multiphase Flow Research Lab. (FUTURE), Department of Mechanical Engineering, King Mongkut's University of Technology Thonburi, Bangmod, Bangkok 10140, Thailand

ARTICLE INFO

Article history:
Received 17 November 2009
Received in revised form 16 April 2010
Accepted 16 April 2010
Available online 9 June 2010

Keywords:
Flow boiling
Mini-channel
Flow pattern
Heat transfer

ABSTRACT

Flow boiling heat transfer of R-134a refrigerant in a circular mini-channel, 600 mm long with a diameter of 1.75 mm, is investigated experimentally in this study. The test section is a stainless steel tube placed horizontally. Flow pattern and heat transfer coefficient data are obtained for a mass flux range of 200–1000 kg/m^2 s, a heat flux range of 1–83 kW/m^2 and saturation pressures of 8, 10, and 13 bar. Five different flow patterns including slug flow, throat-annular flow, churn flow, annular flow and annular-rivulet flow are observed and the heat transfer coefficient data for different flow patterns are presented. The heat transfer coefficient increases with increasing heat flux but is mostly independent of mass flux and vapour quality. In addition, it is indicated from the experiments that the higher the saturation pressure, the lower is the heat transfer coefficient. Comparisons of the present data with the existing correlations are also presented.

© 2010 Elsevier Ltd. All rights reserved.

1. Introduction

Research on two-phase compact heat exchangers has gained increasing attention over the years because of the advantages of using small channels as summarised in Ribatski et al. [1]. Definitions for various channels have been given by several investigators who proposed channel classifications which are often based on different dimensionless parameters. For instance, arbitrary channel classifications associated with the hydraulic diameter D_h have been proposed. Mehendale et al. [2] employed the hydraulic diameter as an important parameter for defining heat exchangers and Kandlikar [3] proposed criteria for small flow channels used in engineering applications. Most of the criteria based on the hydraulic diameter, however, cannot relate the channel diameter to fluid flow mechanisms. Regarding the experimental data obtained from flow visualisation studies in small channels, Chung and Kawaji [4] found that diameters between 100 and 250 μm seemed to be in the range corresponding to mini-to-micro-scale transitions. Their findings were also confirmed by Saisorn and Wongwises [5]. According to existing criteria which are unclear, further investigation is still required to meet a more general definition dealing with channel classification.

Two-phase flow of refrigerants during flow boiling in ordinarily sized channels has been investigated by various investigators. Greco [6], for instance, conducted experiments to study the major parameters affecting the heat transfer characteristics. The results of more than 2000 data points were obtained based on 250 different operating conditions. The effects of vapour quality, heat flux mass flux, saturation temperature and thermo-physical properties on the heat transfer behavior were analyzed in detail. Compared to the reported two-phase flow and heat transfer characteristics in ordinarily sized channels, which are available in a relatively large number of publications, flow boiling phenomena in mini- and micro-channels tend to show different behaviors due to the effects of the limited and confined space. Also, a scaling analysis of different forces, as discussed in Kandlikar [7], pointed out that surface tension and evaporation momentum forces were significant for two-phase flow phenomena at micro-scale. Although some relevant information is currently available in the literature, a complete understanding has not yet been clarified with regard to the trends and parameters dominating the phase-change heat transfer mechanism in these small-scale channels.

In what follows, recent studies associated with flow boiling heat transfer in small channels are briefly outlined.

Brutin and Tadrist [8] carried out experiments on flow boiling in a rectangular mini-channel with hydraulic diameter of 0.89 mm to investigate the two-phase flow stability. They indicated that a maximum value of the average heat transfer coefficient was obtained under the unsteady state regime. The stability criterion was found to be dependent upon heat flux and mass flow rate.

* Corresponding author. Tel.: +66 2 470 9115; fax: +66 2 470 9111.
E-mail address: somchai.won@kmutt.ac.th (S. Wongwises).

0017-9310/$ - see front matter © 2010 Elsevier Ltd. All rights reserved.
doi:10.1016/j.ijheatmasstransfer.2010.05.022

Nomenclature

B_o	Boiling number, $B_o = q/Gi_{LG}$
C	constant
C_{CO}	convection number, $C_{CO} = (\rho_G/\rho_L)^{0.5}((1-x)/x)^{0.8}$
C_o	confinement number
C_p	specific heat at constant pressure (J/kg K)
D	channel diameter (m)
D_b	capillary length (m)
D_h	hydraulic diameter (m)
F	two-phase convection multiplier
F_{Fl}	fluid-surface parameter
f	fanning friction factor
G	mass flux (kg/m^2 s)
h	heat transfer coefficient (W/m^2 K)
i	specific enthalpy (J/kg)
i_{LG}	latent heat of vapourisation (J/kg)
j	superficial velocity (m/s)
k	thermal conductivity (W/mK)
M	molecular weight (kg/kmol)
MAE	mean absolute error, $\mathrm{MAE} = \frac{1}{N}\sum_1^N \left(\frac{\lvert h_{\mathrm{pre}} - h_{\mathrm{mea}}\rvert}{h_{\mathrm{mea}}} \times 100\right)$
N	number of experimental data
Nu	Nusselt number, $Nu = hD_h/k$
P	pressure (Pa)
P_r	reduced pressure
Pr	Prandtl number, $Pr = \mu C_p/k$
ΔP_{sat}	saturation pressure difference (Pa)
q	heat flux (W/m^2)
Re	Reynolds number, $Re = GD_h/\mu$
S	nucleate boiling suppression factor
T	temperature (°C)
ΔT_{sat}	wall superheat (K)
We	Weber number, $We = G^2 D_{\mathrm{h}}/\rho\sigma$
x	vapour quality

Greek symbols

χ	Lockhart–Martinelli parameter
φ^2	two-phase frictional multiplier
μ	dynamic viscosity (Ns/m^2)
ρ	density (kg/m^3)
σ	surface tension (N/m)

Subscripts

A	annular flow
avg	average
CB	coalescing bubble flow
CBC	convection boiling contribution
G	vapour phase
GO	all-vapour
IB	isolated bubble flow
L	liquid phase
LO	all-liquid
mea	experimental value
NBC	nucleate boiling contribution
pre	predicted value
sat	saturation
wall,in	inner wall

Huo et al. [9] studied experimentally boiling heat transfer of R-134a fluid in small vertical tubes of 2.01 and 4.26 mm in diameter. In the low vapour quality range, the heat transfer coefficient in both tubes increased with increasing heat flux and saturated pressure but was independent of vapour quality. These results were attributed to nucleate boiling being the dominant heat transfer mode. In other ranges of vapour quality, however, the dominant heat transfer mode was not addressed as a result of inconsistency in the experimental data. Under the same controlled conditions, they found that the nucleate boiling heat transfer coefficient was higher for the 2.01 mm tube than for the 4.26 mm tube.

Flow boiling heat transfer characteristics in micro-channels of 540 mm length with 25 circular flow channels of 0.81 mm diameter were investigated by Pettersen [10]. They reported that the increase in heat flux resulted in higher heat transfer coefficient, which could be explained according to the dominant role of nucleate boiling over the low/moderate vapour quality region. Another point observed was that the dry-out temperature became much more significant at higher mass flux and temperature, resulting in a rapidly reduced heat transfer coefficient at high vapour qualities. Besides, pressure drop increased with mass flux and vapour quality but decreased as temperature increased. The comparison of measured data and various correlations was also discussed.

Yun et al. [11] were concerned with flow boiling heat transfer characteristics in rectangular multi-channels with hydraulic diameters ranging from 1.08 to 1.54 mm. Working fluids tested were CO_2 and R-134a. Generally, the average heat transfer coefficient of CO_2 increased around 53% when compared with that of R-134a. The influences of heat flux on the heat transfer coefficient were much more obvious for CO_2 than for R-134a. Dry-out phenomenon was promoted with an increase in mass flux and it was also noted that the effects of mass flux on heat transfer coefficient were less significant than those of heat flux. As expected, heat transfer coefficient increased with a decrease in the hydraulic diameter.

Heat transfer of R-134a refrigerant during flow boiling in horizontal tubes with different diameters including 0.51, 1.12 and 3.1 mm was studied experimentally by Saitoh et al. [12]. Nucleate boiling was reported in the low vapour quality region whereas convective evaporation was dominant in the high vapour quality region. The latter mechanism was found to be less dominant as the tube diameter decreases. The smaller the tube diameter, the higher is the effect of saturation temperature on the heat transfer coefficient. The flow instability was also discussed in this work.

Evaporation heat transfer in horizontal mini-channels was studied experimentally by Lie et al. [13]. A diameter of 0.83 or 2 mm was used for each channel and the working fluids were R-134a and R-407C. The effects of mass flux, vapour quality, saturation temperature and heat flux on the heat transfer coefficient were investigated. Under given experimental conditions, the use of R-407C gave a higher heat transfer coefficient than R-134a.

The experiments with flow boiling of water in a vertical circular tube having a diameter of 1.5 mm were performed by Boye et al. [14]. The wall temperatures of the tube in which the water flows upward were measured using infrared thermography. Nucleate boiling and convective boiling mechanisms were observed in the experiments.

Choi et al. [15] reported the heat transfer characteristics of CO_2 through horizontal mini-channels having diameters of 1.5 and 3 mm. They indicated that nucleate boiling was predominant in the low vapour quality region and a convective boiling heat transfer contribution appeared in moderate and high vapour quality regions. The variation of local heat transfer coefficient with heat flux, mass flux, vapour quality and saturation temperature was discussed. A more active nucleate boiling was addressed when the tube with smaller diameter was used. Flow boiling heat

transfer of different refrigerants was continually carried out by Choi et al. [16]. They indicated that the use of CO_2 caused the heat transfer coefficient to be higher than that of R-134a and R-22.

Shiferaw et al. [17] compared their flow boiling data with existing correlations. The data points were obtained from experiments with R-134a flowing through small tubes having diameters of 4.26 and 2.01 mm. The comparisons revealed that the existing correlations did not predict well their data. Comments and suggestions were provided by the authors for further development of the prediction. Similar experiments were conducted by Shiferaw et al. [18] to compare the results obtained from a 1.1 mm diameter tube with the three-zone flow boiling model developed by Thome et al. [19] and Dupont et al. [20]. Generally, the model predicted well the experimental data, especially at relatively low pressure. Regarding the heat transfer characteristics, an insignificant influence of mass flux and vapour quality was observed while the heat transfer coefficient increased with increasing heat flux and saturation pressure.

Three different refrigerants, R-134a, R-236fa and R-245fa, were tested for flow boiling in a 1.03 mm diameter tube by Ong and Thome [21]. The trends of the data were investigated, showing that the heat transfer coefficient depended on heat flux at low vapour qualities and on mass flux at high vapour qualities. Regarding the refrigerants tested at low vapour qualities, R-134a gave the highest heat transfer coefficient followed by R-236fa and R-245fa, respectively.

From the above review of the literature, relatively little information has been reported on flow boiling in mini-channels under high mass flow conditions ($G > 500$ kg/m^2 s) and the detailed investigations concentrating on the relevance of the two-phase flow structures to the heat transfer characteristics are still lacking. The main objective of the present work is therefore to extend the database to high mass flux conditions corresponding to a value of up to around 1000 kg/m^2 s. In this paper, the typical features of the flow patterns and the relevant heat transfer characteristics are described. The present data will subsequently be compared with prediction methods of different researchers.

2. Experimental apparatus and procedure

The present experimental apparatus, which is modified from that developed by Kaew-On and Wongwises [22] and is shown schematically in Fig. 1, is designed to investigate flow boiling of R-134a in a circular mini-channel placed horizontally. The main components of the system include a test section, refrigerant loop, sub-cooling loop, and a data acquisition system.

For the refrigerant circulating loop, as seen in Fig. 1, liquid refrigerant is pumped by a gear pump which can be regulated by means of an inverter. The refrigerant then passes in series through a filter/dryer, a refrigerant flow meter, pre-heater, sight glass tube, and enters the test section. The inlet quality before entering the test section is controlled by the pre-heater with a DC power supply used to apply heat. Leaving the test section, the refrigerant vapour subsequently condenses in a sub-cooler and then is collected in a receiver; it eventually returns to the refrigerant pump to complete the cycle. Instrumentation is installed at various positions, as shown in Fig. 1, to monitor the state of the refrigerant. All the signals from the thermocouples and differential pressure transducer are recorded by a data logger.

Fig. 2 shows a schematic diagram of the test section, a stainless steel tube which is 600 mm long and 1.75 mm in diameter. The regulated DC power supply generating 80 A at 12 V is used to apply heat to the test section. The voltage and electric current values are measured by a multimeter (Fluke 336 meter) which has an uncertainty of ±2% for voltage and ±1% for current. T-type thermocouples are installed at the inlet and outlet of the test section to measure the system temperature. The 10 thermocouples are installed on the top and bottom sides at equal distances along the tube to measure the wall temperature. All thermocouples on the tube surface are fixed with special glue. The test section is well insulated by using rubber foam with a thermal conductivity of 0.04 W/mK. A variable area type flow meter is specially calibrated in the range 0.02–0.2 LPM for R-134a by the manufacturer. All thermocouples,

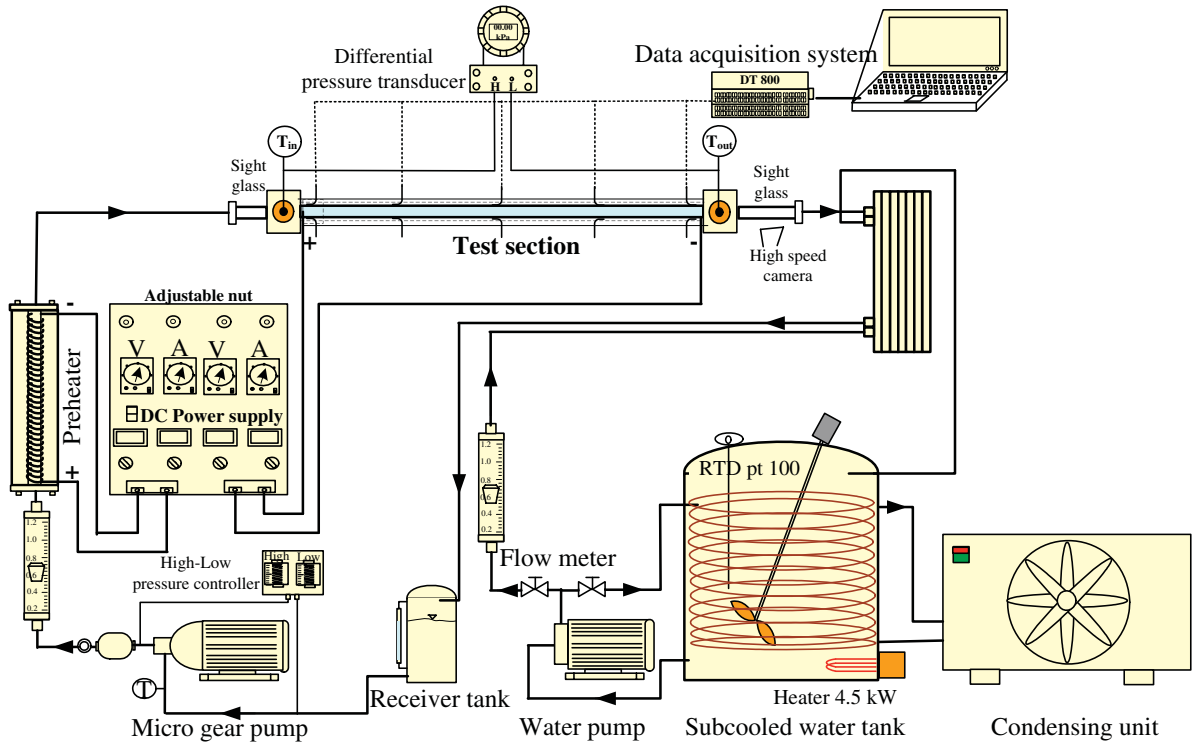

Fig. 1. Schematic diagram of experimental apparatus.

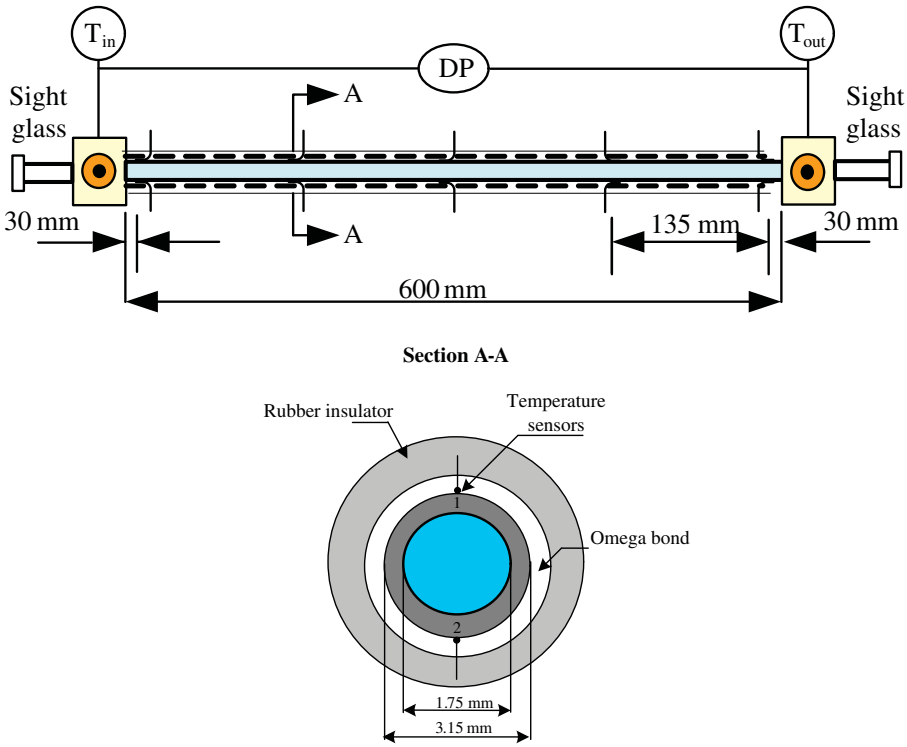

Fig. 2. Schematic diagram of test section.

differential pressure transducer and relevant instruments installed in the experimental apparatus are well calibrated.

A 1.75 mm diameter transparent tube is installed to match up with the test section outlet and to serve as a viewing window for flow visualisation. The detailed formation of each flow pattern is registered by a high quality camera (Fujifilm FinePix S7000) having shutter speeds of 1/15 to 1/10,000 s. The camera together with an adjustable light source consisting of 150 W halogen lamp and dimmer are placed horizontally and normal to the viewing section.

In this work, the experiments are conducted in such a way that the heat applied to the test section is varied by small increments, while the refrigerant flow rate, saturation pressure, and inlet vapour quality in the test section are kept constant at the desired value. The system is allowed to approach a steady state before the flow pattern and relevant data are recorded. During the experiment, the temperature and pressure drop are continuously recorded along the test section by the data logger. The profiles of the temperature help us to know the limit of useful data because a large increase in wall temperature and outlet saturation temperature is observed when dry-out occurs. The range of experimental conditions is presented in Table 1. The uncertainties in the measured quantities and calculated parameters are shown in Table 2.

Table 1
Experimental conditions.

Refrigerant	R-134a
Diameter (mm)	1.75
Length (mm)	600
Mass flux (kg/m^2 s)	200–1000
Heat flux (kW/m^2)	1–83
Saturation pressure (bar)	8–13
Test section material	Stainless steel

Table 2
Uncertainties of measured quantities and calculated parameters.

Parameter	Uncertainty
Temperature	±0.1 (°C)
Mass flow rate of refrigerant	±0.1 **(%)** full scale
Heat transfer rate of test section	±2.25%
Heat transfer rate of pre-heater	±2.25%
Heat transfer coefficient	±8.12%

3. Results and discussion

3.1. Flow pattern

Flow pattern is expected to influence the heat transfer and flow characteristics during the phase-change heat transfer process. A clear understanding of the flow patterns encountered as well as the ability to accurately predict the type of flow are necessary before relevant calculation techniques can be developed. Flow visualisation studies for small channels such as micro- and mini-channels have been carried out by different investigators. A number of the studies concern with flow patterns for gas–liquid flow in small channels and the others concern with those for phase-change process. The flow visualisation for gas–liquid flow in mini- or micro-channel is also considered to be a tool for studying the two-phase flow characteristics because it is not very difficult to control the flow conditions. Gas–liquid flow phenomena are found to be compatible with flow mechanisms based on phase-change process in different aspects. In small channels, for instance, Saisorn and Wongwises [5] indicated that their frictional pressure drop data associated with two-phase gas–liquid flow were fairly predicted by the Muller-Steinhagen and Heck correlation [23] which is working for refrigerants under certain conditions. They also reported the fair agreement between their gas–liquid flow pattern data and the transition lines of Garimella et al. [24] for condensation flow. According to the previous discussion, the present flow

pattern data, which corresponds to flow boiling phenomena, will be subsequently compared with those obtained from gas–liquid flow data to check for the compatibility. The data of Triplett et al. [25] were chosen because of their tube diameter which is comparable to the present one.

In the present study, the boiling flow pattern observations are carried out at system pressures of 8 and 10 bar. The superficial velocities of gas and liquid vary from 0.69 to 16.60 m/s and 0.01 to 0.81 m/s, respectively. By keeping the refrigerant flow rate, saturation pressure and inlet vapour quality constant at a desired value, and increasing the imposed heat flux to the test section by small increments, typical photographs are obtained from the viewing window located downstream of the test section as shown in Fig. 3. The observations show that five different flow patterns are indicated as follows.

Slug flow: elongated bubbles which are larger in length than the channel diameter are developed from small bubbles.

Throat-annular flow: the two consecutive elongated bubbles coalesce into a throat-like gas core.

Churn flow: a disruptive region develops due to the distortion of the elongated bubbles.

Annular flow: liquid film flows on the tube wall and the tube core is occupied by continuous vapour flow.

Annular-rivulet flow: annular flow is observed alternately with flowing of a rivulet-like liquid stream on the tube surface.

It should be noted that peculiar flows such as throat-annular flow and annular-rivulet flow, which have never been observed in ordinarily sized channels, are also reported by Saisorn and Wongwises [26]. However, some discrepancies are normally observed because the present flow patterns are generated by the flow boiling process not by the adiabatic two-phase gas–liquid system used in their experiments.

The usual method in the presentation of flow pattern data is to classify the flow pattern by visual observation and plot the data as a flow pattern map in terms of system parameters. Figs. 4 and 5 illustrate the flow pattern maps which are presented in the superficial velocity of liquid (j_L) versus superficial velocity of vapour (j_G) format. The phase superficial velocities are determined as follows:

$$j_G = \frac{xG}{\rho_G} \tag{1}$$

$$j_L = \frac{(1-x)G}{\rho_L} \tag{2}$$

where x is vapour quality, G is mass flux, ρ_G is vapour density, and ρ_L is liquid density.

The present data are compared with the flow pattern transitions obtained by Triplett et al. [25] for two-phase air–water flow through a 1.45 mm diameter channel. The solid lines along with the flow pattern names indicated on these figures refer to their transition boundaries. In general, the comparisons show inconsistencies between the flow pattern map established from two-phase gas–liquid flow and that from flow boiling. Such inconsistencies were also reported by Martin-Callizo et al. [27] who conducted the visualisation of R-134a during flow boiling in a vertical tube with a diameter of 1.33 mm. Their test section is made from a quartz glass tube coated externally by indium tin oxide (ITO)

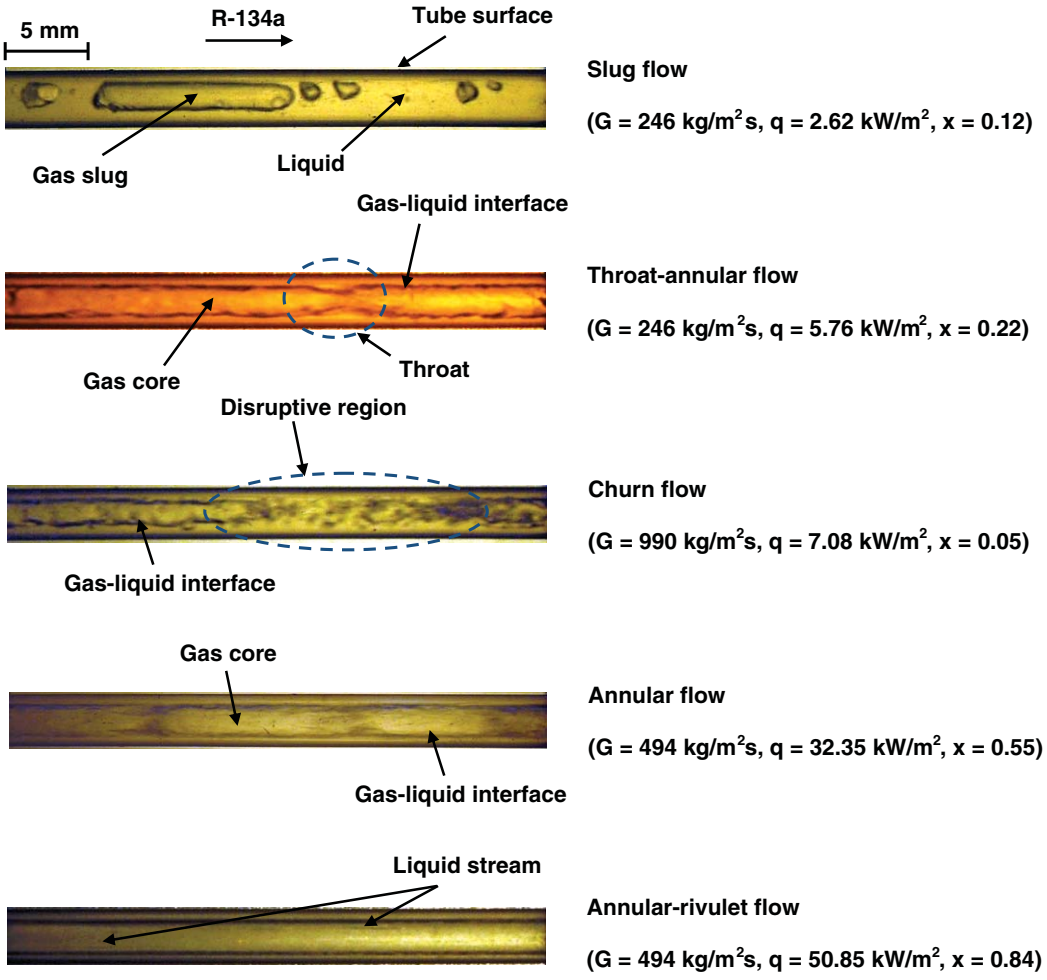

Fig. 3. Flow patterns in flow boiling of R-134a through a 1.75 mm diameter channel under system pressure of 8 bar.

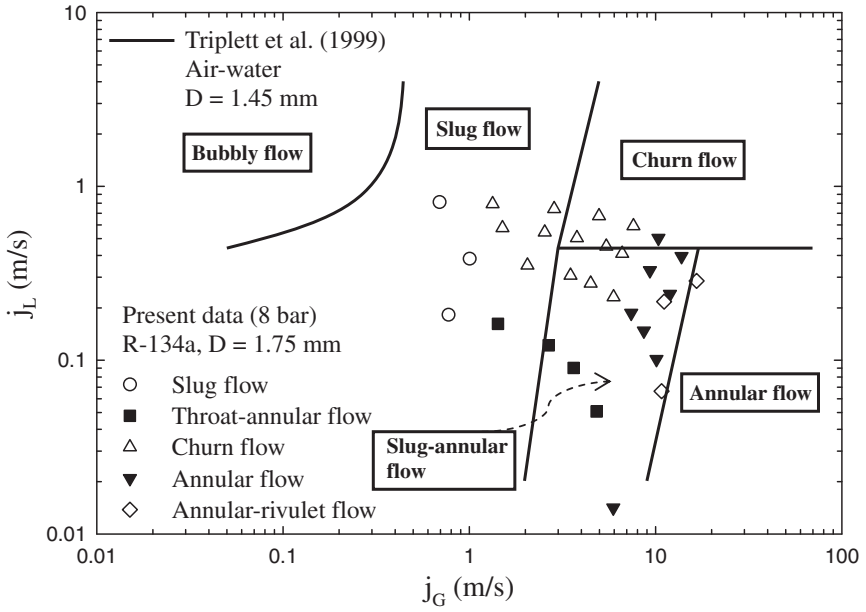

Fig. 4. Comparison of the observed flow patterns at 8 bar with the transition lines by Triplett et al. [25].

which is served as the resistive coating over which a potential difference generated by a DC power supply is applied. Their flow pattern data were also compared with the transition lines of Triplett et al. [25], indicating that the agreement is not satisfactory.

The disagreement can be explained by (i) for gas–liquid flow, the working fluids such as an air–water mixture possess thermophysical properties that are substantially different from the refrigerants used in flow boiling process, (ii) flow patterns generated by an air–water flow system may be possibly based on hydrodynamics of the upstream gas–liquid mixer design, and (iii) the effect of evaporation of the liquid phase taking place in the gas–liquid system could be quite significant in small channels as indicated by Kandlikar [3].

In addition, when the system pressure increases as seen in Fig. 5, a decrease in surface tension results in a degradation of throat-annular flow, especially at high vapour quality.

Recently, a new type of two-phase flow pattern map for flow boiling in micro-channels was developed by Revellin and Thome [28]. The proposed flow regime map comprises different zones according to the bubble coalescence phenomena. The followings are a brief description of each zone located in the flow map.

The isolated bubble (IB) regime corresponds to a relatively high bubble generation rate when compared with the bubble coalescence rate. Either or both of bubbly flow and slug flow are included in this regime. The coalescing bubble (CB) regime is defined when the bubble generation rate is smaller than the bubble coalescence rate.

The isolated bubble (IB) flow to coalescing bubble (CB) flow transition is given by

$$x_{IB/CB} = 0.763\left(\frac{Re_{LO}B_o}{We_{GO}}\right)^{0.41} \tag{3}$$

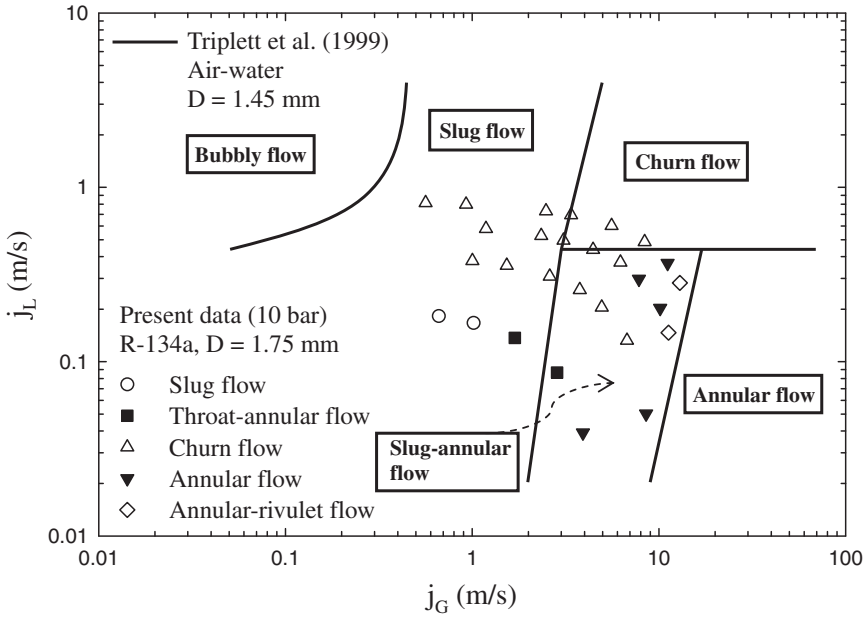

Fig. 5. Comparison of the observed flow patterns at 10 bar with the transition lines by Triplett et al. [25].

where B_o stands for Boiling number, Re_{LO} represents all-liquid Reynolds number and We_{GO} is all-vapour Weber number.

The transition from coalescing bubble flow to annular flow is determined by

$$x_{CB/A} = 0.00014 Re_{LO}^{1.47} We_{LO}^{-1.23} \quad (4)$$

where We_{LO} is all-liquid Weber number.

This correlation takes into account different effects including heat flux, viscosity and surface tension which are represented, respectively, by Boiling number, Reynolds number and Weber number.

The present flow pattern maps in terms of mass flux and vapour quality are presented in Figs. 6 and 7 which are compared with their transition zones. It is found that, in general, the present data correspond well with the transition zones proposed by Revellin and Thome [28]. The regions of churn flow and throat-annular flow obtained from the present study agree fairly well with their coalescing bubble regime whereas our annular flow and annular-rivulet flow are located in their annular region. The present slug flow data are found near the transition zone between their isolated bubble and coalescing bubble regions.

3.2. Flow boiling heat transfer

During two-phase heat transfer experiments, the flow rate, system pressure and inlet vapour quality were set to the desired value and the imposed heat flux was then varied by small increments until dry-out, noticed by a large increase in wall temperature and outlet saturation temperature.

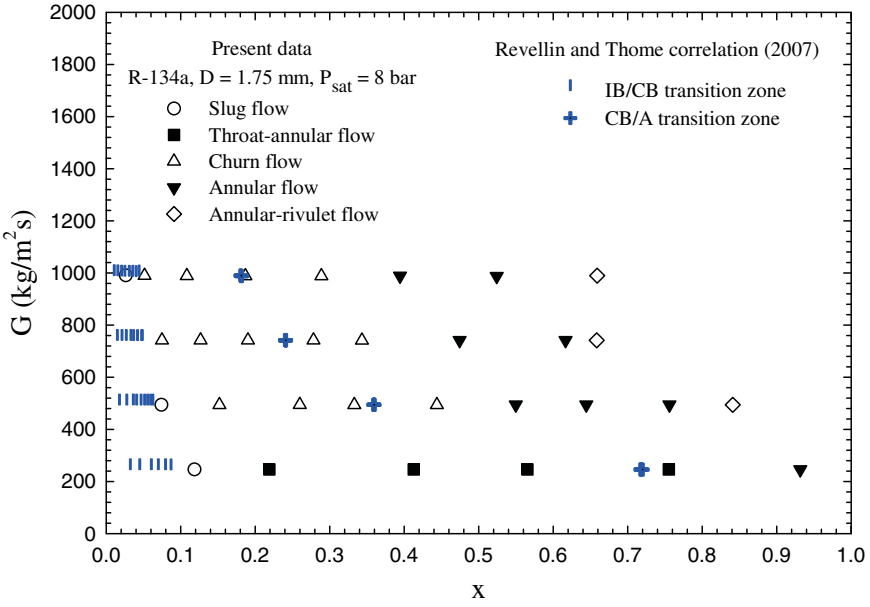

Fig. 6. Comparison of the observed flow patterns at 8 bar with the transition lines by Revellin and Thome correlation [28].

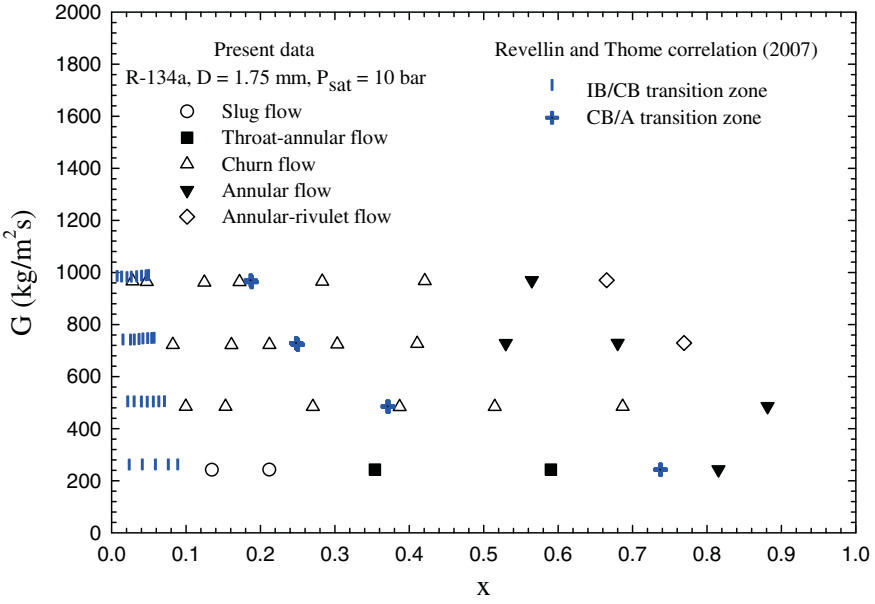

Fig. 7. Comparison of the observed flow patterns at 10 bar with the transition lines by Revellin and Thome correlation [28].

3.2.1. Local heat transfer coefficient

Heat flux, q, transferred to the test section is provided by the regulated DC power supply generating 80 A at 12 V. T-type thermocouples are installed at the inlet and outlet of the test section to measure the refrigerant temperatures. Since, during experiments, the two-phase conditions for flow boiling are provided at the test section inlet by using pre-heater as shown in Fig. 1, the saturation pressures at the test section inlet and outlet are obtained based on the corresponding saturation temperatures. Regarding the assumption of a linear variation of the saturation pressure along the tube, the local saturation temperatures, $T_{sat,loc}$, can subsequently be obtained.

As presented in Fig. 2, the 10 T-type thermocouples are installed on the top and bottom sides at equal distances along the tube to measure the tube surface temperature. For each position where the thermocouple is installed on the tube surface, the inner wall temperature at a given position is determined using the equations for steady-state one-dimensional heat conduction through the tube wall with internal heat generation. At a given distance, hence, the average temperature of the inner wall at the top and bottom sides stands for the local temperature on the inner wall, $T_{wall,in,loc}$. Finally, the local heat transfer coefficient, h_{loc}, for flow boiling of R-134a along the test section is determined using the following equation:

$$h_{loc} = \frac{q}{(T_{wall,in,loc} - T_{sat,loc})} \tag{5}$$

The local vapour quality is determined based on thermodynamic properties, i.e.

$$x = \frac{(i - i_L)}{i_{LG}} \tag{6}$$

where i_L is the specific enthalpy of the saturated liquid, i_{LG} represents the latent heat of vaporisation and the local fluid enthalpy, i is determined from an energy balance.

In the present work, the heat transfer results were taken simultaneously with the flow pattern data. Fig. 8 shows local heat transfer coefficients for different flow patterns. It is found that slug flow appears with the lowest heat transfer coefficient in comparison to the other flow regimes. Although the annular-rivulet flow shows a relatively high heat transfer coefficient, a local dry-out region is observed at high vapour qualities, which is undesirable for a thermal design approach dealing with a cooling system implemented with small channels. Moderate values of heat transfer coefficient are given by throat-annular flow, churn flow and annular flow which might be good choices for the development of these systems. It can be seen from the figure that the flow patterns are expected to influence the flow boiling heat transfer process.

In addition to the flow pattern, the effects of heat flux, mass flux, vapour quality and saturation pressure on the heat transfer characteristics are also addressed as follows.

The dependence of heat transfer coefficients on heat flux is presented in Fig. 9. Regarding the experimental range, the measured results increase with increasing heat flux and are less affected by vapour quality.

In Fig. 10, the heat transfer coefficient is depicted with various values of mass flux. The figure reveals an insignificant effect of mass flux on the measured heat transfer coefficient.

The observed characteristics, presented in Figs. 9 and 10, seem to be the case that nucleate boiling contribution plays an important role on flow boiling heat transfer in mini-channel. Similar observations were also reported by different researchers such as Saitoh et al. [12], Choi et al. [16], Lazarek and Black [29], Wambsganss et al. [30], Bao et al. [31] and Tran et al. [32].

Fig. 11 presents the variation of heat transfer coefficient with vapour quality for saturation pressures of 8, 10 and 13 bar. There is a decrease in heat transfer coefficient with increasing saturation pressure across the experimental range of vapour quality. This may be attributed to the fact that, with an increase in saturation pressure, which corresponds to the smaller latent heat of vaporisation, the lower liquid viscosity can contribute the thinner liquid film on the tube wall to become easily broken and, hence, a decrease in heat transfer coefficient is established. A similar trend regarding the effect of saturation pressure on heat transfer coefficient was also reported by Choi et al. [15] and Kaew-On and Wongwises [22].

3.2.2. Average heat transfer coefficient

The average heat transfer coefficient for the entire 0.6 m long tube is defined as

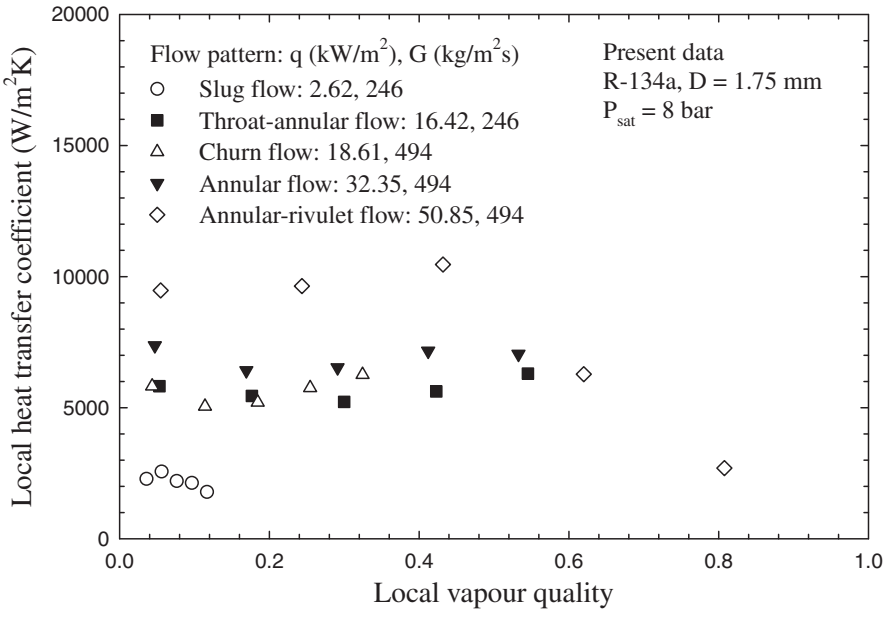

Fig. 8. Local heat transfer coefficient data for various flow patterns.

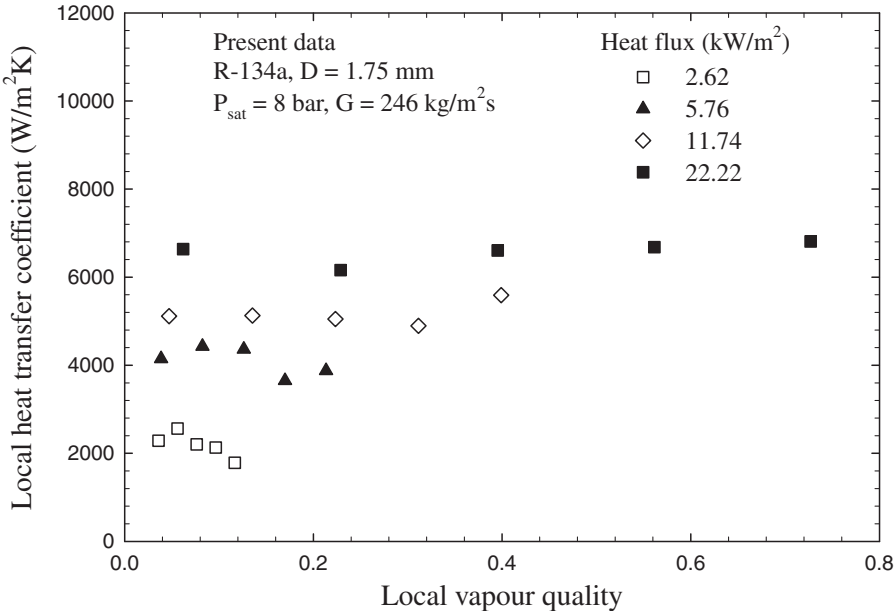

Fig. 9. Local vapour quality versus local heat transfer coefficient for various heat flux values.

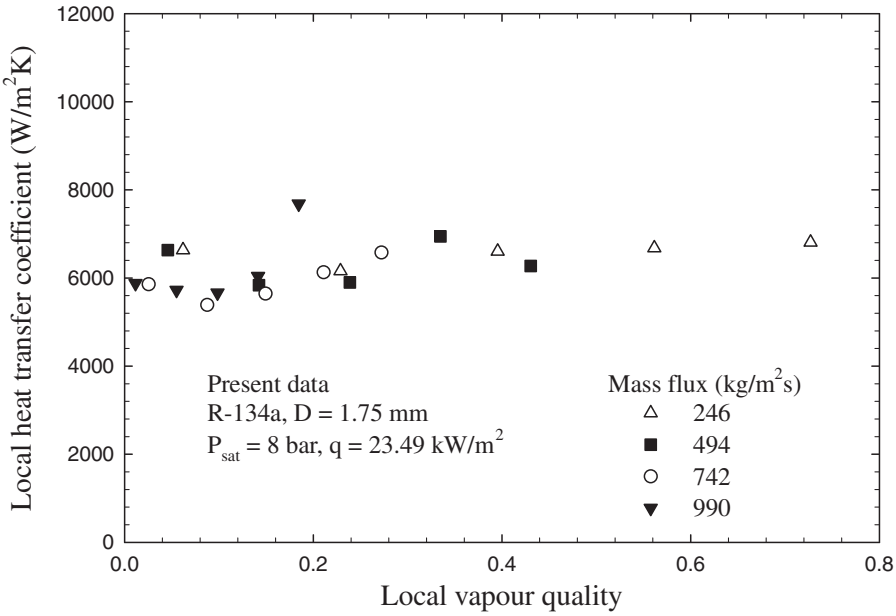

Fig. 10. Local vapour quality versus local heat transfer coefficient for various mass flux values.

$$h_{avg} = \frac{q}{(T_{wall,in,avg} - T_{sat,avg})} \quad (7)$$

There are 10 positions along the tube, at which the inner wall temperatures are determined and thus the average value of the inner wall surface temperature, $T_{wall,in,avg}$, of the test section is obtained using the arithmetic mean of the temperatures along the tube. $T_{sat,avg}$ represents the average temperature of the refrigerant at the test section inlet and outlet.

Fig. 12 presents average heat transfer coefficients plotted as a function of heat flux for different constant values of mass flux. For each mass flux value, the results depend strongly on heat flux. The decreases in heat transfer coefficient which result from the partial dry-out region appearing in the annular-rivulet flow are indicated under mass flux values of 494, 742 and 989 kg/m^2 s.

The interesting point observed from Fig. 12 is that the heat transfer coefficient data are mostly less dependent on mass flux, especially, under heat flux values up to around 40 kW/m^2. This observed behavior reveals that convective contribution does not play dominant role on the heat transfer mechanisms although liquid-turbulent and vapour-turbulent flow are established in the mass flux ranging between 494 and 989 kg/m^2 s (a mass flux value of 246 kg/m^2 s falls in the liquid-laminar and vapour-turbulent region which is a common flow pattern in many applications of mini-channel [33]). To examine such behavior, the confinement number recommended by Kew and Cornwell [34] is used as the transition

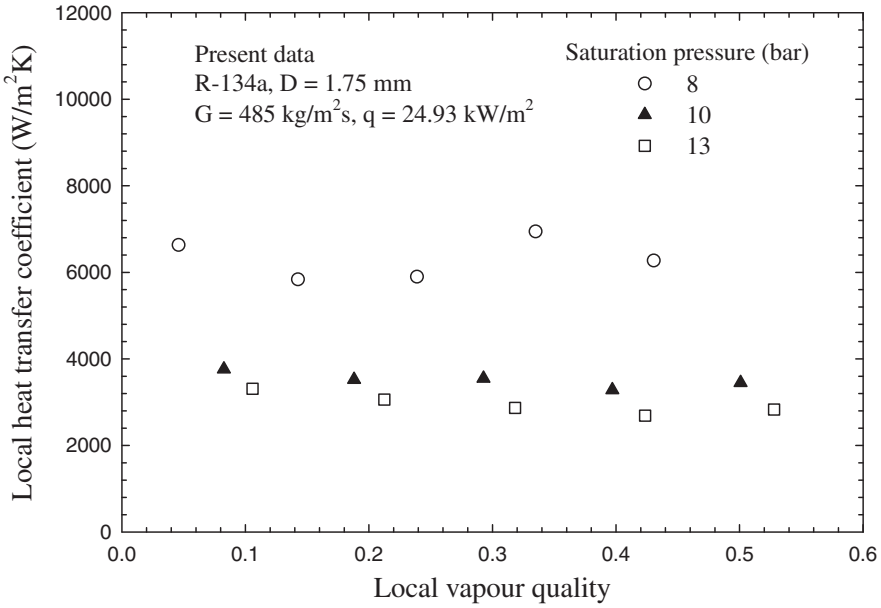

Fig. 11. Local vapour quality versus local heat transfer coefficient for various pressures.

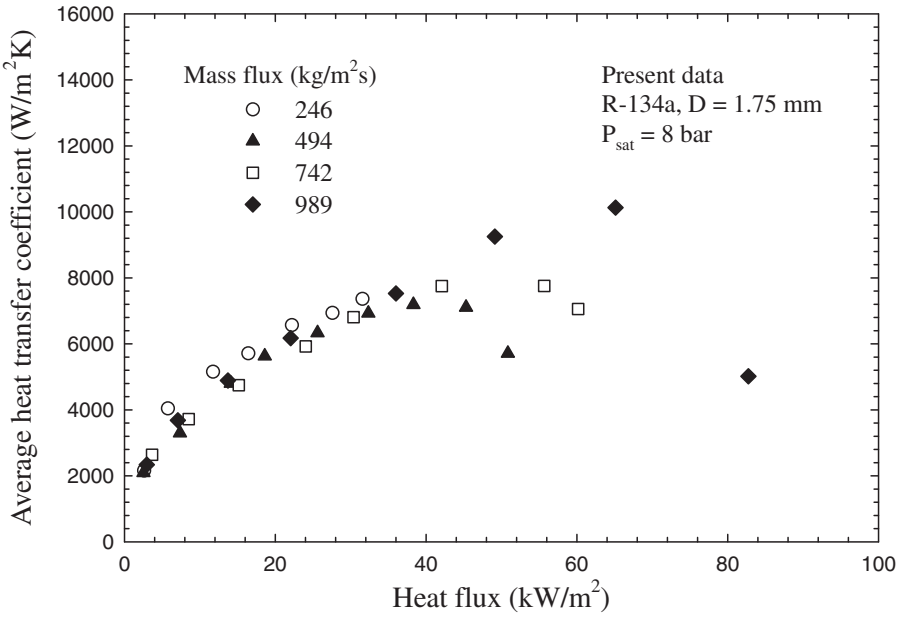

Fig. 12. Heat flux versus average heat transfer coefficient for various mass flux values at P_{sat} = 8 bar.

criterion for checking whether the micro-scale effects are important. The confinement number is defined as

$$C_o = \frac{D_b}{D_h} \tag{8}$$

where D_b is the nominal bubble size or capillary length which is expressed by

$$D_b = \sqrt{\frac{\sigma}{g(\rho_L - \rho_G)}} \tag{9}$$

The confinement number below 0.5 stands for ordinarily sized channel. In the present study, the confinement number for all mass flux values under a saturation pressure of 8 bar is slightly above 0.5, presumably indicating a mini-channel flow.

As heat flux is increased to values larger than 40 kW/m^2, nevertheless, the increase in evaporation momentum force exerted at the evaporating interface tends to enhance convective heat transfer mechanisms, leading to the variation of heat transfer coefficient with mass flux.

For a saturation pressure of 10 bar, the heat flux versus average heat transfer coefficient for various mass flux is illustrated in Fig. 13. The variation of heat transfer coefficient with mass flux is more obvious than that presented in Fig. 12. As expected, the criterion proposed by Kew and Cornwell [34] indicates the macro-scale flow region in which the values of the confinement number are less than 0.5 for all mass flux values.

The results presented in Fig. 14, for heat transfer coefficient plotted against heat flux for different values of saturation pressure show the decrease in heat transfer coefficient with increasing sat-

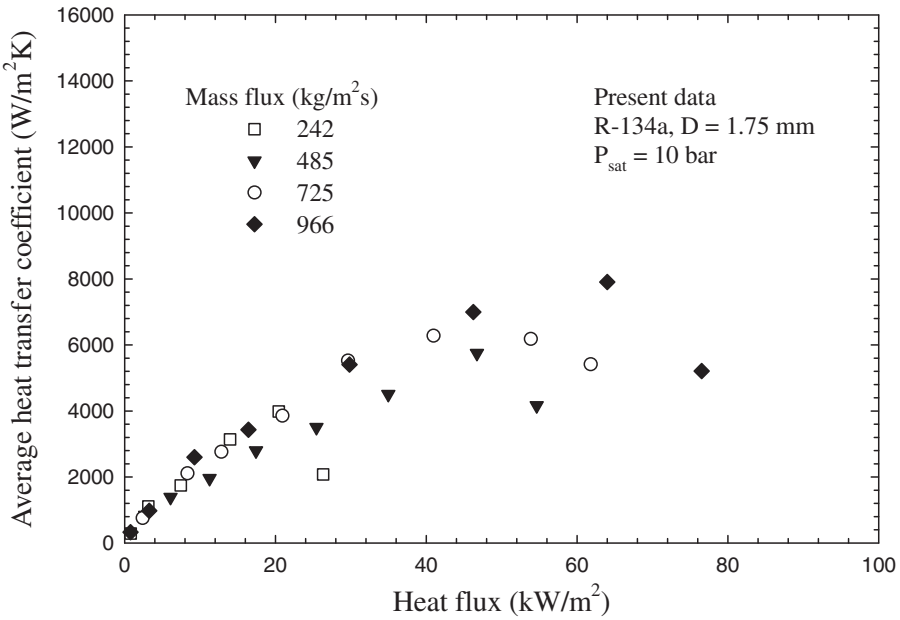

Fig. 13. Heat flux versus average heat transfer coefficient for various mass flux values at P_{sat} = 10 bar.

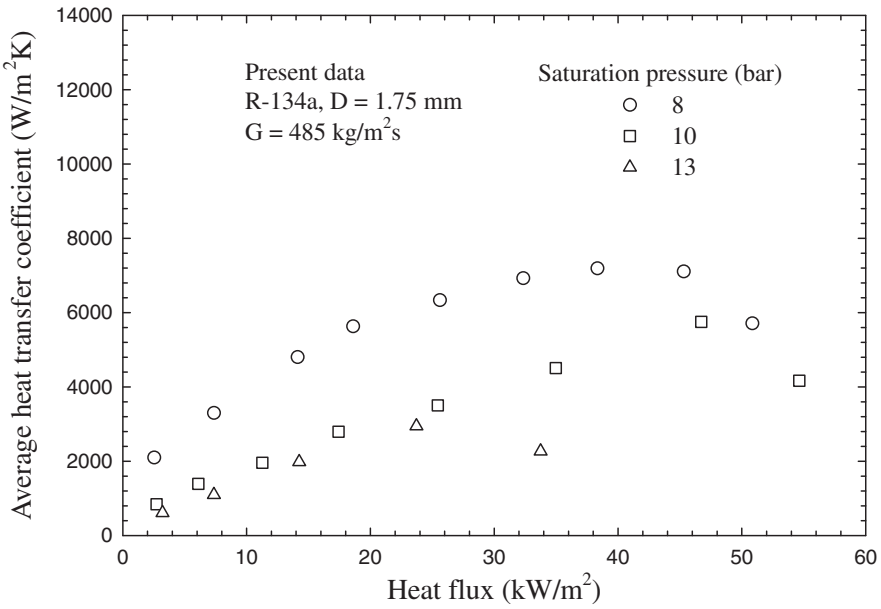

Fig. 14. Heat flux versus average heat transfer coefficient for various pressures.

uration pressure. The results support the trend which is previously discussed as illustrated in Fig. 11. The lower liquid viscosity due to the increment of saturation pressure also leads to the decrease in frictional pressure drop as illustrated in Fig. 15. The frictional pressure drop is determined by subtracting the accelerational pressure drop from the total one which is monitored by the differential pressure transducer.

The average heat transfer coefficient data obtained from the present study are compared with one well-known heat transfer prediction recommended for flow boiling in ordinarily sized channels and with three boiling heat transfer correlations proposed for small flow channels.

One of the widely used correlations for ordinarily sized channels, which is taken as a benchmark in the flow boiling literature, was proposed by Chen [35]. An additive concept for nucleate boiling and forced convective mechanisms was introduced in the correlation which is expressed as

$$h = h_{NBC}S + h_L F \tag{10}$$

where F is a two-phase convection multiplier which is calculated as

$$F = \begin{cases} 1 & \text{for } \frac{1}{\chi} \leqslant 0.1 \\ 2.35\left(\frac{1}{\chi} + 0.213\right)^{0.736} & \text{for } \frac{1}{\chi} > 0.1 \end{cases} \tag{11}$$

χ in Eq. (11) represents the Lockhart–Martinelli parameter determined by:

$$\chi = \left(\frac{1-x}{x}\right)^{0.9}\left(\frac{\rho_G}{\rho_L}\right)^{0.5}\left(\frac{\mu_L}{\mu_G}\right)^{0.1} \tag{12}$$

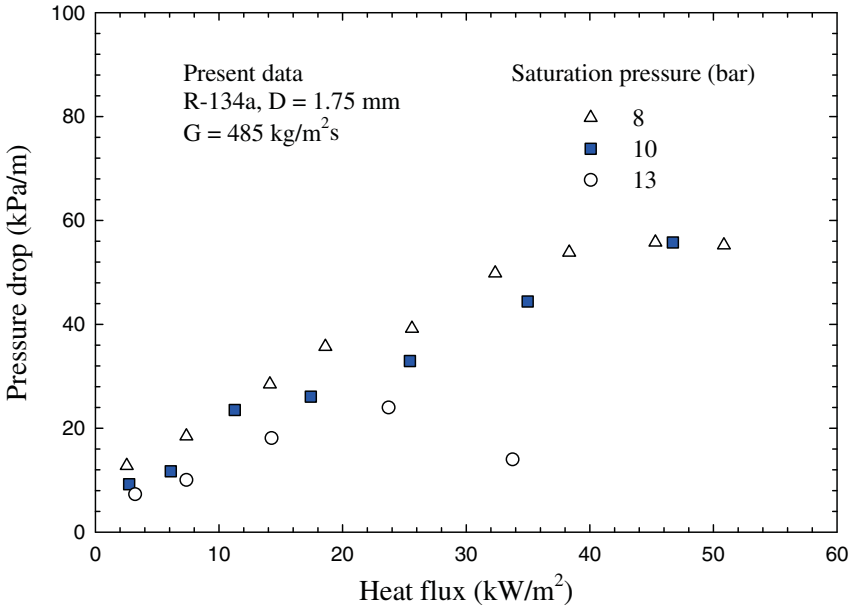

Fig. 15. Heat flux versus frictional pressure drop for various pressures.

The nucleate boiling suppression factor, S, is expressed as

$$S = \frac{1}{1 + 2.53 \times 10^{-6} Re_L^{1.17}} \tag{13}$$

The liquid-phase heat transfer coefficient, h_L, is given by:

$$h_L = 0.023 Re_L^{0.8} \left(\frac{\mu_L C_{pL}}{k_L}\right)^{0.4} \left(\frac{k_L}{D}\right) \tag{14}$$

and nucleate boiling heat transfer coefficient, h_{NBC}, is determined from the following equation:

$$h_{NBC} = 0.00122 \Delta T_{sat}^{0.24} \Delta P_{sat}^{0.75} \left(\frac{k_L^{0.79} C_{pL}^{0.45} \rho_L^{0.49}}{\sigma^{0.5} \mu_L^{0.29} i_{LG}^{0.24} \rho_G^{0.24}}\right) \tag{15}$$

In Eqs. (12)–(15), μ_L is liquid viscosity, μ_G is vapour viscosity, Re_L is liquid Reynolds number, C_{pL} is liquid specific heat capacity, k_L is liquid thermal conductivity, D is channel diameter, σ is surface tension, ΔT_{sat} is wall superheat and ΔP_{sat} stands for the difference between the saturation pressures calculated from wall temperature and fluid temperature.

Later, the Chen correlation [35] was improved by Choi et al. [16] to make it more applicable to small channels. The two-phase convection multiplier, F, which can be related to the two-phase frictional multiplier as indicated in Zhang et al. [36], and the nucleate boiling suppression factor, S, were modified by Choi et al. [16] using a regression method corresponding to their experimental data for mini-channels.

The proposed two-phase convection multiplier and nucleate boiling suppression factor are expressed in Eqs. (16) and (17), respectively:

$$F = 0.042 \phi_L^2 + 0.958 \tag{16}$$

$$S = 469.1689 (\phi_L^2)^{-0.2093} B_o^{0.7402} \tag{17}$$

where ϕ_L^2 represents the two-phase frictional multiplier given by:

$$\phi_L^2 = 1 + \frac{C}{\chi} + \frac{1}{\chi^2} \tag{18}$$

The constant C in this equation is a parameter which indicates the two-phase flow condition. The value of this parameter proposed by Chisholm [37], varying from 5 to 20, depends on the flow condition of the vapour and liquid. $C = 20$ for turbulent liquid and turbulent vapour, $C = 12$ for laminar liquid and turbulent vapour, $C = 10$ for turbulent liquid and laminar vapour, $C = 5$ for laminar liquid and laminar vapour.

Based on the Cooper correlation [38], the nucleate boiling heat transfer coefficient is given by

$$h_{NBC} = 55 P_r^{0.12} (-0.4343 \ln P_r)^{-0.55} M^{-0.5} q^{0.67} \tag{19}$$

where P_r is reduced pressure and M is molecular weight.

Finally, the predicted heat transfer coefficient can be obtained by substituting Eqs. (14), (16), (17), and (19) into (10).

Tran et al. [32] proposed a correlation for flow boiling in circular and rectangular mini-channels. The dominant heat transfer mechanism associated with nucleate boiling was considered to develop a correlation which is written as

$$h = 8.4 \times 10^5 \left(B_o^2 We_{LO}\right)^{0.3} \left(\frac{\rho_L}{\rho_G}\right)^{-0.4} \tag{20}$$

Kandlikar and Balasubramanian [39] modified the correlation proposed by Kandlikar [40] for ordinarily sized channels to extend the prediction to mini- and micro-channels which correspond to the neglected Froude number.

For all-liquid Reynolds numbers higher than 100, their correlation can be expressed as shown below

$$h = \text{larger of} \begin{cases} h_{NBC} \\ h_{CBC} \end{cases} \tag{21}$$

where the heat transfer coefficient based on nucleate boiling contribution, h_{NBC}, and that on forced convective contribution, h_{CBC}, are given by Eqs. (22) and (23), respectively

$$h_{NBC} = 0.6683 C_{CO}^{-0.2} (1-x)^{0.8} h_{LO} + 1058.0 B_o^{0.7} (1-x)^{0.8} F_{FI} h_{LO} \tag{22}$$

$$h_{CBC} = 1.136 C_{CO}^{-0.9} (1-x)^{0.8} h_{LO} + 667.2 B_o^{0.7} (1-x)^{0.8} F_{FI} h_{LO} \tag{23}$$

where C_{CO} represents convection number, F_{FI} stands for a fluid-surface dependent parameter which is equal to 1 for all fluids tested with stainless steel tubes, and h_{LO} for all-liquid flow heat transfer coefficient which is found from Eqs. (24)–(26):

$$h_{LO} = \frac{Re_{LO} Pr_L (f/2)(k_L/D)}{1 + 12.7(Pr_L^{2/3} - 1)(f/2)^{0.5}} \quad \text{for } 10^4 \leqslant Re_{LO} \leqslant 5 \times 10^6 \tag{24}$$

$$h_{LO} = \frac{(Re_{LO} - 1000) Pr_L (f/2)(k_L/D)}{1 + 12.7(Pr_L^{2/3} - 1)(f/2)^{0.5}} \quad \text{for } 3000 \leqslant Re_{LO} \leqslant 10^4 \tag{25}$$

$$h_{LO} = \frac{Nuk_L}{D} \quad \text{for } Re_{LO} \leqslant 1600 \tag{26}$$

Pr_L is the liquid Prandtl number and f appearing in Eqs. (24) and (25) is the friction factor determined by:

$$f = [1.58 \ln(Re_{LO}) - 3.28]^{-2} \tag{27}$$

It is noted that, for laminar flow in a circular channel with constant surface heat flux, the Nusselt number indicated in Eq. (26) is equal to 4.36. In the case of the transition region, the all-liquid flow heat transfer coefficient is established using a linear interpolation between Re_{LO} of 1600 and 3000.

They also proposed a two-phase heat transfer coefficient for very low Reynolds number ($Re_{LO} \leqslant 100$) which is recommended as

$$h = h_{NBC} = 0.6683 C_{CO}^{-0.2} (1-x)^{0.8} h_{LO} + 1058.0 B_o^{0.7} (1-x)^{0.8} F_{FI} h_{LO} \tag{28}$$

where h_{LO} is found from Eq. (26).

Comparisons between the average heat transfer coefficient data and existing correlations are presented in Figs. 16–19 which contain the mean absolute error (MAE) providing the predictive accuracy of the corresponding correlations.

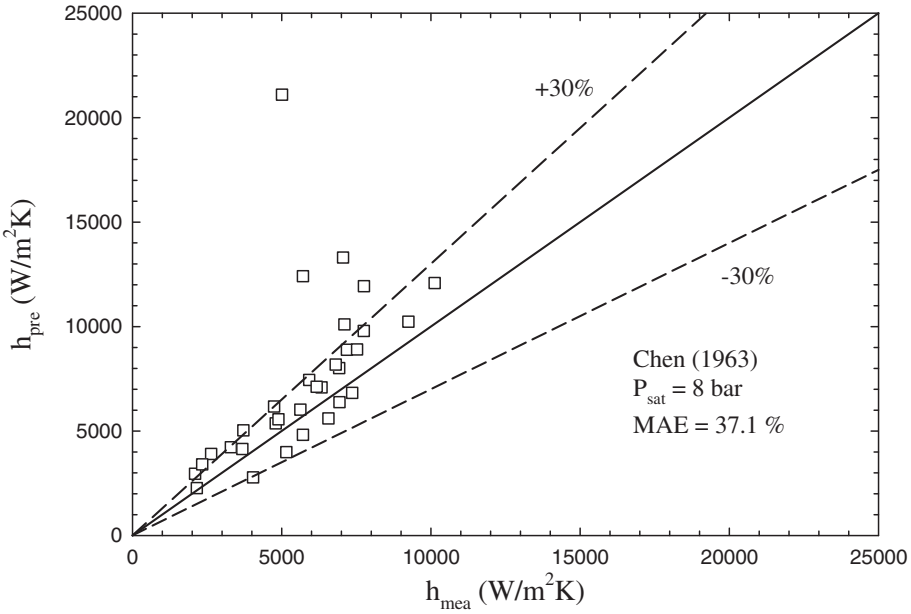

Fig. 16. Comparison between measured and calculated heat transfer coefficient using Chen correlation [35].

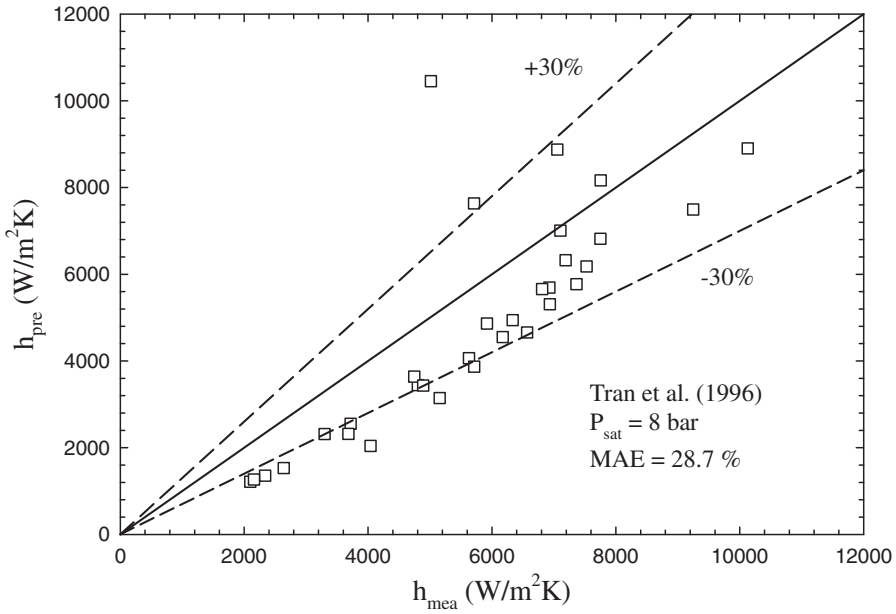

Fig. 17. Comparison between measured and calculated heat transfer coefficient using Tran et al. correlation [32].

The correlations mentioned above were proposed for two-phase heat transfer prediction. The method of Chen [35] were done by assuming that saturated nucleate boiling mechanism and two-phase forced convection mechanism take place to some degree for the entire range of the correlation. The contributions from both mechanisms were also assumed to be additive. Although the method of Chen [35] was developed based on the ordinarily sized channel placed vertically, the applicability of this correlation is examined here. The ordinarily sized channel is often referred to as the channel possessing Bond number (which is in inverse relation to the confinement number) higher than 4.0 for which the effect of the gravitational force is not expected to be small when compared with the surface tension force. In Fig. 16, the correlation proposed by Chen [35] roughly predicts the data. With MAE of 37.1%, the method of Chen [35] captures 68.75% of the data within ±30% error band. The method developed by Tran et al. [32], which is one of the most popular existing correlations, was developed based on flow boiling heat transfer experiments with R-22 in channels having hydraulic diameters of around 2.46 mm, and on the nucleation-dominant mechanism rather than the convection contribution. As presented in Fig. 17, a lower MAE (28.7%) in comparison to that for Chen correlation [35] is due to their method which associates with small channels. However, the Trans et al. correlation [32], which predicts about 65.63% of the data within ±30% error band, deals with the experimental conditions having the Bond number of 9.8 which is nearly three times larger than that for the

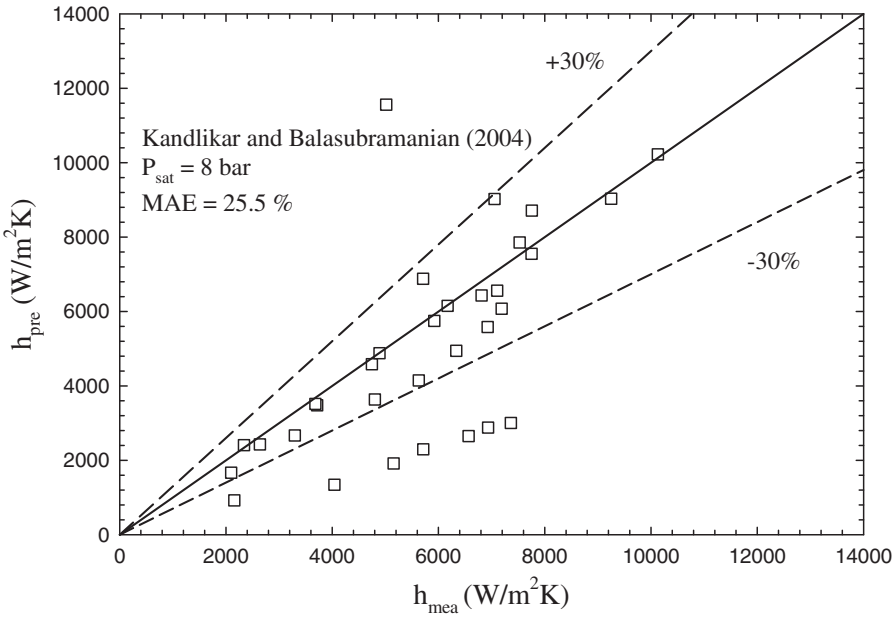

Fig. 18. Comparison between measured and calculated heat transfer coefficient using Kandlikar and Balasubramanian correlation [39].

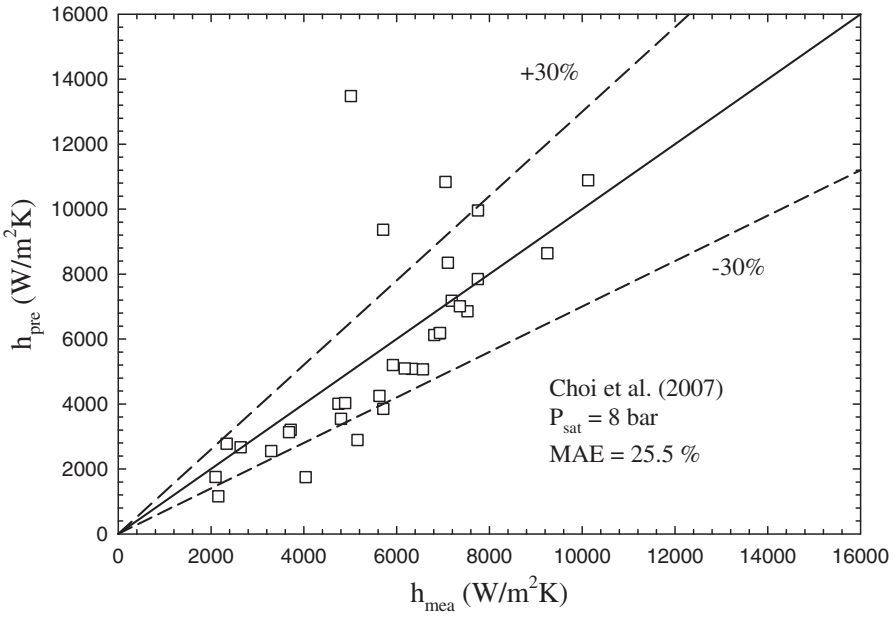

Fig. 19. Comparison between measured and calculated heat transfer coefficient using Choi et al. correlation [16].

Table 3
Mean absolute error (MAE) for different prediction methods.

Prediction method	MAE	
	10 bar	13 bar
Chen [35]	305.5%	670.4%
Tran et al. [32]	71.9%	215.7%
Kandlikar and Balasubramanian [39]	86.5%	154.3%
Choi et al. [15,16]	111.8%	189.7%

present work. The method combining both nucleate boiling and forced convective mechanisms was proposed by Kandlikar and Balasubramanian [39] for predicting heat transfer coefficient in mini- and micro-channels. At a given condition, either heat transfer coefficient based on nucleate boiling contribution or that with respect to forced convective mechanism is representative for the prediction, depending upon which one is larger. With MAE of 25.5%, the correlation developed by Kandlikar and Balasubramanian [39] can predict 75% of the data within ±30% error band as illustrated in Fig. 18. Unlike the method of Kandlikar and Balasubramanian [39], the method for mini-channels proposed by Choi et al. [16] is based on additive concept for nucleate boiling and forced convective contributions under a given condition. In Fig. 19, it seems that the correlation developed by Choi et al. [16] presents the best prediction, with MAE of 25.5% and 78.12% of the predicted data falling within ±30% error band.

The values associated with mean absolute error (MAE) for different prediction methods based on system pressures higher than 8 bar are given in Table 3. As previously discussed, the liquid film under high saturation pressure tends to break up easily, leading to the unstable condition near the tube wall. Such condition, which is not taken into account in these correlations, results in large mean absolute error (MAE) as seen in Table 3.

4. Conclusion

This experimental investigation was conducted to study flow visualisation and heat transfer characteristics of R-134a refrigerant during flow boiling in a stainless steel tube with inner diameter of 1.75 mm and a length of 600 mm. For the flow visualisation study, the flow pattern map is developed from the observed flow patterns, i.e., slug flow, throat-annular flow, churn flow, annular flow and annular-rivulet flow, and is compared with existing transition lines obtained from different working fluids. The heat transfer results for a given flow pattern are presented and the effects of heat flux, mass flux, vapour quality and saturation pressure on the heat transfer coefficient are also discussed in this study. Calculations based on existing heat transfer prediction methods available for ordinarily sized channels and small channels are made to compare the results with the experimental data.

Acknowledgements

The authors would like to express their appreciation to King Mongkut's University of Technology Thonburi, the Thailand Research Fund (TRF) and the Office of Higher Education Commission for providing financial support for this study.

References

[1] G. Ribatski, L. Wojtan, J.R. Thome, An analysis of experimental data and prediction methods for two-phase frictional pressure drop and flow boiling heat transfer in micro-scale channels, Exp. Therm. Fluid Sci. 31 (1) (2006) 1–19.
[2] S.S. Mehendale, A.M. Jacobi, R.K. Ahah, Fluid flow and heat transfer at micro- and meso-scales with application to heat exchanger design, Appl. Mech. Rev. 53 (2000) 175–193.
[3] S.G. Kandlikar, Fundamental issues related to flow boiling in mini-channels and micro-channels, Exp. Therm. Fluid Sci. 26 (7) (2002) 389–407.
[4] P.M.-Y. Chung, M. Kawaji, The effect of channel diameter on adiabatic two-phase flow characteristics in microchannels, Int. J. Multiphase Flow 30 (7–8) (2004) 735–761.
[5] S. Saisorn, S. Wongwises, The effects of channel diameter on flow pattern, void fraction and pressure drop of two-phase air–water flow in circular micro-channels, Exp. Therm. Fluid Sci. 34 (4) (2010) 454–462.
[6] A. Greco, Convective boiling of pure and mixed refrigerants: an experimental study of the major parameters affecting heat transfer, Int. J. Heat Mass Transfer 51 (3–4) (2008) 896–909.
[7] S.G. Kandlikar, Scale effects on flow boiling heat transfer in microchannels: a fundamental perspective, Int. J. Therm. Sci. 49 (7) (2010) 1073–1085.
[8] D. Brutin, L. Tadrist, Pressure drop and heat transfer analysis of flow boiling in a minichannel: influence of the inlet condition on two-phase flow stability, Int. J. Heat Mass Transfer 47 (10–11) (2004) 2365–2377.
[9] X. Huo, L. Chen, Y.S. Tian, T.G. Karayiannis, Flow boiling and flow regimes in small diameter tubes, Appl. Therm. Eng. 24 (8–9) (2004) 1225–1239.
[10] J. Pettersen, Flow vaporization of CO_2 in microchannel tubes, Exp. Therm. Fluid Sci. 28 (2–3) (2004) 111–121.
[11] R. Yun, Y. Kim, M.S. Kim, Convective boiling heat transfer characteristics of CO_2 in microchannels, Int. J. Heat Mass Transfer 48 (2) (2005) 235–242.
[12] S. Saitoh, H. Daiguji, E. Hihara, Effect of tube diameter on boiling heat transfer of R-134a in horizontal small-diameter tubes, Int. J. Heat Mass Transfer 48 (23–24) (2005) 4973–4984.
[13] Y.M. Lie, F.Q. Su, R.L. Lai, T.F. Lin, Experimental study of evaporation heat transfer characteristics of refrigerants R-134a and R-407C, Int. J. Heat Mass Transfer 49 (1–2) (2006) 207–218.
[14] H. Boye, Y. Staate, J. Schmidt, Experimental investigation and modeling of heat transfer during convective boiling in a minichannel, Int. J. Heat Mass Transfer 50 (1–2) (2007) 208–215.
[15] K.I. Choi, A.S. Pamitran, J.T. Oh, Two-phase flow heat transfer of CO_2 vaporization in smooth horizontal minichannels, Int. J. Refrigeration 30 (5) (2007) 767–777.
[16] K.I. Choi, A.S. Pamitran, C.Y. Oh, J.T. Oh, Boiling heat transfer of R-22, R-134a, and CO_2 in horizontal smooth minichannels, Int. J. Refrigeration 30 (8) (2007) 1336–1346.
[17] D. Shiferaw, X. Huo, T.G. Karayiannis, D.B.R. Kenning, Examination of heat transfer correlations and a model for flow boiling of R134a in small diameter tubes, Int. J. Heat Mass Transfer 50 (25–26) (2007) 5177–5193.
[18] D. Shiferaw, T.G. Karayiannis, D.B.R. Kenning, Flow boiling in a 1.1 mm tube with R134a: experimental results and comparison with model, Int. J. Therm. Sci. 48 (2) (2009) 331–341.
[19] J.R. Thome, V. Dupont, A.M. Jacobi, Heat transfer model for evaporation in microchannels. Part I: presentation of the model, Int. J. Heat Mass Transfer 47 (14–16) (2004) 3375–3385.
[20] V. Dupont, J.R. Thome, A.M. Jacobi, Heat transfer model for evaporation in microchannels. Part II: comparison with the database, Int. J. Heat Mass Transfer 47 (14–16) (2004) 3387–3401.
[21] C.L. Ong, J.R. Thome, Flow boiling heat transfer of R134a, R236fa and R245fa in a horizontal 1.030 mm circular channel, Exp. Therm. Fluid Sci. 33 (4) (2009) 651–663.
[22] J. Kaew-On, S. Wongwises, Experimental investigation of evaporation heat transfer coefficient and pressure drop of R-410A in a multiport mini-channel, Int. J. Refrigeration 32 (1) (2009) 124–137.
[23] M. Muller-Steinhagen, K. Heck, A simple friction pressure drop correlation for two-phase flow in pipes, Chem. Eng. Process. 20 (6) (1986) 297–308.
[24] S. Garimella, J.D. Killion, J.W. Coleman, An experimentally validated model for two-phase pressure drop in the intermittent flow regime for circular microchannels, J. Fluid Eng. 124 (1) (2002) 205–214.
[25] K.A. Triplett, S.M. Ghiaasiaan, S.I. Abdel-Khalik, D.L. Sadowski, Gas–liquid two-phase flow in microchannels. Part I: two-phase flow patterns, Int. J. Multiphase Flow 25 (3) (1999) 377–394.
[26] S. Saisorn, S. Wongwises, Flow pattern, void fraction and pressure drop of two-phase air–water flow in a horizontal circular micro-channel, Exp. Therm. Fluid Sci. 32 (3) (2008) 748–760.
[27] C. Martin-Callizo, B. Palm, W. Owhaib, R. Ali, Flow boiling visualization of R-134a in a vertical channel of small diameter, J. Heat Transfer 132 (3) (2010) 1–8.
[28] R. Revellin, J.R. Thome, A new type of diabatic flow pattern map for boiling heat transfer in microchannels, J. Micromech. Microeng. 17 (4) (2007) 788–796.
[29] G.M. Lazarek, S.H. Black, Evaporative heat transfer, pressure drop and critical heat flux in a small diameter vertical tube with R-113, Int. J. Heat Mass Transfer 25 (7) (1982) 945–960.
[30] M.W. Wambsganss, D.M. France, J.A. Jendrzejczyk, T.N. Tran, Boiling heat transfer in a horizontal small-diameter tube, J. Heat Transfer 115 (4) (1993) 963–972.
[31] Z.Y. Bao, D.F. Fletcher, B.S. Haynes, Flow boiling heat transfer of Freon R11 and HCFC123 in narrow passages, Int. J. Heat Mass Transfer 43 (18) (2000) 3347–3358.
[32] T.N. Tran, M.W. Wambsganss, D.M. France, Small circular- and rectangular-channel boiling with two refrigerants, Int. J. Multiphase Flow 22 (3) (1996) 485–498.
[33] W. Li, Z. Wu, A general criterion for evaporative heat transfer in micro/mini-channels, Int. J. Heat Mass Transfer 53 (9–10) (2010) 1967–1976.

[34] P.A. Kew, K. Cornwell, Correlations for the prediction of boiling heat transfer in small-diameter channels, Appl. Therm. Eng. 17 (8–10) (1997) 705–715.
[35] J.C. Chen, A Correlation for Boiling Heat Transfer to Saturated Fluid in Convective Flow, ASME Paper, 63-HT-34, 1963, pp. 1–11.
[36] W. Zhang, T. Hibiki, K. Mishima, Correlation for flow boiling heat transfer in mini-channels, Int. J. Heat Mass Transfer 47 (26) (2004) 5749–5763.
[37] D. Chisholm, A theoretical basis for the Lockhart–Martinelli correlation for two-phase flow, Int. J. Heat Mass Transfer 10 (12) (1967) 1767–1778.
[38] M.G. Cooper, Heat flow rates in saturated nucleate pool boiling – a wide-ranging examination using reduced properties, Adv. Heat Transfer 16 (1984) 157–239.
[39] S.G. Kandlikar, P. Balasubramanian, An extension of the flow boiling correlation to transition, laminar, and deep laminar flows in minichannels and microchannels, Heat Transfer Eng. 25 (3) (2004) 86–93.
[40] S.G. Kandlikar, A general correlation for two-phase flow boiling heat transfer coefficient inside horizontal and vertical tubes, J. Heat Transfer 112 (1) (1990) 219–228.

Applied Thermal Engineering 30 (2010) 1927–1936

Contents lists available at ScienceDirect

Applied Thermal Engineering

journal homepage: www.elsevier.com/locate/apthermeng

Two-phase flow model of refrigerants flowing through helically coiled capillary tubes

Sukkarin Chingulpitak [a,b], Somchai Wongwises [b,*]

[a] The joint Graduate School of Energy and Environment, King Mongkut's University of Technology Thonburi, Bangmod, Bangkok 10140, Thailand
[b] Fluid Mechanics, Thermal Engineering and Multiphase Flow Research Lab. (FUTURE), Department of Mechanical Engineering, King Mongkut's University of Technology Thonburi, Bangmod, Bangkok 10140, Thailand

ARTICLE INFO

Article history:
Received 11 November 2009
Accepted 9 April 2010
Available online 17 June 2010

Keywords:
Capillary tube
Adiabatic
Coiled tube
Friction factor
Homogeneous flow model

ABSTRACT

This paper presents a numerical study of the flow characteristics of refrigerants flowing through adiabatic helically coiled capillary tubes. The theoretical model is based on conservation of mass, energy and momentum of the fluids in the capillary tube. The two-phase flow model developed was based on the homogeneous flow assumption. The viscosity model was also based on recommendations from the literature. The developed model can be considered as an effective tool for designing and optimizing capillary tubes working with newer alternative refrigerants. The model is validated by comparison with the experimental data of Kim et al. (2002) for R-22, R-407C and R-410A, and Zhou and Zhang (2006) for R-22. The results obtained from the present model show reasonable agreement with the experimental data. The proposed model can be used to design helical capillary tubes working with various refrigerants.
© 2010 Elsevier Ltd. All rights reserved.

1. Introduction

In many small refrigeration systems, a capillary tube is used as the expansion device due to its low cost, low starting torque and low maintenance. Normally, it is used in refrigeration systems with cooling capacities less than 10 kW such as household refrigerators and air conditioners. The nominal size of the capillary tube typically ranges between 0.5 and 2.0 mm in diameter and 2–5 m in length.

Several decades ago, the flow characteristics of various refrigerants flowing through capillary tubes were studied both experimentally and theoretically. The most recent articles describing investigations of capillary tubes are summarized as follows:

Wong and Ooi [1] presented comparisons between the predicted results from homogeneous and separated flow models and experimental results from a number of researchers. The separated flow model which uses Miropolskiy's slip ratio combined with Lin's equation for frictional pressure gradient gave better predictions compared to the homogeneous flow model.

Bansal and Rupasinghe [2] investigated a homogeneous two-phase flow model which is called the "CAPIL model" to study the performance of adiabatic capillary tubes using R-134a as working fluid. The REFPROP program was used to calculate the refrigerant properties.

Sami and Tribes [3] reported a numerical model for predicting capillary tube performance for some azeotropic and zeotropic binary mixtures as well as pure HFC refrigerants.

In 1999, Melo et al. [4] studied experimentally the effect of capillary length, diameter, refrigerant subcooling, condensing pressure and type of refrigerant (CFC-12, HFC-134a and HC-600a) on the mass flow rates through capillary tubes. In addition, they proposed correlations to predict the mass flow rate of various refrigerants. The proposed correlations were found to be in good agreement with those obtained from the measured data and other studies in the open literature.

Wongwises et al. [5] developed a two-phase flow model based on homogeneous flow to study the flow characteristics of many pairs of refrigerants flowing through adiabatic capillary tubes. The Colebrook equation was used to determine the two-phase friction factor. It was found that the traditional refrigerants consistently gave lower pressure drops for both single-phase and two-phase regions which resulted from longer capillary tube lengths.

Wongwises et al. [6] presented a two-phase separated flow model to describe the refrigerant flow characteristics in the capillary tubes of refrigeration systems. The agreement between experimental data and simulation results obtained for flows of R-12, R-22 and R-134a through capillary tubes indicated that the separated flow model with appropriate correlations of the frictional pressure gradient and slip ratio can be used to predict the two-phase flow behaviour of refrigerant flowing through capillary tubes.

* Corresponding author. Tel.: +66 2 470 9115; fax: +66 2 470 9111.
E-mail address: somchai.won@kmutt.ac.th (S. Wongwises).

1359-4311/$ – see front matter © 2010 Elsevier Ltd. All rights reserved.
doi:10.1016/j.applthermaleng.2010.04.026

Nomenclature

A	cross sectional area of capillary tube (m^2)
d_i	capillary tube internal diameter (m)
D_C	coil diameter (m)
De	Dean Number, $De = \mathrm{Re}\sqrt{(d_i/D_C)}$
e/d_i	relative roughness
$\triangle T_{sub}$	degree of subcooling (°C)
f	friction factor
g	gravitational acceleration (m/s^2)
G	mass flow rate per unit area ($kg/s\text{-}m^2$)
h	specific enthalpy (J/kg)
H_{loss}	head loss (m)
He	Helical number, $He = \mathrm{Re}[(d_i/D_C)/\{1+(p/\pi D_C)^2\}]^{1/2}$
k	entrance loss coefficient
L	length (m)
m	mass flow rate (kg/s)
P	pressure (Pa)
Re	Reynolds number
s	specific entropy (J/kg-K)
T	temperature (°C)
V	velocity (m/s)
x	quality

Greek letters

τ_w	shear stress at wall (N/m^2)
v	specific volume (m^3/kg)
μ	dynamic viscosity (kg/m-s)
ρ	density (kg/m^3)

Subscripts

cond, evap	condenser and evaporator, respectively
f, g	liquid phase and gas phase, respectively
h	homogeneous flow
i	capillary inlet condition
sp, tp	single-phase and two-phase, respective

Wongwises and Pirompak [7] studied the flow characteristics of alternative refrigerants in adiabatic capillary tubes by using an adiabatic capillary tube model. Moreover, they also proposed selection charts for selecting the size of capillary tube based on the flow rate and flow condition. In addition to tube size, the charts are very useful for determining the mass flow rate directly.

In 2001, Liang and Wong [8] introduced the homogeneous flow model based on a drift flux model to predict the flow characteristics of R-134a flowing through an adiabatic capillary tube. This model was validated by comparisons between numerical and experimental results by Li et al. [9] and Mikol et al. [10] using R-12 as working fluid.

Jung et al. [11] proposed a model to calculate the size of capillary tubes for various refrigerants of R-22, R-134a, R-407C and R-410A. In their model, the Stocker model was modified and took several factors into account such as area contraction, different equations for viscosity and friction factors, and mixing effects. Numerical results indicated that using the McAdam model for the viscosity equation gave a better calculation than the Dukler model. Finally, semi-empirical correlations for predicting mass flow rate, condensing temperature and subcooling of refrigerant were proposed.

Sinpiboon and Wongwises [12] presented a model to study the flow characteristics in non-adiabatic capillary tubes. In this study, the mathematical model was categorized into three different cases, depending on the position of the heat exchange process. The first case is used when the heat exchange process starts in the single-phase flow region. The second case is determined when the heat exchange process starts at the end of the single-phase flow region. Finally, the last case is considered when the heat exchange process takes place in the two-phase flow region. A set of differential equations were solved by an explicit method in a finite-difference scheme.

Fiorelli et al. [13] performed an experimental study to evaluate the performance of R-22 and its alternatives, such as R-407C and R-410A flowing through adiabatic capillary tubes. The results showed that the performance of capillary tubes for R-410A and R-407C were similar under given conditions. Moreover, they also determined the effect of geometry on the behaviour of capillary tubes. Finally, differences in the flow behaviour of R-410A and R-407C were evaluated.

Bansal and Wang [14] presented a homogeneous and metastable simulation model. The first law of thermodynamics, some fluid mechanics and empirical relations were incorporated into this model. Compared with published experimental data, this model shows good agreement within ±7% for R-22, R-134a and R-600. Moreover, a new numerical analysis for simulating the choked flow of refrigerant under adiabatic conditions was proposed.

Choi et al. [15] presented a generalized mass flow rate correlation based on their experimental data for R-22, R-290 and R-407C. Dimensionless parameters were derived from the Buckingham π theorem by considering the effect of refrigerant properties, capillary tube geometry and inlet conditions.

Similarly, Yang and Wang [16] proposed a generalized mass flow rate correlation based on extensive data for R-12, R-22, R-134a, R-290, R-600a, R-410A, R-407C, and R-404A. The simulation conditions used in their study are as follows: 1) the inner diameter ranges between 0.5 and 2 mm, 2) the tube length ranges between 0.5 and 5 m, 3) the condensing temperature ranges between 20 °C and 60 °C, 4) the subcooling temperature is between 0 °C and 20 °C and 5) Inlet quality varies approximately in the range from 0 to 0.3. Their results showed that the predicted values agree well with the experimental data in the open literature for R-12, R-22, R-134a, R-290, R-407C, R-410A and R-404A refrigerants. Moreover, the model presented gave average and standard deviations of 0.83% and 9.02% compared with the ASHRAE [17] and Choi et al. [15] equations, respectively.

Seixlack and Barbazelli [18] presented a numerical model to predict refrigerant flow along non-adiabatic capillary tubes using a two-fluid model. The flow along the straight and horizontal capillary tube is divided into two regions: single-phase and two-phase flow regions. In comparisons between numerical results and experimental data, the results gave good predictions of the refrigerant mass flow rate. In addition, comparisons with a homogeneous model were also made.

It can be noted that the theoretical and experimental investigations found in the literature and described above have focused on the study of the flow characteristics in horizontal straight capillary tubes; the flow characteristics in coiled capillary tubes has received comparatively little attention in the literature. The most productive studies of coiled capillary tubes have been continuously carried out by the following researchers.

Ali [19] proposed pressure drop correlations which were developed in terms of fluid properties (ρ and μ), flow rate (V) and tube geometry (d_i, D_C, p and L). It should be noted that in most of the

previous works, the relevant correlations were developed in terms of Dean number (*De*), Helical number (*He*), curvature ratio (D_C/d_i), Euler number (*Eu*), Reynolds number, *Re*, and the obtained geometrical group.

Kim et al. [20] presented a mass flow rate correlation based on the Buckingham π theorem for R-22 and its alternatives, R-407C and R-410A. Their results indicated that the mass flow rates of R-407C and R-410A were higher than those of R-22 by about 4.0% and 23%, respectively. In addition, the mass flow rates in straight capillary tubes are quite a lot higher than those in coiled capillary tubes, especially at smaller coil diameters. For instance, mass flow rates through a 40 mm coil diameter are smaller than through straight capillary tubes by approximately 9.0%.

Zhou and Zhang [21,22] studied the performance of coiled adiabatic capillary tubes both theoretically and experimentally. The results were compared with the straight capillary data. The results showed that the refrigerant mass flow rate substantially increases with increasing coil diameter. However, little change was observed for coil diameters larger than 300 mm.

Park et al. [23] studied the flow characteristics of coiled capillary tubes for R-22 and developed a mass flow rate correlation for coiled capillary tubes. Under the same operating conditions, they found that the mass flow rates of coiled capillary tubes decreased by 5–16% more than those of straight capillary tubes. The Buckingham π theorem was used to form a generalized correlation to calculate the refrigerant mass flow rate for both straight and coiled capillary tubes. The effects of inlet condition, refrigerant property, and coiled tube geometry were considered. For both straight and coiled capillary tubes, the results showed that the proposed correlation gave satisfactory agreement with the experimental data for R-22, R-407C and R-410A. The average and standard deviations were around 0.24% and 4.4%, respectively.

García-Valladares [24] presented numerical simulations based on a finite volume formulation for describing the flow characteristics of coiled adiabatic capillary tubes. The numerical model considered various aspects such as geometry, type of fluid (pure substances and mixtures), critical or non-critical flow conditions, metastable region, and transient behaviour.

Although some information is currently available on the flow characteristics of refrigerants in coiled capillary tubes, there still remains room for further research, especially in discussing which friction factor used in the calculation will give reliable predictions of flow characteristics. The purpose of this work is to develop a mathematical model to describe the flow characteristics of a refrigerant flowing through an adiabatic helically coiled capillary tube. A number of relevant friction factors, which have never been seen before, are collected together and used in the mathematical model. The simulation results are verified against the limited data available in the literature.

2. Mathematical modelling

As shown in Fig. 1, the flow of refrigerant through a capillary tube can be divided into two distinct regions; single-phase subcooled liquid and two-phase flow. In the model, the physical method used to describe the flow characteristics is developed from the conservation of mass, energy and momentum. Moreover, the model includes the effects of the condenser and evaporator temperatures, inner diameter, degree of subcooling and mass flow rate of refrigerant.

As shown in Fig. 1, the portion between points 1 and 2 is the capillary tube inlet where there is a pressure drop due to the sudden contraction. Similarly, the portion between points 2 and 3 is the single-phase subcooled liquid region and the portion between points 3 and 4 is the two-phase region where liquid and vapour coexist. The developed model is based on the following assumptions:

- the horizontal helical coiled tube has constant diameter
- the inner diameter and surface roughness of the capillary tube are constant
- adiabatic and homogeneous two-phase flow
- non-metastable liquid region
- one-dimensional steady flow
- thermodynamic equilibrium through the capillary tube

The governing equations used in describing the flow characteristics in the single-phase and two-phase flow regions are presented next.

2.1. Single-phase flow region

The pressure loss due to the sudden contraction at the inlet between points 1 and 2 is determined from:

$$P_1 - P_2 = k\frac{\rho V^2}{2g}, \tag{1}$$

where k is the entrance loss coefficient (for square edge, $k = 0.5$).

The steady flow energy equation between points 2 and 3 can be expressed as.

$$\frac{P_2}{\rho_2 g} + \frac{V_2^2}{2g} + z_2 = \frac{P_3}{\rho_3 g} + \frac{V_3^2}{2g} + z_3 + H_{loss}, \tag{2}$$

The head loss can be determined from:

$$H_{loss} = f_{sp}\frac{L_{sp}}{d_i}\frac{V^2}{2g}. \tag{3}$$

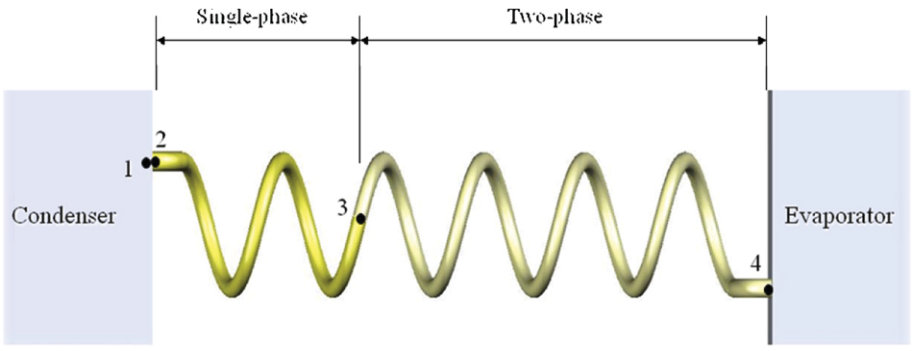

Fig. 1. Schematic diagram of an adiabatic helical capillary tube.

where H_{loss} is the head loss due to friction along the capillary tube and f_{sp} is the single-phase friction factor.

For an incompressible fluid, $\rho_2 \cong \rho_3 = \rho$ the continuity equation is presented in the following equation:

$$m = \rho_2 V_2 A = \rho_3 V_3 A = \rho V A. \tag{4}$$

Re-arranging Eqs. (2)–(4) yields:

$$P_2 = P_3 + \rho g(z_3 - z_2) + \left(\frac{f_{sp}L}{d_i}\right)\left(\frac{\rho V^2}{2}\right), \tag{5}$$

For $z_2 = z_3$ (horizontal tube), substituting Eq. (5) into Eq. (1), gives:

$$L_{sp} = \frac{d_i}{f_{sp}}\left[\frac{2}{\rho V^2}(P_1 - P_3) - (k+1)\right]. \tag{6}$$

The important parameter is the single-phase friction factor (f_{sp}), which can be calculated from twenty six different friction factor models. These equations are expressed as follows (where f_c is the friction factor for a coiled capillary tube and f_s is the friction factor for a straight capillary tube):

1. Dean [25]

$$f_c/f_s = 1.03058\left(De^2/288\right)^2 + 0.01195\left(De^2/288\right)^4, \tag{7}$$

where $De = \mathrm{Re}\sqrt{(d_i/D_C)}$

2. White [26]

$$f_s/f_c = 1 - \left[1 - (11.6/De)^{0.45}\right]^{1/0.45}, \tag{8}$$

3. White [27]

$$f_c = 0.08\mathrm{Re}^{-1/4} + 0.012\sqrt{(d_i/D_C)}, \tag{9}$$

4. Adler [28]

$$f_c/f_s = 0.1064\sqrt{De}, \tag{10}$$

5. Prandtl [29]

$$f_c/f_s = 0.37(0.5De)^{0.36}, \tag{11}$$

6. Hasson [30]

$$f_c/f_s = 0.556 + 0.0969\sqrt{De}, \tag{12}$$

7. Ito [31]

$$f_c/f_s = 21.5De/[1.56 + \log_{10}De]^{5.73}, \tag{13}$$

$$f_c\sqrt{(D_C/d_i)} = 0.0791\left[\mathrm{Re}(d_i/D_C)^2\right]^{-0.2}, \tag{14}$$

$$4f_c\sqrt{(D_C/d_i)} = 0.029 + 0.304 \times \left\{\mathrm{Re}(d_i/D_C)^2\right\}^{-1/4}, \tag{15}$$

8. Kubair and Varrier [32]

$$f_c = 0.7716\exp(3.553d_i/D_C)\mathrm{Re}^{-0.5}, \tag{16}$$

$$f_c = 0.003538\mathrm{Re}^{0.09}\exp(1.887d_i/D_C), \tag{17}$$

9. Barua [33]

$$f_c/f_s = 0.509 + 0.0918\sqrt{De}, \tag{18}$$

10. Mori and Nakayama [34]

$$f_c/f_s = 0.1080\sqrt{De}/\left[1 - 3.253/\sqrt{De}\right], \tag{19}$$

11. Mori and Nakayama [35]

$$f_c\sqrt{(D_C/d_i)} = 0.075\left[\mathrm{Re}(d_i/D_C)^2\right] - 0.2\left\{1 + 0.112 \times \left[\mathrm{Re}(d_i/D_C)^2\right]\right\}^{-0.2}, \tag{20}$$

$$f_c = \frac{0.192(d_i/D_C)^{0.5}}{\left[\mathrm{Re}(d_i/D_C)^{2.5}\right]^{1/6}}\left\{1 + \frac{0.068}{\left[\mathrm{Re}(d_i/D_C)^{2.5}\right]^{1/6}}\right\}, \tag{21}$$

$$f_c = \frac{C_1(d_i/D_C)^{0.5}}{\left[\mathrm{Re}(d_i/D_C)^{2.5}\right]^{1/6}}\left\{1 + \frac{C_2}{\left[\mathrm{Re}(d_i/D_C)^{2.5}\right]^{1/6}}\right\}, \tag{22}$$

$$C_1 = 1.88411177 \times 10^{-1} + 85.2472168(\varepsilon/d_i) - 4.63030629 \times 10^4(\varepsilon/d_i)^2 + 1.31570014 \times 10^7(\varepsilon/d_i)^3,$$

$$C_2 = 6.79778633 \times 10^{-2} + 25.3880380(\varepsilon/d_i) - 1.06133140 \times 10^4(\varepsilon/d_i)^2 + 2.54555343 \times 10^6(\varepsilon/d_i)^3,$$

12. Schmidt [36]

$$f_c/f_s = 1 + 0.14\mathrm{Re}^x, \tag{23}$$

where $x = [1 - 0.0644/(D_C/d_i)^{0.312}]/(D_C/d_i)^{0.97}$,

13. Srinivasan et al. [37]

(a) $$f_c = 5.22\left(\mathrm{Re}\sqrt{(D_C/d_i)}\right)^{-0.6}, \tag{24}$$

(b) $$f_c = 1.8\left(\mathrm{Re}\sqrt{(D_C/d_i)}\right)^{-0.5}, \tag{25}$$

(c) $$f_c = 1.084\left(\mathrm{Re}\sqrt{(D_C/d_i)}\right)^{-0.2}, \tag{26}$$

14. Ito [38]

$$f_c/f_s = 0.1033\sqrt{De}\left[(1 + 1.729/De)^{0.5} - (1.729/De)^{0.5}\right]^{-3}, \tag{27}$$

15. Collins and Dennis [39]

$$f_c/f_s = 0.38 + 0.1028\sqrt{De}, \tag{28}$$

16. Van Dyke [40]

$$f_c/f_s = 0.47136De^{1/4}, \tag{29}$$

17. Mishra and Gupta [41]

$$f_c/f_s = 1 + 0.033[\log_{10}He]^4, \tag{30}$$

$$f_c = 0.0791\mathrm{Re}^{-1/4} + 0.0075\sqrt{(d_i/D_C)}, \tag{31}$$

where $He = \mathrm{Re}[(d_i/D_C)/\{1 + (p/\pi D_C)^2\}]^{1/2}$,

18. Dennis [42]

$$f_c/f_s = 0.388 + 0.1015\sqrt{De}, \tag{32}$$

19. Manlapaz and Churchill [43]

$$f_c/f_s = \left[\left(1 - 0.18/\left\{1 + (35/He)^2\right\}^{0.5}\right)^m + (1 + d_i/\{3D_C\})^2(He/88.33)\right]^{0.5}, \tag{33}$$

where $m = 2$ for $De < 20$, $m = 1$ for $20 < De < 40$, $m = 0$ for $De > 40$,

20. Yanase et al. [44]

$$f_c/f_s = 0.557 + 0.0938\sqrt{De}, \tag{34}$$

21. Giri [45]

$$f_c = 1.1258/\left[\mathrm{Re}^{0.1938}(D_C/d_i)^{0.5391}\right], \tag{35}$$

22. Liu and Masliyah [46]

$$f_c\mathrm{Re} = \left[16 + \left(0.378\mathrm{De}\lambda^{1/4} + 12.1\right)\mathrm{De}^{1/2}\lambda^{1/2}\gamma^2\right] \times \left[1 + \left\{\left(0.0908 + 0.0233\lambda^{1/2}\right)\mathrm{De}^{1/2} - 0.132\lambda^{1/2} + 0.37\lambda - 0.2\right\}/(1 + 49/\mathrm{De})\right], \tag{36}$$

where $\lambda = (D_C/2)/[(D_C/2)^2 + (p/2\pi)^2]$,

$\gamma = \eta/(\lambda De)^{1/2}$,

$\eta = (p/2\pi)/\left[(D_C/2)^2 + (p/2\pi)^2\right]$.

2.2. Two-phase flow region

In this region, the capillary tube is divided into a number of elements as shown in Fig. 2. The following equations are based on control volume considerations in the two-phase region.

The conservation of mass can be calculated using the following equation:

$$m = \frac{AV_i}{v_i} = \frac{AV_{i+1}}{v_{i+1}}. \tag{37}$$

By neglecting the difference in elevation, the conservation of energy for steady-state adiabatic conditions without external work can be expressed as follows:

$$\left(\frac{P_3}{\rho_3 g} + z_3 + \frac{V_3^2}{2g} + u_3\right) = \left(\frac{P_i}{\rho_i g} + z_i + \frac{V_i^2}{2g} + u_i\right). \tag{38}$$

where u is internal energy. Re-arranging Eq. (38) and using the relation $h = Pv + u$,

$$\left(h_3 + gz_3 + \frac{V_3^2}{2}\right) = \left(h_i + gz_i + \frac{V_i^2}{2}\right) = \text{constant},$$

$$h + \frac{V^2}{2} = \text{constant} \tag{39}$$

where h and V are the enthalpy and fluid velocity at any point, respectively.

Due to the fact that the refrigerant flows along the capillary tube, the pressure gradually drops and the liquid flashes into vapour arising purely from the reduced pressure, at any point. Hence,

$$h_i = h_{fi}(1 - x_i) + h_{gi}x_i, \quad v_i = v_{fi}(1 - x_i) + v_{gi}x_i. \tag{40}$$

also, $m = \rho VA = \text{constant}$

$$V = \frac{m}{\rho A} = \frac{G}{\rho} = Gv. \tag{41}$$

The energy balance between point 3 and at any point along the capillary tube in the two-phase flow region can be calculated by substituting Eqs. (40) and (41) into Eq. (39) to give:

$$h_3 + \frac{V_3^2}{2} = h_f + x\left(h_g - h_f\right) + \frac{G^2}{2}\left(v_f(1 - x) + v_g x\right)^2. \tag{42}$$

Expanding the right-hand side of Eq. (42) and rearranging, yields:

$$\left[\left(v_g - v_f\right)^2\frac{G^2}{2}\right]x^2 + \left[G^2 v_f\left(v_g - v_f\right) + \left(h_g - h_f\right)\right]x + \left[\frac{G^2 v_f^2}{2} - h_3 - \frac{V_3^2}{2} + h_f\right] = 0. \tag{43}$$

The quality (x) can be expressed in the form of a quadratic equation as shown in Eq. (44).

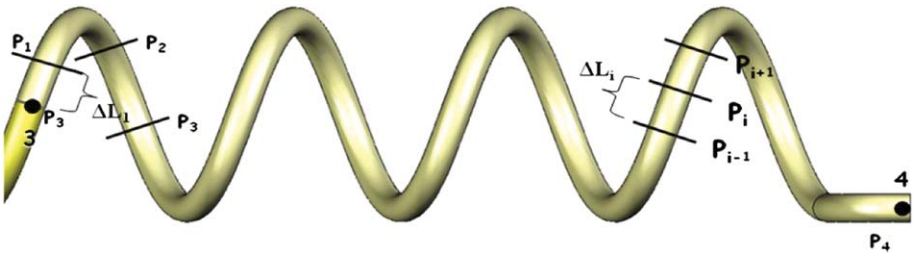

Fig. 2. Schematic diagram of simulation approach for an adiabatic two-phase flow region.

$$x = \frac{-h_{fg} - G^2 v_f v_{fg} + \sqrt{\left(G^2 v_f v_{fg} + h_{fg}\right)^2 - \left(2G^2 v_{fg}^2\right)\left[\frac{G^2 v_f^2}{2} - h_3 - \frac{V_3^2}{2} + h_f\right]}}{G^2 v_{fg}^2}, \quad (44)$$

where $h_{fg} = h_g - h_f$ and $v_{fg} = v_g - v_f$.

Again, the conservation of momentum can be expressed by reconsidering the element of fluid as shown in Fig. 2.

$$\left(P\frac{\pi d_i^2}{4}\right) - (P + dP)\frac{\pi d_i^2}{4} - \tau_w d_i \pi dL = mdV, \quad (45)$$

where τ_w is the wall shear stress which is defined as follows:

$$\tau_w = \frac{f_{tp}\rho V^2}{8}. \quad (46)$$

Substituting Eq. (46) into Eq. (45), we get.

$$-\frac{\pi d_i^2}{4}dP - \frac{f_{tp}}{8}\rho V^2 d_i \pi dL = mdV \quad (47)$$

or:

$$dL = \frac{d_i}{f_{tp}}\left[\frac{2dP}{\rho V^2} + \frac{2mdV}{\rho A V^2}\right]. \quad (48)$$

where f_{tp} is the two-phase friction factor

For constant mass flow rate, $dm = 0$, Eq. (49) is obtained.

$$\frac{-dV}{V} = \frac{d\rho}{\rho}. \quad (49)$$

Substituting Eq. (49) into Eq. (48) gives.

$$dL = \frac{2d_i}{f_{tp}}\left[\frac{-\rho dP}{\rho V^2} + \frac{d\rho}{\rho}\right]. \quad (50)$$

3. Solution method

As shown in Fig. 2, the capillary tube between points 3 and 4 can be divided into numerous sections. Since P_3 is known (saturated liquid), the pressure at any section 'i' can be calculated from the following equation:

$$P_i = P_3 - i\triangle P. \quad (51)$$

With the pressure (P_i) and the quality (x_i) calculated from Eq. (44), the entropy of each section can be calculated from:

$$s_i = s_{if}(1 - x) + s_{ig}x. \quad (52)$$

The Reynolds number in the two-phase region is determined by:

$$\mathrm{Re}_{tp} = \frac{Vd_i}{\mu_{tp} v_{tp}}, \quad (53)$$

where

$$V = Gv_{tp} = G(xv_g) + (1 - x)v_f. \quad (54)$$

The two-phase dynamic viscosity correlation proposed by McAdams [47] is presented as follows:

$$\frac{1}{\mu_{tp}} = \frac{x}{\mu_g} + \frac{1 - x}{\mu_f}. \quad (55)$$

A gradual increase of entropy is obtained along the capillary tube. When the entropy reaches the maximum value, the fluid velocity is equal to the local speed of sound and the flow is choked. As a consequence, the calculation is ended at this point.

The pressure of the element where the entropy has a maximum value $(P_i)_{s\ max}$, is then compared to the evaporator pressure (P_{evap}) given by.

if $P_{i,smax} = P_{evap}$ then $P_4 = P_{evap}$,
if $P_{i,smax} \neq P_{evap}$ then $P_4 = P_{i,smax}$

Thus, from Eq. (50), the two-phase length can be expressed as follows:

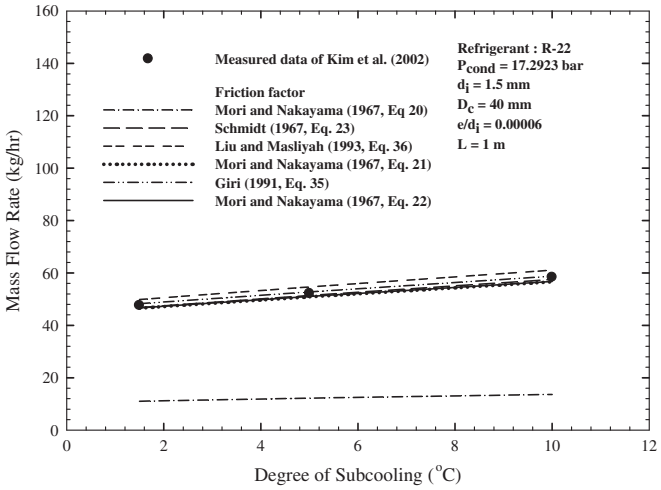

Fig. 3. Comparison of the present numerical results with the measured mass flow rates.

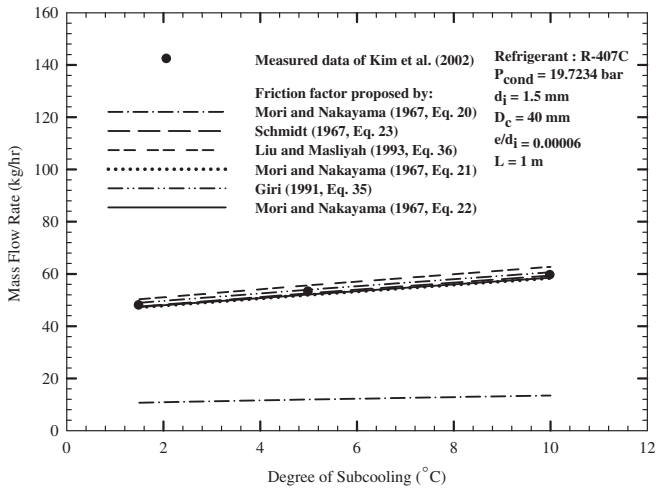

Fig. 4. Comparison of the present numerical results with the measured mass flow rates.

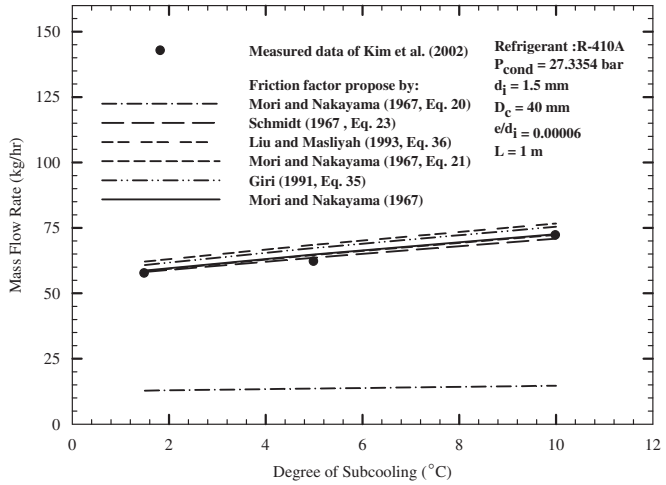

Fig. 5. Comparison of the present numerical results with the measured mass flow rates.

$$L_{tp} = d_i\left[\frac{-2}{G^2}\int_{P_3}^{P_{smax}}\frac{\rho}{f_{tp}}dp + 2\int_{P_3}^{P_{smax}}\frac{d\rho}{\rho f_{tp}}\right], \tag{56}$$

The capillary length of each section is calculated from:

$$\Delta L_i = \frac{2d_i}{f_{tp,i}}\left(\frac{-\rho_i \Delta P}{G^2} + \frac{\Delta \rho}{\rho_i}\right). \tag{57}$$

The total length of the two-phase region is determined from:

$$L_{tp} = \sum_{i=1}^{n} \Delta L_i, \tag{58}$$

Finally, the total length of capillary tube is the sum of the single-phase and two-phase lengths which are defined as follows:

$$L_{total} = L_{sp} + L_{tp}. \tag{59}$$

All refrigerant properties are taken from the REFPROP computer program [48] and are developed in the function of pressure.

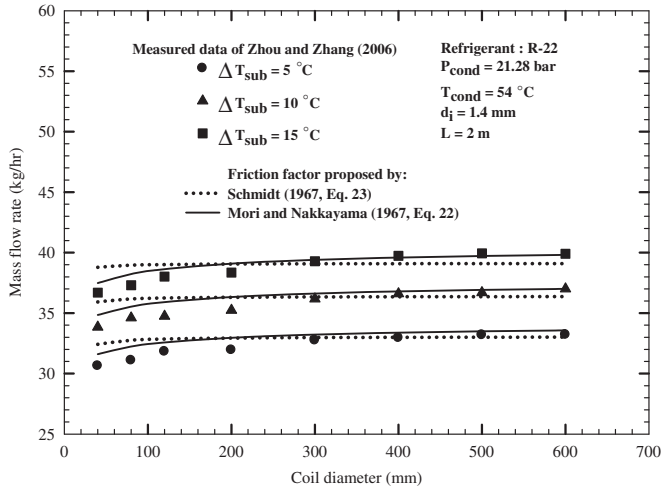

Fig. 6. Comparison of the present numerical results with the measured mass flow rate at different coil diameters and degrees of subcooling.

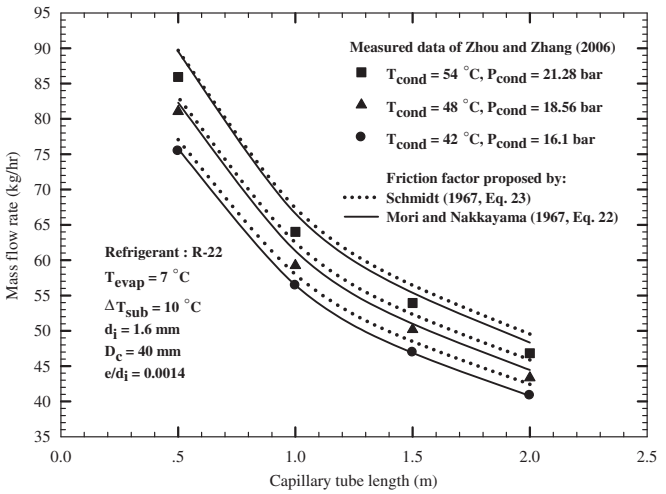

Fig. 7. Comparison of the present numerical results with the measured mass flow rates at different capillary tube lengths and condensing temperatures.

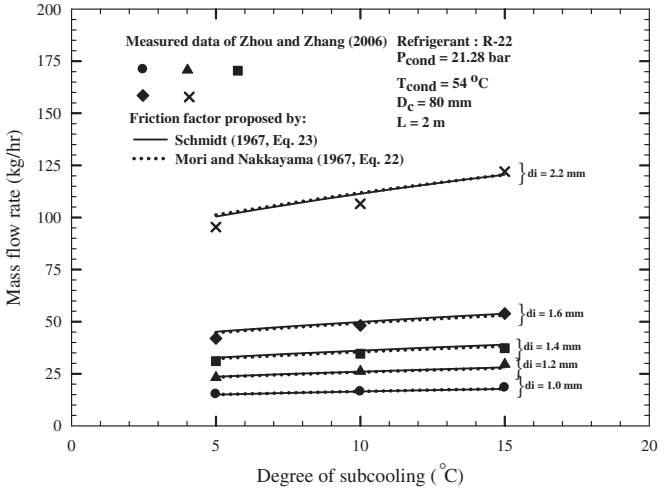

Fig. 8. Comparison of the present numerical results with the measured mass flow rates at different capillary tube diameters and degrees of subcooling.

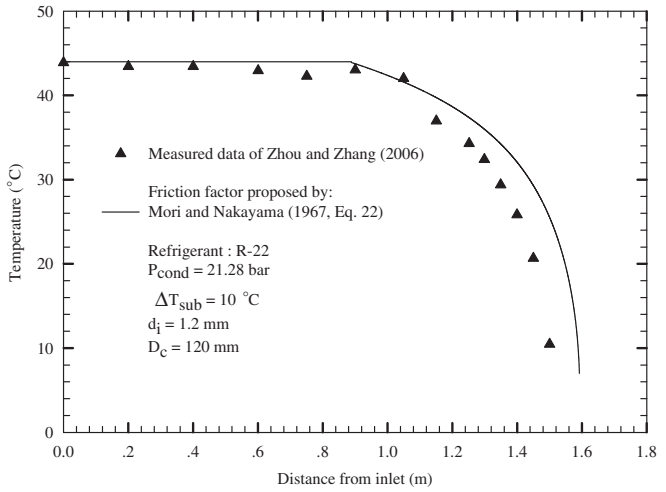

Fig. 9. Comparison of measured temperature distributions with present numerical results.

4. Results and discussion

In order to validate the present model, comparisons are made with the limited available experimental data of Kim et al. [15] for R-22, R-407C and R-410A and of Zhou and Zhang [21] for R-22.

Figs. 3–5 present the mass flow rate variation versus degree of subcooling by comparing the numerical results with the experimental data of Kim et al. [15] for R-22 ($D_c = 200, 120$ and 40 mm). In the present model, friction factors are calculated by the twenty six different models presented in Section 2.1. In this case, the mass flow rate is plotted with the degree of subcooling for fixed total lengths of the helical capillary tube. It is clearly seen that mass flow rate decreases with decreasing subcooling temperature. This is due to the friction loss in the capillary tube increases as the temperature increases which results in the decrease of the refrigerant mass flow rate entering the tube. The model is found to fit the data very well and, in particular, the friction factor models of Mori and Nakayama [35] (Eqs. (20–22)) and Schmidt [36] (Eq. (23)) agree well with the data of Kim et al. [15] for R-22.

Fig. 6 presents comparisons between the present results and the experimental data of Zhou and Zhang [21] for R-22 at different coil diameters and degrees of subcooling. The results show that the calculated mass flow rate of R-22 deviates from the experimental results. Moreover, the results also indicate that the mass flow rate obtained from the present model is fitted very well with the data and in particular, the friction factor of Mori and Nakayama [35] (Eq.

Table 1
Comparison of the present numerical results with the experimental data of Kim et al. [15] for R-22.

Conditions	L (m)	d_i (mm)	ε/d_i	P_{con} (bar)	T_{con} (°C)	ΔT_{sc} (°C)	D_c (mm)	$\dot{m}_{exp}$ (kg/h)
No.1	1.0	1.5	6×10^{-5}	17.2923	45	1.5	200	50.65
No.2						5.0	200	55.04
No.3						10.0	200	61.85
No.4						1.5	120	49.10
No.5						5.0	120	53.68
No.6						10.0	120	60.26
No.7						1.5	40	47.56
No.8						5.0	40	52.20
No.9						10.0	40	58.36

Author	Error (%)									MAE
Conditions	No.1	No.2	No.3	No.4	No.5	No.6	No.7	No.8	No.9	
1. Dean [25] Eq. (7)	−99.10	−99.08	−99.10	−99.25	−99.25	−99.26	−99.53	−99.52	−99.53	99.3
2. White [26] Eq. (8)	−59.55	−59.18	−59.59	−60.40	−60.25	−60.61	−63.16	−63.18	−63.36	61.0
3. White [27] Eq. (9)	50.98	56.32	65.90	53.06	57.17	65.57	50.14	52.65	58.66	56.7
4. Adler [28] Eq. (10)	−60.30	−59.87	−60.23	−61.21	−61.03	−61.35	−64.37	−64.36	−64.52	61.9
5. Prandtl [29] Eq. (11)	−57.16	−56.78	−57.24	−57.58	−57.47	−57.89	−59.93	−59.99	−60.23	58.3
6. Hasson [30] Eq. (12)	−60.17	−59.77	−60.14	−60.95	−60.78	−61.12	−63.90	−63.91	−64.07	61.6
7. Ito [31] Eq. (13)	−61.17	−60.75	−61.09	−62.14	−61.95	−62.25	−65.45	−65.42	−65.55	62.9
8. Ito [31] Eq. (14)	56.94	63.51	77.76	59.51	64.79	77.43	59.45	63.23	73.41	66.2
9. Ito [31] Eq. (15)	56.81	63.33	77.60	59.86	65.21	78.19	59.28	63.07	73.09	66.3
10. Kubair and Varrier [32]										
(a) Eq. (16)	95.51	127.09	209.53	100.81	130.41	213.93	102.84	126.17	205.55	145.8
(b) Eq. (17)	20.87	23.16	24.16	24.29	25.89	26.98	26.36	27.36	28.84	25.3
11. Barua [33] Eq. (18)	−59.18	−58.77	−59.15	−59.98	−59.81	−60.16	−63.01	−63.02	−63.18	60.7
12. Mori and Nakayama [34] Eq. (19)	−61.43	−61.03	−61.39	−62.23	−62.07	−62.39	−65.18	−65.18	−65.33	62.9
13. Mori and Nakayama [35] Eq. (20)	−6.87	−4.76	−5.07	−40.99	−40.19	−40.39	−76.81	−76.64	−76.64	40.9
14. Mori and Nakayama [35] Eq. (21)	−4.33	−3.77	−4.58	−2.46	−2.48	−3.26	−2.10	−2.57	−3.03	**3.2**
15. Mori and Nakayama [35] Eq. (22)	−4.01	−3.43	−4.23	−2.14	−2.14	−2.91	−1.79	−2.25	−2.70	**2.8**
16. Schmidt [36] Eq. (23)	−5.73	−5.38	−6.41	−3.05	−3.17	−4.05	−1.59	−1.55	−1.51	**3.6**
17. Srinivasan et al. [37]										
(a) Eq. (24)	134.41	304.72	466.72	133.83	271.99	421.31	124.37	202.28	325.43	265.0
(b) Eq. (25)	114.62	196.93	304.88	115.14	179.65	281.61	108.26	139.52	228.15	185.4
(c) Eq. (26)	−44.22	−44.13	−45.04	−43.92	−44.16	−45.04	−45.22	−45.69	−46.33	44.86
18. Ito [38] Eq. (27)	−60.84	−60.44	−60.81	−61.64	−61.47	−61.81	−64.61	−64.61	−64.77	62.3
19. Collins and Dennis [39] Eq. (28)	−60.67	−60.12	−60.51	−61.32	−61.18	−61.52	−64.33	−64.34	−64.51	62.1
20. Van Dyke [40] Eq. (29)	−47.40	−47.05	−47.68	−47.29	−47.25	−47.85	−48.89	−49.08	−49.45	48.0
21. Mishra and Gupta [41]										
(a) Eq. (30)	−41.45	−40.86	−41.39	−36.94	−36.68	−37.18	−28.68	−28.66	−28.89	35.6
(b) Eq. (31)	55.04	61.17	73.81	58.05	63.04	74.59	57.46	60.95	70.01	63.8
22. Dennis [42] Eq. (32)	−60.33	−59.94	−60.32	−61.14	−60.99	−61.34	−64.15	−64.17	−64.34	61.9
23. Manlapaz and Churchill [43]										
(a) m=2 Eq. (33)	−39.79	−39.13	−39.63	−34.96	−34.64	−35.11	−26.18	−26.11	−26.29	33.5
(b) m=1 Eq. (33)	−39.98	−39.34	−39.83	−35.21	−34.90	−35.37	−26.59	−26.53	−26.73	33.8
(c) m=0 Eq. (33)	−40.21	−39.58	−40.08	−35.51	−35.21	−35.69	−27.07	−27.03	−27.24	34.2
24. Yanase et al. [44] Eq. (34)	−59.49	−59.11	−59.50	−60.28	−60.13	−60.49	−63.27	−63.29	−63.47	61.0
25. Giri [45] Eq. (35)	31.12	33.71	36.15	23.07	23.99	24.77	1.48	1.03	0.65	19.6
26. Liu and Masliyah [46] Eq. (36)	41.08	44.97	49.93	31.25	32.95	34.88	4.82	4.68	4.61	27.7

$$\text{Error}(\%) = \left(\frac{M_{num} - M_{exp}}{M_{exp}}\right) \times 100$$

$$\text{MAE}(\%) = \frac{1}{N}\sum_{N}\frac{\|M_{num} - M_{exp}\|}{M_{exp}} \times 100$$

(22)) gives the best result which is in agreement with the results of Zhou and Zhang [21] for R-22. Moreover, the friction factor of Mori and Nakayama [35] (Eq. (22)) gives a mean absolute error of 1.58%. In case of a coil diameter less than 300 mm, the experimental data show that the mass flow rate of refrigerant decreases with decreasing coil diameter. Between the coil diameters of 40 and 300 mm, the change in the mass flow rate is about 6–7%.

On the other hand, the mass flow rate of refrigerants is increased by a minuscule amount around 1–2% for a coil diameter ranging between 300 and 600 mm.

Fig. 7 shows a comparison of mass flow rate between the present model and the experimental data of Zhou and Zhang [21] for R-22 flowing through a coiled capillary tube with different capillary tube lengths and condensing temperatures. Similar to the straight tube, the mass flow rate of the coiled capillary decreases rapidly as the tube length increases, but it increases with increasing condensing temperature. The figure also shows that the friction factor of Mori and Nakayama [35] (Eq. (22)) gives reasonable predictions compared with the experimental data.

Similarly, Fig. 8 shows a comparison of mass flow rate between the present model and the experimental data of Zhou and Zhang [21] for R-22 flowing through a coiled capillary tube with different capillary tube diameters and degrees of subcooling. Similarly, the mass flow rate of the coiled capillary tube increases rapidly as the capillary tube diameter increases. Moreover, the results show that the friction factor of Mori and Nakayama [35] (Eq. (22)) gives reasonable predictions compared with experimental data. The results from the present model using the friction factor of Mori and Nakayama [22] are compared with the measured data of Zhou and Zhang [21] as shown in Fig. 8. The results give the mean absolute error of 3%. While comparison between the measured data of Zhou and Zhang [21] and their simulation results give an average deviation of −4.53%. It is clear that the present model shows good prediction than the model of Zhou and Zhang [22].

Fig. 9 shows comparisons between the present model and the experimental data of Zhou and Zhang [21] to validate the temperature distribution along the capillary tube length. In the subcooled liquid region, the temperature remains nearly constant along the tube, while it decreases rapidly after the refrigerant flashes. The deviations between the simulated results with the measured values may be due to the fact that the model was developed based on many assumptions, for example, the metastable liquid region is neglected. This phenomena occurs when the pressure of the liquid approach to the saturation pressure, but the fluid is still in the liquid phase. It can be clearly seen from Fig. 9 that the metastable phenomena may occur. Moreover, the viscosities calculated from various models may cause the error, for example, the McAdam equation which was used to calculate the viscosity of the refrigerant was established under the different conditions compared with the Zhou and Zhang [21] experiment.

Table 1 gives comparisons between the present results and the experimental data of Kim et al. [15] for R-22 ($L = 1.0$ m, $d_i = 1.5$ mm, $\varepsilon/d_i = 6$ and $T_{cond} = 45$ °C) at various coil diameters and degrees of subcooling, using the twenty six friction factor equations. From this table, it is evident that the Mori and Nakayama and Schmidt equations give the smallest error values compared with the other equations.

It is clear that the Mori and Nakayama [35] and Schmidt [36] correlations fit the best to experimental data. This is due to the fact that the correlations were obtained from the measured data at the d_i/D_c ranging between 0.02 and 0.3 which correspond to the experimental conditions performed by Kim et al. [15] and Zhou and Zhang [21]. Other correlations presented in the manuscript were developed based on the curvature ratios which are different from the measured data.

5. Conclusion

In the present study, a model has been developed to determine the refrigerant flow characteristics in adiabatic helical capillary tubes. From the results, it is evident that the most suitable equations for calculating the friction factor are those due to Mori and Nakayama [35] (Eqs. (21,22)) and Schmidt [36] (Eq. (23)). These equations gave a deviation ranging between 1 and 4%. The present model was validated by comparing the results with the experimental data of Kim et al. [15] for R-22, R-407C and R-410A, and the data of Zhou and Zhang [21] for R-22, and was found to give an average discrepancy of around 4%.

Acknowledgement

The authors are indebted to King Mongkut's University of Technology Thonburi (KMUTT), the Thailand Research Fund (TRF) and the Office of the Higher Education Commission for supporting this study.

References

[1] T.N. Wong, K.T. Ooi, Adiabatic capillary tube expansion devices: a comparison of the homogeneous flow and the separated flow models. Applied Thermal Engineering 16 (7) (1996) 625–634.
[2] P.K. Bansal, A.S. Rupasinghe, A homogeneous model for adiabatic capillary tubes. Applied Thermal Engineering 18 (3–4) (1998) 207–219.
[3] S.M. Sami, C. Tribes, Numerical prediction of capillary tube behavior with pure and binary alternative refrigerants. Applied Thermal Engineering 18 (1998) 491–502.
[4] C. Melo, R.T.S. Ferreira, C. Boabaid Neto, J.M. Goncalves, M.M. Mezavi, An experimental analysis of adiabatic capillary tubes. Applied Thermal Engineering 19 (1999) 669–684.
[5] S. Wongwises, T. Songnetichaovalit, N. Lokathada, P. Kritsadathikarn, M. Suchatawat, W. Pirompak, A comparison of the flow characteristics of refrigerants flowing through adiabatic capillary tubes. International Communications in Heat and Mass Transfer 27 (2000) 611–621.
[6] S. Wongwises, P. Chan, N. Luesuwanatat, T. Purattanarak, Two-phase separated flow model of refrigerants flowing through capillary tubes. International Communications in Heat and Mass Transfer 27 (2000) 343–356.
[7] S. Wongwises, W. Pirompak, Flow characteristics of pure refrigerants and refrigerant mixtures in adiabatic capillary tubes. Applied Thermal Engineering 21 (8) (2001) 845–861.
[8] S.M. Liang, T.N. Wong, Numerical modeling of two-phase refrigerant flow through adiabatic capillary tubes. Applied Thermal Engineering 21 (2001) 1035–1048.
[9] R.Y. Li, S. Lin, Z.H. Chen, Numerical modeling of thermodynamic non-equilibrium flow of refrigerant through capillary tubes. ASHRAE Transaction 96 (1990) 542–549.
[10] E.P. Mikol, Adiabatic single and two-phase flow in small bore tubes. ASHRAE Journal 5 (1963) 75–86.
[11] D. Jung, C. Park, B. Park, Capillary tube selection for HCFC22 alternatives. International Journal of Refrigeration 22 (1999) 604–614.
[12] J. Sinpiboon, S. Wongwises, Numerical investigation of refrigerant flow through non-adiabatic capillary tubes. Applied Thermal Engineering 22 (2002) 2015–2032.
[13] F.A.S. Fiorelli, A.A.S. Huerta, O.M. Silvares, Experimental analysis of refrigerant mixtures flow through adiabatic capillary tubes. Experimental Thermal and Fluid Science 26 (2002) 499–512.
[14] P.K. Bansal, G. Wang, Numerical analysis of choked refrigerant flow in adiabatic capillary tubes. Applied Thermal Engineering 24 (2004) 851–863.
[15] J. Choi, Y. Kim, J.T. Chung, An empirical correlation and rating charts for the performance of adiabatic capillary tubes with alternative refrigerants. Applied Thermal Engineering 24 (2004) 29–41.
[16] L. Yang, W. Wang, A generalized correlation for the characteristics of adiabatic capillary tubes. International Journal of Refrigeration 31 (2008) 197–203.
[17] ASHRAE Handbook – Refrigeration. American Society of Heating, Refrigerating and Air-Conditioning Engineer Inc, 2002, (Chapter 45).
[18] A.L. Seixlack, M.R. Barbazelli, Numerical analysis of refrigerant flow along non-adiabatic capillary tubes using a two-fluid model. Applied Thermal Engineering 29 (2009) 523–531.
[19] S. Ali, Pressure drop correlations for flow through regular helical coil tubes. Fluid Dynamics Research 28 (2001) 295–310.
[20] S.G. Kim, S.T. Ro, M.S. Kim, Experimental investigation of the performance of R-22, R-407C and R-410A in several capillary tubes for air-conditioners. International Journal of Refrigeration 25 (2002) 521–531.
[21] G. Zhou, Y. Zhang, Experimental investigation on hysteresis effect of refrigerant flowing through a coiled adiabatic capillary tube. Energy Conversion and Management 47 (2006) 3084–3093.

[22] G. Zhou, Y. Zhang, Numerical and experimental investigations on the performance of coiled adiabatic capillary tubes. Applied Thermal Engineering 26 (2006) 1106–1114.
[23] C. Park, S. Lee, H. Kang, Y. Kim, Experimentation and odelling of refrigerant flow through coiled capillary tubes. International Journal of Refrigeration 30 (2007) 1168–1175.
[24] G. Valladares, Numerical simulation and experimental validation of coiled adiabatic capillary tubes. Applied Thermal Engineering 27 (2007) 1062–1071.
[25] W.R. Dean, The streamline motion of fluid in a curved pipe. Philosophy Magazine 5 (1928) 673–695.
[26] C.M. White, Streamline flow through curved pipe. Proceedings of the Royal Society of London Series A 123 (1929) 645–663.
[27] C.M. White, Fluid Friction and Its Relation to Heat Transfer, vol. 10, Transactions of Institution of Chemical Engineering, London, 1932, pp. 66–86.
[28] M. Adler, Stromung in Gekrummten Rohren. ZAMM-Journal of Applied Mathematics and Mechanics 14 (1934) 257–275.
[29] L. Prandtl, Fuhrer Dmchdie Stromungslehre 1954, , In: Braunsschweigh; English Transl., Essentials of Fluid Dynamics, third ed., vol. 168, Blackie and Son, London, 1949, 159.
[30] D. Hasson, Streamline flow resistance in coils, Research Correspondence 1 S1 (1955).
[31] H. Ito, Friction factors for turbulent flow in curved pipes. ASME Journal of Basic Engineering 81 (1959) 123–134.
[32] V. Kubair, C.B.S. Varrier, Pressure drop for liquid flow in helical coils. Indian Institute of Chemical Engineer Journal, Transactions 14 (1961/1962) 93–97.
[33] S.N. Barua, On secondary flow in stationary curved pipes. The Quarterly Journal of Mechanics and Applied Mathematics 16 (1963) 61–77.
[34] Y. Mori, W. Nakayama, Study on forced convective heat transfer in curve pipes I. International Journal of Heat and Mass Transfer 8 (1965) 67–82.
[35] Y. Mori, W. Nakayama, Study on forced convective heat transfer in curve pipes II. International Journal of Heat and Mass Transfer 10 (1967) 37–59.
[36] E.F. Schmidt, Warmeubergang and Druckverlust in Rohrschlangen. The Chemical Engineering and Technology 13 (1967) 781–789.
[37] P.S. Srinivasan, S.S. Nandapurkar, F.A. Holland, Pressure drop and heat transfer in coils. The Chemical Engineering (London) 218 (1968) 113–119.
[38] H. Ito, Laminar flow in curved pipes. ZAMM Journal of Applied Mathematics and Mechanics 11 (1969) 653–663.
[39] W.M. Collins, S.C.R. Dennis, The steady motion of a viscous fluid in a curved tube. The Quarterly Journal of Mechanics and Applied Mathematics 28 (1975) 133–156.
[40] M. Van Dyke, Extended stokes-series laminar flow through a loosely coiled pipe. Journal of Fluid Mechanics 86 (1978) 129–145.
[41] P. Mishra, S.N. Gupta, Momentum transfer in curved pipes 1. Newtonian fluids; 2. Non-Newtonian fluids. Industrial and Engineering Chemistry Process Design and Development 18 (1979) 130–142.
[42] S.C.R. Dennis, Calculation of the steady flow through a curved tube using a new finite difference method. Journal of Fluid Mechanics 99 (1980) 449–467.
[43] R.L. Manlapaz, S.E.W. Churchill, Fully developed laminar flow in a helically coiled tube of finite pitch. Chemical Engineering Communications 7 (1980) 57–78.
[44] S. Yanase, N. Goto, K. Yamamoto, Dual solutions of the flow through a curved tube. Fluid Dynamics Research 5 (1989) 191–201.
[45] J.N. Gorasia, N. Dubey, K.K. Jain, Computer-aided design of capillaries of different configurations. ASHRAE Transactions(pt 1) (1991) 132–138.
[46] S. Liu, J.M. Masliyah, Axially invariant laminar flow in helical pipes with finite pitch. Journal of Fluid Mechanics 251 (1993) 315–353.
[47] W.H. McAdams, W.K. Wood, R.L. Bryan, Vaporization inside horizontal tubes. II, Benzence-oil mixture. Transaction ASME 64 (1942) 193.
[48] McLinden, M.O., Klein, S.A., Lemmon, E.W., 1998. REFPROP – thermodynamic and transport properties of refrigerants and refrigerant mixtures, NIST Standard Reference Database – version 6.01.

Provided for non-commercial research and education use.
Not for reproduction, distribution or commercial use.

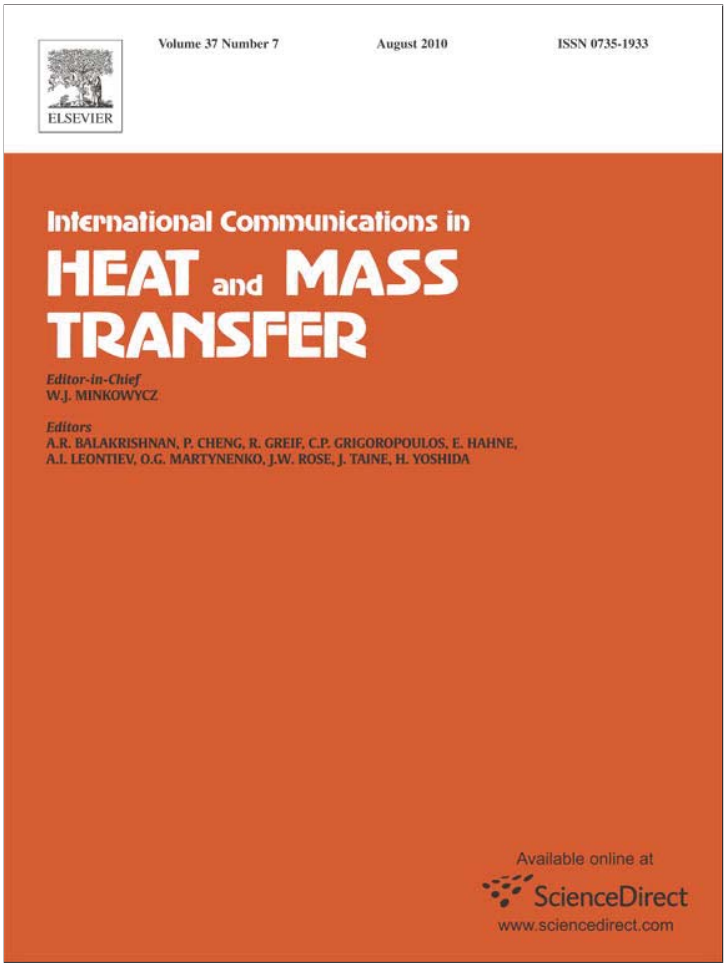

This article appeared in a journal published by Elsevier. The attached copy is furnished to the author for internal non-commercial research and education use, including for instruction at the authors institution and sharing with colleagues.

Other uses, including reproduction and distribution, or selling or licensing copies, or posting to personal, institutional or third party websites are prohibited.

In most cases authors are permitted to post their version of the article (e.g. in Word or Tex form) to their personal website or institutional repository. Authors requiring further information regarding Elsevier's archiving and manuscript policies are encouraged to visit:

http://www.elsevier.com/copyright

Author's personal copy

International Communications in Heat and Mass Transfer 37 (2010) 827–834

Contents lists available at ScienceDirect

International Communications in Heat and Mass Transfer

journal homepage: www.elsevier.com/locate/ichmt

Validation of void fraction models and correlations using a flow pattern transition mechanism model in relation to the identification of annular vertical downflow in-tube condensation of R134a ☆

A.S. Dalkilic [a,*], S. Wongwises [b,*]

[a] Heat and Thermodynamics Division, Department of Mechanical Engineering, Yildiz Technical University (YTU), Yildiz, Besiktas, Istanbul, 34349, Turkey
[b] Fluid Mechanics, Thermal Engineering and Multiphase Flow Research Laboratory (FUTURE), Department of Mechanical Engineering, King Mongkut's University of Technology Thonburi (KMUTT), Bangmod, Bangkok 10140, Thailand

ARTICLE INFO

Available online 7 July 2010

Keywords:
Condensation
Flow regime map
Vertical down flow
R134a
Phase change

ABSTRACT

This paper reports the experimental investigation of a model for predicting flow pattern transitions and for the validation of void fraction models and correlations proposed in the authors' previous publications and for the identification of flow regimes in data corresponding to annular flow downward condensation of R134a in a vertical smooth copper tube having an inner diameter of 8.1 mm and a length of 500 mm. R134a and water are used as working fluids on the tube side and annular side, respectively, of a double tube heat exchanger. Condensation experiments are done at mass fluxes of 260 and 515 kg m^{-2} s^{-1} in the high mass flux region of R134a. The condensing temperatures are between 40 and 50 °C; heat fluxes are between 10.16 and 66.61 kW m^{-2}. A mathematical model proposed by Soliman based on the models of Kosky and Lockhart–Martinelli is used to determine the condensation film thickness of R134a. Comparative void fraction values are determined indirectly using the measured data under laminar and turbulent flow conditions together with various void fraction models and correlations reported in the literature. There is good agreement between the void fraction results obtained from the theoretical model and those obtained from the void fraction models of Soliman, Chisholm and Armand, Turner and Wallis, Smith, Spedding and Spence previously proposed in the authors' publications and tested against their experimental database. Various well-known flow regime correlations from the literature are investigated to identify the flow regime occurring in the test tube, the correlations of Taitel and Dukler, Dobson, Akbar et al., Breber et al., Cavallini et al., and Sardesai et al. can provide accurate estimates of the annular flow conditions in spite of their different working conditions.

© 2010 Published by Elsevier Ltd.

1. Introduction

Many industrial applications are concerned with heat exchange in two-phase flow occurring in condensers and evaporators. The correct calculation of heat transfer rates and pressure drops are necessary for the accurate design of compact heat exchangers. The pressure drop and heat transfer characteristics are strongly dependent on the two-phase flow patterns, their transitions and void fraction during condensation. Most of the analytical or empirical two-phase heat transfer correlations available in the literature are developed for a certain flow pattern. For this reason, the use of specific heat transfer correlations, developed for a certain flow pattern, under incompatible operating conditions can cause significant errors in magnitude and trend. Finally, flow pattern identification inside a condenser and determination of void fraction are important to investigate heat transfer characteristics under certain flow conditions. Although there are a large number of flow pattern identifications by means of maps or correlations and also void fraction studies of horizontal and upward flow, few researchers have examined them for downward flow using new generation refrigerants in small diameter tubes. The most widely recommended flow pattern maps for vertical tubes are those of Barnea et al. [1], Fair [2], Hewitt and Roberts [3], Chen et al. [4] and Zahao and Bi [5].

The orientation and interaction of the liquid and vapor phases inside the tubes are among the most significant characteristics of two-phase flow. These phenomena are related to flow regime and flow pattern. A specific kind of geometric distribution of the phases is called a flow pattern or flow regime. The interfacial area of the phases is affected by geometry, and thus mass, momentum, and energy exchange between phases have come to play important roles in design. Different flow patterns may occur depending on tube position, tube geometry, flow rates, superficial velocities and physical properties such as density, viscosity, and surface tension of the two phases.

☆ Communicated by W.J. Minkowycz.

* Corresponding authors.
E-mail addresses: dalkilic@yildiz.edu.tr (A.S. Dalkilic), somchai.won@kmutt.ac.th (S. Wongwises).

0735-1933/$ – see front matter © 2010 Published by Elsevier Ltd.
doi:10.1016/j.icheatmasstransfer.2010.02.010

Author's personal copy

Nomenclature

A	inside surface area, m^{-2}
c_p	specific heat, J kg^{-1} K^{-1}
d	internal tube diameter, m
F_r	Froude rate parameter
G	mass flux, kg m^{-2} s^{-1}
Ga	Galileo number
g	gravitational constant, m s^{-2}
h	heat transfer coefficient, W m^{-2} K^{-1}
i	enthalpy, J kg^{-1}
i_{fg}	latent heat of condensation, J kg^{-1}
K	coefficient in Smith correlation
L	length of test tube, m
m	mass flow rate, kg s^{-1}
r	internal tube radius, m
Re	Reynolds number
S	slip ratio
T	temperature, °C
Q	heat transfer rate, W
u	velocity, m s^{-1}
u^*	frictional velocity, m s^{-1}
x	mean vapor quality
X	Lockhart–Martinelli parameter
We	Weber number
ΔP	pressure drop, Pa
ΔT	vapor side temperature difference, $T_{sat} - T_{wi}$, °C

Greek symbols

σ	surface tension, N m^{-1}
ρ	density, kg m^{-3}
μ	dynamic viscosity, kg m^{-1} s^{-1}
δ	film thickness, m
δ^+	dimensionless form of film thickness
α	void fraction
τ	shear stress, N m^{-2}
ν	kinematics viscosity m^2 s^{-1}
ϕ	two-phase multiplier

Subscripts

cond	condensate
exp	measured
f	frictional
g	gas/vapor
H	homogen
h	hydraulic
i	inlet
l	liquid
o	outlet
ph	preheater
ref	refrigerant
s	superficial for one phase flow alone in the pipe
sat	saturation
so	Soliman
T	total
TS	test section
w	water
wi	inner wall

Generally, flow patterns are observed by visual inspection and include bubble flow, slug flow, churn flow, wispy–annular flow, and annular flow in a vertical configuration, and bubble flow, plug flow, stratified flow, wavy flow, slug flow, and annular flow in a horizontal configuration. However, Hubbard and Dukler [6] classified the flow patterns as separated flow patterns (stratified flow, annular flow), intermittent flow patterns (elongated bubble flow, slug/plug flow, churn/froth flow), and dispersed flow patterns (bubble flow, dispersed bubble flow). The prediction of flow patterns during gas–liquid flow is achieved by one of three approaches: empirical correlations, visual examination, flow regime maps. In this paper, the applicability of some well-known empirical correlations such as Jaster and Kosky [7], Traviss and Rohsenow [8], Taitel and Dukler [9], Dobson [10], Akbar et al. [11], Breber et al. [12], Cavallini et al. [13], Chisholm and Sutherland [14], Soliman [15], Tandon et al. [16], Sardesai et al. [17], and Soliman [18] in Table 1 are investigated to determine the flow pattern during condensation of R134a in the test tube.

Two-phase annular flow occurs widely in film heating and cooling processes, particularly in power generation and especially in nuclear reactors. This flow regime has received the most attention, both analytically and experimentally, because of its practical importance and the relative ease with which analytical treatment may be applied. Annular two-phase flow is characterized by a phase interface separating a thin liquid film from the gas flow in the core region. In addition to this, the condensate distribution inside the tube wall is almost symmetric and there is high velocity vapor flow in the core during annular flow.

Void fraction is an important parameter and is always used to determine the flow pattern transition, heat transfer coefficient and two-phase pressure drop, and is defined as the cross-sectional area occupied by the vapor in relation to the area of the flow channel. Two-phase separated flow is commonly analyzed using the slip flow model. In this model, it is assumed that the separated phases have different uniform velocities. By contrast, the homogeneous model is defined as an ideal case, as it assumes a homogeneous mixture providing uniform velocities for both phases, and for that reason it is the simplest method of determination of the void fraction.

In the technical literature, numerous studies have been carried out on the modeling of the void fraction and can be divided into several groups: general void fraction models and correlations, $K\varepsilon_H$ parameter-based void fraction models and correlations, flow regime-based void fraction models and correlations, Lockhart and Martinelli parameter-based void fraction models and correlations and slip ratio void fraction models and correlations. It should be noted that the most predictive void fraction models and correlations according to the authors' experimental database, revealed in the authors' previous publications, such as Chisholm [19], Turner and Wallis [20], Smith [21], Spedding and Spence [22] in Table 2, are used for comparison in this paper. A brief and comprehensive overview of these works is presented in the authors' previous publications [23–26].

This paper gives a validation of the most agreeable void fraction models and correlations, previously explained in the authors' publications, against the heat transfer database in relation to a flow transition model having a relationship between the film thickness and void fraction models and correlations. The experiments include a wide range of high mass fluxes with different saturation temperatures as they relate to 380 data points of R134a belonging to the condensation heat transfer database of FUTURE Lab in KMUTT. Apart from the authors' previous publications [23–36], few studies exist in the literature on the investigation of heat transfer characteristics in a small diameter vertical tube during co-current down flow condensation, and besides this, there is no study with the experimental parameters of this work and its content in the open literature. In this study, determination of the void fraction is presented by means of the model of Soliman [18] and verified by relating the void fraction models and correlations. In addition to this, flow regime identification is performed using various flow pattern correlations valid for horizontal and vertical tubes to show the independence of the annular flow regime from tube orientation [33,35].

Author's personal copy

Table 1
Flow pattern correlations.

Number	Flow pattern correlation	Model/correlation
1	Jaster and Kosky [7]	$\tau'>29$ for annular flow regime $\tau' = \frac{\tau_{wall}}{(\rho_l g\delta)}$ Eq. (7) is used for τ_{wall}, Eq. (5) is used for δ
2	Traviss and Rohsenow [8]	Fr>45 for annular/semi-annular flow regime $Fr = \frac{u_l}{\sqrt{g\delta}}$ Eq. (5) is used for δ
3	Taitel and Dukler [9]	F>1.5 for annular flow regime $F = \sqrt{\frac{\rho_g}{(\rho_l-\rho_g)}}\left(\frac{u_{vs}}{\sqrt{gd}}\right)$ $u_{vs} = 14.63\rho_g^{-0.23}u_{ls}^{-0.287}d^{0.414}[\sigma(\rho_l-\rho_g)]^{0.115}$ $u_l = \frac{u_{ls}}{4\left(\bar{\delta}-\bar{\delta}^2\right)}$ $m_{cond} = \rho_l A_l u_l$ $\delta^+ = \frac{\delta}{d}$ Eq. (5) is used for δ
4	Dobson [10]	Fr_{so}>20 for annular flow regime $Fr_{so} = 0.025\mathrm{Re}_l^{1.59}\left(\frac{1+1.09X^{0.039}}{X}\right)1.5\frac{1}{Ga^{0.5}}$ for $Re_l \le 1250$ $Fr_{so} = 1.26Re_l^{1.04}\left(\frac{1+1.09X^{0.039}}{X}\right)1.5\frac{1}{Ga^{0.5}}$ for $Re_l > 1250$ $Ga = g\rho_l(\rho_l-\rho_g)\frac{(\sqrt{\alpha}d)^3}{\mu_l^2}X = \left(\frac{1-x}{x}\right)^{0.9}\left(\frac{\rho_g}{\rho_l}\right)^{0.5}\left(\frac{\mu_l}{\mu_g}\right)^{0.1}$ $\alpha = \left[1+\frac{1-x}{x}\left(\frac{\rho_g}{\rho_l}\right)^{\frac{2}{3}}\right]^{-1}$ $Re_l = \frac{Gd(1-x)}{\mu_l}$
5	Akbar et al. [11]	$\mathrm{We}_{gs} \ge 11.0\mathrm{We}_{ls}^{0.14}$ and $\mathrm{We}_{ls} \le 3.0$ for annular flow regime $We_{ls} = \frac{u_{ls}^2 d_h \rho_l}{\sigma}$ $We_{gs} = \frac{u_{gs}^2 d\rho_g}{\sigma}$ $u_l = \frac{u_{ls}}{4(\delta^+-\delta^{+2})}$ $m_{cond} = \rho_l A_l u_l$ $\delta^+ = \frac{\delta}{d}$ Eq. (5) is used for δ
6	Breber et al. [12]	j_g^*>1.5 and X<1.0 for annular regime $j_g^* = \frac{Gx}{\sqrt{(dg\rho_g(\rho_l-\rho_g)}}$ and $X = \left(\frac{1-x}{x}\right)^{0.9}\left(\frac{\rho_g}{\rho_l}\right)^{0.5}\left(\frac{\mu_l}{\mu_g}\right)^{0.1}$
7	Cavallini et al. [13]	j_g^*>2.5 and X<1.6 for annular regime $j_g^* = \frac{Gx}{\sqrt{(dg\rho_g(\rho_l-\rho_g)}}$ and $X = \left(\frac{1-x}{x}\right)^{0.9}\left(\frac{\rho_g}{\rho_l}\right)^{0.5}\left(\frac{\mu_l}{\mu_g}\right)^{0.1}$
8	Chisholm and Sutherland [14]	$\phi_g^2 F$>1.75 for annular flow regime $\phi_g^2 = 0.7X^2+2X+0.85$ and $X = \left(\frac{1-x}{x}\right)^{0.9}\left(\frac{\rho_g}{\rho_l}\right)^{0.5}\left(\frac{\mu_l}{\mu_g}\right)^{0.1}$ $F = \sqrt{\frac{\rho_g}{\rho_l-\rho_g}}\frac{u_{gs}}{\sqrt{dg}}$ $u_g = \frac{4u_{gs}}{1-4\delta^+ + 4\delta^{+2}}$ $m_g = \rho_g A_g u_g$ $m_g = xm_T$ $x = \frac{x_{TS,i}+x_{TS,o}}{2}$ $\delta^+ = \frac{\delta}{d}$
9	Soliman [15]	We<20 for annular flow regime $We = 2.45Re_g^{0.64}\left(\frac{\mu_g^2}{\rho_g\sigma d}\right)^{0.3}\phi_g^{-0.4}$ for $Re_l \le 1250$ $We = 0.85Re_g^{0.79}\left(\frac{\mu_g^2}{\rho_g\sigma d}\right)^{0.3}\left[\left(\frac{\mu_g^2}{\rho_g\sigma d}\right)^2\left(\frac{\rho_l}{\rho_g}\right)\right]^{0.0884}\left(X/\phi_g^{2.55}\right)^{0.157}$ for $Re_l > 1250X = \left(\frac{1-x}{x}\right)^{0.9}\left(\frac{\rho_g}{\rho_l}\right)^{0.5}\left(\frac{\mu_l}{\mu_g}\right)^{0.1}$ Eqs. (1) and (2) are used for Re_l and Re_g respectively. Eq. (12) is used for ϕ_g
10	Tandon et al. [16]	$1 \le j_g^* \le 6$ and $\frac{1-\alpha}{\alpha} \le 0.5$ for annular/semi-annular regime $j_g^* = \frac{Gx}{\sqrt{(dg\rho_g(\rho_l-\rho_g)}}$ $\alpha = \left\{1+\left(\frac{\rho_g}{\rho_l}\right)K\left(\frac{1}{x}-1\right)+\left(\frac{\rho_g}{\rho_l}\right)(1-K)\left(\frac{1}{x}-1\right)\left[\frac{\left(\frac{\rho_l}{\rho_g}\right)+K\left(\frac{1}{x}-1\right)}{1+K\left(\frac{1}{x}-1\right)}\right]\right\}^{-1}$ $K = 0.4$
11	Sardesai et al. [17]	$\beta \ge 1.75$ for annular flow regime $\beta = (0.7X^2+2X+0.85)F$ $X = \left(\frac{1-x}{x}\right)^{0.9}\left(\frac{\rho_g}{\rho_l}\right)^{0.5}\left(\frac{\mu_l}{\mu_g}\right)^{0.1}$ $F = \sqrt{\frac{\rho_g}{\rho_l-\rho_g}}\frac{j_g}{\sqrt{dg}}$ $j_g = \frac{xG}{\rho_g}$
12	Soliman [18]	Fr>45 for annular/semi-annular flow regime $Fr = \frac{0.25Re_l\left(\frac{u^*}{\delta^+}\right)^{1.5}}{\sqrt{gv_l}}$ $Re_l = \frac{Gd(1-x)}{\mu_l}$ Eq. (6) is used for u^*, Eqs. (3) and (4) are used for δ^+

Author's personal copy

Table 2
Void fraction models and correlations.

Number	Void fraction model/correlation	Model/correlation
1	Homogeneous model	$\alpha_H = \frac{1}{1+\left(\frac{1-x}{x}\right)\left(\frac{\rho_g}{\rho_l}\right)S} \quad S=1$
2	Soliman [18]	$G(1-x) = 4\rho_l u_l\left(\frac{\delta}{d}\right) \quad \alpha = 1-\frac{4\delta}{d}$
3	Chisholm [19]	$\alpha = \frac{1}{\alpha_H + (1-\alpha_H)^{0.5}}\alpha_H$
4	Turner and Wallis [20]	$\frac{1-\alpha}{\alpha} = A\left(\frac{1-x}{x}\right)^p\left(\frac{\rho_g}{\rho_l}\right)^q\left(\frac{\mu_l}{\mu_g}\right)^r$

Correlation or model	A	p	q	r
Homogeneous	1	1	1	0
Zivi	1	1	0.67	0
Turner–Wallis	1	0.72	0.4	0.08
Lockhart–Martinelli	0.28	0.64	0.36	0.07
Thom	1	1	0.89	0.18
Baroczy	1	0.74	0.65	0.13

5	Smith [21]	$\alpha = \left\{1+\left(\frac{\rho_g}{\rho_l}\right)K\left(\frac{1}{x}-1\right)+\left(\frac{\rho_g}{\rho_l}\right)(1-K)\left(\frac{1}{x}-1\right)\left[\frac{\left(\frac{\rho_l}{\rho_g}\right)+K\left(\frac{1}{x}-1\right)}{1+K\left(\frac{1}{x}-1\right)}\right]\right\}^{-1}$ $K=0.4$
6	Spedding and Spence [22]	$\alpha = \left(1+2.22\left(\frac{1-x}{x}\right)^{0.65}\left(\frac{\rho_g}{\rho_l}\right)^{0.65}\right)^{-1}$

2. Experimental apparatus and method

Due to space limitations, detailed descriptions of the experimental apparatus and test section for studying the condensation of R134a inside a vertical tube can be found in the authors' previous publications.

3. Data reduction

The data reduction of the measured results such as inlet and outlet vapor qualities of the test section, average heat transfer coefficient can be seen from the authors' previous publications in detail.

3.1. Calculation procedure for annular flow model

To confirm the annular flow pattern during condensation of refrigerant in the test section, the experimental results at a mass flux of 260–515 kg m^{-2} s^{-1} and condensing temperature of 40–50 °C are checked with the flow regime maps of Hewitt and Roberts [3], Chen et al. [4], Barnea et al. [38], Baker [39], Thome [40] and Kattan et al. [41], and they are also checked through sight glasses at the inlet and outlet of the test section. Plotting the data points on this flow regime map, it is found to be in very good agreement qualitatively. The data points are located in the region of the annular flow pattern although some flow regime maps are developed for two-phase flow in horizontal tubes. Hence, the discussion section will address only the heat transfer mechanism in this flow pattern.

In the present study, annular flow pattern models and correlations are used to show the similarity of annular flow correlations which are independent of tube orientation (horizontal or vertical). Chen et al. [37] also mentioned this similarity in their article. They developed a general correlation by relating the interfacial shear stress to flow conditions for annular film condensation inside horizontal and vertical tubes using correction factors.

Details of the development of the relationship between film thickness, void fraction and flow parameters on one hand, and flow pattern transition mechanisms on the other, can be seen in Soliman [18], Kosky [42], Lockhart–Martinelli [43] and Azer et al. [44].

Liquid and vapor Reynolds numbers can be determined respectively as follows:

$$Re_l = \frac{Gd(1-x)}{\mu_l} \tag{1}$$

$$Re_g = \frac{Gdx}{\mu_g} \tag{2}$$

Kosky [42] developed a model for the determination of liquid film thickness in co-current flow under simultaneous shear and gravity forces which has also been validated experimentally by Soliman [18]. Calculation of liquid film thickness is defined as follows:

$$\delta^+ = 0.707(Re_l)^{0.5} \quad \text{for} \quad Re_l \le 1250 \tag{3}$$

$$\delta^+ = 0.0504Re_l^{0.875} \quad \text{for} \quad Re_l > 1250 \tag{4}$$

where the dimensionless film thickness value is shown in Eq. (5):

$$\delta^+ = \frac{\delta u^*}{\nu_l} \tag{5}$$

Table 3
Standard deviation and mean error between predicted void fraction values for $T_{sat}=40$ °C and $G=300$–515 kg m^{-2} s^{-1}.

Void fraction models and correlations	$G=300$ kg m^{-2} s^{-1}		$G=515$ kg m^{-2} s^{-1}	
	Mean error (%)	Standard deviation	Mean error (%)	Standard deviation
Soliman [18]	−0.376	0.021	−0.845	0.0137
Chisholm [19]	−4.63	0.022	−4.38	0.013
Turner and Wallis [20]	−5.861	0.035	−4.791	0.02
Smith [21]	−6.384	0.045	−4.564	0.025
Spedding and Spence [22]	−5.123	0.03	−4.397	0.017

Author's personal copy

and the frictional velocity is determined as:

$$u^* = \sqrt{\frac{\tau_{wall}}{\rho_l}} \tag{6}$$

where the wall shear stress can be calculated as follows:

$$\tau_{wall} = \frac{-d\left(\frac{dp}{dz}\right)_f}{4} \tag{7}$$

Mandhane et al. [45] reported that the determination of the two-phase frictional pressure drop depends strongly on the flow pattern. Lockhart and Martinelli's correlation [43] is recommended for the annular flow regime and shown in Eq. (8):

$$\left(\frac{dp}{dz}\right)_f = \phi_g^2 \left(\frac{dp}{dz}\right)_{gs} \tag{8}$$

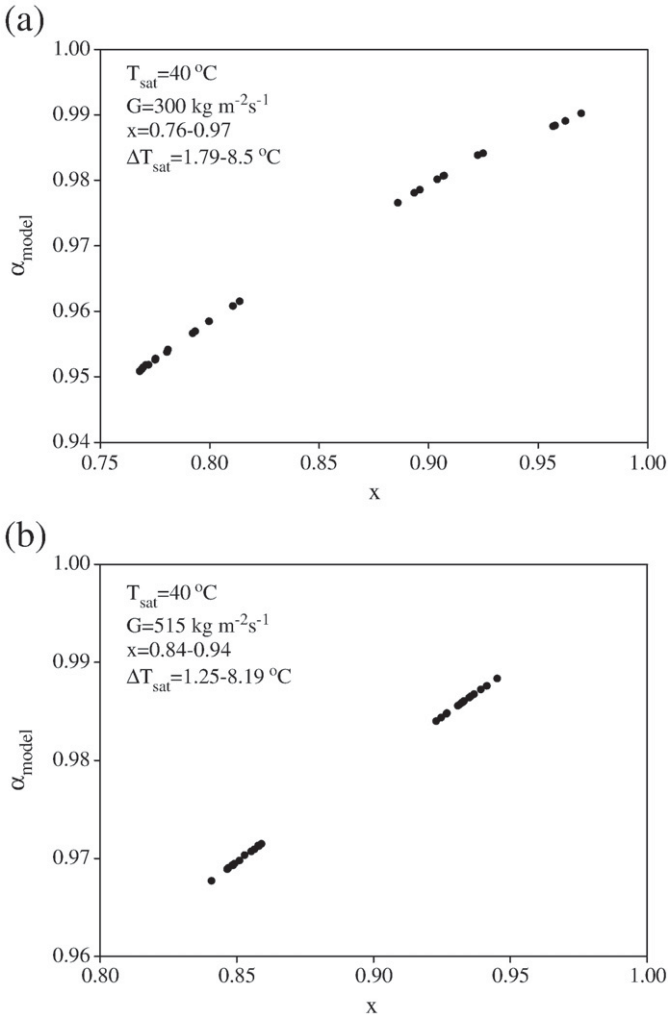

Fig. 1. Void fraction values from model vs. average vapor quality for $G = 300$ kg m^{-2} s^{-1} (a) and 515 kg m^{-2} s^{-1} (b) at the condensing temperature of 40 °C using laminar and turbulent flow data.

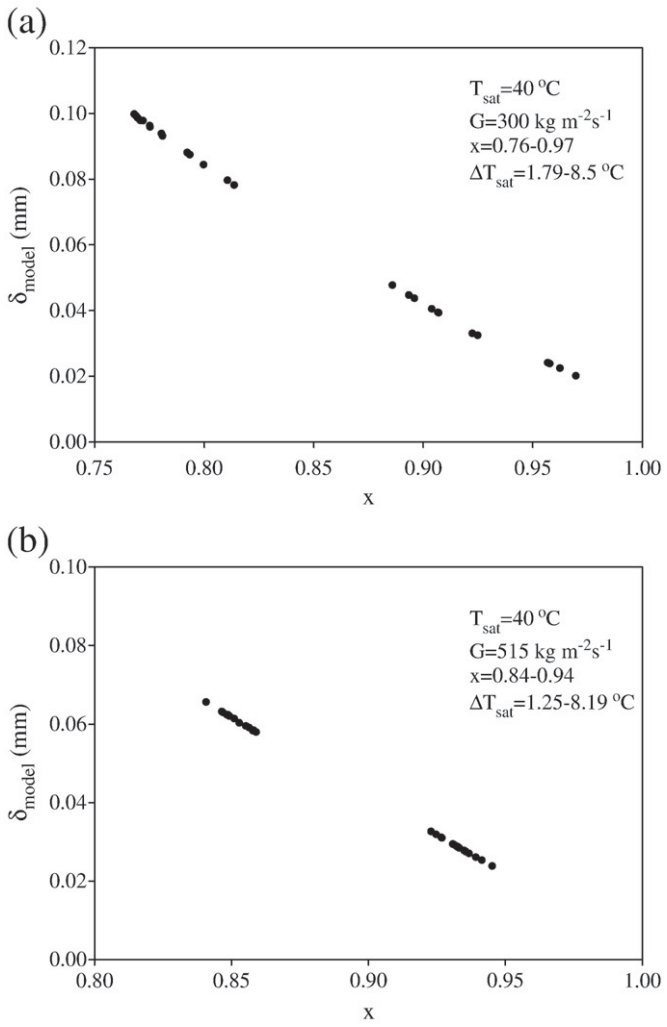

Fig. 2. Film thickness values from model vs. average vapor quality for $G = 300$ kg m^{-2} s^{-1} (a) and 515 kg m^{-2} s^{-1} (b) at the condensing temperature of 40 °C using laminar and turbulent flow data.

where the superficial vapor pressure drop is obtained as follows:

$$\left(\frac{dp}{dz}\right)_{gs} = -\left(\frac{2}{d}\right)\left(\frac{0.045}{Re_g^{0.2}}\right)\left(\frac{G^2x^2}{\rho_g}\right) \tag{9}$$

Substituting Eqs. (7)–(9) into Eq. (6), and simplifying gives:

$$u^* = 0.15\left(\frac{\nu_l}{d}\right)\left(\frac{\phi_g}{X}\right)Re_l^{10.9} \tag{10}$$

where the Lockhart–Martinelli [43] parameter is expressed as follows:

$$X = \left(\frac{1-x}{x}\right)^{0.9}\left(\frac{\rho_g}{\rho_l}\right)^{0.5}\left(\frac{\mu_l}{\mu_g}\right)^{0.1} \tag{11}$$

Soliman [18] used the two-phase multiplier of Azer et al. [44] in his analysis and reported that it was the most consistent one for data of annular flow condensation inside a horizontal tube, it should be noted that Eqs. (6) and (10) give exactly the same results as the two-phase multiplier of Azer et al. [44]. On the other hand, it is found that other two-phase multiplier correlations do not give satisfactory results according to the authors' analysis and the most predictive two-phase

Author's personal copy

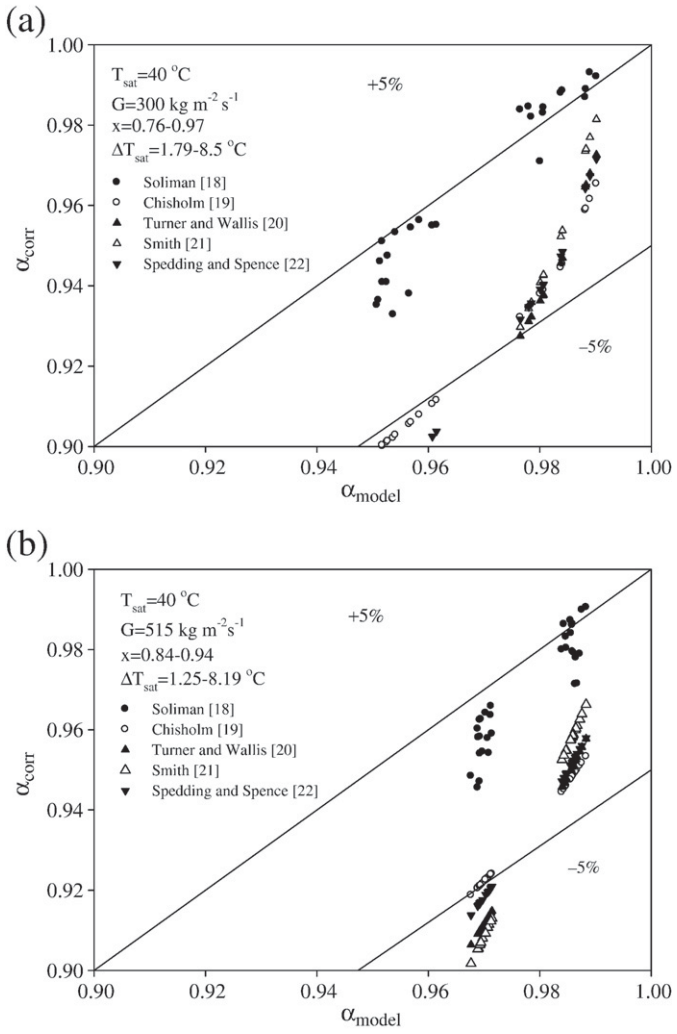

Fig. 3. Comparisons between the model and calculated void fraction values for the mass flux of 300 kg m^{-2} s^{-1} (a) and 515 kg m^{-2} s^{-1} (b) at the condensing temperature of 40 °C using laminar and turbulent flow data.

multiplier for this model by Azer et al. [44] can be seen from Eq. (12) as follows:

$$\phi_g = 1 + 1.09X^{0.039} \tag{12}$$

The void fraction value from the model is estimated using an estimated film thickness value calculated by Eq. (5), assuming $\delta \ll d$ as follows [23–26]:

$$\alpha = \frac{A_g}{A} = \left(1-\frac{\delta}{r}\right)^2 = 1-\frac{4\delta}{d} \tag{13}$$

Moreover mean errors between predicted void fraction values are shown in Table 3 and are calculated as follows:

$$\text{Error} = \left(\frac{\alpha_{corr}-\alpha_{model}}{\alpha_{model}}\right)100 \tag{14}$$

$$\text{Mean Error} = \frac{\sum \text{Error}}{\text{data}} \tag{15}$$

It should also be noted that void fraction values obtained from the model by means of Eq. (13) are assumed as comparative values for the error analysis.

Table 4
Prediction analysis of annular flow pattern for T_{sat} = 40 °C and G = 300–515 kg m^{-2} s^{-1}.

Flow pattern correlation	Predictability of data points	
	G = 300 kg m^{-2} s^{-1}	G = 515 kg m^{-2} s^{-1}
Jaster and Kosky [7]	6/26	32/32
Traviss and Rohsenow [8]	0/26	0/32
Taitel and Dukler [9]	26/26	32/32
Dobson [10]	26/26	32/32
Akbar et al. [11]	26/26	32/32
Breber et al. [12]	26/26	32/32
Cavallini et al. [13]	26/26	32/32
Chisholm and Sutherland [14]	0/26	29/32
Soliman [15]	0/26	0/32
Tandon et al. [16]	26/26	0/32
Sardesai et al. [17]	26/26	0/32
Soliman [18]	12/26	32/32

3.2. Uncertainties

The uncertainties in the Nusselt number and condensation heat transfer coefficient in the test tube varied from ±7.64% to ±10.71%. It should be noted that a similar range of uncertainty with minimum and maximum values exists in the literature. The procedures of Kline and McClintock [46] were used for the calculation of all uncertainties. Various uncertainty values of the study can be seen in the authors' previous works [28,31,33].

4. Results and discussion

In order to investigate the validation of the void fraction models and correlations proposed in the authors' previous publications in the annular flow regime, checked by sight glasses located at the inlet and outlet of the test tube, using a large number of experimental data points for the downward two-phase flow of R134a in a vertical round tube with an inner diameter of 8.1 mm, the present study was performed at the Fluid Mechanics, Thermal Engineering and Multiphase Flow Research Lab. (FUTURE) in KMUTT. Pure HFC-134a was used in the experiments. Discussion of the results will be given in turn as follows:

The present study was performed to study the relationship between void fraction models and the annular flow model of Soliman [18] and to investigate the well-known flow pattern correlations to verify the annular flow conditions of experimental data for downward two-phase flow of R134a in a vertical round tube. The effects of the temperature difference between the saturated temperature of the vapor and the inlet wall temperature of the tube (ΔT_{sat}), mass flux, vapor quality, and condensation temperature on the heat transfer coefficients, pressure drop and void fraction can be seen in the authors' previous studies in detail [23–34]. It should be noted that R134a enters the test section as a pure saturated vapor during laminar flow experiments. Verification of the reliability of the calculated film thickness, void fraction from the model and annular flow pattern identification are checked using different condensing temperatures and mass fluxes.

Figs. 1 and 2 show the relationship between void fraction (Eq. (13)) and film thickness (Eq. (5)) obtained from the model of Soliman [18] and vapor quality in the test tube for mass fluxes of 300 kg m^{-2} s^{-1} (a) and 515 kg m^{-2} s^{-1} (b) and a condensing temperature of 40 °C. Comparison of the void fraction at higher and lower average vapor qualities and smaller liquid film thickness together with higher vapor velocity at the vapor–liquid interface shows an increase in the void fraction when the average quality is higher. In addition to this, the film thickness values increase with decreasing vapor quality. Trend lines of data are in accordance with this basic knowledge of in-tube condensation. It is shown in the authors' previous publications that film thickness decreases with increasing heat transfer coefficient; in other words, film thickness

Author's personal copy

decreases with decreases in ΔT_{sat} for similar test conditions. The increase in heat flux in relation to ΔT_{sat} increases the condensation rate. In other words, the film thickness on the tube wall increases due to the constant latent heat of condensation for a specific saturation temperature of condensation.

In Fig. 3, comparison of the void fraction values obtained from the model of Soliman [18] with the most predictive void fraction and correlations shown in Table 2 are presented with a 5% deviation line for the minimum mass flux of 300 kg m^{-2} s^{-1} (Fig. 3a) and the maximum mass flux of 515 kg m^{-2} s^{-1} (Fig. 3b) according to the condensation temperature of 40 °C. It is clearly seen from the figures that the void fraction models and correlations of Chisholm [19], Turner and Wallis [20], Smith [21] and Spedding and Chen [22] give the best predictability of experimental data among 35 void fraction models and correlations given in the authors' previous publications [23–26]. In addition to this, the majority of the data calculated by the void fraction models and correlations of them fall within ±5% and are in good agreement with experimental data. Table 3 also shows the accuracy of investigated void fraction models and correlations for the tested experimental conditions.

In Table 1, well-known flow pattern models and correlations valid for horizontal and vertical tube orientations are presented with the plotted experimental data of the current study. Verification by visual control of the flow regime in the test tube is done using these flow pattern models and correlations in the literature. Table 4 shows the comparison of annular flow regime correlations for mass fluxes of 300–515 kg m^{-2} s^{-1} at a condensing temperature of 40 °C. The predictability ratio of Jaster and Kosky [7] for the determination of annular flow regime is 6 out of 26 data points for a mass flux of 300 kg m^{-2} s^{-1}, whereas it is 32 of 32 data points for a mass flux of 515 kg m^{-2} s^{-1}. A heat-momentum transfer analogy (for annular flow) is developed for the two-phase multiplier for shear stress using steam in a 12.5 mm i.d. horizontal tube for mass fluxes between 12.6 and 145 kg m^{-2} s^{-1}. Traviss and Rohsenow's model [8] cannot predict the annular flow regime for the tested experimental conditions. They condensed R12 in an 8 mm i.d. horizontal tube for mass fluxes between 100 and 990 kg m^{-2} s^{-1} at saturation temperatures of 10–40.6 °C. Dispersed, annular, semi-annular and slug flow are observed in their study. The Froude number and von Karman velocity profile are used in their condensation analysis. Taitel and Dukler's [9] model predicts all the tested data successfully for annular flow conditions. They investigated adiabatic flow of air–water in conventional tubes developing a theoretical approach to flow regime mapping using a momentum balance on a stratified flow pattern. Many researchers benefited from their analysis in the literature. Dobson's model [10] is found to be consistent with experimental data for the determination of the annular flow regime. He used R12, R134a, R22, R32/R125 as condensing test fluids in 3.14, 4.6, 7.04 mm i.d. horizontal tubes at mass fluxes between 25 and 800 kg m^{-2} s^{-1} at condensing temperatures of 35–60 °C. His results were in good agreement with the flow regime map of Mandhane et al. [45]. A modified Soliman number and mass flux are used in his analysis. The model of Akbar et al. [11] predicts annular flow experimental data successfully. They divided the entire flow regime map into four regions: the surface tension-dominated region, including bubble, plug, and slug, inertia-dominated zone 1, annular and wavy–annular regimes, inertia-dominated zone 2, and dispersed flow regimes and a transition zone. The model of Breber et al. [12] is good at predicting annular flow experimental data. He performed condensation experiments using R11, R12, R113, steam, n-pentane in several tubes with i.d.'s between 4.8 and 50.8 mm at mass fluxes between 17.6 and 990 kg m^{-2} s^{-1}. They benefited from Taitel and Dukler's flow regime map [9] to develop simple criteria for condensation in horizontal tubes. The analysis of Cavallini et al. [13] is successful at predicting annular flow experimental data. They performed condensation tests using data of R22, R134a, R125, R32, R236ea, R407C, R 410A in an 8 mm i.d. horizontal tube for mass flux between 100 and 750 kg m^{-2} s^{-1} at condensation temperatures of 30–50 °C. Kosky and Staub's model [47] is recommended for annular flow and the model of Breber et al. [12] is considered for the observed flow regimes of annular, stratified, wavy, and slug. Chisholm and Sutherland's model [14] was not successful for the minimum mass flux of R134a, whereas it was successful for the maximum mass flux of R134a. They developed a model using a two-phase multiplier and Froude number for gravity-controlled condensation and annular flow. Soliman's model [15] could not predict annular flow experimental data. Soliman condensed R12, R113 and steam in 4.8–15.9 mm i.d. tubes. He used a Froude number for annular–wavy flow and Weber number for mist–annular flow. Soliman's model [18] also has poor predictability for annular flow experimental data. The model of Tandon et al. [16] was not successful for the maximum mass flux of R134a, whereas it was successful for the minimum mass flux of R134a. They did experiments using several refrigerants such as R12, R113, and R22 in 4.8–15.9 mm i.d. horizontal tubes at pressures between 570 and1960 kPa. They observed annular, semi-annular and wavy flows during their experiments. The model of Sardesai et al. [17] was not successful for the maximum mass flux of R134a, whereas it was successful for the minimum mass flux of R134a. They condensed R113, steam, propane, methanol, n-pentane in a 24.4 mm i.d. horizontal tube. An annular-stratified/wavy transition is investigated in their analysis based on Taitel and Dukler [9].

A large number of graphs could be generated from the output of the calculations; however, due to space limitations, only typical results are shown for limited data. It should also be noted that detailed information on the explanations above and some additional figures with different experimental parameters related to this study can be seen in the authors' previous publications [23–36].

5. Conclusion

Co-current downward condensation heat transfer of R134a was experimentally investigated in an 8.1 mm i.d. vertical smooth tube. Accurate and repeatable heat transfer data during annular flow were obtained. There are few research studies on the parameters and content of such cases in the literature. For this reason, the results of this study are expected to fill a gap. This paper provides a comprehensive review of the published literature on flow regime correlations in relation to a flow transition model connected to film thickness and void fraction models and correlations. Validation of the annular flow model was accomplished by using a large number of data points. The following results were obtained:

1– A study of the theoretical model of the flow regime transition mechanism of Soliman [18], performed for condensation in horizontal tubes, was done using experimental data to determine accurate film thickness and void fraction values under various test conditions. Calculated void fraction and film thickness values from the model are found to be in good agreement in the range of ±5%.
2– The effect of vapor quality on film thickness and void fraction is discussed and investigated in detail. Void fraction values obtained from the theoretical model increase with increasing vapor quality and film thickness values obtained from the theoretical model increase with decreasing vapor quality as expected.
3– In order to verify the results of calculations, the data obtained from void fraction correlations previously proposed in the authors' publications with void fraction values from the mode were compared. The majority of data obtained from the void fraction models and correlations of Chisholm [19], Turner and Wallis [20], Smith [21] and Spedding and Chen [22] are found to be in good agreement with the void fraction values obtained from the model of Soliman [18] within the ±5% error band. These results also validate the accuracy of previously proposed consistent void

Author's personal copy

fraction correlations with the condensation database of KMUTT by the authors.

4– According to the analysis of flow regime identification in this paper, the flow pattern correlations of Taitel and Dukler [9], Dobson [10], Akbar et al. [11], Breber et al. [12], Cavallini et al. [13] and Sardesai et al. [17] are capable of predicting the annular flow regime conditions, as verified through sight glasses in the experimental apparatus and also checked with various flow regime maps for the high mass region of R134a in a vertical tube.

5– According to the analysis in this paper, it is shown that the annular flow model does not depend on tube orientation provided that an annular flow regime exists along the tube length and is capable of predicting condensation film thickness, void fraction and flow pattern inside the test tube.

Acknowledgements

The authors are indebted to King Mongkut's University of Technology Thonburi (KMUTT), the Thailand Research Fund and the Office of Higher Education Commission for supporting this study. Especially, the first author wishes to thank KMUTT for providing him with a Post-doctoral fellowship.

References

[1] D. Barnea, O. Shoham, Y. Taitel, Flow pattern transition for vertical downward two phase flow, Chemical Engineering Science 37 (1982) 741–744.
[2] J.R. Fair, What you need to know to design thermosyphon reboilers, Petroleum Refiner, 39 no:2, 1960, p. 105.
[3] G.F. Hewitt, D.N. Robertson, Studies of two-phase flow patterns by simultaneous x-ray and flash photography, Rept AERE-M2159, UKAEA, Harwell, 1969.
[4] L. Chen, Y.S. Tian, T.G. Karayiannis, The effect of tube diameter on vertical two-phase flow regimes in small tubes, International Journal of Heat and Mass Transfer 49 (2006) 4220–4230.
[5] T.S. Zhao, Q.C. Bi, Co-current air–water two-phase flow patterns in vertical triangular microchannels, International Journal of Multiphase Flow 27 (2001) 765–782.
[6] M.G. Hubbard, A.E. Dukler, The characterization of flow regimes for horizontal twophase flow, Proc. Heat Transfer and Fluid Mech. Inst., Standford University Press, 1966.
[7] H. Jaster, P.G. Kosky, Condensation heat transfer in a mixed flow regime, International Journal of Heat and Mass Transfer 19 (1976) 95–99.
[8] D.P. Traviss, W.M. Rohsenow, Flow regimes in horizontal two-phase flow with condensation, ASHRAE Transactions 79 (1973) 31–39.
[9] Y. Taitel, A.E. Dukler, A model for predicting flow regime transitions in horizontal and near horizontal gas–liquid flow, AIChE Journal 22 (1976) 47–55.
[10] M.K. Dobson, Heat transfer and flow regimes during condensation in horizontal tubes, PhD Thesis, Mechanical and Industrial Engineering, University of Illinois at Urbana-Champaign, Urbana-Champaign, IL, 1994.
[11] M.K. Akbar, D.A. Plummer, S.M. Ghiaasiaan, On gas–liquid two-phase flow regimes in microchannels, International Journal of Multiphase Flow 29 (2003) 855–865.
[12] G. Breber, J.W. Palen, J. Taborek, Prediction of horizontal tube side condensation of pure components using flow regime criteria, Journal of Heat Transfer Transactions of ASME 102 (1980) 471–476.
[13] A. Cavallini, G. Censi, D. Del Col, L. Doretti, G.A. Longo, L. Rossetto, Experimental investigation on condensation heat transfer and pressure drop of new HFC refrigerants (R134a, R125, R32, R410A, R236ea) in a horizontal smooth tube, International Journal of Refrigeration 24 (2001) 73–87.
[14] D. Chisholm, L.A. Sutherland, Prediction of pressure gradients in pipeline systems during two-phase flow, Proceedings of the Institution of Mechanical Engineering 184 (1969–1970) 24–32.
[15] H.M. Soliman, Mist–annular transition during condensation and its influence on the heat transfer mechanism, International Journal of Multiphase Flow 12 (1986) 277–288.
[16] T.N. Tandon, H.K. Varma, C.P. Gupta, New flow regimes map for condensation inside horizontal tubes, Journal of Heat Transfer 104 (1982) 763–768.
[17] R.G. Sardesai, R.G. Owen, D.J. Pulling, Flow regimes for condensation of a vapour inside a horizontal tube, Chemical Engineering Science 36 (1981) 1173–1180.
[18] H.M. Soliman, On the annular-to-wavy flow pattern transition during condensation inside horizontal tubes, The Canadian Journal of Chemical Engineering 60 (1982) 475–481.
[19] D. Chisholm, Two Phase Flow in Pipelines and Heat Exchangers, George Godwin in association with The Institution of Chemical Engineers, London, 1983.
[20] J.M. Turner, G.B. Wallis, The Separate-Cylinders Model of Two-Phase Flow, Paper No. NYO-3114-6, Thayer's School Eng.,Dartmouth College, Hanover, NH, USA, 1965.
[21] S.L. Smith, Void fractions in two-phase flow: a correlation based upon an equal velocity head model, Proceedings of the Institution of Mechanical Engineers 36 (1969) 647–664.
[22] P.L. Spedding, D.R. Spence, Prediction of holdup in two phase flow, International Journal of Engineering Fluid Mechanics 2 (1989) 109–118.
[23] A.S. Dalkilic, S. Laohalertdecha, S. Wongwises, Effect of void fraction models on the two-phase friction factor of R134a during condensation in vertical downward flow in a smooth tube, International Communications in Heat and Mass Transfer 35 (2008) 921–927.
[24] A.S. Dalkilic, S. Laohalertdecha, S. Wongwises, Effect of void fraction models on the film thickness of R134a during downward condensation in a vertical smooth tube, International Communications in Heat and Mass Transfer 36 (2009) 172–179.
[25] A.S. Dalkilic, S. Laohalertdecha, S. Wongwises, A comparison of the void fraction correlations of R134a during condensation in vertical downward laminar flow in a smooth and micro-fin tube, Proceedings of the 1st International Conference on Micro/Nanoscale Heat Transfer, ASME, 2008, January 06-09, Taiwan.
[26] A.S. Dalkilic, S. Laohalertdecha, S. Wongwises, Two-phase friction factor obtained from various void fraction models of R-134a during condensation in vertical downward flow at high mass flux, Proceedings of the 1st International Conference on Heat Transfer, ASME, 2008, August 10–14, USA.
[27] A.S. Dalkilic, S. Wongwises, Intensive literature review of condensation inside smooth and enhanced tubes, International Heat and Mass Transfer 52 (2009) 3409–3426.
[28] A.S. Dalkilic, S. Yildiz, S. Wongwises, Experimental investigation of convective heat transfer coefficient during downward laminar flow condensation of R134a in a vertical smooth tube, International Journal of Heat and Mass Transfer 52 (2009) 142–150.
[29] A.S. Dalkilic, S. Laohalertdecha, S. Wongwises, Two-phase friction factor in vertical downward flow in high mass flux region of refrigerant HFC-134a during condensation, International Communications in Heat and Mass Transfer 35 (2008) 1147–1152.
[30] A.S. Dalkilic, S. Laohalertdecha, S. Wongwises, Experimental investigation on heat transfer coefficient of R134a during condensation in vertical downward flow at high mass flux in a smooth tube, International Communications in Heat and Mass Transfer 36 (2009) 1036–1043.
[31] A.S. Dalkilic, S. Laohalertdecha, S. Wongwises, Experimental investigation on the condensation heat transfer and pressure drop characteristics of R134a at high mass flux conditions during annular flow regime inside a vertical smooth tube, Summer Heat Transfer Conference, ASME, July 19–23, USA, 2009.
[32] A.S. Dalkilic, O. Agra, Experimental apparatus for the determination of condensation heat transfer coefficient for R134a and R600a flowing inside vertical and horizontal tubes, Summer Heat Transfer Conference, ASME, July 19–23, USA, 2009.
[33] A.S. Dalkilic, S. Laohalertdecha, S. Wongwises, Experimental research on the similarity of annular flow models and correlations for the condensation of R134a at high mass flux inside vertical and horizontal tubes, International Mechanical Engineering Congress and Exposition, ASME, November 13–19, USA, 2009.
[34] A.S. Dalkilic, S. Wongwises, A heat transfer model for co-current downward laminar film condensation of R134a in a vertical micro-fin tube during annular flow regime, Eleventh UK National Heat Transfer Conference, September 6–8, Queen Mary University of London, 2009.
[35] A.S. Dalkilic, O. Agra, I. Teke, S. Wongwises, Comparison of frictional pressure drop models during annular flow condensation of R600a in a horizontal tube at low mass flux and of R134a in a vertical tube at high mass flux, International Journal of Heat and Mass Transfer, http://dx.doi.org/10.1016/j.ijheatmasstransfer.2009.12.051, 2010.
[36] A.S. Dalkilic, S. Wongwises, An investigation of a model of the flow pattern transition mechanism in relation to the identification of annular flow of R134a in a vertical tube using various void fraction models and flow regime maps, Experimental Thermal and Fluid Science, http://dx.doi.org/10.1016/j.expthermflusci.2009.12.011, 2010.
[37] S.L. Chen, F.M. Gerner, C.L. Tien, General film condensation correlations, Experimental Heat Transfer 1 (1987) 93–107.
[38] D. Barnea, O. Shoham, Y. Taitel, Flow pattern transition for vertical downward two phase flow, Chemical Engineering Science 37 (1982) 741–744.
[39] O. Baker, Design of pipe lines for simultaneous flow of oil and gas, Oil and Gas Journal 26 (1954) 185–195.
[40] J.R. Thome, Update on advances in flow pattern based two-phase heat transfer models, International Journal of Heat and Mass Transfer 29 (2005) 341–349.
[41] N. Kattan, J.R. Thome, D. Favrat, Flow boiling in horizontal tubes. Part 1: development of a diabatic two-phase flow pattern map, Journal of Heat Transfer 120 (1998) 140–147.
[42] P.G. Kosky, Thin liquid films under simultaneous shear and gravity forces, International Journal of Heat Mass Transfer 14 (1971) 1220–1224.
[43] R.W. Lockhart, R.C. Martinelli, Proposed correlation of data for isothermal two-phase, two-component flow in pipes, Chemical Engineering Progress 45 (1949) 39–45.
[44] N.Z. Azer, L.V. Abis, H.M. Soliman, Local heat transfer coefficients during annular flow condensation, ASHRAE Transactions 78 (1972) 135–143.
[45] J.M. Mandhane, G.A. Gregory, K. Aziz, Critical evaluation of friction pressure drop prediction methods for gas–liquid flow in horizontal pipes, Journal of Petroleum Technology 29 (1977) 1348–1358.
[46] S.J. Kline, F.A. McClintock, Describing uncertainties in single sample experiments, Mechanical Engineering 75 (1953) 3–8.
[47] P.G. Kosky, F.W. Staub, Local condensing heat transfer coefficients in the annular flow regime, AIChE Journal 17 (1971) 1037–1043.

International Communications in Heat and Mass Transfer 37 (2010) 822–826

Contents lists available at ScienceDirect

International Communications in Heat and Mass Transfer

journal homepage: www.elsevier.com/locate/ichmt

Investigation on the jet liquid impingement heat transfer for the central processing unit of personal computers ☆

Paisarn Naphon [a,*], Somchai Wongwises [b]

[a] Thermo-Fluids and Heat Transfer Enhancement Lab. (TFHT), Department of Mechanical Engineering, Faculty of Engineering, Srinakharinwirot University, 63 Rangsit-Nakhornnayok Rd., Ongkharak, Nakhorn-Nayok, 26120, Thailand

[b] Fluid Mechanics, Thermal Engineering and Multiphase Flow Research Lab. (FUTURE), Department of Mechanical Engineering, King Mongkut's University of Technology Thonburi, 91 Suksawas 48, Bangmod, Bangkok 10140, Thailand

ARTICLE INFO

Available online 10 June 2010

Keywords:
Jet impingement
Mini-rectangular fin heat sink
Central processing unit

ABSTRACT

In this paper, the jet liquid impingement heat transfer characteristics in the mini-rectangular fin heat sink for the central processing unit of a personal computer are experimentally investigated. The experiments are tested with three different channel width heat sinks under real operating conditions: no load and full load conditions. The jet liquid impingement cooling with mini-rectangular fin heat sink system is introduced as the active and passive heat transfer enhancement techniques. Effects of relevant parameters on the central processing unit temperature are considered. It is found that the central processing unit temperatures obtained from the jet liquid impingement cooling system are lower than those from the conventional liquid cooling system; however, the energy consumption also increases. The results of this study are of technological importance for the efficient design of cooling systems of personal computers or electronic devices to enhance cooling performance.

© 2010 Elsevier Ltd. All rights reserved.

1. Introduction

In order to ensure reliable operation, the personal computer (PC) or electronic devices must be operated in specific temperature ranges. The exceeding maximum allowable temperature is a serious problem for these devices. Therefore, in order to keep the operated temperature constant, the cooling system must dissipate generated heat equal or higher than the generated heat of these devices. There are many techniques to dissipate the generated heat. The development of the miniaturized technology, mini and micro-components has been introduced as one of the techniques. The heat transfer and pressure drop in the mini and micro-channel have been widely studied by researchers. Guglielmini et al. [1] studied the pool boiling heat transfer of the finned copper surfaces immersed in a dielectric fluid. Zhao and Lu [2] analytically and numerically studied the effect of porosity on the thermal performance of the micro channel heat sink. Bhowmil [3] investigated on the convective heat transfer of electronic chips in a vertical rectangular channel. Zhang et al. [4] reported the study of a single-phase heat transfer of micro channel heat sink. Yu [5] studied on the thermal performance of a plate-pin fin heat sink and a plate fin heat sink. Peles et al. [6] investigated on the heat transfer and pressure drop over a bank of micro pin fins. Kosar and Peles [7,8] considered the single-phase and two-phase heat transfer, and pressure drop of R-123 over a bank of the micro pin fins. Yakut et al. [9] considered effects of the heights, widths of the hexagonal fins on thermal resistance and pressure drop characteristics. Mohamed [10] investigated on air-cooling characteristics of an electronic device with various square modules array heat sinks. Didarul [11] investigated on the heat transfer and fluid flow characteristics of finned surfaces. Chein and Chuang [12] studied on the micro channel heat sink performance with and without thermoelectric using nanofluids as coolants. Jeng and Tzeng [13] determined the pressure drop and heat transfer of a square pin-fin array. Lie et al. [14] investigated the flow boiling heat transfer of FC-72 on a heated micro-pin-finned silicon chip. Naphon et al. [15,16] numerically and experimentally studied on the heat transfer and flow characteristics in the mini-fin heat sink for CPU with and without thermoelectric. There is reasonable agreement from the comparison between the measured data and the predicted results.

The numerous papers presented the jet impingement heat transfer enhancement. Kobus and Oshio [17] studied on the thermal performance of a pin-fin heat sink with various geometrical. Li et al. [18] determined the thermal performance of heat sinks with confined impingement cooling. The effects of the impinging Reynolds number, the width and the height of the fins, the distance between the nozzle and the tip of the fins on the thermal resistance were investigated. Geedipalli et al. [19] simulated the combination heating of food using microwave and jet impingement by coupling Maxwell's equations. Sung and Mudawar [20,21] studied on the jet impingement single-phase and two-phase heat transfer characteristics. Reasonable

☆ Communicated by W.J. Minkowycz.

* Corresponding author.
E-mail address: paisarnn@swu.ac.th (P. Naphon).

0735-1933/$ – see front matter © 2010 Elsevier Ltd. All rights reserved.
doi:10.1016/j.icheatmasstransfer.2010.05.004

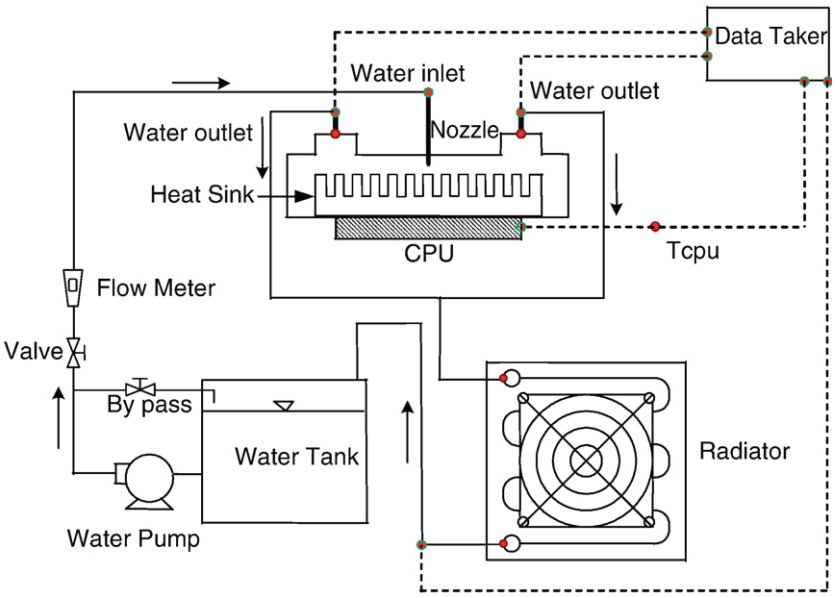

Fig. 1. Schematic diagram of experimental apparatus.

agreement was obtained between the predicted results and the measured data. Koseoglu and Baskaya [22] applied Laser Doppler Anemometry to observe the jet flow field and turbulence on heat transfer characteristics. Katti and Prabhu [23] carried out to study the jet heat transfer enhancement from a flat surface. Kanna and Das [24] simulated the heat transfer from the flat plate by a two-dimensional laminar incompressible offset jet. Goodro et al. [25] considered effects of the hole spacing on the spatially-resolved jet array impingement heat transfer. Cirillo and Isopi [26] experimentally and numerically studied air jet heat transfer characteristics on a flat plate. Effects of jet diameter, air velocity, jet-to-jet spacing, jet-to-plate distance and nozzle height were considered. Jeng et al. [27] experimentally investigated on the jet air flow and heat transfer behaviors of a rotating heat sink. Wong and Saeid [28,29] applied the Brinkman-extended Darcy model to simulate the mixed convection on jet impingement cooling in a horizontal porous layer. Hewakandamby [30] numerically studied on the enhanced heat transfer of oscillatory impinging jets. Nguyen et al. [31] performed to study the enhanced heat transfer of nanofluid in a confined and submerged impinging jet on a flat, horizontal and circular heated surface. Koseoglu and Baskaya [32] experimentally and numerically investigated on the impinging jet heat transfer. Chang et al. [33] studied the jet-array impingement heat transfer in a concentric annular channel with rotating inner cylinder. Sharif and Banerjee [34] applied the k–ε turbulence model to analyze the heat transfer of the confined slot-jet impingement on a moving plate. Whelan and Robinson [35] used the jet liquid impingement for cooling the electronic devices.

As mentioned above, the numerous papers presented the study on heat transfer and pressure drop in the mini-and micro-channel or jet impingement heat transfer on the flat plate. Almost all the works reported on the study of jet air impingement heat transfer. However, heat transfer capability is limited by the working fluid transport properties. At present there is limited data available for jet liquid impingement heat transfer especially for the central processing unit (CPU) of personal computers (PC). Furthermore, the paper focuses on the experimental study on the jet liquid impingement heat transfer characteristics of the mini-rectangular fin heat sink of a CPU based on the real operating conditions of a PC. Effects of channel width, nozzle diameter, and coolant flow rate on the CPU temperature are considered. The results obtained from the jet liquid impingement cooling system are compared with those from the conventional liquid cooling system.

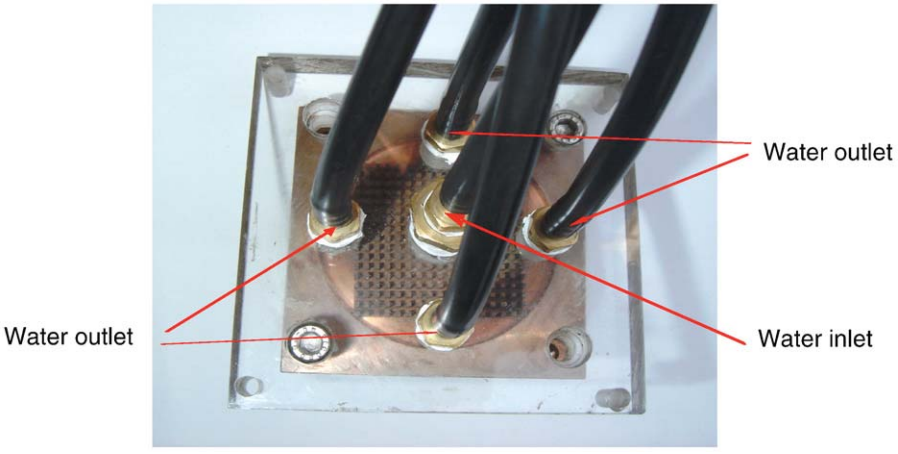

Fig. 2. Photograph of the mini-rectangular fin heat sink unit for cooling the CPU of the PC.

Table 1
Accuracy and uncertainty of measurements.

Instruments	Accuracy	Uncertainty
Voltage supplied by power source (volt)	0.2%	±0.5
Current supplied by power source (ampere)	0.2%	±0.5
Water flow meter	0.2%	±0.5
Thermocouple type T, data logger, (°C)	0.1%	±0.1

2. Experimental apparatus and method

A schematic diagram of the experimental apparatus is shown in Fig. 1. The test loop consists of a set of PC, cooling de-ionized water loop and data acquisition system. The close-loop of de-ionized water consists of a 10^{-3} m^3 storage tank, water pump, flow meter, and radiator. The de-ionized water in the radiator is chilled by the atmospheric air. After the temperatures of the water are cooled to achieve the desired level, the cooling water is pumped out of the storage tank, passed through a flow meter and the CPU, and returned to the storage tank. Three nozzles with diameters of 1.00, 1.40, and 1.80 mm are tested. The flow rates of the cooling water are controlled by adjusting the valve and measured by the flow meter with an accuracy of ±0.2% of full scale. The test sections are fabricated from the blocks of copper by a wire electrical discharge machine (WEDM) with channel widths of 0.50, 1.00, and 1.25 mm. The inlet and outlet plenums are shown in Fig. 2. In Fig.1, the type T copper-constantan thermocouples with an accuracy of 0.1% of full scale are employed to measure the temperatures at various positions. The CPU temperatures are measured by two type-T copper-constantan thermocouples. All thermocouples are pre-calibrated with a dry box temperature calibrator.

The de-ionized water was pumped into the mini-rectangular fin heat sink which was installed on the CPU of the PC in the normal direction. The inlet temperature of coolant water before entering the cooling section was kept nearly constant at 28–30 °C. Experiments were conducted with various cooling water flow rates, channel width of heat sink, and operating condition of PC. The supplied load into the CPU was adjusted to achieve the desired level by setting the operating conditions of the PC. The operating conditions of the computer can be controlled by setting the software of computer system. The energy consumption of the PC was measured by the watt–hour meter. The temperatures at each position and energy consumption were recorded in the period time of 200 min. Data collection was carried out using a data acquisition system (DataTaker). The uncertainty and accuracy of the measurement are given in Table 1.

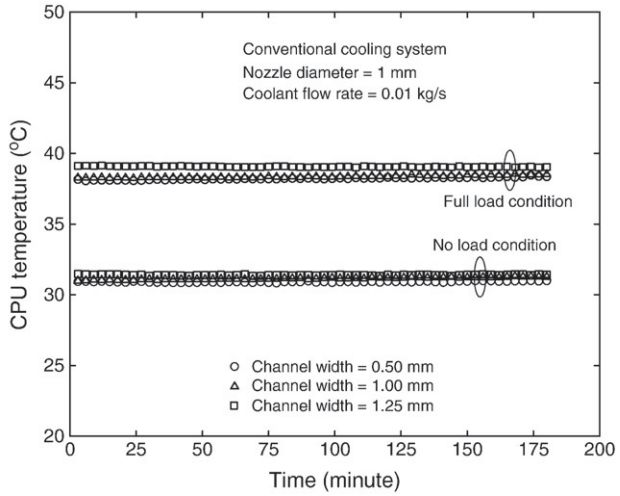

Fig. 3. Effects of channel width of heat sink on CPU temperature of the conventional cooling system for no load and full load conditions.

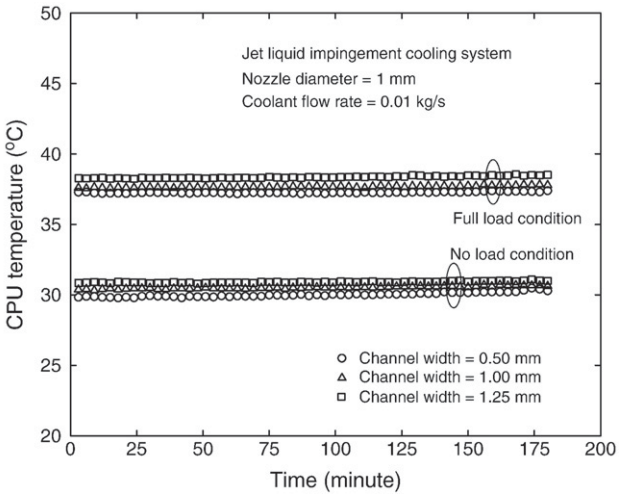

Fig. 4. Effects of channel width of heat sink on CPU temperature of the jet liquid impingement cooling system for no load and full load conditions.

3. Results and discussion

The supplied load into the CPU was adjusted by setting the operating condition of the PC: full load and no load conditions. The relevant parameters are measured in the period time of 200 min. In general, based on the real operating conditions of a PC, it is difficult to know the generated heat of the CPU. In the present experiment, average CPU temperature is measured with type-T copper-constantan thermocouples in the period time of 200 min. Figs. 3–4 show the effect of the channel width of the heat sink on the CPU temperatures for the conventional liquid cooling system and for the jet liquid impingement cooling system, respectively. Due to higher surface area, the heat transfer rate from the CPU to the heat sink increases. Therefore, the CPU temperatures obtained from the heat sink with the channel width of 0.5 mm are lower than those from the higher ones. As expected, the CPU temperatures from the full load condition are higher than those from the no load condition for the whole range of the period time. At the same condition, the CPU temperatures obtained from the jet liquid impingement cooling system are lower than those from the conventional liquid cooling system. From Fig. 2, it can be seen that fluid flows in and flows out the heat sink in the normal direction. At the inlet plenum, it looks like a jet impinging on the bottom of the

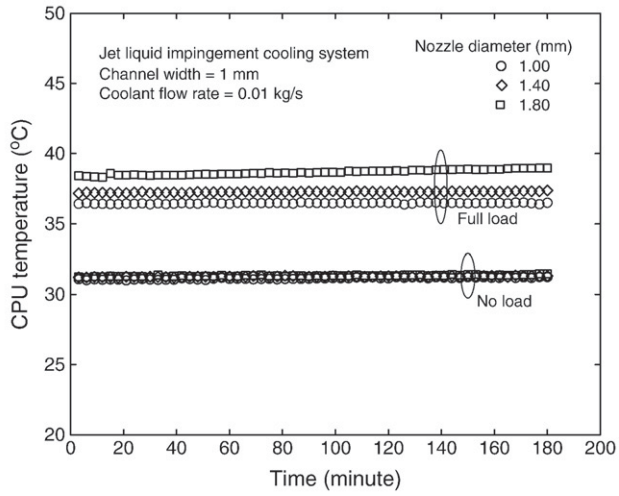

Fig. 5. Effects of nozzle diameter on the CPU temperature for no load and full load conditions.

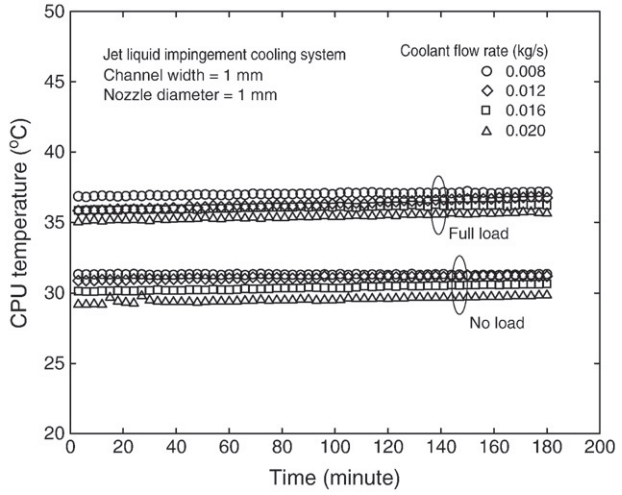

Fig. 6. Effects of coolant flow rate on the CPU temperature for no load and full load conditions.

heat sink. The recirculation zones appear in the inlet and outlet plenums.

In addition, a larger velocity in the heat sink results in higher heat transfer coefficient. Therefore, the jet liquid impingement cooling system gives CPU temperatures lower than the conventional liquid cooling system. Fig. 5 shows the variation of the CPU temperature from the jet liquid impingement cooling system for different nozzle diameters. Due to higher velocity, the heat transfer rate increases with decreasing nozzle diameter. Therefore, the lower nozzle diameter gives CPU temperatures lower than the higher ones. Effects of coolant flow rate on the CPU temperatures for different load conditions are shown in Fig. 6. For the four different coolant flow rates, a larger CPU temperature drop is found for a larger coolant flow rate. The reason for this is because a larger coolant flow rate results in lower capacity resistance and consequently lower heat sink thermal resistance ($R = \Delta T/Q$) as shown in Fig. 7.

The CPU temperature and the energy consumption obtained from the jet liquid impingement cooling system are compared with those from the conventional liquid cooling system. As seen in Table 2, the plus symbol represented the higher values while the minus symbol represented the lower values as compared with those from the

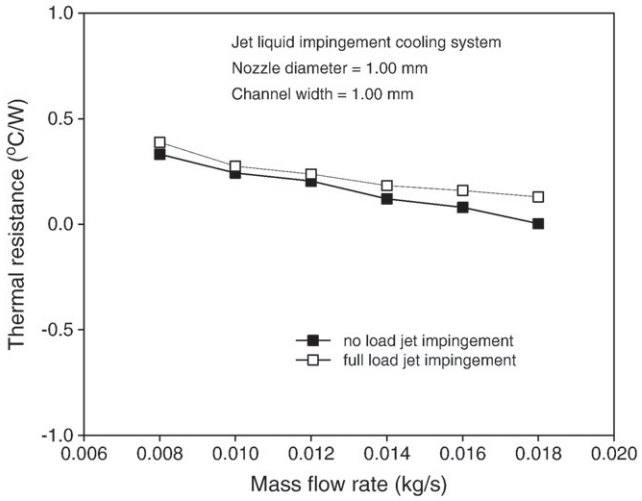

Fig. 7. Variation of thermal resistance with coolant mass flow rate.

Table 2
Comparison of the energy consumption between jet liquid impingement cooling system with conventional liquid cooling system.

Cooling techniques	CPU temperature		Energy consumption	
	No load	Full load	No load	Full load
Jet liquid impingement heat transfer system with the channel width of 0.5 mm	−2.90%	−2.36%	+9.30%	+16.67%
Jet liquid impingement heat transfer system with the channel width of 1.00 mm	−2.04%	−2.26%	+9.30%	+16.67%
Jet liquid impingement heat transfer system with the channel width of 1.25 mm	−1.57%	−3.59%	+9.30%	+16.67%

conventional liquid cooling system. It can be seen that the CPU temperatures obtained from the jet liquid impingement cooling system are lower than those from the conventional liquid system and with the same explanation as mentioned above. However, the energy consumption also increases.

4. Conclusions

Due to high levels of heat generation, space limitation for the set up of the cooling system, and air cooling limitation, the jet liquid impingement cooling in the mini-rectangular fin channel heat sink for CPUs of PCs has been investigated. The jet liquid impingement cooling with mini-rectangular fin heat sink system is introduced as the couple active and passive heat transfer enhancement techniques. The effect of channel width of heat sink, coolant flow rate and operating condition of the PC on the CPU temperature are considered. It is found that the CPU temperatures obtained from the jet liquid impingement cooling system are lower than those from the conventional liquid system. However, this technique requires higher energy consumption. The results of this study are expected to lead to guidelines that will allow the design of a cooling system with improved thermal cooling performance for ensuring that these devices are in the specific temperature ranges.

Acknowledgements

The authors would like to express their appreciation to the Thailand Research Fund (TRF) and Srinakharinwirot University (SWU) for providing financial support for this study.

References

[1] G. Guglielmini, M. Misale, C. Schenone, Boiling of saturated FC-72 on square pin fin arrays, International Journal of Thermal Sciences 41 (2002) 599–608.
[2] C.Y. Zhao, T.J. Lu, Analysis of microchannel heat sink for electronics cooling, International Journal of Heat and Mass Transfer 45 (2002) 4857–4869.
[3] H. Bhowmil, Convection heat transfer from discrete heat sourced in a liquid cooled rectangular channel, Applied Thermal Engineering 25 (2005) 2532–2542.
[4] H.Y. Zhang, D. Pingala, T.N. Wong, K.C. Toh, Y.K. Joshi, Single-phase liquid cooled micro channel heat sink for electronic packages, Applied Thermal Engineering 25 (2005) 1472–1487.
[5] X. Yu, Development of a plate-pin fin heat sink and its performance comparisons with a plate fin heat sink, Applied Thermal Engineering 25 (2005) 173–182.
[6] Y. Peles, A. Kosor, C. Mishra, C.J. Kuo, B. Schneider, Forced convective heat transfer across a pin fin micro heat sink, International Journal of Heat and Mass Transfer 48 (2005) 3615–3627.
[7] A. Kosar, Y. Peles, Convective flow of refrigerant (R123) across a bank of micro pin fins, International Journal of Heat and Mass Transfer 49 (2006) 3142–3155.
[8] A. Kosar, Y. Peles, Boiling heat transfer in a hydrofoil-based micro pin fin heat sink, International Journal of Heat and Mass Transfer 50 (2007) 1018–1034.
[9] K. Yukut, Experimental investigation of thermal resistance of a heat sink with hexagonal fins, Applied Thermal Engineering 26 (2006) 2262–2271.
[10] M.M. Mohamed, Air cooling characteristics of a uniform square modules array for electronic device heat sink, Applied Thermal Engineering 26 (2006) 486–493.

[11] I.M. Didarul, Study on heat transfer and fluid flow characteristics with short rectangular plate fin of different pattern, Experimental Thermal and Fluid Science 31 (2007) 367–379.
[12] R. Chein, J. Chuang, Experimental microchannel heat sink performance studies using nanofluids, International Journal of Thermal Sciences 46 (2007) 57–66.
[13] T.M. Jeng, S.C. Tzeng, Pressure drop and heat transfer of square pin-fin arrays in in-line and staggered arrangements, International Journal of Heat and Mass Transfer 50 (2007) 2364–2375.
[14] Y.M. Lie, Saturated flow boiling heat transfer and associated bubble characteristics of FC-72 on a heated micro-pin-fined silicon chip, International Journal of Heat and Mass Transfer 50 (2007) 3862–3876.
[15] P. Naphon, S. Wiriyasart, Liquid cooling in the mini-rectangular fin heat sink with and without thermoelectric for CPU, International Communications in Heat and Mass Transfer 36 (2009) 166–171.
[16] P. Naphon, S. Klangchart, S. Wongwises, Numerical investigation on the heat transfer and flow in the mini-fin heat sink for CPU, International Communications in Heat and Mass Transfer 36 (2009) 834–840.
[17] C.J. Kobus, T. Oshio, Development of a theoretical model for predicting the thermal performance characteristics of a vertical pin-fin array heat sink under combined forced and natural convection with impinging flow, International Journal of Heat and Mass Transfer 48 (2005) 1053–1063.
[18] H.Y. Li, S.M. Chao, G.L. Tsai, Thermal performance measurement of Heat sinks with confined impinging jet by infrared thermography, International Journal of Heat and Mass Transfer 48 (2005) 5386–5394.
[19] S. Geedipalli, A.K. Datta, V. Rakesh, Heat transfer in a combination microwave–jet impingement oven, Food and Bioproducts Processing 86 (2008) 53–63.
[20] M.K. Sung, I. Mudawar, Single-phase and two-phase heat transfer characteristics of low temperature hybrid micro-channel/micro-jet impingement cooling module, International Journal of Heat and Mass Transfer 51 (2008) 3882–3895.
[21] M.K. Sung, I. Mudawar, Single-phase hybrid micro-channel/micro-jet impingement cooling, International Journal of Heat and Mass Transfer 51 (2008) 4342–4352.
[22] M.F. Koseoglu, S. Baskaya, The effect of flow field and turbulence on heat transfer characteristics of confined circular and elliptic impinging jets, International Journal of Thermal Sciences 47 (2008) 1332–1346.
[23] V. Katti, S.V. Prabhu, Heat transfer enhancement on a flat surface with axisymmetric detached ribs by normal impingement of circular air jet, International Journal of Heat and Fluid Flow 29 (2008) 1279–1294.
[24] P.R. Kanna, M.K. Das, Heat transfer study of two-dimensional laminar incompressible offset jet flows, International Journal of Thermal Sciences 47 (2008) 1620–1629.
[25] M. Goodro, J. Park, P. Ligrani, M. Fox, H.K. Moon, Effects of hole spacing on spatially-resolved jet array impingement heat transfer, International Journal of Heat and Mass Transfer 51 (2008) 6243–6253.
[26] F. Cirillo, G.M. Isopi, Glass tempering heat transfer coefficient evaluation and air jets parameter optimization, Applied Thermal Engineering 29 (2009) 1173–1179.
[27] T.M. Jeng, S.C. Tzeng, H.R. Liao, Flow visualizations and heat transfer measurements for a rotating pin-fin heat sink with a circular impinging jet, International Journal of Heat and Mass Transfer 52 (2009) 2119–2131.
[28] K.C. Wong, N.H. Saeid, Numerical study of mixed convection on jet impingement cooling in a horizontal porous layer-using Brinkman-extended Darcy model, International Journal of Thermal Sciences 48 (2009) 96–104.
[29] K.C. Wong, N.H. Saeid, Numerical study of non-Darcian effects on jet impingement cooling in a horizontal porous layer in the mixed convection regime, International Communications in Heat and Mass Transfer 36 (2009) 45–50.
[30] B.N. Hewakandamby, A numerical study of heat transfer performance of oscillatory impinging jets, International Journal of Heat and Mass Transfer 52 (2009) 396–406.
[31] C.T. Nguyen, N. Galanis, G. Polidori, S. Fohanno, C.V. Popa, A.L. Bechec, An experimental study of a confined and submerged impinging jet heat transfer using Al2O3-water nanofluids, International Journal of Thermal Sciences 48 (2009) 401–411.
[32] M.F. Koseoglu, S. Baskaya, Experimental and numerical investigation of natural convection effects on confined impinging jet heat transfer, International Journal of Heat and Mass Transfer 52 (2009) 1326–1336.
[33] S.W. Chang, T.L. Yang, D.W. Shih, Jet-array impingement heat transfer in a concentric annular channel with rotating inner cylinder, International Journal of Heat and Mass Transfer 52 (2009) 1254–1267.
[34] M.A.R. Sharif, A. Banerjee, Numerical analysis of heat transfer due to confined slot-jet impingement on a moving plate, Applied Thermal Engineering 29 (2009) 532–540.
[35] B.P. Whelan, A.J. Robinson, Nozzle geometry effects in liquid jet array impingement, Applied Thermal Engineering 29 (2009) 2211–2221.

This article was downloaded by: *[INFLIBNET India Order]*
On: *2 September 2010*
Access details: *Access Details: [subscription number 920455929]*
Publisher *Taylor & Francis*
Informa Ltd Registered in England and Wales Registered Number: 1072954 Registered office: Mortimer House, 37-41 Mortimer Street, London W1T 3JH, UK

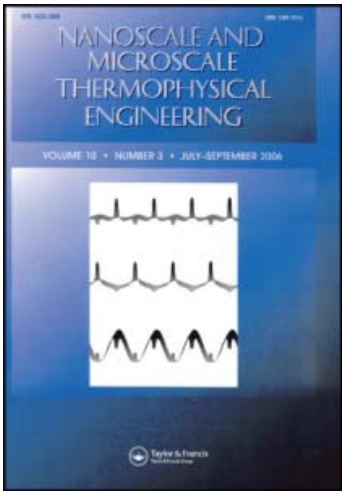

Nanoscale and Microscale Thermophysical Engineering
Publication details, including instructions for authors and subscription information:
http://www.informaworld.com/smpp/title~content=t713774103

Measurement of Thermo Physical Properties of Metallic Nanofluids for High Temperature Applications

Lazarus Godson[a]; D. Mohan Lal[a]; Somchai Wongwises[b]
[a] R&AC Division, Department of Mechanical Engineering, College of Engineering, Guindy, Anna University, Chennai, India [b] Fluid Mechanics, Thermal Engineering and Multiphase Flow Research Lab (FUTURE), Department of Mechanical Engineering, King Mongkut's University of Technology Thonburi, Bangmod, Bangkok, Thailand

Online publication date: 25 August 2010

To cite this Article Godson, Lazarus , Lal, D. Mohan and Wongwises, Somchai(2010) 'Measurement of Thermo Physical Properties of Metallic Nanofluids for High Temperature Applications', Nanoscale and Microscale Thermophysical Engineering, 14: 3, 152 — 173
To link to this Article: DOI: 10.1080/15567265.2010.500319
URL: http://dx.doi.org/10.1080/15567265.2010.500319

PLEASE SCROLL DOWN FOR ARTICLE

Full terms and conditions of use: http://www.informaworld.com/terms-and-conditions-of-access.pdf

This article may be used for research, teaching and private study purposes. Any substantial or systematic reproduction, re-distribution, re-selling, loan or sub-licensing, systematic supply or distribution in any form to anyone is expressly forbidden.

The publisher does not give any warranty express or implied or make any representation that the contents will be complete or accurate or up to date. The accuracy of any instructions, formulae and drug doses should be independently verified with primary sources. The publisher shall not be liable for any loss, actions, claims, proceedings, demand or costs or damages whatsoever or howsoever caused arising directly or indirectly in connection with or arising out of the use of this material.

Nanoscale and Microscale Thermophysical Engineering, 14: 152–173, 2010
Copyright © Taylor & Francis Group, LLC
ISSN: 1556-7265 print / 1556-7273 online
DOI: 10.1080/15567265.2010.500319

Taylor & Francis
Taylor & Francis Group

Downloaded By: [INFLIBNET India Order] At: 07:09 2 September 2010

MEASUREMENT OF THERMO PHYSICAL PROPERTIES OF METALLIC NANOFLUIDS FOR HIGH TEMPERATURE APPLICATIONS

Lazarus Godson[1], D. Mohan Lal[1], and Somchai Wongwises[2]
[1]*R&AC Division, Department of Mechanical Engineering, College of Engineering, Guindy, Anna University, Chennai, India*
[2]*Fluid Mechanics, Thermal Engineering and Multiphase Flow Research Lab (FUTURE), Department of Mechanical Engineering, King Mongkut's University of Technology Thonburi, Bangmod, Bangkok, Thailand*

This article presents the measurement of thermal conductivity and viscosity of nanofluids experimentally. Silver nanoparticles dispersed in water with volume concentrations of 0.3, 0.4, 0.6, 0.8, 0.9, and 1.2 vol% are used in the present study. A transient hot-wire apparatus is used for measuring the thermal conductivity of nanofluids and a Cannon-Fenske viscometer is used to measure the kinematic viscosity of nanofluids. The data are collected for temperatures ranging from 50 to 90°C. The results have shown an increase in the measured thermal conductivity and viscosity of nanofluids as the particle concentrations increase, and the values are higher than the values of the base liquids. The minimum enhancement of 27% for 0.3 vol% and a maximum enhancement of 115% for 1.2 vol% are observed at an average temperature of 70°C when compared with pure water for the same temperature. Further, the thermal conductivity of nanofluids increases with the increase in nanofluid temperatures and, conversely, the viscosity of nanofluids decreases with the increase in temperature of nanofluids. An experimental correlation is developed based on the experimental data for thermal conductivity and viscosity that relates the particle volume concentration and nanofluid temperature.

KEY WORDS: thermal conductivity, viscosity, silver, nanofluid, temperature, nanoparticle enhancement

INTRODUCTION

Conventional heat transfer fluids such as water, mineral oil, and ethylene glycol play a vital role in many industrial applications, including power generation, chemical processes, heating or cooling processes, and microelectronic devices. The operational speed of these devices depends on the cooling rate. Low heat transfer performance of these conventional fluids affects the enhancement of performance and in turn the compactness of heat exchangers. Therefore, further enhancement in heat transfer is always in demand. Energy-efficient fluids with greater potential to improve flow and

Manuscript received 2 July 2009.
The third author would like to thank the Thailand Research Fund and the Office of Higher Education Commission for their support.
Address correspondence to Lazarus Godson, R&AC Division, Department of Mechanical Engineering, College of Engineering, Anna University, Chennai, Tamil Nadu, 600 025, India. E-mail: godasir@yahoo.co.in

NOMENCLATURE

A	surface area, m^2
g	acceleration of gravity, m s^{-2}
h	free surface elevation difference, m
k	thermal conductivity, W/mK
l	length of the capillary section, m
n	empirical shape factor
q	heat flux, W/m
r	radial distance, m
T	final temperature, °C
T_0	initial temperature, °C
t	time, s

Greek Symbols

γ	particle size, nm
μ	dynamic viscosity, mPa.s
ν	kinematic viscosity, m^2/s
ρ	density, kg/m^3
φ	volume fraction

Subscripts

nf	nanofluid
p	particle
w	water

Downloaded By: [INFLIBNET India Order] At: 07:09 2 September 2010

thermal characteristics are the option to enhance heat transfer rate. In the development of any energy-efficient heat transfer fluids for enhanced heat transfer performance, in practical applications, a detailed study on the thermophysical properties such as thermal conductivity and viscosity is necessary. Improving the thermophysical properties is the key idea to improve the heat transfer characteristics of the conventional fluids.

The use of nanosize solid particles as an additive suspended in the base fluid (nanofluids) is a technique for the heat transfer enhancement [1]. Besides the enhancement it is found that the nanofluids eliminate most of the problems arising with microsize slurries, like sedimentation, clogging of small channels, erosion, excessive pressure drop, etc. Thus, nanofluids have greater potential for heat transfer enhancement and are highly suited to application in practical heat transfer processes. Nanofluid thermophysical properties such as thermal conductivity and dynamic viscosity are of significant importance in every heat transfer application involving a fluid system. The heat transfer resistance of a flowing fluid is often represented by a Nusselt number, which takes into account the fluid thermal conductivity sometimes directly and usually indirectly as well through the Prandtl number. Thus, the first assessment of the heat transfer potential of a nanofluid is to consider its thermal conductivity.

The thermal conductivity of nanofluids is more temperature sensitive than that of the base fluid. Consequently, the thermal conductivity enhancement of nanofluids is temperature sensitive. Recently, many researchers have investigated the enhancement of thermal conductivity and observed that the thermal conductivity of the suspension of nanoparticles has increased more than 20% even with the low nanoparticle concentrations [2, 3]. Maxwell's theoretical model showed that the effective thermal conductivity of suspensions containing spherical particles increases with particle volume concentration [4]. Hamilton and Crosser's and the modified Maxwell model showed the effect of particle shape and particle volume concentration on thermal conductivity of fluid containing solid particles [5]. Recent research has focused on both the effect of particle size on the heat transport mechanism and the effect of a solid–-liquid interface and temperature effect on thermal conductivity enhancement. Lee et al. [6] investigated the effective thermal conductivity and viscosities of Al_2O_3 nanoparticles with volume fraction of 0.01–0.3 vol% dispersed in water. The transient hot-wire technique was used to measure the thermal conductivity and an oscillation viscometer was used to measure the viscosity of nanofluids. All data were collected for temperatures ranging between 20 and 40°C. The results showed that the thermal

conductivity of nanofluids increases nearly linearly with the particle volume fraction. The viscosity of nanofluids significantly decreases with increasing temperature. Moreover, the authors found that the measured viscosities of nanofluids exhibited a nonlinear relation with the particle concentration and increase with increase in particle concentrations. Das et al. [7] investigated the thermal conductivity of Al_2O_3 and CuO nanoparticles suspended in water as a function of temperature. The temperature oscillation technique was used for measuring the thermal conductivity of nanofluids at different temperatures ranging from 21 to 51°C. The results showed that the thermal conductivity increased with increase in nanofluid temperature as well as particle concentrations. Thus, fluids containing suspended metal particles are found to manifest enhanced thermal conductivities compared to pure fluids [8]. Masuda et al. [9] dispersed oxide nanoparticles (γ-Al_2O_3 and TiO_2 with $\varphi = 4.3\%$) in liquid and showed the increase in the thermal conductivity to be 32 and 11%, respectively. Grimm [10] dispersed aluminum particles ($\gamma = 80$ nm to 1 μm) in a fluid and claimed a 100% increase in the thermal conductivity of the fluid for $\varphi = 0.5$–10 vol%.

Choi and Eastman [11] measured the thermal conductivity of multiwalled carbon nanotubes (MWCNTs) of diameter 25 nm and length 50 μm. The thermal conductivity was measured by a transient hot-wire method for 1 vol% nanotube loading. The results showed 159% enhancement in the thermal conductivity with 1 vol% fraction of MWCNT. The important feature of this enhancement was the increasing slope of the enhancement curve. Eastman et al. [3] showed that Cu-ethylene glycol (nanoparticles coated with thioglycolic acid) with $\varphi = 0.3\%$ gave a 40% increase in thermal conductivity. Recently, an investigation on thermal conductivity of magnetic nanoparticles (Fe_3O_4 coated with oleic acid) suspended in the base fluid (hexadecane) was conducted at the Indira Gandhi Centre for Atomic Research (IGCAR). The results showed 300% enhancement in the thermal conductivity of nanofluids containing magnetic nanoparticles [12]. Further, it was proved that the thermal properties are tunable for magnetically polarizable nanofluids that consist of a colloidal suspension of magnetite nanoparticles. These enhancements depend on factors such as particle shape, particle size, and volume fraction of particles and temperature and thermal properties of solid and liquid materials.

Viscosity is an important parameter for fluid flow. Determining the viscosity of the nanofluid is essential in establishing adequate pumping power as well as the convective heat transfer coefficient, because the Prandtl and Reynolds numbers (functions of viscosity) will be influenced by these. Until now, only a few studies have addressed the viscous properties of nanoparticle suspensions at different temperatures. Masuda et al. [9] were the first who measured viscosity of water-based nanofluids for temperatures varying from the ambient to 60°C, which was then followed by Pak and Cho [13], who presented some additional data for Al_2O_3–water nanofluid. Wang et al. [14] measured the viscosity using three different dispersion techniques for Al_2O_3–water and Al_2O_3–ethylene glycol mixtures at ambient temperature. Putra et al. [15] have provided some limited data showing the temperature effect on Al_2O_3–water nanofluid viscosity. Recently, Maré et al. [16] have obtained some new temperature-dependent viscosity data for Al_2O_3–water with relatively high particle concentrations. Lu and Fan [17], Kwak and Kim [18], Nguyen et al. [19], Namburu et al. [20], and Avsec and Oblak [21] have studied the viscosity of nanofluids with various metallic and oxide nanoparticles and found that the viscosity of nanofluids increases with particle loading and decreases with increase in temperature. Lee et al. [6] measured viscosity of

Downloaded By: [INFLIBNET India Order] At: 07:09 2 September 2010

Al_2O_3–water nanofluids with low volume concentrations ranging from 0.01 to 0.3%. Results showed that the viscosity decreased with increasing temperature. Furthermore, the measured viscosities of the Al_2O_3–water nanofluids showed a nonlinear relation even in the low volume concentration, whereas the Einstein viscosity model clearly predicts a linear relation. Murshed et al. [22] measured the viscosity of nanofluids and found that the viscosity increased with the volumetric loading of nanoparticles. The results were compared with different models and experimental data. The results showed a substantial increase in the viscosity. Such enhancement of viscosity may diminish the potential benefits of nanofluids. Most recently, Duangthongsuk and Wongwises [23] experimentally investigated the thermal conductivity and dynamic viscosity of TiO_2 nanoparticles dispersed in water with volume concentration of 0.2–2 vol% for temperatures ranging from 15 to 35°C. Detailed information regarding measurement techniques of thermal conductivity, viscosity, and particle size are shown in Duangthongsuk and Wongwises [23], which belong to one of coauthors. The results showed that the measured viscosity and thermal conductivity of nanofluids increased as the particle concentrations increased and are higher than the values of the base liquids. Finally, new thermophysical correlations are proposed for predicting the thermal conductivity and viscosity of nanofluids [23].

Based on the above, it is clearly seen that the nanofluids show higher thermal conductivity and viscosity than the base fluids. However, the inconsistency has been the subject of many published literature works with respect to the thermal conductivity and viscosity of nanofluids. For example, some researchers have suggested that the existing theoretical models can be used to predict the thermal conductivity and viscosity of nanofluids, whereas many other researchers have indicated that these models fail to predict the thermophysical properties of nanofluids. Likewise, the enhancements of the thermophysical properties of nanofluids have been explained by a number of mechanisms and models but no agreement has been reached between the experimental and theoretical results. Also, the thermophysical properties of nanofluids depend on various factors such as particle size, particle shape, metallic or nonmetallic (oxide) material, pH value, etc. For example, nanoparticles with a cylindrical shape have higher thermal conductivity enhancement than spherical-shaped nanoparticles. Nanofluids with smaller nanoparticle size exhibit greater thermal conductivity [24]. Nanofluids with metallic nanoparticles give higher thermal conductivity than nanofluids with nonmetallic nanoparticles [22]. The lower pH value gives higher heat transport than the higher pH value [25]. Furthermore, the thermophysical properties of nanofluids are strongly dependent on temperature. Only a few articles [6, 7, 22, 26] have reported the effect of temperature on the thermal conductivity and viscosity of nanofluids and more experimental investigations are needed to address the effect of the temperature and particle volume concentrations on the thermophysical properties of nanofluids. Therefore, in the present work, the temperature-dependent properties such as the thermal conductivity and viscosity of silver nanoparticles suspended in water are measured. The experiments were carried out over temperatures ranging from 50 to 90°C with 0.3, 0.4, 0.6, 0.8, 0.9, and 1.2% volume concentrations. The thermal conductivity was measured by the transient hot-wire method and the viscosity was measured with a Cannon-Fenske viscometer (Shambhavi Impex, Mumbai, India). Further, the measured data of the thermal conductivity and viscosity of nanofluids are used for comparison with the predicted values of the existing classical models. Finally, new correlations for predicting the thermal conductivity and viscosity of silver–water nanofluids are proposed.

Downloaded By: [INFLIBNET India Order] At: 07:09 2 September 2010

PREPARATION AND CHARACTERIZATION OF SILVER–WATER NANOFLUID

Some important conditions in the preparation of nanofluid are stable suspension ability to withstand any chemical change and low agglomeration of particles. Common methods used for the preparation of nanofluids are (1) addition of acid or base to change the pH value of the suspension; (2) addition of surfactants to disperse particles into fluid; and (3) the use of ultrasonic vibration. Addition of some other materials (surfactants) may have negative effects because of the structural change of solid–liquid interface. Therefore, the ultrasonic vibration method is used for the preparation of nanofluids and also to prevent the structural change of nanofluids in this experiment. The ultrasonic vibration is carried out for 5 h using an ultrasonic processor (Roop-Telsonic TEC-40 model [Roop Telsonic Ultrasonix Limited, USA]; power density 750 W, frequency 20 kHz). The silver nanoparticles were directly purchased from Sigma Aldrich, Bangalore, India (product number 576832, xilver nanopowder, $<$100 nm, 99.5% metals). The silver nanoparticles were mixed directly with deionized water under ultrasonic vibration without any additive or stabilizer. The nanofluid was not transparent and it was black in color. The long-term stability of nanoparticles in suspension is not important to measure the thermal conductivity of nanofluid by the transient hot-wire method because the thermal conductivity measurement is carried out within 10 s. Moreover, the nanofluid used in this experiment was not settled for one day. To validate this, a stability test was conducted by taking a small sample of nanofluid with the maximum concentration of 1.2% volume fraction and physically observing to see whether any settling occurred. Photos were taken 1 h after preparing the sample and after 24 h as shown in Figure 1. From the figure it is clearly seen that settling did not occur in 24 h. Hence, the nanofluid is assumed as a stable fluid in the experiment. The pH value of the nanofluid is also measured by using a pH meter (ELICO, LI120, Elico Limited, Hyderabad, India), which is capable of measuring pH values ranging from 2 to 14. The glass electrode that is connected to the pH meter is inserted into the liquid and the measured value is displayed in the indicator of the pH meter. The desired volume concentrations used in this study are 0.3, 0.4, 0.6, 0.8, 0.9,

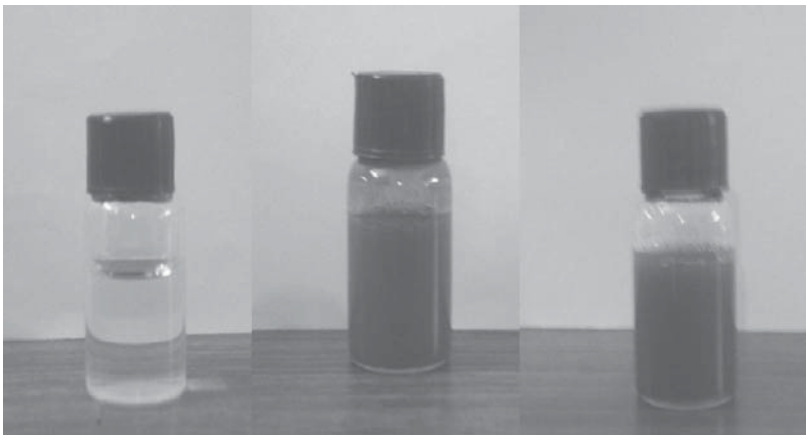

Figure 1 Stability test of silver–water nanofluids.

Downloaded By: [INFLIBNET India Order] At: 07:09 2 September 2010

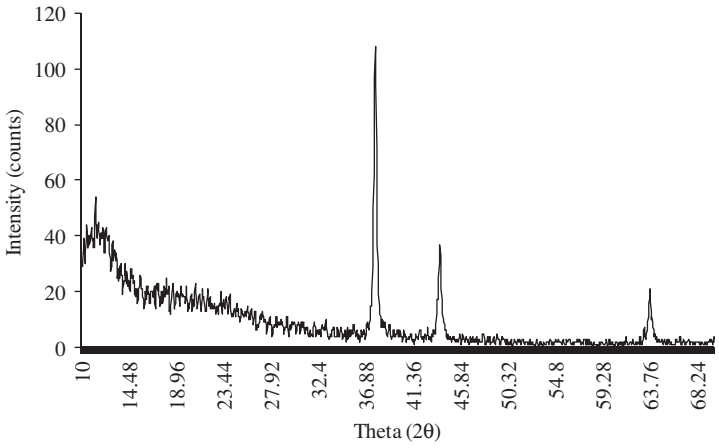

Figure 2 XRD patterns of silver nanoparticles.

Downloaded By: [INFLIBNET India Order] At: 07:09 2 September 2010

and 1.2 vol% with pH values of 7.4, 7.3, 7.1, 6.9, 6.8, and 6.7, respectively. From the pH values, it can be seen that the solution chemistry of nanofluids is nearly neutral in nature. Powder X-ray diffraction (PXRD) as shown in Figure 2 is used in the present study for characterizing silver nanoparticles. As the name suggests, the sample is in powder form, consisting of fine grains in the form of single crystallites. The term *powder* really means that the crystalline domains are randomly oriented in the sample. In Figure 2, The XRD plot is between the intensity (counts) and 2θ, in degrees. The wavelength is 1.54 nm and the shape factor is 0.9. When a two-dimensional (2D) diffraction pattern is recorded, it shows concentric rings of scattering peaks corresponding to the various *d*-spacings in the crystalline lattice. The positions and the intensities of the peaks are used for identifying the underlying structure (or phase) of a solid material. From the Scherrer equation the average size of calculated silver nanoparticles was 63 nm, which is consistent with the identified value from the manufacturer.

THERMAL CONDUCTIVITY MEASUREMENT

Description of the Transient Hot-Wire Method/Apparatus

A transient hot-wire method is the most appropriate and widely used method to determine the thermal conductivity of liquids. This method eliminates the effects of natural convection, whose unwanted presence creates problems for measurements made with a steady-state apparatus. A constant current is supplied to the wire (platinum) to generate the essential temperature rise. The wire serves as both the heat source and the temperature sensor. The wire is surrounded by a liquid, whose thermal conductivity is to be measured. The heat dissipated in the wire increases the temperature of the wire and that of the liquid. The rise in temperature of the wire depends on the thermal conductivity of the liquid in which the wire is immersed.

Normally a platinum wire is chosen because of its capable resistance–temperature relationship over a wide temperature range. The resistance–temperature coefficient of platinum wire is 0.0039092°C. A 75-μm diameter is used in the present study.

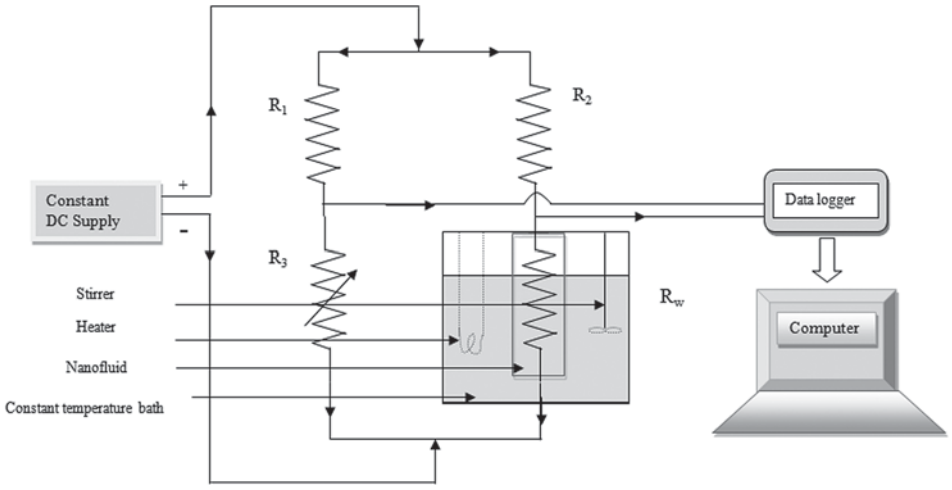

Figure 3 Transient hot-wire setup for measuring the thermal conductivity of nanofluids.

Downloaded By: [INFLIBNET India Order] At: 07:09 2 September 2010

Because the nanofluids are electrically conductive, Teflon spray is used for easy and convenient coating of the platinum wire to act as an electric insulation. The Teflon-coated platinum wire was directly purchased and the 7.5-μm Teflon coating was given as per the specification from the manufacturer. A schematic diagram of the transient hot-wire apparatus is shown in Figure 3. The main experimental cell is actually a part of the Wheatstone bridge circuit because the wire (hot-wire) is used as one arm of the bridge circuit. In the bridge R_1 and R_2 are the fixed resistors having 1,000Ω and 16Ω resistance; R_3 is the variable resistor with maximum of 1,000Ω resistance connected to the Wheatstone bridge circuit; and R_w is the resistance of the wire that is to be measured. A 100-mL glass tube having a cylinder cavity of 2.9 cm in diameter and 23 cm length is used as the nanofluid container, which is filled with fluid whose thermal conductivity is to be measured. The Pplatinum wire is placed at the center of the nanofluid container and is placed inside the constant-temperature bath. The size of the bath is 17.5 cm diameter and 24.5 cm length. The constant-temperature bath consists of a heater, a stirrer, and temperature sensors to ensure that a constant temperature is maintained in the bath. Water is used as the heating fluid in the bath. The constant-temperature bath is also thermally insulated.

Principle of Transient Hot-Wire Method

Because the experiment lasts for just 5 s, the total quantity of heat going to the liquid per second is very small. Hence, the diameter of the container is sufficient to assume the liquid to be a thermally semi-infinite medium. An infinitely long and thin wire is used as a line source for dissipating heat into a semi-infinite medium, with constant heat generation. The working equation is based on a specific solution of Fourier's law [27].

Following is the general Fourier's equation for one-dimensional radial heat conduction:

$$\frac{1}{\alpha_f}\frac{\partial \Delta T}{\partial t} = \frac{1}{r}\frac{\partial}{\partial r}\left(r\frac{\partial \Delta T}{\partial r}\right) \tag{1}$$

with boundary conditions

$$\lim_{r\to 0}\left\{r\left(\frac{\partial T}{\partial r}\right)\right\} = -\frac{q}{2\pi k_f} \tag{2}$$

where $t = 0$ and $r = 0$.

$$\lim_{r\to\infty}\{\Delta T(r,t)\} = 0 \tag{3}$$

where $t \geq 0$ and $r = \infty$ and $\Delta T = T - T_0$.

If temperatures of the heat source at time t_1 and t_2 are T_1 and T_2, respectively, then the thermal conductivity of liquid may be given as

$$k = \frac{q}{4\pi(T_2 - T_1)}\ln\frac{t_2}{t_1} \tag{4}$$

Experimental Procedure

Initially, the experiment was conducted and the readings were recorded up to 10 s and the actual calculation was carried out for less than 5 s after reaching the required temperature in the bath in order to avoid natural convection of the wire and fluid. Measurements were taken at different temperatures ranging from 50 to 90°C. It took nearly 15 to 20 min to reach each temperature range chosen for the study. The nanofluid was heated to the desired temperature after sonication. After taking the reading for each concentration, the nanofluid was taken out and sonicated well before conducting the experiment for the next concentration. During the experimentation, we did not find any agglomeration for the nanofluid tested. However, some particles stuck to the glass tube.

Once the required temperature was reached in the constant-temperature bath, the power supply was switched ON. The Wheatstone bridge circuit was balanced (i.e., until the galvanometer showed zero deflection) by adjusting the variable resistor R_3. Then the DC supply was given to the bridge, which caused a change of voltage in the bridge through the platinum wire. As the current flowed through the circuit the resistance of the wire increased, which in turn produced an emf between the arms, thus causing an unbalanced condition in the circuit. This change in voltage over time was recorded by the data logger (Agilent Technologies Ltd.) at the sampling rate of 10 readings per second. The change in resistance of the wire was calculated from the Ohm's law using the measured voltage change over time. From the temperature–resistance relation of the platinum wire the temperature variation of the wire was calculated. The calculated temperature variation vs. natural logarithm of time was plotted and a sample plot

Downloaded By: [INFLIBNET India Order] At: 07:09 2 September 2010

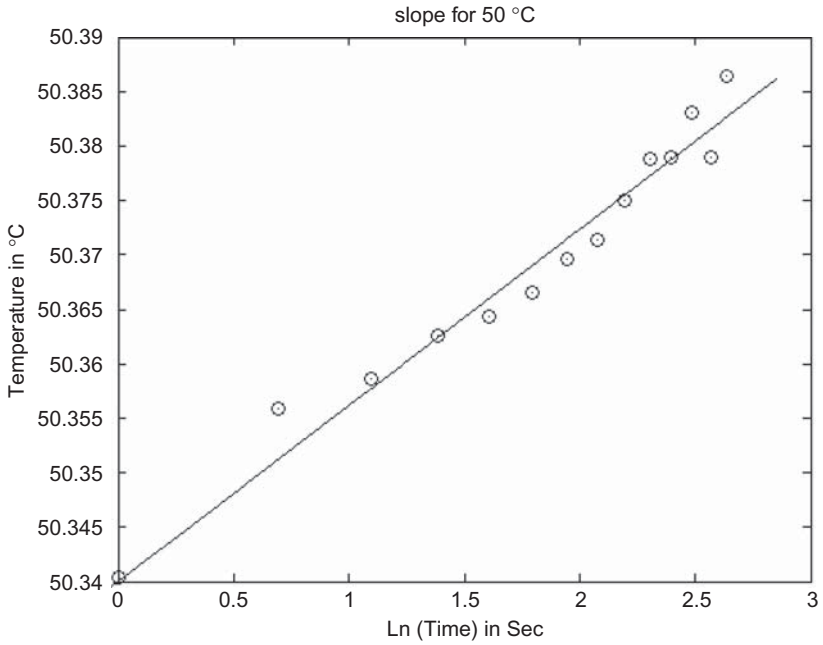

Figure 4 Plot of the temperature variation vs. natural logarithm of time.

Downloaded By: [INFLIBNET India Order] At: 07:09 2 September 2010

of the same is shown in Figure 4. The thermal conductivity was then calculated from the slope of the linear fitted curve and the other known parameters. For every concentration of the nanofluid measurement the glass tube for measuring the thermal conductivity was cleaned and kept for some time to be dried. Then the measurements awere taken for different concentrations. The above procedure was repeated for different temperatures and different volume concentrations of silver water nanofluid.

Uncertainty Analysis

Various measured entities with their average values and uncertainties are as given below, including resistances:

$$\sigma_{\Delta R_W} = \pm\sqrt{\left(\frac{\partial \Delta R_W}{\partial V}\sigma_V\right)^2 + \left(\frac{\partial \Delta R_W}{\partial R_3}\sigma_{R_3}\right)^2 + \left(\frac{\partial \Delta R_W}{\partial R_W}\sigma_{Rw}\right)^2 + \left(\frac{\partial \Delta R_W}{\partial \Delta V}\sigma_{\Delta V}\right)^2} \quad (5)$$

$$\sigma_{\Delta R_W} = \pm 5.0227 \times 10 \times \mathrm{e}^{-4}\ \Omega$$

For example, the thermal conductivity of water at 70°C is calculated as $k = 0.6616$ W/mK, which is the average value from 50 to 90°C. The uncertainty in this value is calculated as

$$\sigma_k = \pm\sqrt{\left(\frac{\partial k}{\partial q}\sigma_q\right)^2 + \left(\frac{\partial k}{\partial slope}\sigma_{slope}\right)^2} = \pm 0.01013\,\mathrm{W/mK}. \tag{6}$$

$$\mathrm{k} = 0.6616 \pm 0.01013\ \mathrm{W/mK}$$

Thus, the uncertainty in the value of thermal conductivity of liquid measured by this equipment is less than 1.6% of its mean value. Then, the measured thermal conductivity of nanofluids is used for comparison with those obtained from the existing correlations, which are defined as follows.

Hamilton and Crosser [5] proposed a model for calculating the thermal conductivity of nanofluids for spherical and nonspherical (cylindrical) particles where $n = 3$ for spheres, $n = 6$ for cylinders, which is expressed in the following form:

$$\frac{k_{nf}}{k_w} = \frac{k_p + (n-1)k_w - (n-1)\varphi(k_w - k_p)}{k_p + (n-1)k_w + \varphi(k_w - k_p)} \tag{7}$$

Timofeeva et al. [28] suggested the effective medium theory to calculate thermal conductivity of nanofluids, which is expressed as follows:

$$k_{nf} = (1 + 3\varphi)k_w \tag{8}$$

Wasp [29] proposed a model for calculating the thermal conductivity of nanofluids, which is expressed as follows:

$$\frac{k_{nf}}{k_w} = \frac{k_p + 2k_w - 2\varphi(k_w - k_p)}{k_p + 2k_w + \varphi(k_w - k_p)} \tag{9}$$

VISCOSITY MEASUREMENT

Principle of Cannon-Fenske Viscometer

Various methods can be used for the experimental determination of viscosity. Concentric cylinders or cone and plate methods are very similar to the parallel plate visualization for measuring the shear viscosity.

The capillary viscometer follows Oswald flow where the kinematic viscosity is given by the formula

$$\nu = \frac{4\pi r^4 gh/8l}{dv/dt} \tag{10}$$

Each glass viscometer size has a coefficient of calibration. The coefficient is multiplied by the time taken for the fluid sample to pass between the different marks on the viscometer. This value determines the kinematic viscosity, which can be converted into the dynamic viscosity by multiplying the density of the fluid. An

Downloaded By: [INFLIBNET India Order] At: 07:09 2 September 2010

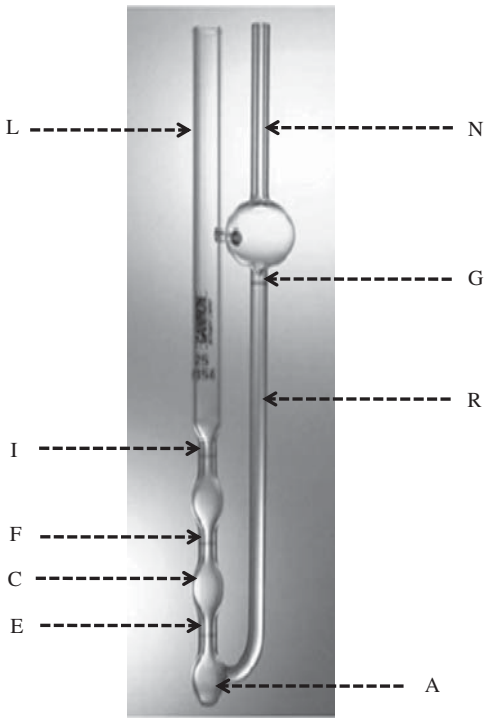

Figure 5 Cannon-Fenske Opaque (reverse-flow) viscometer (height 8 in.).

Downloaded By: [INFLIBNET India Order] At: 07:09 2 September 2010

investigation of the dependence of viscosity on temperature and particle loading for the nanofluids is conducted using the Cannon-Fenske Opaque capillary viscometer. With this instrument it is possible to measure the kinematic viscosity of a fluid in a range from 1 to 15 cSt (1 cSt = 1 mm^2/s). In order to have experimental data at different temperatures the viscometer is placed in a closed transparent container, which is maintained at constant temperature as shown in Figure 5.

Experimental Procedure

Initially the viscometer was cleaned using suitable solvents (ammonia) and dried by passing clean, dry, filtered air through the instrument to remove the final traces of solvents. After cleaning, the sample was charged into the viscometer by inverting the instrument and immersing the tube N in the liquid sample; suction was applied to the tube arm L, and the sample liquid was drawn up to the mark G. After charging the sample, the instrument was turned back to its normal vertical position. Then the sample was allowed to flow through the capillary tube *R* approximately until the bulb *A* was half filled. A rubber stopper was used in the tube arm *L* in order to stop the liquid sample meniscus in bulb *A*. Before taking the readings, the rubber stopper was removed from the tube arm *L* and the liquid sample was allowed to travel upwards into the bulb *C*, and the efflux time was measured for the meniscus to pass from mark *E* to mark *F*. From the measured efflux time in seconds, the kinematic viscosity of the liquid sample was calculated by multiplying the viscometer

constant for bulb C (the viscometer constant was given as 0.015 m^2/S^2). Finally, the dynamic viscosity was calculated by multiplying the kinematic viscosity and the density of the fluid. The density of the nanofluid was calculated according to Pak and Cho's equation as given below [30]:

$$\rho_{nf} = \phi\rho_P + (1 - \phi)\rho_W \tag{11}$$

where ϕ is the volume fraction of the nanoparticles, ρ_p is the density of the nanoparticles, and ρ_w is the density of the base fluid. For every concentration of the nanofluid measurement for measuring the viscosity the viscometer was cleaned and kept for some time to be dried. Then the measurements were taken for different concentrations. The same procedure was repeated for temperatures ranging from 50 to 90°C with 0.3, 0.4, 0.6, 0.8, 0.9, and 1.2% volume concentrations.

Then, the measured viscosities of nanofluids were compared with those obtained from the existing well-known models, as follows: The effective dynamic viscosity of nanofluids can be calculated using Einstein's equation for a viscous fluid containing a dilute suspension of small, rigid, spherical particles [31]:

$$\mu_{nf} = \mu_w(1 + 2.5\varphi) \tag{12}$$

However, Brinkman [32] extended the relation for the viscosity of nanofluids to a more generalized form becausee the above relation has been found valid for relatively low particle loading ($\varphi \leq 2\%$). The following relation can be used to find the viscosity of nanofluids for higher and lower concentrations.

$$\mu_{nf} = \frac{1}{(1 - \varphi)^{2.5}}\mu_w \tag{13}$$

Batchelor [33] proposed a correlation to predict the viscosity of nanofluids with spherical-shaped nanoparticles, which is defined as:

$$\mu_{nf} = (1 + 2.5\varphi + 6.2\varphi^2)\mu_w \tag{14}$$

Wang et al. [14] conducted experiments to find the viscosity of nanofluids, and based on the experimental data, the following correlation has been proposed:

$$\mu_{nf} = \mu_w(123\,\varphi^2 + 7.3\,\varphi + 1) \tag{15}$$

RESULTS AND DISCUSSION

The Thermal Conductivity of Nanofluids

Before measuring the thermal conductivity of silver–water nanofluids, the thermal conductivity of pure deionized water was measured at temperatures ranging from 50 to 90°C to validate the transient hot-wire system. The measured data were then compared with the reference data presented in Incropera and DeWitt [34]. As shown in

Downloaded By: [INFLIBNET India Order] At: 07:09 2 September 2010

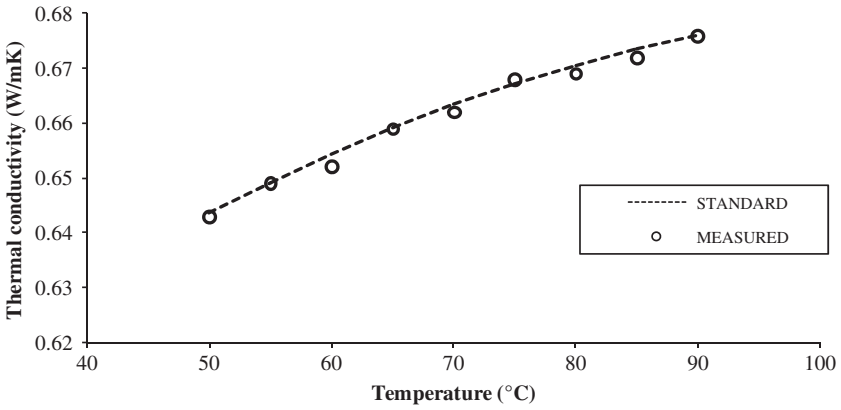

Figure 6 Comparison of the measured thermal conductivity with reference data.

Downloaded By: [INFLIBNET India Order] At: 07:09 2 September 2010

Figure 6, the results showed relatively good agreement between the experimentally measured values and the reference values and the uncertainty of the thermal conductivity measurement was around 1.5%.

Figure 7 shows the thermal conductivity of silver–water nanofluids as a function of particle volume concentration and temperature. The results show that the thermal conductivity of nanofluids significantly increased with increase in the nanofluid temperature and particle volume concentration. For example, the minimum enhancement of 27% for 0.3 vol% and a maximum enhancement of 115% for 1.2 vol% were observed at an average temperature of 70°C when compared with pure water for the same temperature. The thermal conductivity enhancement increased with increase in the particle volume concentration and temperature. W. Yu et al. [24] reported that the metal oxide particle volume concentrations below $\varphi = 4$–5% produces an enhancement level up to about 30%, and metal particles with less than $\varphi < 1.5\%$ provide an enhancement up to 40%. This shows that the enhancement of thermal conductivity

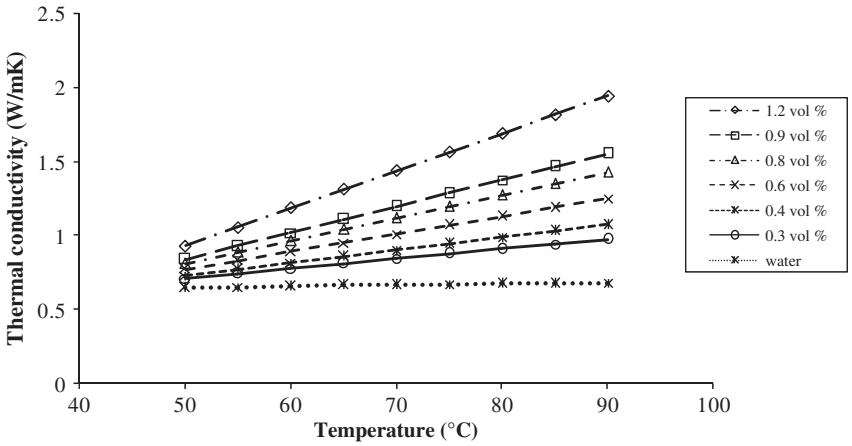

Figure 7 Thermal conductivity of silver–water nanofluids as a function of temperature and volume fraction.

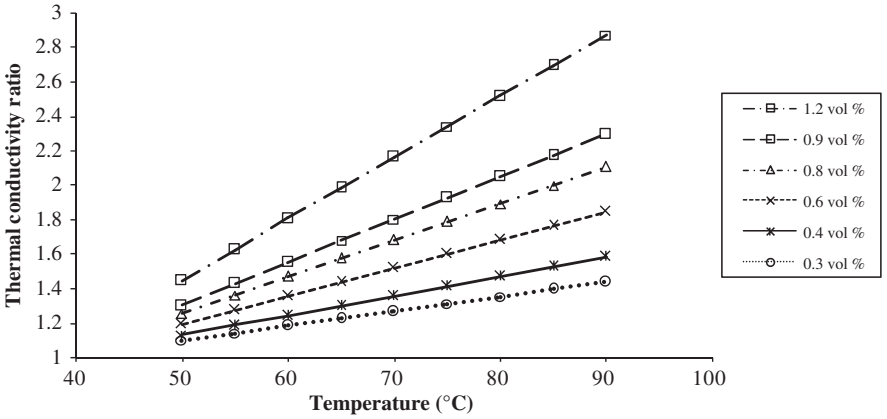

Figure 8 Thermal conductivity ratio of silver–water nanofluids as a function of temperature.

Downloaded By: [INFLIBNET India Order] At: 07:09 2 September 2010

using metal particles is higher than that of the metal oxide particles even at low concentrations. The thermal conductivity of nanoparticles is more temperature sensitive than that of the base fluid. Consequently, the thermal conductivity enhancement of nanofluids is temperature sensitive, and the dependence of nanofluid thermal conductivity is due to the random motion of nanoparticles. Figures 8 and 9 show the thermal conductivity ratio as a function of volume concentration and temperature. It can be clearly seen that the use of nanoparticles dispersed in the base liquid gave higher thermal conductivity than the base fluid. For example, the thermal conductivity ratio for 0.3 vol% concentration of silver nanofluid increased from 1.09 to 1.43 as the temperature increased from 50 to 90°C; similarly, for 1.2 vol% concentration the ratio increased from 1.44 to 2.87 for the temperatures ranging from 50 to 90°C. Further, the observed results show that the measured thermal conductivity ratio from the present study is larger than that of Masuda et al. [9] and Zhang et al. [26].

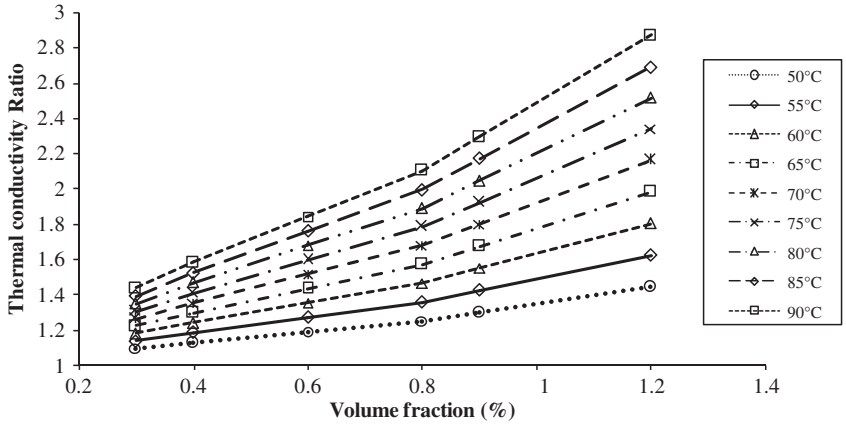

Figure 9 Thermal conductivity ratio of silver–water nanofluids as a function of volume fraction.

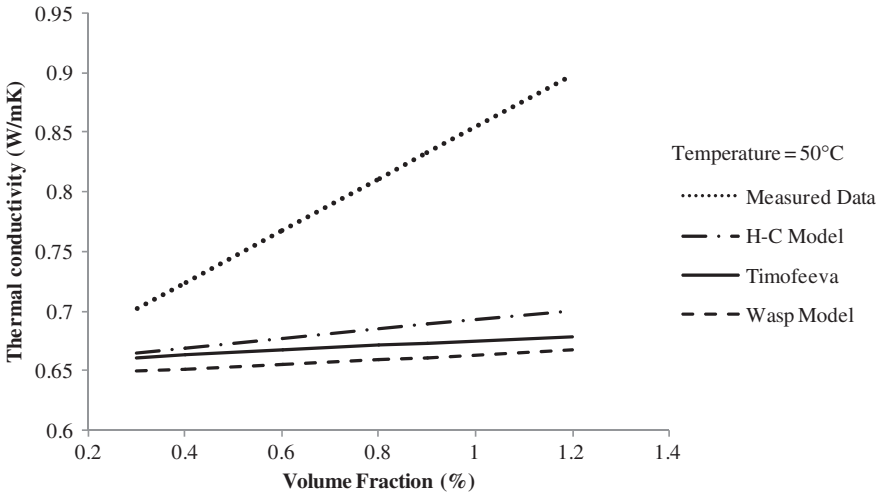

Figure 10 Comparison of the measured thermal conductivities with those obtained from various correlations.

Downloaded By: [INFLIBNET India Order] At: 07:09 2 September 2010

Figure 10 shows a comparison between the measured values of thermal conductivity of silver–water nanofluids and the predicted values of existing correlations at 50°C. As shown in Figure 10, the measured thermal conductivity of nanofluids is much higher than those predicted by the H-C model [5], Timofeeva [28] and Wasp models [29]. The results also show that the thermal conductivity enhancement of measured values mainly depends on the material, size and shape of the particle, volume concentration, and the operating temperature itself. From Figure 10, it is clear that the observed data for the thermal conductivity models proposed by other researchers are quite different from those of the present study, because of the several factors such as difference in the particle size, particle preparation, particle source, particle material, or even the measurement technique. The use of metallic nanoparticles even with low concentrations has an order of magnitude higher enhancement of thermal conductivity than that of oxide nanofluids with high concentration because the thermal conductivity of metallic particles is higher than the oxide ones. Also, it depends on the operating temperature itself. Therefore, more experimental works are needed to exactly predict the thermal behavior of nanofluids. As described above, it is evident that the thermal conductivity is a function of temperature and particle volume concentration. It is also seen that the existing correlations gave inappropriate predictions of the thermal conductivity of nanofluids. Thus, a new equation for calculating the effective thermal conductivity of nanofluids has been proposed as a function of temperature in the following form:

$$\frac{k_{nf}}{k_w} = a + b\varphi \tag{16}$$

where a and b are the coefficients of the slope plotted between the thermal conductivity and temperature on an Excel sheet. R^2 is the root mean square value described as follows:

Temperature (°C)	*a*	*b*	R^2
50	0.625	0.241	0.985
55	0.626	0.342	0.987
60	0.627	0.443	0.987
65	0.628	0.544	0.985
70	0.629	0.645	0.988
75	0.63	0.746	0.988
80	0.63	0.847	0.989
85	0.631	0.948	0.989
90	0.629	1.056	0.989

Downloaded By: [INFLIBNET India Order] At: 07:09 2 September 2010

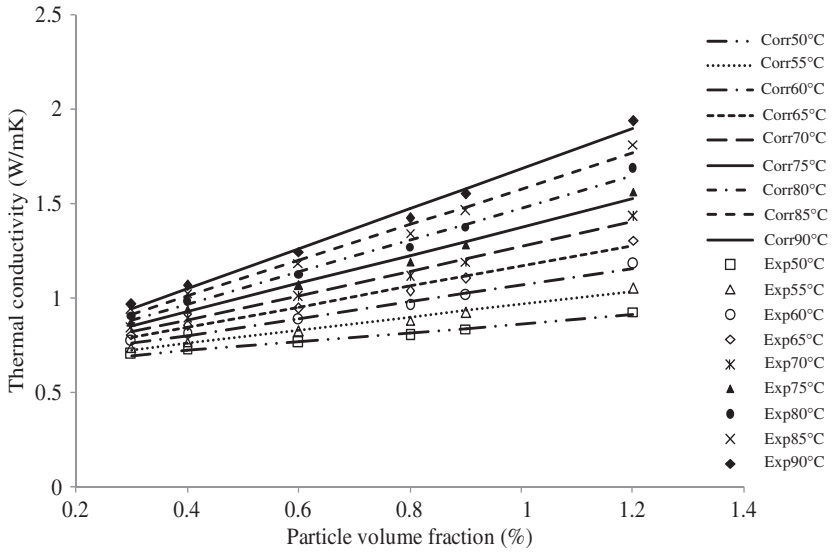

Figure 11 Comparison of the measured thermal conductivity ratio with the proposed correlation.

The authors would like to suggest that this equation is formed by the data on silver–water nanofluids. This equation can be used for (1) temperature range between 50 and 90°C and (2) particle volume concentration range between 0.3 and 1.2 vol%. Figure 11 shows comparisons between the thermal conductivity ratio obtained from the present correlation (Eq. (13)) and those obtained from the experiment. The results show that the present model gives reasonably good agreement with the experimental data.

The Viscosity of Nanofluids

Similar to the thermal conductivity measurement, the viscosity of the base fluid (water) is first measured to validate the experimental apparatus. The viscosity of pure water is measured at temperatures ranging from 50 to 90°C. Then, the measured data

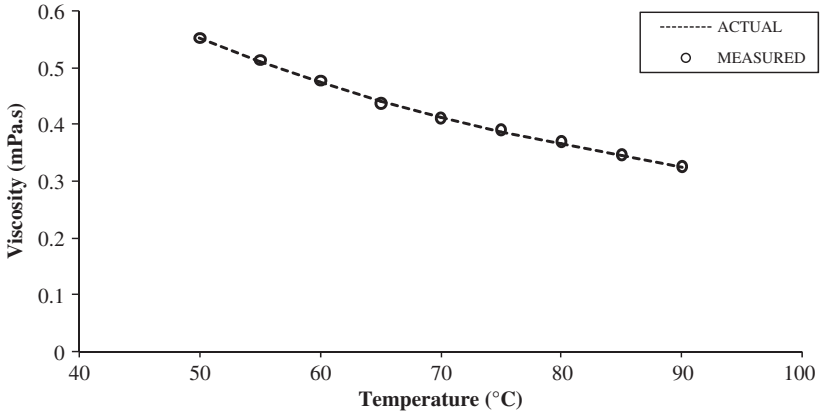

Figure 12 Comparison of the measured viscosity with reference data.

Downloaded By: [INFLIBNET India Order] At: 07:09 2 September 2010

are compared with the reference data from the REFPROP software (REFPROP Version 6.01, NIST Standard Reference Database 23, Gaithersburg, MD: National Institute of Standards and Technology). As shown in Figure 12, the results show good agreement between the measured values and the reference values, and the uncertainty of the viscosities measurement is within 1.5%. Figure 13 shows the viscosity of silver–water nanofluids as a function of particle volume concentration and temperature. The results indicate that the viscosity of nanofluids significantly increases as the concentration of the nanoparticles increases and at the same time the viscosity of nanofluids decreases as the temperature increases. This is because the density of the fluid decreases as the temperature increases and thereby leads to a decrease in the shearing force between the fluid layers. Figure 14 shows the viscosity ratio as a function of volume concentration and temperature. It is clearly seen that the use of nanoparticles dispersed in base liquid gives higher viscosity than the base fluid. For example, the

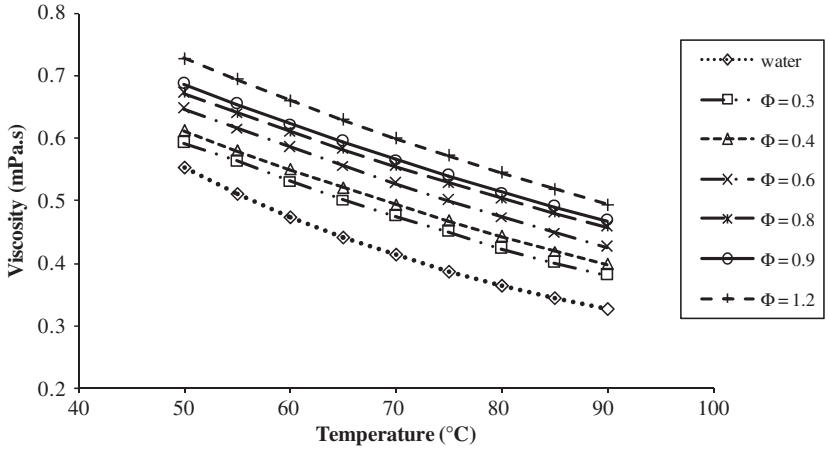

Figure 13 Viscosity of silver–water nanofluids as a function of temperature and volume fraction.

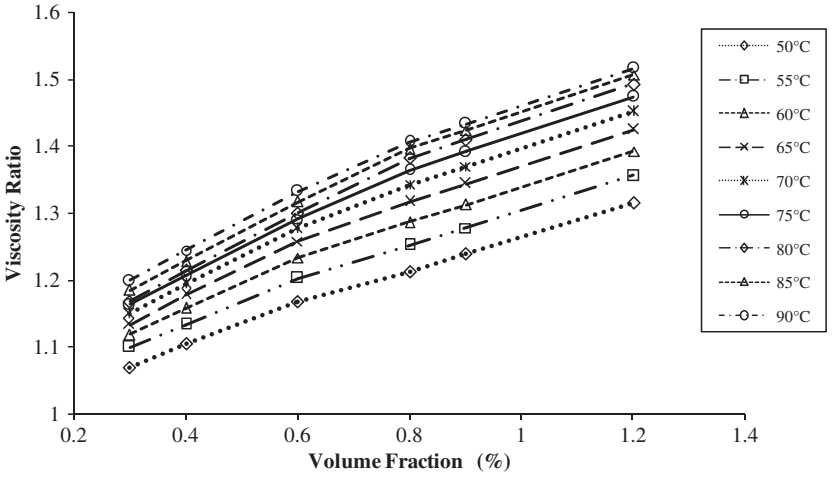

Figure 14 Viscosity ratio of silver–water nanofluids as a function of volume fraction and temperature.

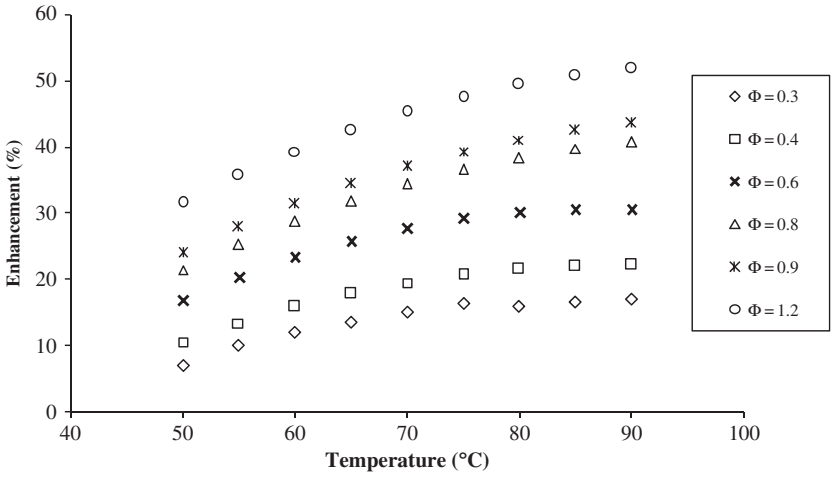

Figure 15 Viscosity enhancement of silver–water nanofluids as a function of temperature and volume fraction.

viscosity ratio for 0.3 vol% concentration of silver nanofluid increases from 1.06 to 1.2 as the temperature increases from 50 to 90°C and similarly for 1.2 vol% concentration the ratio increases from 1.31 to 1.51 for temperatures ranging from 50 to 90°C. Figure 15 shows the viscosity enhancement percentage of the measured data as a function of volume concentration and temperature. The viscosity increase is 13% for 0.3 vol%, 18% for 0.4 vol%, and 48% for 1.2 vol% of silver nanofluids and the average increase in the viscosity for volume fractions ranging from 0.3 to 1.2 is 28.39%. From the present study it is clearly seen that the viscosity of nanofluids is higher than the base fluid by about 13 to 28.39% with percentage volume fractions ranging from 0.3 to 1.2. Figure 16 shows a comparison of measured values at 50°C with the predicted values

Downloaded By: [INFLIBNET India Order] At: 07:09 2 September 2010

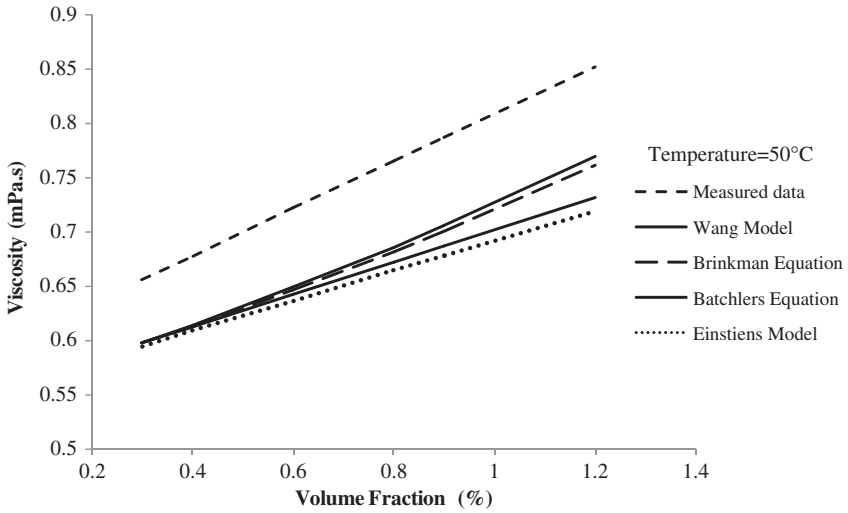

Figure 16 Comparison of the measured viscosity with those obtained from various correlations.

Downloaded By: [INFLIBNET India Order] At: 07:09 2 September 2010

from existing correlations. As shown in Figure 16, the measured data of nanofluids are much higher than those of the predicted values using Einstein's equation, Brinkman's equation, and Batchelor's and modified Einstein's equations. It is also observed that the measured data of silver water nanofluids did not match with any of the above viscosity models. It is also found that the existing correlations give inaccurate calculations of the viscosity of nanofluids. Therefore, the following equation for predicting the viscosity of the silver–water nanofluids has been proposed:

$$\frac{\mu_{nf}}{\mu_w} = (a + b\phi + c\phi^2) \tag{17}$$

where a and b are the coefficients of the slope plotted between the viscosity of nanofluids and temperature on an Excel sheet. R^2 is the root mean square value described as follows:

Temperature (°C)	*a*	*b*	*c*	R^2
50	0.9733	0.3474	–0.1478	0.983
55	0.9955	0.3745	–0.1487	0.988
60	0.9985	0.4363	–0.1514	0.9988
65	0.9993	0.4925	–0.1353	0.99
70	1.0046	0.527	–0.1291	0.995
75	1.0105	0.5492	–0.116	0.98
80	1.0047	0.5892	–0.0907	0.9818
85	1.0225	0.5829	–0.0622	0.9996
90	1.0405	0.5745	–0.1478	0.9997

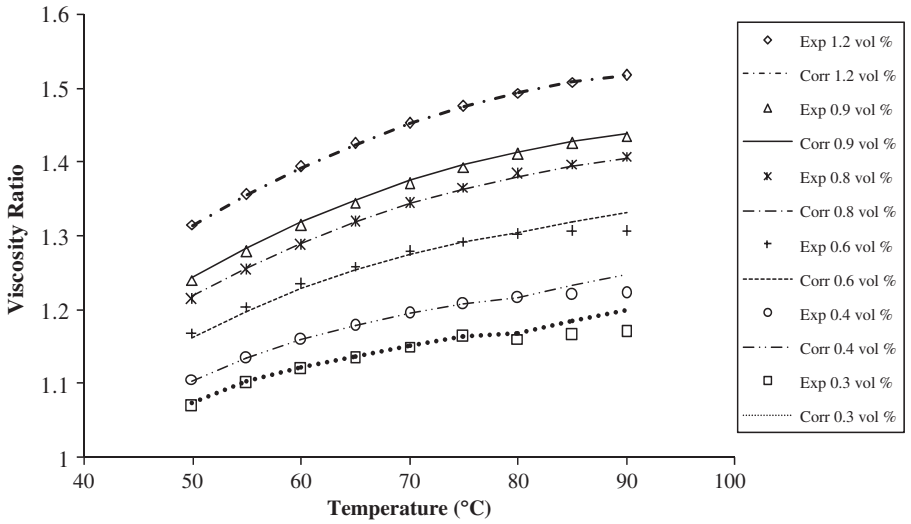

Figure 17 Comparison of the measured viscosity ratio with the proposed correlation.

The range for the above equation is the same as that of the thermal conductivity equation. Figure 17 shows that the measured data are compared with the predicted values of the present equation. The proposed equation for finding the viscosity agrees well with the experimental data from the present study.

CONCLUSION

The present study experimentally investigated the effective thermal conductivity and effective viscosity of silver–water nanofluids with particle volume concentrations of 0.3, 0.4, 0.6, 0.8, 0.9, and 1.2 vol% and temperatures ranging from 50 to 90°C. The nanofluids provided by a commercial source (Sigma Aldrich) were used for measuring the thermal conductivity and viscosity of nanofluids. From the thermal conductivity measurement, the results show that the thermal conductivity of nanofluids increases with increase in the particle volume concentration and temperature. It is also observed that the existing correlations for predicting the thermal conductivity of nanofluids give lower values than the experimental values. In contrast with thermal conductivity data, the viscosity of nanofluids significantly decreases with increase in temperature and increases with increase in the particle volume concentration. Moreover, the existing correlations for calculating the viscosity of nanofluids are found to be not suitable for the nanofluids tested. With regard to both the thermal conductivity and viscosity data, the results indicate that the measured data are quite different from those obtained by the other researchers, because of the various parameters such as particle size, particle shape, material (metal or nonmetallic), particle preparation, measurement technique, and the different particle sources. It is inferred that the proposed correlations for predicting the thermal conductivity and viscosity of nanofluids in the ranges of temperature and volume concentration taken in the present study show a significantly good agreement with the experimental results.

Downloaded By: [INFLIBNET India Order] At: 07:09 2 September 2010

Downloaded By: [INFLIBNET India Order] At: 07:09 2 September 2010

REFERENCES

1. S. Lee, S. Choi, S. Lee, and J. Eastman, Measuring Thermal Conductivity of Fluids Containing Oxide Nanoparticles, *Journal of Heat Transfer*, Vol. 121, pp. 280–289, 1999.
2. M.-S. Liu, M.C.-C. Lin, I.-T. Huang, and C.-C. Wang, Enhancement of Thermal Conductivity with Carbon Nanotube for Nanofluids, *International Communications in Heat and Mass Transfer*, Vol. 32, pp. 1202–1210, 2005.
3. J. Eastman, S. Choi, S. Li, W. Yu, and L. Thompson, Anomalously Increased Effective Thermal Conductivities of Ethylene Glycol-Based Nanofluids Containing Copper Nanoparticles, *Applied Physics Letters*, Vol. 78, pp. 718–720, 2001.
4. J.C. Maxwell, *A Treatise on Electricity and Magnetism*, Clarendon Press, Oxford, UK, 1873.
5. R.L. Hamilton and O.K. Crosser, Thermal Conductivity of Heterogeneous Two-Component Systems, *I & EC Fundamentals*, Vol. 1, pp. 187–191, 1962.
6. J.H. Lee, K.S. Hwang, S.P. Jang, B.H. Lee, J.H. Kim, S.U.S. Choi, and C.J. Choi, Effective Viscosities and Thermal Conductivities of Aqueous Nanofluids Containing Low Volume Concentrations of Al_2O_3 Nanoparticles, *International Journal of Heat and Mass Transfer*, Vol. 51, pp. 2651–2656, 2008.
7. S. Das, N. Putra, P. Thiesen, and W. Roetzel, Temperature Dependence of Thermal Conductivity Enhancement for Nanofluids, *Journal of Heat Transfer*, Vol. 125, pp. 567–574, 2003.
8. S.U.S. Choi, *Nanofluid Technology: Current Status and Future Research*, Paper presented at the Korea-U.S. Technical Conference on Strategic Technologies, Vienna, VA, October 20, 1998.
9. H. Masuda, A. Ebata, K. Teramae, and N. Hishinuma, Alteration of Thermal Conductivity and Viscosity of Liquid by Dispersion of Ultra-fine Particles. *Netsu Bussei (Japan)*, Vol. 4, pp. 227–233, 1993.
10. A. Grimm, *Powdered Aluminum-Containing Heat Transfer Fluids*, German patent DE 4131516 A1, 1993.
11. S.U.S. Choi and J.A. Eastman, U.S. Enhanced heat transfer using nanofluids, Patent 6221275, 2001.
12. J. Philip, J.M. Laskar, and B. Raj, Magnetic Field Induced Extinction of Light in a Suspension of Fe_3O_4 Nanoparticles, *Applied Physics Letters*, Vol. 92, 221911 (2008); doi:10.1063/1.2939100.
13. B.C. Pak and Y.I. Cho, Hydrodynamic and Heat Transfer Study of Dispersed Fluids with Submicron Metallic Oxide Particles, *Experimental Heat Transfer*, Vol. 11, pp. 151–170, 1998.
14. X. Wang, X. Xu, and S.U.S. Choi, Thermal Conductivity of Nanoparticles-Fluid Mixture, *Journal of Thermophysics and Heat Transfer*, Vol. 13, No. 4, pp. 474–480, 1999.
15. N. Putra, W. Roetzel, and S.K. Das, Temperature Dependent Viscosity of Al_2O_3-Water Nanofluids, *Heat and Mass Transfer*, Vol. 39, pp. 775–784, 2003.
16. T. Maré, A.G. Schmitt, C.T. Nguyen, J. Miriel, and G. Roy, Experimental Heat Transfer and Viscosity Study of Nanofluids: Water–γ Al_2O_3. Paper presented at the 2nd International Conference on Thermal Engineering, Theory and Applications, Al Ain, United Arab Emirates, January 3–6, 2006, Paper No. 93.
17. W.-Q. Lu and Q.-M. Fan, Study for the Particle's Scale Effect on Some Thermo Physical Properties of Nanofluids by a Simplified Molecular Dynamics Method, *Engineering Analysis with Boundary Elements*, Vol. 32, pp. 282–289, 2008.
18. K. Kwak and C. Kim, Viscosity and Thermal Conductivity of Copper Oxide Nanofluid Dispersed in Ethylene Glycol, *Korea-Australia Rheology Journal*, Vol. 17, No. 2, pp. 35–40, 2005.
19. C.T. Nguyen, F. Desgrangesb, N. Galanisc, G. Roya, T. Maréd, S. Bouchera, and H. Angue Mintsa, Viscosity Data for Al_2O_3–Water Nanofluid—Hysteresis: Is Heat Transfer Enhancement Using Nanofluids Reliable? *International Journal of Thermal Sciences*, Vol. 47, pp. 103–111, 2008.

20. K. Praveen and Namburu, Viscosity of Copper Oxide Nanoparticles Dispersed in Ethylene Glycol and Water Mixture, *Experimental Thermal and Fluid Science*, Vol. 32, pp. 397–402, 2007.
21. J. Avsec and M. Oblak, The Calculation of Thermal Conductivity, Viscosity and Thermodynamic Properties for Nanofluids on the Basis of Statistical Nanomechanics, *International Journal of Heat and Mass Transfer*, Vol. 50, pp. 4331–4341, 2007.
22. S.M.S. Murshed, K.C. Leong, and C. Yang, Investigations of Thermal Conductivity and Viscosity of Nanofluids, *International Journal of Thermal Sciences*, Vol. 47, No. 5, pp. 560–568, 2008.
23. W. Duangthongsuk and S. Wongwises, Measurement of Temperature-Dependent Thermal Conductivity and Viscosity of TiO_2-Water Nanofluids, *Experimental Thermal and Fluid*, Vol. 33, pp. 706–714.
24. W. Yu, D.M. France, S.U.S. Choi, and J.L. Routbort, Review and Assessment of Nanofluid Technology for Transportation and Other Applications, ANL/ESD/07–9, Energy Systems Division, Argonne National Laboratory, U.S. Department of Energy, http://www.osti.gov/bridge. April 2007.
25. S.M.S. Murshed, K.C. Leong, and C. Yang, Enhanced Thermal Conductivity of TiO_2-Water Based Nanofluids, *International Journal of Thermal Sciences*, Vol. 44, p. 367, 2005.
26. X. Zhang, H. Gu, and M. Fujii, Effective Thermal Conductivity and Thermal Diffusivity of Nanofluids Containing Spherical and Cylindrical Nanoparticles, *Experimental Thermal and Fluid Science*, Vol. 31, pp. 593–599, 2007.
27. H.S. Carslaw and J.C. Jaeger, *Conduction of Heat in Solids*, Oxford University Press, New York, 1959.
28. E.V. Timofeeva, A.N. Gavrilov, J.M. McCloskey, and Y.V. Tolmachev, Thermal Conductivity and Particle Agglomeration in Alumina Nanofluids: Experiment and Theory, *Physical Review*, Vol. 76, pp. 061203, 2007.
29. F.J. Wasp, *Solid-Liquid Slurry Pipeline Transportation*, Trans. Tech, Publications Inc., Berlin, 1977.
30. B.C. Pak and I.Y. Cho, Hydrodynamic and Heat Transfer Study of Dispersed Fluids with Sub-micron Metallic Oxide Particles, *Experimental Heat Transfer*, Vol. 11, pp. 151–170, 1998.
31. D.A. Drew and S.L. Passman, *Theory of Multi Component Fluids*, Springer, Berlin, 1999.
32. H.C. Brinkman, The Viscosity of Concentrated Suspensions and Solution, *Journal of Chemical Physics*, Vol. 20, pp. 571–581, 1952.
33. G.K. Batchelor, The Effect of Brownian Motion on the Bulk Stress in a Suspension of Spherical Particles, *Journal of Fluid Mechanics*, Vol. 83, No. 1, pp. 97–117, 1977.
34. F.P. Incropera and D.P. DeWitt, *Fundamentals of Heat and Mass Transfer*, John Wiley & Sons, New York, 1996.

Downloaded By: [INFLIBNET India Order] At: 07:09 2 September 2010

Provided for non-commercial research and education use.
Not for reproduction, distribution or commercial use.

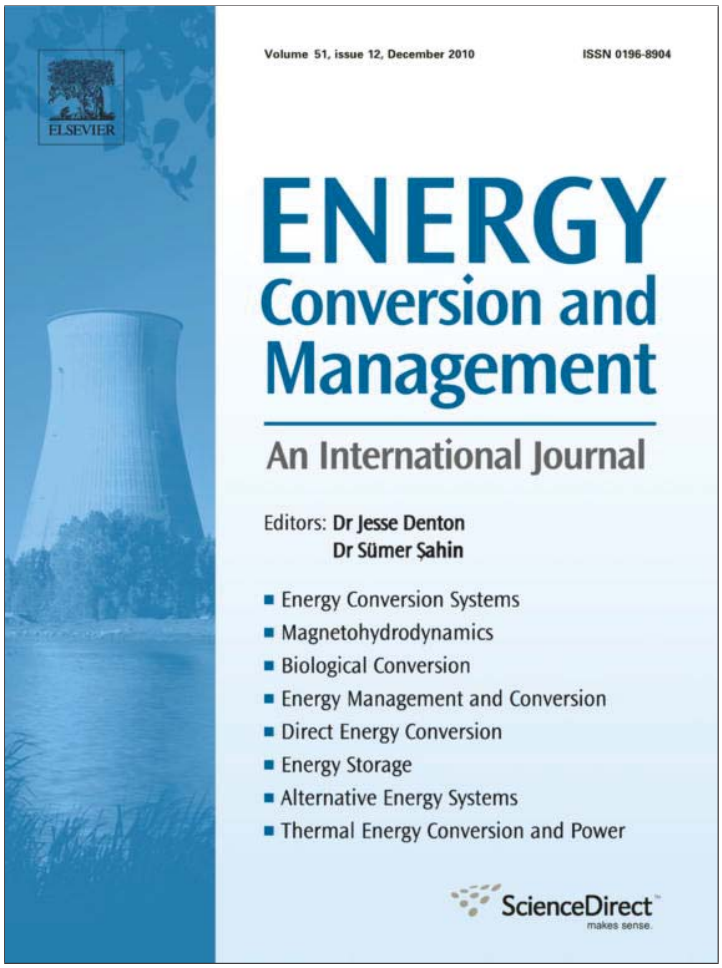

This article appeared in a journal published by Elsevier. The attached copy is furnished to the author for internal non-commercial research and education use, including for instruction at the authors institution and sharing with colleagues.

Other uses, including reproduction and distribution, or selling or licensing copies, or posting to personal, institutional or third party websites are prohibited.

In most cases authors are permitted to post their version of the article (e.g. in Word or Tex form) to their personal website or institutional repository. Authors requiring further information regarding Elsevier's archiving and manuscript policies are encouraged to visit:

http://www.elsevier.com/copyright

Author's personal copy

Energy Conversion and Management 51 (2010) 2535–2547

Contents lists available at ScienceDirect

Energy Conversion and Management

journal homepage: www.elsevier.com/locate/enconman

New experimental approach on the determination of condensation heat transfer coefficient using frictional pressure drop and void fraction models in a vertical tube

A.S. Dalkilic [a,*], S. Wongwises [b,**]

[a] Heat and Thermodynamics Division, Department of Mechanical Engineering, Yildiz Technical University, Yildiz, Besiktas, Istanbul 34349, Turkey
[b] Fluid Mechanics, Thermal Engineering and Multiphase Flow Research Lab. (FUTURE), Department of Mechanical Engineering, King Mongkut's University of Technology Thonburi (KMUTT), Bangmod, Bangkok 10140, Thailand

ARTICLE INFO

Article history:
Received 28 August 2009
Accepted 11 May 2010
Available online 17 June 2010

Keywords:
Two-phase flow
Condensation
Pressure drop
Heat transfer coefficient
R134a

ABSTRACT

The comparison of 35 void fraction and 13 two-phase frictional pressure drop models and correlations with experimental results for the condensation of R134a in a 0.5 m vertical copper tube with an inner diameter of 8.1 mm and outer diameter of 9.52 mm are presented. The most predictive ones having a relation with the heat transfer coefficient at different vapor qualities (0.69–0.96), various mass fluxes (260 and 515 kg m^{-2} s^{-1}), and different condensing temperatures (40 and 50 °C) are proposed. Three of 13 models belonging to the determination of two-phase frictional pressure drop and 8 of 35 models belonging to the determination of void fraction are found to be in good agreement, predicting the condensation heat transfer coefficient by means of von Karman's universal velocity distribution and Kosky–Staub's annular flow film thickness model with their deviations being within the range of ±30% for all tested conditions.

© 2010 Elsevier Ltd. All rights reserved.

1. Introduction

In-tube condensation of refrigerants is a crucial event in many applications such as condensers used in air-conditioning, refrigeration, and heat pumps. The struggle against the depletion of the stratospheric ozone layer and global warming caused by chemical compounds started a short period of time ago. To this end, condenser producers have been trying to change working fluids and to use enhanced geometries while considering energy efficiency. These kinds of improvements will continue to be given attention and to have an important impact on the HVAC industry in the future. Nowadays, new condensers have been designed to work with alternative refrigerants to replace R12 and R22 inside enhanced tubes due to ozone crises and efficiency requirements.

Annular flow conditions along the tube length include convective condensation which occurs for many applications inside tubes. Annular two-phase flow is one of the most important flow regimes and is characterized by a phase interface separating a thin liquid film from the gas flow in the core region. Two-phase annular flow occurs widely in film heating and cooling processes, particularly in power generation and especially in nuclear reactors. This flow regime has received the most attention, both analytically and experimentally, because of its practical importance and the relative ease with which analytical treatment may be applied. In addition to this, condensate distribution inside the tube wall is almost symmetric and there is high velocity vapor flow in the core during annular flow. In this flow regime, it is generally true that due to the breakup of the disturbance wave, part of the liquid phase is entrained as droplets into the gas core. It is also accepted that mass, momentum, and energy transfers are strongly affected by entrainment of the droplets to the gas core.

Void fraction, defined as the cross-sectional area occupied by the vapor in relation to the area of the flow channel, is an important parameter and is always used to determine the flow pattern transition, heat transfer coefficient, and two-phase pressure drop. Gas–liquid two-phase separated flow is commonly analyzed using the slip flow model. In this model, it is assumed that the two-phases are separated with different uniform velocities. In contrast, the homogeneous model is defined as an ideal case; it assumes a homogeneous mixture flowing with the same velocity, and besides this it is the simplest one for the determination of void fraction.

In the technical literature, numerous studies have been carried out on the modeling of the void fraction and can be divided into several groups: general void fraction models and correlations (Huq and Loth [1], Armand [2], Chisholm and Laird [3], Steiner

* Corresponding author. Tel.: +90 2123832819; fax: +90 2122616659.
** Corresponding author. Tel.: +66 24709115; fax: +66 24709111.
E-mail addresses: dalkilic@yildiz.edu.tr (A.S. Dalkilic), somchai.won@kmutt.ac.th (S. Wongwises).

0196-8904/$ - see front matter © 2010 Elsevier Ltd. All rights reserved.
doi:10.1016/j.enconman.2010.05.019

Author's personal copy

Nomenclature

A	area, m^2
Bo	Bond number
c_p	specific heat, J kg^{-1} K^{-1}
d	internal tube diameter, m
f	friction factor
Fr	Froude number
G	mass flux, kg m^{-2} s^{-1}
g	gravitational acceleration, m s^{-2}
h	heat transfer coefficient, W m^{-2} K^{-1}
i	enthalpy, J kg^{-1}
j	superficial velocity
L	length of test tube, m
m	mass flow rate, kg s^{-1}
N_{coff}	confinement number
P	pressure, N m^{-2}
Pr	Prandtl number
Re	Reynolds number
S	slip ratio
T	temperature, °C
T_σ^+	dimensionless parameter
q	mean heat flux, Kw m^{-2}
Q	heat transfer rate, W
We	Weber number
x	average vapor quality
X	Lockhart Martinelli parameter
z	axial coordinate, m
ΔP	pressure drop, Pa
ΔT_{sat}	T_{sat}–T_{wi}, °C

Greek symbols

δ^+	dimensionless film thickness
α	void fraction
ϕ	two-phase multiplier
δ	film thickness, m
ψ	surface tension parameter
ε	height of roughness
Ω	modifier to the Friedel correlation
σ	surface tension, N m^{-1}
ρ	density, kg m^{-3}
μ	dynamic viscosity, Pa s
τ	shear stress, N m^{-2}

Subscripts

avg	average
exp	experimental
evap	evaporator
F	frictional term
G	gravitational term
g	gas/vapor
go	gas only
H	homogeneous
i	inlet
int	interfacial
l	liquid
lo	liquid only
M	momentum term
o	outlet
ph	pre-heater
ref	refrigerant
sat	saturation
t	test section
TP	two-phase
TS	test section
w	water
wi	inner wall

[4], Harms et al. [5], Chisholm [6], $K\varepsilon_H$ parameter-based void fraction models and correlations (Armand and Treschev [7], Bangkoff [8], Czop et al. [9], flow regime-based void fraction models and correlations (Tandon et al. [10], Graham et al. [11], Hughmark [12], Lockhart and Martinelli parameter-based void fraction models and correlations (Hamersma and Hart [13], Lockhart and Martinelli [14], Turner and Wallis [15], Wallis [16], Domanski and Didion [17], Wilson et al. [18], Yashar et al. [19], Premoli et al. [20], Kawahara et al. [21], and slip ratio void fraction models and correlations (El Hajal et al. [22], Zivi [23], Rigot [24], Smith [25], Levy [26], Fauske [27], Thom [28], Baroczy [29], Chisholm [30], Madsen [31], Ahrens [32], Spedding and Spence [33], Chen, [34]. A brief and comprehensive overview of these works is presented in the authors' previous publication [55] and shown in Table 1.

The two-phase pressure drop is a significant design parameter in many engineering applications, such as in the chemical process industry, nuclear industry, petroleum industry, refrigeration and air-conditioning applications, and space applications. There have been a number of investigations into this subject in the literature due to its importance. The frictional, acceleration, and gravitational components form the two-phase total pressure drop in-tubes. Determination of the void fraction is necessary for computing the acceleration and gravitational components, and in a similar way, determination of either the two-phase friction factor or the two-phase frictional multiplier is necessary for computing the frictional component of pressure drop.

The Lockhart and Martinelli [14], Chisholm [30], and Friedel [35,36] correlations are generally used for the determination of pressure drop in conventional channels. Some modifications to account for the specific geometry or flow conditions are made in these correlations. In spite of their large deviations from the data for small channels in the condensation process, they are still used as the basis for many of the recent correlations. Well-known frictional pressure drop models and correlations (Lockhart and Martinelli [14], Chisholm [30], Friedel [35,36], Chen et al. [37], Cavallini et al. [38,39], Garimella [40], Garimella et al. [41], Mishima and Hibiki [42], Wang et al. [43], Wilson et al. [44], Sauza and Pimenta [45], Tran et al. [46], Lee and Lee [47]) are intensively summarized and shown in Table 2.

Performances of the smooth tubes have been determined by many researchers with pure refrigerants as operating fluids. Generally, empirical methods have been offered to compute the condensation heat transfer coefficients in smooth tubes. Most of these proposed models are modifications of the Dittus–Boelter single-phase forced convection correlation [48], such as Akers et al. [49], Cavallini and Zecchin [50], and Shah [51].

Kosky and Staub [52] investigated condensation of steam in a horizontal 12.57 mm i.d. tube at low pressure (20–152 kPa) during annular flow regime. The mass fluxes were between 2.7 and 149.2 kg m^{-2} s^{-1}. They presented a model based on the Friedel [35] correlation and supported by Martinelli's analogy [14] between heat and momentum transfer during turbulent flow and studied the calculation of thermal resistance of a flowing film of condensate assuming the entrainment is negligible and the film is thin and smooth. They showed the relation between the heat transfer coefficient and the frictional pressure gradient through

Author's personal copy

Table 1
Void fraction models and correlations.

Number	Void fraction model/correlation	Model/correlation
1	Homogeneous model	$\alpha_H = \frac{1}{1+\left(\frac{1-x}{x}\right)\left(\frac{\rho_g}{\rho_l}\right)S}\ S = 1$
2	Huq and Loth correlation [1]	$\alpha = 1 - \frac{2(1-x)^2}{1-2x+\left[1+4x(1-x)\left(\frac{\rho_l}{\rho_g}-1\right)\right]^{0.5}}$
3	Armand–Massina correlation [2]	$\alpha = (0.833 + 0.167x)\alpha_H$
4	Chisholm and Laird correlation [3]	$\alpha = 1 + \left[0.8/\left(1+\frac{21}{X}+\frac{1}{X^2}\right)\right]^{1.75}$
5	Steiner correlation [4]	$\alpha = \frac{x}{\rho_g}\left([1+0.12(1-x)]\left[\frac{x}{\rho_g}+\frac{1-x}{\rho_l}\right]+\frac{1.18(1-x)[g\sigma(\rho_l-\rho_g)]^{0.25}}{G\rho_l^{0.5}}\right)^{-1}$
6	Harms et al. model [5]	$\alpha = \left[1-10.06\mathrm{Re}_l^{-0.875}(1.74+0.104\mathrm{Re}_l^{0.5})^2\left(1.376+\frac{7.242}{X^{1.655}}\right)^{-1/2}\right]^2$
7	Chisholm and Armand [6]	$\alpha = \frac{1}{\alpha_H+(1-\alpha_H)^{0.5}}\alpha_H$
8	Armand–Treschev correlation [7]	$\alpha = 0.833\alpha_H$
9	Bangkoff correlation [8]	$\alpha = [0.71 + (0.0145)P]\alpha_H$
10	Czop et al. correlation [9]	$\alpha = -0.285 + 1.097\alpha_H$
11	Tandon model [10]	$50 < \mathrm{Re}_l < 1125\ \alpha = 1 - 1.928\frac{\mathrm{Re}_l^{-0.315}}{F(X)} + 0.9293\frac{\mathrm{Re}_l^{-0.63}}{F(X)^2}\ \mathrm{Re}_l > 1125\ \alpha = 1 - 0.38\frac{\mathrm{Re}_l^{-0.088}}{F(X)} + 0.0361\frac{\mathrm{Re}_l^{-0.176}}{F(X)^2}\ \mathrm{Re}_l = \frac{Gd}{\mu_l}$ $X = \left(\frac{1-x}{x}\right)^{0.9}\left(\frac{\rho_g}{\rho_l}\right)^{0.5}\left(\frac{\mu_l}{\mu_g}\right)^{0.1}\ F(X) = 0.015\left(\frac{1}{X}+\frac{2.85}{X^{0.476}}\right)$
12	Graham correlation [11]	$F_t > 0.01032\ \alpha = 1 - \exp(-1 - 0.3\ln(F_t) - 0.0328(\ln(F_t))^2)\ F_t < 0.01032\ \alpha = 0\ F_t = \left(\frac{x^3G^2}{\rho_g^2gd(1-x)}\right)^{1/2}$
13	Hughmark model [12]	$\alpha = \frac{K_H}{1+\left(\frac{1-x}{x}\right)\left(\frac{\rho_g}{\rho_l}\right)}\ K_H = 0.71 + 0.0001P$
14	Hamersma and Hart correlation [13]	$\alpha = \left(1+0.26\left(\frac{1-x}{x}\right)^{0.67}\left(\frac{\rho_g}{\rho_l}\right)^{0.33}\right)^{-1}$
15	Lockhart and Martinelli correlation [14]	$\frac{1-\alpha}{\alpha} = 0.28\left(\frac{1-x}{x}\right)^{0.64}\left(\frac{\rho_g}{\rho_l}\right)^{0.36}\left(\frac{\mu_l}{\mu_g}\right)^{0.07}$
16	Turner and Wallis two-cylinder model [15]	$\frac{1-\alpha}{\alpha} = A\left(\frac{1-x}{x}\right)^p\left(\frac{\rho_g}{\rho_l}\right)^q\left(\frac{\mu_l}{\mu_g}\right)^r$
17	Wallis correlation [16]	$\alpha = (1+X^{0.8})^{-0.378}\ X = \left(\frac{1-x}{x}\right)^{0.9}\left(\frac{\rho_g}{\rho_l}\right)^{0.5}\left(\frac{\mu_l}{\mu_g}\right)^{0.1}$
18	Domanski and Didion correlation [17]	$\alpha = 0.823 - 0.157\ln(X)\ X = \left(\frac{1-x}{x}\right)^{0.9}\left(\frac{\rho_g}{\rho_l}\right)^{0.5}\left(\frac{\mu_l}{\mu_g}\right)^{0.1}$
19	Wilson et al. correlation [18]	$\alpha = (1+a/F_t+bX)^n\ F_t = \left(\frac{x^3G^2}{\rho_g^2gd(1-x)}\right)^{0.5}$
20	Yashar correlation [19]	$\alpha = (1+F_t^{-1}+X)^{-0.321}\ F_t = \left(\frac{x^3G^2}{\rho_g^2gd(1-x)}\right)^{0.5}\ X = \left(\frac{1-x}{x}\right)^{0.9}\left(\frac{\rho_g}{\rho_l}\right)^{0.5}\left(\frac{\mu_l}{\mu_g}\right)^{0.1}$
21	Premoli model [20]	$\alpha = \frac{1}{1+\left(\frac{1-x}{x}\right)\left(\frac{\rho_g}{\rho_l}\right)S}\ S = 1 + K1\left(\frac{Y}{1+CY}-CY\right)^{1/2}\ K1 = 1.578 + \mathrm{Re}_l^{-0.19}\left(\frac{\rho_l}{\rho_g}\right)^{0.22}\ C = 0.0273\mathrm{We}_l\mathrm{Re}_l^{-0.51}\left(\frac{\rho_l}{\rho_g}\right)^{-0.08}$ $Y = \frac{\beta}{1-\beta}\ \mathrm{We}_l = \frac{G^2d}{\sigma\rho_lg}\ \mathrm{Re}_l = \frac{Gd}{\mu_l}\ \beta = \frac{1}{1+\left(\frac{1-x}{x}\right)\left(\frac{\rho_g}{\rho_l}\right)}$
22	Kawahara correlation [21]	$\alpha = \frac{C_1\alpha_h^{0.5}}{1-C_2\alpha_h^{0.5}}\ C_1 = \begin{cases} 0.03 \text{ for } d = 100\ \mu m \\ 0.02 \text{ for } d = 50\ \mu m \end{cases}\ C_2 = \begin{cases} 0.97 \text{ for } d = 100\ \mu m \\ 0.98 \text{ for } d = 50\ \mu m \end{cases}\ d > 250\ \mu m\ \alpha = \alpha_H$
23	El hajal correlation [22]	$\alpha = \frac{\alpha_H - \alpha_{steiner}}{\ln\left(\frac{\alpha_H}{\alpha_{steiner}}\right)}$
24	Zivi model [23]	$\alpha = \frac{1}{1+\left(\frac{1-x}{x}\right)\left(\frac{\rho_g}{\rho_l}\right)^{2/3}}$
25	Rigot correlation [24]	$\alpha = \frac{1}{1+\left(\frac{1-x}{x}\right)\left(\frac{\rho_g}{\rho_l}\right)S}\ S = 2$

Correlation or model	A	p	q	r
Homogeneous	1	1	1	0
Zivi	1	1	0.67	0
Turner-Wallis	1	0.72	0.4	0.08
Lockhart-Martinelli	0.28	0.64	0.36	0.07
Thom	1	1	0.89	0.18
Baroczy	1	0.74	0.65	0.13

Tube	X_{tt}+1/F_t	a	b	n
Smooth	<2.00	1.84	3.11	-0.21
	>2.00	0,5	1.2	-0.35
18° Helix	<2.00	5.80	8.60	-0.16
	>2.00	1.50	2.70	-0.31
0° Helix	<2.00	1.38	3.30	-0.26
	>2.00	2.26	2.50	-0.26

(continued on next page)

Author's personal copy

Table 1 (*continued*)

Number	Void fraction model/correlation	Model/correlation
26	Smith model [25]	$\alpha = \left\{1 + \left(\frac{\rho_g}{\rho_l}\right)K\left(\frac{1}{x}-1\right) + \left(\frac{\rho_g}{\rho_l}\right)(1-K)\left(\frac{1}{x}-1\right)\left[\frac{\left(\frac{\rho_l}{\rho_g}\right)+K\left(\frac{1}{x}-1\right)}{1+K\left(\frac{1}{x}-1\right)}\right]\right\}^{-1}$ $K = 0.4$
27	Levy correlation [26]	$x = \frac{\alpha(1-\alpha)+\alpha\sqrt{(1-2\alpha)^2+\alpha\left[2\left(\frac{\rho_l}{\rho_g}\right)(1-\alpha)^2+\alpha(1-2\alpha)\right]}}{\left[2\left(\frac{\rho_l}{\rho_g}\right)(1-\alpha)^2+\alpha(1-2\alpha)\right]}$
28	Fauske correlation [27]	$\alpha = \left(1 + \left(\frac{1-x}{x}\right)\left(\frac{\rho_g}{\rho_l}\right)^{0.5}\right)^{-1}$
29	Thom correlation [28]	$\alpha = \frac{\gamma x}{1+x(\gamma-1)}$ $\gamma = Z^{1.6}$ $Z = \left(\frac{\rho_l}{\rho_g}\right)^{0.555}\left(\frac{\mu_g}{\mu_l}\right)^{0.111}$
30	Baroczy model [29]	$\alpha = \left[1 + \left(\frac{1-x}{x}\right)^{0.74}\left(\frac{\rho_g}{\rho_l}\right)^{0.65}\left(\frac{\eta_l}{eta_g}\right)^{0.13}\right]^{-1}$
31	Chisholm correlation [30]	$\alpha = \frac{1}{1+\left(\frac{1-x}{x}\right)\left(\frac{\rho_g}{\rho_l}\right)S}$ $S = \left(1 - x + \frac{x\rho_l}{\rho_g}\right)^{1/2}$
32	Madsen correlation [31]	$\alpha = \left(1 + \left(\frac{1-x}{x}\right)^{b}\left(\frac{\rho_g}{\rho_l}\right)^{-0.5}\right)^{-1}$ $b = 1 + \log\left(\frac{\rho_l}{\rho_g}\right)\left(\log\left(\frac{1-x}{x}\right)\right)^{-1}$
33	Ahren correlation [32]	$\text{P.I.2} = \left(\frac{\mu_l}{\mu_g}\right)^{0.2}\left(\frac{\rho_g}{\rho_l}\right)$ P.I.2 numbers versus slip ratio for Ahren correlation can be obtained from their article
34	Spedding and Chen correlation [33]	$\alpha = \left(1 + 2.22\left(\frac{1-x}{x}\right)^{0.65}\left(\frac{\rho_g}{\rho_l}\right)^{0.65}\right)^{-1}$
35	Chen correlation [34]	$\alpha = \left(1 + 0.18\left(\frac{1-x}{x}\right)^{0.6}\left(\frac{\rho_g}{\rho_l}\right)^{0.33}\left(\frac{\mu_l}{\mu_g}\right)^{0.07}\right)^{-1}$

the shear velocity for the annular flow regime. The model is independent from tube orientation as long as annular flow conditions exist inside the tube.

Jaster and Kosky [53] benefited from Kosky and Staub's data [52] which are valid for the annular-stratified transition and fully stratified flow regimes. The mass fluxes were between 12.6 and 145 kg m^{-2} s^{-1}. The two-phase experimental frictional pressure drop value can be calculated from Table 2 and can be seen as model 1 in this table. They reported that the transition of annular-to-stratified flow had the ratio of axial shear force to gravitational body force. They defined a parameter to decide the flow pattern. In addition to this, they proposed correlations for the heat transfer coefficient during annular and stratified flow. Thermal resistance of boundary layers was calculated using the Martinelli analogy [14] for fully annular flow in their analysis.

The aim of this work is to show the independency of void fraction, frictional pressure drop, and heat transfer annular flow models from tube orientation (Chen [54]), the general applicability for a vertical short tube, and the experimental procedure for a specific data to have the most accurate validation process using the combination of alternative models for the determination of heat transfer coefficient. The experiments include a wide range of high mass fluxes with different saturation temperatures, as they concern 122 data points of R134a belonging to the condensation heat transfer database of FUTURE Lab. In KMUTT. Apart from the authors' previous publications [54–66], there are few studies in the literature related to the heat transfer and pressure drop characteristics of the condensation in a small diameter vertical tube during co-current down flow; besides this, there is no study with the experimental parameters of this work and its content in the open literature. In this study, determination of the shear-dominated heat transfer coefficients for refrigerant 134a is presented by means of the model of Kosky and Staub and von Karman universal velocity distribution correlations [52] by relating the heat transfer to the friction pressure gradient and void fraction during annular flow. Gravity dominated condensation heat transfer data should be treated with a different procedure [56,67].

2. Experimental apparatus and procedure

A schematic diagram of the test apparatus is shown in Fig. 1. The refrigerant loop consists of a pre-heating loop, test section, cooling loop and chilling loop. The refrigerant is circulated by a gear pump controlled by an inverter. The refrigerant flows in series through a filter/dryer, a sight glass tube, a refrigerant flow meter and a pre-heater and enters the test section. A spiral counter flow double tube heat exchanger is designed to supply heat to control the inlet quality of the refrigerant before entering the test section. After exiting the test section, the chilling loop condenses and sub-cools the refrigerant and removes the heat input from the pre-heater and test section, and ejects the heat to the surroundings. Leaving the chilling loop, the refrigerant returns from two-phase refrigerant to a sub-cooled state. Eventually, the refrigerant returns to the refrigerant pump to complete the cycle.

The test section is a vertical counter-flow tube-in-tube heat exchanger with refrigerant flowing downward in the inner tube and cooling water flowing upward in the annulus. The inner and outer tubes are made from smooth vertical copper having inner diameters of 8.1 and 26 mm respectively. The length of the heat exchanger is 0.5 m. Fig. 2 shows the detailed dimensions of the heat exchanger and the location of thermocouples. A thermostat is used to control the inlet temperature of the water. Pressure drop is measured by a differential pressure transducer installed between the inlet and outlet of the test section. Temperatures across the test section are measured by thermocouples. The length between pressure taps is 0.7 m. A low temperature thermostat is used to control the system pressure of the refrigerant flow.

T-type thermocouples are used to measure refrigerant temperature and the tube wall temperatures in the test section. Fig. 2 shows a total of ten thermocouples located at the side wall at five points along the test tube. All the temperature measuring devices are well calibrated in a controlled temperature bath using standard precision mercury glass thermometers. The uncertainty of the temperature measurements is ±0.1 °C. All static pressure taps are mounted on the tube wall. The refrigerant flow meter is a variable area type. The flow meter is specially calibrated in the range of 0–2.2 gal min^{-1} for HFC-134a by the manufacturer. The differential pressure transducer and pressure gauges are calibrated against a primary standard, the dead weight tester.

3. Data reduction

The data reduction of the measured results can be analyzed as follows:

Author's personal copy

Table 2
Frictional pressure drop models and correlations.

Number	Frictional pressure drop model/correlation	Model/correlation
1	Experimental frictional pressure drop	$(\Delta P)_G = g(\alpha\rho_g + (1-\alpha)\rho_l)L$ $\left(\frac{dP}{dz}\right)_M = -G^2\frac{d}{dz}\left[\frac{x^2}{\rho_g\alpha} + \frac{(1-x)^2}{\rho_l(1-\alpha)}\right]$ $\left(\frac{dP}{dz}\right)_F = \left(\frac{dP}{dz}\right)_{Exp} - \left(\frac{dP}{dz}\right)_G - \left(\frac{dP}{dz}\right)_M$
2	Lockhart and Martinelli [14]	$X = \left[\frac{(dP/dz)_l}{(dP/dz)_g}\right]^{1/2}$ $\phi_l^2 = 1 + \frac{C}{X} + \frac{1}{X^2}$ $\left(\frac{dP}{dz}\right)_l = \frac{f_l G^2(1-x)^2}{2d\rho_l}$ $\left(\frac{dP}{dz}\right)_g = \frac{f_g G^2 x^2}{2d\rho_g}$ $\mathrm{Re}_l = \frac{Gd(1-x)}{\mu_l}$ $f_l = \frac{64}{\mathrm{Re}}$ (laminar) $f_l = \frac{0.316}{(\mathrm{Re}_l^{0.25})}$ (turbulent) $\mathrm{Re}_g = \frac{Gdx}{\mu_g}$ $f_g = \frac{0.184}{\mathrm{Re}_g^{0.2}}$ (turbulent) $\left(\frac{\Delta P}{L}\right)_F = \phi_l^2\left(\frac{dP}{dz}\right)_l$
3	Chisholm [30]	$Y = \sqrt{\frac{(dP/dz)_{go}}{(dP/dz)_{lo}}}$ $\left(\frac{dP}{dz}\right)_{lo} = \frac{f_{lo}G^2}{2d\rho_l}$ $\left(\frac{dP}{dz}\right)_{go} = \frac{f_{go}G^2}{2d\rho_g}$ $\phi_{lo}^2 = 1 + (Y^2-1)[Bx^{(2-n)/2}(1-x)^{(2-n)/2} + x^{(2-n)}]$ $n = \begin{cases} \mathrm{Re}_{lo} \leqslant 2100 \\ \mathrm{Re}_{lo} > 2100 \end{cases}$ $f = 8\left[\left(\frac{8}{\mathrm{Re}}\right)^{12} + \left\{\left[2.457\ln\left(\frac{1}{\left(\frac{7}{\mathrm{Re}}\right)^{0.9} + 0.27\varepsilon/d}\right)\right]^{16} + \left(\frac{37530}{\mathrm{Re}}\right)^{16}\right\}^{-1.5}\right]^{1/12}$ $B = \begin{cases} 55/\sqrt{G} & 0 < Y < 9.5 \\ 520/(Y\sqrt{G}) & \text{for } 9.5 < Y < 28 \\ 15000/(Y^2\sqrt{G}) & 28 < Y \end{cases}$ $\left(\frac{\Delta P}{L}\right)_F = \phi_{lo}^2\left(\frac{dP}{dz}\right)_{lo}$
4	Friedel et al. [35,36]	$E = (1-x)^2 + x^2\frac{\rho_l f_{vo}}{\rho_g f_{lo}}$ $F = x^{0.78}(1-x)^{0.24}$ $H = \left(\frac{\rho_l}{\rho_g}\right)^{0.91}\left(\frac{\mu_g}{\mu_l}\right)^{0.19}\left(1-\frac{\mu_g}{\mu_l}\right)$ $\rho_{TP} = \left(\frac{x}{\rho_g} + \frac{1-x}{\rho_l}\right)^{-1}$ $Fr = \frac{G^2}{gd\rho_{TP}^2}$ $\mathrm{We} = \frac{G^2 d}{\rho_{TP}\sigma}$ $\phi_{lo}^2 = E + \frac{3.24FH}{Fr^{0.045}\mathrm{We}^{0.035}}$ $\left(\frac{\Delta P}{L}\right)_F = \phi_{lo}^2\left(\frac{dP}{dz}\right)_{lo}$
5	Chen et al. [37]	$\Omega = \begin{cases} \frac{0.0333\mathrm{Re}_{lo}^{0.45}}{\mathrm{Re}_g^{0.09}(1+0.4\exp(-\mathrm{Bo}))} & \mathrm{Bo} < 2.5 \\ \frac{\mathrm{We}^{0.2}}{(2.5+0.06\mathrm{Bo})} & \mathrm{Bo} \geqslant 2.5 \end{cases}$ $\mathrm{We} = \frac{G^2 d}{\sigma\rho_{TP}}$ $\mathrm{Bo} = g(\rho_l - \rho_g)\left(\frac{(d/2)^2}{\sigma}\right)$ $\frac{dP}{dz} = \left(\frac{dP}{dz}\right)_{\mathrm{Friedel}}\Omega$
6	Cavallini et al. [38,39]	$E = (1-x)^2 + x^2\frac{\rho_l f_{vo}}{\rho_v f_{lo}}$ $F = x^{0.6978}$ $H = \left(\frac{\rho_l}{\rho_g}\right)^{0.3278}\left(\frac{\mu_g}{\mu_l}\right)^{-1.181}\left(1-\frac{\mu_g}{\mu_l}\right)^{3.477}$ $\mathrm{We} = \frac{G^2 d}{\sigma\rho_{avg}}$ $\phi_{lo}^2 = E + \frac{1.262FH}{\mathrm{We}^{0.1458}}$ $\left(\frac{\Delta P}{L}\right)_F = \phi_{lo}^2\left(\frac{dP}{dz}\right)_{lo}$
7	Garimella et al. [40,41]	$\alpha = \left[1 + \left(\frac{1-x}{x}\right)^{0.74}\left(\frac{\rho_v}{\rho_l}\right)^{0.65}\left(\frac{\mu_l}{\mu_v}\right)^{0.13}\right]^{-1}$ $\mathrm{Re}_l = \frac{Gd(1-x)}{\mu_l(1+\sqrt{\alpha})}$ $\mathrm{Re}_g = \frac{Gdx}{\mu_g\sqrt{\alpha}}$ $f = \frac{64}{\mathrm{Re}}$ (laminar) $\psi = \frac{j_l\mu_l}{\sigma}$ $f = \frac{0.316}{\mathrm{Re}^{0.25}}$(turbulent) $\left(\frac{dP}{dz}\right)_l = \frac{f_l G^2(1-x)^2}{2d\rho_l}$ $\left(\frac{dP}{dz}\right)_g = \frac{f_g G^2 x^2}{2d\rho_g}$ $X = \left[\frac{(dP/dz)_l}{(dP/dz)_g}\right]^{1/2}$ $j_l = \frac{G(1-x)}{\rho_l(1-\alpha)}$ $\frac{f_{tpl}}{f_l} = Ax^a\mathrm{Re}_l^b\psi^c$ $\mathrm{Re}_l < 2100$ $A = 1.308\times10^{-3}$ $a = 0.4273$ $b = 0.9295$ $c = -0.1211$ $\frac{\Delta P}{L} = \frac{1}{2}f_{tt}\frac{G^2X^2}{\rho_g\alpha^{2.5}}\frac{1}{d}$
8	Mishima and Hibiki [42]	$\phi_l^2 = 1 + \frac{C}{X} + \frac{1}{X^2}$ $C = 21(1-e^{-0.319d})$ $\left(\frac{\Delta P}{L}\right)_F = \phi_l^2\left(\frac{dP}{dz}\right)_l$ X should be calculated from Lockhart and Martinelli [14].
9	Wang et al. [43]	$G > 200$ kg m^{-2} s^{-1} $C = 4.566\ 10^{-6}X^{0.128}\mathrm{Re}_{lo}^{0.938}\left(\frac{\rho_l}{\rho_g}\right)^{-2.15}\left(\frac{\mu_l}{\mu_g}\right)^{5.1}$ $\mathrm{Re}_{lo} = \frac{Gd}{\mu_l}$ $\left(\frac{\Delta P}{L}\right)_F = \phi_l^2\left(\frac{dP}{dz}\right)_l$ $G < 200$ kg m^{-2} s^{-1} $\phi_g^2 = 1 + 9.4X^{0.62} + 0.564X^{2.45}$ $\left(\frac{\Delta P}{L}\right)_F = \phi_g^2\left(\frac{dP}{dz}\right)_g$ $\phi_l^2 = 1 + \frac{C}{X} + \frac{1}{X^2}$ $(dp/dz)_l$ and $(dp/dz)_g$ should be calculated from Lockhart and Martinelli [14]
10	Wilson et al. [44]	$\phi_{lo}^2 = 12.82Xtt^{-1.47}(1-x)^{1.8}$ $X_{tt} = \left(\frac{(1-x)}{x}\right)^{0.9}\left(\frac{\rho_g}{\rho_l}\right)^{0.5}\left(\frac{\mu_l}{\mu_g}\right)^{0.1}$ $\left(\frac{\Delta P}{L}\right)_F = \phi_{lo}^2\left(\frac{dP}{dz}\right)_{lo}$
11	Souza et al. [45]	$\phi_l^2 = 1.376 + C_1X_{tt}^{-C_2}$ $Fr_l < 0.7$ $\begin{cases} C_1 = 4.172 + 5.48Fr_l \\ C_2 = 1.773 - 0.169Fr_l \end{cases}$ $Fr_l \geqslant 0.7$ $C_1 = 7.242$ $C_2 = 1.655$ $Fr_l = \frac{G}{\rho_l\sqrt{gd}}$ $\left(\frac{dP}{dz}\right)_l = \frac{f_l G^2(1-x)^2}{2d\rho_l}$ $\frac{1}{\sqrt{f_l}} = -2\log\left(\frac{(\varepsilon/d)}{3.7} + \frac{2.51}{\mathrm{Re}_l\sqrt{f_l}}\right)$ $\mathrm{Re}_l = \frac{Gd(1-x)}{\mu_l}$ $\left(\frac{\Delta P}{L}\right)_F = \phi_l^2\left(\frac{dP}{dz}\right)_l$
12	Tran et al. [46]	$\phi_l^2 = 1 + (4.3Y^2-1)N_{conf}x^{0.875} + x^{1.75}$ $N_{conf} = \frac{\left[\frac{\sigma}{g(\rho_l-\rho_g)}\right]^{1/2}}{d}$ $\left(\frac{\Delta P}{L}\right)_F = \phi_{lo}^2\left(\frac{dP}{dz}\right)_{lo}$ $(dp/dz)_{lo}$ should be calculated from Chisholm [30]
13	Lee and Lee [47]	$\phi_l^2 = 1 + \frac{C}{X} + \frac{1}{X^2}$ $C = A\lambda^q\psi^r\mathrm{Re}_{lo}^s$ $\lambda = \frac{\mu_l^2}{\rho_l\sigma d}$ $\psi = \frac{\mu_l j}{\sigma}$ $\left(\frac{\Delta P}{L}\right)_F = \phi_l^2\left(\frac{dP}{dz}\right)_l$

Liquid	Vapor	A	q	r	s	X Range	Re_{lo} Range
Laminar	Laminar	$6.833\ 10^{-8}$	-1.317	0.719	0.557	0.776-14.176	175-1480
Laminar	Turbulent	$6.185\ 10^{-2}$	0	0	0.726	0.303-1.426	293-1506
Turbulent	Laminar	3.627	0	0	0.174	3.276-79.415	2606-17642
Turbulent	Turbulent	0.408	0	0	0.451	1.309-14.781	2675-17757

3.1. The inlet vapor quality of the test section ($x_{TS,i}$)

$$x_{TS,i} = \frac{i_{TS,i} - i_{l@T_{TS,i}}}{i_{fg@T_{TS,i}}} \quad (1)$$

where $i_{l@T_{TS,i}}$ is the enthalpy of the saturated liquid based on the temperature of the test section inlet, $i_{fg@T_{TS,i}}$ is the enthalpy of vaporization based on the temperature of the test section inlet and $i_{TS,i}$ is the refrigerant enthalpy at the test section inlet and is given by:

$$i_{TS,i} = i_{ph,i} + \frac{Q_{ph}}{m_{ref}} \quad (2)$$

where $i_{ph,i}$ is the inlet enthalpy of the liquid refrigerant before entering the pre-heater, m_{ref} the mass flow rate of the refrigerant and Q_{ph} is the heat transfer rate in the pre-heater:

$$Q_{ph} = m_{w,ph}c_{p,w}(T_{w,i} - T_{w,o})_{ph} \quad (3)$$

Author's personal copy

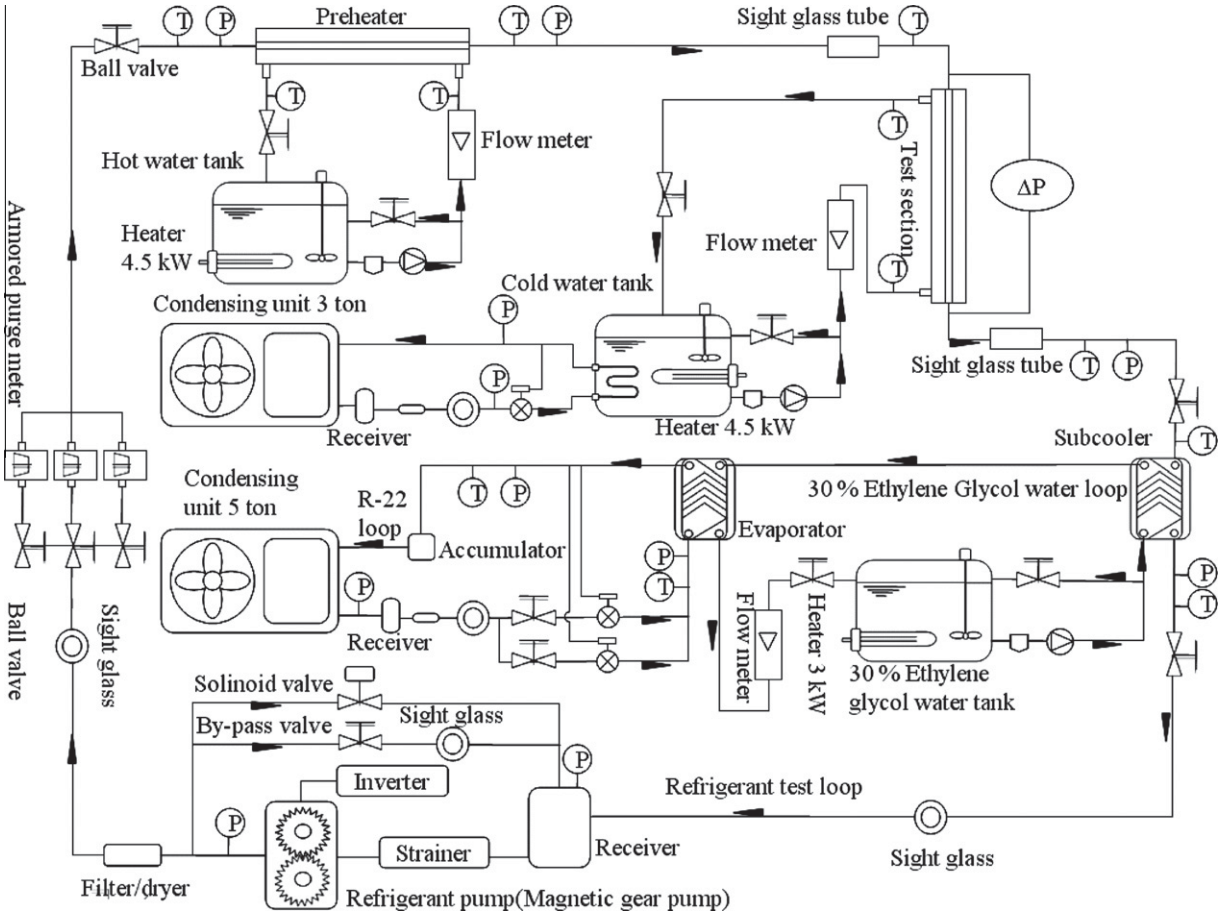

Fig. 1. Schematic diagram of experimental apparatus.

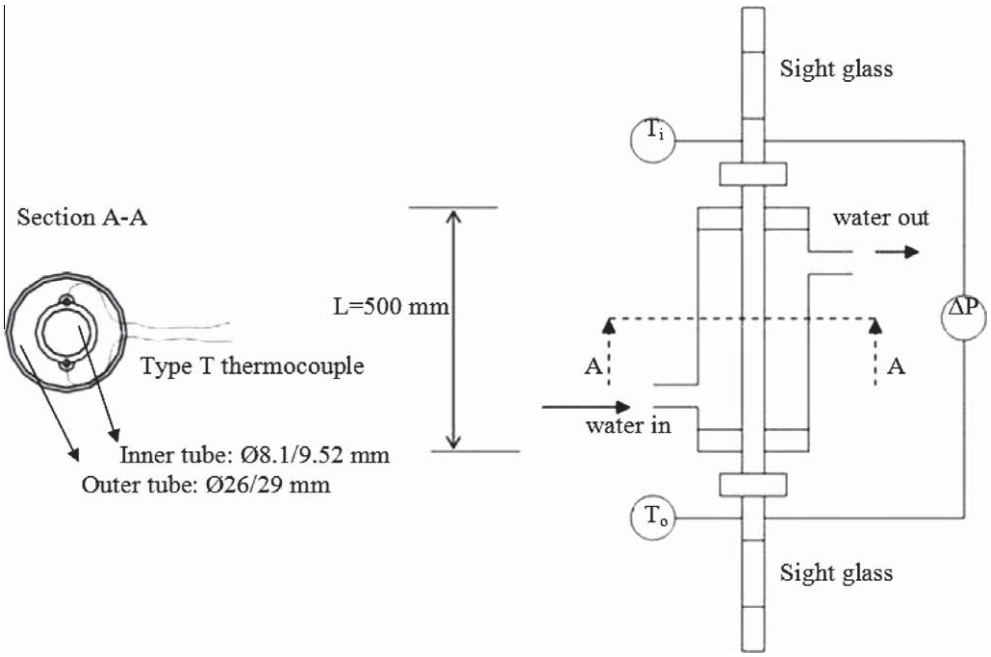

Fig. 2. Schematic diagram of test section.

where $m_{w,ph}$ is the mass flow rate of the water entering the pre-heater, $c_{p,w}$ the specific heat of the water and $(T_{w,i} - T_{w,o})_{ph}$ is the temperature difference between the inlet and outlet positions of the pre-heater.

Author's personal copy

Table 3
Uncertainty of experimental parameters.

Parameters	Uncertainty
T_{sat} (°C)	0.19
$x_{t,i}$	±6.96–8.24%
ΔT_{sat} (K)	±0.191
$(T_{w,o}-T_{w,i})_t$ (K)	±0.045
$(T_{w,i}-T_{w,o})_{evap}$ (K)	±0.13
m_r (g s^{-1})	±0.023
$m_{w,t}$ (g s^{-1})	±0.35 g/s
$m_{w,evap}$ (g s^{-1})	±0.38 g/s
q_t (Kw m^{-2})	±6.55–8.93%
q_{evap} (Kw m^{-2})	±12–14.81%
Nu	±7.64–10.71%
h_r (W m^{-2} K^{-1})	±7.64–10.71%
ΔP (kPa)	±0.15

Table 4
Operating conditions of the study.

Refrigerant	HFC-134a
Test tube material, inner diameter d, length L	Copper, ϕ8.1 mm, 500 mm
Range of condensing pressure, P_{sat} (bar)	10–12
Range of condensing temperature, T_{sat} (°C)	40–50
Range of mass flux, G (kg m^{-2} s^{-1})	260–515
Range of heat flux, q (kW m^{-2})	10.16–66.61
Range of temperature difference, $\Delta T = T_{sat} - T_{wi}$, K	1.26–8.98
Range of average vapor quality, x	0.69–0.96

3.2. The outlet vapor quality of the test section ($x_{TS,o}$)

$$x_{TS,o} = \frac{i_{TS,o} - i_{l@T_{TS,o}}}{i_{fg@T_{TS,o}}} \tag{4}$$

where $i_{TS,o}$ is the refrigerant enthalpy at the test section outlet, $i_{l@T_{TS,o}}$ the enthalpy of the saturated liquid based on the temperature of the test section outlet and $i_{fg@T_{TS,o}}$ is the enthalpy of vaporization. The outlet enthalpy of the refrigerant flow is calculated as follows:

$$i_{TS,o} = i_{TS,i} - \frac{Q_{TS}}{m_{ref}} \tag{5}$$

where the heat transfer rate, Q_{TS}, in the test section is obtained from:

$$Q_{TS} = m_{w,TS} c_{p,w} (T_{w,o} - T_{w,i})_{TS} \tag{6}$$

where $m_{w,TS}$ is the mass flow rate of the water entering the test section, and $(T_{w,o} - T_{w,i})_{TS}$ is the temperature difference between the outlet and inlet positions of the test section.

3.3. The average experimental heat transfer coefficient

$$h_{\exp} = \frac{Q_{TS}}{A_{inside}(T_{ref,sat} - T_{avg,wi})} \tag{7}$$

where h_{exp} is the average heat transfer coefficient, Q_{TS} the heat transfer rate in the test section, $T_{avg,wi}$ the average temperature of the wall, $T_{ref,sat}$ the average temperature of the refrigerant at the test section inlet and outlet and A_{inside} is the inside surface area of the test section:

$$A_{inside} = \pi d L \tag{8}$$

Table 5
Prediction analysis of frictional pressure drop and void fraction models for T_{sat} = 40 °C and G = 260 kg m^{-2} s^{-1} (deviations ⩽ ±30%).

ΔP_F models	*(15/29)2*	3	4	*(20/29)5*	6	7	8	*(17/29)9*	10	11	12	13
α models												
1	14/28	1/28	6/28	8/28	14/28	0/28	17/28	1/28	21/28	20/28	–	–
2	15/28	12/28	23/28	27/28	26/28	15/28	14/28	15/28	22/28	8/28	–	–
(8/11) 3	16/28	8/28	23/28	28/28	28/28	22/28	14/28	15/28	27/28	9/28	–	–
4	–	–	–	–	–	–	–	–	–	–	–	–
5	–	–	–	–	–	–	–	–	–	–	–	–
(8/11) 6	16/28	14/28	28/28	28/28	27/28	21/28	4/28	15/28	14/28	9/28	–	–
(7/11) 7	8/28	17/28	28/28	28/28	23/28	14/28	0/28	20/28	14/28	9/29	–	–
8	14/28	14/28	7/28	0/28	0/28	0/28	0/28	14/28	2/28	4/28	–	–
9	–	–	–	–	–	–	–	–	–	–	–	–
10	14/28	14/28	0/28	0/28	0/28	0/28	0/28	14/28	0/28	1/28	–	–
11	4/28	4/28	0/28	0/28	0/28	0/28	0/28	3/28	0/28	3/28	–	–
12	0/28	1/28	0/28	0/28	0/28	0/28	0/28	0/28	0/28	0/28	–	–
13	0/28	1/28	0/28	0/28	0/28	0/28	0/28	0/28	0/28	0/28	–	–
(8/11) 14	16/28	15/28	28/28	28/28	28/28	16/28	12/28	16/28	20/28	9/28	–	–
(8/11) 15	16/28	14/28	28/28	28/28	28/28	18/28	5/28	16/28	14/28	9/28	–	–
16	8/28	13/28	18/28	16/28	14/28	14/28	0/28	6/28	14/28	9/28	–	–
17	16/28	14/28	28/28	28/28	28/28	18/28	5/28	16/28	14/28	9/28	–	–
18	–	–	–	–	–	–	–	–	–	–	–	–
19	12/28	14/28	28/28	28/28	28/28	21/28	0/28	16/28	14/28	9/28	–	–
20	14/28	14/28	14/28	14/28	0/28	3/28	0/28	14/28	12/28	7/28	–	–
(7/11) 21	4/28	15/28	28/28	28/28	28/28	15/28	0/28	15/28	14/28	9/28	–	–
22	14/28	0/28	7/28	8/28	14/28	1/28	17/28	1/28	21/28	20/28	–	–
23	0/28	0/28	0/28	0/28	0/28	0/28	0/28	0/28	0/28	0/28	–	–
24	16/28	16/28	27/28	27/28	26/28	16/28	12/28	16/28	21/28	9/28	–	–
25	15/28	6/28	16/28	22/28	27/28	14/28	14/28	13/28	26/28	8/28	–	–
26	7/28	2/28	14/28	14/28	14/28	14/28	0/28	3/28	14/28	9/28	–	–
27	–	–	–	–	–	–	–	–	–	–	–	–
(7/11) 28	12/28	15/28	28/28	28/28	27/28	15/28	0/28	16/28	14/28	9/28	–	–
29	6/28	2/28	14/28	14/28	12/28	2/28	11/28	2/28	28/28	23/28	–	–
30	8/28	15/28	28/28	28/28	28/28	23/28	0/28	15/28	15/28	9/28	–	–
(8/11) 31	15/28	15/28	28/28	28/28	28/28	17/28	2/28	16/28	14/28	9/28	–	–
32	–	–	–	–	–	–	–	–	–	–	–	–
33	15/28	3/28	12/28	19/28	26/28	7/28	15/28	10/28	25/28	13/28	–	–
34	8/28	16/28	27/28	24/28	14/28	14/28	0/28	15/28	14/28	9/28	–	–
35	1/28	0/28	5/28	7/28	9/28	0/28	4/28	1/28	9/28	15/28	–	–

Author's personal copy

where d is the inside diameter of the test tube. L is the length of the test tube.

3.4. Calculation procedure for the annular flow model

Based on Hewitt and Robertson's flow pattern map [68], the data used in all tables were collected in an annular flow regime and also checked by sight glass at the inlet and outlet of the test section. In the present study, these correlations are used to show the similarity of annular flow correlations which are independent of tube orientation (horizontal or vertical). Chen et al. [54] also mentioned this similarity in their article.

Considering the annular flow theory of Chen et al. [54] for the condensation inside a relatively short vertical test tube having average vapor qualities between 0.96 and 0.7 to enable annular flow conditions along the tube length, the interfacial shear stress is determined using frictional pressure drop models in Table 2 by means of Eq. (9) as follows:

$$\tau = \left(-\frac{dP}{dz}\right)_F \frac{d}{4} \tag{9}$$

The liquid Reynolds number can be defined as follows:

$$\mathrm{Re}_l = \frac{Gd(1-x)}{\mu_l} \tag{10}$$

Dimensionless film thickness is calculated according to Kosky and Staub [52]:

$$\delta^+ = \left(\frac{\mathrm{Re}_l}{2}\right)^{0.5} \quad \text{for } \mathrm{Re}_l \leqslant 1145 \tag{11}$$

$$\delta^+ = 0.0504\mathrm{Re}_l^{7/8} \quad \text{for } \mathrm{Re}_l > 1145 \tag{12}$$

From the derivation of the von Karman universal velocity distribution inside a tube, T_δ^+ can be obtained as follows:

$$T_\delta^+ = \delta^+ \mathrm{Pr}_l \quad \text{for } \delta^+ \leqslant 5 \tag{13}$$

$$T_\delta^+ = 5\mathrm{Pr}_l + 5\ln[1 + \mathrm{Pr}_l(\delta^+/5 - 1)] \quad \text{for } 5 < \delta^+ < 30 \tag{14}$$

$$T_\delta^+ = 5\mathrm{Pr}_l + 5\ln[1 + 5\mathrm{Pr}_l] + 2.5\ln(\delta^+/30) \quad \text{for } \delta^+ \geqslant 30 \tag{15}$$

The heat transfer coefficient during annular flow is shown below applying the momentum-heat transfer analogy for the calculation of liquid layer thermal resistance:

$$h = \frac{q/A}{T_{sat} - T_{wi}} = \frac{c_{pl}(\rho_l \tau)^{0.5}}{T_\delta^+} \tag{16}$$

It should be noted that detailed information on the von Karman analysis and Eq. (16) can be obtained from Mago et al.'s study [69] and Cavallini et al.'s study [38] respectively.

3.5. Uncertainties

The procedure of Kline & McClintock [70] was used for the calculation of all uncertainties. The maximum uncertainties of experimental parameters are shown in Table 3. The largest uncertainties occurred in the low mass flux region. The uncertainties for the Nusselt number and condensation heat transfer coefficient in the test tube varied from ±7.64% to ±10.71%. Moreover, operating conditions of the study can be seen from Table 4.

4. Results and discussion

The following paragraphs present a summary of the operating conditions of frictional pressure drop models and correlations

Table 6
Prediction analysis of frictional pressure drop and void fraction models for T_{sat} = 50 °C and G = 260 kg m^{-2} s^{-1} (deviations ⩽ ±30%).

ΔP_F models	*(15/29)2*	3	4	*(19/29)5*	6	7	8	*(19/29)9*	10	11	12	13
α models												
1	21/28	6/28	10/28	9/28	17/28	12/28	16/28	9/28	22/28	9/28	–	–
2	11/28	21/28	28/28	28/28	23/28	16/28	0/28	20/28	11/28	7/28	–	–
(7/11) 3	24/28	23/28	28/28	28/28	23/28	27/28	3/28	24/28	13/28	9/28	–	–
4	–	–	–	–	–	–	–	–	–	–	–	–
5	–	–	–	–	–	–	–	–	–	–	–	–
(8/11) 6	14/28	24/24	28/28	28/28	20/28	15/28	0/28	26/28	12/28	8/28	–	–
(6/11) 7	14/28	14/28	14/28	14/28	0/28	14/28	0/28	14/28	6/28	4/28	–	–
8	0/28	0/28	0/28	0/28	0/28	0/28	0/28	0/28	0/28	0/28	–	–
9	–	–	–	–	–	–	–	–	–	–	–	–
10	0/28	0/28	0/28	0/28	0/28	0/28	0/28	0/28	0/28	0/28	–	–
11	0/28	0/28	0/28	0/28	0/28	0/28	0/28	0/28	0/28	0/28	–	–
12	0/28	0/28	0/28	0/28	0/28	0/28	0/28	0/28	0/28	0/28	–	–
13	0/28	0/28	0/28	0/28	0/28	0/28	0/28	0/28	0/28	0/28	–	–
(6/11) 14	13/28	22/28	28/28	28/28	23/28	24/28	0/28	24/28	13/28	9/28	–	–
(7/11) 15	14/28	23/28	28/28	28/28	21/28	15/28	0/28	26/28	13/28	9/28	–	–
16	14/28	14/28	14/28	14/28	0/28	12/28	0/28	14/28	7/28	5/28	–	–
17	14/28	24/28	28/28	28/28	21/28	15/28	0/28	26/28	13/28	8/28	–	–
18	–	–	–	–	–	–	–	–	–	–	–	–
19	14/28	21/28	21/28	22/28	9/28	15/28	0/28	16/28	12/28	8/28	–	–
20	13/28	14/28	2/28	1/28	0/28	0/28	0/28	14/28	2/28	3/28	–	–
(6/11) 21	14/28	17/28	14/28	14/28	1/28	15/28	0/28	15/28	11/28	7/28	–	–
22	22/28	6/28	10/28	9/28	17/28	12/28	16/28	9/28	22/28	9/28	–	–
23	0/28	0/28	0/28	0/28	0/28	0/28	0/28	0/28	0/28	0/28	–	–
24	11/28	20/28	28/28	28/28	23/28	14/28	0/28	22/28	14/28	9/28	–	–
25	13/28	21/28	28/28	28/28	24/28	19/28	0/28	21/28	13/28	9/28	–	–
26	14/28	14/28	14/28	14/28	0/28	14/28	0/28	14/28	10/28	6/28	–	–
27	–	–	–	–	–	–	–	–	–	–	–	–
(5/11) 28	12/28	19/28	17/28	21/28	10/28	15/28	0/28	14/28	13/28	9/28	–	–
29	15/28	6/28	13/28	14/28	9/28	7/28	12/28	7/28	28/28	24/28	–	–
30	14/28	16/28	15/28	16/28	8/28	15/28	0/28	16/28	12/28	8/28	–	–
(6/11) 31	12/28	22/28	26/28	26/28	15/28	15/28	0/28	20/28	13/28	9/28	–	–
32	–	–	–	–	–	–	–	–	–	–	–	–
33	20/28	20/28	28/28	28/28	23/28	19/28	5/28	20/28	12/28	8/28	–	–
34	14/28	14/28	14/28	14/28	0/28	11/28	0/28	14/28	8/28	5/28	–	–
35	5/28	2/28	6/28	6/28	7/28	2/28	2/28	3/28	9/28	16/28	–	–

Author's personal copy

mentioned in Table 1; it should be noted that explanations on the void fraction models and correlations in Table 1 can be seen from the authors' previous publications [55,58,61,62].

Frictional pressure drop can be determined using the Lockhart and Martinelli method [14] which expresses the ratio of viscous drag to vapor kinetic energy in horizontal and vertical tubes. This method was developed for adiabatic flow of air–benzene, kerosene, and water inside 1.5–26 mm tubes. Chisholm [30] developed a two-phase multiplier based on the Lockhart and Martinelli parameter [14] using steam in a tube. It is used for vertical and horizontal tubes in the literature. Friedel [35,36] proposed a two-phase multiplier considering surface tension effects with 25,000 data points during adiabatic flow through the vertical and horizontal channels with hydraulic diameters of more than 1 mm. Besides, the proportion of vapor dynamic viscosity to liquid dynamic viscosity was below 1000 in his study. Chen et al. [37] accounted for the effect of surface tension and mass flux including Bond and Weber numbers in their model. They condensed R410A at 5–15 °C in several horizontal tubes ranging between 3.17 and 9 mm i.d. for the mass fluxes of 50–600 kg m^{-2} s^{-1} and studied the condensation of air–water at room temperature in several horizontal tubes ranging between 1.02 and 7.02 mm i.d. for the mass fluxes of 50–3000 kg m^{-2} s^{-1}. Cavallini et al. [38,39] modified Friedel's correlation [35,36] to develop an annular flow model during the condensation of R22, R134a, R125, R32, R236ea, R407C, and R410A in an 8 mm i.d. horizontal tube for the mass fluxes of 100–750 kg m^{-2} s^{-1} at saturation temperatures between 30 and 50 °C. As a result of the study, a model for predicting condensing heat transfer coefficient was developed by means of frictional pressure drop. Garimella [40] and Garimella et al. [41] developed a flow regime based model for intermittent and annular/mist/disperse flow regimes regarding the condensation of R134a in 0.5–4.91 mm i.d. horizontal tubes at the condensing temperature of 52 °C for mass fluxes between 150 and 750 kg m^{-2} s^{-1}. Mishima and Hibiki [42] investigated two-phase upward flow of air–water in 1–4 mm i.d. vertical tubes. Their model has limitations accounting for the superficial velocities of vapor and liquid of phases. Wang et al. [43] studied the two-phase flow pattern of R22, R134a, and R407C in a 6.5 mm i.d. horizontal tube for mass fluxes of 50–700 kg m^{-2} s^{-1} at the condensing temperatures of 2.6–20 °C. Wilson et al. [44] condensed R134a and R410A in several 1.84–7.79 mm i.d. horizontal flattened round smooth, axial, and helical micro-fin-tubes for the mass fluxes between 75 and 400 kg m^{-2} s^{-1} at the saturation temperatures of 35 °C. Souza et al. [45] showed the effect of oil in R12 and R134a on the pressure drop in a hydraulic diameter of 10.9 mm horizontal flattened tube for the mass fluxes of 200–600 kg m^{-2} s^{-1}. Tran et al. [46] boiled R134a, R12, and R113 in small diameter horizontal circular (2.4, 2.46, and 2.92 mm) and rectangular (4.06 × 1.7 mm) tubes at boiling pressures between 138 and 836 kPa and for mass fluxes between 33 and 832 kg m^{-2} s^{-1}. They proposed a pressure drop correlation modifying Chisholm's correlation [30] to consider surface tension effects. Lee and Lee [47] studied the air–water two-phase flow to develop a two-phase multiplier in a small hydraulic diameter (0.4 × 20 mm, 1.2 × 20 mm, 4 × 20 mm) rectangular horizontal channel. Their model has limitations with the Reynolds number and Lockhart and Martinelli [14] parameter.

The two-phase experimental frictional pressure drop value is defined as model 1 in Table 2 and obtained by means of extraction of the gravitational component and the component due to momentum

Table 7
Prediction analysis of frictional pressure drop and void fraction models for T_{sat} = 40 °C and G = 515 kg m^{-2} s^{-1} (deviations ⩽ ±30%).

ΔP_F models	*(20/29)2*	3	4	*(26/29)5*	6	7	8	*(22/29)9*	10	11	12	13
α models												
1	4/32	4/32	2/32	12/32	4/32	2/32	21/32	3/32	10/32	24/32	–	–
2	3/32	1/32	5/32	29/32	16/32	1/32	17/32	9/32	23/32	23/32	–	–
(7/11) 3	16/32	0/32	15/32	32/32	32/32	16/32	15/32	16/32	32/32	19/32	–	–
4	–	–	–	–	–	–	–	–	–	–	–	–
5	–	–	–	–	–	–	–	–	–	–	–	–
(6/11) 6	16/32	0/32	15/32	32/32	32/32	16/32	11/32	16/32	32/32	11/32	–	–
(7/11) 7	16/32	0/32	21/32	32/32	32/32	24/32	0/32	18/32	31/32	3/32	–	–
8	20/32	0/32	29/32	30/32	32/32	13/32	0/32	23/32	31/32	2/32	–	–
9	–	–	–	–	–	–	–	–	–	–	–	–
10	21/32	1/32	30/32	30/32	32/32	9/32	0/32	24/32	31/32	0/32	–	–
11	20/32	8/32	32/32	26/32	32/32	2/32	0/32	23/32	25/32	0/32	–	–
12	21/32	0/32	32/32	29/32	32/32	6/32	0/32	24/32	29/32	2/32	–	–
13	25/32	6/32	32/32	26/32	30/32	0/32	0/32	26/32	29/32	2/32	–	–
(7/11) 14	16/32	0/32	12/32	32/32	32/32	16/32	15/32	18/32	32/32	20/32	–	–
(6/11) 15	16/32	0/32	15/32	32/32	32/32	16/32	8/32	16/32	32/32	7/32	–	–
16	16/32	0/32	23/32	32/32	32/32	23/23	0/32	18/32	31/32	0/32	–	–
17	6/32	0/32	15/32	32/32	32/32	16/32	8/32	16/32	32/32	7/32	–	–
18	–	–	–	–	–	–	–	–	–	–	–	–
19	16/32	0/32	16/32	32/32	32/32	16/32	6/32	16/32	32/32	7/32	–	–
20	16/32	0/32	22/32	32/32	32/32	26/32	0/32	18/32	31/32	3/32	–	–
(7/11) 21	16/32	0/32	16/32	32/32	32/32	16/32	0/32	16/32	32/32	7/32	–	–
22	4/32	4/32	3/32	12/32	4/32	2/32	22/32	3/32	10/32	24/32	–	–
23	21/32	10/32	30/32	25/32	32/32	2/32	0/32	22/32	25/32	2/32	–	–
24	7/32	2/32	7/32	30/32	23/32	2/32	15/32	20/32	28/32	22/32	–	–
25	4/32	2/32	5/32	29/32	16/32	2/32	15/32	10/32	24/32	22/32	–	–
26	16/32	0/32	25/32	32/32	32/32	16/32	0/32	17/32	32/32	3/32	–	–
27	–	–	–	–	–	–	–	–	–	–	–	–
(6/11) 28	16/32	0/32	9/32	32/32	32/32	16/32	9/32	18/32	32/32	8/32	–	–
29	0/32	0/32	7/32	28/32	18/32	0/32	15/32	6/32	31/32	22/32	–	–
30	16/32	0/32	18/32	0/32	0/32	16/32	0/32	16/32	32/32	3/32	–	–
(6/11) 31	16/32	0/32	8/32	32/32	32/32	16/32	9/32	18/32	32/32	13/32	–	–
32	–	–	–	–	–	–	–	–	–	–	–	–
33	3/32	2/32	5/32	30/32	14/32	1/32	17/32	8/32	23/32	23/32	–	–
34	16/32	0/32	21/32	32/32	32/32	23/32	18/32	18/32	31/32	3/32	–	–
35	2/32	2/32	2/32	5/32	2/32	3/32	13/32	2/32	4/32	16/32	–	–

Author's personal copy

Table 8
Prediction analysis of frictional pressure drop and void fraction models for T_{sat} = 50 °C and G = 515 kg m^{-2} s^{-1} (deviations ⩽ ±30%).

ΔP_F models	*(24/29)2*	3	4	*(26/29)5*	6	7	8	*(24/29)9*	10	11	12	13
α models												
1	6/34	0/34	5/34	19/34	10/34	3/34	20/34	9/34	21/34	24/34	–	–
2	22/34	0/34	7/34	34/34	21/34	13/34	17/34	21/34	30/34	8/34	–	–
(6/11) 3	29/34	0/34	16/34	34/34	30/34	18/34	8/34	25/34	34/34	0/34	–	–
4	–	–	–	–	–	–	–	–	–	–	–	–
5	–	–	–	–	–	–	–	–	–	–	–	–
(7/11) 6	30/34	0/34	34/34	34/34	34/34	18/34	0/34	25/34	34/34	0/34	–	–
(7/11) 7	34/34	3/34	34/34	34/34	34/34	17/34	0/34	34/34	31/34	0/34	–	–
8	34/34	17/34	34/34	25/34	32/34	6/34	0/34	31/34	17/34	0/34	–	–
9	–	–	–	–	–	–	–	–	–	–	–	–
10	31/34	23/34	34/34	22/34	32/34	0/34	0/34	9/34	17/34	0/34	–	–
11	20/34	24/34	31/34	8/34	21/34	0/34	0/34	21/34	15/34	0/34	–	–
12	3/34	26/34	34/34	17/34	32/34	0/34	0/34	31/34	16/34	0/34	–	–
13	30/34	28/34	34/34	13/34	25/34	0/34	0/34	31/34	11/34	0/34	–	–
(7/11) 14	28/34	0/34	19/34	34/34	34/34	18/34	0/34	25/34	34/34	0/34	–	–
(7/11) 15	30/34	0/34	34/34	34/34	34/34	18/34	0/34	25/34	34/34	0/34	–	–
16	34/34	3/34	34/34	34/34	34/34	17/34	0/34	34/34	29/34	0/34	–	–
17	30/34	0/34	34/34	34/34	34/34	18/34	0/34	25/34	34/34	0/34	–	–
18	–	–	–	–	–	–	–	–	–	–	–	–
19	30/34	0/34	34/34	34/34	34/34	18/34	0/34	25/34	34/34	0/34	–	–
20	34/34	3/34	34/34	34/34	34/34	17/34	0/34	34/34	34/34	0/34	–	–
(6/11) 21	30/34	0/34	34/34	34/34	34/34	12/34	0/34	25/34	34/34	0/34	–	–
22	8/34	0/34	5/34	19/34	10/34	3/34	20/34	9/34	21/34	25/34	–	–
23	26/34	0/34	12/34	34/34	32/34	17/34	7/34	24/34	34/34	3/34	–	–
24	26/34	0/34	12/34	34/34	32/34	17/34	7/34	24/34	34/34	3/34	–	–
25	22/34	0/34	8/34	34/34	22/34	14/34	16/34	21/34	32/34	6/34	–	–
26	32/34	3/34	34/34	34/34	34/34	17/34	0/34	34/34	29/34	0/34	–	–
27	–	–	–	–	–	–	–	–	–	–	–	–
(7/11) 28	28/34	0/34	34/34	34/34	34/34	18/34	0/34	25/34	34/34	0/34	–	–
29	9/34	0/34	13/34	23/34	16/34	3/34	18/34	10/34	31/34	18/34	–	–
30	32/34	0/34	34/34	34/34	34/34	17/34	0/34	31/34	34/34	0/34	–	–
(7/11) 31	27/34	0/34	32/34	34/34	34/34	18/34	0/34	25/34	34/34	0/34	–	–
32	–	–	–	–	–	–	–	–	–	–	–	–
33	21/34	0/34	8/34	34/34	17/34	11/34	18/34	20/34	31/34	13/34	–	–
34	34/34	3/34	34/34	34/34	34/34	17/34	0/34	34/34	29/34	0/34	–	–
35	5/34	0/34	4/34	10/34	7/34	0/34	15/34	5/34	9/34	22/34	–	–

Table 9
Most predictive models for the determination of condensation heat transfer coefficient of R134a inside vertical test tube (deviations ⩽ ±30%).

α (model number)	G (kg m^{-2} s^{-1})	T_{sat} (°C)	ΔP_F (model 2)	ΔP_F (model 5)	ΔP_F (model 9)
3	260	40	22/28	24/28	19/28
3	515	40	21/32	29/32	24/32
3	260	50	22/28	21/28	18/28
3	515	50	27/32	26/32	25/32
6	260	40	20/28	23/28	29/28
6	515	40	21/32	29/32	24/32
6	260	50	22/28	21/28	18/28
6	515	50	27/32	29/32	25/32
7	260	40	20/28	23/28	19/28
7	515	40	21/32	29/32	24/32
7	260	50	21/28	20/28	18/28
7	515	50	27/32	29/32	25/32
14	260	40	21/28	24/28	20/28
14	515	40	21/32	29/32	24/32
14	260	50	22/28	20/28	18/28
14	515	50	27/32	29/32	25/32
15	260	40	19/28	22/28	18/28
15	515	40	19/32	25/32	21/32
15	260	50	22/28	21/28	18/28
15	515	50	27/32	29/32	25/32
21	260	40	21/28	24/28	20/28
21	515	40	21/32	29/32	24/32
21	260	50	22/28	21/28	18/28
21	515	50	27/32	29/32	25/32
28	260	40	21/28	24/28	20/28
28	515	40	21/32	29/32	24/32
28	260	50	22/28	21/28	18/28
28	515	50	27/32	29/32	25/32
31	260	40	21/28	24/28	20/28
31	515	40	21/32	29/32	24/32
31	260	50	22/28	21/28	18/28
31	515	50	27/32	29/32	25/32

Author's personal copy

change from the total measured pressure drop regarding the condensing fluid of R134a in a vertical tube. It should be noticed that void fraction values from the authors' previous publication [59] were used to determine the gravitational and momentum pressure drop terms. The results of this calculation process were used as comparative values for the validation of frictional pressure drop models in Tables 5–8 including void fraction models in Table 1.

When the majority of data belonging to a result of the model fall within ±30% deviation, it is assumed to be a successful model in the paper. Relying on this assumption, the predicted values of frictional pressure drop and void fraction models can be seen in Tables 5–8 in bold round brackets. Tables 5 and 6 are prepared for the mass flux of 260 kg m^{-2} s^{-1} and condensing temperatures of 40 and 50 °C respectively; Tables 7 and 8 are prepared for the mass flux of 515 kg m^{-2} s^{-1} and condensing temperatures of 40 and 50 °C. It was found that 29 of 35 void fraction models and 11 of 13 frictional pressure drop models are predictable for the data and 6 of 35 void fraction models and 2 of 13 frictional pressure drop models are not accounted for by the validation process due to having values which are extremely high or low in comparison to others. It is possible to decide the most predictive combinations for the frictional pressure drop and void fraction models from Tables 5–8. When the direction of top to bottom is followed in Tables 5–8, prediction performance of void fractions can be seen for a constant frictional pressure drop model. Besides this, prediction performance of frictional pressure drop can be seen for a constant void fraction model when the direction of left to right is followed in Tables 5–8. For instance, it can be clearly seen by following Table 6 from top to bottom that the frictional pressure drop model of Chen et al. [37] has the majority of results (20 of 29) obtained from predictable void fraction models considering ±30% deviation for the calculated frictional pressure drop values compared to the experimental one. In addition to this, the model by Armand [2] can be given as an example of the majority of results (8/11) being

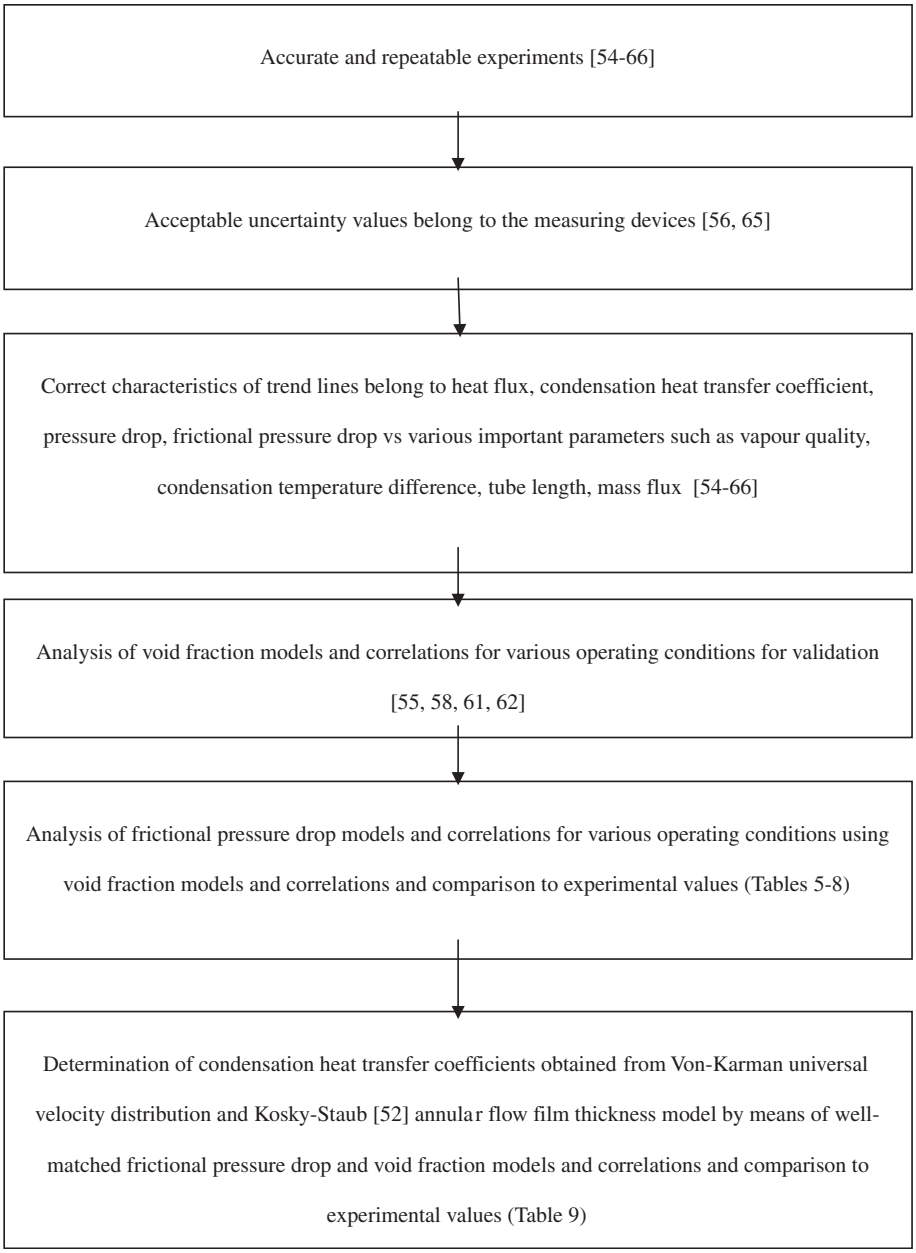

Fig. 3. Experimental validation procedure of the proposed model.

Author's personal copy

obtained from predictable frictional pressure drop models considering ±30% deviation for the calculated frictional pressure drop values compared to the experimental one explained above paragraph from left to right direction in Table 5. As a result of these tables, 3 of 13 models belonging to the determination of two-phase frictional pressure drop and 8 of 35 models belonging to the determination of void fraction are chosen for the determination of the condensation heat transfer coefficient due to their good agreement with the experimental frictional pressure drop values.

As expected, it can be clearly seen from Table 9 that the majority of the calculated condensation heat transfer coefficients obtained from Eq. (16) by means of all the chosen successful frictional pressure drop and void fraction models from the analysis in Tables 5–8 are in good agreement within ±30% deviation compared to experimental heat transfer coefficients defined in the authors' previous publications [54–66]. These results prove the proposed experimental treatment's success by means of the elimination process in Tables 5–8.

A summary of the work as an experimental treatment is shown in Fig. 3 which includes necessary knowledge for a study to be scientific from its starting point to its end point. It should be also noted that detailed information on the characteristics of heat transfer and pressure drop belonging to the data in this study and some additional figures with different experimental parameters related to this study can be seen in the authors' previous publications [54–66].

5. Conclusion

In this study, accurate and repeatable in-tube condensation data belonging to the co-current downward flow of R134a in an 8.1 mm i.d. vertical smooth tube were taken and an examination was conducted of their applicability to the combination of various void fraction, frictional pressure drop, and heat transfer coefficient models having two different mass fluxes and condensing temperatures as operating conditions shown in Table 4 regarding 122 data points for validation. Moreover, there is little research on the parameters used in this study in the current literature. The content of this study is expected to fill this gap in the literature.

Thirty-five void fraction correlations are used to calculate the gravitational and momentum pressure drop. Frictional pressure drop is obtained from measured total pressure drop data and also calculated by means of 13 frictional pressure drop models for comparison.

Most predictive models and correlations belonging to the void fraction and frictional pressure drop to determine the condensation heat transfer coefficient by a theoretical model are investigated in this study. According to the analysis in this paper, the combination of the frictional pressure drop models by Lockhart and Martinelli [14], Chen et al. [37], and Wang et al. [43] with the void fraction models by Armand [2], Harms et al. [5], Chisholm [6], Hamersma and Hart [13], Lockhart and Martinelli [14], Premoli et al. [20], Fauske [27], and Chisholm [30] can determine condensation heat transfer coefficient values of R134a fairly well after the elimination process; on the other hand, it can be seen that, due to their incompatible operating conditions and their values which are extremely high or low in comparison to others, models of frictional pressure drop by Tran et al. [46] and Lee and Lee [47] and models of void fraction by Chisholm and Laird [3], Steiner [4], Bangkoff [8], Domanski and Didion [17], Levy [26], and Madsen [31] disappear in Tables 5–9.

Kosky and Staub's [52] heat transfer correlations with the von Karman universal velocity distribution for the test tube were used to evaluate the condensation heat transfer coefficient during annular flow. As a result of the analysis in this paper, in spite of the use of interfacial shear stress valid for horizontal tubes, it is shown that an annular flow model is not dependent on the tube orientation provided that an annular flow regime exists along the tube length and the model is capable of predicting condensation heat transfer coefficients inside the test tube. Moreover, an essential generalized model for an accurate experimental study regarding the calculation procedure in the paper is shown in Fig. 3.

Acknowledgements

The present study was financially supported by Yildiz Technical University (YTU) and King Mongkut's University of Technology Thonburi (KMUTT). The first author wishes to thank KMUTT for providing him with a Post-doctoral fellowship, while the second author wish to acknowledge the financial support provided by the Thailand Research Fund.

References

[1] Huq RH, Loth JL. Analytical two-phase flow void fraction prediction method. J Thermo Phys 1992;6:139–44.
[2] Armand AA. The resistance during the movement of a two-phase system in horizontal pipes. Izv Vses Tepl, Inst, AERA-Lib/Trans 1946;828:16–23.
[3] Chisholm D, Laird ADK. Two phase flow in rough tubes. Trans ASME 1958;80:276–86.
[4] Steiner D. Heat transfer to boiling saturated liquids. In: Verein Deutscher Ingenieure, editor. VDI-Warmeatlas (VDI Heat Atlas), VDI-Gessellschaft Verfahrenstechnik und Chemie-ingenieurwesen (GCV) [Fullarton JW, Trans.]. Dusseldorf, 1993.
[5] Harms T, Eckart D, Groll A, Braun J. A void fraction model for annular flow in horizontal tubes. Int J Heat Mass Transfer 2003;46:4051–7.
[6] Chisholm D. Two phase flow in pipelines and heat exchangers. George Godwin in association with The Institution of Chemical Engineers, London; 1983.
[7] Armand AA, Treschev GG. The resistance during the movement of a two-phase system in horizontal pipes. Izv Vses Tepl Inst 1946;1:16–23.
[8] Bankoff SG. A variable density single-fluid model for two-phase flow with particular reference to steam-water flow. Trans ASME J Heat Transfer 1960;82:265–72.
[9] Czop V, Barbier D, Dong S. Pressure drop, void fraction and shear stress measurements in adiabatic two-phase flow in coiled tube. Nucl Eng Des 1994;149:323–33.
[10] Tandon TN, Varma HK, Gupta CP. A void fraction model for annular two-phase flow. Int J Heat Mass Transfer 1985;28:191–8.
[11] Graham D, Chato JC, Newell TA. Heat transfer and pressure drop during condensation of refrigerant 134a in an axially grooved tube. Int J Heat Mass Transfer 1999;42:1935–44.
[12] Hughmark GA. Holdup in gas–liquid flow. Chem Eng Prog 1962;58:62–5.
[13] Hamersma PJ, Hart J. A pressure drop correlation for gas/liquid pipe flow with a small liquid holdup. Chem Eng Sci 1987;42:1187–96.
[14] Lockhart RW, Martinelli RC. Proposed correlation of data for isothermal two-phase, two-component flow in pipes. Chem Eng Prog 1949;45:39–48.
[15] Turner JM, Wallis GB. The separate-cylinders model of two-phase flow, paper no. NYO-3114-6. Thayer's School Eng, Dartmouth College, Hanover, NH, USA; 1965.
[16] Wallis GB. One-dimensional two-phase flow. McGraw-Hill; 1965. p. 51–4.
[17] Domanski P, Didion D. Computer modeling of the vapor compression cycle with constant flow area expansion device. Building Science Series, National Bureau of Standards of USA; 1983.
[18] Wilson MJ, Newell TA, Chato JC, Infante Ferreira CA. Refrigerant charge, pressure drop and condensation heat transfer in flattened tubes. Int J Refrig 2003;26:442–51.
[19] Yashar DA, Newell TA, Chato JC. Experimental investigation of void fraction during horizontal flow in smaller diameter refrigeration applications, ACRC TR-141, Air Conditioning and Refrigeration Center, University of Illinois, Urbana-Champaign, IL; 1998.
[20] Premoli A, Francesco D, Prima A. An empirical correlation for evaluating two-phase mixture density under adiabatic conditions. In: European two-phase flow group meeting, Milan, Italy; 1970.
[21] Kawahara A, Kawaji M, Chung PMY, Sadatomi M, Okayama K. Effects of channel diameter and liquid properties on void fraction in adiabatic two-phase flow through microchannels. Heat Transfer Eng 2005;26:13–9.
[22] El Hajal J, Thome JR, Cavallini A. Condensation in horizontal tubes, part 1: two-phase flow pattern map. Int J Heat Mass Transfer 2003;46:3349–63.
[23] Zivi SM. Estimation of steady-state steam void-fraction by means of the principle of minimum entropy production. Trans ASME J Heat Transfer Ser C 1975;86:247–52.
[24] Rigot G. Fluid capacity of an evaporator in direct expansion. Plomberie 1973;328:133–44.
[25] Smith SL. Void fractions in two-phase flow: a correlation based upon an equal velocity head model. Proc Inst Mech Eng 1969;36:647–64.

Author's personal copy

[26] Levy S. Steam slip theoretical prediction from momentum model. Trans ASME J Heat Transfer Ser C 1960;82:113–24.
[27] Fauske H. Critical two-phase, steam–water flows. In: Proceedings of the 1961 heat transfer and fluid mechanics institute. Stanford (CA): Stanford University Press; 1961. p. 79–89.
[28] Thom JRS. Prediction of pressure drop during forced circulation boiling of water. Int J Heat Mass Transfer 1964;7:709–24.
[29] Baroczy CJ. Correlation of liquid fraction in two-phase flow with application to liquid metals. Chem Eng Prog Symp Series 1965;61:179–91.
[30] Chisholm D. Pressure gradients due to friction during the flow of evaporating two-phase mixtures in smooth tubes and channels. Int J Heat Mass Transfer 1973;16:347–58.
[31] Madsen N. A void fraction correlation for vertical and horizontal bulk-boiling of water. AIChE J 1975;21:607–8.
[32] Ahrens FW. Heat pump modeling, simulation and design. In: Proceedings of the NATO advanced study institute on heat pump fundamentals, Espinho, Spain; 1980.
[33] Spedding PL, Spence DR. Prediction of holdup in two phase flow. Int J Eng Fluid Mech 1989;2:109–18.
[34] Chen JJJ. A further examination of void-fraction in annular two-phase flow. Int J Heat Mass Transfer 1986;29:1760–3.
[35] Friedel L. Improved friction pressure drop correlation for horizontal and vertical two-phase pipe flow. European Two-phase Flow Group Meeting Paper E2, vol. 18; 1979. p. 485–92.
[36] Friedel L. Pressure drop during gas/vapor–liquid flow in pipes. Int J Chem Eng 1980;20:352–67.
[37] Chen IY, Yang KS, Chang YJ, Wang CC. Two-phase pressure drop of air-water and R-410a in small horizontal tubes. Int J Multiphase Flow 2001;27:1293–9.
[38] Cavallini A, Censi G, Del Col D, Doretti L, Longo GA, Rossetto L. Experimental investigation on condensation heat transfer and pressure drop of new HFC refrigerants (R134a, R125, R32, R410A, R236ea) in a horizontal smooth tube. Int J Refrig 2007;24:73–87.
[39] Cavallini A, Censi G, Del Col D, Doretti L, Longo GA, Rossetto L. Condensation of halogenated refrigerants inside smooth tubes. HVAC R Research 2002;8:429–51.
[40] Garimella S. Condensation flow mechanisms, pressure drop and heat transfer in microchannels. In: Kakac S, Vasiliev LL, Bayazitoglu Y, Yener Y, editors. Microscale heat transfer – fundamental and applications. The Netherlands: Kluwer Academic Publishers; 2005.
[41] Garimella S, Agarwal A, Killion JD. Condensation pressure drop in circular microchannels. Heat Transfer Eng 2005;26:1–8.
[42] Mishima K, Hibiki T. Some characteristics of air-water two-phase flow in small diameter vertical tubes. Int J Multiphase Flow 1996;22:703–12.
[43] Wang CC, Chiang CS, Lu DC. Visual observation of two-phase flow pattern of R-22, R-134a, and R-407C in a 6.5-mm smooth tube. Exp Therm Fluid Sc 1997;15:395–405.
[44] Wilson MJ, Newell TA, Chato JC, Infante Ferreira CA. Refrigerant charge pressure drop, and condensation heat transfer in flattened tubes. Int J Refrig 2003;26:442–51.
[45] Souza DAL, Pimenta MDM. Prediction of pressure drop during horizontal two-phase flow of pure and mixed refrigerants. In: Proceedings of the 1995 ASME/JSME fluids engineering and laser anemometry conference and exhibition, August 13–18 1995, Hilton Head, SC, ASME, New York, NY; 1995. p. 161–71.
[46] Tran TN, Chyu MC, Wambsganss MW, France DM. Two-phase pressure drop of refrigerants during flow boiling in small channels: an experimental investigation and correlation development. Int J Multiphase Flow 2000;26:1739–54.
[47] Lee HJ, Lee SY. Pressure drop correlations for two-phase flow within horizontal rectangular channels with small heights. Int J Multiphase Flow 2001;27:783–96.
[48] Dittus FW, Boelter LME. Engineering publication, vol. 2, University of California; 1930. p. 443.
[49] Akers WW, Deans HA, Crosser OK. Condensation heat transfer within horizontal tubes. Chem Eng Prog Symp Series 1959;55:171–6.
[50] Cavallini A, Zecchin RA. A dimensionless correlation for heat transfer in forced convection condensation. Proc Sixth Int Heat Transfer Conf 1974;3:309–13.
[51] Shah MM. A general correlation for heat transfer during film condensation inside pipes. Int J Heat Mass Transfer 1979;22:547–56.
[52] Kosky PG, Staub FW. Local condensing heat transfer coefficients in the annular flow regime. AIChE J 1971;17.
[53] Jaster H, Kosky PG. Condensation heat transfer in a mixed flow regime. Int J Heat Mass Transfer 1976;19:95–9.
[54] Chen SL, Gerner FM, Tien CL. General film condensation correlations. Exp Heat Transfer 1987;1:93–107.
[55] Dalkilic AS, Laohalertdecha S, Wongwises S. Effect of void fraction models on the two-phase friction factor of R134a during condensation in vertical downward flow in a smooth tube. Int Commun Heat Mass Transfer 2008;35:921–7.
[56] Dalkilic AS, Yildiz S, Wongwises S. Experimental investigation of convective heat transfer coefficient during downward laminar flow condensation of R134a in a vertical smooth tube. Int J Heat Mass Transfer 2009;52:142–50.
[57] Dalkilic AS, Laohalertdecha S, Wongwises S. Two-phase friction factor in vertical downward flow in high mass flux region of refrigerant HFC-134a during condensation. Int Commun Heat Mass Transfer 2008;35:1147–52.
[58] Dalkilic AS, Laohalertdecha S, Wongwises S. Effect of void fraction models on the film thickness of R134a during downward condensation in a vertical smooth tube. Int Commun Heat Mass Transfer 2009;36:172–9.
[59] Dalkilic AS, Wongwises S. Intensive literature review of condensation inside smooth and enhanced tubes. Int Heat Mass Transfer 2009;52:3409–26.
[60] Dalkilic AS, Laohalertdecha S, Wongwises S. Experimental investigation on heat transfer coefficient of R134a during condensation in vertical downward flow at high mass flux in a smooth tube. Int Commun Heat Mass Transfer 2009;36:1036–43.
[61] Dalkilic AS, Laohalertdecha S, Wongwises S. A comparison of the void fraction correlations of R134a during condensation in vertical downward laminar flow in a smoth and micro-fin tube. In: Proceedings of the 1st international conference on micro/nanoscale heat transfer. ASME January 06–09, Taiwan; 2008.
[62] Dalkilic AS, Laohalertdecha S, Wongwises S. Two-phase friction factor obtained from various void fraction models of R-134a during condensation in vertical downward flow at high mass flux. In: Proceedings of the 1st international conference on heat transfer, ASME, August 10–14, USA; 2008.
[63] Dalkilic AS, Laohalertdecha S, Wongwises S. Experimental investigation on the condensation heat transfer and pressure drop characteristics of R134a at high mass flux conditions during annular flow regime inside a vertical smooth tube. Summer Heat Transfer Conference, ASME, July 19–23, USA; 2009.
[64] Dalkilic AS, Agra O. Experimental apparatus for the determination of condensation heat transfer coefficient for R134a and R600a flowing inside vertical and horizontal tubes, Summer heat transfer conference, ASME, July 19–23, USA; 2009.
[65] Dalkilic AS, Laohalertdecha S, Wongwises S. Experimental research on the similarity of annular flow models and correlations for the condensation of R134a at high mass flux inside vertical and horizontal tubes. International mechanical engineering congress and exposition, ASME, November 13–19, USA; 2009.
[66] Dalkilic AS, Wongwises S. A heat transfer model for co-current downward laminar film condensation of R134a in a vertical micro-fin tube during annular flow regime. In: Eleventh UK national heat transfer conference, September 6–8, Queen Mary University of London; 2009.
[67] Garcia-Valladeres O. Review of in-tube condensation heat transfer correlations for smooth and micro-fin tubes. Heat Transfer Eng 2003;24:6–24.
[68] Hewitt GF, Robertson DN. Studies of two-phase flow patterns by simultaneous x-ray and flash photography, Rept AERE-M2159, UKAEA, Harwell; 1969.
[69] Chamra LM, Mago PJ, Tan M, Kung C. Modeling of condensation heat transfer of pure refrigerants in micro-fin tubes. Int J Heat Mass Transfer 2005;48:1293–302.
[70] Kline SJ, McClintock FA. Describing uncertainties in single sample experiments. Mech Eng 1953.

Springer

KSME

Journal of Mechanical Science and Technology 24 (9) (2010) 1809~1818
www.springerlink.com/content/1738-494x
DOI 10.1007/s12206-010-0626-7

Numerical investigation of an axi-symmetric laminar jet impinging on a dimpled surface under uniform heat flux using a finite element method †

Koonlaya Kanokjaruvijit[1,*], Chakkraphan Thawonngamyingsakul[2] and Somchai Wongwises[3]

[1]*Department of Mechanical Engineering, Naresuan University, Phitsanulok 65000 Thailand*
[2]*Department of Mechanical Engineering, Rajamangala University of Technology Lanna Tak, Tak 63000, Thailand*
[3]*Department of Mechanical Engineering, King Mongkut's University of Technology Thonburi, Bangmod, Bangkok 10140 Thailand*

(Manuscript Received April 13, 2009; Revised March 17, 2010; Accepted May 11, 2010)

Abstract

The purpose of this study is to numerically investigate heat transfer and flow field in a semi-confined axi-symmetric laminar air jet impinging on a concave surface, or dimple, with uniform heat flux. A commercial software package relying on the finite element method was used for the simulation, and mesh convergence was examined in order to minimize computational cost. Jet impingement on a flat plate was used as a baseline reference case, and flat plate results were validated against previously published experimental data with good agreement. The effects of various parameters involved in dimple impingement –such as Reynolds number (Re) between 100–1,400; jet-to-plate spacing (H/D_j) ranging from 2 to 6 jet diameters; dimple depths (d/D_d) of 0.1, 0.15, and 0.2; and the ratio of jet diameter and dimple projected diameter (D_j/D_d) from 0.25 to 1– were all studied. Comparisons show that heat transfer reduction occurs in the presence of dimples because of the larger impingement area, which results in less momentum flux. The dimple curvature lifts the post-impinging fluid and creates a backflow, instead of allowing it to maintain contact with the surface, as is the case with flat plate impingement.

Keywords: Jet impingement ; Dimple ; Finite element

1. Introduction

Jet impingement is one of the most effective heat transfer augmenting techniques in heating, cooling, and drying applications. Although most articles related to jet impingement deal with turbulence, knowledge of its laminar flow is crucial in understanding the physics of turbulence, especially at the stagnation region where static pressure is sufficiently high to induce viscous effect in the turbulent jet. Bergthorson et al. [1] scrutinized a round impinging jet through experiments and numerical analysis using three formulas: axi-symmetric unsteady Navier-Stokes equations with the use of spectral-element method, potential-flow formulation using second-order centered finite difference, and streamfunction formulation. Results of their study, in the form of jet centerline velocities, were compared with the calculated results obtained from the current study. Angioletti et al. [2] examined heat transfer in laminar and transitional unconfined jet impingement between Reynolds numbers (Re) 1,000 and 4,000, experimentally and numerically. Different jet shapes have been investigated. Chattanopadhyay [3] employed the finite volume method and found 20% less heat transfer in an annular jet compared to a round jet. Furthermore, a three-dimensional three-by-three array of laminar impinging square jets with spent fluid removal was examined numerically by Aldabbagh and Sezai [4].

Dimples have been considered as heat transfer enhancers to jet impingement. However, heat transfer results were not consistent among the various studies. Azad et al. [5] found higher heat transfer results compared with those for flat plates for Re values between 4,850 and 18,300. Ekkad and Controvitz [6] reported that the presence of dimples resulted in a lower heat transfer for Re = 4,800–14,800. Kanokjaruvijit and Martinez-Botas [7-9] showed enhanced heat transfer in the presence of dimples with strong crossflows for Re = 5,000–11,500. None of these works gave detailed information on flow visualization.

This investigation started by validating the flow and heat transfer results of an axi-symmetric laminar jet impinging on a uniform heat flux surface, which was obtained from a calculation using the finite element method, against experimental results and those obtained from the finite difference method in literature. Using the flat plate impingement results as baseline cases, dimple impingement was studied together with various parametric effects, such as Re, jet-to-plate spacing (H/D_j), dimple depth (d/D_d), and ratio of nozzle exit diameter to dimple projected diameter (D_j/D_d). Due to the scarcity of informa-

† This paper was recommended for publication in revised form by Associate Editor Gihun Son

*Corresponding author. Tel.: +66 5526 1000, Fax: +66 5526 1062
E-mail address: koonlaya@gmail.com

© KSME & Springer 2010

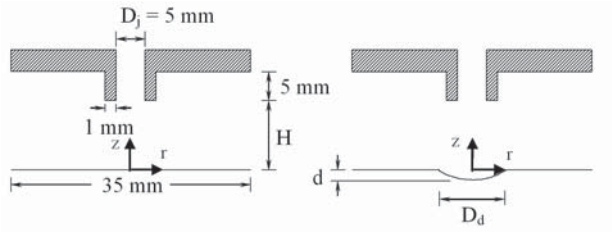

(a) Flat plate (b) Dimpled plate

Fig. 1. Dimension and tested parameters (not to scale).

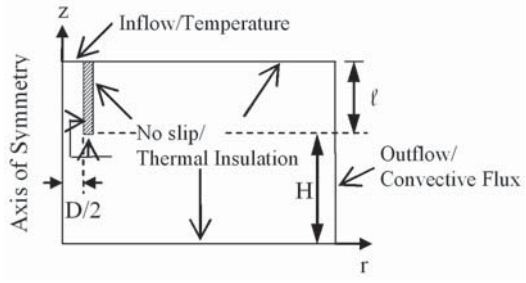

(a) Flat plate

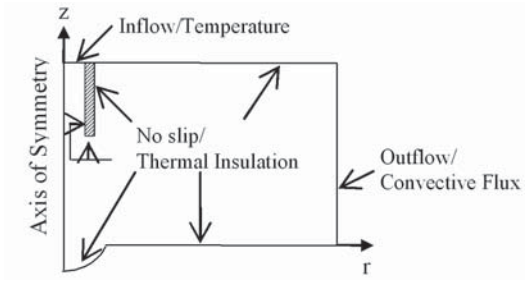

(b) Dimpled plate

Fig. 2. Dimensions and boundary conditions.

tion on heat transfer and flow of a laminar jet impinging onto a dimple, this study intends to provide computational data for better understanding of the experimental results found by previous researchers [5-9].

2. Numerical models

2.1 Computational domain

Fig. 1 shows sketches of the problem set-ups for the flat plate and dimple impingements with a jet diameter of 5 mm extruding from the nozzle plate and a nozzle wall of 1 mm thickness. Initially, the target plate is set at 35 mm long, but the domain is lengthened later in some cases in order to achieve valid results.

Because the problem is two-dimensional (2D) axisymmetric, the computational domain is reduced to half (Fig. 2), allowing for less time and memory usages. Throughout this investigation, a commercial software package for finite element analysis called COMSOL, which is available at the Naresuan University, is used. It pre-defines physical partial differential equations (PDEs) through multiphysics features. Hence, boundary conditions for both problems must be defined simultaneously as shown in the figure. For the flow problem, all solid walls are assigned "no-slip" conditions, which are mathematically written as $v_r = v_z = 0$. The nozzle exit, where the jet is issued, is given an "inflow" condition, $v = U_j$, assigned by the required jet velocity. The post impinging jet leaves the domain to go to the ambient environment. Thus, the domain end is assigned the "outflow" or "do nothing" boundary condition, which means the pressure of the boundary is zero.

Considering the heat transfer cases, an air jet with flat velocity profile at a temperature of 300 K is discharged through the nozzle, whose walls and adjacent walls are assigned by a Neumann boundary condition of "thermal insulation" or $\left.\frac{\partial T}{\partial r}\right|_{nozzle\ wall} = 0$. The target plate associated with heat transfer through the jet is given a constant heat flux of 500 W/m^2. The post-impinging jet leaves the domain to "convective flux" as it exits to the ambient environment, similar to that in the flow problem.

2.2 Governing equations

Computation throughout this investigation is based on the three conservation laws: mass, momentum, and energy. A number of assumptions are made, such as steady state, incompressible Newtonian fluid, neglecting gravitation, and 2D axisymmetry. Hence, throughout this study, the buoyancy effect is not taken into account. Air is used as the working fluid with Pr = 0.71. The conservation laws for the current study are as follows:

Continuity equation:

$$\frac{1}{r}\frac{\partial}{\partial r}(rv_r)+\frac{\partial v_z}{\partial z}=0 \tag{1}$$

Momentum equation in radial direction:

$$\rho\left(v_r\frac{\partial v_r}{\partial r}+v_z\frac{\partial v_r}{\partial z}\right)=-\frac{\partial p}{\partial r}+\mu\left[\frac{\partial}{\partial r}\left(\frac{1}{r}\frac{\partial(rv_r)}{\partial r}\right)+\frac{\partial^2 v_r}{\partial z^2}\right] \tag{2}$$

Momentum equation in axial direction:

$$\rho\left(v_r\frac{\partial v_z}{\partial r}+v_z\frac{\partial v_z}{\partial z}\right)=-\frac{\partial p}{\partial z}+\mu\left[\frac{1}{r}\frac{\partial}{\partial r}\left(r\frac{\partial v_z}{\partial r}\right)+\frac{\partial^2 v_z}{\partial z^2}\right] \tag{3}$$

Energy equation:

$$\rho c_p\left(v_r\frac{\partial T}{\partial r}+v_z\frac{\partial T}{\partial z}\right)=k\left[\frac{1}{r}\frac{\partial}{\partial r}\left(r\frac{\partial T}{\partial r}\right)+\frac{\partial^2 T}{\partial z^2}\right] \tag{4}$$

The local heat transfer coefficient is defined as follows:

$$h=\frac{q_s''}{T_s-T_j} \tag{5}$$

The local Nusselt number (Nu) is defined as follows:

$$Nu = \frac{h D_j}{k} \tag{6}$$

Because it is considered a 2D problem, the average Nu is calculated from a length integral.

2.3 Finite element method for the flow field

Once the computational domain was set, unstructured triangle meshes were generated using the Delaunay algorithm, which maximizes the minimum angle of all the angles of the triangles. The circumcircles of a triangle formed by three points from the original point set is empty if it does not contain vertices other than the three that form it. For the incompressible Navier-Stokes, Lagrange elements of order 2 or quadratic elements model the velocity components, and linear elements model the pressure. A second-order Lagrange triangle consists of six node points at the vertices and side midpoints (Fig. 3). For each of these node points P_i, there is a degree of freedom $N_i = n(P_i)$ and basis function ϕ_i. Restriction of the basis function ϕ_i to an element is a polynomial with a degree of 2 in the local coordinates, such that $\phi_i = 1$ at node i and $\phi_i = 0$ at all other nodes. Thus, the basis functions are continuous, as shown in the system of equations below:

$$\phi(x,y) = \sum N_i(x,y)\,\phi_i \tag{7}$$

where ϕ represents basis functions, such as u, v.

The interpolation function N is dependent on a function of area coordinates L_1, L_2, and L_3, as follows:

$$N_1 = L_1^2 - L_1(L_2 + L_3) \quad N_4 = 4L_2L_3$$
$$N_2 = L_2^2 - L_2(L_3 + L_1) \quad N_5 = 4L_3L_1$$
$$N_3 = L_3^2 - L_3(L_1 + L_2) \quad N_6 = 4L_1L_2$$

where $L_i = \frac{1}{2A}(a_i + b_i x + c_i y)$

$$a_1 = x_2y_3 - x_3y_2 \quad b_1 = y_2 - y_3 \quad c_1 = x_3 - x_2$$
$$a_2 = x_3y_1 - x_1y_3 \quad b_2 = y_3 - y_1 \quad c_2 = x_1 - x_3$$
$$a_3 = x_1y_2 - x_2y_1 \quad b_3 = y_1 - y_2 \quad c_3 = x_2 - x_1$$

The variable A represents an area of each element and is calculated from the following equation:

$$A = \frac{1}{2}\left[x_2(y_3 - y_1) + x_1(y_2 - y_3) + x_3(y_1 - y_2)\right]$$

Note that COMSOL developed the code in Cartesian coordinates despite the fact that the computational domain is constructed in cylindrical coordinates.

For pressure distribution on each Lagrange element, the polynomial is of the order of 1, indicating that three nodes are contained on the triangular vertices (labeled 1, 2, and 3; Fig. 3). The basis function is as follows:

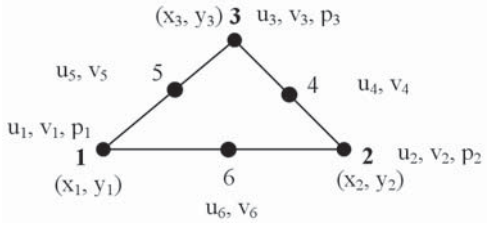

Fig. 3. Labels of nodes and dependent variables for a Lagrange element.

$$p = H_j p_j \text{ ; j = 1,2,3} \tag{8}$$

where H_j is an interpolation function or function of the area coordinates. such that the following hold true:

$$H_1 = L_1 \qquad H_2 = L_2 \qquad H_3 = L_3$$

The Galerkin method was then used, which means that the interpolation function is a weighted function. Applying this function to continuity and x-momentum and y-momentum conservation equations and integrating them gave the following:

$$\int_A H_i\left(\frac{\partial u}{\partial x} + \frac{\partial v}{\partial y}\right)dA = 0 \tag{9a}$$

$$\int_A N_i\left[\rho\left(u\frac{\partial u}{\partial x} + v\frac{\partial u}{\partial y}\right) - \left(2\mu\frac{\partial^2 u}{\partial x^2} - \frac{\partial P}{\partial x} + \mu\frac{\partial^2 u}{\partial y^2} + \frac{\partial^2 v}{\partial x \partial y}\right)\right]dA = 0 \tag{9b}$$

$$\int_A N_i\left[\rho\left(u\frac{\partial v}{\partial x} + v\frac{\partial v}{\partial y}\right) - \left(2\mu\frac{\partial^2 u}{\partial y^2} - \frac{\partial P}{\partial y} + \mu\frac{\partial^2 u}{\partial x \partial y} + \frac{\partial^2 v}{\partial x^2}\right)\right]dA = 0 \tag{9c}$$

Finally, after applying boundary conditions using the UMFPACK algorithm, which is a highly efficient direct solver for asymmetric systems using the asymmetric-pattern multifrontal method and direct LU factorization of the sparse matrix, as a solver with a tolerance of 10^{-6}, matrices of the solution (u, v, p) are obtained.

2.4 Finite element method for the heat transfer

The procedure is similar to that in the previous section, except for the fact that the software uses linear elements (three-node element) to model the heat transfer problem. Applying the Galerkin method to the heat transfer equation yields the following:

$$-\int_A W_i k\left(\frac{\partial^2 T}{\partial x^2} + \frac{\partial^2 T}{\partial y^2}\right)dA + \int_A W_i \rho c\left(u\frac{\partial T}{\partial x} + v\frac{\partial T}{\partial y}\right)dA = 0 \tag{10}$$

where W_i represents the interpolation function. Then, applying the thermal boundary conditions and using the UMFPACK solver, the matrix of temperatures is obtained.

2.5 Meshing

Unstructured meshes or triangular meshes are chosen for the entire study. Meshes near the nozzle exit and the dimple and its edge are denser than anywhere else in the domain. The maximum element size is 1/15 of the maximum distance in the geometry. The element growth rate is 1.3, and the tested mesh densities are 17.32, 21.32, and 23.14 meshes/mm^2. These results are validated in the following section.

3. Validation of flat plate impingement

Validation of the computational results on the flat plate impingement is performed against the experimental results and the computational results from the finite volume method, prior to analyzing the dimple impingement. Appropriate computational domains are selected by taking into account the effects of mesh density and nozzle confinement.

3.1 Validation against experimental results

In this study, the jet exit diameter D_j measures 5 mm, the length (ℓ) of the nozzle is 10 mm, and its thickness is 1 mm. No-slip boundary conditions are given to all walls for the flow problem. Outflow means that the post-impinging jet is leaving the domain to the atmosphere (1 atm). The velocity profile at the nozzle exit is parabolic, and Re is defined as follows:

$$\mathrm{Re} = \frac{\rho D_j U_j}{\mu} \tag{11}$$

where U_j is the average jet exit velocity. For the thermal boundary conditions, the upper plate and the nozzle surface are assigned thermal insulation, and the temperature of the jet issuing from the nozzle is 293 K. The impingement plate has a uniform heat flux of 500 W/m^2. The post-impinging jet then leaves the domain to the atmospheric air. Thermal properties of air are found at 293 K.

According to the finite element analyses of Fagan [10] and Decha-ampai [11], higher mesh density leads to higher accuracy and consumes more computer memory. However, the main concern in the current examination is the limitation in the capacity of the personal computer with the specification of Pentium (R) CPU 3.00 GHz and 2 GB of RAM. COMSOL produces evenly distributed meshes in a particular domain, but different mesh densities can be set. Hence, the optimum mesh density must be determined by testing three values of mesh densities: 17.32, 21.32, and 23.14 meshes/mm^2, which are respectively called models A, B, and C for reference purpose. Fig. 4(a) compares the local Nu obtained from each model. The average Nussult numbers of models A and B are compared to that of model C. Differences between the average Nu of models A and B from those of model C are 0.4937% and 0.2523%, respectively. The local Nus of model B are chosen to be compared with those obtained from experiments of Angioletti [2], as presented in Fig. 4(b), at Re = 1,000 and H/D_j = 4.5. Results are in good agreement, with the difference in the average Nu at 1.0443%.

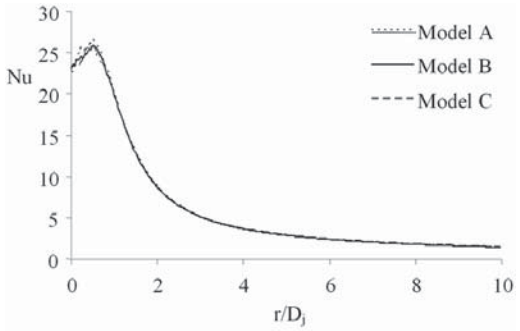

(a) Comparison of local Nus obtained from each model with different mesh densities

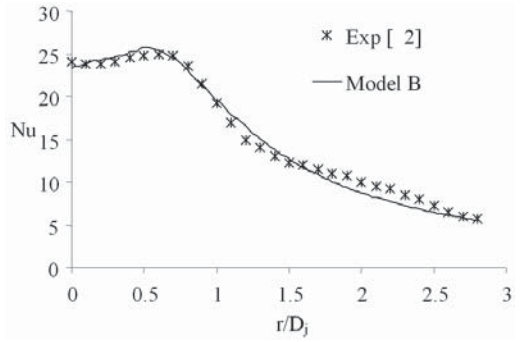

(b) Comparison of local Nus of model B

Fig. 4. Comparison of local Nus with the experimental results of Angioletti et al. [2] at Re = 1,000 and H/D_j = 4.5 after mesh density dependency.

3.2 Validation against results from finite volume method

Because the finite volume method has been used widely, the solution obtained from this study is also compared with those from this method. The work of Chattopadhyay [3] used a SIMPLE algorithm on a 2D axi-symmetric jet impingement. The Re was defined as

$$\mathrm{Re} = \frac{\rho U_j D_j}{\mu} \tag{12}$$

where U_j is the average exit velocity of the jet. Similar to the previous validation, the appropriate model is found when the mesh density and time consumed are considered. In addition, an additional domain is applied in order for the calculation to converge.

The computational domain performed by Chattopadhyay [3] is given as follows: the nozzle length = $0.5D_j$, the distance is measured perpendicularly from the nozzle exit to the impingement plate = $2D_j$, and the impingement plate length = $10D_j$. Furthermore, the nozzle wall is assigned to be a very thin line. The thermal properties of air were set at 303 K.

Set-up of the calculation domain in accordance with Chattopadhyay [3] leads the software to divergence. This is

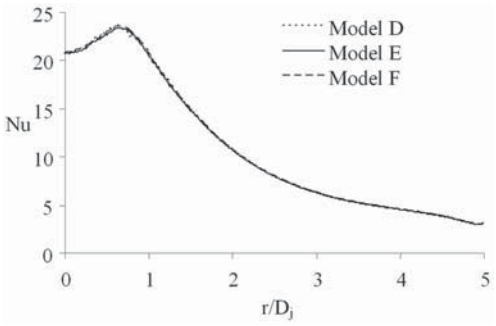

(a) Mesh density dependency check

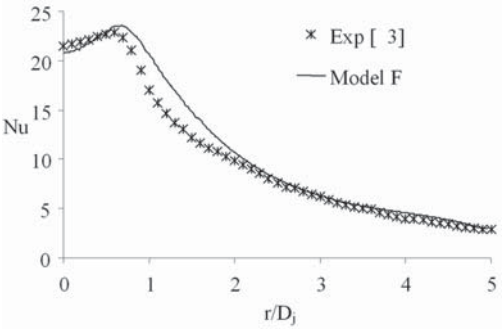

(b) Comparison with experimental results

Fig. 5. Mesh density dependency check on heat transfer and comparison with experimental results of Chattopadhyay [3] at Re = 1,000 and $H/D_j = 2$.

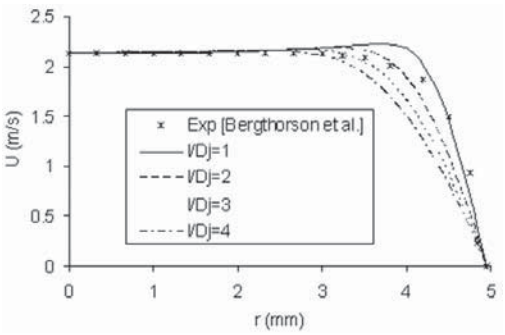

Fig. 6. Comparison of jet exit velocities at the centerline of various values of l/D_j with experimental results of Bergthorson et al. [11] at Re = 1,400.

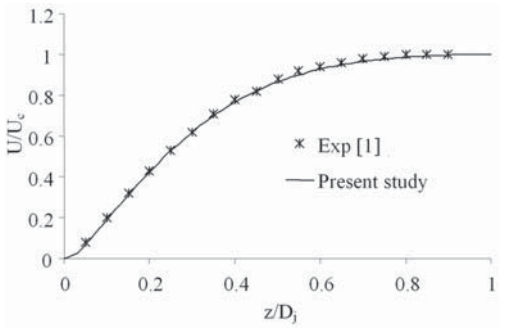

Fig. 7. Comparison of the dimensionless centerline velocities with the results of Bergthorson et al. [1] at Re = 400.

thought to be due to the fact that the length of the impingement surface is too short compared to the jet diameter, causing an end effect. Therefore, an additional domain with the length of $5D_j$ is attached to the first one, which presents new flow and boundary conditions. This does not extend the impingement surface but expands the computational domain. Boundary conditions for the additional domain are set to be exposed to the ambient environment.

The next step is to check mesh density dependency on local Nu by examining three models. The first one, model D, has a mesh density of 35.12 meshes/mm^2 for both domains. The mesh density for model E equals 48.12 meshes/mm^2 for both domains. However, because the first domain is thought to be more significant, the first domain in model F has the same mesh density as that of model E, and the second one is assigned course meshes with a low density of 5.90 meshes/mm^2. The heat transfer results obtained from all three models are plotted in Fig. 5(a), and they show good agreement. Among the three models, model E gives the highest accuracy ([10], [11]) but consumes the highest time and memory. Comparison of the average Nus of models D and F with model E gives 0.3342% and 0.1861%, respectively. Consequently, model F is chosen to validate the results of Chattophadhay [3], as shown in Fig. 5(b), at Re = 1,000 and $H/D_j = 2$. The results agree well near the stagnation zone ($0 < r/D_j < 0.8$) and the wall jet zone starting from $r/D_j > 3$. The difference in the region of $0.8 < r/D_j < 3$ can be due to the fact that the values of the nozzle length and diameter are different. For Re = 500, the difference in the average Nu is 3.6394%, whereas that for Re = 1,000 is 6.8539 %.

3.3 Validation of centerline velocity

Validation begins with comparing computational outcomes with those obtained from Bergthorson et al. [1], who employed an unconfined jet impingement. The results were reported in terms of dimensionless centerline velocity at Re = 400, 700, and 1,400 at $H/D_j = 1$, and Re is defined as follows:

$$\mathrm{Re} = \frac{\rho U_c D_j}{\mu} \tag{13}$$

where U_c represents the jet exit velocity measured at the centerline. The nozzle diameter is given at 9.9 mm, and the diameter of the circular impingement plate is 72.6 mm. The thermal properties of the air jet are observed at 293 K. Length and wall thickness of the nozzle are not given. For the case of unconfined impinging jet, the upper wall is designated as outflow. In addition, it must be sufficiently higher than the nozzle exit to ensure an unconfined problem. Note that due to the lack of information, the nozzle is designed to be cylindrical.

The nozzle lengths of 1, 2, 3, and 4 jet diameters are tested at Re = 1,400 in order to find the appropriate value (Fig. 6). All values give agreeable results along the radial direction with the experimental ones until $r \approx 2.7$. After this,

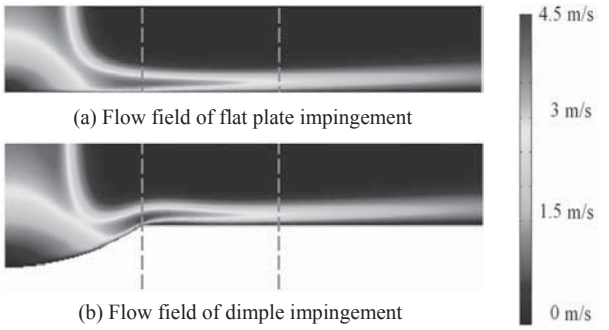

(a) Flow field of flat plate impingement

(b) Flow field of dimple impingement

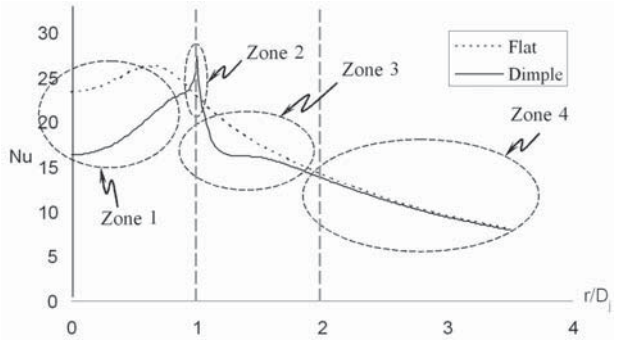

(c) Comparison of local heat transfer and dimple impingement to that of flat plate impingement (circles represent zones of interest)

Fig. 8. Comparison between flat plate and dimple impingement at Re = 1,200 and $H/D_j = 2$ and the dimpled surface of $d/D_d = 0.15$ and $D_j/D_d = 0.5$.

the position of the nozzle of $l/D_j = 2$ provides the best result with a 6.9994% difference from literature. This is subsequently selected for further investigation. In addition, validation for Re = 400 (Fig. 7) and 700 is also tested, and both cases are consistent with the experimental results.

4. Results and discussions

Since experimental data for a laminar jet impinging on a dimpled surface are not available, computational results for dimple impingement in the current study are presented without validation. However, mesh density in the vicinity of a dimple is higher than that in other places of the domain to maintain good accuracy. Apart from comparing the heat transfer results of dimple impingement to those of the flat plate, various parameters were considered, such as the Re, H/D_j, d/D_d, and ratio of jet diameter and dimple projected diameter (D_j/D_d).

4.1 Comparison with flat plate impingement

Fig. 8 shows a comparison of local heat transfer and flow field of the jet impinging on the dimpled surface for $d/D_d = 0.15$ and $D_j/D_d = 0.5$ with that on the flat plate at Re = 1,200, $H/D_j = 2$. Zone 1, which was circled in Fig. 8(c), shows the results of the stagnation region, where flat plate impingement gives a higher heat transfer than that of the dimple impingement. Due to the dimple curvature, the post-impinging fluid

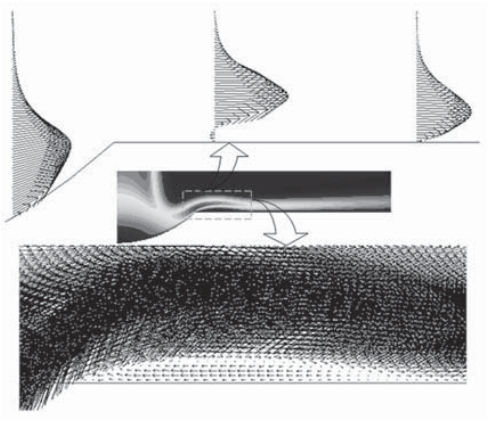

Fig. 9. Velocity profiles in the vicinity of the flat portion adjacent to the dimple.

attempts to traverse downstream, leading to excessive momentum loss near the dimple wall. Thus, its flow velocity gradients become negative. The surface discontinuity presented by the dimple edge in zone 2 causes the high velocity region in Fig. 8(b) and the local heat transfer jump in Fig. 9(c). In zone 3, the local Nu abruptly drops compared to that of the flat plate because the flow separation or back flow is found (Fig. 9). Finally, in zone 4, heat transfer results and flow fields for both cases are similar. The average Nu for the flat plate is 16.6334662, whereas that for the dimpled plate is 14.518827.

4.2 Mesh density independence check

Due to the lack of experimental data for jet impinging on a dimple, mesh density independence check was introduced. Fig. 10(a) shows a comparison of the centerline velocities for the case of Re = 1,200, $H/D_j = 2$, $d/D_d = 0.1$, and $D_j/D_d = 0.5$ at various mesh densities of 17.09 meshes/m, 34.67 meshes/m, and 107.12 meshes/mm^2, which are labeled S, T, and U, respectively. The results are in good agreement. Compared to the data of model U, model S gives a 1.7601% difference, and model T yields a 0.6428% difference. Furthermore, Fig. 10(b) shows a comparison of the Nus for the same case. The vicinity of the dimple is quite crucial because model S does not collapse, compared to the others. Data from models T and U agree well and have a 1.0781% difference, whereas model S is 4.1954% different from that of model U. Therefore, for the entire study on dimple jet impingement, model U with a mesh density of 107.12 meshes/mm^2 was employed.

4.3 Effect of Reynolds number

Although the influence of Reynolds number (Re) on the heat transfer of jet impingement is commonly known, it is still worth investigating. According to Polat [12], a fully developed jet takes place when Re is greater than 3,000. In this study, the Re's tested are in the range of 400-1,200. Fig. 11 shows the local heat transfer of various Re values for $H/D_j = 2$, $d/D_d = 0.2$, and $D_j/D_d = 0.5$. A Re of 1,200 leads to the highest

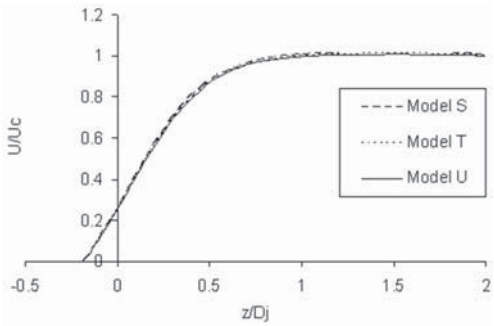

(a) Comparison of centerline velocities from models with different mesh densities

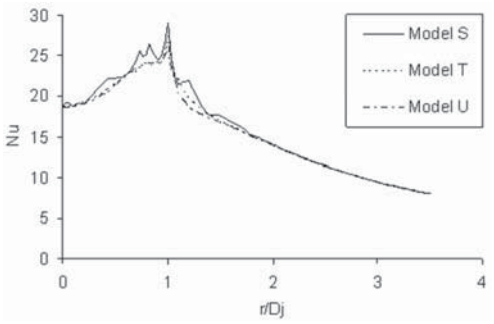

(b) Comparison of local Nus

Fig. 10. Mesh density independence check for dimple impingement: Re = 1,000; $H/D_j = 2$; $d/D_d = 0.15$; $D_j/D_d = 0.5$.

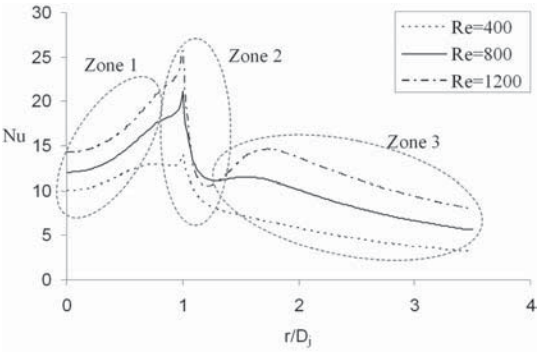

(a) Local Nu distribution divided into three zones

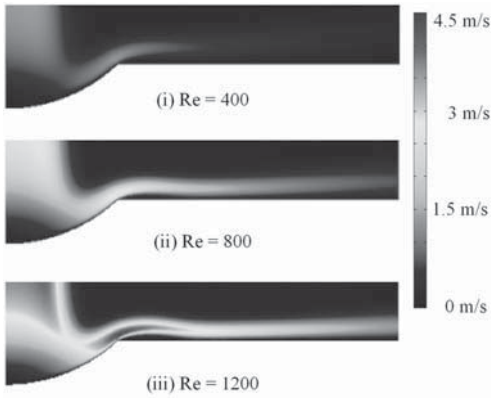

(b) Flow fields of dimple impingement

Fig. 11. Dimple impingement at various Re for $H/D_j = 2$, $d/D_d = 0.2$, and $D_j/D_d = 0.5$.

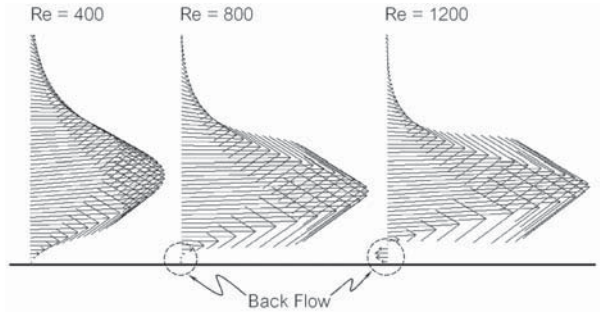

Fig. 12. Velocity profiles for various Re.

heat transfer everywhere, except for the vicinity of the dimple edge where the wall jet begins to form. This is because the oncoming jet with Re = 1,200 carries the highest momentum and thus exchanges that with the target area in the stagnation zone (zone 1). Afterwards, the post-impinging jet accelerates to escape from the indentation toward zone 2. Crossover points are detected in this zone between the Nu plots of Re = 800 and 1,200. This is because the boundary layer flow for Re = 1,200 undergoes adverse pressure gradient earlier and consumes more momentum than that for Re = 800. Therefore, the flow for Re = 1,200 decelerates faster. In addition, close-up velocity profiles on the flat portion next to the dimple in Fig. 12 shows backflow in both cases. Finally, when the wall jet reaches the flat surface (zone 3), Re = 1,200 gives the highest heat transfer, followed by Re = 800 and Re = 400. The flow is similar to a laminar layer flow past a flat plate.

4.4 Effect of jet-to-plate spacing

Fig. 13 presents the local heat transfer distribution for jet impingement on a dimpled plate of $d/D_d = 0.1$ and $D_j/D_d = 0.5$ at Re = 1,200 for various values of jet-to-plate spacing (H/D_j). The curves almost collapse, except at the stagnation region, where $H/D_j = 8$ gives a slightly higher heat transfer result than those of $H/D_j = 2$ and 4. The flow fields in Fig. 18 suggests that the width of the stagnation region represented by the blue color, or the low velocity zone for the case of $H/D_j = 8$, is smaller than the other two cases. Moreover, the jet width upon the target surface for $H/D_j = 8$ is relatively larger because of the expansion of the jet. In addition, because the jet is laminar, it transfers a small amount of momentum to the stagnant surrounding air on its way toward the target surface. In the wall jet zone, the local Nu distribution shows a collapse of all three cases.

4.5 Effect of dimple depth

Dimple depth (d/D_d) remarkably influences heat transfer of the impinging jet on a dimpled plate. This is shown in the plots of local Nus for all tested values of d/D_d for Re = 1,200, $H/D_j = 4$ and $D_j/D_d = 0.5$ (Fig. 14). A significant difference can be observed in the stagnation zone (Zone 1). However, the heat transfer values are similar at the dimple edge. They then decrease in the adjacent flat portions, where backflow is

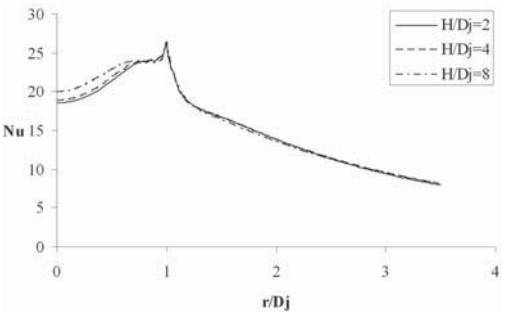

(a) Local Nus

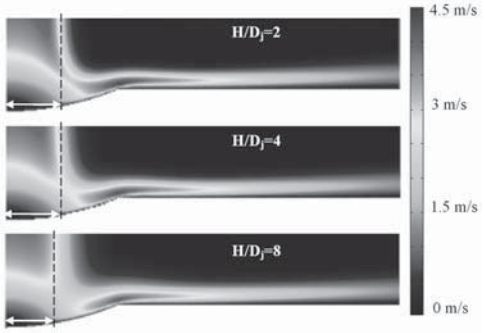

(b) Flow fields

Fig. 13. Dimple impingement at different H/D_j for Re = 1,200, d/D_d = 0.1, and D_j/D_d = 0.5.

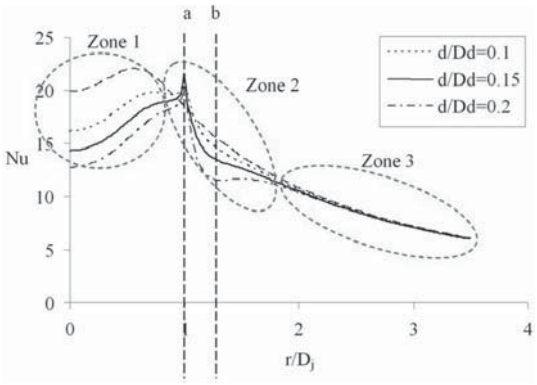

(a) Local Nu distribution zoning

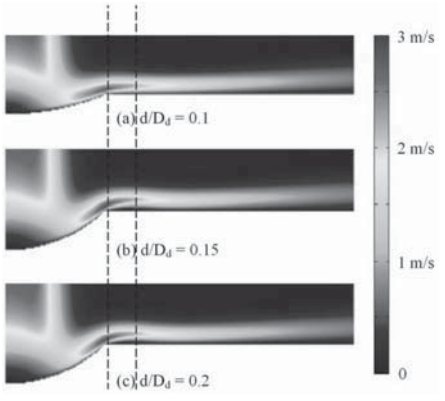

(b) Flow fields

Fig. 14. Comparison of jet impingement on different d/D_d and flat plate for Re = 1,200, H/D_j = 4, and D_j/D_d = 0.5.

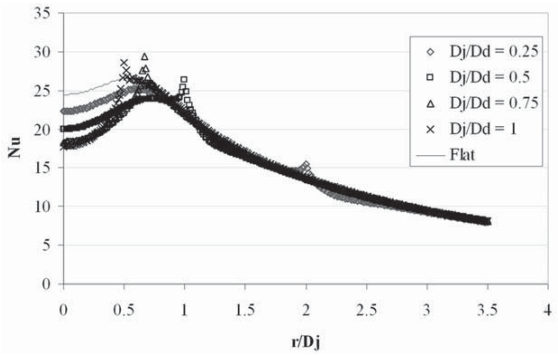

(a) Local Nus for cases of flat plate and dimple impingement

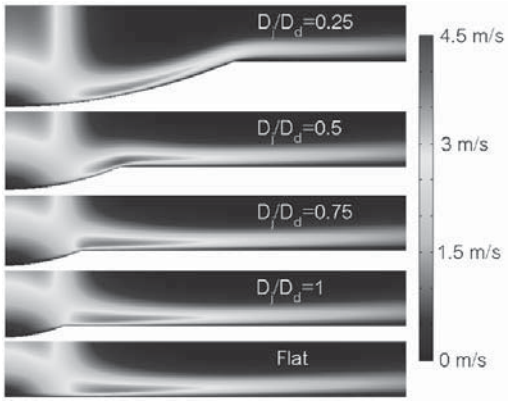

(b) Flow fields

Fig. 15. Local Nu distribution and flow fields for different ratios of jet diameter to dimple projected diameter (D_j/D_d) for Re = 1,200, H/D_j = 8, and d/D_d = 0.1.

acquired. Afterwards, the local heat transfer curves collapse. The deepest dimple of d/D_d = 0.2 gives the lowest heat transfer because of the highest degree of curvature, from which fluid escapes with more difficulty, causing the fluid to lose more momentum. Hence, a higher degree of flow separation occurs at the deeper dimple. The average Nus for d/D_d = 0 (flat plate), 0.1, 0.15, and 0.2 are 16.633466, 15.568294, 14.785281, and 13.427107, respectively.

4.6 Effect of ratio of jet diameter to dimple projected diameter

The tested ratios of jet diameter to dimple projected diameter are 0.25, 0.5, 0.75, and 1.0, measured by varying D_d and fixing D_j at 5 mm. The heat transfer results in Fig. 15(a) show a strong influence of D_j/D_d, especially in the stagnation zone. The figure also presents a comparison with the flat plate impingement. For all four values of D_j/D_d, the curves can be grouped into two shapes. The first group resembles that of the flat plate, except where the dimple edge appears: D_j/D_d = 0.25 and 0.5. Also, the oncoming jet impinges entirely inside the dimple. The second group is for those where the stagnation zone covers the entire dimple: D_j/D_d = 0.75 and 1.

Considering group 1 (impingement inside the dimple), even though the local heat transfer curve shapes of $D_j/D_d = 0.25$ and 0.5 are similar to that of the flat plate, the levels of heat transfer are less. A remarkable difference in the result is found at the dimple edge position, where the local heat transfer jumps. Because the dimple edge for $D_j/D_d = 0.5$ appears earlier than that for $D_j/D_d = 0.25$, the jump occurs earlier in the high-velocity zone, as shown by its flow field in Fig. 15(b), causing high loss in momentum. In contrast, the dimple edge of $D_j/D_d = 0.25$ occurs in the low-momentum zone as displayed in the yellowish region in the flow field. Thus, its jet loses less momentum than $D_j/D_d = 0.5$.

Group 2 represents the case of the impingement zone covering the entire dimple, and this occurs to the impingement on $D_j/D_d = 0.75$ and 1. As aforementioned, presence of the dimple edge causes heat transfer reduction compared to transfer on the flat plate because the fluid attempts to escape from the curvature. Significant heat transfer reduction occurs in the stagnation zone. After jumping at the dimple edge, the local heat transfer curve collapses to that of the flat plate heat transfer.

5. Conclusions

This study uses the commercial software package called COMSOL that uese a finite element method to process the flow and heat transfer problems of an axi-symmetric laminar jet impinging on a flat and a dimpled surface. The work is divided into two main parts: (1) validation of the software against the experimental results obtained from literature and (2) investigation of parametric effects on dimple impingement.

For the validation, only results from flat plate impingement were compared to the experimental and computational results obtained from literature. The effect of mesh density dependency was closely examined. Mesh density does not affect heat transfer and flow problems. However, the mesh densities that help save computational memory and time were selected. Experimental and computational results obtained from literature were compared with those from the current investigation, and a good agreement was found.

Various parametric effects of dimple impingement were considered, such as Re, H/D_j, d/D_d, and the ratio of dimple projected diameter and jet diameter (D_j/D_d):

The Re significantly affects heat transfer of the dimple impingement. An oncoming jet with higher Re carries a higher amount of momentum, so the stagnation heat transfer is higher.

H/D_j does not significantly affect heat transfer because the oncoming viscous laminar jet exchanges a small amount of momentum with the ambient air before impinging on the target plate.

A deeper dimple presents a decrease in heat transfer because the dimple possesses a higher degree of curvature, as well as a larger wetted area. The larger wetted area, thus, leads to less momentum flux.

When considering the influence of D_j/D_d, heat transfer results can be divided into two groups: (1) jet impinging within the dimple and (2) impinging jet covering the dimple. The first case has a similar local Nu distribution trend as that of the flat plate, except where the dimple is present, at which point mild heat transfer reduction is found. The second group gives a higher degree of heat transfer reduction, which occurs at the indentation.

Finally, heat transfer results of dimple impingement were compared to those of flat plate impingement. Heat transfer reduction occurs in the vicinity of the indentation and the dimple edge. The flow fields show that the dimple edge lifts the post-impinging jet, and backflow is found in some cases of dimple impingement. Thus, the presence of a dimple causes overall heat transfer reduction to a laminar impinging jet.

Acknowledgements

This research is financially supported by the Thailand Research Fund (TRF), whose guidance and assistance are gratefully acknowledged. The authors thank Dr. Markus Huebscher for providing relevant documents. In addition, the third author would like to thank King Mongkut's University of Technology Thonburi and the Office of the Higher Education Commission for their support.

Nomenclature

d : Dimple depth, m
g : Gravitation acceleration, m/s^2
h : Heat transfer coefficient
k : Jet thermal conductivity
l : Nozzle length, m
p : Pressure, Pa
q" : Heat flux, W/m^2
r : Radial direction
v : Velocity, m/s
z : Axial direction
A : Area of an element
D : Diameter, m
H : Distance between nozzle exit and target plate (flat portion level for dimpled plate)/Interpolation function for pressure
L : Area coordinates of an element
N : Interpolation function for velocities
Nu : Nusselt number, $\frac{hD_j}{k}$
Re : Reynolds number, $\frac{\rho UD_j}{\mu}$
S : Nozzle thickness, m
W : Interpolation function for temperature

Subscripts

c : Centerline
d : Dimple plate

i : Index for node in an element
j : Jet
s : Of surface

Greek symbols

ϕ : Basis function
μ : Jet viscosity
ρ : Jet density

References

[1] J. M. Bergthorson, K. Sone, T. W. Mattner, P. E. Dimotakis, D. G. Goodwin and D. I. Meiron, Impinging laminar jets at moderate Reynolds numbers and separation distances. *Phy. Rev. E*, 72 (6) (2005) 066307-1-12.

[2] M. E. Angioletti, E. Nino and G. Ruocco, CFD turbulent modelling of jet impingement and its validation by particle image velocimetry and mass transfer measurements, *Int. J. Ther.* Sc. 44 (2005) 349-356.

[3] H. Chattopadhyay, Numerical investigations of heat transfer from impinging annular jet, *Int. J. Heat Mass* 47 (2004) 3197-3201.

[4] L. B. Y. Aldabbagh and I. Sezai, Three-dimensional numerical simulation of an array of impinging laminar square jets with spent fluid removal, *Int. J. Ther. Sc.* 43 (2004) 241-247.

[5] Gm., S. Azad, Y. Huang and J. Han, Impingement heat transfer on dimpled surfaces using a transient liquid crystal technique, *J. Thermophy Heat Tran.* 14 (2000) 186-193.

[6] S. V. Ekkad and D. Controvitz, Jet impingement heat transfer on dimpled target surfaces, *Int. J. Heat Fluid Flow,* 23 (2002) 22-28.

[7] K. Kanokjaruvijit and R. F. Martinez-Botas, Jet impingement on a dimpled surface with different crossflow schemes, *Int. J. Heat Mass Tran.* 48 (2004) 161-170.

[8] K. Kanokjaruvijit and R. F. Martinez-Botas, Parametric effects of heat transfer of impingement on dimpled surface, *J. Turbomach.* 127 (2005) 287-296.

[9] K. Kanokjaruvijit and R. F. Martinez-Botas, Heat Transfer and pressure investigation of dimple impingement, *J. Turbomach.* 130 (2008) 011003-1-9.

[10] M. J. Fagan, Finite element analysis: theory and practice, Prentice Hall, New Jersey, (1992).

[11] P. Decha-ampai, Finite element method for fluid dynamics (in Thai), Chulalongkorn Press, Bangkok, Thailand, (2002).

[12] S. Polat, B. Huang, A. S. Mujumdar and W. J. M. Douglas, Numerical flow and heat transfer under impinging jets: a review, Annual review of Numerical Fluid Mechanics and Heat Transfer, 2 (1989) 157-197.

Koonlaya Kanokjaruvijit received her PhD in Mechanical Engineering from Imperial College London, UK in 2004. She is now an assistant professor at Naresuan University, Phitsanulok Thailand. Her research interests include design of cooling schemes in gas turbine engine and hemodynamics

Chakkraphan Thawonngamyingsakul is a lecturer in the Department of Mechanical Engineering, Rajamangala University of Technology Lanna Tak, Thailand. He received his MEng in Mechanical Engineering from Naresuan University, Thailand in 2007. His research is in thermal system design and heat transfer enhancement. He is currently pursuing a PhD in Energy Engineering at Chiengmai University, Thailand.

Somchai Wongwises is currently a Professor of Mechanical Engineering at King Mongkut's University of Technology Thonburi, Bangmod, Thailand. He received his Doktor Ingenieur (Dr.-Ing.) in Mechanical Engineering from the University of Hannover, Germany, in 1994. His research interests include Gas-Liquid Two-Phase Flow, Heat Transfer Enhancement, and Thermal System Design. Professor Wongwises is the head of the Fluid Mechanics, Thermal Engineering and Multiphase Flow Research Laboratory (FUTURE).

Experimental Thermal and Fluid Science 34 (2010) 1217–1229

Contents lists available at ScienceDirect

Experimental Thermal and Fluid Science

journal homepage: www.elsevier.com/locate/etfs

Two-phase gas–liquid flow characteristics inside a plate heat exchanger

Kitti Nilpueng [a], Somchai Wongwises [b,*]

[a] Department of Mechanical Engineering, South East Asia University, Bangkok 10160, Thailand
[b] Fluid Mechanics, Thermal Engineering and Multiphase Flow Research Lab (FUTURE), Department of Mechanical Engineering, King Mongkut's University of Technology Thonburi, Bangmod, Bangkok 10140, Thailand

ARTICLE INFO

Article history:
Received 16 November 2009
Received in revised form 6 May 2010
Accepted 6 May 2010

Keywords:
Flow pattern
Pressure drop
Corrugated channel
Two-phase multiplier

ABSTRACT

In the present study, the air–water two-phase flow characteristics including flow pattern and pressure drop inside a plate heat exchanger are experimentally investigated. A plate heat exchanger with single pass under the condition of counter flow is operated for the experiment. Three stainless steel commercial plates with a corrugated sinusoidal shape of unsymmetrical chevron angles of 55° and 10° are utilized for the pressure drop measurement. A transparent plate having the same configuration as the stainless steel plates is cast and used as a cover plate in order to observe the flow pattern inside the plate heat exchanger. The air–water mixture flow which is used as a cold stream is tested in vertical downward and upward flow. The results from the present experiment show that the annular-liquid bridge flow pattern appeared in both upward and downward flows. However, the bubbly flow pattern and the slug flow pattern are only found in upward flow and downward flow, respectively. The variation of the water and air velocity has a significant effect on the two-phase pressure drop. Based on the present data, a two-phase multiplier correlation is proposed for practical application.

© 2010 Elsevier Inc. All rights reserved.

1. Introduction

Plate heat exchangers have been utilized in several engineering applications including food processing, chemical processes, and cooling systems of various types of equipment, for example the evaporator and condenser in refrigeration and air conditioning systems. The main advantages of using a plate heat exchanger are high efficiency, compactness, and ease of inspection and cleaning. Because the plate heat exchanger is mostly used for liquid–liquid flow, the single-phase flow characteristics inside the plate heat exchanger have been widely studied and reported in open literature.

It is not possible to understand the two-phase thermohydraulics without a clear understanding of the flow patterns encountered, as it is expected that the flow patterns will influence the two-phase pressure drop, holdup, system stability, exchange rates of momentum, and the heat and mass transfer during the phase change. Therefore, in order to achieve the high heat transfer rate and low pressure drop condition, knowledge of two-phase flow pattern inside the plate heat exchanger is necessary. Up to now, there have been only the following few studies investigating two-phase flow inside a plate heat exchanger.

Rush et al. [1] studied the local heat transfer and flow behavior inside sinusoidal wavy passages under laminar and transition flow. The test section was a horizontal channel having an aspect ratio of 10:1 and bound by two wavy walls. They paid special attention to the onset of macroscopic mixing in both the steady and unsteady flows. The results showed that the location of the onset of macroscopic mixing was dependent on the channel geometry and the Reynolds number, and the onset of mixing corresponded to the increase of the heat transfer.

Vlasogiannis et al. [2] investigated the flow pattern and heat transfer coefficient of air–water two-phase flow in a plate heat exchanger. The test section used in the study was the Alfa-Laval P-01. The plate having a length of 0.43 m and a width of 0.123 m was used in the experiment. The corrugation form of plate was a herringbone pattern with an angle of 60° relative to the direction of flow. The test runs were performed at superficial liquid velocity ranging between 0.01 and 0.25 m/s and superficial liquid velocity ranging between 0.3 and 10 m/s. They reported that the flow regime with a gas continuous phase covering the core of the channel and liquid flowing in the form of rivulets inside the furrows showed particularly favorable heat transfer characteristics.

Hsieh et al. [3] experimentally studied the subcooled flow boiling heat transfer characteristics of HFC-134a in a vertical plate heat exchanger. The effects of the boiling heat flux, refrigerant mass flux, system pressure and inlet subcooling were reported. The results showed that the mass flux of the refrigerant has a significant effect on the subcooled boiling heat transfer coefficient. However, the increase of the inlet subcooling and saturation temperature resulted in only a slight change of the boiling heat transfer coeffi-

* Corresponding author. Tel.: +66 2 470 9115; fax: +66 2 470 9111.
E-mail address: somchai.won@kmutt.ac.th (S. Wongwises).

0894-1777/$ - see front matter © 2010 Elsevier Inc. All rights reserved.
doi:10.1016/j.expthermflusci.2010.05.001

Nomenclature

A	flow area of channel (m^2)
b_c	mean spacing between plates (m)
C	Chisholm's factor
D_h	hydraulic diameter (m)
dP_A	accelerational pressure drop (Pa)
dP_F	frictional pressure drop (Pa)
dP_G	gravitational pressure drop (Pa)
dP_M	pressure loss at the entry and exit (Pa)
dP_T	total pressure drop (Pa)
dP_F/dz	frictional pressure gradient (Pa/m)
f	friction factor
G	mass flux (kg/m^2 s)
g	gravitational acceleration (m/s^2)
J_G	superficial gas velocity (m/s)
J_L	superficial liquid velocity (m/s)
L	length between the centres of entry and exit tubes (m)
N	the number of channels per a stream
Q_G	volumetric flow rate of gas (m^3/s)
Q_L	volumetric flow rate of liquid (m^3/s)
Re	Reynolds number
V	velocity of fluid (m/s)
w	plate width inside gasket (m)
X	Martinelli parameter

Greek symbols

Δx	total quality change in the exchanger
υ	specific volume (m^3/kg)
υ_f	specific volume of liquid phase (m^3/kg)
υ_m	average specific volume (m^3/kg)
υ_{fg}	difference of specific volume between gas and liquid phase (m^3/kg)
μ	viscosity (N s/m^2)
ρ	density (kg/m^3)
ϕ_L	two-phase frictional multiplier based on liquid flow alone

Subscripts

L	liquid-phase
G	gas-phase
TP	two-phase

cient. The visual results showed that the frequency of bubble generation was substantially higher when increasing the heat flux.

Hsieh and Lin [4] investigated the saturated flow boiling heat transfer and frictional pressure drop of HFC-410A in a vertical plate heat exchanger. They reported that both the pressure drop and the heat transfer coefficient increase with increasing heat flux. The saturated flow boiling heat transfer coefficient was significantly affected by the refrigerant mass flux only at high heat flux. An empirical correlation for saturated flow boiling heat transfer coefficient and friction factor were proposed as a function of Boiling number and equivalent Reynolds number.

Shiomi et al. [5] presented the experimental results of liquid single- phase flow and gas–liquid two-phase flow in channels formed by chevron plates. Four combinations of corrugation angle which were 30–30°, 30–60°, 60–30°, and 60–60° were used in the experiments. They found that stratified flow and dispersed flow were observed for horizontal orientation and only dispersed flow was observed for vertical orientation.

Metwally and Manglik [6] investigated the single-phase heat transfer in the sinusoidal corrugated-plate channels with the corrugation aspect ratio ranging between 0 and 1. The control-volume finite-difference method is used to calculate the temperature distribution, local wall heat flux and Nusselt number. The results showed that the flow field is strongly influenced by the corrugation aspect ratio and Reynolds number. It was also found that the heat transfer was enhanced by the mixing of fluid produced by transverse vortices.

Kuo et al. [7] experimentally investigated the heat transfer and frictional pressure drop of HFC-410A in a vertical plate heat exchanger. Three plates of commercial geometry with a corrugated sinusoidal shape and a chevron angle of 60° were used as the test section. They stated that the condensation heat transfer coefficient and frictional pressure drop increased almost linearly with the mean vapor quality, but the system pressure only exhibited a rather slight effect.

Nilpueng and Wongwises [8] experimentally investigated the flow patterns and pressure drop of upward liquid single-phase flow and air–water two-phase flow in sinusoidal wavy channels. Different phase shifts between the side walls of the wavy channel of 0°, 90° and 180° are investigated. The slug flow pattern was only found in the test sections with phase shifts of 0° and 90°. Recirculating gas bubbles were always found in the troughs of the corrugations. The recirculating was higher when the phase shifts were larger.

Longo and Gasparella [9–11] presented heat transfer coefficients and pressure drop measured during vaporization of HFC-134a, HFC-410A, and HFC-236fa inside a small brazed plate heat exchanger. The effect of relevant parameters including heat flux, refrigerant mass flux, saturation temperature and outlet conditions on the heat transfer coefficients and pressure drop were investigated. They found that the heat transfer coefficients showed high sensitivity to the heat flux and outlet conditions and showed weak sensitivity to the saturation temperature. The frictional pressure drop varied in direct proportion to the kinetic energy per unit volume.

The heat transfer and flow characteristic, including Nusselt number, pressure drop, and thermal performance factor in a furrowed channel with transverse and skewed sinusoidal wavy wall were studied by Chang et al. [12]. The steady-state infrared thermo-graphic method was used to measure the heat transfer over the sinusoidal wavy wall. They reported that the heat transfer performance obtained from the skewed wavy wall was higher than those obtained from the transverse wavy wall.

Longo [13] experimentally investigated the heat transfer coefficients and pressure drop during condensation of HFC-410A inside a plate heat exchanger. The effects of saturation temperature, refrigerant mass flux and vapor super-heating on the heat transfer coefficients and pressure drop were reported. The experimental results indicated that at low mass fluxes there is no dependence, while at higher mass flux there is.

As mentioned above, it is found that most of previous studies were concentrated on the plate heat exchangers with symmetrical chevron angles such as 45–45° and 60–60°. Experimental data of two-phase flow characteristics inside a plate heat exchanger with the unsymmetrical chevron angle plate is still lacking, especially, the plate SWEP GX-7 which is commonly used in the commercial applications. In this paper, the main concern is to study the two-phase flow characteristics, i.e. the flow pattern and the pressure drop inside a commercial unsymmetrical plate heat exchanger. A two-phase multiplier correlation for predicting the two-phase pressure drop is also proposed.

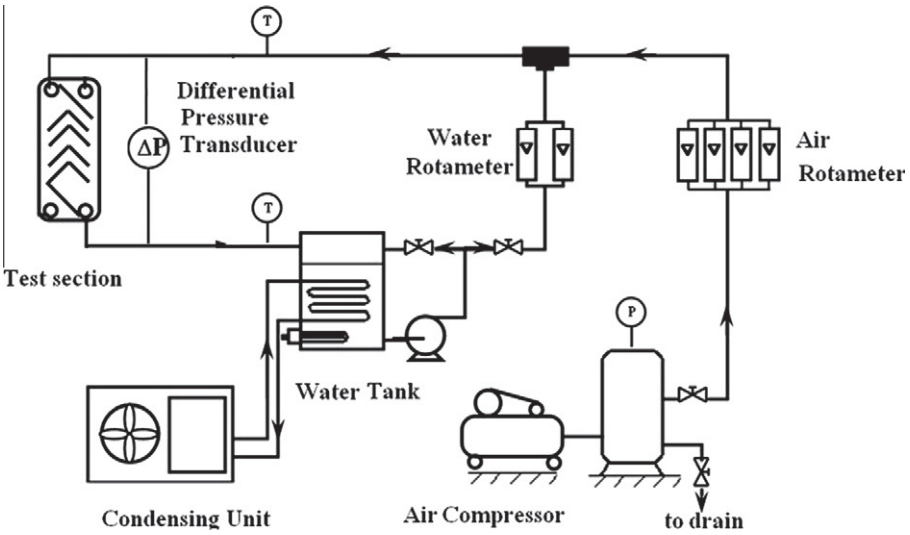

Fig. 1. Schematic diagram of experimental apparatus.

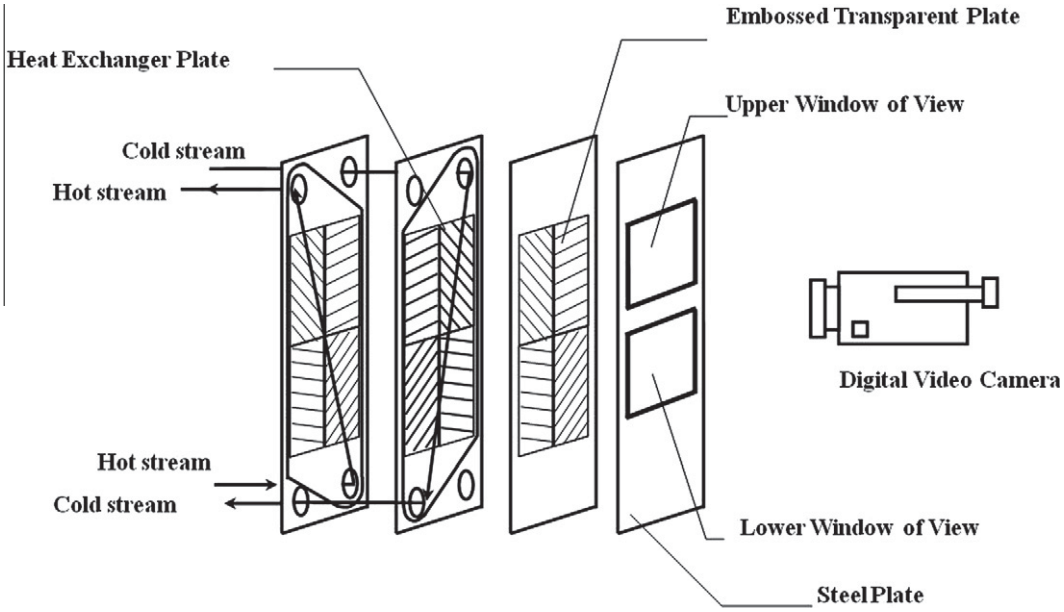

Fig. 2. Schematic diagram of test section.

2. Experimental apparatus

A schematic diagram of the test facility is shown in Fig. 1. The main components of the system are a test section, a hot stream loop, and a cold stream loop. A plate heat exchanger with single pass under the condition of counter flow is operated in this experiment (Fig. 2). The cold stream is the air–water mixture while the hot stream is water. Three stainless steel commercial plates with a corrugated sinusoidal shape with unsymmetrical chevron angles of 55° and 10° are utilized for the pressure drop measurement. The physical configuration of a plate is shown in Fig. 3. The main dimensions of the plates are presented in Table 1. In order to observe the flow pattern of air–water two-phase flow inside the plate heat exchanger, a transparent plate having the same configuration as the stainless steel plates is cast and used as a cover plate. The material of transparent plate is polyurethane resin. The plate thickness is 30 mm. In addition, it is attached by a plain steel plate with a viewing window.

In the cold stream loop, the high pressure air is sent into the system through the air pressure regulator to control the stability of pressure. The cold water temperature is controlled by the refrigeration system together with the electric heater. The cold water is mixed with the air in a T-joint; this is used as the mixture and then passed through the test section co-currently. The hot water which is heated by the electric heater is pumped from a storage tank through the rotameter and the test section. The surplus water is sent back to the storage tank through the control valve. In this experiment, vertical upward and downward flow directions are used for the cold streams. The air flow rate is increased by small increments while the water flow rate is kept constant at a pre-selected value. The system is allowed to approach steady conditions before the air and water flow rates, flow pattern, and pressure drop are recorded. The air flow rate is measured by four sets of rotameters within the ranges 0.2–2, 2–5, 2–20, and 20–200 CFH, respectively. The flow rates of water are measured by two sets of rotameters within the ranges 0.4–4 and 2–20 LPM, respectively.

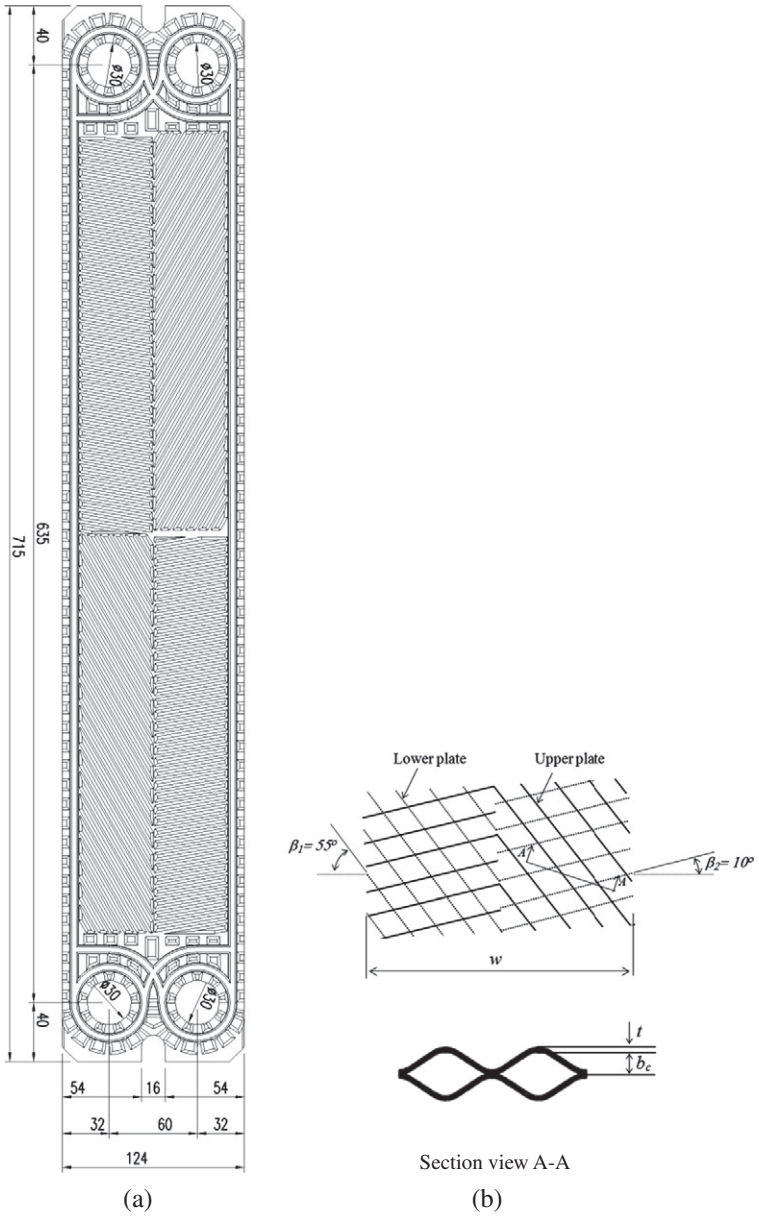

Fig. 3. Schematic diagram of heat exchanger plate.

Table 1
Dimensions of a heat exchanger plate.

Parameters	Dimension
Plate length, m	0.715
Plate width, m	0.124
Mean spacing between plates (b_c), m	0.0025
Plate sheet thickness (t), m	0.0005
Port-to-port length, m	0.635
Port diameter, m	0.03
Plate width inside gasket (w), m	0.1
Heat transfer area per plate, m^2	0.07

The accuracy of the air and water volumetric flow rates is ±2%. A T-type thermocouple is utilized to measure the fluid temperature. The uncertainty of temperature measurements is ±0.1 °C. A differential pressure transducer (YOKOGAWA, EJA110A) is installed in the test section between inlet and outlet port in order to measure the pressure drop across the test section. The transducer had an accuracy of ±0.1% of its calibrated span. The refrigerant flow pattern inside the short-tube orifice is registered by a digital camera (Sumsung DigimaxV3) with a shutter speed of 1/2000 s.

3. Results and discussion

3.1. Flow patterns

The identification of two-phase flow pattern is reported in terms of superficial gas and liquid velocities which are calculated from the following equations:

$$J_G = \frac{Q_G}{A} \tag{1}$$

$$J_L = \frac{Q_L}{A} \tag{2}$$

where Q_G is volumetric flow rate of gas (m^3/s), Q_L is volumetric flow rate of liquid (m^3/s) and A is average cross-sectional flow area (m^2) which can be determined from

$$A = wb_cN \quad (3)$$

where w is the plate width inside the gasket (m), b_c is the mean spacing between plates (m) and N is the number of channels per a stream.

Observation of two-phase air–water flow patterns inside the plate heat exchanger can be done through a digital camera and digital video camera. Examples of photos and sketch drawings are used to explain the flow patterns. The flow pattern at the side view cannot be seen directly from the transparent plate, but it is analyzed and sketched based on the optical visualization, still images and animated images. In this study, the results of two-phase air–water flow can be divided into two directions: vertical upward flow and vertical downward flow.

3.1.1. Flow patterns for vertical upward flow

3.1.1.1. Bubbly flow. This flow pattern contains air bubbles of indefinite size and shape together with water that fills the flow channel. The directions of air bubble flow could be divided into two directions at the same time. The first direction is along the corrugation trough of the heat exchanger plate which has a corrugation angle of 55°. Air bubbles move upward and downward according to features of the wavy flow channel. The second direction is upward flow through the spacing in between plates, as shown in Fig. 4. The reason for the certain directions of the bubble may be because the flow resistance in the spacing between plate and the trough which has corrugation angle 55° is less than the flow resistance in the trough which has corrugation angle 10°.

3.1.1.2. Bubble recirculation flow. This flow pattern continues from the bubbly flow. When the air flow rate increases, it is found that the bubble flow velocity in the upward direction through the spacing between plates increases. This causes an increase of interfacial shear between bubbles flowing in the middle of the channel and those in the trough region which results in the recirculation flow of bubbles in the trough. Therefore, the air bubbles are spun between the troughs along the corrugation angle of 55° (Fig. 5). The size of air bubbles decreases due to collisions of large air bubbles and collisions between air bubbles and contact point.

3.1.1.3. Annular-liquid bridge flow. In this flow pattern, a thin water film is present on the whole surface while the air flows between the water films. However, it is found that some part of the water forms liquid bridges which will spin from the corrugation crests of the heat exchanger plate (10°) to the trough on the other side of the channel (55°), as shown by photos and sketch drawings in Fig. 6. This pattern appears as the small bubbles which flow at the trough and those at the spacing in between plates are combined. As a result, the air flow covers at the middle of the flow channel and a liquid film exists at the plate surface. Due to the shear stress between the air and liquid film, some part of the water

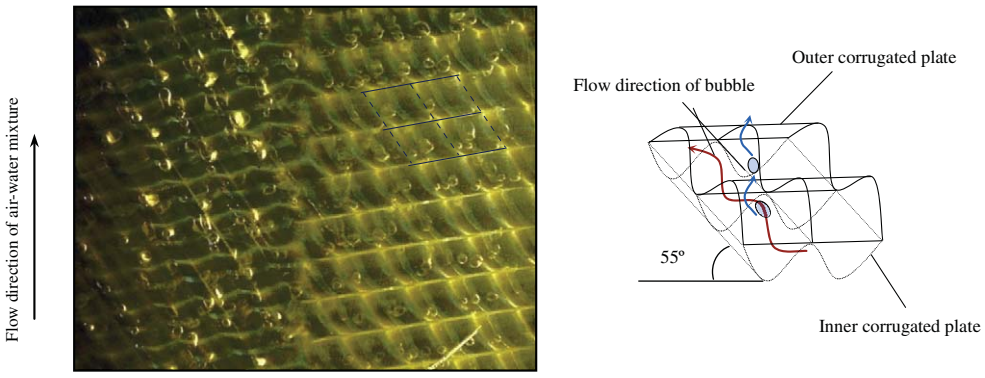

Fig. 4. Bubbly flow at J_L = 0.196 m/s and J_G = 0.126 m/s.

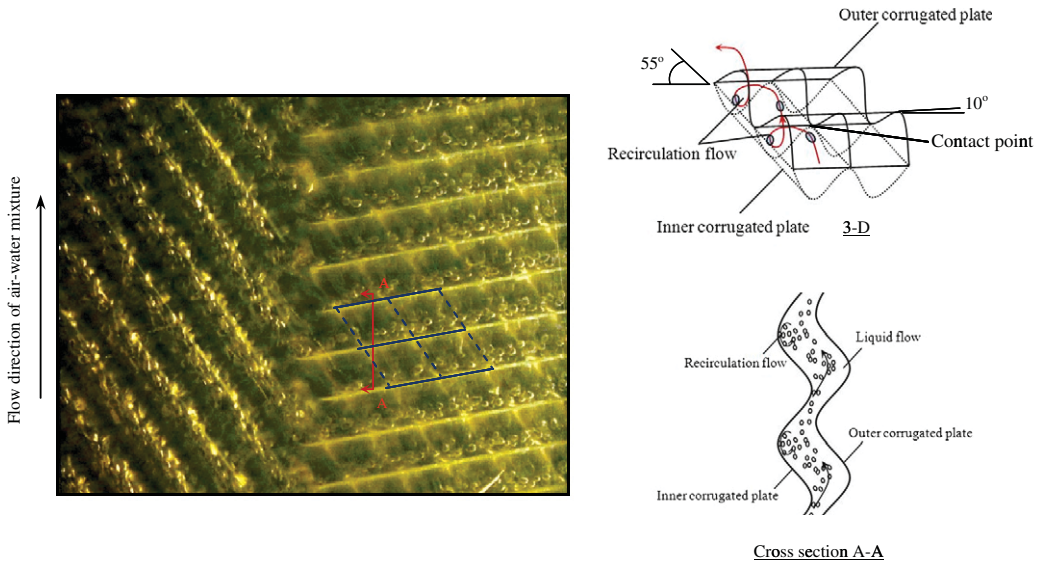

Fig. 5. Bubble recirculation flow at J_L = 0.131 m/s and J_G = 0.252 m/s.

film is spun from a trough (10°) on one side to a trough (55°) on the other side of the channel. The flow behavior of the liquid film may be because the water film thickness at the trough is high when the corrugation angle is low. Conversely, it is found that the water film thickness is very low as corrugation angle is high. Therefore, in general, the thick liquid film from the trough with a corrugation angle of 10° is transported by shear forces from the upward air flow from one side to other side of the channel.

3.1.2. Flow patterns for vertical downward flow

3.1.2.1. Slug flow. This flow pattern is similar to a slug flow in a circular tube; that is, alternating full water flow and air flow in the flow channel. In Fig. 7a, a dashed line represents the interfacial surface between air flow (lower part of the figure) and water (upper part of the figure). A water-only full-channel flow occurs at $t = 0.8$ s (Fig. 7b) while the flow of air and water occurs at $t = 1.36$ s (Fig. 7c). Fig. 7d shows air-only full-channel flow.

3.1.2.2. Annular-liquid bridge flow/air-alone flow. The flow that occurs inside the channel could be divided into two flow patterns. It is found that air-alone flow occurs on the left side of the heat exchanger plate. This may be because the dispersion of water is low when the liquid flow rate is low. In other areas, however, there is a water-film flow between both heat exchanger plates, with air flow in the middle of the flow channel. Some parts of the water are spun from corrugation crests of the heat exchanger plate which has a corrugation angle of 10° to the corrugation trough of the heat ex-

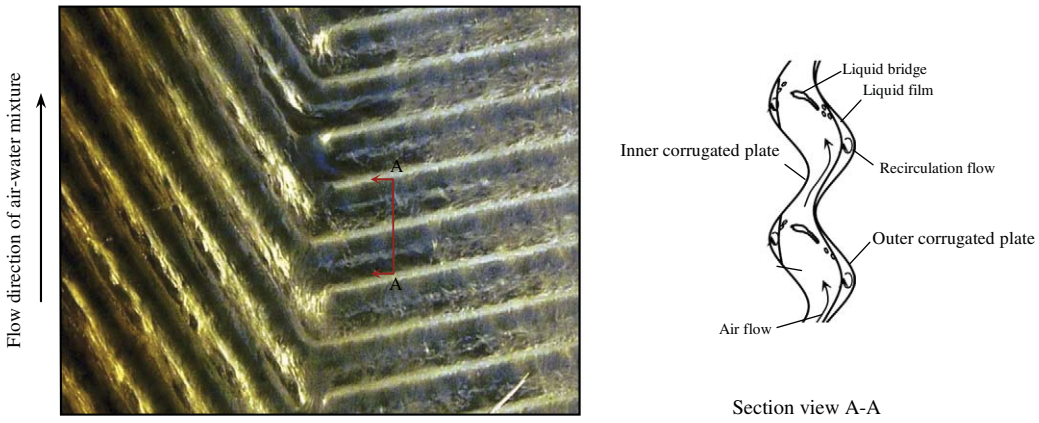

Fig. 6. Annular-liquid bridge flow at $J_L = 0.11$ m/s and $J_G = 1.573$ m/s.

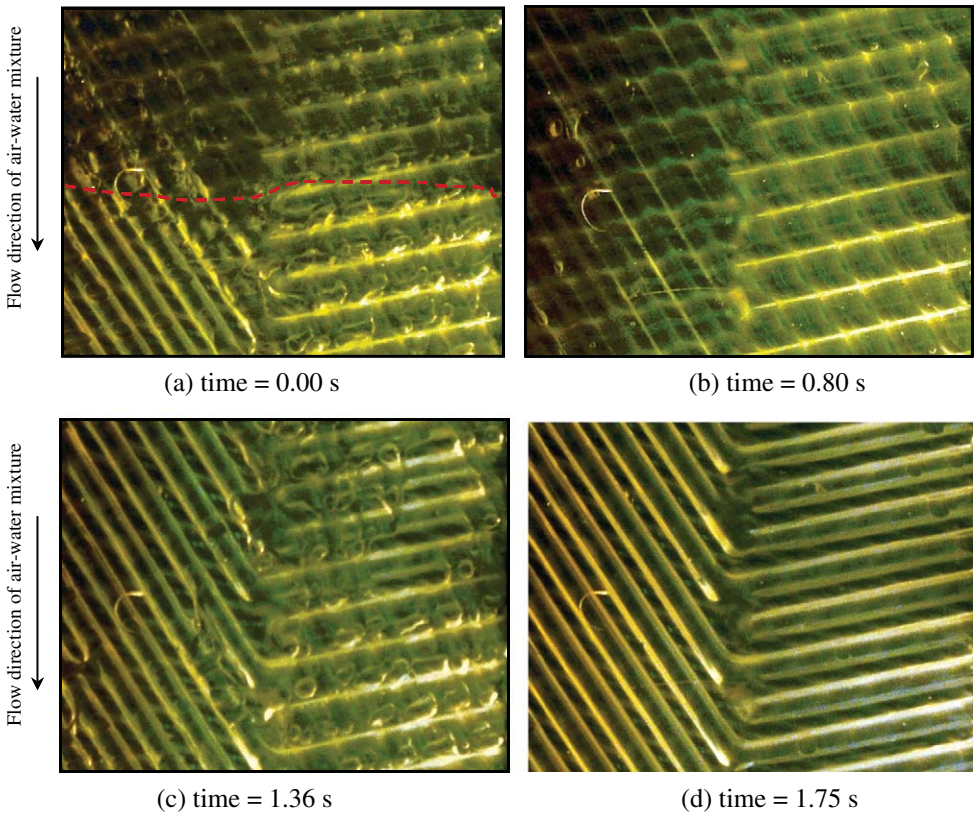

Fig. 7. Slug flow at $J_L = 0.18$ m/s and $J_G = 0.252$ m/s.

changer plate which has a corrugation angle of 55°, as shown in Fig. 8. The reason for this is similar to the one as described above.

3.1.2.3. Annular-liquid bridge flow. This flow pattern continues from the annular-liquid bridge flow/air-alone flow. When the velocity of water increases, water film covers the surface of the whole heat exchanger plate. This means that the occurrence of air-alone flow on the left side of heat exchanger plate has disappeared and the annular-liquid bridge flow covers the entire heat exchanger plate, as shown by photos and sketch drawings in Fig. 9.

In this study, a map of two-phase flow patterns in vertical upward and vertical downward directions is presented. Fig. 10 shows a map of the vertical upward two-phase flow pattern. In this figure, lines inside the graph show the scope of flow pattern inside the flow channel. The results of the study indicate that at a certain water velocity, an increase in air causes the flow pattern to change from bubbly flow to bubble recirculation flow and annular-liquid bridge flow, respectively. Actually, due to the uncertainty at the vicinity of the transitions between flow patterns, the flow patterns do not change suddenly. Therefore, the transition lines should be represented as broad transition bands. From the map of the vertical downward flow pattern in Fig. 11, it can be seen that annular-liquid bridge flow/air-alone flow occurs at a low velocity of water throughout the velocity continuum of air, whereas the annular-liquid bridge flow occurs at a high velocity of water and air. Considering, the study on two-phase flow in a circular tube, Collier [14] reported that the flow patterns in the case of phase change process and the adiabatic two-phase flow at the same flow condition are similar. Therefore, at the same superficial gas and liquid velocity, the flow pattern maps obtained from this study are expected to be usable for phase change processes as well.

3.2. Pressure drop

3.2.1. Single-phase pressure drop

This section discusses frictional pressure drop (dP_F) and friction factors of water flow through the heat exchanger. The frictional pressure drop inside the plate heat exchanger could be calculated by subtracting the gravitational pressure drop (dP_G) and pressure loss at the entry and exit of the test unit (dP_M) from total pressure drop (dP_T) as in the formula below:

$$dP_F = dP_T \pm dP_G - dP_M \tag{4}$$

The gravitational pressure drop could be calculated from the formula:

$$dP_G = \pm \frac{gL}{\upsilon} \tag{5}$$

where L is length between the centres of entry and exit tubes (m), υ is specific volume of liquid (m^3/kg), g is gravitational acceleration (m/s^2).

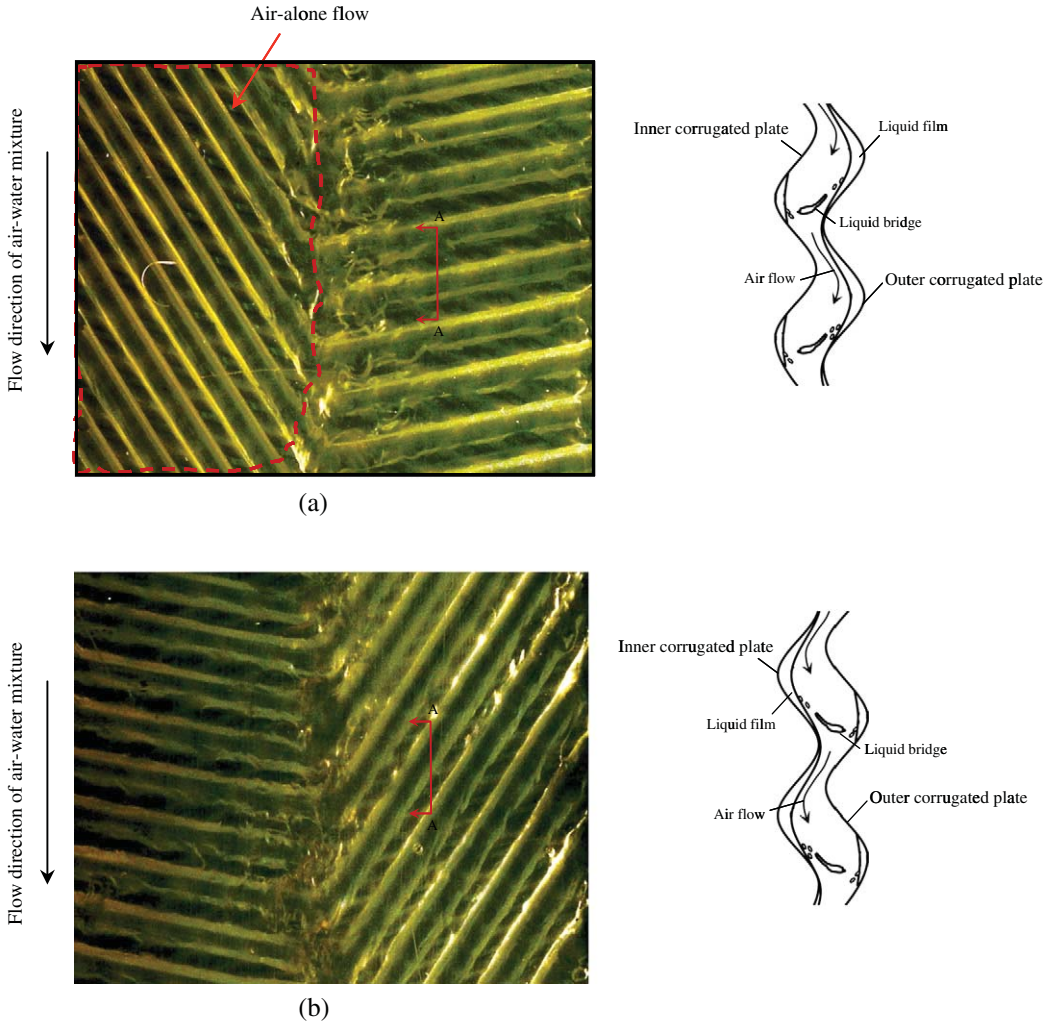

Fig. 8. Annular-liquid bridge flow/air-alone flow at J_L = 0.066 m/s and J_G = 0.944 m/s. (a) Upper window of view and (b) lower window of view.

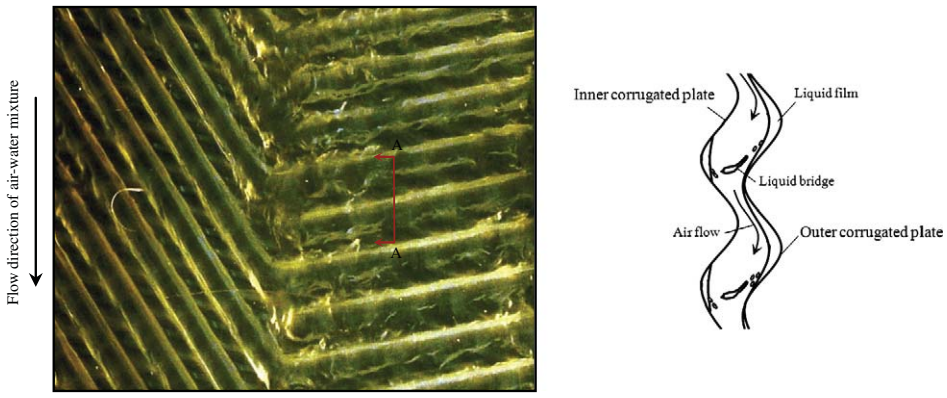

Fig. 9. Annular-liquid bridge flow at J_L = 0.18 m/s and J_G = 2.52 m/s.

The plus sign (+) is used in the case of vertical downward flow while the minus sign (−) is used in the case of vertical upward flow.

Pressure loss at the entry and exit of the heat exchanger could be calculated from a correlation of Shah and Focke [15].

$$dP_M \cong 1.5\left(\frac{V^2}{2\upsilon}\right) \tag{6}$$

where V is the velocity of liquid (m/s).

The friction factor could be calculated from the formula:

$$f = \frac{dP_F}{4\left(\frac{L}{D_h}\frac{V^2}{2}\rho_L\right)} \tag{7}$$

The Reynolds number of water is calculated from the following equations

$$\mathrm{Re} = \frac{\rho V D_h}{\mu} \tag{8}$$

where ρ is density of water (kg/m^3), μ is viscosity (Pa s), V is velocity of water (m/s)and D_h is hydraulic diameter (m). The properties of fluid are calculated based on the average fluid temperature at the inlet and outlet of plate heat exchanger.

Hydraulic diameter could be calculated from the formula:

$$D_h = \frac{2wb_c}{w + b_c} \approx 2b_c \tag{9}$$

For the calculation of the single phase friction factor, the properties of substance are calculated based on the average temperature between the inlet and outlet temperature. The average uncertainties of single phase friction factor are ±0.186 and ±16.1% for the absolute uncertainty and relative uncertainty, respectively. Fig. 12 shows a relationship between friction factors and Reynolds numbers. As expected, friction factors decrease when the Reynolds number increases. Moreover, friction factors gained from this study are compared with the friction factor formula of laminar flow inside a smooth tube and a flow through a plate heat

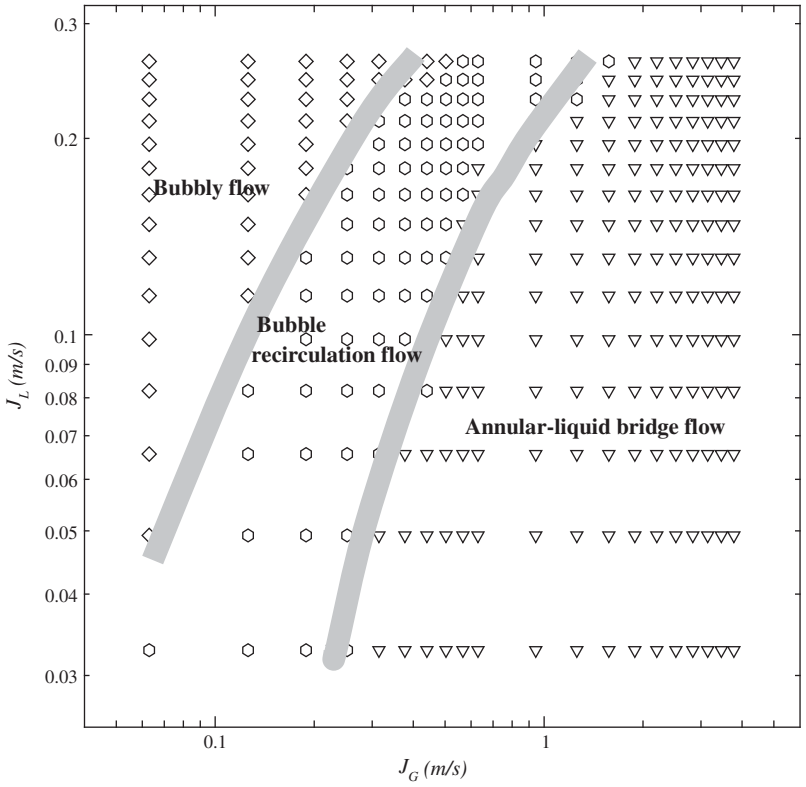

Fig. 10. Flow pattern map for vertical upward flow of air–water mixture.

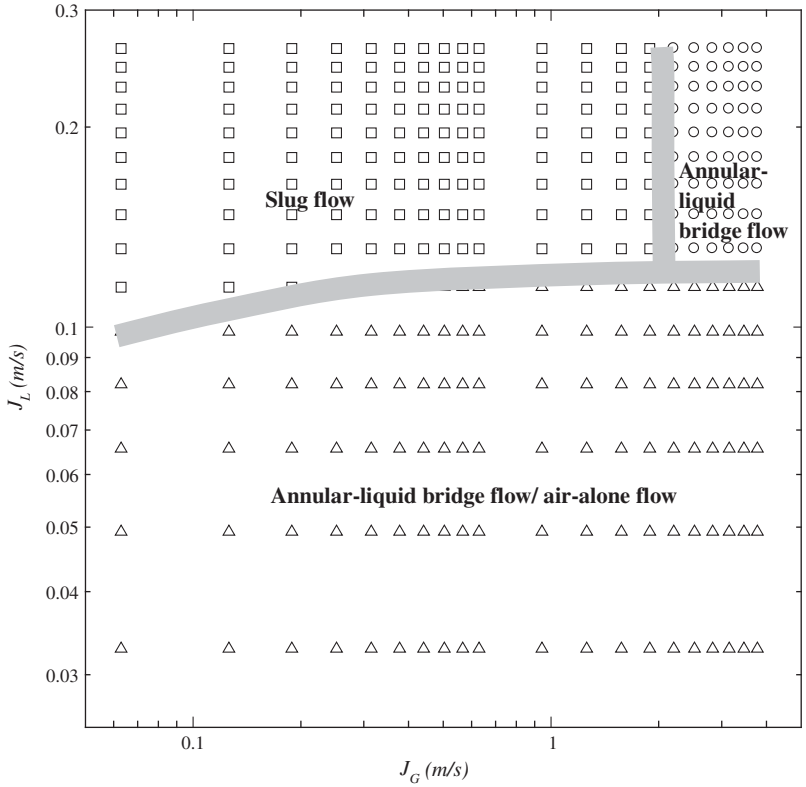

Fig. 11. Flow pattern map for vertical downward flow of air–water mixture.

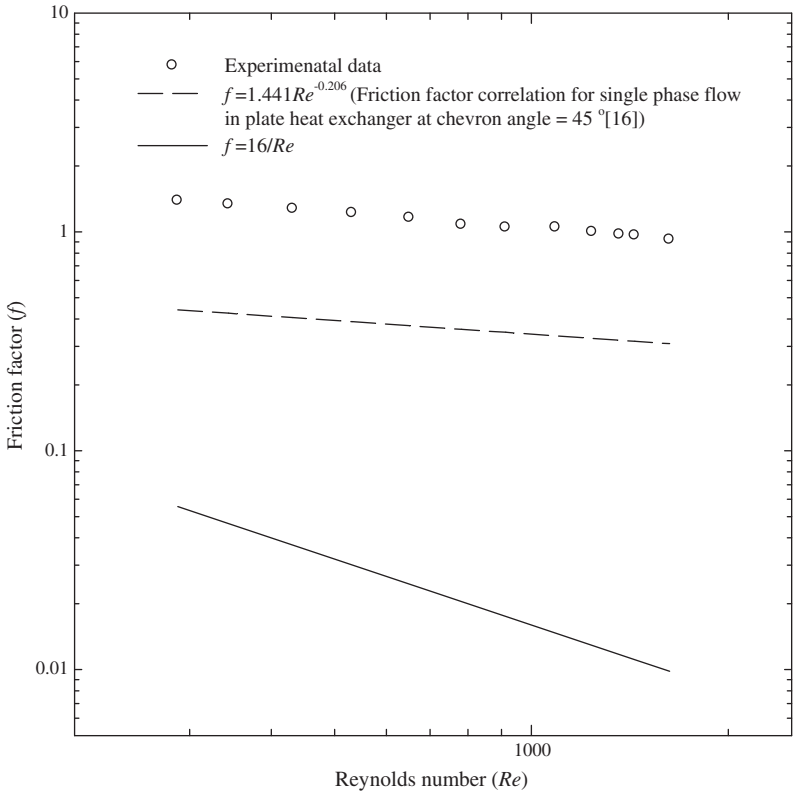

Fig. 12. Relationship between friction factor and Reynolds number for liquid single-phase flow.

exchanger at a corrugation angle of 45° [16]. The results of the study indicate that friction factors gained from this study are higher than that inside a smooth tube. This could occur because the corrugated trough causes spin inside the plate heat exchanger

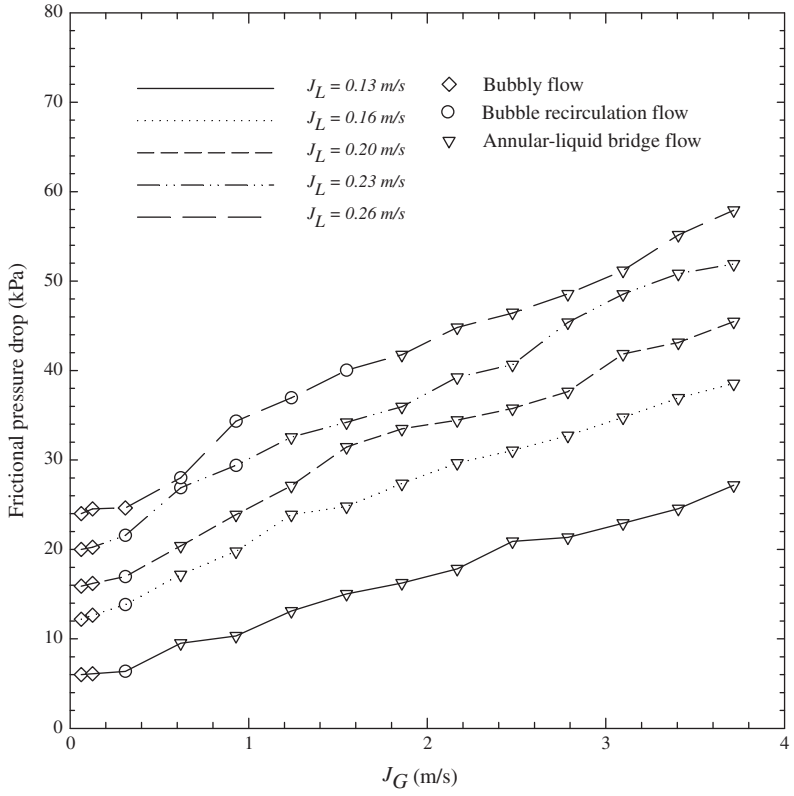

Fig. 13. Relationship between pressure drop and superficial gas velocity for air–water upward flow.

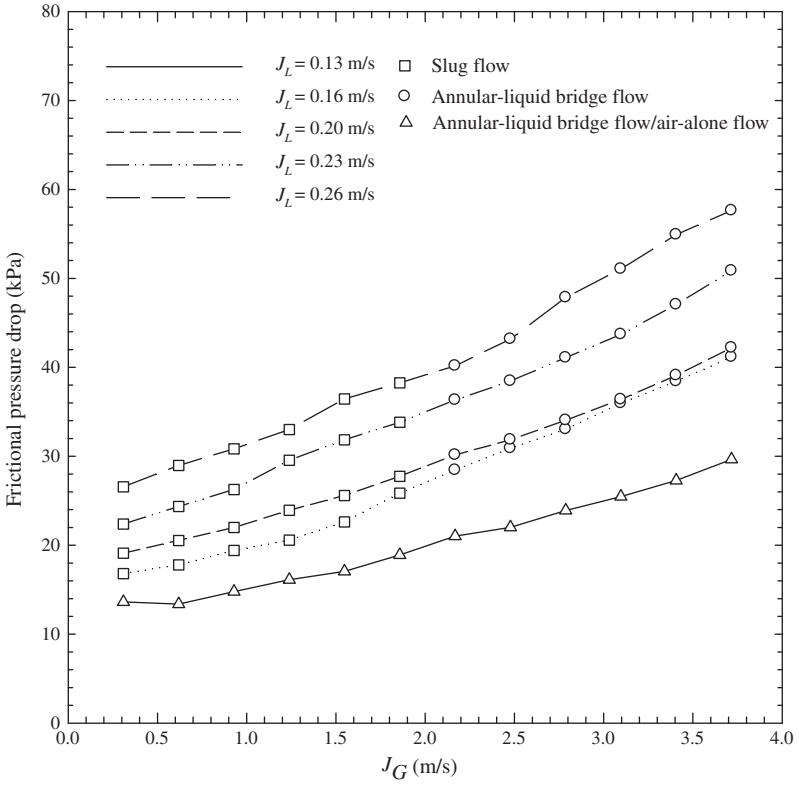

Fig. 14. Relationship between pressure drop and superficial gas velocity for air–water downward flow.

and makes turbulent flow higher than in a smooth tube. In addition, it is also found that the pressure drop of water inside the plate heat exchanger which has asymmetric corrugation angles (corrugation angle 55–10°) is higher than the pressure drop of the heat

exchanger plate which has a symmetric corrugation angle of 45°. For this study, a correlation of the friction factor used in a calculation for the two-phase multiplier of two-phase air and water flow is:

$$f = 4.929\mathrm{Re}^{-0.22} \tag{10}$$

when considering the accuracy of friction factor correlation, it is also found that the predicted friction factor shows good agreement with the measured friction factor with a mean deviation of 3.32%.

3.2.2. Two-phase pressure drop

The frictional pressure drop of the two-phase air and water flow inside the plate heat exchanger can be calculated with Eqs. (4)–(6). The specific volume of the two-phase flow is calculated from:

$$\upsilon_m = \upsilon_f + x_m \upsilon_{fg} \tag{11}$$

where υ_m is an average specific volume, υ_f is specific volume in the liquid phase, and υ_{fg} is the difference in specific volume between vapor and liquid phases. However, in case of phase change process, it is necessary to include the accelerational pressure drop into the total pressure drop. Normally, the accelerational pressure drop is calculated based on the homogeneous flow model using the following equation:

$$dP_A = G^2 \upsilon_{fg} \Delta x \tag{12}$$

where G is mass flux, υ_{fg} is the difference in specific volume between vapor and liquid phase, and Δx is total quality change in the exchanger.

The results of frictional pressure drop at superficial gas velocity and superficial liquid velocity reveal a difference in vertical upward and downward flow as shown in Figs. 13 and 14. The results obtained from the study indicate that an increase in water and air velocities causes the pressure drop to be higher. This is because the higher velocity of liquid results in the higher flow turbulence which leads to higher pressure drop. It is also found that the flow direction and flow pattern are also the cause of the change in pressure drop. Regarding a relationship between pressure drop and flow pattern, it is found that pressure drop reaches the highest level in annular-liquid bridge flow for the vertical upward flow and vertical downward flow. This could be due to the spin of the liquid bridge interfering with the main flow of air and causing the pressure drop in this flow pattern to be higher. The pressure drop reaches the lowest level in the bubbly flow for the vertical upward flow.

Data of frictional pressure drop inside the plate heat exchanger are presented in terms of the two-phase multiplier and Martinelli parameter [17]. In this study, the two-phase multiplier is a ratio of two-phase frictional pressure gradient $(dP/dz)_{TP}$ and liquid pressure gradient $(dP/dz)_L$ as follows:

$$\phi_L^2 = \frac{(dP_F/dz)_{TP}}{(dP_F/dz)_L} \tag{13}$$

The Martinelli parameter is defined as a ratio of liquid pressure gradient $(dP/dz)_L$ and gas pressure gradient $(dP/dz)_G$, as shown in the following formula:

$$X^2 = \frac{(dP_F/dz)_L}{(dP_F/dz)_G} \tag{14}$$

when

$$\left(\frac{dP_F}{dz}\right)_L = \frac{2f_L G_L^2}{\rho_L D_h} \tag{15}$$

$$\left(\frac{dP_F}{dz}\right)_G = \frac{2f_G G_G^2}{\rho_G D_h} \tag{16}$$

As shown above, in order to calculate the two-phase multiplier and the Martinelli parameter, the two-phase frictional pressure gradient is measured directly by differential pressure transducer,

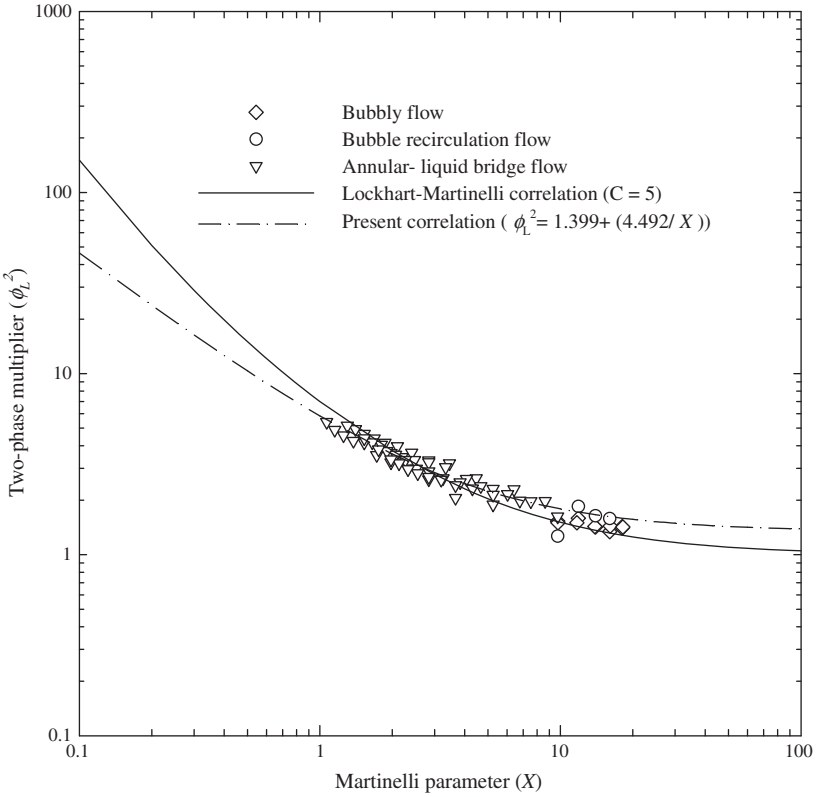

Fig. 15. Martinelli parameter versus the two-phase multiplier for air–water upward flow.

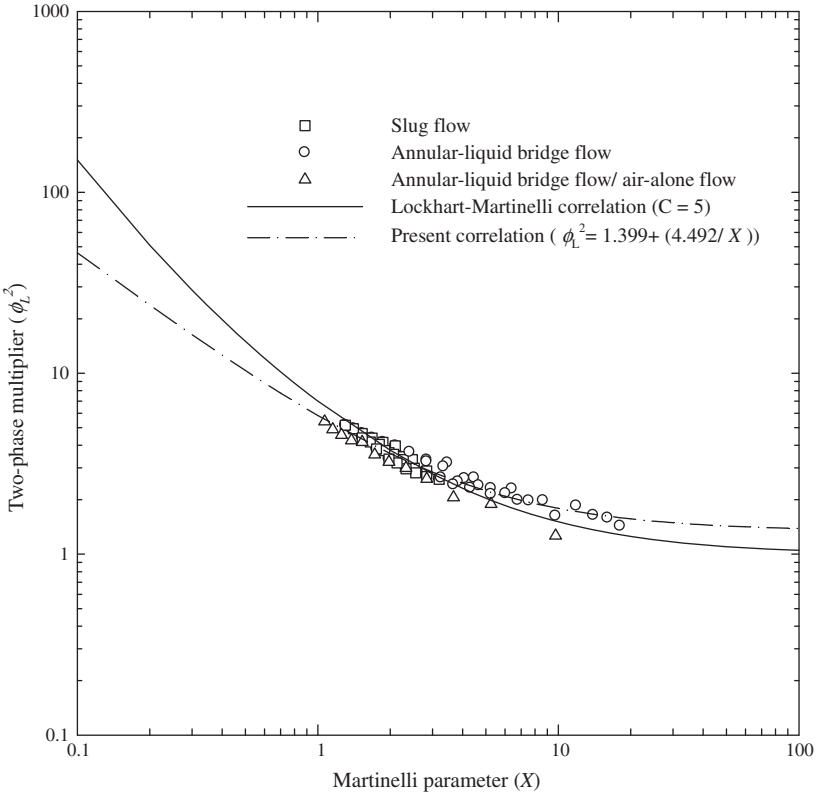

Fig. 16. Martinelli parameter versus the two-phase multiplier for air–water downward flow.

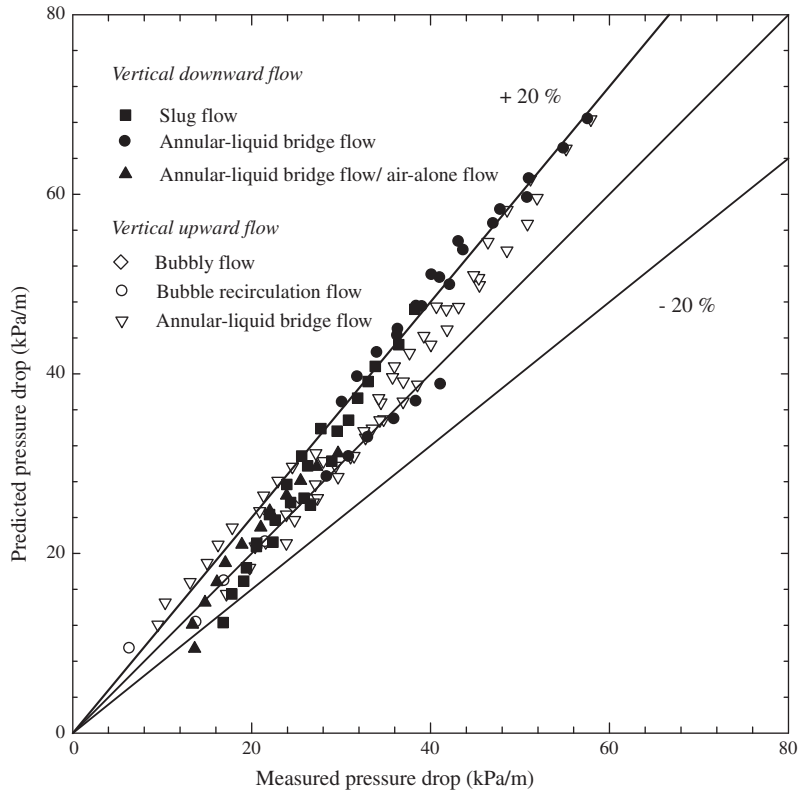

Fig. 17. Predicted pressure drop versus the measured pressure drop.

while the frictional pressure gradient for gas and liquid flows alone is calculated by using the friction factor obtained from proposed correlations.

For flow through a smooth tube, the two-phase multiplier is presented by Lockhart and Martinelli as:

$$\phi_L^2 = 1 + \frac{C}{X} + \frac{1}{X^2} \tag{17}$$

where a constant C by Chisholm [18] ranges from 5 to 20.

For the calculation of two-phase multiplier, the substance properties are determined by the average temperature. The average uncertainty of two-phase multiplier is ±0.138 and ±5.1% for the absolute uncertainty and relative uncertainty, respectively. Figs. 15 and 16 show the relationship between the two-phase multiplier and the Martinelli parameter of two-phase flow through the plate heat exchanger in the upward and downward flow, respectively. The results of the study reveal that the two-phase multiplier decreases when the Martinelli parameter increases. The results are compared with the Lockhart-Martinelli correlation for a flow in a smooth tube. It is found that the data correspond with a correlation where C equals 5. A new correlation for predicting the two-phase multiplier is generated based on the entire data from this study and presented as the following equation:

$$\phi_L^2 = 1.339 + \frac{4.492}{X} \tag{18}$$

The predicted results obtained from the correlation agree well with the experimental results with the mean deviation of 7.49%.

The relationship between the predicted pressure drop calculated from two-phase multiplier correlation and measured pressure drop is presented in Fig. 17. It is found from this figure that the majority of the data falls within ±25% of the proposed correlation. A mean deviation obtained from a correlation is 12.7%.

4. Conclusion

This article presents the results of a study of flow patterns and pressure drop of air–water two-phase flow in a plate heat exchanger. The plate used in the heat exchanger has a V-shaped corrugation with asymmetric corrugation angles of 55° and 10°. There are two flow directions of fluids: vertical upward and vertical downward. The results of the study reveal that two-phase flow direction causes different flow patterns. There are bubbly flow, bubble recirculation flow, and annular-liquid bridge flow for the vertical upward direction, while there are slug flow, annular-liquid bridge flow/air-alone flow, and annular-liquid bridge flow for the vertical downward direction. It is found that annular-liquid bridge flow occurs in both flow directions. However, bubbly flow pattern is found in vertical upward flow only. Similarly, slug flow appears in vertical downward flow only. The results of the study indicate that velocity of water and air has a significant effect on the change in pressure drop. However, the flow pattern shows little effect on the change in pressure drop. The maximum pressure drop occurs in the annular-liquid bridge flow pattern. Two-phase multipliers calculated from the study are found to correspond with the correlation of Lockhart–Martinelli in the case of laminar–laminar flow.

Acknowledgements

The present study was supported financially by King Mongkut's University of Technology Thonburi, the Office of Higher Education Commission and the Thailand Research Fund whose guidance and assistance are gratefully acknowledged.

References

[1] T.A. Rush, T.A. Nuwell, A.M. Jacobi, An experimental study of flow and heat transfer in sinusoidal wavy passages, International Journal of Heat and Mass transfer 42 (1999) 1541–1553.
[2] P. Vlasogiannis, G. Karagiannis, P. Argyropoulos, V. Bontozoglou, Air–water two-phase flow and heat transfer in plate heat exchanger, International Journal of Multiphase flow 28 (2002) 757–772.
[3] Y.Y. Hsieh, L.J. Chiang, T.F. Lin, Subcooled flow boiling heat transfer of R-134a and the associated bubble characteristics in a vertical plate heat exchanger, International Journal of Heat and Mass Transfer 45 (2002) 1791–1806.
[4] Y.Y. Hsieh, T.F. Lin, Saturated flow boiling heat transfer and pressure drop of refrigerant R-410A in a vertical plate heat exchanger, International Journal of Heat and Mass Transfer 45 (2002) 1033–1044.
[5] Y. Shiomi, S. Nakamishi, T. Uehara, Characteristics of two-phase flow in a channel form by chevron type plates, Experimental Thermal and Fluid Science 28 (2004) 231–235.
[6] H.M. Metwally, R.M. Manglik, Enhanced heat transfer due to curvature-induced lateral vortices in laminar flows in sinusoidal corrugated-plate channels, International Journal of Heat and Mass transfer 47 (2004) 2283–2292.
[7] W.S. Kuo, Y.M. Lie, Y.Y. Hsieh, T.F. Lin, Condensation heat transfer and pressure drop of refrigerant R-410A flow in a vertical plate heat exchanger, International Journal of Heat and Mass Transfer 48 (2005) 5205–5220.
[8] K. Nilpueng, S. Wongwises, Flow pattern and pressure drop of vertical upward gas–liquid flow in sinusoidal wavy channels, Experimental Thermal and Fluid Science 30 (2006) 523–534.
[9] G.A. Longo, A. Gasparella, Refrigerant R134a vaporisation heat transfer and pressure drop inside a small brazed plate heat exchanger, International Journal of Refrigeration 30 (2007) 821–830.
[10] G.A. Longo, A. Gasparella, HFC-410A vaporisation inside a commercial brazed plate heat exchanger, Experimental Thermal and Fluid Science 32 (2007) 107–116.
[11] G.A. Longo, A. Gasparella, Heat transfer and pressure drop during HFC refrigerant vaporisation inside a brazed plate heat exchanger, International Journal of Heat and Mass Transfer 50 (2007) 5194–5203.
[12] S.W. Chang, A.W. Lees, T.C. Chou, Enhanced heat transfer due to curvature-induced lateral vortices in laminar flows in sinusoidal corrugated-plate channels, International Journal of Heat and Mass transfer 52 (2009) 4592–4603.
[13] G.A. Longo, R410A condensation inside a commercial brazed plate heat exchanger, Experimental Thermal and Fluid Science 33 (2009) 284–291.
[14] J.G. Collier, Convective Boiling and Condensation, McGraw-Hill, London, 1972.
[15] R.K. Shah, W.W. Focke, Plate heat exchangers and their design theory, in: R.K. Shah, E.C. Subbarao, R.A. Mashelkar (Eds.), Heat Transfer Equipment Design, Hemisphere, Washington, DC, 1988.
[16] S. Kakac, H. Liu, Heat Exchanger: Selection, Rating, and Thermal Design, CRC Press, New York, 2002.
[17] R.W. Lockhart, R.C. Martinelli, Proposed correlation of data for isothermal two-phase two-component flow in pipes, Chemical Engineering Progress 45 (1949) 39–48.
[18] D. Chisholm, A theoretical basis for the Lockhart–Martinelli correlation for two-phase flow, International Journal of Multiphase Flow 10 (1967) 1767–1778.

Experimental Thermal and Fluid Science 34 (2010) 992–999

Contents lists available at ScienceDirect

Experimental Thermal and Fluid Science

journal homepage: www.elsevier.com/locate/etfs

Nucleate pool boiling heat transfer characteristics of TiO_2–water nanofluids at very low concentrations

Adirek Suriyawong, Somchai Wongwises *

Fluid Mechanics, Thermal Engineering and Multiphase Flow Research Lab. (FUTURE), Department of Mechanical Engineering, King Mongkut's University of Technology Thonburi, Bangmod, Bangkok 10140, Thailand

ARTICLE INFO

Article history:
Received 29 June 2009
Received in revised form 9 March 2010
Accepted 9 March 2010

Keywords:
Nucleate boiling
Nanofluids
Nanoparticles
Heat transfer
Heat flux

ABSTRACT

A study of nucleate pool boiling heat transfer of TiO_2–water nanofluids is experimentally conducted. Nanofluids with various concentrations of 0.00005, 0.0001, 0.0005, 0.005, and 0.01 vol.% are employed. Horizontal circular plates made from copper and aluminium with different roughness values of 0.2 and 4 μm are used as heating surfaces. The experiments are performed to explore the effects of nanofluids concentration as well as heating surface material and roughness on nucleate pool boiling characteristics and the heat transfer coefficient under ambient pressure. The results show that based on the copper heated surface which is tested with a concentration of 0.0001 vol.%, higher nucleate pool boiling heat transfer coefficient is obtained when compared with the base fluid. A 15% increase is obtained for the surface roughness of 0.2 μm and a 4% increase is obtained for roughness of 4 μm. For concentrations higher than 0.0001 vol.%, however, the higher the concentration, the lower the heat transfer coefficient. In the case of aluminium heated surface, the corresponding heat transfer coefficients are larger than for the copper surface by around 30% with a roughness of 0.2 μm and around 27% with a roughness of 4 μm. Moreover, the results also indicate that the heat transfer coefficient obtained based on a roughness of 4 μm is higher than that for a roughness of 0.2 μm by around 12% for aluminium and by around 13% for copper.
© 2010 Published by Elsevier Inc.

1. Introduction

At the current time, energy consumption is tending to increase. However, energy sources are tending to decrease rapidly. Thus, many countries are trying to create energy policies to reduce energy consumption. A number of researchers intend to design and develop devices to reduce energy consumption in order to achieve the highest possible efficiency. In general, the working fluids inside a heat exchanger may be single-phase or two-phase flow. Heat transfer with phase change gave more efficiency than that in single-phase. Pool boiling is one kind of heat transfer with phase change. Normally, pool boiling heat transfer can be developed in two aspects as follows: (1) improvement in the heating surface and (2) improvement in the working fluids. Focusing on improving the heat transfer fluids by suspending the small solid particles in the base fluid to increase the thermal conductivity is an innovative method.

The examples of recent publications involving pool boiling heat transfer of nanofluids are summarized as follows.

Das et al. [1,2] studied the nucleate pool boiling heat transfer characteristics of nanofluids using horizontal cylinders with different surface roughness values as heating surfaces. Heating surfaces with diameters of 4, 6.5, and 20 mm were used in this study. The results indicated that the boiling heat transfer coefficient of water deteriorated with the addition of nanoparticles. In addition, the deterioration in heat transfer was dependent on the heating surface roughness and the particle volume concentration.

You et al. [3] investigated the pool boiling curve and critical heat flux (CHF) of a square flat copper heating surface immersed in Al_2O_3–water nanofluids. Nanofluids with volume concentrations ranging from 0.001 g/l to 0.05 g/l were used. The experimental results showed that the CHF increased dramatically (doubled) when compared with the case of pure water.

Vassallo et al. [4] experimentally studied the pool boiling heat transfer of Si–water nanofluids and the results were compared with those of water. An NiCr wire heater having a 0.4 mm diameter and length of about 120 mm were used as the test section. The experimental results showed that both nano- and micro-solutions dramatically increased the CHF when compared with pure water.

Bang and Chang [5] conducted an experiment to study the boiling heat transfer characteristics of Al_2O_3–water nanofluids at different volume concentrations of 0.5, 1.0, 2.0, and 4.0 vol.%, respectively. Smooth horizontal flat surfaces having a roughness of a few tens of nanometers were used as the test section. The experimental results demonstrated that the nanofluids reduced the heat transfer performance compared with pure water for both natural convection and nucleate boiling heat transfer. An increase

* Corresponding author. Tel.: +66 2 470 9115; fax: +66 2 470 9111.
E-mail address: somchai.won@kmutt.ac.th (S. Wongwises).

0894-1777/$ - see front matter © 2010 Published by Elsevier Inc.
doi:10.1016/j.expthermflusci.2010.03.002

Nomenclature

A	area, m^2
C_p	specific heat, kJ/kg °C
C_{sf}	empirical constant used in Eq. (4), dimensionless
g	gravitational acceleration, m/s^2
h_b	boiling heat transfer coefficient, W/m^2 °C
h_{fg}	heat of vaporization, kJ/kg
I	electric current, amps
Pr	Prandtl number, dimensionless
q	heat flux, W/m^2
Ra	average roughness, μm
Rz	mean peak-to-valley height roughness, μm
T	temperature, °C
V	voltage, volts
x	position of temperature on test section, m

Greek symbols

μ	dynamic viscosity, kg/m s
ρ	density, kg/m^3
σ	surface tension of liquid–vapor interface, N/m

Subscripts

l	liquid phase
v	vapor phase
s	heating surface
sat	saturation

Superscript

m	empirical constant used in Eq. (4), dimensionless

in volume concentration tended to reduce the heat transfer coefficient. The heat transfer coefficient decreased with increasing particle volume fraction. In contrast, delay of the boiling activity caused an increase in the CHF performance.

Kim et al. [6,7] experimentally studied the CHF characteristics of TiO_2– and Al_2O_3–water nanofluids with volume concentrations ranging from 0.00001 to 0.1 vol.%. In their study, NiCr wire 0.2 mm in diameter and Ti wire 0.25 mm in diameter were used as the heating surfaces. The results showed that use of nanofluids increased the CHF compared with use of pure water.

Kim et al. [8] conducted an experiment to study the pool boiling characteristics of Al, ZrO, and Si nanoparticles suspended in water with volume concentrations of 0.001, 0.01, and 0.1 vol.%. A stainless steel wire of 0.381 mm diameter and 120 mm length was used as the heating surface. The experimental results indicated that some nanoparticles were coated on the heating surface during nucleate boiling to form a porous layer. This layer significantly improves the surface wettability through a reduction in the static contact angle on the heating surfaces.

Golubovic et al. [9] investigated CHF enhancement of nanofluids experimentally. The BiO_2 and Al_2O_3 nanoparticles dispersed in water were used as working fluids. The test section was made from a NiCr wire heater 0.64 mm in diameter and 50 mm in length. The experimental results indicated that the CHF increased with increases in the volume concentrations.

Liu and Liao [10] presented the nucleate pool boiling heat transfer of nanofluids, experimentally. In this study, CuO and SiO_2 nanoparticles were dispersed in water (H_2O) and alcohol (C_2H_5OH) based fluids. A plain copper surface was used as the test section. The boiling heat transfer characteristics of the nanofluids were slightly poor compared with those of the water and alcohol.

Trisaksri and Wongwises [11] studied nucleate pool boiling heat transfer of a refrigerant based-nanofluid at different nanoparticle concentrations and pressures. The working fluids were TiO_2 nanoparticles mixed with R141b at volume concentrations of 0.01, 0.03, and 0.05 vol.%, respectively. The test was conducted using a cylindrical copper tube as the heating surface. The results indicated that the boiling heat transfer coefficient decreased with increasing volume concentrations. The results also indicated that the effect of pressure on the boiling heat transfer coefficient at lower particle concentrations was more than that at higher concentrations.

Although some information is currently available on the pool boiling of nanofluids, it should be noted that nucleate pool boiling of nanofluids at very low concentrations has received comparatively little attention in the literature, and in particular detailed investigations are lacking on the effects of heating surface material and surface roughness. The purpose of this work is to obtain experimental results on the effect of concentration of nanofluids, heating surface roughness, and heating surface material on the nucleate pool boiling characteristics of nanofluids at very low concentrations. The nucleate pool boiling curves of TiO_2–water nanofluids at very low concentrations, especially those obtained from an aluminium heating surface, which have never before appeared in open literature, are presented.

2. Preparation of nanofluids

Generally, a preparation of nanofluids is an important step in experiments on nanofluids. In general, the preparation of nanofluids can be divided into three parts: pH control, addition of surfactants, and use of ultrasonic vibration. The preparation of nanofluids aims to make nanoparticles suspend in base fluids with stability, without sedimentation. In this study, the nanofluids used were supplied by DEGUSSA Company from Germany (VP Disp. W740). The fluids have TiO_2 nanoparticles with average diameters of 21 nm, suspended in water base fluid which has concentration of 40 wt.%. In the experiment, the nanofluids were diluted by adding water to achieve the desired concentration levels of 0.00005, 0.0001, 0.0005, 0.005, and 0.01 vol.%. After that, the fluids were treated with ultrasonic vibration for 2 h to distribute the nanoparticles evenly.

Sample photographs of nanofluids used in the experiment were taken from a transmission electron microscope (TEM) shown in Fig. 1. An initial analysis of the nanoparticles' sizes revealed an

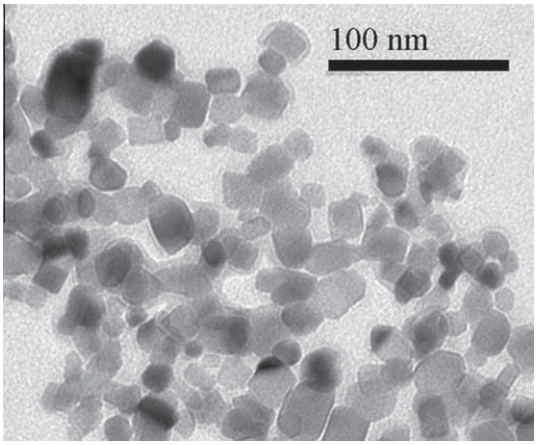

Fig. 1. TEM image of dispersed TiO_2 nanoparticles in water.

almost circular shape with average diameter of 21 nm, corresponding with data from the manufacturer.

3. Experimental apparatus and procedure

This study is an experimental study on nucleate pool boiling heat transfer with a horizontal circular plate heating surface. Fig. 2a shows the experimental apparatus which consists of three main sections: test section, heating device for the test section, and pressure control in the pressure vessel.

The test section was placed inside the twin-layered pressure vessel which was made with stainless steel. The inner layer of the pressure vessel contained the nanofluid used in the experiment. The outer layer contained water heated by a preheater (1.5 kW) to keep the temperature of the nanofluids inside the inner tank stable at saturation temperature. The temperature of the nanofluids was measured by a T-type sheath thermocouple with a diameter of 1 mm, length of 28 cm, and deviation of ±0.1 °C. During operation, the pressure inside both layers of the tank is kept at atmospheric condition.

Fig. 2b shows the boiling test section which consists of a heater (1.2 kW) placed inside a copper bar which will transfer heat from the heater to the test section installed at the upper end of the copper bar. Heat from the heater will be transferred only to the upper test section. The copper bar and the test section are covered with calcium silicate insulator which is 50 mm thick to prevent lateral heat loss. The test section used in this experiment was made from two materials: copper and aluminium. The heating surfaces have average roughness of 0.2 and 4 μm. The roughness can be measured by a Mahr Marsurf PS1 model roughness meter. Average roughness (Ra) and mean peak-to-valley height roughness (Rz) are shown in Table 1. The test section area contains four holes for installing sheath thermocouples with average diameter of 1 mm and length of 16 mm. Thermocouples are placed at intervals of 10 mm. The distance between the uppermost sheath thermocouple and the heating surface is 20 mm. Temperatures at various locations in the test section would be used to calculate the temperature of the heating surface.

Pressure inside the inner tank was controlled by adjusting the water flow in the cooling coil to control the condensation rate of vapor at the outer surface of the cooling coil. Pressure inside the tank was controlled at atmospheric condition throughout the experiment.

In the experiment with high heat flux, there was film boiling which created film at the heating surface. When this happened, temperatures at various points of the test section increased rapidly. This condition can cause harm to the apparatus. Therefore, a wind blower was installed to eradicate film boiling on the heating surface; hence, the surface temperature decreased.

After experimenting under each condition, the experimental apparatus was dissected and cleaned to get rid of nanoparticles on various parts. The apparatus can be cleaned by using a high-pressure water injector to inject water on the heating surface. After that, the apparatus was dried with a blower before being assembled for use in experiments under other conditions.

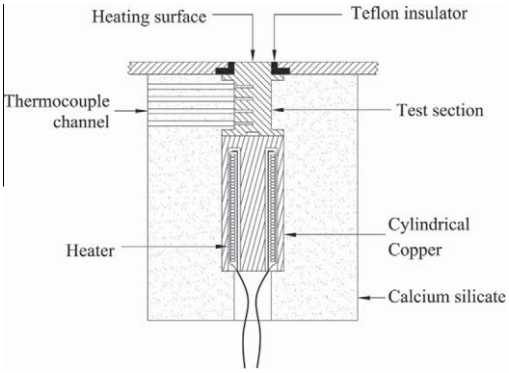

Fig. 2b. Cross-sectional view of the boiling test section.

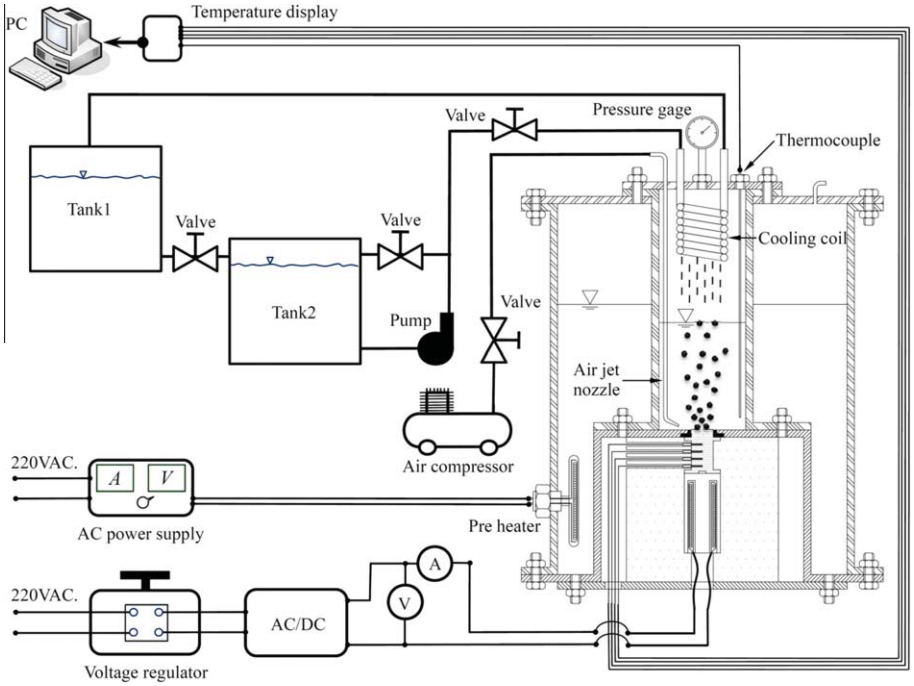

Fig. 2a. Schematic diagram of experimental apparatus.

Table 1
Roughness of copper and aluminium heating surface.

No.	Copper, Ra = 0.2 μm		Copper, Ra = 4 μm		Aluminium, Ra = 0.2 μm		Aluminium, Ra = 4 μm	
	Ra (μm)	Rz (μm)	Ra (μm)	Rz (μm)	Ra (μm)	Rz (μm)	Ra (μm)	Rz (μm)
1	0.237	1.104	4.088	23.000	0.192	1.073	4.219	22.200
2	0.191	1.078	3.224	22.300	0.213	1.088	5.343	30.500
3	0.194	1.061	3.710	20.100	0.227	1.092	4.227	25.000
4	0.200	1.067	3.892	24.500	0.220	1.090	3.538	25.300
5	0.201	1.068	4.231	24.100	0.211	1.087	3.984	24.300
6	0.191	1.078	4.325	26.100	0.202	1.084	3.978	23.300
7	0.171	1.094	4.409	25.500	0.172	1.065	3.891	22.200
8	0.196	1.063	4.328	25.000	0.194	1.076	3.499	21.000

4. Data reduction

Experimental investigations were carried out to observe the boiling characteristics using the flat plate heater. The heat fluxes, q (W/m^2), were calculated from the following equation:

$$q = \frac{IV}{A} \tag{1}$$

where I is the current (amps), V is the voltage (volts), and A is the heating surface area (m^2).

The average boiling heat transfer coefficient, h_b (W/m^2 °C), is defined as:

$$h_b = \frac{q}{T_s - T_{sat}} \tag{2}$$

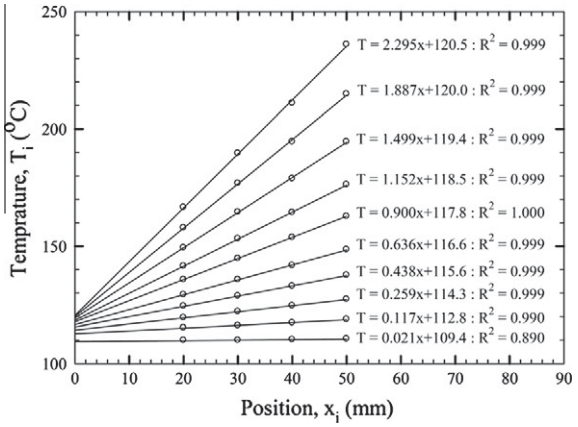

Fig. 3. Axial temperature distribution for the flat plate experiment.

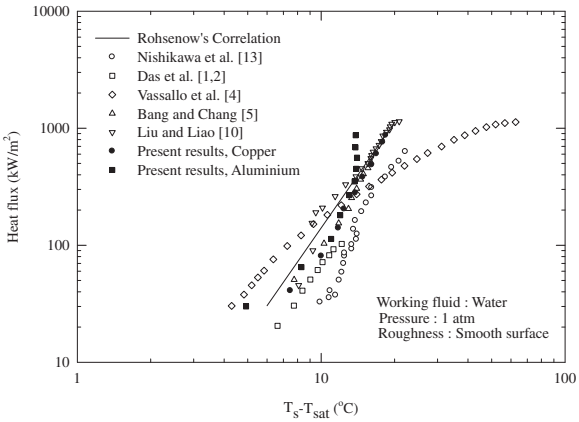

Fig. 4. Comparison of present data with Rohsenow's correlation and other researchers. (See above-mentioned references for further information.)

where T_s is the average heater surface temperature (°C) calculated from Eq. (3), and T_{sat} is the liquid saturation temperature (°C):

$$T_s = \frac{\sum_{i=1}^{4} T_i \sum_{i=1}^{4} x_i^2 - \sum_{i=1}^{4} x_i \sum_{i=1}^{4} x_i T_i}{4\sum_{i=1}^{4} x_i^2 - \left(\sum_{i=1}^{4} x_i\right)^2} \tag{3}$$

where T_i is the local temperature (°C) and x is the position of the temperature measurement (m) on the test section. Fig. 2b shows the cross-sectional view of the boiling test section, and Fig. 3 shows examples of the axial temperature distribution in the copper test section.

The uncertainties of the heat flux, heating surface temperature and heat transfer coefficient are ±2.2%, ±3.7% and ±11.6%, respectively.

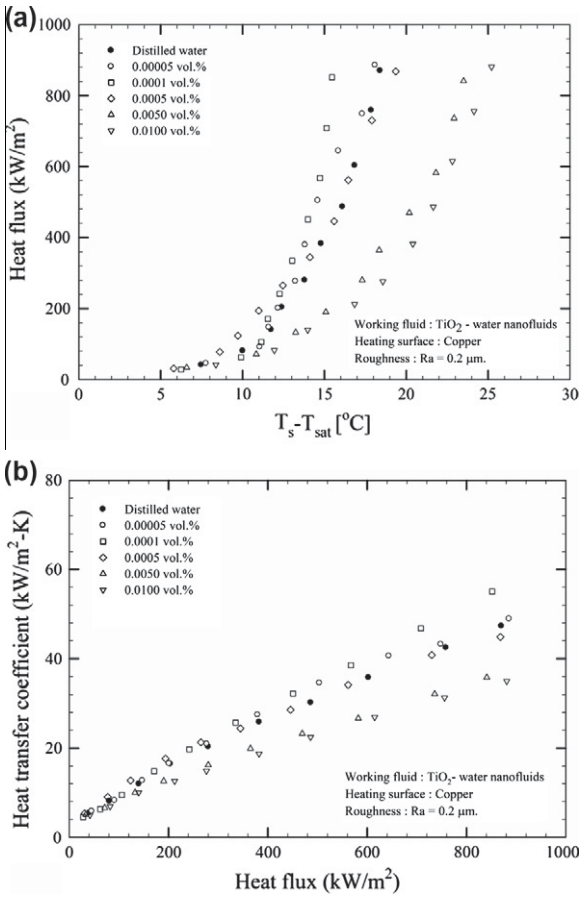

Fig. 5. Nucleate pool boiling heat transfer of TiO_2–water nanofluids for copper heating surface with roughness 0.2 μm at 1 atm.

5. Results and discussion

This research studied the heat transfer characteristic of nucleate pool boiling at atmospheric pressure using distilled water and TiO_2–water nanofluids at various concentration levels as working fluids. The heating surfaces were made from copper and aluminium with surface roughness of 0.2 and 4 μm. Figs. 5–13 show the pool boiling curve in the form of relationships between heat flux and $T_s - T_{sat}$ (which is the heating surface temperature minus the liquid saturation temperature), and in form of relationships between heat flux and heat transfer coefficient. The details of the experimental results are as follows.

5.1. Comparison with pool boiling curve of water

In calibration of the tested unit made to predict the heat transfer characteristic of nucleate pool boiling, the experimental unit was tested with heating surfaces made from copper using water as the working fluid. After that, the experimental results were compared with experimental results reported in related literature and also compared with Rohsenow's correlation [12] as shown in Eq. (4):

$$\frac{C_{p,l}(T_s - T_{sat})}{h_{fg}\mathrm{Pr}_l^m} = C_{sf}\left(\frac{q}{\mu_l h_{fg}}\sqrt{\frac{\sigma}{g(\rho_l - \rho_v)}}\right)^{0.33} \quad (4)$$

where m and C_{sf} – which are constants in Rohsenow's correlation – have values of 1 and 0.031, respectively.

Fig. 4 shows the pool boiling curve that indicated a relationship between heat flux and $T_s - T_{sat}$ obtained from a test with water. From the calibration, it was found that the results obtained from the experiment tend to go in the same direction as Rohsenow's correlation and belong among the experimental data of Das et al. [1,2], Bang and Chang [5], Liu and Liao [10], and Trisaksri and Wongwises [11].

5.2. Effect of nanofluid concentration

This part presents the effect of nanofluids concentration on the pool boiling curve and heat transfer coefficient. The test used nanofluids concentrations of 0.00005, 0.0001, 0.0005, 0.005, and 0.01 vol.%. The results are shown in Figs. 5–8.

With regard to heat transfer on a copper surface with a surface roughness of 0.2 μm as shown in Fig. 5, it was found that at nanofluids concentrations of not more than 0.0001 vol.%, there was an increase in heat transfer, compared with base fluid. At the concentration of 0.00005 vol.%, the heat transfer coefficient increased by about 7% and at the concentration of 0.0001 vol.%, the heat transfer coefficient increased by about 15%. In contrast, when the concentration of nanofluids was more than 0.0001 vol.%, the heat transfer decreased when compared with base fluid.

Fig. 6 shows the heat transfer characteristic on a copper surface with surface roughness of 4 μm. The results tend to be similar to the experimental result for the surface with 0.2 μm roughness. That is, at nanofluids concentrations of not more that 0.0001 vol.%, there was an increase in heat transfer. On the other hand, when the nanofluids concentration was more than 0.0001 vol.%, the heat transfer decreased when compared with base fluid. At concentrations of 0.00005 and 0.0001 vol.%, the heat transfer coefficient increased by about 2% and 4%, respectively.

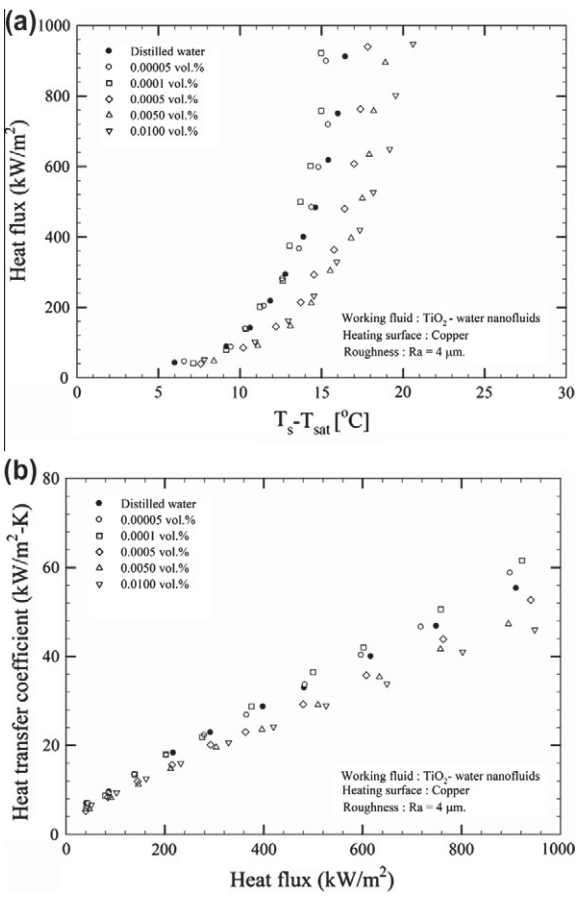

Fig. 6. Nucleate pool boiling heat transfer of TiO_2–water nanofluids for copper heating surface with roughness 4 μm at 1 atm.

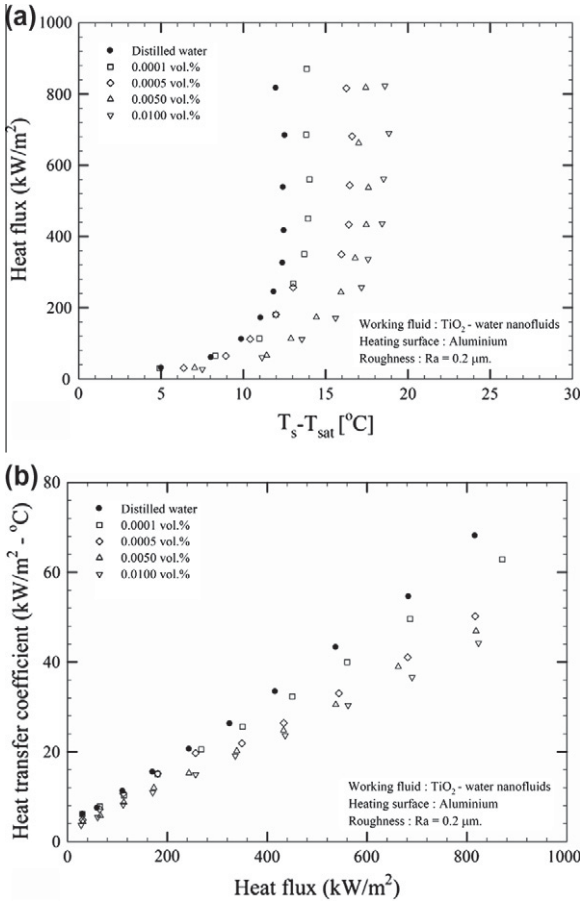

Fig. 7. Nucleate pool boiling heat transfer of TiO_2–water nanofluids for aluminium heating surface with roughness 0.2 μm at 1 atm.

The increase in heat transfer when the nanofluids concentration was not more than 0.0001 vol.% may have occurred because the effect of upward-flow caused by boiling was more than the result of gravity. Thus, nanoparticles did not cause sedimentation on the heating surface, which helps improve heat transfer when compared with base fluids. In contrast, at concentrations of 0.0005, 0.005, and 0.01 vol.%, the heat transfer decreased when compared with base fluids. This may result from the sedimentation of nanoparticles on the heating surface leading to a decrease in the nucleation sites. Moreover, nanoparticle sediment on the heating surface would also increase the resistance of heat transfer between the heating surface and the nanofluids, causing, in turn, a decrease in the heat transfer.

Figs. 7 and 8 show the experimental results of heat transfer of TiO_2–water nanofluids at various concentration levels using heating surfaces made from aluminium with roughness of 0.2 and 4 μm. It was found from the results that, at the same heat flux, the increase in the nanofluids' concentration caused a decrease in the heat transfer when compared with the base fluid. However, considering each pool boiling curve of TiO_2–water nanofluids and base fluid as shown in Figs. 7a and 8a, there were special characteristics which differ from those in Figs. 5a and 6a. That is, at the surface roughness of 0.2 μm and low $T_s - T_{sat}$, a relationship between heat flux and $T_s - T_{sat}$ was similar to an exponential function. The heat flux of 400 kW/m^2 seemed to be the last point of this phase. After that, $T_s - T_{sat}$ was mostly constant while the heat flux increased. At the surface roughness of 4 μm at low $T_s - T_{sat}$, a relationship between heat flux and $T_s - T_{sat}$ was similar to that for the roughness of 0.2 μm. However, $T_s - T_{sat}$ decreased when the heat flux was more than 400 kW/m^2.

Figs. 7b and 8b show relationships between the heat flux and the heat transfer coefficient. The results indicate that the increase in the nanofluids' concentration caused the heat transfer coefficient to decrease. This is because the heating surface was covered with nanoparticles which decreased the nucleation sites and increased heat transfer resistance between the surface and the working fluids as mentioned above.

5.3. Effect of surface roughness and surface material

Fig. 9 shows a comparison of experimental results at atmospheric pressure between surfaces made from copper and from aluminium with surface roughness of 0.2 and 4 μm, using distilled water as the working fluid. The results indicate that, at the same roughness, the aluminium surface gave a higher heat transfer coefficient than the copper surface. At the roughness of 0.2 μm, the heat transfer coefficient was higher by about 30%, and at the roughness of 4 μm, the coefficient was higher by about 27%. The high heat flux gave a higher heat transfer than the low heat flux. With the same heating surface material, it was found that the roughness of 4 μm gave a higher heat transfer coefficient than the roughness of 0.2 μm by about 12%. The higher roughness especially gave better heat transfer than the lower roughness because the high roughness surface has more nucleation sites and more cavities, which can contain more gas. This improved the boiling characteristics.

Figs. 10–13 show the experimental results for nanofluids at various concentration levels with heating surfaces made from copper and aluminium. In general, the results of this experiment are similar to those of the experiment with distilled water shown

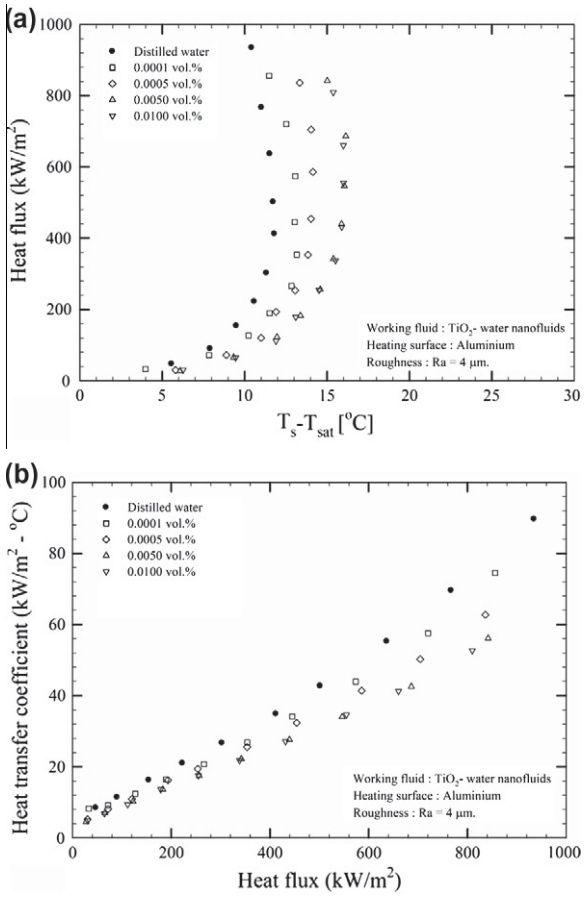

Fig. 8. Nucleate pool boiling heat transfer of TiO_2–water nanofluids for aluminium heating surface with roughness 4 μm at 1 atm.

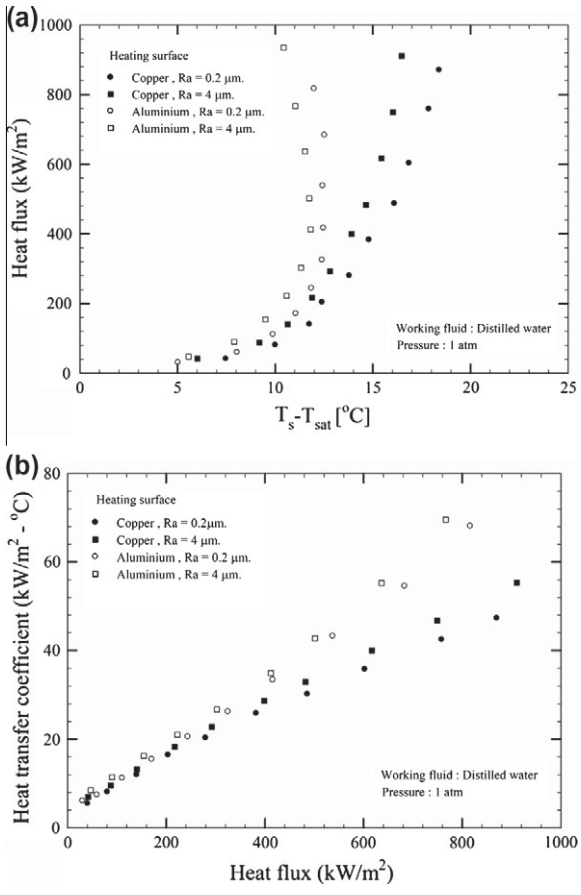

Fig. 9. Nucleate pool boiling heat transfer of distill water at 1 atm.

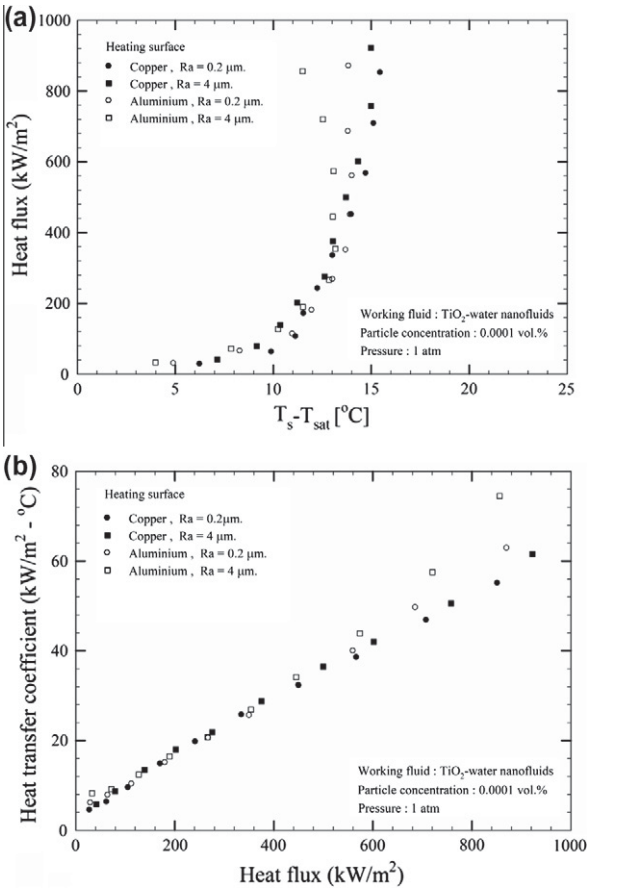

Fig. 10. Nucleate pool boiling heat transfer of TiO_2–water nanofluids with concentration of 0.0001 vol.% at 1 atm.

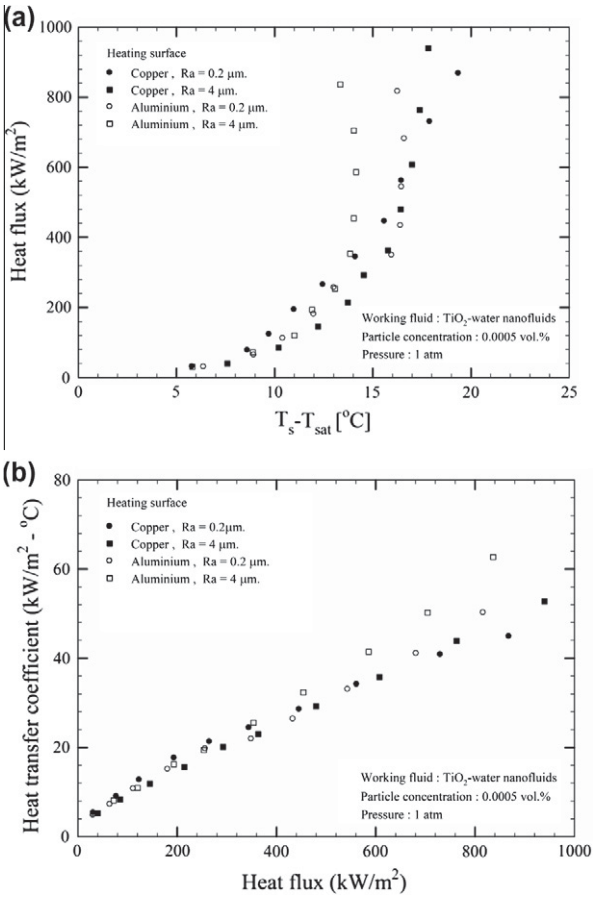

Fig. 11. Nucleate pool boiling heat transfer of TiO_2–water nanofluids with concentration of 0.0005 vol.% at 1 atm.

in Fig. 9. As seen in Fig. 10, which shows the experiment at a concentration of 0.0001 vol.%, the increase in the heat transfer coefficient was clearly observed when the heat flux was higher than 400 kW/m^2. This is because a strong boiling characteristic caused nanofluids to flow in base fluid without sedimentation, and this led to a good heat transfer. In contrast, when the heat flux was lower than 400 kW/m^2, the heat transfer coefficients were only slightly different. This is because the similar clustering of nanoparticles at the heating surface made the heat transfer slightly different.

Fig. 11 shows the experimental results for nanofluids at a concentration of 0.0005 vol.% with heating surfaces made from copper and aluminium. With the same material, the surface roughness of 4 μm gave better heat transfer than the surface roughness of 0.2 μm. When the heat flux was more than 250 kW/m^2, the heat transfer coefficient increased dramatically due to the strong boiling characteristic. In contrast, heat flux below 250 kW/m^2 gave a slightly different heat transfer coefficient as described in Fig. 10. Similarly, Figs. 12 and 13 show experimental results for concentrations of 0.005 and 0.01 vol.%. In general, the results show similar trends, but the differentiated heat fluxes were 300 and 240 kW/m^2, respectively.

6. Conclusions

In the present study, the heat transfer characteristics for nucleate pool boiling of TiO_2–water nanofluids at concentrations of 0.00005, 0.0001, 0.0005, 0.005, and 0.01 vol.% at atmospheric pressure are experimentally investigated. Copper and aluminium surfaces with roughness of 0.2 and 4 μm are used in the experiments. The conclusions drawn from the experiment can be summarized as follows:

1. *For copper surfaces*:
   It was found that with a nanofluids concentration of 0.0001 vol.%, the heat transfer coefficient increased, compared with base fluid. The heat transfer increased at an average of 15% with a surface roughness of 0.2 μm and at 4% with a surface roughness of 4 μm.
   On the other hand, with nanofluids' concentrations of more than 0.0001 vol.%, the heat transfer coefficient was found to be less than that of the base fluid at every level of surface roughness.
2. *For aluminium surfaces*:
   The boiling curve was found to be different from a general boiling curve in that the excess temperature would vary in accordance with the heat flux only for a certain amount of time. After that, it tended to decrease while the heat flux rose. This could be seen from the experimental with pure water and nanofluid at lower concentrations.
   The heat transfer coefficient was found to be less than that of base fluids at every level of nanofluids concentration and surface roughness.
3. When comparing copper with aluminium surfaces using nanofluids and base fluid as experimental substances, it was found that aluminium surfaces yielded higher heat transfer coefficients than copper surfaces. This difference was apparent at high heat flux levels.

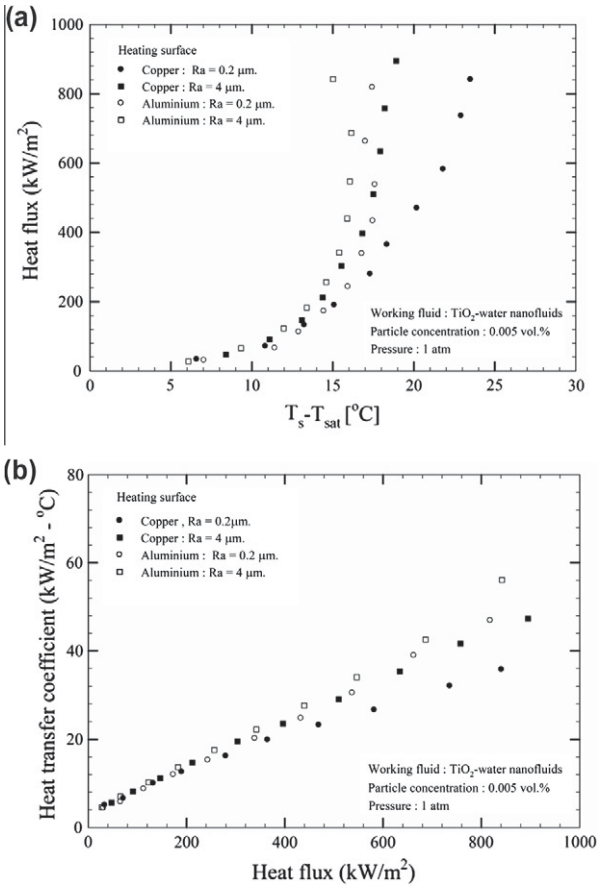

Fig. 12. Nucleate pool boiling heat transfer of TiO_2–water nanofluids with concentration of 0.005 vol.% at 1 atm.

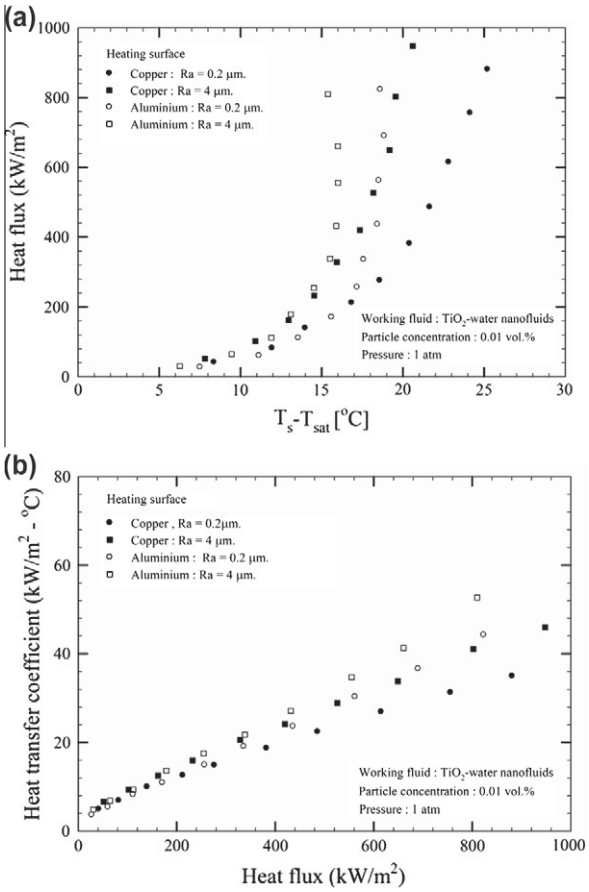

Fig. 13. Nucleate pool boiling heat transfer of TiO_2–water nanofluids with concentration of 0.01 vol.% at 1 atm.

4. When comparing surface roughness of 0.2 μm with 4 μm using nanofluids and base fluid as experimental substances, it was found that the surface roughness of 4 μm yielded a higher heat transfer coefficient than the surface roughness of 0.2 μm. This difference could also be seen at high heat flux levels.

Acknowledgments

The present study was supported by King Mongkut's University of Technology Thonburi, the Thailand Research Fund (TRF), and the Office of the Higher Education Commission whose guidance and assistance are gratefully acknowledged.

References

[1] S.K. Das, N. Putra, W. Roetzel, Pool boiling characteristics of nano-fluids, International Journal Heat and Mass Transfer 46 (2003) 851–862.
[2] S.K. Das, N. Putra, W. Roetzel, Pool boiling of nano-fluids on horizontal narrow tube, International Journal Multiphase Flow 29 (2003) 1237–1247.
[3] S.M. You, J.H. Kim, K.H. Kim, Effect of nanoparticles on critical heat flux of water in pool boiling heat transfer, Applied Physics Letters 83 (2003) 3374–3376.
[4] P. Vassallo, R. Kumar, S.D. Amico, Pool boiling heat transfer experiments in silica–water nano-fluids, International Journal Heat and Mass Transfer 47 (2004) 407–411.
[5] I.C. Bang, S.H. Chang, Boiling heat transfer performance and phenomena of Al_2O_3–water nano-fluids from a plain surface in a pool, International Journal Heat and Mass Transfer 48 (2005) 2407–2419.
[6] H. Kim, J. Kim, M. Kim, Experimental study on characteristics of water–TiO_2 nano-fluids, Nuclear Engineering and Technology 38 (2006) 61–68.
[7] H. Kim, J. Kim, M. Kim, Effect of nanoparticles on CHF enhancement in pool boiling of nano-fluids, International Journal Heat and Mass Transfer 49 (2006) 5070–5074.
[8] S.J. Kim, I.C. Bang, J. Buongiorno, L.W. Hu, Surface wettability change during pool boiling of nanofluids and its effect on critical heat flux, International Journal Heat and Mass Transfer 50 (2007) 4105–4116.
[9] M.N. Golubovic, H.D. Madhawa Hettiarachchi, W.M. Worek, W.J. Minkowycz, Nanofluids and critical heat flux, experimental and analytical study, Applied Thermal Engineering 29 (2009) 1281–1288.
[10] Z. Liu, L. Liao, Sorption and agglutination phenomenon of Nanofluids on a plain heating surface during pool boiling, International Journal Heat and Mass Transfer 51 (2008) 2593–2602.
[11] V. Trisaksri, S. Wongwises, Nucleate pool boiling heat transfer of TiO_2–R141b nanofluids, International Journal Heat and Mass Transfer 52 (2009) 1582–1588.
[12] W.M. Rohsenow, A method of correlating heat transfer data for surface boiling of liquids, ASME Transactions 74 (1952) 969.
[13] K. Nishikawa, Y. Fujita, S. Uchida, H. Ohta, Effect of surface configuration on nucleate boiling heat transfer, International Journal Heat and Mass Transfer 27 (1984) 1559–1571.

International Communications in Heat and Mass Transfer 37 (2010) 1340–1349

Contents lists available at ScienceDirect

International Communications in Heat and Mass Transfer

journal homepage: www.elsevier.com/locate/ichmt

A performance comparison of vapour-compression refrigeration system using various alternative refrigerants ☆

A.S. Dalkilic [a,*], S. Wongwises [b,*]

[a] Heat and Thermodynamics Division, Department of Mechanical Engineering, Yildiz Technical University, Yildiz, Besiktas, Istanbul, 34349, Turkey
[b] Fluid Mechanics, Thermal Engineering and Multiphase Flow Research Lab. (FUTURE), Department of Mechanical Engineering, King Mongkut's University of Technology Thonburi (KMUTT), Bangmod, Bangkok, 10140, Thailand

ARTICLE INFO

Available online 3 August 2010

Keywords:
Refrigeration
Alternative refrigerants
Propane
Butane
Isobutane
Hydrocarbon mixture
R32
R134a
R12
R22

ABSTRACT

A theoretical performance study on a traditional vapour-compression refrigeration system with refrigerant mixtures based on HFC134a, HFC152a, HFC32, HC290, HC1270, HC600, and HC600a was done for various ratios and their results are compared with CFC12, CFC22, and HFC134a as possible alternative replacements. In spite of the HC refrigerants' highly flammable characteristics, they are used in many applications, with attention being paid to the safety of the leakage from the system, as other refrigerants in recent years are not related with any effect on the depletion of the ozone layer and increase in global warming. Theoretical results showed that all of the alternative refrigerants investigated in the analysis have a slightly lower performance coefficient (COP) than CFC12, CFC22, and HFC134a for the condensation temperature of 50 °C and evaporating temperatures ranging between −30 °C and 10 °C. Refrigerant blends of HC290/HC600a (40/60 by wt.%) instead of CFC12 and HC290/HC1270 (20/80 by wt.%) instead of CFC22 are found to be replacement refrigerants among other alternatives in this paper as a result of the analysis. The effects of the main parameters of performance analysis such as refrigerant type, degree of subcooling, and superheating on the refrigerating effect, coefficient of performance and volumetric refrigeration capacity are also investigated for various evaporating temperatures.

© 2010 Published by Elsevier Ltd.

1. Introduction

Recently, the ozone depleting potential (ODP) and global warming potential (GWP) have become the most important criteria in the development of new refrigerants apart from the refrigerant CFCs and HCFCs, both of which have high ODP and GWP, due to the their contribution to ozone layer depletion and global warming. In spite of their high GWP, alternatives to refrigerant CFCs and HCFCs such as hydro fluorocarbon (HFC) refrigerants with their zero ODP have been preferred for use in many industrial and domestic applications intensively for a decade. HFC refrigerants also have suitable specifications such as non-flammability, stability, and similar vapour pressure to the refrigerant CFCs and HCFCs. The problems of the depletion of ozone layer and increase in global warming caused scientists to investigate more environmentally friendly refrigerants than HFC refrigerants for the protection of the environment such as hydrocarbon (HC) refrigerants of propane, isobutene, n-butane, or hydrocarbon mixtures as working fluids in refrigeration and air-conditioning systems. Although HC refrigerants have highly flammable characteristics (A3) according to the standards of ASHRAE as a negative specification, they have not only several preferable specifications such as zero ozone depletion potential, very low global warming, non-toxicity, and higher performance than other refrigerant types but also high miscibility with mineral oil and good accordance with the existing refrigerating systems. They are used in many applications with attention being paid to safety of the leakage from the system as for other refrigerants in recent years.

Many investigations have been conducted in the research into substitutes for CFC12 and CFC22. Wongwises et al. [1] presented an experimental study on the application of hydrocarbon mixtures to replace HFC134a in automotive air conditioners. The hydrocarbons investigated are propane (R290), butane (R600), and isobutane (R600a). The measured data are obtained from an automotive air-conditioning test facility utilizing HFC134a as the refrigerant. Wongwises and Chimres [2] presented an experimental study on the application of a mixture of propane, butane, and isobutene to replace HFC134a in a domestic refrigerator. The results showed that a 60%/40% propane/butane mixture was the most appropriate alternative refrigerant. Hammad and Alsaad [3] investigated the performance of a domestic refrigerator using LPG (24.4% propane, 56.4% butane, and 17.2% isobutane), which is available locally in

☆ Communicated by W.J. Minkowycz.

* Corresponding authors.
E-mail addresses: dalkilic@yildiz.edu.tr (A.S. Dalkilic), somchai.won@kmutt.ac.th (S. Wongwises).

0735-1933/$ – see front matter © 2010 Published by Elsevier Ltd.
doi:10.1016/j.icheatmasstransfer.2010.07.006

Nomenclature

atm	atmosphere
CFCs	chlorofluorocarbons
COP	coefficient of performance
GWP	global warming potential
h	enthalpy, kg kJ^{-1}
h_{fg}	latent heat of condensation, kJ kg^{-1}
HCFCs	hydro chlorofluorocarbons
HCs	hydrocarbons
HFCs	hydro fluorocarbons
ODP	ozone depletion potential
P	pressure, MPa
RE	refrigerating effect, kJ kg^{-1}
SVFR	suction vapour flow per kW of refrigeration, L s^{-1}
T	temperature, °C or K
W	isentropic compression work, kNm kg^{-1}
VRC	volumetric refrigerating capacity, kJ m^{-3}

Greek symbols

ρ	density, kg m^{-3}

Subscripts

cod	condensing/condenser
evap	evaporating/evaporator
comp	compressor
1	evaporator superheat
2	compressor superheat
3	condenser saturated liquid
4	evaporator saturated mixture

many countries, is cheap, and possesses an environmentally friendly nature with no ozone depletion potential (ODP), as an alternative refrigerant to CFC12. Jung et al. [4] used a propane/isobutane (R290/R600a) mixture to determine their performance for domestic refrigerators. According to their thermodynamic cycle analysis, the propane/isobutane blend in the composition range from 0.2 to 0.6 mass fraction of propane yields an increase in the coefficient of performance (COP) of up to 2.3% compared to CFC12. Granryd [5] mentioned the possibilities and problems of using hydrocarbons as working fluids in refrigeration equipment. In spite of their flammability specification, it is shown in his paper that alternative refrigerants can be obtained by means of hydrocarbons for energy efficient and environmentally friendly refrigerating equipment and heat pumps. Han et al. [6] studied a new hydrocarbon refrigerant mixture instead of R407C for vapour-compression refrigeration systems experimentally. As a result of the experimental and theoretical analyses, their new ternary non-azeotropic mixture of R32/R125/R161, whose ODP and GWP are zero and lower than R407C respectively, showed better refrigerating capacity and coefficient of performance (COP) than R407C. Park et al. [7] tested two pure hydrocarbons and seven mixtures composed of propylene, propane, HFC152a, and dimethylether as an alternative to HCFC22 in residential air-conditioners and heat pumps. Their experimental results show that the coefficient of performance (COP) of these mixtures is up to 5.7% higher than that of HCFC22. Mani and Selladurai [8] performed experiments using a vapour-compression refrigeration system with the new R290/R600a refrigerant mixture as a substitute refrigerant for CFC12 and HFC134a. According to the results of their experiments, the refrigerant R290/R600a had a refrigerating capacity 19.9% to 50.1% higher than that of R12 and 28.6% to 87.2% than that of R134a. The R290/R600a blend's performance coefficient (COP) is improved by 3.9–25.1% compared to that of R12 at lower evaporating temperatures and by 11.8–17.6% at higher evaporating temperatures. The refrigerant R134a had a slightly lower coefficient of performance (COP) than R12. Chen and Yu [9] presented a new refrigeration cycle, introduced as an alternative refrigeration cycle applied in residential air-conditioners, using the binary non-azeotropic refrigerant mixture R32/R134a. As a result of the comparison between the conventional cycle configuration and the new one, the coefficient of performance (COP) increases by 8% to 9% compared to the conventional cycle configuration, and the volumetric refrigerating capacity is increased by approximately 9.5%.

In this paper, a vapour-compression refrigeration cycle for binary non-azeotropic mixed refrigerants is used in order to obtain better performance. The present study mostly concentrates on a theoretical investigation of the performance of the vapour-compression refrigeration cycle. The binary non-azeotropic mixtures R-290/R-600, R-290/R-600a, R-290/R-1270, R-290/R-152a, and R-32/R-134a in various concentrations such as R-290/R-600(50/50), R-290/R-600(60/40), R-290/R-600(70/30), R-290/R-600(80/20), R-290/R-600a(40/60), R-290/R-600a(50/50), R-290/R-600a(60/40), R-290/R-600a(70/30), R-290/R-1270(20/80), R-290/R-1270(50/50), R-290/R-1270(60/40), R-290/R-1270(80/20), R-290/R-152a(60/40), R-290/R-152a(70/30), R-290/R-152a(80/20), and R-32/R-134a(30/70) are used as the working fluid for the comparison with the conventional refrigerants R12, R134a, and R22. The effects of the main parameters of performance analysis such as

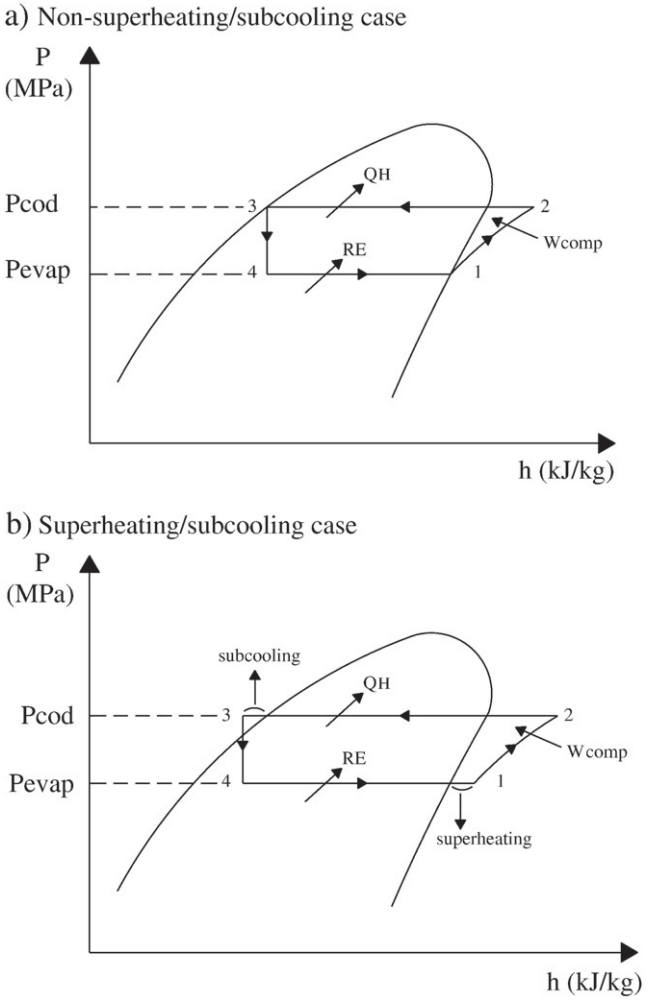

Fig. 1. Traditional vapour-compression refrigeration cycle used in the analysis for the cases of (a) non-superheating/subcooling and (b) superheating/subcooling.

refrigerant type and degree of subcooling and superheating on the refrigerating effect (RE), coefficient of performance (COP) and volumetric refrigeration capacity (VRC) are investigated for various evaporating temperatures ranging between −30 and 5 °C and a constant condensation temperature of 50 °C.

2. Caculation method

The pressure–enthalpy diagram prepared for theoretical data for two different cases is shown in Fig. 1. The ideal refrigeration cycle in Fig. 1 is considered for the working substances that

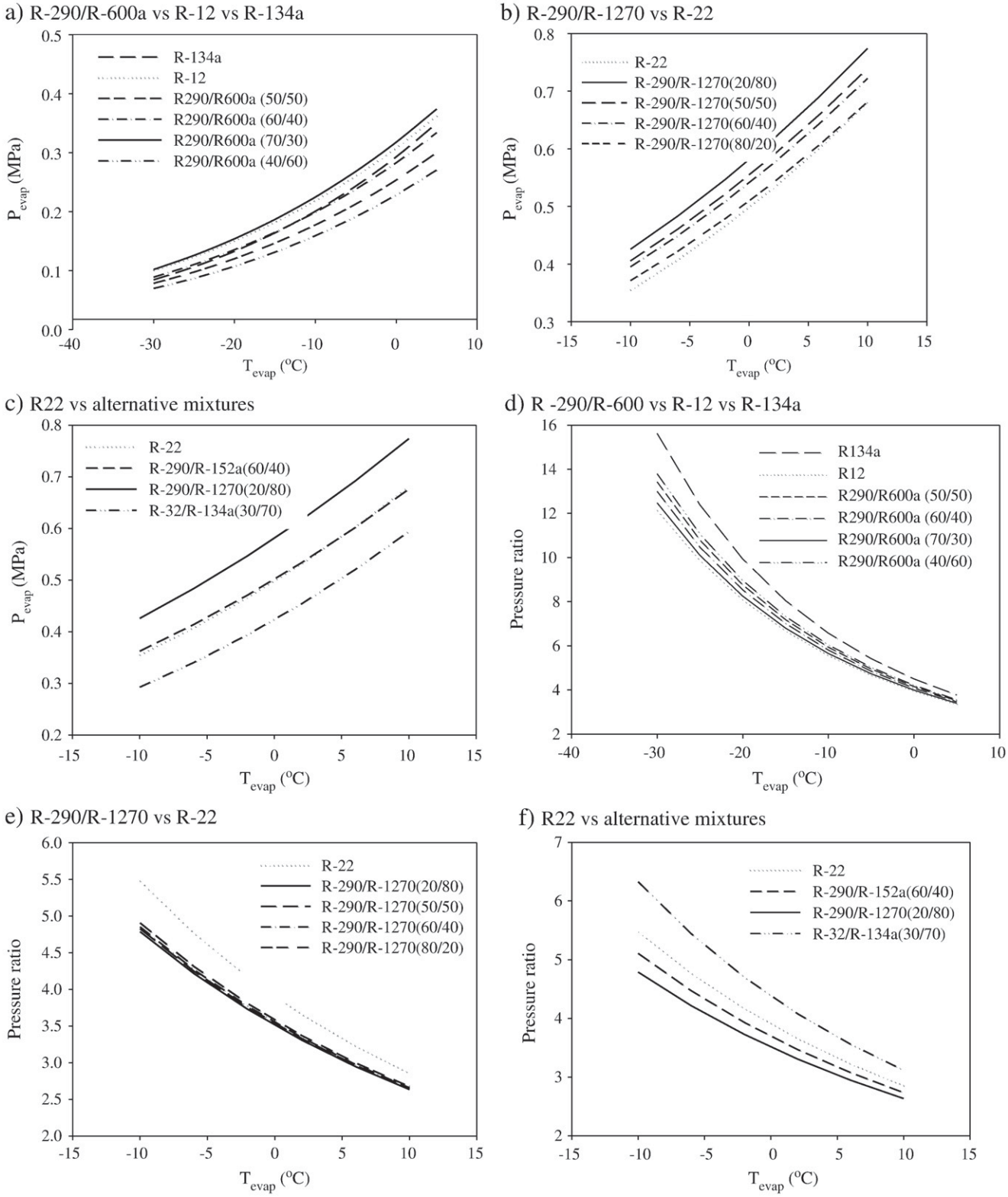

Fig. 2. Evaporating pressure (a, b, c) and pressure ratio (d, e, f) vs evaporating temperature.

change phase during the cycle. It is known that the actual refrigeration cycle systems have some deviations from the ideal one due to pressure losses of fluid flow and heat transfer exchange between the surroundings. The superheated state of vapour exists at the inlet part of the compressor as shown in Fig. 1b, the pressure of the liquid at the exit part of the condenser is lower than the pressure at the inlet part of it, there is a pressure drop greater than the ideal one between the condenser and expansion valve, and also a larger pressure drop occurs on the evaporation line.

Cycle performance determination is performed to ease the theoretical calculations by means of some assumptions as follows: neglect of the pressure drops and the heat losses to the environment from the devices of evaporators, recuperators, subcooler, phase separator and condensers; saturated vapour at the low boiling point stream (vapour phase) from the separator and saturated liquid at the high boiling point

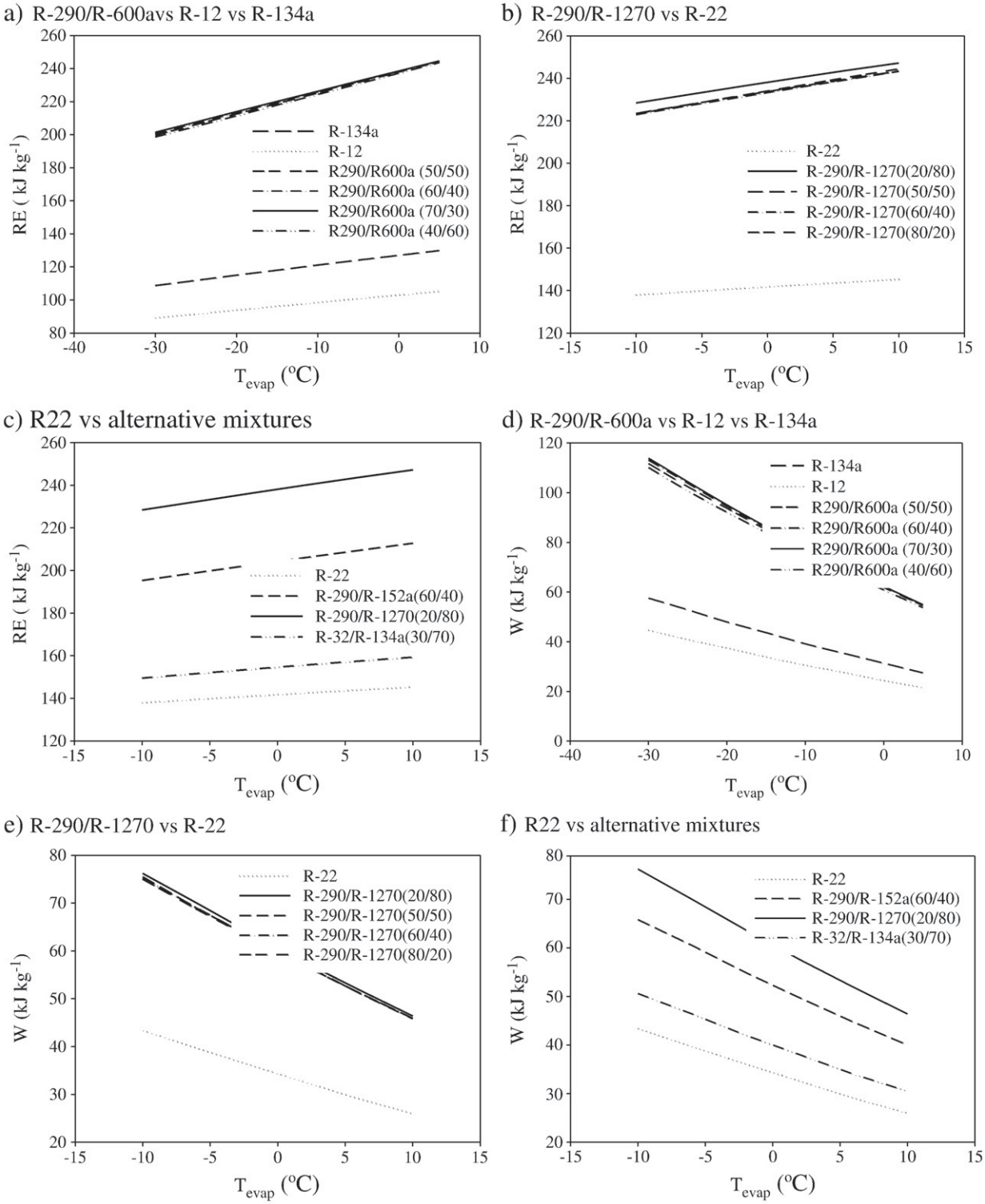

Fig. 3. Refrigerating effect (a, b, c) and isentropic compression work (d, e, f) vs evaporating temperature.

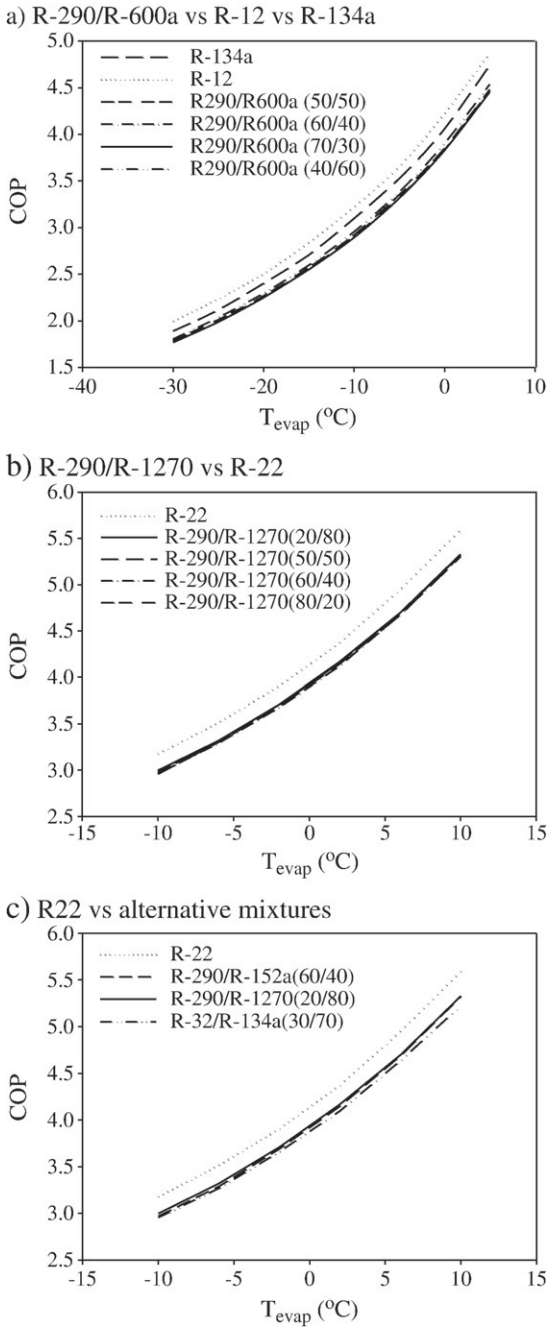

Fig. 4. Coefficient of performance (a, b, c) vs evaporating temperature.

stream (liquid phase) from the separator in Fig. 1a; the isenthalpic flow across the expansion valves; and the considered isentropic efficiency for the compressor. When the thermodynamic properties of each state of the cycle are determined, the equations for the cycle analysis can be obtained by means of mass and energy conservation. The data reduction of the theoretical results can be analysed below.

The pressure ratio of the cycle can be seen below as follows:

$$The\,pressure\,ratio = P_{cod} / P_{evap}. \quad (1)$$

Isentropic compression work of the compressor (W_{comp}) is expressed as follows:

$$W_{comp} = h_2 - h_1. \quad (2)$$

The refrigerating effect (RE), in other words, the heat transfer rate of the evaporator (Q_{evap}), is calculated as follows:

$$RE = Q_{evap} = h_1 - h_4. \quad (3)$$

Power per ton of refrigeration is calculated as follows:

$$Power\,per\,ton\,of\,refrigeration (P/TR) = 3.5 W_{comp} / RE. \quad (4)$$

In the vapour-compression system in Fig. 1, volumetric refrigerating capacity (VRC) is given as:

$$VRC = \rho_1 \cdot RE. \quad (5)$$

Suction vapour flow per kW of refrigeration can be determined as:

$$SVFR = 1 / (\rho_1 \cdot RE). \quad (6)$$

The coefficient of performance (COP) of the refrigeration system's cycle can be determined by:

$$COP = RE / W_{comp}. \quad (7)$$

3. Results and discussion

The dependency on the composition of refrigerant mixtures makes the pressure–temperature relationship in the cycle significant for condensers and evaporators. Cycle performance is affected by the pressure alterations while the ratios of the blend vary at the given temperature. For that reason, the proportion of the components in the mixture is one of the significant factors in the cycle. For comparison of the theoretical data, R12 and R22 are chosen in this paper as reference fluids due to their common usage in cooling systems and prohibition by the Montreal Protocol.

The analysis of the variation of physical properties of pure and blend refrigerants such as evaporation pressure (P_{evap}), pressure ratio, isentropic compression work (W), refrigerating effect (RE), power per ton of refrigeration, volumetric refrigeration capacity (VRC), suction vapor flow rate (SVFR) and coefficient of performance (COP) is investigated in this theoretical study, and they are plotted against the evaporating temperature (T_{evap}) as shown in Figs. 2-6c for the ideal refrigeration cycle in Fig. 1a, and in Figs. 6d-9b for comparison of the superheating/subcooling case in Fig. 1b with the non-superheating/subcooling case in Fig. 1a. Considering the evaporation and condensation temperatures of studies in the literature, the example case studies in Tables 1 and 2 as shown in Stoecker and Jones [10] are shown for the determination of mixed alternative refrigerants for the traditional pure refrigerants R12 and R22 respectively. Tables 3 and 4 shows deviations of alternative refrigerants from the values of R12 and R22 numerically.

The changes in evaporation pressure (P_{evap}) and pressure ratio with the evaporation temperature (T_{evap}) are shown in Fig. 2 for listed refrigerant mixtures with different proportions as follows: R-290/R-600a vs R-12 vs R-134a (Fig. 2a), R-290/R-1270 vs R-22 (Fig. 2b), and R22 vs R290/152a vs R290/R1270 vs R32 vs R134a (Fig. 2c). The nearest pressure ratio of substitute refrigerant to base one belongs to R290/R600a (70/30 by wt.%), whose pressure ratio is 1.63% higher than that of R12 and R290/R152a (60/40 by wt.%), whose pressure ratio is 7.21% lower than that of R22 as shown in Tables 3 and 4 for the constant condensation and evaporation temperatures of 50 °C and −10 °C respectively. In addition to this, R290/R600 (50/50 by wt.%) and R32/R134a (30/70 by wt.%) give the highest ratios as substitutes for R12 and R22 respectively according to the same table. It can be seen from

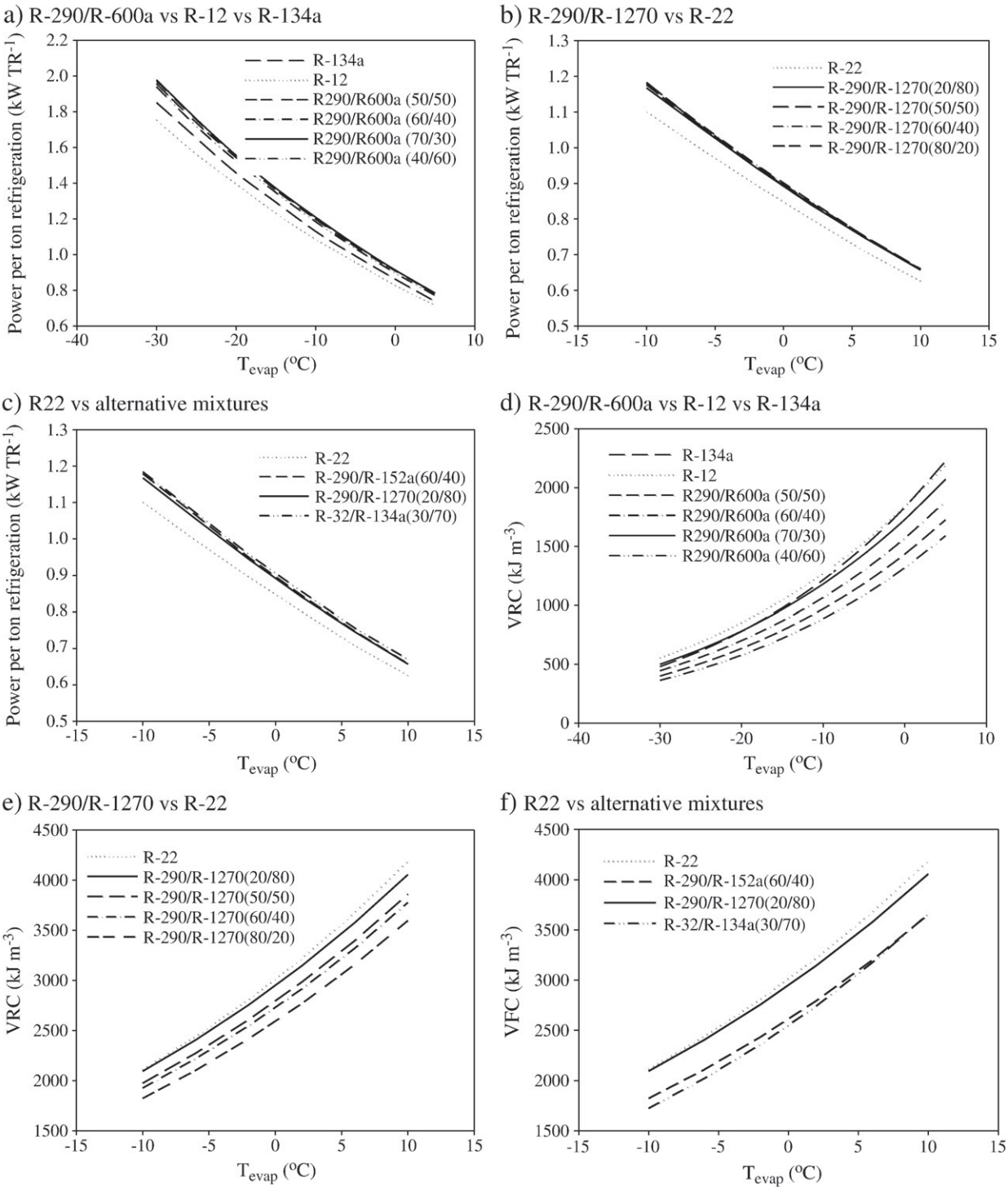

Fig. 5. Power per ton of refrigeration (a, b, c) and volumetric refrigerating capacity (d, e, f) vs evaporating temperature.

Fig. 2a and c that the saturated vapour pressures for R290/R600a (70/30 by wt.%) and R290/R152a (60/40 by wt.%) are closer than others to the vapour pressure curve of the refrigerants R12 and R22 respectively.

In Tables 1 and 2, significant parameters of cycle performance under different conditions are calculated as case studies of R12 and R22 respectively for the same condensing and evaporation temperatures obtained from the literature review. In addition to this, it can be seen that the evaluation of cycle performance results under different working conditions agrees with those under real working conditions.

Fig. 3 shows that the refrigerating effect (RE) increases with increasing evaporation temperature (T_{evap}) while the compressor power (W_{comp}) decreases with increasing T_{evap} for the constant condensation temperature of 50 °C and the evaporation temperatures ranging from −30 °C to 5 °C. Apart from the mixture of R290/R600a (50/50 by wt.%) and R32/R134a (30/70 by wt.%), other tested alternative refrigerants have much higher refrigerating effects than those of R12 and R22 in Fig. 3a, b, c respectively. All of the tested refrigerants at various concentrations apart from R134a and R32/R134a (30/70 by wt.%) have much higher values of isentropic

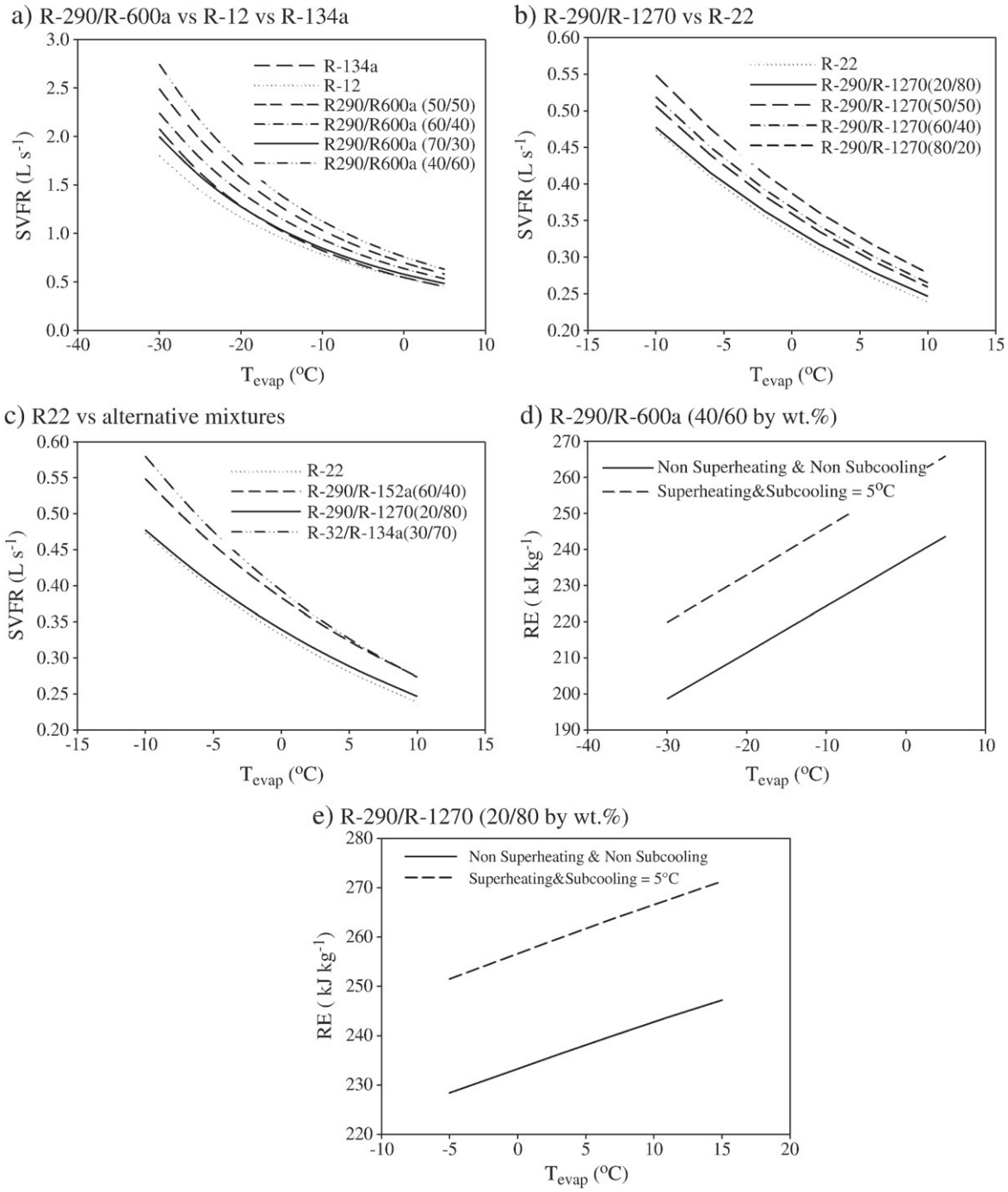

Fig. 6. Suction vapour flow rate (a, b, c) and refrigerating effect (d, e) vs evaporating temperature.

compression work than R12 and R22 respectively in Fig. 3d, e, f and as shown in Tables 3 and 4.

The variation of performance coefficient (COP) with evaporation temperature (T_{evap}) is illustrated in Fig. 4a, b, c. From this figure, the coefficient of performance (COP) increases as the evaporation temperature (T_{evap}) increases for the constant condensation temperature of 50 °C and evaporation temperatures ranging from −30 °C to 5 °C, and this alteration also can be understood from Eq. (4), considering an increase in refrigerating effect (RE) and a decrease in compressor power (W_{comp}) for the case. The decrease in pressure ratio for the compressor also improves the efficiency. All the performance coefficients (COP) of the alternative refrigerants tested are found to be lower than those of R12 and R22 for the simulation conditions. In addition to this, the coefficient of performance (COP) has some alterations with the decrease or increase in the components' ratios in the composition due to the changes in the thermodynamic physical properties of the refrigerant mixture as the composition of the mixture varies.

The changes in power needed for refrigeration with evaporation temperature (T_{evap}) in Fig. 5a, b, c, volumetric refrigeration capacity (VRC) with evaporation temperature (T_{ev}) in Fig. 5d, e, f, and suction vapour flow needed for refrigeration (SVFR) with evaporation temperature (T_{evap}) in Fig. 6a, b, c are shown in order to verify the cycle performance advantages of alternative refrigerants. The specific volume of the suction vapour decreases, causing the

Table 1
Operation on a standard vapor-compression cycle using R12 and various refrigerants at $T_{cod}=50$ °C and $T_{evap}=-10$ °C.

Refrigerant (by wt.%)	P_{evap} (MPa)	P_{cod} (MPa)	Pressure ratio	W_{comp} (kJ kg^{-1})	RE (kJ kg^{-1})	Power per ton refrigeration (kW TR^{-1})	VRC (kJ m^{-3})	SVFR (L s^{-1})	COP
R-12	0.219	1.217	5.562	30.500	98.600	1.083	1273.912	0.785	3.233
R-134a	0.201	1.318	6.570	39.100	121.100	1.130	1215.844	0.822	3.097
20%R600 + 80%R290	0.213	1.268	5.953	83.800	234.500	1.251	1120.676	0.892	2.798
30%R600 + 70%R290	0.176	1.102	6.261	84.900	237.700	1.250	959.357	1.042	2.800
40%R600 + 60%R290	0.149	0.965	6.492	85.000	240.200	1.239	836.376	1.195	2.826
50%R600 + 50%R290	0.128	0.852	6.668	84.000	242.400	1.213	742.229	1.347	2.886
30%R600a + 70%R290	0.225	1.270	5.654	78.200	226.200	1.210	1180.764	0.846	2.893
40%R600a + 60%R290	0.199	1.155	5.807	77.700	225.900	1.204	1066.248	0.937	2.907
50%R600a + 50%R290	0.177	1.053	5.936	77.100	225.200	1.198	969.936	1.031	2.921
60%R600a + 40%R290	0.225	1.270	5.654	78.200	226.200	1.210	1180.764	0.846	2.893

Table 2
Operation on a standard vapor-compression cycle using R22 and various refrigerants at $T_{cod}=50$ °C and $T_{evap}=-10$ °C.

Refrigerant (by wt.%)	P_{evap} (Mpa)	P_{cod} (MPa)	Pressure ratio	W_{comp} (kJ kg^{-1})	RE (kJ kg^{-1})	Power per ton refrigeration (kW TR^{-1})	VRC (kJ m^{-3})	SVFR (L s^{-1})	COP
R-22	0.355	1.943	5.476	43.400	138.000	1.101	1273.912	0.473	3.180
80%R1270 + 20%R290	0.426	2.039	4.789	76.200	228.400	1.168	1215.844	0.478	2.997
50%R1270 + 50%R290	0.406	1.958	4.829	75.500	223.400	1.183	1120.676	0.506	2.959
40%R1270 + 60%R290	0.395	1.918	4.853	75.200	222.900	1.181	959.357	0.519	2.964
20%R1270 + 80%R290	0.371	1.822	4.908	75.000	223.200	1.176	836.376	0.549	2.976
40%R152a + 60%R290	0.362	1.850	5.108	65.800	195.300	1.179	742.229	0.549	2.968
30%R152a + 70%R290	0.366	1.835	5.019	67.700	201.300	1.177	1180.764	0.587	2.973
20%R152a + 80%R290	0.362	1.815	5.025	70.000	197.400	1.241	1066.248	0.587	2.820
70%R134a + 30%R32	0.293	1.851	6.328	50.600	149.500	1.185	969.936	0.580	2.955

increase in the mass flow rate as the evaporation temperature (T_{evap}) increases. The effects of changed concentrations on the performance parameters can be seen from these figures and also from Tables 1–4. The volumetric cooling effect, in other words, the volumetric capacity, is defined as the cooling capacity per unit of vapour volume at the exit of the evaporator. A high cooling capacity can be obtained from a high volumetric capacity refrigerant for a given swept volume in the compressor.

The cycle performance can be improved by the subcooling and superheating application. In this paper, the effects of the degree of subcooling and superheating are calculated respectively. The comparison of the superheating/subcooling case in Fig. 1b with the non-superheating/subcooling case in Fig. 1a is illustrated in Fig. 6d, e and Figs. 7-9 for the blend refrigerants of R-290/R-600a (40/60 by wt.%) and R-290/R-1270 (20/80 by wt.%). It should be noted that the characteristics of trend lines belonging to each refrigerant are similar to those from Figs. 2a-6c and the performance coefficient (COP) values of the superheating/subcooling case are found to be higher than those of the non-superheating/subcooling case. The reason for the improvement is the increase in the compressor inlet temperature, and thus the increases in the refrigerating effect and volumetric refrigerating capacity.

The thermo-physical properties, restrictions related to safety, environmental impact, and associated legislation are the most

Table 3
Some deviation values of alternative refrigerants from R12.

R12 at $T_{cod}=50$ °C and $T_{evap}=-10$ °C							
Refrigerant	Pressure ratio %	W_{comp} %	RE %	Power per ton refrigeration %	VRC %	SVFR %	COP %
R-134a	6.57	21.73	18.57	3.88	−4.77	4.55	−4.03
50%R600 + 50%R290	16.58	63.69	59.32	10.73	−71.63	41.73	−12.02
30%R600a + 70%R290	1.63	60.86	56.41	10.23	−7.88	7.31	−11.39
40%R600a + 60%R290	4.21	60.61	56.35	9.77	−19.47	16.3	−10.83
50%R600a + 50%R290	6.29	60.31	56.21	9.35	−31.33	23.86	−10.31
60%R600a + 40%R290	7.99	59.81	56.04	8.58	−43.38	30.25	-9.39

Table 4
Some deviation values of alternative refrigerants from R22.

R22 at $T_{cod}=50$ °C and $T_{evap}=-10$ °C							
Refrigerant	Pressure ratio %	W_{comp} %	RE %	Power per ton refrigeration %	VRC %	SVFR %	COP %
80%R1270 + 20%R290	−14.36	43.04	39.57	5.73	−0.95	0.94	−6.08
40%R152a + 60%R290	−7.21	34.04	29.33	6.65	−16.01	13.8	−7.13
30%R152a + 70%R290	−9.1	35.89	31.44	6.48	−16.25	13.99	−6.93
20%R152a + 80%R290	−8.98	38	30.09	11.31	−24.13	19.44	−12.75
70%R134a + 30%R32	13.46	14.22	7.69	7.08	−22.64	72.4	−7.62

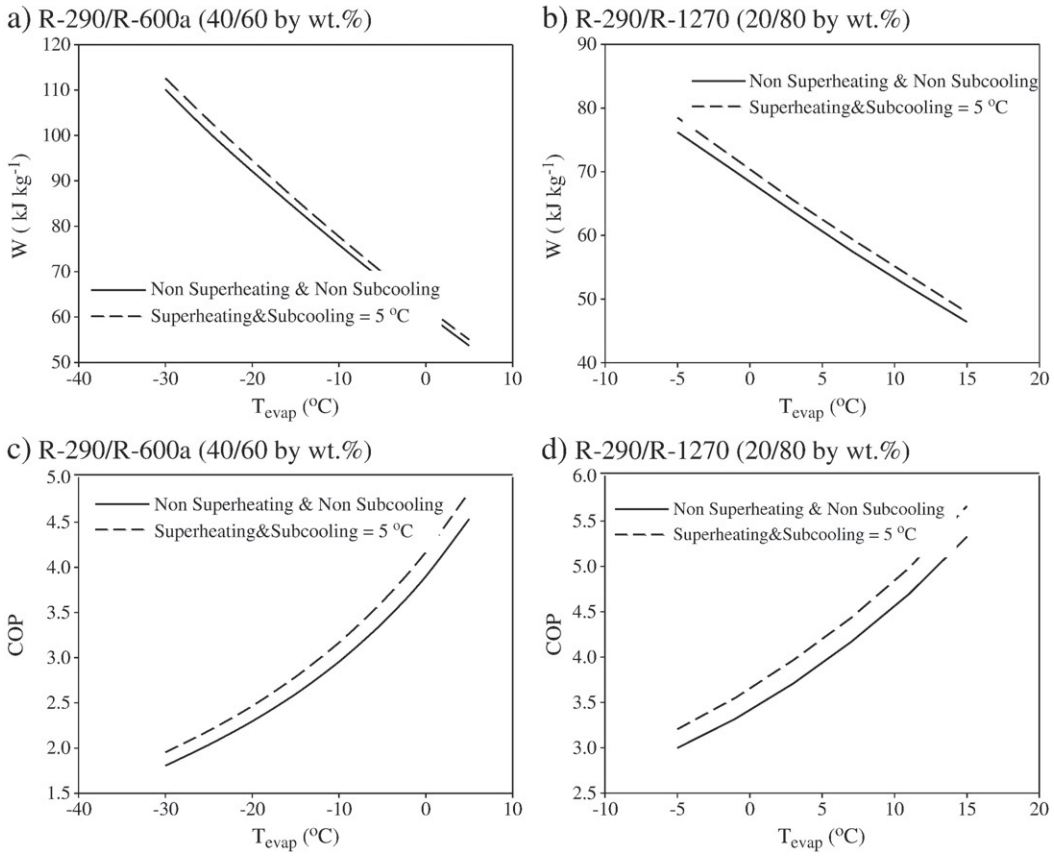

Fig. 7. Isentropic compression work (a, b) and coefficient of performance (c, d) vs evaporating temperature.

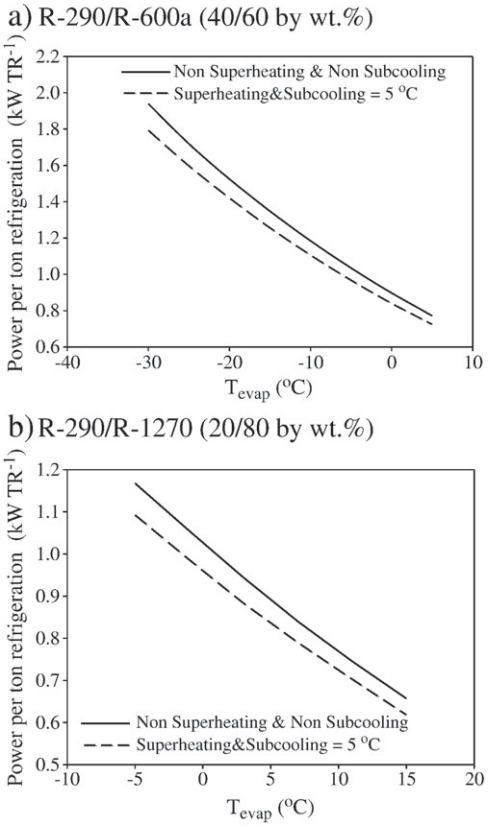

Fig. 8. Power per ton of refrigeration (a, b) vs evaporating temperature.

significant factors in choosing a new refrigerant. Low viscosities of liquid and vapour phases, high liquid specific heat, high thermal conductivities of liquid and vapour phases, high latent heat, and small temperature glide are the desired thermo-physical properties of refrigerant mixtures in the literature. As a result of the analysis in this paper, HC290/HC600a (40/60 by wt.%) instead of R12 and HC290/HC1270 (20/80 by wt.%) instead of R22 seem to be the best alternative refrigerants in terms of the factors in choosing a new refrigerant.

4. Conclusions

In this study, an ideal vapour-compression refrigeration system is used for the performance analysis of alternative new refrigerant mixtures as substitutes for CFC12, HFC134a, and CFC22. Considering the comparison of performance coefficients (COP) and pressure ratios of the tested refrigerants and also the main environmental impacts of ozone layer depletion and global warming, refrigerant blends of HC290/HC600a (40/60 by wt.%) and HC290/HC1270 (20/80 by wt.%) are found to be the most suitable alternatives among refrigerants tested for R12 and R22 respectively. The refrigeration efficiency, the performance coefficient (COP) of the system, increases with increasing evaporating temperature for a constant condensing temperature in the analysis. All systems including various refrigerant blends were improved by analysing the effect of the superheating/subcooling case. Better performance coefficient values (COP) than those of the non-superheating/subcooling case are obtained as a result of this optimization.

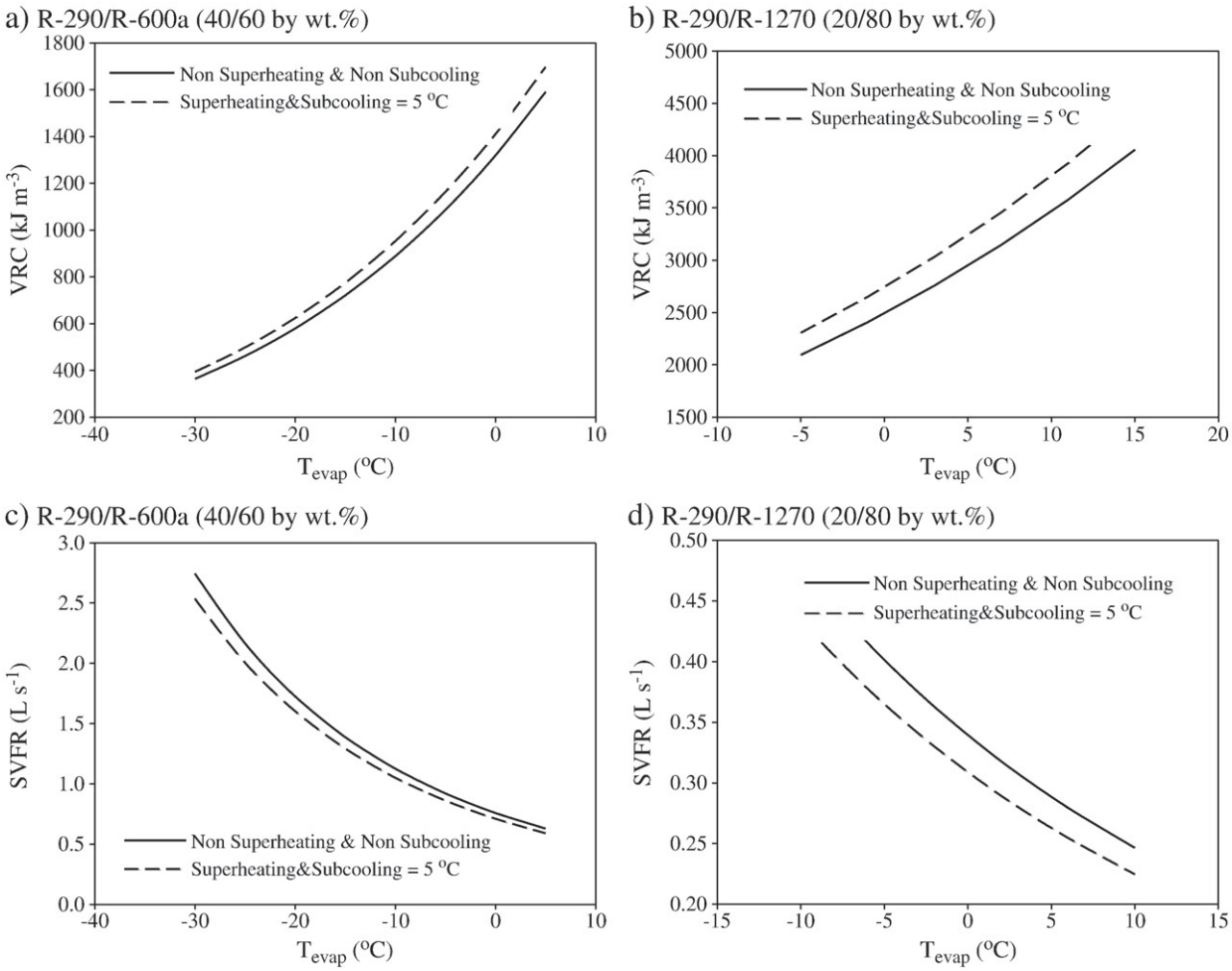

Fig. 9. Volumetric refrigerating (a, b) and suction vapour flow rate (c, d) vs evaporating temperature.

Acknowledgements

The authors are indebted to King Mongkut's University of Technology Thonburi (KMUTT), the Thailand Research Fund, the Office of the Higher Education Commission and the National Research University Project for supporting this study. Especially, the first author wishes to thank KMUTT for providing him with a Post-doctoral fellowship.

References

[1] S. Wongwises, A. Kamboon, B. Orachon, Experimental investigation of hydrocarbon mixtures to replace HFC-134a in an automotive air conditioning system, Energy Conversion and Management 47 (2006) 1644–1659.
[2] S. Wongwises, N. Chimres, Experimental study of hydrocarbon mixtures to replace HFC-134a in a domestic refrigerator, Energy Conversion and Management 46 (2005) 85–100.
[3] M.A. Hammad, M.A. Alsaad, The use of hydrocarbon mixtures as refrigerants in domestic refrigerators, Applied Thermal Engineering 19 (1999) 1181–1189.
[4] D. Jung, C.B. Kim, B.H. Lim, H.W. Lee, Testing of a hydrocarbon mixture in domestic refrigerators, ASHRAE Transactions 3 (1996) 1077–1084.
[5] E. Granryd, Hydrocarbons—an overview, International Journal of Refrigeration 24 (2001) 15–24.
[6] X.H. Han, Q. Wang, Z.W. Zhu, G.M. Chen, Cycle performance study on R-32/R-125/R-161 as alternative refrigerant to R-407C, Applied Thermal Engineering 27 (2007) 2559–2565.
[7] K.J. Park, T. Seo, D. Jung, Performance of alternative refrigerants for residential air-conditioning applications, Applied Energy 84 (2007) 985–991.
[8] K. Mani, V. Selladurai, Experimental analysis of a new refrigerant mixture as drop-in replacement for CFC12 and HFC134a, International Journal of Thermal Sciences 47 (2008) 1490–1495.
[9] J. Chen, J. Yu, Performance of new refrigerant cycle using refrigerant mixture R32/R134a for residential air-conditioner applications, Energy and Buildings 40 (2008) 2022–2027.
[10] W.F. Stoecker, J.W. Jones, Refrigeration and Air Conditioning, second ed., McGraw-Hill, 1982, pp. 298–299.

This article was downloaded by: *[Wongwises, Somchai]*
On: *23 September 2010*
Access details: *Access Details: [subscription number 927229492]*
Publisher *Taylor & Francis*
Informa Ltd Registered in England and Wales Registered Number: 1072954 Registered office: Mortimer House, 37-41 Mortimer Street, London W1T 3JH, UK

Experimental Heat Transfer
Publication details, including instructions for authors and subscription information: http://www-intra.informaworld.com/smpp/title~content=t713770473

Experimental Investigation on the Thermal Conductivity and Viscosity of Silver-Deionized Water Nanofluid

L. Godson[a]; B. Raja[b]; D. Mohan Lal[a]; S. Wongwises[c]
[a] R&AC Division, Department of Mechanical Engineering, College of Engineering, Guindy, Anna University, Chennai, Tamil Nadu, India [b] Indian Institute of Information Technology, Design and Manufacturing, Indian Institute of Technology, Madras, Chennai, Tamil Nadu, India [c] Fluid Mechanics, Thermal Engineering and Multiphase Flow Research Lab (FUTURE), Department of Mechanical Engineering, King Mongkut's University of Technology Thonburi, Bangmod, Bangkok, Thailand

Online publication date: 22 September 2010

To cite this Article Godson, L. , Raja, B. , Lal, D. Mohan and Wongwises, S.(2010) 'Experimental Investigation on the Thermal Conductivity and Viscosity of Silver-Deionized Water Nanofluid', Experimental Heat Transfer, 23: 4, 317 — 332
To link to this Article: DOI: 10.1080/08916150903564796
URL: http://dx.doi.org/10.1080/08916150903564796

PLEASE SCROLL DOWN FOR ARTICLE

Full terms and conditions of use: http://www-intra.informaworld.com/terms-and-conditions-of-access.pdf

This article may be used for research, teaching and private study purposes. Any substantial or systematic reproduction, re-distribution, re-selling, loan or sub-licensing, systematic supply or distribution in any form to anyone is expressly forbidden.

The publisher does not give any warranty express or implied or make any representation that the contents will be complete or accurate or up to date. The accuracy of any instructions, formulae and drug doses should be independently verified with primary sources. The publisher shall not be liable for any loss, actions, claims, proceedings, demand or costs or damages whatsoever or howsoever caused arising directly or indirectly in connection with or arising out of the use of this material.

Experimental Heat Transfer, 23:317–332, 2010
Copyright © Taylor & Francis Group, LLC
ISSN: 0891-6152 print/1521-0480 online
DOI: 10.1080/08916150903564796

Downloaded By: [Wongwises, Somchai] At: 10:43 23 September 2010

EXPERIMENTAL INVESTIGATION ON THE THERMAL CONDUCTIVITY AND VISCOSITY OF SILVER-DEIONIZED WATER NANOFLUID

L. Godson,[1] B. Raja,[2] D. Mohan Lal,[1] S. Wongwises[3]

[1]R&AC Division, Department of Mechanical Engineering, College of Engineering, Guindy, Anna University, Chennai, Tamil Nadu, India
[2]Indian Institute of Information Technology, Design and Manufacturing, Indian Institute of Technology, Madras, Chennai, Tamil Nadu, India
[3]Fluid Mechanics, Thermal Engineering and Multiphase Flow Research Lab (FUTURE), Department of Mechanical Engineering, King Mongkut's University of Technology Thonburi, Bangmod, Bangkok, Thailand

This article presents an experimental investigation where the thermal conductivity and viscosity of silver-deionized water nanofluid is measured and studied. The mixture consists of silver nanoparticles of 0.3, 0.6, and 0.9% of volume concentrations and studied for temperatures between 50°C and 90°C. The transient hot-wire apparatus and Cannon-Fenske viscometer are used to measure the thermal conductivity and kinematic viscosity of nanofluid, respectively. The thermal conductivity increases with the increase in temperature and particle concentrations. A minimum and maximum enhancement of 27% at 0.3 vol% and 80% at 0.9 vol% are observed at an average temperature of 70°C. The viscosity decreases with the increase in temperature and increases with the increase in particle concentrations. The effect of Brownian motion and thermophoresis on the thermo-physical properties is discussed. Thus, an experimental correlation for thermal conductivity and viscosity, which relates the volume concentration and temperature, is developed, and the proposed correlation is found to be in good agreement with the experimental results.

Keywords thermal conductivity, viscosity, silver, nanofluid, temperature, nanoparticle enhancement

INTRODUCTION

Heat transfer fluids, such as water, oil, ethylene glycol, etc., have been playing an important role in the working of many thermal systems for centuries. The scope for the design of thermal systems, like heat exchangers, with respect to the thermo-physical properties is limited since these liquids possess low values of thermal conductivity. Low heat transfer characteristics of these fluids affect the enhancement of performance and in turn the compactness of heat exchangers. However, it is possible to engineer fluids with suspended metallic particles to artificially enhance the thermal conductivity. Particles in the order of millimeter and micrometer suspended in fluids were earlier

Received 10 August 2009; accepted 11 December 2009.
Address correspondence to Lazarus Godson, R&AC Division, Department of Mechanical Engineering, College of Engineering, Guindy, Anna University, Chennai, 600 025, Tamil Nadu, India. E-mail: godasir@yahoo.co.in

NOMENCLATURE

A	surface area (m^2)
D	diffusion coefficient
g	acceleration of gravity (m s^{-2})
h	free surface elevation difference (m)
J	mass flux (kg/m^2s)
k	thermal conductivity (W/mK)
l	length of the capillary section (m)
n	empirical shape factor
q	heat flux (W/m)
r	radial distance (m)
T	final temperature (°C)
t	time (sec)
T_0	initial temperature (°C)
V	velocity (m/s)

Greek Symbols

μ	dynamic viscosity, (mPa.s)
β	proportionality factor
γ	particle size (nm)
ν	kinematic viscosity (m^2/s)
ρ	density (kg/m^3)
φ	volume fraction
∇	gradient

Subscript

B	Brownian
nf	nanofluid
p	particle
T	thermophoresis
w	water

Abbreviation

CNT	carbon nanotube

Downloaded By: [Wongwises, Somchai] At: 10:43 23 September 2010

recommended, but problems, such as the clogging of fluid paths, abrasion, pressure drop, etc., are the major negative features. With the unprecedented increase in the heat loads and heat fluxes caused by a variety of products, such as computers, defense and high-powered lasers, X-rays, Klystron tubes, etc., efficient cooling is the need of the hour. Thus, there is a growing demand for better heat transfer fluids with significantly higher thermal conductivities and improved heat transfer characteristics. A nanofluid (nanoparticle fluid suspensions in a base fluid), a term first suggested by Choi (1995) and later experimented by notable researchers, is a new type of heat transfer fluid that exhibits thermo-physical properties superior to those of the conventional fluid and microparticle-fluid [1]. Besides the enhanced heat transfer, nanofluids eliminate the problems arising with the microparticle fluids. Thus, nanofluids have greater potential ability for heat transfer enhancement and are highly suited to the application in practical heat transfer processes. The thermophysical properties of nanofluids, such as thermal conductivity and viscosity are of significant importance in every heat transfer application involving a fluid system.

First, the thermal conductivity of nanofluids is more temperature sensitive than that of the base fluid. Recent investigations on the enhancement of thermal conductivity have revealed an enhancement with the metallic nanoparticles and oxide nanoparticles from 5 to 60% for φ = 0.1 to 5% [2]. Lee et al. [3] measured thermal conductivity of Al_2O_3–water and CuO–water nanofluids for a temperature between 20°C and 40°C and found a three-fold enhancement in the thermal conductivity. Das et al. [4] reported that the thermal conductivity of Al_2O_3 and CuO nanoparticles in water, for temperature ranging from 21°C to 51°C, increases with an increase in temperature and particle concentrations. Masuda et al. [5] dispersed oxide nanoparticles (γ-Al_2O_3 and TiO_2 with $\varphi = 4.3\%$) in liquid and showed the increase in the thermal conductivity to be 32% and 11%, respectively. Grimm [6] dispersed aluminum particles ($\gamma = 80$ to 1 μm) in water and reported a 100% increase in the thermal conductivity for $\varphi = 0.5$ to 10%. Choi and Eastman [7]

Downloaded By: [Wongwises, Somchai] At: 10:43 23 September 2010

and Eastman et al. [8] showed that the thermal conductivity of Cu-water and CNT-water nanofluids was higher compared to that of their base liquids. Eastman et al. [9] showed that Cu-ethylene glycol (nanoparticles coated with thioglycolic acid) with $\varphi = 0.3\%$ resulted in 40% enhancement in thermal conductivity. Thus, the enhancements depend on factors such as particle shape, particle size, and volume fraction of particles and temperature and thermal properties of solid and liquid materials.

Second, determining the viscosity of the nanofluid is essential in establishing adequate skin friction and a convective heat transfer coefficient. Until now, only a few studies have addressed the viscous properties of nanoparticle suspensions at different temperatures. Masuda et al. [5] measured the temperature-dependent viscosity of water-based nanofluids; Pak and Cho [10] presented additional viscosity data for Al_2O_3–water nanofluid. Wang et al. [11] measured the viscosity for Al_2O_3–water and Al_2O_3–ethylene glycol nanofluids at ambient temperature.

He et al. [12] measured the thermal conductivity and viscosity of TiO_2–distilled water nanofluids ($\gamma = 95$ nm) and investigated the heat transfer performance in a vertical pipe flowing in an upward direction under a constant heat flux boundary condition in both laminar and turbulent flow regimes. The results showed that the thermal conductivity of nanofluids increases with the increasing volume fraction, and the viscosity also increases with an increase in particle concentration as well as the particle size of the nanoparticles. Putra et al. [13] studied the influence of temperature on viscosity of Al_2O_3–water. Recently, Maré et al. [14] have obtained the temperature-dependent viscosity data for Al_2O_3–water with relatively high particle concentrations.

Lu and Fan [15], Kwak and Kim [16], Nguyen et al. [17], Namburu et al. [18], and Avsec and Oblak [19] have presented the viscosity of nanofluids with various metallic and oxide nanoparticles and reported that the viscosity of nanofluids increases with particle loading and decreases with increase in temperature. Lee et al. [3] measured the viscosity of Al_2O_3–water nanofluids with $\varphi = 0.01$–0.3% and found that the viscosity decreases with an increase in temperature. Murshed et al. [20] measured the viscosity of nanofluids and observed an increase in viscosity with the volumetric loading of nanoparticles.

There is always a second opinion on leveraging theoretical models to predict the thermal conductivity and viscosity of nanofluids. Since the thermo-physical properties of nanofluids depend on various factors, such as particle size, particle shape, nature of material, and pH value, it is hard to develop a universal model. For example, nanofluids with spherical-shaped particles provide only slight enhancements in thermal conductivity than with the cylindrical-shaped particles. Also, nanofluids with smaller nanoparticle size exhibit greater thermal conductivity. Nanofluids with metallic nanoparticles give higher thermal conductivity than nanofluids with non metallic nanoparticles [20]. Besides this, the thermo-physical properties of nanofluids are strongly dependent on temperature [17, 21–23].

Most recently, Buongiorno et al. [24] reported a study on resolving the issue of a possible anomaly in the behavior of the thermal conductivity nanofluids claimed by some authors in the past. The thermal conductivity of identical samples of nanofluids was measured by over 30 organizations worldwide, using a variety of experimental approaches. Various types of nanofluids comprised of aqueous and non aqueous base fluids, metal and metal oxide particles, near-spherical and elongated particles, at low and high particle concentrations were tested. The results from the analysis revealed that

the data from most organizations lie within ± 10%. Also, the thermal conductivity of the nanofluids was found to increase with particle concentration and aspect ratio, as expected from classical theory, and was found to be in good agreement with the experimental data, suggesting that no anomalous enhancement of thermal conductivity was achieved in the nanofluids tested. However, in the above-mentioned investigation, the authors only one nanofluid with metallic nanoparticles was tested, and only at very low concentration. Also, the temperature effect on thermal conductivity was not investigated.

Das et al. [4] reported that there exists an extremely strong temperature effect on the thermal conductivity enhancement of nanofluids; also, the enhancement was more than three times higher. The other important observation form this study is that at elevated temperatures, neither Al_2O_3 nor CuO nanofluids comply with the Hamilton–Crosser (H–C) model. This is because the model is completely insensitive to temperature variations between 21°C and 55°C. However, the H–C model agreed well in the experiments conducted by Lee et al. [25] with Al_2O_3–water nanofluids at room temperature. Murshed et al. [20] investigated the thermal conductivity and viscosity of TiO_2 and Al_2O_3 nanofluids and found the thermal conductivity of nanofluids to be strongly dependent on temperature and that the H–C model gave under-predictions of the measured data.

Duangthongsuk and Wongwises [26] investigated the thermal conductivity and viscosity of TiO_2–water nanofluids ($\varphi = 0.2$–2%) over the temperatures ranging from 15°C to 35°C. The results show that the measured viscosity and thermal conductivity of nanofluids increased as the particle concentrations increased and were higher than the values of the base liquids. The results obtained from this study with regard to the thermophysical properties have been used to study the heat transfer performance of the above-mentioned nanofluid in a heat exchanger and found a heat transfer enhancement up to 11% when compared with the pure water [27, 28]. Thus, the experimentation reveals that the nanofluids show higher thermal conductivity and viscosity than the base fluids. Furthermore, the results have also shown that the measured thermal conductivity of nanofluids is much higher than the predicted value of the H–C model, Wasp model, Bruggeman model, and effective medium theory.

From the above, it is evident that nanofluids show substantially higher thermal conductivity and viscosity than the base fluids. Furthermore, the thermo-physical properties of nanofluids are strongly dependent on temperature. Also, there is no controversy about the non applicability of traditional models, such as those of Maxwell [29] and Hamilton and Crosser [30], at elevated temperatures. However, these models agree well only for room temperatures (20°C to 30°C) as reported by Buongiorno et al. [24].

So far, most of the researchers have measured the thermal conductivity and viscosity of nanofluids with metal oxides for $\varphi > 1\%$. However, not much research has been done on the effective thermal conductivities and viscosities of nanofluids at very low volume concentration, say $\varphi < 1\%$, using pure metal nanoparticles tested at higher temperature. Hence, this study is found to be significant in the present context. Therefore, in the present work, the temperature-dependent properties of silver nanoparticles (Ag) suspended in deionized water are measured with $\varphi < 1\%$. The objectives of the article are (1) to measure thermal conductivity and viscosity for temperatures between 50°C and 90°C and $\varphi = 0.3$ vol%, 0.6 vol%, and 0.9 vol%; (2) to bring out the influence of Brownian motion and thermo-phoresis with respect to the temperature on the properties; and (3) to develop correlations for thermal conductivity and viscosity using the experimental data.

Downloaded By: [Wongwises, Somchai] At: 10:43 23 September 2010

Downloaded By: [Wongwises, Somchai] At: 10:43 23 September 2010

PREPARATION OF Ag-WATER NANOFLUID AND MEASUREMENT TEST FACILITIES

The Ag-water nanopowder of $\gamma = 60$ nm is prepared using the ultrasonic vibration method [31]. The ultrasonic vibration is carried out for 5 h using an ultrasonic processor (TEC-40 model, Roop-Telsonic Ultrasonics Limited, USA; power density, 750 watts; frequency, 20 kHz). The silver nanoparticles were directly purchased from Sigma Aldrich (product number 576832, Bangalore, India; silver nanopowder, < 100 nm, 99.5% metals). The Ag particles are directly mixed into deionized water under ultrasonic vibration without adding any surfactant to prepare the nanofluid. For the desired $\varphi = 0.3$, 0.6, and 0.9%, the pH values were measured to be 7.4, 7.1, and 6.8, respectively, which prove that the solution is neutral. The powder x-ray diffraction (PXRD) shown in Figure 1 is used for characterizing silver nanoparticles. The 2-D diffraction pattern is recorded; it shows concentric rings of scattering peaks corresponding to the various d-spacings in the crystalline lattice. The positions and the intensities of the peaks are used for identifying the underlying structure (or phase) of a solid material. From the Scherer equation [32], the average size of the calculated silver nanoparticles was 60 nm, which is consistent with the identified value of the manufacturer.

Measurement of Thermal Conductivity and Viscosity

The schematic diagram of the transient hot-wire apparatus is shown in Figure 2. The platinum wire (hot wire) of unknown resistance R_w, which is one arm of the bridge circuit, is 75 μm in diameter with a resistance-temperature coefficient of 0.0039092°C. The wire serves as both the heat source and the temperature sensor. The platinum wire, which is Teflon sprayed to provide electric insulation, is placed at the center of the

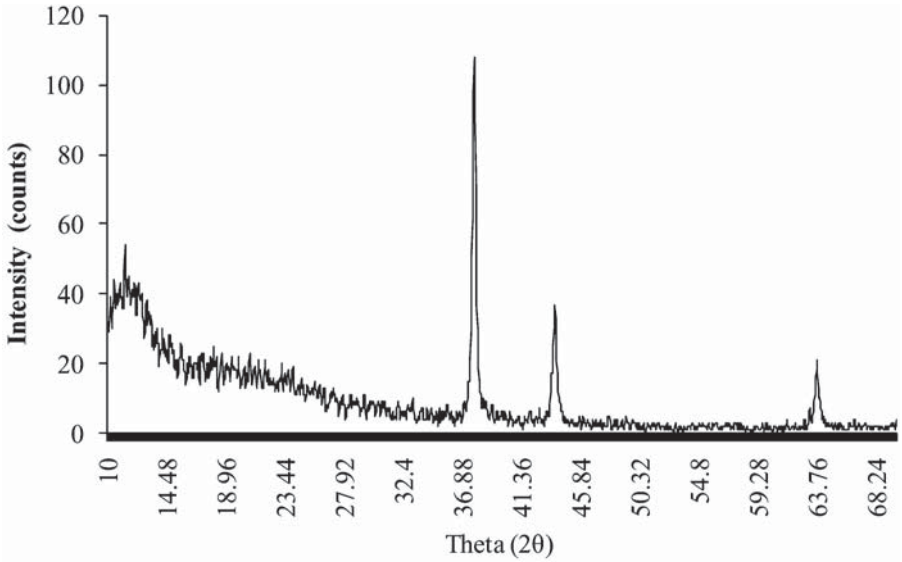

Figure 1. The x-ray diffraction patterns of silver nanoparticles.

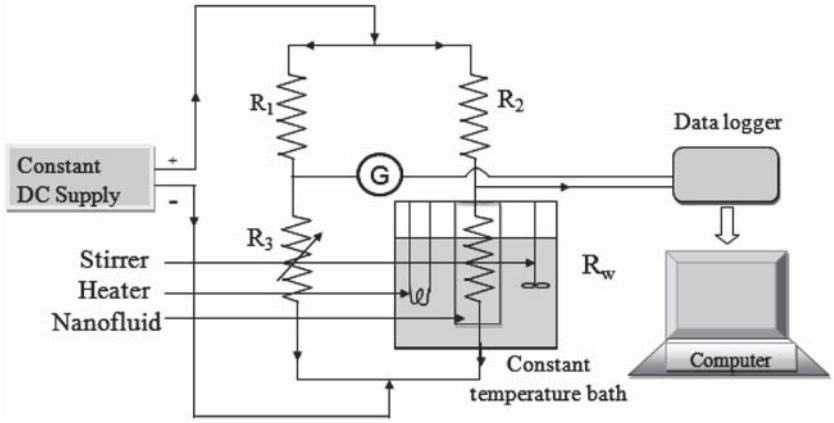

Figure 2. Transient hot-wire set-up for measuring the thermal conductivity of nanofluid.

Downloaded By: [Wongwises, Somchai] At: 10:43 23 September 2010

100-ml glass tube. R_1 and R_2 are the fixed resistors having 1,000-Ω and 16-Ω resistance, respectively; R_3 is the variable resistor with maximum of 1,000-Ω resistance connected to the Wheatstone bridge circuit. A constant current is supplied to the wire (platinum) to generate the essential temperature rise. The insulated constant temperature bath consists of a heater, a stirrer, and suitable temperature sensors. The experiment is conducted within 10 sec in order to avoid the natural convection of the wire and the fluid. The unknown resistance R_w is measured for different temperatures ranging from 50°C to 90°C. The Wheatstone bridge circuit is balanced (i.e., until the galvanometer shows zero deflection) by adjusting the variable resistor R_3. Then the DC supply is given to the bridge, which causes the change of voltage in the bridge through the platinum wire. As the current flows through the circuit, the resistance of the wire increases, which, in turn, produces an emf between the arms, thus causing an unbalanced condition in the circuit. This change in voltage over time is recorded by the data logger at the sampling rate of ten readings per second. The thermal conductivity is then calculated based on a specific solution of Fourier's law [33], as given in Eq. (1). The uncertainty of the measured value is estimated using Moffat [34]. The uncertainty in thermal conductivity measurement is ± 0.013 W/mK or ± 1.6%:

$$k = \frac{q}{4\pi(T_2 - T_1)} \ln \frac{t_2}{t_1}. \tag{1}$$

Cannon-Fenske opaque, also called a reverse-flow viscometer, is used to measure the kinematic viscosity of the Ag-water nanofluid. These viscometers are preferred when the meniscus of the fluid is opaque and for the viscosity range from 1 to 15 cSt. The capillary viscometer follows the Oswald flow, where the kinematic viscosity is calculated using Eq. (2). Each glass viscometer size has a coefficient of calibration, which is multiplied by the time taken for the fluid sample to pass between the different marks on the viscometer to achieve the kinematic viscosity, which is then converted into the dynamic viscosity by multiplying the density of the fluid. In order to have experimental data at different temperatures, the viscometer is placed in a closed transparent container

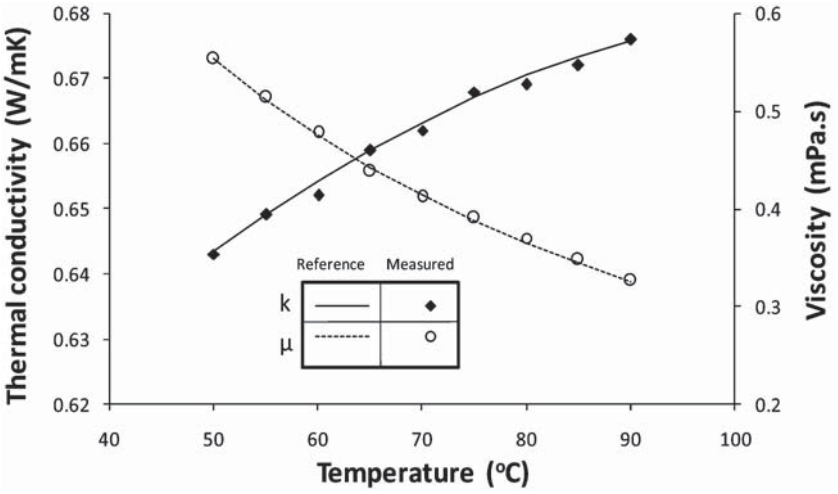

Figure 3. Comparison of the measured thermal conductivity and viscosity with reference data.

Downloaded By: [Wongwises, Somchai] At: 10:43 23 September 2010

that is maintained at constant temperature:

$$\nu = \frac{4\pi r^4 gh/8l}{du/dt}. \tag{2}$$

The transient hot-wire apparatus and viscometer is first validated with deionized water for temperatures between 50°C and 90°C. The measured data for thermal conductivity are then compared with the reference data presented in Incropera and DeWitt [35]. The measured data for viscosity are compared with REFPROP [36], an NIST database. Figure 3 shows a good agreement between the experimentally measured values and the reference values for thermal conductivity and viscosity with the base fluid. The uncertainty of the thermal conductivity and viscosity measurements is found to be around 1.5% and 2%, respectively, and the confidence level is found to be 95%. Similarly, the uncertainties of temperature and volume fraction measurements are estimated to be within $\pm$ 1° and 1%, respectively.

RESULTS AND DISCUSSION

The thermal conductivity and viscosity of Ag-water as a function of particle volume concentration and temperature is shown in Figure 4. The thermal conductivity of the nanofluid is observed to increase with an increase in temperature and particle volume concentration. The minimum enhancement of 27% for $\varphi = 0.3$ vol% and a maximum enhancement of 80% for 0.9 vol% are observed at an average temperature of 70°C when compared with pure water for the same temperature. The viscosity of the nanofluid increases with an increase in particle volume concentration and decreases with an increase in the temperature.

The thermal conductivity and viscosity ratios as a function of volume concentration and temperature are shown in Figure 5. The use of nanoparticles dispersed in the base liquid gives higher thermal conductivity and viscosity than the base fluid. The thermal

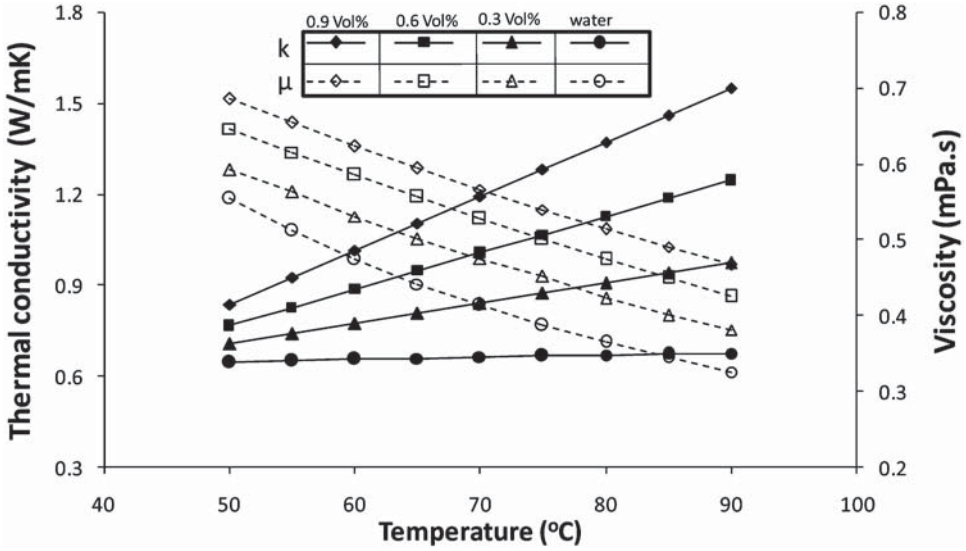

Figure 4. Thermal conductivity and viscosity of silver-water nanofluids as a function of temperature and volume fraction.

Downloaded By: [Wongwises, Somchai] At: 10:43 23 September 2010

conductivity ratio for $\varphi = 0.3$ vol% increases from 1.09 to 1.43 as the temperature increases from 50°C to 90°C; and similarly for $\varphi = 0.9\%$, the ratio increases from 1.29 to 2.29. The viscosity ratio for $\varphi = 0.3\%$ increases from 1.06 to 1.2, and for $\varphi = 0.9\%$, the ratio increases from 1.23 to 1.43 for the above temperature range. Further, the observed results from the present study have shown that the measured thermal conductivity ratio is larger than that of Masuda et al. [5] and Zhang et al. [37]. Yu et al. [38] reported

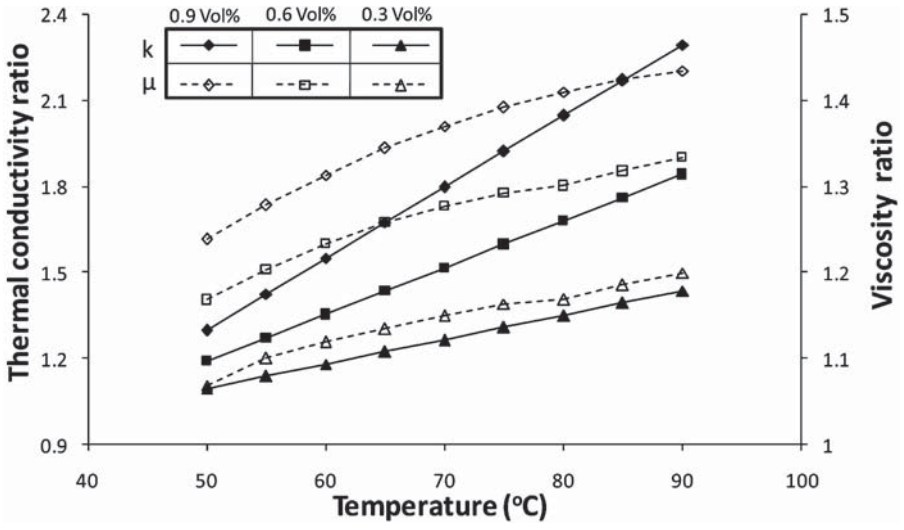

Figure 5. Thermal conductivity ratio and viscosity ratio of silver-water nanofluids as a function of temperature.

that the metal oxide particle for $\varphi = 4$–5% produces an enhancement level up to 30%, and the metal particles with less than $\varphi < 1.5\%$ give an enhancement up to 40%. However, the results from the present study show an enhancement of 80%, even with $\varphi < 0.9\%$. This shows that the enhancement of thermal conductivity using metal particles is higher than that of the metal oxide particles even at low concentrations.

A comparison of the measured values of thermal conductivity and viscosity of silver-water nanofluids and the predicted values of existing correlations at 50°C is shown in Figure 6. The measured thermal conductivity of nanofluids is much higher than the predicted value of Hamilton and Crosser [39], Timofeeva et al. [40], and Wasp [41] (abbreviated, respectively, as HC, T, and W in the figure). Also, the measured data for viscosity of the nanofluids are much higher than those of the predicted values using the Einstein equation in Drew and Passman [42], Brinkman [43], and Wang et al. [11] (abbreviated, respectively, as E, B, and W in the figure). It is also observed that the measured data for thermal conductivity and viscosity of the nanofluid show a far deviation with the models. The results show that the thermal conductivity enhancement and viscosity depend on the material, size, and shape of the particle, volume concentration, random motion of the particles, and the operating temperature itself. Therefore, more experimental works are required before concrete conclusions can be inferred from the thermal behavior of nanofluids.

Since the existing models are far deviating from the experimental ones, a new equation for calculating the effective thermal conductivity and viscosity of nanofluids has been proposed in the following form, as given in Eqs. (3) and (4). The thermal conductivity and viscosity are correlated as linear and quadratic functions of volume fraction, respectively. And the coefficients of the Ag-water nanofluid for the tested

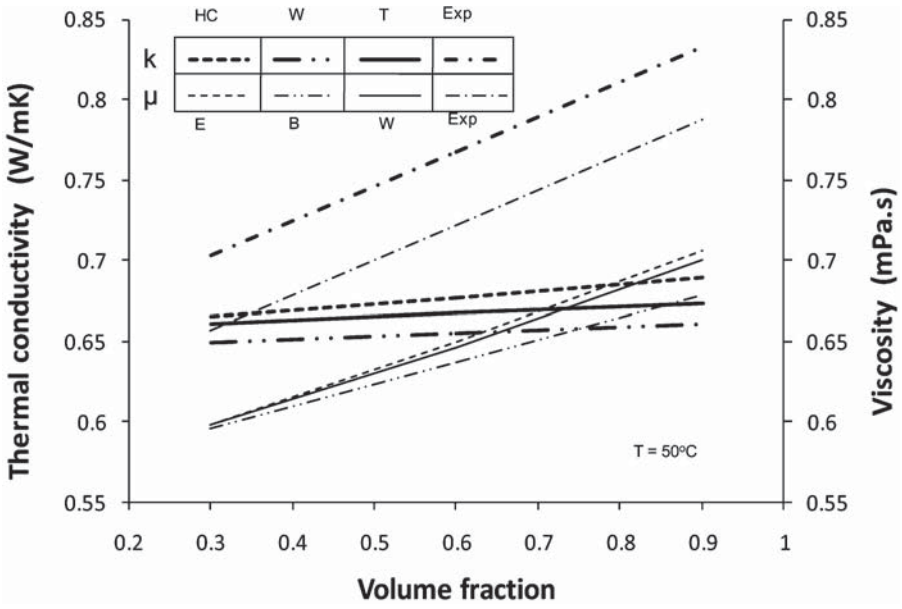

Figure 6. Comparison of the measured thermal conductivities and viscosities with those obtained from various correlations.

Downloaded By: [Wongwises, Somchai] At: 10:43 23 September 2010

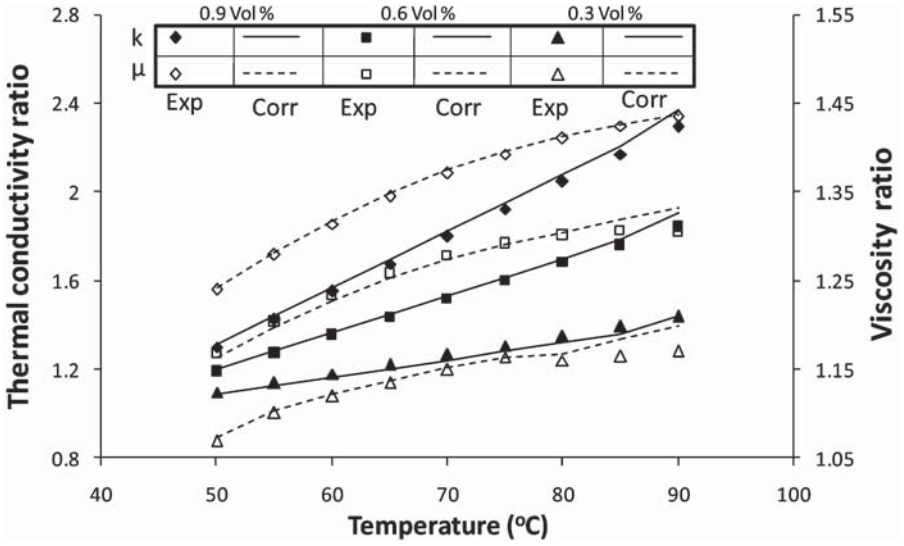

Figure 7. Comparison of the measured thermal conductivity ratio and viscosity ratio with the proposed correlation.

Downloaded By: [Wongwises, Somchai] At: 10:43 23 September 2010

volume concentration and temperature are achieved using linear regression, shown as

$$\frac{k_{nf}}{k_w} = (0.9692\varphi + 0.9508), \tag{3}$$

$$\frac{\mu_{nf}}{\mu_w} = (1.005 + 0.497\varphi - 0.1149\varphi^2). \tag{4}$$

A comparison between the thermal conductivity ratio and viscosity ratio obtained from the present correlations and the data obtained from the experiment are shown in Figure 7. The present thermal conductivity and viscosity models give a reasonably good agreement with the experimental data. It is also observed that the use of metal nanoparticles with low volume concentration gives a higher thermal conductivity enhancement than the high concentration metal oxide nanoparticles.

Brownian Diffusion and Thermophoresis

Brownian motion is defined as the random walk motion of nanoparticles within the base fluid, which results from the continuous collisions between the nanoparticles and the molecules of the base fluid. The nanoparticles themselves can be identified effectively as large molecules when compared with fluid molecules. Also, the nanoparticles are moving with an average kinetic energy equal to that of the fluid molecules with a considerable lower velocity. The Brownian diffusion is found to be the potential mechanism for enhancement of thermal conductivity in the absence of turbulent eddies. Thus, the Brownian motion intensifies with an increase in temperature as per the kinetic theory of particles. The effectiveness of the Brownian motion decreases with an increase in the bulk viscosity. The nanoparticle mass flux due to Brownian diffusion $J_{p,B}$ (kg/m^{2}s)

can be calculated as

$$J_{p,B} = \rho_p D_B \nabla \varphi. \tag{5}$$

Thermophoresis or the Sorét effect is a phenomenon that is explained as the diffusion of particles under the effect of a temperature gradient. This phenomenon is found to be significant in the enhancement of thermal conductivity with nanoparticle mixture, where the flow is driven by buoyancy and temperature. The particles travel in the direction of decreasing temperature, and the process of heat transfer increases with a decrease in the bulk density. The nanoparticle mass flux due to thermophoretic effects, $J_{p,T}$, can be calculated as

$$J_{p,T} = \rho_p \varphi V_T = -\rho_p D_T \frac{\nabla T}{T}, \tag{6}$$

where $D_T = \beta \frac{\mu}{\rho} \varphi$.

The calculated velocity and mass fluxes due to the Brownian motion and thermophoresis is shown, respectively, in Figures 8 and 9. It is observed from Figure 8 that the Brownian velocity varies linearly against the temperature, and the slope increases as the volume concentration is increased. For every increase in concentration of 0.3%, the Brownian velocity increases by 40–60%. When extrapolated to lower temperature (0°C), the velocity almost approaches zero because of higher fluid viscosity. The velocity due to thermophoresis has also exhibited a similar trend, and for every increase in φ of 0.3%, the velocity increases by 40–80%. An extrapolation to 0°C will certainly result in logarithmic decrease toward zero velocity. When compared to the two mechanisms, it is obvious that the thermophoretic velocity is significantly higher than the Brownian velocity.

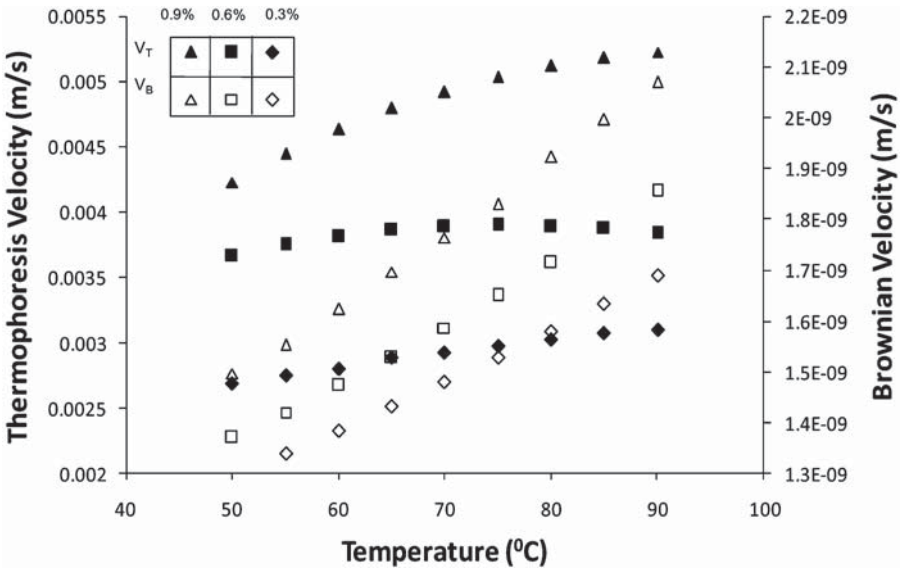

Figure 8. Brownian and thermophoresis velocities of silver-water nanofluids as a function of temperature and volume concentrations.

Downloaded By: [Wongwises, Somchai] At: 10:43 23 September 2010

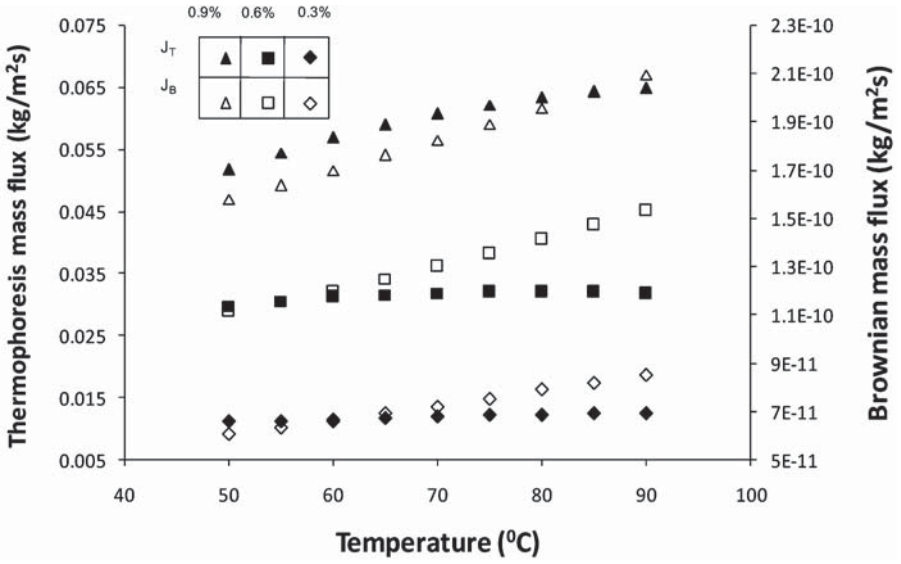

Figure 9. Brownian and thermophoresis mass flux of silver-water nanofluids as a function of temperature and volume concentrations.

Downloaded By: [Wongwises, Somchai] At: 10:43 23 September 2010

A comparison of the Brownian and thermophoresis mass flux for Ag-water at $\varphi = 0.3$–0.9% and the temperature between 50°C to 90°C is shown in Figure 9. The mass fluxes, due to both the mechanisms, increase with an increase in temperature and particle concentration. It is observed from Figure 9 for the lowest tested concentration ($\varphi = 0.3\%$), the mass flux due to thermophoresis is almost flat. This is because the quantity of particle that is required to augment heat transport through buoyancy diffusion is less. An increase in random motion causes increased collision between the particles, which is the primary reason for the increase in thermal conductivity. Even though the presence of the metal particles should result in increased viscosity, due to very low concentration, the nanofluid behaves just like a normal fluid from a viscosity point of view. The mass flux due to Brownian motion is negligible when compared to thermophoresis, especially at a higher temperature. It is observed from the present study that the thermophoretic velocity is one of the mechanisms that are responsible for the enhancement of the thermal conductivity, and its contribution is higher than the Brownian motion. This is the primary reason for the turbulence intensification and for the enhancement of thermal conductivity.

CONCLUSION

The thermal conductivity and effective viscosity of silver-water nanofluids increase with the increase in the particle volume concentrations of 0.3, 0.6, and 0.9%. The thermal conductivity of silver-water nanofluids increases as the temperature increases from 50 to 90°C, and conversely, the viscosity of nanofluids decreases with the increase in temperature. The existing correlations for thermal conductivity and viscosity of nanofluids give lower values than the experimental values of Ag-water, and therefore, new correlations

for the properties are proposed. The thermal conductivity enhancement ratio is higher than the viscosity enhancement ratio for the same volume concentration. Among the Brownian motion and thermophoresis, the latter plays a vital role in the enhancement of thermal conductivity than the former at higher temperature for metallic particle. Finally, it is inferred from this study that the thermophoretic effect should be considered as one of the important mechanisms with the use of nanofluids for high-temperature applications.

APPENDIX

Models for Thermal Conductivity

Hamilton and Crosser [39] proposed a model for calculating the thermal conductivity of nanofluids for spherical and non spherical (cylindrical) particles ($n = 3$ for spheres, $n = 6$ for cylinders):

$$\frac{k_{nf}}{k_w} = \frac{k_p + (n-1)k_w - (n-1)\varphi(k_w - k_p)}{k_p + (n-1)k_w + \varphi(k_w - k_p)}. \tag{A1}$$

Timofeeva et al. [40] suggested the effective medium theory to calculate thermal conductivity of nanofluids, which is expressed as follows:

$$k_{nf} = (1 + 3\varphi)k_w. \tag{A2}$$

Wasp [41] proposed a model for calculating the thermal conductivity of nanofluids, which is expressed as follows:

$$\frac{k_{nf}}{k_w} = \frac{k_p + 2k_w - 2\varphi(k_w - k_p)}{k_p + 2k_w + \varphi(k_w - k_p)}. \tag{A3}$$

Models for Dynamic Viscosity

Drew and Passman [42] proposed a model for effective dynamic viscosity of nanofluids that can be calculated using Einstein's equation for a viscous fluid containing a dilute suspension of small, rigid, spherical particles as follows:

$$\mu_{nf} = \mu_w(1 + 2.5\varphi). \tag{A4}$$

Brinkman [43] extended the relation for the viscosity of nanofluids to a more generalized form, since the above relation has been found valid for relatively low particle loading ($\varphi \leq 2\%$) as follows:

$$\mu_{nf} = \frac{1}{(1-\varphi)^{2.5}}\mu_w. \tag{A5}$$

Wang et al. [11] conducted experiments for finding the viscosity of nanofluids, and, based on the experimental data, the following correlation has been proposed:

$$\mu_{nf} = \mu_w(123\varphi^2 + 7.3\varphi + 1). \tag{A6}$$

Downloaded By: [Wongwises, Somchai] At: 10:43 23 September 2010

Downloaded By: [Wongwises, Somchai] At: 10:43 23 September 2010

ACKNOWLEDGMENTS

S. Wongwises would like to thank the Thailand Research Fund, the Office of Higher Education Commission, and the National Research University Project for their financial support.

REFERENCES

1. S. U. S. Choi, Enhancing Thermal Conductivity of Fluids with Nanoparticles, *Developments and Applications of Non-Newtonian Flows* (ASME FED 231/MD), vol. 66, pp. 99–103, 1995.
2. Y. Xuan, Q. Li, and W. Hu, Aggregation Structure and Thermal Conductivity of Nanofluids, *AIChE J.*, vol. 49, pp. 1038–1043, 2003.
3. J. H. Lee, K. S. Hwang, S. P. Jang, B. H. Lee, J. H. Kim, S. U. S. Choi, and C. J. Choi, Effective Viscosities and Thermal Conductivities of Aqueous Nanofluids Containing Low Volume Concentrations of Al_2O_3 Nanoparticles, *Intl. J. Heat Mass Transf.*, vol. 51, pp. 2651–2656, 2008.
4. S. Das, N. Putra, P. Thiesen, and W. Roetzel, Temperature Dependence of Thermal Conductivity Enhancement for Nanofluids, *J. Heat Transf.*, vol. 125, pp. 567–574, 2003.
5. H. Masuda, A. Ebata, K. Teramae, and N. Hishinuma, Alteration of Thermal Conductivity and Viscosity of Liquid by Dispersion of Ultra-Fine Particles, *Netsu Bussei (Japan)*, vol. 4, pp. 227–233, 1993.
6. A. Grimm, *Powdered Aluminum-Containing Heat Transfer Fluids*, German patent DE 4131516 A1, 1993.
7. S. U. S. Choi and J. A. Eastman, *Enhanced Heat Transfer Using Nanofluids*, U.S. Patent 6221275, April 2001.
8. J. A. Eastman, S. U. S. Choi, S. Li, and L. J. Thompson, Enhanced Thermal Conductivity Through the Development of Nanofluids, *Proceedings of the Symposium on Nanophase and Nanocomposite Materials II, Materials Research Society*, vol. 457 pp. 3–11, Boston, 1997.
9. J. A. Eastman, S. U. S. Choi, S. Li, W. Yu, and L. J. Thompson, Anomalously Increased Effective Thermal Conductivities of Ethylene Glycol Based Nanofluids Containing Copper Nanoparticles, *Appl. Phys. Lett.*, vol. 78, pp. 718–720, 2001.
10. B. C. Pak and Y. I. Cho, Hydrodynamic and Heat Transfer Study of Dispersed Fluids with Submicron Metallic Oxide Particles, *Exp. Heat Transf.*, vol. 11, pp. 151–170, 1998.
11. X. Wang, X. Xu, and S. U. S. Choi, Thermal Conductivity of Nanoparticles-Fluid Mixture, *J. Thermophys. Heat Transf.*, vol. 13, pp. 474–480, 1999.
12. Y. He, Y. Jin, H. Chen, Y. Ding, D. Cang, and H. Lu, Heat Transfer and Flow Behavior of Aqueous Suspensions of TiO_2 Nanoparticles (Nanofluids) Flowing Upward Through a Vertical Pipe, *Intl. J. Heat Mass Transf.*, vol. 50, p. 2272, 2007.
13. N. Putra, W. Roetzel, and S. K. Das, Temperature Dependent Viscosity of Al_2O_3-Water Nanofluids, *Intl. J. Heat Mass Transf.*, vol. 39, pp. 775–784, 2003.
14. T. Maré, A. G. Schmitt, C. T. Nguyen, J. Miriel, and G. Roy, Experimental Heat Transfer and Viscosity Study of Nanofluids: Water–γ Al_2O_3, *Proceedings of the 2nd International Conference on Thermal Engineering Theory and Applications*, Paper no. 93, Al Ain, United Arab Emirates, January 3–6, 2006.
15. W.-Q. Lu and Q.-M. Fan, Study for the Particle's Scale Effect on Some Thermo Physical Properties of Nanofluids by a Simplified Molecular Dynamics Method, *Eng. Analysis Boundary Elements*, vol. 32, pp. 282–289, 2008.
16. K. Kwak and C. Kim, Viscosity and Thermal Conductivity of Copper Oxide Nanofluid Dispersed in Ethylene Glycol, *Korea-Australia Rheol. J.*, vol. 17, pp. 35–40, 2005.
17. C. T. Nguyen, F. Desgranges, N. Galanis, G. Roy, and T. Mare, Viscosity Data for Al_2O_3–Water Nanofluid—Hysteresis: Is Heat Transfer Enhancement Using Nanofluids Reliable? *Intl. J. Thermal Sci.*, vol. 47, pp. 103–111, 2008.

Downloaded By: [Wongwises, Somchai] At: 10:43 23 September 2010

18. P. K. Namburu, D. P. Kulkarni, O. Misra, and D. K. Das, Viscosity of Copper Oxide Nanoparticles Dispersed in Ethylene Glycol and Water Mixture, *Exp. Thermal Fluid Sci.*, vol. 32, pp. 397–402, 2007.
19. J. Avsec and M. Oblak, The Calculation of Thermal Conductivity, Viscosity and Thermodynamic Properties for Nanofluids on the Basis of Statistical Nanomechanics, *Intl. J. Heat Mass Transf.*, vol. 50, pp. 4331–4341, 2007.
20. S. M. S. Murshed, K. C. Leong, and C. Yang, Investigations of Thermal Conductivity and Viscosity of Nanofluids, *Intl. J. Thermal Sci.*, 47, pp. 560–568, 2008.
21. C. H. Chonand K. D. Kihm, Thermal Conductivity Enhancement of Nanofluids by Brownian Motion, *J. Heat Transf.*, vol. 127, p. 810, 2005.
22. C. H. Li and G. P. Peterson, Experimental Investigation of Temperature and Volume Fraction Variations on the Effective Thermal Conductivity of Nanoparticle Suspensions (Nanofluids), *J. Appl. Phys.*, vol. 99, p. 084314, 2006.
23. S. K. Das, S. U. S. Choi, W. Yu, and T. Pradeep, *Nanofluids: Science and Technology*, John Wiley & Sons, Inc., Hoboken, NJ, 2008.
24. J. Buongiorno, D. C. Venerus, N. Prabhat, T. McKrell, J. Townsend, R. Christianson, Y. V. Tolmachev, P. Keblinski, L. Hu, J. L. Alvarado, I. C. Bang, S. W. Bishnoi, M. Bonetti, F. Botz, A. Cecere, Y. Chang, G. Chen, H. Chen, S. J. Chung, M. K. Chyu, S. K. Das, R. D. Paola, Y. Ding, F. Dubois, G. Dzido, J. Eapen, W. Escher, D. Funfschilling, Q. Galand, J. Gao, P. E. Gharagozloo, K. E. Goodson, J. G. Gutierrez, H. Hong, M. Horton, K. S. Hwang, C. S. Iorio, S. P. Jang, A. B. Jarzebski, Y. Jiang, L. Jin, S. Kabelac, A. Kamath, M. A. Kedzierski, L. G. Kieng, C. Kim, J. Kim, S. Kim, S. H. Lee, K. C. Leong, I. Manna, B. Michel, R. Ni, H. E. Patel, J. Philip, D. Poulikakos, C. Reynaud, R. Savino, P. K. Singh, P. Song, T. Sundararajan, E. Timofeeva, T. Tritcak, A. N. Turanov, S. V. Vaerenbergh, D. Wen, S. Witharana, C. Yang, W.-H. Yeh, X. Z. Zhao, and S. Q. Zhou, A Benchmark Study on the Thermal Conductivity of Nanofluids, *J. Appl. Physics*, vol. 106, p. 094312, 2009.
25. S. Lee, S. U. S. Choi, S. Li, and J. A. Eastman, Measuring Thermal Conductivity of Fluids Containing Oxide Nanoparticles, *J. Heat Transf.*, vol. 121, pp. 280–289, 1999.
26. W. Duangthongsuk and S. Wongwises, Measurement of Temperature-Dependent Thermal Conductivity and Viscosity of TiO_2-Water Nanofluids, *Exp. Thermal Fluid Sci.*, vol. 33, pp. 706–714, 2009.
27. W. Duangthongsuk and S. Wongwises, Effect of Thermophysical Properties Models on the Prediction of the Convective Heat Transfer Coefficient for Low Concentration Nanofluid, *Intl. Comm. Heat Mass Transf.*, vol. 35, pp. 1320–1326, 2008.
28. W. Duangthongsuk and S. Wongwises, Heat Transfer Enhancement and Pressure Drop Characteristics of TiO2-Water Nanofluid in a Double-Tube Counter Flow Heat Exchanger, *Intl. J. Heat Mass Transf.*, vol. 52, pp. 2059–2067, 2009.
29. J. C. Maxwell, *Treatise on Electricity and Magnetism*, Clarendon Press, Oxford, UK, 1873.
30. R. L. Hamilton and O. K. Crosser, Thermal Conductivity of Heterogeneous Two-Component Systems, *Ind. Eng. Chem. Fundament. 1*, vol. 1, pp. 187–191, 1962.
31. Y. Xuan and Q. Li, Heat Transfer Enhancement of Nanofluids, *Intl. J. Heat Fluid Flow*, vol. 21, pp. 58–64, 2000.
32. P. Scherrer, *Göttinger Nachrichten Gesell*, vol. 2, p. 98, 1918; R. Zsigmondy, *Kolloidchemie*, 3rd ed., p. 394, 1920.
33. H. S. Carslaw and J. C. Jaeger, *Conduction of Heat in Solids*, Oxford University Press, New York, 1959.
34. R. J. Moffat, Describing the Uncertainties in Experimental Results, *Exp. Thermal Fluid Sci.*, vol. 1, pp. 3–17, 1988.
35. F. P. Incropera and D. P. DeWitt, *Fundamentals of Heat and Mass Transfer*, John Wiley & Sons, New York, 1996.
36. M. O. McLinden, S. A. Klein, E. W. Lemmon, and A. P. Peskin, *NIST Thermodynamic and Transport Properties of Refrigerant Mixtures—REFPROP, Version 6.01, NIST Standard*

Reference Database 23, National Institute of Standards and Technology, Gaithersburg, MD, 1998.
37. X. Zhang, H. Gu, and M. Fujii, Effective Thermal Conductivity and Thermal Diffusivity of Nanofluids Containing Spherical and Cylindrical Nanoparticles, *Exp. Thermal Fluid Sci.*, vol. 31, pp. 593–599, 2007.
38. W. Yu, D. M. France, S. U. S. Choi, and J. L. Routbort, *Review and Assessment of Nanofluid Technology for Transportation and Other Applications*, Argonne National Laboratory, pp. 1–78, 2007.
39. R. L. Hamilton and O. K. Crosser, Thermal Conductivity of Heterogeneous Two-Component Systems, *I & EC Fundamentals*, vol. 1, pp. 187–191, 1962.
40. E. V. Timofeeva, A. N. Gavrilov, J. M. McCloskey, and Y. V. Tolmachev, Thermal Conductivity and Particle Agglomeration in Alumina Nanofluids: Experiment and Theory, *Physical Rev.*, vol. 76, p. 061203, 2007.
41. F. J. Wasp, *Solid-Liquid Slurry Pipeline Transportation*, Trans. Tech, Berlin, 1977.
42. D. A. Drew and S. L. Passman, *Theory of Multi Component Fluids*, Springer, Berlin. 1999.
43. H. C. Brinkman, The Viscosity of Concentrated Suspensions and Solution, *J. Chem. Physics*, vol. 20, pp. 571–581, 1952.

Downloaded By: [Wongwises, Somchai] At: 10:43 23 September 2010

International Communications in Heat and Mass Transfer 37 (2010) 1305–1311

Contents lists available at ScienceDirect

International Communications in Heat and Mass Transfer

journal homepage: www.elsevier.com/locate/ichmt

Effects of coil diameter and pitch on the flow characteristics of alternative refrigerants flowing through adiabatic helical capillary tubes ☆

Sukkarin Chingulpitak [a,b], Somchai Wongwises [b,*]

[a] The joint Graduate School of Energy and Environment, King Mongkut's University of Technology Thonburi, Bangmod, Bangkok 10140, Thailand
[b] Fluid Mechanics, Thermal Engineering and Multiphase Flow Research Lab. (FUTURE), Department of Mechanical Engineering, King Mongkut's University of Technology Thonburi, Bangmod, Bangkok 10140, Thailand

ARTICLE INFO

Available online 3 August 2010

Keywords:
Capillary tube
Coiled tube
Adiabatic
Homogeneous flow
Coil diameter
Pitch
Alternative refrigerant

ABSTRACT

This paper presents the effects of various geometries of helical capillary tubes on the flow characteristics of alternative refrigerants flowing through adiabatic helical capillary tubes. The theoretical model is based on the conservation of mass, energy and momentum of fluids in the capillary tube. The two-phase flow model developed was based on a homogenous flow assumption. The model was validated by comparing it with the experimental data of published in literature for R-22, particularly various pairs of refrigerants. It was found conventional refrigerants had lower capillary lengths than alternative refrigerants. For all pairs, the numerical results showed that the traditional refrigerants consistently gave lower pressure drops for both single-phase and two-phase flows, which resulted in longer tube lengths. The results show that coil diameter variation (less than 300 mm) for helical capillary tube geometries affected the length of helical capillary tubes. However, pitch variation (more than 300 mm) had no significant effect on the length of helical capillary tubes. This adiabatic helical capillary tube model can be used to integrate system models working with alternative refrigerants for design and optimisation.

© 2010 Elsevier Ltd. All rights reserved.

1. Introduction

In small refrigeration systems, the capillary tube is used as the expansion device because of its low cost, low starting torque and low maintenance. Normally, it is used in refrigeration systems with a cooling capacity less than 10 kW such as household refrigerators and air conditioners. The nominal size of the capillary tube ranges between 0.5–2.0 mm in diameter and 2–5 m in length. Several decades ago, the flow characteristics flowing through the straight capillary tube of various refrigerants were both experimentally and theoretically studied. In practical applications, however, capillary tubes are generally coiled to save space. The most productive studies have been continuously carried out by the following researchers.

Zhou and Zhang [1] theoretically and experimentally studied the performance of coiled adiabatic capillary tubes and compared the results with straight capillary data. These results showed that the mass flow rate of a refrigerant substantially increases by increasing the coil diameter. However, little change was observed for coil diameters larger than 300 mm.

Ali [2] proposed the pressure drop correlations developed in terms of fluid properties (ρ and μ), flow rate (V) and tube geometry (d_i, D_C, p and L). In most previous works, the relevant correlations were developed in terms of Dean number (De), Helical number (He), curvature ratio (D_C/d_i) and Euler number (Eu), Reynolds number (Re) and the obtained geometrical group.

Kim et al. [3] presented a mass flow rate correlation based on the Buckingham π theorem for R-22 and its alternatives, R-407C and R-410A. Their results indicated that the mass flow rates of R-407C and R-410A were higher than those of R-22 by about 4% and 23%, respectively. In addition, the mass flow rates of straight capillary tubes are higher than those of coiled capillary tubes, especially at smaller coiled diameters. For instance, mass flow rates for 40 mm coiled diameter tubes are smaller than the straight capillary tubes by approximately 9%.

Park et al. [4] studied the flow characteristics of coiled capillary tubes for R-22 and developed a mass flow rate correlation for coiled capillary tubes. At the same operating condition, they found that the mass flow rates of the coiled capillary tubes decreased by 5–16% more than those of the straight capillary tubes. The Buckingham π theorem was used to form a generalised correlation to calculate the refrigerant mass flow rate for both straight and coiled capillary tubes. The effects of inlet condition, refrigerant property and coiled tube geometry were considered. For both straight and coiled capillary tubes, the results showed that the proposed correlation gave a satisfactory agreement with the experimental data for R-22, R-407C and R-410A. The average and standard deviations were around 0.24% and 4.4%, respectively.

García-Valladares [5] presented a numerical simulation based on finite volume formulation for describing the flow characteristics of

☆ Communicated by W.J. Minkowycz.

* Corresponding author.
E-mail address: somchai.won@kmutt.ac.th (S. Wongwises).

0735-1933/$ – see front matter © 2010 Elsevier Ltd. All rights reserved.
doi:10.1016/j.icheatmasstransfer.2010.07.005

Nomenclature

A	cross sectional area of capillary tube (m^2)
d_i	capillary tube internal diameter (m)
D_C	coil diameter (m)
De	Dean number $De = \mathrm{Re}\sqrt{d_i / D_C}$
e/d_i	relative roughness
ΔT_{sub}	degree of subcooling (°C)
f	friction factor
g	gravitational acceleration (m/s^2)
G	mass flow rate per unit area ($kg/s\ m^2$)
h	specific enthalpy (J/kg)
H_{loss}	total head loss (m)
He	Helical number $He = \mathrm{Re}\left[(d_i/D_C)/\left\{1 + (p/\pi D_C)^2\right\}\right]^{1/2}$
p	pitch of coil (m)
k	entrance loss coefficient
L	length (m)
m	mass flow rate (kg/s)
P	pressure (Pa)
Re	Reynolds number
s	specific entropy (J/kg K)
T	temperature (°C)
V	velocity (m/s)
x	quality

Greek letters

τ_w	shear stress at wall (N/m^2)
ν	specific volume (m^3/kg)
μ	dynamic viscosity (kg/m s)
ρ	density (kg/m^3)

Subscripts

cond, evap	condenser and evaporator, respectively
f, g	liquid phase and gas phase, respectively
h	homogeneous flow
i	capillary inlet condition
sp, tp	single-phase and two-phase, respectively

coiled adiabatic capillary tubes. The numerical model was considered for various aspects such as geometry, type of fluid (pure substances and mixtures), critical or non-critical flow conditions, metastable region and transient behaviour.

Mittal et al. [6] presented an experimental investigation of coiling effect on the flow characteristics of R-407C in an adiabatic helical capillary tube. It was observed that the coiling of capillary tubes (coil diameters 60 mm, 100 mm and 140 mm) significantly influenced the mass flow rate of R-407C. From the experimental results, the mass flow rates of coiled capillary tubes were about 5–10% less than those of straight capillary tubes. In addition, they also proposed correlations to predict the mass flow rate of R-407C flowing through straight and helical capillary tubes. Compared with the experimental data, it could clearly be seen that the majority of the data fell within 10% of their proposed correlation.

Although some information is available on the flow characteristics in helical capillary tubes, there remains room for further research, for example the effect of the relevant parameters on flow characteristics. In this study, the aim is to analyse the effect of coil diameters and pitch on flow characteristics of refrigerants flowing through the adiabatic helical capillary tubes. Moreover, this investigation will aim to compare various alternative mixtures of refrigerants, particularly between the following pairs of HCFCs with HFCs:

- R-502 (R-22/R-115; 48.8.51.2) and R-404A (R-125/R-143a/R-134a; 44%/52%/4%);
- R-502 (R-22/R-115; 48.8.51.2) and R-507A (R-125/R-143a; 50%/50%);
- R-22 and R-407B (R-32/R-125/R-134a; 10%/70%/20%);
- R-22 and R-407C (R-32/R-125/R-134a; 23%/25%/52%);
- R-22 and R-410A (R-32/R-125; 50%/50%); and
- R-22 and R-410B (R-32/R-125; 45%/55%).

2. Mathematical modelling

As shown in Fig. 1, the flow of refrigerants through a capillary tube can be divided into two distinct regions: the single-phase subcooled liquid and two-phase regions. In modelling, the physical method, which is used to describe flow characteristics, is developed from the conservations of mass, energy and momentum. Moreover, the model includes the effect of the condenser and evaporator temperatures, inner diameter, degree of subcooling and mass flow rate of refrigerant.

The position between points 1 and 2 indicated in Fig. 1 is the capillary tube inlet associated with a pressure drop because of sudden contraction. Similarly, the position between points 2 and 3 is the single-phase subcooled liquid region and the position between points 3 and 4 corresponds to the two-phase region consisting of the liquid–vapour two-phase region. The developed model is based on the following assumptions:

- The horizontal helical coiled tube has a constant diameter;
- The inner diameter and roughness of the capillary tube are constant;
- Adiabatic and homogeneous two-phase flow;
- Non-metastable liquid region;
- One-dimensional and steady flow;
- Oil-free refrigerant; and
- The thermodynamic equilibrium through the capillary tube.

The governing equations for describing flow characteristics for the single-phase and two-phase flow regions are presented below.

2.1. Single-phase flow region

A pressure loss because of an inlet sudden contraction between points 1 and 2 is determined from:

$$P_1 - P_2 = k\frac{\rho V^2}{2g}, \tag{1}$$

where k is the entrance loss coefficient (for square edged, $k = 0.5$). The steady flow energy equation between points 2 and 3 can be expressed as:

$$\frac{P_2}{\rho_2 g} + \frac{V_2^2}{2g} + z_2 = \frac{P_3}{\rho_3 g} + \frac{V_3^2}{2g} + z_3 + f_{sp}\frac{L_{sp}}{d_i}\frac{V^2}{2g}. \tag{2}$$

For an incompressible fluid, $\rho_2 \cong \rho_3 = \rho$, the continuity equation is presented as:

$$m = \rho_2 V_2 A = \rho_3 V_3 A = \rho V A. \tag{3}$$

Rearranging Eqs. (2)–(3) yield:

$$P_2 = P_3 + \rho g(z_3 - z_2) + \left(\frac{f_{sp}L_{sp}}{d_i}\right)\left(\frac{\rho V^2}{2}\right). \tag{4}$$

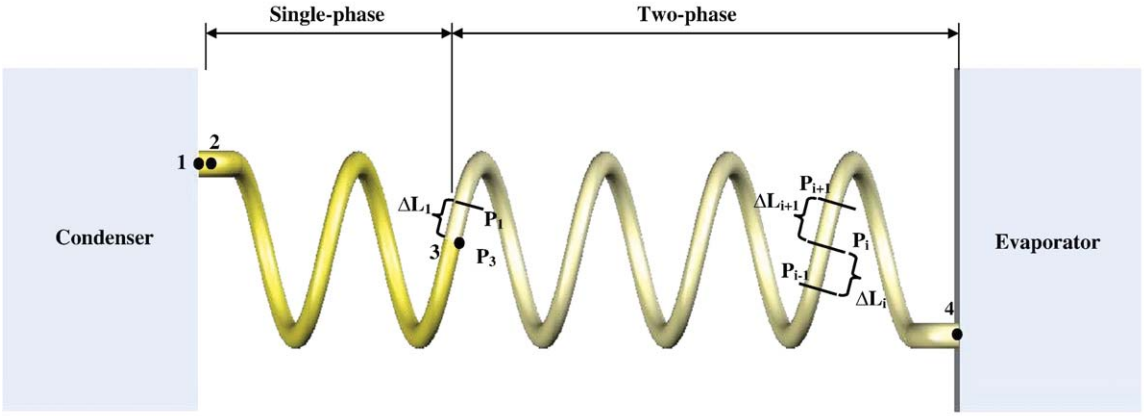

Fig. 1. Schematic diagram of an adiabatic helical capillary tube.

For $z_2 = z_3$, substituting Eq. (4) into Eq. (1) gives:

$$L_{sp} = \frac{d_i}{f_{sp}}\left[\frac{2\rho}{G^2}(P_1 - P_3) - k - 1\right] \tag{5}$$

where

$$G = \rho V \tag{6}$$

The important parameter is the single-phase friction factor (f_{sp}), which can be calculated from three different friction factor models. These equations are expressed as follows (where f_c is the friction factor for coiled capillary tubes and f_s is the friction factor for straight capillary tubes):Schmidt [7]

$$f_c / f_s = 1 + 0.14\mathrm{Re}^x, \tag{7}$$

where $x = [1 - 0.0644/(D_C/d_i)^{0.312}]/(D_C/d_i)^{0.97}$. Mori and Nakayama [8]

$$f_c = \frac{C_1(d_i/D_C)^{0.5}}{[\mathrm{Re}(d_i/D_C)^{2.5}]^{1/6}}\left\{1 + \frac{C_2}{[\mathrm{Re}(d_i/D_C)^{2.5}]^{1/6}}\right\} \tag{8}$$

$C_1 = 1.88411177\times10^{-1} + 85.2472168(\varepsilon/d_i) - 4.63030629\times10^4(\varepsilon/d_i)^2 + 1.31570014\times10^7(\varepsilon/d_i)^3 C_2 = 6.79778633\times10^{-2} + 25.3880380(\varepsilon/d_i) - 1.06133140\times10^4(\varepsilon/d_i)^2 + 2.54555343\times10^6(\varepsilon/d_i)^3$ Manlapaz and Churchill [9]

$$f_c / f_s = \left[(1 - 0.18/\{1 + (35/\mathrm{He})^2\}^{0.5})^m + (1 + d_i/\{3D_C\})^2(\mathrm{He}/88.33)\right]^{0.5} \tag{9}$$

where $m = 0$ for De > 40

$$He = \mathrm{Re}\left[(d_i/D_C)/\{1 + (p/\pi D_C)^2\}\right]^{1/2}.$$

2.2. Two-phase flow region

In this region, the capillary tube is divided into a number of elements as shown in Fig. 1. The following equations are based on the control volume considerations in the two-phase region. The conservation of mass can be calculated using the following equation:

$$m = \frac{AV_i}{v_i} = \frac{AV_{i+1}}{v_{i+1}}. \tag{10}$$

The conservation of energy for the steady-state adiabatic condition without external work can be expressed as follows:

$$\left(h_3 + gz_3 + \frac{V_3^2}{2}\right) = \left(h_i + gz_i + \frac{V_i^2}{2}\right) \tag{11}$$

If the elevation difference is neglected, we get:

$$h + \frac{V^2}{2} = \text{constant} \tag{12}$$

where h and V are the enthalpy and velocity of fluid at any point, respectively.

Because the refrigerant flows along the capillary tube, the pressure gradually drops and the liquid flashes into vapour arising purely from the reduced pressure at any point. Hence:

$$h_i = h_{fi}(1 - x_i) + h_{gi}x_i, v_i = v_{fi}(1 - x_i) + v_{gi}x_i \tag{13}$$

Also, $m = \rho VA = \text{constant}$

$$V = \frac{m}{\rho A} = \frac{G}{\rho} = Gv \tag{14}$$

The energy balance between point 3 and at any point along the capillary tube in the two-phase flow region can be calculated by substituting Eqs. (13) and (14) into Eq. (12):

$$h_3 + \frac{V_3^2}{2} = h_f + x\left(h_g - h_f\right) + \frac{G^2}{2}\left(v_f(1 - x) + v_g x\right)^2 \tag{15}$$

Expanding the right-hand side of Eq. (15) and rearranging yields:

$$\left[\left(v_g - v_f\right)^2\frac{G^2}{2}\right]x^2 + \left[G^2 v_f\left(v_g - v_f\right) + \left(h_g - h_f\right)\right]x + \left[\frac{G^2 v_f^2}{2} - h_3 - \frac{V_3^2}{2} + h_f\right] = 0 \tag{16}$$

The quality (x) can be expressed in the form of a quadratic equation as shown in Eq. (17):

$$x = \frac{-h_{fg} - G^2 v_f v_{fg} + \sqrt{\left(G^2 v_f v_{fg} + h_{fg}\right)^2 - \left(2G^2 v_{fg}^2\right)\left[\frac{G^2 v_f^2}{2} - h_3 - \frac{V_3^2}{2} + h_f\right]}}{G^2 v_{fg}^2} \tag{17}$$

where $h_{fg} = h_g - h_f$ and $v_{fg} = v_g - v_f$.

Again, the conservation of momentum can be expressed by reconsidering the element of fluid as shown in Fig. 1.

$$\left(P\frac{\pi d_i^2}{4}\right) - (P + dP)\frac{\pi d_i^2}{4} - \tau_w \pi d_i dL = mdV \tag{18}$$

where τ_w is the wall shear stress which is defined as follows:

$$\tau_w = \frac{f\rho V^2}{8} \tag{19}$$

substituting Eq. (19) into Eq. (18), we get:

$$-\frac{\pi d_i^2}{4} dP - \frac{f_{tp}}{8}\rho V^2 \pi d_i dL = mdV \tag{20}$$

or

$$dL = \frac{d_i}{f_{tp}}\left[\frac{2dP}{\rho V^2} + \frac{2md_i V}{\rho A V^2}\right]. \tag{21}$$

For the constant mass flow rate, $dm = 0$, Eq. (22) is obtained:

$$\frac{-dV}{V} = \frac{d\rho}{\rho}. \tag{22}$$

Substituting Eq. (22) into Eq. (21) gives:

$$dL = \frac{2d_i}{f_{tp}}\left[\frac{-\rho dP}{\rho V^2} + \frac{d\rho}{\rho}\right]. \tag{23}$$

3. Solution method

As shown in Fig. 1, the capillary tube between points 3 and 4 can be divided into numerous sections. Because P_3 is known (saturated liquid), the pressure at any section 'i' can be calculated from the following equation:

$$P_i = P_3 - i\Delta P. \tag{24}$$

The pressure (P_i) and quality (x_i) can be calculated from Eq. (16). So, the entropy of each section can be calculated from:

$$s_i = s_{if}(1-x) + s_{ig}x. \tag{25}$$

The Reynolds number in the two-phase region is determined by:

$$\mathrm{Re}_{tp} = \frac{Vd_i}{\mu_{tp} v_{tp}} \tag{26}$$

where

$$V = G v_{tp} = G\left(x v_g + (1-x)v_f\right). \tag{27}$$

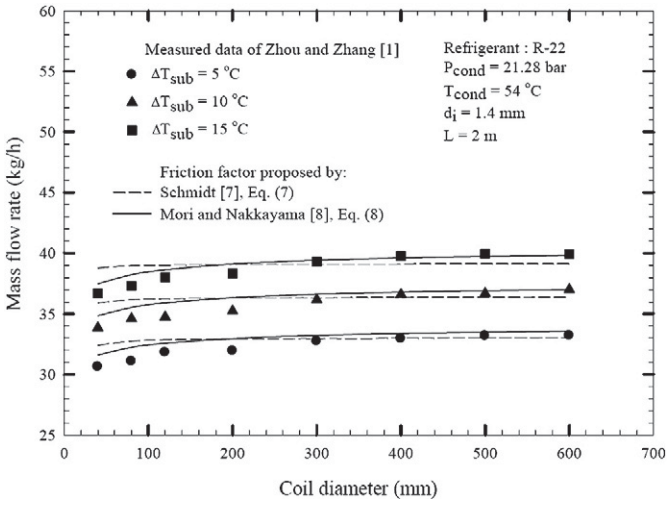

Fig. 2. Comparison of the present numerical results with the measured mass flow rate at different coil diameters and degrees of subcooling.

The two-phase dynamic viscosity correlation proposed by McAdams et al. [10] is presented as follows:

$$\frac{1}{\mu_{tp}} = \frac{x}{\mu_g} + \frac{1-x}{\mu_f}. \tag{28}$$

The gradual increase of the entropy is obtained along the capillary tube. When the entropy reaches its maximum value, the fluid velocity is equal to the local speed of sound and the flow is choked. As a consequence, the calculation is ended at this point. The pressure of the element, where the entropy has the maximum value $(P_i)_{s\,\max}$, is then compared with the evaporator pressure (P_{evap}) given by:

if $P_{i,s\max} = P_{\mathrm{evap}}$ then $P_4 = P_{\mathrm{evap}}$

if $P_{i,s\max} \neq P_{\mathrm{evap}}$ then $P_4 = P_{i,s\max}$.

Thus, from Eq. (23) the two-phase length can be expressed as follows:

$$L_{tp} = d_i\left[\frac{-2}{G^2}\int_{P_3}^{P_{s\max}} \frac{\rho}{f_{tp}} dp + 2\int_{P_3}^{P_{s\max}} \frac{d\rho}{\rho f_{tp}}\right]. \tag{29}$$

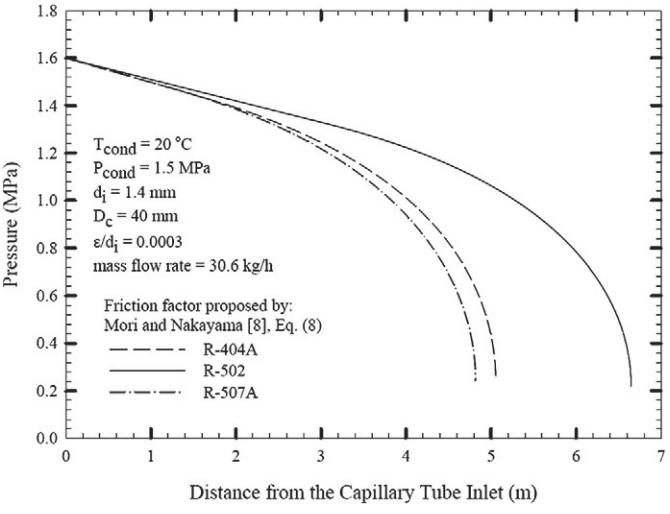

Fig. 3. Comparison of pressure distributions along the capillary tube for R-502, R-404A and R-507A.

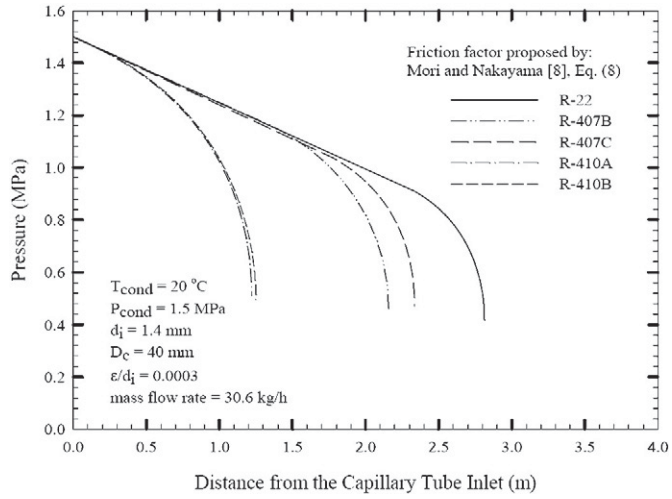

Fig. 4. Comparison of pressure distributions along the capillary tube for R-22, R-407B, R-407C, R-410A and R-410B.

The capillary length of each section is calculated by:

$$\Delta L_i = \frac{2d_i}{f_{tp,i}}\left(\frac{-\rho_i \Delta P}{G^2} + \frac{\Delta \rho}{\rho_i}\right). \tag{30}$$

The total length of the two-phase region is determined from:

$$L_{tp} = \sum_{i=1}^{n} \Delta L_i \,. \tag{31}$$

Finally, the total length of the capillary tube is a summation of the single-phase and two-phase lengths, which is defined as follows:

$$L_{\text{total}} = L_{\text{sp}} + L_{\text{tp}} \,. \tag{32}$$

4. Results and discussion

With the suitable friction factor equations, the straight capillary tube model can also be applied to the coiled capillary tubes. The viscosity model is calculated with the McAdams et al. [10] model (recommended by Wongwises and Pirompak [11]).

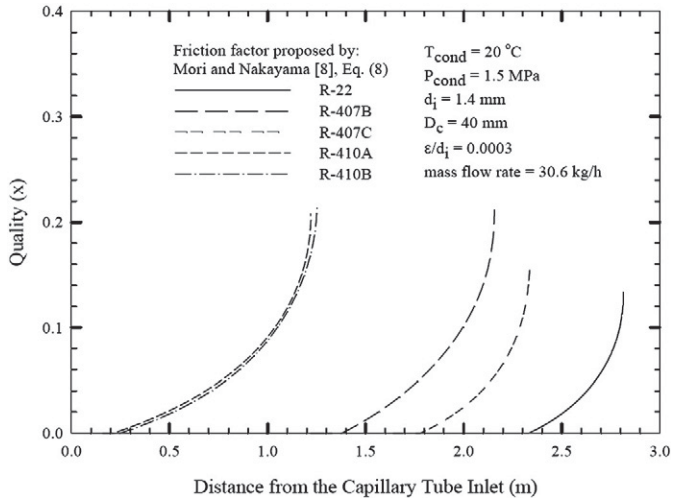

Fig. 5. Comparison of quality distributions along the capillary tube for R-22, R-407B, R-407C, R-410A and R-410B.

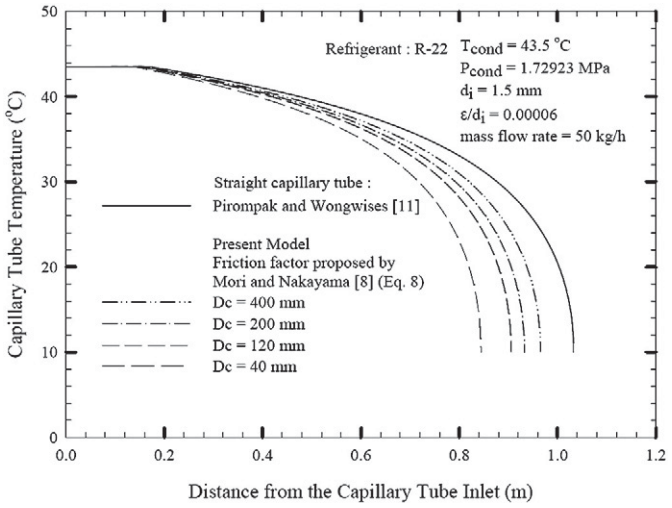

Fig. 6. Comparison of pressure distributions along the capillary tube for R-22 at different coil diameters.

4.1. Mathematical model verification

To validate the present model, comparisons are made with the available experimental data of Zhou and Zhang [1] for R-22. Fig. 2 shows the comparisons between the present results and experimental data of Zhou and Zhang [1] for R-22 at different coil diameters and degrees of subcooling. The results show that the calculated mass flow rate of R-22 deviates from the experimental results. Moreover, the results also indicate that the mass flow rate obtained from the present model fits very well with the data. In particular, the friction factor of Mori and Nakayama [8] gives the best result, which is in agreement with the results of Zhou and Zhang [1] for R-22. Moreover, the friction factor of Mori and Nakayama [8] gives a mean absolute error of 1.58%.

4.2. Alternative refrigerants

As shown in Figs. 3 and 4, comparing the pressure drop characteristics for the rest of the pairs of refrigerant types shows that for all cases in the single-phase region the conventional refrigerant flowing through capillary tubes gives a slightly lower pressure drop than the newer alternative refrigerants because of the higher viscosity of the alternative refrigerant. In the two-phase

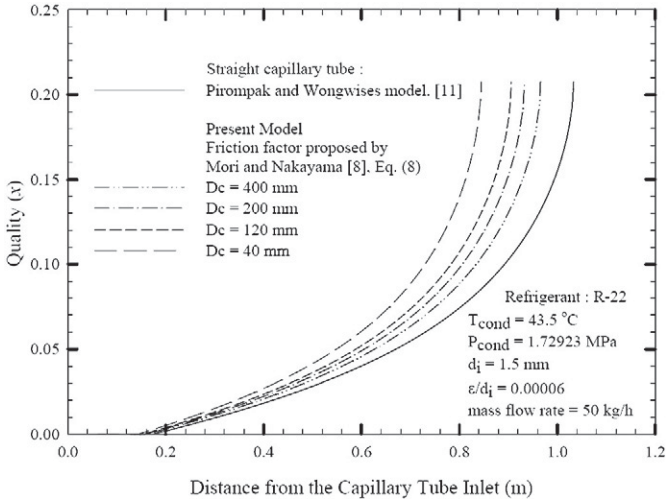

Fig. 7. Comparison of quality distributions along the capillary tube for R-22.

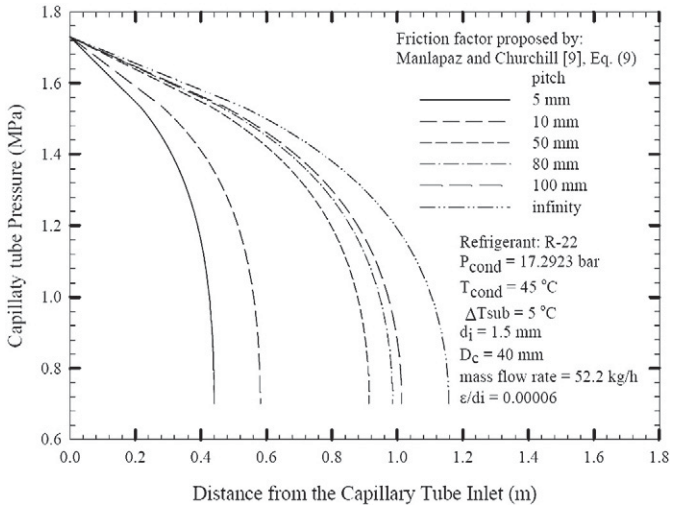

Fig. 8. Comparison of pressure distributions along the capillary tube for R-22.

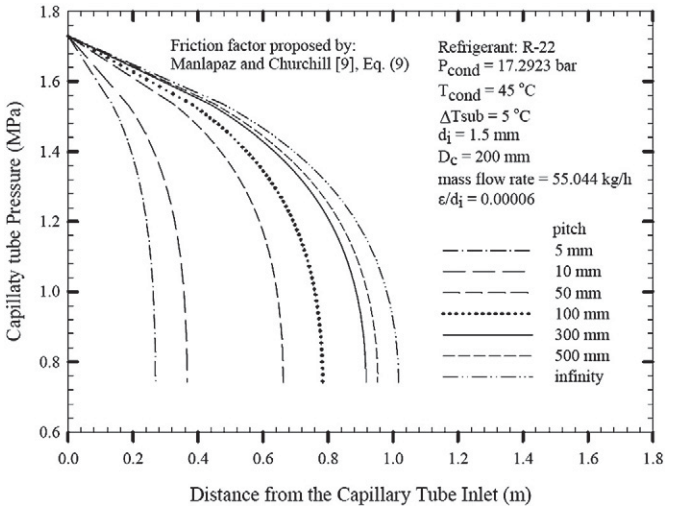

Fig. 10. Comparison of pressure distributions along the capillary tube for R-22.

flow region, however, the conventional refrigerant gives a significantly lower pressure drop than the alternative refrigerant, resulting in a longer total tube length. This result indicates that although both refrigerants have differences in composition, the pressure distributions along the capillary tube are almost the same.

Fig. 5 shows the change in quality with position along the capillary tube length. For all refrigerants, as expected, the quality is zero up to the flash point and then increases in a non-linear fashion, rising more rapidly as the critical length is approached. It also shows that all alternative refrigerants vaporise earlier than their corresponding conventional refrigerants.

4.3. Effects of coil diameter on helical capillary tube

As shown in Figs. 2 and 6, in the case of coil diameters less than 300 mm, the experimental data showed that the mass flow rate of refrigerants rapidly increases by about 6–7%. On the contrary, the mass flow rate increase of refrigerants is small (around 1–2%) for coil diameters between 300 mm and 600 mm.

Fig. 7 illustrates the change in quality with position along the capillary tube length. The observed trend for geometry consideration is similar to that corresponding to the refrigerant consideration previously mentioned. The quality is zero up to the flash point and then increases in a non-linear fashion, rising more rapidly as the critical length is approached. In addition, the total tube length of the helical capillary tube is shorter than the straight capillary tube by about 20% (at a coil diameter of 40 mm).

4.4. Effects of pitch on helical capillary tube

Figs. 8–12 present the pressure distributions at different pitches along the helical capillary tube. The friction factor can be calculated from Manlapaz and Churchill [9] because their correlation includes pitch parameter (p) in the calculation. In the case of pitches less than 300 mm, the numerical results show that the total tube length rapidly increases by about 260–290%. On the contrary, the total tube length slightly decreases by around 9–15% for pitches from 300 mm to more than 900 mm (to infinity).

5. Conclusion

This paper presents the effects of coil diameter and pitch on the flow characteristics of alternative refrigerants flowing through the adiabatic helical capillary tubes. From the results, it is evident that the most suitable equations for calculating the friction factor are Schmidt [7] and Mori and Nakayama [8]. These equations provided a deviation of 1–4%. This model was validated by comparing it with the experimental data of Zhou and Zhang [1] R-22 and was found to

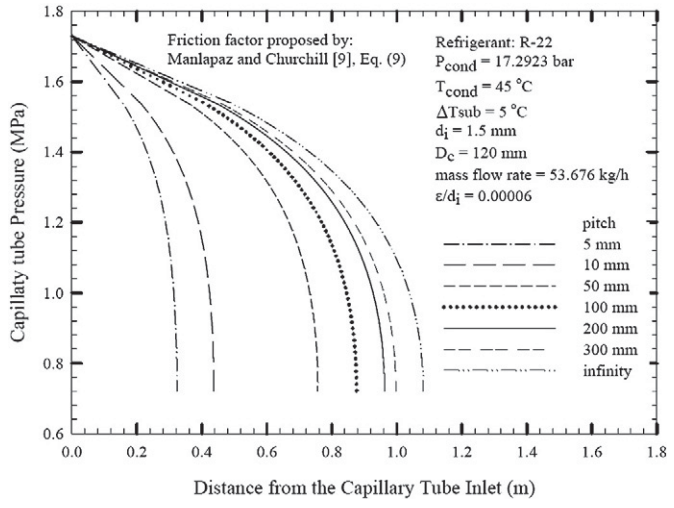

Fig. 9. Comparison of pressure distributions along the capillary tube for R-22.

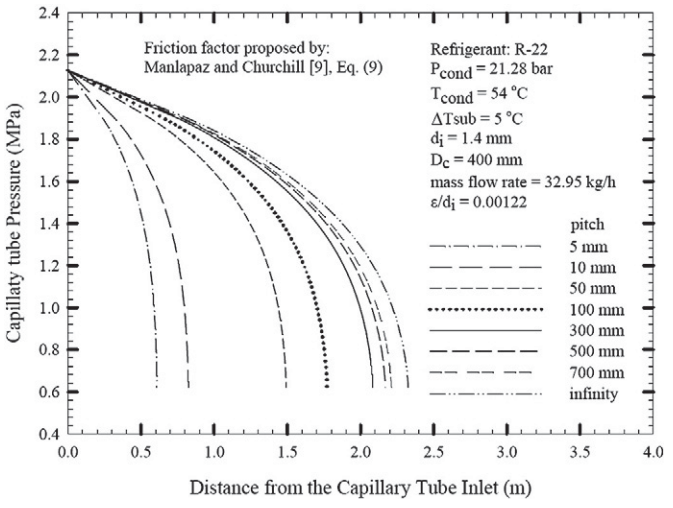

Fig. 11. Comparison of pressure distributions along the capillary tube for R-22.

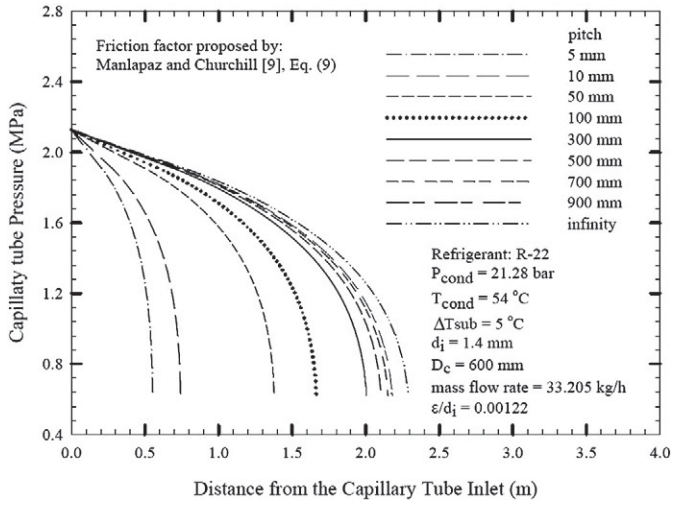

Fig. 12. Comparison of pressure distributions along the capillary tube for R-22.

give an average discrepancy of around 4%. The obtained results show that coil diameter variation (less than 300 mm) affects the length of the helical capillary tube. Nevertheless, pitch variation (more than 300 mm) has no significant effect on the length of the helical capillary tube because the geometries of helical capillary tubes have similar shapes to straight capillary tubes. By varying the model input parameters for all pairs, it was found that new alternative refrigerants consistently gave lower pressure drops for both single-phase and two-phase regions, resulting in longer capillary tube lengths.

Acknowledgements

The authors are indebted to King Mongkut's University of Technology Thonburi (KMUTT), the Office of Higher Education Commission, the Thailand Research Fund (TRF) and National Research University Project for supporting this study.

References

[1] G. Zhou, Y. Zhang, Numerical and experimental investigations on the performance of coiled adiabatic capillary tubes, Applied Thermal Engineering 26 (11–12) (2006) 1106–1114.
[2] S. Ali, Pressure drop correlations for flow through regular helical coil tubes, Fluid Dynamics Research 28 (5) (2001) 295–310.
[3] S.G. Kim, S.T. Ro, M.S. Kim, Experimental investigation of the performance of R-22, R-407C and R-410A in several capillary tubes for air-conditioners, International Journal of Refrigeration 25 (5) (2002) 521–531.
[4] C. Park, S. Lee, H. Kang, Y. Kim, Experimentation and modelling of refrigerant flow through coiled capillary tubes, International Journal of Refrigeration 30 (7) (2007) 1168–1175.
[5] G. Valladares, Numerical simulation and experimental validation of coiled adiabatic capillary tubes, Applied Thermal Engineering 27 (5–6) (2007) 1062–1071.
[6] M.K. Mittal, R. Kumar, A. Gupta, An experimental study of the flow of R-407C in an adiabatic helical capillary tube, International Journal of Refrigeration 33 (4) (2010) 840–847.
[7] E.F. Schmidt, Warmeubergang and Druckverlust in Rohrschlangen, The Chemical Engineering and Technology 39 (13) (1967) 781–789.
[8] Y. Mori, W. Nakayama, Study on forced convective heat transfer in curve pipes II, International Journal of Heat and Mass Transfer 10 (1) (1967) 37–59.
[9] R.L. Manlapaz, S.E.W. Churchill, Fully developed laminar flow in a helically coiled tube of finite pitch, Chemical Engineering Communications 7 (1–3) (1980) 57–78.
[10] W.H. McAdams, W.K. Wood, R.L. Bryan, Vaporization inside horizontal tubes. II. Benzene–oil mixture, Transaction ASME 64 (1942) 193–200.
[11] S. Wongwises, W. Pirompak, Flow characteristics of pure refrigerants and refrigerant mixtures in adiabatic capillary tubes, Applied Thermal Engineering 21 (8) (2001) 845–861.

International Communications in Heat and Mass Transfer 37 (2010) 1238–1245

Contents lists available at ScienceDirect

International Communications in Heat and Mass Transfer

journal homepage: www.elsevier.com/locate/ichmt

Operating design conditions of a solar-powered vapor absorption cooling system with an absorber plate having different profiles: An analytical study ☆

B. Kundu [a,b,*], P.K. Mondal [a], S.P. Datta [a], S. Wongwises [c]

[a] Department of Mechanical Engineering, Jadavpur University, Kolkata 700 032, India
[b] School of Mechanical Engineering, Hanyang University, 17 Haengdang-dong, Seongdong-gu, Seoul, 133-791, Republic of Korea
[c] Fluid Mechanics, Thermal Engineering and Multiphase Flow Research Lab (FUTURE), Department of Mechanical Engineering, Faculty of Engineering King Mongkut's University Thonburi (KMUTT), Bangkok 10140, Thailand

ARTICLE INFO

Keywords:
Absorber
Absorption system
COP
Performance
Refrigerating system
Solar collector
Water–lithium bromide

ABSTRACT

An effort has been devoted to analyze the collector performance parameters of a solar-assisted LiBr/H_2O vapor absorption cooling system with a flat-plate collector consisting of an absorber plate of different profiles. The effect of the collector fluid inlet temperature on the performance of solar collector, vapor absorption cycle, vapor absorption system and refrigerating efficiency has been studied for a wide range of design variables. A comparative study has also been made among the performance parameters of an absorber plate of different shapes with the variation of collector fluid inlet temperature. From the result, it can be highlighted that, at a particular collector fluid inlet temperature, the performances of a vapor absorption system attain a maximum value. Finally, an optimum collector fluid inlet temperature is determined by satisfying the minimization of volume of an absorber plate without affecting the cooling rate in the evaporator.

© 2010 Elsevier Ltd. All rights reserved.

1. Introduction

The uses of nonconventional energy sources are becoming more important than the conventional sources. Utilization of solar energy in practical applications, among the nonconventional sources, has grown up exponentially. In particular, its application plays an important role to places where very strong solar radiation intensity is available almost over the years. It has been seen that there are so many areas where the supply of electricity either for human comfort or food preservation is no longer possible due to some infrastructural hindrance; the solar operated system for cooling only provides the way to short out that problem. Vapor absorption cycles formed one of the early developments of the refrigeration system becoming the most significant application of cooling using solar energy. Recently, they have achieved renewed interest with their potential as a "greener" refrigeration system. Moreover, the requirement of high-grade energy for the operation of mechanical vapor compression refrigeration systems grows more interest to researchers to put their thought for the continuous development of absorption refrigeration systems. The capability to produce a cooling effect by utilizing low-grade energy makes the absorption refrigeration system more attractive to researchers; thus, solar energy, of course, has a very promising potential to compete with conventional vapor compression and absorption technologies. Fortunately, with the development of science and technology, new materials and new techniques are emerging continually. Such refrigeration technologies recently have been attractive extensively, increasing attention from the experts all over the world because of their simple structure, fast refrigeration, and low-level powering energy source without generating the greenhouse effect.

Among the approaches available and used for the absorption cooler that is solar assisted, the first one is used for continuous cooling and the last one is for intermittent cooling. In both approaches of absorption cooling, the energy from the solar collector is supplied to the generator. Flat-plate collectors having different profiles such as rectangular, triangular, trapezoidal, and parabolic (convex and concave) are usually used for the first approach as mentioned above. Flat-plate collectors have the capability to provide very low temperature to the generator, which, in turn, allows a water–lithium bromide mixture, which can be used as the working fluid in the absorption system. However, with the use of water as a refrigerant in place of CFC and HCFC, the water–lithium bromide absorption system becomes very attractive as far as environmental issues are concerned. In the collector, the solar energy is converted to the useful energy to heat up the generator.

The individual performance of the solar collector and absorption system guides the performance of the solar-operated absorption cooling system as a whole. However, this performance evaluation has two directions, i.e., on an instantaneous basis and with the performance integrated over the full day of operation. The performance of the total

☆ Communicated by: A.R. Balakrishnan.

* Corresponding author. Department of Mechanical Engineering, Jadavpur University, Kolkata 700 032, India.
E-mail address: bkundu123@rediffmail.com (B. Kundu).

0735-1933/$ – see front matter © 2010 Elsevier Ltd. All rights reserved.
doi:10.1016/j.icheatmasstransfer.2010.08.012

system greatly depends on the energy transfer characteristics of the solar collector. The energy transfer from the collector to the generator takes place mainly due to conduction and convection. Convective energy transfer has no role to vary the performance of the system until the flow of a characteristic through the collector pipe is getting changed significantly. However, the conductive energy transfer can be enhanced by changing the collector area, i.e., by changing its shape, and thus plays an important role in the enhancement of the overall system performance. A number of research activities [1–4] have considered different profile shapes, i.e., rectangular, rectotrapezoidal, straight trapezoidal, straight triangular, rectangular with a step change in the local thickness, parabolic, for the design of the collector.

Among the different shapes of the flat-plate collector mentioned above, only a few are found to be used for the design of the collector. First, an investigation was done by Hollands and Stedman [2] for the design of a step-fin flat-plate collector although their study was focused on the determination of fin efficiency. Kundu [4] modified the work of Hollands and Stedman and developed a generalized methodology for the determination of the optimum fin dimensions. Varol and Oztop [5] studied numerically to compare the heat transfer rate in flat and wavy collectors. It has been mentioned above that the overall performance of the system depends on the individual performance of the collector and absorption system. It is therefore necessary to study the performance of the collector and the thermodynamic analysis of the absorption system separately for the improvement of the performance of the system altogether.

Many researchers have studied the solar-powered absorption refrigeration system. Li and Sumathy [6] performed the simulation study of a solar-powered absorption system considering the $H_2O + LiBr$ solution as a refrigerant–absorbent pair. Florides et al. [7] have revealed a method for the evaluation of the characteristics and performance of a single-stage $LiBr–H_2O$ absorption machine. Kaynakali and Kilic [8] have studied the effect of all the parameter on the performance of the absorption refrigeration system and they have showed that the use of the solution heat exchanger (SHE) in between the condenser and the evaporator increases the COP of the system remarkably. Balghouthi et al. [9] had demonstrated the application of solar-powered air conditioning as a solution to reduce the environmental pollution.

The available literature on solar-powered cooling system summarized above indicates that the previous works in this area were mainly concentrated on the performance analysis of the individual unit separately. However, in real-life cases, the solar collector acts as a heat source and the absorption unit acts as a heat sink for the solar-assisted absorption cooling system. Hence, an analysis of the collector and the absorption cooling unit and the dependency of the performance of the absorption unit on the performance of the collector are provided to estimate the overall system performance and optimum design parameters. Generally, solution heat exchangers are employed between the generator and the absorber to increase the performance of an absorption system. The addition of refrigerant heat exchangers between the condenser and the evaporator may increase the system performance also. No analysis has, so far, been made to predict the performance and the design criteria of the absorption system with an absorber plate of variable thickness. These facts are motivated in the present analysis.

In this study, the thermal performance of flat-plate collectors of different profiles has been established analytically. A parametric thermodynamic analysis of a single-stage absorption refrigeration cycle with solution and refrigerant heat exchangers (SHE and RHE) coupled with a solar collector is performed. For this purpose, an analytical model has been developed to determine the system's overall performance. Various profile shapes, namely, rectangular, trapezoidal, triangular, convex parabolic and concave parabolic, of the collector has been considered in the present model. A comparative study on system performances using different profiles has been made. An operating collector fluid inlet temperature is determined and subjected to minimize the collector volume.

2. Thermal analysis of a solar-powered absorption cooling system

The schematic diagram of a single-stage solar-assisted absorption refrigeration system has been shown in Fig. 1. The various components of the system are basically: a flat-plate collector, a generator, an absorber, a condenser, an evaporator, a pump, expansion valves, a solution heat exchanger (SHE) and a refrigerant heat exchanger (RHE). To establish the thermodynamic analysis of an absorption system, it can be highlighted that, due to the imposition of the two heat exchangers (SHE and RHE) in the present study, the analysis of the vapor absorption cycle is to be modified. The cycle efficiency and operation characteristics of an ab>sorption refrigeration system depend on the working fluids, temperatures and effectiveness of the heat exchanger. The SHE increases the COP of the cycle, reducing the heat load of the generator. On the other hand, in the RHE, which is the refrigerant side of the cycle, the refrigerant leaving the condenser is cooled by the vapor coming from the evaporator. Thus, the RHE decreases the enthalpy of the liquid, and the cooling capacity increases, which, in turn, increases the COP value of the cycle. In the absorber, the strong solution absorbs the water vapor leaving the evaporator.

The collector fluid heats the generator, and hence, the refrigerant is separated from the absorbent in the generator. The generator acts as a heat exchanger due to heat transfer between the collector fluid and the solution of refrigerant–absorbent. For a design application, the temperatures of the condenser($T_c = 32^0C$), absorber ($T_a = 30^0C$) and evaporator ($T_e = 5^0C$) are kept constant. In this regard, it can be mentioned that the evaporator temperature depends on the design application, and the condenser and absorber temperature can be fixed, depending on the ambient condition. Therefore, the generator temperature can be varied due to the change in the collector fluid inlet temperature. The present analysis is focused on obtaining an optimum design condition with the variation of collector fluid inlet temperature for a design condition. The calculations are done for one ton of refrigeration effect ($Q_e = 3.861$ kW). The mass flow rates of the refrigerant (m_r) and the mass flow rate of a strong solution (m_s) based on the concentration of the refrigerant can be determined from the expression given below:

$$(m_r;\ m_s) = (Q_e / (h_5 - h_4);\quad \xi_w m_r / (\xi_s - \xi_w)) \tag{1}$$

where ξ_s and ξ_w are the concentration of LiBr at state points 7 and 10 (Fig. 1a), respectively. The heat exchange rate in the generator (Q_g), condenser (Q_c) and absorber (Q_a) can then be evaluated from the expression below:

$$\begin{aligned}\left(Q_g;\quad Q_c;\ Q_a\right) = (&m_s(h_{10} - h_9) \\ &+ m_r(h_1 - h_{10});\ m_r(h_1 - h_2);\quad m_s(h_{12} - h_7) \\ &+ m_r(h_6 - h_{12}))\end{aligned} \tag{2}$$

where h'sare the enthalpies at respective states. The pump work for the solution leaving the absorber to feed the generator can be expressed as

$$w_{pump} = m_r(p_c - p_e)v_s \tag{3}$$

The performance of the cycle is understandable from the value of the coefficient of performance (COP):

$$\left((COP)_{\max};\quad (COP)_{cycle}\right) = \left(T_e\left(T_g - T_a\right) / \left\{T_g(T_a - T_e)\right\};\quad Q_e / \left(Q_g + w_{pump}\right)\right) \tag{4}$$

The energy balance for the solution heat exchanger yields the following expression of enthalpy.

$$h_{11} = h_{10}(1 - \varepsilon_{SHE}) + h_8\varepsilon_{SHE} = h_8 + \varepsilon_{SHE}(m_s - m_r)(h_{10} - h_8) / m_s \tag{5}$$

The RHE, which is located in between the condenser and evaporator, is in the refrigerant side of the system and allows the

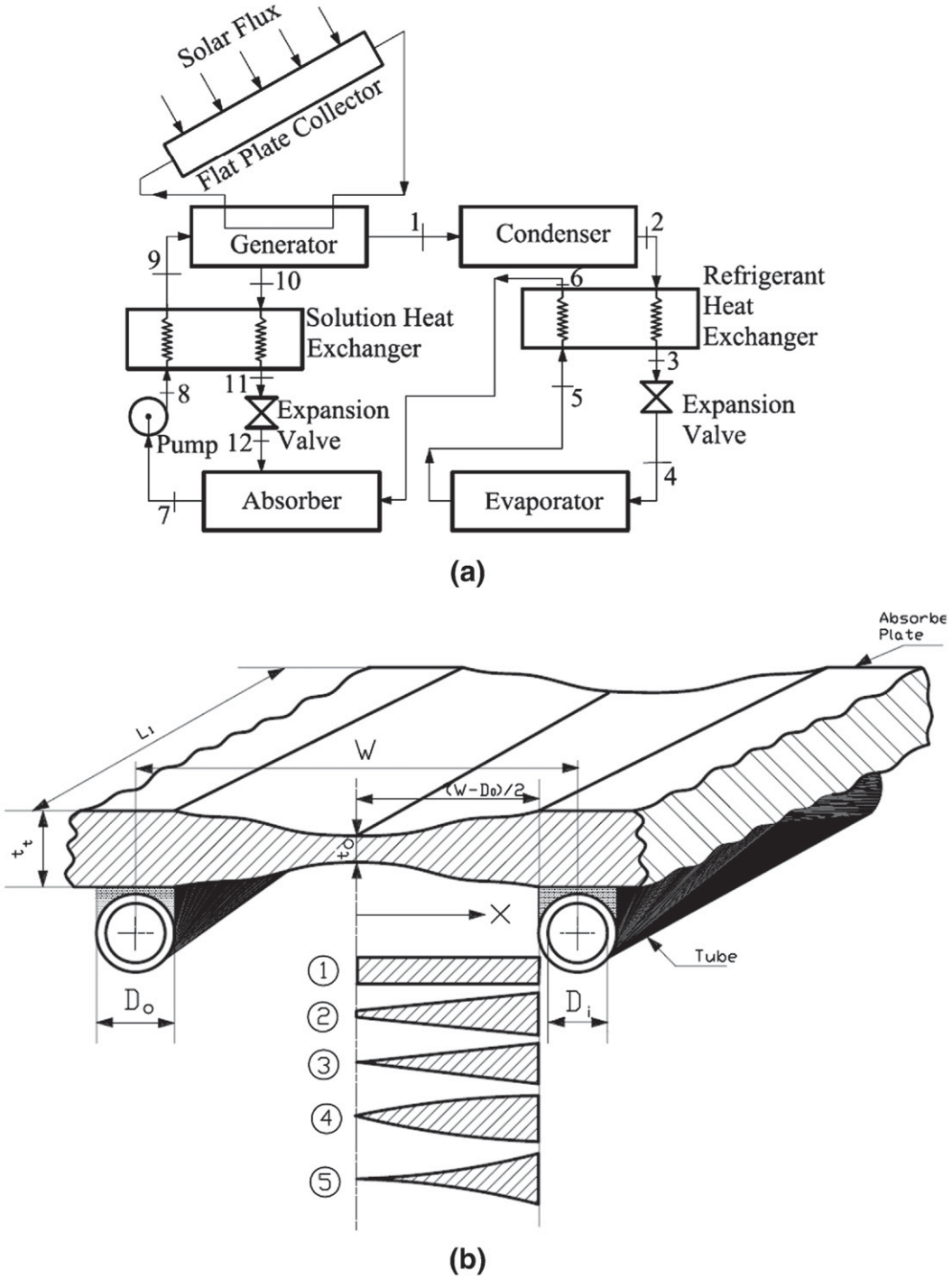

Fig. 1. (a) Schematic diagram of an absorption refrigeration system and (b) schematic diagram of a flat-plate collector with an absorber plate of different profiles: (1) rectangular; (2) trapezoidal; (3) triangular; (4) convex parabolic; (5) concave parabolic.

heat to transfer from the saturated liquid, leaving the condenser to the saturated vapor coming out from evaporator. The saturated vapor becomes heated, receiving heat from the liquid leaving condenser, and then enters into the absorber. The energy balance equation for the RHE can be written as

$$(h_6;\quad h_3) = \left(h_5 + \varepsilon_{RHE}(h_{2^*} - h_5)\,;\ \ h_{2^*} - \varepsilon_{RHE}(h_2 - h_5)\right) \tag{6}$$

where h_2* is the superheated vapor enthalpy of the refrigerant at the condenser temperature (T_c), since the vapor temperature leaving the evaporator increases up to the condenser temperature.

The amount of generator heat rate (Q_g) is supplied by the collector. Under the steady-state condition, the collector area (A_p) required to supply this energy is obtained from an energy balance:

$$A_p = m_w c_{pw} \ln\left[\left(1 - Q_g / \left\{m_w c_{pw}(I_A / U_l - T_{WI} + T_\infty)\right\}\right)\right] / \left(U_l \eta_F\right) \tag{7}$$

where m_w and C_{pw} are the mass flow rate and the specific heat of the collector fluid, respectively. From the above expression, it is obvious that, for the determination of A_p, the collector efficiency factor (η_F) is

provided. For the thermal analysis of the collector to determine η_F, the following steps can be followed.

The schematic diagram of a flat-plate collector of different absorber plate profiles is shown in Fig. 1b. The solar collectors are basically the heat exchanger that converts radiation energy into the transport medium as a useful form of energy. The energy obtained from the solar collector mainly depends on the collector performance, which is directly associated with the plate temperature distribution. However, the collector performance is the function of the collector efficiency factor (η_F), heat removal factor (F_R) and instantaneous collector efficiency (η_i). To estimate the collector performance, the above parameters are to be determined first. For this, an energy balance equation has been developed for a solar collector of unit length in the direction of the fluid flow under the steady-state condition. This energy balance gives the following differential equation in a normalized form:

$$d(Yd\theta/dX)/dX = Z_0^2\theta \tag{8}$$

where

$$[Z_0;\theta;X;Y;\ \mathrm{Bi};\varphi] = [\sqrt{\mathrm{Bi}}/\varphi;\left(T_p - T_\infty - I_A/U_l\right) / \left(T_{pt} - T_\infty - I_A/U_l\right);2x / (W - D_0);t/t_t;\ U_l t_t/k_p;\ 2t_t/(W - D_0)] \tag{9}$$

Considering a general profile of the collector plate (Y) can be expressed as follows:

$$[Y;\ \lambda] = \left[(1-\lambda)X^n + \lambda;\ t_0/t_t\right] \tag{10}$$

Putting the Y value in Eq. (8) and the governing equation reduces to

$$\left[(1-\lambda)X^n + \lambda\right]d^2\theta/dX^2 + n(1-\lambda)X^{n-1}d\theta/dX - Z_0^2\theta = 0 \tag{11}$$

The above-mentioned governing equation satisfies all the absorber profiles considered in the present study by selecting the respective n and λ values. These (n,λ) values for rectangular, trapezoidal, triangular, convex parabolic and concave parabolic profiles can be taken as (0,1), (1,0 < λ < 1), (1,0), (1/2,0) and (2,0), respectively. Eq. (11) is subjected to the following boundary conditions:

$$\text{at } X = 0,\ d\theta/dX = 0 \text{ and at } X = 1,\ \theta = 1 \tag{12}$$

In order to determine the temperature distribution in an absorber plate of different profiles, Eq. (11) can be solved with the above boundary conditions. The temperature profile in an absorber plate of rectangular, trapezoidal, triangular, convex parabolic and concave parabolic profiles is derived separately:

$$\theta = \begin{cases} \cosh(Z_0X)/\cosh(Z_0) & \text{Rectangular Profile} \\ D_1/D_2 & \text{Trapezoidal Profile} \\ I_0\left(2Z_0Y^{1/2}\right)/I_0(2Z_0) & \text{Triangular Profile} \\ X^{1/4}I_{-1/3}\left(4Z_0X^{3/4}/3\right)/I_{-1/3}(4Z_0/3) & \text{Convex Parabolic} \\ X^{\left(-1+\sqrt{1+4Z_0^2}\right)/2} & \text{Concave Parabolic} \end{cases} \tag{13}$$

where

$$(D_1;\ D_2;\ Z_1) = \left(I_0\left(2Z_1Y^{1/2}\right)K_1\left(2Z_1\lambda^{1/2}\right) + I_1\left(2Z_1\lambda^{1/2}\right)K_0\left(2Z_1Y^{1/2}\right);\ I_0(2Z_1)K_1\left(2Z_1\lambda^{1/2}\right) + I_1\left(2Z_1\lambda^{1/2}\right)K_0(2Z_1);\ Z_0/(1-\lambda)\right) \tag{14}$$

The absorber plate acts as a fin. The performance of an absorber plate is the ratio of the actual energy transfer rate through the plate to the ideal energy transfer rate. It can be expressed as

$$\eta = \begin{cases} \tanh(Z_0)/Z_0 & \text{Rectangular Profile} \\ D_3/D_2 & \text{Trapezoidal Profile} \\ I_1(2Z_0)/[Z_0I_0(2Z_0)] & \text{Triangular Profile} \\ I_{2/3}(4Z_0/3)/\left[Z_0I_{-1/3}(4Z_0/3)\right] & \text{Convecx Parabolic} \\ 2\Big/\left[1+\sqrt{1+4Z_0^2}\right] & \text{Concave Parabolic} \end{cases} \tag{15}$$

where

$$D_3 = \left[I_1(2Z_1)K_1\left(2Z_1\lambda^{1/2}\right) - I_1\left(2Z_1\lambda^{1/2}\right)K_1(2Z_1)\right]/Z_0 \tag{16}$$

The thermal resistance of the system will not allow the transferring of the heat being absorbed by the collector to the fluid in the tube. Thus, the useful heat gain by the collector will conceive the term of collector efficiency factor, which can be written as

$$\eta_F = (WU_l)^{-1}\left[\{U_l[D_0 + \eta(W-D_0)]\}^{-1} + C_b^{-1} + (\pi D_i h_l)^{-1} + (2\pi k_t)^{-1}\ln(D_0/D_i)\right]^{-1} \tag{17}$$

where the center-to-center distance between two tubes W, the inner diameter of the tube D_i, the outer diameter of the tube D_0, the thermal conductivity of the tube material k_t, the heat transfer coefficient at the collector fluid side h_l and the bonding conduction C_b are taken as 0.1 m, 0.014 m, 0.016 m, 100 W K^{-1}m^{-1}, 300 W K^{-1}m^{-2} and 50 W K^{-1}m^{-1}, respectively, to take the result.

The above equation gives the useful energy gain per unit flow length of the collector fluid in a tube. The fluid temperature increases in the direction of flow, receiving the thermal energy from the plate. The heat removal factor (F_R) can symbolically be expressed as

$$F_R = \dot{m}_W c_{PW}\left(A_pU_l\right)^{-1}\left[1 - \exp\left\{-A_p\eta_F U_l(m_W c_{PW})^{-1}\right\}\right] \tag{18}$$

where the mass flow rate of the collector fluid through each tube m_W is taken as 0.05 Kg s^{-1}.

The instantaneous efficiency of a flat-plate solar collector is given by

$$\eta_i = F_R[I_A - U_l(T_{WI} - T_\infty]/I_T \tag{19}$$

From Eq. (19), it is obvious that the instantaneous efficiency can be determined if the incident solar heat flux (I_T) and the absorbed solar heat flux (I_a) and U_l are known [1].

After getting the surface area of the collector (A_p), the heat removal factor (F_R) can be determined using Eq. (18). In this connection, it may be noted that the overall loss coefficient U_l can be determined if the plate mean temperature is known. The plate mean temperature can be achievable by integrating the temperature distribution T_p expressed in Eq. (13) over the plate area. Thus

$$\left(T_{pm} - T_\infty - I_A/U_l\right)/\left[T_{WI} + (1-F_R)q_g/\left(A_pU_lF_R\right) - T_\infty - I_A/U_l\right] = \int_{X=0}^{1}\theta dX \Big/ \int_{X=0}^{1}dX \tag{20}$$

It may further be noted that the plate mean temperature T_{pm} is a function of the overall loss coefficient U_l, which is also a function of T_{pm}. Thus, iteration is required for the solution until a desired accuracy has been reached. The iteration can be started from a guess value. The temperature of the generator varies during iteration. The collector

fluid outlet temperature (T_{WO}) and the generator temperature (T_1) can be determined from the following expression:

$$T_{WO} = T_9 + Q_g / \left(C_{\min}\varepsilon_g\right);\ C_{\min} = \text{Min}\{m_r c_r, m_w c_w\};\quad T_1 = T_9 + \varepsilon_g (T_{WO} - T_9) \tag{21}$$

The repetition of the above process is continued until the difference between two successive iterative temperature T_1 is negligibly small.

Now, the system COP and the refrigerating efficiency are determined from the following expression:

$$\left((COP)_{system};\ (\eta_R)_{system}\right) = \left(Q_e / \left(A_p I_T\right);\ (COP)_{system} / (COP)_{\max}\right) \tag{22}$$

The plate volume (V_p) between two tubes is required for a ton of refrigeration effect, which can be expressed as

$$V_p = \begin{cases} A_p t_t & \text{Rectangular Profile} \\ (A_p t_t)[(1+\lambda)(W - D_0)/(2W) + D_0/W] & \text{Trapezoidal Profile} \\ (A_p t_t)(W + D_0)/(2W) & \text{Triangular Profile} \\ (A_p t_t)(2W + D_0)/(3W) & \text{Convecx Parabolic} \\ (A_p t_t)(W + 2D_0)/(W) & \text{Concave Parabolic} \end{cases} \tag{23}$$

3. Results and discussion

Based on the above analysis, results have been taken systematically. The design condition of a solar-assisted vapor absorption system depends on the application. For a design condition, condenser and absorber temperatures are kept constant, depending on the ambient temperature. To find out a design criterion, the generator temperature can be varied by coupling a solar collector with the generator in the absorption unit. The generator temperature mainly depends on the amount of solar energy absorbed in the collector and the generator temperature can also be varied to change the collector fluid condition. This event may be made by varying the mass flow rate and the collector fluid inlet temperature. In the present study, an effort has been made to examine the performance parameters of a solar-assisted vapor absorption cooling system with the variation of collector fluid inlet temperature (T_{WI}). The solar flux incident on the absorbed plate of a collector depends on many factors. Among these factors, place and time are more depended on. The present analysis is carried out in Kolkata, India, at which the latitude angle = 22.5^0 north. The analysis is performed on 10th June. For the simulation of the solar powered system, the design parameters considered in the present analysis are taken as follows: convective heat transfer coefficient over the glass cover = 10W $K^{-1}m^{-2}$, thermal conductivity of insulation = 0.045W $K^{-1}m^{-1}$, thermal conductivity of the absorber plate material = 200W $K^{-1}m^{-1}$, thermal conductivity of the tube material = 100W $K^{-1}m^{-1}$, number of glass cover = 2, tilt angle = 20^0, thickness of insulation = 0.05 m, absorber plate thickness above the tube = 0.0016 m, ambient temperature = 30^0C, emissivity of glass = 0.9, emissivity of plate = 0.1, effectiveness of solution heat exchanger (ε_{SHE})=0.85, effectiveness of refrigerant heat exchanger (ε_{RHE})=0.85, λ=0.3 and effectiveness due to heat exchange in the generator (ε_g)=0.85.

The collector analysis has been furnished for different profiles. A comparative study of their performance parameters has been done by plotting the collector efficiency as a function of Z_0. Fig. 2 is illustrated for the above-mentioned purpose. The absorber plate efficiency for all types of profiles decreases with the increase in Z_0. The maximum efficiency closes to 100% when Z_0 tends to zero, irrespective of the profiles considered. The increasing Z_0 from its zero value makes an unequal absorber plate efficiency of different profiles. The maximum efficiency is obtained from the rectangular profile and a minimum value is noticed for the concave parabolic profile for a given Z_0. The

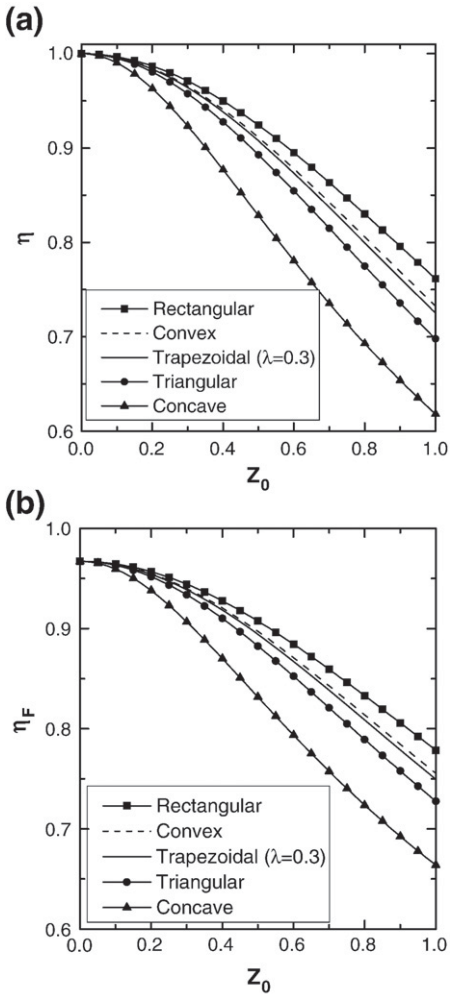

Fig. 2. Collector efficiency as a function of Z_0. (a) Efficiency of the absorber plate. (b) Collector efficiency factor.

efficiency for other profiles, such as convex parabolic, trapezoidal and triangular, is found in between in decreasing order. It may be noted that the efficiency of the trapezoidal profile depends on the geometrical parameter λ also and the effect of λon the efficiency is an incremental function. The same nature of curve has been obtained for the variation of collector efficiency factor with Z_0, as shown in Fig. 2b. However, the collector efficiency factor is slightly less than the absorber plate efficiency due to an addition of conductive–convective resistance for heat flow from the plate to the fluid carrying tubes.

Fig. 3 depicts the absorber plate efficiency factors, heat removal factor and instantaneous collector efficiency for different profiles as a function of T_{WI}. From Fig. 3a and b, an increase in T_{WI} declines both the fin efficiency and collector efficiency factor for all geometric fins considered in the present study. With the increase in fluid inlet temperature, the absorber plate mean temperature increases as a result and the effective heat absorbed in the plate decreases by increasing the rate of heat loss from the plate to the surrounding. The increase in the overall loss coefficient factor with the increase in T_{WI} can surely be attributed for the decrement in the collector efficiency. However, this declining effect changes marginally with the increase in T_{WI}. From the graph, it is again worth mentioning that the value of the fin efficiency parameter is a maximum for the rectangular profile absorber plate and is a minimum for the concave parabolic profile. The efficiency parameter for the convex parabolic profile is lower than the rectangular profile and is slightly higher than the trapezoidal profile. The efficiency of the triangular profile is always lower than the

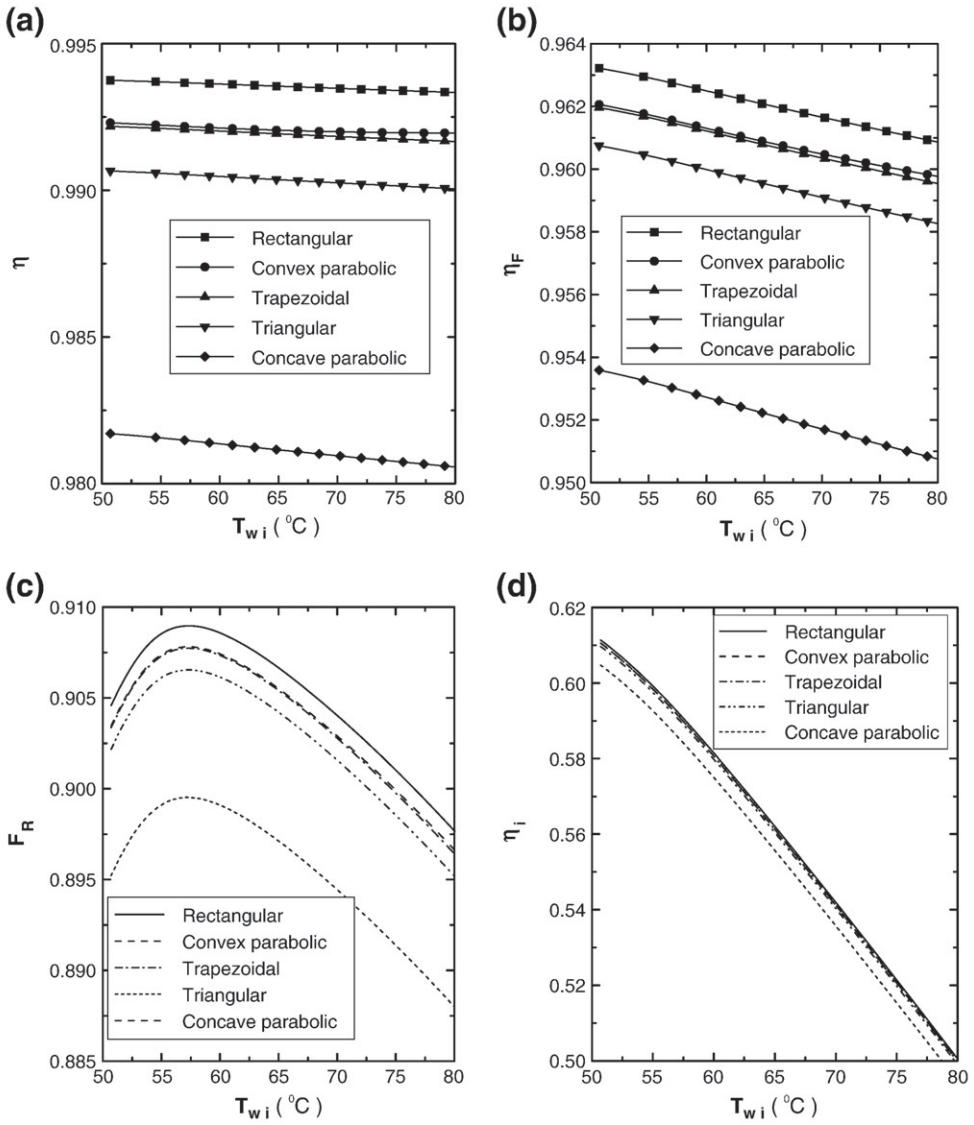

Fig. 3. Comparison of the collector performance factors for different profiles with the variation of collector fluid inlet temperature: (a) fin efficiency, (b) collector efficiency factor, (c) heat removal factor, and (d) instantaneous collector efficiency.

trapezoidal profile. Fig. 3c and d depicts the effect of T_{WI} on the heat removal factor and instantaneous collector efficiency having different geometrical shapes, respectively. In contrast to the collector efficiency and collector efficiency factor, a different profile is seen for this case. Initially, a gradual rise in the heat removal factor with T_{WI} is seen for all the profiles. However, attaining a peak value, followed by a continuous decrease in the profile, is seen to be associated for a constant surface area with an increase in T_{WI}. On the other hand, the instantaneous collector efficiency for all the profiles decreases monotonically with the increase in T_{WI}. From the graph, it can be demonstrated that the instantaneous efficiency does not depend much on the geometry of the absorber plate in comparison to the variation with T_{WI}.

The variation of the cycle COP and the cycle refrigerating efficiency with T_{wI} has been shown in Fig. 4a and b, respectively. It is seen that, for all the profiles, the COP value increases continuously with the increase in T_{WI}. However, an interesting observation is seen, i.e., the COP reaches an almost-constant value for all the profiles with the increase in T_{WI} at high values of T_{WI}. Therefore, it may be pointed out that T_{WI} is to be selected to a minimum value in such a way that the cycle COP reaches almost a maximum. In Fig. 4b, the refrigerating efficiency of the cycle has been depicted with the T_{WI}, and it is seen that following a gradual increase for a duration, there is a continuous decrease in the refrigerating efficiency with the increase in temperature. Thus, the refrigerating efficiency for all profiles attains a maximum for a particular T_{WI}, which may be of great importance from a design point of view. In Fig. 4c and d, the effect of T_{WI} has been shown on the system COP and the system refrigerating efficiency, respectively. Initially, both the system COP and refrigerating efficiency are seen to be increasing with the increase in T_{WI}. However, the figure also reveals that both the COP and refrigerating efficiency reach a maximum value at a particular temperature T_{WI} for all the profiles, followed by a continuous decrease in nature. The systems COP for different profiles are of comparable magnitude for a same T_{WI}, whereas a slight variation is noticed when they are compared to that obtained from the concave parabolic profile.

The variation of the plate volume of the collector of different profiles has been shown in Fig. 4e with T_{WI}. It is seen that the nature is the same for all the profile shapes considered in this study. A minimum value of the plate volume for each profile has also been determined separately at an optimum collector fluid inlet temperature. In other words, with the increase in T_{WI}, the plate volume decreases initially and reaches a minimum value and further increases with T_{WI} for every profile shape of an absorber plate adopted in the

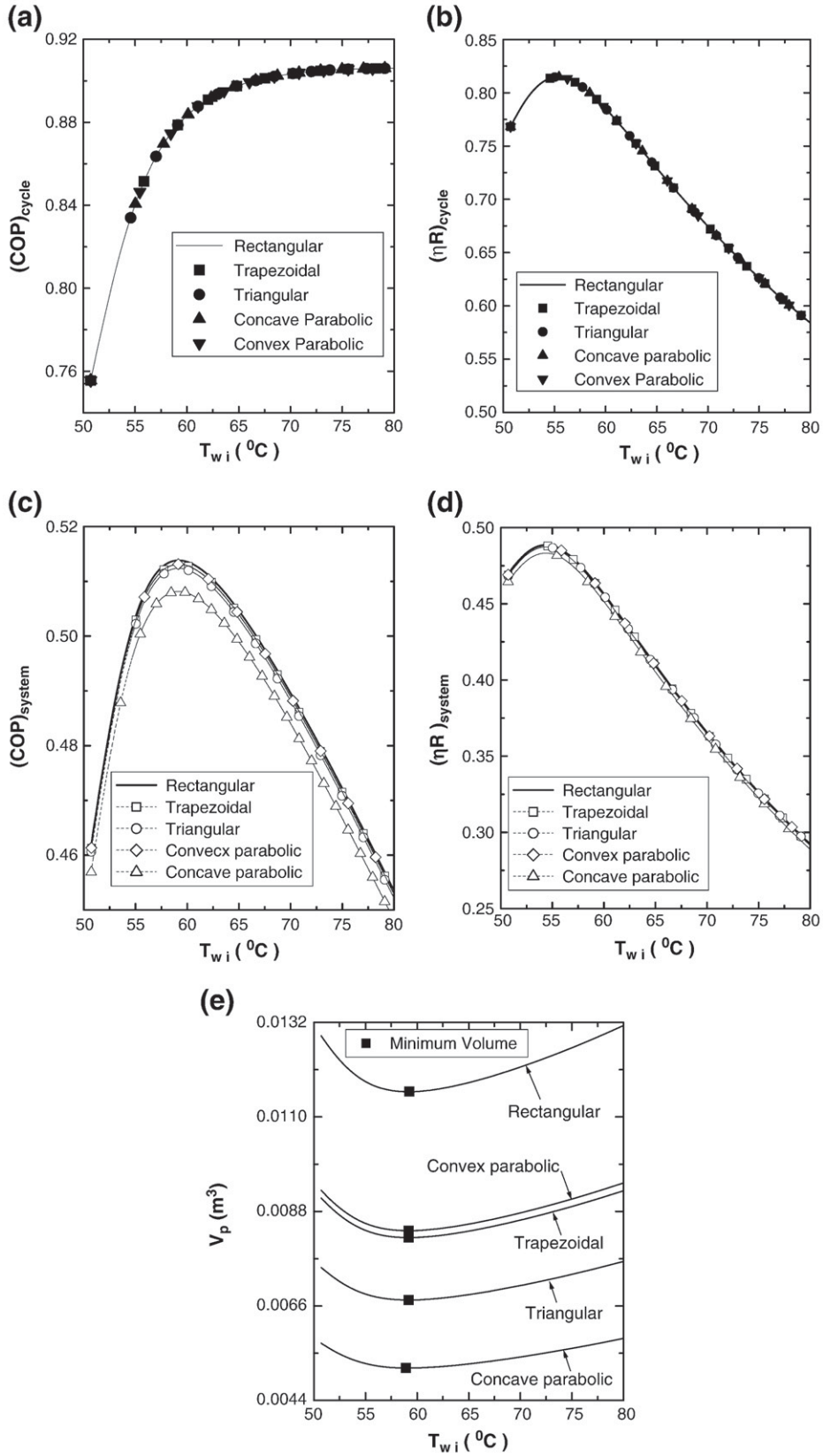

Fig. 4. Comparison of COP, refrigerating efficiency and plate volume of different shapes of an absorber plate with the variation of the collector fluid inlet temperature: (a) $(COP)_{cycle}$, (b) $(\eta_R)_{cycle}$, (c) $(COP)_{system}$, (d) $(\eta_R)_{system}$, and (e) V_p.

present study. The volume is the highest for the collector plate having a rectangular profile and the lowest for the concave parabolic profile. Therefore, from the design point of view, it can be demonstrated that the solar-operated vapor absorption system requires a minimum of absorber plate volume if the system is operated at a particular collector fluid inlet temperature. In comparison to the absorber plate

of different shapes, the minimum plate volume is required when a concave parabolic profile is employed. With the variation of T_{WI} on the plate volume, the nature of variation is the same for all profiles. However, a relatively strong function is obtained when the plate volume is correlated with T_{WI} for the rectangular profile.

4. Conclusion

An analytical method has been suggested for the performance analysis of a flat-plate collector of an absorber plate having different profiles. The analysis of the LiBr–H_2O absorption cycle has been demonstrated with the consideration of the solution and refrigerant heat exchanges for increasing the cycle performances. A simulation has been made for the variation of the collector fluid inlet temperature on the performance of a solar-operated absorption system. An optimum system COP and system refrigerating efficiency are obtained if the system operates under an optimum collector fluid inlet temperature. The performance of a solar-assisted absorption system depends significantly on the T_{WI}, and it does not depend considerably on the shape of the absorber plate adopted. On the other hand, the plate volume required for obtaining a desired effect is very much dependent on the shape of the absorber plate. The concave parabolic shape gives a minimum plate volume. For each shape, the plate volume is also strong function with the T_{WI}. An operating T_{WI} can be obtained by satisfying a minimum plate volume required for a given profiled shape and a desired cooling effect.

Acknowledgement

The authors would like to thank KMUTT for financial support.

References

[1] J.A. Duffie, W.A. Beckman, Solar Engineering of Thermal Process, Wiley Interscience, New York, 1991.
[2] K.G.T. Hollands, B.A. Stedman, Optimization of an absorber plate fin having a step-change in local thickness, Solar Energy 49 (1992) 493–495.
[3] M. Kovarik, Optimal distribution of heat-conducting material in the finned-pipe solar energy collector, Solar Energy 49 (1978) 477–484.
[4] B. Kundu, Performance analysis and optimization of absorber plates of different geometry for a flat-plate solar collector: A comparative study, Applied Thermal Engineering 22 (2002) 999–1012.
[5] Y. Varol, H.F.A. Oztop, Comparative numerical study on natural convection in inclined wavy and flat-plate solar collectors, Building and Environment 43 (2008) 1535–1544.
[6] J.F. Li, K. Sumathy, Simulation of a solar absorption air-conditioning system, Energy Conversion and Management 42 (2001) 313–327.
[7] G.A. Florides, S.A. Kalogirou, S.A. Tassou, L.C. Wrobel, Design and construction of a LiBr–H_2O absorption machine, Energy Conversion and Management 44 (2003) 2483–2508.
[8] O. Kaynakli, M. Kilic, Theoretical study on the effect of operating conditions on performance of absorption refrigeration system, Energy Conversion and Management 48 (2006) 599–607.
[9] M. Balghouthi, M.H. Chahbani, A. Guizani, Solar-powered air conditioning as a solution to reduce environmental pollution in Tunisia, Desalination 185 (2005) 105–110.

American J. of Engineering and Applied Sciences 3 (2): 470-475, 2010
ISSN 1941-7020
© 2010 Science Publications

Assessment of Useful Life of Lubricants Using Analytical Hierarchy Process (AHP) and Vector Projection Approach (VPA)

Surachai Bovornsethanant and Somchai Wongwises
Department of Mechanical Engineering, King Mongkut's University of Technology Thonburi, Bangmod, Bangkok 10140

Abstract: Problem statement: In general, engine oil is usually changed as defined by car or lubricant manufacturers, which is according to mileage. However, it was found from past researches that, at the predefined mileage or timeframe, most lubricant is still acceptably usable and efficient. **Approach:** This research aimed to calculate useful life of lubricant in order to reach its maximum usefulness. The method of study began by collecting data that indicates deterioration of lubricant by increasing mileage which includes total base number, viscosity, iron and flash point. Then the data was analyzed by means of Analysis Hierarchy Process (AHP). These variables were used to construct a model for calculating appropriate useful life of lubricant by using vector projection approach. It was found from this study that the defined mileage for changing lubricant, which is generally at 5,000 km, is not appropriate. **Results:** Results of the study suggest that the most appropriate mileage for change of lubricant is at 12,000 km. **Conclusion:** It could be concluded that collection of data about characteristics of lubricant and use of model for calculating useful life of lubricant can define appropriate interval change of lubricant.

Key words: Analytical hierarchy process, vector projection approach, useful life of lubricant

INTRODUCTION

An interval changing lubricant of engines is very important in maintenance work because lubricant helps prevent wear and tear of frictional parts. Deterioration of lubricant can be analyzed from changing characteristics of lubricant according to duration of use. The characteristics considered include Viscosity, TAN or TBN, Flash Point and fire Point and increased amount of metal particles in lubricant-which in this study Iron is used to signalize wear and tear of various parts. Since there are several indicators of deterioration of lubricant, in traditional method, used lubricant from several timeframes were tested against acceptable standard. If any characteristic exceeds the specified standard, it is time to change lubricant. In this research, Multi-criteria decision-making method was used to determine an interval change of lubricant. Analytical Hierarchy Process (AHP) is one of popular methods which can be applied to solve multi-indicators problems. Because in this method indicators are weighted according to importance of characteristic in use, more rational relationship can be specified.

Lubrication is very important for engines. At present, car manufacturers, oil manufacturers, including feeling of cars' users, are major factors in defining suitable interval change of lubricant. However, suitable timeframe or mileage for change of lubricant has never been clearly defined.

Up to the present, there are only some previous studies concerning this problem as follows:

Sinha *et al*. (2000) studied the useful life of lubricants using the artificial neural network method. In this study, the critical properties of oil such as viscosity, flash point, water content, insoluble rating were used as the input value to the network. Matlab version 5 with ANN toolbox was used to run the program and the network model was trained for viscosity. The result obtained from this study indicated that the estimated rejection time was 308 h.

Mukherjee *et al*. (2000) analyzed the remaining useful life of lubricant by the Fourier Transform Infrared (FTIR). A case study on Heavy Earth Moving Machinery (HEMM) in Indian mines was studied. They concluded that this method was simple and the result obtained from this method was reliable. However, this method can be utilized as the total life of the lubricant was identified.

The application of the Analytic Hierarchy Process (AHP) for selecting the best maintenance strategy was

Corresponding Author: Surachai Bovornsethanant, Department of Mechanical Engineering, King Mongkut's University of Technology Thonburi, Bangmod, Bangkok 10140

presented by Bevilacqua and Braglia (2000) for oil refinery. The preventive, predictive, condition-based, corrective and opportunistic maintenance which were the possible alternative were analyzed. They noted that AHP was coupled with a sensitivity analysis in order to correct the effectiveness of the procedure.

Al-Harbi (2001) applied the Analytic Hierarchy Process (AHP) in the project management. An example of contractor prequalification was presented. A sensitivity analysis was used to check the sensitivity of the final decisions. In order to simplify the methodology, the professional software (Expert choice) which was available commercially was used in this analysis.

The assessment of Remaining Useful Life (RUL) of lube oil using AHP and vector projection approach was studied by Sharma and Gandhi (2006). They used this method to identify the degradation of lubricants at an accelerated rate by operating system. The physical and chemical properties related to degradation of the lube oil were investigated. They reported that the result obtained from this study will help the maintenance and operational personnel.

Chen and Cai (2003) developed the methodology for evaluating the maintainability of the mechanical system. A number of standard guidelines were presented in this study and used to develop a set of maintainability factor. The developed methodology was called vector projection method. An example of mechanism of valve-driving system was discussed. They reported that this procedure provided a convenient method to estimate the best design.

The combination of the Analytic Hierarchy Process (AHP) and Technique for Order Preference by Similarity to Ideal Solution (TOPSIS) were developed to select an optimum maintenance strategy for a textile industry by Shyjith *et al*. (2008). They stated that the multifaceted factors were involved in the maintenance strategy selection. Therefore, it required the multi criteria decision-making to estimate the strategies. The results showed the most accurate decision when a maintenance policy was used.

Change of lubricant according to mileage predefined by manufacturers could be done while the lubricant is still usable. Currently, Thailand uses about 292 L of lubricant per year. Each change of lubricant produces waste which should be disposed of and loss from ineffective use. Moreover, engines have been improved to have higher performance and lubricant has also been improved to have higher efficiency. Hence, lubricant should have longer useful life.

The objective of this research is to apply the Analytical Hierarchy Process (AHP) and Vector Projection Approach to determine remaining useful life of lubricant in order to achieve its maximum usefulness as well as to conserve valuable resources and save production cost.

Theories used for calculating useful life of lubricant: All variables were weighted by using Analytical Hierarchy Process (AHP) to define significant weight of each variable (Saaty, 1994). The method consists of the following steps:

- Define weight for each variable according to its importance:

$$V = \{P_1, P_2, P_3, P_4, \ldots\ldots, P_i\},\ i = 1,2,3,\ldots,n$$

where n is number of variable used in AHP process.

- Construct a matrix of n×n to compare against decision-making criteria:

$$P = \begin{array}{c} \\ P_1 \\ P_2 \\ . \\ . \\ P_n \end{array} \begin{array}{c} \begin{array}{cccccc} P_1 & P_2 & . & . & P_n \end{array} \\ \begin{bmatrix} a_{11} & a_{12} & - & - & a_{1n} \\ a_{21} & a_{22} & - & - & a_{2n} \\ - & - & - & - & - \\ - & - & - & - & - \\ a_{n1} & a_{n2} & - & - & a_{nn} \end{bmatrix} \end{array}$$

Matrix P contains members of a_{ij} which derived from a comparison of importance of P_1 which is higher than the importance of P_2 according to Table 1. Values of a_{ji} will be reversed values of a_{ij} ($a_{ji} = 1/a_{ij}$). This matrix is called "reciprocal matrix".

- Use the reciprocal matrix to calculate Consistency Ratio (CR) of data by:
  - Find value of λ_{max}
  - Find Consistency Index (CI) using $CI = \frac{\lambda_{max} - n}{n-1}$ (Table 2)

Table 1: Pair wise comparison in AHP preferences (Saaty, 1994)

Ratings	Judgment/preference
9	Extremely preferred
7	Very strongly preferred
5	Strongly preferred
3	Moderately preferred
1	Equally preferred

Note: 2,4,6,8 are in the middle scale

Table 2: Assigning of random consistency Index (RI) (Saaty, 1994; Saaty and Kearns, 1991)

Size of matrix	1	2	3	4	5	6	7	8	9	10
Random consistency index	0	0	0.58	0.90	1.12	1.24	1.32	1.41	1.45	1.49

- Find Consistency Ratio (CR) from $CR = \frac{CI}{RI}$ by using RI value from Table 3. If CR is <0.1, weight of variable is accurate.

- Find importance value of each variable from Normalized matrix:

$$W = \begin{bmatrix} W_1 \\ W_2 \\ W_3 \\ W_4 \end{bmatrix}$$

Vector projection approach: Value of each variable at increased kilometer does not show similar trend. Some variable has downward trend while some has upward trend. From the field test, value of each variable could be written into the following matrix:

$$B = \begin{array}{c} \\ P_1 \\ P_2 \\ . \\ . \\ P_i \end{array} \begin{array}{c} \begin{array}{ccccc} S_1 & S_2 & . & . & S_j \end{array} \\ \begin{bmatrix} b_{11} & a_{12} & - & - & a_{1j} \\ b_{21} & a_{22} & - & - & a_{2j} \\ - & - & - & - & - \\ - & - & - & - & - \\ b_{i1} & a_{12} & - & - & a_{ij} \end{bmatrix} \end{array}$$

b_{ij} is a value from field test.

Therefore, all variables have to be made to show the same trend in order to summarize into one conclusion and compare to acceptable value of the oil.

From the formula:

For variables with upward trend:

$$D_{ij} = \left[\frac{b_{ij} - \text{UpperLimit}}{\text{LowerLimit} - \text{UpperLimit}} \right]$$

For variables with downward trend:

$$D_{ij} = \left[\frac{b_{ij} - \text{LowerLimit}}{\text{UpperLimit} - \text{LowerLimit}} \right]$$

A matrix which compares increased mileage (S) with various variables (P) is as follows:

Table 3: Comparison of matrix of pair wise and its reciprocal

Criterion for decision making	P1	P2	P3	P4
TBN P1	1	1	7	8
Kinematic viscosity at 100°C P2	1	1	6	7
Flash point P3	1/7	1/6	1	1
Iron P4	1/8	1/7	1	1
Summation	2.2678	2.3095	15	17

$$D = \begin{array}{c} \\ P_1 \\ P_2 \\ . \\ . \\ P_i \end{array} \begin{array}{c} \begin{array}{ccccc} S_1 & S_2 & . & . & S_j \end{array} \\ \begin{bmatrix} D_{11} & D_{12} & - & - & D_{1j} \\ D_{21} & D_{22} & - & - & D_{2j} \\ - & - & - & - & - \\ - & - & - & - & - \\ D_{i1} & D_{i2} & - & - & D_{ij} \end{bmatrix} \end{array}$$

Matrix D and matrix W are used to calculate remaining useful life of lubricant by finding matrix E from multiplying matrix W with matrix D:

$$[E] = [W][D]$$

$$E = \begin{array}{c} \\ P_1 \\ P_2 \\ P_3 \\ . \\ . \\ P_i \end{array} \begin{array}{c} \begin{array}{ccccc} S_1 & S_2 & . & . & S_j \end{array} \\ \begin{bmatrix} W_1D_{11} & W_1D_{12} & . & . & W_1D_{1j} \\ W_2D_{21} & W_2D_{22} & . & . & W_2D_{2j} \\ . & . & . & . & . \\ . & . & . & . & . \\ . & . & . & . & . \\ W_jD_{i1} & W_jD_{i2} & . & . & W_jD_{ij} \end{bmatrix} \end{array}$$

Then, find the following values:

d_j = Modulus at time interval/kilometer "j"
α_j = Angle between modulus and projection
T_j = Projection at time interval/kilometer "j"

The relations of these three values are shown in Fig. 1.

By using the following formula:

$$\text{Cos}(\alpha) = r_j = \frac{\sum_{i=1}^{n} W_iD_{ij} \times W_i}{\sqrt{\sum_{i=1}^{n} [W_iD_{ij}]^2} \times \sqrt{\sum_{i=1}^{n} [W_i]^2}}$$

and:

$$d_j = \sqrt{[\sum_{i=1}^{n} W_iD_{ij}]^2} \quad i = 1,2,...,n \text{ and } j = 1,2,...,m$$

$$T_j = d_j \times r_j = d_j \times \cos(\alpha) \quad j = 1,2,...,m$$

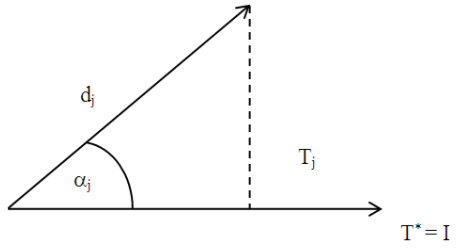

Fig. 1: The relation among d_j, α_j and T_j

The gained T_j value is a Remaining Useful Life (RUL) of the lubricant, which should be converted to 100% when compared against mileage of cars.

MATERIALS AND METHODS

The used BP SAE 40 API CD/SF lubricant from 4, 6 and 10-wheel trucks at the mileages of 0, 5000, 7500 and 10000 km was tested for its remaining useful life. After that, the sampling mileage was increased 1000 km at a time. Four variables which affect useful life of lubricant-Total Base Number (TBN), kinematic viscosity, flash point and amount of Iron-were studied.

RESULTS

Use of Analytical Hierarchy Process (AHP): The vector projection approach could be used to define an interval change of lubricant when certain variable is deteriorated. Lubricant is best changed when the viscosity is deteriorated in order to preserve the engine. On the contrary, change of lubricant according to value of metals' deterioration does not preserve the engine and can cause engine's damage. Thus, the AHP is used to define a suitable interval change of lubricant in order to achieve maximum efficiency and to preserve the engine.

Step 1: Define weight for each variable.

From the study, variables should be weighted as follow:

TBN = 9
Viscosity = 8
Flash Point = 2
Iron = 1

Step 2: Construct a matrix for paired-comparison against decision-making criteria:

$P_{12} = 1$ from $P_1 - P_2 = 9 - 8 = 1$
$P_{21} = 1/P_{12} = 1$ is a reversed value

As shown in Table 3.

Step 3: Use the sum value of each position to divide all values in the position: e.g., sum value of the 1st position:

$$1+1+1/7+1/8 = 2.268$$

Use this sum value to divide all values in the 1st position: e.g., $P_{11} = 1/2.268 = 0.441$ and find average value of each row as shown in Table 4.

Step 4: Find average value of the horizontal sum of each row: e.g., average sum of the 1st row is:

$$(0.441+0.433+0.467+0.471)/4 = 0.453$$

Step 5: Multiply value from Step 2 with value from Step 4:

$$\begin{bmatrix}0.453 & 0.421 & 0.065 & 0.061\end{bmatrix}\times\begin{bmatrix}1 & 1 & 7 & 8\\ 1 & 1 & 6 & 7\\ 1/7 & 1/6 & 1 & 1\\ 1/8 & 1/7 & 1 & 1\end{bmatrix}$$

Results should be as shown in Table 5.

Step 6: Divide value from Step 5 with value from Step 4:

$1.815/0.453 = 4.006, 1.690/0.421 = 4.014, 0.261/0.065 = 4.015, 0.243/0.061 = 3.983$

Then, find Eigen value:

$$\lambda_{max} = (4.006+4.014+4.015+3.983)/4 = 4.005$$

Step 7: Find Consistency Index (CI):

$$CI = \frac{\lambda_{max} - n}{n-1} = (4.005-4)/(4-1) = 0.002$$

Step 8: Check Consistency Ratio (CR) of variables.

Using RI value from Table 3 with a matrix of 4×4 = 0.9:

$$CR = \frac{CI}{RI} = 0.002 / 0.9 = 0.002$$

Table 4: Percentage of each attribution and their average (priority vector)

Criterion for decision making	P1	P2	P3	P4	Mean
TBN P1	0.441	0.433	0.467	0.471	0.453
Kinematic viscosity at 100°C P2	0.441	0.433	0.400	0.412	0.421
Flash point P3	0.063	0.072	0.067	0.059	0.065
Iron P4	0.055	0.062	0.067	0.059	0.061

Table 5: The priority vector multiply the reciprocal matrix expression

Criterion for decision making	
TBN P1	1.815
Kinematic viscosity at 100°C P2	1.690
Flash point P3	0.261
Iron P4	0.243
Summation	4.008

Note if CR is <0.1, variables are given accurate weights.

Step 9: Gain weight of variable used to define interval change of lubricant.

By finding vertical sum value of Step 5:

$$1.815+1.690+0.261+0.243 = 4.008$$

$$\begin{bmatrix} W_1 \\ W_2 \\ W_3 \\ W_4 \end{bmatrix} = \begin{bmatrix} 1.815/4.008 \\ 1.690/4.008 \\ 0.261/4.008 \\ 0.243/4.008 \end{bmatrix} = \begin{bmatrix} 0.453 \\ 0.422 \\ 0.065 \\ 0.061 \end{bmatrix}$$

This gives weights of variables used to define interval change of lubricant, as shown in Table 6.

From Table 6, the lubricant's life of 100% consists of TBN = 45.3%, Viscosity = 42.2%, Flash Point = 6.5% and Iron = 6.1% according to AHP process.

Lubricant's life gained from AHP process is a single sum of various variables that affect the use of lubricant.

Use of vector projection approach: Some variables that affect condition of lubricant show upward trend to deteriorate beyond acceptable value (e.g., contamination of sand and wear-and-tear of metal) while some variables show downward trend to deteriorate beyond acceptable value (e.g., viscosity, flash point and total base number). Thus, the Vector Projection Approach can make all variables deteriorate in the same trend:

Step 1: Test variables that affect condition of lubricant according to changing mileage as shown in Table 7.

Step 2: Compare the tested value with acceptable value of the lubricant as in Table 8.

Table 6: Percentage with weighting of each attribution

TBN	P1	0.453
Viscosity	P2	0.422
Flash point	P3	0.065
Iron	P4	0.061
Summation		1.000

Table 7: Values of lubricant attribution of the tested vehicle

Criterion for decision making	Distance (km) 0	5.000	7.543	11.513	Unit
TBN	7.60	5.80	5.20	4.76	mgKOH g^{-1}
Kinematic viscosity at 100°C	14.39	12.54	11.28	10.20	cSt°
Flash point	240.00	228.00	223.00	221.00	C
Iron	0.00	16.00	21.00	33.00	ppm

Step 3: Compare the tested value with acceptable value using the formula of vector projection approach.

Formula of vector projection approach:

For variables with upward trend: (Silicon and Iron):

$$D_{ij} = \left[\frac{b_{ij} - \text{UpperLimit}}{\text{LowerLimit} - \text{UpperLimit}} \right]$$

For variables with downward trend: (Viscosity, flash point and TBN):

$$D_{ij} = \left[\frac{b_{ij} - \text{LowerLimit}}{\text{UpperLimit} - \text{LowerLimit}} \right]$$

b_{ij} is value gained from the field test.

Step 4: From Step 3, percentage of variables that affect condition of lubricant could be gained as in Table 9.

Step 5: Find suitable interval change of lubricant with AHP and vector projection approach.

Multiply weight of variables from AHP with results from vector projection approach to gain useful life of lubricant which changes with mileage. After that, use lubricant's life to define suitable interval as shown in Table 10.

Table 8: The acceptable limits and their working range of the lubricant attribution

Oil property	Standard	Unit	Limitation	Standard of BP SAE 40 CD/SF
Kinematic viscosity at 100°C	ASTM D445	cSt	±25%	14.39
Flash point	ASTM D92	°C	270-160	240
TBN	ASTM D4739	mgKOH g^{-1}	-50% new oil	7.60
Iron	ASTM D6595	ppm	<200	0.00

Table 9: The normalized quantitative value of attribution

D_{ij}			
0 km	5000 km	7500 km	11513 km
1	0.526	0.368	0.252
1	0.486	0.136	-0.163
0.72	0.618	0.572	0.554
1	0.920	0.895	0.835

Table 10: Conversion of the normalized quantitative value to weight normalized value

E = [D][W]			
0 km	5,000 km	7,543 km	11,513 km
0.453	0.238	0.166	0.114
0.422	0.205	0.057	-0.068
0.046	0.040	0.034	0.036
0.061	0.056	0.054	0.050

Table 11: Calculations of parameters along with the distance

Distance (km)	0	5,000	7,543	11,513
d_j	0.624	0.321	0.186	0.146
Cos (α)	1.000	0.998	0.897	0.307
T_j	0.624	0.320	0.167	0.045
RUL in percentage	62.4	32.0	16.7	4.5
Corrected RUL	100	51.28	26.76	7.2

Step 6: Find the following values:

d_j = Modulus at time interval/kilometerage
α_j = Angle between modulus and projection
T_j = Projection at time interval /kilometerage

Lubricant's life by mileage could be gained as shown in Table 11.

DISCUSSION

The advantage of this method is to show trends in characteristic change of various indicators, thus, remaining useful life can be predicted. Consequently, maintenance is more effective. Results from the study for one logistic company which used to change lubricant every 5,000 km reveal that, when AHP and Projection Approach were used for analysis, the suitable interval change of lubricant was at every 12,000 km. Hence, about 50% of usable lubricant was wasted. Besides the cost of lubricant, other additional losses, such as opportunities in goods transport which may be more than the cost of lubricant itself, were also wasted.

CONCLUSION

This research used AHP to find relationship between indicators and used Projection Approach to convert the relationship values of indicators into values of lubricant's characteristics measured by mileage. When these values were compared against acceptable values of the lubricant, remaining useful life of lubricant by mileage could be defined. The remaining useful life of 0% indicates that the characteristics of lubricant are not sufficient for use. The result from the present study shows that the multi criteria decision making can be used to determine the useful life of the lubricant oil. The method is reasonable rather than the use of any one variable.

REFERENCES

Al-Harbi, K.M.A.S., 2001. Application of the AHP in project management. Int. J. Project Manage., 19: 19-27. DOI: 10.1016/S0263-7863(99)00038-1

Bevilacqua, M. and M. Braglia, 2000. The analytic hierarchy process applied to maintenance strategy selection. Reliab. Eng. Syst. Safe., 70: 71-83.

Chen, L. and J. Cai, 2003. Using vector projection method to evaluate maintainability of mechanical system in design review. Reliab. Eng. Syst. Safe., 81: 147-154.

Mukherjee, P.S., A.M. Sinha and A. De, 2000. RULL assessment by FTIR- a case study on HEMM in Indian mines. Ind. Lubricat. Tribol., 52: 61-66.

Saaty, T.L., 1994. The Fundamentals of Decision-Making and Priority Theory with the Analytic Hierarchy Process. RWS Publication, Pittsburg.

Saaty, T.L. and K.P. Kearns, 1991. Analytical Planning: The Organization of System: The Analytical Hierarchy Process Series. RWS Publication, Pittsburg.

Sharma, B.C. and O.P. Gandhi, 2006. RUL assessment of lube oil using AHP and vector projection approach. Ind. Lubricat. Tribol., 58: 187-194.

Shyjith, K., M. Ilangkumaran and S. Kumanan, 2008. Methodology and theory multi-criteria decision-making approach to evaluate optimum maintenance strategy in textile industry. J. Qual. Mainten. Eng., 14: 375-386.

Sinha, A.N., P.S. Mukherjee and A. De, 2000. Assessment of useful life of lubricants using artificial neural network. Ind. Lubricat. Tribol., 52: 105-109.

Provided for non-commercial research and education use.
Not for reproduction, distribution or commercial use.

This article appeared in a journal published by Elsevier. The attached copy is furnished to the author for internal non-commercial research and education use, including for instruction at the authors institution and sharing with colleagues.

Other uses, including reproduction and distribution, or selling or licensing copies, or posting to personal, institutional or third party websites are prohibited.

In most cases authors are permitted to post their version of the article (e.g. in Word or Tex form) to their personal website or institutional repository. Authors requiring further information regarding Elsevier's archiving and manuscript policies are encouraged to visit:

http://www.elsevier.com/copyright

Author's personal copy

Experimental Thermal and Fluid Science 35 (2011) 20–28

Contents lists available at ScienceDirect

Experimental Thermal and Fluid Science

journal homepage: www.elsevier.com/locate/etfs

Evaporation heat transfer and friction characteristics of R-134a flowing downward in a vertical corrugated tube

Kanit Aroonrat, Somchai Wongwises *

Fluid Mechanics, Thermal Engineering and Multiphase Flow Research Lab. (FUTURE), Department of Mechanical Engineering, King Mongkut's University of Technology Thonburi, Bangmod, Bangkok 10140, Thailand

ARTICLE INFO

Article history:
Received 2 May 2010
Received in revised form 4 August 2010
Accepted 4 August 2010

Keywords:
Vertical
Evaporation
Nusselt number
Two-phase friction factor
Corrugated tube

ABSTRACT

Differently from most previous studies, the heat transfer and friction characteristics of the pure refrigerant HFC-134a during evaporation inside a vertical corrugated tube are experimentally investigated. The double tube test sections are 0.5 m long with refrigerant flowing in the inner tube and heating water flowing in the annulus. The inner tubes are one smooth tube and two corrugated tubes, which are constructed from smooth copper tube of 8.7 mm inner diameter. The test runs are performed at evaporating temperatures of 10, 15, and 20 °C, heat fluxes of 20, 25, and 30 kW/m^2, and mass fluxes of 200, 300, and 400 kg/m^2 s. The quality of the refrigerant in the test section is calculated using the temperature and pressure obtained from the experiment. The pressure drop across the test section is measured directly by a differential pressure transducer. The effects of heat flux, mass flux, and evaporation temperature on the heat transfer coefficient and two-phase friction factor are also discussed. It is found that the percentage increases of the heat transfer coefficient and the two-phase friction factor of the corrugated tubes compared with those of the smooth tube are approximately 0–10% and 70–140%, respectively.

© 2010 Elsevier Inc. All rights reserved.

1. Introduction

Since the depletion of the ozone layer and global warming have been discovered, many conventional refrigerants are being phased out from industries. Consequently, the refrigeration industry has switched over to "ozone-friendly" refrigerants such as R-134a. Therefore, improving the performance of heat transfer equipment which uses R-134a is necessary. The thermal performance of heat transfer equipment can be improved by using heat transfer enhancement techniques. In general, heat transfer enhancement techniques are classified into two groups: active methods and passive methods. Active methods are those that use the addition of external power essentially to facilitate the desired flow modification and concomitant improvement in the rate of heat transfer such as mechanical vibration, injection, and electric field. The second group is passive methods which do not require direct input of external power such as surface modification.

The rough surface technique is a passive method that usually involves surface modification to promote turbulent flow and increases the heat transfer surface area. Normally, smooth tubes are replaced by corrugated tubes in many heat exchangers to increase the heat transfer rate by mixing and also limiting the fluid boundary layers close to the heat transfer surfaces. Moreover, they can promote two-phase heat transfer enhancement.

Over the years, the heat transfer and flow characteristics of refrigerants have been studied by a large number of researchers, both experimentally and analytically, mostly in horizontal straight tubes (Goldstein et al. [1]). Study of the heat transfer and pressure drop of refrigerant in vertical tubes has received comparatively little attention in the literature. Publications on the heat transfer and flow characteristics of refrigerant flow in vertical tubes are summarized as follows.

Ma et al. [2] experimentally studied the heat transfer and pressure drop characteristics for condensation of downward flow of R113 in vertical smooth and micro-fin tubes. Lee and Chang [3] investigated the heat transfer characteristics in the post-dryout region for the boiling of up-flow of R-134a in vertical smooth tubes and rifled tubes. Cheung et al. [4] studied the EHD-assisted external condensation of R-134a in vertical and horizontal smooth tubes. Experimental results demonstrated a remarkable potential in utilizing EHD to enhance external condensation heat transfer. Among all these studies, extensive studies concerning the condensation of R-134a in vertical smooth tubes have been continually performed by Dalkilic et al. [5]. The two-phase pressure drop during condensation of R-134a was studied. A new correlation for the two-phase friction factor was presented by means of the equivalent Reynolds number. In a series of studies, Dalkilic et al. [6,7] presented the effect of void fraction models on the two-phase friction

* Corresponding author. Tel.: +66 2 470 9115; fax: +66 2 470 9111.
E-mail address: somchai.won@kmutt.ac.th (S. Wongwises).

0894-1777/$ - see front matter © 2010 Elsevier Inc. All rights reserved.
doi:10.1016/j.expthermflusci.2010.08.002

Author's personal copy

Nomenclature

A	surface area of the test section (m^2)
c_p	specific heat at constant pressure (J/kg K)
G	mass flux (kg/m^2 s)
h	heat transfer coefficient (W/m^2 K)
i	specific enthalpy (J/kg)
i_{fg}	specific enthalpy of vaporization (J/kg)
k	thermal conductivity (W/m K)
m	mass flow rate (kg/s)
Q	heat transfer rate (W)
q''	heat flux (W/m^2)
T	temperature (K)
x	quality
Re	Reynolds number
d	tube diameter (m)
g	gravitational acceleration (m/s^2)
P	pressure (Pa)
z	axial coordinate (m)
f	friction factor
e	depth of corrugation (m)
p	pitch of corrugation (m)

Greek symbols

α	void fraction
μ	dynamic viscosity (kg/m s)
θ	helix angle (°)
ρ	density (kg/m^3)

Subscripts

avg	average
in	inlet
i	inside
out	outlet
o	outside
ph	pre-heater
ref	refrigerant
sat	saturation
TS	test section
g	gas/vapor
l	liquid
w	water
wi	inner wall
tp	two-phase
eq	equivalent
F	frictional term
G	gravitational term
M	omentum term

factor and film thickness during condensation of R-134a. The friction factors and film thickness values obtained from various void fraction models and correlations were compared with each other. Dalkilic et al. [8,9] studied the heat transfer coefficient, film thickness, and condensation rate during downward condensing of film. A new correlation for the heat transfer coefficient was proposed for practical applications.

Most of the experimental investigations described above focused on the heat transfer and flow characteristics of refrigerant flow inside vertical smooth tubes, particularly during condensation. There have been very few works dealing with the flow in vertical enhanced tubes. However, it can be noted that the heat transfer and flow characteristics of refrigerant during downward flow and evaporation in corrugated tubes remain unstudied

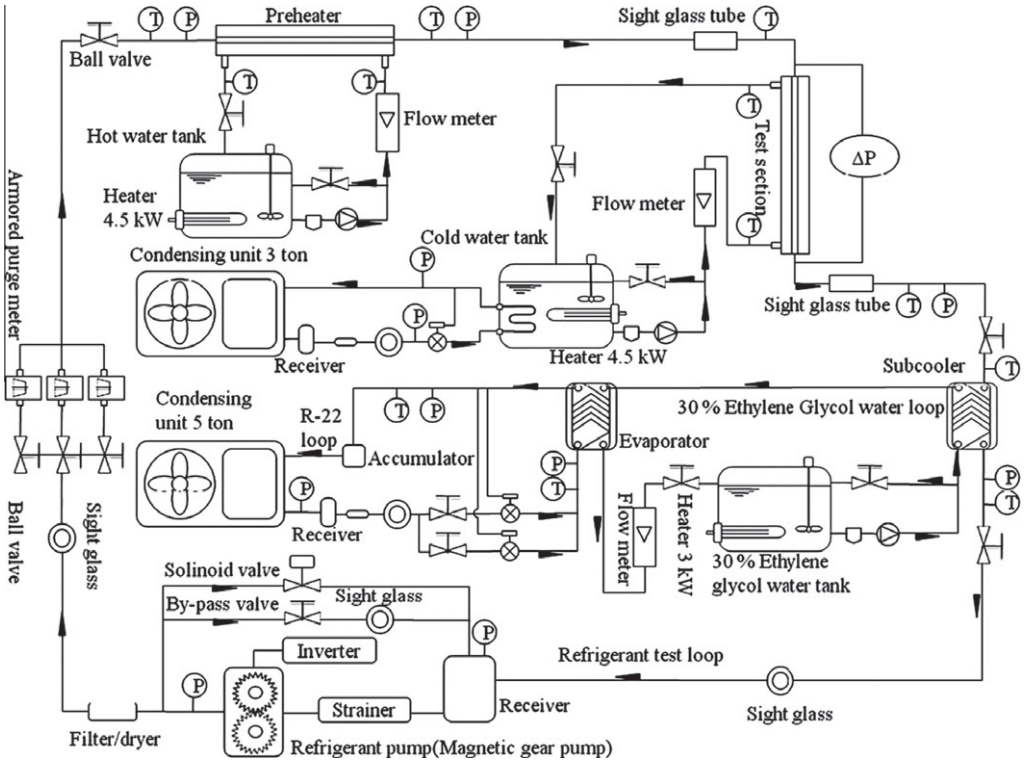

Fig. 1. Schematic diagram of the experimental apparatus.

Author's personal copy

despite their possible importance in many refrigeration applications. Therefore the main concern of this work is to study the heat transfer and flow characteristics of R-134a during downward evaporation inside vertical corrugated tube. Experimental data that have never been seen before on heat transfer and pressure drop are presented.

2. Experimental apparatus and method

A schematic diagram of the test apparatus is shown in Fig. 1. The refrigerant loop consists of a pre-heating loop, test section, heating loop, and chilling loop. For the refrigerant circulating loop, liquid refrigerant is forced by a gear pump which can be adjusted to the flow rate using an inverter. The refrigerant then passes in series through a filter/dryer, a refrigerant flow meter, a pre-heater, and a sight glass and enters the test section. The pre-heater controls the inlet quality before entering the test section. It consists of a spiral counter-flow tube-in-tube heat exchanger which is designed to supply heat in order to prepare an inlet quality for the vaporization of the refrigerant. Leaving the test section, the refrigerant vapor then condenses inside a sub-cooler and is collected in a receiver. After leaving the chilling loop, the refrigerant returns from a two-phase refrigerant to a sub-cooled state. Eventually, the refrigerant returns to the refrigerant pump to complete the cycle.

Details of the test section are shown schematically in Fig. 2. The test section is a vertical counter-flow double tube heat exchanger with refrigerant flowing downward in the inner tube and heating water flowing upward in the annulus. The test sections are one smooth tube and two corrugated tubes, which are made from copper. The inner diameter and outer diameter of the inner tube are 8.7 and 9.52 mm, respectively. The length of the test section is 500 mm. Fig. 3 shows a sketch of a corrugated tube. The dimensions of the test section are listed in Table 1. T-type thermocouples are installed at the inlet and outlet of the test section to measure the saturation temperature of the refrigerant. Similarly, the

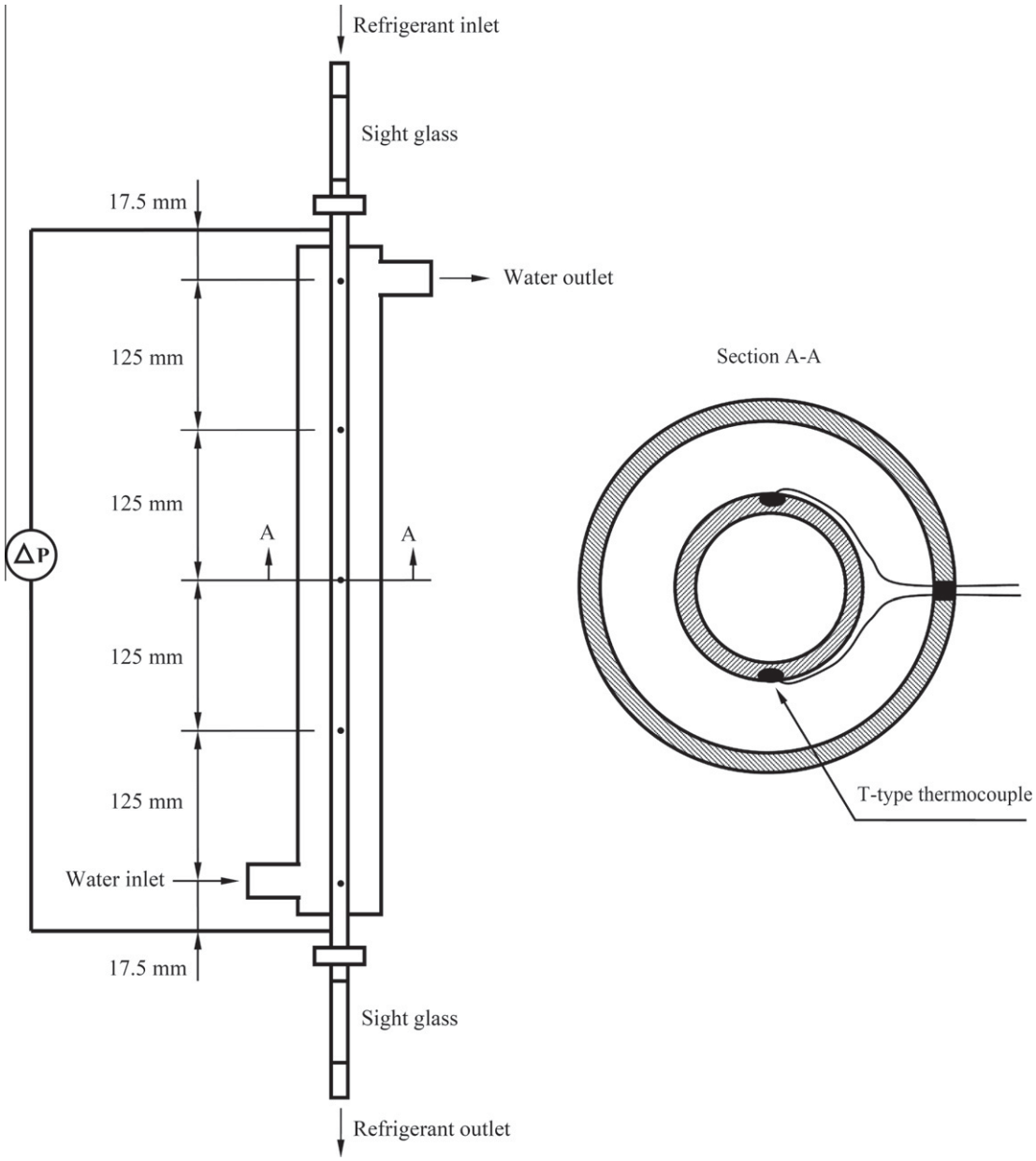

Fig. 2. Schematic diagram of the test section.

Author's personal copy

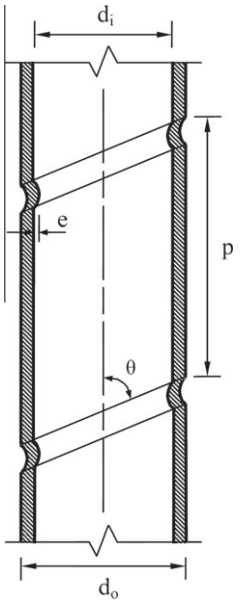

Fig. 3. Sketch of the corrugated tube.

Table 1
The Dimensions of the test sections.

Parameters	Smooth tube	Corrugated tube (A)	Corrugated tube (B)
Outer diameter (mm)	9.52	9.52	9.52
Inner diameter (mm)	8.7	8.7	8.7
Length of test section (mm)	500	500	500
Inside tube area (mm^2)	13665.9	14,514	14938.1
Pitch of corrugation (mm)	–	12.7	12.7
Depth of corrugation (mm)	–	0.5	0.75
Helix angle (°)	–	53.875	53.875

differential pressure transducer is installed in order to measure the pressure drop across the test section. The length between the pressure taps is 850 mm. There are 10 thermocouples located at five positions along the test section. All of the wall thermocouples are fixed with special glue having low thermal conductivity. The test section is insulated with rubber foam with a thermal conductivity of 0.04 W/mK. All of the thermocouples are well calibrated by standard thermometers with a precision of 0.1 °C. The refrigerant flow meter is a variable area type and is specially calibrated in the range of 0.2–3.4 LPM for R-134a by the manufacturer, as is the differential pressure transducer.

In the experiments, the inlet quality of the test section is varied by small increments. The imposed heat flux, mass flux, and saturation temperature are kept constantly at the desired values. The system is allowed to approach a steady state before any data are recorded. During experiments, the temperature and pressure are continuously recorded along the test section by the data acquisition system. The range of experimental conditions tested in this study is listed in Table 2. The uncertainties of measured quantities and calculated parameters, which are calculated from the root mean sum square method are shown in Table 3.

Table 2
Experimental conditions.

Controlled variable	Range
Mass flux (kg/m^2 s)	200, 300, 400
Heat flux (kW/m^2)	20, 25, 30
Saturation temperature (°C)	10, 15, 20
Tested tube material	Copper
Refrigerant	R-134a

Table 3
Uncertainties of measured quantities and calculated parameters.

Parameter	Uncertainty
Temperature, T (°C)	±0.1
Pressure drop, ΔP (kPa)	±0.37
Mass flow rate of refrigerant, m_{ref} (%)	±2 Full scale
Heat transfer rate of test section, Q_{TS} (%)	±15.01
Heat transfer rate of pre-heater, Q_{ph} (%)	±10.04
Average heat transfer coefficient, h_{avg} (%)	±15.01
Two-phase friction factor, f_{tp} (%)	±13.52
Average quality, x_{avg} (%)	±7.63
Equivalent Reynolds number, Re_{eq} (%)	±6.03

3. Data reduction

The data reduction of the measured results can be analysed as follows:

3.1. The inlet vapor quality of the test section ($x_{TS,in}$)

$$x_{TS,in} = \frac{i_{TS,in} - i_{lT_{TS,in}}}{i_{fgT_{TS,in}}} \tag{1}$$

where $i_{lT_{TS,in}}$ and $i_{fgT_{TS,in}}$ are the enthalpy of the saturated liquid and the enthalpy of vaporization, respectively, based on the temperature at the test section inlet, and $i_{TS,in}$ is the enthalpy of refrigerant at the test section inlet, which is calculated by the following equation:

$$i_{TS,in} = i_{ph,in} + \frac{Q_{ph}}{m_{ref}} \tag{2}$$

where $i_{ph,in}$ is the inlet enthalpy of the liquid refrigerant before entering the pre-heater, m_{ref} is the mass flow rate of the refrigerant, and Q_{ph} is the heat transfer rate in the pre-heater:

$$Q_{ph} = m_{w,ph} c_{p,w} (T_{w,in} - T_{w,out})_{ph} \tag{3}$$

with $m_{w,ph}$ the mass flow rate of water entering the pre-heater.

3.2. The outlet vapor quality of the test section ($x_{TS,out}$)

$$x_{TS,out} = \frac{i_{TS,out} - i_{lT_{TS,out}}}{i_{fgT_{TS,out}}} \tag{4}$$

where $i_{TS,out}$ is the refrigerant enthalpy at the test section outlet, $i_{lT_{TS,out}}$ is the enthalpy of the saturated liquid based on the temperature at the test section outlet, and $i_{fgT_{TS,out}}$ is the enthalpy of vaporization based on the temperature at the test section outlet. As a consequence, the outlet enthalpy of the refrigerant flow is calculated as:

$$i_{TS,out} = i_{TS,in} + \frac{Q_{TS}}{m_{ref}} \tag{5}$$

where the heat transfer rate, Q_{TS}, in the test section is obtained from:

$$Q_{TS} = m_{w,TS} c_{p,w} (T_{w,in} - T_{w,out})_{TS} \tag{6}$$

where $m_{w,TS}$ is the mass flow rate of the water entering the test section, and $(T_{w,in} - T_{w,out})_{TS}$ is the difference in water temperature between the outlet and the inlet positions.

Author's personal copy

3.3. Average heat transfer coefficient (h_{avg})

The average heat transfer coefficient (h_{avg}) can be calculated using the following equation:

$$h_{avg} = \frac{Q_{TS}}{A_i(T_{i,avg,wi} - T_{avg,sat})} \tag{7}$$

where $T_{avg,sat}$ is the average temperature of the refrigerant at the test section inlet and outlet, $T_{i,avg,wi}$ is the average temperature of the inner wall, and A_i is the inside surface area of the test section.

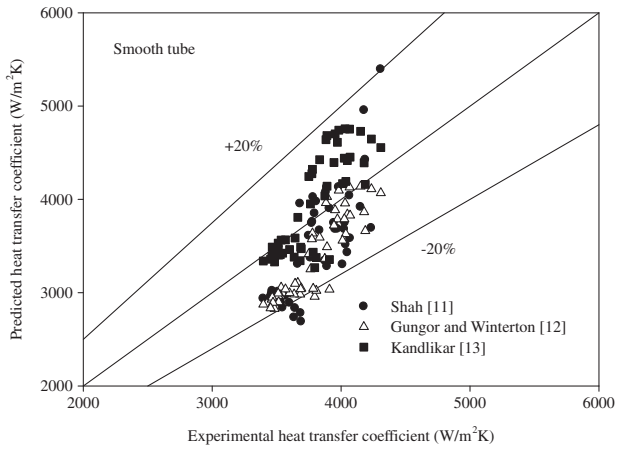

Fig. 4. Comparison of present R-134a heat transfer coefficient data with existing correlation.

3.4. Two-phase friction factor (f_{tp})

The total pressure gradient is the sum of three contributions: the gravitational pressure gradient, the momentum pressure gradient, and the frictional pressure gradient as follows:

$$\left(\frac{dP}{dz}\right)_T = \left(\frac{dP}{dz}\right)_F + \left(\frac{dP}{dz}\right)_G + \left(\frac{dP}{dz}\right)_M \tag{8}$$

Pressure drop due to gravity can be determined from:

$$\left(\frac{dP}{dz}\right)_G = -g[(1-\alpha)\rho_l + \alpha\rho_g] \tag{9}$$

where the void fraction, α, can be determined from the Zivi correlation [10] below:

$$\alpha = \frac{1}{1 + \frac{(1-x)}{x}\left(\frac{\rho_g}{\rho_l}\right)^{2/3}} \tag{10}$$

The momentum pressure gradient can be defined as follows:

$$\left(\frac{dP}{dz}\right)_M = G^2 \frac{d}{dz}\left[\frac{(1-x)^2}{\rho_l(1-\alpha)} + \frac{x^2}{\rho_g \alpha}\right] \tag{11}$$

The two-phase frictional pressure gradient can be obtained by subtracting the gravitational and momentum terms from the total measured pressure drop as follows:

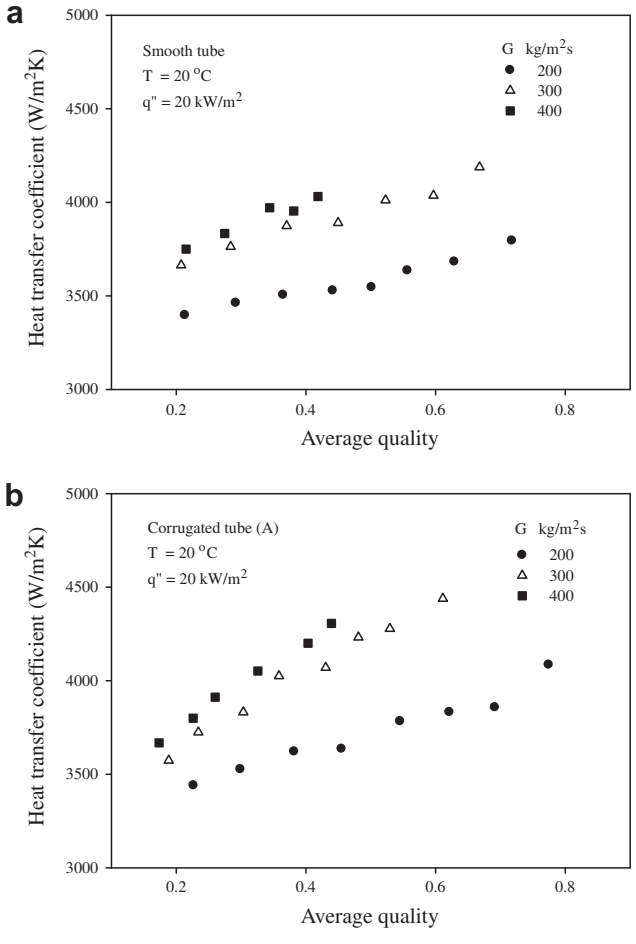

Fig. 5. Effect of mass flux on heat transfer coefficient.

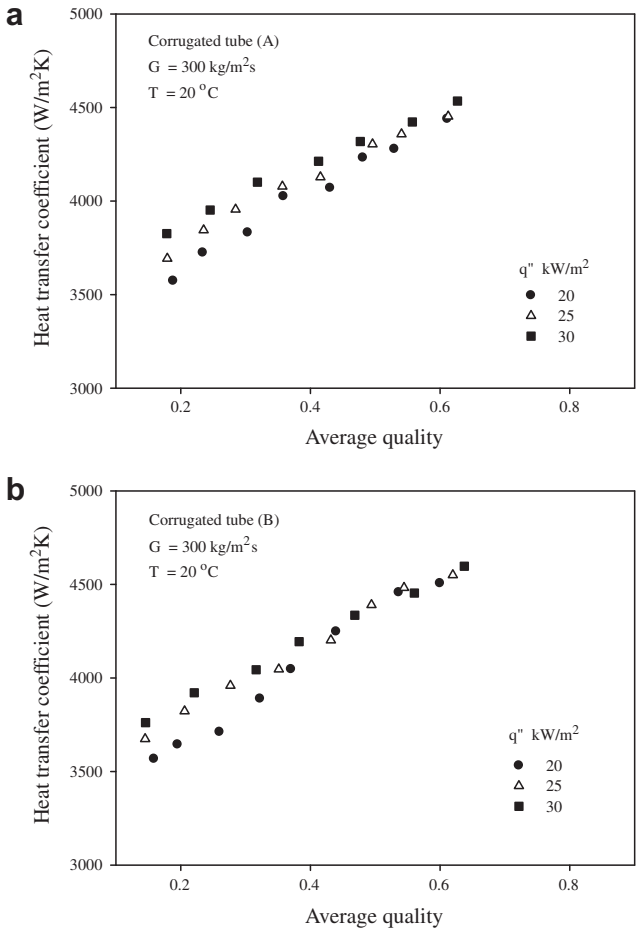

Fig. 6. Effect of heat flux on heat transfer coefficient.

Author's personal copy

$$\left(\frac{dP}{dz}\right)_F = \left(\frac{dP}{dz}\right)_T - \left(\frac{dP}{dz}\right)_G - \left(\frac{dP}{dz}\right)_M \quad (12)$$

The two-phase friction factor is calculated by the following equation based on the equivalent Reynolds number:

$$f_{tp} = \left(\frac{dP}{dz}\right)_F \frac{\rho_l d_i^3}{2\mathrm{Re}_{eq}^2 \mu_l^2} \quad (13)$$

where the equivalent Reynolds number is determined from:

$$\mathrm{Re}_{eq} = \frac{G_{eq} d_i}{\mu_l} \quad (14)$$

and equivalent mass flux is defined as:

$$G_{eq} = G\left[(1-x) + x\sqrt{\frac{\rho_l}{\rho_g}}\right] \quad (15)$$

4. Results and discussion

Data are presented in the forms of average heat transfer coefficient and two-phase friction factor. The effects of mass flux, heat flux, and evaporating temperature on the average heat transfer coefficient and two-phase friction factor are investigated.

4.1. Average heat transfer coefficient

The average heat transfer coefficient obtained from the smooth tube is compared with the results calculated from the correlations proposed by Shah [11], Gungor and Winterton [12] and Kandlikar [13]. As shown in Fig. 4, these correlations can describe almost all of the heat transfer coefficient within 20%.

The effect of the mass flux on the average heat transfer coefficient can be observed from Fig. 5. It shows the variation of the average heat transfer coefficient as a function of average quality at constant saturation temperature and heat flux for different mass fluxes of 200, 300, and 400 kg/m^2 s. The average quality is shown in the present work; it is averaged from the inlet quality and outlet quality of the test section. During evaporation, the liquid film thickness gradually decreases, and the thermal resistance is therefore decreased, resulting in an increase in the heat transfer rate. As a result, the average heat transfer coefficient increases with increasing average quality. In addition, the average heat transfer coefficient increases with a rise in the mass flux. This is because the increase in the mass flux also increased the velocity of the vapor and liquid film and the flow turbulence as a result of enhancing the convective heat transfer.

Fig. 6 shows the relationship between the average heat transfer coefficient and the average quality at constant mass flux and saturation temperature. The figure shows the results of three different values of heat flux: 20, 25, and 30 kW/m^2. In this experiment, as the heat flux increases, the heat transfer coefficient also increases. The increase in heat transfer rate which is caused by the increase of the heat flux causes the number of bubbles to increase. These bubbles can induce turbulent flow in the liquid film, which resulting in the increasing heat transfer coefficient. At low or moderate quality, the heat transfer enhancement in the variation of the heat flux was more remarkable than at high quality. This is due to the nucleate

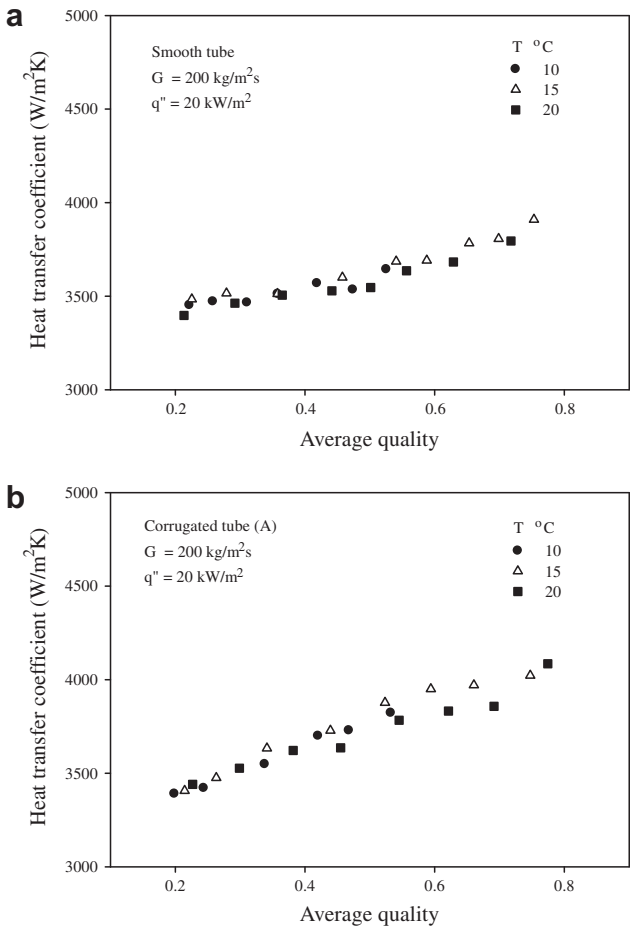

Fig. 7. Effect of saturation temperature on heat transfer coefficient.

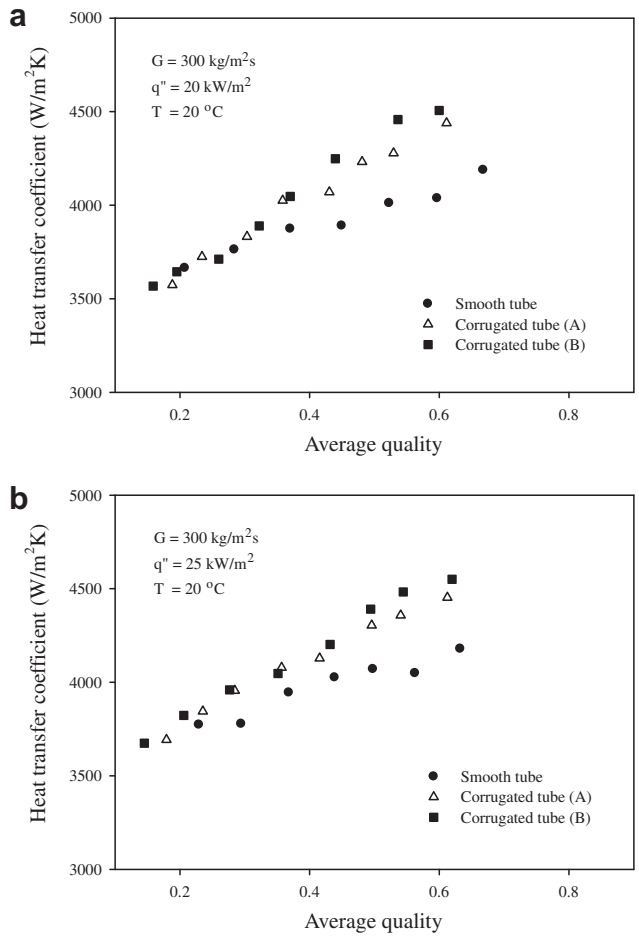

Fig. 8. Comparison of heat transfer coefficient.

Author's personal copy

boiling mechanism is very stronger than the effect of force convective at low quality. In the other hand, it becomes weaker at high quality.

Fig. 7 presents the variation in the average heat transfer coefficient versus the average quality at constant mass flux and heat flux for different saturation temperatures of 10, 15, and 20 °C, respectively. It can be seen from the figure that the heat transfer coefficient is changed by a relatively small amount with increasing evaporating temperature.

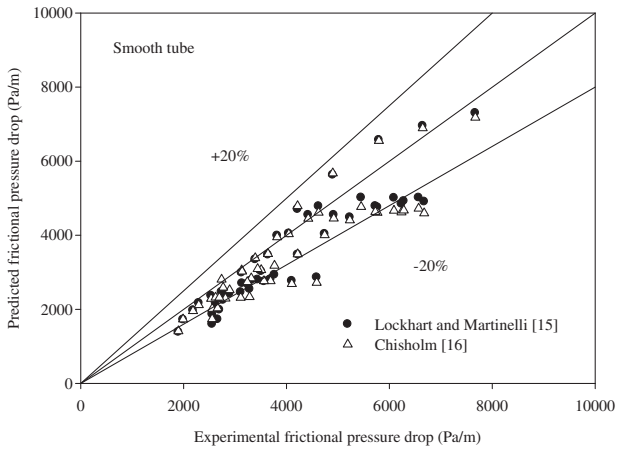

Fig. 9. Comparison of present R-134a frictional pressure drop data with existing correlation.

The comparisons of the evaporative heat transfer coefficient between the smooth and the corrugated tubes at a mass flux of 300 kg/m^2 s and an evaporating temperature of 20 °C for the different heat fluxes of 20 and 25 kW/m^2 are shown in Fig. 8. The results show that the heat transfer coefficient for both corrugated tubes are approximately 0–10% higher than that for the smooth tubes. This is due to an increase in the heat transfer area and more turbulence induced by corrugated surface. The corrugated tubes may provide periodic redevelopment of the boundary layers, causing more effective heat transfer. In other words, the thermal boundary layers inside the corrugated tubes became thinner than that in the case of the smooth tube (Bilen et al. [14]).

4.2. Two-phase friction factor

The comparisons of the experimental results for the smooth tube to those correlations proposed by Lockhart and Martinelli [15] and Chisholm [16] are displayed in Fig. 9. The figure shows that more than 70% of the data measured from the present study fall within ±20% of the proposed correlation.

The effect of mass flux on the two-phase friction factor of evaporation is shown in Fig. 10. These graphs show the relationship between the two-phase friction factor and the equivalent Reynolds number at constant saturation temperature of evaporation and heat flux values for mass fluxes of 200, 300, and 400 kg/m^2 s. These plots show that the two-phase friction factor decreases with increasing equivalent Reynolds number. The reason for this can be given in two aspects. Firstly, the frictional pressure drop increases with increasing vapor quality. This is because at higher

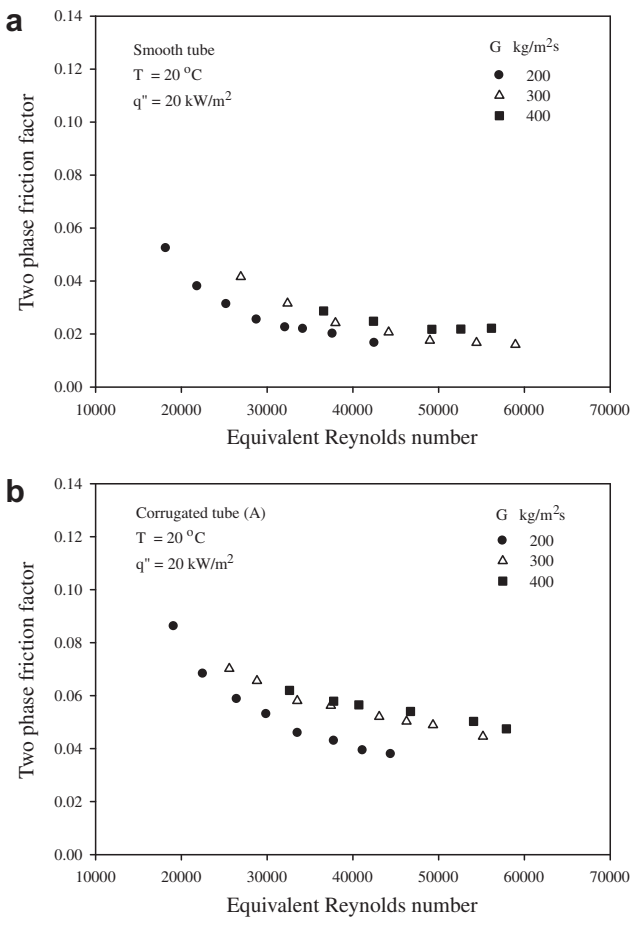

Fig. 10. Effect of mass flux on two-phase friction factor.

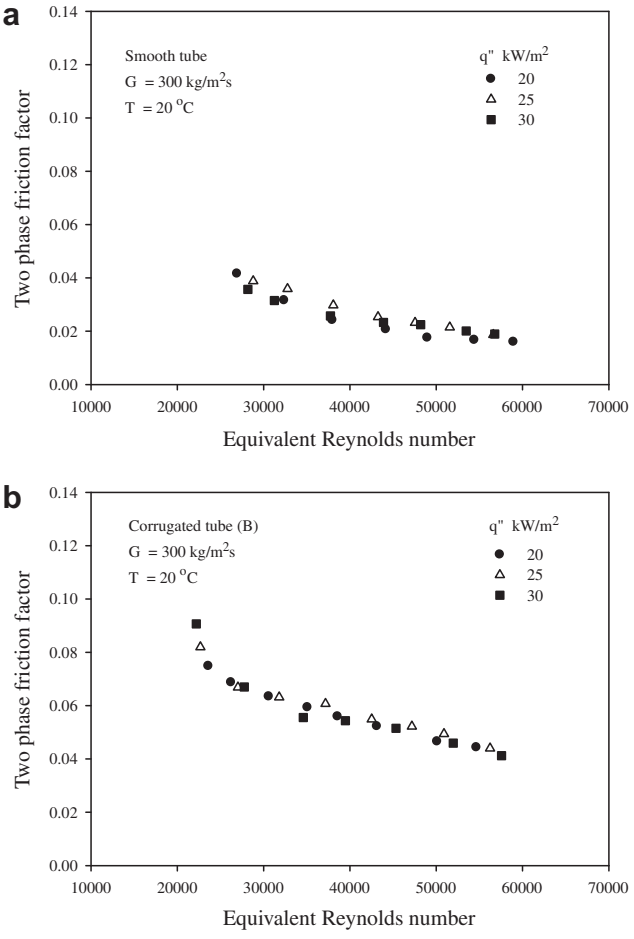

Fig. 11. Effect of heat flux on two-phase friction factor.

Author's personal copy

vapor quality, the higher velocity of vapor flow causes more shear stress at the interface of the vapor and liquid film. Moreover, the secondary flow that becomes stronger at higher vapor velocity will produce more entrainment and redeposition of droplets, causing more flow turbulence. Secondly, the equivalent Reynolds number increases with increasing vapor quality. This is because the increasing in average quality increases the equivalent mass flux, according to Eq. (15). As the equivalent mass flux increase, the equivalent Reynolds number also increases, according to Eq. (14). It can be seen that both frictional pressure drop and equivalent Reynolds number increase with an increase in average quality. According to Eq. (13), it is found that the equivalent Reynolds number dominates the two-phase friction factor. Therefore, the increase in average quality causes the two-phase friction factor to decrease. The results also indicate that the two-phase friction factor at higher mass flux is always higher than that at lower mass flux for a given equivalent Reynolds number.

Fig. 11 presents the variation of the two-phase friction factor with equivalent Reynolds number at a mass flux of 300 kg/m^2 s and a saturation temperature of 20 °C for heat fluxes of 20, 25, and 30 kW/m^2. These graphs show that the heat flux has an insignificant effect on the two-phase friction factor.

Fig. 12 shows the relationship between the two-phase friction factor and the equivalent Reynolds number at constant values of heat flux and mass flux for different saturation temperatures of 10, 15, and 20 °C. It is found that the saturation temperature has an unremarkable effect on the two-phase friction factor in the range of evaporating temperatures investigated.

Fig. 13 shows the variation of the two-phase friction factor with equivalent Reynolds number in smooth and corrugated tubes at a heat flux of 20 kW/m^2 and an evaporating temperature of 20 °C for the different mass fluxes of 200 and 300 kg/m^2 s. It can be seen from the figure that the two-phase friction factor for both corrugated tubes are approximately 70–140% higher than that for the smooth tube.

Fig. 14 presents the relationship between the two-phase friction factor versus the equivalent Reynolds number. The results show that the two-phase friction factor increases with decreasing equivalent Reynolds numbers. The same trend was also seen by Ma et al.

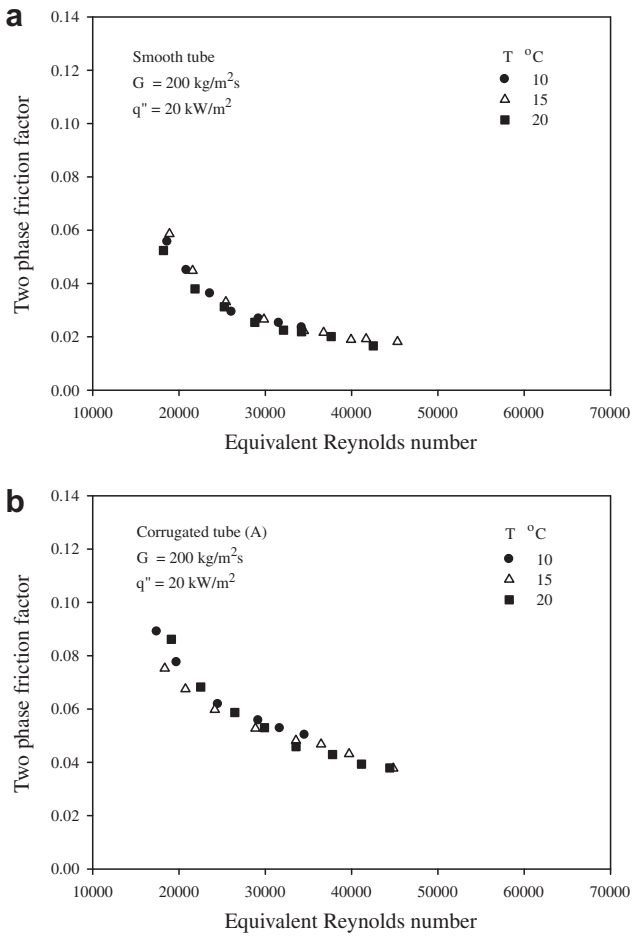

Fig. 12. Effect of saturation temperature on two-phase friction factor.

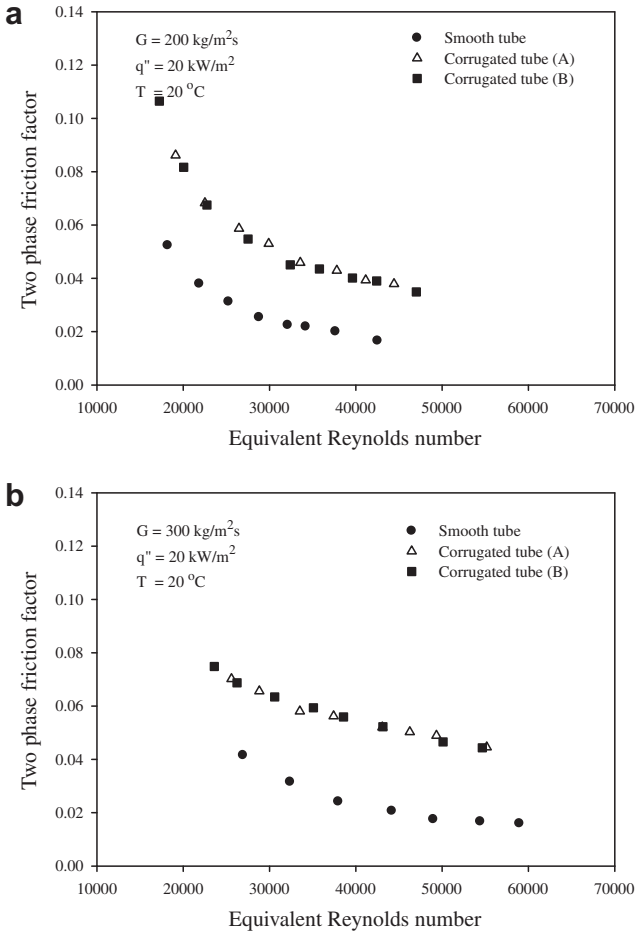

Fig. 13. Comparison of the two-phase friction factor.

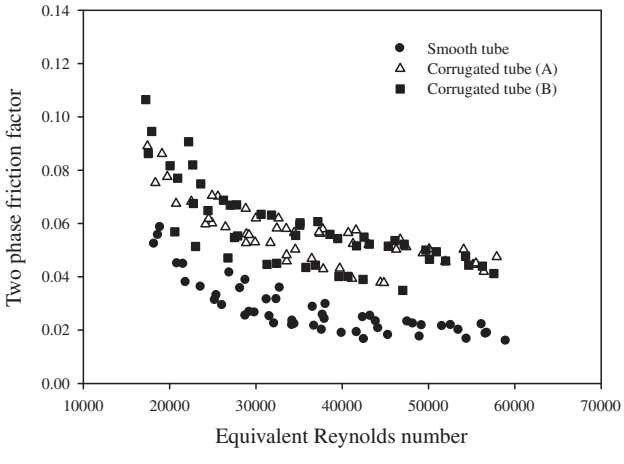

Fig. 14. Two-phase friction factor versus equivalent Reynolds number.

Author's personal copy

[2] and Dalkilic et al. [5] with different experimental conditions and parameters.

5. Conclusions

The present paper reports heat transfer and flow characteristics of R-134a during evaporation inside vertical smooth and corrugated tubes, and the following results are obtained:

1. For smooth tube and corrugated tubes, the average heat transfer coefficient tends to increase with increases in average quality, mass flux, and heat flux. At low or moderate quality, the heat transfer enhancement in the variation of the heat flux was more remarkable than at high quality. As the evaporation temperature increased, the heat transfer coefficient is changed by a relatively small amount.
2. For smooth tube and corrugated tube, the two-phase friction factor decreases with increasing equivalent Reynolds number. The two-phase friction factor at higher mass flux is always higher than that at lower mass flux for a given equivalent Reynolds number. However, the heat flux and evaporating temperature have unremarkable effects on the two-phase friction factor.
3. Comparing the heat transfer coefficient of the evaporation process in the corrugated tubes with that in the smooth tube under the same conditions, it is found that the heat transfer coefficient in corrugated tubes are approximately 0–10% higher and the two-phase friction factor are approximately 70–140% higher.

Acknowledgement

The present study was supported financially by King Mongkut's University of Technology Thonburi, the Thailand Research Fund, the Office of the Higher Education Commission and National Research University Project, whose guidance and assistance are gratefully acknowledged.

References

[1] R.J. Goldstein, E.R.G. Eckert, W.E. Ibele, S.V. Patankar, T.W. Simon, T.H. Kuehn, P.J. Strykowski, K.K. Tamma, A. Bar-Cohen, J.V.R. Heberlein, J.H. Davidson, J. Bischof, F.A. Kulacki, U. Kortshagen, S. Garrick, V. Srinivasan, Heat transfer—a review of 2002 literature, International Journal of Heat and Mass Transfer 48 (2005) 819–927.
[2] X. Ma, A. Briggs, J.W. Rose, Heat transfer and pressure drop characteristics for condensation of R113 in a vertical micro-finned tube with wire insert, International Communications in Heat and Mass Transfer 31 (5) (2004) 619–627.
[3] S.K. Lee, S.H. Chang, Experimental study of post-dryout with R-134a upward flow in smooth tube and rifled tubes, International Journal of Heat and Mass Transfer 51 (11–12) (2008) 3153–3163.
[4] K. Cheung, M.M. Ohadi, S.V. Dessiatoun, EHD-assisted external condensation of R-134a on smooth horizontal and vertical tubes, International Journal of Heat and Mass Transfer 42 (10) (1999) 1747–1755.
[5] A.S. Dalkilic, S. Laohalertdecha, S. Wongwises, Two-phase friction factor in vertical downward flow in high mass flux region of refrigerant HFC-134a during condensation, International Communications in Heat and Mass Transfer 35 (9) (2008) 1147–1152.
[6] A.S. Dalkilic, S. Laohalertdecha, S. Wongwises, Effect of void fraction models on the two-phase friction factor of R134a during condensation in vertical downward flow in a smooth tube, International Communications in Heat and Mass Transfer 35 (8) (2008) 921–927.
[7] A.S. Dalkilic, S. Laohalertdecha, S. Wongwises, Effect of void fraction models on the film thickness of R134a during downward condensation in a vertical smooth tube, International Communications in Heat and Mass Transfer 36 (2) (2009) 172–179.
[8] A.S. Dalkilic, S. Yildiz, S. Wongwises, Experimental investigation of convective heat transfer coefficient during downward laminar flow condensation of R134a in a vertical smooth tube, International Journal of Heat and Mass Transfer 52 (1–2) (2009) 142–150.
[9] A.S. Dalkilic, S. Laohalertdecha, S. Wongwises, Experimental investigation of heat transfer coefficient of R134a during condensation in vertical downward flow at high mass flux in a smooth tube, International Communications in Heat and Mass Transfer 36 (10) (2009) 1036–1043.
[10] S.M. Zivi, Estimation of steady-state steam void-fraction by means of the principle of minimum entropy production, Transactions ASME Journal of Heat Transfer Series C 86 (1975) 247–252.
[11] M.M. Shah, Chart correlation for saturated boiling heat transfer equation and further study, ASHRAE Transactions 88 (1982) 185–196.
[12] K.E. Gungor, R.H.S. Winterton, A general correlation for flow boiling in tubes and annuli, International Journal of Heat and Mass Transfer 29 (1986) 351–358.
[13] S.G. Kandlikar, A general correlation for saturated two-phase flow boiling heat transfer inside horizontal and vertical tubes, ASME Journal of Heat Transfer 112 (1990) 219–228.
[14] K. Bilen, M. Cetin, H. Gul, T. Balta, The investigation of groove geometry effect on heat transfer for internally grooved tubes, Applied Thermal Engineering 29 (2009) 753–761.
[15] R.W. Lockhart, R.C. Martinelli, Proposed correlation of data for isothermal two-phase two component flow in pipes, Chemical Engineering Progress 45 (1949) 39–48.
[16] D. Chisholm, Pressure gradients due to friction during the flow of evaporating two-phase mixtures in smooth tubes and channels, International Journal of Heat and Mass Transfer 16 (1973) 347–358.

Heat Transfer Engineering, 32(1):33–44, 2011
Copyright © Taylor and Francis Group, LLC
ISSN: 0145-7632 print / 1521-0537 online
DOI: 10.1080/01457631003732839

Taylor & Francis
Taylor & Francis Group

Experimental Study on the Modeling of Condensation Heat Transfer Coefficients in High Mass Flux Region of Refrigerant HFC-134a Inside the Vertical Smooth Tube in Annular Flow Regime

AHMET S. DALKILIC[1] and SOMCHAI WONGWISES[2]

[1]Department of Mechanical Engineering, Yildiz Technical University, Yildiz, Besiktas, Istanbul, Turkey
[2]Department of Mechanical Engineering, King Mongkut's University of Technology Thonburi, Bangmod, Bangkok, Thailand

This article presents an experimental investigation on the co-current downward condensation of R134a in a vertical smooth copper tube having inner diameter of 8.1 mm and a length of 500 mm. Condensation experiments are done at mass fluxes varying between 260 and 515 kg/m^2-s. The condensing temperatures are 40°C and 50°C; heat fluxes are between 10.16 and 66.61 kW/m^2. The quality of the refrigerant in the test section is calculated considering the temperature and pressure obtained from the experiment. The pressure drop across the test section is directly measured by a differential pressure transducer. The average experimental heat transfer coefficient of the refrigerant is calculated by applying an energy balance based on the energy transferred from the test section. The average predicted heat transfer coefficient of the refrigerant is determined by means of the model of Kosky and Staub, and Von Karman universal velocity distribution correlations using different interfacial shear stress equations valid for annular flow in horizontal and vertical tubes to investigate the Chen et al. annular flow theory. The effects of heat flux, mass flux, and condensation temperature on the pressure drop are also discussed. A new correlation using a large number of data points for the turbulent condensation heat transfer coefficient is proposed.

INTRODUCTION

In-tube condensation of refrigerants is a crucial event in many applications such as condensers used in air-conditioning, refrigeration, and heat pumps. Struggling with the depletion of the stratospheric ozone layer and global warming caused by chemical compounds started a short time ago. To this end, condenser producers have been trying to change working fluids and use enhanced geometries while thinking over energy efficiency. These kinds of improvements will continue taking attention and will have an important impact on the heating, ventilation, and air-conditioning (HVAC) industry in the future. Nowadays, due to ozone crises and efficiency requirements, new condensers have been designed to work with alternative refrigerants to replace R12 and R22 inside enhanced tubes.

Several recognizable flow structures are seen for the distribution of the liquid–gas phases for co-current flow of the phases in a vertical tube, such as bubbly flow, slug flow, churn flow, annular flow, wispy annular flow, and mist flow. The most widely recommended flow pattern maps for vertical tubes are Fair [1] and Hewitt and Roberts [2], and the earliest studies belong to Kosky and Staub [3], Traviss et al. [4], and Shah [5], who paid attention to the condensation heat transfer of pure refrigerants during an annular flow regime.

The authors are indebted to King Mongkut's University of Technology Thonburi (KMUTT), the Thailand Research Fund, the Office of the Higher Education Commission and the National Research University Project for supporting this study. Especially, the first author wishes to thank KMUTT for providing him with a Post-doctoral fellowship.

Address correspondence to Professor Somchai Wongwises, Fluid Mechanics, Thermal Engineering and Multiphase Flow Research Laboratory (FUTURE), Department of Mechanical Engineering, King Mongkut's University of Technology Thonburi, Bangmod, Bangkok 10140, Thailand. E-mail: somchai.won@kmutt.ac.th

Annular flow conditions along the tube length include convective condensation, which occurs for many applications inside tubes. Annular two-phase flow is one of the most important flow regimes and is characterized by a phase interface separating a thin liquid film from the gas flow in the core region. Two-phase annular flow occurs widely in film heating and cooling processes, particularly in power generation and especially in nuclear reactors. This flow regime has received the most attention, both analytically and experimentally, because of its practical importance and the relative ease with which analytical treatment may be applied. In addition to this, condensate distribution inside tube wall is almost symmetric and there is high-velocity vapor flow in the core during annular flow. In this flow regime, it is generally true that due to the breakup of the disturbance wave, part of the liquid phase is entrained as droplets into the gas core. It is also accepted that mass, momentum, and energy transfers are strongly affected by entrainment of the droplets to the gas core.

Heat transfer and pressure drop characteristics of refrigerants have been studied by a large number of researchers, mostly in horizontal tubes. The study of the heat transfer and pressure drop of refrigerants during downward condensation in small-diameter vertical tubes has received comparatively little attention in literature. A brief summary of studies for downward condensation is given next.

Goodykoontz and Dorsch [6] investigated the local condensation heat transfer coefficients and pressure distribution of R113 for the mass fluxes of 21–455 kg/m^2-s in a 7.4–15.9 mm ID vertical tube. Kim and No [7] developed a turbulent film condensation model including pressure drop for high-pressure steam in a 46 mm ID vertical tube. Ma et al. [8] studied the two-phase friction factors of downward R113 flow for mass fluxes from 400 to 800 kg/m^2-s in a 20.8 mm ID smooth and finned tube. Levich [9] and Blangetti et al. [10] used a model to estimate the local heat transfer coefficients of the film. An empirical relationship between the Fanning friction factor and vapor Reynolds number for an annular flow regime was proposed by Bergelin et al. [11]. They studied the pressure drop of air–water and several organic vapors for the downward turbulent flow through a vertical 25.4 mm ID tube.

Performance of the smooth tubes was determined by many researchers with pure refrigerants as operating fluids. Generally, empirical methods have been offered to compute the condensation heat transfer coefficients in smooth tubes. Most of these proposed models are modifications of the Dittus–Boelter single-phase forced convection correlation [12], such as Akers et al. [13], Cavallini and Zecchin [14], and Shah [5].

Kosky and Staub [3] investigated condensation of steam in a horizontal 12.57 mm ID tube at low pressure (20–152 kPa) during an annular flow regime. The mass fluxes were between 2.7 and 149.2 kg m^{-2} s^{-1}. They presented a model based on the Wallis [15] correlation and supported by the Lockhart and Martinelli analogy [16] between heat and momentum transfer during turbulent flow and studied the calculation of thermal resistance of a flowing film of condensate, assuming the entrainment is negligible and the film is thin and smooth. They showed the relation between the heat transfer coefficient and the frictional pressure gradient through the shear velocity for the annular flow regime. The model is independent of tube orientation as long as annular flow conditions exist inside the tube.

Jaster and Kosky [17] benefited from Kosky and Staub's [3] data valid for the annular-stratified transition and fully stratified flow regimes. The mass fluxes were between 12.6 and 145 kg/m^2-s. They reported that the transition of annular-to-stratified flow had a ratio of axial shear force to gravitational body forces (stress ratio). They defined a parameter to decide the flow pattern. In addition to this, they proposed correlations for the heat transfer coefficient during annular and stratified flow. Thermal resistances of boundary layers were calculated using the Lockhart and Martinelli analogy for fully annular flow in their analysis.

Rufer and Kezios [18] developed a simple model for the fully stratified flow. They neglected the heat transfer in the liquid pool. A successful linear interpolation was suggested for the transition region of fully annular and stratified flow.

Dobson and Chato [19] investigated condensation of pure refrigerants and near-azeotropic blends over a wide range of mass flux in horizontal tubes. They stated that heat transfer coefficient increased with mass flux and quality in annular flow due to increased shear and thinner liquid film than for other flow regimes. They used a two-phase multiplier approach for annular flow. Sweeney [20] extended their model for R407C, using mass flux-based modification.

Cavallini and Zecchin [14] presented a theoretical analysis based on a simple hydrodynamic model of the annular flow pattern and on the momentum and heat transfer analogy using a large number of data for the condensation of pure refrigerants inside tubes. Recently, Cavallini et al. [21] reviewed the most recent work in the open literature on the condensation inside and outside smooth and enhanced tubes. In addition to this, Cavallini et al. [22] tested high-pressure fluids to predict the condensation heat transfer coefficients by using the Kosky and Staub [3] analysis. They used the Friedel [23] correlation for two-phase pressure drop and suggested the Kosky and Staub [3] correlation in the annular flow regime and the Jaster and Kosky [17] correlation in the stratified flow regime. Cavallini et al. [24] also proposed a generalized method including 5478 data points from independent laboratories all over the world to use in heat exchanger modeling and design applications for the condensation of hydrochlorofluorocarbons (HCFCs), hydrofluorocarbons (HFC)s, hydrocarbons (HCs), carbon dioxide, ammonia, water, and zeotropic mixtures with two and three components inside horizontal smooth tubes with internal diameters $d > 3$ mm. In addition to this, El Hajal et al. [25] and Thome et al. [26] developed a new flow pattern map [25] and flow pattern-based heat transfer model [26] for the condensation of many refrigerants inside horizontal smooth tubes using 2771 data points from other researchers in the literature.

The aim of this work is to show the independency of an annular flow model from tube orientation and general applicability

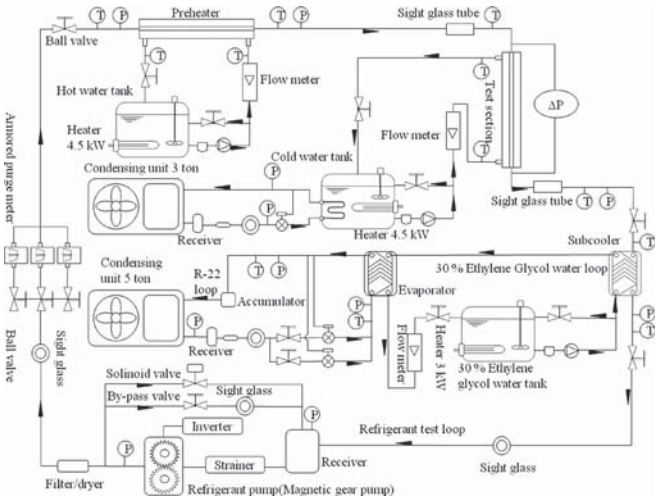

Figure 1 Schematic diagram of experimental apparatus.

for a vertical relatively short tube. The experiments include a wide range of high mass fluxes with different saturation temperatures. Apart from the authors' previous publications [27–38], few studies exist in the literature for the investigation of heat transfer characteristics in a small-diameter vertical tube during co-current down-flow condensation; moreover, there is no study with the experimental parameters of this work and its content in the open literature. In this study, determination of the shear-dominated heat transfer coefficients for refrigerant 134a is presented by means of the model of Kosky and Staub [3] and Von Karman universal velocity distribution correlations by relating the heat transfer to the pressure gradient depending on the shear stress between phases during annular flow. It should be noted that gravity-dominated condensation heat transfer data should be treated with a different procedure [28, 39]. In addition, a new correlation is developed adding some significant variables into the Dittus and Boelter's [12] correlation for the turbulent flow conditions to determine the convective condensation heat transfer coefficient.

EXPERIMENTAL APPARATUS AND METHOD

A schematic diagram of the test apparatus is shown in Figure 1. The refrigerant loop consists of a preheating loop, test section, cooling loop, and chilling loop. The refrigerant is circulated by a gear pump controlled by an inverter. The refrigerant flows in series through a filter/dryer, a sight glass tube, a refrigerant flow meter, and a preheater and enters the test section. A spiral counterflow double-tube heat exchanger is designed to supply heat to control the inlet quality of the refrigerant before entering the test section. After exiting the test section, the chilling loop condenses and subcools the refrigerant and removes the heat input from the preheater and test section, ejecting it into the surroundings. After leaving the chilling loop, the refrigerant changes from the two-phase refrigerant to a subcooled

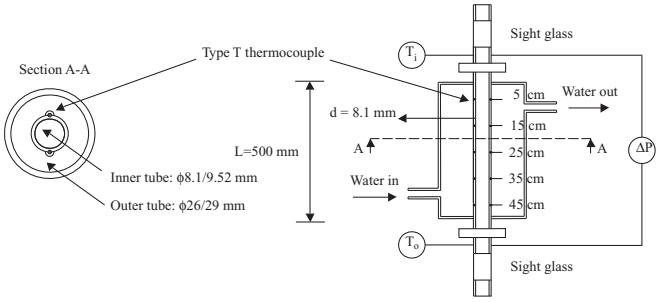

Figure 2 Schematic diagram of test section.

state. Eventually, the refrigerant returns to the refrigerant pump to complete the cycle.

The test section, well insulated with a proper material to minimize the heat loss, is a vertical counterflow tube-in-tube heat exchanger with refrigerant flowing downward (co-current liquid and vapor of R134a's down flow) in the inner tube and cooling water flowing upward in the annulus. The inner and outer tubes are made from smooth vertical copper having inner diameters of 8.1 and 26 mm, respectively. The length of the heat exchanger is 0.5 m. Figure 2 shows the detailed dimensions of the heat exchanger and the location of the thermocouples.

T-type thermocouples are used to measure refrigerant temperature and the tube wall temperatures in the test section. In total, 10 thermocouples are located on the sidewall at five points along the test tube. A thermostat is used to control the inlet temperature of the water. All the temperature measuring devices are calibrated in a controlled temperature bath using standard-precision mercury–glass thermometers. The uncertainty of the temperature measurements is $\pm 0.1^{\circ}$C. All static pressure taps are mounted on the tube wall. The refrigerant flow meter is a variable area type. The flow meter was calibrated in the range of 0–2.2 gal min^{-1} for HFC-134a by the manufacturer. Pressure drop is measured by a differential pressure transducer installed between the inlet and outlet of the test section. The length between pressure taps is 0.7 m. A low-temperature thermostat is used to control the system pressure of the refrigerant flow. The differential pressure transducer and pressure gauges are calibrated against a primary standard, the dead weight tester. All signals from thermocouples and pressure transducers are recorded by a data logger. Tests are performed in the steady state.

DATA REDUCTION AND EXPERIMENTAL UNCERTAINTY

The data reduction of the measured results can be analyzed as follows:

The inlet vapor quality of the test section ($x_{TS,i}$) is

$$x_{TS,i} = \frac{i_{TS,i} - i_{l@T_{TS,i}}}{i_{fg@T_{TS,i}}} \tag{1}$$

where $i_{l@T_{TS,i}}$ is the enthalpy of the saturated liquid based on the inlet temperature of the test section, $i_{fg@T_{TS,i}}$ is the enthalpy of

vaporization based on the inlet temperature of the test section, and $i_{TS,i}$ is the refrigerant enthalpy at the test section inlet and is given by:

$$i_{TS,i} = i_{ph,i} + \frac{Q_{ph}}{m_{ref}} \tag{2}$$

where $i_{ph,i}$ is the inlet enthalpy of the liquid refrigerant before entering the preheater, m_{ref} is the mass flow rate of the refrigerant, and Q_{ph} is the heat transfer rate in the preheater:

$$Q_{ph} = m_{w,ph} c_{p,w} (T_{w,i} - T_{w,o})_{ph} \tag{3}$$

where $m_{w,ph}$ is the mass flow rate of the water entering the preheater, $c_{p,w}$ is the specific heat of water, and $(T_{w,i} - T_{w,o})_{ph}$ is the temperature difference between inlet and outlet positions of the preheater.

The outlet vapor quality of the test section ($x_{TS,o}$) is

$$x_{TS,o} = \frac{i_{TS,o} - i_{l@T_{TS,o}}}{i_{fg@T_{TS,o}}} \tag{4}$$

where $i_{TS,o}$ is the refrigerant enthalpy at the test section outlet, $i_{l@T_{TS,o}}$ is the enthalpy of the saturated liquid based on the outlet temperature of the test section, and $i_{fg@T_{TS,o}}$ is the enthalpy of vaporization. The outlet enthalpy of the refrigerant flow is calculated as follows:

$$i_{TS,o} = i_{TS,i} - \frac{Q_{TS}}{m_{ref}} \tag{5}$$

where the heat transfer rate, Q_{TS}, in the test section is obtained from:

$$Q_{TS} = m_{w,TS} c_{p,w} (T_{w,o} - T_{w,i})_{TS} \tag{6}$$

where $m_{w,TS}$ is the mass flow rate of the water entering the test section and $(T_{w,o} - T_{w,i})_{TS}$ is temperature difference between outlet and inlet position of the test section.

The average heat transfer coefficient is

$$h_{exp} = \frac{Q_{TS}}{A_{wi}(T_{ref,sat} - T_{wi})} \tag{7}$$

where h_{exp} is the experimental average heat transfer coefficient, Q_{TS} is the heat transfer rate in the test section, T_{wi} is the average temperature of the inner wall, $T_{ref,sat}$ is the average saturation temperature of the refrigerant at the test section inlet and outlet, and A_{wi} is the inside surface area of the test section:

$$A_{wi} = \pi d L \tag{8}$$

where d is the inside diameter of the test tube. L is the length of the test tube.

Calculation Procedure for the Annular Flow Model

The two-phase pressure gradient is the sum of three contributions: the gravitational pressure gradient, the momentum pressure gradient, and the frictional pressure gradient, as follows:

$$\frac{dP}{dz} = \left(\frac{dP}{dz}\right)_G + \left(\frac{dP}{dz}\right)_M + \left(\frac{dP}{dz}\right)_F \tag{9}$$

Pressure drop due to gravity can be determined from [40]:

$$(\Delta P)_G = g \rho_g L \tag{10}$$

The momentum transfer term contributes to the overall pressure drop during condensation due to the mass transfer that occurs at the phase's interface. It was reported by Honda et al. [41] and Sami and Schnotale [42] that the momentum pressure gradient can be neglected for the condensation; on the other hand, the momentum pressure gradient can be written according to the results of the one-dimensional two-phase separated-flow analysis, which can be defined as follows [40]:

$$\left(\frac{dP}{dz}\right)_M = -G^2 \frac{d}{dz}\left[\frac{x^2}{\rho_g \alpha} + \frac{(1-x)^2}{\rho_l (1-\alpha)}\right] \tag{11}$$

Equation (11) can be rearranged as follows:

$$\Delta P_M = G^2 \left[\left\{\frac{(1-x)^2}{\rho_l (1-\alpha)} + \frac{x^2}{\rho_g \alpha}\right\}_o - \left\{\frac{(1-x)^2}{\rho_l (1-\alpha)} + \frac{x^2}{\rho_g \alpha}\right\}_i\right] \tag{12}$$

where the void fraction, α, can be determined from Chisholm [43] correlation, as:

$$\alpha = \frac{1}{1 + \left(\frac{1-x}{x}\right)\left(\frac{\rho_g}{\rho_l}\right) S} \tag{13}$$

where the slip ratio, S, is defined as:

$$S = \left(1 - x + x\frac{\rho_l}{\rho_g}\right)^{1/2} \tag{14}$$

The two-phase frictional pressure drop can be obtained by subtracting the gravitational and momentum terms from the total measured pressure drop as follows:

$$\left(\frac{dP}{dz}\right)_F = \left(\frac{dP}{dz}\right)_{exp} - \left(\frac{dP}{dz}\right)_G - \left(\frac{dP}{dz}\right)_M \tag{15}$$

To confirm the flow pattern during the condensation of refrigerant in the test section, the experimental results at a mass flux of 260–515 kg/m^2-s are checked with the flow regime map of Hewitt and Roberts [2] and also checked by sight glass at the inlet and outlet of the test section. Plotting the data points on this flow regime map, it is found to be in very good agreement qualitatively. The data points are located in the region of the annular flow pattern. Hence, the discussion section addresses only the heat transfer mechanism in this flow pattern.

In the present study, these correlations are used to show the similarity of annular flow correlations that are independent of tube orientation (horizontal or vertical). Chen et al. [44] also mentioned this similarity in their article. They developed a general correlation by relating the interfacial shear stress to

flow conditions for annular film condensation inside horizontal and vertical tubes using correction factors.

The interfacial shear stress is determined for the annular flow in horizontal tubes as follows [22]:

$$\tau = \left(-\frac{dP}{dz}\right)_F \frac{d}{4} \tag{16}$$

The interfacial shear stress is determined for the annular downward flow in vertical tubes as follows [45, 46]:

$$\tau = \left(-\frac{dP}{dz} + \rho_g g\right) \frac{d}{4} \tag{17}$$

The liquid Reynolds number can be defined as follows:

$$Re_l = \frac{Gd(1-x)}{\mu_l} \tag{18}$$

The dimensionless film thickness is calculated according to Kosky and Staub [3]:

$$\delta^+ = \left(\frac{Re_l}{2}\right)^{0.5} \quad \text{for} \quad Re_l \le 1145 \tag{19}$$

$$\delta^+ = 0.0504 Re_l^{7/8} \quad \text{for} \quad Re_l > 1145 \tag{20}$$

From the derivation of the Von Karman universal velocity distribution inside a tube, $T_\delta{}^+$ can be obtained as follows:

$$T_\delta^+ = \delta^+ \Pr_l \quad \text{for} \quad \delta^+ \le 5 \tag{21}$$

$$T_\delta^+ = 5\Pr_l + 5\ln\left[1 + \Pr_l(\delta^+/5 - 1)\right] \quad \text{for} \quad 5 < \delta + < 30 \tag{22}$$

$$T_\delta^+ = 5\Pr_l + 5\ln\left[1 + 5\Pr_l\right] + 2.5\ln(\delta^+/30) \quad \text{for} \quad \delta \ge 30 \tag{23}$$

The heat transfer coefficient during annular flow is shown next, applying the momentum–heat transfer analogy for the calculation of liquid layer thermal resistance:

$$h = \frac{c_{pl}(\rho_l \tau)^{0.5}}{T_\delta^+} \tag{24}$$

Correlation Development

The present correlation for the turbulent flow inside the test tube was developed as a form of Dittus and Boelter's [12] correlation by means of several dimensionless numbers that were defined and used by Akers et al. [13] for the Reynolds equivalent number in Eq. (26), by Koyama et al. [47] for the ratio of density to dynamic viscosity in Eq. (27), by Lockhart and Martinelli [16] for their parameter in Eq. (29), by Dobson and Chato [48] for the form of Lockhart and Martinelli's [16] parameter with specific constant numbers in Eq. (25), and by Cavallini et al. [49, 50] for the usage of Bond and Froude numbers together in Eqs. (30) and (31). The Reynolds equivalent number, R number, Lockhart and Martinelli parameter, and Bond and Froude numbers were used as the most significant variables in the proposed correlation. The Reynolds number gives a measure of the ratio of inertial forces to viscous forces characterizing different flow regimes such as laminar or turbulent flow. The Lockhart and Martinelli parameter is used in internal two-phase flow calculations expressing the liquid fraction of a flowing fluid. The Bond number expresses the ratio of body forces to surface tension forces; low Bond numbers indicate the surface tension domination on the system. The Froude number is used to compare inertial and gravitational forces. The effects of other important parameters belong to the fluid properties such as liquid and vapor phases of density, dynamic viscosity, kinematic viscosity, and thermal diffusivity in R and Prandtl numbers.

The majority of the data, 90% of 198 data points, fall within ±20% of the proposed correlation. Regression analysis was performed with these variables just described and gave a convincing correlation. From the experimental results, the two-phase convective heat transfer coefficient of R134a in a copper smooth tube having an inner diameter of 8.1 mm and length of 0.5 m during downward condensation is correlated based on 198 turbulent flow data points regarding two different condensing temperatures (40, 50°C) and 6 different mass fluxes (260, 300, 340, 400, 456, 515 kg/m^2-s) and expressed as follows:

$$h = 0.0315\left(\frac{k_l}{d}\right) Re_{eq}^{0.893} (Pr\,R)^{0.292} \times \left[\frac{0.42}{X_{tt}^{0.665}} + 1.15\right] (BoFr)^{-0.357} \tag{25}$$

where the all liquid equivalent Re number is determined from:

$$Re_{eq} = \frac{G_{eq} d}{\mu_l} \tag{26}$$

and equivalent liquid mass flux is defined as:

$$G_{eq} = G\left((1-x) + x\left(\frac{\rho_l}{\rho_g}\right)^{0,5}\right) \tag{27}$$

and the ratio of density to dynamic viscosity is defined as:

$$R = \frac{\rho_l \mu_l}{\rho_g \mu_g} \tag{28}$$

The Lockhart and Martinelli [16] parameter is expressed as:

$$X_{tt} = \left(\frac{1-x}{x}\right)^{0.9} \left(\frac{\rho_g}{\rho_l}\right)^{0.5} \left(\frac{\mu_l}{\mu_g}\right)^{0.1} \tag{29}$$

The Bond number is defined as:

$$Bo = g(\rho_l - \rho_g)\left(\frac{(d/2)^2}{\sigma}\right) \tag{30}$$

Table 1 Uncertainty of experimental parameters

Parameters	Uncertainty
$T_{ref,\,sat}$ (°C)	0.19
x_i	±6.96–8.24%
ΔT (K)	±0.191
$(T_{w,o} - T_{w,i})_{TS}$ (K)	±0.045
$(T_{w,i} - T_{w,o})_{ph}$ (K)	±0.13
m_{ref} (g/s)	±0.023
$m_{w,TS}$ (g/s)	±0.35
$m_{w,ph}$ (g/s)	±0.38
q_{TS} (kW/m^2)	±6.55–8.93%
q_{ph} (kW/m^2)	±12–14.81%
h_{ref} (W/m^2-K)	±7.64–10.71%.
ΔP (kPa)	±0.15

The Froude number is defined as:

$$\mathrm{Fr} = \frac{G^2}{gd\rho_{TP}^2} \tag{31}$$

where the two-phase density is determined from:

$$\rho_{TP} = \left(\frac{x}{\rho_g} + \frac{1-x}{\rho_l}\right)^{-1} \tag{32}$$

Uncertainties

The uncertainties of the Nusselt number and condensation heat transfer coefficient in the test tube varied from ±7.64% to ±10.71%. It should be noted that similar ranges of uncertainty with minimum and maximum values exist in the literature. The procedures of Kline and McClintock [51] were used for the calculation of all uncertainties. Various uncertainty values of the study can be seen from the authors' previous works [28, 35, 37], and the details are given in Table 1.

RESULTS AND DISCUSSION

In order to develop the empirical convective condensation heat transfer coefficient correlation and investigate the well-known annular flow model for the downward two-phase flow of R134a in a vertical round tube with inner diameter of 8.1 mm, the present study was performed at the Fluid Mechanics, Thermal Engineering and Multiphase Flow Research Laboratory (FUTURE) in KMUTT. Pure HFC-134a was used in the experiments. Operating conditions of the study are given in Table 2. Discussion of the results is given next.

Figure 3 shows the relationship between the mean heat flux and the condensation temperature difference ($T_{sat} - T_{wi}$) for the condensation temperature of 40°C at various mass fluxes in a smooth tube. It can be seen that heat flux increases with increasing temperature difference (or condensation rate). The increase in heat flux increases the condensation rate. In other words, film thickness on the tube wall increases due to the constant latent heat of condensation for a specific saturation temperature of condensation (Eqs. (5) and (6)). It can also be seen that heat flux increases with increasing mass flux due to the increase in condensation rate. It should be noted that vapor quality decreases with increasing heat flux and condensation temperature difference ($T_{sat} - T_{wi}$) in this figure.

Table 2 Operating conditions of the study

Refrigerant	HFC-134a
Test tube material, inner diameter d, length L	Copper, φ8.1 mm, 500 mm
Range of condensing pressure, P_{sat} (bar)	10–12
Range of condensing temperature, T_{sat} (°C)	40–50
Range of mass flux, G (kg/m^2-s)	260–515
Range of heat flux, q (kW/m^2)	10.16–66.61
Range of temperature difference, $\Delta T = T_{sat} - T_{wi}$, K	1.26–8.98
Range of average vapor quality, x	0.69–0.96

Figure 4 shows the change in total pressure drop with various mass fluxes for the condensation temperature of 50°C at various temperature differences. Due to the increase in shear stress at the interface of the phases, total pressure drop increases with increasing mass fluxes. Hence, increasing heat flux increases with increasing condensation rate decreases the vapor quality, and as a result, pressure drop is decreased.

Figure 5 shows the relationship between total measured pressure drop and quality for the condensation temperature of 40°C at various mass fluxes. At high vapor quality, the higher velocity of vapor flow causes more shear stress at the interface of the vapor and liquid film. As a consequence, the total pressure drop increases with increasing vapor quality.

The pressure drop per unit length shown in Figure 6 is obtained from dividing the measured pressure drop by the length between pressure taps. Figure 6 shows the effect of condensation temperature (40–50°C) on the total measured pressure drop per

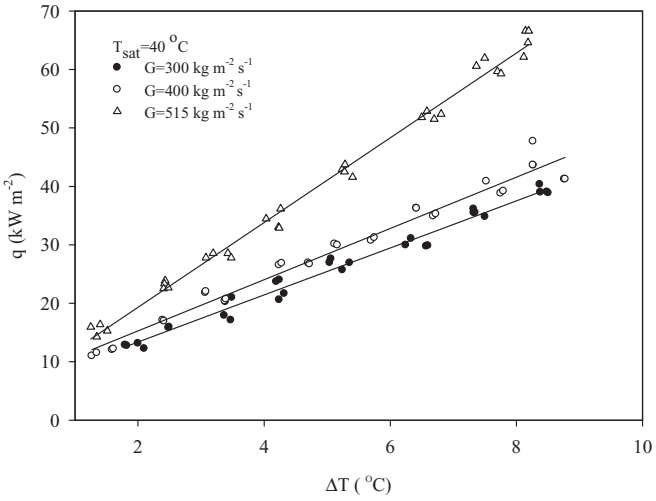

Figure 3 Comparison of heat flux for various mass fluxes of R134a at T_{sat} = 40°C.

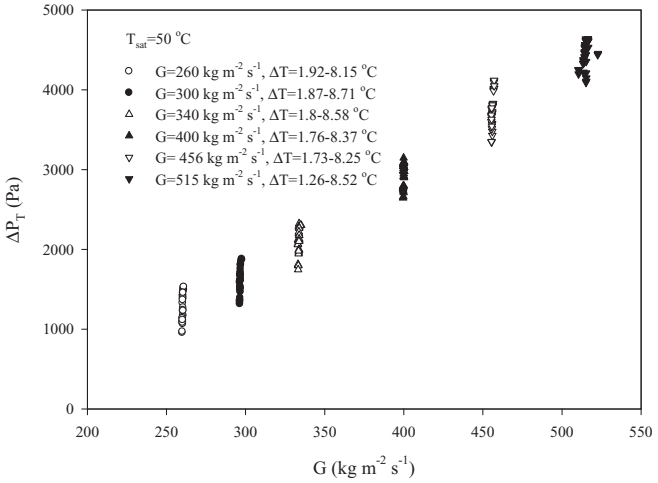

Figure 4 Change in measured total pressure drop for all mass fluxes of R134a at $T_{sat} = 50°C$ and various condensation temperature differences.

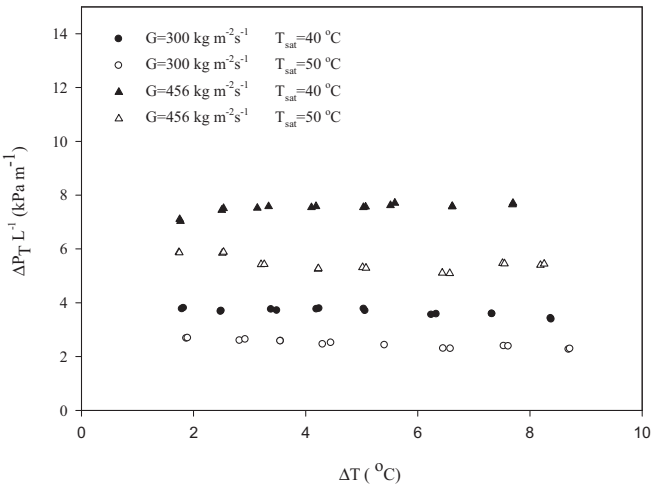

Figure 6 Effect of condensation temperatures of R134a on measured total pressure drop for G = 300 and 456 kg/m^2-s and $x_{inlet} = 1$.

length for low and high mass fluxes (300 and 456 kg/m^2-s). Low mass flux conditions give less condensation pressure drop per length than high mass flux conditions at the same condensing temperature. In addition to this, it is also shown that an increase in system pressure or condensing temperature leads to some decrease in pressure drop at the same mass flux. Yan and Lin [54] also stated similar results in their research.

Figures 7 and 8 show the variation of the average condensation heat transfer coefficient of R134a with average quality in the 8.1 mm ID smooth copper tube at saturation temperatures of 50 and 40°C and mass fluxes of 300 and 400 kg/m^2-s, respectively. During the condensation, the liquid film thickness gradually increases and the thermal resistance is therefore increased, which results in a decrease in the heat transfer rate. Comparison of the heat transfer coefficient at higher average vapor quality with a smaller liquid film thickness, and higher vapor velocity at the vapor–liquid interface and those at lower average vapor quality reveals an increase of the heat transfer coefficient when the average quality is higher. The result is that the average heat transfer coefficient increases with increasing average quality.

In spite of different experimental conditions, trends similar to those shown in Figures 3–8 were presented by Ma et al. [8], Park et al. [52], Kuo et al. [53], and Yan and Lin [54]. Ma et al. [8] showed the alteration of heat flux versus the condensation temperature difference ($T_{sat} - T_{wi}$), and frictional pressure drop versus average vapor quality, in their diagrams. Park et al. [52] investigated the heat transfer coefficients and pressure drop of R22, propylene, propane, dimethyl ether (DME), and isobutene and reported that the pressure drop increases as the mass flux and quality increase, and also showed the alteration of heat transfer coefficients with vapor quality with diagrams. Kuo et al. [53] studied the heat transfer characteristics and associated frictional pressure drop in the condensing flow of R410A and Yan and

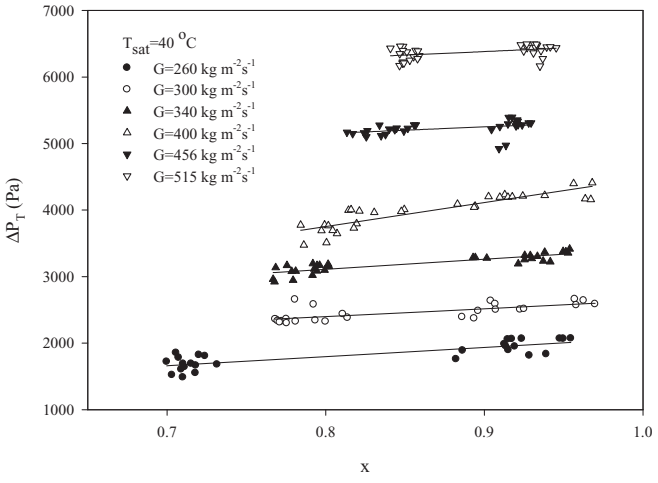

Figure 5 Effect of various mass flux of R134a on measured pressure drop at $T_{sat} = 40°C$.

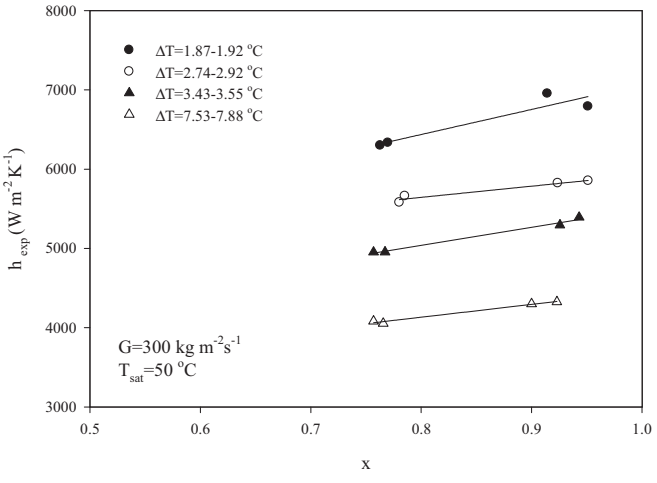

Figure 7 Experimental condensation heat transfer coefficient vs. average vapor quality for G = 300 kg/m^2-s and $T_{sat} = 50°C$.

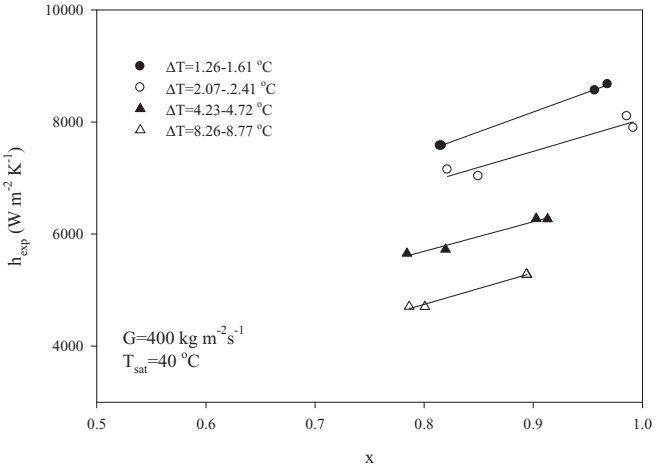

Figure 8 Experimental condensation heat transfer coefficient vs. average vapor quality for G = 400 kg/m^2-s and T_{sat} = 40°C.

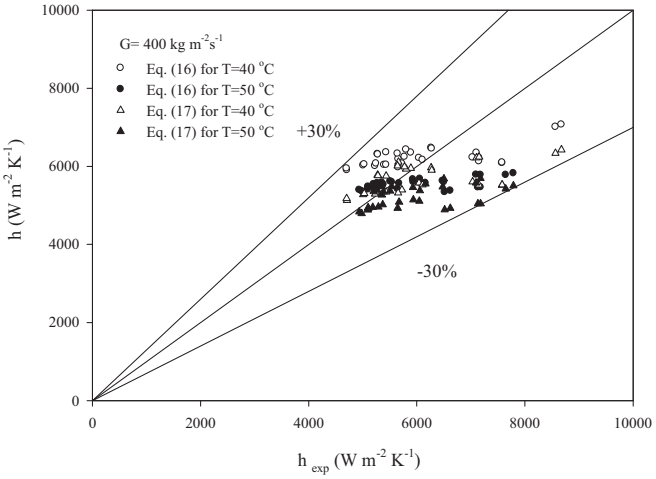

Figure 10 Comparison of experimental and calculated condensation heat transfer coefficients for G = 400 kg/m^2-s and T_{sat} = 40, 50°C.

Lin [54] condensed R134a in a horizontal small circular pipe to investigate the characteristics of condensation heat transfer and pressure drop. The effects of the heat flux, mass flux, and vapor quality and saturation temperature of refrigerants on the measured condensation heat transfer and pressure drop were examined in detail in these works [53, 54]. The similarity in the characteristics of trends of the data obtained from this work and the former studies shows the accuracy and reliability of the database in the current study. A large number of experimental data points for the validation process and variations of these important measured parameters such as heat flux, heat transfer coefficient, pressure drop, and vapor quality are shown in this article.

Figures 9 to 11 present the comparison of average condensation heat transfer coefficients of R134a obtained from Eqs. (16) and (17) to show the independence of annular flow conditions from the tube orientation at high mass flux inside the test tube according to condensation temperatures of 40 and 50°C. Low condensation temperature conditions (40°C) give larger condensation heat transfer coefficients than high condensation temperature conditions (50°C) at the same condensing temperature differences. It can be clearly seen that heat transfer coefficients increase with increasing mass fluxes. In addition to this, it is found that the majority of the calculated data using Eqs. (16) and (17), which are valid for horizontal and vertical tubes, respectively, fall within ±30% for the mass fluxes of 300, 400, and 515 kg/m^2-s and all condensing saturation temperatures of R134a.

Comparisons of the proposed condensation heat transfer coefficient correlation in Eq. (25) and experimental heat transfer correlation in Eq. (7) are shown in Figures 12 and 13. It can be seen from Figures 12 and 13 that the majority of the measured data falls within ±20% by the means of proposed correlation (Eq. (25)) for all the mass fluxes (260, 300, 340, 400, 456, and 515 kg/m^2-s) and saturation temperatures (40°C and 50°C) of

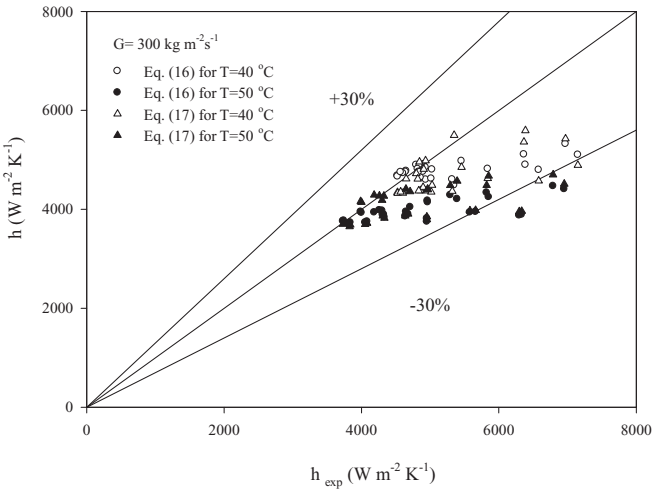

Figure 9 Comparison of experimental and calculated condensation heat transfer coefficients for G = 300 kg/m^2-s and T_{sat} = 40, 50°C.

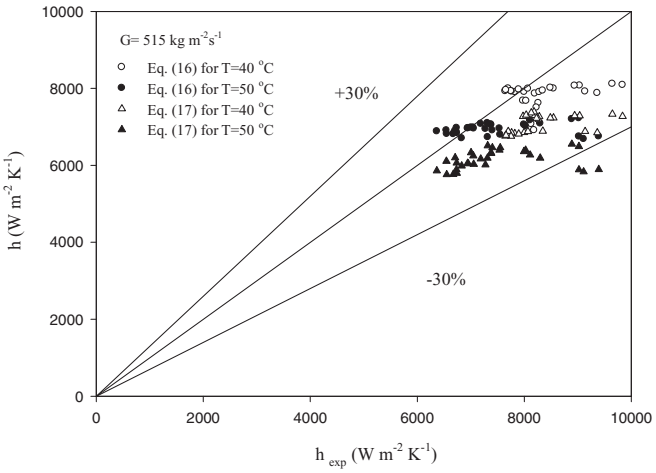

Figure 11 Comparison of experimental and calculated condensation heat transfer coefficients for G = 515 kg/m^2-s and T_{sat} = 40, 50°C.

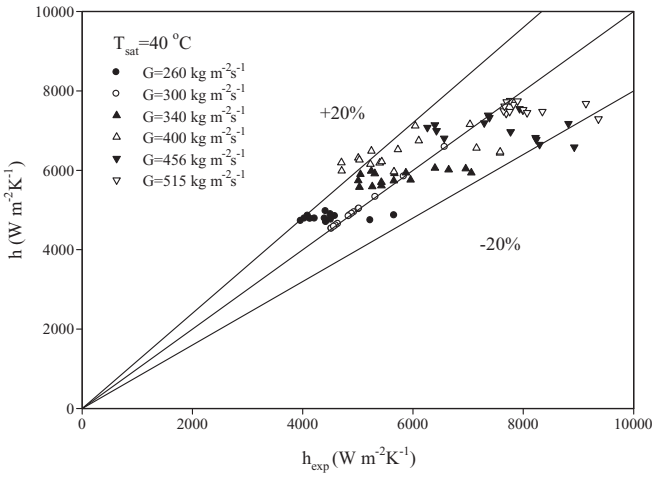

Figure 12 Comparison of the experimental convective heat transfer coefficient with the proposed empirical heat transfer correlation in Eq. (25) under the experimental conditions G = 260–515 kg/m^2-s, P = 0.1 MPa, T_{sat} = 40°C for the turbulent condensation of R134a in a vertical smooth copper tube 8.1 mm ID and 0.5 m long.

R134a. It should be noted that all turbulent flow data fall within the ±30% deviation band. It can be also seen from Figures 12 and 13 that heat transfer coefficient increases with increasing mass flux and decreasing condensing temperature, as explained in earlier. It should be also noted that the characteristic length is used as tube diameter in the proposed equation (Eq. (25)) instead of the tube length.

A large number of graphics could be generated from the output of the calculations; however, due to space limitation, only typical results are shown for limited data. Detailed information on the explanations presented here and some additional figures with different experimental parameters related to this study can also be seen in the authors' previous publications [27–38].

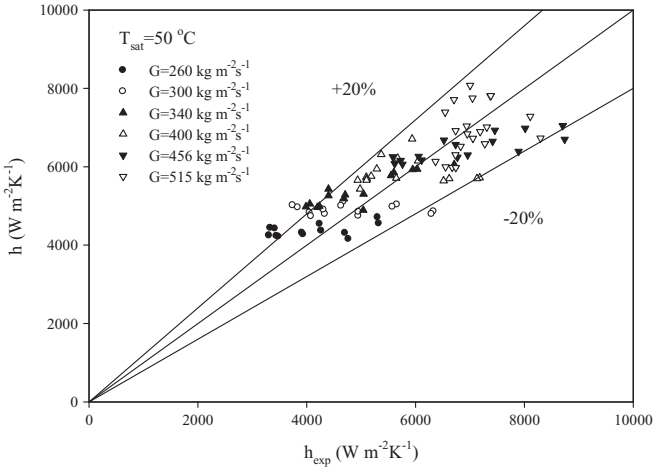

Figure 13 Comparison of the experimental convective heat transfer coefficient with the proposed empirical heat transfer correlation in Eq. (25) under the experimental conditions G = 260–515 kg/m^2-s, P = 0.12, MPa, T_{sat} = 50°C for the turbulent condensation of R134a in a vertical smooth copper tube 8.1 mm ID and 0.5 m long.

CONCLUSIONS

Co-current downward condensation heat transfer and pressure drop of R134a were experimentally investigated in an 8.1 mm ID vertical smooth tube. Accurate and repeatable heat transfer data were obtained. There is limited research on the parameters of such cases in the literature. For this reason, results of this study are expected to fill a gap in the literature. The validation process of investigated annular flow model and correlation development was accomplished by 380 and 198 data points, respectively. The following results were obtained:

1. Heat flux increased with increasing temperature difference (or condensation rate).
2. Total pressure drop increased with increasing vapor quality and mass flux.
3. The average heat transfer coefficient increased with increasing average quality.
4. The annular flow model is not dependent on the tube orientation, provided that an annular flow regime exists along the tube length. The model predicted condensation heat transfer coefficients inside the test tube within the deviation line of ±30%.
5. The proposed correlation has still a limited validity range since it covers a large number of annular flow data at the high mass region of R134a condensing in a relatively short vertical tube.

NOMENCLATURE

A	inside surface area, m^2
Bo	Bond number
c_p	specific heat, J/kg-K
d	internal tube diameter, m
Fr	Froude number
G	mass flux, kg/m^2-s
g	gravitational constant, m/s^2
h	heat transfer coefficient, W/m^2-K
i	enthalpy, J/kg
i_{fg}	latent heat of condensation, J/kg
L	length of test tube, m
k	thermal conductivity, W/m-K
m	mass flow rate, kg/s
P	pressure, MPa
Pr	Prandtl number
R	ρ/μ ratio
Re	Reynolds number
S	slip ratio
T	temperature, °C
T_δ^+	dimensionless parameter evaluated at the vapor–liquid interface
Q	heat transfer rate, W
q	mean heat flux, kW/m^2
X_{tt}	Lockhart and Martinelli parameter

x mean vapor quality
z axial coordinate
ΔP pressure drop, Pa
ΔT vapor side temperature difference, T_{sat}—T_{wi}, K

Greek Symbols

σ surface tension, N/m
ρ density, kg/m^3
μ dynamic viscosity, kg/ms
δ film thickness, m
δ^+ dimensionless film thickness
α void fraction
τ shear stress, N/m^2

Subscripts

eq equivalent
exp measured
F frictional term
g gas/vapor
G gravitational term
i inlet
l liquid
M momentum term
o outlet
ph preheater
ref refrigerant
sat saturation
T total
TS test section
TP two-phase
w water
wi inner wall

REFERENCES

[1] Fair, J. R., What You Need to Know to Design Thermosyphon Reboilers, *Petroleum Refiner*, vol. 39, no. 2, pp. 105–123, 1960.

[2] Hewitt, G. F., and Roberts, D. N., *Studies of Two-Phase Flow Patterns by Simultaneous X-Ray and Flash Photography*, Report AERE-M2159, UKAEA, Harwell, 1969.

[3] Kosky P. G., and Staub, F. W., Local Condensing Heat Transfer Coefficients in the Annular Flow Regime, *AIChE Journal*, vol. 17, no. 5, pp. 1037–1043, 1971.

[4] Traviss, D. P., Rohsenow, W. M., and Baron, A. B., Forced-Convection Condensation inside Tubes: A Heat Transfer Equation for Condenser Design, *ASHRAE Transactions*, vol. 79, no. 1, pp. 157–165, 1972.

[5] Shah, M. M., A General Correlation for Heat Transfer During Film Condensation Inside Pipes, *International Journal of Heat and Mass Transfer*, vol. 22, no. 4, pp. 547–556, 1979.

[6] Goodykoontz, J. H., and Dorsch, R. G., *Local Heat Transfer and Pressure Distributions for Freon-113 Condensing in Downward Flow in a Vertical Tube*, NASA TN D-3952, Glenn Research Center, Washington, 1967.

[7] Kim, S. J., and No, H. C., Turbulent Film Condensation of High Pressure Steam in a Vertical Tube, *International Journal of Heat and Mass Transfer*, vol. 43, no. 21, pp. 4031–4042, 2000.

[8] Ma, X., Briggs, A., and Rose, J. W., Heat Transfer and Pressure Drop Characteristics for Condensation of R113 in a Vertical Micro-Finned Tube with Wire Insert, *International Communications in Heat and Mass Transfer*, vol. 31, no. 5, pp. 619–627, 2004.

[9] Levich, V. G., *Physicochemical Hydrodynamics*, Prentice Hall, Englewood Cliffs, NJ, 1962.

[10] Blangetti, F., Krebs, R., and Schlunder, E., Condensation in Vertical Tubes—Experimental Results and Modelling, *Chemical Engineering Fundamentals*, vol. 1, no. 1, pp. 20–63, 1982.

[11] Bergelin, O. P., Kegel, P. K., Carpenter, F. G., and Gazley, C., *Co-Current Gas–Liquid Flow. II. Flow in Vertical Tubes*, ASME Heat Transfer and Fluid Mechanic Institute, Berkeley, CA, pp. 19–28, 1946.

[12] Dittus, F. W., and Boelter, L. M. E., *Engineering Publication*, vol. 2, p. 443, University of California Press, Berkeley, 1930.

[13] Akers, W. W., Deans, H. A., and Crosser, O. K., Condensation Heat Transfer Within Horizontal Tubes, *Chemical Engineering Progress Symposium Series*, vol. 55, no. 29, pp. 171–176, 1959.

[14] Cavallini, A., and Zecchin, R. A., A Dimensionless Correlation for Heat Transfer in Forced Convection Condensation, *Proceedings of the Sixth International Heat Transfer Conference*, vol. 3, pp. 309–313, 1974.

[15] Wallis, G. B., *One-Dimensional Two Phase Flow*, McGraw-Hill, New York, 1969.

[16] Lockhart, R. W., and Martinelli, R. C., Proposed Correlation of Data for Isothermal Two-Phase, Two-Component Flow in Pipes, *Chemical Engineering Progress*, vol. 45, no. 1, pp. 39–48, 1949.

[17] Jaster H., and Kosky, P. G., Condensation Heat Transfer in a Mixed Flow Regime, *International Journal of Heat and Mass Transfer*, vol. 19, pp. 95–99, 1976.

[18] Rufer, C. E., and Kezios, S. P., Analysis of Two-Phase, One-Component Stratified Flow with Condensation, *ASME Journal of Heat Transfer*, vol. 88, pp. 265–275, 1966.

[19] Dobson, M. K., and Chato, J. C., Condensation in Smooth Horizontal Tubes, *Journal of Heat Transfer, Transactions of ASME*, vol. 120, no. 1, pp. 193–213, 1998.

[20] Sweeney, K. A., *The Heat Transfer and Pressure Drop Behavior of a Zeotropic Refrigerant Mixture in a*

Micro-Finned Tube, M.S. thesis, University of Illinois, Urbana, 1996.

[21] Cavallini, A., Censi, G., Del Col, D., Doretti, L., Longo, G. A., Rossetto, L., and Zilio, C., Condensation Inside and Outside Smooth and Enhanced Tubes—A Review of Recent Research, *International Journal of Refrigeration*, vol. 26, no. 4, pp. 373–392, 2003.

[22] Cavallini, A., Censi, G., Del Col, D., Doretti, L., Longo, G. A., and Rossetto, L., Experimental Investigation on Condensation Heat Transfer and Pressure Drop of New HFC Refrigerants (R134a, R125, R32, R410A, R236ea) in a Horizontal Smooth Tube, *International Journal of Refrigeration*, vol. 24, pp. 73–87, 2001.

[23] Friedel, L., *Improved Friction Pressure Drop Correlations for Horizontal and Vertical Two-Phase Pipe Flow*, European Two-Phase Group Meeting, Ispra, Italy, Paper E2, 1979.

[24] Cavallini, A., Del Col, D., Doretti, L., Matkovic, M., Rossetto, L., Zilio, C., and Censi, G., Condensation in Horizontal Smooth Tubes: A New Heat Transfer Model for Heat Exchanger Design, *Heat Transfer Engineering*, vol. 27, no. 8, pp. 31–38, 2006.

[25] El Hajal, J., Thome, J. R., and Cavallini, A., Condensation in Horizontal Tubes, Part 1: Two-Phase Flow Pattern Map, *International Journal of Heat and Mass Transfer*, vol. 46, no. 18, pp. 3349–3363, 2003.

[26] Thome, J. R., El Hajal, J., and Cavallini, A., Condensation in Horizontal Tubes, Part 2: New Heat Transfer Model Based on Flow Regimes, *International Journal of Heat and Mass Transfer*, vol. 46, no. 18, pp. 3365–3387, 2003.

[27] Dalkilic, A. S., Laohalertdecha, S., and Wongwises, S., Effect of Void Fraction Models on The Two-Phase Friction Factor of R134a During Condensation in Vertical Downward Flow in a Smooth Tube, *International Communications in Heat and Mass Transfer*, vol. 35, no. 8, pp. 921–927, 2008.

[28] Dalkilic, A. S., Yildiz, S., and Wongwises, S., Experimental Investigation of Convective Heat Transfer Coefficient During Downward Laminar Flow Condensation of R134a in a Vertical Smooth Tube, *International Journal of Heat and Mass Transfer*, vol. 52, no. 1–2, pp. 142–150, 2009.

[29] Dalkilic, A. S., Laohalertdecha, S., and Wongwises, S., Two-Phase Friction Factor in Vertical Downward Flow in High Mass Flux Region of Refrigerant HFC-134a During Condensation, *International Communications in Heat and Mass Transfer*, vol. 35, no. 9, pp. 1147–1152, 2008.

[30] Dalkilic, A. S., Laohalertdecha, S., and Wongwises, S., Effect of Void Fraction Models on The Film Thickness of R134a During Downward Condensation in a Vertical Smooth Tube, *International Communications in Heat and Mass Transfer*, vol. 36, no. 2, pp. 172–179, 2009.

[31] Dalkilic, A. S., and Wongwises, S., Intensive Literature Review of Condensation Inside Smooth and Enhanced Tubes, *International Journal Heat and Mass Transfer*, vol. 52, no. 15–16, pp. 3409–3426, 2009.

[32] Dalkilic, A. S., Laohalertdecha, S., and Wongwises, S., A Comparison of the Void Fraction Correlations of R134a During Condensation in Vertical Downward Laminar Flow in a Smooth and Micro-Fin Tube, *ASME Proceedings of the 1st International Conference on Micro/Nanoscale Heat Transfer*, Tainan, Taiwan, vol. A–B, pp. 1029–1040, 2008.

[33] Dalkilic, A. S., Laohalertdecha, S., and Wongwises, S., Two-Phase Friction Factor Obtained From Various Void Fraction Models of R-134a During Condensation in Vertical Downward Flow at High Mass Flux, *ASME Proceedings of the 1st International Conference on Heat Transfer*, Jacksonville, FL, vol. 2, pp. 193–206, 2008.

[34] Dalkilic, A. S., Laohalertdecha, S., and Wongwises, S., Experimental Investigation on Heat Transfer Coefficient of R134a During Condensation in Vertical Downward Flow at High Mass Flux in a Smooth Tube, *International Communications in Heat and Mass Transfer*, vol. 36, no. 10, pp. 1036–1043, 2009.

[35] Dalkilic, A. S., Laohalertdecha, S., and Wongwises, S., Experimental Investigation on the Condensation Heat Transfer and Pressure Drop Characteristics of R134a at High Mass Flux Conditions During Annular Flow Regime Inside a Vertical Smooth Tube, *ASME Summer Heat Transfer Conference*, San Francisco, CA, 2009.

[36] Dalkilic, A. S., and Agra, O., Experimental Apparatus for the Determination of Condensation Heat Transfer Coefficient for R134a and R600a Flowing Inside Vertical and Horizontal Tubes, *ASME Summer Heat Transfer Conference*, San Francisco, CA, 2009.

[37] Dalkilic, A. S., Laohalertdecha, S., and Wongwises, S., Experimental Research on the Similarity of Annular Flow Models and Correlations for the Condensation of R134a at High Mass Flux Inside Vertical and Horizontal Tubes, *ASME International Mechanical Engineering Congress and Exposition*, Lake Buena Vista, FL, 2009.

[38] Dalkilic, A. S., and Wongwises, S., *A Heat Transfer Model for Co-Current Downward Laminar Film Condensation of R134a in a Vertical Micro-Fin Tube During Annular Flow Regime*, Eleventh UK National Heat Transfer Conference, London, UK, 2009.

[39] Garcia-Valladares, O., Review of In-Tube Condensation Heat Transfer Correlations for Smooth and Microfin Tubes, *Heat Transfer Engineering*, vol. 24, no. 4, pp. 6–24, 2003.

[40] Carey, V. P., *Liquid–Vapor Phase Change Phenomena*, Hemisphere, New York, 1992.

[41] Honda, H., Nozu, S., Matsuoka, Y., and Nakata, H., Condensation of R-11 and R-113 in the Annuli of Horizontal Double-Tube Condensers with an Enhanced Inner Tube, *Experimental Thermal and Fluid Science*, vol. 2, pp. 173–182, 1989.

[42] Sami, S. M., and Schnotale, J., Prediction of Forced Convective Condensation of Non-Azeotropic Refrigerant Mixtures Inside Enhanced Surface Tubing, *Applied Scientific Research Journal*, vol. 50, pp. 149–168, 1993.

[43] Chisholm, D., *Two Phase Flow in Pipelines and Heat Exchangers*, George Godwin in association with The Institution of Chemical Engineers, London, 1983.
[44] Chen, S. L., Gerner, F. M., and Tien, C. L., General Film Condensation Correlations, *Experimental Heat Transfer*, vol. 1, pp. 93–107, 1987.
[45] Collier, J. G., and Thome, J. R., *Convective Boiling and Condensation*, Clarendon Press, Oxford, UK, 1994.
[46] Whalley, P. B., *Boiling, Condensation, and Gas-Liquid Flow*, Clarendon Press, Oxford, UK, 1987.
[47] Koyama, S., Miyara, A., Takamatsu, H., and Fujii, T., Condensation Heat Transfer of Binary Refrigerant Mixtures of R22 and R114 Inside a Horizontal Tube with Internal Spiral Grooves, *International Journal of Refrigeration*, vol. 13, no. 3, pp. 256–263, 1990.
[48] Dobson, M. K., and Chato, J. C., Condensation in Smooth Horizontal Tubes, *Journal of Heat Transfer*, vol. 120, no. 1, pp. 193–213, 1998.
[49] Cavallini, A., Longo, G. A., and Rossetto, L., Condensation Heat Transfer and Pressure Drop of Refrigerants in Tubes of Finned Tube Heat Exchangers, *in Recent Developments in Finned Tube Heat Exchangers, Theoretical and Practical Aspects*, DTI, Tastrup, Denmark, pp. 160–204, 1993.
[50] Cavallini, A., Doretti, L., Klammsteiner, N., Longo, G. A., and Rossetto, L., Condensation of New Refrigerants Inside Smooth and Enhanced Tubes, *Proceedings 19th International Congress of Refrigeration*, The Hague, Holland, vol. 4, pp. 105–114, 1995.
[51] Kline, S. J., and McClintock, F. A., Describing Uncertainties in Single Sample Experiments, *Mechanical Engineering*, vol. 75, no. 1, pp. 3–8, 1953.
[52] Park, K. J., Jung, D., and Seo, T., Flow Condensation Heat Transfer Characteristics of Hydrocarbon Refrigerants and Dimethyl Ether Inside a Horizontal Plain Tube, *International Journal of Multiphase Flow*, vol. 34, no. 7, pp. 628–635, 2008.
[53] Kuo, K. S., Lie, Y. M., Hsieh, Y. Y., and Lin, T. F., Condensation Heat Transfer and Pressure Drop of Refrigerant R-410A Flow in a Vertical Plate Heat Exchanger, *International Journal of Heat and Mass Transfer*, vol. 48, no. 25–26, pp. 5205–5220, 2005.
[54] Yan, Y., and Lin, T., Condensation Heat Transfer and Pressure Drop of Refrigerant R134a in a Small Pipe, *International Journal of Heat and Mass Transfer*, vol. 42, no. 4, pp. 697–708, 1999.

Ahmet Selim Dalkılıç is currently a research assistant in mechanical engineering at Yildiz Technical University, İstanbul, Turkey. He received his Ph.D. degree in mechanical engineering from the same university. His current research interest is on enhanced heat transfer, convection heat transfer, condensation, evaporation, boiling heat transfer of new refrigerants and mixture refrigerants, and applications in heat exchangers. He is a member of the Innovation Explorer for Scientific Researchers Community sponsored by Elsevier and American Society of Mechanical Engineers (ASME).

Somchai Wongwises is currently a professor of mechanical engineering at King Mongkut's University of Technology Thonburi, Bangmod, Thailand. He received his Doktor-Ingenieur (Dr.-Ing.) in mechanical engineering from the University of Hannover, Germany, in 1994. His research interests include two-phase flow, heat transfer enhancement, and thermal system design. He is the head of the Fluid Mechanics, Thermal Engineering and Multiphase Flow Research Labarotory (FUTURE).

Provided for non-commercial research and education use.
Not for reproduction, distribution or commercial use.

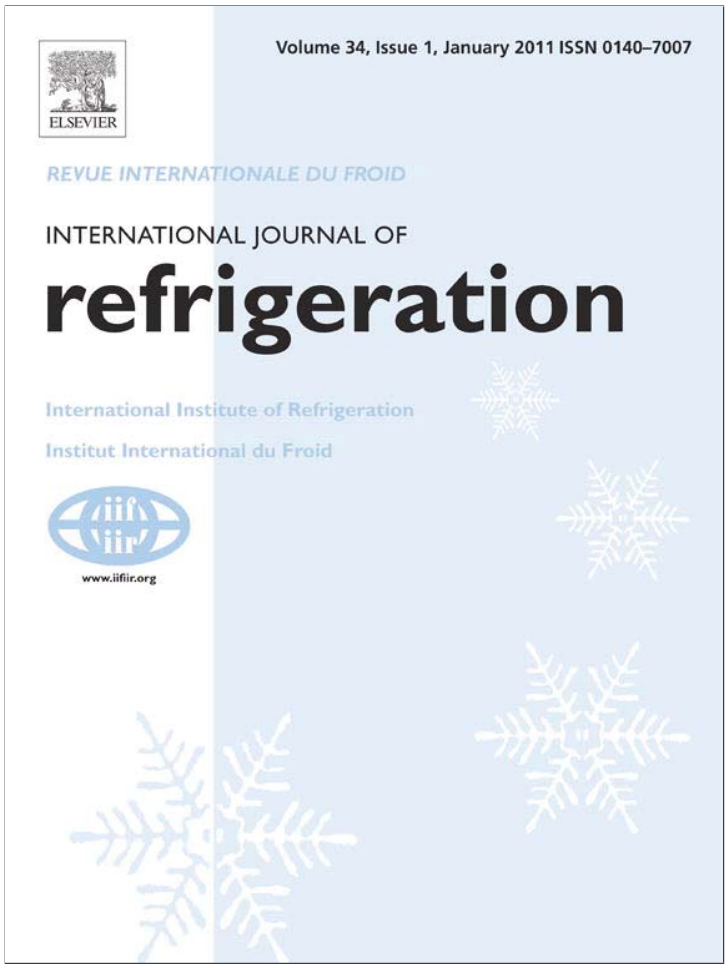

This article appeared in a journal published by Elsevier. The attached copy is furnished to the author for internal non-commercial research and education use, including for instruction at the authors institution and sharing with colleagues.

Other uses, including reproduction and distribution, or selling or licensing copies, or posting to personal, institutional or third party websites are prohibited.

In most cases authors are permitted to post their version of the article (e.g. in Word or Tex form) to their personal website or institutional repository. Authors requiring further information regarding Elsevier's archiving and manuscript policies are encouraged to visit:

http://www.elsevier.com/copyright

Author's personal copy

INTERNATIONAL JOURNAL OF REFRIGERATION 34 (2011) 280–291

available at www.sciencedirect.com

ScienceDirect

journal homepage: www.elsevier.com/locate/ijrefrig

An experimental study into the evaporation heat transfer and flow characteristics of R-134a refrigerant flowing through corrugated tubes

Suriyan Laohalertdecha [a], *Somchai Wongwises* [b,*]

[a] *The Joint Graduate School of Energy and Environment (JGSEE), King Mongkut's University of Technology Thonburi, Bangmod, Bangkok 10140, Thailand*

[b] *Fluid Mechanics, Thermal Engineering and Multiphase Flow Research Lab. (FUTURE), Department of Mechanical Engineering, King Mongkut's University of Technology Thonburi, Bangmod, Bangkok 10140, Thailand*

ARTICLE INFO

Article history:
Received 28 October 2009
Received in revised form
4 July 2010
Accepted 12 July 2010
Available online 29 July 2010

Keywords:
Two-phase flow
Pressure
Temperature
R-134a
Heat transfer
enhancement
Corrugated tube

ABSTRACT

The effects of corrugation pitch on the evaporation of R-134a flowing inside horizontal corrugated tubes are investigated. The test section is a tube-in-tube heat exchanger with refrigerant flowing in the inner tube and hot water flowing in the annulus. Smooth and corrugated tubes having similar inside diameters are used as the inner tube. Three corrugated tubes having a corrugation depth fixed at 1.5 mm and corrugation pitches of 5.08, 6.35 and 8.46 mm are examined. The data obtained from smooth tube are plotted and compared with the flow pattern map established by Censi et al. (2003) and Zurcher et al. (2002). The effects of average vapour quality, equivalent Reynolds number and corrugation pitch are discussed. The maximum ratios of heat transfer enhancement factor to pressure drop penalty factor $(Nu_c/Nu_s)/((\Delta P/L)_c/(\Delta P/L)_s)$ is approximately 1.2.

© 2010 Elsevier Ltd and IIR. All rights reserved.

Etude expérimentale sur le transfert de chaleur lors de l'évaporation et les caractéristiques d'écoulement du frigorigène R-134a en écoulement à l'intérieur de tubes ondulés

Mots clés : Écoulement diphasique ; Pression ; Température ; R-134a ; Transfert de chaleur ; Amélioration ; Tube ondulé

* *Corresponding author*. Tel.: +662 470 9115; fax: +662 470 9111.
E-mail address: somchai.won@kmutt.ac.th (S. Wongwises).

0140-7007/$ – see front matter © 2010 Elsevier Ltd and IIR. All rights reserved.
doi:10.1016/j.ijrefrig.2010.07.012

Author's personal copy

Nomenclature

A	surface area of the test section (m^2)
B_o	boiling number
c_p	specific heat at constant pressure (J/kg K)
D	diameter (m)
e	corrugation depth (mm)
f	friction factor
G	mass flux (kg/m^2 s)
h	heat transfer coefficient (W/m^2 K)
i	enthalpy (J/kg)
k	thermal conductivity (W/m K)
LMTD	logarithmic mean temperature difference
m	mass flow rate (kg/s)
Nu	Nusselt number
p	corrugation pitch (mm)
Pr	Prandtl number
Q	heat transfer rate (W)
Re	Reynolds number
q''	heat flux (W/m^2)
T	temperature (^oC)
x	average quality
X_{tt}	Martinelli parameter

Greek letters

α	void fraction
β	helix angle (degree)
ρ	density (kg/m^3)
v	specific volume (m^3/kg)
μ	dynamic viscosity (Pa s)
ΔP	pressure drop (Pa/m)

Subscripts

a	acceleration
avg	average
eq	equivalent liquid
f	friction
in	inlet
i	inside
l	liquid
lo	liquid only
out	outlet
o	outside
ph	pre-heater
ref	refrigerant
sat	saturation
TS	test section
tp	two-phase
v	vapor
w	water

1. Introduction

Heat transfer enhancement techniques necessarily reduce the thermal resistance in a conventional heat exchanger by promoting a higher convection heat transfer coefficient in order to minimise the size of the heat exchanger. Introducing surface roughness, especially corrugated tube, is one of the heat transfer enhancement techniques where the surface is modified in such a way as to promote turbulence in the flow field and increase the heat transfer surface. However, this tube can be employed in many heat exchangers to enhance the heat transfer coefficient of both the inside and outside tubes by mixing and also limiting the fluid boundary layers close to the heat transfer surfaces. Moreover, corrugated tubes are chosen instead of smooth tubes for designing industrial heat exchangers. So far, the heat transfer and flow characteristics of corrugated tubes have been reviewed as described below.

Nozu et al. (1995a,b)investigated local heat transfer and pressure gradients in pure R-114, R-113 and a zeotropic refrigerant mixture during condensation in a tube-in-tube heat exchanger. A corrugated copper tube with an O.D. of 19.1 mm was used as the test section. Mass flows were tested in the range from 80 to 240 kg/m^2s. The results showed that the frictional pressure gradient data and measured heat transfer data were approximately 11% and 13%, respectively.

Dong et al. (2001) investigated turbulent friction and heat transfer characteristics of four spirally corrugated tubes with various geometrical parameters. Water and oil were used as the working fluid. The experimental conditions gave Reynolds numbers ranging from 6000 to 93,000 for water and from 3200 to 19,000 for oil, respectively. Their results showed that the heat transfer coefficient enhancement varied from 30% to 120%, while the friction factor increased from 60% to 160% when compared with a smooth tube.

Barba et al. (2002) studied experimentally the heat transfer and pressure drop for a single-phase in a corrugated tube which could be used in the chemical and food industry. The tested conditions were done at moderate Reynolds numbers in the range 100–800. Ethylene glycol was used as the working fluid. The results gave a heat transfer enhancement around one while the friction factor increased up to 1.83–2.45 folds as compared with the smooth tube. Based on the experimental data, Nusselt number and friction factor correlations were proposed for the fully developed region.

Rainieri and Pagliarini (2002) studied experimentally the thermal performance of corrugated tubes, attempting to increase the convection heat transfer. Helical and transverse corrugated tubes with different pitch values were used as the test section. Ethylene glycol having a strong temperature dependence was employed as the working fluid. The tests were conducted at Reynolds numbers ranging from 90 to 800. A comparison of helical corrugated tubes, transverse corrugated tubes and a smooth tube demonstrated that almost all data for transverse corrugated tubes showed a more strongly enhanced heat transfer rate than the helical corrugated and smooth tubes.

Among all these previous studies, the most productive studies have been performed by Zimparov (2001). The heat transfer enhancement of a combination of three-start spirally corrugated tubes with a twisted tape was investigated. Two three-start spirally corrugated tubes combined with five twisted tape inserts with different relative pitches were

Author's personal copy

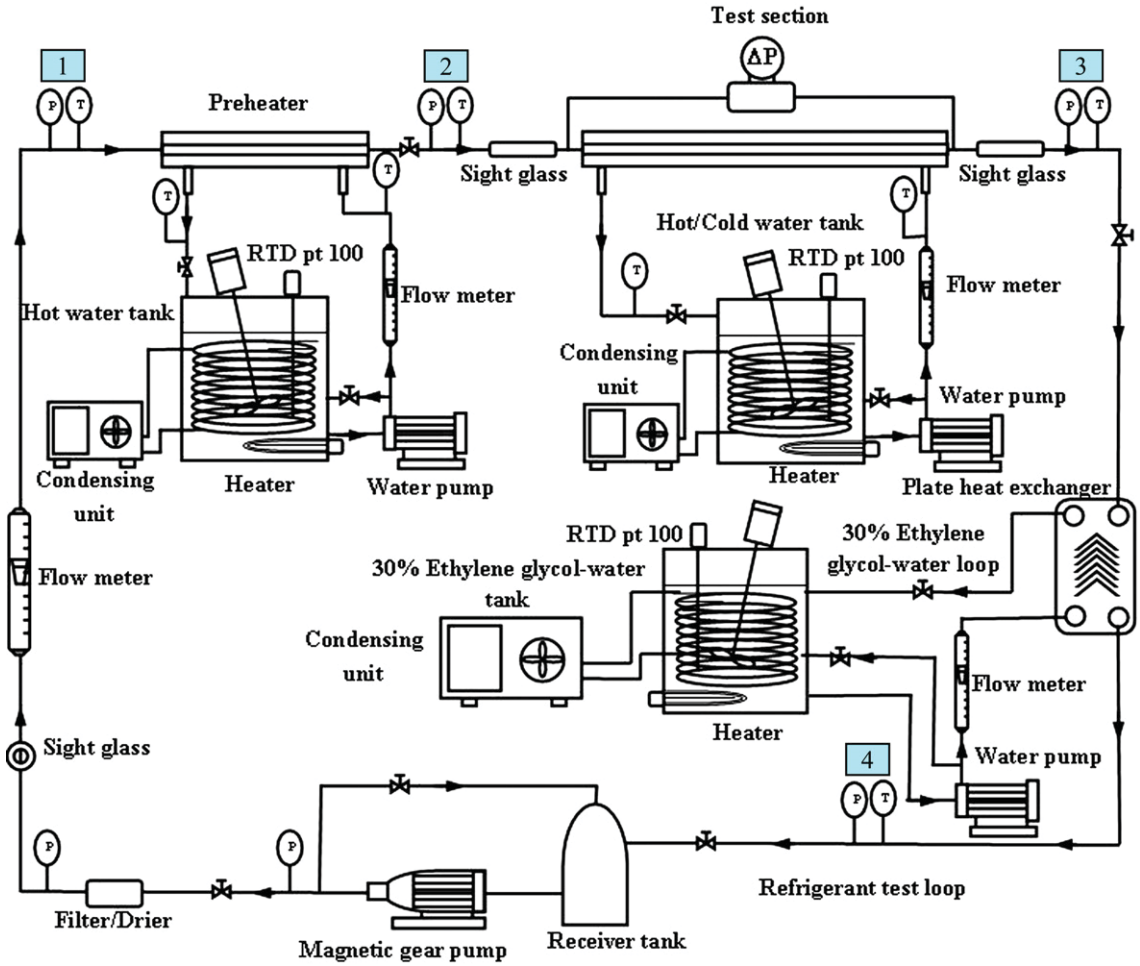

Fig. 1 – Schematic diagram of experimental apparatus.

employed as the test section. The experimental conditions were conducted at Reynolds number ranging from 3000 to 60,000. The height to diameter ratio (e/D_i) and relative pitch (H/D_i) parameters were 0.0407, 0.0569 and 15.3, 12.2, 7.7, 5.8, 4.7, respectively. The results showed that the friction factor and heat transfer coefficients of three-start spirally corrugated tubes with a twisted tape were significantly higher than those of a smooth tube under the same operating conditions.

Zimparov (2002) presented the heat transfer enhancement using a combination of single-start spirally corrugated tubes with a twisted tape. The friction factors and inside heat transfer coefficients obtained from these tubes were higher than those obtained from the smooth tube under the same conditions. In addition, Zimparov (2004a,b) applied a simple mathematical model to predict the friction factors and heat transfer coefficients in a spirally corrugated configuration combined with twisted tape inserts flowing in the turbulent flow regime. The calculated friction factors and heat transfer coefficients were compared with the experimental data. The results showed that the agreement between predicted and experimental data was fairly good.

Vicente et al. (2004a,b) presented measurements of mixed convection heat transfer and isothermal pressure drop in corrugated tubes for laminar, transition and turbulent flow regions. Water and ethylene glycol were used as working fluids. Corrugated tubes gave a higher pressure drop and heat transfer coefficient than the smooth tube under the same flow conditions. The pressure drop obtained from laminar to transition flow and turbulent flow increased by up to 25% and 300%, respectively. The Nusselt number obtained from laminar to transition flow and turbulent flow increased by up to 30% and 250%, respectively.

Targanski and Cieslinski (2007) studied experimentally the heat transfer coefficient and pressure drop of pure R-407C and R-407C/oil mixtures during evaporation inside a smooth stainless steel tube, smooth copper tubes and two enhanced tubes. The inlet and outlet vapour quality were set to 0 and 0.7, respectively, mass flow varied from 250 to 500 kg/m^{2}s and the average saturation temperature was 0 °C. It was found that the heat transfer coefficient and pressure drop for the enhanced tubes were distinctly higher than for the smooth tube. The maximum enhancement factor and penalty factor for corrugated tube were 1.25 and 1.8, respectively.

As mentioned above, it is evident that the corrugated tubes have greater heat transfer potential than smooth tubes. Although there have been a number of studies on the

Author's personal copy

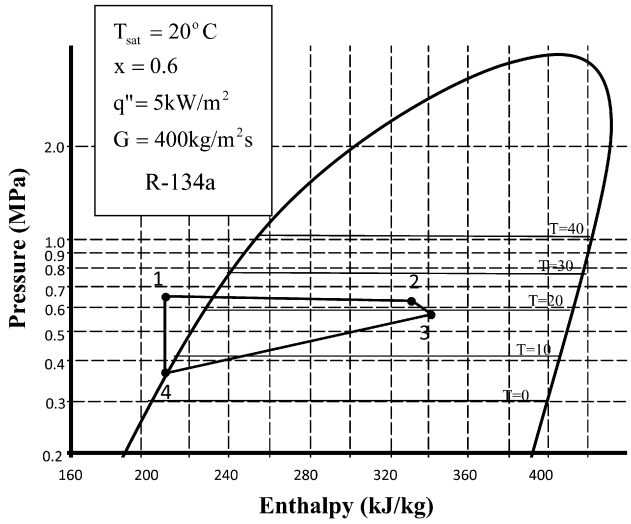

Fig. 2 – Corresponding state point with schematic diagram of experimental apparatus in a pressure–enthalpy diagram.

enhanced tube, there have been only some studies on the heat transfer and pressure drop of the two-phase flow of refrigerants through a corrugated copper tube. However, some information is currently available, there still remains room for further research, e.g. the effects of corrugation pitch on the evaporation of the refrigerant flowing inside horizontal corrugated tubes remain unstudied. As a consequence, this study presents an experimental investigation of the evaporation heat transfer enhancement and pressure drop of R-134a flowing inside corrugated copper tubes.

2. Experimental apparatus

A schematic diagram of the test apparatus is shown in Fig. 1. The experimental apparatus was designed to determine the heat transfer coefficient and pressure drop of pure R-134a over

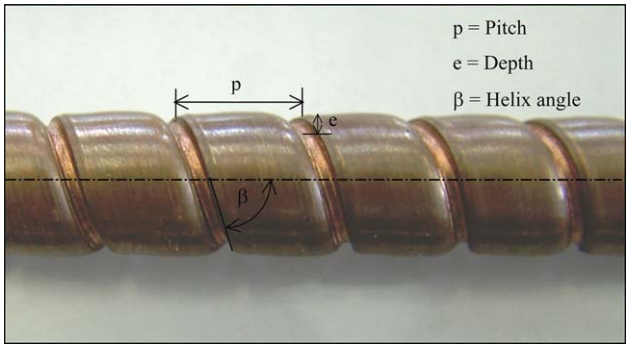

Fig. 4 – Photograph of helically corrugated tube.

the length of the test tube. The test loop consists of a test section, refrigeration loop, heating water flow loops, sub-cooling loop and relevant instrumentation. The objective of the water loop before the test section is to provide a controlled inlet quality. The second water loop located in the test section provides a controlled heat output from the test section. The sub-cooling loop is used to prevent any two-phase flow condition of the refrigerant occurring before it enters the refrigerant pump.

For the refrigeration circulating loop, liquid refrigerant at state 1 is discharged by a gear pump regulated by an inverter. The refrigerant passes in series through a filter/dryer, a sight glass tube, flow meter, pre-heater and enters the test section. The inlet quality before entering the test section at state 2 is controlled by the pre-heater. The pre-heater is a spiral counter-flow heat exchanger that supplies energy to provide a controlled inlet quality for vaporisation of the refrigerant. Leaving the test section at state 3, the refrigerant is then condensed and sub-cooled by a chilling loop that removes the heat input from the pre-heater and test section and then it returns from the two-phase refrigerant to a sub-cooled state and later collects in a receiver at state 4 and eventually returns to the refrigerant pump to complete the cycle. The corresponding state with a schematic diagram of the experimental apparatus is shown on a pressure–enthalpy diagram in Fig. 2.

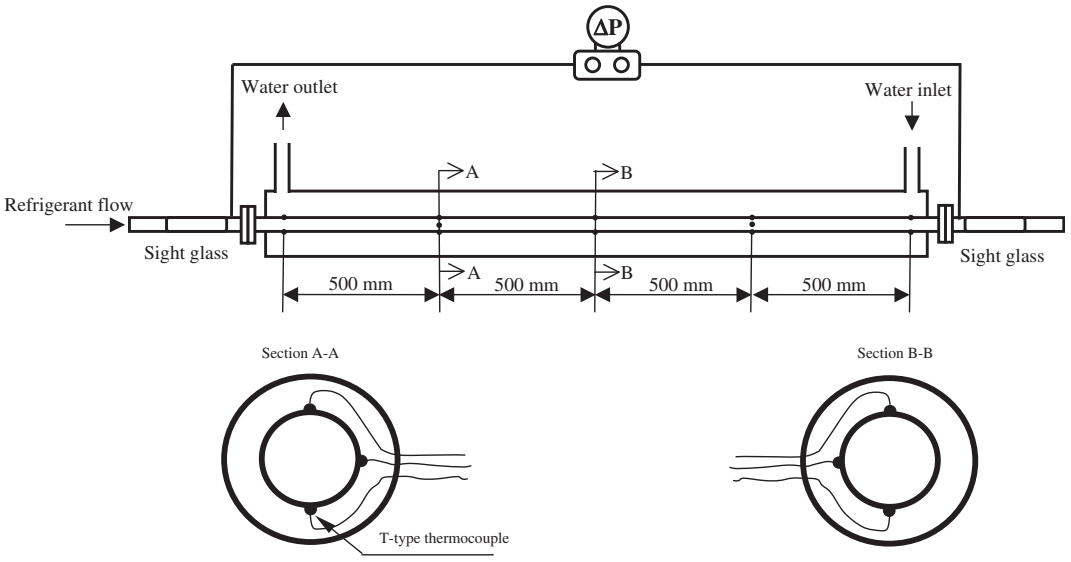

Fig. 3 – Schematic diagram of the test section.

Author's personal copy

Table 1 – Dimensions of the test section.

Parameter	Smooth tube	Corrugated tube		
Depth, e (mm)	–	1.5	1.5	1.5
Pitch, p (mm)	–	5.08	6.35	8.46
Helix angle, β (degree)	–	79.47	76.56	74.20
Outside diameter, D_o (mm)	9.52	9.52	9.52	9.52
Inside diameter, D_i, (mm)	8.7	8.7	8.7	8.7
Inside tube area, A_i, (mm^2)	54,663	82789	76773	72045
Length of the test tube, L (mm)	2000	2000	2000	2000

The test section is a horizontal counter-flow double tube heat exchanger. The length of the heat exchanger is 2.0 m. The detailed dimensions of the heat exchanger and the location of the thermocouples are shown in Fig. 3. Fig. 4 shows a drawing of a helically corrugated tube and nomenclature to describe the geometry. The dimensions of the test section are shown in Table 1.

The inlet temperature of the water is controlled by a thermostat. A differential pressure transducer and thermocouples are installed in the test section to measure the pressure drop and temperature across the test section. The length between pressure taps is 2.5 m. In the present study, the pressure of the refrigerant is mainly controlled by a high-pressure limit switch. High-pressure limit switches (Danfoss Type KP 5) are a device for regulating the pressure of a system so that the system's pressure is maintained near a desired set point pressure in order to prevent the experimental apparatus damage.

The refrigerant temperature and tube wall temperatures in the test section are measured by T type thermocouples. A total of 15 thermocouples are soldered at the top, bottom and side at five points along the tube as shown in Fig. 3. All the temperature-measuring devices are well calibrated in a controlled temperature bath using standard precision mercury glass thermometers. The uncertainty of the temperature measurements as recorded by the data acquisition system is ±0.1 °C. All static pressure taps are mounted in the tube wall. The refrigerant flow meter is a variable area type. The flow meter is specially calibrated in the range 0.2–3.4 LPM for R-134a by the manufacturer. Also, the differential pressure transducer is calibrated by the manufacturer.

Experiments were conducted with various flow rates of refrigerant, vapour qualities of refrigerant entering the test section, heat flows and temperatures of refrigerant condensing in the test section. In the experiments, the refrigerant flow rate in the test section was controlled by adjusting the speed of the magnetic gear pump. To vary the vapour qualities at the inlet of the test section, the heating water flow rate and the cooling water flow rate were varied by small increments while the refrigerant flow rate was kept constant. The hot water in the test section was re-circulated by a centrifugal pump to supply heat from the water to the refrigerant. During each experiment, the heat transferred from the test section was kept at a desired value. This might be obtained by simultaneously adjusting and controlling the temperature and flow rate of the hot water entering the test section. The system was allowed to approach a steady state before any data was recorded. After stabilisation, the temperatures on the tube wall, the temperature of the refrigerant at the locations mentioned above, the inlet and outlet temperatures of the heating water and flow rates of heating water and refrigerant were all recorded. The pressure drop was measured by a pressure transducer installed between the inlet and outlet of the test section. The experiments could be done by increasing the refrigerant flow rate while the saturation temperature in the test section was kept constant. The accuracy of the direct measurements and the uncertainties in the derived experimental values are shown in Table 2.

Table 2 – Uncertainties of measured quantities and calculated parameters.

Parameter	Uncertainty
Temperature, T (°C)	±0.1
Pressure drop, ΔP (kPa)	±0.37
Mass flow rate of refrigerant, m_{ref}	±2%
Mass flow rate of water, m_w	±2%
Heat transfer rate at test section, Q_{TS}	±10%
Heat transfer rate at pre-heater, Q_{ph}	±5%
Evaporation heat transfer coefficient, h	±10%
Average quality, x	±5%

3. Data reduction

The data reduction of the measured results can be summarized as follows.

3.1. The inlet vapour quality of the test section ($x_{TS,in}$)

$$x_{TS,in} = \frac{i_{TS,in} - i_{f@T_{TS,in}}}{i_{fg@T_{TS,in}}} \quad (1)$$

where i_f is the enthalpy of the saturated liquid based on the temperature of the test section inlet, i_{fg} is the enthalpy of vaporisation based on the temperature of the test section inlet, $i_{TS,in}$ is the refrigerant enthalpy at the test section inlet and is given by:

$$i_{TS,in} = i_{ph,in} + \frac{Q_{ph}}{m_{ref}} \quad (2)$$

where $i_{ph,in}$ is the inlet enthalpy of the liquid refrigerant before entering the pre-heater, m_{ref} is the mass flow rate of the refrigerant and Q_{ph} is the heat transfer rate in the pre-heater:

$$Q_{ph} = m_{w,ph}\, c_{p,w} \left(T_{w,in} - T_{w,out}\right)_{ph} \quad (3)$$

where $m_{w,ph}$ is the mass flow rate of water entering the pre-heater.

3.2. The outlet vapour quality of the test section ($x_{TS,out}$)

$$x_{TS,out} = \frac{i_{TS,out} - i_{f@T_{TS,out}}}{i_{fg@T_{TS,out}}} \quad (4)$$

where $i_{TS,out}$ is the refrigerant enthalpy at the test section outlet, i_f is the enthalpy of the saturated liquid based on the temperature of the test section outlet, and i_{fg} is the enthalpy of

Author's personal copy

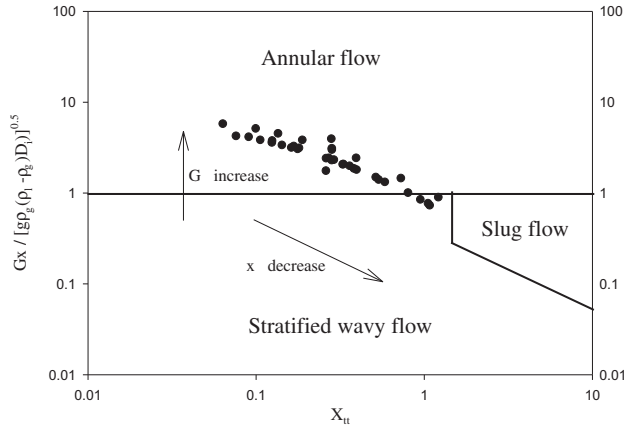

Fig. 5 – The present data plotted in smooth tube flow regime map of Censi et al., (2003)

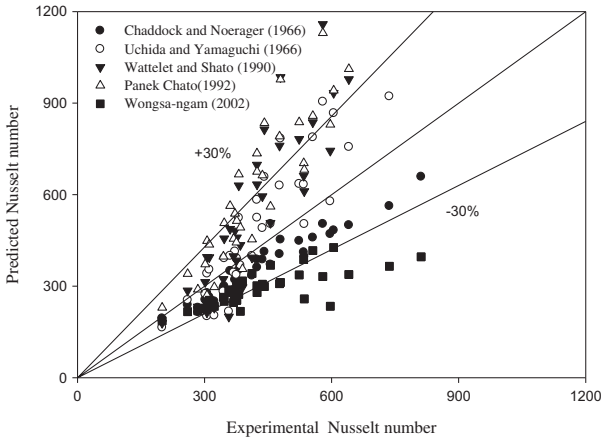

Fig. 7 – Comparison of the Nusselt number with existing correlations for smooth tube.

vaporisation. As a consequence, the outlet enthalpy of the refrigerant flow is calculated as:

$$i_{TS,out} = i_{TS,in} + \frac{Q_{TS}}{m_{ref}} \tag{5}$$

where the heat transfer rate in the test section is obtained from:

$$Q_{TS} = m_{w,TS}\, c_{p,w} \left(T_{w,in} - T_{w,out}\right)_{TS} \tag{6}$$

where $m_{w,\,TS}$ is the mass flow rate of the water entering the test section.

3.3. *The Nusselt number (Nu)*

$$h = \frac{1}{\left(\frac{1}{U_i}\right) - \left(\frac{1}{2k}\right) D_i \ln\left(\frac{D_o}{D_i}\right) - \left(\frac{D_i}{D_o}\right)\left(\frac{1}{h_o}\right)} \tag{7}$$

where U_i is the overall heat transfer coefficient, k is the thermal conductivity of tube material, h_o is the outside heat transfer coefficient.

$$U_i = \frac{Q_{TS}}{A_i (LMTD)} \tag{8}$$

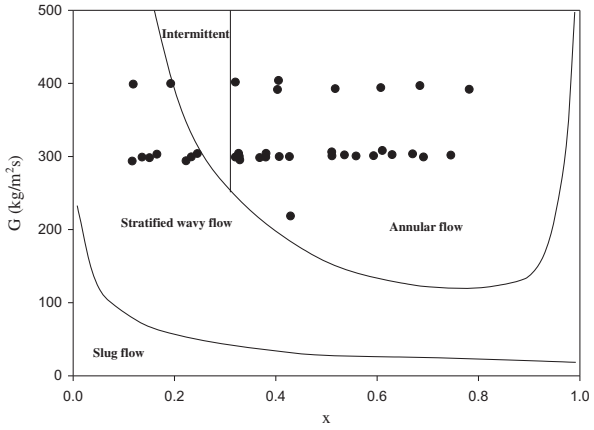

Fig. 6 – The present data plotted in smooth tube flow regime map of (Zurcher et al., 2002).

where A_i is the inside tube surface, LMTD is the logarithmic mean temperature difference.

$$LMTD = \frac{\Delta T_1 - \Delta T_2}{\ln\left(\frac{\Delta T_1}{\Delta T_2}\right)} \tag{9}$$

$$\Delta T_1 = T_{ref,in} - T_{w,out} \tag{10}$$

$$\Delta T_2 = T_{ref,out} - T_{w,in} \tag{11}$$

where $T_{w,in}$ and $T_{w,out}$ denote the inlet and outlet temperature of the water on the annulus. $T_{r,in}$ and $T_{r,out}$ are the inlet and outlet refrigerant temperature, respectively.

$$h_o A_o = \frac{Q_{TS}}{T_{w,avg} - T_{wall,avg}} \tag{12}$$

where A_o is outside tube surface, $T_{wall,avg}$ is average wall temperature and $T_{w,avg}$ is average water temperature.

The Nusselt number is calculated as:

$$Nu = \frac{hD_i}{k_l} \tag{13}$$

where k_l is thermal conductivity of liquid phase refrigerant.

3.4. *The frictional pressure drop (ΔP_f)*

The total pressure drop, ΔP_{total}, is expressed as the sum of the three different components, as follows:

$$\Delta P_{total} = \Delta P_f + \Delta P_a + \Delta P_g \tag{14}$$

The three terms on the right-hand side represent the frictional pressure drop (ΔP_f), acceleration pressure drop (ΔP_a) and gravitational pressure drop (ΔP_g), respectively. The gravitational pressure drop (ΔP_g) is zero in a horizontal tube. The acceleration pressure drop, ΔP_a, is proposed by Tran (1998):

$$\Delta P_a = G^2 \left(\left(\frac{x_{out}^2}{\rho_v \alpha_{out}} + \frac{(1 - x_{out})^2}{\rho_l (1 - \alpha_{out})} \right) - \left(\frac{x_{in}^2}{\rho_v \alpha_{in}} + \frac{(1 - x_{in})^2}{\rho_l (1 - \alpha_{in})} \right) \right) \tag{15}$$

where α is the void fraction and presented by Zivi's (1964) correlation as follows:

Author's personal copy

Table 3 – Existing correlations and standard deviation

Author	Correlation	Standard deviation (SD) %
Chaddock and Noerager (1966)	$h = 1.85h_{lo}((B_o \times 10^4) + 1.5(X_{tt}^{-\frac{2}{3}}))^{0.6}$	6.47
Uchida and Yamaguchi (1966)	$h = 17.5h_{lo}(B_o^{0.2})(X_{tt}^{-\frac{3}{5}})$	26.44
Wattelet and Shato (1990)	$h = \frac{2.9h_{lo}}{X_{tt}^{\frac{2}{3}}}$	37.39
Panek et al. (1992)	$h = \frac{2.9h_{lo}}{X_{tt}^{\frac{2}{3}}}$	31.23
Wongsa-ngam et al. (2002)	$h = 3.1737h_{lo}(B_o \times 10^4)^{0.4}X_{tt}^{-0.17}$	11.44

$h_{lo} = 0.023(\frac{GD_i}{\mu_l})^{0.8}Pr_l^{0.4}(\frac{k_l}{D_i})$
$B_o = \frac{q}{i_{fg}G}$
$X_{tt} = (\frac{1-x}{x})^{0.9}(\frac{\rho_v}{\rho_l})^{0.5}(\frac{\mu_l}{\mu_v})^{0.1}$

$$\alpha = \left(1 + \frac{(1-x)}{x}\left(\frac{\rho_v}{\rho_l}\right)^{\frac{2}{3}}\right)^{-1} \quad (16)$$

The frictional pressure drop, ΔP_f, can be obtained by subtracting the acceleration pressure drop from the total measured pressure drop.

The two-phase friction factor is defined in terms of an equivalent liquid mass flux (G_{eq}) proposed by Akers et al. (1959) as shown in Eq. (17).

$$f_{tp} = \frac{D_i \Delta P_f \rho_l}{2G_{eq}^2} \quad (17)$$

$$G_{eq} = G\left[(1-x) + x\left(\frac{\rho_l}{\rho_v}\right)^{0.5}\right] \quad (18)$$

3.5. *Equivalent Reynolds number (Re_{eq})*

The equivalent Reynolds number is defined as:

$$Re_{eq} = Re_l + Re_v\left(\frac{\mu_v}{\mu_l}\right)\left(\frac{\rho_l}{\rho_v}\right)^{0.5} \quad (19)$$

where Re_l is the liquid Reynolds number defined as:

$$Re_l = \frac{GD_i(1-x)}{\mu_l} \quad (20)$$

where Re_v is the vapour Reynolds number defined as:

$$Re_v = \frac{GD_i x}{\mu_v} \quad (21)$$

4. Results and discussion

4.1. *Flow pattern map for smooth tube*

Many researchers have attempted to visualise the flow pattern inside the tube in order to investigate the flow mechanism. Flow patterns have an important influence on prediction of the heat transfer coefficients and pressure drops of two-phase flow fluids. Normally, a flow pattern map is used to predict the flow pattern for studying two-phase flow phenomena and designing of two-phase equipment. In the present study, the data obtained from smooth tube is firstly plotted and compared with the flow pattern map established by Censi et al. (2003) and Zurcher et al. (2002). Fig. 5 displays the flow pattern map of R-134a in terms of the Lockhart–Martinelli parameter and the modified fluid velocity. The results also indicate that the data fall in the annular flow and stratified-wavy flow regimes, approximately 95 and 5%, respectively. Fig. 6 shows flow regime map of R-134a at saturation temperature of 4 °C, and heat flux of 5 kW/m^2 in term of mass flux and vapour quality. This result illustrated that around 80% of the data fall in the annular flow regime, 20% of the data fall in the stratified-wavy flow regime.

4.2. *Smooth tube*

As illustrated in Fig. 7, the experimental Nusselt number is compared with well-known correlations for predicting the

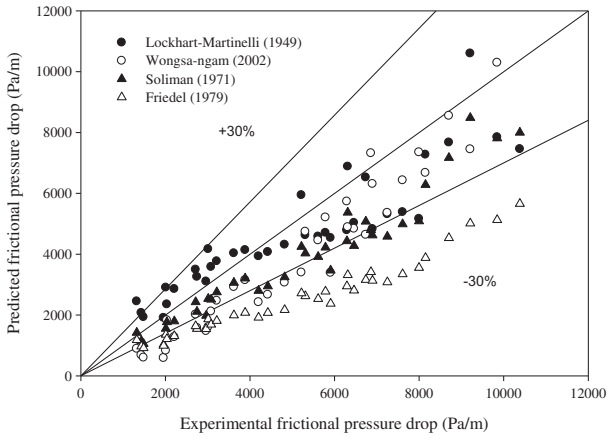

Fig. 8 – Comparison of the experimental frictional pressure drop with existing correlations for smooth tube.

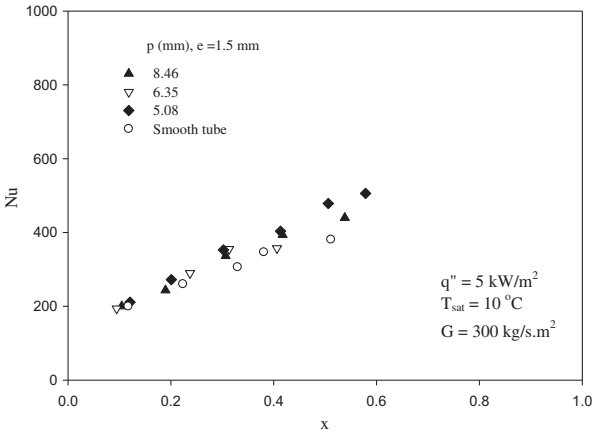

Fig. 9 – Nusselt number versus average quality at $T_{sat} = 10$ °C, $G = 300$ kg/m^{2}s and $q'' = 5$ kW/m^2.

Author's personal copy

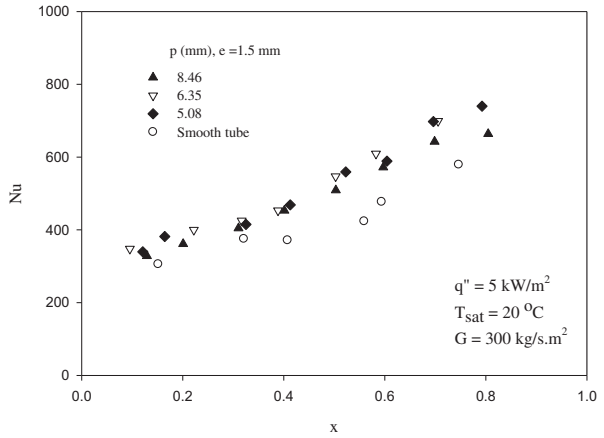

Fig. 10 – Nusselt number versus average quality at T_{sat} = 20 °C, G = 300 kg/m²s and q'' = 5 kW/m².

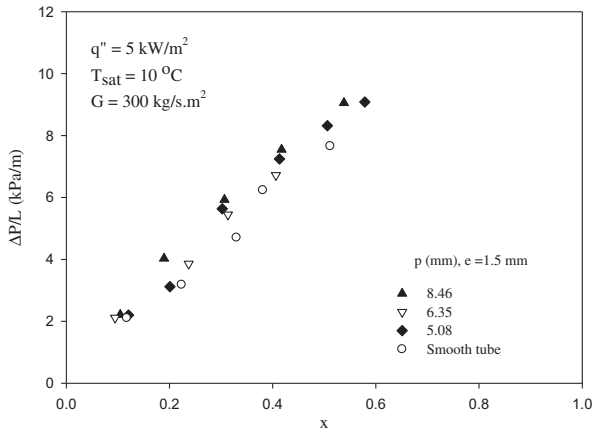

Fig. 12 – Pressure drop versus average quality at T_{sat} = 10 °C, G = 300 kg/m²s and q'' = 5 kW/m².

two-phase heat transfer performance such as Chaddock and Noerager (1966), Uchida and Yamaguchi (1966), Wattelet and Chato (1990), Panek et al. (1992) and Wongsa-ngam et al. (2002). Table 3 shows existing correlation and standard deviation. The smooth tube is tested at saturation temperatures of 10, 15 and 20 °C, heat fluxes of 5 and 10 kW/m² and mass fluxes between 200 and 500 kg/m²s. It is found that approximately 80% of the data are correlated within a deviation of ±30%. Moreover, the frictional pressure drop is also compared with established correlations which are proposed by Lockhart and Martinelli (1949), Wongsa-ngam et al. (2002), Soliman and Azer (1971) and Friedel (1979). Fig. 8 indicates that almost all correlations are in agreement with the present data within 30% except Friedel's (1979) correlation.

4.3. *Nusselt number*

Figs. 9 and 10 demonstrate the variation of the Nusselt number with average quality in the smooth and corrugated tube having different pitches of 5.08, 6.35 and 8.46 mm, respectively. The test condition consists of a mass flux of 300 kg/m²s, heat flux of 5 kW/m² and saturation temperatures of 10 and 20 °C, respectively. The results show that the Nusselt number increases with a rise in average vapour quality for smooth tube and corrugated tubes. This behaviour can be explained as follows. During evaporation, the liquid refrigerant boils and turns to vapour which has a higher specific volume than liquid. This situation leads to an increase in the velocity of the two-phase flow, which results in an increasing heat transfer coefficient. Moreover, as the average quality increases, the liquid film thickness decreases resulting in a decrease in the thermal resistance of the liquid film which is lead to more activity evaporation. Thus, a higher heat transfer coefficient is obtained.

Across the range of average quality, the Nusselt number of corrugated tubes is higher than that of the smooth tube at the same average quality. This is due to the fact that the corrugation of the surface increases mixing of the liquid film at the tube surface which leads to enhancement of the heat transfer and promotes instability in the refrigerant flow. Compared with the smooth tube, the maximum Nusselt number is obtained at 29% for a pitch of 5.08 mm, 28% for a pitch of 6.35 mm and 18% for a pitch of 8.46 mm. This behaviour is

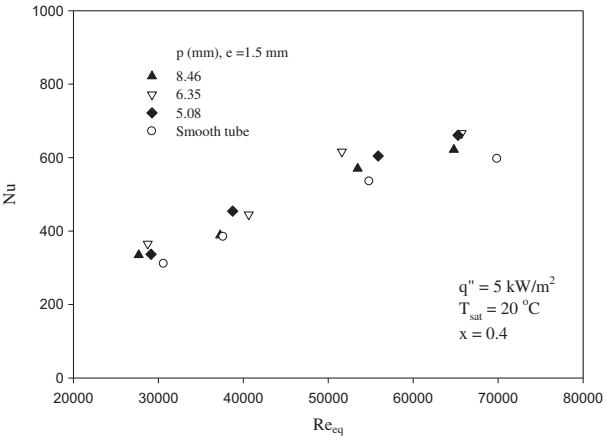

Fig. 11 – Nusselt number versus equivalent Reynolds number at T_{sat} = 20 °C, q'' = 5 kW/m² and x = 0.4.

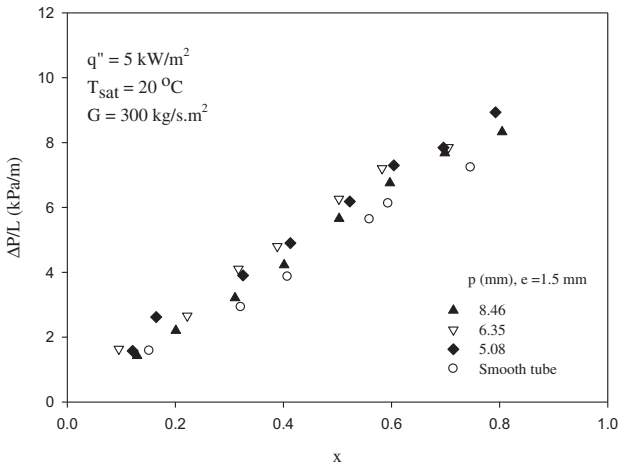

Fig. 13 – Pressure drop versus average quality at T_{sat} = 15 °C, G = 300 kg/m²s and q'' = 5 kW/m².

Author's personal copy

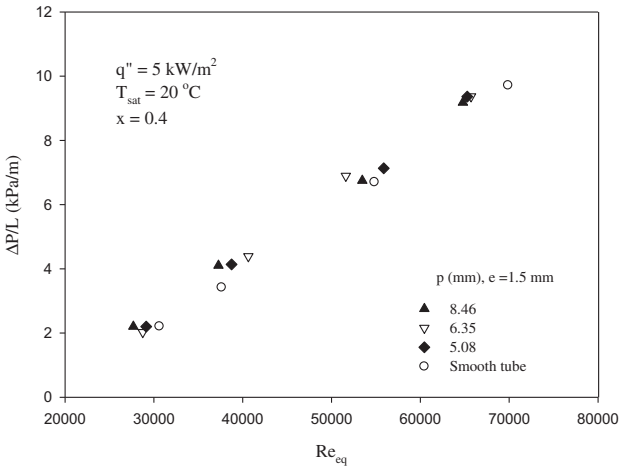

Fig. 14 – Pressure drop versus Reynolds number at $T_{sat} = 20\ ^{o}C$, $q'' = 5\ kW/m^2$ and $x = 0.4$.

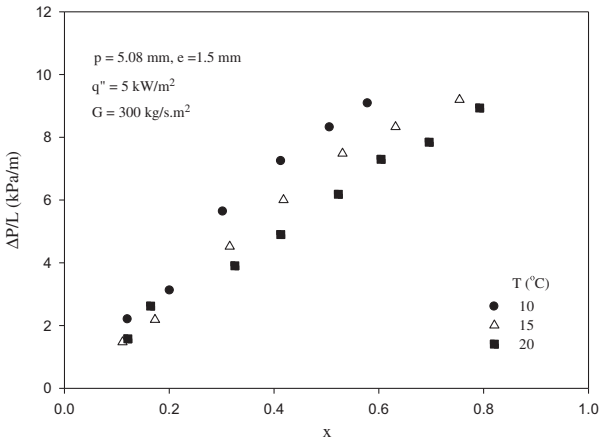

Fig. 16 – Effect of saturation temperature on pressure drop.

obtained at the testing condition of the saturation temperature of 20 °C, mass flux of 300 kg/m^{2}s and heat flux of 5 kW/m^2.

The effect of the pitch on Nusselt number is weak in the low average quality region, however, it becomes stronger at high average quality where the annular flow regime is achieved. This is because at low average quality the liquid film thickness is higher than the corrugation depth which causes the turbulence of refrigerant flow to be reduced. Therefore, the effect of corrugation pitch on Nusselt number obtained from the corrugated tube is insignificant in low average quality.

At higher average quality, the liquid film thickness is smaller than the corrugation depth, which is relatively efficient in an improvement of evaporation heat transfer. Nusselt number from a corrugated tube with a pitch of 5.08 mm is more pronounced than that from a corrugated tube with a pitch of 6.35 and 8.46 mm. This is because tube with lower corrugation pitch produces more turbulence of the refrigerant flow and increases more mixing at the thermal boundary layer which cause the effective heat transfer to be obtained. Therefore, the effect of corrugation pitch on Nusselt number of corrugated tube is significant in high average quality.

Fig. 11 displays the Nusselt number as a function of equivalent Reynolds number at a heat flux of 5 kW/m^2, saturation temperature of 20 °C and average vapour quality of 0.4. The results show that the Nusselt number increases with increasing equivalent Reynolds number. Similarly, the Nusselt numbers obtained from corrugated tubes are somewhat higher than those obtained from a smooth tube, which have been explained previously. The maximum Nusselt number of the corrugated tube is up to 17% higher than that in the smooth tube. Finally, the heat transfer correlation is done as shown in Eq. (22). This correlation is found that approximately 95% of the data are correlated within a deviation of ±20%.

$$Nu = 0.107 Re_{eq}^{0.735} Pr^{0.3} \left(\frac{e \cdot p}{D_i^2}\right)^{-0.1} \quad (22)$$

4.4. *Pressure drop*

Figs. 12 and 13 show the pressure drop plotted against average vapour quality. The pressure drops are obtained by dividing the measured pressure drop by the length of the test section between pressure taps. In this study, the length between pressure taps is 2.5 m while the length of the heat exchanger is

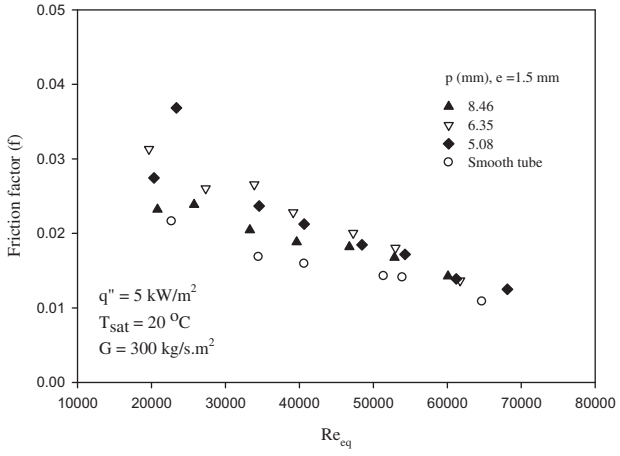

Fig. 15 – Friction factor versus equivalent Reynolds number at $T_{sat} = 20\ ^{o}C$, $q'' = 5\ kW/m^2$ and $G = 300\ kg/m^2\ s$.

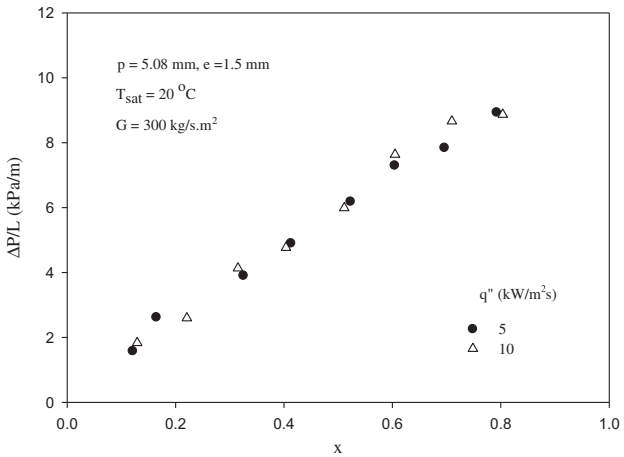

Fig. 17 – Effect of heat flux on pressure drop.

Author's personal copy

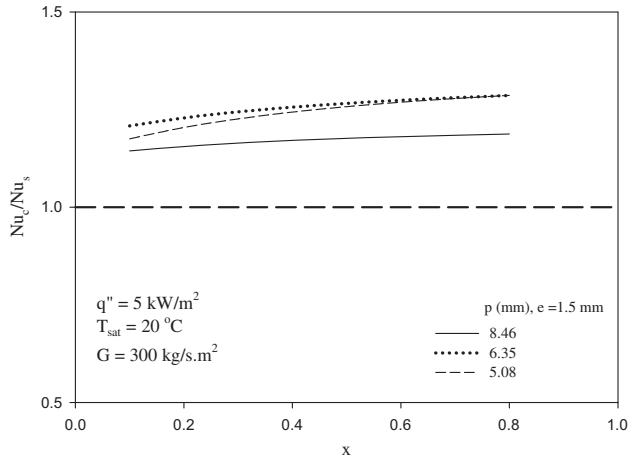

Fig. 18 – Heat transfer enhancement factor versus average quality at T_{sat} = 20 °C, G = 300 kg/m^{2}s and q'' = 5 kW/m^2.

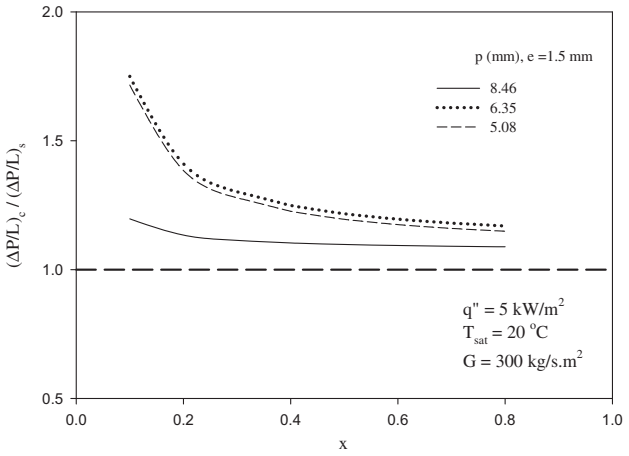

Fig. 19 – Pressure drop penalty factor versus average quality at T_{sat} = 20 °C, G = 300 kg/m^{2}s and q'' = 5 kW/m^2.

2 m. In the smooth tube and corrugated tubes, the increasing pressure drop depends on increasing the average vapour quality. At the same quality, the pressure drop obtained from the corrugated tube is clearly higher than that from a smooth tube. This is due to the fact that the corrugation surface has an effect simultaneously on axial velocity, secondary fluid motion and resulting swirl mixing. Comparing with the smooth tube, the maximum pressure drop is obtained from corrugated tubes up to about 1.75 times. This result is obtained at a saturation temperature of 20 °C, mass flux of 300 kg/m^{2}s and heat flux of 5 kW/m^2. Furthermore, the effect of corrugation pitch on pressure drop is insignificant.

Fig. 14 displays the variation of the pressure drop with equivalent Reynolds number in smooth and corrugated tubes at a heat flux of 5 kW/m^2, saturation temperature of 20 °C and average vapour quality of 0.4. The figure illustrates that the pressure drop increases with increasing mass flux. Similarly, the pressure drop obtained from the corrugated tube is relatively high compared with the smooth tube. However, the maximum pressure drop in the corrugated tube is up to 1.3 times higher than in the smooth tube. This can be explained similarly as mentioned above.

Fig. 15 shows friction factor versus equivalent Reynolds number at T_{sat} = 20 °C, q'' = 5 kW/m^2 and G = 300 kg/m^{2}s. The figure shows a very small dependence of the friction factor on Reynolds number. The present experimental data also show that the friction factors of smooth tube are about 0.01 and friction factors of corrugated tubes are between 0.01 and 0.015.

The effect of the evaporating temperature on the pressure drop is illustrated in Fig. 16. The results indicate that the pressure drop decrease with increasing evaporating temperature. This is mainly due to a decrease in two-phase specific volume which results in a decrease in velocity of the refrigerant. Fig. 17 shows the effect of heat flux on pressure drop. The result illustrates that the effect of heat flux on pressure drop is insignificant. Finally, the pressure drop obtained from the friction factor correlation is done as shown in Eq. (23). This correlation is found that approximately 95% of the data are correlated within a deviation of ±20%.

$$f_{tp} = 27.476 Re_{eq}^{-0.676} \left(\frac{e \cdot p}{D_i^2}\right)^{0.0122} \quad (23)$$

4.5. *Heat transfer enhancement factor (Nu_c/Nu_s)*

The heat transfer characteristics of corrugated tubes are presented in terms of the heat transfer enhancement factor (Nu_c/Nu_s) as shown in Fig. 18. The Nu_c parameter represents the Nusselt number obtained from the corrugated tube and Nu_srepresents the Nusselt number obtained from the smooth tube. The heat transfer enhancement factor is calculated by a linear regression analysis using a least squares method to determine the best-fitting straight line. The heat transfer enhancement ratio is calculated from the measured data in Fig. 10. The heat transfer enhancement ratio increases with increasing average vapour quality as shown in Fig. 10. This is due to the fact that, at lower average quality, the liquid film thickness is higher than the corrugation depth, not only does the liquid film become a thermal resistance but also turbulence effects can be reduced. On the other hand, at higher average vapour quality, the corrugation depth is higher than the liquid film thickness, the increase of heat transfer area and turbulence effects resulting from the increase of corrugation depth are relatively efficient at improving evaporation heat transfer. When the liquid film thickness is close to the corrugation depth, the periodic liquid wave cased by corrugated pitch produces an unstable liquid flow which maximises thermal efficiency and turbulent effects (Yun et al., 2002). The maximum heat transfer enhancement ratio obtained from experiments with a corrugated tube is around 1.3 times.

4.6. *Pressure drop penalty factor ($(\Delta P/L)_c/(\Delta P/L)_s$)*

The pressure drop characteristics of corrugated tubes are investigated in terms of the pressure drop penalty factor ($(\Delta P/L)_c/(\Delta P/L)_s$) as shown in Fig. 19. The ($(\Delta P/L)_c/(\Delta P/L)_s$) are defined in the same manner as Nu_c and Nu_s. The pressure drop penalty factor is calculated as well as the heat transfer enhancement factor. The pressure drop penalty factor is

Author's personal copy

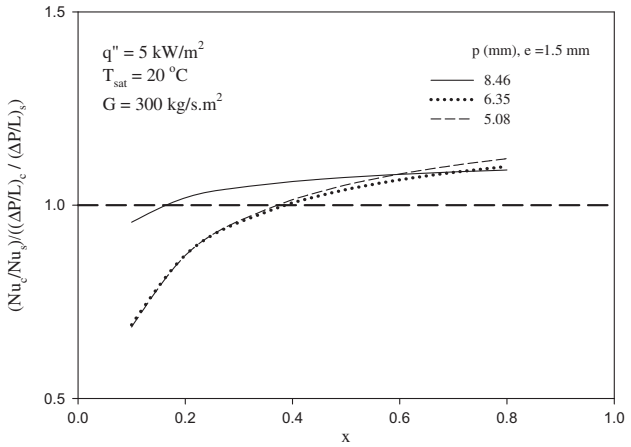

Fig. 20 – Ratio of heat transfer enhancement factor to pressure drop penalty factor with average quality at $T_{sat} = 20\ °C$, $G = 300\ kg/m^2s$ and $q'' = 5\ kW/m^2$.

determined from the measured data in Fig. 13. These figures show that the pressure drop penalty factor increases with decreasing average vapour quality as shown in Fig. 19. The maximum pressure drop penalty factor is around 1.75 times.

4.7. *Ratio of heat transfer enhancement factor to pressure drop penalty factor $(Nu_c/Nu_s)/((\Delta P/L)_c/(\Delta P/L)_s)$*

$(Nu_c/Nu_s)/((\Delta P/L)_c/(\Delta P/L)_s)$ is the ratio of heat transfer enhancement factor to pressure drop penalty factor under the same operating conditions as shown in Fig 20. In this figure, a ratio of $(Nu_c/Nu_s)/((\Delta P/L)_c/(\Delta P/L)_s)$ lower than 1 means a disadvantage and higher than 1 means an advantage. The results show that the maximum $(Nu_c/Nu_s)/((\Delta P/L)_c/(\Delta P/L)_s)$ is around 1.2. It is obtained for a corrugated tube with a corrugation pitch of 5.08 mm at $T_{sat} = 20\ °C$, $G = 300\ kg/m^2s$ and $q'' = 5\ kW/m^2$.

5. Conclusion

The evaporation heat transfer and flow characteristics of R-134a refrigerant flowing inside smooth and corrugated tubes are investigated by experiment. The test section is a tube-in-tube heat exchanger with refrigerant flowing in the inner tube and hot water flowing in the annulus. Three corrugated tubes having depths fixed at 1.5 mm and pitches of 5.08, 6.35 and 8.46 mm, respectively, are examined in this study. The data obtained from smooth tube are plotted and compared with the flow pattern map established by Censi et al. (2003) and Zurcher et al. (2002). The Nusselt number and pressure drop as a function of average vapour quality and equivalent Reynolds number are illustrated. It is found that the Nusselt number and pressure drop increase with increasing average vapour quality and equivalent Reynolds number. The Nusselt number and pressure drop obtained from corrugated tubes are higher than that in a smooth tube under all test conditions. The effect of corrugation pitch on Nusselt number is insignificant at low average quality. Moreover, the effect of corrugation pitches on pressure drop is insignificant for all tested conditions. The maximum (Nu_c/Nu_s), $((\Delta P/L)_c/(\Delta P/L)_s)$ and $(Nu_c/Nu_s)/((\Delta P/L)_c/(\Delta P/L)_s)$ ratios are approximately 1.3, 1.75 and 1.2, respectively.

Acknowledgements

The present study was supported financially by King Mongkut's University of Technology Thonburi, the Thailand Research Fund, the Office of the Higher Education Commission and the National Research University Project, whose guidance and assistance are gratefully acknowledged.

REFERENCES

Akers, W.W., Deans, H.A., Crasser, O.K., 1959. Condensing heat transfer within horizontal tubes, Chem. Eng. Prog. Symp 55, 171–176.

Barba, A., Rainieri, S., Spiga, M., 2002. Heat transfer enhancement in a corrugated tube. Int. Commun. Heat Mass Transfer 29, 313–322.

Censi G., Doretti L., Rossetto L., Zilio C., 2003. Flow pattern visualization during condensation of R134a inside horizontal microfin and smooth tubes. In: Proceedings of the International Congress of Refrigeration, Washington, DC, USA.

Chaddock, J.B., Noerager, J.A., 1966. Evaporation of refrigerant 12 in a horizontal tube with constant wall heat flux. ASHRAE Trans. 72, 90–101.

Dong, Y., Huixiong, L., Tingkuan, C., 2001. Pressure drop, heat transfer and performance of single-phase turbulent flow in spirally corrugated tubes. Exp. Therm. Fluid Sci. 24, 131–138.

Friedel, L., 1979. Improved friction pressure drop correlations for horizontal and vertical two-phase pipe flow. The European Two-Phase Flow Group Meeting, Paper E2, Ispra, Italy.

Lockhart, R.W., Martinelli, R.C., 1949. Proposed correlation of data for isothermal two-phase, two-component flow in pipes. Chem. Eng. Prog. 45, 39–48.

Nozu, S., Honda, H., Nakata, H., 1995a. Condensation of refrigerants CFC11 and CFC113 in the annulus of a double-tube coil with an enhanced inner tube. Exp. Therm. Fluid Sci. 11, 40–51.

Nozu, S., Honda, H., Nishida, S., 1995b. Condensation of a zeotropic CFC 114-CFC 113 refrigerant mixture in the annulus of a double-tube coil with an enhanced inner tube. Exp. Therm. Fluid Sci. 11, 364–371.

Panek, J.S., Chato, J.C., Jarbado, J.M.S., De Souza, A.L., Wattelet, J., 1992. Evaporation Heat Transfer and Pressure Drop in Ozone-safe Refrigerant and Refrigerant–oil Mixture. Air Conditioning and Refrigeration Center, University of Illinois at Urbana-Champaign.

Rainieri, S., Pagliarini, G., 2002. Convective heat transfer to temperature dependent property fluids in the entry region of corrugated tubes. Int. J. Heat Mass Transfer 45, 4525–4536.

Soliman, H.M., Azer, N.Z., 1971. Flow patterns during condensation inside a horizontal tube. ASHRAE Trans. 77, 210–224.

Targanski, T., Cieslinski, J.T., 2007. Evaporation of R407C/oil mixtures inside corrugated and micro-fin tubes. Appl. Therm. Eng 27, 2226–2232.

Tran TN., 1998. Pressure Drop and Heat Transfer Study of Two-phase Flow in Small Channels. Ph.D. Dissertation, Texas Tech University, Texas.

Uchida, H., Yamaguchi, S., 1966. Heat transfer in two-phase flow of refrigerant 12 through a horizontal tube. In: Proceeding of Third International Heat Transfer Conference, vol. 5, 69 pp.

Vicente, P.G., Garcia, A., Viedma, A., 2004a. Experimental investigation on heat transfer and friction factor characteristics of spirally corrugated tubes in turbulent flow at different Prandtl number. Int. J. Heat Mass Transfer 47, 671–681.

Author's personal copy

Vicente, P.G., Garcia, A., Viedma, A., 2004b. Mixed convection heat transfer and isothermal pressure drop in corrugated tubes for laminar and transition flow. Int. Commun. Heat Mass Transfer 31, 651–662.

Wattelet, J., Chato, J.C., 1990. Design, Building, and Baseline Testing of an Apparatus used to Measure Evaporation Characteristics of Ozone-safe Refrigerants. Air Conditioning and Refrigeration Center, University of Illinois at Urbana-Champaign. ACRC-TR-90-02.

Wongsa-ngam, J., Nualboonrueng, T., Wongwises, S., 2002. Performance of smooth and micro-fin tubes in high mass flux region of R-134a during evaporation. Heat Mass Transfer 10, 425–435.

Yun, R., Kim, Y., Seo, K., Kim, H.Y., 2002. A generalized correlation for evaporation heat transfer of refrigerants in micro-fin tubes. Int. J. Heat Mass Transfer 45, 2003–2010.

Zivi, S.M., 1964. Estimation of steady-state steam void-fraction by mean of the principle of minimum entropy production. Trans. ASME, J. Heat Transfer 86, 247–252.

Zimparov, V., 2001. Enhancement of heat transfer by a combination of three-start spirally corrugated tubes with a twisted tape. Int. J. Heat Mass Transfer 44, 551–574.

Zimparov, V., 2002. Enhancement of heat transfer by a combination of a single-start spirally corrugated tubes with a twisted tape. Exp. Therm. Fluid Sci. 25, 535–546.

Zimparov, V., 2004a. Prediction of friction factors and heat transfer coefficients for turbulent flow in corrugated tubes combined with twisted tape inserts. Part 1: friction factors. Int. J. Heat Mass Transfer 47, 589–599.

Zimparov, V., 2004b. Prediction of friction factors and heat transfer coefficients for turbulent flow in corrugated tubes combined with twisted tape inserts. Part 2: heat transfer coefficients. Int. J. Heat Mass Transfer 47, 385–393.

Zurcher, O., Favrat, D., Thome, J.R., 2002. Development of a diabatic two-phase flow pattern map for horizontal flow boiling. Int. J. Heat Mass Transfer 45, 291–301.

Provided for non-commercial research and education use.
Not for reproduction, distribution or commercial use.

This article appeared in a journal published by Elsevier. The attached copy is furnished to the author for internal non-commercial research and education use, including for instruction at the authors institution and sharing with colleagues.

Other uses, including reproduction and distribution, or selling or licensing copies, or posting to personal, institutional or third party websites are prohibited.

In most cases authors are permitted to post their version of the article (e.g. in Word or Tex form) to their personal website or institutional repository. Authors requiring further information regarding Elsevier's archiving and manuscript policies are encouraged to visit:

http://www.elsevier.com/copyright

Author's personal copy

International Journal of Heat and Mass Transfer 54 (2011) 1008–1014

Contents lists available at ScienceDirect

International Journal of Heat and Mass Transfer

journal homepage: www.elsevier.com/locate/ijhmt

Technical Note

Experimental analysis for the determination of the convective heat transfer coefficient by measuring pressure drop directly during annular condensation flow of R134a in a vertical smooth tube

A.S. Dalkilic [a,*], I. Teke [a], S. Wongwises [b,*]

[a] Heat and Thermodynamics Division, Department of Mechanical Engineering, Yildiz Technical University, Yildiz, Besiktas, Istanbul 34349, Turkey
[b] Fluid Mechanics, Thermal Engineering and Multiphase Flow Research Lab. (FUTURE), Department of Mechanical Engineering, King Mongkut's University of Technology Thonburi, Bangmod, Bangkok 10140, Thailand

ARTICLE INFO

Article history:
Received 3 March 2010
Received in revised form 6 September 2010
Accepted 6 September 2010
Available online 9 November 2010

Keywords:
Condensation
Two-phase pressure drop
Heat transfer coefficient
Vertical downward flow
R134a

ABSTRACT

This study investigated the direct relationship between the measured condensation pressure drop and convective heat transfer coefficient of R134a flowing downward inside a vertical smooth copper tube having an inner diameter of 8.1 mm and a length of 500 mm during annular flow. R134a and water were used as working fluids on the tube side and annular side of a double tube heat exchanger, respectively. Condensation experiments were performed at mass fluxes of 260, 300, 340, 400, 456 and 515 kg m^{-2} s^{-1} in the high mass flux region of R134a. The condensing temperatures were around 40 and 50 °C; the heat fluxes were between 10.16 and 66.61 kW m^{-2}. Paliwoda's analysis, which focused mainly on the determination of the two-phase flow factor and two-phase length of evaporators and condensers, was adapted to the in-tube condensation phenomena in the test section to determine the condensation heat transfer coefficient, heat flux, two-phase length and pressure drop experimentally by means of a large number of data points obtained under various experimental conditions.

© 2010 Elsevier Ltd. All rights reserved.

1. Introduction

Over the years, there are a large number of papers on the in-tube condensation heat transfer coefficient and pressure drop. The total pressure drop of two-phase flow in tubes is combination of the frictional, accelerational, and gravitational components. Determination of accelerational and gravitational components depends on the void fraction, and in a similar way, determination of either the two-phase friction factor or the two-phase frictional multiplier is required to compute the frictional component of pressure drop. Commonly, the computation of the condensation heat transfer coefficients in smooth tubes has been performed by empirical methods which are mostly the modifications of the Dittus–Boelter single-phase forced convection correlation [1], as in Akers et al. [2], Cavallini and Zecchin [3], and Shah [4].

The investigation of the characteristics of downward condensation heat transfer and pressure drop of refrigerants in small diameter vertical tubes has received relatively little interest in comparison to those in horizontal tubes. One of the most important flow pattern is annular two-phase flow which is characterized by a phase interface separating a thin liquid film from the gas flow in the core region. Two-phase annular flow occurs usually in the processes of film heating and cooling, mainly in power generation and especially in nuclear reactors. This flow pattern has taken the most notice, both analytically and experimentally regarding with its practical significance.

The aim of this work was to show the independence of an annular flow model from tube orientation and the general applicability for a relatively short vertical tube. Although convective heat transfer coefficient and pressure drop models and correlations have been extensively developed in the past, no attention has been paid to the determination of the convective heat transfer coefficient by direct measurement of the pressure drop. Experiments included a wide range of high mass fluxes with different saturation temperatures. Apart from the authors' previous publications [5–15], few studies exist in the literature on the investigation of heat transfer characteristics in a small diameter vertical tube during co-current downflow condensation. Furthermore, there is no study with the experimental parameters and content used here in the open literature. In this study, determination of the shear-dominated forced convective condensation heat transfer coefficients for refrigerant 134a is presented by means of Paliwoda's model [16], by relating the heat transfer to the pressure gradient depending mainly on the two-phase flow parameter during annular flow. In addition, the measured heat flux and two-phase length were validated by

* Corresponding authors. Tel.: +90 212 3832819; fax: +90 212 2616659 (A.S. Dalkilic), tel.: +66 2 470 9115; fax. +66 2 470 9111 (S. Wongwises).
E-mail addresses: dalkilic@yildiz.edu.tr (A.S. Dalkilic), somchai.won@kmutt.ac.th (S. Wongwises).

0017-9310/$ - see front matter © 2010 Elsevier Ltd. All rights reserved.
doi:10.1016/j.ijheatmasstransfer.2010.06.057

Author's personal copy

Nomenclature

A	inside surface area (m^{-2})
d	internal tube diameter (m)
f	friction coefficient
G	mass flux ($kg\,m^{-2}\,s^{-1}$)
h	heat transfer coefficient ($W\,m^{-2}\,K^{-1}$)
i_{fg}	latent heat of condensation ($J\,kg^{-1}$)
L	length of test tube (m)
m	mass flow rate ($kg\,s^{-1}$)
Re	Reynolds number
T	temperature (°C)
Q	heat transfer rate (W)
x	mean vapour quality
z	axial coordinate
ΔP	pressure drop (Pa)

Greek symbols

μ	dynamic viscosity ($kg\,m^{-1}\,s^{-1}$)
υ	specific volume ($m^3\,kg^{-1}$)
β	two-phase flow factor
θ	dimensionless ratio of liquid–vapour pressure gradient
ε	dimensionless two-phase parameter

Subscripts

exp	measured
F	frictional
g	gas/vapour
i	inlet
l	liquid
o	outlet
ph	preheater
ref	refrigerant
sat	saturation
TS	test section
w	water
wi	inner wall

means of a large number of data points obtained under various experimental conditions.

2. Experimental apparatus and method

The detailed information on the experimental apparatus and test section can be seen from authors' previous publications [5–13].

3. Data reduction and experimental uncertainty

The equations of data reduction section regarding the inlet vapour quality of the test section, the outlet vapour quality of the test section, the average heat transfer coefficient and uncertainty analysis can be obtained from authors' previous publications [5–13].

3.1. The average heat transfer coefficient

$$h_{exp} = \frac{Q_{TS}}{A_{wi}(T_{ref,sat} - T_{wi})} \tag{1}$$

where h_{exp} is the experimental average heat transfer coefficient, Q_{TS} is the heat transfer rate in the test section, T_{wi} is the average temperature of the inner wall, $T_{ref,sat}$ is the average saturation temperature of the refrigerant at the test section inlet and outlet, and A_{wi} is the inside surface area of the test section:

$$A_{wi} = \pi\, d L \tag{2}$$

4. Calculation procedure for the generalized two-phase model

According to Paliwoda [16], the pressure gradient of any two-phase flow depends on liquid and vapour phase gradients and the mixture quality of the liquid–vapour phases, and he used Müller-Steinhagen and Heck's correlation [17] in his analysis due to its simple mathematical form. This can be seen in Eq. (3), which has the minimum number of correlating parameters, for the prediction of a two-phase flow gradient as follows:

$$\frac{dP_F}{dL} = \left[\left(\frac{dP_F}{dL}\right)_l + 2\left\{\left(\frac{dP_F}{dL}\right)_g - \left(\frac{dP_F}{dL}\right)_l\right\}x\right](1-x)^{1/3} + \left(\frac{dP_F}{dL}\right)_g x^3 \tag{3}$$

where the Darcy–Weisbach equation is used to calculate the liquid phase gradient $\left(\frac{dP_F}{dL}\right)_l$ and the vapour phase gradient $\left(\frac{dP_F}{dL}\right)_g$ as follows:

$$\frac{dP_F}{dL} = f\frac{G^2\upsilon}{2d} \tag{4}$$

where the friction coefficient can be calculated by means of the Hagen-Poiseulle and Blasius equations according to the Reynolds numbers of the liquid or vapour as follows:

$$f = \frac{64}{Re} \quad \text{for } Re = \frac{Gd}{\mu} \leqslant 1187 \tag{5}$$

$$f = \frac{0.3164}{Re^{0.25}} \quad \text{for } Re = \frac{Gd}{\mu} > 1187 \tag{6}$$

Paliwoda [16] defined the two-phase flow factor (β) regarding the transformation of two-phase flow pressure gradients from any vapour phase pressure gradient at any temperature using mixture quality with the liquid–vapour pressure ratio parameter of θ. He paid attention to the validation range of his model developed for boiling and condensing refrigerants for a wide range of saturation temperatures. For that reason, he developed Müller-Steinhagen and Heck's correlation [17] due to its limited operating range of pressures. His two-phase flow factor can be seen in Eq. (7) as:

$$\beta = \frac{\left(\frac{dP_F}{dL}\right)}{\left(\frac{dP_F}{dL}\right)_g} \tag{7}$$

Eq. (7) is obtained by dividing both sides by the liquid phase gradient $\left(\frac{dP_F}{dL}\right)_l$ in Eq. (3), and is presented in Eq. (8) after some rearrangements as follows:

$$\beta = [\theta + 2(1-\theta)x](1-x)^{1/3} + x^3 \tag{8}$$

where the dimensionless ratio of the liquid–vapour pressure gradient (θ) can be calculated by means of the Hagen-Poiseulle and Blasius equations according to the Reynolds numbers of liquid or vapour as follows:

$$\theta = \frac{64}{0.3164}\frac{\mu_l}{\mu_g^{0.25}}\frac{\upsilon_l}{\upsilon_g}(Gd)^{-0.75} \quad \text{for } Re_l \leqslant 1187 \text{ and } Re_g > 1187 \tag{9}$$

$$\theta = \frac{\upsilon_l}{\upsilon_g}\left(\frac{\mu_l}{\mu_g}\right)^{0.25} \quad \text{for } Re_l > 1187 \text{ and } Re_g > 1187 \tag{10}$$

Author's personal copy

Paliwoda [16] presented the flow resistance (ΔP) taking place over the tube length (ΔL), in the following form:

$$\frac{\Delta P}{\Delta L} = \beta\left(\frac{dP_F}{dL}\right)_g \tag{11}$$

Eq. (12) is obtained from the combination of Eqs. (4) and (6) as follows:

$$\left(\frac{\Delta P}{\Delta L}\right)_g = \frac{0.3164}{2} G^{1.75} \upsilon_g \mu_g^{0.25} d^{-1.25} \tag{12}$$

Mass flux (G) can be calculated from the evaporator heat balance as follows:

$$G = \frac{4}{\pi}\frac{Q_o}{r(x_o - x_i)d^2} = 1.23\frac{qA_oL}{i_{fg}(x_o - x_i)d^2} \tag{13}$$

Rearrangement of Eqs. (12) and (13) with Eq. (11) gives the actual pressure drop (ΔP) over a straight horizontal tube of length (ΔL) = L as follows:

$$\Delta P = 0.2414\varepsilon_{\Delta P(b)}\left(\frac{qA_o}{i_{fg}}\right)^{1.75}\upsilon_g\mu_g^{0.25}d^{-4.75}L^{2.75} \tag{14}$$

where the dimensionless two-phase parameter ($\varepsilon_{\Delta P(b)}$) is determined as follows:

$$\varepsilon_{\Delta P(b)} = \frac{\beta}{(x_o - x_i)^{1.75}} \tag{15}$$

The expression "two-phase length" proposed by Paliwoda [16] refers to that part of the evaporator or condenser in which two-phase flow takes place. It is obtained by rearranging Eq. (14):

$$\frac{L}{d} = 1.675\varepsilon_{L(b)}\left(\frac{i_{fg}}{qA_o}\right)^{0.636}\mu_g^{-0.096}d^{0.727}\left(\frac{\Delta P}{\upsilon_g}\right)^{0.364} \tag{16}$$

where the dimensionless two-phase parameter ($\varepsilon_{\Delta P(b)}$) is determined as follows:

$$\varepsilon_{L(b)} = \frac{(x_o - x_i)^{0.636}}{\beta^{0.364}} \tag{17}$$

It should be noted that the mean heat flux in Eqs. (14) and (16) is taken as shown in Eq. (18) to calculate the pressure drop, and ($x_i - x_o$) is used instead of ($x_o - x_i$) shown in Eqs. (15) and (17) to adapt Paliwoda's model [16] to the in-tube condensation:

$$q = \frac{Q_{TS}}{A_{wi}} \tag{18}$$

The tube unit length external heat transfer area in Eqs. (14) and (16) is calculated as follows:

$$A_o = \frac{A_{wi}}{L} \tag{19}$$

In spite of their negligible effect on the results, the liquid and vapour Reynolds numbers for the condensation process are calculated respectively as follows:

$$Re_l = \frac{Gd(1-x)}{\mu_l} \tag{20}$$

$$Re_g = \frac{Gdx}{\mu_g} \tag{21}$$

The heat flux transferred from the inner tube (R134a) to the annulus (cooling water) is determined from the model as follows:

$$q_{model} = \frac{\left(\dfrac{\Delta P}{0.2414\left\{\frac{[(\theta+2(1-\theta)x](1-x)^{1/3}+x^3\}}{(x_i-x_o)^{1.75}}\right\}\upsilon_g\mu_g^{0.25}d^{-4.75}L^{2.75}}\right)^{1/1.75}}{\left(\frac{A_o}{i_{fg}}\right)} \tag{22}$$

The convective heat transfer coefficient of the model is determined by means of Eqs. (1) and (14) as follows:

$$h_{model} = \frac{\left(\dfrac{\Delta P}{0.2414\left\{\frac{[(\theta+2(1-\theta)x](1-x)^{1/3}+x^3\}}{(x_i-x_o)^{1.75}}\right\}\upsilon_g\mu_g^{0.25}d^{-4.75}L^{2.75}}\right)^{1/1.75}}{\left(\frac{A_o(T_{ref,sat}-T_{wi})}{i_{fg}}\right)} \tag{23}$$

It should also be noted that the derivation of all equations above and additional information on the model, proposed as a universal method of pressure drop and horizontal tube length calculation with boiling and condensing refrigerants, can be seen in Paliwoda [16]. In addition, there are also some alternative equations for the two-phase parameter (ε) for different types of evaporators and condensers listed in his paper. In this paper, only correlations that were consistent with the authors' experimental data were used in the model for the adaptation of the annular flow of the in-tube condensation process.

5. Results and discussion

The main concern of the present study is to adapt Paliwoda's [16] generalized two-phase model to the annular downward condensation flow of R134a in a vertical round tube with an inner diameter of 8.1 mm and to investigate the direct relationship between pressure drop and the convective heat transfer coefficient. Pure HFC-134a was used in the experiments.

Comparisons of the pressure drop calculated from the model (Eq. (14)) and the measured pressure drop are shown in Fig. 1a and b. It can be seen from these figures that all of the measured data falls within ±30% of the proposed correlation (Eq. (14)) for all the mass fluxes (260, 300, 340, 400, 456, 515 kg m^{-2} s^{-1}) and saturation temperatures (40 and 50 °C) of R134a respectively. It should be noted that the measured heat flux in Eq. (18) was used to determine the pressure drop value from Eq. (14). Fig. 1 shows the change in the measured pressure drop with various mass fluxes of R134a for the condensation temperatures of 40–50 °C at various temperature differences. Due to the increase in shear stress at the interface of the phases, the total measured pressure drop increases with increasing mass fluxes. Hence, heat flux increases with increasing condensation rate, and the vapour quality decreases; as a result, the pressure drop is decreased.

Table 1 illustrates the maximum and minimum error rates for the determination of the two-phase length between the calculated value (Eq. (16)) and the actual tube length (L = 0.5 m). It can be seen from the table that all of the measured data falls within ±10% of the proposed correlation (Eq. (16)) for all mass fluxes (260, 300, 340, 400, 456, 515 kg m^{-2} s^{-1}) and saturation temperatures (40 and 50 °C) of R134a respectively. It should be noted that the experimental heat flux in Eq. (18) and measured pressure drop were used to determine the two-phase length value from Eq. (16).

Fig. 2a and b shows the comparison of measured heat flux (Eq. (18)) with the calculated flux (Eq. (14)) during condensation in the test tube at saturation temperatures of 40–50 °C for all mass fluxes of 260, 300, 340, 400, 456 and 515 kg m^{-2} s^{-1} respectively within a 15% deviation line. It should be noted that the measured pressure drop was used to determine the heat flux value from Eq. (22).

Comparisons of the proposed condensation heat transfer coefficient correlation in Eq. (23) and experimental heat transfer correlation in Eq. (1) are shown in Fig. 3a and b. It can be seen that all

Author's personal copy

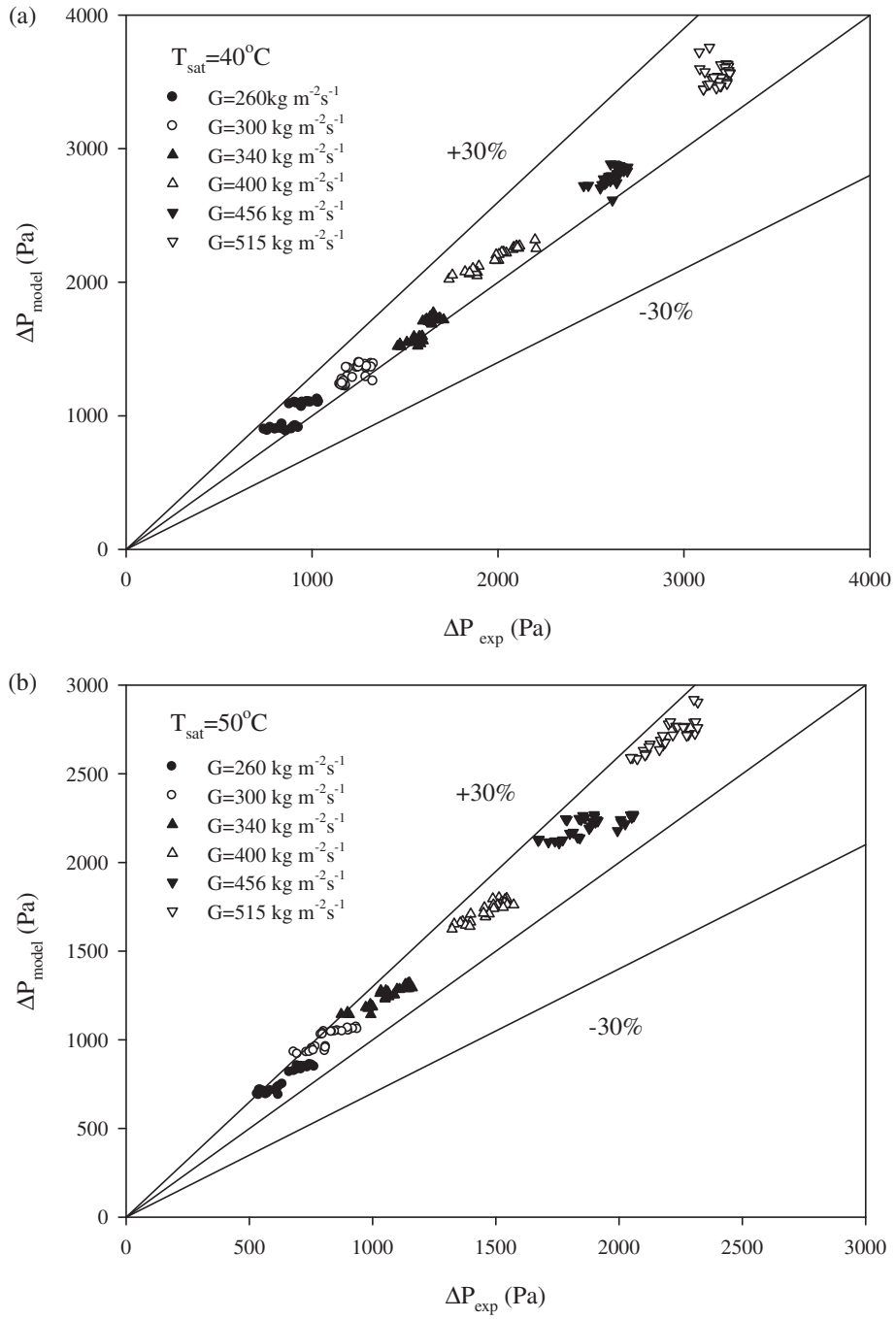

Fig. 1. Comparison of measured and calculated (Eq. (20)) pressure drops for all mass flux of R134a at T_{sat} = 40 °C (a) and 50 °C (b).

Table 1
Maximum and minimum error rates for the determination of two-phase length between the calculated one (Eq. (22)) and actual tube length (L = 0.5 m).

$T_{ref,sat}$ = 40 °C		$T_{ref,sat}$ = 50 °C	
Mass flux (kg m^{-2} s^{-1})	Error rate range (%)	Mass flux (kg m^{-2} s^{-1})	Error band range (%)
260	−6.34 to 0.94	260	−9.28 to −3.27
300	−4.58 to 2.31	300	−10.34 to −3.88
340	−2.13 to 1.45	340	−9.03 to −3.49
400	−5.22 to 0.39	400	−7.21 to −3.66
456	−3.21 to 0.39	456	−7.99 to −2.79
515	−6.26 to −2.33	515	−7.81 to −5.5

of the measured data falls within ±15% of the proposed correlation (Eq. (23)) for all the mass fluxes (260, 300, 340, 400, 456, 515 kg m^{-2} s^{-1}) and saturation temperatures (40 and 50 °C) of R134a respectively. It should be noted that the temperature difference between the saturated temperature of the vapour and the inlet wall temperature of the tube and measured pressure drop was used to determine the convective heat transfer coefficient value from Eq. (23). Fig. 3a and b also shows the effect of mass flux on the average condensation heat transfer coefficient with a temperature difference of pure R-134a during condensation in the test tube at saturation temperatures of 40–50 °C for all mass fluxes in the database. These figures show that the heat transfer coefficient decreases with decreasing mass flux. This is due to the increase in

Author's personal copy

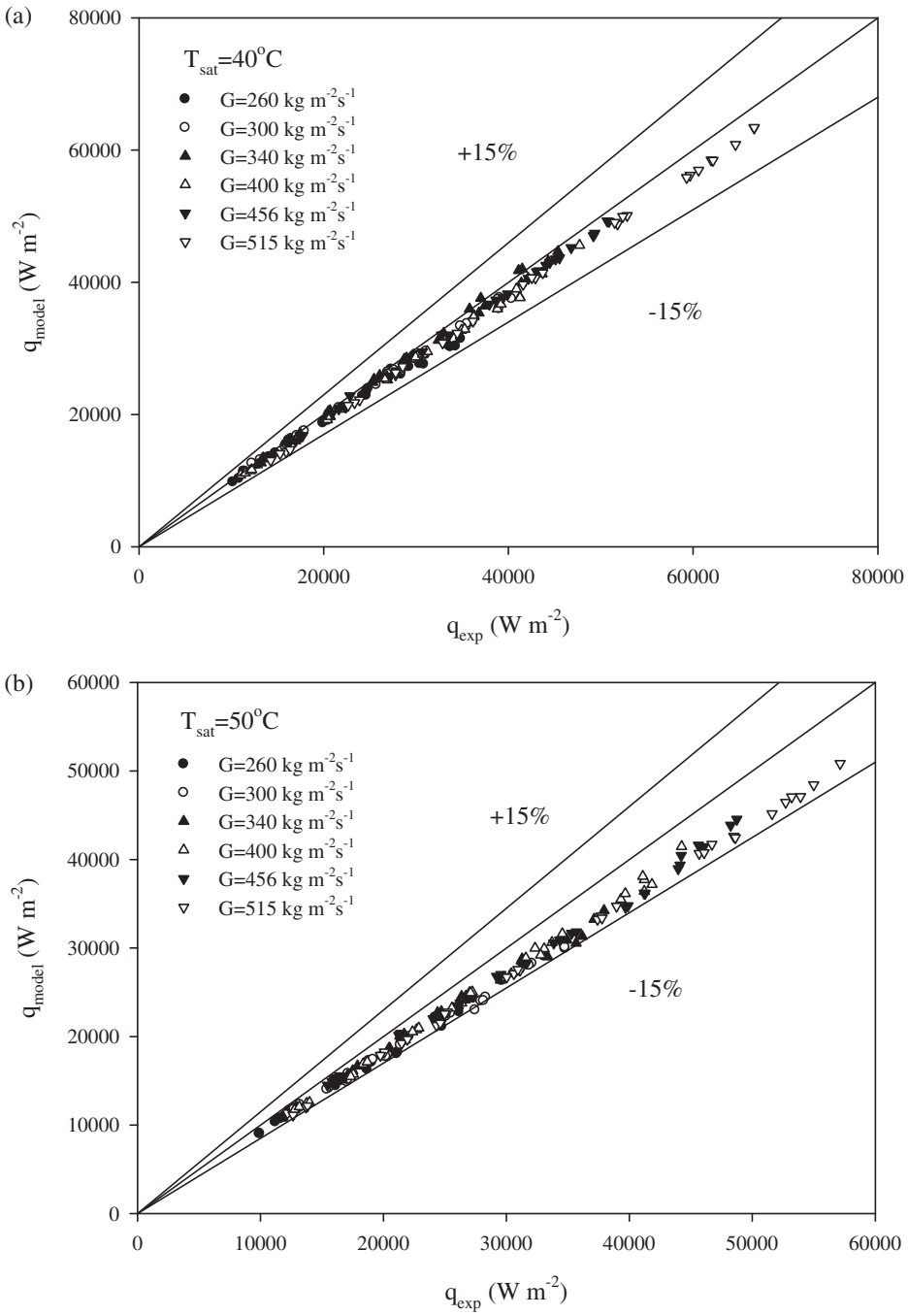

Fig. 2. Comparison of experimental (Eq. (18)) and calculated (Eq. (22)) heat fluxes for all mass flux of R134a at T_{sat} = 40 °C (a) and 50 °C (b).

the vapour velocity of R134a. In addition to this, it can be seen that the average condensation heat transfer coefficient of R134a decreases with increasing condensation temperature difference as explained in the authors' previous publications.

All results described above show that the calculated pressure drop, two-phase length, heat flux and convective heat transfer coefficient calculated by means of the improved Paliwoda model [16] are consistent with experimental data in spite of the different operating conditions and tube orientation in the original model.

6. Conclusions

The experimental investigation of co-current downward condensation heat transfer and pressure drop of R134a were performed in an 8.1 mm i.d. vertical smooth tube. Accurate and repeatable heat transfer data were obtained. In the literature, there is not much knowledge related with the studied cases' parameters and content. Therefore, this investigation's results are anticipated to complete a space in the literature. The studied annular flow model and correlation was validated using 380 data points. The conclusions were obtained as follows:

1. Paliwoda's [14] generalized two-phase model was successfully adapted to the in-tube condensation phenomenon. The adopted model predicts the two-phase length of the test section, measured pressure drop, heat flux from the test tube to the annulus and condensation heat transfer coefficient within the limits of reasonable deviation.

Author's personal copy

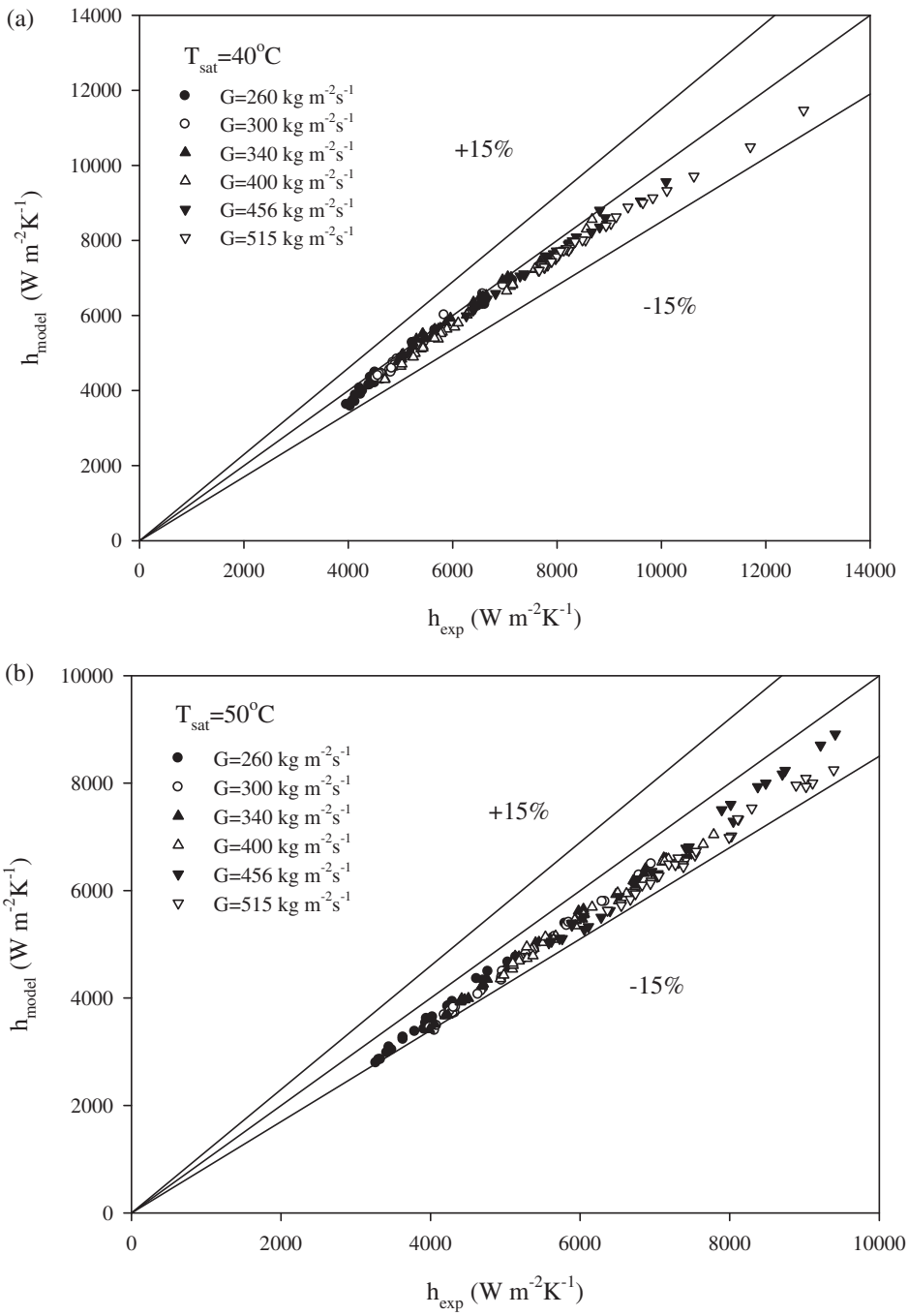

Fig. 3. Comparison of experimental (Eq. (1)) and calculated (Eq. (23)) heat transfer coefficients for all mass flux of R134a at T_{sat} = 40 °C (a) and 50 °C (b).

2. It should be noted that the original Paliwoda's [14] model without any correction factor is developed successfully for prediction analysis in the paper. The results also show that his model is adaptable to two-phase flows accurately.
3. The independency of the annular flow model on the tube orientation model is shown in the paper. It should be noted that an annular flow pattern exists along the tube length during experiments. The improved annular flow model of Paliwoda [14] is capable of predicting the condensation heat transfer coefficients inside the test tube within the deviation limit of ±30%.
4. It should be also noted that the valid range of the proposed correlation is still limited in spite of the usage of a large number of annular flow data in the high mass region of R134a condensing in a relatively short vertical tube.

Acknowledgements

The authors are indebted to the King Mongkut's University of Technology Thonburi (KMUTT), and the Thailand Research Fund, the Commission of Higher Education and the National Research University Project for supporting this study. Especially, the first author wishes to thank KMUTT for providing him with a post-doctoral fellowship.

References

[1] F.W. Dittus, L.M.E. Boelter, Engineering Publication, vol. 2, University of California, 1930, p. 443.
[2] W.W. Akers, H.A. Deans, O.K. Crosser, Condensation heat transfer within horizontal tubes, in: Chemical Engineering Progress Symposium Series, vol. 55, 1959, pp. 171–176.

Author's personal copy

[3] A. Cavallini, R. Zecchin, A dimensionless correlation for heat transfer in forced convection condensation, in: Proceedings of the Sixth International Heat Transfer Conference, vol. 3, 1974, pp. 309–313.
[4] M.M. Shah, A general correlation for heat transfer during film condensation inside pipes, Int. J. Heat Mass Transfer 22 (1979) 547–556.
[5] A.S. Dalkilic, O. Agra, I. Teke, S. Wongwises, Comparison of frictional pressure drop models during annular flow condensation of R600a in a horizontal tube at low mass flux and of R134a in a vertical tube at high mass flux, Int. J. Heat Mass Transfer 53 (2010) 2052–2064.
[6] A.S. Dalkilic, S. Laohalertdecha, S. Wongwises, Two-phase friction factor in vertical downward flow in high mass flux region of refrigerant HFC-134a during condensation, Int. Commun. Heat Mass Transfer 35 (2008) 1147–1152.
[7] A.S. Dalkilic, S. Laohalertdecha, S. Wongwises, Experimental investigation of heat transfer coefficient of R134a during condensation in vertical downward flow at high mass flux in a smooth tube, Int. Commun. Heat Mass Transfer 36 (2009) 1036–1043.
[8] A.S. Dalkilic, S. Yildiz, S. Wongwises, Experimental investigation of convective heat transfer coefficient during downward laminar flow condensation of R134a in a vertical smooth tube, Int. J. Heat Mass Transfer 52 (2009) 142–150.
[9] A.S. Dalkilic, S. Laohalertdecha, S. Wongwises, Effect of void fraction models on the two-phase friction factor of R134a during condensation in vertical downward flow in a smooth tube, Int. Commun. Heat Mass Transfer 35 (2008) 921–927.
[10] A.S. Dalkilic, S. Laohalertdecha, S. Wongwises, Effect of void fraction models on the film thickness of R134a during downward condensation in a vertical smooth tube, Int. Commun. Heat Mass Transfer 36 (2009) 172–179.
[11] A.S. Dalkilic, S. Wongwises, An investigation of a model of the flow pattern transition mechanism in relation to the identification of annular flow of R134a in a vertical tube using various void fraction models and flow regime maps, Exp. Thermal Fluid Sci. 34 (2010) 2052–2064.
[12] A.S. Dalkilic, S. Wongwises, Experimental study on the modeling of condensation heat transfer coefficients in high mass flux region of refrigerant HFC-134a inside the vertical smooth tube in annular flow regime, Heat Transfer Eng. 32 (2011) 33–44.
[13] A.S. Dalkilic, S. Wongwises, Intensive literature review of condensation inside smooth and enhanced tubes, Int. J. Heat Mass Transfer 52 (2009) 3409–3426.
[14] A.S. Dalkilic, S. Laohalertdecha, S. Wongwises, Validation of void fraction models and correlations using a flow pattern transition mechanism model in relation to the identification of annular vertical downflow in-tube condensation of R134a, Int. Commun. Heat Mass Transfer 37 (2010) 827–834.
[15] A.S. Dalkilic, S. Laohalertdecha, S. Wongwises, New experimental approach on the determination of condensation heat transfer coefficient using frictional pressure drop and void fraction models in a vertical tube, Energy Convers. Manage. 51 (2010) 2535–2547.
[16] A. Paliwoda, Generalized method of pressure drop and tube length calculation with boiling and condensing refrigerants within the entire zone of saturation, Int. J. Refrig. 12 (1989) 314–322.
[17] H. Müller-Steinhagen, K.A. Heck, A simple friction pressure drop correlation for two-phase flow in pipes, Chem. Eng. Prog. 20 (1986) 297–308.

Experimental Thermal and Fluid Science 35 (2011) 347–354

Contents lists available at ScienceDirect

Experimental Thermal and Fluid Science

journal homepage: www.elsevier.com/locate/etfs

Choked flow mechanism of HFC-134a flowing through short-tube orifices

Kitti Nilpueng, Somchai Wongwises *

Fluid Mechanics, Thermal Engineering and Multiphase Flow Research Lab (FUTURE), Department of Mechanical Engineering, King Mongkut's University of Technology Thonburi, Bangmod, Bangkok 10140, Thailand

ARTICLE INFO

Article history:
Received 10 July 2010
Received in revised form 30 September 2010
Accepted 12 October 2010

Keywords:
Refrigerant
Vapour-compression refrigeration system
Two-phase flow
Critical mass flow rate

ABSTRACT

This paper is a continuation of the author's previous work. New experimental data on the occurrence of choked flow phenomenon and mass flow rate of HFC-134a inside short-tube orifices under choked flow condition are presented. Short-tube orifices diameters ranging from 0.406 mm to 0.686 mm with lengths ranging from 1 mm to 3 mm which can be applied to a miniature vapour-compression refrigeration system are examined. The experimental results indicated that the occurrence of choked flow phenomena inside short-tube orifices is different from that obtained from short-tube orifice diameters of greater than 1 mm, which are typically used in air-conditioner. The beginning of choked flow is dependent on the downstream pressure, degree of subcooling, and length-to-diameter ratio. Under choked flow condition, the mass flow rate is greatly varied with the short-tube orifice dimension, but it is slightly affected by the operating conditions. A correlation of mass flow rate through short-tube orifices is proposed in terms of the dimensionless parameters. The predicted results show good agreement with experimental data with a mean deviation of 4.69%.

© 2010 Elsevier Inc. All rights reserved.

1. Introduction

During the past decade, two-phase gas–liquid flows through small channels have been encountered in a wide variety of applications including medical devices, high heat-flux compact heat exchangers, and cooling systems for various types of equipment, such as high performance micro-electronics, supercomputers, and high-power lasers. For two-phase flow inside small channels, it found that the flow characteristics strongly depend on surface tension in addition to viscosity and inertia forces. As a result, the flow behaviour inside channels is different from that in channels of ordinary size [1]. In order to achieve optimum design and process control of small systems, a comprehensive understanding of flow and heat transfer characteristics inside small channels is very necessary.

An expansion device is an important component in the basic elements of a refrigeration system. The purpose of the expansion device is to reduce the pressure of the refrigerant from the condenser pressure to the evaporator pressure and to regulate the mass flow rate of refrigerant flowing from the condenser to the evaporator. During the flow of liquid refrigerant through the expansion device, pressure is rapidly decreased below the saturation pressure and the refrigerant is changed from subcooled liquid or saturated liquid to liquid–vapour mixture. This phase-change mechanism is described as a flashing process. The short-tube orifice is one type of expansion device popularly used in residential and automotive air-conditioning systems. Its simplicity, low initial cost, high reliability, and ease of maintenance are the main reasons for its use. Normally, the diameters of short-tube orifices which is utilized the normal air-conditioner are larger than or close to 1 mm. However, in the recent years, a miniature vapour-compression refrigeration system has been developed and applied for the cooling of high power components in computers and several electronic devices such as power supplies, microprocessors, integrated circuits, and microcontrollers [2,3]. Some of these miniature systems will employ the smaller diameter short-tube orifices being studied and reported herein. In order to obtain appropriate operation and performance of systems, the flow of refrigerant inside the short-tube orifice should be choked flow [4]. Under this condition, the flow of refrigerant through the short-tube orifice corresponds to the critical flow rate, which is the maximum flow rate that can be attained by reducing the downstream pressure under given upstream conditions. Therefore, the comprehensive knowledge of the appearance of choked flow phenomena and the critical flow rate that can be produced at a given operating conditions is useful for designing of the miniature refrigeration system.

In the past, studies associated with performance characteristics of short-tube orifices have been conducted by a number of researchers. Early experimental investigations on flashing flow inside short-tube orifices focused exclusively on CFC-12 and HCFC-22 [4–8]. Pasqua [5] examined the flow characteristics of subcooled and saturated liquid CFC-12 through glass short-tube

* Corresponding author. Tel.: +66 2 470 9115; fax: +66 2 470 9111.
E-mail address: somchai.won@kmutt.ac.th (S. Wongwises).

0894-1777/$ - see front matter © 2010 Elsevier Inc. All rights reserved.
doi:10.1016/j.expthermflusci.2010.10.004

Nomenclature

A	cross section area of short-tube orifice, m^2
C	discharge coefficient
L	length, m
D	diameter, m
$\dot{m}$	mass flow rate, kg/s
P	pressure, Pa
T_c	critical temperature, K
ΔT_{sub}	degree of subcooling, K

Greek symbols

ρ	density, kg/m^3
β	short-tube orifice diameter to the tube diameter ratio
μ	viscosity, Pa s

Subscripts

down	downstream
f	saturated liquid
g	saturated vapour
meas	measurement
pred	prediction
sat	saturation
up	upstream

orifices with length-to-diameter ratios ranging between 4 and 24. He discovered that flashing of liquid refrigerant appeared inside the short-tube orifices when the downstream pressure was near or below the saturation pressure. His mass flow rate data indicated that, after the first-stage choking, the flow rate is increased and is insensitive by changing the pressure difference between upstream and downstream. Under this condition, the flow is defined as second-stage choking. Mei [6] experimentally studied the flow of subcooled liquid HCFC-22 through short tubes with $7.5 < L/D < 11.9$. He reported that first-stage choking occurred at the degree of subcooling of 22.2 °C. However, there was no indication of second-stage choking in the normal heat pump operating range. Aaron and Domanski [7] observed the flow characteristics, including flow pattern, mass flow rate, and pressure distribution of subcooled liquid HCFC-22 inside short tubes with $5 < L/D < 20$. The flow indicated a very weak dependence upon the downstream pressure within a normal heat pump operating range. Kim [4] experimentally investigated the flow of two-phase and subcooled HCFC-22 through short-tube orifices with length-to-diameter ratios ranging between 7 and 20. The results showed that the mass flow rate was dependent on upstream pressure and upstream subcooling, but that it was insensitive to downstream pressure due to approximate choking. Kim et al. [8] experimentally investigated the flow of HCFC-22 through flexible short-tube orifices. They stated that the flexible short-tube orifice provided better control of air-conditioning systems than the conventional fixed short-tube orifice, but the flow control with the flexible short-tube orifice was not as good as with a thermal expansion valve. Kim et al. [8] experimentally investigated the flow of HCFC-22 through flexible short-tube orifices. They stated that the flexible short-tube orifice provided better control of air-conditioning systems than the conventional fixed short-tube orifice, but the flow control with the flexible short-tube orifice was not as good as with a thermal expansion valve.

Due to environmental concerns about the depletion of the ozone layer and global warming, CFC and HCFC refrigerants were replaced by the alternative refrigerants. Therefore, several researchers concentrated on HFC-134a, HFC-407C, R744, and HFC-410A [4,9–14]. Kim [4] experimentally investigated the flow of two-phase and subcooled HFC-134a through short-tube orifices with diameter ranging between 1.09 and 1.72 mm. For two-phase flow entering the short tube, he noticed that the mass flow rate decreased with increases in the dryness fraction. The flow characteristics of HFC-407C through short-tube orifices with diameters of 1.09–1.94 mm were studied by Payne and O'Neal [9]. They found that the addition of oil into refrigerant increased the mass flow rate by more than 12% for a two-phase flow entering the short tube but had little effect on mass flow rate at a high degree of subcooling. Singh et al. [10] presented experimental data on refrigerant HFC-134a flow through short-tube orifices with and without inlet and outlet screens. The experimental results indicated that the inlet and outlet screens had an insignificant effect on the mass flow rate. Liu et al. [11] explored the characteristics of R744 flow through short-tube orifices. The experimental results showed that choked flow existed under a wide range of operating conditions. They reported that the inlet and outlet chamfer depths had no apparent effects on the mass flow rate. Kim et al. [12] examined the mass flow rate of HFC-410A through short-tube orifices at upstream pressures approaching the critical point. They found that the decrease in mass flow rate with a reduction in subcooling became more significant when upstream pressure increased beyond 3604 kPa, due to a greater density change. Tu et al. [13] presented the experimental results of HFC-134a flowing through orifices with diameters of 31.0 and 52.0 μm. The experimental results indicated that flow was not choked, even when the downstream pressure was reduced to more than 400 kPa below the saturation pressure for liquid-upstream/two-phase-downstream flow. Nilpueng and Wongwises [14] experimentally investigated the two-phase flow characteristics of HFC-134a, including flow pattern, mass flow rate, pressure distribution, and temperature distribution through short-tube orifices. The results indicated that metastable flow and choked flow phenomena exist inside short-tube orifices over the whole range of experimental conditions.

To predict the mass flow rate of two-phase refrigerant flow through short-tube orifices, several procedures were generated by many researchers. Most previous researchers have developed short-tube orifice flow models based on a single-phase orifice equation [15]. The single-phase orifice equation is expressed as follows:

$$\dot{m} = CA\sqrt{\frac{2\rho(P_{up} - P_{down})}{(1-\beta^4)}} \quad (1)$$

where C is the discharge coefficient, A is the cross-sectional area of a short-tube orifice, ρ is the upstream density of fluid, P_{up} is upstream pressure, P_{down} is downstream pressure, and β is the ratio of the orifice diameter to the upstream tube diameter. The proposed correlation which is included in the single-phase orifice equation can be divided into two groups. The first group is the orifice constant correlation (C). This correlation was generated as a function of relevant parameters such as degree of subcooling, pressure difference between upstream and downstream, length-to-diameter ratio, and downstream vapour quality [5,6,13]. The other group is downstream pressure correlation. The upstream pressure, downstream pressure, upstream temperature, diameter and length-to-diameter ratio were included in the downstream pressure correlation [4,7,8,11]. A few researchers proposed a generalized correlation for predicting the mass flow rate of two-phase flow of alternative refrigerant through short-tube orifices [16]. The correlation is

presented in a power law form of dimensionless parameters. Dimensionless parameters are generated by using the Buckingham Pi theorem.

As mentioned above, it can be noted that most of the previous works studied two-phase flow characteristics inside the short-tube orifice diameter of greater than 1 mm which is normally used in residential and mobile air-conditioner. Only a few researchers focused on the short-tube orifice of less than 1 mm, which can be applied to a miniature vapour-compression refrigeration system. In addition, there remains room for further research, in particular, detailed investigations of the occurrence of choked flow, which has a significant effect on the flow behaviour inside a short-tube orifice. This paper is the third in a series and is a continuation of the authors' previous work. The main aim of the present study is to observe the occurrence of choked flow and study the effects of relevant parameters, e.g. upstream pressure, degree of subcooling, short-tube orifice diameter, and short-tube orifice length on the mass flow rate inside short-tube orifices diameter of less than 1 mm under choked flow condition. A mass flow rate correlation which is formed in the power law pattern of a dimensionless parameter is also proposed.

2. Experimental apparatus

In this experiment, a vapour-compression refrigeration system which use the short-tube orifice as expansion device is established and illustrated in Fig. 1. A detailed description of the experimental setup can be seen in Nilpueng and Wongwises [14]. It consists of the main refrigeration system components: compressor, condenser, short-tube orifice (test section) and evaporator, and other accessory parts. A commercial HFC-134a is used as the working fluid. A two-cylinder single stage reciprocating compressor, driven by an electric motor, is used to discharge the refrigerant. The speed of the motor is varied so as to provide a wide range of mass flow rates by means of an inverter. Compact plate heat exchangers are used as condenser, evaporator, and subcooler.

The hot water (heat load) is supplied from the hot water tank to pass through the flow meter and the evaporator by the circulating pump. The downstream pressure of the test section is controlled by adjusting the temperature and the flow rate of hot water. The condenser rejects heat to the water coming from a cold water tank. The upstream pressure of the test section is regulated by adjusting the temperature of cold water. The degree of subcooling of refrigerant entering the test section is set by varying the flow rate of water to the subcooler. The upstream pressures are set at 1000, 1100, and 1200 kPa, while downstream pressures are varied between 320 and 480 kPa. The degree of subcooling is varied from 8 to 22.1 °C. T-type thermocouples were used to measure fluid temperature. The uncertainty of the temperature measurement was ±0.1 °C. The differential pressure transducer had an accuracy of ±0.1% of its calibrated span. The flow rate of refrigerant through the short-tube orifice was measured by a coriolis mass flow meter (ABB FCM2000) with an accuracy of ±0.25%.

Fig. 2 shows a schematic diagram of the test section. It consists of a brass connector, o-ring rubber, short-tube orifice, and attachment set. The o-ring rubbers are inserted between the brass connector and the short-tube orifice in order to give protection from refrigerant leakage. The short-tube orifice is supported by an attachment set to resist the high pressure. The copper tube is connected to the brass connector by soft soldering. Two points of pressure and temperature taps are drilled to 0.5 mm at upstream and downstream of short-tube orifice. In order to avoid the disturbance in the flow field, as shown in Fig. 2, the thermocouples are inserted into the temperature taps having a 0.5 mm diameter hole. The thermocouples are insulated with a 6.4 mm thick Aeroflex standard sheet to reduce the effect of heat transfer on the measurement errors. The short-tube orifice's diameter is drilled by using a wire cutting machine. Table 1 lists the short-tube orifices used in this study. A microscope (Olympus BX51) is used to measure the diameter of the short-tube orifice. The length of the short tube is measured with a digital calliper. The accuracies of diameter and length measurements are ±0.001 mm and ±0.01 mm, respectively.

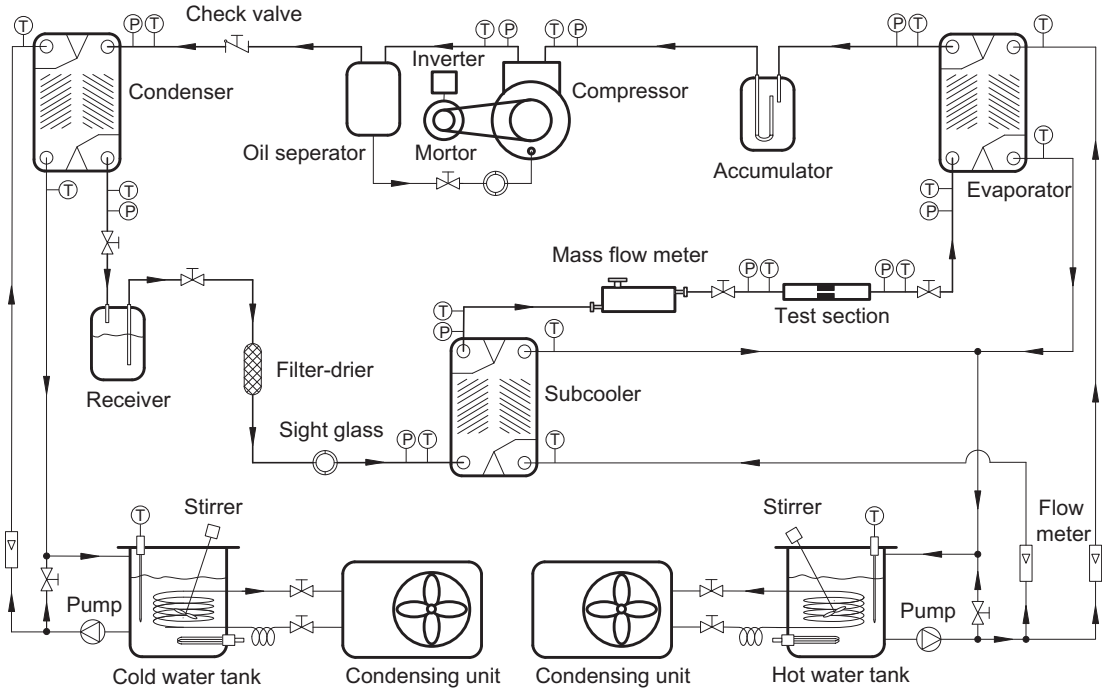

Fig. 1. Schematic diagram of test facility.

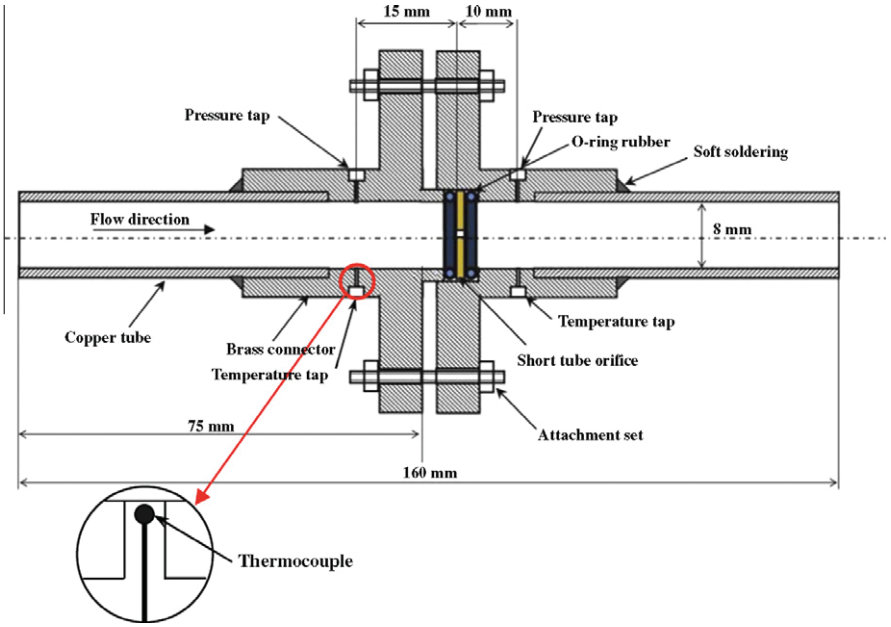

Fig. 2. Schematic diagram of test section.

Table 1
Dimension of the short-tube orifices.

Short tube	Diameter (mm)	Length (mm)	*L*/*D*
1	0.424	1	2.36
2	0.412	2	4.85
3	0.406	3	7.38
4	0.474	1	2.11
5	0.443	2	4.51
6	0.462	3	6.49
7	0.686	1	1.46
8	0.686	2	2.91
9	0.685	3	4.37

3. Results and discussion

3.1. The occurrence of choked flow phenomena inside short-tube orifices

Choked flow is a limiting condition which occurs when the mass flow rate of fluid inside the channel does not increase with reductions in the downstream pressure under given upstream conditions. Under this condition, the refrigerant flow through the short-tube orifice corresponds to the maximum flow rate. Therefore, the flow of refrigerant inside the short-tube orifice should be choked flow in order to achieve an appropriate operation and performance of refrigeration systems [4]. In this section, the effect of relevant parameters on the occurrence of choked flow inside the short-tube orifices is examined.

In this experiment, the relationship between the mass flow rate and downstream pressure inside short-tube orifices is used to verify the existence of choked flow phenomenon. As shown in Fig. 3, it is found that the measured mass flow rate inside the short-tube orifice can be divided into two different flow regions as depicted by the dash line. In the first region, the mass flow rate of refrigerant increases proportionally with the downstream pressure. In the second region, the trend is still the same but the variation in flow rate is little affected by the downstream pressure. It is found to increase by about 2.37%. This may be because the refrigerant velocity is suddenly increased when the liquid refrigerant is changed into a liquid–vapour mixture inside short-tube orifice. As a result, the

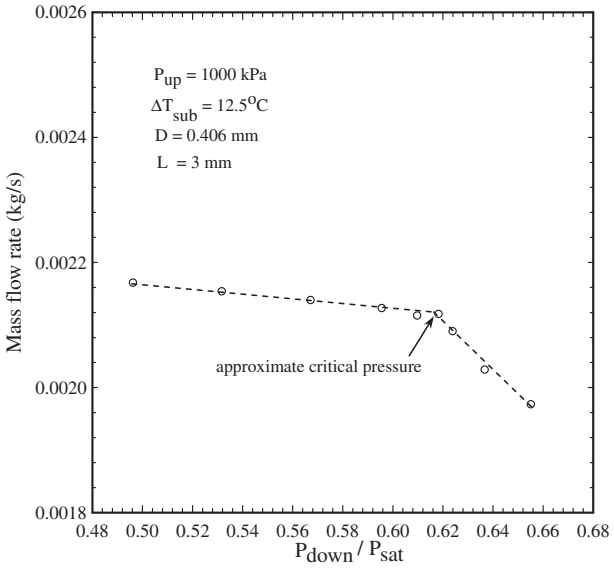

Fig. 3. Effect of downstream pressure on mass flow rate inside the short-tube orifice.

refrigerant velocity at the exit plane approaches to sonic velocity. This flow mechanism is similar to choked flow phenomenon for compressible fluid flowing through a converging nozzle and a straight pipe (Fanno and Rayleigh flows). Moreover, it is found that the beginning of choked flow inside the short-tube orifice is appeared at the ratio of downstream pressure to saturation pressure corresponding to the upstream temperature (P_{down}/P_{sat}) of 0.62.

In order to verify the effect of length-to-diameter ratio on the occurrence of choked flow, the experiment is performed at the entire general operating condition (P_{up} = 1000–1200 kPa, ΔT_{sub} = 8–16 °C and P_{down} = 320–480 kPa). The effect of downstream pressure on the mass flow rate at different length-to-diameter ratio is typically plotted in Fig. 4. It is found that at the length-to-diameter ratio ranging from 1.46 to 4.37, the critical pressure slightly decreases and two different flow behaviours appears as the

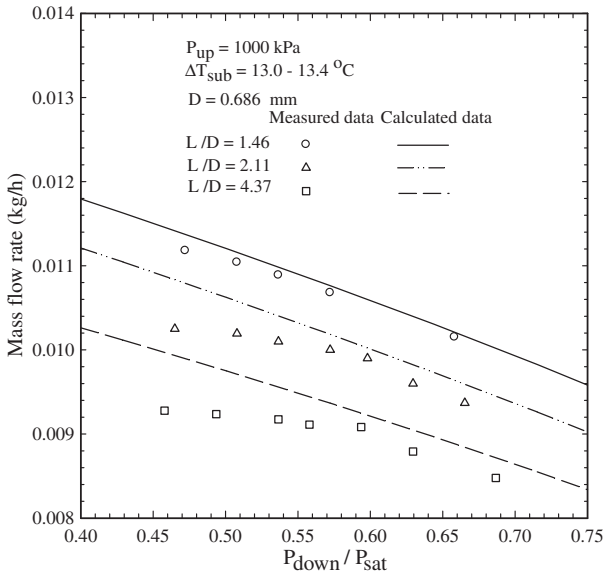

Fig. 4. Effect of downstream pressure on mass flow rate at different length-to-diameter ratio.

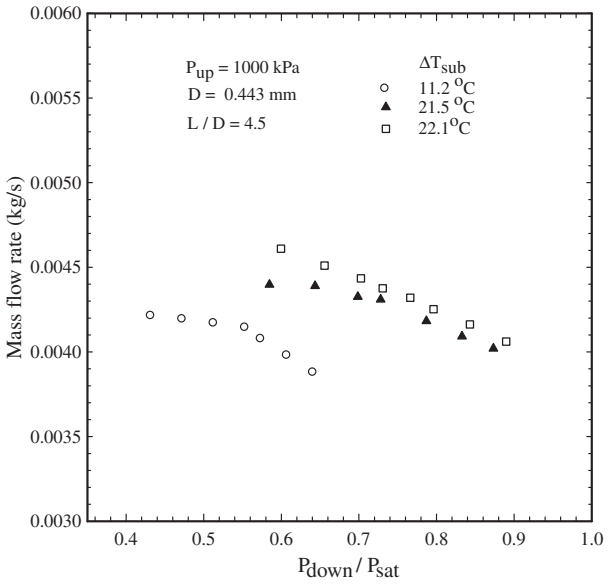

Fig. 5. Effect of downstream pressure on mass flow rate at different degree of subcooling.

length-to-diameter ratio is reduced. It is also found that the data tend to change the shape at low downstream pressure. At a length-to-diameter ratio of less than 2.11, the flow rate increased monotonically with the decrease in downstream pressure. At a length-to-diameter ratio of more than 2.11, when the downstream pressure decreased, the flow rate increased proportionally over a short length and remained almost constant thereafter. As shown in this figure, it also found that the measured mass flow rate is compared with the predicted mass flow rate which is calculated from the single-phase orifice equation. The results show good agreement at length-to-diameter ratios of less than 2.11. However, the trend of measured data diverges from that of calculated data at length-to-diameter ratios of more than 2.11. These results are consistent with the results of Nilpueng and Wongwises [17] which is examined at the short-tube diameter ranging between 0.605 mm and 1.2 mm. The present results imply that the flow of refrigerant does not choke at length-to-diameter ratios of less than 2.11, but the choked flow phenomenon is appeared at length-to-diameter ratios of higher than 2.11. This is because at small length-to-diameter ratio, the accelerational pressure drop due to sudden contraction and frictional pressure drop may not be high enough for flashing of the metastable liquid inside the short-tube orifice which results in the existence of liquid refrigerant inside the orifice and the disappearance of choked flow.

The effect of degree of subcooling at the length-to-diameter ratio of above 2.11 under the normal upstream and downstream pressure on the onset of choked flow is investigated. The data shown in Fig. 5 are used to represent the data from all experiments. It can be seen that the mass flow rate increased proportionally and remained almost constant thereafter as the downstream pressure was decreased at degrees of subcooling below 21.5 °C. On the other hand, it is increased monotonically with the decreasing the downstream pressure at a degree of subcooling above 21.5 °C. The results showed that the flow behaviour is similar to that obtained from Fig. 4. Consequently, it can be concluded that the choked flow disappeared inside the short-tube orifice when degrees of subcooling is higher than 21.5 °C. This may be because the saturation temperature of refrigerant decreases with increasing degree of subcooling. Similarly, the metastable liquid length inside short-tube orifice is extended as degree of subcooling is increased. These two impacts lead to the existence of liquid refrigerant inside the short-tube orifice. As a result, Mach number of refrigerant at the exit plane is less than one and the choked flow does not occur inside short-tube orifice.

As mentioned above, it can be seen from Figs. 3–5 that at the short-tube orifice ranging between 0.406 mm and 0.686 mm and the length-to-diameter ratio ranging between 2.11 and 7.38, the beginning of choked flow appeared at the ratio of downstream pressure to saturation pressure corresponding to the upstream temperature (P_{down}/P_{sat}) ranging between 0.53 and 0.72. However, based on the diameter size above 1 mm, the ratio of length-to-diameter ranging between 5 and 20, the same refrigerant and similar experimental conditions, Kim [4] summarized that the choked flow occurred when the downstream pressure is closed to saturation pressure ($P_{down}/P_{sat} \approx 1$). Therefore, it may be noted that the ratio of downstream pressure to saturation pressure corresponding to upstream temperature of refrigerant tend to reduce when the short-tube diameter is smaller. Based on the experimental results obtained from the previous researchers [13,17], it is found that the metastable liquid length inside the short-tube orifice increases as the short-tube orifice diameter decreases. This means that the vapourization of refrigerant is delayed with reducing of the diameter. Therefore, the flashing may not be able to be initiated at saturation pressure corresponding to upstream temperature in smaller short-tube orifice.

3.2. Mass flow rate

Under choked flow condition, although the mass flow rate is insensitive to the downstream pressure, it is varied with changing the upstream pressure, degree of subcooling, short-tube orifice diameter, and short-tube orifice length. In this section, the influence of relevant parameters on the mass flow rate is examined.

As shown in Fig. 6, the mass flow rate is nearly constant as the degree of subcooling is varied. However, based on the linear curve fitting for all diameters and upstream pressure, it is found that the mass flow rate increases by about 1.8–4.3% with increases in the degree of subcooling ranging from 8 °C to 15 °C. This is because the density of the refrigerant is increased when increasing the degree of subcooling, which results in an increase of the mass flow rate.

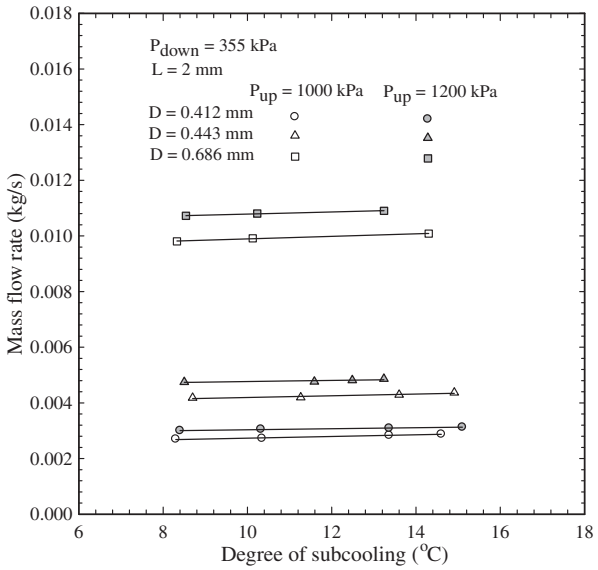

Fig. 6. Effect of degree of subcooling on mass flow rate.

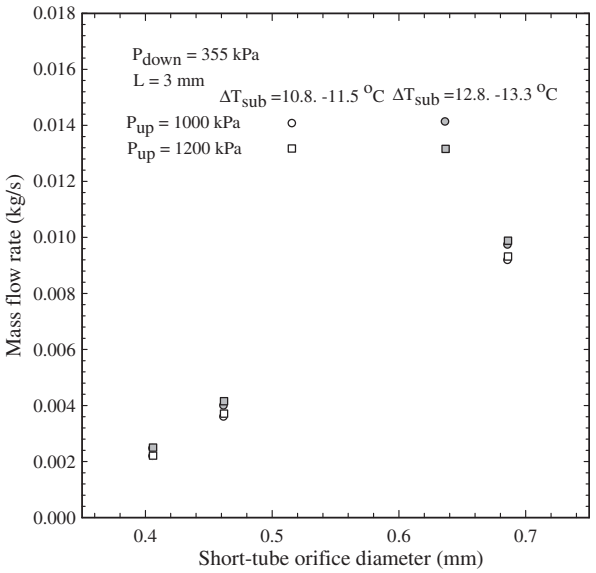

Fig. 8. Effect of short-tube orifice diameter on mass flow rate.

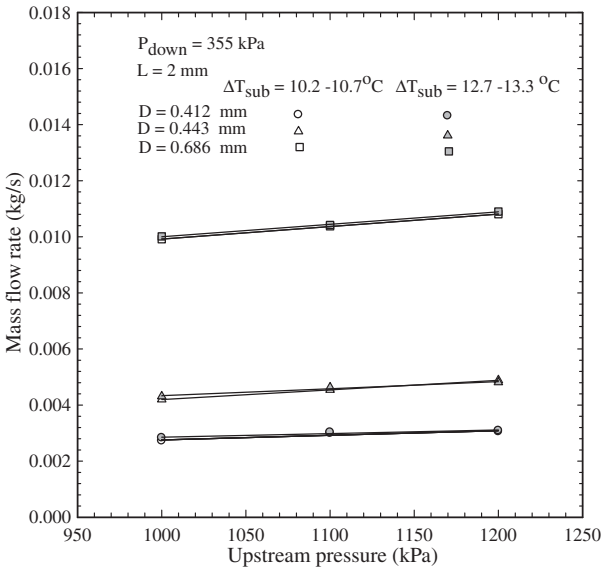

Fig. 7. Effect of upstream pressure on mass flow rate.

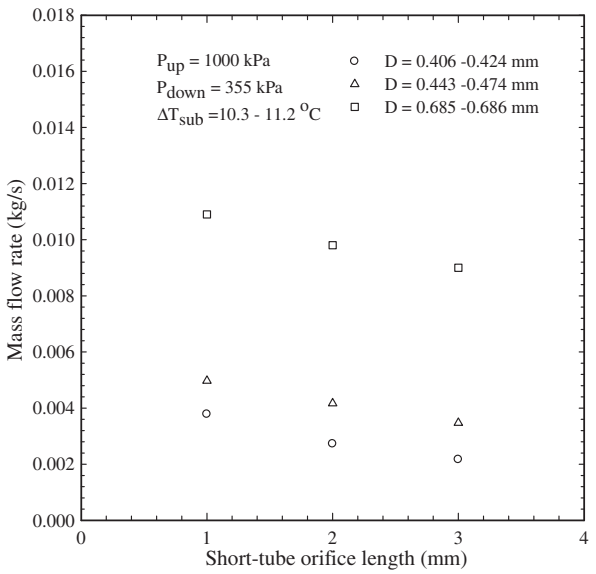

Fig. 9. Effect of short-tube orifice length on mass flow rate.

Fig. 7 shows the relationship between mass flow rate and upstream pressure at different short-tube orifice diameters. Based on the linear curve fitting for all diameters and degree of subcooling, it can be seen that the flow rate increases with the upstream pressure. The flow rate increases by about 8.5–11% as upstream pressure is varied between 1000 kPa and 1200 kPa. This can be attributed to the increment of the difference between upstream pressure and downstream pressure which lead to the augmentation of refrigerant velocity inside short-tube orifices. Moreover, it is noticed that the steepness of data is slightly higher when the short-tube orifice diameter increases.

The impacts of short-tube orifice diameter and length on the mass flow rate are shown in Figs. 8 and 9. As expected, the mass flow rate is increased with increasing the diameter and it is reduced when the length extended. The increase of short-tube orifice diameter leads to an increase of mass flow rate by about 25.91 kg/s/m. It is also found that the extension of short-tube orifice length causes a decrease of mass flow rate by about 0.88 kg/s/m. This is because the friction between the refrigerant and the tube wall increases when the short-tube length increases which produce the reduction of refrigerant velocity and mass flow rate inside the short-tube orifice.

3.3. Mass flow rate correlation

For predicting the mass flow rate through the short-tube orifice, a correlation is generated by using the dimensional analysis [12]. The relevant parameters which are used for this analysis consist of three groups: operating parameters, short-tube orifice geometry, and refrigerant property. For the operating parameters group, the upstream pressure (P_{up}), degree of subcooling (ΔT_{sub}) and the subcooled liquid pressure difference (P_{up}–P_{sat}) which has a significant effect on the mass flow rate [7] are considered. However, the downstream pressure is excluded because the correlation is developed under the choked flow conditions. In addition, to non-dimensionalize the degree of subcooling, the critical temperature

(T_c) is included. The short-tube orifice diameter (D) and short-tube orifice length (L) are used to indicate the effect of short-tube orifice geometry. Because the mass flow rate strongly depends on the upstream density and the friction inside the short-tube orifice, the viscosity and density of refrigerant liquid and vapour are included into the refrigerant property group. The refrigerant properties are evaluated at the saturation temperature. A list of the parameters associated with mass flow rate could be established in the following form:

$$\dot{m} = f(\Delta T_{sub}, P_{up} - P_{sat}, D, L, \rho_f, \rho_g, \mu_f, \mu_g, T_c) \quad (2)$$

The Buckingham Pi theorem is used to generate the dimensionless groups. The variables of D, ρ_f, μ_f and T_c are selected as the repeating variable. Six π-groups are presented in Table 2. However, in dimensionless π_2 group, it is found that the repeating variable ($\mu_f^2/\rho_f D^2$) is complicated. In order to obtain the simple form, the repeating variable is replaced by critical pressure (P_c) in the modified parameter. In addition, because the term of $(\mu_f-\mu_g)/\mu_g$ indicate the better dependence on the flow rate, π_5 is also modified as described in Kim et al. [12]. The relationship between dimensionless parameters is expressed as follows:

$$\pi_1 = \phi(\pi_2, \pi_3, \pi_4, \pi_5, \pi_6) \quad (3)$$

$$\frac{\dot{m}}{D^2\sqrt{\rho_f P_{up}}} = \phi\left(\frac{(P_{up} - P_{sat})}{P_c}, \frac{\Delta T_{sub}}{T_c}, \frac{L}{D}, \frac{\rho_g}{\rho_f}, \frac{(\mu_f - \mu_g)}{\mu_g}\right) \quad (4)$$

As shown in Eq. (4) and Table 2, the term of $(P_{up}-P_{sat})/P_c$ indicates the subcooled liquid pressure drop with respect to the critical pressure, $\Delta T_{sub}/T_c$ implies the degree of subcooling of refrigerant with respect to the critical temperature, L/D shows the geometric parameter of short-tube orifice, ρ_g/ρ_f is used as indicator of the slip ratio between phases at the exit plane of short-tube orifice, and $(\mu_f-\mu_g)/\mu_g$ accounts the variation of viscosity due to the difference of velocity between phases. Based on the database obtained from the present study and those obtained from Nilpueng and Wongwises [14] (D = 0.406–1.2 mm, P_{up} = 1000–1200 kPa, P_{down} = 300–400 kPa and ΔT_{sub} = 3–16 °C), a proposed correlation covered the calculation of the flow of refrigerant HFC-134a in short-tube orifice diameter ranging between 0.406 and 1.2 mm. This database contains a total of 280 data points. The correlation is produced in power law form. The nonlinear regression method is used to calculate the coefficient and exponent of the dimensionless parameters. The refrigerant properties are computed by using REFPROP [18]. A mass flow rate correlation can be expresses as

$$\pi_1 = 3330.5\pi_2^{0.192}\pi_3^{-0.0185}\pi_4^{-0.199}\pi_5^{-6.48}\pi_6^{-11.43} \quad (5)$$

Fig. 10 shows the measured mass flow rate plotted against the calculated mass flow rate. In this figure, the measured data obtained from Kim [4] are also compared. It is found that the entire data fall within ±15% of the proposed correlation. A mean deviation of prediction $\left(1/n\sum_1^n\left[\frac{|\dot{m}_{meas}-\dot{m}_{pred}|\times 100}{\dot{m}_{meas}}\right]\right)$ is 4.69%.

Table 2
Dimensionless groups.

Dimensionless groups	Original parameter	Modified parameter
π_1	$\dot{m}/D\mu_f$	$\dot{m}/D^2\sqrt{\rho_f P_{up}}$
π_2	$(P_{up} - P_{sat})\rho_f D^2/\mu_f^2$	$(P_{up} - P_{sat})/P_c$
π_3	$\Delta T_{sub}/T_c$	$\Delta T_{sub}/T_c$
π_4	L/D	L/D
π_5	ρ_g/ρ_f	ρ_g/ρ_f
π_6	μ_g/μ_f	$(\mu_f - \mu_g)/\mu_g$

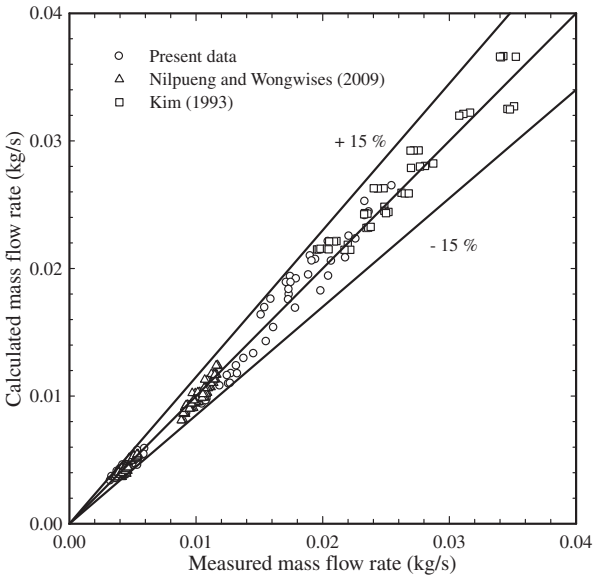

Fig. 10. Measured mass flow rate versus calculated mass flow rate.

4. Conclusion

This paper provides the new experimental data on the HFC-134a flow mechanism through short-tube orifices. The influence of operating conditions and short-tube orifice dimension on the choked flow mechanisms, i.e., occurrence of choked flow phenomenon and mass flow rate under choked flow condition are presented. The experimental results indicate that the choked flow phenomenon initially appeared inside the short-tube orifice at length-to-diameter ratios of more than 2.11, a degree of subcooling of less than 21.5 °C, and a ratio of downstream pressure to saturation pressure corresponding to upstream temperature ranging between 0.53 and 0.72. The mass flow rate increases with increasing upstream pressure, degree of subcooling, and short-tube orifice diameter, but decreases with increasing short-tube orifice length. A proposed correlation shows good agreement with measured data obtained from the present study and previous researchers with a mean deviation of 4.69%.

Acknowledgements

The authors would like to express their appreciation to King Mongkut's University of Technology Thonburi, the Thailand Research Fund, the Office of Higher Education Commission and the National Research University Project for providing financial support for this study.

References

[1] S. Saisorn, S. Wongwises, An experimental investigation of two-phase air–water flow through a horizontal circular micro-channel, Exp. Therm. Fluid Sci. 33 (2009) 306–315.
[2] R.C. Chu, The challenges of electronic cooling: past, current and future, J. Electron. Packag. 126 (2004) 491–500.
[3] S. Trutassanawin, E.A. Groll, S.V. Garimella, L. Cremaschi, Experimental investigation of a miniature-scale refrigeration system for electronics cooling, IEEE Trans. Compon. Packag. Technol. 29 (2006) 678–687.
[4] Y. Kim, Two-phase flow of HFC134a and HCFC22 through short tube orifices, PhD Thesis, Texas A&M University, USA, 1993.
[5] P.F. Pasqua, Metastable flow of Freon-12, Refrig. Eng. 61 (1953) 1084–1088.
[6] V.C. Mei, Short-tube refrigerant flow restrictors, ASHRAE Trans. 88 (1982) 157–169.
[7] A.A. Aaron, P.A. Domanski, Experimentation analysis and correlation of refrigerant-22 flow through short tube restrictors, ASHRAE Trans. 96 (1990) 729–742.

[8] Y.C. Kim, W.V. Payne, D.L. O'Neal, M. Farzad, Refrigerant flow through flexible short tube orifices, Int. J. HVAC Res. 8 (2002) 179–190.
[9] W.V. Payne, D.L. O'Neal, Mass flow characteristics of R407C through short-tube orifices, ASHRAE Trans. 104 (1998) 197–209.
[10] G.M. Singh, P.S. Hrnjak, C.W. Bullard, Flow of refrigerant R134a through orifice tubes, Int. J. HVAC&R Res. 7 (2001) 245–262.
[11] J.P. Liu, Y.M. Niu, J.P. Chen, Z.J. Chen, X. Feng, Experimental and correlation of R744 two-phase flow through short tubes, Exp. Therm. Fluid Sci. 28 (2004) 565–573.
[12] Y. Kim, V. Payne, J. Choi, P. Domanski, Mass flow of R410A through short tube working near the critical point, Int. J. Refrig. 28 (2005) 547–553.
[13] X. Tu, P.S. Hrnjak, C.W. Bullard, Refrigerant 134a liquid flow through micro-scale short tube orifices with/without phase change, Exp. Therm. Fluid Sci. 30 (2006) 253–262.
[14] K. Nilpueng, S. Wongwises, Experimental investigation of two-phase flow characteristics of HFC-134a through short-tube orifices, Int. J. Refrig. 32 (2009) 854–864.
[15] ASME, Fluid Meters – Their Theory and Application, American Society of Mechanical Engineers, New York, 1971.
[16] J. Choi, J.T. Chung, Y. Kim, A generalized correlation for two-phase flow of alternative refrigerants through short tube orifices, Int. J. Refrig. 27 (2004) 393–400.
[17] K. Nilpueng, C. Supavarasuwat, S. Wongwises, Flow pattern, mass flow rate, pressure distribution, and temperature distribution of two-phase flow of HFC-134a inside short-tube orifices, Int. J. Refrig. 32 (2009) 1864–1875.
[18] M.O. McLinden, S.A. Klein, E.W. Lemmon, REFPROP – Thermodynamic and Transport Properties of Refrigerant and Refrigerant Mixtures, NIST Standard Reference Database – Version 6.01, 1998.

Experimental Thermal and Fluid Science 35 (2011) 364–374

Contents lists available at ScienceDirect

Experimental Thermal and Fluid Science

journal homepage: www.elsevier.com/locate/etfs

Flow boiling heat transfer of R134a in the multiport minichannel heat exchangers

Jatuporn Kaew-On [a,b], Kittipong Sakamatapan [b], Somchai Wongwises [b,*]

[a] The Joint Graduate School of Energy and Environment, King Mongkut's University of Technology Thonburi, Bangmod, Bangkok 10140, Thailand
[b] Fluid Mechanics, Thermal Engineering and Multiphase Flow Research Lab. (FUTURE), Department of Mechanical Engineering, King Mongkut's University of Technology Thonburi, Bangmod, Bangkok 10140, Thailand

ARTICLE INFO

Article history:
Received 14 July 2010
Received in revised form 19 October 2010
Accepted 20 October 2010

Keywords:
Flow boiling heat transfer
Multiport minichannels
Tube-in-tube heat exchangers
LMTD
R134a

ABSTRACT

The flow boiling heat transfer characteristics of R134a in the multiport minichannel heat exchangers are presented. The heat exchanger was designed as the counter flow tube-in-tube heat exchanger with refrigerant flowing in the inner tube and hot water in the gap between the outer and inner tubes. Two inner tubes were made from extruded multiport aluminium with the internal hydraulic diameter of 1.1 mm for 14 numbers of channels and 1.2 mm for eight numbers of channels. The outer surface areas of two inner test sections are 5979 mm^2 and 6171 m^2, while the inner surface areas are 13,545 mm^2 and 8856 mm^2 for 14 and eight numbers of channels, respectively. The outer tube of heat exchanger was made from circular acrylic tube with an internal hydraulic diameter of 25.4 mm. The experiments were performed at the heat fluxes between 15 and 65 kW/m^2, mass flux of refrigerant between 300 and 800 kg/m^2 s and saturation pressure ranging from 4 to 6 bar. For instance the boiling curve, average heat transfer coefficients are discussed. The comparison results of two test sections with different the number of channels are investigated. The results are also compared with nine existing correlations. The new correlation for predicting the heat transfer coefficient was also proposed.

© 2010 Elsevier Inc. All rights reserved.

1. Introduction

Multiport minichannels have been considered to be of great interest in compact evaporator applications in both automotive air conditioning and heat pump systems. There are many advantages over both the conventional tube and the single channel such as more compact size, low refrigerant charge, light weight, and reduced pressure drop. Thus, designs of multiport minichannels used as evaporators in air conditioning or heat pumps need to overcome the practical obstructions related to flow boiling in small channels. However, the heat transfer and flow characteristics of refrigerant in small channels have been studied by a number of researchers, mostly in single ports. The heat transfer and flow characteristics of refrigerant in multiport minichannels have received little attention in the open literature.

State-of-the-art and some examples of the most productive studies of single ports and multiports are summarized and described below.

Yan and Lin [1] determined the evaporation heat transfer coefficient and pressure drop of R134a in a tube with an inner diameter of 2 mm. The test section consisted of 28 parallel pipes with outer diameter of 3 mm and length of 0.2 m. They found that the heat transfer coefficients were quite different from those of larger pipes. The heat transfer coefficient increased with increases in the wall heat flux except in high quality regions. However, reverse results were obtained in the case of the high vapour quality region for high wall heat flux. Moreover, their results indicated that the heat transfer coefficients in small tubes are higher than that of conventional tubes ($d_i > 8$ mm) by around 30–80%. In the case of pressure drop, the experimental results showed that the measured pressure drop increased with increases in the mass flux as well as the imposed heat flux. Finally, they also proposed empirical correlations to predict the evaporation heat transfer coefficient and friction factors.

Owhaib et al. [2] presented new experimental results on saturated flow boiling of R134a in vertical circular tubes with internal diameters of 1.7, 1.224, and 0.826 mm. From their results, they concluded that wall heat flux and system pressure have more significant effects on the heat transfer coefficients, while mass flux and vapour quality had no significant effect on the heat transfer coefficient. They also strongly recommended that the heat transfer coefficients were dominated by nucleate boiling.

In 2004, Huai et al. [3] performed an experimental study of boiling heat transfer and pressure drop of CO_2 flowing through a multiport extruded aluminium tube with 10 circular channels, each with an inner diameter of 1.31 mm. The heating effect was obtained by hot water flowing inside copper blocks attached on both sides of the test section. The experiments were performed for either subcooled liquid or two-phase of CO_2 being fed to the inlet of the test section. They found that both a larger mass flux and a higher heat flux led to larger heat transfer coefficients.

* Corresponding author. Tel.: +66 2 470 9115; fax: +66 2 470 9111.
E-mail address: somchai.won@kmutt.ac.th (S. Wongwises).

0894-1777/$ - see front matter © 2010 Elsevier Inc. All rights reserved.
doi:10.1016/j.expthermflusci.2010.10.007

Nomenclature

A	area (m^2)
Bo	Boiling number, $Bo = \frac{q''}{Gi_{fg}}$
c_p	specific heat at constant pressure (kJ kg^{-1} K^{-1})
d_h	hydraulic diameter (m)
G	mass flux (kg m^{-2} s^{-1})
h	heat transfer coefficient (W m^{-2} K^{-1})
i	enthalpy (kJ kg^{-1})
$LMTD$	log mean temperature difference (°C)
$\dot{m}$	mass flow rate (kg s^{-1})
N	number of thermocouples
n	number of channels
P	pressure (kPa)
P	perimeter (m)
Pr	Prandtl number, $Pr = \frac{C_p \mu}{k}$
$\dot{Q}$	heat transfer rate (kW)
q''	heat flux (kW m^{-2})
Re	Reynolds number, $Re = \frac{Gd}{\mu}$
T	temperature (°C)
U	overall heat transfer coefficient (W m^{-2} K^{-1})
We	Weber number, $We = \frac{G^2 d}{\rho \sigma}$
x	vapour quality

Greek letters

β	aspect ratio
μ	dynamic viscosity (Pa s)
α	void fraction
ε	roughness (m)
ρ	density (kg m^{-3})
σ	surface tension (N m^{-1})
δ	wall thickness (m)
ϕ^2	two-phase frictional multiplier

Subscripts

avg	average
c	cross section
cir	circular
cont	contraction
exp	expansion
i	inner
in	inlet
l	liquid
v	vapour
o	outter
out	outlet
rec	rectangular
ref	refrigerant
s	surface
sat	saturation
TS	test section
w	water

Pettersen [4] investigated the flow boiling heat transfer coefficients and pressure drops of CO_2 in extruded aluminium with 25 circular channels, 0.8 mm internal diameter, and 0.5 m length. The hot water was used as the heating source to his test section. He modified the Wilson plot technique to calculate the flow boiling heat transfer coefficients. His experimental results showed that nucleate boiling dominated at low/medium vapour qualities, where the heat transfer coefficient increased with heat flux but was less affected by varying mass flux and vapour quality. He also observed that the dryout effects became very important at higher mass flux and higher temperature.

Zhang et al. [5] proposed a new correlation to predict the heat transfer coefficient in minichannels. Their equation is based on the correlation proposed by Chen [6]. From experiments, they stated that the liquid-laminar and gas-turbulent flows are simple cases in many minichannel applications. In contrast with conventional channels, most correlations were generally formulated from liquid-turbulent and gas-turbulent flow conditions. Therefore, they modified the Chen correlation (1966) to predict the heat transfer coefficient. The new correlation was in good agreement with the experimental results.

Saitoh et al. [7] investigated the heat transfer coefficient of R134a flowing through channels with three different diameters of 0.51, 1.12, and 3.1 mm. They found that the heat transfer coefficient for the 3.1 mm channels depended upon both heat flux and mass flux. In contrast, the heat transfer coefficient for the 0.51 mm channels increased with increasing heat flux but was not significantly affected by mass flux. They also concluded that the decrease in the channel diameter resulted in a decrease in the contribution of forced convection. Moreover, for the small channels, the influence of surface tension became a more important parameter which resulted in the occurrence of dryout at lower quality.

In a series of studies, Yun et al. [8] determined the convective boiling heat transfer characteristics of CO_2 flowing through micro-channels. They used rectangular micro-channels with hydraulic diameters varying from 1.08 to 1.54 mm. The mass flux and heat flux varied from 200 to 400 kg/m^2 s and 10–20 kW/m^2, respectively. Similarly, the saturation temperatures were set at 0, 5, and 10 °C. The results showed that the heat transfer coefficient of CO_2 was 53% higher than that of R134a. Furthermore, they found that the heat transfer coefficient increased by 5% and 31% with a reduction in hydraulic diameter from 1.54 mm to 1.27 mm and from 1.27 mm to 1.08 mm, respectively.

Yun et al. [9], in a paper continuing from Yun et al. [8], investigated convective boiling heat transfer coefficients of R410A in rectangular micro-channels having hydraulic diameters of 1.36 and 1.44 mm. They concluded that when the flow distribution to each channel was uniform, the effects of heat flux, mass flux, and saturation on heat transfer coefficients were very small. In addition to considering the effect of the number of channels on the heat transfer coefficients, those of the eight-hole micro-channel were 25% higher than those of the seven-hole micro-channel under the same conditions. They also presented a heat transfer coefficient correlation which was developed using the non-dimensional parameters Bo, We_l and Re_l, and given 18% deviation.

Lie et al. [10] conducted an experimental study on the evaporation heat transfer characteristics of refrigerants R134a and R407C in two multiport channels with hydraulic diameters of 0.83 m and 2.0 mm. From their results, the data clearly showed that the heat transfer coefficients of both R134a and R407C increased almost linearly with the vapour quality except at low mass flux and high heat flux. Their results also showed that the heat transfer coefficient increased substantially with increases in heat flux, mass flux, and saturation temperature. At a given condition, they found that the heat transfer coefficient of R407C was higher than that of R134a. They did not directly mention the comparison of the heat transfer coefficient between hydraulic diameters of 0.83 mm and 2.0 mm due to the difference in the mass flux range. Finally, they also proposed the empirical correlation for calculating the heat transfer coefficient of small channels as a function of the Reynolds number and boiling number.

Shiferaw et al. [11] conducted experiments on the flow boiling heat transfer of R134a in two stainless steel tubes with internal diameters of 4.26 mm and 2.01 mm under different conditions. They concluded that in the low vapour quality region, the local heat transfer coefficient was independent of vapour quality, while in the high vapour quality region, the heat transfer coefficient decreased with increasing vapour quality. They explained that at low quality the heat transfer coefficient was dominated by nucleate boiling and that partial dryout occurred at high vapour quality.

In a series of studies, Fernando et al. [12–14] investigated the heat transfer coefficient of a minichannel aluminium tube heat exchanger. They separated their works into three parts as follows. In the first part, they studied the single-phase water-to-water heat transfer coefficient by the Wilson plot method. In the second, the heat transfer coefficient of propane operating as evaporator was investigated. In the third, the heat transfer coefficient of propane operating as condenser was studied. From the single-phase studied, they concluded that the Wilson method was successfully applied to determine the liquid-to-liquid heat transfer coefficients under laminar and transition flow regimes. Moreover, the Gnielinski equation [15] showed good agreement with the experimental data. Fourteen existing correlations for both conventional tubes and small tubes were selected and then compared with the experimental results. They recommended that correlations emphasizing nucleate boiling were in better agreement with the experimental data than correlations emphasizing convective evaporation. In the third paper, they investigated the heat transfer coefficient of propane during condensation flowing through the minichannel aluminium tube heat exchanger.

Ong and Thome [16] experimentally investigated the flow boiling heat transfer of R134a, R236fa, and R245fa in a horizontal circular channel with 1.030 mm. They modified an isolated bubble (IB)/coalescing bubble (CB)/annular flow map to investigate the influence of flow pattern on the heat transfer coefficient. At low mass flow rates, the results indicated that the heat transfer coefficients of R134a and R236fa increase with increasing heat flux for a wide rage of qualities. At low qualities, R134a gave the highest heat transfer coefficient, followed by R236fa and R245fa, respectively. At high qualities, the heat transfer coefficient of R236fa and 245fa continued to increase until close to the value of R134a. However, they recommended that the flow mechanisms of nucleate boiling and forced convection in small channels are not fully understood and more research work is still required.

In 2009, Kaew-On and Wongwises [17] experimentally studied the evaporation of 410A in a three-port minichannel with a 3.48 mm hydraulic diameter. The experimental results indicated that the average heat transfer coefficient tended to increase with increasing average quality, mass flux, and heat flux. In contrast, the heat transfer coefficient tended to decrease with increasing saturation temperature. Moreover, the pressure drop increased with increasing mass flux and decreased with increasing saturation temperature. The results also showed that the heat flux has no significant effect on the pressure drop. Finally, correlations for predicting the heat transfer coefficient and frictional pressure drop were also proposed.

As mentioned above, it is clearly seen that there is some information available on the boiling flow characteristics in minichannels and micro-channels, especially single channels. Despite worthwhile industrial applications, the flow boiling characteristics in multiport minichannels have received comparatively little attention in literature. As a consequence, the present paper aims to determine the heat transfer and flow characteristics of refrigerant R134a during flow boiling. The effects of mass flux, heat flux, and saturation pressure on average heat transfer coefficients which have never seen before in the open literature are presented. In addition, the correlation for predicting heat transfer coefficients is also proposed for practical applications.

2. Experimental apparatus and method

The experimental apparatus is schematically presented in Fig. 1. The main components of the system are: a test section, refrigerant loop, hot water loop, subcooling loop, and data acquisition system.

For the refrigerant circulating loop, as shown in Fig. 1, liquid refrigerant is pumped by a gear pump regulated flow rate by means of an inverter. The refrigerant then passes in series through a filter/dryer, refrigerant flow meter, pre-heater, and sight glass tube, and enters the test section. The inlet quality before entering the test section is controlled by the pre-heater. The DC power supply is used to supply the imposed heat flux to the pre-heater,

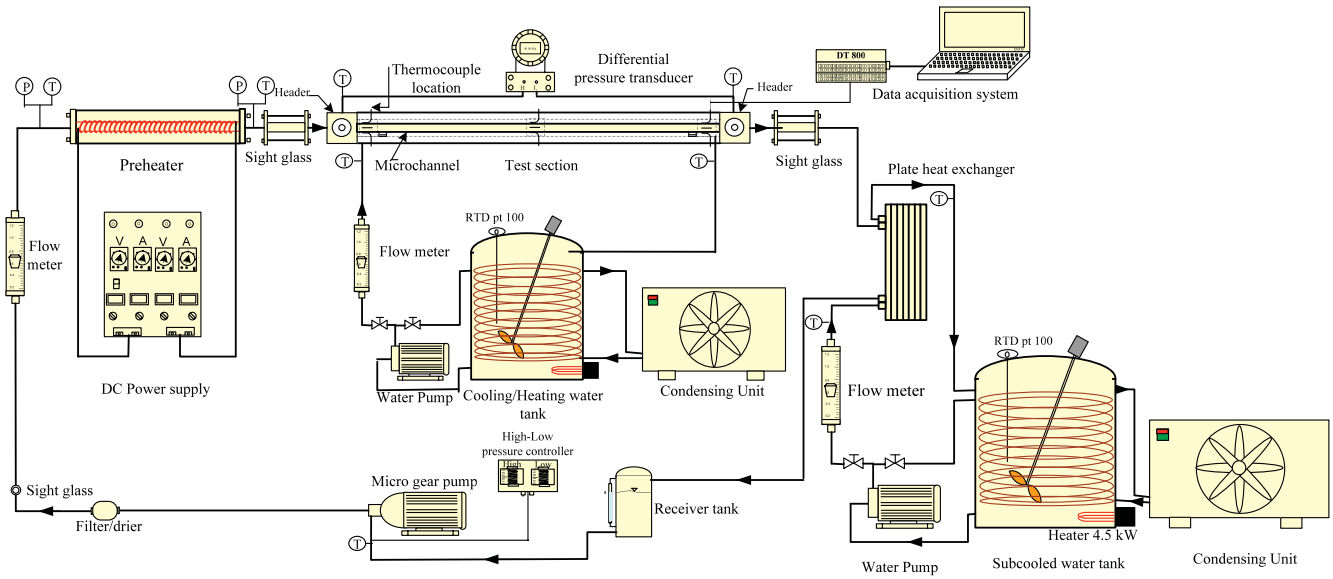

Fig. 1. Schematic diagrams of the experimental apparatus.

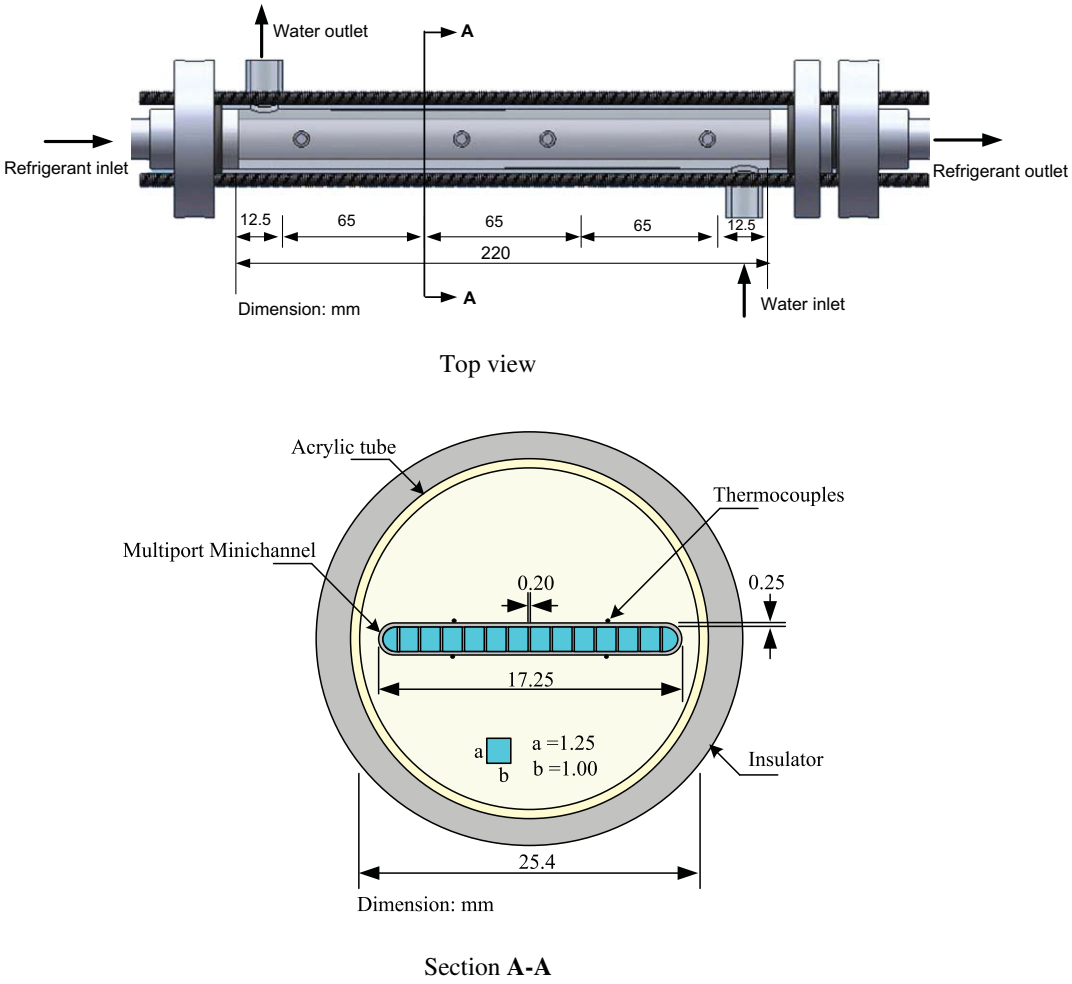

Fig. 2. Schematic diagram of the test section.

which can be controlled by adjusting the supply voltage and current. For all conditions, the inlet quality of the refrigerant entering the test sections is controlled about 0.05–0.1. Leaving the test section, the refrigerant vapour then condenses in a subcooler and is later collected in a receiver; it eventually returns to the refrigerant pump to complete the cycle. Instrumentation is installed at various positions, as clearly shown in Fig. 1, to monitor the refrigerant state. All the signals from the thermocouples and pressure transducer were recorded by a data logger.

The complete schematic diagram of the test section is shown in Fig. 2. The test section is a counter flow tube-in-the tube heat exchanger. Two refrigerant sides are the aluminium rectangular multiport minichannel with the hydraulic diameter of 1.1 mm for 14 channels, and 1.2 mm for eight channels with similar outer surface areas. The hot water sides are made from the circular transparent acrylic tube with internal hydraulic diameter of 25.4 mm and are used to provide the heat flux to the test tubes. The details of test sections are presented in Table 2.

The test section is connected with a header at the inlet and outlet. T-type thermocouples are installed at the inlet and outlet at the side of header to measure the saturation temperature of the refrigerant. At the other side of the header, the differential pressure transducer was installed in order to measure the pressure drop across the test section. The length between pressure taps is 250 mm. The accuracy of the differential pressure transducer is ±0.25% of full scale or ±0.125 kPa. The sixteen thermocouples were installed at the top and bottom at four points along the multiport minichannel to measure the wall temperature of the test section. All of the wall thermocouples are fixed with special glue having low thermal conductivity. With this method, the thermocouples are not biased by the heat from hot water. The water outside the test section was insulated by using rubber foam with a thermal conductivity of 0.04 W/m K. All the thermocouples were well calibrated. The refrigerant flow meter is a variable area type. The flow meter was specially calibrated in the range of 0.2–1.8 LPM for R134a by the manufacturer. The details of the test conditions are presented in Table 3.

3. Data reduction

For all calculations, the thermophysical properties of refrigerant are evaluated by using REFPROP, Version 6.01 (1998). The data reduction of the measured results is summarized in the following procedures.

The log mean temperature difference (*LMTD*) method was applied to calculate the overall heat transfer rate, which is expressed as follows:

$$\dot{Q} = UA \cdot LMTD \tag{1}$$

where U is the overall heat transfer coefficient of the heat exchanger, A is the surface area based on the outside surface of the heat exchanger, and *LMTD* is the log mean temperature difference, which is defined as follows:

$$LMTD = \frac{(T_{w,in} - T_{ref,out}) - (T_{w,out} - T_{ref,in})}{\ln\left(\frac{T_{w,in} - T_{ref,out}}{T_{w,out} - T_{ref,in}}\right)} \quad (2)$$

where T_w and T_{ref} are the water and refrigerant temperatures, respectively.

Consider the test section as presented in Fig. 2. Assuming no heat loss to the surroundings, the heat transfer rate from the hot water to the refrigerant past the wall of the multiport minichannel can be calculated by:

$$\dot{Q} = \dot{m}_w c_{p,w}(T_{w,in} - T_{w,out}) = \dot{m}_{ref}(i_{ref,out} - i_{ref,in}) \quad (3)$$

where $\dot{Q}$ is the heat transfer rate, $\dot{m}_w$ and $\dot{m}_{ref}$ are the mass flow rate of the hot water and refrigerant, respectively, and $i_{ref,in}$ and $i_{ref,out}$ are the enthalpy at the inlet and outlet of the test section, respectively.

Finally, the total thermal resistance of the multiport minichannel heat exchanger can be expressed as:

$$\frac{1}{UA} = \frac{1}{h_o A_o} + \frac{\delta_t}{k_t A_m} + \frac{1}{h_i A_i} \quad (4)$$

where h_o is the heat transfer coefficient of hot water and can be calculated from the following equation:

$$h_o = \frac{\dot{Q}}{A_o(T_{w,avg} - T_{wall,avg})} \quad (5)$$

where A_o is the outer surface area of the tested tube, $T_{w,avg}$ is the average water temperature measured at the inlet and outlet of the water side, and $T_{wall,avg}$ are the average wall temperatures and can be calculated by:

Table 1
Correlations from literature.

No.	Author(s)	Correlation	Conditions
1	Chen [6]	$h_{tp} = Fh_l + Sh_{pool}$ where, $F = 1$ for $\frac{1}{X_{tt}} \leqslant 0.1,\ F = 2.35\left(0.213 + \frac{1}{X_{tt}}\right)^{0.736}$ for $\frac{1}{X_{tt}} \geqslant 0.1$ $h_l = 0.023Re_l^{0.8}Pr_l^{0.4}\left(\frac{k_l}{d_h}\right),\ S = \frac{1}{1+2.53Re_{tp}^{1.17}10^{-6}},\ Re_{tp} = Re_lF^{1.25}$ $h_{pool} = 0.00122\left(\frac{k_l^{0.79}Cp_l^{0.45}\rho_l^{0.24}}{\sigma^{0.5}\mu_l^{0.29}h_{lv}^{0.24}\rho_v^{0.24}}\right)(T_w - T_{sat})^{0.24}(P_w - P_{sat})^{0.75}$ Pressure in Pascal	Conventional channel
2	Lazarek and Black [26]	$h_{tp} = 30Re_l^{0.857}Bo^{0.714}\frac{k_l}{d_h}$ where, $Re_l = \frac{Gd_h}{\mu_l},\ Bo = \frac{q''}{Gh_{lv}},\ d_h = \frac{4A_c}{P}$	Round tube, d_h = 0.31 mm, R113, local HTC
3	Malek and Colin [27]	For vertical orientation $h_{tp} = 2460G^{0.017}q''^{0.515}Pr^{0.25}$ For horizontal orientation $h_{tp} = 1590G^{-0.08}q''^{0.53}Pr^{0.18}$ where q'' in kW m^{-2}, and h_{tp} in W m^{-2} K^{-1}	Conventional channel, circular tube, d = 21 mm, ammonia, average HTC
4	Kenning and Cooper [18]	$h_{tp} = Eh_l$ where, $E = (1 + 1.8\left(\frac{1}{X_{tt}}\right)^{0.87},\ h_l = 0.023Re_l^{0.8}Pr_l^{0.4}\left(\frac{k_l}{d_h}\right)$	Circular tubes, d = 9.6 and 14.4 mm, water
5	Tran et al. [28]	$h_{tp} = 840,000(Bo^2We_l)^{0.3}\left(\frac{\rho_L}{\rho_v}\right)^{-0.4}$ where, $We_l = \frac{G^2d_h}{\rho_l\sigma},\ Bo = \frac{q''}{Gh_{lv}},\ d_h = \frac{4A_c}{P}$	Circular and rectangular, d_h = 2.40 mm, R12 and R133, average HTC
6	Kew and Cornwell [29]	$h_{tp} = 30Re_l^{0.857}Bo^{0.714}\frac{k_l}{d_h}(1-x)^{-0.143}$ where, $Re_l = \frac{Gd_h}{\mu_l},\ Bo = \frac{q''}{Gh_{lv}},\ d_h = \frac{4A_c}{P}$	Modified Lazararek and Black [26]
7	Warrier et al. [19]	$h_{tp} = Eh_l$ where, $E = (1 + 6Bo^{1/16} - 5.3(1 - 855Bo)x^{0.65}$ $h_l = 0.023Re_l^{0.8}Pr_l^{0.4}\left(\frac{k_l}{d_h}\right)$ Validity: $0.03 \leqslant x \leqslant 0.55;\ 0.00027 \leqslant Bo \leqslant 0.00089$	Rectangular channel, d_h = 0.75 mm, average HTC, FC-84
8	Yu et al. [30]	$h_{tp} = 6.4 \cdot 10^6(Bo^2We_{lo})^{0.27}\left(\frac{\rho_L}{\rho_v}\right)^{-0.2}$ where, $E = (1 + 6Bo^{1/16} - 5.3(1 - 855Bo)x^{0.65}$ $h_l = 0.023Re_l^{0.8}Pr_l^{0.4}\left(\frac{k_l}{d_h}\right)$ Validity: $0.03 \leqslant x \leqslant 0.55;\ 0.00027 \leqslant Bo \leqslant 0.00089$	Circular channel, d = 2.98 mm, average HTC, water
9	Kaew-On and Wongwises [17]	$h_{TP} = Sh_{sp}$ $h_l = 0.023Re_l^{0.8}Pr_l^{0.4}\frac{k_l}{d_h},\ S = 1.737 + 0.97(\beta\phi_l^2)^{0.523}$ $\phi_l^2 = 1 + \frac{C}{X} + \frac{1}{X^2},\ C = -3.356 + 41.863e^A + B$ $A = -69.475\beta f_l d_h,\ B = 498\beta f_l d_h$ $X = \left(\left(\frac{dp}{dz}f\right)_l \Big/ \left(\frac{dp}{dz}f\right)_v\right)^{1/2}$ $4f_l = (1/(-1.8Log(6.9/Re_l + ((\varepsilon/d_h)/3.7)^{1.11})))^2$ $Re_l = \frac{Gd_h(1-x)}{\mu_l}$	Multiport minichannel, d_h = 3.5 mm, n = 3 channels, average HTC, R410A
10	Proposed new correlation	$h_{TP} = SBo^{0.185}We_l^{0.0013}h_l$ $Bo = \frac{q''}{Gh_{lv}},\ We_l = \frac{G^2d_h}{\rho_l\sigma}$	Multiport minichannel, d_h = 1.1 and 1.2 mm, n = 8 and 14 channels, average HTC, R134a

Table 2
The details of test sections.

Test No.	Hydraulic diameter (mm)	Number of channel	Channel width (mm)	Channel height (mm)	Aspect ratio	Inner surface (mm^2)	Outer surface (mm^2)
1	1.1	14	1	1.25	1.25	13,545	5979
2	1.2	8	1.8	0.9	0.5	8856	6171

Table 3
Experimental conditions.

Refrigerant	R134a
Hydraulic diameter (mm)	1.1 and 1.2
Number of channels, N	14 and 8
Mass flux ($kg/m^2\,s$)	300–800
Heat flux (kW/m^2)	15–65
Saturation pressure (bars)	4, 5, 6

$$T_{wall,avg} = \frac{1}{N}\sum_{i=1}^{N} T_{wall,i} \tag{6}$$

where $T_{wall,i}$ is the local wall temperature at each section of the heat exchanger.

From Eq. (4), the inside heat transfer coefficient can be calculated by:

$$\frac{1}{h_i A_i} = \frac{1}{UA} - \frac{1}{h_o A_o} - \frac{\delta_t}{k_t A_m} \tag{7}$$

where h_i is the inside heat transfer coefficient or the refrigerant side heat transfer coefficient. A_i is the inside surface area and can be calculated by:

$$A_i = [2n_{rec}(a+b) + n_{cir}(a+\pi b)]L \tag{8}$$

where a is the width of the channel, b is the height of the channel, n_{rec} is the number of rectangular channel, n_{cir} is the number of the circular channel, and L is the length of the test section.

3.1. The existing correlations from the literature

The boiling heat transfer coefficients experimentally determined from the present studies are compared with those obtained from the existing correlations. These correlations can be classified into three forms. First, the two-phase heat transfer can be calculated from single-phase heat transfer, normally using the Disttus–Boeter correlation, multiplied by a multiplier factor. The correlations proposed here are from studies such as Kenning and Cooper [18], Warier et al. [19], and Kaew-On and Wongwises [17]. Second, the convective boiling and nucleate boiling contributions are combined due to two important mechanisms mainly governed by the flow boiling heat transfer. Chen [6], the pioneer who formulated this form, used the addition of two components corresponding to the two mechanisms with a suppression factor, S, and a multiplier factor; F. Chen's correlation [6] is one of the well known and widely used correlations. Many researchers, for example Gungor and Winterton [20], developed their correlations based on modifications of Chen's correlation [6] which was taken as a benchmark for developing a new correlation. The final form combines the two mechanisms of boiling using a power-type asymptotic model, which was presented by Kutateladze [21]. From the literature, the correlations are summarized in Table 1.

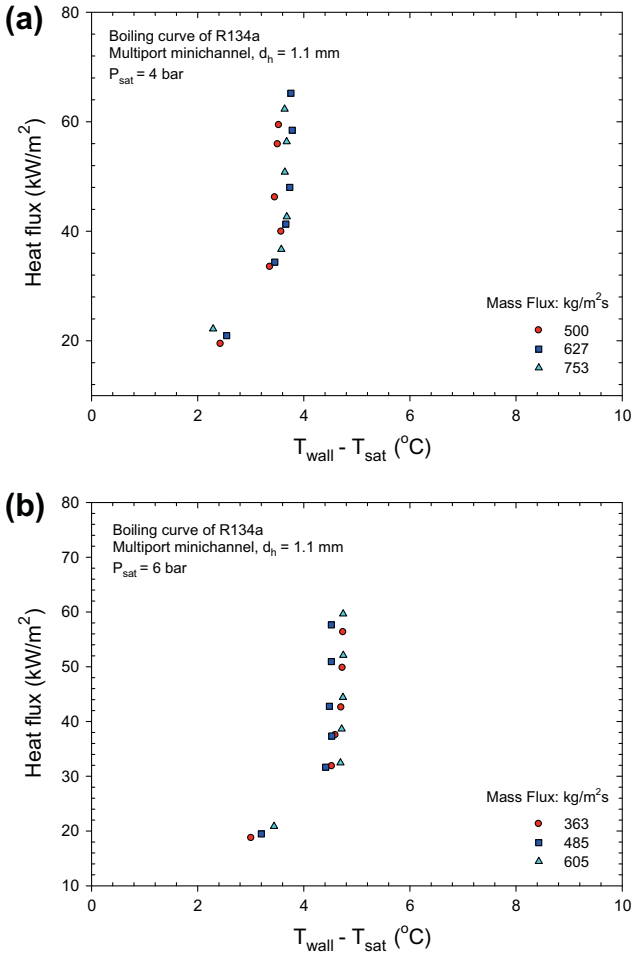

Fig. 3. The boiling curve of R134a in multiport minichannel: (a) P_{sat} = 4 bar and (b) P_{sat} = 6 bar.

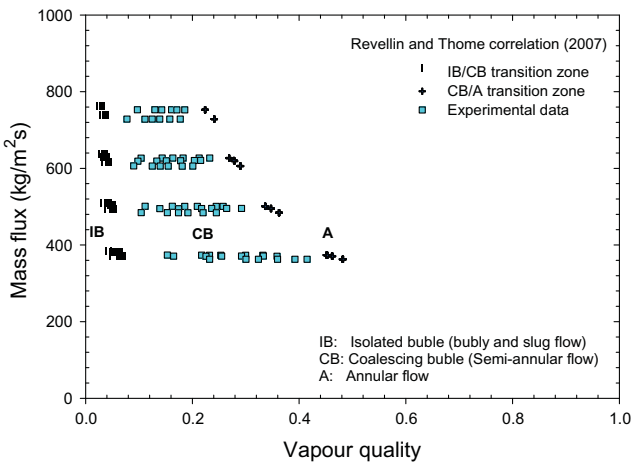

Fig. 4. Flow pattern maps with the experimental transition zone of Revellin and Thome [22] correlation.

4. Results and discussion

4.1. The boiling curve

The boiling curves of R134a flowing through multiport minichannels are plotted in terms of the variation of the wall heat flux with the temperature difference between the wall and saturation temperatures or excess temperature as presented in Fig. 3. The results are obtained at three different mass fluxes in the ranges of 363–753 kg/m^2 s, heat fluxes of 15–60 kW/m^2, and saturation pressures of 4 bar (Fig. 3a) and 6 bar (Fig. 3b). The inlet qualities of the refrigerant before entering the test section were kept constant at approximately 0.05. As indicated in Fig. 3, the boiling curves correspond to the nucleate boiling regime. Nucleate boiling is generally associated with bubbly, slug, or low velocity annular flow patterns which normal flow patterns are occurring in small channels. In the present study, a new type of two-phase flow pattern map for flow boiling in mini and micro-channel developed by Revellin and Thome [22] was applied to identify the flow regime. As shown in Fig. 4, it is found that all experimental data are in the coalescence bubble (CB) zone. The coalescing bubble (CB) regime is defined when bubble generation rate is smaller than the bubble coalescence rate. The flow pattern in this regime is semi-annular flow pattern. In general in nucleate boiling, bubbles are formed by nucleation in the superheated liquid near the walls. The heat transfer coefficient in this type of boiling is a function of the heat flux, but is almost independent of vapour quality or mass flux. Fig. 3 also clearly shows that mass flux has an insignificant effect on the boiling curve. When the results at different saturation pressures are compared, it is found that the excess temperature increases with increases in the saturation pressure.

4.2. Average heat transfer coefficient

In order to investigate the overall performance of the heat exchanger, average heat transfer coefficients are required. So, the heat transfer coefficients of R134a in an extruded multiport minichannel are examined as an average value over the entire length. The relevant parameters such as mass flux, heat flux, and saturation pressure for the average heat transfer coefficient are examined and discussed. The experiments were conducted by varying the heat fluxes while the saturation pressure, mass flux, and inlet quality of each condition were kept constant.

Fig. 4 shows the variation in the average heat transfer coefficient with a heat flux of R134a in the multiport minichannel at saturation pressure of 5 bar (Fig. 5a) and 6 bar (Fig. 5b) and quality at the test section inlet of 0.05 for different mass fluxes of 360–878 kg/m^2 s. The results indicate that the heat transfer coefficients increase according to increases in heat flux, especially at high heat flux and low saturation temperature conditions. Furthermore, Fig. 5 also shows the effect of mass fluxes on the heat transfer coefficient. The results show that the increase in mass flux has no significant effect on the heat transfer coefficient whether saturation pressure increases or decreases.

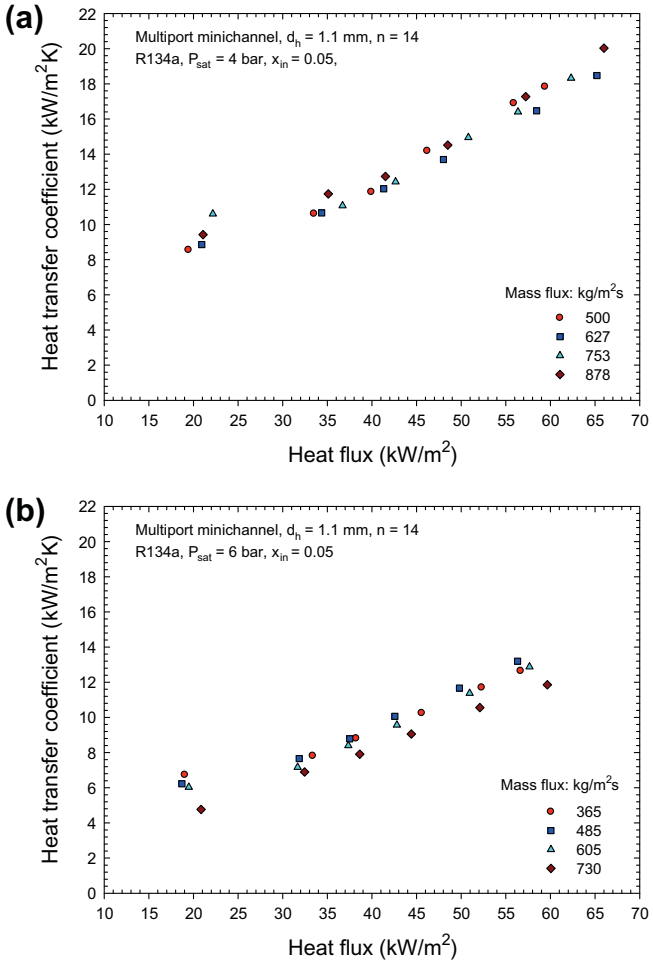

Fig. 5. Average heat transfer coefficient as a function of heat flux for different mass fluxes: (a) P_{sat} = 4 bar and (b) P_{sat} = 6 bar.

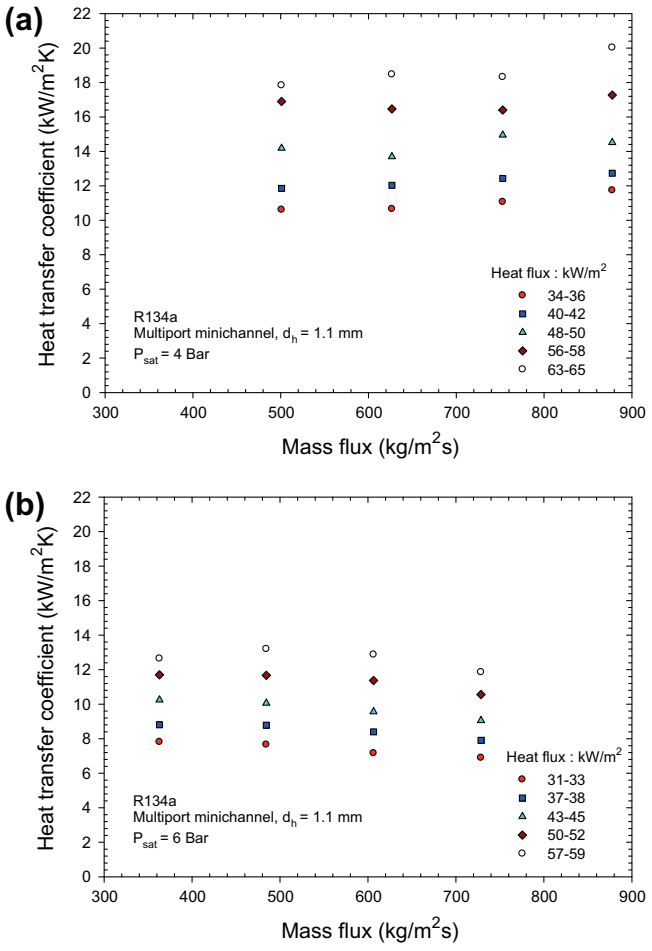

Fig. 6. Average heat transfer coefficient as a function of mass flux for different heat fluxes: (a) P_{sat} = 4 bar and (b) P_{sat} = 6 bar.

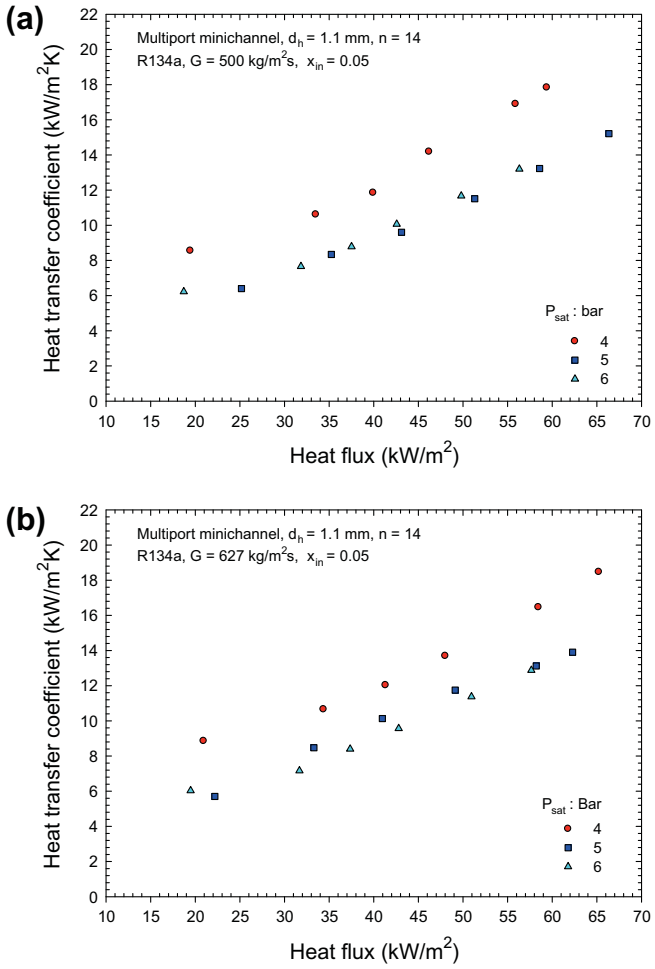

Fig. 7. Average heat transfer coefficient as a function of heat flux for different saturation pressures: (a) P_{sat} = 4 bar and (b) P_{sat} = 6 bar.

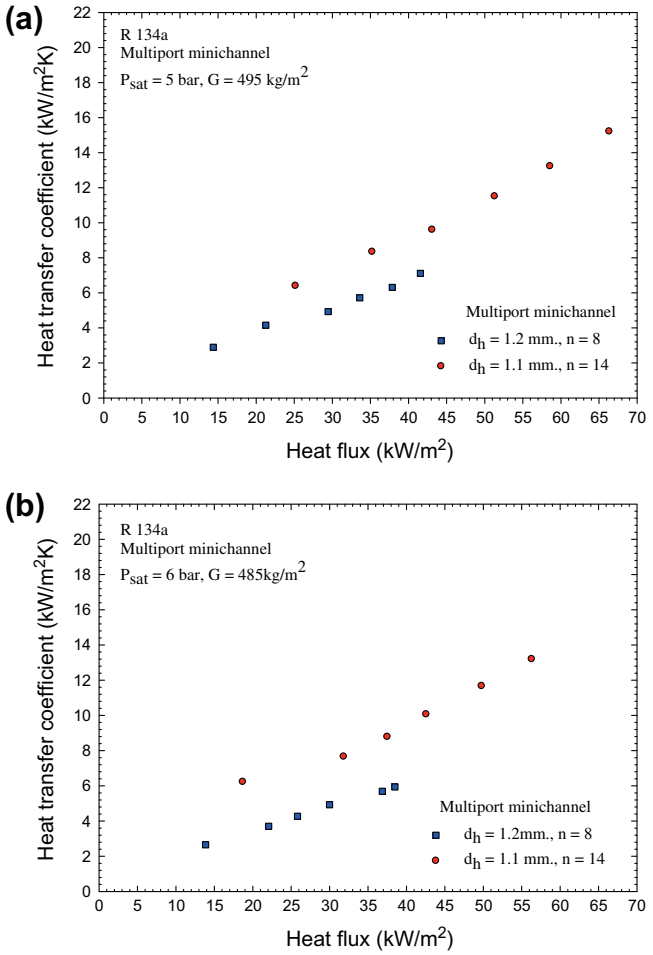

Fig. 8. Average heat transfer coefficient as a function of heat flux for different number of channels: (a) P_{sat} = 4 bar and (b) P_{sat} = 6 bar.

The average heat transfer coefficient plotted against the mass flux for different of heat flux are represented in Fig. 6. The experiment was performed at saturation pressure of 4 bar (Fig. 6a), and 6 bar (Fig. 6b) with inlet quality of 0.05, and heat flux ranging between 30 to 65 kW/m^2. It is clearly seen that the heat flux has a strong effect on the average heat transfer coefficient, and increases with increasing heat flux. The dependence of the heat flux on the heat transfer coefficient and its independence upon the mass flux suggests that the contribution of forced convection heat transfer to the overall flow boiling heat transfer is small; the mechanism of heat transfer is dominated by nucleate boiling. Therefore, the average heat transfer coefficient is a function of the heat flux, but almost independent of vapour quality and mass flux. This behavior is rather distinguished from that of the conventional channels, which are dependent upon mass flux, vapour quality, and saturation pressure, but independent of heat flux. It can be also explained by the fact that the increase in heat flux attributes to the increase in the number of bubbles results in an increase in the entrainment of droplets and the degree of turbulence, which led to the increase in the heat transfer coefficient.

In order to investigate the effect of saturation pressure on the average heat transfer coefficient, experimental measurements were carried out by increasing and decreasing the system pressure at constant mass flux and inlet quality. Fig. 7 shows the experimental data for three saturation pressures of 4 bar, 5 bar, and 6 bar at two mass fluxes of 500 kg/m^2 s (Fig. 7a) and 620 kg/m^2 s (Fig. 7b). The experimental data show that the heat transfer coefficient of 4 bar is significantly higher than that of 5 bar and 6 bar. The reason is that heat transferred through the liquid film covering around inner wall surface depends on the thermal conductivity of liquid film, and that the liquid refrigerant film at 6 bar has a lower thermal conductivity than at 4 bar (6.2% lower). This results in a decrease in the heat transfer coefficient as the evaporation pressure is increased. Moreover, density of vapour increases with increasing pressure which strongly affects the velocity of generated vapour. Therefore convective heat transfer is expected to be lower with higher pressure. This results in a decrease of the heat transfer coefficient as the evaporation pressure is increased. A similar trend regarding the effect of saturation pressure on the heat transfer coefficient was also reported by Choi et al. [23], Bertsch et al. [24] and Kaew-On and Wongwises [17].

The comparisons of heat transfer coefficient carried out of two heat exchangers with different of inner tubes whereas same outer tubes are presented in Fig. 8. The inner tube No. 1 is the tube that have hydraulic diameter of 1.1 mm, 14 numbers of channels, 1.25 of aspect ratio, and inner surface area is 13,545 mm^2, while, the tube No. 2 having hydraulic diameter of 1.2 mm, eight numbers of channels, 0.5 of aspect ratio, and inner surface area of 8856 mm^2. The outer surface area of two inner tubes are 5979 mm^2 and 6171 mm^2 for tube No. 1 and No. 2, respectively. The more details of the test sections are presented in Table 2. At similar experimental conditions of 4 bar (Fig. 8a) and 6 bar (Fig. 8b), the results show that heat transfer coefficients for tube No. 1 are higher than those for tube No. 2 about 50–70%. This is due to the different inner surface area. It can

be indicated that the inner surface of inner tube No. 1 is about 1.5 time of tube No. 2. The increasing of inner surface area (better load distribution) results in the increase of number of bubbles at the inner wall surface which causes the heat transfer coefficient to increase. Moreover, from the description of Cengel [25], regarding the nucleate boiling, he explained that the bubbles are formed at the surface, and then these bubbles are dissipated in the liquid shortly after they separate from the surface. The space vacated by the rising bubbles is filled by the liquid in the vicinity of the heater surface, and the process is repeated. The stirring and agitation caused by the entrainment of the liquid to the heat transfer surface is primarily responsible for the increase of the heat transfer coefficient in nucleate boiling region.

4.3. Comparison of experimental data with existing correlations

In this section, the heat transfer coefficient is compared to that predicted from the existing correlations. Nine correlations, proposed by Chen [6], Lazarek and Black [26], Malek and Colin [27], Kenning and Cooper [18], Tran et al. [28], Kew and Cornwell [29],

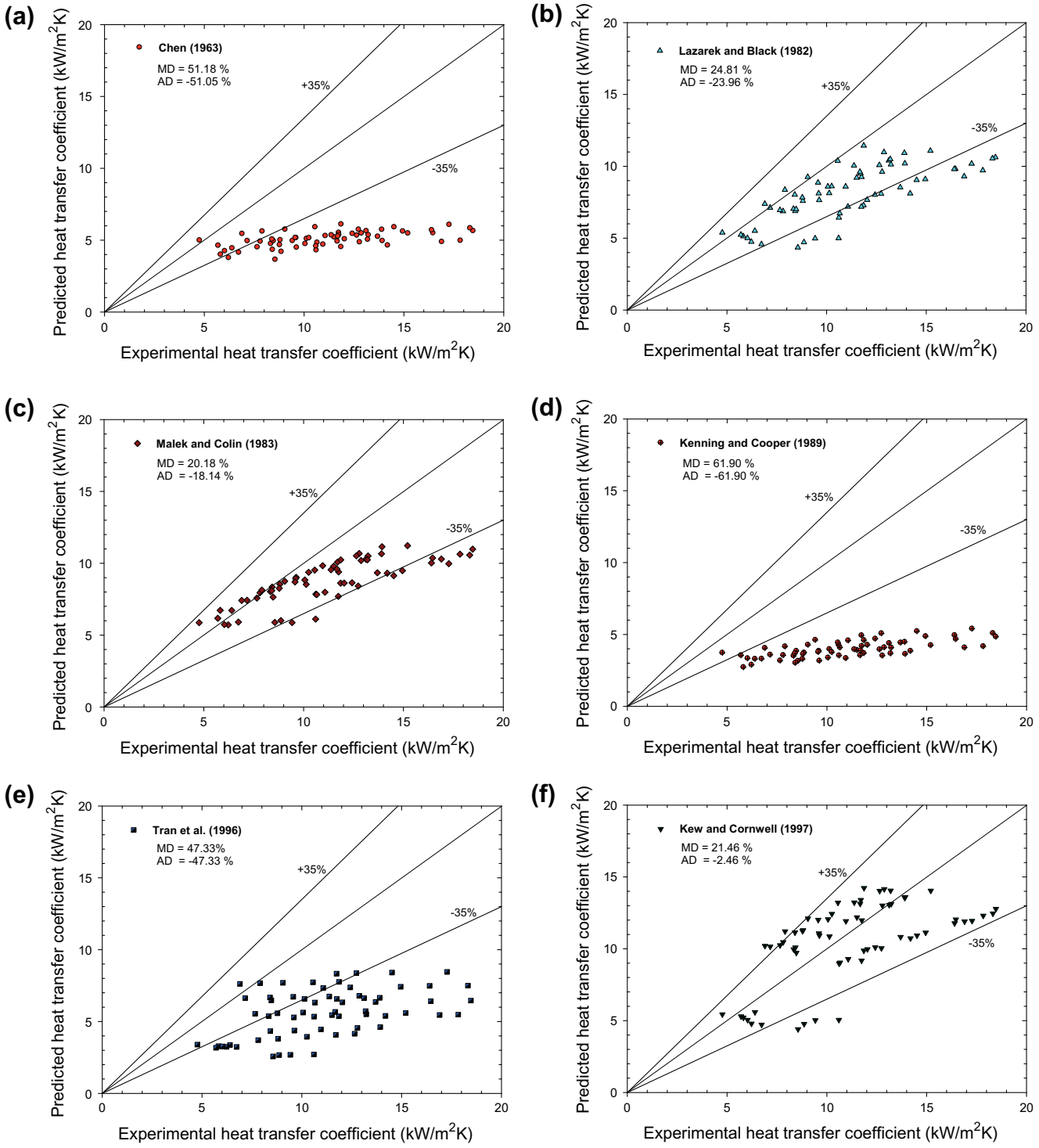

Fig. 9. Comparison of experimental average heat transfer coefficient with existing correlations: (a) Chen [6], (b) Lazarek and Black [26], (c) Malek and Colin [27], (d) Kenning and Cooper [18], (e) Tran et al. [28], (f) Kew and Cornwell [29], (g) Warrier et al. [19], (h) Yu et al. [30] and (i) Kaew-On and Wongwises [17].

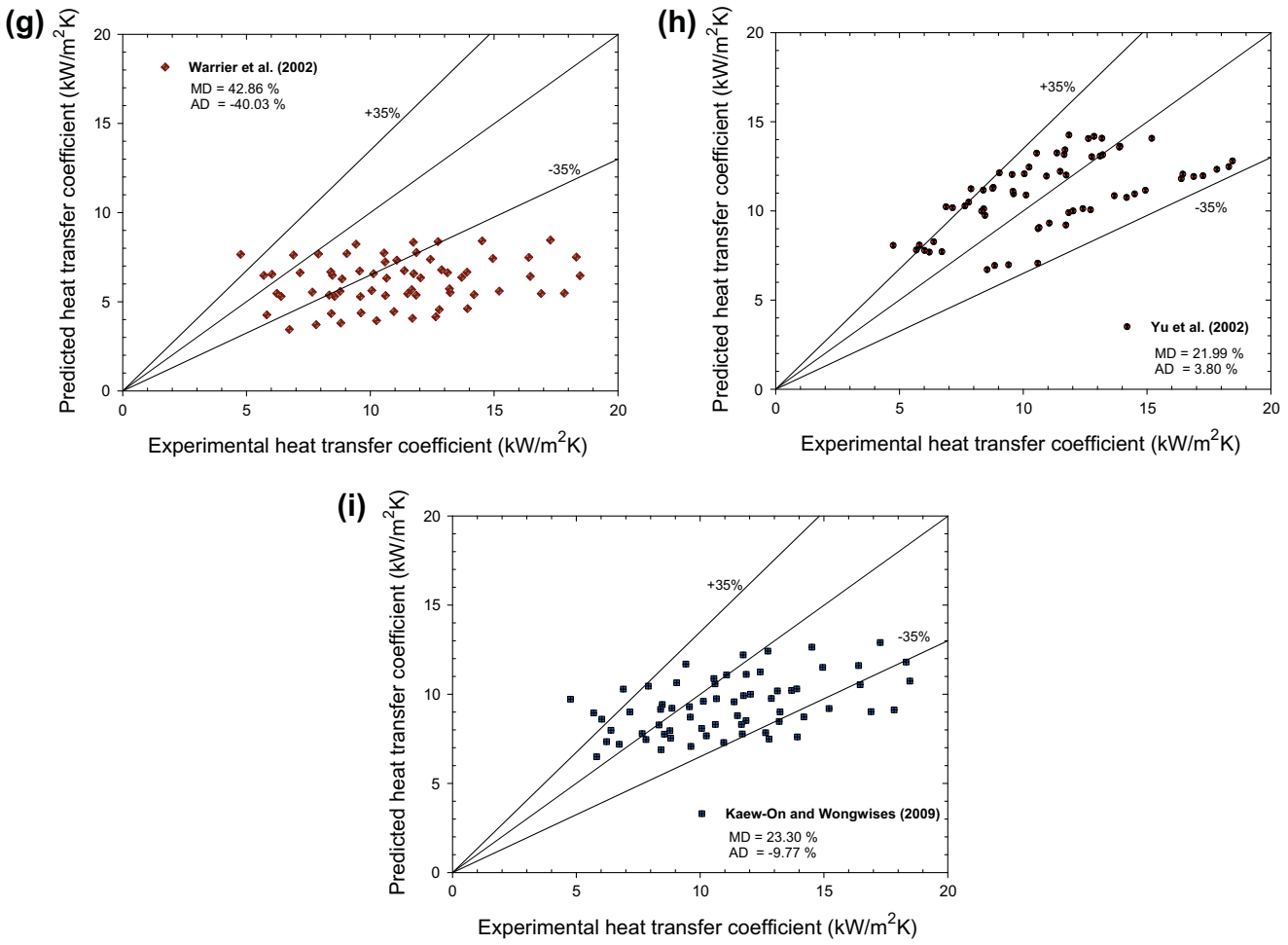

Fig. 9 (*continued*)

Warrier et al. [19], Yu et al. [30], and Kaew-On and Wongwises [17], are presented as equations in Table 1. Comparisons of the experimental data with the predicted heat transfer coefficients are shown in Fig. 9. The mean and average deviations of the comparisons between the experimental data and predicted values are summarized in Table 5. The correlations of Chen [6], Kenning and Cooper [18], Tran et al. [28], and Warrier et al. [19] showed results whose mean deviations from the present data were greater than 50%. These large deviations may be attributed to the limitations of tube diameter and working fluids used in developing their models. The proposed correlations of Lazarek and Black [26], Malek and Colin [27], Kew and Cornwell [29], Yu et al. [30], and Kaew-On and Wongwises [17], presented fairly good predictions of the present data with mean deviations of 20–25%. These deviations may be due to the existence of a mal-distribution of multiport channels, which yield the differences of heat transfer coefficients between multiport channels and single channel even though the tests were conducted at similar operating conditions.

4.4. Development of a new correlation for predicting the heat transfer coefficient

The modified Kaew-On and Wongwises [17] correlation obtained by adding two dimensionless terms, *Bo* and *We*, is presented as follows:

$$h_{TP} = SBo^{0.185} We_l^{0.0013} h_l \quad (9)$$

where *Bo* and We_l are the boiling number and Webber number, respectively, defined as follows:

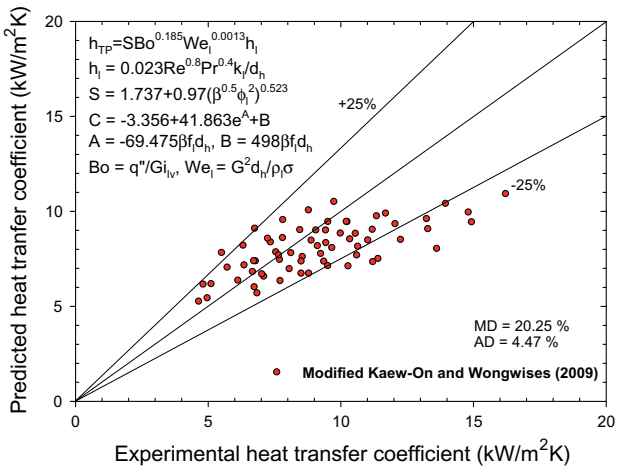

Fig. 10. Comparison of experimental average heat transfer coefficient with new correlation based on Kaew-On and Wongwises.

Table 4
Uncertainties of measured quantities and calculated parameters.

Parameter	Uncertainty
Temperature	±0.1 (°C)
Mass flow rate of refrigerant	±0.1 (%) full scale
Heat transfer rate of test section	±8.50%
Heat transfer rate of pre-heater	±2.25%
Heat transfer coefficient	±12.25%

Table 5
Deviation of the heat transfer coefficient comparison between the present data and the existing correlations.

Correlation	Mean deviation%	Average deviation%
Chen [6]	51.48	−51.05
Lazarek and Black [26]	24.51	−23.96
Malek and Colin [27]	20.18	−18.14
Kenning and Cooper [18]	61.90	−61.90
Tran et al. [26]	47.33	−47.33
Kew and Cornwell [29]	21.46	−2.46
Warrier et al. [19]	42.86	−40.03
Yu et al. [30]	21.99	3.80
Kaew-On and Wongwises [17]	23.30	−9.77
Proposed new correlation	20.25	4.75

$$Bo = \frac{q''}{Gi_{lv}}, \tag{10}$$

$$We_l = \frac{G^2 d_h}{\rho_l \sigma} \tag{11}$$

The comparison of the experimental heat transfer coefficient with the predicted heat transfer coefficients calculated from the new correlation is presented in Fig. 10 and tabulated in Table 4. The new correlation showed good agreement, with a mean deviation of 20.25% and average deviation of 4.47%.

5. Conclusion

Experiments were performed with an aluminium multiport minichannel counter flow heat exchanger with refrigerant flow inside the tube while the hot water flows outside. System pressures ranged from 4 to 6 bar, heat fluxes ranged from 15 to 65 kW/m^2, and mass fluxes ranged from 300 to 800 kg/m^2 s. The main findings of the present study are summarized as follows.

According to the boiling curves, the flow boiling regime corresponds to nucleate boiling. Therefore, the average heat transfer coefficients increase with increasing heat flux while being independent of mass flux. At similar tested conditions, the results show that when the number of channel decreases from 14 to 8 channels, the average heat transfer coefficients increase by 50–70%. Comparisons of the experimental data with nine existing correlations found that the correlations of Chen [6], Kenning and Cooper [18], Tran et al. [28], and Warrier et al. [19], failed to predict the heat transfer coefficient of presented study. While, the correlations of Lazarek and Black [26], Malek and Colin [27], Kew and Cornwell [29], Yu et al. [30], and Kaew-On and Wongwises [17], presented fairly good predictions of the present data with mean deviations of 20–25%. The new heat transfer coefficient correlation based on the modified Kaew-On and Wongwises [17] correlation showed good agreement with the experimental data.

Acknowledgements

The authors would like to acknowledge the Thailand Research Fund (TRF), the Joint Graduate School of Energy and Environment (JGSEE), the Office of Higher Education Commission and the National Research University Project for financial support.

References

[1] Y.Y. Yan, T.F. Lin, Evaporation heat transfer and pressure drop of refrigerant R-134a in a small pipe, International Journal of Heat and Mass Transfer 41 (1998) 4183–4194.
[2] W. Owhaib, C. Martin-Callizo, B. Palm, Evaporative heat transfer in vertical circular microchannels, Applied Thermal Engineering 24 (2004) 1241–1253.
[3] X. Huai, S. Koyama, T.S. Zhao, E. Shinmura, K. Hidehiko, M. Masaki, An experimental study of flow boiling characteristics of carbon dioxide in multiport mini channels, Applied Thermal Engineering 24 (2004) 1443–1463.
[4] J. Pettersen, Flow vaporization of CO_2 in microchannel tubes, Experimental Thermal and Fluid Science 28 (2004) 111–121.
[5] W. Zhang, T. Hibiki, K. Mishima, Correlation for flow boiling heat transfer in mini-channels, International Journal of Heat and Mass Transfer 47 (2004) 5749–5763.
[6] J.C. Chen, A correlation for boiling heat transfer to saturated fluid in convective flow, ASME Paper, 63-HT-34, 1963, pp. 1–11.
[7] S. Saitoh, H. Daiguji, E. Hihara, Effect of tube diameter on boiling heat transfer of R134a in horizontal small-diameter tubes, International Journal of Heat and Mass Transfer 48 (2005) 4973–4984.
[8] R. Yun, Y. Kim, M.S. Kim, Convective boiling heat transfer characteristics of CO_2 in micro-channels, International Journal of Heat and Mass Transfer 48 (2005) 335–342.
[9] R. Yun, J.H. Heo, Y. Kim, Evaporative heat transfer and pressure drop of R-410A in micro-channels, International of Refrigeration 29 (2006) 92–100.
[10] Y.M. Lie, F.Q. Su, R.L. Lai, T.F. Lin, Experimental study of evaporation heat transfer characteristics of refrigerants R134a and R407C in horizontal small tubes, International Journal of Heat and Mass Transfer 49 (2006) 207–218.
[11] D. Shiferaw, X. Huo, T.G. Karayiannis, D.B.R. Kenning, Examination of heat transfer and a model for flow boiling of R134a in small diameter tubes, International Journal of Heat and Mass Transfer 50 (2007) 5177–5193.
[12] P. Fernando, B. Palm, T. Ameel, P. Lundquist, E. Granryd, A minichannel aluminium tube heat exchanger-part I: evaluation of single-phase heat transfer coefficients by the Wilson plot method, International Journal of Refrigeration 31 (2008) 669–680.
[13] P. Fernando, B. Palm, T. Ameel, P. Lundquist, E. Granryd, A minichannel aluminium tube heat exchanger-part II: evaporation performance with propane, International Journal of Refrigeration 31 (2008) 681–695.
[14] P. Fernando, B. Palm, T. Ameel, P. Lundquist, E. Granryd, A minichannel aluminium tube heat exchanger-part III: condenser performance with propane, International Journal of Refrigeration 31 (2008) 696–708.
[15] V. Gnielinski, New equations for heat and mass transfer in turbulent pipe and channel flow, Institution of Chemical Engineers 16 (1936) 359–368.
[16] C.L. Ong, J.R. Thome, Flow boiling heat transfer of R134a, R236fa and R245fa in a horizontal 1.030 mm circular channel, Experimental Thermal and Fluid Science 33 (2009) 651–663.
[17] J. Kaew-On, S. Wongwises, Experimental investigation of evaporation heat transfer coefficient and pressure of R410A in multiport minichannel, International Journal of Refrigeration 32 (2009) 124–137.
[18] D.B.R. Kenning, M.G. Cooper, Saturated flow boiling of water in vertical tubes, International Journal of Heat and Mass Transfer 32 (1989) 445–458.
[19] G.R. Warrier, V.K. Dhir, L.A. Momoda, Heat transfer and pressure drop in narrow rectangular channels, Experimental Thermal and Fluid Science 26 (2002) 53–64.
[20] K.E. Gungor, R.H.S. Winterton, A general correlation for flow boiling in tubes and annuli, International Journal of Heat and Mass Transfer 29 (1986) 351–358.
[21] S.S. Kutateladze, Fundamentals of Heat Transfer, Edward Arnold, 1963. pp. 1–11.
[22] R. Revellin, J.R. Thome, A new type of adiabatic flow pattern map for boiling heat transfer in microchannels, Journal of Micromechanics and Microengineering 17 (2007) 788–796.
[23] K.I. Choi, A.S. Pamitran, C.Y. Oh, J.T. Oh, Boiling heat transfer of R-22, R-134a, and CO_2 in horizontal smooth minichannels, International Journal of Refrigeration 30 (2007) 1336–1346.
[24] S.S. Bertsch, E.A. Groll, A.V. Garimella, Refrigerant flow boiling in parallel microchannels as a function of local vapor quality, International Journal of Heat and Mass Transfer 51 (2008) 4775–4787.
[25] Y.A. Cengel, Heat and Mass Transfer: A Practical Approach, third ed., McGraw-Hill, New York, 2006.
[26] G.M. Lazarek, S.H. Black, Evaporative heat transfer, pressure drop and critical heat flux in small vertical tube with R-113, International Journal of Heat and Mass Transfer 25 (1982) 945–960.
[27] A. Malek, R. Colin, Ebullition de l'ammoniac en tube long, Transfert de chaleur et ertes de charges en tubes vertical et horizontal, Centre Technique des Industries Mecanniques, Senlis France, CETIM-14-011, 1983, pp. 1–65.
[28] T.N. Tran, M.W. Wambsganss, D.M. France, Small circular- and rectangular-channel boiling with two refrigerants, International Journal of Multiphase Flow 22 (1996) 485–498.
[29] P.A. Kew, K. Cornwell, Correlations for prediction of boiling heat transfer in small-diameter channels, Applied Thermal Engineering 17A (1997) 705–715.
[30] W. Yu, D.M. France, M.W. Wambganss, J.R. Hull, Two-phase pressure drop, boiling heat transfer, and critical heat flux to water in a small-diameter horizontal tube, International Journal of Multiphase Flow 28 (2002) 927–942.

Provided for non-commercial research and education use.
Not for reproduction, distribution or commercial use.

This article appeared in a journal published by Elsevier. The attached copy is furnished to the author for internal non-commercial research and education use, including for instruction at the authors institution and sharing with colleagues.

Other uses, including reproduction and distribution, or selling or licensing copies, or posting to personal, institutional or third party websites are prohibited.

In most cases authors are permitted to post their version of the article (e.g. in Word or Tex form) to their personal website or institutional repository. Authors requiring further information regarding Elsevier's archiving and manuscript policies are encouraged to visit:

http://www.elsevier.com/copyright

Author's personal copy

International Communications in Heat and Mass Transfer 38 (2011) 75–84

Contents lists available at ScienceDirect

International Communications in Heat and Mass Transfer

journal homepage: www.elsevier.com/locate/ichmt

Artificial neural network techniques for the determination of condensation heat transfer characteristics during downward annular flow of R134a inside a vertical smooth tube ☆

M. Balcilar [a], A.S. Dalkilic [b,*], S. Wongwises [c,*]

[a] Computer Engineering Department, Yildiz Technical University, Yildiz, Besiktas, Istanbul 34349, Turkey
[b] Heat and Thermodynamics Division, Department of Mechanical Engineering, Yildiz Technical University, Yildiz, Besiktas, Istanbul 34349, Turkey
[c] Fluid Mechanics, Thermal Engineering and Multiphase Flow Research Lab. (FUTURE), Department of Mechanical Engineering, King Mongkut's University of Technology Thonburi, Bangmod, Bangkok 10140, Thailand

ARTICLE INFO

Available online 18 November 2010

Keywords:
Condensation
Heat transfer coefficient
Pressure drop
Modeling
Neural network

ABSTRACT

In this study, the best artificial intelligence method is investigated to estimate the measured convective heat transfer coefficient and pressure drop of R134a flowing downward inside a vertical smooth copper tube having an inner diameter of 8.1 mm and a length of 500 mm during annular flow numerically. R134a and water are used as working fluids in the tube side and annular side of a double tube heat exchanger, respectively. The ANN training sets have the experimental data of in-tube condensation tests including six different mass fluxes of R134a such as 260, 300, 340, 400, 456 and 515 kg m^{-2} s^{-1}, two different saturation temperatures of R134a such as 40 and 50 °C and heat fluxes ranging from 10.16 to 66.61 kW m^{-2}. The quality of the refrigerant in the test section is calculated considering the temperature and pressure obtained from the experiment. The pressure drop across the test section is directly measured by a differential pressure transducer. Input of the ANNs are the measured values of test section such as mass flux, heat flux, the temperature difference between the tube wall and saturation temperature, average vapor quality, while the outputs of the ANNs are the experimental condensation heat transfer coefficient and measured pressure drop in the analysis. Condensation heat transfer characteristics of R134a are modeled to decide the best approach using several artificial neural network (ANN) methods such as multilayer perceptron (MLP), radial basis networks (RBFN), generalized regression neural network (GRNN) and adaptive neuro-fuzzy inference system (ANFIS). Elimination process of the ANN methods is performed by means of 183 data points, divided into two sets randomly, obtained in the experiments. Sets of test and training/validation include 33 and 120/30 data points respectively for the elimination process. Validation process, in terms of various experimental conditions, is done by means of 368 experimental data points having 68 data points for test set and 300 data points for training set. In training phase, 5-fold cross validation is used to determine the best value of ANNs control parameters. The ANNs performances were measured by means of relative error criteria with the usage of unknown test sets. The performance of the method of multi layer perceptron (MLP) with 5-13-1 architecture and radial basis function networks (RBFN) were found to be in good agreement, predicting the experimental condensation heat transfer coefficient and pressure drop with their deviations being within the range of ±5% for all tested conditions. Dependency of outputs of the ANNs from input values is also investigated in the paper.

© 2010 Elsevier Ltd. All rights reserved.

1. Introduction

Determination of heat transfer characteristics of compact systems such as heat transfer coefficient, frictional pressure drop, flow type between the fluids, heat transfer surface area in heat exchangers should be known accurately for the optimum design. The two-phase heat transfer systems have higher thermal heat transfer performance than single-phase heat transfer systems in limited apparatus volumes. The advantage of high thermal performance in comparison to the single-phase applications includes smaller, more compact systems regarding tube length, tube diameter, internal tube geometry shape in a wide variety of applications, e.g. refrigeration and air conditioning systems, power engineering and other thermal processing plants. Before doing any numerical work on this subject, validation process of the experimental setup and data is a very significant for reliability of the study. The correctness of experimental data should be evaluated by either graphics regarding the characteristics of trend lines such as

☆ Communicated by W.J. Minkowycz.

* Corresponding authors.
E-mail addresses: dalkilic@yildiz.edu.tr (A.S. Dalkilic), somchai.won@kmutt.ac.th (S. Wongwises).

0735-1933/$ – see front matter © 2010 Elsevier Ltd. All rights reserved.
doi:10.1016/j.icheatmasstransfer.2010.10.009

Author's personal copy

alteration of heat transfer coefficient vs quality, heat flux vs temperature difference between the vapor and inlet wall temperature, pressure drop vs vapor quality etc. or widely accepted correlations in the literature and desired working conditions should be agreeable with the heat balance correlations and flow type observations by means of sight glasses at the different points of experimental apparatus.

There have been a number of studies on the in-tube condensation heat transfer coefficient and pressure drop. The frictional, acceleration, and gravitational components determine the two-phase total pressure drop in tubes. Determination of the void fraction is required to compute the acceleration and gravitational components, and in a similar way, determination of either the two-phase friction factor or the two-phase frictional multiplier is required to compute the frictional component of pressure drop. Generally, empirical methods have been used to compute the condensation heat transfer coefficients and pressure drops in tubes. Most of these proposed models are modifications of the Dittus–Boelter single-phase forced convection correlation [1], as in Akers et al. [2], Cavallini and Zecchin [3], and Shah [4].

Dalkilic et al. [5] compared thirteen well-known two-phase pressure drop models with the experimental results of a condensation pressure drop of R600a and R134a in horizontal and vertical smooth copper tubes respectively and discussed the main parameters of related models and correlations. Dalkilic et al. [6] proposed a new correlation for the two-phase friction factor of R134a flow based on the equivalent Reynolds number model [7] and also showed the effects of heat flux, mass flux and condensation temperature on the pressure drop. Dalkilic et al. [8] compared eleven well-known correlations for annular flow to each other using a large amount of data obtained under various experimental conditions and proposed a new correlation based on Bellinghausen and Renz's method [9] for the condensation heat transfer coefficient of high mass flux flow of R134a. They also reported the effects of heat flux, mass flux and condensation temperature on the heat transfer coefficients in their paper. Dalkilic et al. [10] emphasized that an interfacial shear effect is significant for the laminar condensation heat transfer of R134a using Carey's analysis [11], which is the improved version of Nusselt's theory [12], and proposed a new correlation based on Bellinghausen and Renz's method [9] for the condensation heat transfer coefficient during annular flow of R134a at low mass flux in a vertical tube. Dalkilic et al. [13] reviewed thirty-three void fraction models and correlations, determined using relevant data from the available literature. They calculated the friction factors, based on the analysis of Ma et al. [14], obtained from various void fraction models and correlations, and compared these with each other and also with those determined from graphical information provided by Bergelin et al. [15]. The effect of void fraction alteration on the momentum pressure drop was also presented in their paper. Dalkilic et al.'s [16] analysis based on simple void fraction models of the annular flow pattern was presented for the forced convection condensation of pure R134a, taking into account the effect of the different saturation temperatures in high mass flux conditions. The comparisons of calculated film thickness from void fraction models and correlations with those from Whalley's annular flow model [17] were made using their experimental database. Dalkilic and Wongwises [18] studied a mathematical model, developed by Barnea et al. [19], and based on the momentum balance of liquid and vapor phases, in order to determine the condensation film thickness of R134a in their paper. The effects of heat flux, mass flux and condensation temperature on the film thickness and condensation heat transfer coefficient were also discussed for laminar and turbulent flow conditions. Six well-known flow regime maps from the literature were found to be predictive for the annular flow conditions in the test tube in spite of their different operating conditions.

Dalkilic et al. [20] reports the experimental investigation of Kosky's model [21] for predicting flow pattern transitions and for the validation of void fraction models and correlations proposed in their previous publications and for the identification of flow regimes in data corresponding to annular flow downward condensation of R134a in a vertical smooth copper tube. In addition to this, 12 number of well-known flow regime correlations from the literature are investigated to identify the flow regime occurring in the test tube. Dalkilic et al. [22] determined the average predicted heat transfer coefficient of the refrigerant by means of Kosky and Staub's model [23] and the Von Karman universal velocity distribution correlations using different interfacial shear stress equations valid for annular flow in horizontal and vertical tubes in order to investigate Chen et al.'s annular flow theory [24]. The effects of heat flux, mass flux and condensation temperature on the pressure drop were also discussed. A new correlation, based on dimensionless parameters such as the equivalent Reynolds number, Prandtl number, R number (ρ-μ ratio), Lockhart and Martinelli parameter, Bond number and Froude number, using a large number of data points for the turbulent condensation heat transfer coefficient, was proposed in their paper. Dalkilic et al. [25] presented a new experimental approach on the determination of condensation heat transfer coefficient using 13 number of frictional pressure drop models and 35 number of void fraction models in a vertical tube by means of von Karman's universal velocity distribution and Kosky and Staub's annular flow film thickness model [23]. Dalkilic and Wongwises [26] presented a detailed review of research on in-tube condensation due to its significance in refrigeration, air conditioning and heat pump applications. Their review considered heat transfer and pressure drop investigations during in-tube condensation. Almost all relevant research subjects were summarized, such as condensation heat transfer and pressure drop studies according to tube orientation (horizontal, vertical, inclined tubes) and tube geometry (smooth and enhanced tubes), flow pattern studies of condensation, void fraction studies, and refrigerants with oil. Dalkilic and Wongwises [27] performed a theoretical performance study on a traditional vapor-compression refrigeration system with refrigerant mixtures based on HFC134a, HFC152a, HFC32, HC290, HC1270, HC600, and HC600a for various ratios and their results are compared with CFC12, CFC22, and HFC134a as possible alternative replacements. Dalkilic et al. [28] investigated the direct relationship between the measured condensation pressure drop and convective heat transfer coefficient of R134a to determine the condensation heat transfer coefficient, heat flux, two-phase length and pressure drop experimentally. In addition to the above, various other papers [29–36] support and validate the proposed models and correlations in their papers.

To the best of the authors' knowledge, there has been only one work just for the condensation of R600a in a horizontal tube, recently carried out by Demir et al. [37] dealing with numerical solution using neural network analysis of heat transfer coefficient, and no work regarding the numerical solution using neural network analysis for the condensation heat transfer coefficient and pressure drop of HFC-134a either in a horizontal or vertical tube. For these reasons, there remains room for further research. Especially, it can be noted that all of the numerical investigations of neural network analysis do not have any that are concerned with the study. As a consequence, in the present study, the main concern is to fill the gap in the literature. The results for the solution of neural network analysis on the two-phase heat transfer coefficient and pressure drop which have never before appeared in

Table 1
Operating conditions of the study.

Refrigerant	HFC-134a
Test tube material, inner diameter d, length L	Copper, ϕ8.1 mm, 500 mm
Range of condensing pressure, P_{sat} (bar)	10–12
Range of condensing temperature, T_{sat} (°C)	40–50
Range of mass flux, G (kg m^{-2} s^{-1})	260–515
Range of heat flux, q (kW m^{-2})	10.16–66.61
Range of temperature difference, $\Delta T = T_{sat} - T_{wi}$, K	1.26–8.98
Range of average vapor quality, x	0.69–0.96

Author's personal copy

Table 2
Uncertainty of experimental parameters.

Parameters	Uncertainty
$T_{ref,\ sat}$ (°C)	0.19
x_i	±6.96–8.24%
ΔT (K)	±0.191
$(T_{w,o}-T_{w,i})_{TS}$ (K)	±0.045
$(T_{w,i}-T_{w,o})_{ph}$ (K)	±0.13
m_{ref} (g s^{-1})	±0.023
$m_{w,TS}$ (g s^{-1})	±0.35
$m_{w,ph}$ (g s^{-1})	±0.38
q_{TS} (kW m^{-2})	±6.55–8.93%
q_{ph} (kW m−2)	±12–14.81%
h_{ref} (W m^{-2} K^{-1})	±7.64–10.71%.
ΔP (kPa)	±0.15

open literature are presented. The large amount of measured data obtained from the experimental study regarding with the convective heat transfer coefficient and pressure drop is compared with the results from artificial neural networks' methods such as multi layer perceptron (MLP), radial basis function networks (RBFN), generalized regression neural network (GRNN) and adaptive neuro-fuzzy inference system (ANFIS). In addition to this, the effect of input parameters (mass flux (G), heat flux (q), saturation temperature (T_{sat}), temperature difference between the condensing temperature and inlet tube wall temperature (ΔT_{sat}), vapor quality (x)) on the output parameters (convective heat transfer coefficient (h), pressure drop (ΔP)) is also shown and discussed as a first study on this subject in the literature.

2. Experimental apparatus and method

Detailed descriptions of the experimental apparatus for studying condensation of R134a inside a vertical tube can be found in the authors' previous publications.

3. Data reduction and experimental uncertainty

The data reduction of the measured results can be analyzed as follows:

3.1. The inlet vapor quality of the test section ($x_{TS,i}$)

$$x_{TS,i} = \frac{i_{TS,i} - i_{l@T_{TS,i}}}{i_{fg@T_{TS,i}}} \quad (1)$$

where $i_{l@T_{TS,i}}$ is the enthalpy of the saturated liquid based on the temperature of the test section inlet, $i_{fg@T_{TS,i}}$ is the enthalpy of

Table 3
Elimination of ANN methods according to the error rates for the determination of condensation heat transfer coefficient (a) and pressure drop (b) for the mass fluxes of 260, 340, 456 kg m^{-2} s^{-1} and T_{sat} = 40 and 50 °C.

Error analysis/ ANN methods	h (W m^{-2} K^{-1})			
	MLP	RBFN	ANFIS	GRNNN
a)				
R square	0.999	0.992	0.994	0.056
Proportional (%)	0.588	1.558	1.182	16.062
Square law	39.452	113.617	103.296	1293.76
	ΔP (Pa)			
	MLP	RBFN	ANFIS	GRNNN
b)				
R square	0.997	0.998	0.989	0.432
Proportional (%)	2.127	1.74	4.15	37.608
Square law	64.895	55.208	147.85	1148.447

Table 4
Effect of the experimental data number on the error rates for the determination of condensation heat transfer coefficient (a) and pressure drop (b) for the mass fluxes of 300, 400, 515 kg m^{-2} s^{-1} and T_{sat} = 40 and 50 °C.

Experimental data number	35		68	
error analysis/ANN methods	MLP	RBFN	MLP	RBFN
a)				
h (W m^{-2} K^{-1})				
R square	0.999	0.988	0.999	0.99
Proportional (%)	0.059	1.295	0.061	1.444
Square law	6.048	144.952	5.551	132.68
b)				
ΔP (Pa)				
R square	0.998	0.997	0.998	0.997
Proportional (%)	1.793	2.28	1.754	2.017
Square law	67.702	78.77	64.581	71.11

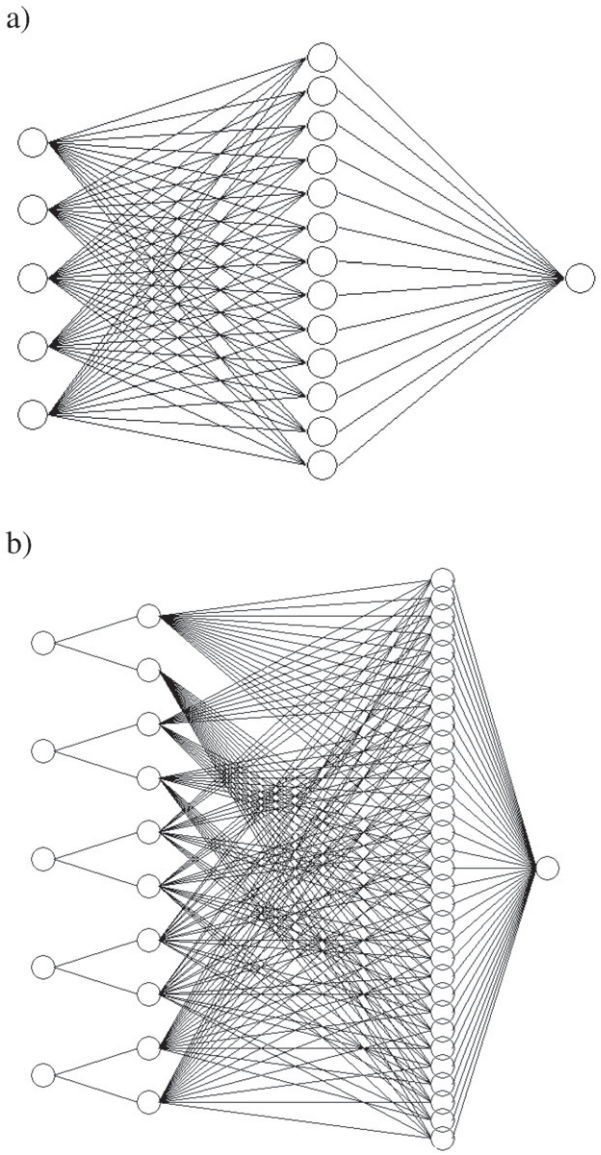

Fig. 1. Schematic diagrams of artificial intelligence models used in the analysis. a) Multi layer perceptron (MLP) with 5-13-1 architecture. b) Artificial neural fuzzy inference system (ANFIS).

Author's personal copy

vaporization based on the temperature of the test section inlet, $i_{TS,i}$ is the refrigerant enthalpy at the test section inlet and is given by:

$$i_{TS,i} = i_{ph,i} + \frac{Q_{ph}}{m_{ref}} \tag{2}$$

where $i_{ph,i}$ is the inlet enthalpy of the liquid refrigerant before entering the preheater, m_{ref} is the mass flow rate of the refrigerant, and Q_{ph} is the heat transfer rate in the preheater:

$$Q_{ph} = m_{w,ph} c_{p,w} \left(T_{w,i} - T_{w,o}\right)_{ph} \tag{3}$$

where $m_{w,ph}$ is the mass flow rate of the water entering the preheater, $c_{p,w}$ is the specific heat of water, $\left(T_{w,i} - T_{w,o}\right)_{ph}$ is the temperature difference between inlet and outlet positions of the preheater.

3.2. The outlet vapor quality of the test section ($x_{TS,o}$)

$$x_{TS,o} = \frac{i_{TS,o} - i_{l@T_{TS,o}}}{i_{fg@T_{TS,o}}} \tag{4}$$

where $i_{TS,o}$ is the refrigerant enthalpy at the test section outlet, $i_{l@T_{TS,o}}$ is the enthalpy of the saturated liquid based on the temperature of the test section outlet, and $i_{fg@T_{TS,o}}$ is the enthalpy of vaporization. The outlet enthalpy of the refrigerant flow is calculated as follows:

$$i_{TS,o} = i_{TS,i} - \frac{Q_{TS}}{m_{ref}} \tag{5}$$

where the heat transfer rate, Q_{TS}, in the test section is obtained from:

$$Q_{TS} = m_{w,TS} c_{p,w} \left(T_{w,o} - T_{w,i}\right)_{TS} \tag{6}$$

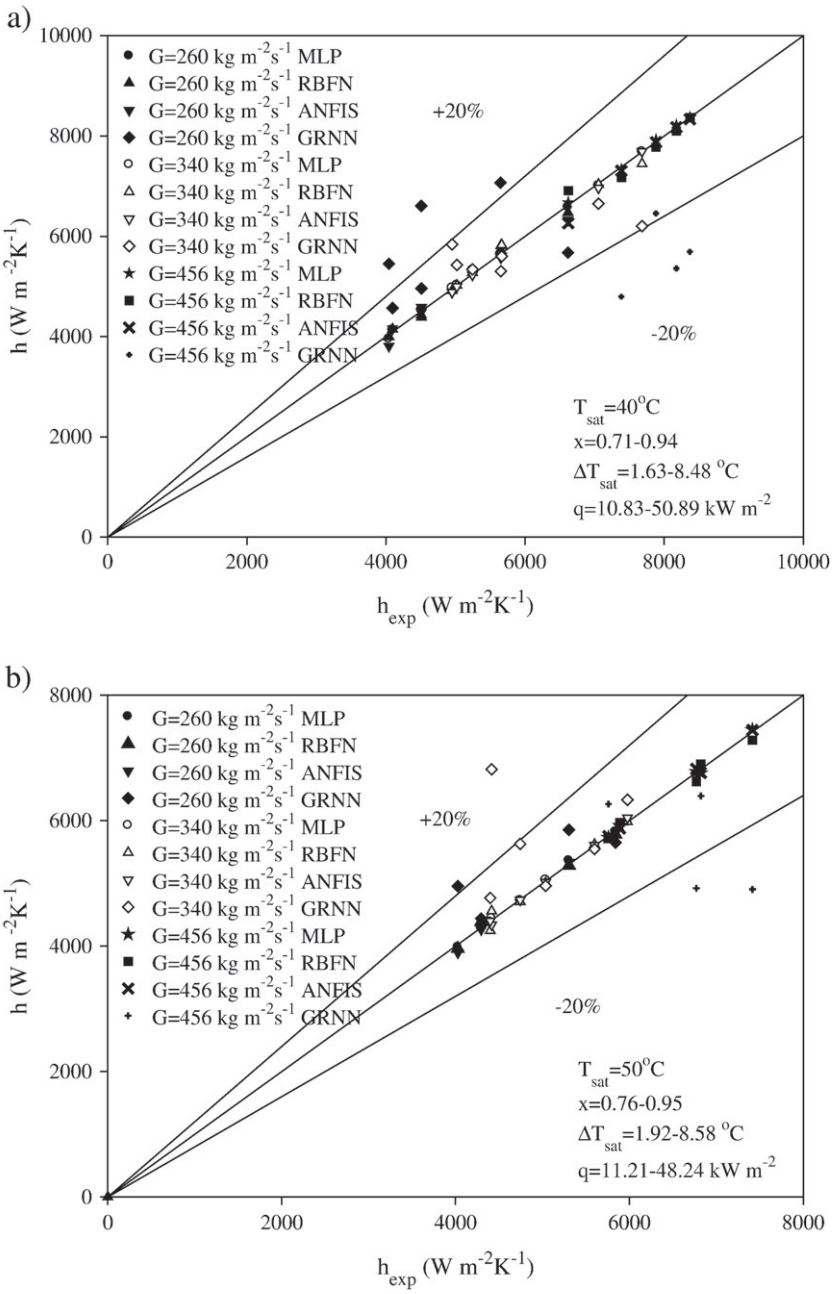

Fig. 2. Comparisons of experimental convective heat transfer coefficients with the artificial neural network methods using 33 number of experimental data points as ANN test group for the mass fluxes of 260, 340, 456 kg m^{-2} s^{-1} and T_{sat} = 40 °C (a) and 50 °C (b).

Author's personal copy

where $m_{w,TS}$ is the mass flow rate of the water entering the test section, and $\left(T_{w,o}-T_{w,i}\right)_{TS}$ is temperature difference between outlet and inlet position of the test section.

3.3. The average heat transfer coefficient

$$h_{exp}=\frac{Q_{TS}}{A_{wi}\left(T_{ref,sat}-T_{wi}\right)} \tag{7}$$

where h_{exp} is the experimental average heat transfer coefficient, Q_{TS} is the heat transfer rate in the test section, T_{wi} is the average temperature of the inner wall, $T_{ref,sat}$ is the average temperature of the refrigerant at the test section inlet and outlet, and A_{wi} is the inside surface area of the test section:

$$A_{wi}=\pi dL \tag{8}$$

where d is the inside diameter of the test tube. L is the length of the test tube.

3.4. Uncertainties

The uncertainties of the Nusselt number and condensation heat transfer coefficient in the test tube varied from ±7.64% to ±10.71%. It should be noted that similar range of uncertainty with minimum and maximum values are exist in the literature. The procedures of Kline and McClintock [38] were used for the calculation of all uncertainties. Various uncertainty values of the study for the operating conditions in Table 1 can be seen from authors' previous works and in Table 2 in detail.

3.5. Error analysis

Error analysis of the study is performed by means of Eqs. (9), (10) and (11) and results of them were given in Tables 3 and 4. In these

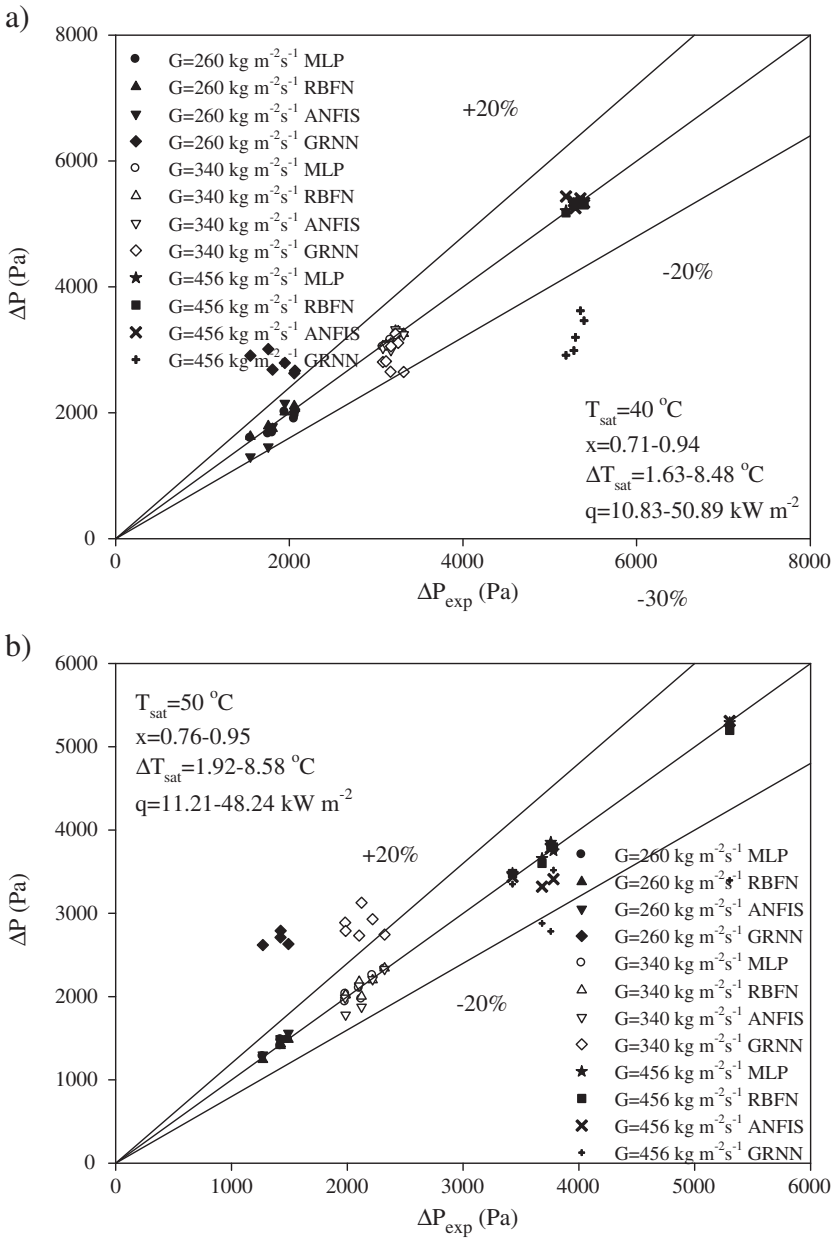

Fig. 3. Comparisons of measured two-phase pressure drops with the artificial neural network methods using 33 number of experimental data points as ANN test group for the mass fluxes of 260, 340, 456 kg m^{-2} s^{-1} and T_{sat} = 40 °C (a) and 50 °C (b).

Author's personal copy

equations, N is the element number of test group, h^i_{exp} and h^i_{calc} are the experimental and calculated results of heat transfer coefficient obtained from "i" number of test data respectively and h_{exp} and h_{calc} are the average values of experimental and calculated results of heat transfer coefficient obtained from the numerical analysis. It should be noted that error analysis of pressure drop was done similarly. R square error is determined as follows:

$$E_{Rsquare} = \frac{\left(\sum_{i=1}^{N}\left(h^i_{exp}-\overline{h_{exp}}\right)\left(h^i_{calc}-\overline{h_{calc}}\right)\right)^2}{\left(\sum_{i=1}^{N}\left(h^i_{exp}-\overline{h_{exp}}\right)^2\right)\left(\sum_{i=1}^{N}\left(\left(h^i_{calc}-\overline{h_{calc}}\right)^2\right)\right)} \quad (9)$$

Proportional error is calculated as follows:

$$E_{ratio} = \frac{100}{N}\sum_{i=1}^{N}\frac{\left|h^i_{exp}-h^i_{calc}\right|}{h^i_{exp}} \quad (10)$$

Square law error is estimated as follows:

$$E_{square} = \sqrt{\frac{1}{N}\cdot\sum_{i=1}^{N}\left(h^i_{exp}-h^i_{calc}\right)^2} \quad (11)$$

3.6. Calculation procedure for the generalized artificial neural networks (ANNs) model

An artificial neural network is an information-processing system that has certain performance characteristics in common with biological neural networks. Artificial neural networks have been developed as generalizations of mathematical models of human cognition or neural biology, based on the assumptions that: (1) Information processing occurs at many simple elements called neurons (2) Signals are passed between neurons over connection links (3) Each connection link has an associated weight, which, in a typical neural net, multiplies the signal transmitted (4) Each neuron applies an activation function (usually non-linear) to its net input (sum of weighted input signals) to determine its output signal [39].

As the artificial neural networks (ANNs) are one of the commonly used and developed models to investigate the relationship between linear or non-linear input–output patterns, they try to generalize the training group and then estimate the test group. Performance of ANNs is measured with the success of the prediction. There are many described ANN types related with the function approximation in the literature. The most known methods are multi layer perceptron (MLP), radial basis functions networks (RBFN), generalized regression neural networks (GRNN) and artificial neural fuzzy inference system (ANFIS) which is the combination of fuzzy logic decision systems and ANNs. Schematic diagrams of some artificial intelligence models used in the analysis are shown in Fig. 1.

3.6.1. Multi layer perceptron (MLP)

MLP is the member of feed-forward network family. According to this method, number of input and output neurons is equal to the number of input and output parameters respectively and there are some layers including neurons between them. Specification of non-linearity and calculation process increase with increasing numbers of hidden layer and neurons. Different architectures of MLP were used for the calculation of heat transfer coefficient and pressure drop. All neurons of MLP are connected with another neurons and the way of connections is forward. Levenberg–Marquardt algorithm, based on the method of back propagation, was used for the training process.

3.6.2. Radial basis function networks (RBFN)

RBFN architecture has a single hidden layer and some similarities with MLP method. On the other hand, it has different calculation process for the determination of neuron number, different activation function and difference in neuron number in hidden layer. RBFN architecture's of single layer has equal neuron numbers with the element numbers in training group. Bias numbers are the control parameters of RBFN architecture and should be given by the user. Training of this architecture, in other words, values of neuron connections is calculated using training group by means of least square method.

3.6.3. Generalized regression neural networks (GRNN)

A generalized regression neural network (GRNN) is often used for function approximation. It has a radial basis layer and a special linear layer. It performs regression rather than classification tasks. GRNNs can only be used for regression problems and trains almost instantly, but tends to be large and slow. Like an RBFN network, a GRNN does not extrapolate. Detailed information can be seen from [40].

3.6.4. Artificial neural fuzzy inference system (ANFIS)

ANFIS is an adaptive network which permits the usage of neural network topology together with fuzzy logic. It not only includes the characteristics of both methods, but also eliminates some disadvantages of their lonely-used case.

4. Results and discussion

The present study's experiments were performed at the Fluid Mechanics, Thermal Engineering and Multiphase Flow Research Lab. (FUTURE) in KMUTT. Pure HFC-134a was used in the experiments. Special attention was paid on the accuracy of the measurements during experiments as can be seen from authors' previous publications on in-tube condensation process.

Numerical analysis of artificial intelligence includes 5 dimensional input parameters such as mass flux (G, kg m^{-2} s^{-1}), heat flux (q, kW m^{-2}), saturation temperature (T_{sat}), temperature difference between the saturation and inlet wall temperatures ($\Delta T_{sat} = T_{sat} - T_{wi}$) and average vapor quality of R134a (x), 2 dimensional output parameters such as convective heat transfer (h, W m^{-2} K^{-1}) and pressure drop (ΔP, Pa).

Table 5
The most predictive combinations of input parameters according to the error rates for the determination of condensation heat transfer coefficient (h) and pressure drop (ΔP).

Inputs					Input number	Outputs	
G (kg m^{-2} s^{-1})	q (kW m^{-2})	T_{sat} (°C)	ΔT_{sat} (K)	x		R^2-h (%)	$R^2-\Delta P$ (%)
1	0	0	0	0	1	0.616	0.886
0	**1**	**0**	**1**	**0**	**2**	**0.999**	**0.897**
1	0	0	1	0	2	0.93	0.807
1	0	1	0	0	2	0.656	0.988
1	1	0	0	0	2	0.895	0.82
0	1	0	1	1	3	0.999	0.894
0	**1**	**1**	**1**	**0**	**3**	**0.998**	**0.945**
1	0	0	1	1	3	0.939	0.801
1	0	1	0	1	3	0.696	0.994
1	0	1	1	0	3	0.954	0.989
1	1	0	0	1	3	0.893	0.83
1	1	0	1	0	3	0.999	0.915
1	1	1	0	0	3	0.914	0.989
0	1	1	1	1	4	0.999	0.938
1	0	1	1	1	4	0.969	0.996
1	1	0	1	1	4	0.999	0.92
1	1	1	0	1	4	0.95	0.995
1	**1**	**1**	**1**	**0**	**4**	**0.999**	**0.994**
1	1	1	1	1	5	0.998	0.996

Author's personal copy

In terms of the elimination process of several ANN methods such as neural network (ANN) methods such as multilayer perceptron (MLP), radial basis networks (RBFN), generalized regression neural network (GRNN) and adaptive neuro-fuzzy inference system (ANFIS), random sets of test and training/validation were determined as 33 and 120/30 among 183 data points by means of Matlab software [40] respectively. The best value of ANNs control parameters is determined using 5-fold cross validation in training phase. During the calculation process of heat transfer coefficient and pressure drop, the most agreeable hidden layer number value was found as 13 (h and ΔP) among the numbers from 1 to 30 for the method of multi layer perceptron (MLP), the most agreeable spread numbers (sp) were found as 12,000 (h) and 40,000 (ΔP) for the radial basis function networks (RBFN). The experimental data includes the mass fluxes of 260, 340 and 456 kg m^{-2} s^{-1} belong to the saturation temperatures of 40 and 50 °C in Table 3 and also in Figs. 2 and 3. Table 3 shows the best predictive method for the convective heat transfer coefficient (a) and pressure drop (b) accurately according to the their low average values of test group of 33 data points' results using several error analysis. The performance of the method of multi layer perceptron (MLP) with 5-13-1 architecture and radial basis function networks (RBFN) with the spread coefficient (sp) of 40,000, shown in Figs. 2 and 3, were found to be superior to other methods and architectures by means of satisfactory results with their deviations within the range of ±0.58% for the estimated condensation heat transfer coefficient and ±1.74% for the estimated pressure drop respectively. In addition to this, according to the condensation temperatures of 40 and 50 °C, comparison of experimental heat transfer coefficients and pressure drops with those from various artificial neural network methods of test groups are shown in Figs. 2 and 3 in a 20% deviation line for the mass fluxes of 260, 340 and 456 kg m^{-2} s^{-1}respectively. It can be clearly seen from these figures that the generalized regression neural

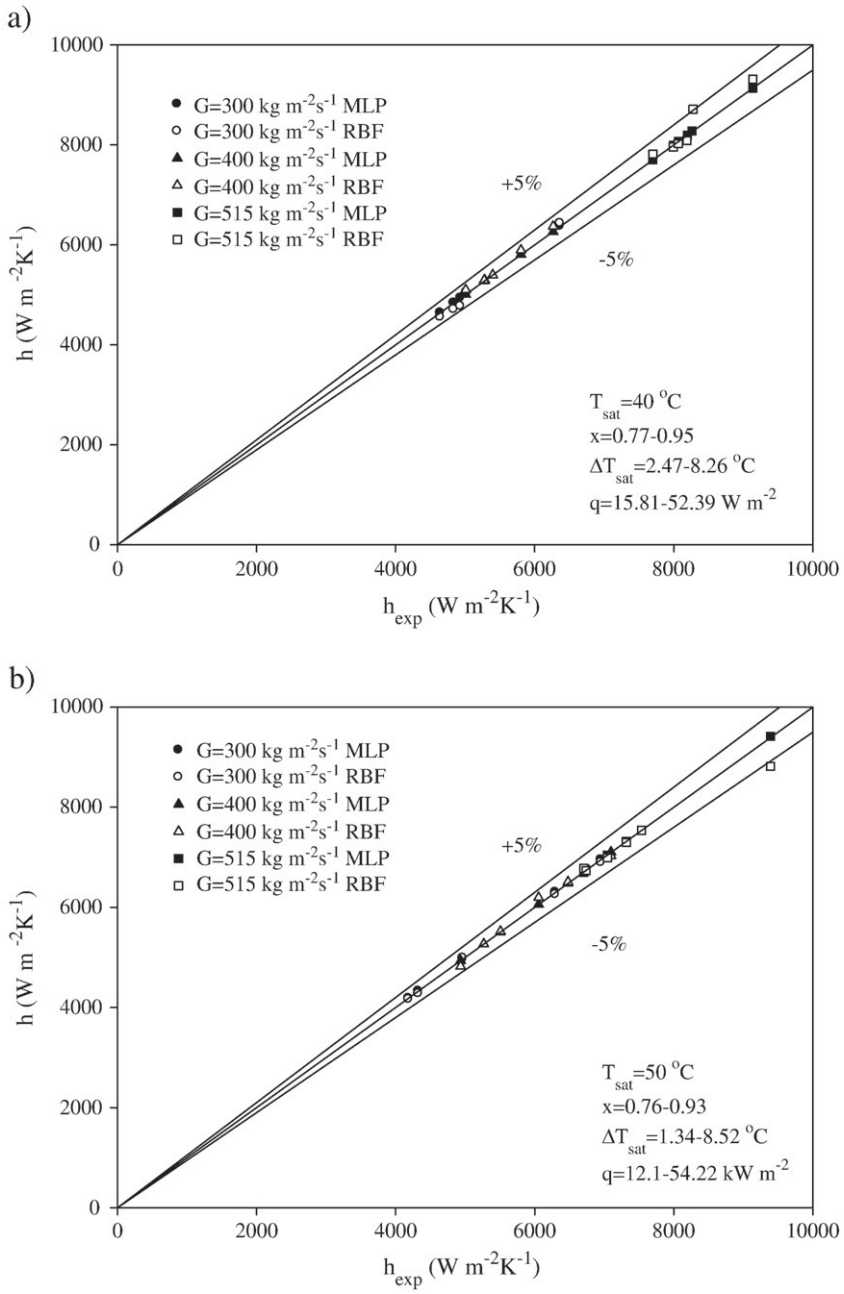

Fig. 4. Comparisons of experimental convective heat transfer coefficients with the most predictive artificial neural network methods using 35 number of experimental data points as ANN test group for the mass fluxes of 300, 400, 515 kg m^{-2} s^{-1} and T_{sat} = 40 °C (a) and 50 °C (b).

Author's personal copy

networks (GRNN) method has the poorest predictability of experimental data.

In terms of the increase in data number for the accuracy and validation process of the experiments, numerical calculations is done by means of 368 experimental data points having 68 data points for test set and 300 data points for training set in Tables 4 and 5. Table 4 shows the effect of the experimental data number on the error rates of the test group of ANN according to the most predictive ANN methods, determined from Table 3 and Figs. 2 and 3, for the determination of condensation heat transfer coefficient (a) and pressure drop (b) for the mass fluxes of 300, 400, 515 kg m^{-2} s^{-1} and condensation temperatures of 40 and 50 °C. According to Table 3, results of error analysis decrease with increasing data number due to the result of learning process of artificial intelligence. Figs. 4 and 5 show the success of determined compatible artificial neural network methods for the prediction of convective heat transfer coefficient and pressure drop according to the condensing temperatures of 40 °C (a) and 50 °C (b) respectively with their deviations being within the range of ±5% for all tested conditions. Table 5 shows the most predictive combinations of input parameters, whose deviations are over 0.5%, according to the error rates for the determination of condensation heat transfer coefficient (h) and pressure drop (ΔP) using the method of multi layer perceptron (MLP) with 5-13-1 architecture including 68 experimental data points. When the input parameter number is 2, heat flux (q) and temperature difference between the condensing temperature and inlet wall temperatures (ΔT_{sat}) seem to be dominant on the prediction of convective heat transfer coefficient with the deviation of 0.999% and pressure drop with the deviation of 0.897%. When there are 3 known input parameters, heat flux (q), temperature difference between the condensing temperature and inlet wall temperatures (ΔT_{sat}), and saturation temperature (T_{sat}) has the best predictability for the prediction of convective heat transfer coefficient with the deviation of

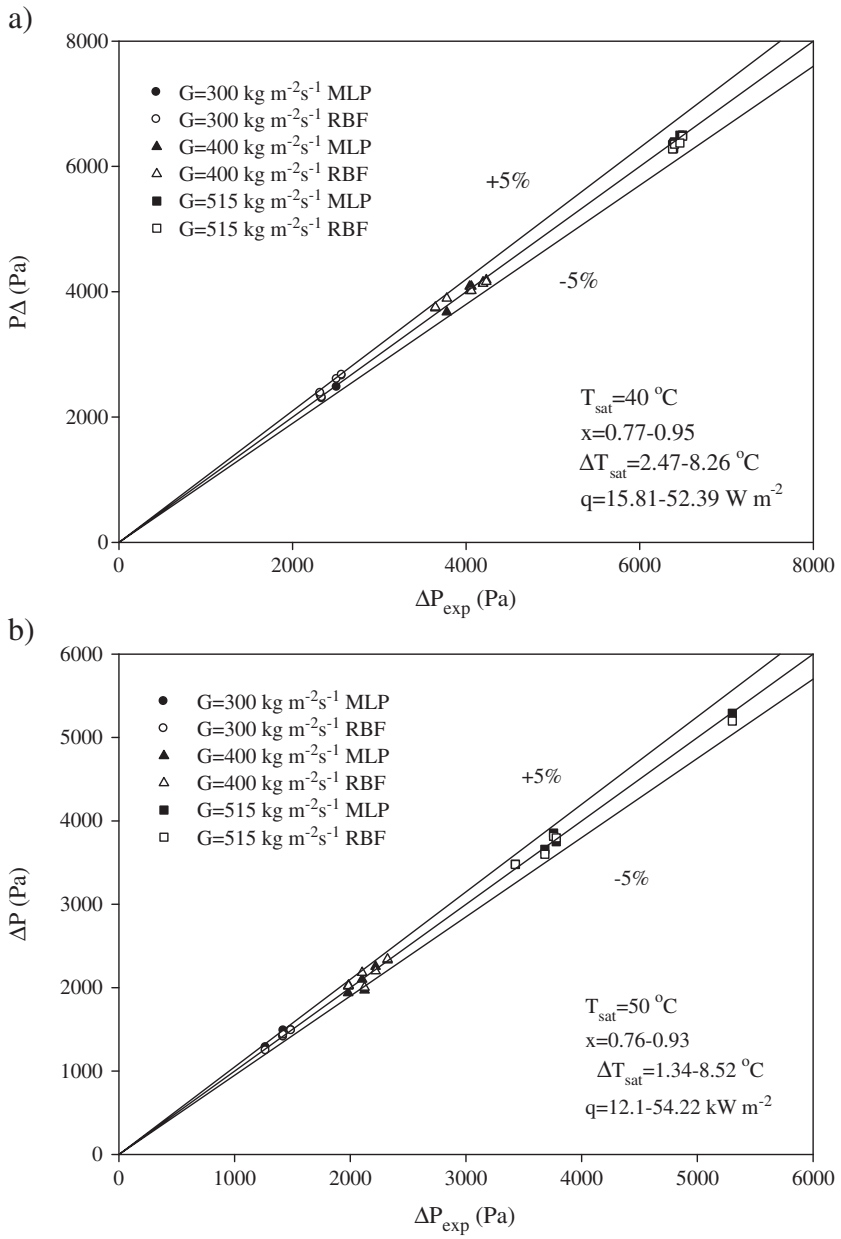

Fig. 5. Comparisons of measured two-phase pressure drops with the most predictive artificial neural network methods using 35 number of experimental data points as ANN test group for the mass fluxes of 300, 400, 515 kg m^{-2} s^{-1} and T_{sat} = 40 °C (a) and 50 °C (b).

Author's personal copy

0.998% and pressure drop with the deviation of 0.945%. It shows that the accuracy of the estimated output values by means of input values increases with increasing added proper input parameters.

A large number of graphics could be generated from the output of the calculations, however, due to space limitation, only typical results are shown for limited data of the experimental database of the authors. It should be also noted that detailed information on the heat transfer characteristics of the study with some additional figures and different experimental parameters can be seen from the authors' previous publications.

5. Conclusion

Comparison of the numerical condensation heat transfer coefficient and pressure drop values with the measured values by means of artificial intelligence methods was performed in this paper. There is no research on the content of this paper considering its parameters in current literature. The results of this study are expected to fill this gap in the literature.

Except from the generalized regression neural network (GRNN), the artificial neural network (ANN) methods of multilayer perceptron (MLP), radial basis networks (RBFN) and adaptive neuro-fuzzy inference system (ANFIS) are found to be capable of predicting the condensation heat transfer coefficient and pressure drop for the high mass region of R134a in a vertical tube within the range of $\pm 20\%$ and also within the slightly small error rates.

The performance of the method of multi layer perceptron (MLP) and radial basis function networks (RBFN) were the most predictive methods with their deviations within the range of $\pm 5\%$ for the estimated condensation heat transfer coefficient and pressure drop. It should be noted that these artificial intelligence methods have better results on the prediction of condensation heat transfer coefficient and pressure drop than the empirical models and correlations proposed in the authors' previous publications.

Convective heat transfer coefficient and pressure drop of R134a in the paper are found to be dependent to the heat flux and temperature difference between the condensing temperature and inlet wall temperatures strongly according to the results of analysis.

Nomenclature

A	surface area, m^2
c_p	specific heat, J kg^{-1} K^{-1}
d	internal tube diameter, m
E	error
G	mass flux, kg m^{-2} s^{-1}
h	heat transfer coefficient, W m^{-2} K^{-1}
i	enthalpy, J kg^{-1}
i_{fg}	latent heat of condensation, J kg^{-1}
L	length of test tube, m
m	mass flow rate, kg s^{-1}
N	element number
P	Pressure, N m^{-2}
ΔP	pressure drop, N m^{-2}
Q	heat transfer rate, W
q	heat flux, kW m^{-2}
T	temperature, °C
ΔT	temperature difference, K
x	average vapor quality

Subscripts

avg	average
calc	calculated
cond	condensate
exp	experimental
g	gas/vapor
i	inlet
l	liquid
ph	preheater
o	outlet
ref	refrigerant
sat	saturation
TS	test section
w	water

Acknowledgements

The first author is indebted to the Department of Mechanical Engineering, Yildiz Technical University (YTU). The second author wishes to thank King Mongkut's University of Technology Thonburi (KMUTT) for providing him with a Post-doctoral fellowship. The third author wishes to thank the Thailand Research Fund, the Office of the Higher Education Commission and the National Research University Project for financial support for this study.

References

[1] F.W. Dittus, L.M.E. Boelter, Engineering Publication, 2, University of California, 1930, p. 443.
[2] W.W. Akers, H.A. Deans, O.K. Crosser, Condensation heat transfer within horizontal tubes, Chemical Engineering Progress Symposium Series 55 (1959) 171–176.
[3] A. Cavallini, R. Zecchin, A dimensionless correlation for heat transfer in forced convection condensation, Proceedings of the Sixth International Heat Transfer Conference 3 (1974) 309–313.
[4] M.M. Shah, A general correlation for heat transfer during film condensation inside pipes, International Journal of Heat and Mass Transfer 22 (1979) 547–556.
[5] A.S. Dalkilic, O. Agra, I. Teke, S. Wongwises, Comparison of frictional pressure drop models during annular flow condensation of R600a in a horizontal tube at low mass flux and of R134a in a vertical tube at high mass flux, International Journal of Heat and Mass Transfer 53 (2010) 2052–2064.
[6] A.S. Dalkilic, S. Laohalertdecha, S. Wongwises, Two-phase friction factor in vertical downward flow in high mass flux region of refrigerant HFC-134a during condensation, International Communications in Heat and Mass Transfer 35 (2008) 1147–1152.
[7] K. Moser, R.L. Webb, B. Na, A new equivalent Reynolds number model for condensation in smooth tubes, International Journal of Heat Transfer 120 (1998) 410–417.
[8] A.S. Dalkilic, S. Laohalertdecha, S. Wongwises, Experimental investigation of heat transfer coefficient of R134a during condensation in vertical downward flow at high mass flux in a smooth tube, International Communications in Heat and Mass Transfer 36 (2009) 1036–1043.
[9] R. Bellinghausen, U. Renz, Heat transfer and film thickness during condensation of steam flowing at high velocity in a vertical pipe, International Journal of Heat and Mass Transfer 35 (1992) 683–689.
[10] A.S. Dalkilic, S. Yildiz, S. Wongwises, Experimental investigation of convective heat transfer coefficient during downward laminar flow condensation of R134a in a vertical smooth tube, International Journal of Heat and Mass Transfer 52 (2009) 142–150.
[11] V.P. Carey, Liquid–Vapor Phase Change Phenomena, Hemisphere Publishing, 1992.
[12] W. Nusselt, Die Oberflachen Kondenastion des Wasserdamfes, Z. Vereines Dtsch. Ingenieure 60 (1916) 541–546, 569–575.
[13] A.S. Dalkilic, S. Laohalertdecha, S. Wongwises, Effect of void fraction models on the two-phase friction factor of R134a during condensation in vertical downward flow in a smooth tube, International Communications in Heat and Mass Transfer 35 (2008) 921–927.
[14] X. Ma, A. Briggs, J.W. Rose, Heat transfer and pressure drop characteristics for condensation of R113 in a vertical micro-finned tube with wire insert, International Communications in Heat and Mass Transfer 31 (2004) 619–627.
[15] O.P. Bergelin, P.K. Kegel, F.G. Carpenter, C. Gazley, Co-current gas–liquid flow. II. Flow in vertical tubes. Meeting at Berkeley, Cal. (USA) June, ASME, Heat Transfer and Fluid Mechanic Institute (1946) 19–28.
[16] A.S. Dalkilic, S. Laohalertdecha, S. Wongwises, Effect of void fraction models on the film thickness of R134a during downward condensation in a vertical smooth tube, International Communications in Heat and Mass Transfer 36 (2009) 172–179.
[17] P.B. Whalley, Boiling, Condensation, and Gas–Liquid Flow, Oxford University Press, 1987.
[18] A.S. Dalkilic, S. Wongwises, An investigation of a model of the flow pattern transition mechanism in relation to the identification of annular flow of R134a in a vertical tube using various void fraction models and flow regime maps, Experimental Thermal and Fluid Science 34 (2010) 692–705.
[19] D. Barnea, O. Shoham, Y. Taitel, Flow pattern transition for vertical downward two phase flow, Chemical Engineering Science 37 (1982) 741–744.
[20] A.S. Dalkilic, S. Laohalertdecha, S. Wongwises, Validation of void fraction models and correlations using a flow pattern transition mechanism model in relation to the identification of annular vertical downflow in-tube condensation of R134a.

Author's personal copy

International Communications in Heat and Mass Transfer, International Communications in Heat and Mass Transfer 37 (2010) 827–834.
[21] P.G. Kosky, Thin liquid films under simultaneous shear and gravity forces, International Journal of Heat Mass Transfer 14 (1971) 1220–1224.
[22] A.S. Dalkilic, S. Wongwises, Experimental study on the modeling of condensation heat transfer coefficients in high mass flux region of refrigerant HFC-134a inside the vertical smooth tube during annular flow regime, Heat Transfer Engineering 32 (2011) 1–12.
[23] P.G. Kosky, F.W. Staub, Local condensing heat transfer coefficients in the annular flow regime, AIChE Journal 17 (1971) 1037–1043.
[24] S.L. Chen, F.M. Gerner, C.L. Tien, General film condensation correlations, Experimental Heat Transfer 1 (1987) 93–107.
[25] A.S. Dalkilic, S. Laohalertdecha, S. Wongwises, New experimental approach on the determination of condensation heat transfer coefficient using frictional pressure drop and void fraction models in a vertical tube, Energy Conversion and Management 51 (2010) 2535–2547.
[26] A.S. Dalkilic, S. Wongwises, Intensive literature review of condensation inside smooth and enhanced tubes, International Journal of Heat and Mass Transfer 52 (2009) 3409–3426.
[27] A.S. Dalkilic, S. Wongwises, A performance comparison of vapour compression refrigeration system using various alternative refrigerants, International Communications in Heat and Mass Transfer 37 (2010) 1340–1349.
[28] A.S. Dalkilic, I. Teke, S. Wongwises, Experimental analysis for the determination of the convective heat transfer coefficient by measuring pressure drop directly during annular condensation flow of R134a in a vertical smooth tube, International Journal of Heat and Mass Transfer (in press).
[29] A.S. Dalkilic, S. Laohalertdecha, S. Wongwises, A comparison of the void fraction correlations of R134a during condensation in vertical downward laminar flow in a smooth and microfin tube, MNHT2008: Proceedings of the Micro/Nanoscale Heat Transfer International Conference-2008 Parts A–B, 2008, pp. 1029–1040.
[30] A.S. Dalkilic, S. Laohalertdecha, S. Wongwises, Two-phase friction factor obtained from various void fraction models of R-134a during condensation in vertical downward flow at high mass flux, HT2008: Proceedings of the ASME Summer Heat Transfer Conference-2008 2, 2009, pp. 193–206.
[31] A.S. Dalkilic, S. Laohalertdecha, S. Wongwises, Experimental investigation on the condensation heat transfer and pressure drop characteristics of R134a at high mass flux conditions during annular flow regime inside a vertical smooth tube, Summer Heat Transfer Conference, ASME (2009), July 19–23, USA, 2009.
[32] A.S. Dalkilic, O. Agra, Experimental apparatus for the determination of condensation heat transfer coefficient for R134a and R600a flowing inside vertical and horizontal tubes, Summer Heat Transfer Conference, ASME (2009), July 19–23, USA, 2009.
[33] A.S. Dalkilic, S. Laohalertdecha, S. Wongwises, Experimental research on the similarity of annular flow models and correlations for the condensation of R134a at high mass flux inside vertical and horizontal tubes, International Mechanical Engineering Congress and Exposition, ASME (2009), November 13–19, USA, 2009.
[34] A.S. Dalkilic, S. Laohalertdecha, S. Wongwises, Comparison of condensation frictional pressure drop models and correlations during annular flow of R134a inside a vertical tube, Thermal and Environmental Issues in Energy Systems, ASME-ATI-UTI, (2010), May 16–19, Italy, 2010.
[35] A.S. Dalkilic, S. Wongwises, Experimental study on the flow regime identification in the case of co-current condensation of R134a in a vertical smooth tube, International Heat Transfer Conference, ASME, (2010), August 8–13, USA, 2010.
[36] A.S. Dalkilic, S. Wongwises, Experimental study on the flow regime identification in the case of co-current condensation of R134a in a vertical smooth tube, International Heat Transfer Conference, ASME, (2010), August 8–13, USA, 2010.
[37] H. Demir, Ö. Ağra, Ş.Ö. Atayılmaz, Generalized neural network model of alternative refrigerant (R600a) inside a smooth tube, International Communications in Heat and Mass Transfer 36 (2009) 744–749.
[38] S.J. Kline, F.A. McClintock, Describing uncertainties in single sample experiments, Mechanical Engineering 75 (1953) 3–8.
[39] L. Fausett, Fundamentals of Neural Networks, Architectures, Algorithms, and Applications, Prentice-Hall, Inc. Press, 1994.
[40] Matlab R2010a, 2010, http://mathworks.com/.

Provided for non-commercial research and education use.
Not for reproduction, distribution or commercial use.

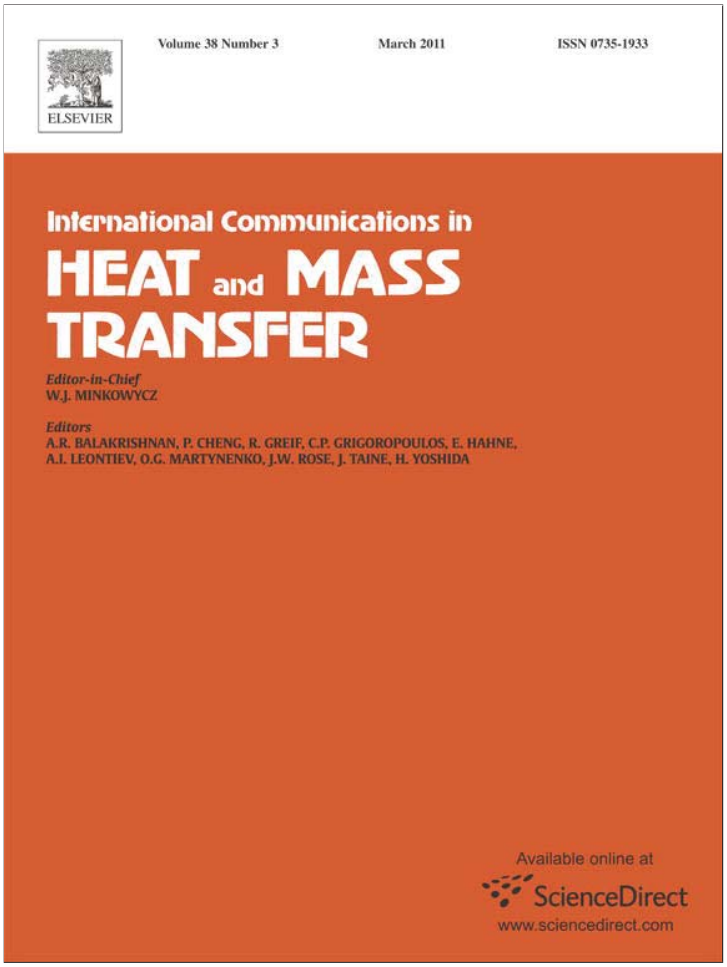

This article appeared in a journal published by Elsevier. The attached copy is furnished to the author for internal non-commercial research and education use, including for instruction at the authors institution and sharing with colleagues.

Other uses, including reproduction and distribution, or selling or licensing copies, or posting to personal, institutional or third party websites are prohibited.

In most cases authors are permitted to post their version of the article (e.g. in Word or Tex form) to their personal website or institutional repository. Authors requiring further information regarding Elsevier's archiving and manuscript policies are encouraged to visit:

http://www.elsevier.com/copyright

Author's personal copy

International Communications in Heat and Mass Transfer 38 (2011) 398–404

Contents lists available at ScienceDirect

International Communications in Heat and Mass Transfer

journal homepage: www.elsevier.com/locate/ichmt

A comparison of flow characteristics of refrigerants flowing through adiabatic straight and helical capillary tubes ☆

Sukkarin Chingulpitak [a,b], Somchai Wongwises [b,*]

[a] The joint Graduate School of Energy and Environment, King Mongkut's University of Technology Thonburi, Bangmod, Bangkok 10140, Thailand
[b] Fluid Mechanics, Thermal Engineering and Multiphase Flow Research Lab. (FUTURE), Department of Mechanical Engineering, King Mongkut's University of Technology Thonburi, Bangmod, Bangkok 10140, Thailand

ARTICLE INFO

Available online 17 December 2010

Keywords:
Capillary tube
Helical tube
Straight tube
Adiabatic
Homogeneous flow model
Alternative refrigerant

ABSTRACT

This paper presents a numerical investigation of the flow characteristics of helical capillary tubes compared with straight capillary tubes. The homogenous two-phase flow model developed is based on the conservation of mass, energy, and momentum of the fluids in the capillary tube. This model is validated by comparing it with the experimental data of both straight and helical capillary tubes. Comparisons of the predicted results between the straight and helical capillary tubes are presented, together with the experimental results for straight capillary tubes obtained by previous researchers. The results show that the refrigerant flowing through the straight capillary tube provides a slightly lower pressure drop than that in the helical capillary tube, which resulted in a total tube length that was longer by about 20%. In addition, for the same tube length, the mass flow rate in the helical capillary tube with a coil diameter of 40 mm is 9% less than that in the straight tube. Finally, the results obtained from the present model show reasonable agreement with the experimental data of helical capillary tubes and can also be applied to predict the flow characteristics of straight capillary tubes by changing to straight tube friction factors, for which Churchill's equation was used in the present study.

© 2010 Elsevier Ltd. All rights reserved.

1. Introduction

A capillary tube is commonly used as an expansion device in small refrigeration systems with cooling capacities below 10 kW because it has the lowest cost and a low starting torque and requires no maintenance. It is the simplest means of flow control of refrigerant from the condenser to the evaporator and also maintains the required operating pressure differential between the two units. Nominal size of the capillary tube is ranging between 0.5–2.0 mm in diameter and 1–6 m in length. In the past decades, the design and analysis of capillary tubes have been studied both numerically and experimentally, mostly for straight capillary tubes [1–20]. However, in practical applications, domestic refrigerator systems use a helical capillary tube in order to construct a compact unit. The works reviewed that use helical coils are summarized as follows:

Ali [21] proposed the pressure drop correlations for helical coil tube which were developed in terms of the flow rate (V), the tube geometry (d_i, D_c, p and L) and fluid properties (ρ and μ). It should be noted that in most of the previous works, the relevant correlations were developed in terms of Reynolds number (Re), curvature ratio (d_i/D_c), Dean number (De), Helical number (He) and Euler number (Eu) and the obtained geometrical group.

Kim et al. [22] presented experimental results of mass flow rate and proposed a correlation based on the Buckingham-π-theorem for predicting the mass flow rate of R-22, R-407 °C, and R-410A. Their results indicated that the mass flow rates of R-407 °C and R-410A were higher than those of R-22 about 4.0% and 23%, respectively. In addition, the mass flow rates of the coiled capillary tubes are quite lower than those of straight capillary tubes, especially at smaller coiled diameter. For example, mass flow rates for 40 mm coiled diameter are lower than the straight capillary tubes approximately 9.0%.

In 2006, Zhou and Zhang [23] studied the performance of coiled adiabatic capillary tubes both theoretically and experimentally. The results were used for comparison with straight capillary data, and showed that the mass flow rate of the refrigerant increased significantly with increases in the coil diameter. However, little change was observed for the coil diameter larger than 300 mm. Valladares [24] presented numerical simulation based on finite volume formulation for describing the flow characteristics of coiled adiabatic capillary tubes. The numerical model was considered for various aspects such as geometry, type of fluid (pure substances and mixtures), critical or non-critical flow conditions, metastable region, and transient behaviour. The prediction showed an agreement of 97.7% of 211 data points evaluated within an error of ± 10%. Park et al. [25] studied the flow characteristics of coiled capillary tubes for R-22 and developed mass flow rate correlation for coiled capillary tubes. At the same operating condition, they found that the mass flow rates of

☆ Communicated by W.J. Minkowycz.

* Corresponding author.
E-mail address: somchai.won@kmutt.ac.th (S. Wongwises).

0735-1933/$ – see front matter © 2010 Elsevier Ltd. All rights reserved.
doi:10.1016/j.icheatmasstransfer.2010.12.014

Author's personal copy

Nomenclature

A	cross sectional area of capillary tube (m^2)
d_i	capillary tube internal diameter (m)
D_c	coil diameter (m)
De	Dean Number, $De = \mathrm{Re}\sqrt{(d_i / D_C)}$
f	friction factor
g	gravitational acceleration (m/s^2)
G	mass flow rate per unit area ($kg/s\ m^2$)
h	specific enthalpy (J/kg)
H_{loss}	head loss (m)
He	Helical number, $He = \mathrm{Re}[(d_i/D_C)/\{1+(p/\pi D_C)^2\}]^{1/2}$
k	entrance loss coefficient
L	length (m)
m	mass flow rate (kg/s)
p	pitch of coil (m)
P	pressure (Pa)
Re	Reynolds number
s	specific entropy (J/kg K)
ΔT_{sub}	degree of subcooling (°C)
T	temperature (°C)
V	velocity (m/s)
x	quality

Greek letters

τ	shear stress at wall (N/m^2)
v	specific volume (m^3/kg)
μ	dynamic viscosity (kg/m s)
ρ	density (kg/m^3)
ϵ	surface roughness (m)

Subscripts

cond, evap	condenser and evaporator, respectively
f, g	liquid phase and gas phase, respectively
i	capillary inlet condition
sp, tp	single-phase and two-phase, respective
w	wall

the coiled capillary tubes decreased by about 5–16% more than those of the straight capillary tubes. The Buckingham-π-theorem was used to form a generalized correlation to calculate the refrigerant mass flow rate for both straight and coiled capillary tubes. The effects of inlet condition, refrigerant property, and coiled tube geometry are considered. For both straight and coiled capillary tubes, the results showed that the proposed correlation gave satisfactory agreement with the experimental data for R-22, R-407 °C and R-410A. The average and standard deviations were around 0.24% and 4.4%, respectively. Mittal et al. [26] presented an experimental investigation of coiling effect on the flow characteristics of R-407 °C in an adiabatic helical capillary tube. It was observed that the coiling of capillary tubes (coil diameters 60 mm, 100 mm and 140 mm) significantly influenced the mass flow rate of R-407 °C. From the experimental results, the mass flow rates of coiled capillary tubes were about 5–10% less than those of straight capillary tubes. In addition, they also proposed correlations to predict the mass flow rate of R-407 °C flowing through straight and helical capillary tubes. Compared with the experimental data, it could clearly be seen that the majority of the data fell within 10% of their proposed correlation.

As shown above, most of the previous works have presented the flow characteristics of refrigerants in helical capillary tubes by comparing predicted values with experimental data to validate the proposed models. Moreover, there are only a few articles which reported the flow behaviours of helical capillary tubes and compared them with straight capillary tubes. Thus, in this study, a comparison of the refrigerant flow characteristics between a helical capillary tube and a straight capillary tube is investigated. The effect of coil diameters on mass flow rate and pressure profile is also presented.

2. Mathematical modelling

In the modelling, the physical method, which is used to describe the flow characteristics, is developed from the conservation of mass, energy, and momentum. As shown in Fig. 1, the flow of refrigerant through a capillary tube can be divided into two distinct regions; single-phase subcooled liquid and two-phase regions. Moreover, the model includes the effect of the condenser and evaporator temperatures, inner tube diameter, degree of subcooling and mass flow rate of refrigerant.

As shown in Fig. 1, the position between points 1 and 2 is the capillary tube inlet having a pressure drop due to sudden contraction. Similarly, the position between points 2 and 3 is the single-phase subcooled liquid region and the position between points 3 and 4 is the two-phase region consisting of a liquid–vapour two-phase region. The developed model is based on the following assumptions:

- horizontal helical coiled tube has constant diameter
- inner diameter and roughness of capillary tube are constant
- adiabatic and homogeneous two-phase flow
- non-metastable liquid region
- one-dimensional and steady flow
- oil-free refrigerant, and
- the thermodynamic equilibrium through the capillary tube.

The governing equations used in describing the flow characteristics for the single-phase and the two-phase flow regions are presented as follows:

2.1. Single-phase flow region

The steady flow energy equation between points 1 and 3 can be expressed as

$$\frac{P_1}{\rho_1} + \frac{V_1^2}{2} + gz_1 = \frac{P_3}{\rho_3} + \frac{V_3^2}{2} + gz_3 + H_{loss}. \tag{1}$$

The head loss can be determined from

$$H_{loss} = f_{sp}\frac{L_{sp}}{d_i}\frac{V^2}{2g} + k\frac{V^2}{2g} \tag{2}$$

where H_{loss} is the total head loss due to friction along the capillary tube and sudden contraction, f_{sp} is the single phase friction factor and k is the entrance loss coefficient (for square edged, $k = 0.5$).

Substituting Eq. (2) into Eq. (1) and rearranging (in head form), gave

$$\frac{P_1}{\rho_1 g} + \frac{V_1^2}{2g} + z_1 = \frac{P_3}{\rho_3 g} + \frac{V_3^2}{2g} + z_3 + f_{sp}\frac{L_{sp}}{d_i}\frac{V^2}{2g} + k\frac{V^2}{2g}. \tag{3}$$

For an incompressible fluid, $\rho_1 \cong \rho_3 = \rho$, the continuity equation is presented in the following equation

$$m = \rho_1 V_1 A = \rho_3 V_3 A = \rho V A. \tag{4}$$

For $z_1 = z_3$ (horizontal tube), rearranging Eq. (3), yields

$$L_{sp} = \frac{d_i}{f_{sp}}\left[\frac{2}{\rho V^2}(P_1 - P_3) - k - 1\right]. \tag{5}$$

Author's personal copy

The single-phase friction factor (f_{sp}) can be calculated from different friction factor models. In case of the straight capillary tubes, the Churchill friction factor model is used to calculate the friction factors. It is defined as follows:

Churchill [27]

$$f_s = 8\left[\left(\frac{8}{\mathrm{Re}}\right)^{12} + \frac{1}{(A+B)^{1.5}}\right]^{1/12} \tag{6}$$

where $A = \left\{2.457\ ln\left[\frac{1}{(7/\mathrm{Re})^{0.9} + 0.27(\varepsilon/d_i)}\right]\right\}^{16}$, $B = \left(\frac{37530}{\mathrm{Re}}\right)^{16}$

and f_s is the friction factor for straight capillary tube.

In the case of the helical capillary tubes, models of Schmidt [28] and, Mori and Nakayama [29] can be used to predict the friction factors.

Schmidt [28]

$$f_c/f_s = 1 + 0.14\mathrm{Re}^x \tag{7}$$

where $x = [1 - 0.0644/(D_c/d_i)^{0.312}]/(D_c/d_i)^{0.97}$ and f_c is friction factor for coiled capillary tube.

Mori and Nakayama [29]

$$f_c = \frac{C_1(d_i/D_c)^{0.5}}{\left[\mathrm{Re}(d_i/D_c)^{2.5}\right]^{1/6}}\left\{1 + \frac{C_2}{\left[\mathrm{Re}(d_i/D_c)^{2.5}\right]^{1/6}}\right\} \tag{8}$$

where

$$C_1 = 1.88411177 \times 10^{-1} + 85.2472168(\varepsilon/d_i) - 4.63030629 \times 10^4(\varepsilon/d_i)^2 + 1.31570014 \times 10^7(\varepsilon/d_i)^3$$

$$C_2 = 6.79778633 \times 10^{-2} + 25.3880380(\varepsilon/d_i) - 1.06133140 \times 10^4(\varepsilon/d_i)^2 + 2.54555343 \times 10^6(\varepsilon/d_i)^3.$$

2.2. Two-phase flow region

In this region, the capillary tube is divided into a number of elements as shown in Fig. 1. The following equations are based on the control volume considerations in the two-phase region.

The conservation of mass can be calculated using the following equation:

$$m = \frac{AV_i}{v_i} = \frac{AV_{i+1}}{v_{i+1}} \tag{9}$$

where v_i is specific volume of fluid at any point.

By neglecting the elevation difference, the conservation of energy for steady-state adiabatic condition without external work can be expressed as follows:

$$\left(h_3 + gz_3 + \frac{V_3^2}{2}\right) = \left(h_i + gz_i + \frac{V_i^2}{2}\right) \tag{10}$$

$$h + \frac{V^2}{2} = \text{constant} \tag{11}$$

where h and V are the enthalpy and velocity of fluid at any point, respectively.

Due to the fact that the refrigerant flows along the capillary tube, the pressure gradually drops and the liquid flashes into vapour arising purely from the reduced pressure, at any point. Hence,

$$h_i = h_{fi}(1-x_i) + h_{gi}x_i,\ v_i = v_{fi}(1-x_i) + v_{gi}x_i. \tag{12}$$

Also, $m = \rho VA = \text{constant}$

$$V = \frac{m}{\rho A} = \frac{G}{\rho} = Gv. \tag{13}$$

The energy balance between point 3 and at any point along the capillary tube in the two-phase flow region can be calculated by substituting Eqs. (12) and (13) into Eq. (11) giving

$$h_3 + \frac{V_3^2}{2} = h_f + x\left(h_g - h_f\right) + \frac{G^2}{2}\left(v_f(1-x) + v_g x\right)^2. \tag{14}$$

Expanding the right-hand side of Eq. (14) and rearranging, yield

$$\left[\left(v_g - v_f\right)^2\frac{G^2}{2}\right]x^2 + \left[G^2 v_f\left(v_g - v_f\right) + \left(h_g - h_f\right)\right]x + \left[\frac{G^2 v_f^2}{2} - h_3 - \frac{V_3^2}{2} + h_f\right] = 0. \tag{15}$$

The quality (x) can be expressed in the form of a quadratic equation as shown in Eq. (16).

$$x = \frac{-h_{fg} - G^2 v_f v_{fg} + \sqrt{\left(G^2 v_f v_{fg} + h_{fg}\right)^2 - \left(2G^2 v_{fg}^2\right)\left[\frac{G^2 v_f^2}{2} - h_3 - \frac{V_3^2}{2} + h_f\right]}}{G^2 v_{fg}^2} \tag{16}$$

where $h_{fg} = h_g - h_f$ and $v_{fg} = v_g - v_f$.

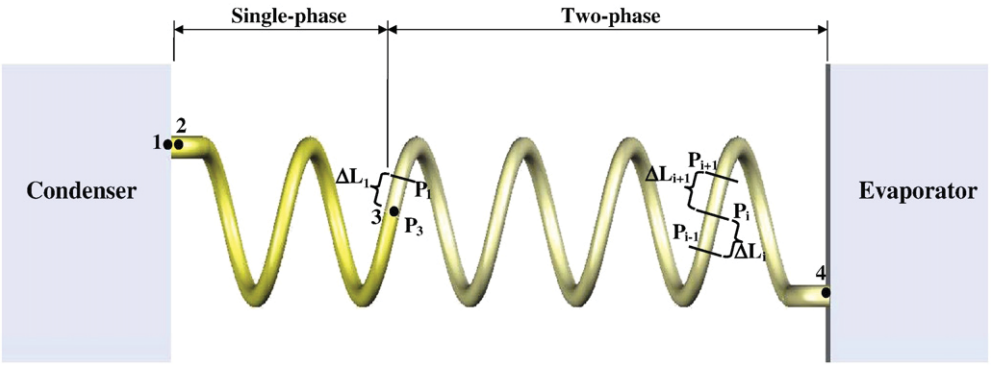

Fig. 1. Schematic diagram of an adiabatic helical capillary tube.

Author's personal copy

Again, the conservation of momentum can be expressed by reconsidering the element of fluid as shown in Fig. 1.

$$\left(P\frac{\pi d_i^2}{4}\right)-(P+dP)\frac{\pi d_i^2}{4}-\tau_w \pi d_i dL = mdV \tag{17}$$

where τ_w is the wall shear stress which is defined as follows:

$$\tau_w = \frac{f_{tp}\rho V^2}{8}. \tag{18}$$

The two-phase friction factor (f_{tp}) is calculated from the same equation as shown in the case of the single-phase flow region.

Substituting Eq. (18) into Eq. (17), we get

$$-\frac{\pi d_i^2}{4}dP-\frac{f_{tp}}{8}\rho V^2 d_i \pi dL = mdV \tag{19}$$

or

$$dL = -\frac{d_i}{f_{tp}}\left[\frac{2dP}{\rho V^2}+\frac{2mdV}{\rho A V^2}\right]. \tag{20}$$

For constant mass flow rate, $dm=0$, Eq. (21) is obtained.

$$\frac{dV}{V} = -\frac{d\rho}{\rho} \tag{21}$$

Substituting Eq. (21) into Eq. (20) gives

$$dL = \frac{2d_i}{f_{tp}}\left[\frac{-\rho dP}{\rho V^2}+\frac{d\rho}{\rho}\right]. \tag{22}$$

3. Solution method

As shown in Fig. 1, the capillary tube between points 3 and 4 can be divided into numerous sections. Since P_3 is known (saturated liquid), the pressure at any section 'i' can be calculated from the following equation.

$$P_i = P_3 - i\Delta P \tag{23}$$

With the pressure (P_i) and the quality (x_i) can be calculated from Eq. (16). So, the entropy of each section can be calculated from:

$$s_i = s_{fi}(1-x)+s_{gi}x. \tag{24}$$

The Reynolds number in the two-phase region is determined by

$$\mathrm{Re}_{tp} = \frac{Vd_i}{\mu_{tp}v_{tp}} \tag{25}$$

where

$$V = Gv_{tp} = G\left(xv_g+(1-x)v_f\right). \tag{26}$$

The two-phase dynamic viscosity correlation proposed by McAdams [30] is presented as follows:

$$\frac{1}{\mu_{tp}} = \frac{x}{\mu_g}+\frac{1-x}{\mu_f}. \tag{27}$$

The gradual increase of the entropy is obtained along the capillary tube. When the entropy reaches to the maximum value, the fluid velocity is equal to the local speed of sound and the flow is choked. As a consequence, the calculation is ended at this point.

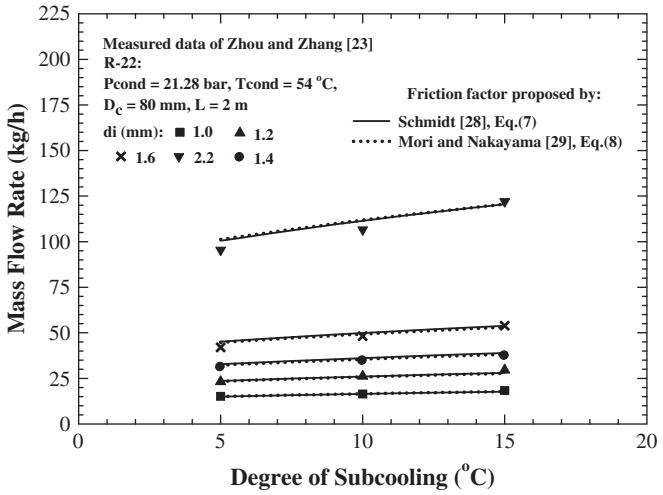

Fig. 2. Comparison of the present numerical results with the measured mass flow rates at different capillary tube diameters and degrees of subcooling.

The pressure of the element, where the entropy has the maximum value $(P_i)_{s\ max}$, is then compared to the evaporator pressure (P_{evap}) given by

$$\begin{array}{ll} \text{if} & P_{i,smax} = P_{evap} \quad \text{then} \quad P_4 = P_{evap} \\ \text{if} & P_{i,smax} \neq P_{evap} \quad \text{then} \quad P_4 = P_{i,smax}. \end{array}$$

Thus, from Eq. (22) the two-phase length can be expressed as follows:

$$L_{tp} = d_i\left[\frac{-2}{G^2}\int_{P_3}^{P_{s,\,max}}\frac{\rho}{f_{tp}}dp+\int_{P_3}^{P_{s,\,max}}\frac{d\rho}{\rho f_{tp}}\right]. \tag{28}$$

The capillary length of each section is calculated by

$$\Delta L_i = \frac{2d_i}{f_{tp,i}}\left(\frac{-\rho_i \Delta P}{G^2}+\frac{\Delta\rho}{\rho_i}\right). \tag{29}$$

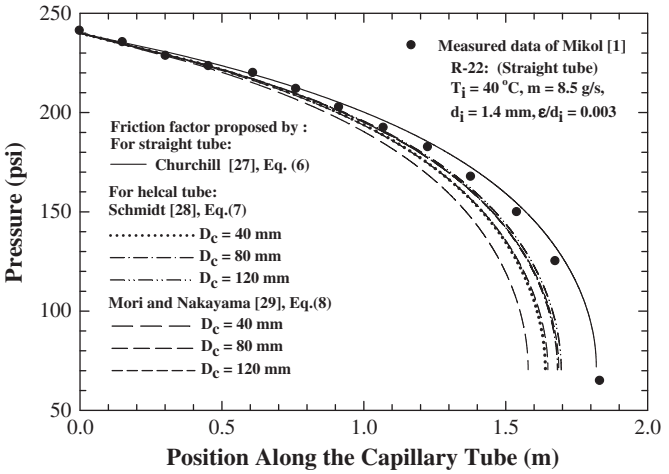

Fig. 3. Comparison of measured pressure distributions with present numerical results at different coil diameters.

Author's personal copy

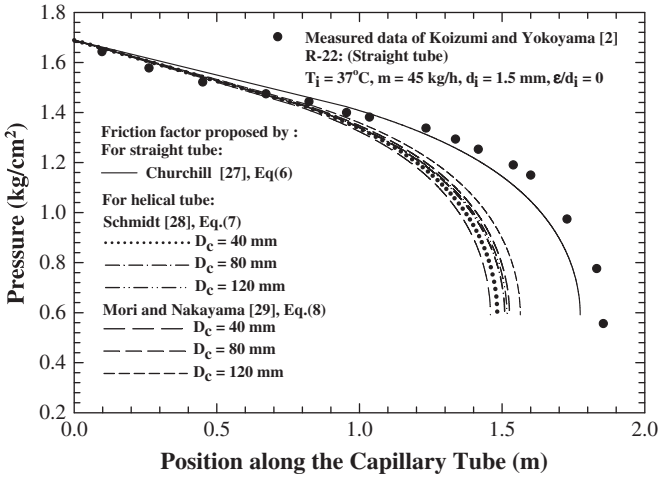

Fig. 4. Comparison of measured pressure distributions with the present numerical results at different coil diameters.

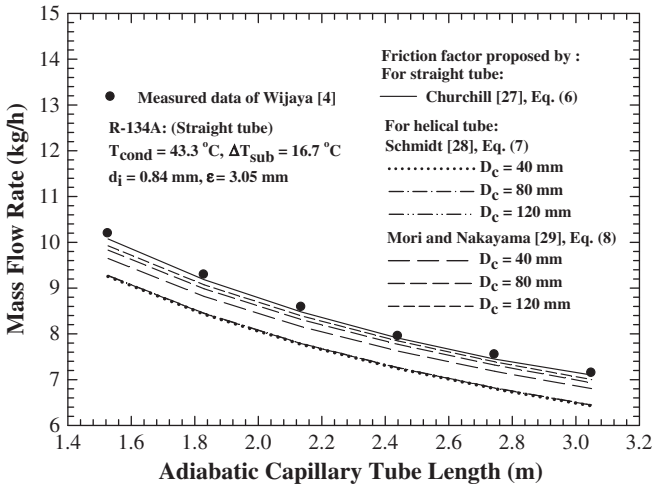

Fig. 6. Comparison of the present numerical results with the measured mass flow rates.

The total length of the two-phase region is determined from

$$L_{tp} = \sum_{i=1}^{n} \Delta L_i. \tag{30}$$

Finally, the total length of capillary tube is the summation of the single-phase and the two-phase lengths which is defined as follows:

$$L_{total} = L_{sp} + L_{tp}. \tag{31}$$

4. Results and discussion

4.1. Mathematical model verification

In order to validate the proposed model, comparisons are made with the available experimental data of Zhou and Zhang [23] for R-22. Fig. 2 shows a comparison of mass flow rate between the present model and the experimental data of Zhou and Zhang [23] for R-22 flowing through coiled capillary tubes with different capillary tube diameters and degrees of subcooling. Similarly to the straight capillary tube, the mass flow rate of the coiled capillary tube increases rapidly with an increase in capillary tube diameter.

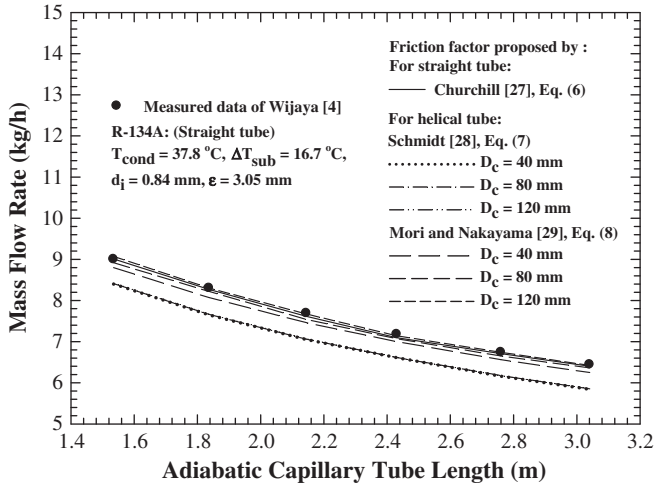

Fig. 5. Comparison of the present numerical results with the measured mass flow rates.

Moreover, the results show that the friction factor of Mori and Nakayama [29] gives reasonable predictions compared with the experimental data. The results from the present model using the friction factor of Mori and Nakayama [29] are compared with the measured data of Zhou and Zhang [23] as shown in Fig. 2. The results give the mean absolute error of 3%.

4.2. Comparison of the numerical results with measured data of the straight capillary tube

Figs. 3 and 4 show the pressure distributions along the helical capillary tubes with different coil diameters obtained from the present model compared with those of the straight capillary tubes obtained from the experimental data of Mikol [1] and Koizumi and Yokoyama [2] for R-22. In the case of the straight capillary tube simulation results, the friction factors are calculated by the Churchill equation [27]. The results of the present model using the friction factor of the Churchill equation [27] give reasonable predictions compared with the measured data of Mikol [1] and Koizumi and Yokoyama [2] as shown in Figs. 3 and 4. For the helical capillary tube, the results show that the total tube length of the helical capillary tube with a coil diameter of 40 mm is shorter than that of the straight capillary tube by about 20%. This is because the friction loss in the helical capillary tube is higher than that in the straight capillary tube.

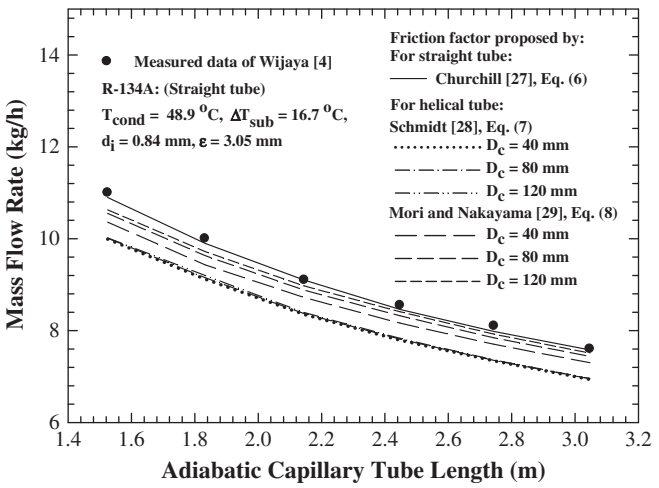

Fig. 7. Comparison of the present numerical results with the measured mass flow rates.

Author's personal copy

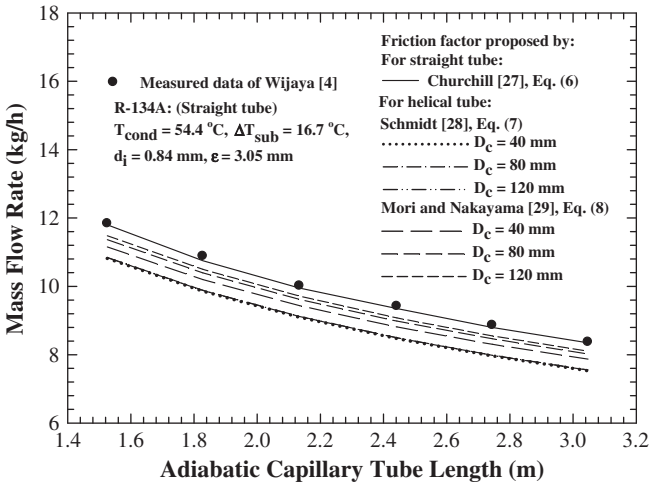

Fig. 8. Comparison of the present numerical results with the measured mass flow rates.

Figs. 5–8 present the variation in mass flow rates versus capillary tube lengths by comparing the numerical results with the experimental data of the straight capillary tube of Wijaya [4] for R-134a. These figures show the variation in mass flow rate versus tube length ($L = 1.52$ to 3.05 m) and condensing temperature ($T_{cond} = 37.8$ to 54.4 °C) for $d_i = 0.84$ mm and $\Delta T_{sub} = 16.7$ °C. It is evidently seen that the mass flow rate of the capillary tube decreases with increases in the condenser temperature as well as the capillary tube length. In the case of the helical capillary tube simulation results, friction factors are calculated by Schmidt [28] and Mori and Nakayama [29]. As the coil diameter (D_c) decreases, the curvature ratio (d_i/D_c) increases, which results in an increase in resistance to the refrigerant flow. Moreover, the results also indicated that the mass flow rate of the helical capillary tube with a coil diameter of 40 mm is reduced by an average of 9% compared with the mass flow rate in the straight capillary tube.

Fig. 9 shows a comparison of mass flow rate between the present model and the experimental data of Mittal et al. [26] for R-407 °C flowing through straight capillary tubes with different capillary tube diameters and degrees of subcooling. In the case of the straight capillary tube simulation results, friction factors are calculated by the Churchill equation [27]. The results obtained with the present model using the friction factor of the Churchill equation [27] give reasonable

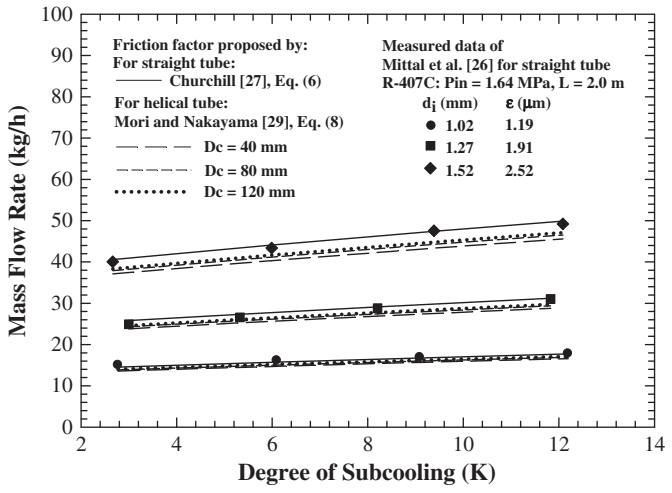

Fig. 9. Comparison of the present numerical results with the measured mass flow rates at different capillary tube diameters and degrees of subcooling.

predictions compared with the measured data of Mittal et al. (2010), as shown in Fig. 9. The comparison results also showed that the mean absolute percentage error of the refrigerant's mass flow rate is about 1.6%. Moreover, it is clearly seen that mass flow rate increases with increasing subcooling temperature. This is due to the friction loss in the capillary tube increases as the temperature increases which results in a decrease in the refrigerant mass flow rate entering the capillary tube.

As compared with the mass flow rate of R-407 °C in straight capillary tubes, the mass flow rates in helical capillary tubes with coil diameters of 40 mm, 80 mm, and 120 mm are reduced by averages of 7.12%, 5.2%, and 4.14% respectively. For helical capillary tubes, the results show that the mass flow rate of a helical capillary tube with a coil diameter of 40 mm is less than that of a straight capillary tube by about 5–8%.

As shown above, it can be concluded that the present model can be used to calculate the flow characteristics of refrigerants flowing through both straight and helical capillary tubes by changing the corresponding friction factor equations.

5. Conclusion

A homogeneous two-phase flow model has been developed to determine the refrigerant flow characteristics in adiabatic helical capillary tubes. The present model was validated by comparing with the experimental data of Zhou and Zhang [23] for R-22 and was found to give an average discrepancy at around 3%. The mass flow rates of refrigerant flowing through the helical capillary tubes are lower compared with those for the straight capillary tubes, especially for lower coil diameters. The mass flow rates of the helical capillary tubes with coil diameters of 40 mm, 80 mm, and 120 mm are decreased by 5–9% more than those of the straight capillary tubes under given conditions due to increased flow friction resulting from strong coil effects. Under the same operating conditions, the length of the helical capillary tube is 20% shorter than that of the straight capillary tube. Finally, the numerical results for straight capillary tubes give reasonable predictions compared with the measured data of straight capillary tubes. Therefore, the present model can be applied to predict the flow characteristics of refrigerant flowing through straight capillary tubes using the Churchill friction factors equation.

Acknowledgements

The authors are indebted to King Mongkut's University of Technology Thonburi, the Thailand Research Fund, the Commission of Higher Education and the National Research University Project for supporting this study.

References

[1] E.P. Mikol, Adiabatic single and two-phase flow in small bore tubes, ASHRAE Journal 5 (1963) 75–86.
[2] H. Koizumi, K. Yokoyama, Characteristics of refrigerant flow in a capillary tube, ASHRAE Transaction 80 (1980) 19–27.
[3] R.Y. Li, S. Lin, Z.H. Chen, Numerical modeling of thermodynamic non-equilibrium flow of refrigerant through capillary tubes, ASHRAE Transaction 96 (1990) 542–549.
[4] H. Wijaya, Adiabatic capillary tube test data for HFC-134a, Proceeding of the IIR-Purdue Conference, vol. 1, 1992, pp. 63–71,, West Lafayette, USA.
[5] T.N. Wong, K.T. Ooi, Adiabatic capillary tube expansion devices: a comparison of the homogeneous flow and the separated flow models, Applied Thermal Engineering 16 (7) (1996) 625–634.
[6] P.K. Bansal, A.S. Rupasinghe, A homogeneous model for adiabatic capillary tubes, Applied Thermal Engineering 18 (3–4) (1998) 207–219.
[7] S.M. Sami, C. Tribes, Numerical prediction of capillary tube behavior with pure and binary alternative refrigerants, Applied Thermal Engineering 18 (12) (1998) 491–502.
[8] C. Melo, R.T.S. Ferreira, C. Boabaid Neto, J.M. Goncalves, M.M. Mezavi, An experimental analysis of adiabatic capillary tubes, Applied Thermal Engineering 19 (16) (1999) 669–684.

Author's personal copy

[9] D. Jung, C. Park, B. Park, Capillary tube selection for HCFC22 alternatives, International Journal of Refrigeration 22 (8) (1999) 604–614.
[10] S. Wongwises, P. Chan, N. Luesuwanatat, T. Purattanarak, Two-phase separated flow model of refrigerants flowing through capillary tubes, International Communications in Heat and Mass Transfer 27 (3) (2000) 343–356.
[11] S. Wongwises, T. Songnetichaovalit, N. Lokathada, P. Kritsadathikarn, M. Suchatawat, W. Pirompak, A comparison of the flow characteristics of refrigerants flowing through adiabatic capillary tubes, International Communications in Heat and Mass Transfer 27 (5) (2000) 611–621.
[12] S. Wongwises, W. Pirompak, Flow characteristics of pure refrigerants and refrigerant mixtures in adiabatic capillary tubes, Applied Thermal Engineering 21 (8) (2001) 845–861.
[13] S.M. Liang, T.N. Wong, Numerical modeling of two-phase refrigerant flow through adiabatic capillary tubes, Applied Thermal Engineering 21 (10) (2001) 1035–1048.
[14] ASHRAE Handbook—Refrigeration, American Society of Heating, Refrigerating and Air-Conditioning Engineer Inc., 2002, (Chapter 45).
[15] J. Sinpiboon, S. Wongwises, Numerical investigation of refrigerant flow through non-adiabatic capillary tubes, Applied Thermal Engineering 22 (18) (2002) 2015–2032.
[16] F.A.S. Fiorelli, A.A.S. Huerta, O.M. Silvares, Experimental analysis of refrigerant mixtures flow through adiabatic capillary tubes, Experimental Thermal and Fluid Science 26 (5) (2002) 499–512.
[17] J. Choi, Y. Kim, J.T. Chung, An empirical correlation and rating charts for the performance of adiabatic capillary tubes with alternative refrigerants, Applied Thermal Engineering 24 (1) (2004) 29–41.
[18] P.K. Bansal, G. Wang, Numerical analysis of choked refrigerant flow in adiabatic capillary tubes, Applied Thermal Engineering 24 (5–6) (2004) 851–863.
[19] L. Yang, W. Wang, A generalized correlation for the characteristics of adiabatic capillary tubes, International Journal of Refrigeration 31 (2) (2008) 197–203.
[20] A.L. Seixlack, M.R. Barbazelli, Numerical analysis of refrigerant flow along non-adiabatic capillary tubes using a two-fluid model, Applied Thermal Engineering 29 (2–3) (2009) 523–531.
[21] S. Ali, Pressure drop correlations for flow through regular helical coil tubes, Fluid Dynamics Research 28 (4) (2001) 295–310.
[22] S.G. Kim, S.T. Ro, M.S. Kim, Experimental investigation of the performance of R-22, R-407 C and R-410A in several capillary tubes for air-conditioners, International Journal of Refrigeration 25 (5) (2002) 521–531.
[23] G. Zhou, Y. Zhang, Numerical and experimental investigations on the performance of coiled adiabatic capillary tubes, Applied Thermal Engineering 26 (11–12) (2006) 1106–1114.
[24] G. Valladares, Numerical simulation and experimental validation of coiled adiabatic capillary tubes, Applied Thermal Engineering 27 (5–6) (2007) 1062–1071.
[25] C. Park, S. Lee, H. Kang, Y. Kim, Experimentation and odelling of refrigerant flow through coiled capillary tubes, International Journal of Refrigeration 30 (7) (2007) 1168–1175.
[26] M.K. Mittal, R. Kumar, A. Gupta, An experimental study of the flow of R-407 C in an adiabatic helical capillary tube, International Journal of Refrigeration 33 (4) (2010) 840–847.
[27] S.W. Churchill, Frictional equation spans all fluid flow regions, Chemical Engineering 84 (24) (1977) 91–92.
[28] E.F. Schmidt, Warmeubergang and Druckverlust in Rohrschlangen, Chemical Engineering and Technology 39 (13) (1967) 781–789.
[29] Y. Mori, W. Nakayama, Study on forced convective heat transfer in curve pipes II, International Journal of Heat and Mass Transfer 10 (1) (1967) 37–59.
[30] W.H. McAdams, W.K. Wood, R.L. Bryan, Vaporization inside horizontal tubes. II, Benzence-oil mixture, Transaction ASME 64 (1942) 193.

Provided for non-commercial research and education use.
Not for reproduction, distribution or commercial use.

This article appeared in a journal published by Elsevier. The attached copy is furnished to the author for internal non-commercial research and education use, including for instruction at the authors institution and sharing with colleagues.

Other uses, including reproduction and distribution, or selling or licensing copies, or posting to personal, institutional or third party websites are prohibited.

In most cases authors are permitted to post their version of the article (e.g. in Word or Tex form) to their personal website or institutional repository. Authors requiring further information regarding Elsevier's archiving and manuscript policies are encouraged to visit:

http://www.elsevier.com/copyright

Author's personal copy

International Journal of Heat and Mass Transfer 54 (2011) 2234–2240

Contents lists available at ScienceDirect

International Journal of Heat and Mass Transfer

journal homepage: www.elsevier.com/locate/ijhmt

Technical Note

Effect of fin pitches on the air-side performance of crimped spiral fin-and-tube heat exchangers with a multipass parallel and counter cross-flow configuration

Parinya Pongsoi [a], Santi Pikulkajorn [b], Chi-Chuan Wang [c], Somchai Wongwises [a,*]

[a] Fluid Mechanics, Thermal Engineering and Multiphase Flow Research Lab. (FUTURE), Department of Mechanical Engineering, King Mongkut's University of Technology Thonburi, Bangmod, Bangkok 10140, Thailand
[b] Somchai Industry Co., Ltd, Bangkok 10150, Thailand
[c] Department of Mechanical Engineering, National Chiao Tung University, Hsinchu 300, Taiwan

ARTICLE INFO

Article history:
Received 4 November 2010
Received in revised form 3 December 2010
Accepted 3 December 2010
Available online 27 January 2011

Keywords:
Fin
Heat transfer
Heat exchanger
Air–water
Extended surface

ABSTRACT

This study investigates the effect of fin pitches and fin materials on the air-side performance of crimped fin-and-tube heat exchangers in the range of high Reynolds numbers (4000–13000). The test samples are made from copper and aluminium with different fin pitches (f_p = 3.2, 4.2 and 6.2 mm). It is found that the proposed simple average effectiveness equation from the pure counter and parallel circuitry arrangement can well represent the effectiveness-NTU relationship for the current z-shape arrangement. The experimental results reveal that the fin pitch casts insignificant effect on the heat transfer characteristics (Colburn j factor). However, a detectable rise of the friction factor is seen when the fin pitch is increased to f_p = 6.2 mm. On the other hand, the effect of fin material on the airside performance is negligible.

© 2010 Elsevier Ltd. All rights reserved.

1. Introduction

The heat exchanger is a basic equipment for thermal systems in many industrial processes involving heat transfer. One of the most favourable configurations of heat exchanger used in industrial applications takes the form as fin-and-tube heat exchanger. Normally for this type of heat exchanger, the dominant thermal resistance is on the air-side of the heat exchanger. Hence one way to augment the heat transfer performance is via enhanced fin geometry. There have been numerous fin configurations such as plain fin, slit fin, wavy fin, louvered fin, circular fin, annular fin, spiral fin, compounded fin and the like that were already implemented in various industrial applications. Upon the foregoing fin configurations, the spiral fin featuring easy production, is quite common in industrial services. However, there is only a few studies concerning the air-side performance of the spiral fin-and-tube heat exchanger [1–6]. According to these literatures, crimped spiral fin is proved to be quite reliable in industrial applications [1–5]. Upon the foregoing studies, Nuntaphan et al. [1] is the only experimental work that examines the effect of fin pitches on the air-side performance of crimped spiral fin-and-tube heat exchangers. However, this study only discussed the effect at a very low air frontal velocity (0.5–1.5 m/s). In practice, especially in industrial service, the operation velocity is normally much higher [7]. Therefore, it is the main purpose of this study is to extend the applicable range (V_{fr} up to 6 m/s) of the spiral heat exchangers subject to the influence of fin pitch. Moreover, the effect of fin materials on the air-side performance is also examined.

2. Data reduction

This present work is conducted by using the experimental apparatus of Wongwises and Chokeman [8], including the test section, air supply, water loop, instrumentation, and data acquisition. Air and hot water are used as working fluids. Detailed descriptions of the relevant components can be seen from the previous study.

In the experiment, the inlet water temperature and the water flow rate are fixed while varying the air flow rate. Tests are then conducted at the steady state with tested conditions being tabulated in Table 1.

The tests heat exchangers are of fin-and-tube configurations with copper tube being finned with either copper or aluminium. The water-side circuitry arrangement and detailed dimensions of the tested fin-and-tube heat exchangers are shown in Fig. 1. Photos of the crimped spiral fin pattern are shown in Fig. 2. The geometric parameters of the heat exchangers are summarized in Table 2. Tests are performed under steady state condition, and the overall resistance can be obtained from the UA product of transfer units (ε-NTU), yet the total resistance is the sum of the individual resistances as follows:

$$\frac{1}{UA} = \frac{1}{h_i A_i} + \frac{\ln(d_o/d_i)}{2\pi k_t L} + \frac{1}{\eta_o h_o A_o} \quad (1)$$

* Corresponding author. Tel.: +66 24709115.
E-mail address: somchai.won@kmutt.ac.th (S. Wongwises).

0017-9310/$ - see front matter © 2010 Elsevier Ltd. All rights reserved.
doi:10.1016/j.ijheatmasstransfer.2010.12.027

Author's personal copy

Nomenclature

A_{min}	minimum free flow area, m^2
A_o	total surface area, m^2
A_p	cross-sectional or profile area of fin, m^2
Al	aluminium material
C^*	capacity rate ratio, dimensionless
Cu	copper material
f	Fanning friction factor, dimensionless
G_c	mass flux of the air based on minimum free flow area, kg/m^2 s
h	heat transfer coefficient, $W/(m^2 K)$
j	Colburn factor, dimensionless
NTU	number of transfer units, dimensionless
Nu	Nusselt number, dimensionless
Pr	Prandtl number, dimensionless
ΔP	pressure drop, Pa
Re_{d_o}	Reynolds number based on tube outside diameter(d_o)
U	overall heat transfer coefficient, $W/(m^2 K)$
V_{fr}	air frontal velocity, m/s
V_{max}	maximum velocity across heat exchanger, m/s
ε_c	heat exchanger effectiveness for multipass counter cross-flow
ε_p	heat exchanger effectiveness for multipass parallel cross-flow
ε_{pc}	heat exchanger effectiveness for multipass parallel and counter cross-flow
η_f	fin efficiency, dimensionless
ϕ	combination of terms, dimensionless

Table 1
Experimental conditions.

Inlet-air-dry bulb temperature, °C	31.5 ± 0.5
Inlet-air frontal velocity, m/s	2–6 or Re_{d_o}(4000—13000)
Inlet-water temperature, °C	55–70
Water flow rate, LPM	12–14

The ε-NTU relationships with one fluid mixed and one fluid unmixed in cross-flow was employed to determine the overall heat transfer coefficient. From Fig. 1, the present mixed circuitry arrangement is a combination of parallel and counter cross-flow. From the previous discussion, the ε-NTU relationships for multipass parallel cross-flow and multipass counter cross-flow configuration are available from [9–11], as shown in Eqs. (2) and (3):

For multipass counter cross-flow with $N_{row} = 2$:

$$\varepsilon_c = 1 - \left[\frac{K}{2} + \left(1 - \frac{K}{2}\right)e^{2K/C_A^*}\right]^{-1}, \quad K = 1 - e^{NTU_A(C_A^*/2)} \tag{2}$$

For multipass parallel cross-flow with $N_{row} = 2$:

$$\varepsilon_P = \left(1 - \frac{K}{2}\right)\left(1 - e^{-2K/C_A^*}\right), \quad K = 1 - e^{-NTU_A(C_A^*/2)} \tag{3}$$

where $C^* = C_{min}/C_{max}$ is equal to C_c/C_h or C_h/C_c depending on the value of hot and cold fluid heat capacity rates. However, the multipass parallel and counter cross-flow used in this experiment is a combination of multipass parallel cross-flow. Hence it may be reasonable to use the average value of the relationships shown in Eq. (4) as follows:

$$\varepsilon_{pc} = \frac{\varepsilon_P + \varepsilon_C}{2} \quad \text{for } N_{row} = 2 \tag{4}$$

The schematic diagram of circuitry arrangement (parallel, counter, cross) for $N_{row} = 2$ are shown in Fig. 3.

Further details about the data reduction can be seen from Wongwises and Chokeman [8]. The efficiency of a radial fin with rectangular profile is based on the derivation of Gardner [12], i.e.,

$$\eta_f = \frac{2\psi}{\phi(1+\psi)} \frac{I_1(\phi R_o)K_1(\phi R_i) - I_1(\phi R_i)K_1(\phi R_o)}{I_0(\phi R_i)K_1(\phi R_o) + I_1(\phi R_o)K_0(\phi R_i)} \tag{5}$$

where

$$\phi = (r_o - r_i)^{3/2}\left(\frac{2h_o}{k_f A_p}\right)^{1/2} \tag{6}$$

Accordingly, the air-side heat transfer coefficient (h_o) can then be calculated from Eq. (1). The air-side heat transfer characteristics of the heat exchanger are often in terms of dimensionless Colburn j factor:

$$j = \frac{Nu}{Re_{d_o} Pr^{1/3}} = \frac{h_o}{\rho_a V_{max} C_P}(Pr)^{2/3} \tag{7}$$

The frictional characteristics are termed with Fanning friction factor, as depicted by Kays and London [13]:

$$f = \left(\frac{A_{min}}{A_o}\right)\left(\frac{\rho_m}{\rho_1}\right)\left[\frac{2\Delta P \rho_1}{G_c^2} - (1+\sigma^2)\left(\frac{\rho_1}{\rho_2} - 1\right)\right] \tag{8}$$

where G_c is the mass flux of the air based on minimum free flow area, A_o is the total heat transfer area, A_{min} is the minimum free flow area. The experiments are conducted following the ANSI/ASHRAE 33 Standards [14] in which the energy un-balance between air and water of the crimped spiral fin and tube heat exchangers, denoting $|Q_a - Q_w|/Q_{ave}$, is less than 0.05. The uncertainties are calculated from the root mean sum square method, the maximum uncertainties are 12.30% for the j-factor and 11.13% for f-factor.

3. Results and discussion

As aforementioned in Eq. (4) which was used to calculate the Colburn factor (j) for $N_{row} = 2$. The reasons for using Eq. (4) can be explained by Fig. 4(a) which shows the calculation of heat exchanger effectiveness using Eqs. (2)–(4) subject to variation of NTU and C^*. Apparently, it is not suitable to use either counter flow (Eq. (2)) or parallel flow (Eq. (3)) when operating at a high Reynolds number. For the present flow configuration, the heat exchanger effectiveness lies between the multipass parallel cross-flow and counter cross-flow. Note that using inappropriate ε-NTU relationships for complex flow arrangement may lead to an error up to 10% as pointed out by Navarro and Cabezas-Gomez [15]. Moreover, in Fig. 4(a), the heat exchanger effectiveness using Eq. (4) is found to be in excellent agreement with the simulated result of the z-shaped arrangement from [15]. Notice that the z-shape arrangement is analogous to the present circuitry arrangement. As a consequence, Eq. (4) can be proposed as the empirical ε-NTU relationship for the multipass parallel and counter cross-flow arrangement.

Fig. 4(b) and (c) shows the effect of fin pitches on the performance of heat exchangers having a two-row configuration with copper and aluminium fin, respectively. The corresponding fin pitches were 3.2, 4.2 and 6.2 mm. Test results indicated that the effect of fin pitch on the Colburn factor is very small. In contrast, for the effect of the fin pitch on the heat transfer performance, Lee et al. [6] (spiral fin), Mon and Gross [16] (annular fin) and Kim and Kim [17] (plate fin) all revealed a noticeable decline of heat transfer performance with respect to the smaller fin pitch. At the first glance, it seems that there exist some controversies amid

Author's personal copy

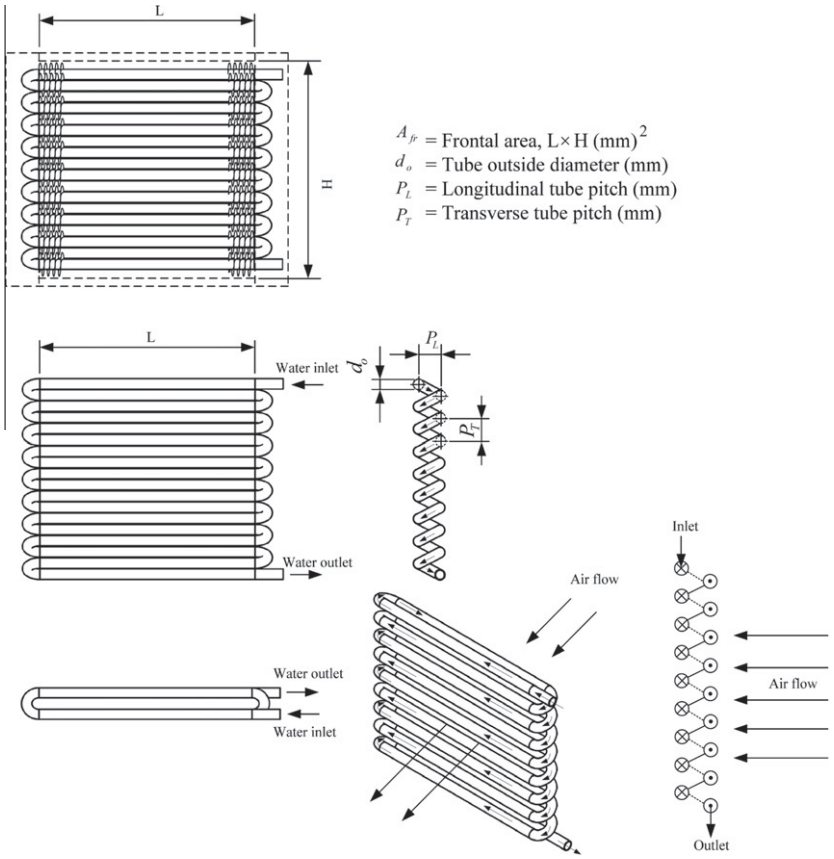

Fig. 1. Geometric details of multipass parallel-and-counter cross flow heat exchangers and water flow circuit inside the heat exchanger. N_{row} = 2 ($\times$ and $\bullet$ signs indicates that water flows into or out of the paper, respectively).

the present study and those studies. The difference arises from two different aspects, and an elaboration is given subsequently.

Firstly, there is a departure of the present Reynolds number and those aforementioned studies. The tests Reynolds number ($Re_{d_o} < 1000$) of previous studies were considerably lower than this study. Note that the present Reynolds number ranges approximately from 4000 to 13000. In this regard, higher operating velocities promote better mixing and lead to a better heat transfer performance, and this phenomenon prevails irrespective of change of fin pitch. Secondly, even for the Reynolds number is low (below 1000), Kim and Kim [17] found that the dependence of Colburn j factor on the fin pitch is rather small for a one row coil. The results are related to the boundary layer development. Kim and Kim [17] provided an analysis of the boundary layer development for the flat plate surface, and concluded that the boundary layer interruption could not occur for a fin-and-tube heat exchanger having large fin pitches, indicating the whole heat exchangers are in the developing region where the corresponding heat transfer performance is high, resulting a negligible dependence of j factor on the fin pitch. This is actually similar to a high operation velocity. Conversely, their 4-row coils show that the Coburn j increases with the rise of fin pitch at the same range of the Reynolds number. With varying fin pitches, the entrance region is in developing region while the rest are in fully developed region. The percentage of the length of developing/fully developed varies for different fin pitches, hence a detectable influence of fin pitch is encountered.

Lee et al. [6] argues that the convection heat transfer coefficient decreases with smaller fin pitches due to the boundary layer becomes thicker with a decrease in fin pitch, which can cause easier boundary layer interruption between the fins. However, this phenomenon diminishes as the high Reynolds number. Moreover, the fact that the effect of fin pitch on the heat transfer characteristics vanishes for the Reynolds numbers is above 1000 can also be found in the louvered fin-and-tube heat exchanger of Wang et al. [18]. In the meantime, Fig. 4(b) and (c) also shows that there is no significant effect of fin pitch on the friction factor for f_p = 3.2 and 4.2 mm. On the other hand, a fin pitch of 6.2 mm casts a noticeable effect on the friction factor (f). The friction factor for a fin pitch of 6.2 mm is higher than those having smaller fin pitch (f_p = 3.2, 4.2 mm). The reason can be seen from Eq. (8), since the friction factor depends on the dynamic effects of the ratio of minimum free-flow area with the total heat transfer area (A_{min}/A_o) and mass flux of air (G_c). Notice that A_o is significantly increased as the fin pitch is varied from 6.2 to 4.2 or 3.2 mm whereas the reduction of A_{min} is comparatively small. On the other hand, there is no significant effect of fin pitch on G_c over the entire area ratio [19]. In summary of the foregoing analysis engenders the detectable rise of friction factor for f_p = 6.2 mm.

For a comparison of the present test samples with previous studies, Fig. 4(b) and (c) also include the Wang and Chang [20], Wang et al. [21] and Briggs and Young [22] correlations for plain and circular fin-and-tube heat exchangers. It is found that crimped spiral fins shows a similar trend with those of circular fins or plate fins when f_p = 4.2 mm. However, due to the corrugated folding at the base of the present fin configuration, it appears that the crimped spiral fins give a higher friction factor (f) than that of plate fins at the same Reynolds number.

The effect of the material on the air-side heat transfer characteristics is shown in Fig. 5(a). The results show that there is an insignificant effect of fin material on either the Colburn factor (j)

Author's personal copy

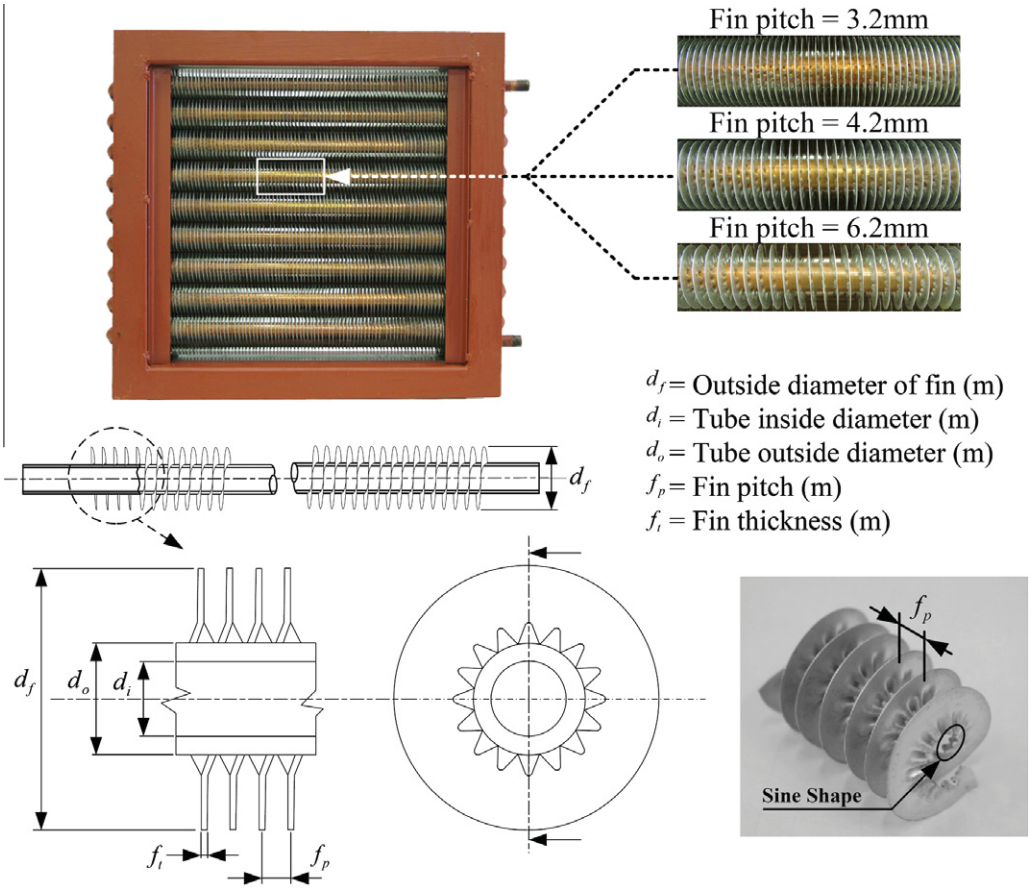

Fig. 2. The photos of the tested crimped spiral fin and tube heat exchangers (f_p = 3.2, 4.2 and 6.2 mm) and schematic diagram of crimped spiral fin.

Table 2
Detailed geometric parameters of the test samples.

No.	Fin type	d_i (mm)	d_o (mm)	d_f (mm)	A_{fr} (mm^2)	P_L (mm)	P_T (mm)	f_t (mm)	n_t	N_{row}	f_p (mm)	Fin material
1&2	Crimped	13.5	16.35	34.8	320 × 350	35	39	0.4	9	2	3.2	Al&Cu
3&4	Crimped	13.5	16.35	34.8	320 × 350	35	39	0.4	9	2	4.2	Al&Cu
5&6	Crimped	13.5	16.35	34.8	320 × 350	35	39	0.4	9	2	6.2	Al&Cu

Remarks: d_f = Outside diameter of fin; d_i = Tube inside diameter; d_o = Tube outside diameter; f_p = Fin pitch; f_t = Fin thickness; P_L = Longitudinal tube pitch; P_T = Transverse tube pitch; n_t = number of tubes in row; N_{row} = number of tube rows; A_{fr} = Frontal area (L × H).
Notes: Tube layouts of all heat exchangers are staggered layout (Al = aluminium, Cu = copper).

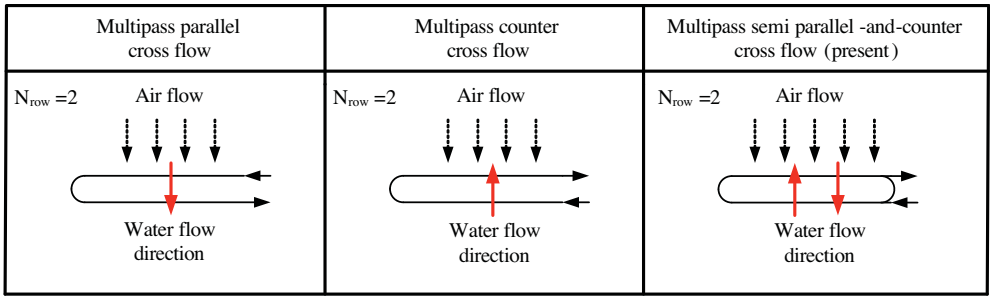

Fig. 3. Schematic diagram of the heat exchangers algorithm for multipass parallel cross flow, multipass counter cross flow and multipass parallel and counter cross-flow (N_{row} = 2).

or friction factor (f) at the same experimental condition. The results are somehow expected for the convection heat transfer performance is independent of fin materials. In contrast, it can be clearly seen that the fin efficiency (η_f) of the copper fin is higher than that of aluminium fin. The reason may be clearly explained by Eqs. (5) and (6) through which a higher thermal conductivity will result in a higher fin efficiency (η_f) accordingly. This phenomenon is confirmed in Fig. 5(b).

Author's personal copy

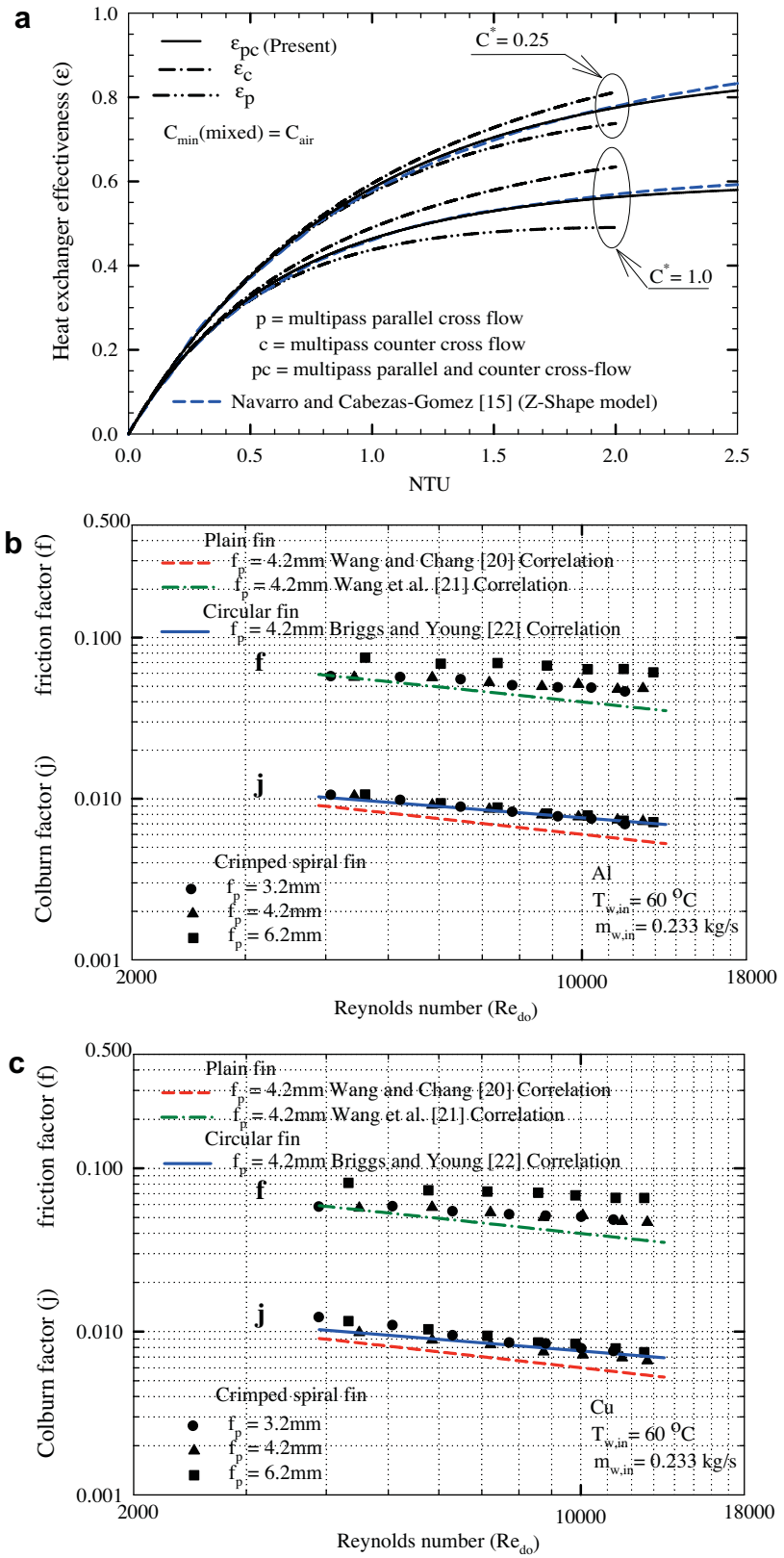

Fig. 4. The comparison chart for ε-NTU relationships graphic (a) and effect of fin pitch on the Colburn factor and friction factor for (b) aluminium fin, and (c) copper fin.

Moreover, the heat transfer rate for both fins is shown in Fig. 5(c). It is clearly seen that the heat transfer rate for copper fin is only marginally higher than that of aluminium fin due to very minor difference in fin efficiency.

4. Conclusion

This study has investigated the effect of fin pitch on the air-side performance of crimped spiral fin-and-tube heat exchangers with

Author's personal copy

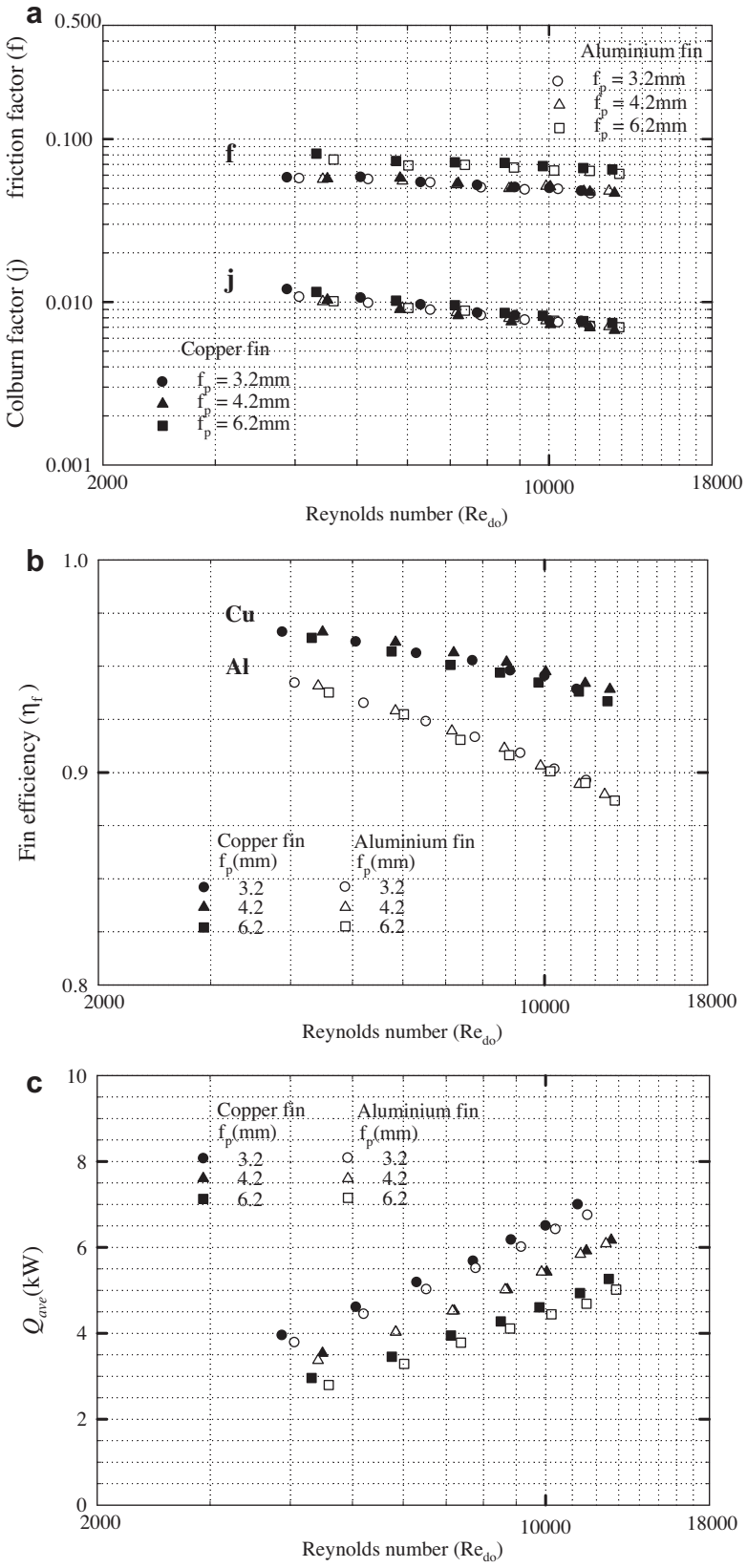

Fig. 5. Effect of fin material on the *j* and *f* factors (a), fin efficiency (b) and heat transfer rate (c) of crimped spiral fin and tube heat exchangers at $T_{w,in}$ = 65 °C and $m_{w,in}$ = 0.2 kg/s.

multipass z-shape cross-flow under sensible heating conditions with Reynolds number ranging from 4000 to 13000. A total of 6 samples were tested with associated fin materials of copper or aluminium, respectively. The associated fin thickness and outside diameter is 0.4 mm and 34.8 mm, respectively. The number of tube rows is two and fin pitches are 3.2, 4.2 and 6.2 mm, respectively. It

Author's personal copy

is found that the proposed simple average effectiveness equation from the pure counter and parallel circuitry arrangement can well represent the effectiveness-NTU relationship for the current z-shape arrangement. Based on the test results, it is found that the effect of fin pitch on the Coburn j factor is insignificant. This is because the high Reynolds number accentuates good mixing, leading to a better heat transfer performance irrespective changes of fin pitch. In the meantime, there is negligible difference for friction factor amid $f_p = 3.2$ and 4.2 mm. However, a detectable increase of friction factor is seen when the fin pitch is increased to 6.2 mm. Moreover, it could be clearly seen that the airside performance is independent of fin material.

Acknowledgments

The authors are indebted to King Mongkat's University of Technology Thonburi, the Thailand Research Fund, the Office of the Higher Education Commission and the National Research University Project for supporting this study. The third author also expresses gratitude for supporting funding from the National Science Council of Taiwan (99-2218-E-009-012-MY2).

References

[1] A. Nuntaphan, T. Kiatsiriroat, C.C. Wang, Air side performance at low Reynolds number of cross-flow heat exchanger using crimped spiral fins, Int. Commun. Heat Mass Transfer 32 (2005) 151–165.
[2] P. Naphon, S. Wongwises, Investigation of the performance of a spiral-coil finned tube heat exchanger under dehumidifying conditions, J. Eng. Phys. Thermophys. 76 (2003) 83–92.
[3] S. Wongwises, P. Naphon, Heat transfer characteristics of a spiral-coil finned tube heat exchanger under dry-surface conditions, Heat Transfer Eng. 27 (2006) 25–34.
[4] S. Wongwises, P. Naphon, Thermal performance of a spiral-coil finned tube heat exchanger under wet-surface conditions, J. Mech. Sci. Technol. 20 (2006) 212–226.
[5] K. Srisawad, S. Wongwises, Heat transfer characteristics of a new helically coiled crimped spiral finned tube heat exchanger, Heat Mass Transfer 45 (2009) 381–391.
[6] M. Lee, T. Kang, Y. Kim, Air-side heat transfer characteristics of spiral-type circular fin-and-tube heat exchangers, Int. J. Refrig. 33 (2010) 313–320.
[7] G. Xie, Q. Wang, B. Sunden, Parametric study and multiple correlations on air-side heat transfer and friction characteristics of fin-and-tube heat exchangers with large number of large-diameter tube rows, Appl. Therm. Eng. 29 (2009) 1–16.
[8] S. Wongwises, Y. Chokeman, Effect of fin pitch and number of tube rows on the air side performance of herringbone wavy fin and tube heat exchangers, Energy Convers. Manage. 46 (2005) 2216–2231.
[9] ESDU 86018, Effectiveness-NTU Relations for the Design and Performance Evaluation of two-stream heat exchangers, Engineering Science Data Unit 86018 with Amendment, London ESDU International plc (1991) 92-107.
[10] H.A. Navarro, L. Cabezas-Gomez, A new approach for thermal performance calculation of cross-flow heat exchanger, Int. J. Heat Mass Transfer 48 (2005) 3880–3888.
[11] L. Cabezas-Gomez, H.A. Navarro, J.M. Saiz-Jabardo, Thermal performance of multipass parallel and counter-cross-flow heat exchangers, J. Heat transfer 129 (2007) 282–290.
[12] K.A. Gardner, Efficient of extended surface, ASME Trans. 67 (1945) 621.
[13] W.M. Kays, A. London, Compact Heat Exchangers, third ed., McGraw-Hill, New York, 1984.
[14] ANSI/ASHRAE Standard 33-2000, Method of Testing Forced Circulation Air Cooling and Air Heating Coils, 2000.
[15] H.A. Navarro, L. Cabezas-Gomez, Effectiveness-NTU computation with a mathematical model for cross-flow heat exchangers, Brazilian J. Chem. Eng 24 (4) (2007) 509–521.
[16] M.S. Mon, U. Gross, Numerical study of fin-spacing effects in annular-finned tube heat exchangers, Int. J. Heat Mass Transfer 47 (2004) 1953–1964.
[17] Y.H. Kim, Y. Kim, Heat transfer characteristics of flat plate finned-tube heat exchangers with large fin pitch, Int. J. Refrig. 28 (2005) 851–858.
[18] C.C. Wang, K-Y. Chi, Y-J. Chang, Y-P. Chang, An experimental study of heat transfer and friction characteristics of typical louver fin-and-tube heat exchangers, Int. J. Heat Mass Transfer 41 (1998).
[19] K. Torikoshi, G.N. Xi, Y. Nakazawa, H. Asano, Flow and heat transfer performance of a plate fin and tube heat exchanger (First Report: Effect of Fin Pitch), Heat Transfer 1994, in: Proceedings of the 10th Int. Heat Transfer Conf. 4, 1994, pp. 411–416.
[20] C.C. Wang, C-T. Chang, Heat and mass transfer for plate fin-and-tube heat exchangers with and without hydrophilic coating, Int. J. Heat Mass Transfer 41 (1998) 3109–3120.
[21] C.C. Wang, Y.J. Chang, Y.C. Hsieh, Y.T. Lin, Sensible heat and friction characteristics of plate fin-and-tube heat exchangers having plane fins, Int. J. Refrig. 19 (4) (1996) 223–230.
[22] D.E. Briggs, E.H. Young, Convective heat transfer and pressure drop of air flowing across triangular pitch banks of finned tubes, Chem. Eng. Prog. Symp. Ser. 59 (41) (1963) 1–10.

Provided for non-commercial research and education use.
Not for reproduction, distribution or commercial use.

This article appeared in a journal published by Elsevier. The attached copy is furnished to the author for internal non-commercial research and education use, including for instruction at the authors institution and sharing with colleagues.

Other uses, including reproduction and distribution, or selling or licensing copies, or posting to personal, institutional or third party websites are prohibited.

In most cases authors are permitted to post their version of the article (e.g. in Word or Tex form) to their personal website or institutional repository. Authors requiring further information regarding Elsevier's archiving and manuscript policies are encouraged to visit:

http://www.elsevier.com/copyright

Author's personal copy

International Journal of Heat and Mass Transfer 54 (2011) 2673–2682

Contents lists available at ScienceDirect

International Journal of Heat and Mass Transfer

journal homepage: www.elsevier.com/locate/ijhmt

Condensation heat transfer and flow characteristics of R-134a flowing through corrugated tubes

Suriyan Laohalertdecha [a,b], Somchai Wongwises [b,*]

[a] The Joint Graduate School of Energy and Environment (JGSEE), King Mongkut's University of Technology Thonburi, Bangmod, Bangkok 10140, Thailand
[b] Fluid Mechanics, Thermal Engineering and Multiphase Flow Research Laboratory (FUTURE), Department of Mechanical Engineering, King Mongkut's University of Technology Thonburi, Bangmod, Bangkok 10140, Thailand

ARTICLE INFO

Article history:
Received 8 March 2010
Received in revised form 14 December 2010
Accepted 14 December 2010
Available online 2 March 2011

Keywords:
Condensation
Nusselt number
Two-phase friction factor
Smooth tube
Corrugated tube

ABSTRACT

This article presents the condensation heat transfer and flow characteristics of R-134a flowing through corrugated tubes experimentally. The test section is a horizontal counter-flow concentric tube-in-tube heat exchanger 2000 mm in length. A smooth copper tube and corrugated copper tubes having inner diameters of 8.7 mm are used as an inner tube. The outer tube is made from smooth copper tube having an inner diameter of 21.2 mm. The corrugation pitches used in this study are 5.08, 6.35, and 8.46 mm. Similarly, the corrugation depths are 1, 1.25, and 1.5 mm, respectively. The test conditions are performed at saturation temperatures of 40–50 °C, heat fluxes of 5–10 kW/m^2, mass fluxes of 200–700 kg/m^2 s, and equivalent Reynolds numbers of 30000–120000. The Nusselt number and two-phase friction factor obtained from the corrugated tubes are significantly higher than those obtained from the smooth tube. Finally, new correlations are developed based on the present experimental data for predicting the Nusselt number and two-phase friction factor for corrugated tubes.

© 2011 Elsevier Ltd. All rights reserved.

1. Introduction

Heat transfer enhancement techniques are the methods used for increasing the heat transfer performance of heat exchangers. Microfin tube is a type of rough surface used in heat transfer enhancement techniques and has been successfully implemented in the air conditioning and refrigeration industries for effective tube-side performance. This success is because of their ability to significantly improve the heat transfer coefficient [1–3] with only a moderate increase of the friction penalty. Moreover, the corrugated tube is another one type that is widely used in heat exchanger applications for the purpose of heat transfer enhancement, size reduction, and an easier manufacturing process. Many researchers have studied heat transfer enhancement using corrugated tubes as shown in Table 1. Some examples of these studies are described below.

Dong et al. [4] investigated the friction factor and heat transfer characteristics of four spirally corrugated tubes with various geometrical parameters. The working fluids are water and oil. The test runs are conducted at Reynolds numbers varying from 6000 to 93000 for water and 3200 to 19000 for oil. Their results indicated that the maximum heat transfer coefficient and friction factor obtained from corrugated tubes increase by approximately 120% and 160% when compared to smooth tubes.

Barba et al. [5] presented the experimental results of single-phase heat transfer and pressure drop of ethylene glycol flowing in a corrugated tube at moderate Reynolds numbers varying from 100 to 800. The inside heat transfer coefficient in the corrugated tube increases up to 4.27–16.79 times higher than that of the smooth tube, while the friction factor increases up to a factor of 1.83–2.45. Based on the experimental data, Nusselt number and friction factor correlations are proposed for the periodically fully developed region.

Rainieri and Pagliarini [6] studied the thermal performances of corrugated tubes. Axial symmetrical and helical corrugated tubes with different pitch values were considered. The tests were conducted at Reynolds numbers ranging between 90 and 800. Ethylene glycol is used as the working fluid. The results showed that the helical corrugation induces significant swirl components.

Among all these previous studies, the most productive studies have continually been performed by Zimparov [7]. Extended performance evaluation criteria for enhanced heat transfer surfaces at constant wall temperature were studied. Zimparov [8] presented heat transfer and isothermal friction pressure drop results of two single-start spirally corrugated tubes combined with five twisted tape inserts with different relative pitches. The friction factors and inside heat transfer coefficients obtained from these tubes were higher than those obtained from the smooth tube. Moreover, Zimparov [9,10] applied a simple mathematical model for predicting the friction factors and heat transfer coefficients in a spirally corrugated configuration combined with a twisted tape insert flowing in the turbulent flow regime. The calculated friction factors

* Corresponding author. Tel.: +662 470 9115; fax: +662 470 9111.
E-mail address: somchai.won@kmutt.ac.th (S. Wongwises).

0017-9310/$ - see front matter © 2011 Elsevier Ltd. All rights reserved.
doi:10.1016/j.ijheatmasstransfer.2010.12.034

Author's personal copy

Nomenclature

A	surface area of the test section (m^2)
C	Chisholm parameter
c_p	specific heat at constant pressure (J/kg K)
D	diameter (m)
e	corrugation depth (m)
f	friction factor
G	mass flux (kg/m^2 s)
h	heat transfer coefficient (W/m^2 K)
i	specific enthalpy (J/kg)
k	thermal conductivity (W/m K)
L	length of the test tube (m)
LMTD	logarithmic mean temperature difference
m	mass flow rate (kg/s)
Nu	Nusselt number
p	corrugation pitch (m)
Pr	Prandtl number
Q	heat transfer rate (W)
Re	Reynolds number
q''	heat flux (W/m^2)
T	temperature (°C)
v	specific volume (m^3/kg)
w	corrugation width (m)
x	average quality
X	Martinelli parameter

Greek letters

α	void fraction
β	helix angle (degree)
ε	relative roughness (m)
ρ	density (kg/m^3)
ϕ_l^2	two-phase multiplier
μ	dynamic viscosity (Pa s)
ΔP	pressure drop (Pa/m)

Subscripts

a	acceleration
avg	average
c	corrugated tube
f	friction
in	inlet
i	inside
l	liquid
out	outlet
o	outside
ph	pre-heater
ref	refrigerant
s	smooth tube
sat	saturation
tp	two-phase
TS	test section
v	vapor
w	water

and heat transfer coefficients were compared with the experimental data. The results showed that the agreement between predicted and experimental data is fairly good.

Vicente et al. [11,12] experimentally studied the mixed convection heat transfer and isothermal pressure drop in corrugated tubes for laminar, transition, and turbulent flow regions. At a high Rayleigh number, the Nusselt number obtained from these tubes is 30% higher than that obtained from the smooth tube. The friction factors of the corrugated tube were between 5% and 25% higher than those of the smooth tube.

Naphon et al. [13] studied the heat transfer and pressure drop characteristics of water flowing in horizontal double pipes with helical ribs. Nine test sections with different characteristic parameters were tested, namely helical rib height to diameter $h/d = 0.12$, 0.15, and 0.19 and helical rib pitch to diameter $p/d = 1.05$, 0.78, and 0.63. It was found that the helical ribs have a significant effect on the heat transfer and pressure drop augmentations. Both the proposed correlations for the heat transfer coefficient and friction factor give good agreement with the present data to within 15%.

Targanski and Cieslinski [14] studied the evaporation for the pure R407C and R407C/oil mixtures in two smooth tubes and two enhanced tubes experimentally. The advantages of the micro-fin tube and corrugated tube were quantified and discussed. Test runs were performed as follows: inlet and outlet vapour quality were set at 0 and 0.7, respectively, and mass flux density ranged from 250 to 500 kg/m^2 s. The experiments were conducted at an average saturation temperature of 0 °C. It was found that the corrugated tube and micro-fin tube had a significant effect on the heat transfer coefficient and pressure drop augmentations.

Bilen et al. [15] experimentally investigated the heat transfer and friction characteristics of air flow in different grooved tubes under turbulent flow regime. Reynolds numbers ranging from 10000 to 38000 were tested. The circular, trapezoidal, and rectangular grooves were used as the test section. The tube's length-

Table 1
Experimental investigation on the corrugated tube with various working fluid and tube configurations.

Sources	D_i (mm)	e/D_i	p/D_i	β (degree)	Phase
Dong et al. [4]	16.04–22.82	0.0243–0.0398	0.438–0.623	78.8–82.1	Single phase
Barba et al. [5]	14.5	0.103	0.793	45	Single phase
Rainieri and Pagliarini [6]	14	0.107	1.143–4.571	–	Single phase
Zimparov [7]	13.68–13.73	0.0407–0.0569	4.7–15.3	67.4–68	Single phase
Zimparov [8]	13.39–13.65	0.0371–0.0441	2.4–7.7	79.3–82.2	Single phase
Zimparov [9]	12.44–13.90	0.0224–0.0569	7.45–21.17	67.4–90	Single phase
Zimparov [10]	12.44–13.90	0.0224–0.0569	7.45–21.17	67.4–90	Single phase
Vicente et al. [11]	18	0.0239–0.0572	0.608–1.229	68–80	Single phase
Vicente et al. [12]	18	0.0239–0.0572	0.608–1.229	68–80	Single phase
Naphon et al. [13]	8.1	0.12–0.19	0.63–1.05	45	Single phase
Targanski and Cieslinski [14]	8.8	0.0511	0.681	77.75	Two phase (evaporation)
Bilen et al. [15]	36	0.0833	0.333–0.416	90	Single phase
Laohalertdecha and Wongwises [16]	8.7	0.1724	0.584–0.9724	74.2–79.47	Two phase (condensation)
Laohalertdecha and Wongwises [17]	8.7	0.1724	0.584–0.9724	74.2–79.47	Two phase (evaporation)

Author's personal copy

to-diameter ratio was 33. The maximum heat transfer enhancements were up to 63% for the circular groove, 58% for the trapezoidal groove, and 47% for the rectangular groove in comparison with the smooth tube at the given Reynolds number.

Laohalertdecha and Wongwises [16,17] experimentally studied the effects of pitch on heat transfer coefficient and pressure drop of R134a flowing in corrugated tubes during condensation and evaporation. The results showed that the heat transfer coefficient and pressure drop obtained from corrugated tube are higher than those of the smooth tube for all experimental condition.

As mentioned above, almost all of the literature reviews report the effects of the corrugation surface on the heat transfer coefficient and pressure drop of single-phase flows in corrugated tubes. However, although many papers have been published on two-phase heat transfer enhancement, there are some articles concerning the evaporation and condensation of refrigerants inside corrugated tubes. Moreover, it can also be noted that most of the works lack the condensation Nusselt number and two-phase friction factor data for corrugated tubes. Similarly, the *C* factor and two-phase friction factor of corrugated tubes are not reported in previous studies. As a consequence, this study mainly aims to study the Nusselt number and two-phase friction factor during condensation of R-134a inside horizontal corrugated tubes. In addition, the new correlations are developed based on the present experimental data for predicting the Nusselt number and two-phase friction factor for corrugated tubes.

2. Experimental apparatus

A schematic diagram of the experimental apparatus is shown in Fig. 1. The experimental apparatus was designed in order to determine the heat transfer coefficient and pressure drop of pure R-134a over the length of the test tube. The test loop consists of a test section, refrigeration loop, cooling water flow loops, subcooling loop, and the relevant instrumentation. The objective of the water loop before the test section is to provide controlled inlet quality. The second water loop located in the test section can provide controlled heat output from the test section. The subcooling loop is used to prevent any two-phase flow condition of the refrigerant occurring before it enters the refrigerant pump.

For the refrigeration circulating loop, liquid refrigerant is discharged by a gear pump regulated by an inverter. The refrigerant passes in series through a filter/dryer, sight glass tube, flow meter, and pre-heater and enters the test section. The inlet quality before entering the test section is controlled by the pre-heater. The pre-heater is a spiral counter-flow heat exchanger that supplies energy to provide a controlled inlet quality for vaporization of the refrigerant. Leaving the test section, the refrigerant is then condensed and subcooled by the chilling loop that removes the heat input from the pre-heater and test section, returns from the two-phase refrigerant to a subcooled state, collects later in a receiver, and eventually returns to the refrigerant pump to complete the cycle.

The test section is a horizontal counter-flow double tube heat exchanger. The length of the heat exchanger is 2.0 m. The detailed dimensions of the heat exchanger and the location of the thermocouples can be seen in Fig. 2. Fig. 3 shows schematic diagram and photograph of corrugated tubes together with nomenclature to describe the geometry. The dimensions of the test section are shown in Table 2.

The inlet temperature of the water is controlled by a thermostat. A differential pressure transducer and thermocouples are installed in the test section to measure the pressure drop and temperature across the test section. The length between pressure taps is 2.5 m. In the present study, the pressure of the refrigerant is mainly controlled by a high-pressure limit switch. High-pressure limit switches (Danfoss Type KP 5) are a device for regulating the

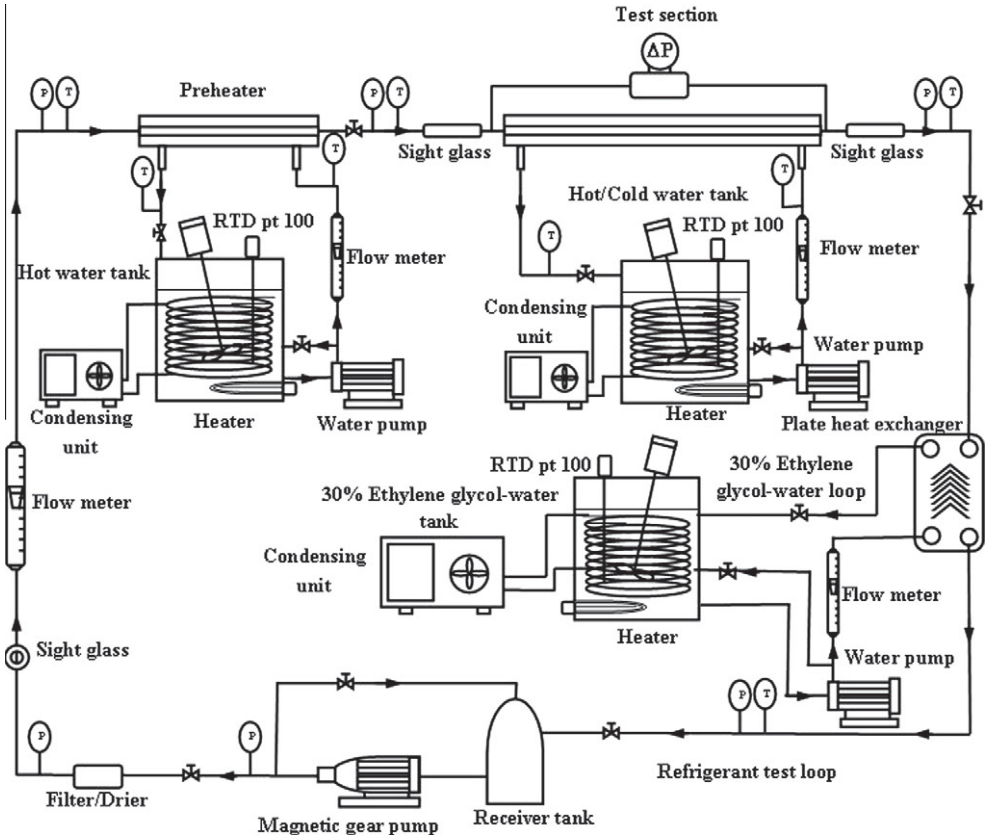

Fig. 1. Schematic diagram of experimental apparatus.

Author's personal copy

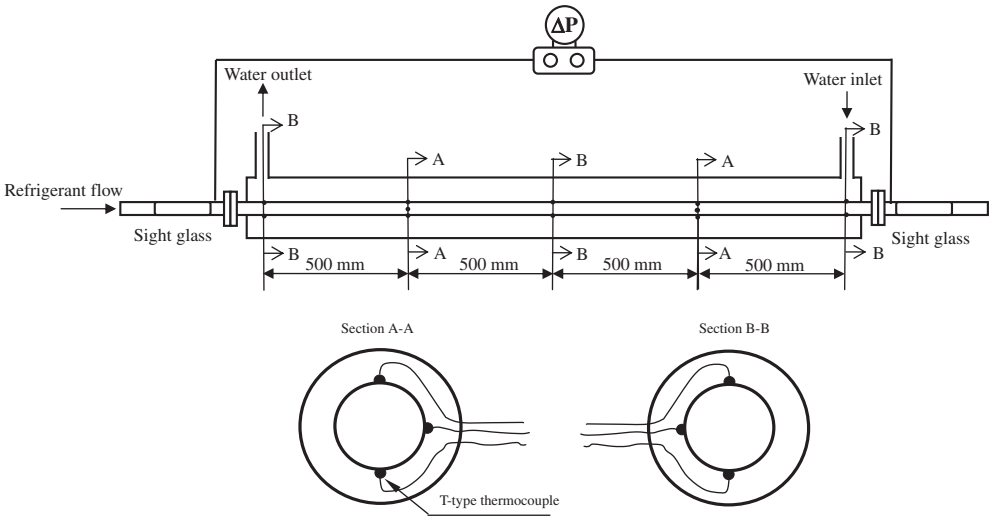

Fig. 2. Schematic diagram of the test section.

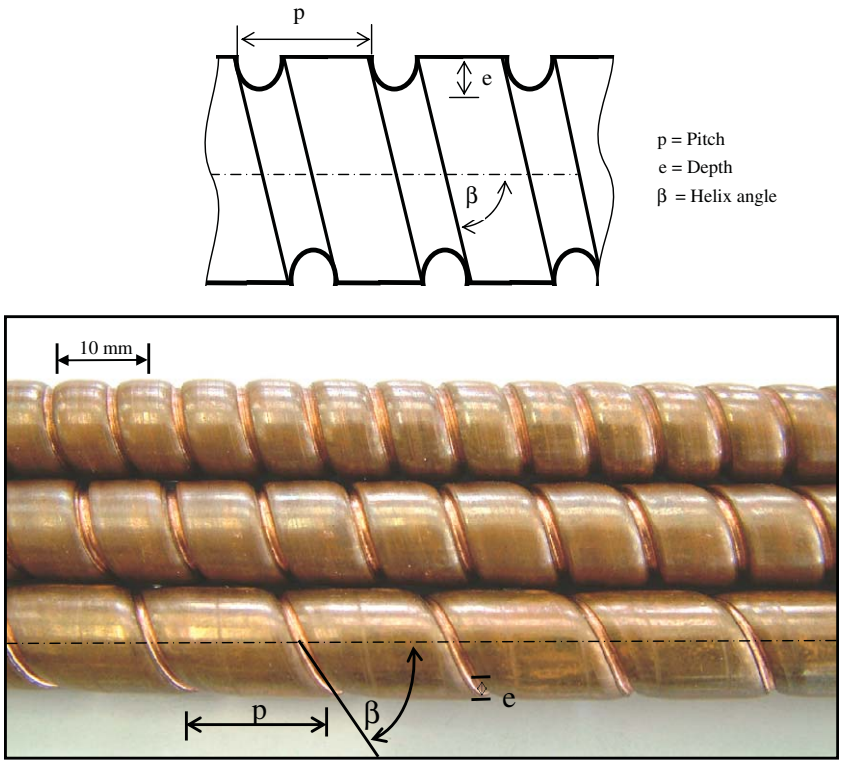

Fig. 3. Schematic diagram and photograph of corrugated tubes.

Table 2
The dimensions of the test section.

Number	p (mm)	e (mm)	w (mm)	β (degree)	D_i (mm)	L (mm)
1	5.08	1	1	79.47	8.7	2000
2	5.08	1.25	1	79.47	8.7	2000
3	5.08	1.5	1	79.47	8.7	2000
4	8.46	1.5	1	74.20	8.7	2000
5	6.35	1.5	1	76.56	8.7	2000
6	Smooth tube				8.7	2000

pressure of a system so that the system's pressure is maintained near a desired set point pressure in order to prevent the experimental apparatus damage.

The refrigerant temperature and tube wall temperatures along the test section are measured by T type thermocouples. As shown in Fig. 2, a total of 15 thermocouples are soldered at the top, bottom, and side at five points along the tube. All the temperature measuring devices are well calibrated in a controlled temperature bath using standard precision mercury glass thermometers. The uncertainty of the temperature measurements after considering the data acquisition system is ±0.1 °C. The refrigerant flow meter is a variable area type. The flow meter is specially calibrated in the range of 0.2–3.4 LPM for R-134a by the manufacturer. The differential pressure transducer is also calibrated by the manufacturer.

Author's personal copy

Table 3
Uncertainties of measured quantities and calculated parameters.

Parameter	Uncertainty
Temperature, T (°C)	±0.1%
Pressure drop, ΔP (kPa)	±0.075%
Mass flow rate of refrigerant, m_{ref}	±2% Full scale
Mass flow rate of water, m_w	±5% Full scale
Heat transfer rate at test section, Q_{TS}	±12.9%
Heat transfer rate at pre-heater, Q_{ph}	±8.5%
Condensation heat transfer coefficient, h	±18.8%
Average quality, x	±5.2%

Experiments were conducted with various flow rates of refrigerant, vapour qualities of refrigerant entering the test section, heat fluxes, and temperatures of refrigerant condensing in the test section. In the experiments, the refrigerant flow rate in the test section was controlled by adjusting the speed of the magnetic gear pump. To vary the vapour qualities at the inlet of the test section, the heating water flow rate was varied by small increments while the refrigerant flow rate was kept constant. The cold water in the test section was circulated by centrifugal pump to remove heat from the refrigerant to the water. Moreover, the vapour quality along test section is kept at lower than 0.2 for all experimental conditions. During each experiment, the heat transferred from the test section was kept at a desired value. This might be obtained by simultaneously adjusting and controlling the temperature and flow rate of the cold water entering the test section. The system was allowed to approach the steady state before any data were recorded. After stabilization, temperatures on the tube wall, refrigerant temperatures at the locations mentioned above, inlet and outlet temperatures of the heating water and cooling water, and flow rates of heating water, cooling water, and refrigerant were recorded. The pressure drop was measured by a pressure transducer installed between the inlet and outlet of the test section. It was possible to carry out the experiments by increasing the refrigerant flow rate while the saturation temperature in the test section was kept constant. The accuracies of the direct measurements and the uncertainties, which are calculated using the root mean sum square method, are shown in Table 3.

3. Data reduction

The data reduction of the measured results can be summarized as follows:

3.1. The vapour quality at the test section inlet ($x_{TS,in}$)

The vapour quality at the test section inlet is calculated as follows:

$$x_{TS,in} = \frac{i_{TS,in} - i_{f,T_{TS,in}}}{i_{fg,T_{TS,in}}} \tag{1}$$

where $i_{f,T_{TS,in}}$ is the enthalpy of the saturated liquid based on the temperature of the test section inlet, $i_{fg,T_{TS,in}}$ is the enthalpy of vaporization based on the temperature of the test section inlet, and $i_{TS,in}$ is the refrigerant enthalpy at the test section inlet given by

$$i_{TS,in} = i_{ph,in} + \frac{Q_{ph}}{m_{ref}} \tag{2}$$

where $i_{ph,in}$ is the inlet enthalpy of the liquid refrigerant before entering the pre-heater, m_{ref} is the mass flow rate of the refrigerant, and Q_{ph} is the heat transfer rate in the pre-heater, which is calculated by the following equation:

$$Q_{ph} = m_{w,ph} c_{p,w} \left(T_{w+,in} - T_{w,out}\right)_{ph} \tag{3}$$

where $m_{w,ph}$ is the mass flow rate of water entering the pre-heater.

3.2. The vapour quality at the test section outlet ($x_{TS,out}$)

The vapour quality at the test section outlet is calculated as follows:

$$x_{TS,out} = \frac{i_{TS,out} - i_{f,T_{TS,out}}}{i_{fg,T_{TS,out}}} \tag{4}$$

where $i_{TS,out}$ is the refrigerant enthalpy at the test section outlet, $i_{f,T_{TS,out}}$ is the enthalpy of the saturated liquid based on the temperature of the test section outlet, and $i_{fg,T_{TS,out}}$ is the enthalpy of vaporization based on the temperature of the test section outlet. As a consequence, the outlet enthalpy of the refrigerant flow is calculated as:

$$i_{TS,out} = i_{TS,in} - \frac{Q_{TS}}{m_{ref}} \tag{5}$$

where the heat transfer rate Q_{TS} in the test section is obtained from:

$$Q_{TS} = m_{w,TS} c_{p,w} \left(T_{w,out} - T_{w,in}\right)_{TS} \tag{6}$$

where $m_{w,TS}$ is the mass flow rate of the water entering the test section.

3.3. Equivalent Reynolds number (Re_{eq})

The equivalent Reynolds number is calculated as follows:

$$Re_{eq} = Re_l + Re_v \left(\frac{\mu_v}{\mu_l}\right)\left(\frac{\rho_l}{\rho_v}\right)^{0.5} \tag{7}$$

where Re_l is the liquid Reynolds number defined as:

$$Re_l = \frac{GD_i(1-x)}{\mu_l} \tag{8}$$

where Re_v is the vapour Reynolds number defined as:

$$Re_v = \frac{GD_i x}{\mu_v} \tag{9}$$

3.4. The inside heat transfer coefficient (h_i)

The inside heat transfer coefficient is determined by the following equation:

$$h_i = \frac{1}{\left(\frac{1}{U_i}\right) - \left(\frac{1}{2k}\right) D_i \ln\left(\frac{D_o}{D_i}\right) - \left(\frac{D_i}{D_o}\right)\left(\frac{1}{h_o}\right)} \tag{10}$$

where U_i is the overall heat transfer coefficient based on the internal heat transfer area. k is the thermal conductivity of the tube material, and h_o is the outside heat transfer coefficient:

$$U_i = \frac{Q_{TS}}{A_i(\mathrm{LMTD})} \tag{11}$$

where A_i is the inside tube surface and LMTD is the logarithmic mean temperature difference, defined as follows:

$$\mathrm{LMTD} = \frac{\Delta T_1 - \Delta T_2}{\ln\left(\frac{\Delta T_1}{\Delta T_2}\right)} \tag{12}$$

$$\Delta T_1 = T_{ref,in} - T_{w,out} \tag{13}$$

$$\Delta T_2 = T_{ref,out} - T_{w,in} \tag{14}$$

where $T_{w,in}$ and $T_{w,out}$ denote the inlet and outlet temperatures of the water in the annulus. $T_{ref,in}$ and $T_{ref,out}$ are the inlet and outlet refrigerant temperatures.

Moreover, the average outside heat transfer coefficient is calculated as:

Author's personal copy

$$h_o A_o = \frac{Q_{TS}}{T_{wall,avg} - T_{w,avg}} \tag{15}$$

where A_o is the outside test tube surface, $T_{wall,avg}$ is the average wall temperature, and $T_{w,avg}$ is the average cooling water temperature flowing inside the annulus.

3.5. The Nusselt number (Nu)

The Nusselt number is calculated as follows:

$$Nu = \frac{h_i D_i}{k_l} \tag{16}$$

where k_l is thermal conductivity of liquid refrigerant.

3.6. The frictional pressure drop (ΔP_f)

The total pressure drop, ΔP_{total}, is expressed as the sum of two important components, as follows:

$$\Delta P_{total} = \Delta P_f + \Delta P_a \tag{17}$$

The two terms on the right-hand side represent the frictional pressure drop (ΔP_f) and accelerational pressure drop (ΔP_a). The accelerational pressure drop, ΔP_a, was proposed by Tran [18] as follows:

$$\Delta P_a = G^2 \left(\left(\frac{x_{out}^2}{\rho_v \alpha_{out}} + \frac{(1-x_{out})^2}{\rho_l (1-\alpha_{out})} \right) - \left(\frac{x_{in}^2}{\rho_v \alpha_{in}} + \frac{(1-x_{in})^2}{\rho_l (1-\alpha_{in})} \right) \right) \tag{18}$$

where α is the void fraction and is presented by Zivi's correlation [19] as follows:

$$\alpha = \left(1 + \frac{(1-x)}{x} \left(\frac{\rho_v}{\rho_l} \right)^{\frac{2}{3}} \right)^{-1} \tag{19}$$

So far, the frictional pressure drop, ΔP_f, can be obtained by subtracting the accelerational pressure drop from the total measured pressure drop.

3.7. Two-phase friction factor (f_{tp})

The two-phase friction factor is calculated as follows:

$$f_{tp} = \frac{D_i \Delta P_f \rho_l}{2 G_{eq}^2} \tag{20}$$

where the equivalent mass flux, G_{eq}, is presented by Akers [21] as shown below:

$$G_{eq} = G \left[(1-x) + x \left(\frac{\rho_l}{\rho_v} \right)^{0.5} \right] \tag{21}$$

4. Results and discussion

In this study, the effects of corrugation pitch and corrugation depth on the Nusselt number and two-phase friction factor were experimentally investigated as a function of saturation temperature, heat flux, average quality, mass flux, and equivalent Reynolds number. The physical properties of the refrigerants were obtained by REFPROP, Version 6.01 [20]. The data cover five corrugated tubes and a smooth tube. The analysis of the data reported in Table 2 focuses on the effects of corrugation pitch and depth on the Nusselt number and two-phase friction factor.

4.1. Nusselt number

The experimental data for the smooth tube were validated by comparing the present heat transfer coefficient in terms of the Nusselt number with those taken from existing correlations such as those obtained by Akers et al. [21], Traviss et al. [22], Nualboonrueng et al. [23], Chen et al. [24], Cavallini and Zechin [25], Dobson and Chato [26], and Bassi and Bansal [27], as demonstrated in Fig. 4. It is found that around 90% of the data are correlated within the deviation of ±30%.

4.1.1. Effect of pitch on the Nusselt number

Fig. 5 illustrates the Nusselt number with average quality at various corrugation pitches (p = 5.08, 6.35, and 8.46 mm) with a constant corrugation depth of 1.5 mm at G = 400 kg/m^2 s, q'' = 10 kW/m^2, and T_{sat} = 40 °C. The results show that the Nusselt number increases with increasing average quality. At the same average quality, the Nusselt number obtained from the corrugated tubes is evidently higher than that from the smooth tube across the range of the average quality. Moreover, this figure shows that the Nusselt number at a lower corrugation pitch is higher than that at a higher one. This is because the corrugation pitch has a significant effect on mixing of the condensate film in the boundary layer

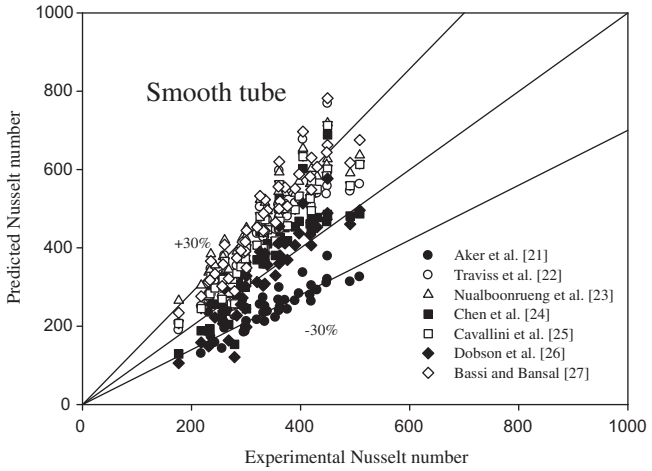

Fig. 4. Comparison of present R-134a Nusselt number data with existing correlation.

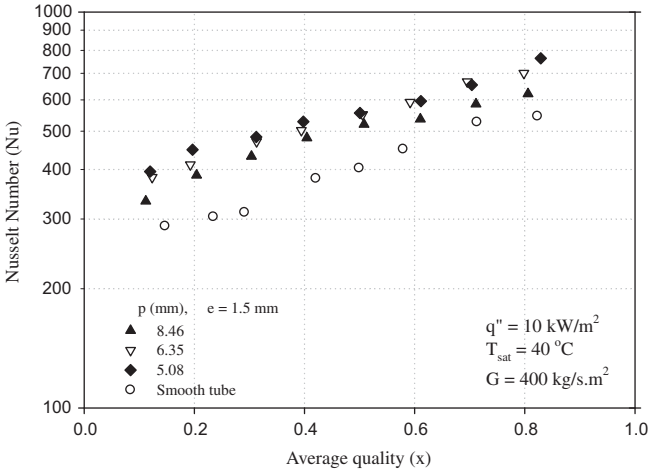

Fig. 5. Nusselt number vs average quality at T_{sat} = 40 °C, G = 400 kg/m^{2}s and q'' = 10 kW/m^2 for different pitches.

Author's personal copy

at the tube wall which causes the turbulence to increase. Therefore, the Nusselt number increases with decreasing corrugation pitch.

4.1.2. Effect of depth on the Nusselt number

Figs. 6 and 7 illustrate the Nusselt number with average quality and equivalent Reynolds number for different corrugation depths of 1, 1.25 and 1.5 mm, respectively with a constant corrugation pitch of 5.08 mm. As shown, the Nusselt number increases with increasing average quality and equivalent Reynolds number. At the same quality, the Nusselt number obtained from corrugation depth of 1.25 and 1.5 mm is obviously higher than that obtained from smooth tube. This is due to (1) drag forces exerted on the flow field by the corrugation, (2) flow blockage due to area reduction, (3) turbulence augmentation, and (4) rotational flow produced by the corrugation depth [11–12]. However, the Nusselt number obtained from corrugation depth of 1 mm is nearly same as the Nusselt number obtained from the smooth tube. This is because the axial momentum dominates the rotational flow produced by the corrugation depth of 1 mm.

4.1.3. Comparison of experimental data with proposed correlations

Fig. 8 shows a comparison of the experimental data for the corrugated tube with the proposed correlations. The proposed correlation is established from the Buckingham's Pi theorem in terms of Nusselt number, equivalent Reynolds number, Prandtl number, corrugation pitch and depth, and inside diameter. The proposed correlation is shown as follows:

$$Nu = 0.007\ Re_{eq}^{0.557} Pr^{3.8} \left(\frac{ep}{D_i^2}\right)^{0.02} \quad (22)$$

As illustrated in Fig. 8, the results show that approximately 90% of data fall within a deviation of ±10%.

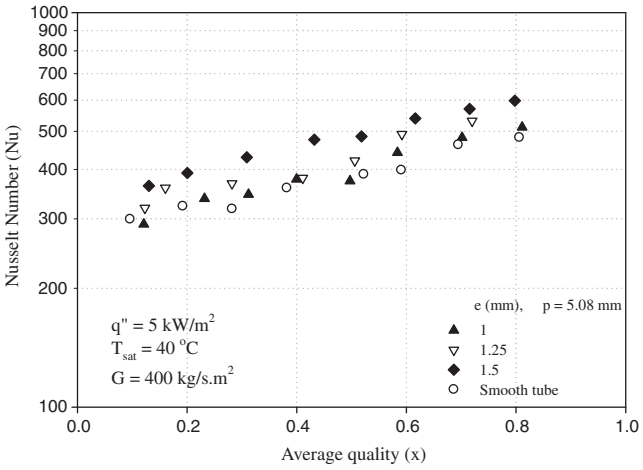

Fig. 6. Nusselt number vs average quality at T_{sat} = 40 °C, G = 400 kg/m^{2}s and q'' = 5 kW/m^2 for different depths.

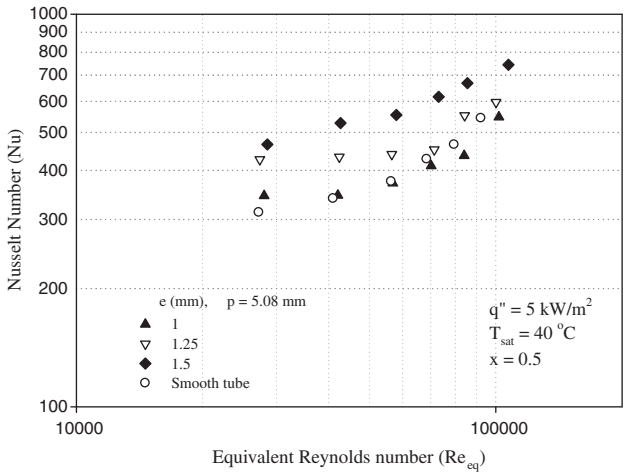

Fig. 7. Nusselt number vs equivalent Reynolds number at T_{sat} = 40 °C, q'' = 5 kW/m^2 and x = 0.5 for different depths.

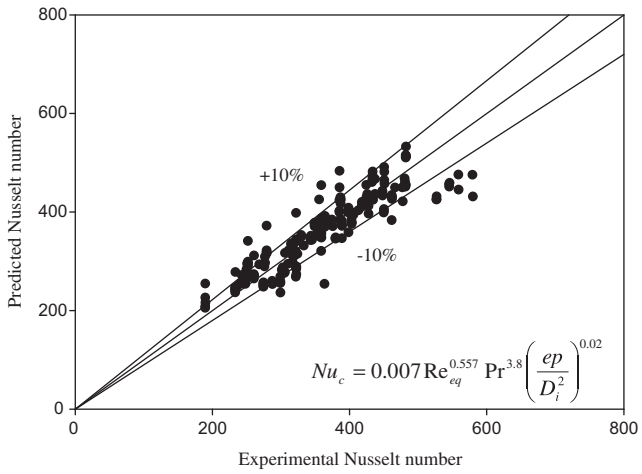

Fig. 8. Predicted Nusselt number using the proposed correlation vs the experimental data.

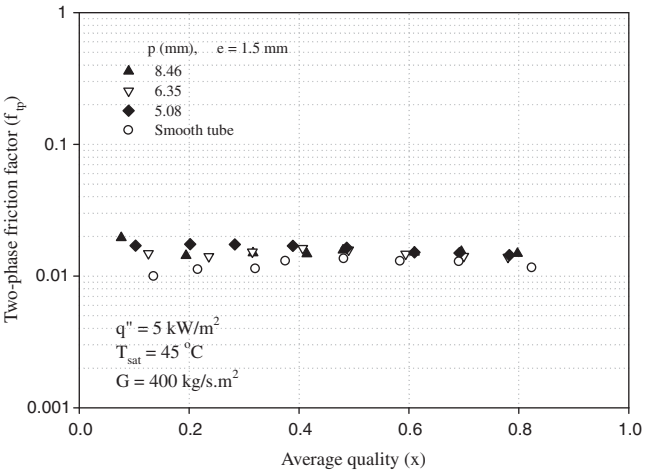

Fig. 9. Two-phase friction factor vs average quality at T_{sat} = 45 °C, G = 400 kg/m^{2}s and q'' = 5 kW/m^2 for different pitches.

4.2. Two-phase friction factor

The total condensation pressure drop was directly measured by the differential pressure transducer mounted on the header at the inlet and outlet of the test section. In our apparatus, the length between headers is 2.5 m while the length of the test section is 2 m. The frictional pressure drop can be obtained by subtracting the accelerational pressure drop from the total measured pressure drop. The results show the frictional pressure drop obtained from smooth and corrugated tubes in term of the Fanning two-phase friction factor.

Author's personal copy

4.2.1. Effect of pitch on two-phase friction factor

Fig. 9 illustrates the frictional pressure drop obtained from smooth and corrugated tubes in term of the Fanning two-phase friction factor. This plot shows that the two-phase friction factor slightly decreases with increasing average quality. The reason for this can be given in two aspects. Firstly, the frictional pressure drop increases with increasing average quality. This is because at higher average quality, the higher velocity of vapor flow causes more shear stress at the interface of the vapor and liquid film. Moreover, the secondary flow that becomes stronger at higher vapor velocity will produce more entrainment and redeposition of droplets, causing more flow turbulence. Secondly, the equivalent mass flux increases with increasing average quality. This is because the increasing in average quality increases the equivalent mass flux, according to Eq. (21). As the equivalent mass flux increase, the two-phase friction factor also decreases, according to Eq. (20). Therefore, the increase in average quality causes the two-phase friction factor to decrease. In addition, from the comparison of smooth and corrugated tubes, the two-phase friction factors obtained from corrugated tubes are higher than those obtained from smooth tube, under the same experimental condition. However, the effect of pitch on the two-phase friction factor is very small for all average quality.

4.2.2. Effect of depth on two-phase friction factor

Figs. 10 and 11 show the variations of the two-phase friction factor with average quality and the two-phase friction factor with equivalent Reynolds number, respectively. The experimental results show that the two-phase friction factor of the corrugated tube is greater than that of the smooth tube. The reason for this is similar to the reason given for Fig. 9. As shown in Figs. 10 and 11, the difference between two-phase friction factor obtained from corrugated tubes and smooth tube is reduced with increasing average quality and equivalent Reynolds number, respectively. This is because the secondary motion in refrigerant decreases as the axial momentum increases. However, from the present data, the effect of depth on the two-phase friction factor is insignificant.

4.2.3. The two-phase frictional multiplier (ϕ_l^2)

The two-phase frictional multiplier (ϕ_l^2) for the smooth tube is proposed by Chisholm [28] as follows:

$$\phi_l^2 = 1 + \frac{C}{X} + \frac{1}{X^2} \tag{23}$$

where X is the Martinelli parameter, which is given by

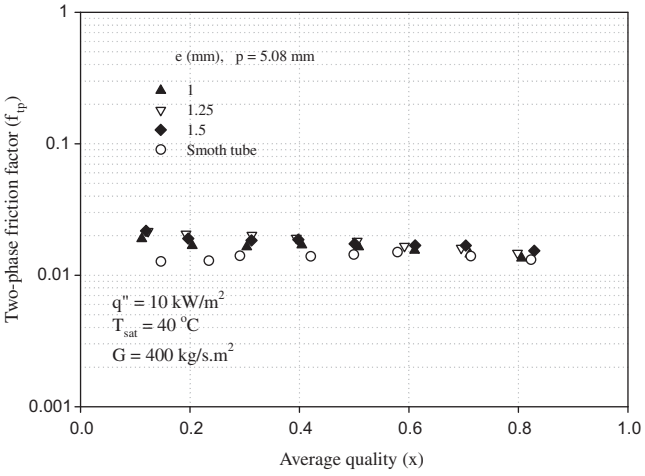

Fig. 10. Two-phase friction factor vs average quality at T_{sat} = 40 °C, G = 400 kg/m^{2}s and q'' = 10 kW/m^2 for different depths.

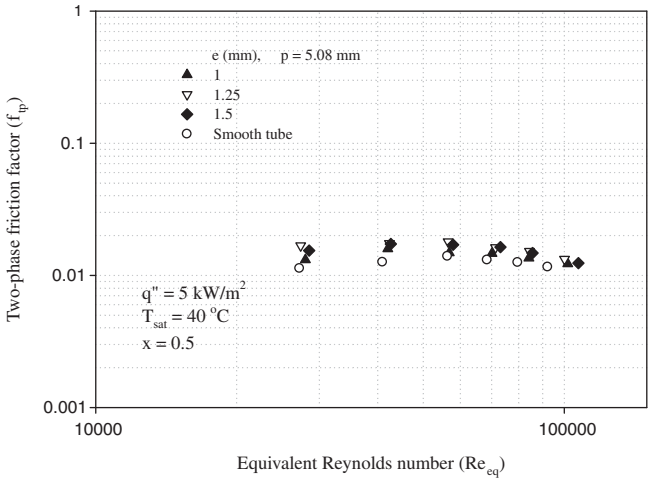

Fig. 11. Two-phase friction factor vs equivalent Reynolds number at T_{sat} = 40 °C, x = 0.5 and q'' = 5 kW/m^2 for different depths.

$$X^2 = \frac{\left(\frac{dp}{dz}\right)_l}{\left(\frac{dp}{dz}\right)_g} \tag{24}$$

The constant C in Eq. (23) is the parameter which indicates the two-phase flow condition.

Fig. 12 shows the comparison of the two-phase friction multiplier with the Martinelli parameter for different tubes. The predicted lines at values of constant C of 5, 10, and 20 are calculated by the Chisholm method. The constant value of C varies from 5 to 20 depending on the flow condition of the vapour and liquid. For instance, the constant C = 20 when the vapour and liquid flow is in the turbulent region. C = 10 when the vapour and liquid are laminar and turbulent, respectively. The value of C = 5 when the two-phase flow is in the laminar region. This figure shows that a smooth tube has a two-phase friction multiplier lower than that of the corrugated tube at the same Martinelli parameter. As shown in Fig. 13, almost all values of constant C obtained from the smooth tube are lower than those obtained from the corrugated tube at the same Martinelli parameter. However, the constant C depends not only on the Martinelli parameter but also on the Reynolds number and tube configurations. Therefore, constant C values can be correlated as follows:

$$\text{For smooth tube}: \quad C_s = 15.75\, X^{-0.5} Re_l^{-0.1} \tag{25}$$

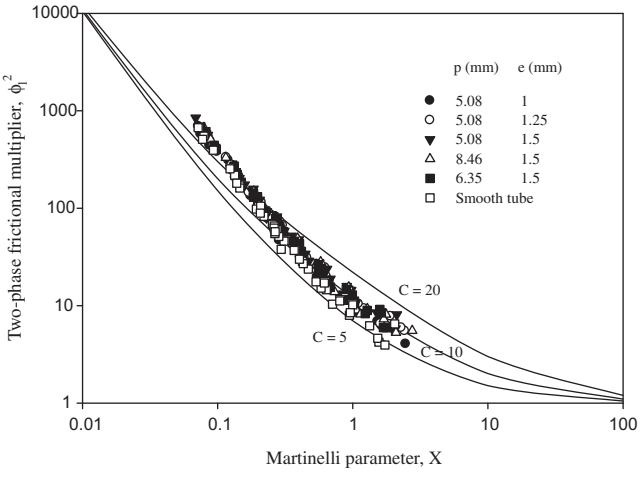

Fig. 12. Two-phase frictional multiplier vs Martinelli parameter.

Author's personal copy

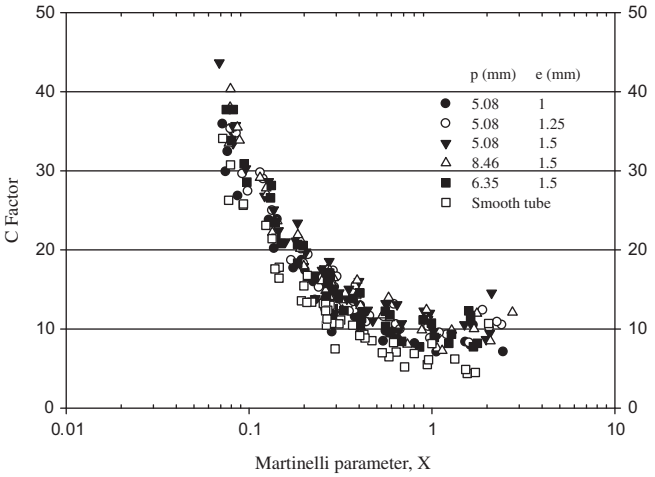

Fig. 13. Experimentally calculated *C* factors.

$$\text{For corrugated tube}: \quad C_c = 304.73X^{-0.254}Re_l^{-0.33}\left(\frac{ep}{D_i^2}\right)^{0.117} \tag{26}$$

The frictional pressure drops using the proposed *C* correlation are plotted with the experimental frictional pressure drop as shown in Fig. 14. It is found that about 95% of the data fall within a deviation of ±20%.

Fig. 15 shows the variation of the two-phase friction factor with equivalent Reynolds number for smooth tube and corrugated tubes. The experimental two-phase friction factor obtained from smooth tube is around 0.012. Moreover, Fig. 15 also shows that the two-phase friction factor obtained from corrugated tubes depends on the equivalent Reynolds number and tube geometry. The two-phase friction factor for corrugated tube is presented as follows:

$$\text{For corrugated tube}: \quad f_{tp,c} = 0.172Re_{eq}^{-0.2}\left(\frac{ep}{D_i^2}\right)^{0.09} \tag{27}$$

Fig. 16 shows the predicted frictional pressure drop of corrugated tubes using the proposed two-phase friction factor correlation versus the experimental data. However, the two-phase frictional pressure drop can be determined from Eqs. (27). Moreover, it is found that more than 90% of the data fall within a deviation of ±10%.

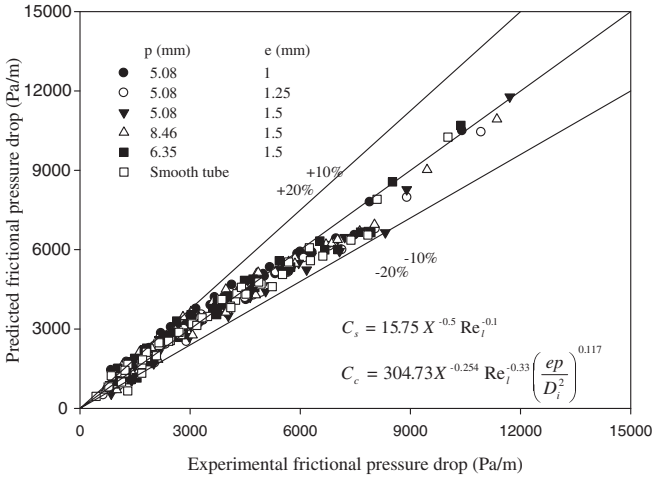

Fig. 14. Predicted frictional pressure drop using the proposed *C* factor correlation vs the experimental data.

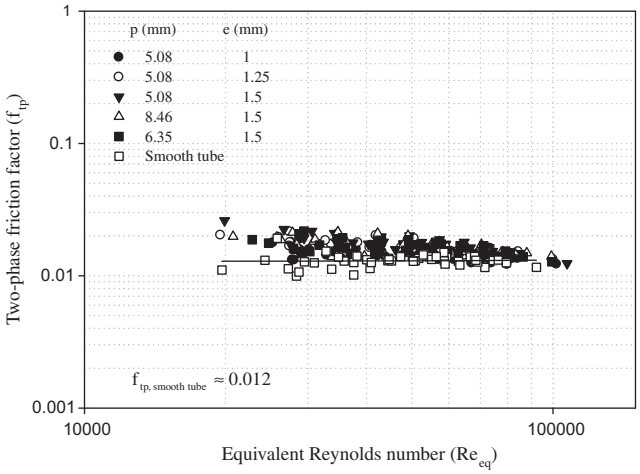

Fig. 15. Two-phase flow friction factor vs equivalent Reynolds number for smooth and corrugated tubes.

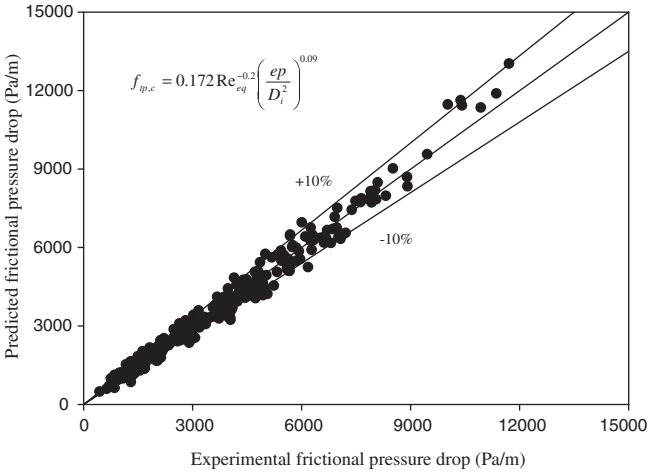

Fig. 16. Predicted frictional pressure drop using the proposed two-phase friction factor correlation vs the experimental data.

5. Conclusion

The experimental apparatus is designed to determine the Nusselt number and two-phase friction factor of R-134a using copper smooth and corrugated tubes. The test section is a counter-flow concentric tube-in-tube heat exchanger 2000 mm in length. A smooth tube and corrugated tubes having inner diameters of 8.7 mm are used as the inner tube. The corrugation pitches are 5.08, 6.35, and 8.46 mm. The corrugation depths are 1, 1.25, and 1.5 mm, respectively. The results obtained from the corrugated tubes are compared with those obtained from the smooth tube. Since the corrugation at the surface promotes turbulence of the refrigerant flow and mixing of the condensate film, it is evident that the Nusselt number and two-phase friction factor obtained from the corrugated tubes are significantly higher than those obtained from the smooth tube. The effect of pitch and depth on Nusselt number is significant. The Nusselt number increases with decreasing corrugation pitch and increases with increasing corrugation depth. On the other hand, the effect of pitch and depth on two-phase friction factor is insignificant. The new correlations are developed based on the present experimental data for predicting the Nusselt number and two-phase friction factor for corrugated tubes.

Author's personal copy

Acknowledgements

The present study was supported financially by King Mongkut's University of Technology Thonburi, the Thailand Research Fund, the Office of the Higher Education Commission and the National Research University Project, whose guidance and assistance are gratefully acknowledged.

References

[1] L.M. Schlager, M.P. Pate, A.E. Bergles, Evaporation and condensation heat transfer and pressure drop in horizontal 12.7-mm micro-fin tubes with refrigerant 22, J. Heat Transfer 112 (1989) 1041–1047.
[2] C.S. Kuo, C.C. Wang, In-tube evaporation of HCFC-22 in a 9.52 mm micro-fin/smooth tube, Int. J. Heat Mass Transfer 39 (1996) 2559–2569.
[3] Y. Kim, K. Seo, J.T. Chung, Evaporation heat transfer characteristics of R-410A in 7 and 9.52 mm smooth/micro-fin tubes., Int. J. Refrig. 25 (2002) 716–730.
[4] Y. Dong, L. Huixiong, C. Tingkuan, Pressure drop heat transfer and performance of single-phase turbulent flow in spirally corrugated tubes, Exp. Therm. Fluid Sci. 24 (2001) 131–138.
[5] A. Barba, S. Rainieri, M. Spiga, Heat transfer enhancement in a corrugated tube, Int. Commun. Heat Mass Transfer 29 (2002) 313–322.
[6] S. Rainieri, G. Pagliarini, Convective heat transfer to temperature dependent property fluids in the entry region of corrugated tubes, Int. J. Heat Mass Transfer 45 (2002) 4525–4536.
[7] V. Zimparov, Enhancement of heat transfer by a combination of three-start spirally corrugated tubes with a twisted tape, Int. J. Heat Mass Transfer 44 (2001) 551–574.
[8] V. Zimparov, Enhancement of heat transfer by a combination of a single-start spirally corrugated tubes with a twisted tape, Exp. Therm. Fluid Sci. 25 (2002) 535–546.
[9] V. Zimparov, Prediction of friction factors and heat transfer coefficients for turbulent flow in corrugated tubes combined with twisted tape inserts. Part 1: friction factors, Int. J. Heat Mass Transfer 47 (2004) 589–599.
[10] V. Zimparov, Prediction of friction factors and heat transfer coefficients for turbulent flow in corrugated tubes combined with twisted tape inserts. Part 2: heat transfer coefficients, Int. J. Heat Mass Transfer 47 (2004) 385–393.
[11] P.G. Vicente, A. Garcia, A. Viedma, Experimental investigation on heat transfer and friction factor characteristics of spirally corrugated tubes in turbulent flow at different Prandtl number, Int. J. Heat Mass Transfer 47 (2004) 671–681.
[12] P.G. Vicente, A. Garcia, A. Viedma, Mixed convection heat transfer and isothermal pressure drop in corrugated tubes for laminar and transition flow, Int. Commun. Heat Mass Transfer 31 (2004) 651–662.
[13] P. Naphon, M. Nuchjapo, J. Kurujareon, Tube side heat transfer coefficient and friction factor characteristics of horizontal tubes with helical rib, Energ. Convers. Manage. 47 (2006) 3031–3044.
[14] T. Targanski, J.T. Cieslinski, Evaporation of R407C/oil mixtures inside corrugated and micro-fin tubes, Appl. Therm. Eng. 27 (2007) 2226–2232.
[15] K. Bilen, M. Cetin, H. Gul, T. Balta, The investigation of groove geometry effect on heat transfer for internally grooved tubes, Appl. Therm. Eng. 29 (2009) 753–761.
[16] S. Laohalertdecha, S. Wongwises, The effects of corrugation pitch on the condensation heat transfer coefficient and pressure drop of R-134a inside horizontal corrugated tube, Int. J. Heat Mass Transfer 53 (2010) 2924–2931.
[17] S. Laohalertdecha, S. Wongwises, An experimental study into the evaporation heat transfer and flow characteristics of R-134a refrigerant flowing through corrugated tubes, Int. J. Refrig. 34 (2011) 280–291.
[18] T.N. Tran, Pressure drop and heat transfer study of two-phase flow in small channels, Ph.D. Dissertation, Texas Tech University, Lubbock, Texas, 1998.
[19] S.M. Zivi, Estimation of steady-state steam void-fraction by mean of the principle of minimum entropy production, J. Heat Transfer – Trans. ASME 86 (1964) 247–252.
[20] REFPROP, Refrigerant Properties Database, Version 6.01, NIST, Gaithersburg, MD, 1998.
[21] W.W. Akers, H.A. Beans, O.K. Crosser, Condensation heat transfer within horizontal tubes, Chem. Eng. Prog. Symp. 55 (1959) 29.
[22] D.P. Traviss, W.M. Rohsenow, A.B. Baron, Forced-convection condensation inside tubes: a heat transfer equation for condenser design, ASHRAE Trans. 79 (1973) 157–165.
[23] T. Nualboonrueng, J. Kaew-on, S. Wongwises, Two-phase condensation heat transfer coefficients of HFC-134a at high mass flux in smooth and micro-tubes, Int. Commun. Heat Mass Transfer 30 (2003) 577–590.
[24] S.L. Chen, F.M. Gerner, C.L. Tien, General film condensation correlation, Exp. Heat Transfer 1 (1987) 93–107.
[25] A. Cavallini, R. Zechin, A dimensionless correlation for heat transfer coefficient in forced-convection condensation, in: Proceedings of the 5th International Heat Transfer Conference, Japan, vol. 3, 1974, pp. 309–313.
[26] M.K. Dobson, J.C. Chato, Condensation in smooth horizontal tubes, J. Heat Transfer 120 (1998) 193–213.
[27] R. Bassi, P.K. Bansal, In-tube condensation of mixture of R134a and ester oil: empirical correlations, Int. J. Refrig. 26 (2003) 402–409.
[28] D. Chisholm, Pressure gradients due to friction during the flow of evaporating two-phase mixtures in smooth tubes and channels, Int. J. Heat Mass Transfer 16 (1973) 347–358.

Journal of Electronics Cooling and Thermal Control, 2011, 1, 38-44
doi:10.4236/jectc.2011.13005 Published Online December 2011 (http://www.SciRP.org/journal/jectc)

Experimental Study of Jet Nanofluids Impingement System for Cooling Computer Processing Unit

Paisarn Naphon[1*], Somchai Wongwises[2]
[1]*Thermo-Fluids and Heat Transfer Enhancement Lab, Department of Mechanical Engineering, Faculty of Engineering, Srinakharinwirot University, Ongkharak, Thailand*
[2]*Fluid Mechanics, Thermal Engineering and Multiphase Flow Research Lab, Department of Mechanical Engineering, King Mongkut's University of Technology Thonburi, Suksawas, Bangkok, Thailand*
E-mail: [*]*paisarnn@swu.ac.th*
Received September 20, 2011; *revised November* 15, 2011; *accepted November* 25, 2011

Abstract

An experimental investigation of the jet nanofluids impingement heat transfer characteristics of mini-channel heat sink for cooling computer processing unit of personal computer is performed. The experiments are tested under the real personal computer operating conditions: no load and full load conditions. The experiments are performed for the following ranges of the parameters: coolant flow rate varies from 0.008 to 0.020 kg/s, the nozzle diameter is set to 1.00, 1.40, 1.80 mm, the distance nozzle-to-fins tip is 2.00 mm, the channel width of the mini-channel heat sink is 1.00 mm. The nanofluids with suspending of TiO_2 particles in base fluid are used as a working fluids. It was observed that the average CPU temperatures obtained from the jet nanofluids impingement cooling system are 3.0%, 6.25% lower than those from the jet liquid impingement and from the conventional liquid cooling systems, respectively. However, this cooling system requires higher energy consumption.

Keywords: Jet Impingement, Nanofluids Cooling, Cooling CPU, Mini-Rectangular Fin Heat Sink

1. Introduction

In order to ensure reliable operation, the PCs or electronics devices must be operated in the specific temperature ranges which the exceeding maximum allowable temperature is the serious problem of these devices. There are many techniques to dissipate the generated heat. The development of the miniaturized technology, mini and micro-components has been introduced as one of heat transfer enhancement techniques. The study of a single phase heat transfer of the various geometrical heat sinks for cooling electronic devices are reported by Zhange *et al*.,[1]; Yu [2]; Peles [3]; Kosar and Peles [4]; Yakut *et al*. [5]; Mohamed [6]. Didarul [7] investigated the heat transfer and fluid flow characteristics of finned surfaces. Chein and Chuang [8] applied the thermoelectric with microchannel heat sink by using nanofluids as coolant for cooling electric components. Jeng and Tzeng [9] experimentally studied the pressure drop and heat transfer of a square pin-fin array. These studies indicated that the various geometrical heat sinks are possible for cooling electronics devices.

The most frequently used coolants in the heat transfer devices study are air, water, and fluoro-chemicals. However, the heat transfer capability is limited by the working fluid transport properties. One of the methods for the heat transfer enhancement is the application of additives to the working fluids to change the fluid transport properties and flow features. Therefore, in order to further enhance thermal performance of heat transfer devices, the use of nanofluids is proposed. The numerous papers presented on the single phase convective heat transfer of nanofluids, boiling heat transfer of nanofluids and heat transfer enhancement using nanofluids are continuously reviewed by Duangtongsuk and Wongwises [10]; Trisaksri and Wonwises [11]; Godson *et al*. [12]. However, improving the cooling performance had been continuously performed by using the jet liquid impingement technique. Thermal performance of a pin-fin heat sink with various geometrical with impingement cooling was considered by Kobus and Oshio [13]; Li *et al*. [14]. Geedipalli *et al.* [15] simulated the combination heating of food using microwave and jet impingement by coupling Maxwell's equation. Sung and Mudawar [16,17] studied the jet impingement single-phase and two-phase heat transfer characteristics. Reasonable

Copyright © 2011 SciRes.

agreement was obtained between the predicted results and the measured data. Koseoglu and Baskaya [18] used a Laser Doppler Anemometry to observe the jet flow field and turbulence on heat transfer characteristics. The jet heat transfer enhancement from a flat surface was simulated by Katti and Prabhu [19]; Kanna and Das [20]; Cirillo and Isopi [21]. Goodro *et al*. [22] considered effects of the hole spacing on the spatially-resolved jet array impingement heat transfer. Jeng *et al*. [23] and Hewakandamby [24] investigated the jet air flow and heat transfer behaviors of the rotating heat sink and oscillation impinging jet. Nguyen *et al.* [25] studied the enhanced heat transfer with of nanofluids in a confined and submerged impinging jet on a flat, horizontal and circular heated surface. Koseoglu and Baskaya [26] experimentally and numerically investigated the impinging jet heat transfer. Chang *et al*. [27] studied the jet-array impingement heat transfer in a concentric annular channel with rotating inner cylinder. Sharif and Banerjee [28] applied the k-ε turbulence model to analyze the heat transfer of the confined slot-jet impingement on a moving plate. Whelan and Robinson [29] used the jet liquid impingement for cooling the electronics devices. Several studies showed that thermal conductivity of the nanofluids is higher than that of the base fluids and therefore great potential for the enhancement of heat transfer.

As mentioned above, the numerous papers presented the study on the heat transfer and pressure drop in the mini- and micro-channel, nanofluids heat transfer enhancement, jet impingement heat transfer characteristics. However, only one work [25] reported the passive and active heat transfer enhancement techniques by using the jet nanofluids impingement heat transfer characteristics of the heat sinks. Therefore, the present work focus on the experimental study of the jet nanofluids impingement heat transfer characteristics of the mini-rectangular fin heat sink for cooling computer processing unit (CPU) of personal computer (PC) based on the real operating conditions of PC. This is because it has an excellent chemical and physical stability, a safe material for human, produced commercially available products, and cheap. The TiO_2 nanoparticles are used in the present experiments. The results obtained from the jet nanofluids impingement cooling system are compared with those from the jet liquid impingement and the conventional liquid cooling systems.

2. Experimental Apparatus and Method

2.1. Test Loop

This paper primary tries to investigate the jet nanofluids impingement heat transfer of the mini-rectangular channel heat sinks for CPU of PC. A schematic diagram of the experimental apparatus is shown in **Figure 1**. The test loop consists of a set of ultrasonic system, cooling nanofluids loop and data acquisition system. The close-loop

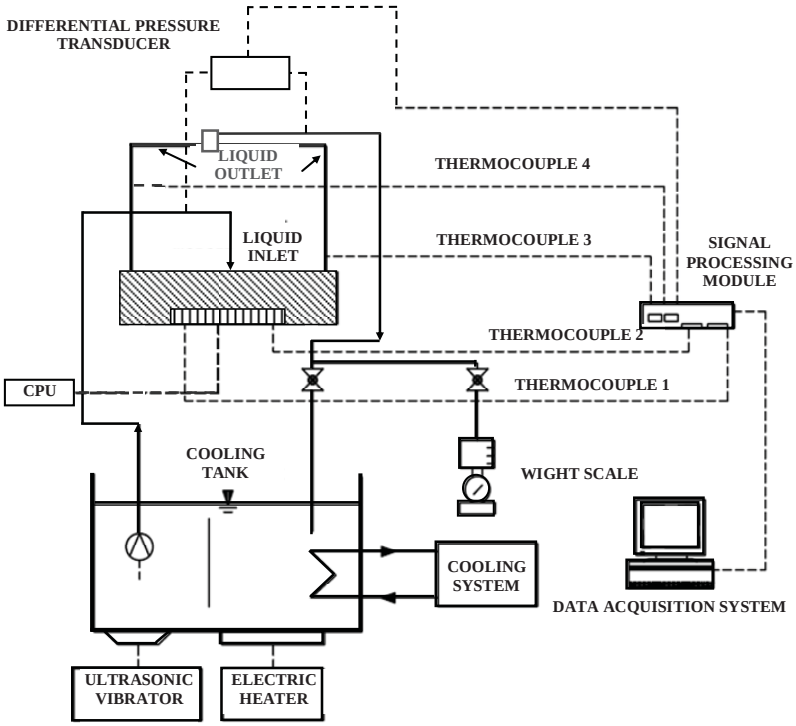

Figure 1. Schematic diagram of experimental apparatus.

Copyright © 2011 SciRes.

of nanofluids consists of a 10^{-3} m^3 storage tank, pump, and the flow rate measurement system. After the temperatures of the nanofluids are cooled to achieve the desired level, the nanofluids is pumped out of the storage tank, passed through the mini-rectangular fin heat sink, and returned to the storage tank. The flow rates are varied during a set of experiments with the help of a dimmerstat connected to the pump. The flow rates of the cooling nanofluids are controlled by adjusting the valve and measured by collecting the nanofluids with the precise cylinder for a period of time during 15 min and the nanofluids mass is measured by an electronic weight scale. The maximum variation of the mass flow rate of nanofluids as determined by such simple technique has been estimated to be ±3.5%. The nanofluids with suspending TiO_2 nanoparticles in base fluids are used as working fluids. An average spherical particle size of TiO_2 nanoparticles is about 21 nm. In the present study, the base fluids are the deionized water. The nanofluids are prepared by ultrasonic method with the constant nanoparticles concentration of 0.4% by volume without using surfactant. The heat sink is fabricated from the block of copper by the wire electrical discharge machine (WEDM) with the channel width of 1.00 mm. In order to minimize thermal resistance between the CPU-cooling block, cooling block-heat sink, a thin film of high thermal conductivity grease is applied at their junction interface. In **Figure 1**, the type T copper-constantan thermocouples with an accuracy of 0.1% of full scale are employed to measure the temperatures at various positions. The CPU temperature is measured by two type-T copper-constantan thermocouples. All thermocouples are pre-calibrated with dry box temperature calibrator.

2.2. Experimental Method

Nanofluids were used as coolant in the present experiments. The nanofluids were pumped into the mini-rectangular fin heat sink which installed on the CPU of PC in the normal direction with the base bottom as shown on **Figure 2** and then returned to the storage tank. Experiments were conducted with various cooling nanofluids flow rates and operating condition of PC. The supplied load into the CPU was adjusted to achieve the desired level by setting the operating conditions of PC: no load and full load conditions. The energy consumption of the PC was measured by the watt-hour meter. The temperatures at each position and energy consumption were recorded in the period time of 200 minutes. Data collection was carried out using a data acquisition system (Data Taker).

3. Data Reduction

The heat transfer into the nanofluids is calculated from:

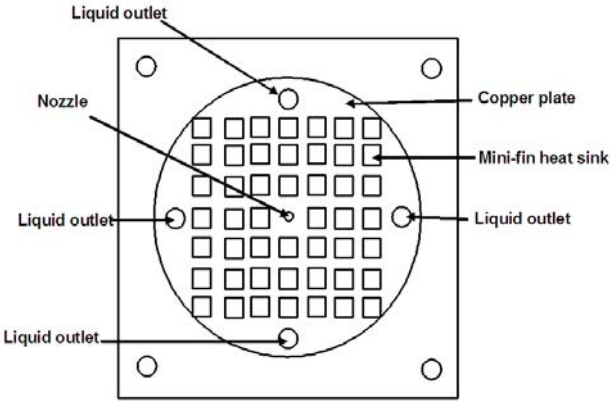

Figure 2. Schematic diagram of the inlet and outlet positions of the coolant.

$$Q_{nf} = \dot{m}_{nf} \times C_{p_{nf}} \times \left(T_{in,nf} - T_{out,nf}\right) \tag{1}$$

where Q_{nf} is the heat transfer by the nanofluids, $\dot{m}_{nf}$ is the mass flow rate of the nanofluids and $T_{in,nf}$, $T_{out,nf}$ are the inlet and outlet temperatures of the nanofluids.

The heat transfer coefficient is calculated from the following equation:

$$\overline{h} = \frac{Q_{nf}}{A_s\left(\Delta T_{LMTD}\right)} \tag{2}$$

where h is the average heat transfer coefficient, A_s is the total heat transfer surface area of the heat sink and ΔT_{LMTD} is the logarithm mean temperature difference which is given by:

$$\Delta T_{LMTD} = \frac{\left(T_b - T_{in,nf}\right) - \left(T_b - T_{out,nf}\right)}{\ln\left(\dfrac{\left(T_b - T_{in,nf}\right)}{\left(T_b - T_{out,nf}\right)}\right)} \tag{3}$$

where T_b is the temperature of the heat sink.

The average base temperature of the heat sink can be calculated from:

$$T_b = \overline{T}_{CPU} - \left(\frac{q_{in}L}{k_{hs}}\right) \tag{4}$$

where T_b is the base temperature of the heat sink, $\overline{T}_{CPU}$ is the CPU temperature, q_{in} is the heat flux, L is the base thickness of the heat sink and k_{hs} is the thermal conductivity of the heat sink.

The Nusselt number based on the nozzle diameter is calculated from the following equation:

$$\overline{N}u = \frac{\overline{h}D_{nozzle}}{k_{nf}} \tag{5}$$

where $\overline{N}u$ is the Nusselt number and D_{nozzle} is the diameter of the nozzle.

The thermal conductivity of the nanofluids is calculated

Copyright © 2011 SciRes.

from Yu and Choi [30] using the following equation:

$$k_{nf} = \left[\frac{k_p + 2k_w - 2\phi\left(k_w - k_p\right)}{k_p + 2k_w + \phi\left(k_w - k_p\right)} \right] k_w \quad (6)$$

where k_{nf} is the thermal conductivity of the nanofluids, k_w is the thermal conductivity of the base fluid and k_p is the thermal conductivity of the nanoparticles.

The density of the nanofluids is calculated from Pak and Cho [31] using the following equation:

$$\rho_{nf} = \phi\rho_P + (1-\phi)\rho_w \quad (7)$$

where ρ_{nf} is the density of the nanofluids, ρ_p is the density of the nanoparticles, ρ_w is the density of the base fluid and ϕ is the volume fraction of the nanoparticles.

While the specific heat is calculated from Xuan and Roetzel [32] as follows:

$$\left(\rho C_p\right)_{nf} = \phi\left(\rho C_p\right)_p + (1-\phi)\left(\rho C_p\right)_w \quad (8)$$

where $\left(\rho C_p\right)_{nf}$ is the heat capacity of the nanofluids, $\left(\rho C_p\right)_w$ is the heat capacity of the base fluid and $\left(\rho C_p\right)_p$ is the heat capacity of the nanoparticles.

Analysis of the thermal resistance of the convective heat transfer of the nanofluids can be defined as

$$R_{th} = \frac{T_b - T_{nf,ave}}{Q_{nf}} \quad (9)$$

The uncertainties of measurements data and the relevant parameters obtained from the data reduction process are calculated. The maximum uncertainties of the relevant parameters in the data calculation are based on Coleman and Steel method [33]. The maximum uncertainties of relevant parameters are ±10% for heat transfer coefficient, ±10% for Nusselt number and ±5% for thermal resistance.

4. Results and Discussion

The supplied load into the CPU was adjusted by setting the operating condition of PC: full load and no load conditions. The relevant parameters are measured in the period time of 200 minutes. **Figure 3** shows effect of coolant flow rate on the variation of CPU temperature for the jet nanofluids impingement cooling systems. The full load operating condition generates the heat higher than the no load operating condition. Therefore, the CPU temperatures from the full load condition are higher than those from the no load condition for the whole range of the period time. For the four different coolant flow rates, a larger CPU temperature drop is found for a larger coolant flow rate. The reason for this is because a larger coolant flow rate results in higher heat transfer rate and consequently lower CPU temperature.

Figure 4 shows the comparison between the CPU temperatures obtained from the jet nanofluids impingement technique, the jet liquid impingement and the conventional liquid cooling techniques. The thermal conductivity of nanofluids depends on the sizes and species of the nanoparticles, the concentration of nanoparticles in the base fluid and the combination of the nanoparticles and the base fluid properties. However, there are various correlations are proposed to predict the thermal conductivity and

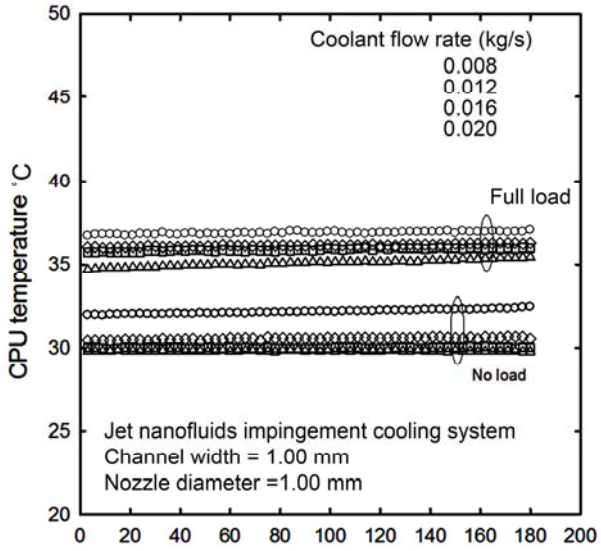

Figure 3. Effect of coolant flow rate on the CPU temperature for jet nanofluids impingement cooling system.

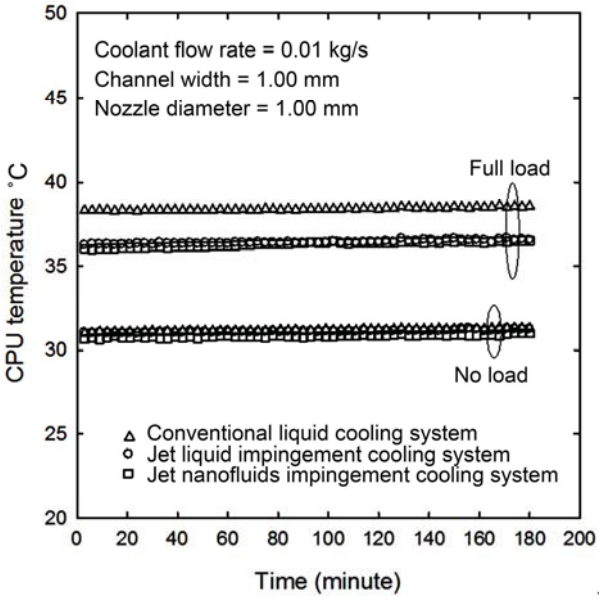

Figure 4. Comparison of CPU temperatures for different cooling techniques.

Copyright © 2011 SciRes.

others properties of the nanofluids. Due to particle migration inside the heat sink, non-uniformity of the nanoparticles concentration has significant effect on the thermal conductivity and viscosity of the fluid. Therefore, in the present study, an average heat transfer characteristics are presented. At the same operating condition of CP, the CPU temperatures obtained from the jet nanofluids impingement cooling system are lower than those from the jet liquid impingement and from the conventional cooling systems, respectively. This is because the thermal conductivity of the nanofluids is higher than that of the base fluids therefore great potential for the enhancement of heat transfer.

Figure 5 shows the variation of the Nusselt number with nanofluids mass flow rate. As expected, the heat transfer rate is directly proportional to the nanofluids mass flow rate. In addition, **Figure 5** also shows the comparison of the average Nusselt number obtained from the jet nanofluids impingement cooling technique, jet liquid impingement cooling technique, and conventional liquid cooling technique. It can be seen that the jet nanofluids impingement technique gives the Nusselt number higher than two other cooling techniques. The application of the nanofluids to the working fluid has significantly changed the fluid transport properties and flow characteristics. Therefore, the Nusselt number obtained from the jet nanofluids impingement are higher than those obtained from two other cooling techniques.

In this study, the overall heat sink performance can be shown in the thermal resistance form. The heat sink thermal resistance is defined as shown in Equation (9). Using this definition, thermal resistance of heat sink is a function of heat transfer coefficient. Due to higher heat transfer rate, the heat sink thermal resistance decreases with increasing flow rate. Based on results shown in **Figure 6**, it is seen that the thermal resistance obtained from the jet nanofluids impingement cooling technique are lower than those from the jet liquid impingement and from the conventional cooling techniques. This result can be realized from Equation (9) and nanofluids transport properties. Due to the increase in thermal conductivity, the contribution to the thermal resistance is mainly improved. In addition, the reduction of the thermal resistance is clearly due to the thermal dispersion.

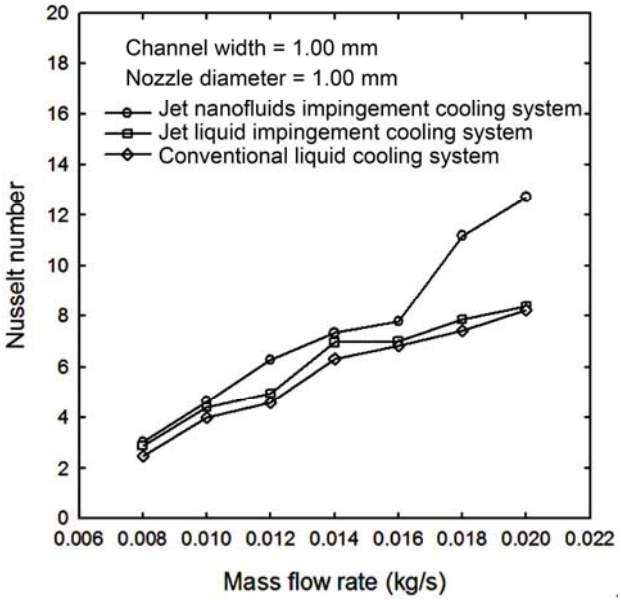

Figure 5. Variation of the Nusselt number versus mass flow rate for different cooling techniques.

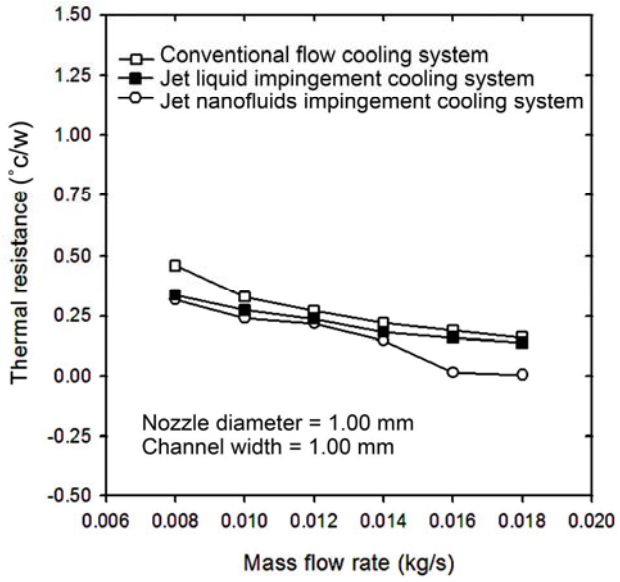

Figure 6. Comparison of thermal resistance versus mass flow rate for different cooling techniques.

5. Conclusions

Due to high level of heat generation, space limitation for set up the cooling system, and air cooling limitation, the jet nanofluids impingement cooling in the mini-rectangular fin channel heat sink for CPU of PC has been investigated. The jet nanofluids impingement cooling with mini-rectangular fin heat sink system is introduced as the couple active and passive heat transfer enhancement techniques. It is found that the CPU temperatures obtained from the jet nanofluids impingement cooling system are lower than those from the jet liquid impingement cooling system and the conventional liquid cooling system. However, this technique requires higher energy consumption. The results of this study are expected to lead to guidelines that will allow the design of the cooling system with improved thermal cooling performance for obtaining these devices in the specific temperature ranges.

Copyright © 2011 SciRes.

6. Acknowledgements

The authors would like to express their appreciation to the Thailand Research Fund (TRF), the Srinakharinwirot University (SWU), and the King Mongkut's University of Technology Thonburi (KMUTT) for providing financial support for this study.

7. References

[1] H. Y. Zhang, D. Pingala, T. N. Wong, K. C. Toh and Y. K. Joshi, "Single-Phase Liquid Cooled Micro Channel Heat Sink for Electronic Packages," *Applied Thermal Engineering*, Vol. 25, No. 2, 2005, pp. 1472-1487. doi:10.1016/j.applthermaleng.2004.09.014

[2] X. Yu, "Development of a Plate-Pin Fin Heat Sink and Its Performance Comparisons with a Plate Fin Heat Sink," *Applied Thermal Engineering*, Vol. 25, No.1, 2005, pp. 173-182. doi:10.1016/j.applthermaleng.2004.06.016

[3] Y. Peles, A. Kosor, C. Mishra, C. J. Kuo and B. Schneider, "Forced Convective Heat Transfer across a Pin Fin Micro Heat Sink," *International Journal of Heat and Mass Transfer*, Vol. 48, No. 2, 2005, pp. 3615-3627. doi:10.1016/j.ijheatmasstransfer.2005.03.017

[4] A. Kosar and Y. Peles, "Convective Flow of Refrigerant (R123) across a Bank of Micro Pin," *International Journal of Heat and Mass Transfer*, Vol. 50, No. 1, 2007, pp. 1018-1034.

[5] K. Yukut, "Experimental Investigation of Thermal Resistance of a Heat Sink with Hexagonal Fins," *Applied Thermal Engineering*, Vol. 26, No. 2, 2006, pp. 2262-2271. doi:10.1016/j.applthermaleng.2006.03.008

[6] M. M. Mohamed, "Air Cooling Characteristics of a Uniform Square Modules Array for Electronic Device Heat Sink," *Applied Thermal Engineering*, Vol. 26, No. 2, 2006, pp. 486-493. doi:10.1016/j.applthermaleng.2005.07.013

[7] I. M. Didarul, "Study on Heat Transfer and Fluid Flow Characteristics with Short Rectangular Plate Fin of Different Pattern," *Experimental Thermal and Fluid Science*, Vol. 31, No. 1, 2007, pp. 367-379. doi:10.1016/j.expthermflusci.2006.05.009

[8] R. Chein and J. Chuang, "Experimental Microchannel Heat Sink Performance Studies Using Nanofluids," *International Journal of Thermal Sciences*, Vol. 46, No. 1, 2007, pp. 57-66. doi:10.1016/j.ijthermalsci.2006.03.009

[9] T. M. Jeng and S. C. Tzeng, "Pressure Drop and Heat Transfer of Square Pin-Fin Arrays in In-Line and Staggered Arrangements," *International Journal of Heat and Mass Transfer*, Vol. 50, No. 1, 2007, pp. 2364-2375. doi:10.1016/j.ijheatmasstransfer.2006.10.028

[10] W. Duangtongsuk and S. Wongwises, "A Critical Review of Convective Heat Transfer of Nanofluids," *Renewable and Sustainable Energy Review*, Vol. 11, No. 1, 2007, pp. 797-817. doi:10.1016/j.rser.2005.06.005

[11] V. Trisaksri and S, Wonwises, "Critical Review of Heat Transfer Characteristics of Nanofluids Review," *Renewable and Sustainable Energy Reviews*, Vol. 11, No. 2, 2007, pp. 512-523. doi:10.1016/j.rser.2005.01.010

[12] L. Godson, B. Raja, D. M. Lal and S. Wongwises, "Enhancement of Heat Transfer Using Nanofluids—An Overview," *Renewable and Sustainable Energy Reviews*, Vol. 14, No. 1, 2010, pp. 629-641. doi:10.1016/j.rser.2009.10.004

[13] C. J. Kobus and T. Oshio, "Development of a Theoretical Model for Predicting the Thermal Performance Characteristics of a Vertical Pin-Fin Array Heat Sink under Combined Forced and Natural Convection with Impinging Flow," *International Journal of Heat and Mass Transfer*, Vol. 48, No. 3, 2005, pp. 1053-1063. doi:10.1016/j.ijheatmasstransfer.2004.09.042

[14] H. Y. Li, S. M. Chao and G. L. Tsai, "Thermal Performance Measurement of Heat Sinks with Confined Impinging Jet by Infrared Thermography," *International Journal of Heat and Mass Transfer*, Vol. 48, Vol. 1, 2005, pp. 5386-5394.

[15] S. Geedipalli, A. K. Datta and V. Rakesh, "Heat Transfer in a Combination Microwave-Jet Impingement Oven," *Food and Bioproducts Processing*, Vol. 86, No. 1, 2008, pp. 53-63. doi:10.1016/j.fbp.2007.10.016

[16] M. K. Sung and I. Mudawar, "Single-Phase and Two-Phase Heat Transfer Characteristics of Low Temperature Hybrid Micro-Channel/Micro-Jet Impingement Cooling Module," *International Journal of Heat and Mass Transfer*, Vol. 51, No. 2, 2008, pp. 3882-3895. doi:10.1016/j.ijheatmasstransfer.2007.12.016

[17] M. K. Sung and I. Mudawar, "Single-Phase Hybrid Micro-Channel/Micro-Jet Impingement Cooling," *International Journal of Heat and Mass Transfer*, Vol. 51, No. 1, 2008, pp. 4342-4352. doi:10.1016/j.ijheatmasstransfer.2008.02.023

[18] M. F. Koseoglu and S. Baskaya, "The Effect of Flow Field and Turbulence on Heat Transfer Characteristics of Confined Circular and Elliptic Impinging Jets," *International Journal of Thermal Sciences*, Vol. 47, No. 2, 2008, pp. 1332-1346. doi:10.1016/j.ijthermalsci.2007.10.015

[19] V. Katti and S. V. Prabhu, "Heat Transfer Enhancement on a Flat Surface with Axisymmetric Detached Ribs by Normal Impingement of Circular Air Jet," *International Journal of Heat and Fluid Flow*, Vol. 29, No. 1, 2008, pp. 1279-1294. doi:10.1016/j.ijheatfluidflow.2008.05.003

[20] P. R. Kanna and M. K. Das, "Heat Transfer Study of Two-Dimensional Laminar Incompressible Offset Jet Flows," *International Journal of Thermal Sciences*, Vol. 47, No. 1, 2008, pp. 1620-1629. doi:10.1016/j.ijthermalsci.2008.01.003

[21] F. Cirillo and G. M. Isopi, "Glass Tempering Heat Transfer Coefficient Evaluation and Air Jets Parameter Optimization," *Applied Thermal Engineering*, Vol. 29, No. 2, 2009, pp. 1173-1179. doi:10.1016/j.applthermaleng.2008.06.005

[22] M. Goodro, J. Park, P. Ligrani, M. Fox and H. K. Moon, "Effects of Hole Spacing on Spatially-Resolved Jet Array

Copyright © 2011 SciRes.

Impingement Heat Transfer," *International Journal of Heat and Mass Transfer*, Vol. 51, No. 1, 2008, pp. 6243-6253. doi:10.1016/j.ijheatmasstransfer.2008.05.004

[23] T. M. Jeng, S. C. Tzeng and H. R. Liao, "Flow Visualizations and Heat Transfer Measurements for a Rotating Pin-Fin Heat Sink with a Circular Impinging Jet," *International Journal of Heat and Mass Transfer*, Vol. 52, No. 2, 2009, pp. 2119-2131. doi:10.1016/j.ijheatmasstransfer.2008.10.028

[24] B. N. Hewakandamby, "A Numerical Study of Heat Transfer Performance of Oscillatory Impinging Jets," *International Journal of Heat and Mass Transfer*, Vol. 52, No. 2, 2009, pp. 396-406.

[25] C. T. Nguyen, N. Galanis, G. Polidori, S. Fohanno, C. V. Popa and A. L. Bechec, "An Experimental Study of a Confined and Submerged Impinging Jet Heat Transfer Using Al_2O_3-Water Nanofluids," *International Journal of Thermal Sciences*, Vol. 48, No. 3, 2009, pp. 401-411. doi:10.1016/j.ijthermalsci.2008.10.007

[26] M. F. Koseoglu and S. Baskaya, "Experimental and Numerical Investigation of Natural Convection Effects on Confined Impinging Jet Heat Transfer," *International Journal of Heat and Mass Transfer*, Vol. 52, No. 1, 2009, pp. 1326-1336. doi:10.1016/j.ijheatmasstransfer.2008.07.051

[27] S. W. Chang, T. L. Yang and D. W. Shih, "Jet-Array Impingement Heat Transfer in a Concentric Annular Channel with Rotating Inner Cylinder," *International Journal of Heat and Mass Transfer*, Vol. 52, No. 1, 2009, pp. 1254-1267. doi:10.1016/j.ijheatmasstransfer.2008.08.023

[28] M. A. R. Sharif and A. Banerjee, "Numerical Analysis of Heat Transfer Due to Confined Slot-Jet Impingement on a Moving Plate," *Applied Thermal Engineering*, Vol. 29, No. 1, 2009, pp. 532-540. doi:10.1016/j.applthermaleng.2008.03.011

[29] B. P. Whelan and A. J. Robinson, "Nozzle Geometry Effects in Liquid Jet Array Impingement," *Applied Thermal Engineering*, Vol. 29, No. 1, 2009, pp. 2211-2221. doi:10.1016/j.applthermaleng.2008.11.003

[30] W. Yu and S. U. S. Choi, "The Role of Interfacial Layers in the Enhanced Thermal Conductivity of Nanofluids: A Renovated Maxvell Model," *Journal of Nanoparticle Research*, Vol. 5, No. 1, 2003, pp. 167-171. doi:10.1023/A:1024438603801

[31] B. C. Pak and Y. I. Cho, "Hydrodynamic and Heat Transfer Study of Dispersed Fluids with Submicron Metallic Oxide Particles," *Experimental Heat Transfer*, Vol. 11, No. 2, 1998, pp. 151-170. doi:10.1080/08916159808946559

[32] Y. Xuan and W. Roetzel, "Conceptions of Heat Transfer Correlation of Nanofluids," *International Journal of Heat and Mass Transfer*, Vol. 43, No. 19, 2000, pp. 3701-3707. doi:10.1016/S0017-9310(99)00369-5

[33] H. W. Coleman and W. G. Steele, "Experimental and Uncertainty Analysis for Engineers," John Wiley & Sons, New York, 1989.

Nomenclatures

A_s : total heat transfer surface area of the heat sink, m^2.
D_{nozzle} : nozzle diameter, m.
$\bar{h}$: average heat transfer coefficient, $W/(m^2 K)$.
k_{nf} : thermal conductivity of the nanofluids, W/(m K).
$\bar{Nu}$: Nusselt number.
q_{nf} : heat flux, W/m^2.
R_{th} : thermal resistance, K/W.
T_b : the base temperature of the heat sink, ˚C.
$\bar{T}_{CPU}$: CPU temperature, ˚C.
ΔT_{LMTD} : logarithm mean temperature difference, ˚C.

Greek Symbols

ρ_{nf} : density of the nanofluids.
$(\rho c_p)_{nf}$: heat capacity of the nanofluids.
$(\rho c_p)_p$: heat capacity of the nanoparticles.
μ_{nf} : viscosity of the nanofluids.

Copyright © 2011 SciRes.

International Communications in Heat and Mass Transfer 38 (2011) 218–228

Contents lists available at ScienceDirect

International Communications in Heat and Mass Transfer

journal homepage: www.elsevier.com/locate/ichmt

Numerical investigation on the single phase forced convection heat transfer characteristics of TiO_2 nanofluids in a double-tube counter flow heat exchanger ☆

H. Demir [a,*], A.S. Dalkilic [a], N.A. Kürekci [a], W. Duangthongsuk [b], S. Wongwises [b,*]

[a] Heat and Thermodynamics Division, Department of Mechanical Engineering, Yildiz Technical University (YTU), Yildiz, Besiktas, Istanbul 34349, Turkey
[b] Fluid Mechanics, Thermal Engineering and Multiphase Flow Research Lab. (FUTURE), Department of Mechanical Engineering, King Mongkut's University of Technology Thonburi (KMUTT), Bangmod, Bangkok 10140, Thailand

ARTICLE INFO

Available online 21 December 2010

Keywords:
Heat transfer coefficient
Pressure drop
Wall shear stress
Nanofluid
Heat exchanger

ABSTRACT

In this study, forced convection flows of nanofluids consisting of water with TiO_2 and Al_2O_3 nanoparticles in a horizontal tube with constant wall temperature are investigated numerically. The horizontal test section is modeled and solved using a CFD program. Palm et al.'s correlations are used to determine the nanofluid properties. A single-phase model having two-dimensional equations is employed with either constant or temperature dependent properties to study the hydrodynamics and thermal behaviors of the nanofluid flow. The numerical investigation is performed for a constant particle size of Al_2O_3 as a case study after the validation of its model by means of the experimental data of Duangthongsuk and Wongwises with TiO_2 nanoparticles. The velocity and temperature vectors are presented in the entrance and fully developed region. The variations of the fluid temperature, local heat transfer coefficient and pressure drop along tube length are shown in the paper. Effects of nanoparticles concentration and Reynolds number on the wall shear stress, Nusselt number, heat transfer coefficient and pressure drop are presented. Numerical results show the heat transfer enhancement due to presence of the nanoparticles in the fluid in accordance with the results of the experimental study used for the validation process of the numerical model.

© 2010 Elsevier Ltd. All rights reserved.

1. Introduction

Water, oil, and ethylene glycol mixture is one of the low thermal conductivity of widely used conventional heat transfer fluids that limits the enhancement of the performance and compactness of these devices belong to the electronic, automotive and aerospace industries. Improvements on the thermal conductivity by suspending small solid particles in the fluid are one of the solutions to prevent this disadvantage. Thermal conductivity is an important parameter in enhancing the heat transfer performance of a heat transfer fluid. Since the thermal conductivity of solid metals is higher than that of fluids, the suspended particles are expected to be able to increase the thermal conductivity and heat transfer performance. Many researchers have reported experimental studies on the thermal conductivity of nanofluids. Metallic, non-metallic and polymeric particles are used to form slurries by adding into fluids. Some of problems such as abrasion and clogging can be seen due to the suspended particles' sizes that are of millimeter dimensions. For that reason, these kinds of large particles are not suitable for heat transfer enhancement. Recently, advances in manufacturing technologies have made the production of particles in the nanometer scale possible (i.e., 10 nm<particle diameter<100 nm). The uniform and stable suspensions are obtained by means of these smaller sized particles. Thus, the nanofluids provide higher heat transfer enhancement than existing techniques. The use of particles of nanometer dimension was first continuously studied by a research group at the Argonne National Laboratory around a decade ago. Choi [1] was probably the first one who called the fluids with particles of nanometer dimensions 'nano-fluids'. The term 'nanofluid' refers to a two-phase mixture usually composed of a continuous liquid phase and dispersed nanoparticles in suspension.

In spite of the two phase mixture specialty of nanofluids, they are easily fluidized and can be nearly considered to behave as a fluid [2] due to the tiny size of solid particles. For that reason, it is possible for nanofluids to be treated as single phase flow. It is assumed that the fluid phase and particles are in thermal equilibrium and moving with the same velocity in certain conditions [3] considering the ultrafine and low volume fraction of the solid particles. The advantage of single phase flow is about its simplicity and required less computational time. It should be noted that experimental, numerical and theoretical solutions are strongly affected by physical properties of nanofluids. In addition, there is some inconsistency on this subject in the literature.

The most well-known nanoparticles are Al_2O_3, CuO, TiO_2 and they are used by many researchers in their experimental works together with the base fluids of water and ethylene glycol. In spite of the different size of the particles and type of base fluids, the enhancement

☆ Communicated by W.J. Minkowycz.

* Corresponding authors.
E-mail addresses: hdemir@yildiz.edu.tr (H. Demir), somchai.won@kmutt.ac.th (S. Wongwises).

0735-1933/$ – see front matter © 2010 Elsevier Ltd. All rights reserved.
doi:10.1016/j.icheatmasstransfer.2010.12.009

Nomenclature

Cp	specific heat, J kg^{-1} K^{-1}
CFD	Computational Fluid Dynamics
d	internal tube diameter, m
h	heat transfer coefficient, W m^{-2} K^{-1}
k	thermal conductivity, W m^{-1} K^{-1}
L	length of test tube, m
m	mass flow rate, kg s^{-1}
Nu	Nusselt number
ΔP	pressure drop, Pa
Pr	Prandtl number
Re	Reynolds number
Q	heat transfer rate, W
q''	heat flux, W m^{-2}
T	temperature, °C
μ	dynamic viscosity, Pa s
ρ	density, kg m^{-3}
τ	shear stress, N m^{-2}
φ	volume fraction, %
ν	kinematic viscosity, m^2 s^{-1}

Subscripts

avg	average
bf	base fluid
exp	experimental
ext	external
f	fluid
h	hot
i	inlet
m	mean
nf	nanofluid
num	numerical
p	particle
s	surface
o	outlet
w	water

of the thermal conductivity was seen during all the experimental conditions. Firstly, Maxwell [3,4] mentioned the enhancement on the thermal conductivity of a mixture by increasing volume fraction of solid particles. Besides this, the first empirical correlations for the determination of Nusselt number for laminar and turbulent flow of a nanofluid inside a tube were developed by Pak and Cho [5] and Xuan and Li [2,6] using the mixture of water and Cu, TiO_2 and Al_2O_3 nanoparticles. A significant increase in heat transfer performance was obtained in comparison to the water for the same Reynolds number. Liu et al. [7] conducted experiments on an industrial application and studied the effects of flow rates on the slurry pressure drop and heat transfer behavior. Choi [8] investigated augmentation of heat transfer that occurred by means of nanofluids considering little or no penalty in the pressure drop. Lee et al. [9] reported increase in thermal conductivity of the nanofluid approximately 20% at the volume concentration of 4% using oxide ceramic nanofluids consisting of CuO nanoparticles having a mean diameter of 35 nm in ethylene glycol, whereas an increase up to 10% was observed using larger particles with an average diameter of 40 nm. Masuda et al. [10] reported thermal conductivity enhancement by 30% using water–Al_2O_3 nanofluid having 13 nm mean diameter particles at 4.3% volume fraction. Rea et al. [11] investigated laminar convective heat transfer and viscous pressure loss for alumina–water and zirconia–water nanofluids in a flow loop with a vertical heated tube. The heat transfer

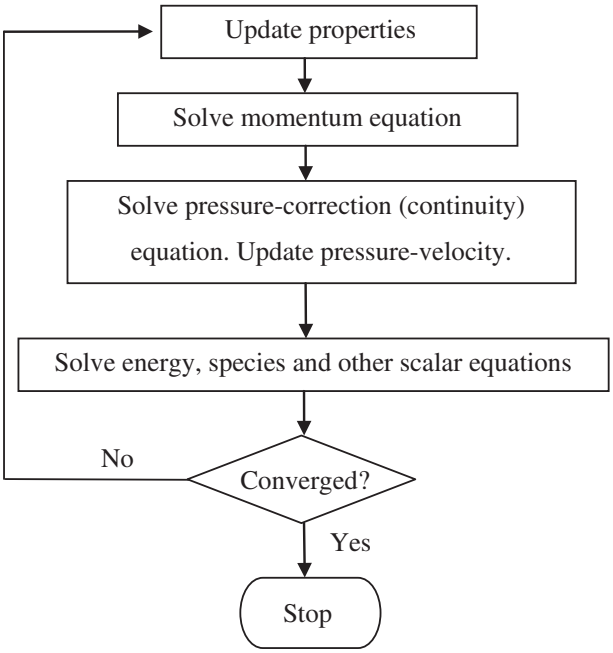

Fig. 1. Overview of the segregated method.

coefficients in the entrance region and in the fully developed region are found to be increased in 17% and 27%, respectively, for alumina–water nanofluid at 6 vol.% with respect to pure water. Bianco et al. [12] obtained heat transfer coefficient for the developing laminar forced convection flow of a water–Al_2O_3 nanofluid in a circular tube using single and two-phase models which have the maximum difference between them is about 11%. They also stated that convective heat transfer coefficient for nanofluids is greater than that of the base liquid. Heat transfer enhancement increases with the particle volume concentration, but it is accompanied by increasing wall shear stress values. Fard et al. [13] used CFD approach regarding single-phase and two-phase models to predict temperature, flow field, and calculation of heat transfer coefficient for the laminar convective heat transfer of nanofluids in a circular tube under constant wall temperature condition. Comparisons among two-phase model, single-phase model, theoretical models and experimental data were done and

Table 1
Operating conditions of the study.

Experimental study for the validation of numerical model	
Nanoparticle type, d_p	TiO_2, 21 nm
Test tube material, d, L	Copper, φ8.13 mm, 1500 mm
φ (wt.%)	0, 0.2, 0.6, 1
$T_{avg,f}$ (°C)	25–29–26.94
$T_{avg,s}$ (°C)	26.75–29.39
$T_{avg,h,w}$ (°C)	26.75–29.39
Re	4516.13–15,681.36
q'' (W m^{-2})	7233.13–13,340.99
Numerical study for the simulation of the case study	
Nanoparticle type, d_p	Al_2O_3, TiO_2, 21 nm
Test tube material, d, L	Copper, φ8 mm, 1000 m
φ (wt.%)	0, 1, 4
$T_{avg,f}$ (°C)	25.78, 28.34
$T_{avg,s}$ (°C)	26.19, 28.79
$T_{avg,h,w}$ (°C)	34.64, 36,64
Re	1000, 5000, 15,000, 25,000, 50,000, 75,000
q'' (W m^{-2})	1000, 5000, 10,000, 50,000

they reported that heat transfer coefficient clearly increases with an increase in particle concentration and two-phase model shows better agreement with experimental measurements.

Recently, Daungthongsuk and Wongwises [14] summarized the published subjects with respect to the forced convective heat transfer of the nanofluids both of experimental and numerical investigation in their review paper. Daungthongsuk and Wongwises [15] reported that thermal conductivity of nanofluids increased with increasing nanofluid temperatures and, conversely, the viscosity of nanofluids decreased with increasing temperature of nanofluids. Daungthongsuk and Wongwises [16] investigated the differences between using measured and computed thermophysical properties to describe the heat transfer performance of TiO_2–water nanofluids. Their results show that use of the models of thermo physical properties for calculating the Nusselt number of nanofluids gave similar results to use of the measured data. Daungthongsuk and Wongwises [17] presented the heat transfer coefficient and friction factor of the TiO_2–water nanofluids flowing in a horizontal double tube counter-flow

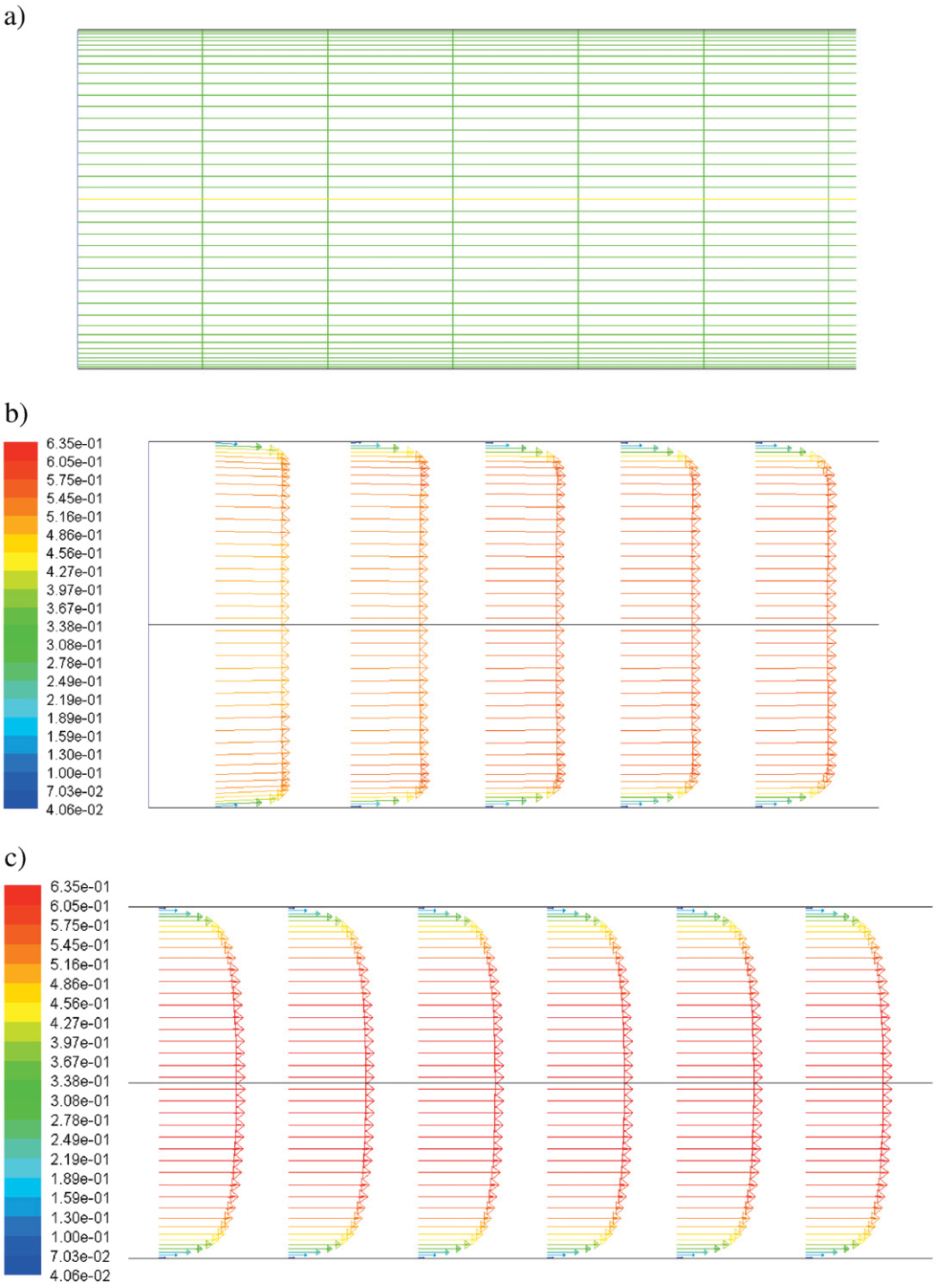

Fig. 2. Grid and velocity vectors for pure water ($Re = 4731$, $Q = 7233$ W). a) Solution grid generated in GAMBIT and used in the present analysis, axis-symmetric about *x*-axis. b) Velocity vectors at the inlet section of the test tube (m/s). c) Velocity vectors at the middle section of the test tube (m/s).

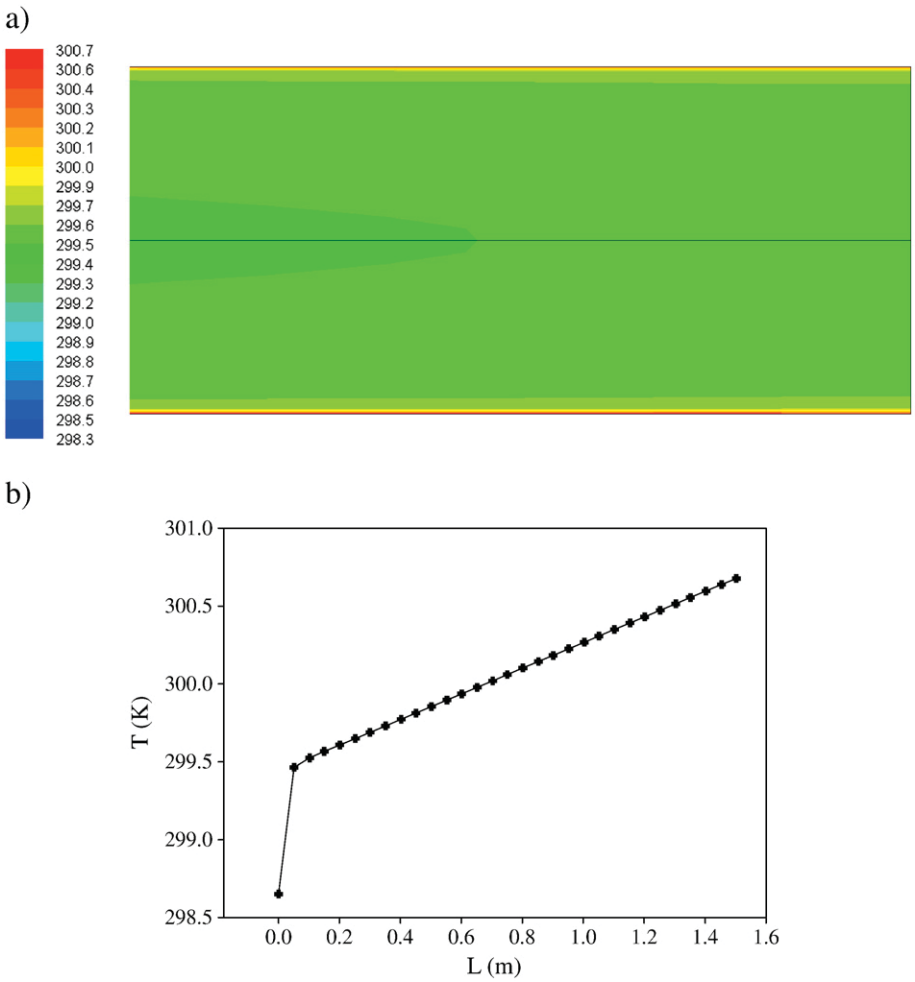

Fig. 3. Temperature distributions of outlet section and pipe surface for water and 0.6% TiO_2 nanoparticles ($Re = 14{,}880$, $Q = 11{,}862$ W). a) Temperature distribution at the outlet section of the tube. b) Surface temperature distribution along pipe.

heat exchanger under turbulent flow conditions, experimentally. Their results show that the heat transfer coefficient of nanofluid is higher than that of the base liquid and increased with increasing the Reynolds number and particle concentrations. Daungthongsuk and Wongwises [18] reported an experimental study on the forced convective heat transfer and flow characteristics of a nanofluid consisting of water and 0.2 vol.% TiO_2 nanoparticles. According to their experimental results, the heat transfer coefficient of the nanofluid increases with an increase in the mass flow rate of the hot water and nanofluid, and increases with a decrease in the nanofluid temperature, and the temperature of the heating fluid has no significant effect on the heat transfer coefficient of the nanofluid. Daungthongsuk and Wongwises [19] aimed in their paper to summarize the various models for predicting the thermophysical properties of nanofluids which have been commonly cited by a number of researchers and use them to calculate the experimental convective heat transfer coefficient of the nanofluid flowing in a double-tube counter flow heat exchanger. Daungthongsuk and Wongwises [20] summarized the published subjects with respect to the forced convective heat transfer of the nanofluids both of experimental and numerical investigation. Demir et al. [21] investigated laminar and turbulent forced convection flows of a nanofluid consisting of water and Al_2O_3 in a horizontal smooth tube with constant wall temperature numerically. Their numerical results show the heat transfer enhancement due to presence of the nanoparticles in the fluid.

Over the years, many studies have focused on the development of a model to predict the heat transfer enhancement of nanofluids. In the present work, the heat transfer behavior of a circular pipe flow has been modeled numerically in comparison to the distilled water as the base fluid with the nanofluid that is composed of distilled water and Al_2O_3 nanoparticles for a constant particle diameter and fluid temperature and various volume concentrations. Besides this, some significant experimental results reported in the study of Palm et al. [22] are used in the numerical solution. Before the modeling process in Fluent CFD program [23], validation of the model is performed using the experimental data belonging to the forced convection of nanofluids consisting of TiO_2 particles [16] regarding the comparison of calculated and measured Nusselt numbers, heat transfer coefficients and pressure drops. In addition to this, temperature distributions of inner surface and the fluids at the inlet and outlet sections of the tube, alteration of wall shear stress, Nusselt numbers, heat transfer coefficients and pressure drops with Reynolds numbers and particle concentrations, local heat transfer coefficients and pressure drops are also obtained from the numerical study and presented in the paper.

2. Sample preparation

In the present study, nanofluids provided by a commercial source (DEGUSSA, VP Disp. W740x) are used as working fluid. The detailed image of dispersed TiO_2 nanoparticles in water, taken by TEM, and

details of preparation of nanofluids can be seen from Duangthongsuk and Wongwises [16].

3. Experimental apparatus

Detailed descriptions of the experimental apparatus for studying single phase heat transfer performance of nanofluids inside a horizontal tube can be found in Duangthongsuk and Wongwises [16].

4. Data reduction

4.1. Thermal and physical properties of nanofluids

It is known that the determination of the nanofluid properties is problematic in the literature. There are also some correlations developed for this aim by Williams et al. [24]. Measurement of physical properties is performed by several researchers in the literature such as Rea et al. [11] and Duangthongsuk and Wongwises [15]. Calculation of the thermal and physical properties of the nanofluids can be done as follows:

Constant-value temperature independent densities based on nanoparticle volume fraction can be seen as follows:

$$\rho_{nf} = (1-\varphi)\rho_{bf} + \varphi\rho_p \quad (1)$$

The effective specific heat can be calculated as follows:

$$Cp_{nf} = (1-\varphi)Cp_{bf} + \varphi Cp_p \quad (2)$$

There is an alternate approach based on heat capacity concept to determine specific heat of nanofluids as follows:

$$(\rho Cp_{nf}) = (1-\varphi)(\rho Cp_{bf}) + \varphi\left(\rho Cp_p\right) \quad (3)$$

It should be noted that it is possible to have different results from Eqs. (2) and (3). Palm et al. [22] preferred to use Eq. (2) to calculate specific heat of nanofluids due to lack of experimental data on this subject.

Putra et al.'s [25] experimental data gives following equations, obtained by Palm et al.'s [22] analysis, to compute the nanofluid effective viscosity as a function of the local temperature for H_2O–Al_2O_3 nanofluid with 1% and H_2O–Al_2O_3 nanofluid with 4% respectively as follows:

$$\mu_{nf} = 2.910^{-7}T^2 - 2.10^{-4}T + 3.4.10^{-2} \quad (4)$$

$$\mu_{nf} = 3.410^{-7}T^2 - 2.310^{-4}T + 3.910^{-2} \quad (5)$$

According to the results of Palm et al.'s [22] study based on Putra et al.'s [25] experimental data, the effective thermal conductivity is determined for H_2O–Al_2O_3 nanofluid with 1% and H_2O–Al_2O_3 nanofluid with 4% respectively as follows:

$$k_{nf} = 0.003352T - 0.3708 \quad (6)$$

$$k_{nf} = 0.004961T - 0.8078 \quad (7)$$

4.2. Governing dimensionless numbers, heat flux, heat transfer coefficient and Nusselt number

In flow through ducts, the heat transfer surface surrounds and guides the stream, and the convection process is said to be internal. The velocity distribution in a duct has two distinct regions in laminar flow: first, the entrance region, where the walls are lined up by growing boundary layers, and, farther downstream, the fully developed region, where the longitudinal velocity is independent of the position along the duct. It is assumed that the duct geometry does not change with the longitudinal position. The flow through a straight duct ceases to be laminar when *Re* number exceeds approximately 2300. It is also observed that the turbulent flow becomes fully developed hydro dynamically and thermally after a relatively short entrance distance [26].

Reynolds number, Prandtl number are used in the theoretical analysis [22], the particle volume fraction (φ) and the ratios k_p/k_{bf} and

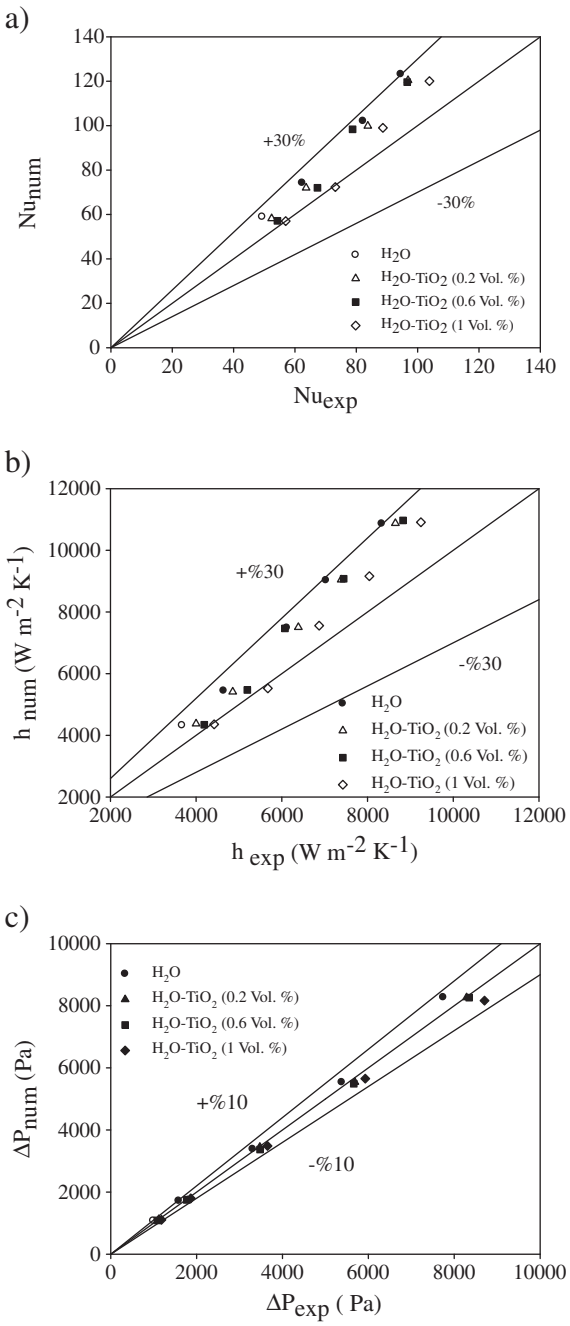

Fig. 4. Comparison of experimental and numerical Nusselt numbers, heat transfer coefficients and pressure drops using pure water with 0.2%, 0.6% and 1% TiO_2 particles data [21]. a) Experimental Nusselt numbers vs. numerical Nusselt numbers. b) Experimental heat transfer coefficient vs. numerical heat transfer coefficient. c) Experimental pressure drop vs. numerical pressure drop.

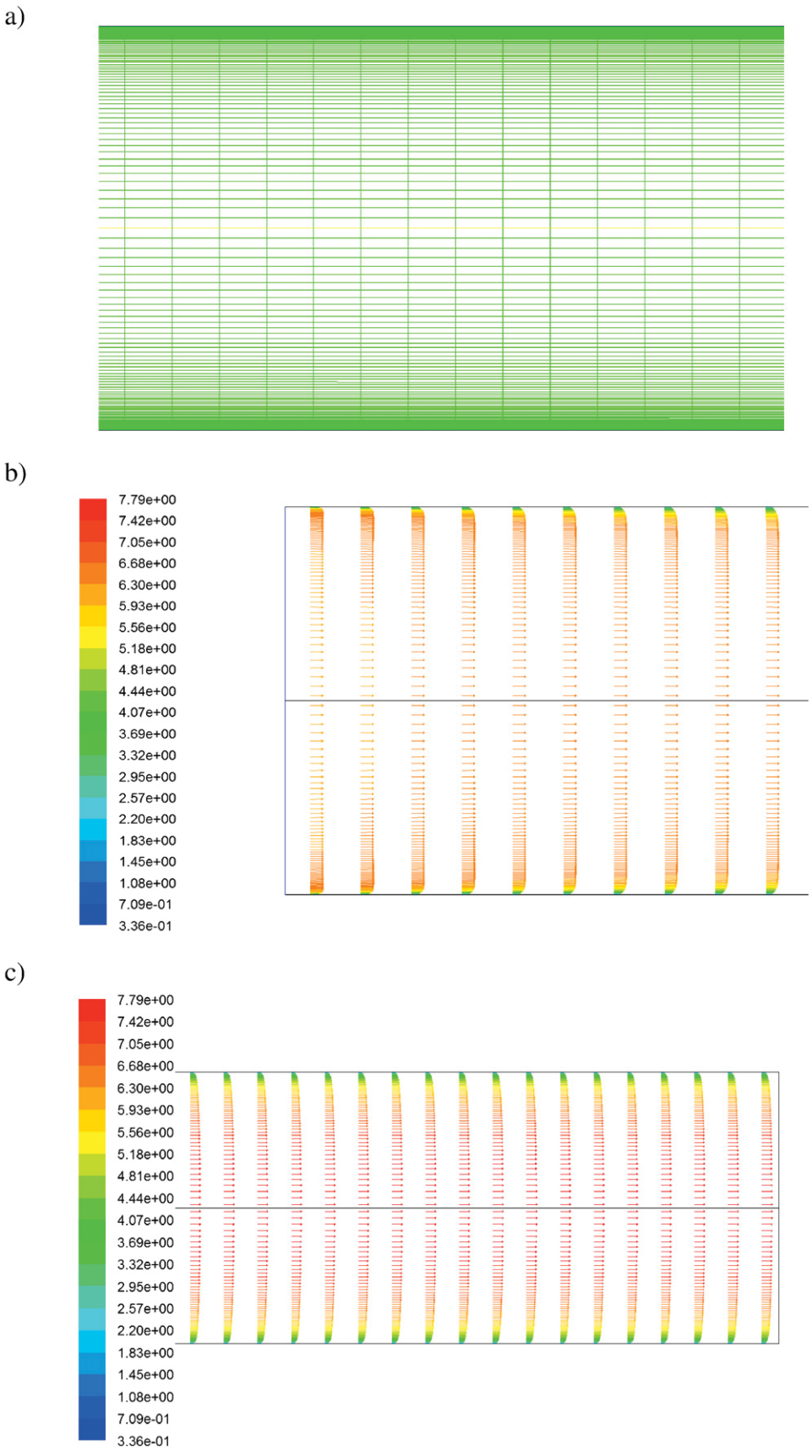

Fig. 5. Grid and velocity vectors layout obtained in the present analysis ($Re = 50{,}000$, $q'' = 10{,}000$ W m^{-2}, $T = 20$ °C). a) Solution grid generated in GAMBIT and used in the present analysis, axis-symmetric about x-axis. b) Velocity vectors at the inlet section of the test tube (m s^{-1}). c) Velocity vectors at the middle section of the test tube (m s^{-1}).

Cp_p/Cp_{bf} are used to characterize the problem and can be calculated as follows:

$$Re = \frac{2Q}{\pi d v} \tag{8}$$

$$Pr = \frac{Cp\mu}{k} \tag{9}$$

Heat flux in the test section is determined as follows:

$$q'' = \frac{m_w Cp_w (T_i - T_o)}{\pi d L} \tag{10}$$

Heat transfer coefficient of the base fluid and nanofluid can be calculated as follows:

$$h = \frac{q''}{\left(T_w - T_{f,m}\right)} \tag{11}$$

Nusselt number belongs to the base fluid and nanofluid can be calculated as follows:

$$Nu = \frac{hd}{k} \tag{12}$$

4.3. Numerical method

This problem was solved by means of the processes in Fluent CFD program [23]. FLUENT is commonly used software in CFD analysis in the literature and a detailed description of the mathematical model can be found in the Fluent User's Guide. This program uses a technique based on control volume theory to convert the governing equations to algebraic equations so they can be solved numerically. The control volume technique works by performing the integration of the governing equations about each control volume, and then generates discrimination of the equations which conserve each quantity based on control volume. The results are obtained thanks to the segregated solver algorithm shown in Fig. 1 in order to

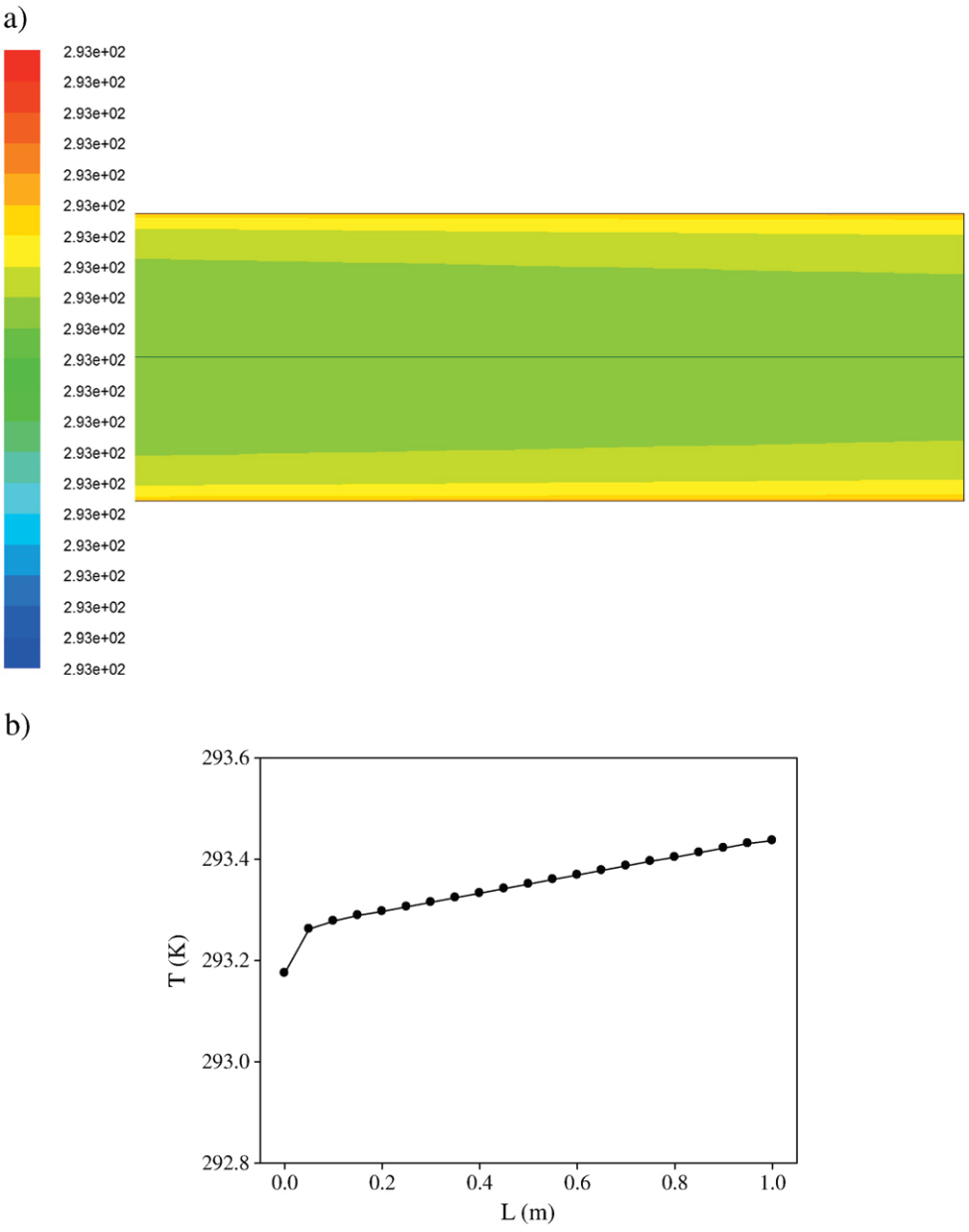

Fig. 6. Temperature distributions of inner surface and fluid in the tube ($Re = 50{,}000$, $q'' = 10{,}000\ W\ m^{-2}$, $T = 20\ °C$). a) Temperature distribution at the outlet section of the tube. b) Inner surface temperature distribution of the tube.

benefit from the experimental data reported in Palm et al.'s [22] study. According to this method the governing equations are solved sequentially, segregated one another. By means of this technique, each discrete equation is linearized implicitly respecting the equations dependent. Gambit program is used to form the model which is used for analyzing problems.

Classic single phase conservation equations were solved by control volume approach which makes possible numerical solution of governing equations by converting them to a set of algebraic equations. Governing equations have some results regarding convection terms, diffusion terms and other quantities which were discredited by second order upwind scheme. All scalar values and velocity components of the problem are calculated at the center of control volume interfaces where the grid schemes are used intensively. Semi Implicit Method for Pressure Linked Equations (SIMPLE) was used to pair the pressure and velocity. A point implicit (Gauss–Seidel) linear equation solver in conjunction with an algebraic multigrid method was used by Fluent CFD program [23] to solve the linear systems resulting from discretization schemes. Boundary conditions defined as velocity inlet at the pipe inlet and pressure outlet for the pipe exit. Turbulence intensity and hydraulic diameter defined for turbulence parameters. Constant heat flux applied to the pipe surface.

Monitor of the residuals was done during the iterative process thoroughly. All solutions were assumed to be converged when the residuals for all governing equations were lower than 10^{-6}. Optimal sizes of grid numbers were selected as 1000 (axial)×80 (radial) considering computation times and low variation with mesh size in temperature and pressure values for all conditions studied in this paper and they are placed highly near the radial flow channel entrance, as well as on all walls. Thus, it is provided that the solution became independent from the mesh size. This grid size was validated by our CFD results in all figures in the paper.

The equation for conservation of mass, or continuity equation, can be expressed as follows [23]:

$$\frac{\partial \rho}{\partial T} + \nabla\left(\rho \vec{\upsilon}\right) = S_m \tag{13}$$

Eq. (13) is the general form of the mass conservation equation and is valid for incompressible as well as compressible flows. The source S_m is the mass added to the continuous phase from the dispersed second phase and any user-defined sources.

For 2D axisymmetric geometries, the continuity equation is given by [23]

$$\frac{\partial \rho}{\partial T} + \frac{\partial}{\partial x}(\rho \upsilon_x) + \frac{\partial}{\partial r}(\rho \upsilon_r) + \frac{\rho \upsilon_r}{r}(\rho \upsilon_r) = S_m \tag{14}$$

where x is the axial coordinate, r is the radial coordinate, υ_r is the radial velocity.

5. Results and discussion

A commercial software package FLUENT [23] is employed in the numerical study. It uses control volume technique to convert the governing equations to algebraic equations so they can be solved numerically. The control volume technique works by performing the integration of the governing equations about each control volume, and then generates discretization of the equations which conserve each quantity based on control volume [23]. GAMBIT was used to plot and mesh the model of the test tube. The problem under investigation is a two-dimensional (axisymmetric) steady, forced turbulent convection flow of nanofluid flowing inside a straight circular tube having diameter of 0.00813 m and a length of 1.5 m for TiO_2 and 0.008 m and 1 m for Al_2O_3. The operating conditions of the study can be seen from Table 1. The fluid enters the circular tube with uniform axial velocity and temperature. The flow and thermal fields are assumed to be axisymmetric with respect to the horizontal plane parallel to x-axis as shown in Fig. 2 for the validation study of the numerical model and Fig. 5 for the simulation study. The main frame of the grid is preferred to be intense near by the tube wall in order to investigate the alteration of boundary layer as shown in Figs. 2a and 5a.

Velocity vectors of the problems for the validation study using experimental data [16] and the simulation study using correlations of physical properties proposed by Palm et al. [22] based on the experimental data of Putra et al. [25] can be seen from Figs. 2a–b and 5a–b respectively. It should be noted that the uniformity of the flow at the inlet section of the tube and fully developed flow at the middle section of the tube can be seen from these figures respectively.

Fig. 3a for the validation study and Fig. 6a for the simulation study illustrate the temperature distribution of the flow in the outlet section of test tube. Due to the given heat flux applied to the surface of the tube, temperature values increased from center of the tube to the surface of the tube and this situation is shown in Figs. 3a and 6a. In accordance with these figures, inner surface temperature distributions of the tube can be seen from Figs. 3b and 6b for the single phase flow of the nanofluids consisting of TiO_2 particles and Al_2O_3 particles respectively.

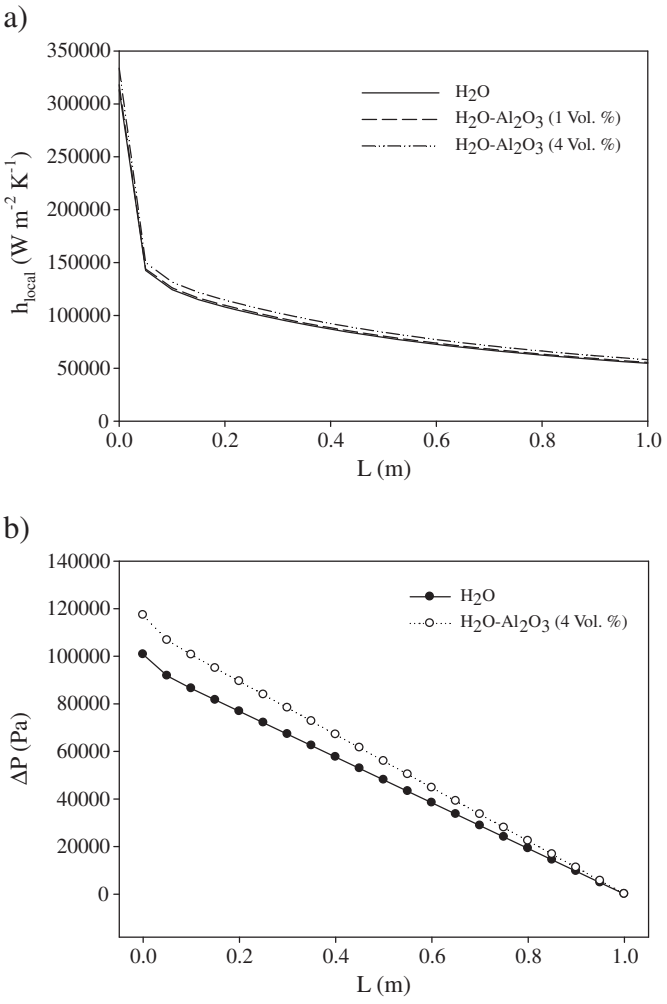

Fig. 7. Variation of local heat transfer coefficient and Pressure drop of water and nanofluid (Re = 50,000, q'' = 10,000 W, T = 20 °C, 4% concentration). a) Heat transfer coefficient—L. b) Pressure drop—L.

Validation process of numerical model is performed by means of the experimental data [16] as shown in Fig. 4 for some heat transfer characteristics of the problem. According to Fig 4, it can be clearly seen that the numerical model of Fluent [23] is in good agreement with the experimental values [16] in terms of the calculation of average Nusselt number within the range of ±30%, heat transfer coefficient within the range of ±30%, and pressure drop within the range of ±10% for the in-tube single phase flow of pure water and nanofluids with TiO_2 volume concentrations of 0.2%, 0.6% and 1%. Experimental and numerical studies are conducted for *Re* numbers between 4516 and 15681 and surface heat fluxes between 7233 and 13340 W m^{-2} (Figs. 2 and 3).

Fig. 7 shows the variation in local heat transfer coefficient and pressure drop along the length of the tube. The characteristics of the trend lines are found to be compatible with others in the literature. In addition to this, heat transfer enhancement due to nanoparticles can be seen from this figure. It is also noticed that a higher slope of relative local heat transfer coefficient can be seen at the entrance region of the tube in Fig. 7a. Fig. 7b shows the pressure drop distribution in the test tube including pure water and nanofluid with 4% Al_2O_3 concentration respectively. It can be seen from Fig. 7b that the volume concentration difference in small Reynolds numbers does not cause a significant effect, on the contrary, pressure drop increases with increasing Al_2O_3 concentration and Reynolds number in Fig. 7b.

From Fig. 8a, it is observed that wall shear stress increases with the increasing Reynolds number of the flow and also volume concentration of the nanoparticles in the tube as the mixture viscosity is increased strongly due to inclusion of nanoparticles. Fig. 8b and c displays the increase in Nusselt number, the heat transfer coefficient respectively by the various nanofluid volume concentrations over the base fluid of pure water for a fixed heat flux of 10,000 W m^{-2}. The increase in heat transfer coefficient is high for Al_2O_3, this is due to the higher Prandtl number and thermal conductivity of nanoparticles than the base fluid and also a large energy exchange process resulting from the chaotic movement of nanoparticles [27]. It should be noted that Nusselt number and heat transfer coefficient increase with increasing Reynolds number in these figures. The results complied with those obtained from Pak and Cho [5], Xuan and Li [28] and He et al. [29]. It can be seen from Fig. 8d that pressure drop increases with increasing the particle loading parameter and Reynolds number because of increasing velocity and viscosity of nanofluid.

From Fig. 9a, it is observed that wall shear stress increases with the increasing volume concentration of the nanofluid and Reynolds numbers. The shear stress has a significant increase at high Reynolds numbers. The effect of the particle concentration on the average Nusselt number and heat transfer coefficient can be clearly seen from Fig. 9b and c respectively. Nusselt number and heat transfer coefficient increase with increasing nanoparticle concentration and also Reynolds number in these figures. This shows the effect of particle concentration. It is evident that nanofluids give higher heat transfer coefficients compared to the base fluid. It can be clearly seen from Fig. 9d that there is a significant increase in pressure drop values especially at high Reynolds numbers and volume concentrations. From Fig. 9d, pressure drop increases with increasing Reynolds number and the particle loading parameter.

A large number of graphics could be generated from the output of the calculations; however, due to space limitations, only typical results are shown for limited data. It should also be noted that detailed

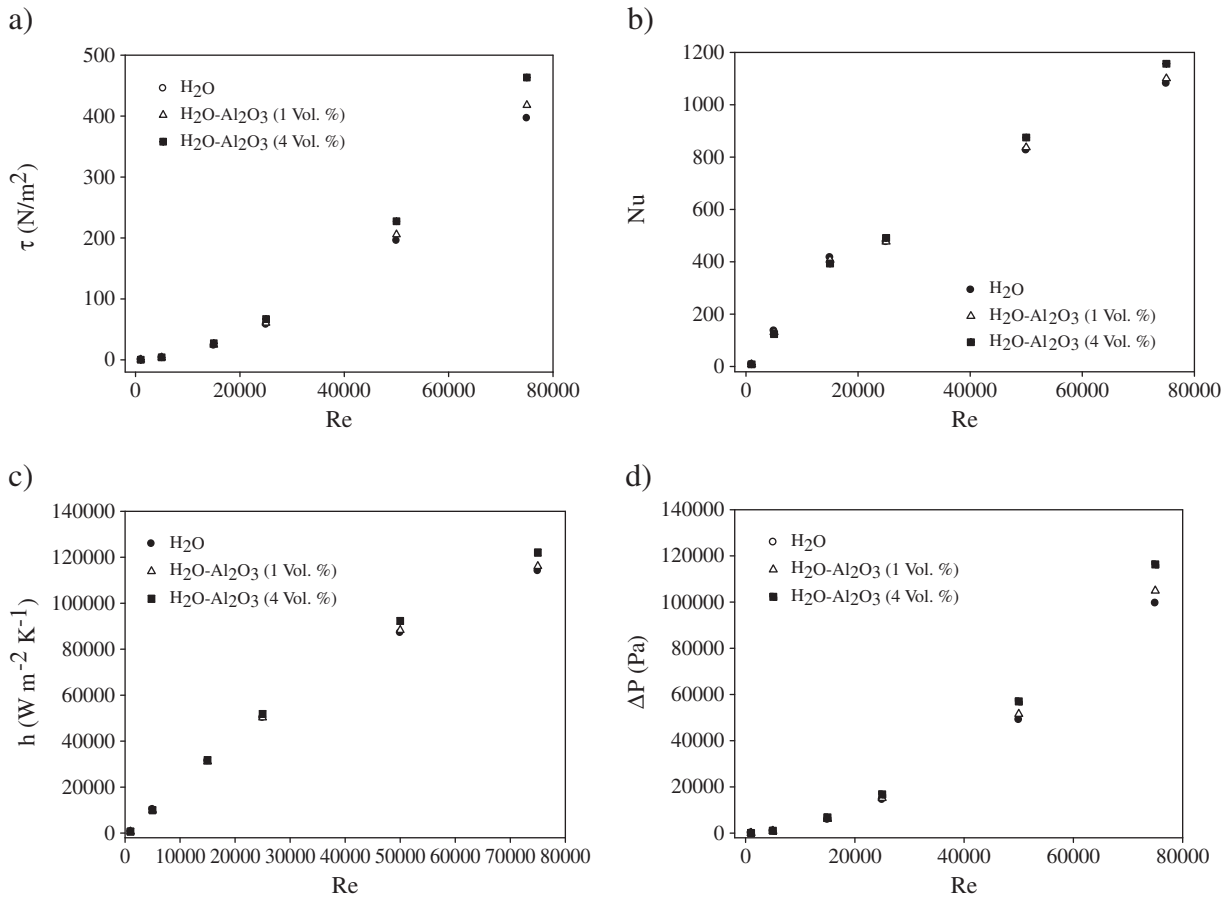

Fig. 8. Comparison of some heat transfer characteristics of different nanofluid concentrations over the base fluid of water ($q'' = 10{,}000$ W m^{-2}, $T = 20$ °C). a) Numerical wall shear stress vs. Re numbers. b) Numerical Nusselt numbers vs. Re numbers. c) Numerical heat transfer coefficient vs. Reynolds numbers. d) Numerical pressure drops vs. Reynolds numbers.

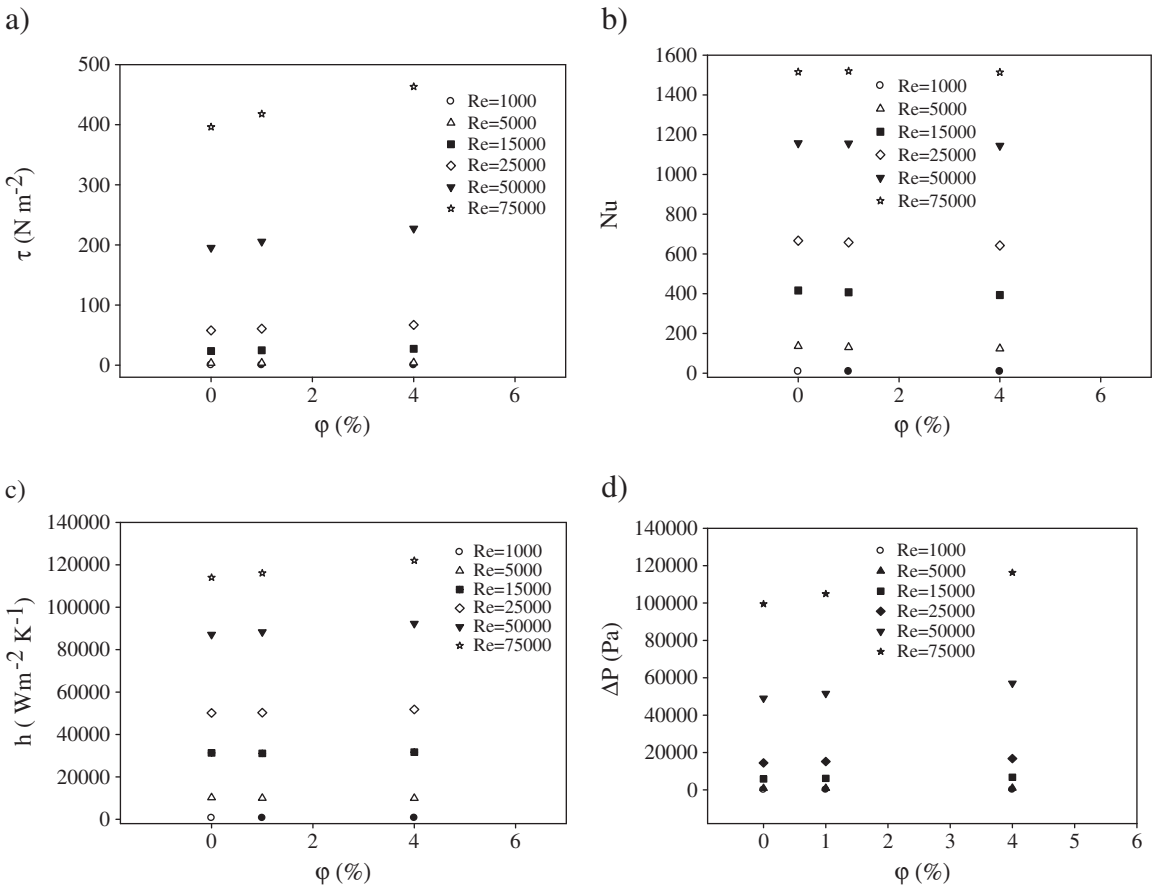

Fig. 9. Effect of particle loading φ on the some in laminar and turbulent flow ($q'' = 10{,}000\ \mathrm{W\,m^{-2}}$, $T = 20\ ^{\circ}\mathrm{C}$). a) Numerical wall shear stress vs. particle loading. b) Numerical Nusselt numbers vs. particle loading. c) Numerical heat transfer coefficient vs. particle loading. d) Numerical pressure drop vs. particle loading.

information on the explanations above and some additional figures with different experimental parameters related to this study can be seen in the authors' previous publications [14–21].

6. Conclusion

The heat transfer enhancement capabilities of nanofluids consisting of water–TiO_2 for a validation study and water–Al_2O_3 for a simulation study with various volume concentrations in a horizontal smooth tube have been investigated for forced flow conditions numerically using two dimensional governing equations.

Numerical results have clearly shown that the use of nanofluids can significantly increase heat transfer capabilities of nanofluids even for relatively small particle volume fractions.

Nanofluids with higher volume concentration have higher heat transfer enhancement and also have higher pressure drop. Therefore, judicious decision should be taken when selecting a nanofluid that will balance the heat transfer enhancement and the pressure drop penalty.

Although the nanofluid is actually a two-phase fluid in nature, the results show that the nanofluid behaves more like a pure fluid than a liquid–solid mixture.

Acknowledgments

The authors wish to thank DEGUSSA AG, Germany for the valuable donation of the nanoparticles used in the present study. The second author wishes to thank KMUTT for providing him with a Post-doctoral fellowship. The fifth author would like to thank the Thailand Research Fund, the Commission of Higher Education and the National Research University Project for providing financial support.

References

[1] U.S. Choi, Enhancing thermal conductivity of fluids with nanoparticles, ASME FED 231 (1995) 99–103.
[2] Y. Xuan, Q. Li, Heat transfer enhancement of nanofluids, Internatnal Journal of Heat Fluid Flow 21 (2000) 58–64.
[3] J.C. Maxwell, Electricity and Magnetism, Clarendon Press, Oxford, UK, 1873.
[4] J.C. Maxwell, A Treatise on Electricity and Magnetism, second ed., Oxford University Press, Cambridge, 1904, pp. 435–441.
[5] B.C. Pak, Y.I. Cho, Hydrodynamic and heat transfer study of dispersed fluids with submicron metallic oxide particles, Experimental Heat Transfer 11 (1998) 151–170.
[6] Y.M. Xuan, Q. Li, Investigation on convective heat transfer and flow features of nanofluids, Journal of Heat Transfer 125 (2003) 151–155.
[7] K.V. Liu, S.U.S. Choi, K.E. Kasza, Measurement of pressure drop and heat transfer in turbulent pipe flows of particulate slurries, Argonne National Laboratory Report, ANL-88-15, 1988.
[8] U.S. Choi, Enhancing thermal conductivity of fluid with nanoparticles, in: D.A. Singiner, H.P. Wang (Eds.), Development and Application of Non-Newtonian Flows, ASME, 231, 1995, pp. 99–105.
[9] S. Lee, S.U.S. Choi, S. Li, J.A. Eastman, Measuring thermal conductivity of fluids containing oxide nanoparticles, ASME Journal Heat Transfer 121 (1999) 280–288.
[10] H. Masuda, A. Ebata, K. Teramae, N. Hishinuma, Alteration of thermal conductivity and viscosity of liquid by dispersing ultra-fine particles (dispersions of c-Al_2O_3, SiO_2, and TiO_2 ultra-fine particles), Netsu Bussei (Japan) 4 (1993) 227–233.
[11] U. Rea, T. McKrell, L. Hu, J. Buongiorno, Laminar convective heat transfer and viscous pressure loss of alumina–water and zirconia–water nanofluids, International Journal of Heat and Mass Transfer 52 (2009) 2042–2048.
[12] V. Bianco, F. Chiacchio, O. Manca, S. Nardini, Numerical investigation of nanofluids forced convection in circular tubes, Applied Thermal Engineering 29 (2009) 3632–3642.
[13] M. H. Fard, M. N. Esfahany, M.R. Talaie, Numerical study of convective heat transfer of nanofluids in a circular tube two-phase model versus single-phase model, International Communications in Heat and Mass Transfer 37 (2010) 91–97.
[14] W. Daungthongsuk, S. Wongwises, A critical review of convective heat transfer of nanofluids, Renewable & Sustainable Energy Reviews 11 (2007) 797–817.
[15] W. Duangthongsuk, S. Wongwises, Measurement of temperature-dependent thermal conductivity and viscosity of TiO_2–water nanofluids, Experimental Thermal and Fluid Science 32 (2009) 706–714.

[16] W. Duangthongsuk, S. Wongwises, Comparison of the effects of measured and computed thermophysical properties of nanofluids on heat transfer performance, Experimental Thermal and Fluid Science 34 (2010) 616–624.
[17] W. Duangthongsuk, S. Wongwises, An experimental study on the heat transfer performance and pressure drop of TiO_2–water nanofluids flowing under a turbulent flow regime, International Journal of Heat and Mass Transfer 53 (2010) 334–344.
[18] W. Duangthongsuk, S. Wongwises, Heat transfer enhancement and pressure drop characteristics of TiO_2–water nanofluid in a double-tube counter flow heat exchanger, International Journal of Heat and Mass Transfer 52 (2009) 2059–2067.
[19] W. Duangthongsuk, S. Wongwises, Effect of thermophysical properties models on the predicting of the convective heat transfer coefficient for low concentration nanofluid, International Communications in Heat and Mass Transfer 35 (2008) 1320–1326.
[20] W. Duangthongsuk, S. Wongwises, A critical review of convective heat transfer of nanofluids, Renewable & Sustainable Energy Reviews 11 (2007) 797–817.
[21] H. Demir, A.S. Dalkilic, N.A. Kurekci, B. Kelesoglu, S. Wongwises, A numerical investigation of nanofluids forced convection flow in a horizontal smooth tube, International Heat Transfer Conference, ASME, 2010, August 8–13, USA.
[22] S.J. Palm, G. Roy, C.T. Nguyen, Heat transfer enhancement with the use of nanofluids in radial flow cooling systems considering temperature-dependent properties, Applied Thermal Engineering 26 (2006) 2209–2218.
[23] Fluent release 6.2.16, Fluent Incorporated, 2005.
[24] W.C. Williams, J. Buongiorno, L.W. Hu, Experimental investigation of turbulent convective heat transfer and pressure loss of alumina/water and zirconia/water nanoparticle colloids (nanofluids) in horizontal tubes, Journal of Heat Transfer 130 (2008) 042412.
[25] N. Putra, W. Roetzel, S.K. Das, Natural convection of nanofluids, Heat and Mass Transfer 39 (2003) 775–784.
[26] A. Bejan, G. Tsatsaronics, M. Moran, Thermal Design and Optimization, Wiley-Interscience Publication, 1996.
[27] Y. Xuan, W. Roetzel, Conceptions for heat transfer correlation of nanofluids, International Journal of Heat and Mass Transfer 43 (2000) 3701–3707.
[28] Y. Xuan, Q. Li, Investigation on convective heat transfer and flow features of nanofluids, ASME Journal of Heat Transfer 125 (2003) 151–155.
[29] Y. He, Y. Jin, H. Chen, Y. Ding, D. Cang, H. Lu, Heat transfer and flow behavior of aqueous suspensions of TiO_2 nanoparticles (nanofluids) flowing upward through a vertical pipe, International Journal of Heat and Mass Transfer 50 (2007) 2272–2281.

International Communications in Heat and Mass Transfer 38 (2011) 212–217

Contents lists available at ScienceDirect

International Communications in Heat and Mass Transfer

journal homepage: www.elsevier.com/locate/ichmt

Two-phase air–water flow in micro-channels: An investigation of the viscosity models for pressure drop prediction ☆

Sira Saisorn [a,b], Somchai Wongwises [b,*]

[a] Department of Engineering, King Mongkut's Institute of Technology Ladkrabang Chumphon Campus, Chumphon 86160, Thailand
[b] Fluid Mechanics, Thermal Engineering and Multiphase Flow Research Lab. (FUTURE), Department of Mechanical Engineering, King Mongkut's University of Technology Thonburi, Bangmod, Bangkok 10140, Thailand

ARTICLE INFO

Available online 16 December 2010

Keywords:
Two-phase flow
Micro-channel
Void fraction
Pressure drop

ABSTRACT

Adiabatic two-phase air–water flow is experimentally studied in this work. Two channels, made of fused silica, with different diameters of 0.53 and 0.15 mm are used as test sections. The void fraction data for both tubes are obtained by image analysis. For the larger channel, the void fraction is found to be a linear relationship with the volumetric quality. In the case of the smaller one, however, the non-linear void fraction is obtained. The measured frictional pressure drop data are compared with the predictions regarding the homogeneous flow assumption. Several well-known two-phase viscosity models are subsequently evaluated for applicability to micro-channels.

© 2010 Elsevier Ltd. All rights reserved.

1. Introduction

Two-phase flow in micro-channel flow passages has been studied over the years. Clarification of micro-scale effects on two-phase flow and heat transfer characteristics has become more necessary due to the rapid development of microstructure devices used for several engineering applications including medical devices, high heat-flux compact heat exchangers, and cooling systems of various types of equipment such as high performance micro-electronics, supercomputers, and high-powered lasers.

Several investigators have proposed criteria to address the definition of a micro-channel. The proposed channel classifications are often based on different dimensionless parameters. For instance, arbitrary channel classifications based on the hydraulic diameter D_h have been proposed. Mehendale et al. [1] employed the hydraulic diameter as an important parameter for defining heat exchangers and Kandlikar [2] proposed criteria for small flow channels used in engineering applications.

Two-phase flow and heat transfer characteristics in small channels such as micro-channels and mini-channels are likely to be strongly dependent on surface tension effects in addition to viscosity and inertia forces, resulting in significant differences in two-phase flow phenomena between ordinarily sized channels and small channels.

In the past decade, a relatively small amount of publications have been available for both mini-channels and micro-channels compared to those for ordinarily sized channels.

Triplett et al. [3,4] studied adiabatic two-phase air-deionized water (DI water) flow characteristics in micro-channels with hydraulic diameters ranging from 1.1 to 1.5 mm. The flow patterns observed were bubbly, slug, churn, slug-annular, and annular. The measured void fraction and two-phase pressure drop in the relevant flow regimes were also investigated. The void fraction data were obtained based on image analysis.

Serizawa et al. [5] investigated the visualization of the two-phase flow pattern in circular micro-channels. The flowing mixture of air and water in channels 20, 25, and 100 μm in diameter and that of steam and water in a channel of 50 μm in diameter were studied experimentally. Two-phase flow patterns obtained from both air–water and steam–water flows were quite similar and their detailed structures were described. The study confirmed that the surface wettability had a significant effect on the two-phase flow patterns in very small channels.

Chung and Kawaji [6] performed an experiment to distinguish the two-phase flow characteristics in micro-channels from those in mini-channels. Four different circular diameters ranging from 50 to 526 μm were employed to examine a scaling effect on nitrogen-DI water two-phase flow. The results including the flow patterns, void fraction, and two-phase pressure drop were analysed.

A flow visualization study to clarify the flow patterns of a vertical upward gas–liquid two-phase flow in rectangular mini-channels with hydraulic diameters ranging from 1.95 to 5.58 mm was carried out by Satitchaicharoen and Wongwises [7]. Air–water, air — 20 wt.% glycerol solution, and air — 40 wt.% glycerol solution were used as working fluids. In the experiments, they employed various rectangular test sections: 20 mm × 2 mm, 40 mm × 1 mm, 40 mm × 2 mm, 40 mm × 3 mm, and 60 mm × 2 mm with an equal length of 1 m. The flow phenomena, which were classified as bubbly flow, cap-bubbly

☆ Communicated by W.J. Minkowycz.

* Corresponding author.
E-mail address: somchai.won@kmutt.ac.th (S. Wongwises).

0735-1933/$ – see front matter © 2010 Elsevier Ltd. All rights reserved.
doi:10.1016/j.icheatmasstransfer.2010.12.008

Nomenclature

C_o	confinement number
D	channel diameter (m)
D_b	capillary length (m)
D_h	hydraulic diameter (m)
f	friction factor
G	mass flux (kg/m^2s)
g	gravitational acceleration (m/s^2)
MAE	mean absolute error
$-dP_f/dz$	frictional pressure gradient (Pa/m)
Re	Reynolds number
x	mass quality

Greek symbols

α	void fraction
β	volumetric quality
μ	dynamic viscosity (Ns/m^2)
ρ	density (kg/m^3)
σ	surface tension (N/m)

Subscripts

G	gas phase
H	homogeneous
L	liquid phase
TP	two-phase

flow, slug flow, churn flow, and annular flow, were observed and recorded by a high-speed camera. The effects of gap size, channel width, and liquid viscosity on the flow pattern transitions were also discussed.

Saisorn and Wongwises [8] reported the influence of the working fluid on flow characteristics in a 0.53 mm diameter channel. Air, nitrogen gas, water and deionized water were used as working fluids. The results of the two-phase air–water system were found to agree with those of working fluids other than air–water mixture. A new correlation was also developed based on their experimental data.

From the previously mentioned review of the literature, it is noted that two-phase flow phenomena in micro-channels are not entirely consistent with those in ordinarily sized channels. However, some experimental data for micro-channels showed fair agreement with predictions developed based on ordinarily sized channels. In general, the prediction methods derived from the separated flow assumption were considered to be comparable with the data whereas the homogeneous flow assumption seemed to be unattractive to previous researchers. This is possibly due to the fact that the observed flow patterns are much less homogeneous under different conditions. Interestingly, it should be noted from Chung and Kawaji [6] and Saisorn and Wongwises [8] that although their observed flow patterns in micro-channels were not perfectly homogeneous, the linear void fraction is found to take place at a certain size of the channel. Such a linear relationship between the void fraction and volumetric quality indicates the homogeneous flow assumption, which may possibly be able to predict the two-phase flow behaviour in micro-channels. This work is, therefore, aimed at examining the applicability of several widely used viscosity models to the pressure drop prediction of air–water flow through different circular micro-channels.

2. Experimental apparatus and procedure

The experiments dealing with pressure drop measurements are carried out using the apparatus along with the instruments as shown in Fig. 1. Air and water are used as working fluids in the system. Instead of a conventional pump, which may contribute to pulsation and fluid contamination, air and the liquid-filled tank are combined and operated as a pneumatic pump to supply a constant flow rate of liquid through the test section. The mixing chamber is designed to introduce the air–water mixture smoothly along the channel. The mixture flows freely from the channel outlet where atmospheric pressure is realized. The gas flow rates can be measured by four sets of rotameters within the ranges of 5–50 sccm, 0.05–0.5, 0.2–2.0, and 1–10 SCFH, respectively. For liquid flow rate measurements, an electronic balance (320 ± 0.001 g) is used to measure the weight of the liquid flowing freely from the outlet over a time period. Test sections made of fused silica with two different inner diameters of 0.53 and 0.15 mm with corresponding lengths of 320 and 104 mm, respectively, are used in this work. The single-phase and two-phase pressure drops across the test section are determined by two pressure transducers installed at the channel inlet. The low range pressure transducer is calibrated from 0 to 250 kPa with a ± 0.5 kPa accuracy and the high range one is calibrated from 0 to 1000 kPa with a ± 2 kPa accuracy. Type T thermocouples are used to measure fluid temperatures. The degree of uncertainty of the temperature measurements is ± 0.1 °C.

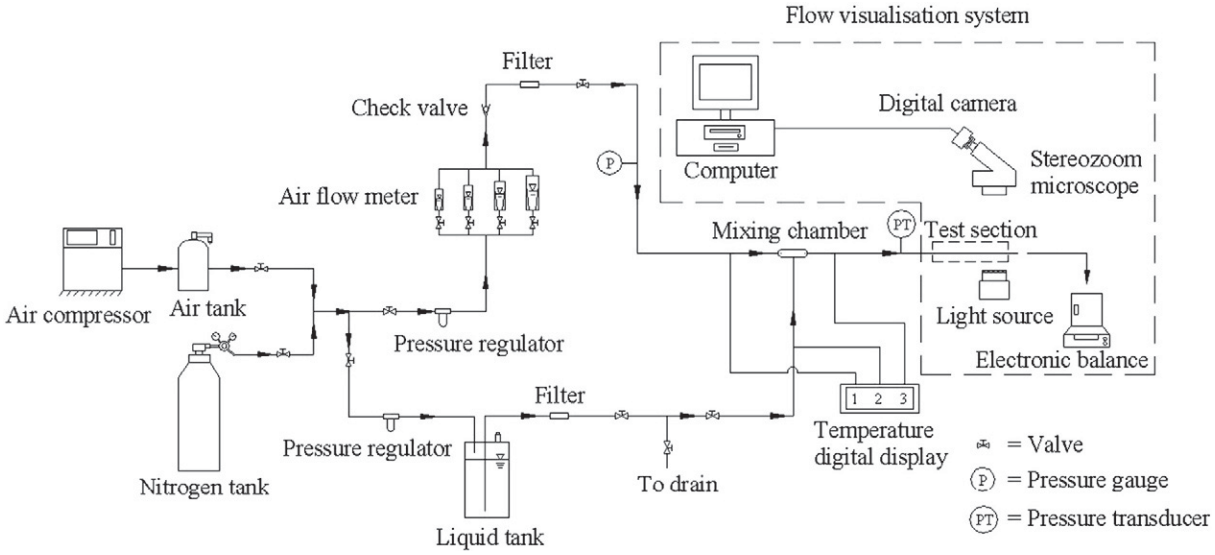

Fig. 1. Experimental apparatus.

Single-phase flow experiments with different fluids were the first to be performed. Following this, two-phase flow experiments were conducted at various gas and liquid flow rates. In this work, the gas flow rate was increased by small increments, while the liquid flow rate was kept constant at a pre-selected value. The system was allowed to approach steady conditions before the fluid flow rates, flow patterns, and pressure drops were recorded.

3. Results and discussion

3.1. Void fraction

Void fraction, the fraction of the channel cross-sectional volume that is occupied by the gas phase, is one of the most important parameters used to evaluate the pressure drop components existing in two-phase flows in various channels. In the case of a horizontal channel, for instance, the void fraction is required before the accelerational pressure drop can be calculated.

Different methods available for void fraction estimation have been used by previous researchers.

Conventional methods such as a constant electric current method generally used to measure void fraction in ordinarily sized channels were carried out by Kariyasaki et al. [9] to obtain void fractions in channels with three different diameters of 1, 2.4, and 4.9 mm. In a method based on quick-closing valves, Wongwises and Pipathattakul [10] measured the void fraction in an inclined narrow annular channel with a hydraulic diameter of 4.5 mm.

For channels with hydraulic diameters of less than 1 mm, it may be convenient to estimate volumetric void fraction by image analysis.

Prior to obtaining the present void fraction data based on image analysis, the detailed formation of each flow pattern has to be registered by a precise stereozoom microscope (Nikon SMZ-1) mounted together with a camera system having shutter speeds of 1/15 to 1/10,000 s. This flow visualization system provides continuous zoom so that the appropriate view field (L/D = 10) is obtained for channels with diameters of 0.53 and 0.15 mm. The region near the channel outlet is always selected as the viewing window.

In this work, the void fraction is the average value estimated from around 50–70 photographed images of flow pattern at a given flow condition. Slug flow, throat-annular flow, annular-rivulet flow, annular flow, liquid-alone flow, and serpentine-like gas core flow are taken into account in the estimation. However, the void fraction regarding churn flow is not measured due to the highly disruptive characteristics. The image analysis is considered by assuming symmetrical volumes, covering spherical and ellipsoidal segments as well as cylinders, formed by the gas–liquid interface. The volumetric void fraction is determined based on a micrometer scale with an accuracy of ±0.05 mm, and the effect of the curvature radius of the tube, which was first introduced by Kawahara et al. [11], is carefully considered in the analysis.

The void fraction data for the channel having a diameter of 0.53 mm are well compatible with the homogeneous flow model ($\alpha = \beta$), while a 0.15 mm diameter channel, in contrast, provides the non-linear void fraction as shown in Eq. (1).

$$\alpha = \frac{0.036\beta^{0.5}}{1-0.945\beta^{0.5}} \tag{1}$$

The non-linear relationship between the void fraction (α) and volumetric quality (β) was also reported by Kawahara et al. [11] and Kwak et al. [12]. Such non-linear characteristics may be contributed by the highly frequent appearance of the gas core flow patterns which have inherent flow with large slip ratios. Due to such different behaviours between the two channel sizes, the confinement number recommended by Kew and Cornwell [13] is used for checking whether the micro-scale effects are still important. The confinement number is defined as

$$C_o = \frac{D_b}{D_h}, \tag{2}$$

where D_b stands for capillary length, which is determined by

$$D_b = \sqrt{\frac{\sigma}{g(\rho_L - \rho_G)}}, \tag{3}$$

where σ is surface tension, g represents gravitational acceleration, and ρ_L and ρ_G are liquid and gas densities, respectively.

A confinement number below 0.5 refers to ordinarily sized channels. For all the present experimental conditions, channels with diameters of 0.53 and 0.15 mm correspond respectively to confinement numbers of around 5.07 and 17.98. These values of the confinement number indicate that surface tension plays a dominant role in the flow mechanisms, which implies the micro-scale point of view.

3.2. Frictional pressure drop

Prior to obtaining data for the two-phase frictional pressure drop, measurements of the total pressure drop are taken under various different conditions. In this work, the total pressure drop of two-phase flow in a horizontal channel is composed of three terms: frictional

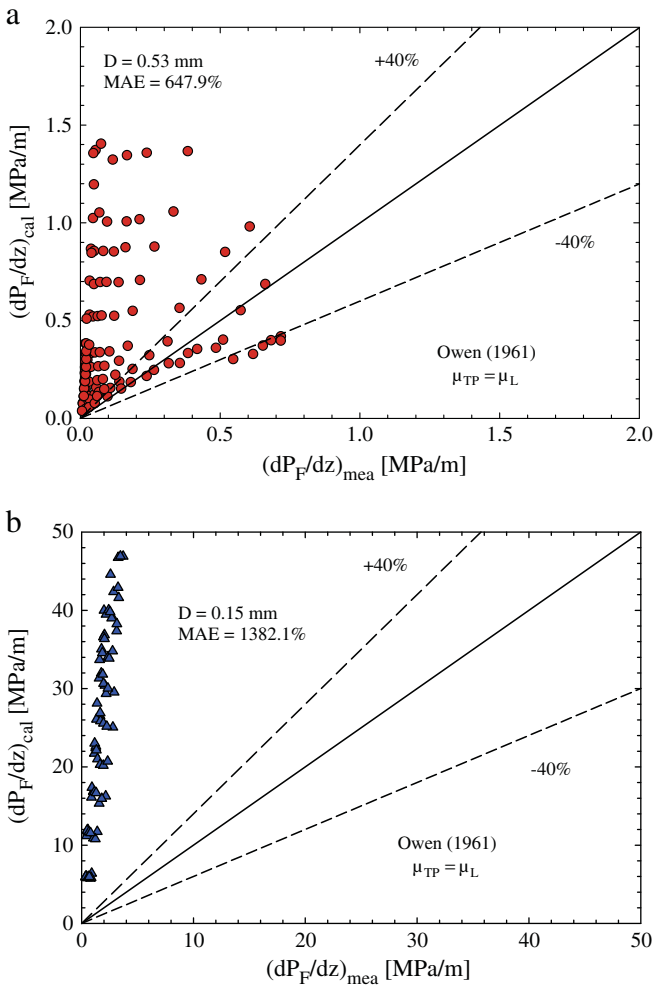

Fig. 2. Experimental data plotted against the predictions by Owen [16].

pressure drop, accelerational pressure drop, and pressure drop caused by an abrupt flow area. The latter component can be evaluated from an empirical correlation proposed by Abdelall et al. [14]. By subtracting the accelerational term and sudden contraction component from the total pressure drop, the frictional pressure drop data are obtained. Further details regarding the calculation method are available in Saisorn and Wongwises [15]. The obtained frictional pressure drop data are subsequently compared with the homogeneous flow predictions, taking into account several existing viscosity models.

The homogeneous flow model assumes that gas and liquid phases flow with equal velocity. The gas–liquid mixture is considered as a single-phase flow with average fluid properties.

For pressure drop calculations based on the homogeneous flow, it follows that

$$-\frac{dP_f}{dz} = \frac{f_{TP}G^2}{2D\rho_H} \tag{4}$$

$$\rho_H = \left[\frac{x}{\rho_G} + \frac{(1-x)}{\rho_L}\right]^{-1}. \tag{5}$$

In Eqs. (4) and (5), $(-dP_f/dz)$ is the two-phase frictional pressure gradient, G is the mass flux, D is the channel diameter, x is the mass quality, ρ_H is the average density of the homogeneous fluid, and ρ_L and ρ_G are liquid and gas densities, respectively. f_{TP} shown in Eq. (4) represents the two-phase Darcy friction factor, which is a function of the two-phase Reynolds number:

$$Re_{TP} = \frac{GD}{\mu_{TP}}. \tag{6}$$

For laminar flow ($Re_{TP} \leq 2100$),

$$f_{TP} = \frac{64}{Re_{TP}}. \tag{7}$$

For turbulent flow ($Re_{TP} < 100{,}000$) in a smooth channel,

$$f_{TP} = \frac{0.3164}{Re_{TP}^{0.25}}, \tag{8}$$

where μ_{TP} presented in Eq. (6) is the two-phase viscosity, for which various forms were proposed by different researchers as follows.

The two-phase viscosity was assumed by Owen [16] to be equal to the liquid viscosity as shown in Eq. (9).

$$\mu_{TP} = \mu_L \tag{9}$$

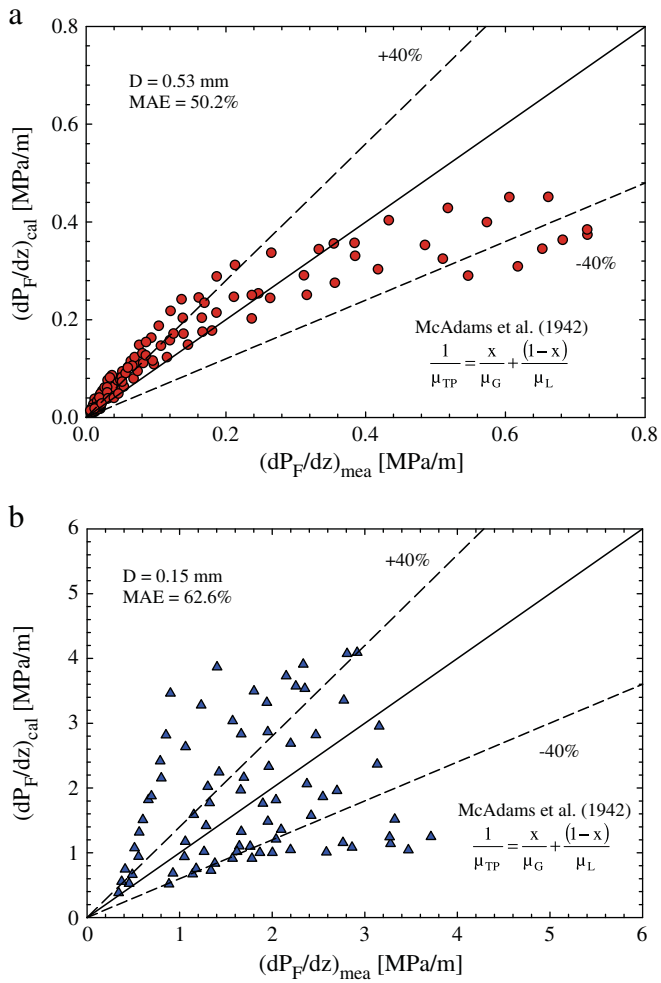

Fig. 3. Experimental data plotted against the predictions by McAdams et al. [17].

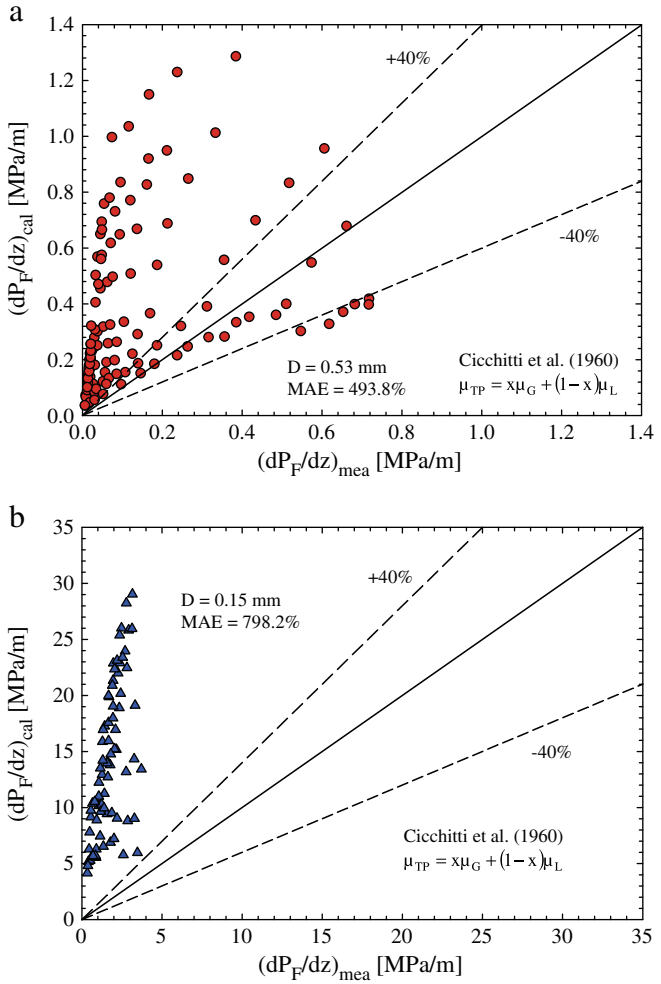

Fig. 4. Experimental data plotted against the predictions by Cicchitti et al. [18].

McAdams et al. [17] proposed the two-phase viscosity presented in Eq. (10), in which the viscosities of each phase are weighted by their corresponding mass quality.

$$\frac{1}{\mu_{TP}} = \frac{x}{\mu_G} + \frac{(1-x)}{\mu_L} \tag{10}$$

The two-phase viscosity of Eq. (11) was proposed by Cicchitti et al. [18] and the mass quality is an important parameter for the calculation.

$$\mu_{TP} = x\mu_G + (1-x)\mu_L \tag{11}$$

With the experimental data obtained from R-12 during vaporization in a capillary tube, Lin et al. [19] proposed the two-phase viscosity as follows.

$$\mu_{TP} = \frac{\mu_L \mu_G}{\mu_G + x^{1.4}(\mu_L - \mu_G)} \tag{12}$$

Dukler et al. [20] and Beattie and Whalley [21] developed two-phase viscosity models based on volumetric quality (β) as expressed respectively in Eqs. (13) and (14).

Dukler et al. [20]:

$$\mu_{TP} = \beta\mu_G + (1-\beta)\mu_L. \tag{13}$$

Beattie and Whalley [21]:

$$\mu_{TP} = \beta\mu_G + (1-\beta)(1 + 2.5\beta)\mu_L \tag{14}$$

In order to examine the applicability of the two-phase viscosity predictions for both tubes, the experimental pressure drop data are plotted against the values predicted by the corresponding models as presented in Figs. 2–7. The mean absolute error (MAE) indicated on these figures refers to the predictive accuracy of a given model. In general, the agreement between the experimental data and the predicted pressure drops is not good for a 0.15 mm diameter channel in which a non-linear void fraction is obtained. Nevertheless, better predictions are observed when a tube with a diameter of 0.53 mm, associated with the linear void fraction, is used. According to the previous discussion, different void fraction characteristics for the two channel sizes may result in the discrepancy in predictions. The comparisons shown in Figs. 2–7 also indicate that only the methods proposed by Beattie and Whalley [21] and by McAdams et al. [17] are roughly predictable. The prediction by Beattie and Whalley [21] is shown to be the best. The MAE values of 37.3% and 38.3% as well as 57.7% and 48.1% of the predicted data falling within a ±40% error band are obtained respectively for a 0.53 mm diameter channel and a 0.15 mm diameter channel. For the second best prediction, which is obtained by the method developed by McAdams et al. [17], the channels with diameters of 0.53 and 0.15 mm correspond respectively to the MAE values of 50.2% and 62.6%. Accordingly, 50.4% and 44.2% of the predicted values fall in the range of a ±40% error band.

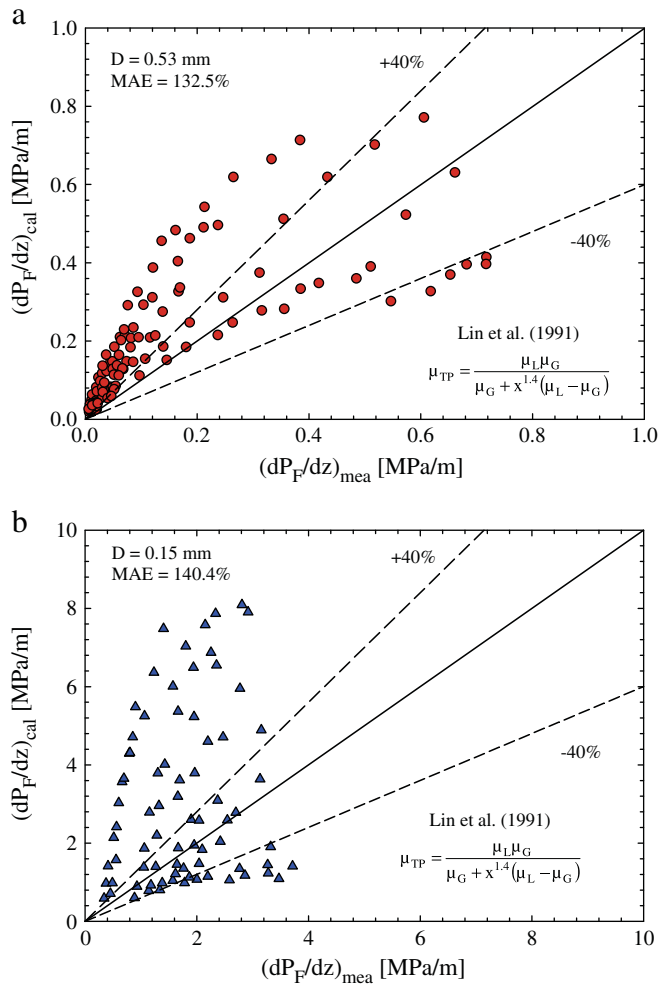

Fig. 5. Experimental data plotted against the predictions by Lin et al. [19].

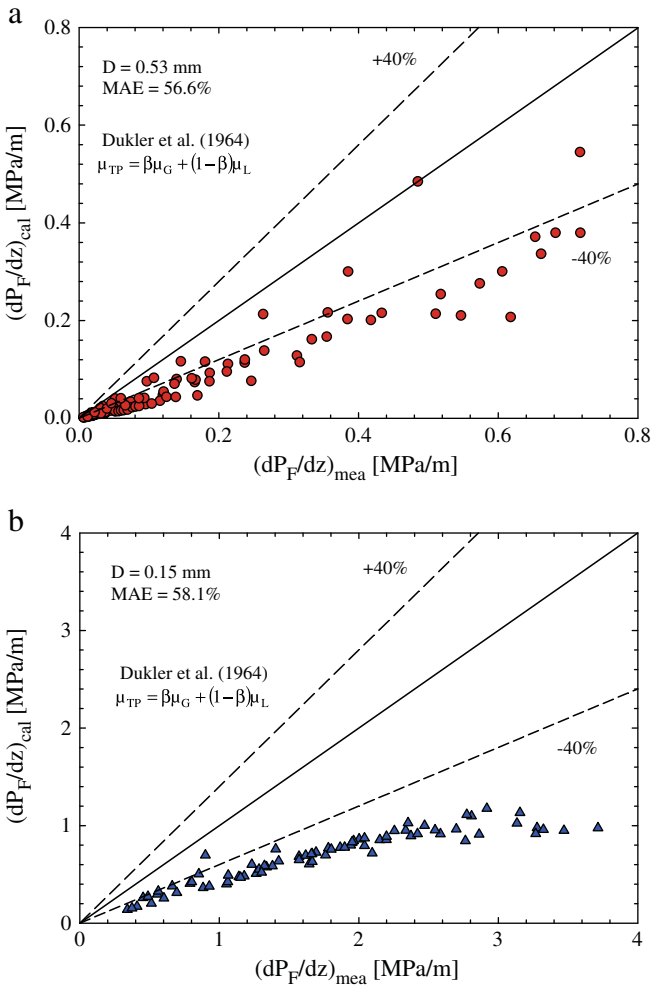

Fig. 6. Experimental data plotted against the predictions by Dukler et al. [20].

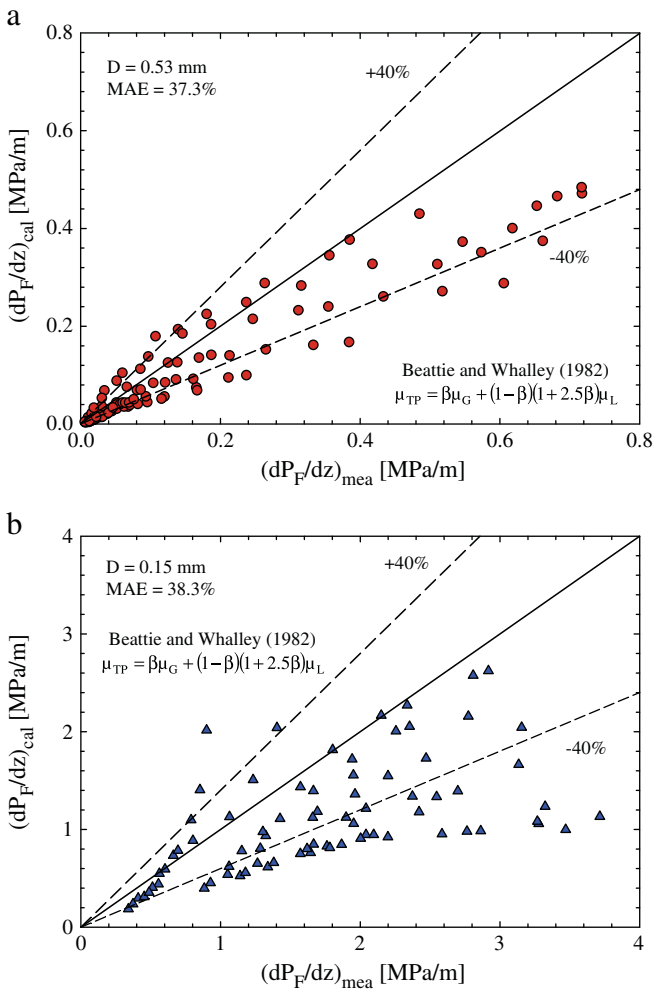

Fig. 7. Experimental data plotted against the predictions by Beattie and Whalley [21].

4. Conclusion

Two-phase pressure drop of air–water flow through circular channels having different diameters of 0.53 and 0.15 mm is experimentally investigated in this study. The test sections are made of fused silica. Void fraction data for both tubes are obtained by using a method based on image analysis. The linear void fraction is observed for the channel with a diameter of 0.53 mm whereas the non-linear void fraction is identified in the smaller channel. The frictional pressure drop data, determined by subtracting the accelerational component and the sudden contraction term from the total pressure drop, are compared with the predictions of several well-known two-phase viscosity models. The homogeneous flow assumption seems to unsatisfactorily predict the data corresponding to the channel with a diameter of 0.15 mm. However, better predictions are obtained for a 0.53 mm diameter channel in which the linear void fraction characteristics occur.

Acknowledgements

The authors would like to express their appreciation to the Thailand Research Fund, the Commission of Higher Education and the National Research University Project for providing financial support for this study.

References

[1] S.S. Mehendale, A.M. Jacobi, R.K. Ahah, Fluid flow and heat transfer at micro- and meso-scales with application to heat exchanger design, Appl. Mech. Rev. 53 (2000) 175–193.
[2] S.G. Kandlikar, Fundamental issues related to flow boiling in mini-channels and micro-channels, Exp. Therm. Fluid Sci. 26 (2002) 389–407.
[3] K.A. Triplett, S.M. Ghiaasiaan, S.I. Abdel-Khalik, D.L. Sadowski, Gas–liquid two-phase flow in microchannels Part I: two-phase flow patterns, Int. J. Multiphase Flow 25 (1999) 377–394.
[4] K.A. Triplett, S.M. Ghiaasiaan, S.I. Abdel-Khalik, A. LeMouel, B.N. McCord, Gas–liquid two-phase flow in microchannels Part II: void fraction and pressure drop, Int. J. Multiphase Flow 25 (1999) 395–410.
[5] A. Serizawa, Z. Feng, Z. Kawara, Two-phase flow in micro-channels, Exp. Therm. Fluid Sci. 26 (2002) 703–714.
[6] P.M.-Y. Chung, M. Kawaji, The effect of channel diameter on adiabatic two-phase flow characteristics in microchannels, Int. J. Multiphase Flow 30 (2004) 735–761.
[7] P. Satitchaicharoen, S. Wongwises, Two-phase flow pattern maps for vertical upward gas–liquid flow in mini-gap channels, Int. J. Multiphase Flow 30 (2004) 225–236.
[8] S. Saisorn, S. Wongwises, Flow pattern, void fraction and pressure drop of two-phase air–water flow in a horizontal circular micro-channel, Exp. Therm. Fluid Sci. 32 (2008) 748–760.
[9] A. Kariyasaki, T. Fukano, A. Ousaka, M. Kagawa, Characteristics of time-varying void fraction in isothermal air–water co-current flow in horizontal capillary tube, Trans. JSME 57 (1991) 4036–4043.
[10] S. Wongwises, M. Pipathattakul, Flow pattern, pressure drop and void fraction of two-phase gas–liquid flow in an inclined narrow annular channel, Exp. Therm. Fluid Sci. 30 (2006) 345–354.
[11] A. Kawahara, P.M.-Y. Chung, M. Kawaji, Investigation of two-phase flow pattern, void fraction and pressure drop in a microchannel, Int. J. Multiphase Flow 28 (2002) 1411–1435.
[12] Y. Kwak, D. Pence, J. Liburdy, V. Narayanan, Gas–liquid flows in a fractal-like branching flow network, Engineering Conference International Heat Transfer and Fluid Flow in Microscale III, Whistler, BC, Canada, 2008., September 21–26.
[13] P.A. Kew, K. Cornwell, Correlations for the prediction of boiling heat transfer in small-diameter channels, Appl. Therm. Eng. 17 (8–10) (1997) 705–715.
[14] F.F. Abdelall, G. Hahn, S.M. Ghiaasiaan, S.I. Abdel-Khalik, S.S. Jeter, M. Yoda, D.L. Sadowski, Pressure drop caused by abrupt flow area changes in small channels, Exp. Therm. Fluid Sci. 29 (2005) 425–434.
[15] S. Saisorn, S. Wongwises, An experimental investigation of two-phase air–water flow through a horizontal circular micro-channel, Exp. Therm. Fluid Sci. 33 (2009) 306–315.
[16] W.L. Owen, Two-phase pressure gradient, Int. Dev. Heat Transfer, Pt II, ASME, New York, 1961.
[17] W.H. McAdams, W.K. Woods, L.C. Heroman, Vaporization inside horizontal tubes-III, Benzene-Oil Mixtures. Trans. ASME. 64 (1942) 193.
[18] A. Cicchitti, C. Lombardi, M. Silvestri, G. Solddaini, R. Zavalluilli, Two-phase cooling experiments — pressure drop, heat transfer and burnout measurement, Energy Nucl. 7 (1990) 407–425.
[19] S. Lin, C.C.K. Kwok, R.Y. Li, Z.H. Chen, Z.Y. Chen, Local frictional pressure drop during vaporization for R-22 through capillary tubes, Int. J. Multiphase Flow 17 (1991) 95–102.
[20] A.E. Dukler, M. Wicks III, R.G. Cleveland, Pressure drop and hold-up in two-phase flow, AIChE J. 10 (1964) 38–51.
[21] D.R.H. Beattie, P.B. Whalley, A simple two-phase flow frictional pressure drop calculation method, Int. J. Multiphase Flow 8 (1982) 83–87.

Heat Mass Transfer (2011) 47:629–640
DOI 10.1007/s00231-010-0748-6

ORIGINAL

Evaporation heat transfer and flow characteristics of R-134a flowing through internally grooved tubes

Somchai Wongwises · Suriyan Laohalertdecha · Jatuporn Kaew-on · Weerapun Duangthongsuk · Kanit Aroonrat · Kittipong Sakamatapan

Received: 8 November 2009 / Accepted: 29 November 2010 / Published online: 4 January 2011
© Springer-Verlag 2010

Abstract This article describes experimental investigations of the heat transfer coefficient and pressure drop of R-134a flowing inside internally grooved tubes. The test tubes are one smooth tube and four grooved tubes. All test tubes are made from type 304 stainless steel, have an inner diameter of 7.1 mm, are 2,000 mm long and are installed horizontally. The test section is uniformly heated by a DC power supply to create evaporation conditions. The groove depth of all grooved tubes is fixed at 0.2 mm. The experimental conditions are conducted at saturation temperatures of 20, 25 and 30°C, heat fluxes of 5, 10 and 15 kW/m^2, and mass fluxes of 300, 500 and 700 kg/m^2 s. The effects of groove pitch, mass flux, heat flux, and saturation temperature on heat transfer coefficient and frictional pressure drop are discussed. The results illustrate that the grooved tubes have a significant effect on the heat transfer coefficient and frictional pressure drop augmentations.

S. Wongwises (✉) · S. Laohalertdecha · J. Kaew-on · W. Duangthongsuk · K. Aroonrat · K. Sakamatapan
Fluid Mechanics, Thermal Engineering and Multiphase Flow Research Lab. (FUTURE), Department of Mechanical Engineering, King Mongkut's University of Technology Thonburi, Bangmod, Bangkok 10140, Thailand
e-mail: somchai.won@kmutt.ac.th

S. Laohalertdecha
The Joint Graduate School of Energy and Environment (JGSEE), King Mongkut's University of Technology Thonburi, Bangmod, Bangkok 10140, Thailand

J. Kaew-on
Department of Physics, Faculty of Science, Thaksin University, Papayom, Phattalung 93110, Thailand

W. Duangthongsuk
Department of Mechanical Engineering, South-East Asia University, Bangkok 10160, Thailand

List of symbols

A	surface area of the test section (m^2)
c_p	specific heat at constant pressure (J/kg K)
G	mass flux (kg/m^2 s)
h	heat transfer coefficient (W/m^2 K)
I	current (A)
i	enthalpy (J/kg)
k	thermal conductivity (W/m K)
L	length of the test tube (m)
$\dot{m}$	mass flow rate (kg/s)
N	number of the thermocouples on the inner wall surface
ΔP	pressure drop (Pa)
$\dot{Q}$	heat transfer rate (W)
q''	heat flux (W/m^2)
r	radius (m)
T	temperature (^{o}C)
V	voltage (V)
x	average vapour quality
X	position of the test section (m)

Greek symbols

ρ	density (kg/m^3)
α	void fraction

Subscripts

a	acceleration
avg	average
f	friction
g	gravity
in	inlet
i	inside
l	liquid
out	outlet
o	outside

ph pre-heater
ref refrigerant
sat saturation
TS test section
v vapor
w water
wall wall surface

1 Introduction

Nowadays, global warming and energy saving are major issues which many countries are addressing. All fluorocarbons, for example CFCs, HCFCs, HFCs are major sources of the global warming problem. Normally, Fluorocarbons are divided into two categories. The first group is the chemical substance containing chlorine or bromine, for example CFCs (R-11, R-12, R-502, etc.) and HCFCs (R-22, etc.), which are regulated by the Montreal Protocol. The production of CFCs and HCFCs have been or will be prohibited in developed countries from 1995 to 2030, respectively. The second group does not contain chlorine or bromine, for example HFCs (R-134a, R-404A, R-407C, etc.). The index for indicating the global warming problem is called "Global Warming Potential (GWP)". GWP is a measure of how much a given mass of greenhouse gas contributes to global warming. The details of GWPs for CFCs, HCFCs and HFCs are provided by IRR [1] as shown in Table 1. It is evident that R-134a shows the minimum value of GWP.

In order to reduce energy consumption, the thermal performance of heat transfer equipment should be improved. The rough surface technique is a heat transfer enhancement technique, which generally involves surface modification to promote turbulence in the flow field and increases the heat transfer surface area. In general, internally grooved tubes are used instead of smooth tubes in many heat exchangers to increase heat transfer performance by mixing and also limiting the fluid boundary layers close to the heat transfer surfaces. Moreover, they can promote two-phase heat transfer enhancement.

Table 1 GWPs of CFCs, HCFCs and HFCs [1]

CFCs		HCFCs		HFCs	
Refrigerant	GWP	Refrigerant	GWP	Refrigerant	GWP
R-11	3,800	R-22	1,500	R-134a	1,300
R-12	8,100			R-404A	3,260
R-502	5,500			R-407C	1,520
				R-410A	1,725
				R-507	3,300

Publications on the heat transfer and flow characteristics of single-phase flow in internally grooved tubes are summarized as follows:

Herman and Kang [2] investigated the heat transfer enhancement in a grooved channel with curved vanes. The unsteady temperature fields in the grooved channel with curved vanes were visualized by holographic interferometry. Air was used as the working fluid. The results demonstrated that heat transfer and pressure drop were enhanced by up to 1.5–3.5 and 3–5 times, respectively, compared to the basic grooved channel.

Bilen et al. [3] investigated the effect of groove shapes on heat transfer and friction characteristics in the turbulent flow regime. The experimental conditions corresponded to Reynolds numbers of 10,000–38,000. Circular, trapezoidal and rectangular grooved tubes with a ratio of tube length-to-diameter fixed at 33 were used in this study. Under given conditions, the experimental results showed that the maximum heat transfer coefficients were obtained from the circular groove, trapezoidal groove and rectangular groove, with enhancements of up to 63, 58 and 47%, respectively, in comparison with the smooth tube.

Bharadwaj et al. [4] studied experimentally the heat transfer and flow characteristics of water flowing in 75-start spirally grooved tube with a twisted tape insert. The test sections were internally grooved copper tubes, 1,040 mm long with 15.875 mm OD, inserted with clockwise and anticlockwise twist tape. The results illustrated that the maximum heat transfer enhancement obtained from the laminar range without and with twisted tape were 400 and 600%, respectively. In the turbulent range, the experimental results also showed that both maximum heat transfer enhancement without and with twisted tape is 140%.

Besides these, there are some publications concerned with the heat transfer and pressure drop characteristics of two-phase flow inside grooved tubes such as Graham et al. [5], Goto et al. [6] and Zhang et al. [7]. In 1999, Graham et al. [5] investigated the heat transfer and pressure drop characteristics of R-134a during condensation in an axially grooved tube. The experiment was performed at mass fluxes ranging between 75 and 450 kg/m^{2}s. Grooved tubes with 0 and 18^o helix angle were used as the inner tube. The results showed that the heat transfer coefficient and pressure drop obtained from grooved tubes were higher than from smooth tubes by factors of about 3 and 2, respectively.

Goto et al. [6] studied experimentally the condensation heat transfer of R-410A and R-22 fluids inside internally grooved horizontal tubes with an O.D. of 8.0 mm. The length of the test section was 1.0 m. The test conditions were run as follows: mass flux of 130–400 kg/m^{2}s, vapour pressure of 2.41 MPa for R-410A and 1.53 MPa for R-22. The new empirical correlation was proposed. The results

found that the majority of the data fall within ±20% of the proposed correlations.

The heat transfer coefficient of R-417A (R-125/R-134a/R-600) during evaporation flowing inside horizontal smooth and internally grooved tubes was investigated by Zhang et al. [7]. The test conditions were conducted with mass fluxes of 176–344 kg/m^{2}s, heat fluxes of 11–32 kW/m^2, saturation temperature of 0–5.5°C and vapour quality of 0.2–1. The test section was the three double tube type of heat exchangers. The results showed that the heat transfer coefficient of the grooved tube was much higher than the smooth tube. Moreover, R-22 was characterised by a higher heat transfer coefficient than R-417A, especially for the grooved tube.

Despite the heat transfer enhancement potential of grooved tube, as shown above, there are only few studies dealing with the heat transfer and pressure drop of flow of refrigerant changing the phase in grooved tubes. In the present study, the main concern is to experimentally study heat transfer enhancement and two-phase flow characteristics during evaporation of R134a in internally grooved tubes. Experimental data that have never been seen before on local heat transfer coefficient, average heat transfer coefficient and pressure drop under constant heat flux are presented.

2 Experimental apparatus and method

The experimental system consists mainly of a test section, refrigerant circulating loop, sub-cooling loop, a DC power supply and a data acquisition system as shown in Fig. 1.

For the refrigerant circulating loop, liquid refrigerant is forced by a gear pump which can be adjusted to the flow rate using an inverter. The refrigerant then passes in series through a filter/dryer, a refrigerant flow meter, pre-heater, a sight glass, and enters the test section. The inlet quality before entering the test section is controlled by the pre-heater. The heating water is used to apply the heat flux to the pre-heater, which can be controlled by adjusting the flow rate or the temperature of the hot water. Leaving the test section, the refrigerant vapour then condenses inside a sub-cooler and is collected in a receiver, returning to the refrigerant pump to complete the cycle. Instrumentation is installed at various positions, as shown in Fig. 1, to monitor the state of the refrigerant. All signals from the thermocouples and differential pressure transducer are recorded by a data acquisition system.

Details of the test section are shown schematically in Fig. 2. The dimensions of the test section are listed in Table 2. The test sections are a smooth tube (SMT), a straight grooved tube (SGT), a grooved tube with 8″ pitch (GT8), a grooved tube with 10″ pitch (GT10) and a grooved tube with 12″ pitch (GT12), which are made from type 304 stainless steel type. The cross section of grooved tube is shown in Fig. 3. The regulated DC power supply is used to provide the voltage for the test section. The voltage and electrical current values are measured by a multi-meter (Fluke 336 meter) which has an uncertainty of ±2% for voltage and ±1% for current. T-type thermocouples are installed at the inlet and outlet of the test section to measure the saturation temperature of the refrigerant. Similarly, the differential pressure transducer is installed in order to measure the pressure drop across the test section. The length between pressure taps is 2,000 mm. The twelve thermocouples are installed at the top, bottom, and side at four points along the test section to measure the wall temperatures. All of the thermocouples are fixed at the outer surface of the test section by the special glue (OMEGABOND 101) having a thermal conductivity of 1 W/mK. The test section is insulated with rubber foam with a thermal conductivity of 0.04 W/mK. All of the thermocouples are well calibrated with standard thermometers with a precision of 0.05°C. The refrigerant flow meter is a variable area type and is specially calibrated in the range of 0.2–1.8 LPM for R-134a by the manufacturer as was the differential pressure transducer.

In the experiments, the inlet quality of the test section is varied by small increments. The imposed heat flux, mass flux, and saturation temperature are kept constant at the desired values. The system is allowed to approach a steady state before any data are recorded. During experiments, the temperature and pressure are continuously recorded along the test section by the data acquisition system. The temperature profiles help us to know the limit of useful data because a large increase in wall temperature and outlet saturation temperature is noticed when dry-out takes place. The range of experimental conditions tested in this study is listed in Table 3. The uncertainties of measured quantities and calculated parameters are shown in Table 4.

3 Data reduction

In order to calculate the heat transfer performance of R-134a under evaporation conditions, the conversion of measured data into meaningful quantities is defined in the following equations.

The inlet vapour quality of the test section ($x_{\mathrm{TS,in}}$) can be calculated as follows:

$$x_{\mathrm{TS,in}} = \frac{i_{\mathrm{TS,in}} - i_{f@T_{\mathrm{TS,in}}}}{i_{\mathrm{fg}@T_{\mathrm{TS,in}}}} \quad (1)$$

where $i_{f@T_{\mathrm{TS,in}}}$ and $i_{fg@T_{\mathrm{TS,in}}}$ are the enthalpy of the saturated liquid and the enthalpy of vaporization, respectively, based

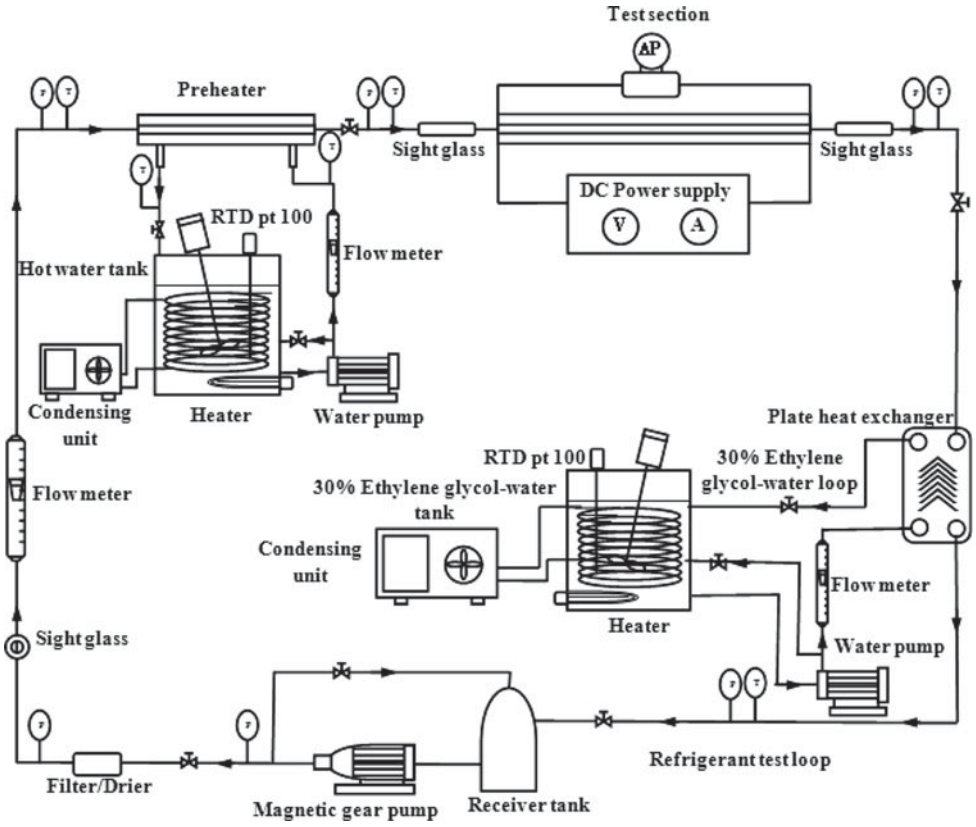

Fig. 1 Schematic diagram of the experimental apparatus

on the temperature at the test section inlet, and $i_{TS,in}$ is the enthalpy of refrigerant at the test section inlet which is calculated by the following equation:

$$i_{TS,in} = i_{ph,in} + \frac{\dot{Q}_{ph}}{\dot{m}_{ref}} \tag{2}$$

where $i_{ph,in}$ is the inlet enthalpy of the liquid refrigerant before entering the pre-heater, $\dot{m}_{ref}$ is the mass flow rate of the refrigerant and $\dot{Q}_{ph}$ is the heat transfer rate in the pre-heater:

$$\dot{Q}_{ph} = \dot{m}_{w,ph} c_{p,w} (T_{w,in} - T_{w,out})_{ph} \tag{3}$$

with $\dot{m}_{w,ph}$ the mass flow rate of water entering the pre-heater.

The outlet vapour quality of the test section ($x_{TS,out}$) can be calculated as follows:

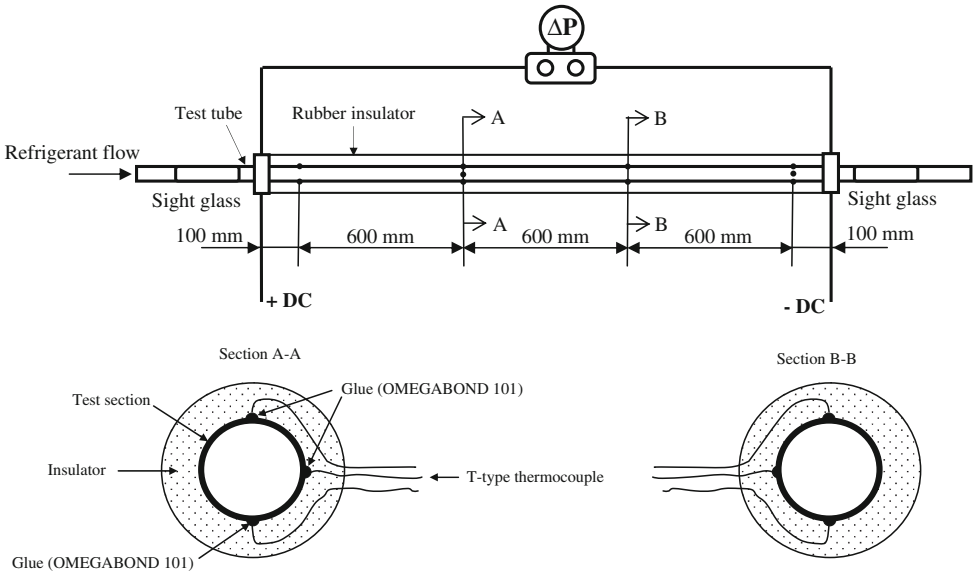

Fig. 2 Schematic diagram of the test section

Table 2 The details of the test sections

Parameter	Smooth tube (SMT)	Straight grooved tube (SGT)	Grooved tube with 8″ pitch (GT8)	Grooved tube with 10″ pitch (GT10)	Grooved tube with 12″ pitch (GT12)
Depth, e (mm)	–	0.2	0.2	0.2	0.2
Pitch, p (mm)	–	–	203	254	305
Outside diameter, D_o (mm)	9.5	9.5	9.5	9.5	9.5
Inside diameter, D_i (mm)	7.1	7.1	7.1	7.1	7.1
Actual inside cross section area (mm^2)	396	420	416	416	416
Actual inside tube area, A (mm^2)	44,611	54,210	52,658	52,641	52,632
Length of the test tube, L (mm)	2,000	2,000	2,000	2,000	2,000

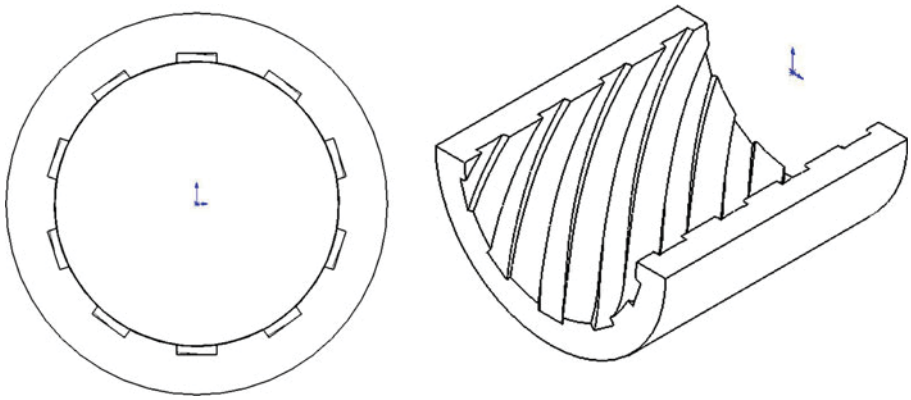

Fig. 3 The cross section of grooved tube

Table 3 Experimental conditions

Controlled variable	Range
Mass flux (kg/m^2s)	300, 500, 700
Heat flux (kW/m^2)	5, 10, 15
Saturation temperature (°C)	20, 25, 30
Tested tube material	Stainless steel type 304
Refrigerant	R-134a

Table 4 Uncertainties of measured quantities and calculated parameters

Parameter	Uncertainty
Temperature (°C)	±0.1
Pressure drop (Pa)	±370
Mass flow rate of refrigerant	±2% Full scale
Heat transfer rate of test section	±2.24%
Heat transfer rate of pre-heater	±2.24%
Heat transfer coefficient	±10%

$$x_{TS,out} = \frac{i_{TS,out} - i_{f@T_{TS,out}}}{i_{fg@T_{TS,out}}} \tag{4}$$

where $i_{\mathrm{TS,out}}$ is the refrigerant enthalpy at the test section outlet, $i_{f@T_{\mathrm{TS,out}}}$ is the enthalpy of the saturated liquid based on the temperature at the test section outlet, and $i_{fg@T_{\mathrm{TS,out}}}$ is the enthalpy of vaporization based on the temperature at the test section outlet. As a consequence, the outlet enthalpy of the refrigerant flow is calculated as:

$$i_{\mathrm{TS,out}} = i_{\mathrm{TS,in}} + \frac{\dot{Q}_{\mathrm{TS}}}{\dot{m}_{\mathrm{ref}}} \tag{5}$$

where the heat transfer rate in the test section is obtained from

$$\dot{Q}_{\mathrm{TS}} = IV \tag{6}$$

with I and V the current and voltage of the electric heater, respectively.

The average heat transfer coefficient can be calculated using the following equation:

$$h_{\mathrm{avg}} = \frac{\dot{Q}_{\mathrm{TS}}}{A_{\mathrm{i}}(T_{\mathrm{i,avg,wall}} - T_{\mathrm{avg,sat}})} \tag{7}$$

where $\dot{Q}_{\mathrm{TS}}$ is the heat transfer rate at the test section, $T_{\mathrm{avg,sat}}$ is the average temperature of the refrigerant at the test section inlet and outlet and A_i is the actual inside surface area of the test section. h_{avg} is the heat transfer coefficient averaged over the entire 2 m long tube. A total of 12 thermocouples are soldered to the outer wall of the tube at the top, bottom, and side (as shown in Fig. 2) at four

positions along the test section to measure the outer wall temperature ($T_{wall,o}$). These outer wall temperatures will be used to determine the inner wall temperatures. At each section, the temperatures at the inside wall of the tube ($T_{wall,i}$) at each position (top, bottom, and side of the tube) are determined based on heat conduction through the wall as follows:

$$T_{i,wall} = T_{o,wall} - \frac{q''_{TS} r_i \ln\left(\frac{r_o}{r_i}\right)}{k} \quad (8)$$

The circumferentially averaged values of the inner wall surface temperatures ($T_{i,avg,wall}$) of the test section are taken as the arithmetical mean of the 12 measurement points as follows:

$$T_{i,avg,wall} = \frac{\sum_{j=1}^{N} T_{i,wall}}{N} \quad (9)$$

The total pressure drop (ΔP_{total}) is measured by a pressure transducer installed between the inlet and outlet of the test section. The total pressure drop is expressed as the sum of the three different components, as follows:

$$\Delta P_{total} = \Delta P_f + \Delta P_a + \Delta P_g \quad (10)$$

The three terms on the right-hand side represent the frictional pressure drop (ΔP_f), acceleration pressure drop (ΔP_a) and gravitational pressure drop (ΔP_g), respectively. The gravitational pressure drop (ΔP_g) is zero in a horizontal tube. The acceleration pressure drop, ΔP_a, is proposed by Tran [8]:

$$\Delta P_a = G^2 \left(\left(\frac{x_{out}^2}{\rho_v \alpha_{out}} + \frac{(1-x_{out})^2}{\rho_l (1-\alpha_{out})} \right) - \left(\frac{x_{in}^2}{\rho_v \alpha_{in}} + \frac{(1-x_{in})^2}{\rho_l (1-\alpha_{in})} \right) \right) \quad (11)$$

where α is the void fraction and presented by Zivi's correlation [9] as follows:

$$\alpha = \left(1 + \frac{(1-x)}{x} \left(\frac{\rho_v}{\rho_l} \right)^{\frac{2}{3}} \right)^{-1} \quad (12)$$

The frictional pressure drop, ΔP_f, can be obtained by subtracting the acceleration pressure drop from the total measured pressure drop.

4 Results and discussion

4.1 Heat transfer coefficient

The comparison of the experimental data with published correlations proposed by Chaddock and Noerager [10], Choi et al. [11] and Wongsa-ngam et al. [12] for smooth tubes is shown in Fig. 4. Most of the correlations are in agreement with the present data to within 20%. How the heat transfer coefficient depends on flow regime, must first be observed. The flow pattern can be seen via sight glasses which are placed on the inlet and outlet of the test section. This observation found that the stratified flow pattern occurred at an average quality lower than 0.3 and the annular flow pattern occurred at an average quality higher than 0.3.

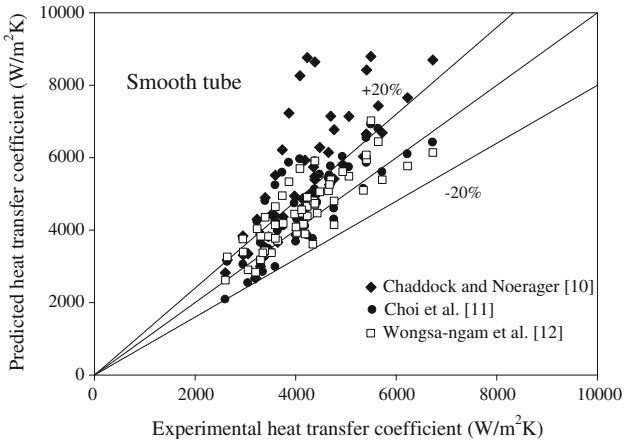

Fig. 4 Comparison of the heat transfer coefficient with existing correlations for the smooth tube

4.1.1 *Local heat transfer coefficient*

The variation of the measured inside wall temperature and refrigerant temperature along the test section (X/L) during evaporation of R-134a in internally grooved tubes at saturation temperatures between 30–32°C, mass flux of 500 kg/m^{2}s, and for different heat fluxes of 5 kW/m^2 (Fig. 5a) and 10 kW/m^2 (Fig. 5b) is shown in Fig. 5. Almost all the inside wall temperatures measured on the grooved tube are higher than those measured on a smooth tube. The results can be described in terms of the liquid film thickness decreasing as thermal resistance decreases. This is due to the fact that a grooved tube strongly increases the swirl flow. Moreover, the refrigerant temperature decreases with increasing (X/L) due to the effect of pressure drop.

Figure 6 illustrates the local heat transfer coefficient along the test section of R-134a during evaporation based on the inside wall temperature and refrigerant temperature obtained from Fig. 5. The result demonstrates that the local heat transfer coefficient gradually decreases with increasing (X/L) due to the effect of the entrance region. In the case of a grooved tube, the local heat transfer coefficient is higher than that obtained from a smooth tube. This is caused by the grooved tube promoting turbulence of the refrigerant flow.

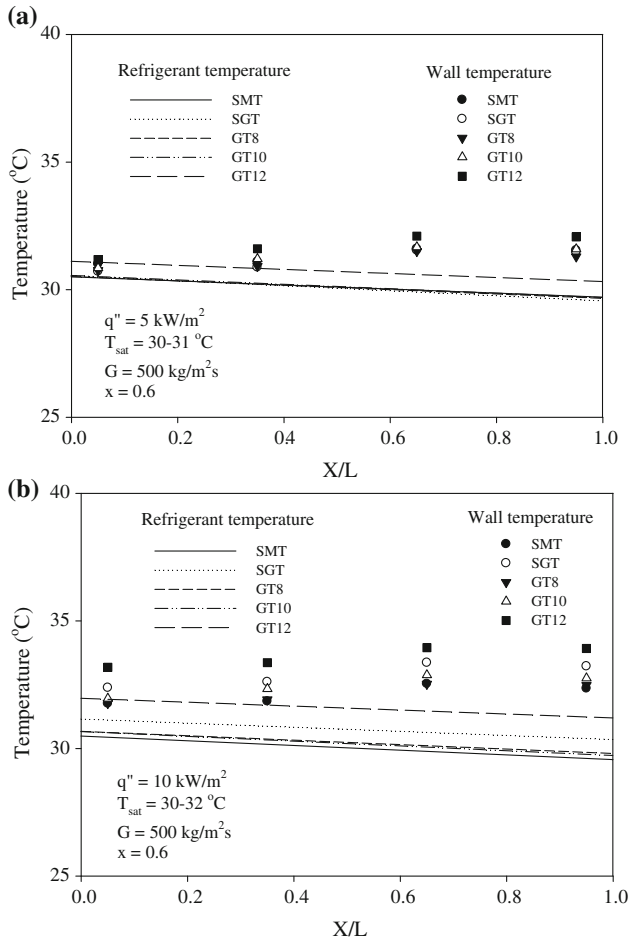

Fig. 5 The variation of the measured inside wall and refrigerant temperature along the test section

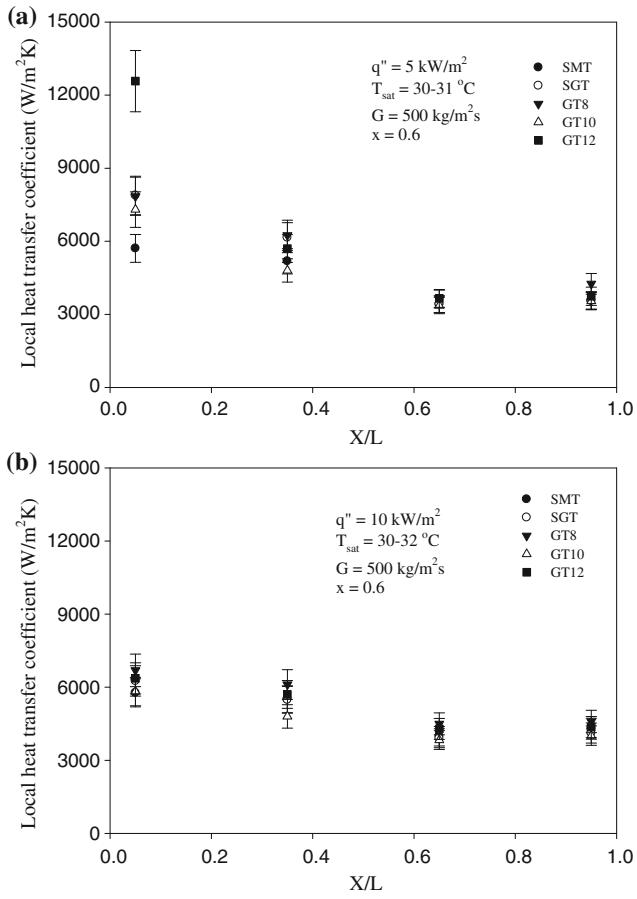

Fig. 6 The local heat transfer coefficient versus the position of the test section

4.1.2 *Effect of groove pitch on average heat transfer coefficient*

Figure 7 shows the variation of average evaporation heat transfer coefficient with average vapour quality of R134a at a saturation temperature of 30°C, mass flux of 500 kg/m^{2}s, and heat fluxes of 5 kW/m^2 (Fig. 7a) and 10 kW/m^2 (Fig. 7b). As shown in the figures, the heat transfer coefficient increase with an increase of average quality. However, at the same average quality, the groove pitch has only a small effect on the heat transfer coefficient. This may be caused by the spiral angles and small groove depth being too small. Similar trends of heat transfer coefficient are obtained under other test conditions.

4.1.3 *Effect of mass flux on average heat transfer coefficient*

Figure 8 shows the heat transfer coefficient as a function of average vapour quality of R-134 at constant saturation temperature and heat flux, for different mass fluxes of 300, 500, and 700 kg/m^{2}s. The results show that the heat transfer coefficient tends to increase with increasing average quality and mass flux. Moreover, the increase of the heat transfer coefficient becomes relatively smaller as the mass flux decreases.

The heat transfer coefficient increases significantly with increasing average vapour quality until the maximum heat transfer coefficient is reached ($x \approx 0.8$), and then decreases with increasing average vapour quality. This is due to dry-out taking place, so the wall temperature becomes higher and the heat transfer coefficient is reduced.

4.1.4 *Effect of heat flux on average heat transfer coefficient*

Figure 9 shows the experimental heat transfer coefficients plotted against average vapour quality at constant mass flux and saturation temperature for the different heat fluxes of 5, 10, 15 kW/m^2. As expected, an increase of heat flux results in an increase of the heat transfer

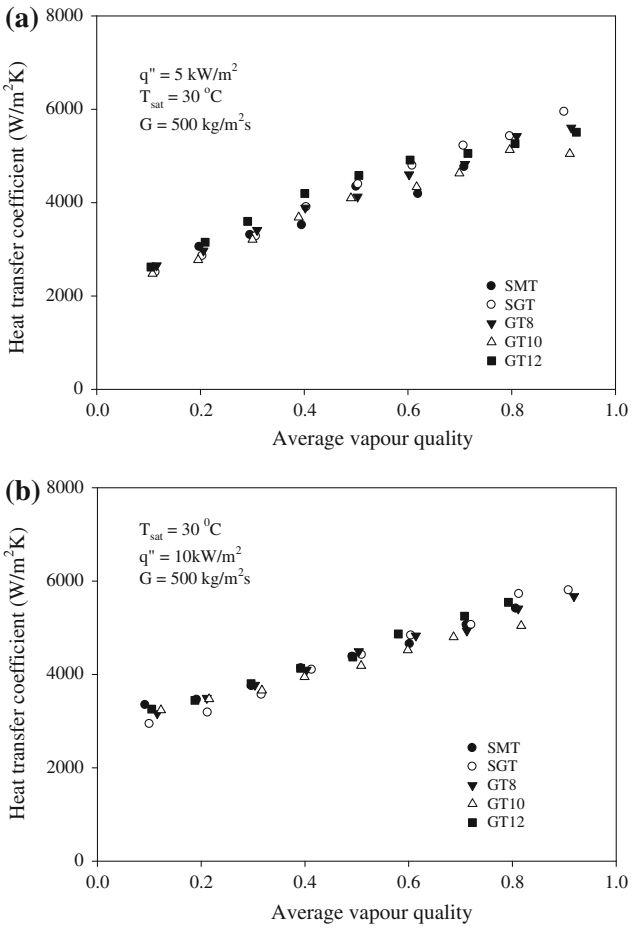

Fig. 7 Effect of groove pitch on average heat transfer coefficient

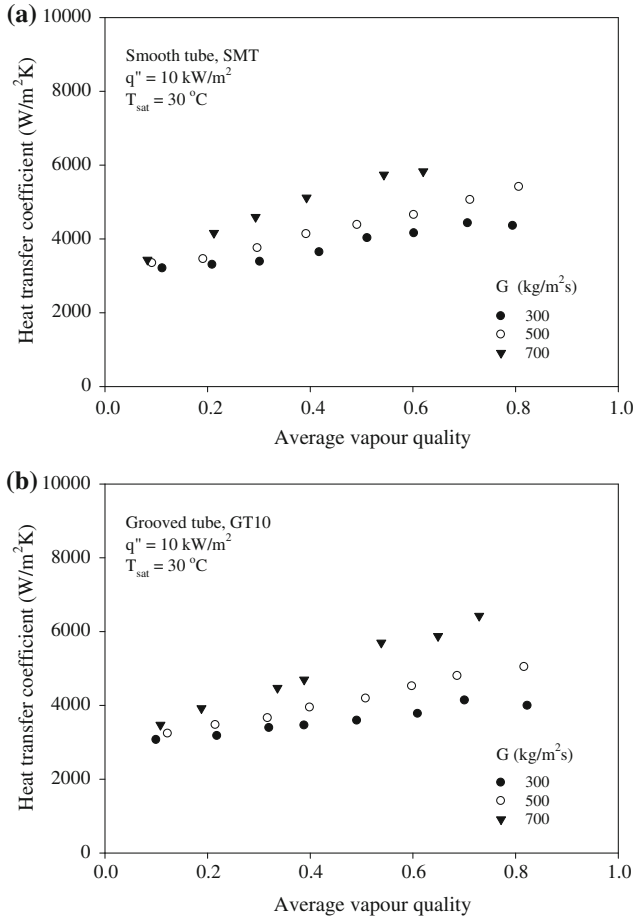

Fig. 8 Effect of mass flux on heat transfer coefficient

coefficients, before dry-out occurs. This can be explained by the increase in heat flux increasing the number of bubbles. These bubbles can induce turbulent flow in the liquid film, which accelerates the two-phase velocity and promotes the entrainment of droplet. On the other hand, the increase in the number of bubbles results in an increased entrainment of droplets and greater turbulence, resulting in a higher heat transfer coefficient.

4.1.5 Effect of saturation temperature on average heat transfer coefficient

Figure 10 presents the variation of heat transfer coefficient versus average vapour quality at constant mass flux and heat flux, for different saturation temperatures of 20, 25, and 30°C, respectively. The heat transfer coefficient increases with increasing saturation temperature across the range of quality. This is due to the evaporating temperature increasing and the two-phase viscosity decreasing. This results in increase of velocity and heat transfer coefficient.

4.2 Frictional pressure drop

The pressure drop is directly measured by the differential pressure transducer installed between the inlet and outlet of the test section. The comparison of the experimental data with well-known correlations proposed by Lockhart-Martinelli [13], Soliman and Azer [14], Friedel [15] and Wongsa-ngam et al. [12], for smooth tubes, is shown in Fig. 11. Most of the correlations are in agreement with the present data to within 30%.

4.2.1 Effect of grooved pitch on frictional pressure drop

Figure 12 shows the variation of the frictional pressure drop with average vapour quality during evaporation of R134a at a saturation temperature of 30°C, mass flux of 500 kg/m^{2}s, and heat fluxes of 5 kW/m^2 (Fig. 12a) and 10 kW/m^2 (Fig. 12b). Similar to the heat transfer coefficient, the frictional pressure drop increases with increasing average quality. At a given average quality, most of the frictional pressure drop in the grooved tube are slightly

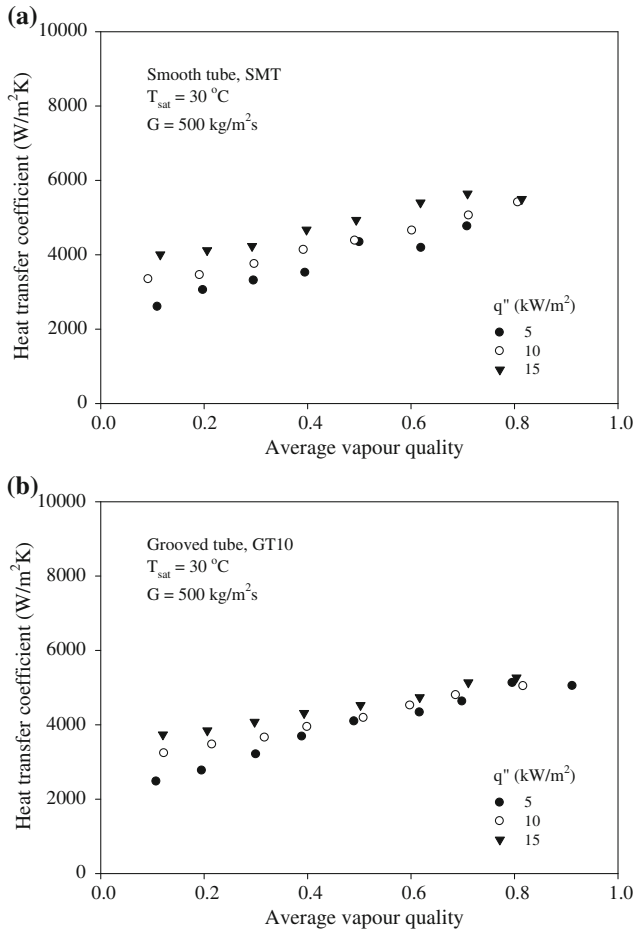

Fig. 9 Effect of heat flux on heat transfer coefficient

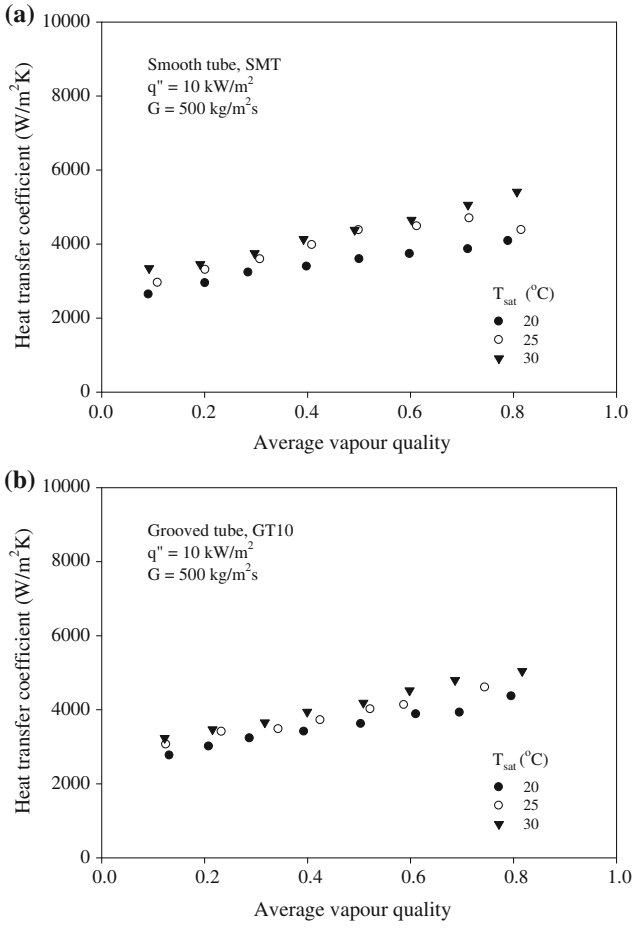

Fig. 10 Effect of saturation temperature on heat transfer coefficient

higher than those measured on the smooth tube. This may result from small differences in spiral angle or small groove depth. Similar trends of frictional pressure drop were found under the other test conditions.

4.2.2 *Effect of mass flux on frictional pressure drop*

Figure 13 shows the frictional pressure drop plotted against average vapour quality at constant saturation temperature and heat flux for mass fluxes of 300, 500, and 700 kg/m^{2}s. As shown, the frictional pressure drop increases with increasing average quality.

4.2.3 *Effect of heat flux on frictional pressure drop*

Figure 14 presents the variation of the measured frictional pressure drop with average vapour quality at mass flux of 500 kg/m^{2}s and saturation temperature of 30°C for heat fluxes of 5, 10 and 15 kW/m^2. These figures show that the frictional pressure drop increases significantly with increasing quality until the maximum frictional pressure drop is reached, and then reduces. Furthermore, it is also found that the heat flux has no significant effect on frictional pressure drop. This is because the increase in total rate of liquid film vaporization close to the wall surface is very small compared with the vapour flow rate at the inlet.

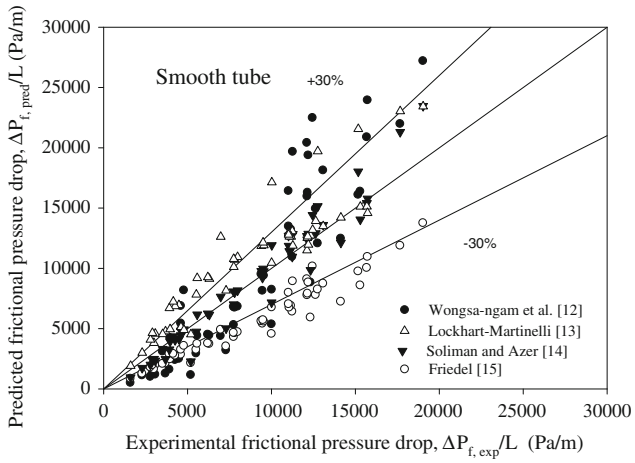

Fig. 11 Comparison of the experimental frictional pressure drop with existing correlations for the smooth tube

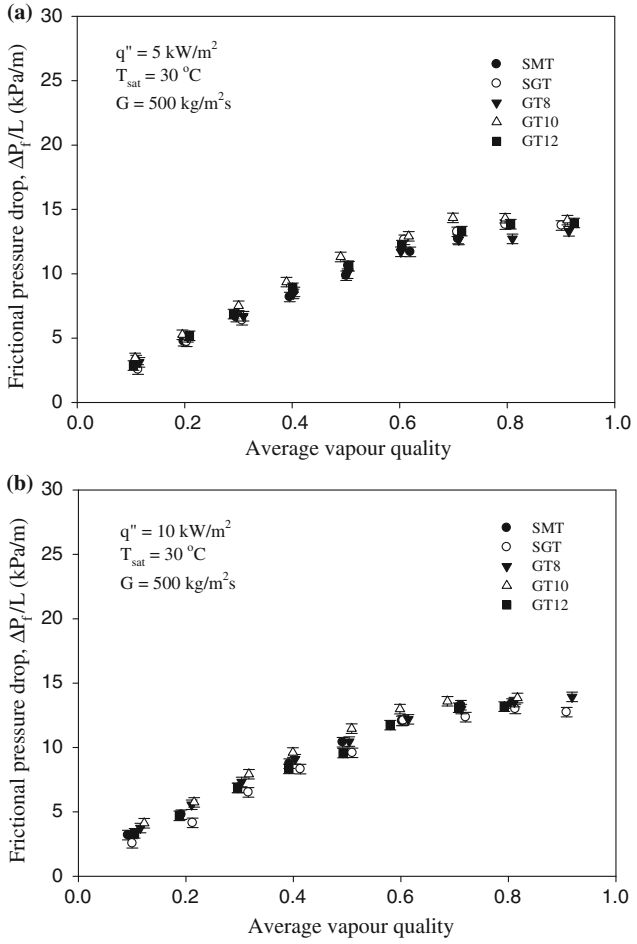

Fig. 12 Effect of grooved pitch on frictional pressure drop

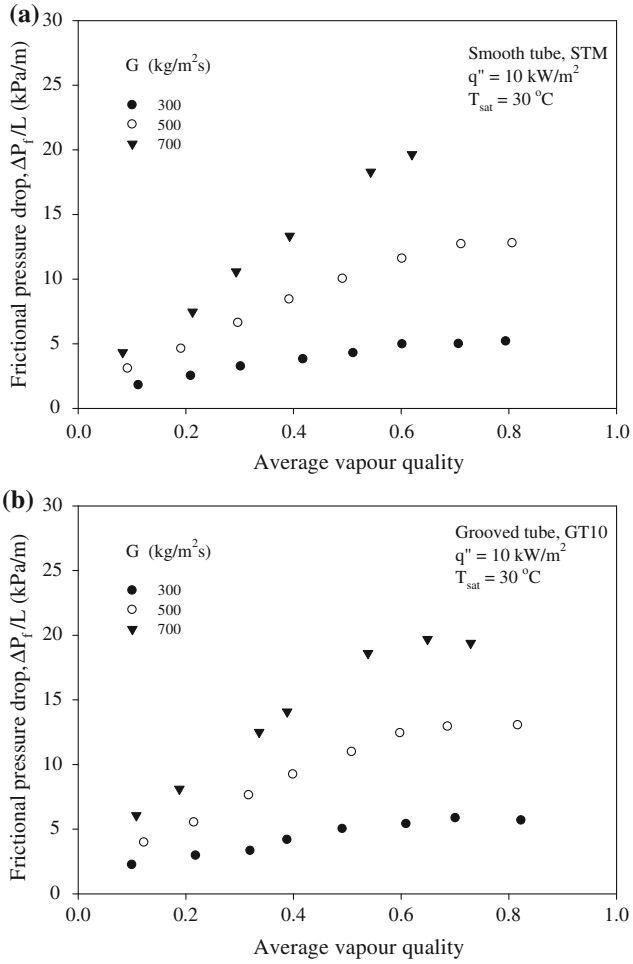

Fig. 13 Effect of mass flux on frictional pressure drop

4.2.4 *Effect of saturation temperature on frictional pressure drop*

Figure 15 shows the variation of frictional pressure drop versus average vapour quality at constant heat flux and mass flux for different saturation temperatures of 20, 25 and 30°C. It is found that the frictional pressure drop increases with a decrease in evaporation temperature. This is mainly due to a decrease in two-phase specific volume which results in a decrease in the velocity of the refrigerant.

5 Conclusions

In this work, the heat transfer coefficient and frictional pressure drop in grooved tubes during evaporation of R-134a were investigated experimentally. The tested tube configurations are as follows: smooth tube (SMT); straight grooved tube (SGT); grooved tube with 8″ pitch (GT8); grooved tube with 10″ pitch (GT10); and grooved tube with 12″ pitch (GT12). The tested tubes are made from type 304 stainless steel. The local heat transfer coefficient along the test section with (X/L) is presented. Moreover, the effects of groove pitch, mass flux, heat flux, and saturation temperature on the heat transfer coefficient and pressure drop are discussed. The ranges of mass flux, saturation temperature and heat flux studies were 300–700 kg/m^{2}s, 20–30°C and 5–15 kW/m^2, respectively. The important experimental results are concluded as follows:

1. The local heat transfer coefficient of R134a fluid during evaporation decreases with increasing (X/L), and is affected significantly by groove pitch.
2. The average heat transfer coefficient increases with increasing average quality, mass flux, and heat flux, but is little affected by groove pitch.
3. The frictional pressure drop increases with increasing average quality and mass flux, but decreases with increasing saturation temperature. Also, the heat flux has no significant effect on frictional pressure drop.

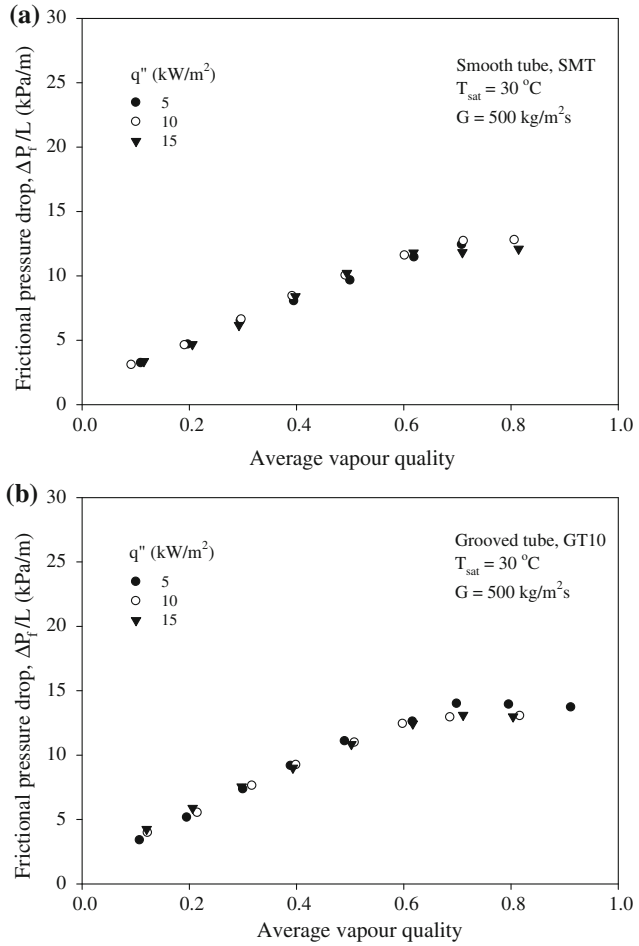

Fig. 14 Effect of heat flux on frictional pressure drop

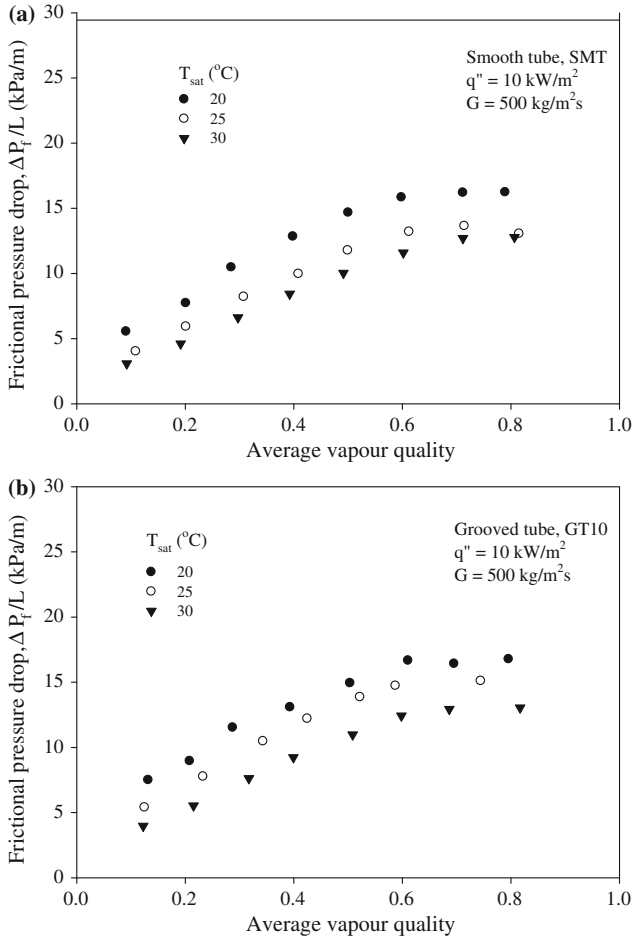

Fig. 15 Effect of saturation temperature on the frictional pressure drop

Finally, the frictional pressure drop increases slightly with increasing groove pitch.

Acknowledgments The present study was supported financially by the Thailand Research Fund (TRF), the Office of the Higher Education Commission and the National Research University Project, whose guidance and assistance are gratefully acknowledged. The authors also wish to acknowledge Thai-German Products Public Company Limited for providing the test tubes.

References

1. International Institute of Refrigerant (1997) 12th Informatory Note on Fluorocabons and Refrigeration
2. Herman C, Kang E (2002) Heat transfer enhancement in a grooved channel with curved vanes. Int J Heat Mass Transfer 45:3741–3757
3. Bilen K, Cetin M, Gul H, Balta T (2009) The investigation of groove geometry effect on heat transfer for internally grooved tubes. Appl Thermal Eng 29:753–761
4. Bharadwaj P, Khondge AD, Date AW (2009) Heat transfer and pressure drop in a spirally grooved tube with twisted tape insert. Int J Heat Mass Transfer 52:1938–1944
5. Graham D, Chato JC, Newell T (1999) Heat transfer and pressure drop during condensation of refrigerant 134a in an axially grooved tube. Int J Heat Mass Transfer 42:1935–1944
6. Goto M, Inoue N, Yonemoto R (2003) Condensation heat transfer of R410A inside internally grooved horizontal tubes. Int J Refrig 26:410–416
7. Zhang X, Zhang X, Chen Y, Yuan X (2008) Heat transfer characteristics for evaporation of R417A flowing inside horizontal smooth and internally grooved tubes. Energy Convers Managet 49:1731–1739
8. Tran TN (1998) Pressure drop and heat transfer study of two-phase flow in small channels. Ph.D. Dissertation, Texas Tech University, Lubbock
9. Zivi SM (1964) Estimation of steady-state steam void-fraction by mean of the principle of minimum entropy production. Trans ASME J Heat Transfer 86:247–252
10. Chaddock JB, Noerager JA (1966) Evaporation of refrigerant 12 in a horizontal tube with constant wall heat flux. ASHRAE Trans 72:90–101
11. Choi TY, Kim YJ, Kim MS, Ro ST (2000) Evaporation heat transfer of R-32, R-134a, R-32/134a, and R-32/125/134a inside a horizontal smooth tube. Int J Heat Mass Transfer 43:3651–3660
12. Wongsa-ngam J, Nualboonrueng T, Wongwises S (2004) Performance of smooth and micro-fin tubes in high mass flux region of R-134a during evaporation. Heat Mass Transfer 10:425–435

13. Lockhart RW, Martinelli RC (1949) Proposed correlation of data for isothermal two-phase, two-component flow in pipes. Chem Eng Prog 45:39–48
14. Soliman HM, Azer NZ (1971) Flow patterns during condensation inside a horizontal tube. ASHRAE Trans 77:210–224
15. Friedel L (1979) Improved friction pressure drop correlations for horizontal and vertical two-phase pipe flow. The European Two-Phase Flow Group Meeting, Paper E2. Ispra, Italy

Applied Mathematics and Computation 217 (2011) 8640–8654

Contents lists available at ScienceDirect

Applied Mathematics and Computation

journal homepage: www.elsevier.com/locate/amc

Study of storm surge due to Typhoon Linda (1997) in the Gulf of Thailand using a three dimensional ocean model

N. Aschariyaphotha [a,b], P. Wongwises [a], U.W. Humphries [b], S. Wongwises [c,*]

[a] The Joint Graduate School of Energy and Environment, King Mongkut's University of Technology Thonburi, Bangkok 10140, Thailand
[b] Department of Mathematics, King Mongkut's University of Technology Thonburi, Bangkok 10140, Thailand
[c] Department of Mechanical Engineering, King Mongkut's University of Technology Thonburi, Bangkok 10140, Thailand

ARTICLE INFO

Keywords:
Gulf of Thailand
Three dimensional ocean model
Storm surge
Typhoon Linda

ABSTRACT

Numerical integrations using the three dimensional ocean model based on the princeton ocean model (POM) were applied for the study of both sea level elevation and ocean circulation patterns forced by the wind fields during typhoons that moved over the Gulf of Thailand (GoT). The simulation concerned a case of Typhoon Linda which occurred during November 1–4, 1997. Typhoon Linda was one of the worst storms that passed the Gulf of Thailand and hit the southern coastal provinces of Thailand on November 3, 1997. It caused flooding and a strong wind covering large areas of agriculture and fisheries, which destroyed households, utilities and even human lives. The model is the time-dependent, primitive equation, Cartesian coordinates in a horizontal and sigma coordinate in the vertical. The model grid has 37×97 orthogonal curvilinear grid points in the horizontal, with variable spacing from 2 km near the head of the GoT to 55 km at the eastern boundary, with 10 sigma levels in the vertical conforming to a realistic bottom topography. Open boundary conditions are determined by using radiation conditions, and the sea surface elevation is prescribed from the archiving, validation and interpretation of satellite oceanographic data (AVISO). The initial condition is determined from the spin up phase of the first model run, which was executed by using wind stress calculated from climatological monthly mean wind, restoring-type surface heat and salt and climatological monthly mean freshwater flux. The model was run in spin up phase until an ocean model reached an equilibrium state under the applied force. A spatially variable wind field taken from the European Centre for Medium-Range Weather Forecasts (ECMWF) is used to compute the wind stress directly from the velocity fluctuations. Comparison of tendency between the sea surface elevations from model and the observed significant wave heights of moored buoys in the Gulf of Thailand under Seawatch project is investigated. The model predicts the sea level elevation up to 68.5 cm at the Cha-Am area located in the north of where the typhoon strands to the shore. Results of sea level elevation show that there is an area of peak set-up in the upper gulf, particularly in the western coast, and the effects of the storm surge are small at the lower gulf. During the entire period of this study, the surge in the gulf was induced by the northeasterly wind blowing over it.

© 2011 Elsevier Inc. All rights reserved.

1. Introduction

The Gulf of Thailand is located in Southeast Asia immediately to the west of the South China Sea (SCS). The gulf is a semi-enclosed sea that measures approximately 400- km by 800- km, covering an area of about 320,000 square km. Its location in

* Corresponding author.
E-mail address: somchai.won@kmutt.ac.th (S. Wongwises).

0096-3003/$ - see front matter © 2011 Elsevier Inc. All rights reserved.
doi:10.1016/j.amc.2011.03.105

the global map is between 6°N to 14°N latitudes and 99°E to 105°E longitudes surrounded by the kingdom of Cambodia, Malaysia, the kingdom of Thailand and the socialist republic of Vietnam (Fig. 1). It is a part of the sunda shelf which is a submerged connection between Southeast Asia, Malaysia, Sumatra, Java and Borneo, and is relatively shallow. The mean and maximum depths in the central part in the GoT are about 45 m and 80 m respectively. The living and non-living resources of the gulf are of great value to the people of four littoral countries.

The Gulf of Thailand is subjected to the monsoon system of the Western North Pacific Ocean or the South China Sea. Monsoons influence the surface currents, being clockwise during the southwest monsoon and counterclockwise during the northeast monsoon. There are several POM-based studied in the SCS connected to the GoT e.g. Yang et al. [5] used the POM to study the seasonal mean SCS circulation and its formation mechanisms. It reproduced well the observed sea surface height (SSH) annual cycle, and the sensitivity experiments show that the wind forcing dominates the seasonal variability of the SCS SSH, while the buoyancy forcing is of minor importance. The model also indicated that the Kuroshio current affects the SCS circulation by creating a loop current that exists throughout the year. Gan et al. [6] had studied the circulation and its seasonal variation in the SCS in response to the forcing of the Asian monsoon and the Kuroshio intrusion by using a three-dimensional ocean model. They found that the seasonal circulation in the SCS is mainly driven by the monsoonal wind stress and greatly influenced by the inflow from the Kuroshio intrusion.

Chu et al. [10] used POM to simulate the circulation and thermohaline variability for the SCS covering the GoT. They verified that the wind effect is the key factor for the generation of the SCS deep basin warm/cool eddy and that the lateral boundary forcing is the major factor for the formation of the strong western boundary currents. Afterwards, Chu et al. [11] simulated the SCS thermohaline structure, as well as the circulation, and investigated physical processes causing seasonal variability by using POM. They revealed that the POM model has the capability for simulating seasonal variations of the SCS circulation and thermohaline structure. The simulated SCS surface circulation is generally clockwise during the summer, and counterclockwise during the winter monsoon period with the strong western boundary currents.

In the early 1960's, a Typhoon name was not recorded for one that hit the Laem Talumpuk area located in Nakhon Si Thammarat province. This event was not announced in advance, hence it devastated human life and utilities. In 1989, Typhoon Gay originated in the southern part of GoT as a depression and then strengthened quickly to become a tropical storm. Typhoon Gay caused storm surge and enormous damage on the coast of Chumphon province and neighboring areas. Typhoon Linda in 1997 also caused a storm surge. Typhoon Linda, which formed in a westward pattern in the SCS, was one of the worst storms to hit Vietnam. Southern Vietnam was devastated by Typhoon Linda during the first two days of November 1997. The rapid development of the storm in the East Sea not far from the Vietnamese coast

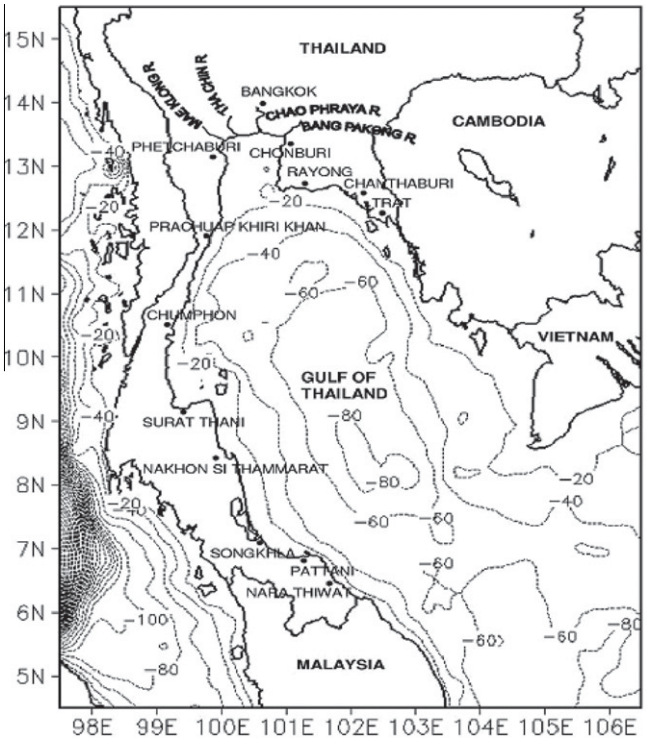

Fig. 1. Bathymetry (m) of the Gulf of Thailand.

meant that there was little time for warnings to be issued and acted upon. Over 600 people are known to have died in the storm's passing. Typhoon Linda, shown in Fig. 2, moved across the southern tip of Vietnam and was expected to hit Thailand's southern coastal provinces on November 3, 1997. When the storm passed over the southernmost coast of Vietnam it was estimated that the winds were reaching 28 ms^{-1} through the Gulf of Thailand, winds at its center were still over 25 ms^{-1}. As the storm tracked west through the Gulf of Thailand into the Bay of Bengal, it continued to wreak destruction, killing over 30 people in Cambodia and Thailand with around 200 fishermen reported missing. At least 330 people were killed in Vietnam and Thailand with approximately 2,250 people still missing. Regardless of its causes, Typhoon Linda demonstrated that even with a highly developed civil protection system, many thousands of individuals remain at risk when the warning time is limited by rapid storm development. Improved monitoring and prediction of storms such as Typhoon Linda must be a high priority.

Very few researches have been made about Typhoon Linda and its storm surge in the GoT. Schjølberg [12] used the Seawatch 3D model which is the three dimension model in vertical sigma coordinate developed in cooperation with Putch Company for studying the Typhoon Linda case. The research was run by two simulations, one with only the wind field forcing and another one with both wind and tide. The open boundary was applied by tidal forcing and used about 3 days of simulation before the typhoon actually entered the GoT in the sense of to spin up circulation. The model using the atmospheric forcing predicted the increase in sea level less than using the tidal forcing, and the result of the current speed compared with the buoy observation. Schjølberg concluded that the event quite well described when the Typhoon passed, although the maximum speed is underestimated by the model. In 2001, Kanbua et al.[20] used the wave analysis model (WAM), a third generation wave model, to forecast the significant wave height during the attack of Typhoon Linda in 1997 in the GoT. The WAM model is one of the best-tested wave models. Their results were also compared with the buoy observation in the Gulf of Thailand and Andaman Sea under the Seawatch project. The results indicated that the model fairly reproduces the observed characteristics of waves. Kanbua et al. [21] studied an investigation of wave field during Typhoon Linda in the GoT by two modeling approaches which were the WAM cycle 4.0 and the general regression neural network (GRNN) model. The results showed that the WAM model underestimates the wave height as much as 20%, while The GRNN gave the better forecasting results than the WAM model. They concluded that for short-term prediction within 24 h, the data-driven model, such as the GRNN, should be viewed as a strong alternative in operational forecasting.

The objective of this paper is to simulate the sea level and the ocean circulation patterns during the attack of Typhoon Linda for the GoT by using the POM model. In this paper, the focus is on how much of the surge generated due to meteorological forcing (wind forcing fields) and where the wind forcing fields affect the sea water elevation. During the entire period of this research, the northeasterly wind field was continuous and significant for determination of the sea level and ocean circulation patterns. The effects of atmospheric pressure differences are negligible. Consequences of difference parameter are presented along with the results of simulations illustrated in terms of sea surface elevations and sea surface anomalies. In this research, there are no observations of the sea surface height of the GoT to compare with the model results. The contents study only the effects of the Typhoon passing and illustrated the application of the three dimensional oceanic model. Comparison of tendency between the sea surface elevations from the model and the observed significant wave heights of moored buoys in the GoT under Seawatch project is investigated.

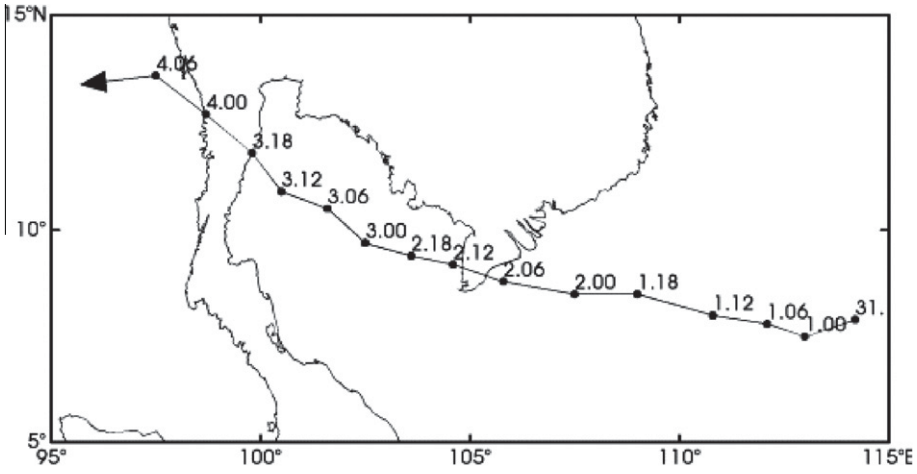

Fig. 2. The track of Typhoon Linda [18].

2. Model description

POM model is the time-dependent, primitive equation model formulated in Cartesian coordinates and vertical sigma coordinates. The model has been applied to simulate the storm surge and current patterns in the GoT. The model includes hydrostatic and Boussinesq approximations, realistic topography, a second-order turbulence closure model [4], horizontal diffusivity coefficients calculated by the Smagorinsky parameterization [7] and splitting modes, but the model does not include tidal forcing and river outflow. The Smagorinsky form of the horizontal viscosity is used to obtain a significantly smoother flow field which could be resolved on a model grid.

2.1. Three dimensional ocean model

Two approximations are used; first is the hydrostatic assumption, and second is the Boussinesq approximation [8]. The basic equations consist of the continuity, momentum, hydrostatic, temperature, salinity, density and by assuming that the ocean is incompressible.

In order to save computational time, the equations can be solved by the mode splitting method [13,17]. This method involves separating out the external (vertically averaged) and the internal (three dimension) modes and solving each of them separately at appropriate time steps. The vertical averaged currents (barotropic) are defined by:

$$\bar{u} = \int_{-1}^{0} u d\sigma \quad \text{and} \quad \bar{v} = \int_{-1}^{0} v d\sigma, \tag{2.1}$$

where u and v are the corresponding current components in the eastward and northward respectively. The value of σ ranges from $\sigma = 0$ at $z = \eta$ to $\sigma = -1$ at $z = -H(x,y)$, where $H(x,y)$ is the bottom topography, and η is the sea surface elevation. The barotropic equations are:

$$\frac{\partial \bar{u} D}{\partial x} + \frac{\partial \bar{v} D}{\partial y} + \frac{\partial \eta}{\partial t} = 0, \tag{2.2}$$

$$\frac{\partial \bar{u} D}{\partial t} + \frac{\partial \bar{u}^2 D}{\partial x} + \frac{\partial \bar{u}\bar{v} D}{\partial y} - \widetilde{F}^x - f\bar{v}D + gD\frac{\partial \eta}{\partial x} = - < wu(0) > + < wu(-1) > + G_x - \frac{gD}{\rho_0}\int_{-1}^{0}\int_{\sigma}^{0}\left(D\frac{\partial \rho'}{\partial x} - \sigma'\frac{\partial \rho'}{\partial \sigma'}\frac{\partial D}{\partial x}\right)d\sigma' d\sigma, \tag{2.3}$$

$$\frac{\partial \bar{v} D}{\partial t} + \frac{\partial \bar{u}\bar{v} D}{\partial x} + \frac{\partial \bar{v}^2 D}{\partial y} - \widetilde{F}^y + f\bar{u}D + gD\frac{\partial \eta}{\partial y} = - < wv(0) > + < wv(-1) > + G_y - \frac{gD}{\rho_0}\int_{-1}^{0}\int_{\sigma}^{0}\left(D\frac{\partial \rho'}{\partial y} - \sigma'\frac{\partial \rho'}{\partial \sigma'}\frac{\partial D}{\partial y}\right)d\sigma' d\sigma, \tag{2.4}$$

where $D = H + \eta$; t is time; ρ_0 is a reference density of the ocean; ρ is the density of sea water given by UNESCO [19]; $f = 2\Omega\sin\theta$ is the Coriolis parameter; Ω is the angular speed of the earth's rotation (7.2921×10^{-5} rad s^{-1}); g is magnitude of gravitational acceleration; the terms ($< wu(0) >$, $< wv(0) >$) and ($< wu(-1) >$, $< wv(-1) >$) are the transformed surface and bottom stresses (the stress components are opposite in sign) respectively. The terms $G_x, G_y, \widetilde{F}^x$ and $\widetilde{F}^y$ represent the horizontal viscosity and diffusion terms.

For the model grid, the rectangular horizontal grid was replaced by an orthogonal curvilinear grid to improve coastline representations with 37×97 horizontal grid points, as shown in Fig. 3. The horizontal grid spacing has ranged from 2 to 55 km. The vertical sigma coordinate has 10 levels. Aschariyaphotha et al. [9] has described the techniques that generate the model grid and interpolated the initial data by using cubic spline and bilinear interpolations.

2.2. Initialization

The bathymetry for the model was derived from the digital bathymetric data base 5- min (DBDB5) binary data file developed by the Naval Oceanographic Office (NAVOCEANO) with 1/12 degree longitude-latitude grided resolution. The numerical model integration was divided into spin up and simulation phases. In the spin up phase of the model run, the model was integrated with all three components of velocity initially set to zero, while the temperature and salinity were indicated by interpolating climatological monthly mean fields from Levitus94 [14,15] to the model grid. The spin up phase of the first model run was executed using wind stress calculated from climatological monthly mean wind, restoring-type surface temperature and salinity and climatological monthly mean freshwater flux taken from the European Centre for Medium-Range Weather Forecasts (ECMWF). The drag coefficient for wind stress (C_D) suggested by Matthias and Godfrey [16] is used in this paper. The C_D is calculated by

$$C_D = Min\{0.001 + 0.00007|\vec{V}_a|, 0.0025\}. \tag{2.5}$$

For spin up phase of the first model run, the wind velocities, $\vec{V}_a$, were taken from ECMWF climatological monthly mean wind velocity measured from 10 m above the sea surface.

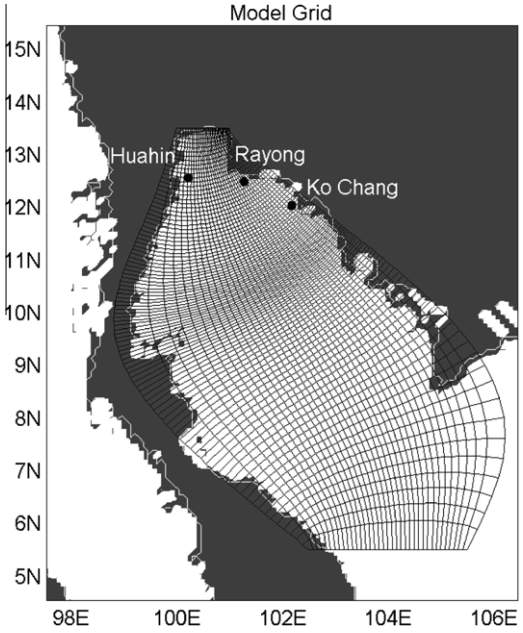

Fig. 3. The curvilinear model grid and three buoy locations in the Gulf of Thailand.

On the bottom of the gulf, the normal gradients of T and S are zero. Nevertheless there is an additional bottom friction force depending on the velocity adjacent to the boundary. A coefficient of bottom friction, C_z, will increase in value when wave effects are presented. This value taken from Blumberg and Mellor [1] can be obtained from the following expression:

$$C_z = Max\left\{\frac{\kappa^2}{\left[\ln\left\{\frac{(1+\sigma_{kb-1})H}{z_0}\right\}\right]^2}, 0.0025\right\}, \tag{2.6}$$

where κ is the Von Kraman constant; H is the bottom topography; kb is the total number of sigma vertical level, and z_0 is the bottom roughness parameter. In this paper, κ is taken to be 0.4, while $z_0 = 0.01$ m is used from Weatherly and Martin [2].

A radiation type of condition prescribes the normal currents across the open sea boundaries. As usual it is assumed that the motion in the sea is generated from an initial state of rest. Along the open boundaries the radiation conditions were applied

$$\frac{\partial}{\partial t}(T,S) + U_n\frac{\partial}{\partial n}(T,S) = 0, \tag{2.7}$$

where the subscript n is the direction normal to the boundary. The velocities and elevations at the open lateral boundary may be taken from observations if observed current and elevation data are available. In this paper, the boundary conditions of sea surface elevation are prescribed from You's model results [22]. The velocities at the open lateral boundary when inflow occur are calculated from the radiation condition for the $u-$ component and $v-$ component [3] as follows:

$$\frac{\partial u}{\partial t} \pm c_i\frac{\partial u}{\partial x} = 0, \tag{2.8}$$

$$\frac{\partial v}{\partial t} \pm c_i\frac{\partial v}{\partial y} = 0, \tag{2.9}$$

where c_i is the baroclinic phase speed.

In this paper, You's model outputs [22] are used as the value at the open boundary for the velocity. His model was run for simulating the circulation in the SCS covering the GoT with model resolution $1.125^\circ \times 1.125^\circ$ and $z-$ coordinate in the vertical. These data have been interpolated to the model grid. The model domain has two open boundaries, i.e. eastern boundary and southern boundary. At the eastern boundary the $u-$ component of the velocities was calculated from the radiation condition, and the $v-$ component was prescribed from You's results, while at the southern boundary the $u-$ component of the velocities was prescribed from You's results, and the $v-$ component was calculated from the radiation condition. The lateral boundary values of velocity and elevation taken from You's results are gradually increased from zero to the full values over the first 1/3 of a total runtime. The model was run with internal time step 900 s and 30 s for external time step until all variables were stable under the applied force. The results from this run were used as the initial data for simulation of storm surge, and the sea surface elevations and currents assumed to be the climatological value.

After spin up phase, the initial data for typhoon Linda simulation was wind field measured from 10 m above sea surface provided by ECMWF. The 6- h wind fields were taken from the period 00UTC on October 31 to 18UTC on November 7, 1997 with 1.125×1.1213 degree longitude-latitude grid resolution, and were interpolated by using cubic spline and bilinear interpolations to specify wind components at the model grid point. The sea surface elevation is prescribed from the AVISO sea surface height data.

2.3. Integration

The computation starts at 00UTC on October 31 and ends at 23UTC on November 7, 1997. The wind forcing field was added every 6 h, and the results were saved every one hour. Time steps used in this phase for the Typhoon Linda event were the internal time step 300 s and 10 s for the external time step.

3. Wind of Typhoon Linda

Fig. 4 shows the time series of the observed atmospheric pressure taken from ECMWF at the central part of the GoT (102.5°E, 10°N) and the typhoon's core passing. For Typhoon Linda, the atmospheric pressure in the center of the typhoon was only of the order of 10 hPa which is less than from the surroundings, consequently the effect from the pressure was very small. In addition, the GoT is shallow; the main effect is due to the strong wind stress. The effects of atmospheric pressure differences are negligible in this paper. The intense winds cause the sea water to pile up on the coast, leading to sudden inundation and flooding of coastal regions.

The availability of a wind field allows us to access how much and where the wind affects the sea levels in the gulf. The 6- h atmospheric wind fields during the Typhoon Linda period of from 00UTC on October 31 to 18UTC on November 7, 1997 shown in Fig. 5 were used to investigate the generated storm surge. These wind fields were obtained from ECMWF with 1.125×1.1213 degree longitude-latitude grid resolution. The wind in this event was a northeasterly wind. Typhoon Linda moved passing the southern tip of Vietnam on November 2. There is a strong counterclockwise wind circulation influenced by the northeasterly monsoon. The Typhoon moved into the GoT on the next day with the wind speed approximately 11.8 ms^{-1}, and then moved passing the center of the gulf with a speed of 12.7 ms^{-1}. At 18UTC on November 3, it was moving to the west and was approaching toward Huahin area with a maximum wind speed of 15.5 ms^{-1}. It was very close to Huahin 6 h later with the wind speed increasing up to 16.3 ms^{-1}, and then it moved passing further to the Bay of Bangal. The wind speed reduced after the Typhoon passed across the gulf.

4. Results

Although a three dimensional model is necessary to examine wind induced currents in the majority of storm surge calculations, the main emphasis is on changes in sea surface elevations and two dimensional models are used by Eqs. (2.2)–(2.4). For the results from the model run we will examine the time series of currents and sea surface elevations at only a limited number of locations, and consider for the whole GoT at the time during when the surge occurred. Three buoys, i.e. Huahin, Rayong and Ko Chang, located at the upper part of the gulf, as shown in Fig. 3, collected the significant wave height, so the simulated results at these three locations are examined. The positions of Huahin, Rayong and Ko Chang buoys are (100.17°E, 12.52°N), (101.23°E, 12.51°N) and (102.21°E, 12°N) respectively.

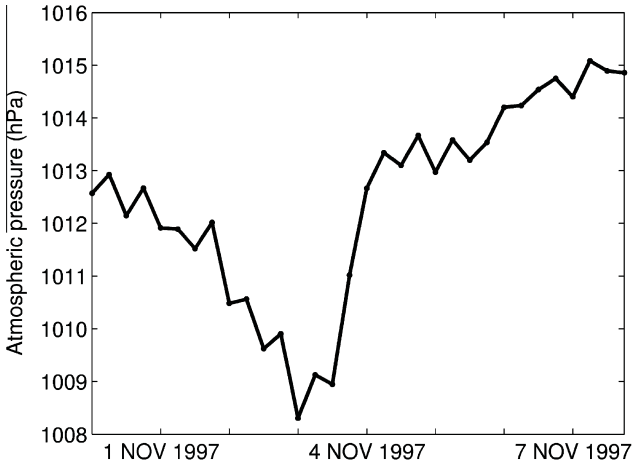

Fig. 4. The time series of the observed atmospheric pressure at point (102.5°E, 10°N).

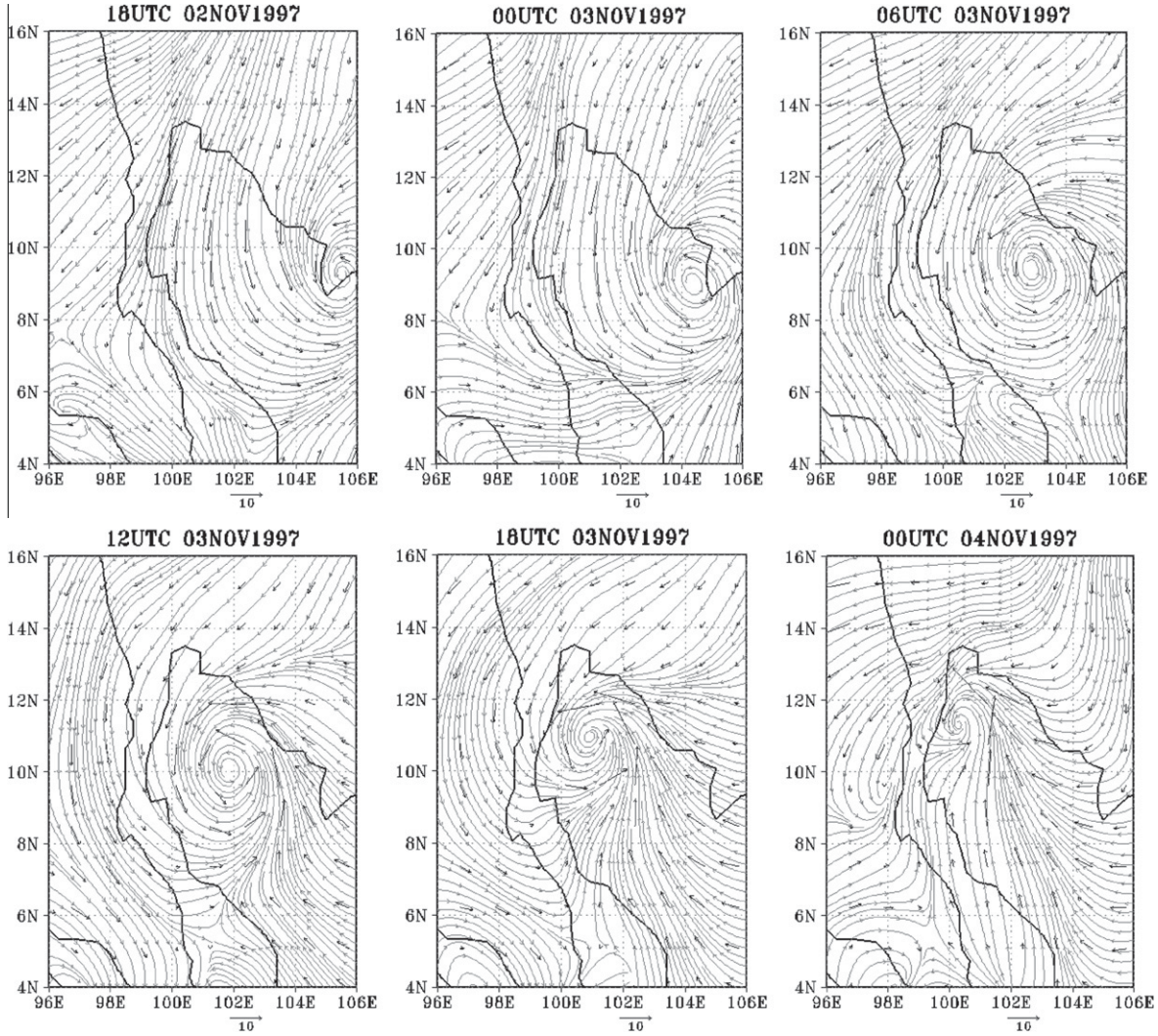

Fig. 5. The observed 6- h wind fields (ms^{-1}) of 18UTC on November 2 to 00UTC on November 4, 1997.

4.1. Determinations of drag coefficient

The formula of drag coefficient due to Matthias and Godfrey [16], which emphasize the dependency on wind speed, has been often used in oceanic models. On the other hand, the models with a constant drag coefficient have been mostly used for determination of the design heights of the sea level. For determining C_D, it may be appropriate to calculate wind stress and to produce sea surface elevation. In this paper, the observed sea surface anomaly on November 5, 1997 was used to determine the appropriate value of the drag coefficient. Fig. 6 shows the observed sea surface anomaly on November 5, 1997 taken from AVISO. The simulated sea surface anomalies on November 5 calculated using the drag coefficient as 1.3×10^{-3}, depending on the wind speed and 2.5×10^{-3} are shown in Fig. 7. The sea surface anomaly from the cases carried out using a constant drag coefficient, 1.3×10^{-3} and 2.5×10^{-3}, are compared with those using the drag coefficient depending on the wind speed. Using 1.3×10^{-3} for C_D gives a tendency to underestimate the sea surface anomaly, while using 2.5×10^{-3} was overestimated. It can be seen that the values from using C_D depending on the wind speed close to the observation. From the results, it may be concluded that the drag coefficient is reasonably taken for the calculation of storm surges in this research as C_D depending on the wind speed due to Mathias and Godfrey [16], and the sea surface elevation is substantially affected by the change of the drag coefficient. The value of drag coefficient can enhance or reduce the magnitude of the storm surge elevation.

In Fig. 8, the time series of sea surface elevations are shown for Huahin, Rayong and Ko Chang calculated in three cases; case 1 is calculated using bottom roughness parameter (z_0) as 0.01 m and bottom coefficient (C_z) calculated from the formula suggested by Mellor [3], case 2 estimated using $z_0 =$ 0.1 m and C_z also calculated from the same formula, and case 3

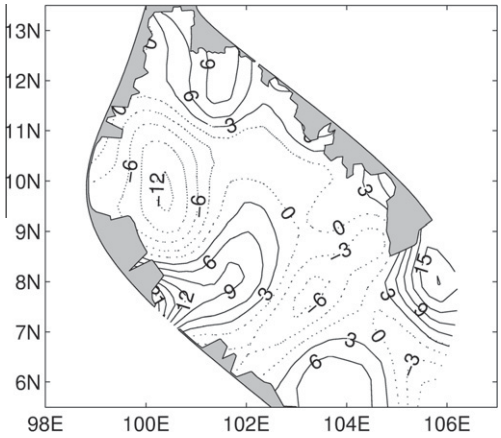

Fig. 6. The contours of observed sea surface anomaly (cm) taken from the AVISO near real-time sea surface anomaly data on November 5, 1997.

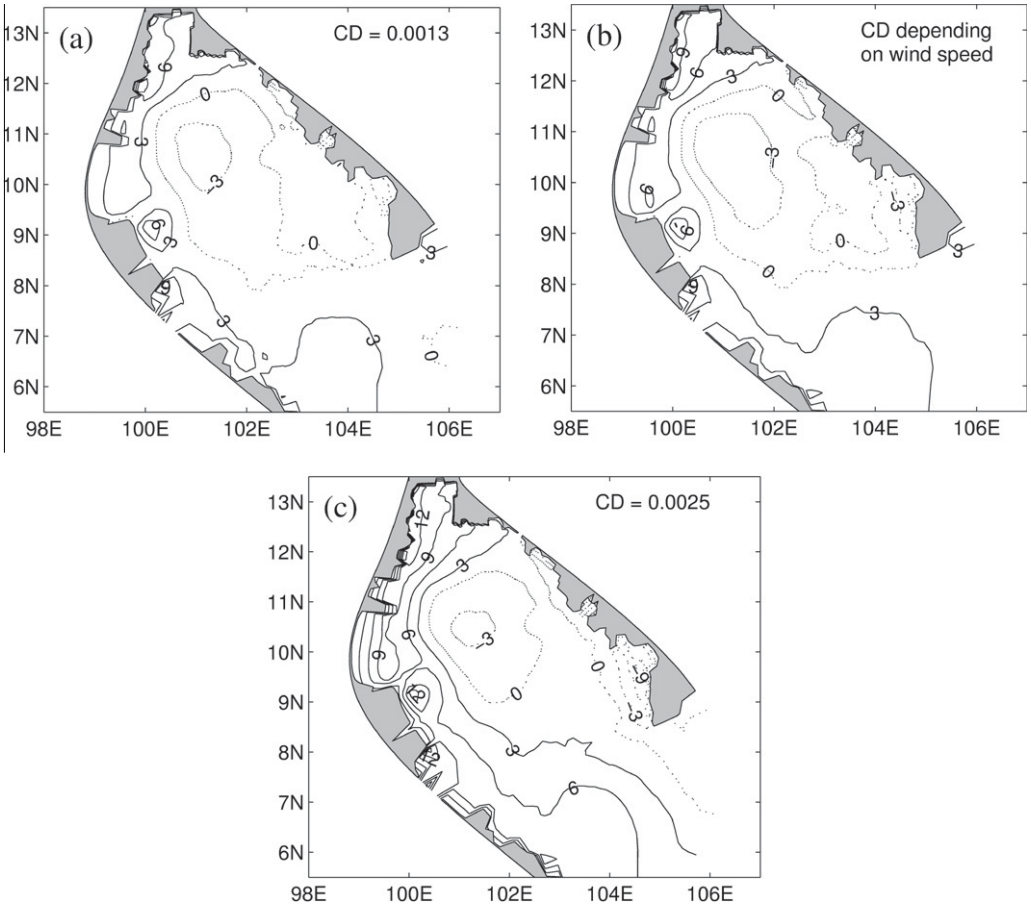

Fig. 7. The contours of simulated sea surface anomaly (cm) calculated using (a) $C_D = 1.3 \times 10^{-3}$, (b) C_D depending on the wind speed and (c) $C_D = 2.5 \times 10^{-3}$ on November 5, 1997.

estimated using $z_0 = 0.01$ m and constant $C_z = 3.3 \times 10^{-3}$. All three cases use the drag coefficient depending on the wind speed. The sea surface elevations of all three cases are the same. So that the changes of the bottom roughness parameter and bottom coefficient are insignificant to influence the calculation of sea surface elevation in the present study.

The results shown in the following were calculated using the drag coefficient due to the formula of Matthias and Godfrey [16], bottom roughness parameter as 0.01 m suggested by Weatherly and Martin [2] and bottom coefficient from calculation based on the logarithm law of the wall suggested by Mellor [3].

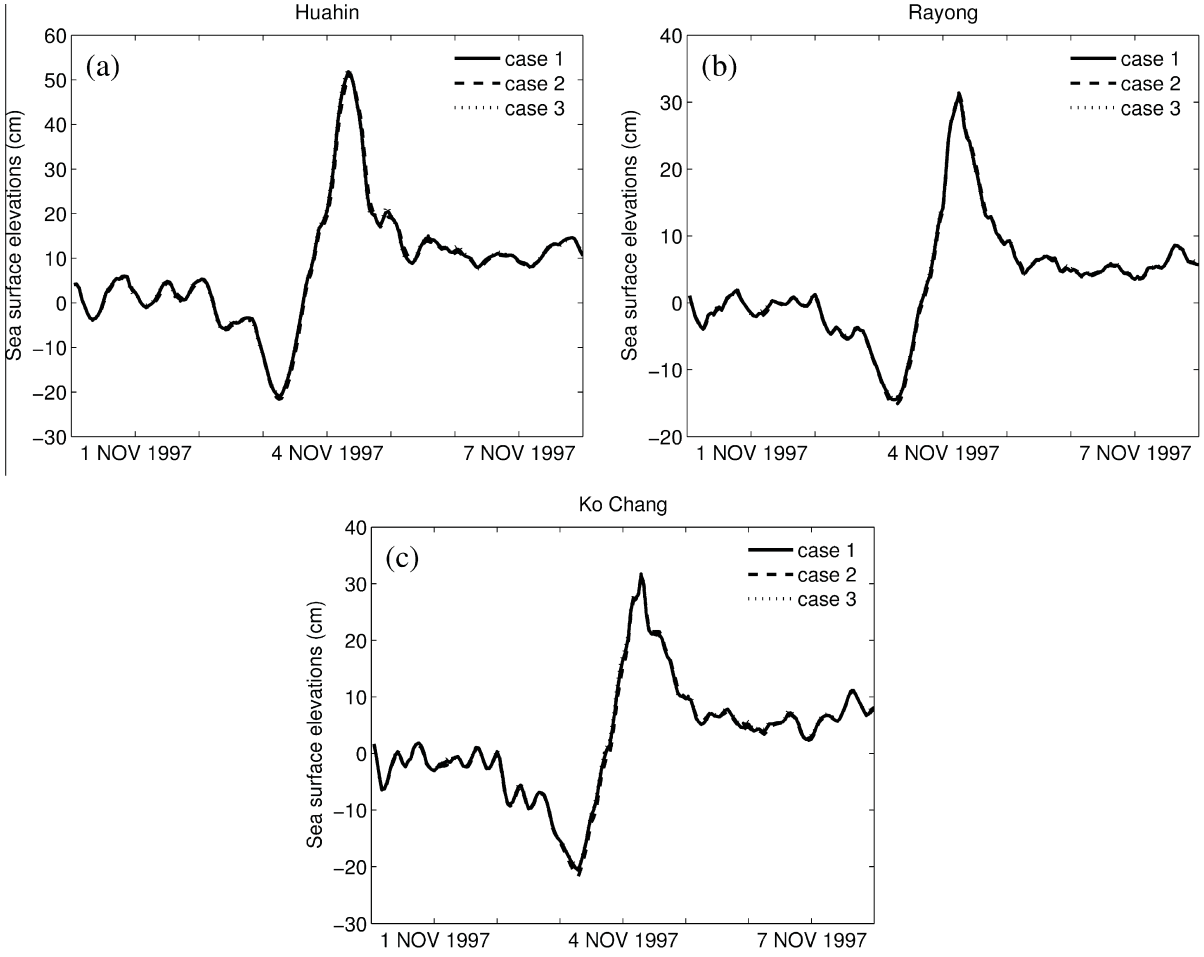

Fig. 8. The time series of sea surface elevations (cm) where case 1 estimated using $z_0 = 0.01$ m and C_z calculated from the formula suggested by Mellor [3], case 2 estimated using $z_0 = 0.1$ m and C_z also from calculation, and case 3 estimated using $z_0 = 0.01$ m and constant $C_z = 3.3 \times 10^{-3}$ at (a) Huahin (b) Rayong and (c) Ko Chang positions.

4.2. Simulated results of the current circulations

The simulated currents at the surface level induced by wind from observations are shown in Fig. 9. The actual storm surge is produced directly by the wind force. The wind induced circulation inside the gulf is characterized by the migration of water from the southeast to the north of the gulf as an effect of the wind force. It can be seen that the current circulation is counterclockwise during the typhoon passing. The positions of the center of the current circulation at the surface level correspond to the center of the typhoon at various times. When the typhoon moves northwestward from the SCS through the northern GoT, the current circulation also moves northwestward. A wind from the northeast drives a surface flow towards the land. The currents at the surface level, nearest surface, in offshore regions show a counterclockwise flow to the western coast with currents in some areas exceeding 0.8 ms^{-1} on November 4. A peak of the currents appeared to be associated with variations in wind stress. The currents in the area near the center of circulation are very low speeds which correspond to the existence of the area at the center of the typhoon where there is no relevant wind induced surge level.

Fig. 10 shows vectors of simulated currents at the surface level computed at 08UTC on November 4, 1997, around 8 h after the typhoon landfalls. The sea surface elevation rose to the maximum height at this time. The center of the counterclockwise circulation is quite a long way away from the shore, about 100 km south of Huahin. During this time, the counterclockwise circulation flow splits into two branches, one branch that flows directly toward the northeastern coast of the GoT, and another branch that flows directly to the north of Huahin with a speed of 0.8 ms^{-1}. A near-coast easterly flow is apparent along the northwestern coast of the GoT.

4.3. Simulated results of the sea surface elevations

The simulated sea surface elevations are shown in Fig. 11. As the wind blows, the water is pushed from the southwest to the north of the gulf. The area of set-up is permanently established in the northern part of the gulf. Following the spatial

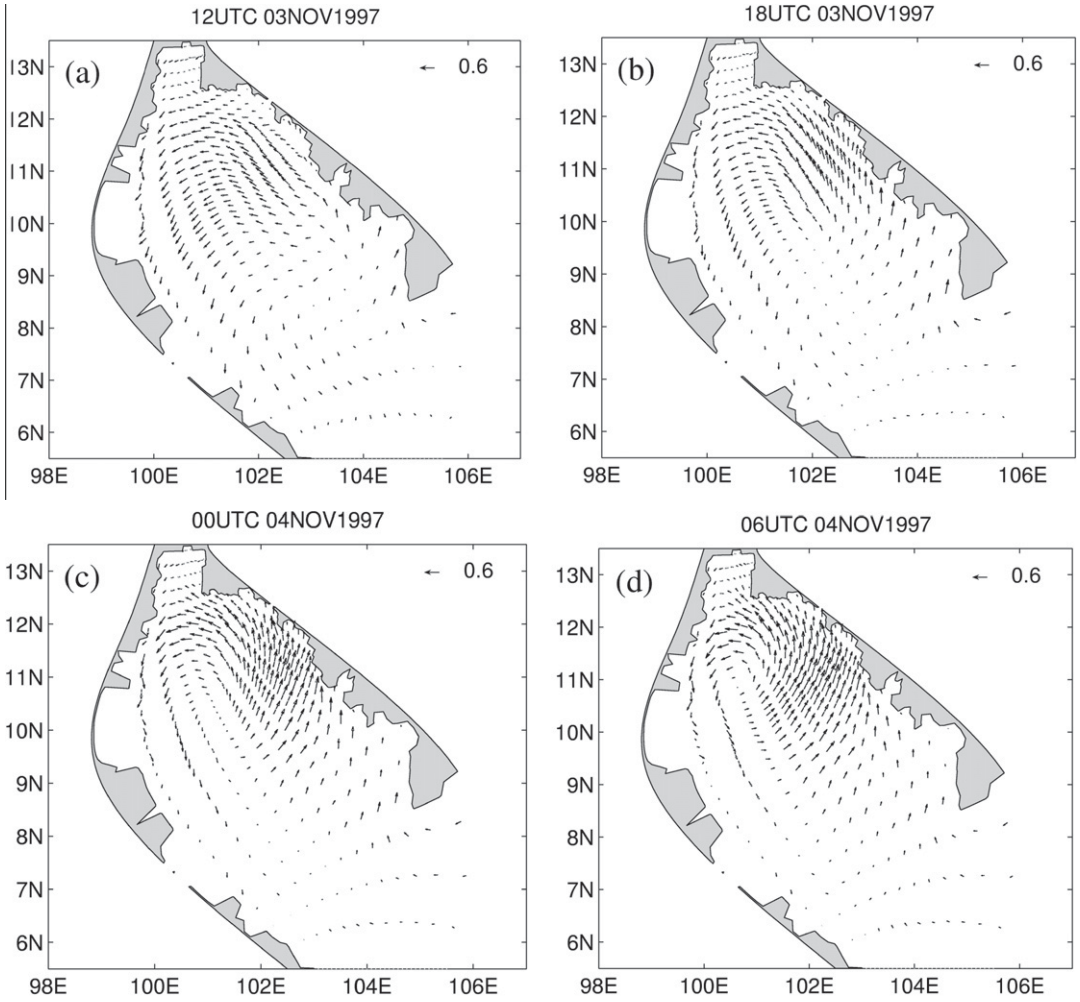

Fig. 9. The simulated the surface level current vectors (ms^{-1}) of 12UTC on November 3 to 06UTC on November 4, 1997.

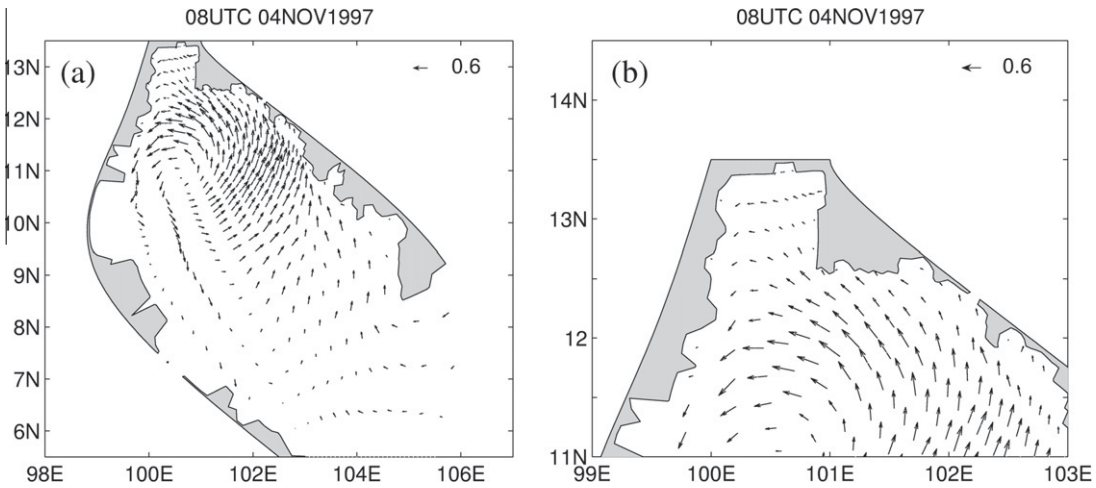

Fig. 10. The simulated (a) the surface level current vectors (ms^{-1}) and (b) the current vectors (ms^{-1}) in the upper of the GoT at 08UTC on November 4, 1997.

pattern of wind stress related to wind field, the gradient of sea levels is almost southwest-north. While the wind stress over the GoT increased, the sea level rose with very rapid increasing in the near-shore regions such as Cha-Am and Huahin.

Comparisons of the observed significant wave height provided by a network of moored data buoys called Seawatch buoys with the simulated sea surface height for three buoys, including the buoy at Huahin, Rayong and Ko Chang, are shown in Fig. 12. A peak has occurred in this observed wave height. At Huahin the peak of wave height, which appears to be 406.2 cm, appropriate to time of the peak of simulated sea surface elevation, which is 50.1 cm. At Rayong the peak of wave height, which is 296.9 cm, occurs at the same time as the peak of simulated sea surface elevation, which is 30.4 cm. At Ko Chang the peak of simulated sea surface elevation occurs after the peak of wave height by around 6 h. The 6- h delay may be caused by the errors in observation of initial wind. The peaks of wave height and simulated sea surface elevation at Ko Chang are 234.4 cm and 34.9 cm respectively. The Seawatch project, which was run by Schjølberg [12] using only the wind field, predicted an increase in sea level at 06UTC on November 4, 1997 to be 61 cm, calculated somewhere north of Cha-Am in the upper part of the gulf. In the model results, the highest sea surface elevation at this time was 61.4 cm. It agrees well with the Seawatch project. But the observation could not trace it. It is justified that the sea level does not elevate dramatically until the storm approaches the coast.

Fig. 13 shows the simulated sea surface heights in the upper part of the gulf at 08UTC on November 4, 1997. The time of peak surge agrees well with the time of peak wave height. The sea level raised to a maximum at this time at about 70 cm in the Cha-Am area, around latitude 12.8°N in the western coast of the upper GoT, very close to north of Huahin. For the Huahin position the maximum sea level was more than 51 cm. For the Rayong and Ko Chang positions located on the eastern coast of the upper GoT, the sea level calculated diminished down to 25 and 22 cm at this time, which is the time after the peak surge of these two locations occurring. It can be seen that the storm surge attains maximum values at the coastal region in the immediate vicinity of a storm's center slightly after storm passage. The climatological sea surface elevation taken from

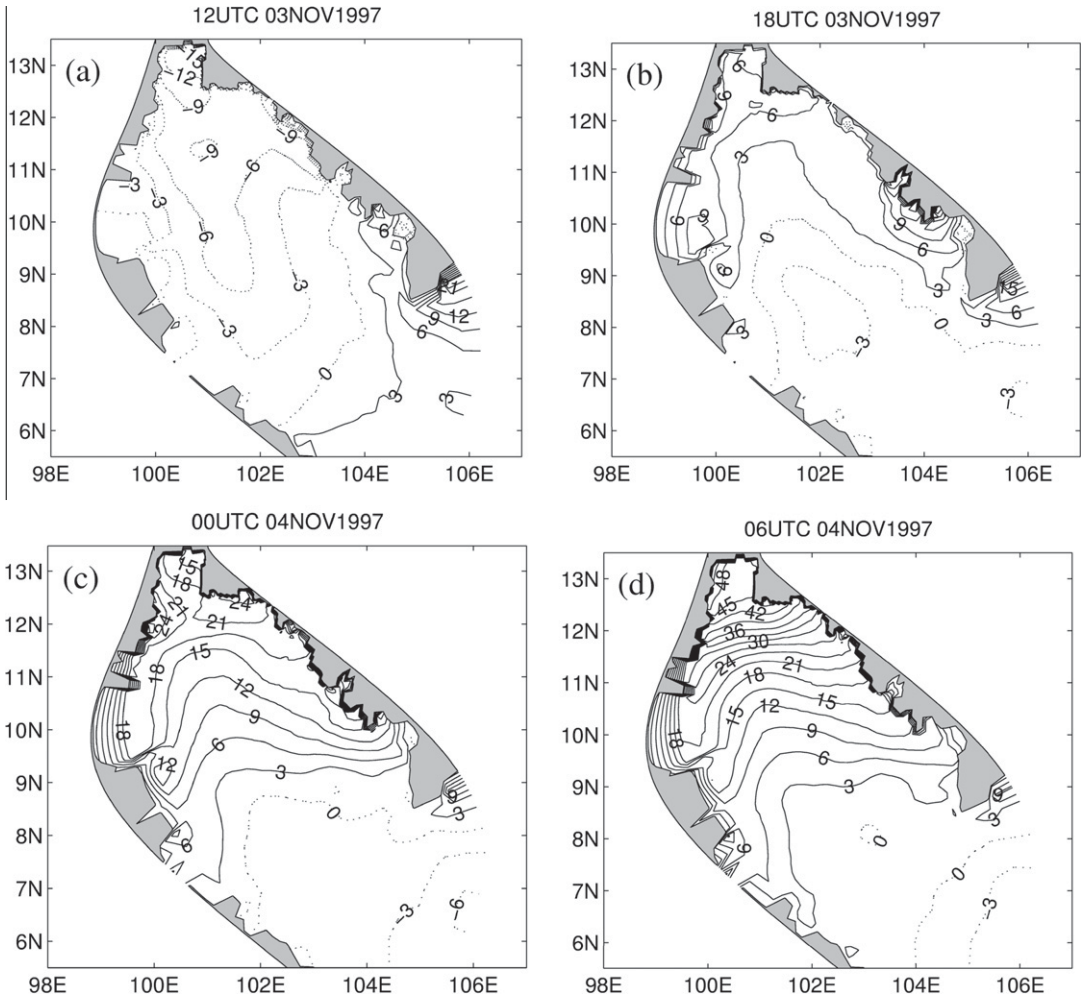

Fig. 11. The contours of simulated sea surface elevation (cm) of 12UTC on November 3 to 06UTC on November 4, 1997.

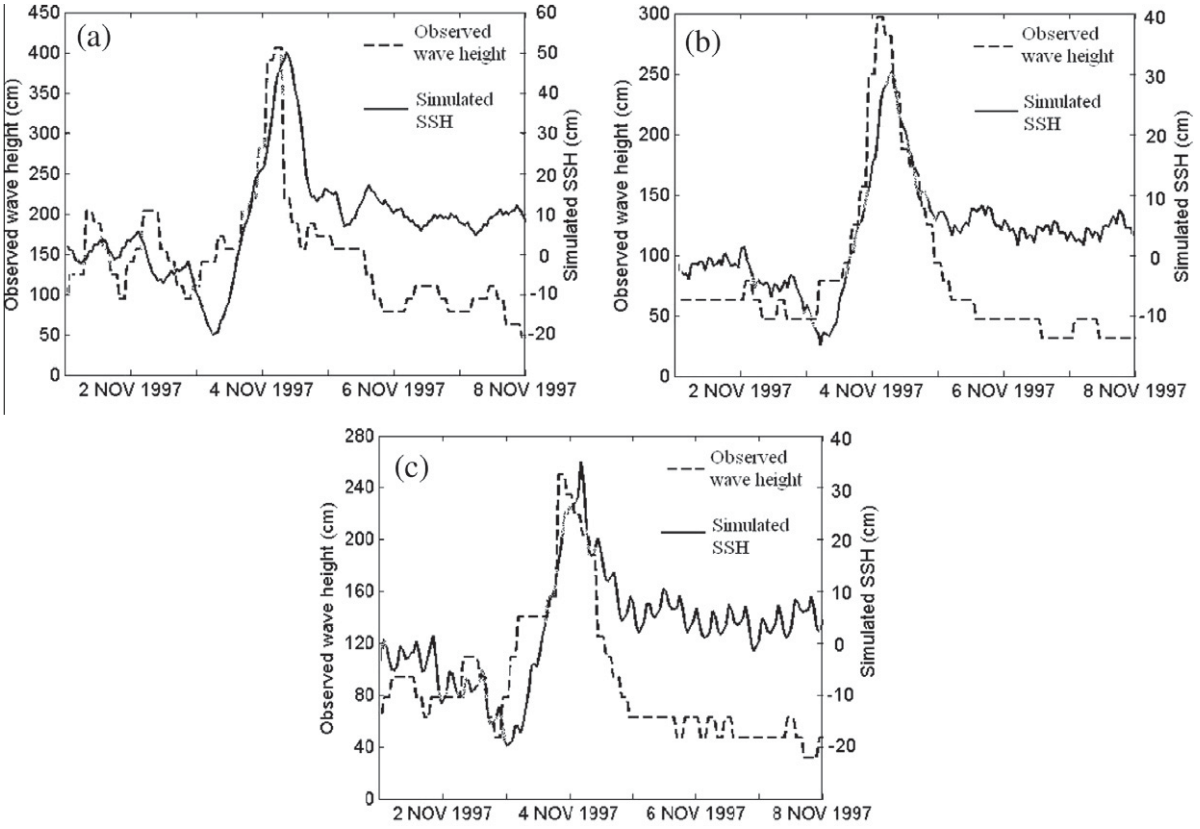

Fig. 12. The time series of the significant wave height (cm) from observation and the simulated sea surface elevation (cm) at (a) Huahin, (b) Rayong and (c) Ko Chang.

the spin up run on November and the simulated sea surface anomaly at 08UTC on November 4, 1997 are shown in Fig. 14. The big anomaly occurred in the upper part of the GoT in which the typhoon was passing toward the coast. The highest value of sea surface anomaly is about 60 cm in the Cha-Am area. At Huahin, Rayong and Ko Chang the sea surface anomalies are 46, 33 and 25 cm respectively. The averaged sea surface anomaly in the lower GoT is 5 cm, and in the upper GoT is 23 cm. It can be clearly concluded that the effects of the storm surge are a serious concern at the upper gulf when the typhoon moves northwestward through the northern GoT.

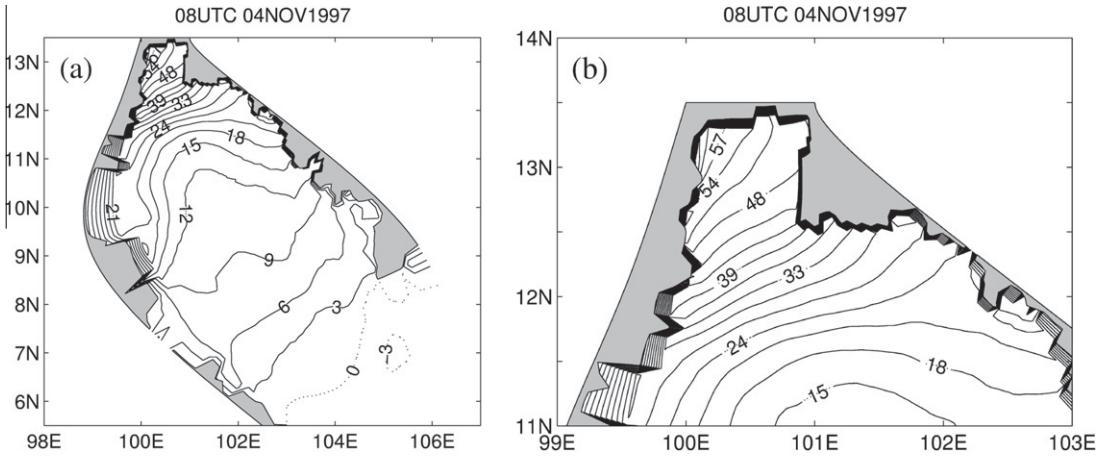

Fig. 13. The simulated (a) the contours of sea surface elevation (cm) and (b) the sea surface elevation (cm) in the upper of the GoT at 08UTC on November 4, 1997.

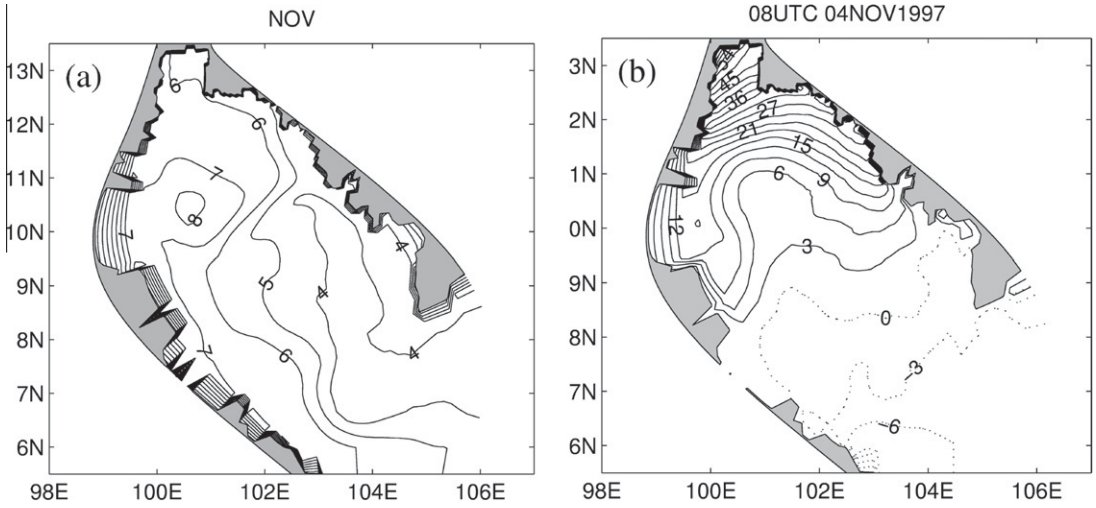

Fig. 14. The contours of (a) climatological sea surface elevation (cm) from spin up run for November and (b) simulated sea surface anomaly (cm) at 08UTC on November 4, 1997.

As we mentioned on the Cha-Am area, shown in Fig. 15, at a point near the shore the sea level elevations exceeded 70 cm. The maximum water set-up occurs at 08UTC on November 4, the maximum set-down at 08UTC on November 3. Thus around 24 h of time lag between the two maximum set-up and set-down with twenty-four hours of time lag correspond to the time between the high wave peak and the minimum taken from observation. The surges at the western coast region such as Hua-hin and Cha-Am rise higher than the eastern coast. The current speeds at this area are quite weak, the maximum current speed is 0.28 ms^{-1} occurring at 19UTC on November 3 which is the time before the typhoon landfalls. At the time of peak elevation, 08UTC on November 4, the current speed at Cha-Am is only 0.21 ms^{-1}, but the strong speed occur at the area around Cha-Am. That means the peak surge is not generated by the speed at that point, but it influenced by the strong speed around the peak area.

The variations of sea surface height can be divided into 3 stages that is the stage before storm surge occurred, the stage when storm surge existed, and the stage after the storm had passed. On November 3–4, a predominantly northeasterly wind was blowing over the GoT producing the surface elevation gradients, in which the surface elevation increases in the near coastal region.

The model contains the non-linear terms, and these terms are particularly important in shallow water, so we should be considering the energy for this study. Fig. 16 illustrates the kinetic energy and potential energy in units of Nm at various times in the GoT. Notice that potential energy is small compared to kinetic energy until the storm's center invades the gulf. Not that until the storm passes the coast does potential surpass kinetic energy. This suggests that the core of the storm when distant from the coast exclusively elevates the surface hydrostatically.

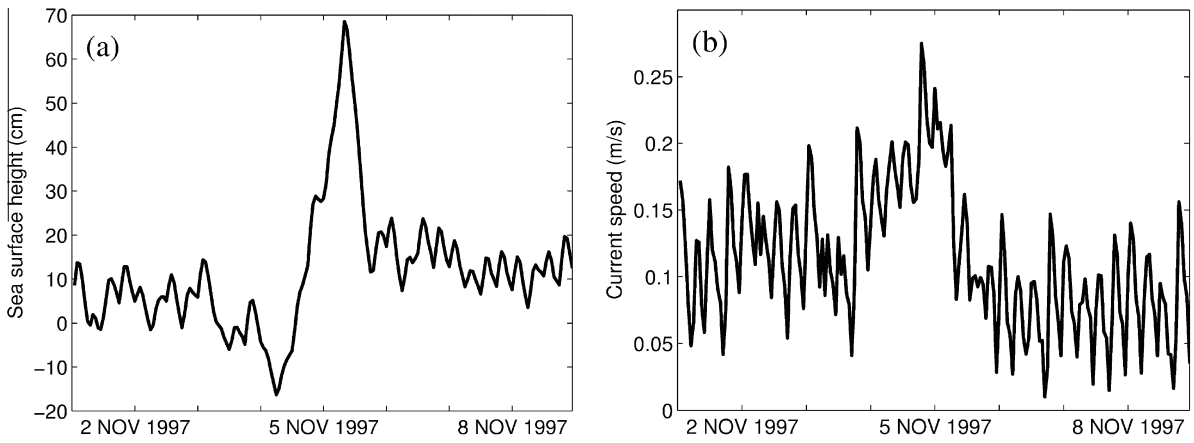

Fig. 15. The time series of (a) the simulated sea surface height (cm) and (b) the simulated first level current speed (ms^{-1}) at Cha-Am.

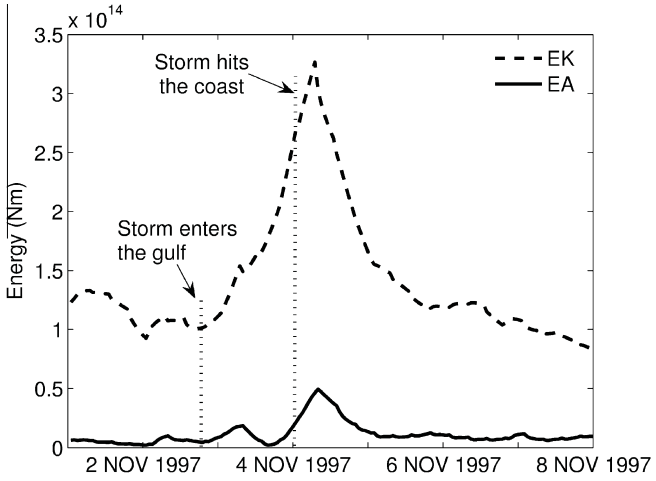

Fig. 16. The time series of kinetic energy (EK) and potential energy (EA) in units of Nm.

5. Conclusion

Numerical hindcast of storm surge caused by the Typhoon Linda in the Gulf of Thailand is conducted by using the three-dimensional ocean model (POM). In this case, the appropriate magnitude of drag coefficient depending on the wind speed is taken from the formula due to Matthias and Godfrey [16] which has been often used in storm surge models. It should be also noted that changes of bottom roughness parameter and bottom coefficient are checked not to influence the calculation of storm surge in this study. During the storm event, a northeasterly wind blew strongly over the southeastern coast of Thailand, which caused sea level elevation to rise in the northwestern part of GoT reaching a maximum value of 70 cm. Under the northeasterly wind, there is a contribution of sea water from the SCS into the GoT. A simulation has clearly revealed that the maximum sea elevation at the coast occurs not at the time of storm passage, but slightly after the storm strikes the coast. The wind forcing of a storm surge is the influential in controlling storm surges at a coastal region, whereas the initial value taken from the spin up phase is of minor importance. It is suitable to describe the storm from considerations presumed to hold at and near its center where the wind has the greatest effects.

The study of coastal storm surges for difference storm should be considered in the future. The results would be of immediate qualitative value to the typhoon warning service, and would provide insight on the relative importance of various mechanisms involved in storm surge generation.

Acknowledgements

This research was supported by the Thailand Research Fund (TRF), the Joint Graduate School of Energy and Environment (JGSEE) and the National Research University Project. The authors are greatly indebted to Prof. Dr. Jiang Zhu and Prof. Dr. Suphat Vongvisessomjai for valuable comments. We express our sincere thanks to the Institute of Atmospheric Physics (IAP), Chinese Academy of Sciences (CAS) and Department of Mathematics, King Mongkut's University of Technology Thonburi (KMUTT) for the facilities during this research and geo-informatics and space technology development agency (GISTDA) for the buoy data.

References

[1] A.F. Blumberg, G.L. Mellor, A description of a three-dimensional coastal ocean circulation model, in: N.S. Heaps (Ed.), Three Dimensional Coastal Ocean Models, American Geophysical Union, 1987, pp. 1–16.
[2] G. Weatherly, P.J. Martin, On the structure and dynamics of the ocean bottom boundary layer, Journal of Physical Oceanography 8 (1978) 557–570.
[3] G.L. Mellor, User's Guide for a Three-Dimensional, Primitive Equation, Numerical Ocean Model, Princeton University, New Jersey, 2004.
[4] G.L. Mellor, T. Yamada, Develop of a turbulence closure model for geophysical fluid problems, Reviews of Geophysics and Space Physics 20 (1982) 851–875.
[5] H.J. Yang, Q. Liu, Z. Liu, D. Wang, X. Liu, A general circulation model study of the upper ocean circulation of the South China Sea, Journal of Geophysical Research 107 (2002) C7.
[6] J. Gan, H. Li, E.N. Curchitser, D.B. Haidvogel, modeling South China Sea circulation: response to seasonal forcing regimes, Journal of Geophysical Research 111 (2006).
[7] J. Smagorinsky, General circulation experiments with the primitive equations, Monthly Weather Review 91 (1963) 99–164.
[8] K. Bryan, A numerical method for the study of circulation of the world ocean, Journal of Computing Physics 4 (1969) 357–376.
[9] N. Aschariyaphotha, P. Wongwises, U.W. Humphries, Interpolation of climatological data to numerical ocean modeling for the Gulf of Thailand, in: Proceedings of the Joint International Conference on Sustainable Energy and Environment, Huahin, Thailand, 2004, pp.784–789.
[10] P.C. Chu, Y. Chen, S. Lu, Wind-driven South China Sea deep basin warm-core/cool-core eddies, Journal of Oceanography 54 (1998) 347–360.
[11] P.C. Chu, N.L. Edmons, C.W. Fan, Dynamics mechanisms for the South China Sea seasonal circulation and thermohaline variabilities, Journal of Physical Oceanography 29 (1999) 2971–2989.

[12] P. Schjølberg, An operational ocean circulation model in the Gulf of Thailand: the Typhoon Linda case, in: Proceedings of the Seminar on The Seawatch Programmes in Asian Countries, Bangkok, Thailand, 2002, pp. 98–121.
[13] R.V. Madala, S.A. Piacsek, A semi-implicit numerical model for Baroclinic oceans, Journal of Computing Physics 23 (1977) 167–178.
[14] S. Levitus, T. Boyer, World ocean atlas, temperature, NOAA Atlas NESDIS, vol.4, U.S. Government Printing Office, Wasington, D.C., 1994.
[15] S. Levitus, R. Burgett, T. Boyer, World Ocean Atlas, Salinity, NOAA Atlas NESDIS, vol. 3, U.S. Government Printing Office, Wasington, D.C., 1994.
[16] T. Matthias, J.S. Godfrey, Regional Oceanography: An Introduction, Pergamon, Australia, 1994.
[17] T.J. Simons, Verification of numerical models of lake Ontario, Part I: circulation in spring and early summer, Journal of Physical Oceanography 4 (1974) 507–523.
[18] Tiempo Climate Cyberlibrary, Typhoon Linda hits Vietnam. Available from: <http://www.cru.uea.ac.uk/tiempo/floor0/recent/issue26/t26art5.htm>, 1997.
[19] UNESCO, Tenth Report of the Joint Panel on Oceanographic Tables and Standards, UNESCO Technical Pap. in Marine Science, UNESCO, Paris, 1981.
[20] W. Kanbua, I.W. Tang, B. Wiwatanapataphee, A study on ocean wave forecasting from Typhoon Linda by using the WAM model, in: Proceedings of ANSCES 2001, Bangkok, Thailand, 2001, pp. 22–28.
[21] W. Kanbua, S. Supharatid, I.W. Tang, Ocean wave forecasting in the Gulf of Thailand during Typhoon Linda 1997: WAM and neural network approaches, Science Asia 31 (2005) 243–250.
[22] X.B. You, R.F. Li, Q.C. Zeng, Numerical simulation of the current system in the China Sea by using a nested mesh model, Proceedings of the Nineth Asian Congress of Fluid Mechanics, Isfahan, Iran, 2002.

Provided for non-commercial research and education use.
Not for reproduction, distribution or commercial use.

This article appeared in a journal published by Elsevier. The attached copy is furnished to the author for internal non-commercial research and education use, including for instruction at the authors institution and sharing with colleagues.

Other uses, including reproduction and distribution, or selling or licensing copies, or posting to personal, institutional or third party websites are prohibited.

In most cases authors are permitted to post their version of the article (e.g. in Word or Tex form) to their personal website or institutional repository. Authors requiring further information regarding Elsevier's archiving and manuscript policies are encouraged to visit:

http://www.elsevier.com/copyright

Author's personal copy

Experimental Thermal and Fluid Science 35 (2011) 887–895

Contents lists available at ScienceDirect

Experimental Thermal and Fluid Science

journal homepage: www.elsevier.com/locate/etfs

Two-phase flow of R-134a refrigerant during flow boiling through a horizontal circular mini-channel

Sira Saisorn [a,c], Jatuporn Kaew-On [b,c], Somchai Wongwises [c,*]

[a] King Mongkut's Institute of Technology Ladkrabang Chumphon Campus Chumphon 86160, Thailand
[b] Department of Physics, Faculty of Science, Thaksin University, Phattalung 93110, Thailand
[c] Fluid Mechanics, Thermal Engineering and Multiphase Flow Research Lab. (FUTURE), Department of Mechanical Engineering, King Mongkut's University of Technology Thonburi, Bangmod, Bangkok 10140, Thailand

ARTICLE INFO

Article history:
Received 18 December 2009
Received in revised form 24 October 2010
Accepted 21 January 2011
Available online 31 January 2011

Keywords:
Flow boiling
Mini-channel
Flow pattern
Heat transfer

ABSTRACT

This research focuses on heat transfer to R-134a during flow boiling in a 1.75 mm internal diameter tube. Flow visualisation and heat transfer experiments are conducted to obtain heat transfer coefficients for different flow patterns. The measured data in each flow regime are compared with predictions from a three-zone flow boiling model. The calculations are in fair agreement with the experimental results which correspond in particular to slug flow, throat-annular flow and churn flow regimes under conditions of low heat flux.

© 2011 Elsevier Inc. All rights reserved.

1. Introduction

In recent years, intense research effort has been devoted to the flow boiling heat transfer characteristics of small flow passages such as mini- and micro-channels owing to the rapid development of micro-scale devices used for several engineering applications including medical devices, high heat-flux compact heat exchangers, and cooling systems for various types of equipment.

Several advantages can be obtained when small channels are selected for applications. In compact heat exchanger implementations, for instance, small channels can provide a larger contact area with the fluid per unit volume and support high pressure operating conditions. Capillary force or surface tension is likely to play an important role in two-phase flow and heat transfer characteristics, resulting in significant differences in the flow phenomena between ordinarily sized channels and small channels.

The criteria for the classification of small channels have been given by different investigators as reported in Saisorn and Wongwises [1]. For instance, arbitrary channel classifications associated with the hydraulic diameter, D_h have been proposed. Mehendale et al. [2] employed the hydraulic diameter as an important parameter for defining the heat exchangers as follows:

- Micro-heat exchanger: 1 μm $\leqslant D_h \leqslant$ 100 μm
- Meso-heat exchanger: 100 μm $\leqslant D_h \leqslant$ 1 mm
- Compact heat exchanger: 1 mm $\leqslant D_h \leqslant$ 6 mm
- Conventional heat exchanger: $D_h >$ 6 mm

Kandlikar [3] proposed criteria for different-sized channels used in engineering applications:

- Micro-channels: 10 μm $\leqslant D_h \leqslant$ 200 μm
- Mini-channels: 200 μm $\leqslant D_h \leqslant$ 3 mm
- Conventional channels: $D_h >$ 3 mm

With regard to two-phase flow research, there have been a relatively small number of publications in the area of small channels compared with those done for ordinarily sized channels. Hydrodynamic and transport phenomena in small channels, which have limited and confined space, are less well understood compared to those in larger channels. Recent works concerned with two-phase heat transfer characteristics in mini- and micro-channels are outlined in the following paragraphs.

Huo et al. [4] studied experimentally boiling heat transfer of R-134a fluid flowing in small vertical tubes of 2.01 and 4.26 mm internal diameter. In the range of low vapour quality, the heat transfer coefficient in both tubes increased with increasing heat flux and saturated pressure but was independent of vapour quality. These results were attributed to nucleate boiling being the dominant heat transfer mode. Over other ranges of vapour quality, however, the dominant heat transfer mode was not addressed as a

* Corresponding author. Tel.: +66 2 470 9115; fax: +66 2 470 9111.
E-mail address: somchai.won@kmutt.ac.th (S. Wongwises).

0894-1777/$ - see front matter © 2011 Elsevier Inc. All rights reserved.
doi:10.1016/j.expthermflusci.2011.01.008

Author's personal copy

Nomenclature

Bo	boiling number
D	channel diameter (m)
G	mass flux (kg/m^{2}s)
h	heat transfer coefficient (W/m^2 K)
i	specific enthalpy (J/kg)
i_{LG}	latent heat of vapourization (J/kg)
MAE	mean absolute error
q	heat flux (W/m^2)
Re	Reynolds number
T	temperature (°C)
t	time (s)
We	Weber number
x	vapour quality
z	axial distance (m)

Greek symbols

τ	pair period (s)

Subscripts

A	annular flow
CB	coalescing bubble flow
dry	dry-out zone
film	liquid film between bubble and wall
G	vapour phase
GO	all-vapour
IB	isolated bubble flow
L	liquid phase
LO	all-liquid
sat	saturation
wall,in	inner wall

result of inconsistency in the experimental data. Under the same controlled conditions, they found that the nucleate boiling heat transfer coefficient was higher for the 2.01 mm tube than for the 4.26 mm tube.

Flow boiling heat transfer characteristics in micro-channels of 540 mm length with 25 circular flow channels of 0.81 mm diameter were investigated by Pettersen [5]. They reported that the increase in heat flux resulted in a higher heat transfer coefficient, which can be explained according to the dominant role of nucleate boiling over the low/moderate vapour quality region. Another point observed was that the dry-out effects were more noticeable at higher mass flux and temperature, resulting in a substantially reduced heat transfer coefficient at high vapour qualities. Besides, the pressure drop increased with mass flow and vapour quality but decreased as temperature increased. The measured heat transfer coefficient data corresponding to low vapour quality region were compared with various heat transfer correlations based on nucleate boiling mechanism. The frictional pressure drop data were also compared with the existing correlations.

Yun et al. [6] were concerned with flow boiling heat transfer characteristics in rectangular multi-channels with hydraulic diameters ranging from 1.08 to 1.54 mm. Working fluids tested were CO_2 and R-134a. Generally, the average heat transfer coefficient of CO_2 increased by around 53% as compared with that of R-134a. The effect of heat flux on heat transfer coefficient was much more obvious for CO_2 than for R-134a. The dry-out phenomenon was promoted by an increase in mass flux and it was also noted that the effect of mass flux on heat transfer coefficient was less sig-

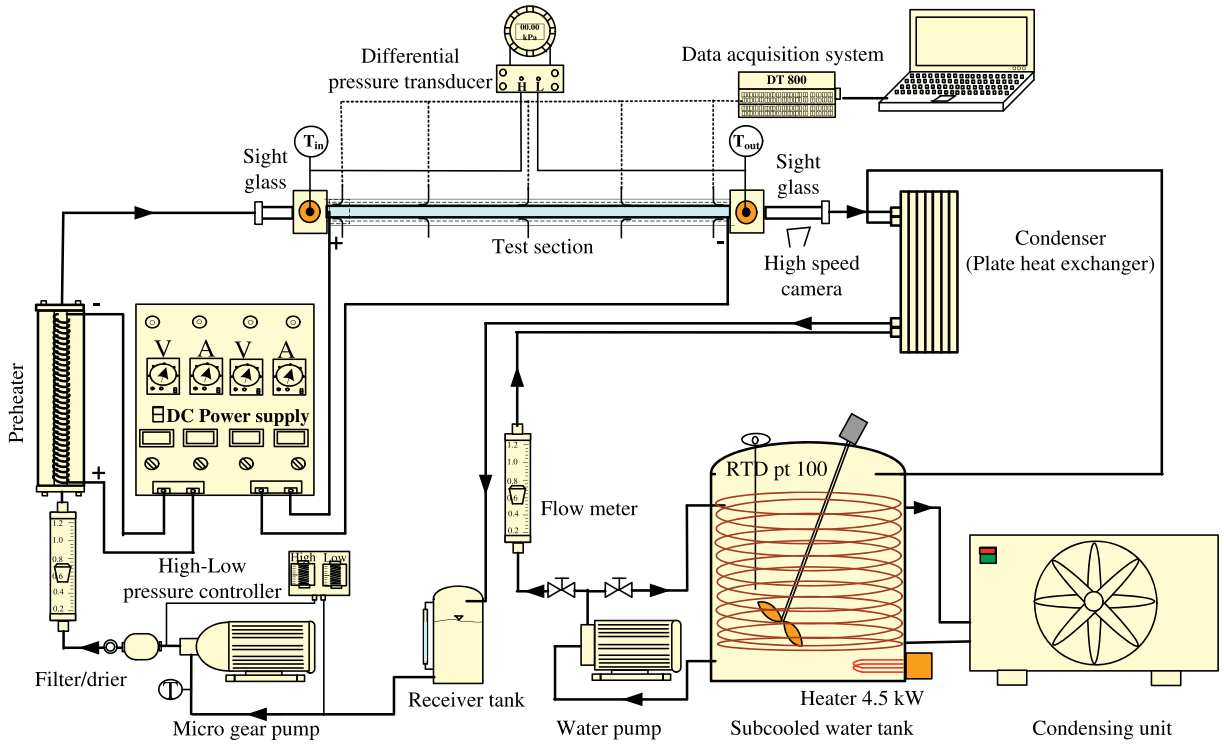

Fig. 1. Schematic diagram of experimental apparatus.

Author's personal copy

nificant than that of heat flux. As expected, the heat transfer coefficient increased with a decrease in hydraulic diameter.

Heat transfer of R-134a refrigerant during flow boiling in horizontal tubes with different diameters including 0.51, 1.12 and 3.1 mm was studied experimentally by Saitoh et al. [7]. Nucleate boiling was reported in the low vapour quality region whereas convective evaporation was dominant in the high vapour quality region. The latter mechanism was found to be less dominant as the tube diameter decreased. The smaller the tube diameter, the higher is the effect of saturation temperature on heat transfer coefficient. Flow instability was also discussed in this work.

Choi et al. [8] reported the heat transfer characteristics of CO_2 through horizontal mini-channels having diameters of 1.5 and 3 mm. They indicated that nucleate boiling was predominant in the low vapour quality region and a convective boiling heat transfer contribution appeared in moderate and high vapour quality regions. The variation of local heat transfer coefficient with heat flux, mass flux, vapour quality and saturation temperature was discussed. More vigorous nucleate boiling was observed and studied when the smaller diameter tube was used. Flow boiling heat transfer experiments with different refrigerants were continually carried out by Choi et al. [9]. They indicated that the use of CO_2 caused the heat transfer coefficient to be higher than with R-134a and R-22 fluids.

Shiferaw et al. [10] compared their flow boiling data with existing correlations. The data points were obtained from experiments with R-134a fluid flowing through small tubes with diameters of 4.26 and 2.01 mm. The comparison revealed that existing correlations do not predict their data very well. Comments and suggestions were provided by the authors for further development of the prediction. Similar experiments were conducted by Shiferaw et al. [11] to obtain data from a 1.1 mm diameter tube. Generally, the heat transfer characteristics showed that the heat transfer coefficient was not affected by mass flux or vapour quality, but increased with increasing heat flux and saturation pressure.

Three different refrigerants, R-134a, R-236fa and R-245fa, were tested for flow boiling in a 1.03 mm diameter tube by Ong and Thome [12]. Trends apparent in the data were investigated, showing that the heat transfer coefficient depended on heat flux at low vapour quality and on mass flux at high vapour quality. In terms of the refrigerants tested at low vapour quality, R-134a exhibited the highest heat transfer coefficient followed by R-236fa and R-245fa, respectively.

Interestingly, a number of researchers such as Lee and Lee [13], Sumith et al. [14] and Qu and Mudawar [15] have reported that flow boiling heat transfer is substantially controlled by convective boiling.

In addition to the mechanisms corresponding to nucleate boiling and convective boiling contributions, recently, a three-zone flow boiling model based on the elongated bubble flow regime, was developed by Thome et al. [16] and Dupont et al. [17] to predict heat transfer characteristics in micro-channels. The point they make is that heat transfer is controlled primarily by conduction through the evaporation film trapped between the elongated bubble and the tube wall.

From the above review of the literature, the characteristics of flow boiling heat transfer in small channels are not entirely consistent with those in ordinarily sized channel. Moreover, there is inconsistency in the micro-scale heat transfer results obtained from different researchers and, as a result, the major heat transfer mechanisms behind the phase-change phenomena are still unclear for small flow passages. Flow patterns have been expected to affect the heat transfer phenomena. Different flow patterns may give differences in flow boiling mechanisms. The current work is, therefore, aimed at examining the three-zone flow boiling model for various flow patterns observed in R-134a refrigerant flow boiling through a 1.75 mm tube.

2. Experimental apparatus and procedure

The present experimental apparatus, which is modified from that developed by Kaew-On and Wongwises [18] and is shown schematically in Fig. 1, is designed to investigate flow boiling of R-134a in a circular mini-channel placed horizontally. The main

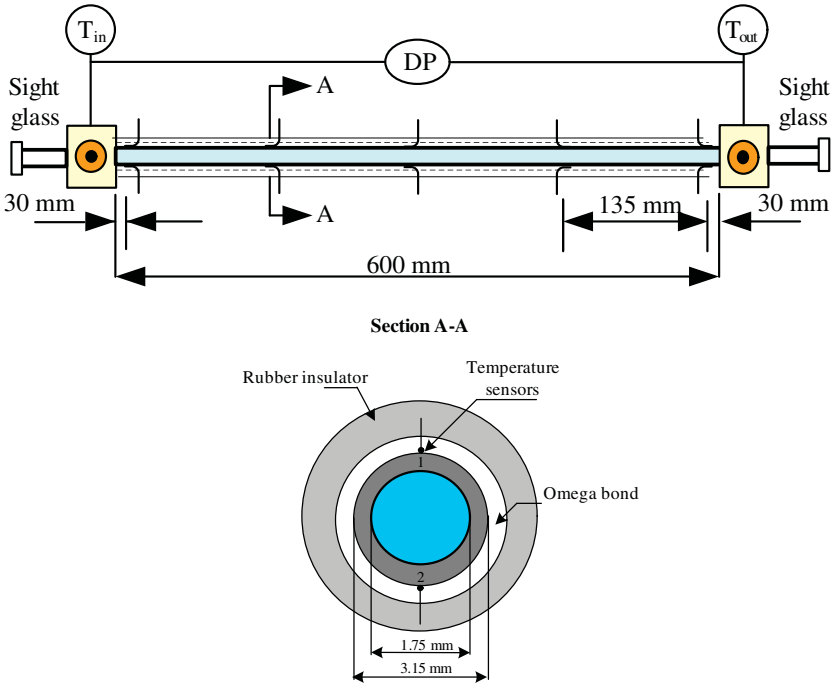

Fig. 2. Schematic diagram of the test section.

Author's personal copy

Table 1
Experimental conditions.

Refrigerant	R-134a
Diameter (mm)	1.75
Length (mm)	600
Mass flux (kg/m^2 s)	200–1000
Heat flux (kW/m^2)	1–83
Saturation pressure (bar)	8–13
Test section material	Stainless steel

Table 2
Uncertainties of measured quantities and calculated parameters.

Parameter	Uncertainty
Temperature	±0.1 (°C)
Mass flow rate of refrigerant	±0.1 (%) Full scale
Heat transfer rate of test section	±2.25%
Heat transfer rate of pre-heater	±2.25%
Heat transfer coefficient	±8.12%

components of the system include a test section, refrigerant loop, sub-cooling loop, and a data acquisition system.

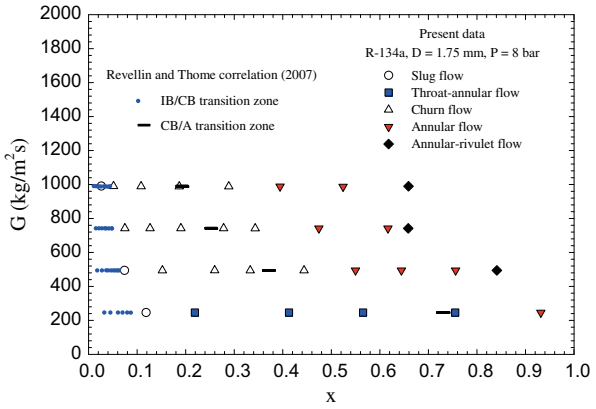

Fig. 4. The present flow regime map compared with the transition zones by Revellin and Thome [20].

For the refrigerant circulating loop, as seen in Fig. 1, liquid refrigerant is pumped by a gear pump which can be regulated by means of an inverter. The refrigerant then passes in series through a filter/dryer, a refrigerant flow metre, pre-heater, sight glass tube, and enters the test section. The inlet quality before entering the test section is controlled by the pre-heater with a DC power supply used to apply heat. Leaving the test section, the refrigerant vapour

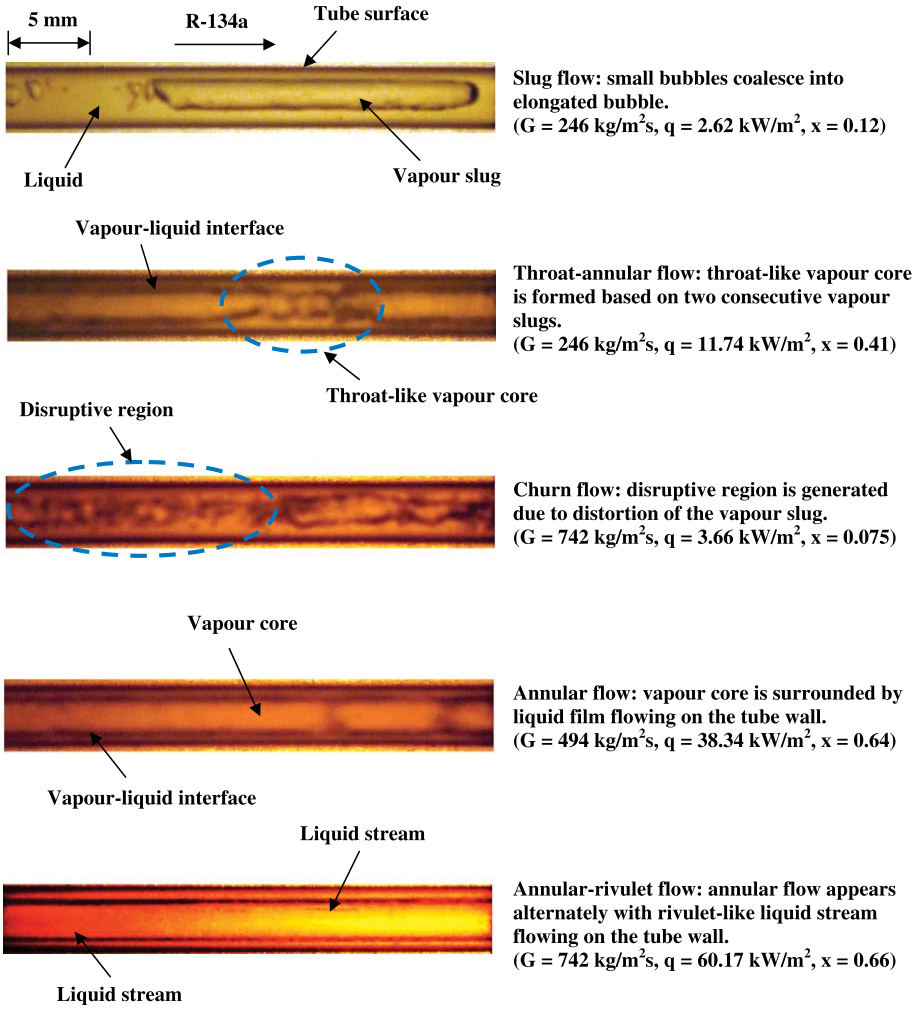

Fig. 3. Flow patterns for R-134a during flow boiling in a mini-channel with diameter of 1.75 mm (saturation pressure = 8 bar).

Author's personal copy

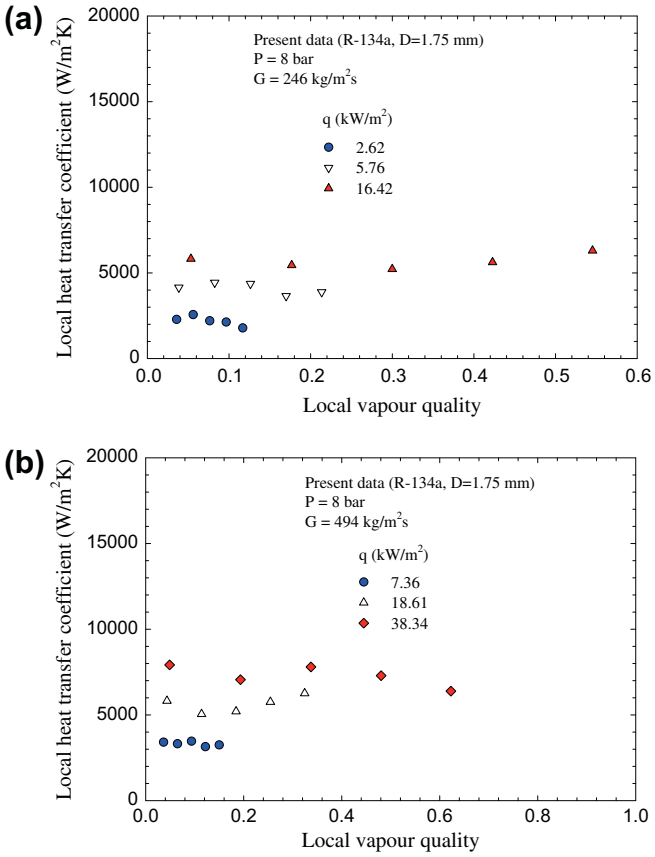

Fig. 5. Local vapour quality versus local heat transfer coefficient for various heat flux values.

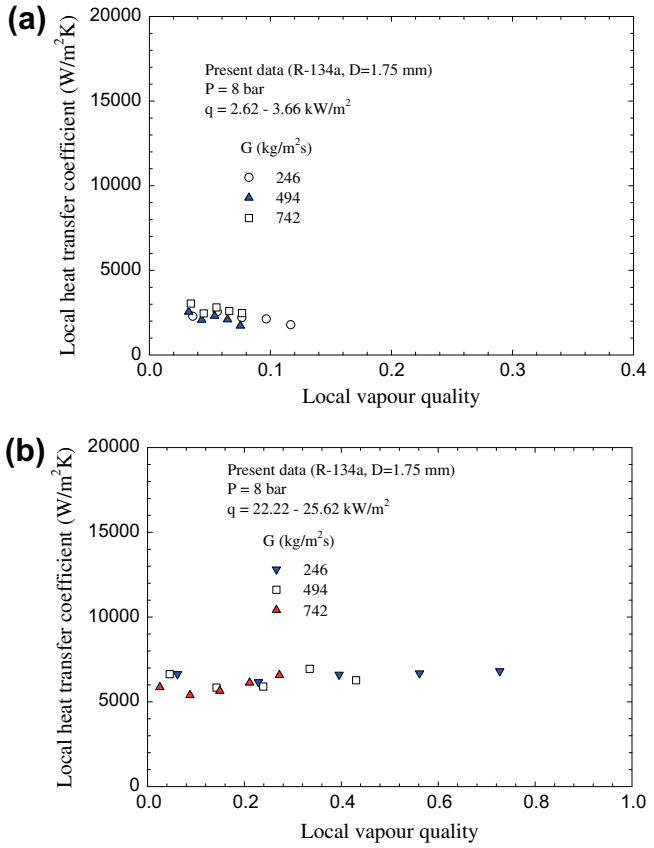

Fig. 6. Local vapour quality versus local heat transfer coefficient for various mass flux values.

subsequently condenses in a condenser which is a plate heat exchanger and then is collected in a receiver and returns to the refrigerant pump to complete the cycle. Instrumentation is installed at various positions, as shown in Fig. 1, to monitor the state of the refrigerant. All the signals from the thermocouples and pressure transducer are recorded by the data acquisition system.

Fig. 2 shows a schematic diagram of the test section, a stainless steel tube which is 600 mm long and 1.75 mm in diameter. A regulated DC power supply generating 80 A at 12 V is used to apply heat to the test section. The voltage and electric current values are measured by a multi-metre (Fluke 336 model) which has an uncertainty of ±2% for voltage and ±1% for current. T-type thermocouples are installed at the inlet and outlet of the test section to measure the system temperature. The 10 thermocouples are installed on the top and bottom sides at equal distances along the tube to measure the wall temperature. All thermocouples on the tube surface are fixed with special glue. The test section is well insulated by means of rubber foam with a thermal conductivity of 0.04 W/mK. A variable area type flow metre is specially calibrated in the range 0.02–0.2 LPM for R-134a by the manufacturer. All relevant instruments installed in the experimental apparatus, including the thermocouples and pressure transducer are well calibrated.

A 1.75 mm diameter transparent tube is installed to match up with the test section outlet and to serve as a viewing window for flow visualisation. The detailed formation of each flow pattern is registered by a high quality camera (Fujifilm FinePix S7000) having shutter speeds of 1/15–1/10,000 s. The camera, together with an adjustable light source consisting of 150 W halogen lamp and dimmer, are placed horizontally and normal to the viewing section.

In this work, the experiments were conducted in such a way that the heat applied to the test section is varied in small increments, while the refrigerant flow rate, saturation pressure, and inlet vapour quality in the test section are kept constant at the desired value. The system is allowed to approach a steady state before the flow pattern and relevant data are recorded. The steady state condition is verified by plotting a number of temperatures measured by the T-type thermocouples installed at pre-heater and test section, against time. Their variations are within the error range for a time of at least 120 s. During the experiment, the temperature and pressure are continuously recorded along the test section on the data acquisition system. The temperature profiles help us to know the limits of useful data because a large increase in wall temperature and outlet saturation temperature is observed when dry-out occurs. The range of experimental conditions is presented in Table 1. The uncertainties in the measured quantities and calculated parameters are shown in Table 2.

3. Results and discussion

Flow boiling of R-134a fluid in a horizontal tube of 1.75 mm inner diameter is carried out to obtain flow pattern and heat transfer coefficient data.

Photographs of the flow pattern are obtained through the viewing window located downstream of the test section. Fig. 3 illustrates the observed flow patterns which can be summarised as follows.

Slug flow: elongated bubbles which are larger in length than the channel diameter are developed from small bubbles.

Throat-annular flow: the two consecutive elongated bubbles coalesce into a throat like gas core.

Author's personal copy

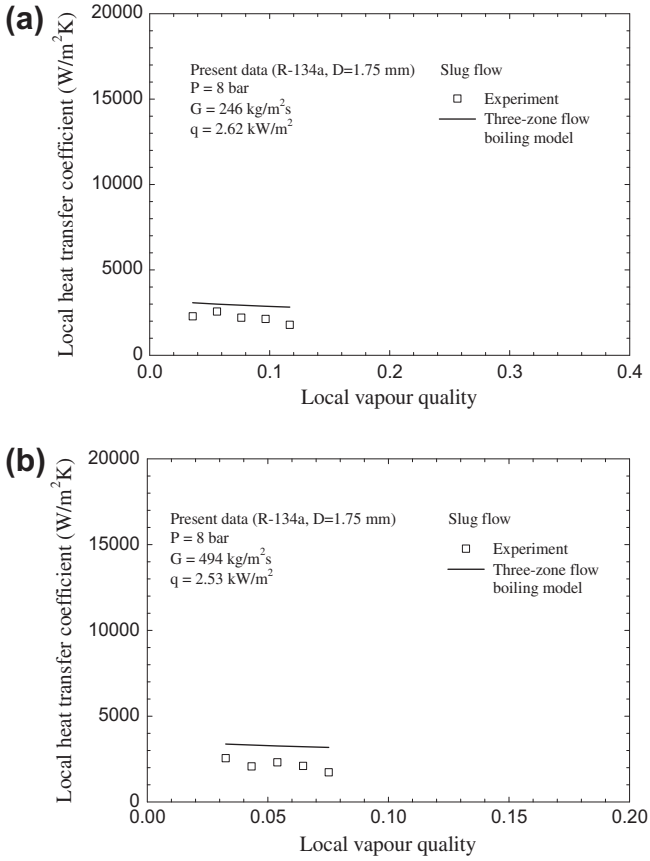

Fig. 7. Comparison of the local heat transfer coefficient data for slug flow regime with the three-zone flow boiling model.

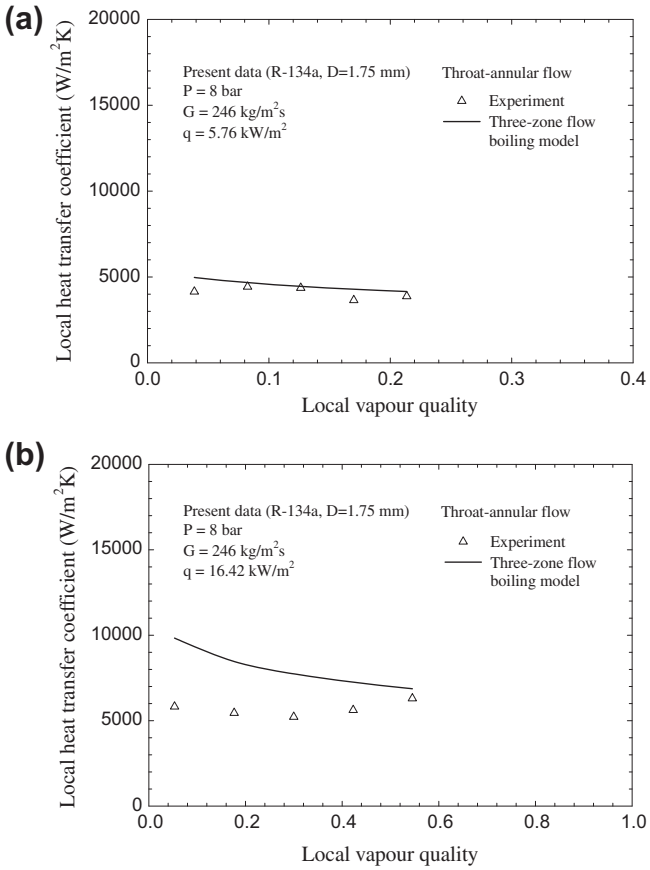

Fig. 8. Comparison of the local heat transfer coefficient data for throat-annular flow regime with the three-zone flow boiling model.

Churn flow: a disruptive region develops due to the distortion of the elongated bubbles.

Annular flow: liquid film flows on the tube wall and the tube core is occupied by continuous vapour flow.

Annular-rivulet flow: annular flow is observed alternately with flowing of a rivulet-like liquid stream on the tube surface.

It is remarkable to note from the figure that peculiar flow patterns, throat-annular flow and annular-rivulet flow, are also observed in the two-phase gas–liquid system for small channels as reported by Saisorn and Wongwises [19]. Such flow patterns have never been observed in ordinarily sized channels.

The usual method in the presentation of flow pattern data is to classify the flow pattern by visual observation and plot the data as a flow pattern map in terms of system parameters. The flow pattern map in terms of mass flux and vapour quality is presented in Fig. 4. The present data are also compared with the flow pattern map developed by Revellin and Thome [20] for flow boiling in micro-channels. Their flow regime map comprises different zones according to the bubble coalescence phenomena. The followings are a brief description of each zone located in the flow pattern map.

The isolated bubble (IB) regime corresponds to a relatively high bubble generation rate when compared with the bubble coalescence rate. Either or both of bubbly flow and slug flow are included in this regime. The coalescing bubble (CB) regime is defined when the bubble generation rate is smaller than the bubble coalescence rate.

The isolated bubble (IB) flow to coalescing bubble (CB) flow transition is given by

$$x_{IB/CB} = 0.763\left(\frac{Re_{LO}Bo}{We_{GO}}\right)^{0.41} \quad (1)$$

where Bo stands for Boiling number, Re_{LO} represents all-liquid Reynolds number and We_{GO} is all-vapour Weber number.

The transition from coalescing bubble flow to annular flow is determined by

$$x_{CB/A} = 0.00014Re_{LO}^{1.47}We_{LO}^{-1.23} \quad (2)$$

where We_{LO} is all-liquid Weber number.

These correlations take into account different effects including heat flux, viscosity and surface tension which are represented, respectively, by Boiling number, Reynolds number and Weber number. Their correlations were remarkably developed to generate a number of points representing the zone or vicinity of the transitions between flow regimes.

The comparison as indicated in Fig. 4 reveals that, in general, the present data correspond well with the transition zones proposed by Revellin and Thome [20]. The regions of churn flow and throat-annular flow obtained from the present study agree fairly well with their coalescing bubble regime whereas our annular flow and annular-rivulet flow are located in their annular region. The present slug flow data are found near the transition zone between their isolated bubble and coalescing bubble regions.

Heat flux, q, transferred to the test section is provided by the regulated DC power supply generating 80 A at 12 V. T-type thermocouples are installed at the inlet and outlet of the test section to measure the refrigerant temperatures. The two-phase conditions for flow boiling are provided at the test section inlet by using pre-heater as shown in Fig. 1. The saturation pressures at the test section inlet and outlet are obtained based on the corresponding saturation temperatures. Regarding the assumption of a linear

Author's personal copy

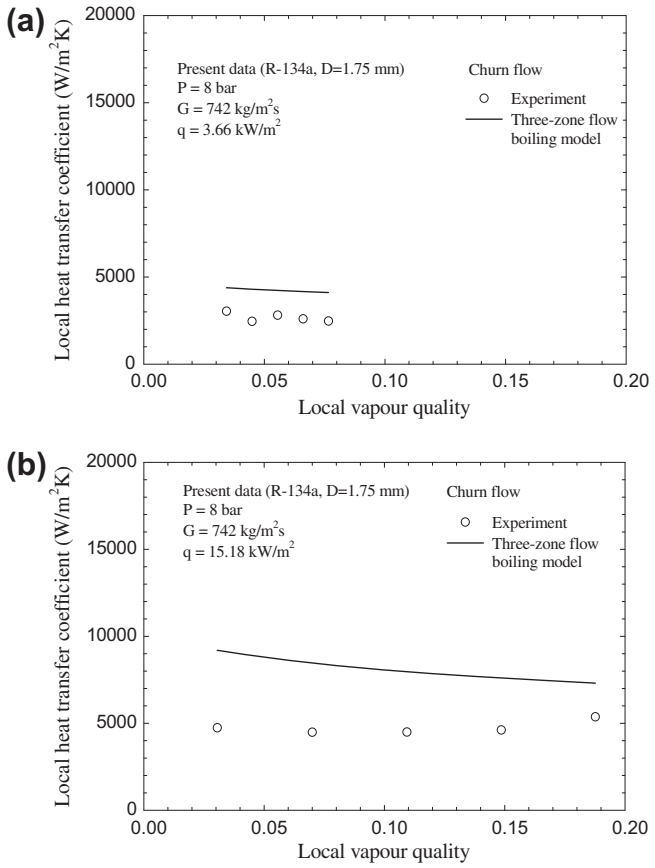

Fig. 9. Comparison of the local heat transfer coefficient data for churn flow regime with the three-zone flow boiling model.

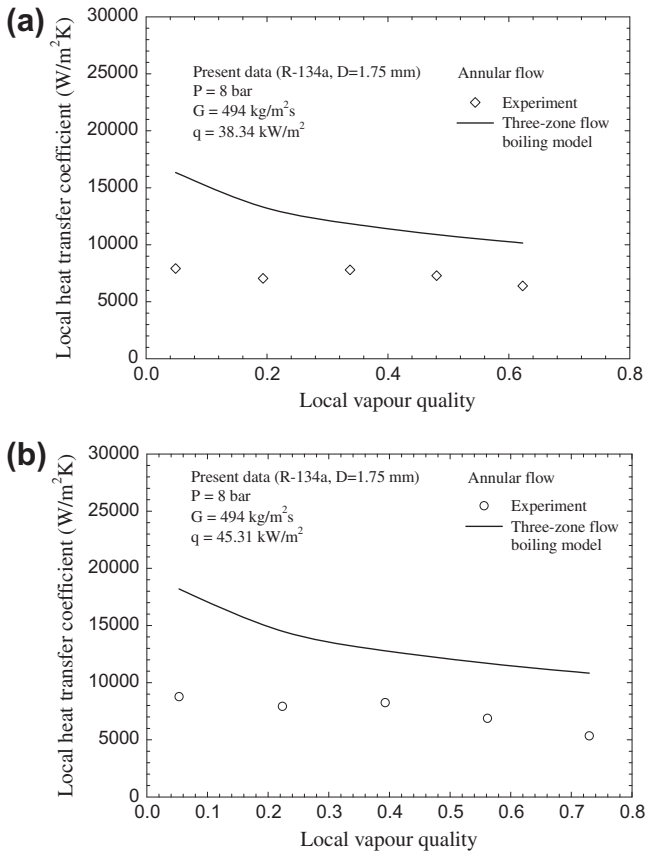

Fig. 10. Comparison of the local heat transfer coefficient data for annular flow regime with the three-zone flow boiling model.

variation of the saturation pressure along the tube, the local saturation temperatures, $T_{sat,loc}$, can subsequently be obtained.

As shown in Fig. 2, the 10 T-type thermocouples are installed on the top and bottom sides at equal distances along the tube to measure the tube surface temperature. For each position where the thermocouple is installed on the tube surface, the inner wall temperature at a given position is determined using the equations for steady state one-dimensional heat conduction through the tube wall with internal heat generation. At a given distance, hence, the average temperature of the inner wall at the top and bottom sides stands for the local temperature on the inner wall, $T_{wall,in,loc}$. Finally, the local heat transfer coefficient, h_{loc}, for flow boiling of R-134a along the test section is determined using the following equation.

$$h_{loc} = \frac{q}{(T_{wall,in,loc} - T_{sat,loc})} \tag{3}$$

The local vapour quality is determined based on thermodynamic properties, i.e.

$$x = \frac{(i - i_L)}{i_{LG}} \tag{4}$$

where i_L is the specific enthalpy of the saturated liquid, i_{LG} represents the latent heat of vaporisation and the local fluid enthalpy, i, is determined from an energy balance.

Figs. 5 and 6 show the variation of the heat transfer coefficient with vapour quality for different heat flux and mass flux values. Based on the experimental range, Fig. 5 shows the dependence of heat transfer coefficients on heat flux. The measured results increase with increasing heat flux and are less affected by vapour quality. Fig. 6 depicts the variation of the heat transfer coefficient with different values of mass flux. The results indicate that the measured heat transfer coefficients are mostly less dependent on mass flux. The similar behaviours as presented in Figs. 5 and 6 were also reported by different researchers such as Saitoh et al. [7] and Shiferaw et al. [11].

The experimental heat transfer coefficients for different flow patterns will be subsequently compared with predictions made with the three-zone flow boiling model which is discussed briefly next.

The modelling approach based on the elongated bubble flow regime, also known as the three-zone flow boiling model, was recently proposed by Thome et al. [16] and Dupont et al. [17]. It is a mechanistic flow boiling heat transfer model comprising heat transfer zones including a pair of liquid slug and elongated bubble zones, followed by vapour slug if dry-out occurs. Each zone is modelled as passing at a fixed location sequentially and cyclically. Rather than nucleate boiling, the heat transfer was proposed to be dominated by conduction through the thin liquid film trapped between the elongated bubble and the tube wall.

To describe the cyclic passage through each zone, a time-averaged local heat transfer coefficient is obtained as follows:

$$h(z) = \frac{t_L}{\tau} h_L(z) + \frac{t_{film}}{\tau} h_{film}(z) + \frac{t_{dry}}{\tau} h_G(z) \tag{5}$$

where the period of bubble generation, τ, which is the reciprocal of the frequency was determined empirically by Dupont et al. [17]. t_L represents the time needed for the liquid slug to pass by a fixed location z along the tube. t_{film} and t_{dry} are the times needed, respectively, for film formation and local wall dry-out. h_{film} stands for the heat transfer coefficient in the film, which is assumed to be

Author's personal copy

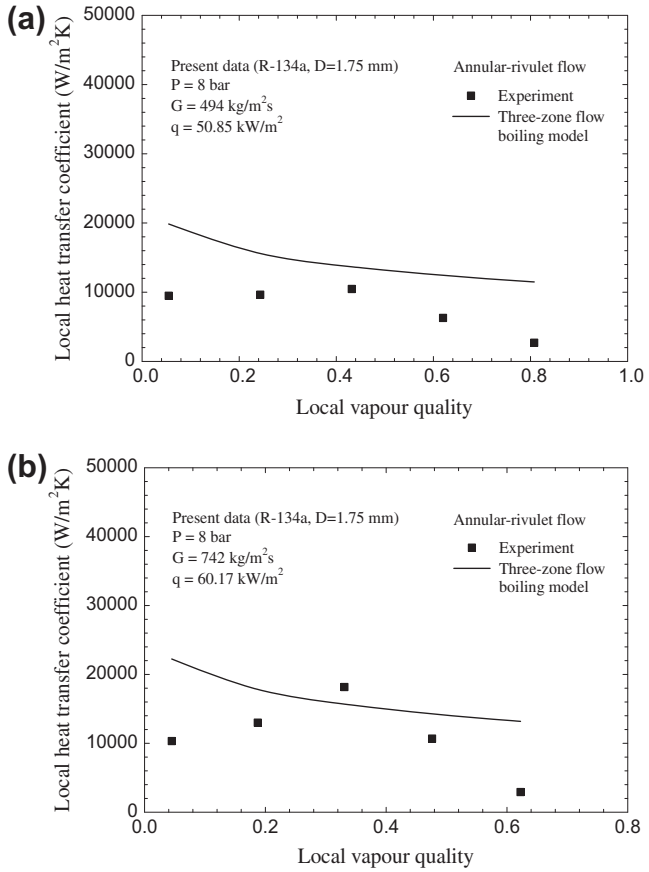

Fig. 11. Comparison of the local heat transfer coefficient data for annular-rivulet flow regime with the three-zone flow boiling model.

stagnant, across which one-dimensional conduction takes place. h_L and h_G are heat transfer coefficients in the liquid and vapour slugs, respectively, and are determined from their local Nusselt numbers.

Based on the general values for relevant parameters presented by Thome et al. [16] and Dupont et al. [17], our calculation is performed in order to examine the applicability of such a heat transfer model, whose dominant mechanism is transient conduction through the thin liquid film surrounding the confined and elongated bubble, to flow boiling heat transfer in different flow regimes.

Figs. 7–11 show a comparison of the present heat transfer coefficients for different flow regimes with predictions made with the three-zone flow boiling model.

Regarding the present flow pattern map shown in Fig. 4, the slug flow regime can be observed only in low vapour quality region. It is noted that the measured heat transfer coefficient for slug flow pattern tends to be not dependent with vapour quality. This corresponds well with the trends predicted by the model, excluding a contribution from nucleate boiling, as seen in Fig. 7.

In the throat-annular flow regime, which is developed from two consecutive vapour slugs (or elongated bubbles) coalescing into a throat-like vapour core, the measured heat transfer coefficient is not dependent on vapour quality but found to increase with heat flux as illustrated in Fig. 8. The observed characteristics, presented in Figs. 7 and 8, appear likely to agree with macro-scale ideas which suggest that nucleate boiling plays an important role in flow boiling heat transfer when the heat transfer coefficient is found to be strongly dependent on heat flux.

With regard to the predicted behaviour at increased heat flux, a relatively large enhancement of the predicted heat transfer coefficient is obtained when compared with the measured value, as indicated in Fig. 8. Based on transient conduction across the thin film being the dominant heat transfer mechanism, the heat transfer enhancement is due to the frequency of bubble generation which is strongly dependent on heat flux [17]. The model assumption seems to be compatible with the present results under low heat flux condition as seen in Fig. 8a.

The throat-annular flow is developed from the two consecutive elongated bubbles (vapour slugs) which coalesce to form the ripple, leading to a throat-like vapour core. As heat flux increases, however, the ripple appearing at the throat-like vapour core becomes thinner, and the annular flow is eventually established as illustrated by the flow regime map shown in Fig. 4. For throat-annular flow regime under a heat flux of 16.42 kW/m^2, the relevant position on the flow regime map is located near the transition from coalescing bubble flow to annular flow (CB/A transition zone). Such location is far from slug flow pattern from which the model was developed. As a consequence, the significant deviations of model predictions from the experimental results are observed in Fig. 8b.

Churn flow is characterised by a disruptive region caused by distortion of the vapour slug. This unstable condition, not included in the model which assumes a stagnant thin liquid film where one-dimensional conduction plays an important role in determining the local heat transfer coefficient, may explain why the prediction does not represent satisfactorily the experimental data as presented in Fig. 9. The deviation between measured and predicted values seems to get smaller as the heat flux decreases.

Up to this point, it is likely that the three-zone flow boiling model could also be roughly applicable to the throat-annular flow and churn flow regimes, in addition to the slug flow pattern from which the model was developed. It should be noted however, that the prediction is fairly reasonable under low heat flux conditions.

Figs. 10 and 11 show, respectively, the predictions compared with measured heat transfer coefficients for annular flow and annular-rivulet flow. In contrast to the results mentioned previously, the applicability of the model cannot extend to both annular and annular-rivulet flow regimes appearing under the present experimental range. In Fig. 11, a significant drop in the measured heat transfer coefficient near the test section outlet may be mainly attributed to partial dry-out intermittently appearing in annular-rivulet flow.

For the saturation pressure higher than 8 bar, the three-zone flow boiling model failed to predict the experimental data. Mean absolute error (MAE) of above 150% was obtained for all conditions as well as all flow patterns. As discussed in Saisorn et al. [21] and Choi et al. [9], the liquid film under high saturation pressure tends to break up easily, leading to the unstable condition near the tube wall. Such condition, which is not taken into account in the model assumption, results in the disagreement of the data with the model prediction.

4. Conclusion

Boiling of R-134a flowing through a mini-channel with diameter of 1.75 mm is studied. Five different flow patterns, including slug flow, throat-annular flow, churn flow, annular flow and annular-rivulet flow, are identified. The heat transfer coefficient increases with increasing heat flux but is mostly independent of mass flux and vapour quality. The heat transfer coefficients for each flow pattern are also compared with the predictions based on the three-zone flow boiling model. Although the model was developed to describe the slug flow regime, the comparison illustrates that the model tends to become roughly applicable for throat-annular flow and churn flow patterns, especially at low heat flux conditions.

Author's personal copy

Acknowledgements

The authors would like to express their appreciation to King Mongkut's University of Technology Thonburi, the Thailand Research Fund, the Office of the Higher Education Commission and the National Research University Project for providing financial support for this study.

References

[1] S. Saisorn, S. Wongwises, A review of two-phase gas–liquid adiabatic flow characteristics in micro-channels, Renew. Sust. Energy Rev. 12 (2008) 824–838.
[2] S.S. Mehendale, A.M. Jacobi, R.K. Ahah, Fluid flow and heat transfer at micro- and meso-scales with application to heat exchanger design, Appl. Mech. Rev. 53 (2000) 175–193.
[3] S.G. Kandlikar, Fundamental issues related to flow boiling in mini-channels and micro-channels, Exp. Therm. Fluid Sci. 26 (2002) 389–407.
[4] X. Huo, L. Chen, Y.S. Tian, T.G. Karayiannis, Flow boiling and flow regimes in small diameter tubes, Appl. Therm. Eng. 24 (2004) 1225–1239.
[5] J. Pettersen, Flow vaporization of CO_2 in microchannel tubes, Exp. Therm. Fluid Sci. 28 (2004) 111–121.
[6] R. Yun, Y. Kim, M.S. Kim, Convective boiling heat transfer characteristics of CO_2 in microchannels, Int. J. Heat Mass Transfer 48 (2005) 235–242.
[7] S. Saitoh, H. Daiguji, E. Hihara, Effect of tube diameter on boiling heat transfer of R-134a in horizontal small-diameter tubes, Int. J. Heat Mass Transfer 48 (2005) 4973–4984.
[8] K.I. Choi, A.S. Pamitran, J.T. Oh, Two-phase flow heat transfer of CO_2 vaporization in smooth horizontal minichannels, Int. J. Refrig. 30 (2007) 767–777.
[9] K.I. Choi, A.S. Pamitran, C.Y. Oh, J.T. Oh, Boiling heat transfer of R-22, R-134a, and CO_2 in horizontal smooth minichannels, Int. J. Refrig. 30 (2007) 1336–1346.
[10] D. Shiferaw, X. Huo, T.G. Karayiannis, D.B.R. Kenning, Examination of heat transfer correlations and a model for flow boiling of R134a in small diameter tubes, Int. J. Heat Mass Transfer 50 (2007) 5177–5193.
[11] D. Shiferaw, T.G. Karayiannis, D.B.R. Kenning, Flow boiling in a 1.1 mm tube with R134a: experimental results and comparison with model, Int. J. Therm. Sci. 48 (2009) 331–341.
[12] C.L. Ong, J.R. Thome, Flow boiling heat transfer of R134a, R236fa and R245fa in a horizontal 1.030 mm circular channel, Exp. Therm. Fluid Sci. 33 (2009) 651–663.
[13] H.J. Lee, S.Y. Lee, Heat transfer correlation for boiling flows in small rectangular horizontal channels with low aspect ratios, Int. J. Multiphase Flow 27 (2001) 2043–2062.
[14] B. Sumith, F. Kaminaga, K. Matsumura, Saturated flow boiling of water in a vertical small tube, Exp. Therm. Fluid Sci. 27 (2003) 789–801.
[15] W. Qu, I. Mudawar, Flow boiling heat transfer in two-phase microchannel heat sinks; experimental investigation and assessment of correlation methods, Int. J. Heat Mass Transfer 46 (2003) 2755–2771.
[16] J.R. Thome, V. Dupont, A.M. Jacobi, Heat transfer model for evaporation in microchannels. Part I: presentation of the model, Int. J. Heat Mass Transfer 47 (2004) 3375–3385.
[17] V. Dupont, J.R. Thome, A.M. Jacobi, Heat transfer model for evaporation in microchannels. Part II: comparison with the database, Int. J. Heat Mass Transfer 47 (2004) 3387–3401.
[18] J. Kaew-On, S. Wongwises, Experimental investigation of evaporation heat transfer coefficient and pressure drop of R-410A in a multiport mini-channel, Int. J. Refrig. 32 (2009) 124–137.
[19] S. Saisorn, S. Wongwises, Flow pattern, void fraction and pressure drop of two-phase air-water flow in a horizontal circular micro-channel, Exp. Therm. Fluid Sci. 32 (2008) 748–760.
[20] R. Revellin, J.R. Thome, A new type of diabetic flow pattern map for boiling heat transfer in microchannels, J. Micromech. Microeng. 17 (2007) 788–796.
[21] S. Saisorn, J. Kaew-On, S. Wongwises, Flow pattern and heat transfer characteristics of R-134a refrigerant during flow boiling in a horizontal circular mini-channel, Int. J. Heat Mass Transfer 53 (2010) 4023–4038.

International Journal of Heat and Mass Transfer 54 (2011) 4376–4388

Contents lists available at ScienceDirect

International Journal of Heat and Mass Transfer

journal homepage: www.elsevier.com/locate/ijhmt

Numerical investigation of effective parameters in convective heat transfer of nanofluids flowing under a laminar flow regime

Ehsan Ebrahimnia-Bajestan [a,*], Hamid Niazmand [a], Weerapun Duangthongsuk [b], Somchai Wongwises [c,d]

[a] Department of Mechanical Engineering, Ferdowsi University of Mashhad, Mashhad, Iran
[b] Department of Mechanical Engineering, South-East Asia University, Bangkok, Thailand
[c] Fluid Mechanics, Thermal Engineering and Multiphase Flow Research Laboratory (FUTURE), Department of Mechanical Engineering, King Mongkut's University of Technology Thonburi, Bangmod, Bangkok 10140, Thailand
[d] The Royal Institute of Thailand, Academy of Science, Sanam Sueapa, Dusit, Bangkok 10300, Thailand.

ARTICLE INFO

Article history:
Received 3 December 2010
Received in revised form 29 April 2011
Accepted 29 April 2011
Available online 27 May 2011

Keywords:
Nanofluids
Heat transfer performance
Pressure drop
Numerical study
Thermal conductivity

ABSTRACT

This article presents a numerical investigation on heat transfer performance and pressure drop of nanofluids flows through a straight circular pipe in a laminar flow regime and constant heat flux boundary condition. Al_2O_3, CuO, carbon nanotube (CNT) and titanate nanotube (TNT) nanoparticles dispersed in water and ethylene glycol/water with particle concentrations ranging between 0 and 6 vol.% were used as working fluids for simulating the heat transfer and flow behaviours of nanofluids. The proposed model has been validated with the available experimental data and correlations. The effects of particle concentrations, particle diameter, particles Brownian motions, Reynolds number, type of the nanoparticles and base fluid on the heat transfer coefficient and pressure drop of nanofluids were determined and discussed in details. The results indicated that the particle volume concentration, Brownian motion and aspect ratio of nanoparticles similar to flow Reynolds number increase the heat transfer coefficient, while the nanoparticle diameter has an opposite effect on the heat transfer coefficient. Finally, the present study provides some considerations for the appropriate choice of the nanofluids for practical applications.

© 2011 Elsevier Ltd. All rights reserved.

1. Introduction

Common heat transfer fluids such as oil, water and ethylene glycol have inherently poor thermal conductivity compared to most solids. This problem is the primary obstacle to the high compactness, light in weight and effectiveness of heat exchangers. In order to enhance the thermal conductivity of conventional heat transfer fluids, it has been tried to develop a new type of modern heat transfer fluid by suspending ultrafine solid particles in base fluids. In 1993, Masuda et al. [1] studied the heat transfer performance of liquids with solid nanoparticles suspension. However, the term of "nanofluid" was first named by Choi [2] in 1995, and successively gained popularity. Because of the extensively greater thermal conductivity and heat transfer performance of the nanofluids as compared to the base fluids, they are expected to be ideally suited for practical applications.

Since a decade ago, research publications related to the use of nanofluids as working fluids have been reported both numerically and experimentally. There are also some review papers that elaborate on the current stage in the thermal behaviours, thermophysical properties and flow characteristics of nanofluids [3–6]. However, this article is aimed at reviewing only the novel literature considering convective heat transfer of nanofluids with a numerical approach. These studies are briefly described as follows.

Mirmasoumi and Behzadmehr [7] reported the effect of nanoparticle diameter on convective heat transfer performance of Al_2O_3/water nanofluid flowing under a fully developed laminar flow regime numerically. In their study, a two-phase mixture model was used. The results demonstrated that the heat transfer coefficient of the nanofluid dramatically increases with decreasing the diameter of nanoparticle. Moreover, the results also indicated that nanoparticle diameter has no significant effect on the skin friction coefficient.

Kalteh et al. [8] numerically studied forced convective heat transfer of Cu/water nanofluid inside an isothermally heated microchannel under a laminar flow regime. An Eulerian two-fluid model was used to simulate the heat transfer characteristic of the nanofluid. The results indicated that the heat transfer performance increases with increasing Reynolds number as well as particle volume fraction. On the contrary, heat transfer enhancement increases with decreasing nanoparticle diameter. Finally, the results also showed that the pressure drop of nanofluids is slightly higher than that of base fluids.

* Corresponding author. Tel.: +98 915 300 6795; fax: +98 511 876 3304.
E-mail address: ehsan.ebrahimnia@gmail.com (E. Ebrahimnia-Bajestan).

0017-9310/$ - see front matter © 2011 Elsevier Ltd. All rights reserved.
doi:10.1016/j.ijheatmasstransfer.2011.05.006

Mirmasoumi and Behzadmehr [9] investigated the laminar mixed convection heat transfer of Al_2O_3/water nanofluid flowing through a horizontal tube numerically. A two-phase mixture model was used to describe the hydrodynamic and thermal behaviour of the nanofluid. The numerical results indicated that in the fully developed region the particle concentration has insignificant effects on the hydrodynamic parameters, while it has important effects on the thermal parameters. Moreover, the results showed that nanoparticle concentration is higher at the bottom of the test tube and at the near wall region.

Akbarinia [10] and Akbarinia and Behzadmehr [11] numerically investigated the fully developed laminar mixed convection of Al_2O_3/water nanofluid flowing through a horizontal curved tube. In their studies, three-dimensional elliptic governing equations were used. The effects of the buoyancy force, centrifugal force and particle concentration on the heat transfer performance were presented. The results showed that the particle concentration has no direct effect on the secondary flow, axial velocity and skin friction coefficient. However, when the buoyancy force is more important than the centrifugal force, the effect of particle concentration on the entire fluid temperature can affect the hydrodynamic parameters. Moreover, the results also indicated that the buoyancy force decreases the Nusselt number whereas the particle concentration has a positive effect on the heat transfer enhancement and on the skin friction reduction.

Izadi et al. [12] studied the hydrodynamic and thermal behaviours of an Al_2O_3/water nanofluid flowing through an annulus under a laminar flow regime. In their study, a single-phase model was used for nanofluid simulation. The results indicated that the particle volume concentration has no significant effect on the dimensionless axial velocity, but affects the temperature field and increases the heat transfer coefficient.

He et al. [13] numerically studied the convective heat transfer of a nanofluid with TiO_2 nanoparticles dispersed in water under laminar flow conditions. A single-phase model and combined Euler and Lagrange methods were used to investigate the effects of volume concentration, Reynolds number and aggregate size on the convective heat transfer and flow behaviour of the nanofluid. Their results indicated that the nanofluid significantly enhances the Nusselt number, especially in the entrance region. Moreover, the numerical results were consistent with experimental data.

Bianco et al. [14] investigated the heat transfer performance of an Al_2O_3/water nanofluid flowing through a circular tube under a laminar flow regime numerically. A single-phase model and two-phase model were used to determine the heat transfer coefficient of the nanofluid. The results demonstrated that the heat transfer performance increases with increasing Reynolds number as well as particle volume concentration. Moreover, differences in the average heat transfer coefficient between the single-phase and two-phase models were observed as approximately 11%.

Kumar et al. [15] used a single-phase thermal dispersion model to numerically investigate the thermal properties and flow field of a Cu/water nanofluid in a thermally driven cavity. The results indicated that the Grashof number, particle volume fraction and particle shape factor augment the average Nusselt number of nanofluids.

Talebi et al. [16] presented the numerical formulation to evaluate the laminar mixed convection heat transfer of Cu/water nanofluid flowing through a square lid-driven cavity. They found that, at a given Reynolds number, the particle concentration affects the thermal behaviour and flow characteristic at larger Rayleigh numbers. Moreover, the effect of particle concentration decreased with increasing Reynolds number.

Shahi et al. [17] reported a numerical investigation to simulate the heat transfer performance of Cu/water nanofluid flowing through a square cavity under a laminar flow regime. Their results indicated that the average Nusselt number of the nanofluid increases with increasing particle concentration. In contrast, the results also showed that the bulk temperature of the nanofluid decreases with increasing particle concentration.

Akbarinia and Laur [18] presented the laminar mixed convection heat transfer of Al_2O_3/water nanofluid flows in a circular curved tube numerically. A two-phase mixture model and the control-volume technique were used to investigate the effect of particle diameter on the hydrodynamic and thermal parameters. Their results indicated that the Nusselt number and secondary flow decrease with increasing the particle diameter and uniform distribution of nanoparticles is observed.

Zeinali Heris et al. [19] numerically investigated the convective heat transfer of nanofluid in a circular tube with constant wall temperature, employing a dispersion model. Their results showed that decreasing nanoparticle size and increasing nanoparticle concentration augment the heat transfer coefficient.

Raisi et al. [20] carried out a numerical study on laminar convective heat transfer of Cu/water nanofluid inside a microchannel with slip and no slip boundary conditions. They investigated the effect of different parameters such as Reynolds number, particle concentration, and slip velocity coefficient on the nanofluid heat transfer characteristics. The results indicated that the particle concentration and slip velocity coefficient have significant effects on the heat transfer rate at high Reynolds numbers.

Ghasemi and Aminossadati [21] investigated the natural convective heat transfer of CuO/water nanofluid inside an inclined enclosure with top and bottom wall at different temperatures. The effects of Rayleigh number, inclination angle, and particle concentration on heat transfer performance were studied. The results showed that the flow pattern, temperature field and heat transfer rate are affected by inclination angle at high Rayleigh numbers. Furthermore, it was found that the heat transfer rate is maximised at specific particle concentration and inclination angle.

Zhou et al. [22] presented the lattice Boltzman method (LB method) to study the microscale characteristics of the multicomponent flow of nanofluids. In this method, the computation domain was separated into fine mesh and coarse mesh regions, respectively. The multicomponent LB method was used in the fine mesh region and the single-component LB method was applied in the coarse mesh region. The results indicated that the present model can be used to predict the microscopic characteristics of the nanofluid and the computational efficiency can be significantly improved.

Although numerous papers are currently available on the numerical study of laminar convective heat transfer of nanofluids, there is no comprehensive study on different effective parameters in this field. The effect of several parameters such as nanoparticle shape, based fluid type and nanoparticle material are not considered in literature. On the other hand, naturally the increase in heat transfer performance due to the nanofluids is accompanied by several undesirable effects such as an increase in pressure drop. Therefore, it needs to find the suitable nanofluid for optimum operation. No significant attention is paid to find some criteria for the choice of appropriate nanofluids in different heat transfer applications. In the present study a modified single-phase model for predicting the heat transfer performance of nanofluids is proposed and a home-made FORTRAN computer program is developed. The model has been validated against the measured data of Kim et al. [23] and the predicted values from Shah and London [24] for the base fluid. The effects of particle concentration, mean particle diameter, Reynolds number, Brownian motion, nanoparticle material and shape, and type of base fluid on the heat transfer performance of nanofluids are then investigated in detail. Finally, some guidelines related to choice of the appropriate nanofluid for particular applications are provided.

2. Mathematical modelling

Normally, two different approaches can be used in predicting the heat transfer performance of nanofluids. One is the two-phase model, where solid particles are treated as a solid phase in the base fluid, and the other is the single-phase model, where the presence of the nanoparticles is accounted for by introducing the effective thermophysical properties for the nanofluid. A single-phase model is simpler to implement and requires less computational time, and therefore, adopted here to describe the heat transfer characteristics of nanofluids flowing through a straight circular tube under constant wall heat flux and laminar flow regime, as shown in Fig. 1. On the basis of this model, the governing equations are as follows.

For continuity equation:

$$\iint \rho_e \vec{V} \cdot d\vec{A} = 0. \tag{1}$$

For momentum equation:

$$\int_{\forall} \rho_e \frac{\partial \vec{V}}{\partial t} d\forall + \iint \vec{V} \rho_e \vec{V} \cdot d\vec{A} = -\iint p\vec{n} \cdot d\vec{A} + \iint \mu_e \vec{\nabla} \vec{V} \cdot d\vec{A} \tag{2}$$

For energy equation:

$$\int_{\forall} (\rho C_p)_e \frac{\partial T}{\partial t} d\forall + \iint (\rho C_p)_e T\vec{V} \cdot d\vec{A} = \iint k_e \vec{\nabla} T \cdot d\vec{A} \tag{3}$$

where $\vec{V}$, p, T, t, $\forall$, $\vec{A}$ and $\vec{n}$ are the velocity vector, pressure, temperature, time, volume, cross-sectional area vector and normal unit vector, respectively. The effective thermophysical properties of the nanofluid indicated by the subscript e are density (ρ), thermal conductivity (k), dynamic viscosity (μ), and heat capacity (C_p). These effective properties are modelled as temperature dependent variables using available correlations and experimental data as follows.

Density:

$$\rho_e(\phi, T) = (1-\phi)\rho_f(T) + \phi\rho_p \tag{4}$$

Heat capacity:

$$C_{p,e}(\phi, T) = \frac{(1-\phi)(\rho(T)C_p(T))_f + \phi(\rho_p C_p)_p}{(1-\phi)\rho_f(T) + \phi\rho_p} \tag{5}$$

where ϕ is the volume fraction of the nanoparticles, and the subscripts p and f indicate the nanoparticle and base fluid, respectively.

Regarding the dynamic viscosity and thermal conductivity of nanofluids two different methods have been considered. In the first method, available measured data of these properties in static condition are used. However, in the second method, available models for dynamic viscosity and thermal conductivity of nanofluids, where different effects such as base fluid type, Brownian motions, volume concentration, and nanoparticle diameters are also included are employed. Clearly, these models are designed to accurately predict the heat transfer coefficient.

In the present study, the measured data of Kim et al. [23] is used to develop the following correlations for predicting the effective thermal conductivity and viscosity of the nanofluids according to the first method.

$$\mu_e = -0.0001953 + \frac{0.0475745}{T} - \frac{0.42561}{T^2} \quad \text{for } 20\,^\circ\text{C} \leqslant T \leqslant 80\,^\circ\text{C} \tag{6}$$

$$k_e = 0.65 + 4.864 \times 10^{-7} T^3 \quad \text{for } 22\,^\circ\text{C} \leqslant T \leqslant 52\,^\circ\text{C} \tag{7}$$

where T is the temperature in Celsius. However, it should be mentioned that above correlations are valid only for Al_2O_3/water nanofluid containing 3 vol.% of suspended particles.

As for the second method, the Vajjha et al.'s [25] model is taken for viscosity with two parameters A and B, which are determined according to the experimental data of Kim et al. [23].

$$\mu_e = \mu_f(T) A \exp(B\phi) \tag{8}$$

This correlation applies for $20\,^\circ\text{C} \leqslant T \leqslant 90\,^\circ\text{C}$ and $1\% \leqslant \phi \leqslant 10\%$, with $A = 0.9$ and $B = 10.0359$.

For thermal conductivity, the model presented by Koo and Kleinstreuer [26] and modified by Vajjha and Das [27] is employed. The model consists of static thermal conductivity based on the Maxwell's theory and dynamic thermal conductivity to include Brownian motion of nanoparticles. This model is expressed as follows:

$$k_e = \left[\frac{k_p + 2k_f - 2(k_f - k_p)\phi}{k_p + 2k_f + (k_f - k_p)\phi}\right] k_f + (5 \times 10^4 \beta \phi \rho_f C_{p,f}) \times \sqrt{\frac{\kappa(T + 273.15)}{\rho_p d_p}} f(T, \phi) \tag{9}$$

$$f(T, \phi) = (2.8217 \times 10^{-2}\phi + 3.917 \times 10^{-3}) \frac{(T + 273.15)}{(T_0 + 273.15)} + (-3.0669 \times 10^{-2}\phi - 3.91123 \times 10^{-3}) \tag{10}$$

$$\beta = 8.4407(100\phi)^{-1.07304} \tag{11}$$

where κ is the Boltzmann constant (1.381×10^{-23} J/K), d_p is the nanoparticle diameter (m), and T is the temperature (°C). $T_0 = 0\,^\circ\text{C}$ is the reference temperature. The correlation is valid for $25\,^\circ\text{C} \leqslant T \leqslant 90\,^\circ\text{C}$ and the volume fractions between 1% and 10% for Al_2O_3 nanofluids [27]. It should be mentioned that all thermophysical properties of the base fluid (μ_f, k_f, $C_{p,f}$ and ρ_f) are considered as functions of temperature. For water as the base fluid, density, heat capacity and thermal conductivity are obtained from the curve-fits applied to available data [28], while for dynamic viscosity the following correlation is employed [29]:

$$\mu_{water} = 0.00002414 \times 10^{[247.8/(T+133)]} \tag{12}$$

The above methods for effective viscosity (Eqs. (6) and (8)) have been compared with measured data of Kim et al. [23] for 3.0 vol.% Al_2O_3/water nanofluids, where reasonable agreements are observed (Fig. 2). Similarly, the temperature variations of thermal

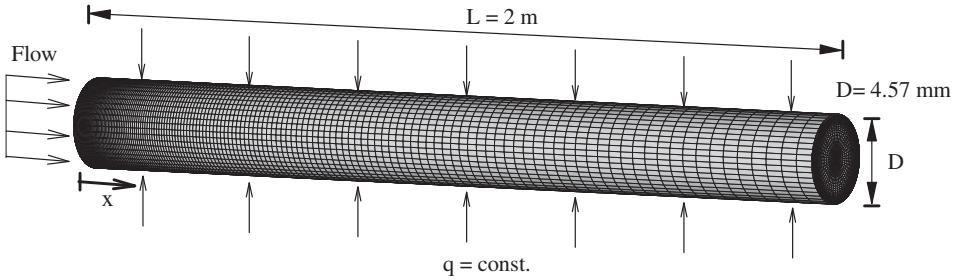

Fig. 1. Flow geometry and numerical grid distributions.

conductivity according to Eqs. (7) and (9) have been compared with the measured data of Kim et al. [23] as shown in Fig. 3. It can be seen that Eq. (9) over predicts the thermal conductivity as compared to the measured data, however it can predict the heat transfer coefficient more accurately as compared to Eq. (7) as will be discussed later.

3. Solution methodology

In order to evaluate the heat transfer coefficient of nanofluids numerically, the following assumptions are required.

As for boundary conditions for velocity filed, a uniform velocity profile is assumed at the inlet, while zero gradients are applied to all hydrodynamic variables at the outlet, with no-slip condition at walls. For the thermal field, constant heat flux of 60 W (2089.56 W/m^2) and the inlet temperature of 22 °C are employed corresponding to the data of Kim et al. [23], while constant temperature gradient is applied at the outlet.

In order to simulate the nanofluid flow, pipe geometry with 4.57 mm in diameter and 2 m long has been adopted according to the flow geometry in the experimental work of Kim et al. [23] as shown in Fig. 1. The problem under investigation is steady, however, in the numerical scheme the steady solution is obtained through sufficient integrations in time. The governing equations are solved numerically in a body-fitted coordinate system using a control-volume technique. The numerical solution is based on a projection-type method which solves the flow field in two steps. Firstly, an intermediate velocity field is obtained using the available pressure field. Secondly, velocity and pressure corrections

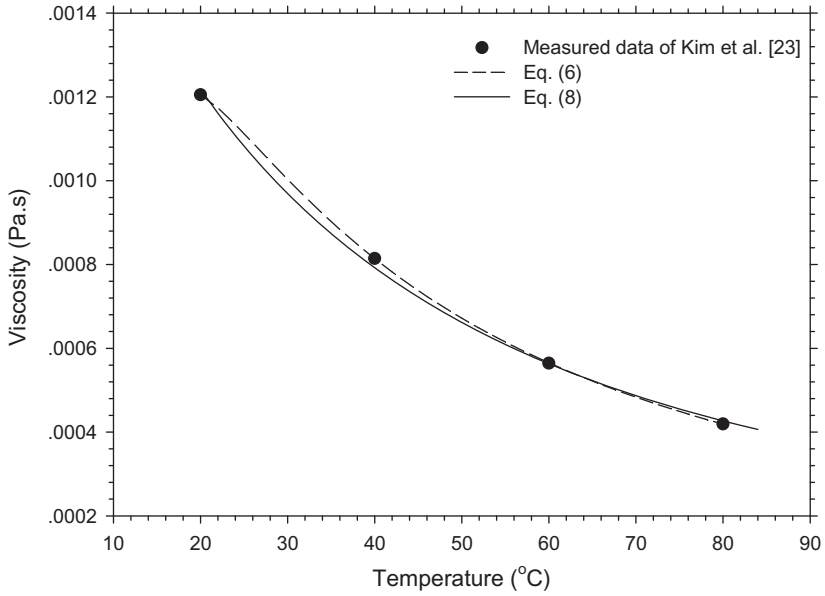

Fig. 2. Comparison of the predicted viscosity using Eqs. (6) and (8) with the measured data.

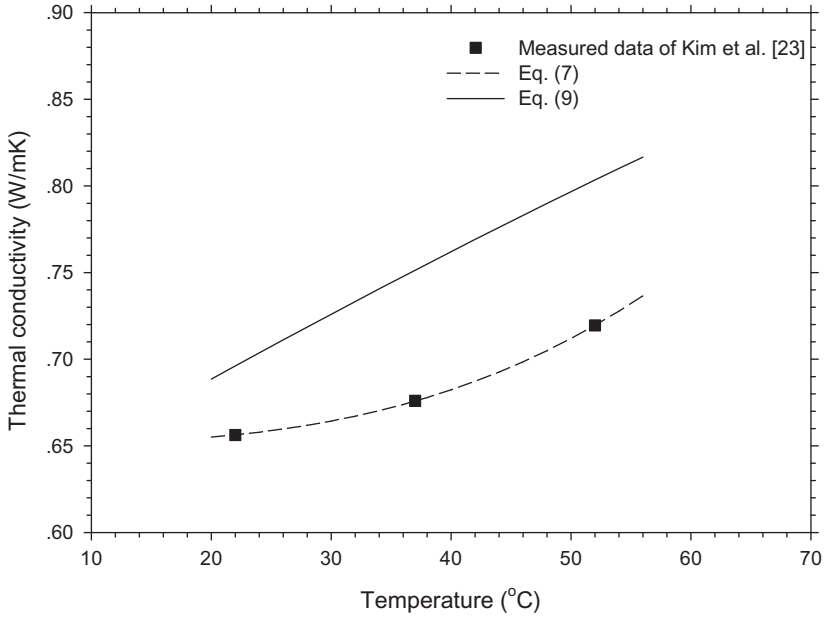

Fig. 3. Comparison of the predicted thermal conductivity using Eqs. (7) and (9) with the measured data.

are calculated from a Poisson equation designed to satisfy the continuity equation. The numerical scheme was originally developed by Chorin [30] and improved further by Dwyer [31] as well as Renksizbulut and Niazmand [32].

Moreover, extensive computations have been performed to identify the number of grid points that produce reasonably grid independent results. In Fig. 4 the grid resolution effects on the axial variations of the centreline velocity (nondimensionalized with the inlet velocity) and the heat transfer coefficient for just four different mesh distributions are presented. It is clear that the grid system of $41 \times 50 \times 150$ points in respective directions of radial, azimuthal, and axial adequately resolve the velocity and thermal fields with reasonable accuracy. Uniform grid spacing is used in the azimuthal direction, while the expansion ratios of 1.15 and 1.02 are employed in the radial and axial directions.

4. Model validation

For validating the present numerical scheme, the axial variations of the local Nusselt number have been compared with the experimental data of Kim et al. [23] and the results of Shah and London [24] as shown in Fig. 5. A laminar water flow in a straight circular pipe geometry, as mentioned above, has been considered under the constant heat flux condition of 60 W (2089.56 W/m^2) at Reynolds number of 1620. The Shah and London [24] equation for the axial variations of the local Nusselt number is expressed as:

$$Nu(x) = \begin{cases} 3.302x_*^{-1/3} - 1; & x_* \leqslant 0.00005 \\ 1.302x_*^{-1/3} - 0.5; & 0.00005 < x_* < 0.0015 \\ 4.264 + 8.68(10^3 x_*)^{-0.506}\exp(-41x_*); & x_* > 0.001 \end{cases} \quad (13)$$

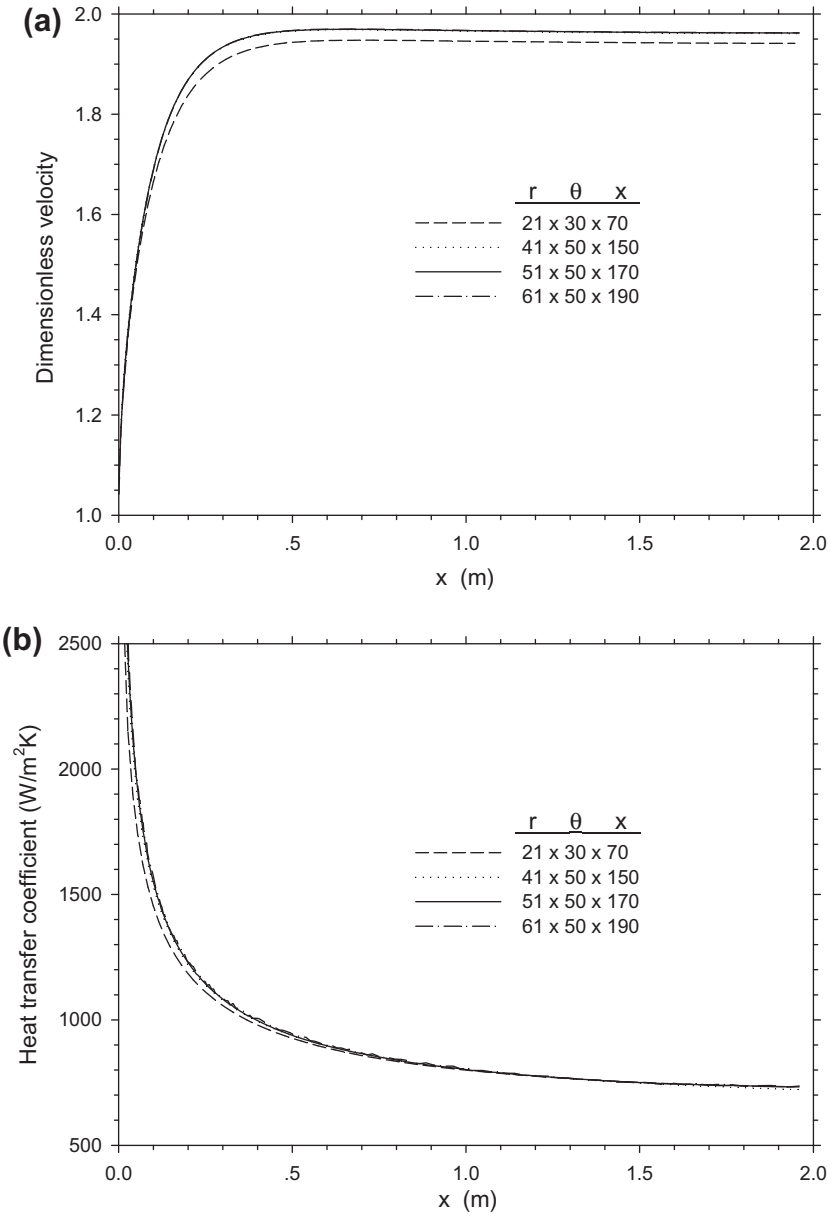

Fig. 4. Grid resolution effects on the axial variations of (a) dimensionless centreline velocity and (b) heat transfer coefficient for 6.0 vol.% Al_2O_3/water nanofluid at Reynolds number of 1460.

where $x_* = \frac{x/D}{\mathrm{Re}\,\mathrm{Pr}}$. Excellent agreements between the results can be observed in Fig. 5.

For the validation of the effective nanofluid properties models, the convective heat transfer of nanofluid in a straight pipe has been considered. Fig. 6 shows the axial variations of heat transfer coefficient of Al_2O_3/water nanofluid containing 3.0 vol.% of nanoparticles for Reynolds number of 1460. The results indicate that the second method (Eqs. (8) and (9)) agrees better with the measured data of Kim et al. [23] as compared to the first method (Eqs. (6) and (7)). This implies that the changes in thermal conductivity of nanofluids at static condition cannot justify the enhancement in heat transfer coefficient of nanofluids and a model, which adjusts the thermal conductivity to accurately estimate the heat transfer coefficient, is required.

Other numerical scheme validations for nanofluids can be found in Ebrahimnia-Bajestan et al. [33], which are not repeated here for conciseness.

5. Results and discussion

As shown in Fig. 6, the second method of nanofluid properties models predicts the heat transfer coefficient more accurately than the first method. In addition, the second method is more general than the first method, which is only valid for 3.0 vol.% Al_2O_3/water. Therefore, the second method has been employed for the evaluations of the effective thermal conductivity and viscosity in all numerical computations reported here. Moreover, the effects of

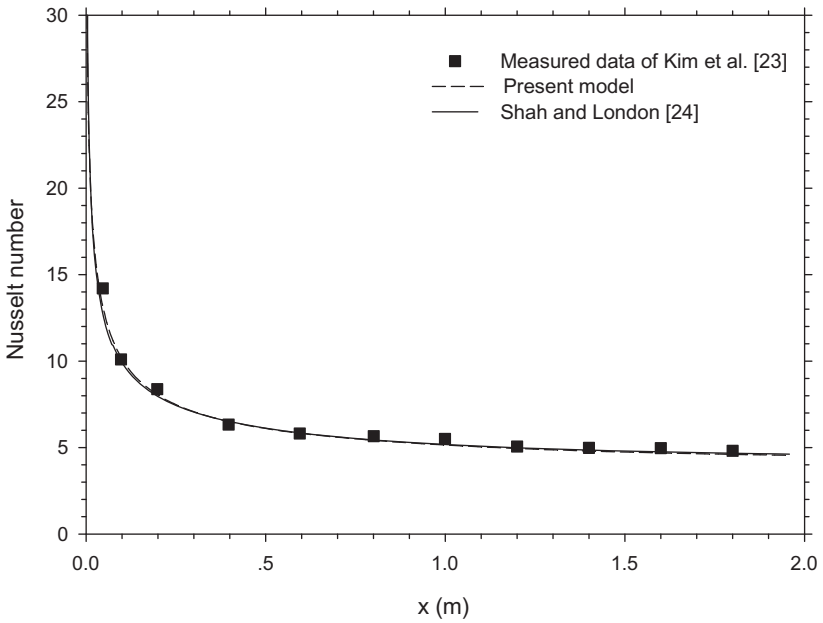

Fig. 5. Comparison of the axial variations of the Nusselt number with available data in literature at Reynolds number of 1620.

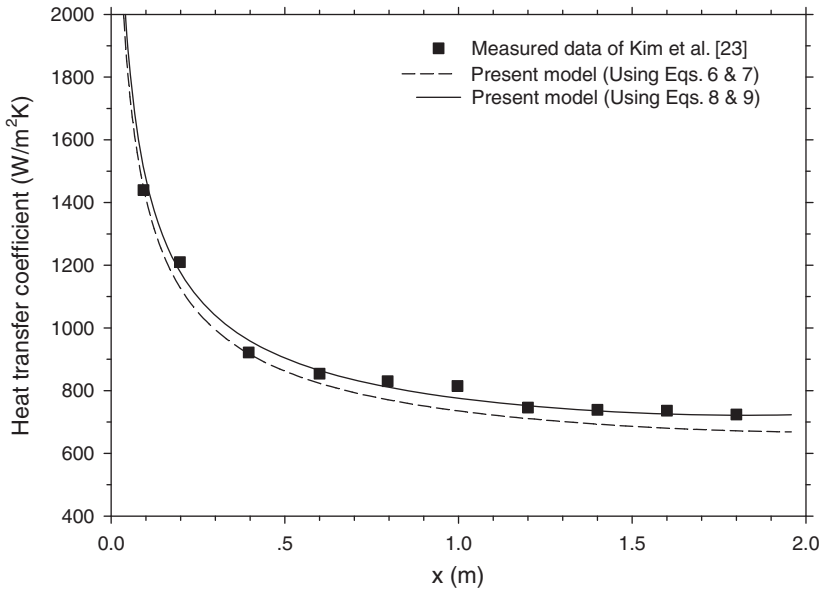

Fig. 6. Comparison of the local heat transfer coefficient with measured data of 3.0 vol.% Al_2O_3/water nanofluid at Reynolds number of 1460.

several parameters on the convective heat transfer characteristics of nanofluids will be examined in detail.

5.1. The effect of nanoparticle concentration

Fig. 7 shows the effect of particle volume concentration on the heat transfer coefficient along the pipe for Reynolds number of 1460 and heat flux of 2089.56 W/m^2. The results indicate that the heat transfer coefficient of nanofluid increases with increasing particle volume concentration. According to Eq. (9), nanofluids with higher particle concentrations have higher static and dynamic thermal conductivities, which in turn increase the heat transfer coefficient. For example, in the case of 6.0 vol.%, the local heat transfer coefficient is about 22% larger than pure water at the end of the pipe.

5.2. The effect of nanoparticle diameter

The effect of nanoparticle diameter on the heat transfer performance of nanofluid for Reynolds number of 1460 and heat flux of 2089.56 W/m^2 is shown in Fig. 8. The results show that the nanofluid with smaller nanoparticle diameter slightly increases the heat transfer coefficient as compared to the larger particle diameter, especially at lower volume concentrations. In general, according to Eq. (9) the nanoparticle diameter has a negative effect on the thermal conductivity and consequently on the heat transfer coefficient.

5.3. The effect of Reynolds number

Fig. 9 presents the effect of Reynolds number on the heat transfer coefficient along the pipe for Al_2O_3/water nanofluid with

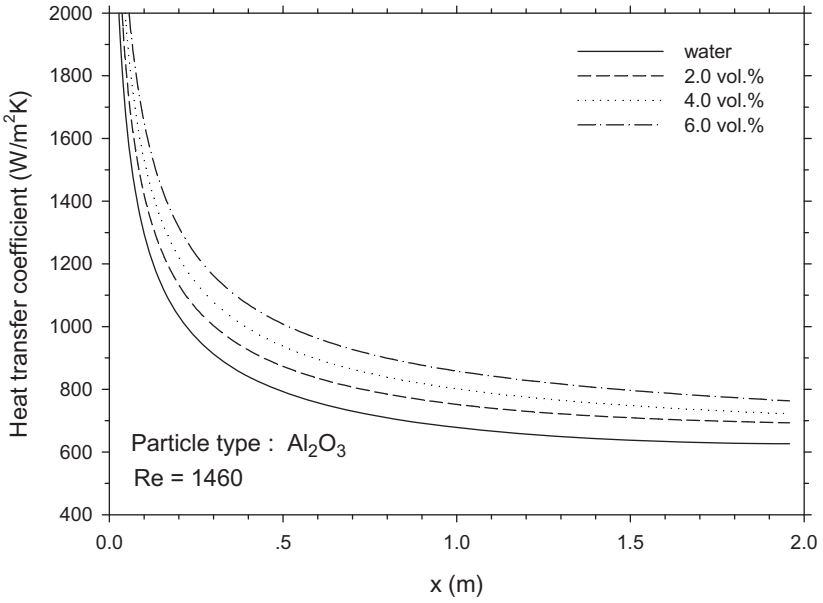

Fig. 7. Axial variations of heat transfer coefficient for different particle volume concentrations of Al_2O_3/water nanofluid at Reynolds number of 1460.

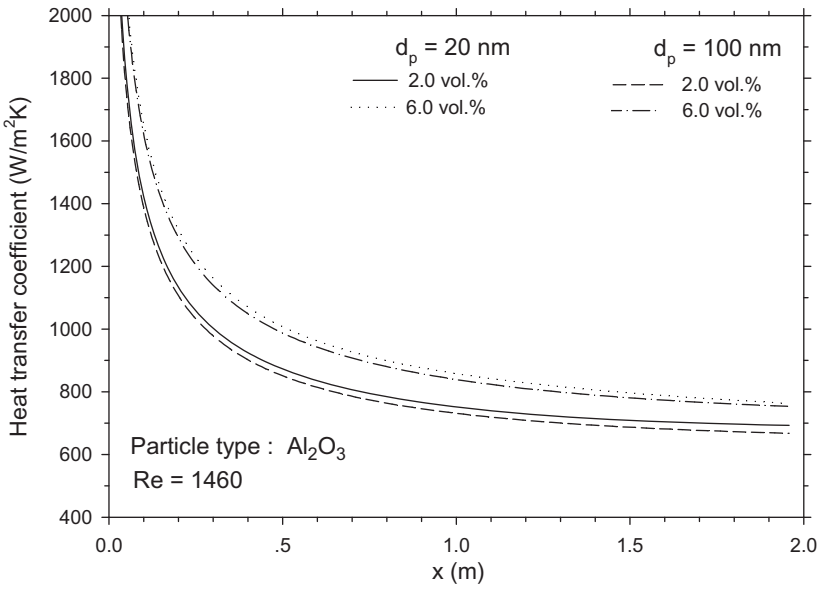

Fig. 8. Axial variations of heat transfer coefficient for different particle diameters and concentrations of Al_2O_3/water nanofluid at Reynolds number of 1460.

particle diameter of 20 nm. The results indicate that the heat transfer coefficient of nanofluid increases with increasing Reynolds number. This is due to the fact that higher Reynolds numbers lead to higher velocity and temperature gradients at the pipe wall.

5.4. The effect of Brownian motion of nanoparticles

According to Eq. (9), the second term is related to the dynamic thermal conductivity and reflects the Brownian motion effects on the thermal characteristics of nanofluids. In order to study the effects of Brownian motion on the heat transfer performance of nanofluids, Eq. (9) without the dynamic thermal conductivity term is used to simulate the convective heat transfer. It means that the classical two-phase model of Maxwell is employed and compared with the new nanofluid thermal conductivity model. Fig. 10 compares the axial variations of the heat transfer coefficient of Al_2O_3/water nanofluid with and without Brownian motion effects on thermal conductivity model for various particle concentrations at Reynolds number of 1460 and particle diameter of 20 nm. It is clearly seen that the Brownian motion has significant effects on the heat transfer coefficient of the nanofluids.

5.5. The effect of nanoparticle material

The nanoparticle material affects the nanofluid properties and consequently is an important factor in heat transfer performance. In order to study the effect of nanoparticle material, the CuO/water nanofluid is selected to compare with the results of the Al_2O_3/

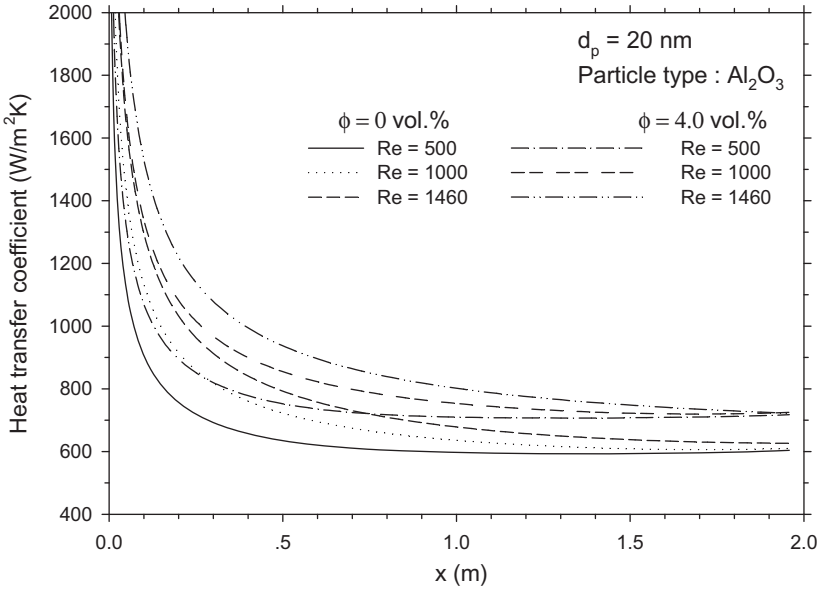

Fig. 9. Axial variations of heat transfer coefficient for different Reynolds numbers and particle concentrations of Al_2O_3/water nanofluid.

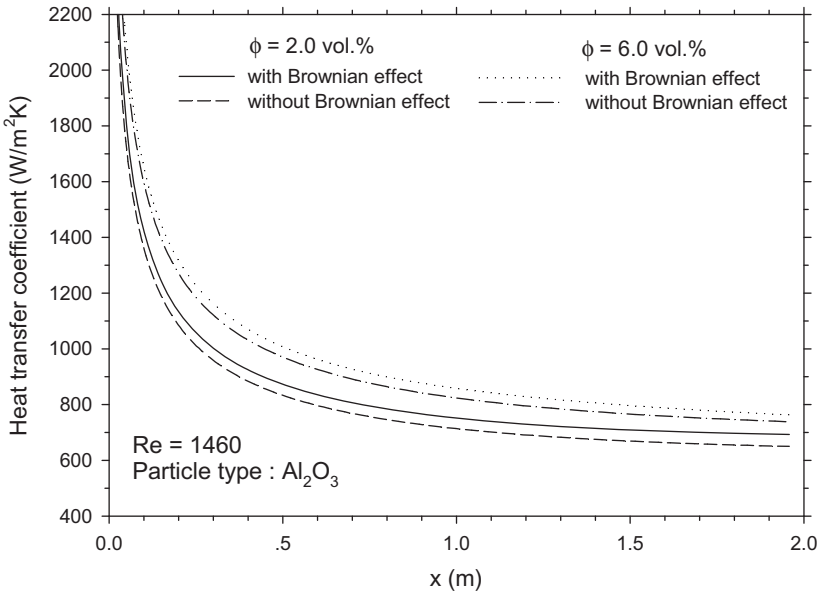

Fig. 10. Effects of Brownian motion on the local heat transfer coefficient as a function of particle concentration for Al_2O_3/water nanofluid at Reynolds number of 1460.

water nanofluid. For the viscosity of the CuO/water nanofluid, Eq. (8) is employed, where constants $A = 0.9197$ and $B = 22.8539$ are obtained following Vajjha et al. [25]. The thermal conductivity of CuO/water is evaluated based on Eqs. (9) and (10), however, the parameter β is determined from [27] as expressed below, which is valid for $25\ ^\circ C \leqslant T \leqslant 90\ ^\circ C$ and $1\% \leqslant \phi \leqslant 6\%$.

$$\beta = 9.881(100\phi)^{-0.9446} \tag{14}$$

As shown in Fig. 11, CuO/water nanofluids give higher convective heat transfer coefficients than the Al_2O_3/water nanofluids. For example, the heat transfer coefficient of 4.0 vol.% CuO/water nanofluids is greater than that of the 6.0 vol.% Al_2O_3/water nanofluids. This is because of the fact that the thermal conductivity of CuO nanoparticles is much larger than the thermal conductivity of Al_2O_3 nanoparticles.

5.6. The effect of base fluid properties

Another important factor in the heat transfer characteristics of nanofluids is the type of base fluid. In addition to water, a common base fluid consists of 60% ethylene glycol and 40% water (60% EG/water) by mass has also been considered. This kind of heat transfer fluid is common in cold regions of the world because of its low freezing point. The thermophysical properties of 60% EG/water as functions of temperature are obtained from [34] as follows:

$$\rho_{60\%EG/water} = -2.475 \times 10^{-3}T^2 - 0.35T + 1090.93 \tag{15}$$

$$C_{p,60\%EG/water} = 4.248T + 3042.74 \tag{16}$$

$$k_{60\%EG/water} = -3.196 \times 10^{-6}T^2 + 7.54 \times 10^{-4}T + 0.34 \tag{17}$$

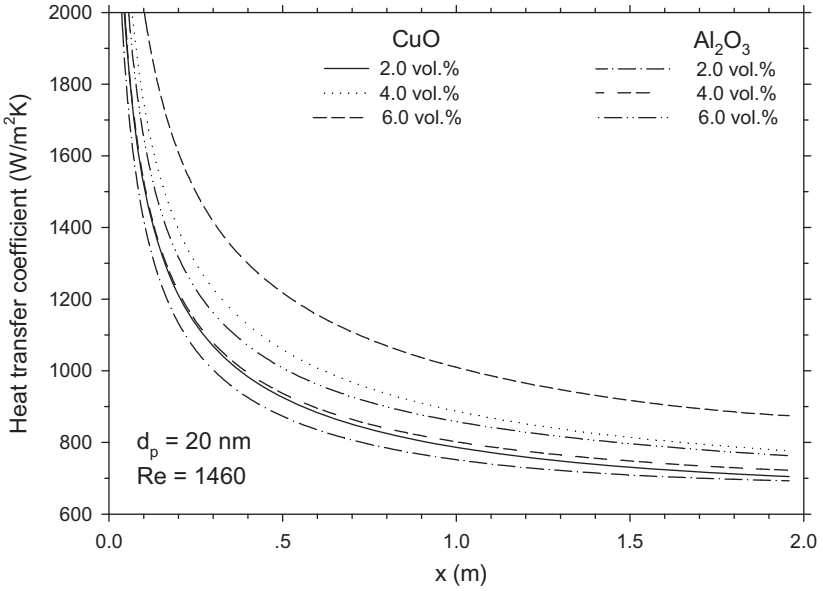

Fig. 11. Effects of particle type and particle concentration on the local heat transfer coefficient at Reynolds number of 1460 and particle diameter of 20 nm.

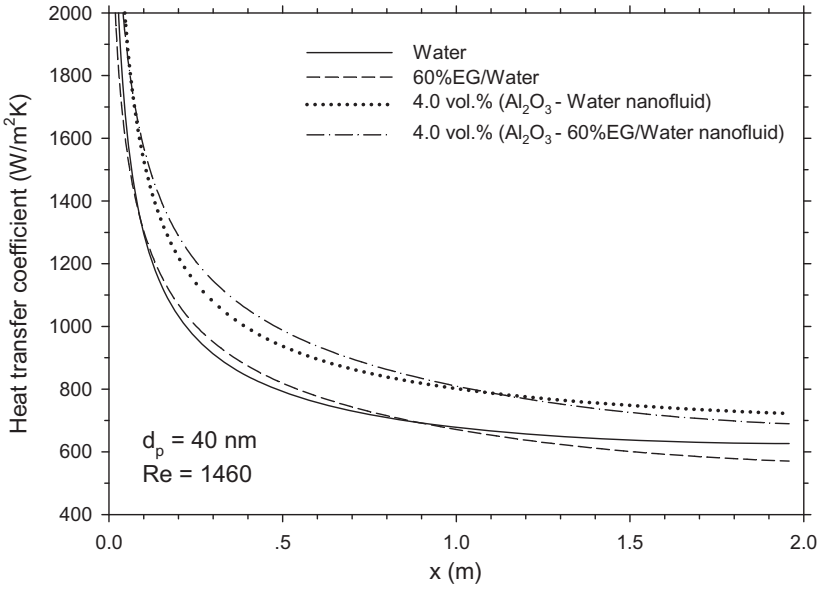

Fig. 12. Axial variations of heat transfer coefficient for different base fluids at Reynolds number of 1460 and particle diameter of 20 nm.

Table 1
Properties of CNT/water and TNT/water nanofluids.

Nanofluids	Nanoparticles aspect ratio	Nanoparticles concentration (vol.%)	Viscosity (Pa s)	Thermal conductivity (W/m K) $k = a + bT + cT^2$		
				a	b	c
CNT/water	>100	0.0384	0.00308	51.88156	−0.35487	6.14×10^{-4}
TNT/water	≈10	0.6	0.0015	0.42548	6.4×10^{-4}	0

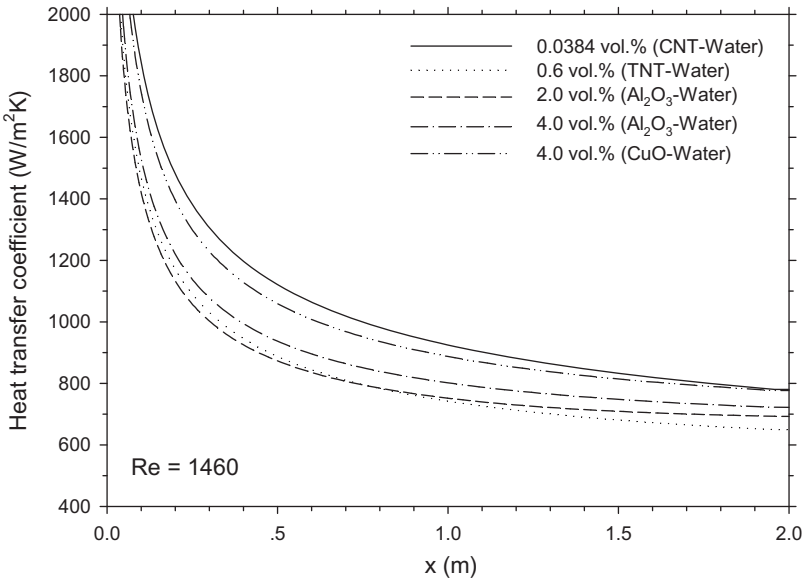

Fig. 13. Effects of particle shape on the local heat transfer coefficient at Reynolds number of 1460.

$$\mu_{60\%EG/water} = 0.001 \exp\left(\frac{3135.6}{T + 273.15} - 8.9367\right) \quad (18)$$

These correlations are valid for $0\ ^\circ C \leqslant T \leqslant 97\ ^\circ C$.

According to Vajjha and Das [27], Eqs. (8)–(11) are still applicable for the evaluation of viscosity and thermal conductivity of 60% EG/water base nanofluids.

In Fig. 12, the heat transfer coefficients of Al_2O_3 nanoparticles in both water and 60% EG/water base fluids are compared. The results indicate that the heat transfer characteristics of nanofluids are strongly influenced by the type of the base fluid.

5.7. The effect of nanoparticle shape

It has been shown that nanofluids containing nanoparticles with a higher aspect ratio have better thermal properties [35,36]. For example, the cylindrical nanoparticles give higher thermal conductivity and heat transfer coefficient than the spherical nanoparticles. To study the effect of nanoparticle shape, two kinds of cylindrical nanoparticles, which are CNT and TNT are used and then compared with the nanofluids with spherical nanoparticles. He et al. [35] studied the heat transfer performance of CNT/water nanofluid containing 0.1 wt.% (0.0384 vol.%) and TNT/water nanofluid containing 2.5 wt.% (0.6 vol.%) numerically and experimentally. They indicated that, at a given temperature, the shear viscosity of both nanofluids decreases with increasing shear rate, exhibiting a shear thinning behaviour. Moreover, the shear viscosity approaches a constant minimum value at higher shear rate. The measured viscosity did not show an important change versus share rate, more than the shear rates of 200 1/s and 500 1/s for the CNT/water and TNT/water nanofluids, respectively. They simulated the convective heat transfer of nanofluids as both Newtonian and non-Newtonian fluids. Their results showed that the heat transfer coefficients based on the non-Newtonian model agree well with the measured data. Furthermore, they indicated that, when the

Table 2
Different nanofluids flow conditions simulated in the present study and their corresponding temperature increase, pressure drop, and pumping power.

Type of working fluids	Re	d_p (nm)	ϕ (vol.%)	ΔT (°C)	ΔP (Pa)	Pump power (W)
Al_2O_3/60% EG/water	1460	20	4	0.56	43240	1.38
60% EG/water	1460	–	–	0.68	26240	0.69
CNT/water	1460	$L_p/d_p > 100$	0.038	0.9	9625	0.16
CuO/water	1460	20	6	1.05	8838	0.12
CuO/water	1460	20	4	1.52	3830	0.04
TNT/water	1460	$d_p = 10$, $L_p = 100$	0.6	1.8	2241	0.017
Al_2O_3/water	1460	100	6	2.05	2020	0.014
Al_2O_3/water	1460	40	6	2.06	2020	0.014
Al_2O_3/water	1460	20	6	2.08	2020	0.014
CuO/water	1460	20	2	2.18	1670	0.011
Al_2O_3/water	1460	40	4	2.39	1416	0.008
Al_2O_3/water	1460	20	4	2.39	1417	0.008
Al_2O_3/water	1460	20	3	2.52	1188	0.007
Water	1620	–	–	2.6	974	0.005
Al_2O_3/water	1460	20	2	2.72	996	0.005
Al_2O_3/water	1460	100	2	2.72	995	0.005
Al_2O_3/water	1460	40	2	2.73	995	0.005
Water	1460	–	–	2.78	869	0.004
Al_2O_3/water	1000	20	4	3.44	936	0.004
Water	1000	–	–	4.08	572	0.002
Al_2O_3/water	500	20	4	6.91	438	0.0009
Water	500	–	–	8.19	266	0.0004

nanofluid is considered as Newtonian with the constant minimum value of viscosity, the heat transfer coefficient has also reasonable agreement with the result of non-Newtonian model.

In the present work, the constant minimum value of viscosity presented by He et al. [35] was adopted as the effective viscosity. Similarly, the thermal conductivity of nanofluids as a function of temperature is taken from [35] as listed in Table 1.

Fig. 13 presents the comparison of axial heat transfer coefficients for nanoparticles with different aspect ratios at Reynolds number of 1460. The results show that the heat transfer coefficient of the CNT/water nanofluid is significantly greater than that of the other nanofluids, which can be attributed to its large aspect ratio (>100) as listed in Table 1. In addition to the nanoparticle shape, the higher thermal conductivity of CNTs compared with Al_2O_3 and CuO is the reason of substantial thermal characteristics enhancement of CNT/water nanofluids, even at low concentrations.

On the other hand, because of the low aspect ratio of TNT (≈10) and its lower thermal conductivity as compared with Al_2O_3, CuO and CNT, the heat transfer coefficient of TNT/water nanofluid is lower than those. Yet, it should be mentioned that the concentration of TNT is lower than Al_2O_3, CuO. The TNT/water nanofluid containing 0.6 vol.% nanoparticle shows approximately the same heat transfer coefficient as that of Al_2O_3/water nanofluid containing 2 vol.%, which also indicates the considerable effect of nanoparticle shape on the heat transfer characteristics of nanofluids.

Thus far, several influential parameters on the heat transfer of nanofluids are investigated; yet the important question is which nanofluid is more appropriate for a specific application. In this article, considering a constant wall heat flux condition, two important factors are considered as the criteria for the choice of proper nanofluids. These factors are pressure drop and temperature difference along the pipe. For a constant wall heat flux condition with a given

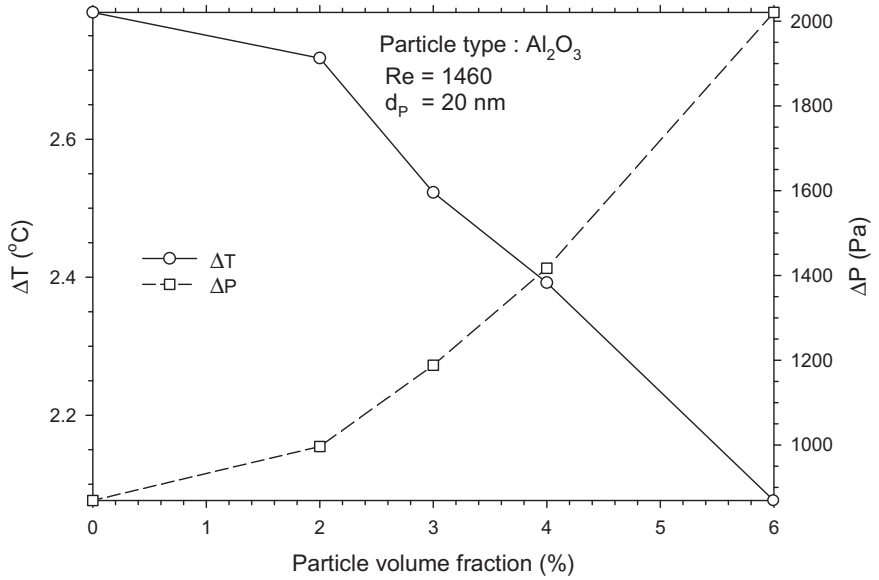

Fig. 14. Temperature differences and pressure drops for different particle volume concentrations of Al_2O_3/water nanofluid at Reynolds number of 1460 and particle diameter of 20 nm.

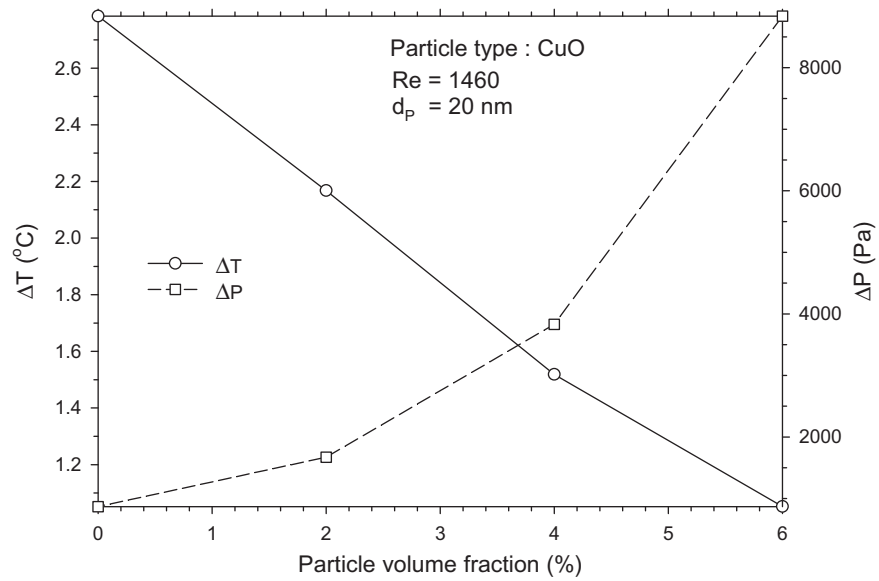

Fig. 15. Temperature differences and pressure drops for different particle volume concentrations of CuO/water nanofluid at Reynolds number of 1460 and particle diameter of 20 nm.

amount of heat transfer to the fluid, the lower temperature difference along the pipe can be considered as an advantage in some applications. On the other hand, lower pressure drop reduces the pumping cost.

In the view of these two criteria, all cases simulated in the present study are listed in Table 2, which have been sorted by pressure drop. It can be concluded from the table that almost all cases with lower pressure drops have higher temperature differences, which also implies that nanofluids should be selected according to the application requirements.

From Table 2 it is observed that considerable pressure drop are associated with high particle concentration of nanofluids, while much less pressure drop has been reported in numerical studies of [37,38] for similar flow conditions. It must be emphasised that the viscosity model, $\mu_e = \mu_f(1-\phi)^{-2.5}$, which has been used in these studies produces much lower values for viscosity as compared to the present experimental data [23] and consequently leads to relatively lower pressure drops. However, the applied viscosity model in the present study (Eq. (8)) represents the experimental data with reasonable accuracy and therefore, the resulting pressure drops are higher.

Another related issue to the pressure drop is the relative increase in viscosity with respect to thermal conductivity as the nanoparticle concentration increases. In general, the advantage of the nanofluids for the heat transfer applications is directly related to the amount of the thermal conductivity increase, leading to the heat transfer enhancement, to the amount of the viscosity increase associated with higher pressure drops. For the nanofluids used in the present study, the viscosity of the base fluid increases faster than its thermal conductivity as nanoparticle concentration increases, and therefore, the heat transfer enhancements come at the expense of relatively considerable pressure drop.

Considering Table 2, the temperature increase along the pipe and the pressure drop behave in an opposite manner. In Figs. 14 and 15 these parameters are plotted versus the particle volume fraction to see if an optimum nanoparticle concentration for a specific application can be identified. Fig. 14 shows the Al_2O_3 nanoparticles in water with particle diameter of 20 nm and Reynolds number of 1460. From this figure, the optimum choice for the Al_2O_3/water nanofluid is the volume fraction of about 4 vol.%, which has more reasonable temperature increase and pressure drop. Similarly, Fig. 15 indicates that for the case of the CuO/water nanofluid with particle diameter of 20 nm and Reynolds number of 1460, the proper choice is the volume fraction of about 3.7 vol.%.

Another limitation for nanofluids applications is the toxicity of nanoparticles. Clearly, the green nanofluids with no environmental, health and safety dangers are desirable. There are some studies on toxicity of nanoparticles considered in this article, Al_2O_3 [39], CuO [40], CNT [41,42] and TiO_2 [40]. Among them, the high toxicity of CuO nanoparticles has been reported [40]. Moreover, Bottini et al. [42] indicated that CNTs nanofluids can be very toxic at high particle concentrations.

In addition, the economical justification is one of the important considerations in nanofluid selection. In the present study, CNT/water nanofluid with a low concentration of 0.038 vol.% but high heat transfer coefficient seems to be a low cost nanofluid as compared with the others. Finally, the chemical reaction of nanofluids with the pipe wall is a consideration, especially in the case of surfactants, which may affect the nanofluids applications.

6. Conclusions

The laminar convective heat transfer performance and pressure drop of different nanofluids flowing in a straight circular pipe under a constant heat flux condition were numerically investigated. The effects of particle concentration, Reynolds number, Brownian motion, particle diameter, particle shape, particle material and type of base fluid on the heat transfer performance of nanofluids are examined in details. Major findings can be summarised as follows:

- The predicted heat transfer coefficients based on the thermophysical properties of nanofluids in a static condition are lower than the experimental data. This means that the static thermal conductivity increase is not the only reason of convective heat transfer enhancement of nanofluids.
- A thermal conductivity model which considers the effect of Brownian motion of nanoparticles predicts the heat transfer coefficient of nanofluids more accurately as compared to the models based on the pure static conditions of the nanofluids.
- The particle volume concentration, Brownian motion and aspect ratio of nanoparticles similar to the flow Reynolds number increase the heat transfer coefficient of nanofluids, while the particle diameter has an opposite effect. Moreover, the heat transfer characteristics of nanofluids are strongly influenced by the type of both base fluid and nanoparticle.
- There are several parameters to select the proper nanofluids for convective heat transfer of nanofluids in pipes. These parameters are the amount of heat transfer enhancement, pump power, stability, cost, toxicity and chemical corrosion of pipe wall. Also, there are some other restrictions in the special applications such as low freezing temperature nanofluids as the anti-refrigerant fluids in cold region.

Acknowledgements

The authors wish to thank Ferdowsi University of Mashhad (Iran), South-East Asia University (Thailand), King Mongkut's University of Technology Thonburi (Thailand) for the valuable support in the present study. The fourth author would like to acknowledge the Thailand Research Fund and the National Research University Project for financial supporting.

References

[1] H. Masuda, A. Ebata, K. Teramae, N. Hishinuma, Alteration of thermal conductivity and viscosity of liquid by dispersing ultra-fine particles (dispersion of Al_2O_3, SiO_2 and TiO_2 ultra-fine particles), Netsu Bussei (in Japanese) 7 (4) (1993) 227–233.
[2] S.U.S. Choi, Enhancing thermal conductivity of fluids with nanoparticles, in: Proceedings of the 1995 ASME International Mechanical Engineering Congress and Exposition, ASME, New York, 1995, pp. 99–105.
[3] W. Duangthongsuk, S. Wongwises, A critical review of convective heat transfer of nanofluids, Renew. Sustain. Energy Rev. 11 (2007) 797–817.
[4] V. Trisaksri, S. Wongwises, Critical review of heat transfer characteristics of the nanofluids, Renew. Sustain. Energy Rev. 11 (3) (2007) 512–523.
[5] X.Q. Wang, A.S. Mujumdar, Heat transfer characteristics of nanofluids: a review, Int. J. Therm. Sci. 46 (1) (2007) 1–19.
[6] L. Godson, B. Raja, D. Mohan Lal, S. Wongwises, Enhancement of heat transfer using nanofluids – an overview, Renew. Sustain. Energy Rev. 14 (2) (2010) 629–641.
[7] S. Mirmasoumi, A. Behzadmehr, Effect of nanoparticles mean diameter on mixed convection heat transfer of a nanofluid in a horizontal tube, Int. J. Heat Fluid Flow 29 (2) (2008) 557–566.
[8] M. Kalteh, A. Abbassi, M. Saffar-Avval, J. Harting, Eulerian–Eulerian two-phase numerical simulation of nanofluid laminar forced convection in a microchannel, Int. J. Heat Fluid Flow 32 (1) (2011) 107–116.
[9] S. Mirmasoumi, A. Behzadmehr, Numerical study of laminar mixed convection of a nanofluid in a horizontal tube using two-phase mixture model, Appl. Therm. Eng. 28 (7) (2008) 717–727.
[10] A. Akbarinia, Impacts of nanofluid flow on skin friction factor and Nusselt number in curved tubes with constant mass flow, Int. J. Heat Fluid Flow 29 (1) (2008) 229–241.
[11] A. Akbarinia, A. Behzadmehr, Numerical study of laminar mixed convection of a nanofluid in horizontal curved tubes, Appl. Therm. Eng. 27 (8–9) (2007) 1327–1337.
[12] M. Izadi, A. Behzadmehr, D. Jalali-Vahida, Numerical study of developing laminar forced convection of a nanofluid in an annulus, Int. J. Therm. Sci. 48 (11) (2009) 2119–2129.

[13] Y. He, Y. Men, Y. Zhao, H. Lu, Y. Ding, Numerical investigation into the convective heat transfer of TiO_2 nanofluids flowing through a straight tube under the laminar flow conditions, Appl. Therm. Eng. 29 (10) (2009) 1965–1972.
[14] V. Bianco, F. Chiacchio, O. Manca, S. Nardini, Numerical investigation of nanofluids forced convection in circular tubes, Appl. Therm. Eng. 29 (17) (2009) 3632–3642.
[15] S. Kumar, S.K. Prasad, J. Banerjee, Analysis of flow and thermal field in nanofluid using a single phase thermal dispersion model, Appl. Math. Model. 34 (3) (2010) 573–592.
[16] F. Talebi, A.H. Mahmoudi, M. Shahi, Numerical study of mixed convection flows in a square lid-driven cavity utilizing nanofluid, Int. Commun. Heat Mass Transfer 37 (1) (2010) 79–90.
[17] M. Shahi, A.H. Mahmoudi, F. Talebi, Numerical study of mixed convective cooling in a square cavity ventilated and partially heated from the below utilizing nanofluid, Int. Commun. Heat Mass Transfer 37 (2) (2010) 201–213.
[18] A. Akbarinia, R. Laur, Investigating the diameter of solid particles effects on a laminar nanofluid flow in a curved tube using a two phase approach, Int. J. Heat Fluid Flow 30 (4) (2009) 706–714.
[19] S. Zeinali Heris, M. Nasr Esfahany, G. Etemad, Numerical investigation of nanofluid laminar convective heat transfer through a circular tube, Numer. Heat Transfer, Part A: Appl. 52 (11) (2007) 1043–1058.
[20] A. Raisi, B. Ghasemi, S.M. Aminossadati, A numerical study on the forced convection of laminar nanofluid in a microchannel with both slip and no-slip conditions, Numer. Heat Transfer, Part A: Appl. 59 (2) (2011) 114–129.
[21] B. Ghasemi, S.M. Aminossadati, Natural convection heat transfer in an inclined enclosure filled with a water–CuO, Numer. Heat Transfer, Part A: Appl. 55 (8) (2009) 807–823.
[22] L. Zhou, Y. Xuan, Q. Li, Multiscale simulation of flow and heat transfer of nanofluid with lattice Boltzmann method, Int. J. Multiphase Flow 36 (5) (2010) 364–374.
[23] D. Kim, Y. Kwon, Y. Cho, C. Li, S. Cheong, Y. Hwang, J. Lee, D. Hong, S. Moon, Convective heat transfer characteristics of nanofluids under laminar and turbulent flow conditions, Curr. Appl Phys. 9 (2) (2009) e119–e123.
[24] R.K. Shah, A.L. London, Laminar Flow Forced Convection in Ducts, Academic Press, New York, 1978. p.128.
[25] R.S. Vajjha, D.K. Das, P.K. Namburu, Numerical study of fluid dynamic and heat transfer performance of Al_2 O_3 and CuO nanofluids in the flat tubes of a radiator, Int. J. Heat Fluid Flow 31 (4) (2010) 613–621.
[26] J. Koo, C. Kleinstreuer, A new thermal conductivity model for nanofluids, J. Nanopart. Res. 6 (6) (2004) 577–588.
[27] R.S. Vajjha, D.K. Das, Experimental determination of thermal conductivity of three nanofluids and development of new correlations, Int. J. Heat Mass Transfer 52 (21–22) (2009) 4675–4682.
[28] F.P. Incropera, D.P. DeWitt, T.L. Bergman, A.S. Lavine, Fundamentals of Heat and Mass Transfer, sixth ed., John Wiley & Sons, 2006. p. 949.
[29] R.W. Fox, A.T. McDonald, P.J. Pritchard, Introduction to Fluid Mechanics, sixth ed., John Wiley & Sons, Berlin, 2004. p. 724.
[30] A.J. Chorin, Numerical solution of the Navier–Stokes equations for an incompressible fluid, Math. Comput. 22 (104) (1968) 745–762.
[31] H.A. Dwyer, Calculations of droplet dynamics in high temperature environments, Prog. Energy Combust. Sci. 15 (2) (1989) 131–158.
[32] M. Renksizbulut, H. Niazmand, Laminar flow and heat transfer in the entrance region of trapezoidal channels with constant wall temperature, J. Heat Transfer 128 (1) (2006) 63–74.
[33] E. Ebrahimnia-Bajestan, H. Niazmand, M. Renksizbulut, Flow and heat transfer of nanofluids with temperature dependent properties, in: Proceedings of the ASME 2010 Third Joint US–European Fluids Engineering Summer Meeting and Eighth International Conference on Nanochannels, Microchannels, and Minichannels, Montreal, 2010.
[34] R. Strandberg, D.K. Das, Finned tube performance evaluation with nanofluids and conventional heat transfer fluids, Int. J. Therm. Sci. 49 (3) (2010) 580–588.
[35] Y. He, Y. Men, X. Liu, H. Lu, H. Chen, Y. Ding, Study on forced convective heat transfer of non-Newtonian nanofluids, J. Therm. Sci. 18 (1) (2009) 20–26.
[36] H. Chen, W. Yang, Y. He, Y. Ding, L. Zhang, C. Tan, A.A. Lapkin, D.V. Bavykin, Heat transfer and flow behaviour of aqueous suspensions of titanate nanotubes (nanofluids), Powder Technol. 183 (1) (2008) 63–72.
[37] J. Li, C. Kleinstreuer, Thermal performance of nanofluid flow in microchannels, Int. J. Heat Fluid Flow 29 (4) (2008) 1221–1232.
[38] R. Chein, G. Huang, Analysis of microchannel heat sink performance using nanofluids, Appl. Therm. Eng. 25 (17–18) (2005) 3104–3114.
[39] W. Lin, I. Stayton, Y. Huang, X.D. Zhou, Y. Ma, Cytotoxicity and cell membrane depolarization induced by aluminum oxide nanoparticles in human lung epithelial cells A549, Toxicol. Environ. Chem. 90 (5) (2008) 983–996.
[40] V. Aruoja, H.C. Dubourguiera, K. Kasemets, A. Kahru, Toxicity of nanoparticles of CuO, ZnO and TiO_2 to microalgae Pseudokirchneriella subcapitata, Sci. Total Environ. 407 (4) (2009) 1461–1468.
[41] J. Miyawaki, M. Yudasaka, T. Azami, Y. Kubo, S. Iijima, Toxicity of single-walled carbon nanohorns, ACS Nano 2 (2) (2008) 213–226.
[42] M. Bottini, S. Bruckner, K. Nika, N. Bottini, S. Bellucci, A. Magrini, A. Bergamaschi, T. Mustelin, Multi-walled carbon nanotubes induce T lymphocyte apoptosis, Toxicol. Lett. 160 (2) (2006) 121–126.

Heat Mass Transfer (2011) 47:1219–1227
DOI 10.1007/s00231-011-0783-y

ORIGINAL

Performance characteristics of HFC-134a and HFC-410A refrigeration system using a short-tube orifice as an expansion device

Kitti Nilpueng · Chietta Supavarasuwat · Somchai Wongwises

Received: 24 March 2010 / Accepted: 8 March 2011 / Published online: 27 March 2011
© Springer-Verlag 2011

Abstract In the present article, the effect of heat source temperature, heat sink temperature, short-tube orifice diameter and short-tube orifice length on the performance characteristics of HFC-140A and HFC-134a refrigeration system using a short-tube orifice as expansion device, i.e., mass flow rate, cooling capacity, compressor pressure ratio, power consumption, and second law efficiency are experimentally studied. The short-tube orifices diameters ranging from 0.849 to 1.085 mm with length ranging from 10 to 20 mm are used in this examination. The test run are done at heat source temperature ranging between 16.5 and 18.5°C, and heat sink temperature ranging between 30 and 35°C. The results show that the tendency of second law efficiency is increased as the short-tube orifice diameter and heat source temperature are enhanced, but it is decreased by increasing the short-tube orifice length and heat sink temperature. Under the similar conditions, the mass flow rate, cooling capacity, and compressor power consumption obtained from HFC-410A are higher than those obtained from HFC-134a.

List of symbols

COP_{actual}	Actual coefficient of performance
COP_{carnot}	Carnot coefficient of performance
$c_{p,\ hw}$	Specific heat at constant pressure of the hot water, kJ/kg K
D	Short-tube orifice diameter, m
L	Short-tube orifice length, m
$\dot{m}_{hw}$	Mass flow rate of hot water, kg/s
$\dot{m}_{cw}$	Mass flow rate of cold water, kg/s
Q_{evap}	Heat transfer rate at evaporator, kW
T_{sink}	Heat sink temperature, °C
T_{source}	Heat source temperature, °C
$T_{hw,\ in}$	Hot water temperature at the inlet of the evaporator, °C
$T_{hw,\ out}$	Hot water temperature at the outlet of the evaporator, °C
ΔT_{sub}	Degree of subcooling, °C
ΔT_{sup}	Degree of superheat, °C
W_{comp}	Electrical power supplied to the compressor, kW

1 Introduction

Due to the destruction of the earth's ozone layer by chlorine molecules from chlorofluorocarbon (CFC), many companies have been developed the alternative refrigerants to replace CFC refrigerant and hydrochlorofluorocarbon (HCFC) refrigerant in the refrigeration and air-conditioning applications for example, HFC-417A, HFC-404A, HFC-407C, HFC-134a, and HFC-410A. However, since the properties of refrigerant are changed, it may cause the variation of system performance. Therefore, the inspection in the performance of refrigeration system with using the new hydrofluorocarbon (HFC) refrigerants is very important.

An expansion device is a necessary element in the refrigeration system which is utilized to reduce the pressure of the refrigerant from the condenser pressure to the evaporator pressure and to regulate the mass flow rate of refrigerant flowing from the condenser to the evaporator.

K. Nilpueng · S. Wongwises (✉)
Fluid Mechanics, Thermal Engineering and Multiphase Flow Research Lab (FUTURE), Department of Mechanical Engineering, King Mongkut's University of Technology Thonburi, Bangmod, Bangkok 10140, Thailand
e-mail: somchai.won@kmutt.ac.th

C. Supavarasuwat
C Aircon Tech Co., Ltd., Bangkae, Bangkok 10160, Thailand

Basically, it can be divided into two main categories: variable-restriction type and constant-restriction type. In the prior, the flow area can be adjusted by the control system for example the automatic expansion valve and thermostatic expansion valve. In the latter, the flow area of the expansion device is fixed. An instance of most popular device of this type is capillary tube, ejector and short-tube orifice. Recently, however, it is discovered that the short-tube orifice have been widely used as the expansion device in residential and automotive air-conditioning systems. This is because of its simplicity, low initial cost, high reliability and ease of maintenance. Accordingly, a clear understanding of performance characteristics of air-conditioning system using as expansion device is more important.

In the past decade, the experimental investigation about the performance of vapour compression refrigeration system working with new HFC refrigerants and the refrigerant flow behaviour inside short-tube orifices have been investigated by the a number of researchers which are described in the following paragraphs.

1.1 Performance of the vapour compression refrigeration system with new HFC refrigerants

The performance characteristic of water chiller and heat pump and cold storage were experimentally studied by Aprea et al. [2] and Aprea and Renno [1]. HCFC-22 and HFC-417A were used as working fluid. The effect of cold storage air temperature on the coefficient of performance, compression ratio, volumetric efficiency, discharge temperature, and exergy destroy were presented. The results showed that *COP* and exergetic efficiency obtained from HFCF-22 was higher than those obtained from HFC-417A. Navarro-Esbrı′ et al. [13] estimated the effect of internal heat exchanger on the energy efficiency of a vapour compression plant working with HCFC-22, HFC-134a, and HFC-407C. The comparison between the results obtained from an experimental compression vapour plant with and without the internal heat exchanger was reported. They stated that the internal heat exchanger can have positive or negative effects on the plant efficiency, depending on the working fluid and the operating conditions. Cabello et al. [3] developed the mathematical model for analyzing the effect of operating conditions on performance of a single-stage vapour compression plant, including mass flow rate, cooling capacity, compressor power consumption and coefficient of performance. The results indicated that evaporating or condensing conditions have no significant effect on the change of mass flow rate and other energetic parameter. Llopis et al. [12] evaluated the performance of HFC-404A and HFC-507A in a double-stage vapour compression plant. The experiment was performed at evaporating temperature range between −36 and −20°C for a constant condensing temperature of 40°C. They reported that the performance of the HFC-404A was higher than that gained from the HFC-507A when the plant was operated without inter- stage systems. The performance of refrigeration system using an ejector as expansion device was experimentally investigated by Disawas and Wongwises [6], Wongwises and Disawas [19], Chaiwongsa and Wongwises, [4], and Chaiwongsa and Wongwises [5]. The impact of the external parameters, i.e., heat sink and heat source temperature on primary mass flow rate of refrigerant, secondary mass flow rate of refrigerant, compressor ratio, discharge temperature, cooling capacity and coefficient of performance were reported. The results indicated that the use of two-phase ejector enabled the evaporator to be flooded by refrigerant. Thus, the heat transfer rate in the evaporator was increased comparing with the standard cycle. However, although the ejector cycle has higher performance over the standard cycle, some disadvantage such as high refrigerant charge, high refrigerant flow, piping insulation and installation cost should be considered.

1.2 Flow characteristics of refrigerant through the short-tube orifices

Kim [9] experimentally investigated the flow of two-phase and subcooled HFC-134a through short-tube orifices with length-to-diameter ratios ranging between 7 and 20. For two-phase flow entering the short tube, he noticed that the mass flow rate decreased with increases in the dryness fraction. The flow characteristics of HFC-407C through mini short-tube orifices with diameters of 1.09–1.94 mm were studied by Payne and O'Neal [16]. They found that the addition of oil into refrigerant increased the mass flow rate by more than 12% for a two-phase flow entering the short tube but had little effect on mass flow rate at a high degree of subcooling. Singh et al. [17] presented experimental data on refrigerant HFC-134a flow through short-tube orifices with and without inlet and outlet screens. The experimental results indicated that the inlet and outlet screens had an insignificant effect on the mass flow rate. Liu et al. [11] explored the characteristics of R744 flow through short-tube orifices. The experimental results showed that choked flow existed under a wide range of operating conditions. They reported that the inlet and outlet chamfer depths had no evident effects on the mass flow rate. Kim et al. [10] examined the mass flow rate of HFC-410A through short-tube orifices at upstream pressures approaching the critical point. They found that the decrease in mass flow rate with a reduction in subcooling became more significant when upstream pressure increased beyond 3,604 kPa, due to a greater density change. Tu et al. [18]

presented the experimental results of HFC-134a flowing through micro-orifices with diameters of 31.0 and 52.0 mm. The experimental results indicated that flow was not choked, even when the downstream pressure was reduced to more than 400 kPa below the saturation pressure for liquid-upstream/two-phase-downstream flow. Nilpueng and Wongwises [14] and Nilpueng et al. [15] experimentally investigated the two-phase flow characteristics of HFC-134a, including flow pattern, mass flow rate, pressure distribution, and temperature distribution through short-tube orifices. The results indicated that metastable flow exists inside short-tube orifices over the whole range of testing conditions. However, the choked flow phenomenon disappears inside the short-tube orifice when L/D is less than 2.91.

As mentioned above, the studies about the performance of vapour compression refrigeration system with HFC refrigerants which is used to replace the CFC and HCFC refrigerants is currently available. However, there are still limited on the inspection of the system performance by using the short-tube orifice as expansion device; especially, HFC-134a and HFC-410A which is popularly used in the residential and automobile air conditioner. Therefore, the knowledge about performance characteristics is important for designing the air-conditioning system. The main aim of this article is to explore the impacts of short-tube orifice diameter, short-tube orifice length, heat source temperature, and heat sink temperature on the performance characteristics of refrigeration system, i.e., mass flow rate, cooling capacity, compressor pressure ratio, compressor power consumption, and second law efficiency. The comparison of vapour compression refrigeration system performance obtained from HFC-134a to HFC-410A are also presented.

2 Experimental apparatus

The experimental apparatus used for testing the performance of refrigeration system is setup as shown in Fig. 1. It consists of the three main loops: the refrigerant loop, the hot water loop and the cold water loop. The refrigerant loop consists of the main refrigeration system components: compressor, condenser, short-tube orifice (expansion device), evaporator, and other accessory parts: oil separator, liquid receiver, filter/drier, sight glass, sub-cooler and accumulator. Refrigerant is circulated by a two-cylinder single stage reciprocating compressor along with an inverter. The compressor speed is maintained at 450 rpm by controlling the inverter frequency. A helical oil separator is used to minimize the effect of lubricating oil on refrigerant which is discharged from the compressor. Compact plate heat exchangers are used as condenser, evaporator and sub-cooler. A schematic diagram of the short-tube orifice which is used as an expansion device is illustrated in Fig. 2. As shown in this figure, in order to fix the brass short-tube orifice with the copper tube, it is pressed by pressing machine. The short-tube orifice diameter ranging between 0.849 and 1.085 mm with length ranging between 10 and 20 mm are used in this experiment. The hot water loop and cold water loop are used for transferring heat to evaporator and from condenser, respectively. The hot water is heated by electric heater inside an insulated tank and supplied through the evaporator by the circulating pump. The cold water is cooled by a separated refrigeration system.

Normally, the examination of the cycle performance can be made by two approaches. The first one is based on internal parameters i.e., evaporating and condensing temperatures. The second one is based on external parameters such as the inlet temperature and the flow rate of the heat transfer fluid [7, 8]. In this paper, the cycle performance is examined by using the second method because it is more likely in real life. Thus, hot water acts as a heat source of the evaporator and heat source temperature means temperature of hot water. While cold water acts as a heat sink of the condenser and heat sink temperature means temperature of cold water. The test runs are done at heat source temperatures ranging between 16.5 and 18.5°C and heat sink temperatures ranging between 30 and 35°C. The volume flow rate of hot water and cold water are kept constant at 8 LPM and 6 LPM, respectively.

A microscope (Olympus BX51) is used to measure the diameter of the short-tube orifice. The length of the short-tube orifice is measured with a digital calliper. The accuracies of diameter and length measurements are ±0.001 and ±0.01 mm, respectively. The flow of hot water and cold water are measured by the rotameters within the ranges 2–20 LPM. The accuracy of the water volumetric flow rates is ±2%. The pressure is detected by pressure transducers calibrated from 0 to 30 bar with ±20 mbar accuracy. *T*-type thermocouples are used to measure fluid temperature. The uncertainty of the temperature measurement is ±0.1°C. The differential transducer had an accuracy of ±0.1% of its calibrated span. The flow rate of refrigerant through the short-tube orifice is measured by a Coriolis mass flow meter (ABB FCM2000) with an accuracy of ±0.25%. The uncertainty of the calculation of cooling capacity is ±13.2%.

3 Results and discussion

In this section, the performance characteristics of refrigeration system using short-tube orifice as expansion device

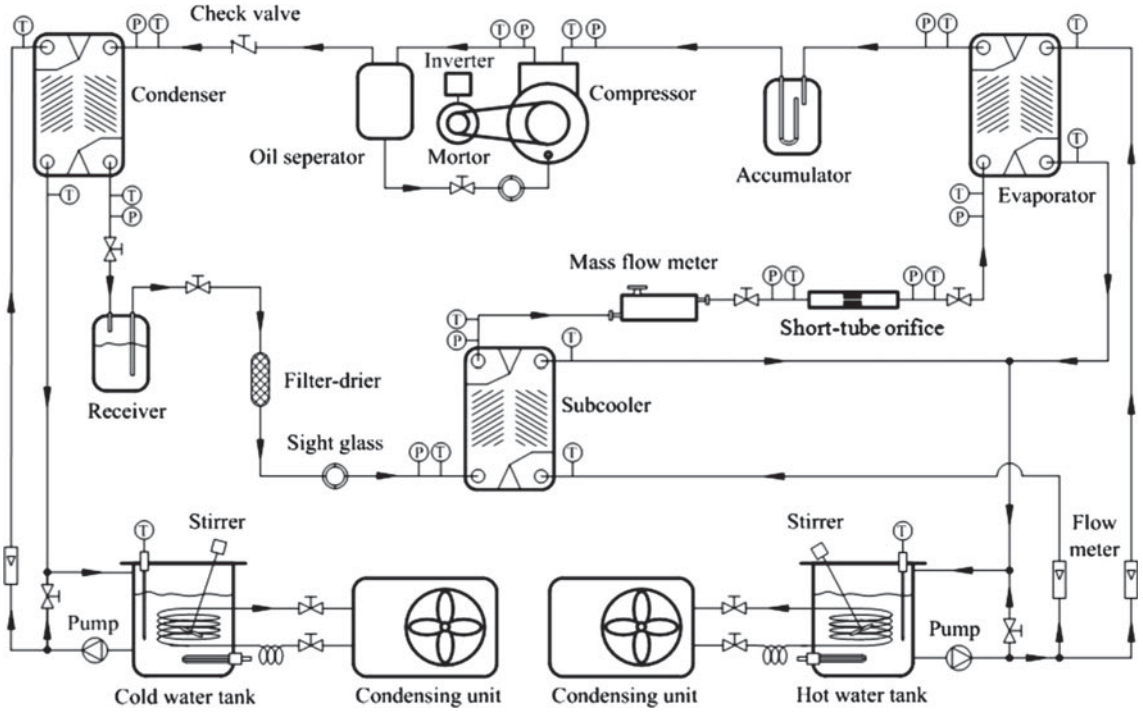

Fig. 1 Schematic diagram of experimental apparatus

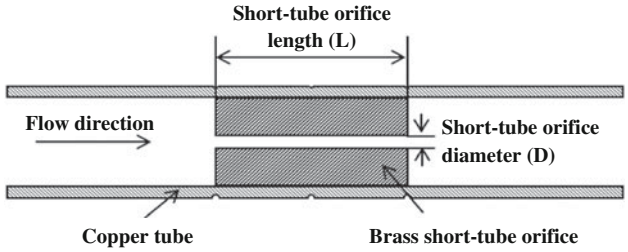

Fig. 2 Schematic diagram of the short-tube orifice

are described. The impacts of relevant parameters, i.e., heat source temperature, heat sink temperature, short-tube orifice diameter and short-tube orifice length on the mass flow rate, cooling capacity, compressor power consumption, and second law efficiency are explained.

3.1 Refrigerant mass flow rate

The variation of refrigerant mass flow rate with the heat source temperature is illustrated in Fig. 3. The results indicate that the mass flow rate is very little affected by the change of heat source temperature. However, it is found that the drop of heat source temperature causes the flow rate to increase by 1.03–1.60%. In this case, there are two explanations about the change of mass flow rate. The first one is related to the refrigerant density at the compressor inlet. When heat source temperature is reduced, the evaporation pressure is reduced whereas the degree of superheating is slightly increased. This leads to the decrease of refrigerant density which leads to a decrease of mass flow rate through compressor. The second reason is associated to the refrigerant velocity inside the short-tube orifice. The drop of heat source temperature causes the decrease of evaporation pressure which results in an increase of the pressure difference across the short-tube orifice. Therefore, refrigerant velocity and mass flow rate through short-tube orifice slightly increases. The reduction of mass flow rate inside compressor dominates the increase of mass flow rate inside the short tube orifice. As a result, the reduction of heat source temperature results in a very slight increase of mass flow rate in the refrigeration system. As shown in Fig. 3, it also can be seen that, when lifting the heat sink temperature, the mass flow rate is increased. The reason for this is similar to the one as mentioned above. That is, the increase of heat sink temperature leads to the rise of condensing pressure and pressure difference across the short-tube orifices, resulting in a higher refrigerant velocity and mass flow rate along the short-tube orifice. On the other hand, the increase of condensing pressure causes an increase of the compressor pressure ratio which results in the decrease of volumetric efficiency of compressor. As a result, the mass flow rate through the compressor is slightly reduced. Consequently, at the steady condition, the mass flow rate in the refrigeration system increases with increasing the heat sink temperature. In addition, at the same conditions, the mass flow rate of HFC-410A is higher than that of HFC-134a by about 85.3%.

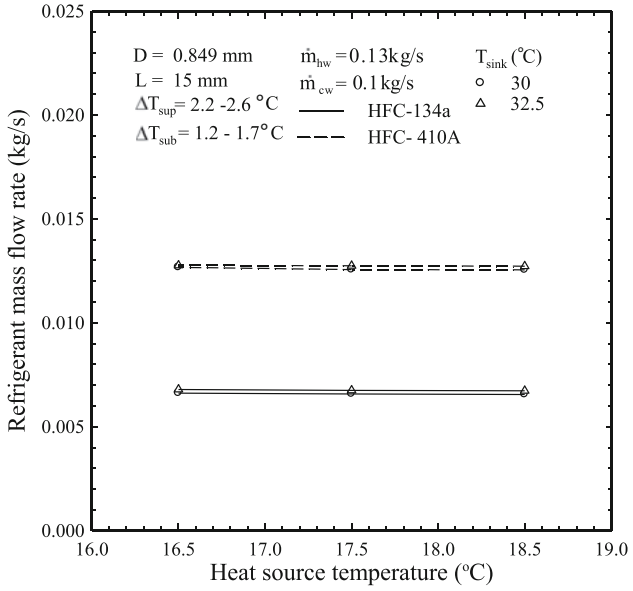

Fig. 3 Effect of heat source temperature on the refrigerant mass flow rate

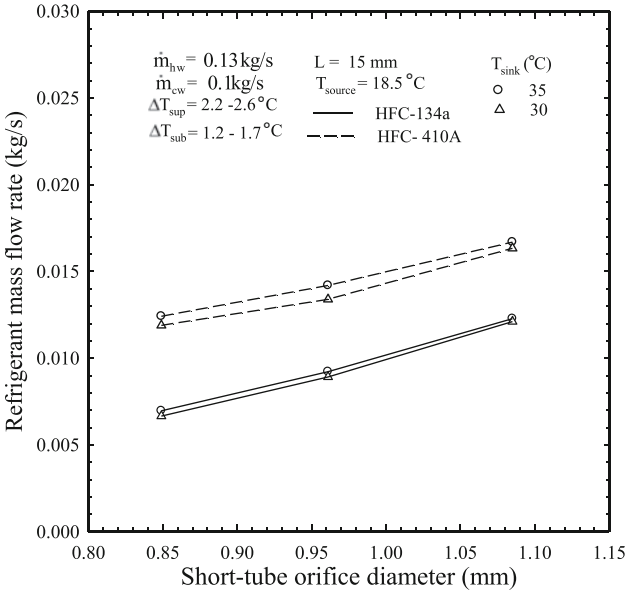

Fig. 4 Effect of short-tube orifice diameter on the refrigerant mass flow rate

The relationship between the refrigerant mass flow rate and short-tube orifice diameter is illustrated in Fig. 4. As expected, the refrigerant mass flow rate is greatly enhanced as the orifice diameter increases. This is because the enlargement of orifice diameter leads to an increase of mass flow rates of refrigerant flowing through short-tube orifice and evaporator. In addition to this, the density of suction vapour at the compressor inlet also increases due to a decrease of degree of superheating, resulting in a higher mass flow rate along the compressor. Consequently, the refrigerant flow rate in the air-conditioning system is increased.

As shown in Fig. 5, it is found that the decrease of refrigerant mass flow rate is the result of the enlargement of short-tube orifice length. The mass flow rate is found to decrease by about 0.31 and 0.38 kg/h/mm for HFC-134a and HFC-410A, respectively. This is due to the fact that the extension of length causes the increase of frictional pressure drop which lead to the drop of velocity and mass flow rate along the short-tube orifice. In addition, at this condition, the density of vapour at the evaporator outlet decreases because the evaporation pressure is reduced whereas the degree of superheating is slightly increased. The volumetric efficiency of compressor is also decreased as the pressure ratio enlarged. As a result, the mass flow rate of refrigerant flowing through compressor is also decreased. These two impacts cause the refrigerant flow rate to decrease.

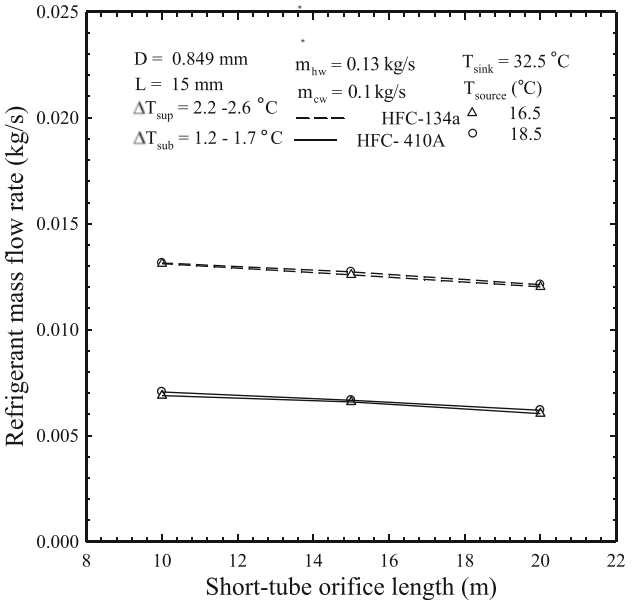

Fig. 5 Effect of short-tube orifice length on the refrigerant mass flow rate

3.2 Cooling capacity

In this experiment, the cooling capacity of the refrigeration system can be calculated from the following equation:

$$Q_{\text{evap}} = \dot{m}_{\text{hw}} c_{\text{p,hw}} (T_{\text{hw,in}} - T_{\text{hw,out}}) \quad (1)$$

where $\dot{m}_{\text{hw}}$ is mass flow rate of hot water (kg/s), $c_{\text{p,hw}}$ is specific heat at constant pressure of hot water (kJ/kg K), $T_{\text{hw,in}}$ is hot water temperature at the inlet of evaporator (°C), $T_{\text{hw,out}}$ is hot water temperature at the outlet of evaporator (°C).

As seen in Fig. 6, the cooling capacity is reduced by increasing the heat sink temperature. This is because, the

increase in heat sink temperature leads to a decrease of temperature difference between refrigerant inside the condenser and cold water, resulting in a decrease of the heat rejection from condenser. Therefore, based on the energy conservation, the cooling capacity is also decreased. This figure also shows that the rise of heat source temperature leads to an increase of cooling capacity. An increase of the heat source temperature leads to a slight increase of the evaporating pressure. As a result, the refrigerating effect and the density of the suction vapour at the compressor are increased. These effects lead to an increase of cooling capacity.

As seen in Fig. 7, it can be seen that the cooling capacity increases when the orifice diameter is enlarged. This is due to the fact that, at the similar operating conditions, the increase of short-tube orifice diameter results in an enhancement of refrigerant mass flow rate. Therefore, the heat absorption into the evaporator or cooling capacity is also increased.

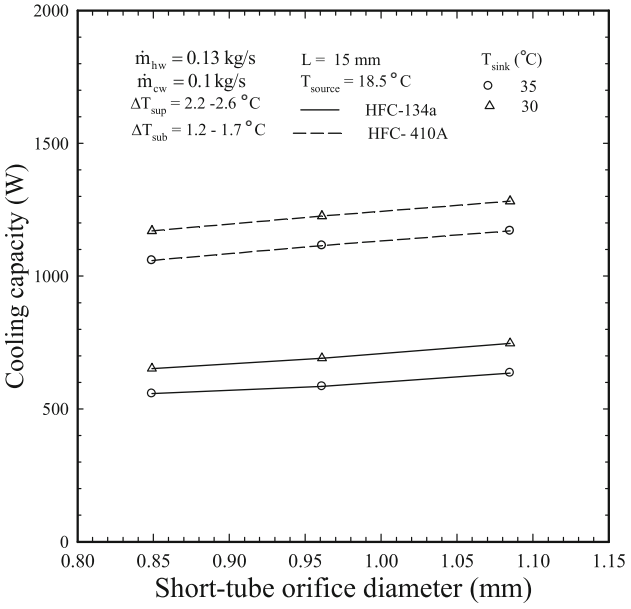

Fig. 7 Effect of short-tube orifice diameter on the cooling capacity

3.3 Compressor power consumption

The variation of compressor pressure ratio and electrical power consumption of compressor with the heat sink temperature is shown in Fig. 8. In this study, the electrical power consumption of compressor is directly measured by the built-in function of the inverter. The plots show that the electrical power consumption of compressor increases with increasing heat sink temperature, but it tends to decrease when the heat source temperature increases. This is because, as the heat sink temperature increases, the pressure ratio is increased. As we known, the volumetric efficiency of compressor is directly proportional with the pressure ratio. Conversely, it is found that the pressure ratio is decreased by increasing heat source temperature which results in an increase of volumetric efficiency of compressor. Therefore, the power consumption of compressor is reduced as the heat source temperature increases.

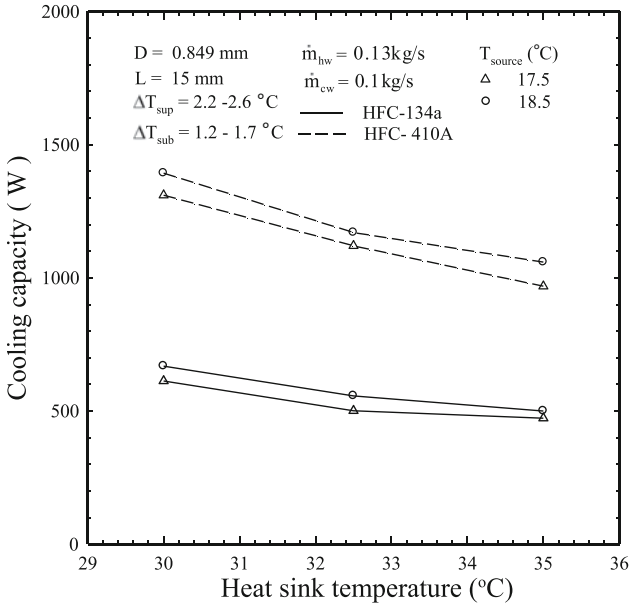

Fig. 6 Effect of heat sink temperature on the cooling capacity

As shown in Fig. 9, the power consumption of compressor slightly decreases with increasing the short-tube orifice diameter. This is because the expansion of diameter is the cause of the decrease of pressure drop due to sudden contraction which leads to the higher average evaporation pressure. This results in the decrease of compressor pressure ratio which leads to an increase of volumetric efficiency of compressor. Accordingly, the power consumption of compressor is lessened with enlarging the short-tube orifice diameter.

3.4 Second law efficiency

The identification of refrigeration system performance is presented by the second law efficiency (η_{II}) which is defined as the ratio of actual coefficient of performance (COP_{actual}) to the Carnot coefficient of performance (COP_{Carnot}) as shown by the following equation:

$$\eta_{II} = \frac{COP_{actual}}{COP_{Carnot}} \tag{2}$$

$$COP_{Carnot} = \frac{1}{\frac{T_H}{T_L} - 1} \tag{3}$$

where T_H is temperature of refrigerant inside the condenser (K) and T_L is temperature refrigerant inside the evaporator

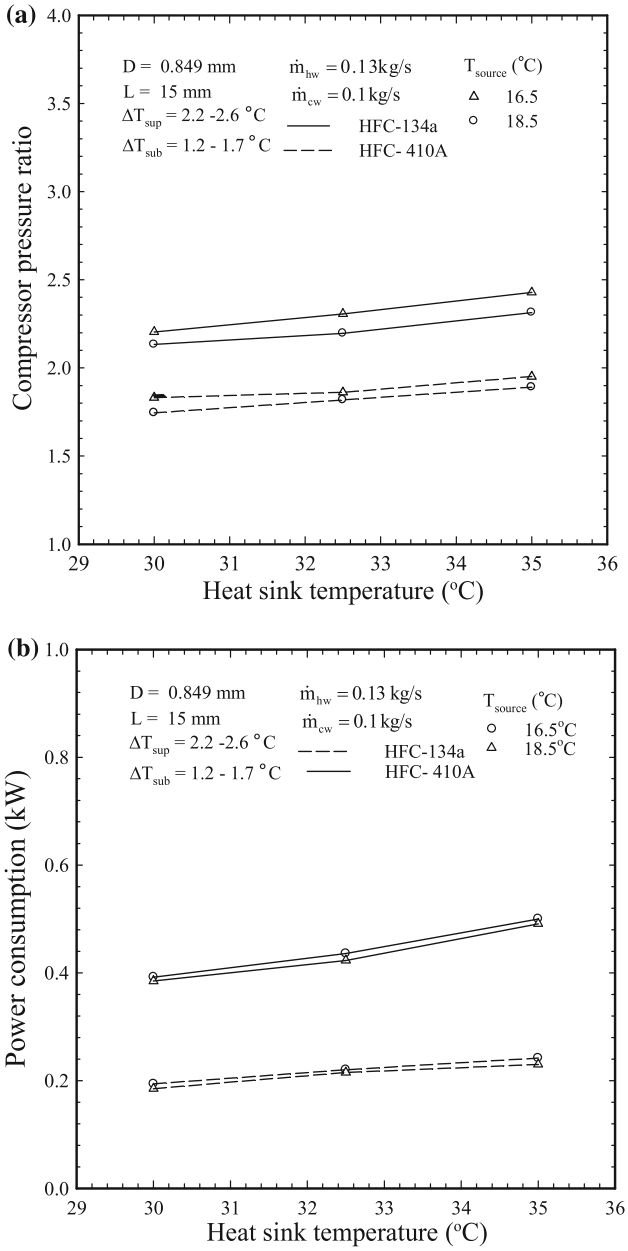

Fig. 8 Effect of heat sink temperature on the compressor pressure ratio and power consumption

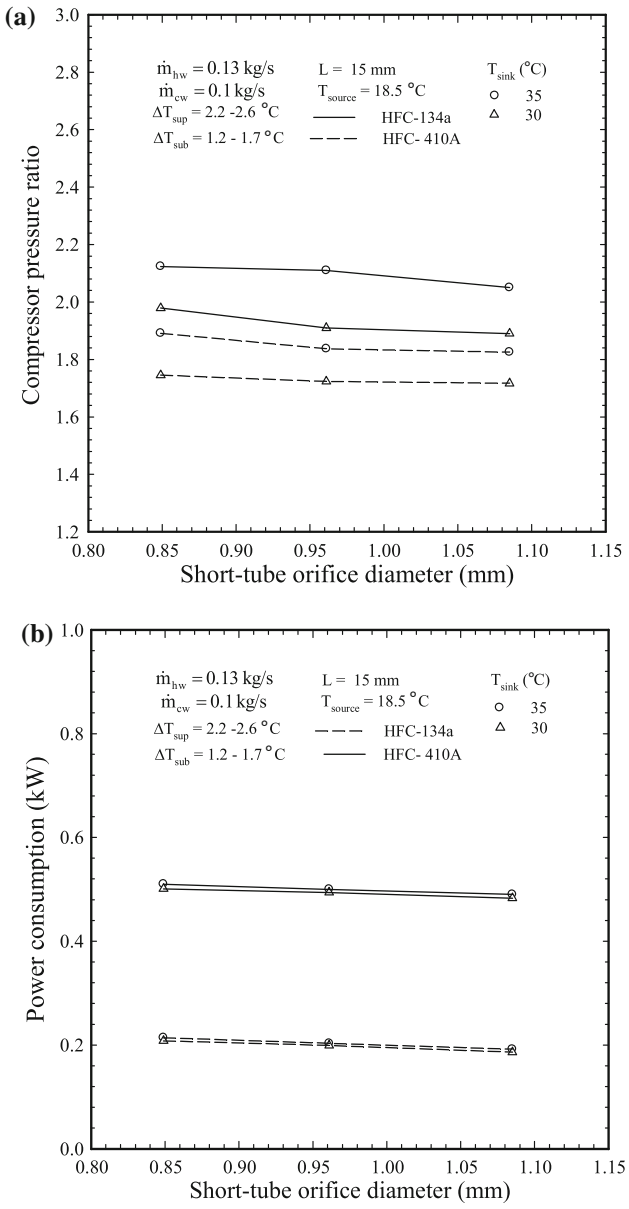

Fig. 9 Effect of short-tube orifice diameter on the compressor pressure ratio and power consumption

(*K*). The actual coefficient of performance is the ratio between the cooling capacity (Q_{evap}) and the electrical power supplied to the compressor (W_{comp}) as follows:

$$COP_{\text{actual}} = \frac{Q_{\text{evap}}}{W_{\text{comp}}} \tag{4}$$

The effect of heat source temperature on the second law efficiency is shown in Fig. 10. The results show that the second law efficiency is augmented when the heat source temperature increases. The average second law efficiency is 24.21 and 27.39% for HFC-410A and HFC-134a, respectively. This is because the refrigerant temperature inside evaporator slightly increases with increasing heat source temperature which produces an increase of Carnot *COP*. The increase of heat source temperature causes the actual *COP* of HFC-134a and HFC-410A to increase. The reason for this is that, when the heat source temperature increases, the cooling capacity also increases due to an increase of refrigerating effect. Conversely, the power consumption of compressor is reduced because the pressure ratio decreased. These influences lead to an increase of actual *COP*. However, the increment of actual *COP* is

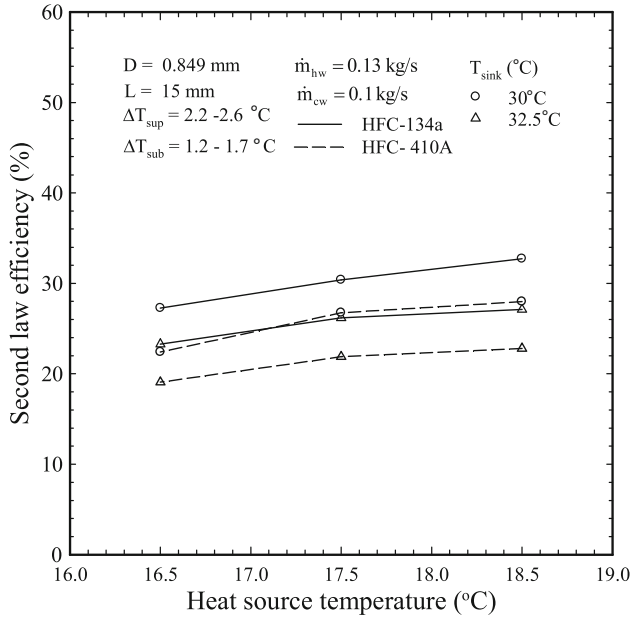

Fig. 10 Effect of heat source temperature on the second law efficiency

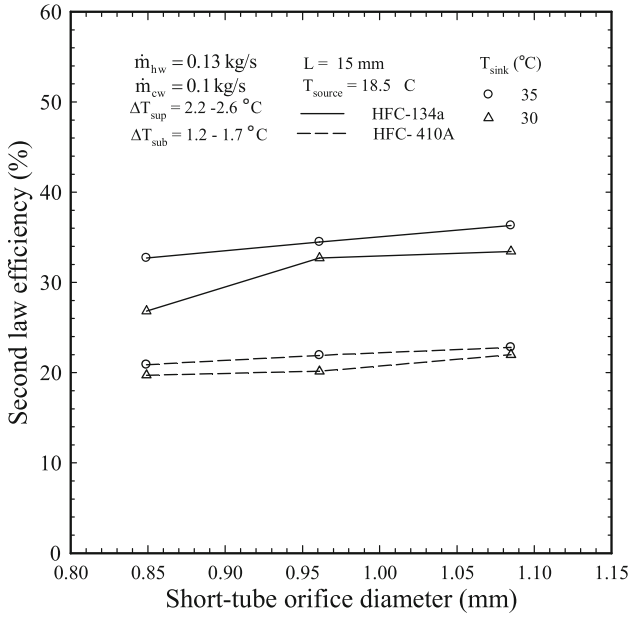

Fig. 11 Effect of short-tube orifice diameter on the second law efficiency

higher than the increment Carnot *COP* which causes the increase of second law efficiency.

Considering the second law efficiency of the short-tube orifice diameters ranging between 0.849 and 1.085 mm (Fig. 11), it is found that the average second law efficiency is 21.25 and 32.75% for HFC-410A and HFC-134a, respectively. As aforementioned from Figs. 4, 7 and 9, it is found that the enlargement of orifice diameter leads to an increase of refrigerant mass flow rate and cooling capacity. Conversely, the power consumption is slightly reduced as the orifice diameter is expanded due to the decrease of pressure ratio. This leads to the increase of actual *COP*. As a result, second law efficiency slightly increases with increasing short-tube orifice diameters.

As shown in Fig. 12, the second law efficiency tends to decrease as the short-tube orifice length increases. As described earlier, it is indicated that the wall friction increases when short-tube orifice length increases which leads to a decrease of the mass flow rate and cooling capacity. In addition, it is also found that electrical power consumption becomes higher when pressure ratio is higher due to the extension of short-tube orifice length. Similarly, the increase of short-tube orifice length results in the slight reduction of refrigerant temperature inside evaporator, resulting in a slight decrease of Carnot *COP*. Therefore, both actual *COP* and Carnot *COP* tend to decrease as the short-tube orifice length increases. Finally, the second law efficiency tends to decrease with increasing short-tube orifice length.

4 Conclusion

New experimental data of the performance characteristics of refrigeration system using a short-tube orifice as expansion device is presented. The impacts of working conditions and short-tube orifice dimension on mass flow rate, cooling capacity, compressor pressure ratio, compressor power consumption, and second law efficiency are

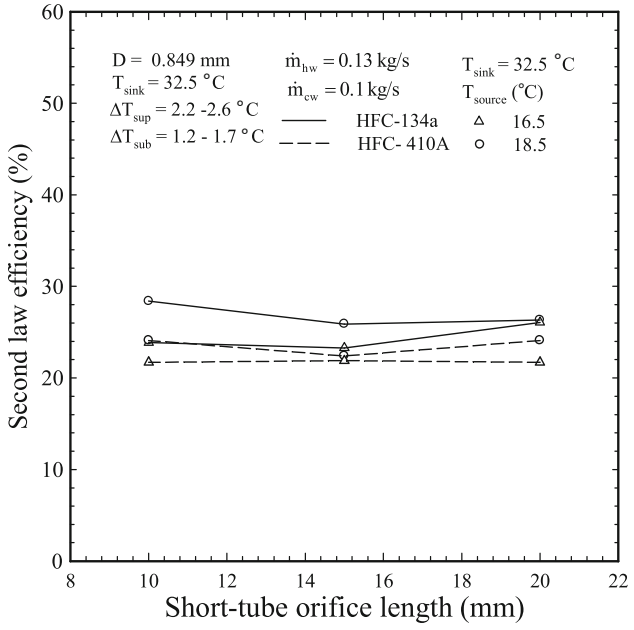

Fig. 12 Effect of short-tube orifice length on the second law efficiency

described. The performance characteristics of refrigeration system obtained from HFC-410A and HFC-134a are also compared. The short-tube orifice having diameter of 0.849, 0.961 and 1.085 mm with the length of 10, 15, and 20 mm are used in this experiment. Based on the foregoing discussions, the following summaries can be given:

1. The increases of short-tube orifice diameter and heat source temperature result in an increase of cooling capacity, but the increases of heat sink temperature lead to a reduction of cooling capacity.
2. The compressor power consumption is increased by increasing the heat sink temperature, but it is decreased with increasing the short-tube orifice diameter and heat source temperature.
3. Under the similar conditions, the mass flow rate, cooling capacity, and power consumption of compressor obtained from HFC-410A are higher than those obtained from HFC-134a.
4. Based on the testing conditions, the tendency of second law efficiency is increased when increasing short-tube orifice diameter and heat source temperature. On the other hand, it is decreased by increasing short-tube orifice length and heat sink temperature.

Acknowledgments The authors would like to express their appreciation to the Thailand Research Fund (TRF), the Office of the Higher Education Commission and the National Research University Project for providing financial support for this study.

References

1. Aprea C, Renno C (2004) Experimental comparison of R22 with R417A performance in a vapour compression refrigeration plant subjected to a cold store. Energy Convers Manag 45:1807–1819
2. Aprea C, Mastrullo R, Renno C (2004) An analysis of the performances of a vapour compression plant working both as a water chiller and a heat pump using R22 and R417A. Appl Therm Eng 24:487–499
3. Cabello R, Navarro-Esbrı′ J, Llopis R, Torrella E (2007) Analysis of the variation mechanism in the main energetic parameters in a single-stage vapour compression plant. Appl Therm Eng 27:167–176
4. Chaiwongsa P, Wongwises S (2007) Effect of throat diameters of the ejector on the performance of the refrigeration cycle using a two-phase ejector as an expansion device. Int J Refrig 30:601–608
5. Chaiwongsa P, Wongwises S (2008) Experimental study on R-134a refrigeration system using a two-phase ejector as an expansion device. Appl Therm Eng 28:467–477
6. Disawas S, Wongwises S (2004) Experimental investigation on the performance of the refrigeration cycle using a two-phase ejector as an expansion device. Int J Refrig 27(6):587–594
7. Giuliani G, Hewitt NJ, Marchesi Donati F, Polonara F (1999) Composition shift in liquid-recirculation refrigeration systems: an experimental investigation for the pure fluid R134a and the mixture R32/134a. Int J Refrig 22(6):486–498
8. Hoegberg M, Vamling L, Berntsson T (1993) Calculation methods for comparing the performance of pure and mixed working fluids in heat pump applications. Int J Refrig 16(6):403–413
9. Kim Y (1993) Two-phase flow of HFC134a and HCFC22 through short tube orifices PhD thesis. Texas A&M University, USA
10. Kim Y, Payne V, Choi J, Domanski P (2005) Mass flow of R410A through short tube working near the critical point. Int J Refrig 28:547–553
11. Liu JP, Niu YM, Chen JP, Chen ZJ, Feng X (2004) Experimental and correlation of R744 two-phase flow through short tubes. Exp Therm Fluid Sci 28:565–573
12. Llopis R, Torrella E, Cabello R, S′anchez D (2009) Performance evaluation of R404A and R507A refrigerant mixtures in an experimental double-stage vapour compression plant. Appl Energy, (in press)
13. Navarro-Esbrı′ J, Cabello R, Torrella E (2005) Experimental evaluation of the internal heat exchanger influence on a vapour compression plant energy efficiency working with R22, R134a and R407C. Energy 30:621–636
14. Nilpueng K, Wongwises S (2009) Experimental investigation of two-phase flow characteristics of HFC-134a through short-tube orifices. Int J Refrig 32:854–864
15. Nilpueng K, Supavarasuwat C, Wongwises S (2009) Flow pattern, mass flow rate, pressure distribution, and temperature distribution of two-phase flow of HFC-134a inside short-tube orifices. Int J Refrig 32:1864–1875
16. Payne WV, O'Neal DL (1998) Mass flow characteristics of R407C through short-tube orifices. ASHRAE Trans 104(3):197–209
17. Singh GM, Hrnjak PS, Bullard CW (2001) Flow of refrigerant R134a through orifice tubes. Int J HVAC&R Res 7:245–262
18. Tu X, Hrnjak PS, Bullard CW (2006) Refrigerant 134a liquid flow through micro-scale short tube orifices with/without phase change. Exp. Therm. Fluid Sci 30(3):253–262
19. Wongwises S, Disawas S (2005) Performance of the two-phase ejector expansion refrigeration cycle. Int J Heat Mass Trans 48:4282–4286

Springer

KSME

Journal of Mechanical Science and Technology 25 (10) (2011) 2683~2701
www.springerlink.com/content/1738-494x
DOI 10.1007/s12206-011-0618-2

Investigation of empirical correlations on the determination of condensation heat transfer characteristics during downward annular flow of R134a inside a vertical smooth tube using artificial intelligence algorithms †

Muhammet Balcılar[1], Ahmet Selim Dalkılıç[2,*], Berna Bolat[3] and Somchai Wongwises[4,5,**]

[1]*Computer Engineering Department, Yildiz Technical University, Yildiz, Besiktas, Istanbul 34349, Turkey*
[2]*Heat and Thermodynamics Division, Department of Mechanical Engineering, Yildiz Technical University, Yildiz, Besiktas, Istanbul 34349, Turkey*
[3]*Design Division, Department of Mechanical Engineering, Yildiz Technical University,Yildiz, Besiktas, Istanbul 34349, Turkey*
[4]*Fluid Mechanics, Thermal Engineering and Multiphase Flow Research Lab. (FUTURE), Department of Mechanical Engineering, King Mongkut's University of Technology Thonburi, Bangmod, Bangkok 10140, Thailand*
[5]*Academy of Science, The Royal Institute of Thailand, Sanam Suea Pa, Dusit, Bangkok 10300, Thailand*

(Manuscript Received November 3, 2010; Revised June 7, 2011; Accepted June 15, 2011)

Abstract

The heat transfer characteristics of R134a during downward condensation are investigated experimentally and numerically. While the convective heat transfer coefficient, two-phase multiplier and frictional pressure drop are considered to be the significant variables as output for the analysis, inputs of the computational numerical techniques include the important two-phase flow parameters such as equivalent Reynolds number, Prandtl number, Bond number, Froude number, Lockhart and Martinelli number. Genetic algorithm technique (GA), unconstrained nonlinear minimization algorithm-Nelder-Mead method (NM) and non-linear least squares error method (NLS) are applied for the optimization of these significant variables in this study. Regression analysis gave convincing correlations on the prediction of condensation heat transfer characteristics using ±30% deviation band for practical applications. The most suitable coefficients of the proposed correlations are depicted to be compatible with the large number of experimental data by means of the computational numerical methods. Validation process of the proposed correlations is accomplished by means of the comparison between the various correlations reported in the literature.

Keywords: Condensation; Heat transfer coefficient; Pressure drop; Genetic algorithm; Unconstrained nonlinear minimization algorithm; Nelder-mead method; Non-linear least squares

1. Introduction

Artificial intelligence methods such as genetic algorithm (GA) and artificial neural network (ANN) modeling validated by the experimental works have been gaining increased popularity in correlating two-phase flows in tubes. However, there still are not enough investigations on the prediction of in-tube condensation's characteristics by means of artificial intelligence techniques in the literature. Existing numerical studies in this subject regarding the two-phase flows in the literature are summarized in the following paragraphs.

Jenkins [1] mentioned the definition of the GA as "survival of the fittest" and ANN as "human brain activity" in his study. The principal subject of his paper is on application of the GA to find the optimum combination of design variables of a space condensation heuristic.

Akin and Demiral [2] defined the primary flow parameters required to model multiphase flow in porous media as relative permeability and capillary pressure and showed that the performance of the algorithm depends on the probabilities of crossover and mutation, and the proper usage of the fitness function of genetic algorithm.

Alizadehdakhel et al. [3] studied the two-phase flow regimes and pressure drops in a 2 cm diameter and 6 m length tube, and the flow in the test tube is modeled using a computational fluid dynamics (CFD) program and also ANN analysis. As a result of their analysis, the CFD results are more accurate than the ANN evaluations compared to their experimental results.

Magee and Boyle [4] presented a system, based on re-sampling condensation proposed by Isard and Blakes [5], for the tracking and classification of livestock movements. They reported that re-sampling condensation relies on the variation within the shape model being separated into pseudo-

† This paper was recommended for publication in revised form by Associate Editor Jae Dong Chung

* Corresponding author. Tel.: +902123832819, Fax.: +902122616659
** Co-corresponding author. Tel.: +6624709115, Fax.: +6624709111
E-mail address: dalkilic@yildiz.edu.tr, somchai.won@kmutt.ac.th

© KSME & Springer 2011

independent components regarding analogous to genes.

Nasseh et al. [6] focused on the two-phase pressure drop, which is the most important factor affecting the dust collection efficiency in venturi scrubbers in their paper. As a conclusion of their study, their neural network model is optimized by genetic algorithm, and it was selected as the best model due to its compatibility with experimental data and easier usage than the mathematical models.

Salgado et al. [7] presented a new approach, based on gamma-ray pulse height distributions pattern recognition by means of ANNs, for the identification of flow regimes and prediction of volume fraction in water-gas-oil multiphase systems. Their ideal and static theoretical models are developed for annular, stratified and homogeneous regimes using MCNP-X mathematical code. The training, test and validation data for the ANNs was performed using their mathematical code. Finally, their proposed ANNs were in good agreement related with the identification of all three different regimes and prediction of the volume fraction in water-gas-oil multiphase system.

Shang [8] developed a new numerical calculation method, a novel algorithm for CFD using the concept of artificial intelligence, based on the nonlinear analysis characteristics of ANN. Finally, they applied the model to the determination of the vapor-water two-phase flows in a tube with uniform and no uniform heating successfully.

Sunde et al. [9] investigated a non-intrusive method of two-phase flow identification for the bubbly and slug flow regimes in their measurements. Consequently, they classified the flow regime types by an ANN algorithm in agreement with their experimental work.

Tambouratzis and Pazsit [10] proposed a general regression ANN for the identification of the two-phase flow in the coolant channels of boiling water reactors. In conclusion, their cross validation tests validated accurate on-line flow regime identification.

Tarca et al. [11] used ANN validated with experimental data successfully for the modeling of multiphase reactors. They correlated the two-phase pressure drop in randomly packed beds with countercurrent flow by means of the new approach illustrated in their paper as a case study.

Vins and Vacek [12] presented some experimental results of fluorinate refrigerant R218, used in some special vapor cooling circuits, e.g., in various particle detectors, two-phase flow through a capillary tube. They compared two approaches such as the conventional power law function with the correlation determined with the use of an ANN in their paper.

Zhang et al. [13] investigated the alternative correlations of two-phase friction pressure drop and void fraction for mini-channels based on the separated flow model and drift-flux model by applying the artificial neural network on the dominant parameters to correlate the two-phase friction multiplier and void fraction.

Allen et al. [14] presented a procedure for the design of the components of a heat exchanger network including condensers using a GA in order to minimize its total annual cost. Eleven design variables related to the exchanger geometry are considered in their study. In consequence of their study, the optimal solution is determined for the minimum temperature difference providing the more economical heat exchanger network.

Wang et al. [15] developed an ANN correlation for boiling heat transfer coefficient of R22 and its alternative refrigerants R134a, R407C and R410A inside horizontal smooth tubes in their paper. They compared the trained ANN with the experimental data in terms of the average, mean and root-mean-square deviations successfully.

Demir et al. [16] presented an ANN correlation for the experimental data belonging to the condensation heat transfer coefficient of alternative refrigerant R600a inside horizontal tube in their paper. Eventually, the results from the trained network showed good agreement with the experimental data and better results than the some well-known correlations in the literature.

In this study, the main idea is to determine the proper coefficients of correlations, related with heat transfer coefficient and frictional pressure drop, characterizing the two-phase annular downward condensation flow in a vertical tube by means of computational numerical methods such as genetic algorithm (GA), unconstrained nonlinear minimization algorithm- Nelder-Mead method (NM) and non-linear least squares error method (NLS). However, there is no work regarding the numerical solution using GA, NM and NLS for the condensation heat transfer coefficient and frictional pressure drop of HFC-134a either in a horizontal or vertical tube apart from the ANN work just for the condensation of R600a in a horizontal tube, recently carried out by Demir et al. [16]. For these reasons, there remains room for further research. Especially, it can be also noted that all of the numerical and experimental investigations on in-tube condensation do not have any, considering contents and operating parameters, which are concerned with the authors' previous studies [17-29]. Finally, in the present study, the main concern is to fill the gap in the literature. The results for the solution of computational numerical methods on the two-phase heat transfer coefficient, frictional pressure drop, two-phase friction factor which have never before appeared in open literature are presented and compared with the results from the in-tube condensation database of KMUTT whose accuracy was proven in many papers in the literature. The results are evaluated with a genetic algorithm (GA), unconstrained nonlinear minimization algorithm-Nelder-Mead method (NM) and a non-linear least squares (NLS) method, and a least squares error method (LS), respectively.

2. Experimental apparatus and method

A schematic diagram of the test apparatus is shown in Fig. 1. The refrigerant loop consists of a pre-heating loop, test section, cooling loop and chilling loop. The refrigerant is circulated by

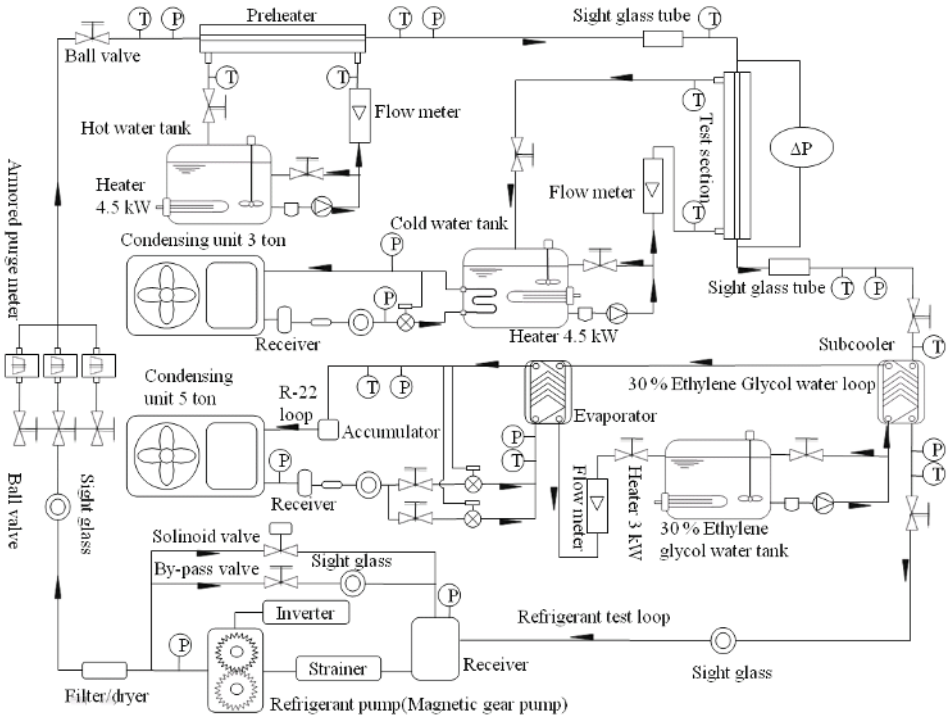

Fig. 1. Schematic diagram of experimental apparatus.

a gear pump controlled by an inverter. The refrigerant flows in series through a filter/dryer, a sight glass tube, a refrigerant flow meter and a preheater and enters the test section. A spiral counter-flow double tube heat exchanger is designed to supply heat to control the inlet quality of the refrigerant before entering the test section. After exiting the test section, the chilling loop condenses and sub-cools the refrigerant and removes the heat input from the pre-heater and test section, and ejects it into the surroundings. After leaving the chilling loop, the refrigerant changes from the two-phase refrigerant to a subcooled state. Eventually, the refrigerant returns to the refrigerant pump to complete the cycle.

The test section, well insulated with a proper material to minimize the heat loss, is a vertical counter-flow tube-in-tube heat exchanger with refrigerant flowing downward (co-current liquid and vapor of R134a's down flow) in the inner tube and cooling water flowing upward in the annulus. The inner and outer tubes are made from smooth vertical copper having inner diameters of 8.1 and 26 mm, respectively. The length of the heat exchanger is 0.5 m. Fig. 2 shows the detailed dimensions of the heat exchanger and the location of the thermocouples.

T-type thermocouples are used to measure refrigerant temperature and the tube wall temperatures in the test section. A total of ten thermocouples are located on the sidewall at five points along the test tube. A thermostat is used to control the inlet temperature of the water. All the temperature-measuring devices are calibrated in a controlled temperature bath using standard precision mercury glass thermometers. The uncertainty of the temperature measurements is ±0.1 °C. All static pressure taps are mounted on the tube wall. The refrigerant flow meter is a variable area type. The flow meter was calibrated in the range of 0-2.2 gal min^{-1} for HFC-134a by the manufacturer. Pressure drop is measured by a differential pressure transducer installed between the inlet and outlet of the test section. The length between pressure taps is 0.7 m. A low temperature thermostat is used to control the system pressure of the refrigerant flow. The differential pressure transducer and pressure gauges are calibrated against a primary standard, the dead weight tester. All signals from thermocouples and pressure transducers are recorded by a data logger. Tests are performed in the steady state.

The test runs were performed at average condensing temperatures of 40°C and 50°C in a copper smooth tube having an inner diameter of 8.1 mm and length of 0.5 m. The mass fluxes were varied from 260 to 515 kg $m^{-2}s^{-1}$ and the heat fluxes were between 10.16 and 66.61 kW m^{-2}. Accuracy of the dataset was proven in many papers in the literature.

3. Data reduction and experimental uncertainty

The data reductions of the measured results such as inlet and outlet vapor quality of the test section are presented in detail in the authors' previous publications in the literature.

3.1 The average heat transfer coefficient

$$h_{exp} = \frac{Q_{TS}}{A_i(T_{ref,sat} - T_{wi})} \quad (1)$$

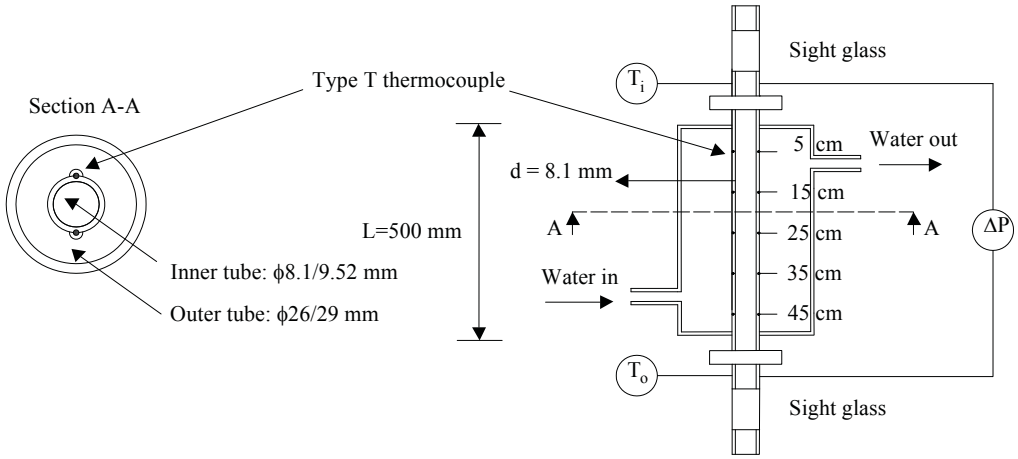

Fig. 2. Schematic diagram of test section.

where h_{exp} is the experimental average heat transfer coefficient, Q_{TS} is the heat transfer rate in the test section, T_{wi} is the average temperature of the inner wall, $T_{ref,sat}$ is the average temperature of the refrigerant at the test section inlet and outlet, and Ai is the inside surface area of the test section:

$$A_i = \pi dL \tag{2}$$

where d is the inside diameter of the test tube. L is the length of the test tube.

3.2 Error analysis

Error analysis of the study is performed by means of Eqs. (3), (4) and (5). In these equations, N is the element number of test group, h^i_{exp} and h^i_{calc} are the experimental and calculated results of heat transfer coefficient obtained from "i" number of test data, respectively, and h_{exp} and h_{calc} are the average values of experimental and calculated results of heat transfer coefficient obtained from the numerical analysis. It should be noted that error analysis of frictional pressure drop and two-phase multiplier was done similarly.

R square error is determined as follows:

$$E_{Rsquare} = \frac{\left(\sum_{i=1}^{N}(h^i_{exp} - \overline{h_{exp}})(h^i_{calc} - \overline{h_{calc}})\right)^2}{\left(\sum_{i=1}^{N}(h^i_{exp} - \overline{h_{exp}})^2\right)\left(\sum_{i=1}^{N}((h^i_{calc} - \overline{h_{calc}})^2\right)} \tag{3}$$

$$E_{ratio} = \frac{100}{N}\sum_{i=1}^{N}\frac{\left|h^i_{exp} - h^i_{calc}\right|}{h^i_{exp}} \tag{4}$$

$$E_{square} = \sqrt{\frac{1}{N}\cdot\sum_{i=1}^{N}(h^i_{exp} - h^i_{calc})^2}\,. \tag{5}$$

3.3 Calculation procedure for the genetic algorithm (GA)

GA is a search technique used in computing to find good solutions for optimization and search problems. GA uses the techniques inspired by Darwin's evolution theory and it is a particular class of evolutionary algorithms that solves hard problems quickly, reliably and accurately [30-32]. GA is applied to find a good solution that meets the system requirements. GA strongly differs in conception from other stochastic search methods and traditional optimization methods. While other methods always process single points in the search space, the GA maintains a population of potential solutions [33] as a basic difference. The GA starts with a large number of randomly generated chromosomes which are necessary for the problem, and each chromosome represents different solutions of the problem. Chromosomes are created to encode the potential solutions as a mathematical representation for solutions according to the type of problem. Each solution in the population is evaluated from the fitness function which is always dependent to the problem. The chromosomes are selected from best to worst by means of an objective function. In every generation, the genetic operators are applied to create a new population. GA uses the operators of reproduction, crossover and mutation. Reproduction selects and recombines the individuals from the population and produces offspring for the next generation. There are several techniques for the usage of reproduction operators. The most frequently used reproduction methods are roulette wheel and linear selection methods. Crossover is used to change the information between randomly selected two parents without losing any important information. There are also many crossover techniques which are one-point, two-point, multiple point, shuffle-exchange and uniform. One of the operators of GA is the mutation which is applied to chromosomes by changing the gene values. The basic steps of genetic algorithm are as follows:

(1) The initial population type and number is determined.
(2) Initial population is generated.
(3) Each individual's fitness function value of the population is calculated.
(4) The fitness is determined according to the scale method.
(5) All individuals of the population are binary matched ac-

cording to the selection method.
(6) New individuals are created among the individuals who are binary matched, by the crossing over operators.
(7) A mutation is applied to the newly formed individual.
(8) Fitness value of the mutated individual is calculated and added to population.
(9) The most well-defined number of individuals (elitism) are stored for the next generation.
(10) To fix the increased number of population to the initially defined number, individuals with high fitness values (poor individuals) are removed from the population randomly.
(11) And the individual with the lowest fitness value (best individual) is assigned as the global best.
(12) If the stop condition is not fulfilled then step 4 is followed again.

Genetic algorithms are search and optimization methods, working in a similar way as the evolutionary process observed in nature. They look for the best global solution, according to the principle of survival of the good, in a complex multi-dimensional search space. Basic principles of genetic algorithms have been first proposed by John Holland at the University of Michigan. First, Holland used the laws of evolution in genetic algorithms for optimization problems [34].

Genetic algorithms produce a set of solutions to problems, rather than a single solution. Thus, many points are evaluated in the search space at the same time while the possibility of reaching ultimately global solution increases. The solutions in the solution set are completely independent of each other. Each one is a vector of multi-dimensional space.

In practice, a bit-based population was used, consisting of 200 individuals. Each coefficient candidate has been expressed by 20 bits. Each parameter was searched between -5 to +5. If all of the bits, corresponding to any parameter, are 1, it means that this parameter is at 5, and if all of the bits are 0, then this means that it's at -5. Since, 2^{20} -1 different states can be expressed by 20 bits, the sensitivity for each parameter becomes (5- (-5)) / (2^{20} -1). The used population is simulated in Table 1.

Bit sequence of the individuals in initial population was determined in a uniform random manner. And the fitness function is square error (MSE) between the calculated value and the actual value. Therefore, the genetic algorithm searches the formula coefficients, which give the smallest MSE, between experimentally obtained values and the output of the heuristic formula.

The rank scale method, which is used as the scale method, is based on calculation of the fitness in accordance with the individual's rank number, after sorting each individual by their fitness. The roulette selection method is used as the selection method. According to this method, individuals are selected by a lottery with the odds being maximum for the best individual and the odds being minimum for the worst individual. In this way, even the worst individuals have the possibility to produce new individuals and to remain in the next generation.

A crossing-over process is performed among selected pairs

Table 1. The simulated population for GA analysis.

	20 bits															
	1.coefficient				2.coefficient				3.coefficient				4.coefficient			
1. individual	0	1	....	0	1	1	....	1	0	1	....	0	0	1	....	1
2. individual	0	0	....	1	1	1	....	0	0	1	....	1	0	0	....	1
3. individual	1	1	....	0	0	1	....	1	0	0	....	0	1	1	....	0
	⋮	⋮	⋮	⋮	⋮	⋮	⋮	⋮	⋮	⋮	⋮	⋮	⋮	⋮	⋮	⋮
200.individual	1	1	....	0	1	0	....	1	0	1	....	0	0	1	....	1

to maintain diversity. This process is the process of creating a new individual, with a mixture of the two selected individual's bit sequences. In practice, scatter crossing-over is used. This process is to rearrange every bit of the new individual by 50% probability from the first individual and by 50% probability from the second individual.

Mutation is a procedure that increases the diversity in new individuals. In this step, any randomly selected bit of randomly selected 10% of individuals is changed from 0 to 1 or 1 to 0.

The elitism number is taken as 2 in the algorithm. Thus, the best two individuals in each generation are always guaranteed to remain in the next generation. The individuals which are not going to be in the next generation are again selected according to the selection method, by determining their fitness. Thus, 1 generation is completed.

In practice, the determined stopping condition should be 1000 generations, or the best value should never be changed for consecutive 200 generations. This algorithm stops when one of these two stop conditions is fulfilled, and the globally best known individual so far is presented as the solution.

3.4 Unconstrained nonlinear minimization algorithm Nelder-Mead method (NM)

Nelder and Mead developed a simplex method to determine a local minimum of a function of several variables. It is a good alternative method when the differential of the fitness function is complex either analytically or numerically. A simplex forms triangle for two variables and function values at the three vertices of this triangle are compared by means of the pattern search method. The new vertex is found by replacing with the rejected worst vertex where f (x, y) is largest. Then, the search is continued when the new vertex is formed. A sequence of triangles, which might have different shapes, is generated by each iteration when values at the vertices get smaller and smaller. Reduction of the size of the triangles is performed and the coordinates of the minimum point are found. Generally, this effective method begins to the simplex having “n+1” vertex for the minimization of the fitness function having “n” variables.

The Nelder-Mead algorithm is a local optimization method which attempts to find better points by removing the worst of m+1 points at each step of its iterative methods, that starts

with m+1 initial guesses in an m dimension space, without using a derivative information. The Nelder-Mead technique is a technique for minimizing a fitness function in a many-dimensional space.

It is used to find the optimal value of the predetermined function parameters, which expresses the experimental data collected from the environment, in this study. For this, an error function was coded, and minimization of this error function with desired parameters is provided by the above mentioned method.

Assume we have n data points with 3 inputs and 1 output. Where, input parameters are denoted by x, y, z and the output parameter is denoted by f. In this case, our data points can be expressed as follows:

$$(x_1,y_1,z_1,f_1),(x_2,y_2,z_2,f_2),(x_3,y_3,z_3,f_3)\ldots(x_n,y_n,z_n,f_n). \quad (6)$$

The non-linear function to be fitted to these points is denoted by g, and if the m coefficients to be found are β_1, β_2, $\beta_3\ldots\beta_m$ then it can be expressed as $f_i = g(x_i,y_i,z_i,\beta)$. Here, f_i is the real value and $g(x_i,y_i,z_i,\beta)$ are the calculated values. If we call total squared error as E, between these two values, equivalent of E becomes as follows:

$$E(\beta) = \sum_{i=1}^{n} (f_i - g(x_i,y_i,z_i,\beta))^2 . \quad (7)$$

The goal of the method is to find the β value which makes the E(β) function minimum.

There are five operators in the Nelder-Mead algorithm used for this purpose as shown in Fig. 3. These operators are briefly described as follows:

Reflection: Its operation, where the worst candidate among m+1 guesses is moved to a symmetrical point according to the center of gravity of other remaining m candidates.

Expansion: The worst candidate point is to be moved beyond its point of reflection. The distance of expansion point to the reflection point equals the distance of the worst candidate to the center of gravity of the remaining points.

Inside contraction: The worst candidate point is to be moved to the exact center, where it is the center of gravity of other points together with itself.

Outside contraction: The worst candidate point is to be moved to the exact center, where it is the center of gravity of other points together with the reflection point.

Shrink: Except the best point, is to be moved to the exact center of all points and itself.

The steps of the algorithm are as follows [36]:

(1) Determine m+1 starting point for m parameter guess.

$x_1 = [\beta_1^1, \beta_2^1, \beta_m^1]$, $x_2 = [\beta_1^2, \beta_2^2, \beta_m^2]$,

$x_{m+1} = [\beta_1^{m+1}, \beta_2^{m+1}, \beta_m^{m+1}]$.

(2) Sort by fitness function $E(x_1)<E(x_2)<E(x_3)\ldots<E(x_{m+1})$.

(3) Calculate the reflection point x_r of the point x_{m+1}.

(4) If $E(x_1) \le E(x_r) < E(x_m)$ then $x_{m+1}=x_r$.

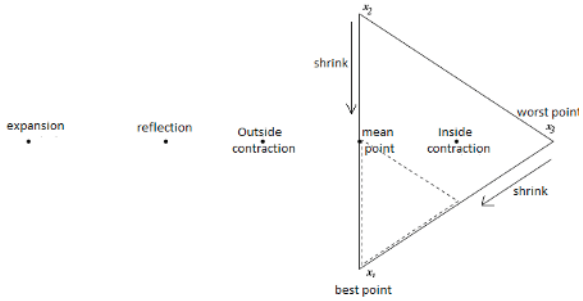

Fig. 3. Operators in Nelder-Mead algorithm.

(5) Else if $E(x_r) < E(x_1)$ then calculate the expansion point x_θ.

If $E(x_\theta) < E(x_r)$ then $x_{m+1} = x_\theta$ else $x_{m+1}=x_r$.

(6) Else if $E(x_r) \ge E(x_m)$ then

a. If $E(x_m) \le E(x_r) < E(x_{m+1})$ then

i. Calculate inside contraction x_{ic} and outside contraction x_{oc}.

ii. If $E(x_{oc}) < E(x_r)$ then $x_{m+1}=x_{oc}$.

iii. Else if $E(x_{ic}) < E(x_{m+1})$ then $x_{m+1}=x_{ic}$.

iv. Else shrink.

b. Else shrink.

(7) If var $(x_1,x_2,x_3\ldots x_{m+1}) > \varepsilon$ go to step 2.

(8) Take the x_1 as candidate solution.

The stop condition in this algorithm is that the variance of m+1 candidate solution points is smaller than a certain epsilon. As the algorithm progresses, each m+1 candidate solution points will approach mutually. When the loop ends, the best of the m+1 candidate is determined as the result.

3.5 Calculation procedure for the non-linear least squares algorithm (NLS)

Gauss [37] described the LS method, which is one of the standard approaches to the approximate solution of over determined systems or inexactly specified systems of equations in an approximate sense. It can be used when the sets of equations in which there are fewer unknowns than equations. LS means that the overall solution minimizes the sum of the squares of the errors made in solving every single equation instead of solving the equations exactly.

The data fitting is the most important application of LS. The minimization of the sum of squared residuals is sensed by the best fit in the LS and a residual causes the difference between an observed value and the value provided by a model. LS matches with the maximum probability criterion if there is a normal distribution of the experimental errors.

LS problems consist of linear least squares and non-linear least squares (NLS) depending on whether or not the residuals are linear in all unknowns. Most statistical regression analysis has linear LS problems; it has a closed form solution. The non-linear problem, usually solved by iterative refinement, has no closed solution. The system is approximated by a linear one at each iteration in order to have similar results for the

core calculation in both cases.

The non-linear least square (NLS) method allows determination of the most optimal non-linear function coefficients, in order to fit data collected from an experimental environment to a non-linear function (non-linear curve fitting). This method tries to minimize the mean square error, beginning from the first estimated values determined by the user [38]. Since it advances step by step by optimizing this point, starting from this initial point, it finds the local minimum and not the global minimum. The method is tested by starting from different initial points, and the point which finds global minimum is tried to be predicted.

Mathematical basis of the method is as follows:

Assume we have n data points with 3 inputs and 1 output, where input parameters are denoted by x, y, z and the output parameter is denoted by f. In this case, our data points can be expressed as in Eq. (6).

The non-linear function to be fitted to these points is denoted by g, and if the m coefficients to be found are $\beta_1,\beta_2,\beta_3 \ldots \beta_m$ then it can be expressed as $f_i=g(x_i, y_i, z_i, \beta)$. Here, f_i is the real value and $g(x_i, y_i, z_i, \beta)$ are the calculated values. If we say that the total squared error between these two values is S, then equivalent of S is as follows:

$$S=\sum_{i=1}^{n}(f_i-g(x_i,y_i,z_i,\beta))^2 \quad . \tag{8}$$

The β values, which make the S value minimum, are the coefficient vectors to be found. The point where S is minimum is the point where the partial derivatives of S are equal to zero. Therefore the following equation is written, where j=1...m

$$\frac{\partial S}{\partial \beta_j}=2.\sum_{j=1}^{n}(f_i-g(x_i,y_i,z_i,\beta)).\frac{(f_i-g(x_i,y_i,z_i,\beta))}{\partial \beta_j}=0. \tag{9}$$

The iterative steps to be applied in order to find the β values, which equate the above equation to zero, are as follows:

(1) k is determined as the iteration counter and k=0 value is assigned.
(2) The β^k initial values are determined randomly.
(3) The vector with n elements $\Delta f_i = f_i - g(x_i, y_i, z_i, \beta^k)$ is calculated (i=1..n).
(4) If the $J_{i,j}$ expression is stated in terms of a partial derivative of the error function according to β_j, with the values at i^{th} data point, then that J matrix becomes the Jacobian matrix (i=1..n, j=1..m).
(5) $\beta^{k+1} = \beta^k + (J^T J)^{-1} J^T \Delta f$ is updated.
(6) If $\left|\beta^{k+1} - \beta^k\right| > \varepsilon$ then k is increased by one, and continued from the 3rd step.
(7) The searched coefficients are found as β^{k+1}.

In the study, coefficients are searched by starting the above algorithm for each problem at 100 different initial points. The results of these 100 experiments, which give the best curve fits, are presented as the output.

3.6 Correlation development

Determination of heat transfer characteristics of compact systems such as heat transfer coefficient, frictional pressure drop, flow type between the fluids, heat transfer surface area in heat exchangers should be known accurately for the optimum design. The two-phase heat transfer systems have higher thermal heat transfer performance than single-phase heat transfer systems in limited apparatus volumes. Advantage of high thermal performance in comparison to the single-phase applications includes smaller, more compact systems regarding tube length, tube diameter, and internal tube geometry shape in a wide variety of applications, e.g., refrigeration and air conditioning systems, power engineering and other thermal processing plants. Before doing any numerical work on this subject, validation process of the experimental setup and data is a very significant for reliability of the study. The correctness of experimental data should be evaluated by either graphics regarding the characteristics of trend lines [17-29] such as alteration of heat transfer coefficient vs. quality, heat flux vs. temperature difference between the vapor and inlet wall temperature, pressure drop vs. vapor quality etc., or widely accepted correlations in the literature and desired working conditions should be agreeable with the heat balance correlations and flow type observations by means of sight glasses at the different points of experimental apparatus.

There have been a number of studies on the in-tube condensation heat transfer coefficient and pressure drop. The frictional, acceleration, and gravitational components determine the two-phase total pressure drop in tubes. Determination of the void fraction is required to compute the acceleration and gravitational components, and in a similar way, determination of either the two-phase friction factor or the two-phase frictional multiplier is required to compute the frictional component of pressure drop. Generally, empirical methods have been used to compute the condensation heat transfer coefficients and pressure drops in tubes. Most of these proposed models are modifications of the Dittus-Boelter single-phase forced convection correlation [39], as in Akers et al. [40], Cavallini and Zecchin [41], and Shah [42].

3.6.1 Correlation proposal for the convective condensation heat transfer coefficient

The correlation for the laminar and turbulent flow inside the test tube was developed as a form of Dittus and Boelter's [39] correlation in Eq. (10) by means of several dimensionless numbers which were defined and used by Akers et al. [40] for Reynolds equivalent number in Eq. (11), by Koyama et al. [43] for the ratio of density to dynamic viscosity in Eq. (12), by Lockhart and Martinelli [44] for their parameter in Eq. (14), by Dobson and Chato [41] for the form of Lockhart and Martinelli's [44] parameter with specific constant numbers in Eq. (10) and by Cavallini et al. [46, 47] for the usage of Bond and Froude numbers together in Eqs. (15)-(16). As a result, Eq. (10) is formed to predict the convective condensation heat

transfer coefficient in terms of the above explanations as follows:

$$h = A\left(\frac{k_l}{d}\right)Re_{eq}{}^{B}(PrR)^{C}\left[\frac{D}{X^{E}}+F\right](BoFr)^{G} \tag{10}$$

where the all liquid equivalent Re number is determined from:

$$Re_{eq} = \frac{G_{eq}d}{\mu_l} \tag{11}$$

and equivalent liquid mass flux is defined as:

$$G_{eq} = G\left((1-x)+x(\frac{\rho_l}{\rho_g})^{0,5}\right) \tag{12}$$

and the ratio of density to dynamic viscosity is defined as:

$$R = \frac{\rho_l \mu_l}{\rho_g \mu_g} \tag{13}$$

and Bond number is defined as:

$$Bo = g(\rho_l - \rho_g)\left(\frac{(d/2)^2}{\sigma}\right) \tag{14}$$

and Froude number is defined as:

$$Fr = \frac{G^2}{gd\rho_{TP}{}^2} \tag{15}$$

where the two-phase density is determined from:

$$\rho_{TP} = \left(\frac{x}{\rho_g}+\frac{1-x}{\rho_l}\right)^{-1} \tag{16}$$

and Lockhart and Martinelli [44] parameter is expressed as:

$$X = \sqrt{\frac{\left(\frac{dp}{dz}\right)_l}{\left(\frac{dp}{dz}\right)_g}} \tag{17}$$

where the two-phase frictional pressure gradient can be related to the Fanning friction factor [48] in terms of mass flux and mass quality for liquid flowing alone as follows:

$$\left(\frac{dp}{dz}\right)_l = \frac{f_l G^2(1-x)^2}{2d\rho_l} \tag{18}$$

and liquid phase's friction factors are determined for laminar flow by Darcy and Weisbach [49, 50] in Eq. (19) and turbulent flow by Blasius [51] in Eq. (20) as follows:

$$f_l = \frac{64}{Re_l}, \tag{19}$$

$$f_l = \frac{0.316}{Re_l^{0.25}} \tag{20}$$

where the Reynolds number equation can be expressed in terms of mass flux and mass quality for liquid flowing alone as:

$$Re_l = \frac{Gd(1-x)}{\mu_l} \tag{21}$$

and the gas phase's pressure drop in Eq. (17) is calculated in a similar way with Eq. (14) as:

$$\left(\frac{dp}{dz}\right)_g = \frac{f_g G^2 x^2}{2d\rho_g} \tag{22}$$

where all of the gas phase's friction factors, valid for Re_g>20000, are determined by Blasius [51] for turbulent flow in this study as:

$$f_g = \frac{0.184}{Re_g^{0.2}} \tag{23}$$

and the two-phase gas Reynolds number is defined as:

$$Re_g = \frac{Gdx}{\mu_g}. \tag{24}$$

It should be noted that Lockhart and Martinelli [44] parameter in Eq. (17) is calculated by means of the equations from 17 to 24 according to the situation for the laminar or turbulent flows of liquid and gas phases of R134a in the test tube. The detailed information on the basis of Lockhart and Martinelli's development [44] can be obtained from Chisholm [52]'s investigation.

3.6.2 Correlation proposal for the two phase multiplier

The separated flow model is the most used method to calculate heat transfer characteristics. Lockhart and Martinelli's [44] method is one of the most well-known for the determination of two-phase frictional pressure drop. It is a combination of the inertial and viscous forces of both phases. Chisholm and Laird's [53] two-phase frictional multiplier is commonly used in the literature as follows:

$$\phi_l^2 = \frac{\left(\frac{dp}{dz}\right)_F}{\left(\frac{dp}{dz}\right)_l} = 1+\frac{C}{X}+\frac{1}{X^2} \tag{25}$$

where Chisholm parameter C varies from 5 to 20 depending on whether the phases of liquid and gas are laminar or turbulent for conventional channels. As a result, Eq. (25) is modified to predict the frictional pressure drop regarding with the explanations above as follows:

$$\phi_l^2 = A + \frac{B}{X^C} + \frac{D}{X^E}. \quad (26)$$

The two-phase frictional pressure drop can be obtained by subtracting the gravitational and momentum terms from the total measured pressure drop as follows:

$$\left(\frac{dP}{dz}\right)_F = \left(\frac{dP}{dz}\right)_{exp} - \left(\frac{dP}{dz}\right)_G - \left(\frac{dP}{dz}\right)_M. \quad (27)$$

Pressure drop due to gravity can be determined from:

$$(\Delta P)_G = g(\alpha\rho_g + (1-\alpha)\rho_l)L \quad (28)$$

where the void fraction, α, can be determined from Chisholm [54] correlation below:

$$\alpha = \frac{1}{1 + \left(\frac{1-x}{x}\right)\left(\frac{\rho_g}{\rho_l}\right)S}, \quad (29)$$

$$S = \left(1 - x + x\frac{\rho_l}{\rho_g}\right)^{1/2}. \quad (30)$$

The momentum transfer term contributes to the overall pressure drop during condensation due to the mass transfer that occurs at the phase's interface. The momentum pressure gradient can be written according to the results of the one-dimensional two-phase separated-flow analysis which can be defined as follows:

$$\left(\frac{dP}{dz}\right)_M = -G^2 \frac{d}{dz}\left[\frac{x^2}{\rho_g\alpha} + \frac{(1-x)^2}{\rho_l(1-\alpha)}\right]. \quad (31)$$

Eq. (31) can be rearranged as follows:

$$\Delta P_M = G^2\left[\left\{\frac{(1-x)^2}{\rho_l(1-\alpha)} + \frac{x^2}{\rho_g\alpha}\right\}_o - \left\{\frac{(1-x)^2}{\rho_l(1-\alpha)} + \frac{x^2}{\rho_g\alpha}\right\}_i\right]. \quad (32)$$

3.6.3 Validation of the proposed correlations by means of heat transfer correlations

The Shah correlation [55] has been investigated by researchers commonly for turbulent condensation conditions especially in vertical tubes [56] and is considered to be the most comparative condensation model for annular flow regime in a tube [57]. The Shah correlation is based on the liquid heat transfer coefficient, which is valid for $Re_l \geq 350$. It has a two-phase multiplier for annular flow regime of high pressure steam and refrigerants [56, 57]. Dobson and Chato [58] developed a correlation using a two-phase multiplier for an annular flow regime. They also provided a correlation for a wavy flow regime. Their correlations are commonly used in the literature for zeotropic refrigerants. Chato [59] developed Dittus and Boelter's correlation [39] using a two-phase multiplier for an annular flow regime. Sweeney [60] provided a modification of the Dobson and Chato model [58]. He studied zeotropic mixtures for annular flow. He also offered a correlation for wavy flow. Cavallini et al. [61] developed a semi empirical correlation for the condensation of various organic refrigerants in both vertical and horizontal orientations. Fujii [62] developed the following correlation for smooth tubes. He also offered a correlation for gravity controlled regimes. His equation was used for shear-controlled regimes in Table 5. Tang et al. [63] modified the Shah [55] equation for annular flow condensation of R410A, R134a and R22 in i.d. 8.81 mm tube with Frso > 7. Bivens and Yokozeki [64] modified Shah correlation [3] for various flow patterns of R22, R502, R32/R134a, R32/R125/R134a. Tandon et al. [65] modified the Akers and Rosson [66] correlation for shear controlled annular and semi-annular flows with $Re_g > 30000$. It should be noted that there is another correlation for gravity-controlled wavy flows with $Re_g < 30000$ which belongs to Tandon et al. [65]. Traviss et al. [66] investigated flow regime maps for condensation inside tubes. Their correlation was suggested for the condensation of R134a inside tubes specifically. Variation in the quality of the refrigerant was considered using Lockhart-Martinelli parameter [44]. Akers and Rosson [67] modified the Dittus and Boelter [39] single-phase forced convection correlation. Their correlation was recommended for turbulent annular flow in small diameter circular tubes and rectangular channels. Table 2 shows the correlations mentioned above.

3.7 Uncertainties

The uncertainties of the Nusselt number and condensation heat transfer coefficient in the test tube varied from ±7.64% to ±10.71%. It should be noted that similar ranges of uncertainty with minimum and maximum values exist in the literature. The procedures of Kline and McClintock [68] were used for the calculation of all uncertainties. Various uncertainty values of the study can be seen from authors' previous works and the details are given in Table 3.

4. Results and discussion

The present study was done at the Fluid Mechanics, Thermal Engineering and Multiphase Flow Research Lab. (FUTURE) in KMUTT for the correlation development belong to the convective heat transfer coefficient and two-phase multiplier during the downward two-phase flow of pure R134a in a vertical round tube with inner diameter of 8.1 mm.

Table 2. The existing heat transfer coefficient correlations from literature for the comparison.

Researcher	Correlation
Shah [55]	$h_{shah} = h_{sf}\left(\frac{1.8}{Co^{0.8}}\right)$ $Co = \left(\frac{1}{x}-1\right)^{0.8}\left(\frac{\rho_g}{\rho_l}\right)^{0.5}$ $h_{sf} = h_l(1-x)^{0.8}$ $h_l = \frac{k_l}{d}\left(0.023\left(\frac{Re_l}{1-x}\right)^{0.8} Pr_l^{0.4}\right)$ $P_{red} = P_{sat}/P_{critic}$ $Re_l = \frac{Gd(1-x)}{\mu_l}$
Dobson and Chato [58]	for $G > 500$ kg m^{-2} s^{-1} $Nu = 0.023Re_l^{0.8}Pr_l^{0.4}\left[1+\frac{2.22}{X^{0.89}}\right]$ for $Re_l > 1250$ and $Fr_{so}>18$ $Nu = 0.023Re_l^{0.8}Pr_l^{0.3}\frac{2.61}{X^{0.805}}$ $X = \left(\frac{1-x}{x}\right)^{0.9}\left(\frac{\rho_g}{\rho_l}\right)^{0.5}\left(\frac{\mu_l}{\mu_g}\right)^{0.1}$
Chato [59]	$Nu = 0.023Re_l^{0.8}Pr_l^{0.4}\left[\frac{2.47}{X^{1.96}}\right]$
Sweeney [60]	$Nu = 0.7\left(\frac{G}{300}\right)^{0.3} Nu_{Dobson,Chato}$
Cavallini et al. [61]	$Nu_l = 0.05Re_{eq}^{0.8}Pr^{0.33}$ $Re_{eq} = Re_g\left(\mu_g/\mu_l\right)\left(\rho_l/\rho_g\right)^{0.5} Re_l$
Fujii [62]	$Nu_l = 0.0125\left(Re_l\sqrt{\rho_l/\rho_g}\right)^{0.9}\left(\frac{x}{1-x}\right)^{0.1x+0.8} Pr_l^{0.63}$
Tang et al. [63]	$Nu = 0.023Re_l^{0.8}Pr_l^{0.4}\left[1+4.863\left(\left(-\ln(P_{red})\frac{x}{1-x}\right)^{0.836}\right]\right.$ $Fr_{so} = c_3Re_l^{c_4}\left(\frac{1+1.09X^{0.039}}{X}\right)^{1.5}\frac{1}{Ga^{0.5}}$ $Ga = \frac{\rho_l(\rho_l-\rho_g)gd^3}{\mu_l^2}$ $R_{el} \leq 1250$ $c_3 = 0.025c_4 = 1.59$ $R_{el}>1250$ $c_3 = 1.26$ $c_4 = 1.04$
Bivens and Yokozeki [64]	$Nu = Nu_{Shah}\left(0.78738+\frac{6187.89}{G^2}\right)$ $Nu_{Shah} = 0.023Re_l^{0.8}Pr_l^{0.4}\left[1+\frac{3.8}{P_{red}^{0.38}}\left(\frac{x}{1-x}\right)^{0.76}\right]$
Tandon et al [65]	$Nu = 0.084Re_g^{0.67}Pr_l^{1/3}\left[\frac{1}{Ja_l}\right]^{1/6}$
Travis et al. [66]	$Nu = Re_l^{0.9}Pr_l\frac{F_l(X)}{F_2(Re_l,Pr_l)}$ $F_l(X) = 0.15\left[\frac{1}{X}+\frac{2.83}{X^{0.476}}\right]$ $F_2 = 5Pr_l+5\ln(1+5Pr_l)+2.5\ln(0.00313Re_l^{0.812})$ for $Re_l>1125$
Akers and Rosson [67]	$Nu = 0.0265Re_{eq}^{0.8}Pr_l^{1/3}$ $Re_{eq} = \frac{G_{eq}d}{\mu_l}$ $G_{eq} = G\left[(1-x)+x\left(\rho_l/\rho_g\right)^{0.5}\right]$

The results will be discussed in turn as follows.

The determination of convective heat transfer coefficient and frictional pressure drop by means of computational numerical techniques is presented in the following paragraphs using relevant measured data such as 178 numbers of 40°C data and 191 numbers of 50°C data during the downward laminar and turbulent condensation of R134a at a high mass flux in a vertical smooth tube over a wide range of experimental conditions. 89 of 178 at 40°C data and 95 of 191 at 50°C data were separated from others to form the test group. The rest of them were used to form the training group.

The thermal resistance is increased due to the increase in film thickness during condensation, hence, the heat transfer rate decreases. The heat transfer coefficient is larger when the inlet quality is higher. This is due to the result of smaller liquid film thickness together with higher vapor velocity at the

Table 3. Uncertainty of experimental parameters.

Parameters	Uncertainty
$T_{ref,sat}$ (°C)	0.19
x_i	±6.96-8.24%
ΔT (K)	±0.191
$(T_{w,o}-T_{w,i})_{TS}$ (K)	±0.045
$(T_{w,i}-T_{w,o})_{ph}$ (K)	±0.13
m_{ref} (g s^{-1})	±0.023
$m_{w,TS}$ (g s^{-1})	±0.35
$m_{w,ph}$ (g s^{-1})	±0.38
q_{TS} (kW m^{-2})	±6.55-8.93%
q_{ph} (kW m^{-2})	±12-14.81%
h_{ref} (W m^{-2}K^{-1})	±7.64-10.71%.
ΔP (kPa)	±0.15

vapor-liquid interface in comparison to the lower inlet quality with larger film thickness. Finally, the average heat transfer coefficient increases with increasing inlet quality. The heat transfer coefficient decreases with decreasing mass flux. This is due to the increase of vapor velocity of R134a. On the contrary, it decreases with increasing saturation temperature due to alteration of the physical properties of refrigerant by condensation temperature or pressure. Therefore, film thickness at high saturation temperature is thicker than that of low saturation temperature. The increase in condensation temperature difference between saturation and inner wall temperature, condensation rate and heat flux increases the film thickness due to the constant latent heat of condensation for a specific saturation temperature of condensation. Therefore, the average convective condensation heat transfer coefficient decreases with increasing condensation temperature difference regarding Eq. (1). It is also known that the increase in condensation rate causes an increase in mass flux and heat flux. Besides this, vapor quality decreases with decreasing void fraction. The increase in mass flux increases the total pressure drop at the same condensing temperature due to the increase of shear stress at the interface of phases. It is also known that the pressure drop decreases with increasing with system pressure or condensing at the same mass flux. In the same way, frictional pressure drop increases with increasing mass flux as well. Thus, the specific volume of R-134a vapor and the viscosity of R134a are decreased by the increase of saturation temperature. For that reason, the flow resistance is also decreased. All of these factors lower the pressure drop due to the increase in condensing pressure. Also, the pressure drop decreases with decreasing vapor quality generally. The decrease in vapor quality can occur by the increase in heat flux, which increases with increasing condensation rate. Also, total pressure drop increases with increasing mass flux at the same condensing temperature difference. The increase in the vapor velocity and the flow turbulence can occur by the increase of mass flux at a specific vapor quality. As a result of the increase in the shear stress at the interface of the vapor and liquid film, there is an increase in pressure drop. It can be noted that two-phase friction factor increases with decreasing equivalent Reynolds numbers. The results of correlation development study in this paper are found to be in good agreement with this fundamental knowledge of in-tube condensation as expected.

Table 4 shows the detailed results of the study. First, the convective heat transfer coefficient was obtained by means of the computational numerical methods such as genetic algorithm (GA), unconstrained nonlinear minimization algorithm- Nelder-Mead method (NM) and non-linear least squares method (NLS), and their correlations can be seen from the table separately. All the results of the computational numerical methods seem to have low proportional error rate values calculated from Eqs. (3) to (5). The unconstrained nonlinear minimization algorithm-Nelder-Mead method (NM) has the lowest proportional error rates as a result of the analysis. For that reason, dependency analysis was only done for this method. Second, the term (k_l/d), obtained by the division of the liquid thermal conductivity (k_l) to inner tube diameter (d), was a constant parameter in Eq. (10) due to its unit of "W $m^{-2}K^{-1}$". Other parameters such as equivalent Reynolds number, Prandtl number, Lockhart and Martinelli number, Bond number and Froude number are changed in Table 4 to show the dependency of convective heat transfer coefficient to them. It can be seen clearly from Table 4 that the convective heat transfer coefficient has the highest dependency to equivalent Reynolds number among others together with the ratio of liquid thermal conductivity to inner tube diameter; in other words, equivalent Reynolds number is found to be the dominant parameter for the determination of convective heat transfer coefficient by means of Eq. (10).

Figs. 4 to 6 show the comparison of convective condensation heat transfer coefficients obtained by the computational numerical methods of GA, NM, NLS and experiment (Eq. (1)) for all mean mass fluxes from 260 to 515 kg m^{-2} s^{-1} at the saturation temperatures of 40-50°C separately. These figures clearly show that the distribution of the data between the errors bands of ±30% seems quite balanced as expected from the results shown in Table 4. In addition, it is also shown that convective heat transfer coefficients increase with increasing mass flux of R134a as explained above. This result also shows that results of the numerical analysis are reasonable and compatible with the fundamental issues of condensation heat transfer.

Table 5 demonstrates the proposed equations for the two-phase multipliers and their error rates obtained from Eqs. (3) to (5). Lockhart and Martinelli parameter was the single parameter regarding with the form of Chisholm and Laird [53]'s two-phase frictional multiplier in Eq. (26). All proposed correlations' results using computational numerical methods are found to be successful according to their error rates in Table 5. NM method seems the most predictive one among others as a result of the analysis. For that reason, the last two equations' development is performed using NM in a different form from Chisholm and Laird's [53] two-phase frictional multiplier. It can be clearly seen from Table 5 that the last correlation in this table has the lowest proportional error rate.

Figs. 7 to 9 illustrate the comparison of the two-phase multipliers calculated from the computational numerical methods of GA, NM, NLS and experiment (Eq. (21)) for all mean mass fluxes from 260 to 515 kg m^{-2} s^{-1} at the saturation temperatures of 40-50°C separately. The 98.36% of the data for GA and NM, and 96.73% of the data for LS falls within the ±30% deviation line in these figures. The results also show the success due to the usage of Lockhart and Martinelli parameter in Eq. (25).

Figs. 10 to 12 show the comparison of frictional pressure drops between the computational numerical methods and the experiment (Eq. (23)) for condensation of R134a inside the vertical tube at the mean mass fluxes from 260 to 515 kg m^{-2} s^{-1} at the saturation temperatures of 40-50°C. The 89.66% of the data falls within the ±30% deviation line in these figures for all investigated computational numerical methods. It can be clearly seen from figures that the distribution of the data between the error bands of ±30% seems quite balanced apart

Table 4. The most predictive combinations of input parameters for Eq. (10) and proposed correlations for the condensation heat transfer coefficient.

Inputs for Eq. (10)					Input number	Error analysis			Proposed equations	Method		
k_l/d ($W\,m^{-2}K^{-1}$)	Re_{eq}	PrR	X	BoFr		R^2	Prop. (%)	Square law	h ($W\,m^{-2}K^{-1}$)	GA	NM	NLS
1	1	0	0	0	2	0.683	12.154	923.252	$h = 0.0436\left(\frac{k_l}{d}\right)Re_{eq}^{0.85}$	0	1	0
1	0	1	0	0	2	0.623	23.158	1622.576	$h = 404.86\left(\frac{k_l}{d}\right)(PrR)^{0.08}$	0	1	0
1	0	0	1	0	2	0.685	22.428	1569.877	$h = 12.64\left(\frac{k_l}{d}\right)\left[\frac{0.000172}{X^{2.914}} + 52.886\right]$	0	1	0
1	0	0	0	1	2	0.619	12.712	1012.119	$h = 21.479\left(\frac{k_l}{d}\right)(BoFr)^{0.368}$	0	1	0
1	1	1	1	1	4	0.675	12.389	934.468	$h = 0.332\left(\frac{k_l}{d}\right)Re_{eq}^{0.619}(PrR)^{0.032}\left[\frac{0.648}{X^{-0.00152}} + 0.127\right](BoFr)^{0.0713}$	1	0	0
1	1	1	1	1	4	0.688	11.969	916.376	$h = 0.0536\left(\frac{k_l}{d}\right)Re_{eq}^{0.999}(PrR)^{-0.06}\left[\frac{-0.739}{X^{-0.0239}} + 1.248\right](BoFr)^{-0.0875}$	0	1	0
1	1	1	1	1	4	0.647	12.388	974.128	$h = 0.591\left(\frac{k_l}{d}\right)Re_{eq}^{0.327}(PrR)^{0.297}\left[\frac{0.222}{X^{-0.0815}} + 0.0782\right](BoFr)^{0.281}$	0	0	1

Table 5. The most predictive coefficients of the proposed correlations for two-phase multiplier by means of the computational numerical methods.

Inputs for Eq. (25)	Input number	Error analysis			Proposed equations	Method		
X		R^2	Prop. (%)	Square law	φ_l^2	GA	NM	NLS
1	1	0.965	18.624	269.826	$\varphi_l^2 = -2.272 + \frac{2.188}{X^{1.987}} + \frac{0.337}{X^{1.553}}$	1	0	0
1	1	0.965	18.43	270.42	$\varphi_l^2 = -0.0283 + \frac{2.253}{X^{1.988}} - \frac{0.351}{X^{0.247}}$	0	1	0
1	1	0.965	18.604	270.215	$\varphi_l^2 = -29.483 + \frac{28.283}{X^{0.0166}} + \frac{2.314}{X^{1.98}}$	0	0	1
1	1	0.966	16.114	267.695	$\varphi_l^2 = 46462.2e^{-125.788X} + 2746.01e^{-24.944X}$	0	1	0
1	1	0.966	13.608	267.122	$\varphi_l^2 = 6019149e^{(-((X+0.1034)/0.0456)^2)} + 2045.276e^{(-((24.944X+0.0377)/0.09)^2)}$	0	1	0

from the data belonging to the mass flux of 260 kg $m^{-2}s^{-1}$ at 50°C. As explained above, the frictional pressure drop increases with increasing mass flux in these figures, and this situation shows the compatibility of the computational numerical models with the condensation heat transfer fundamental issues. As a result of the analysis of the authors' previous publications on the prediction of the proper void faction models and correlations, the reported agreeable void fraction correlations give quite similar frictional pressure drops. For that reason, the Chisholm correlation [54] is used as a constant void faction correlation in this numerical study.

The fitness function is defined to perform the optimization process considering its maximization in the GA analysis. The performances of the method of GA, NM and NLS with suitable architecture were found to be in good agreement predicting the experimental condensation heat transfer coefficient, two-phase friction multiplier and frictional pressure drop for all tested conditions. In addition, their prediction success can be realized and comparable with the results published in the authors' previous publications, especially for the condensation heat transfer coefficient [22] and pressure drop [23].

Table 6 shows the deviations of investigated heat transfer coefficient correlations shown in Table 2. The first proposed heat transfer coefficient correlation shown in Table 4, which depends only on k_l/d and Re_{eq} , and obtained from NM analysis, is also selected for the comparison. A large number of data points are used to show the success of the proposed correlation. The deviations of the different condensing temperatures are found to be similar with each other. For that reason, Table 6 also shows the accuracy of the experiments according to different condensing temperatures of 40 and 50°C in terms of the consistency of the deviations. Considering all data points, the proposed correlation has the best predictability among the reported correlations with the deviation of 2.52%. Akers and Rosson's [67] correlation has the largest one with the deviation of 50.39%. As explained above, artificial intelligence techniques have a learning process including test and training processes using a limited number of experimental data. As shown in Table 4, the proposed correlation in Table 6 has the $E_{Rsquare}$ (R^2) value of 0.683. In spite of its low R^2 value obtained from the testing process, it has lower deviations in comparison to the most of the correlations in Table 6. The

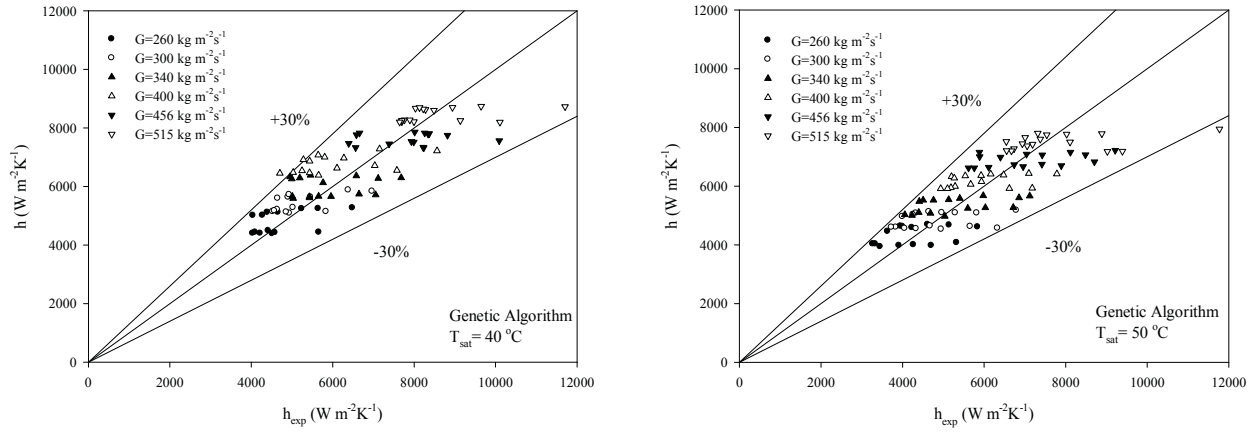

Fig. 4. Comparisons of experimental convective heat transfer coefficients with the method of genetic algorithm for the mass fluxes of 260, 340, 456 kg $m^{-2}s^{-1}$ and (a) T_{sat}=40°C and (b) 50°C.

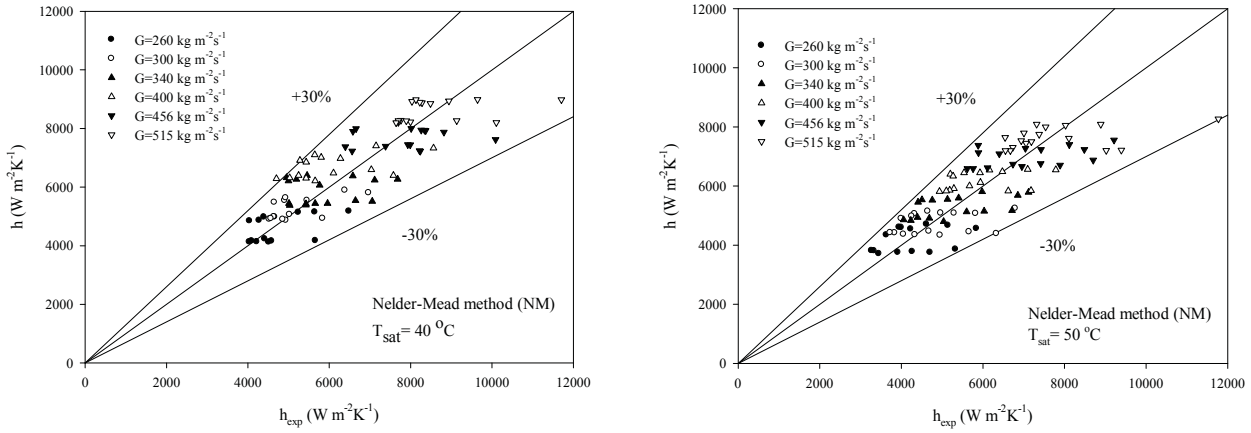

Fig. 5. Comparisons of experimental convective heat transfer coefficients with the method of non-linear least squares for the mass fluxes of 260, 340, 456 kg $m^{-2}s^{-1}$ and (a) T_{sat}=40°C and (b) 50°C.

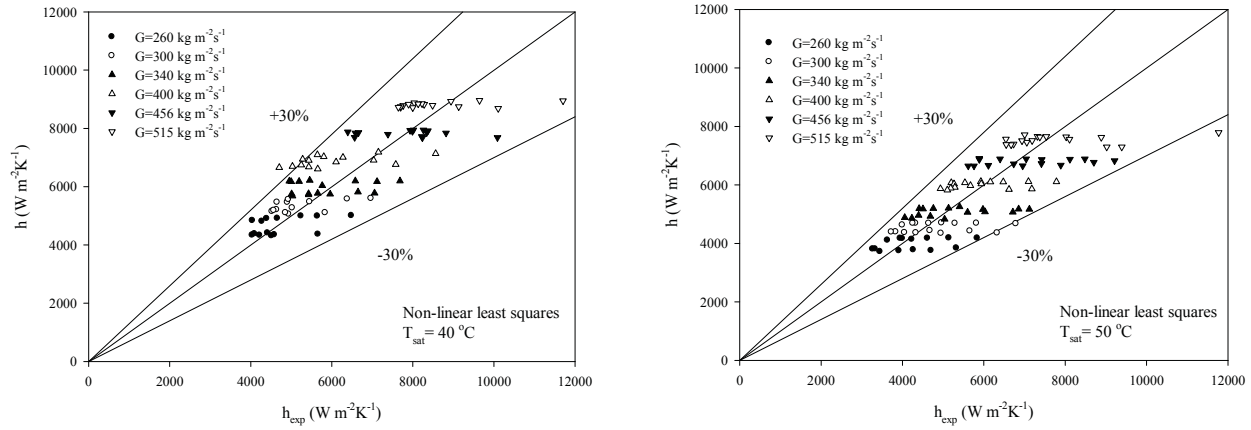

Fig. 6. Comparisons of experimental convective heat transfer coefficients with the method of least squares for the mass fluxes of 260, 340, 456 kg $m^{-2}s^{-1}$ and (a) T_{sat}=40°C and (b) 50°C.

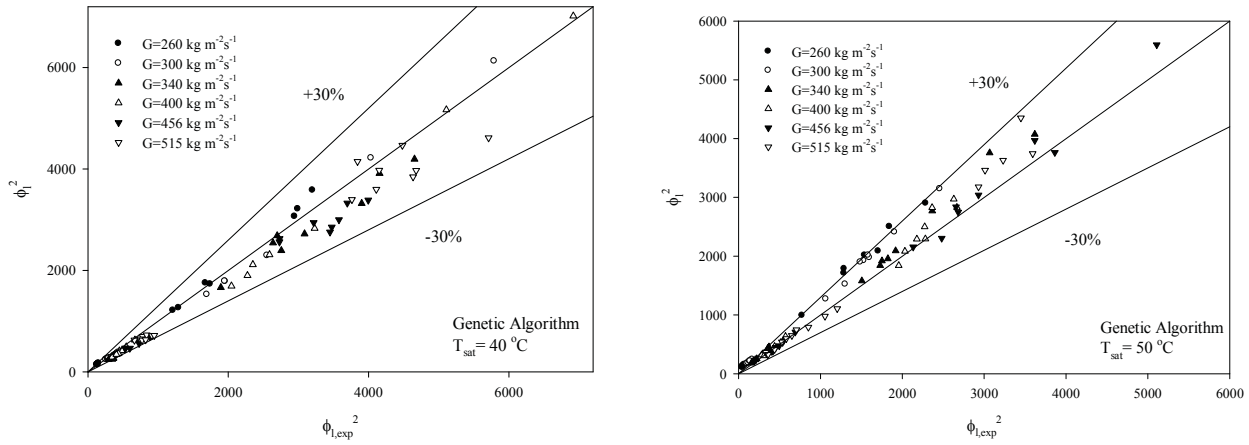

Fig. 7. Comparisons of experimental two-phase multiplier with the method of genetic algorithm for the mass fluxes of 260, 340, 456 kg $m^{-2}s^{-1}$ and (a) T_{sat}=40°C and (b) 50°C.

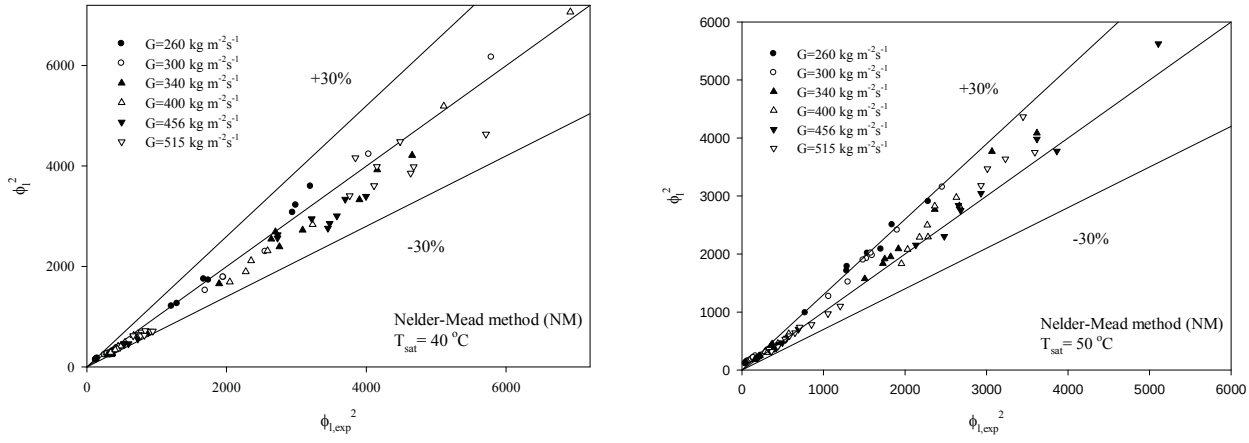

Fig. 8. Comparisons of experimental two-phase multiplier with the method of non-linear least squares for the mass fluxes of 260, 340, 456 kg $m^{-2}s^{-1}$ and (a) T_{sat}=40°C and (b) 50°C.

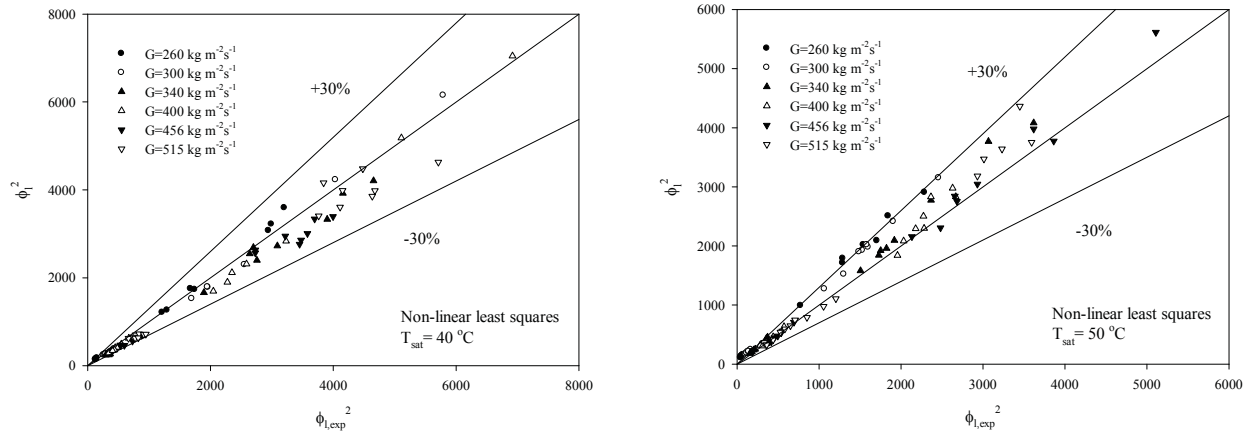

Fig. 9. Comparisons of experimental two-phase multiplier with the method of least squares for the mass fluxes of 260, 340, 456 kg $m^{-2}s^{-1}$ and (a) T_{sat}=40°C and (b) 50°C.

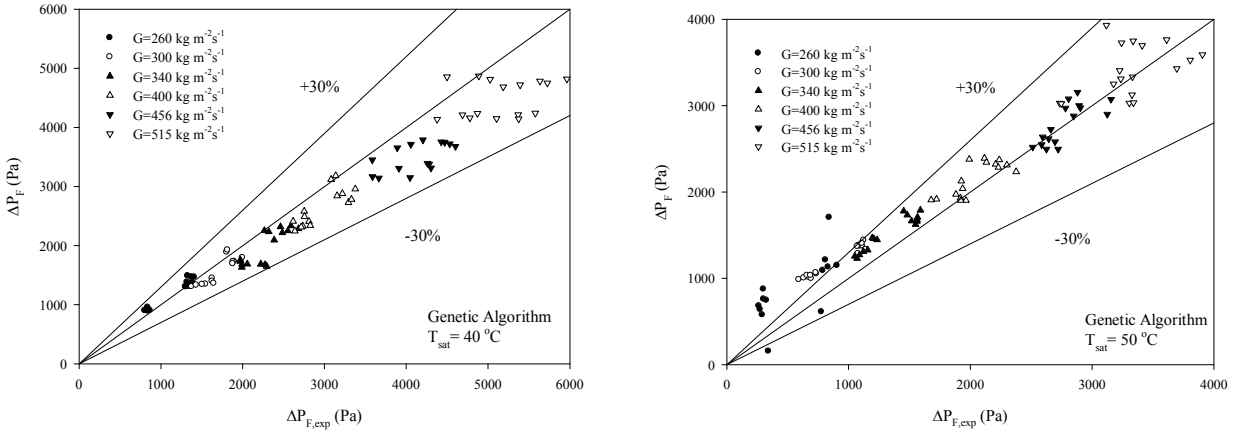

Fig. 10. Comparisons of experimental frictional pressure drop with the method of genetic algorithm for the mass fluxes of 260, 340, 456 kg $m^{-2}s^{-1}$ and (a) T_{sat}=40°C and (b) 50°C.

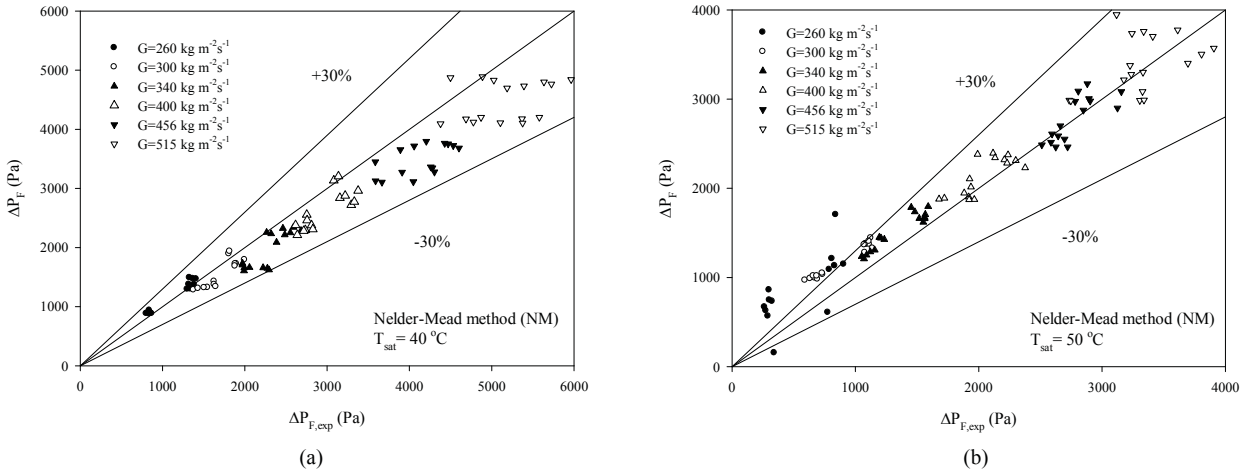

Fig. 11. Comparisons of experimental frictional pressure drop with the method of non-linear least squares for the mass fluxes of 260, 340, 456 kg $m^{-2}s^{-1}$ and (a) T_{sat}=40°C and (b) 50°C.

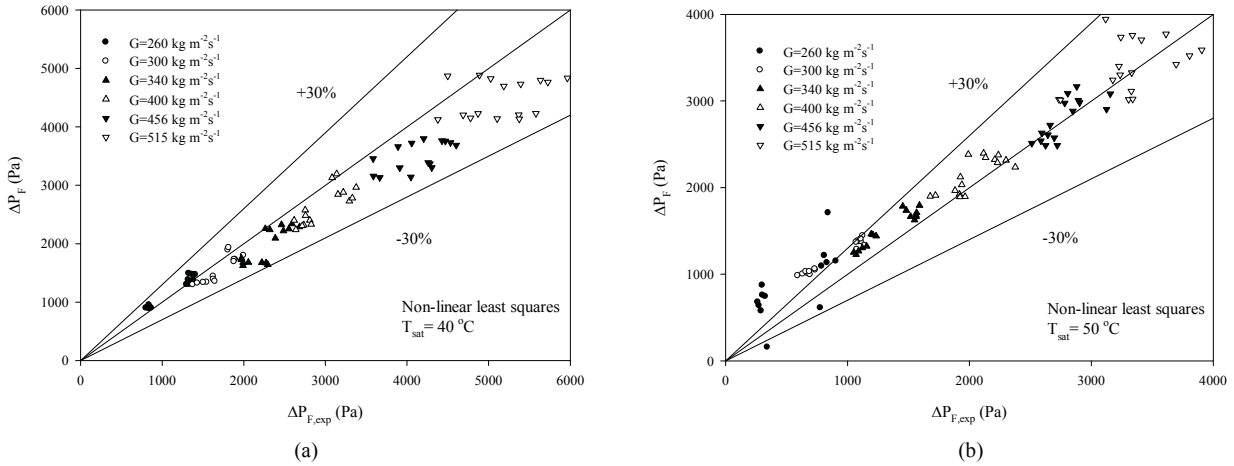

Fig. 12. Comparisons of experimental frictional pressure drop with the method of least squares for the mass fluxes of 260, 340, 456 kg $m^{-2}s^{-1}$ and (a) T_{sat}=40°C and (b) 50°C.

Table 6. The existing heat transfer coefficient correlations and one of the proposed correlations for the validation for the mass fluxes ranging between 260 and 515 kg $m^{-2}s^{-1}$.

Researcher	Data of 40 °C (178 data points) deviation (%)	Data of 50 °C (191 data points) deviation (%)	All data (369 data point) deviation (%)
Shah [55]	21.29	18.89	20.09
Dobson and Chato [58]	5.08	3.76	4.42
Dobson and Chato [58]	26.19	24.34	25.26
Chato [59]	27.22	26.2	26.71
Sweeney [60]	28.9	28.05	28.47
Cavallini et al. [61]	-4.34	-5.56	-4.95
Fujii [62]	3.08	3.25	3.16
Tang et al. [63]	8.88	12.07	10.48
Bivens and Yokozeki [64]	34.13	32.04	33.09
Tandon et al. [65]	40.43	40.91	40.67
Travis et al. [66]	17.29	15.07	16.18
Akers and Rosson [67]	50.73	50.04	50.39
Proposed correlation $h = 0.0436\left(\frac{k_l}{d}\right)Re_{eq}^{0.85}$	3.73	1.31	2.52

two-phase friction multipliers shown in Table 4 have the average deviation of 0.96%. It is obvious that they are supposed to predict the measured pressure drop values better than other correlations.

In addition, detailed explanations and some additional figures and tables with different experimental parameters related to the study on the void fraction models and correlations, film thickness models, friction factors and frictional pressure drop models, heat transfer and pressure drop characteristics can be seen from the series of the authors' previous publications [17-29]. A general application of computational numerical techniques to in-tube condensation on the correlation development is performed in this paper.

A large number of graphics could be generated from the output of the calculations; however, due to space limitation, only typical results are shown for limited data of the experimental database of the authors. It should be also noted that detailed information on the heat transfer characteristics of the study with some additional figures and different experimental parameters can be seen from the authors' previous publications.

5. Conclusion

Experiments have been conducted to determine the convective condensation heat transfer coefficient, two-phase friction factor and frictional pressure drop by means of computational numerical techniques. This paper reports that in spite of the numerous studies on the determination of convective condensation heat transfer coefficient in tubes, application of computational numerical techniques to the in-tube condensation for the aim of correlation development does not exist in the literature. For that reason, the content of this study is expected to fill this gap in the literature.

The calculated heat transfer coefficients, two-phase friction factors and frictional pressure drops by means of all computational numerical methods such as genetic algorithm (GA), unconstrained nonlinear minimization algorithm- Nelder-Mead method (NM) and non-linear squares error method (NLS) are found to be quite near to each other and also be in good agreement with the 369 numbers of laminar and turbulent flow experimental data.

It is shown clearly that the proposed correlations, obtained from artificial intelligence algorithms, have better predictability of heat transfer characteristics than the existing correlations in the literature.

Acknowledgments

The second author wishes to thank King Mongkut's University of Technology Thonburi for providing him with a Post-doctoral fellowship and Yıldız Technical University (Research Project No: 29-06-01-01). The fourth author would like to thank the Thailand Research Fund and the National Research University Project, for the financial support.

Nomenclature

A : Surface area, m^2
ANN : Artificial neural network
Bo : Bond number
CFD : Computational fluid dynamics
Co : Parameter in Shah correlation
D : Internal tube diameter, m
E : Error

f : Friction factor
Fr : Froude number
G : Mass flux, kg m^{-2} s^{-1}
GA : Genetic algorithm
Ga : Galileo number
h : Heat transfer coefficient, W $m^{-2}K^{-1}$
k : Thermal conductivity, W $m^{-1}K^{-1}$
L : Length of test tube, m
LS : Least square
N : Element number
NLS : Non-linear least squares
NM : Nelder-Mead method
Nu : Nusselt number
P : Pressure, N m^{-2}
ΔP : Pressure drop, N m^{-2}
Pr : Prandtl number
$Prop$: Proportional
R : ρ-μ ratio
Re : Reynolds number
S : Slip ratio
Q : Heat transfer rate, W
T : Temperature, °C
X : Lockhart and Martinelli parameter
x : Average vapor quality

Greek symbols

φ_l^2 : Two-phase multiplier
ρ : Density, kg m^{-3}
μ : Dynamic viscosity, kg m^{-1} s^{-1}
α : Void fraction
σ : Surface tension, N m^{-1}

Subscripts

$calc$: Calculated
$critic$: Critical
eq : Equivalent
exp : Experimental
F : Frictional term
G : Gravitational term
g : Gas/vapor
sf : Superficial
so : Soliman
i : Inlet
l : Liquid
M : Momentum term
ph : Preheater
o : Outlet
red : Reduced
ref : Refrigerant
sat : Saturation
TP : Two-phase
TS : Test section
wi : Inner wall

References

[1] W. M. Jenkins, On the application of natural algorithms to structural design optimization, *Eng. St.,* 19 (4) (1997) 302-308.

[2] S. Akin, B. Demiral, Genetic algorithm for estimating multi-phase flow functions from unsteady-state displacement experiments, *Comp. and Geosci.,* 24 (3) (1998) 251-258.

[3] A. Alizadehdakhel, M. Rahimi, J. Sanjari and A. A. Alsairafi, CFD and artificial neural network modeling of two-phase flow pressure drop, *Int. Comm. in Heat and Mass Tr.,* 36 (8) (2009) 850-856.

[4] D. R. Magee and R. D. Boyle, Detecting lameness using 'Re-sampling Condensation' and 'multi-stream cyclic hidden Markov models', *Im. and Vis. Comp.,* 20 (8) (2002) 581-594.

[5] M. Isard and A. Blake, Condensation-conditional density propagation for visual tracking, *Int. J. of Comp. Vis.,* 29 (1) (1998) 5-28.

[6] S. Nasseh, A. Mohebbi, A. Sarrafi and M. Taheri, Estimation of pressure drop in venturi scrubbers based on annular two-phase flow model, artificial neural networks and genetic algorithm, *Chem. Eng. J.,* 150 (1) (2009) 131-138.

[7] C. M. Salgado, C. M. N. A. Pereira, R. Schirru and L. E. B. Brandao, Flow regime identification and volume fraction prediction in multiphase flows by means of gamma-ray attenuation and artificial neural networks, *Prog. in Nuc. En.,* 52 (6) (2010) 555-562.

[8] Z. Shang, Application of artificial intelligence CFD based on neural network in vapor-water two-phase flow, *Eng.App. of Artificial Int.,* 18 (6) (2005) 663-671.

[9] C. Sunde, S. Avdic and I. Pazsit, Classification of two-phase flow regimes via image analysis and neuro-wavelet approach, *Prog. in Nuc. En.,* 46 (3-4) (2005) 348-358.

[10] T. Tambouratzis and I. Pazsit, A general regression artificial neural network for two-phase flow regime identification, *Ann. of Nuc. En.,* 37 (5) (2010) 672-680.

[11] L. A. Tarca, B. P. A. Grandjean and F. Larachi, Reinforcing the phenomenological consistency in artificial neural network modeling of multiphase reactors, *Chem. Eng. and Proc.,* 42 (8-9) (2003) 653-662.

[12] V. Vins and V. Vacek, Mass flow rate correlation for two-phase flow of R218 through a capillary tube, *Appl. Th. Eng.,* 29 (14-15) (2009) 2816-2823.

[13] W. Zhang, T. Hibiki and K. Mishima, Correlations of two-phase frictional pressure drop and void fraction in mini-channel, *Int. J. of Heat and Mass Tr.,* 53 (1-3) (2010) 453-465.

[14] B. Allen, M. Savard-Goguen and L. Gosselin, Optimizing heat exchanger networks with genetic algorithms for designing each heat exchanger including condensers, *Appl. Th. Eng.*, 29 (16) (2009) 3437-3444.

[15] W. Wang, L. X. Zhao and C. L. Zhang, Generalized neural network correlation for flow boiling heat transfer of R22 and its alternative refrigerants inside horizontal smooth tubes, *Int. J. of Heat and Mass Tr.,* 49 (15-16) (2006) 2458-2465.

[16] H. Demir, Ö. Agra and Ş. Ö. Atayılmaz, Generalized neural network model of alternative refrigerant (R600a) inside a

smooth tube, *Int. Comm. in Heat and Mass Tr.,* 36 (2) (2009) 744-749.

[17] A. S. Dalkilic, S. Laohalertdecha and S. Wongwises, Effect of void fraction models on the two-phase friction factor of R134a during condensation in vertical downward flow in a smooth tube, *Int. Comm. in Heat and Mass Tr.,* 35 (8) (2008) 921-927.

[18] A. S. Dalkilic, S. Yildiz and S. Wongwises, Experimental investigation of convective heat transfer coefficient during downward laminar flow condensation of R134a in a vertical smooth tube, *Int. J. of Heat and Mass Tr.,* 52 (1-2) (2009) 142-150.

[19] A. S. Dalkilic, S. Laohalertdecha and S. Wongwises, Two-phase friction factor in vertical downward flow in high mass flux region of refrigerant HFC-134a during condensation, *Int. Comm. in Heat and Mass Tr.,* 35 (9) (2008) 1147-1152.

[20] A. S. Dalkilic, S. Laohalertdecha and S. Wongwises, Effect of void fraction models on the film thickness of R134a during downward condensation in a vertical smooth tube, *Int. Comm. in Heat and Mass Tr.,* 36 (2) (2009) 172-179.

[21] A. S. Dalkilic and S. Wongwises, Intensive literature review of condensation inside smooth and enhanced tubes, *Int. J. of Heat and Mass Tr.,* 52 (15-16) (2009) 3409-3426.

[22] A. S. Dalkilic, S. Laohalertdecha and S. Wongwises, Experimental investigation on heat transfer coefficient of R134a during condensation in vertical downward flow at high mass flux in a smooth tube*, Int. Comm. in Heat and Mass Tr.,* 36 (10) (2009) 1036-1043.

[23] A. S. Dalkilic, O. Agra, I. Teke and S. Wongwises, Comparison of frictional pressure drop models during annular flow condensation of R600a in a horizontal tube at low mass flux and of R134a in a vertical tube at high mass flux, *Int. J. of Heat and Mass Tr.,* 53 (9-10) (2010) 2052-2064.

[24] A. S. Dalkilic and S. Wongwises, An investigation of a model of the flow pattern transition mechanism in relation to the identification of annular flow of R134a in a vertical tube using various void fraction models and flow regime maps, *Exp. Th. and Fl. Sci.,* 34 (6) (2010) 692-705.

[25] A. S. Dalkilic, S. Laohalertdecha and S. Wongwises, Validation of void fraction models and correlations using a flow pattern transition mechanism model in relation to the identification of annular vertical downflow in-tube condensation of R134a, *Int. Comm. in Heat and Mass Tr.*, 37 (7) (2010) 827-834.

[26] A. S. Dalkilic, S. Laohalertdecha and S. Wongwises, New experimental approach on the determination of condensation heat transfer coefficient using frictional pressure drop and void fraction models in a vertical tube, *En. Conv. and Man.,* 51 (12)(2010) 2535-2547.

[27] A. S. Dalkilic and S. Wongwises, A performance comparison of vapour compression refrigeration system using various alternative refrigerants, *Int. Comm. in Heat and Mass Tr.,* 37 (9) (2010) 1340-1349.

[28] A. S. Dalkilic, S. Laohalertdecha and S. Wongwises, Experimental study of the condensation heat transfer coefficients in high mass flux region in annular flow regime of HFC-134a inside the vertical smooth tube, *H. Tr. Eng.,* 32 (1) (2011) 1-12.

[29] A. S. Dalkilic, I. Teke and S. Wongwises, Experimental analysis for the determination of the convective heat transfer coefficient by measuring pressure drop directly during annular condensation flow of R134a in a vertical smooth tube, *Int. J. of Heat and Mass Tr.,* 54 (4) (2011) 1008-1014.

[30] J. H. Holland, *Adaptation in natural and artificial systems*, University of Michigan Press, Michigan, USA (1975).

[31] J. Koza, *Genetic programming: on the programming of computers by means of natural selection*, MIT Press/ Cambridge, Massachusetts, USA (1992).

[32] D. E., Goldberg, *Genetic algorithms in search optimization and machine learning*, Addison Wesley Longman Publishing Co., Boston (1989).

[33] G. Renner, A. Ekart, Genetic algorithms in computer aided design, *Comp.-Aided Des.,* 35 (2003) 709-726.

[34] J. H. Holland, *Adaptation in natural and artificial systems: an introductory analysis with applications to biology*, *Control and Artificial Intelligence*, MIT Press/Bradford Books Ed., USA (1992).

[35] J. A. Nelder and R. Mead, A simplex method for function minimization, *Comp. J.,* 7 (15) (1965) 308-313.

[36] J. Nocedal and S. J. Wright, *Numerical optimization*, Springer, New York, USA (2006).

[37] C. F. Gauss, Theory of the combination of observations least subject to errors: part one, part two, supplement (repost), translated by G.W. Stewart, *Soc. for Ind. Engi.*, 1987.

[38] M. J. Box, D. Davies and W. H. Swann, *Non-linear optimization techniques,* Oliver and Boyd, Edinburg, Scotland (1969).

[39] F. W. Dittus and L. M. E. Boelter, Heat transfer in automobile radiators of the tubular type, *Univ. of California* Pub. on Eng., 2 (1930) 443-461.

[40] W. W. Akers, H. A. Deans and O. K. Crosser, Condensation heat transfer within horizontal tubes, *Chemical Engineering Prog. Sym. Ser.,* 55 (1959) 171-176.

[41] A. Cavallini and R. Zecchin, A dimensionless correlation for heat transfer in forced convection condensation, *Proceedings of the Sixth Int. Heat Tr. Conf.,* 3 (1974) 309-313.

[42] M. M. Shah, A general correlation for heat transfer during film condensation inside pipes, *Int. J. of Heat and Mass Tr.,* 22 (1979) 547-556.

[43] S. Koyama, A. Miyara, H. Takamatsu and T. Fujii, Condensation heat transfer of binary refrigerant mixtures of R22 and R114 inside a horizontal tube with internal spiral grooves, *Int. J. of Ref.,* 13 (4) (1990) 256-263.

[44] R. W. Lockhart and R. C. Martinelli, Proposed correlation of data for isothermal two-phase, two-component flow in pipes, *Chem. Eng. Prog.,* 45 (1949) 39-48.

[45] M. K. Dobson and J. C. Chato, Condensation in smooth horizontal tubes, J. of Heat Tr., 120 (1998) 193-213.

[46] A. Cavallini, G. A. Longo and L. Rossetto, Condensation heat transfer and pressure drop of refrigerants in tubes of finned tube heat exchangers, *Rec. Dev. in Finned Tube Heat Exc., Theo. and Prac. Aspects*, Denmark (1993) 160-204.

[47] A. Cavallini, L. Doretti, N. Klammsteiner, G. A. Longo and L. Rossetto, Condensation of new refrigerants inside smooth and enhanced tubes, *Proceedings 19th Int. Cong. of Ref.,* Holland, 4 (1995) 105-114.
[48] J. T. Fanning, *A practical treatise on hydraulic and water supply engineering*, *Van Nostrand*, New York, USA (1877) Revised ed. 1886.
[49] H. Darcy, *Recherches experimentales relatives au mouvement de l'Eau dans les Tuyaux, Mallet-Bachelier*, Paris, France (1857).
[50] J. Weisbach, Lehrbuch der ingenieur und maschinen-mechanik, *Braunschwieg*, 1845.
[51] H. Blasius, Grenzschichten in Flüssigkeiten mit kleiner Reibung, *Z. Math. u. Phys*., 56 (1908) 1-37.
[52] D. Chisholm, A theoretical basis for the Lockhart-Martinelli correlation for two-phase flow, *Int. J. of Heat and Mass Tr.,* 10 (1967) 1767-1778.
[53] D. Chisholm and A. D. K. Laird, Two-phase flow in rough tubes, *Trans. of ASME,* 80 (2) (1958) 276-286.
[54] D. Chisholm, *Two phase flow in pipelines and heat exchangers*, George Godwin in association with The Institution of Chemical Engineers, *London*, UK (1983).
[55] M. M. Shah, A general correlation for heat transfer during film condensation inside pipes, *Int. J. of Heat and Mass Tr.,* 22 (4) (1979) 547-556.
[56] S. J. Kim and H. C. No, Turbulent film condensation of high pressure steam in a vertical tube, *Int. J. of Heat and Mass Tr.,* 43 (21) (2000) 4031-4042.
[57] L. Lienberg, J. P. Bukasa, M. F. K. Holm, J. P. Meyer and A. E. Bergles, Towards a unified approach for modelling of refrigerant condensation in smooth tubes, *Proc. of the Int. Sym. on Comp. Heat Exch.,* (2002) 457-462.
[58] M. K. Dobson and J. C. Chato, Condensation in smooth horizontal tubes, *J. of Heat Tr., Trans. of ASME,* 120 (2) (1998) 193-213.
[59] J. C. Chato, Laminar Condensation inside horizontal and inclined tubes, *ASHRAE J.,* 4 (2) (1962) 52-60.
[60] K. A. Sweeney, *The heat transfer and pressure drop behavior of a zeotropic refrigerant mixture in a micro-finned tube*, M.S. thesis, Dept. of Mech. and Ind. Eng., Univ. of Illinois at Urbana-Champaign, Illinois, USA (1996).
[61] A. Cavallini, J. R. Smith and R. Zecchin, A dimensionless correlation for heat transfer in forced convection condensation, *6th Int. Heat Tr. Conf*., Tokyo, Japan (1974) 309-313.
[62] T. Fujii, Enhancement to condensing heat transfer-new developments, *J. of Enhanced Heat Tr.,* 2 (1-2) (1995) 127-137.
[63] L. Tang, M. M. Ohadi and A. T. Johnson, Flow condensation in smooth and microfin tubes with HCFC-22, HFC-134a, and HFC-410 refrigerants. part II: Design equations, *Journal of Enh. Heat Tr.,* 7 (5) (2000) 311-325.
[64] D. B. Bivens and A. Yokozeki, Heat transfer coefficient and transport properties for alternative refrigerants, *Proc. 1994 Int. Ref. Conf.* (1994) 299-304.
[65] T. N. Tandon, H. K. Varma and C. P. Gupta, Heat transfer during forced convection condensation inside horizontal tube, *Int. J. of* Ref., 18 (3) (1995) 210-214.
[66] D. P. Travis, W. M. Rohsenow and A. B. Baron, Forced convection inside tubes: a heat transfer equation for condenser design, *ASHRAE Trans.,* 79 (1) (1973) 157-165.
[67] W. W. Akers and H. F. Rosson, Condensation inside a horizontal tube, *Chem. Eng. Prog.* Symp. Series, 56 (30) (1960) 145-149.
[68] S. J. Kline and F. A. McClintock, Describing uncertainties in single sample experiments, *Mech. Eng.,* 75 (1) (1953) 3-8.

Muhammet Balcılar is currently a Research Assistant of Computer Engineering at Yildiz Technical University, İstanbul, Turkey. He is a Ph.D student in Computer Engineering from the same university. His research interest is on artificial intelligence, video editing, optimization and signal processing.

Ahmet Selim Dalkılıç is currently an Assistant Professor of Mechanical Engineering at Yildiz Technical University, İstanbul, Turkey. He received his Ph.D in Mechanical Engineering from the same university. His current research interest is in enhanced heat transfer, convection heat transfer, two-phase flow of new refrigerants and mixture refrigerants and applications in heat exchangers. Dr. Ahmet Selim Dalkılıç is the member of Innovation Explorer for Scientific Researchers Community sponsored by Elsevier and American Society of Mechanical Engineers.

Berna Bolat is currently an Assistant Professor of Mechanical Engineering at Yildiz Technical University, İstanbul, Turkey. She received her Ph.D in Mechanical Engineering from the same university. Her current research interest is in computer aided design, vertical transportation, elevator traffic modeling and simulation and genetic algorithms.

Somchai Wongwises is currently a Professor of Mechanical Engineering at King Mongkut's University of Technology Thonburi, Bangmod, Thailand. He received his Doktor-Ingenieur (Dr.-Ing.) in Mechanical Engineering from the University of Hannover, Germany, in 1994. His research interests include two-phase flow, heat transfer enhancement, and thermal system design. He is the head of the Fluid Mechanics, Thermal Engineering and Multiphase Flow Research Labarotory (FUTURE).

Particuology 9 (2011) 626–631

Contents lists available at SciVerse ScienceDirect

Particuology

journal homepage: www.elsevier.com/locate/partic

Convective heat transfer of nanofluids with correlations

Lazarus Godson Asirvatham[a,*], Balakrishnan Raja[b], Dhasan Mohan Lal[a], Somchai Wongwises[c,d]

[a] R&AC Division, Department of Mechanical Engineering, College of Engineering, Guindy, Anna University, Chennai 600 025, Tamil Nadu, India
[b] Indian Institute of Information Technology, Design and Manufacturing (IIITD&M)-Kancheepuram, Chennai 600 048, India
[c] Fluid Mechanics, Thermal Engineering and Multiphase Flow Research Lab (FUTURE), Department of Mechanical Engineering, King Mongkut's University of Technology Thonburi, 126 Bangmod, Tongkru, Bangkok 10140, Thailand
[d] The Academy of Science, The Royal Institute of Thailand, Sanam Suea Pa, Dusit, Bangkok 10300, Thailand

ARTICLE INFO

Article history:
Received 1 May 2010
Received in revised form 17 February 2011
Accepted 31 March 2011

Keywords:
Convective heat transfer
Silver
Nanofluid
Correlation
Laminar
Turbulent
Transition

ABSTRACT

To investigate the convective heat transfer of nanofluids, experiments were performed using silver–water nanofluids under laminar, transition and turbulent flow regimes in a horizontal 4.3 mm inner-diameter tube-in-tube counter-current heat transfer test section. The volume concentration of the nanoparticles varied from 0.3% to 0.9% in steps of 0.3%, and the effects of thermo-physical properties, inlet temperature, volume concentration, and mass flow rate on heat transfer coefficient were investigated. Experiments showed that the suspended nanoparticles remarkably increased the convective heat transfer coefficient, by as much as 28.7% and 69.3% for 0.3% and 0.9% of silver content, respectively. Based on the experimental results a correlation was developed to predict the Nusselt number of the silver–water nanofluid, with ±10% agreement between experiments and prediction.

© 2011 Chinese Society of Particuology and Institute of Process Engineering, Chinese Academy of Sciences. Published by Elsevier B.V. All rights reserved.

1. Introduction

Energy costs have soared rapidly in the last decade and there is tremendous need for new kinds of heating/cooling fluids, to improve heating system performance and to reduce equipment size and energy consumption. Nanofluids are new-generation heat transfer fluids for various industrial and automotive applications because of their excellent thermal performance (Eastman, Phillpot, Choi, & Keblinski, 2004). Nanofluids consist of nanometer-sized particles (<100 nm) dispersed in a base fluid such as water, engine oil or ethylene glycol. Addition of high thermal-conductivity metallic nanoparticles (e.g., copper, aluminum, silicon and silver) increases the thermal conductivity of such mixtures, thus enhancing their overall energy transport capability (Xuan & Li, 2003).

Eastman, Choi, Li, Yu, and Thompson (2001) showed a 40% increase in thermal conductivity by adding 0.3 vol% copper nanoparticles to ethylene glycol. For convective heat transfer, Xuan and Li (2004) studied the single phase heat transfer of Cu–water nanofluid with volume fraction of Cu, $\varphi = 0.3$–2.0% in the turbulent flow regime (Reynolds number between 10,000 and 25,000), and proposed a heat transfer correlation. The convective heat transfer coefficient increased by more than 60% with increase in Cu volume–fraction and flow velocity, yet with negligible penalty in pumping power. Li, Xuan, Jiang, and Xu (2005) measured the convective heat transfer of the Cu–water nanofluid in a small-hydraulic-diameter flat tube under laminar flow and found that the Nusselt number of the nanofluid with $\varphi = 1.5\%$ increased by more than 39% as compared to pure water. Zhou (2004) investigated the enhancement of heat transfer of Cu–acetone nanofluids with average Cu particle sizes in the range of $\gamma = 80$–100 nm and concentrations up to 4.0 g/L, and found that the heat transfer coefficient was much higher when compared to that of the base fluid. Faulkner, Rector, Davison, and Shekarriz (2004) investigated the convective heat transfer of a carbon nanotube (CNT)–water nanofluid in a micro channel, with a hydraulic diameter of 355 μm, at a Reynolds number between 2 and 17 and $\varphi = 1.1\%$, 2.2% and 4.4%, showing enhanced heat transfer coefficient of CNT–water at the higher concentrations. Yang, Zhang, Grulke, Anderson, and Wu (2005) investigated the convective heat transfer of graphite nanoparticles dispersed in a liquid in laminar flow in a horizontal tubular heat exchanger, and reported that at 2.5 wt% the heat transfer coefficient of the nanofluids increased by 22%. Ding, Alias, Wen, and Williams (2006) tested nanofluids with multi-walled carbon nanotubes (MCNT with $\varphi = 0.1$–1.0% with 0.5 wt% in aqueous solution) in a horizontal tube, and obtained a maximum enhancement of heat transfer of 350% at a Reynolds number of 800.

* Corresponding author. Tel.: +91 42 22614430; fax: +91 42 2615615.
E-mail addresses: godasir@yahoo.co.in (L.G. Asirvatham), rajab@iiitdm.ac.in (B. Raja), mohanlal@annauniv.edu (D. Mohan Lal), somchai.won@kmutt.ac.th (S. Wongwises).

1674-2001/$ – see front matter © 2011 Chinese Society of Particuology and Institute of Process Engineering, Chinese Academy of Sciences. Published by Elsevier B.V. All rights reserved.
doi:10.1016/j.partic.2011.03.014

Nomenclature

A	cross sectional area, m^2
C_p	specific heat, J/(kg K)
D	tube diameter, m
h	heat transfer coefficient, W/(m^2 K)
k	thermal conductivity, W/(m K)
m	mass flow rate, kg/s
Nu	Nusselt number
Pr	Prandtl number
Re	Reynolds number
T	temperature, K

Greek symbols

φ	volume fraction
ρ	density, kg/m^3
μ	dynamic viscosity, kg/m s
γ	particle size (nm)

Subscript

bf	base fluid
i	inner wall
nf	nanofluid
o	outer wall
p	nanoparticle
x	axial distance
w	tube wall

In this study, the enhancement of convective heat transfer of a silver–water nanofluid flowing in a concentric-tube countercurrent flow heat exchanger in which the heated nanofluid flowed in the inner tube while chilled water flowed through the annulus was experimentally studied. The effect of inlet temperature, concentration of silver, friction factor and flow rate on convective heat transfer was investigated.

2. Experimental

2.1. Nanofluid preparation

The silver nanoparticles manufactured by Sigma Aldrich (product number-576832, 99.5% metal, particle size <100 nm) were mixed with deionized water without any additive or stabilizer for 12 h under ultrasonic vibration using a Roop-Telsonic TEC-40 Model mixer with power density of 750 W at frequency of 20 kHz, to ensure complete dispersion of the nanoparticles in water. The volume concentrations used in this study were 0.3%, 0.6%, and 0.9% with pH values of 7.4, 7.1 and 6.8, respectively. A scanning electron microscope (SEM) was used to monitor the dispersion and size of the silver nanoparticles, as shown in Fig. 1. The figure shows that the nanoparticles were nearly spherical in shape, with a size of about 80 nm and the distribution in the base fluid was essentially uniform, though not without some agglomeration of the particles.

2.2. Measurement of thermal conductivity and viscosity

In this study, the transient-hot-wire method, which involves measuring the slope of the rise in the wire's temperature against the logarithmic time interval, was used to measure the effective thermal conductivity of the nanofluids. And the Cannon-Fenske Opaque reverse-flow viscometer was used to measure the viscosity of the Ag–water nanofluid. The uncertainty of the thermal conductivity and viscosity measurements was around 1.5% and 2%,

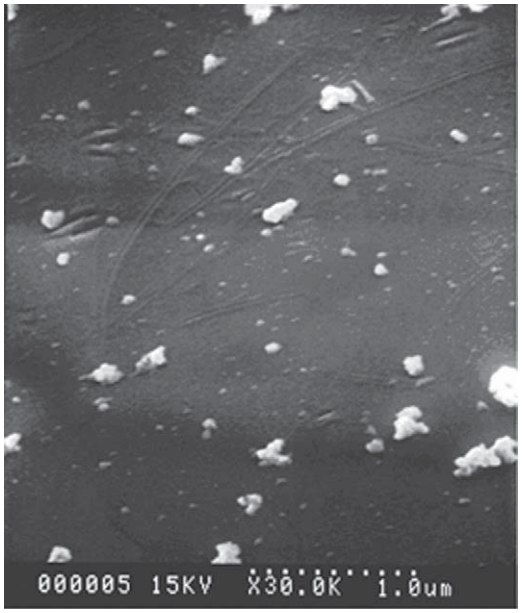

Fig. 1. SEM image of 0.6 vol% dispersed silver nanoparticles in water.

respectively, while the uncertainties of temperature and volume fraction measurements were estimated to be ±0.15 °C and $\pm 10^{-5}$ g, respectively. Details on these measurements were given in a previous paper of the present authors (Godson, Raja, Mohan Lal, & Wongwises, 2010).

2.3. Convective heat transfer coefficient

Fig. 2 shows the schematic layout of the test facility to measure convective heat transfer coefficient, which comprises two flow circuits, chilled water and nanofluid. Each circuit consists of a constant temperature bath, of chilled water and of nanofluid bath respectively, with its own temperature controller, pump and flow meter. The test section is a 2.94 m long counter flow horizontal concentric-tube heat exchanger with nanofluid flowing inside the inner tube and chilled water inside the annular space. The inner tube is 4.3 mm in inside diameter, while the outer tube, 10.5 mm in inside diameter. The test section is thermally insulated by ceramic wool to reduce heat loss. A differential pressure transducer with 0.075% accuracy and two RTDs are mounted at both ends of the test section to measure respectively the pressure drop between the inlet and outlet and the bulk temperatures of the nanofluid. Six RTDs (PT100 RTD sensors with ±0.15 °C accuracy) are mounted longitudinally on the surface of the outside wall to measure the temperature distributions along the length of the test section. The nanofluid is heated in an insulated cylindrical tank with a 0.5 kW electric heater coupled to a proportional-integral-derivative controller (PID-C). Heated nanofluid is tapped out from the bottom of the tank and pumped by a centrifugal pump through a mass flow meter into the test section, counter-current to the chilled water. The nanofluid flow rate is measured using a Coriolis type mass flow meter with ±0.1% accuracy. Similarly, the outflowing water is cooled in a chilling unit of 0.5 TR (refrigeration ton) capacity with a 1 kW heater coupled to a PID controller in order to keep the temperature of the chilled water constant. A stirrer operating at 1500 rpm is mounted inside the chilled water tank to ensure uniform temperature. All inter connecting tubes for the nanofluid and chilled water are insulated to avoid heat loss to the surroundings. Error analysis for the heat transfer coefficient of the nanofluid is carried out by applying the uncertainty analysis suggested by Moffat

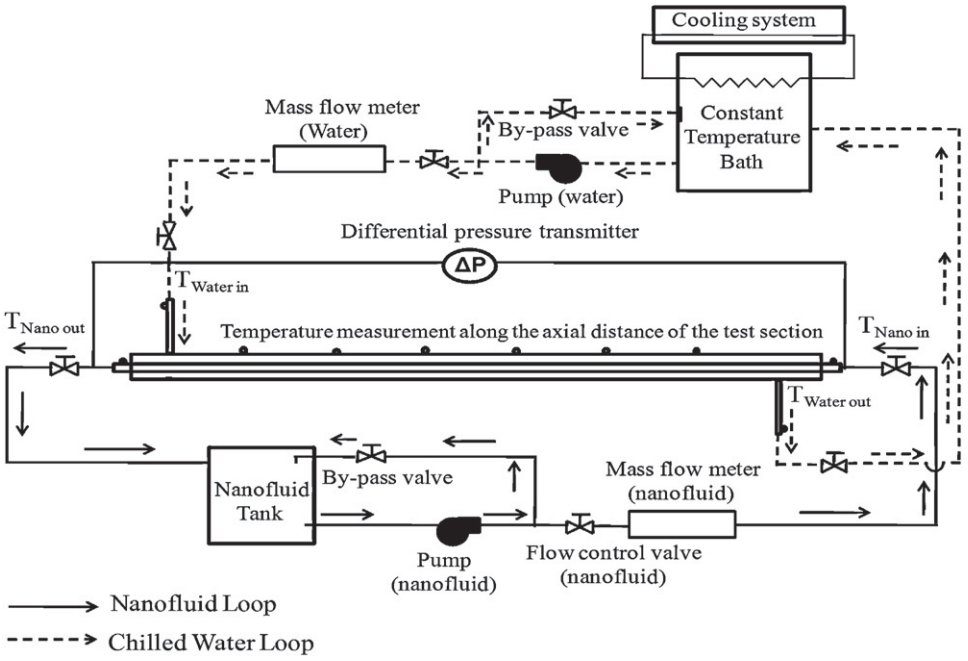

Fig. 2. Schematic diagram of the experimental apparatus.

Table 1
Experimental conditions.

D (mm)	Re	T_{nano} (°C)	T_{water} (°C)	m_{water} (kg/s)
4.3	900–12,000	48, 57, 65	26, 30, 35	0.016

(1988). The uncertainty of the heat transfer coefficient was found to be 4.44%. During a test run, the inlet and exit temperatures of the chilled water and nanofluids, and temperatures of the wall of the test tubes, mass flow rates of the chilled water and nanofluid, and the pressure difference in the nanofluid are measured. Table 1 lists the experimental conditions used in this study.

2.4. Data reduction

The heat transfer rate from the hot fluid is defined as:

$$Q_{h_{nf}} = m_{h_{nf}} C_{P_{h_{nf}}} (T_{in_{nf}} - T_{out_{nf}}), \tag{1}$$

$$\frac{1}{U_i A_i} = \frac{1}{h_i A_i} + \frac{\ln\,(d_o/d_i)}{2\pi kL} + \frac{1}{h_o A_o}, \tag{2}$$

$$Nu_{nf} = \frac{h_{nf} D}{k_{nf}}, \tag{3}$$

where $Q_{h_{nf}}$ is the heat transfer rate of the hot nanofluid, $m_{h_{nf}}$ is the mass flow rate of the hot nanofluid, $h_i = h_{nf}$ is the heat transfer coefficient of the nanofluid, h_o the heat transfer coefficient of chilled water in the annulus, k is the thermal conductivity of the copper tube, U_i is the overall heat transfer coefficient of the inner tube, Nu_{nf} is the Nusselt number of the nanofluid, D is the inner diameter of the test tube and k_{nf} is the thermal conductivity of the nanofluid.

The thermo-physical properties such as density, specific heat, thermal conductivity and viscosity of the nanofluid are calculated using the following published correlations.

Density is calculated from Pak and Cho (1998) using the following equation:

$$\rho_{nf} = \varphi\rho_p + (1-\varphi)\rho_w. \tag{4}$$

Specific heat is calculated from Xuan and Roetzel (2000) as follows:

$$(\rho C_p)_{nf} = \varphi(\rho C_p)_p + (1-\varphi)(\rho C_p)_w, \tag{5}$$

Where $(\rho C_p)_{nf}$ is the heat capacity of the nanofluid, $(\rho C_p)_p$ the heat capacity of the nanoparticles and $(\rho C_p)_w$ the heat capacity of the base fluid.

The thermal conductivity and viscosity of the nanofluid are calculated by correlations developed elsewhere by the present authors (Godson et al., 2010), both correlated as linear and quadratic functions of particle volume fraction. And the coefficients of silver–water nanofluid for the tested volume concentration and temperature are achieved using linear regression as shown below for water and nanofluid at their average bulk temperature:

$$\frac{k_{nf}}{k_w} = (0.9692\varphi + 0.9508), \tag{6}$$

$$\frac{\mu_{nf}}{\mu_w} = (1.005 + 0.497\varphi - 0.1149\varphi^2). \tag{7}$$

3. Correlation

The heat transfer coefficient, Nusselt number, of the nanofluid depends on various factors such as thermal conductivity, heat capacity of both the base fluid and the nanoparticles, viscosity of the nanofluid, volume fraction of the suspended particles, and dimension and shape of the particles, and can be expressed as follows:

$$Nu_{nf} = f\left(Re,\ Pr,\ \frac{k_{nf}}{k_w} \times \frac{(\rho C_p)_{nf}}{(\rho C_p)_w},\ \varphi,\ \text{dimension and shape of particles}\right).$$

In the present study, an additive method is used for developing a correlation to predict the Nusselt number with closest fit to

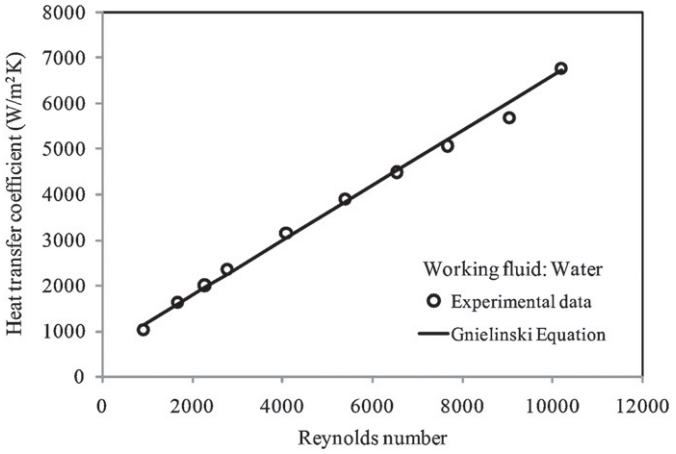

Fig. 3. Comparison between measured heat transfer coefficients and those calculated from Gnielinski (1976) equation.

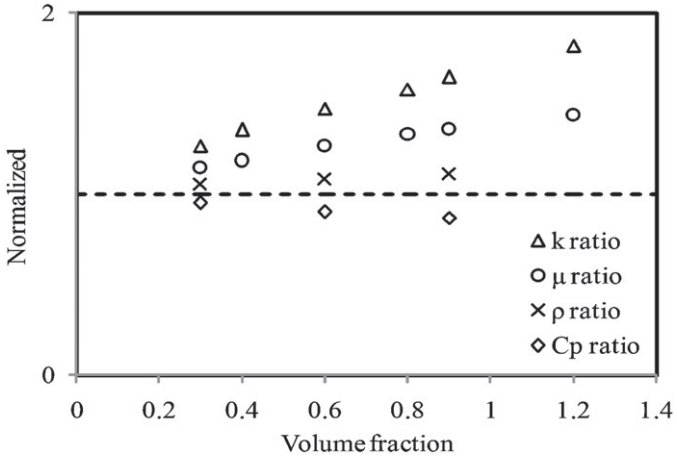

Fig. 4. Thermo-physical property ratios against silver nanoparticle volume fraction.

experimental data for silver–water nanofluid. The present correlation includes the effect of Reynolds number, Prandtl number, volume concentration and the temperature-dependent thermo-physical properties of silver–water nanofluid. The experimental data are correlated against Reynolds and Prandtl numbers ($Nu = C\ Re^a\ Pr^b$), in a manner resembling that of Pak and Cho (1998) and of Maiga et al. (2006). Such technique is used for the entire database for experimental values for Ag concentrations of 0.3%, 0.6% and 0.9%. The coefficient C and exponents a and b are calculated using multiple regression techniques. The difference between the nanofluid experimental Nusselt numbers and the single phase Nusselt number calculated using Dittus and Boelter (1930) correlation is then used to develop the new correlation. The current experiments showed that the Nusselt number of the nanofluid under test conditions is always higher than that for the single-phase base fluid. The difference in Nusselt numbers is thus once again correlated against Reynolds and Prandtl number ($Nu = C\ Re^a\ Pr^b$) and the coefficient C and exponents a and b are calculated using multiple regression. Hence, a generalized correlation is developed, where the constant and exponents of the correlation are functions of volume concentration in percentage. The coefficient of determination, R^2, is used in the context of correlation models with the main purpose of predicting Nusselt number on the basis of other related information. It is the proportion of variability in a data set that is accounted for by the statistical model, and provides a measure of how well outcomes are likely to be predicted by the model. The value of the coefficient of determination for all the correlations was above 0.98, thus testifying to the credibility of the correlation. The following is the correlation developed using the experimental data after careful removal of outliers from the database. Detailed comparisons of the predicted correlation with those from existing correlations and experimental results are discussed in the following sections. $Nu_{nf} = 0.023\,Re^{0.8}\ Pr^{0.3} + (0.617\ \varphi - 0.135)Re^{(0.445\varphi - 0.37)}Pr^{(1.081\varphi - 1.305)}$

4. Results and discussion

Experiments were carried out for the conditions given in Table 1. The effect of thermo-physical properties, mass flow rate, heat flux and concentration on the heat transfer coefficient to develop a new correlation are discussed in the following subsections. The experimental results for water are compared with those obtained from the Gnielinski (1976) equation as shown in Fig. 3, showing agreement within ±4.5%, thus validating the test facility for its repeatability and accuracy.

4.1. Dependence of thermo-physical properties on volume fraction of nanoparticles

Dependence of the thermo-physical property ratios on volume fraction of silver nanoparticles is shown in Fig. 4. All the observed values of the thermo-physical property data are normalized. It can be seen that the dependence of thermal conductivity k ratio on volume fraction of silver nanoparticles is significantly higher than the other thermo-physical properties such as ratios of density, viscosity and heat capacity. For 0.3% volume concentration, the thermal conductivity ratio is 1.27. Similarly for the same concentration the ratios for density, viscosity and heat capacity are 1.05, 1.14 and 0.95, respectively. Likewise, the thermal conductivity ratio enhancement increases to 1.64 for 0.9% volume concentration, whereas the ratio enhancement for density, viscosity and heat capacity are 1.1, 1.36 and 0.87, respectively, much lower than that for the thermal conductivity ratio. Evidently, the influence on thermal conductivity plays a major role in heat transfer enhancement. Both Brownian diffusion and thermophoresis are found to be the potential mechanisms for enhancement of thermal conductivity in the absence of turbulent eddies, that is, these mechanisms are responsible for an increase in temperature which leads to the enhancement in convective heat transfer coefficient at higher Reynolds number as well as with higher volume concentration of the nanoparticles (Xuan & Roetzel, 2000).

4.2. Effects of Reynolds number, Nusselt number and silver nanoparticle volume fraction on heat transfer coefficient

Fig. 5 shows increases of average heat transfer coefficients of nanofluids with Reynolds number and volume concentration, for example, as much as 28.3%, 47.6% and 69.3% for 0.3%, 0.6% and 0.9% volume concentration respectively at Reynolds number of 11,000. Similar enhancement has been observed by Xuan and Li (2004) who investigated convective heat transfer characteristics of copper–water nanofluid finding that the Nusselt number of the nanofluid with $\varphi = 1.5\%$ increased by 60% as compared to pure water. A possible reason for this enhancement is the enhancement of thermal conductivity by the chaotic movement of the nanoparticles, as reported by Xuan and Roetzel (2000). Fig. 6 shows the variation of the average Nusselt number with Reynolds number and volume concentration of nanoparticles, e.g., an increase by 47%

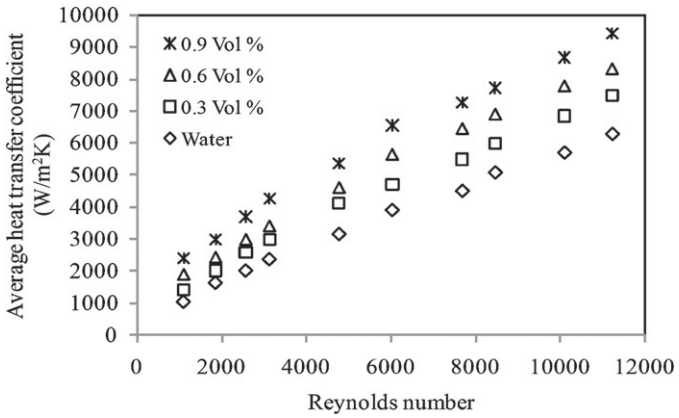

Fig. 5. Variation of the average heat transfer coefficient against Reynolds number.

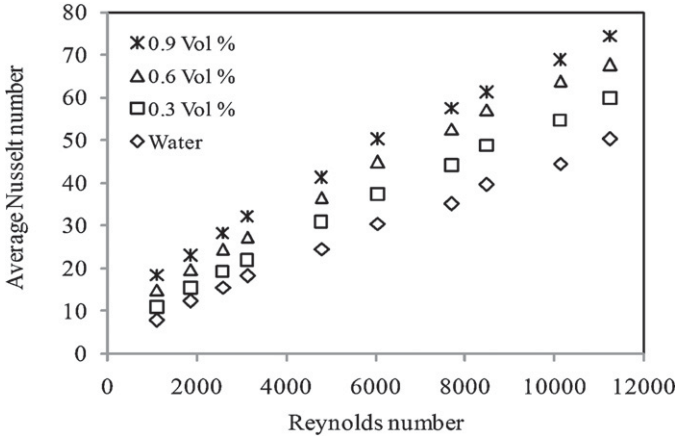

Fig. 6. Variation of the average Nusselt number against Reynolds number.

in the turbulent region, by 33% in the transition region and by 25% in the laminar region, even for the small volume concentration of 0.6% of silver nanoparticles.

Fig. 7 shows the significant variation of heat transfer coefficient with volume fraction for Reynolds numbers of 1800, 4600 and 9500, corresponding to a flow regime transition from laminar through transition to turbulent. Also, for a given Reynolds number, heat transfer coefficient clearly augments with increasing particle loading, e.g. for laminar flow condition with $Re = 1800$, the heat

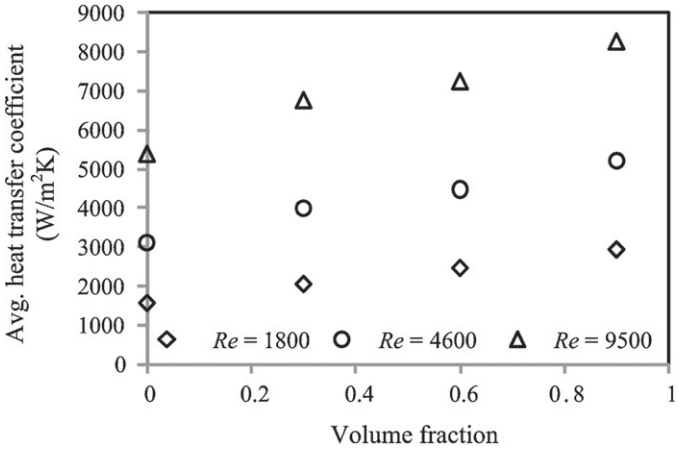

Fig. 7. Variation of heat transfer coefficient against volume fraction.

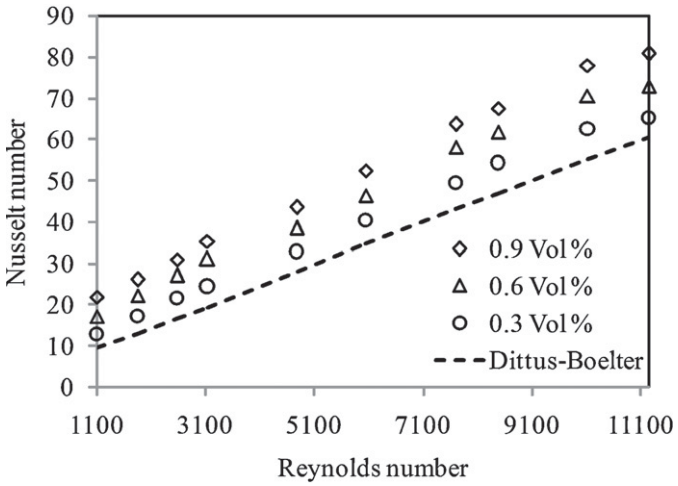

Fig. 8. Comparison between experimental Nusselt number and Dittus–Boelter correlation against Reynolds number.

transfer coefficient increases from 1560 W/(m^2 K) at 0% nanoparticles to 2930 W/(m^2 K) at 0.9%. Combination of particle loading and Reynolds number can produce rather high wall heat transfer rate, a conclusion very useful for advanced and special thermal applications.

4.3. Correlation results

Fig. 8 compares experimental Nusselt number for nanofluid with the Dittus and Boelter (1930) correlation for a single phase fluid (i.e. 0% volume concentration) against Reynolds number, showing how the Nusselt number increases with increasing nanoparticle concentration. For 0.9% volume concentration of nanoparticles, an average increase of 50.5% is observed for Nusselt number with respect to the pure fluid. The observed experimental results for Nusselt number are compared with those obtained by Dittus and Boelter (1930), Pak and Cho (1998), Gnielinski (1976), Xuan and Li (2003) as shown in Fig. 9.

A comparison of the experimental Nusselt number with that predicted from the familiar existing correlations for nanofluids such as Pak and Cho (1998) and Maiga et al. (2006), respectively, are shown in Fig. 10(a) and (b). It is clearly observed that the Pak and Cho (1998) correlation under predicts the experimental data

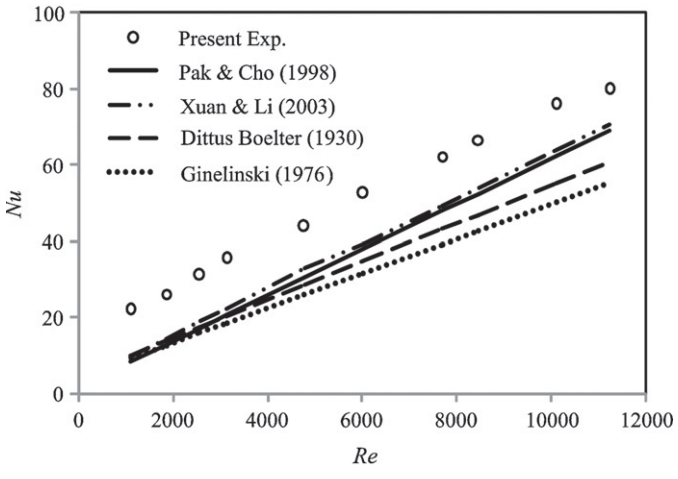

Fig. 9. Comparison of experimental and theoretical Nusselt number obtained from various correlations.

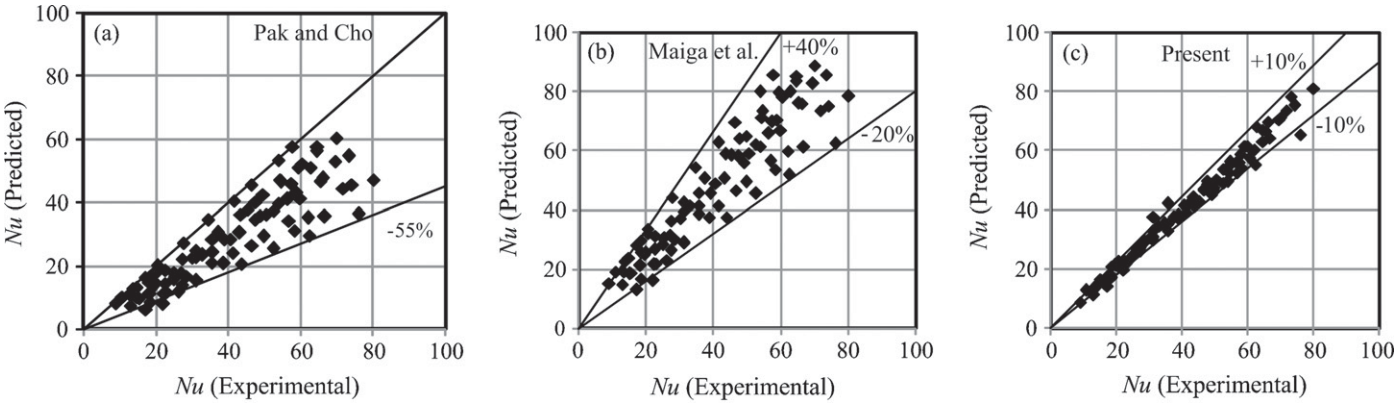

Fig. 10. Mean deviation between predicted Nusselt number (a) by Pak and Cho (1998) correlation, (b) by Maiga et al. (2006) correlation, and (c) by the proposed correlation, with experimental Nusselt number.

by 50%. Likewise, Maiga et al. (2006) correlation predicts fairly well with present experimental data of silver–water nanofluid, and the deviation of the predicted data and the experimental ones lies between +40% and −20%. In both case, the prediction accuracy of the correlation is poor as the volume concentration increases. However, the latter predicts better than the former. The distribution of the percentage deviation of the new correlation between the predicted and the experimental Nusselt number for the entire database is shown in Fig. 10(c). This new correlation is generalized for all the volume concentration. The date from the new correlation predicts the Nusselt number reasonably well within ±10% deviation. This correlation can be used for predicting the Nusselt number for the following ranges of the parameters: Reynolds number from 800 to 12,000; Prandtl number from 4 to 10 and volume concentration from 0 to 2%.

5. Conclusions

The convective heat transfer coefficient of silver–water nanofluids was investigated experimentally in a 4.3 mm inside diameter tube. Experimental results show that the suspended nanoparticles remarkably increase the heat transfer performance of the base fluid, water, under the same Reynolds number. The addition of 0.9 vol% silver particles in water enhances the heat transfer coefficients by 69.3%. Considering the factors affecting convective heat transfer characteristics of nanofluids, such as flow velocity, transport properties, volume fraction of nanoparticles, a new convective heat transfer correlation for nanofluids suspending metal nanoparticles has been developed. Comparison between experimental data and calculated results indicates that the correlation could take into account the main factors that affect heat transfer of the nanofluid and could be used to predict heat transfer coefficient of nanofluids with ±10% deviation.

Acknowledgements

The fourth author wishes to express his indebtedness to King Mongkut's University of Technology Thonburi, the Thailand Research Fund, the Office of the Higher Education Commission and the National Research University Project for supporting his study.

References

Ding, Y., Alias, G., Wen, D. & Williams, R. A. (2006). Heat transfer of aqueous suspensions of carbon nanotubes (CNT nanofluids). *International Journal of Heat and Mass Transfer*, *49*, 240–250.

Dittus, F. W. & Boelter, L. M. K. (1930). *Heat transfer in automobile radiators of the tubular type* Berkeley: University of California Publications in Engineering., pp. 443–461.

Eastman, J. A., Choi, S. U. S., Li, S., Yu, W. & Thompson, L. J. (2001). Anomalously increased effective thermal conductivities of ethylene glycol-based nanofluids containing copper nanoparticles. *Applied Physics Letters*, *78*, 718–720.

Eastman, J. A., Phillpot, S. R., Choi, S. U. S. & Keblinski, P. K. (2004). Thermal transport in nanofluids. *Annual Review of Materials Research*, *34*, 219–246.

Faulkner, D. J., Rector, D. R., Davison, J. J. & Shekarriz, R. (2004). Enhanced heat transfer through the use of nanofluids in forced convection. In *Proceedings of the ASME International Mechanical Engineering Congress and Exposition (IMECE '04)* Anaheim, USA, (pp. 219–224).

Gnielinski, V. (1976). New equations for heat and mass transfer in turbulent pipe and channel flow. *International Chemical Engineering*, *16*, 359–368.

Godson, L., Raja, B., Mohan Lal, D. & Wongwises, S. (2010). Experimental investigation on the thermal conductivity and viscosity of silver-deionized water nanofluid. *Experimental Heat Transfer*, *23*(4), 317–332.

Li, Q., Xuan, Y., Jiang, J. & Xu, J. W. (2005). Experimental investigation on flow and convective heat transfer feature of a nanofluid for aerospace thermal management. *Journal of Astronautics*, *26*, 391–394 (in Chinese).

Maiga, S. B., Nguyen, C. T., Galanis, N., Roy, G., Mare, T. & Coqueux, M. (2006). Heat transfer enhancement in turbulent tube flow using Al_2O_3 nanoparticle suspension. *International Journal of Numerical Methods for Heat and Fluid Flow*, *16*, 275–292.

Moffat, R. J. (1988). Describing the uncertainties in experimental results. *Experimental Thermal and Fluid Science*, *1*, 3–17.

Pak, B. C. & Cho, Y. I. (1998). Hydrodynamic and heat transfer study of dispersed fluids with sub-micron metallic oxide particles. *Experimental Heat Transfer*, *11*, 151–170.

Xuan, Y. & Li, Q. (2003). Investigation on convective heat transfer and flow features of nanofluids. *ASME Journal of Heat Transfer*, *125*, 151–155.

Xuan, Y. & Li, Q. (2004). Flow and heat transfer performances of nanofluids inside small hydraulic diameter flat tube. *Journal of Engineering Thermophysics*, *25*, 305–307.

Xuan, Y. & Roetzel, W. (2000). Conceptions for heat transfer correlation of nanofluids. *International Journal of Heat and Mass Transfer*, *43*, 3701–3707.

Yang, Y., Zhang, Z. G., Grulke, E. A., Anderson, W. B. & Wu, G. (2005). Heat transfer properties of nanoparticle-in-fluid dispersions (nanofluids) in laminar flow. *International Journal of Heat and Mass Transfer*, *48*, 1107–1116.

Zhou, D. W. (2004). Heat transfer enhancement of copper nanofluid with acoustic cavitation. *International Journal of Heat and Mass Transfer*, *47*, 3109–3117.

International Communications in Heat and Mass Transfer 38 (2011) 1406–1413

Contents lists available at SciVerse ScienceDirect

International Communications in Heat and Mass Transfer

journal homepage: www.elsevier.com/locate/ichmt

Correlations for evaporation heat transfer coefficient and two-phase friction factor for R-134a flowing through horizontal corrugated tubes ☆

Suriyan Laohalertdecha [a,b], Ahmet Selim Dalkilic [c], Somchai Wongwises [b,d,*]

[a] The Joint Graduate School of Energy and Environment (JGSEE), King Mongkut's University of Technology Thonburi, Bangmod, Bangkok 10140, Thailand
[b] Fluid Mechanics, Thermal Engineering and Multiphase Flow Research Lab. (FUTURE), Department of Mechanical Engineering, King Mongkut's University of Technology Thonburi, Bangmod, Bangkok 10140, Thailand
[c] Heat and Thermodynamics Division, Department of Mechanical Engineering, Yildiz Technical University (YTU), Yildiz, Besiktas, Istanbul 34349, Turkey
[d] The Academy of Science, The Royal Institute of Thailand, Sanam Suea Pa, Dusit, Bangkok 10300, Thailand

ARTICLE INFO

Available online 27 August 2011

Keywords:
Two-phase friction factor
Heat transfer
Temperature
R-134a
Corrugated tube

ABSTRACT

Correlations for the evaporation heat transfer coefficient and two-phase friction factor of R-134a flowing through horizontal corrugated tubes are proposed. In the present study, the test section is a horizontal counter-flow concentric tube-in-tube heat exchanger with R-134a flowing in the inner tube and hot water flowing in the annulus. Smooth tube and corrugated tubes with inner diameters of 8.7 mm and lengths of 2000 mm are used as the inner tube. The corrugation pitches are 5.08, 6.35, and 8.46 mm and the corrugation depths are 1, 1.25, and 1.5 mm, respectively. The outer tube is made from smooth copper tube with an inner diameter of 21.2 mm. The correlations presented are formed by using approximately 200 data points for five different corrugated tube geometries and are then proposed in terms of Nusselt number, equivalent Reynolds number, Prandtl number, corrugation pitch and depth, and inside diameter.

© 2011 Elsevier Ltd. All rights reserved.

1. Introduction

Heat transfer enhancement techniques can produce superior heat exchanger performance. One such technique is the use of corrugated tube instead of smooth tube. Corrugated tubes can enhance the heat transfer coefficient on both the outer and inner heat transfer surface area without a significant increase in pressure drop. Typically, corrugated tubes can improve the heat transfer performance of the heat exchanger by increasing fluid mixing, unsteadiness, turbulence flow or by limiting the growth of fluid boundary layers close to the heat transfer surface. Corrugated tubes are sometimes chosen for the design of industrial shell-and-tube heat exchangers in order to reduce the size of the heat exchangers. However, use of corrugated tubes to replace conventional smooth tubes has only been reported over the past two decades. It is still a new method for improving the heat transfer performance of heat transfer equipment. So far, the heat transfer and flow characteristics of corrugated tube have been reviewed as described in the following subsections and in Table 1.

Nozu et al. [1,2] investigated local heat transfer and pressure gradients of pure R-114, R-113 and a zeotropic refrigerant mixture during condensation in the annulus of a double-tube coil consisting of three U-bends and four straight lengths. A corrugated copper tube with an ID of 17.2 mm was used as the test section. Mass fluxes were tested in the range of 80 to 240 kg/sm^2. The results showed that the local heat transfer coefficient decreased along the tube length and that the U-bends showed higher heat transfer coefficients than straight lengths.

Dong et al. [3] experimentally determined the turbulent friction and heat transfer characteristics for four spirally corrugated tubes with various geometrical parameters. Water and oil were used as the working fluid. The experimental conditions were tested at Reynolds numbers ranging between 6000 and 93,000 for water, and from 3200 to 19,000 for oil. Compared with a smooth tube, their results showed that the heat transfer coefficient enhancement varied from 30% to 120%, while the friction factor increased from 60% to 160%.

Barba et al. [4] experimentally studied single-phase heat transfer and flow behaviour of corrugated tube used in the chemical and food industry. The tested conditions were done at moderate Reynolds numbers ranging from 100 to 800. In this study, ethylene glycol was used as the working fluid. The results offered a heat transfer enhancement ranging from 4.27 to 16.79, while the friction factor increased by up to 1.83–2.45 times compared to the smooth tube. Based on the experimental data, Nusselt number and friction factor correlations were proposed.

Rainieri and Pagliarini [5] experimentally investigated the thermal performance of corrugated tubes. Helical and transverse corrugated tubes with different pitches were used as the test section. Ethylene glycol was employed as the working fluid. The experimental conditions were conducted at Reynolds numbers ranging from 90 to 800.

☆ Communicated by W.J. Minkowycz.

* Corresponding author at: Fluid Mechanics, Thermal Engineering and Multiphase Flow Research Lab. (FUTURE), Department of Mechanical Engineering, King Mongkut's University of Technology Thonburi, Bangmod, Bangkok 10140, Thailand. Tel.: +66 2 470 9115; fax: +66 2 470 9111.
E-mail address: somchai.won@kmutt.ac.th (S. Wongwises).

0735-1933/$ – see front matter © 2011 Elsevier Ltd. All rights reserved.
doi:10.1016/j.icheatmasstransfer.2011.08.014

Nomenclature

A	surface area of the test section (m^2)
c_p	specific heat at constant pressure (J/kg K)
d	inner diameter (m)
D	outer diameter (m)
e	corrugation depth (mm)
f	friction factor
G	mass flux (kg/m^2 s)
h	heat transfer coefficient (W/m^2 K)
i	enthalpy (J/kg)
i_f	enthalpy of the saturated liquid (J/kg)
i_{fg}	enthalpy of the vaporisation (J/kg)
k	thermal conductivity (W/m K)
L	length of test section (m)
$LMTD$	logarithmic mean temperature difference
m	mass flow rate (kg/s)
Nu	Nusselt number
p	corrugation pitch (mm)
Pr	Prandtl number
ΔP	pressure drop (Pa/m)
Q	heat transfer rate (W)
Re	Reynolds number
q''	heat flux (W/m^2)
T	temperature (°C)
U	overall heat transfer coefficient (W/m^2 K)
w	corrugation wide (mm)
x	average vapour quality

Greek letters

α	void fraction
β	helix angle (degree)
ρ	density (kg/m^3)
u	dynamic viscosity (Pa.s)

Subscripts

a	acceleration
avg	average
c	corrugated tube
eq	equivalent
f	friction
g	gravitation
in	inlet
i	inside
l	liquid
out	outlet
o	outside
ph	pre-heater
ref	refrigerant
s	smooth tube
sat	saturation
tp	two-phase
TS	test section
v	vapour
w	water

As a comparison of helical corrugated tubes, transverse corrugated tubes and a smooth tube, the results demonstrated that the transverse corrugated tubes showed greater heat transfer enhancement than the helical corrugated and smooth tubes.

Among all of these previous studies, the most productive studies have been performed by Zimparov [6]. The heat transfer enhancement of a combination of three-start spirally corrugated tubes with a twisted tape was investigated. Two three-start spirally corrugated tubes combined with five twisted tape inserts with different relative pitches were employed as the test section. The experimental conditions were conducted at Reynolds number ranging from 3000 to 60,000. The height to diameter ratio (e/d_i) and relative pitch (p/d_i) parameters were 0.0407, 0.0569 and 15.3, 12.2, 7.7, 5.8, 4.7, respectively.

Zimparov [7] presented the heat transfer enhancement using a combination of single-start spirally corrugated tubes with a twisted tape. The friction factors and heat transfer coefficients obtained from these tubes were higher than those of the smooth tube under the same conditions. In addition, Zimparov [8,9] applied a simple mathematical model to predict the friction factor and heat transfer coefficient for a spirally corrugated configuration combined with twisted tape inserts flowing in a turbulent flow regime. The friction factors and heat transfer coefficients calculated were compared with the experimental data. The results showed good agreement between the predicted and experimental data.

Vicente et al. [10,11] presented measurements of mixed convection heat transfer and isothermal pressure drop in corrugated tubes for laminar, transition and turbulent flow regions. Water and ethylene glycol were used as the working fluids. Their results indicated that the corrugated tubes gave a higher pressure drop and heat transfer coefficient than the smooth tube under given conditions. Moreover, the pressure drop obtained from laminar flow to transition flow and from transition flow to turbulent flow increased by up to 25% and 300%, respectively. Similarly, the Nusselt number obtained from laminar flow to transition flow and transition flow to turbulent flow increased by up to 30% and 250%, respectively.

Targanski and Cieslinski [12] experimentally studied the heat transfer coefficient and pressure drop of pure R-407C and R-407C/oil mixtures during evaporation inside a smooth stainless steel tube, smooth copper tubes and two enhanced tubes. The inlet and exit vapour quality were controlled at 0 and 0.7, respectively, the mass flow varied from 250 to 500 $kg/m^2.s$, and the average saturation temperature was controlled at 0 °C. It was found that the heat transfer coefficient and pressure drop for the enhanced tubes were distinctly higher than those of the smooth tube. The maximum enhancement factor and penalty factor for corrugated tube were 1.25 and 1.8, respectively.

Laohalertdecha and Wongwises [13,14] experimentally investigated the effect of pitch on the heat transfer coefficient and pressure drop of R-134a flowing in corrugated tubes during condensation and evaporation conditions. The results demonstrated that the heat transfer coefficient and pressure drop obtained from corrugated tube are higher than those of the smooth tube for all experimental conditions. Moreover, the results also showed that the corrugation surface significantly promotes turbulent flow. However, the effect of pitch on the heat transfer coefficient absolutely has significance at high average quality. On the other hand, the effect of pitch on the pressure drop was insignificant.

In 2011, Laohalertdecha and Wongwises [15] continuously studied the condensation heat transfer and flow characteristics of R-134a flowing through corrugated tubes. The test section was a horizontal counter-flow concentric tube-in-tube heat exchanger, 2000 mm in length. A smooth copper tube and corrugated copper tubes with inner diameters of 8.7 mm were used as the inner tube. The outer tube was made from smooth copper tube with an inner diameter of 21.2 mm. The corrugation pitches used in this study were 5.08, 6.35, and 8.46 mm. Similarly, the corrugation depths were 1, 1.25, and 1.5 mm, respectively. The results found that the Nusselt number and two-phase friction factor obtained from the corrugated tubes were significantly higher than those obtained from the smooth tube. Moreover, new correlations were proposed for predicting the Nusselt number and two-phase friction factor of the corrugated tubes.

Table 1
Experimental investigations on the corrugated tube.

Sources	d_i (mm)	e/d_i	p/d_i	β (deg)	Phase
Nozu et al. [1,2]	17.2	0.0174	0.407	–	Two-phase (Condensation)
Dong et al. [3]	16.04–22.82	0.0243–0.0398	0.438–0.623	78.8–82.1	Single phase
Barba et al. [4]	14.5	0.103	0.793	45	Single phase
Rainieri and Pagliarini [5]	14	0.107	1.143–4.571	–	Single phase
Zimparov [6]	13.68–13.73	0.0407–0.0569	4.7–15.3	67.4–68	Single phase
Zimparov [7]	13.39–13.65	0.0371–0.0441	2.4–7.7	79.3–82.2	Single phase
Zimparov [8,9]	12.44–13.90	0.0224–0.0569	7.45–21.17	67.4–90	Single phase
Vicente et al. [10,11]	18	0.0239–0.0572	0.608–1.229	68–80	Single phase
Targanski and Cieslinski [12]	8.8	0.0511	0.681	77.75	Two phase (Evaporation)
Laohalertdecha and Wongwises [13]	8.7	0.1724	0.584–0.9724	74.2–79.47	Two phase (Condensation)
Laohalertdecha and Wongwises [14]	8.7	0.1724	0.584–0.9724	74.2–79.47	Two phase (Evaporation)
Laohalertdecha and Wongwises [15]	8.7	0.115–0.1724	0.584–0.9724	74.2–79.47	Two phase (Condensation)

As described above, most of the papers to date examine single-phase heat transfer in corrugated tube. There are very few studies, however, dealing with heat transfer enhancement using a corrugated tube in two-phase flow. However, although some information is currently available on two-phase heat transfer enhancement by using corrugated tube, there are no suitable correlations including important relevant parameters yet available for heat transfer and pressure drop characteristics. In the present study, correlations for predicting the heat transfer coefficient and two-phase friction factor for R-134a flowing in horizontal corrugated tubes during the evaporation process, are presented. These correlations, which have never before appeared in open literature, include several important relevant parameters such as corrugation depth and corrugation pitch.

2. Experimental apparatus

A schematic diagram of the test apparatus is shown in Fig. 1. The experimental apparatus was designed to determine the heat transfer coefficient and pressure drop of pure R-134a over the length of the test tube. The test loop consists of a test section, refrigeration loop, cooling water flow loops, sub-cooling loop and relevant instrumentation. The objective of the water loop before the test section is to provide a controlled inlet vapour quality. The second water loop located in the test section provides a controlled heat output from the test section. The sub-cooling loop is used to prevent any two-phase flow condition of the refrigerant occurring before it enters the refrigerant pump.

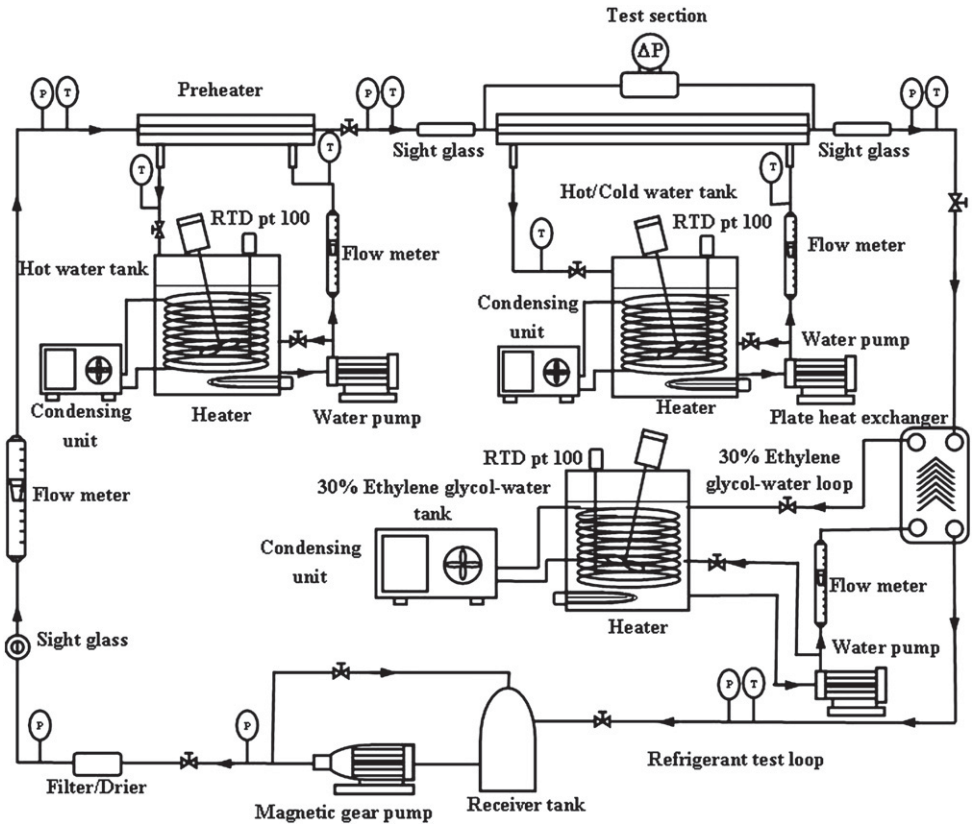

Fig. 1. Schematic diagram of the experimental apparatus.

For the refrigeration circulating loop, liquid refrigerant is discharged by a gear pump regulated by an inverter. The refrigerant passes in series through a filter/dryer, a sight glass tube, flow metre, pre-heater and enters the test section. The inlet vapour quality before entering the test section is controlled by the pre-heater. The pre-heater is a spiral counter flow heat exchanger that supplies energy to provide a controlled inlet vapour quality for vaporisation of the refrigerant. On leaving the test section, the refrigerant is then condensed and sub-cooled by a chilling loop that removes the heat input from the pre-heater and test section and then it returns from the two-phase refrigerant to a sub-cooled state, which later collects in a receiver and eventually returns to the refrigerant pump to complete the cycle.

The test section is a horizontal counter-flow double tube heat exchanger. The length of the heat exchanger is 2000 mm. The detailed dimensions of the heat exchanger and the location of the thermocouples are shown in Fig. 2. A photograph of a corrugated tube and nomenclature to describe the geometry is shown in Fig. 3. The dimensions of the test section are shown in Table 2.

The inlet temperature of the water is controlled by a thermostat. A differential pressure transducer and thermocouples are installed in the test section to measure the pressure drop and temperature across the test section. The length between pressure taps is 2500 mm. In the present study, the pressure of the refrigerant is mainly controlled by a high-pressure limit switch. High-pressure limit switches (Danfoss Type KP 5) are devices for regulating the pressure of a system so that the pressure is maintained near a desired set point pressure in order to prevent the damage to the apparatus.

The refrigerant temperature and tube wall temperature in the test section are measured by Type T thermocouples. A total of 15 thermocouples are soldered to the top, bottom and at five points along side of the tube as shown in Fig. 2. All the temperature measuring devices are well calibrated in a controlled temperature bath using standard precision mercury glass thermometers. The uncertainty of the temperature measurements as recorded by the data acquisition system is ±0.1 °C. All static pressure taps are mounted on the tube wall. The refrigerant flow metre is a variable area type and specially calibrated in the range 0.2–3.4 LPM for R-134a by the manufacturer. Also, the differential pressure transducer is calibrated by the manufacturer.

Experiments were conducted with various flow rates of refrigerant, vapour qualities of refrigerant entering the test section, heat flows and temperatures of refrigerant condensing in the test section. In the experiments, the refrigerant flow rate in the test section was controlled by adjusting the speed of the magnetic gear pump. To vary the vapour quality at the inlet of the test section, the heating water flow and the cooling water flow rates were varied by small increments while the refrigerant flow rate was kept constant. The hot water in the test section was re-circulated by a centrifugal pump to supply heat from the water to the refrigerant. During each experiment, the heat transferred from the test section was kept at a desired value. This might be obtained by simultaneously adjusting and controlling the temperature and flow rate of the hot water entering the test section. The system was allowed to approach a steady state before any data was recorded. After stabilisation, the temperature on the tube wall, the temperature of the refrigerant at the locations mentioned above, the inlet and outlet temperatures of the heating water and flow rates of heating water and refrigerant were all recorded. The pressure drop was measured by a differential pressure transducer installed between the inlet and outlet of the test section. The experiments could be carried out by increasing the refrigerant flow rate while the saturation temperature in the test section was kept constant. The accuracy of the direct measurements and the uncertainties in the derived experimental values are shown in Table 3.

3. Data reduction

The data reduction for calculating the two-phase heat transfer coefficient and pressure drop of R-134a flowing in horizontal smooth and corrugated tubes under evaporation conditions can be summarised as follows.

3.1. The inlet vapour quality of the test section ($x_{TS,in}$)

The inlet vapour quality entering the test section can be calculated as follows:

$$x_{TS,in} = \frac{i_{TS,in} - i_{f,T_{TS,in}}}{i_{fg,T_{TS,in}}} \tag{1}$$

where i_f is the enthalpy of the saturated liquid based on the temperature of the test section inlet, i_{fg} is the enthalpy of vaporisation based on the temperature of the test section inlet, $i_{TS,in}$ is the refrigerant enthalpy at the test section inlet and is given by:

$$i_{TS,in} = i_{ph,in} + \frac{Q_{ph}}{m_{ref}} \tag{2}$$

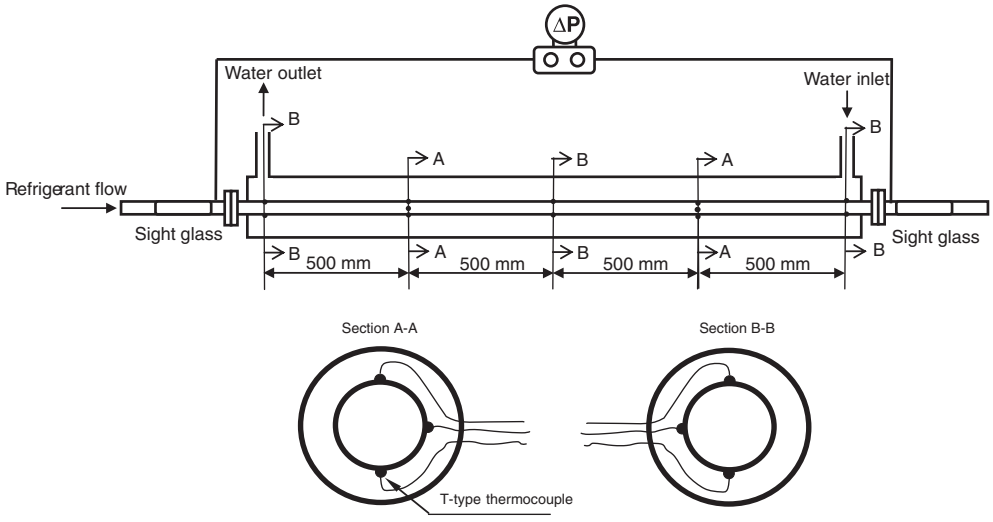

Fig. 2. Schematic diagram of the test section.

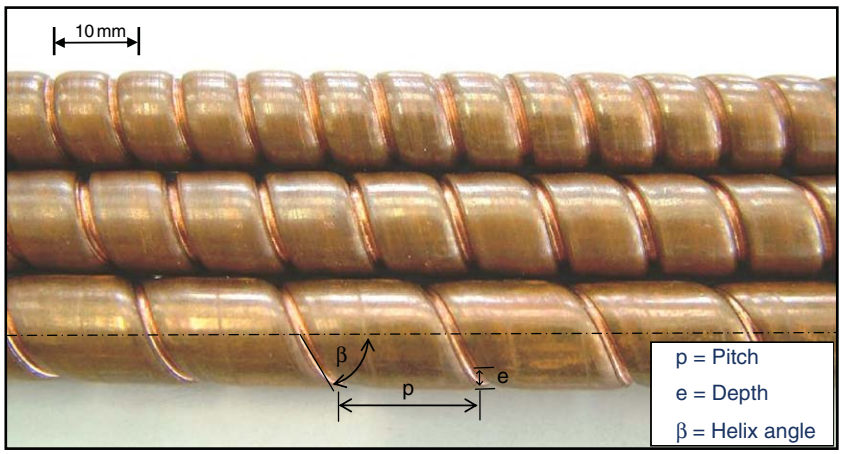

Fig. 3. Photograph of corrugated tubes.

where $i_{ph,in}$ is the inlet enthalpy of the liquid refrigerant before entering the pre-heater, m_{ref} is the mass flow rate of the refrigerant and Q_{ph} is the heat transfer rate in the pre-heater which is calculated by Eq. (3)

$$Q_{ph} = m_{w,ph}c_{p,w}\left(T_{w,in} - T_{w,out}\right)_{ph} \tag{3}$$

where $m_{w,ph}$ is the mass flow rate of water entering the pre-heater.

3.2. The outlet vapour quality of the test section ($x_{TS,out}$)

Similarly, Eq. (4) was used to calculate the exit vapour quality of the test section.

$$x_{TS,out} = \frac{i_{TS,out} - i_{f,T_{TS,out}}}{i_{fg,T_{TS,out}}} \tag{4}$$

where $i_{TS,out}$ is the refrigerant enthalpy at the test section outlet, i_f is the enthalpy of the saturated liquid based on the temperature of the test section outlet, and i_{fg} is the enthalpy of vaporisation. As a consequence, the outlet enthalpy of the refrigerant flow is calculated as:

$$i_{TS,out} = i_{TS,in} + \frac{Q_{TS}}{m_{ref}} \tag{5}$$

where the heat transfer rate in the test section is obtained from:

$$Q_{TS} = m_{w,TS}c_{p,w}\left(T_{w,in} - T_{w,out}\right)_{TS} \tag{6}$$

where $m_{w,\ TS}$ is the mass flow rate of the water entering the test section.

3.3. The inside heat transfer coefficient (h_i)

The inside heat transfer coefficient is calculated as follows:

$$h_i = \frac{1}{\left(\frac{1}{U_i}\right) - \left(\frac{1}{2k}\right)d_i \ln\left(\frac{d_o}{d_i}\right) - \left(\frac{d_i}{d_o}\right)\left(\frac{1}{h_o}\right)} \tag{7}$$

where U_i is the overall heat transfer coefficient based on inside surface area, k is the thermal conductivity of tube material and h_o is the outside heat transfer coefficient.

$$U_i = \frac{Q_{TS}}{A_i(LMTD)} \tag{8}$$

where A_i is the inside tube surface, $LMTD$ is the logarithmic mean temperature difference which is defined as follows:

$$LMTD = \frac{\Delta T_1 - \Delta T_2}{\ln\left(\frac{\Delta T_1}{\Delta T_2}\right)} \tag{9}$$

$$\Delta T_1 = T_{w,out} - T_{ref,in} \tag{10}$$

$$\Delta T_2 = T_{w,in} - T_{ref,out} \tag{11}$$

where $T_{w,in}$ and $T_{w,out}$ denote the inlet and outlet temperatures of the water on the annulus. $T_{ref,in}$ and $T_{ref,out}$ are the inlet and outlet refrigerant temperatures.

$$h_o A_o = \frac{Q_{TS}}{T_{w,avg} - T_{wall,avg}} \tag{12}$$

where Ao is the outside tube surface, $T_{wall,avg}$ is average wall temperature and $T_{w,avg}$ is average water temperature.

Table 2
The dimensions of the test section.

Number	p (mm)	e (mm)	w (mm)	β (degree)	d_i (mm)	L (mm)
1	5.08	1	1	79.47	8.7	2000
2	5.08	1.25	1	79.47	8.7	2000
3	5.08	1.5	1	79.47	8.7	2000
4	8.46	1.5	1	74.20	8.7	2000
5	6.35	1.5	1	76.56	8.7	2000
6	Smooth tube				8.7	2000

Table 3
Uncertainties of measured quantities and calculated parameters.

Parameter	Uncertainty
Temperature, T (°C)	±0.1
Pressure drop, ΔP (kPa)	±0.37
Mass flow rate of refrigerant, m_{ref}	±2%
Mass flow rate of water, m_w	±2%
Heat transfer rate at test section, Q_{TS}	±10%
Heat transfer rate at pre-heater, Q_{ph}	±5%
Evaporation heat transfer coefficient, h	±10%
Average vapour quality, x	±5%

The Nusselt number is determined as:

$$Nu = \frac{hd}{k_l} \tag{13}$$

where k_l is thermal conductivity of the liquid phase refrigerant.

3.4. The frictional pressure drop (ΔP_f)

The total pressure drop, ΔP_{total}, is expressed as the sum of the three different components, as follows:

$$\Delta P_{total} = \Delta P_f + \Delta P_a + \Delta P_g. \tag{14}$$

The three terms on the right-hand side represent the frictional pressure drop (ΔP_f), acceleration pressure drop (ΔP_a) and gravitational pressure drop (ΔP_g). The gravitational pressure drop (ΔP_g) is zero in a horizontal tube. The acceleration pressure drop, ΔP_a, is as proposed by Tran [16]:

$$\Delta P_a = G^2\left(\left(\frac{x^2{}_{out}}{\rho_v\alpha_{out}} + \frac{(1-x_{out})^2}{\rho_l(1-\alpha_{out})}\right) - \left(\frac{x^2{}_{in}}{\rho_v\alpha_{in}} + \frac{(1-x_{in})^2}{\rho_l(1-\alpha_{in})}\right)\right) \tag{15}$$

where α is the void fraction and presented by Zivi's correlation [17] as follows:

$$\alpha = \left(1 + \frac{(1-x)}{x}\left(\frac{\rho_v}{\rho_l}\right)^{\frac{2}{3}}\right)^{-1}. \tag{16}$$

The frictional pressure drop, ΔP_f, can be obtained by subtracting the acceleration pressure drop from the total measured pressure drop.

The two-phase friction factor is defined in terms of equivalent mass flux (G_{eq}) as proposed by Akers et al. [18] and shown in Eq. (17).

$$f_{tp} = \frac{d_i\Delta P_f\rho_l}{2G_{eq}^2} \tag{17}$$

$$G_{eq} = G\left[(1-x) + \left(\frac{\rho_l}{\rho_v}\right)^{0.5}\right] \tag{18}$$

3.5. Equivalent Reynolds number (Re_{eq})

The equivalent Reynolds number is defined as:

$$\mathrm{Re}_{eq} = \mathrm{Re}_l + \mathrm{Re}_v\left(\frac{\mu_v}{\mu_l}\right)\left(\frac{\rho_l}{\rho_v}\right)^{0.5} \tag{19}$$

where Re_l is the liquid Reynolds number defined as:

$$\mathrm{Re}_l = \frac{Gd_i(1-x)}{\mu_l} \tag{20}$$

where Re_v is the vapour Reynolds number defined as:

$$\mathrm{Re}_v = \frac{Gd_ix}{\mu_v} \tag{21}$$

4. Results and discussion

In this study, correlations for evaporation heat transfer coefficient and two-phase friction factor of R-134a flowing through horizontal corrugated tubes are proposed as a function of Nusselt number, equivalent Reynolds number, Prandtl number, corrugation pitch and depth, and inside diameter. The corrugation pitches used in this study are 5.08, 6.35, and 8.46 mm. Similarly, the corrugation depths are 1, 1.25, and 1.5 mm, respectively. The database of the present correlation includes about 200 data points for five different corrugation geometries. The physical properties of the refrigerants are obtained from REFPROP, Version 6.01 [19]. The important results are presented as follows.

4.1. Comparison of experimental heat transfer coefficient and frictional pressure drop for smooth tube with exiting data

Comparison between the experimental data and the data of heat transfer coefficient obtained from Wongsa-ngam et al. [20], Silva Lima et al. [21] and Rossi et al. [22] are shown in Fig. 4a. Almost all the existing data yield relatively good agreement with the experimental data, except Rossi's data which produces a relatively high difference in heat transfer coefficient compared to the experimental data, especially at higher average vapour quality. This may be due to differences in the saturation temperature. Similarly, the frictional pressure drop data are compared with existing data obtained from Filho et al. [23] and Wellsandt and Vamling [24] as shown in Fig. 4b. In this figure, the frictional pressure drops of experimental data give good agreement with existing data.

4.2. Comparison of experimental Nusselt number with the proposed correlations

Fig. 5 shows a comparison of the experimental Nusselt number for the smooth tube and corrugated tube with the proposed correlations.

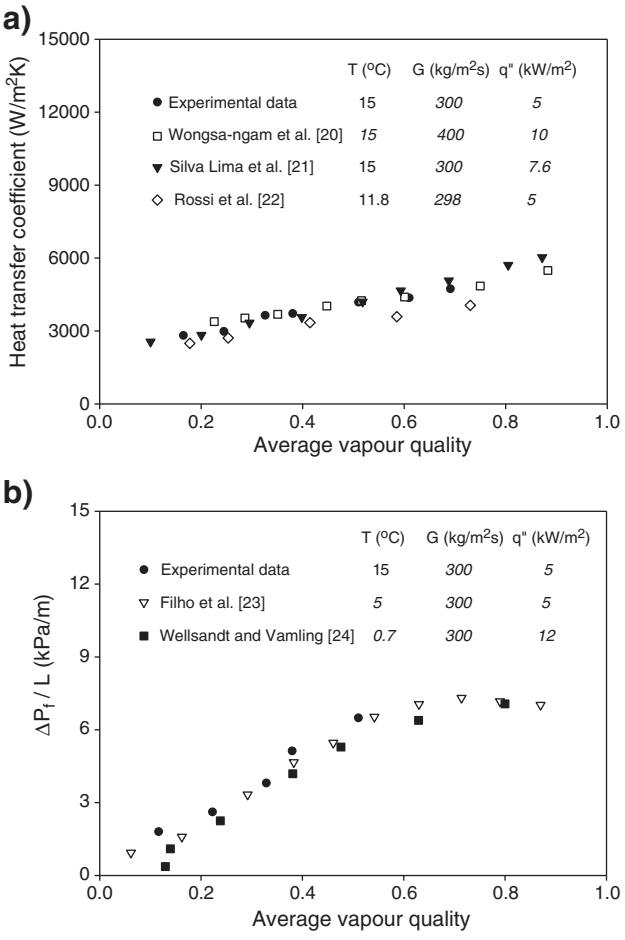

Fig. 4. Comparisons of experimental heat transfer coefficient and frictional pressure drop data for smooth tube with data obtained from literature.

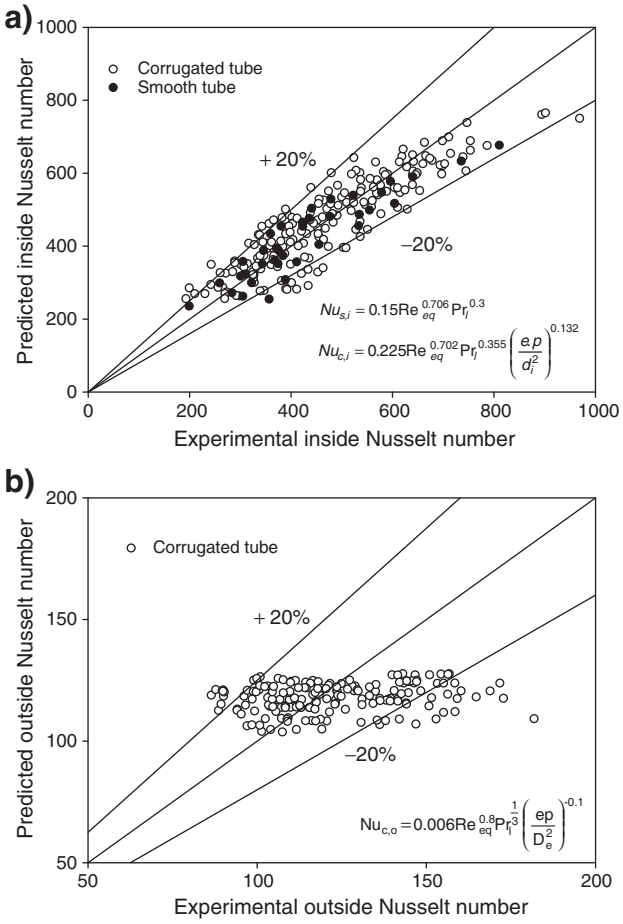

Fig. 5. Inside and outside Nusselt number obtained from the proposed correlations versus the experimental data.

The tests are performed at saturation temperatures of 10–20 °C, heat fluxes of 5–10 kW/m^2, mass fluxes of 300–500 kg/m^2.s, and equivalent Reynolds numbers of 20,000–90,000. The proposed correlations are established based on the Buckingham's Pi theorem and presented in terms of Nusselt number, equivalent Reynolds number, Prandtl number, corrugation pitch and depth, and inside diameter. The Nusselt number correlations for flow in smooth and corrugated tubes are expressed as follows:

- For smooth tube

$$Nu_{s,i} = 0.15\,\mathrm{Re}_{eq}^{0.706}\,\mathrm{Pr}_l^{0.3} \tag{22}$$

- For corrugated tube

$$Nu_{c,i} = 0.225\,\mathrm{Re}_{eq}^{0.702}\,\mathrm{Pr}_l^{0.355}\left(\frac{ep}{d_i^2}\right)^{0.132} \tag{23}$$

The inside Nusselt number is determined from

$$Nu_i = \frac{h_i d_i}{k_{l,ref}}. \tag{24}$$

Similarly, the Nusselt number correlation for flow outside the corrugated tubes is defined as follows:

$$Nu_{c,o} = 0.006\mathrm{Re}_{eq}^{0.8}\mathrm{Pr}_l^{\frac{1}{3}}\left(\frac{ep}{D_{eq}^2}\right)^{-0.1} \tag{25}$$

The outside Nusselt number is determined from

$$Nu_o = \frac{h_o D_{eq}}{k_w} \tag{26}$$

where D_{eq} is the equivalent diameter which is defined as follows:

$$D_{eq} = \frac{D_i^2 - d_o^2}{d_o}. \tag{27}$$

The inside Nusselt number correlations for smooth tube and corrugated tubes are displayed in Fig. 5a. The results show that approximately 90% of data fall within a deviation of ±20%. Equally, the outside Nusselt number correlation for corrugated tube is shown in Fig. 5b. The results show that approximately 85% of the data are correlated within a deviation of 20%.

4.3. Comparison of experimental frictional pressure drop with proposed correlations

The pressure drops are obtained by dividing the measured pressure drop by the length of the test section between pressure taps. In this study, the length between pressure taps is 2500 mm while the length of the heat exchanger is 2000 mm.

Fig. 6 shows the variation of the two-phase friction factor with equivalent Reynolds number for smooth tube and corrugated tubes. The result shows the two-phase friction factor obtained from corrugated tubes depends on the equivalent Reynolds number and tube geometry. Moreover, the result also shows that the two-phase friction factors obtained from smooth and corrugated tubes increase by decreasing the equivalent Reynolds number.

Similar to the Nusselt number, the proposed correlations are presented as function of equivalent Reynolds number, corrugation pitch and depth, and inside diameter. The proposed correlations are shown as follows:

- For smooth tube

$$f_{tp,s} = 13.64\mathrm{Re}_{eq}^{-0.625} \tag{28}$$

- For corrugated tube

$$f_{tp,c} = 33.368\mathrm{Re}_{eq}^{-0.68}\left(\frac{ep}{d_i^2}\right)^{0.1}. \tag{29}$$

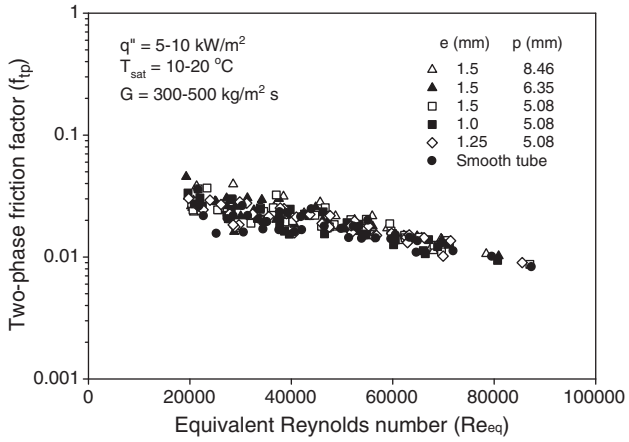

Fig. 6. Two-phase flow friction factor versus equivalent Reynolds number for smooth and corrugated tubes.

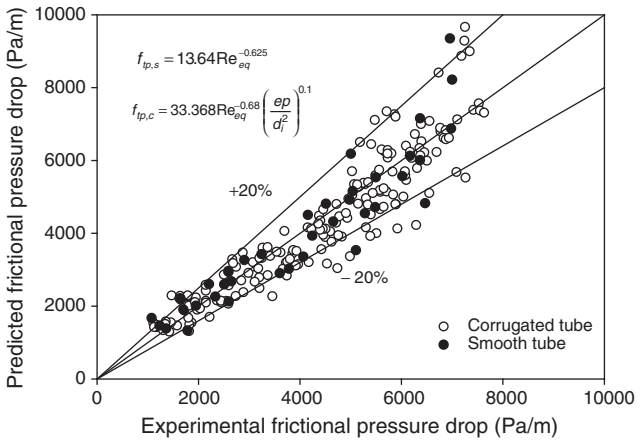

Fig. 7. Frictional pressure drop obtained from the proposed two-phase friction factor correlations versus the experimental data.

Fig. 7 illustrates a comparison of the experimental frictional pressure drop for the smooth tube and corrugated tubes with the proposed correlations. As illustrated in Fig. 7, the results show that approximately 95% of data fall within a deviation of ±20%.

5. Conclusion

Correlations for evaporation heat transfer coefficient and two-phase friction factor of R-134a flowing through horizontal corrugated tubes have been proposed. The test section is a horizontal counter-flow concentric tube-in-tube heat exchanger with R-134a flowing in the inner tube and hot water flowing in the annulus. The Buckingham's *Pi* theorem was used to analyse and form the correlations, and were then presented in terms of Nusselt number as a function of equivalent Reynolds number, Prandtl number, corrugation pitch and depth, and inside diameter. The results show that approximately 85–90% of Nusselt number data fall within a deviation of ±20%. Similarly, the two-phase friction factor results show that approximately 95% of data fall within a deviation of ±20%.

Acknowledgements

The present study was supported financially by the Thailand Research Fund, the Office of the Higher Education Commission and the National Research University Project, whose guidance and assistance are gratefully acknowledged.

References

[1] S. Nozu, H. Honda, H. Nakata, Condensation of refrigerants CFC11 and CFC113 in the annulus of a double-tube coil with an enhanced inner tube, Exp. Therm. Fluid Sci. 11 (1995) 40–51.
[2] S. Nozu, H. Honda, S. Nishida, Condensation of a zeotropic CFC 114–CFC 113 refrigerant mixture in the annulus of a double-tube coil with an enhanced inner tube, Exp. Therm. Fluid Sci. 11 (1995) 364–371.
[3] Y. Dong, L. Huixiong, C. Tingkuan, Pressure drop, heat transfer and performance of single-phase turbulent flow in spirally corrugated tubes, Exp. Therm. Fluid Sci. 24 (2001) 131–138.
[4] A. Barba, S. Rainieri, M. Spiga, Heat transfer enhancement in a corrugated tube, Int. Commun. Heat Mass Transfer 29 (2002) 313–322.
[5] S. Rainieri, G. Pagliarini, Convective heat transfer to temperature dependent property fluids in the entry region of corrugated tubes, Int. J. Heat Mass Transfer 45 (2002) 4525–4536.
[6] V. Zimparov, Enhancement of heat transfer by a combination of three-start spirally corrugated tubes with a twisted tape, Int. J. Heat Mass Transfer 44 (2001) 551–574.
[7] V. Zimparov, Enhancement of heat transfer by a combination of a single-start spirally corrugated tubes with a twisted tape, Exp. Therm. Fluid Sci. 25 (2002) 535–546.
[8] V. Zimparov, Prediction of friction factors and heat transfer coefficients for turbulent flow in corrugated tubes combined with twisted tape inserts. Part 1: friction factors, Int. J. Heat Mass Transfer 47 (2004) 589–599.
[9] V. Zimparov, Prediction of friction factors and heat transfer coefficients for turbulent flow in corrugated tubes combined with twisted tape inserts. Part 2: heat transfer coefficients, Int. J. Heat Mass Transfer 47 (2004) 385–393.
[10] P.G. Vicente, A. Garcia, A. Viedma, Experimental investigation on heat transfer and friction factor characteristics of spirally corrugated tubes in turbulent flow at different Prandtl number, Int. J. Heat Mass Transfer 47 (2004) 671–681.
[11] P.G. Vicente, A. Garcia, A. Viedma, Mixed convection heat transfer and isothermal pressure drop in corrugated tubes for laminar and transition flow, Int. Commun. Heat Mass Transfer 31 (2004) 651–662.
[12] T. Targanski, J.T. Cieslinski, Evaporation of R407C/oil mixtures inside corrugated and micro-fin tubes, Appl. Therm. Eng. 27 (2007) 2226–2232.
[13] S. Laohalertdecha, S. Wongwises, The effects of corrugation pitch on the condensation heat transfer coefficient and pressure drop of R-134a inside horizontal corrugated tube, Int. J. Heat Mass Transfer 53 (2010) 2924–2931.
[14] S. Laohalertdecha, S. Wongwises, An experimental study into the evaporation heat transfer and flow characteristics of R-134a refrigerant flowing through corrugated tubes, Int. J. Refrig. 34 (2011) 280–291.
[15] S. Laohalertdecha, S. Wongwises, Condensation heat transfer and flow characteristics of R-134a flowing through corrugated tubes, Int. J. Heat Mass Transfer 54 (2011) 2673–2682.
[16] T.N. Tran, Pressure drop and heat transfer study of two-phase flow in small channels. Ph.D. Dissertation, Texas Tech University, Lubbock, Texas, 1998
[17] S.M. Zivi, Estimation of steady-state steam void-fraction by mean of the principle of minimum entropy production, Trans. ASME, J. Heat Transfer 86 (1964) 247–252.
[18] W.W. Akers, H.A. Deans, O.K. Crasser, Condensing heat transfer within horizontal tubes, Chem. Eng. Prog. Symp. 55 (1959) 171–176.
[19] REFPROP, Refrigerant Properties Database Version 6.01, NIST, Gaithersburg, MD, 1998.
[20] J. Wongsa-ngam, T. Nualboonrueng, S. Wongwises, Performance of smooth and micro-fin tubes in high mass flux region of R-134a during evaporation, Heat Mass Transfer 10 (2002) 425–435.
[21] R.J. Silva Lima, J.M.Q. Quibén, J.R. Thome, Flow boiling in horizontal smooth tubes: New heat transfer results for R-134a at three saturation temperatures, Appl. Therm. Eng. 29 (2009) 1289–1298.
[22] F. Rossi, A.W. Mauro, A. Rosato, Local heat transfer coefficients and pressure gradients for R-134a during flow boiling at temperatures between −9 °C and +20 °C, Energy Convers. Manage. 50 (2009) 1714–1721.
[23] E.P.B. Filho, J.M.S. Jabardo, P.E.L. Barbieri, Convective boiling pressure drop of refrigerant R-134a in horizontal smooth and micro-fin tubes, Int. J. Refrig. 27 (2004) 895–903.
[24] S. Wellsandt, L. Vamling, Evaporation of R134a in a horizontal herringbone micro-fin tube heat transfer and pressure drop, Int. J. Refrig. 28 (2005) 889–900.

American J. of Engineering and Applied Sciences 4 (4): 540-547, 2011
ISSN 1941-7020
© 2011 Science Publications

Improvement of the Runner Design of Francis Turbine using Computational Fluid Dynamics

[1]Suthep Kaewnai and [1,2]Somchai Wongwises
[1]Department of Mechanical Engineering,
Thermal Engineering and Multiphase Flow Research Lab (FUTURE),
Faculty of Engineering, King Mongkut's University of Technology Thonburi,
Bangkok 10140, Thailand
[2]The Academy of Science, the Royal Institute of Thailand,
Sanam Suea Pa, Dusit, Bangkok 10300, Thailand

Abstract: Problem statement: The objective of this study is to improve runner design of the Francis turbine and analyze its performance with the Computational Fluid Dynamics (CFD) technique. **Approach:** A runner design process uses a direct method with the following design conditions: flow rate of 3.12m^3/sec head of 46.4 m and speed of 750 rpm or dimensionless specific speed of 0.472. **Results:** The first stage involves the calculation of various dimensions such as the blade inlet and exit angle at hub and the mean and shroud positions to depict the meridional plane. The second stage deals with the CFD simulation. Various results were calculated and analyzed for factors affecting runner's performance. Results indicated that the head rise of the runner at the design point was approximately 39 m, which is lower than the specified head. Based on past experiences, the meridional plane was modified and blade inlet and lean angles were corrected. The process of meridional plane modification was repeated until the head rise was nearly equal to the specified head. Velocity vector and streamline should be a uniform stream. **Conclusion/Recommendations:** Results from calculating runner's performance were approximately 90% at design point. Existing absolute velocity component from CFD simulation pointed out that swirling flow occurred at the exit of runner. Based on the comparison of runner's performance between simulation results and experimental data from previous work reported in the literature, it is possible to use this method to simulate runner's performance of the Francis turbine.

Key words: Meridional plane, Francis turbine, runner, theoretical calculation, Best Efficiency Point (BEP), streamline

INTRODUCTION

Difficulty in construction of large dams to produce electricity leads to the study of the small turbine. Owing to the progress of the numerical method and computer capacity, a runner design of the Francis turbine can be analyzed by computer programs such as 3D-Navier-Stokes or CFD code to predict its performance before real production. Nevertheless, both the prediction and the design cannot be done easily without an existing database and past experiences. If results from the CFD predictions differ from the design, the turbine should be redesigned before real production. During the past decades, the Francis turbine was studied by many researchers.

Sebestyen and Keck studied flow in the Francis turbine at low head for EGLISU electrical plant (Sebestyen and Keck, 1995). The runner design was improved to fit with existing casing and draft tube by analyzing with CFD technique. The efficiency was improved by 7% and its real efficiency was measured by 5% at design point.

Milos and Barglazan explained that the hydraulic runner design process for Francis turbine usually took a long duration, even for experienced designers (Milos and Barglazan, 2004). They proposed a streamline function of the flow through the runner to enable a quicker design process (Keck *et al*., 1996; 1997; Krishna, 1997; Vu and Shy, 1994; Wu *et al*., 2007).

MATERIALS AND METHODS

There are explanations for runner design processes and CFD prediction techniques, there is no available

Corresponding Author: Suthep Kaewnai, Department of Mechanical Engineering, Thermal Engineering and Multiphase Flow Research Lab (FUTURE), Faculty of Engineering, King Mongkut's University of Technology Thonburi, Bangmod, Bangkok 10140, Thailand

data for one-dimensional hydraulic runner design, which is a starting point of the design process. Even though there is much research on the Francis turbine, there is still a large gap for further study. Therefore, this study focuses on the following main issues:

- Data for improvement of runner design
- Prediction of total head rise at various flow rates
- Checking of speed and streamline through the runner
- Checking of speed distribution along meridian plane at the runner inlet and outlet
- Checking of circumferential component at the absolute velocity to determine swirling flow at the runner outlet

Runner design process: In general, there are two approaches to runner design: the direct method and the inverse method. This study uses a direct method. Figure 1 show the runner design process that begins with the setting of Q (volume flow rate), H (head) and n (speed).

Basic equation in runner design: Basic theory in runner design assumes that flow occurs in one dimension. A momentum equation is applied to determine the runner's head Euler Eq. 1:

$$H = \frac{U_l C_{u1}}{g} \quad (1)$$

The Free vortex used in the design assumes that head is static with no swirl at the runner blade outlet.

Dimensionless specific speed Eq. 2:

$$\nu = \frac{\omega\sqrt{(Q/\pi)}}{(2gH)^{0.75}} \quad (2)$$

Meridional component of absolute velocity Eq. 3:

$$C_m = \frac{Q}{A_v} \quad (3)$$

Inlet or outlet area with blockage Eq. 4:

$$A_v = \pi Db - ZS_u b \quad (4)$$

Blade blockage Eq. 5:

$$S_u = \frac{S}{\sin(\beta)} \quad (5)$$

Average diameter Eq. 6:

$$D_{ave} = \frac{D_{hub} + D_{shroud}}{2} \quad (6)$$

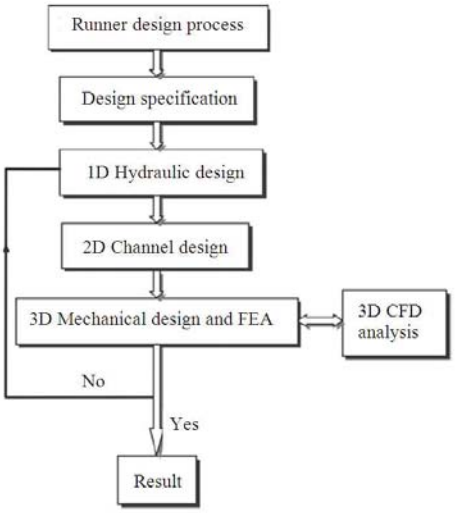

Fig. 1: Design process of runner

Circumferential speed Eq. 7:

$$U = \frac{\pi Dn}{60} \quad (7)$$

Basic mathematical equation of the model: This study uses CFX 5.5 software for three-dimensional flow. The fluid is incompressible and unsteady. The mass conservation and momentum equations for coordinate rotation system can be described as follows:

Mass conservation Eq. 8:

$$\frac{\partial \rho}{\partial t} + \vec{\nabla} \cdot \rho \vec{V} = 0 \quad (8)$$

Momentum Eq. 9:

$$\rho \frac{d\vec{V}}{dt} + \vec{\nabla} P = \rho \vec{g} + \mu\left(\nabla^2 \cdot \vec{V}\right) - 2\rho\vec{\Omega} \times \vec{V} - \rho\vec{\Omega} \times \left(\vec{\Omega} \times \vec{r}\right) \quad (9)$$

Parameters for efficiency calculation: In CFD-code analysis, speed and pressure on the controlled surface at the runner's upstream and downstream could be determined by Eq. 10.

Total head rise:

$$H_{total} = \left(\frac{\overline{P_{1total}} - \overline{P_{2total}}}{\rho g}\right) \quad (10)$$

Table 1: Details at runner inlet

Position	Hub	Mean	Shroud
Circumferential speed (m/sec)	23.562	26.196	28.588
Circumferential component of the absolute velocity (m/sec)	19.277	17.339	15.888
Blade angle (Degree)	61.112	41.245	31.446

Table 2: Details at runner outlet without preswirl

Position	Hub	Mean	Shroud
Circumferential speed (m/sec)	12.802	22.408	28.431
Blade angle (Degree)	30.22	18.109	14.697

Table 3: Conditions used for the simulation

Parameters	CFD Code, CFX 5.5
Flow simulation domain	Single runner flow channel
Mesh	Structured
Fluid	Water at 25°C
Inlet	Total pressure
Outlet	Mass flow rate, Variable (kg/sec)
Wall	No slip
Turbulence model	k,ε
Maximum residual convergence	10^{-4} (RMS)

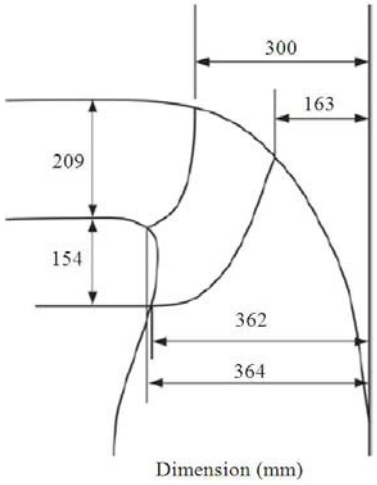

Fig. 2: Dimension of Francis turbine runner in meridional plane (Dimension: mm)

Theoretical head Eq. 11:

$$H_{th} = \frac{\overline{U_1C_{u1}} - \overline{U_2C_{u2}}}{g} \quad (11)$$

Runner efficiency Eq. 12:

$$\eta_{runner} = \frac{\text{Total head rise}}{\text{Theoretical head}} \quad (12)$$

Analysis of runner's flow: Analysis of the Francis turbine runner was done on the given design quantities: volume flow rate of 3.12 m^3/sec, head of 46.4 m, circumferential speed of 750 rpm or dimensionless specific speed of 0.472 and 11 blades of runner. The calculation shows that the Meridional component of the absolute velocity at the runner inlet, C_{m1} is 7.766 m/sec and Meridional component of the absolute velocity at the runner outlet, C_{m2} is 7.457 m/sec. Various dimensions of the runner are shown in Fig. 2. Blade angle, circumferential speed and the circumferential component of the absolute velocity at the runner inlet and outlet could be summarized in Table 1 and 2.

Dimension of runner in meridional plane is shown in Fig. 2. The analysis began with mesh generation and mesh refinement on runner domain. (The domain is the runner channel through which the fluid flows). Secondly, initial conditions and boundary conditions were specified for the mesh-refined domain. Finally, several calculations were made and displayed to determine factors affecting runner's performance. Results from CFD code included pressure; speed on x, y and z axes and specific data that could be further analyzed. If the CFD code prediction gives incorrect results, the runner design can be corrected. Regarding the simulation using CFD code, the conditions used are shown in Table 3.

RESULTS AND DISCUSSION

Drafting domain of runner channel by 3D-CAD programs began as shown in Fig. 4. Then, the domain was entered into CFD code analysis to generate mesh, as shown in Fig. 5.

Analysis of simulation results: In this study, only the inlet and outlet of the fluid were considered to determine the effect on domain. To get better results, a finer mesh should be generated. Figure 6 shows the streamline distribution of the fluid and Fig. 7 shows the velocity distribution on the domain. Notably, the distributions are non-uniform. The results from simulation using CFD Code before improving the runner of Francis turbine are concluded in Table 4 and 5.

Runner design process: At the specified flow rate, results from simulation showed that the head rise was lower than specified head in the design:

- The design improvement process began by reshaping the meridian plane. The shape of the meridian plane is the first priority in designing fluid machinery that requires much experience. In Fig. 8, the shorter length of the meridian plane, compared to Fig. 3, does not signify the shorter length of the runner blade. The length of the runner blade depends on wrap angle (λ), which is normally between 20-80 degrees.

Table 4: Results from the simulation before runner improvement

Mass flow rate	3120	kg /sec
Volume flow rate	3.12	m^3/sec
Head rise	39.00	m

Table 5: Results from simulation after runner improvement at design point

Mass flow rate	3120	kg /sec
Volume flow rate	3.12	m^3/sec
Head rise	46.3	m

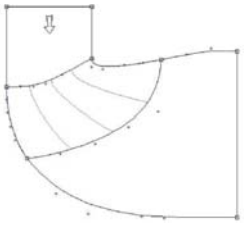

Fig. 3: Meridional plane of Fig. 2 corresponding to CFD Code

Fig. 4: Domain of runner channel

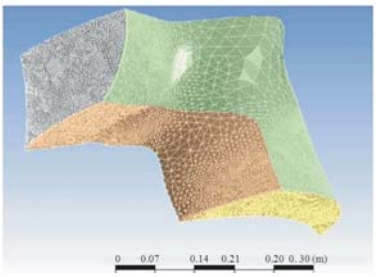

Fig. 5: Mesh on domain for numerical calculation

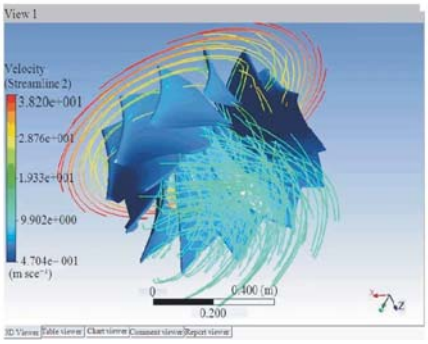

Fig. 6: Streamline distribution on runner

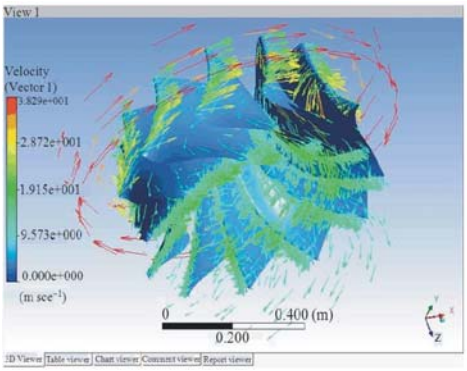

Fig. 7: Velocity distribution on runner

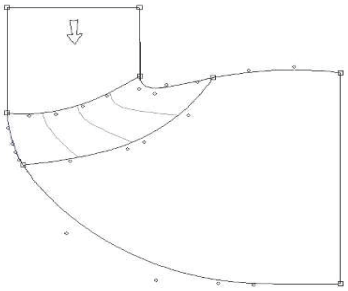

Fig. 8: Meridional plane after improvement

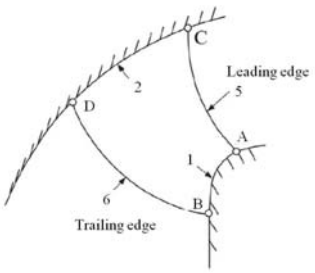

Fig. 9: Location of Meridional plane for Fig. 10

- Lean angle (β) at runner blade inlet was adjusted to 10-30 degrees. Characteristic of lean angle is shown in Fig. 9-10
- Plan view of runner blade was adjusted as shown in Fig. 10
- Inlet angle of runner blade was adjusted to the value shown in Fig. 11. At the dimensionless specific speed 0.472, the angles at the Hub and Shroud were changed to 64 and 73 Degrees, respectively. It is noticeable that the shroud angle is larger than the hub angle, which is contrary to the results from the theoretical calculation given in Table 1

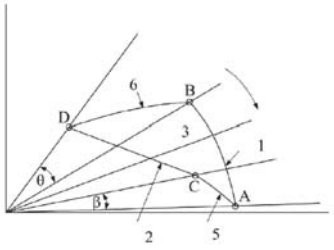

Fig. 10: Plan view of a runner blade

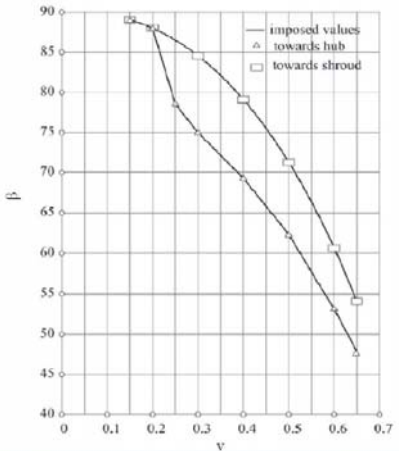

Fig. 11: Inlet and outlet angle of runner blade

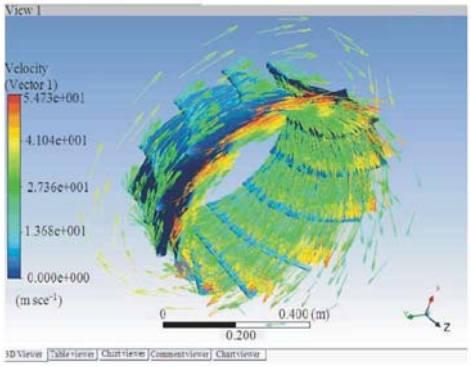

Fig. 12: Velocity distribution on runner after improvement

Results from runner design process: Figure 12 and 13 show that the velocity and streamline distributions on domain are uniform.

Runner performance: Runner performance from this study is shown in Fig. 14-17. Head rise at the specified design point is 46.4 m. From Fig. 14, the head rise is 46.3 m at the same flow rate.

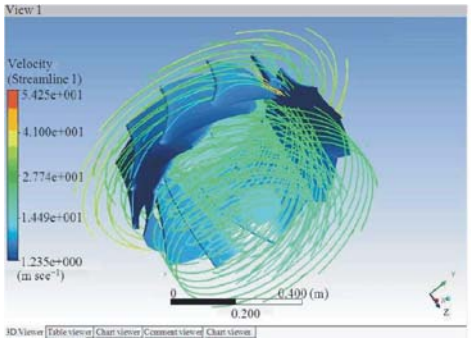

Fig. 13: Streamline distribution on runner after improvement

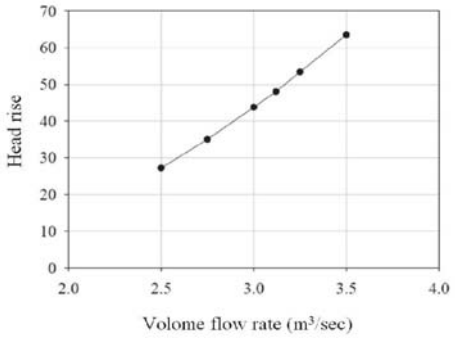

Fig. 14: Head rise Vs volume flow rate

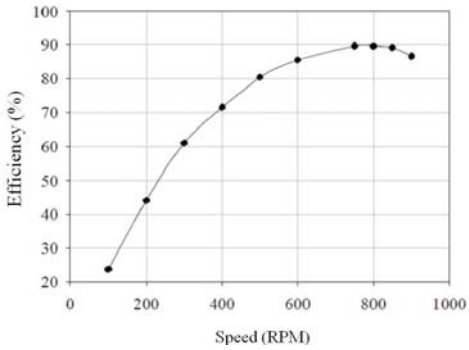

Fig. 15: Runner efficiency Vs speed

It could be seen that improvement of runner design leads to better head rise and head obtained from the simulation is close to the specified design point.

Figure 15 shows that, at the speed of 750 rpm, the runner's efficiency is 90%. In real use, the runner is assembled with casing, draft tube and bearing; thus, the turbine's overall efficiency might be reduced because of friction. Figure 16 shows a relationship between head rise and speed.

It is found that at the designed speed, the head rise that has occurred is not the maximum head, which should be rotated at 400 rpm.

Figure 17 shows the speed of the meridian plane from CFD code from hub to shroud. One notices that the speed of meridian plane is maximum at the hub and minimum at the shroud, with an average of 6.931 m/sec. This differs slightly from the value gained from theoretical calculation.

Figure 18 shows that the circumferential component of the absolute velocity, at the runner inlet decreases from hub to shroud. Figure 19 shows that the speed of the meridian plane at the runner outlet is nearly stable.

Figure 20-21 show that the circumferential component of the absolute velocity at the runner outlet and distance from Hub is not equal to zero.

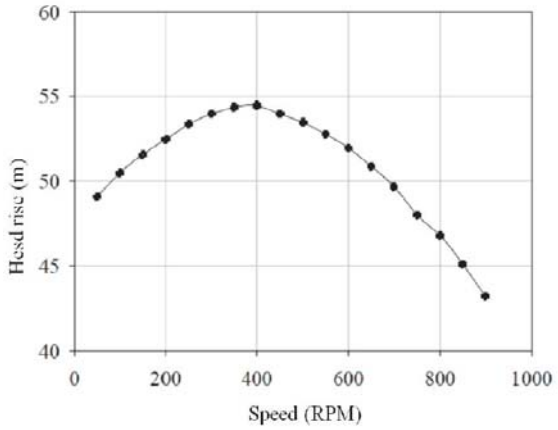

Fig. 16: Head rise Vs speed

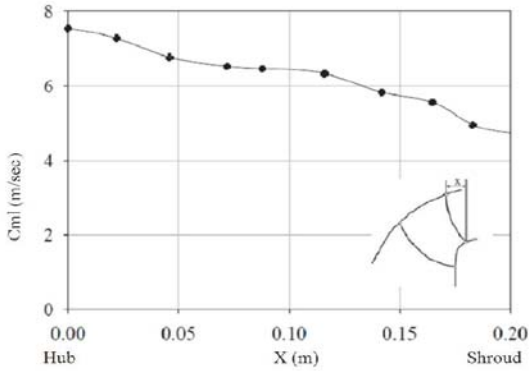

Fig. 17: Variation of meridional component of the absolute velocity at runner inlet with distance from hub

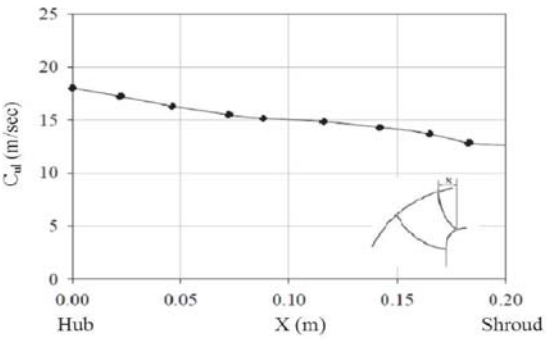

Fig. 18: Variation of circumferential component of the absolute velocity at runner inlet with distance from hub

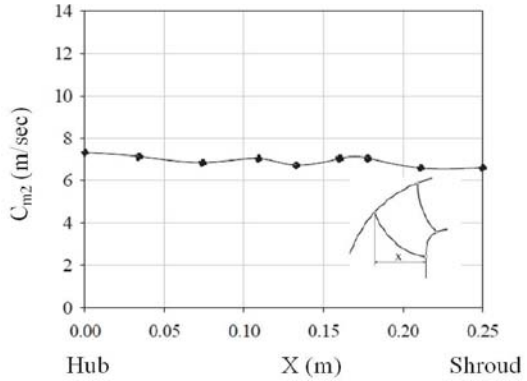

Fig. 19: Variation of meridional component of the absolute velocity at runner outlet with distance from hub

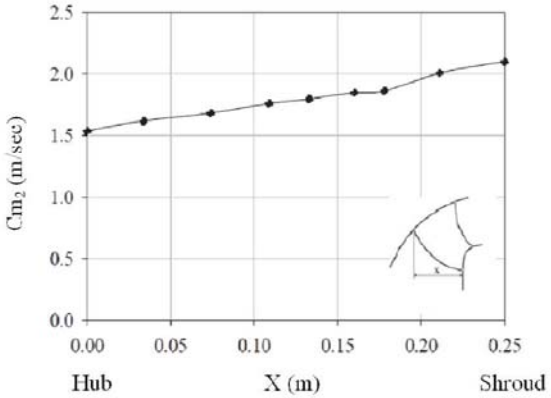

Fig. 20: Variation of circumferential component of the absolute velocity at runner outlet with distance from hub

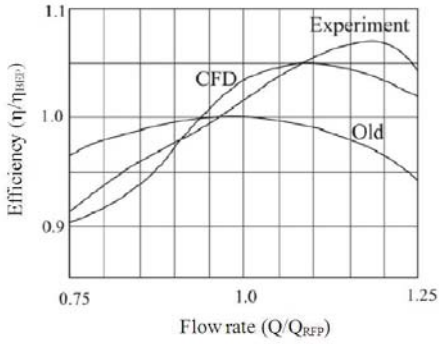

Fig. 21: Comparison between calculation and measurement; efficiency and volume flow rate referred to best efficiency point

This means that there is a pre-swirl at the runner outlet. Hence, the design that sets to zero is not correct.

Confirmation from CFD: This study did not conduct any experiment because of the high cost. However, the study by Sebestyen and Keck shows corresponding results between analysis and test (Sebestyen and Keck, 1995). The runner is redesigned for EGLISU electrical plant. CFD analysis indicated higher efficiency by 7%. Then, the new runner was installed into the old casing and tested. It was found that the efficiency of the new runner-not including friction in casing, draft tube and bearing-was better by 5%, close to results from CFD analysis. The highest point of efficiency was at.

CONCLUSION

The improvement of runner design of the Francis turbine to get the desired head rise and high efficiency relied on experienced correction of meridional plane and angle of runner blade inlet as shown in Fig. 11. It took a long time to complete this step. CFD analysis indicated that the runner efficiency at the design point was 90%. At the flow rate close to the Best Efficiency Point (BEP), the runner's efficiency was quite high and became lower when the flow rate was far from the BEP. Checking the speed from CFD code revealed that the circumferential component of the absolute velocity at runner outlet was not equal to zero. Thus, the flow at the runner outlet caused swirl. However, the analysis only gave very small value. On the other hand, the meridional component of the absolute velocity at the runner outlet was nearly stable.

ACKNOWLEDGMENT

The researchers would like to express their appreciation to the Thailand Research Fund (TRF), the Office of Higher Education Commission and the National Research University Project for providing financial support for this study.

List of symbols:

A_v	Inlet or outlet area (m^2)
b	Width of channel in the meridional section (m)
C_{m1}	Meridional component of the absolute velocity at runner inlet (m/sec)
C_{m2}	Meridional component of the absolute velocity at runner outlet (m/sec)
C_{u1}	Circumferential component of the absolute velocity at runner inlet (m/sec)
C_{u2}	Circumferential component of the absolute velocity at runner outlet (m/sec)
CFD	Computational Fluid Dynamics
D	Diameter (m)
FEA	Finite element analysis
G	Gravitational acceleration (m/sec^2)
H	Design head of runner (m)
H_{total}	Total head rise
H_{th}	Theoretical head
K	Turbulence kinetic energy
n	Speed (rpm)
P	Pressure (N/m^2)
p_w	Power (Watt)
P_{1total}	Total pressure at runner inlet (N/m^2)
p_{2total}	Total pressure at runner outlet ($N\ m^2$)
Q	Volume flow rate (m^3/sec)
R	Radius from the reference point (m)
S	Blade thickness (m)
S_u	Blade thickness with blockage (m)
U_1	Circumferential speed at runner inlet (m/sec)
U_2	Circumferential speed at runner outlet (m/sec)
$\vec{V}$	Velocity vector (m)
Z	Number of blade
β	Blade angle
η	Efficiency
ν	Dimensionless specific speed
ε	Turbulence eddy dissipation
ρ	Density of water (kg/m^3)
$\vec{\Omega}$	Angular velocity (rad/sec)
$\vec{\nabla}$	Operator

REFERENCES

Keck, H., P. Drtina and M. Sick, 1996. Numerical hill chart prediction by mean of CFD stage simulation for a complete Francis turbine. Porceedings of the IAHR Symposium Hydraulic Machinery and Cavitation, (HMC' 96), Valencia.

Keck, H., P. Drtina and M. Sick, 1997. A breakthrough–CFD flow simulation for a complete turbine. Sulzer Hydro Ltd., Switzerland.

Krishna, H.C.R., 1997. Hydraulic Design of Hydraulic Machinery. 1st Edn., Avebury, Aldershot, ISBN: 0291398510, pp: 570.

Milos, T. and M. Barglazan, 2004. CAD technique used to optimize the francis runner design. Proceedings of the 6th International Conference on Hydraulic Machinery and Hydrodynamics Timisoara, Oct. 21-22, Politehnica University, Romania, pp: 125-130.

Sebestyen, A. and H. Keck, 1995. Uprating of ultra-low francis units based on numerical flow analysis. Sulzer Hydro Ltd., Switzerland.

Vu, T.C. and W. Shy, 1994. Performance prediction by viscous flow analysis for francis turbine runner. J. Fluid Eng., 116: 116-120.

Wu, J., K. Shimmei, K. Tani, K. Niikura and J. Sato, 2007. CFD-based design optimization for hydro turbines. J. Fluid Eng. ASME, 129: 159-168.

Experimental Thermal and Fluid Science 36 (2012) 107–117

Contents lists available at SciVerse ScienceDirect

Experimental Thermal and Fluid Science

journal homepage: www.elsevier.com/locate/etfs

Flow boiling pressure drop of R134a in the counter flow multiport minichannel heat exchangers

Jatuporn Kaew-On [a,b], Kittipong Sakamatapan [b], Somchai Wongwises [b,c,*]

[a] The Joint Graduate School of Energy and Environment (JGSEE), King Mongkut's University of Technology Thonburi, Bangmod, Bangkok 10140, Thailand
[b] Fluid Mechanics, Thermal Engineering and Multiphase Flow Research Lab. (FUTURE), Department of Mechanical Engineering, King Mongkut's University of Technology Thonburi, Bangmod, Bangkok 10140, Thailand
[c] The Academy of Science, The Royal Institute of Thailand, Sanam Suea Pa, Dusit, Bangkok 10300, Thailand

ARTICLE INFO

Article history:
Received 8 April 2011
Received in revised form 29 July 2011
Accepted 4 September 2011
Available online 22 September 2011

Keywords:
Flow boiling pressure drop
Multiport minichannels
Tube-in-tube heat exchanger
R134a

ABSTRACT

In the present study, the pressure drop characteristics during the boiling of R134a as it flows through the multiport minichannel heat exchangers are presented. The heat exchangers are counter flow tube-in-tubes. The refrigerant flow runs through the inner tube, while the hot water flows through the 25.4 mm round tube at outer edge of the heat exchanger. Two inner test sections are made from aluminium tubing with hydraulic diameters of 1.1 mm for 14 channels and 1.2 mm for eight channels. The experiments were carried out at mass fluxes ranging from 350 to 980 kg/(m^2 s), heat fluxes ranging from 18 to 80 kW/m^2, and saturation pressures of 4, 5 and 6 bar, at constant inlet quality of 0.05. The effect of relevant parameters on the frictional pressure drop, such as the saturation pressure, mass flux, heat flux, and aspect ratio, are examined and discussed in detail. Finally, the nine existing correlations that are based on both conventional tubes and small tubes are selected for comparison with the experimental results.

© 2011 Elsevier Inc. All rights reserved.

1. Introduction

Multiport minichannels have been considered to be of great interest in the compact evaporator applications of both automotive air-conditioning and heat pump systems. The greatest advantages of the minichannels are their high heat transfer coefficient, high compactness, and lower required fluid mass. The greater heat transfer in minichannels is obtained by a higher surface area. The decreasing size also allows heat exchangers to achieve a significant weight reduction, a lower fluid inventory, a low capital and installation cost, and enhanced energy savings. Despite such advantages, the pressure drop in the minichannels is still higher than that which occurs with a conventional tube due to the increased wall friction. Thus, the designs of multiport minichannels that are used as evaporators for air conditioning or heat pumps are needed in order to overcome the practical obstructions that relate to flow boiling. In the last decade, the pressure drop characteristics of refrigerant in small channels have been studied by a number of researchers. However, most of them were studied with a singleport minichannel. Thus, the pressure drop and flow characteristics of refrigerant in multiport minichannels have received little attention in existing literature. So far, some examples of the most productive studies that address both single port and multiport minichannels are summarized as follows:

Zhang and Webb [1] measured the single phase and adiabatic two-phase flow pressure drop of R134a, R22, and R404A flowing in a multiport extruded aluminium minichannel with a hydraulic diameter of 2.13 mm. They concluded that the Blasius friction correlation gave supported the experimental data for a single-phase flow. In contrast, Friedel's [2] correlation showed over-predicted values for two-phase data. They also proposed the two-phase multiplier based on their experimental results as a function of the refrigerant quality and reduced pressure.

In 2002, Ould Didi et al. [3] presented experimental data for evaporation in two horizontal test sections of 10.92 and 12.00 mm diameter for five refrigerants (i.e., R134a, R123, R402A, R404A and R502) over mass fluxes from 100 to 500 kg/(m^2 s). They showed the comparisons between the experimental results and the seven two-phase frictional pressure drop predictions method. From the comparisons, they concluded that the method of Müller-Steinhagen and Heck [4] and the method of Gronnerud [5] consistently gave the best predictions, while the Friedel [2] method was the third best in comparisons of seven leading predictive methods.

In 2005, Cavallini et al. [6] investigated the pressure drop characteristics in multiport minichannels during the adiabatic

* Corresponding author at: Fluid Mechanics, Thermal Engineering and Multiphase Flow Research Lab. (FUTURE), Department of Mechanical Engineering, King Mongkut's University of Technology Thonburi, Bangmod, Bangkok 10140, Thailand. Tel.: +662 470 9115; fax: +662 470 9111.
E-mail address: somchai.won@kmutt.ac.th (S. Wongwises).

0894-1777/$ - see front matter © 2011 Elsevier Inc. All rights reserved.
doi:10.1016/j.expthermflusci.2011.09.002

Nomenclature

Bo	boiling number, $Bo = \frac{q''}{Gi_{lv}}$
C_c	coefficient of sudden contraction (−)
d_h	hydraulic diameter (m)
f	fanning friction factor (−)
G	mass flux (kg/(m^2 s))
i	enthalpy (kJ/kg)
k	thermal conductivity (W/(m K))
N	number of channel
P	pressure (kPa)
q''	heat flux (kW/m^2)
Re	Reynolds number, $Re = \frac{Gd}{\mu}$
v	specific volume (m^3/kg)
We	Weber number, $We = \frac{G^2 d}{\rho\sigma}$
X	Lockhart–Martinelli parameter (−)
x	vapor quality

Greek letters

α	void fraction
β	aspect ratio
$\frac{\Delta P}{\Delta z}$	pressure gradient (kPa/m)
μ	dynamic viscosity (Pa s)
ρ	density (kg/m^3)
σ	surface tension (N/m)
σ_c	the ratio of A_1/A_2 in sudden contraction equation (−)
σ_e	the ratio of A_1/A_2 in sudden expansion equation (−)
ϕ^2	two-phase frictional multiplier (−)

Subscripts

A	annular
a	acceleration
CB	coalescing bubble
$cont$	contraction
cr	critical
exp	expansion
f	friction
l	liquid
lo	all liquid
lv	liquid–vapor
v	vapor
vo	all vapor
IB	isolated bubble
in	inlet
out	outlet
tot	total
tp	two-phase

two-phase flow of R236ea, R134a, and R410A. They performed the wide range of the reduced pressure (varying from 0.1 up to 0.5). Their results showed that the frictional pressure drop of R410A gave the lowest values when comparison with those of R134a and R234ea at the same conditions. Moreover, the experimental results were used to compare with the existing correlations. The results showed that the frictional pressure drop of R134a supported the available correlations.

Nino et al. [7] proposed correlations based on a flow-regime for predicting the frictional pressure drop in the intermittent and annular flow regime. For the intermittent flow regime, the average kinetic energy of the mixture was used to develop the correlation based on the homogenous flow model. They found that the relation between the two-phase pressure drop and the average kinetic energy of the mixture is linear. For the annular flow regime, they developed the new separated flow model by using the correlation of Lockhart and Martinelli [8].

Mauro et al. [9] compared their experimental pressure drop data for different refrigerants (R22, R134a, R404A, R407C, R417A, and R507A) and different experimental conditions to the prediction method by using a general model. They found that the method by Quiben and Thome [10] was able to yield reliable predictions in the annular, intermittent, and dry-out flow regime, while the Gronnerud [5] method worked well up to the annular flow regime.

In 2008, Pamitran et al. [11] studied the two-phase pressure drop of CO_2 during vaporization in horizontal smooth minichannels. The test section was made of stainless steel tubes with inner diameters of 1.5 mm and 3.0 mm and lengths of 2000 and 3000 mm. The electric current was supplied to the test section directly in order to meet the uniform wall heat flux. They concluded that the pressure drop is higher for a smaller inner tube diameter, lower saturation temperature, and for higher mass flux and heat flux. They also showed that the two-phase pressure drop is a function of mass flux, inner diameter, surface tension, density and viscosity. Finally, the new correlation based on the Lockhart–Martinelli [8] method was presented.

Revellin and Haberschill [12] compared the experimental frictional pressure drop database for smooth tubes to four well-known correlations (Gronnerud [5], Friedel [2], Müller-Steinhagen and Heck [4], and Jung and Radermacher [13]) and the model proposed by Quibem and Thome [10]. They found that the Gronnerud [5] correlation and the model of Quiben and Thome [10] displayed the best prediction.

Kaew-On and Wongwises [14] experimentally studied the evaporation of 410A in three ports minichannels with a 3.48 mm hydraulic diameter. The experimental results indicated that the average heat transfer coefficient tended to increase with increasing average quality, mass flux, and heat flux. On the contrary, the heat transfer coefficient tended to decrease with increasing saturation temperature. Moreover, the pressure drop increased with increasing mass flux and decreased with an increased saturation temperature. The results also showed that the heat flux has no significant effect on the pressure drop. Finally, the correlations for predicting the heat transfer coefficient and frictional pressure drop were also proposed. The comparison of the frictional pressure drop of R134a and 410A in multiport are reported by the studied of Kaew-On and Wongwises [15]. They found that the frictional pressure drops of R410A were lower than those of R134a by approximately 30–50%.

In recently, Zhang et al. [16] proposed the new method to correlate the two-phase friction multiplier by applying the artificial neural network. They found that the newly developed correlations are extensively evaluated with a variety of data sets collected from the literature.

1.1. The existing correlations for predicting frictional pressure drop

The overview of two-phase frictional pressure drop correlations for both conventional channels and small channels are presented as follows:

1.2. Conventional channel correlations

The existing correlations for conventional channel are frequently seen in the open literature are follows:

1.2.1. Lockhart and Martinelli correlation [8]

For calculating the frictional pressure drop of two-phase flow, Martinelli and Nelson [17] and Lockhart and Martinelli [8] defined

key multipliers which are ratios of a two-phase to single-phase pressure drop. These two-phase multipliers, ϕ_l^2, ϕ_v^2, ϕ_{lo}^2 and ϕ_{vo}^2 are defined as follows:

$$\phi_l^2 = \frac{(dp_f/dz)_{tp}}{(dp_f/dz)_l}, \quad \phi_v^2 = \frac{(dp_f/dz)_{tp}}{(dp_f/dz)_v}, \\ \phi_{lo}^2 = \frac{(dp_f/dz)_{tp}}{(dp_f/dz)_{lo}}, \quad \phi_{vo}^2 = \frac{(dp_f/dz)_{tp}}{(dp_f/dz)_{vo}}. \tag{1}$$

The single-phase frictional pressure gradient, $(dp_f/dz)_l$, $(dp_f/dz)_v$, $(dp_f/dz)_{lo}$ and $(dp_f/dz)_{vo}$ are defined as:

$$(dp_f/dz)_l = \frac{2f_l(1-x)^2G^2}{d\rho_l}, \quad (dp_f/dz)_v = \frac{2f_v x^2 G^2}{d\rho_v}, \\ (dp_f/dz)_{lo} = \frac{2f_{lo}G^2}{d\rho_l}, \qquad (dp_f/dz)_{lo} = \frac{2f_{lo}G^2}{d\rho_l}. \tag{2}$$

Factors f_{lo} and f_{vo} are the fanning friction factors which assume that only liquid or only vapor is flowing alone at the same mass flux of the two-phase flow. Further, f_l and f_v are Fanning friction factors which assume that only liquid or only vapor is flowing alone at the same superficial velocity of the phase. Moreover, Lockhart and Martinelli [8] proposed the parameter to correlate their experimental results, well known as the Lockhart–Martinelli parameter.

$$X = \left(\frac{1-x}{x}\right)^{0.875}\left(\frac{\rho_v}{\rho_l}\right)^{0.5}\left(\frac{\mu_l}{\mu_v}\right)^{0.125}. \tag{3}$$

1.2.2. Chisholm correlation [18]

The two-phase multiplier is related to the Lockhart–Martinelli parameter through the Chisholm correlation [18], which is defined as:

$$\phi_l^2 = 1 + \frac{C}{X} + \frac{1}{X^2}, \tag{4}$$

where the value C depends on the flow regime of the liquid and vapor.

1.2.3. Friedel correlation [2]

One of the most widely used correlations for predicting the two-phase frictional pressure drop was suggested by Friedel [2]. He proposed correlation based on 25,000 data points. He correlated his experimental data with ϕ_{lo}^2 as a function of the Lockhart–Martinelli parameter, Froude number, Weber number, quality, friction factor, and physical properties.

$$\phi_{lo}^2 = E + \frac{3.24FX}{F_r^{0.045}We_l^{0.035}}, \tag{5}$$

where

$$F_r = \frac{G^2}{gd\rho_{tp}}, \quad F = x^{0.78}(1-x)^{0.224}, \quad We_l = \frac{G^2 d}{\sigma\rho_l}, \tag{6}$$

$$E = (1-x)^2 + x^2\frac{\rho_l f_{vo}}{\rho_v f_{lo}}. \tag{7}$$

1.2.4. Müller-Steinhagen and Heck correlation [4]

$$(dP_f/dz)_{tp} = F(1-x)^{1/3} + (dP_f/dz)_{lo}x^3, \tag{8}$$

where

$$F = (dP_f/dz)_{lo} + [(dP_f/dz)_{vo} - (dP_f/dz)_{lo}]. \tag{9}$$

1.3. Small channel correlations

There are many correlations for predicting the frictional pressure drop in a small channel. The following correlations for small channels were presented in extant literatures.

1.3.1. Mishima and Hibiki correlation [19]

Mishima and Hibiki [19] proposed the correlation based on the Lockhart–Martinelli correlation [8]. They modified the constant C as a function of hydraulic diameter, which is presented as follows:

$$C = 21(1 - e^{-319d_h}); \quad (d_h \text{ in mm}). \tag{10}$$

The constant C proposed by Mishima and Hibiki [19] was developed using the available air–water two-phase data, which was obtained in circular and rectangular channels with a hydraulic diameter of 1–4 mm.

1.3.2. Zhang and Webb correlation [1]

In 2000, Zhang and Webb [1] proposed the two-phase multiplier based only on liquid flow as a function of the refrigerant quality and reduced pressure.

$$\phi_{lo}^2 = (1-x)^2 + 2.87x^2\left(\frac{P}{P_{cr}}\right)^{-1} + 1.68x^{0.25}(1-x)^2\left(\frac{P}{P_{cr}}\right)^{-1.64}. \tag{11}$$

1.3.3. Lee and Mudawar correlation [20]

Lee and Mudawar [20] proposed two correlations for calculating the constant C values which depend on the flow regimes of liquid and vapor.

For laminar liquid and laminar vapor flows

$$C = 2.16Re_{lo}^{0.047}We_{lo}^{0.23}. \tag{12}$$

For laminar liquid and turbulent vapor flows

$$C = 1.45Re_{lo}^{0.25}We_{lo}^{0.23}. \tag{13}$$

1.3.4. Saisorn and Wongwises correlation [21]

Saisorn and Wongwises [21] developed the correlation for predicting the two-phase frictional multiplier according to their experimental data of adiabatic two-phase air–water flowing through 0.53 mm inner diameter. The correlation they presented is as follow:

$$\phi_l^2 = 1 + \frac{6.627}{X^{0.761}}. \tag{14}$$

1.3.5. Kaew-On and Wongwises correlation [14]

Recently, Kaew-On and Wongwises [14] proposed the correlation for predicting the frictional pressure drop as a function of constant C, which was defined as follows:

$$C = -3.356 + 41.863e^A + B, \tag{15}$$

where A and B were defined as

$$A = -69.475\beta f_l d_h, \tag{16}$$

$$B = 498\beta f_l d_h. \tag{17}$$

1.3.6. Zhang et al. correlation [16]

Zhang et al. [16] developed the correlations for predicting the pressure drop in minichannels and microchannels.

For an adiabatic liquid–vapor two-phase flow:

$$C = 21[1 - e^{(-0.674/Lo^*)}]. \tag{18}$$

For a diabatic liquid–gas two-phase flow:

$$C = 21[1 - e^{(-0.142/Lo^*)}], \tag{19}$$

where Lo^* is the non-dimensional Laplace constant, which is defined as

$$Lo^* = \left[\frac{\sigma}{g(\rho_l - \rho_v)}\right]^{0.5} / d_h. \tag{20}$$

They recommended that the application ranges of their correlation are as follows:

$0.014 \leqslant d_h \leqslant 6.25$ mm, $Re_l \leqslant 2000$ and $Re_g \leqslant 2000$.

As previously mentioned, it is clearly evident that some information is available on the boiling flow characteristics in minichannels and microchannels, especially which pertains to the single port channel. However, despite worthwhile applications in industrials, relatively little information is currently available on flow boiling characteristics in a multiport minichannel. As a consequence, this article, which is a continuation of our previous paper (Kaew-On et al. [22]), is aimed at determining the frictional pressure drop of refrigerant R134a during a flow boiling condition. The effects of the mass flux, heat flux, and saturation pressure on the frictional pressure drop are presented. Moreover, the comparisons of a frictional pressure drop at a different aspect ratio of the channel are also presented. In addition, the nine existing correlations for predicting frictional pressure drop are compared with the present data.

2. Experimental apparatus and method

The experimental apparatus is schematically presented in Fig. 1. The main components of the system are the test section, refrigerant flow loop, hot water flow loop, subcooling loop, and a data acquisition system.

As indicated by Fig. 1, which portrays the refrigerant circulating loop, liquid refrigerant is pumped by a gear pump with a regulated flow rate by means of an inverter. The refrigerant then passes in a series through a filter/dryer, refrigerant flow meter, pre-heater, and sight glass tube and enters the test section. The inlet quality before entering the test section is controlled by the pre-heater. The DC power supply is used to supply the imposed heat flux to the pre-heater, which can be controlled by adjusting the supply voltage and current. Leaving the test section, the refrigerant vapor then condenses in a subcooler and is later collected in a receiver; it eventually returns to the refrigerant pump to complete the cycle. Instrumentation is installed at various positions, as is also clearly shown in Fig. 1, to monitor the refrigerant state. All of the signals from the thermocouples and pressure transducer are recorded by a data logger.

The complete schematic diagram and the drawing of the test section are shown in Figs. 2 and 3, respectively. The heat exchanger was designed as the counter flow tube-in-tube heat exchanger with refrigerant flowing in the inner tube and heating water in the gap between the outer and inner tubes. Therefore, the supply heat fluxes from the heating water to the refrigerant are based on the outer surface area of the multiport minichannel test section. Two inner tubes were made from extruded multiport aluminium with the internal hydraulic diameter of 1.1 mm for 14 numbers of channels (tube No. 1) and 1.2 mm for eight numbers of channels (tube No. 2). The outer surface areas of two inner test sections are 5979 mm^2 and 6171 mm^2, while the inner surface areas are 13,545 mm^2 and 8856 mm^2 for tube No. 1 and tube No. 2, respectively. Additional details about the test sections are presented in Table 1. The outer tube of the heat exchanger was made from a circular acrylic tube with an internal hydraulic diameter of 25.4 mm. The test section is connected with a header at the inlet and outlet. T-type thermocouples are installed at the inlet and outlet on the side of header to measure the saturation temperature of the refrigerant. At the other side of the header, the differential pressure transducer is installed in order to measure the pressure drop across the test section. The accuracy of the differential pressure transducer is ±0.25% of the full scale or ±0.125 kPa. The water outside of the test section is insulated through the use of rubber foam with a thermal conductivity of 0.04 W/(mK). The refrigerant flow meter is a variable area type. The flow meter is specially calibrated in the range of 0.2–1.8 LPM for R134a by the manufacturer. The details of the test conditions and the uncertainties of measured quantities and calculated parameters are presented in Tables 2 and 3, respectively.

3. Data reduction

For all calculations, the thermophysical properties of the refrigerant are evaluated by using the REFPROP, Version 6.01 [23]. The

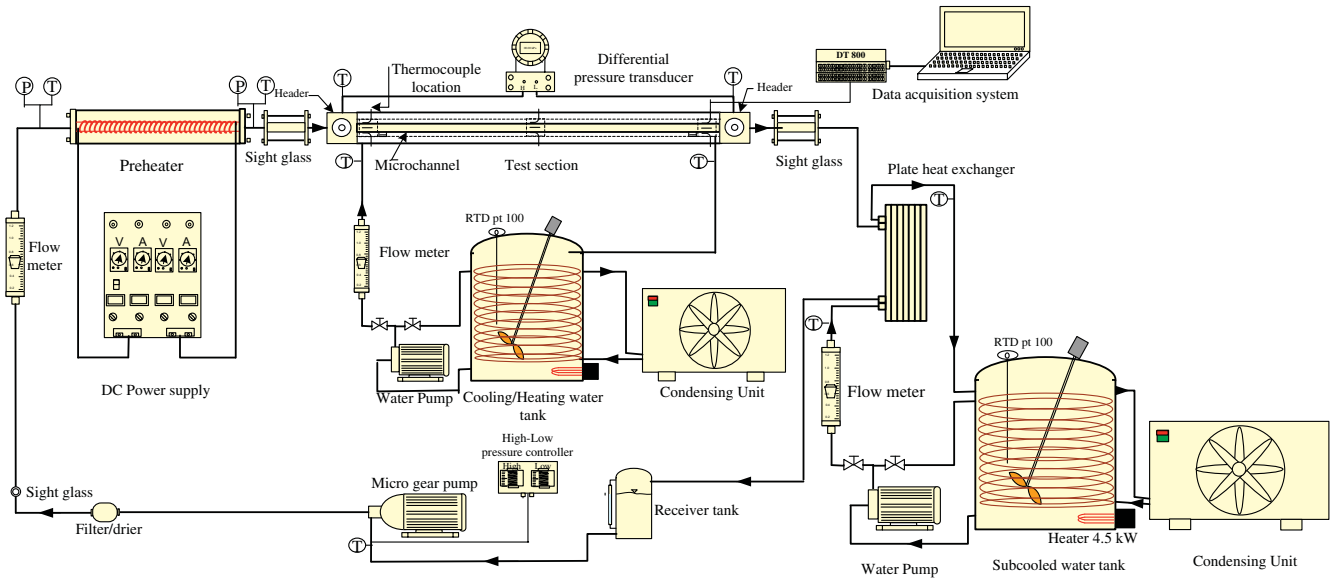

Fig. 1. Schematic diagrams of the experimental apparatus.

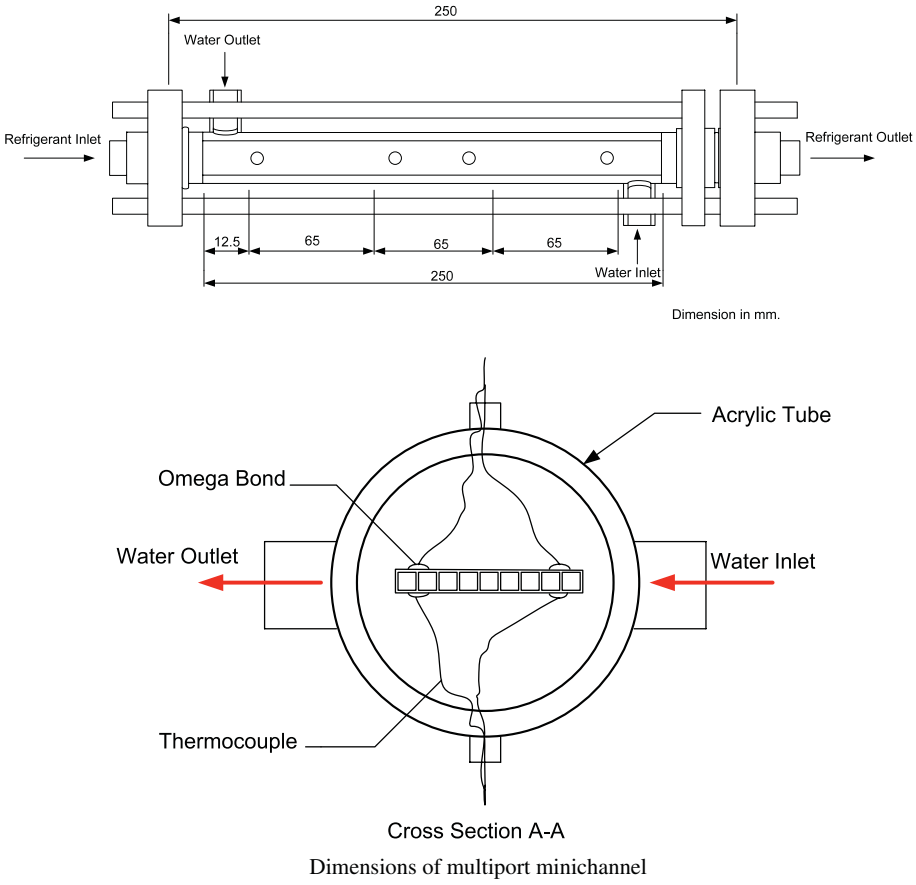

Fig. 2. Schematic diagram of the test section.

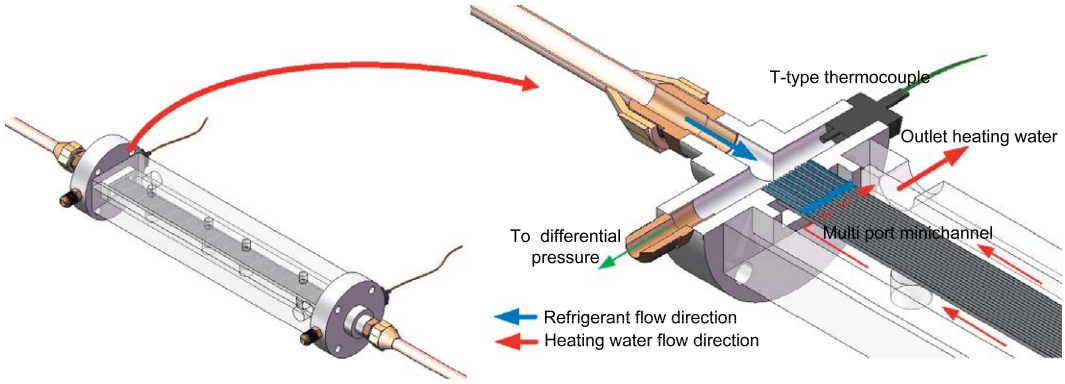

(a) Overall test section (b) Inlet manifold

Fig. 3. Illustration of the test section, (a) overall test section, and (b) inlet manifold.

Table 1
The details of test sections.

Test no.	Hydraulic diameter (mm)	Number of channel	Channel width (mm)	Channel height (mm)	Aspect ratio	Inner surface (mm^2)	Outer surface (mm^2)
1	1.1	14	1	1.25	1.25	13,545	5979
2	1.2	8	1.8	0.9	0.5	8856	6171

data reduction of the measured results is summarized in the following procedures.

The total boiling pressure drop was measured by the differential pressure transducer which was installed between the inlet and exit of the test section. The main components of the total pressure gradient are the frictional pressure gradient, the sudden contraction pressure gradient or the loss at the minichannels inlet, the sudden expansion pressure gradient and the acceleration or momentum

Table 2
Experimental conditions.

Refrigerant	R134a
Mass flux (kg/m^2 s)	350–980
Heat flux (kW/m^2)	18–80
Saturation pressure (bars)	4, 5, 6

Table 3
Uncertainties of measured quantities and calculated parameters.

Parameter	Uncertainty
Temperature	±0.1 °C
Differential pressure transducer	±0.25% of full scale
Mass flow rate of refrigerant	±0.1% of full scale
Heat transfer rate of pre-heater	±2.25%
Heat transfer rate of the test section	±8.5%
Vapor quality inlet	±3.25%
Vapor quality outlet	±9.00%

pressure gradient. Therefore, the total pressure gradient between the upstream and downstream portion of the test section can be expressed as follows:

$$(\Delta p/\Delta z)_{tot} = (\Delta p_f/\Delta z) + (\Delta p_{cont}/\Delta z) + (\Delta p_{\exp}/\Delta z) + (\Delta p_a/\Delta z). \tag{21}$$

The sudden contraction pressure gradient is calculated from the following correlation that Collier and Thome proposed [24].

$$(\Delta p_{cont}/\Delta z) = \frac{G^2 v_l}{2}\left[\left(\frac{1}{C_c}-1\right)^2 + \left(1-\frac{1}{\sigma_c^2}\right)^2\right]\left[1+\frac{v_{lv}x_{in}}{v_l}\right]. \tag{22}$$

Similarly, the sudden expansion pressure gradient is also determined from Collier and Thome [24], which is expressed as follows:

$$(\Delta P_{exp}/\Delta z) = G^2\sigma_e(1-\sigma_e)v_l\left[1+\frac{v_{lv}x_{out}}{v_l}\right]. \tag{23}$$

The acceleration or momentum pressure gradient is the loss due to the phase change which can be determined from following equation.

$$(\Delta p_a/\Delta z) = G^2\left\{\left[\frac{(1-x)^2}{\rho_l(1-\alpha)}+\frac{x^2}{\rho_v\alpha}\right]_{out} - \left[\frac{(1-x)^2}{\rho_l(1-\alpha)}+\frac{x^2}{\rho_v\alpha}\right]_{in}\right\}, \tag{24}$$

where the void fraction, α, can be calculated by the correlation of Zivi [25] as follows:

$$\alpha = \left[1+\frac{(1-x)}{x}\left(\frac{\rho_v}{\rho_l}\right)\right]^{-1}. \tag{25}$$

The frictional pressure gradient can be obtained through the Eqs. (22)–(26). The experimental frictional pressure gradient results are then compared with values predicted by the existing correlation for both the conventional channel correlations and small channel correlations.

4. Results and discussion

4.1. Flow patterns

The patterns of the refrigerant as it flows through the multiport minichannel are a very important parameter which influences the changing pressure drop. Therefore, an investigation into the flow patterns is necessary. Due to the visualized investigation of the flow patterns, additional instruments are needed and the material of the test section must be transparent. Therefore, this study cannot be performed through the observation of the flow pattern. However, the available existing flow regimes map the correlation in previous studies and can be used to estimate the flow patterns. In 2007, the two-phase flow pattern map for flow boiling in a micro-channel was developed by Revellin and Thome [26]. They proposed a flow regime map comprised of different zones according to the bubble coalescence phenomena. The following is a brief description of each zone located in the flow map.

The isolated bubble (IB) regime corresponds to a relatively high bubble generation rate in comparison to the bubble coalescence rate. Either or both of the bubbly flow and the slug flow are included in this regime. The coalescing bubble (CB) regime is defined when the bubble generation rate is smaller than the bubble coalescence rate.

The isolated bubble (IB) flow to coalescing bubble (CB) flow transition is given by

$$x_{IB/CB} = 0.763\left(\frac{Re_{lo}Bo}{We_{vo}}\right)^{0.41}, \tag{26}$$

where Bo stands for the boiling number, Re_{lo} represents the all-liquid Reynolds number, and We_{vo} is the all-vapor Weber number.

The transition from the coalescing bubble flow to the annular flow is determined by

$$x_{CB/A} = 0.00014Re_{lo}^{1.47}We_{lo}^{-1.23}. \tag{27}$$

where We_{vo} is the all-liquid Weber number.

Fig. 4 presents flow pattern maps in terms of mass flux and vapor quality which are compared with Revellin and Thome [26] transition zones. It was found that all of the present experimental data is located in the coalescence bubble (CB) or semi-annular zone.

Recently, a new update macro-to-micro scale flow pattern map was proposed by Ong and Thome [27]. They proposed new flow pattern transition lines as follows:

1. Isolated bubble/coalescing bubble (IB/CB)

$$x_{IB/CB} = 0.36Co^{0.20}\left(\frac{\mu_v}{\mu_l}\right)^{0.65}\left(\frac{\rho_v}{\rho_l}\right)^{0.9}Re_v^{0.75}Bo^{0.25}We_l^{-0.91}. \tag{28}$$

2. Coalescing bubble/annular (CB/A)

$$x_{CB/A} = 0.047Co^{0.05}\left(\frac{\mu_v}{\mu_l}\right)^{0.7}\left(\frac{\rho_v}{\rho_l}\right)^{0.6}Re_v^{0.8}We_l^{-0.91}. \tag{29}$$

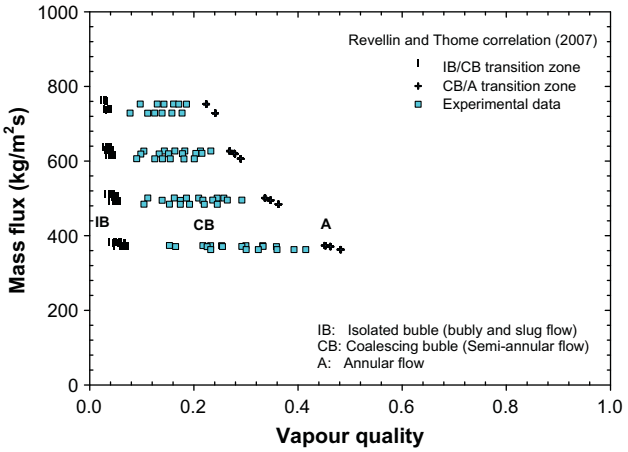

Fig. 4. The comparison of the experimental flow patterns with the transition lines by Revellin and Thome correlation [26].

3. Plug–slug/coalescing bubble (S–P/CB) if ($x_{S-P/CB} < x_{CB/A}$)

$$x_{S-P/CB} = 9(Co^{0.20})\left(\frac{\rho_v}{\rho_l}\right)^{0.9} Fr_l^{-1.2} Re_l^{0.1}. \quad (30)$$

4. Plug–slug/annular (S–P/A) if ($x_{S-P/CB} > x_{CB/A}$)

$$x_{S-P/A} = x_{CB/A}, \quad (31)$$

where Re_v, Re_l, Bo, We_l and Fr_l are respectively defined as:

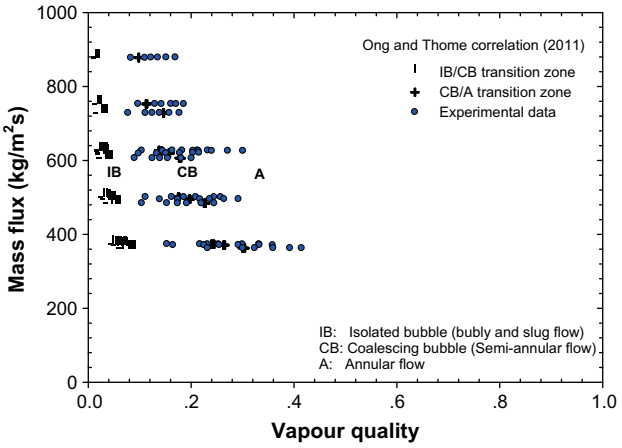

Fig. 5. The comparison of the experimental flow patterns with the transition lines by Ong and Thome correlation [27].

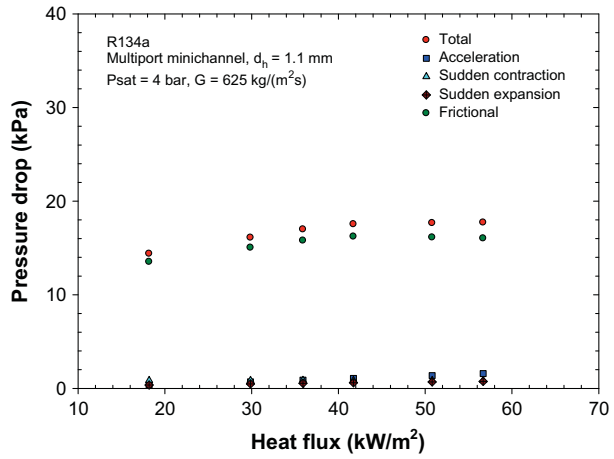

Fig. 6. The pressure drop components as a function of heat flux.

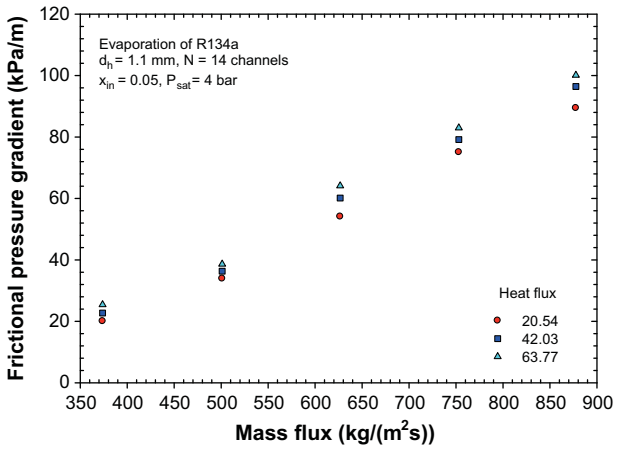

Fig. 7. The frictional pressure gradient as a function of mass flux for different levels of heat flux.

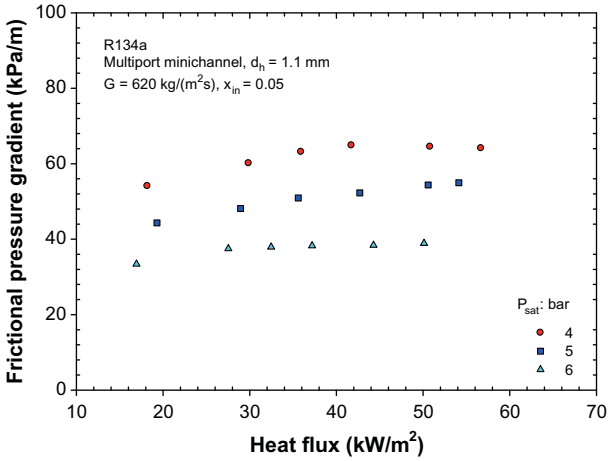

Fig. 8. The frictional pressure gradient as a function of heat flux for different levels of saturation pressure.

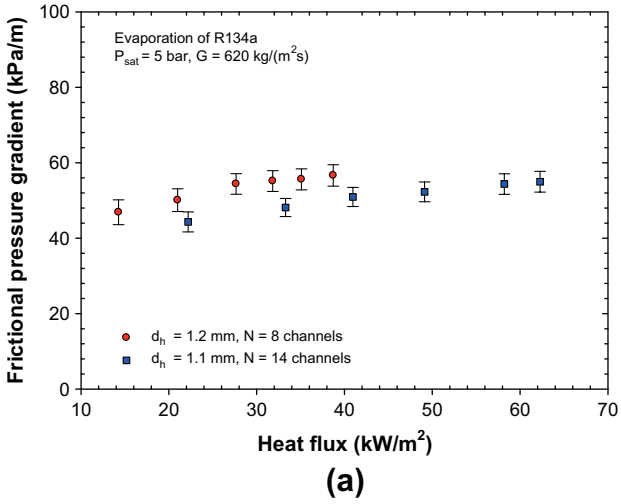

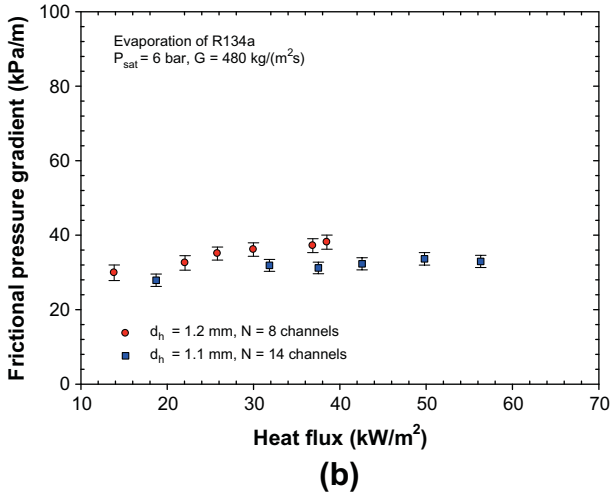

Fig. 9. Comparison the frictional pressure gradient as a function of heat flux for different numbers of channels.

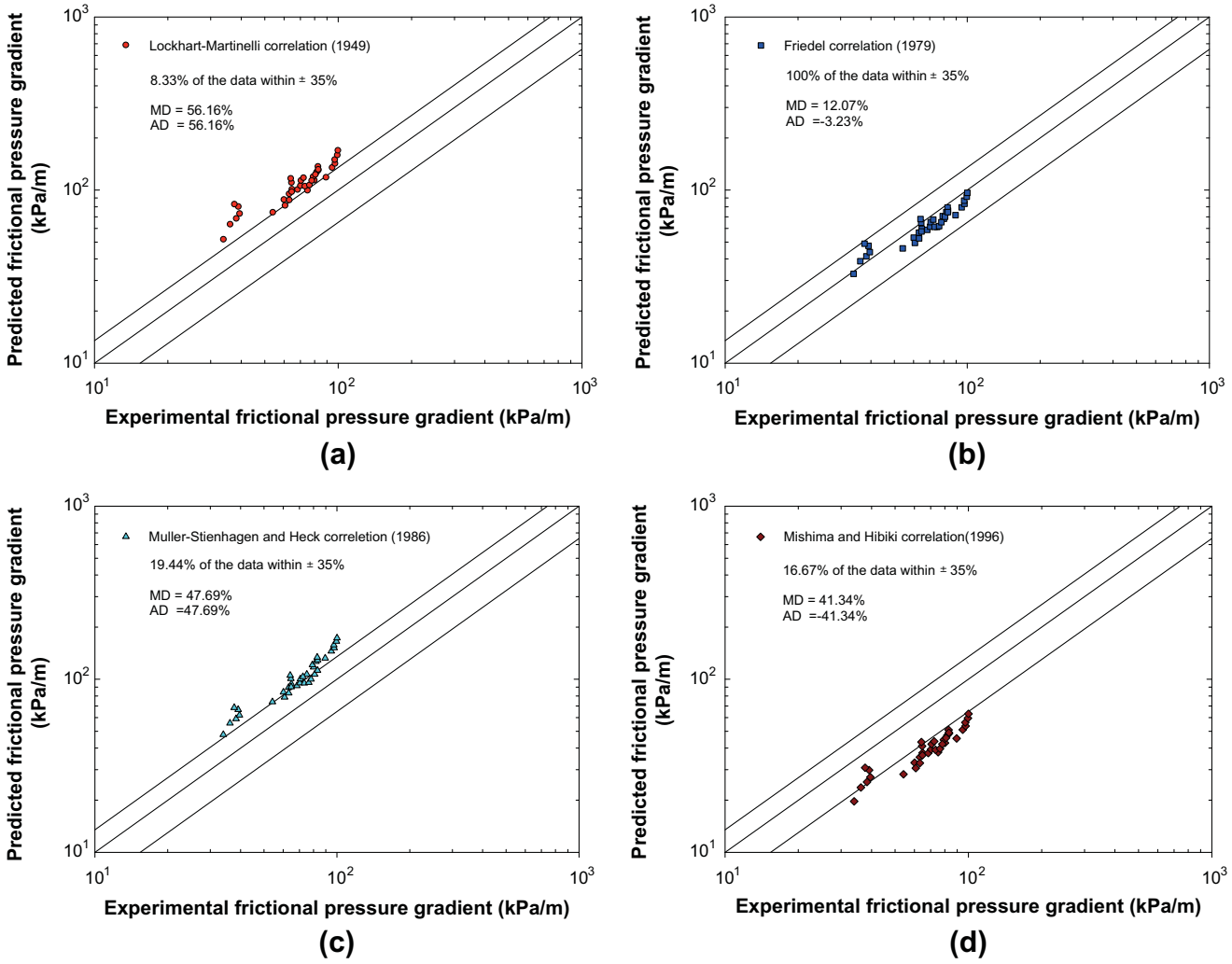

Fig. 10. Comparison of experimental pressure gradient with existing correlations proposed by (a) Lockhart–Martinelli [8], (b) Friedel [2] (c) Müller-Steinhagen and Heck [4], (d) Mishima and Hibiki [19], (e) Zhang and Webb [1], (f) Lee and Mudawar [20], (g) Saisorn and Wongwises [21], (h) Kaew-On and Wongwises [14] and (i) Zhang et al. [16].

$$Re_v = \frac{Gd_h}{\mu_v},\ Re_l = \frac{Gd_h}{\mu_l},\ Bo = \frac{q''}{Gh_{lv}},\ We_l = \frac{G^2 d_h}{\sigma\rho_l},\ Fr_l = \frac{G^2}{\rho_l^2 g d_h}.$$

From the comparison with the flow patterns map of Ong and Thome [27], as presented in Fig. 5, it is found that all experimental data are in all three transition zones (i.e., the isolated bubble zone, coalescing bubble zone, and annular flow zone). From the comparisons of the two flow pattern models, therefore, it can be concluded that the most experimental data in this study are semi-annular and annular flow patterns.

4.2. The pressure drop components

The total pressure drops are composed of the frictional pressure drop, the momentum pressure drop, the sudden contraction pressure drop, and the sudden expansion pressure drop. The components of the pressure drop with the variation of heat fluxes are presented in Fig. 6. The results were obtained at a mass flux of 625 kg/(m^2 s) and the saturation pressure was kept constant at 4 bar. The results show that the frictional pressure drop dominates all other pressure drop components which possess values ranging between 90% and 95% of the total pressure drop. The acceleration pressure drop that is attributed to the change of momentum is about 4–5% of the total pressure drop. In addition, the sudden contraction pressure drop and sudden expansion pressure drop are between 3–5% and 2–4% of the total pressure drop, respectively. This figure also shows that the frictional pressure drop slightly increases with an increase in the supposed heat flux. This is due to the increase of the heat fluxes, which causes the vapor-phase fraction and mean quality to increase. Therefore, the frictional pressure drop increases with an increasing heat flux.

4.3. Frictional pressure gradient

The variations of the frictional pressure gradient with mass flux are presented in Fig. 7. The experiment carried out by varying mass flux from 370 to 980 kg/(m^2 s) for various heat fluxes of 20.54, 42.03, and 63.77 kW/m^2 at a constant saturation pressure of 4 bar and inlet quality of 0.05. The results indicate that the frictional pressure gradient increase when the mass flux increases. This is due to higher shear stress at the tube wall and interfacial shear at the liquid–vapor interface. Moreover, this figure also illustrates that the pressure gradient slightly increases with an increasing heat flux. The increasing heat flux results in a higher vaporization and then leads to an increase in the average fluid vapor quality and flow velocity.

Fig. 8 presents the influence of saturation pressure on the frictional pressure gradient. At constant mass flux and heat flux, the

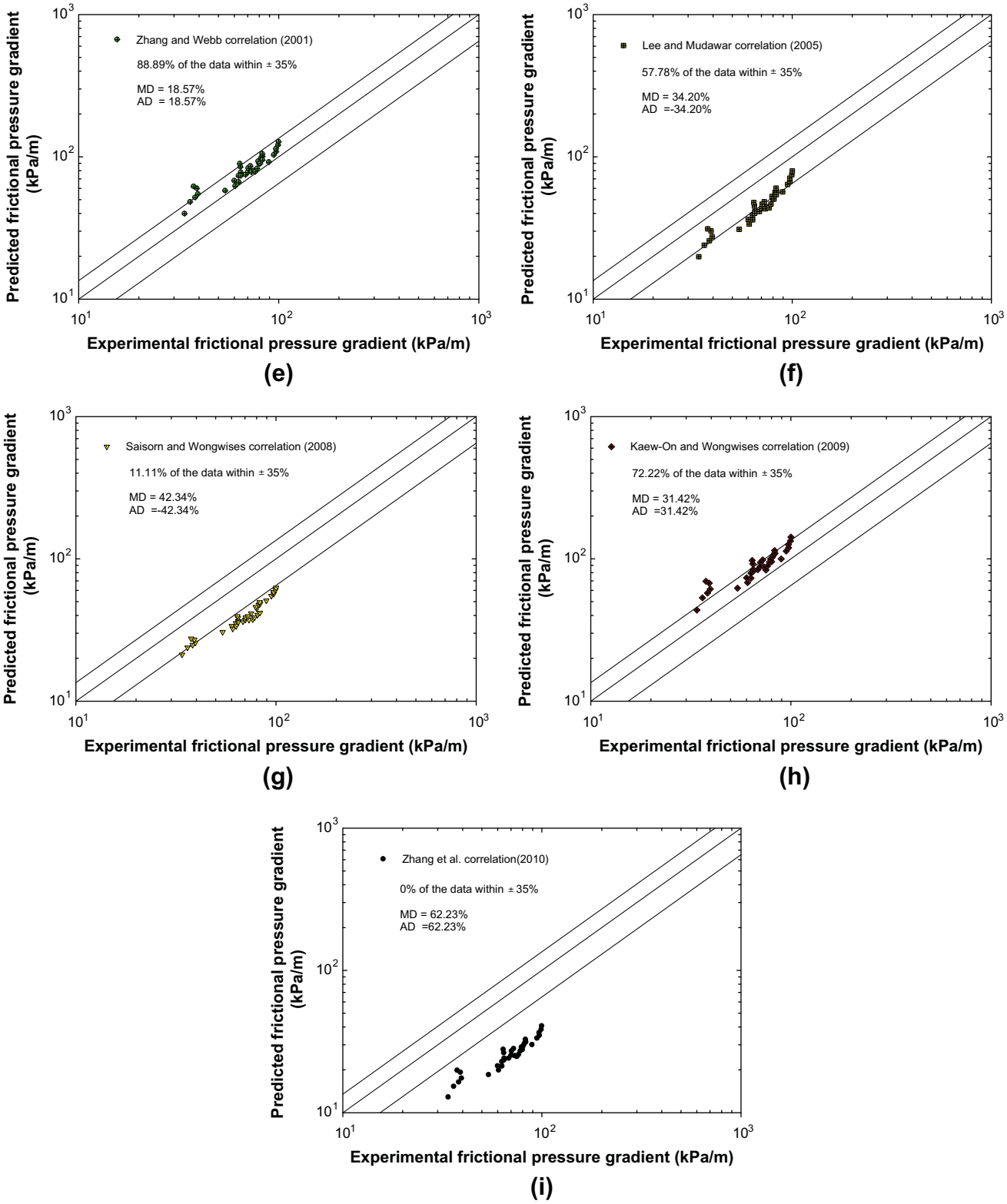

Fig. 10 (*continued*)

results indicate that the frictional pressure gradient increases with decreasing saturation pressure. This can be explained by the difference in the properties of the liquid and vapor phases. Considering that the saturation pressure decreased from 6 to 4 bar, it found that the viscosity ratio, μ_l/μ_v, increased from 17.73 to 21.81 (22.99%), similarity, the density ratio, ρ_l/ρ_{lv}, increase from 41.85 to 64.77 (54.76%). The increasing liquid density and liquid viscosity resulted in a lower liquid velocity, whereas the decreasing vapor density and vapor viscosity result in higher vapor velocity. Moreover, surface tension forces are more dominant at lower pressures, thus the interface between liquid and vapor is less wavy. At lower pressures, the pressure drop increases because of higher liquid

viscosity and an increase relative phase densities. The result is a higher interfacial shear. Therefore, the frictional pressure gradients increase when saturation pressure decreases.

4.4. Comparison results at two different inner tubes

Fig. 7 presents the comparison results that were obtained from the two heat exchangers that contain different inner tube geometries. Two inner tubes were made from extruded multiport aluminium with internal hydraulic diameters of 1.1 mm for 14 numbers of channels (tube No.1) and 1.2 mm for eight numbers of channels (tube No.2). Additional details about the test section are presented in Table. 1. As shown in Fig. 9, the results show that the frictional pressure drop of tube No. 1 is lower than that of tube No. 2 (i.e., approximately 15–20% for Fig. 9a and 10–15% for Fig. 9b). This finding can be explained by the different of geometries of the tubes that were tested. According to the details of the test section as shown in Table 1, although the two test sections are of a similar hydraulic diameter, but there are so different of the aspect ratio, 1.25 for tube No. 1 and 0.5 for tube No. 2. In their investigation, Akbari et al. [28] defined the term of the Poiseuille number, *fRe*, for the microchannel rectangular cross section as follows:

$$fRe = \frac{4\pi^2(1+\beta^2)}{3\sqrt{\beta}(1+\beta)}. \tag{32}$$

As the same mass flux condition, it can be seen from their correlation that the friction factor is only a function of the aspect ratio, β; that is, in support of the present experimental data, the friction factor increased when the aspect ratio decreased. The experimental result in Fig. 9a also reveals similar trends that emerged in Fig. 9b.

4.5. Comparison of experimental data with existing correlations

In this section, the frictional pressure drop obtained from the presented study is compared with the values predicted by both conventional and minichannel tubes. The nine well-known correlations, proposed by Lockhart–Martinelli [8], Friedel [2], Müller-Steinhagen and Heck[4], Mishima and Hibiki [19], Zhang and Webb [1], Lee and Mudawar [20], Saisorn and Wongwises [21], Kaew-On and Wongwises [14], and Zhang et al. [16] are compared to this author's experimental results. The results of the comparisons between the predicted and experimental frictional pressure gradient are presented in Fig. 10. The error band of ±35% is also presented by the solid lines in these figures. The mean and average deviations of the comparisons between the experimental data and predicted values are summarized in Table 4. For all of the comparisons, the Friedel correlation [2] predicted the current experimental data better than the other correlations (i.e., mean and average deviations of 12.07% and −3.23%, respectively). The correlations of Zhang and Webb [1] and Kaew-On and Wongwises [14] reasonably correlated to the current experimental data (i.e., 88.89% and 72.22% fell within ±35% of the error band, respectively). The correlations of Mishima and Hibiki [19], Lee and Mudawar [20], Saisorn and Wongwises [21], and Zhang et al. [16] are under-predicted, while the correlation of Lockhart–Martinelli [8] and Müller-Steinhagen and Heck [4] are over-predicted.

Table 4
Deviation of the frictional pressure gradient comparison between the present data and the existing correlations.

Correlation	Mean deviation %	Average deviation %
Lockhart–Martinelli [8]	56.16	56.16
Friedel [2]	12.07	−3.23
Muller-Stienhagen and Heck [4]	47.69	47.69
Mishima and Hibiki [19]	41.34	−41.34
Zhang and Webb [1]	18.57	18.57
Lee and Mudawar [20]	34.20	−34.20
Saisorn and Wongwises [21]	42.34	−42.34
Kaew-On and Wongwises [14]	31.42	31.42
Zhang et al. [16]	62.23	−62.23

5. Conclusions

This study presents the experimental investigations of the pressure drop of R134a flowing through the two multiport heat exchangers. The heat exchangers include the counter flow tube-in-tube heat exchangers. The experimental process has been applied for a wide range of experimental conditions: Mass fluxes from 350 to 980 kg/(m^2 s), heat fluxes from 18 to 80 kW/m^2, and saturation pressures from 4 to 6 bar. The major finding of this study are summarized as follows:

1. The results of Revelin and Thome [26] and Ong and Thome [27] are applied to determine the flow patterns of the present data. It was determined that most of the experimental data are located within semi-annular and annular flow patterns.
2. According to the total pressure drop components, the frictional pressure drop, acceleration pressure drop, sudden contraction pressure drop, and sudden expansion pressure drop are 90–95%, 4–10%, 3–5%, and 2–4% of the total pressure drop, respectively.
3. According to the effects of the relevant parameters on the frictional pressure drop, the mass flux has a more significant influence on the frictional pressure drop over the others, whereas the frictional pressure drop slightly increases with increasing heat flux. In addition, the frictional pressure drop decreases as the saturation pressure increase.
4. From the comparisons of the frictional pressure drop of two types of heat exchange inner tubes, it was found that the frictional pressure drops of tube No. 1 are lower than those of tube No. 2 (i.e., approximately 10–20%).
5. The Friedel correlation [2] provided the best predictions with the mean deviation of 12.07% and the average deviation of −3.23%, while the Zhang and Webb correlation [1] and Kaew-On and Wongwises correlation [14] satisfactorily predicted all of the data.

Acknowledgements

The present study was supported financially by the Thailand Research Fund, the Office of Higher Education Commission and the National Research University Project, whose guidance and assistance are gratefully acknowledged.

References

[1] M. Zhang, R.L. Webb, Correlation of two-phase friction for refrigerants in small-diameter tubes, Exp. Thermal Fluid Sci. 25 (2001) 131–139.
[2] L. Friedel, Improved frictional pressure drop correlation for horizontal and vertical two-phase flow, European two-phase flow group meeting, 1979.
[3] M.B. Ould Didi, N. Kattan, J.R. Thome, Prediction of two-phase pressure gradients of refrigerants in horizontal tubes, Int. J. Refrig. 25 (2002) 935–947.
[4] H. Müller-Steinhagen, K. Heck, A simple friction pressure drop correlation for two-phase flow in pipes, Chem. Eng. Process 20 (1986) 297–300.
[5] R. Gronnerud, Investigation of liquid hold-up, flow resistance and heat transfer in circulation type evaporators, part iv: two-phase flow resistance in boiling refrigerants, Bull de 1'Inst. Du Froid, 1979 (Annexe, 1972-1).
[6] A. Cavallini, D. Del Col, L. Doretti, M. Matkovic, L. Rossetto, C. Zilio, Two-phase frictional pressure gradient of R236ea, R134a and R410A, Exp. Thermal Fluid Sci. 29 (2005) 861–870.

[7] V.G. Nino, E.W. Jassim, P.S. Hrnjak, T.A. Newell, Flow-regime-based model for pressure drop predictions in microchannels, HVAC&R Research 12 (2005) 17–34.
[8] R.W. Lockhart, R.C. Martinelli, Proposed correlation of data for isothermal two-phase, Two-component flow in pipes, Chemical Engineering Progress 45 (1949) 39–48.
[9] A.W. Mauro, J.M. Quiben, J.R. Thome, Comparison of experimental pressure drop data for two phase flows to prediction methods using a general model, Int. J. Refrig. 30 (2007) 1358–1367.
[10] J.M. Quiben, J.R. Thome, Flow pattern based two-phase frictional pressure drop model for horizontal tubes, part II: new phenomenological model, Int. J. Heat fluid flow 28 (2007) 1060–1072.
[11] A.S. Pamitran, K.-I. Choi, J.-T. Oh, H.-K. Oh, Two-phase pressure drop during CO_2 vaporization in horizontal smooth minichannels, Int. J. Refrig. 31 (2008) 1375–1383.
[12] R. Revellin, P. Haberschill, Prediction of frictional pressure drop during flow boiling of refrigerants in horizontal tubes: Comparison to an experimental database, Int. J. Refrig. 32 (2009) 487–497.
[13] D.S. Jung, R. Radermacher, Prediction of pressure drop during horizontal annular flow boiling of pure and mixed refrigerants, Int. J. Heat Mass Transfer 32 (1989) 2435–2446.
[14] J. Kaew-On, S. Wongwises, Experimental investigation of evaporation heat transfer coefficient and pressure of R410A in multiport minichannel, Int. J. Refrig. 32 (2009) 124–137.
[15] J. Kaew-On, S. Wongwises, Experimental study of evaporation heat transfer characteristics and pressure drops of R410A and R134a in a multiport mini-channel, Proceedings of the 7th International Conference on Nanochannels, Microchannels and Minichannels 2009, ICNMM2009 (PART A), 581–588.
[16] M. Zhang, T. Hibiki, K. Mishima, Correlation of two-phase frictional pressure drop and void fraction in min-channel, Int. Heat and Mass Transfer 53 (2010) 453–465.
[17] R.C. Martinelli, D.B. Nelson, Prediction of pressure drop during forced circulation boiling of water, Trans. ASME 70 (1948) 695–702.
[18] D. Chisholm, Pressure gradients due to friction during the flow of evaporating two-phase mixtures in smooth tubes and channels, Int. Heat and Mass Transfer 16 (1973) 347–358.
[19] K. Mishima, T. Hibiki, Some characteristics of air-water two-phase flow in small diameter tube, J. Multiphase Flow 22 (1996) 703–712.
[20] J. Lee, I. Mudawar, Two-phase flow in high-heat-flux micro-channel heat sink for refrigeration cooling applications: Part I—pressure drop characteristics, Int. J. Heat Mass Transfer 48 (2005) 928–940.
[21] S. Saisorn, S. Wongwises, Flow pattern, void fraction and pressure drop of two-phase air–water flow in a horizontal circular micro-channel, Exp. Thermal Fluid Sci. 32 (2008) 748–760.
[22] J. Kaew-On, K. Sakamatapan, S. Wongwises, Flow Boiling Heat Transfer of R134a in the Multiport Minichannel Heat Exchangers, Exp. Thermal Fluid Sci. 35 (2011) 364–374.
[23] REFPROP, NIST, Refrigerant Properties Database 23, Gaithersburg, MD, 1998, Version 6.01.
[24] J.G. Collier, J.R. Thome, Convective boiling and condensation, 3rd ed., Oxford University Press, Oxford, U.K., 1994.
[25] S.M. Zivi, Estimation of steady-state steam void–fraction by mean of the principle of minimum entropy production, Trans. ASME, J. Heat Transfer 86 (1964) 247–252.
[26] R. Revellin, J.R. Thome, A new type of diabatic flow pattern map for boiling heat transfer in microchannels, J. Micromech. Microeng 17 (2007) 788–796.
[27] C.L. Ong, J. Thome, Macro-to-microchannel transition in two-phase flow: part 1 – two-phase flow patterns and film thickness measurements, Exp. Thermal Fluid Sci. 35 (2011) 37–47.
[28] M. Akbari, D. Sinton, M. Bahrami, Pressure drop in rectangular microchannels as compared with theory based on arbitrary cross section, J. Fluid Eng. 131 (2009) 1–8.

This article was downloaded by: [Mr Sujoy K. Saha]
On: 18 November 2011, At: 08:10
Publisher: Taylor & Francis
Informa Ltd Registered in England and Wales Registered Number: 1072954 Registered office: Mortimer House, 37-41 Mortimer Street, London W1T 3JH, UK

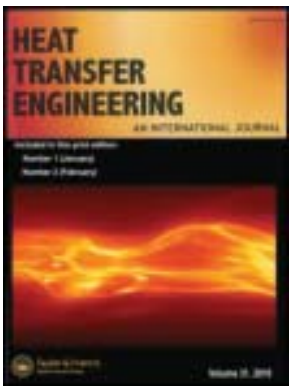

Heat Transfer Engineering
Publication details, including instructions for authors and subscription information:
http://www.tandfonline.com/loi/uhte20

Selected Papers on Advances in Heat Transfer

Sujoy K. Saha [a] , Gian P. Celata [b] & Somchai Wongwises [c]

[a] Mechanical Engineering Department, Bengal Engineering and Science University, West Bengal, India

[b] ENEA, Energy Department, Institute of Thermal Fluid Dynamics, Rome, Italy

[c] Department of Mechanical Engineering, King Mongkut's University of Technology Thonburi, Bangmod, Bangkok, Thailand

Available online: 18 Nov 2011

To cite this article: Sujoy K. Saha, Gian P. Celata & Somchai Wongwises (2012): Selected Papers on Advances in Heat Transfer, Heat Transfer Engineering, 33:4-5, 281-283

To link to this article: http://dx.doi.org/10.1080/01457632.2012.614157

PLEASE SCROLL DOWN FOR ARTICLE

Full terms and conditions of use: http://www.tandfonline.com/page/terms-and-conditions

This article may be used for research, teaching, and private study purposes. Any substantial or systematic reproduction, redistribution, reselling, loan, sub-licensing, systematic supply, or distribution in any form to anyone is expressly forbidden.

The publisher does not give any warranty express or implied or make any representation that the contents will be complete or accurate or up to date. The accuracy of any instructions, formulae, and drug doses should be independently verified with primary sources. The publisher shall not be liable for any loss, actions, claims, proceedings, demand, or costs or damages whatsoever or howsoever caused arising directly or indirectly in connection with or arising out of the use of this material.

Heat Transfer Engineering, 33(4–5):281–283, 2012
Copyright © Taylor and Francis Group, LLC
ISSN: 0145-7632 print / 1521-0537 online
DOI: 10.1080/01457632.2012.614157

Taylor & Francis
Taylor & Francis Group

Downloaded by [Mr Sujoy K. Saha] at 08:10 18 November 2011

editorial

Selected Papers on Advances in Heat Transfer

SUJOY K. SAHA,[1] GIAN P. CELATA,[2] and SOMCHAI WONGWISES[3]

[1]Mechanical Engineering Department, Bengal Engineering and Science University, West Bengal, India
[2]ENEA, Energy Department, Institute of Thermal Fluid Dynamics, Rome, Italy
[3]Department of Mechanical Engineering, King Mongkut's University of Technology Thonburi, Bangmod, Bangkok, Thailand

Advancement of technology in virtually all fields, in one way or another, has been due to simultaneous advances in thermal engineering. Design objectives of space stations, hazardous-waste destruction, high-speed transport, electronics, materials processing and manufacturing, etc. are fulfilled by proper energy management, heat-flow control, and temperature control.

The scale of thermal engineering ranges from the very large to the near-molecular level and from very high temperatures of thousands of degrees to very low ones approaching absolute zero. Thermal energy transport occurs in every walk of human existence.

In the recent past and of course with the passage of time, tremendous progress has been made in the field of thermal science and engineering. It is a continuous process and the quest of knowledge is truly unending.

In this special issue of the journal, an attempt has been made to collate some scattered knowledge in the advances in heat transfer. Leading international heat transfer experts from the diverse fields of heat transfer have contributed in this special issue. It should be useful to the readers of the journal. This special issue is a compendium of the following 10 papers.

- The first paper is "Thermal Design of Multistream Plate Fin Heat Exchangers—A State-of-the-Art Review" by Prasanta Kumar Das and Indranil Ghosh:

Address correspondence to Professor Sujoy K. Saha, Mechanical Engineering Department, Bengal Engineering and Science University, Shibpur, Howrah 711 103, West Bengal, India. E-mail: sujoy_k_saha@hotmail.com

Multistream plate fin heat exchangers are useful and important innovations in the design of heat exchangers. These heat exchangers encounter direct/indirect crossover in temperatures due to several thermal communications among the fluid streams, and their thermal performance depends on "stacking pattern." Extension of the commonly used design/simulation techniques like ε-NTU or the LMTD method, applicable for two-stream heat exchangers, fails miserably in case of multistream units. Though several techniques have been suggested over the years, the "thermal design" method of multistream plate fin heat exchangers is far from being perfect even today.

A state-of-the-art review of the thermal design of multistream plate fin heat exchangers is presented by the authors. Different methods of analysis including "area splitting" and "successive partitioning" along with their merits and demerits are discussed. Basic thermal design methodology and its optimization, the techniques adopted for accounting variable fluid properties, axial heat conduction in the solid matrix, and thermal communication with the environment are discussed. Need for further research is emphasized.

- The second paper is "Dropwise Condensation Studies on Multiple Scales" by Basant Singh Sikarwar, Sameer Khandekar, Smita Agarwal, Sumeet Kumar, and K. Murlidhar:

New surfaces are being engineered by nanotechnology, chemical texturing technologies, thin film coatings, and physical texturing using advanced manufacturing techniques. Dropwise condensation rather than film condensation occurs on those special surfaces. Superior experimental techniques are now available to study the thermo-fluid dynamics of dropwise condensation. Phenomena at different hierarchical length

scales, e.g., surface modification at the microscale, nuclei formation, formation of clusters, macroscopic droplet ensemble, and drop coalescence, are involved. Atomistic modeling of initial nucleation, droplet–substrate interaction, surface preparation, preliminary results on simulation of fluid motion inside sliding drops, experimental determination of the local and average heat transfer coefficient, and a macroscopic model of the complete dropwise condensation process underneath horizontal and inclined surfaces are discussed.

- The third paper is "Modified Wilson Plots for Enhanced Heat Transfer Experiments: Current Status and Future Perspectives" by E. van Rooyen, M. Christians, and J. R. Thome:

Performance of enhanced heat transfer tubes is evaluated indirectly using the "Wilson plot" method to first characterize the thermal performance of one side (heating or cooling supply) and then obtaining the heat transfer data for the enhanced side based on the Wilson plot results. Wilson plot evolution and alternative methods to the Wilson plot including the advantages and disadvantages are discussed. The existing method has been modified so that the experimental errors can be propagated through the method and the error in the generated correlations may be estimated. A new method based on unconstrained minimization is proposed as an alternative to the least-squares regression.

- The fourth paper is "A State-of-the-Art Review of Compact Vapor Compression Refrigeration Systems and Their Applications" by Jader R. Barbosa, Jr., Guilherme B. Ribeiro, and Pablo A. de Oliveira:

Literature on the fundamentals, design, and application aspects of compact and miniature mechanical vapor compression refrigeration systems has been critically reviewed. Vapor compression enables the attainment of low evaporating temperatures while maintaining a large cooling capacity per unit power input to the system. Miniaturization of system components, particularly the compressor, has been the significant development. When compared with competing cooling technologies, such as flow boiling in microchannels, jet impingement and spray cooling refrigeration is the only one capable of lowering the junction temperature to values below the ambient temperature. The simultaneous use of vapor compression refrigeration with the aforementioned technologies is also possible, necessary, and beneficial, since it increases greatly the potential for reducing the system size. The paper sheds some light on the thermodynamic and thermal aspects of the cooling cycle and on the recent developments regarding its components (compressor, heat exchangers and expansion device). Issues and challenges associated with the different cycle designs have been addressed. An overview of the ongoing efforts in competing technologies is also presented.

- The fifth paper is "Modeling of Evaporation and Combustion of Droplets in a Spray Using the Unit Cell Approach: A Review" by Achintya Mukhopadhyay and Dipankar Sanyal:

Modeling of evaporation and combustion of liquid fuel droplets using "unit cell" approach has been reviewed extensively. Different regimes of droplet combustion and other techniques used for evaluating mutual interaction of droplets are discussed first, followed by the detailed presentation of the cell model. Gas-phase convection, high pressure, and multicomponent composition of fuels are reviewed for both dense and dilute sprays.

- The sixth paper is "Loop Heat Pipes: A Review of Fundamentals, Operation, and Design" by Amrit Ambirajan, Abhijit A. Adoni, Jasvanth S. Vaidya, Anand A. Rajendran, Dinesh Kumar, and Pradip Dutta:

The loop heat pipe (LHP) is a passive two-phase heat transport device. LHPs are used in spacecraft thermal control system and in avionics cooling and submarines. A major advantage of a loop heat pipe is that that the porous wick structure is confined to the evaporator section, and connection between the evaporator and condenser sections is by smooth tubes, thus minimizing pressure drop. Basic fundamentals, construction details, operating principles, typical operating characteristics, and current developments in modeling of thermohydraulics and design methodologies of LHPs are discussed.

- The seventh paper is "Augmentation of Heat Transfer by Creation of Streamwise Longitudinal Vortices Using Vortex Generators" by Gautam Biswas, Himadri Chattopadhyay, and Anupam Sinha:

A state-of-the-art review of improving heat exchanger surfaces using streamwise longitudinal vortices is presented. Fin-tube cross-flow heat exchangers and the plate-fin heat exchangers are focused on. Protrusions in certain forms such as delta wing or winglet pairs and rectangular winglet pairs act as vortex generators, creating longitudinal vortices, disrupting growth of the thermal boundary layer, and promoting mixing between fluid layers, resulting in enhanced heat transfer from the flat or louvered surfaces. The flow fields are dominated by a swirling motion associated with a modest pressure penalty. Both computational and experimental investigations on flow and heat transfer in the heat exchanger passages with built-in vortex generators are reviewed.

- The eighth paper is "Frictional and Heat Transfer Characteristics of Single-Phase Microchannel Liquid Flows" by Ranabir Dey, Tamal Das, and Suman Chakraborty:

The literature on friction and heat transfer characteristics of single-phase liquid flows through microchannels has been reviewed. The disagreement of experimental results with theoretical predictions has been brought to the fore. Theoretical models and empirical correlations are highlighted. Aspects of microscale liquid flow and heat transfer requiring further scrutiny are identified and possible future research directions are prescribed.

Downloaded by [Mr Sujoy K. Saha] at 08:10 18 November 2011

- The ninth paper is "Recent Trends in Computation of Turbulent Jet Impingement Heat Transfer" by Anupam Dewan, Rabijit Dutta, and Balaji Srinivasan:

> A review of the current status of computation of turbulent impinging jet heat transfer has been made. Flow and heat transfer characteristics of single jet impingement on a flat surface are considered. The effect of different sub-grid scale models, boundary conditions, numerical schemes, grid distribution, and size of the computational domain adopted in various large eddy simulations of this flow configuration is dealt with in detail. Direct numerical simulation and Reynolds-averaged Navier–Stokes modeling of the same geometry are discussed. Other complex impinging flows are also presented. A listing of some important findings and future directions in the computation of impinging flows is presented.

- The tenth paper is "Two-Phase Natural Circulation Loops: A Review of the Recent Advances" by Souvik Bhattacharyya, Dipankar N. Basu, and Prasanta K. Das:

> Experimental and theoretical studies of two-phase natural circulation loops abound in the literature. A comprehensive review has been made by the authors. Different forms of thermal-hydraulic instabilities and coupled nuclear instabilities are discussed. Further research direction is delineated.

We thank the authors for their contributions, and the reviewers, who have played a great role in improving the quality of the papers. We also thank the editor-in-chief of *Heat Transfer Engineering*, Professor Afshin Ghajar, for his willingness to publish this special issue highlighting the current research going on worldwide.

Sujoy K. Saha is a professor of mechanical engineering at Bengal Engineering and Science University Shibpur, India. He specializes in heat transfer enhancement, heat transfer in microchannels, biomimetics, and circulating fluidized bed. Prof. Saha is an associate editor of *ASME Journal of Heat Transfer*, editor of *Experimental Thermal and Fluid Science*, associate editor of *Heat Transfer Engineering*, regional editor of the *Journal of Enhanced Heat Transfer,* and guest editor of *Frontiers of Heat and Mass Transfer*. Prof. Saha has published about 60 articles in international and national peer-reviewed journals and conferences.

Gian P. Celata is director of the Division of Advanced Technologies for Energy and Industry of ENEA, Italy. He is a member of the European Academy of Sciences, of several scientific boards in Italy (UIT, past-President, ANIMP, AIDIC), and also of international scientific boards (EUROTHERM, past president, AIHTC, AWC, vice-president, ICHMT, Executive Committee). Dr. Celata is also the editor-in-chief of the *Journal of Experimental Thermal and Fluid Science* and associate editor of the *International Journal of Thermal Sciences*. He is also the editor of *Thermopedia and Heat Exchangers Design Handbook*. His areas of expertise are heat transfer and two-phase flow, CHEx, microscale heat transfer, bubbly flow, two-phase critical flow, and CHF. He has about 200 articles in international journals and international conferences, and one patent, and is the editor of many scientific books.

Somchai Wongwises is a professor of mechanical engineering at King Mongkut's University of Technology Thonburi, Bangmod, Thailand. He received his Dr.-Ing. (Doktor Ingenieur) in mechanical engineering from the University of Hannover, Germany, in 1994. His research interests include two-phase flow, heat transfer enhancement, and thermal system design. Professor Wongwises is the head of the Fluid Mechanics, Thermal Engineering and Multiphase Flow Research Laboratory (FUTURE).

Downloaded by [Mr Sujoy K. Saha] at 08:10 18 November 2011

INTERNATIONAL JOURNAL OF REFRIGERATION 35 (2012) 27–35

Available online at www.sciencedirect.com

SciVerse ScienceDirect

journal homepage: www.elsevier.com/locate/ijrefrig

Review

Review on the experimental studies of refrigerant flow mechanisms inside short-tube orifices

Kitti Nilpueng [a], Somchai Wongwises [a,b,*]

[a] Fluid Mechanics, Thermal Engineering and Multiphase Flow Research Lab (FUTURE), Department of Mechanical Engineering, King Mongkut's University of Technology Thonburi, Bangmod, Bangkok 10140, Thailand

[b] The Academy of Science, The Royal Institute of Thailand, Sanam Suea Pa, Dusit, Bangkok 10300, Thailand

ARTICLE INFO

Article history:
Received 24 May 2011
Received in revised form
7 September 2011
Accepted 24 September 2011
Available online 2 October 2011

Keywords:
Expansion valve
Flow rate
Critical pressure
Temperature variation

ABSTRACT

A short-tube orifice is a kind of an expansion device. The advantages of a short-tube orifice are simplicity, low cost, and low starting torque of the compressor as the pressures across the short-tube orifice equalise during the off-cycle. The two-phase flow mechanisms of refrigerant inside the short-tube orifice are very complicated although its physical configurations are simple. During the past decade, investigations of the mass flow rate of various refrigerants inside short-tube orifices, which is useful for selecting the proper size in practical applications, have been reported by many researchers. However, few researchers focused on the flow pattern, choked flow, and metastable flow phenomena inside short-tube orifices, which are necessary for a clear understanding of the flow behaviour and developing suitable calculation techniques. The aim of this paper is to summarise the evolution of the experimental research on refrigerant flow characteristics inside short-tube orifices to provide guidelines for future research.

© 2011 Elsevier Ltd and IIR. All rights reserved.

Passage en revue des études expérimentales sur les mécanismes du débit du frigorigène dans les orifices de tubes courts

Mots clés : détendeur ; débit ; pression critique ; variation de température

1. Introduction

An expansion device is one of the four important components of the vapour compression refrigeration system. The main purposes of the expansion device are to reduce the pressure of the refrigerant from the condenser pressure to the evaporator pressure and to regulate the mass flow rate of refrigerant flowing from the condenser to the evaporator at a rate equal to

* *Corresponding author*. Fluid Mechanics, Thermal Engineering and Multiphase Flow Research Lab (FUTURE), Department of Mechanical Engineering, King Mongkut's University of Technology Thonburi, Bangmod, Bangkok 10140, Thailand. Tel.: +662 470 9115; fax: +662 470 9111.
E-mail address: somchai.won@kmutt.ac.th (S. Wongwises).

0140-7007/$ – see front matter © 2011 Elsevier Ltd and IIR. All rights reserved.
doi:10.1016/j.ijrefrig.2011.09.011

Nomenclature

D	diameter, m
f	fanning friction factor
G	mass flux, kg m^{-2} s^{-1}
P_v	actual vapourisation pressure, Pa
P_{inlet}	inlet pressure, Pa
P_c	critical pressure, Pa
z_m	length of short-tube orifice in metastable region, mm

Greek symbols

ρ	density, kg m^{-3}
v	specific volume, m^3 kg^{-1}
μ	viscosity, kg m^{-1} s^{-1}

Subscripts

c	critical
f	liquid-phase
g	gas-phase

the evaporation rate in the evaporator. During the flow of liquid refrigerant through the expansion device, the pressure decreases rapidly below the saturation pressure and the refrigerant is changed from a subcooled liquid or saturated liquid to a liquid–vapour mixture. This behaviour is defined as a flashing process.

Basically, there are two types of expansion devices: the variable-restriction type and the constant-restriction type. In the former, the flow area can be varied depending on the control system, such as automatic expansion valve or thermostatic expansion valve. In the latter, the flow area of the expansion device, for example, a capillary tube, ejector, or short-tube orifice, is fixed.

In recent years, the short-tube orifice has been popularly used as an expansion device in residential and automotive air conditioners. The short-tube orifices used in small residential air conditioners are made from extremely small bore hollow brass ingots with lengths of 10–13 mm and L/D = 3–20, while the diameter and L/D of short-tube orifices for automotive applications are 1–2 mm and 21–35, respectively (Fang, 2001). The advantages of the short-tube orifice over the thermostatic expansion valve are simplicity, low initial cost, and low starting torque of the compressor, as the pressures across the short-tube orifice equalise during the off-cycle.

Although the short-tube orifice's physical configuration is very simple, the two-phase flow behaviours inside the tube are complicated. Experimental results from previous studies (Aaron and Domanski, 1990; Kim, 1993; Liu et al., 2004; Nilpueng and Wongwises, 2009a) indicated that the choked flow and metastable flow phenomena existed inside a short-tube orifice under the normal operating conditions of an air conditioner and heat pump. As a result, the refrigerant flow characteristics inside a short-tube orifice not only depended on the working conditions, but were also significantly affected by these flow phenomena.

The aim of this paper is to review the literature on the refrigerant flow characteristics including flow pattern, pressure and temperature distribution, metastable flow, choked flow, and mass flow rate inside short-tube orifices and to suggest guidelines for future research work.

2. Flow pattern

During the flashing process, the flow of liquid refrigerant changes from a subcooled liquid or saturated liquid to a liquid–vapour two-phase flow. It is not possible to understand the refrigerant flow mechanism without a clear understanding of the flow patterns encountered, as it is expected that the flow patterns will influence the two-phase pressure drop, holdup, system stability, exchange rates of momentum, and heat and mass transfer during the phase change. Therefore, investigation of the flow pattern inside the channel is very useful.

Pasqua (1953) studied the flow behaviour of subcooled and saturated liquid CFC-12 through glass short tubes with length to diameter ratios ranging between 4 and 24. He found four distinct flow patterns when the pressure differential between upstream and downstream was increased as shown in Fig. 1. At a very low pressure differential (Regime AB), the flow of refrigerant remained in the liquid state at the entrance and exit of the short-tube orifice. It was also observed that the vena contracta appeared inside the short-tube orifice. When the pressure differential was increased (Regime BC), the liquid refrigerant started to evaporate between the vena contracta and the solid wall because the refrigerant pressure reached the saturation pressure. The flow pattern was in the form of a liquid jet encircled by a ring of two-phase mixture as the pressure differential was higher (Regime CD). He noted that the refrigerant at the central core of the tube was in a metastable state. At a high pressure differential (Regime DE), it was seen that the liquid refrigerant at the vena contracta changed into the mist jet of a two-phase mixture. He stated that the liquid refrigerant began to flash inside the short-tube orifice when the downstream pressure was approximately at or below the saturation pressure. In addition, he concluded that the metastable liquid diameter decreased as the fluids proceeded to the exit. According to Pasqua's results, it may be concluded that the flow pattern in regimes CD and DE appeared in the short-tube orifice when the downstream pressure used in the common air conditioner was lower than the saturation pressure.

The flow pattern of saturated and nearly saturated water flowing through a short-tube orifice with a ratio of length to diameter less than 6 was also observed by Zaloudek (1963). He reported that the results were similar to the photograph obtained by Pasqua (1953).

Fauske (1965) and Henry (1970) investigated the flow pattern of subcooled and saturated liquid inside sharp-edged short-tube orifices with different length to diameter ratios. They found that three flow patterns appeared inside the short-tube orifice when the length to diameter ratio was varied (Fig. 2). For L/D < 3, a superheated liquid commonly flowed at the central core of the tube in the form of a free streamline jet and was surrounded by a vapour annulus. For the short-tube orifice with 3 < L/D < 12, the liquid jet at the

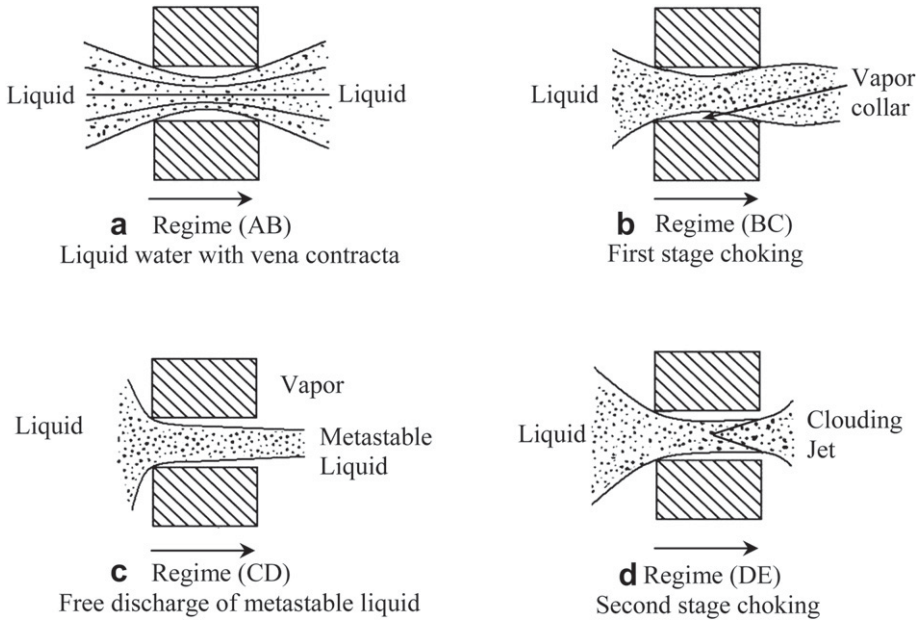

Fig. 1 – Flow patterns inside the short-tube orifice (Pasqua, 1953).

exit region of the tube was broken and changed into bubbles at the surface of the jet. When the length to diameter ratio was higher than 12,it was found that the flow pattern was divided into two regions: a superheated liquid jet flow region and a dispersed two-phase flow region. In the superheated liquid jet flow region, a liquid jet flowed at the central core of the tube and was surrounded by a vapour annulus. In the dispersed two-phase flow region, the mixture of the two-phase flow covered the entire cross-sectional flow area.

Aaron and Domanski (1990) observed the flow pattern of subcooled liquid HCFC-22 at the inlet and outlet of short-tube orifices with $5 < L/D < 20$. In order to fix a brass short-tube orifice with a glass short-tube and prevent refrigerant leakage, the perimeter of the brass short-tube orifice was tightened by a rubber o-ring. The results indicated that the refrigerant existed in the liquid state at the inlet and outlet of short-tube orifices even though the downstream pressure reached saturation pressure. They explained that under this condition, the two-phase mixture recondensed into liquid refrigerant inside the tube. However, under the normal downstream pressure of an air conditioner, the microscopic bubbles suspended in the liquid covered the short-tube orifice outlet in a homogeneous form over several inches.

The flow behaviours of HCFC-22 and HFC-134a along the short-tube orifice were visually investigated by Kim (1993). In order to observe the refrigerant flow at the entrance region, exit region, and inside the short-tube orifice, a glass short-tube orifice was connected with two glass tubes using frame solder. The glass short-tube orifice was attached to a copper tube using a Swagelok connector and Teflon ferrule to prevent leakage of the refrigerant. The results obtained from HFC-134a showed that the metastable liquid core which was enclosed by the two-phase mixture appeared inside the short-tube orifice when subcooled liquid entered the short-tube orifice. It was also found that the flashing point of refrigerant moved to the inlet section as the degree of subcooling decreased. In the case of a two-phase flow entering the short-tube orifice, bubbly flow and stratified wavy flow occurred at low inlet quality ($x < 4\%$) and high inlet quality ($x > 4\%$), respectively. Considering the effect of oil concentration on the flow pattern at a high degree of subcooling ($\Delta T_{sub} > 8.3\ ^{\circ}C$), the flashing point of refrigerant moved slightly to the exit region as the oil concentration increased. They stated that the variations in flow pattern of HCFC-22 and HFC-134a inside the short-tube orifice were similar.

Nilpueng and Wongwises (2009a) and Nilpueng and Wongwises (2009b) investigated the flow pattern of HFC-134a inside short-tube orifices under general operating conditions. Glass tubes without flame solder were specially designed to ensure that the entrance and exit of the short-tube orifice were sharp-edged. In order to prevent leakage of the refrigerant, the glass short-tube orifice and the glass tube were fitted into an acrylic tube and rubber o-rings were inserted between the glass tubes. The flow pattern of refrigerant inside the short-tube orifice was registered by a digital camera with a shutter speed of 1/2000 s mounted together with a 20X magnification lens. The flow pattern of refrigerant inside the short-tube orifice was divided into two regions: the metastable liquid flow region and the two-phase flow region (Fig. 3). From the images in this study, the light (white) area represented the liquid refrigerant flow while the dark (black) area represented the two-phase refrigerant flow of liquid and vapour. In the metastable liquid flow region, the liquid refrigerant, which had the appearance of a cone shape, flowed in the central core of the tube while the two-phase flow, which had many tiny bubbles mixed in the liquid refrigerant, covered the liquid refrigerant. In the two-phase flow region, there were many tiny bubbles mixed with the liquid refrigerant so that it looked misty. They reported that the length of metastable liquid flow increased when the upstream pressure

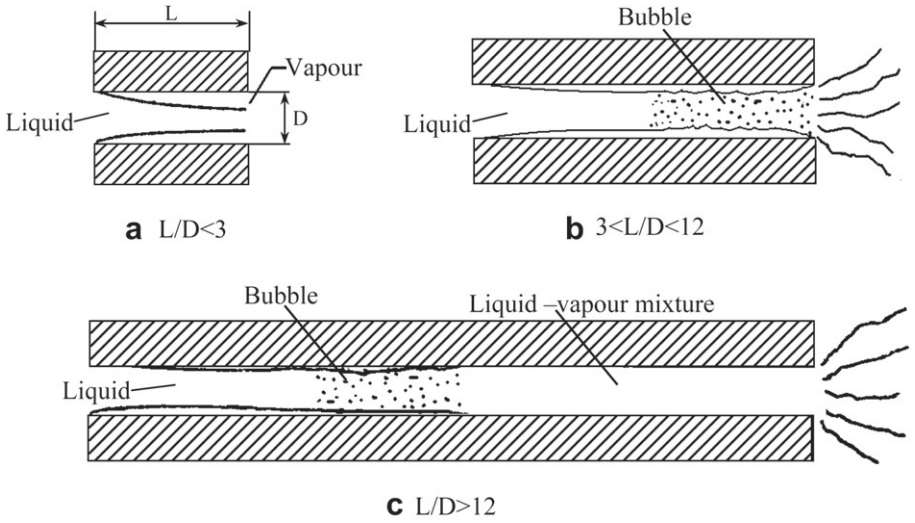

Fig. 2 – Flow patterns of saturated or subcooled liquid through sharp-edge orifices at different ratio of length to diameter (Fauske, 1965; Henry, 1970).

and degree of subcooling were increased. In addition, it was also found from Fig. 4 that at length-to-diameter ratios ranging between 1.87 and 33 the metastable liquid flow inside the short-tube orifice was divided into three different forms: metastable liquid core flow ($L/D < 2.91$), conical metastable liquid core flow ($2.91 \leq L/D < 24.9$), and full metastable liquid flow ($L/D \geq 24.9$).

3. Pressure and temperature distribution

One of the purposes of a refrigerant expansion device is to reduce the refrigerant pressure from the condenser pressure to the evaporator pressure, which also results in a temperature drop. Over the years, pressure and temperature distributions inside short-tube orifices have been studied and published by some researchers (Aaron and Domanski, 1990; Kim, 1993; Liu et al., 2004; Nilpueng and Wongwises, 2009a,b; Chen et al., 2004).

The pressure distribution of HCFC-22 through a short-tube orifice with $L = 12.7$ mm and $D = 1.35$ mm was presented by Aaron and Domanski (1990). Six pressure taps having diameters of 0.08 mm were drilled along the tube length. Pressure transducers with an accuracy of ±0.15% were used to measure the pressure distribution.

Kim (1993) investigated the pressure distribution inside three short-tube orifices: (1) $L = 12.83$ mm and $D = 1.33$ mm, (2) $L = 25.35$ mm and $D = 1.34$ mm, and (3) $L = 12.69$ mm and $D = 1.63$ mm. HCFC-22 and HFC-134a were used as working fluids. Five or six pressure taps with diameter of 0.2 mm were drilled along the length of the short-tube.

The pressure and temperature distributions of carbon dioxide in a short-tube orifice with $D = 1.35$ mm and $L = 12.92$ mm were studied by Liu et al. (2004) and Chen et al. (2004). In order to decrease the effect of taps on the measurement of refrigerant flow rate, low pressure and low temperature taps ($D = 0.1$ mm) were bored by laser equipment. The difference in mass flow rate in cases before and after perforation was measured. It was discovered that the deviation in measurement was ±1.5%.

Nilpueng and Wongwises (2009a) and Nilpueng and Wongwises (2009b) observed the pressure and temperature distribution of HFC-134a inside short-tube orifice. A short-tube orifice diameter of 0.961 mm and lengths of 10 mm, 15 mm, and 20 mm were used in the experiment. Along the short-tube length, six pressure and temperature taps were bored to 0.2 mm using a wire cutting machine. Based on the results obtained from the above researchers, it was found that the pressure distribution along the short-tube orifice could be divided into three regions: inlet section, constant cross-section, and

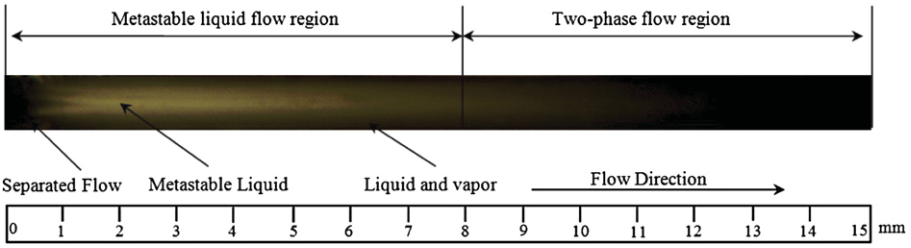

Fig. 3 – Flow pattern of HFC-134a inside a short-tube orifice (Nilpueng and Wongwises, 2009a).

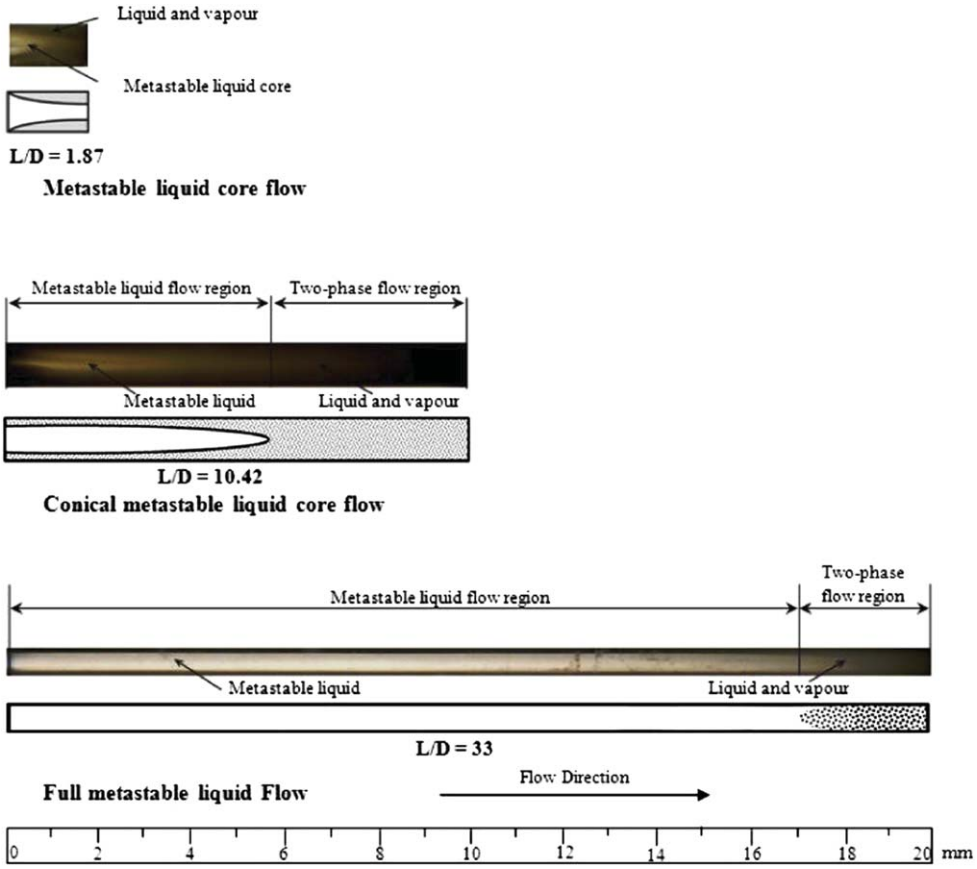

Fig. 4 – Effect of length-to-diameter ratio of short-tube orifice on flow pattern inside a short-tube orifice (Nilpueng and Wongwises, 2009b).

outlet section. The typical pressure and temperature distribution of HFC-134a along a short-tube orifice is illustrated in Fig. 5. It was clear that the pressure decreased rapidly at the inlet and outlet sections, while the pressure decreased slightly inside the constant cross-section under the normal working conditions of the air conditioner (P_{down} = 300–400 kPa). The reason for the enormous pressure drop at the inlet section was explained by the rapid change in acceleration and the loss of flow due to sudden contraction. That is, the upstream pressure was suddenly converted into kinetic energy and the pressure loss was produced due to an inertial effect and wall shear stress at the inlet section. With a constant cross-section, the pressure of HCFC-22 and HFC-134a increased slightly and then decreased steadily inside the constant cross-section. The reason for this was explained by the slight increase in the refrigerant flow area at the beginning of the constant cross-section and the shear stress between the refrigerant and tube wall along the constant cross-section, respectively. They also concluded that the vena contracta appeared at the beginning of the constant cross-section (Aaron and Domanski, 1990; Kim, 1993; Nilpueng and Wongwises, 2009a,b).

However, for carbon dioxide, the refrigerant pressure along the constant cross-section gradually decreased. That is, the increase in pressure at the beginning of the constant cross-section did not appear (Liu et al., 2004; Chen et al., 2004). When considering the pressure variation at the outlet section, it was found that the pressure decreased greatly. This implied that the flow behaviour of the refrigerant was not in agreement with the incompressible fluid flow theory but was similar to compressible flow through a converging nozzle when the velocity in the exit plane reached sonic speed. Under this condition, they stated that the pressure decreased discontinuously from the exit plane to the downstream pressure value. This behaviour was defined as the choked flow phenomenon. Conversely, the refrigerant flow behaviour agreed with incompressible flow when the downstream pressure was higher than the saturation pressure.

Considering the change in temperature inside the short-tube orifice, it was discovered that the temperature distribution was related to the pressure distribution. This means that the temperature decreased rapidly at the inlet and outlet sections, while it decreased slightly inside the constant cross-section. This was because the refrigerant pressure was lower than the saturation pressure corresponding to the upstream pressure when refrigerant passed the inlet plane. Therefore, refrigerant temperature varied directly with refrigerant pressure (Nilpueng and Wongwises, 2009a,b).

4. Metastable flow

During the refrigerant flow through the expansion device, the liquid refrigerant changes into a liquid–vapour mixture. Under thermodynamic equilibrium, the refrigerant inside the

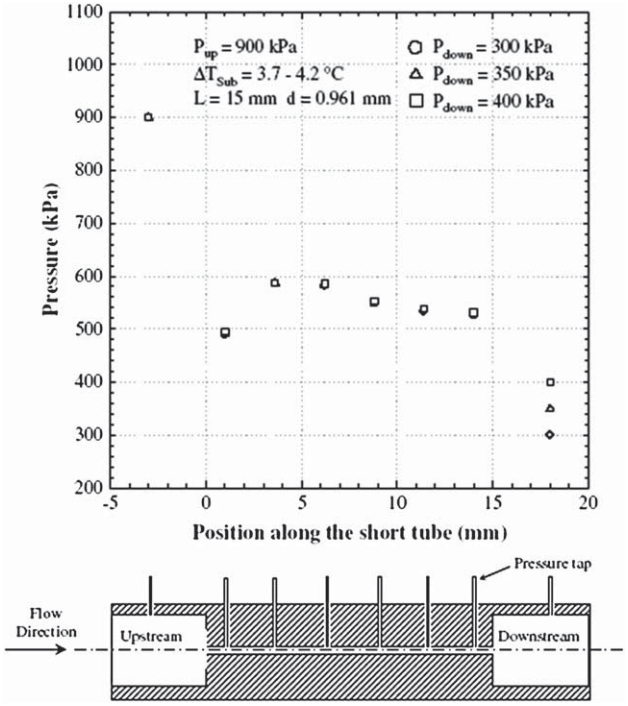

Fig. 5 – Pressure profile along short-tube orifice with L = 15 mm and D = 0.961 mm (Nilpueng and Wongwises, 2009a).

short-tube orifice was evaporated under the saturated condition. However, previous studies of metastable flow inside short-tube orifices have been discussed and reported by some publications.

Pasqua (1953) explored the appearance of metastable flow of CFC-12 inside a short-tube orifice. The photograph of the flow pattern showed that although the pressure was lower than the saturation pressure, the flow of liquid refrigerant was in the form of a liquid core along the tube length. His results implied that the metastable flow phenomenon existed inside the short-tube orifice. This phenomenon was consistent with the results of water flow through short-tube orifices observed by past researches (Fauske, 1965; Henry, 1970; Baily, 1951). He concluded that the flow rate increased in the metastable liquid core flow compared with the flashing flow of refrigerant inside the tube.

The existence of metastable flow of HCFC-22 inside a short-tube orifice was reported by Kim (1993) and Kim and O'Neal (1994). The relationship between the pressure distribution and visual studies along the short-tube orifice was used to identify the metastable flow. Their results showed that the refrigerant pressure was lower than the saturation pressure corresponding to the upstream temperature when it passed the inlet section. However, the visual studies indicated that the refrigerant remained in a liquid state. They noted that the flashing of refrigerant inside the short-tube orifice was delayed. In order to develop a mathematical model for calculating the mass flow rate inside the short-tube orifice, the location of inception of vapourisation was presented in terms of a single-phase frictional pressure drop as follows.

$$z_m = \frac{2D\rho_f(P_v - P_{inlet})}{fG^2} \quad (1)$$

where

$$\frac{P_v - P_{inlet}}{P_c} = 0.000693\left(\frac{GD}{\mu_f}\right)^{3.1146} - 0.3165\left(\frac{v_g}{v_g - v_f} - 1.0469\right) \quad (2)$$

$$f = 1.7649\left(\frac{GD}{\mu_f}\right)^{-0.1685} \quad (3)$$

Where z_m is the fraction of the short-tube length in the metastable region (mm), D is the short-tube orifice diameter (mm), P_v is actual vapourisation pressure (kPa), P_{inlet} is inlet pressure (kPa), P_c is critical pressure (kPa), f is the fanning friction factor, G is mass flux (kg m^{-2} s^{-1}), ρ_f is liquid density (kg m^{-3}), μ_f is liquid dynamic viscosity (kg m^{-1} s^{-1}), v_f is liquid specific volume (m^3 kg^{-1}), and v_g is vapour specific volume (m^3 kg^{-1}).

Nilpueng and Wongwises (2009a) and Nilpueng and Wongwises (2009b) observed the metastable flow of HFC-134a inside short-tube orifices. The existence of metastable flow inside the short-tube orifice was verified by considering the relation of flow pattern, pressure distribution, and temperature distribution. The results showed similar behaviour to that found by previous researchers. That is, the refrigerant remained in the liquid state although the pressure was lower than saturation pressure. The metastable liquid which flowed at the central core of the tube in a cone shape existed inside the short-tube orifice under the general operating conditions of the air conditioner. They stated that with the same short-tube orifice size, the mass flow rate increased as the metastable liquid flow region increased. Moreover, it was also reported that metastable two-phase flow occurred inside the short-tube orifice.

5. Choked flow

Choked flow is a limiting condition which occurs inside a short-tube orifice when the velocity of refrigerant is increased to sonic velocity. Under this condition, the flow of refrigerant through the short-tube orifice corresponds to the critical flow rate, which is the maximum flow rate that can be attained by reducing the downstream pressure under given upstream conditions.

In order to use a short-tube orifice as an expanding device in an air-conditioning system, it is found that the flow of refrigerant should be choked flow to achieve an appropriate distribution of refrigerant under working conditions. This is because under non-choked flow, the refrigerant mass flow rate which is discharged to the evaporator is reduced when the evaporator pressure or cooling load of the system increases, but is increased as the evaporator pressure or cooling load of the system decreases. This flow behaviour is inappropriate for air-conditioning systems. Therefore, to achieve proper performance and reliability, the short-tube orifice should be insensitive to the downstream pressure.

Over the years, the choked flow phenomenon inside short-tube orifices has been investigated and carried out by

a number of researchers. Baily (1951) investigated the occurrence of choked flow of saturated and nearly saturated water through a short tube with $5 < L/D < 20$. In the experiment, the upstream pressure was kept at atmospheric pressure, while the downstream pressure was varied by using a vacuum pump. The flow behaviour was divided into three regions as shown in Fig. 6.In regime AB, the flow rate increased approximately as a function of the square root of the pressure differential across the short-tube orifice. He reported that the instability of the flow appeared near point B before the curve AB moved to curve CD. However, the relationships between the mass flow rate and the pressure differential across the short-tube orifice of the two curves were similar. Beyond this point, the mass flow rate remained constant although the pressure differential was augmented. Therefore, he concluded that critical flow or choked flow occurred in the region DE.

The choked flow phenomenon of water through a short-tube orifice with $L/D < 6$ was studied by Zaloudek (1963). He stated that his results showed the same behaviour as those obtained by Baily (1951). However, the instability between curve AB and curve CD did not appear, but the mass flow rate in this region remained constant as shown by a dotted line. This flow phenomenon was named as the first-stage critical flow. It was also discovered that the same flow behaviour occurred in the region DE. He stated that this flow phenomenon was established at the end of the tube when the downstream pressure was below the saturation pressure, and termed it the second-stage critical flow.

Mei (1982) explored the choked flow phenomenon of HCFC-22 along a short-tube orifice with $7 < L/D < 12$. The results within the normal heat pump operating range indicated that first-stage choking appeared at a degree of subcooling ranging between 19.4 and 22.2 °C, but the second-stage choking disappeared inside the short-tube orifice. Therefore, under any operating condition, the refrigerant flow rate through the short-tube orifice was related to the square root of the pressure differential.

An investigation of the choked flow of HCFC-22 inside a short-tube orifice with $5 < L/D < 12$ was reported by Aaron and Domanski (1990). The experiment was run at upstream pressures ranging from 1448 to 2006 kPa, downstream pressures ranging from 345 to 827 kPa, and degrees of subcooling ranging from 5.6 to 13.9 °C, which were the normal working conditions of the heat pump. The results showed that the mass flow rate was insensitive to the downstream pressure

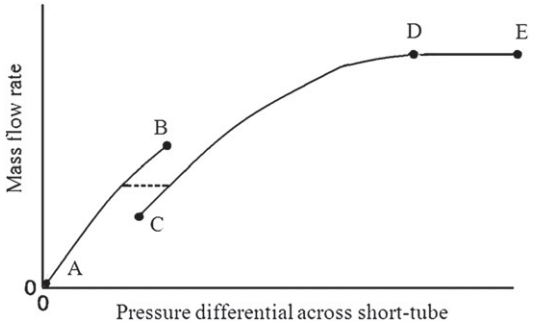

Fig. 6 – Relationship between mass flow rate and pressure differential across short-tube orifice (Baily, 1951).

when the downstream pressure was reduced below saturation pressure. They noted that the tendency of the mass flow rate was similar to curve CDE presented by Baily (1951). However, the flow rate was found to increase by about 3–8% with the downstream pressure. Therefore, the flow behaviour was defined as non-ideal choked flow. They concluded that non-ideal choked flow appeared inside the short-tube orifice used in the heat pump because the evaporator pressure under working conditions was lower than the saturation pressure. In addition, under these conditions, it was noted that the pressure drop in the exit region was large.

Kim (1993) and Kim and O'Neal (1994) observed the existence of choked flow of two-phase HCFC-22 flowing through short-tube orifices. The experiment was performed at upstream pressures ranging from 1448 to 2006 kPa, qualities ranging from 0 to 10%, and degrees of subcooling ranging from 0 to 13.9 °C. The effect of downstream pressure on the relevant parameter, including the flow rate change, pressure distribution change, and flow pattern change, was used to identify the choked flow phenomenon. The results indicated that the mass flow rate depended on the downstream pressure when the pressure was above the saturation pressure. Conversely, when the downstream pressure was below the saturation pressure, the mass flow rate changed slightly. It was also found that the pressure drop at the exit region decreased greatly when the downstream pressure was lower than the saturation pressure. Under this condition, they concluded that the refrigerant flow was choked.

The choked flow of HFC-134a inside short-tube orifices was studied by Kim (1993), Nilpueng and Wongwises (2009a,b). The change in mass flow rate, pressure distribution, and flow pattern with downstream pressure was used to confirm the appearance of choked flow. The results demonstrated that the mass flow rate, pressure distribution, and length of metastable liquid flow inside the short-tube orifice were affected very little by the change in downstream pressure. This flow behaviour agreed well with the theory of compressible flow through a converging nozzle. Therefore, they concluded that there was a choked flow phenomenon in HFC-134a flow through a short-tube orifice. However, Nilpueng and Wongwises (2009b) reported that choked flow appeared inside a short-tube orifice with $L/D > 2.91$ but disappeared with $L/D < 2.91$.

In addition, the existence of choked flow of other refrigerants such as HFC-407C, HFC-410A, and carbon dioxide was confirmed by Payne and O'Neal (1998), Payne and O'Neal (1999) and Kim et al. (2005). According to all the experimental results obtained from previous publications, it was indicated that the mass flow rate was very little affected by the change in downstream pressure. Therefore, they concluded that choked flow appeared inside short-tube orifices under the normal operating conditions of an air conditioner and heat pump. This was because the liquid refrigerant suddenly changed to a liquid and vapour mixture. As a result, the refrigerant velocity accelerated until it reached sonic velocity at the exit plane of the short-tube orifice. Moreover, it was obvious that the inception of choked flow occurred when the downstream pressure was nearly at saturation pressure. Nonetheless, the investigation of HFC-134a flowing through micro-orifices with diameters of 31.0 and 52.0 μm showed different flow

behaviours. That is, the flow was not choked even though the downstream pressure was reduced to more than 400 kPa below the saturation pressure. They recorded that the refrigerant cannot flash in a micro-tube when the downstream pressure is equal to saturation pressure. The reason for this was attributed to the strengthening of the metastable effect in a micro-tube (Tu et al., 2006).

6. Mass flow rate

As mentioned earlier, although the refrigerant mass flow rate is insensitive to downstream pressure under the choked flow condition, it depends on the relevant parameters, for example upstream pressure, degree of subcooling, upstream quality, short-tube orifice length, short-tube orifice diameter, and inlet and outlet chamfering. The data of mass flow rate obtained from the experiments are directly useful for selecting the proper short-tube orifice size in air conditioners. Therefore, the impacts of the operating conditions and short-tube orifice dimensions on the refrigerant mass flow rate are studied and presented in most published researches.

Early experimental investigations of refrigerant flow inside short-tube orifices focused exclusively on CFC-12 and HCFC-22. Kim et al. (1994) investigated the flow rate of CFC-12 through short-tube orifices with $5 < L/D < 20$. They reported that the mass flow rate was greatly affected by the upstream condition. The refrigerant mass flow rate was augmented when the degree of subcooling increased and reduced when the upstream quality increased. Also, changes in the short-tube orifice diameter resulted in large changes in mass flow rate. However, the effect of diameter on the flow rate was lower when the two-phase flow entered the short-tube orifice.

The influence of relevant parameters on the mass flow rate of HCFC-22 was explored by Mei (1982), Aaron and Domanski (1990), Kuehl and Goldschmidt (1992), Kim (1993), and Kim and O'Neal (1994). It was found that the mass flow rate was directly proportional to the cross-sectional area, upstream pressure, and degree of subcooling and was greatly affected by the inlet and outlet chamfering. Conversely, the mass flow rate was inversely proportional to the short-tube orifice length. For two-phase flow entering the short-tube orifice, it could be seen that increases in the upstream quality led to decreases in the mass flow rate.

Due to environmental concerns about depletion of the ozone layer and global warming, CFC and HCFC refrigerants have been replaced by alternative refrigerants. Therefore, several researchers have concentrated on HFC-134a, HFC-407C, R744, and HFC-410A.

The mass flow rate of HFC-134a inside short-tube orifices has been studied by Kim and O'Neal (1994), Singh et al. (2001), Nilpueng and Wongwises (2009a,b). The results indicated that the variation in mass flow rate with relevant parameters was similar to those obtained in previous works. That is, the mass flow rate strongly increased with the upstream pressure and degree of subcooling but decreased with increases in the short-tube orifice length. The flow rate increased approximately as a function of the square of the short-tube orifice diameter. In addition, a change in the orientation of the short-tube orifice and the installation of upstream and downstream screens had negligible effects on the mass flow rate.

Payne and O'Neal (1998) and Payne and O'Neal (1999) presented results for the mass flow rates of HFC-407C and HFC-410A through short-tube orifices. The effects of upstream subcooling, upstream pressure, downstream pressure, tube length, tube diameter, and lubricant concentration on the mass flow rate were tested. They reported that the variation in refrigerant mass flow rate with operating conditions and short-tube orifice sizes for the refrigerant mixtures followed the same trend as those achieved with HCFC-22 and HFC-134a. However, for two-phase flow entering the short-tube orifice, the flow rate was directly related to the short-tube orifice diameter. Moreover, they found that the addition of oil to the refrigerant led to an increase in the mass flow rate for two-phase flow entering the short-tube orifice but had little effect on the mass flow rate at a high degree of subcooling. The mass flow rate result of HFC-410A inside short-tube orifices at upstream pressures approaching the critical point was reported by Kim et al. (2005). Test runs were performed at upstream pressures ranging from 2619 to 4551 kPa, degrees of subcooling ranging from 2.8 to 11.1 °C, and downstream pressures ranging from 772 to 1274 kPa. They reported that the flow rate varied greatly with upstream pressure, degree of subcooling, and short-tube diameter. This was similar to the normal condition in general air-conditioning system. Nonetheless, they found that the decrease in the mass flow rate with a reduction in subcooling became more significant when the upstream pressure increased beyond 3604 kPa, due to a higher density change.

The flow of carbon dioxide through short-tube orifices was observed by Liu et al. (2004) and Chen et al. (2004). They stated that the flow characteristics of carbon dioxide through short-tube orifices differed from those obtained from conventional refrigerants such as HFC-134a when the trans-critical fluid was not directly changed into the two-phase region. The results showed that the mass flow rate decreased as the upstream temperature increased but was insignificantly affected by the inlet and outlet chamfer depths.

7. Conclusions

Recent developments in research work on refrigerant flow mechanisms inside short-tube orifices are presented in this paper. Based on a review of the open literature, the conclusions can be summarised as follows:

- Most of the research works have been focused on the mass flow rate inside short-tube orifices, but studies of flow pattern, pressure distribution, temperature distribution, and metastable flow have rarely been reported.
- The refrigerant pressure and temperature decreased suddenly at the inlet and outlet of the short-tube orifice, but gradually decreased along the constant cross-section.
- Only one correlation which is generated for predicting the HFC-134a metastable liquid length inside short-tube orifice has been reported in the literature.
- The experimental results indicated that choked flow and metastable flow phenomena exist inside short-tube orifices

under the normal operating conditions of an air conditioner and heat pump. Under the choked flow condition, the refrigerant flow rate through the short-tube orifice is increased with increases in the upstream pressure, degree of subcooling, short-tube orifice diameter, and chamfer depth.

At the present time, although short-tube orifices have been popularly used in residential and automobile air conditioners, a clear understanding of the refrigerant flow phenomena, especially, flow pattern, choked flow and metastable flow are still needed for developing suitable calculation techniques. Therefore, future research work on refrigerant flow mechanisms inside short-tube orifices remains important.

Acknowledgements

The authors would like to express their appreciation to the Thailand Research Fund (TRF), the Office of Higher Education Commission and the National Research University Project for providing financial support for this study.

REFERENCES

Aaron, A.A., Domanski, P.A., 1990. Experimentation, analysis, and correlation of refrigerant-22 flow through short tube restrictors. ASHRAE Trans. 96, 729–742.

Baily, J.F., 1951. Metastable flow of saturated water. Trans. ASME 73, 1109–1116.

Chen, J.P., Liu, J.P., Chen, Z.J., Niu, Y.M., 2004. Trans-critical R744 and two-phase flow through short tube orifices. Int. J. Thermal Sci. 43, 623–630.

Fang, X., 2001. Flow calculations for fixed- area expansion device. ASHRAE Trans. 107, 130–139.

Fauske, H.K., 1965. The discharge of saturated water through tube. Chem. Eng. Symp. 61, 210–216.

Henry, R.E., 1970. The two-phase critical discharge of initially saturated or subcooled liquid. Nucl. Sci. Eng. 41, 336–343.

Kim, Y., 1993. Two-phase flow of HFC134a and HCFC22 through short tube orifices. PhD thesis, Texas A&M University, USA.

Kim, Y., O'Neal, D.L., 1994. Two-phase flow of refrigerant-22 through short tube orifices. ASHRAE Trans. 100, 323–334.

Kim, Y., O'Neal, D.L., Yuan, X., 1994. Two-phase flow of HFC-134a and CFC-12 through short-tube orifices. ASHRAE Trans. 100, 582–591.

Kim, Y., Payne, V., Choi, J., Domanski, P., 2005. Mass flow of R410A through short tube working near the critical point. Int. J. Refrig. 28, 547–553.

Kuehl, S.J., Goldschmidt, V.W., 1992. Flow of R-22 through short-tube restrictors. ASHRAE Trans. 98, 59–64.

Liu, J.P., Niu, Y.M., Chen, J.P., Chen, Z.J., Feng, X., 2004. Experimental and correlation of R744 two-phase flow through short tubes. Exp. Therm. Fluid Sci. 28, 565–573.

Mei, V.C., 1982. Short tube refrigerant flow restrictors. ASHRAE Trans. 88, 157–169.

Nilpueng, K., Wongwises, S., 2009a. Experimental investigation of two-phase flow characteristics of HFC-134a through short-tube orifices. Int. J. Refrig. 32, 854–864.

Nilpueng, K., Wongwises, S., 2009b. Flow pattern, mass flow rate, pressure distribution, and temperature distribution of two-phase flow of HFC-134a inside short-tube orifices. Int. J. Refrig. 32, 1864–1875.

Pasqua, P.F., 1953. Metastable flow of Freon-12. Refrig. Eng. 61, 1084–1088.

Payne, W.V., O'Neal, D.L., 1998. Mass flow characteristics of R407C through short-tube orifices. ASHRAE Trans. 104, 197–209.

Payne, W.V., O'Neal, D.L., 1999. Multiphase flow of refrigerant 410A through short tube orifices. ASHRAE Trans. 105, 66–74.

Singh, G.M., Hrnjak, P.S., Bullard, C.W., 2001. Flow of refrigerant R134a through orifice tubes. HVAC&R Res. 7, 245–262.

Tu, X., Hrnjak, P.S., Bullard, C.W., 2006. Refrigerant 134a liquid flow through micro-scale short tube orifices with/without phase change. Exp. Therm. Fluid Sci. 30, 253–262.

Zaloudek, R.R., 1963. The Critical Flow of Hot Water through Short Tube. HW77594, Hanford Lab. Richland, Washington.

International Journal of Heat and Mass Transfer 55 (2012) 1403–1411

Contents lists available at SciVerse ScienceDirect

International Journal of Heat and Mass Transfer

journal homepage: www.elsevier.com/locate/ijhmt

Technical Note

Effect of number of tube rows on the air-side performance of crimped spiral fin-and-tube heat exchanger with a multipass parallel and counter cross-flow configuration

Parinya Pongsoi [a], Santi Pikulkajorn [b], Chi-Chuan Wang [c], Somchai Wongwises [a,d,*]

[a] Fluid Mechanics, Thermal Engineering and Multiphase Flow Research Lab. (FUTURE), Department of Mechanical Engineering, King Mongkut's University of Technology, Thonburi, Bangmod, Bangkok 10140, Thailand
[b] Somchai Industry Co., Ltd., Bangkok 10150, Thailand
[c] Department of Mechanical Engineering, National Chiao Tung University, Hsinchu 300, Taiwan
[d] The Royal Institute of Thailand, Academy of Science, Sanam Suea Pa, Dusit, Bangkok 10300, Thailand

ARTICLE INFO

Article history:
Received 11 March 2011
Received in revised form 23 June 2011
Accepted 23 June 2011
Available online 21 October 2011

Keywords:
Crimped fin
Heat transfer
Heat exchanger
Air–water
Extended surface

ABSTRACT

The air-side performance of crimped spiral fin and tube heat exchangers at high Reynolds number (3000–13,000) is investigated in this study. The test heat exchangers have a new type of multipass parallel and counter cross-flow water flow arrangement which is a combination of parallel cross-flow and counter cross-flow. The test samples are made from copper and aluminium with different number of tube rows (N_{row} = 2, 3, 4 and 5). The effects of number of tube rows and fin material on the heat transfer and friction characteristics are studied. The results show that no significant effect for either number of tube rows or fin materials on the heat transfer performance is found at high Reynolds number. In addition, the correlation of the air-side performances of this type of the heat exchangers at high Reynolds number is developed for industrial applications.

© 2011 Elsevier Ltd. All rights reserved.

1. Introduction

The heat exchanger is a basic component that is used for thermal systems in many industrial processes involving heat transfer. The most favourable type of heat exchanger used in industrial applications is the fin-and-tube heat exchanger. It is very important to consider the heat transfer rate, which is normally limited by the thermal resistance on the air-side of the heat exchanger. One way to augment the heat transfer rate on the air-side of the heat exchanger is to improve the fin geometry. However, this method may lead to the need for increased fan power because of the penalty associated with the pressure drop. Many researchers had studied the effect of the plate fin geometry, such as plain fin, slit fin, wavy fin, louvered fin, compounded fin, etc., on the heat transfer performance and frictional characteristic. On the other hand, there are only few researches on the crimped spiral fin-and-tube heat exchanger as found in [1–4].

Nuntaphan et al. [1] studied the air-side of crimped spiral fin heat exchanger to analyse the effect of tube diameter, fin spacing, transfer tube pitch, and tube arrangement and proposed correlations between heat transfer and friction characteristics in the case of low Reynolds numbers. Moreover, heat exchangers using crimped spiral finned tubes were investigated by Srisawad and Wongwises [2] who focused on the air-side performance of helically coiled crimped spiral finned tube heat exchangers in dry-surface conditions. Pongsoi et al. [3] studied the effect of fin pitch on the air-side heat transfer characteristics of crimped spiral fin-tube heat exchangers having multipass parallel and counter cross-flow under sensible heating conditions and purpose the ε–*NTU* relation equation for this new water flow arrangement. Tang et al. [4] studied the air-side heat transfer and friction characteristics of five kinds of fin-and-tube heat exchangers i.e. crimped spiral fin, plain fin, slit fin, fin with delta-wing longitudinal vortex generators, and mixed fin. The number of tube rows (N_{row}) was 12. The diameter of tubes (d_o) was 18 mm. Reynolds number was varied from 4000 to 10,000. According to their results, although the crimped spiral fin gave high pressure drop, it provided higher air-side heat transfer performance than several types of heat exchangers.

According to these literatures, crimped spiral fin is proved to be quite reliable in industrial applications. The crimped spiral fin

* Corresponding author at: Fluid Mechanics, Thermal Engineering and Multiphase Flow Research Lab. (FUTURE), Department of Mechanical Engineering, King Mongkut's University of Technology, Thonburi, Bangmod, Bangkok 10140, Thailand. Tel.: +66 24709115.
E-mail address: Somchai.won@kmutt.ac.th (S. Wongwises).

0017-9310/$ - see front matter © 2011 Elsevier Ltd. All rights reserved.
doi:10.1016/j.ijheatmasstransfer.2011.09.064

Nomenclature

A_{min}	minimum free flow area, m^2
A_o	total surface area, m^2
A_p	cross-sectional or profile area of fin, m^2
Al	aluminium material
C^*	capacity rate ratio, dimensionless
Cu	copper material
f	Fanning friction factor, dimensionless
Gc	mass flux of the air based on minimum free flow area, kg/m^2 s
h	heat transfer coefficient, $W/(m^2 K)$
j	Colburn factor, dimensionless
NTU	number of transfer units, dimensionless
Nu	Nusselt number, dimensionless
Pr	Prandtl number, dimensionless
ΔP	pressure drop, Pa
Re_{do}	Reynolds number based on tube outside diameter (d_o)
U	overall heat transfer coefficient, $W/(m^2 K)$
V_{fr}	air frontal velocity, m/s
V_{max}	maximum velocity across heat exchanger, m/s
ε_c	heat exchanger effectiveness for multipass counter cross-flow
ε_p	heat exchanger effectiveness for multipass parallel cross-flow
ε_{pc}	heat exchanger effectiveness for multipass parallel and counter cross-flow
η_f	fin efficiency, dimensionless
ϕ	combination of terms, dimensionless

Table 1
Experimental conditions.

Inlet-air-dry bulb temperature, °C	31.5 ± 0.5
Inlet-air frontal velocity, m/s	2–6 or Re_{do}(3000–13,000)
Inlet-water temperature, °C	55–70
Water flow rate, LPM	12–14

features a sine-shaped fin which gives rise to a higher heat transfer rate on the air-side through the increase in the contact surface between the fin base and tube. However, up to now, none of the experimental investigations found in the literature had reported the effect of the number of tube rows on the air-side performance of crimped spiral fin-and-tube heat exchangers. Upon the foregoing studies, Nuntaphan et al. [1] is the only experimental work that examined the effect of fin geometry and tube arrangement on the air-side performance of crimped spiral fin-and-tube heat

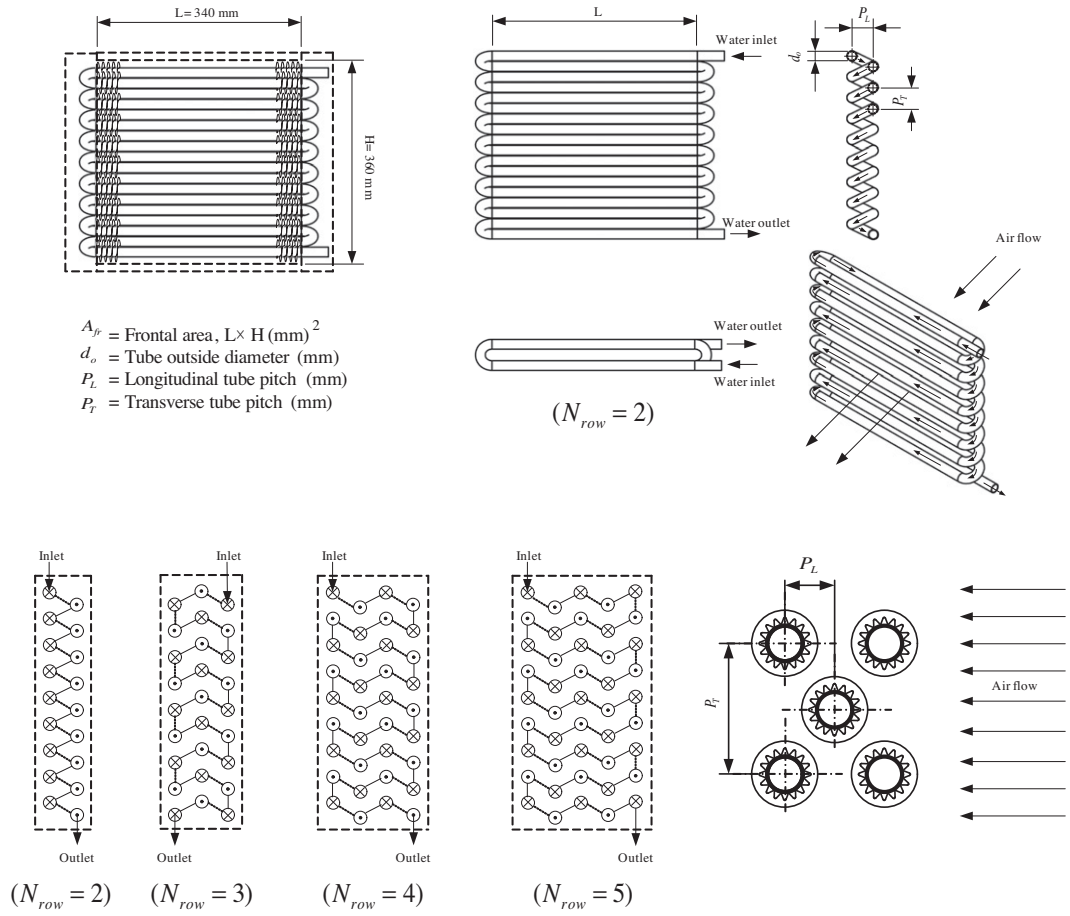

Fig. 1. Geometric details of multipass parallel-and-counter cross flow heat exchangers and water flow circuit inside the heat exchanger. N_{row} = 2, 3, 4 and 5 (× and • signs indicates that water flows into or out of the paper, respectively).

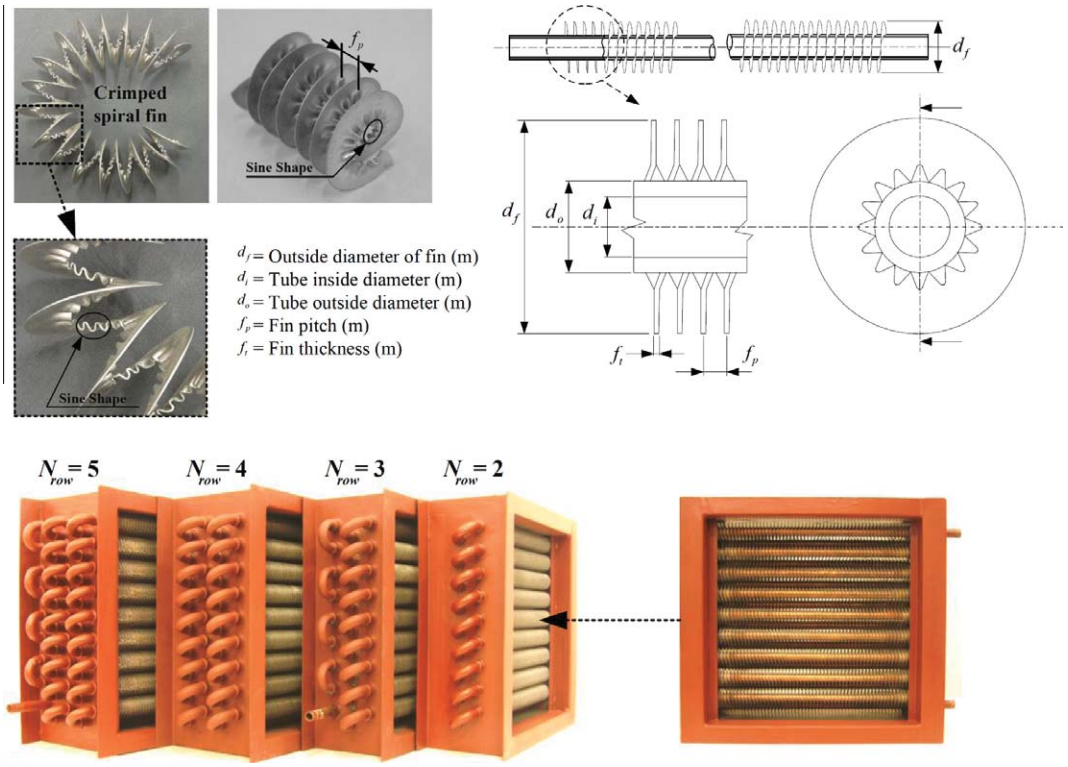

Fig. 2. The photos of the tested crimped spiral fin and tube heat exchangers and schematic diagram of crimped spiral fin.

exchangers. However, their tests were conducted at a very low air frontal velocity (0.5–1.5 m/s) which limited the applicability of the test results. In practice, especially in industrial service, the operation velocity is normally much higher as reported by Xie et al. [5]. Therefore, it is the main purpose of this study is to extend the applicable range (V_{fr} up to 6 m/s) of the crimped spiral fin-and-tube heat exchangers subject to the influence of the number of tube rows and fin materials. Moreover, the test samples are of this study is of large diameter tubes (about 16 mm) which are very popularly used in ventilator and fan-coil units [6,7].

2. Data reduction

This present work is conducted by using the experimental apparatus of Wongwises and Chokeman [8], including the test section, air supply, water loop, instrumentation, and data acquisition. Air and hot water are used as working fluids. Detailed descriptions of the relevant components can be seen from the previous study.

In the experiment, the inlet water temperature and the water flow rate are fixed while varying the air flow rate. Tests are then conducted at the steady state with tested conditions being tabulated in Table 1.

The tests heat exchangers are of fin-and-tube configurations with copper tube being finned with either copper or aluminium. The water-side circuitry arrangement and detailed dimensions of the tested fin-and-tube heat exchangers are shown in Fig. 1. Photos of the crimped spiral fin pattern are shown in Fig. 2. The geometric parameters of the heat exchangers are summarized in Table 2. Tests are performed under steady state condition, and the overall resistance can be obtained from the *UA* product of transfer units (ε–*NTU*), yet the total resistance is the sum of the individual resistances as follows:

$$\frac{1}{UA} = \frac{1}{h_i A_i} + \frac{\ln(d_o/d_i)}{2\pi k_t L} + \frac{1}{\eta_o h_o A_o} \tag{1}$$

The ε–*NTU* relationships with one fluid mixed and one fluid unmixed in cross-flow was employed to determine the overall heat transfer coefficient. From Fig. 1, the present mixed circuitry arrangement is a combination of parallel and counter cross-flow. Therefore, the ε–*NTU* relationships developed by Pongsoi et al. [3] is selected to calculate the heat exchanger effectiveness. This relation combines both effect of parallel and counter cross-flow configuration of water flow arrangement from [9–11], as shown in Eqs. (2)–(9):

For multipass parallel cross-flow with N_{row} = 2, 3, 4 and 5:

$$(N_{row} = 2), \quad \varepsilon_P \left(1 - \frac{K}{2}\right)\left(1 - e^{-2K/C_A^*}\right), \quad K = 1 - e^{-NTU_A(C_A^*/2)} \tag{2}$$

Table 2
Detailed geometric parameters of the test samples.

No.	Fin type	d_i (mm)	d_o (mm)	d_f (mm)	P_L (mm)	P_T (mm)	f_t (mm)	n_t	N_{row}	f_p (mm)	Fin material
1, 2	Crimped	13.5	16.35	35.0	35	40	0.5	9	3, 4	6.3	Cu
3–6	Crimped	13.5	16.35	35.0	35	40	0.5	9	2, 3, 4, 5	6.3	Al

d_f = outside diameter of fin; d_i = tube inside diameter; d_o = tube outside diameter; f_p = fin pitch; f_t = fin thickness; P_L = longitudinal tube pitch; P_T = transverse tube pitch; n_t = number of tubes in row; N_{row} = number of tube rows. Tube layouts of all heat exchangers are staggered layout (Al = aluminium, Cu = copper).

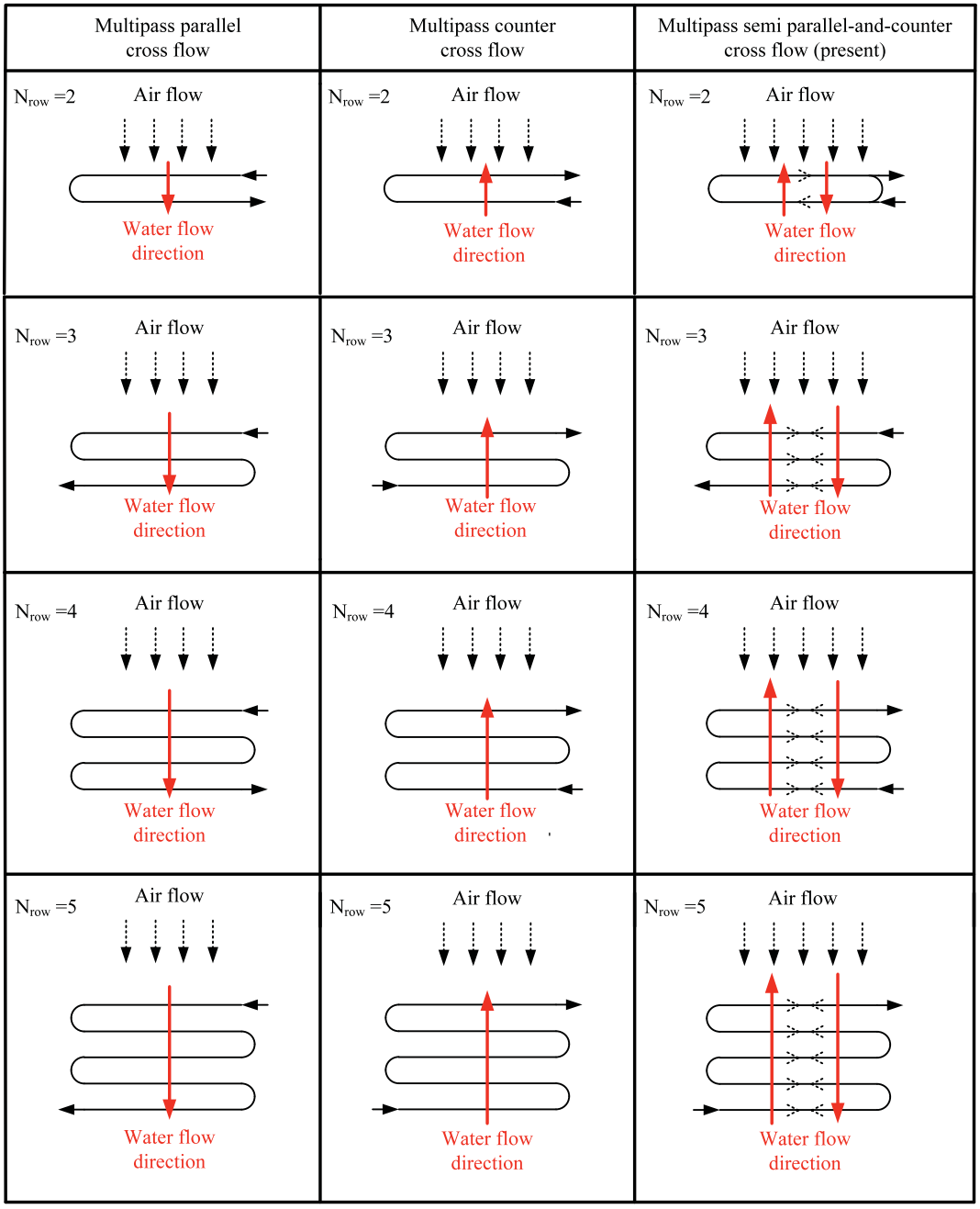

Fig. 3. Schematic diagram of the heat exchangers algorithm for multipass parallel cross flow, multipass counter cross flow and multipass parallel and counter cross-flow (N_{row} = 2, 3, 4 and 5).

$$(N_{row}=3),\quad \varepsilon_P = 1-\left(1-\frac{K}{2}\right)^2 e^{-3K/C_A^*} - K\left[1-\frac{K}{4}+\frac{K}{C_A^*}\left(1-\frac{K}{2}\right)\right]e^{-K/C_A^*},\quad K=1-e^{-NTU_A(C_A^*/3)} \tag{3}$$

$$(N_{row}=4),\quad \varepsilon_P = 1-\frac{K}{2}\left(1-\frac{K}{2}+\frac{K^2}{4}\right)-K\left(1-\frac{K}{2}\right)\left(1+2\frac{K}{C_A^*}\left[1-\frac{K}{2}\right]\right)e^{-2K/C_A^*}-\left(1-\frac{K}{2}\right)^3 e^{-4K/C_A^*},\quad K=1-e^{-NTU_A(C_A^*/4)} \tag{4}$$

$$(N_{row}=5 \text{ or } \infty),\quad \varepsilon_P = \frac{1-e^{-NTU_A(1+C_A^*)}}{1+C_A^*} \tag{5}$$

For multipass counter cross-flow with N_{row} = 2, 3, 4 and 5:

$$(N_{row}=2),\quad \varepsilon_c = 1-\left[\frac{K}{2}+\left(1-\frac{K}{2}\right)e^{2K/C_A^*}\right]^{-1},\quad K=1-e^{-NTU_A(C_A^*/2)} \tag{6}$$

$$(N_{row}=3),\quad \varepsilon_c = 1-\left\{\left(1-\frac{K}{2}\right)^2 e^{3K/C_A^*} + k\left[K\left(1-\frac{K}{4}\right)-\left(1-\frac{K}{2}\right)\frac{K^2}{C_A^*}\right]e^{K/C_A^*}\right\}^{-1},\quad K=1-e^{-NTU_A(C_A^*/3)} \tag{7}$$

$$(N_{row}=4),\quad \varepsilon_c = 1-\left\{\frac{K}{2}\left(1-\frac{K}{2}+\frac{K^2}{4}\right)+K\left(1-\frac{K}{2}\right)\times\left[1-2\frac{K}{C_A^*}\left(1-\frac{K}{2}\right)\right]e^{2K/C_A^*}+\left(1-\frac{K}{2}\right)^3 e^{4K/C_A^*}\right\}^{-1},\quad \times K=1-e^{-NTU_A(C_A^*/4)} \tag{8}$$

$$(N_{row} = 5 \text{ or } \infty), \quad \varepsilon_c = \frac{1 - e^{-NTU_A(1-C_A^*)}}{1 - C_A^* e^{-NTU_A(1-C_A^*)}} \tag{9}$$

where $C^* = C_{min}/C_{max}$ is equal to C_c/C_h or C_h/C_c depending on the value of hot and cold fluid heat capacity rates

$$\varepsilon_{pc} = \frac{\varepsilon_P + \varepsilon_C}{2} \quad \text{for } N_{row} = 2, 3, 4 \text{ and } 5 \tag{10}$$

The schematic diagram of circuitry arrangement for $N_{row} = 2$, 3, 4 and 5 are shown in Fig. 3.

The heat transfer performance is calculated by the method of Kays and London. Further details about the data reduction can be seen from Wongwises and Chokeman [8], The efficiency of a radial fin with rectangular profile is based on the derivation of Gardner [12], i.e.,

$$\eta_f = \frac{2\psi}{\phi(1+\psi)} \frac{I_1(\phi R_o)K_1(\phi R_i) - I_1(\phi R_i)K_1(\phi R_o)}{I_0(\phi R_i)K_1(\phi R_o) + I_1(\phi R_o)K_0(\phi R_i)} \tag{11}$$

where

$$\phi = (r_o - r_i)^{3/2} \left(\frac{2h_o}{k_f A_p}\right)^{1/2} \tag{12}$$

Accordingly, the air-side heat transfer coefficient (h_o) can be calculated from Eq. (1). The air-side heat transfer characteristics of the heat exchanger are often in terms of dimensionless Colburn j factor:

$$j = \frac{Nu}{Re_{do}\Pr^{1/3}} = \frac{h_o}{\rho_a V_{\max} c_P}(\Pr)^{2/3} \tag{13}$$

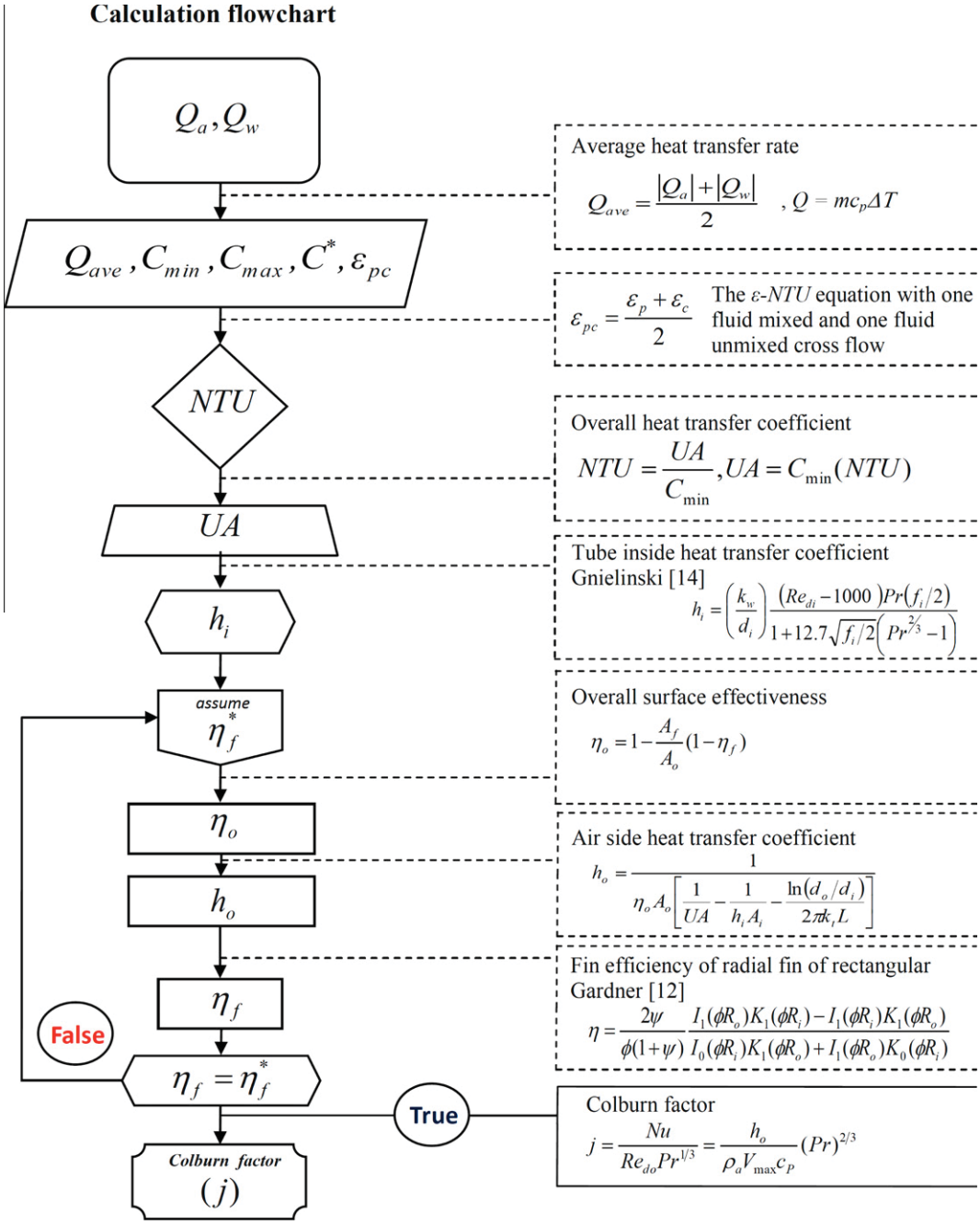

Fig. 4. Flowchart of the data reduction for air-side heat transfer performance (j-factor). (See above-mentioned reference for further information.)

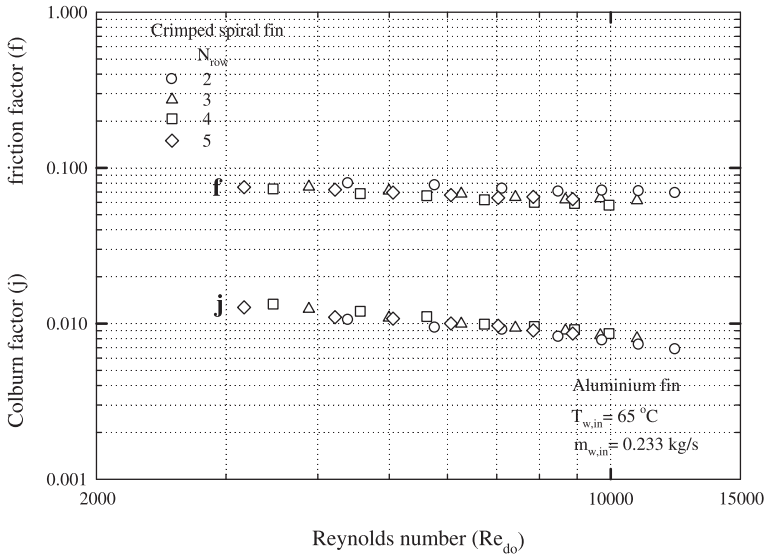

Fig. 5. Effect of number of tube rows on the Colburn factor and friction factor of crimped spiral fin and tube heat exchangers.

The frictional characteristics are termed with Fanning friction factor, as depicted by Kays and London [13]:

$$f = \left(\frac{A_{\min}}{A_o}\right)\left(\frac{\rho_m}{\rho_1}\right)\left[\frac{2\Delta P\rho_1}{G_c^2} - (1+\sigma^2)\left(\frac{\rho_1}{\rho_2} - 1\right)\right] \tag{14}$$

where G_c is the mass flux of the air based on minimum free flow area, A_o is the total heat transfer area, A_{min} is the minimum free flow area. The flow chart showing the reduction of the data is shown in Fig. 4.

The experiments are conducted following the ANSI/ASHRAE 33 Standards [15] in which the energy un-balance between air and water of the crimped spiral fin-and-tube heat exchangers, denoting $|Q_a - Q_w|/Q_{ave}$, is less than 0.05. The uncertainties are calculated from the root mean sum square method, the maximum uncertainties are 3.5% for the Re_{do}, 13.0% for the j-factor and 11.5% for f-factor. The uncertainties decreased as Reynolds number increased.

3. Results and discussion

In experiments, the analysis of air-side heat transfer and friction characteristics of all the heat exchangers examined are presented in terms of a dimensionless number including the Colburn factor (j) and friction factor (f) plotted against the Reynolds number (Re_{do}) and the Reynolds number based on the outside diameter of the tube. As expected, both the Colburn factor (j) and the friction factor (f) decrease an increasing Reynolds number.

Fig. 5 shows the effect of the number of tube rows on the heat transfer and friction characteristic. The number of tube row of the heat exchangers are from 2 to 5. As can be seen in Fig. 5, the number of tube rows casts no significant effect on the Colburn factor (j) at high Reynolds numbers (3000–13,000). This phenomenon is similar to the plain fin data as reported by Rich [16] and Wang et al. [17] in which the effect of the number of tube rows diminishes as the Reynolds number is increased over 2000. This is due to the downstream turbulence eddies shed from the tubes that

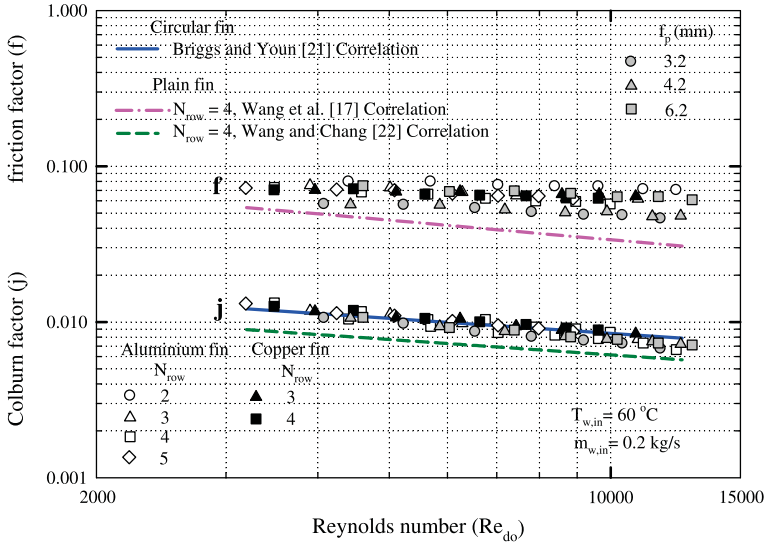

Fig. 6. The comparison of j and f factors between presented data with correlation of plain fin and circular fin.

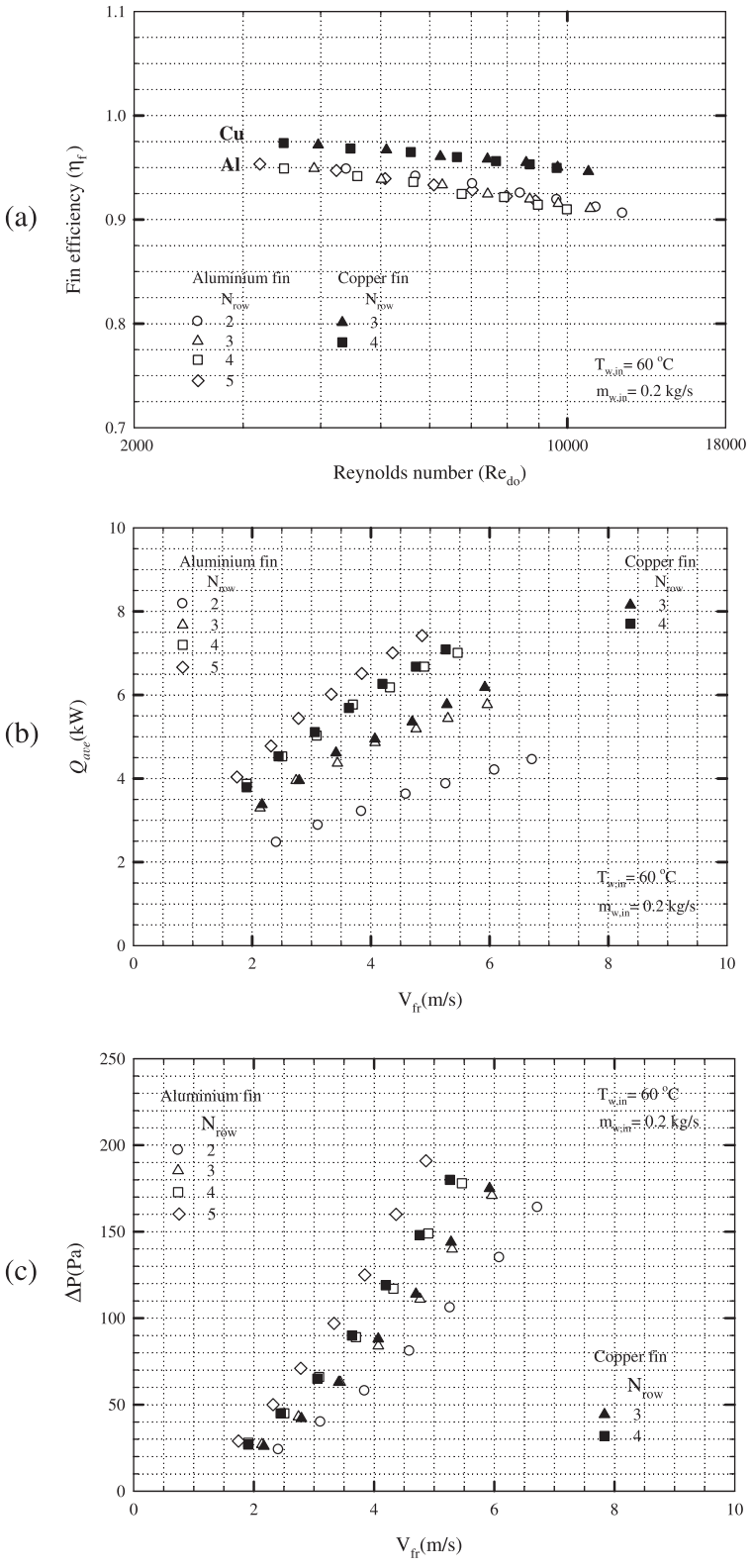

Fig. 7. Effect of number of tube rows on the fin efficiency (a), heat transfer rate (b) and pressure drop (c) of crimped spiral fin and tube heat exchangers (N_{row} = 2, 3, 4 and 5).

cause good mixing in the downstream fin region. Moreover, the fact that the effect of the number of tube rows on the heat transfer characteristics vanishes for Reynolds numbers over 2000 can also be found in the works of [18–20] with fin-and-tube heat exchangers having wavy, louver and slit geometry, respectively. The data point in Fig. 5 shows that the number of tube row (N_{row}) does not affect the friction factor (f) over the range of Reynolds numbers being examined.

For a comparison of the present test samples with previous studies, the Briggs and Young [21] correlation for circular fin-and-tube heat exchanger is chosen to compare with the present experimental results as illustrated in Fig. 6. Note that the configu-

ration of circular fin is very similar to that of the tested crimped spiral fin. Therefore, the calculated Colburn factor (j) of circular fins reveals a similar trend and magnitude as the present crimped spiral fins. Also, the Colburn factor (j) and friction factor (f) correlations of plain fin-and-tube heat exchangers, which is proposed by Wang and Chang [22] and Wang et al. [17], respectively, are selected to compare with the tested results. As shown in Fig. 6, it is found that crimped spiral fins have a similar trend with the plain fins as well. However, due to the corrugated folding at the base of the present fin configuration, it appears that crimped spiral fins give a higher friction factor (f) than that plain fins at the same Reynolds number. Moreover, as shown in Fig. 6, there is no significant effect of fin material on both the Colburn factor (j) and friction factor (f).

Fig. 7(a) illustrated the effect of the number of tube rows on the fin efficiency (η_f) of both fin material. It can be seen that no significant effect of number of tube rows is found under the same experimental conditions. The reason may be explained by Eqs. (11) and (12), which show that an increase in the number of tube rows has no significant differences in terms of ϕ and fin efficiency (η_f) at the same Reynolds number because the fin efficiency depends only on size, shape and material of fin. In the meantime, it can be clearly seen that the fin efficiency (η_f) of the copper fin is higher than that of aluminium fin due to a higher thermal conductivity of copper.

Moreover, the heat transfer rate for both fins is shown in Fig. 7(b). It seems that the heat transfer rate for copper fin only marginally higher than that of aluminium fin due to its very minor difference in fin efficiency. On the other hand, the number of tube rows had significant effect on average heat transfer rate at the same air frontal velocity.

A comparison of the results for the effect of the number of tube rows on the pressure drop of crimped spiral fin-and-tube heat exchangers is presented in Fig. 7(c). As seen, the pressure drop increases with the frontal air velocity while the friction factor decreases with increasing Reynolds number. It can be seen that the pressure drop for $N_{row} = 5$ is two times higher than those for $N_{row} = 2$. The reason for this result can be explained by the increase in the blocking flow area when N_{row} is increased.

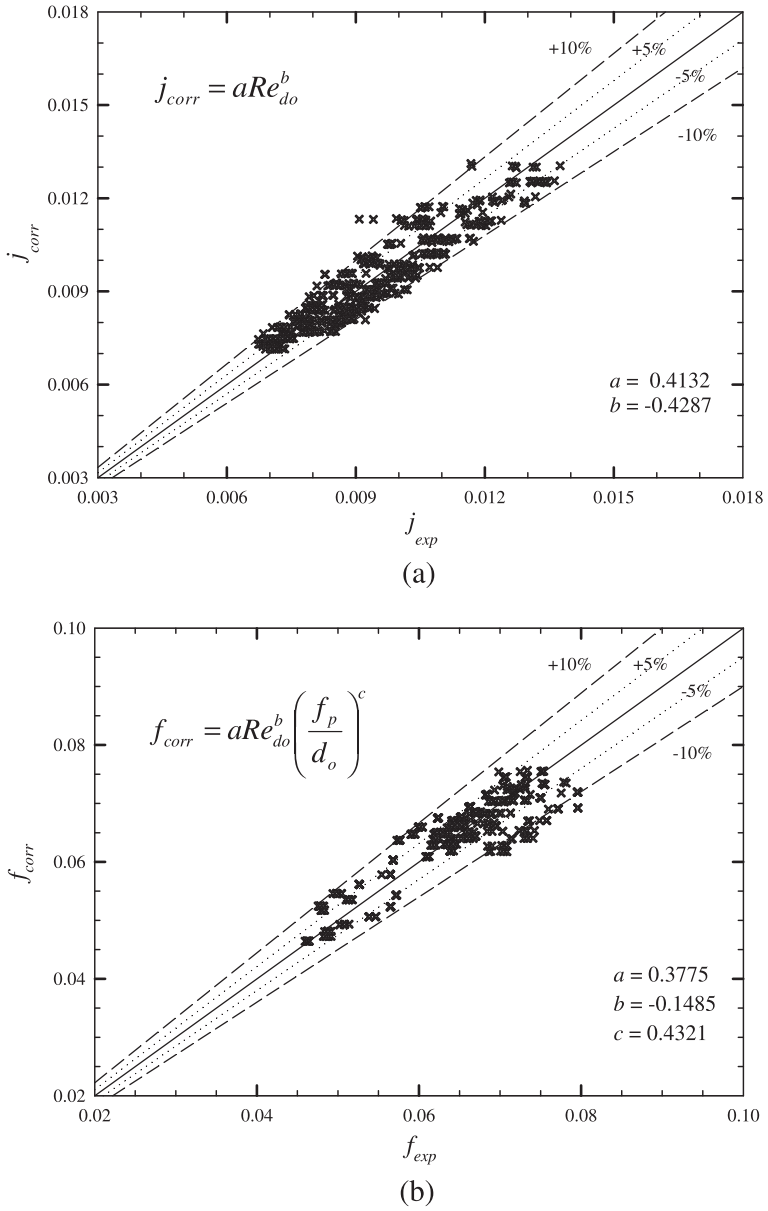

Fig. 8. Comparison of the proposed correlations with experimental data: (a) Colburn factor and (b) friction factor.

To determine the heat transfer coefficient of crimped spiral fin-and-tube heat exchangers, an empirical correlation between the Colburn factor (j) and the friction factor (f) is proposed in this work. The correlations may be valuable for industrial usage in order to design the heat exchangers operating at air flows of high Reynolds number.

An empirical correlation for j and f factors for crimped spiral fin-and-tube heat exchanger is developed in this work. The correlation also includes the experimental data used to study the effect of fin pitch as reported in Pongsoi et al. [3]. It must be noted that number of tube rows cast negligible influence on both j and f factors as foregoing discussions. As a result, the number of tube row is not included in the correlations. The test results are correlated as suggested by Wang et al. [23] in the form of $j = aRe_{do}^{b}$ and $f = aRe_{do}^{b}$ where a and b are the empirical constants obtained from least-square fitting of the experimental data. Furthermore, based on the data analysis, the f factor of crimped spiral fin-and-tube heat exchanger were also proportional to the fin pitch. Therefore, the present correlation for f factor is modified by including the dimensionless fin pitch (f_p) normalized by the tube outside diameter (d_o). The final correlation for the j and f factors takes the following form:

$$j_{corr} = 0.4132Re_{do}^{-0.4287} \tag{15}$$

$$f_{corr} = 0.3775Re_{do}^{-0.1485}\left(\frac{f_p}{d_o}\right)^{0.4321} \tag{16}$$

$$\text{Mean deviations} = \frac{1}{M}\left[\sum_{1}^{M}\frac{|\Phi_{corr} - \Phi_{exp}|}{\Phi_{exp}}\right] \times 100\% \tag{17}$$

As shown in Fig. 8, the proposed heat transfer and friction correlations Eqs. (15) and (16) can describe 95.04% and 91.07% of the j and f factors to be within ±10%, respectively. The mean deviations Eq. (17) of the proposed heat transfer and friction correlations are 5.09% and 4.53%, respectively. However, Eq. (15) and (16) can be used only (N_{row} = 2–5), (f_p = 3.2–6.3 mm) when staggered arrangement.

4. Conclusion

This study has investigated the effect of number of tube rows on the air-side performance of crimped spiral fin and tube heat exchangers having multipass parallel and counter cross-flow under sensible heating conditions at high Reynolds number (3000–13,000) based on the tube outside diameter. The following conclusions based on the tests are obtained:

- The number of tube rows cast a negligible influence on the air-side heat transfer performance at high Reynolds number (3000–13,000). Moreover, it could be clearly seen that the airside performance is independent of fin material.
- The average heat transfer rate and pressure drop increase with increasing the number of tube rows.
- The correlation of Colburn factor (j) and friction factor (f) of crimped spiral fin-and-tube heat exchangers at high Reynolds number are proposed in this paper. The mean deviations of the proposed heat transfer and friction correlations are 5.09% and 4.53%, respectively.

Acknowledgments

The authors are indebted to the Thailand Research Fund and the National Research University Project for supporting this study. The third author also expresses gratitude for support funding from the National Science Council of Taiwan (99-2218-E-009-012-MY2).

References

[1] A. Nuntaphan, T. Kiatsiriroat, C.C. Wang, Air side performance at low Reynolds number of cross-flow heat exchanger using crimped spiral fins, Int. Commun. Heat Mass Transfer 32 (1-2) (2005) 151–165.
[2] K. Srisawad, S. Wongwises, Heat transfer characteristics of a new helically coiled crimped spiral finned tube heat exchanger, Heat Mass Transfer 45 (4) (2009) 381–391.
[3] P. Pongsoi, S. Pikulkajorn, C.C. Wang, S. Wongwises, Effect of fin pitches on the air-side performance of crimped spiral fin-and-tube heat exchangers with a multipass parallel and counter cross-flow configuration, Int. J. Heat Mass Transfer 54 (9–10) (2011) 2234–2240.
[4] L.H. Tang, M. Zeng, Q.W. Wang, Experimental and numerical investigation on air-side performance of fin-and-tube heat exchangers with various fin patterns, Exp. Thermal Fluid Sci. 33 (2009) 818–827.
[5] G. Xie, Q. Wang, B. Sunden, Parametric study and multiple correlations on air-side heat transfer and friction characteristics of fin-and-tube heat exchangers with large number of large-diameter tube rows, Appl. Therm. Eng. 29 (1) (2009) 1–16.
[6] Y.C. Liu, S. Wongwises, W.J. Chang, C.C. Wang, Airside performance of fin-and-tube heat exchangers in dehumidifying conditions – data with larger diameter, Int. J. Heat Mass Transfer 53 (7-8) (2010) 1603–1608.
[7] C.C. Wang, J.S. Liaw, B.C. Yang, Airside performance of herringbone wavy fin-and-tube heat exchangers – data with larger diameter tube, Int. J. Heat Mass Transfer 54 (5–6) (2011) 1024–1029.
[8] S. Wongwises, Y. Chokeman, Effect of fin pitch and number of tube rows on the air side performance of herringbone wavy fin and tube heat exchangers, Energy Convers. Manage. 46 (13–14) (2005) 2216–2231.
[9] ESDU 86018, Effectiveness-NTU Relations for the Design and Performance Evaluation of two-stream heat exchangers, Engineering Science Data Unit 86018 with Amendment, London ESDU International plc, 1991, pp. 92–107.
[10] H.A. Navarro, L. Cabezas-Gomez, A new approach for thermal performance calculation of cross-flow heat exchanger, Int. J. Heat Mass Transfer 48 (18) (2005) 3880–3888.
[11] L. Cabezas-Gomez, H.A. Navarro, J.M. Saiz-Jabardo, Thermal performance of multipass parallel and counter-cross-flow heat exchangers, J. Heat Transfer 129 (3) (2007) 282–290.
[12] K.A. Gardner, Efficient of extended surface, ASME Trans. 67 (1945) 621.
[13] W.M. Kays, A. London, Compact Heat Exchangers, third ed., McGraw-Hill, New York, 1984.
[14] V. Gnielinski, New equation for heat and mass transfer in turbulent pipe and channel flow, Int. Chem. Eng. 16 (1976) 359–368.
[15] ANSI/ASHRAE Standard 33-2000, Method of Testing Forced Circulation Air Cooling and Air Heating Coils, 2000.
[16] D.G. Rich, The effect of the number of tube rows on heat transfer performance of smooth plate fin-and-tube heat, ASHRAE Trans. 81 (1) (1975) 307–317.
[17] C.C. Wang, Y.J. Chang, Y.C. Hsieh, Y.T. Lin, Sensible heat and friction characteristics of plate fin-and-tube heat exchangers having plane fins, Int. J. Refrig. 19 (4) (1996) 223–230.
[18] C.C. Wang, W.L. Fu, C.T. Chang, Heat transfer and friction characteristics of typical wavy fin-and-tube heat exchangers, Exp. Thermal Fluid Sci. 14 (2) (1997) 174–186.
[19] C.C. Wang, K.-Y. Chi, Y.-J. Chang, Y.-P. Chang, An experimental study of heat transfer and friction characteristics of typical louver fin-and-tube heat exchangers, Int. J. Heat Mass Transfer 41 (4-5) (1998) 817–822.
[20] Y.J. Du, C.C. Wang, An experimental study of the airside performance of the superslit fin-and-tube heat exchangers, Int. J. Heat Mass Transfer 43 (24) (2000) 4475–4482.
[21] D.E. Briggs, E.H. Young, Convective heat transfer and pressure drop of air flowing across triangular pitch banks of finned tubes, Chem. Eng. Prog. Symp. Ser. 59 (41) (1963) 1–10.
[22] C.C. Wang, C.T. Chang, Heat and mass transfer for plate fin-and-tube heat exchangers, with and without hydrophilic coating, Int. J. Heat Mass Transfer 41 (20) (1998) 3109–3120.
[23] C.C. Wang, K.Y. Chi, C.J. Chang, Heat transfer and friction characteristics of plain fin-and-tube heat exchangers: Part II. Correlation, Int. J. Heat Mass Transfer 43 (15) (2000) 2693–2700.

International Journal of Heat and Mass Transfer 55 (2012) 1475–1485

Contents lists available at SciVerse ScienceDirect

International Journal of Heat and Mass Transfer

journal homepage: www.elsevier.com/locate/ijhmt

Unconfined laminar nanofluid flow and heat transfer around a square cylinder

Vahid Etminan-Farooji [a], Ehsan Ebrahimnia-Bajestan [a,*], Hamid Niazmand [a], Somchai Wongwises [b,c]

[a] Department of Mechanical Engineering, Ferdowsi University of Mashhad, Mashhad, Iran
[b] Fluid Mechanics, Thermal Engineering and Multiphase Flow Research Lab. (FUTURE), Department of Mechanical Engineering, King Mongkut's University of Technology Thonburi, Bangmod, Bangkok, Thailand
[c] The Academy of Science, The Royal Institute of Thailand, SanamSueaPa, Dusit, Bangkok 10300, Thailand

ARTICLE INFO

Article history:
Received 13 April 2011
Received in revised form 10 October 2011
Accepted 10 October 2011
Available online 12 December 2011

Keywords:
Nanofluid
Square cylinder
Peclet number
Thermophysical properties
Unconfined flow
Heat transfer enhancement

ABSTRACT

The momentum and forced convection heat transfer for a laminar and steady free stream flow of nanofluids past an isolated square cylinder have been studied numerically. Different nanofluids consisting of Al_2O_3 and CuO with base fluids of water and a 60:40 (by mass) ethylene glycol and water mixture were selected to evaluate their superiority over conventional fluids. Recent correlations for the thermal conductivity and viscosity of nanofluids, which are functions of particle volumetric concentration as well as temperature, have been employed in this paper. The simulations have been conducted for $Pe = 25$, 50, 100 and 200, with nanoparticle diameters of 30 and 100 nm and particle volumetric concentrations ranging from 0% to 4%. The results of heat transfer characteristics of nanofluid flow over a square cylinder showed marked improvement comparing with the base fluids. This improvement is more evident in flows with higher Peclet numbers and higher particle volume concentration, while the particle diameter imposes an adverse effect on the heat transfer characteristics. In addition, it was shown that for any given particle diameter there is an optimum value of particle concentration that results in the highest heat transfer coefficient.

© 2011 Elsevier Ltd. All rights reserved.

1. Introduction

Due to the immense theoretical and practical importance of cross flow past bluff bodies, this field of study has received substantial attention from researchers. Common examples of this kind of flow include flow in tubular and pin-type heat exchangers, the use of thin cylinders as measuring probes as well as sensors, and in the continuous thermal treatment of food particles (such as slices and chips of carrots and potatoes) in viscous fluids (high Prandtl number). Over the years, a considerable amount of information dealing with different aspects of the heat transfer and flow over bluff bodies has been added to the literature, a great majority of which relates to the flow over a circular cylinder [1–5]. In contrast to much theoretical, experimental and numerical data on the flow around circular cylinders over a wide range of Reynolds numbers, there are a limited number of similar studies and information available on flow around square bodies. However, in recent years there have been some efforts to expand the knowledge of flow over square cylinders in the literature. Turki et al. [6] presented a numerical study to analyse the unsteady flow field and heat transfer characteristics in a horizontal channel with a built-in heated square cylinder. The study was carried out for two channel blockage ratios ($B = 1/4$ and 1/8), and different Reynolds and Richardson numbers ranging from 62 to 200 and from 0 to 0.1 respectively at $Pr = 0.71$. They showed that the overall heat transfer of a square cylinder was slightly affected by the blockage ratio and presented correlations for $B = 1/4$ and $B = 1/8$.

Sharma and Eswaran [7] have carried out a detailed study on heat and fluid flow over square cylinders. In a study concerning the unconfined two dimensional laminar regime for Reynolds numbers between 1 and 160, they showed that the transition to unsteadiness occurs between $Re = 40$ and 50. The results indicated that the heat transfer characteristics in the steady flow regime ($Re \leqslant 40$) and unsteady periodic 2-D flow regime ($50 \leqslant Re \leqslant 160$) are markedly different. The time-averaged rear-surface Nusselt number is more strongly dependent on Reynolds numbers in the periodic flow regime, in contrast to the other faces of the cylinder. Finally, heat transfer correlations for both constant temperature and constant-heat-flux boundary conditions were proposed.

Dihman et al. [8] researched the flow and heat transfer characteristics of an isolated square cylinder in a crossflow placed symmetrically in a channel for the range of conditions of $1 \leqslant Re \leqslant 45$, $0.7 \leqslant Pr \leqslant 4000$, $Pe \leqslant 4000$ and $B = 1/8$, 1/6 and 1/4. It was shown

* Corresponding author. Tel.: +98 915 300 6795; fax: +98 511 876 3304.
E-mail address: ehsan.ebrahimnia@gmail.com (E. Ebrahimnia-Bajestan).

0017-9310/$ - see front matter © 2011 Elsevier Ltd. All rights reserved.
doi:10.1016/j.ijheatmasstransfer.2011.10.030

Nomenclature

B	blockage ratio, $B = L/H$
c_d	drag coefficient
c_p	specific heat, J/kg K
d	diameter, m
h	heat transfer coefficient, W/m^2 K
H	height of the computational domain, m
k	thermal conductivity, W/m K
L	side of the square cylinder, m
n	normal direction to the surface, m
Nu	Nusselt number, $Nu = hL/k$
P	pressure, Pa
Pe	Peclet number, $Pe = Re \times Pr$
Pr	Prandtl number, $Pr = \mu c_p/k$
Re	Reynolds number, $Re = \rho u_\infty L/\mu$
T	temperature, K
V	velocity, m/s
x	streamwise coordinate, $x = x'/L$
X_d	downstream face distance of the cylinder from the outlet, m
X_u	upstream face distance of the cylinder from the inlet, m
y	transverse coordinate, $y = y'/L$

Greek symbols

δ	size of the CV clustered around the cylinder, m
Δ	size of the CV far away from the cylinder, m
μ	dynamic viscosity, kg/m s
Φ	particle volumetric concentration, %
ρ	density, kg/m^3
κ	Boltzmann constant, 1.381×10^{-23} J/K

Subscripts

∞	inlet condition
bf	base fluid
nf	nanofluid
np	nanoparticle
w	wall

that under the same conditions of B, Re and Pr, the use of the constant heat flux boundary condition yields slightly higher values of the Nusselt number than constant temperature case. The results indicated that for a fixed block ratio, the increase in Prandtl and/or Reynolds number ends in the enhancement of the average Nusselt number. Finally, heat transfer correlations were obtained for the constant temperature and constant heat flux cases of the solid square cylinder in the previously mentioned range of physical parameters. In a recent study [9] on the effects of Reynolds and Prandtl numbers on the heat transfer from a square cylinder, a numerical study has been carried out in a 2D unsteady crossflow for the range of conditions $60 \leqslant Re \leqslant 160$ and $0.7 \leqslant Pr \leqslant 50$ (the maximum value of Peclet number being 4000). The results showed that the overall mean Nusselt number increases with the Reynolds and Prandtl numbers. It was also shown that the Nusselt number profiles for the two boundary conditions were qualitatively similar, though the constant heat flux case had a numerically higher mean Nu, for identical conditions. The front surface of the cylinder exhibited the highest value of the surface average Nusselt number; however the value for the rear face exceeded the values at the top or bottom surfaces at high Reynolds and Prandtl numbers.

One of the main difficulties with industrial fluids such as water, mineral oils and ethylene glycol is their poor heat transfer properties that impose a limitation in improving the heat transfer augmentation and compactness of the heat exchangers. There are several methods to improve the heat transfer characteristics, such as employing the flow inserts and nanofluids. Recently, much research [10,11] has been done on the suspension of nanoparticles in conventional heat transfer fluids named nanofluid, due to their anomalous thermal conductivity enhancement. Applying this new generation of heat transfer fluids eliminates the limitation of low thermal conductivity of conventional heat transfer fluids. Several effective parameters on the thermal conductivity of nanofluids have been presented, such as nanofluid temperature [12,13], nanoparticle size [12], concentration [12,13], shape [14] and materials [13]. Furthermore, some researchers believe that the Brownian motion of nanoparticles inside the fluid is a key mechanism of heat transfer in nanofluids [15]. A number of models are presented to consider these different effective parameters on the conductive heat transfer of nanofluids [13,15,16] and other thermophysical properties such as viscosity [17,18].

Ding et al. [19] conducted experiments on the laminar convective heat transfer of a Carbone nanotube-water mixture flowing through a horizontal tube. They reported a maximum enhancement of 3.5 times the heat transfer coefficient of the nanofluid relative to pure water. They showed that the effect of shape and concentration of nanoparticles is significant in determining the convective heat transfer coefficient. An experimental investigation on the convective heat transfer characteristics in the developing region of tube flow was carried out by using water/Al_2O_3 nanofluids by Anoop et al. [20]. Their results indicated that nanofluids with a smaller average particle size result in higher heat transfer coefficient.

The effect of types of nanoparticle on the laminar convective heat transfer of nanofluids was studied by Rea et al. [21]. They showed that water/Al_2O_3 nanofluid increases the heat transfer coefficient more than water/ZrO_2 nanofluid. Zeinali et al. [22] investigated the heat transfer performance of water/Al_2O_3 and water/CuO nanofluids flowing through a circular tube under a laminar flow regime. The results of their experiments indicated that the water/Al_2O_3 nanofluids cause a greater enhancement in heat transfer coefficient compared with CuO/water. They suggested that it may result from the large particle size of CuO nanoparticles compared with Al_2O_3. Ebrahimnia-Bajestan et al. [23] carried out a numerical study on the effects of different parameters on the convective heat transfer of nanofluids inside a straight circular pipe. Their results indicated that increasing particle concentration, aspect ratio of nanoparticles and flow Reynolds number enhance the heat transfer while increasing nanoparticle diameter reduces the heat transfer coefficient. Furthermore, the results demonstrated that the heat transfer characteristics of nanofluids are significantly affected by Brownian motion of particles as well as types of base fluid and nanoparticles.

Due to the outstanding potential of nanofluids in enhancing heat transfer many researchers have studied their effects and characteristics, but most of these studies are oriented toward simple geometries. To the best of the authors' knowledge, no research on nanofluids flow and heat transfer over bluff bodies has been documented in the literature. In this study, the unconfined flows of two conventional fluids as well as various types of nanofluids over a square cylinder are numerically simulated. The convective heat transfer coefficients of these flows are determined and the

effect of using nanofluids in enhancing the heat transfer from the cylinder to the flow is carefully studied. The conventional fluids (also base fluids) were chosen to be water and a 60% ethylene glycol and 40% water mixture by mass (EG:W) which are widely used as the heat transfer fluid in heat exchangers, building heating and automobile radiators. The material of the nanoparticles were selected as Al_2O_3 and CuO with two different diameters of d_{np} = 30 and 100 nm. The values of the nanoparticle volumetric concentration φ were also chosen to be 2% and 4%. All the simulations were conducted at four different Peclet numbers of 25, 50, 100 and 200.

2. Mathematical modelling

2.1. Geometrical configuration

The system of interest in this case is the unconfined flow around a two-dimensional square cylinder with side L, which is also the non-dimensionalising length scale. In this system, the square cylinder (block) is placed symmetrically between the upper and lower boundaries and is maintained at a constant temperature T_w. The block is exposed to a free stream with uniform velocity u_∞ and temperature T_∞ (Fig. 1). In addition, the free slip condition is used for artificial confining boundaries. Sohankar et al. [24] have shown that for avoiding the misleading effects of the presence of the upper and lower boundaries on the flow characteristics near the cylinder, the blockage ratio B which is defined as L/H should not be more than 5. Therefore, H/L = 20 has been used in the present work as the channel blockage ratio. Moreover, the non-dimensional upstream distance between the channel inlet and the front surface of the cylinder, X_u/L, is taken as 8 and the non-dimensional downstream distance between the rear surface of the cylinder and channel outlet, X_d/L, is taken as 15. More details on the procedure of choosing these values are presented in Section 2.4.

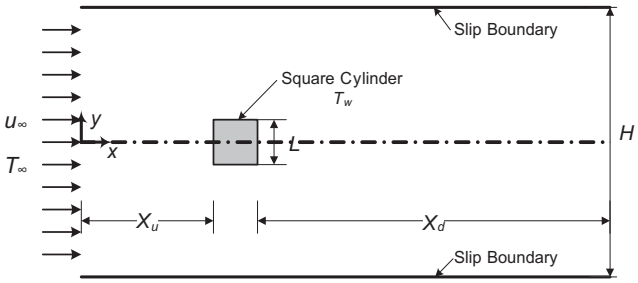

Fig. 1. Schematics of the flow and the computational domain.

2.2. Governing equations

The unconfined flow of water and the mixture of ethylene glycol and water (60:40 EG:W)can be considered to be incompressible. It is also reasonable to neglect viscous dissipation. Under these conditions, the following conservation equations were solved numerically in a two-dimensional flow field using the computational fluid dynamics software Fluent6.3 [25]:

– *Continuity*

$$(\nabla \cdot V) = 0, \tag{1}$$

– *Momentum*

$$\rho_{nf}(\nabla \cdot V)V = -\nabla P + \nabla.(\mu_{nf}\nabla V), \tag{2}$$

– *Energy*

$$\rho_{nf}c_{P,nf}(V \cdot \nabla)T = \nabla.(k_{nf}\nabla T). \tag{3}$$

2.3. Numerical method

The system of governing Eqs. (1)–(3) was solved by the control volume method using Fluent [25]. Discretization of convection terms, diffusion terms, and other quantities resulting from the governing equations was carried out using the first-order upwind scheme. The pressure–velocity coupling was modelled with the SIMPLE algorithm. Fluent uses a point implicit linear equation in conjunction with an algebraic multi-grid (AMG) method to solve the resultant block system of equations for all dependent variables in each cell. For all the simulations performed in this study, the solutions were only considered to be converged when the residuals were lower than 10^{-9}. The resulting data were then post-processed to obtain the streamlines, temperature field and convective heat transfer coefficients of the block walls.

2.4. Choice of numerical parameters

It has been shown that in numerical simulations of flow around bluff bodies, the numerical parameters such as blockage ratio B, upstream computational domain X_u, downstream computational domain X_d and grid size, $M \times N$, are of great importance and should be chosen carefully [24,26]. Since there is no available information on nanofluids flow around a square cylinder, the values of aforementioned parameters used when studying the air flow over bluff bodies were used as initial guesses. In order to study the confining upper and lower boundaries, three blockage ratios of 1/15, 1/20 and 1/25 were tested for nanofluid EG:W/Al_2O_3 4% (d_{np} = 30 nm) at the lowest Peclet number (Pe = 25). A monotonic behaviour was discovered in the variation of c_d and Nu with blockage ratio, and the changes in the values of c_d and Nu were 1.68% and 0.47%, respectively as the blockage ratio reduced from 1/20 to 1/25. Therefore, B = 1/20 was found to be adequate to simulate nanofluid unconfined flow.

In order to explore the influence of the upstream distance between the inlet and the front surface of the cylinder, four values of X_u/L = 5, 8, 10 and 15 were studied while keeping X_d/L constant at 40. Once again the nanofluid EG:W/Al_2O_3 4% (d_{np} = 30 nm) was simulated at Pe = 25 and results showed that relative percentage changes in the values of c_d and Nu were about 0.042% and 0.012% for X_u/L = 8 with respect to X_u/L = 15, respectively. Thus X_u/L = 8 was found to be an appropriate value, which is consistent with earlier research [7,8,27].

An extensive study on the influence of the downstream distance of the cylinder from the outlet X_d is carried out in [24] and also in a number of other studies including [8,28]. Based on the values used in these papers, four values of X_d/L = 10, 15, 20 and 30 were tested for water/CuO 4% (d_{np} = 100 nm) at the highest Peclet number (Pe = 200), while keeping X_u/L constant at 8. This experiment revealed that the resulting gain in the accuracy of c_d and Nu were as small as 0.019% and 0.01%, respectively, at the expense of a considerable increase in CPU time when increasing the X_d/L from 15 to 30. As a result, X_d/L = 15 is used for all the calculations in this study.

2.5. Grid structure

The grid structure approach adopted in [7,8] was found to be adequate for simulating the unconfined flow of interest. First, a uniform fine grid with constant cell size δ was distributed around the cylinder over a distance of 1.5 units to adequately capture wake-wall interactions. A much coarser mesh with constant cell size Δ was made outside the region around the cylinder that extended 4 units upstream, downstream, and to the sides. An

Table 1
Details of the grids used at $Pe = 200$ for grid independence study.

	δ	Δ	X_u	X_d	B	Size (M × N)
Grid 1	0.015	0.5	8	15	1/20	163 × 67
Grid 2	0.01	0.25	8	15	1/20	274 × 129
Grid 3	0.008	0.2	8	15	1/20	342 × 162
Grid 4	0.006	0.15	8	15	1/20	458 × 210

algebraic expression was used to generate the grid between these two regions.

2.6. Grid independence study

A grid independence study was carried out using the different non-uniform grids listed in Table 1. Four values of δ and Δ were tested to study the effects of near-region and far-field grid resolution for $Pe = 200$ and a blockage ratio of $B = 1/20$. The fluid was chosen to be water/CuO4% ($d_{np} = 100$ nm) and the upstream distance X_u/L and downstream distance X_d/L were kept constant at 8 and 15, respectively. The results of grids 1 and 2 demonstrate considerable differences while the relative changes in the value of c_d and Nu for grid 3 relative to grid 4 is only 0.31% and 0.74%, respectively. The excessive computation time taken to solve grid 4 justifies the small errors involved in using grid 3. Therefore, grid 3 is used in this study for unconfined ($B = 1/20$) flow. The grid structure was generated using Gambit [29] and is shown in Fig. 2. It shows the non-uniform grid for the whole computational domain (Fig. 2(a)) and a magnified view near the block (Fig. 2(b)).

2.7. Nanofluid modelling

The thermophysical properties of nanofluids such as density, specific heat, thermal conductivity and viscosity are calculated based on relationships presented in the literature. These formulas are listed below:

- *Density*
  The density of the nanofluids is calculated based on the equation proposed by Pak and Cho [30]:

$$\rho_{nf} = (1-\phi)\rho_{bf} + \phi\rho_{np}. \tag{4}$$

- *Specific heat*
  The specific heat of nanofluids is determined using the equation given by Xuan and Roetzel [31] that assumes thermal equilibrium between the base fluid and the nanoparticles:

$$C_{p,nf} = \frac{(1-\phi)(\rho c_p)_{bf} + \phi(\rho c_p)_{np}}{(1-\phi)\rho_{bf} + \phi\rho_{np}}. \tag{5}$$

- *Thermal conductivity*
  Koo and Kleinstreuer [15] presented their thermal conductivity model as a two-term function which takes into account the effect of particle size d_{np}, particle volumetric concentration ϕ, temperature T and the properties of the base fluid as well as the effect of the Brownian motion of nanoparticles. Later, Vajjha and Das [32] revised this relation using a broader set of data:

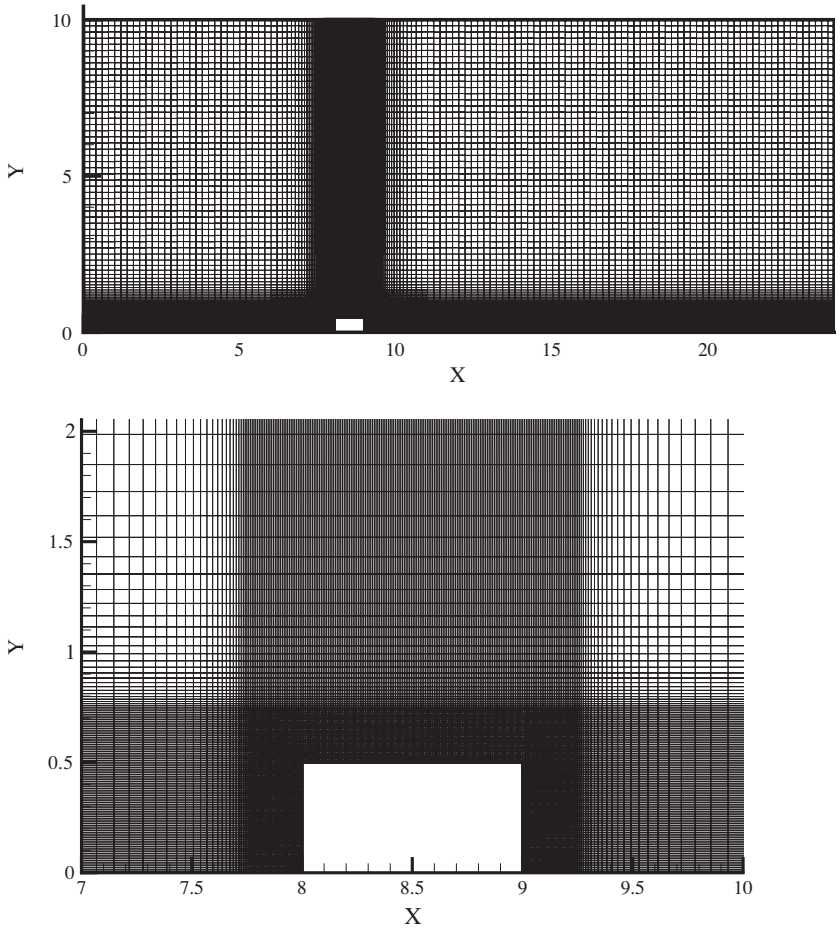

Fig. 2. Non-uniform computational grid structure.

Table 2
Curve-fit relations proposed by Vajjha and Das [32].

Type of particles	β	Concentration
Al_2O_3	$8.4407(100\phi)^{-1.07304}$	$1\% \leqslant \phi \leqslant 10\%$
CuO	$9.881(100\phi)^{-0.9446}$	$1\% \leqslant \phi \leqslant 6\%$

Table 3
Physical properties of nanoparticles.

Material	ρ (kg/m^3)	Cp (J/kg·K)	k (W/m K)
Al_2O_3	3970	765	40
CuO_2	6350	535.6	76.5

$$k_{nf} = \frac{k_{np} + 2k_{bf} - 2(k_{bf} - k_{np})\phi}{k_{np} + 2k_{bf} + (k_{bf} - k_{np})\phi} k_{bf} + 5 \times 10^4 \beta\phi\rho c_{p,bf} \times \sqrt{\frac{\kappa T}{\rho_{np} d_{np}}} f(T,\phi), \tag{6a}$$

where

$$f(T,\phi) = \left(2.8217 \times 10^{-2}\phi + 3.917 \times 10^{-3}\right)\frac{T}{T_0} + \left(-3.0669 \times 10^{-2}\phi - 3.91123 \times 10^{-3}\right). \tag{6b}$$

In the above equation, T_0 is set at 273 K and also the expressions of β for Al_2O_3 and CuO nanoparticles are given in Table 2. These relations are valid for 298 K $\leqslant T \leqslant$ 363 K.

– *Viscosity*

In a recent paper, Masoumi et al. [17] developed a theoretical model for the prediction of the effective viscosity of nanofluids based on Brownian motion. They showed that their presented model could accurately predict the effective viscosity of different nanofluids. Their model is:

$$\mu_{nf} = \mu_{bf} + \frac{\rho_{np} V_B d_{np}^2}{72C\delta}, \tag{7a}$$

in which:

$$V_B = \frac{1}{d_{np}}\sqrt{\frac{18\kappa T}{\pi\rho_{np} d_{np}}}, \tag{7b}$$

$$\delta = \sqrt[3]{\frac{\pi}{6\phi}} d_{np}, \tag{7c}$$

$$C = \mu_{bf}^{-1}\left[\left(c_1 d_{np} \times 10^9 + c_2\right)\phi + \left(c_3 d_{np} \times 10^9 + c_4\right)\right], \tag{7d}$$

where:

$$c_1 = -0.000001133,$$
$$c_2 = -0.000002771,$$
$$c_3 = 0.00000009,$$
$$c_4 = -0.000000393.$$

The thermophysical properties equations summarised in the previous sections require the values of the properties of the base fluid as well as nanoparticles. The properties of nanoparticles are taken to be constant in the present operating range of 300 K to about 320 K (Table 3).

The thermophysical properties of water and EG:W were obtained from the ASHRAE Handbook [33] were curve fitted as a function of the temperature with the following equations.

– *Thermophysical properties of water*

$$\rho_{bf} = -0.0036T^2 + 1.9159T + 748.19, \tag{8}$$
$$c_{p,nf} = -0.0001T^3 + 0.1155T^2 - 41.296T + 9017.8, \tag{9}$$
$$k_{bf} = -8 \times 10^{-6}T^2 + 0.0062T - 0.5388, \tag{10}$$
$$\mu_{bf} = 0.00002414 \times 10^{(247.8/(T-140))}, \tag{11}$$

– *Thermophysical properties of EG:W*

$$\rho_{bf} = -0.002475T^2 + 0.9998T + 1002.5, \tag{12}$$
$$C_{p,bf} = 4.248T + 1882.4, \tag{13}$$
$$k_{bf} = -3.196 \times 10^{-6}T^2 + 0.0025T - 0.1054, \tag{14}$$
$$\mu_{bf} = 0.001 \times \exp\left(3135.6 \times \frac{1}{T} - 8.9367\right). \tag{15}$$

Then they were substituted into the density, specific heat, thermal conductivity and viscosity equations, Eqs. (4)–(7), to evaluate the properties of nanofluids at different temperatures, concentrations and nanoparticle diameters. This was done by developing various User Defined Functions (UDFs) in C language which were then interpreted and incorporated into the main solver. Hence, in this study the properties of nanofluids are temperature dependent. Tables 4 and 5 show the physical properties of nanofluids based on water and EG:W at T = 300 K, respectively.

2.8. Validation of results

The results were validated using the available data in the literature which are mostly oriented to air (Pr = 0.7). Separate runs were necessary to determine the results at specific Reynolds numbers of 5, 20 and 40. Table 6 compares the drag coefficient c_d and overall Nusselt number of the cylinder $\overline{Nu}$ obtained in the present research with those from references [7,26]. It is clear that the results are in very good agreement with previous studies.

3. Results and discussion

Computations were carried out in a complete laminar and steady regime. The Peclet numbers were chosen to be 25, 50, 100 and 200 so the corresponding Reynolds numbers would not exceed 45 (for Re > 50 the flow becomes unsteady). A total number of 72 simulations were carried out for four nanofluids of water/Al_2O_3, water/

Table 4
Physical properties of nanofluids with the base fluid of water at T = 300 K.

Nanofluid	d_{np} (nm)	ϕ (%)	ρ (kg/m^3)	c_p (J/kg K)	k (W/m K)	μ (kg/m s)	Pr
Water/Al_2O_3	30	2	1056.0	3924.3	0.6857	9.942E−04	5.689
		4	1115.5	3694.8	0.7215	1.188E−03	6.086
	100	2	1056.0	3924.3	0.6679	8.715E−04	5.121
		4	1115.5	3694.8	0.7043	8.909E−04	4.674
Water/CuO	30	2	1103.6	3761.7	0.6870	1.032E−03	5.650
		4	1210.7	3416.3	0.7272	1.277E−03	6.001
	100	2	1103.6	3761.7	0.6689	8.767E−04	4.930
		4	1210.7	3416.3	0.7082	9.012E−04	4.348

Table 5
Physical properties of nanofluids with the base fluid of EG:water (60:40) at $T = 300$ K.

Nanofluid	d_{np} (nm)	φ (%)	ρ (kg/m^3)	c_p (J/kgK)	k (W/mK)	μ (kg/ms)	Pr
EG:Water/Al_2O_3	30	2	1137.5	2989.8	0.4143	5.310E−03	38.320
		4	1195.3	2839.0	0.4356	6.347E−03	41.374
	100	2	1137.5	2989.8	0.3997	4.655E−03	34.819
		4	1195.3	2839.0	0.4215	4.758E−03	32.055
EG:Water/CuO	30	2	1185.1	2875.9	0.4149	5.511E−03	38.193
		4	1290.5	2640.9	0.4394	6.823E−03	41.003
	100	2	1185.1	2875.9	0.4002	4.682E−03	33.649
		4	1290.5	2640.9	0.4238	4.813E−03	29.991

Table 6
Comparing the values of $\overline{Nu}$ and C_D with the data in the literature (air, $Pr = 0.7$).

	$Re = 5$		$Re = 20$		$Re = 40$	
	$\overline{Nu}$	c_d	$\overline{Nu}$	c_d	$\overline{Nu}$	c_d
Present study	1.27	4.83	2.07	2.43	2.72	1.83
Paliwali et al. [26]	1.22	–	2.07	–	2.71	1.98
Sharma and Eswaran [7]	1.24	4.86	2.05	2.35	2.71	1.75

CuO, EG:W/Al_2O_3, and EG:W/CuO using values of $d_{np} = 30$ and 100 as well as $\phi = 0$, 2% and 4%. Twelve extra simulations were also conducted to determine the required values for presenting Fig. 10.

Fig. 3 shows the streamlines plots in the vicinity of the square cylinder at $Pe = 25$, 50, 100 and 200 for water/CuO4% ($d_{np} = 30$ nm). It is clear from Fig. 3(a)–(d) that the flow is attached to the block until it reaches the trailing edge of the upper surface. At this point, the flow separates from the block and forms a recirculation region behind the cylinder. At $Pe = 25$ (Fig. 3(a)), this region is small but by increasing the Peclet number the recirculation region develops and at $Pe = 200$ (Fig. 3(d)) extends to less than 3 times L. In the case of

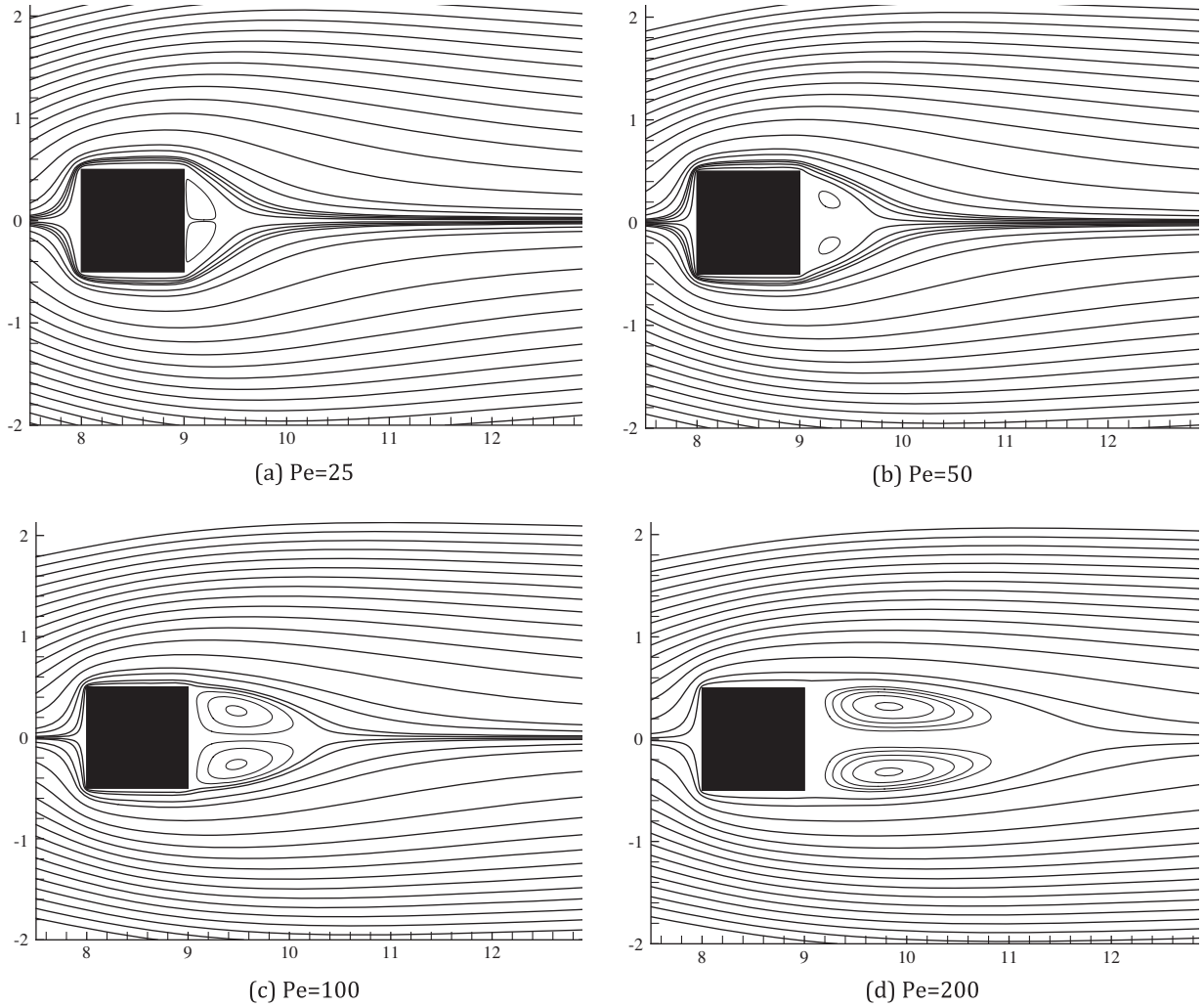

Fig. 3. Streamlines of water/CuO 4% ($d_{np} = 30$ nm) at different Peclet numbers.

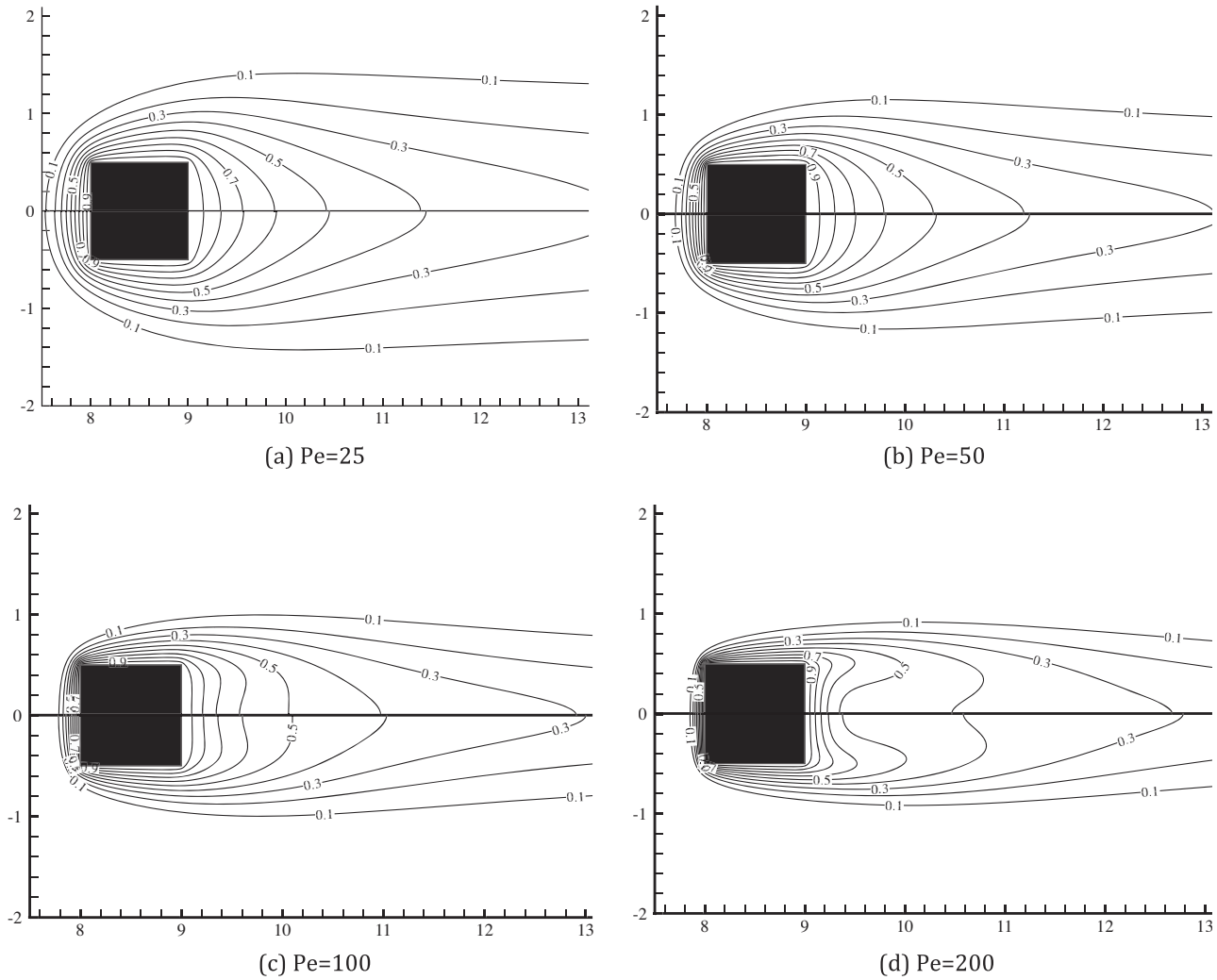

Fig. 4. Temperature contours of water (upper half) and water/CuO 4% (d_{np} = 30 nm, lower half) at different Peclet numbers.

water/CuO 4% (d_{np} = 30 nm), the Peclet numbers of 25, 50, 100 and 200 correspond to Reynolds numbers of 4.2, 8.3, 16.7 and 33.3.

Fig. 4 depicts the non-dimensional temperature contours (temperature is non-dimensionalised as $\theta = (T - T_\infty)/(T_w - T_\infty)$) around the block for different Peclet numbers. The top half and the lower half show the isotherms of water and water/CuO4% (d_{np} = 30 nm), respectively. Clearly, the contours of both fluids have the same pattern but the nanofluids show a higher capability of transferring the heat from the cylinder, particularly at higher Peclet numbers. It is evident from Fig. 4 that temperature contours are much denser near the front surface of the block. This indicates the higher temperature gradient and, subsequently, greater heat transfer coefficient. At the trailing edge of the upper surface of the cylinder, where the flow separates from the block, the temperature contours start to disperse. As the Pe increases and the recirculation region behind the cylinder grows, this dispersion reduces and the isotherms become closer to the rear side of the block.

Fig. 5 shows the local heat transfer coefficient along the cylinder surfaces for water/CuO 4% (d_{np} = 30 nm) at different Peclet numbers. The heat transfer coefficient around the block is defined as:

$$h = \frac{k_{nf}\partial T/\partial n}{T_w - T_\infty}. \tag{16}$$

As expected, the h values increase with increasing the Peclet number. Generally, the front surface has the highest heat transfer coefficient which is predictable according to Fig. 4. It is also clear that heat transfer coefficient curve reaches a peak at the corners of the block which is due to the high temperature gradients at these points. The averaged values of h over the rear surface of the cylinder is lower than the front and upper surfaces as the temperature contours are less crowded behind the block.

Fig. 6 presents the average heat transfer coefficient around the block at different Peclet numbers, nanoparticles volume fractions and diameters for the cases of Al_2O_3/water and CuO/water nanofluids. The results indicate that the average heat transfer coefficient of nanofluid rises with increasing Peclet number as well as the particle volume fraction and decreases with an increase in particle diameter.

Since the denominator of Eq. (16) is constant, the effect of nanofluids on the heat transfer coefficient can be explained based on the variation in thermal conductivity and wall temperature gradient.

In this paper the inlet velocity is adjusted to achieve a constant Peclet number ($Pe = \frac{\rho u_\infty L C_p}{k}$) for different cases of nanofluids. According to Table 4, at higher concentration levels, the values of thermal conductivity and density increase and the heat capacity reduces. However, the overall interaction of these parameters is such that the inlet velocity should increase to achieve a constant Peclet number which may lead to a higher velocity gradient and as a result, depending on the Prandtl behaviour, the temperature gradient around the block changes. On the other hand, increasing the particle concentration boosts the viscosity which may tend to decrease the velocity gradient near the block. Therefore, these

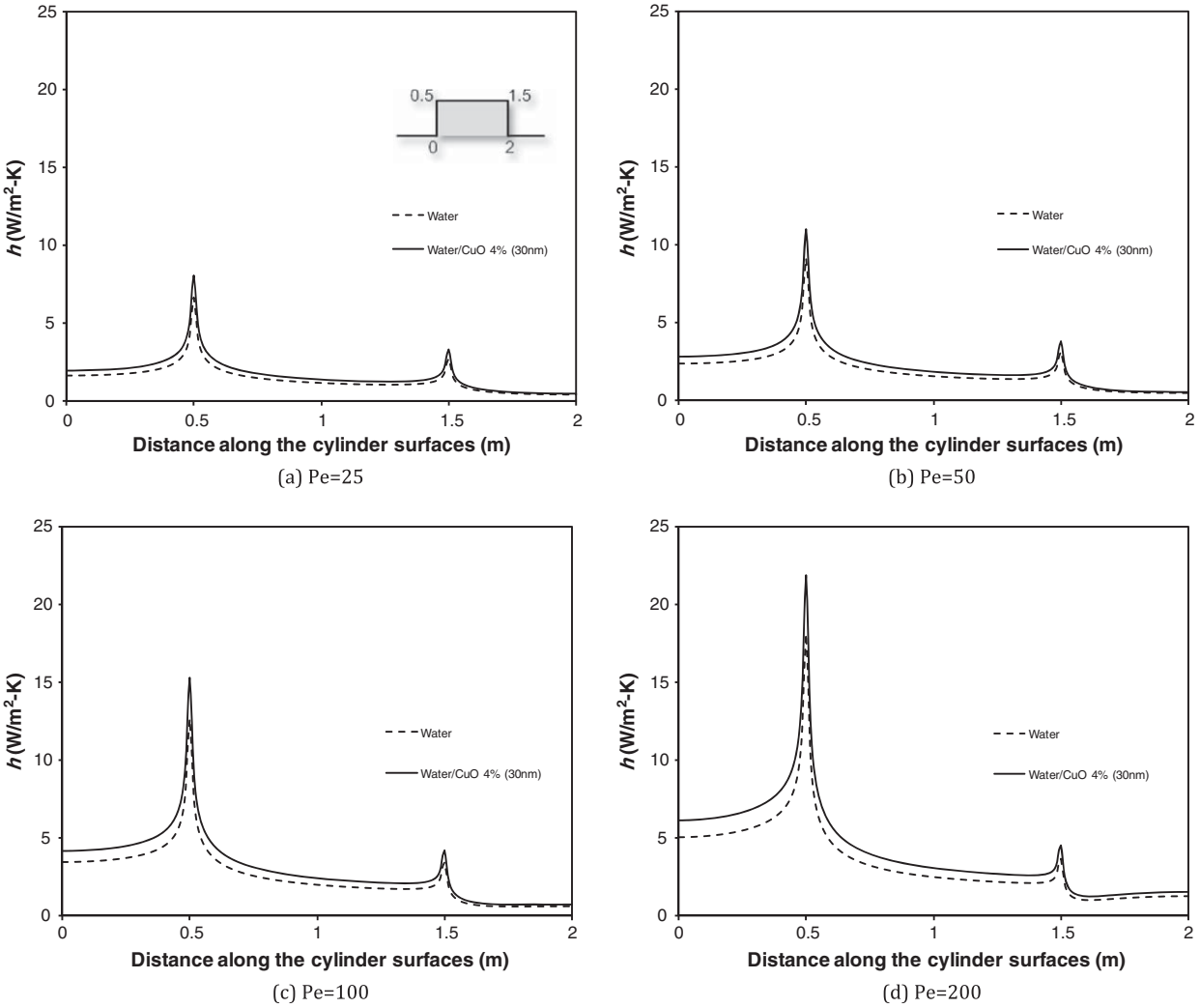

Fig. 5. Local heat transfer coefficient of water and water/CuO 4% (d_{np} = 30 nm) along the cylinder surfaces at different Peclet numbers.

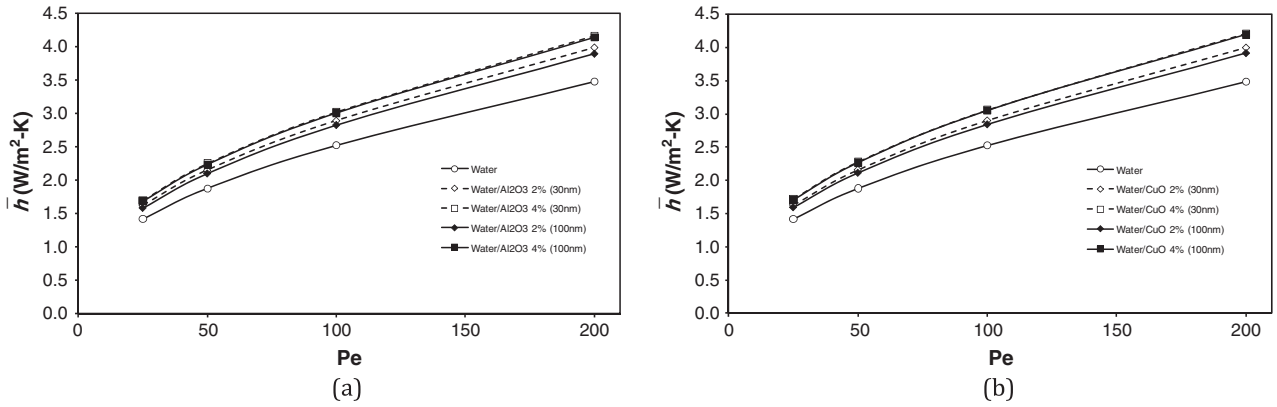

Fig. 6. Average heat transfer coefficient of the cylinder as a function of Peclet number for water and different nanofluids with base fluid of water.

opposing behaviours during particle concentration enhancement should be considered to realise the resultant heat transfer characteristics of nanofluids.

Fig. 6 shows that, at any given *Pe*, the heat transfer coefficient is enhanced as the particle concentration increases. According to Eq. (16), this manner proves that for the nanofluids shown in this figure, the upward trend of thermal conductivity dominates the heat transfer coefficient behaviour. It can also be seen that the effect of particle concentration becomes more significant at higher Peclet numbers.

Similarly, for a given particle concentration the heat transfer coefficient increases at a higher *Pe*. That is due to the fact that for constant thermophysical properties and a fixed geometry the only way to increase the Peclet number is to increase the inlet

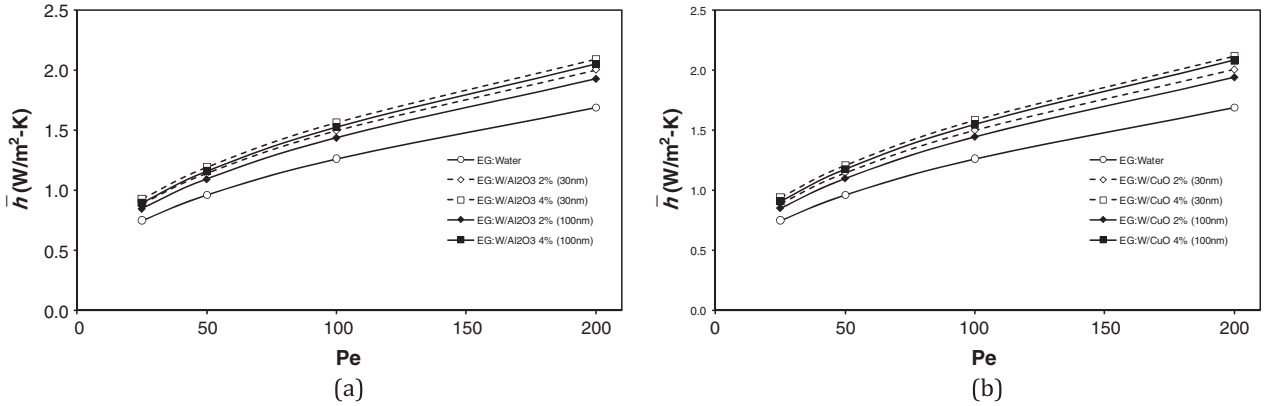

Fig. 7. Average heat transfer coefficient of the cylinder as a function of Peclet number for ethylene glycol:water (EG:W) and different nanofluids with base fluid of EG:W.

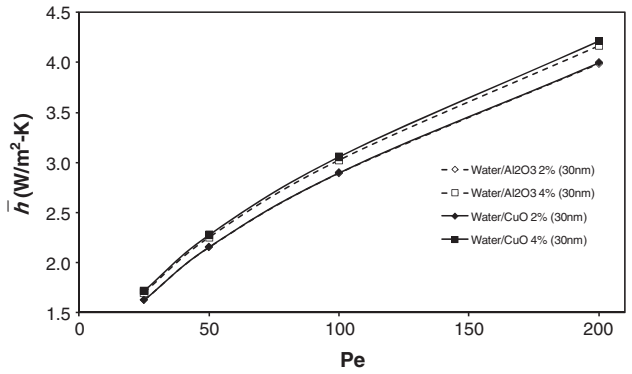

Fig. 8. Average heat transfer coefficient of the cylinder as a function of Peclet number for different water based nanofluids.

velocity which leads to a higher velocity and temperature gradient near the block.

On the other hand, the particle diameter has an inverse effect on heat transfer characteristics, which is obvious in Fig. 6, especially at lower particle concentrations.

Similarly, Fig. 7 presents the effects of particle concentration and diameter on averaged heat transfer coefficients at different values of Peclet number. In this figure the base fluid is a 60:40 mixture of ethylene glycol and water (EG:W).

Comparison of Figs. 6 and 7 indicates that the effect of nanoparticle diameter on the heat transfer coefficient is more significant in the cases of nanofluids with the base fluid of EG:W. Since the Prandtl number of EG:W is noticeably higher than water at the same *Pe* number (see Tables 4 and 5), the heat transfer coefficient of water based nanofluids is higher than that of EG:W based nanofluids.

The effect of nanoparticle material on heat transfer coefficient of nanofluids is shown in Fig. 8. The results indicate that the heat transfer coefficient of water/CuO nanofluid is a little higher than water/Al_2O_3 at higher particle concentrations and Peclet number due to the more noticeable difference in the thermophysical properties of CuO as compared with Al_2O_3.

Fig. 9 presents the ratio of overall heat transfer rate of nanofluids to the corresponding base fluids (at the same Peclet number) for different particle concentrations and diameters. The results show that the ratio of heat transfer rate increases with increasing particle concentration ϕ and decreases with particle diameter d_{np}. As Fig. 9 shows, the effect of particle concentration in enhancing the heat transfer is more significant than that of particle diameter and the effect of particle diameter is more considerable in lower particle concentrations. The enhancement of heat transfer rate is nearly constant at different Peclet number flows, especially at higher Peclet numbers. Comparison of Fig. 9(a) and (b) demonstrates that the effect of nanofluids on the heat transfer rate enhancement is considerably greater for the case of EG:W based nanofluids than water based nanofluids.

Fig. 10 shows the effect of particle diameter on the heat transfer coefficient for different particle concentrations at *Pe* = 100. The results indicate that the effect of particle diameter is substantial at lower particle concentrations. As aforementioned, in order to maintain a constant Peclet number the inlet velocity should be increased with respect to the particle concentration and consequently the heat transfer coefficient enhances. However, in the case of the particle diameter of 15 nm, there is an optimum particle

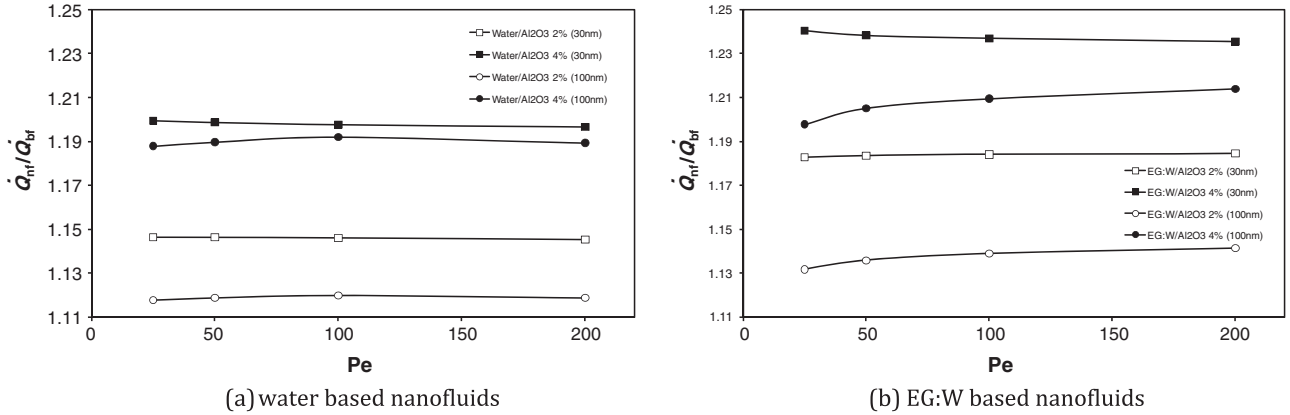

Fig. 9. Heat transfer coefficient ratio of nanofluids to the base fluids.

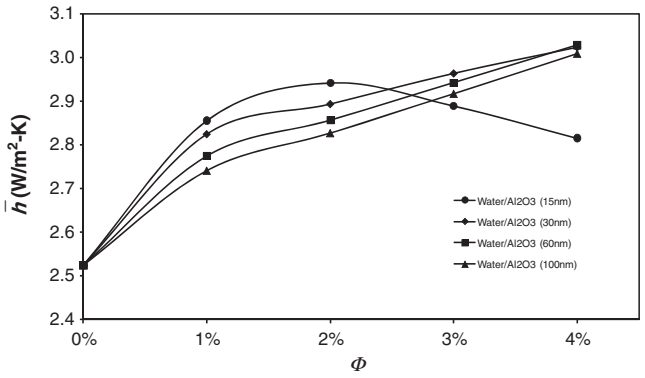

Fig. 10. Average heat transfer coefficient of the cylinder as a function of volumetric ratio for different Al_2O_3 nanoparticle diameters at $Pe = 100$.

concentration with the largest heat transfer coefficient and for higher particle concentrations the heat transfer decreases.

In the explanation of Fig. 6, two opposing behaviours of the wall velocity gradient were observed during particle concentration enhancement which should be considered to realise the resultant heat transfer characteristics of nanofluids. For a given *Pe*, increasing the particle concentration enhances the thermal conductivity of the nanofluid, but based on Eq. (7a) and Table 5 the viscosity increase is more dominant at small particle diameters which can govern the wall velocity gradient behaviour. Higher viscosity causes a lower velocity gradient near the block which results in a lower temperature gradient. Therefore, in the nominator of Eq. (16) the thermal conductivity increases with particle diameter and the temperature gradient decreases, which denotes that there is a certain particle concentration with better heat transfer characteristics as shown in Fig. 10 for $d_p = 15$ nm. Considering Fig. 10, this behaviour is expected to be observed at higher particle concentrations for other particle diameters.

4. Conclusion

The effects of using nanofluids instead of conventional fluids in the unconfined flow and heat transfer over a square cylinder were investigated numerically. Heat transfer characteristics of Al_2O_3 and CuO nanofluids were studied by varying effective parameters such as particle volumetric concentrations ϕ, nanoparticle diameters d_{np} and base fluids. For example, at a Peclet number of 200, using nanofluids water/CuO 4% ($d_p = 30$) and water/Al_2O_3 4% ($d_p = 30$) increases the heat transfer by 21% and 19.66% relative to water. For the same value of *Pe*, EG:W/CuO 4% ($d_p = 30$) and EG:W/Al_2O_3 4% ($d_p = 30$) augmented heat transfer by 25.1% and 23.6% relative to EG:W, respectively.

It was also concluded that heat transfer enhancement rises with the Peclet number as well as particle concentration, but falls with increasing nanoparticle diameter d_{np}. The results show that the effect of particle concentration on the heat transfer is more significant than the particle diameter.

Finally, studying the variation of heat transfer coefficient h versus ϕ revealed that for any given particle diameter there is an optimum value of nanoparticle concentration that results the maximum heat transfer coefficient. Therefore, extreme care should be taken in choosing the values of ϕ and d_{np}.

Acknowledgements

The second author spent one year for this research work at Fluid Mechanics, Thermal Engineering and Multiphase Flow Research Lab. (FUTURE), Department of Mechanical Engineering, King Mongkut's University of Technology Thonburi, whose guidance and assistance are gratefully acknowledged. The fourth author would like to thank the Thailand Research Fund and the National Research University Project for the support.

References

[1] R.A. Ahmad, Steady-state numerical solution of the Navier–Stokes and energy equations around a horizontal cylinder at moderate Reynolds numbers from 100 to 500, Heat Transfer Eng. 17 (1) (1996) 31–81.
[2] C.F. Lange, F. Durst, M. Breuer, Momentum and heat transfer from cylinders in laminar crossflow at $10^{-4} \leqslant Re \leqslant 200$, Int. J. Heat Mass Transfer 41 (22) (1998) 3409–3430.
[3] C. Norberg, Fluctuating lift on a circular cylinder: review and new measurements, J. Fluids Struct. 17 (1) (2003) 57–96.
[4] M.M. Zdravkovich, Flow Around Circular Cylinders: Fundamentals, Oxford University Press, New York, 1997.
[5] M.M. Zdravkovich, Flow Around Circular Cylinders: Applications, Oxford University Press, New York, 2003.
[6] S. Turki, H. Abbassi, S. Ben Nasrallah, Two-dimensional laminar fluid flow and heat transfer in a channel with a built-in heated square cylinder, Int. J. Therm. Sci. 42 (12) (2003) 1105–1113.
[7] A. Sharma, V. Eswaran, Heat and fluid flow across a square cylinder in the two-dimensional laminar flow regime, Numer. Heat Transfer A 45 (3) (2004) 247–269.
[8] A.K. Dhiman, R.P. Chhabra, V. Eswaran, Flow and heat transfer across a confined square cylinder in the steady flow regime: effect of Peclet number, Int. J. Heat Mass Transfer 48 (21–22) (2005) 4598–4614.
[9] A.K. Sahu, R.P. Chhabra, V. Eswaran, Effects of Reynolds and Prandtl numbers on heat transfer from a square cylinder in the unsteady flow regime, Int. J. Heat Mass Transfer 52 (3–4) (2009) 839–850.
[10] W. Daungthongsuk, S. Wongwises, A critical review of convective heat transfer of nanofluids, Renew. Sustain. Energ. Rev. 11 (5) (2007) 797–817.
[11] V. Trisaksri, S. Wongwises, Critical review of heat transfer characteristics of nanofluids, Renew. Sustain. Energ. Rev. 11 (3) (2007) 512–523.
[12] C.H. Li, G.P. Peterson, The effect of particle size on the effective thermal conductivity of Al_2O_3-water nanofluids, J. Appl. Phys. 101 (4) (2007) 044312–044315.
[13] S.M.S. Murshed, K.C. Leong, C. Yang, Investigations of thermal conductivity and viscosity of nanofluids, Int. J. Therm. Sci. 47 (5) (2008) 560–568.
[14] S.M.S. Murshed, K.C. Leong, C. Yang, Enhanced thermal conductivity of TiO_2 – water based nanofluids, Int. J. Therm. Sci. 44 (4) (2005) 367–373.
[15] J. Koo, C. Kleinstreuer, A new thermal conductivity model for nanofluids, J. Nanopart. Res. 6 (6) (2004) 577–588.
[16] C.H. Chon, K.D. Kihm, S.P. Lee, S.U.S. Choi, Empirical correlation finding the role of temperature and particle size for nanofluid (A_2O_3) thermal conductivity enhancement, Appl. Phys. Lett. 87 (15) (2005) 153107.
[17] N. Masoumi, N. Sohrabi, A. Behzadmehr, A new model for calculating the effective viscosity of nanofluids, J. Phys. D. Appl. Phys. 42 (5) (2009) 055501.
[18] B.C. Sahoo, R.S. Vajjha, R. Ganguli, G.A. Chukwu, D.K. Das, Determination of rheological behavior of aluminum oxide nanofluid and development of new viscosity correlations, Pet. Sci. Technol. 27 (15) (2009) 1757–1770.
[19] Y. Ding, H. Alias, D. Wen, R.A. Williams, Heat transfer of aqueous suspensions of carbon nanotubes (CNT nanofluids), Int. J. Heat Mass Transfer 49 (1–2) (2006) 240–250.
[20] K.B. Anoop, T. Sundararajan, S.K. Das, Effect of particle size on the convective heat transfer in nanofluid in the developing region, Int. J. Heat Mass Transfer 52 (9–10) (2009) 2189–2195.
[21] U. Rea, T. McKrell, L.-W. Hu, J. Buongiorno, Laminar convective heat transfer and viscous pressure loss of alumina–water and zirconia–water nanofluids, Int. J. Heat Mass Transfer 52 (7–8) (2009) 2042–2048.
[22] S. Zeinali Heris, S.G. Etemad, M. Nasr Esfahany, Experimental investigation of oxide nanofluids laminar flow convective heat transfer, Int. Commun. Heat Mass Transfer 33 (4) (2006) 529–535.
[23] E. Ebrahimnia-Bajestan, H. Niazmand, W. Duangthongsuk, S. Wongwises, M. Renksizbulut, Numerical investigation of effective parameters in convective heat transfer of nanofluids flowing under laminar flow regime, Int. J. Heat Mass Transfer 54 (19–20) (2011) 4376–4388.
[24] A. Sohankar, C. Norberg, L. Davidson, Low-Reynolds-number flow around a square cylinder at incidence: study of blockage, onset of vortex shedding and outlet boundary condition, Int. J. Numer. Methods Fluids 26 (1) (1998) 39–56.
[25] Fluent 6.3 User's Guide, Fluent Inc., Lebanon, New Hampshire, 2006.
[26] B. Paliwal, A. Sharma, R.P. Chhabra, V. Eswaran, Power law fluid flow past a square cylinder: momentum and heat transfer characteristics, Chem. Eng. Sci. 58 (23–24) (2003) 5315–5329.
[27] A. Sharma, V. Eswaran, Effect of channel confinement on the two-dimensional laminar flow and heat transfer across a square cylinder, Numer. Heat Transfer A 47 (1) (2004) 79–107.
[28] A.K. Dhiman, R.P. Chhabra, V. Eswaran, Steady flow of power-law fluids across a square cylinder, Chem. Eng. Res. Des. 84 (4) (2006) 300–310.
[29] Gambit User's Guide, Fluent Inc., Lebanon, New Hampshire, 2006.

[30] B.C. Pak, Y.I. Cho, Hydrodynamic and heat transfer study of dispersed fluids with submicron metallic oxide particles, Exp. Heat Transfer 11 (2) (1998) 151–170.
[31] Y. Xuan, W. Roetzel, Conceptions for heat transfer correlation of nanofluids, Int. J. Heat Mass Transfer 43 (19) (2000) 3701–3707.
[32] R.S. Vajjha, D.K. Das, Experimental determination of thermal conductivity of three nanofluids and development of new correlations, Int. J. Heat Mass Transfer 52 (21–22) (2009) 4675–4682.
[33] ASHRAE Handbook: Fundamentals, American Society of Heating, Refrigerating and Air-Conditioning Engineers Inc., Atlanta, GA, 2005.

Heat Mass Transfer (2012) 48:123–139
DOI 10.1007/s00231-011-0854-0

ORIGINAL

Effect of void fraction and friction factor models on the prediction of pressure drop of R134a during downward condensation in a vertical tube

A. S. Dalkilic · N. A. Kürekci · S. Wongwises

Received: 10 November 2010 / Accepted: 28 June 2011 / Published online: 10 July 2011
© Springer-Verlag 2011

Abstract The theoretical flow models of homogeneous and separated flow are applied to in-tube condensation to predict the pressure drop characteristics of R134a. The homogeneous flow model is modified by ten different dynamic viscosity correlations and various alternative correlations of total, frictional and momentum pressure drops to take account of the partial condensation inside the tube. Numerical analyses were performed to determine the average and local homogeneous wall shear stresses and friction factors by means of a CFD program. The equivalent Reynolds number model is modified by six different two-phase friction factors to determine the total condensation pressure drop in the separated flow model. The refrigerant side total pressure drops, frictional pressure drops, friction factors and wall shear stresses are determined within a ±30% error band. The importance of using the alternative total, momentum and frictional pressure drop correlations for the homogeneous flow model is also shown.

A. S. Dalkilic (✉) · N. A. Kürekci
Heat and Thermodynamics Division,
Department of Mechanical Engineering,
Yildiz Technical University (YTU),
Yildiz, Besiktas, Istanbul 34349, Turkey
e-mail: dalkilic@yildiz.edu.tr

S. Wongwises (✉)
Fluid Mechanics, Thermal Engineering and Multiphase Flow Research Lab. (FUTURE), Department of Mechanical Engineering, King Mongkut's University of Technology Thonburi (KMUTT), Bangmod, Bangkok 10140, Thailand
e-mail: somchai.won@kmutt.ac.th

S. Wongwises
The Royal Institute, Academy of Science,
Sanam Suea Pa, Dusit, Bangkok 10300, Thailand

List of symbols

A	Inside surface area (m^2)
CFD	Computational fluid dynamics
C_f	Non-dimensional skin friction coefficient
c_p	Specific heat (J/kg K)
d	Internal tube diameter (m)
f	Friction factor
G	Mass flux (kg/m^2s)
g	Gravitational constant (m/s^2)
i	Enthalpy (J/kg)
i_{fg}	Latent heat of condensation (J/kg)
L	Length of test tube (m)
m	Mass flow rate (kg/s)
P	Pressure (MPa)
Re	Reynolds number
S	Slip ratio
T	Temperature (°C)
u	Velocity (m/s)
U_∞	Free stream velocity (m/s)
Q	Heat transfer rate (W)
q	Mean heat flux (kW/m)
x	Mean vapor quality
y	Wall coordinate
z	Wall coordinate
ΔP	Pressure drop (Pa)
ΔT	Vapor side temperature difference ($T_{sat} - T_{wi}$, K)

Greek symbols

ϕ_l^2	Two-phase multiplier
ρ	Density (kg/m^3)
μ	Dynamic viscosity (kg/ms)
α	Void fraction
δ	Film thickness (m)
τ	Shear stress (N/m)
v	Specific volume (m^3/kg)

Subscripts

eq	Equivalent
exp	Measured
F	Frictional term
G	Gravitational term
g	Gas/vapor
hom	Homogeneous
i	Inlet
l	Liquid
loc	Local
o	Outlet
ph	Preheater
ref	Refrigerant
sat	Saturation
TS	Test section
tp	Two-phase
w	Water

1 Introduction

Many conventional refrigerants are being phased out from industrial use since the depletion of the earth's ozone layer and global warming has been discovered. Consequently, a lot of corporations have been required to find substitute chemicals. To meet the demand for saving the environment and also improving the performance of refrigerating equipment, re-examination of the individual components is essential. The correct size of the condenser is one of the significant issues for the optimal performance of refrigerating and air conditioning systems. The design and analysis of flow and heat transfer characteristics is complicated. The condensation of refrigerant has been investigated by numerous researchers, generally through experimental investigations. A good understanding of the two-phase flow characteristic should be included in the studies of the two-phase flow regimes, void fraction, and pressure drop. The model simulation for condensation of the refrigerant in vertical tube has received comparatively less attention in the literature.

The hydrodynamics of the condensate at the start of the tube are controlled by the shearing effect of the vapour phase if the inlet vapour flow rate is large enough. At the same time as the condensation is continuous in the tube, the vapour flow rate decreases and thus the condensate increases correspondingly. Due to this process in the tube, a conversion caused by the effect of gravity between flow patterns appears gradually. Therefore, there is annular or mist/annular flow at the beginning of the tube and a transition to other flow patterns along the tube length. A big difference exists between the heat transfer behaviours of the shear and gravity controlled regimes, and for this reason the developed models and correlations' exactness is dependent on the correct determination of the flow patterns. The main flow regime is the annular one, according to the studies in the literature, particularly during condensation inside tubes for high vapour qualities. It can be obtained from the literature that annular flow inside tubes can exist until the vapour quality reaches a value of 0.25. As a result, the annular flow has been the focus of various theoretical and experimental two-phase flow investigations. By means of these investigations in the literature, the designers can solve the in-tube condensation phenomena easily.

The heat transfer characteristics of the flow in condenser tubes are affected by the heat transfer resistance of the condensate. The local heat flux and the film thickness are one of the main parameters. First of all, Nusselt [1] presented a well-known model that is valid for smooth films at low vapour velocities regarding the prediction of the Nusselt number and film thickness for laminar films. Wasten and Dukler [2] performed the first numerical study on the calculation of a two-dimensional wavy surface using measured film thickness during turbulent film flow. Kritsadathikarn et al. [3] modified a homogeneous two-phase flow model to investigate the flow characteristics of some refrigerants flowing in adiabatic capillary tubes. The basic governing equations are derived from the conservations of mass, energy and momentum. The Runge–Kutta method is used to solve the differential equations obtained. According to their numerical results, the traditional refrigerants give lower pressure gradients than the alternative refrigerants used as examples in their study. Choi et al. [4] proposed a correlation from a database consisting of the following pure and mixed refrigerants: R125, R134a, R32, R410A, R22, R407C and R32/R134a (25/75% mass). The new correlation was derived by replacing the friction factor and the tube-diameter in the Bo Pierre [5] correlation with a friction factor obtained from pressure drop data for a micro-fin tube and the hydraulic diameter, respectively. Choi et al. [6] did convective boiling pressure drop experiments using horizontal minichannels with a binary mixture refrigerant, R-410A. Their experimental results were compared against 15 two-phase pressure drop prediction methods. The experimental pressure drop was predicted by the homogeneous model successfully. A new pressure drop prediction method based on the Lockhart–Martinelli [7] method was developed with 4.02% mean deviation. In Baudouy [8], pressure drop estimation was done with the momentum balance equation including subcooling. The homogeneous model and Friedel's friction multiplier [9] related with the Huq and Loth [10] void fraction correlations determined the data to within 15%. Dutkowski [11] investigated the frictional pressure drop in horizontal minichannels and compared his experimental

results with the theoretical values obtained from a homogeneous equilibrium model. The dynamic viscosity correlations of McAdams et al. [12], Cicchitti et al. [13], Dukler et al. [14], Owens [15], Ackers et al. [16], Beattie and Whalley [17], and Lin et al. [18] were used in his analysis. As a result of his analysis, none of the tested correlations can determine accurately the two-phase pressure drop gradient. The homogeneous model was modified with a correction factor proposed by Chen [19]. Yadigaroglu and Lahey [20] presented an alternative form for the conservation equations for one dimensional time-dependent two-phase flow. The model included the effects of the radial distributions of void fraction, velocity, and enthalpy, which were taken into account through the use of spatial correlation coefficients. Later, their model was modified by Wang [21] to analyze the thermally non-equilibrium condensing flow in a double-pipe condenser. Bhramara et al. [22] did investigations at different saturation temperatures and at different flow rates to determine the local frictional pressure drop using the homogeneous model. Each of the refrigerants' average properties is calculated assuming that they are considered as single phase pseudo fluid. The thus obtained pressure drop data is compared with the separated flow models available in the literature. Rahimi et al. [23] reported experimental and CFD investigations on the friction factor, Nusselt number, and thermal–hydraulic performance of a tube equipped with the classic and three modified twisted tape inserts. According to their results, the Nusselt number and performance of the jagged insert were higher than the other ones.

To the best of the authors' knowledge, no information in the open literature is currently available on the combination of mathematical models of refrigerant flow and numerical solutions such as CFD during in-tube condensation for the prediction of the pressure drop characteristics in vertical tubes. In the present study, the mathematical models of homogeneous and separated flow are modified to study the adiabatic steady-state one-dimensional flow of refrigerants condensing under various heat fluxes and condensing temperatures in a vertical tube. The physical properties of pure R134a belonging to the homogeneous model are provided by means of various correlations. In addition to this, apart from the authors' previous publications in the literature, there are few studies in the literature using the experimental parameters of this study related with the heat transfer and pressure drop characteristics for condensation in a small diameter vertical tube during co-current down flow of R134a. As a result, the main concern of this study is to apply these models to annular flow condensation in a vertical tube by means of the void fraction correlation reported in the authors' previous studies, dynamic viscosity correlations, equivalent Reynolds number model [24], and some well-known two-phase friction factors from the literature using a large number of experimental pressure drops to determine the wall shear stress, friction factor, frictional, and total pressure drops. A comparison of pressure drop characteristics belonging to the model and experiment is performed, and their results are also in agreement with the Fluent CFD program [25] in terms of the agreed correlations. The independence of pressure drop calculations from tube orientation [26] is also shown by means of the correlations valid for different tube orientations and agreed results. The local distributions of the wall shear stress and friction factor of R134a along the tube length, calculated by the Fluent CFD program [25], flowing in the test tube is also shown.

2 Experimental apparatus and method

A schematic diagram of the test apparatus is shown in Fig. 1. The refrigerant loop consists of a pre-heating loop, test section, cooling loop, and chilling loop. The refrigerant is circulated by a gear pump controlled by an inverter. The refrigerant flows in series through a filter/dryer, a sight glass tube, a refrigerant flow meter, and a preheater, and enters the test section. A spiral counter-flow double tube heat exchanger is designed to supply heat to control the inlet quality of the refrigerant before entering the test section. After exiting the test section, the chilling loop condenses and sub-cools the refrigerant and removes the heat input from the pre-heater and test section, and ejects it into the surroundings. After leaving the chilling loop, the refrigerant changes from the two-phase refrigerant to a sub-cooled state. Eventually, the refrigerant returns to the refrigerant pump to complete the cycle.

The test section, well insulated with suitable material to minimize the heat loss, is a vertical counter-flow tube-in-tube heat exchanger with refrigerant flowing downward (co-current liquid and vapour of R134a's down flow) in the inner tube and cooling water flowing upward in the annulus. The inner and outer tubes are made from smooth vertical copper having inner diameters of 8.1 and 26 mm, respectively. The length of the heat exchanger is 0.5 m. Figure 2 shows the detailed dimensions of the heat exchanger and the location of the thermocouples.

T-type thermocouples are used to measure the refrigerant temperature and the tube wall temperatures in the test section. A total of ten thermocouples are located on the sidewall at five points along the test tube. A thermostat is used to control the inlet temperature of the water. All the temperature measuring devices are calibrated in a controlled temperature bath using standard precision mercury glass thermometers. The uncertainty of the temperature measurements is $\pm 0.1^{\circ}C$. All static pressure taps are mounted on the tube wall. The refrigerant flow meter is a

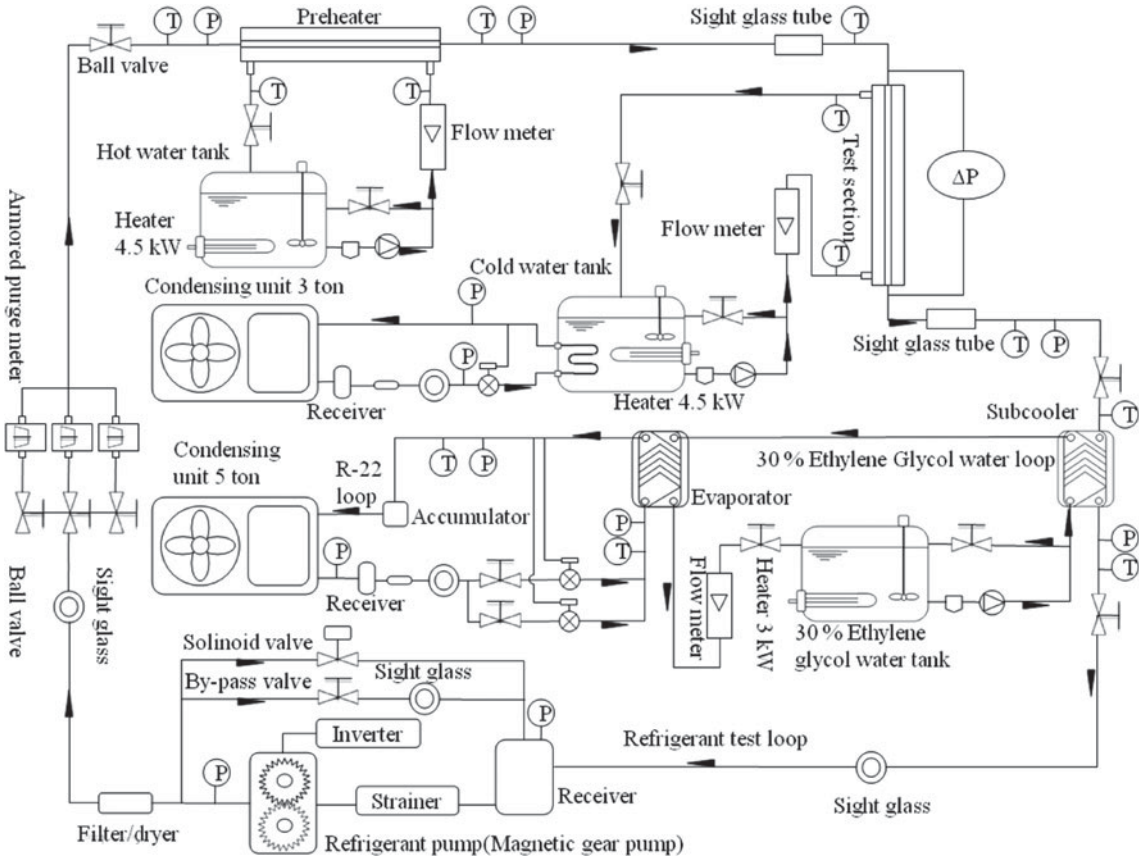

Fig. 1 Schematic diagram of experimental apparatus

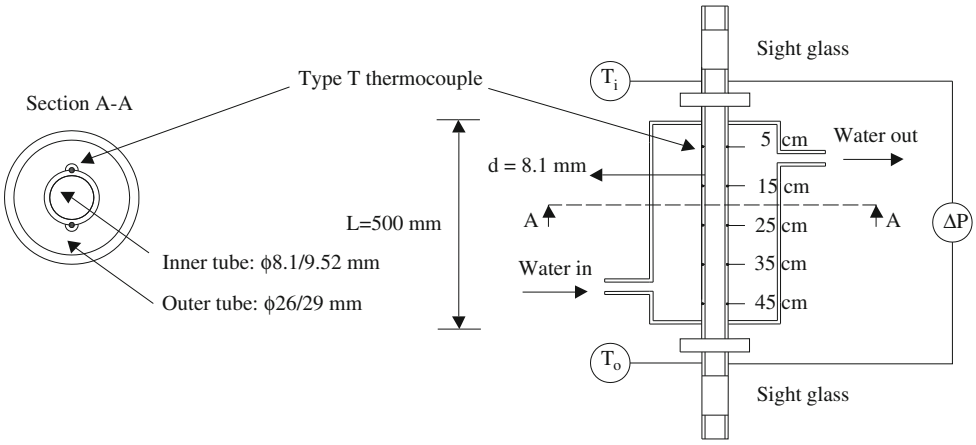

Fig. 2 Schematic diagram of test section

variable area type. The flow meter was calibrated in the range of 0–2.2 gal/min for HFC-134a by the manufacturer. The pressure drop is measured by a differential pressure transducer installed between the inlet and outlet of the test section. The length between pressure taps is 0.7 m. A low temperature thermostat is used to control the system pressure of the refrigerant flow. The differential pressure transducer and pressure gauges are calibrated against a primary standard, the dead weight tester. All signals from thermocouples and pressure transducers are recorded by a data logger. Tests are performed in the steady state.

The test runs were performed at average condensing temperatures of 40 and 50°C in a copper smooth tube having an inner diameter of 8.1 mm and length of 0.5 m. The mass fluxes were varied from 260 to 515 kg/m^2/s and the heat fluxes were between 10.16 and 66.61 kW/m^2. The accuracy of the dataset was proven in many papers in the literature.

3 Data reduction and experimental uncertainty

The following equations are used to prepare the system for experiments which have saturated vapour of R134a at the inlet of test section during steady-state regime conditions. Energy balances are written for evaporator and test section separately. Data reduction of measured results is summarized in the following procedures

3.1 The inlet vapour quality of the test section ($x_{TS,i}$)

$$x_{TS,i} = \frac{i_{TS,i} - i_{l@T_{TS,i}}}{i_{fg@T_{TS,i}}} \quad (1)$$

where $i_{l@T_{TS,i}}$ is the enthalpy of the saturated liquid based on the inlet temperature of the test section, $i_{fg@T_{TS,i}}$ is the enthalpy of vaporization based on the inlet temperature of the test section, $i_{TS,i}$ is the refrigerant enthalpy at the test section inlet and is given by:

$$i_{TS,i} = i_{ph,i} + \frac{Q_{ph}}{m_{ref}} \quad (2)$$

where $i_{ph,i}$ is the inlet enthalpy of the liquid refrigerant before entering the pre-heater, m_{ref} is the mass flow rate of the refrigerant, and Q_{ph} is the heat transfer rate in the pre-heater:

$$Q_{ph} = m_{w,ph} c_{p,w} (T_{w,i} - T_{w,o})_{ph} \quad (3)$$

where $m_{w,ph}$ is the mass flow rate of the water entering the preheater, $c_{p,w}$ is the specific heat of water, and $(T_{w,i} - T_{w,o})_{ph}$ is the temperature difference between inlet and outlet positions of the preheater.

3.2 The outlet vapour quality of the test section ($x_{TS,o}$)

$$x_{TS,o} = \frac{i_{TS,o} - i_{l@T_{TS,o}}}{i_{fg@T_{TS,o}}} \quad (4)$$

where $i_{TS,o}$ is the refrigerant enthalpy at the test section outlet, $i_{l@T_{TS,o}}$ is the enthalpy of the saturated liquid based on the outlet temperature of the test section, and $i_{fg@T_{TS,o}}$ is the enthalpy of vaporization. The outlet enthalpy of the refrigerant flow is calculated as follows:

$$i_{TS,o} = i_{TS,i} - \frac{Q_{TS}}{m_{ref}} \quad (5)$$

where the heat transfer rate, Q_{TS}, in the test section is obtained from

$$Q_{TS} = m_{w,TS} c_{p,w} (T_{w,o} - T_{w,i})_{TS} \quad (6)$$

where $m_{w,TS}$ is the mass flow rate of the water entering the test section, and $(T_{w,o} - T_{w,i})_{TS}$ is temperature difference between outlet and inlet position of the test section.

3.3 Uncertainties

The procedures of Kline and McClintock [27] were used for the calculation of all uncertainties. Various uncertainty values of the study can be seen from the authors' previous works and the details are given in Table 1. It should be noted that similar ranges of uncertainty with minimum and maximum values exist in the literature.

3.4 Modeling of the condensation in a vertical tube

The homogeneous and separated flow models are the most important types of flow models in developing frictional pressure drop. The separated flow model assumes that there are two artificially separated streams, each flowing in its own tube. According to this model, the velocities of each phase are constant and different from each other in their cross-sections in the tube. Most of the two-phase frictional pressure drop models are related to the separated flow analysis. Moreover, it is essential to apply a properly defined single-phase friction factor to a two-phase friction factor according to the homogeneous model, which assumes an equilibrium for the flow of both phases and also equal vapour and liquid velocities ($S = 1$). The homogeneous model is also known as the friction factor model [28] and the frictional pressure drop is computed as if the flow were a single-phase flow according to this model.

3.4.1 Homogeneous flow model

The momentum pressure drop can be expressed either by means of Eq. 7 as in Revellin [29] or Eq. 8 in Pope [30] as follows:

$$-\left(\frac{dP}{dz}\right)_M = \frac{G^2(x_i - x_o)}{L(\rho_l - \rho_g)} \quad (7)$$

Table 1 Uncertainty of experimental parameters

Parameters	Uncertainty
$T_{ref,\ sat}$ (°C)	0.19
x_i	±6.96–8.24%
ΔT (K)	±0.191
$(T_{w,o} - T_{w,i})_{TS}$ (K)	±0.045
$(T_{w,i} - T_{w,o})_{ph}$ (K)	±0.13
m_{ref} (g/s)	±0.023
$m_{w,TS}$ (g/s)	±0.35
$m_{w,ph}$ (g/s)	±0.38
q_{TS} (kW/m^2)	±6.55–8.93%
q_{ph} (kW/m^2)	±12–14.81%
ΔP (kPa)	±0.15

Table 2 Homogeneous dynamic viscosity correlations

Number	Homogeneous dynamic viscosity correlation	Correlation
1	Mc Adams et al. [12]	$\frac{1}{\mu_{tp}} = \frac{x}{\mu_g} + \frac{(1-x)}{\mu_l}$
2	Cicchitti et al. [13]	$\mu_{tp} = x\mu_g + (1-x)\mu_l$
3	Dukler et al. [14]	$\mu_{tp} = \rho_{tp}\left[xv_g\mu_g + (1-x)v_l\mu_l\right] = \rho_{tp}\left[x\frac{\mu_g}{\rho_g} + (1-x)\frac{\mu_l}{\rho_l}\right]$
4	Ovens [15]	$\mu_{tp} = \mu_l$
5	Ackers [16]	$\mu_{tp} = \frac{\mu_l}{(1-X)+X\left(\frac{\rho_l}{\rho_g}\right)^{0.5}}$
6	Beattie and Whalley [17]	$\mu_{tp} = \alpha_H\mu_g + \mu_l(1-\alpha_H)(1+2.5\alpha_H) \quad \alpha_H = \frac{x\rho_l}{X\rho_l+(1+X)\rho_g}$ $\mu_{tp} = \mu_l - 2.5\mu_l\left(\frac{x\rho_l}{X\rho_l+(1-X)\rho_g}\right)^2 + \left(\frac{x\rho_l\left(1.5\mu_l+\mu_g\right)}{X\rho l+(1-X)\rho_g}\right)$
7	Lin et al. [18]	$\mu_{tp} = \frac{\mu_l\mu_g}{\mu_g+X^{1.4}\left(\mu_l-\mu_g\right)}$
8	Fourar and Bories [32]	$\mu_{tp} = \rho_H\left(x\eta_g + (1-x)\eta_l + 2\sqrt{x(1-x)\eta_g\eta_l}\right) = \rho_H\left(\sqrt{x\eta_g} + \sqrt{(1-x)\eta_l}\right)$ $\eta_{tp} = \left(\sqrt{x\eta_g} + \sqrt{(1-x)\eta_g\eta_l}\right)^2$
9	Davidson [33]	$\mu_{tp} = \mu_l\left[1 + x\left(\frac{\rho_l}{\rho_g} - 1\right)\right]$
10	Garcia et al. [34]	$\mu_{tp} = \mu_l\left(\frac{\rho_H}{\rho_l}\right) = \frac{\mu_l\rho_g}{X\rho_l+(1-X)\rho_g}$

Table 3 Void fraction models and correlations

Number	Void fraction model/correlation	Model/correlation
1	Homogeneous model	$\alpha_H = \frac{1}{1+\left(\frac{1-x}{X}\right)\left(\frac{\rho_g}{\rho_l}\right)S} \quad S = 1$
2	Chisholm [38]	$\alpha = \frac{1}{\alpha_H+(1-\alpha_H)^{0.5}}\alpha_{hom} \quad \alpha = 1 - \frac{4\delta}{d}$
3	Soliman [39]	$G(1-x) = 4\rho_l u_l\left(\frac{\delta}{d}\right)$
4	Smith [40]	$\alpha = \left\{1 + \left(\frac{\rho_g}{\rho_l}\right)K\left(\frac{1}{X}-1\right) + \left(\frac{\rho_g}{\rho_l}\right)(1-K)\left(\frac{1}{X}-1\right)\left[\frac{\left(\frac{\rho_l}{\rho_g}\right)+K\left(\frac{1}{x}-1\right)}{1+K\left(\frac{1}{X}-1\right)}\right]\right\}^{-1} \quad K = 0.4$
5	Turner and Wallis [41]	$\frac{1-\alpha}{\alpha} = A\left(\frac{1-x}{X}\right)^p\left(\frac{\rho_g}{\rho_l}\right)^q\left(\frac{\mu_l}{\mu_g}\right)^r$
6	Spedding and Spence [42]	$\alpha = \left(1 + 2.22\left(\frac{1-x}{X}\right)^{0.65}\left(\frac{\rho_g}{\rho_l}\right)^{0.65}\right)^{-1}$

Correlation or model	A	p	q	r
Homogeneous	1	1	1	0
Zivi	1	1	0.67	0
Turner-Wallis	1	0.72	0.4	0.08
Lockhart-Martinelli	0.28	0.64	0.36	0.07
Thom	1	1	0.89	0.18
Baroczy	1	0.74	0.65	0.13

Table 4 Friction factor models and correlations

Number	Void fraction model/correlation	Model/correlation
1	Fukano and Furukawa [48]	$f_i = 0.425\left[12 + \left(\frac{v_l}{v_w}\right)\right]^{-1.33}\left(1 + 12\left(\frac{\delta}{d}\right)\right)$
2	Moeck [49]	$f_i = 0.005\left[1 + 1458\left(\frac{\delta}{d}\right)^{1.42}\right]$
3	Fore et al. [50]	$f_i = 0.005\left[1 + 300\left(\frac{\delta}{d} - 0.0015\right)\right]$
4	Choi et al. [6]	$f = 0.00506\,Re_{fo}^{-0.0951}K_f^{0.1554}\quad Re = \frac{Gd}{\mu_l}\quad K_f = \frac{\Delta xi_{fg}}{Lg}$
5	Carey [37]	$f_g = 0.079\left[\frac{Gx(d-\delta)}{\mu_g(1-4\delta/d)}\right]^{-0.25}$

Table 5 Details of the modelling in Fluent CFD program [25]

Viscos model		K-epsilon standard model
Pressure–velocity coupling		SIMPLE model
Pressure		PRESTO
Momentum		Second order upwind model
Turbulent kinetic energy		Second order upwind model
Turbulent dissipation rate		Second order upwind model
Energy		Second order upwind model
Residual	Fluent absolute criteria	Criteria in the solution
Some important critic values (iteration number: 2500)		
Continuity	10^{-3}	10^{-8}
x-velocity	10^{-3}	10^{-12}
y-velocity	10^{-3}	10^{-12}
Energy	10^{-3}	10^{-12}
k	10^{-3}	10^{-12}
Epsilon	10^{-3}	10^{-12}

$$-\left(\frac{dP}{dz}\right)_M = \frac{G^2}{L}\left(\frac{1}{\rho_o} - \frac{1}{\rho_i}\right) \tag{8}$$

The pressure drop due to gravity can be determined from Eq. 9:

$$-\left(\frac{dP}{dz}\right)_G = \rho_{tp} g \tag{9}$$

The experimental frictional pressure drop is calculated as follows.

$$\left(\frac{dP}{dz}\right)_F = \left(\frac{dP}{dz}\right)_{exp} - \left(\frac{dP}{dz}\right)_G - \left(\frac{dP}{dz}\right)_M \tag{10}$$

The frictional pressure drop correlations in Wong and Ooi [31] and Revellin [29] can be used to determine the two-phase friction factors in Eqs. 11 and 12 respectively:

$$-\left(\frac{dP}{dz}\right)_F = \frac{2f_{tp}G^2}{d\rho_{tp}} \tag{11}$$

$$-\left(\frac{dP}{dz}\right)_F = \frac{2f_{tp}G^2}{d\rho_{tp}}\left[1 + \frac{\Delta x}{2}\left(\frac{\rho_g}{\rho_l - \rho_g}\right)\right] \tag{12}$$

In addition to this, it is possible to calculate the frictional pressure drop by means of the approach of two-phase multiplier according to Collier and Thome [28]:

$$-\left(\frac{dP}{dz}\right)_F = \frac{2f_{tp}G^2}{d\rho_l}\phi_l^2 \tag{13}$$

where the two-phase friction factor is

$$\phi_l^2 = \left(1 + x\left(\frac{v_g - v_l}{v_l}\right)\right)\left(1 + x\left(\frac{\mu_l - \mu_g}{\mu_g}\right)\right)^{-0.25} \tag{14}$$

The wall shear stress from Collier and Thome [28] is

$$\tau_{wall} = \frac{f_{tp}\rho_{tp}u_{hom}^2}{2} \tag{15}$$

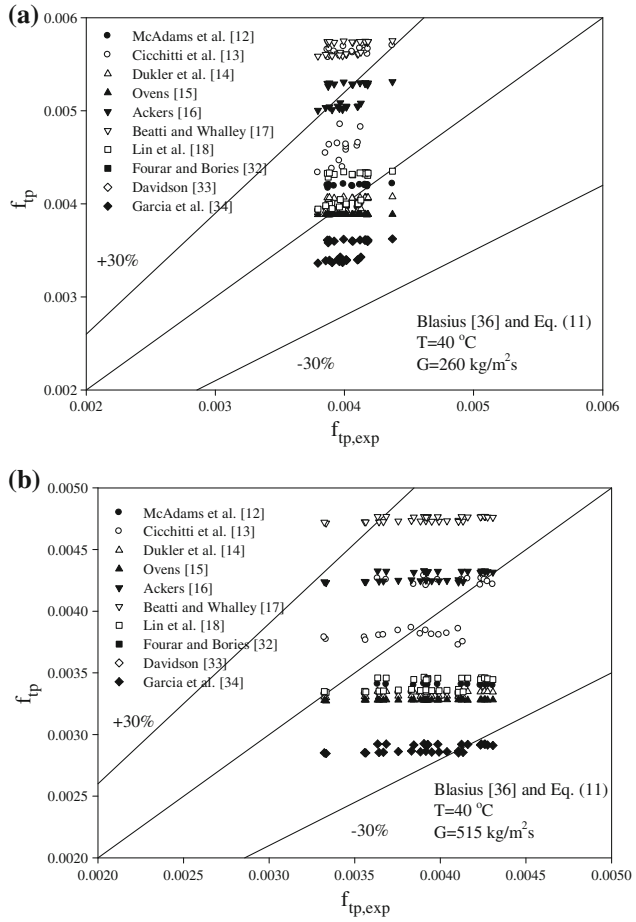

Fig. 3 Comparison of two-phase friction factors obtained from Blasius [36] equation and Eq. 11

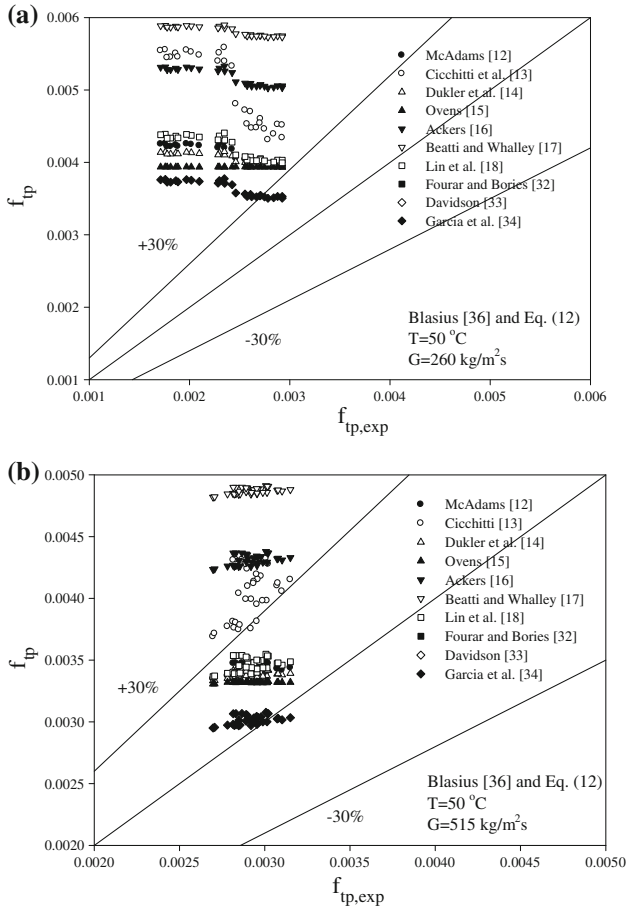

Fig. 4 Comparison of two-phase friction factors obtained from Blasius [36] equation and Eq. 12

where the homogeneous velocity is calculated from Dutkowski [11]:

$$u_{hom} = \frac{m_{total}}{\rho_{tp} A} \tag{16}$$

where the total mass flow is

$$m_{total} = GA \tag{17}$$

and the area of the flow is

$$A = \frac{\pi d^2}{4}. \tag{18}$$

The homogeneous dynamic viscosity correlations (μ_{tp}) in the literature are summarized in Table 2. They were the variable parameters in the related equations in the study and also numerical solution of the study.

The Fanning friction factor can be calculated using the Hagen-Poiseuille flow [35] in Eq. 19 for laminar–laminar flow and the Blasius equation [36] in Eq. 20 for turbulent–turbulent flow respectively as follows:

$$Re_{hom} < 2,300 \quad f_{tp} = \frac{16}{Re_{hom}} \tag{19}$$

$$Re_{hom} > 2,300 \quad f_{tp} = \frac{0.079}{Re_{hom}^{0.25}} \tag{20}$$

where the homogeneous Reynolds number can be determined as:

$$Re_{hom} = \frac{Gd}{\mu_{tp}} \tag{21}$$

3.4.2 *Separated flow model*

The two-phase pressure gradient is the sum of three contributions: the gravitational pressure gradient, the momentum pressure gradient, and the frictional pressure gradient:

$$\frac{dP}{dz} = \left(\frac{dP}{dz}\right)_G + \left(\frac{dP}{dz}\right)_M + \left(\frac{dP}{dz}\right)_F \tag{22}$$

Pressure drop due to gravity can be determined as in [37]:

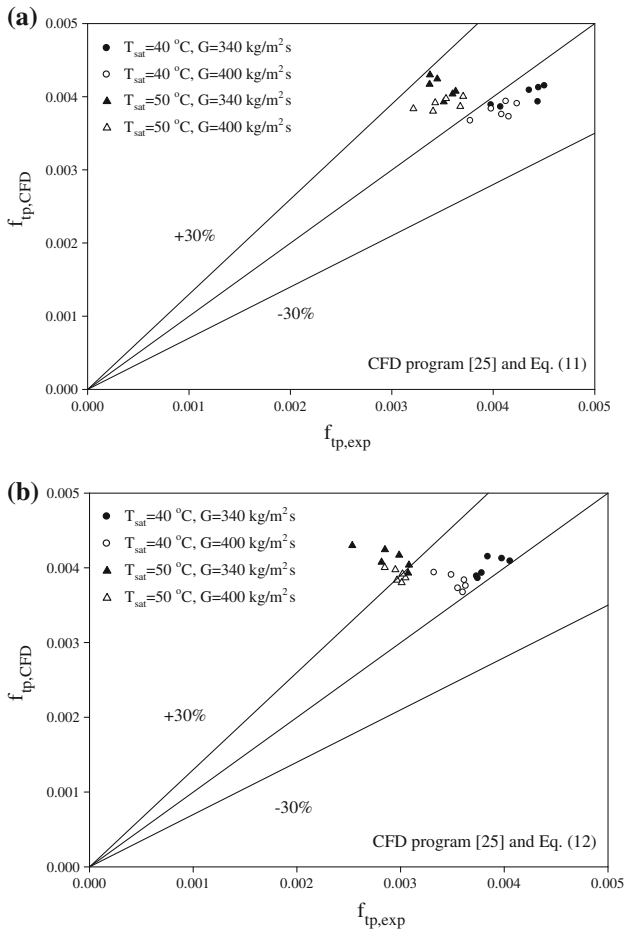

Fig. 5 Comparison of two-phase friction factors obtained from Eq. 11 (**a**) and (**b**) Eq. 12 and CFD program [25]

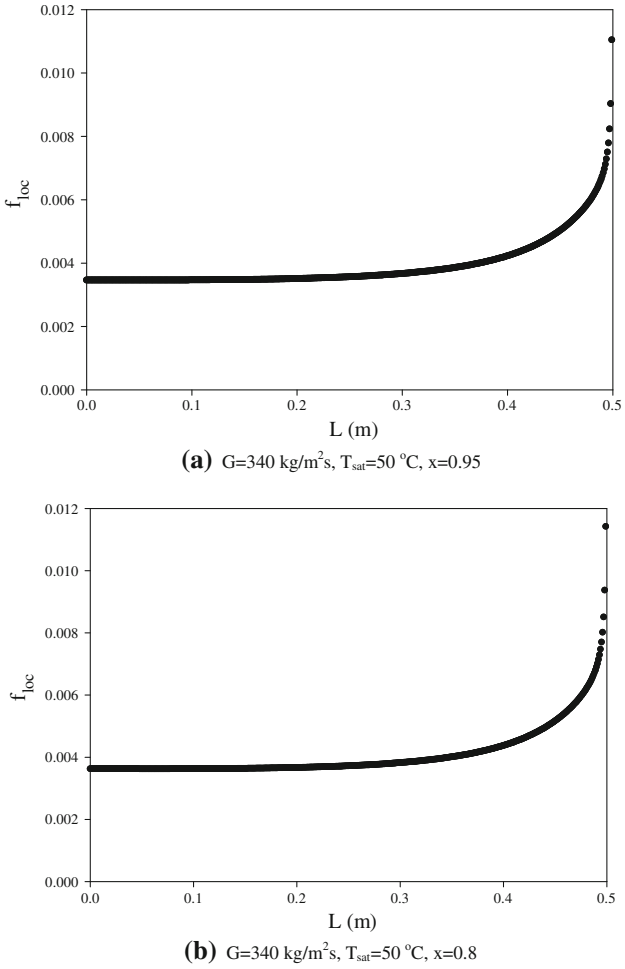

Fig. 6 Local alterations of two-phase friction factors obtained from CFD program [25] for various experimental conditions

$$(\Delta P)_G = g(\alpha\rho_g + (1-\alpha)\rho_l)L \tag{23}$$

where the void fraction, α, can be determined from the Chisholm [38] correlation shown in Table 3.

Generally, the characterization of two-phase flows depends on the void fraction which is an important value for the calculation of various parameters regarding the heat transfer and pressure drop. Accordingly, researchers have performed intensive studies to develop void fraction correlations for two-phase flows. In consequence of their efforts in the literature, Woldesemayat and Ghajar [43] stated that void fraction models and correlations can be specified as local, chordal, cross-sectional, and volumetric for different flow regimes. It should be noted that the determination of the proper void fraction models and correlations belonging to the authors' experimental database was performed in the authors' previous publications and these void fraction models and correlations are summarized in Table 3.

The momentum transfer term contributes to the overall pressure drop during condensation due to the mass transfer that occurs at the phase's interface. It was reported by Honda et al. [44] and Sami et al. [45] that the momentum pressure gradient can be neglected for the condensation, on the other hand, the momentum pressure gradient can be written according to the results of the one-dimensional two-phase separated-flow analysis which can be defined as follows [37]:

$$\left(\frac{dP}{dz}\right)_M = -G^2\frac{d}{dz}\left[\frac{x^2}{\rho_g\alpha} + \frac{(1-x)^2}{\rho_l(1-\alpha)}\right] \tag{24}$$

Equation 24 can be rearranged as follows:

$$\Delta P_M = G^2\left[\left\{\frac{(1-x)^2}{\rho_l(1-\alpha)} + \frac{x^2}{\rho_g\alpha}\right\}_o - \left\{\frac{(1-x)^2}{\rho_l(1-\alpha)} + \frac{x^2}{\rho_g\alpha}\right\}_i\right] \tag{25}$$

Akers et al. [46] developed a two-phase multiplier with the assumption that two-phase flows were similar to a single-phase flow. He predicted the frictional two-phase pressure drop by means of a multiplying factor, using the

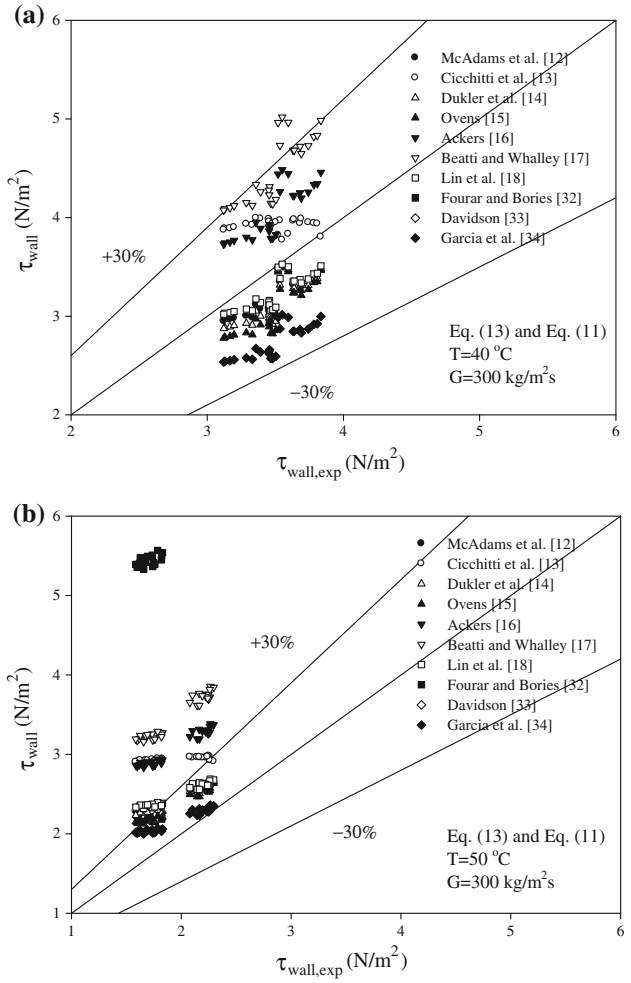

Fig. 7 Comparison of wall shear stresses obtained from Eqs. 13 and 11

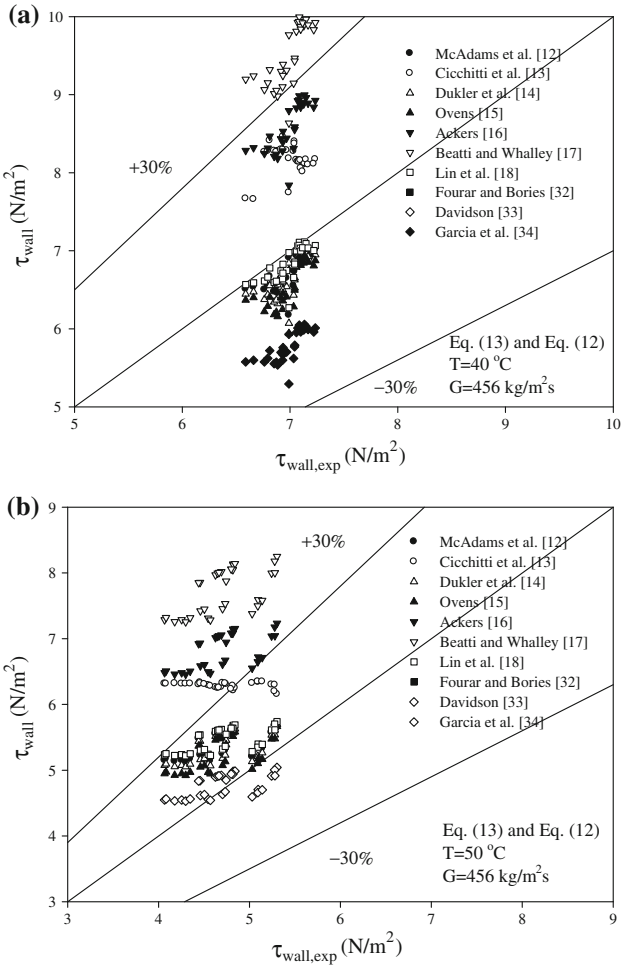

Fig. 8 Comparison of wall shear stresses obtained from Eqs. 13 and 12

same rationale as that behind the Lockhart Martinelli multiplier [7]. His model is known as the "equivalent Reynolds number model". It can be used for an annular flow regime which could be replaced by an equivalent all liquid flow that produces the same wall shear stress as that of the two-phase flow according to this model. Later, several researchers used this model, for example Moser et al. [24] and Ma et al. [47]. The two-phase frictional pressure drop is calculated from two-phase friction factor by the following equation based on all liquid *Re* number [46]:

$$f_{tp} = \frac{(\Delta P)_F}{G_{eq}^2/2\rho_l}\frac{d}{4L} = \frac{(\Delta P)_F 2\rho_l d^3}{Re_{eq}^2 \mu_l^2 4L} \tag{26}$$

where the all liquid equivalent *Re* number is

$$Re_{eq} = \frac{G_{eq} d}{\mu_l} \tag{27}$$

and equivalent liquid mass flux is

$$G_{eq} = G\left((1-x) + x\left(\frac{\rho_l}{\rho_g}\right)^{0,5}\right) \tag{28}$$

and two-phase friction factors are calculated by means of the correlations in Table 4.

Fukano and Furukawa [48] investigated the effects of liquid viscosity on the mean liquid film thickness, wave heights, and gas–liquid interfacial stresses in the vertical upward co-current annular flow in a 26 mm inner diameter tube using water and glycerol solutions as working fluids. Moeck [49] performed experiments on the diameter of entrained liquid droplets for air–water annular flow. Fore et al. [50] has obtained the film thickness and pressure gradient data for co-current upward flow of nitrogen and water under high pressure in a rectangular duct. Carey [37] developed Blasius's [36] friction factor and reported that the vapour flow in the tube can be treated as a single phase flow. Because the film is thin, the mean velocity of the

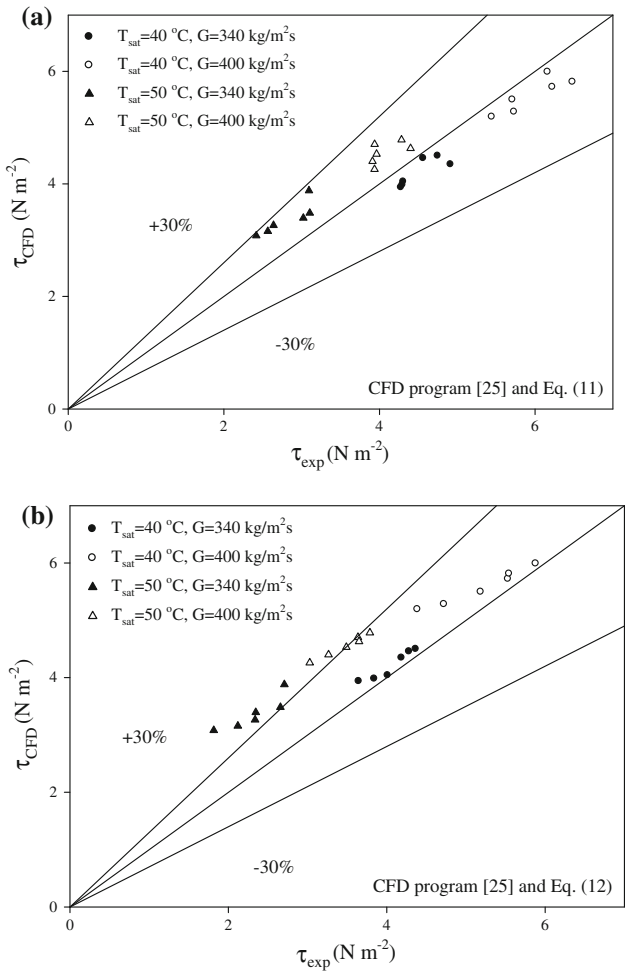

Fig. 9 Comparison of wall shear stresses obtained from Eq. 11 (**a**) and (**b**) Eq. 12 and CFD program [25]

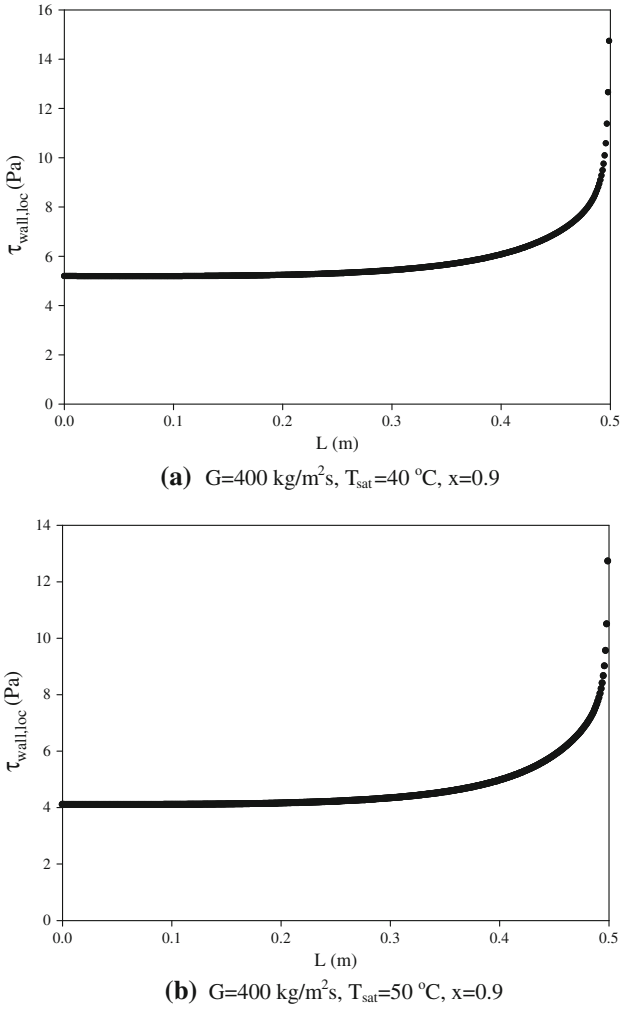

Fig. 10 Local alterations of wall shear stresses obtained from CFD program [25] for various experimental conditions

vapour is much larger than the liquid velocity at the interface due to the high viscosity of the liquid phase compared to the vapour phase. Moreover, the vapour velocity is assumed to be zero between the phases. The interfacial shear can be computed using the conventional single phase correlation by using these assumptions. The interfacial shear stress in annular two-phase flow is one of the main parameters governing transport phenomena and is required for modeling the flow. It has been intensively studied, especially for the flow assuming that all liquid travels in the liquid film. Some of the earliest works were performed by Cousins et al. [51], Wallis [52], Webb [53], Whalley [54, 55], Hewitt and Hall-Taylor [56], Asali et al. [57], Azzopardi and Teixeira [58], Fukano and Furukawa [48], Moeck [49], and Fore et al. [50].

3.4.3 Numerical model

This problem was solved by means of the processes in the Fluent CFD program [25]. Fluent is a commonly used software in CFD analysis in the literature and a detailed description of the mathematical model can be found in the Fluent User's Guide. This program uses a technique based on control volume theory to convert the governing equations to algebraic equations so they can be solved numerically. The control volume technique works by performing the integration of the governing equations about each control volume, and then generates discrimination of the equations which conserve each quantity based on control volume. Details of the selections in CFD program is given in Table 5. The necessary input values for the CFD program to run are obtained from the homogeneous flow model's correlations such as dynamic viscosity from Lin et al. [18].

The skin friction coefficient is defined by

$$C_f = \frac{\tau_{wall}}{\frac{1}{2}\rho U_\infty^2} \quad (29)$$

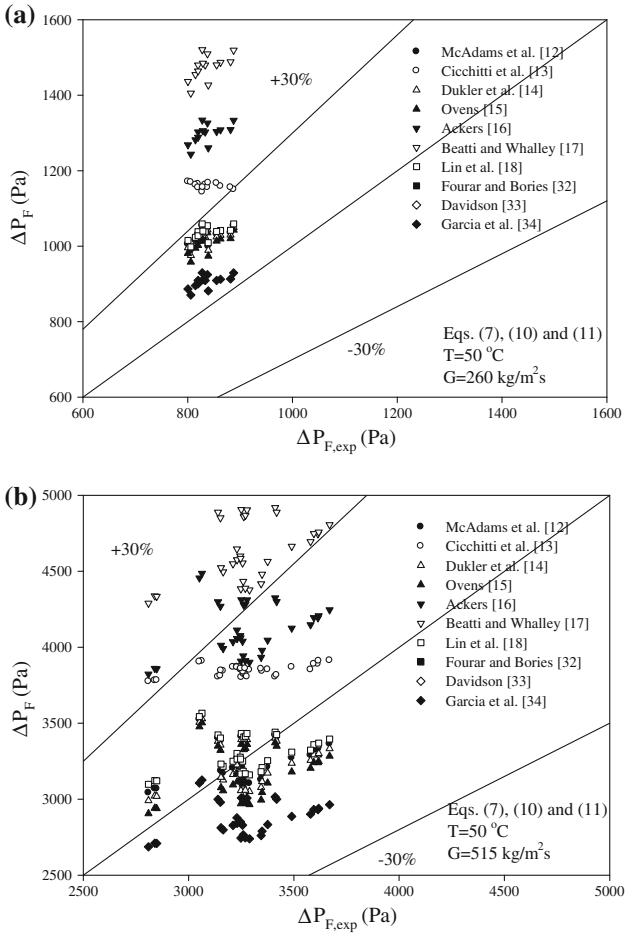

Fig. 11 Comparison of frictional pressure drops obtained from Eqs. 7, 10 and 11

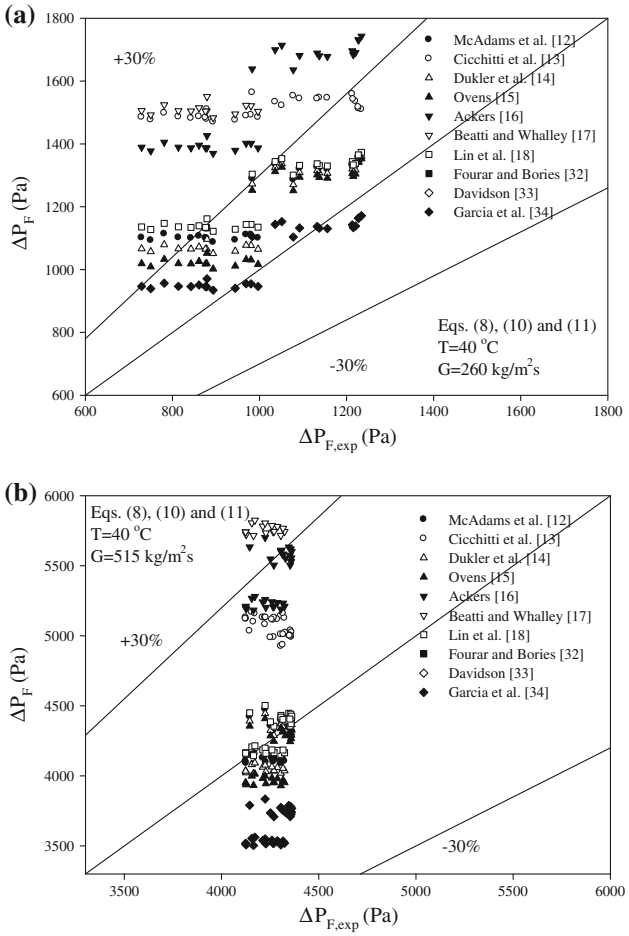

Fig. 12 Comparison of frictional pressure drops obtained from Eqs. 8, 10 and 11

where τ_{wall} is the local wall shear stress, ρ is the fluid density and U_{∞} is the free-stream velocity (usually taken outside of the boundary layer or at the inlet).

The wall shear stress, τ_{wall}, is given by

$$\tau_{wall} = \mu\left(\frac{\partial u}{\partial y}\right)_{y=0} \tag{30}$$

where μ is the dynamic viscosity, u is the flow velocity parallel to the wall, and y is the distance to the wall.

4 Results and discussion

The indirectly determined void fraction, wall shear stress, friction factor, frictional pressure drop, and total pressure drop were presented in the following paragraphs using a large number of measured data during the downward laminar condensation of R134a at a high mass flux in a vertical smooth tube over a range of experimental conditions shown in authors' previous publications. It should be noted that detailed explanations and some additional figures and tables with different experimental parameters related to this study on the void fraction models and correlations, film thickness models, friction factor and frictional pressure drop models, and heat transfer and pressure drop characteristics of data belonging to the experimental apparati can be seen in the authors' previous publications.

The experiments were performed to investigate the effect of empirical correlations such as dynamic viscosity correlations and friction factor correlations on the pressure drop characteristics using well-known flow models for the downward two-phase flow of R134a in a vertical round tube with an inner diameter of 8.1 mm. Pure HFC-134a was used in the experiments. The heat fluxes are between 10.16 and 66.61 kW/m^2 while the mass fluxes are between 260 and 515 kg/m^{2}s.

The data shown in all tables and figures for the study of R134a condensation in a vertical tube were found in the annular flow section according to the authors' investigation of flow identification studies using various flow pattern

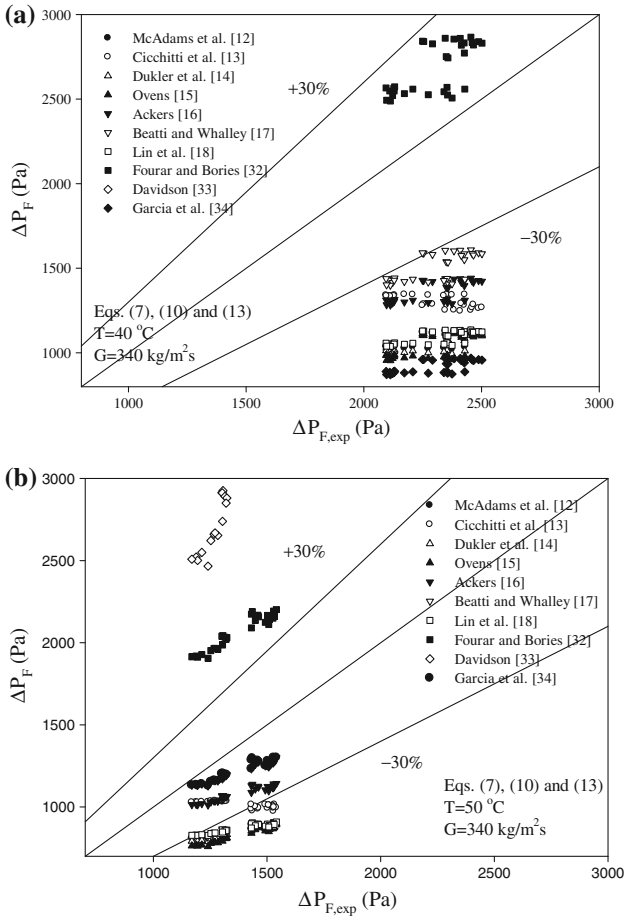

Fig. 13 Comparison of frictional pressure drops obtained from Eqs. 7, 10 and 13

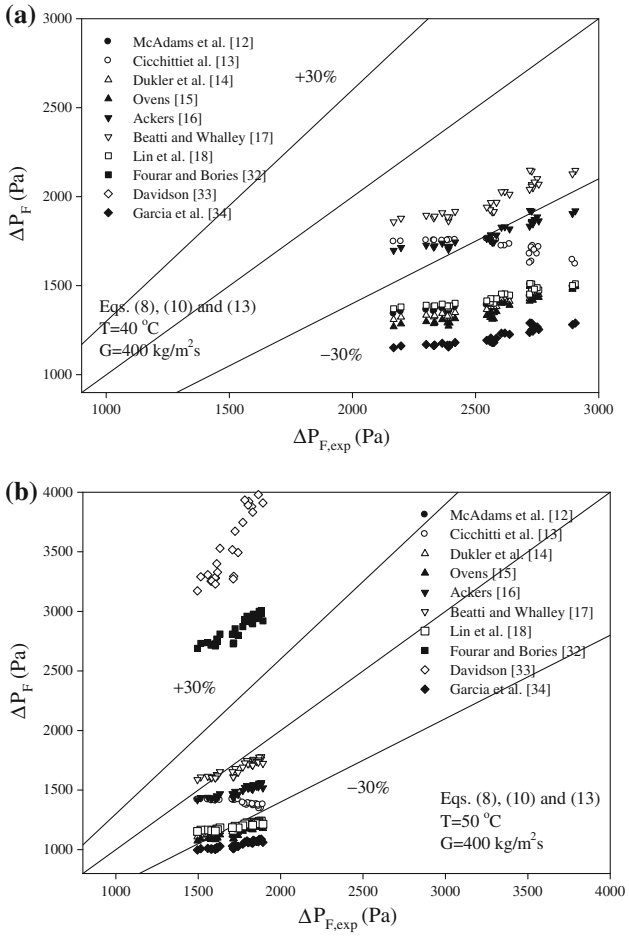

Fig. 14 Comparison of frictional pressure drops obtained from Eqs. 8, 10 and 13

maps and correlations and also checked by sight glass at the inlet and outlet of the test section.

The pressure drop is obtained by dividing the measured pressure drop by the length between pressure taps. In the vertical test section, the length between pressure taps is 0.7 m while the length of the heat exchanger is 0.5 m.

Table 3 shows the void fraction models and correlations that agree with the experimental database according to the authors' investigation of void fraction studies. As a result of the analysis, these void faction models and correlations give quite similar values such as gravitational and momentum pressure drops. For that reason, the Chisholm correlation [38] is used as a constant void faction correlation in the analysis.

Plots of the results belong to the homogeneous flow model are given from Figs. 3, 4, 5, 6, 7, 8, 9, 10, 11, 12, 13, and 14. The variations in these figures to calculate the two-phase friction factor, wall shear stress, frictional pressure drop and total pressure drop are generated by means of the two-phase homogeneous dynamic viscosity correlations such as Mc Adams et al. [12], Cicchitti et al. [13], Dukler et al. [14], Ovens [15], Ackers [16], Beattie and Whalley [17], Lin et al. [18], Fourar and Bories [32], Davidson [33], and Garcia et al. [34]. Alternative correlations from the literature are gathered for the determination of momentum pressure drop in Eqs. 7 and 8, and frictional pressure drop in Eqs. 11 and 12. The effects of these equations on the determined values are investigated in the paper. It should be noted that the two-phase homogeneous dynamic viscosity correlations of Fourar and Bories [31], and Davidson [32] have considerably large deviations from the experimental data due to their incompatible operating conditions; therefore, they are not presented in most of the figures.

Figures 3 and 4 show the comparison of two-phase friction factors calculated based on the Blasius [36] equation according to the dynamic viscosity correlations in Table 2 and different frictional pressure drop correlations in Eqs. 11 and 12. As a result of these plots, the two-phase friction factor obtained from Eq. 11 is found to be more predictive than those obtained by Eq. 12 according to the two-phase homogeneous dynamic viscosity correlations of

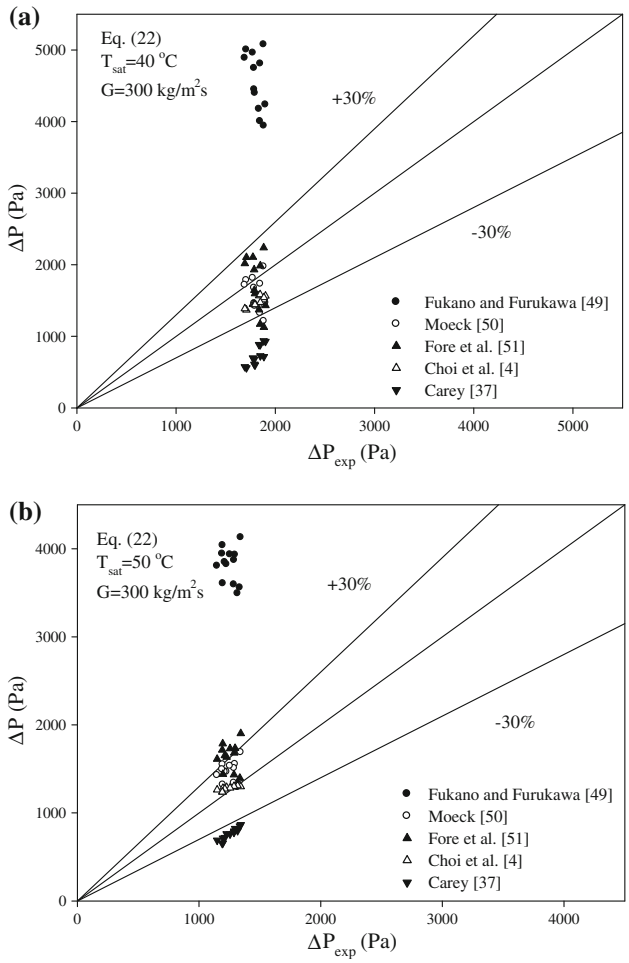

Fig. 15 Comparison of total pressure drop values between measured and calculated ones obtained from Eq. 22 during laminar flow of R134a

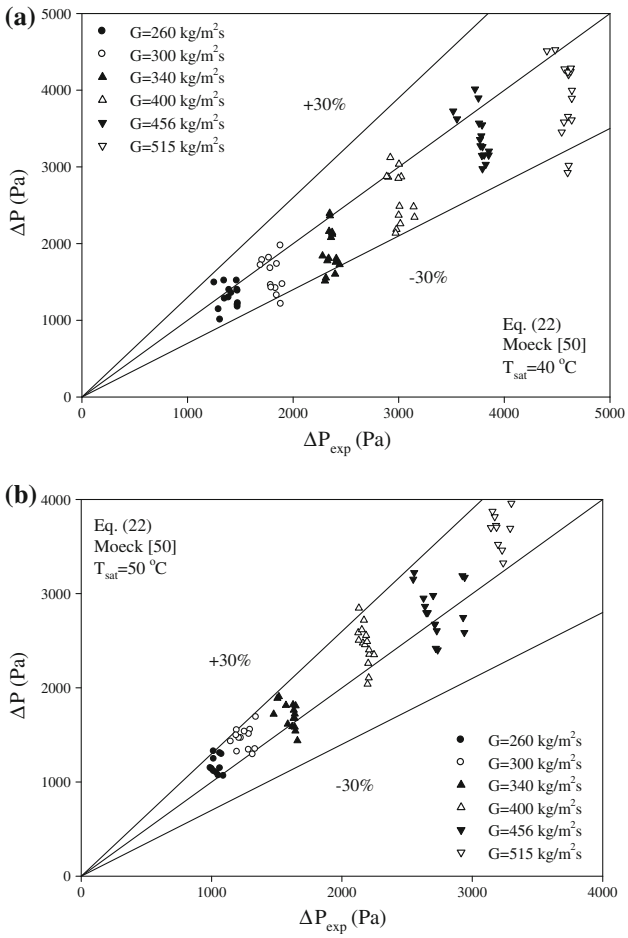

Fig. 16 Comparison of total pressure drop values between measured and calculated ones obtained from Eq. 22 and Moeck [49]'s two-phase friction factor during laminar flow of R134a

Mc Adams et al. [12], Dukler et al. [14], Ovens [15], Lin et al. [18] and Garcia et al. [34].

For the same purpose, in Figs. 3 and 4, the two-phase homogeneous friction factors are determined by means of the CFD program [25] in Fig. 5 according to the dynamic viscosity correlation of Lin et al. [18]. The numerical results are found to be in good agreement with those obtained from Eq. 11 and the same with the theoretical results. Figure 6 shows local variation of the two-phase homogeneous friction factors obtained from the numerical study. Their local values increase gradually along the tube length as expected.

In a similar way to the last figures, Figs. 7 and 8 show the comparison between the calculated wall shear stresses obtained from Eq. 13 and experimental ones. Figure 9 shows the numerical results for the determination of the wall shear stress. Consequently, similar results to the previous one, where the majority of the data belong to agreed correlations fall within the ±30% deviation band, are also obtained from these figures. Figure 10 illustrates the local wall shear stress values obtained from the CFD program [25]. The characteristics of the trend lines in the figure are in good agreement with those in the literature.

It can be clearly seen from Figs. 11 and 12 that the closest agreement comes from the two-phase homogeneous dynamic viscosity of Mc Adams et al. [12], Dukler et al. [14], Ovens [15], Lin et al. [18] and Garcia et al. [34] as explained before. The effect of the use of the different momentum pressure drop correlations in Eqs. 7 and 8 are also shown in these figures. A similar prediction performance is seen for the momentum pressure drop equations. The frictional pressure drop correlation in Eq. 11 is used in this figures.

Another frictional pressure drop correlation in Eq. 13 is used for the calculations in Figs. 13 and 14. The same variables with the previous figure are also used in these figures to investigate their effects. Although the dynamic viscosity correlations of Cicchitti et al. [13], Ackers [16], and Beattie and Whalley [17] have better prediction performance than others, none of them has satisfactory results for all experimental conditions in these figures.

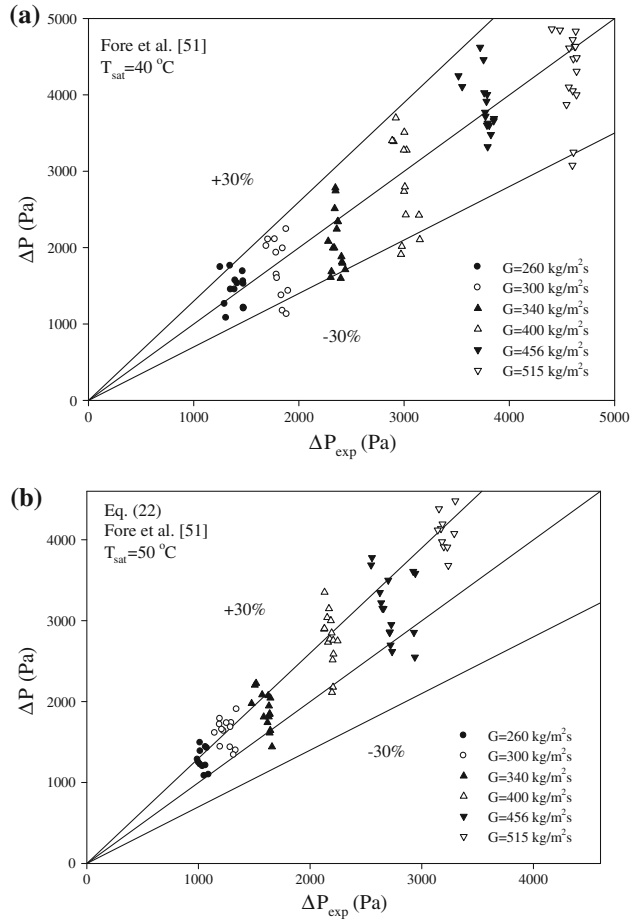

Fig. 17 Comparison of total pressure drop values between measured and calculated ones obtained from Eq. 22 and Fore et al. [50]'s two-phase friction factor during laminar flow of R134a

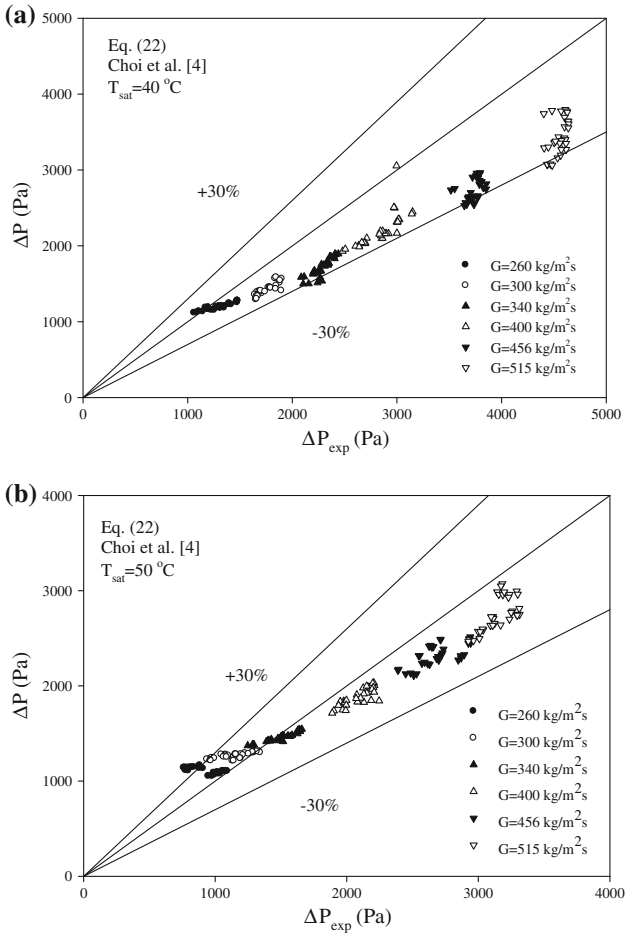

Fig. 18 Comparison of total pressure drop values between measured and calculated ones obtained from Eq. 22 and Choi et al. [6]'s two-phase friction factor during laminar and turbulent flows of R134a

Plots of the results from the separated flow model are given in Figs. 15, 16, and 17. The variations in these figures to calculate the two-phase total pressure drop are generated by means of the two-phase friction factor correlations such as Fukano and Furukawa [48], Moeck [49], Fore et al. [50], Choi et al. [6], and Carey [37]. An elimination process was performed in Fig. 15 to determine the best predictive friction factors. As a result, the friction factors of Moeck [49], Fore et al. [50] and Choi et al. [6] are found to be better than the others. It can be clearly seen from Figs. 16 and 17 that the distribution of the data between the error bands of ±30% seems quite balanced. It should be noted that the data in these figures belong to the laminar flow and none of these friction factors apart from Choi et al. [6] in Fig. 18 could predict well the total pressure drop during turbulent flow due to their large deviations from the experimental values. The prediction success of Choi et al. [6]'s correlation can be seen from Fig. 18 for laminar and turbulent flow data within ±30%. The total pressure drop increases with increasing mass fluxes in all figures as expected.

5 Conclusion

Experiments have been performed to predict the pressure drop characteristics using homogeneous and separated flow models by means of the proper two-phase dynamic viscosity correlations, some alternative correlations of momentum and pressure drop, and various two-phase friction factors and void fraction models and correlations. There is little research on the parameters and content used in this study in the current literature. The content of this study is expected to fill this gap in the literature. Accurate experiments were done for annular flow heat transfer data in a vertical tube for the condensation of R134a at high mass flux. The importance of the use of a large number of data with different experimental conditions is shown during the validation process of the results.

The calculated homogeneous two-phase friction factors, wall shear stresses, frictional pressure drops and total pressure drops by means of the two-phase homogeneous dynamic viscosity correlations of Mc Adams et al., Dukler

et al., Ovens, Lin et al. and Garcia et al. are found to be in good agreement with the experimental data: within ±30%.

Moreover, the correlations of the two-phase friction factors of Moeck and Fore et al. for the laminar flow and Choi et al. for the laminar and turbulent flows are the best predictive models, within ±30%, for the investigation of the separated flow model's total pressure drop correlation and could reflect the effect of mass flux on the total pressure drop.

Acknowledgments The authors would like to thank King Mongkut's University of Technology Thonburi (KMUTT), the Thailand Research Fund, and the National Research University Project for the financial support. Especially, the first author wishes to thank KMUTT for providing him with a Post-doctoral fellowship.

References

1. Nusselt W (1916) Die Oberflachen Kondenastion des Wasserdamfes. Zeitschrift des Vereines Deutscher Ingenieure 60:541–546 (569–575)
2. Wasden FK, Dukler AE (1989) Insights into the hydrodynamics of free falling wavy films. AIChE J 35:187–195
3. Kritsadathikarn P, Songnetichaovalit T, Lokathada N, Wongwises S (2002) Pressure distribution of refrigerant flow in an adiabatic capillary tube. Sci Asia 28:71–76
4. Choi JY, Kedzierski MA, Domanski PA (1999) A generalized pressure drop correlation for evaporation and condensation of alternative refrigerants in smooth and micro-fin tubes. NISTIR 6333:1–50
5. Pierre B (1964) Flow resistance with boiling refrigerants-part 1. ASHRAE J 6:58–65
6. Choi K, Pamitran AS, Oh CY, Oh JT (2008) Two-phase pressure drop of R-410A in horizontal smooth minichannels. Int J Refrig 31:119–129
7. Lockhart RW, Martnelli RC (1949) Proposed correlation of data for isothermal two-phase, two-component flow in pipes. Chem Eng Prog 45:39–48
8. Baudouy B (2002) Pressure drop in two-phase He I natural circulation loop at low vapor quality. In: Gistau Baguer PSG (ed) International cryogenic engineering proceedings, vol 19, France, pp 817–820
9. Friedel L (1979) Improved friction pressure drop correlations for horizontal and vertical two phase pipe flow. Eur Two-phase Flow Group Meet 18:485–491
10. Huq RH, Loth JL (1992) Analytical two-phase flow void prediction method. J Thermophys 6:139–144
11. Dutkowski K (2010) Air-water two-phase frictional pressure drop in minichannels. Heat Transf Eng 31:321–330
12. McAdams WH, Woods WK, Heroman LC (1942) Vaporization inside horizontal tubes II-benzene-oil mixtures. Trans ASME 64:193–200
13. Cicchitti A, Lombaradi C, Silversti M, Soldaini G, Zavattarlli R (1960) Two-phase cooling experiments- pressure drop heat transfer burnout measurements. Energia Nucl 7:407–425
14. Dukler AE, Wicks M, Cleveland RG (1964) Frictional pressure drop in two-phase flow. Part A: a comparison of existing correlations for pressure loss and holdup, and Part B: an approach through similarity analysis. AIChE J 10:38–51
15. Owens WL (1961) Two-phase pressure gradient. In: ASME International Developments in Heat Transfer, Part II, pp 363–368
16. Lee J, Mudawar I (2005) Two-phase flow in high-heat-flux micro-channel heat sink for refrigeration cooling applications: part II-heat transfer characteristics. Int J Heat Mass Transf 48:941–955
17. Beattie DRH, Whalley PB (1982) Simple two-phase frictional pressure drop calculation method. Int J Multiph Flow 8:83–87
18. Lin S, Kwok CCK, Li RY, Chen ZH, Chen ZY (1991) Local frictional pressure drop during vaporization for R-12 through capillary tubes. Int J Multiph Flow 17:95–102
19. Chen IY, Yang KS, Chang YJ, Wang CC (2001) Two- phase pressure drop of air-water and R-410A in small horizontal tubes. Int J Multiph Flow 27:1293–1299
20. Yadigaroglu H, Lahey RT Jr (1976) On the various forms of the conservation equations in two-phase flow. Int J Multiph Flow 2:477–494
21. Wang CC (1997) A numerical method for thermally non-equilibrium condensing flow in a double-pipe condenser. Appl Thermal Eng 17:647–660
22. Bhramara P, Rao VD, Sharma KV, Reddy TKK (2009) CFD analysis of two phase flow in a horizontal pipe-prediction of pressure drop. Int J Mech Ind Aerosp Eng 3:81–87
23. Rahimi M, Shabaniana SR, Alsairafi AA (2009) Experimental and CFD studies on heat transfer and friction factor characteristics of a tube equipped with modified twisted tape inserts. Chem Eng Process 48:762–770
24. Moser K, Webb RL, Na B (1998) A new equivalent Reynolds number model for condensation in smooth tubes. Int J Heat Transf 120:410–417
25. Fluent release 6.2.16, Fluent Incorporated (2005)
26. Chen SL, Gerner FM, Tien CL (1987) General film condensation correlations. Exp Heat Transf 1:93–107
27. Kline SJ, McClintock FA (1953) Describing uncertainties in single sample experiments. Mech Eng 75:3–8
28. Collier JG, Thome JR (2001) Convective boiling and condensation. Oxford Science Publications, Oxford
29. Revellin R (2005) Experimental two-phase fluid flow in microchannel. Ph.D. thesis, Ecole Polytechnique Federale De Lausanne, Lyon, France
30. Pope JE (1996) Rules of thumb for mechanical engineers. Gulf professional publishing, Houston
31. Wong TN, Ooi KT (1995) Refrigerant flow in capillary tube: an assessment of the two-phase viscosity correlations on model prediction. Int Commun Heat Mass Transf 22:595–604
32. Fourar M, Bories S (1995) Experimental study of air–water two-phase flow through a fracture (narrow channel). Int J Multiph Flow 21:621–637
33. Davidson WF, Hardie PH, Humphreys CGR, Markson AA, Mumford AR, Ravese T (1943) Studies of heat transmission through boiler tubing at pressures from 500 to 3, 300 Lbs. Trans ASME 65:553–591
34. García F, García R, Padrino JC, Mata C, Trallero JL, Joseph DD (2003) Power law composite power law friction factor correlations for laminar turbulent gas- liquid flow in horizontal pipelines. Int J Multiph Flow 29:1605–1624
35. White FM (2005) Viscous fluid flow. McGraw-Hill, New York
36. Blasius H (1913) Das Ähnlichkeitsgesetz bei Reibungsvorgängen in Flüssikeiten, Forsch. Gebiete Ingenieurw 131
37. Carey VP (1992) Liquid-vapor phase change phenomena. Hemisphere Publishing, New York
38. Chisholm D (1983) Two phase flow in pipelines and heat exchangers. George Godwin in association with The Institution of Chemical Engineers, London
39. Soliman HM (1982) On the annular-to-wavy flow pattern transition during condensation inside horizontal tubes. Can J Chem Eng 60:475–481

40. Smith SL (1969) Void fractions in two-phase flow: a correlation based upon an equal velocity head model. Proc Inst Mech Eng 36:647–664
41. Turner JM, Wallis GB (1965) The separate-cylinders model of two-phase flow, paper no. NYO-3114-6. Thayer's School Eng., Dartmouth College, Hanover
42. Spedding PL, Spence DR (1989) Prediction of holdup in two phase flow. Int J Eng Fluid Mech 2:109–118
43. Woldesemayat MA, Ghajar AJ (2007) Comparison of void fraction correlations for different flow patterns in horizontal and upward inclined pipes. Int J Multiph Flow 33:347–370
44. Honda H, Nozu S, Matsuoka Y, Nakata H (1989) Condensation of R-11 and R-113 in the annuli of horizontal double-tube condensers with an enhanced inner tube. Exp Thermal Fluid Sci 2:173–182
45. Sami SM, Schnotale J (1993) Prediction of forced convective condensation of non-azeotropic refrigerant mixtures inside enhanced surface tubing. Appl Sci Res J 50:149–168
46. Akers WW, Deans A, Crosser OK (1959) Condensing heat transfer within horizontal tubes. Chem Eng Prog Symp Ser 55:171–176
47. Ma X, Briggs A, Rose JW (2004) Heat transfer and pressure drop characteristics for condensation of R113 in a vertical micro-finned tube with wire insert. Int Commun Heat Mass Transf 31:619–627
48. Fukano T, Furukawa T (1998) Prediction of the effects of liquid viscosity on interfacial shear and frictional pressure drop in vertical upward gas-liquid annular flow. Int J Multiph Flow 24:587–603
49. Moeck EO (1970) Annular-dispersed two-phase flow and critical heat flux. AECL 3656:337
50. Fore LB, Beus SG, Bauer RC (2000) Interfacial friction in gas-liquid annular flow: analogies to full and transition roughness. Int J Multiph Flow 26:1755–1769
51. Cousin LB, Dcnton WH, Hewitt GF (1965) Liquid mass transfer in annular two-phase flow. AERE-R4926
52. Wallis GB (1969) One-dimensional two-phase flow. McGraw-Hill, New York
53. Webb D (1970) Studies of the characteristics of downward annular two-phase flow: measurements of entrainment rate, pressure gradient, probability distribution of film thickness and disturbance wave inception. AERE-R6426
54. Whalley PB, Hewitt GF, Hutchinson P (1973) Experimental wave and entrainment measurements in vertical annular two-phase flow. AERE-R7521
55. Whalley PB, Hewitt GF (1978) The correlation of liquid entrainment fraction and entrainment rate in annular two-phase flow. AERE-R9187
56. Hewitt GF, Hall-Taylor NS (1970) Annular two-phase flow. Pergamon Press, Oxford
57. Asali JC, Hanratty TJ, Andreussi P (1985) Interfacial drag and film height for vertical annular flow. AIChE J 31:895–902
58. Azzopardi BJ, Teixeira JCF (1994) Detailed measurements of vertical annular two-phase flow-Part II: gas core turbulence. Trans ASME 116:796–800

Frontiers in Heat and Mass Transfer (FHMT), 3, 013006 (2012)
DOI: 10.5098/hmt.v3.1.3006

Global Digital Central
ISSN: 2151-8629

Frontiers in Heat and Mass Transfer

Available at www.ThermalFluidsCentral.org

A CRITICAL REVIEW OF RECENT INVESTIGATIONS ON FLOW PATTERN AND HEAT TRANSFER DURING FLOW BOILING IN MICRO-CHANNELS

Sira Saisorn[a,b], Somchai Wongwises[b,c*]

[a]*King Mongkut's Institute of Technology Ladkrabang Chumphon Campus Chumphon 86160, Thailand*
[b]*Fluid Mechanics, Thermal Engineering and Multiphase Flow Research Lab. (FUTURE)*
Department of Mechanical Engineering, King Mongkut's University of Technology Thonburi, Bangmod, Bangkok 10140, Thailand
[c]*The Academy of Science, The Royal Institute of Thailand, Sanam Suea Pa, Dusit, Bangkok 10300, Thailand*

ABSTRACT

A summary of recent research on flow boiling in micro-channels is provided in this article. This review aims to survey and identify new findings arising in this important area, which may contribute to optimum design and process control of high performance miniature devices comprising extremely small channels. Several criteria for defining a micro-channel are presented at first and the recent works on micro-scale flow boiling are subsequently described into two parts including flow visualization and two-phase heat transfer. The results obtained from a number of previous studies show that the flow behaviours and heat transfer mechanisms in micro-channels deviate significantly from those in ordinarily sized channels. Future research with numerous aspects of flow boiling phenomena necessary to answer the fundamental questions is still required.

Keywords: *flow boiling, micro-channel, heat transfer*

1. INTRODUCTION

In the past 10 years, investigations on flow boiling heat transfer and flow characteristics in micro-channel flow passages have gained significant attention in engineering community. Flow boiling in micro-channel has been applied to energy and process systems including high heat-flux compact heat exchangers, and cooling devices of various types of equipment such as high performance micro-electronics, high-powered lasers, and so on.

Several advantages can be obtained when micro-channels are selected for applications. In compact heat exchanger implementations, for instance, such small channels can provide a larger contact area with the fluid per unit volume and support high pressure operating conditions. Unfortunately, a comprehensive understanding is still lacking on the trend and parameters dominating the phase-change behavior in micro-channel. The fundamental data corresponding to flow pattern, heat transfer coefficient and pressure drop during flow boiling are therefore essential for designing and operating compact heat exchangers as well as micro-electro-mechanical systems (MEMS).

A scaling analysis of different forces, as recently discussed in Kandlikar (2010), pointed out that surface tension and evaporation momentum forces were significant for two-phase flow phenomena at micro-scale, resulting in the flow behaviors substantially different from those of ordinarily sized channels. Currently, it seems rather vague to identify whether or not the flow passages are micro-channels. Several criteria have been established in order to define a micro-channel.

The classifications with respect to the absolute diameter of channel were presented by Mehendale et al. (2000) and Kandlikar and Grande (2003). Mehendale et al. (2000) defined a channel with a hydraulic diameter ranging from 1 to 100 μm as micro-channel. Kandlikar and Grande (2003), however, divided the range from 10 to 200 μm as micro-channel.

The flow mechanisms in a confined space may be different according to cross-sectional shape. Accordingly, the circular micro-channels cannot give the same results as those in most practical applications which are rectangular in shape and, hence, the micro-channel is not likely to be characterized by only absolute diameter.

The criteria based on different dimensionless parameters have also been proposed in the literature. For instance, the confinement number recommended by Kew and Cornwell (1997) was proposed to be related with some physical aspects of flow boiling. The confinement number is defined as

$$C_o = \frac{D_b}{D_h} \tag{1}$$

where D_h is hydraulic diameter and D_b is nominal bubble size or capillary length which is expressed by

$$D_b = \sqrt{\frac{\sigma}{g(\rho_L - \rho_G)}} \tag{2}$$

The confinement number above 0.5 implies that the micro-scale effects are important for a given channel diameter. In Eq.(2), σ stands for surface tension, g is gravitational acceleration, ρ_L and ρ_G are, respectively, liquid and vapour densities.

Recently, a criterion developed based on flow boiling heat transfer data was proposed by Li and Wu (2010). 4228 data points were collected from the literature. According to their data analysis,

* Corresponding author: E-mail: somchai.won@kmutt.ac.th

the authors found that the transitional threshold from macro- to micro-channels could be represented as a combined non-dimensional number, $\lambda \times Re_L^{0.5} = 200$. λ and Re_L stand, respectively, for Bond number and liquid Reynolds number. The micro-scale effects are dominant when such combined non-dimensional number is lower than 200. The combination of non-dimensional number was also used by Harirchian and Garimella (2010) to propose the transition criterion. They indicated a micro-channel corresponding to the flow conditions for which $\lambda^{0.5} \times Re_L$ is lower than 160.

It is interesting to note from Tibirica and Ribatski (2010) that the channel with a diameter of 2.3 mm was considered as the one in which the transition between macro- and micro-scale flow boiling phenomena took place when halocarbon refrigerants were used as working fluids under Earth's gravity. With visualization study, they detected stratification effects in this channel size. Ong and Thome (2011a) investigated experiments to address the macro-to-micro-scale transition for flow boiling of refrigerants in different channel sizes. They indicated the dependence of the threshold of the transition on flow regime and confinement number. As illustrated in Fig. 1, the lower threshold of macro-scale flow corresponded to confinement number ranging from 0.3 to 0.4 whereas the confinement number of around 1.0 stood for the upper threshold of micro-scale flow. It was noted that the transition region, frequently corresponding to as mini-channels in literature, was located in between the two boundaries.

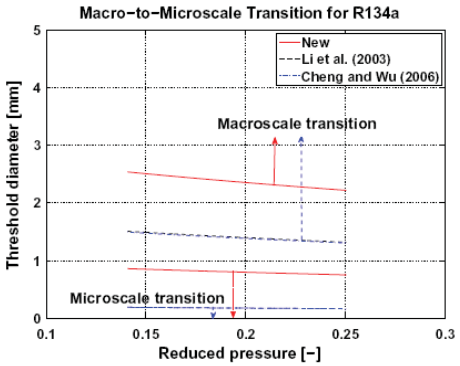

Fig. 1 Transition criterion of Ong and Thome (2011a). "Reprinted from Experimental Thermal and Fluid Science, 35(1), Ong, C.L., and Thome, J.R., Macro-to-microchannel transition in two-phase flow: Part 1-Two-phase flow patterns and film thickness measurements, pp. 37-47 (2011), with permission from Elsevier."

Regarding the experimental data obtained from two-phase gas-liquid adiabatic flow, Chung and Kawaji (2004) found that diameters between 100 and 250 μm seemed to be in the range corresponding to mini-to-micro-scale transitions. Their findings were in agreement with Saisorn and Wongwises (2010).

Despite a number of criteria being proposed, a clear physical criterion that relates the channel diameter to the fluid flow mechanisms is still not available and, hence, further investigation should be performed to meet a more general definition dealing with channel classification.

The foregoing is an introduction and some important tentative criterions which are given in brief. This research field has gained broad interest in the heat transfer community and there have been several major concerns for flow boiling in micro-channels. In this paper, however, the following explorations are carried out to review recent studies on flow patterns and heat transfer characteristics during flow boiling in micro-channels.

2. FLOW BOILING CHARACTERISTICS IN MICRO-CHANNELS

During the past years, a number of investigations pertaining to micro-scale flow phenomena have been published in the literature. Table 1 lists the important investigations on micro-scale flow boiling, recently done by various researchers.

In this section, the recent research works on micro-channel flow boiling are reviewed and are categorized into two main areas. Flow visualization studies are explored and the micro-scale heat transfer characteristics together with the relevant prediction methods are subsequently presented.

2.1. Flow visualization

Lee and Mudawar (2005) conducted flow visualization in rectangular micro-channels with width and depth of 231 μm and 713 μm, respectively. Bubbly/slug flow, slug flow and annular flow were observed for flow boiling of R-134a refrigerant. Not only did the flow regime transition was dependent on vapour quality, the transition behavior was also affected by surface tension and channel configuration.

Kandlikar and Balasubramanian (2005) studied experimentally the flow boiling of water in micro-channels. Hydraulic diameter for each channel was 0.333 mm. The observed flow patterns including bubbly flow, plug flow, churn flow and annular flow tend to appear alternately with time even at a given flow condition. Regarding the experimental data, they indicated the gravitational orientation affecting the flow pattern transitions.

Flow boiling of HCFC123 in micro-channels with different shaped cross-sections was carried out by Yen et al. (2006). They reported that at low vapour quality region, bubbly flow and annular flow were observed in the square micro-channel having hydraulic diameter of 214 μm. In comparison to the square channel, the constitution of flow patterns in the circular channel with nearly the same diameter became more complicated. Capillary flow, representing independent droplets moving along the channel wall, annular flow, bubbly flow and dry-out region were reported for the circular micro-channel. In contrast, the flow patterns at high vapour quality region only comprised annular flow and dry-out region for both circular and square micro-channels.

It should be noted from Jiang and Wong (1999) and Zhang et al. (2002) that bubbly flow was not reported when flow boiling was established in micro-channels with hydraulic diameters ranging from 25 to 60 μm. The channels with triangular cross-sections were used by Jiang and Wong (1999), and those with rectangular cross-sections were examined by Zhang et al. (2002).

Recently, a new type of two-phase flow pattern map for flow boiling in micro-channels was developed by Revellin and Thome (2007). The proposed flow regime map comprises different zones according to the bubble coalescence phenomena. The following are a brief description of each zone located in the flow map.

The isolated bubble (IB) regime corresponds to a relatively high bubble generation rate when compared with the bubble coalescence rate. Either or both of bubbly flow and slug flow are included in this regime. The coalescing bubble (CB) regime is defined when the bubble generation rate is smaller than the bubble coalescence rate. The isolated bubble (IB) flow to coalescing bubble (CB) flow transition is given by

$$x_{IB/CB} = 0.763\left(\frac{Re_{LO}B_o}{We_{GO}}\right)^{0.41} \quad (3)$$

where B_o stands for boiling number, Re_{LO} represents all-liquid Reynolds number and We_{GO} is all-vapour Weber number.

The transition from coalescing bubble flow to annular flow is determined by

DOI: 10.5098/hmt.v3.1.3006 ISSN: 2151-8629

Table 1 Summary of recent investigations on micro-scale flow boiling.

Reference	*Fluid and parameter ranges* G [kg/m^{2}s], q [kW/m^2] P [kPa], T [^{o}C]	*Channel geometry/ substrate/orientation/ diameter* [mm]	*Remarks*
Yang and Shieh (2001)	R-134a G = 300-1600, x = 0.003- 0.92 T_{sat} = 30	Single circular/Pyrex glass/horizontal/ D = 2, 3	Inconsistencies between the flow pattern map established from two-phase air-water and that from two-phase R-134a were addressed.
Lee and Lee (2001)	R-113 G = 50-200, x = 0.15-0.75 q = 0-1.5 P_{sat} = 100	Single rectangular/stainless steel/horizontal/ D_h = 0.78-3.63	Heat transfer coefficient increased with increasing mass flux and vapour quality.
Sumith et al. (2003)	Water G = 23-153, x = 0-0.8 q = 10-715 T_{in} = 97.5, 98	Single circular/stainless steel/vertical D = 1.45	Convective boiling was likely to dominate heat transfer phenomena.
Qu and Mudawar (2003)	Water G = 135-402, x = 0-0.2 T_{in} = 30, 60	21 parallel rectangular/ copper/horizontal D_h = 0.35	Heat transfer mechanisms were compatible with convective boiling contribution.
Huo et al. (2004)	R-114a G = 100-500, x = 0-0.9 q = 13-150 P_{sat} = 800-1200	Single circular/stainless steel/vertical/ D = 2.01, 4.26	Heat transfer mechanism over low vapour quality region was compatible with nucleate boiling contribution. Heat transfer coefficient was higher for the 2.01 mm tube than for the 4.26 mm tube.
Pettersen (2004)	CO_2 G = 190-570, x = 0.12-1 q = 5-20 T_{sat} = 0, 10, 20, 25	25 parallel circular/ aluminum/horizontal/ D = 0.81	The results were discussed according to the dominant role of nucleate boiling over low/moderate vapour quality region. Dry-out effects were obvious at high mass flux and temperature.
Lee and Mudawar (2005)	R-134a G = 127-654, x = 0.26-0.87 q = 159-938 P_{in} = 144-660	53 parallel rectangular/ copper/horizontal/ D_h = 0.35	Bubbly/slug flow, slug flow and annular flow were observed. Different heat transfer mechanisms were addressed for three different vapour quality regions.
Kandlikar and Balasubramanian (2005)	Water G = 120, x = 0.18-0.36 q = 317 T_s = 110-114	6 parallel rectangular/ copper/horizontal and vertical/ D_h = 0.333	Bubbly flow, plug flow, churn flow and annular flow were reported. The gravitational orientation affected the flow pattern transition and heat transfer coefficients.
Yun et al. (2005)	CO_2, R-134a G = 200-400, x = 0-0.9 q= 10 – 20 T_{sat} = 0, 5, 10	6-10 parallel rectangular/ -/horizontal/ D_h = 1.08-1.54	The effect of heat flux on heat transfer coefficient was much more obvious for CO_2 than for R-134a.
Saitoh et al. (2005)	R-134a G = 150-450, x=0-0.2 q = 5-39 T_{sat} = 5, 15	Single circular/-/horizontal/ D = 0.51, 1.12, 3.1	Nucleate boiling was reported in low vapour quality region whereas convective evaporation was dominant in high vapour quality region. The smaller the tube diameter, the higher was the effect of saturation temperature on heat transfer coefficient.
Lie et al. (2006)	R-134a, R-407C G = 200-1500, x = 0.2-0.8 q = 5, 10, 15 T_{sat} = 5, 10, 15	28 parallel circular/copper/ horizontal/ D = 0.83, 2.0	The use of R-407C gave a higher heat transfer coefficient when compared with R-134a.
Yen et al. (2006)	R-123 G = 100-800, x = 0.07-0.8 q = 25-90 P_{in} = 163	Single circular and single square/Pyrex glass/horizontal/ D_h = 0.2	Different shaped cross-sections gave different flow characteristics. The shape of the cross-section had no significant influence on the heat transfer coefficient when high vapour quality region was established.

DOI: 10.5098/hmt.v3.1.3006 ISSN: 2151-8629

Table 1 Summary of recent investigations on micro-scale flow boiling (continued).

Reference	*Fluid and parameter ranges* G [kg/m^{2}s], q [kW/m^2] P [kPa], T [^{o}C]	*Channel geometry/ substrate/orientation/ diameter* [mm]	*Remarks*
Revellin and Thome (2007)	R-134a, R-245fa G = 210-2094, x = 0-0.95 q = 3.1-597 T_{sat} = 26, 30, 35	Single circular/stainless steel/ horizontal/ D = 0.509, 0.79	Two-phase flow regime map was developed, including isolated bubble regime, coalescing bubble regime and annular regime.
Choi et al. (2007a)	CO_2 G = 200-600, x = 0-1 q = 20-40 T_{sat} = -10, -5, 0, 10	Single circular/stainless steel/ horizontal/ D = 1.5, 3	More vigorous nucleate boiling was observed when the smaller diameter tube was used.
Choi et al. (2007b)	R-22, R-134a, CO_2 G = 200-600, x = 0-1 q = 10-40 T_{sat} = 10	Single circular/stainless steel/ horizontal/ D = 1.5, 3	The use of CO_2 caused the heat transfer coefficient higher than the case of R-134a and R-22 fluids.
Agostini et al. (2008a, 2008b)	R-236fa, R-245fa G = 280-1500, x = 0.02-0.78 q = 36-2220 P_{sat} = 141-273	66 parallel rectangular/ silicon/horizontal/ D_h = 0.336	Heat transfer coefficient for R-245fa was dependent on mass flux in comparison to the case for R-236fa. The effect of the saturation pressure on the heat transfer coefficient was obvious for R-236fa.
Lee and Mudawar (2008)	HFE 7100 G = 670-6730 q = 0-7500 P_{out} = 113.8	11-24 parallel rectangular/ copper/horizontal/ D_h = 0.176, 0.2, 0.334, 0.416	Heat transfer coefficient did not monotonously increase with the decrease in hydraulic diameter.
Lee and Garimella (2008)	Water G = 368-738, x = 0-0.2 q = 100-3400 T_{in} = 90.6-95.1	10-60 parallel rectangular/ Silicon/horizontal/ D_h = 0.16-0.54	At high heat flux region, the heat transfer coefficient was nearly independent with heat flux.
Bertsch et al. (2008)	R-134a G = 20.3-81, x = 0-0.85 q = 0-200 T_{sat} = 8.9, 18.7, 29	17 parallel rectangular/ copper/horizontal/ D_h = 1.09	Vapour quality showed significant influence on the heat transfer coefficient whereas the saturation pressure played insignificant role on the heat transfer coefficient. The higher the mass flux, the higher was the heat transfer coefficient.
Shiferaw et al. (2009)	R-134a G = 100-600, x = 0-0.9 q = 16-150 P_{sat} = 600-1200	Single circular/stainless steel/ vertical/ D = 1.1	Heat transfer coefficient increased with increasing heat flux and saturation pressure.
Ong and Thome (2009)	R-134a, R-236fa, R-245fa G = 100-1500, x = 0-1 q = 2.3-250 T_{sat} = 29, 31, 33	Single circular/stainless steel/ horizontal/ D = 1.03	Two-phase flow regime map was developed and worked well for mass flux values larger than 200 kg/m^{2}s and reduced pressure ranging from 1.842 to 7.926. R-134a gave the highest heat transfer coefficient followed by R-236fa and R-245fa, respectively.
Bertsch et al. (2009a)	R-134a, R-245fa G = 20-350, x = 0-0.8 q = 0-220 T_{sat} = 8.9, 18.7, 29	17-33 parallel rectangular/ copper/horizontal/ D_h = 0.54, 1.09	The use of R-134a resulted in high heat transfer coefficient when compared with R-245fa. The heat transfer coefficient was not affected by the variation of the hydraulic diameter.
Choi et al. (2009)	C_3H_8 G = 50-400, x = 0-1 q = 5-20 T_{sat} = 0, 5, 10	Single circular/stainless steel/ horizontal/ D = 1.5, 3	The smaller channel diameter yielded a higher heat transfer coefficient. The heat transfer coefficient increased with increasing saturation temperature.
Tibirica and Ribatski (2010)	R-134a, R-245fa G = 50-700, x = 0.05-0.99 q = 5-55 T_{sat} = 22, 31, 41	Single circular/stainless steel/ horizontal/ D = 2.3	The variation of the heat transfer coefficient with the saturation temperature for R-245fa was more obvious than that for R-134a. R-134a provided high heat transfer coefficients in comparison to R-245fa.

DOI: 10.5098/hmt.v3.1.3006 ISSN: 2151-8629

Table 1 Summary of recent investigations on micro-scale flow boiling (continued).

Reference	*Fluid and parameter ranges* G [kg/m^{2}s], q [kW/m^2] P [kPa], T [^{o}C]	*Channel geometry/ substrate/orientation/ diameter* [mm]	*Remarks*
Arcanjo et al. (2010)	R-134a, R-245fa G = 50-600, x = 0-0.95 T_{sat} = 22, 31, 41	Single circular/stainless steel/ horizontal/ D = 2.32	Slug flow, churn flow and annular flow were observed. The flow pattern transitions were affected by working fluid and saturation temperature.
Celata et al. (2010)	FC-72 G = 500-1500 q = 50-150	Single circular/-/horizontal/ D = 0.48	Stable flows including bubbly/slug flow, slug/annular flow and annular/mist flow were observed at high mass flux and heat flux values
Saisorn et al. (2010)	R-134a G = 200-1000, x = 0.05-0.95 q = 1-83 P_{sat} = 800, 1000, 1300	Single circular/stainless steel/ horizontal/ D = 1.75	Slug flow, throat-annular flow, churn flow, annular flow and annular-rivulet flow were observed and found to influence heat transfer process.
Martin-Callizo et al. (2010)	R-134a G = 100-500, x= 0-0.97 q = 5-45 T_{sat} = 30, 35	Single circular/quartz tube/ vertical/ D = 1.33	Seven two-phase flow patterns were observed including isolated bubbly flow, confined bubbly flow, slug flow, churn flow, slug-annular flow, annular flow and mist flow.
Oh et al. (2011)	R-22, R-134a, R-410A, C_3H_8, CO_2 G = 50-600, x = 0-1 q = 5-40 T_{sat} = 0-15	Single circular/stainless steel/ horizontal/ D = 0.5, 1.5, 3	Heat transfer coefficient increases with the decrease in channel diameter. The heat transfer coefficient of CO_2 was highest in comparison to the other four refrigerants.
Bang et al. (2011)	Water G = 100, x= 0-1 q = 50-160 P_{sat} = 200, 1600	Single circular/stainless steel/ horizontal/ D = 1.73	Heat transfer coefficient was slightly affected by pressure. The dominance of forced convection was reported.
Soupremanien et al. (2011)	Forane®365 HX G = 200-400, x= 0-0.6 q = 25-62 T_{sat} = 56	Single rectangular/stainless steel/horizontal/ D_h = 1.4	Bubbly flow, plug flow, plug/slug flow, churn/annular flow and annular flow were observed. Heat transfer coefficient was influenced by aspect ratio.
Copetti et al. (2011)	R-134a G = 240-930, x= 0-0.8 q = 10-100 T_{sat} = 12, 22	Single circular/stainless steel/ horizontal/ D = 2.62	Heat transfer coefficient was strongly dependent on mass flux only for low heat flux conditions. Flow pattern was reported to play important role on the heat transfer coefficient.
Ong and Thome (2011a, 2011b)	R-134a, R-236fa, R-245fa G = 100-1500, x = 0-1 q = 4.8-250 T_{sat} = 25, 31, 35	Single circular/stainless steel/ horizontal/ D = 1.03, 2.2, 3.04	Flow pattern transition lines were developed to predict both macro-scale and micro-scale flow patterns. The heat transfer coefficient for R-134a showed the highest dependence on heat flux.

$$x_{CB/A} = 0.00014 Re_{LO}^{1.47} We_{LO}^{-1.23} \quad (4)$$

where We_{LO} is all-liquid Weber number.

The proposed correlations take into account different effects including heat flux, viscosity and surface tension which are represented, respectively, by boiling number, Reynolds number and Weber number.

With the data for three refrigerants including R-134a, R-236fa and R-245fa in channels with diameters ranging from 0.509 to 1.03 mm, the Revellin and Thome correlation (2007) was subsequently modified by Ong and Thome (2009) as follows.

The isolated bubble (IB) flow to coalescing bubble (CB) flow transition was modified as

$$x_{IB/CB} = 0.763 \left(\frac{Re_{LO} B_o}{We_{GO}} \right)^{0.39} \quad (5)$$

The transition from coalescing bubble flow to annular flow was modified to account for reduced pressure as follow.

$$x_{CB/A} = \left(\frac{P_r}{P_{sat,R-134a}} \right)^{0.45} 0.00014 Re_{LO}^{1.47} We_{LO}^{-1.23} \quad (6)$$

where P_r stands for reduced pressure and $P_{sat,\ R\text{-}134a}$ represents saturation pressure with respect to refrigerant R-134a. Ong and Thome (2009) also pointed out that their correlations worked well for mass flux values larger than 200 kg /m^{2}s and reduced pressures ranging from 1.842 to 7.926.

Ong and Thome (2011a) continually developed the flow pattern transition lines in order to predict both macro-scale and micro-scale flow patterns as follows.

Isolated bubble/coalescing bubble (IB/CB) was presented by

$$x_{IB/CB} = 0.36 C_o^{0.2} \left(\frac{\mu_G}{\mu_L} \right)^{0.65} \left(\frac{\rho_G}{\rho_L} \right)^{0.9} Re_{GO}^{0.75} B_o^{0.25} We_{LO}^{-0.91} \quad (7)$$

Coalescing bubble/annular (CB/A) was denoted as

$$x_{CB/A} = 0.047 C_o^{0.05} \left(\frac{\mu_G}{\mu_L}\right)^{0.7} \left(\frac{\rho_G}{\rho_L}\right)^{0.6} Re_{GO}^{0.8} We_{LO}^{-0.91} \quad (8)$$

Plug-slug/coalescing bubble (S-P/CB) was expressed in Eq.(9) when $x_{S\text{-}P/CB} < x_{CB/A}$ as shown below.

$$x_{S\text{-}P/CB} = 9 C_o^{0.2} \left(\frac{\rho_G}{\rho_L}\right)^{0.9} Fr_{LO}^{-1.2} Re_{LO}^{0.1} \quad (9)$$

Plug-slug/annular (S-P/A) was established when $x_{S\text{-}P/CB} > x_{CB/A}$ as seen in Eq.(10) .

$$x_{S\text{-}P/A} = x_{CB/A} \quad (10)$$

Notably, Eqs.(9) and (10) are applicable when confinement number is lower than 0.34.

Arcanjo et al. (2010) obtained flow visualization data for flow boiling of R-134a and R-245fa in a horizontal tube having a diameter of 2.32 mm. Slug flow, churn flow and annular flow were observed. According to their report, the flow pattern transitions were affected by working fluid and saturation temperature. Different existing flow pattern maps for micro-channels were discussed and compared with their flow regime maps.

During flow boiling of FC-72 in horizontal circular micro-channel with a diameter of 0.48 mm, Celata et al. (2010) indicated stable flow at high mass flux and heat flux values. In such region, the flow patterns including bubbly/slug flow, slug/annular flow and annular/mist flow were reported.

Saisorn et al. (2010) performed flow visualization study for R-134a refrigerant during flow boiling in a circular channel having a diameter of 1.75 mm. Slug flow, throat-annular flow, churn flow, annular flow and annular-rivulet flow were observed and found to influence the flow boiling heat transfer process as seen in Fig. 2. Slug flow appeared with the lowest heat transfer coefficient in comparison to the other flow regimes. Annular-rivulet flow showed a relatively high heat transfer coefficient but a local dry-out region was observed at high vapour qualities, which has been undesirable for a thermal design approach dealing with a cooling system implemented with small channels. Moderate values of heat transfer coefficient were given by throat-annular flow, churn flow and annular flow which might be good choices for the development of the micro-scale devices. Besides, their flow pattern data were compared with the transition lines by Triplett et al. (1999) for two-phase air-water flow through a 1.45 mm diameter channel. In general, the comparisons showed inconsistencies between the flow pattern map established from two-phase gas-liquid flow and that from phase-change process. Such inconsistencies were also reported by Yang and Shieh (2001) and Martin-Callizo et al. (2010). Yang and Shieh (2001) performed flow visualization with air-water mixture and refrigerant R-134a, and the comparison between such two cases were discussed. Martin-Callizo et al. (2010) conducted the visualization of R-134a during flow boiling in a tube with a diameter of 1.33 mm. Their test section was made from a quartz glass tube coated externally by Indium Tin Oxide (ITO) which was served as the resistive coating over which a potential difference generated by a DC power supply was applied. Their flow pattern data were also compared with the transition lines by Triplett et al. (1999), indicating that the agreement was not satisfactory. However, two-phase gas-liquid flow phenomena tend to be compatible with flow mechanisms based on phase-change process in different aspects. In micro-channels, for instance, Saisorn and Wongwises (2010) reported the fair agreement between their gas-liquid flow pattern data and the transition lines of Garimella et al. (2002) for condensation flow.

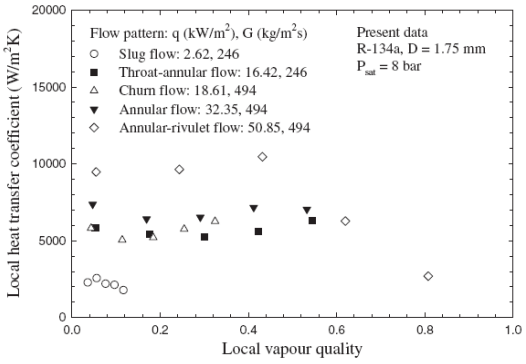

Fig. 2 Flow boiling data of Saisorn et al. (2010). "Reprinted from International Journal of Heat and Mass Transfer, 53(19-20), Saisorn, S., Kaew-On, J., and Wongwises, S., Flow pattern and heat transfer characteristics of R-134a refrigerant during flow boiling in a horizontal circular mini-channel, pp. 4023-4038 (2010), with permission from Elsevier."

Flow boiling visualization study was carried out by Soupremanien et al. (2011). In their work, the test section having hydraulic diameter of 1.4 mm was employed and the Forane® 365 HX was used as working fluid. They observed bubbly flow, plug flow, plug/slug flow, churn/annular flow and annular flow.

2.2. Two-phase heat transfer

Huo et al. (2004) studied experimentally boiling heat transfer of R-134a flowing in 2.01 and 4.26 mm diameter channels. In the range of low vapour quality, the heat transfer coefficient in both tubes increased with increasing heat flux and saturated pressure but was independent of vapour quality. These results were attributed to nucleate boiling being the dominant heat transfer mode. Over other ranges of vapour quality, however, the dominant heat transfer mode was not addressed as a result of inconsistency in the experimental data. Under the same controlled conditions, they found that the nucleate boiling heat transfer coefficient was higher for the 2.01 mm tube than for the 4.26 mm tube.

Flow boiling heat transfer characteristics in micro-channels of 540 mm length with 25 circular flow channels of 0.81 mm diameter were investigated by Pettersen (2004). The author reported that the increase in heat flux resulted in a higher heat transfer coefficient, which was explained according to the dominant role of nucleate boiling over the low/moderate vapour quality region. Another point observed was that the dry-out effects were more noticeable at higher mass flux and temperature, resulting in a substantially reduced heat transfer coefficient at high vapour qualities. The measured heat transfer coefficient data corresponding to low vapour quality region were compared with various heat transfer correlations based on nucleate boiling mechanism.

Kandlikar and Balasubramanian (2004) modified the correlation proposed by Kandlikar (1990) for ordinarily sized channels to extend the prediction to micro-channels which correspond to the neglected Froude number.

For all-liquid Reynolds numbers higher than 100, their correlation can be expressed as shown below.

$$h = \text{larger of} \begin{cases} h_{nb} \\ h_{conv} \end{cases} \quad (11)$$

where the heat transfer coefficient based on nucleate boiling contribution, h_{nb}, and that on forced convective contribution, h_{conv}, are given by Eqs.(12) and (13), respectively.

$$h_{nb} = 0.6683 C_{CO}^{-0.2} (1-x)^{0.8} h_{LO} + 1058.0 B_o^{0.7} (1-x)^{0.8} F_{FI} h_{LO} \quad (12)$$

$$h_{conv} = 1.136C_{CO}^{-0.9}(1-x)^{0.8}h_{LO} + 667.2B_o^{0.7}(1-x)^{0.8}F_{FI}h_{LO} \quad (13)$$

where C_{CO} represents convection number, F_{FI} stands for a fluid-surface dependent parameter which is equal to 1 for all fluids tested with stainless steel tubes, and h_{LO} for all-liquid flow heat transfer coefficient which is found from Eqs.(14) – (16):

$$h_{LO} = \frac{Re_{LO}Pr_L(f/2)(k_L/D)}{1+12.7(Pr_L^{2/3}-1)(f/2)^{0.5}} \quad \text{for } 10^4 \le Re_{LO} \le 5\times 10 \quad (14)$$

$$h_{LO} = \frac{(Re_{LO}-1000)Pr_L(f/2)(k_L/D)}{1+12.7(Pr_L^{2/3}-1)(f/2)^{0.5}} \quad \text{for } 3000 \le Re_{LO} \le 10 \quad (15)$$

$$h_{LO} = \frac{Nuk_L}{D} \quad \text{for } Re_{LO} \le 1600 \quad (16)$$

Pr_L is the liquid Prandtl number and f appearing in Eqs. (14) and (15) is the friction factor determined by:

$$f = [1.58\ln(Re_{LO}) - 3.28]^{-2} \quad (17)$$

It is noted that, for laminar flow in a circular channel with constant surface heat flux, the Nusselt number indicated in Eq. (16) is equal to 4.36. In the case of the transition region, the all-liquid flow heat transfer coefficient is established using a linear interpolation between Re_{LO} of 1600 and 3000.

They also proposed a two-phase heat transfer coefficient for very low Reynolds number ($Re_{LO} \le 100$) which is recommended as:

$$h = h_{nb} = 0.6683C_{CO}^{-0.2}(1-x)^{0.8}h_{LO} + 1058.0B_o^{0.7}(1-x)^{0.8}F_{FI}h_{LO} \quad (18)$$

where h_{LO} is found from Eq. (16).

A number of researchers such as Lee and Lee (2001), Sumith et al. (2003) and Qu and Mudawar (2003) have reported that flow boiling heat transfer is substantially controlled by convective boiling. Inconsistently, there were such publications as Lazarek and Black (1982), Wambsganss et al. (1993), Tran et al. (1996), Kew and Cornwell (1997) and Bao et al. (2000), which indicated nucleate boiling as predominant heat transfer mechanism. Noting that, the analysis of the experimental data based on studies published before 2007 was provided by Thome (2004) and Ribatski et al. (2006).

In addition to nucleate boiling and convective boiling contributions, recently, a three-zone flow boiling model based on the elongated bubble flow regime, was developed by Thome et al. (2004) and Dupont et al. (2004) to predict heat transfer characteristics in micro-channels. The point they make was that heat transfer is controlled primarily by conduction through the evaporation film trapped between the elongated bubble and the tube wall. The prediction is a mechanistic flow boiling heat transfer model comprising heat transfer zones including a pair of liquid slug and elongated bubble zones, followed by vapour slug if dry-out occurs. Each zone is modelled as passing at a fixed location sequentially and cyclically. Rather than nucleate boiling, the heat transfer was proposed to be dominated by conduction through the thin liquid film trapped between the elongated bubble and the tube wall.

To describe the cyclic passage through each zone, a time-averaged local heat transfer coefficient is obtained as follows:

$$h(z) = \frac{t_L}{\tau}h_L(z) + \frac{t_{film}}{\tau}h_{film}(z) + \frac{t_{dry}}{\tau}h_G(z) \quad (19)$$

where the period of bubble generation, τ, which is the reciprocal of the frequency was determined empirically by Dupont et al. (2004). t_L represents the time needed for the liquid slug to pass by a fixed location z along the tube. t_{film} and t_{dry} are the times needed, respectively, for film formation and local wall dry-out. h_{film} stands for the heat transfer coefficient in the film, which is assumed to be stagnant, across which one-dimensional conduction takes place. h_L and h_G are heat transfer coefficients in the liquid and vapour slugs, respectively, and are determined from their local Nusselt numbers. Ribatski et al. (2006) collected the experimental results, dealing with micro-scale flow boiling heat transfer, from the literature and compared them with different prediction methods. Among Zhang et al. (2004), Kandlikar and Balasubramanian (2004), and Thome et al. (2004), Ribatski et al. (2006) concluded, by analysing the selected database, that the three zone flow boiling model developed by Thome et al. (2004) seems to be good choice for flow boiling heat transfer prediction as illustrated in Fig. 3.

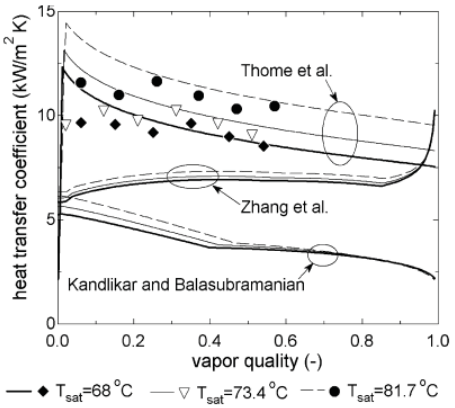

Fig. 3 Comparison of the micro-scale prediction methods and the experimental data of Bao et al. (2000) (Ribatski et al., 2006). "Reprinted from Experimental Thermal and Fluid Science, 31(1), Ribatski, G., Wojtan, L., and Thome, J.R., An analysis of experimental data and prediction methods for two-phase frictional pressure drop and flow boiling heat transfer in micro-scale channels, pp. 1-19 (2006), with permission from Elsevier."

Yun et al. (2005) were concerned with flow boiling heat transfer characteristics in rectangular channels with hydraulic diameters ranging from 1.08 to 1.54 mm. Working fluids tested were CO_2 and R-134a. Generally, the average heat transfer coefficient of CO_2 increased by around 53% as compared with that of R-134a. The effect of heat flux on heat transfer coefficient was much more obvious for CO_2 than for R-134a. The dry-out phenomenon was promoted by an increase in mass flux and it was also noted that the effect of mass flux on heat transfer coefficient was less significant than that of heat flux. As expected, the heat transfer coefficient increased with a decrease in hydraulic diameter.

Heat transfer of refrigerant R-134a during flow boiling in circular channels with different diameters including 0.51, 1.12 and 3.1 mm was studied experimentally by Saitoh et al. (2005). Nucleate boiling was reported in the low vapour quality region whereas convective evaporation was dominant in the high vapour quality region. The latter mechanism was found to be less dominant as the tube diameter decreased. The smaller the tube diameter, the higher was the effect of saturation temperature on heat transfer coefficient.

Effect of gravitational orientation on heat transfer characteristics during flow boiling of water in micro-channels was experimentally investigated by Kandlikar and Balasubramanian (2005). The heat transfer coefficient was affected by the gravitational orientation and found to be compatible with nucleate boiling mechanism.

Lee and Mudawar (2005) carried out experiments to explore flow boiling heat transfer characteristics of R-134a refrigerant in rectangular micro-channels having 231 μm wide and 713 μm deep. In this study, different heat transfer mechanisms were addressed for

Global Digital Central
ISSN: 2151-8629

three different vapour quality regions. According to this finding, they proposed heat transfer correlations for different vapour quality ranges as follows.

For vapour quality ranging from 0 to 0.05, corresponding to bubble nucleation, the relevant correlation as shown in Eq.(20) was developed based only on water flow boiling data of Qu and Mudawar (2003).

$$h_{TP} = 3.856\chi^{0.267} h_L \tag{20}$$

The Martinelli parameter, χ, can be determined according to two-phase flow condition. Laminar liquid-laminar vapour flow and laminar liquid-turbulent vapour flow correspond respectively to Eqs.(21) and (22).

$$\chi_{vv} = \left(\frac{\mu_L}{\mu_G}\right)^{0.5}\left(\frac{1-x}{x}\right)^{0.5}\left(\frac{\rho_G}{\rho_L}\right)^{0.5} \tag{21}$$

$$\chi_{vt} = \left(\frac{f_L Re_G^{0.25}}{0.079}\right)^{0.5}\left(\frac{1-x}{x}\right)^{0.5}\left(\frac{\rho_G}{\rho_L}\right)^{0.5} \tag{22}$$

The heat transfer coefficient for single-phase liquid, h_L, is given by

$$h_L = \frac{Nu_3 k_L}{D_h} \tag{23}$$

where Nu_3 is single-phase Nusselt number for laminar flow with three-sides wall heating and is expressed in terms of aspect ratio (β) or ratio of channel depth to width as shown below.

$$Nu_3 = 8.235\left(1 - 1.883\beta + 3.767\beta^2 - 5.814\beta^3 + 5.361\beta^4 - 2.0\beta^5\right) \tag{24}$$

The correlation for moderate vapour quality range (x = 0.05 - 0.55, bubbly/slug flow) as presented in Eq.(25) was developed from both R-134a and water data points.

$$h_{TP} = 436.48 B_o^{0.522} We_{LO}^{0.351} \chi^{0.665} h_L \tag{25}$$

The annular flow with local dry-out was located in the last vapour quality range (x = 0.55 - 1.0) and the correlation pertaining to this region was based only on R-134a data points as presented below.

$$h_{TP} = \max\left\{\left(108.6\chi^{1.665} h_G\right), h_G\right\} \tag{26}$$

The heat transfer coefficient for single-phase vapour flow, h_G, is evaluated according to vapour flow condition.

For laminar vapour flow:

$$h_G = \frac{Nu_3 k_G}{D_h} \tag{27}$$

For turbulent vapour flow:

$$h_G = 0.023 Re_G^{0.8} Pr_G^{0.4} \tag{28}$$

Yen et al. (2006) experimentally studied flow boiling heat transfer characteristics of HCFC123 in circular and square micro-channels with the same hydraulic diameter of around 210 μm. The heat transfer coefficient for the square channel was relatively high in low vapour quality region when compared with that for the circular channel. In high vapour quality region, however, the shape of the cross-section had no significant influence on the heat transfer coefficient. The corresponding results are illustrated in Fig. 4. The authors explained that the very large number of nucleation sites due to the existence of corners in the square channel resulted in the improved heat transfer coefficients, especially in the region controlled by bubble nucleation mechanism.

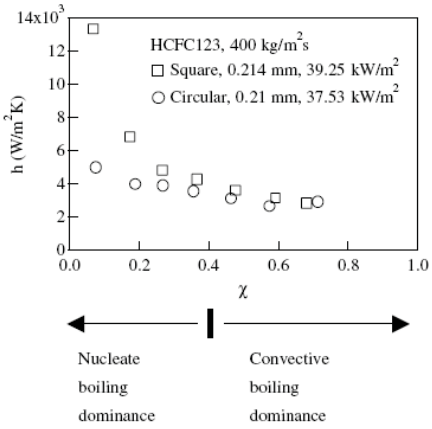

Fig. 4 Heat transfer coefficient data for different shaped cross-sections of Yen et al. (2006). "Reprinted from International Journal of Heat and Mass Transfer, 49(21-22), Yen, T.-H., Shoji, M., Takemura, F., Suzuki, Y., and Kasagi, N., Visualization of convective boiling heat transfer in single microchannels with different shaped cross-sections, pp. 3884-3894 (2006), with permission from Elsevier."

Evaporation heat transfer in tubes was studied experimentally by Lie et al. (2006). A diameter of 0.83 or 2 mm was used for each test section and the working fluids were R-134a and R-407C. The effects of mass flux, vapour quality, saturation temperature and heat flux on the heat transfer coefficient were investigated. Under given experimental conditions, the use of R-407C gave a higher heat transfer coefficient than R-134a.

The experiments with flow boiling of water in a circular tube having a diameter of 1.5 mm were performed by Boye et al. (2007). The wall temperatures of the tube in which the water flows upward were measured using infrared thermography. Nucleate boiling and convective boiling mechanisms were observed in the experiments.

Choi et al. (2007a) reported the heat transfer characteristics of CO_2 through circular channels having diameters of 1.5 and 3 mm. They indicated that nucleate boiling was predominant in the low vapour quality region and a convective boiling heat transfer contribution appeared in moderate and high vapour quality regions. The variation of local heat transfer coefficient with heat flux, mass flux, vapour quality and saturation temperature was discussed. More vigorous nucleate boiling was observed when the smaller diameter tube was used. Flow boiling heat transfer experiments with different refrigerants were continually carried out by Choi et al. (2007b). They indicated that the use of CO_2 caused the heat transfer coefficient to be higher than the case of R-134a and R-22 fluids.

Shiferaw et al. (2007) compared their flow boiling data with existing correlations. Their data points were obtained from experiments with R-134a fluid flowing through circular channels with diameters of 4.26 and 2.01 mm. The comparison revealed that existing correlations did not predict their data very well. Comments and suggestions were provided by the authors for further development of the prediction. Similar experiments were conducted by Shiferaw et al. (2009) to obtain data for a 1.1 mm diameter tube. An insignificant influence of mass flux and vapour quality on heat transfer coefficient was observed. However, the heat transfer coefficient increased with increasing heat flux and saturation pressure.

Heat transfer coefficient data for flow boiling of R-236fa in micro-channels were measured and presented by Agostini et al. (2008a). The channels are 0.223 mm wide and 0.68 mm high. The heat transfer enhancement resulted from the increase in heat flux, and the variation of vapour quality or mass flux had insignificant effect on the heat transfer coefficient. Their next publication referring to Agostini et al. (2008b) concentrated on R-245fa refrigerant during flow boiling condition in the same test section. The results showed that the heat transfer trends were similar to those for R-236fa refrigerant. Notably, the heat transfer coefficient for R-245fa was quite dependent on mass flux in comparison to the case for R-236fa. On the other hand, the effect of the saturation pressure on the heat transfer coefficient was relatively obvious for R-236fa. According to the comparisons based on different experimental conditions, they concluded that R-245fa provided heat transfer performance slightly higher than that for R-236fa.

Lee and Mudawar (2008) carried out experiments to investigate flow boiling in four different rectangular micro-channels. The heat transfer coefficient did not monotonously increase with the decrease in hydraulic diameter. This complex trend was explained with respect to sidewall thickness, channel width and aspect ratio.

The experiments for boiling heat transfer of water flow through rectangular micro-channels were carried out by Lee and Garimella (2008). The channel width ranging from 102 to 997 μm with the channel depth of around 400 μm was considered in this work and working fluid was deionized water. They found that at heat flux larger than 30 W/cm^2, the heat transfer coefficient was nearly independent with heat flux. According to their data and the asymptotic model developed by Steiner and Taborek (1992), the proposed heat transfer correlations were presented as follows.

$$h_{TP} = \frac{Nu_3}{Nu_4}\left[\left(F_{conv}h_L\right)^3 + \left(F_{nb}h_{nb}\right)^3\right]^{\frac{1}{3}} \tag{29}$$

where h_L represents single-phase liquid heat transfer coefficient, proposed by Lee and Garimella (2006), for laminar and thermally developing flow in rectangular micro-channels, and is expressed as

$$h_L = \left[1.766\left(Re_L Pr_L \frac{D_h}{L}\right)^{0.378}\beta^{0.1224}\right]\frac{k_L}{D_h} \tag{30}$$

The convective enhancement factor, F_{conv}, appearing in Eq.(29) can be determined by Eq.(31).

$$F_{conv} = \left(\phi_L^2\right)^{0.2743}\left(\frac{c_{p,TP}}{c_{p,L}}\right)^{0.2743}\left(\frac{k_{TP}}{k_L}\right)^{0.7257} \tag{31}$$

The two-phase frictional multiplier is given in the form of the Lockhart-Martinelli correlation as shown in Eq.(32).

$$\phi_L^2 = 1 + \frac{2566G^{0.5466}D_h^{0.8819}\left(1-e^{-319D_h}\right)}{\chi_{vv}} + \frac{1}{\chi_{vv}^2} \tag{32}$$

The Martinelli parameter for two-phase flow, which is in laminar region, is given by

$$\chi_{vv} = \left(\frac{1-x}{x}\right)^{0.5}\left(\frac{\rho_G}{\rho_L}\right)^{0.5}\left(\frac{\mu_L}{\mu_G}\right)^{0.5} \tag{33}$$

Any two-phase thermophysical properties can be evaluated based on arithmetic mean of those for the two phases.

Regarding Gorenflo (1993) for water, the nucleate boiling heat transfer coefficient is given by the following equation.

$$h_{nb} = 5600\left[1.73P_r^{0.27} + \left(6.1 + \frac{0.68}{1-P_r}\right)P_r^2\right]\left(\frac{q}{20000}\right)^{0.9-0.3P_r^{0.15}} \tag{34}$$

Finally, the nucleate boiling correction factor is obtained by

$$F_{nb} = 4.6809 - 0.6705\log\left(\frac{q}{1\times10^6}\right) + 3.908\left(\frac{D_h}{0.001}\right) \tag{35}$$

Heat transfer characteristics of R-134a for flow boiling in rectangular micro-channels were experimentally investigated by Bertsch et al. (2008). Their test section was micro-channels with a hydraulic diameter of 1.09 mm. Vapour quality showed significant influence on the heat transfer coefficient whereas the saturation pressure played insignificant role on the heat transfer coefficient. The higher the mass flux, the higher was the heat transfer coefficient. Similar to several previous works, the heat transfer coefficient was strongly dependent on the heat flux. With the same experimental apparatus, their next publication referring to Bertsch et al. (2009a) concerned with flow boiling heat transfer phenomena of R-245fa in addition to those of R-134a. In general, the use of R-134a for flow boiling in micro-channels resulted in relatively high heat transfer coefficient compared with R-245fa. Such discrepancy was explained based on the thermodynamic fluid properties. The comparisons between heat transfer results for two different hydraulic diameters of 1.09 and 0.54 mm were carried out for R-134a. The data shown in Fig. 5 revealed that the heat transfer coefficient was not affected by the variation of the hydraulic diameter. The similar manner was also reported by Harirchian and Garimella (2008). In contrast, the obvious effects of heat flux and vapour quality on the heat transfer coefficient were identified. The dominant heat transfer mechanism was considered to be nucleate boiling, due to the experimental data which were well predicted by pool boiling equation of Cooper (1984).

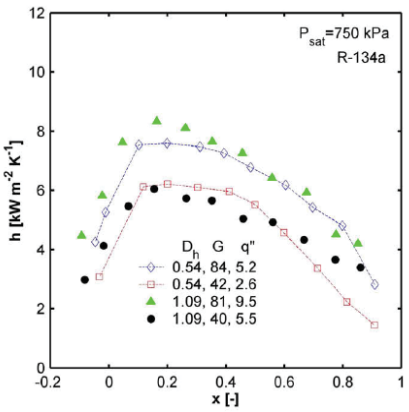

Fig. 5 Heat transfer coefficient data for different hydraulic diameters of Bertsch et al. (2009a). "Reprinted from International Journal of Multiphase Flow, 35(2), Bertsch, S.S., Groll, E.A., and Garimella, S.V., Effects of heat flux, mass flux, vapor quality, and saturation temperature on flow boiling heat transfer in microchannels, pp. 142-154 (2009), with permission from Elsevier."

Bertsch et al. (2009b) proposed a heat transfer correlation for flow boiling in micro-channels. Their correlation was based on the method of Chen (1966), which was done by accounting for nucleate boiling mechanism and two-phase force convection contribution for predicting heat transfer coefficient. The proposed correlation is presented in Eq.(36).

$$h_{TP} = h_{nb}\left(1-x\right) + h_{conv}\left(1 + 80\left(x^2 - x^6\right)e^{-0.6C_o}\right) \tag{36}$$

The nucleate boiling heat transfer coefficient is evaluated using Cooper correlation (1984) as expressed in Eq.(37) and convective heat transfer coefficient is given by Eq.(38).

$$h_{nb} = 55P_r^{0.12-0.2\log R_p}\left(-\log P_r\right)^{-0.55} M^{-0.5} q^{0.67} \tag{37}$$

$$h_{conv} = h_L(1-x) + h_G x \tag{38}$$

Surface roughness parameter, R_p, in Eq.(37) is equal to 1 if the surface roughness is unknown and M denotes molecular weight. The convective heat transfer coefficients for liquid and vapour phases appearing in Eq.(38) can be predicted using Hausen correlation (1943) as shown below.

$$h = \left(3.66 + \frac{0.0668\frac{D_h}{L}RePr}{1+0.04\left(\frac{D_h}{L}RePr\right)^{\frac{2}{3}}} \right)\frac{k}{D_h} \tag{39}$$

As seen in the above equation, liquid-phase heat transfer coefficient is therefore obtained regarding the properties of saturated liquid whereas the similar manner can be done for the vapour-phase heat transfer coefficient.

Three different refrigerants, R-134a, R-236fa and R-245fa, were tested for flow boiling in a 1.03 mm diameter tube by Ong and Thome (2009). Trends apparent in the data were investigated, showing that the heat transfer coefficient depended on heat flux at low vapour quality and on mass flux at high vapour quality. In terms of the refrigerants tested at low vapour quality, R-134a exhibited the highest heat transfer coefficient followed by R-236fa and R-245fa, respectively.

Choi et al. (2009) conducted experiments to obtain the data for two-phase flow vapourization of propane in circular channels. Two different channels with diameters of 1.5 and 3.0 mm were employed in this work. The effects of mass flux, heat flux, channel diameter and saturation temperature on the heat transfer coefficient were addressed. For low vapour quality region, the heat transfer coefficient was less affected by mass flux but substantially dependent on heat flux, showing nucleation-dominant mechanism. At higher quality region, however, an increase of forced convective mechanism was detected. As expected, the smaller channel diameter yielded a higher heat transfer coefficient. The heat transfer coefficient also increased with increasing the saturation temperature. For this work, the modification was done in the basis of Chen correlation (1966). The convective enhancement factor and nucleate boiling correction factor were proposed as shown in Eqs.(40) – (42).

The convective enhancement factor was given by

$$F_{conv} = \max\left(0.5\phi_L, 1\right) \tag{40}$$

where the two-phase multiplier was proposed in the form of the Lockhart-Martinelli correlation with Chisholm parameter expressed as

$$C = 1732.953 Re_{TP}^{-0.323} We_{TP}^{-0.24} \tag{41}$$

The nucleate boiling correction factor was presented in Eq.(42).

$$F_{nb} = 181.458\left(\phi_L^2\right)^{0.002} B_o^{0.816} \tag{42}$$

Sun and Mishima (2009) modified Lazarek and Black correlation (1982) to predict the heat transfer coefficient. Weber number was taken into account in the proposed correlation. Their correlation was not able to predict the trend of the heat transfer coefficient with vapour quality variation. The following is their proposed correlation.

$$h_{TP} = \frac{6Re_{LO}^{1.05} B_o^{0.54} k_L}{D_h We_{LO}^{0.191}\left(\frac{\rho_L}{\rho_G}\right)^{0.142}} \tag{43}$$

Tibirica and Ribatski (2010) presented experimental results for flow boiling heat transfer in a tube having a diameter of 2.3 mm. The results were obtained based on two different refrigerants, R-134a and R-245fa, which were used as working fluids. The heat transfer coefficient generally increased with increasing heat flux, saturation temperature, mass flux and vapour quality. The variation of the heat transfer coefficient with the saturation temperature for R-245fa was more obvious than that for R-134a. Nevertheless, R-134a provided high heat transfer coefficients in comparison to R-245fa.

Lee et al. (2010) collected existing 1623 data points from the literature to develop heat transfer correlations for evaporative micro-channels. The correlations of Lee and Mudawar (2005) were modified in this study as presented in Eqs.(44) – (46).

$$h_{TP} = \frac{3.856\chi^{0.267} h_L}{0.958e^{\left(\frac{-\lambda}{1.537}\right)} + 0.126}; \quad 0 \le x < 0.05 \tag{44}$$

$$h_{TP} = \frac{436.48 B_o^{0.522} We_{LO}^{0.351} \chi^{0.665} h_L}{0.958e^{\left(\frac{-\lambda}{1.537}\right)} + 0.126}; \quad 0.05 \le x < 0.55 \tag{45}$$

$$h_{TP} = \frac{\max\left\{\left(108.6\chi^{1.665} h_G\right), h_G\right\}}{0.958e^{\left(\frac{-\lambda}{1.537}\right)} + 0.126}; \quad 0.55 \le x < 1 \tag{46}$$

Convective boiling heat transfer experiments were carried out by Oh et al. (2011) for tubes with diameters of 0.5, 1.5 and 3.0 mm. There were five refrigerants used in their study, i.e. R-22, R-134a, R-410A, C_3H_8 and CO_2. Based on an insignificant effect of mass flux on the heat transfer coefficient in low vapour quality region, the dominance of nucleate boiling mechanism was indicated. However, forced convective contribution was addressed as dominant in moderate-high quality region due to the mass flux dependency. The smaller diameter tube resulted in the higher heat transfer coefficient, especially at low vapour quality region. The heat transfer coefficient of CO_2 was highest in comparison to the other four refrigerants.

Bang et al. (2011) reported slight effect of pressure on heat transfer coefficient of water during flow boiling in a 1.73 mm diameter channel. The dominance of forced convection was observed during their experiments.

Copetti et al. (2011) presented the experimental work for flow boiling of R-134a in a tube with a diameter of 2.6 mm. Heat transfer characteristics under the variation of different parameters were discussed. They reported the dependence of heat transfer coefficient on heat flux, especially at low vapour quality region. At high quality region, however, the heat flux dependency became lower. The heat transfer coefficient was strongly dependent on mass flux only for low heat flux conditions. Flow pattern was reported to play important role on the heat transfer coefficient.

Influence of the aspect ratio on flow boiling heat transfer characteristics in rectangular channels were reported by Soupremanien et al. (2011). The results showed that for a low aspect ratio of 0.143, the heat transfer coefficient was not dependent on the vapour quality for a heat flux range of 25 to 45 kW/m^2. As heat flux increased above 45 kW/m^2, the heat transfer coefficient tended to decrease with increasing vapour quality. However, the heat transfer coefficient was not affected by the variation of vapour quality when the channel with higher aspect ratio of 0.43 was used in the experiments. Another point to note was that the heat transfer

DOI: 10.5098/hmt.v3.1.3006 ISSN: 2151-8629

coefficient was higher for the aspect ratio of 0.143 than that of 0.43 under low heat flux conditions. The opposite trend was addressed for high heat flux conditions.

Ong and Thome (2011b) experimentally investigated flow boiling heat transfer of three refrigerants in channels of 1.03, 2.20 and 3.04 mm diameters. R-134a, R-236fa and R-245fa were used as working fluids in their study. The channel with higher confinement number, i.e. smaller diameter, gave heat transfer coefficients with lower dependency on heat flux. The heat transfer coefficient was also found to strongly depend on flow pattern. The coalescing bubble flow regime posed heat transfer mechanism compatible with three-zone flow boiling model proposed by Thome et al. (2004) whereas the dominance of forced convection was observed in the annular flow regime. The heat transfer coefficient for R-134a showed the highest dependence on heat flux but R-245fa yielded the lowest heat flux dependency while R-236fa was positioned in between the other two refrigerants. It was noted from the authors that surface roughness played important role on micro-scale flow boiling.

In summary, this emerging field is very attractive and may enable us to develop powerful miniature devices which seem to be unfeasible in the past. Although a number of studies have been reported for micro-channels, micro-scale phenomena with respect to phase-change mechanisms are still open questions for which systematic answers are of importance. Based on this, further investigations should be performed as follows.

1. The existing models and correlations for flow pattern and heat transfer predictions should be examined based on different sources of the experimental data
2. Conduct more experiments to address the macro-to-micro-scale transition for flow boiling of refrigerants in different channel sizes and channel orientations. The threshold of the transition would be addressed according to the dependence of the channel orientation on flow regime and heat transfer characteristics.
3. Heat transfer behaviors in parallel channels are different from those in single channel under a given set of experimental conditions. The discrepancies are possibly due to instabilities resulting from flow reversal in the channels. The details corresponding to instabilities encountered in narrow spaces were reviewed by Tadrist (2007). Referring to Kandlikar et al. (2006), the surface condition was found to influence on the instabilities. The introduction of artificial nucleation cavities fabricated on the micro-channel surface together with inlet header having restriction holes was recommended to obtain a good heat transfer performance without instabilities. The surface effects during flow boiling in micro-channels were also discussed in Mahmoud et al. (2011). Additionally, the effect of conduction heat transfer over the partitions in the parallel channels may cause the difference in the heat transfer characteristics between single and parallel channels. The previous studies imply that the parametric studies regarding the comparisons of the heat transfer performance in single channel and that in parallel channels should be further performed to explain the cause of the discrepancies.
4. Although the topics such as critical heat flux, flow instability and two-phase pressure drop are not included in this paper due to the restricted space, the relevant experimental data are of importance for developing the miniature devices.

3. CONCLUSION

A state-of-the-art review of flow boiling in micro-channels is presented. Recent researches on flow pattern, heat transfer characteristics are described in this paper. Different criteria are presented at first to give definition for micro-channel. The explorations indicate that the existing channel classifications cannot relate the channel diameter to the fluid flow and heat transfer mechanisms. Further works should be conducted to meet a more general definition dealing with the channel classification. Then, flow visualization studies and investigations on heat transfer characteristics are reviewed. Obviously, the research work in this area is still rare so far. As a consequence, a great deal of systematic investigations remain to be done to meet general conclusions needed for the appropriate design and process control of several engineering applications.

ACKNOWLEDGEMENTS

The authors would like to express their appreciation to the Thailand Research Fund, KMITL Research Fund, the Office of Higher Education Commission and the National Research University Project for providing financial support.

NOMENCLATURE

B_o	boiling number, $B_o = q/Gi_{LG}$
C	Chisholm parameter
C_{CO}	convection number, $C_{CO} = (\rho_G/\rho_L)^{0.5}((1-x)/x)^{0.8}$
C_o	confinement number as defined in Eq.(1)
C_p	specific heat at constant pressure (J/kgK)
D	channel diameter (m)
D_b	capillary length (m)
D_h	hydraulic diameter (m)
F	factor
Fr	Froude number, $Fr = G^2/\rho^2 gD$
F_{Fl}	fluid-surface parameter
f	friction factor
G	mass flux (kg/m^2s)
g	gravitational acceleration (m/s^2)
h	heat transfer coefficient (W/m^2K)
i	specific enthalpy (J/kg)
k	thermal conductivity (W/mK)
L	length (m)
M	molecular weight (kg/kmol)
Nu	Nusselt number, $Nu = hD_h/k$
P	pressure (Pa)
P_r	reduced pressure
Pr	Prandtl number, $Pr = \mu C_p/k$
q	heat flux (W/m^2)
Re	Reynolds number, $Re = GD_h/\mu$
R_p	surface roughness parameter
T	temperature (^oC)
t	time (s)
We	Weber number, $We = G^2 D_h/\rho\sigma$
x	vapour quality
z	axial distance (m)

Greek symbols

β	ratio of channel dept to width
χ	Lockhart-Martinelli parameter
ϕ	two-phase multiplier
λ	Bond number, $\lambda = g(\rho_L - \rho_G)D_h^2/\sigma$
μ	dynamic viscosity (Ns/m^2)
ρ	density (kg/m^3)
σ	surface tension (N/m)
τ	pair period (s)

Subscripts

3	three-sided wall heating
4	four-sided wall heating
A	annular flow

CB	coalescing bubble flow
conv	convection boiling contribution
dry	dry-out zone
eq	equivalent
film	liquid film between bubble and wall
G	vapour phase
GO	all-vapour
IB	isolated bubble flow
in	inlet
L	liquid phase
LO	all-liquid
nb	nucleate boiling contribution
out	outlet
s	surface
sat	saturation
TP	two-phase
vt	Laminar liquid-turbulent vapour flow
vv	laminar liquid-laminar vapour flow

REFERENCES

Agostini, B., Thome, J.R., Fabbri, M., Michel, B., Calmi, D., and Kloter, U., 2008a, "High heat flux flow boiling in silicon multi-microchannels – Part I: Heat transfer characteristics of refrigerant R236fa," *International Journal of Heat and Mass Transfer,* 51, 5400-5414.
http://dx.doi.org/10.1016/j.ijheatmasstransfer.2008.03.006

Agostini, B., Thome, J.R., Fabbri, M., Michel, B., Calmi, D., and Kloter, U., 2008b, "High heat flux flow boiling in silicon multi-microchannels – Part II: Heat transfer characteristics of refrigerant R245fa," *International Journal of Heat and Mass Transfer,* 51, 5415-5425.
http://dx.doi.org/10.1016/j.ijheatmasstransfer.2008.03.007

Arcanjo, A.A., Tibirica, C.B., and Ribatski, G., 2010, "Evaluation of flow patterns and elongated bubble characteristics during the flow boiling of halocarbon refrigerants in a micro-scale channel," *Experimental Thermal and Fluid Science,* 34, 766-775.
http://dx.doi.org/10.1016/j.expthermflusci.2010.01.006

Bang, K.H., Kim, K.K., Lee, S.K., and Lee, B.W., 2011, "Pressure effect on flow boiling heat transfer of water in minichannels," *International Journal of Thermal Sciences,* 50, 280-286.
http://dx.doi.org/10.1016/j.ijthermalsci.2010.03.011

Bao, Z.Y., Fletcher, D.F., and Haynes, B.S., 2000, "Flow boiling heat transfer of Freon R11 and HCFC123 in narrow passages," *International Journal of Heat and Mass Transfer,* 43, 3347-3358.
http://dx.doi.org/10.1016/S0017-9310(99)00379-8

Bertsch, S.S., Groll, E.A., and Garimella, S.V., 2008, "Refrigerant flow boiling heat transfer in parallel microchannels as a function of local vapor quality," *International Journal of Heat and Mass Transfer,* 51, 4775-4787.
http://dx.doi.org/10.1016/j.ijheatmasstransfer.2008.01.026

Bertsch, S.S., Groll, E.A., and Garimella, S.V., 2009a, "Effects of heat flux, mass flux, vapor quality, and saturation temperature on flow boiling heat transfer in microchannels," *International Journal of Multiphase Flow,* 35, 142-154.
http://dx.doi.org/10.1016/j.ijmultiphaseflow.2008.10.004

Bertsch, S.S., Groll, E.A., and Garimella, S.V., 2009b, "A composite heat transfer correlation for saturated flow boiling in small channels," *International Journal of Heat and Mass Transfer,* 52, 2110-2118.
http://dx.doi.org/10.1016/j.ijheatmasstransfer.2008.10.022

Boye, H., Staate, Y., and Schmidt, J., 2007, "Experimental investigation and modeling of heat transfer during convective boiling in a minichannel," *International Journal of Heat and Mass Transfer,* 50, 208-215.
http://dx.doi.org/10.1016/j.ijheatmasstransfer.2006.06.017

Celata, G.P., Saha, S.K., Zummo, G., and Dossevi, D., 2010, "Heat transfer characteristics of flow boiling in a single horizontal microchannel," *International Journal of Thermal Sciences,* 49, 1086-1094.
http://dx.doi.org/10.1016/j.ijthermalsci.2010.01.019

Chen, J.C., 1966, "Correlation for boiling heat transfer to saturated fluids in convective flow," I&EC Process Des. Dev., 5, 322-329.

Choi, K.-I., Pamitran, A.S., and Oh, J.-T., 2007a, "Two-phase flow heat transfer of CO_2 vaporization in smooth horizontal minichannels," *International Journal of Refrigeration,* 30, 767-777.
http://dx.doi.org/10.1016/j.ijrefrig.2006.12.006

Choi, K.-I., Pamitran, A.S., Oh, C.-Y., and Oh, J.-T., 2007b, "Boiling heat transfer of R-22, R-134a, and CO_2 in horizontal smooth minichannels," *International Journal of Refrigeration,* 30, 1336-1346.
http://dx.doi.org/10.1016/j.ijrefrig.2007.04.007

Choi, K.-I., Pamitran, A.S., Oh, J.-T., and Saito, K., 2009, "Pressure drop and heat transfer during two-phase flow vaporization of propane in horizontal smooth minichannels," *International Journal of Refrigeration,* 32, 837-845.
http://dx.doi.org/10.1016/j.ijrefrig.2008.12.005

Chung, P.M.-Y., and Kawaji, M., 2004, "The effect of channel diameter on adiabatic two-phase flow characteristics in microchannels," *International Journal of Multiphase Flow,* 30, 735-761.
http://dx.doi.org/10.1016/j.ijmultiphaseflow.2004.05.002

Cooper, M.G., 1984, "Heat flow rates in saturated nucleate pool boiling – A wide ranging examination using reduced properties," *Advances in Heat Transfer,* 16, 157-239.
http://dx.doi.org/10.1016/S0065-2717(08)70205-3

Copetti, J.B., Macagnan, M.H., Zinani, F., and Kunsler, N.L.F., 2011, "Flow boiling heat transfer and pressure drop of R-134a in a mini tube: an experimental investigation," *Experimental Thermal and Fluid Science,* 35, 636-644.
http://dx.doi.org/10.1016/j.expthermflusci.2010.12.013

Dupont, V., Thome, J.R., and Jacobi, A.M., 2004, "Heat transfer model for evaporation in microchannels. Part II: comparison with the database," *International Journal of Heat and Mass Transfer,* 47, 3387-3401.
http://dx.doi.org/10.1016/j.ijheatmasstransfer.2004.01.007

Garimella, S., Killion, J.D., and Coleman, J.W., 2002, "An experimentally validated model for two-phase pressure drop in the intermittent flow regime for circular microchannels," *Journal of Fluids Engineering,* 124, 205-214.
http://dx.doi.org/10.1115/1.1428327

Gorenflo, D., 1993, "Pool Boiling," VDI-Heat Atlas, VDI-Verlag, Dusseldorf, Germany.

Harirchian, T., and Garimella, S.V., 2008, "Microchannel size effects on local flow boiling heat transfer to a dielectric fluid," *International Journal of Heat and Mass Transfer,* 51, 3724-3735.

http://dx.doi.org/10.1016/j.ijheatmasstransfer.2008.03.013

Harirchian, T., and Garimella, S.V., 2010, "A comprehensive flow regime map for microchannel flow boiling with quantitative transition criteria," *International Journal of Heat and Mass Transfer,* 53, 2694-2702.
http://dx.doi.org/10.1016/j.ijheatmasstransfer.2010.02.039

Hausen, H., Warmeuberganges 1943, "Darstellung des in Rohren durch verallgemeinerte Potenzbeziehungen," Z. VDI Beiheft Verfahrenstechnik, 4, 91-102.

Huo, X., Chen, L., Tian, Y.S., and Karayiannis, T.G., 2004, "Flow boiling and flow regimes in small diameter tubes," *Applied Thermal Engineering,* 24, 1225-1239.
http://dx.doi.org/10.1016/j.applthermaleng.2003.11.027

Jiang, L., and Wong, M., 1999, "Phase change in microchannel heat-sinks with integrated temperature sensors," *Journal of Microelectromechanical Systems,* 8, 358-365.
http://dx.doi.org/10.1109/84.809049

Kandlikar, S.G., 1990, "A general correlation for two-phase flow boiling heat transfer coefficient inside horizontal and vertical tubes," *Journal of Heat Transfer,* 112, 219-228.
http://dx.doi.org/10.1115/1.2910348

Kandlikar, S.G., and Grande, W.J., 2003, "Evolution of microchannel flow passages – thermohydraulic performance and fabrication technology," *Heat Transfer Engineering,* 24, 3-17.
http://dx.doi.org/10.1080/01457630304040

Kandlikar, S.G., and Balasubramanian, P., 2004, "An extension of the flow boiling correlation to transition, laminar, and deep laminar flows in minichannels and microchannels," *Heat Transfer Engineering,* 25, 86-93.
http://dx.doi.org/10.1080/01457630490280425

Kandlikar, S.G., and Balasubramanian, P., 2005, "An experimental study on the effect of gravitational orientation on flow boiling of water in 1054 × 197 μm parallel minichannels," *Journal of Heat Transfer,* 127, 820–829.
http://dx.doi.org/10.1115/1.1928911

Kandlikar, S.G., Kuan, W.K., Willistein, D.A., and Borrelli, J., 2006, "Stabilization of flow boiling in microchannels using pressure drop elements and fabricated nucleation sites," *Journal of Heat Transfer,* 128, 389-396.
http://dx.doi.org/10.1115/1.2165208

Kandlikar, S.G., 2010, "Scale effects on flow boiling heat transfer in microchannels: A fundamental perspective," *International Journal of Thermal Sciences,* 49, 1073-1085.
http://dx.doi.org/10.1016/j.ijthermalsci.2009.12.016

Kew, P.A., and Cornwell, K., 1997, "Correlations for the prediction of boiling heat transfer in small-diameter channels," *Applied Thermal Engineering,* 17, 705-715.
http://dx.doi.org/10.1016/S1359-4311(96)00071-3

Lazarek, G.M., and Black, S.H., 1982, "Evaporative heat transfer, pressure drop and critical heat flux in a small diameter vertical tube with R-113," *International Journal of Heat and Mass Transfer,* 25, 945-960.
http://dx.doi.org/10.1016/0017-9310(82)90070-9

Lee, H.J., and Lee, S.Y., 2001, "Heat transfer correlation for boiling flows in small rectangular horizontal channels with low aspect ratios," *International Journal of Multiphase Flow,* 27, 2043-2062.
http://dx.doi.org/10.1016/S0301-9322(01)00054-4

Lee, J., and Mudawar, I., 2005, "Two-phase flow in high-heat-flux micro-channel heat sink for refrigeration cooling applications: Part II – heat transfer characteristics," *International Journal of Heat and Mass Transfer,* 48, 941-955.
http://dx.doi.org/10.1016/j.ijheatmasstransfer.2004.09.019

Lee, P.-S., and Garimella, S.V., 2006, "Thermally developing flow and heat transfer in rectangular microchannels of different aspect ratios," *International Journal of Heat and Mass Transfer,* 49, 3060-3067.
http://dx.doi.org/10.1016/j.ijheatmasstransfer.2006.02.011

Lee, P.-S., and Garimella, S.V., 2008, "Saturated flow boiling heat transfer and pressure drop in silicon microchannel arrays," *International Journal of Heat and Mass Transfer,* 51, 789-806.
http://dx.doi.org/10.1016/j.ijheatmasstransfer.2007.04.019

Lee, J., and Mudawar, I., 2008, "Fluid flow and heat transfer characteristics of low temperature two-phase micro-channel heat sinks – Part 2. Subcooled boiling pressure drop and heat transfer," *International Journal of Heat and Mass Transfer,* 51, 4327-4341.
http://dx.doi.org/10.1016/j.ijheatmasstransfer.2008.02.013

Lee, H.J., Liu, D.Y., Alyousef, Y., and Yao, S., 2010, "Generalized two-phase pressure drop and heat transfer correlations in evaporative micro/minichannels," *Journal of Heat Transfer,* 132, 1-9.
http://dx.doi.org/10.1115/1.4000861

Li, W., and Wu, Z., 2010, "A general criterion for evaporative heat transfer in micro/mini-channels," *International Journal of Heat and Mass Transfer,* 53, 1967-1976.
http://dx.doi.org/10.1016/j.ijheatmasstransfer.2009.12.059

Lie, Y.M., Su, F.Q., Lai, R.L., and Lin, T.F., 2006, "Experimental study of evaporation heat transfer characteristics of refrigerants R-134a and R-407C," *International Journal of Heat and Mass Transfer,* 49, 207-218.
http://dx.doi.org/10.1016/j.ijheatmasstransfer.2005.07.018

Mahmoud, M.M., Karayiannis, T.G., and Kenning, D.B.R., 2011, "Surface effects in flow boiling of R134a in microtubes," *International Journal of Heat and Mass Transfer, 54*, 3334-3346.
http://dx.doi.org/10.1016/j.ijheatmasstransfer.2011.03.052

Martin-Callizo, C., Palm, B., Owhaib, W., and Ali, R., 2010, "Flow boiling visualization of R-134a in a vertical channel of small diameter," *Journal of Heat Transfer,* 132, 1-8.
http://dx.doi.org/10.1115/1.4000012

Mehendale, S.S., Jacobi, A.M., and Ahah, R.K., 2000, "Fluid flow and heat transfer at micro- and meso-scales with application to heat exchanger design," *Applied Mechanics Reviews,* 53, 175-193.
http://dx.doi.org/10.1115/1.3097347

Oh, J.-T., Pamitran, A.S., Choi, K.-I., and Hrnjak, P., 2011, "Experimental investigation on two-phase flow boiling heat transfer of five refrigerants in horizontal small tubes of 0.5, 1.5 and 3.0 mm inner diameters," *International Journal of Heat and Mass Transfer,* 54, 2080-2088.
http://dx.doi.org/10.1016/j.ijheatmasstransfer.2010.12.021

Ong, C.L., and Thome, J.R., 2009, "Flow boiling heat transfer of R134a, R236fa and R245fa in a horizontal 1.030 mm circular channel," *Experimental Thermal and Fluid Science,* 33, 651-663.
http://dx.doi.org/10.1016/j.expthermflusci.2009.01.002

Ong, C.L., and Thome, J.R., 2011a, "Macro-to-microchannel transition in two-phase flow: Part 1-Two-phase flow patterns and film thickness measurements," *Experimental Thermal and Fluid Science,* 35, 37-47.
http://dx.doi.org/10.1016/j.expthermflusci.2010.08.004

Ong, C.L., and Thome, J.R., 2011b, "Macro-to-microchannel transition in two-phase flow: Part 2-Flow boiling heat transfer and critical heat flux," *Experimental Thermal and Fluid Science,* 35, 873-886.
http://dx.doi.org/10.1016/j.expthermflusci.2010.12.003

Pettersen, J., 2004, "Flow vaporization of CO_2 in microchannel tubes," *Experimental Thermal and Fluid Science,* 28, 111-121.
http://dx.doi.org/10.1016/S0894-1777(03)00029-3

Qu, W., and Mudawar, I., 2003, "Flow boiling heat transfer in two-phase microchannel heat sinks; experimental investigation and assessment of correlation methods," *International Journal of Heat and Mass Transfer,* 46, 2755-2771.
http://dx.doi.org/10.1016/S0017-9310(03)00041-3

Revellin, R., and Thome, J.R., 2007, "A new type of diabatic flow pattern map for boiling heat transfer in microchannels," *Journal of Micromechanics and Microengineering,* 17, 788-796.
http://dx.doi.org/10.1088/0960-1317/17/4/016

Ribatski, G., Wojtan, L., and Thome, J.R., 2006, "An analysis of experimental data and prediction methods for two-phase frictional pressure drop and flow boiling heat transfer in micro-scale channels," *Experimental Thermal and Fluid Science,* **31**, 1-19.
http://dx.doi.org/10.1016/j.expthermflusci.2006.01.006

Saisorn, S., and Wongwises, S., 2010, "The effects of channel diameter on flow pattern, void fraction and pressure drop of two-phase air-water flow in circular micro-channels," *Experimental Thermal and Fluid Science,* 34, 454-462.
http://dx.doi.org/10.1016/j.expthermflusci.2009.02.006

Saisorn, S., Kaew-On, J., and Wongwises, S., 2010, "Flow pattern and heat transfer characteristics of R-134a refrigerant during flow boiling in a horizontal circular mini-channel," *International Journal of Heat and Mass Transfer,* 53, 4023-4038.
http://dx.doi.org/10.1016/j.ijheatmasstransfer.2010.05.022

Saitoh, S., Daiguji, H., and Hihara, E., 2005, "Effect of tube diameter on boiling heat transfer of R-134a in horizontal small-diameter tubes," *International Journal of Heat and Mass Transfer,* 48, 4973-4984.
http://dx.doi.org/10.1016/j.ijheatmasstransfer.2005.03.035

Shiferaw, D., Huo, X., Karayiannis, T.G., and Kenning, D.B.R., 2007, "Examination of heat transfer correlations and a model for flow boiling of R134a in small diameter tubes," *International Journal of Heat and Mass Transfer,* 50, 5177-5193.
http://dx.doi.org/10.1016/j.ijheatmasstransfer.2007.07.002

Shiferaw, D., Karayiannis, T.G., and Kenning, D.B.R., 2009, "Flow boiling in a 1.1 mm tube with R134a: Experimental results and comparison with model," *International Journal of Thermal Sciences,* 48, 331-341.
http://dx.doi.org/10.1016/j.ijthermalsci.2008.02.009

Soupremanien, U., Person, S.L., Favre-Marinet, M., and Bultel, Y., 2011, "Influence of the aspect ratio on boiling flows in rectangular mini-channels," *Experimental Thermal and Fluid Science,* 35, 797-809.
http://dx.doi.org/10.1016/j.expthermflusci.2010.06.014

Steiner, D., and Taborek, J., 1992, "Flow boiling heat transfer in vertical tubes correlated by an asymptotic model," *Heat Transfer Engineering,* 13, 43-68.
http://dx.doi.org/10.1080/01457639208939774

Sumith, B., Kaminaga, F., and Matsumura, K., 2003, "Saturated flow boiling of water in a vertical small tube," *Experimental Thermal and Fluid Science,* 27, 789-801.
http://dx.doi.org/10.1016/S0894-1777(02)00317-5

Sun, L., and Mishima, K., 2009, "An evaluation of prediction methods for saturated flow boiling heat transfer in mini-channels," *International Journal of Heat and Mass Transfer,* 52, 5323-5329.
http://dx.doi.org/10.1016/j.ijheatmasstransfer.2009.06.041

Tadrist, L., 2007, "Review on two-phase flow instabilities in narrow spaces," *International Journal of Heat and Fluid Flow, 28*, 54-62.
http://dx.doi.org/10.1016/j.ijheatfluidflow.2006.06.004

Thome, J.R., 2004, "Boiling in microchannels: a review of experiment and theory," *International Journal of Heat and Fluid Flow, 25*, 128-139.
http://dx.doi.org/10.1016/j.ijheatfluidflow.2003.11.005

Thome, J.R., Dupont, V., and Jacobi, A.M., 2004, "Heat transfer model for evaporation in microchannels. Part I: presentation of the model," *International Journal of Heat and Mass Transfer,* 47 3375-3385.
http://dx.doi.org/10.1016/j.ijheatmasstransfer.2004.01.006

Tibirica, C.B., and Ribatski, G., 2010, "Flow boiling heat transfer of R134a and R245fa in a 2.3 mm tube," *International Journal of Heat and Mass Transfer,* 53, 2459-2468.
http://dx.doi.org/10.1016/j.ijheatmasstransfer.2010.01.038

Tran, T.N., Wambsganss, M.W., and France, D.M., 1996, "Small circular- and rectangular-channel boiling with two refrigerants," *International Journal of Multiphase Flow,* 22, 485-498.
http://dx.doi.org/10.1016/0301-9322(96)00002-X

Triplett, K.A., Ghiaasiaan, S.M., Abdel-Khalik, S.I., and Sadowski, D.L., 1999, "Gas-liquid two-phase flow in microchannels Part I: two-phase flow patterns," *International Journal of Multiphase Flow,* 25, 377-394.
http://dx.doi.org/10.1016/S0301-9322(98)00054-8

Wambsganss, M.W., France, D.M., Jendrzejczyk, J.A., and Tran, T.N., 1993, "Boiling heat transfer in a horizontal small-diameter tube," *Journal of Heat Transfer,* 115, 963-972.
http://dx.doi.org/10.1115/1.2911393

Yang, C.-Y., and Shieh, C.-C., 2001, "Flow pattern of air-water and two-phase R-134a in small circular tubes," *International Journal of Multiphase Flow,* 27, 1163-1177.
http://dx.doi.org/10.1016/S0301-9322(00)00070-7

Yen, T.-H., Shoji, M., Takemura, F., Suzuki, Y., and Kasagi, N., 2006, "Visualization of convective boiling heat transfer in single microchannels with different shaped cross-sections," *International Journal of Heat and Mass Transfer,* 49, 3884-3894.
http://dx.doi.org/10.1016/j.ijheatmasstransfer.2005.12.024

Yun, R., Kim, Y., and Kim, M.S., 2005, "Convective boiling heat transfer characteristics of CO_2 in microchannels," *International Journal of Heat and Mass Transfer,* 48, 235-242. http://dx.doi.org/10.1016/j.ijheatmasstransfer.2004.08.019

Zhang, L., Koo, J.M., Jiang, L., Asheghi, M., Goodson, K.E., and Santiago, J.G., 2002, "Measurements and modeling of two-phase flow in microchannels with nearly constant heat flux boundary conditions," *Journal of Microelectromechanical Systems,* 11, 12-19. http://dx.doi.org/10.1109/84.982858

Zhang, W., Hibiki, T., and Mishima, K., 2004, "Correlation for flow boiling heat transfer in mini-channels," *International Journal of Heat and Mass Transfer,* 47, 5749-5763. http://dx.doi.org/10.1016/j.ijheatmasstransfer.2004.07.034

Frontiers in Heat and Mass Transfer (FHMT), 3, 013007 (2012)
DOI: 10.5098/hmt.v3.1.3007

Global Digital Central
ISSN: 2151-8629

Frontiers in Heat and Mass Transfer

Available at www.ThermalFluidsCentral.org

A CRITICAL REVIEW OF RECENT INVESTIGATIONS ON TWO-PHASE PRESSURE DROP IN FLOW BOILING MICRO-CHANNELS

Sira Saisorn[a,b], Somchai Wongwises[b,c*]

[a]*King Mongkut's Institute of Technology Ladkrabang Chumphon Campus Chumphon 86160, Thailand*
[b]*Fluid Mechanics, Thermal Engineering and Multiphase Flow Research Lab. (FUTURE)*
Department of Mechanical Engineering, King Mongkut's University of Technology Thonburi, Bangmod, Bangkok 10140, Thailand
[c]*The Academy of Science, The Royal Institute of Thailand, Sanam Suea Pa, Dusit, Bangkok 10300, Thailand*

ABSTRACT

Two-phase pressure drop during flow boiling has been studied for several decades. Obviously, the publications available on micro-channels are relatively small compared with those for ordinarily sized channels. Although the use of micro-channels yields several advantages, the pressure drop takingp lace in these extremely small channels is higher than that in the ordinarily sized channels because of the increased wall friction. The knowledge of the two-phase pressure drop characteristics in addition to heat transfer phenomena is essential to the design and evaluation of the micro-systems. In this paper, recent research on the flow boiling pressure drop in micro-scale channels is reviewed. The experimental results as well as the relevant prediction methods based on different researchers are presented.

Keywords: *flow boiling, micro-channel, pressure drop, heat transfer*

1. INTRODUCTION

In the past 10 years, investigations on flow boiling heat transfer and flow characteristics in micro-channel flow passages have gained significant attention in engineering community. Because of their large heat transfer surface area, the utilization of micro-channels can result in relatively high heat transfer coefficient when compared with the application of ordinarily sized channels. Flow boiling in micro-channel has been applied to energy and process systems including high heat-flux compact heat exchangers, and cooling devices of various types of equipment such as high performance micro-electronics, high-powered lasers, and so on.

Although there are several advantages arising in micro-channel applications, a considerable penalty is relatively high pressure drop due to the increased wall friction, resulting in the increment of power consumption. The applicable range of the flow in miniature devices is restricted by this main drawback. It is therefore important to understand pressure drop characteristics in addition to heat transfer phenomena in micro-channels, which is of necessity for operating and evaluating the system performance.

A scaling analysis of different forces, as recently discussed in Kandlikar (2010), pointed out that surface tension and evaporation momentum forces were significant for two-phase flow phenomena at micro-scale, resulting in the flow behaviors substantially different from those of ordinarily sized channels.

Currently, it seems rather vague to identify whether or not the flow passages are micro-channels. The followings are some important tentative criterions which are given in brief.

The criteria based on different dimensionless parameters have been proposed in the literature. The confinement number recommended by Kew and Cornwell (1997) was proposed to be related with some physical aspects of flow boiling. The confinement number is defined as

$$C_o = \frac{D_b}{D_h} \tag{1}$$

where D_h is hydraulic diameter and D_b is nominal bubble size or capillary length which is expressed by

$$D_b = \sqrt{\frac{\sigma}{g(\rho_L - \rho_G)}} \tag{2}$$

The confinement number above 0.5 implies that the micro-scale effects are important for a given channel diameter. In Eq.(2), σ stands for surface tension, g is gravitational acceleration, ρ_L and ρ_G are, respectively, liquid and vapour densities.

Based on 4228 data points gathered from the literature, Li and Wu (2010a) showed the transitional threshold from macro- to micro-channels during flow boiling to be represented as a combined non-dimensional number, $B_o \times Re_L^{0.5} = 200$. B_o and Re_L stand, respectively, for Bond number and liquid Reynolds number. The micro-scale effects are dominant when such combined non-dimensional number is lower than 200.

It is interesting to note from Tibirica and Ribatski (2010) that the channel with a diameter of 2.3 mm was considered as the one in which the transition between macro- and micro-scale flow boiling phenomena took place when halocarbon refrigerants were used as working fluids under Earth's gravity. With visualization study, they detected stratification effects in this channel size. Recently, Ong and

* *Corresponding author: E-mail: somchai.won@kmutt.ac.th*

Thome (2011) investigated experiments to address the macro-to-micro-scale transition for flow boiling of refrigerants in different channel sizes. They indicated the dependence of the threshold of the transition on flow regime and confinement number. As illustrated in Fig. 1, the lower threshold of macro-scale flow corresponded to confinement number ranging from 0.3 to 0.4 whereas the confinement number of around 1.0 stood for the upper threshold of micro-scale flow. It was noted that the transition region, frequently corresponding to as mini-channels in literature, was located in between the two boundaries.

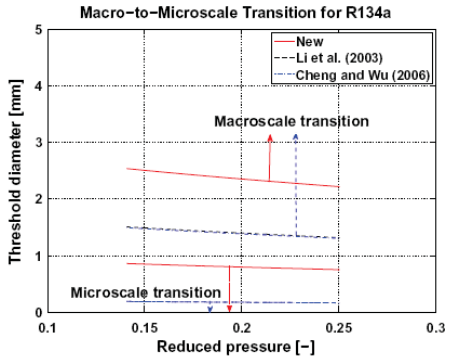

Fig. 1 Transition criterion of Ong and Thome (2011). "Reprinted from Experimental Thermal and Fluid Science, 35(1), Ong, C.L., and Thome, J.R., Macro-to-microchannel transition in two-phase flow: Part 1-Two-phase flow patterns and film thickness measurements, pp. 37-47 (2011), with permission from Elsevier."

Noting from Kandlikar (2010) that as the mass flux substantially increases, the inertia force becomes larger and tends to be of importance as shown in Fig. 2. In the region of very high mass flux, therefore, the inertia force in addition to surface tension and buoyancy (gravity) forces should be taken into account for developing the criteria.

Despite a number of criteria being proposed, a clear physical criterion that relates the channel diameter to the fluid flow mechanisms is still not available and, hence, further investigation should be performed to meet a more general definition dealing with channel classification.

2. TWO-PHASE PRESSURE DROP

Although there are several advantages arising in micro-channel applications, a considerable penalty is relatively high pressure drop, due to the increased wall friction, when compared with the ordinarily sized channels. It is therefore important to understand pressure drop characteristics in addition to heat transfer phenomena in micro-channels, which is of necessity for operating and evaluating the system performance.

Recent studies dealing with flow boiling pressure drop characteristics, excluding flow instability, in micro-channels are reviewed in this section. During the past years, investigations of two-phase pressure drop during micro-scale flow have been published in the literature and Table 1 lists the selected investigations recently done by various researchers.

Two-phase pressure drop across micro-channels were measured by Lee and Mudawar (2005). Flow boiling of R-134a in rectangular channels was established in their study. The measured pressure drops were not well predicted by the existing correlations. To improve the accuracy of the prediction, the parameters including liquid viscosity and surface tension were incorporated in their correlation as seen in Eqs.(3) and (4).

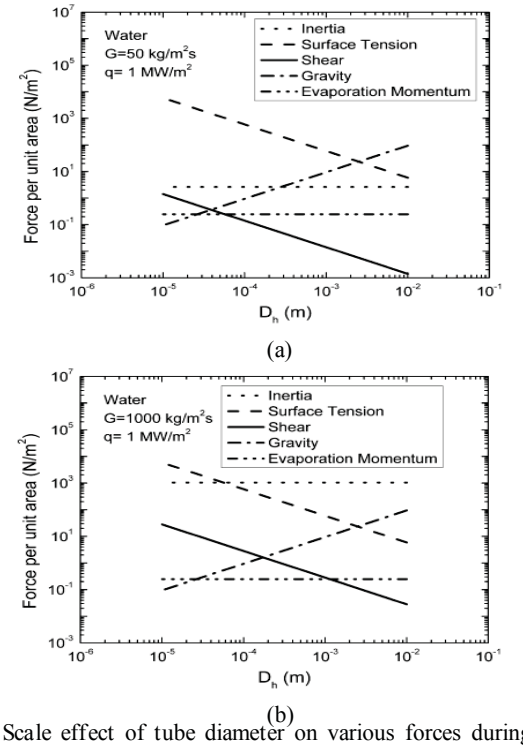

Fig. 2 Scale effect of tube diameter on various forces during flow boiling by Kandlikar (2010). "Reprinted from International Journal of Thermal Science, 49(7), Kandlikar, S.G., Scale effects on flow boiling heat transfer in microchannels: A fundamental perspective, pp. 1073-1085 (2010), with permission from Elsevier."

For laminar liquid-laminar vapour flow:

$$\phi_L^2 = 1 + \frac{2.16 Re_{LO}^{0.047} We_{LO}^{0.6}}{\chi} + \frac{1}{\chi^2} \tag{3}$$

For laminar liquid-turbulent vapour flow:

$$\phi_L^2 = 1 + \frac{1.45 Re_{LO}^{0.25} We_{LO}^{0.23}}{\chi} + \frac{1}{\chi^2} \tag{4}$$

Lee and Garimella (2008) experimentally investigated two-phase pressure drop in rectangular micro-channels. The measured pressure drop strongly depended on heat flux. The comparisons between the experimental data and the existing correlations were discussed. They also proposed a correlation for pressure drop prediction based on the method by Mishima and Hibiki (1996) as follows.

$$\phi_L^2 = 1 + \frac{2566 G^{0.5466} D_h^{0.8819} \left(1 - e^{-319 D_h}\right)}{\chi_{vv}} + \frac{1}{\chi_{vv}^2} \tag{5}$$

For laminar liquid-laminar vapour flow, the Martinelli parameter is expressed as

$$\chi_{vv} = \left(\frac{1-x}{x}\right)^{0.5} \left(\frac{\rho_G}{\rho_L}\right)^{0.5} \left(\frac{\mu_L}{\mu_G}\right)^{0.5} \tag{6}$$

Choi et al. (2008) performed flow boiling pressure drop experiments. R-410A was used as working fluid flowing in stainless steel tubes with diameters of 1.5 and 3 mm. The results indicated that the two-phase pressure drop increased with the increase in mass flux

DOI: 10.5098/hmt.v3.1.3007 ISSN: 2151-8629

Table 1 Summary of recent investigations on pressure drop during micro-scale flow boiling

Reference	Fluid and parameter ranges G [kg/m^{2}s], q [kW/m^2] P [kPa], T [^{o}C]	Channel geometry/ substrate/orientation/ diameter [mm]	Remarks
Lee and Mudawar (2005)	R-134a G = 127-654, x = 0.001-0.25 q = 316-938 P_{in} = 144-660	53 parallel rectangular/ copper/horizontal/ D_h = 0.35	The proposed correlation incorporated liquid viscosity and surface tension effects.
Lee and Garimella (2008)	water G = 368-738, x = 0-0.2 q = 100-3400 T_{in} = 90.6-95.1	10-60 parallel rectangular/ silicon/horizontal/ D_h = 0.16-0.54	Pressure drop strongly depended on heat flux.
Choi et al. (2008)	R-410A G = 300-600, x = 0-1 q = 10-40 T_{in} = 10	Single circular/stainless steel/horizontal/ D = 1.5, 3	Pressure drop increased with increasing mass flux and vapour quality.
Pamitran et al. (2008)	CO_2 G = 200-600 q = 10-30 T_{sat} = -10, -5, 10	Single circular/stainless steel/horizontal/ D = 1.5, 3	Channel diameter, mass flux, surface tension, density and viscosity had influence on pressure drop.
Agostini et al. (2008)	R-236fa G = 276-992, x = 0.5-1.0 q = 1120-2500 T_{sat} = 20.31-34.27	66 parallel rectangular/ silicon/horizontal/ D_h = 0.336	Homogeneous flow model worked well with the measured pressure drop.
Singh et al. (2008)	water G = 82-126, x = 0.29 q = 290-366	Single rectangular/silicon/ horizontal/ D_h = 0.142	Two-phase pressure drop was found to be lower than the single-phase value when a certain mass flux and heat flux range was established.
Lie et al. (2008)	R-134a, R-407C G = 200-400, x = 0.2-0.8 q = 5-15 T_{sat} = 5-15	28 parallel circular/ copper/horizontal/ D = 0.83, 2	The use of R-134a as working fluid caused pressure drop relatively high in comparison to R-407C
Choi et al. (2009)	C_3H_8 G = 50-400, x = 0-1 q = 5-20 T_{sat} = 0, 5, 10	Single circular/stainless steel/horizontal/ D = 1.5, 3	An increase in mass flux or heat flux resulted in higher pressure drop.
Coppetti et al. (2011)	R-134a G = 240-930, x = 0-0.8 q= 10 – 100 T_{sat} = 12, 22	Single circular/stainless steel/horizontal/ D = 2.62	Pressure drop depended on mass flux and vapour quality.
Soupremanien et al. (2011)	Forane®365 HX G = 200-400, x = 0-0.6 q = 25-62 T_{sat} = 56	Single rectangular/stainless steel/horizontal/ D_h = 1.4	Pressure drop characteristics were affected by aspect ratio.
Costa-Patry et al. (2011)	R-236fa, R-245fa G = 499-1100, x = 0.03-0.53 q = 130-1400 T_{sat} = 30.5	135 parallel rectangular/ silicon/horizontal/ D_h = 0.148	The experimental technique was presented to measure the outlet pressure losses.

and vapour quality. The pressure drop was also strongly dependent on the channel diameter.

The two-phase pressure drop experiments similar to Choi et al. (2008) were carried out by Pamitran et al. (2008). The stainless steel tubes having diameters of 1.5 and 3 mm were used as test sections in which flow vapourization of CO_2 was established. According to their experimental data, the pressure drop was in relation with channel diameter, mass flux, surface tension, density and viscosity.

Agostini et al. (2008) carried out experiments to investigate pressure drop of R-236fa and R-245fa during flow boiling in micro-channels. They reported that flow boiling of R-245fa induced pressure drop higher than R-236fa. The prediction method on the basis of homogeneous flow assumption predicted well their measured results.

Singh et al. (2008) investigated two-phase pressure drop characteristics for flow boiling of water in micro-channels with different aspect ratios. All test sections had rectangular cross-section having a constant hydraulic diameter of 142 μm. The experiments were performed for the aspect ratio range of 1.23 to 3.75. The aspect ratio of around 1.56 provided the minimum two-phase pressure drop. Moreover, at this value of aspect ratio, the two-phase pressure drop was found to be lower than the single-phase value when a certain condition was established as presented in Fig. 3.

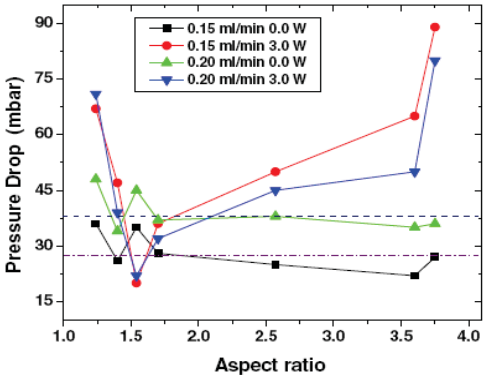

Fig. 3 Pressure drop data of Singh et al. (2008). "Reprinted from Experimental Thermal and Fluid Science, 33(1), Singh, S.G., Kulkarni, A., Duttagupta, S.P., Puranik, B.P., and Agrawal, A., Impact of aspect ratio on flow boiling of water in rectangular microchannels, pp. 153-160 (2008), with permission from Elsevier."

Lie et al. (2008) studied experimentally flow boiling of refrigerants in micro-channels. The frictional pressure drop characteristics of R-134a and R-407C were reported in their work. The results showed the increase in pressure drop with increasing vapour quality and mass flux. The reduction in pressure drop was observed as the saturation temperature was increased. In their study, the pressure drop was less dependent with heat flux. The use of R-134a as working fluid caused pressure drop relatively high in comparison to R-407C. They also proposed pressure drop correlation in the form of friction factor as expressed below.

$$f_{TP} = -0.037 - 147341 Re_{eq}^{-1.859} + 0.039 C_o^{-0.508} + 327726 Re_{eq}^{-1.859} C_o^{-0.508} \quad (7)$$

Re_{eq} in the above equation refers to equivalent Reynolds number expressed as

$$Re_{eq} = \frac{G_{eq} D_h}{\mu_L} \quad (8)$$

The equivalent mass flux, G_{eq}, is determined by

$$G_{eq} = G\left[(1 - x_{in}) + x_{in}\left(\frac{\rho_L}{\rho_G}\right)^{0.5}\right] \quad (9)$$

Pressure drop during flow boiling of propane in horizontal channels was studied by Choi et al. (2009). An increase in mass flux or heat flux resulted in the higher pressure drop. A decrease in channel diameter, corresponding to a higher wall shear stress, leaded to an increase in the pressure drop. They indicated that the lower the saturation temperature, the higher was the pressure drop, which was explained according to the change in density and viscosity. In addition, they developed a pressure drop correlation on the basis of the Lockhart-Martinelli method and the Chisholm parameter was proposed by the following equation.

$$C = 1732.953 Re_{TP}^{-0.323} We_{TP}^{-0.24} \quad (10)$$

Sun and Mishima (2009) analysed 2092 data points collected from several previous studies. They found that in laminar flow region ($Re_L < 2000$ and $Re_G < 2000$), the Chisholm parameter was found to be significantly affected by liquid Reynolds number and confinement number, and expressed as follow.

$$C = 26\left(1 + \frac{Re_L}{1000}\right)\left[1 - e^{\left(\frac{-0.153}{0.27 C_o + 0.8}\right)}\right] \quad (11)$$

For $Re_L > 2000$ or $Re_G > 2000$, the ratio of Re_G to Re_L was found to play dominant role on the Chisholm correlation which was modified as presented below.

$$\phi_L^2 = 1 + \frac{1.79\left(\frac{Re_G}{Re_L}\right)^{0.4}\left(\frac{1-x}{x}\right)^{0.5}}{\chi^{1.19}} + \frac{1}{\chi^2} \quad (12)$$

Zhang et al. (2010) proposed correlations for two-phase flow in micro-channels. The Chisholm parameter needed for pressure drop calculations was correlated by the following equations.

For boiling flow:

$$C = 21\left[1 - e^{\left(\frac{-0.358}{C_o}\right)}\right] \quad (13)$$

For two-phase gas-liquid adiabatic flow:

$$C = 21\left[1 - e^{\left(\frac{-0.674}{C_o}\right)}\right] \quad (14)$$

For two-phase vapour-liquid adiabatic flow:

$$C = 21\left[1 - e^{\left(\frac{-0.142}{C_o}\right)}\right] \quad (15)$$

These correlations were developed based on the method of Mishima and Hibiki (1996). Remarkably, the above correlations are applicable when the experimental conditions comply with the following ranges; $0.014 \leq D_h \leq 6.25$ mm, $Re_L \leq 2000$ and $Re_G \leq 2000$.

Referring to the above three equations, the relevant processes were defined as follows. The gas-liquid adiabatic flow was denoted as two fluids without heat and mass transfers. The vapour-liquid adiabatic flow was dealt only with one fluid appearing in two-phase condition. Flow boiling represented the most complex two-phase flow pertaining to thermal and hydraulic coupling.

The experimental investigation for R-134a refrigerant during flow boiling in a tube having a diameter of 1.75 mm was performed by Saisorn et al. (2010). They reported that the lower liquid viscosity due to the increment of saturation pressure lead to the decrease in frictional pressure drop.

Lee et al. (2010) reported that Bond number and outlet vapour quality played important role on the pressure drop prediction for flow boiling in micro-channels. They also proposed the correlation as seen below.

$$\phi_L^2 = 1 + \frac{121.6\left(1 - e^{-22.7\lambda}\right)x_{out}^{1.85}}{\chi} + \frac{1}{\chi^2} \tag{16}$$

The two-phase pressure drop characteristics in micro-channels were reported by Li and Wu (2010b). Concerning the database containing 769 data points available in the literature, they indicated the significant role of Bond number on the pressure drop prediction, and the Chisholm parameter was modified as follows.

$$C = 11.9B_o^{0.45}; \quad B_o \le 1.5 \tag{17}$$

$$C = 109.4\left(B_o Re_L^{0.5}\right)^{-0.56}; \quad 1.5 < B_o \le 11 \tag{18}$$

For Bond number greater than 11, there was no obvious relationship between the Chisholm parameter and the Bond number. In such region (B_o > 11), however, they recommended the Beattie and Whalley correlation (1982), which is prediction method based on homogeneous flow assumption, as a good choice for predicting the pressure drop. As also reported by Ribatski et al. (2006) and Revellin et al. (2006), the methods on the basis of homogeneous flow model were able to tentatively apply for micro-channels under a certain range of experimental condition. Moreover, the homogeneous flow model was adopted by Chen et al. (2009) and Wang et al. (2010) to predict the pressure drop for two-phase flow through abrupt area change.

The correlation for two-phase pressure change due to sudden expansion in small flow passages was proposed by Wang et al. (2010). With 282 data collected from the literature, their prediction method based on the modified homogeneous model is given by the following equation.

$$\Delta P_e = G^2\sigma_A\left(1-\sigma_A\right)\left[\frac{(1-x)}{\rho_L} + \frac{x}{\rho_G}\right]\left(1+\Omega_1-\Omega_2\right)\left(1+\Omega_3\right) \tag{19}$$

where σ_A represents flow cross-sectional area expansion ratio, 0 < σ_A < 1, and the correction factors, Ω_1, Ω_2, and Ω_3, are expressed as follows.

$$\Omega_1 = \frac{1}{Fr^{0.8}}\left(\frac{We \times B_o}{Re_{LO}}\right)^2\left(\frac{1-x}{x}\right)^{0.3} \tag{20}$$

$$\Omega_2 = 0.2\left(\frac{\mu_G}{\mu_L}\right)^{0.4} \tag{21}$$

$$\Omega_3 = 0.4\left(\frac{x}{1-x}\right)^{0.3} + 0.3e^{\frac{16}{Re_{LO}^{0.1}}} - 0.4\left(\frac{\rho_L}{\rho_G}\right)^{0.2} \tag{22}$$

Instead of using prediction methods, the developed measurement technique, under which flow boiling of R-236fa and R-245fa in rectangular micro-channels having hydraulic diameter of 0.148 mm was studied, was addressed by Costa-Patry et al. (2011) to measure the outlet pressure losses. As presented in Figs. 4 and 5, their measurements indicated that such pressure losses possessed up to 30% of the total pressure drop, tending to be non-negligible.

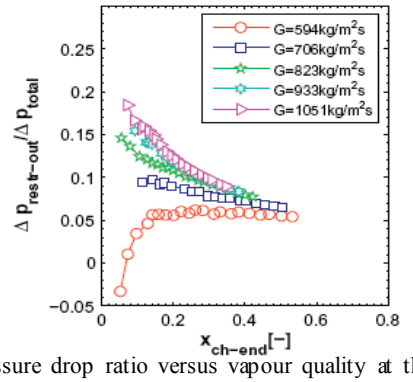

Fig. 4 Pressure drop ratio versus vapour quality at the end of the channel: R-236fa (Costa-Patry et al., 2011). "Reprinted from International Journal of Heat and Fluid Flow, 32(2), Costa-Patry, E., Olivier, J., Nichita, B.A., Michel, B., and Thome, J.R., 2011, Two-phase flow of refrigerants in 85 μm-wide multi-microchannels: Part I – Pressure drop, pp. 451-463 (2011), with permission from Elsevier."

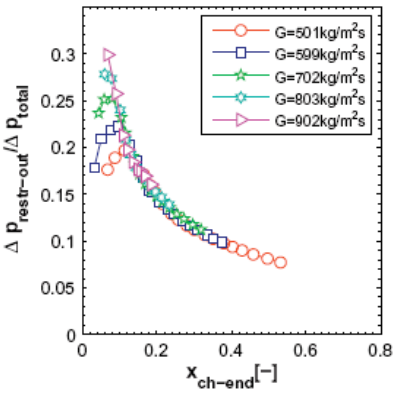

Fig. 5 Pressure drop ratio versus vapour quality at the end of the channel: R-245fa (Costa-Patry et al., 2011). "Reprinted from International Journal of Heat and Fluid Flow, 32(2), Costa-Patry, E., Olivier, J., Nichita, B.A., Michel, B., and Thome, J.R., 2011, Two-phase flow of refrigerants in 85 μm-wide multi-microchannels: Part I – Pressure drop, pp. 451-463 (2011), with permission from Elsevier."

Copetti et al. (2011) reported the two-phase pressure drop results of flow boiling experiment with R-134a flowing in a 2.6 mm diameter tube. The results showed relatively strong dependence of pressure drop on mass flux and vapour quality.

Soupremanien et al. (2011) indicated that aspect ratio had influence on pressure drop characteristics during flow boiling in rectangular channels. The pressure drop became lower as aspect ratio was decreased. In their work, the test sections with the same hydraulic diameter of 1.4 mm were examined.

In summary, this research field is still in its infancy. Although a number of studies have been reported for micro-channels, the pressure drop during micro-scale phenomena with respect to flow boiling mechanisms are still open questions for which systematic answers are of importance. Based on this, further investigations should be performed as follows.

1. Systematic flow boiling experiments should be carried out to obtain the macro-to-micro-scale transition. The threshold of the transition would be addressed according to the dependence of the channel orientation on pressure drop in addition to flow regime and heat transfer characteristics.

Global Digital Central
ISSN: 2151-8629

2. Conduct more investigations for pressure change across inlet and outlet of the micro-channel evaporator to obtain precise prediction methods.
3. The existing models and correlations for two-phase pressure drop prediction should be examined based on different sources of the experimental data
4. Comparisons of flow boiling pressure drop characteristics in parallel channels with those in single channel should be performed under systematic parameters.
5. Void fraction is an important parameter for estimating two-phase pressure drop. Several studies employed the existing correlations, based on ordinarily sized channels, to calculate void fractions which were subsequently used to evaluate the pressure drop in micro-channels. Instead of conventional correlations for macro-scale flow, the prediction method should be developed from the micro-channel flow data. Recently, a small number of investigations were reported for micro-channel void fractions which were experimentally obtained, leading to the correlations. It is noted, however, that the experimental data mainly correspond to adiabatic two-phase gas-liquid flow systems. According to the lacking information, the flow boiling experiments with micro-channels should be designed to obtain the void fraction data for developing an appropriate correlation.
6. Several studies reported that separated flow model predicted well the pressure drop data. In contrast, the homogeneous flow assumption was also found to be in agreement with the measured results as reported by a number of publications. To meet a general conclusion, the systematic experiments during flow boiling in micro-channels should be performed over a wide range of experimental conditions to identify when a given prediction method is applicable to the micro-scale flow boiling.

3. CONCLUSION

Recent studies on pressure drop during micro-scale flow boiling are reviewed in this article to provide information applicable for developing miniature flow devices. Although micro-scale flow has been defined by different criteria, the existing channel classifications cannot relate the channel diameter to the flow boiling mechanisms. On the basis of different previous investigations, the two-phase pressure drop characteristics in micro-channels are not completely compatible with those in ordinarily sized channels. Moreover, the existing two-phase pressure drop predictions are needed to be examined based on different sources of the experimental data.

ACKNOWLEDGEMENTS

The authors would like to express their appreciation to the Thailand Research Fund, KMITL Research Fund, the Office of Higher Education Commission and the National Research University Project for providing financial support.

NOMENCLATURE

B_o	bond number, $B_o = g(\rho_L-\rho_G)D^2/\sigma$
C	Chisholm parameter
C_o	confinement number as defined in Eq.(1)
D	channel diameter (m)
D_b	capillary length (m)
D_h	hydraulic diameter (m)
f	friction factor
G	mass flux (kg/m^2s)
g	gravitational acceleration (m/s^2)
P	pressure (Pa)
ΔP_e	pressure change due to sudden expansion (Pa)
Re	Reynolds number, $Re = GD_h/\mu$
We	Weber number, $We = G^2D_h/\rho\sigma$
x	vapour quality

Greek symbols

χ	Lockhart-Martinelli parameter
ϕ	two-phase multiplier
μ	dynamic viscosity (Ns/m^2)
ρ	density (kg/m^3)
σ	surface tension (N/m)
σ_A	flow cross-sectional area expansion ratio
Ω	correction factors given in Eqs. (20) – (22)

Subscripts

eq	equivalent
G	vapour phase
GO	all-vapour
in	inlet
L	liquid phase
LO	all-liquid
out	outlet
restr-out	outlet restriction
sat	saturation
TP	two-phase
vv	laminar liquid-laminar vapour flow

REFERENCES

Agostini, B., Revellin, R., Thome, J.R., Fabbri, M., Michel, B., Calmi, D., and Kloter, U., 2008, "High heat flux flow boiling in silicon multi-microchannels – Part III: Saturated critical heat flux of R236fa and two-phase pressure drops," *International Journal of Heat and Mass Transfer,* **51**, 5426-5442.
http://dx.doi.org/10.1016/j.ijheatmasstransfer.2008.03.005

Beattie, D.H., and Whalley, P.B., 1982, "Simple two-phase frictional pressure drop calculation method," *International Journal of Multiphase Flow,* **8**, 83-87.
http://dx.doi.org/10.1016/0301-9322(82)90009-X

Chen, I.Y., Tseng, C.-Y., Lin, Y.-T., and Wang, C.-C., 2009, "Two-phase flow pressure change subject to sudden contraction in small rectangular channels," *International Journal of Multiphase Flow,* **35**, 297-306.
http://dx.doi.org/10.1016/j.ijmultiphaseflow.2008.10.008

Choi, K-I., Pamitran, A.S., Oh, C.-Y., and Oh, J.-T., 2008, "Two-phase pressure drop of R-410A in horizontal smooth minichannels," *International Journal of Refrigeration,* **31**, 119-129.
http://dx.doi.org/10.1016/j.ijrefrig.2007.06.006

Choi, K.-I., Pamitran, A.S., Oh, J.-T., and Saito, K., 2009, "Pressure drop and heat transfer during two-phase flow vaporization of propane in horizontal smooth minichannels," *International Journal of Refrigeration,* **32**, 837-845.
http://dx.doi.org/10.1016/j.ijrefrig.2008.12.005

Copetti, J.B., Macagnan, M.H., Zinani, F., and Kunsler, N.L.F., 2011, "Flow boiling heat transfer and pressure drop of R-134a in a mini tube: an experimental investigation," *Experimental Thermal and Fluid Science,* **35**, 636-644.
http://dx.doi.org/10.1016/j.expthermflusci.2010.12.013

Costa-Patry, E., Olivier, J., Nichita, B.A., Michel, B., and Thome, J.R., 2011, "Two-phase flow of refrigerants in 85 μm-wide multi-

microchannels: Part I – Pressure drop," *International Journal of Heat and Fluid Flow*, **32**, 451-463.
http://dx.doi.org/10.1016/j.ijheatfluidflow.2011.01.005

Kandlikar, S.G., 2010, "Scale effects on flow boiling heat transfer in microchannels: A fundamental perspective," *International Journal of Thermal Sciences,* **49**, 1073-1085.
http://dx.doi.org/10.1016/j.ijthermalsci.2009.12.016

Kew, P.A., and Cornwell, K., 1997, "Correlations for the prediction of boiling heat transfer in small-diameter channels," *Applied Thermal Engineering,* **17**, 705-715.
http://dx.doi.org/10.1016/S1359-4311(96)00071-3

Lee, J., and Mudawar, I., 2005, "Two-phase flow in high-heat-flux micro-channel heat sink for refrigeration cooling applications: Part I – pressure drop characteristics," *International Journal of Heat and Mass Transfer,* **48**, 928-940.
http://dx.doi.org/10.1016/j.ijheatmasstransfer.2004.09.018

Lee, P.-S., and Garimella, S.V., 2008, "Saturated flow boiling heat transfer and pressure drop in silicon microchannel arrays," *International Journal of Heat and Mass Transfer,* 51, 789-806.
http://dx.doi.org/10.1016/j.ijheatmasstransfer.2007.04.019

Lee, H.J., Liu, D.Y., Alyousef, Y., and Yao, S., 2010, "Generalized two-phase pressure drop and heat transfer correlations in evaporative micro/minichannels," *Journal of Heat Transfer,* **132**, 1-9.
http://dx.doi.org/10.1115/1.4000861

Li, W., and Wu, Z., 2010a, "A general criterion for evaporative heat transfer in micro/mini-channels," *International Journal of Heat and Mass Transfer,* **53**, 1967-1976.
http://dx.doi.org/10.1016/j.ijheatmasstransfer.2009.12.059

Li, W., and Wu, Z., 2010b, "A general correlation for adiabatic two-phase pressure drop in micro/mini-channels," *International Journal of Heat and Mass Transfer,* **53**, 2732-2739.
http://dx.doi.org/10.1016/j.ijheatmasstransfer.2010.02.029

Lie, Y.M., Su, F.Q., Lai, R.L., and Lin, T.F., 2008, "Experimental study of evaporation pressure drop characteristics of refrigerants R-134a and R-407C in horizontal small tubes," *International Journal of Heat and Mass Transfer,* **51**, 294-301.
http://dx.doi.org/10.1016/j.ijheatmasstransfer.2007.03.046

Mishima, K., and Hibiki, T., 1996, "Some characteristics of air-water two-phase flow in small diameter vertical tubes," *International Journal of Multiphase Flow,* **22**, 703-712.
http://dx.doi.org/10.1016/0301-9322(96)00010-9

Ong, C.L., and Thome, J.R., 2011, "Macro-to-microchannel transition in two-phase flow: Part 1-Two-phase flow patterns and film thickness measurements," *Experimental Thermal and Fluid Science,* **35**, 37-47.
http://dx.doi.org/10.1016/j.expthermflusci.2010.08.004

Pamitran, A.S., Choi, K.-I., Oh, J.-T., and Oh, H.-K., 2008, "Two-phase pressure drop during CO_2 vaporization in horizontal smooth minichannels," *International Journal of Refrigeration,* **31**, 1375-1383.
http://dx.doi.org/10.1016/j.ijrefrig.2008.04.004

Revellin, R., Dupont, V., Ursenbacher, T., Thome, J.R., and Zun, I., 2006, "Characterization of diabatic two-phase flows in microchannels: Flow parameter results for R134a in a 0.5 mm channel," *International Journal of Multiphase Flow,* **32**, 755-774.
http://dx.doi.org/10.1016/j.ijmultiphaseflow.2006.02.016

Ribatski, G., Wojtan, L., and Thome, J.R., 2006, "An analysis of experimental data and prediction methods for two-phase frictional pressure drop and flow boiling heat transfer in micro-scale channels," *Experimental Thermal and Fluid Science,* **31**, 1-19.
http://dx.doi.org/10.1016/j.expthermflusci.2006.01.006

Saisorn, S., Kaew-On, J., and Wongwises, S., 2010, "Flow pattern and heat transfer characteristics of R-134a refrigerant during flow boiling in a horizontal circular mini-channel," *International Journal of Heat and Mass Transfer,* **53**, 4023-4038.
http://dx.doi.org/10.1016/j.ijheatmasstransfer.2010.05.022

Singh, S.G., Kulkarni, A., Duttagupta, S.P., Puranik, B.P., and Agrawal, A., 2008, "Impact of aspect ratio on flow boiling of water in rectangular microchannels," *Experimental Thermal and Fluid Science,* **33**, 153-160.
http://dx.doi.org/10.1016/j.expthermflusci.2008.07.014

Soupremanien, U., Person, S.L., Favre-Marinet, M., and Bultel, Y., 2011, "Influence of the aspect ratio on boiling flows in rectangular mini-channels," *Experimental Thermal and Fluid Science,* **35**, 797-809.
http://dx.doi.org/10.1016/j.expthermflusci.2010.06.014

Sun, L., and Mishima, K., 2009, "Evaluation analysis of prediction methods for two-phase flow pressure drop in mini-channels," *International Journal of Multiphase Flow,* **35**, 47-54.
http://dx.doi.org/10.1016/j.ijmultiphaseflow.2008.08.003

Tibirica, C.B., and Ribatski, G., 2010, "Flow boiling heat transfer of R134a and R245fa in a 2.3 mm tube," *International Journal of Heat and Mass Transfer,* **53**, 2459-2468.
http://dx.doi.org/10.1016/j.ijheatmasstransfer.2010.01.038

Wang, C.-C., Tseng, C.-Y., and Chen, I.Y., 2010, "A new correlation and the review of two-phase flow pressure change across sudden expansion in small channels," *International Journal of Heat and Mass Transfer,* **53**, 4287-4295.
http://dx.doi.org/10.1016/j.ijheatmasstransfer.2010.05.057

Zhang, W., Hibiki, T., and Mishima, K., 2010, "Correlations of two-phase frictional pressure drop and void fraction in mini-channel," *International Journal of Heat and Mass Transfer,* **53**, 453-465.
http://dx.doi.org/10.1016/j.ijheatmasstransfer.2009.09.011

Available online at www.sciencedirect.com

SciVerse ScienceDirect

Journal of the Franklin Institute 349 (2012) 966–984

Journal of The Franklin Institute

www.elsevier.com/locate/jfranklin

A decomposition analysis on convecting–radiating rectangular plate fins for variable thermal conductivity and heat transfer coefficient

Balaram Kundu[a,c], Somchai Wongwises[b,d,*]

[a]*Department of Mechanical Engineering, Jadavpur University, Kolkata 700032, India*
[b]*Fluid Mechanics, Thermal Engineering and Multiphase Flow Research Lab (FUTURE), Department of Mechanical Engineering, King Mongkut's University of Technology Thonburi (KMUTT) Bangmod, Bangkok 10140, Thailand*
[c]*School of Mechanical Engineering, Hanyang University, 17 Haengdang-dong, Sungdong-gu, Seoul, 133-791, Korea*
[d]*The Academy of Science, The Royal Institute of Thailand, Sanam Suea Pa, Dusit, Bangkok 10300, Thailand*

Received 27 February 2011; received in revised form 2 March 2011; accepted 6 December 2011
Available online 13 December 2011

Abstract

The present study concentrates to make a complete thermal analysis on a rectangular fin with its primary surface by taking into consideration of radiation heat exchange with the surrounding along with the convective mode of heat transfer. The one side of the primary surface is heated by a fluid with high temperature which may be required to dissipate heat quickly by a fin array system. To analyze an actual case study, the thermal conductivity of the fin material and convective heat transfer coefficient over the surface are treated as a variable and they are as a function of the local fin surface temperature. With the aforementioned condition, the energy equations for both the fin and primary surface become nonlinear. The decomposition method is suggested to solve these highly nonlinear equations to obtain a closed form temperature distribution. The result of temperature distribution determined by the present analysis is compared with that of the numerical values. With the adaptation of the simplified case, the present method is also compared with the exactly closed form results. From both of these comparisons, an exact matching of results is found. The fin performances, namely, fin efficiency, surface efficiency and augmentation factor are evaluated for a wide range of thermogeometric parameters.
© 2011 The Franklin Institute. Published by Elsevier Ltd. All rights reserved.

*Corresponding author. Tel.: +66 2 470 9115; fax: +66 2 470 9111.
E-mail addresses: bkundu123@rediffmail.com (B. Kundu), somchai.won@kmutt.ac.th (S. Wongwises).

0016-0032/$32.00 © 2011 The Franklin Institute. Published by Elsevier Ltd. All rights reserved.
doi:10.1016/j.jfranklin.2011.12.002

Nomenclature

A_i	adomian ploynomial
Aug	augmentation factor
Bi	Biot number based on dry surface heat transfer coefficient, $h_0 t/k_{f0}$
g_0, g_1, g_2, g_3	variables, defined in Eq. (20)
h	convective heat transfer coefficient on the fin side, W m^{-2} K^{-1}
h_L	convective heat transfer coefficient on the hot fluid side, W m^{-2} K^{-1}
h_0	constant value of convective heat transfer coefficient on the fin side, W m^{-2} K^{-1}
k	thermal conductivity, W m^{-1} K^{-1}
k_{f0}	thermal conductivity of the fin material corresponding to ambient temperature, W m^{-1} K^{-1}
K_r	thermal conductivity ratio, k_{w0}/k_{f0}
k_{w0}	thermal conductivity of the wall material corresponding to ambient temperature, W m^{-1} K^{-1}
L	length of the fin, m
m_1, m_2, m_3, m_4	parameters see Eqs. (13) and (34)
Nu_L	Nusselt number, $h_L L/k_L$
P	wall length, m
P^*	dimensionless wall length, P/t
q	actual heat transfer rate through the primary surface attached with a fin, W
Q	dimensionless heat transfer rate, see Eq. (25)
q_f	actual heat transfer rate through the fin, W
Q_f	dimensionless heat transfer rate through the fin, see Eq. (29)
q_i	ideal heat transfer rate through the fin-wall system, W
Q_i	dimensionless ideal heat transfer rate, see Eq. (27)
$q_{f\,i}$	ideal heat transfer rate through the fin, W
$Q_{f\,i}$	dimensionless ideal heat transfer rate through the fin, see Eq. (30)
q_0	actual heat transfer rate through the primary surface with considering no fin condition, W
Q_0	dimensionless heat transfer rate, see Eq. (38)
t	semi-fin thickness, m
T_f	Local fin surface temperature ($0 \le x \le L$), K
T_w	Local wall temperature [$L \le x \le (L+w)$], K
T_a	surrounding temperature, K
T_L	hot liquid temperature, K
w	wall thickness, m
x	coordinate, m
X	dimensionless coordinate, x/L
Z_0	dimensionless fin parameter, $\sqrt{Bi}/\psi$

Greek letters

α	coefficient of thermal conductivity, K^{-1}
β	dimensionless variable thermal conductivity parameter, $(T_L - T_a)\alpha$

γ	Temperature ratio, T_L/T_a
δ	dimensionless temperature factor, $T_a/(T_L-T_a)$
ε	dimensionless radiation parameter, $\sigma\varepsilon'(T_L-T_a)^3/h_0$
ε'	emissivity of the fin material
η	surface efficiency
η_f	fin efficiency
λ	variable, see Eq. (28)
σ	Boltzmann constant, W m^{-2} K^{-4}
θ	dimensionless fin temperature, $(T_f-T_a)/(T_L-T_a)$
θ_0	dimensionless tip temperature
τ	dimensionless base temperature
ϕ	dimensionless wall temperature, $(T_w-T_a)/(T_L-T_a)$
Φ	dimensionless wall temperature when there is no fin attached, $(T'_w-T_a)/(T_L-T_a)$
ψ	aspect ratio, t/L
ω	dimensionless wall thickness, w/L

Subscripts

f	fin
w	wall

1. Introduction

The transfer of heat from a heated fluid to surrounding is essentially needed to avoid overheating of the apparatus in industrial applications. A hot fluid flowing through a passage separated it from surrounding air by a solid wall. As the heat transfer coefficient in the air side is low, fins or extended surfaces are attached to the wall to enhance the heat transfer rate. If the hot fluid temperature is very high heat dissipation from the wall and fin surfaces takes place not only due to convection but also radiation mode of heat transfer. Only fin surface is never used in practice. A fin with the attachment of supporting structure, known as fin-wall assembly, is commonly used. To account for the effect of supporting structure, the analysis becomes complicated.

Sparrow and Le [1] studied in a multi-fin array in order to determine the temperature distribution at the fin base and heat flux. Using finite difference formulation Suryanarayana [2] analyzed the heat transfer in an array of longitudinal rectangular fins with insulated tip. Heggs and Stone [3] determined the performance of fin assemblies of longitudinal and annular fins of uniform cross-section. They have used one- and two-dimensional formulation for comparison. In the one-dimensional model, the overall resistance of the fin wall was determined by the analogy of electrical net work. In the two-dimensional analysis, a numerical technique was adopted for obtaining the temperature distribution both in the wall and in the fin. A significant difference between the results predicted by the two types of analysis has been reported. Heggs et al. [4] proposed a semi-analytical solution to evaluate the temperature distribution in the fin array. Recently, performance and optimum design analysis of convective fin arrays attached to

flat and curved primary surfaces has been carried out by Kundu and Das [5]. By an analytical determination, the performance of a fin assembly under dehumidifying conditions was determined by Kundu and Miyara [6] and results have been presented in a comparative ways.

Chung and Zhung [7] demonstrated a novel design for a radiative fin array system. An analysis of heat transfer in rectangular fin arrays was conducted by Elazhary and Soliman [8] with taking into consideration of convection and radiation. The analysis was done based on diffuse nongray surfaces. From the result, they highlighted that convection is more effective mode of heat transfer in fin arrays and the effectiveness of the array decreases as the contribution of the radiative component increases. Recently, Kundu and Aziz [9] determined numerically the performance of a convectively heated rectangular fin with a step change in cross-sectional area when losing heat by simultaneous convection and radiation. Aziz and Khani [10] established an analytic model based on the homototopy analysis method (HAM) for heat transfer in a moving fin of variable thermal conductivity which is losing heat by simultaneous convection and radiation to its surroundings. With the correlation of the fin profile and temperature distribution, the nonlinear heat transfer equation for convective–radiative spines was integrated analytically [11].

From the literature survey mentioned in a summarized way above, a very few works has been devoted to analyze fin-array heat transfer with considering radiation heat exchange. In general, if the supporting wall temperature is high, radiation heat transfer from the supporting wall and fin surfaces cannot be ignored. Due to high temperature variation, thermal conductivity of the wall and fin materials may not be a constant. In addition, there is always possibility to have variable heat transfer coefficients along the fin surface. These have been made to motivate for carrying out the present analysis.

An approximate analytical model has been established to analyze heat transfer through a fin of rectangular fin attached with a flat primary surface. For the analysis, three modes of heat transfer are taken into account. A variable thermal conductivity of the fin as well as wall material has been adopted. The convective heat transfer coefficient is as a power function of temperature taken for an actual analysis. A decomposition method has been applied to solve the governing fin and supporting structure equations to determine the temperature distributions. The surface efficiency and augmentation factor are evaluated. The effects of thermophysical and radiation parameters on fin–wall performances are exhibited.

2. Analysis

A schematic diagram of a plate fin with primary surface is shown in Fig. 1. The present work considers combined convection and radiation modes of heat transfer from a fin of rectangular profile attached to a flat base which is heated by hot liquid with a constant temperature, T_L and convective heat transfer coefficient, h_L. The rectangular fins are attached with the primary surface to the gas side in order to increase the heat transfer rate. The surface temperature of the fin and wall is so high that the radiation mode of heat transfer cannot be neglected. However, there is negligible interaction of radiation heat assumed between wall and fin surfaces. For the high fin surface temperature, variable thermal conductivity is considered. The heat is rejected from the fin surface to the surrounding fluid with a constant temperature T_a. The heat transfer coefficient over the fin surface changes and it is a function of local fin surface temperature. The energy balance

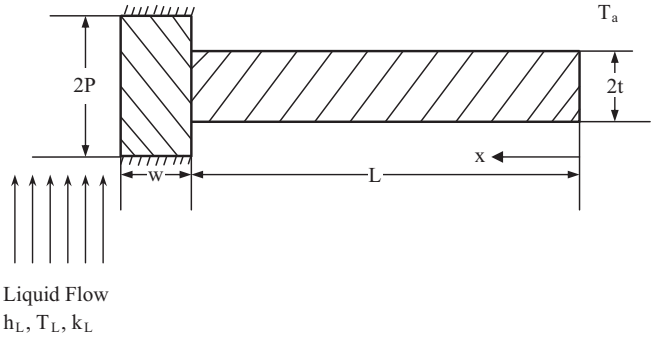

Fig. 1. Diagram of a fin attached with a primary surface.

equation for differential elements of fins and the primary surface for one-dimensional heat conduction is given as

$$\begin{bmatrix} d/dx(k_w dT_w/dx) \\ d/dx(k_f dT_f/dx) - h(T_f - T_a)/t - \sigma\varepsilon_f'(T_f^4 - T_a^4)/t \end{bmatrix} = \begin{bmatrix} 0 \\ 0 \end{bmatrix} \quad \begin{matrix} L \le x \le (L+w) \\ 0 \le x \le L \end{matrix} \tag{1a,1b}$$

The variable thermal conductivity and heat transfer coefficient are assumed in the following:

$$k_f = k_{f0}[1 + \alpha_f(T_f - T_a)]; \quad k_w = k_{w0}[1 + \alpha_w(T_w - T_a)]; \quad h = h_0\theta^n \tag{2}$$

Eq. (1) can be written by Eq. (2) in dimensionless form as

$$\begin{bmatrix} (1+\beta_w\phi)d^2\phi/dX^2 + \beta_w(d\phi/dX)^2 \\ d^2\theta/dX^2 + \beta_f(d\theta/dX)^2 + \beta_f\theta(d^2\theta/dX^2) - Z_0^2\theta(\theta^n + 4\delta^3\varepsilon_f + 6\delta^2\varepsilon_f\theta + 4\delta\varepsilon_f\theta^2 + \varepsilon_f\theta^3) \end{bmatrix} = \begin{bmatrix} 0 \\ 0 \end{bmatrix} \text{for} \quad \begin{matrix} 1 \le X \le (1+\omega) \\ 0 \le X \le 1 \end{matrix} \tag{3a,3b}$$

where

$$\beta_w = \alpha_w(T_L - T_a); \quad \beta_f = \alpha_f(T_L - T_a); \quad Z_0 = \sqrt{Bi}/\psi; \quad Bi = h_0 t/k_{f0};$$
$$\psi = t/L; \quad \gamma = T_L/T_a; \quad \delta = 1/(\gamma - 1); \quad \varepsilon_f = \sigma(T_L - T_a)^3\varepsilon_f'/h_0;$$
$$\varepsilon_w = \sigma(T_L - T_a)^3\varepsilon_w'/h_0; \quad X = x/L; \quad \theta = (T_f - T_a)/(T_L - T_a);$$
$$\text{and} \quad \varphi = (T_w - T_a)/(T_L - T_a) \tag{4}$$

Eq. (3) is subjected to the following boundary conditions:

$$\text{at } X = 0, \quad d\theta/dX = 0 \tag{5a}$$

$$\text{at } X = 1, \quad \theta = \phi \tag{5b}$$

$$\text{at } X = 1, \quad (1+\beta_f\theta)\psi d\theta/dX + Bi(P^* - 1)\theta^{n+1} + Bi\varepsilon_w\phi(P^* - 1)(4\delta^3 + 6\delta^2\varphi + 4\delta\phi^2 + \phi^3) = K_r P^*\psi(1+\beta_w\phi)d\phi/dX \tag{5c}$$

and

$$\text{at } X = 1 + \omega, \quad d\phi/dX = Nu_L(1 - \phi) \tag{5d}$$

where

$$Nu_L = h_L L/k_L; \quad P^* = P/t; \quad \text{and} \quad K_r = k_{w0}k_{f0} \tag{6}$$

The wall temperature can be determined from Eq. (3a) by integrating

$$\beta_w \phi^2 + 2\phi - (m_1 X + m_2) = 0 \tag{7}$$

where m_1 and m_2 are constants determined from boundary conditions. The above equation is a quadratic equation and thus the temperature ϕ can be determined directly. However, for smaller values of β_w, it may not give correct result due to β_w in denominator. Alternatively, the temperature ϕ can be determined by the decomposition method [12] which can give exact results whatever β_w value is selected in the design process. Eq. (7) can be expressed in the following:

$$\phi = (m_1 X + m_2)/2 - (\beta_w/2)\phi^2 \tag{8}$$

The Adomian method consists of calculating ϕ as an infinite series

$$\phi = \sum_{i=0}^{\infty} \phi_i \tag{9}$$

The nonlinear function ϕ^2 is decomposed as

$$\theta^2 = \sum_{i=0}^{\infty} A_i \tag{10}$$

where the Adomian polynomials A_i's are given by

$$A_n(\theta_0, \theta_1, \cdots, \theta_m) = (1/m!) = (d^m/d\zeta^m)\theta^2 \left(\sum \theta_m \zeta^m \right)\Big|_{\zeta = 0} \tag{11}$$

From Eqs. (10) and (11), the Adomian polynomials are written in the following:

$$\begin{aligned} &\begin{bmatrix} A_0 & A_1 & A_2 & A_3 & A_4 & \cdots \end{bmatrix} \\ &\quad = \begin{bmatrix} \varphi_0^2 & 2\phi_0\phi_1 & 2\phi_0\phi_2 + \phi_1^2 & 2\phi_0\phi_3 + 2\phi_1\phi_2 & 2\phi_0\phi_4 + 2\phi_1\phi_3 + \phi_2^2 & \cdots \end{bmatrix} \end{aligned} \tag{12}$$

Using Eqs. (8), (9) and (12), temperature profile in the supporting structure can be written as

$$\begin{aligned} \phi = (m_1 X + m_2) \Bigg[1 - \frac{\beta_w}{2}(m_1 X + m_2) + \frac{\beta_w^2}{2}(m_1 X + m_2)^2 - \frac{5\beta_w^3}{8}(m_1 X + m_2)^3 \\ + \frac{7\beta_w^4}{8}(m_1 X + m_2)^4 - \frac{21\beta_w^5}{16}(m_1 X + m_2)^5 + \cdots \Bigg] \quad (1 \le X \le 1 + \omega) \end{aligned} \tag{13}$$

The temperature distribution in the fin is obtained from Eq. (3b) which is highly nonlinear. For its solution, decomposition method can be employed. To avoid in calculating Adomian polynomials in the Adomian decomposition method, Shang et al. [13] and Biazar et al. [14] implemented variational iteration method (VIM) to solve linear and nonlinear equations. For solving quadratic Riccati differential equations, Legendre wavelet method [15,16] is advantageous because of a fast convergent series of easily computable components found. However, the solution of nonlinear equations with

adopting Adomian decomposition method is still a great interest as convergence becomes rapidly. Introducing the operator $L_X = d^2/dX^2$, Eq. (3b) takes the form below for the Adomian decomposition method

$$L_X\theta = Z_0^2\theta(\theta^n + 4\delta^3\varepsilon_f + 6\delta^2\varepsilon_f\theta + 4\delta\varepsilon_f\theta^2 + \varepsilon_f\theta^3) - \beta_f(d\theta/dX)^2 - \beta_f\theta(d^2\theta/dX^2) \tag{14}$$

Applying inverse operator L_X^{-1} to both sides of Eq. (14) and boundary condition (5a) yields

$$\theta = \theta_0 + Z_0^2 L_X^{-1}[\theta(\theta^n + 4\delta^3\varepsilon_f + 6\delta^2\varepsilon_f\theta + 4\delta\varepsilon_f\theta^2 + \varepsilon_f\theta^3)] - \beta_f L_X^{-1}[(d\theta/dX)^2] - \beta_f L_X^{-1}[\theta(d^2\theta/dX^2)] \tag{15}$$

Three terms of right-hand side in Eq. (15) are nonlinear and they can be decomposed by Adomian polynomials (A_j, B_j and C_j for $j = 0,1,\cdots,\infty$). The temperature terms can then be written in the following:

$$\begin{bmatrix} \theta_1 \\ \theta_2 \\ \vdots \\ \theta_m \end{bmatrix} = \begin{bmatrix} Z_0^2 L_X^{-1} A_0 - \beta_f L_X^{-1} B_0 - \beta_f L_X^{-1} C_0 \\ Z_0^2 L_X^{-1} A_1 - \beta_f L_X^{-1} B_1 - \beta_f L_X^{-1} C_1 \\ \vdots \\ Z_0^2 L_X^{-1} A_{m-1} - \beta_f L_X^{-1} B_{m-1} - \beta_f L_X^{-1} C_{m-1} \end{bmatrix} \tag{16}$$

The Adomian polynomials are computed as follows:

$$\begin{aligned} A_0 &= \theta_0^{n+1} + 6\delta^2\varepsilon_f\theta_0^2 + 4\delta\varepsilon_f\theta_0^3 + \varepsilon_f\theta_0^4; \quad A_1 = Z_0^2\theta_0^2 g_0 g_1 X^2/2!; \\ A_2 &= Z_0^2\theta_0^2 g_0[-\beta_f\theta_0 g_1 X^2/2! + g_1 Z_0^2(4\delta^3\varepsilon_f + \theta_1 g_1 + 3Z_0^2 g_0 g_2)X^4/4!]; \\ A_3 &= \beta_f^2 g_0 g_1 Z_0^2\theta_0^4 X^2/2! - \beta_f Z_0^4\theta_0^3 g_0(3g_0 g_1 + 2\theta_0 g_1^2 + 8\delta^3\varepsilon_f g_1 + 6g_0 g_2)X^4/4! \\ &\quad + Z_0^6 g_0\theta_0^2\lfloor g_1(4\delta^3\varepsilon_f + \theta_0 g_1)^2 + 3\theta_0 g_0 g_1 g_2 + 15g_0 g_2(4\delta^3\varepsilon_f + \theta_0 g_1) \\ &\quad + 15\theta_0 g_0^2 g_3]X^6/6!; \cdots \end{aligned} \tag{17}$$

$$\begin{aligned} &B_0 = 0; \quad B_1 = 0; \quad B_2 = 2Z_0^4\theta_0^2 g_0^2 X^2/2!; \\ &B_3 = -4\beta_f Z_0^4\theta_0^3 g_0^2 X^2/2! + 8Z_0^6 g_0^2\theta_0^2(4\delta^3\varepsilon_f + \theta_0 g_1)X^4/4!; \cdots \end{aligned} \tag{18}$$

and

$$\begin{aligned} &C_0 = 0; \quad C_1 = Z_0^2\theta_0^2 g_0; \quad C_2 = -\beta_f Z_0^2\theta_0^3 g_0 + Z_0^4 g_0\theta_0^2(g_0 + \theta_0 g_1 + 4\delta^3\varepsilon_1)X^2/2; \\ &C_3 = \beta_f^2 Z_0^2\theta_0^3 g_0 - \beta_f Z_0^6 g_0\theta_0^3(5g_0 + 8\delta^3\varepsilon_f + 2\theta_0 g_1)X^2/2! + Z_0^6 g_0\theta_0^2\lfloor 28\delta^3\varepsilon_f g_0 + 7\theta_0 g_0 g_1 \\ &\quad + (4\delta^3\varepsilon_f + \theta_0 g_1)^2 + 3\theta_0 g_0 g_2]X^4/4! \end{aligned} \tag{19}$$

where

$$\begin{bmatrix} g_0 \\ g_1 \\ g_2 \\ g_3 \end{bmatrix} = \begin{bmatrix} 4\delta^3\varepsilon_f + \theta_0^n + 6\delta^2\varepsilon_f\theta_0 + 4\delta\varepsilon_f\theta_0^2 + \varepsilon_f\theta_0^3 \\ (n+1)\theta_0^{n-1} + 12\delta^2\varepsilon_f + 12\delta\varepsilon_f\theta_0 + 4\varepsilon_f\theta_0^2 \\ (n+1)n\theta_0^{n-1} + 12\delta^2\varepsilon_f + 24\delta\varepsilon_f\theta_0 + 12\varepsilon_f\theta_0^2 \\ (n+1)n(n-1)\theta_0^{n-2} + 24\delta\varepsilon_f + 24\varepsilon_f\theta_0 \end{bmatrix} \tag{20}$$

The temperature terms can be determined from Eq. (16) using Adomian polynomials as

$$\theta_1 = Z_0^2 g_0 \theta_0 X^2/2! \tag{21a}$$

$$\theta_2 = -\beta_f Z_0^2 \theta_0^2 g_0 X^2/2! + Z_0^4 g_0 \theta_0 (4\delta^3 \varepsilon_f + \theta_0 g_1) X^4/4! \tag{21b}$$

$$\begin{aligned}\theta_3 = {} & \beta_f^2 Z_0^2 g_0 \theta_0^3 X^2/2! - \beta_f Z_0^4 g_0 \theta_0^2 (3g_0 + 2\theta_0 g_1 \\ & + 8\delta^3 \varepsilon_f) X^4/4! + Z_0^6 g_0 \theta_0 \lfloor (4\delta^3 \varepsilon_f + \theta_0 g_1)^2 + 3\theta_0 g_0 g_2 \rfloor X^6/6\,!\end{aligned} \tag{21c}$$

$$\begin{aligned}\theta_4 = {} & \beta_f^3 Z_0^2 g_0 \theta_0^4 X^2/2! + 3\beta_f^2 Z_0^4 g_0 \theta_0^3 (3g_0 + \theta_0 g_1 + 4\delta^3 \varepsilon_f) X^4/4! \\ & - 3\beta_f Z_0^6 \theta_0^2 g_0 (24\delta^3 \varepsilon_f g_0 + 8\delta^3 \varepsilon_f \theta_0 g_1 + 16\delta^6 \varepsilon_f^2 + 8\theta_0 g_0 g_1 + \theta_0^2 g_1^2 + \theta_0 g_0 g_2) X^6/6! \\ & + Z_0^8 \theta_0 g_0 (64\delta^9 \varepsilon_f^3 + 48\delta^6 \varepsilon_f^2 \theta_0 g_1 + 12\delta^3 \varepsilon_f \theta_0^2 g_1^2 + 72\delta^3 \varepsilon_f \theta_0 g_0 g_2 + \theta_0^3 g_1^3 \\ & + 18\theta_0^2 g_0 g_1 g_2 + 15\theta_0^2 g_0^2 g_3) X^8/8! \\ & \vdots \quad = \quad \vdots\end{aligned} \tag{21d}$$

Thus the temperature distribution in fins is

$$\begin{aligned}\theta = {} & Z_0^2 g_0 \theta_0 (1 - \beta_f \theta_0 + \beta_f^2 \theta_0^2 + \beta_f^3 \theta_0^3 + \cdots) X^2/2! \\ & + Z_0^4 g_0 \theta_0 [4\delta^3 \varepsilon_f + \theta_0 g_1 - \beta_f \theta_0 (3g_0 + 2\theta_0 g_1 + 8\delta^3 \varepsilon_f) \\ & + 3\beta_f^2 \theta_0^2 (3g_0 + \theta_0 g_1 + 4\delta^3 \varepsilon_f) + \cdots] X^4/4! \\ & + Z_0^6 g_0 \theta_0 \lfloor (4\delta^3 \varepsilon_f + \theta_0 g_1)^2 + 3\theta_0 g_0 g_2 - 3\beta_f \theta_0 (24\delta^3 \varepsilon_f g_0 + 8\delta^3 \varepsilon_f \theta_0 g_1 + 16\delta^6 \varepsilon_f^2 \\ & + 8\theta_0 g_0 g_1 + \theta_0^2 g_1^2 + \theta_0 g_0 g_2) + \cdots] X^6/6! \\ & + Z_0^8 \theta_0 g_0 (64\delta^9 \varepsilon_f^3 + 48\delta^6 \varepsilon_f^2 \theta_0 g_1 + 12\delta^3 \varepsilon_f \theta_0^2 g_1^2 + 72\delta^3 \varepsilon_f \theta_0 g_0 g_2 + \theta_0^3 g_1^3 \\ & + 18\theta_0^2 g_0 g_1 g_2 + 15\theta_0^2 g_0^2 g_3) X^8/8! + \cdots\end{aligned} \tag{22}$$

The temperature distribution in fin assemblies expressed in Eqs. (13) and (22) are unknown constants m_1 and m_2 in supporting structure energy equation and θ_0 in fin energy equation. These three unknown can be determined using boundary conditions (5b)–(5d). For a tip temperature θ_0, it is to calculate the fin base temperature from Eqs. (13) and (22) and then equating to ease other, the following expression can be obtained:

$$\begin{aligned}& (m_1 + m_2)\left[1 - \frac{\beta_w}{2}(m_1 + m_2) + \frac{\beta_w^2}{2}(m_1 + m_2)^2 - \frac{5\beta_w^3}{8}(m_1 + m_2)^3 + \frac{7\beta_w^4}{8}(m_1 + m_2)^4 - \frac{21\beta_w^5}{16}(m_1 + m_2)^5 + \cdots\right] \\ & - Z_0^2 g_0 \theta_0 (1 - \beta_f \theta_0 + \beta_f^2 \theta_0^2 + \beta_f^3 \theta_0^3 + \cdots) 1/2! - Z_0^4 g_0 \theta_0 [4\delta^3 \varepsilon_f + \theta_0 g_1 - \beta_f \theta_0 (3g_0 + 2\theta_0 g_1 + 8\delta^3 \varepsilon_f) \\ & + 3\beta_f^2 \theta_0^2 (3g_0 + \theta_0 g_1 + 4\delta^3 \varepsilon_f) + \cdots] 1/4! - Z_0^6 g_0 \theta_0 [(4\delta^3 \varepsilon_f + \theta_0 g_1)^2 + 3\theta_0 g_0 g_2 - 3\beta_f \theta_0 (24\delta^3 \varepsilon_f g_0 \\ & + 8\delta^3 \varepsilon_f \theta_0 g_1 + 16\delta^6 \varepsilon_f^2 + 8\theta_0 g_0 g_1 + \theta_0^2 g_1^2 + \theta_0 g_0 g_2) + \cdots] 1/6! - Z_0^8 \theta_0 g_0 (64\delta^9 \varepsilon_f^3 + 48\delta^6 \varepsilon_f^2 \theta_0 g_1 \\ & + 12\delta^3 \varepsilon_f \theta_0^2 g_1^2 + 72\delta^3 \varepsilon_f \theta_0 g_0 g_2 + \theta_0^3 g_1^3 + 18\theta_0^2 g_0 g_1 g_2 + 15\theta_0^2 g_0^2 g_3) 1/8! + \cdots = 0\end{aligned} \tag{23}$$

From boundary condition (5d), one can write

$$\begin{aligned}& \left[m_1 - \beta_w m_1 (m_1 + m_2 + m_1 \omega) + \frac{3\beta_w^2 m_1}{2}(m_1 + m_2 + m_1 \omega)^2 - \frac{5\beta_w^3 m_1}{2}(m_1 + m_2 + m_1 \omega)^3\right. \\ & \left. + \frac{35\beta_w^4 m_1}{8}(m_1 + m_2 + m_1 \omega)^4 - \frac{63\beta_w^5 m_1}{8}(m_1 + m_2 + m_1 \omega)^5 + \cdots\right] \\ & + Nu_L (m_1 + m_2 + m_1 \omega)\left[1 - \frac{\beta_w}{2}(m_1 + m_2 + m_1 \omega) + \frac{\beta_w^2}{2}(m_1 + m_2 + m_1 \omega)^2\right.\end{aligned}$$

$$-\frac{5\beta_w^3}{8}(m_1+m_2+m_1\omega)^3+\frac{7\beta_w^4}{8}(m_1+m_2+m_1\omega)^4-\frac{21\beta_w^5}{16}(m_1+m_2+m_1\omega)^5+\cdots\Big]$$

$$-Nu_L=0 \tag{24}$$

A generalized Newton–Raphson method can be used to solve Eqs. (23) and (24) simultaneously to determine the unknown constants, m_1 and m_2 for a guess value of θ_0. Using boundary condition (5c), tip temperature θ_0 is evaluated from the previously calculated m_1 and m_2. The final values of these unknowns are estimated by iteration.

The actual heat transfer rate through the fin-supporting structure system is obtained by applying Fourier's law of heat conduction at the liquid side of the primary surface and it can be written in dimensionless form as

$$Q=\frac{q}{2k_{w0}(T_L-T_a)}=P^*\psi(1+\beta_w\phi_{X=1+\omega})\frac{d\phi}{dX}\Big|_{X=1+\omega} \tag{25}$$

Eq. (25) is expanded using Eq. (13) as

$$\begin{aligned}Q=P^*\psi\Big\{&1+\beta_w[m_1(1+\omega)+m_2]-\frac{\beta_w^2}{2}[m_1(1+\omega)+m_2]^2+\frac{\beta_w^3}{2}[m_1(1+\omega)+m_2]^3\\&-\frac{5\beta_w^4}{8}[m_1(1+\omega)+m_2]^4+\frac{7\beta_w^5}{8}[m_1(1+\omega)+m_2]^5-\frac{21\beta_w^6}{16}[m_1(1+\omega)+m_2]^6\Big\}\\&\times\Big\{m_1-\beta_w m_1[m_1(1+\omega)+m_2]+\frac{3\beta_w^2m_1}{2}[m_1(1+\omega)+m_2]^2\\&-\frac{5\beta_w^3m_1}{2}[m_1(1+\omega)+m_2]^3+\frac{35\beta_w^4m_1}{8}[m_1(1+\omega)+m_2]^4\\&-\frac{63\beta_w^5m_1}{8}[m_1(1+\omega)+m_2]^5\Big\}+\cdots\end{aligned} \tag{26}$$

The ideal heat transfer rate through the fin system can be determined by assuming the entire fin–wall surfaces maintaining a uniform temperature which is assumed to be equal to the wall temperature adjacent to the liquid. Mathematically, the ideal heat transfer rate can be expressed in dimensionless form as

$$\begin{aligned}Q_i=\frac{q_i}{2k_{w0}(T_L-T_a)}&=Bi(P^*-1)\left[\lambda^{n+1}+\varepsilon_w\lambda\,(4\delta^3+6\delta^2\lambda+4\delta\lambda^2+\lambda^3)\right]'\\&+\frac{Bi}{\psi}\left[\lambda^{n+1}+\varepsilon_f\lambda(4\delta^3+6\delta^2\lambda+4\delta\lambda^2+\lambda^3)\right]\end{aligned} \tag{27}$$

where

$$\begin{aligned}\lambda=&[m_1(1+\omega)+m_2]-\frac{\beta_w}{2}[m_1(1+\omega)+m_2]^2+\frac{\beta_w^2}{2}[m_1(1+\omega)+m_2]^3\\&-\frac{5\beta_w^3}{8}[m_1(1+\omega)+m_2]^4+\frac{7\beta_w^4}{8}[m_1(1+\omega)+m_2]^5-\frac{21\beta_w^5}{16}[m_1(1+\omega)+m_2]^6+\cdots\end{aligned} \tag{28}$$

The actual heat transfer rate through a fin can be calculated from the following expression:

$$\begin{aligned}Q_f=\frac{q_f}{2k_{w0}(T_L-T_a)}=\psi(1+\beta_f\tau)K_r\Big\{&Z_0^2g_0\theta_0(1-\beta_f\theta_0+\beta_f^2\theta_0^2+\beta_f^3\theta_0^3+\cdots)\\&+Z_0^4g_0\theta_0[4\delta^3\varepsilon_f+\theta_0g_1-\beta_f\theta_0(3g_0+2\theta_0g_1+8\delta^3\varepsilon_f)+3\beta_f^2\theta_0^2(3g_0+\theta_0g_1+4\delta^3\varepsilon_f)\end{aligned}$$

$$+\cdots]1/3! + Z_0^6 g_0\theta_0[(4\delta^3\varepsilon_f + \theta_0 g_1)^2 + 3\theta_0 g_0 g_2 - 3\beta_f\theta_0(24\delta^3\varepsilon_f g_0 + 8\delta^3\varepsilon_f\theta_0 g_1 + 16\delta^6\varepsilon_f^2 + 8\theta_0 g_0 g_1 + \theta_0^2 g_1^2 + \theta_0 g_0 g_2) + \cdots]1/5! + Z_0^8\theta_0 g_0(64\delta^9\varepsilon_f^3 + 48\delta^6\varepsilon_f^2\theta_0 g_1 + 12\delta^3\varepsilon_f\theta_0^2 g_1^2 + 72\delta^3\varepsilon_f\theta_0 g_0 g_2 + \theta_0^3 g_1^3 + 18\theta_0^2 g_0 g_1 g_2 + 15\theta_0^2 g_0^2 g_3)1/7! + \cdots\} \quad (29)$$

where τ is the temperature at the fin base. It can be determined from Eq. (22) by putting $X=1$.

The ideal heat transfer rate through a fin is determined from the following equation:

$$Q_{fi} = \frac{q_{fi}}{2k_{w0}(T_L - T_a)} = \frac{BiK_r\tau}{\psi}\left[\tau^n + \varepsilon_f(4\delta^3 + 6\delta^2\tau + 4\delta\tau^2 + \tau^3)\right] \quad (30)$$

Thus from definition of fin efficiency yields

$$\eta_f = Q/Q_{fi} \quad (31)$$

The performance of a fin attached with the primary surface is conveniently expressed by augmentation factor. It is defined as the ratio of the heat transfer rate to that of the unfinned wall operating under the same condition. The heat transfer rate through the unfinned wall can be determined from the following mathematical steps:

The governing equation in the unfinned wall is given by

$$(1 + \beta_w\Phi)d^2\Phi/dX^2 + \beta_w(d\Phi/dX)^2 = 0 \quad \text{for } 0 \le X \le \omega \quad (32)$$

For the solution of Eq. (32), the following boundary conditions are taken:

$$\text{at } X = 0, \quad (1 + \beta_w\Phi)\frac{d\Phi}{dX} = \frac{Bi}{\psi}\left[\Phi^{n+1} + \varepsilon_w\Phi(4\delta^3 + 6\delta^2\Phi + 4\delta\Phi^2 + \Phi^3)\right] \quad (33a)$$

and

$$\text{at } X = \omega, \quad \frac{d\Phi}{dX} = Nu_L(1-\Phi) \quad (33b)$$

By solving Eq. (32), the following temperature distribution can be obtained:

$$\Phi = (m_3X + m_4)\left[1 - \frac{\beta_w}{2}(m_3X + m_4) + \frac{\beta_w^2}{2}(m_3X + m_4)^2 - \frac{5\beta_w^3}{8}(m_3X + m_4)^3 + \frac{7\beta_w^4}{8}(m_3X + m_4)^4 - \frac{21\beta_w^5}{16}(m_3X + m_4)^5 + \cdots\right] \quad (0 \le X \le \omega) \quad (34)$$

The integration constants m_3 and m_4 are determined from boundary conditions (33). The temperature at $X=0$, Φ_0, is calculated first from Eq. (34) by assuming suitable m_4 value

$$\Phi_0 = m_4 - \beta_w m_4^2/2 + \beta_w^2 m_4^3/2 - 5\beta_w^3 m_4^4/8 + 7\beta_w^4 m_4^5/8 - 21\beta_w^5 m_4^6/16 + \cdots \quad (35)$$

From Eqs. (33a) and (33b), one can get

$$m_3 = \frac{Bi\lfloor\Phi_0^{n+1} + \varepsilon_w\Phi_0(4\delta^3 + 6\delta^2\Phi_0 + 4\delta\Phi_0^2 + \Phi_0^3)\rfloor}{\psi(1 + \beta_w\Phi_0)(1 - \beta_w m_4 + 3\beta_w^2 m_4^2/2 - 5\beta_w^3 m_4^3/2 + 35\beta_w^4 m_4^4/8 - 63\beta_w^5 m_4^5/8 + \cdots)} \quad (36)$$

and

$$m_3[1 - \beta_w(m_3\omega + m_4) + 3\beta_w^2(m_3\omega + m_4)^2/2 - 5\beta_w^3(m_3\omega + m_4)^3/2 + 35\beta_w^4(m_3\omega + m_4)^4/8 - 63\beta_w^5(m_3\omega + m_4)^5/8] - Nu_L[1 - m_3\omega - m_4 + \beta_w(m_3\omega + m_4)^2/2 - \beta_w^2(m_3\omega + m_4)^3/2 + 5\beta_w^3(m_3\omega + m_4)^4/8 - 7\beta_w^4(m_3\omega + m_4)^5/8 + 21\beta_w^5(m_3\omega + m_4)^6/16 - \cdots] = 0 \quad (37)$$

In order to determine the constant m_4, Eq. (37) can be solved by Newton–Raphson iterative method and final m_3 and m_4 are obtained by simultaneous solution of Eqs. (35)–(37) iteratively.

The actual heat transfer rate through unfinned wall can be evaluated from the following expression:

$$Q_0 = \frac{q_0}{2k_{w0}(T_L - T_a)} = P^*\psi\, m_3(1 + \beta_w m_4 - \beta_w^2 m_4^2/2 + \beta_w^3 m_4^3/2 - 5\beta_w^4 m_4^4/8 + 7\beta_w^5 m_4^5/8 - 21\beta_w^6 m_4^6/16)$$
$$(1 - \beta_w m_4 + 3\beta_w^2 m_4^2/2 - 5\beta_w^3 m_4^3/2 + 35\beta_w^4 m_4^4/8 - 63\beta_w^5 m_4^5/8) + \cdots \quad (38)$$

From definition of augmentation factor, it is given by

$$Aug = Q/Q_0 \quad (39)$$

3. Results and discussion

The present analysis is done with considering variable all thermo-physical parameters involved in the heat transfer process to determine analytically thermal performance of a fin attached with a wall. However, the present theoretical model can handle to analyze for an ideal case also where all the thermophysical properties are to be taken constant. For the validation purpose, this ideal condition can be adopted. The temperature distribution in the fin–wall assembly for the ideal condition can be written in nondimensional form as

$$\theta = \frac{K_r P^*\psi\, Nu_L \cosh(Z_0 X)}{\cos Z_0\{(1 + \omega Nu_L)[\psi Z_0 \tanh Z_0 + Bi(P^* - 1)] + K_r P^*\psi Nu_L\}} \quad (0 \le X \le 1) \quad (40)$$

and

$$\phi = \frac{Nu_L(X-1)}{(1+\omega Nu_L)} + \frac{K_r P^*\psi Nu_L(1 - XNu_L + \omega Nu_L + Nu_L)}{(1+\omega Nu_L)\{(1+\omega Nu_L)[\psi z_0 \tanh Z_0 + Bi(P^*-1)] + K_r P^*\psi Nu_L\}} \quad (1 \le X \le 1+\omega) \quad (41)$$

Fig. 2A is drawn for temperature distribution in fin–wall assembly for an ideal case predicted by exact analytical, present analytical and numerical methods. The results obtained from the exact analytical and present analytical methods are matched perfectly whereas a slight deviation in results especially near to the fin tip is found when they are determined by a numerical technique. The finite difference method is used for determining the numerical result. The temperature distribution obtained from the present analytical model with consideration of an actual case is depicted in Fig. 2B. For comparison of results, numerical values have been plotted. A satisfactorily matching of results obtained from both the methods has been found.

The effect of radiation parameter ε_f or ε_w, temperature ratio δ, variable heat transfer coefficient parameter n and variable thermal conductivity parameter β on the temperature distribution in a fin–wall assembly is illustrated in Fig. 3. In Fig. 3A, the influence of radiation is exhibited. The temperature in fin–wall assembly for the condition of no radiation from a fin surface is always higher in comparison to any radiated surface. With the increase in radiation effect, fin array temperature gradually decreases. However, the decreasing effect is slowdown with the increase in radiation parameter. Therefore, the fin surface temperature is extremely dependent on radiation parameter whereas temperature in supporting structure does not have much dependence on it. This fact is due to conduction heat transfer taking place in the supporting structure without losing any heat

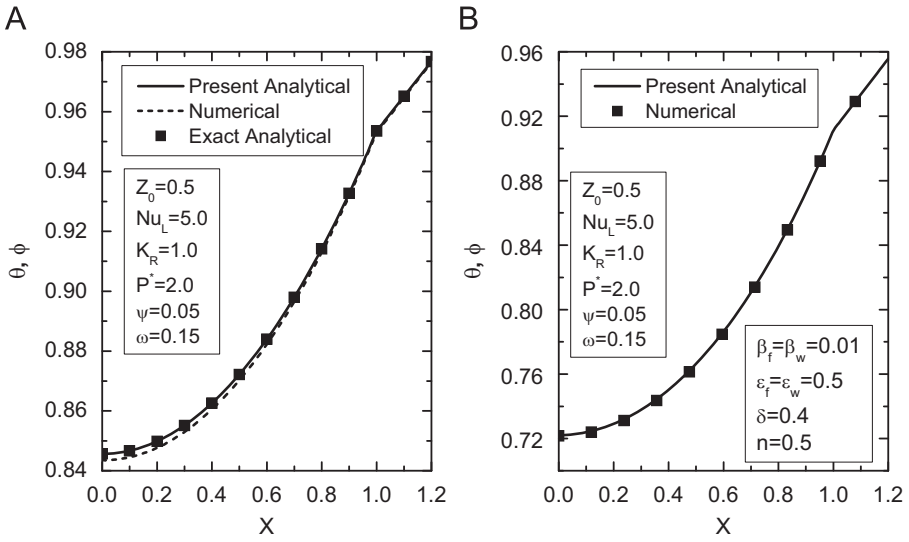

Fig. 2. Temperature distribution in a fin for simplified and actual conditions determined by different methods: (A) simplest study and (B) actual study.

except the boundaries opened to expose to the surrounding. Fig. 3B depicts the effect of temperature ratio parameter δ on temperature distribution in a fin-wall assembly. This parameter has made the same impact with variation of radiation parameters as shown in Fig. 3A. The only difference is temperature dependency effect gradually enhances with the increase in parameter from its zero value. The temperature distribution in a fin assembly is plotted with different values of heat transfer coefficient as illustrated in Fig. 3C. The dependency factor n taken for plotting are 0.5, 2 and 4. The wide range of n value is taken which may be within any practical value. The maximum temperature variation in the fin is found in the case of $n=0.5$. With the increase in n value, variation in temperature in fin assemblies is an incremented function. However, this dependency effect does not have significant impact on the temperature in the supporting structure. The influence of variable thermal conductivity on the temperature distribution has been shown in Fig. 3D. It is obvious from this figure that the variation of thermal conductivity on temperature distribution in the fin assembly may not have any significant change.

Fig. 4 is drawn to show the effect of Nu_L, K_R, P^* and Z_0 on the temperature profile in the fin–wall assembly. Fig. 4A depicts this effect with the variation of Nu_L. An increase in Nu_L means either increase in h_L or decrease in k_L for a constant fin length. For a higher value of Nu_L, convective resistance to the fluid side is to be a lower one and it may be desirable in fin design applications. With the higher Nu_L, the variation of dimensionless temperature in the fin-wall structure is also higher. With the decrease in Nu_L, it decreases as well. For a certain lower value of Nu_L, temperature in fin arrays may be uniform and effectiveness for transferring heat may be a minimum value. The variation of temperature distribution is shown in Fig. 4B with different thermal conductivity ratio K_R. The fin–wall temperature enhances with an increasing K_R value. From temperature distribution, it may be mentioned that for K_R value greater than and equal to one, temperature distribution in the fin and wall structure is clearly distinguishable. But this effect minimizes with the decrease in K_R.

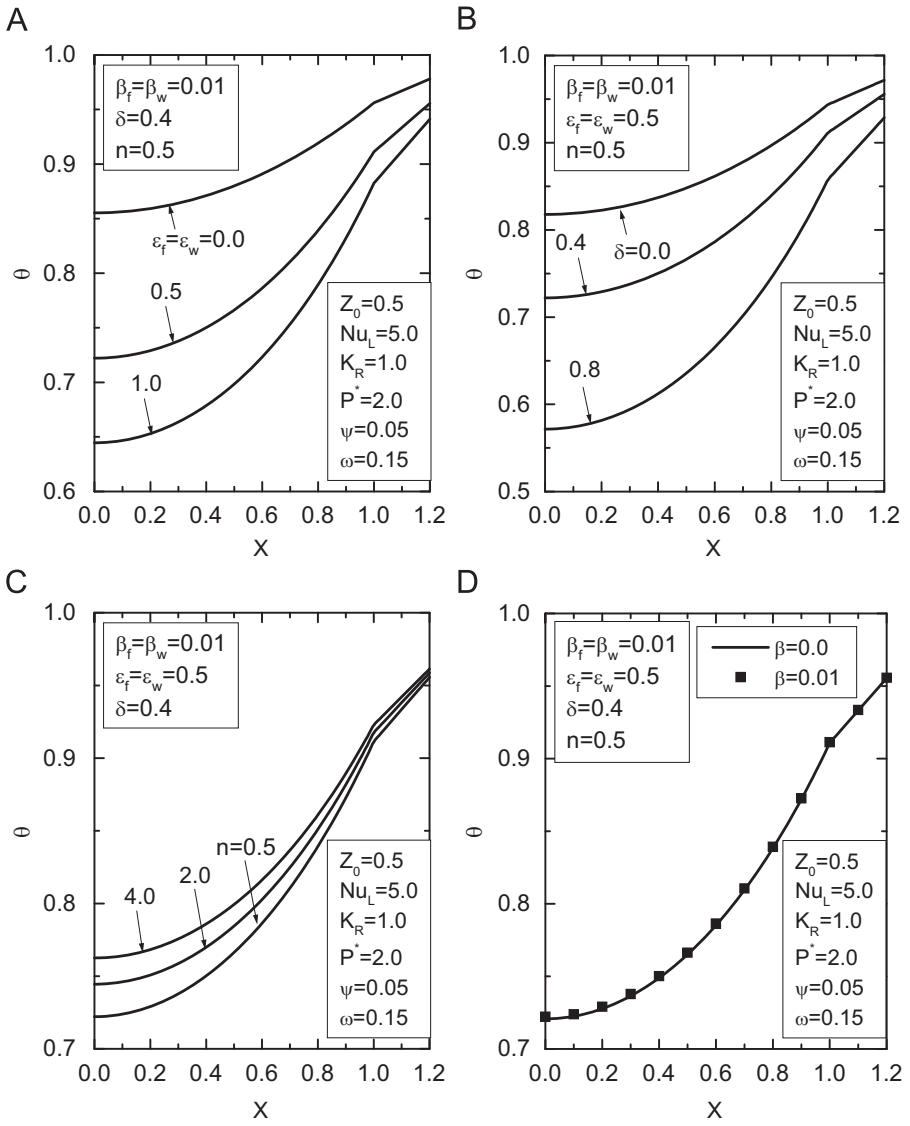

Fig. 3. Effects of different heat transfer parameters on temperature distribution in a fin-wall system: (A) radiation parameter ε, (B) temperature ratio δ, (C) variable heat transfer coefficient parameter n, and (D) variable thermal conductivity parameter β.

The nondimensional wall length P^*effects the temperature distribution in fin arrays as shown in Fig. 4C. With increase in dimensionless wall length, the conductive resistance in the fin array enhances and hence the fin–wall temperature increases. The conductive–convective parameter Z_0 is changed significantly the fin temperature as displayed in Fig. 4D. A smaller value of Z_0 magnifies the fin array temperature. Thus from design point of view, small value of Z_0 and higher value of Nu_L, K_R and P^* may be desirable for the better transfer of heat through a fin–wall assembly.

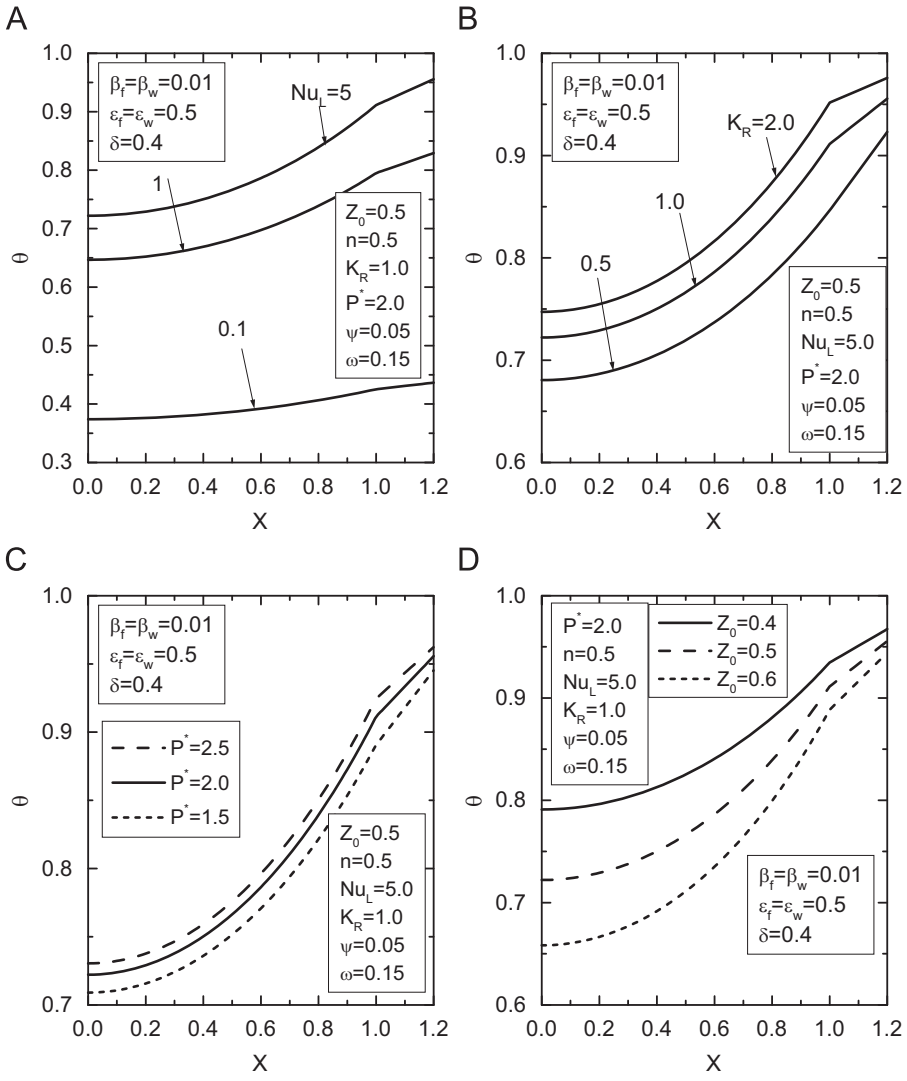

Fig. 4. Effects of thermophysical and geometric parameters on temperature distribution in a fin-wall assembly: (A) radiation parameter ε, (B) Biot number, Bi_L, (C) thermal conductivity ratio, K_R, and (D) conduction–convection parameter, Z_0.

Fin–wall assembly performance, namely, surface efficiency, fin efficiency and augmentation factor are determined based on the present analysis. Fig. 5 is prepared for showing the dependency effect on these performances, by varying δ and Z_0 parameters. The surface efficiency and fin efficiencies decrease with an increasing δ for a constant Z_0 shown in Fig. 5A. The surface efficiency is always lower than the fin efficiency for practical design conditions. However, the nature of curves is almost identical. It may be mentioned that the thermal efficiency of fin–wall system is always less comparison to that of the fin efficiency. Both the surface efficiency and fin efficiency decrement with the increase in Z_0 value. It is less worthy to demonstrate that the difference in efficiencies between fin and

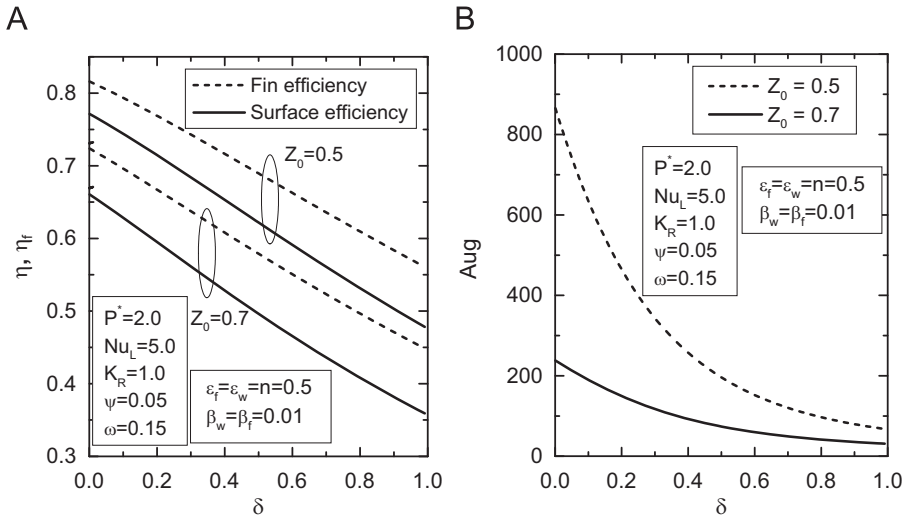

Fig. 5. Performance parameters as a function of δ for different Z_0: (A) fin and surface efficiency and (B) augmentation factor.

surface gradually amplifies with δ but this difference is marginal. The augmentation factor is plotted as a function of δ for different constants Z_0 shown in Fig. 5B. An incremented either δ or Z_0 gives a lower augmentation factor. The diminishing augmentation factor with δ is pronounced at a little value of δ.

Fig. 6 depicts the performances of fin–wall assembly as a function of radiative parameter ε_f. It is obvious that the heat transfer rate is an increasing function with ε_f. The temperature range in the fin–wall is more for an incremented ε_f. Hence, the performances of assembly decline with the radiative parameter. For the lower value of Z_0, decrement of the surface efficiency is always more with that of the fin efficiency for an increase in ε_f. The variation of augmentation factor as a function of ε_f is plotted here for a constant Z_0. The augmentation factor is greatly dependent on the magnitude of Z_0 and the value of ε_f. For a lesser value of Z_0 and ε_f, augmentation factor becomes high due to more heat transfer taken place through the fin-wall than the supporting structure with unfinned condition. The augmentation factor is almost invariable for higher values of Z_0 with variation of ε_f.

Fig. 7 is drawn for showing the fin–wall assembly performances with the variation of index of variable heat transfer coefficient n. It may be mentioned that n value is zero indicating a uniform heat transfer coefficient. With increase in n from its zero value, fin array performances decrease. The decrease in performance namely fin assembly efficiency and fin efficiency are more rapidly with n in comparison to decrease in the augmentation factor. On the other hand, the effect of Z_0 on fin performances is significant especially in the case of augmentation factor.

In every fin design, fin wall plays an important role to augment the heat transfer. Actually depending upon the wall length surface heat transfer coefficient may depend. Fig. 8 is illustrated to execute the effect of projected wall length on fin array performances. An increase in projected wall length decreases both fin efficiency and augmentation factor well which are shown in Figs. 8A and B, respectively. However, the surface efficiency increases with this parameter. It is obvious that for a higher value of wall height, surface

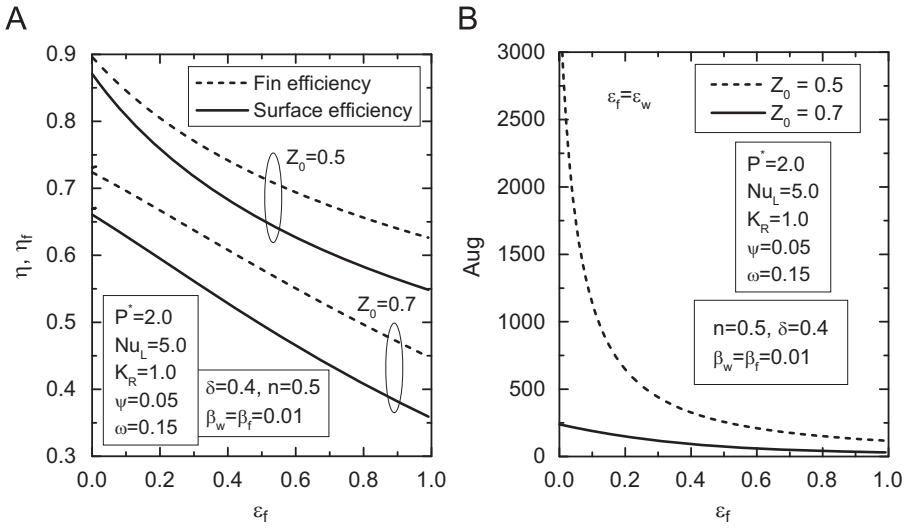

Fig. 6. Effects of radiation parameters ε_f and ε_w on fin performances: (A) fin and surface efficiencies and (B) augmentation factor.

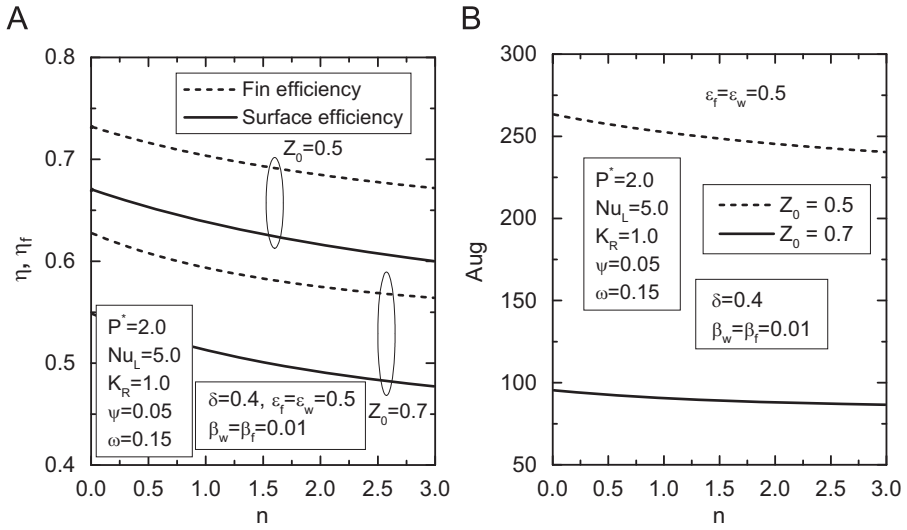

Fig. 7. Effects of variable heat transfer coefficient index n on fin performances: (A) fin and surface efficiencies and (B) augmentation factor.

efficiency is very closer to the fin efficiency. This closeness is dependent also on the magnitude of Z_0 in the design application. The augmentation factor diminishes with the dimensionless wall height P^* as an expected observation. The decremented augmentation factor is a relatively strong function with P^* at lower values of Z_0.

The effect of Nusselt number at the liquid side on the performance of fin array is displayed in Fig. 9. Both surface and fin efficiency decrease with Nu_L due to increase in

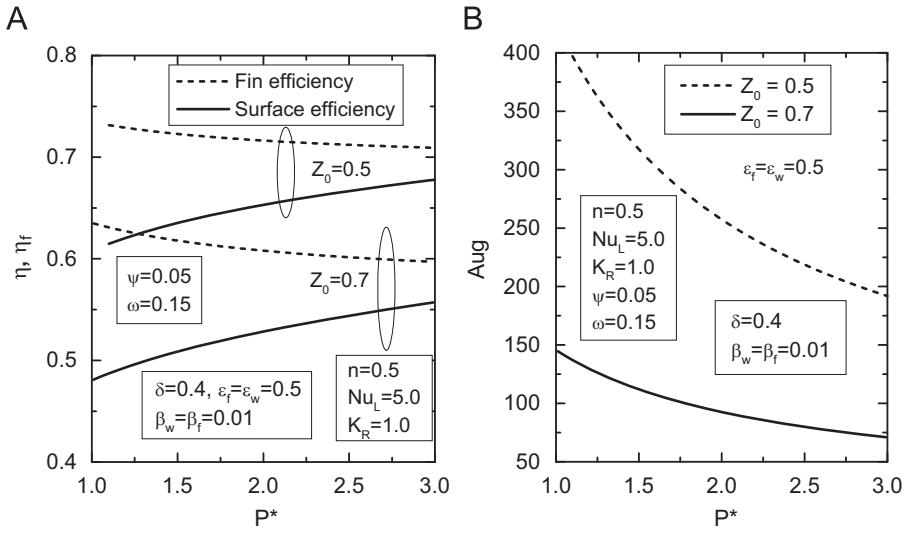

Fig. 8. Fin performances as a function of pitch length P^*: (A) fin and surface efficiencies and (B) augmentation factor.

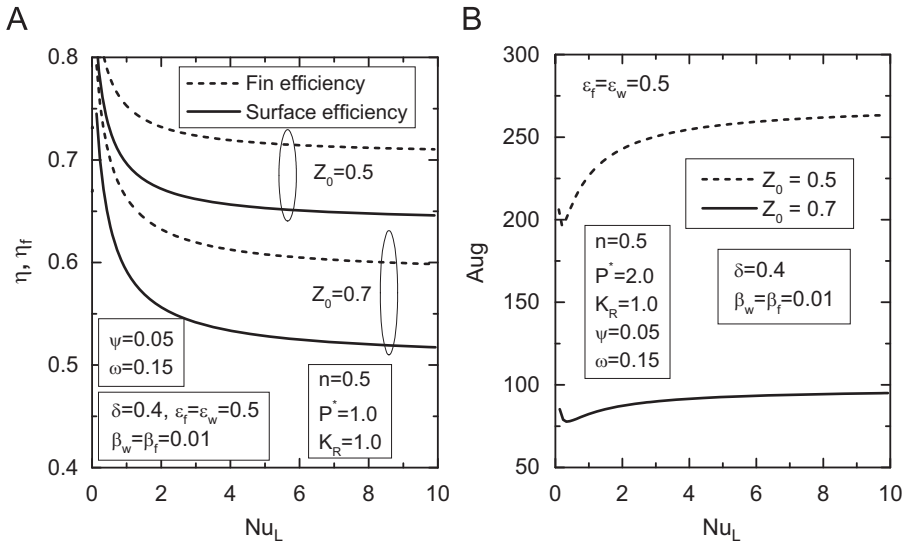

Fig. 9. Variation of fin performances with Biot number Bi_L: (A) fin and surface efficiencies and (B) augmentation factor.

temperature range in the fin–wall assembly. The drop in surface and fin efficiency is more for lower values of Nusselt number. With the increase in Nu_L, this drop rate gradually decreases. The difference between fin and surface efficiency is as an increasing function with Nu_L. On the other hand, AUG decreases with Nu_L for a very small range of Nu_L and then increases monotonically with Nusselt number. But the increment rate depends upon the magnitude of Z_0 also.

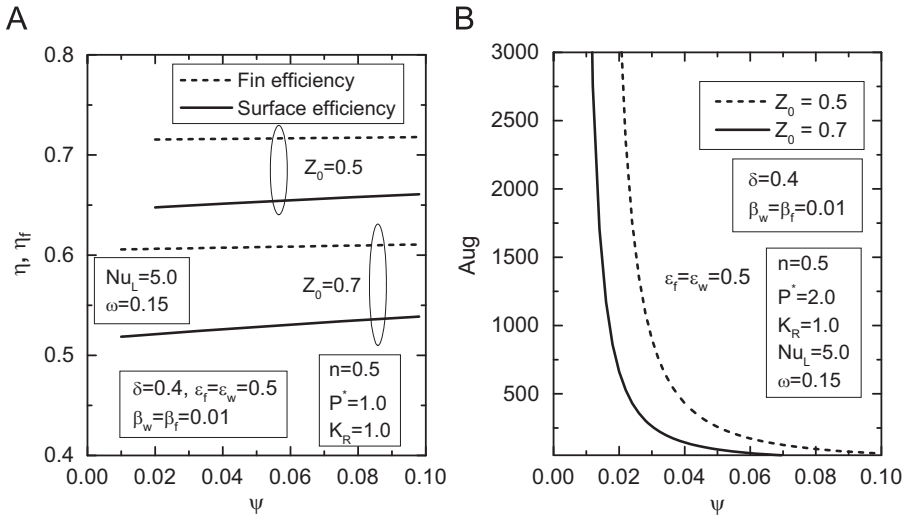

Fig. 10. Variation of fin performances with fin thickness to length ratio ψ: (A) fin and surface efficiencies and (B) augmentation factor.

The fin–wall performance is depicted with the variation of geometrical parameter ψ. The fin and surface efficiency are marginally dependent on this geometric ratio as shown in Fig. 10A. However, this dependency may be treated as a linear. But the fin and surface efficiency are always an increasing function. The augmentation factor with ψ is strongly dependent as shown in Fig. 10B. For higher value of ψ, AUG becomes near to one whatever the design condition is imposed. Naturally for practical utilization of fins, the geometrics of a fin is constructed in such a way that AUG value is high as possible. It may be noted that this is only achievable for a lower value of ψ.

4. Conclusions

From the present analysis, following concluding remarks can be drawn:

1. The proposed approximate analytical model can estimate the temperature distribution and performances of fin–wall assembly under both convective and radiative environments.
2. The analysis has been made into account of the actual situation adopted by considering variable thermophysical parameters.
3. The radiation effect declines both surface temperature and fin–wall performances.
4. With the increase in index of variable heat transfer coefficient n, fin performances decrease slowly.
5. The variable thermal conductivity does not make role significantly on the temperature and fin–wall performances under radiative–convective environment.
6. An increase in Nu_L increases augmentation factor and decreases both the fin and surface efficiencies.
7. The geometrical parameter ψ does not make remarkable impact on fin and surface efficiencies whereas the augmentation factor depends very much upon the ψ.

8. The influence of dimensionless wall height P^* on the fin efficiency and augmentation factor is diminished but the surface efficiency is enhanced as well.

Acknowledgment

The authors must acknowledge King Mongkut's University of Technology Thonburi, the Thailand Research Fund, the Office of the Higher Education Commission and the National Research University Project for providing financial support to complete this work.

References

[1] E.M. Sparrow, L. Lee, Effect of fin base temperature depression in a multi-fin array, ASME J. Heat Transfer 97 (1975) 463–465.
[2] N.V. Suryanarayan, Two-dimensional effects on heat transfer from an array of straight fins, ASME J. Heat Transfer 99 (1977) 129–132.
[3] P.J. Heggs, R.R. Stone, The effects of dimensions of heat flow rates through extended surfaces, ASME J. Heat Transfer 102 (1980) 180–182.
[4] P.J. Heggs, D.B. Ingham, M. Manzoor, The analysis of fin assembly heat transfer by series truncation method, ASME J. Heat Transfer 104 (1982) 210–212.
[5] B. Kundu, P.K. Das, Performance and optimum design analysis of convective fin arrays attached to flat and curved primary surfaces, Int. J. Refrig. 32 (2009) 430–443.
[6] B. Kundu, A. Miyara, An analytical method for determination of the performance of a fin assembly under dehumidifying conditions: A comparative study, Int. J. Refrig. 32 (2009) 369–380.
[7] B.T.F. Chung, B.X. Zhung, A novel design for a radiative fin array system, J. Franklin Inst. 330 (1993) 465–478.
[8] A.M. Elazhary, H.M. Soliman, A nongray analysis of radiating-convecting rectangular plate-fin arrays, Heat Mass Transfer 44 (2008) 413–420.
[9] B. Kundu, A. Aziz, Performance of a convectively heated rectangular fin with a step change in cross-sectional area and losing heat by simultaneous convection and radiation, ASME J. Heat Transfer 132 (2010) 104502-1–104502-6.
[10] A. Aziz, F. Khani, Convection–radiation from a continuously moving fin of variable thermal conductivity, J. Franklin Inst. 348 (2011) 640–651.
[11] A. Razani, H. Zohoor, Optimum dimensions of convective-radiative spines using a temperature correlated profile, J. Franklin Inst. 328 (1991) 471–486.
[12] G. Adomian, in: Non-linear Stochastic System Theory and Application to Physics, Kluwer Academic Publisher, Dordrecht, 1988.
[13] X. Shang, P Wu, X. Shao, An efficient method for solving Emden–Fowler equations, J. Franklin Inst. 346 (2009) 889–897.
[14] J. Biazar, P. Gholamin, K. Hosseini, Variational iteration method for solving Fokker–Planck equation, J. Franklin Inst. 347 (2010) 1137–1147.
[15] P.Y. Tsai, C.K. Chen, An approximate analytic solution of the nonlinear Riccati differential equation, J. Franklin Inst. 347 (2010) 1850–1862.
[16] F. Mohammadi, M.M. Hosseini, A comparative study of numerical methods for solving quadratic Riccati differential equations, J. Franklin Inst. 348 (2011) 158–164.

Provided for non-commercial research and education use.
Not for reproduction, distribution or commercial use.

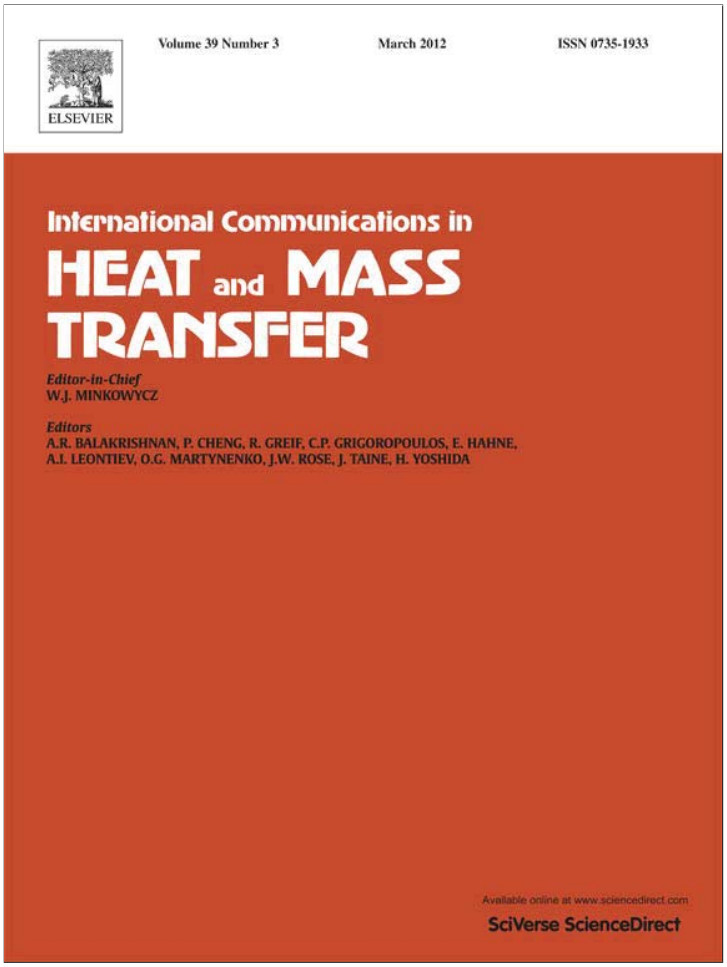

This article appeared in a journal published by Elsevier. The attached copy is furnished to the author for internal non-commercial research and education use, including for instruction at the authors institution and sharing with colleagues.

Other uses, including reproduction and distribution, or selling or licensing copies, or posting to personal, institutional or third party websites are prohibited.

In most cases authors are permitted to post their version of the article (e.g. in Word or Tex form) to their personal website or institutional repository. Authors requiring further information regarding Elsevier's archiving and manuscript policies are encouraged to visit:

http://www.elsevier.com/copyright

Author's personal copy

International Communications in Heat and Mass Transfer 39 (2012) 424–431

Contents lists available at SciVerse ScienceDirect

International Communications in Heat and Mass Transfer

journal homepage: www.elsevier.com/locate/ichmt

Investigation of pool boiling of nanofluids using artificial neural networks and correlation development techniques ☆

M. Balcilar [a], A.S. Dalkilic [b,*], A. Suriyawong [c], T. Yiamsawas [c], S. Wongwises [c,d,**]

[a] Computer Engineering Department, Yildiz Technical University, Yildiz, Besiktas, Istanbul 34349, Turkey
[b] Heat and Thermodynamics Division, Department of Mechanical Engineering, Yildiz Technical University, Yildiz, Besiktas, Istanbul 34349, Turkey
[c] Fluid Mechanics, Thermal Engineering and Multiphase Flow Research Lab. (FUTURE), Department of Mechanical Engineering, King Mongkut's University of Technology Thonburi, Bangmod, Bangkok 10140, Thailand
[d] The Academy of Science, The Royal Institute of Thailand, Sanam Suea Pa, Dusit, Bangkok 10300, Thailand

ARTICLE INFO

Available online 31 January 2012

Keywords:
Pool boiling
Heat transfer coefficient
Nanofluid
Modeling
Neural network

ABSTRACT

The nucleate pool boiling heat transfer characteristics of TiO_2 nanofluids are investigated to determine the important parameters' effects on the heat transfer coefficient and also to have reliable empirical correlations based on the neural network analysis. Nanofluids with various concentrations of 0.0001, 0.0005, 0.005, and 0.01 vol.% are employed. The horizontal circular test plate, made from copper with different roughness values of 0.2, 2.5 and 4 μm, is used as a heating surface. The artificial neural network (ANN) training sets have the experimental data of nucleate pool boiling tests, including temperature differences between the temperatures of the average heater surface and the liquid saturation from 5.8 to 25.21 K, heat fluxes from 28.14 to 948.03 kW m^{-2}. The pool boiling heat transfer coefficient is calculated using the measured results such as current, voltage, and temperatures from the experiments. Input of the ANNs are the 8 numbers of dimensional and dimensionless values of the test section, such as thermal conductivity, particle size, physical properties of the fluid, surface roughness, concentration rate of nanoparticles and wall superheating, while the outputs of the ANNs are the heat flux and experimental pool boiling heat transfer coefficient from the analysis. The nucleate pool boiling heat transfer characteristics of TiO_2 nanofluids are modeled to decide the best approach, using several ANN methods such as multi-layer perceptron (MLP), generalized regression neural network (GRNN) and radial basis networks (RBF). Elimination process of the ANN methods is performed together with the copper and aluminum test sections by means of a 4-fold cross validation algorithm. The ANNs performances are measured by mean relative error criteria with the use of unknown test sets. The performance of the method of MLP with 10-20-1 architecture, GRNN with the spread coefficient 0.7 and RBFs with the spread coefficient of 1000 and a hidden layer neuron number of 80 are found to be in good agreement, predicting the experimental pool boiling heat transfer coefficient with deviations within the range of ±5% for all tested conditions. Dependency of output of the ANNs from input values is investigated and new ANN based heat transfer coefficient correlations are developed, taking into account the input parameters of ANNs in the paper.

© 2012 Elsevier Ltd. All rights reserved.

1. Introduction

The existence of a moving and deforming phase interface affects the heat transfer in two-phase flows concerning gas and liquid phases. Two-phase flows occur during boiler operation in a power plant, nuclear reactors, evaporator performance in refrigeration systems, quenching in materials processing, and condensers in power and refrigeration systems. In this paper, artificial neural network analyses were used as one of the numerical solution techniques to determine the important characteristics of pool boiling heat transfer.

Das and Kishor [1] used a modeling technique based on fuzzy system to determine the heat transfer coefficient in pool boiling of distilled water. They performed an experimental study to develop an empirical correlation for saturated boiling of distilled water from a plain copper heating tube surface at atmospheric and sub-atmospheric pressures. Their experimental data has been compared with those determined from the zero-order adaptive fuzzy model with heat flux as input variable and also Matlab based adaptive neuro-fuzzy inference system (ANFIS) function.

Liu et al., [2] developed a numerical model using artificial neural network (ANN) technology to investigate boiling heat transfer enhancement using additives. Their model was validated by 30 additives tested by the authors and other researchers on the augmentation of boiling heat transfer experimentally.

☆ Communicated by W.J. Minkowycz.
* Corresponding author.
** Correspondence to: S. Wongwises, The Academy of Science, The Royal Institute of Thailand, Sanam Suea Pa, Dusit, Bangkok 10300, Thailand.
E-mail addresses: dalkilic@yildiz.edu.tr (A.S. Dalkilic), somchai.won@kmutt.ac.th (S. Wongwises).

0735-1933/$ – see front matter © 2012 Elsevier Ltd. All rights reserved.
doi:10.1016/j.icheatmasstransfer.2012.01.008

Author's personal copy

Nomenclature

A	area, m^2
C_p	specific heat, kJ kg^{-1} °C
g	gravitational acceleration, m s^{-2}
h	boiling heat transfer coefficient, W m^{-2} K
h_{fg}	heat of vaporization, kJ kg^{-1}
I	electric current, amps
i	number of test data
k	thermal conductivity, W m^{-1} K^{-1}
Nu	Nusselt number
P	pressure, kPa
P_c	critical pressure, kPa
Pr	Prandtl number
R_a	average roughness, μm
Re	Reynolds number
R_p	particle size, nm
q	heat flux, kW m^{-2}
T_c	critical temperature, K
V	voltage, volts
ΔT	wall superheat, $T_s - T_{sat}$, K

Greek symbols

μ	dynamic viscosity, kg m^{-1} s^{-1}
ρ	density, kg m^{-3}
σ	surface tension, N m^{-1}

Subscripts

exp	experimental
l	liquid phase
s	heating surface
sat	saturation
v	vapor phase

Scalabrin et al., [3] studied the heat transfer modeling of flow boiling inside horizontal tubes at saturation conditions using eight pure fluids and a constant composition ternary mixture. ANNs were used to characterize conventional heat transfer surfaces. Their model's performance was validated by five conventional correlations. Scalabrin et al., [4] investigated the flow boiling inside horizontal smooth tubes for mixtures. They proposed a new modeling technique for the heat transfer. They improved their model to mixtures in their former work. Directly-accessible physical quantities controlling the phenomenon were selected for the correlation architectures considered for the ANN functions. They stated that they obtained considerable increase of prediction capability with respect to the conventional methods by means of their numerical model.

Wang et al., [5] developed a generalized neural network correlation for boiling heat transfer coefficient of R22 and its alternative refrigerants R134a, R407C and R410A inside horizontal smooth tubes using the experimental data in the literature. The inputs of the neural network consisted of four kinds of dimensionless parameter groups from existing generalized correlations, while the output was a Nusselt number. As a result of their analyses, the input parameter group based on the Gungor–Winterton [6] correlation has the highest predictability in the tested groups.

Suriyawong and Wongwises [7] studied nucleate pool boiling heat transfer of TiO_2–water nanofluids experimentally. Nanofluids with various concentrations of 0.00005, 0.0001, 0.0005, 0.005, and 0.01 vol.% were employed in their study. The experiments were performed to explore the effects of nanofluids concentration as well as heating surface material and roughness on nucleate pool boiling characteristics and the heat transfer coefficient under ambient pressure. Their results showed that based on the copper heated surface which was tested with a concentration of 0.0001 vol.%, higher nucleate pool boiling heat transfer coefficient was obtained when compared with the base fluid.

Trisaksri and Wongwises [8] investigated nucleate pool boiling heat transfer of a refrigerant-based-nano-fluid at different nanoparticle concentrations and pressures. TiO_2 nanoparticles were mixed with the refrigerant HCFC 141b at 0.01, 0.03 and 0.05 vol%. Pool boiling experiments of nano-fluid were conducted and compared with that of the base refrigerant. Their results indicated that the nucleate pool boiling heat transfer deteriorated with increasing particle concentrations, especially at high heat fluxes.

The correct prediction of refrigerant boiling heat transfer performance is important for the design of evaporators. Information on the pool boiling characteristics of refrigerant-based nanofluids is still limited. Moreover, there remains room for further research, especially on the point at which the presence of the nanoparticle can enhance or deteriorate heat transfer. As a consequence, the main aim of the present study was to have reliable empirical correlations, based on numerical and experimental studies, to cover the wide range important parameters on the pool boiling. The effect of various TiO_2–water nanoparticle concentrations using a copper-based heating material with various surface roughness values on the boiling heat transfer coefficient is considered in the numerical analyses to achieve the main aim thoroughly. In addition to this, the effect of input parameters (thermal conductivity, particle size, physical properties of the fluid, surface roughness, concentration rate of nanoparticles and wall superheating) on the output parameters (heat flux and pool boiling heat transfer coefficient) is shown and discussed as a primary study on this subject in the literature.

2. Sample preparation and experimental apparatus

In the present study, nanofluids provided by a commercial source (DEGUSSA, VP Disp. W740x) are used as working fluid. The detailed image of dispersed TiO_2 nanoparticles in water, taken by Transmission electron microscopy (TEM), details of preparation of nanofluids and details of experimental apparatus can be seen from Suriyawong and Wongwises [7].

3. Data reduction

3.1. Experimental pool boiling heat transfer coefficient

Experimental investigations were carried out to observe the boiling characteristics using the flat plate heater. The heat fluxes, q (W m^{-2}), were calculated from the following equation:

$$q = \frac{IV}{A} \tag{1}$$

where I is the current (amps), V is the voltage (volts), and A is the heating surface area (m^2).

The average boiling heat transfer coefficient, h_b (W m^{-2} °C), is defined as:

$$h_b = \frac{q}{(T_s - T_{sat})} \tag{2}$$

where T_s is the average heater surface temperature (°C) calculated from Eq. (3), and T_{sat} is the liquid saturation temperature (°C):

$$T_s = \frac{\sum_{i=1}^{4} T_i \sum_{i=1}^{4} x^2{}_i - \sum_{i=1}^{4} x_i \sum_{i=1}^{4} x_i T_i}{4\sum_{i=1}^{4} x^2{}_i - \left(\sum_{i=1}^{4} x_i\right)^2} \tag{3}$$

where T_i is the local temperature (°C) and x is the position of the temperature measurement (m) on the test section. The examples of the

Author's personal copy

axial temperature distribution in the copper test section can be seen from Suriyawong and Wongwises [7].

The uncertainties of the heat flux, heating surface temperature and heat transfer coefficient are ±2.2%, ±3.7% and ±11.6%, respectively.

3.2. Calculation procedure for the Generalized Artificial Neural Networks (ANNs) model

ANNs are such factors that can utilize machine learning for the duty of considered necessary mapping of the inputs to the outputs. A dataset is divided into three parts such as training, testing and validation. ANNs determine a function between the inputs and outputs generalizing the training group. The success of this group is calculated using the test group. The training duration of ANNs is determined by the validation group. When the training group has over-fitting as a result of long time training, ANNs memorize the training group and its success on the test group reduces. The optimum point for the stop of training is determined by using a validation group. Performance of ANNs is measured by the success of the prediction. There are many described ANN types and their architectures (different size of layers, neuron numbers and spread coefficients) related to function approximation in the literature. The most known methods are multi-layer perceptron (MLP), radial basis functions networks (RBF), generalized regression neural networks (GRNN) and artificial neural fuzzy inference system (ANFIS), which is the combination of fuzzy logic decision systems and ANNs. Schematic diagrams of artificial intelligence models used in the analysis, obtained by Matlab software, and detailed information can be seen from the authors' previous publication [9].

Nelder and Mead developed a simplex method to determine a local minimum of a function of several variables. It is a good alternative method when the differential of the fitness function is complex either analytically or numerically. A simplex forms triangle for two variables and function values at the three vertices of this triangle are compared by means of the pattern search method. The new vertex is found by replacing with the rejected worst vertex where f (x, y) is largest. Then, the search is continued when the new vertex is formed. A sequence of triangles, which might have different shapes, is generated by each iteration when values at the vertices get smaller and smaller. Reduction of the size of the triangles is performed and the coordinates of the minimum point are found. The Nelder–Mead technique was proposed by Nelder and Mead [10] and is a technique for minimizing a fitness function in a many-dimensional space. Operators in Nelder–Mead algorithm is shown in [11].

The least square (LS) method is one of the standard approaches to the approximate solution of over-determined systems or inexactly specified systems of equations in an approximate sense. It can be used when the sets of equations in which there are fewer unknowns than equations. LS means that the overall solution minimizes the sum of the squares of the errors made in solving every single equation instead of solving the equations exactly. The data fitting is the most important application of LS. The minimization of the sum of squared residuals is sensed by the best fit in the LS and a residual causes the difference between an observed value and the value provided by a model. LS match with the maximum probability criterion if there is a normal distribution of the experimental errors.

LS problems consist of linear least squares and non-linear least squares (NLS) depending on whether or not the residuals are linear in all unknowns. Most statistical regression analyses have linear LS problems; it has a closed form solution. The non-linear problem, usually solved by iterative refinement, has no closed solution. The system is approximated by a linear one at each iteration in order to have similar results for the core calculation in both cases. The Non-Linear Least Square (NLS) method allows determination of the most optimal non-linear function coefficients, in order to fit data collected from an experimental environment to a non-linear function (non-linear curve fitting). This method tries to minimize the mean square error, beginning from the first estimated values determined by the user. Mathematical basis of the investigated methods and details are shown in [11].

3.3. Correlation development

Rhosenow [12] proposed the following equations from Eqs. (4)–(7) for pool nucleate boiling considering surface characteristics. His correlations are widely accepted in the literature. Narayan et al. [13] used Eq. (4) to investigate the effect of surface orientation on pool boiling heat transfer of nanoparticle suspensions. They stated that m should be taken as 1 for water in Eq. (4). Suriyawong and Wongwises [7] also used Eq. (4) to study nucleate pool boiling heat transfer characteristics of TiO_2–water nanofluids at very low concentrations. Taylor and Phelan [14] benefitted from Eq. (5) to prepare their review on the pool boiling of nanofluids. Bang and Chang [15] used Rhosenow [12]'s equations of 6 and 7 to determine boiling heat transfer performance and phenomena of Al_2O_3–water nanofluids from a plain surface in a pool

$$\frac{C_{p,l}(T_s-T_{sat})}{h_{fg}\mathrm{Pr}_l^{\,m}} = C_{sf}\left(\frac{q}{\mu_l h_{fg}}\sqrt{\frac{\sigma}{g(\rho_l-\rho_v)}}\right)^{0.33} \tag{4}$$

$$q = \mu_l h_{fg}\left[\frac{\sigma}{g(\rho_l-\rho_v)}\right]^{-1/2}\left(\frac{1}{C_{sf}}\right)^{1/r}\mathrm{Pr}_l^{\,s/r}\left[\frac{C_{p,l}(T_s-T_{sat})}{h_{fg}}\right] \tag{5}$$

$$Nu = \frac{1}{C_{sf}}\mathrm{Re}^{(1-n)}\mathrm{Pr}_l^{\,-m} \tag{6}$$

$$h = \left(\frac{1}{C_{sf}}\right)\left[\frac{C_{p,l}q}{h_{fg}}\right]\left[\frac{q}{\mu_l h_{fg}}\left(\frac{\sigma}{g(\rho_l-\rho_v)}\right)^{1/2}\right]^{-n}\left[\frac{Cp_l\mu_l}{k_l}\right]^{-(m+1)} \tag{7}$$

Zhaohu et al., [16] developed some correlation structures similar with Eqs. (8) and (9) to investigate the nucleate pool boiling heat transfer coefficients of pure HFC134a, HC290, HC600a and their binary and ternary mixtures.

$$h = \frac{AP_c^{\,B}}{M^C T_c^{\,D}}(ER_a)^{F\left(1-\frac{P}{P_c}\right)}\frac{\left(\frac{P}{P_c}\right)^G}{\left[1-H\left(\frac{P}{P_c}\right)\right]^I}\mathrm{q}^J \tag{8}$$

$$h = A\mathrm{q}^B \tag{9}$$

It should be noted that Cornwell and Houston [17] developed convective type correlation for the nucleate pool boiling on horizontal tubes. Das et al., [18,19] benefitted from Cornwell and Houston [17]'s correlation to determine pool boiling characteristics of nanofluids and developed correlations for the smooth and rough surfaces and also various nanoparticles concentrations separately.

3.4. Error analysis

The error analyses' calculation procedure for the average values of the experimental and calculated results regarding with R square error, proportional error and Mean square error (MSE) can be seen from authors' previous publication [9].

4. Results and discussion

The experiments of the present study were done at the Fluid Mechanics, Thermal Engineering and Multiphase Flow Research Lab. (FUTURE) in KMUTT for the determination of heat transfer

Author's personal copy

enhancement during pool boiling of nanofluids. The heat transfer enhancement obtained by the use of nanoparticles, pool boiling curve in the form of relationships between heat flux and $T_s - T_{sat}$ and in the form of relationships between heat flux and heat transfer coefficient can be seen from Suriyawong and Wongwises [7]. This numerical research studied the heat transfer characteristic of nucleate pool boiling at atmospheric pressure using distilled water and TiO_2–water nanofluids at various concentration levels as working fluids by means of various methods of Artificial Neural Networks. Special attention was paid on the accuracy of the measurements during experiments as can be seen from authors' previous publications on two-phase flow in the literature. Discussion of the results will be given in turn as follows:

Numerical analysis of artificial intelligence includes 7 dimensional input parameters, such as thermal conductivity (k, W m^{-1} K^{-1}), particle size (nm), density (ρ, kg m^{-3}), dynamic viscosity (μ, kg m^{-1} s^{-1}), specific heat at constant pressure, (C_p, kJ kg^{-1} K^{-1}), roughness of heating surface (Ra, μm) and wall superheat ($\Delta T = T_s - T_{sat}$), and 1 dimensionless input parameter of nanoparticle concentration (%), 2 dimensional output parameters such as pool boiling heat transfer coefficient (h, kW m^{-2} K^{-1}) and heat flux (q, kW m^{-2}).

Regarding the elimination process of several artificial neural network (ANN) methods such as multi-layer perceptron (MLP), radial basis networks (RBF) and generalized regression neural network (GRNN), train and test sets are determined by the way of 4-fold cross validation. According to 4-fold cross validation, all data points are divided into 4 different sets randomly. The first set is determined as test and the others are determined as train set. After this iteration the second set is determined test and the other is train too. Hence all individual sets are determined test receptively. At the train section, %20 of train data is selected as validation set to prevent over-fitting. The best value of ANNs control parameters is determined using 4-fold cross validation in training phase.

During the calculation process of pool boiling heat transfer coefficient and heat flux, the most agreeable multi-layer perceptron (MLP) has 2 hidden layers. First hidden layer has 20 neurons and second hidden layer has 10 neurons. The most agreeable spread numbers (s_p) were found as 1000 and hidden layers neurons were 80 for the radial basis function networks (RBF). The most agreeable spread numbers (s_p) were found as 0.7 for the generalized regression neural networks (GRNN). Table 1 shows the best predictive method for the pool boiling heat transfer coefficient and heat flux accurately according to the their low average values of all test points' results using several error analysis methods. According to Table 1, the method of multi-layer perceptron (MLP) for the heat flux and the method of generalized regression neural network (GRNN) were found as the most predictive methods with their higher R^2 values than others.

Table 1
Elimination of ANN methods according to the error rates for the determination of heat flux and pool boiling heat transfer coefficient.

Output 1 – q (kW m^{-2})			
ANN Methods	Error Analysis		
	R square	Proportional (%)	Square law
MLP	0.916	23.2994	6251.2506
GRNN	0.8846	23.3829	8543.5481
RBF	0.8989	37.8096	7401.877
Output 2 – h (kW m^{-2} K^{-1})			
ANN Methods	Error Analysis		
	R square	Proportional (%)	Square law
MLP	0.8638	23.9805	28.1906
GRNN	0.8795	19.3751	23.3867
RBF	0.8472	24.05128	29.2348

The performance comparisons of the investigated ANN methods were shown in Figs. 1–3 for the heat flux and in Figs. 4–6 for the pool boiling heat transfer coefficient regarding the surface roughness of the heater separately. From these figures, all tested ANN methods seem to have similar results with each other by means of satisfactory results with their deviations within the range of ±30% for the estimated pool boiling heat transfer coefficient and the estimated heat flux, respectively.

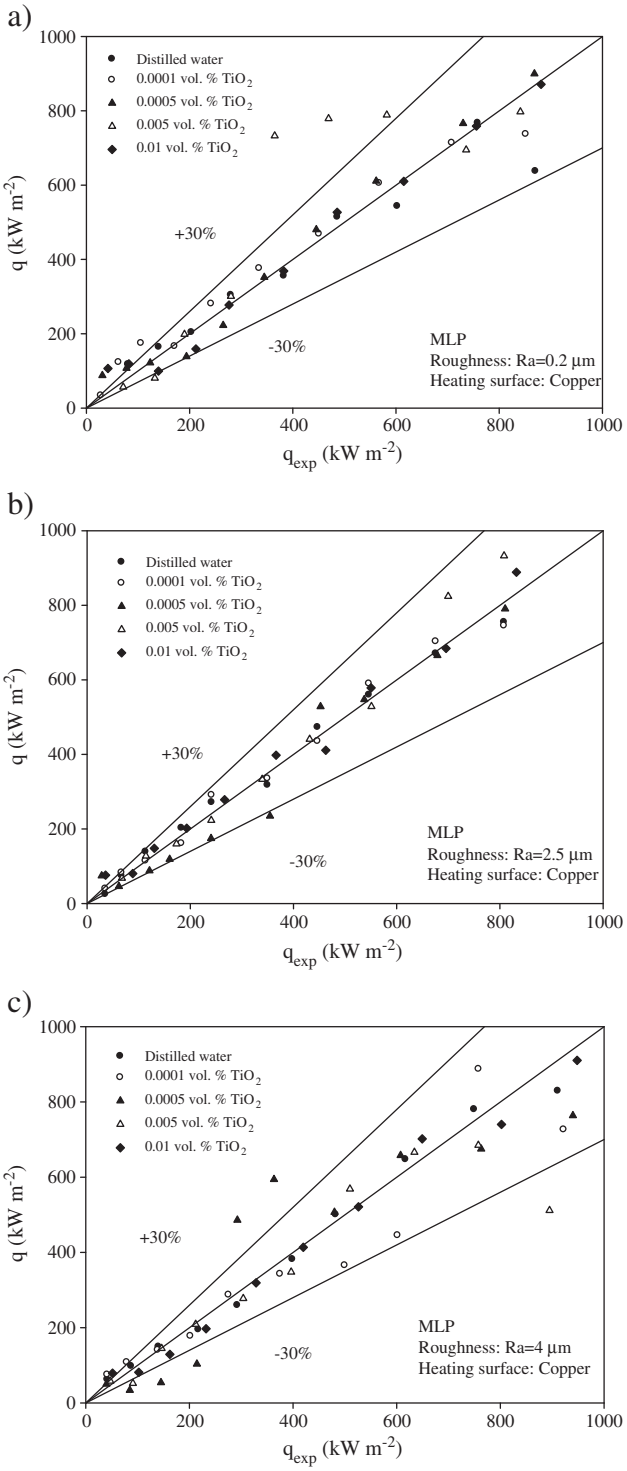

Fig. 1. Comparison of experimental and numerical heat fluxes obtained from artificial neural network prediction method of MLP for the various surface roughness values of heater.

Author's personal copy

Table 2 shows the most predictive combinations of input parameters, whose deviations are quite low, according to the error rates for the determination of pool boiling heat transfer coefficient (h) and heat flux (q) using the method of multi-layer perceptron (MLP) with 10-20-1 architecture which was found as the most successful architecture as a results of the analyses. They also show the dependency of the each input parameters on the outputs of the study separately according to the error rates of the test group of ANN, as a result of

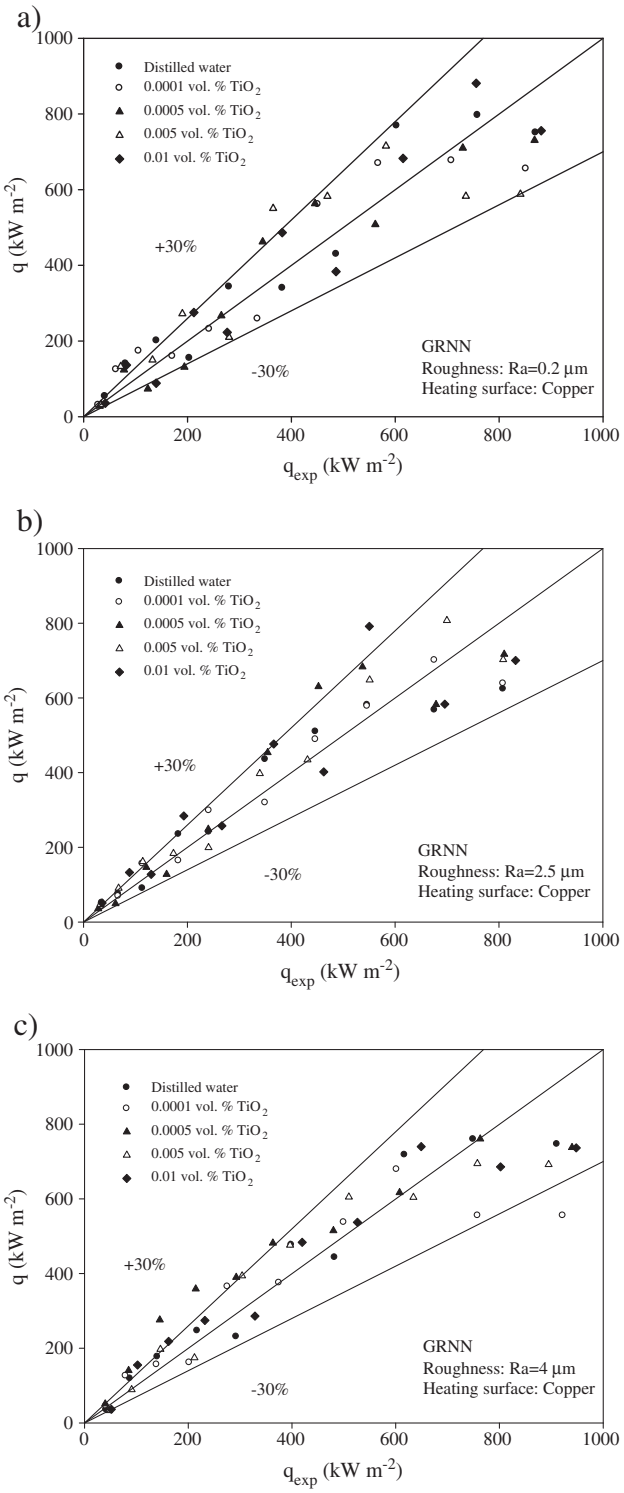

Fig. 2. Comparison of experimental and numerical heat fluxes obtained from artificial neural network prediction method of GRNN for the various surface roughness values of heater.

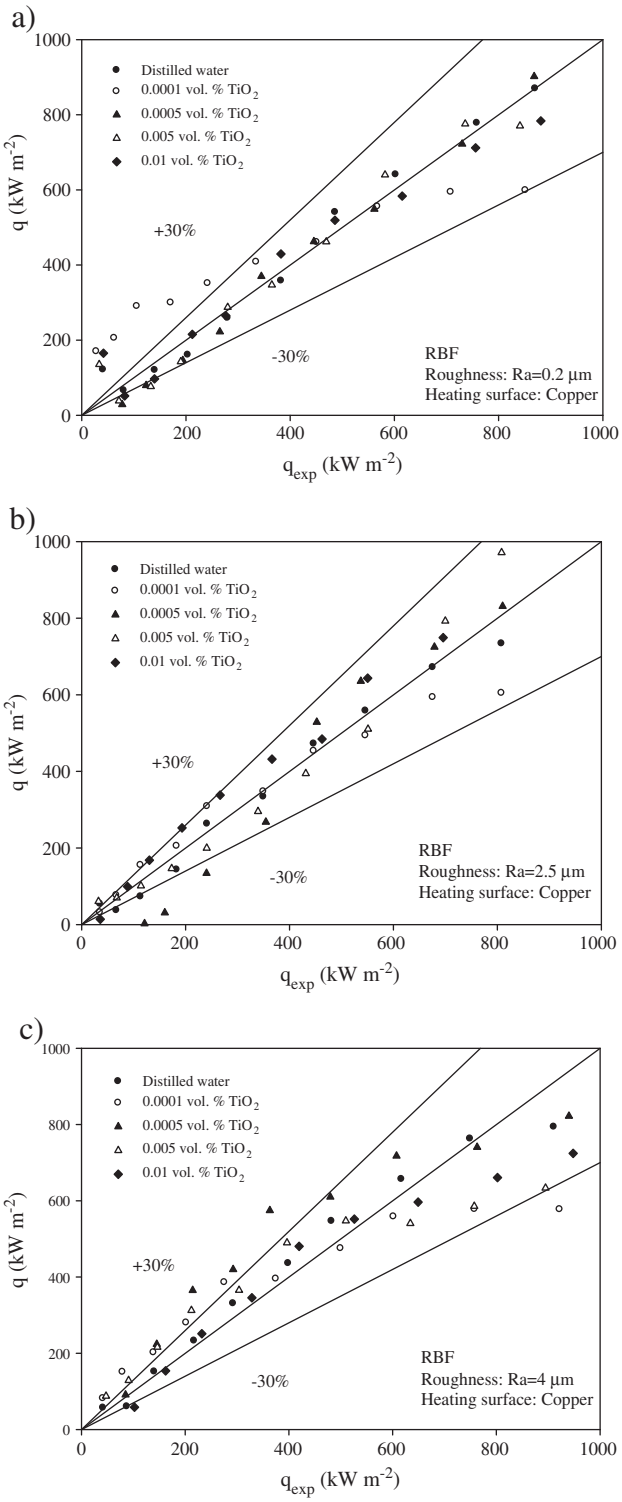

Fig. 3. Comparison of experimental and numerical heat fluxes obtained from artificial neural network prediction method of RBF for the various surface roughness values of heater.

the most predictive ANN method of the MLP 10-20-1 architecture for the operating conditions shown in all figures. The input parameters are shown with numbers in this table as follows: thermal conductivity (I), particle size (II), liquid density of the fluid (III), liquid dynamic viscosity (IV), liquid specific heat at constant pressure (V), roughness of heating surface (VI), nanoparticle concentration (VII) and wall superheat (VIII). When the input parameter number is 1, wall superheat (VIII) seems to be the most dominant parameter on

Author's personal copy

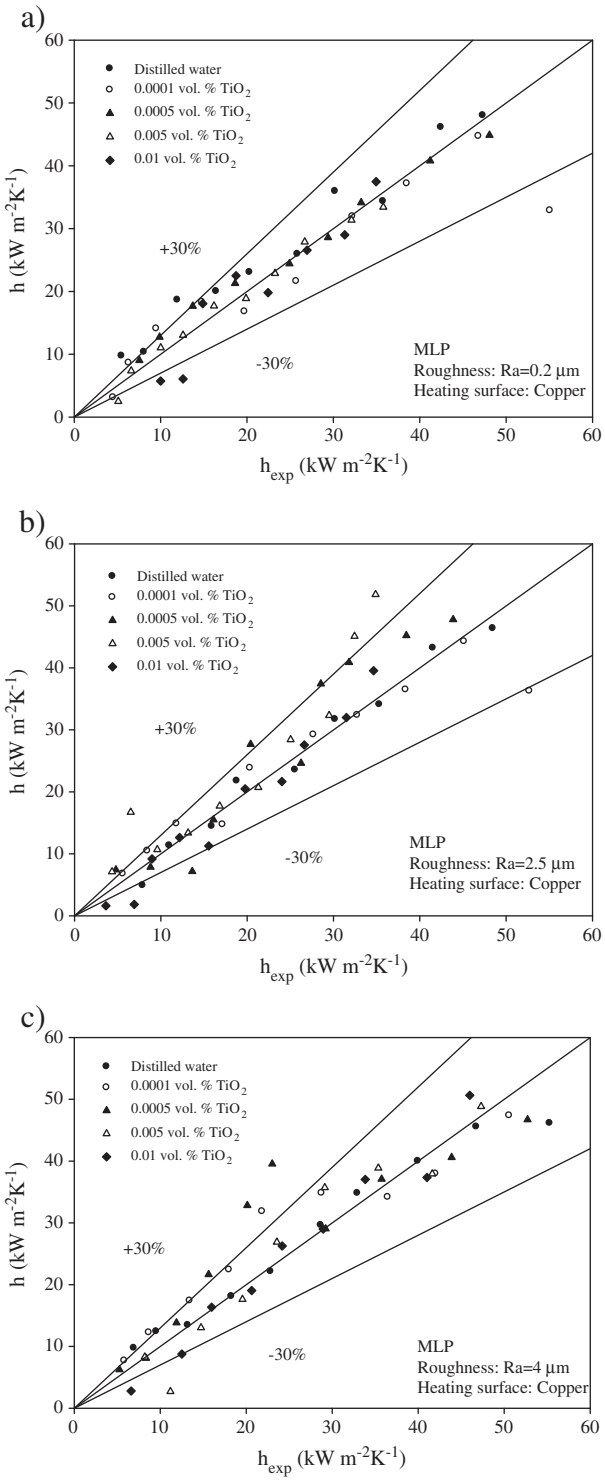

Fig. 4. Comparison of experimental and numerical pool boiling heat transfer coefficients obtained from artificial neural network prediction method of MLP for the various surface roughness values of heater.

the prediction of pool boiling heat flux and heat transfer coefficient with the deviations of 0.6087% and 50.85% in Table 2 respectively. When the input parameter number is 3, liquid dynamic viscosity (IV), roughness of heating surface (VI) and wall superheat (VIII) seem to be dominant on the prediction of heat flux with the deviation of 0.8474% and liquid density of the fluid (III), nanoparticle concentration (VII) and wall superheat (VIII) have the success on the heat transfer coefficient with the deviation of 0.7827% in Table 2. It shows that the accuracy of the estimated output values by means of input values increases with increasing added proper input parameters due to the result of the learning process of the artificial intelligence. As a result, it is possible to derive many results from this table on the input combinations' performance.

The correlation development study's results are shown in Table 3 and also in Fig. 7. The main frames of the proposed correlations are shown from Eqs. (4)–(9), which have many possible dominant parameters on the pool boiling heat transfer coefficient. Artificial

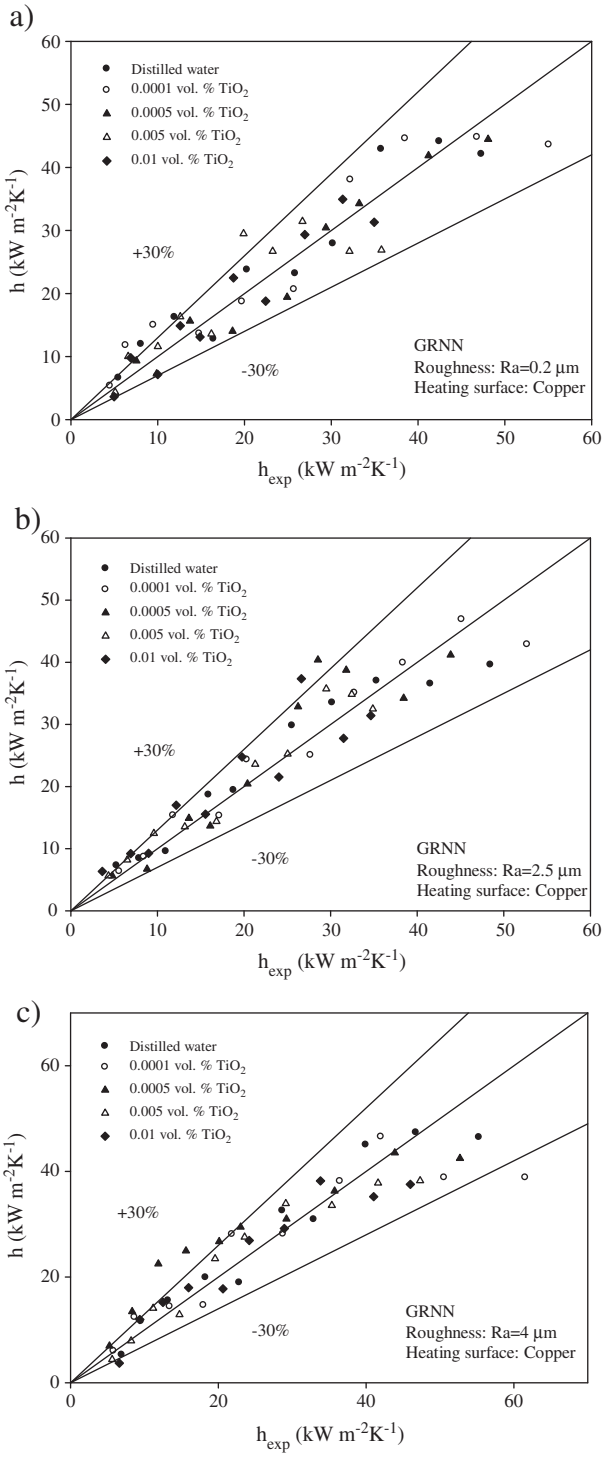

Fig. 5. Comparison of experimental and numerical pool boiling heat transfer coefficients obtained from artificial neural network prediction method of GRNN for the various surface roughness values of heater.

Author's personal copy

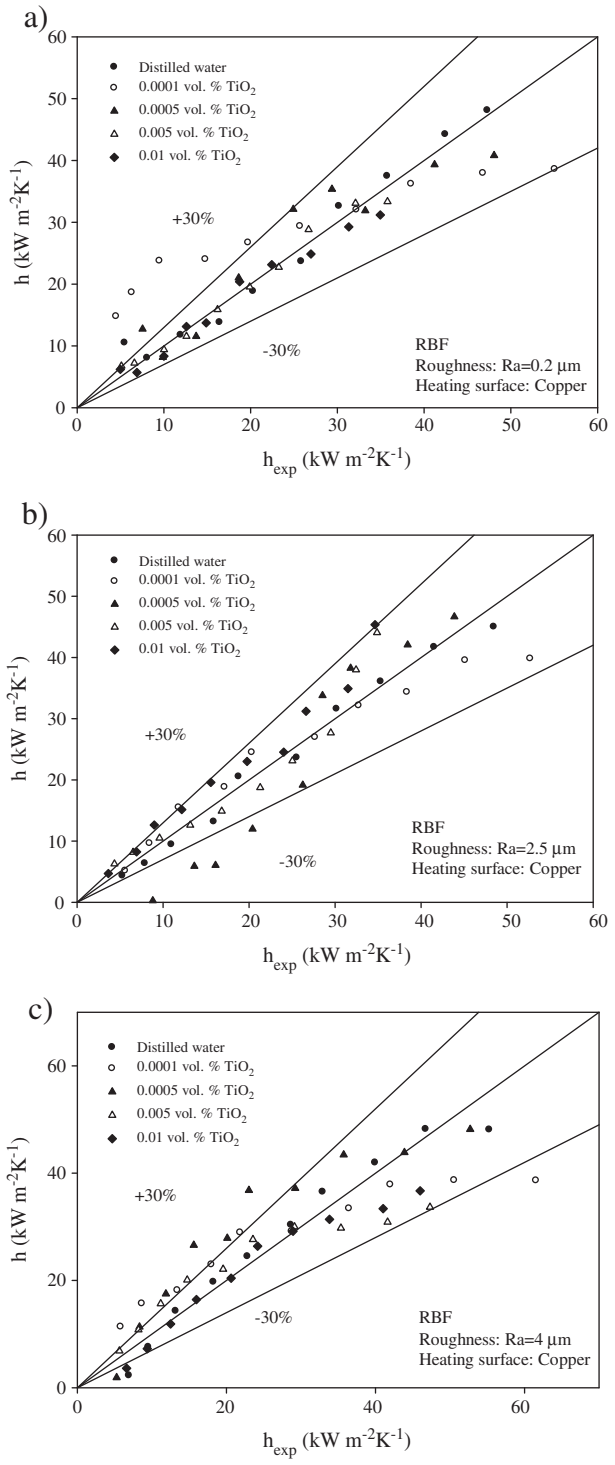

Fig. 6. Comparison of experimental and numerical pool boiling heat transfer coefficients obtained from artificial neural network prediction method of MLP for the various surface roughness values of heater.

intelligence decided the coefficients of these significant parameters step by step in Table 3 and their error rates can be seen in the same Table. All of the data obtained from the optimization methods of pool boiling heat transfer coefficient fall between the deviations of ± 30% in Table 3. It can be seen that Eq. (7) has the best proposed correlation formula by means of NLS method of optimization analyses according to all error criteria calculated by Eqs. (10)–(12) on the prediction of the pool boiling heat transfer coefficient and its results are shown in Fig. 7. It should be noted that measured heat flux is used in Eqs. (7) and (9).

Table 2
Dependency analyses regarding with the inputs on the output as heat flux of the artificial neural networks.

INPUTS								Input Number	OUTPUTS
I	II	III	IV	V	VI	VII	VIII		R^2 – q
							X	1	0.6087
					X		X	2	0.6328
			X		X		X	3	0.8474
X			X		X		X	4	0.8970
X			X		X	X	X	5	0.8992
X		X	X		X	X	X	6	0.9122
X	X	X	X		X	X	X	7	0.9152
X	X	X	X	X	X	X	X	8	0.9160
I	II	III	IV	V	VI	VII	VIII	Input Number	R^2 – h
							X	1	0.5085
						X	X	2	0.5190
		X				X	X	3	0.7827
		X		X		X	X	4	0.7842
X		X		X		X	X	5	0.7958
X		X	X	X		X	X	6	0.8082
X		X	X	X	X	X	X	7	0.8223
X	X	X	X	X	X	X	X	8	0.8795

5. Conclusion

The numerical pool boiling heat transfer coefficient and heat flux values with the measured values by means of artificial intelligence methods were compared in this paper. It should be noted that there is no research on the content of this paper considering its parameters in current literature. For that reason, the results of this study are expected to fill this gap in the literature.

The artificial neural network (ANN) methods of multi-layer perceptron (MLP), radial basis networks (RBF) and the generalized regression neural network (GRNN) are found to be capable of predicting the heat transfer coefficient and heat flux for the pool boiling of water–TiO_2 nano-fluid within the range of ± 30% and also within the slightly small error rates.

The performance of the method of multi-layer perceptron (MLP), radial basis function networks (RBF) and the generalized regression neural network (GRNN) on the correlation development have the similar and satisfactory results with their deviations with the average R^2 values about 92% for the estimated pool boiling heat transfer coefficient using the artificial neural network methods of unconstrained nonlinear minimization Nelder–Mead algorithm (NM) and the nonlinear least squares algorithm (NLS). It should be noted that these artificial intelligence methods have better results on the prediction of pool boiling heat transfer coefficient and heat flux than the empirical models and correlations proposed in the authors' previous publications.

Pool boiling heat flux of nano-fluid in the paper are found to be dependent on the nano-liquid dynamic viscosity (IV), roughness of heating surface (VI) and wall superheat (VIII) while liquid density of the fluid (III), nanoparticle concentration (VII) and wall superheat (VIII) are for the pool boiling heat transfer coefficient strongly according to the results of analysis.

Acknowledgements

The second author wishes to thank King Mongkut's University of Technology Thonburi for providing him with a Post-doctoral fellowship. The third, fourth and fifth authors wish to thank the Thailand Research Fund, the Office of Higher Education Commission and the National Research University Project for financial support.

Author's personal copy

Table 3
Error rates for the correlation development study.

Optimization methods	Proposed Correlations	Error Analysis		
		R square	Proportional (%)	Square law
NM	$h = \left(\frac{1}{45.49}\right)\left[\frac{C_{pl}q}{h_{fg}}\right]\left[\frac{q}{\mu_l h_{fg}}\left(\frac{\sigma}{g(\rho_l-\rho_v)}\right)^{1/2}\right]^{-0.2445}\left[\frac{Cp_l\mu_l}{k_l}\right]^{-1.179}$	0.9294	11.9546	13.5719
NLS	$h = \left(\frac{1}{7741.22}\right)\left[\frac{C_{pl}q}{h_{fg}}\right]\left[\frac{q}{\mu_l h_{fg}}\left(\frac{\sigma}{g(\rho_l-\rho_v)}\right)^{1/2}\right]^{-0.248}\left[\frac{Cp_l\mu_l}{k_l}\right]^{-1.989}$	0.938	11.1037	11.8737
NM	$h = \frac{1.1132P_c^{0.24}}{M^{0.312}T_c^{0.417}}(0.478R_a)^{0.03\left(1-\frac{p}{p_c}\right)}\frac{\left(\frac{p}{p_c}\right)^{0.318}}{\left[1-0.61\left(\frac{p}{p_c}\right)\right]^{-0.012}}q^{0.737}$	0.9258	12.6739	14.1924
NLS	$h = \frac{0.544P_c^{0.411}}{M^{0.817}T_c^{0.747}}(0.716R_a)^{0.03\left(1-\frac{p}{p_c}\right)}\frac{\left(\frac{p}{p_c}\right)^{0.058}}{\left[1-0.629\left(\frac{p}{p_c}\right)\right]^{-0.849}}q^{0.737}$	0.9258	12.6739	14.1924
NM-NLS	$h = 0.311q^{0.738}$	0.92	12.4595	15.3066

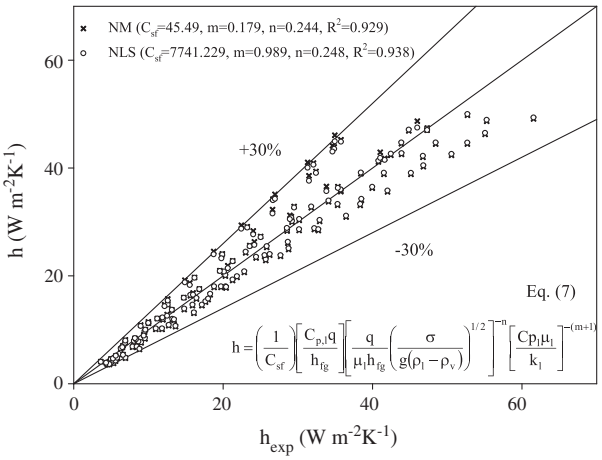

Fig. 7. Comparisons of experimental convective heat transfer coefficients with the most predictive proposed correlation obtained from optimization methods using 150 number of experimental data points.

References

[1] M.K. Das, N. Kishor, Adaptive fuzzy model identification to predict the heat transfer coefficient in pool boiling of distilled water, Expert Systems with Applications 36 (2009) 1142–1154.

[2] T. Liu, X. Sun, X. Li, H. Wang, Neural network analysis of boiling heat transfer enhancement using additives, International Journal of Heat and Mass Transfer 45 (2002) 5083–5089.

[3] G. Scalabrin, M. Condosta, P. Marchi, Modeling flow boiling heat transfer of pure fluids through artificial neural networks, International Journal of Thermal Sciences 45 (2006) 643–663.

[4] G. Scalabrin, M. Condosta, P. Marchi, Mixtures flow boiling: modeling heat transfer through artificial neural networks, International Journal of Thermal Sciences 45 (2006) 664–680.

[5] W.J. Wang, L.X. Zhao, C.L. Zhang, Generalized neural network correlation for flow boiling heat transfer of R22 and its alternative refrigerants inside horizontal smooth tubes, International Journal of Heat and Mass Transfer 49 (2006) 2458–2465.

[6] K.E. Gungor, R.H.S. Winterton, A general correlation for flow boiling in tubes and annuli, International Journal of Heat Mass Transfer 29 (1986) 351–358.

[7] A. Suriyawong, S. Wongwises, Nucleate pool boiling heat transfer characteristics of TiO_2–water nanofluids at very low concentrations, Experimental Thermal and Fluid Science 34 (2010) 992–999.

[8] V. Trisaksri, S. Wongwises, Nucleate pool boiling heat transfer of TiO_2–R141b nanofluids, International Journal of Heat and Mass Transfer 52 (2009) 1582–1588.

[9] M. Balcilar, A.S. Dalkilic, S. Wongwises, Artificial neural network (ANN) techniques for the determination of condensation heat transfer characteristics during downward annular flow of R134a inside a vertical smooth tube, International Communications in Heat and Mass Transfer 38 (2011) 75–84.

[10] J.A. Nelder, R. Mead, A simplex method for function minimization, Computer Journal 7 (1965) 308–313.

[11] M. Balcilar, A.S. Dalkilic, B. Bolat, S. Wongwises, Investigation of empirical correlations on the determination of condensation heat transfer characteristics using computational numerical methods during downward annular flow of R134a inside a vertical smooth tube, Journal of Mechanical Science and Technology 25 (2011) 1–20.

[12] W.M. Rhosenow, A method of correlating heat transfer data for surface boiling of liquids, Transactions of ASME 74 (1952) 969–975.

[13] G.P. Narayan, K.B. Anoop, G. Sateesh, S.K. Das, Effect of surface orientation on pool boiling heat transfer of nanoparticle suspensions, International Journal of Multiphase Flow 34 (2008) 145–160.

[14] R.A. Taylor, P.E. Phelan, Pool boiling of nanofluids: comprehensive review of existing data and limited new data, International Journal of Heat and Mass Transfer 52 (2009) 5339–5347.

[15] I.C. Bang, S.H. Chang, Boiling heat transfer performance and phenomena of Al_2O_3–water nano-fluids from a plain surface in a pool, International Journal of Heat and Mass Transfer 48 (2005) 2407–2419.

[16] S. Zhaohu, G. Maoqiong, L. Zhijian, W. Jianfeng, Nucleate pool boiling heat transfer coefficients of pure HFC134a, HC290, HC600a and their binary and ternary mixtures, International Journal of Heat and Mass Transfer 50 (2007) 94–104.

[17] K. Cornwell, S.D. Houston, Nucleate pool boiling on horizontal tubes: a convection-based correlation, International Journal of Heat Mass Transfer 37 (1994) 303–309.

[18] S.K. Das, N. Putra, W. Roetzel, Pool boiling characteristics of nano-fluids, International Journal of Heat and Mass Transfer 46 (2003) 851–862.

[19] S.K. Das, N. Putra, W. Roetzel, Pool boiling of nano-fluids on horizontal narrow tubes, International Journal of Multiphase Flow 29 (2003) 1237–1247.

International Journal of Heat and Mass Transfer 55 (2012) 3138–3146

Contents lists available at SciVerse ScienceDirect

International Journal of Heat and Mass Transfer

journal homepage: www.elsevier.com/locate/ijhmt

A dispersion model for predicting the heat transfer performance of TiO_2–water nanofluids under a laminar flow regime

Weerapun Duangthongsuk [a,b], Somchai Wongwises [b,c,*]

[a] Department of Mechanical Engineering, South-East Asia University, Bangkok, Thailand
[b] Fluid Mechanics, Thermal Engineering and Multiphase Flow Research Laboratory (FUTURE), Department of Mechanical Engineering, King Mongkut's University of Technology Thonburi, Bangmod, Bangkok 10140, Thailand
[c] The Academy of Science, The Royal Institute of Thailand, Sanam Suea Pa, Dusit, Bangkok 10300, Thailand

ARTICLE INFO

Article history:
Received 22 April 2011
Received in revised form 3 February 2012
Accepted 3 February 2012
Available online 22 March 2012

Keywords:
Nanofluids
Heat transfer performance
Thermal conductivity
Dispersion model

ABSTRACT

Nanofluids are a suspension of particles with ultrafine size in a conventional base fluid that increases the heat transfer performance of the original base fluid. They show higher thermal performance than base fluids especially in terms of the thermal conductivity and heat transfer coefficient. During the last decade, many studies have been carried out on the heat transfer and flow characteristics of nanofluids, both experimentally and theoretically. The purpose of this article is to propose a dispersion model for predicting the heat transfer coefficient of nanofluids under laminar flow conditions. TiO_2 nanoparticles dispersed in water with various volume fractions and flowing in a horizontal straight tube under constant wall heat flux were used. In addition, the predicted values were compared with the experimental data from He et al. [14]. In the present study, the results show that the proposed model can be used to predict the heat transfer behaviour of nanofluids with reasonable accuracy. Moreover, the results also indicate that the predicted values of the heat transfer coefficient obtained from the present model differ from those obtained by using the Li and Xuan equation by about 3.5% at a particle volume fraction of 2.0%.

© 2012 Elsevier Ltd. All rights reserved.

1. Introduction

Conventional heat transfer fluids such as oil, water and ethylene glycol have inherently poor thermal properties. Thus, over the past ten years, many researchers have attempted to rectify the poor heat transfer properties of these fluids, in particular their thermal conductivity. In general, solids have several hundred-fold greater thermal conductivity than common fluids. In order to overcome this problem, ultrafine solid particles can be suspended in base fluids to increase their thermal performance. The earliest studies of the thermal performance of liquids with a nanoparticle suspension were reported by Masuda et al. [1] in 1993. However, the term nanofluids was introduced by Choi [2] in 1995, and subsequently gained popularity. Nanofluids were expected to be ideally suited for practical application because they have a substantially higher thermal conductivity and convective heat transfer coefficient relative to the base fluids.

Over the past decade, many researchers have reported the heat transfer and flow behaviour of various types of nanofluids, especially their thermal conductivity and heat transfer coefficient. A number of researchers have attempted to investigate the thermal behaviour of nanofluids both theoretically and experimentally. The available literature with respect to the heat transfer performance and flow characteristics of nanofluids is summarized elsewhere [3–5]. However, such reviews are not up to date. Recent papers dealing with the heat transfer and flow features of nanofluids both experimentally and theoretically are summarized below.

He et al. [6] experimentally studied the heat transfer and flow behaviours of TiO_2–distilled water nanofluids flowing through a vertical pipe in an upward direction under a constant heat flux in both a laminar and a turbulent flow regime. The experimental results showed that the local heat transfer coefficient increased with increasing particle concentration in both laminar and turbulent flow regimes in a given condition. They also showed that the pressure drop of the nanofluids was similar to that of the base fluid.

Nguyen et al. [7] experimentally investigated the heat transfer coefficient of an Al_2O_3–water nanofluid flowing through a small liquid cooling system of microprocessors under a turbulent flow regime. The results showed a much higher heat transfer coefficient for nanofluids than for the base liquid, with a nanofluid with a 36 nm particle diameter giving a higher heat transfer coefficient than that with a 47 nm particle diameter.

* Corresponding author at: Fluid Mechanics, Thermal Engineering and Multiphase Flow Research Laboratory (FUTURE), Department of Mechanical Engineering, King Mongkut's University of Technology Thonburi, Bangmod, Bangkok 10140, Thailand. Tel: +662 470 9115; fax: +662 470 9111.
E-mail address: somchai.won@kmutt.ac.th (S. Wongwises).

0017-9310/$ - see front matter © 2012 Elsevier Ltd. All rights reserved.
doi:10.1016/j.ijheatmasstransfer.2012.02.016

Nomenclature

C_p	specific heat, J/kgK
d	nanoparticle diameter, m
D	tube diameter, m
h	heat transfer coefficient, W/m^{2}K
k	thermal conductivity, W/mK
L	length of the test tube, m
Nu	Nusselt number
Pe	Peclet number
Pr	Prandtl number
q	heat flux, W/m^2
R	tube radius, m
Re	Reynolds number
T	temperature, K
u	mean velocity, m/s

Greek symbols

β	dispersion coefficient, W/mK
ϕ	volume fraction
κ_B	Boltzmann constant (1.3807×10^{-23} m^2 kg/ s^{2}K)
ρ	density, kg/m^3
α	thermal diffusivity, m^2/s
μ	viscosity, kg/ms

Subscript

ave	average
o	inlet
p	particles
nf	nanofluid
w	water or wall

Ko et al. [8] reported on an experiment in which the viscosity and pressure drop of CNT nanoparticles was dispersed in distilled water flowing through a horizontal tube. The effect of the CNT concentrations and preparation methods on the viscosity of nanofluids was also reported. Under laminar flow conditions, the results indicated that the nanofluids had larger friction factors than the base fluid. In contrast, under turbulent flow conditions, the friction factor of the nanofluids was very close to that of the base fluids.

Chein and Chuang [9] reported the performance of the microchannel heat sink (MCHS) using CuO–water nanofluids as coolants. At a low flow rate, the experimental results showed that nanofluids absorbed more energy than the base fluid. However, there was no contribution from heat absorption when the flow rate was high.

Duangthongsuk and Wongwises [10,11] studied the effect of thermophysical properties on the prediction of the heat transfer coefficient and also reported the heat transfer performance and friction characteristics of a TiO_2–water nanofluid. The results indicated that a number of thermophysical models have an insignificant effect on the calculated Nusselt number of the nanofluid. Moreover, the results also showed that the presence of nanoparticles leads to a higher heat transfer coefficient than that of water and that the pressure drop of the nanofluid is similar to that of the base fluid.

Nguyen et al. [12] studied the heat transfer performance of Al_2O_3–water nanofluids in a confined and submerged jet impinging on a horizontal and circular heated surface. The experimental results indicated that nanofluids with high particle fractions (6.0 vol.% and even 2.8 vol.%) do not seem to be appropriate for heat transfer enhancement purposes under such a configuration. Moreover, their results also showed that the use of nanofluids does not increase heat transfer, and in the worst cases, there was a clear decrease in the heat transfer coefficient. Thus, the use of nanofluids does not always guarantee enhancement of heat transfer.

Izadi et al. [13] numerically investigated the hydrodynamics and thermal behaviours of an Al_2O_3–water nanofluid flowing through an annulus under a laminar flow regime, using a single-phase model. The numerical results showed that the convective heat transfer coefficient increased with increasing particle concentration. Moreover, the results also indicated that the particle volume concentration has no significant effect on the dimensionless axial velocity, but does affect the temperature profile.

He et al. [14] numerically studied the convective heat transfer of a nanofluid with TiO_2 nanoparticles dispersed in water under laminar flow conditions. A single-phase model and combined Euler and Lagrange method (Discrete method) were used to determine the effects of volume concentrations, Reynolds number and aggregate sizes on the convective heat transfer and flow behaviour of the nanofluid. Their results indicated that the nanofluid significantly enhanced the Nusselt number, especially in the entrance region. Moreover, the numerical results were consistent with experimental data.

Bianco et al. [15] numerically investigated the heat transfer performance of an Al_2O_3–water nanofluid flowing through a circular tube under a laminar flow regime. A single-phase model and two-phase model were employed to describe the heat transfer coefficient of the nanofluid. The results showed that the heat transfer coefficient increased with increasing particle volume fraction as well as Reynolds number and was higher than that of the base fluid. Moreover, there was an approximately 11% difference in the average heat transfer coefficient between the single-phase and two-phase model.

Kumar et al. [16] used a single-phase thermal dispersion model to analyse the thermal properties and flow field of a nanofluid numerically. The results showed that suspended nanoparticles increased the heat capacity and surface area of the conventional base liquid, which led to an increase in the Nusselt number, especially at high volume fractions.

The review of literature shown above includes all studies of nanofluids flowing in channels, both experimental and theoretical. However, most of the models used involved commercial software and few compared the simulation results with the experimental data. In the present study, main concern is to develop a mathematical model to describe the convective heat transfer characteristics of nanofluids under a laminar flow conditions, and then compare the results with experimental data. This dispersion model is different from that proposed by He et al. [14] which is based on single phase method and combined Euler and Lagrange method.

2. Mathematical model and data reduction

2.1. Mathematical model

There are two different approaches to analysing the heat transfer enhancement of nanofluids. One is the two-phase model and the other is the single-phase model. Although the former describes the functions of both the liquid phase and solid phase in the heat transfer process, it requires a long time for computation and a high performance computer. The second model, assuming that both the liquid and particle phases are in thermal equilibrium and flow at the same velocity, is simpler and requires less computation time. However, although the behaviour of a nanofluid is more similar to a liquid than solid–liquid mixtures, several factors such as gravity, Brownian forces, friction between the liquid and solid particles, sedimentation and dispersion may coexist in the main flow of

nanofluids. So, this means that the slip velocity between the fluid and solid particles may not be zero and random movement of the particles in the main flow must be taken into account [17]. This model was first introduced by Taylor [18] in 1953. However, Xuan and Li [17] were the first to apply this model to describing the heat transfer characteristics of nanofluids under constant wall temperature boundary conditions. As mentioned above, the purpose of this work was to use the modified single-phase model (Dispersion model) to investigate the heat transfer performance of nanofluids flowing through a horizontal tube under a laminar flow regime and constant wall heat flux boundary conditions. On the basis of this model, the governing equation under steady state conditions and a negligible axial temperature gradient is as follows:

$$u\frac{\partial T}{\partial x}=\frac{1}{r}\frac{\partial}{\partial r}\left[\alpha_{nf}+\frac{\beta}{(\rho Cp)_{nf}}\right]r\frac{\partial T}{\partial r} \tag{1}$$

where u is the velocity of nanofluid which is assumed constant along the test section, α_{nf} is the thermal diffusivity of the nanofluid, and β is the thermal dispersion coefficient, which considers the contribution of hydrodynamic dispersion and the irregular movement of the ultra-fine particles.

Unfortunately, to date, there has been no theoretical or experimental work on the dispersion coefficient of nanofluids. However, the dispersion coefficient (β) appearing in Eq. (1) can be calculated by Einstein–Strokes's equation, which was introduced by Buongiorno [19]. The form of this equation is as follows:

$$\beta=\frac{\kappa_B T_{nf}}{3\pi\mu_{nf}d_P} \tag{2}$$

in which κ_B is Boltzmann's constant (1.3807×10^{-23} m^2 kg/s^{2}K) and d_P is the nanoparticle diameter (m). In general, the dispersion coefficient for water-based nanofluids at room temperature ranges between 4×10^{-10} to 4×10^{-12} m^2/s [19].

In order to find the solution for Eq. (1), the following boundary conditions are required:

$$T=T(r,x)$$
$$T(r,0)=T_0 \tag{3}$$
$$\frac{\partial T}{\partial r}(0,x)=0 \tag{4}$$
$$\frac{\partial T}{\partial r}(r,x)=\frac{q_w}{k} \tag{5}$$

where T_0 is the inlet temperature of fluid (K), q_w is the wall heat flux and k is the thermal conductivity of the nanofluid.

Applying the following dimensionless parameters

$$\theta=\frac{T-T_0}{T_w-T_0} \tag{6}$$
$$\bar{r}=r/R \quad \text{and} \quad \bar{x}=x/L \tag{7}$$

and rearranging the left-hand side and right-hand side of Eq. (1), we obtain the following expressions:

$$u\frac{\partial T}{\partial x}=\frac{u(T_w-T_0)}{L}\frac{\partial\theta}{\partial\bar{x}} \tag{8}$$

and

$$\frac{1}{r}\frac{\partial}{\partial r}\left[\frac{k^*_{eff}}{\rho Cp}\right]r\frac{\partial T}{\partial r}=\frac{1}{R^2\bar{r}}\frac{\partial}{\partial\bar{r}}\left[\frac{k^*_{eff}}{\rho Cp}\bar{r}(T_w-T_0)\frac{\partial\theta}{\partial\bar{r}}\right] \tag{9}$$

where $k^*_{eff}=\alpha_{nf}+\beta$

Substituting Eqs. (8) and (9) into Eq. (1) yields,

$$\frac{u(T_w-T_0)}{L}\frac{\partial\theta}{\partial\bar{x}}=\frac{1}{R^2\bar{r}}\frac{\partial}{\partial\bar{r}}\left[\frac{k^*_{eff}}{\rho Cp}\bar{r}(T_w-T_0)\frac{\partial\theta}{\partial\bar{r}}\right] \tag{10}$$

By rearranging Eq. (10), we obtain

$$\frac{u}{L}\frac{\partial\theta}{\partial\bar{x}}=\frac{1}{R^2\bar{r}}\frac{\partial}{\partial\bar{r}}\left[\frac{k^*_{eff}}{\rho Cp}\bar{r}\frac{\partial\theta}{\partial\bar{r}}\right] \tag{11}$$

Rearranging the above equation yields

$$\frac{uL}{L^2}\frac{\partial\theta}{\partial\bar{x}}=\frac{1}{R^2\bar{r}}\frac{k^*_{eff}}{\rho Cp}\frac{\partial}{\partial\bar{r}}\bar{r}\frac{\partial\theta}{\partial\bar{r}} \tag{12}$$

let

$$\frac{k^*_{eff}}{\rho Cp}=\alpha^*_{eff} \tag{13}$$

Substituting Eq. (13) into Eq. (12), we obtain

$$\frac{uL}{\alpha^*_{eff}}\frac{\partial\theta}{\partial\bar{x}}=\frac{L^2}{R^2\bar{r}}\frac{\partial}{\partial\bar{r}}\left[\bar{r}\frac{\partial\theta}{\partial\bar{r}}\right] \tag{14}$$

Let

$$\frac{uL}{\alpha^*_{eff}}=Pe^* \tag{15}$$

Substituting Eq. (15) into Eq. (14), yields

$$Pe^*\frac{R^2}{L^2}\frac{\partial\theta}{\partial\bar{x}}=\frac{1}{\bar{r}}\frac{\partial}{\partial\bar{r}}\left[\bar{r}\frac{\partial\theta}{\partial\bar{r}}\right] \tag{16}$$

let

$$Pe^*\frac{R^2}{L^2}=\overline{Pe} \tag{17}$$

Substituting the above equation into Eq. (16) yields

$$\overline{Pe}\frac{\partial\theta}{\partial\bar{x}}=\frac{1}{\bar{r}}\frac{\partial}{\partial\bar{r}}\left[\bar{r}\frac{\partial\theta}{\partial\bar{r}}\right] \tag{18}$$

Applying the separation method yields

$$\theta(\bar{r},\bar{x})=R_1(\bar{r})X_1(\bar{x})+R_2(\bar{r})+X_2(\bar{x}) \tag{19}$$

The new boundary conditions are expressed as follows:

$$\theta(\bar{r},0)=0 \tag{20}$$
$$\theta(0,\bar{x})=\text{finite} \tag{21}$$
$$\frac{\partial\theta}{\partial\bar{r}}(1,\bar{x})=1 \tag{22}$$

By rearranging Eq. (18), we obtain

$$\frac{\partial\theta}{\partial\bar{x}}=R_1\frac{dX_1}{d\bar{x}}+\frac{dX_2}{d\bar{x}} \tag{23}$$

and

$$\frac{\partial}{\partial\bar{r}}\bar{r}\frac{\partial\theta}{\partial\bar{r}}=\frac{d}{d\bar{r}}\bar{r}X_1\frac{dR_1}{d\bar{r}}+\frac{d}{d\bar{r}}\bar{r}\frac{dR_2}{d\bar{r}} \tag{24}$$

Substituting Eqs. (23) and (24) into Eq. (18), we obtain

$$\overline{Pe}\left[R_1\frac{dX_1}{d\bar{x}}+\frac{dX_2}{d\bar{x}}\right]=\frac{X_1}{\bar{r}}\frac{d}{d\bar{r}}\bar{r}\frac{dR_1}{d\bar{r}}+\frac{1}{\bar{r}}\frac{d}{d\bar{r}}\bar{r}\frac{dR_2}{d\bar{r}} \tag{25}$$

By arranging Eq. (25), we obtain

$$\overline{Pe}R_1\frac{dX_1}{d\bar{x}}=\frac{X_1}{\bar{r}}\frac{d}{d\bar{r}}\bar{r}\frac{dR_1}{d\bar{r}} \tag{26}$$

Rearranging again yields

$$\frac{\overline{Pe}}{X_1}\frac{dX_1}{d\bar{x}}=\frac{1}{R_1\bar{r}}\frac{d}{d\bar{r}}\bar{r}\frac{dR_1}{d\bar{r}}=-\lambda^2 \tag{27}$$

According to Eq. (27), rearranging yields

$$\frac{1}{R_1\bar{r}}\frac{d}{d\bar{r}}\bar{r}\frac{dR_1}{d\bar{r}}+\lambda^2=0$$

$$\frac{1}{R_1\bar{r}}\left[\bar{r}\frac{d^2R_1}{d\bar{r}^2}+\frac{dR_1}{d\bar{r}}\right]+\lambda^2=0$$

$$\frac{1}{R_1}\frac{d^2R_1}{d\bar{r}^2}+\frac{1}{R_1\bar{r}}\frac{dR_1}{d\bar{r}}+\lambda^2=0$$

$$\frac{d^2R_1}{d\bar{r}^2}+\frac{1}{\bar{r}}\frac{dR_1}{d\bar{r}}+\lambda^2R_1=0 \tag{28}$$

The general solution of the above equation is

$$R_1=C_1J_0(\lambda\bar{r})+C_2Y_0(\lambda\bar{r}) \tag{29}$$

The remaining term in Eq. (27) is

$$\frac{\overline{Pe}}{X_1}\frac{dX_1}{d\bar{x}}+\lambda^2=0$$

$$\frac{1}{X_1}dX_1+\frac{\lambda^2}{\overline{Pe}}d\bar{x}=0 \tag{30}$$

The general solution of this equation is

$$X_1=C_3e^{-\lambda^2\bar{x}/\overline{Pe}} \tag{31}$$

The remaining term in Eq. (25) is

$$\overline{Pe}\frac{dX_2}{d\bar{x}}=\frac{1}{\bar{r}}\frac{d}{d\bar{r}}\bar{r}\frac{dR_2}{d\bar{r}}=C_4 \tag{32}$$

$$X_2=\frac{C_4}{\overline{Pe}}\bar{x}+C_5 \tag{33}$$

and

$$R_2=\frac{C_4}{4}\bar{r}^2+C_5\ln\bar{r}+C_6 \tag{34}$$

Substituting Eq. (21) into Eq. (29), we obtain

$$R_1=C_1J_0(0)+C_2Y_0(0)$$
$$C_2=0$$

Substituting Eq. (21) into Eq. (34) yields

$$C_5=0$$

From the above expressions, Eq. (19) can be changed as follows:

$$\theta(\bar{r},\bar{x})=C_1C_3e^{-\lambda_n^2\bar{x}/\overline{Pe}}J_0(\lambda_n\bar{r})+\frac{C_4}{4}\bar{r}^2+C_6+\frac{C_4}{\overline{Pe}}\bar{x} \tag{35}$$

Substituting Eq. (20) into Eq. (35), we obtain

$$0=C_1C_3J_0(\lambda_n\bar{r})+\frac{C_4}{4}\bar{r}^2+C_6 \tag{36}$$

From the linearly independent relation, this yields

$$C_6=0$$

Differentiating Eq. (35) yields

$$\frac{\partial\theta}{\partial\bar{r}}=C_1C_3e^{-\lambda_n^2\bar{x}/\overline{Pe}}(-\lambda_n)J_1(\lambda_n\bar{r})+\frac{C_4}{2}\bar{r} \tag{37}$$

Substituting Eq. (22) into Eq. (37), we obtain

$$1=-\lambda_nC_1C_3e^{-\lambda_n^2\bar{x}/\overline{Pe}}J_1(\lambda_n)+\frac{C_4}{2}$$
$$C_4=2 \tag{38}$$

where λ_n are eigen values that are the positive roots of the $J_1(\lambda_n)=0$

Then, substituting $C_4=2$ into Eq. (36), we obtain

$$0=C_1C_3J_0(\lambda_n\bar{r})+\frac{\bar{r}^2}{2}$$
$$-\frac{\bar{r}^2}{2}=\sum_{n=0}^{\infty}C_nJ_0(\lambda_n\bar{r}) \tag{39}$$

Rearranging the above equation yields

$$-\frac{\bar{r}^2}{2}=C_0J_0(\lambda_n\bar{r})+\sum_{n=1}^{\infty}C_nJ_0(\lambda_n\bar{r}) \tag{40}$$

Considering a part of Eq. (40)

$$-\frac{\bar{r}^2}{2}=\sum_{n=1}^{\infty}C_nJ_0(\lambda_n\bar{r})$$

Multiplying the above equation by $\bar{r}J_0(\lambda_n\bar{r})d\bar{r}$ and then integrating from 0 to 1, yields

$$-\int_0^1\frac{\bar{r}^2}{2}\bar{r}J_0(\lambda_n\bar{r})d\bar{r}=\int_0^1\sum_{n=1}^{\infty}C_nJ_0(\lambda_n\bar{r})\bar{r}J_0(\lambda_n\bar{r})d\bar{r}$$
$$-\frac{1}{2}\int_0^1\bar{r}^2\bar{r}J_0(\lambda_n\bar{r})d\bar{r}=\frac{1}{2}\sum_{n=1}^{\infty}C_nJ_0^2(\lambda_n) \tag{41}$$

Taking the right-hand term of Eq. (41) into account and applying the method of bypass integration, we obtain

$$w=\bar{r}^2,\quad dw=2\bar{r}d\bar{r}\quad\text{and}\quad dv=\bar{r}J_0(\lambda_n\bar{r})d\bar{r}$$

This yields

$$v=\int dv=\int\bar{r}J_o(\lambda_n\bar{r})d\bar{r}=\frac{1}{\lambda_n}\int\lambda_n\bar{r}J_o(\lambda_n\bar{r})d\bar{r}=\frac{1}{\lambda_n}\bar{r}J_1(\lambda_n\bar{r})$$

Applying the relation $\int wdv=wv-\int vdw$ yields

$$\int_0^1\bar{r}^2\bar{r}J_0(\lambda_n\bar{r})d\bar{r}=\frac{\bar{r}}{\lambda_n}\bar{r}J_1(\lambda_n\bar{r})\Big|_0^1-\int_0^1\frac{\bar{r}}{\lambda_n}J_1(\lambda_n\bar{r})2\bar{r}d\bar{r}$$
$$=\frac{1}{\lambda_n}J_1(\lambda_n)-\frac{2}{\lambda_n^2}\int_0^1\lambda_n\bar{r}^2J_1(\lambda_n\bar{r})d\bar{r}$$
$$=-\frac{2}{\lambda_n^2}\bar{r}^2J_2(\lambda_n\bar{r})\Big|_0^1$$
$$\int_0^1\bar{r}^2\bar{r}J_0(\lambda_n\bar{r})d\bar{r}=-\frac{2}{\lambda_n^2}J_2(\lambda_n)$$

Substituting the above equation into Eq. (41), we obtain

$$-\frac{1}{2}\frac{2}{\lambda_n^2}J_2(\lambda_n\bar{r})=\frac{1}{2}J_0^2(\lambda_n)\sum_{n=1}^{\infty}C_n$$
$$C_n=\sum_{n=1}^{\infty}\frac{2}{\lambda_n^2}\frac{J_2(\lambda_n)}{J_0^2(\lambda_n)} \tag{42}$$

since

$$J_{v+1}(x)=\frac{2v}{x}J_v(x)-J_{v-1}(x)$$

And given $v=1$, we obtain

$$J_2(x)=\frac{2}{x}J_1(x)-J_0(x)$$

Rearranging Eq. (42) yields

$$C_n=\sum_{n=1}^{\infty}\frac{2}{\lambda_n^2}\left[\frac{2}{\lambda_n}J_1(\lambda_n)-J_0(\lambda_n)\right]\frac{1}{J_0^2(\lambda_n)}$$
$$C_n=-\sum_{n=1}^{\infty}\frac{2}{\lambda_n^2}\frac{J_0(\lambda_n)}{J_0^2(\lambda_n)}=-\sum_{n=1}^{\infty}\frac{2}{\lambda_n^2}\frac{1}{J_0(\lambda_n)} \tag{43}$$

The remaining term in Eq. (40) is

$$-\frac{\bar{r}^2}{2}=C_0J_0(\lambda_n\bar{r})$$

Multiplying by $\bar{r}J_0(\lambda_n\bar{r})d\bar{r}$ and integration from 0 to 1 yields

$$-\frac{1}{2}\int_0^1 \bar{r}^2\bar{r}J_0(\lambda_n\bar{r})d\bar{r} = C_0\int_0^1 J_0(\lambda_0\bar{r})\bar{r}J_0(\lambda_0\bar{r})d\bar{r}$$

Applying the relations $J_0(\lambda_n\bar{r}) = 0$ and $J_0(\lambda_0\bar{r}) = 1$ yields

$$-\frac{1}{2}\frac{\bar{r}^4}{4}\Big|_0^1 = C_0\frac{\bar{r}^2}{2}\Big|_0^1$$

$$C_0 = -\frac{1}{4} \tag{44}$$

Eventually, the final solution of Eq. (19) is as follows:

$$\theta = \frac{T-T_0}{T_w-T_0} = \frac{2\bar{x}}{\overline{Pe}} + \frac{\bar{r}^2}{2} - \frac{1}{4} - 2\sum_{n=1}^{\infty} e^{-\lambda_n^2\bar{x}/\overline{Pe}}\frac{J_0(\lambda_n\bar{r})}{\lambda_n^2 J_0(\lambda_n)} \tag{45}$$

For the constant heat flux boundary condition, the heat transfer equation at the tube wall is defined as follows:

$$q_w = k_{eff}^*\frac{\partial T}{\partial r}\Big|_{r=R}$$

By rearranging the above equation, we obtain

$$\frac{q_w R}{k_{eff}^*} = (T_w - T_o) \tag{46}$$

Substituting the above equation into Eq. (45) yields

$$\frac{T-T_0}{\frac{q_w R}{k_{eff}^*}} = \frac{2\bar{x}}{\overline{Pe}} + \frac{\bar{r}^2}{2} - \frac{1}{4} - 2\sum_{n=1}^{\infty} e^{-\lambda_n^2\bar{x}/\overline{Pe}}\frac{J_0(\lambda_n\bar{r})}{\lambda_n^2 J_0(\lambda_n)} \tag{47}$$

In this situation, the wall heat flux is known. So, the variation in wall temperature along the test section can be expressed as follows:

$$\frac{T_w-T_0}{\frac{q_w R}{k_{eff}^*}} = \frac{2\bar{x}}{\overline{Pe}} + \frac{1}{2} - \frac{1}{4} - 2\sum_{n=1}^{\infty} e^{-\lambda_n^2\bar{x}/\overline{Pe}}\frac{J_0(\lambda_n)}{\lambda_n^2 J_0(\lambda_n)}$$

$$\frac{T_w-T_0}{\frac{q_w R}{k_{eff}^*}} = \frac{2\bar{x}}{\overline{Pe}} + \frac{1}{4} - 2\sum_{n=1}^{\infty} \frac{e^{-\lambda_n^2\bar{x}/\overline{Pe}}}{\lambda_n^2} \tag{48}$$

By applying the energy balance

$$\rho A_t u Cp(T_b - T_o) = q_w A_w$$

From the above equation, the variation in bulk fluid temperature along the test section can be expressed as follows:

$$T_b(x) - T_o = \frac{2q_w x}{\rho RuCp} \tag{49}$$

Multiplying the above equation by $\frac{Rk_{eff}^*}{Rk_{eff}^*}$ yields

$$T_b(x) - T_o = \frac{2q_w x}{\rho RuCp}\frac{Rk_{eff}^*}{Rk_{eff}^*} = \frac{2xk_{eff}^*}{\rho uCpR^2}\frac{q_w R}{k_{eff}^*} \tag{50}$$

Dividing this equation by $\frac{q_w R}{k_{eff}^*}$, we obtain

$$\frac{T_b(x) - T_o}{\frac{q_w R}{k_{eff}^*}} = \frac{2xk_{eff}^*}{\rho uCpR^2} \tag{51}$$

where $x = \bar{x}L$

Subtracting Eq. (51) from Eq. (48), we obtain

$$\frac{T_w - T_b(\bar{x})}{\frac{q_w R}{k_{eff}^*}} = \frac{2\bar{x}}{\overline{Pe}} + \frac{1}{4} - 2\sum_{n=1}^{\infty}\frac{e^{-\lambda_n^2\bar{x}/\overline{Pe}}}{\lambda_n^2} - \frac{2\bar{x}Lk_{eff}^*}{\rho uCpR^2} \tag{52}$$

Considering the first term of the right hand side of Eq. (52) and applying the relations in Eq. (17), yields

$$\frac{2\bar{x}}{\overline{Pe}} = \frac{2\bar{x}}{Pe^*}\frac{L^2}{R^2}$$

By rearranging the above equation, we obtain

$$\frac{2\bar{x}}{\overline{Pe}} = \frac{2\bar{x}L^2}{R^2}\frac{\alpha_{eff}^*}{uL} = \frac{2\bar{x}L^2}{R^2uL}\frac{k_{eff}^*}{\rho Cp} = \frac{2\bar{x}Lk_{eff}^*}{R^2u\rho Cp} \tag{53}$$

Substituting the above equation into Eq. (52) yields

$$\frac{T_w - T_b(\bar{x})}{\frac{q_w R}{k_{eff}^*}} = \frac{1}{4} - 2\sum_{n=1}^{\infty}\frac{e^{-\lambda_n^2\bar{x}/\overline{Pe}}}{\lambda_n^2} \tag{54}$$

From the Newton Cooling laws:

$$h = \frac{q_w}{(T_w - T_b)}$$

On rearranging, we obtain

$$\frac{T_w - T_b}{q_w} = \frac{1}{h}$$

Substituting the above equation into Eq. (54), the analytical correlation of the local Nusselt number of the nanofluid is obtained as follows:

$$\frac{k_{eff}^*}{h_x R} = \frac{1}{4} - 2\sum_{n=1}^{\infty}\frac{e^{-\lambda_n^2\bar{x}/\overline{Pe}}}{\lambda_n^2}$$

$$\frac{2k_{eff}^*}{h_x D} = \frac{1}{4} - 2\sum_{n=1}^{\infty}\frac{e^{-\lambda_n^2\bar{x}/\overline{Pe}}}{\lambda_n^2}$$

$$\frac{h_x D}{k_{eff}^*} = Nu_x = \frac{8}{1 - 8\sum_{n=1}^{\infty}\frac{e^{-\lambda_n^2\bar{x}/\overline{Pe}}}{\lambda_n^2}} \tag{55}$$

Moreover, the average heat transfer coefficient can be calculated using the following equation:

$$h_{ave} = \frac{1}{L}\int_{x_1}^{x_2} h_x dx \tag{56}$$

In order to calculate the local heat transfer coefficient Eq. (55) along the test section, the distance along the test tube is divided into numerous sections. The eigenvalues (λ_n) are the positive roots of the equation of $J_1(\lambda_n) = 0$. The $\overline{Pe}$ number that appears in Eq. (55) can be calculated using Eq. (17).

Finally, the average heat transfer coefficient obtained from the present model was compared with the correlation proposed by Li and Xuan [20] as follows:

Table 1
The thermophysical properties of nanofluids used in the present study.

Properties	Particle volume fraction (%)						
	0	**0.24**	**0.6**	**1.18**	**2.0**	**4.0**	**6.0**
ρ (kg/m^3)	998	1004.2	1016.9	1035.3	1061.3	1124.7	1188.2
Cp (J/kgK)	4180.8	4174	4160	4140	4111.5	4042.1	3972.7
μ (kg/ms)	0.000922	0.000927	0.000937	0.000951	0.000971	0.00103	0.00108
k (W/mK)	0.592	0.595	0.601	0.610	0.623	0.655	0.689

$$h_{nf} = 0.4328(k_{nf}/D)(1.0 + 11.285\phi^{0.754}Pe_d^{0.218})Re_{nf}^{0.333}\mathrm{Pr}_{nf}^{0.4} \quad (57)$$

The physical properties such as the density, viscosity, and specific heat and thermal conductivity of the nanofluid were calculated using the following published correlations:

The density and specific heat were calculated from equations in Pak and Cho [21], which are as follows:

$$\rho_{nf} = \phi\rho_p + (1-\phi)\rho_w \quad (58)$$

and

$$Cp_{nf} = \phi Cp_p + (1-\phi)Cp_w \quad (59)$$

Brinkman [22] suggested an equation to calculate the viscosity of the suspension, which is defined as follows:

$$\mu_{nf} = \frac{1}{(1-\phi)^{2.5}}\mu_w \quad (60)$$

Similarly, one well-known equation for calculating the thermal conductivity of a nanofluid is the Hamilton and Crosser [23] model, which is expressed in the following form:

$$k_{nf} = \left[\frac{k_p + (n-1)k_w - (n-1)\phi(k_w - k_p)}{k_p + (n-1)k_w + \phi(k_w - k_p)}\right]k_w \quad (61)$$

$$n = 3/\psi \quad (62)$$

where n is the empirical shape factor and ψ is the sphericity, defined as the ratio of the surface area of a sphere (with the same volume as the given particle) to the surface area of the particle. The sphericity is 1 and 0.5 for the spherical and cylindrical shapes, respectively. Moreover, ϕ is the volume concentration, k is the thermal conductivity.

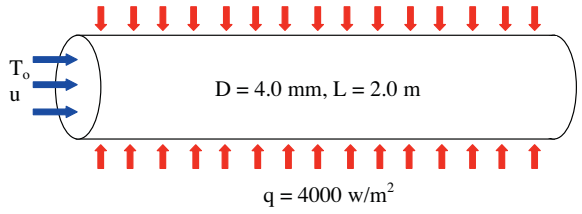

Fig. 1. Schematic diagram of the simulation domain.

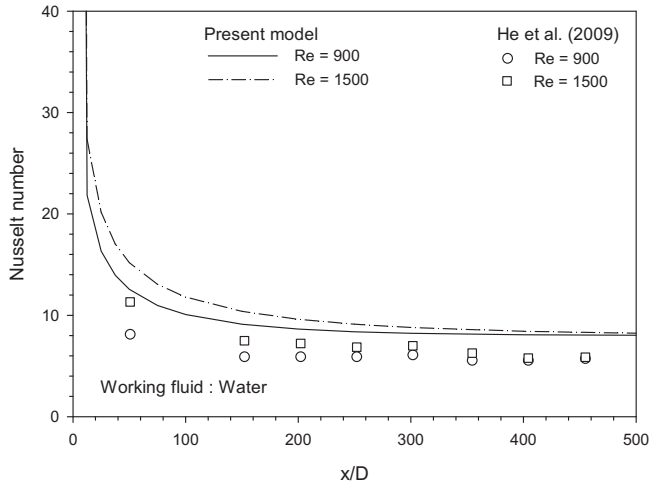

Fig. 2. Comparison of the Nusselt number between the measured data of He et al. [14] and the predicted values for water.

It should be noted that the above equation can be used to estimate the Nusselt number of a nanofluid under constant heat flux boundary conditions. However, other aspects of the heat transfer condition can be seen in Xuan and Li [17]. It is evident that the dispersion effect of the nanoparticles resulting from their random

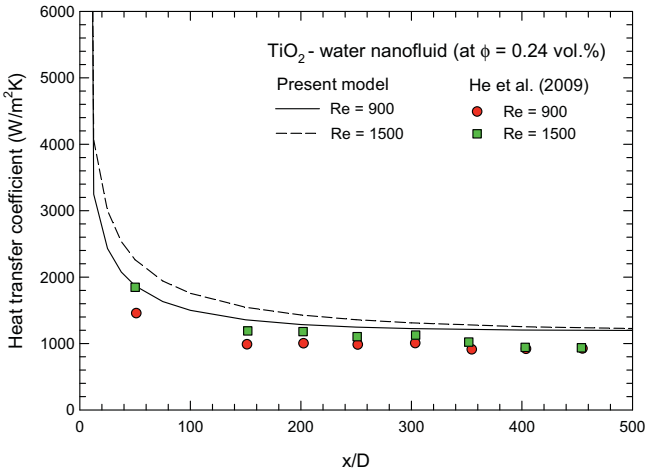

(a) at particle concentration of 0.24 vol.%

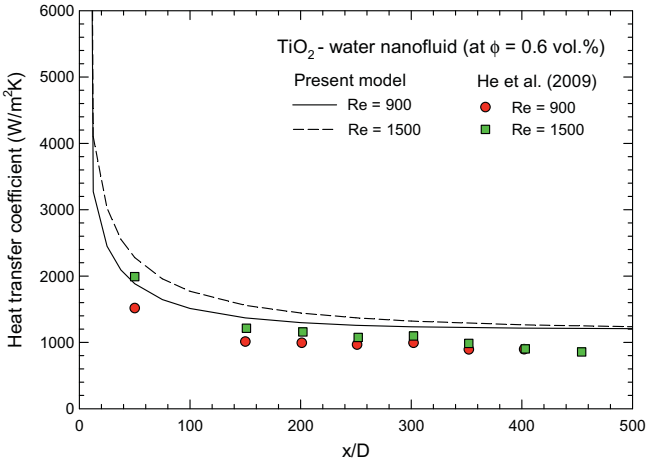

(b) at particle concentration of 0.60 vol.%

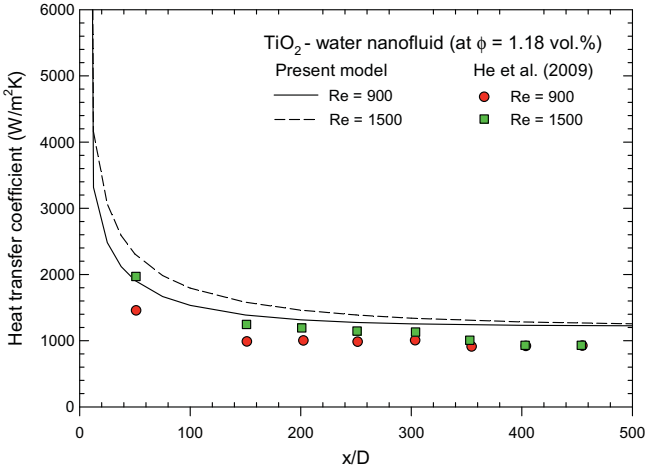

(c) at particle concentration of 1.18 vol.%

Fig. 3. Comparison of the predicted local heat transfer coefficients with those obtained from measured data of He et al. [14] for nanofluids with various volume fractions and Reynolds number.

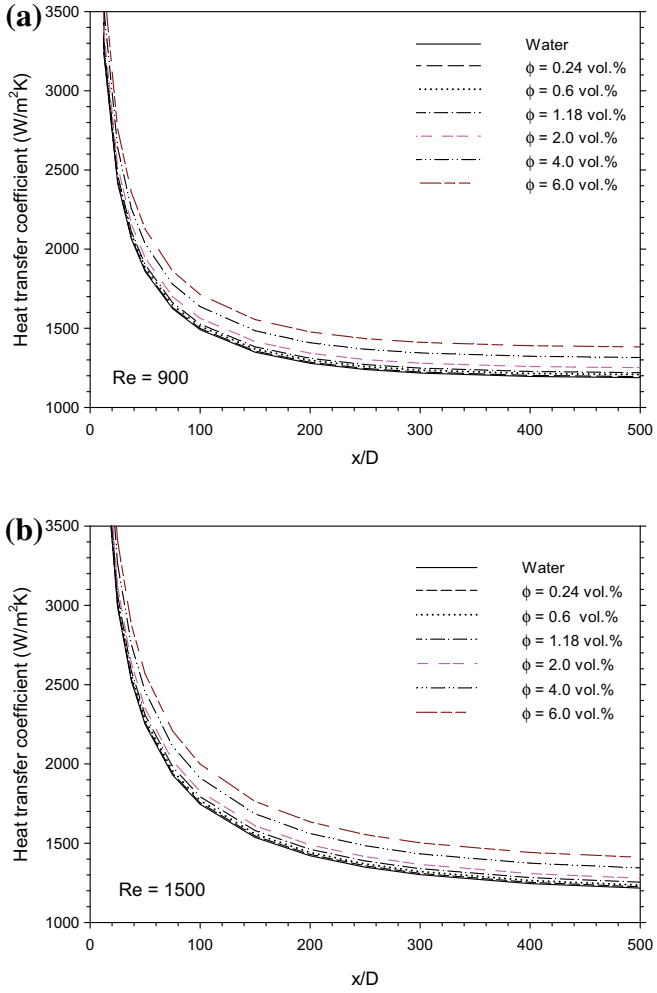

Fig. 4. Local heat transfer coefficient obtained from the present model as a function of particle concentrations at Reynolds number of 900 and 1500.

movement should be included in the model. However, a comparison of this model with the experimental data is still lacking, and was thus the main objective of this study.

2.2. Simulation conditions

For comparison with available experimental data, the data of He et al. [14] were used. In their study, a straight pipe with a 2.0 m length and 4.00 mm inner diameter was used as a test section. TiO_2 nanoparticles dispersed in water with volume concentrations of 0.24%, 0.6% and 1.18% were used to determine the heat transfer coefficient of a nanofluid. The wall heat flux was kept constant at 4000 W/m^2. Similarly, the Reynolds number was kept constant at 900 and 1500. The thermophysical properties of nanofluids used in the present study are shown in Table 1 and the geometrical configuration used in the simulation is shown in Fig. 1.

3. Results and discussion

Fig. 2 shows a comparison of the Nusselt number obtained from the simulation results and the experimental data of He et al. [14]. The data are obtained from pure water. It can be seen that the proposed model gives about a 25% higher predicted Nusselt number than the measured data.

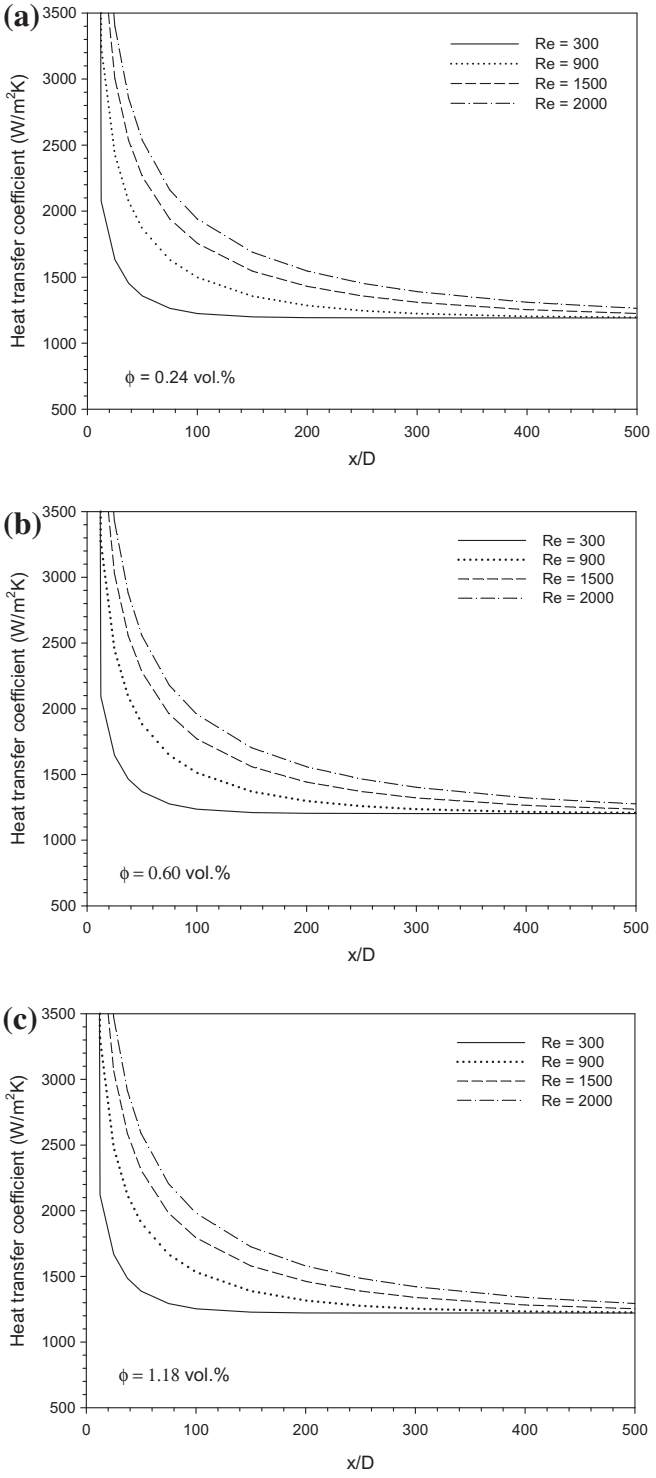

Fig. 5. Local heat transfer coefficient obtained from the present model as a function of Reynolds number at various particle concentration (a) 0.24 vol.%. (b) 0.6 vol.% (c) 1.18 vol.%.

Similarly, Fig. 3a–c shows a comparison of the predicted heat transfer coefficient of nanofluids obtained from the present model and the measured values of He et al. [14]. As shown in Fig. 3, the data from the present model give a 25–30% larger heat transfer coefficient than the experimental data. However, although the present model shows moderate over-prediction of the heat transfer coefficient compared with the measured data, this approach is easier and consumes less computational time compared with

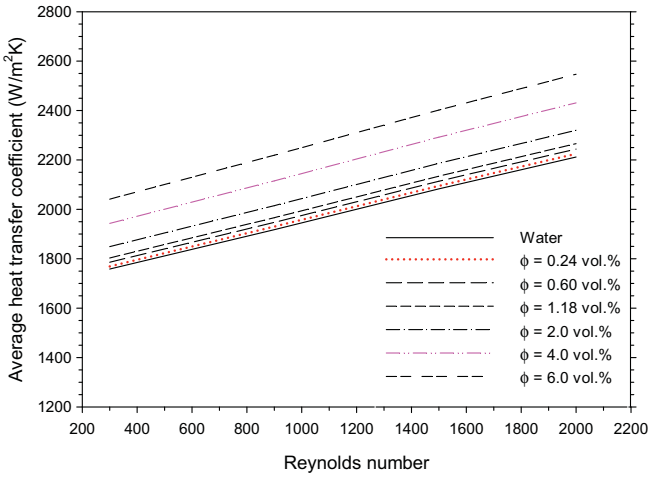

Fig. 6. Predicted average heat transfer coefficient as a function of Reynolds number and particle concentrations.

other models proposed by a number of researchers using commercial software.

Fig. 4a and b shows the effect of particle concentration on the heat transfer coefficient of nanofluids for a Re of 900 and 1500. The results indicate that the heat transfer coefficient of nanofluids increases with increasing particle volume fractions and decreases with increasing tube length, as expected. This behavior occurs because adding nanoparticles to a base fluid leads to an increase in the thermal conductivity of the base liquid. Moreover, the chaotic movement of nanoparticles in the main flow brings to large energy exchange process [24].

Fig. 5a–c shows the variation in the local heat transfer coefficient obtained from the present model as a function of Reynolds number at a particle volume fraction of 0.24, 0.6 and 1.18 vol.%, respectively. The increasing of the Reynolds number leads to an increasing of heat transfer rate and results in an increase in the heat transfer coefficient.

Similarly, Fig. 6 also shows the average heat transfer coefficient as a function of Reynolds number and particle concentrations. The simulation results show that the average heat transfer coefficient of nanofluids increases with increasing Reynolds number as well as with particle concentration. The reason for this is given in the preceding section.

Fig. 7a–c shows a comparison of the predicted average heat transfer coefficient obtained from the proposed model and the calculated values from obtained from Li and Xuan [2] for particle volume fractions of 0.6, 1.0 and 2.0%, respectively. At Reynolds numbers ranging between 1200 and 2000, the use of the present model to evaluate the heat transfer coefficient of nanofluids gives different values compared with the Li and Xuan correlation [20], by around 13% (at ϕ = 1.0 vol.%) and 3.5% (at ϕ = 2.0 vol.%).

Besides the difference in the nanoparticles used in both studies, the proposed model is also analyzed by the means of analytical approach whereas the Li and Xuan correlation was established based on their experimental data. Therefore it is impossible that both results will be equal. In general, for experimental approach, the complicated phenomena such as agglomeration, random movement of the nanoparticle, the slip velocity between the solid–liquid mixture, sedimentation and deposition on the tube wall will be coexisting in the main flow. These phenomenon rather differ from the assumption used in the present model which cause some different between the proposed model and the Li and Xuan correlation. However there is a good agreement with respect to the shapes of the heat transfer coefficient profile.

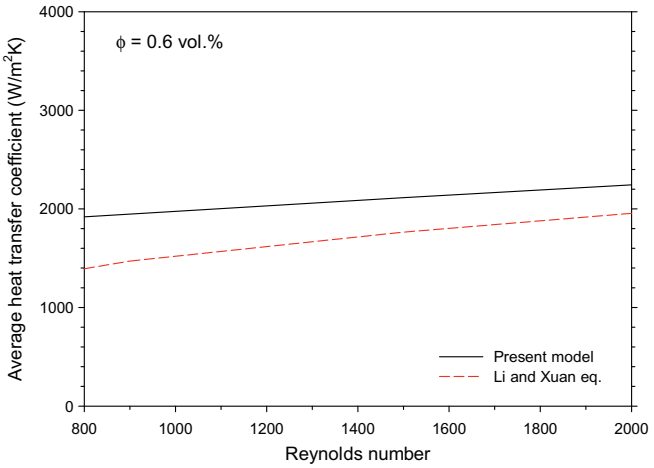

(a) at particle concentration of 0.60 vol.%

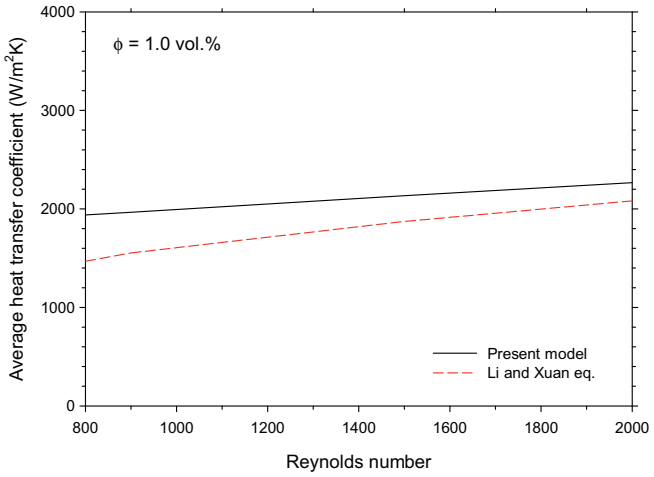

(b) at particle concentration of 1.0 vol.%

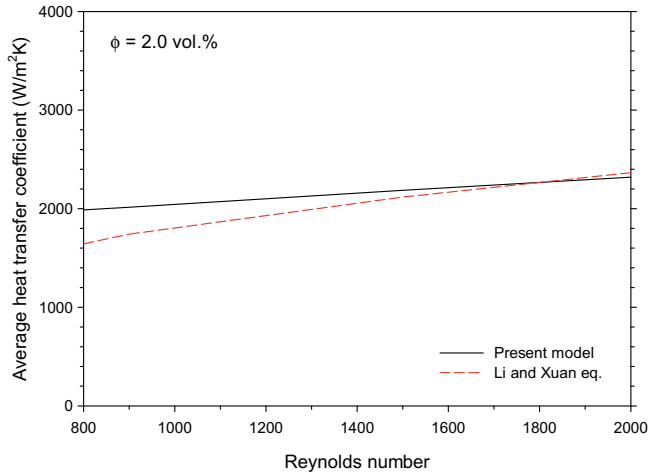

(c) at particle concentration of 2.0 vol.%

Fig. 7. Comparison of the average heat transfer coefficient of nanofluids between present model and the Li and Xuan correlation.

4. Conclusions

In the present study, the dispersion model for predicting the heat transfer performance of TiO_2–water nanofluids flowing under a laminar flow regime and constant heat flux is proposed. The Einstein–Strokes's equation is used to calculate the dispersion coefficient of nanofluids. The results from the present model are

compared with the data of He et al. [14]. The simulation results indicate that the heat transfer coefficient obtained from the proposed model is higher than the experimental data by around 25–30%. However, the advantages of this model are that it is easy to use, easy to understand and that it consumes less computational time. The model results also show that the heat transfer coefficient of nanofluids increases with increasing Reynolds number and particle concentration. In contrast, the heat transfer coefficient decreases with increasing length of the test tube. Moreover, the results from the present model differ from those obtained using the Li and Xuan correlation [20] by approximately 3.5% at a particle concentration of 2.0 vol.%.

Acknowledgments

The authors would like to express their appreciation to the Thailand Research Fund (TRF), the office of the Higher Education Commission and the National Research University Project for providing financial support.

References

[1] H. Masuda, A. Ebata, K. Teramae, N. Hishinuma, Alteration of thermal conductivity and viscosity of liquid by dispersing ultra-fine particles (dispersion of Al_2O_3, SiO_2 and TiO_2 ultra-fine particles), Netsu Bussei (Japan) 7 (4) (1993) 227–233.
[2] S.U.S. Choi, Enhancing thermal conductivity of fluids with nanoparticle, ASME FED 231 (1995) 99.
[3] W. Duangthongsuk, S. Wongwises, A critical review of convective heat transfer of nanofluids, Renew. Sust. Energ. Rev. 11 (2007) 797–817.
[4] V. Trisaksri, S. Wongwises, Critical review of heat transfer characteristics of the nanofluids, Renew. Sust. Energ. Rev. 11 (3) (2007) 512–523.
[5] X.Q. Wang, A.S. Mujumdar, Heat transfer characteristics of nanofluids: a review, Int. J. Thermal Sci. 46 (2007) 1–19.
[6] Y. He, Y. Jin, H. Chen, Y. Ding, D. Cang, H. Lu, Heat transfer and flow behavior of aqueous suspensions of TiO_2 nanoparticles (nanofluids) flowing upward through a vertical pipe, Int. J. Heat Mass Transfer 50 (2007) 2272.
[7] C.T. Nguyen, G. Roy, C. Gauthier, N. Galanis, Heat transfer enhancement using Al_2O_3–water nanofluid for electronic liquid cooling system, Appl. Thermal Eng. 28 (2007) 1501.
[8] G.H. Ko, K. Ho, K. Lee, D.S. Kim, C. Kim, Y. Sohn, M. Choi, An experimental study on the pressure drop of nanofluids containing carbon nanotubes in the horizontal tube, Int. J. Heat Mass Transfer 50 (2007) 4749.
[9] R. Chein, J. Chuang, Experimental microchannel heat sink performance studies using nanofluids, Int. J. Thermal Sci. 46 (1) (2007) 57.
[10] W. Duangthongsuk, S. Wongwises, Effect of thermophysical properties models on the prediction of the convective heat transfer coefficient for low concentration nanofluid, Int. Commun. Heat Mass Transfer 35 (2008) 1320.
[11] W. Duangthongsuk, S. Wongwises, Heat transfer enhancement and pressure drop characteristics of TiO_2–water nanofluid in a double-tube counter flow heat exchanger, Int. J. Heat Mass Transfer 52 (2009) 2059–2067.
[12] C.T. Nguyen, N. Galanis, G. Polidori, S. Fohanno, C.V. Popa, A.L. Bechec, An experimental study of a confined and submerged impinging jet heat transfer using Al_2O_3–water nanofluid, Int. J. Thermal Sci. 48 (2009) 401–411.
[13] M. Izadi, A. Behzadmehr, D. Jajali-Vahida, Numerical study of developing laminar forced convection of a nanofluid in an annulus, Int. J. Thermal Sci. (2009) 1–11.
[14] Y. He, Y. Men, Y. Zhao, H. Lu, Y. Ding, Numerical investigation into the convection heat transfer of TiO_2 nanofluids flowing through a straight tube under the laminar flow conditions, Appl. Thermal Eng. 29 (2009) 1965–1972.
[15] V. Bianco, F. Chiacchio, O. Manca, S. Nardini, Numerical investigation of nanofluids forced convection in circular tubes, Appl. Thermal Eng. 29 (17–18) (2009) 3632–3642.
[16] S. Kumar, S.K. Prasad, J. Banerjee, Analysis of flow and thermal field in nanoflui using a single phase thermal dispersion model, Appl. Math. Model. 34 (3) (2010) 573–592.
[17] Y. Xuan, Q. Li, Heat transfer emhancement of nanofluids, Int. J. Heat Fluid Flow 21 (2000) 58–68.
[18] G.I. Taylor, Dispersion of soluble matter in solvent flowing through a tube, Proc. Royal Soci. (London) A219 (1953) 186–203.
[19] J. Buongiorno, Convective transport in nanofluids, Transaction of the ASME, J. Heat Transfer 128 (2006) 240–250.
[20] Q. Li, Y. Xuan, Convective heat transfer and flow characteristics of Cu-water nanofluid, Sci. China (Ser. E) 45 (4) (2002) 408–416.
[21] B.C. Pak, Y.I. Cho, Hydrodynamic and heat transfer study of dispersed fluids with submicron metallic oxide particles, Exp. Heat Transfer 11 (1998) 151–170.
[22] H.C. Brinkman, The viscosity of concentrated suspensions and solution, J. Chem. Phys. 20 (1952) 571–581.
[23] R.L. Hamilton, O.K. Crosser, Thermal conductivity of heterogeneous two-component systems, Indust. Eng. Chem. Fundament. 1 (3) (1962) 187–191.
[24] Y. Xuan, W. Roetzel, Conceptions for heat transfer correlation of nanofluids, Int. J. Heat Mass Transfer 43 (2000) 3701–3707.

International Journal of Air-Conditioning and Refrigeration
Vol. 20, No. 1 (2012) 1250001 (11 pages)
© World Scientific Publishing Company
DOI: 10.1142/S2010132512500010

World Scientific
www.worldscientific.com

EXPERIMENTAL INVESTIGATION OF R134a FLOWING THROUGH ADIABATIC HELICALLY COILED CAPILLARY TUBES

JATUPORN KAEW-ON[*,†], SAKARIN CHINGULPITAK[†] and SOMCHAI WONGWISES[†,‡,§]

[*]*Physics Department, Thaksin University*
Papayom, Phattalung 93110, Thailand

[†]*Fluid Mechanics, Thermal Engineering and Multiphase Flow Research Laboratory (FUTURE)*
Department of Mechanical Engineering
King Mongkut's University of Technology Thonburi
Bangmod, Bangkok 10140, Thailand

[‡]*The Academy of Science, The Royal Institute of Thailand*
Sanam Suea Pa, Dusit, Bangkok 10300, Thailand
[§]*somchai.won@kmutt.ac.th*

Received 5 August 2011
Accepted 29 November 2011
Published 31 March 2012

The effects of the relevant parameters on the flow characteristic of R134a flowing through adiabatic helical capillary tubes were experimentally studied. The capillary tubes' diameter, coil diameter, and parameters relating to flow conditions such as inlet pressures and degree of subcooling were the major parameters investigated. The test section was made from copper tubing with inner diameters of 1.07, 1.27, and 1.62 mm. The coil diameters were 25, 50, and 100 mm. The local pressure and temperature distributions along the length of the capillary tubes were measured at inlet pressures ranging from 10 to 14 bar, mass flow rates from 8 to 20 kg/h, and degrees of subcooling from 0.5°C to 15°C. The metastable flow and the delay of vaporization of R134a are also presented and discussed. The results showed that the capillary diameter had more of a significant effect on the mass flow rate than the other variables.

Keywords: Capillary; pressure drop; R134a; subcooling; temperature; two-phase flow.

Nomenclature

AD : Average deviation, %
C_p : Specific heat, J kg^{-1} K^{-1}
D : Coil diameter, mm
d : Capillary diameter, mm
i : Enthalpy, J kg^{-1}
L : Capillary tube length, m
$\dot{m}$: Mass flow rate, kg s^{-1}
MD : Mean deviation, %
P : Pressure, Pa
p : Pitch of coil, mm
T : Temperature, °C

Greek Letters

μ : Viscosity, Pa s
π : Dimensionless parameter
ρ : Density, kg m^{-3}
σ : Surface tension, N m^{-1}

Subscripts

aprox : Approximately
cond : Condenser
crit : Critical point
in : Inlet
l : Liquid phase
out : Outlet
sat : Saturation
sub : Subcooled
v : Vapor phase

1. Introduction

A capillary tube is one of the expansion devices that are widely used in household refrigerators and window-type air conditioners. Normally, it is a long hollow tube of drawn copper with an inside diameter of between 0.5 and 2.0 mm and a length from 2 to 6 m that is connected at the outlet of the condenser and the inlet of the evaporator. The advantages of a capillary tube are its simplicity, low expense, zero maintenance cost, and that it has no moving parts. Moreover, it allows the pressures between the condenser and evaporator to equalize during the off cycle, thus decreasing the starting torque requirements of the compressor. Consequently, a capillary tube is suitable for household refrigerators or freezers, where the cooling load and refrigerant charge remain slightly constant.

Over the years, there have been a number of studies on the flow characteristic of refrigerants in capillary tubes. However, it should be noted that the studies found in the literature focused on the flow in horizontal tubes. Information on helically coiled capillary tubes is still limited, especially with regard to experimental data.

To the best of the authors' knowledge, up to now there has been minimal experimental investigation carried out by researchers on this issue. The available papers regarding experimental investigation of refrigerant flow in coiled capillary tubes are summarized as follows:

Kim *et al.*[1] studied the performance of R22, R407C, and R410A in several capillary tubes for air conditioners. They performed tests at 40°C, 45°C, and 50°C of the condensing temperature, and 1.5°C, 5°C, and 10°C of the subcooling temperature. They used the Buckingham π theorem to develop the correlation for predicting the mass flow rate through the capillary tubes. They concluded that the mass flow rates of R407C were greater by 4.0%, and those of R410A were greater by 23%, than those of R22. The mass flow rates in helical capillary tubes were smaller compared with those of straight tubes, especially in the cases of smaller the coil diameters. The deviation of experimental results for R22, R407C, and R410A from the dimensionless correlation in this study was between $\pm 12\%$ for all test conditions.

Zhou and Zhang[2] experimentally and numerically investigated the mass flow rate of R22 flowing through a capillary coil tube. They found that the mass flow rate of the refrigerant with coil diameter of 40 mm is approximately 10% less than that of a straight tube. They also found that the change in mass flow rate for coil diameters beyond 300 mm was insignificant.

Park *et al.*[3] studied the flow characteristics of coil capillary tubes in order to develop a generalized correlation for the mass flow rate through coil capillary tubes. The resulting correlation showed good predictions with the present database for R22, R407C, and R410A in the straight and coil capillary tubes, yielding average and standard deviations of 0.24% and 4.4%, respectively.

Khan *et al.*[4] investigated the flow of R134a inside an adiabatic helical capillary tube. The main study parameters were capillary tube diameter, length, coil pitch, and inlet subcoolings. They concluded that the effect of coiled capillary tubes reduces the mass flow rate by 5% to 15%, as compared to those of straight capillary tubes operating under similar conditions. They also proposed a correlation to predict the mass flow rate in spiral coil capillary tubes. Khan *et al.*[4] found that the correlation could predict more than 91% of the mass flow rate. The data were in agreement with measured data in an error band of $\pm 10\%$.

Mittal *et al.*[5] studied the coiling effect on the flow of R407C in an adiabatic helical capillary tube. They observed that coiling the capillary tube had a strong effect on the mass flow rate of R407C through the tube. They also found that the mass flow rates in coiled capillary tubes were 5%−10% less than those in straight ones. The correlations based on the

Buckingham π theorem were developed for predicting mass flow rates in straight and helically coiled capillary tubes. The error band of comparison between experimental data and their correlation was $\pm 10\%$.

Over the years, many studies have focused on the horizontal capillary tube while coiled capillary tube has received comparatively little attention. Experimental investigation in coiled capillary tubes has not attracted much attention despite its importance in real practical use. Although some information is currently available on this issue, there still remains room to discuss. In particular, detailed investigation is lacking on the effects of various relevant parameters on flow characteristics, specifically local pressure and local temperature distributions along the capillary tube. In this paper, the main concern was to study the influence of parameters such as inlet pressure, degree of subcooling, capillary tube diameters, and coil diameters on local pressure, local temperature distribution, and mass flow rate along the capillary tube length. The behavior of the flashing process and the delay of refrigerant vaporization are also presented.

2. Experimental Apparatus and Method

The experiment used a vapor-compression refrigeration system that included a capillary tube as the expansion device. Figure 1 shows a schematic diagram of the test apparatus. It consisted of the main refrigeration system components: Compressor, condenser, capillary tube, evaporator, and other accessory parts: the oil separator, liquid receiver, filter/drier, sight glass, subcooler, and accumulator. A two-cylinder single stage reciprocating compressor, driven by an electric motor, was used to circulate the refrigerant. The speed of the motor was varied so as to provide a wide range of mass flow rates by means of an inverter. The Alco AW-55824 helical oil separator was used to minimize the effect of lubricating oil on refrigerant flow through capillary tube. The efficiency of oil separation was approximately 99%. Compact plate heat exchangers were used as a condenser, evaporator, and subcooler.

An electric heater and a separate refrigeration system were installed in the water tank so as to control the water temperature. The hot water was supplied from a hot water tank by the circulating pump and passed through the flow meter and evaporator. The downstream pressure of the test section was controlled by adjusting the temperature and the flow rate of hot water. A condenser was used to reject heat to the water coming from a cold water tank. The upstream pressure of the test section was set by varying the flow rate of water to the subcooler.

The upstream pressure of the test section was regulated by adjusting the temperature of cold water. The degree of refrigerant subcooling entering the test section was set by varying the flow rate of

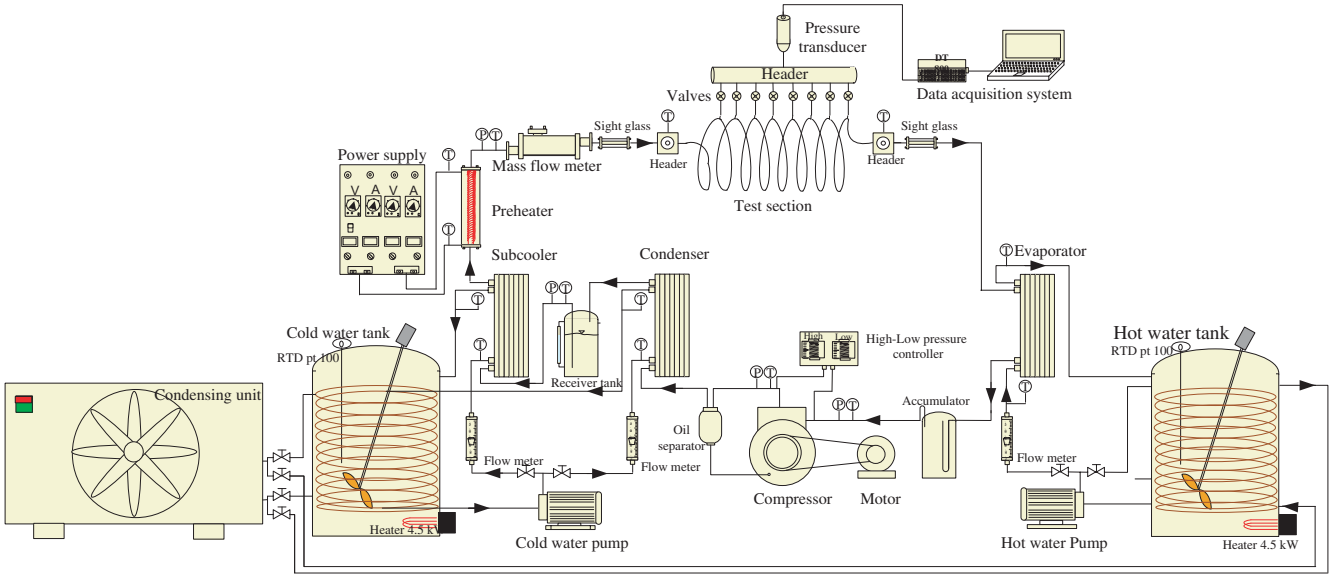

Fig. 1. Schematic diagram of the experimental apparatus.

water to the subcooler. The test runs were chosen to cover a wide range of working conditions of an air conditioner. The upstream pressures were set at 10, 12 and 14 bar, while the downstream pressures were varied between 3.5 to 4.5 bar. The degree of subcooling was varied from 0.5°C to 10.5°C.

The pressure distribution inside the capillary tube was measured by the pressure transducer calibrated from 0 to 22 bar within a ±20 mbar accuracy. The T-type thermocouple with an accuracy of ±0.1°C was installed to measure the temperature distribution along the test section. A total of nine thermocouples were soldered on the outer surface wall of the capillary tube at nine sections along the test tube to measure the outer wall temperatures. These outer wall temperatures were used to determine the inner wall temperatures based on heat conduction through the wall. The flow rate of the refrigerant through the capillary tube was measured by a coriolis mass flow meter (ABB FCM2000) with an accuracy of ±0.25%.

The details of the dimension of the test capillary tubes are presented in Fig. 2. The inlet pressure and inlet temperature were measured at the inlet header. Similarly, the outlet pressure and outlet temperature were obtained from the outlet header. Seven points of the capillary tube were drilled for the installation of pressure taps. Also, the seven T-type thermocouples were installed in the same sections as the pressure taps. The thermocouples were insulated with the Aeroflex standard sheet to reduce the effect of heat transfer on the measurement errors. The range of experimental conditions tested and the details of test sections are listed in Table 1.

3. Results and Discussion

The results are divided in three sections. First, the flow characteristics inside the capillary tubes are discussed. Next, the profiles of pressure and temperature distributions along the adiabatic helical capillary tubes are presented. Finally, the geometric and test conditions' effects on the mass flow rate of the refrigerant are shown and discussed in detail.

3.1. *Flow characteristics inside the capillary tube*

Figure 3 shows the measured pressure profiles and saturation pressure profiles along the capillary tube for a capillary diameter of 1.27 mm, coil diameter of 50 mm, condenser outlet pressure of 12 bar, and degree of subcooling of 8.5°C. The saturation pressures were calculated from measured temperatures, obtained from the T-type thermocouples installed in the same sections as the pressure tabs along the capillary tubes. As shown in Fig. 3, the refrigerant entered the capillary tube as a subcooled liquid. The measured pressure gradually decreased towards the end of the tube, at which point it rapidly decreased. On the other hand, the measured temperatures along the tube were nearly constant, but suddenly decreased at the end of the tube. The coincident point of the measured pressure and saturation pressure is called the theoretical flash point. The saturation pressure remains constant after it has passed the theoretical flash point, but then rapidly decreases. The delay in refrigerant vaporization is called the metastable region. Therefore, this phenomenon confirmed that refrigerant flow inside the capillary tube can be divided into three regions: Subcooled liquid region, metastable liquid region, and metastable two-phase region. In the subcooled liquid region, the measured pressure was higher than the saturation pressure. However, in the metastable liquid region, the measured pressure was lower than the near-constant saturation pressure. This behavior indicated that the refrigerant existed

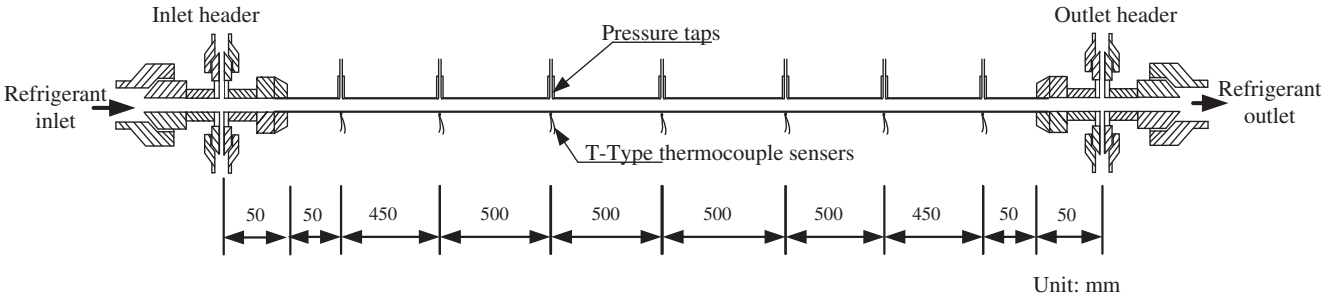

Fig. 2. Schematic diagram of the test section.

Table 1. The details of test sections and experimental conditions.

Items	Details
Refrigerant	R134a
Capillary diameter (mm)	1.07, 1.27, 1.62
Coil diameter (mm)	25, 50, 100
Capillary length (m)	3.05
Inlet pressure (bar)	10, 12, 14
Degree of subcooling	0.5−10.5

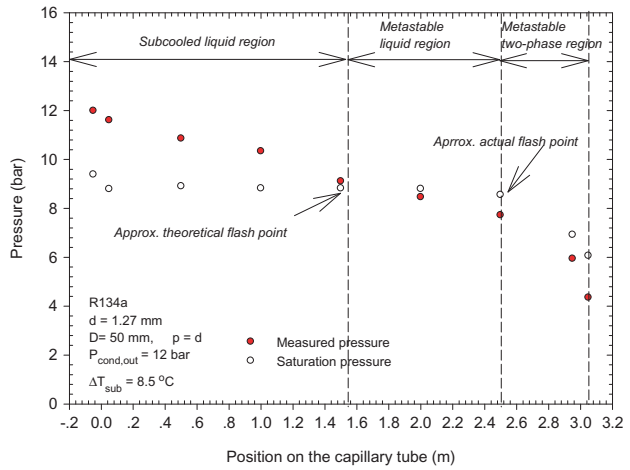

(a)

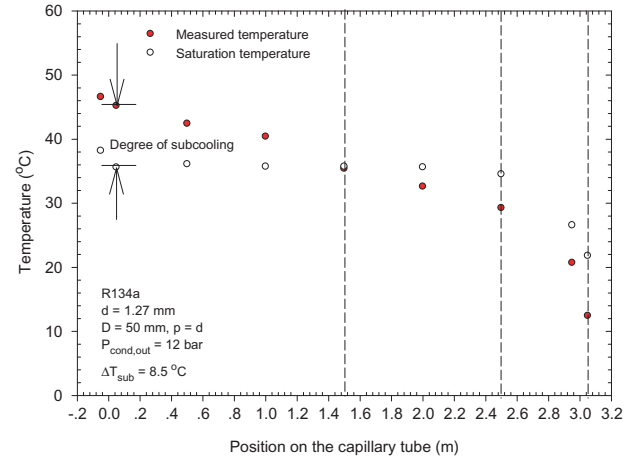

(b)

Fig. 3. Flow phenomena inside the capillary tube (a) pressure distribution and (b) temperature distribution.

in a liquid state, and lead to nonthermodynamic equilibrium. Therefore, the flow phenomenon in this region was called the metastable liquid flow. In the metastable two-phase region, the measured temperature suddenly decreased. This was a result of the velocity of the refrigerant greatly increasing when the liquid refrigerant changed to a liquid−vapor mixture. This phenomenon led to a decrease in refrigerant pressure and temperature. In addition, it was also found that the measured pressure was lower than the saturation pressure. As described above, this means that the state of refrigerant was a two-phase (liquid/vapor) mixture and did not exist in thermodynamic equilibrium. This flow phenomenon was consistent with the results of Valladares.[6]

3.2. *Pressure and temperature distributions*

Figure 4 presents the relevant influence parameters on pressure and temperature distributions along the adiabatic helical capillary tube length. The experiment was conducted for capillary diameters of 1.07, 1.27, and 1.52 mm, subcooling temperature ranges of 2.5°C to 10.5°C, and inlet pressures of 10, 12, and 14 bar. The coil diameters were 25, 50, and 100 mm. The results and discussion of the main relevant effects on the variation of pressure along the helical capillary tube length are as follows:

3.2.1. *Effect of inlet pressure on pressure and temperature distributions*

The variations of refrigerant pressure and temperature along the capillary tube at different inlet pressure are depicted in Fig. 4(a). The pressure and temperature drop was enhanced by increasing the inlet pressure. The possible reason for this could be that the enlargement of inlet pressure led to an increased difference between inlet and outlet pressure, which resulted in an increase of refrigerant mass flow rate and velocity. Consequently, the frictional and acceleration-related pressure drop inside the capillary tube was increased. It was also found that temperature distribution was directly related to pressure distribution. This was due to the fact that the increase in saturation pressure resulted in an increase of saturation temperature, at the same degree of subcooling and capillary tube configuration.

3.2.2. *Effect of degree of subcooling on pressure and temperature distributions*

The effect of degree of subcooling on pressure and temperature distributions along the capillary tube at the same inlet pressure and capillary tube configuration

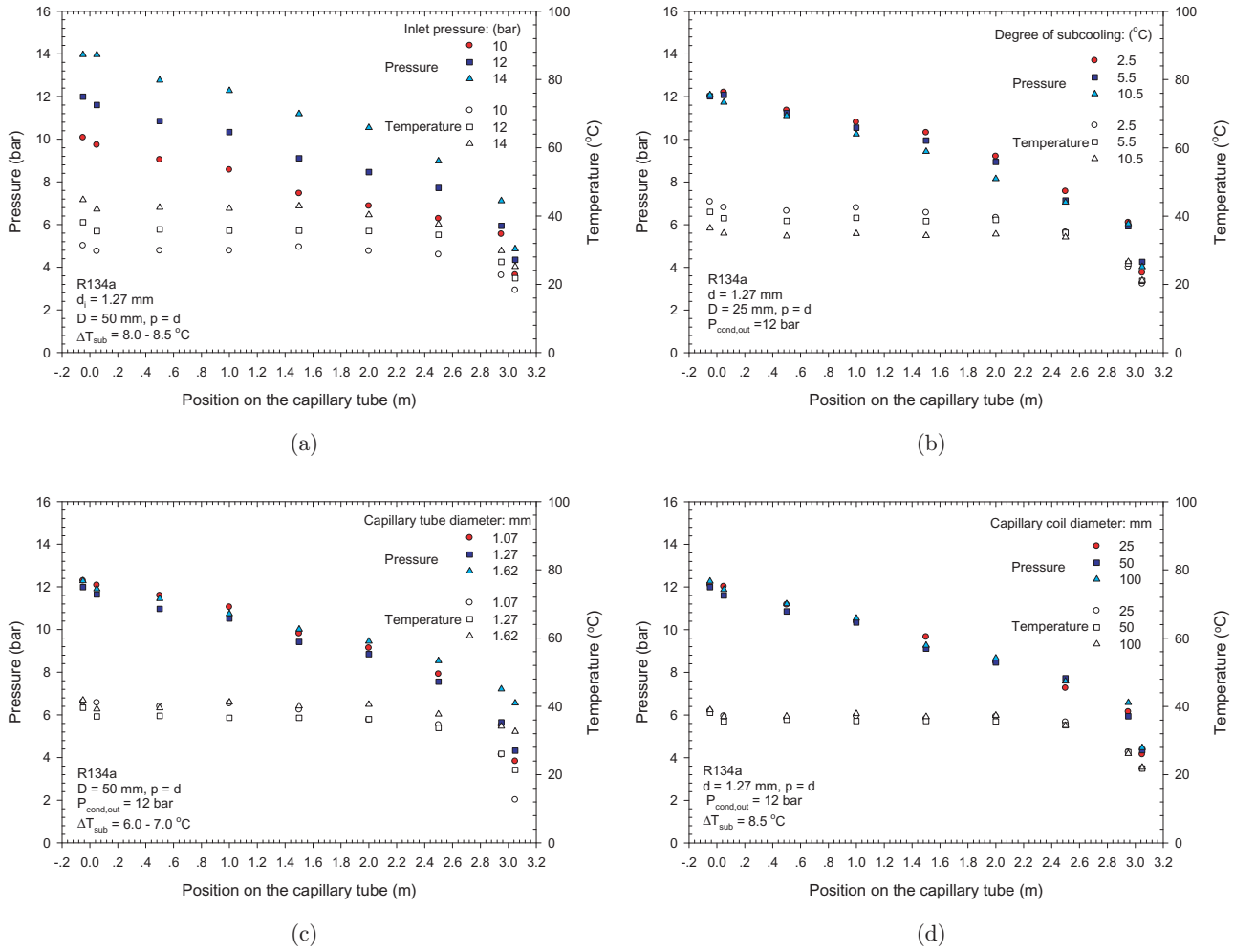

Fig. 4. Effect of the relevant parameter on the pressure and temperature distribution along the capillary length: (a) Effect of inlet pressure, (b) effect of degree of subcooling, (c) effect of capillary tube diameter, and (d) effect of coil diameter.

is presented in Fig. 4(b). The results show that the average pressure and temperature along the capillary tube was reduced as the degree of subcooling decreased. This was due to the fact that the density and velocity of refrigerant is boosted as the degree of subcooling increased, which resulted in an increase in frictional pressure drop inside the helical capillary tube. However, at the end of the capillary tube, the pressure drop was highest when the degree of subcooling was low. This may be due to a decrease in acceleration-related pressure when the quality at the end of the capillary tube is higher.

3.2.3. *Effect of capillary tube diameter on pressure and temperature distributions*

As shown in Fig. 4(c), the pressure and temperature drop along the capillary tube was decreased with an increase in the capillary tube diameter. This was due to the fact that the frictional pressure drop was increased by decreasing the capillary tube diameter. The reason for the variation of temperature at different capillary tube diameters is similar to that described above.

3.2.4. *Effect of coil diameter on pressure and temperature distributions*

The effect of coil diameter on pressure and temperature distribution is presented in Fig. 4(d). The results show that decrease in pressure and temperature was similar for all test conditions. Thus, it can be concluded that coil diameter has no significant effect on pressure and temperature distribution.

3.3. *The mass flow rate*

The coriolis mass flow meter (ABB FCM2000), with an accuracy of $\pm 0.25\%$, was installed to measure the mass flow rate of the refrigerant flowing through the capillary tubes. The effect of capillary tube geometry, such as tube diameter and coil diameter, as well as the operating conditions, such as inlet pressure and degree of subcooling on the mass flow rate of the refrigerant through adiabatic helical capillary tubes, were investigated. The results from the experimental investigation are as follow:

3.3.1. *Effect of degree of subcooling on mass flow rate*

Figure 5 plots the variations of mass flow rate against the degree of subcooling for various conditions. These figures show that for all conditions, the mass flow rate increased with an increased degree of subcooling. This phenomenon can be explained by the fact that the increase in mass flow rate was a result of increased liquid length for high inlet subcooling, since resistance of the liquid flow was less than that for the two-phase flow.

3.3.2. *Effect of inlet pressure on mass flow rate*

The variation of mass flow rates for capillary inlet pressures of 10, 12, and 14 bar with varying degrees of subcooling is presented in Fig. 5(a). The results show that for a given capillary diameter, the mass flow rate increased with an increase in the inlet pressure. At higher inlet pressures, the driving force

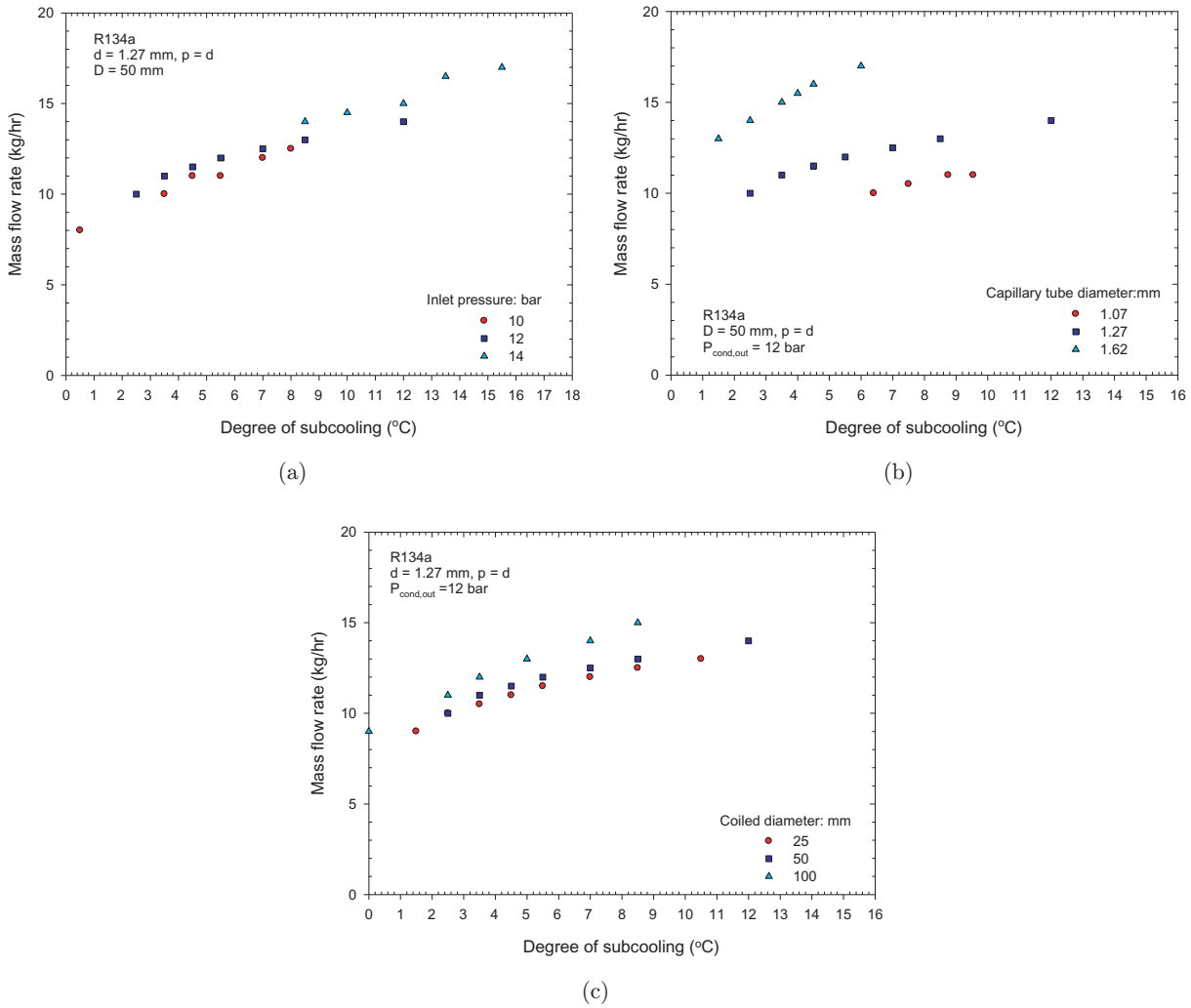

Fig. 5. Effect of the relevant parameter on the mass flow rate of the R134a through the capillary tubes: (a) Effect of inlet pressure, (b) effect of capillary tube diameter, and (c) effect of coil diameter.

was also higher and resulted in an increase of mass flow rate. As seen in Fig. 5(a), at identical degrees of subcooling, increasing inlet pressure from 10 to 12 bar increases the mass flow rate by 5% to 10%.

3.3.3. *Effect of capillary tube diameter on mass flow rate*

Figure 5(b) presents mass flow rates and degrees of subcooling for capillary tube diameters of 1.07, 1.27, and 1.62 mm, inlet pressure of 12 bar, and coil diameter of 50 mm. The effect of capillary tube diameter on refrigerant mass flow rate is clearly seen and significant. The results show that the mass flow rates dramatically increased with an increase in capillary tube diameter. Figure 5(b) shows that for 6.5°C of subcooling, as the capillary tube diameter was increased from 1.07 mm to 1.27 mm, and from 1.27 mm to 1.62 mm, the refrigerant mass flow rate increased by 26.3% and 41.7%, respectively. This was due to smaller frictional effects as the internal diameter of the capillary tube increased.

Table 2. The relevant dimensionless parameters.

π-group	Dimensionless parameters	Consideration	References
π_1	$\pi_1 = (P_{in} - P_{sat})/P_{crit}$	Inlet pressure	Choi *et al.*,[9,10] Zhang[11]
π_2	$\pi_2 = \Delta T_{sub}/T_{crit}$	Subcooling	Choi *et al.*,[9,10] Zhang[11]
π_3	$\pi_3 = L/d$	Tube geometry	ASHRAE,[7] Melo *et al.*,[8] Kim *et al.*,[1] Choi *et al.*,[9,10] Zhang,[11] Mittal *et al.*[5]
π_4, π'_4	$\pi_4 = \rho_l/\rho_v, \pi'_4 = \rho_v/\rho_l$	Density	ASHRAE,[7] Choi *et al.*,[9,10] Zhang,[11] Mittal *et al.*[5]
π_5, π'_5	$\pi_5 = (\mu_l - \mu_v)/\mu_v, \pi'_5 = \mu_v/\mu_l$	Viscosity	ASHRAE,[7] Choi *et al.*,[9,10] Zhang,[11] Mittal *et al.*[5]
π_6	$\pi_6 = \sigma/(P_{in}d)$	Bubble growth	Choi *et al.*,[9,10] Zhang[11]
π_7	$\pi_7 = \rho_l i_{vl}/P_{sat}$	Vaporization	Choi *et al.*,[9,10] Zhang[11]
π_8	$\pi_8 = \dot{m}/(d^2\sqrt{\rho_l P_{in}})$	Mass flow rate	Choi *et al.*,[9,10] Zhang[11]
π_9	$\pi_9 = \dot{m}/(d\mu_l)$	Mass flow rate	ASHRAE,[7] Melo *et al.*,[8] Kim *et al.*,[1] Mittal *et al.*[5]
π_{10}	$\pi_{10} = d^2\rho_l P_{in}/\mu_l^2$	Inlet pressure	ASHRAE,[7] Melo *et al.*,[8] Kim *et al.*,[1] Mittal *et al.*[5]
π_{11}	$\pi_{11} = d^2\rho_l^2 Cp_l \Delta T_{sub}/\mu_l^2$	Subcooling	ASHRAE,[7] Melo *et al.*,[8] Kim *et al.*,[1] Mittal *et al.*[5]
π_{12}	$\pi_{12} = d^2 h_{lv}\rho_l^2/\mu_l^2$	Vaporization	Kim *et al.*,[1] Mittal *et al.*[5]
π_{13}	$\pi_{13} = d\rho_l\sigma/\mu_l^2$	Bubble growth	Kim *et al.*,[1] Mittal *et al.*[5]
π_{14}	$\pi_{14} = D/d$	Geometry	Mittal *et al.*[5]

Table 3. The summary of the existing correlations for predicting the mass flow rate.

No	Author(s)	Correlation	Conditions
1	ASHRAE[7]	$\pi_9 = 1.8925\pi_3^{-0.484}\pi_4^{0.773}\pi_5^{0.265}\pi_{10}^{1.369}\pi_{11}^{0.0187}$	Straight tube, R134a, R22, R410A
2	Melo *et al.*[8]	$\pi_9 = 1.95\pi_3^{-0.528}\pi_{10}^{0.448}\pi_{11}^{0.164}$	Straight tube, R12, R134a, R600a
3	Kim *et al.*[1]	$\pi_9 = 1.5104\pi_3^{-0.3785}\pi_{10}^{0.5351}\pi_{11}^{0.1074}\pi_{12}^{-0.1596}\pi_{13}^{0.096}$	Helical and Straight tube, R22, R407C, R410A
4	Choi *et al.*[9]	$\pi_8 = 1.313 \times 10^{-3}\pi_1^{-0.087}\pi_2^{0.188}\pi_3^{-0.412}\pi_4^{-0.834}\pi_5^{0.199}\pi_6^{-0.368}\pi_7^{0.992}$	Straight tube, R12, R22
5	Choi *et al.*[10]	$\pi_8 = 0.5782 \times 10^{-4}\pi_1^{-0.315}\pi_2^{0.369}\pi_3^{-0.344}\pi_4^{-0.034}\pi_5^{0.040}\pi_6^{-0.458}\pi_7^{0.376}$	Straight tube, R12, R22, R134a, R152a, R407C, R410A
6	Zhang[11]	$\pi_8 = 1/[1 + \exp(2.956h - 0.064)]h = 1/[1 + \exp(0.654 - 5.371\pi_1 + 7.332\pi_2 - 9.541 \times 10^{-4}\pi_3 - 0.1588\pi_4 + 2.277 \times 10^{-2}\pi_5 - 5.202 \times 10^4\pi_6 + 1.731 \times 10^{-2}\pi_7)]$	Straight tube, R12, R134a, R22, R290, R407C, R410A, and R600a
7	Mittal *et al.*[5]	$\pi_9 = 0.0087\pi_3^{-0.351}\pi_4'^{-0.507}\pi_5'^{-1.235}\pi_{10}^{1.538}\pi_{11}^{0.003}\pi_{12}^{-0.463}\pi_{13}^{-0.965}\pi_{14}^{0.098}$	Helical tube R407C

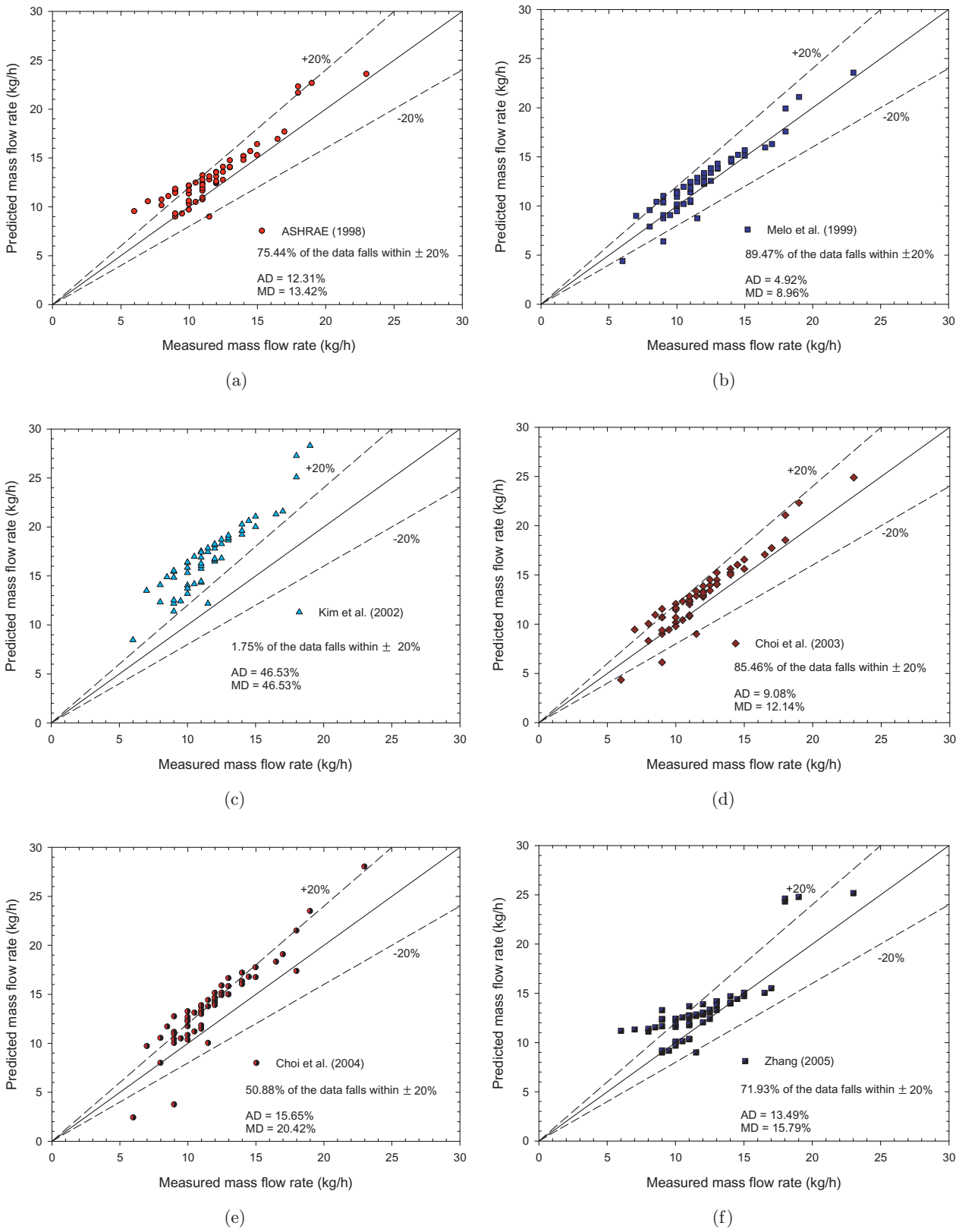

Fig. 6. Comparison of the present measured mass flow rate with existing correlations: (a) ASHARE,[7] (b) Melo *et al.*,[8] (c) Kim *et al.*,[1] (d) Choi *et al.*,[9] (e) Choi *et al.*,[10] (f) Zhang,[11] and (g) Mittal *et al.*[5]

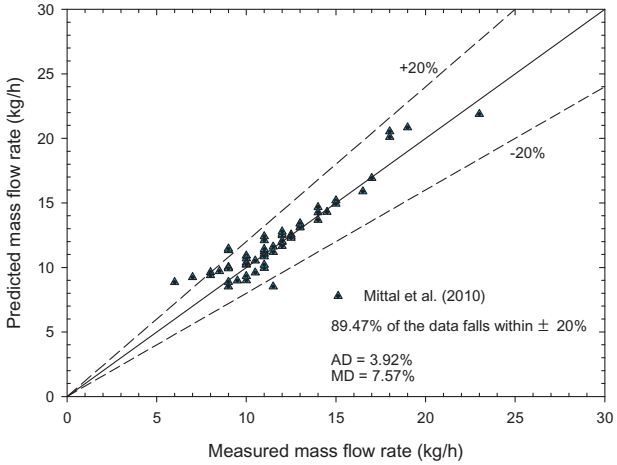

(g)

Fig. 6. (*Continued*)

Table 4. The percentage of the data falls within ±20% and deviations of the predicted and measured mass flow rate.

Correlation	% of the data falls within ±20%	Average deviation (%)	Mean deviation (%)
ASHRAE[7]	75.44	12.31	13.42
Melo *et al.*[8]	**89.47**	**4.92**	**8.96**
Kim *et al.*[1]	1.75	46.53	46.53
Choi *et al.*[9]	85.96	9.08	12.14
Choi *et al.*[10]	50.88	15.65	20.42
Zhang[11]	71.93	13.49	15.75
Mittal *et al.*[5]	**89.47**	**3.92**	**7.57**

3.3.4. *Effect of coil diameter on mass flow rate*

The variation of mass flow rates with coil diameters of 25, 50, and 100 mm is presented in Fig. 5(c). It can be clearly observed that the refrigerant mass flow rate increased with an increase in coil diameter. For 8.5°C of subcooling, as the coil diameter increased from 25 mm to 50 mm, and from 50 mm to 100 mm, the refrigerant mass flow rate increased by 7.5% and 15%, respectively.

3.3.5. *Comparison with the mass flow rate correlations*

The correlations for predicting the refrigerant mass flow rate in the capillary tube have been proposed by several researchers. In general, these correlations are presented as a function of the dimensionless parameters. The summary of the most common dimensionless parameters with descriptions is presented in Table 2. The seven selected mass flow rate correlations, proposed by ASHRAE,[7] Melo *et al.*,[8] Kim *et al.*,[1] Choi *et al.*,[9] Choi *et al.*,[10] Zhang[11] and Mittal *et al.*,[5] are presented as equations in Table 3. Comparisons of the measured mass flow rates with the predicted mass flow rates are shown in Fig. 6. The deviations obtained from the comparisons are summarized in Table 4. The correlations of Mittal *et al.*[5] presented the best predictions with average and mean deviations of 3.92% and 7.57%.

4. Conclusion

In this paper, the flow characteristics of R134a flowing through adiabatic helical capillary tubes were experimentally investigated. Copper tubes with inside diameters of 1.07 mm, 1.27 mm, and 1.62 mm, with coil diameters of 25 mm, 50 mm, and

100 mm, and length of 3.05 m, were used as the test sections. Conclusions can be drawn as follows:

(1) The refrigerant flow inside the capillary tube can be divided into three regions: Subcooled liquid region, metastable liquid region, and metastable two-phase region. The subcooled liquid region was extended by increasing the inlet pressure and degree of subcooling.
(2) The effect of relevant parameters on pressure and temperature distributions showed that the average pressure and temperature along the capillary tube was reduced as the degree of subcooling decreased. Additionally, the pressure and temperature drop along the capillary tube decreased by increasing the capillary tube diameter.
(3) Capillary diameter, capillary coil diameter, degree of refrigerant subcooling, and condensing pressure had varying effects on refrigerant mass flow rate in adiabatic capillary tubes. The results show that capillary diameter has more of a significant effect on mass flow rate than the other variables. For instance, at 6.5°C of subcooling, as the capillary tube diameter increased from 1.07 mm to 1.27 mm, and from 1.27 mm to 1.62 mm, the refrigerant mass flow rate increased by 26.3% and 41.7%, respectively. Similarly, at 8.5°C of subcooling, as the coil diameter increased from 25 mm to 50 mm, and from 50 mm to 100 mm, the refrigerant mass flow rate increased by 7.5% and 15%, respectively.
(4) The Mittal *et al.*[5] correlation gives the best predictions with the average deviation of 3.92% and the mean deviation of 7.57%.

Acknowledgments

The authors would like to acknowledge the Thailand Research Fund, The Office of the Higher Education Commission and The National Research University project for financial support.

References

1. S. G. Kim, M. S. Kim and S. T. Ro, Experimental investigation of the performance of R22 R407C and R410A in several capillary tubes for air-conditioners, *Int. J. Ref.* **25** (2002) 521−531.
2. G. Zhou and Y. Zhang, Experimental investigation on hysteresis effect of refrigerant flowing through a coiled adiabatic capillary tube, *Energy Convers. Manage.* **47** (2006) 3084−3093.
3. C. Park, S. Lee, H. Kang and Y. Kim, Experimentation and modeling of refrigerant flow through coiled capillary tubes, *Int. J. Ref.* **30** (2007) 1168−1175.
4. M. K. Khan, R. Kumar and P. K. Sahoo, An experimental study of the flow of R-134a inside an adiabatic spirally coiled capillary tube, *Int. J. Ref.* **31** (2008) 970−978.
5. M. K. Mittal, R. Kumar and A. Gupta, An experimental study of the flow of R-407C in an adiabatic helical capillary tube, *Int. J. Ref.* **33** (2010) 840−847.
6. O. G. Valladares, Numerical simulation and experimental validation of coiled adiabatic capillary tubes, *Appl. Therm. Eng.* **27** (2007) 1062−1071.
7. *ASHRAE Handbook*: *Refrigeration/SI edition*, Chapter 45 (ASHRAE, 1998).
8. C. Melo, R. T. S. Ferreira, C. B. Neto, J. M. Goncalves and M. M. Mezavila, An experimental analysis of adiabatic tubes, *Appl. Therm. Eng.* **19** (1999) 669−684.
9. J. Choi, Y. Kim and H. Y. Kim, A generalized correlation for refrigerant mass flow rate through adiabatic capillary tube, *Int. J. Ref.* **26** (2003) 881−888.
10. J. Choi, Y. Kim and J. T. Chung, An empirical correlation and rating charts for the performance of adiabatic capillary tubes with alternative refrigerants, *Appl. Therm. Eng.* **24** (2004) 29−41.
11. C. L. Zhang, Generalized correlation of refrigerant mass flow rate through adiabatic capillary tubes using artificial neural network, *Int. J. Ref.* **28** (2005) 506−514.

Isı Bilimi ve Tekniği Dergisi, 32, 1, 19-31, 2012
J. of Thermal Science and Technology
©2012 TIBTD Printed in Turkey
ISSN 1300-3615

HEAT TRANSFER ENHANCEMENT DURING DOWNWARD LAMINAR FLOW CONDENSATION OF R134A IN VERTICAL SMOOTH AND MICROFIN TUBES

Ahmet Selim DALKILIÇ*, İsmail TEKE* and Somchai WONGWISES**
*Yildiz Technical University Mechanical Engineering Faculty Department of Mechanical Engineering
34349 Beşiktaş, İstanbul, Turkey, dalkilic@yildiz.edu.tr
**King Mongkut's University of Technology Thonburi Engineering Faculty Department of Mechanical Engineering
10140 Bangmod, Bangkok, Thailand, somchai.won@kmutt.ac.th

(Geliş Tarihi: 04. 08. 2010, Kabul Tarihi: 08. 11. 2010)

Abstract: This paper presents an experimental comparison of the laminar film condensation heat transfer coefficients of R134a in vertical smooth and micro-fin tubes having inner diameters of 7 mm and lengths of 500 mm. Condensation experiments were performed at a mass flux of 29 kg m^{-2} s^{-1}. The pressures were between 0.8 and 0.9 MPa. The original smooth tube heat transfer model was modified by a well-known friction factor to account for the heat transfer enhancement effects due to the presence of micro-fins on the internal wall surface during annular flow regime conditions. Alterations of the local heat transfer coefficient, and condensation rate along the tube length during downward condensing film were determined, considering the effects of the temperature difference between the saturation temperature and the inner wall temperature of the test tubes, and the condensing temperature on these items. The results show that the interfacial shear stress is found to have significance for the laminar condensation heat transfer of R134a under the given conditions due to its better predictive performance than the classical solution neglecting the interfacial shear stress effect. A comparison of the condensation heat transfer coefficients was also done according to the condensing pressures. New empirical correlations of the condensation heat transfer coefficient belonging to the test tubes are proposed for practical applications.
Keywords: Condensation, Heat transfer coefficient, Downward flow, Laminar flow, Micro-fin tube, Nusselt theory, Annular flow.

İÇ YÜZEYİ PÜRÜZSÜZ VE MİKRO KANATLI DÜŞEY BORULARDA R134A'NIN LAMİNER AKIŞINDAKİ YOĞUŞMASI SIRASINDA MEYDANA GELEN ISI TRANSFERİ İYİLEŞMESİNİN ARAŞTIRILMASI

Özet: Bu çalışmada, iç çapı 7 mm ve uzunluğu 500 mm olan iç yüzeyi pürüzsüz ve mikro kanatlı borular içinde akan R134a'nın laminar film yoğuşması ısı transferi katsayısının deneysel karşılaştırılması sunulmuştur. Yoğuşma deneyleri 29 kg $m^{-2}s^{-1}$ kütlesel akılarında yapılmıştır. Basınçlar 0.8-0.9 MPa değerleri arasındadır. Halka akışı şartlarında geçerli olan iç yüzeyi pürüzsüz boruya ait olan ısı transferi modeli, literatürde yaygın olarak kullanılan bir sürtünme katsayısı ile boru iç yüzeyindeki mikro kanatların varlığından ötürü meydana gelen ısı transferi iyileşmesini hesaba katacak şekilde modifiye edilmiştir. Düşey olarak yoğuşan film esansındaki yerel ısı transferi katsayılarındaki değişim ve boru boyunca oluşan yoğuşma miktarı, doyma sıcaklığı ile boru iç yüzeyindeki sıcaklık farkı ve yoğuşma sıcaklığı da dikkate alınarak bulunmuştur.Sonuçlar arayüzey kayma gerilmesinin çalışmada belirtilen şartlarda R134a'nın laminer yoğuşma ısı transferi üzerinde öneme sahip olduğunu ve önerilen modelin arayüzey kayma gerilmesinin etkisinin ihmal edildiği geleneksel çözümden daha iyi sonuçlar vermesiyle göstermiştir. Ayrıca, yoğuşma basınçlarına göre ısı transferi katsayıları da karşılaştırılmıştır. Pratik uygulamalar için test edilen borulara ait yeni amprik yoğuşma ısı transferi eşitlikleri önerilmiştir.
Anahtar Kelimeler: Yoğuşma, Isı transferi katsayısı, Düşey akış, Laminer akış, Micro kanatlı boru, Nusselt teorisi, Halka akış.

NOMENCLATURE

A_i	tube inside surface area, m^2
A_{mf}/A_s	augmentation ratio
c_p	specific heat capacity at constant pressure, J $kg^{-1}K^{-1}$
d	inside diameter of tube, m
Exp	experiment
G	mass flux, kg $m^{-2}s^{-1}$
g	gravitational acceleration, m s^{-2}
h	heat transfer coefficient, W $m^{-2}K^{-1}$
i	specific enthalpy, j kg^{-1}

i_{fg} latent heat of condensation, J kg^{-1}
i_{fg}' correction factor included latent heat of condensation, J kg^{-1}
k thermal conductivity, W $m^{-1}K^{-1}$
l tube length, m
L characteristic length
l_f fin length, m
m mass flow rate, kg s^{-1}
n number of fins per unit length
Nu Nusselt number
P pressure, MPa
Pr Prandtl number
Re Reynolds number
Q heat transfer rate, W
T temperature, °C
u axial velocity, m s^{-1}
w tube thickness, m
x vapour quality
y wall coordinate
z axial coordinate
$\Delta T_{r,sat}$ $T_{r,sat}$-T_{wi} , K

Greek symbols
δ film thickness, m
δ* dimensionless film thickness
μ dynamic viscosity, kg $m^{-1}s^{-1}$
ρ density, kg m^{-3}
ρ_g* fictitious vapour density defined by Carey (1992), kg m^{-3}
β spiral angle, rad
τ shear stress, N m^{-2}

Subscripts
avg average
cond condensate
corr correlation
eq equivalent
exp experimental
F frictional term
G gravitational term
g gas/vapour
i inlet
l liquid
M momentum term
o outlet
ph preheater
r refrigerant
sat saturation
T total
TS test section
w water
wi inner wall

INTRODUCTION

The taking cognisance of the need to increase the thermal performance of heat exchangers, thereby effecting savings of energy, material and cost, as well as a consequential mitigation of environmental degradation, has led to the development and use of many heat transfer enhancement techniques. In general, enhancement techniques can be divided into two groups: active and passive. Active techniques require external forces, e.g., electrical field, acoustic or surface vibration. Passive techniques require special surface geometries, such as rough surface, extended surface for liquids etc., or fluid additives. Both techniques have been used by researchers for 140 years to increase heat transfer rates in heat exchangers. If two or more of these techniques are utilised together to achieve enhancement, this is referred to as compound enhancement.

The usage of micro-fin tubes has increased the heat transfer performance of tubes with relatively low pressure drop increases in commercial and air conditioning applications since the 1980s. Micro-fins improve heat transfer in both single-phase and two-phase applications, and are one of the most efficient and common heat transfer enhancement mechanisms for heat exchangers due to their superior heat transfer performance.

Many experimental investigations have been performed to determine the effects of fin geometry, tube diameter, refrigerant, etc., on the condensation heat transfer and pressure drop performance of micro-fin tubes. The presence of the micro-fins inside the tube enhances the heat transfer by providing an increased surface area. They cause not only uniform liquid film distribution around the circumference of the tube, but also turbulence induced in the liquid film.

Many studies on condensation have been done with horizontal micro-fin tubes. Wang and Honda (2003), Cavallini et al. (1999), Chamra et al. (1996), and Schlager (1990) have proposed correlations and theoretical models to predict the heat transfer, and they have made intensive comparisons of previously proposed correlations with a large body of experimental data at the same time. Helically grooved, 18° helix angled, horizontal micro-fin tubes have been used in air conditioners recently, because of their better heat transfer performance compared to smooth tubes.

However, there are few studies on the condensation of R134a with down flow in vertical micro-fin tubes. Briggs et al. (1998) have used large diameter tubes around 20.8 mm with CFC113. The Shah (1979) correlation has commonly been used by researchers for turbulent condensation conditions.

The flow pattern occurring in many real convective condensation applications is that of an annular flow along a tube length, which is characterised by a phase interface separating a thin liquid film from the gas flow in the core region. Researchers, in relation to both analytical and experimental work, have paid attention to this flow regime due to its practical importance.

The first theoretical solution for predicting heat transfer coefficients was proposed by Nusselt (1916). A linear temperature profile through a laminar film flowing downwards without entrainment on a vertical plate was assumed, waves and an interfacial shear effect between the phases were neglected in his analysis. Nusselt-type analysis can be used for convective condensation in round tubes under these conditions. Detailed information on the studies in the literature regarding modifications of the Nusselt theory can be seen in the authors' previous publications (Dalkilic et al., 2009a, 2009b).

Carey (1992) developed a theoretical model to investigate convective condensation in round tubes during an annular flow regime. He modified Nusselt's theory (1916) by taking into account the interfacial shear stress and new simplified equations. An iterative technique for the calculation of the interfacial shear and the determination of the local heat transfer coefficients were proposed in this study. Any alteration of the thermo-physical properties of the refrigerant for condensation was also neglected due to the small pressure drop along the test tube. But it is reported that the analysis in his study cannot be applicable to fully or partially turbulent film flow.

Dalkilic et al. (2009a) used Carey's (1992) theoretical model for the downward condensation of R134a to investigate the local and average heat transfer coefficients in a vertical smooth tube at low mass flux conditions. The calculated results obtained from the modified Nusselt model incorporating interfacial shear stress, the modified Nusselt model with the McAdams correction factor (1954), and the classical Nusselt model (1916), were compared with the experimental data. Comparisons with the data for laminar flow at low mass flux show that the modified Nusselt model without a correction factor predicts the data well. Experimental results show that the interfacial shear stress that was incorporated into the modified Nusselt model (1916) affects the condensation process of R134a in a vertical smooth tube.

The most common passive heat transfer enhancement technique nowadays for condensers is the use of helical micro-fin tubes. In the present study, tests are performed in smooth and micro-fin tubes with the same dimensions and conditions for the purpose of comparison. The helical micro-fin tube, which was produced for commercial usage, used as test tube has a 0.5 m length, 7.94 mm outside diameter, 18° helix angle and 50 fins. To the best of the authors' knowledge, there has been insufficient work dealing with condensation heat transfer of HFC-134a in small diameter micro-fin tubes during downward flow. Although some information is currently available, there still remains room for further research. Moreover, it should also be noted that the reported mass fluxes, heat fluxes, condensation pressures and dimensions of the test tube do not include the parameters presently studied (except for the authors' previous publications (Balcilar et al. (2010a, 2010b), Dalkilic et al. (2007, 2008, 2009, 2010)). The aim of the present study is to determine the heat transfer enhancement, comparing smooth and micro-fin tubes, and investigate the alteration of the local heat transfer coefficients, film thicknesses, and condensation rates along the test tubes. In addition to this, the effect of different experimental parameters such as condensing temperature difference between saturation and wall inlet temperature of the test tube, condensation pressure on the convective heat transfer coefficient of R134a and condensation rate are also shown and then discussed. Moreover, new correlations for the condensation heat transfer coefficient are proposed for practical applications for smooth and micro-fin tubes separately.

EXPERIMENTAL SETUP

A schematic diagram of the test apparatus is shown in Figure 1. The refrigerant loop consists of an evaporator, test section and condenser loop. The refrigerant is circulated by a gear pump controlled by an inverter. The refrigerant flows in series through the bypass line, a coriolis type refrigerant flow meter which has a sensitivity of 0.1%, an evaporator, a separator, and a sight glass tube, and then enters the test section. The evaporator controls the inlet quality before entering the test section, and consists of a plate heat exchanger designed to supply heat to adjust the inlet quality for the vaporisation of the refrigerant. The circulated water flow rate of the evaporator is measured by a turbine-type flow meter which has a sensitivity of 2%. After exiting the test section, the vapour phase of R134a, which comes from the liquid-gas separator, continues to the condenser. The flow rate of liquid R134a from the liquid-gas separator is measured in a vessel to check the condition of the apparatus. A plate heat exchanger is used as a condenser. The liquid phase of R134a, from the condenser and separator, is collected in a reserve tank which has a water coil to balance the pressure of liquid R134a. There is another sight glass to check the saturated liquid R134a before the refrigerant pump. The pressures are measured by pressure transducers which have sensitivities of 0.5%.

The test section is a vertical counter-flow tube-in-tube heat exchanger with refrigerant flowing in the inner tube and cooling water flowing in the annulus. The inner and outer tubes are made from copper having inner diameters of 7 mm and 16 mm, respectively. The length of the heat exchanger is 0.5 m. A thermostat is used to control the inlet temperature of the water. The flow rate of cooling water is measured using a turbine-type flow meter which has a sensitivity of 1%. The pressure drop is measured by a differential pressure transducer, which has a sensitivity of 0.05%, installed between the inlet and outlet of the test section. The temperatures of the inlet and outlet of the test section are measured by pt100 sensors and T-type thermocouples. A band-type heater is

wrapped around the copper tube line from the exit of the evaporator to the inlet of the test tube to control the system pressure of the refrigerant flow.

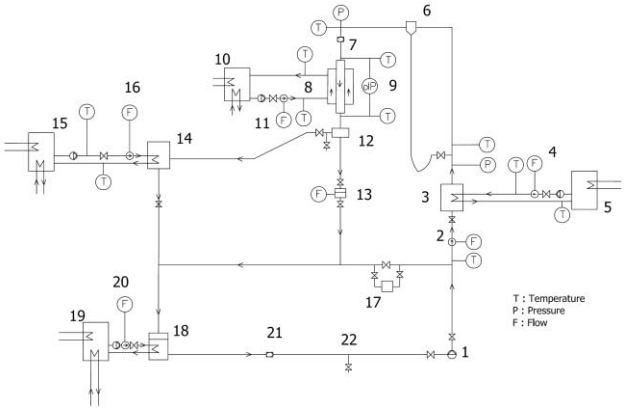

1- Refrigerant Pump 2- Coriolis Flow Meter 3- Evaporator 4- Turbine Flow Meter 5- Thermostat System 6- Liquid/Gas Separator 7- Sight Glass 8- Test Section 9- Differential Pressure Transmitter 10- Thermostat System 11- Turbine Flow Meter 12- Liquid/Gas Separator 13- Scaled Vessel 14- Condenser 15- Thermostat System 16- Rotameter 17- Filter/Dryer 18- R134a Reserve Tank 19- Thermostat System 20- Rotameter 21- Sight Glass 22- R134a Charging Point

Figure 1. Schematic diagram of experimental apparatus.

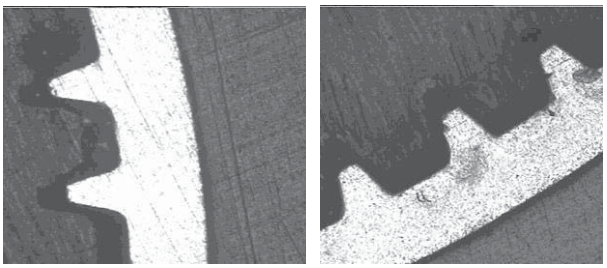

(a) Cross-section of the micro-fin tube by electron microscope (100x) (Dalkilic, 2007)

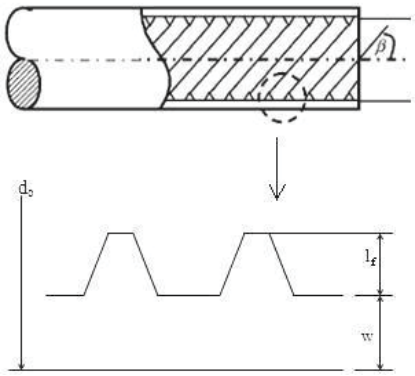

(b) Schematic cross-section of the micro-fin tube (Dalkilic and Wongwises, 2009t)

Figure 2. Detailed cross-section of the test tube.

A Panasonic-Nais PLC device was used to record and collect data from all flow meters, pressure transducers and differential pressure transmitters. The computer programme collected 10 types of data and recorded the average values each second using an MS Excel programme spreadsheet.

Figure 2 shows detailed cross section of the tested micro-fin tube which was produced for commercial usage and its geometric parameters can be seen in Table 1.

Table 1. Geometry of the tested micro-fin tube.

Test tube	Micro-fin tube
l (mm)	500
d_o (mm)	7.94
w (mm)	0.28
l_f (mm)	0.15
ß (°)	18
n	100
A_{mf}/A_s	1.38

DATA REDUCTION

The data reduction of the measured results can be analysed as follows:

The Inlet Vapour Quality of The Test Section ($x_{TS,i}$)

$$x_{TS,i} = \frac{i_{TS,i} - i_{l@T_{TS,i}}}{i_{fg@T_{TS,i}}} \quad (1)$$

where $i_{l@T_{TS,i}}$ is the specific enthalpy of the saturated liquid based on the inlet temperature of the test section, $i_{fg@T_{TS,i}}$ is the specific enthalpy of vaporization based on the inlet temperature of the test section, $i_{TS,i}$ is the refrigerant specific enthalpy at the test section inlet and is given by:

$$i_{TS,i} = i_{ph,i} + \frac{Q_{ph}}{m_r} \quad (2)$$

where $i_{ph,i}$ is the inlet specific enthalpy of the liquid refrigerant before entering the pre-heater, m_r is the mass flow rate of the refrigerant, and Q_{ph} is the heat transfer rate in the pre-heater:

$$Q_{ph} = m_{w,ph} c_{p,w} (T_{w,i} - T_{w,o})_{ph} \quad (3)$$

where $m_{w,ph}$ is the mass flow rate of the water entering the preheater, cp,w is the specific heat of water, $(T_{w,i} - T_{w,o})_{ph}$ is the temperature difference between inlet and outlet positions of the preheater.

The Outlet Vapour Quality of The Test Section ($x_{TS,o}$)

$$x_{TS,o} = \frac{i_{TS,o} - i_{l@T_{TS,o}}}{i_{fg@T_{TS,o}}} \quad (4)$$

where $i_{TS,o}$ is the refrigerant specific enthalpy at the test section outlet, $i_{l@T_{TS,o}}$ is the specific enthalpy of the saturated liquid based on the outlet temperature of the test section, and $i_{fg@T_{TS,o}}$ is the specific enthalpy of vaporization. The outlet specific enthalpy of the refrigerant flow is calculated as follows:

$$i_{TS,o} = i_{TS,i} - \frac{Q_{TS}}{m_{ref}} \quad (5)$$

where the heat transfer rate, Q_{TS}, in the test section is obtained from:

$$Q_{TS} = m_{w,TS} c_{p,w} (T_{w,o} - T_{w,i})_{TS} \quad (6)$$

where $m_{w,TS}$ is the mass flow rate of the water entering the test section, and $(T_{w,o} - T_{w,i})_{TS}$ is temperature difference between outlet and inlet position of the test section.

The Average Heat Transfer Coefficient

$$h_{exp} = \frac{Q_{TS}}{A_{wi}(T_{r,sat} - T_{wi})} \quad (7)$$

where h_{exp} is the experimental average heat transfer coefficient, Q_{TS} is the heat transfer rate in the test section, T_{wi} is the average temperature of the inner wall, $T_{r,sat}$ is the saturation temperature of the refrigerant, and A_{wi} is the inside surface area of the test section:

$$A_{wi} = \pi d l \quad (8)$$

where d is the inside diameter of the test tube. l is the length of the test tube. It should be noted that the increase in tube area (A_{mf}/A_s) in Table 1 is considered for the surface area of the micro-fin tube during calculation process.

THE LAMINAR ANNULAR FILM CONDENSATION MODEL

Figure 3 shows the steady-state physical model of downward film condensation of R134a in a vertical tube. The assumptions were made as follows: laminar film flow; saturated state for the vapour of R134a; condensed film of R134a along the tube surface; constant physical properties corresponding to inlet pressure and temperature conditions; no entrainment. A Nusselt-type analysis is valid under these assumptions for the internal convective condensation in a round tube. The interfacial shear effect at the liquid-vapour interface is taken account due to the much greater vapour velocity than the film velocity. It should be noticed that the inertia and downstream diffusion contributions were also neglected.

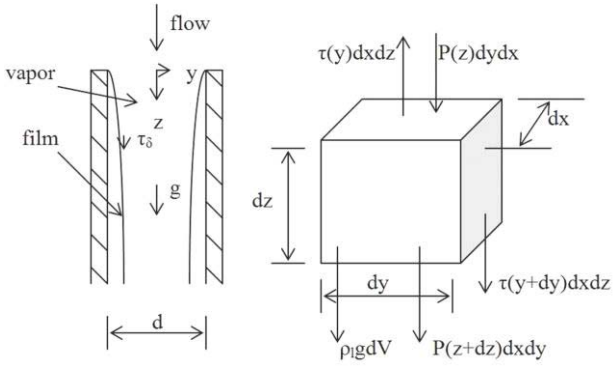

Figure 3. System model for analysis of downward condensation (Dalkilic et al., 2009a).

The differential element's force balance in the control volume is given as follows:

$$\rho_l g dx dy dz + \tau_\delta (y + dy) dx dz + P(z) dx dy = \tau_\delta (y) dx dz + P(z + dz) dx dy \quad (9)$$

The hydrostatic pressure gradient, the frictional pressure gradient and the momentum pressure gradient composes the total two-phase pressure gradient and it can be seen as:

$$\left(\frac{dP}{dz}\right)_T = \left(\frac{dP}{dz}\right)_G + \left(\frac{dP}{dz}\right)_F + \left(\frac{dP}{dz}\right)_M \quad (10)$$

where the hydrostatic pressure gradient is:

$$\left(\frac{dP}{dz}\right)_G = \rho_g g \quad (11)$$

The interfacial shear stress causes the occurrence of the frictional pressure gradient in the vapour (Carey, 1992) and it can be expressed as follows:

$$\left(\frac{dP}{dz}\right)_F = -\frac{4\tau_\delta}{(d - 2\delta)} \quad (12)$$

As a result of the one-dimensional two-phase separated-flow analysis, the momentum pressure gradient can be calculated as follows:

$$\left(\frac{dP}{dz}\right)_M = -G^2 \frac{d}{dz}\left[\frac{x^2}{\rho_g \alpha} + \frac{(1-x)^2}{\rho_l (1-\alpha)}\right] \quad (13)$$

Eq. (14) is obtained from Eq. (13) under the following assumptions: liquid density of R134a is much greater than its vapour density; the variation in vapour quality is bigger than the variation in the void fraction along the test tube (Carey, 1992):

$$\left(\frac{dP}{dz}\right)_M = -\frac{2xdG^2}{\rho_g(d-2\delta)}\frac{dx}{dz} \quad (14)$$

Carey (1992) modified this by means of the usual idealisation on pressure gradient According to his theory; pressure gradient has an equal value in the vapour phase and in the liquid film as expected. A fictitious vapour density is defined to facilitate analysis of the momentum transport in the liquid film, as reported below (Carey, 1992):

$$\rho_g^* g = \rho_g g - \frac{4\tau_\delta}{d-2\delta} - \frac{2xdG^2}{\rho_g(d-2\delta)}\left(\frac{dx}{dz}\right) \quad (15)$$

The velocity gradient can be obtained from Eq. (16) using interfacial shear stress as follows:

$$\frac{du}{dy} = \frac{(\delta - y)(\rho_l - \rho_g^*)g}{\mu_l} + \frac{\tau_\delta}{\mu_l} \quad (16)$$

Integration of Eq. (16) gives Eq. (17) using u=0 at y=0:

$$u = \frac{(\rho_l - \rho_g^*)g}{\mu_l}\left(y\delta - \frac{y^2}{2}\right) + \frac{\tau_\delta y}{\mu_l} \quad (17)$$

The liquid flow rate can be derived from the velocity profile as follows:

$$\dot{m} = \pi d\delta u_{avg}\rho_l = \left[\frac{(\rho_l - \rho_g^*)g\delta^2}{3\mu_l} + \frac{\tau_\delta\delta}{2\mu_l}\right]\pi d\delta\rho_l \quad (18)$$

Eq. (19) can be expressed from the overall mass and energy balance in the case of a falling film without sub-cooling (Carey, 1992):

$$k_l\left(\frac{T_{r,sat} - T_{wi}}{\delta}\right)\pi ddz = i_{fg}d\dot{m} \quad (19)$$

The energy balance in Eq. (19) yields quality gradient as (Carey, 1992):

$$\dot{q} = h_l\pi d\Delta z\Delta T_{sat} = \dot{m}_{cond}i_{fg} \quad (20)$$

$$\frac{dx}{dz} = \frac{4q''}{DGi_{fg}} = \frac{4h_l(T_{r,sat} - T_{w,i})}{DGi_{fg}} \quad (21)$$

Eq. (19) can be rearranged using Eq. (21): (δ=0, x=0)

$$\delta^4 + \frac{4}{3}\frac{\tau_\delta\delta^3}{(\rho_l - \rho_g^*)g} = \frac{4k_l\mu_l(T_{r,sat} - T_{wi})z}{\rho_l(\rho_l - \rho_g^*)gi_{fg}} \quad (22)$$

The film thickness equation, belong to Nusselt's analysis (Nusselt, 1916), can be obtained when the interfacial shear stress effects are omitted as shown in Eq. (23):

$$\delta(z) = \left[\frac{4\mu_l k_l z(T_{r,sat} - T_{wi})}{gi_{fg}\rho_l(\rho_l - \rho_g)}\right]^{1/4} \quad (23)$$

Application of the correction factor to the latent heat of vaporisation per unit mass can be seen from Eq. (24) as follows:

$$i_{fg}' = i_{fg}\left[1 + \left(\frac{3}{8}\right)\frac{c_{pl}(T_{r,sat} - T_{wi})}{i_{fg}}\right] \quad (24)$$

The film heat transfer coefficient is shown in Eq. (25) assuming a linear temperature distribution in the film region as:

$$h_l(z) = \frac{k_l}{\delta(z)} \quad (25)$$

The vapour flow can be behaved as a single phase flow in the tube as an approach due to the thin film and the much greater mean velocity of vapour than the liquid velocity at the interface caused by the high viscosity of the liquid phase compared to the vapour phase. Furthermore, vapour velocity is assumed to be zero between the phases in calculations. The interfacial shear can be obtained by means of the conventional single phase correlation with these assumptions (Carey, 1992):

$$\tau_\delta = f_g\left(\frac{\rho_g u_g^2}{2}\right) = f_g\left(\frac{G^2x^2}{2\rho_g(1-4\delta/d)}\right) \quad (26)$$

The friction factor can be expressed for round smooth tubes as (Carey, 1992):

$$f_g = 0.079\left[\frac{Gx(d-\delta)}{\mu_g(1-4\delta/d)}\right]^{-0.25} \quad (27)$$

Cavallini et al. (1997b) proposed a friction factor for round micro-fin tubes including their fin parameters as follows:

$$f_g = \frac{\left[1.74 - 2.\log(2Rx_f)\right]^{-2}}{4} \quad (28)$$

where geometry enhancement factor of micro-fin tube in comparison to the smooth tube is expressed in Eq. (29) as (Cavallini, 1997b):

$$Rx_f = \frac{0.18\left(\frac{l_f}{d}\right)}{(0.1 + \cos\beta)} \quad (29)$$

It is possible for the McAdams correction factor (1954) to be used to consider the effects of the waviness and rippling in the film regarding the increase in heat transfer. It can be used for downward laminar film condensation, and it corrects the Nusselt's equation (1916) in terms of the above explanation as follows:

$$h_{wave} = 1.2\frac{k_l}{\delta(z)} \quad (30)$$

Carey (1992) offered an iterative technique for the determination of film heat transfer coefficient and interfacial shear using specified mass flux, tube wall inlet temperature, and condensation pressure and thermo physical properties. Firstly, a value for a film thickness is guessed, the quality gradient is obtained from Eqs. (21) and (25). The interfacial shear stress value is calculated by means of Eqs. (26) and (28), and Eq. (15) gives the fictitious vapour density.

The substitution of the estimated film thickness values, calculated fictitious vapour density and interfacial shear values are performed into Eq. (22). These values are updated and the film thickness value repeatedly estimated until convergence. The level of accuracy judges the acceptable values of estimated film thickness and calculated film heat transfer coefficient. Figure 4 shows this procedure step by step in detail.

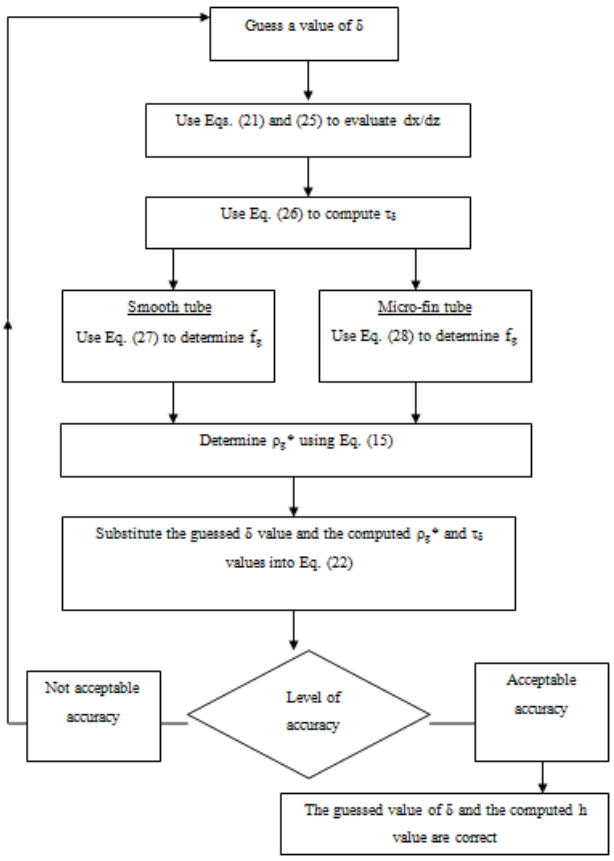

Figure 4. Flow chart of iteration process.

It should be noted that it is possible Nusselt's theory (1916) to be used for both condensation on vertical flat surfaces and condensation outside tubes and also inside the tubes if the tubes are large in diameter, compared with the film thickness. Nusselt (1916) proposed the average convective heat transfer coefficient as follows ($0<Re_l<30$):

$$h_{Nusselt} = 0.943\left[\frac{\rho_l(\rho_l-\rho_g)gi_{fg}k_l^3}{\mu_l l(T_{r,sat}-T_{wi})}\right]^{1/4} \quad (31)$$

RESULTS AND DISCUSSION

The experiments of smooth and micro-fin tubes were done using R134a in tubes at the mass flux of 29 kg $m^{-2}s^{-1}$ and pressures between 0.8-0.9 MPa. The modified Nusselt theory including the interfacial shear effect was used in the calculations of all local heat transfer coefficients. Figures 5-8 show the effect of the temperature difference between the saturated temperature of R134a and inner wall temperature of the micro-fin tube ($\Delta T_{r,sat}$) and the condensation pressure on the local heat transfer coefficients, film thickness and condensation rates along the micro-fin tube's length.

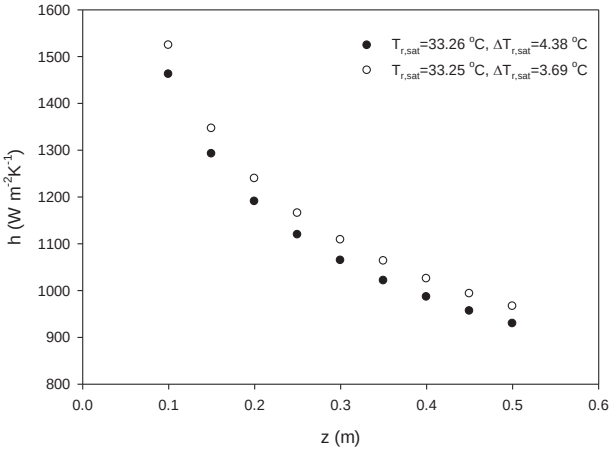

Figure 5. Comparison of local heat transfer coefficients of micro-fin tube at different $\Delta T_{r,sat}$ for the mass flux of 29 kg $m^{-2}s^{-1}$ and a constant condensation temperature.

The decrease in the local condensation heat transfer coefficient and condensation rate of micro-fin tube along the tube length, calculated by the proposed model, can be seen from Figures 5 and 6. It is because of this that the film thickness and hence total condensation rate increase from the top to the bottom of the test tube through the direction of gravity. There is high local condensation rate along the tube length at the tube entrance caused by high vapour velocity and high interfacial shear. It decreases along the tube length with decreasing vapour velocity due to an increase in condensation rate. Oh and Revankar (2005) have the similar characteristics of trend lines in their study.

The effect of pressure, in other saying, the effect of the saturation temperature on the local heat transfer coefficients and condensation rate along the tube length for the micro-fin tube, calculated by the proposed model, can be seen from Figures 7 and 8. Low condensation pressures, in other saying, high temperature differences and change of physical properties at low pressure induce higher local heat transfer coefficients than those of high condensation pressure. These results and the general trend are found

to be compatible with the Nusselt (1916) theory in which the average and local heat transfer coefficients are proportional to $\Delta T_{r,sat}^{-0.25}$ and $z^{-0.25}$.

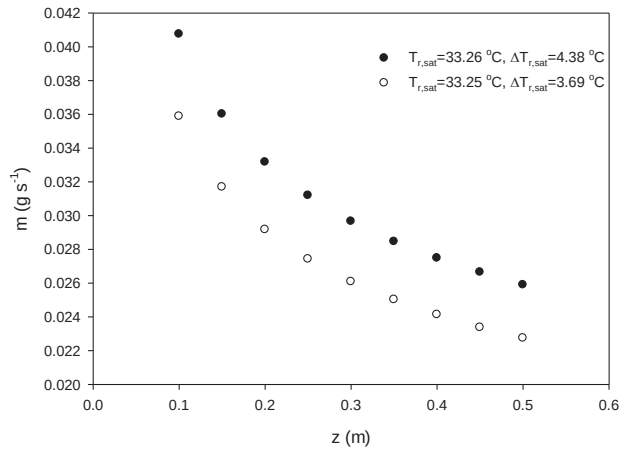

Figure 6. Comparison of local condensation rates of micro-fin tube at different $\Delta T_{r,sat}$ for the mass flux of 29 kg m^{-2}s^{-1} and a constant condensation temperature.

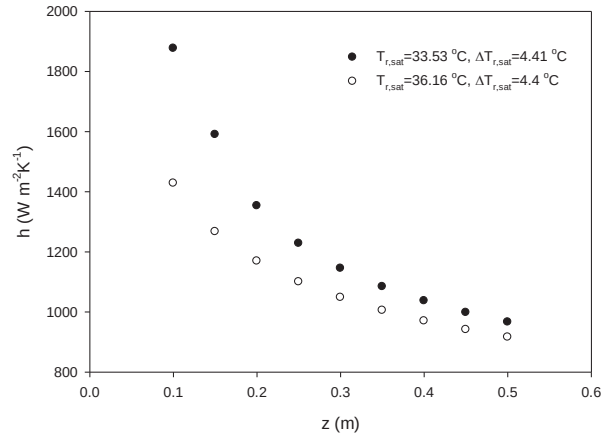

Figure 7. Comparison of local heat transfer coefficients of micro-fin tube at different condensation temperatures (33.53 and 36.16 °C) for the mass flux of 29 kg m^{-2}s^{-1} and $\Delta T_{r,sat}$=4.4 °C.

The data shown in all figures and tables were collected in an annular flow regime in Hewitt and Robertson's (1969) flow pattern map, and also checked by sight glasses at the inlet and outlet of the test section.

The determination of the film heat transfer coefficient for the laminar flow at low mass flux for the smooth and micro-fin tubes was performed by means of the modified Nusselt theory (Carey, 1992), the McAdams correlation (1954) and the classical Nusselt theory (1916).

The modified Nusselt theory in Eq. (22) including the interfacial shear stress effect is found to be the most suitable model for the experimental data from the micro-fin tube according to the analysis of Figure 9. Besides this, it can be also understood from Figure 9 that the investigated experimental conditions do not require the usage of McAdams correction factor (1954) in Eq. (30) to take account the wave effect at the vapour-liquid interface occurred by low mass flux. In addition to this, the classical Nusselt theory in Eq. (31) overestimates the heat transfer coefficients considering the deviation of 30%.

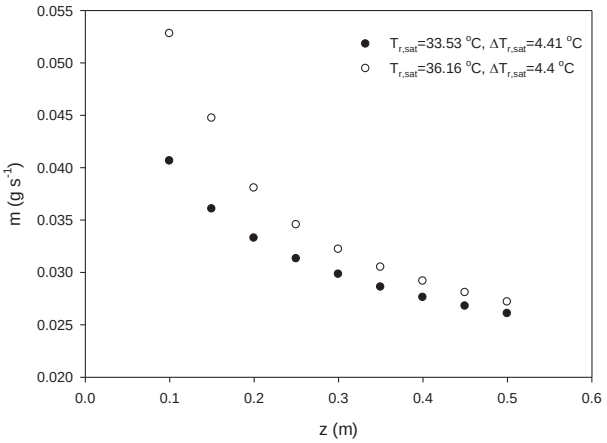

Figure 8. Comparison of local condensation rates of micro-fin tube at different condensation temperatures (33.53 and 36.16 °C) for the mass flux of 29 kg m^{-2}s^{-1}and $\Delta T_{r,sat}$=4.4 °C.

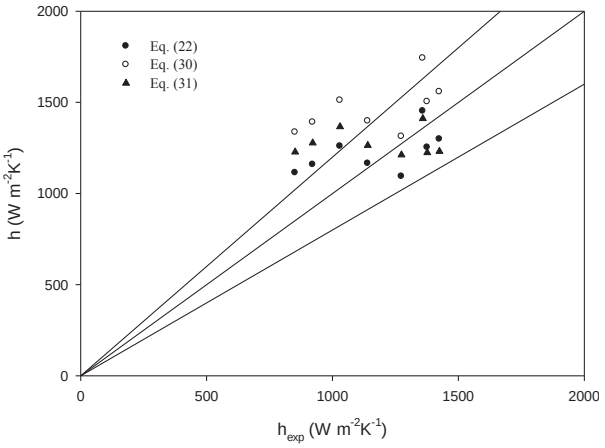

Figure 9. Comparisons between the experimental and calculated condensation heat transfer coefficients for the micro-fin tube under the experimental conditions: G=29 kg m^{-2}s^{-1}, P= 0.8-0.9 MPa, $T_{r,sat}$= 31.73-35.28 ºC, $\Delta T_{r,sat}$= 1.67-4.4 °C, x_{avg} = 0.82-0.99.

The enhancement on the condensation heat transfer coefficients using smooth and micro-fin tubes at the approximately similar experimental conditions, shown in Table 2, such as mass flux, condensing pressure, vapour quality, $\Delta T_{r,sat}$ can be seen from Figure 10. According to the result of analysis, the heat transfer enhancement of 60-82% is gained by means of the usage of micro-fin in comparison to the smooth tube.

Figure 11 shows the effect of the condensation pressure on the heat transfer coefficients. According to Figure 11, the average experimental condensation heat transfer coefficients obtained from Eq. (7) decrease with increasing system pressure as expected.

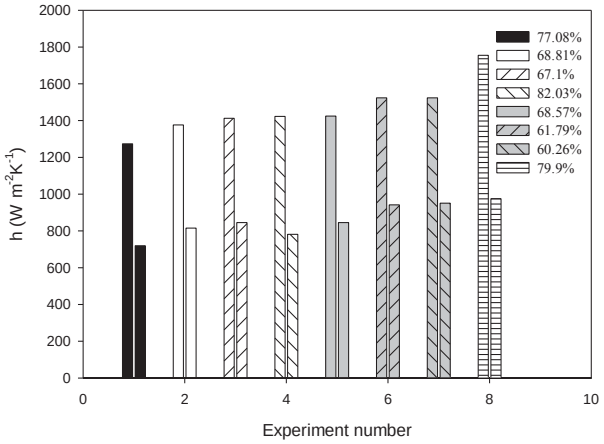

Figure 10. Comparisons between the experimental condensation heat transfer coefficients for the smooth and micro-fin tubes under the experimental conditions:
G=29 kg $m^{-2}s^{-1}$, P= 0.8-0.9 MPa, $T_{r,sat}$= 31.08-36.16 ºC, $\Delta T_{r,sat}$= 2.71-4.86 °C, x_{avg} = 0.8-0.99.

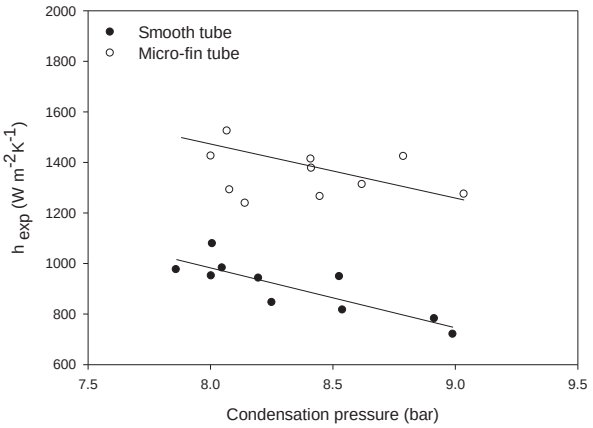

Figure 11. Comparison of average experimental convective heat transfer coefficients of the smooth and micro-fin tubes for the mass flux of 29 kg $m^{-2}s^{-1}$ at pressures of 0.77-0.90 MPa.

Bellinghausen and Renz's (1992) method is used to present correlations for the smooth (Dalkilic, 2009a) and micro-fin tubes separately. Although their correlation's accuracy seems poor with their data (Bellinghausen and Renz, 1992) it can be used in Nusselt-type analysis for the conditions of laminar film with stagnant vapour and a wave-free interface in a smooth tube. Therefore, the low mass flux data (29 kg $m^{-2}s^{-1}$) were used. It should be noted that these correlations simplify the calculations for practical applications. The comparison of the results from the present correlation with the experimental data is shown in Figure 12. The majority of the data fall within ±25% of the proposed correlation.

Table 2. Numerical values used in Figure 10.

Exp. number	Tube type	$T_{r,sat}$ (°C)	G (kg $m^{-2}s^{-1}$)	x	$\Delta T_{r,sat}$ (°C)	h (W $m^{-2}K^{-1}$)	Augmentation rate (h, %)
1	Smooth	35.982	28.434	0.936	3.989	719.413	77.08
1	Micro-fin	36.169	28.664	0.938	4.405	1273.982	
2	Smooth	34.084	28.65	0.99	3.609	815.385	68.81
2	Micro-fin	33.537	28.432	0.8	4.419	1376.521	
3	Smooth	32.836	28.73	0.88	3.69	845.127	67.1
3	Micro-fin	33.527	28.478	0.88	4.56	1412.718	
4	Smooth	35.669	29.74	0.85	4.861	781.32	82.03
4	Micro-fin	35.141	28.72	0.84	4.676	1422.693	
5	Smooth	32.83	28.73	0.88	3.699	845.127	68.57
5	Micro-fin	31.723	29.75	0.82	4.457	1424.652	
6	Smooth	32.59	28.903	0.938	3.09	941.773	61.79
6	Micro-fin	32.019	28.57	0.925	2.904	1523.75	
7	Smooth	31.73	28.79	0.97	2.76	950.782	60.26
7	Micro-fin	32.019	28.57	0.925	2.904	1523.75	
8	Smooth	31.082	28.972	0.864	3.04	975.225	79.9
8	Micro-fin	31.174	28.81	0.98	2.719	1755.282	

The correlations are presented as:

For the smooth tube (Dalkilic et al. (2009a):

$$\delta^* = 7.4.Re_l^{0.018} \quad (32)$$

For the micro-fin tube:

$$\delta^* = 6.19.Re_l^{0.018} \quad (33)$$

$$h_l = (k_l/L).(1/\delta^*) \quad (34)$$

Liquid Reynolds number:

$$Re_l = \dot{m}/(\pi.d.\mu_l) \quad (35)$$

Liquid Nusselt number:

$$Nu_l = 1/\delta^* \quad (36)$$

Dimensionless film thickness:

$$\delta^* = \delta/L \quad (37)$$

Characteristic length:

$$L = (\delta_l^2/g)^{1/3} \quad (38)$$

Nusselt number:

$$Nu_l = h_l.L/k_l \quad (39)$$

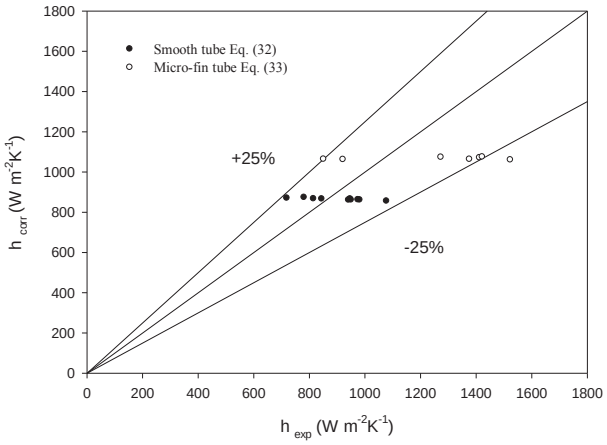

Figure 12. Comparison of the experimental convective heat transfer coefficient with the present heat transfer correlations for the smooth tube and micro-fin tubes.

CONCLUSION

Generally, horizontal micro-fin tubes are used to enhance convective heat transfer during in-tube condensation. According to the review of literature, only a few experimental works (Dalkilic and Wongwises, 2009) have been done for the heat transfer and flow characteristics inside enhanced vertical tubes. There isn't any previous work with the content and parameters in the literature apart from the present paper. Therefore, the present study has a large importance for the development of new types of compact heat exchangers in all industrial fields.

The investigation of the convective heat transfer coefficient of R134a during condensation in vertical downward flow at a low mass flux in smooth and micro-fin tubes was presented in the paper. It should be noted that research on the various parameters used in the present study is still limited. The results from this study are expected to fill the gap in the literature due to the insufficient works regarding condensation inside vertical micro-fin tubes in the literature. The accurate and repeatable heat transfer data for the condensation of R134a in a downward flow at a low mass flux inside smooth and micro-fin tubes were obtained. Detailed investigation and discussion were performed on the effects of various relevant parameters such as condensing temperature, condensation temperature difference, vapour quality and mass flux on the heat transfer.

The investigation of the local and average heat transfer coefficients in vertical smooth and micro-fin tubes at low mass flux conditions were done by means of the theoretical model from Carey (1992). Cavallini et al. (1997b)'s friction factor was added to the model for the micro-fin tube's calculations. The experimental data was compared with the calculated results obtained from the modified Nusselt model incorporating the interfacial shear stress, along with the modified Nusselt model with McAdams correction factor and also with the classical Nusselt model.

As an expected result, the condensation rate reaches the highest value at the pipe entrance where the highest local heat transfer coefficients exist. The film thickness is highest at the end of the tube where the local heat transfer coefficients are lowest. This result also shows the experiments' accuracy and validity.

According to the comparisons with laminar flow at low mass flux data, the modified Nusselt model without a correction factor predicts the data well. As a result of the analysis, the interfacial shear stress that was incorporated into the modified Nusselt model affects the condensation process of R134a in a vertical smooth and micro-fin tube. The classical Nusselt theory and the McAdams heat transfer coefficient cannot predict the data well.

Convective condensation heat transfer coefficients of micro-fin tube are found to be 1.6-1.82 times higher than the smooth tube at the similar experimental conditions.

New correlations for the determination of condensation heat transfer coefficients are proposed belong to the tested tubes separately for practical applications, and as a result of this study, it is possible to simply calculate the condensation heat transfer coefficient with an interfacial shear effect during downward laminar flow in vertical smooth and micro-fin tubes at low mass flux conditions.

ACKNOWLEDGEMENTS

The present study was financially supported by Yildiz Technical University. The first author wishes to thank KMUTT for providing him with a Post-doctoral fellowship, while the third author wish to acknowledge the support provided by the Thailand Research Fund. The authors also wish to thank Wieland-Wilke AG (Ulm, Germany) for valuable donation of the micro-fin tube used in the present study.

REFERENCES

Balcilar, M., Dalkilic, A.S., Wongwises, S., Artificial Neural Network (ANN) Techniques for the Determination of Condensation Heat Transfer Characteristics during Downward Annular Flow of R134a inside a Vertical Smooth Tube, *Int. Communications in Heat and Mass Transfer*, "Accepted for Publication-Article in Press", 2010. (a)

Balcilar, M., Dalkilic, A.S., Wongwises, S., Determination of Condensation Heat Transfer Characteristics of R134a by means of Artificial Intelligence Method, *ASME International Mechanical Engineering Congress and Exposition*, 12-18, 2010. (b)

Bellinghausen. R, Renz, U., Heat Transfer and Film Thickness During Condensation of Steam Flowing at High Velocity in a Vertical Pipe, *Int. J. of Heat and Mass Transfer* 35, 683-689, 1992.

Briggs, A., Kelemenis, C., Rose, J.W., Condensation of CFC-113 with Down Flow in Vertical, Internally Enhanced Tubes, *Proceedings of 11th IHTC*, 23-28, 1998.

Carey, V.P., *Liquid-Vapor Phase Change Phenomena*, Hemisphere Publishing, 1992.

Cavallini, A., Del Col, D., Doretti, L., Longo, G.A., Rossetto, L.A., A New Computational Procedure for Heat Transfer and Pressure Drop during Refrigerant Condensation inside Enhanced Tubes, *Enhanced Heat Transfer* 6, 441-456, 1999. (a)

Cavallini, A., Del Col, D., Doretti, L., Longo, G.A., Rossetto, L., Pressure Drop During Condensation and Vaporisation of Refrigerants Inside Enhanced Tubes, *Heat and Technology* 15, 3-10, 1997. (b)

Chamra, L.M., Webb, R.L., Randlett, M.R., Advanced Micro-fin Tubes for Condensation, *Int. Journal of Heat and Mass Transfer* 39, 1839-1846, 1996.

Dalkilic, A.S., Yildiz, S., Wongwises, S., Experimental Investigation of Convective Heat Transfer Coefficient During Downward Laminar Flow Condensation of R134a in a Vertical Smooth Tube, *Int. Journal of Heat and Mass Transfer* 52, 142-150, 2009. (a)

Dalkilic, A.S., Wongwises, S., Intensive Literature Review of Condensation Inside Smooth and Enhanced Tubes, *Int. Heat and Mass Transfer* 52, 3409-3426, 2009. (b)

Dalkilic, A.S., Laohalertdecha, S., Wongwises, S., Effect of Void Fraction Models on the Two-phase Friction Factor of R134a During Condensation in Vertical Downward Flow in a Smooth Tube, *Int. Communications in Heat and Mass Transfer* 35, 921-927, 2008. (c)

Dalkilic, A.S., Laohalertdecha, S., Wongwises, S., Two-phase Friction Factor in Vertical Downward Flow in High Mass Flux Region of Refrigerant HFC-134a During Condensation, *Int. Communications in Heat and Mass Transfer* 35, 1147-1152, 2008. (d)

Dalkilic, A.S., Laohalertdecha, S., Wongwises, S., Effect of Void Fraction Models on the Film Thickness of R134a During Downward Condensation in a Vertical Smooth Tube, *Int. Communications in Heat and Mass Transfer* 36, 172-179, 2009. (e)

Dalkilic, A.S., Laohalertdecha, S., Wongwises, S., Experimental Investigation on Heat Transfer Coefficient of R134a During Condensation in Vertical Downward Flow at High Mass Flux in a Smooth Tube, *Int. Communications in Heat and Mass Transfer* 36, 1036-1043, 2009. (f)

Dalkilic, A.S., Agra, O., Teke, I., Wongwises, S., Comparison of Frictional Pressure Drop Models During Annular Flow Condensation of R600a in a Horizontal Tube at Low Mass Flux and of R134a in a Vertical Tube at High Mass Flux, *Int. Journal of Heat and Mass Transfer* 53, 2052-2064, 2010. (g)

Dalkilic, A.S., Wongwises, S., An Investigation of a Model of the Flow Pattern Transition Mechanism in Relation to the Identification of Annular Flow of R134a in a Vertical Tube Using Various Void Fraction Models and Flow Regime Maps, *Experimental Thermal and Fluid Science* 34, 692-705, 2010. (h)

Dalkilic, A.S., Laohalertdecha, S., Wongwises, S., Validation of Void Fraction Models and Correlations Using a Flow Pattern Transition Mechanism Model in Relation to the Identification of Annular Vertical Downflow In-tube Condensation of R134a, *Int. Communications in Heat and Mass Transfer* 37, 827-834, 2010. (i)

Dalkilic, A.S., Laohalertdecha, S., Wongwises, S., Experimental Study of the Condensation Heat Transfer Coefficients in High Mass Flux Region in Annular Flow Regime of HFC-134a Inside the Vertical Smooth tube, *Heat Transfer Engineering* 32, 1-12, 2011. (j)

Dalkilic, A.S., Laohalertdecha, S., Wongwises, S., New Experimental Approach on the Determination of Condensation Heat Transfer Coefficient Using Frictional Pressure Drop and Void Fraction Models in a Vertical Tube, *Energy Conversion and Management* 51, 2535-2547, 2010. (k)

Dalkilic, A.S. Dalkilic, Wongwises, S., A Performance Comparison of Vapour Compression Refrigeration System Using Various Alternative Refrigerants, *Int. Communications in Heat and Mass Transfer* 37, 1340-1349, 2010. (l)

Dalkilic, A.S., Teke, I., Wongwises, S., Experimental Analysis for the Determination of the Convective Heat Transfer Coefficient by Measuring Pressure Drop Directly During Annular Condensation Flow of R134a in a Vertical Smooth Tube, *Int. J. of Heat and Mass Transfer*, "Accepted for Publication-Article in Press". (m)

Dalkilic, A.S., Laohalertdecha, S., Wongwises, S., A Comparison of the Void Fraction Correlations of R134a During Condensation in Vertical Downward Laminar Flow in a Smooth and Microfin Tube, *ASME Proceedings of the Micro/Nanoscale Heat Transfer International Conference* Parts A-B, 1029-1040, 2008. (n)

Dalkilic, A.S., Laohalertdecha, S., Wongwises, S., Two-phase Friction Factor Obtained From Various Void Fraction Models of R-134a During Condensation in Vertical Downward Flow at High Mass Flux, *ASME Proceedings of the ASME Summer Heat Transfer Conference* 2, 193-206, 2009. (o)

Dalkilic, A.S., Laohalertdecha, S., Wongwises, S., Experimental Investigation on the Condensation Heat Transfer and Pressure Drop Characteristics of R134a at High Mass Flux Conditions During Annular Flow Regime Inside a Vertical Smooth Tube, *ASME Summer Heat Transfer Conference* 19-23, 2009. (p)

Dalkilic, A.S., Agra, O., Experimental Apparatus for the Determination of Condensation Heat Transfer Coefficient for R134a and R600a Flowing Inside Vertical and Horizontal Tubes, *ASME Summer Heat Transfer Conference* 19-23, 2009. (r)

Dalkilic, A.S., Laohalertdecha, S., Wongwises, S., Experimental Research on the Similarity of Annular Flow Models and Correlations for the Condensation of R134a at High mass Flux Inside Vertical and Horizontal Tubes, *ASME International Mechanical Engineering Congress and Exposition* 13-19, 2009. (s)

Dalkilic, A.S., Wongwises, S., A Heat Transfer Model for Co-current Downward Laminar Film Condensation of R134a in a Vertical Micro-fin Tube During Annular Flow Regime, *the Eleventh UK National Heat Transfer Conference* 6-8, 2009. (t)

Dalkilic, A.S., Laohalertdecha, S., Wongwises, S., Comparison of Condensation Frictional Pressure Drop Models and Correlations During Annular Flow of R134a Inside a Vertical Tube, *ASME-ATI-UTI Thermal and Environmental Issues in Energy Systems* 16-19, 2010. (u)

Dalkilic, A.S., Wongwises, S., Experimental Study on the Flow Regime Identification in the Case of Co-current Condensation of R134a in a Vertical Smooth Tube, *ASME International Heat Transfer Conference* 8-13, 2010. (v)

Dalkilic, A.S., Wongwises, S., Comparison of Various Alternative Refrigerants for Vapour Compression Refrigeration Systems, *ASME/JSME 8th Thermal Engineering Joint Conference* 13-17, 2011. (y)

Dalkilic, A.S., Düşey borularda yoğuşmada ısı taşınım katsayısının araştırılması, *Ph.D. Thesis*, Yildiz Technical University, Istanbul, Turkey, 2007. (z)

Hewitt, G.F., Robertson, D.N., Studies of Two-phase Flow Patterns by Simultaneous X-ray and Flash Photography, *Rept AERE-M2159, UKAEA, Harwell*, 1969.

McAdams, W.H., *Heat Transmission*, 3rd ed., McGraw-Hill, New York Univ. Calif. (Berkeley) Pub. Eng., 443-461, 1954.

Nusselt, W., Die Oberflachen Kondenastion des Wasserdamfes, *Zeitschrift des Vereines Deutscher Ingenieure* 60, 541-546, 569-575, 1916.

Oh, S., Revankar, A., Analysis of the Complete Condensation in a Vertical Tube Passive Condenser, *Int. Communications in Heat and Mass Transfer* 32, 716-727, 2005.

Schlager, L.M., Pate, M.B., Bergles, A.E., Evaporation and Condensation Heat Transfer and Pressure Drop in Horizontal, 12.7-mm Microfin Tubes with Refrigerant 22, *J. of Heat Transfer* 12, 1041-1047, 1990.

Shah, M.M., A General Correlation for Heat Transfer During Film Condensation Inside Pipes, *Int. J. of Heat and Mass Transfer* 22, 547-556, 1979.

Wang, H.S., Honda, H., Condensation of Refrigerants in Horizontal Microfin Tubes: Comparison of Prediction Methods for Heat Transfer, *Int. J. of Refrigeration* 26, 452-460, 2003.

Ahmet Selim DALKILIÇ is currently a Research Assistant of Mechanical Engineering at Yildiz Technical University, İstanbul, Turkey. He received his Ph.D. Degree in Mechanical Engineering from the same university. His current research interest is on enhanced heat transfer, convection heat transfer, condensation, evaporation, boiling heat transfer of new refrigerants and mixture refrigerants and applications in heat exchangers. Dr. Ahmet Selim Dalkılıç is the member of Innovation Explorer for Scientific Researchers Community sponsored by Elsevier and American Society of Mechanical Engineers (ASME). He has been serving as a volunteer associate editor for Scientific Journals International (SJI) - Journal of Mechanical, Aerospace and Industrial Engineering.

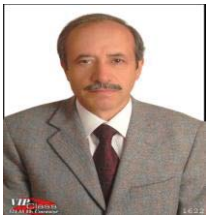

İsmail TEKE is currently a professor of mechanical engineering at Yıldız Technical Üniversity,İstanbul, Turkey. He received his PhD degree in mechanical engineering from the same üniversity in 1981. His current research interest is on two phase flow and heat exchangers.

Somchai Wongwises is currently a professor of mechanical engineering at King Mongkut's University of Technology Thonburi, Bangmod, Thailand. He received his Doktor-Ingenieur (Dr.-Ing.) in mechanical engineering from the University of Hannover, Germany, in 1994. His research interests include two phase flow, heat transfer enhancement, and thermal system design. He is the head of the Fluid Mechanics, Thermal Engineering and Multiphase Flow Research Labarotory (FUTURE). He has been serving as an editor for Experimental Thermal and Fluid Science.

Provided for non-commercial research and education use.
Not for reproduction, distribution or commercial use.

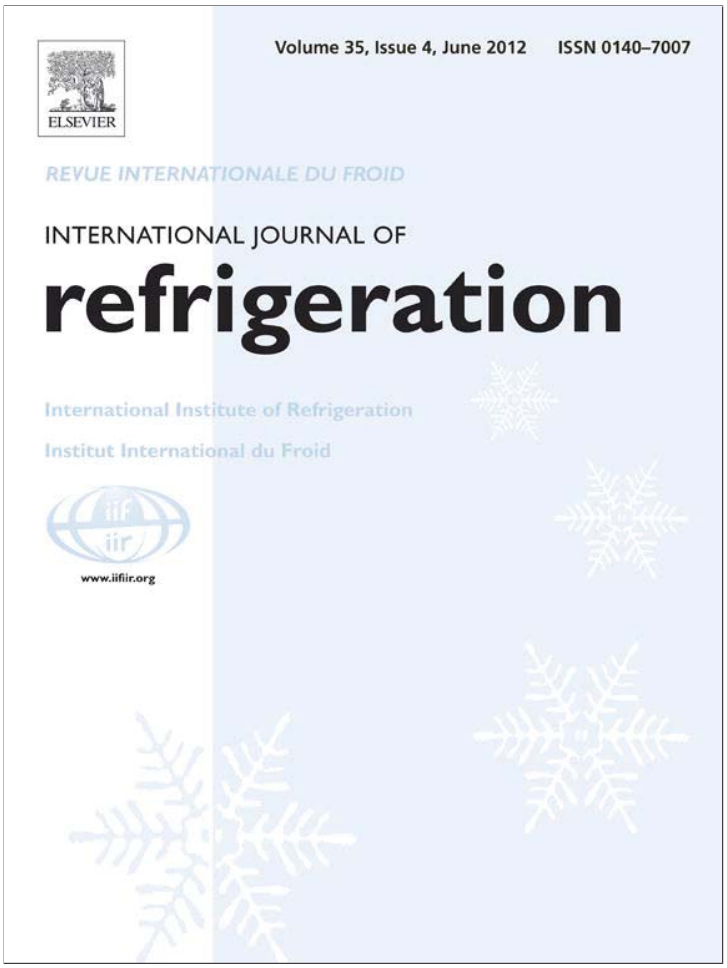

This article appeared in a journal published by Elsevier. The attached copy is furnished to the author for internal non-commercial research and education use, including for instruction at the authors institution and sharing with colleagues.

Other uses, including reproduction and distribution, or selling or licensing copies, or posting to personal, institutional or third party websites are prohibited.

In most cases authors are permitted to post their version of the article (e.g. in Word or Tex form) to their personal website or institutional repository. Authors requiring further information regarding Elsevier's archiving and manuscript policies are encouraged to visit:

http://www.elsevier.com/copyright

Author's personal copy

INTERNATIONAL JOURNAL OF REFRIGERATION 35 (2012) 740–749

Available online at www.sciencedirect.com

SciVerse ScienceDirect

journal homepage: www.elsevier.com/locate/ijrefrig

Review

A review of numerical modelling studies on short-tube orifice performance with applications to air-conditioning systems

Kitti Nilpueng [a,b], *Somchai Wongwises* [b,c,*]

[a] *Department of Mechanical Engineering, South-East Asia University, Bangkok, Thailand*
[b] *Fluid Mechanics, Thermal Engineering and Multiphase Flow Research Lab (FUTURE), Department of Mechanical Engineering, King Mongkut's University of Technology Thonburi, Bangmod, Bangkok 10140, Thailand*
[c] *The Academy of Science, The Royal Institute of Thailand, Sanam Suea Pa, Dusit, Bangkok 10300, Thailand*

ARTICLE INFO

Article history:
Received 25 August 2011
Received in revised form
20 January 2012
Accepted 20 January 2012
Available online 3 February 2012

Keywords:
Expansion valve
Flow rate
Critical pressure
Temperature variation

ABSTRACT

The manufacturers of air conditioners need a precise method for calculating the critical flow rate of refrigerant through the short-tube orifice, and they must select the proper size of short-tube orifice at given operating conditions in order to achieve optimum system performance. The present study divides the research into two main groups: studies conducted under the semi-empirical model and those conducted under the theoretical model. The former model has been developed based on the single-phase orifice equation with the correction factor. The latter model applies the proper governing equations, including conservation of mass, momentum, and energy, to determine the refrigerant flow mechanism inside the short-tube orifice. Because these equations are rather difficult to solve, only a few studies have been conducted. This paper describes the details of the numerical modelling of refrigerant flow characteristics through the short-tube orifice reported in previous publications as well as the guideline for future research.

© 2012 Elsevier Ltd and IIR. All rights reserved.

Etudes sur la modélisation numérique effectuées sur la performance des orifices des tubes courts dans le contexte du conditionnement d'air : passage en revue

Motsclés : détendeur ; débit ; pression critique ; variation de température

* *Corresponding author*. Department of Mechanical Engineering, King Mongkut's University of Technology Thonburi, Bangmod, Bangkok 10140, Thailand. Tel.: +662 4709115; fax: +662 4709111.
E-mail address: somchai.won@kmutt.ac.th (S. Wongwises).
0140-7007/$ – see front matter © 2012 Elsevier Ltd and IIR. All rights reserved.
doi:10.1016/j.ijrefrig.2012.01.019

Author's personal copy

Nomenclature

A	cross-section area of short-tube orifice, m^2
C	discharge coefficient
C_c	correction factor for chamfering
C_p	specific heat at constant pressure, $kJ\,kg^{-1}\,K^{-1}$
C_{tp}	correction factor for two-phase flow
DEPTH	chamfer depth, mm
D	diameter, m
D_{ref}	reference short-tube diameter, m
D_R	normalized diameter
EVAP	normalized downstream pressure
f	fanning friction factor
F_{GL}	interfacial fictional force per unit volume between vapour and liquid, $N\,m^{-3}$
F_{WL}	interfacial fictional force per unit volume between tube wall and liquid phase, $N\,m^{-3}$
G	mass flux, $kg\,m^{-2}\,s^{-1}$
G_{cr}	critical mass flux, $kg\,m^{-2}\,s^{-1}$
g_c	dimensional gravity constant, $1.296 \times 10^{10}\ s^2\,N\,h^{-2}\,kN^{-1}$
h	enthalpy, $kJ\,kg^{-1}$
k	slip ratio
L	length, m
$\dot{m}$	mass flow rate, $kg\,s^{-1}$
P	pressure, Pa
P_f	adjusted downstream pressure, Pa
P_R	normalized upstream pressure
s	entropy, $kJ\,kg^{-1}\,K^{-1}$
SUBC	normalized subcooling
T	temperature, °C
t_R	normalized upstream temperature
u	fluid velocity, $m\,s^{-1}$
u_L	liquid velocity, $m\,s^{-1}$
u_G	vapour velocity, $m\,s^{-1}$
We_d	Weber number, $G^2D/\rho_L\sigma$
x	quality
z	incremental axial length, mm

Greek symbols

ρ	density, $kg\,m^{-3}$
β	short-tube orifice diameter to the tube diameter ratio
υ	specific volume, $m^3\,kg^{-1}$
μ	viscosity, $kg\,m^{-1}\,s^{-1}$
σ	surface tension, $N\,m^{-1}$
Φ	correction factor
Γ	inter-phase mass transfer rate per unit volume, $kg\,m^{-3}\,s^{-1}$
ϕ_{tp}^2	two-phase multiplier

Subscripts

c	critical
down	downstream
f	liquid phase
g	gas-phase
ref	reference
sat	saturation
up	upstream

1. Introduction

A short-tube orifice is a type of expansion device popularly used in residential and automotive air conditioners. It is made from extremely small bore hollow brass with length-to-diameter ratios ranging between 3 and 20. The benefits of a short-tube orifice over a thermostatic expansion valve are the low starting torque of the compressor as the pressures across the short-tube orifice equalize during the off-cycle, simplicity, low initial cost, and absence of any moving parts. However, it has been found that after the size of a short-tube orifice is selected to install into an air-conditioning system, it will be suitable for only one design condition. That is, the mass flow rate and pressure drop would not be adequate under different operating conditions. In addition, the refrigerant flow inside the short-tube orifice should be choked in order to obtain an appropriate distribution of refrigerant under working conditions. This is because, under a non-choked flow condition, the refrigerant mass flow rate discharged into the evaporator will decrease when the evaporator pressure increases with an increase in evaporator load. Conversely, the mass flow rate increases as the evaporator pressure decreases under a decrease in evaporator load. This flow behaviour is inappropriate for air-conditioning systems. Thus, to obtain the optimum performance of the air-conditioning system, engineers must identify proper short-tube orifice size at a given operating condition or quantify the critical flow rate that can be produced through the short-tube orifice.

In the past decade, several short-tube orifice models were developed to calculate the refrigerant flow behaviour inside the short-tube orifice. The models can be divided into two main groups: semi-empirical models and theoretical models. The aim of this paper is to describe the detail of the numerical modelling of refrigerant flow characteristics through the short-tube orifice of previous publications and to suggest guidelines for future research.

2. Semi-empirical models

The semi-empirical models are generated in the form of simple equations with the correction factor created from experimental data. During the past decade, it can be seen that most previous researchers have developed short-tube orifice flow models based on a single-phase orifice equation (ASME, 1971). The single-phase orifice equation is expressed as follows:

$$\dot{m} = CA\sqrt{\frac{2\rho(P_{up} - P_{down})}{(1-\beta^4)}} \tag{1}$$

where C is the discharge coefficient, A is the cross-sectional area of a short-tube orifice, ρ is the density of fluid, P_{up} is

Author's personal copy

upstream pressure, P_{down} is downstream pressure, and β is the ratio of the orifice diameter to the upstream tube diameter.

Mei (1982) proposed two short-tube orifice models with degrees of subcooling over 22.2 °C and below 22.2 °C for HCFC-22 flow through short-tube orifices. The refrigerant mass flux can be estimated by

$$G = C\left[2\rho\left(P_{up} - P_{down}\right)\right]^{1/2} \tag{2}$$

For $\Delta T_{sub} < 22.2\ ^{\circ}C$

$$C = -0.007364\left(\sqrt{\Delta P} - \sqrt{1034.2}\right) + 0.0108\Delta T_{sub} + 0.40 \tag{3}$$

For $\Delta T_{sub} > 22.2\ ^{\circ}C$

$$C = 0.9175 - 0.00585\Delta T_{sub} \tag{4}$$

The correlation of the orifice coefficient (C) was presented as a function of degree of subcooling (ΔT_{sub}) and pressure difference between upstream and downstream (ΔP).

Aaron and Domanski (1990) developed the single-phase orifice equation with a correction factor of adjusted saturation pressure for the purpose of predicting the mass flow rate of HCFC-22 through short-tube orifices. In their model, the discharge coefficient (C) is set equal to unity, while the velocity of approach factor ($1-\beta^4$) is neglected, as shown below.

$$\dot{m} = C_c A\sqrt{2\rho(P_1 - P_2)} \tag{5}$$

where

$$P_2 = P_{sat}\left[1 + 12.599\mathrm{SUB}^{1.293} - 0.1229\exp\left(-0.0169(L/D)^2\right) - 0.04753\mathrm{EVAP}^{0.6192}\right] \tag{6}$$

$$\mathrm{SUB} = \left(T_{sat} - T_{fliud}\right)/T_{sat} \tag{7}$$

$$\mathrm{EVAP} = \left(P_{sat} - P_{down}\right)/P_{sat} \tag{8}$$

A correlation of the chamfered inlet is applied to a short-tube orifice with a chamfered inlet.

$$C_c = 1 + 0.0551(L/D)^{0.5844}(\mathrm{DEPTH}/D)^{0.2967} \tag{9}$$

where DEPTH is the inlet chamfer depth.

The models for calculating the flow rate of saturated liquid and two-phase flow of CFC-12, HCFC-22, HFC-134a, and HFC-407C though a short-tube orifice were developed by Kim et al. (1994), Kim and O'Neal (1994) and Payne and O'Neal (1998). The adjusted downstream pressure correlation was proposed as a function of the upstream pressure, downstream pressure, upstream temperature, diameter, and length-to-diameter ratio. The flow rate can be estimated with the following equation:

$$\dot{m} = C_c C_{tp} A\sqrt{2\rho\left(P_{up} - P_f\right)} \tag{10}$$

where P_f is the pressure before the flashing point, which correlates with the degree of subcooling, the ratio of length to diameter, diameter, and downstream pressure.

$$P_f = P_{sat}\left[b_1 + b_2\left(P_{up}/P_c\right)^{b_3}(L/D)^{b_4}\mathrm{SUBC}^{b_5} + b_6\left(P_{up}/P_c\right)^{b_7} + b_8\exp\left(b_9(D/D_{ref})(L/D)^{b_{10}}\right) + b_{11}\mathrm{EVAP}\right] \tag{11}$$

$$C_c = 1 + \pi_1(L/D)^{\pi_2}(\mathrm{DEPTH}/D)^{\pi_3} \tag{12}$$

Table 1 – Coefficient of correction factor. Reproduced with permission of ASHRAE Transactions: symposia, from Two-phase flow of HFC134a and CFC12 through short tube orifices, Kim, Y.C., O'Neal, D.L., Yuan, Y., 1994; permission conveyed through Copyright Clearance Center, Inc.", "Reproduced with permission of ASHRAE Transactions, from Two-phase flow of R-22 through short tube orifices, Kim, Y., O'Neal, D.L., 100, 1994; permission conveyed through Copyright Clearance Center, Inc.", "Reproduced with permission of ASHRAE Transactions, from Mass flow characteristics of R407C through short-tube orifices, Payne, W.V., O'Neal, D.L., 104 (3), 1998; permission conveyed through Copyright Clearance Center, Inc.

Coefficient	CFC-12	HCFC-22	HFC-134a	HFC-407C (Pure)	HFC-407C (1.1% oil)
a_1	–	–	−2.6519	−4.45974577	−4.349745770
a_2	–	–	5.7705	10.69467130	10.454571210
a_3	–	–	−0.4474	−0.55303036	−0.663120121
a_4	–	–	0.3820	0.39429366	0.323273661
b_1	1.0011	1.0050	1.0156	0.963034325	0.980538238
b_2	11.3523	5.7367	10.0612	4.286408416	4.957604391
b_3	−0.2176	−0.485	−0.3296	−0.278235435	−0.309919995
b_4	−0.2150	−0.179	−0.1758	−0.043090943	−0.116219951
b_5	1.0643	0.9948	1.0831	0.916226528	0.906610038
b_6	0.0000	0.268	0.0000	0.071794702	0.227476573
b_7	0.0000	2.716	0.0000	0.499098698	0.186773583
b_8	−0.1905	−0.226	−0.1802	−0.208417565	−0.398196082
b_9	−0.00615	−0.021	−0.00214	−0.034680678	−0.030711793
b_{10}	2.4291	2.0000	2.9596	1.844061084	1.587754176
b_{11}	−0.0437	−0.092	−0.0745	−0.091235910	−0.134132834
π_1	–	0.02655	–	–	–
π_2	–	0.070775	–	–	–
π_3	–	0.22684	–	–	–

Author's personal copy

$$SUBC = (T_{sat} - T_{up})/T_c \tag{13}$$

$$EVAP = (P_c - P_{down})/P_c \tag{14}$$

For two-phase flow, the correlation (C_{tp}), which includes the effect of upstream quality and short-tube geometry, was added into his model.

$$C_{tp} = \frac{1}{(1 + a_1 x_{up})\left(1 + a_2 (L/D)^{a_3} Y^{a_4 \mathrm{Ln}(L/D)}\right)} \tag{15}$$

$$Y = \frac{x_{up}}{(1 - x_{up})}\left(\frac{\rho_f}{\rho_g}\right)^{0.5} \tag{16}$$

The model for HFC-407C is divided into two cases: pure refrigerant and oil–refrigerant mixtures. Table 1 shows the correction coefficient of various refrigerants used in the flow model.

For practical application, flow charts of HCFC-22 derived from the empirical correlations were generated by Kim and O'Neal (1994) and Aaron and Domanski (1990). Four flow charts, which are a function of upstream pressure, inlet quality, degree of subcooling, short-tube diameter, short-tube length, and chamfer depth, were proposed. The mass flow rate was calculated using the following equation:

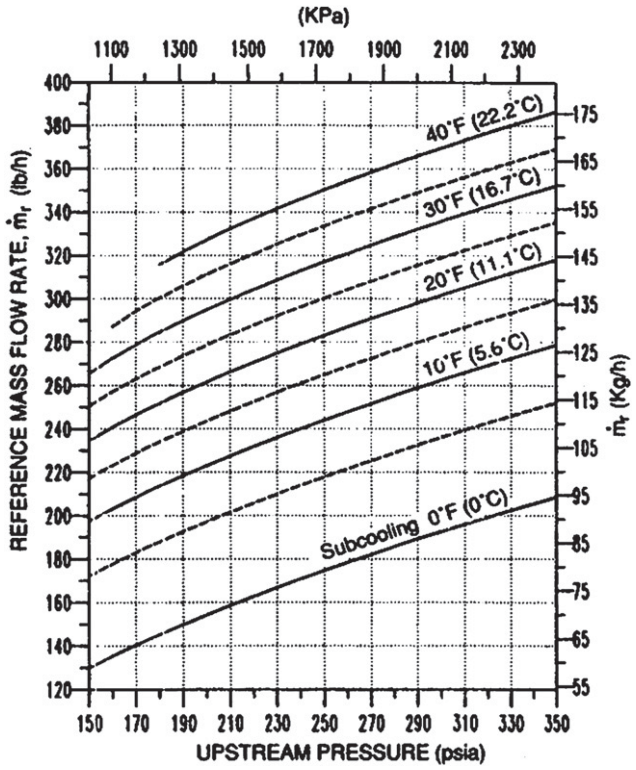

Fig. 1 – Reference mass flow rate for short-tube orifice with HCFC-22: L = 12.70mm and D = 1.35mm. Reproduced with permission of ASHRAE Transactions, from Experimentation analysis and correlation of refrigerant-22 flow through short tube restrictors, Aaron, A.A., Domanski, P.A., 96 (1), 1990; permission conveyed through Copyright Clearance Center, Inc.

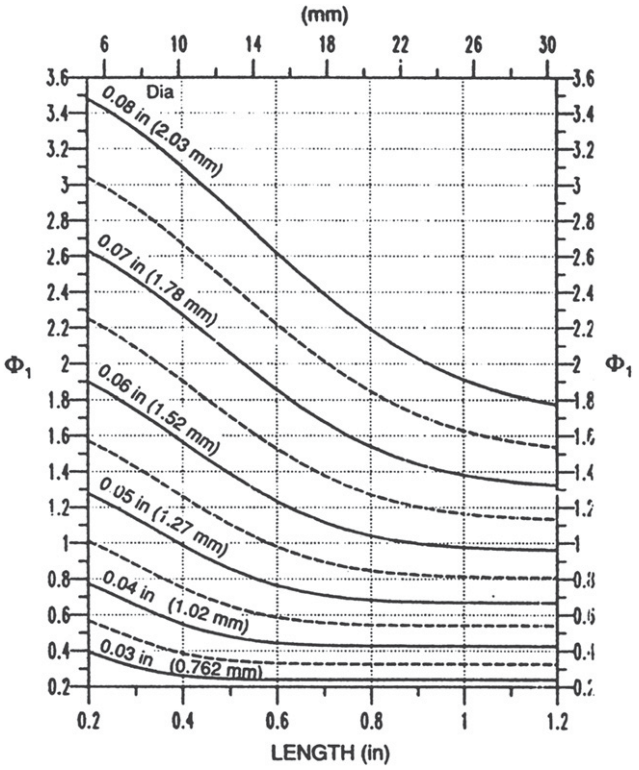

Fig. 2 – Correction factor for short-tube orifice configuration with HCFC-22. Reproduced with permission of ASHRAE Transactions, from Experimentation analysis and correlation of refrigerant-22 flow through short tube restrictors, Aaron, A.A., Domanski, P.A., 96 (1), 1990; permission conveyed through Copyright Clearance Center, Inc.

$$\dot{m}_a = \dot{m}_r \Phi_1 \Phi_2 \Phi_3 \tag{17}$$

where $\dot{m}_a$ is the actual mass flow rate, $\dot{m}_r$ is the reference mass flow rate, Φ_1 is the correction factor for short-tube geometry, Φ_2 is the correction factor for the degree of subcooling or quality, and Φ_3 is the correction factor for the inlet chamfer. The calculated mass flow rate obtained from the flow charts agreed with the actual value. However, Kim and O'Neal (1994), and Aaron and Domanski (1990) reported that the accuracy of calculation cannot be guaranteed when extrapolating beyond the operating conditions of the flow chart. The selection charts for HCFC-22 are shown in Figs. 1–4.

Singh et al. (2001) developed a model for predicting the mass flow rate of HFC-134a inside a short-tube orifice over a wide range of inlet and outlet conditions, that is, liquid, two phase, and vapour. The flow model could be divided into four regimes, namely liquid inlet–liquid outlet flow, liquid inlet–two-phase outlet flow, two-phase inlet–two-phase outlet flow, and single-phase inlet–single-phase outlet flow. However, for predicting the mass flow rate under the choke flow condition, the models were combined together as shown below.

$$\dot{m} = (1 - x_{up})^{c_8} c_1 D^2 \sqrt{2\rho(P_{up} - P_{down}K)} + x_{up}^{c_9} c_{10} P_{up} D^2 M \sqrt{\gamma_{up}/(RT_{up})} \tag{18}$$

Author's personal copy

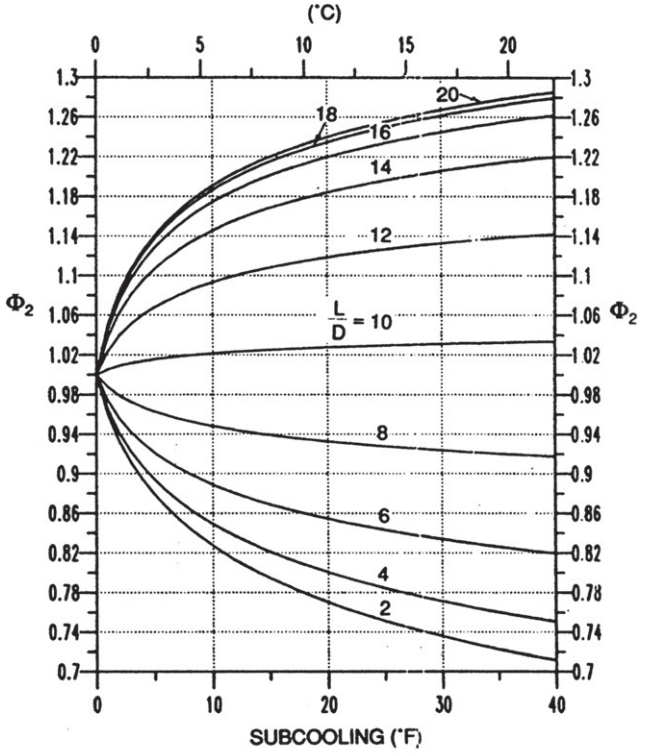

Fig. 3 – Correction factor for inlet subcooling with HCFC-22. Reproduced with permission of ASHRAE Transactions, from Experimentation analysis and correlation of refrigerant-22 flow through short tube restrictors, Aaron, A.A., Domanski, P.A., 96 (1), 1990; permission conveyed through Copyright Clearance Center, Inc.

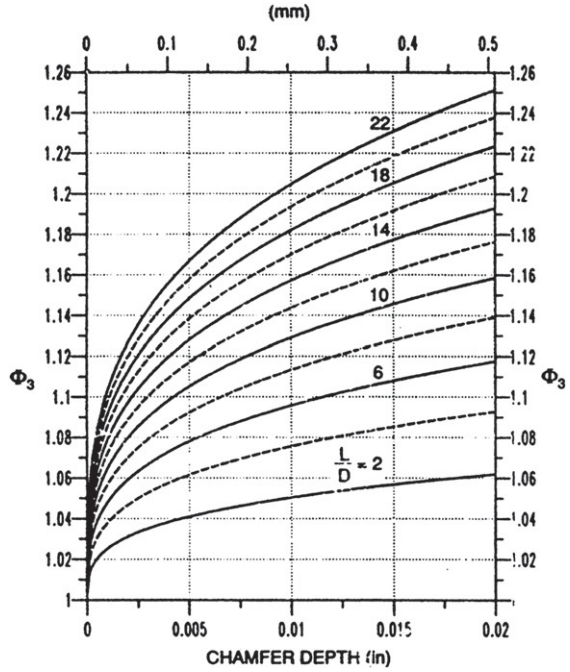

Fig. 4 – Correction factor for chamfering with HCFC-22. Reproduced with permission of ASHRAE Transactions, from Experimentation analysis and correlation of refrigerant-22 flow through short tube restrictors, Aaron, A.A., Domanski, P.A., 96 (1), 1990; permission conveyed through Copyright Clearance Center, Inc.

$$K = c_2\left(\frac{S}{T_c}\right)c_3 + D^{c_4}L^{c_5} + c_6L + c_7\left(\frac{P_c - P_{down}}{P_c}\right) \quad (19)$$

where D is the short-tube orifice diameter, L is the short-tube orifice length, S is inlet subcooling, M is the Mach number, and R is the gas constant. The coefficients included in the model are presented in Table 2.

Kim et al. (2002) have developed the mass flow rate correlation of HCFC-22 through a flexible short-tube orifice, and they presented the single-phase orifice model with a correction factor for the HCFC-22. For each flexible short tube, the proposed flow model is divided into moduli of elasticity of 7063 kPa and 9860 kPa.

$$\dot{m} = CA\sqrt{2\gamma_c\rho(P_{up} - P_f)} \quad (20)$$

$$P_f = P_{sat}\left[b_1 + b_2(PRA)^{b_3}SUB^{b_4} + b_5EVAP^{b_6}\right] \quad (21)$$

where SUB is normalized subcooling, $(T_{sat} - T_{up})/T_c$. EVAP is the normalized downstream pressure, and $(P_c - P_{down})/P_c$. PRA is the ratio of upstream pressure to critical pressure (P_{up}/P_c). γ_c is a dimensional constant, $1.296 \times 10^{10}\ s^2\,N\,h^{-2}\,kN^{-1}$. The coefficients of the correction factor of this model appear in Table 3. The non-linear regression technique was used to determine a correlation between adjusted pressure and normalized parameters.

Liu et al. (2004) formulated a flow model to estimate the mass flow rate of R744 through a short-tube orifice. The upstream pressure, upstream temperature, diameter, and length-to-diameter ratio were included in the adjusted downstream pressure correlation. The mass flow rate was calculated with the followed equation:

$$\dot{m} = A\sqrt{2\rho(P_{up} - P_f)} \quad (22)$$

Table 2 – Coefficient in the mass flow model. Reprinted from HVAC&Research, 7, Singh, G.M., Hrnjak, P.S., Bullard, C.W., Flow of refrigerant R134a through orifice tubes, pp. 245–262 (2001), with permission from Taylor & Francis.

Coefficient	
c_1	0.265249714
c_2	−0.11497189
c_3	0.041465780
c_4	−0.006578346
c_5	0.0039000541
c_6	0.0000218672
c_7	0.0362919356
c_8	1.7562517005
c_9	0.4970578018
c_{10}	25π

Author's personal copy

Table 3 – Coefficient of the correction factor. Reprinted from HVAC&Research, 8(2), Kim, Y.C., Payne, W.V., O'Neal, D.L., Farzad, M., Refrigerant flow through flexible short tube orifices, pp. 179–190 (2004), with permission from Taylor & Francis.

Coefficient	Modulus of elasticity 7063 kPa	Modulus of elasticity 9860 kPa
b_1	0.9187	1.0434
b_2	10.4091	7.4048
b_3	−0.0500	0.0191
b_4	1.1787	1.0421
b_5	−0.0276	−0.1683
b_6	0.9241	−0.7797

$$P_f = P_c\left|0.77213 + 0.86505D_R^{0.42405} - 0.40453P_R^{-4.7025}t_R^{0.12293} + 0.00006(L/D)^{1.6326}\right| \quad (23)$$

where D_R is normalized diameter, (D/D_p), $(D_p = 7.03\ \text{mm})$, and P_R is normalized upstream pressure, (P_{up}/P_c). t_R is normalized upstream temperature $(t_{up} - t_c)/t_c)$.

Tu et al. (2006) presented a semi-empirical flow model for the liquid inlet–two-phase outlet flow of HFC-134a through a micro-scale short-tube orifice based on a single-phase orifice equation with an adjusted discharge coefficient. The discharge coefficient was correlated with downstream vapour quality.

$$\dot{m} = (1 + C_x x_{out})C_d A\sqrt{2\rho\Delta P} \quad (24)$$

where x_{out} is the downstream vapour quality and C_x and C_d are empirical constants. C_d was 0.7 and 0.68 for short-tube diameters of 52 and 31 μm, respectively, and the value of C_x is 0.416.

Nilpueng and Wongwises (2009) proposed a flow model for a small size short-tube orifice ($D = 0.605$–1.2 mm) under critical flow. The flow model is expressed as

Table 4 – Dimensionless π term of the generalized correlation. Reprinted from International Journal of Refrigeration, 27, Choi, J., Chung, J.T., Kim, Y., A generalized correlation for two-phase flow of alternative refrigerants through short tube orifices, pp. 393–400 (2004), with permission from Elsevier.

π term	Parameter	Inlet condition
π_1	$\dot{m}/D^2\sqrt{\rho_f P_{in}}$	Subcooled/two-phase
π_2	$(P_c - P_{in})/P_c$	Subcooled/two-phase
π_3	$(P_c - P_{down})/P_c$	Subcooled/two-phase
π_4	$(P_c - P_{sat})/P_c$	Subcooled
π_5	$\Delta T_{sub}/T_c$	Subcooled
π_6	L/D	Subcooled/two-phase
π_7	ρ_f/ρ_g	Subcooled
π_8	$(\mu_f - \mu_g)/\mu_g$	Subcooled/two-phase
π_9	σ/DP_{in}	Subcooled
π_{10}	$x_{in}/(1 - x_{in})$	Two-phase
π_{11}	ρ_{mean}/ρ_f	Two-phase

$$\dot{m} = A\sqrt{2\rho(P_{up} - P_f)} \quad (25)$$

$$P_f = P_{sat}\left[0.201 + 0.421P_R^{-0.204}(L/D)^{0.218}T_R^{0.398} + 0.244P_R^{-0.458} + 0.203\exp 0.00031D_R(L/D)^{1.55}\right] \quad (26)$$

where D_R is normalized diameter (D/D_{ref}), $(D_{ref} = 0.961\ \text{mm})$, and P_R is normalized upstream pressure (P_{up}/P_c). T_R is normalized upstream temperature $(T_{sat} - T_{up})/T_c)$. The calculated results showed good agreement with the measured results with a mean deviation $(1/n\sum_1^n[|\dot{m}_{meas} - \dot{m}_{cal}| \times 100/\dot{m}_{meas}])$ of 6.3%.

Due to the fact that the semi-empirical models were generated based on their own database, each model cannot be used beyond its condition. Therefore, Choi et al. (2004) developed a generalized correlation in a simple form to calculate the mass flow rate of alternative refrigerants inside short-tube orifices. The relevant parameters consisted of three groups: operating condition, short-tube orifice geometry, and refrigerant property. They developed their correlation based on the dimensional analysis, and produced the correlation in the power law form of dimensionless parameters. The generalized correlation for calculating the refrigerant mass flow rate through the short tube falls into two groups: the subcooled inlet condition and the two-phase inlet condition.

For the subcooled inlet condition

$$\pi_1 = 0.1378\pi_2^{-0.950}\pi_3^{0.033}\pi_4^{0.769}\pi_5^{0.082}\pi_6^{-0.099}\pi_7^{-0.104}\pi_8^{0.554}\pi_9^{-0.034} \quad (27)$$

For the two-phase inlet condition

$$\pi_1 = 0.0720\pi_2^{-0.090}\pi_3^{0.406}\pi_6^{-0.149}\pi_8^{-0.099}\pi_{10}^{-0.013}\pi_{11}^{0.283} \quad (28)$$

Table 4 lists and defines the dimensionless π groups included in the generalized correlation. The coefficient and exponents of the independent Pi-groups are determined from a non-linear regression method. Extensive experimental data for CFC-12, HCFC-22, HFC-134a, HFC-407C, HFC-410A, and HFC-502 were used to create the correlation. The results indicate that the present correlation yielded a good agreement with the database with standard deviations of 6.1% and 5% for subcooled inlet conditions and two-phase inlet conditions, respectively.

3. Theoretical models

As described in the earlier section, the semi-empirical models can be used to calculate the mass flow rate through a short-tube orifice, but they cannot be used to indicate the physical meaning of refrigerant flow mechanism. To fulfil this shortcoming, other researchers have proposed two-phase critical flow models to simulate the refrigerant flow behaviour.

The present study compared eight critical flow models by Kim and O'Neal, (1995) with the measured mass flow rates of HCFC-22 and HFC-134a, and divided these models into three groups: (1) homogeneous equilibrium models (HEM), (2) homogeneous frozen models (HFM), and (3) non-homogeneous equilibrium models (NEM). The details of each group of models are described below.

Author's personal copy

3.1. Homogeneous equilibrium model

This model was generated based on the following assumption: the liquid–vapour mixture is homogeneous, the vapour and liquid velocities are equal, and both phases exist in thermal equilibrium. Based on the interfacial mass transfer between the liquid and vapour phases ($\partial x/\partial P$), the models were divided into three groups: isenthalpic flow path (Lahey and Moody, 1977), isentropic flow path (Lahey and Moody, 1977), and Fanno line (Sajben, 1961). The critical mass flux can be determined by the following model.

3.1.1. Isenthalpic homogeneous equilibrium model

$$G_{cr} = \left(\frac{-1}{\frac{dv_f}{dP} - \left(\frac{v_{fg}}{h_{fg}}\right)\frac{dh_f}{dP} + x\left(\frac{dv_{fg}}{dP} - \left(\frac{v_{fg}}{h_{fg}}\right)\frac{dh_{fg}}{dP}\right)} \right)^{1/2} \tag{29}$$

where v_f is the specific volume of the liquid phase, P is pressure, x is quality, v_{fg} is the difference between vapour and liquid specific volume, and h_{fg} is the difference between vapour and liquid enthalpy. A thermodynamic relation of $h = h_f + xh_{fg}$ was used to calculate the interfacial mass transfer path.

3.1.2. Isentropic homogeneous equilibrium model

$$G_{cr} = \left(\frac{-1}{\frac{dv_f}{dP} - \left(\frac{v_{fg}}{s_{fg}}\right)\frac{ds_f}{dP} + x\left(\frac{dv_{fg}}{dP} - \left(\frac{v_{fg}}{s_{fg}}\right)\frac{ds_{fg}}{dP}\right)} \right)^{1/2} \tag{30}$$

where s_f is the entropy of the liquid phase and s_{fg} is the difference between vapour and liquid enthalpy. $\partial x/\partial P$ was determined by the relation $s = s_f + xs_{fg}$.

3.1.3. Sajben homogeneous equilibrium model

In this model, the assumptions of the flow are adiabatic with friction in a constant area (Fanno line), which was derived from the following equations:

$$\frac{G^2\bar{v}^2}{2} + \frac{h_{fg}\bar{v}}{v_{fg}} - \left[h_t - \left(h_f - \frac{h_{fg}}{v_{fg}}v_f\right)\right] = 0 \tag{31}$$

$$h_t = h_f + xh_{fg} + \frac{u_m^2}{2} = \text{const} \tag{32}$$

Therefore, the critical mass flux was calculated by

$$G_{cr} = \left(\frac{h_{fg}/v_{fg}}{\frac{d\left(h_f - h_{fg}\left(v_f/v_{fg}\right)\right)}{dP} + \left[(1-x)v_f + xv_g\right]\left[\frac{d\left(h_{fg}/v_{fg}\right)}{dP} - 1\right]} \right)^{1/2} \tag{33}$$

3.2. Homogeneous frozen model (HFM)

The homogeneous frozen model was established with the following assumptions: the two-phase flow is homogeneous, the average velocities of each phase are equal, and no mass transfer occurs between phases ($\partial x/\partial P = 0$). The models used in this work were proposed by Wallis (1969) and Smith (1963).

3.2.1. Wallis homogeneous frozen model

Based on the above assumptions, Wallis (1969) presented the mass flux equation of refrigerant flow rate through a short-tube orifice as follows:

$$G_{cr} = \left[-\left(x\frac{dv_g}{dP} + (1-x)\frac{dv_f}{dP} \right)^{-1} \right]^{1/2} \tag{34}$$

3.2.2. Smith homogeneous frozen model

In this model, the pressure–volume relation for an isentropic process was included as follows:

$$P\left[\bar{v} - v_f(1-x)\right]^{\Gamma} = \text{constant} \tag{35}$$

$$\Gamma = \frac{xC_{pg} + (1-x)C_f}{xC_{vg} + (1-x)C_f} \tag{36}$$

Therefore, the governing equation for the model was given by

$$G_c = \left[\frac{xC_{pg} + (1-x)C_f}{xC_{vg} + (1-x)C_f} \left(\frac{P}{xv_g}\right) \right]^{1/2} \tag{37}$$

where C_{pg} is the specific heat at a constant pressure of vapour, C_{vg} is the specific heat at a constant volume of vapour, and C_f is the specific heat of the liquid. Under incompressible liquid flow, the specific heat of liquid was approximated by specific heat at the constant pressure of liquid.

3.3. Non-homogeneous equilibrium model

In non-homogeneous equilibrium models, the velocities of the two phases were not equal. Therefore, the slip ratio was included for calculating the critical mass flow rate inside a short-tube orifice. The other assumptions of the models were the presence of a thermodynamic equilibrium with no heat and no mass transfer between the phases as well as no friction. Two models with different slip ratios, which were used to predict the critical mass flux through a short-tube orifice, were presented.

3.3.1. Fauske non-homogeneous equilibrium model (Fauske, 1962)

$$G_{cr} = \left[\frac{-g_c k}{A}\right]^{1/2} \tag{38}$$

$$A = \left[(1 - x + kx)x\right]\frac{dv_g}{dP} + \left[v_g(1 + 2kx - 2x) + v_f\left(2kx - 2k - 2xk^2 + k^2\right)\right]\frac{dx}{dP} + k\left[1 + x(k-2) - x^2(k-1)\right]\frac{dv_f}{dP} \tag{39}$$

The interfacial mass transfer ($\partial x/\partial P$) was estimated based on the isenthalpic flow path, and the slip ratio was calculated by

$$k = \left(\frac{v_g}{v_f}\right)^{1/2} \tag{40}$$

where k is the slip ratio, v_f is the specific volume of the liquid phase, and v_g is the specific volume of the vapour phase.

Author's personal copy

3.3.2. *Moody non-homogeneous equilibrium model (Moody, 1965)*

$$G_{cr} = \left[\frac{-2g_c\left(\upsilon_f + x\upsilon_{fg}\right)}{a(ad+2be)}\right]^{1/2} \tag{41}$$

$$a = k\upsilon_f + x\left(\upsilon_g - k\upsilon_f\right) \tag{42}$$

$$b = \frac{1}{k^2} + x\left(1 - \frac{1}{k^2}\right) \tag{43}$$

$$d = \left[\frac{1}{k^2 s_{fg}}\frac{\partial s_g}{\partial P} - \frac{1}{s_{fg}}\frac{\partial s_f}{\partial P} - \frac{s_{fg}k^2}{k^4 s_{fg}}\right] + x\left[\frac{1}{k^4 s_{fg}}\frac{\partial\left(s_{fg}k^2\right)}{\partial P} - \frac{1}{s_{fg}}\frac{\partial s_{fg}}{\partial P}\right] \tag{44}$$

$$e = \left[s_{fg}\frac{\partial}{\partial P}\left(\frac{k\upsilon}{s_{fg}}\right) + \left(\frac{k\upsilon_f}{s_{fg}}\right)\frac{\partial s_g}{\partial P} - \left(\frac{\upsilon_g}{s_{fg}}\right)\frac{\partial s_f}{\partial P}\right] + x\left[s_{fg}\frac{\partial}{\partial P}\left(\frac{\upsilon_g}{s_{fg}}\right) - s_{fg}\frac{\partial}{\partial P}\left(\frac{k\upsilon_f}{s_{fg}}\right)\right] \tag{45}$$

Moody (1965) used the criterion of minimum value of the specific kinetic energy to estimate the slip ratio. The resulting expression for the slip ratio was given by

$$k = \left(\frac{\upsilon_g}{\upsilon_f}\right)^{1/3} \tag{46}$$

Based on the experimental results, Kim and O'Neal, (1995) stated that a lack of equilibrium due to a short time of expansion and homogeneous mist flow at the exit plane appeared in the short-tube orifice. The lack of equilibrium indicated that the flow was consistent with the assumptions of the homogeneous frozen model. In addition, a comparison between the calculated results obtained from the critical flow models and the experimental data showed that the homogeneous frozen model gave the best agreement, except at outlet qualities below 0.06.

Yang and Zhang (2005) developed a non-equilibrium, two-fluid model for predicting refrigerant flow behaviour inside a short-tube orifice. Their model is based on the following assumptions: (1) one-dimensional steady flow; (2) constant cross-section flow area; (3) adiabatic flow, and (4) neglect the gravitational force. The governing equations, which consisted of mass, momentum, and energy equations for each phase, are represented by the following equations:

Vapour phase mass equation

$$\frac{\partial}{\partial z}(\varphi\rho_G u_G) = \Gamma_G \tag{47}$$

Liquid phase mass equation

$$\frac{\partial}{\partial z}[(1-\varphi)\rho_L u_L] = \Gamma_L \tag{48}$$

Vapour phase momentum equation

$$\frac{\partial}{\partial z}(\varphi p) + \frac{\partial}{\partial z}\left(\varphi\rho_G u_G^2\right) = F_{GL} + F_{Gi} \tag{49}$$

Total momentum equation

$$\frac{\partial p}{\partial z} + \frac{\partial}{\partial z}\left(\varphi\rho_G u_G^2\right) + \frac{\partial}{\partial z}\left[(1-\varphi)\rho_L u_L^2\right] = -F_{WL} + F_{GL} + F_{LG} + F_{Gi} + F_{Li} \tag{50}$$

Total energy equation

$$\frac{\partial}{\partial z}\left[\varphi\rho_G u_G\left(h_G + \frac{u_G^2}{2}\right)\right] + \frac{\partial}{\partial z}\left[(1-\varphi)\rho_L u_L\left(h_L + \frac{u_L^2}{2}\right)\right] = 0 \tag{51}$$

Energy equation of bubble growth

$$\alpha_i(T_L - T_G)A_i = GA\ dx(h_G - h_L) + xGA\ dh_G \tag{52}$$

where Γ_L is the liquid phase mass transfer rate per unit volume, Γ_G is the vapour phase mass transfer rate per unit volume, F_{GL} and F_{LG} are interfacial frictional forces per unit volume between vapour and liquid, and F_{WL} is the frictional force between the tube wall and liquid phase. α_i is the interfacial heat transfer coefficient, a_i is the interfacial area per unit volume, and A_i is the interfacial area. The supplementary equations in terms of the empirical correlations, including the interfacial frictional force, momentum transfer, heat transfer, bubble diameter, and void fraction in different flow patterns, were included in the model as follows:

(1) The steady-state inter-phase frictional force (F_{LG}, F_{GL})

$$F_{LG} = -F_{GL} = 3C_{fi}\varphi^{1/2}\rho_G(u_G - u_L)|u_G - u_L|/D \tag{53}$$

where C_{fi} is the interfacial frictional factor.

$$C_{fi} = 0.005[1 + 75(1-\varphi)] \tag{54}$$

(2) Interfacial momentum transfer (F_{Gi}, F_{Li})

$$F_{Gi} = -\eta\Gamma_G(u_G - u_L) \tag{55}$$

$$F_{Li} = -(1-\eta)(u_L - u_G) \tag{56}$$

(3) Frictional force per unit volume (F_{WL})

$$F_{WL} = \phi_{tp}^2(dp/dz)F_{Lo} \tag{57}$$

where $(dp/dz)F_{Lo}$ is the friction pressure drop, assuming that the total flow rate is liquid and can be calculated from

$$(dp/dz)F_{Lo} = \frac{f_{Lo}G^2}{(2\rho D)} \tag{58}$$

$$f_{Lo} = (0.79\ln Re_{Lo} - 1.64)^{-2} \tag{59}$$

Table 5 – Interfacial area and heat transfer coefficient at different flow pattern. Reprinted from International Journal of Refrigeration, 28, Yang, L., Zhang, C-L., Two-fluid model of refrigerant two-phase flow through short tube orifice, pp. 419–427 (2005), with permission from Elsevier.

Flow regime	Correlations
Bubble flow	$a = N\pi d^2 = \sqrt[3]{36N\pi\varphi^2}$, $\varphi = N\pi d^3/6$ $\alpha_i = k_L(2 + 0.6Re_b^{1/2}Pr_L^{1/3})/d$
Churn-turbulent	$a = a_b + (a_b - a_a)\cdot(\varphi - \varphi_b)/(\varphi_b - \varphi_a)$ $\alpha_i = (\alpha_b)_{\varphi_b}\cdot\alpha_a/(\alpha)_{\varphi_b}$
Annular flow	$a = 4\varphi^{1/2}/D$ $\alpha_i = 0.5C_{fi}\rho_L c_{pL}(u_G - u_L)Pr^{-2/3}$

Author's personal copy

The empirical two-phase multiplier can be estimated by

$$\phi_{tp}^2 = \left(\frac{1-x}{1-\varphi}\right)^{1.75} \tag{60}$$

The Yang and Zhang (2005) study divided the correlation of interfacial area and heat transfer coefficient into three flow patterns: bubbly flow, churn-turbulent flow, and annular flow (Table 5). They solved the governing equations through the central difference discretization method, and thus computed and presented the mass flow rate, velocity, and temperature distribution of refrigerants through short-tube orifices. In addition, their study verified the effect of non-equilibrium behaviour on the mass flow rate by comparing the predicted results between a two-fluid model and a homogeneous equilibrium model. Based on the measured mass flow rates of HFC-134a, CFC-12, HCFC-22, HFC-410A, and HFC-407C, they found that the two-fluid model gave an acceptable prediction with experimental data with deviation of ±20%, while the homogeneous equilibrium model underestimated the predicted results obtained from two-fluid model by 25–30%. This indicated that the non-equilibrium behaviour coexisted during the flow of refrigerant through the short-tube orifice. However, for the flow of supercritical carbon dioxide (CO_2) through a short-tube orifice, Zhang and Yang (2005) reported that the non-homogeneous and non-equilibrium behaviour was unimportant. They also concluded that the accuracy of the two-fluid model was similar to that of the homogeneous equilibrium model. Therefore, in this case, Zhang and Yang (2005) recommended the homogeneous equilibrium model for calculating the mass flow rate inside the short-tube orifice.

Simulation of the fluid-dynamic flow characteristics of carbon dioxide through short-tube orifices was presented by Garcia-Valladares (2006). To predict the mass flow rate and pressure distribution inside a short-tube orifice, the continuity equation, momentum equation, energy equation, and entropy equation were developed. The hypothesis of the mathematical model was one-dimensional flow, thermodynamic equilibrium between phases, and adiabatic flow. The present review found that the mass flow rate, pressure, and enthalpy at the outlet section can be estimated from the following equations:

- Continuity equation

$$\dot{m}_{i+1} = \dot{m}_i - \frac{A\Delta z}{\Delta t}\left(\bar{\rho}_{tp} - \bar{\rho}_{tp}^0\right) \tag{61}$$

where

$$\rho_{tp} = \varepsilon_g \rho_g + (1-\varepsilon_g)\rho_1 \tag{62}$$

- Momentum equation

$$p_{i+1} = p_i - \frac{\Delta z}{A}\left(\Phi\frac{\bar{f}}{4}\frac{\bar{\dot{m}}^2}{2\bar{\rho}_{tp}A^2}\pi D + \bar{\rho}_{tp}Ag\sin\theta + \frac{\bar{\dot{m}} - \bar{\dot{m}}^0}{\Delta t} + \frac{\left[\dot{m}\left(x_g v_g + (1-x_g)\right)v_1\right]_i^{i+1}}{\Delta z}\right) \tag{63}$$

- Energy equation

$$h_{i+1} = \frac{-a\dot{m}_{i+1} + b\dot{m}_i + cA\Delta z/\Delta t}{\dot{m}_{i+1} + \dot{m}_i + \bar{\rho}_{tp}^0 A\Delta z/\Delta t} \tag{64}$$

$$a = \left(x_g v_g + (1-x_g)v_1\right)_{i+1}^2 + g\sin\theta\Delta z - h_i \tag{65}$$

$$b = \left(x_g v_g + (1-x_g)v_1\right)_i^2 - g\sin\theta\Delta z + h_i \tag{66}$$

$$c = 2\left(\bar{p}_i - \bar{p}_i^0\right) - \bar{\rho}_{tp}^0\left(h_i - 2\bar{h}_i^0\right) - \left(\overline{\rho v_i^2} - \bar{\rho}^0\bar{v}_i^{0^2}\right) \tag{67}$$

where v_1 is the specific volume of the liquid phase, x is the quality, v_g is the specific volume of the vapour phase, Δz is a spatial discretization step, Δt is a temporal discretization step, $\bar{v}_i^0$ is the average specific volume at the previous instant, $\bar{h}_i^0$ is average enthalpy at the previous instant, $\bar{f}$ is the average friction factor, $\dot{m}$ is the mass flow rate, and Φ is the two-phase frictional multiplier. In order to solve the above equations, additional information regarding the friction factor and the two-phase frictional multiplier was necessary, and can be determined with the following equations:

- friction factor

$$f = 0.316Re^{-1/4} \quad \text{for } Re \le 2\times10^4 \tag{68}$$

$$f = 0.184Re^{-1/5} \quad \text{for } Re > 2\times10^4 \tag{69}$$

- two-phase frictional multiplier

$$\Phi_{f,lo}^2 = 1 + 4.2\left(\Gamma^2 - 1\right)\left[\frac{B}{We_D}x_g^{0.875}\left(1-x_g\right)^{0.875} + x_g^{1.75}\right] \tag{70}$$

where

$$\Gamma^2 = \frac{f_{go}v_g}{f_{lo}v_1} \tag{71}$$

Table 6 – Criteria for selecting B. Reprinted from Applied Thermal Engineering, 26, Garcia-Valladares, Numerical simulation of trans-critical carbon dioxide (R744) flow through short tube orifices, pp. 144–151 (2006), with permission from Elsevier.

Γ	G (kg m^{-2} s^{-1})	B
≤9.5	≤500	4.8
	500 < G < 1900	2400/G
	≥1900	55/$G^{0.5}$
9.5 < Γ < 28	≤600	520/($\Gamma G^{0.5}$)
	>600	21/Γ
≥28	–	15,000/($\Gamma^2 G^{0.5}$)

Author's personal copy

where Γ is a dimensionless physical property coefficient, We_D is the Weber number, f_{go} is the friction factor for vapour only, and f_{lo} is the friction factor for liquid only. Table 6 presents the criteria for selecting the coefficient B. In addition, to verify the critical flow condition, the invalidity of entropy equation and $dp/dz \to \infty$ at the short-tube outlet plane were used as the criterion. The results showed good agreement between the numerical simulation and experimental data.

4. Conclusions

This paper presented the details of numerical modelling of two-phase refrigerant flow inside the short-tube orifice. The models can be divided into two groups: semi-empirical models and theoretical models. The present review thus gives the following conclusions for each model:

- The semi-empirical models, which are generated from the single-phase orifice equation, are utilized by most previous researchers. Researchers prefer them because they are easy to create; however, the accuracy of each model is valid only for the testing conditions.
- To cover the wide range of the calculation of mass flow rate under various operating conditions and refrigerants, a generalized correlation in a simple form can be developed through a dimensional analysis. However, the empirical correction factors obtained from this correlation do not imply any physical significance.
- The theoretical model, which is developed from the continuity, momentum and energy equation under the proper assumptions, can describe the physical meaning of refrigerant flow behaviour inside the short-tube orifice. The calculated results obtained from this model agreed well with the experimental data.
- The theoretical model is attractive, because it can show the physical meaning of the refrigerant along the short-tube orifice. Yet the theoretical model is rather difficult to solve when complicated equations and correlations are included. As a result, only a few published studies have used theoretical models, and it is still not clear which one is the best. Therefore, further development of the theoretical model for refrigerant flow through the short-tube orifice is still required.

Acknowledgements

The authors would like to express their appreciation to the Thailand Research Fund (TRF), the Commission of Higher Education and the National Research University Project for providing financial support for this study.

REFERENCES

Aaron, A.A., Domanski, P.A., 1990. Experimentation analysis and correlation of refrigerant-22 flow through short tube restrictors. ASHRAE Trans. 96 (1), 729–742.

ASME, 1971. Fluid Meters – Their Theory and Application, sixth ed. American Society of Mechanical Engineers, New York.

Choi, J., Chung, J.T., Kim, Y., 2004. A generalized correlation for two-phase flow of alternative refrigerants through short tube orifices. Int. J. Refrigeration 27, 393–400.

Fauske, H.K., 1962. Contribution to the Theory of Two-phase, One Component Critical Flow. ANL-6633. ANL Lab., Argonne.

Garcia-Valladares, O., 2006. Numerical simulation of trans-critical carbon dioxide (R744) flow through short tube orifices. Appl. Therm. Eng., 144–151.

Kim, Y., O'Neal, D.L., 1994. Two-phase flow of R-22 through short tube orifices. ASHRAE Trans. 100, 323–334.

Kim, Y., O'Neal, D.L., 1995. A comparison of critical flow models for estimating two-phase flow of HCFC22 and HFC134a through short tube orifices. Int. J. Refrigeration 18, 447–455.

Kim, Y.C., O'Neal, D.L., Yuan, Y., 1994. Two-phase flow of HFC134a and CFC12 through short tube orifices. ASHRAE Trans.: Symposia, 582–591.

Kim, Y.C., Payne, W.V., O'Neal, D.L., Farzad, M., 2002. Refrigerant flow through flexible short tube orifices. HVAC&R Res. 8 (2), 179–190.

Lahey, R.T., Moody, E.J., 1977. The Thermal–Hydraulic of a Boiling Water Nuclear Reactor. American Nuclear Society, Hinsdale, Illinois.

Liu, J.P., Niu, Y.M., Chen, J.P., Chen, Z.J., Feng, X., 2004. Experimental and correlation of R744 two-phase flow through short tubes. Exp. Therm. Fluid Sci. 28, 565–573.

Mei, V.C., 1982. Short tube refrigerant flow restrictors. ASHRAE Trans. 88 (2), 157–169.

Moody, F.J., 1965. Maximum flow rate of a single component two-phase mixture. J. Heat Transf., Trans. ASME, 134–142.

Nilpueng, K., Wongwises, S., 2009. Flow pattern, mass flow rate, pressure distribution, and temperature distribution of two-phase flow of HFC-134a inside short-tube orifices. Int. J. Refrigeration 32, 1864–1875.

Payne, W.V., O'Neal, D.L., 1998. Mass flow characteristics of R407C through short-tube orifices. ASHRAE Trans. 104 (3), 197–209.

Sajben, M., 1961. Adiabatic flow of flashing liquid in pipe. J. Basic Eng. 83, 619–631.

Singh, G.M., Hrnjak, P.S., Bullard, C.W., 2001. Flow of refrigerant R134a through orifice tubes. HVAC&R Res. 7 (3), 245–262.

Smith, R.V., 1963. Some idealized solution for chocking, two-phase flowing hydrogen, nitrogen and oxygen. Adv. Cryog. Eng. 8, 563–573.

Tu, X., Hrnjak, P.S., Bullard, C.W., 2006. Refrigerant 134a liquid flow through micro-scale short tube orifices with/without phase change. Exp. Therm. Fluid Sci. 30 (3), 253–262.

Wallis, G.B., 1969. One-dimensional Two-phase Flow. McGraw Hill Book.

Yang, L., Zhang, C.-L., 2005. Two-fluid model of refrigerant two-phase flow through short tube orifice. Int. J. Refrigeration 28, 419–427.

Zhang, C.-L., Yang, L., 2005. Modeling of supercritical CO_2 flow through short tube orifice. J. Fluid Eng., Trans. ASME, 1194–1198.

Convective Heat Transfer of Al_2O_3-water Nanofluids in a Microchannel Heat Sink

Weerapun Duangthongsuk[a,b] Ahmet Selim Dalkilic[c] and Somchai Wongwises[b,d*]

[a]*Department of Mechanical Engineering, South-East Asia University, Bangkok , Thailand;* [b]*Fluid Mechanics, Thermal Engineering and Multiphase Flow Research Lab. (FUTURE), Department of Mechanical Engineering, King Mongkut's University of Technology Thonburi, Bangmod, Bangkok, Thailand;* [c]*Heat and Thermodynamics Division, Department of Mechanical Engineering, Yildiz Technical University, Yildiz, Istanbul, 34349, Turkey;* [d]*The Academy of Science, The Royal Institute of Thailand, Sanam Suea Pa, Dusit, Bangkok 10300, Thailand*

Abstract: The research presents an experimental study on the heat transfer and pressure drop characteristics of Al_2O_3-water nanofluids flowing through a microchannel heat sink (MCHS). The effects of Reynolds number and particle concentrations on the heat transfer and flow behavior are investigated. Comparison of the heat transfer coefficient obtained from water-cooled MCHS and nanofluids-cooled MCHS is also presented. MCHS with rectangular flow channel made from aluminum with dimension of 50x50 mm is used as the test section. Al_2O_3-water nanofluids with particle concentrations of 1.0, 2.0 and 3.0 wt.% are tested. Two electric heaters each with a capacity of 50 W are used to supply heat to the test section. The results indicate that the heat transfer performance of MCHS increases with increasing Reynolds number as well as particle concentrations. Compared with pure water, the results indicate that at particle concentration of 3.0 wt%, the heat transfer coefficient for nanofluid-cooled MCHS is range between 1,100-1,700 W/m^{2}K which is higher than that of water by about 7 – 15%. The pressure drop is between 8 and 25 kPa which is close to the water.

Keywords: Heat transfer coefficient, microchannel heat sink, nanofluid, pressure drop.

1. INTRODUCTION

The concept of nanofluid is to disperse some solid particles with nanometer size in conventional heat transfer fluids such as water, oil and ethylene glycol. This concept was carried out by Masuda *et al*., [1] who studied the heat transfer performance of liquids with solid nanoparticles suspension in 1993. However, the term "nanofluid" was first introduced by S.U.S Choi [2] in 1995, and successively gained popularity. A number of researchers reported that nanofluids gave higher heat transfer performance than that of common heat transfer fluids [3-18]. Similarly, based on advanced electronic devices, these devices became smaller and employed high speed and high power density such as computers, power electronics, car engines, and high-powered lasers or x-rays. Normally, these devices generate an unprecedented high load, whereas their surface area for heat removal is limited. Thus, proper cooling technologies for advanced electronic devices are necessarily required and it is a challenging task for a number of researchers. As mentioned above, it is the concept of microchannel heat sink (MCHS) for dissipating large amounts of heat from these devices in order to maintain the required performance and reliability.

Two decades ago, pioneer researchers Tuckerman and Pease [19] reported the heat transfer performance of microchannel heat sink (MCHS) for cooling the very-large-scale integrated (VLSI) circuit. However, a single-phase liquid is used as working fluid for cooling the microchannel heat sinks and shows a higher potential for heat removal than an air cooling system. In general, there are three approaches for increasing the cooling performance of advanced electronic devices with a high level of heat generation. The first is to find an optimum geometry of cooling devices in which the cooling performance is maximized. The second is to reduce the channel diameter for enhancing the heat transfer coefficient, which is reported by Tuckerman and Pease [19]. The last is to improve the heat transfer performance of coolants. Thus, the use of MCHS combined with nanofluids as a coolant is an innovative idea for cooling small electronic devices. So far, some existing published articles associated with this idea are described in the following sections.

Lee and Choi [20] investigated the thermal performance of MCHS with NF_2 and NF_3 nanofluids compared with pure water and liquid nitrogen, theoretically. Their results showed that thermal resistances of nanofluids were lower than that of a pure water and liquid nitrogen, respectively. On the contrary, the cooling rate and power density of nanofluids were much larger than those of pure water and liquid nitrogen.

Chein and Huang [21] proposed a mathematical model for predicting the heat transfer performance and pumping power of $MCHS_S$ using nanofluids as working fluids. Cu nanoparticles dispersed in water with various particle concentrations were used as testing fluids. Similarly, two specific geometries of MCHS were tested. Their results indicated that addition of nanoparticles in the base liquid remarkably enhanced the heat transfer performance of the base liquid and there was no penalty in pressure drop.

Koo and Kleinstreuer [22] presented a numerical study on the heat transfer and flow characteristics of MCHS with CuO nanoparticles dispersed in water and ethylene glycol, respectively. Their simulation data showed that heat transfer performance of ethylene glycol was higher than that of water. Moreover, they also suggested that nanoparticles with high thermal conductivity and MCHS with high aspect ratio of flow channel should be used.

Jang and Choi [23] presented the cooling performance of a MCHS by using Cu-water and diamond-water nanofluids as coolants, numerically. The results showed that the diamond–water nanofluids with a particle concentration of 1.0 vol.% gave a higher heat transfer performance than the base fluid by about 10%. Moreover, their results indicated that use of nanofluids can reduce both the thermal resistance and temperature difference between the heated surface of MCHS and the working fluid. They also demonstrated that nanofluids-cooled MCHS is the next generation cooling system for cooling the ultra-high heat flux devices.

Abbassi and Aghanajafi [24] investigated the heat transfer performance of MCHS using Cu-water nanofluids as a coolant, numerically. The thermal dispersion model was adopted for heat transfer analysis and a thermal dispersion coefficient was consid-

*Address correspondence to this author at the Fluid Mechanics, Thermal Engineering and Multiphase Flow Research Lab. (FUTURE), Department of Mechanical Engineering, King Mongkut's University of Technology Thonburi, Bangmod, Bangkok, Thailand; Tel: 024709115; Fax: 024709111;
E-mail: somchai.won@kmutt.ac.th

1875-6786/12 $58.00+.00 © 2012 Bentham Science Publishers

ered. Their data showed that nanofluids gave larger heat transfer enhancement than those of base fluid and this enhancement increased with increasing particle concentration as well as Reynolds number.

Chein and Chuang [25] presented the thermal performance of MCHS using CuO-water nanofluids as a coolant. Particle concentrations of 0.2 and 0.4 vol% were tested in their study. The results showed that the presence of nanoparticles results in a higher energy absorption than that of pure water at a low flow rate. In contrast, there is no contribution from heat absorption when the flow rate is high.

Tsai and Chein [26] analytically investigated the MCHS performance using nanofluids as a coolant. Cu-water and CNT-water nanofluids were used as the working fluids. The porous medium model was used to simulate the MCHS performance. Their simulation results demonstrated that the use of nanofluids can reduce the temperature difference between MCHS surface and fluid temperature compared with that of pure water. Moreover, at the porosity and aspect ratio less than the optimum porosity and aspect ratio, it was clearly seen that heat transfer performance of nanofluids-cooled MCHS was larger than that of base fluid. In contrast, for the case of the porosity and channel aspect ratio greater than optimum porosity and aspect ratio, the use of nanofluids did not create a significant change in thermal resistance of the MCHS.

Jung and colleagues [27] reported an experimental investigation on the heat transfer coefficient and friction factor of Al_2O_3-water nanofluids flowing through MCHS with a rectangular channel under laminar flow condition. Compared with pure water, the results indicated that the heat transfer coefficient of nanofluids was about 32% higher than that of water without penalty in pressure drop. This enhancement increased with increasing Reynolds number and particle concentration.

Ghazvini and Shokouhmand [28] determined the heat transfer performance of a MCHS using CuO-water nanofluids as a coolant, both analytically and numerically. The fin model and the porous media approach were used to analyze the thermal behavior of MCHS. The results showed that the overall heat transfer coefficient of nanofluids was larger than that of pure water and increased with an increasing Reynolds number. The porous media approach gave a higher heat transfer coefficient ratio than the fin model. Moreover, the dimensionless temperature increased with an increasing porosity of the MCHS.

Ho *et al*., [29] investigated the forced convective cooling performance of Al_2O_3-water nanofluids flowing through MCHS under laminar flow regime, experimentally. MCHS made from copper which consists of 25 parallel rectangular microchannels with a length of 50 mm was used as the test section. The results showed that the nanofluids have a much higher average heat transfer coefficient than those of pure water. Moreover, their results also indicated that nanofluids gave a lower thermal resistance and wall temperature than those of base fluid. Finally, use of nanofluids has little penalty in pressure drop.

Ebrahimi *et al*., [30] numerically investigated the cooling performance of a nanofluids-cooled MCHS. Carbon nanotubes (CNTs) dispersed in water were used as a coolant. The results showed that thermal conductivity of nanofluids increases with increasing nanolayer thickness, which leads to a decrease in temperature gradient in MCHS.

As aforementioned, the above literatures have focused on the heat transfer performance of nanofluids-cooled MCHS both experimentally and numerically. Their results showed that nanofluids-cooled MCHS gave a higher heat transfer potential than that of the common base liquid. Moreover, many researchers recommended that MCHS using nanofluids as a coolant is expected to be the next generation of the novel electronic cooling technology. Thus, the authors would like to address the heat transfer performance of MCHS with use of nanofluids as a coolant for dissipating large amounts of heat from a MCHS. Al_2O_3-water nanofluids with particle concentrations of 1 and 3 wt.% are used as working fluids and flow through MCHS with a rectangular flow channel.

2. SAMPLE PREPARATION

In the present study, nanofluids provided by a commercial source (DEGUSSA, Aerodisp. W630) were used as a working fluid. This mixture was composed of Al_2O_3 nanoparticles with an average diameter of 120 nm dispersed in water. The original particle concentration was 30 wt%. In order to produce other required particle volume fractions, dilution with water followed by a stirring action was effected. Moreover, an ultrasonic vibrator was used to sonicate the solution continuously for about two hours in order to break down agglomeration of the nanoparticles. The desired concentrations used in this study were 1.0%, 2.0%, and 3.0 wt%.

3. EXPERIMENTAL APPARATUS AND PROCEDURE

Fig. (**1**) shows schematic diagram of the experimental system used in the present study. It mainly consists of four main parts as follows: a test section (MCHS with rectangular channel configuration), a micro pump with an inverter, two storage tanks, and a receiver tank. A 50x50 mm MCHS with 20 rectangular flow channels is made from aluminum. Focused on the MCHS, the width and height of the channel are 1 mm and 1 mm, respectively. Similarly, hydraulic diameter (D_H) and heat transfer areas of MCHS are 1 mm and 0.003 m^2, respectively. A Schematic diagram of MCHS is shown in Fig. (**2**). Plastic tubes were placed at both ends of the MCHS for reducing the heat loss along the axial direction. Similarly, an acrylic plate was placed on the top of MCHS to prevent heat loss. Two 50 W heaters were used to supply heat load to the MCHS. The pressure drop and the bulk temperature of the nanofluids at inlet and exit of the test section were measured by using the differential pressure transmitter and T-type thermocouples, respectively. Similarly, three positions of wall temperatures measurement were carried out using T-type thermocouples. Two storage tanks with 20 L capacity were made from acrylic plate and used for adjusting the nanofluid temperature and reducing the nanofluid temperature leaving from the test section, respectively. The storage tank No.1 with a 9,000 Btu/hr cooling capacity, 2 kW heaters and a thermostat was used to keep the temperature of nanofluids constant. Similarly, storage tank No. 2 with a 9,000 Btu/hr cooling capacity and a thermostat was used to cool down the nanofluid temperature leaving from the test section to the setting temperature of tank No.1. The speed of the micro pump was controlled by using an inverter for adjusting the flow rate of nanofluids. The receiver tank was used to measure the nanofluid flow rate by the time taken for a given volume of nanofluids to be discharged.

The differential pressure transmitter was calibrated using an air operated dead weight tester. The uncertainty of the pressure measurement is ± 0.030 kPa. The nanofluid flow rates were determined by electronic balance. The uncertainty of the electronic balance was ± 0.001 kg. A standard thermometer was used to calibrate all of the T-type thermocouples with a maximum precision of 0.1 ^oC. Therefore, the uncertainty of the measured Nusselt number was around 5%.

During the test run, the pressure difference in the nanofluids, wall temperatures of the MCHS, mass flow rates of the nanofluids, and the inlet and exit temperatures of the nanofluids were recorded.

4. DATA REDUCTION

In the present study, Al_2O_3-water nanofluids with particle fractions of 1.0%, 2.0%, and 3.0 wt.% are used to evaluate the heat transfer performance of MCHS using nanofluids as a coolant. Thus, the heat transfer performance of nanofluids can be computed from the following equation.

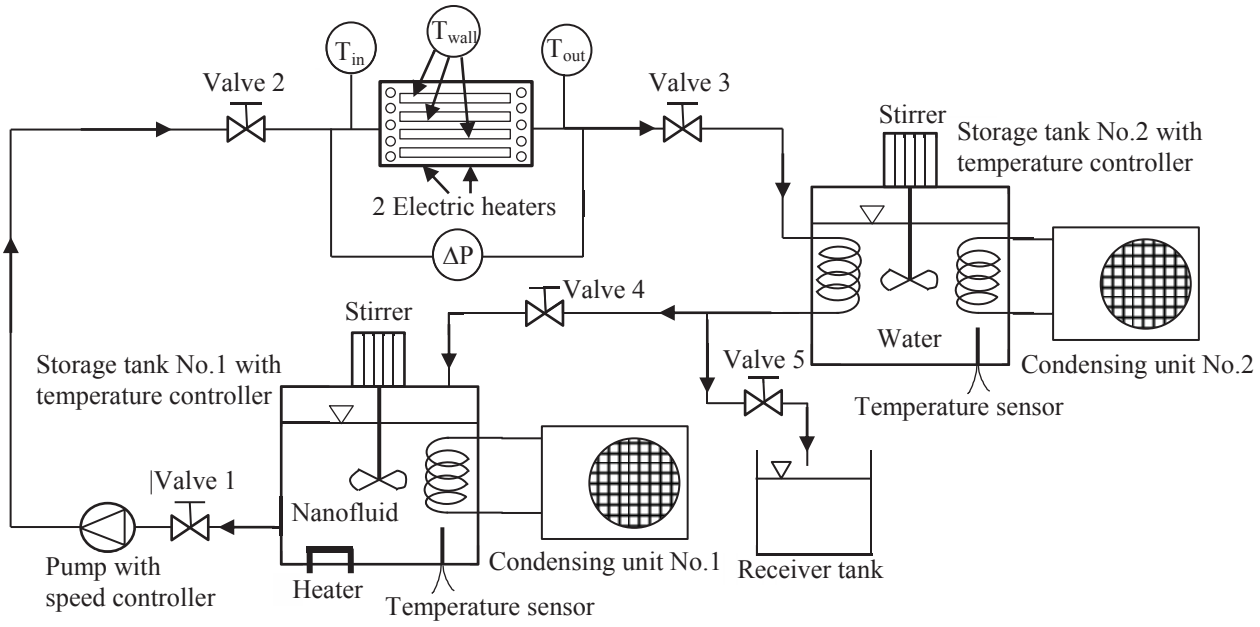

Fig. (1). Schematic diagram of the test apparatus used in the present study.

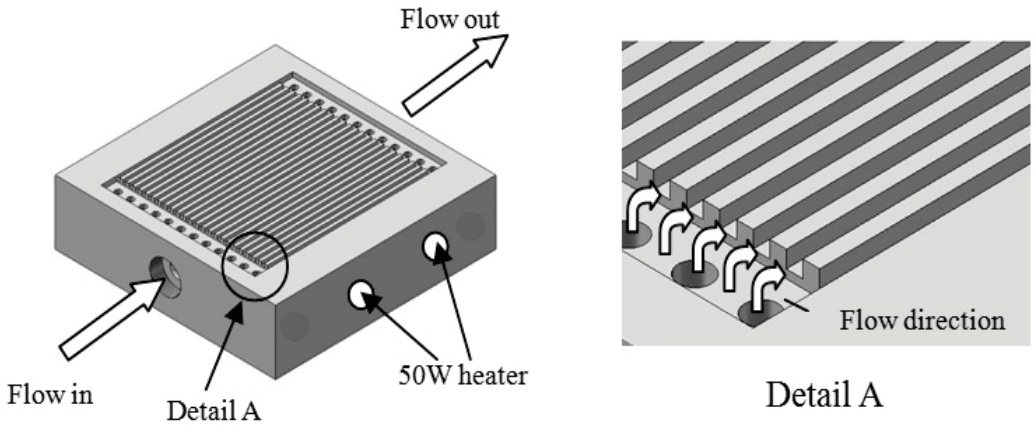

Fig. (2). MCHS used in the present study.

The heat transfer rate into the nanofluids is computed from:

$$Q_{nf} = \dot{m}_{nf} Cp_{nf} (T_{out} - T_{in})_{nf} \quad (1)$$

where Q_{nf} is the heat transfer rate of the nanofluids, $\dot{m}_{nf}$ is the mass flow rate of the nanofluids and T_{in} and T_{out} are the temperature of the nanofluids at inlet and exit of the test section.

The heat transfer coefficient and the Nusselt numbers of the nanofluids are evaluated from the following equations.

$$h_{nf} = \frac{Q_{nf}}{A_S (T_S - T_{nf})} \quad (2)$$

$$Nu_{nf} = \frac{h_{nf} D_H}{k_{nf}} \quad (3)$$

where h_{nf} is the heat transfer coefficient of the nanofluids, T_S is the average temperature of the heated surface of MCHS, T_{nf} is the bulk temperature of the nanofluids, which is the average fluid temperature across the test section, Nu_{nf} is the Nusselt number of the nanofluids, D_H is the Hydraulic diameter of the channel and k_{nf} is the thermal conductivity of the nanofluids.

Moreover, the Reynolds number can be calculated by using the following equation:

$$\mathrm{Re} = \frac{\rho_{nf} u_m D_H}{\mu_{nf}} \quad (4)$$

where ρ_{nf} is the density of the nanofluids, u_m is the mean velocity of the nanofluids and μ_{nf} is the viscosity of the nanofluids.

The density and specific heat of the nanofluids presented in the above equation are computed by use of the Pak and Cho [6] correlations, which are expressed as follows:

$$\rho_{nf} = \phi\rho_p + (1-\phi)\rho_w \tag{5}$$

and

$$Cp_{nf} = \phi Cp_p + (1-\phi)Cp_w \tag{6}$$

where Cp_{nf} is the specific heat of the nanofluids, Cp_p is the specific heat of the nanoparticles, Cp_w is the specific heat of the base fluid and ϕ is the particle volume fraction of the nanoparticles.

Similarly, the thermal conductivity and viscosity of nanofluids are calculated from Hamilton and Crosser model [31] and Einstein equation suggested by Drew and Passman [32] which are expressed as follows:

For thermal conductivity of the nanofluids;

$$k_{nf} = \left[\frac{k_p + (n-1)k_w - (n-1)\phi(k_w - k_p)}{k_p + (n-1)k_w + \phi(k_w - k_p)}\right]k_w \tag{7}$$

$$n = 3/\psi \tag{8}$$

where n is the empirical shape factor and ψ is the sphericity, defined as the ratio of the surface area of a sphere (with the same volume as the given particle) to the surface area of the particle. The sphericity is 1 and 0.5 for the spherical and cylindrical shapes, respectively. Moreover, k_p is the thermal conductivity of the nanoparticles and k_w is the thermal conductivity of the base fluid.

At a temperature of 15 ^{o}C, the thermal conductivity of water is 0.589 W/mK. Similarly, the thermal conductivity of the nanofluids with particle concentrations of 1.0, 2.0 and 3.0 wt.% are 0.594, 0.599 and 0.604 W/mK, respectively.

For viscosity of the nanofluids;

$$\mu_{nf} = (1 + 2.5\phi)\mu_w \tag{9}$$

where μ_w is the viscosity of the base fluid.

The thermophysical properties of the nanofluids shown in the above equations are calculated from water and nanoparticles at average bulk temperature.

For the case of pressure drop, the measured pressure drop of nanofluid-cooled MCHS is compared with the water-cooled MCHS.

5. RESULTS AND DISCUSSION

Fig. (**3**) shows the energy balance ratio, which is the ratio of the energy absorbed by fluid to the energy supplied to the fluid, plotted against Reynolds number for all three concentrations . The plot shows that at higher Reynolds number, both heat transfer rates are almost equal. However, in general, they are nearly 1. In our experiment, the heat loss was kept as small as possible.

In the present study, the experimental data are divided into two groups: 1) heat transfer performance and 2) pressure drop. The detailed results are shown as follows:

As shown in (Figs. (**4**) and (**5**)), the heat transfer coefficient and the Nusselt number of the nanofluids are higher than those of the base liquid, and increase with increasing Reynolds number as well as the particle concentrations. The enhancement range between 7 to 15% is obtained. This is because the nanoparticles presented in the base liquid increase the thermal conductivity. The chaotic movement of nanoparticles also increases the heat transfer rate which leads to an increase in the heat transfer performance. Moreover, increasing the Reynolds number leads to an increase in the heat transfer rate which results in an increase in the heat transfer coefficient.

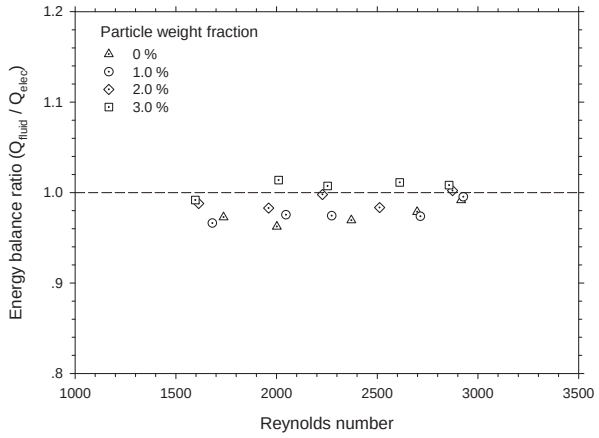

Fig. (3). Energy balance at various Reynolds number and concentrations.

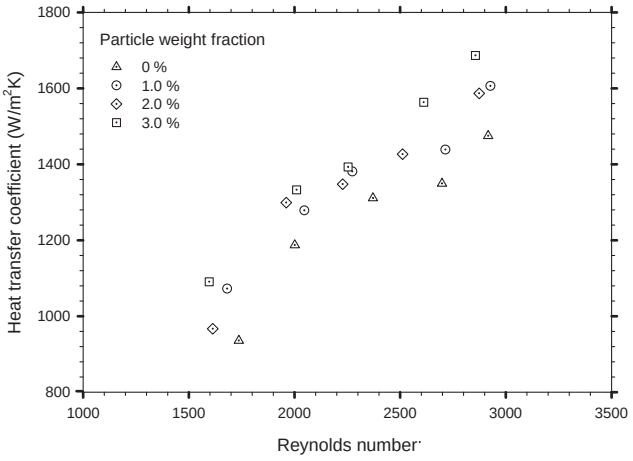

Fig. (4). Measured heat transfer coefficient for water and Al_2O_3-water nanofluids.

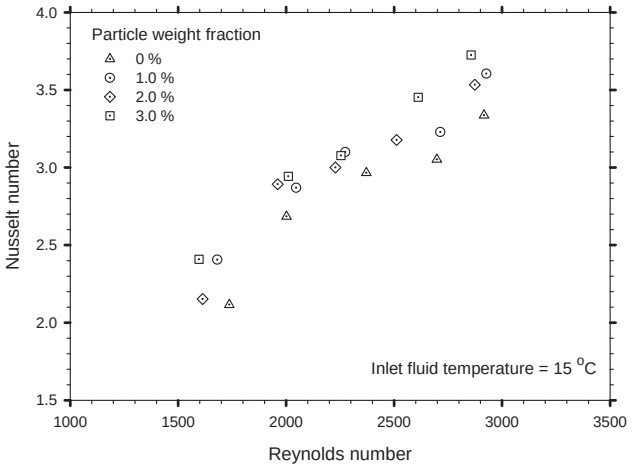

Fig. (5). Nusselt number versus Reynolds number for water-cooled MCHS and nanofluid-cooled MCHS.

Fig. (**6**) shows that the average wall temperature of MCHS decreases with increasing Reynolds number as well as particle concentrations, especially at lower Reynolds number. This is due to the fact that the addition of nanoparticles in the base fluid increases the energy exchange process, which leads to an increase in the heat transfer performance. At a lower Reynolds number, a higher wall temperature difference between water-cooled MCHS and nanofluid-cooled MCHS is obtained. This may be caused by the fact that the heat exchange period for a lower Reynolds number is longer than that for a higher Reynolds number.

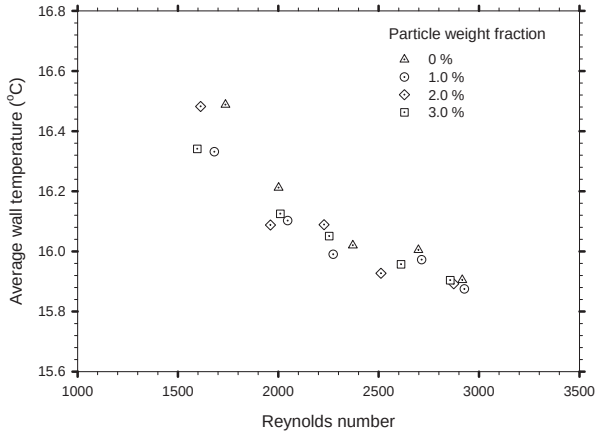

Fig. (6). Effect of particle weight fractions on the average wall temperature of MCHS.

As shown in Fig. (**7**), the results indicate that the pressure drop of the nanofluids increases with increasing Reynolds number and that there is a small increase with increasing particle concentrations. This means that the use of nanofluids will not cause a penalty in pressure drop. This is due to small particle size and very low particle concentrations. This is one of the benefits of using nanofluids as a heat transfer fluid in practical applications.

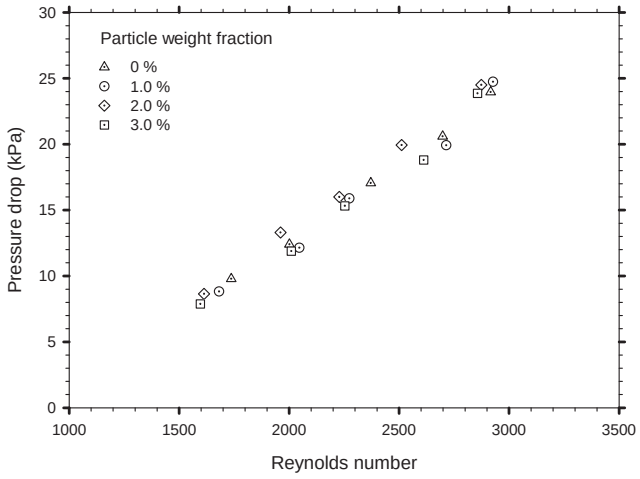

Fig. (7). Comparison of pressure drop between water-cooled MCHS and nanofluid-cooled MCHS.

CONCLUSIONS

The convective heat transfer performance and pressure drop characteristics of MCHS using Al_2O_3-water nanofluids as a coolant were experimentally investigated. The particle concentrations of 1 and 3 wt.% were tested. The effect of particle concentrations and the Reynolds number on the heat transfer performance and pressure drop of nanofluids-cooled MCHS were examined and then compared with the data for water-cooled MCHS. Important conclusions have been obtained and summarized as follows:

- The use of nanofluid-cooled MCHS gives significantly higher heat transfer coefficients than those of the water-cooled MCHS by about 7 - 15%.
- The wall temperature of MCHS decreases with increasing Reynolds number as well as particle concentrations. For the case of nanofluid-cooled MCHS, the average wall temperatures are lower than those of water-cooled MCHS, especially at a lower Reynolds number.
- The pressure drop of water-cooled and nanofluid-cooled MCHS increases with increasing Reynolds number and there is a small increase with increasing particle concentrations.

ACKNOWLEDGEMENTS

The authors would like to express their appreciation to the Office of Research, South-East Asia University, the Thailand Research Fund (TRF), the Office of the Higher Education Commission and the National Research University Project for providing financial support. The authors also wish to thank DEGUSSA AG, (Germany) for the valuable donation of the nanoparticles used in the present study.

CONFLICT OF INTEREST

None declared.

NOMENCLATURE

C_p	=	Specific heat, J/kgK
D_H	=	Hydraulic diameter, m
f	=	Friction factor
h	=	Heat transfer coefficient, W/m^2K
k	=	Thermal conductivity, W/mK
L	=	Length of the test tube, m
m	=	Mass flow rate, kg/s
Nu	=	Nusselt number
ΔP	=	Pressure drop, Pa
Q	=	Heat transfer rate, W
Re	=	Reynolds number
T	=	Temperature, ^oC
u	=	Velocity, m/s

Greek symbols

ϕ	=	Volume fraction
ρ	=	Density, kg/m^3
μ	=	Viscosity, kg/ms

Subscript

f	=	Fluid
in	=	Inlet
m	=	Mean
out	=	Outlet
p	=	Particles
nf	=	Nanofluid
s	=	Surface

REFERENCES

[1] Masuda, H.; Ebata, A.; Teramae, K.; Hishinuma, N. Alteration of thermal conductivity and viscosity of liquid by dispersing ultra-fine particles (Disper-

sion of Al_2O_3, SiO_2 and TiO_2 ultra-fine particles). *Netsu Bussei (Japan)*, **1993**, *7*(4), 227-233.

[2] Choi, S.U.S. Enhancing thermal conductivity of fluids with nanoparticle. *ASME FED.*, **1995**, *231*, 99-105.

[3] Trisaksri, V.; Wongwises, S. Critical review of heat transfer characteristics of the nanofluids. *Renew. Sust. Energ. Rev.*, **2007**, *11*(3), 512-523.

[4] Duangthongsuk, W.; Wongwises, S. A critical review of convective heat transfer of nanofluids. *Renew. Sust. Energ. Rev.*, **2007**, *11*, 797-817.

[5] Wang, X.Q.; Mujumdar, A.S. Heat transfer characteristics of nanofluids: a review. *Int. J. Therm. Sci.,* **2007**, *46*, 1-19.

[6] Pak, B.C.; Cho, Y.I. Hydrodynamic and heat transfer study of dispersed fluids with submicron metallic oxide particles. *Exp. Heat Transf.*, **1998**, *11*, 151-170.

[7] Li, Q.; Xuan, Y. Convective heat transfer and flow characteristics of Cu-water nanofluid. *Sci. China E.*, **2002**, *45*, 408-416.

[8] Xuan, Y.; Li, Q. Investigation on convective heat transfer and flow features of nanofluids. *ASME J. Heat Transf.,* **2003**, *125*, 151-155.

[9] Tsai, C.Y.; Chien, H.T.; Ding, P.P.; Chan, B.; Luh, T.Y.; Chen, P.H. Effect of structural character of gold nanoparticles in nanofluid on heat pipe thermal performance. *Mater. Lett.*, **2004**, *58*, 1461-1465.

[10] Wen, D.; Ding, Y. Experimental investigation into convective heat transfer of nanofluids at the entrance region under laminar flow conditions. *Int. J. Heat Mass Transf.,* **2004**, *47*, 5181-5188.

[11] Yang, Y.; Zhang, Z.G.; Grulke, E.A.; Anderson, W.B.; Wu, G. Heat transfer properties of nanoparticle-in-fluid dispersions (nanofluids) in laminar flow. *Int. J. Heat Mass Transf.,* **2005**, *48*(6), 1107-1116.

[12] Ding, Y.; Alias, H.; Wen, D.; Williams, R.A. Heat transfer of aqueous suspensions of carbon nanotubes (CNT nanofluids). *Int. J. Heat Mass Transf.,* **2005**, *49*(1-2), 240-250.

[13] Heris, S.Z.; Etemad, S.G.; Esfahany, M.N. Experimental investigation of oxide nanofluids laminar flow convective heat transfer. *Int. Commun. Heat Mass Transf.*, **2006**, *33*, 529-535.

[14] Heris, S.Z.; Esfahany, M.N.; Etemad, S.G. Experimental investigation of convective heat transfer of Al_2O_3/water nanofluid in circular tube. *Int. J. Heat Fluids Fl.,* **2007**, *28*(2), 203-210.

[15] He, Y.; Jin, Y.; Chen, H.; Ding, Y.; Cang, D.; Lu, H. Heat transfer and flow behavior of aqueous suspensions of TiO_2 nanoparticles (nanofluids) flowing upward through a vertical pipe. *Int. J. Heat Mass Transf.,* **2007**, *50*, 2272-2281.

[16] Duangthongsuk, W.; Wongwises, S. Effect of thermophysical properties models on the prediction of the convective heat transfer coefficient for low concentration nanofluid. *Int. Commun. Heat Mass Transf.*, **2008**, *35*, 1320-1326.

[17] Duangthongsuk, W.; Wongwises, S. Heat transfer enhancement and pressure drop characteristics of TiO_2-water nanofluid in a double-tube counter flow heat exchanger. *Int. J. Heat Mass Transf.,* **2009**, *52*, 2059-2067.

[18] Duangthongsuk, W.; Wongwises, S. An experimental study on the heat transfer performance and pressure drop of TiO_2-water nanofluids flowing under a turbulent flow regime. *Int. J. Heat Mass Transf.,* **2010**, *53*, 334-344.

[19] Tuckeman, D.B.; Pease, R.F.W. High performance heat sinking for VLSI. *IEEE Electron. Device L.,* **1981**, *2(5),* 126-129

[20] Lee, S.; Choi, S.U.S. *Application of metallic nanoparticle of metallic nanoparticles suspensions in advanced cooling systems*. Proceedings of the International Mechanical Engineering Conference Session on Application of Metallic Materials in Advanced Engineering System, Atlanta, GA, USA, November 17-23, **1996**.

[21] Chein, R.; Huang, G. Analysis of microchannel heat sink performance using nanofluids. *Appl. Therm. Eng.,* **2005**, *25*, 3104-3114.

[22] Koo, J.; Kleinstreuer, C. Laminar nanofluid flow in microheat-sinks. *Int. J. Heat Mass Transf.,* **2005**, *48*, 2652-2661.

[23] Jang, S.P.; Choi, S.U.S. Cooling performance of a microchannel heat sink with nanofluids. *Appl. Therm. Eng.,* **2006**, *26*, 2457-2463.

[24] Abbassi, H.; Aghanajafi, C. Evaluation of Heat Transfer Augmentation in a Nanofluid-Cooled Microchannel Heat Sink. *J. Fusion Energ.,* **2006**, *25*(3/4), 187-196.

[25] Chein, R.; Chuang, J. Experimental microchannel heat sink performance studies using nanofluids. *Int. J. Therm. Sci.*, **2007**, *46*, 57-66.

[26] Tsai, T.S.; Chein, R. Performance analysis of nanofluid-cooled microchannel heat sinks. *Int. J. Heat Fluids Fl.*, **2007**, *28*, 1013-1026.

[27] Jung, J.Y.; Oh, H.S.; Kwak, H.Y. Forced convective heat transfer of nanofluids in microchannels. *Int. J. Heat Mass Tran.,* **2009**, *52*, 466-472.

[28] Ghazvini, M.; Shokouhmand, H. Investigation of a nanofluid-cooled microchannel heat sink using Fin and porous media approaches. *Energ. Convers. Manage.*, **2009**, *50*, 2373-2380.

[29] Ho, C.J.; Wei, L.C.; Li, Z.W. An experimental investigation of forced convective cooling performance of a microchannel heat sink with Al_2O_3/water nanofluid. *Appl. Therm. Eng.,* **2010**, *30*, 96-103.

[30] Ebrahimi, S.; Sabbaghzadeh, J.; Lajevardi, M.; Hadi, I. Cooling performance of a microchannel heat sink with nanofluids containing cylindrical nanoparticles (carbon nanotubes). *Heat Mass Transf.*, **2010**, *46*, 549-553.

[31] Hamilton, R.L.; Crosser, O.K. Thermal conductivity of heterogeneous two-component systems. *Ind. Eng. Chem. Fundam.*, **1962**, *1*(3), 187.

[32] Drew, D.A.; Passman, S.L. *Theory of multicomponent fluids*, Springer: Berlin, **1999**.

Received: December 19, 2011 Revised: January 20, 2012 Accepted: March 11, 2012

Journal of ASTM International, Vol. 9, No. 5
Paper ID JAI104409
Available online at www.astm.org

A. Suriyawong,[1] *A. S. Dalkilic,*[2] *and S. Wongwises*[3]

Nucleate Pool Boiling Heat Transfer Correlation for TiO_2-Water Nanofluids

ABSTRACT: This paper is a continuation of the authors' previous work on the nucleate pool boiling heat transfer of nanofluids [Suriyawong, A. and Wongwises, S., "Nucleate pool boiling heat transfer characteristics of TiO2-water nanofluids at very low concentrations," *Exp. Therm. Fluid Sci.*, Vol. 34, No. 8, 2010, pp. 992–999.] This study presents new correlation for predicting heat transfer coefficient for nucleate pool boiling of TiO_2-water nanofluids at several low concentrations. Unlike most previous studies, the proposed correlation consists of various relevant factors. Two horizontal circular plates made from copper and aluminum with different surface roughness values are used as heating surfaces. Because the calculation concerns with properties of nanofluids, this research uses various correlations from previous studies to find the properties of nanofluids and the best one is selected for the presentation. Compared with measured data of nucleate pool boiling of water and nanofluids from present and previous studies, it was found that the developed correlation could be used for prediction at a certain level.

KEYWORDS: nucleate boiling, nanofluids, nanoparticles, heat transfer, heat flux

Nomenclature

A = Area, m^2
bf = Base fluids
C_p = Specific heat, $kJ/kg \times K$
$cond$ = Conduction heated
$elec$ = Electric power
g = Gravitational acceleration, m/s^2
h_b = Boiling heat transfer coefficient, $W/m^2 \times K$
h_{fg} = Heat of vaporization, kJ/kg
I = Electric current, Amps
k = Thermal conductivity, $W/m \times K$
L_c = Characteristic length, m
l = Liquid phase
nf = Nanofluids
np = Nanoparticles
Pr = Prandtl number, Dimensionless
q'' = Heat flux, W/m^2
Ra = Average roughness, μmRz Mean peak-to-valley height roughness, μm
s = Heating surface
sat = Saturation
T = Temperature, K
V = Voltage, Volts
ν = Vapor phase
x = Position of temperature on test section, m

Manuscript received October 8, 2011; accepted for publication January 27, 2012; published online May 2012.
[1]Fluid Mechanics, Thermal Engineering and Multiphase Flow Research Laboratory (FUTURE), Dept. of Mechanical Engineering, King Mongkut's Univ. of Technology Thonburi, Bangmod, Bangkok 10140, Thailand.
[2]Heat and Thermodynamics Division, Dept. of Mechanical Engineering, Yildiz Technical Univ., Yildiz, Besiktas, Istanbul 34349, Turkey.
[3]Fluid Mechanics, Thermal Engineering and Multiphase Flow Research Lab. (FUTURE) Dept. of Mechanical Engineering, King Mongkut's Univ. of Technology Thonburi, Bangmod, Bangkok 10140, Thailand; and The Academy of Science, The Royal Institute of Thailand, Sanam Suea Pa, Dusit, Bangkok 10300, Thailand (Corresponding author), e-mail: somchai.won@kmutt.ac.th

Copyright © 2012 by ASTM International, 100 Barr Harbor Drive, PO Box C700, West Conshohocken, PA 19428-2959.

Copyright by ASTM Int'l (all rights reserved); Mon Jun 11 12:07:24 EDT 2012
Downloaded/printed by
King Mongkuts Univ. of Tech. Thonburi pursuant to License Agreement. No further reproductions authorized.

ε = Roughness of the heating surface, m
μ = Dynamic viscosity, $\mathrm{kg/m} \times \mathrm{s}$
ρ = Density, $\mathrm{kg/m^3}$
σ = Surface tension of liquid–vapor interface, $\mathrm{N/m}$
ϕ = Volume fraction of the nanoparticles, Dimensionless

Introduction

As a result of the fact that thermal conductivity of nanofluids is higher than that of base fluid, the writers propose to use nanofluids as working fluids in heat exchanger. The study of pool boiling heat transfer characteristics is another important and necessary issue in the development of heat exchanger, in which the working fluid boils. Literature review reveals that, recently, many researchers have had an interest in and conducted experimental studies about pool boiling of nanofluids (as shown in Table 1).

To the best of our knowledge, there are only a few correlations available for predicting heat transfer coefficient for pool boiling of nanofluids. However, although some information is currently available, there still remains room for further research, especially relevant parameters or variables that are taken into account in the correlation. The outstanding feature of this research is the correlation to predict the boiling heat transfer coefficient. The proposed correlation consists of several parameters that contribute to heat transfer characteristics, i.e., nanofluids concentration; thermophysical properties of nanofluids (density, specific heat, viscosity, thermal conductivity); heating surface roughness; and heating surface material.

Preparation of Nanofluids

The preparation of nanofluids can be divided into three parts: *p*H control, addition of surfactants, and use of ultrasonic vibration. The preparation of nanofluids aims to make nanoparticles suspend in base fluids with stability, without sedimentation. The nanofluids used (VP Disp. W740) were supplied by Degussa Company. The fluids have TiO_2 nanoparticles with average diameters of 21 nm, suspended in a water base fluid that has a concentration of 40 wt. %. The nanofluids were diluted by adding water to achieve the desired concentration levels of 0.00005 vol. %, 0.0001 vol. %, 0.0005 vol. %, 0.005 vol. %, and 0.01 vol. %. After that, the fluids were treated with ultrasonic vibration for 2 h to distribute the nanoparticles evenly.

Sample photographs of nanofluids used in the experiment were taken from a transmission electron microscope (TEM) shown in Fig. 1(*a*). An initial analysis of the nanoparticles' sizes revealed an almost circular shape with average diameter of 21 nm (Fig. 1(*b*)), corresponding with data from the manufacturer.

Experimental Apparatus and Procedure

The experimental apparatus as shown in Fig. 2(*a*) consists of three main sections: test section, heating device, and pressure control in the pressure vessel. The test section was placed inside the twin-layered stainless steel pressure vessel. The inner layer of the pressure vessel contained the nanofluids used in the experiment. The outer layer contained water heated by a preheater (1.5 kW) to keep the temperature of the nanofluids inside the inner tank stable at saturation temperature. The temperature of the nanofluids was measured by a T-type sheath thermocouple with deviation of $\pm$ 0.1 °C.

Figure 2(*b*) shows the boiling test section, which consists of a heater (1.2 kW) placed inside a copper bar that will transfer heat from the heater to the test section installed at the upper end of the copper bar. The copper bar and the test section are covered with calcium silicate insulator which is 50 mm thick to prevent lateral heat loss. The test section was made from two materials: copper and aluminum. The heating surfaces have average roughnesses of 0.2 μm and 4 μm. The roughness can be measured by a Mahr Marsurf PS1 model roughness meter. The test section area contains four holes for installing sheath thermocouples. Thermocouples are placed at intervals of 10 mm. The distance between the uppermost sheath thermocouple and the heating surface is 20 mm. Temperatures at various locations in the test section would be used to calculate the temperature of the heating surface.

Pressure inside the inner tank was controlled by adjusting the water flow in the cooling coil to control the condensation rate of vapor at the outer surface of the cooling coil. During operation, the pressure inside both layers of the tank is kept at atmospheric condition.

Copyright by ASTM Int'l (all rights reserved); Mon Jun 11 12:07:24 EDT 2012
Downloaded/printed by
King Mongkuts Univ. of Tech. Thonburi pursuant to License Agreement. No further reproductions authorized.

TABLE 1—*The literature review for pool boiling nanofluids.*

Authors	Heating surface	Nanofluids	Concentration	Remarks
Li et al. [1]	Platinum wire	SiO_2-water	0.05–0.5 wt. %.	There was no subsidence of nanoparticles on Pt wire surface, as suffered on heated tube. The superheat of 0.05 wt. % nanofluids was lower than that of pure water.
Vassallo et al. [2]	Nichrome wire, D = 0.4 mm, L = 120 mm.	Si-water	0.5–9 vol. %.	The experimental data show a marked increase in CHF compared to pure water.
Kim et al. [3,4]	Nichrome wire, D = 0.2 mm. Titanium wire, D = 0.25 mm.	TiO_2-water Al_2O_3-water	0.00001–0.1 vol. %.	The nanofluids increased the CHF compared with pure water. The SEM photograph showed that the nanoparticles were deposited on the heating surface during pool boiling.
Golubovic et al. [5]	Nichrome wire, D = 0.64 mm, L = 50 mm.	BiO_2-water Al_2O_3-water	0.5714–6.4615 mg/l	The CHF increased with increase in the volume concentrations.
You et al. [6]	Square flat copper surfaces	Al_2O_3-water	0.001–0.05 g/l	The CHF increased dramatically (200 %) compared with pure water.
Bang and Chang [7]	Smooth flat copper surfaces	Al_2O_3-water	0.5–4.0 vol. %	The nanofluids have poor heat transfer performance compared to pure water. The HTC was decreased by increasing particle concentration.
Nishikawa et al. [8]	Copper flat plate	Water	-	The effect of surface orientation was remarkable in the low heat flux region, the HTC increased as the inclination angle was increased.
Kim et al. [9]	Stainless steel wire D = 0.381 mm. L = 120 mm.	Al-water ZrO-water Si- water	0.001–0.1 vol. %.	The nanofluids exhibited significant CHF enhancement compared with the base fluid. Some nanoparticles were coated on the heating surface during nucleate boiling to form a porous layer.
Liu and Liao [10]	Plain copper	CuO-water CuO-alcohol	0.5 wt. % and 1 wt. %	The boiling heat transfer characteristics of the nanofluids were slightly poor compared with water and alcohol.
Das et al. [11,12]	Stainless steel cylinders D = 4, 6.5, 20 mm	Al_2O_3-water	1–4 vol. %	The HTC deteriorated with the addition of nanoparticles.
Trisaksri and Wongwises [13]	Cylindrical copper tube	TiO_2-R141b	0.01–0.05 vol. %	The effect of pressure on the HTC was clear at higher heat flux.
Suriyawong and Wongwises [14]	Copper and aluminum flat surfaces.	TiO_2-water	0.00005–0.01 vol. %	For copper, at 0.0001 vol. %, higher nucleate pool boiling heat transfer coefficient was obtained compared with the base fluid. A 15 % increase was obtained for the roughness of 0.2 μm and a 4 % increase was obtained for roughness of 4 μm. For concentrations higher than 0.0001 vol. %, the higher the concentration, the lower the heat transfer coefficient. For aluminum, the corresponding heat transfer coefficients were larger than for the copper surface by around 30 % with a roughness of 0.2 μm and around 27 % with a roughness of 4 μm. The results indicated that the heat transfer coefficient obtained based on a roughness of 4 μm was higher than that for a roughness of 0.2 μm by around 12 % for aluminum and by around 13 % for copper.

Copyright by ASTM Int'l (all rights reserved); Mon Jun 11 12:07:24 EDT 2012
Downloaded/printed by
King Mongkuts Univ. of Tech. Thonburi pursuant to License Agreement. No further reproductions authorized.

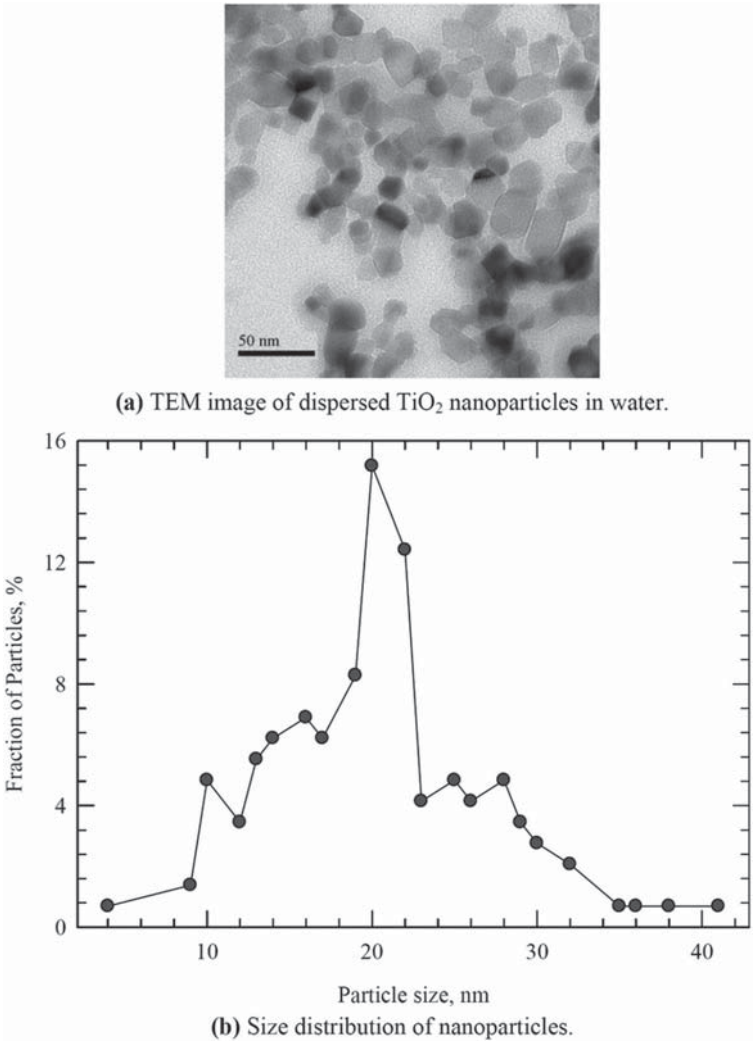

FIG. 1—*Nanofluids used in the present study (a) TEM image of dispersed TiO_2 nanoparticles in water; (b) size distribution of nanoparticles.*

In the experiment with high heat flux there was film boiling, which created film at the heating surface. When this happened, temperatures at various points of the test section increased rapidly. This condition can cause harm to the apparatus. Therefore, a wind blower was installed to eradicate film boiling on the heating surface; hence, the surface temperature decreased.

After experimenting under each condition, the experimental apparatus was dissected and cleaned to get rid of nanoparticles on various parts. The apparatus can be cleaned by using a high-pressure water injector to inject water on the heating surface. After that, the apparatus was dried with a blower before being assembled for use in experiments under other conditions. The experimental conditions for the present study are shown in Table 2.

Data Reduction

The heat fluxes, q (W/m^2), were calculated from the following equation:

$$q = \frac{IV}{A} \tag{1}$$

where:

I is the current (amps),
V is the voltage (volts), and
A is the heating surface area (m^2).

Copyright by ASTM Int'l (all rights reserved); Mon Jun 11 12:07:24 EDT 2012
Downloaded/printed by
King Mongkuts Univ. of Tech. Thonburi pursuant to License Agreement. No further reproductions authorized.

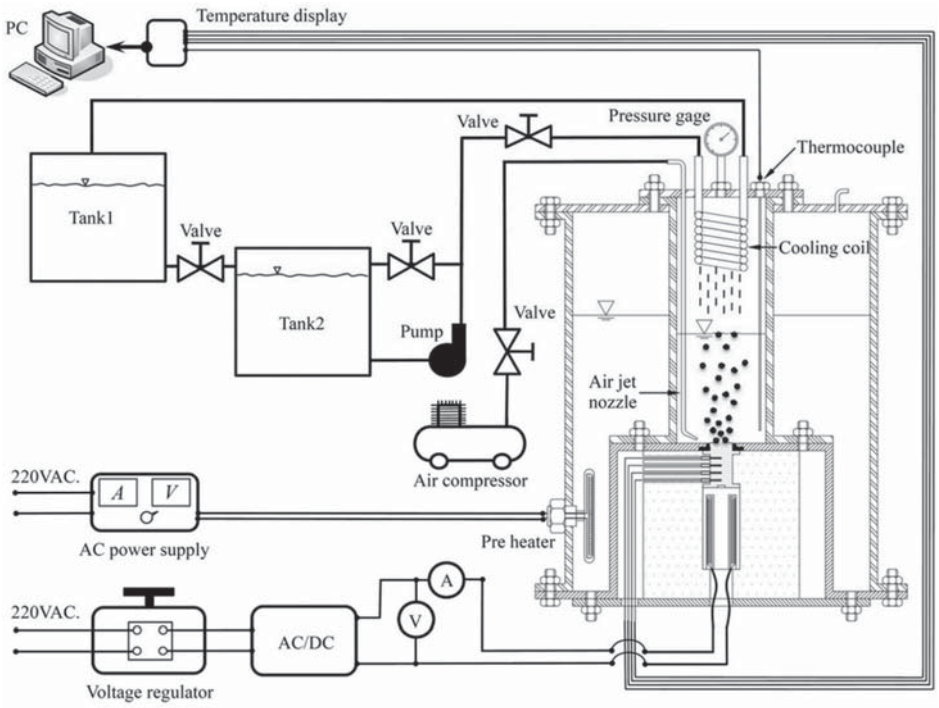

(a) Schematic diagram of the experimental apparatus.

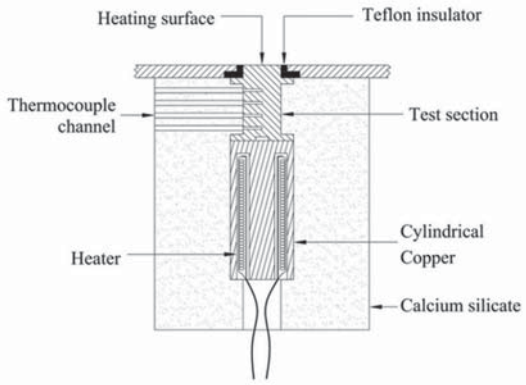

(b) Cross-sectional view of the boiling test section.

FIG. 2—*Experimental apparatus: (a) schematic diagram of experimental apparatus; (b) cross-sectional view of the boiling test section.*

The average boiling heat transfer coefficient, h_b ($W/m^2 \times K$), is defined as

$$h_b = \frac{q}{T_s - T_{sat}} \tag{2}$$

where:

T_s is the average heater surface temperature (°C) calculated from Eq 3, and T_{sat} is the liquid saturation temperature (°C)

$$T_s = \frac{\sum_{i=1}^{4} T_i \sum_{i=1}^{4} x_i^2 - \sum_{i=1}^{4} x_i \sum_{i=1}^{4} x_i T_i}{4\sum_{i=1}^{4} x_i^2 - \left(\sum_{i=1}^{4} x_i\right)^2} \tag{3}$$

where T_i is the local temperature (°C) and x is the position of the temperature measurement (m) on the test section.

Copyright by ASTM Int'l (all rights reserved); Mon Jun 11 12:07:24 EDT 2012
Downloaded/printed by
King Mongkuts Univ. of Tech. Thonburi pursuant to License Agreement. No further reproductions authorized.

TABLE 2—*The present experimental conditions.*

Parameter	Value
Classification of boiling	Saturated pool boiling
Material of heating surface	Copper and Aluminum
Heating surface roughness	0.2–4.0 μm
Type of nanofluids	TiO_2-distilled water
Concentration of nanofluids	0.0001–0.01 vol.%
Heat flux	40–800 kW/m^2
Pressure	1 atm.

The uncertainties of the heat flux, heating surface temperature, and heat transfer coefficient are ±2.2 %, ±3.7 %, and ±11.6 %, respectively.

Results and Discussion

It is quite difficult to develop any general theoretical model for predicting the heat transfer coefficients in nucleate boiling [15]. In this section, the correlation for predicting the pool boiling heat transfer coefficient is developed. The correlation is modified from Rohsenow's correlation [16] for various liquid-surface combinations. The pool boiling heat transfer coefficient of nanofluids, $h_{b,nf}$, is assumed to be a function of the viscosity of nanofluids μ_{nf}, the heat flux q'', the thermal conductivity of nanofluids k_{nf}, the roughness of heating surface ε, the specific heat of nanofluids $C_{p,nf}$, the latent heat of vaporization h_{fg}, the volume fraction of nanoparticles ϕ, the surface tension σ, the gravitational acceleration g, the density of nanofluids ρ_{nf}, and the density of water vapor ρ_v.

The model is of the form

$$h_{b,nf} = f\left(\mu_{nf}, q'', k_{nf}, \varepsilon, C_{p,nf}, h_{fg}, (\phi + m), \frac{\sigma}{g(\rho_{nf} - \rho_v)}\right) \tag{4}$$

TABLE 3—*The thermophysical property models of nanofluids.*

Investigator	Correlation	Remarks
Density of nanofluids		
Pak and Cho [17]	$\rho_{nf} = \phi\rho_{np} + (1-\phi)\rho_{bf}$	For Al_2O_3- and TiO_2-water nanofluids.
Specific heat of nanofluids		
Pak and Cho [17]	$C_{p,nf} = \phi C_{p,np} + (1-\phi)C_{p,bf}$	For Al_2O_3- and TiO_2-water nanofluids.
Xuan and Roetzel [18]	$(\rho C_p)_{nf} = \phi(\rho C_p)_{np} + (1-\phi)(\rho C_p)_{bf}$	For the synthesized nanoparticle-liquid suspension.
Viscosity of nanofluids		
Wang et al. [19]	$\mu_{nf} = (1 + 7.3\phi + 123\phi^2)\mu_{bf}$	For Al_2O_3-water nanofluids, volume fractions less than 6 %.
Einstein's equation suggested by Drew and Passman [20]	$\mu_{nf} = (1 + 2.5\phi)\mu_{bf}$	For small rigid spherical particles in volume fractions less than 5 %.
Brinkman [21]	$\mu_{nf} = \mu_{bf}(1-\phi)^{-2.5}$	For oil-water nanofluids and Cu-water nanofluids.
Thermal conductivity of nanofluids		
Hamilton and Crosser [22]	$k_{nf} = \left(\frac{k_{np}+(n-1)k_{bf}-(n-1)\phi(k_{bf}-k_{np})}{k_{np}+(n-1)k_{bf}+\phi(k_{bf}-k_{np})}\right)k_{bf}$	Empirical shape factor (n = 3/ψ), where ψ is the sphericity, defined as the ratio of the surface area of a sphere per surface area of the particle.
Murshed et al. [23]	$k_{nf} = \frac{1}{4}[(3\phi-1)k_{np} + (2-3\phi)k_{bf}] + \frac{k_{bf}}{4}\sqrt{\Delta}$ $\Delta = \begin{pmatrix}(3\phi-1)^2(k_{np}/k_{bf})^2 + (2-3\phi)^2 \\ +2(2+9\phi-9\phi^2)(k_{np}/k_{bf})\end{pmatrix}$	For the TiO_2-water nanofluids, volume fractions less than 5 %.
Wasp [24]	$k_{nf} = \left(\frac{k_{np}+2k_{bf}-2\phi(k_{bf}-k_{np})}{k_{np}+2k_{bf}+\phi(k_{bf}-k_{np})}\right)k_{bf}$	For particle special case with the sphericity ψ = 1.0.
Yu and Choi [25]	$k_{nf} = \left(\frac{k_{np}+2k_{bf}+2(k_{np}-k_{bf})(1+\beta)^3\phi}{k_{np}+2k_{bf}-(k_{np}-k_{bf})(1+\beta)^3\phi}\right)k_{bf}$	The β is the ratio of the nanolayer thickness to the original particle radius, normally β = 1.

Copyright by ASTM Int'l (all rights reserved); Mon Jun 11 12:07:24 EDT 2012
Downloaded/printed by
King Mongkuts Univ. of Tech. Thonburi pursuant to License Agreement. No further reproductions authorized.

TABLE 4—*The groups of correlations used to determine the thermophysical properties.*

Nanofluids property correlations		
μ_{nf}	$C_{p,nf}$	k_{nf}
Wang et al. [19]	Pak and Cho [17]	Hamilton and Crosser [22]
Wang et al. [19]	Pak and Cho [17]	Yu and Choi [25]
Wang et al. [19]	Xuan and Roetzel [18]	Hamilton and Crosser [22]
Wang et al. [19]	Xuan and Roetzel [18]	Yu and Choi [25]
Einstein's equation [20]	Pak and Cho [17]	Hamilton and Crosser [22]
Einstein's equation [20]	Pak and Cho [17]	Yu and Choi [25]
Einstein's equation [20]	Xuan and Roetzel [18]	Hamilton and Crosser [22]
Einstein's equation [20]	Xuan and Roetzel [18]	Yu and Choi [25]

Using the Buckingham Pi theorem, a set of dimensionless terms was established as follows:

$$Nu_{nf} = a(\mathrm{Pr}_{nf})^b \left(\frac{q''\varepsilon}{\mu_{nf} h_{fg}}\right)^c \left(\frac{\varepsilon^2 g(\rho_{nf} - \rho_v)}{\sigma}\right)^d \left(\frac{L_c}{\varepsilon(\phi + m)^e}\right) \tag{5}$$

where

$$Nu_{nf} = \frac{h_{b,nf} L_c}{k_{nf}} \tag{6}$$

$$\mathrm{Pr}_{nf} = \frac{\mu_{nf} C_{p,nf}}{k_{nf}} \tag{7}$$

L_c is the characteristic length, and a, b, c, d, e, and m are the coefficients.

TABLE 5—*The coefficients for the correlation.*

Coefficient for copper surface						Coefficient for aluminum surface					
a	b	c	d	e	m	a	b	c	d	e	m
28.85	0.59	0.70	0.16	0.12	0.001	46.63	0.55	0.74	0.15	0.05	0.00001

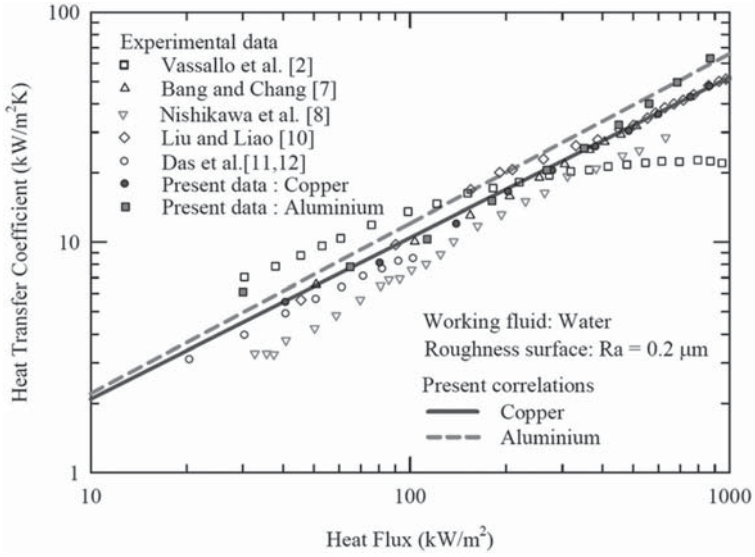

FIG. 3—*Comparison of the results obtained from the proposed correlations with the measured data obtained from several researchers.*

Copyright by ASTM Int'l (all rights reserved); Mon Jun 11 12:07:24 EDT 2012
Downloaded/printed by
King Mongkuts Univ. of Tech. Thonburi pursuant to License Agreement. No further reproductions authorized.

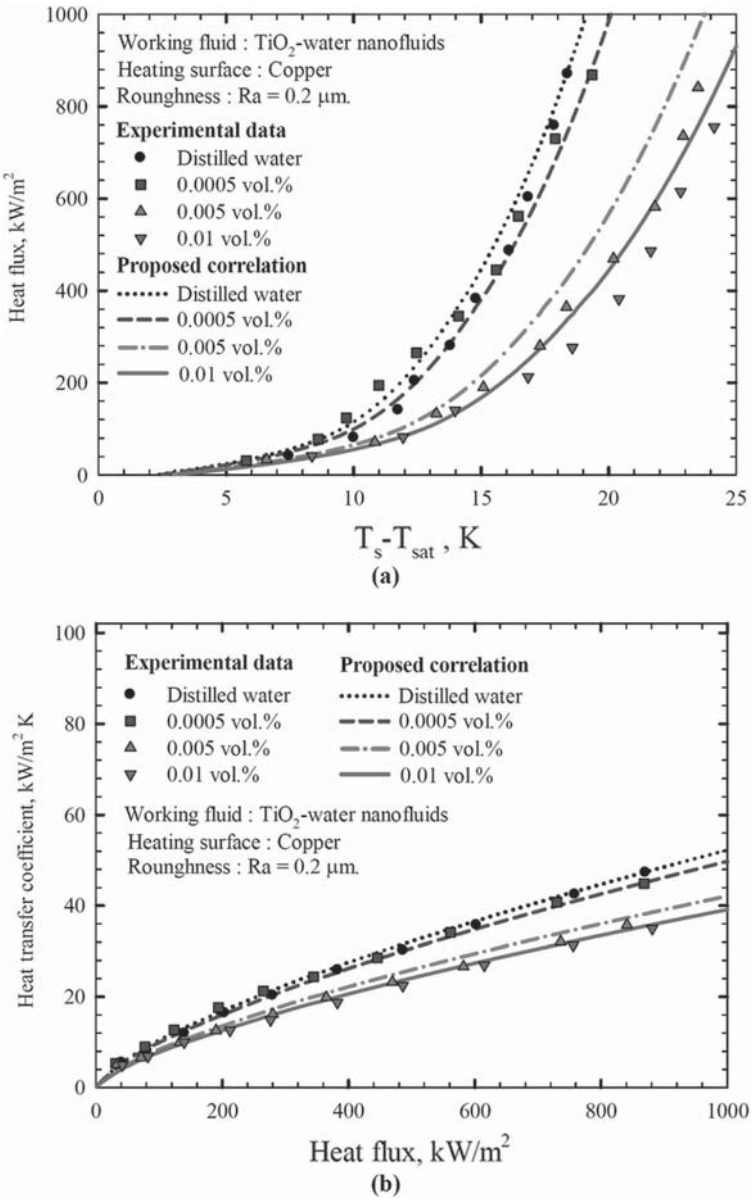

FIG. 4—*Comparison of the measured boiling curve and heat transfer coefficient with the proposed correlation (Copper heating surface, roughness Ra = 0.2 μm).*

The thermophysical properties such as density, viscosity, specific heat, and thermal conductivity of the nanofluid are calculated using different formulae as shown in Table 3. On the basis of the experimental result of Das et al. [11], the surface tension of water is used in the present study.

Because there are several equations for determining various thermophysical properties of nanofluids, the combinations of these equations, as shown in Table 4, are used to determine the coefficients in Eq 5.

The coefficients in Eq 5 are obtained by equation fitting for measured data obtained from the experiments with copper surface and aluminum surface. Comparisons between the heat transfer coefficients obtained from the proposed correlations and those obtained from the experiments show that there is no difference in heat transfer coefficient obtained from various properties. All existing correlations for specific heat, absolute viscosity, and thermal conductivity give very similar predicted results. As a result, in order to make it easy, the viscosity correlation of Wang et al. [19], specific heat correlation of Pak and Cho [17], and thermal conductivity correlation of Hamilton and Crosser [22] are used for the next calculations. The coefficients in Eq 5 for both surfaces are shown in Table 5.

Figure 3 shows comparisons between plots of heat transfer coefficients against heat flux, obtained from the present experiment and those obtained from the proposed correlations. The experimental data of

Copyright by ASTM Int'l (all rights reserved); Mon Jun 11 12:07:24 EDT 2012
Downloaded/printed by
King Mongkuts Univ. of Tech. Thonburi pursuant to License Agreement. No further reproductions authorized.

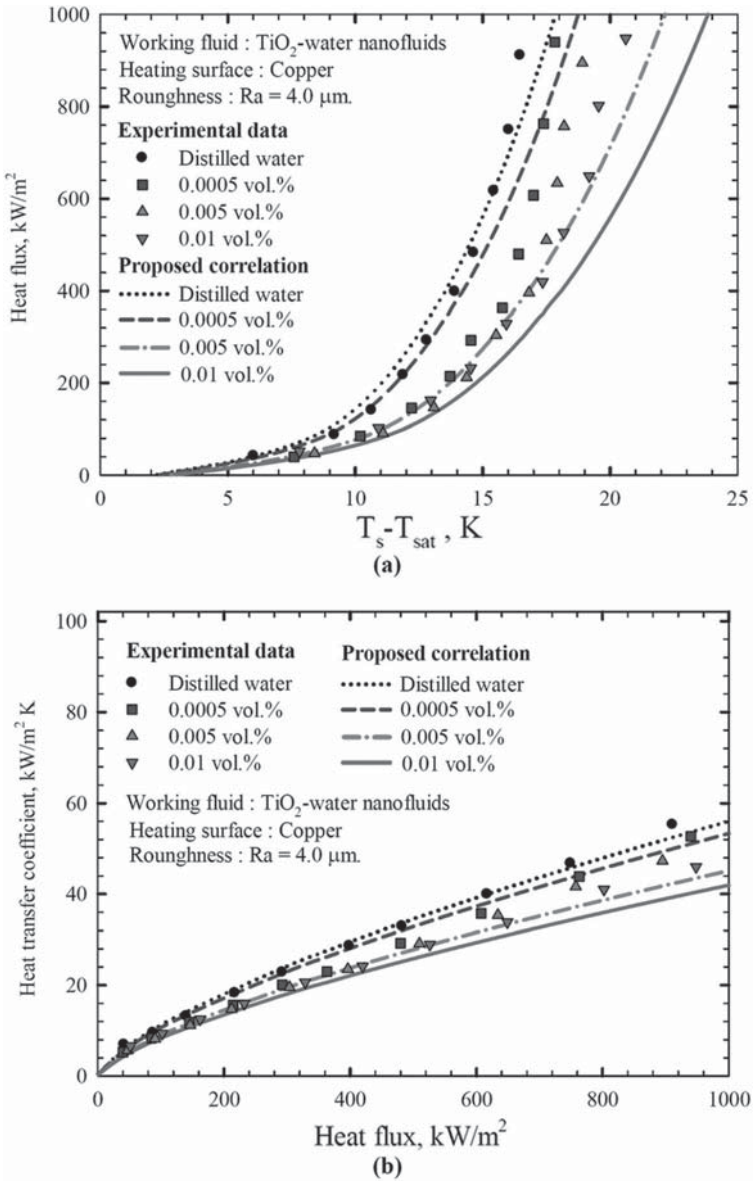

FIG. 5—*Comparison of the measured boiling curve and heat transfer coefficient with the proposed correlation (Copper heating surface, roughness Ra = 4 μm).*

Vassallo et al. [2], Bang and Chang [7], Nishikawa et al. [8], Liu and Liao [10], and Das et al. [11,12] obtained from various heating surface materials, surface roughnesses, nanofluids, and concentrations are also plotted in Fig. 3. From comparison between the measured heat transfer coefficients and the calculated ones for nucleate boiling of water on the horizontal circular plate, it is found that mean absolute error for copper surface and for aluminum surface are 5 % and 14 %, respectively.

Comparisons of the experimental boiling curves and experimental heat transfer coefficient with those calculated by the proposed correlations are shown in Figs. 4 and 5 for copper heating surface and Figs. 6 and 7 for aluminum heating surface.

All boiling curves shown in Figs. 4 through 7 present the experimental heat transfer data of nanofluids at various concentrations. Each data point was taken at steady state and each curve was obtained from the constant pressure experiment. The condition of steady state in pool boiling study is defined as a variation in the system saturation temperature of less than some accepted small temperature.

Considering each curve, we accept that the nanoparticle deposition, which is the transient process associated with boiling time, would occur and affect the nucleation site density. However we believe that

Copyright by ASTM Int'l (all rights reserved); Mon Jun 11 12:07:24 EDT 2012
Downloaded/printed by
King Mongkuts Univ. of Tech. Thonburi pursuant to License Agreement. No further reproductions authorized.

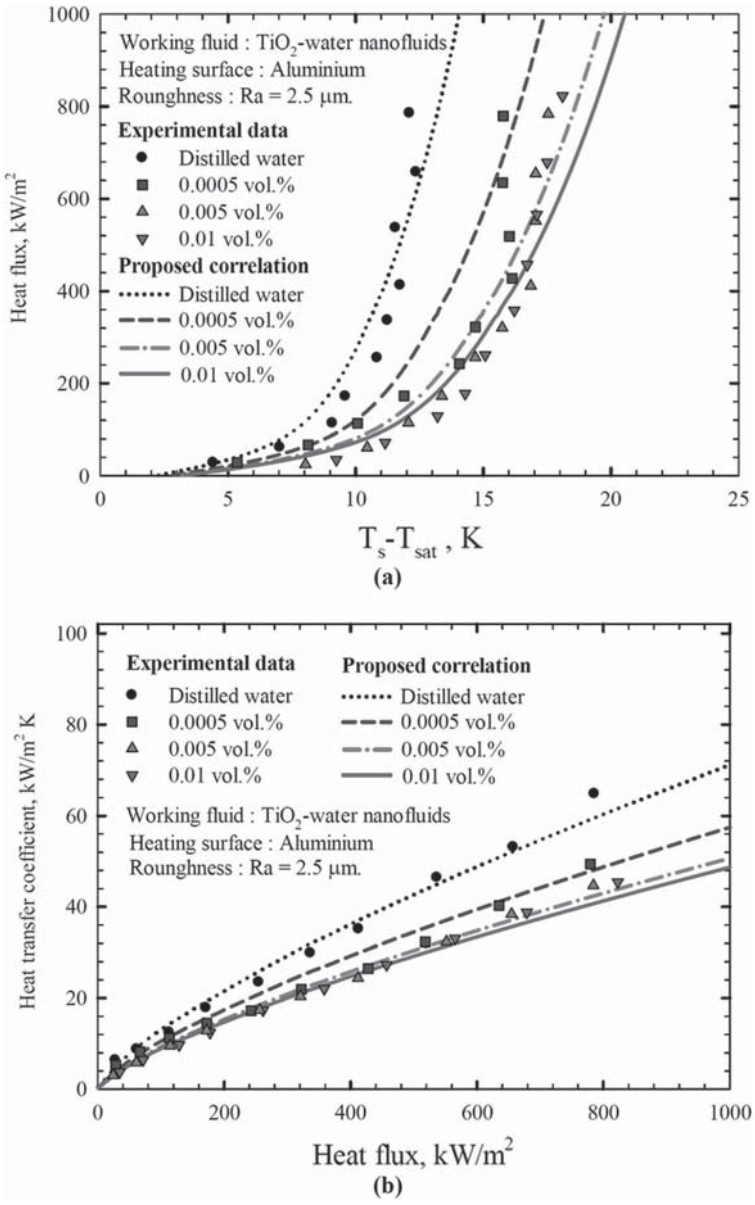

FIG. 6—*Comparison of the measured boiling curve and heat transfer coefficient with the proposed correlation (Aluminum heating surface, roughness Ra = 2.5 μm).*

the boiling curve in this style is still a good graphical presentation and is practical for pool boiling study. In other words, even though deposition occurs on the surface during the experiment and varies with boiling time, this type of curve is still useful and gives some physical information.

Because several parameters are included for the correlation fitting, it is quite hard to make this obtained correlation fit all data curves. However, the results obtained from the correlation tend to go in the same direction as the data, especially the heat transfer coefficient data of the copper surface. We do believe that this correlation will be useful to predict the heat transfer coefficients for nucleate pool boiling of TiO_2-water nanofluids under the same various conditions, and the results will be a guideline for the prediction of boiling heat transfer coefficients for any other nanofluids at various other conditions.

Conclusions

Correlations for nucleate pool boiling heat transfer coefficient for TiO_2-water nanofluids at low concentrations for heating surfaces made from copper and aluminum are proposed. Different from most previous

Copyright by ASTM Int'l (all rights reserved); Mon Jun 11 12:07:24 EDT 2012
Downloaded/printed by
King Mongkuts Univ. of Tech. Thonburi pursuant to License Agreement. No further reproductions authorized.

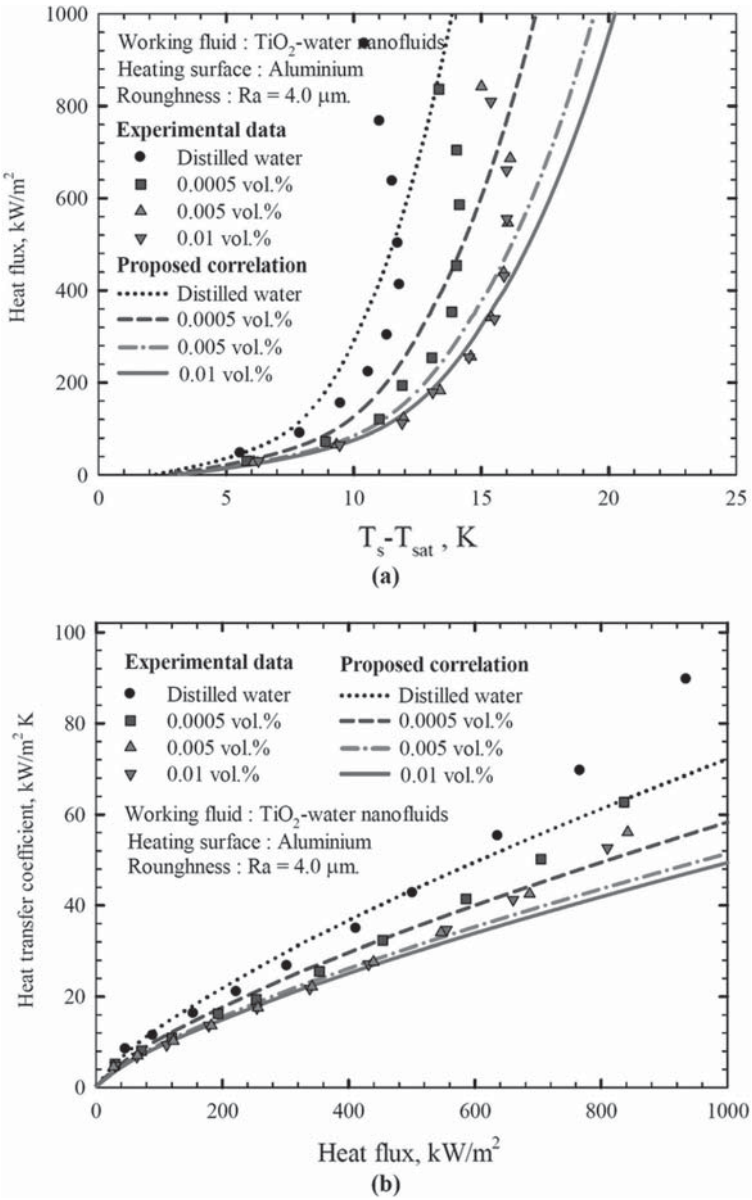

FIG. 7—*Comparison of the measured boiling curve and heat transfer coefficient with the proposed correlation (Aluminum heating surface, roughness Ra = 4 μm).*

correlations, this new correlation includes many relevant variables, i.e., viscosity, heat flux, thermal conductivity, roughness of heating surface, specific heat, latent heat of vaporization, volume fraction of nanoparticles, surface tension, gravitational acceleration, density of nanofluids, and density of water vapor. The viscosity correlation of Wang et al. [19], specific heat correlation of Pak and Cho [17], and thermal conductivity correlation of Hamilton and Crosser [22] are used to determine the coefficients of the correlations. The correlations are shown to fit the data well for the copper surface but show fair agreement for the aluminum surface.

Acknowledgments

The writers would like to express their appreciation to the Thailand Research Fund (TRF), the Office of the Higher Education Commission, and the National Research University Project for providing financial support for this study. The writers also wish to thank Degussa AG, Germany, for the valuable donation of the nanoparticles used in the present study.

Copyright by ASTM Int'l (all rights reserved); Mon Jun 11 12:07:24 EDT 2012
Downloaded/printed by
King Mongkuts Univ. of Tech. Thonburi pursuant to License Agreement. No further reproductions authorized.

References

[1] Li, C. H., Wang, B. X., and Peng, X. F., "On the Pool Boiling of Subcooled Nano-Particle Suspensions," *Proceedings of 6th International Symposium on Heat Transfer*, Beijing, China, June 15–19, 2004, pp. 505–510.

[2] Vassallo, P., Kumar, R., and Amico, S. D., "Pool Boiling Heat Transfer Experiments in Silica–Water Nano-Fluids," *Int. J. Heat Mass Transfer*, Vol. 47, No. 2, 2004, pp. 407–411.

[3] Kim, H., Kim, J., and Kim, M., "Experimental Study on CHF Characteristics of Water-TiO_2 Nano-Fluids, *Nucl. Eng. Tech.*, Vol. 38, No. 1, 2006, pp. 61–68.

[4] Kim, H., Kim, J., and Kim, M., "Effect of Nanoparticles on CHF Enhancement in Pool Boiling of Nano-Fluids," *Int. J. Heat Mass Transfer*, Vol. 49, No. 25–26,2006, pp. 5070–5074.

[5] Golubovic, M. N., Madhawa Hettiarachchi, H. D., Worek, W. M., and Minkowycz, W. J., "Nanofluids and Critical Heat Flux, Experimental and Analytical Study," *Appl. Therm. Eng.*, Vol. 29, No. 7, 2009, pp. 1281–1288.

[6] You, S. M., Kim, J. H., and Kim, K. H., "Effect of Nanoparticles on Critical Heat Flux of Water in Pool Boiling Heat Transfer," *Appl. Phys. Lett.*, Vol. 83, No. 16, 2003, pp. 3374–3376.

[7] Bang, I. C. and Chang, S. H., "Boiling Heat Transfer Performance and Phenomena of Al_2O_3-Water Nano-Fluids from a Plain Surface in a Pool, *Int. J. Heat Mass Transfer*, Vol. 48, No. 12, 2005, pp. 2407–2419.

[8] Nishikawa, K., Fujita, Y., Uchida, S., and Ohta, H., "Effect of Surface Configuration on Nucleate Boiling Heat Transfer," *Int. J. Heat Mass Transfer*, Vol. 27, No. 9, 1984, pp. 1559–1571.

[9] Kim, S. J., Bang, I. C., Buongiorno, J., and Hu, L. W., "Surface Wettability Change During Pool Boiling of Nanofluids and Its Effect on Critical Heat Flux," *Int. J. Heat Mass Transfer*, Vol. 50, No. 19–20, 2007, pp. 4105–4116.

[10] Liu, Z., Liao, L., "Sorption and Agglutination Phenomenon of Nanofluids on a Plain Heating Surface During Pool Boiling," *Int. J. Heat Mass Transfer*, Vol. 51, No. 9–10, 2008, pp. 2593–2602.

[11] Das, S. K., Putra, N., and Roetzel, W., "Pool Boiling Characteristics of Nano-Fluids," *Int. J. Heat Mass Transfer*, Vol. 46, No. 5, 2003, pp. 851–862.

[12] Das, S. K., Putra, N., and Roetzel, W., "Pool Boiling of Nano-Fluids on Horizontal Narrow Tube," *Int. J. Multiphase Flow*, Vol. 29, No. 8, 2003, pp. 1237–1247.

[13] Trisaksri, V. and Wongwises, S., Nucleate Pool Boiling Heat Transfer of TiO_2–R141b Nanofluids," *Int. J. Heat Mass Transfer*, Vol. 52, No. 5–6, 2009, pp. 1582–1588.

[14] Suriyawong, A. Wongwises, S., "Nucleate Pool Boiling Heat Transfer Characteristics of TiO2-Water Nanofluids at Very Low Concentrations," *Exp. Therm. Fluid Sci.*, Vol. 34, No. 8, 2010, pp. 992–999.

[15] Whalley, P. B., *Boiling, Condensation, and Gas-Liquid Flow*, 1st ed., Oxford University Press, New York, 1990, pp. 131–133.

[16] Rohsenow, W. M., "A Method of Correlating Heat Transfer Data for Surface Boiling of Liquids," Trans. ASME, Vol. 74, 1952, pp. 969–975.

[17] Pak, B. C., Cho, Y. I., "Hydrodynamic and Heat Transfer Study of Dispersed Fluids with Submicron Metallic Oxide Particles," *Exp. Heat Transfer*, Vol. 11, No. 2, 1998, pp. 151–170.

[18] Xuan Y., and Roetzel, W., Conceptions for Heat Transfer Correlation of Nanofluids," *Int. J. Heat Mass Transfer*, Vol. 43, No. 19, 2000, pp. 3701–3707.

[19] Wang, X., Xu, X., and Choi, S. U. S., "Thermal Conductivity of Nanoparticles-Fluid Mixture," *J. Thermophys. Heat Transfer*, Vol. 13, No. 4, 1999, pp. 474–480.

[20] Drew, D. A. and Passman, S. L., *Theory of Multicomponent Fluids*, Springer, Berlin, 1999, pp. 121–128.

[21] Brinkman, H. C., "The Viscosity of Concentrated Suspensions and Solution," *J. Chem. Phys.*, Vol. 20, No. 4, 1952, pp. 571–581.

[22] Hamilton, R. L. and Crosser, O. K., "Thermal Conductivity of Heterogeneous Two-Component Systems," *Ind. Eng. Chem. Fundam.*, Vol. 1, No. 3, 1962, pp. 187–191.

[23] Murshed, S. M. S., Leong, K. C., and Yang, C., "Enhanced Thermal Conductivity of TiO_2-Water Based Nanofluids," *Int. J. Therm. Sci.*, Vol. 44, No. 4, 2005, pp. 367–373.

[24] Wasp, F. J., *Solid-Liquid Flow Slurry Pipeline Transportation*, Trans Tech Publications, Clausthal, 1977.

[25] W. Yu and Choi, S. U. S., "The Role of Interfacial Layers in the Enhanced Thermal Conductivity of Nanofluids: A Renovated Maxwell Model, *J. Nanopart. Res.*, Vol. 5, No. 4, 2003, pp. 167–171.

Copyright by ASTM Int'l (all rights reserved); Mon Jun 11 12:07:24 EDT 2012
Downloaded/printed by
King Mongkuts Univ. of Tech. Thonburi pursuant to License Agreement. No further reproductions authorized.

Provided for non-commercial research and education use.
Not for reproduction, distribution or commercial use.

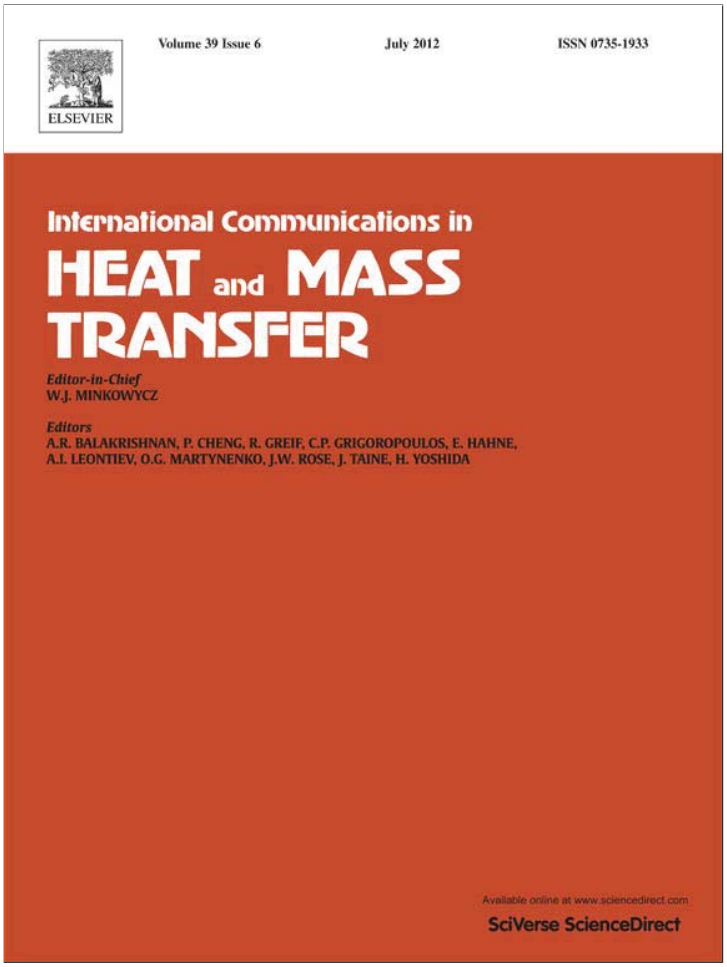

This article appeared in a journal published by Elsevier. The attached copy is furnished to the author for internal non-commercial research and education use, including for instruction at the authors institution and sharing with colleagues.

Other uses, including reproduction and distribution, or selling or licensing copies, or posting to personal, institutional or third party websites are prohibited.

In most cases authors are permitted to post their version of the article (e.g. in Word or Tex form) to their personal website or institutional repository. Authors requiring further information regarding Elsevier's archiving and manuscript policies are encouraged to visit:

http://www.elsevier.com/copyright

Author's personal copy

International Communications in Heat and Mass Transfer 39 (2012) 853–860

Contents lists available at SciVerse ScienceDirect

International Communications in Heat and Mass Transfer

journal homepage: www.elsevier.com/locate/ichmt

New proposed two-phase multiplier and evaporation heat transfer coefficient correlations for R134a flowing at low mass flux in a multiport minichannel ☆

Jatuporn Kaew-On [a], Somchai Wongwises [a,b,*]

[a] Fluid Mechanics, Thermal Engineering and Multiphase Flow Research Lab. (FUTURE), Department of Mechanical Engineering, King Mongkut's University of Technology Thonburi, Bangmod, Bangkok 10140, Thailand
[b] The Academy of Science, The Royal Institute of Thailand, Sanam Suea Pa, Dusit, Bangkok 10300, Thailand

ARTICLE INFO

Available online 4 May 2012

Keywords:
Two-phase multiplier
Heat transfer coefficient
Correlations
Multiport minichannel
Low mass flux
R134a

ABSTRACT

New correlations of the two-phase multiplier and heat transfer coefficient of R134a during evaporation in a multiport minichannel at low mass flux are proposed. The experimental results were obtained from a test using a counter-flow tube-in-tube heat exchanger with refrigerant flowing in the inner tube and hot water in the gap between the outer and inner tubes. Test section is composed of the extruded multiport aluminium inner tube with an internal hydraulic diameter of 1.2 mm and an acrylic outer tube with an internal hydraulic diameter of 25.4 mm. The experiments were performed at heat fluxes between 10 and 35 kW/m^2, and a refrigerant mass flux between 45 and 155 kg/(m^2 s). Some physical parameters that influenced the frictional pressure drop and heat transfer coefficient are examined and discussed in detail. The pressure drop and heat transfer coefficient results are also compared with existing correlations. Finally, new correlations for predicting the frictional pressure drop and heat transfer coefficient at low mass fluxes are proposed.

© 2012 Elsevier Ltd. All rights reserved.

1. Introduction

This study is a continuation of previous studies conducted by Kaew-on and Wongwises [1] and Kaew-on et al. [2]. The main aims of the previous studies were to propose the correlations for predicting the heat transfer coefficient and pressure drop of multiport minichannels at medium-to-high mass flux. In the practical application of mini- or microchannels, such as the evaporator or condenser of an automotive air-conditioning unit, the flow is generally laminar. Therefore, this work focuses on proposing correlations for predicting the heat transfer and pressure drop of R134a in multiport minichannels during evaporation at low mass flux. Heat transfer and pressure drop correlations of a refrigerant in a small channel have been proposed by a number of researchers, mostly at medium to high mass flux. The heat transfer and pressure drop correlations of a refrigerant during evaporation at low mass flux have drawn little attention in the literature. The existing correlations for predicting the heat transfer and pressure drop of a refrigerant during evaporation in a conventional tube and a small tube are summarised and shown in the authors' previous studies.

As mentioned in the summation of correlations presented in Kaew-on and Wongwises [1] and Kaew-on et al. [2], some correlations are available for the boiling flow characteristics in minichannels and microchannels, especially for medium-to-high mass flux or turbulent flow. Despite worthwhile industrial applications, the flow boiling correlations in multiport minichannels, where the flow is generally laminar, have received comparatively little attention in the literature. As a consequence, the present paper aims to investigate the heat transfer and flow characteristics of a refrigerant, R134a, during flow boiling at low mass flux. In addition, the effects of relevant parameters on the heat transfer and pressure drop are presented. Finally, the correlations for predicting the two-phase multiplier and heat transfer coefficients at low mass flux are also proposed for practical applications.

2. Experimental apparatus and method

The present work is conducted using the experimental apparatus of Kaew-On and Wongwises [1]. The main components of the system are: a test section, refrigerant loop, hot water loop, subcooling loop, and data acquisition system. Detailed descriptions of the relevant components can be found in the authors' previous studies.

A schematic diagram of the test section is shown in Fig. 1. The test section is a counter-flow tube-in-the tube heat exchanger. According to this figure, both the inlet and outlet headers of the test section were designed as a calm section at the inlet of the multiport channel. The refrigerant side is an aluminium rectangular multiport minichannel with a hydraulic diameter of 1.2 mm and eight numbers of channels. The hot water side is made from a rectangular transparent acrylic tube with an internal hydraulic diameter of 25.4 mm, used to provide the heat flux to the test tubes. The details of the test

☆ Communicated by W.J. Minkowycz.

* Corresponding author at: Fluid Mechanics, Thermal Engineering and Multiphase Flow Research Lab. (FUTURE), Department of Mechanical Engineering, King Mongkut's University of Technology Thonburi, Bangmod, Bangkok 10140, Thailand.
E-mail address: somchai.won@kmutt.ac.th (S. Wongwises).

0735-1933/$ – see front matter © 2012 Elsevier Ltd. All rights reserved.
doi:10.1016/j.icheatmasstransfer.2012.04.015

Author's personal copy

Nomenclature

A	area (m^2)
Bo	boiling number, $Bo = \frac{q''}{Gi_{fg}}$
Co	convection number, $Co = \frac{(1-x)}{x}^{0.8}\left(\frac{\rho_v}{\rho_l}\right)^{0.5}$
d_h	hydraulic diameter (m)
f	fanning friction factor (-)
G	mass flux ($kg\,m^{-2}\,s^{-1}$)
h	heat transfer coefficient ($W\,m^{-2}\,K^{-1}$)
i	enthalpy ($kJ\,kg^{-1}$)
LMTD	log mean temperature difference (°C)
P	pressure (Pa)
$\dot{Q}$	heat transfer rate (kW)
q''	heat flux (kW/m^2)
Re	Reynolds number, $Re = \frac{Gd}{\mu}$
T	temperature (°C)
U	overall heat transfer coefficient ($W\,m^{-2}\,K^{-1}$)
We	Weber's number, $We = \frac{G^2 d}{\rho\sigma}$
x	vapour quality

Greek letters

β	aspect ratio
μ	dynamic viscosity (Pa s)
ρ	density ($kg\,m^{-3}$)
σ_c	the ratio of A_1/A_2 in sudden contraction equation (-)
σ_e	the ratio of A_1/A_2 in sudden expansion equation (-)
ΔP	pressure drop (Pa)
δ	wall thickness (m)
ϕ^2	two-phase frictional multiplier

Subscripts

avg	average
cont	contraction
exp	expansion
e	exit
f	frictional
i	inner
in	inlet
l	liquid
lo	entire flow as liquid
lv	liquid–vapour
v	vapour
vo	entire flow as vapour
o	outer
sat	saturation
tot	total
tp	two-phase

conditions and the uncertainties of measured quantities and calculated parameters are presented in Tables 1 and 2, respectively.

3. Data reduction

For all calculations, the thermophysical properties of the refrigerant are evaluated using REFPROP, Version 6.01 [3]. The data reduction of the measured results is summarised in the following procedures.

3.1. Frictional pressure drop

The main components of the total pressure drop are the frictional pressure drop, the sudden contraction pressure drop or the loss at the minichannel inlet, the sudden expansion pressure drop, and the acceleration or momentum pressure drop. Therefore, the total pressure drop between the upstream and downstream of the test section can be expressed as follows:

$$\Delta p_{tot} = \Delta p_f + \Delta p_{cont} + \Delta p_{\exp} + \Delta p_a. \tag{1}$$

The sudden contraction pressure drop is calculated from the following correlation proposed by Collier [4]:

$$\Delta P_{con} = \frac{G^2 v_l}{2}\left[\left(\frac{1}{C_c}-1\right)^2 + \left(1-\frac{1}{{\sigma_c}^2}\right)^2\right]\left[1+\frac{v_{lv}x_{e,\mathrm{in}}}{v_l}\right]. \tag{2}$$

Similarly, the sudden expansion pressure drop is also determined based on Collier [4], expressed as follows:

$$\Delta P_{exp} = G^2\sigma_e(1-\sigma_e)v_l\left[1+\frac{v_{lv}x_{e,\mathrm{out}}}{v_l}\right]. \tag{3}$$

The acceleration or momentum pressure drop is the loss due to phase change, which can be determined using the following equation:

$$\Delta P_a = G^2\left\{\left[\frac{(1-x)^2}{\rho_l(1-\alpha)}+\frac{x^2}{\rho_v\alpha}\right]_{\mathrm{out}} - \left[\frac{(1-x)^2}{\rho_l(1-\alpha)}+\frac{x^2}{\rho_v\alpha}\right]_{\mathrm{in}}\right\}. \tag{4}$$

3.2. The inside heat transfer coefficient

The total thermal resistance of the multiport minichannel heat exchanger can be expressed as:

$$\frac{1}{UA} = \frac{1}{h_o A_o} + \frac{\delta_t}{k_t A_m} + \frac{1}{h_i A_i} \tag{5}$$

where h_o is the heat transfer coefficient of hot water and can be calculated from the following equation:

$$h_o = \frac{\dot{Q}}{A_o\left(T_{w,avg}-T_{wall,avg}\right)} \tag{6}$$

where A_o is the outer surface area of the tested tube, $T_{w,avg}$ is the average water temperature measured at the inlet and outlet of the water side, and $T_{wall,avg}$ is the average wall temperatures.

The log mean temperature difference (LMTD) method was applied to calculate the overall heat transfer rate, which is expressed as follows:

$$\dot{Q} = \mathrm{UA}\cdot\mathrm{LMTD}. \tag{7}$$

Finally, the inside heat transfer coefficient can be calculated by:

$$\frac{1}{h_i A_i} = \frac{1}{UA} - \frac{1}{h_o A_o} - \frac{\delta_t}{k_t A_m} \tag{8}$$

where h_i is the inside heat transfer coefficient or the refrigerant side heat transfer coefficient. A_i is the inside surface area.

4. Results and discussion

4.1. Frictional pressure drop

4.1.1. Frictional pressure gradient data

Fig. 2 presents the variation of the measured two-phase frictional pressure gradient with the average quality, x_{avg}, for different imposed wall heat fluxes, 12.84 to 26.44 kW/m^2 of the multiport minichannel heat exchanger. Increasing the average quality at a constant heat flux results in a slight increase in the frictional pressure gradient. According to the previous investigations of Kaew-On and Wongwises [1],

Author's personal copy

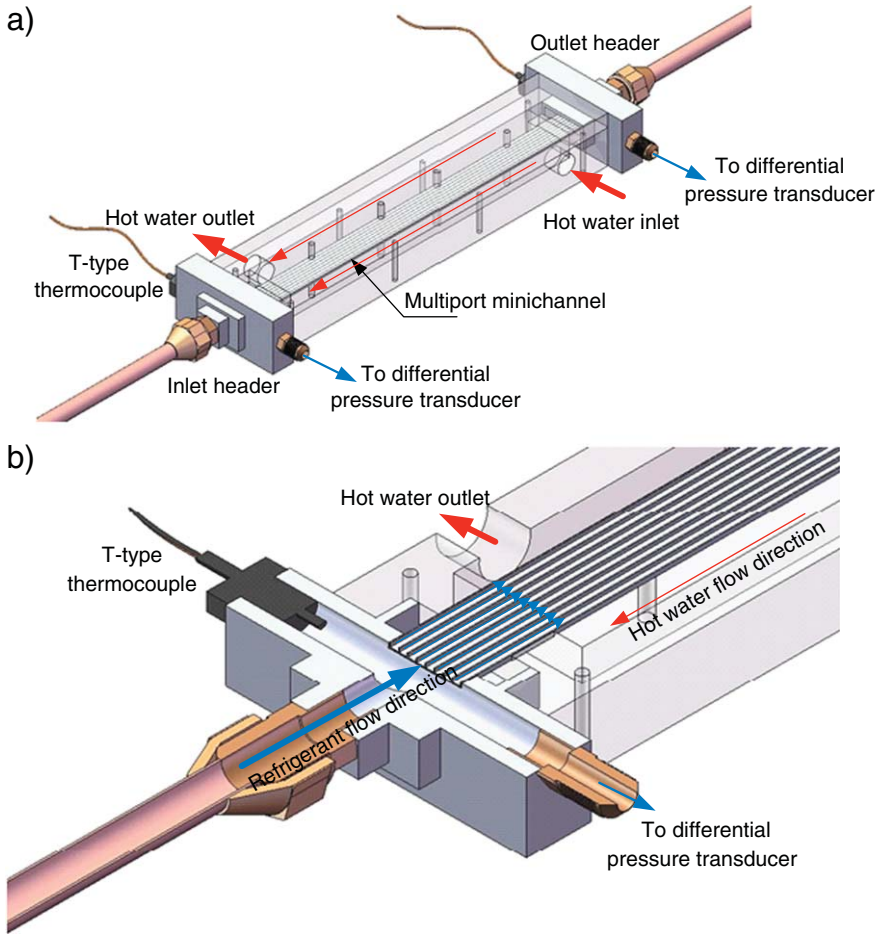

Fig. 1. Drawing of the test section: (a) overview and (b) inlet header.

they found that the frictional pressure gradient slightly increased with increasing heat flux with the reason that the increase of the heat fluxes caused the vapour-phase fraction and mean quality to increase. However, the effect of heat flux on the frictional pressure gradient cannot be seen from this figure due to the small different ranges of the heat flux. As expected, the mass flux has a strong effect on the frictional pressure gradient, as shown in Fig. 3. This is because the increase in mass flux leads to an increase in the shear stress at the tube wall and interfacial shear at the liquid–vapour interface; therefore, the frictional pressure gradient increases with the increase in the mass flux.

Table 1
Experimental conditions.

Refrigerant	R134a
Mass flux (kg/m^{2}s)	45–155
Heat flux (kW/m^2)	10–30
Saturation pressure (bar)	8

Table 2
Uncertainties of measured quantities and calculated parameters.

Parameter	Uncertainty
Temperature	±0.1 (°C)
Mass flow rate of refrigerant	±0.1 (%) Full scale
Heat transfer rate of test section	±8.50%
Heat transfer rate of pre-heater	±2.25%
Heat transfer coefficient	±12.25%

4.1.2. Comparison with existing correlations

The comparisons of the experimental frictional pressure gradient and the pressure gradient calculated from the selected correlations proposed by Kaew-On and Wongwises [1], Lockhart and Martinelli [5], Friedel [6], Muller-Steinhagen and Heck [7], Mishima and Hibiki [8], and Zhang and Webb [9], are shown in Fig. 4. The deviations of the frictional pressure gradient obtained from a comparison of the present data with the existing correlations are presented in Table 3. Friedel's [6] and Zhang and Webb's correlations [9] are the best

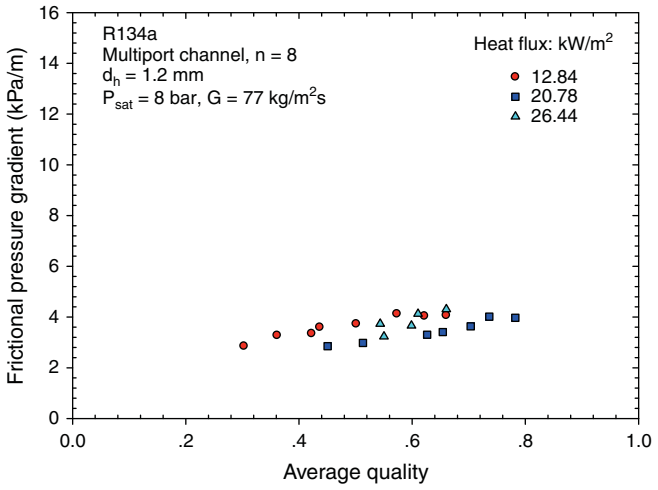

Fig. 2. Frictional pressure gradient versus average quality at various heat fluxes.

Author's personal copy

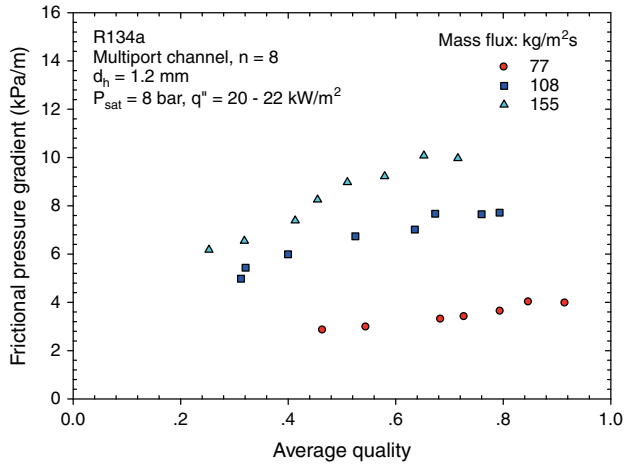

Fig. 3. Frictional pressure gradient versus average quality at various mass fluxes.

among the 6 correlations with a mean deviation of 14.06% and 15.57%, respectively.

4.1.3. Proposed new correlations

Kaew-On and Wongwises' correlation [1] is modified to develop a new pressure drop correlation. The relationships of the two-phase multiplier (ϕ_l^2) for various mass fluxes with the Martinelli parameter (X) are plotted in Fig. 5. The value of the constant, C, proposed by Chisholm [10] to vary from 5 to 20, depends on the flow conditions of the vapour and liquid. As shown in this figure, most of the measured data are in the region between C = 10 and 20. Kaew-On and Wongwises [1] proposed parameter C as a function of hydraulic diameter (d_h), aspect ratio (β), and liquid friction factor (f_l), as follows:

$$C = -3.356 + 41.863e^{A} + B \tag{9}$$

where $A = -69.475\beta f_l d_h$ $B = 498\beta f_l d_h$: d_h in mm.

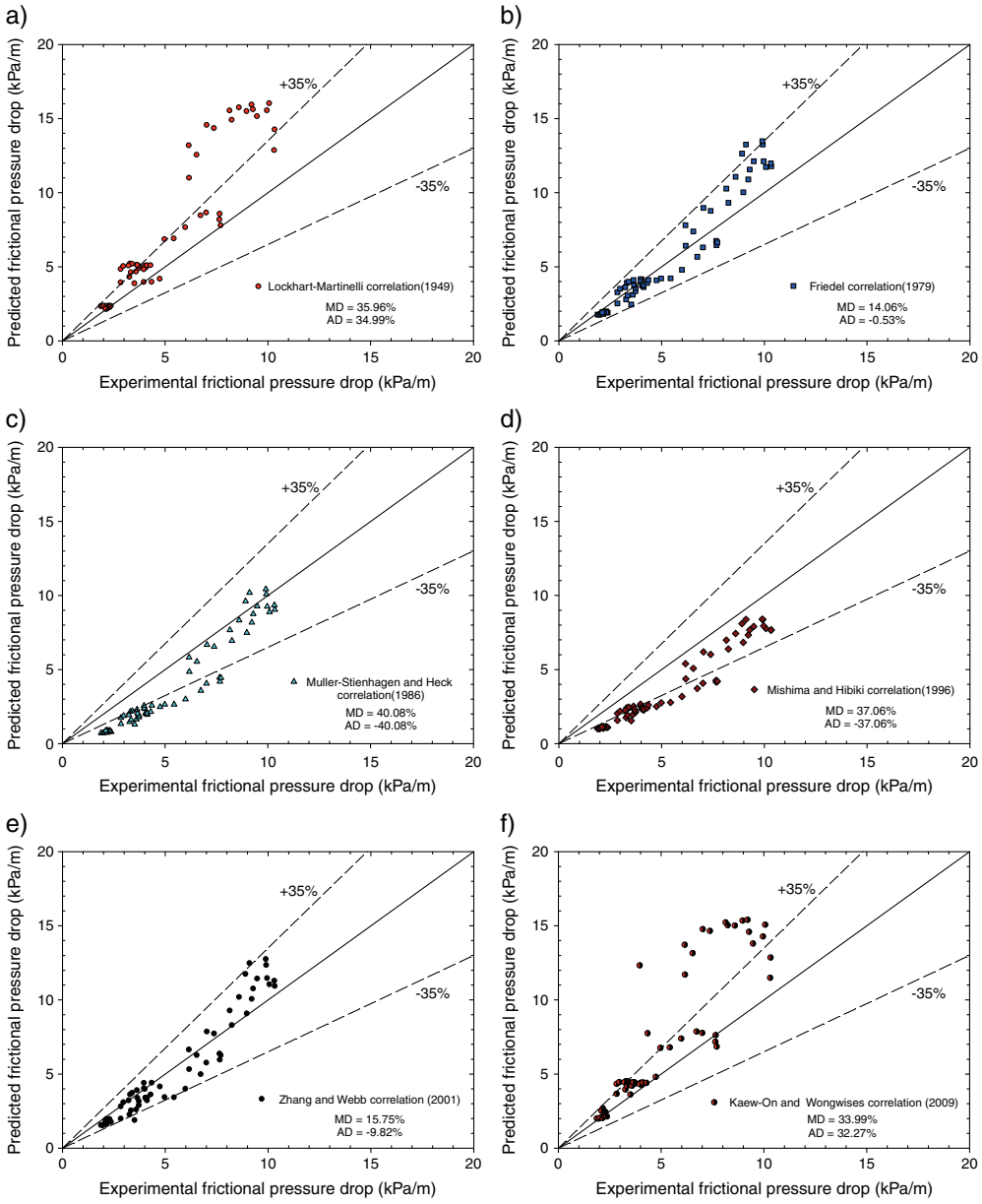

Fig. 4. Comparison between the experimental results and the existing correlations, (a) Lockhart-Martinelli [5], (b) Friedel [6], (c) Muller-Stienhagen and Heck [7], (d) Mishima and Hibiki [8], (e) Zhang and Webb [9] and (f) Kaew-On and Wongwises [1].

Author's personal copy

Table 3
Deviation of the frictional pressure gradient obtained from comparison between the present data and the existing correlations.

Author(s)	Mean deviation (%)	Average deviation (%)
Kaew-on and Wongwises [1]	33.99	32.27
Lockhart and Martinelli [5]	35.96	34.99
Friedel [6]	14.06	−0.53
Muller-Stienhagen and Heck [7]	40.08	−40.08
Mishima and Hibiki [8]	37.06	−37.06
Zhang and Webb [9]	15.75	−9.82
Proposed new correlation	**7.63**	**0.66**

As shown in Fig. 4(f), this correlation is unsatisfactory in predicting the pressure gradient within the mean and average deviation of 34% and 32.27%, respectively. This is because Kaew-On and Wongwises' correlation [1] was proposed for a range of mass fluxes from 300 to 800 kg/(m^2 s) or for turbulent flows. However, in the present study, the correlation is developed based on the experimental data at low mass flux for predicting the two-phase multiplier in the range of $45 \le G \le 155$ as follows:

$$\text{For } 45 < G \le 77 \text{ kg/}\left(\text{m}^2 \text{ s}\right),\ C = 23.23e^{-0.0027\beta Re_l} \tag{10}$$

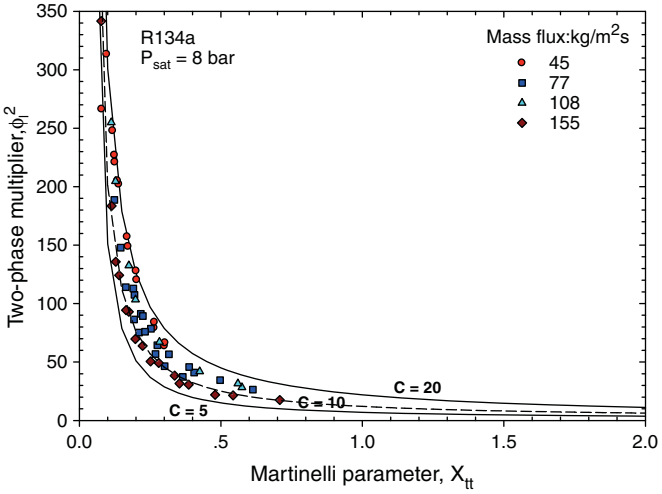

Fig. 5. The relationship between Martinelli's parameter and two-phase multiplier.

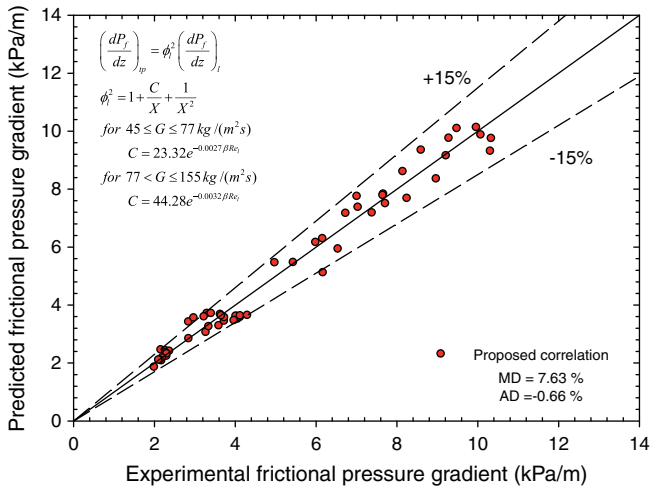

Fig. 6. Comparison between the predicted and experimental frictional pressure gradients.

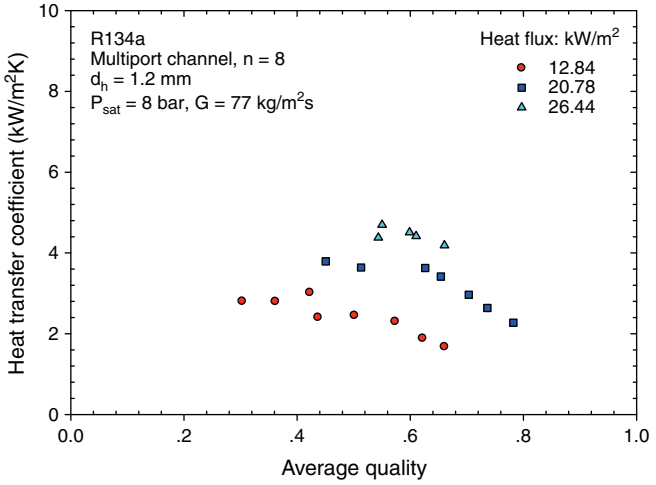

Fig. 7. Heat transfer coefficient versus average quality at various heat fluxes.

$$\text{For } 77 < G \le 155 \text{ kg/}\left(\text{m}^2 \text{ s}\right),\ C = 44.28e^{0.0032\beta Re_l}. \tag{11}$$

Fig. 6 shows an experimental frictional pressure gradient plotted against a predicted frictional pressure gradient. It is clear from this figure that the majority of the data falls within ±15% of the proposed correlation.

4.2. Heat transfer

4.2.1. Heat transfer coefficient

The effect of heat flux on the heat transfer coefficients of R134a is presented in Fig. 7. As shown, the experimental heat transfer coefficients are plotted against average quality at $G = 77$ kg/(m^2 s) and $P_{sat} = 8$ bar for the different heat fluxes of 12.84, 20.78 and 26.44 kW/m^2. This figure shows that a strong dependence of heat flux on the heat transfer coefficients appears throughout the range of average quality. This is because an increase in heat flux corresponds to the increase of the number of bubbles. These bubbles can induce turbulent flow in liquid film, which accelerates the two-phase velocity and increases the droplet entrainment. Hence, the increase in heat transfer coefficient is obtained. A similar trend on the effect of heat flux on the heat transfer coefficient was also reported by Kaew-On and Wongwises [1] and Kaew-On et al. [2].

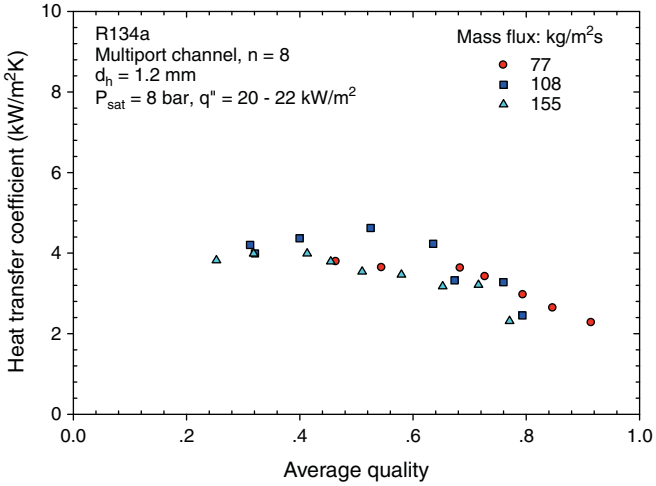

Fig. 8. Heat transfer coefficient versus average quality at various heat fluxes.

Author's personal copy

Fig. 8 shows the variation in the average heat transfer coefficient with average quality during the evaporation of R134a at $P_{sat} = 8$ bar for mass fluxes of 77, 108 and 155 kg/(m^2 s) and a small change in heat flux of 20–22 kW/m^2. The dependence of heat flux on the heat transfer coefficient and its independence upon the mass flux can be seen from Figs. 7 and 8. This is because the nucleate boiling contribution plays a more important role than convection boiling on flow boiling heat transfer in minichannel. Similar observations were also reported by different researchers such as Kaew-On and Wongwises [1], Kaew-On et al. [2], Lazarek and Black [11] and Tran et al. [12].

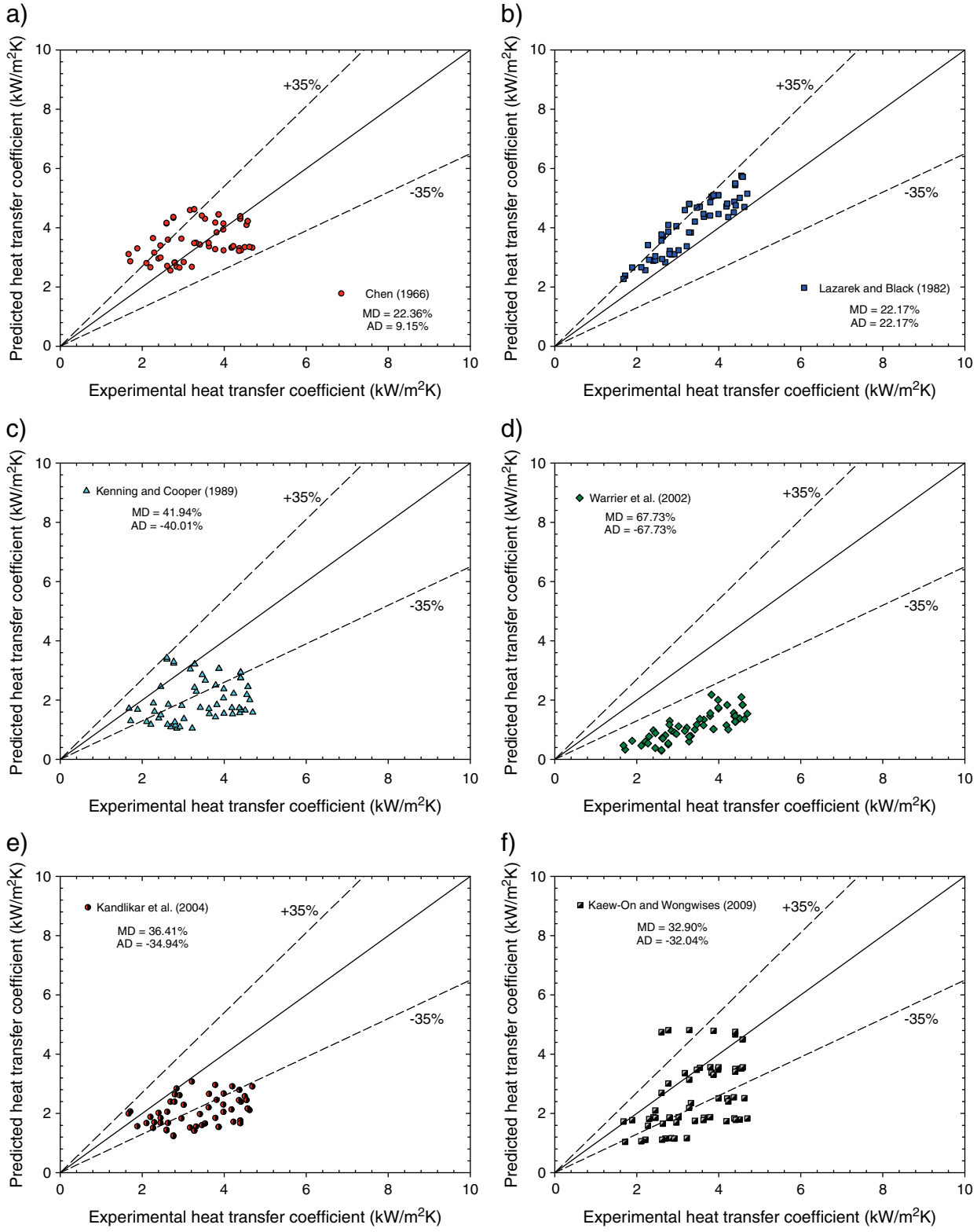

Fig. 9. Comparison between the experimental results and the existing correlations, (a) Chen [13], (b) Lazarek and Black [11], (c) Kenning and Cooper [14], (d) Warrier et al. [15], (e) Kandlikar and Balasubramanian [16], (f) Kaew-On and Wongwises [1] and (g) Kaew-On et al. [2].

Author's personal copy

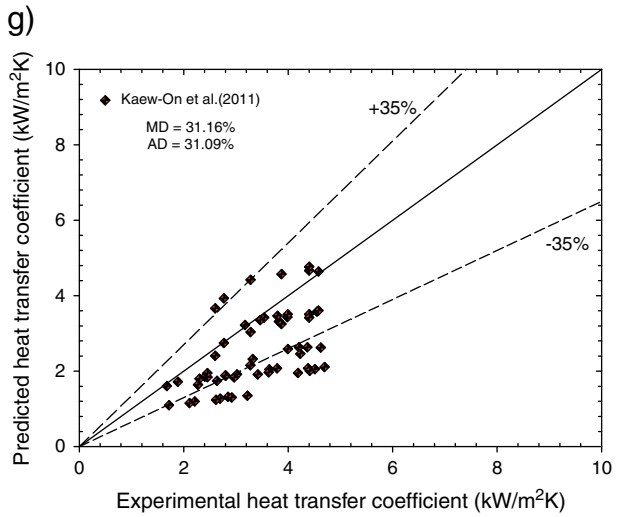

Fig. 9 (*continued*).

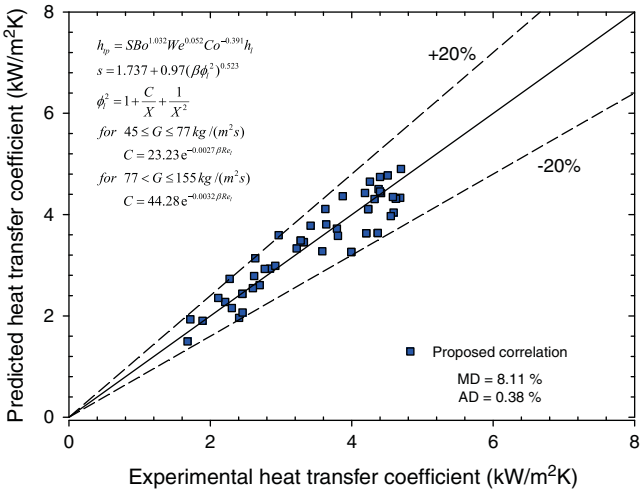

Fig. 10. Comparison between the predicted and experimental heat transfer coefficients.

4.2.2. Comparison with existing correlations

In this section, the heat transfer coefficient is compared to that predicted by the existing correlations. The existing correlations proposed by Kaew-On and Wongwises [1], Kaew-On et al. [2], Chen [13], Lazarek and Black [11], Kenning and Cooper [14], Warrier et al. [15] and Kandlikar and Balasuramanian [16] are selected to compare with the experimental data. Comparisons of the experimental data with the predicted heat transfer coefficients are shown in Fig. 9. The mean and average deviations of the comparisons between the experimental data and predicted values are summarised in Table 4. According to the comparisons, the correlations of Chen [13] and Lazarek and Black [11] are the best correlations, but none of them has a mean deviation of less than 20%.

4.2.3. Development of a new correlation for predicting the heat transfer coefficient

The modified Kaew-On and Wongwises' correlation [1] obtained by adding three dimensionless terms, Bo, We_l and Co, is presented as follows:

$$h_{tp} = SBo^{1.032} We_l^{0.052} Co^{-0.391} h_l \tag{12}$$

$$S = 1.737 + 0.97\left(\beta\phi_l^2\right)^{0.523} \tag{13}$$

where Bo,We_l and Co are defined as follows:

$$Bo = \frac{q''}{Gi_{lv}} \tag{14}$$

$$We_l = \frac{G^2 d_h}{\rho_l \sigma} \tag{15}$$

Table 4
Deviation of the heat transfer coefficient obtained from comparison between the present data and the existing correlations.

Author(s)	Mean deviation (%)	Average deviation (%)
Kaew-On and Wongwises [1]	32.90	32.04
Kaew-On et al. [2]	31.16	31.10
Lazarek and Black [11]	22.17	22.17
Chen [13]	22.36	9.15
Kenning and Cooper [14]	41.94	40.01
Warrier et al. [15]	67.73	67.73
Kandlikar and Balasubramaniam [16]	36.41	34.94
Proposed new correlation	**8.11**	**0.83**

$$Co = \left(\frac{(1-x)}{x}\right)^{0.8}\left(\frac{\rho_v}{\rho_l}\right)^{0.5}. \tag{16}$$

The comparison of the experimental heat transfer coefficient with the predicted heat transfer coefficients calculated from the new proposed correlation is presented in Fig. 10 and tabulated in Table 4. The new correlation shows good agreement, with a mean deviation of 8.11% and an average deviation of 0.38%.

5. Conclusions

The heat transfer coefficients and pressure drops of R134a during evaporation at low mass fluxes are experimentally investigated. The conclusions can be drawn as follows:

1. The pressure gradient increases with increasing mass flux and is less affected by heat flux.
2. The average heat transfer coefficients increase strongly with heat flux and tend to decrease slightly with increasing average quality. In addition, the results indicate the insignificant effects of mass flux on the heat transfer coefficient.
3. From the comparison of the six selected pressure drop correlations, Friedel's [6] and Zhang and Webb's correlations [9] are the best correlations, with a mean deviation of 14.06% and 15.57%, respectively. In addition, the new proposed two-phase multiplier correlation for predicting the pressure gives mean and average deviations of 7.63% and −0.66%, respectively.
4. According to the comparison of the seven selected heat transfer coefficient correlations, those of Chen [13] and Lazarek and Black [11] are fairly consistent with the experimental results, but neither has a mean deviation of less than 20%. The new proposed correlation for predicting the heat transfer coefficient gives mean and average deviations of 8.11% and 0.38%, respectively.

Acknowledgment

The authors would like to acknowledge the Thailand Research Fund, the Office of the Higher Education Commission and the National Research University project for financial support.

References

[1] J. Kaew-On, S. Wongwises, Experimental investigation of evaporation heat transfer coefficient and pressure of R410A in multiport minichannel, International Journal of Refrigeration 32 (2009) 124–137.

Author's personal copy

[2] J. Kaew-On, K. Sakamatapan, S. Wongwises, Flow boiling heat transfer of R134a in the multiport minichannel heat exchangers, Experimental Thermal and Fluid Science 35 (2011) 364–374.
[3] REFPROP, NIST, Refrigerant Properties Database 23, Gaithersburg, MD, 1998, Version 6.01.
[4] J.G. Collier, Convective Boiling and Condensation, Second edition, McGraw-Hill, 1981, pp. 26–108.
[5] R.W. Lockhart, R.C. Martinelli, Proposed correlation of data for isothermal two-phase, two-component flow in pipes, Chemical Engineering Progress 45 (1949) 39–48.
[6] L. Friedel, Improved frictional pressure drop correlation for horizontal and vertical two-phase flow, European Two-phase Flow Group Meeting, 1979.
[7] H. Müller-Steinhagen, K. Heck, A simple friction pressure drop correlation for two-phase flow in pipes, Chemical Engineering and Processing 20 (1986) 297–308.
[8] K. Mishima, T. Hibiki, Some characteristics of air–water two-phase flow in small diameter tube, International Journal of Multiphase Flow 22 (1996) 703–712.
[9] M. Zhang, R.L. Webb, Correlation of two-phase friction for refrigerants in small-diameter tubes, Experimental Thermal and Fluid Science 25 (2001) 131–139.
[10] D. Chisholm, Pressure gradients due to friction during the flow of evaporating two-phase mixtures in smooth tubes and channels, International Journal of Heat and Mass Transfer 16 (1973) 347–358.
[11] G.M. Lazarek, S.H. Black, Evaporative heat transfer, pressure drop and critical heat flux in small vertical tube with R-113, International Journal of Heat and Mass Transfer 25 (1982) 945–960.
[12] T.N. Tran, M.W. Wambsganss, D.M. France, Small circular- and rectangular-channel boiling with two refrigerants, International Journal of Multiphase Flow 22 (1996) 485–498.
[13] J.C. Chen, A correlation for boiling heat transfer to saturated fluid in convective flow, ASME Paper 63-HT-34 (1963) 1–11.
[14] D.B.R. Kenning, M.G. Cooper, Saturated flow boiling of water in vertical tubes, International Journal of Heat and Mass Transfer 32 (1989) 445–458.
[15] G.R. Warrier, V.K. Dhir, L.A. Momoda, Heat transfer and pressure drop in narrow rectangular channels, Experimental Thermal and Fluid Science 26 (2002) 53–64.
[16] S. Kandlikar, P. Balasubramanian, An extension of the flow boiling correlation to transition, laminar, and deep laminar flows in minichannels and microchannels, Heat Transfer Engineering 25 (2004) 86–93.

Simulations of Seasonal Current Circulations and Its Variabilities Forced by Runoff from Freshwater in the Gulf of Thailand

Nitima Aschariyaphotha & Somchai Wongwises

Arabian Journal for Science and Engineering

ISSN 1319-8025
Volume 37
Number 5

Arab J Sci Eng (2012) 37:1389-1404
DOI 10.1007/s13369-012-0246-x

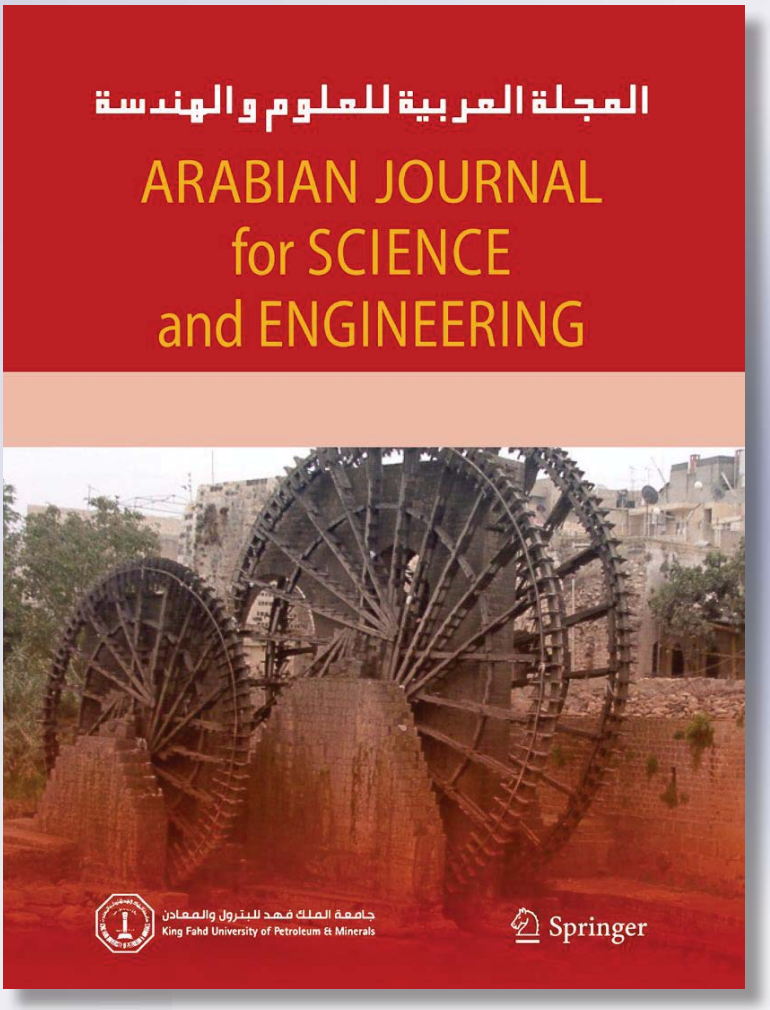

Springer

Your article is protected by copyright and all rights are held exclusively by King Fahd University of Petroleum and Minerals. This e-offprint is for personal use only and shall not be self-archived in electronic repositories. If you wish to self-archive your work, please use the accepted author's version for posting to your own website or your institution's repository. You may further deposit the accepted author's version on a funder's repository at a funder's request, provided it is not made publicly available until 12 months after publication.

Author's personal copy

Arab J Sci Eng (2012) 37:1389–1404
DOI 10.1007/s13369-012-0246-x

RESEARCH ARTICLE – EARTH SCIENCES

Nitima Aschariyaphotha · Somchai Wongwises

Simulations of Seasonal Current Circulations and Its Variabilities Forced by Runoff from Freshwater in the Gulf of Thailand

Received: 5 January 2011 / Accepted: 1 June 2011 / Published online: 12 April 2012
© King Fahd University of Petroleum and Minerals 2012

Abstract This paper presents the seasonal climatology of currents and elevations in the Gulf of Thailand (GoT) derived from a numerical three-dimensional ocean model. A numerical three-dimensional ocean model, based on the Princeton Ocean Model (POM), with rectangular coordinates in horizontal and vertical sigma coordinates was implemented for the GoT, situated between 6° to 14°N latitude and 99° to 105°E longitude. The Gulf is a relatively shallow body of water with a maximum depth of 83 m and an average depth of 45 m. It was driven at the surface by monthly mean sea surface temperature, salinity and wind stress climatology. In this paper, the simulations of current circulations and sea surface elevations for each season are presented, where the winter, summer, rainy season, and end of the rainy season in Thailand are represented by the months January, May, July, and October, respectively. The simulations in the upper GoT are also described. The results show clockwise circulations during summer and rainy seasons of Thailand. They occur in the central GoT. Two experiments were designed to investigate the effects of freshwater runoff. The freshwater runoff is shown to be the important factor for generating current circulation in the upper GoT at the end of the rainy seasons. The current speed is weakened when the runoff is removed. The sea surface elevations also decrease when the freshwater runoff is removed, especially in October, where it is reduced by about 50 %.

Keywords Gulf of Thailand · Runoff · Freshwater · Curvilinear grid

الخلاصة

تعرض هذه الورقة العلمية المواسم المناخية للتيارات المائية والإرتفاعات في خليج تايلند المستمدة من أنموذج ثلاثي الابعاد للمحيط. وقد تم تطبيق الأنموذج ثلاثي الأبعاد المستند الى أنموذج المحيط برينسون (POM مع إحداثيات مستطيلة في إحداثيات سيغما الأفقية والرأسية لخليخ تايلان (GoT) التي تقع بين خطوط العرض N°6 الى N14° وخطوط الطول E 99° الى 105°E. إن مياه الخليج ضحلة نسبياً مع أقصى عمق 83 متراً و متوسط العمق هو 45 متراً. إن التيارات تدفع على السطح بوساطة متوسط درجة حرارة سطح البحر شهرياً والملوحة وعلم المناخ. وفي هذه الورقة العلمية نعرض المحاكاة للتداولات الحالية والارتفاعات السطحية في كل موسم، حيث يتم تمثيل الشتاء والصيف والأمطار ونهاية موسم الأمطار في تايلند بشهر يناير ومايو ويوليو وأكتوبر على التوالي. وتم وصف المحاكمة في خليج تايلاند العلوي أيضاً. وأظهرت النتائج أن التوزيعات هي في إتجاه عقارب الساعة خلال فصل ومواسم الامطار في تايلاند وأن حدوثها هو في وسط خليج تايلاند، حيث صُممت تجربتان لدراسة تأثير الجريان السطحي للمياه العذبة. وأظهرت النتائج أن جريان المياه العذبة هو أهم عامل في توليد التوزيع الحالي في الجزء العلوي من خليج تايلاند في نهاية موسم الامطار، و قد تناقصت السرعة الحالية عندما تم ازالة جريان السطح، كما أن إرتفـاع سطـح البحـر قـد إنخفض أيضـاً عندما تم إيقاف الجريان السطحي وبخاصة في شهر أكتوبر حيث انخفضت بنحو 50 % .

N. Aschariyaphotha (✉)
Department of Mathematics, King Mongkut's University of Technology Thonburi, Bangkok 10140, Thailand
E-mail: nitima.asc@kmutt.ac.th

S. Wongwises
Department of Mechanical Engineering, King Mongkut's University of Technology Thonburi, Bangkok 10140, Thailand

S. Wongwises
The Academy of Science, The Royal Institute of Thailand, Sanam Suea Pa, Dusit, Bangkok 10140, Thailand

Author's personal copy

1 Introduction

The Gulf of Thailand (GoT) is located in Southeast Asia immediately to the west of the South China Sea (SCS). The Gulf is a semi-enclosed sea that measures approximately 400 km × 800 km, covering an area of about 320,000 km^2. Its location in the global map is between 6° to 14°N latitude and 99° to 105°E longitude surrounded by the Kingdom of Cambodia, Malaysia, the Kingdom of Thailand and the Socialist Republic of Vietnam (Fig. 1). It is a part of the Sunda Shelf, which is a submerged connection between Southeast Asia, Malaysia, Sumatra, Java and Borneo, and is relatively shallow. The mean and maximum depths in the central part in the GoT are about 45 and 80 m, respectively. The Chao Phraya, Tha Chin, Mae Klong, and Bang Pakong rivers enter the Gulf near its heads; there are also many rivers that flow along the coast. The strong water inflow from the rivers makes the Gulf low in salinity and rich in sediments.

The upper GoT is located in the tropical region at 13°N and 100°E. It is surrounded by land on the eastern, northern and western sides, and is open to the lower GoT on the southern side. It has an approximate area of 10,000 km^2, with a maximum depth of 40 m in the southern areas.

The Chao Phraya River has the greatest discharge into the upper Gulf (with a 55-year average of about 482 m^3/s) [1]. Stansfield and Garrett [2] stated that several rivers discharge directly into the GoT; the largest is the Chao Phraya which empties into the upper GoT. From 1956 to 1960 the Chao Phraya had an average discharge of 590 m^3/s and a maximum monthly average discharge of about 2,050 m^3/s in October. Information on the discharge of some of the other smaller rivers was available, but no comprehensive source of data was found. The total contribution of freshwater by the other smaller rivers was estimated to be equivalent to six times that of the Chao Phraya (18.5 km^3/yr). This gave a net input of freshwater directly into the GoT by local rivers of 129.5 km^3/yr. They calculated the evaporation rate by using the data of the UWM/COADS, and then concluded that there is a large seasonal cycle in precipitation; 70 % of the annual rainfall occurs between June and November and only 30 % between December and May, while evaporation rates are virtually constant throughout the year.

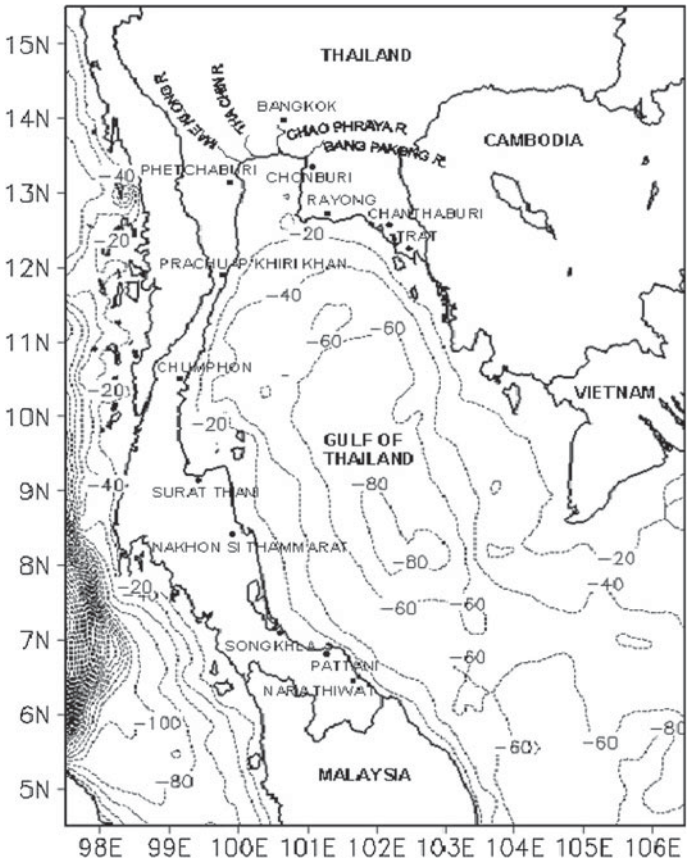

Fig. 1 Geography and bathymetry (m) of the Gulf of Thailand

Author's personal copy

Knowledge of the circulation over the continental shelf is very useful for managing fisheries, oil and gas resource development, maritime scientific research and forecasting, marine environmental protection, sea disaster mitigation, and ocean coastal engineering. According to the importance and problems of the upper GoT, understanding its oceanographic condition has become a vital key to determining the ways to use it sustainably. The GoT is an important resource to the national economy of Thailand, which receives income from the Gulf fishing industry, and tourism and port operations. Fishery is important in such an area. Although overfishing has almost wiped out the high-priced fish species, the income from local fishery is still a major one. Furthermore, maritime activities are rapidly increasing because of industrial development.

The area is strongly influenced by the two-monsoon wind system, the northeast monsoon (November–March) and the southwest monsoon (May–October). Therefore, the discharge and contaminants carried down by the river also display great seasonal variations.

Numerical ocean modeling technologies have been developed in many countries. The general ocean models have become an important tool to study the state of the ocean. Zhang and Liang [3] and Zeng et al. [4,5] at the Institute of Atmospheric Physics (IAP) developed some ocean models, which have been used in previous years for simulating the annual mean circulation of the world's oceans and the seasonal cycle of the circulation in the Pacific Ocean and the China Seas. The Princeton Ocean Model (POM), developed by Blumberg and Mellor [6], is one of the widely used ocean models. The POM model is a free surface model described in Cartesian coordinates. Killworth et al. [7,8] have described the details of the Cox [9] numerical ocean circulation model, which was modified to include a free surface.

Chu et al. [10] used the POM to simulate the circulation and thermohaline variability for the SCS covering the GoT. They verified that the effect of wind is the key factor for the generation of the SCS deep basin's warm/cool eddy and that the lateral boundary force is the major factor for the formation of the strong western boundary currents. Afterwards, Chu et al. [11] simulated the SCS thermohaline structure as well as the circulation, and investigated the physical processes causing seasonal variability by using the POM. They revealed that the POM model has the capability for simulating seasonal variations of the SCS circulation and thermohaline structure.

Aschariyaphotha [12] used the POM to investigate the effects of wind force and open boundary conditions in the GoT. The results show that wind force is the important factor for generating the circulation in the GoT. The lateral velocity at the open boundaries is of considerable importance to the current circulation for the rainy season and the end of the rainy season, with insignificant effect for the winter and summer seasons.

Freshwater input is one of the most critical parameters driving water properties. The freshwater runoff not only has an influence on local estuarine dynamics, but can also be a significant contribution to regional coastal circulation and geographic properties. This paper focuses on simulating the current circulation by modifying the POM model, and studying the effects of runoff from freshwater on the current circulation in the GoT, including the upper GoT.

2 The Numerical Ocean Model

2.1 Model Description

The POM model is a time-dependent, primitive equation model on a three-dimensional grid in Cartesian coordinates and vertical sigma coordinates, which have all been modified to simulate the circulation and to investigate the temperature and salinity in the GoT. The model includes hydrostatic and Boussinesq approximations. The equations of the three-dimensional primitive model are as follows:

$$\frac{\mathrm{d}u}{\mathrm{d}t} = -\frac{1}{\rho_0}\frac{\partial p}{\partial x} + fv + \frac{\partial}{\partial z}\left(A_{mv}\frac{\partial u}{\partial z}\right) + F_x, \tag{1}$$

$$\frac{\mathrm{d}v}{\mathrm{d}t} = -\frac{1}{\rho_0}\frac{\partial p}{\partial y} - fu + \frac{\partial}{\partial z}\left(A_{mv}\frac{\partial v}{\partial z}\right) + F_y, \tag{2}$$

$$\frac{\partial w}{\partial z} + \frac{\partial u}{\partial x} + \frac{\partial v}{\partial y} = 0, \tag{3}$$

Author's personal copy

$$\frac{\partial p}{\partial z} = -\rho g, \tag{4}$$

$$\frac{\mathrm{d}T}{\mathrm{d}t} = \frac{\partial}{\partial z}\left(A_{hv}\frac{\partial T}{\partial z}\right) + F_T, \tag{5}$$

$$\frac{\mathrm{d}S}{\mathrm{d}t} = \frac{\partial}{\partial z}\left(A_{hv}\frac{\partial S}{\partial z}\right) + F_S, \tag{6}$$

$$\rho = \rho(T, S, z), \tag{7}$$

where x, y and z represent the eastward, northward, and upward directions, respectively; u, v and w are the corresponding current components in the eastward, northward and upward directions, respectively; t is time; ρ_0 is the reference density of the sea water; p is the pressure; ρ is the density of sea water given by UNESCO [13]; T is the potential temperature; S is the salinity; $f = 2\Omega \sin\theta$ is the Coriolis parameter; Ω is the angular speed of the earth's rotation (7.2921×10^{-5} rad/s); θ is the latitude; g is the magnitude of gravitational acceleration; A_{mv} is the vertical eddy viscosity coefficient, and A_{hv} is the vertical eddy diffusivity coefficient. The vertical mixing coefficients, A_{mv} and A_{hv}, are obtained by appealing to a second-order turbulence closure scheme, as described by Mellor and Yamada [14].

The governing equations are then transformed from z-coordinates (x, y, z, t) to the vertical sigma coordinates (x^*, y^*, σ, t^*) by the following relation:

$$x^* = x, \quad y^* = y, \quad \sigma = \frac{z-\eta}{H+\eta} \quad \text{and} \quad t^* = t, \tag{8}$$

where $H(x, y)$ is the bottom topography, and η is the sea surface elevation. The value of σ ranges from $\sigma = 0$ at $z = \eta$ to $\sigma = -1$ at $z = -H(x, y)$.

For the model grid, the rectangular horizontal grid was replaced by an orthogonal curvilinear grid to improve coastline representations with 37×97 horizontal grid points, as shown in Fig. 2. The horizontal grid spacing ranges from 2 km near the head of the GoT to 55 km at the eastern boundary. The vertical sigma coordinate has 10 levels. Aschariyaphotha [15] has described the techniques that generate the model grid and interpolate the initial data using cubic spline and bilinear interpolations.

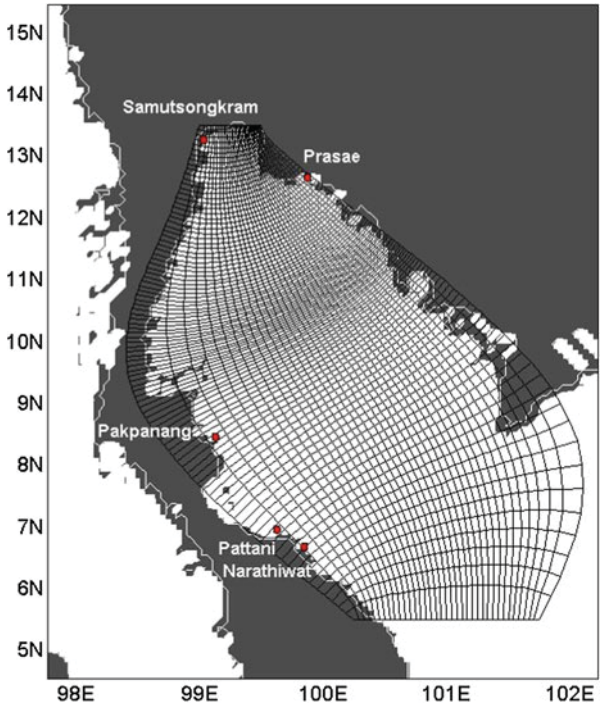

Fig. 2 The curvilinear model grid and five tide gauge stations in the GoT

Author's personal copy

2.2 Boundary Conditions

The model has to be given boundary conditions for motion, temperature and salinity. These consist of boundary conditions at the air–sea interface, bottom friction conditions, and lateral boundary conditions.

Upper surface boundary conditions are required to drive the current. These include the stress acting on the ocean due to the wind, heat flux, salt flux, and fresh water, through the air–sea interface. The wind force at the sea surface, taken from Mellor [16], is described by

$$\rho_0 A_{mv}\left(\frac{\partial u}{\partial z}, \frac{\partial v}{\partial z}\right) = \left(\tau_{0x}, \tau_{0y}\right), \tag{9}$$

where (τ_{0x}, τ_{0y}) are the components of the wind stress vector along the x and y curvilinear coordinates, respectively. The wind stress, obtained from Mellor [16], is specified by

$$\begin{aligned}\left(\tau_{0x}, \tau_{0y}\right) &= \rho_a C_{\mathrm{D}} |V_a - V_l|(U_a - U_l, V_a - V_l) \\ &\approx \rho_a C_{\mathrm{D}} |V_a|(U_a, V_a),\end{aligned} \tag{10}$$

where ρ_a is the sea level air density; (U_a, V_a) is the wind velocity component measured from 10 m above the sea surface; (U_l, V_l) represents the surface layer ocean current velocity component, and C_{D} is the drag coefficient, which varies from about 0.001 to 0.0025 depending on the wind speed itself. The drag coefficient C_{D}, taken from Matthias and Godfrey [17], is calculated by

$$C_{\mathrm{D}} = Min\{0.001 + 0.00007|V_a|, 0.0025\}. \tag{11}$$

Restoring-type surface heat and salt fluxes are adopted for the temperature and salinity equations. The thermal force at the surface, described by Li et al. [18], is depicted by

$$A_{hv}\frac{\partial T}{\partial z} = \mu_1(T_{\mathrm{obs}} - T), \tag{12}$$

$$A_{hv}\frac{\partial S}{\partial z} = Q_s + \mu_2(S_{\mathrm{obs}} - S), \tag{13}$$

where Q_s is the surface net salinity flux, specified from the freshwater runoff surface fluxes; μ_1 and μ_2 are the relaxation factors for temperature and salinity, respectively, and T_{obs} and S_{obs} are the observed surface potential temperature and salinity, respectively.

At the bottom of the Gulf, the normal gradients of T and S are zero; therefore, there are no heat fluxes and salt fluxes across this boundary. The bottom friction condition, obtained from Mellor [16], is described by

$$\rho_0 A_{mv}\left(\frac{\partial u}{\partial z}, \frac{\partial v}{\partial z}\right) = \left(\tau_{bx}, \tau_{by}\right), \tag{14}$$

where (τ_{bx}, τ_{by}) is the component of the bottom stress parameterized as the following expression

$$(\tau_{bx}, \tau_{by}) = \rho_0 C_z |V_b|(V_{bx}, V_{by}), \tag{15}$$

where (V_{bx}, V_{by}) is the horizontal component of the nearest bottom velocity. The coefficient C_z taken from Mellor [16] is calculated by

$$C_z = Max\left\{\frac{\kappa^2}{\left[ln\left\{\frac{(1+\sigma_{kb-1})H}{z_0}\right\}\right]^2}, 0.0025\right\}, \tag{16}$$

where κ is the Von Kraman constant, H is the bottom topography, and z_0 is the bottom roughness. In this study, κ is taken to be 0.4, while $z_0 = 0.01$m is used, as suggested by Weatherly and Martin [19].

Author's personal copy

The western boundary and northern boundary of the model domain are closed boundaries bordered by land. Closed boundaries were defined using a no-slip condition for velocity, non-thermal flow and zero fluxes of heat and salt. Side boundary conditions for the eastern boundary and southern boundary of the model domain are open boundary conditions. There exist two types of open boundaries, inflow and outflow. Whenever inflow occurs at the boundary of the model domain, the boundary condition is applied as follows:

$$\frac{\partial}{\partial t}(T, S) + u\frac{\partial}{\partial x}(T, S) = 0, \tag{17}$$

$$\frac{\partial}{\partial t}(T, S) + v\frac{\partial}{\partial y}(T, S) = 0, \tag{18}$$

$$\frac{\partial u}{\partial t} \pm c_i \frac{\partial u}{\partial x} = 0, \tag{19}$$

$$\frac{\partial v}{\partial t} \pm c_i \frac{\partial v}{\partial y} = 0, \tag{20}$$

where c_i is the baroclinic phase speed.

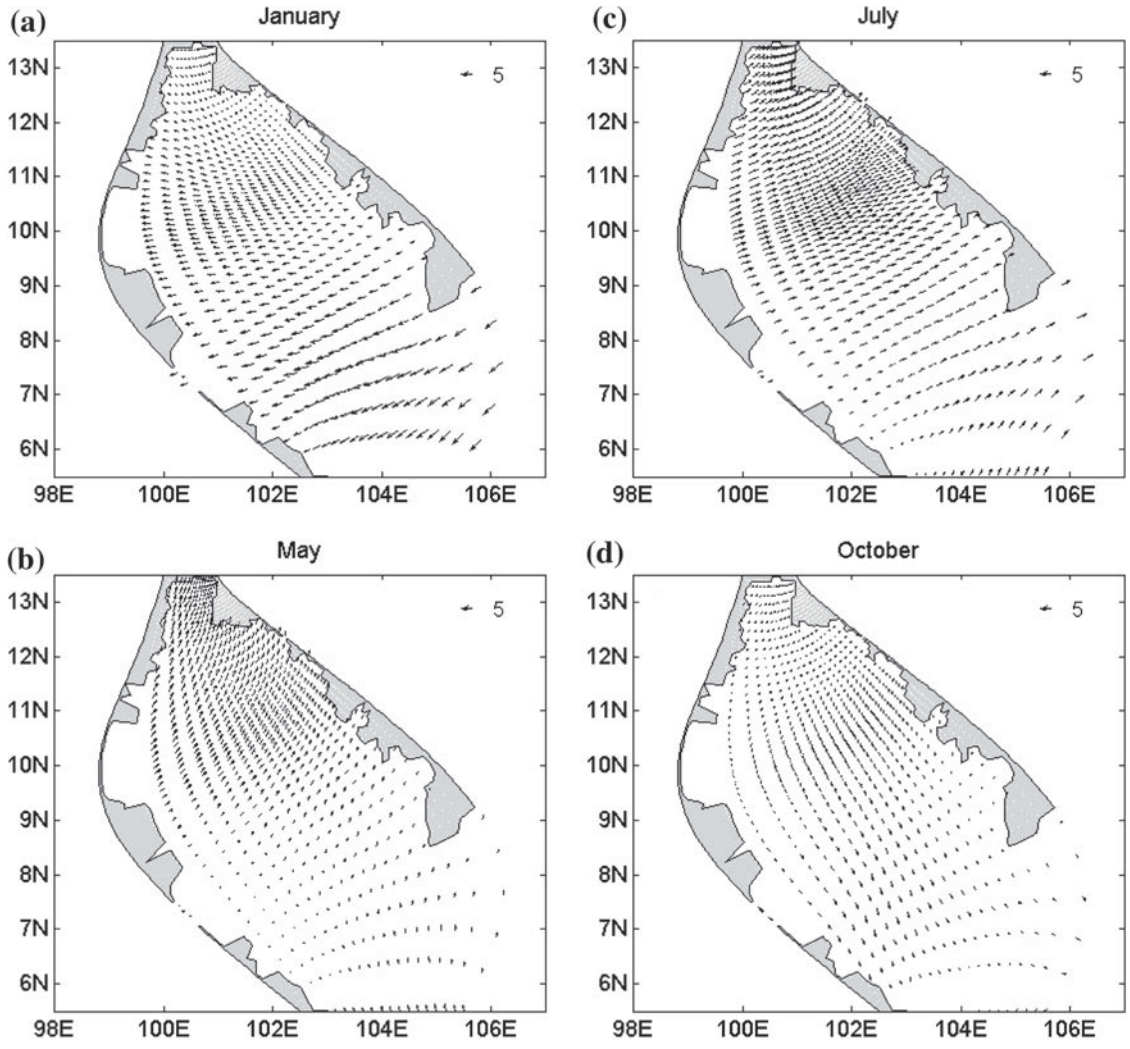

Fig. 3 The monthly mean wind velocities distribution (m/s) for **a** January, **b** May, **c** July, and **d** October

Author's personal copy

Whenever outflow occurs at the boundary of the domain, the radiation condition, obtained from Blumberg and Mellor [6], is applied as follows:

$$\frac{\partial \Theta}{\partial t} + U_n \frac{\partial \Theta}{\partial n} = 0, \tag{21}$$

where Θ can be taken to be T, S, u or v, and the subscript n is the direction normal to the boundary. For velocities normal to land, the lateral boundary conditions are set to zero. The velocities and sea surface elevations at the open lateral boundary may be taken from observations if observed current and elevation data are available. In the case where there are no available observed data, the lateral boundary conditions will be obtained from other ocean models' results. In this paper, You's model outputs [20–22] are used as the values at the open boundary for the velocities and sea surface elevations.

2.3 Initial Conditions and Initialization

In the spin-up phase of the model run, the model was integrated with all three components of velocity initially set to zero, and temperature and salinity were indicated by interpolating climatological monthly mean fields from Levitus94 [23,24] to the model grid. In addition, wind stress was calculated from the European Centre

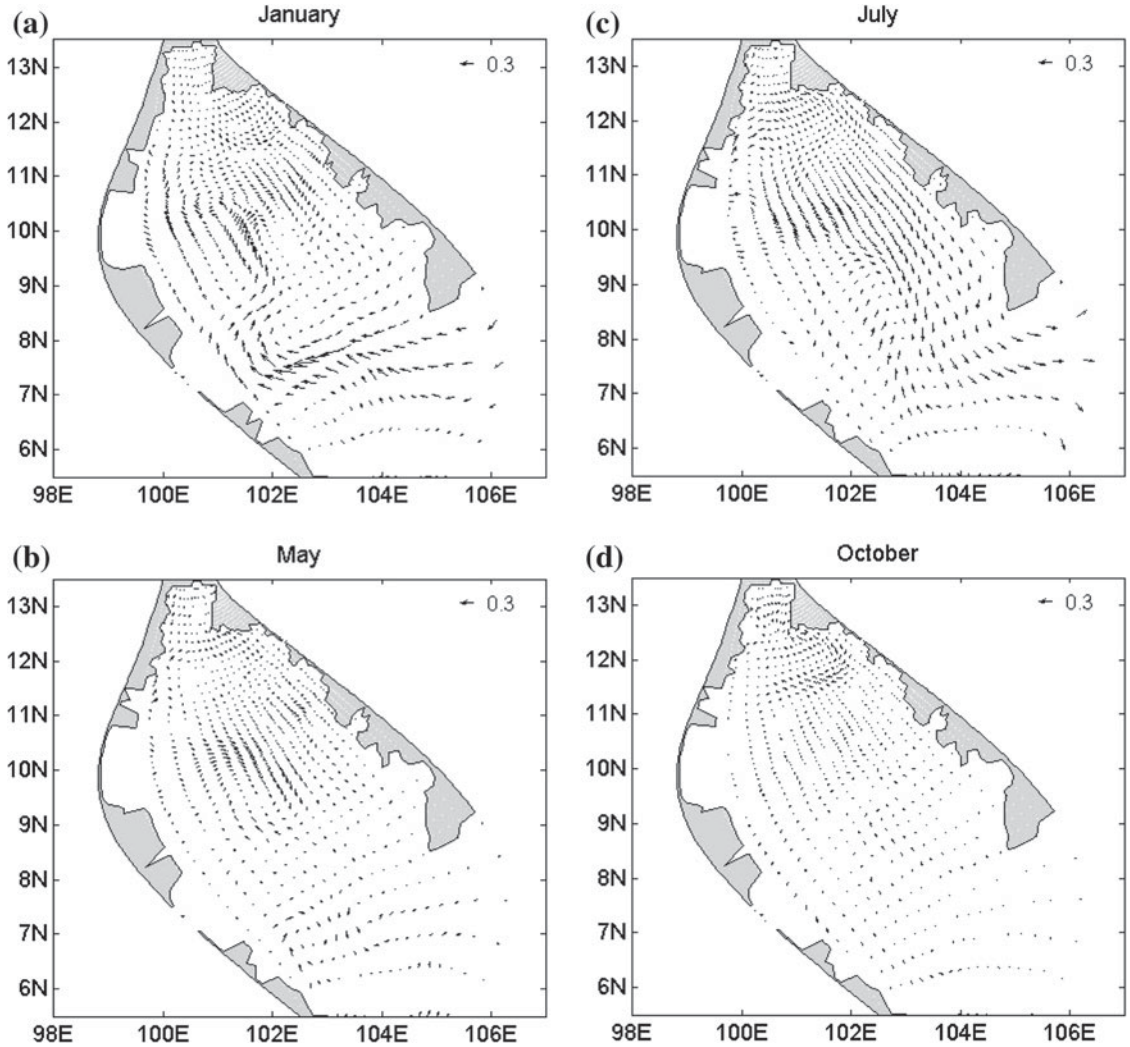

Fig. 4 The simulated current circulation (m/s) from the run with freshwater runoff at surface level for **a** January, **b** May, **c** July, and **d** October

Author's personal copy

for Medium-Range Weather Forecasts (ECMWF) climatological monthly mean wind, as shown in Fig. 3. In January, the northeasterly monsoon is fully developed. Over the whole GoT, the northeasterly monsoon blows. A wind speed of 7.5 m/s is often exceeded over the GoT. The weak south winds prevail over the GoT in May. July brings southwesterly winds, and the winds become stronger reaching speeds of 5 m/s and move over the GoT. In October, a weakening of the winds occurs. The winds move rapidly southward with a maximum wind speed of 1 m/s. The lateral boundary conditions of sea surface elevation and velocity were prescribed from You's model outputs [20–22] and the radiation condition. It was run until all variables were stable, and then the results, assumed to be the climatological values, were used as initial data for the future simulations.

2.4 Mode Splitting Technique

To save computational time, the mode splitting technique [6] is used to separate barotropic modes from baroclinic modes, with a barotropic time step of 30 s based on the Courant–Friederichs–Levy computational stability (CFL) condition and the external wave speed. A baroclinic time step of 900 s is based on the CFL condition and the internal wave speed [25].

2.5 Experimental Design

The model was run in spin-up phase until the ocean model reached an equilibrium state, or in other words, the time series of total kinetic energy, total potential energy and total surface potential energy reached a steady state under the applied force. The model was re-initialized every month with temperature and salinity data from Levitus94 climatology, with sea surface elevation and velocity at zero. Surface forcing includes the monthly climatological sea surface temperature and salinity, also obtained from Levitus94, and monthly climatological wind field and freshwater runoff obtained from ECMWF. The force at the lateral boundary was prescribed from You's results and the radiation condition. It was found that 350, 480, 350 and 480 days were sufficient for

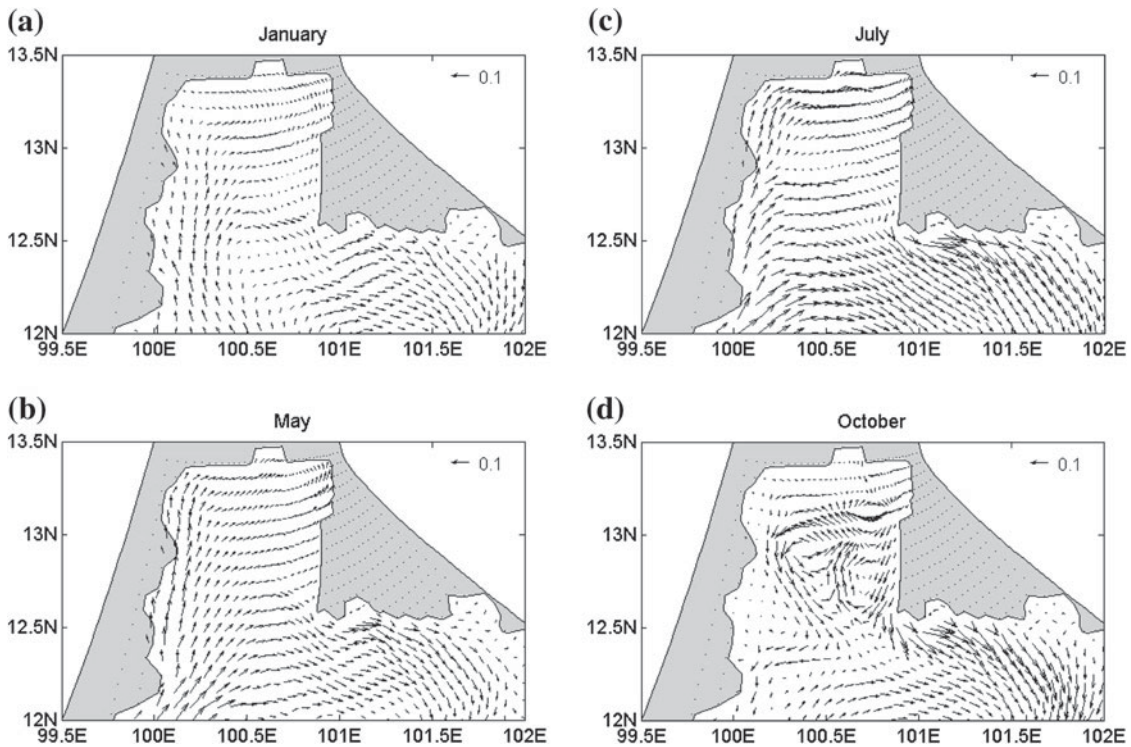

Fig. 5 The simulated current circulation (m/s) from the run with freshwater runoff at surface level in the upper GoT for **a** January, **b** May, **c** July, and **d** October

Author's personal copy

the model energy to reach quasi-steady state under the imposed conditions in January, May, July and October, respectively.

Two numerical experiments were carried out. The model was run with and without freshwater runoff. Other initial conditions remained the same. The difference between two runs at each grid point should then isolate the runoff effects. The circulation patterns will be identified from the run with freshwater runoff for subsequent comparative analysis.

3 Results

3.1 Seasonal Current Circulations

In this paper, the months January, May, July and October represent the winter, summer, rainy season, and end of the rainy season of Thailand, respectively.

The model simulates seasonal circulation for the GoT quite well, compared to the results from Chu et al. [11], which simulated the circulations of the SCS including the GoT for March, May, July, September, October, and December. The circulations from observations by Wyrtki [26] are also considered. Since the GoT is a small area and shallow region, the circulations from Wyrtki for the GoT cannot be clearly seen. Wyrtki stated about

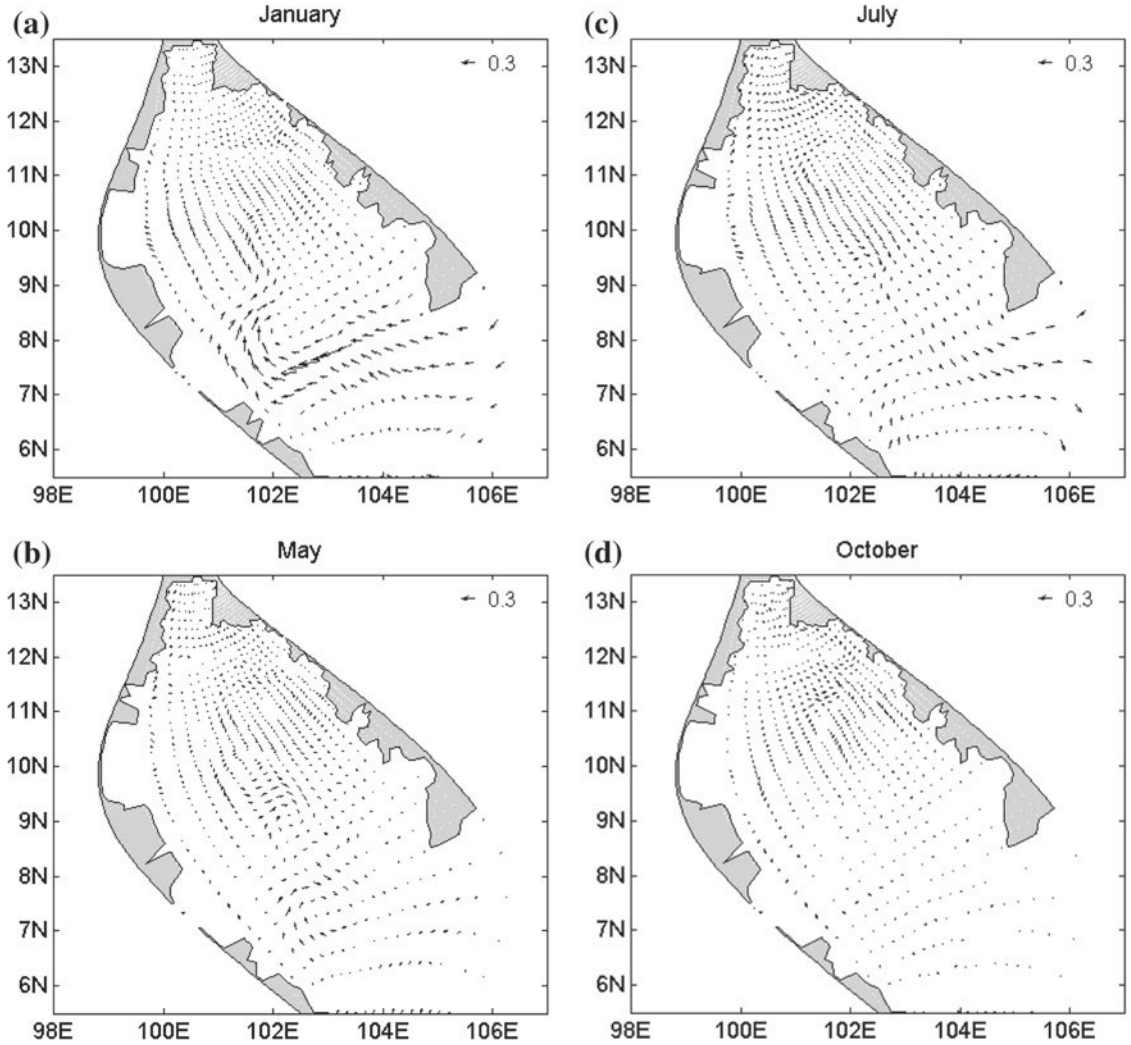

Fig. 6 The simulated current circulation (m/s) from the run without freshwater runoff at surface level for **a** January, **b** May, **c** July, and **d** October

Author's personal copy

the current circulation in the GoT that very few observations have been made in the GoT, but from available data, water movements seem always to be weak. During the southern monsoon, from May to September, they are clockwise and during the northeast monsoon, from October to January, they are counterclockwise. From February to April, movement from the Gulf seems to prevail.

3.1.1 Run with Freshwater Runoff

The simulated current circulations from the model run with freshwater runoff at the surface for January, May, July, and October are shown in Fig. 4. For January, which represents the winter season of Thailand, the currents are strong and off the shore of Vietnam they often exceed 0.3 m/s. The westward intensification is strong when a deflection of the current occurs to the east, caused by the northeast wind. A clockwise current circulation in the southeastern part of the GoT near the coast of Songkla, Pattani and Narathiwat provinces of Thailand, around the area 6.5°–9°N and 101°–103.5°E, is found with current speed exceeding 0.5 m/s. The current pattern for January agrees well with that of Chu et al. [11] for December, which is in the same season. For May, which is the summer period, all currents have decreased. They are soon turned eastward, approximately located 6°–7.5°N and 102°–103.5°E with a speed of about 0.2 m/s. A small clockwise circulation occurs in the central GoT around a point at (9°N, 102°E). There are also inflows from the SCS into the GoT.

During the rainy season, July, winds blow from the southwest. The GoT surface current flows northward from the south, and follows clockwise in the central GoT, and then flows southward along the eastern coast of the GoT. An outflow of water occurs through the SCS at the eastern boundary with a current speed of more than 0.3 m/s. The main circulation for this month agrees with Wyrtki [26] and Chu et al. [11], where the observed circulations from Wyrtki [26] showed that the circulation in the GoT is clockwise with a surface current speed of between 0.12 and 0.25 m/s, and Chu et al. [11] pointed out that the southwesterly monsoon winds drive a clockwise circulation in the GoT. In October, the end of the rainy season, there are no strong currents in the whole GoT due to the weak winds.

The simulated current circulations from the model run with freshwater runoff at the surface in the upper GoT for January, May, July, and October are shown in Fig. 5. For January, the current flows northward along the western coast, while the current near the eastern coast flows southward. For May, stronger currents with a

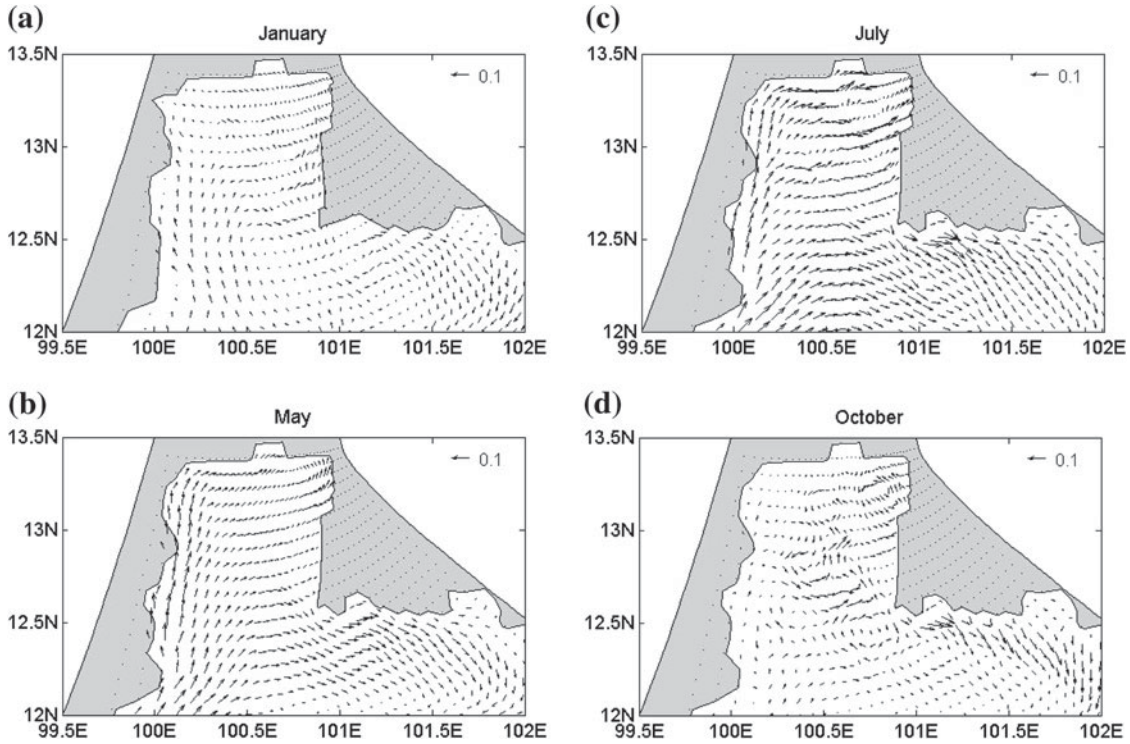

Fig. 7 The simulated current circulation (m/s) from the run without freshwater runoff at surface level in the upper GoT for **a** January, **b** May, **c** July, and **d** October

Author's personal copy

speed of about 0.15 m/s occur, and the currents move northward towards land at the head of the GoT, with a weak speed of only 0.01 m/s. For July, the main current pattern is almost the same as in May. Current speeds of over 0.1 m/s occur in the lower part of the Gulf, and about 0.02 m/s near the head of the GoT. For October, the currents also flow southward along the eastern coast. There is a fully clockwise current circulation near the coast of Chonburi and Rayong provinces of Thailand located at approximately 12.5°–13°N and 100.5°–100.8°E, and there is a counterclockwise current circulation in the western part of the GoT.

3.1.2 Run Without Freshwater Runoff

In order to study the effects of freshwater runoff, the model was run without freshwater runoff. The surface current velocities for January (Fig. 6a) illustrate similar current patterns to the results from the run with runoff (Fig. 4a), which indicates that the runoff from freshwater does not change the general circulation pattern for this month, which is the dry season. The difference between the run with and without freshwater runoff shows the runoff effects on the GoT surface circulation for May and July, which are the summer and rainy seasons, respectively. The main current for May in the run without runoff (Fig. 6b) is almost the same as (Fig. 4b), but this is soon turned eastward, approximately located 6°–8°N and 102°–103.75°E. Small clockwise current circulations occur in the central GoT around the point (9°N, 102.2°E). There are no clockwise circulations in July in the run without runoff (Fig. 6c), and the current speed is weaker than in the run with runoff (Fig. 4c).

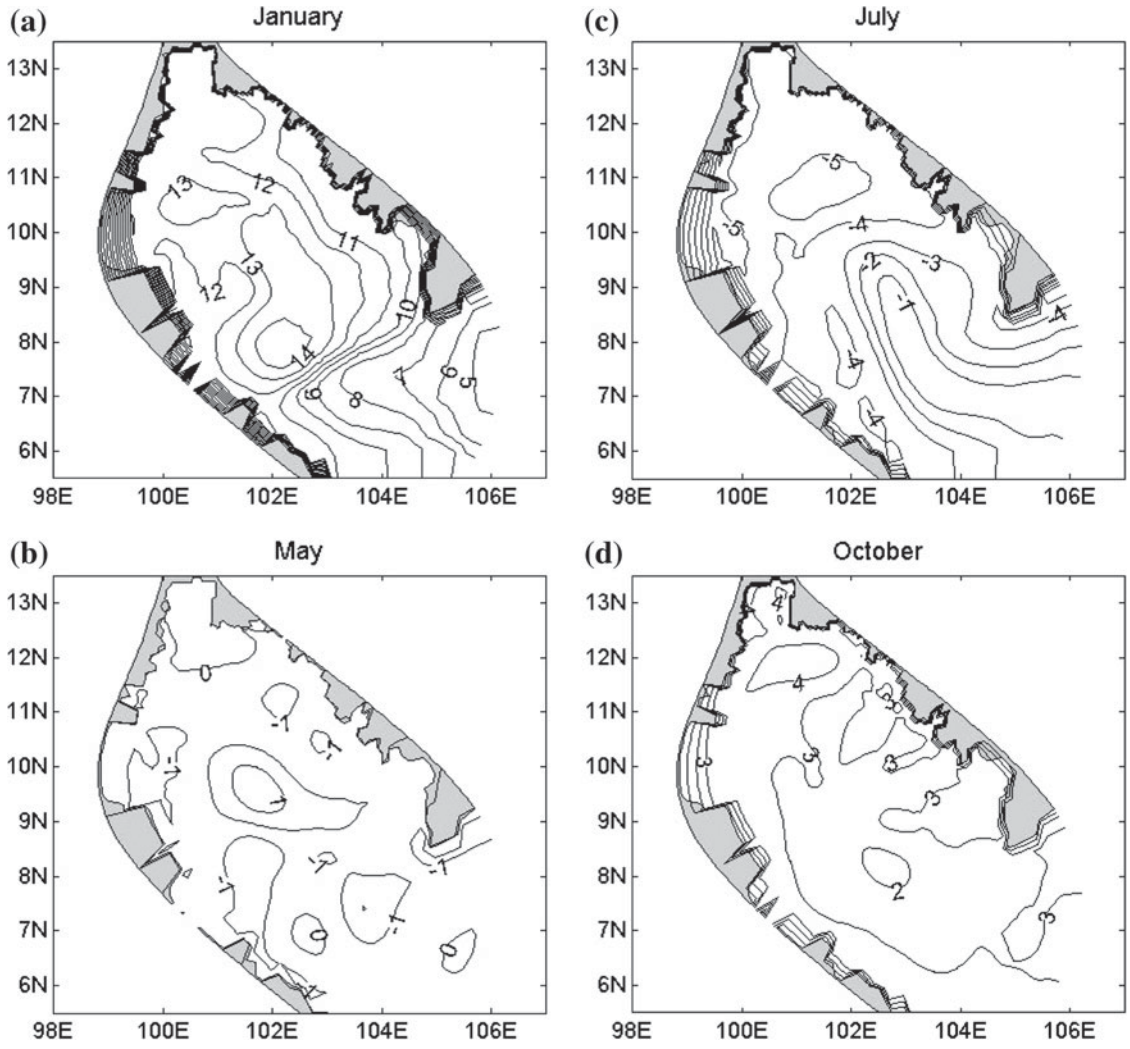

Fig. 8 The simulated sea surface elevation (cm) from the run with freshwater runoff for **a** January, **b** May, **c** July, and **d** October

Author's personal copy

The outflow of water still occurs through the SCS at the eastern boundary with a current speed of less than 0.3 m/s. During October (Fig. 6d), the currents pattern cannot clearly seen due to weak winds.

The results for the run without runoff in the upper GoT for January and May (Fig. 7a, b) retain the same current patterns same as the results with runoff, meaning that the freshwater runoff does not significantly affect the circulation patterns for January and May, which are the winter and summer seasons of Thailand, respectively. Figure 7c shows the circulation by the run without runoff in the upper GoT for July. It can be seen that the current is weaker than the run with runoff, but the current pattern is not changed. Therefore, the runoff is the factor to increase the current speed. The current circulation in the upper GoT for October changes when the freshwater runoff is removed. The surface current velocity for October (Fig. 7d) flows southward on the eastern coast, but circulation does not occur. Hence, freshwater runoff is the important factor for the current pattern in the upper GoT for October, which is the end of rainy season of Thailand.

3.2 Seasonal Elevations

3.2.1 Run with Freshwater Runoff

The simulated sea surface elevations for January, May, July, and October are shown in Fig. 8. Due to the strong winds in January, the highest elevation of 14 cm occurs in the area near the coast of Chumphon province of Thailand. The sea levels for May and July, affected by southwest monsoons, are lower than the reference level. In July, an elevation of less than −5 cm occurs in the northern part of the Gulf. The winds for May and October, which are the transitions between monsoon periods, are weak winds, causing the sea levels to be nearly the reference.

Figure 9 shows the simulated sea surface elevations for January, May, July, and October in the upper GoT. During January and May, the highest elevations are in the western part, including the head of the GoT, while the lowest elevations are in the eastern part. For July, the lowest elevations occur near the Petchaburi's coast. The sea surface elevation of about 4 cm occurs near the head of the GoT, which is higher than the other parts.

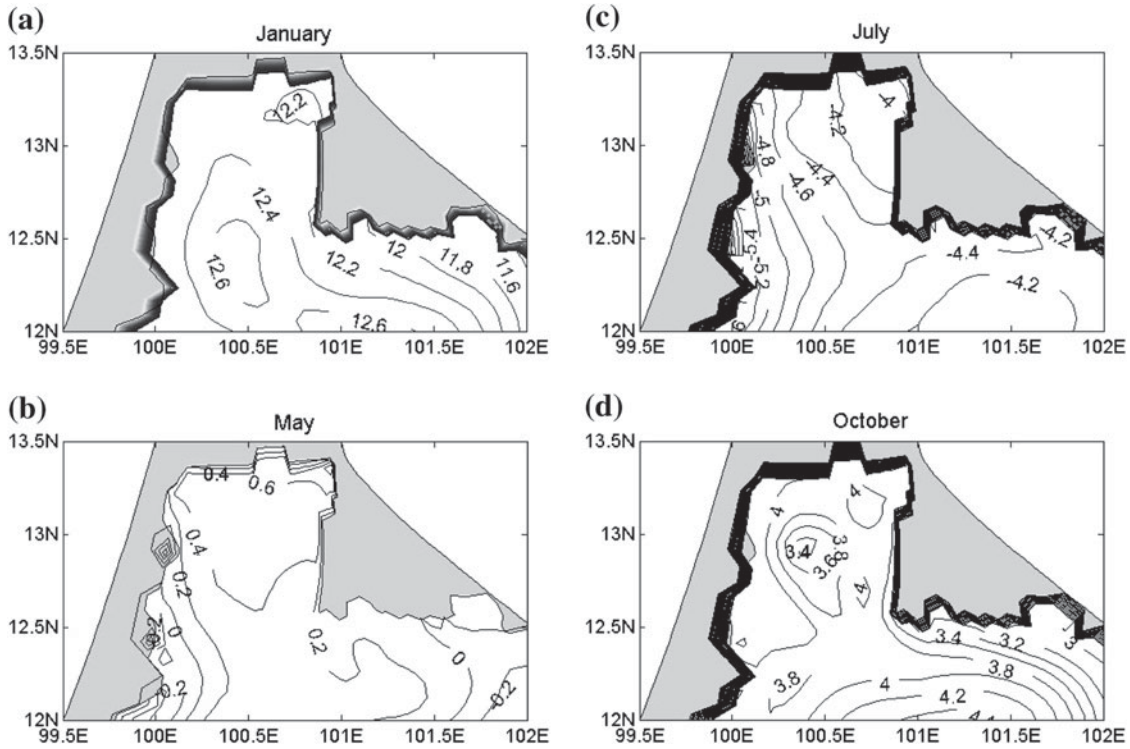

Fig. 9 The simulated sea surface elevation (cm) from the run with freshwater runoff in the upper GoT for **a** January, **b** May, **c** July, and **d** October

Author's personal copy

3.2.2 Run Without Freshwater Runoff

The sea surface elevations from the run without freshwater runoff for the four months (Fig. 10) are not much different from the runoff results, which indicate that the freshwater runoff does not significantly affect the sea level. Due to the strong winds in January, the highest elevation of 13 cm occurs in the same area of runoff run. There are no sea levels higher than the reference level in May and July, and the elevations are lower than the runoff run. When the runoff is removed from the force, the model results show a reduction of sea surface elevation. The maximum sea surface elevations are reduced to 13, 0, −2, and 2 cm for January, May, July, and October, respectively

A large difference in sea level can be seen when the upper GoT (Fig. 11) is considered. For October, the elevations in the area near the head of the Gulf decrease significantly when the runoff is removed. This difference shows the runoff effect on the sea surface elevation for October, which is the end of rainy season of Thailand.

Table 1 shows the average simulated current speed (m/s) and sea surface elevations (cm) from the runs with and without runoff from freshwater in the GoT and upper GoT for the 4 months. Strong current speeds occur during January and July. Weak current speeds occur in October due to the weak wind. In this month the upper GoT current speed is stronger than in the whole Gulf because of the freshwater released from the four

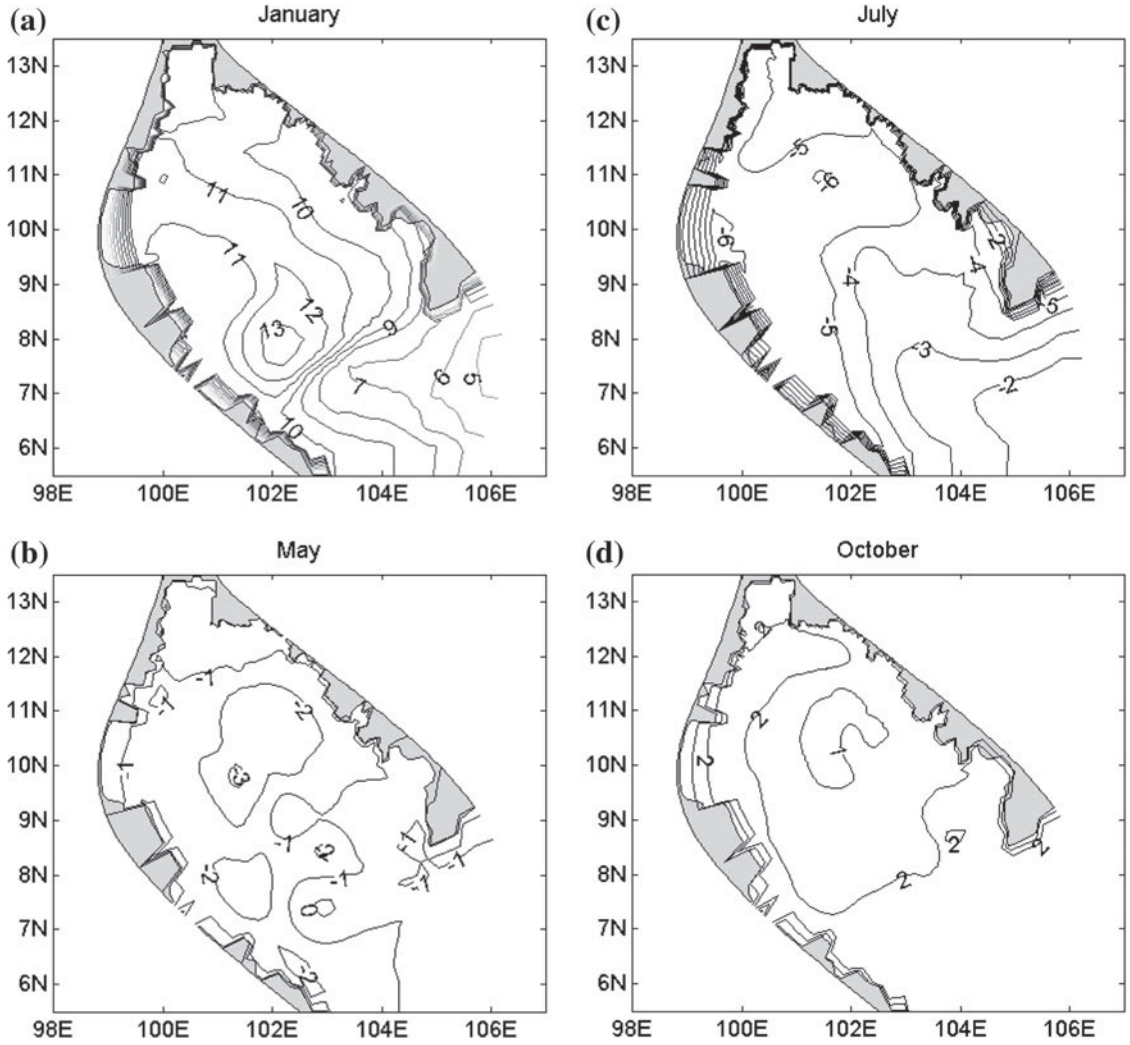

Fig. 10 The simulated sea surface elevation (cm) from the run without freshwater runoff for **a** January, **b** May, **c** July, and **d** October

Author's personal copy

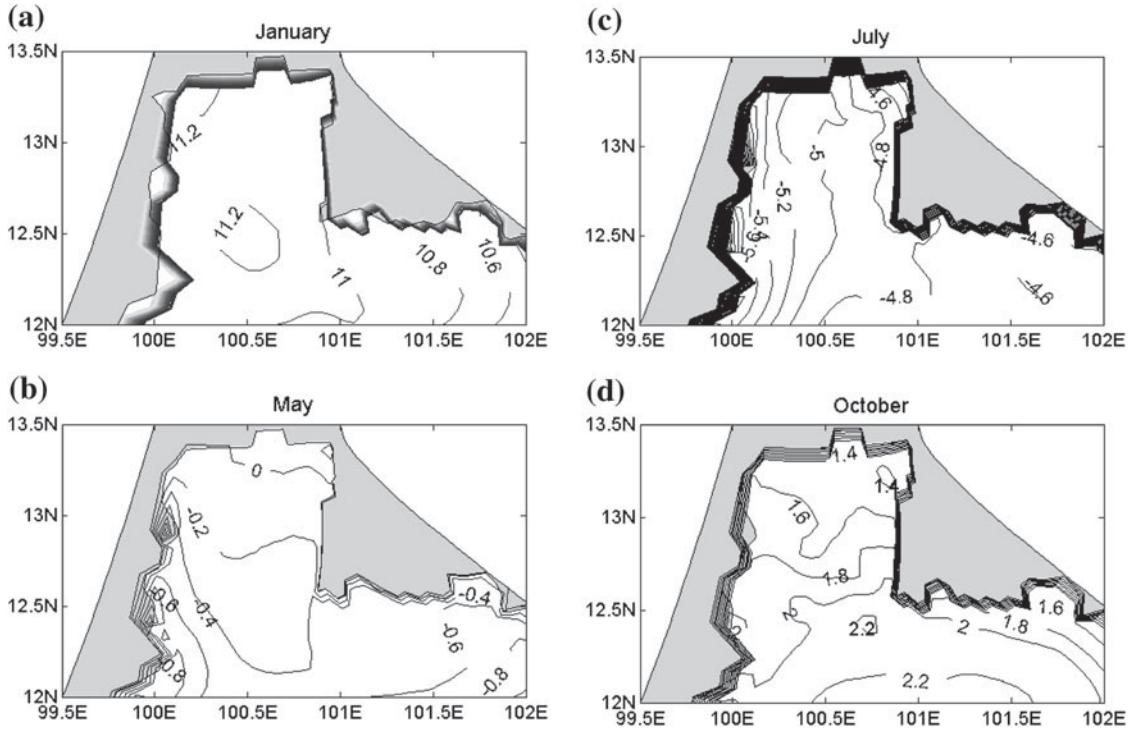

Fig. 11 The simulated sea surface elevation (cm) from the run without freshwater runoff in the upper GoT for **a** January, **b** May, **c** July, and **d** October

Table 1 The average simulated current speed (m/s) and sea surface elevations (cm) from the run with and without freshwater runoff in the GoT and upper GoT

	January	May	July	October
GoT current speed				
Run with runoff	0.0594	0.0370	0.0540	0.0273
Run without runoff	0.0496	0.0343	0.0400	0.0222
Upper GoT current speed				
Run with runoff	0.0237	0.0278	0.0320	0.0360
Run without runoff	0.0158	0.0234	0.0283	0.0176
GoT elevation				
Run with runoff	11.34	−0.36	−3.81	3.06
Run without runoff	10.01	−1.36	−4.62	1.61
Upper GoT elevation				
Run with runoff	11.74	0.33	−4.21	3.68
Run without runoff	10.54	−0.27	−4.68	1.75

main river basins at the head. The current speed is weakened when the freshwater runoff is removed. The sea surface elevations also decrease when the runoff from freshwater is removed, especially in October, where it is reduced by about 50 %.

3.3 Model Verification

The sea level observations obtained from a government organization, the Marine Department, have been used for comparison with the model results. The tide gauge stations are shown in Table 2. Table 3 shows the comparison between the average sea surface elevations from observations and model simulations. There are higher variations of sea level in January and July at Prasae, Pakpanang and Pattani stations, while the lowest variations of sea level occur at Samutsongkram station, which is in the area at the head of the GoT.

Author's personal copy

Table 2 The five tide gauge stations

Station name	Longitude	Latitude	Province of Thailand
Prasae	101°42′21″E	12°31′54″N	Rayong
Samutsongkram	99°59′44″E	13°22′36″N	Samutsongkram
Pakpanang	100°12′08″E	8°21′11″N	Nakhonsithammarat
Pattani	101°14′57″E	6°54′08″N	Pattani
Narathiwat	101°49′48″E	6°25′26″N	Narathiwat

Table 3 The comparison between the average sea surface elevations (cm) from the observation and the model simulations

	January	May	July	October
Prasae				
Observation	14.11	−11.03	−15.89	6.73
Model run with runoff	3.04	0.05	−1.08	0.79
Model run without runoff	2.76	−0.11	−1.15	0.40
Samutsongkram				
Observation	15.04	1.80	−5.15	7.10
Model run with runoff	12.24	0.72	−4.04	3.98
Model run without runoff	11.14	0.14	−4.77	1.52
Pakpanang				
Observation	21.53	−0.78	−11.30	6.21
Model run with runoff	5.21	−0.45	−2.01	1.56
Model run without runoff	4.59	−0.85	−2.58	0.98
Pattani				
Observation	17.01	−4.26	−10.04	4.32
Model run with runoff	7.78	−0.69	−2.67	2.35
Model run without runoff	6.86	−1.13	−3.46	1.66
Narathiwat				
Observation	16.05	−1.64	−5.61	8.19
Model run with runoff	11.33	−0.75	−4.02	3.47
Model run without runoff	10.08	−2.06	−4.95	2.67

4 Conclusions

The current circulation and sea surface elevation in the Gulf of Thailand was simulated by modifying the POM. The model was run under climatological forces. During the winter season of Thailand, January, the GoT surface current circulation is generally clockwise with a strong current in the southwest Gulf, at the coasts of Songkla, Pattani and Narathiwat provinces. During the summer season of Thailand, April, small clockwise circulation occurs in the central GoT. The POM model simulates a clockwise circulation in the central GoT during July, or the rainy season of Thailand. Weak currents occur at the end of the rainy season of Thailand, October. In the upper GoT, the current flows northward along the western coast, while the current near the eastern coast flows southward, during January. For May and July, the currents move northward toward land at the head of GoT. For October, the currents also flow southward along the eastern coast. There is a fully clockwise current circulation near the coast of Chonburi and Rayong provinces of Thailand.

The freshwater runoff does not change the general circulation pattern for January, which is the dry season, while the runoff affects the GoT surface circulation pattern for May and July, which are the summer and rainy seasons, respectively.

The freshwater runoff does not significantly affect the circulation pattern in the upper GoT for January and May, but it is the factor increasing the current speed for July. The water in the upper GoT is freshest at the end of rainy season because of the freshwater released from the four main river basins at the head; therefore, the runoff for October is the important factor for the current pattern in the upper GoT.

The GoT sea surface elevation is higher than the reference level with a maximum elevation around the central Gulf during the winter season of Thailand, January. During May and October, the weak winds cause the sea level to be near the reference. In July, the elevation is lower than the reference level. The runoff affects the sea surface elevation in the upper GoT in October. The model results show a reduction of sea surface elevation, when the runoff is removed from the forcing.

Author's personal copy

Acknowledgments This research was financially supported by a TRF-CHE research grant for new scholar (Grant No. MRG5280146) and the National Research University Project. The authors would like to express their gratitude.

References

1. Burnett, W.C.; Wattayakorn, G.; Taniguchi, M.; Dulaiova, H.; Sojisuporn, P.; Rungsupa, S.; Ishitobi, T.: Groundwater-derived nutrient inputs to the Upper Gulf of Thailand. Cont. Shelf Res. **27**(2), 176–190 (2006)
2. Stansfeld, K.; Garrett, C.: Implications of the salt and heat budgets of the Gulf of Thailand. J. Marine Res. **55**, 935–963 (1997)
3. Zhang, X.H.; Liang, X.Z.: A numerical world ocean general circulation model. Adv. Atmos. Sci. **6**(1), 43–61 (1989)
4. Zeng, Q.C.; Ji, Z.Z.; Li, R.F.: A numerical model of offshore currents and some tests. Adv. Hydrodyn. **2**(1), 67–71 (1987)
5. Zeng, Q.C.; Li, R.F.; Ji, Z.Z.; Gan, Z.J.; Ke, P.H.: Calculations of the monthly ocean currents of the South China Sea. Chin. J. Atmos. Sci. **13**(2), 129–144 (1989)
6. Blumberg, A.F.; Mellor, G.L.: A description of a three-dimensional coastal ocean circulation model. In: Heaps, N.S. (ed.) Three Dimensional Coastal Ocean Models, pp. 1–16, American Geophysical Union, USA (1987)
7. Killworth, P.D.; Stainforth, D.; Webb, D.J.; Paterson, S.M.: A Free Surface Bryan-Cox Semtner Model. Report No. 270 (Reprinted 1993), Institute of Oceanographic Sciences, Deacon Laboratory Internal, p. 87 (1989)
8. Killworth, P.D.; Stainforth, D.; Webb, D.J.; Paterson, S.M.: The development of a free surface Bryan-Cox-Semtner ocean model. J. Physi. Oceanogr. **21**, 1333–1348 (1991)
9. Cox, M.D.: An idealized model of the world ocean, Part I: The global-scale water masses. J. Phys. Oceanogr. **19**, 1730–1752 (1989)
10. Chu, P.C.; Chen, Y.; Lu, S.: Wind-driven South China Sea deep basin warm-core/cool-core eddies. J. Oceanogr. **54**, 347–360 (1998)
11. Chu, P.C.; Edmons, N.L.; Fan, C.: NOTES AND CORRESPONDENCE: Dynamics mechanisms for the South China Sea seasonal circulation and thermohaline variabilities. J. Phys. Oceanogr. **29**, 2971–2989 (1999)
12. Aschariyaphotha, N.; Wongwises, P.; Wongwises, S.; Humphries,U.W.; You, X.B.: Simulation of seasonal circulations and thermohaline variabilities in the Gulf of Thailand. Adv. Atmos. Sci. **25**(3), 489–506 (2008)
13. UNESCO.: Tenth Report of the Joint Panel on Oceanographic Tables and Standards. UNESCO Technical Papers in Marine Sciences 36, Unesco, Paris, p. 25 (1981)
14. Mellor, G.L., Yamada, T.: Develop of a turbulence closure model for geophysical fluid problems. Rev. Geophy. Space Phys. **20**, 851–875 (1982)
15. Aschariyaphotha, N.; Wongwises, P.; Humphries, U.W.: Interpolation of Climatological Data to Numerical Ocean Modeling for the Gulf of Thailand. In: Proceedings of the joint international conference on sustainable energy and environment, Huahin, Thailand, pp. 784–789 (2004)
16. Mellor, G.L.: Users Guide for a Three-Dimensional, Primitive Equation, Numerical Ocean Model. Princeton University, New Jersey, p. 56 (2004)
17. Matthias, T.; Godfrey, J.S.: Regional Oceanography: An Introduction. Pergamon, Australia, p. 430 (1994)
18. Li, R.F.; You, X.B.; Wongwises, P.: A Three-Dimensional Coastal Ocean Circulation Model. King Mongkut's University of Technology Thonburi, p. 59 (2002)
19. Weatherly, G.; Martin, P.J.: On the structure and dynamics of the ocean bottom boundary layer. J. Phys. Oceanogr. **8**, 557–570 (1978)
20. Li, R.F.; You, X.B.: The development and application of the oceanic general circulation model Part II: The regional oceanic general circulation model. Chin. J. Atmos. Sci. **27**, 729–739 (2003)
21. You, X.B.; Li, R.F.; Zhang, M.; Zeng, Q.C.: Numerical calculation of the wintertime circulation in the South China Sea by using a baroclinic model. Acta Oceanologia Sinica **26**, 1–10 (2001)
22. You, X.B.; Li, R.F.; Zeng, Q.C.: Numerical Simulation of the Current System in the China Sea by Using a Nested Mesh Model. In: Proceedings of the Ninth Asian Congress of Fluid Mechanics Isfahan, Iran (2002)
23. Levitus, S., Boyer, T.: World Ocean Atlas, vol. 4: Temperature. NOAA Atlas NESDIS, 4, U.S. Government Printing Office, Wasington, D.C., p. 117 (1994)
24. Levitus, S., Burgett, R., Boyer,T.: World Ocean Atlas, vol. 3: Salinity. NOAA Atlas NESDIS, 3, U.S. Government Printing Office, Wasington, D.C., p. 99 (1994)
25. Oey, L.Y.; Mellor, G.L.; Hires, R.I.: A three-dimensional simulation of the Hudson-Raritan Estuary. Part I: Description of the model and model simulations. J. Phys. Oceanogr. **15**, 1676–1692 (1985)
26. Wyrtki, K.: Scientific Results of Marine Investigations of the South China Sea and the Gulf of Thailand 1959-1961. Naga Report 2, University of California at San Diego, 164–169 (1961)

Provided for non-commercial research and education use.
Not for reproduction, distribution or commercial use.

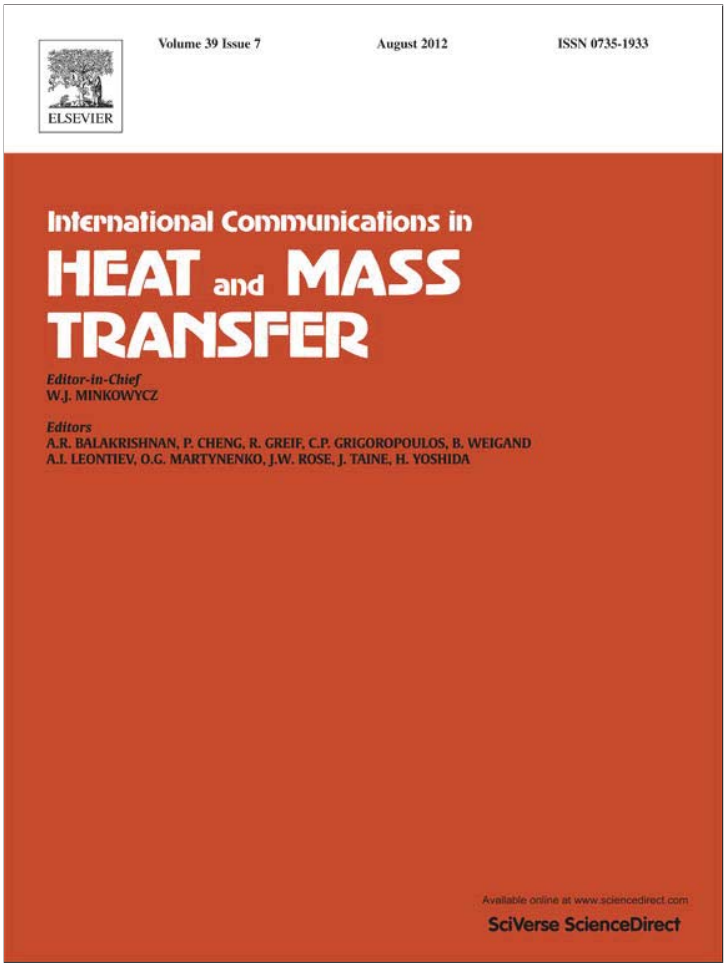

This article appeared in a journal published by Elsevier. The attached copy is furnished to the author for internal non-commercial research and education use, including for instruction at the authors institution and sharing with colleagues.

Other uses, including reproduction and distribution, or selling or licensing copies, or posting to personal, institutional or third party websites are prohibited.

In most cases authors are permitted to post their version of the article (e.g. in Word or Tex form) to their personal website or institutional repository. Authors requiring further information regarding Elsevier's archiving and manuscript policies are encouraged to visit:

http://www.elsevier.com/copyright

Author's personal copy

International Communications in Heat and Mass Transfer 39 (2012) 937–944

Contents lists available at SciVerse ScienceDirect

International Communications in Heat and Mass Transfer

journal homepage: www.elsevier.com/locate/ichmt

A correlation development for predicting the pressure drop of various refrigerants during condensation and evaporation in horizontal smooth and micro-fin tubes ☆

M. Balcilar [a], A.S. Dalkilic [b,*], O. Agra [b], S.O. Atayilmaz [b], S. Wongwises [c,d,**]

[a] Computer Engineering Department, Yildiz Technical University, Yildiz, Besiktas, Istanbul 34349, Turkey
[b] Heat and Thermodynamics Division, Department of Mechanical Engineering, Yildiz Technical University (YTU), Yildiz, Besiktas, Istanbul 34349, Turkey
[c] Fluid Mechanics, Thermal Engineering and Multiphase Flow Research Lab. (FUTURE), Department of Mechanical Engineering, King Mongkut's University of Technology Thonburi, Bangmod, Bangkok 10140, Thailand
[d] The Academy of Science, The Royal Institute of Thailand, Sanam Suea Pa, Dusit, Bangkok 10300, Thailand

ARTICLE INFO

Available online 28 May 2012

Keywords:
Artificial neural network (ANN)
Multi-layer perceptron (MLP)
Non-linear least squares (NLS)
Condensation
Evaporation
Correlation development
Micro-fin
Pressure drop

ABSTRACT

This paper predicts the condensation and evaporation pressure drops of R32, R125, R410A, R134a, R22, R502, R507a, R32/R134a (25/75 by wt%), R407C and R12 flowing inside various horizontal smooth and micro-fin tubes by means of the numerical techniques of artificial neural networks (ANNs) and non-linear least squares (NLS). In its analyses, this paper used experimental data from the National Institute of Standards and Technology (NIST) and Eckels and Pate, as presented in Choi et al.'s study provided by NIST. In their experimental setups, the horizontal test sections have 1.587, 3.78, 3.81 and 3.97 m long countercurrent flow double tube heat exchangers with refrigerant flowing in the inner smooth (8, 8.01 and 11.1 mm i.d.) and micro-fin (4.339, 5.45, 7.43 and 8.443 mm i.d.) copper tubes and cooling water flowing in the annulus. Their test runs cover a wide range saturation temperatures, vapor qualities and mass fluxes. The pressure drops are calculated with 1485 measured data points, together with analyses of artificial neural networks and non-linear least squares numerically. Inputs of the ANNs of the best correlation are the measured values of the test sections, such as mass flux, tube length, inlet and outlet vapor qualities, critical pressure, latent heat of condensation, mass fraction of liquid and vapor phases, dynamic viscosities of liquid and vapor phases, hydraulic diameter, two-phase density and the outputs of the ANNs, which comprise the experimental total pressure drops of the evaporation and condensation data from independent laboratories. The total pressure drops of in-tube condensation and in-tube evaporation tests are modeled using the artificial neural network (ANN) method of multi-layer perceptron (MLP) with 12-40-1 architecture. Its average error rate is 7.085%, which came from the cross validation tests of 1485 evaporation and condensation data points. Dependency of the output of the ANNs from 12 numbers of input values is also shown in detail, and new ANN based empirical pressure drop correlations are developed separately for the conditions of condensation and evaporation in smooth and micro-fin tubes as a result of the analyses. In addition, a single empirical correlation for the determination of both evaporation and condensation pressure drops in smooth and micro-fin tubes is proposed with an error rate of 14.556%.

© 2012 Elsevier Ltd. All rights reserved.

1. Introduction

Artificial intelligence methods, which include the genetic algorithm (GA) and artificial neural network (ANN) modeling that have been validated by experimental works, are increasingly being utilized to correlate two-phase flows in tubes. However, the literature still lacks investigations on the prediction of in-tube condensation and evaporation characteristics by means of artificial intelligence techniques. In this paper, artificial neural network analyses were used as one of the numerical solution techniques to determine the important pressure drop characteristics of condensation and evaporation heat transfer. Existing recent numerical studies in these subjects regarding the two-phase flows in the literature are summarized in the following paragraphs.

Balcilar et al. [1,2] numerically investigated the best artificial intelligence method among multi-layer perceptron (MLP), radial basis networks (RBFN), generalized regression neural network (GRNN) and adaptive neuro-fuzzy inference system (ANFIS) to estimate the experimentally measured convective heat transfer coefficient and pressure drop of R134a flowing downward inside a vertical tube during annular flow. Balcilar et al. [3,4] investigated the heat transfer characteristics

☆ Communicated by W.J. Minkowycz.

* Corresponding author.
** Correspondence to: S. Wongwises, The Academy of Science, The Royal Institute of Thailand, Sanam Suea Pa, Dusit, Bangkok 10300, Thailand.
E-mail addresses: dalkilic@yildiz.edu.tr (AS. Dalkilic), somchai.won@kmutt.ac.th (S. Wongwises).

0735-1933/$ – see front matter © 2012 Elsevier Ltd. All rights reserved.
doi:10.1016/j.icheatmasstransfer.2012.05.005

Author's personal copy

Nomenclature

A	coefficients in Eqs. (5), (6) and (7)
Bo	Bond number
d	internal tube diameter, m
f	function
Fr	Froude number
G	mass flux, kg m^{-2} s^{-1}
h_{fg}	latent heat of condensation, kJ kg^{-1}
j	superficial velocity
K_{num}	numerical correction coefficient
L	tube length, m
Pr	Prandtl number
R	ratio of density to dynamic viscosity
Re	Reynolds number
V	volume of fluid
x	average vapor quality
w	mass fraction, m^3 kg^{-1}
We	Weber number
X_{tt}	Lockhart and Martinelli parameter
ΔP	pressure drop, kPa

Greek symbols

α	void fraction
ρ	density, kg m^{-3}
μ	dynamic viscosity, kg m^{-1} s^{-1}
σ	surface tension, N m^{-1}
Ψ	surface tension parameter

Subscripts

eq	equivalent
exp	experiment
g	gas
h	hydraulic
l	liquid
TP	two-phase

of R134a during downward condensation both experimentally and numerically by using the genetic algorithm technique (GA), the unconstrained nonlinear minimization algorithm Nelder–Mead method (NM) and the non-linear least squares error method (NLS) for the optimization of the variables in the study. Demir et al. [5] numerically investigated the forced convection flows of nanofluids by using a computational fluid dynamics (CFD) program in a horizontal tube with constant wall temperature. In addition, Demir et al. [6] developed a generalized neural network correlation for the condensation heat transfer coefficient of alternative refrigerant R600a inside a horizontal tube in their earlier study. The results from the trained network show good agreement with the experimental data and better results than the well-known correlations in the literature. Agra et al. [7] numerically investigated the passive heat transfer enhancement techniques to determine the distribution of temperature and static pressure in the test tubes, the friction factor, the heat flux, temperature difference between the inlet and outlet fluid temperatures, the pressure drop penalty, and convective heat transfer coefficient using a CFD program. Their results were also in-line with the available experimental data in the literature.

Although two-phase flow characteristics of refrigerants have been extensively investigated experimentally in the past; little attention has been paid to determining those numerically, especially with artificial intelligence and CFD techniques in order to predict accurately the pressure drop and related issues inside horizontal smooth and enhanced tubes. Consequently, the chief aim of this study is to model the condensation and evaporation in smooth and micro-fin tubes in the MATLAB program with the methods of multi-layer perceptron (MLP) and non-linear least squares (NLS), then determine the most affected parameters and develop reliable correlations with several sets of basic heat transfer data [8,9] that belong to the flow in smooth and micro-fin tubes. It is believed that the proposed correlations will be useful in predicting the pressure drop characteristics of new smooth and micro-fin tubes without doing additional experiments due to the use of reliable data from independent laboratories.

2. Experimental apparatus and method

Detailed descriptions of the experimental apparatus and summary of test conditions in terms of flow type, refrigerant, mass flux, average pressure, inlet and outlet vapor qualities and number of data points belonging to the data for studying condensation and evaporation of various refrigerants inside horizontal smooth and micro-fin tubes can be found in Choi et al.'s [8] and Eckels and Pate's [9] publication.

3. Calculation procedure for the analyses

3.1. Error analysis

The error analyses' calculation procedure for the average values of the experimental and calculated results of the two-phase pressure drops regarding with R^2 error, proportional error and mean square error (MSE) can be seen from authors' previous publication [1] and their results appear in Tables 1 and 2.

3.2. The generalized artificial neural networks (ANNs) model

As the artificial neural networks (ANNs) are one of the most commonly used and developed models to investigate the relationship between linear or non-linear input–output patterns. These models try to generalize the training group and then estimate the test group. Performance of ANNs is measured with the success of the prediction. There are many described ANN types related with the function approximation in the literature. The most known methods are multi-layer perceptron (MLP), radial basis functions networks (RBFN), generalized regression neural networks (GRNN) and artificial neural fuzzy inference system (ANFIS). The lattermost method is the combination of fuzzy logic decision systems and ANNs.

The detailed information on the ANN analyses of the determination condensation heat transfer coefficient, pressure drop and correlation development can be seen from the authors' previous publications [1–4,6,7]. It should be noted that the authors benefitted from their own experimental database in these publications.

3.3. The non-linear least squares algorithm (NLS)

The non-linear least square (NLS) method allows the user to determine the most optimal non-linear function coefficients in order to fit data collected from an experimental environment to a non-linear function (non-linear curve fitting). This method tries to minimize the mean square error, beginning from the first estimated values determined by the user. Since it advances step by step through optimizing this point, it finds the local minimum and not the global minimum by starting from this initial point. The method is tested by starting from different initial points, and thus the global minimum value of ANN code is determined.

Author's personal copy

Table 1
Elimination of MLP with the architecture 12-10-10-1 according to the error rates for the determination of pressure drop of data [8,9].

Data set	Data of condensation in micro-fin tubes by NIST [8]					Data set	Data of condensation in micro-fin tubes by Eckels and Pate [9]				
1	Error analysis/MLP architecture	ΔP (kPa)				4	Error analysis/MLP architecture	ΔP (kPa)			
		5-5	10-10	20-20	40-40			5-5	10-10	20-20	40-40
	R^2	0.972	0.975	0.949	0.719		R^2	0.962	0.97	0.965	0.952
	MSE	0.149	0.138	0.2768	2.154		MSE	3.131	2.43	2.834	3.985
	Proportional (%)	17.991	18.183	28.599	60.15		Proportional (%)	22.59	20.526	24.13	31.314
Data set	Data of evaporation in micro-fin tubes by NIST [8]					Data set	Data of evaporation in smooth tubes by Eckels and Pate [9]				
2	Error analysis/MLP architecture	ΔP (kPa)				5	Error analysis/MLP architecture	ΔP (kPa)			
		5-5	10-10	20-20	40-40			5-5	10-10	20-20	40-40
	R^2	0.979	0.978	0.982	0.974		R^2	0.928	0.995	0.991	0.987
	MSE	0.24	0.248	0.204	0.29		MSE	12.005	0.625	1.1362	1.785
	Proportional (%)	5.98	6.142	4.934	5.82		Proportional (%)	34.518	17.609	33.645	62.126
Data set	Data of condensation in smooth tubes by Eckels and Pate [9]					Data set	Data of evaporation in micro-fin tubes by Eckels and Pate [9]				
3	Error analysis/MLP architecture	ΔP (kPa)				6	Error analysis/MLP architecture	ΔP (kPa)			
		5-5	10-10	20-20	40-40			5-5	10-10	20-20	40-40
	R^2	0.969	0.988	0.964	0.869		R^2	0.988	0.9942	0.982	0.988
	MSE	0.825	0.322	1.168	3.609		MSE	1.658	1.433	2.65	1.762
	Proportional (%)	21.168	15.286	22.485	50.108		Proportional (%)	19.124	19.524	17.85	20.122

3.4. Correlation development for the two-phase pressure drop

There have been a number of studies on the in-tube condensation and evaporation pressure drops of smooth and enhanced tubes in the literature. The frictional, acceleration, and gravitational components determine the two-phase total pressure drop in tubes. Determination of the void fraction is required to compute the acceleration and gravitational components, and in a similar way, determination of either the two-phase friction factor or the two-phase frictional multiplier is required to compute the frictional component of pressure drop. Generally, empirical methods have been used to compute the two-phase pressure drops in tubes. As a result, Eq. (1) is formed to predict the pressure drops of evaporation and condensation in terms of the above explanations as follows:

$$\Delta P = \left(\frac{G^2 L}{d\rho_{TP}}\right) K_{num} \tag{1}$$

where the numerical correction coefficient (K_{num}) is calculated using the artificial neural network (ANN) with the architecture of multi-layer perceptron (MLP-12-40-1) and non-linear least squares that appear in all tables and figures labeled as f(MLP) and f(NLS), respectively. The following Eqs. (2) and (3) are determined by means of f(NLS). Their coefficients are shown as A_1 to A_{12} in Table 3,

$$K_{num} = \left(\frac{A_1}{1+e^{(A_2 R + A_3)}} + A_4\right) 10^{-8} \tag{2}$$

$$K_{num} = \left(\frac{A_{11}}{1+e^{-Y}} + A_{12}\right) 10^{-8} \tag{3}$$

where the coefficient of Y is estimated as:

$$Y = A_1 \mathrm{Fr} + A_2 \mathrm{We} + A_3 \mathrm{Bo} + A_4 X_{tt} + A_5 \alpha + A_6 \Psi + A_7 \mathrm{Re}_{eq} + A_8 R + A_9 \mathrm{Pr}_l + A_{10} \tag{4}$$

The inputs of all analyses, including MLP architectures with 12-10-10-1 for the determination of pressure drop directly and 12-40-1 (f(MLP)) for the determination of K_{num} in Eq. (1) and non-linear least squares (NLS) for the determination of K_{num} in Eqs. (3) and (4) are shown as follows.

Table 2
Elimination of ANN methods by means of f(ANN) in Eq. (1) according to the error rates for the determination of pressure drop of data [8,9].

Data set	Data of condensation in micro-fin tubes					Data set	Data of evaporation in smooth and micro-fin tubes				
1	Error analysis/MLP architecture	ΔP (kPa)				4	Error analysis/MLP architecture	ΔP (kPa)			
		40	10-10	20-20	40-40			40	10-10	20-20	40-40
	R^2	0.994	0.989	0.981	0.994		R^2	0.93	0.97	0.974	0.975
	MSE	0.028	0.056	0.097	0.036		MSE	7.841	2.574	2.111	2.0697
	Proportional (%)	5.556	6.653	7.523	5.672		Proportional (%)	13.969	14.483	13.966	14.211
Data set	Data of condensation in smooth and micro-fin tubes					Data set	Data of condensation and evaporation in micro-fin tubes				
2	Error analysis/MLP architecture	ΔP (kPa)				5	Error analysis/MLP architecture	ΔP (kPa)			
		40	10-10	20-20	40-40			40	10-10	20-20	40-40
	R^2	0.986	0.987	0.985	0.987		R^2	0.997	0.997	0.996	0.996256
	MSE	0.16	0.144	0.162	0.152		MSE	0.336	0.603	0.796	0.684
	Proportional (%)	3.735	3.484	3.817	3.735		Proportional (%)	7.887	8.959	10.186	9.369
Data set	Data of evaporation in micro-fin tubes					Data set	Data of condensation and evaporation in smooth tubes				
3	Error analysis/MLP architecture	ΔP (kPa)				6	Error analysis/MLP architecture	ΔP (kPa)			
		40	10-10	20-20	40-40			40	10-10	20-20	40-40
	R^2	0.988	0.991	0.995	0.994		R^2	0.986	0.992	0.992	0.989
	MSE	0.308	0.236	0.126	0.22		MSE	2.238	1.406	1.064	4.591
	Proportional (%)	8.256	8.364	7.539	8.143		Proportional (%)	6.774	9.403	7.6	9.381

Author's personal copy

Table 3
Proposed correlations obtained from f(NLS) for condensation and evaporation in smooth and micro-fin tubes using the data points of [8,9].

Type of two-phase flow	Data set	Proposed correlation: $\Delta P = \left(\frac{G^2 L}{d\rho_{TP}}\right)\left(\frac{A_1}{1+e^{(A_2 R+A_3)}}+A_4\right)10^{-8}$	Tube type		R^2	MSE	% Average error
			Smooth	Micro-fin			
Condensation	1	$A_1=-1.17378$, $A_2=0.000167$, $A_3=-11.2363$, $A_4=1.173774$	–	x	0.982	0.101	12.303
	3	$A_1=-1.16593$, $A_2=0.000144$, $A_3=-10.0917$, $A_4=1.165895$	x	–	0.977	0.621	12.665
	4	$A_1=-1.16862$, $A_2=0.065145$, $A_3=-34.1775$, $A_4=1.168633$	–	x	0.962	3.471	18.697
	1–4	$A_1=-1.169$, $A_2=0.080706$, $A_3=-43.954$, $A_4=1.169006$	–	x	0.966	2.071	16.602
	1–3–4	$A_1=-1.16833$, $A_2=0.045122$, $A_3=-29.4969$, $A_4=1.168344$	x	x	0.966	1.746	15.765
Evaporation	2	$A_1=-2.57E\text{-}06$, $A_2=0.324154$, $A_3=-143.636$, $A_4=1.73E\text{-}05$	–	x	0.954	0.522	9.374
	5	$A_1=-9.11E\text{-}06$, $A_2=0.064966$, $A_3=-23.1589$, $A_4=1.96E\text{-}05$	x	–	0.964	5.181	26.089
	6	$A_1=-5.64E\text{-}06$, $A_2=2.661379$, $A_3=-866.67$, $A_4=1.68E\text{-}05$	–	x	0.95	7.965	23.786
	2–5–6	$A_1=-6.51E\text{-}06$, $A_2=0.047376$, $A_3=-18.699$, $A_4=1.77E\text{-}05$	x	x	0.947	2.431	13.983
Condensation and evaporation	1–2–4–6	$A_1=-6.03E\text{-}06$, $A_2=0.032756$, $A_3=-12.5242$, $A_4=1.72E\text{-}05$	–	x	0.961	1.814	13.607
	3–5	$A_1=-1.13E\text{-}05$, $A_2=0.003371$, $A_3=-2.14455$, $A_4=2.02E\text{-}05$	x	–	0.971	2.208	18.703
	1–2–3–4–5–6	$A_1=-0.58331683$, $A_2=0.053697258$, $A_3=-20.9082209$, $A_4=1.707628765$	x	x	0.957	2.119	14.556
	1–2–3–4–5–6	Proposed correlation : $\Delta P = \left(\frac{G^2 L}{d\rho_{TP}}\right)\left(\frac{A_{11}}{1+e^{-Y}}+A_{12}\right)10^{-8}$ $Y = A_1\mathrm{Fr}+A_2\mathrm{We}+A_3\mathrm{Bo}+A_4X_{tt}+A_5\alpha+A_6\Psi+A_7\mathrm{Re}_{eq}+A_8R+A_9\mathrm{Pr}_l+A_{10}$ $A_1=-0.005195717$, $A_2=0.001339146$, $A_3=-0.037830204$, $A_4=-12.67518703$, $A_5=39.32388258$, $A_6=47.21149639$, $A_7=-0.000167776$, $A_8=0.019563285$, $A_9=-16.38509432$, $A_{10}=2.816148392$, $A_{11}=0.662922688$, $A_{12}=1.134726668$	x	x	0.96	1.966	15.471

The all liquid equivalent Re number is determined from:

$$\mathrm{Re}_{eq} = \frac{G_{eq} d_h}{\mu_l}. \tag{5}$$

Equivalent liquid mass flux is defined as:

$$G_{eq} = G\left((1-x) + x\left(\frac{\rho_l}{\rho_g}\right)^{0.5}\right). \tag{6}$$

The ratio of density to dynamic viscosity is defined as:

$$R = \frac{\rho_l \mu_l}{\rho_g \mu_g}. \tag{7}$$

Bond number is defined as:

$$Bo = g\left(\rho_l - \rho_g\right)\left(\frac{(d_h/2)^2}{\sigma}\right). \tag{8}$$

The Froude number is defined as:

$$\mathrm{Fr} = \frac{G^2}{g d_h {\rho_{TP}}^2} \tag{9}$$

where the two-phase density is determined from:

$$\rho_{TP} = \left(\frac{x}{\rho_g} + \frac{1-x}{\rho_l}\right)^{-1}. \tag{10}$$

The Lockhart and Martinelli parameter is expressed as:

$$X_{tt} = \left(\frac{1-x}{x}\right)^{0.9}\left(\frac{\mu_g}{\mu_l}\right)^{0.1}\left(\frac{\rho_g}{\rho_l}\right)^{0.5}. \tag{11}$$

The all liquid Reynolds number equation can be expressed as:

$$\mathrm{Re}_l = \frac{G d_h}{\mu_l}. \tag{12}$$

All gas Reynolds number is defined as:

$$\mathrm{Re}_g = \frac{G d_h}{\mu_g}. \tag{13}$$

The void fraction, α, can be determined from Butterworth's [10] correlation, which was suggested by Choi et al. [8] for the data as follows:

$$\alpha = \frac{1}{1 + 0.28\left(\frac{1-x}{x}\right)^{0.64}\left(\frac{\rho_g}{\rho_l}\right)^{0.36}\left(\frac{\mu_l}{\mu_g}\right)^{0.07}} \tag{14}$$

Author's personal copy

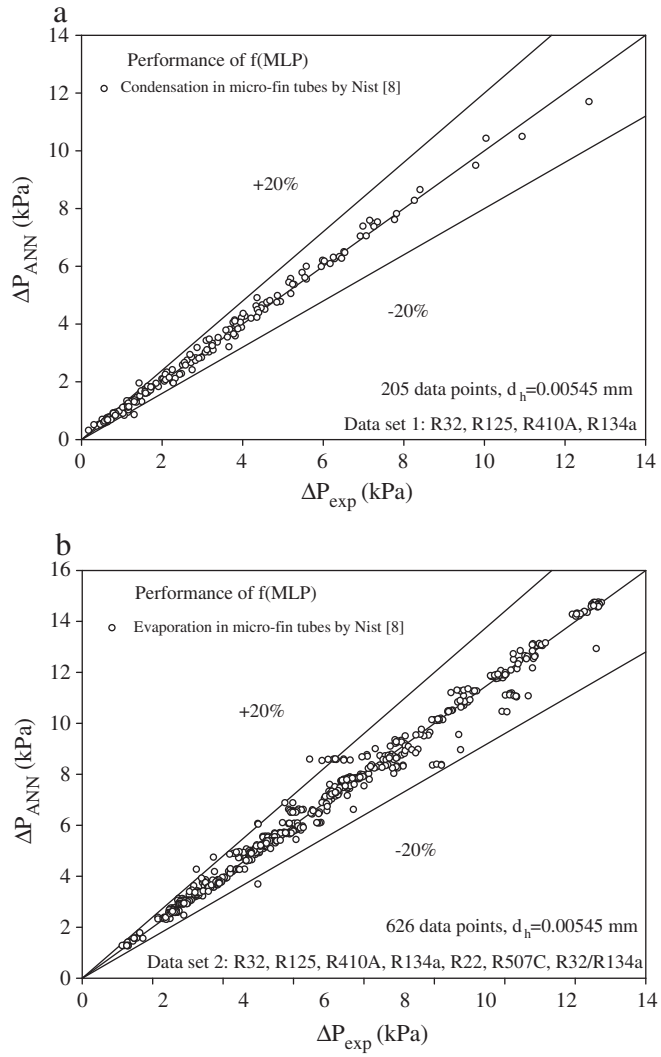

Fig. 1. Comparison of pressure drop values obtained from the condensation (a) and evaporation (b) experiments of NIST [8] in a micro-fin tube and MLP-12-40-1.

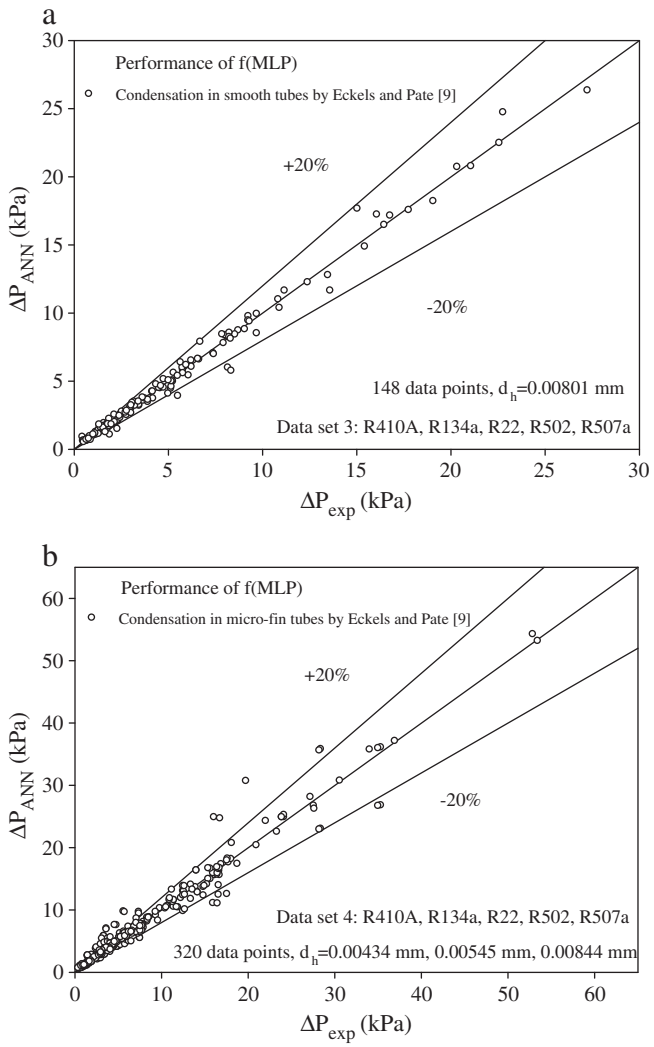

Fig. 2. Comparison of pressure drop values obtained from the condensation experiments of Eckels and Pate [9] in smooth (a) and micro-fin (b) tubes and MLP-12-40-1.

Weber number, We, is used as:

$$\mathrm{We} = \frac{G^2 d_h}{\sigma \rho_{TP}}. \tag{15}$$

Surface tension parameter, ψ, is calculated as:

$$\psi = \frac{j_l \mu_l}{\sigma} \tag{16}$$

where the liquid superficial velocity, j_l, is determined as:

$$j_l = \frac{G(1-x)}{\rho_l (1-\alpha)}. \tag{17}$$

4. Results and discussion

The following paragraphs numerically present the discussion of calculated total pressure drops using the database of National Institute of Standards and Technology (NIST) [8] and Eckels and Pate [9], presented in Choi et al.'s study provided by NIST [8] for the condensation and evaporation of R32, R125, R410A, R134a, R22, R502, R507a, R32/R134a (25/75 by wt%), R407C and R12 in horizontal smooth and micro-fin tubes. It should be noted that detailed explanations and some additional figures and tables containing different experimental parameters related to their studies on the pressure drop calculations can be seen in the applied reference databases [8,9], which demonstrate the accuracy of the experiments. A discussion of the results follows.

There are two-types of neural network analyses in the paper. One of them is developed for the direct determination of the two-phase pressure drop. Its architecture has 2 hidden layers with 10 neurons, and it is shown as MLP 12-10-10-1. This architecture's inputs are mass flux (G), tube length (z), inlet (x_{in}) and outlet (x_{out}) vapor qualities, critical pressure (P_c), latent heat of condensation (h_{fg}), density of liquid (ρ_l) and vapor (ρ_g) phases, dynamic viscosities of liquid (μ_l) and vapor (μ_g) phases, hydraulic diameter (d_h) and the all liquid Reynolds number (Re_l). Another neural network analysis is developed for the calculation of the numerical correction coefficient (K_{num}) in Eq. (1). Its architecture has one hidden layer with forty neurons and it is symbolized as f(MLP) 12-40-1. This architecture's inputs are mass flux (G), tube length (z), inlet (x_{in}) and outlet (x_{out}) vapor qualities, critical pressure (P_c), latent heat of condensation (h_{fg}), mass fraction of liquid (w_l) and vapor (w_g) phases, dynamic viscosities of liquid (μ_l) and vapor (μ_g) phases, hydraulic diameter (d_h) and two-phase density of (ρ_{TP}). These architectures are found as the best architectures of MLP and f(MLP) as a result analyses as shown

Author's personal copy

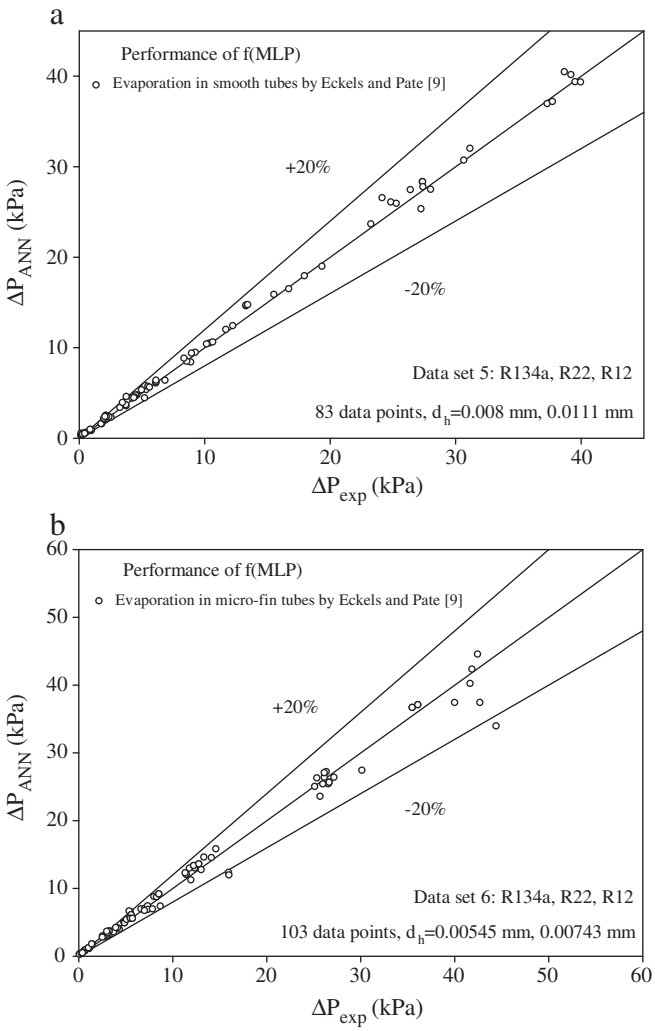

Fig. 3. Comparison of pressure drop values obtained from the evaporation experiments of Eckels and Pate [9] in smooth (a) and micro-fin (b) tubes and MLP-12-40-1.

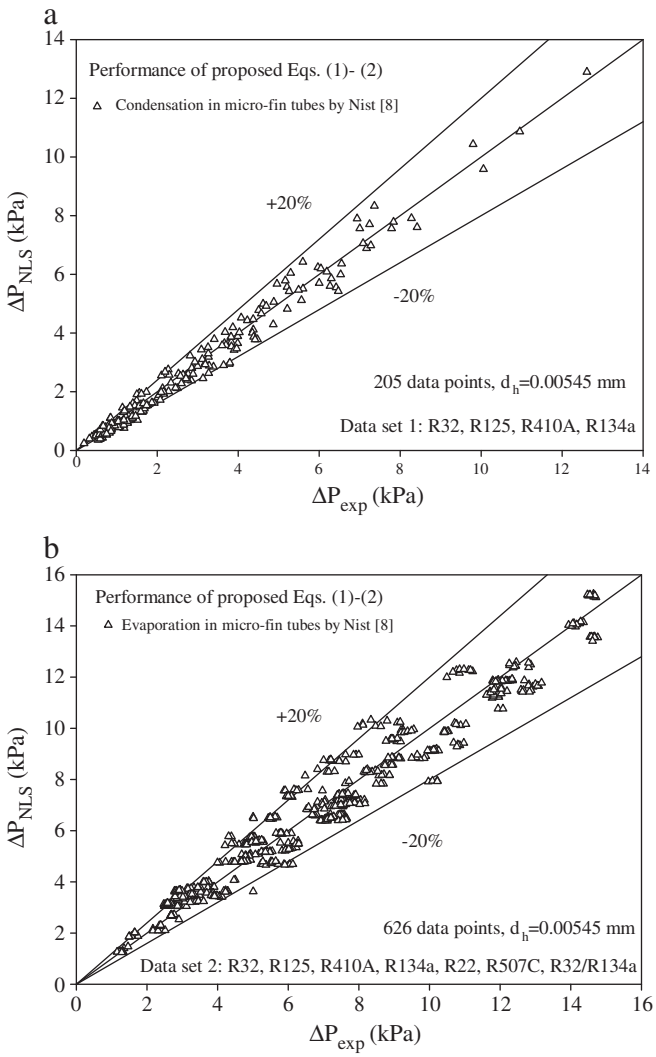

Fig. 4. Comparison of pressure drop values obtained from the comparison of pressure drop values obtained from the condensation (a) and evaporation (b) experiments of NIST [8] in a micro-fin tube and f(NLS).

in Table 2 for MLP and Table 3 for f(MLP). Four-fold cross validation was used for all ANN analyses. It means that 1485 data points (all data of evaporation and condensation in smooth and micro-fin tubes) were divided by four sets randomly and one of the sets selected for the test process, and the rest of them (three sets) were selected for the training process. These processes were continued until there were no untested data sets. Six different data sets of researchers [8,9] are defined in Tables 2 and 3. In terms of the elimination process of different MLPs, the 12-5-5-1, 12-10-10-1, 12-20-20-1 and 12-40-40-1 architectures are tested in Table 2 for MLP, and the 12-40-1, 12-10-10-1, 12-20-20-1 and 12-40-40-1 architectures are tested in Table 3 for f(MLP). It should be noted that although various architectures were tested for elimination, only the typical ones were shown in Tables 2 and 3 due to limited space. Nevertheless, it is possible to derive many results from these tables alone according to the separate databases on the selection of MLP architectures. For instance, the best architecture is found as 12-5-5-1 for data set 1 while the best architecture is found as 12-10-10-1 for data set 4 according to the mean proportional error rates. It should be noted that two of the data sets (one and four) were valid for the condensation in micro-fin tubes. The difference between the results is due to the hardness of generalization in the two-phase flow.

The developed correlations by means of f(NLS) from Eqs. (1) to (4) are the exact form of neural network method of MLP with nine inputs and one hidden neuron. This architecture's inputs are the Froud number (Fr), Weber number (We), Bond number (Bo), Lockhart and Martinelli number (X_{tt}), void fraction, surface tension parameter (Ψ), equivalent Reynolds number (Re_{eq}), the ratio of density to dynamic viscosity (R) and liquid Prandtl number (Pr_l). The initial values of coefficients from Eqs. (2) to (4) were taken from MLP and then they were improved by the method of non-linear least squares (NLS). Approximately 60% and 40% of all data points (1485) were selected for the correlation development set (training) and correlation test set to be used randomly in NLS analyses, respectively. It is obtained from the analyses that f(MLP) with the architecture of 12-40-1 has the lowest mean proportional error rate considering all data with the R^2 value of 0.963. Table 3 shows the coefficients of the proposed equations from Eqs. (1) to (4) according to the flow type, data set, and tube type with the error rates of R^2, MSE and mean proportional error rate in detail. The developed equations of Eqs. (1) and (2) seem to have lower mean deviation than Eqs. (1), (3) and (4) and offer easier applicability with their simpler form than the other ones.

The comparisons between the experimental and predicted values obtained from MLP with the architecture of f(MLP) and the architecture of 12-40-1 and f(NLS) in Eqs. (1) and (2) are illustrated from Figs. 1 to 3 and Figs. 4 to 6, respectively. The condensation and

Author's personal copy

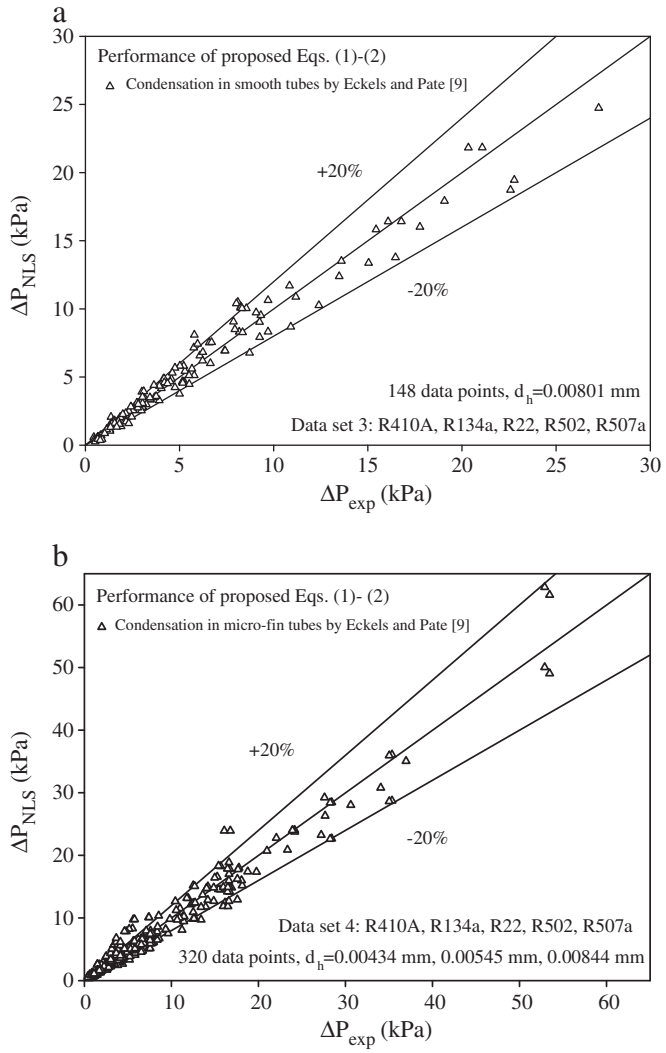

Fig. 5. Comparison of pressure drop values obtained from the condensation experiments of Eckels and Pate [9] in smooth (a) and micro-fin (b) tubes and f(NLS).

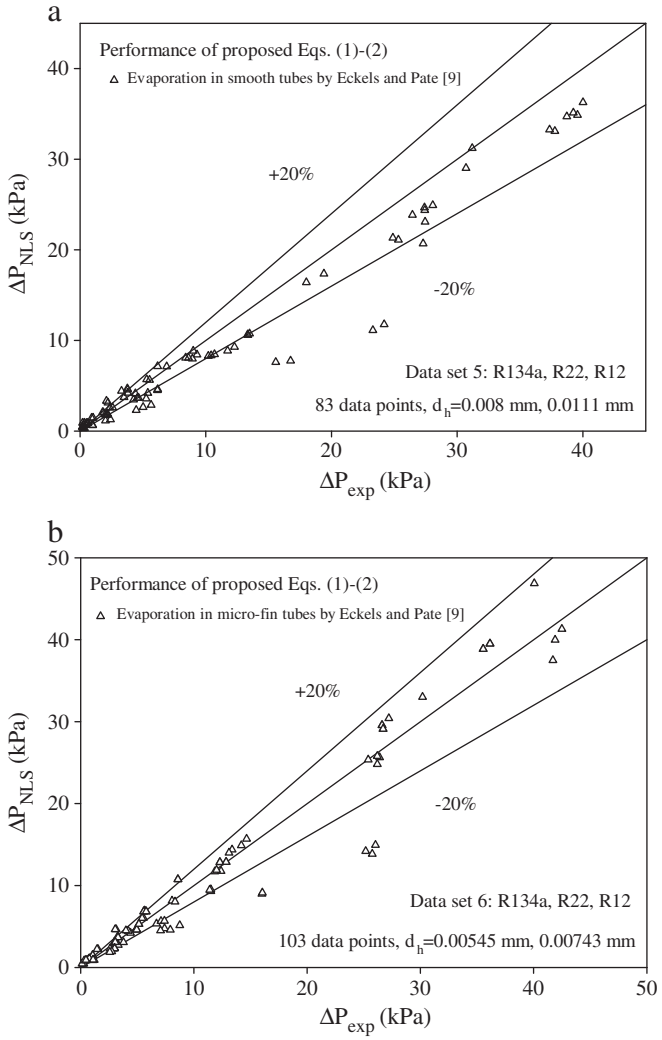

Fig. 6. Comparison of pressure drop values obtained from the evaporation experiments of Eckels and Pate [9] in smooth (a) and micro-fin (b) tubes and f(NLS).

evaporation in micro-fin tube data of NIST [8] are used in Figs. 1 and 4; the condensation in smooth and micro-fin tube data of Eckels and Pate [9] is used in Figs. 2 and 5; the evaporation in smooth and micro-fin tube data of Eckels and Pate [9] is used in Figs. 3 and 6. The data obtained from f(MLP) in Figs. 1 to 3 and NLS in Figs. 4 to 6 have the best results, with a deviation band of ±20%.

Table 4 shows the most predictive combinations of input parameters according to the R^2 values using the method of multi-layer perceptron (MLP) with 12-10-10-1 architecture, including the 1485 experimental data points for condensation and evaporation pressure drop in smooth and micro-fin tubes. In Table 4, when the input parameter number is one, mass flux (G) seems to be dominant on the prediction of pressure drop (ΔP) with the R^2 value of 0.755 for the condensation pressure drop in smooth and micro-fin tubes using data sets 1–3–4. When there are 2 known input parameters, mass flux (G) and the all liquid Reynolds number (Re_l) have the R^2 value of 0.924. When there are 3 known input parameters, mass flux, all liquid Reynolds number (Re_l) and latent vaporization (h_{fg}) have the R^2 value of 0.962. In the same table, when the input parameter number is one, vapor quality (x_{out}) best predicts pressure drop with the R^2 value of 0.473 among others for the evaporation pressure drop in smooth and micro-fin tubes using data sets 2–5–6. When there are 2 known input parameters, mass flux (G) and outlet vapor quality (x_{out}) have the R^2 value of 0.904. This result shows the importance of mass flux. When there are 3 known input parameters, mass flux, outlet vapor quality (x_{out}) and critical pressure have the R^2 value of 0.983. In the same table again, when the input parameter number is one, mass flux (G) best predicts pressure drop with the R^2 value of 0.365 for the evaporation and condensation pressure drops in smooth and micro-fin tubes using data sets 1–2–3–4–5–6. When there are 2 known input parameters, mass flux (G) and liquid dynamic viscosity (μ_l) have the R^2 value of 0.773. This result shows the importance of liquid dynamic viscosity for the investigated data sets. When there are 3 known input parameters, mass flux, mass flux (G), liquid dynamic viscosity (μ_l), and tube length (z) have the R^2 value of 0.88. When there are 4 known input parameters, mass flux, mass flux (G), liquid dynamic viscosity (μ_l), tube length (L) and all liquid Reynolds number (Re_l) have the R^2 value of 0.965. These tables show that the accuracy of the estimated output values by means of input values increases along the increasing number of proper input parameters. In addition, they show the existence of less important input parameters of the method of MLP with the architecture of 12-10-10-1 on the prediction of the pressure drop. Some details on the data sets can be seen on all figures as brief explanations as well as from Choi et al.'s [8] and Eckels and Pate's [9] publications.

5. Conclusion

Numerical analyses have been performed to determine the two-phase pressure drops and to develop reliable correlations of condensation and evaporation in smooth and micro-fin tubes by means of

Author's personal copy

Table 4
The most predictive combinations of input parameters according to the error rates for the determination of measured pressure drop.

Inputs											Input number	Outputs
G	L	x_{in}	x_{out}	P_c	h_{fg}	μ_l	μ_g	d_h	ρ_l	ρ_g	Re_l	R^2 (ΔP)
Condensation pressure drop (ΔP) in smooth and micro-fin tubes using the data sets of 1–3–4 with MLP architecture 12-10-10-1												
						1					1	0.186
1											1	0.755
1							1				2	0.898
1										1	2	0.924
1					1						1	3	0.962
1					1	1					1	4	0.975
1	1				1	1					1	5	0.981
Evaporation pressure drop (ΔP) in smooth and micro-fin tubes using the data sets of 2–5–6 with MLP architecture 12-10-10-1												
						1					1	0.457
			1								1	0.473
			1							1	2	0.865
1			1								2	0.904
1			1	1							3	0.983
1			1	1					1		4	0.990
1			1	1		1			1		5	0.992
Evaporation and condensation pressure drops (ΔP) in smooth and micro-fin tubes using the data sets of 1–2–3–4–5–6 with MLP architecture 12-10-10-1												
						1					1	0.216
1											1	0.365
1										1	2	0.730
1						1					2	0.773
1	1					1					3	0.880
1	1					1				1	4	0.965
1	1					1				1	5	0.978

computational numerical techniques. In order to derive reliable correlations, the well-known experimental databases in the literature [8,9] are used in the analyses. This paper reports that in spite of the numerous studies on the determination of two-phase pressure drop in tubes, application of artificial neural networks (ANN) together with non-linear least squares (NLS) to the in-tube evaporation and condensation for the aim of correlation development does not exist in the literature. For that reason, the content of this study is expected to fill this gap in the literature.

As expected, the neural network approach (MLP) for the aim of correlation development study is found to have equally good results as the non-linear least squares (NLS). The multi-layer perceptron method (f(MLP)) with the architecture of 12-40-1 has better predictability than the classical multi-layer perceptron method (MLP) with the architecture of 12-10-10-1 due to the use of proper input parameters during the correlation development study.

Therefore, this study proposes Eqs. (1) and (2) for practical usage by engineers due to their lower deviation from $\pm 20\%$ and the fact that they are derived for the conditions of evaporation and condensation in smooth and micro-fin tubes separately. These equations are also beneficial for the determination of pressure drops using various databases at the same time that have only one parameter (R). A detailed model of f(MLP) is given to be used in MATLAB directly. This explanation will enable users to predict the two-phase pressure drop with high accuracy.

The pressure drop of evaporation and condensation in smooth and micro-fin tubes is found to be highly dependent upon mass flux, all liquid Reynolds numbers, latent evaporation, outlet vapor quality, critical pressure of refrigerant, liquid dynamic viscosity and tube length as a result of dependency analyses.

Acknowledgments

The second author wishes to thank King Mongkut's University of Technology Thonburi (KMUTT) for providing him with a post-doctoral fellowship. The fifth author is indebted to the Thailand Research Fund and the National Research University Project for their financial support. This paper used NIST's data [8] and Eckels and Pate's [9] experimental data, which were presented in Choi et al.'s [8] study provided by NIST. The authors wish to thank them for their contributions to the subject of in-tube two-phase flow.

References

[1] M. Balcilar, A.S. Dalkilic, S. Wongwises, Artificial neural network (ANN) techniques for the determination of condensation heat transfer characteristics during downward annular flow of R134a inside a vertical smooth tube, International Communications in Heat and Mass Transfer 38 (2011) 75–84.
[2] M. Balcilar, A.S. Dalkilic, S. Wongwises, Determination of condensation heat transfer characteristics of R134a by means of artificial intelligence method, International Mechanical Engineering Congress and Exposition, ASME, November 12–18 2010, USA.
[3] M. Balcilar, A.S. Dalkilic, B. Bolat, S. Wongwises, Investigation of empirical correlations on the determination of condensation heat transfer characteristics using computational numerical methods during downward annular flow of R134a inside a vertical smooth tube, Journal of Mechanical Science and Technology 25 (10) (2011) 1–20.
[4] B. Bolat, M. Balcilar, A.S. Dalkilic, S. Wongwises, Optimization of the relationship between the two-phase friction factor and Reynolds equivalent number model by the means of Genetic Algorithm, ASME/JSME 8th Thermal Engineering Joint Conference, ASME, March 13–17 2011, Hawaii.
[5] H. Demir, A.S. Dalkilic, N.A. Kurekci, W. Duangthongsuk, S. Wongwises, Numerical investigation on the single phase forced convection heat transfer characteristics of TiO_2 nanofluids in a double-tube counter flow heat exchanger, International Communications in Heat and Mass Transfer 38 (2011) 218–228.
[6] H. Demir, O. Agra, Ş.Ö. Atayılmaz, Generalized neural network model of alternative refrigerant (R600a) inside a smooth tube, International Communications in Heat and Mass Transfer 36 (2009) 744–749.
[7] O. Agra, H. Demir, S. Ozgur Atayilmaz, F. Kantas, A.S. Dalkilic, Numerical investigation of heat transfer and pressure drop in enhanced tubes, International Communications in Heat and Mass Transfer 38 (2011) 1384–1391.
[8] J.Y. Choi, M.A. Kedzierski, P.A. Domanski, A generalized pressure drop correlation for evaporation and condensation of alternative refrigerants in smooth and micro-fin tubes, NISTIR 6333 (1999) 1–50.
[9] S.J. Eckels, M.B. Pate, In-tube evaporation and condensation of refrigerant-lubricant mixtures of HFC-134a and CFC-12, ASHRAE Transaction 97 (1991) 62–67.
[10] D. Butterworth, A comparison of some void-fraction relationships for co-current gas–liquid flow, International Journal of Multiphase Flow 1 (1975) 845–850.

Lazarus Godson[1]
Department of Mechanical Engineering,
Karunya University,
Coimbatore, Tamil Nadu 641 114, India
e-mail: godasir@yahoo.co.in

B. Raja
Indian Institute of Information Technology,
Design and Manufacturing (IIITD&M),
Kancheepuram, Chennai,
Tamil Nadu 600 048, India
e-mail: rajab@iiitdm.ac.in

D. Mohan Lal
Department of Mechanical Engineering,
Anna University,
Chennai, Tamil Nadu 600 025, India
e-mail: mohanlal@annauniv.edu

S. Wongwises
Fluid Mechanics, Thermal Engineering and
Multiphase Flow Research Lab. (FUTURE),
Department of Mechanical Engineering,
King Mongkut's University of Technology
Thonburi,
Bangmod, Bangkok 10140, Thailand;
The Academy of Science,
The Royal Institute of Thailand,
Sanam Suea Pa,
Dusit, Bangkok 10300, Thailand
e-mail: somchai.won@kmutt.ac.th

Convective Heat Transfer Characteristics of Silver-Water Nanofluid Under Laminar and Turbulent Flow Conditions

The convective heat transfer coefficient and pressure drop of silver-water nanofluids is measured in a counter flow heat exchanger from laminar to turbulent flow regime. The experimental results show that the convective heat transfer coefficient of the nanofluids increases by up to 69% at a concentration of 0.9 vol. % compared with that of pure water. Furthermore, the experimental results show that the convective heat transfer coefficient enhancement exceeds the thermal conductivity enhancement. It is observed that the measured heat transfer coefficient is higher than that of the predicted ones using Gnielinski equation by at least 40%. The use of the silver nanofluid has a little penalty in pressure drop up to 55% increase 0.9% volume concentration of silver nanoparticles.
[DOI: 10.1115/1.4006027]

Keywords: convective heat transfer, silver, nanofluid, pressure drop, laminar, turbulent, transition

1 Introduction

The last few decades have seen unprecedented growth in field of electronics, communication, and computing technologies, and it is likely to continue unabated into the present century. Recently, high heat flux devices used in avionics and medical engineering demands ultrahigh-performance cooling in thermal management systems. The exponential growth in these areas and their devices through miniaturization and an enhanced rate of operation has brought serious problems in the thermal management of these devices. Conventionally, water, oil and ethylene glycol are used as heat transfer fluids. Though various methods have been used to enhance the performance of a heat transfer device, the poor thermophysical properties affect the enhancement of heat transfer and the compactness of heat exchangers. As a result, there is a strong need to develop advanced heat transfer fluids with higher thermal conductivities and improved heat transfer characteristics. A nanofluid is a new class of heat transfer fluids that manifest enhanced thermal conductivities relative to pure fluids [1]. Besides enhanced heat transfer, nanofluids eliminate most of the problems arising with microsize slurries such as sedimentation, clogging of small channels, erosion, excessive pressure drop, etc. Thus, nanofluids have greater potential for convective heat transfer enhancement and are highly suited to application in practical heat transfer processes.

Focusing on the forced convective heat transfer, the majority of the experimental research focuses on the heat transfer enhancement by using the metal oxide nanoparticles such as aluminum oxide, copper oxide, titanium oxide, silicon oxide, etc., and only a limited research has been done with the use of pure metal nanoparticles such as copper, silver, gold, and carbon nanotube. Pak and Cho [2] investigated the convective heat transfer characteristics of nanofluids (γAl_2O_3–water and TiO_2–water) with $\varphi = 1$–3% in a turbulent regime and showed that the Nusselt number for the nanofluids increased with volume concentration and Reynolds number. Eastman et al. [3] conducted tests to assess the thermal performance of CuO–water with $\varphi = 0.9\%$ under turbulent flow conditions, and the heat transfer coefficient was higher by 15% than that of the base fluid. Wen and Ding [4] assessed the convective heat transfer of nanofluids in the entrance region under laminar flow conditions, γAl_2O_3–water nanofluid ($\gamma = 27$–56 nm; $\varphi = 0.6$–1.6%) under a constant heat flux boundary condition. For nanofluids containing $\varphi = 1.6\%$, the local heat transfer coefficient in the entrance region was found to be 41% higher than that of the base fluid at the same flow rate. It was observed that the enhancement is particularly significant in the entrance region and decreases with axial distance, and the particle migration was found to be the reason for the enhancement. Lai et al. [5] studied the flow behavior of nanofluids (Al_2O_3–deionsed water ; $\gamma = 20$ nm) in a millimeter-sized stainless steel test tube, subjected to constant wall heat flux and a low Reynolds number ($Re < 270$). The maximum Nusselt number enhancement of the nanofluid of 8% at $\varphi = 1\%$ was recorded. Jung et al. [6] conducted convective heat transfer experiments for a nanofluid (Al_2O_3–water) in a rectangular microchannel (50×50 μm) under laminar flow conditions. The convective heat transfer coefficient increased by more than 32% for $\varphi = 1.8\%$ in base fluids. Duangthongsuk and Wongwises [7] reported that the forced convective heat transfer under varied heat flux boundary conditions and pressure drop characteristics of a nanofluid consisting of water and 0.2 vol. % TiO_2 nanoparticles of 21 nm diameter flowing in a horizontal double-pipe counter flow heat exchanger under turbulent flow conditions. The results showed that the convective heat transfer coefficient of nanofluid is slightly higher than that of the base

[1]Corresponding author.

Contributed by the Heat Transfer Division of ASME for publication in the Journal of Thermal Science and Engineering Applications. Manuscript received April 6, 2011; final manuscript received January 24, 2012; published online July 12, 2012. Assoc. Editor: Mehmet Arik.

Copyright © 2012 by ASME

liquid by about 6–11%, and the use of the oxide nanofluid has a little penalty in pressure drop.

Xuan and Li [8] measured the convective heat transfer of the Cu– water nanofluid in a small-hydraulic-diameter flat tube under laminar flow conditions. The Nusselt number of the nanofluid with $\varphi = 0.5\%$ increased by more than 39% compared with that of pure water. Ding et al. [9] tested multiwalled carbon nanotubes (MCNT with $\varphi = 0.1$–1.0% with 0.5 wt % in aqueous solution) in a horizontal tube and obtained a maximum enhancement of heat transfer of 350% at a Reynolds number of 800. Kang et al. [10] investigated heat transfer in a grooved heat pipe using Ag–water and Ag–deionized (DI) water ($\gamma = 10$–35 nm) with particle concentrations ranging from 1 mg/l to 100 mg/l. The results indicated that, after adding a small amount of silver nanoparticles in pure water, the heat pipe wall temperature became lower than that of pipes filled only with pure water. As more nanoparticles became dispersed in the working fluid, the heat pipe wall temperature increase became smaller. The maximum reduction in thermal resistance of a heat pipe operated containing $\gamma = 10$ nm was 52% lower than that of DI–water and while that containing $\gamma = 35$ nm was 81% lower. The enhancement of heat pipe performance was attributed to the increase in effective liquid conductance that flattens the temperature of the fluid.

From the above review, it is observed that the heat transfer enhancement with the use of pure metal nanoparticles with low volume concentration is found to be very much higher than the metal oxide nanoparticles with relatively higher concentrations. This is because the metal nanoparticles posses higher thermal conductivity than the metal oxide ones. High aspect ratio nanoparticles such as carbon nanotubes resulted in greater enhancement in thermal conductivity and the heat transfer coefficient, compared to spherical and low aspect ratio nanoparticles. It is also observed that the use of high concentration metal oxide nanoparticles increases the viscosity and pressure drop leading to the higher pumping power. This issue can be eliminated with the use of low concentration metal nanoparticles. Maiga et al. [11] reported that, with regard to the nanofluid thermal properties, the actual amount of experimental data available in the literature remains surprisingly small, and it is obvious that more works in this area will be published in the near future. So far, all of the convective studies have been performed either in the laminar or turbulent regime or the combination of both. However, no one has studied on the hydrodynamic and heat transfer behavior of nanofluids in the laminar, transition, and the turbulent regime with pure metal nanoparticle such as silver with different concentrations. In this study, the convective heat transfer characteristics of nanofluid suspended with low volume concentrations of silver nanoparticles with 0.3, 0.6, and 0.9 vol. % are investigated. The effect of the Reynolds number and temperature of the flowing nanofluid and mass flow rate and temperature of the chilled water on the heat transfer coefficient are studied.

2 Experiments

2.1 Nanofluid Preparation. In the present study, the two-step method is used for preparation Ag–water nanofluid. The silver nanoparticles are mixed directly with deionized water under ultrasonic vibration without any additive or stabilizer. The ultrasonic vibration is carried out for 8 h using the ultrasonic processor (Roop-Telsonic TEC-40 model, power density-750 W, frequency-20 kHz) in order to make sure complete dispersion of the nanoparticles in the base fluid. The nanofluid was not transparent, and it was looking like black in color. The settling did not occur in 24 h. To validate this, a stability test was conducted by taking some small sample of nanofluid and physically observed if there is any settling occurs. No sedimentation was observed. Hence, the prepared nanofluid is stable for experimentation.

2.2 Effective Thermal Conductivity and Viscosity. A hot wire system is used to measure the thermal conductivity of the nanofluid, which involves a wire suspended symmetrically in a liquid in a vertical cylindrical container. The wire serves both as heating element and as thermometer. Constant current is applied to a thin wire, made of platinum, and the time evolution of its electrical resistance due to the temperature increase is measured. The thermal conductivity of the nanofluid is determined by observing the rate at which the temperature of a very thin platinum wire increases with time after a step change in voltage has been applied to it, thus creating a line source of constant heat flux per unit length. The relative viscosities of nanofluid were measured using Cannon-Fenske Opaque also called as reverse-flow viscometer. It works on the principle of evaluating the time required for a particular quantity of fluid to pass through a capillary bore. The ratio of efflux time of nanofluid to that of base-fluid is regarded as the experimental relative viscosity ratio. The uncertainty of the thermal conductivity and viscosity measurements is found to be around 1.5% and 2%, respectively, and the confidence level is found to be 95%. Detailed methods on the measurement of thermal conductivity and viscosity are given elsewhere in the most recently accepted paper of the present authors [12]. The thermal conductivity and viscosity are correlated as linear and quadratic functions of volume fraction, respectively. The coefficients of silver–water nanofluid for the tested volume concentration and temperature are achieved using linear regression analysis.

2.3 Convective Heat Transfer Coefficient. The experimental setup to measure convective heat transfer coefficient and pressure drop is shown in Fig. 1. The equipment comprises two flow loops: chilled water and nanofluid. Each loop consists of several units such as pump, flow meter, a constant temperature chilled water bath, nanofluid bath with temperature controller, and a test section. The test section is a 2.94 m long tube-in-tube counter flow heat exchanger with heated nanofluid flowing inside the tube while the cooling water flows in the annulus. The inner tube is of 6.3 mm outer diameter and 4.3 mm inner diameter, while the outer tube is having 12.7 mm outer diameter and 10.5 mm as inner diameter. The test section is thermally isolated from its upstream and downstream section by ceramic wool in order to reduce the heat loss along the axial direction. Two RTDs and a differential pressure transmitter are mounted at both ends of the test section to measure the bulk temperatures and pressure drop of the nanofluid. Six RTDs (PT100 RTD sensors with $\pm 0.15\,^{\circ}\mathrm{C}$ accuracy) are mounted on the surface of the wall to measure the temperature distributions along the length of the test section. The nanofluid is heated in an insulated cylindrical tank with a 0.5 kW heating capacity coupled with a proportional integral differential controller (PID-C) to keep the temperature constant inside the nanofluid bath. The hot nanofluid from the bottom of the tank is pumped using a centrifugal pump and then passed through a mass flow meter and fed into the test section in the counter flow direction to the cooling water. The nanofluid flow rate is measured using a Coriolis type mass flow meter with $\pm 0.1\%$ accuracy. Similarly, the water is cooled using an auxiliary cooling system with a 0.5 TR capacity condensing unit and a 1 kW heater coupled with a PID controller in order to keep the temperature of the cooling water constant. The interconnecting tubes in the nanofluid and cooling water loops are provided with necessary insulation to avoid heat loss to the surroundings. The heat infiltration analysis is performed by applying the uncertainty analysis suggested by Moffat [13], and it is seen that the heat leak was less than 5% of the actual heat load, which is insignificant and can be negligible. The inlet and exit temperatures of the cooling water and nanofluids, wall temperatures of the test section, mass flow rates of the cooling water and nanofluid, and the differential pressure in the nanofluid are measured. The experimental test matrix that is used in this study is given below in Table 1.

2.4 Data Reduction. The heat transfer rate from the hot fluid is defined as

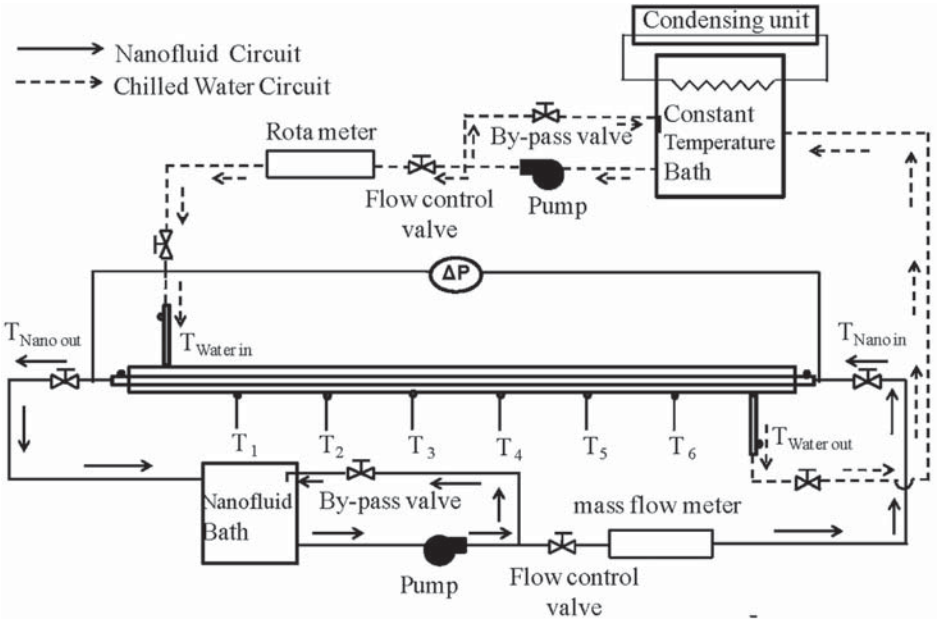

Fig. 1 Schematic diagram of the experimental apparatus

Table 1 Experimental test conditions

D (mm)	Re	T_{nano} (°C)	T_{water} (°C)	m_{water} (kg/s)
4.3	900–12,000	48	26	0.016
		57	30	
		65	35	

$$Q_{h_{nf}} = \dot{m}_{h_{nf}} C_{P_{h_{nf}}} (T_{in_{nf}} - T_{out_{nf}}) \tag{1}$$

where $Q_{h_{nf}}$ is the heat transfer rate of the hot nanofluid and $m_{h_{nf}}$ is the mass flow rate of the hot nanofluid

$$\frac{1}{U_i A_i} = \frac{1}{h_i . Ai} + \frac{\ln(d_o/d_i)}{2\pi kL} + \frac{1}{h_o . A_o} \tag{2}$$

$$Nu_{nf} = \frac{h_{nf} D}{k_{nf}} \tag{3}$$

where $h_i = h_{nf}$ is the heat transfer coefficient of the nanofluid, h_o = heat transfer coefficient of the annulus; k is the thermal conductivity of the copper tube, U_i is the overall heat transfer coefficient of the inner tube, Nu_{nf} is the Nusselt number of the nanofluid, D is the inner diameter of the test tube, and k_{nf} is the thermal conductivity of the nanofluid.

Similar to the heat transfer coefficient, the friction factor of the nanofluid flowing through the test section is calculated using the following equation

$$f_{nf} = \frac{2D\Delta P_{nf}}{L\rho_{nf} u_m^2} \tag{4}$$

where f_{nf} is the friction factor of the nanofluid, ΔP_{nf} is the measured pressure drop of the nanofluid, L is the length of the tube, ρ_{nf} is the density of the nanofluid, and u_m is the mean velocity of the nanofluid.

The thermophysical properties such as the density, specific heat, thermal conductivity, and viscosity of the nanofluid are calculated using the following published correlations.

The density is calculated from Pak and Cho [2] using the following equation

$$\rho_{nf} = \phi\rho_p + (1-\phi)\rho_w \tag{5}$$

The specific heat is calculated from Xuan and Roetzel [14] as follows

$$(\rho C_p)_{nf} = \phi(\rho C_p)_p + (1-\phi)(\rho C_p)_w \tag{6}$$

where $(\rho Cp)_{nf}$ is the heat capacity of the nanofluid, $(\rho Cp)_p$ is the heat capacity of the nanoparticles, and $(\rho Cp)_w$ is the heat capacity of the base fluid.

The thermal conductivity and viscosity of the nanofluid is calculated by the developed correlation given elsewhere in the most recently accepted paper of the present authors in the *Experimental Heat Transfer Journal* [ISSN: 0891-6152]. The thermal conductivity and viscosity are correlated as linear and quadratic functions of volume fraction, respectively. The coefficients of silver–water nanofluid for the tested volume concentration and temperature are achieved using linear regression as shown below

$$\frac{k_{nf}}{k_w} = (0.9692\phi + 0.9508) \tag{7}$$

$$\frac{\mu_{nf}}{\mu_w} = (1.005 + 0.497\phi - 0.1149\phi^2) \tag{8}$$

The properties of the nanofluid shown in the above equations are evaluated from water and nanoparticles at average bulk temperature. The detailed data reduction flow chart is shown below in Fig. 2.

3 Results and Discussion

A data base consisting of 960 data points were generated and the enhancement in heat transfer with respect thermophysical

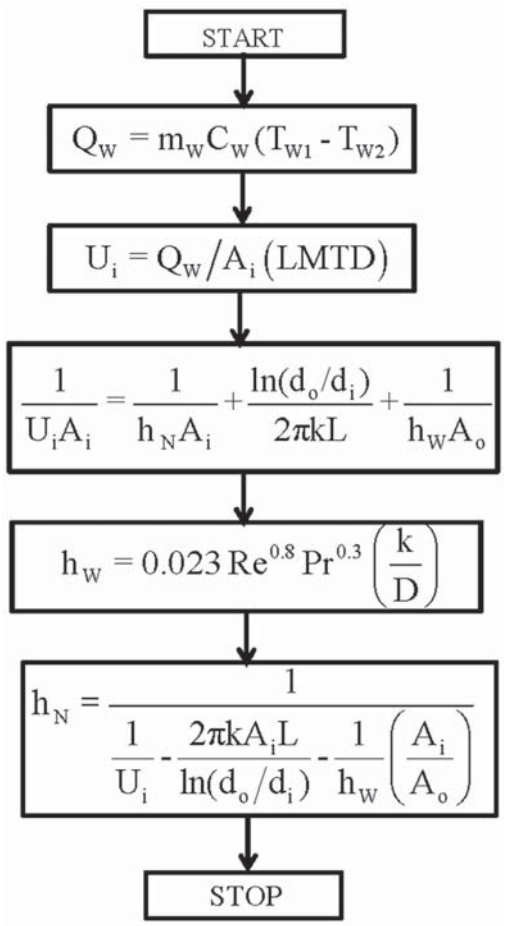

Fig. 2 Data reduction flow chart

properties, mass flow rate, heat flux, concentration, mechanism of heat transfer, etc., are discussed in Secs. 3.1–3.6. The experimental test results of various parameters are shown in Table 2. The test facility is validated with experimental results of water for its repeatability and accuracy. The results are compared with those obtained from the Gnielinski equation [15], and a deviation of ± 4.5% is observed between the experimental and the predicted results.

3.1 Influence of Thermophysical Properties. The thermal conductivity and viscosity ratios as a function of volume concentration and temperature are shown in Fig. 3. The use of nanoparticles dispersed in water gives higher thermal conductivity and viscosity than the base fluid. The thermal conductivity ratio for $\varphi = 0.3$ vol. % increases from 1.09 to 1.43 as the temperature increases from 50 °C to 90 °C; and similarly, for $\varphi = 0.9\%$, the ratio increases from 1.29 to 2.29. This enhancement is expected to reflect in heat transfer coefficient also. The viscosity ratio for $\varphi = 0.3\%$ increases from 1.06 to 1.2, and for $\varphi = 0.9\%$, the ratio increases from 1.23 to 1.43 for the above temperature range. Further, the observed results from the present study have shown that the measured thermal conductivity ratio is larger than that of Masuda et al. [16] and Zhang et al. [17]. Yu et al. [18] reported that the metal oxide particle for $\varphi = 4$–5% produces an enhancement level up to 30%; and the metal particles with less than $\varphi < 1.5\%$ give an enhancement up to 40%. However, the results from the present study show an enhancement of 60% even with $\varphi < 0.9\%$. This shows that the enhancement of thermal conductivity using metal particles is higher than that of the metal oxide particles even at low concentrations. It can be seen the thermal conductivity ratio is significantly higher than the other properties such as density, viscosity, and heat capacity. For 0.3 vol. %, the thermal conductivity ratio is 1.27; and the ratios of density, viscosity, and heat capacity are found to be 1.05, 1.14, and 0.9, respectively. Hence, it clear that the influence of thermal conductivity plays a major role for the heat transfer enhancement.

3.2 Influence of Heat Transfer Mechanism. Brownian motion is a random walk motion of nanoparticles within the base fluid, which results from the collisions between the nanoparticles and the molecules of the base fluid. The nanoparticles themselves can be identified effectively as large molecules when compared with fluid molecules. Also, the nanoparticles are moving with an average kinetic energy equal to that of the fluid molecules with a considerable lower velocity. The Brownian diffusion is found to be the potential mechanism for enhancement of thermal conductivity in the absence of turbulent eddies. Thus, the Brownian motion intensifies with an increase in temperature as per the kinetic theory of particles. The effectiveness of the Brownian motion decreases with an increase in the bulk viscosity and velocity. Heat transfer enhancement through Brownian motion is effective when the bulk flow velocities are very low. At higher flow velocities, the particles travel along with the velocities. It is seen that, with respect to tested flow velocities, the effect of Brownian motion is insignificant. For instant, the required Brownian velocity for silver–water fluid ranges between 0.002 and 0.005 m/s for particle concentration between 0.3% and 0.9%, which is much lower than the lowest tested velocity of 0.12 m/s, which corresponds to a Reynolds number of 800. Even though some literature [19] has exposed the presence of Brownian motion while flow is laminar, the present work reveals that its presence is insignificant under the tested condition. Similarly, the thermophoresis or the Sorét effect, which is due to the diffusion of particles under the effect of a temperature gradient, also seems to be insignificant. The Thermophoresis velocity ranges between 0.0025 and 0.005 m/s, which is very low than the tested flow velocities. Therefore, both effects of thermophoretic and Brownian motion are insignificant under these tested conditions.

3.3 Temperature Distributions. The temperature distribution of the silver–water nanofluid, which flows in the inner tube and the cooling water, which flows in the annulus along the length of the test section for a test condition is shown in Fig. 4. The test mass flow rates 3, 8, and 18 g s^{-1} correspond to laminar, transition, and turbulent flow condition of the nanofluid, respectively. It is observed that, as the mass flow is increased, the logarithmic mean temperature difference (LMTD) decreases. For instance, for a volume concentration of 0.9%, the LMTD is 7.69, 5.63, and 3.73 for laminar, transition, and turbulent regime, respectively. It can also be observed that, for a same flow operating condition, the LMTD decreases as the particle concentration increases. For instance, for a volume concentration of 0.3%, 0.6%, and 0.9%, the LMTD is 4.62, 4.13, and 3.73 for the laminar, transition, and turbulent regime, respectively. Further, it can be noticed that the steepness of the nanofluid curve decreases as the mass flow rate of nanofluid is increased. This steepness in the curve will be reflected in the local and average heat transfer coefficients. The steepness of the curve is higher for entrance region of the laminar flow and lesser for turbulent flow.

3.4 Average Heat Transfer Coefficient. The variation of average heat transfer coefficient ratio on Reynolds number for different concentration is shown in Fig. 5. The heat transfer coefficient ratios for the tested condition are between 1.2 and 1.87 and the ratios increase as Reynolds number increases. The average heat transfer coefficient increases with Reynolds number and particle concentration. For Reynolds number less than 3000, the increase in average heat transfer coefficient with respect to concentration is close to 10% to 15% increase for every increase in

Table 2 Experimental results

			Convective heat transfer coefficient (W/(m^2 K))				Nusselt number				Pressure drop (kPa)			
Re	Mass flow rate (kg/s)	Heat flux (kW/m^2)	Water	0.30%	0.60%	0.90%	Water	0.30%	0.60%	0.90%	Water	0.30%	0.60%	0.90%
$T_{nf}=48\,^{\circ}$C and $T_W=25\,^{\circ}$C														
1107	0.002	3.09	977.57	1198.89	1687.07	1991.90	7.04	8.89	12.19	14.99	0.12	0.31	0.92	1.20
1862	0.003	5.56	1537.92	1834.17	2337.77	2641.00	11.02	13.60	17.28	20.46	0.25	0.45	0.73	1.85
2579	0.004	6.87	1857.12	2299.37	2898.50	3298.55	14.19	17.05	21.66	26.00	0.38	0.68	1.45	2.45
3136	0.005	8.74	2273.91	2773.35	3480.25	3935.93	17.38	20.10	24.21	29.99	0.58	0.92	1.72	3.41
4785	0.008	9.63	3072.34	3723.91	4550.29	4977.12	24.02	28.61	35.57	38.91	1.74	2.11	2.96	4.78
6041	0.011	10.62	3902.91	4414.29	5785.90	6254.69	30.51	34.45	45.24	48.90	3.53	3.92	5.02	5.97
7700	0.014	10.47	4363.73	5134.75	6335.49	6872.25	34.12	41.50	49.53	53.73	5.14	5.80	6.68	7.48
8479	0.017	11.43	5011.34	5739.00	6737.25	7340.27	39.18	46.39	54.24	57.39	7.488	7.92	8.67	9.82
10,115	0.02	11.98	5694.54	6651.48	7631.00	8242.27	44.52	53.06	59.74	64.44	10.69	11.65	12.38	14.07
11,246	0.023	11.51	6176.88	7146.27	8003.65	8771.65	48.29	57.06	63.13	68.74	13.68	15.13	15.14	15.99
$T_{nf}=57\,^{\circ}$C and $T_W=30\,^{\circ}$C														
1107	0.002	3.72	1030.06	1421.87	1975.34	2343.78	8.05	10.99	15.44	18.32	0.09	0.242	0.828	0.94
1862	0.003	6.41	1624.58	1959.01	2496.62	2936.77	12.70	15.38	19.52	22.96	0.16	0.368	0.6555	0.98
2579	0.004	8.63	2028.31	2445.64	3188.32	3647.05	15.86	19.00	24.93	28.51	0.29	0.483	0.7935	1.34
3136	0.005	9.08	2343.51	2720.89	3447.26	3983.24	18.32	20.99	26.95	31.14	0.54	0.777	1.81	2.89
4785	0.008	9.81	3111.99	4119.73	4557.32	5282.83	24.33	31.08	35.63	41.30	1.63	1.932	2.8055	4.74
6041	0.011	9.95	3807.98	4691.56	5509.45	6348.48	29.77	37.26	43.07	49.63	2.89	3.444	4.0595	5.52
7700	0.014	10.63	4462.5	5472.4	6454.32	7256.79	34.89	43.46	50.46	56.73	4.29	5.24	5.4625	7.09
8479	0.017	11.31	4996.61	5984.68	7004.56	7651.32	39.06	47.52	55.33	59.82	6.015	7.14	7.9275	9.65
10,115	0.02	11.74	5577.07	6862.08	7803.36	8463.93	43.60	53.49	61.57	66.17	9.06	10.89	11.431	11.71
11,246	0.023	12.28	6201.98	7461.45	8475.81	9365.81	48.49	58.25	67.19	73.99	13.06	14.16	15.169	15.07
$T_{nf}=65\,^{\circ}$C and $T_W=35\,^{\circ}$C														
1107	0.002	3.82	1105.52	1653.86	2223.24	2715.9	8.64	13	17.23	22.03	0.07	0.21	0.693	0.78
1862	0.003	6.63	1730.89	2257.88	2854.34	3224.43	13.53	17.25	22.35	26.16	0.1	0.294	0.839	0.95
2579	0.004	8.92	2153.36	2879.01	3455.34	3824.94	16.84	21.76	27.22	31.03	0.22	0.357	0.927	2.45
3136	0.005	9.38	2482.25	3198.43	3845.34	4377.78	19.41	24.53	31.20	35.52	0.48	0.567	1.858	3.1
4785	0.008	9.89	3281.26	4289.24	4761.8	5387.36	25.65	32.94	38.63	43.71	1.24	1.523	2.254	4.02
6041	0.011	10.19	4002.12	5275.63	5731.69	6478.47	31.29	40.51	46.50	52.56	2.19	2.457	3.563	5.014
7700	0.014	10.72	4678.09	6175.3	7178.83	7676.71	36.57	47.42	58.24	62.28	4.34	4.125	4.998	6.24
8479	0.017	11.39	5228.52	6574.1	7541.03	8208.71	40.88	52.35	61.99	66.60	4.917	7.01	7.707	8.12
10,115	0.02	12.00	5825.64	7371.69	8633.2	9369.3	45.55	57.7	70.67	76.02	8.79	10.52	10.076	11.36
11,246	0.023	12.42	6467.37	7896.63	8910.69	9861.23	50.56	64.3	73.08	80.88	12.25	13.62	14.355	14.97

concentration of 0.3%. However, for Reynolds numbers between 3000 and 7500, the average heat transfer coefficient increases by 20–30% for the same concentrations. Further, at higher Reynolds number, the average heat transfer coefficient from pure fluid is more than 30%, but with respect to change in concentration, the percentage enhancement is less significant. It can be observed that enhancement in heat transfer with respect to concentration is significant in moderate Reynolds number range from 3000 to 7500, which corresponds to the operating condition for transition from laminar to turbulent. As reported in Ref. [20], the enhancement

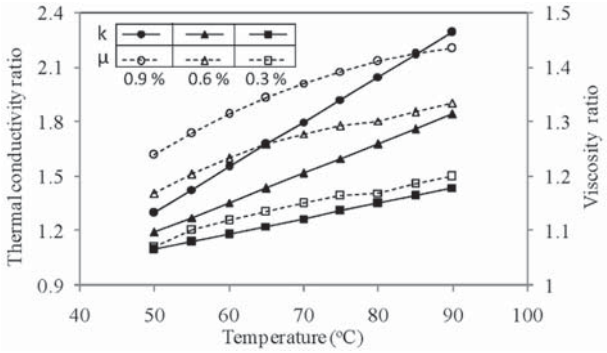

Fig. 3 Thermal conductivity ratio and viscosity ratio of silver-water nanofluids as a function of temperature

heat transfer at Reynolds numbers greater than 7000, which pertains to fully turbulent flow, is less significant.

The comparison between the heat transfer coefficient and the Gnielinski equation is shown in Fig. 6. From the figure, it is clearly seen that the measured heat transfer coefficient of nanofluid is 40% higher than that of the Gnielinski equation. This may be due to the fact that the correlation was established from single phase fluid data and was valid only for the single-phase flow. Similarly, it is observed that the Nu increases with the increase in the Reynolds number and the volume concentration. The enhancement is highly significant in the turbulent region and less significant in the laminar region. Similarly, the enhancement is moderate in the transition region from laminar to turbulent even for small variation in the volume concentration of silver nanoparticles. The attributed reason may be the effect on thermal boundary layer thickness (or thermally fully developed length). Some researchers claimed that one reason for the heat transfer enhancement of nanofluids is reduction of boundary layer thickness and delay in boundary layer development. This effect is more important in turbulent regime. Because, in turbulent regime, the boundary layer develops fast compared to that in laminar flow. For example, for a specific pipe with turbulent flow, the flow along the length of the pipe is almost thermally fully developed. But, with laminar flow, there is a considerable entrance region length. Therefore, using nanofluids, the delay in boundary layer development for turbulent regime is more considerable. Another reason is maybe because of particles migration, which is bigger in turbulent flows. It has been shown in some researches that the nanofluids

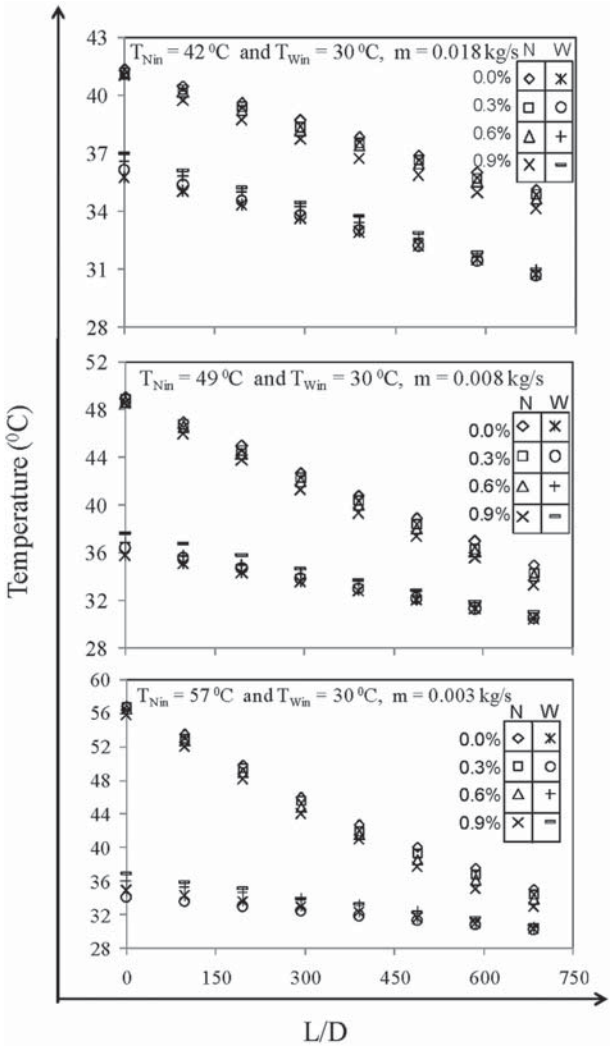

Fig. 4 Variation of temperature of nanofluids against axial positions

are non-Newtonian flows with shear thinning behavior, in which their viscosity decreases when the shear stress increases. Since the wall shear stresses in turbulent regime are so much bigger compared to laminar flow, the viscosity of nanofluid near the wall in

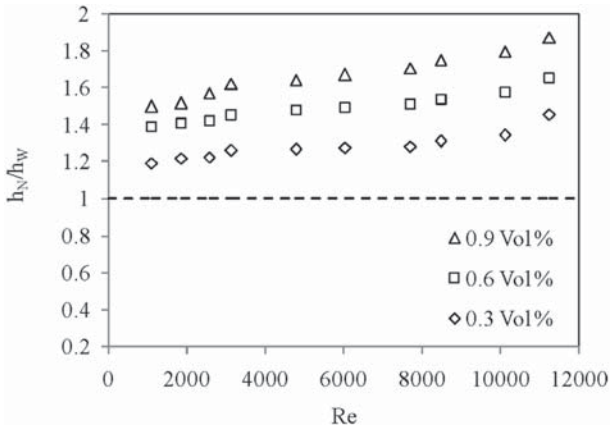

Fig. 5 Variation of heat transfer coefficient ratio (h_{nf}/h_w) against Reynolds number

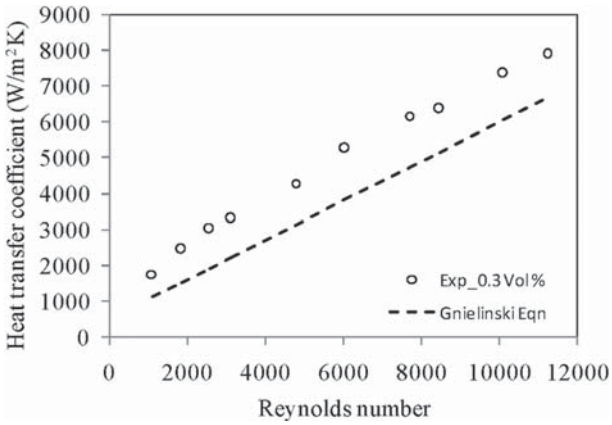

Fig. 6 Comparison of experimental and theoretical heat transfer coefficient

turbulent flow is lower, and as a result, the boundary layer decreases.

Figure 7 shows the variation of the Nusselt number as function of volume fraction and Reynolds numbers of 1800, 4600, and 9500, which corresponds to the laminar, transition, and turbulent flow regimes. It is observed that the Nusselt number increases considerably with both these parameters. Thus, for a given Reynolds number, say Re is 1800, the Nu increases in from 12 to 51 for the lowest tested particle volume fraction of 0.3%. Similarly, the Nusselt number increases from 15 to 55 and 17 to 60 for the Reynolds number varying from of 4600 to 9500, respectively. It is also observed that the increase of Nu with respect to the volume fraction appears less pronounced for low and moderate Reynolds numbers, which is due to the fact that the definition of Nu includes nanofluid thermal conductivity that also increases with particle volume concentration. Further, the Nusselt number increases with the increase in the combination of both high Reynolds number and high particle concentration.

Figure 8 shows the percentage enhancement of heat transfer coefficient with respect to the dimensionless length. The percentage enhancement increases with the increase in the concentration and decreases with the increase in the length. An enhancement of 81.2% and 48.4% is observed at the entrance and the exit regions, respectively, for 0.9 vol. % concentration.

3.5 Local Heat Transfer Coefficient. The variation of local heat transfer coefficient on dimensionless length for different concentration for different flow condition is shown in Fig. 9. The mass flow rates are 3, 8, and 18 g s^{-1} selected in laminar,

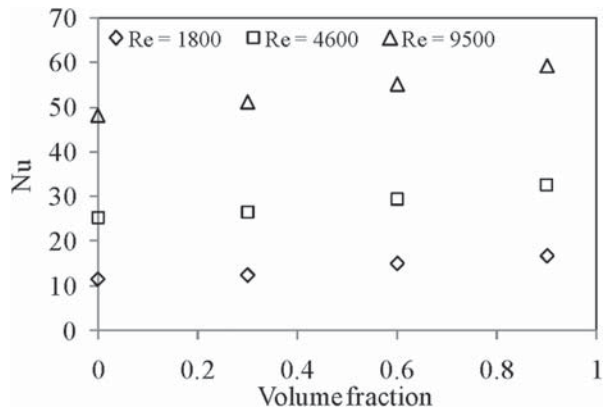

Fig. 7 Effect of volume fraction and Reynolds number on Nusselt number

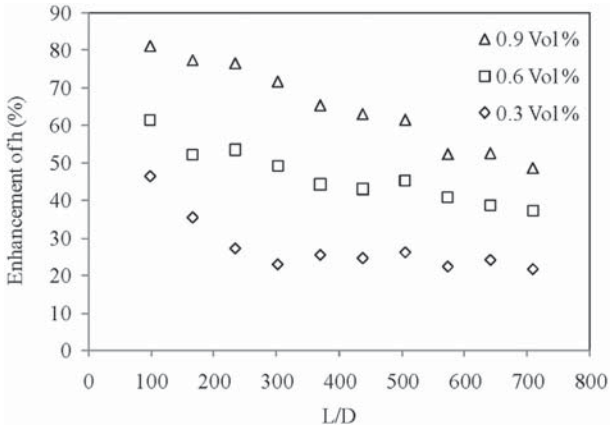

Fig. 8 Enhancement of heat transfer coefficient against axial positions

transition, and turbulent condition, respectively. It can be seen that the local heat transfer coefficient is a strong function of dimensionless length. For the same mass flow rate, the local heat transfer coefficient increases with particle concentration. The decreasing trend of the coefficient is due to the configuration of the test section, which is a counter current heat exchanger. The temperature difference is maximum at a dimensionless length close to 0 and minimum at 1 and so is the heat transfer coefficient. The initial heat transfer coefficient in laminar flow regime cumulatively increases by 15% to 25% from the value of the base fluid. However, in a laminar flow, the percentage increase rapidly decreases as the dimensionless length increases, and the values are almost same at the maximum dimensionless length of 1. Under transition condition, the cumulative percentage increase is spread throughout the dimensionless length as volume concentration is increased, and under the turbulent condition, the increase is drastic. The intense turbulence and thorough mixing of particles at all volume concentration are reasoned for it. Even though, the enhancement of heat transfer is insignificant with respect to Brownian and thermophoresis effects, the particles' capacity of carrying heat in the turbulence flow plays a vital role.

3.6 Pressure Drop. Figure 10 shows the pressure drop as a function of the Reynolds number, which shows that there exists a penalty in pressure drop in the nanofluid used in this study. For instance, a minimum pressure drop of 24% is observed for 0.3 vol. % and, for the nanofluid, average inlet temperature of 57 °C and chilled water temperature of 30 °C. Similarly, a maximum pressure drop of 55% is observed for 0.9 vol. % for the same temperature conditions. The reason may be the use of metal nanoparticles posses a bit higher pressure drop than the use of the metal oxide once, since the viscosity of the pure metal nanoparticles is

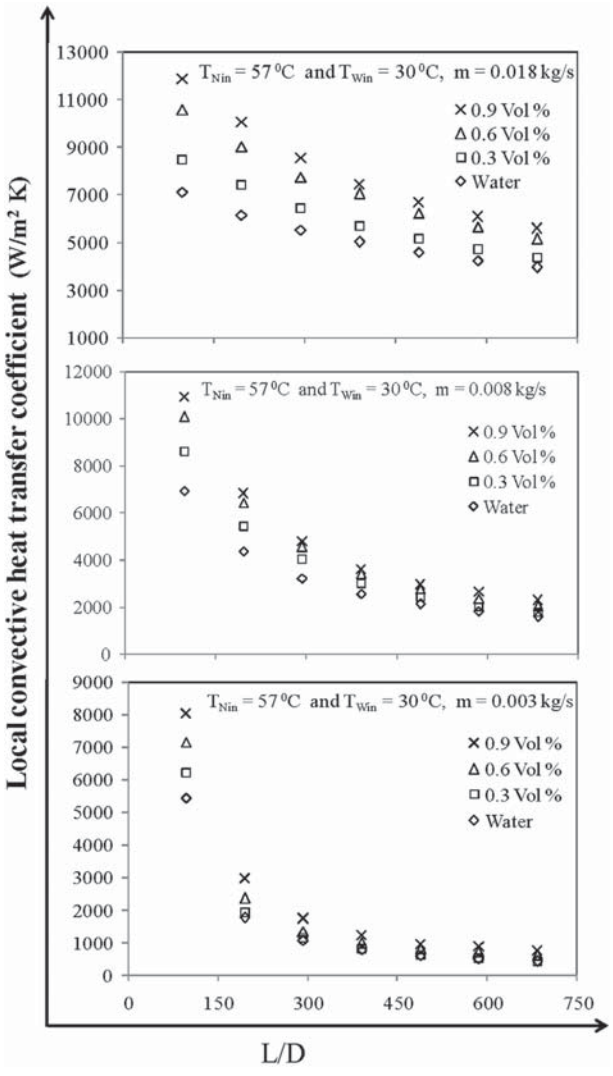

Fig. 9 Variation of local heat transfer coefficients of nanofluids against axial positions

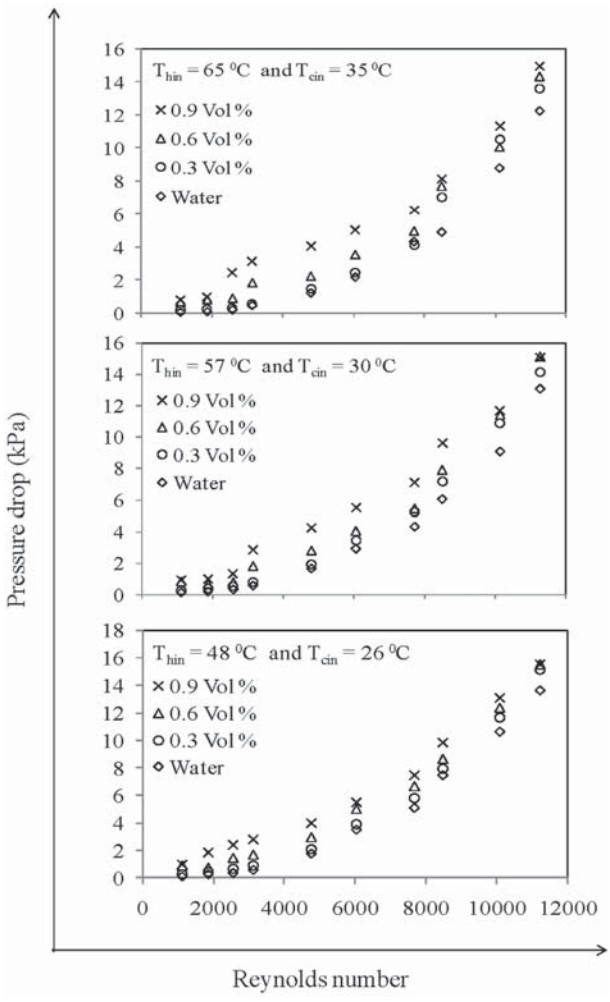

Fig. 10 Variation in pressure drop against Reynolds number

high when compared with that of the oxides. However, it is observed that, for the given conditions, the pressure drop decreases with increase in the temperature. An increase in the nanofluid temperature leads to a decrease in the viscosity of the nanofluid, which results in a reduction in the pressure drop. The important observation is that the nanofluid is actually a two-phase flow, and there need to be more experimental data and correlation to predict the pressure drop of nanofluids, which behaves more like a liquid–solid mixture.

4 Conclusion

The convective heat transfer characteristics of silver–water nanofluid under laminar and turbulent flow conditions are experimentally measured. The use of silver nanoparticles in the base fluid enhances the heat transfer coefficients by 23.5% and 69% for 0.3 and 0.9 vol. % concentrations, respectively. For Reynolds number corresponding to laminar regime, the increase in average heat transfer coefficient with respect to concentration is close to 10% to 15% increase for every increase in concentration of 0.3%. Reynolds numbers corresponding to transition and turbulent regime, the heat transfer coefficient increases by 20% to 30% for the same concentrations. It can be observed that enhancement in heat transfer with respect to concentration is significant in moderate Reynolds number range from 3000 to 7500, which corresponds to the operating condition for transition from laminar to turbulent. The effect of thermophysical properties plays a major role for the heat transfer enhancement. The pressure drop of using the pure metal nanofluid has a little penalty when compared with that of the pure water.

Acknowledgment

The fourth author would like to thank the Thailand Research Fund and the National Research University Project for the financial support.

Nomenclature

A = cross sectional area, m^2
Cp = specific heat, J/(kg K)
D = tube diameter, m
h = heat transfer coefficient, $W/(m^2 K)$
k = thermal conductivity, W/(m K)
m = mass flow rate, kg/s
Nu = Nusselt number
Pr = Prandtl number
q'' = heat flux, W/m^2
Re = Reynolds number
T = temperature, °C

Greek Symbols

β = thermal dispersion coefficient, $N/(m^2 K)$
φ = volume fraction
ρ = density, kg/m^3
μ = dynamic viscosity, kg/(m s)
γ = particle size (nm)

Subscripts

nf = nanofluid
w = tube wall
x = axial distance
bf = base fluid
i = inner wall
o = outer wall

References

[1] Choi, S. U. S., 1995, "Enhancing Thermal Conductivity of Fluids With Nanoparticles in Developments and Applications of Non-Newtonian Flows," ASME FED 231/MD 66, pp. 99–103.
[2] Pak, B. C., and Cho, I. Y., 1998, "Hydrodynamic and Heat Transfer Study of Dispersed Fluids With Sub-Micron Metallic Oxide Particles," Exp. Heat Transfer, **11**, pp. 151–170.
[3] Eastman, J. A, Choi, S. U. S., Li, S., Soyez, G., Thompson, L. J., and DiMelfi, R. J., 1999, "Novel Thermal Properties of Nanostructure Materials," Mater. Sci. Forum, **312**, pp. 629–634.
[4] Wen, D., and Ding, Y., 2005, "Experimental Investigation into the Pool Boiling Heat Transfer of Aqueous Based Alumina Nanofluids," J. Nanopart. Res., **7**, pp. 265–274.
[5] Lai, W. Y., Duculescu, B., Phelan, P. E., and Prasher, R. S., 2006, "Convective Heat Transfer With Nanofluids in a Single 1.02-mm Tube," Proceedings of the ASME International Mechanical Engineering Congress and Exposition, Chicago, pp. 1–8.
[6] Jung, J. Y., Oh, H. S., and Kwak, H. Y., 2006, "Forced Convective Heat Transfer of Nanofluids in Microchannels," Proceedings of the ASME International Mechanical Engineering Congress and Exposition, Chicago, pp. 11–17.
[7] Duangthongsuk, W., and Wongwises, S., 2008, "Effect of Thermo-Physical Properties Models on the Prediction of the Convective Heat Transfer Coefficient for Low Concentration Nanofluid," Int. Commun. Heat Mass Transfer, **35**(10), pp. 1320–1326.
[8] Xuan, Y., and Li, Q., 2004, "Flow and Heat Transfer Performances of Nanofluids Inside Small Hydraulic Diameter Flat Tube," J. Eng. Thermophys., **25**(2), pp. 305–307.
[9] Ding, Y., Alias, G., Wen, D., and Richard, A. W., 2006, "Heat Transfer of Aqueous Suspensions of Carbon Nanotubes (CNT nanofluids)," Int. J. Heat Mass Transfer, **49**, pp. 240–250.
[10] Kang, S. W., Wei, W. C., Tsai, S. H., and Yang, S. Y., 2006, "Experimental Investigation of Silver Nano-Fluid on Heat Pipe Thermal Performance," Appl. Therm. Eng., **26**, pp. 2377–2382.
[11] Maiga, S. E., Palm, S. J., Nguyen, C. T., Roy, G., and Galanis, G., "Heat Transfer Enhancements by Using Nanofluids in Forced Convection Flows," Int. J. Heat Fluid Flow, **26**, pp. 530–546.
[12] Lazarus, G., Raja, B., Lal, D. M., and Wongwises, S., 2010, "Experimental Investigation on the Thermal Conductivity and Viscosity of Silver-Deionized Water Nanofluid," Exp. Heat Transfer, **23**(4), pp. 317–332.
[13] Moffat, R. J., 2000, "Describing the Uncertainties in Experimental Results," Exp. Therm. Fluid Sci., **1**(1), pp. 3–17.
[14] Xuan, Y., and Roetzel, W., 2000, "Conceptions for Heat Transfer Correlation of Nanofluids," Int. J. Heat Mass Transfer, **43**, pp. 3701–3707.
[15] Gnielinski, V., 1976, "New Equations for Heat and Mass Transfer in Turbulent Pipe and Channel Flow," Int. Chem. Eng., **16**, pp. 359–368.
[16] Masuda, H., Ebata, A., Teramae, K., and Hishinuma, N., 1993, "Alteration of Thermal Conductivity and Viscosity of Liquid by Dispersion of Ultra-Fine Particles," Netsu Bussei, **4**, pp. 227–233.
[17] Zhang, X., Gu, H., and Fujii, M., 2007, "Effective Thermal Conductivity and Thermal Diffusivity of Nanofluids Containing Spherical and Cylindrical Nanoparticles," Exp. Therm. Fluid Sci., **31**, pp. 593–599.
[18] Yu, W., France, D. M., Choi, S. U. S., and Routbort, J. L., 2007, "Review and Assessment of Nanofluid Technology for Transportation and Other Applications," Energy Systems Division, Argonne National Laboratory, ANL/ESD/07-9, pp. 1–78.
[19] Buongiorno, J., 2006, "Convective Heat Transfer Enhancement in Nanofluids," Heat and Mass Transfer Conference, HMT-2006-C335, pp. 1–6.
[20] Das, S. K., Choi, S. U. S., Yu, W., and Pradeep, T., 2008, *Nanofluids—Science and Technology*, Wiley, New York.

Provided for non-commercial research and education use.
Not for reproduction, distribution or commercial use.

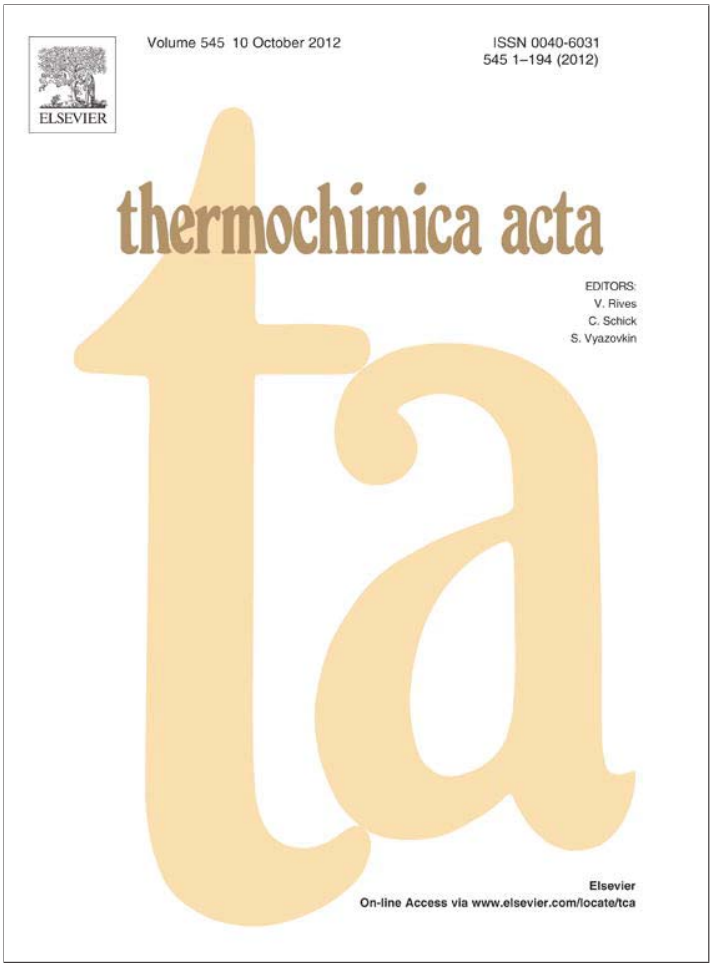

This article appeared in a journal published by Elsevier. The attached copy is furnished to the author for internal non-commercial research and education use, including for instruction at the authors institution and sharing with colleagues.

Other uses, including reproduction and distribution, or selling or licensing copies, or posting to personal, institutional or third party websites are prohibited.

In most cases authors are permitted to post their version of the article (e.g. in Word or Tex form) to their personal website or institutional repository. Authors requiring further information regarding Elsevier's archiving and manuscript policies are encouraged to visit:

http://www.elsevier.com/copyright

Author's personal copy

Thermochimica Acta 545 (2012) 48–56

Contents lists available at SciVerse ScienceDirect

Thermochimica Acta

journal homepage: www.elsevier.com/locate/tca

Measurement of the thermal conductivity of titania and alumina nanofluids

Thakleaw Yiamsawasd[a], Ahmet Selim Dalkilic[b], Somchai Wongwises[a,c,*]

[a] Fluid Mechanics, Thermal Engineering and Multiphase Flow Research Lab. (FUTURE), Department of Mechanical Engineering, King Mongkut's University of Technology Thonburi, Bangmod, Bangkok 10140, Thailand
[b] Heat and Thermodynamics Division, Department of Mechanical Engineering, Yildiz Technical University (YTU), Yildiz, Besiktas, Istanbul 34349, Turkey
[c] The Academy of Science, The Royal Institute of Thailand, Sanam Suea Pa, Dusit, Bangkok 10300, Thailand

ARTICLE INFO

Article history:
Received 21 January 2012
Received in revised form 18 May 2012
Accepted 20 June 2012
Available online 10 July 2012

Keywords:
Thermal conductivity
Nanoparticle
Nanofluids
Transient hot-wire method

ABSTRACT

This article reports the thermal conductivity of nanofluids experimentally. TiO_2 and Al_2O_3 nanoparticles were suspended in base fluids (water and 20/80 by mass of an ethylene glycol–water mixture) with concentration level of 0–8 vol.%, at a temperature of 15–65 °C. The measurement was done by the transient hot-wire method. The results showed that thermal conductivity of nanofluids increased more with respect to the base fluid and increased with increasing concentration and temperature. When compared with predictions from existing models, thermal conductivity ratio could not be predicted by the models in terms of both concentration and temperature. Finally, a useful correlation for predicting thermal conductivity of Al_2O_3 and TiO_2 nanofluids was presented.

© 2012 Elsevier B.V. All rights reserved.

1. Introduction

At present, modern nanotechnology could synthesize or produce various types of nanoparticles quite easily. Nanoparticles have become important components in several technologies or innovations that are very useful for mankind. Similarly, nanoparticles are also used in heat transfer innovation. A new kind of heat transfer fluid or "nanofluid" has been developed (named by Choi [1]) by suspending nanoparticles of solid substance in general heat transfer fluids.

High conduction heat transfer of solid substance is used to enhance the heat transfer of general working fluids. Nanofluids are also expected to be used appropriately in various forms of mini- and micro-scale heat exchanger, such as in electronic devices, in processors of mobile computers, or in high-capacity military communication devices. They are also used in large-scale heat exchangers or systems that require maximum performance like the heat exchangers of nuclear reactors or high-capacity heat transfer systems.

For real application, the thermal and basic transfer properties of nanofluids should be carefully researched. Therefore, many researchers have studied the thermal properties and transfer capacities of nanofluids, such as thermal conductivity, viscosity, convective heat transfer, and boiling heat transfer. However, there is a basic concept that nanofluids with high thermal conductivity help increase heat transfer capacity. Thus, research on the development and measurement of the thermal conductivity of nanofluids gained special attention over other properties. These studies dealt with the impact or effect of various factors on the increase of thermal conductivity of nanofluids, such as temperature, concentration, shape or size of nanoparticles, and pH. Examples of research on the measurement of thermal conductivity follow.

Masuda et al. [2] studied the thermophysical properties of Al_2O_3–water, SiO_2–water and TiO_2–water nanofluids. The transient hot-wire method was used to measure the thermal conductivity of nanofluids. They found that the thermal conductivity of nanofluids increased dramatically compared with the base fluid. The thermal conductivity of Al_2O_3 nanofluid increased by 32% at the concentration of 4.3 vol.%. They concluded that temperature did not have any effect on the increase of relative thermal conductivity (thermal conductivity ratio).

Lee et al. [3] conducted an experiment to measure the thermal conductivity of Al_2O_3 and CuO suspended in water and ethylene glycol. Particle sizes of Al_2O_3 and CuO were 23.6 nm and 38.4 nm, respectively. The transient hot-wire method was used to measure the thermal conductivity of nanofluids at a concentration range of 1–4 vol.%. Their results indicated that nanofluids had higher thermal conductivity than the base fluid, and it increased with the increasing level of concentration. When compared the experimental results with prediction from Hamilton and Crosser model, it was found that the model could predict thermal conductivity of Al_2O_3 nanofluids, but it could not predict for CuO nanofluids.

* Corresponding author at: Fluid Mechanics, Thermal Engineering and Multiphase Flow Research Lab. (FUTURE), Department of Mechanical Engineering, King Mongkut's University of Technology Thonburi, Bangmod, Bangkok 10140, Thailand. Tel.: +66 2 470 9115; fax: +66 2 470 9111.
E-mail address: somchai.won@kmutt.ac.th (S. Wongwises).

0040-6031/$ – see front matter © 2012 Elsevier B.V. All rights reserved.
http://dx.doi.org/10.1016/j.tca.2012.06.026

Author's personal copy

Wang et al. [4] studied thermal conductivity of Al_2O_3 and CuO nanofluids with a particle size of 20 nm. Each was suspended in water, vacuum pump oil, engine oil, and ethylene glycol. A steady state method was used to measure thermal conductivity. Their results showed that the thermal conductivity of both nanofluids were higher than that of the base fluids and varied with concentration level. The engine oil and ethylene glycol base fluids yielded higher enhancement than other types of base fluids. When compared with the theoretical model, a thermal conductivity ratio of the nanofluids was found to be higher.

Eastman et al. [5] conducted an experiment to measure the thermal conductivity of Cu–ethylene glycol nanofluid with an average copper particle size of 10 nm and concentration level of 0.6 vol.%. A transient hot-wire method was used for measurement. They found that nanofluids had higher thermal conductivity when the concentration level increased. Moreover, acid-added nanofluids had increased thermal conductivity. At a concentration level of 0.3 vol.%, thermal conductivity of acid-added Cu nanofluid increased dramatically by 40%. Their experimental results were higher than those obtained from the classical model. The researchers proposed that the shape of particle also had an effect on the increase of thermal conductivity.

Xie et al. [6] studied the effect of particle size and pH on thermal conductivity of Al_2O_3 nanofluid with particle sizes of 12–300 nm. Deionized water, ethylene glycol, and pump oil were used as base fluid. Transient hot-wire apparatus was used to measure thermal conductivity in this experiment. Their results showed the thermal conductivity of Al_2O_3 nanofluid was higher than that of the base fluid. It also increased with the increase of concentration level, but decreased when pH was lower. Regarding the effect of nanoparticle size, thermal conductivity of the nanofluid was found to vary with particle size. The optimal particle size of 60 nm yielded the highest thermal conductivity enhancements. They also found that the enhanced thermal conductivity ratio decreased when the thermal conductivity of the base fluid increased. When compared with predictions from the classic model, the thermal conductivity used in the experiment was higher.

Das et al. [7] studied the effect of temperature on an increase of thermal conductivity of Al_2O_3 and CuO suspended in water, with a concentration range of 1–4 vol.% at temperatures of 21, 36 and 51 °C. They used the temperature oscillation technique. Their resulted indicated the thermal conductivity of nanofluids increased when the temperature increased. In particular, the thermal conductivity of Al_2O_3–water nanofluid at 4 vol.% increased dramatically when the temperature slightly increased. The experimental results tended to be higher than predictions from the classic model.

Chon and Kihm [8] studied the increase of thermal conductivity of a nanofluid from Brownian motion. Al_2O_3–water nanofluid at the concentration of 1 vol.% was used in this experiment. The particle sizes used were 11, 47, and 150 nm in a temperature range of 20–70 °C. They reported the thermal conductivity of the nanofluid increased more than the base fluid and rose with the increase of temperature. They also found that smaller particle sizes gave higher thermal conductivity. They asserted the increase in thermal conductivity of the nanofluid resulted from Brownian motion or micro-convection mechanism. They argued the increase of temperature caused a greater Brownian motion mechanism.

Hwang et al. [9] conducted an experiment to measure the thermal conductivity of nanofluids. They used multiwalled carbon nanotubes (MWCNT) and CuO and SiO_2 with the base fluid of water and ethylene glycol. The average particle size of the MWCNTs was 10–50 μm long with a diameter of 10–30 nm. The average diameters of the CuO and SiO_2 particles were 35.4 nm and 7 nm, respectively. They used a transient hot-wire method to measure thermal conductivity. They found the thermal conductivity of nanofluids was higher than the base fluid and varied with concentration level. They also found that nanofluids with ethylene glycol as the base fluid had a higher increase in thermal conductivity than water. The MWCNT–ethylene glycol had the highest increase of 11.3% at a concentration level of 1 vol.%.

He et al. [10] studied the heat transfer and upward flow patterns in vertical tubes of TiO_2–water nanofluid. They measured the thermal conductivity and viscosity of TiO_2–water nanofluids. The particle sizes of TiO_2 were 95, 145 and 210 nm with concentration ranges of 1–5 wt.%. They measured the thermal conductivity with a transient hot-wire method. They found that when the concentration level increased, the thermal conductivity of the nanofluid also increased to levels higher than the predictions from the H–C model. They also found smaller particle sizes had higher thermal conductivity than larger particle sizes.

Li and Peterson [11] conducted an experiment on the measurement of thermal conductivity of Al_2O_3 nanofluids with particle sizes of 36 and 47 nm. The nanofluids were suspended in distilled water at temperatures of 27–37 °C and concentration levels of 0.5–6.0 vol.%. They used a steady-state method for measurement. Their experimental results showed the thermal conductivity of nanofluids increased more than the base fluid and increased with the rise of concentration level and temperature. However, the increase was nonlinear. They also found that particle size was an important parameter for the increase of thermal conductivity. Smaller particles had higher increase than larger particle. In this experiment, the temperature of 32 °C and concentration levels of 2 vol.% and 4 vol.% were optimal points that had the highest increase of thermal conductivity. Unfortunately, existing theoretical models could not be used for prediction.

Wang et al. [12] measured thermal conductivity and thermal diffusion of TiO_2 (26 nm) and SiO_2 (23 nm) nanoparticles suspended in distilled water, ethanol, and ethylene glycol. They used a 3ω wire method to measure thermal conductivity. The experiment was conducted with concentration ranges of 1–4 vol.% at temperatures of 18–65 °C. The results indicated the thermal conductivity of nanofluids was higher than the base fluids and increased with the rise of temperature and concentration level. The researchers reported temperature had an obvious effect on the increase of thermal conductivity ratio. The Koo model that referred to a Brownian motion effect and the Ren model that referred to micro convection could not be used for prediction, especially at high temperature.

Zhang et al. [13] studied the thermal conductivity and thermal diffusion of Au–toluene Al_2O_3–water, TiO_2–water, CuO/water and CNT/water nanofluids. The diameters of Au, Al_2O_3, TiO_2, and CuO particles were 1.65, 20, 40, and 33 nm, respectively, with CNF of 10 nm × 150 nm. They measured the thermal conductivity of the nanofluids with a transient short-hot-wire technique. They used concentration levels of 0%, 10%, 20%, and 40% by mass at temperatures of 5–50 °C. Their results showed that the thermal conductivity ratio of nanofluids increased only slightly. The results were similar to the predictions from the model of Hamilton and Crosser in the case of spherical nanoparticles, and the prediction of Yamada and Ota in the case of carbon nanofibers.

Murshed et al. [14] measured the thermal conductivity and viscosity of nanofluids which consisted of 80 and 150 nm Al_2O_3 and 15 nm TiO_2 particles suspended in deionized water and ethylene glycol and 80 nm Al suspended in ethylene glycol (EG) and engine oil (EO). The concentrations ranged from 1 to 5 vol.% at temperatures of 20–60 °C. They used a transient hot-wire technique to measure thermal conductivity. They found nanofluids had higher increases of thermal conductivity than the base fluid and this varied with concentration level and temperature. The researchers also proposed a new model to predict the thermal conductivity of nanofluids which referred to nanolayers as factors of the increase. The model yielded predictions similar to the results of the experiment.

Author's personal copy

Duangthongsuk and Wongwises [15] studied the effect of temperature on thermal conductivity and viscosity of TiO_2-water nanofluids. They experimented with 21 nm TiO_2 particles at temperatures of 15–35 °C with concentration levels of 0.2–2 vol.%. They measured thermal conductivity with the transient hot-wire method. They found the thermal conductivity of TiO_2–water nanofluids increased when concentration levels and temperatures increased.

Turgut et al. [16] used a 3ω method to measure thermal conductivity of TiO_2-deionized water nanofluid with an average TiO_2 nanoparticle diameter of 21 nm. They used a concentration level of 3% by volume and temperature ranges from 13 to 55 °C. They found that thermal conductivity increased by about 7.4% when the concentration level was 3 vol.%. The thermal conductivity ratio did not change with temperature. The experimental results were lower than predictions from the classic model.

From all research mentioned above, the thermal conductivity of nanofluids was found to be higher than the base fluid and increased with concentration level. However, certain important details of the experimental results are still different in many studies. For example, some research found that existing classic models like the Hamilton and Crosser model (H–C model) [17] and Bruggeman model [18] could be used to predict thermal conductivity of nanofluids whereas many researchers found that existing classic models could not be used. Similarly, some parameters showed contrasting effects. For example, Masuda et al. [2] concluded that temperature did not have any effect on the increase in thermal conductivity ratio of nanofluids. This corresponds with Turgut et al. [16]. On the contrary, Das et al. [7], Wang et al. [12] and many other researchers stated that temperature clearly had an effect on the increase in thermal conductivity ratio of nanofluids.

In addition, researchers referred to various theories for the increase in thermal conductivity of nanofluids that conclusions could not be drawn. Hence, there are many different newly-developed models for prediction of thermal conductivity of nanofluids, according to the theories used. For instance, Yu and Choi [19,20] and Xie et al. [21] presented a newly-developed model based mainly on the energy transfer mechanism at the liquid/solid interfacial nanolayer. At the same time, a theory that discusses Brownian motion as cause of the increase in thermal conductivity of nanofluids was also used to develop models in many studies such as Xuan et al. [22], Koo and Kleinstreuer [23], and Jang and Choi [24]. The differences in opinion are quite obvious. Therefore, the measurement of thermal conductivity should be further studied in order to draw clear conclusions in various aspects. Hence, this research aims to conduct an experiment to measure the thermal conductivity of TiO_2 and Al_2O_3 nanofluids suspended in water and ethylene glycol–water mixtures. This study also investigates the effect of concentration level and temperature on the increase in thermal conductivity of nanofluids. Moreover, results gained from the measurement of the thermal conductivity of nanofluids will be compared to predictions from various models and to results from other research. Finally, this study will propose a correlation for predicting the thermal conductivity of nanofluids.

2. Sample preparation

A main purpose in preparing nanofluids is to make suspended nanoparticles diffuse well in the base fluids without precipitation of particles in a short time.

Preparation of nanofluids is an important step. In general, it consists of three methods: control of pH, addition of surfactants or dispersants, and the use of an ultrasonic vibration machine. In this experiment, TiO_2 and Al_2O_3 nanofluids used were supported by the DEGUSSA Company, Germany. The average diameter of TiO_2 nanoparticles was 21 nm and the average diameter of Al_2O_3 particles was 120 nm. Water, and ethylene glycol–water (20/80 wt.%) were used as base fluids. Both TiO_2 and Al_2O_3 were suspended in base fluids with concentration levels of 13.8 and 10.6 vol.%, respectively. Before the experiment, nanofluids were mixed and diluted by adding base fluids to the desired concentration level. After that, the nanofluids were sonicated by an ultrasonic vibrator for 2 h. The addition of surfactants were already done by the manufacturer. The pH of the Al_2O_3–water, Al_2O_3–EG/water, TiO_2–water and TiO_2–EG/water nanofluids were 4, 3, 7 and 6, respectively. The particle size distribution of TiO_2 was also estimated via a transmission electron microscope (TEM) as shown in Fig. 1.

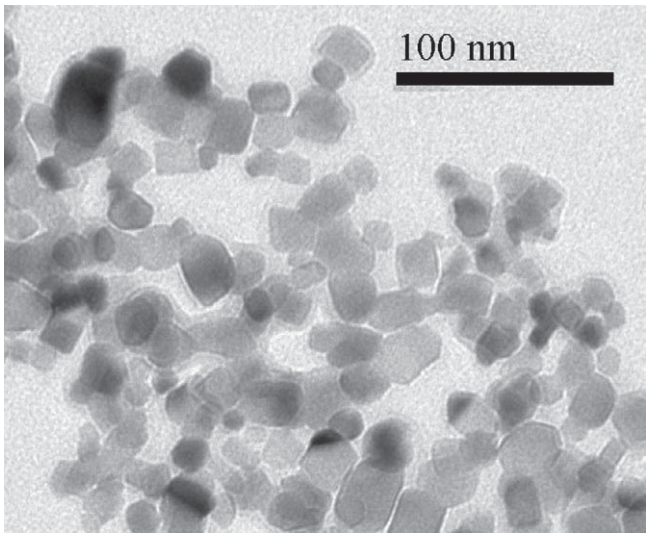

Fig. 1. TEM image of dispersed TiO_2 nanoparticles in water.

3. Experimental apparatus and procedure

The transient hot-wire method is based on measurement of changing temperatures during the heat transfer process of a small-scaled wire which serves both as a heater and temperature sensor of the sample substance. Presumably, small-scale wire has a high thermal diffusion ratio. Heat from the wire will be completely transferred to the surrounding sample substance. When electrical current flows through the wire, it will become a source of heat. The temperature of both the wire and the sample nanofluid will be higher. The increasing rate of temperature depends on the thermal conductivity of the sample substance.

In general, the concept and design for this works are similar to those of Duangthongsuk and Wongwises [15], and Kostic and Simham [25]. The experimental apparatus shown in Fig. 2(a) consists of various main parts. A polypropylene cylinder containing the sample substance is 250 mm long with a diameter of 25 mm. The Teflon-coated platinum wire with a diameter of 76.20 μm and a length of 190 mm was used as a hot wire cell. The thickness of Teflon is 31.75 μm. Based on Healy et al. [26] criteria, the minimum hot wire cell outer boundary diameter was determined as 5.6 mm. The sample substance lump seems to be very large compared with the size of the wire. Based on the 139 mm minimum length of hot-wire recommended by Kierkus et al. [27], the wire seems to be very long and there seems to be no transfer of heat along the wire's length. The both ends of hot wire were well insulated with silicone. The sample substance's temperature is controlled with circulating water in a temperature-control cylinder. The temperature of the sample substance lump was measured with a high-precision thermometer. Changing temperature of the wire was measured using an oscilloscope in form of voltage drops in the bridge resistance

Author's personal copy

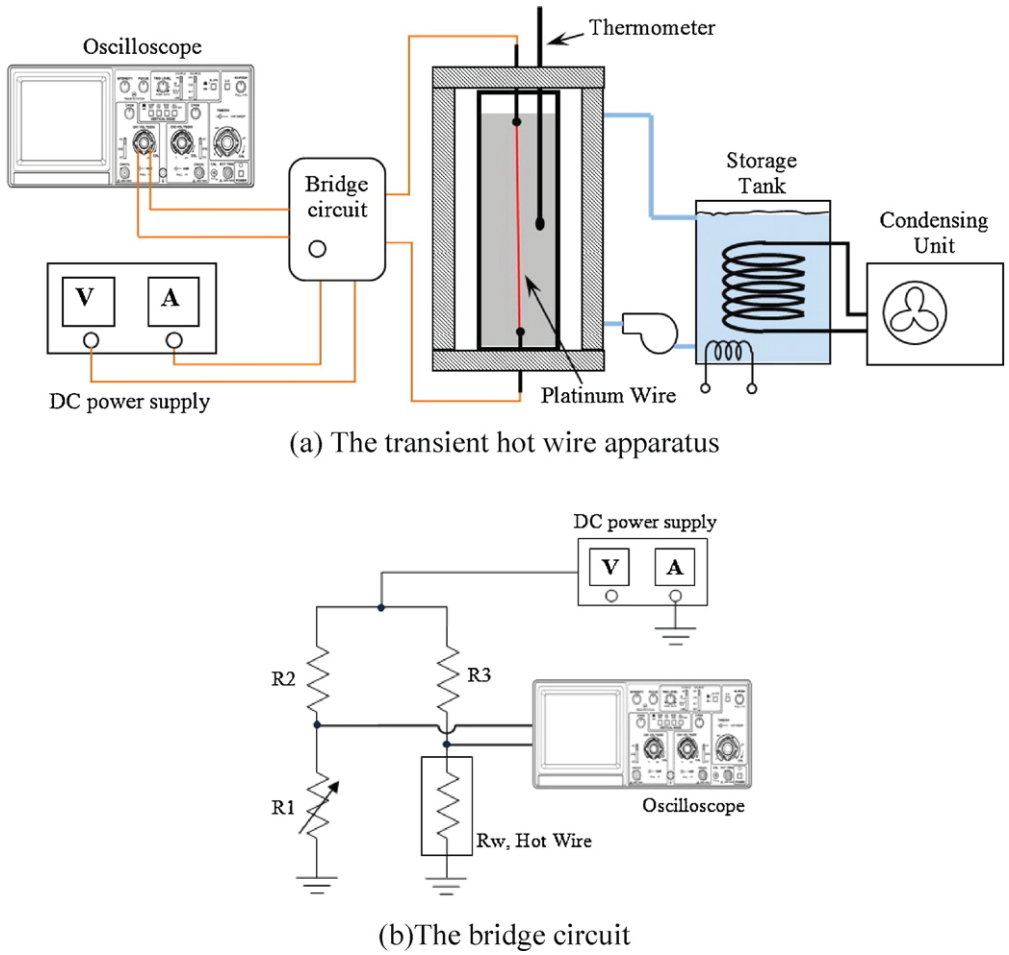

Fig. 2. Schematic diagram of experimental apparatus.

circuit, as shown in Fig. 2(b). A relationship between the temperature and electrical resistance of a platinum wire was presented in Bentley [28]. The thermal conductivity of the sample substance could be calculated from the slope of increase in temperature per logarithmic time interval as follows:

$$k_{nf} = \frac{q}{4\pi(T_2 - T_1)} \ln\left(\frac{t_2}{t_1}\right) \quad (1)$$

where k_{nf} is the thermal conductivity of nanofluids, q is the heat applied to the platinum wire per length unit (W/m), $T_2 - T_1$ (ΔT) is the increased temperature during the test (°C), and t_1 and t_2 are durations of the test (s).

Usually ΔT versus $\ln(t)$ is measured at times from the beginning of heat pulse but only the part which is a straight line is used to calculate the slope which will be used in the calculation of thermal conductivity. The early part of ΔT versus $\ln(t)$ recording is ignored because not only the existence of insulation coating but also the because of the definite C_p of the platinum wire.

4. Results and discussion

Before the measurement of the thermal conductivity of nanofluids, the transient hot-wire method was calibrated by measuring the thermal conductivity of water and the ethylene glycol–water mixture (20/80 wt.%) in temperature ranges of 15–60 °C and comparing the results with the reference standard from ASHRAE [29]. The experimental results tended to correspond with the reference standard. The water sample had the highest deviation of 2.53% with an average deviation of 2.01%. On the other hand, the EG/water (20/80) sample had the highest deviation of 4.04% and an average deviation of 3.46%, as shown in Fig. 3.

The measurement of thermal conductivity of nanofluids with water base fluid shown in Figs. 4 and 5 indicates that thermal conductivity of both Al_2O_3–water and TiO_2–water nanofluids are higher than that of the base fluid and are a function of concentration level and temperature. That is, a higher concentration level of nanoparticles increases the level of thermal conductivity. The

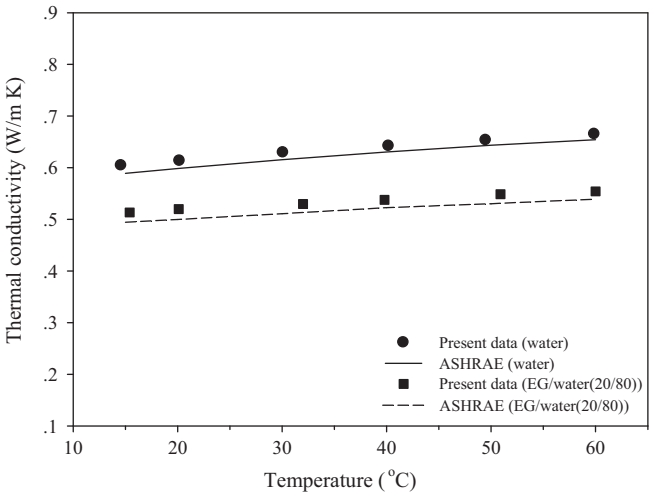

Fig. 3. Comparison of the present data with reference data.

Author's personal copy

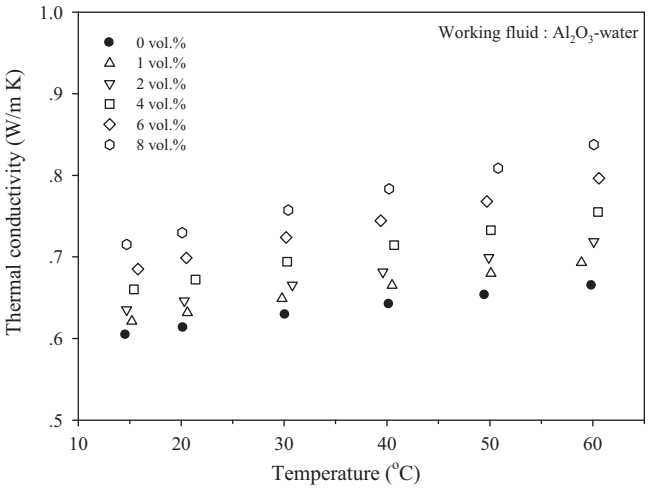

Fig. 4. Thermal conductivity of Al_2O_3–water nanofluid as a function of temperature and concentration.

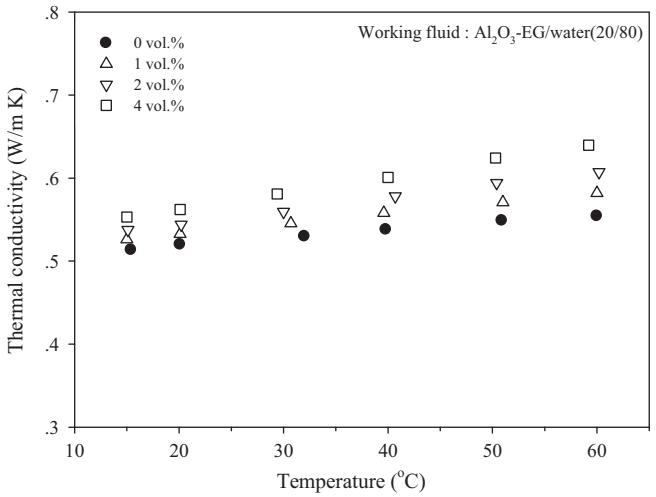

Fig. 6. Thermal conductivity of Al_2O_3–EG/water (20/80) nanofluid as a function of temperature and concentration.

Al_2O_3–water increases by about 5–30% and TiO_2–water increases by about 2–20% in concentration ranges of 1–8 vol.%. Similarly, higher temperature also increases the level of thermal conductivity. Particularly at high concentration level, temperature affects the increase of thermal conductivity more than at low concentration level. However, the effect of increased temperature on the increase of thermal conductivity of TiO_2–water is not great compared to the effect on Al_2O_3–water.

The measurement of the thermal conductivity of nanofluids with an EG/water (20/80) base fluid shown in Figs. 6 and 7 indicates similar results to the water base fluid. The thermal conductivity of Al_2O_3–EG/water (20/80) increases by about 5–20% when the concentration level becomes higher in a range of 1–4 vol.%. The results of TiO_2–EG/water (20/80) show that thermal conductivity increases by about 15% at a concentration level of 4 vol.%. Higher temperature also leads to higher thermal conductivity.

Fig. 8 shows a comparison between the experimental thermal conductivity ratio (relative thermal conductivity) of Al_2O_3–water and results from other studies at various temperatures. The experimental results are different from other studies. Obviously, the experimental thermal conductivity ratio causes lower increases than those from other researches, as evident from the slope of the graph. Particularly, when compared with results from Das et al. [7] and Li and Peterson [11], their results clearly show that the increase of temperature has a dramatic effect on the increase of thermal conductivity ratio of Al_2O_3 nanofluid. Even when compared with results from Murshed et al. [14] and Chon and Kihm [8], who used a similar 150-nm particle size as in this experiment, their thermal conductivity ratio seems to have had higher increases with the rise of temperature.

Similarly, the experimental results of TiO_2–water in Fig. 9 show that the increase of temperature slightly affects the increase of thermal conductivity ratio. This corresponds to results from Masuda et al. [2], Zhang et al. [13], and Turgut al. [16]. In contrast, the results of Wang et al. indicate a higher effect of temperature on the increase of thermal conductivity ratio of TiO_2–water than results from this experiment. It can be seen from Figs. 8 and 9 that the particle size may affect the thermal conductivity of the nanofluid. However, the data are scattered over a large range of the temperature and concentration. Therefore, it is difficult to conclude the trend of the effect of the particle size.

Fig. 10 shows the thermal conductivity ratio of Al_2O_3–water nanofluids at various concentration levels. The thermal conductivity ratio of Al_2O_3–water nanofluid increases when the concentration level increases. The experimental results tend to be similar to those from Wang et al. [4] and Xie et al. [6]. On the

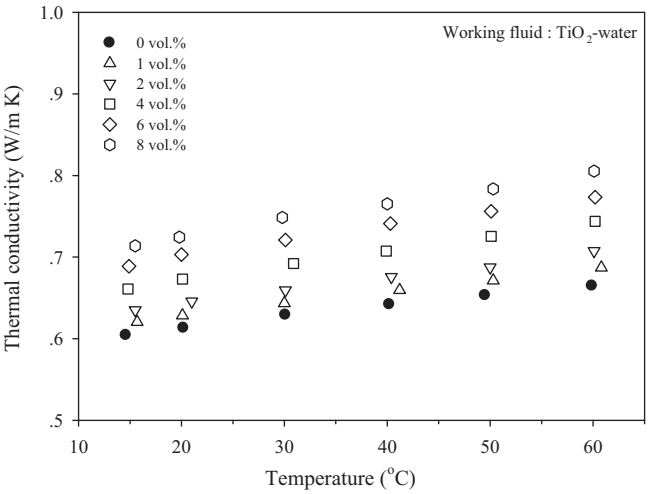

Fig. 5. Thermal conductivity of TiO_2–water nanofluid as a function of temperature and concentration.

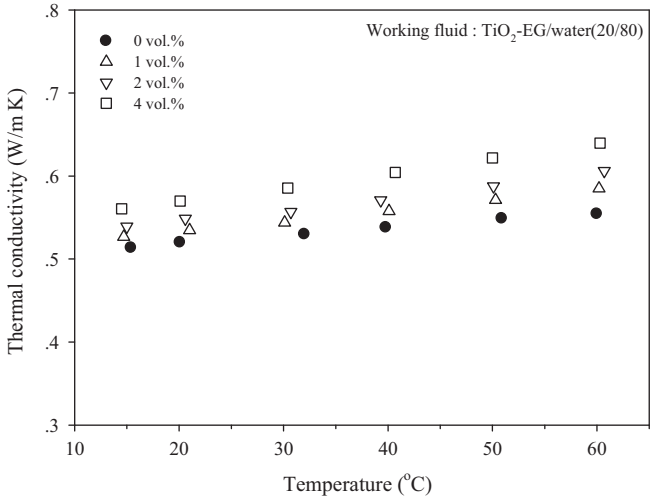

Fig. 7. Thermal conductivity of TiO_2–EG/water (20/80) nanofluid as a function of temperature and concentration.

Author's personal copy

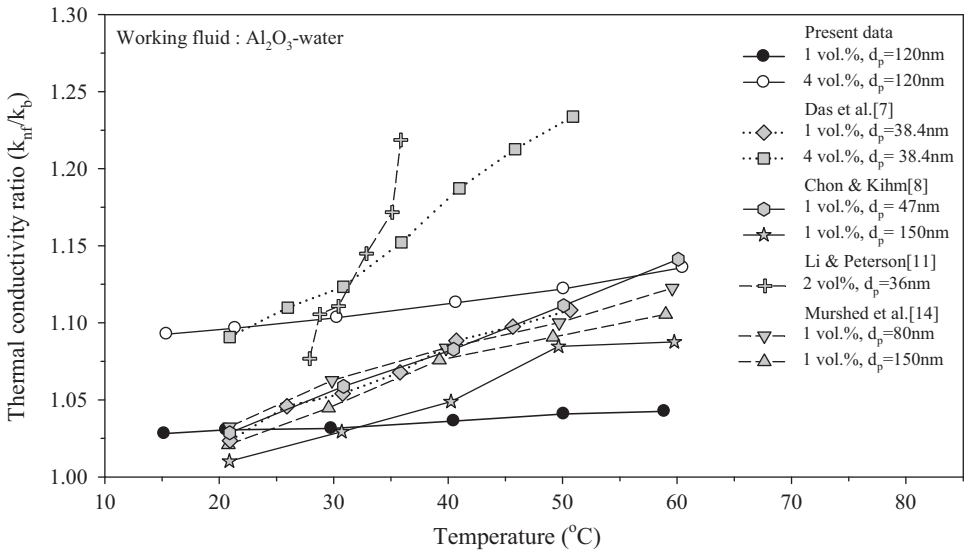

Fig. 8. Effect of temperature on the thermal conductivity ratio of Al_2O_3–water nanofluid.

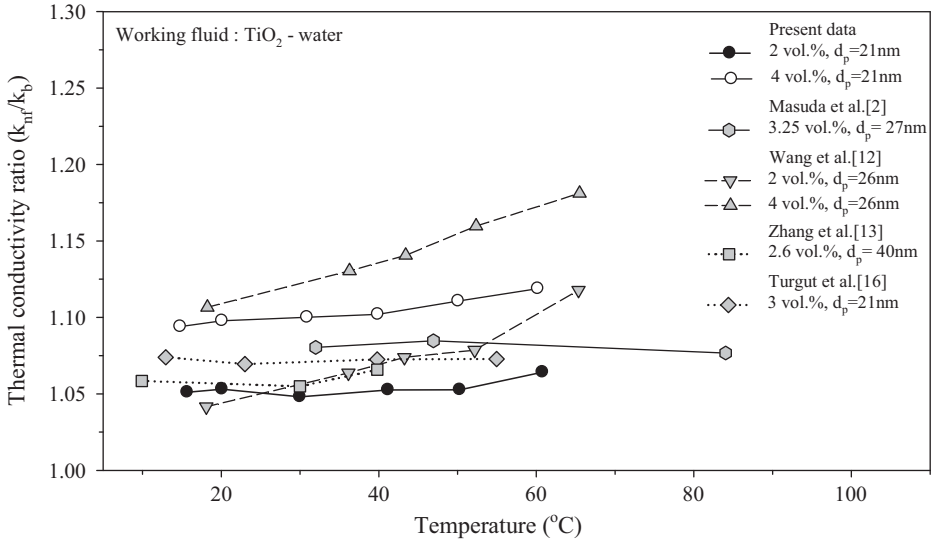

Fig. 9. Effect of temperature on the thermal conductivity ratio of TiO_2–water nanofluid.

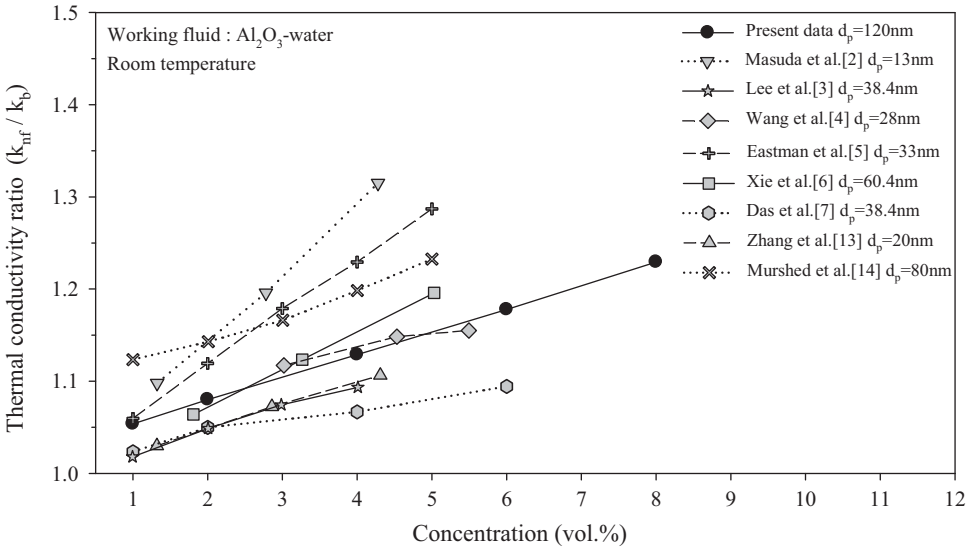

Fig. 10. Effect of concentration on the thermal conductivity ratio of Al_2O_3–water nanofluid.

Author's personal copy

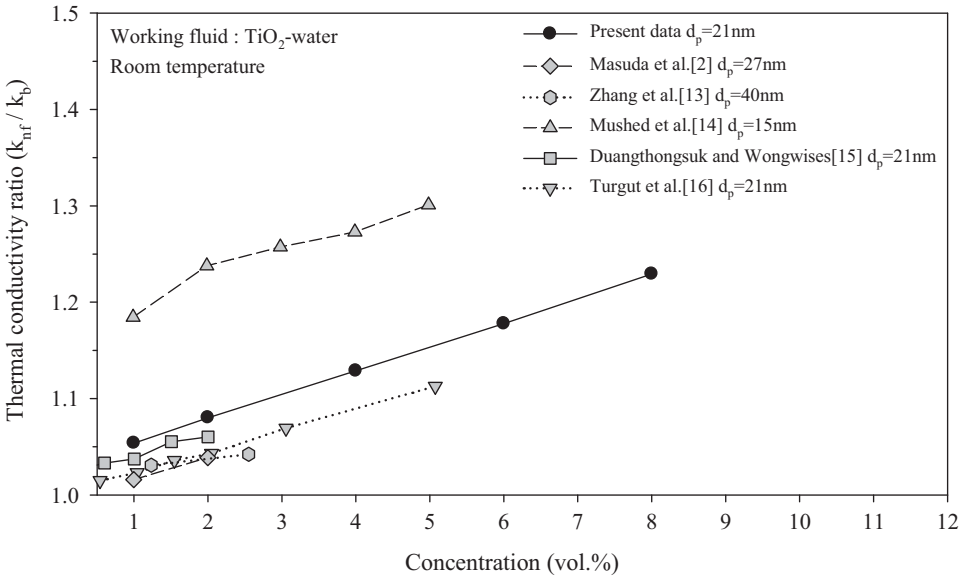

Fig. 11. Effect of concentration on the thermal conductivity ratio of TiO_2–water nanofluid.

other hand, results from Masuda et al. [2], Eastman et al. [5] and Murshed et al. [14] show higher effects. Fig. 11 shows the results of TiO_2–water nanofluids which are similar to those from Masuda et al. [2], Zeng et al. [13], Duangthongsuk and Wongwises [15] and Turgut et al. [16].

Figs. 12–15 show comparisons between the experimental results and predictions from various models popularly used to predict thermal conductivity of nanofluids. For example, the Hamilton and Crosser model (H–C model) [17], popularly used to predict thermal conductivity of two-component mixtures was developed from the Maxwell model [30] by adding a particle shape factor as follows:

$$k_{nf} = \left[\frac{k_p + (n-1)k_b - (n-1)\phi(k_b - k_p)}{k_p + (n-1)k_b + \phi(k_b - k_p)}\right] k_b, \quad \text{when} \quad n = \frac{3}{\psi} \tag{2}$$

where ϕ is the volume fraction, n is a particle shape factor, ψ is the particle sphericity or a ratio of the surface area of a sphere with volume equal to that of the particle, to the surface area of the particle, which are 1 and 0.5 for spherical shape and cylindrical shape, respectively.

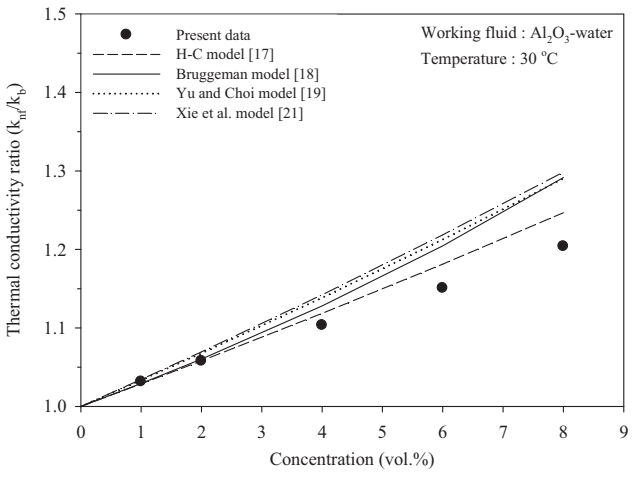

Fig. 12. Comparison of the experimental thermal conductivity ratio of Al_2O_3–water nanofluid with those obtained from various equations.

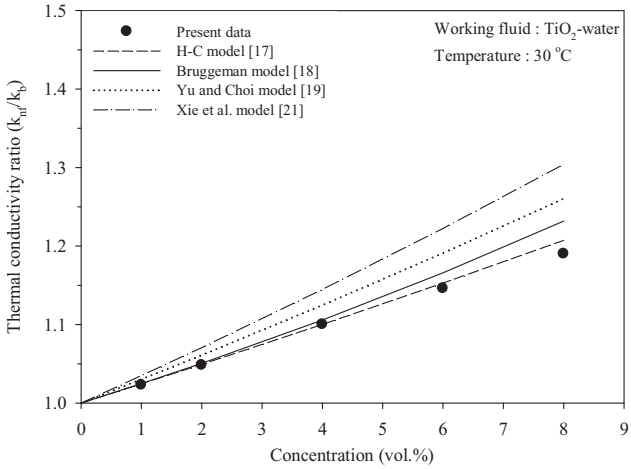

Fig. 13. Comparison of the experimental thermal conductivity ratio of TiO_2–water nanofluid with those obtained from various equations.

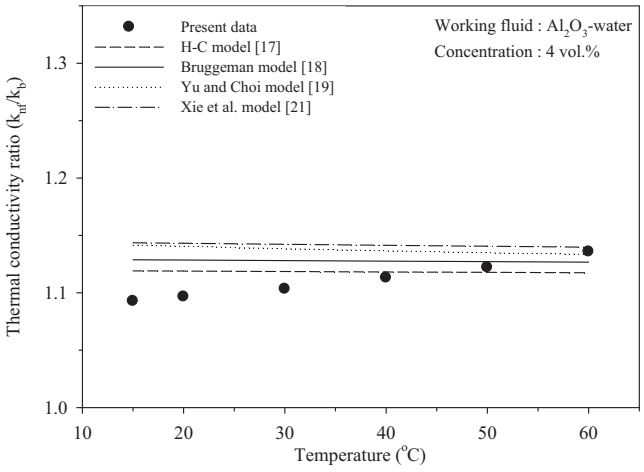

Fig. 14. Comparison of experimental thermal conductivity ratio of Al_2O_3–water nanofluid with those obtained from various equations.

Author's personal copy

Table 1
Coefficients in the correlation for different nanofluids.

Nanofluids	Coefficient				Max. error	Avg. error
	A	*B*	*C*	*D*		
Al_2O_3	0.945867	0.073528	0.036168	−0.00585	2.74%	1.23%
TiO_2	0.916205	0.066817	0.018789	0.016229	2.28%	1.11%

The following Bruggeman's equation [18] is another classic model popularly used to predict thermal conductivity of nanofluids:

$$k_{nf} = \frac{1}{4}[(3\phi-1)k_p + (2-3\phi)k_b] + \frac{k_b}{4}\sqrt{\Delta},$$

$$\text{when } \Delta = \left[(3\phi-1)^2\left(\frac{k_p}{k_b}\right)^2 + (2-3\phi)^2 + 2(2+9\phi-9\phi^2)\left(\frac{k_p}{k_b}\right)\right] \quad (3)$$

The Yu and Choi model [19] is another model that is developed from the Maxwell model. This model includes the mechanism caused by a solid-like nanolayer that coats particles as shown in the following equation:

$$k_{nf} = \left[\frac{k_p + 2k_b + 2\phi(k_p - k_b)(1+\gamma)^3}{k_p + 2k_b + \phi(k_p - k_b)(1+\gamma)^3}\right] k_b \quad (4)$$

where $\gamma = \delta/r_p$ is a ratio of nanolayer thickness ($\delta = 2$ nm) per nanoparticle radius.

Similarly, the Xie et al. model [21] takes the mechanism caused by nanolayer into consideration

$$k_{nf} = \left[1 + 3\Theta\phi_T + \frac{3\Theta^2\phi_T^2}{1-\Theta\phi_T}\right] k_b,$$

$$\text{when } \Theta = \left[\frac{\beta_{llb}(1+\gamma)^3 - \beta_{pl}/\beta_{bl}}{(1+\gamma)^3 + 2\beta_{lb}\beta_{pl}}\right], \quad \beta_{lb} = \left(\frac{k_l - k_b}{k_l + 2k_b}\right),$$

$$\beta_{pl} = \left(\frac{k_p - k_l}{k_p + 2k_l}\right), \quad \beta_{bl} = \left(\frac{k_f - k_l}{k_f + 2k_l}\right) \quad (5)$$

where $\phi_T = \phi(1+\gamma)^3$ is the modified total volume fraction of the original nanoparticle and nanolayer, $k_l = 2k_f$ is the thermal conductivity of nanolayer.

Comparisons on the effect of the concentration show that the increase of thermal conductivity ratio of Al_2O_3–water is different from those obtained by H–C model, Bruggeman model, Yu and Choi model, and Xie et al. model. At low concentration levels, the experimental results are similar to those predicted by the models. However, as shown in Fig. 13, at high concentration levels, the experimental results are lower than those predicted by the models and tend to become steadily lower when the concentration level increases. Comparisons of TiO_2–water in Fig. 13 show that the H–C model could be used to predict the thermal conductivity ratio of TiO_2–water nanofluid with similar results to the experiment, particularly at low concentration levels. However, at high concentration levels, the experimental results tend to be lower than those predicted by the model, similar to the results of the Al_2O_3–water nanofluid.

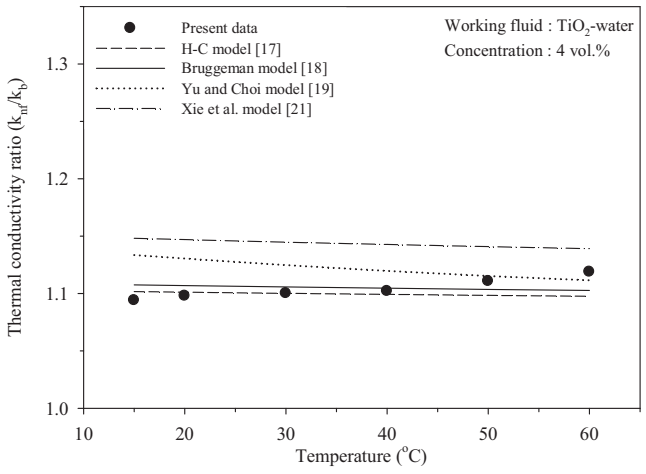

Fig. 15. Comparison of the experimental thermal conductivity ratio of TiO_2–water nanofluid with those obtained from various equations.

Comparisons between experimental results and those obtained from other models, in terms of thermal conductivity ratio of nanofluids with temperature, are shown in Figs. 14 and 15. Fig. 14 shows that other models could not be used to predict the thermal conductivity ratio of the Al_2O_3 nanofluid when temperature changes. The experimental thermal conductivity ratio tends to increase when the temperature increases. On the contrary, predictions from other models show that the thermal conductivity ratio of the Al_2O_3–water nanofluid does not vary with temperature and tends to be lower in some models. However, at low temperature, the experimental results are lower than those predicted by the models. In Fig. 15 which shows the results of TiO_2–water, the experimental results are similar to those predicted by the H–C model and Bruggeman model. However, the experimental thermal conductivity ratio of TiO_2 tends to increase when the temperature increases. On the other hand, the models predict no change with temperature, with a tendency to become lower in Yu and Choi's model.

From comparisons with predictions from other models and with results from other researches mentioned above, the experimental thermal conductivity ratio of nanofluids tends to be lower, especially at high concentration levels. This may be because the nanofluids used in this experiment lack stability in suspension or the nanoparticles cause more clustering with high concentration levels. Taking the increase mechanism of thermal conductivity caused by the solid/liquid nanolayer into account, it could be said that the nanofluids used in this experiment are not influenced by this mechanism, noticeable from a comparison with the models of Yu and Choi and Xie et al. Both models were developed by referring to the mechanism caused by a nanolayer. Reexamination of the effect of temperature shows that thermal conductivity ratio from other models and from some studies does not change with temperature while results from this experiment increase when temperature increases. The increase of the thermal conductivity could result from Brownian motion as discussed by several researchers [7,8,12]. They proposed that when the temperature of the fluid increases, molecules or particles of both liquids and solid will create more turbulence and collision than in low temperature. As a consequence, there is more transfer of energy between molecules or particles which, in turn, affects the thermal property or thermal conductivity.

This paper also presents a correlation for predicting thermal conductivity of the Al_2O_3 and TiO_2 nanofluids in a form of ratio of thermal conductivity between the nanofluid and base fluid ($k_{p,nf}/k_{p,b}$) which can be used in prediction for other base fluids.

Author's personal copy

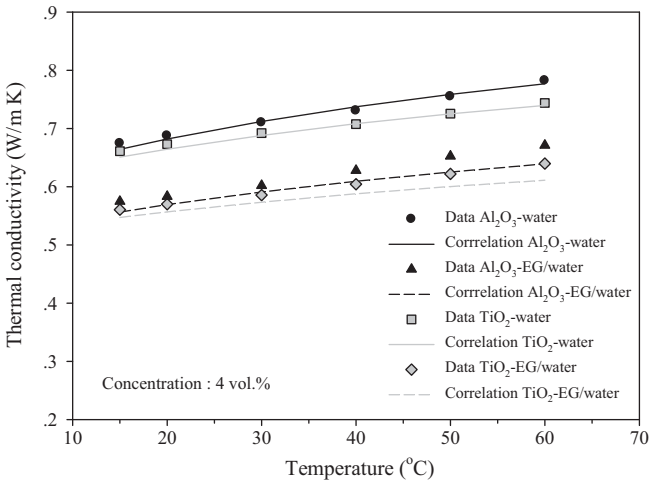

Fig. 16. Comparison of the measured thermal conductivity with proposed correlation.

Effects of temperature, concentration, and thermal conductivity of nanoparticles and base fluid are taken into account in the following equation:

$$\frac{k_{p,nf}}{k_{p,b}} = A\phi^B T^C \left(\frac{k_{p,np}}{k_{p,b}}\right)^D \quad (6)$$

where A, B, C, and D are coefficients of the equation shown in Table 1. This equation could be used with a temperature range of 15–65 °C and a concentration range of 1–8 vol.%. Fig. 16 shows a comparison between thermal conductivity obtained from the experiment and that obtained from the correlation. The results from the predictions are similar to the experimental results with acceptable accuracy.

5. Conclusions

From the calibration by measuring thermal conductivity of water and ethylene glycol, the experimental results are similar to a reference standard from ASHRAE. The developed experimental apparatus for measuring thermal conductivity has acceptable level of precision.

The experimental results show that thermal conductivity of nanofluids is higher than that of the base fluid and varies with temperature and concentration level of nanofluids. The thermal conductivity ratio from this experiment does not correspond with that obtained from predictions using well known models, both in terms of concentration and temperature. The newly- and specifically-developed correlation for predicting thermal conductivity of Al_2O_3 and TiO_2 nanofluids gives similar results to the experiment at acceptable level.

Acknowledgements

The present study was supported financially by the Thailand Research Fund, the Office of the Higher Education Commission and the National Research University Project, whose guidance and assistance are gratefully acknowledged.

References

[1] S.U.S. Choi, Enhancing thermal conductivity of fluids with nanoparticles, ASME Fluids Eng. Div. 231 (1995) 99–103.
[2] H. Masuda, A. Ebata, K. Teramae, N. Hishinuma, Alteration of thermal conductivity and viscosity of liquid by dispersing ultra-fine particles (dispersion of Al_2O_3, SiO_2 and TiO_2 ultra-fine particles), Netsu Bussei (Japan) 7 (4) (1993) 227–233.
[3] S. Lee, S.U.S. Choi, S. Li, J.A. Eastman, Measuring thermal conductivity of fluids containing oxide nanoparticles, J. Heat Transfer 21 (1999) 280–289.
[4] X. Wang, X. Xu, S.U.S. Choi, Thermal conductivity of nanoparticles–fluid mixture, J. Thermophys. Heat Transfer 13 (4) (1999) 474–480.
[5] J.A. Eastman, S.U.S. Choi, S. Li, W. Yu, L.J. Thomson, Anomalously increased effective thermal conductivities of ethylene glycol-based nanofluids containing copper nanoparticles, Appl. Phys. Lett. 78 (2001) 718–720.
[6] H. Xie, J. Wang, T. Xi, Y. Liu, F. Ai, Thermal conductivity enhancement of suspensions containing nanosized alumina particles, J. Appl. Phys. 91 (7) (2002) 4568–4573.
[7] S.K. Das, N. Putta, P. Thiesen, W. Roetzel, Temperature dependence of thermal conductivity enhancement for nanofluids, ASME Trans.: J. Heat Transfer 125 (2003) 567–574.
[8] C.H. Chon, K.D. Kihm, Thermal conductivity enhancement of nanofluids by Brownian motion, J. Heat Transfer 127 (2005) 810.
[9] Y.J. Hwang, Y.C. Ahn, H.S. Shin, C.G. Lee, G.T. Kim, H.S. Park, J.K. Lee, Investigation on characteristics of thermal conductivity enhancement of nanofluids, Curr. Appl. Phys. 6 (2006) 1068–1071.
[10] Y. He, Y. Jin, H. Chen, Y. Ding, D. Cang, H. Lu, Heat transfer and flow behavior of aqueous suspensions of TiO_2 nanoparticles (nanofluids) flowing upward through a vertical pipe, Int. J. Heat Mass Transfer 50 (2007) 2272–2281.
[11] C.H. Li, G.P. Peterson, The effect of particle size on the effective thermal conductivity of Al_2O_3–water nanofluids, J. Appl. Phys. 101 (2007) 044312.
[12] Z.L. Wang, D.W. Tang, S. Liu, X.H. Zheng, N. Araki, Thermal-conductivity and thermal-diffusivity measurements of nanofluids by 3ω method and mechanism analysis of heat transport, Int. J. Thermophys. 28 (2007) 1255–1268.
[13] X. Zhang, H. Gu, M. Fujii, Effective thermal conductivity and thermal diffusivity of nanofluids containing spherical and cylindrical nanoparticles, Exp. Therm. Fluid Sci. 31 (2007) 593–599.
[14] S.M.S. Murshed, K.C. Leong, C. Yang, Investigations of thermal conductivity and viscosity of nanofluids, Int. J. Therm. Sci. 47 (5) (2008) 560–568.
[15] W. Duangthongsuk, S. Wongwises, Measurement of temperature-dependent thermal conductivity and viscosity of TiO_2–water nanofluids, Exp. Therm. Fluid Sci. 33 (2009) 706–714.
[16] A. Turgut, I. Tavman, M. Chirtoc, H.P. Schuchmann, C. Sauter, S. Tavman, Thermal conductivity and viscosity measurements of water-based TiO_2 nanofluids, Int. J. Thermophys. 30 (2009) 1213–1226.
[17] R.L. Hamilton, O.K. Crosser, Thermal conductivity of heterogeneous two component systems, Ind. Eng. Chem. Fundam. 1 (1962) 187–191.
[18] D.A.G. Bruggeman, Berechnung Verschiedener Physikalischer Konstanten von Heterogenen Substanzen I. Dielektrizitatskonstanten und Leitfahigkeiten der Mischkorper aus Isotropen Substanzen, Annalen der Physik 14 (1935) 636–679.
[19] W. Yu, S.U.S. Choi, The role of interfacial layers in the enhanced thermal of nanofluids: a renovated maxwell model, J. Nanopart. Res. 5 (2003) 167–171.
[20] W. Yu, S.U.S. Choi, The role of interfacial layers in the enhanced thermal conductivity of nanofluids: a renovated Hamilton–Crosser model, J. Nanopart. Res. 6 (2004) 355–361.
[21] H. Xie, M. Fujii, X. Zhang, Effect of interfacial nanolayer on the effective thermal conductivity of nanoparticle–fluid mixture, Int. J. Heat Mass Transfer 48 (2005) 2926–2932.
[22] Y. Xuan, Q. Li, W. Hu, Aggregation structure and thermal conductivity of nanofluids, AIChE J. 49 (2003) 1038–1043.
[23] J. Koo, C. Kleinstreuer, A new thermal conductivity model for nanofluids, J. Nanopart. Res. 6 (2004) 577–588.
[24] S.P. Jang, S.U.S. Choi, Role of Brownian motion in the enhanced thermal conductivity of nanofluids, Appl. Phys. Lett. 84 (2004) 4316–4318.
[25] M. Kostic, K.C. Simham, Computerized, transient hot-wire thermal conductivity (HWTC) apparatus for nanofluids, in: Proceedings of the 6th WSEAS International Conference on Heat and Mass Transfer, 2009.
[26] J.J. Healy, J.J. deGroot, J. Kestin, The theory of the transient hot-wire method for measuring thermal conductivity, Physica 82C (1976) 392–408.
[27] W.T. Kierkus, N. Mani, J.E.S. Venart, Radial–axial transient heat conduction in a region bounded internally by a circular cylinder of finite length and appreciable heat capacity, Can. J. Phys. 51 (1973) 1182–1186.
[28] J.P. Bentley, Temperature sensor characteristics and measurement system design, J. Phys. 17 (1984) 430–439.
[29] ASHRAE, ASHRAE Handbook: Fundamentals, American Society of Heating, Refrigerating and Air-Conditioning Engineers Inc., Atlanta, GA, 2005.
[30] J.C. Maxwell, A Treatise on Electricity and Magnetism, vol. 1, third ed., Dover, New York, 1954.

This article was downloaded by: [Uppsala universitetsbibliotek]
On: 19 August 2012, At: 02:19
Publisher: Taylor & Francis
Informa Ltd Registered in England and Wales Registered Number: 1072954 Registered office: Mortimer House, 37-41 Mortimer Street, London W1T 3JH, UK

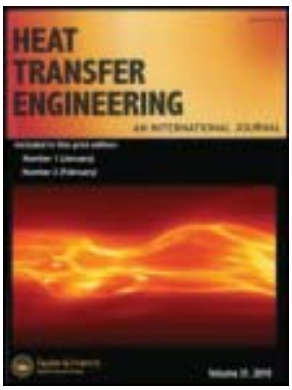

Heat Transfer Engineering
Publication details, including instructions for authors and subscription information:
http://www.tandfonline.com/loi/uhte20

Experimental Study on the Air-Side Performance of a Multipass Parallel and Counter Cross-Flow L-Footed Spiral Fin-and-Tube Heat Exchanger

Parinya Pongsoi [a] , Santi Pikulkajorn [b] & Somchai Wongwises [a c]

[a] Department of Mechanical Engineering, King Mongkut's University of Technology Thonburi, Bangkok, Thailand

[b] Somchai Industry Co., Ltd., Bangkok, Thailand

[c] The Academy of Science, Royal Institute of Thailand, Dusit, Bangkok, Thailand

Accepted author version posted online: 15 May 2012. Version of record first published: 17 Jul 2012

To cite this article: Parinya Pongsoi, Santi Pikulkajorn & Somchai Wongwises (2012): Experimental Study on the Air-Side Performance of a Multipass Parallel and Counter Cross-Flow L-Footed Spiral Fin-and-Tube Heat Exchanger, Heat Transfer Engineering, 33:15, 1251-1263

To link to this article: http://dx.doi.org/10.1080/01457632.2012.692296

PLEASE SCROLL DOWN FOR ARTICLE

Full terms and conditions of use: http://www.tandfonline.com/page/terms-and-conditions

This article may be used for research, teaching, and private study purposes. Any substantial or systematic reproduction, redistribution, reselling, loan, sub-licensing, systematic supply, or distribution in any form to anyone is expressly forbidden.

The publisher does not give any warranty express or implied or make any representation that the contents will be complete or accurate or up to date. The accuracy of any instructions, formulae, and drug doses should be independently verified with primary sources. The publisher shall not be liable for any loss, actions, claims, proceedings, demand, or costs or damages whatsoever or howsoever caused arising directly or indirectly in connection with or arising out of the use of this material.

Heat Transfer Engineering, 33(15):1251–1263, 2012
Copyright © Taylor and Francis Group, LLC
ISSN: 0145-7632 print / 1521-0537 online
DOI: 10.1080/01457632.2012.692296

Downloaded by [Uppsala universitetsbibliotek] at 02:19 19 August 2012

Experimental Study on the Air-Side Performance of a Multipass Parallel and Counter Cross-Flow L-Footed Spiral Fin-and-Tube Heat Exchanger

PARINYA PONGSOI,[1] SANTI PIKULKAJORN,[2] and SOMCHAI WONGWISES[1,3]

[1]Department of Mechanical Engineering, King Mongkut's University of Technology Thonburi, Bangkok, Thailand
[2]Somchai Industry Co., Ltd., Bangkok, Thailand
[3]The Academy of Science, Royal Institute of Thailand, Dusit, Bangkok, Thailand

This study conducted experiments on the air-side performance of novel L-footed spiral fin-and-tube heat exchangers that were faced with airflow at high Reynolds numbers (3500–13,000). The examined heat exchangers have a multipass parallel-and-counter cross-flow type of water flow arrangement. This flow arrangement is a combination of the parallel cross-flow and the counter cross-flow. This type of water flow arrangement may be the best fit for the reverse-flow system, because it can provide constant heat-exchange effectiveness for every flow reversal direction at the same airflow rate. Ambient air was used as a working fluid on the air side and hot water for the tube side. This way the effect of the number of tube rows on the heat transfer and friction characteristics of L-footed spiral fin-and-tube heat exchangers was clearly observed. The effect of the fin's outside diameter on the pressure drop was also studied. The results show that the number of tube rows has no significant effect on the air-side heat transfer or on friction characteristics at high Reynolds numbers. However, the fin's outside diameter shows a significant effect on the pressure drop. The pressure drop increases as the fin's outside diameter increases for the same number of tube rows.

INTRODUCTION

Heat exchangers are devices that are commonly used for exchanging heat between two fluids of different temperatures without mixing those fluids. Many types of heat exchangers are used in industrial processes. However, one of the most favorable types of heat exchangers is the fin-and-tube heat exchanger. In order to improve the heat transfer performance of this type of heat exchanger, it is very important to consider the heat transfer rate, which is normally limited by the thermal resistance on the air side of the heat exchanger. Improving the fin geometry is one way to augment the heat transfer rate on the air side of the heat exchanger.

The authors are indebted to the Thailand Research Fund, the Energy Policy and Planning Office, the Office of the Higher Education Commission, and the National Research University Project for supporting this study.

Address correspondence to Professor Somchai Wongwises, Department of Mechanical Engineering, Fluid Mechanics, Thermal Engineering and Multiphase Flow Research Laboratory (FUTURE), King Mongkut's University of Technology Thonburi, 126 Pracha-utid Road, Bangkok, Bangmod 10140, Thailand. E-mail: somchai.won@kmutt.ac.th

However, this method may lead to the need for increased fan power because of the pressure drop. Many researchers have studied the effect of the plate fin's geometry, such as plain fin, slit fin, wavy fin, louvered fin, compounded fin, and so on, on heat transfer performance and the friction characteristic. These valuable studies on plate fin-and-tube heat exchangers are detailed in the following section to place this experimental work within the context of previous literature.

Wang et al. [1] tested 49 louver fin-and-tube heat exchangers with different geometrical parameters and proposed a correlation between the heat transfer and the friction characteristic for the louver fin. Yan and Sheen [2] examined 36 fin-and-tube heat exchangers, including 12 plain fin, 12 wavy fin, and 12 louver fin geometries, to study the effects of the number of tube rows and fin pitch on air-side performance. Yan and Sheen then compared the air-side performance of plain, wavy, and louver fin-and-tube heat exchangers. Du and Wang [3] tested 31 samples of superslit fin-and-tube heat exchangers to study the effect of the number of tube rows on air-side performance. They found that the number of tube rows is almost negligible for smaller slit length at Reynolds numbers more than 2000, and they found that friction

Downloaded by [Uppsala universitetsbibliotek] at 02:19 19 August 2012

factors are relatively independent of the number of tube rows. Wongwises and Chokeman [4] tested 10 herringbone wavy fin-and-tube heat exchangers to investigate the effect of fin pitch and the number of tube rows on air-side performance. A change in fin pitch does not significantly affect heat transfer performance, even though changing the pitch enough will reverse the friction characteristic. The Colburn factor and friction factor decrease with increasing number of tube rows when the Reynolds number is less than 4000. Chokeman and Wongwises [5] examined three herringbone wavy fin-and-tube heat exchangers and conducted experiments to investigate the effect of fin pattern and edge corrugation on air-side heat transfer and friction characteristics. Wen and Ho [6] tested three fin-and-tube heat exchangers, including a plate fin, wavy fin, and compound fin, in a range of airflows corresponding to Reynolds numbers of 600–1200, and Wen and Ho's results strongly suggest the use of compounded fins in the construction of heat exchangers. Pirompugd et al. [7] tested 15 plain fin-and-tube heat exchangers and 18 wavy fin-and-tube heat exchangers, and found that the percentage of the surface that gets wet increases with increasing fin spacing or an increasing number of tube rows along with a decreasing Reynolds number. Pirompugd et al. used the finite circular fin method for data reduction in their experiment.

It can be seen from the literature that many researchers are interested in studying the plate fin-and-tube heat exchanger. On the other hand, there are very few extant studies on the spiral fin-and-tube heat exchanger, as found in references [8–12].

Nuntaphan et al. [8] tested 23 crimped spiral fin-and-tube heat exchangers to analyze the effect of tube diameter, fin spacing, transfer tube pitch, and tube arrangement, and they proposed correlations between heat transfer and friction characteristics in the case of a low Reynolds number. Wongwises and Naphon [9, 10] studied the heat transfer characteristics and the performance of a spirally coiled finned tube heat exchanger under dry-surface and wet-surface conditions. Moreover, they tested heat exchangers that rely on a crimped spiral finned tube. Then Srisawad and Wongwises [11] tested the helically coiled crimped spiral finned tube heat exchanger, focusing on the air-side heat transfer characteristics in dry-surface conditions. Lee et al. [12] studied the air-side heat transfer characteristics of spiral-type circular fin-tube heat exchangers under nonfrosting conditions. They measured these characteristics by varying the fin pitch, the number of tube rows, and the fin alignment.

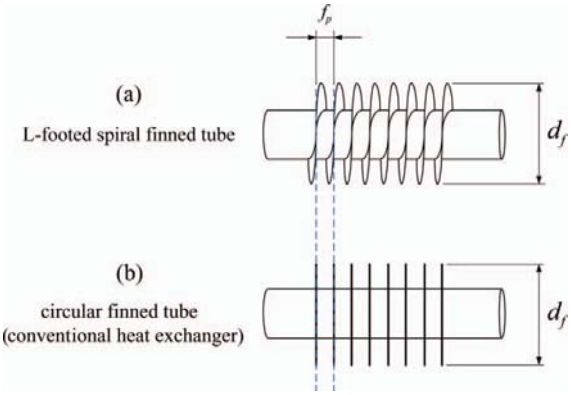

Figure 1 Schematic diagram of (a) the L-footed spiral fin and (b) the circular fin. (Color figure available online.)

The L-footed spiral fin is another type of fin geometry. The base of the fin has an L shape, which provides a large contact area, ensuring a good path for heat transfer from the tube surface to the fin. The spiral fin seems to have a greater heat transfer coefficient than the conventional circular fin, as shown in Figure 1. The L-footed spiral fin-and-tube heat exchanger may be suitable for industrial processes that present a high risk of tube corrosion. To the best of the authors' knowledge, the air-side performance of L-footed spiral fin-and-tube heat exchangers remains unstudied. This study therefore presents the heat transfer performance and frictional characteristics of L-footed spiral fin-and-tube heat exchangers, results that has never before been seen in the literature. Moreover, this study focuses on the effect of the number of tube rows on both copper and aluminum fins with different outside diameters on each fin. The investigation was done at high Reynolds numbers, which correspond to real applications in the industry.

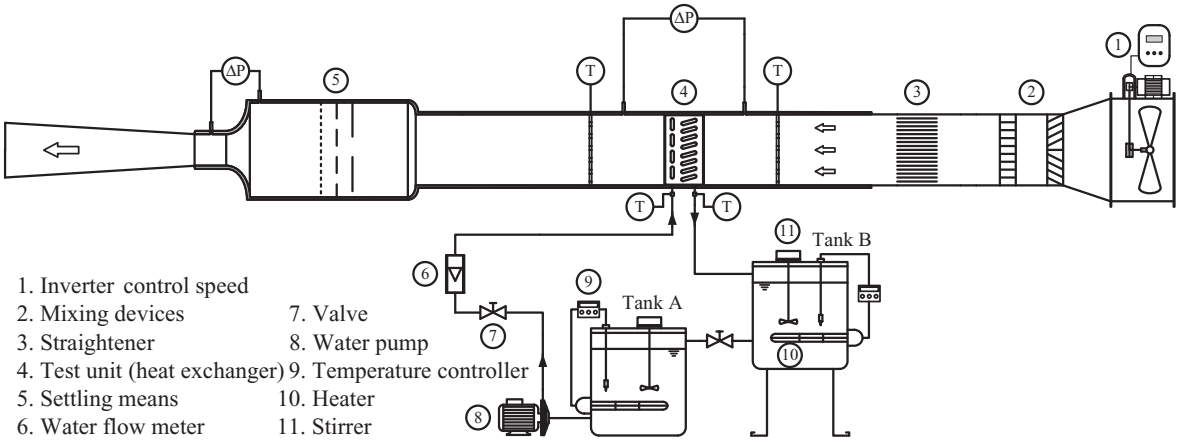

Figure 2 Schematic diagram of the experimental apparatus.

In addition, the multipass parallel and counter cross-flow, which is a type of water flow arrangement, was applied in this work. The heat exchangers tested in this work have a combined configuration between the parallel cross-flow and the counter cross-flow: each layer of water flow alternates between the parallel cross-flow and the counter cross-flow. This type of water flow arrangement may be appropriate for reverse-flow heat exchangers used in recuperative systems, because it provides constant heat exchange effectiveness in every direction of flow reversal, which the original parallel cross-flow and counter cross-flow water flow arrangement cannot provide in reverse flow. However, none of the ε–*NTU* relationships match this geometry of water flow arrangement. In order to apply ε–*NTU* methods to this type of water flow arrangement, this work also discusses the effect of using ε–*NTU* relationships on both the multipass parallel cross-flow and the counter cross-flow for this type of water flow arrangement.

EXPERIMENTAL APPARATUS

Figure 2 shows the schematic diagram of the experimental apparatus. Air and hot water were used as working fluids. The main components of the system were the heat exchanger, water

Downloaded by [Uppsala universitetsbibliotek] at 02:19 19 August 2012

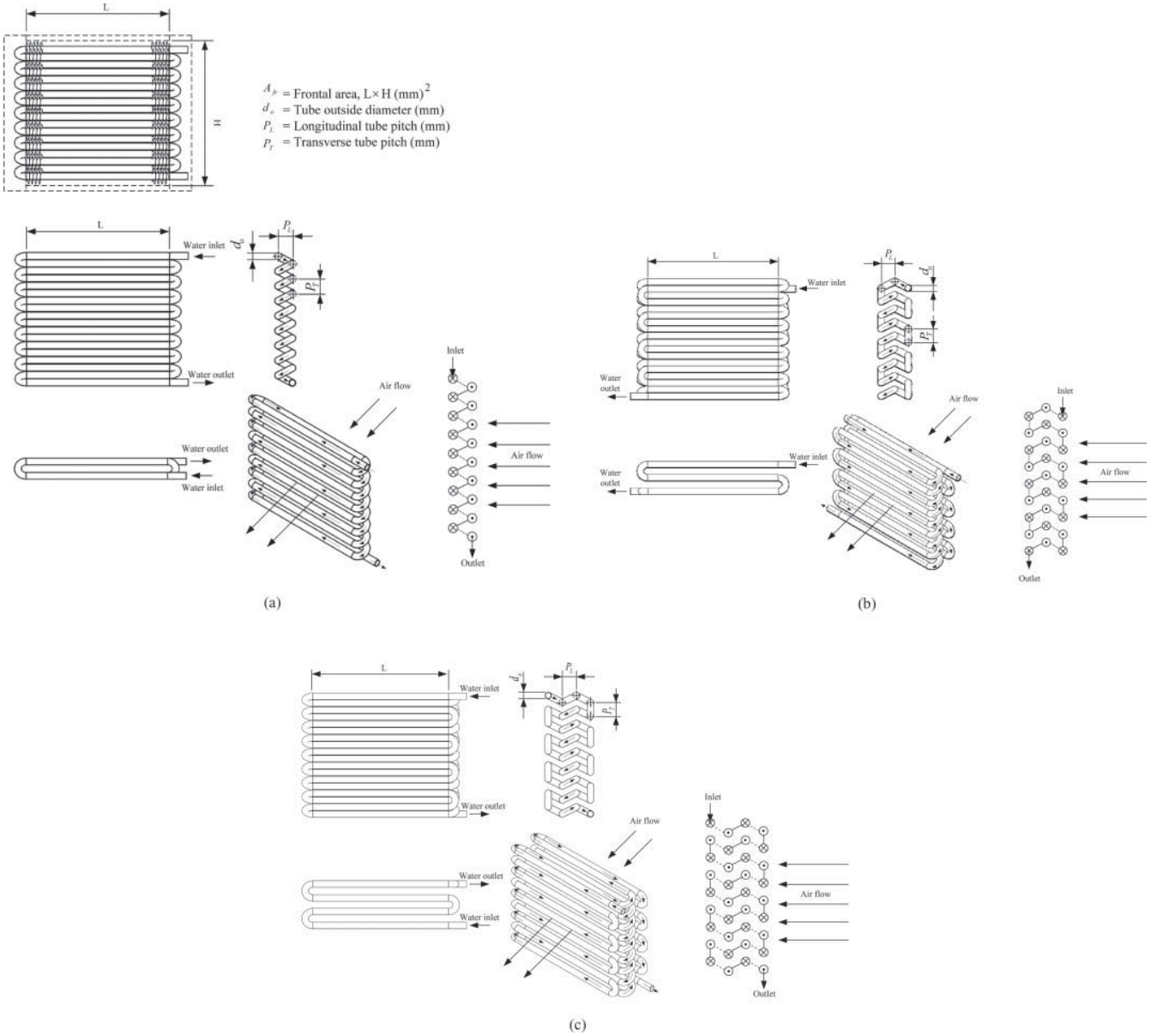

Figure 3 Geometric details of the multipass parallel-and-counter cross-flow heat exchangers and water flow circuit inside the heat exchanger: (a) $N_{row} = 2$, (b) $N_{row} = 3$, and (c) $N_{row} = 4$ (× and • signs indicate that water flows into or out of the paper, respectively).

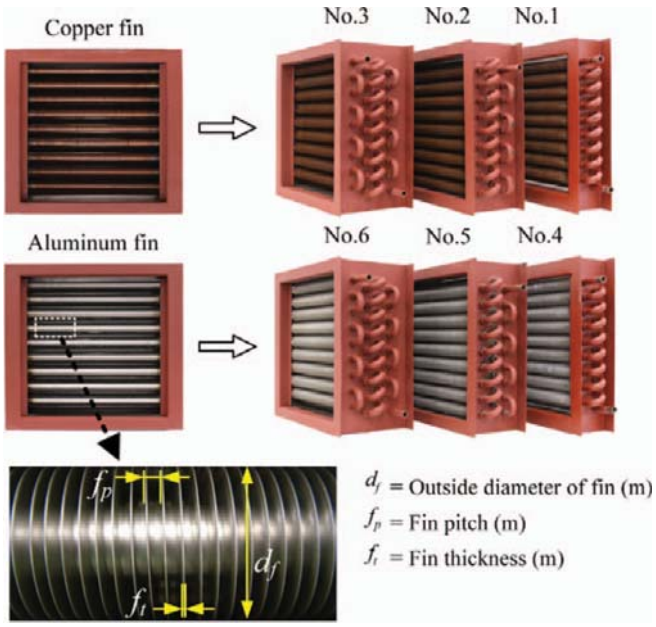

Figure 4 The photos of the tested L-footed spiral fin and tube heat exchangers (numbers 1–6). (Color figure available online.)

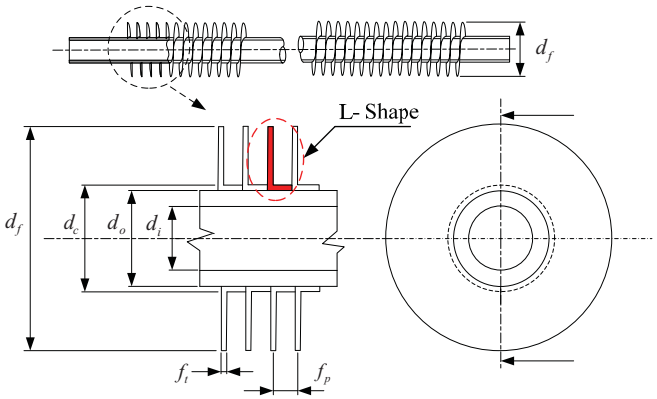

Figure 5 Schematic diagram of the tested L-footed spiral fin. (Color figure available online.)

flow loop, air supply, and the instrumentation and data acquisition system.

The present study's heat exchanger is a type of fin-and-tube heat exchanger. The copper tube is finned with two types of fins: copper fin and aluminum fin. Figure 3 details the water-side circuit and the dimensions of the tested fin and tube heat exchangers. The configuration of the L-footed spiral fin pattern appears in Figures 4 and 5. Finally, the geometric parameters of the heat exchangers are summarized in Table 1.

An open-type wind tunnel was used to push air through the heat exchanger. The connections of the duct were designed so that parts could be changed or repaired quickly and easily. This arrangement operated in a cross-flow with the hot water passing through the heat exchanger. The tunnel was a rectangular air duct fabricated from a steel plate, having the dimensions of 0.43 × 0.48 m. The duct was insulated with a 16-mm-thick Aeroflex standard sheet. Fresh air was drawn into the duct and passed through the mixing device, straightener, and heat exchanger by means of a 2.2-kW axial flow fan. The speed of the fan could be adjusted with an inverter.

Thermocouple probes were located at the air inlet and outlet sections of the heat exchanger. The temperature was measured with 1-mm-diameter probes extending into the duct where the air flowed. The probes consisted of T-type copper–constantan thermocouples grounded to a stainless-steel outer sheath. The measuring points were located at the positions recommended by the ASHRAE standard [13]. The temperature was monitored and recorded continuously. All temperature-measuring devices were well calibrated in a controlled-temperature bath using a standard precision mercury-in-glass thermometer. All sensors were wired directly to terminal control panels mounted on the bench. The airflow rate was detected with a nozzle based on the ISO 5801 standard. The drops in air pressure across the test section and the nozzle were measured with a digital manometer. There were four pressure taps on each wall: an upstream and downstream tap in the test section and in the the nozzle.

To avoid distortion of the air velocity profile, mixing devices and straighteners were installed in the duct. Air velocity and air-velocity fluctuation in the duct were checked with a constant-temperature anemometer 90CN10/C10 (CTA, Dantec) that had an automatic probe setup. Stream Ware software was used to set up the anemometer modules, to perform velocity and directional calibrations, and to provide an experimental platform wherein automatic sequences of hardware setup, data acquisitions, and data reductions could be performed. The probe used in this experiment was a wedge-shaped, right-angled film probe 55R33 with a noncylindrical sensor in a 1 × 0.2-mm sheath. All signals

Table 1 Detailed geometric parameters of the test samples

Number	Fin type	d_i (mm)	d_o (mm)	d_c (mm)	f_p (mm)	f_t (mm)	P_L (mm)	P_T (mm)	d_f (mm)	n_t	A_{fr} (mm)^2	Fin material	N_{row}
1	L-footed	13.5	16.35	16.85	3.25	0.25	35	39	30.5	9	320 × 350	Cu	2
2	L-footed	13.5	16.35	16.85	3.25	0.25	35	40	30.5	9	340 × 360	Cu	3
3	L-footed	13.5	16.35	16.85	3.25	0.25	35	40	30.5	9	340 × 360	Cu	4
4	L-footed	13.5	16.35	16.85	3.25	0.25	35	39	35.0	9	320 × 350	Al	2
5	L-footed	13.5	16.35	16.85	3.25	0.25	35	40	35.0	9	340 × 360	Al	3
6	L-footed	13.5	16.35	16.85	3.25	0.25	35	40	35.0	9	340 × 360	Al	4

Note. Tube layouts of all heat exchangers are staggered layout. Cu = copper, Al = aluminum.

Downloaded by [Uppsala universitetsbibliotek] at 02:19 19 August 2012

Downloaded by [Uppsala universitetsbibliotek] at 02:19 19 August 2012

Table 2 Testing conditions of experimental runs

Inlet-air-dry bulb temperature, °C	31.5 ± 0.5
Inlet-air frontal velocity, m/s	2–6 or Re_{dc} (3500–13,000)
Inlet-water temperature, °C	50–70
Water flow rate, LPM	12–14

were registered by a data acquisition system and finally averaged over the elapsed time.

The hot water flow loop consisted of two storage tanks, an 18-kW electric heater, a centrifugal pump, a control unit and a flow meter with a 0.5 LPM resolution, as shown in Figure 2. The purpose of this loop was to transfer heat to the air flowing through the heat exchanger. The temperature of the hot water in the two tanks was measured with T-type copper–constantan thermocouples and was controlled with the temperature controller. After it had been heated to the required temperature, the hot water was pumped out of storage tank (A), delivered to the heat exchanger, and then returned to storage tank (B), which was used to preheat the water in order to reduce the temperature difference before entering tank (A). The water temperatures at the inlet and outlet of the heat exchanger were measured with 1-mm-diameter probes extending inside the tube where the water flowed. The probes consisted of T-type copper–constantan thermocouples grounded to a stainless-steel outer sheath.

In the experiment, at a specific inlet water temperature, the water flow rate was fixed while the airflow rate was increased. The system was allowed to approach a steady state before any data were recorded. After the system had reached a steady state, the inlet and outlet temperatures of the air passing across the heat exchanger and the water flow rates were determined. All tested conditions of the heat exchangers are shown in Table 2. The accuracies of the direct measurement sensors and uncertainties, which were calculated from the root mean sum square method, are shown in Tables 3 and 4.

DATA REDUCTION

In order to determine the heat transfer characteristics of the heat exchangers from the data recorded under steady-state conditions during each test run, the method of number of transfer units (ε–*NTU*), based on the concept of heat exchanger effectiveness, was applied to determine the *UA* product.

The air-side heat transfer rate is given as:

$$Q_a = m_a c_{P,a} \Delta T_a \tag{1}$$

Table 3 The accuracies of the measurements

Parameters	Accuracy
Inlet-air dry-bulb temperature, °C	±0.1
Pressure drop, Pa	±0.5
Inlet-water temperature, °C	±0.1
Water flow rate, LPM	±0.4 (±0.02 of full scale)

Table 4 Uncertainties of the derived experimental values

Parameters	Maximum uncertainties (%)
Air-side heat transfer rate, Q_a	± 4.96
Water-side heat transfer rate, Q_w	± 3.37
Pressure drop, ΔP	± 2.50
Frontal velocity, V_{fr}	± 3.30
Reynolds number, Re_{dc}	± 3.18
Air-side heat transfer coefficient, h_o	± 8.98
Colburn factor, j	± 12.30
Friction factor, f	± 11.13

The water-side heat transfer rate is given as:

$$Q_w = m_w c_{P,w} \Delta T_w \tag{2}$$

The total rate of heat transfer used in the calculation is averaged from the air side and water side as follows:

$$Q_{ave} = \frac{|Q_a| + |Q_w|}{2} \tag{3}$$

The overall heat transfer coefficient can be written in terms of the total resistance to heat transfer. This total thermal resistance is the sum of the individual thermal resistances, as follows:

$$\frac{1}{UA} = \frac{1}{h_i A_i} + \frac{ln(d_o/d_i)}{2\pi k_t L} + \frac{ln(d_c/d_o)}{2\pi k_f L} + \frac{1}{\eta_o h_o A_o} \tag{4}$$

The ε–*NTU* relationships with one fluid mixed and one fluid unmixed in the cross-flow is employed to determine the overall heat transfer coefficient. According to Figure 3, the multipass parallel and counter cross-flow is a complicated water flow arrangement based on a combination of the multipass parallel cross-flow and the counter cross-flow configurations of water flow. As mentioned earlier, none of the ε–*NTU* relationships match the geometry of the water flow arrangement used in this work. Both relations for the multipass parallel and the counter cross-flow configuration of the water flow arrangement from references [14–19], as shown in Eqs. (5)–(11), were applied in order to calculate the overall heat transfer coefficient. However, the multipass parallel and counter cross-flow used in this experiment is a combination of multipass parallel cross-flow and counter cross-flow. It may be suitable to use the average value of those relations shown in Eq. (11). In addition, the schematic diagram of the heat exchangers algorithm for multipass parallel cross-flow, multipass counter cross-flow, and multipass parallel and counter cross-flow ($N_{row} = 2$, 3, and 4) is shown in Figure 6. In this work, the air-side working fluid (air) is defined as fluid A, and the tube-side working fluid (water) is defined as fluid B. It should be noted that the minimum heat capacity rate (C_{min}) is on the air side (fluid A). Therefore, the following relations are applied in the present calculations.

Multipass parallel cross-flow:

For ($N_{row} = 2$):

$$\varepsilon_p = \left(1 - \frac{K}{2}\right)\left(1 - e^{-2K/C_A^*}\right), \; K = 1 - e^{-NTU_A(C_A^*/2)} \tag{5}$$

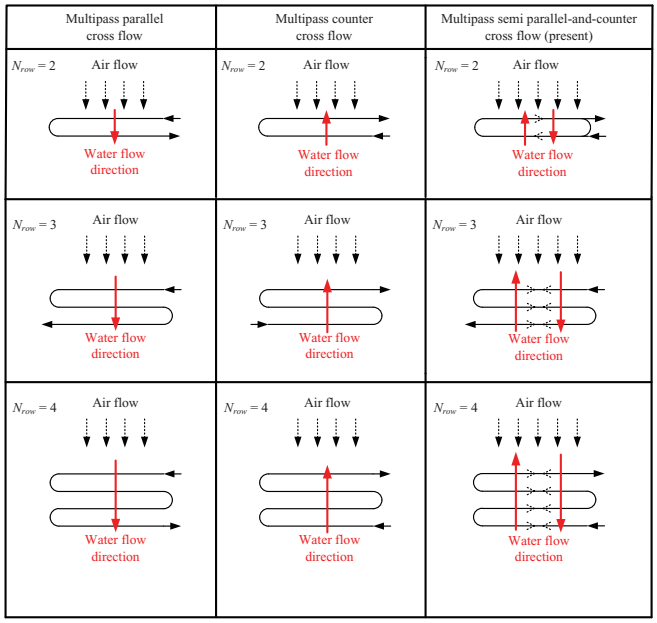

Figure 6 Schematic diagram of the heat exchangers algorithm for multipass parallel cross flow, multipass counter cross flow, and multipass parallel-and-counter cross-flow (N_{row} = 2, 3, and 4). (Color figure available online.)

For ($N_{row}=3$):

$$\varepsilon_p = 1-\left(1-\frac{K}{2}\right)^2 e^{-3K/C_A^*} - K\left[1-\frac{K}{4}+\frac{K}{C_A^*}\left(1-\frac{K}{2}\right)\right] \times e^{-K/C_A^*},\ K = 1-e^{-NTU_A(C_A^*/3)} \tag{6}$$

For ($N_{row}=4$):

$$\varepsilon_p = 1-\frac{K}{2}\left(1-\frac{K}{2}+\frac{K^2}{4}\right) - K\left(1-\frac{K}{2}\right) \times \left(1+2\frac{K}{C_A^*}\left[1-\frac{K}{2}\right]\right)e^{-2K/C_A^*} - \left(1-\frac{K}{2}\right)^3 \times e^{-4K/C_A^*},\ K = 1-e^{-NTU_A(C_A^*/4)} \tag{7}$$

Multipass counter cross-flow:

For ($N_{row}=2$):

$$\varepsilon_c = 1-\left[\frac{K}{2}+\left(1-\frac{K}{2}\right)e^{2K/C_A^*}\right]^{-1},\ K = 1-e^{-NTU_A(C_A^*/2)} \tag{8}$$

For ($N_{row}=3$):

$$\varepsilon_c = 1-\left\{\left(1-\frac{K}{2}\right)^2 e^{3K/C_A^*} + \left[K\left(1-\frac{K}{4}\right) - \left(1-\frac{K}{2}\right)\frac{K^2}{C_A^*}\right]e^{K/C_A^*}\right\}^{-1},\ K = 1-e^{-NTU_A(C_A^*/3)} \tag{9}$$

For ($N_{row}=4$):

$$\varepsilon_c = 1-\left\{\frac{K}{2}\left(1-\frac{K}{2}+\frac{K^2}{4}\right) + K\left(1-\frac{K}{2}\right) \times \left[1-2\frac{K}{C_A^*}\left(1-\frac{K}{2}\right)\right]e^{2K/C_A^*} + \left(1-\frac{K}{2}\right)^3 e^{4K/C_A^*}\right\}^{-1},$$

$$K = 1-e^{-NTU_A(C_A^*/4)} \tag{10}$$

where

$$\varepsilon_A = \frac{\varepsilon_p+\varepsilon_c}{2} \text{ for} N_{row} = 2, 3, \text{ and } 4 \tag{11}$$

Fluid A is mixed (C_{min}); fluid B is unmixed (C_{max}).

$$\varepsilon_A = \varepsilon_B/C_A^* \tag{12}$$

$$C_A^* = \frac{C_A}{C_B} = \frac{1}{C_B^*} \quad \text{for } C^* \le 1 \tag{13}$$

$$NTU_A = \frac{NTU_B}{C_A^*} \tag{14}$$

where $C^* = C_{min}/C_{max}$ is equal to C_c/C_h or C_h/C_c, depending on the value of the hot and cold fluid heat capacity rates.

$$C_{min} = \begin{cases} C_h; C_h < C_c \\ or \\ C_c; C_c < C_h \end{cases} \tag{15}$$

as

$$Q_{max} = (mc_P)_c(T_{h1}-T_{c1}) \text{ if } C_c < C_h \tag{16}$$

or

$$Q_{max} = (mc_P)_h(T_{h1}-T_{c1}) \text{ if } C_h < C_c \tag{17}$$

$$\varepsilon = \frac{Q_{ave}}{Q_{max}} \tag{18}$$

The air-side *UA* tests vary the airflow rate while keeping the water flow rate constant. The *UA* term in Eq. (4) is calculated by using Eq. (20):

$$NTU = \frac{UA}{C_{min}} \tag{19}$$

so that

$$UA = C_{min}(NTU) \tag{20}$$

The tube-side heat transfer coefficient (h_i) is evaluated from the semi-empirical correlation of Gnielinski [20]:

$$h_i = \left(\frac{k_w}{d_i}\right)\frac{(Re_{di}-1000)\,Pr\,(f_i/2)}{1+12.7\sqrt{f_i/2}\left(Pr^{2/3}-1\right)} \tag{21}$$

where the friction factor is given by:

$$f_i = (1.58 ln\, Re_{di} - 3.28)^{-2} \tag{22}$$

Downloaded by [Uppsala universitetsbibliotek] at 02:19 19 August 2012

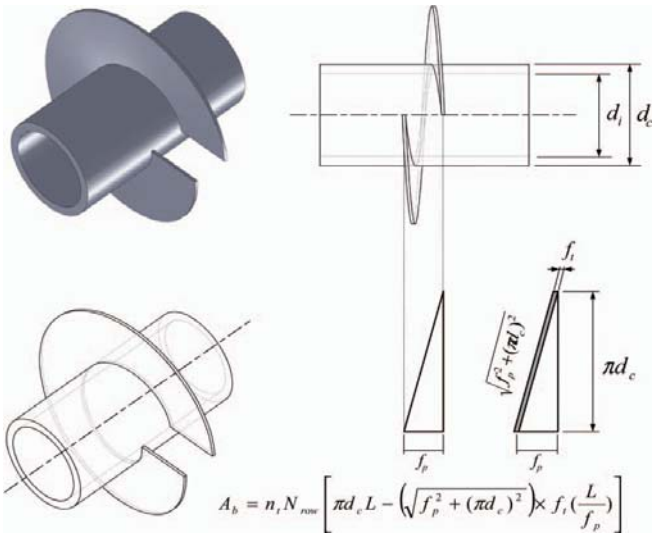

Figure 7 Equation used to determine the unfinned base surface area (A_b). (Color figure available online.)

where $\mathrm{Re}_{di} = \rho V_i d_i/\mu$.

The overall surface effectiveness (η_o), which is defined as the ratio of effective heat transfer area to total heat transfer area, can be expressed in terms of fin efficiency (η), fin surface area (A_f), and total surface area (A_o), as follows:

$$\eta_o = 1 - \frac{A_f}{A_o}(1 - \eta) \tag{23}$$

The relationship among the total surface area of the fin (A_o), the surface area of the fin (A_f), and A_b equals the area of the unfinned base surface (Figure 7). It is determined from Eq. (24).

$$A_b = n_t N_{row}\left[\pi d_c L - \left(\sqrt{f_p^2 + (\pi d_c)^2}\right) \times f_t\left(\frac{L}{f_p}\right)\right] \tag{24}$$

The surface area of fin (A_f) can be estimated by assuming it to be equal to that of the radial fin:

$$A_f = n_t N_{row}\left(\frac{L}{f_p}\right)\left[0.5\pi d_f^2 - 0.5\pi d_c^2 + \pi d_f f_t\right] \tag{25}$$

where $A_o = A_f + A_b$.

The efficiency of a radial fin with a rectangular profile is determined by the method proposed by Gardner [21]:

$$\eta = \frac{2\psi}{\phi(1+\psi)} \frac{I_1(\phi R_o)K_1(\phi R_i) - I_1(\phi R_i)K_1(\phi R_o)}{I_0(\phi R_i)K_1(\phi R_o) + I_1(\phi R_o)K_0(\phi R_i)} \tag{26}$$

where

$$\phi = (r_o - r_i)^{3/2}\left(\frac{2h_o}{k_f A_p}\right)^{1/2} \tag{27}$$

and where A_p is the area in the profile of the fin, as shown in Figure 8:

$$A_p = f_t(r_o - r_i) \tag{28}$$

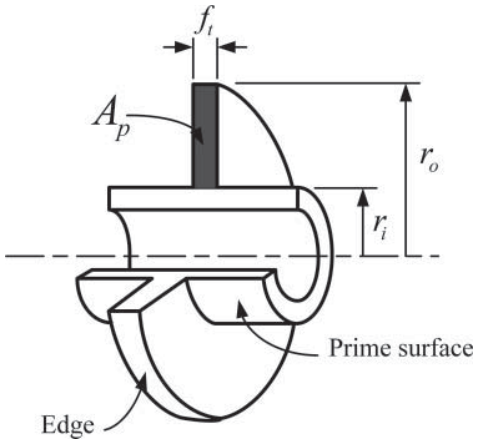

Figure 8 Schematic of the radial fin of the rectangular profile.

The parameters R_o, R_i are given in terms of the radius ratio (ψ):

$$R_o = \frac{1}{1-\psi} \tag{29}$$

and

$$R_i = \frac{\psi}{1-\psi} \tag{30}$$

where

$$\psi = \frac{r_i}{r_o} \tag{31}$$

The air-side heat transfer coefficient (h_o) can then be calculated from Eq. (4).

The air-side heat transfer characteristics of the heat exchanger are presented in terms of nondimensional groups:

$$Re_{dc} = \frac{\rho_a V_{max} d_c}{\mu} \tag{32}$$

$$j = \frac{Nu}{Re_{dc} Pr^{1/3}} = \frac{h_o}{\rho_a V_{max} c_P}(Pr)^{2/3} \tag{33}$$

The flow characteristics determined from the equation proposed by Kays and London [22] are given in terms of the fanning friction factor. The equation includes the entrance and exit pressure losses:

$$f = \left(\frac{A_{min}}{A_o}\right)\left(\frac{\rho_m}{\rho_1}\right)\left[\frac{2\Delta P \rho_1}{G_c^2} - \left(1+\sigma^2\right)\left(\frac{\rho_1}{\rho_2} - 1\right)\right] \tag{34}$$

where σ is the ratio of minimum free flow area to frontal area, A_o is the total heat transfer area and A_{min} is the minimum free flow area.

RESULTS AND DISCUSSION

This section presents the experimental results according to a primary analysis of the energy balance between air and water. The mass flow rate and temperature of both working fluids (air

Downloaded by [Uppsala universitetsbibliotek] at 02:19 19 August 2012

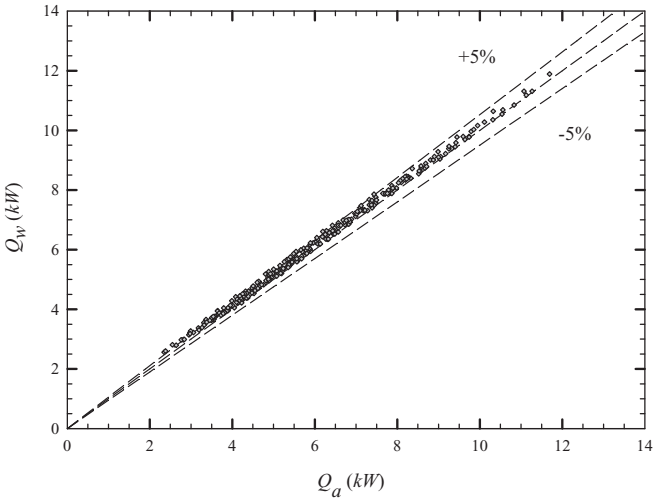

Figure 9 Energy balance between air and water.

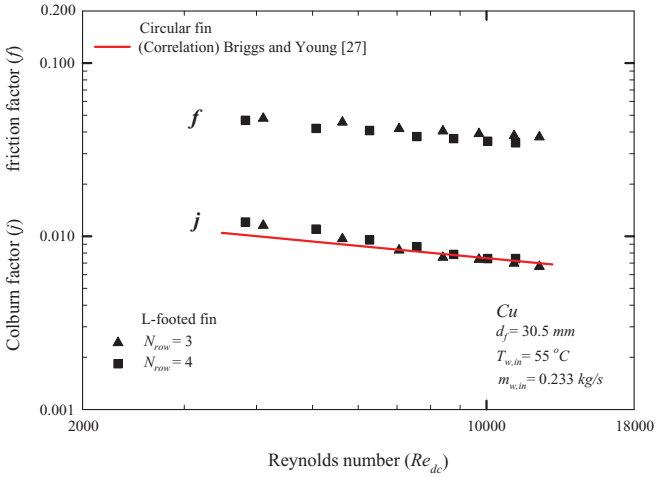

Figure 11 Effect of the number of tube rows on the Colburn factor and the friction factor of L-footed spiral fin-and-tube heat exchangers at $T_{w,in} = 55°C$ and $m_{w,in} = 0.233$ kg/s (copper fin). (Color figure available online.)

and water) were measured to calculate the heat transfer rate using Eqs. (1) and (2). Figure 9 shows that the energy balances between the air and water of the L-footed spiral fin and tube heat exchangers have relative errors of less than 5%. The present database was used to construct the relative errors, and it included 392 data points.

The analyses of air-side heat transfer and friction characteristics of all the heat exchangers examined in this experiment are presented in terms of a dimensionless number that includes the Colburn factor (j) and friction factor (f) plotted against Re_{dc}, which is the Reynolds number based on the fin collar's outside diameter ($d_o + 2f_t$).

As mentioned earlier, Eq. (11) represents the most realistic equation for this multipass parallel and counter cross-flow, so it was used to calculate the Colburn factor (j) for $N_{row} = 2$, 3, and 4. The reason for using Eq. (11) can be explained with Figure 10, which is the comparison chart illustrating the effect of Eqs. (5)–(11) on the variation of heat exchanger effectiveness. The high range of variation of heat exchanger effectiveness between parallel and counter cross-flows occurs at a high value of capacity rate ratio (C^*), which represents a high Reynolds number for the airflow. It may not be suitable for researchers to use one of those equations while operating at high Reynolds numbers. Due to its flow configuration, the heat exchanger effectiveness of multipass parallel cross-flow and counter cross-flow may not be lower or higher than the multipass parallel and the counter cross-flow configuration of the water flow arrangement, respectively. Therefore, Eq. (11) may be the most suitable one for the heat exchanger tested in this work.

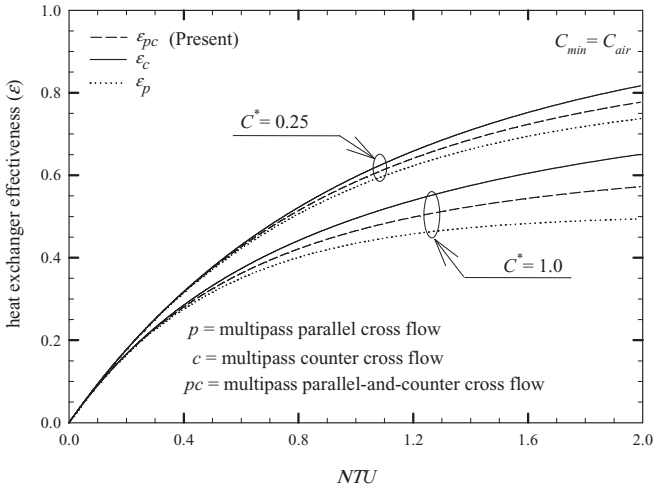

Figure 10 The comparison of the ε–*NTU* relationship at various water flow arrangements.

Figure 11 shows the effect of the number of tube rows on the heat transfer and friction characteristics for a copper fin with an outside diameter of 30.5 mm. The numbers of tube rows of the heat exchanger used in the present work were 3 and 4. As expected, both the Colburn factor (j) and the friction factor (f) decreased with an increasing Reynolds number. However, the number of tube rows has no significant effect on the Colburn factor (j) or the friction factor (f). The present data correspond with those of Rich [23] and Wang et al. [24], who studied the effect of the number of tube rows on the air-side performance of the plain fin. They concluded that the effect of tube rows on the air-side performance diminished as the Reynolds number increased over 2000.

This occurs because the downstream turbulence eddies shed from the tubes and cause good mixing in the downstream fin region. Moreover, the fact that the effect of the number of tube rows on the heat transfer characteristics vanishes for Reynolds numbers over 2000 can also be found in the works of Du and Wang [3] and Wang et al. [25, 26] for the fin-and-tube heat exchangers that have slit, wavy, and louver fins, respectively.

In addition, according to Figure 12, the same phenomenon of the effect of the number of tube rows on the air-side performance

Downloaded by [Uppsala universitetsbibliotek] at 02:19 19 August 2012

Downloaded by [Uppsala universitetsbibliotek] at 02:19 19 August 2012

Table 5 Correlations of the air side performance used for comparing with the experimental data

Round tube				
Authors	Fin types	Surface condition	Correlations	Range of parameters
Wang and Chang [28]	Plain fin	Dry surface	• j – Colburn factor correlation $\frac{j_{N_{row}}}{j_4} = 0.991\left[2.24Re_{dc}^{-0.092}\left(\frac{N_{row}}{4}\right)^{-0.031}\right]^{0.607(4-N_{row})}$ $j_4 = 0.14Re_{dc}^{-0.328}\left(\frac{P_T}{P_L}\right)^{-0.502}\left(\frac{f_p}{d_c}\right)^{0.0312}$; for $N_{row} = 4$	$Re_{dc} = 300 - 8000$ $d_c = 7 - 19.51\,mm$ $f_p = 1.07 - 8.51\,mm$ $N_{row} = 1 - 8$ $P_T = 20.35 - 50.73\,mm$ $P_L = 12.7 - 44.09\,mm$
Wang et al. [24]	Plain fin	Dry surface	• f – Friction factor correlation $f = 1.039Re_{dc}^{-0.418}\left(\frac{f_t}{d_c}\right)^{-0.104}N_{row}^{-0.0935}\left(\frac{f_p}{d_c}\right)^{-0.197}$	$Re_{dc} = 800 - 7500$ $d_c = 10.51\,mm$ $f_p = 1.77 - 3.21\,mm$ $N_{row} = 2 - 6$ $P_T = 25.4\,mm$ $P_L = 22\,mm$
Briggs and Young [27]	Circular fin	Dry surface	• j – Colburn factor correlation $j = 0.134Re_{dc}^{-0.319}\left[\frac{(f_p - f_t)}{\left(\frac{d_f - d_c}{2}\right)}\right]^{0.2}\left[\frac{(f_p - f_t)}{f_t}\right]^{0.11}$	$0.13 \le 2\left[\frac{(f_p - f_t)}{(d_f - d_c)}\right] \le 0.63$ $0.09 \le \frac{1}{2}\left[\frac{(d_f - d_c)}{d_c}\right] \le 0.69$ $0.011 \le \left(\frac{f_t}{d_c}\right) \le 0.15$ $1.54 \le \left(\frac{P_T}{d_c}\right) \le 8.23$

Note. Tube layouts of all correlations are staggered layout.

also occurs with an aluminum fin that has an outside diameter of 35 mm. As shown in Figures 11 and 12, the Briggs and Young correlation [27] (also shown in Table 5) for a circular fin-and-tube heat exchanger was chosen for comparison with the experimental results. It should be noted that the circular fin has the most similar configuration to the tested L-footed spiral fin. However, the difference between these two types of fins is that the tube surface at the base of the circular fin is not covered by the fin, leading to the risk of tube corrosion. As can be seen in Figures 11 and 12, the Briggs and Young correlation [27] gives the same trend of Colburn factor (j) of the circular fin compared with the experimental data with a maximum discrepancy of about 5%.

A comparison of the results for the effect of the number of tube rows on the pressure drop of L-footed spiral fin-and-tube heat exchangers is presented in Figure 13. As expected,

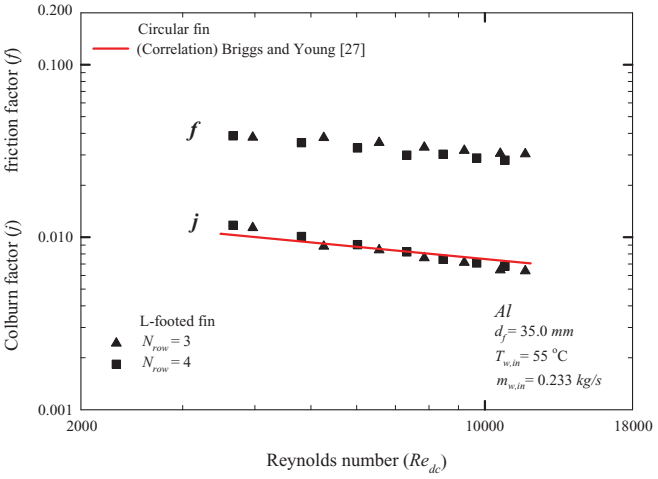

Figure 12 Effect of the number of tube rows on the Colburn factor and friction factor of the L-footed spiral fin and the tube heat exchangers at $T_{w,in} = 55°C$ and $m_{w,in} = 0.233$ kg/s (aluminum fin). (Color figure available online.)

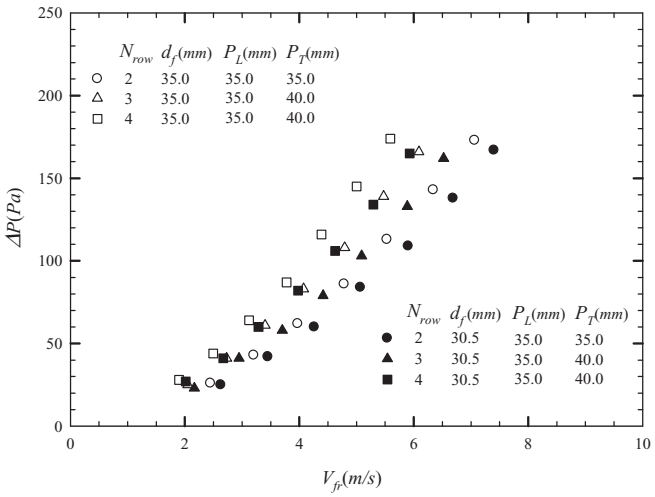

Figure 13 Effect of the fin's outside diameter on the pressure drop of the L-footed spiral fin-and-tube heat exchangers ($N_{row} = 2$, 3, and 4).

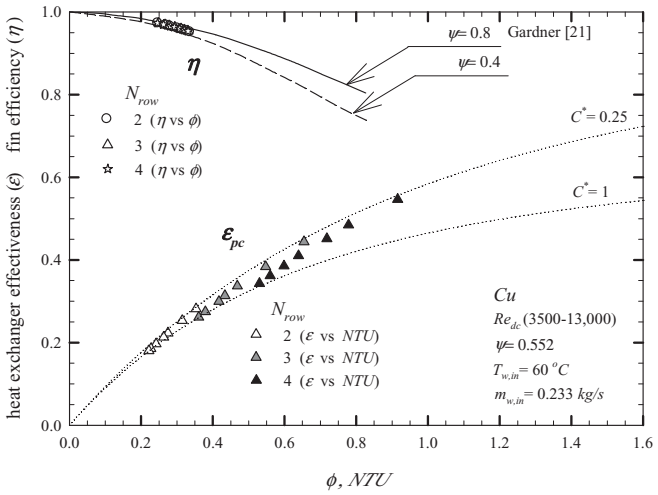

Figure 14 Effect of the number of tube rows on heat exchanger effectiveness (ε) and fin efficiency (η) (copper fin).

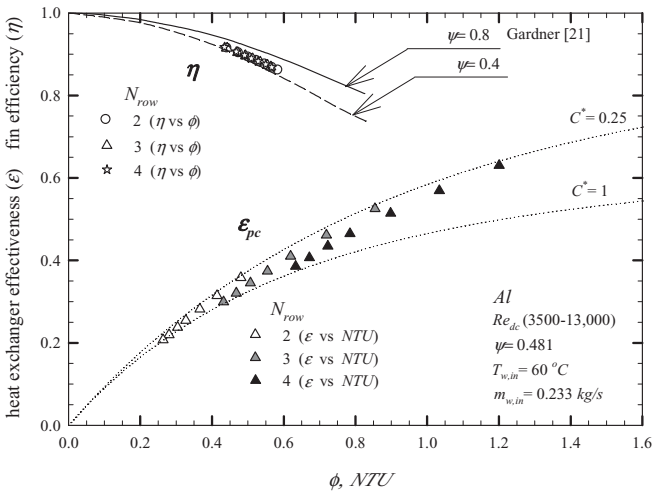

Figure 15 Effect of the number of tube rows on heat exchanger effectiveness (ε) and fin efficiency (η) (aluminum fin).

the pressure drop increases with increasing frontal air velocity while the friction factor, as mentioned earlier, decreases with an increasing Reynolds number. The pressure drop also increases with an increase in the number of tube rows. It can be seen that the pressure drop for $N_{row} = 4$ is higher than for $N_{row} = 3$ by about 22.7–23.4% ($d_f = 30.5$ mm) and 21.5–22.6% ($d_f = 35.0$ mm), respectively. Moreover, the pressure drop increases when d_f increases for the same number of tube rows. When d_f increases from 30.5 mm to 35.0 mm, the pressure drop increases by about 13.3–17.1% (for $N_{row} = 2$), 18.1–18.9% (for $N_{row} = 3$), and 16.3–18.8% (for $N_{row} = 4$) over the range of air frontal velocities (2–6 m/s). The reason for this result can be explained by the increase in the blocking flow area when d_f is increased.

Figure 14 shows the effect of the number of tube rows on the fin efficiency (η) of the copper fin with an outside diameter of 30.5 mm. It can be seen that no significant effect is found under the same experimental conditions. The reason may be explained by Eqs. (26) and (27), which show that an increase in the number of tube rows creates no significant differences in terms of ϕ and fin efficiency (η) at the same Reynolds number because of the characteristics of the efficiency of a radial fin with a rectangular profile, as proposed by Gardner [21].

The plot of heat exchanger effectiveness (ε) for multipass parallel-and-counter cross-flow heat exchangers is also shown in Figure 14. The heat exchanger effectiveness (ε) of a higher number of tube rows is higher than that of a smaller number of tube rows at the same Reynolds number. The causes of this result can be explained by the increase in the heat transfer rate between the air side and the water side with an increase in the number of tube rows. In addition, a trend similar to the one just mentioned occurs with an aluminum fin with an outside diameter of 35 mm, as Figure 15 demonstrates. In addition, Figure 16 shows the influence of the number of tube rows on the average heat transfer rate of L-footed spiral fin and tube heat exchangers. The average heat transfer rate increases with an increasing number of tube rows for both fin materials.

A comparison of the Colburn factor (j) and friction factor (f) is shown in Figure 17 in order to contrast the performance of an L-footed spiral fin to the performances of several plate fin types at high Reynolds numbers. It must be noted that none of the works described in the literature studied radial fins at a high range of Reynolds numbers, so the Colburn factor (j) and friction factor (f) of plate fins in the studies that tested at high Reynolds numbers are used for comparison with the L-footed spiral fin. It was found that the L-footed spiral fin had the same trend in the Colburn factor (j) as a plain fin, slit fin, wavy fin, and louver fin. Moreover, this same trend also occurred in the friction factor (f). It was found that the L-footed spiral fin gave a higher Colburn factor (j) than a plain fin but a lower friction factor than a plain fin. This may be because the L-footed spiral fin mixes the turbulent flow across the spaces between fins more effectively than does a plain fin. Also, the L-footed spiral fin's ability to reduce blockage flow decreases

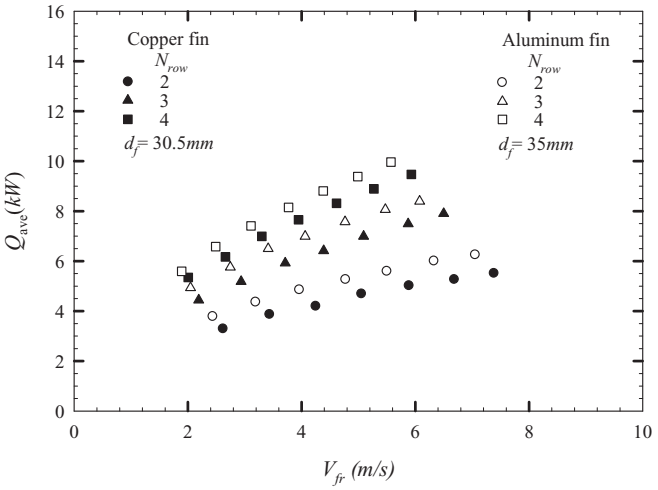

Figure 16 Effect of the number of tube rows on the average heat transfer rate at $T_{w,in} = 65°$C and $m_{w,in} = 0.2$ kg/s.

Downloaded by [Uppsala universitetsbibliotek] at 02:19 19 August 2012

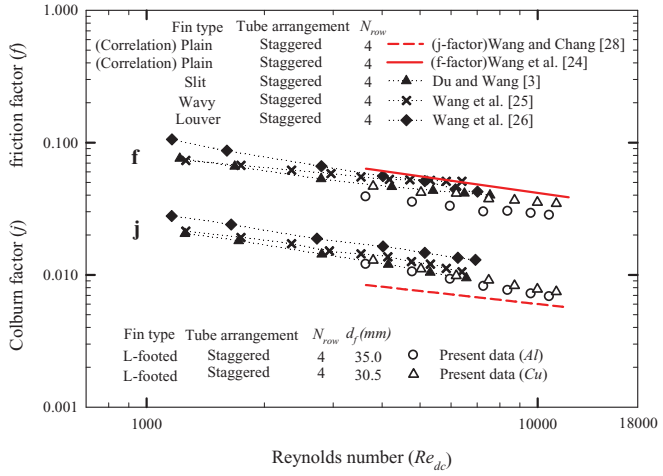

Figure 17 Comparison of j factor and f factor between presented data with correlational and experimental data of several fin types. (Color figure available online.)

with pressure drop, which affects the f factor. Furthermore, the authors found that the j factor and f factor of L-footed spiral fins are about 5–35% and 5–70% different from the plain fin, respectively. As expected, the L-footed spiral fin-and-tube heat exchanger seems to have lower j and f factors when compared to slit, wavy, and louver fin-and-tube heat exchangers, which have more complex fin shapes. In addition, Figure 17 shows only the $N_{row} = 4$ staggered L-footed spiral fins, because N_{row} has no significant effect on the Colburn factor (j) or the friction factor (f), as mentioned earlier. Therefore, the plots for $N_{row} =$ 2 and 3 will result in the same trend, which is not included in this article.

CONCLUSIONS

The objective of this study is to track the heat transfer performance of L-footed spiral fin-and-tube heat exchangers that have multipass parallel-and-counter cross-flows under sensible heating conditions and at a high Reynolds number based on the fin collar's outside diameter (3500–13,000). In total, 6 samples were investigated, each having a fin thickness of 0.25 mm, fin outside diameters (d_f) of 30.5 mm and 35.0 mm, a fin pitch of 3.25 mm, and the number of tube rows (N_{row}) at 2, 3, and 4. The conclusions and related findings of the study are as follows.

- The multipass parallel and counter cross-flow, which is combination of water flow configurations between the parallel cross-flow and the counter cross-flow, was used in this work. This type of multipass parallel-and-counter cross-flow arrangement may be an efficient choice for the reverse-flow heat exchanger that is employed in recuperative systems in modern industrial complexes, because the multipass parallel-and-counter cross-flow heat exchanger provides constant heat exchanger effectiveness under every direction of flow reversal at the same airflow rate.
- This type of water flow arrangement cannot be modeled by only one of the ε–*NTU* relationships for multipass parallel or counter cross-flow configurations because of the high variation in these relations at high Reynolds numbers (the value of C^* approaches 1). On the other hand, at low Reynolds numbers, either relation for the multipass parallel cross-flow or the counter cross-flow arrangement can be used because of the small range of variation. However, this work decided to use the average value of those ε–*NTU* relationships, which may prove to be realistic for this type of water flow arrangement.
- The number of tube rows has no significant effect on the air-side performance (j and f factors) at high Reynolds numbers (3500–13,000).
- The fin's outside diameter has a significant effect on pressure drop. The pressure drop increased as the fin's outside diameter increased for the same number of tube rows.
- It must be noted that all Colburn factors (j) and friction factors (f) calculated in this work use the model of average value of the ε–*NTU* relationships for both the multipass parallel-and-counter cross-flow configurations of water flow arrangement. However, finding the true ε-*NTU* relationships of the multipass parallel-and-counter cross-flow types may present a challenging subject for further investigation.

NOMENCLATURE

A	area, m^2
A_{min}	minimum free flow area, m^2
A_f	surface area of fin, m^2
A_o	total surface area, m^2
A_p	cross-sectional or profile area of fin, m^2
Al	aluminum
c_P	specific heat at constant pressure, J/(kg-K)
C	heat capacity rate, W/K
C^*	capacity rate ratio, dimensionless
C_c	cold-fuid capacity rate, W/K
C_h	hot-fluid capacity rate, W/K
Cu	copper
d_c	fin collar outside diameter, m
d_f	outside diameter of fin, m
d_i	tube inside diameter, m
d_o	tube outside diameter, m
f	Fanning friction factor
f_p	fin pitch, m
f_t	fin thickness, m
G_c	mass flux of the air based on minimum free flow area, kg/m^2-s
H	height, m
h	heat transfer coefficient, W/(m^2-K)
I_0	modified Bessel function solution of the first kind, order 0
I_1	modified Bessel function solution of the first kind, order 1

Downloaded by [Uppsala universitetsbibliotek] at 02:19 19 August 2012

j	Colburn factor
k	thermal conductivity, W/(m-K)
K_0	modified Bessel function solution of the second kind, order 0
K_1	modified Bessel function solution of the second kind, order 1
L	length, m
m	mass flow rate, kg/s
n_t	number of tubes in row
N_{row}	number of tube rows
NTU	number of transfer units, dimensionless
Nu	Nusselt number
P_L	longitudinal tube pitch, m
P_T	transverse tube pitch, m
Pr	Prandtl number
Q	heat transfer rate, W
r_o	radius of tip fin, m
r_i	radius of base fin, m
R	radius function in terms of the radius ratio, dimensionless
Re_{dc}	Reynolds number based on fin collar outside diameter (d_c)
Re_{di}	Reynolds number based on tube inside diameter (d_i)
Re_{do}	Reynolds number based on tube outside diameter (d_o)
T	temperature, °C
T_w	water temperature, °C
U	overall heat transfer coefficient, W/(m^2-K)
V_i	velocity based on tube inside diameter (d_i), m/s
V_{fr}	air frontal velocity, m/s
V_{max}	maximum velocity across heat exchanger, m/s

Greek Symbols

ε	heat exchanger effectiveness
η	fin efficiency
η_o	overall surface effectiveness
ρ	density, kg/m^3
σ	contraction ratio of cross-sectional area
μ	dynamic viscosity of air, Pa-s
ϕ	combination of terms, dimensionless
ψ	radius ratio
ΔP	pressure drop, Pa

Subscripts

1	air-side inlet
2	air-side outlet
a	air
ave	average
b	unfinned base surface
c	multipass counter cross flow or cold fluid
f	fin
fr	frontal ($L \times H$)
h	hot fluid
i	tube-side
in	inlet
m	mean value
max	maximum
min	minimum
o	air-side
p	multipass parallel cross-flow
pc	multipass parallel-and-counter cross-flow
t	tube
w	water

REFERENCES

[1] Wang, C. C., Lee, C. J., Chang, C. T., and Lin, S. P., Heat Transfer and Friction Correlation for Compact Louvered Fin-and-Tube Heat Exchangers, *International Journal of Heat and Mass Transfer*, vol. 42, no. 11, pp. 1945–1956, 1999.

[2] Yan, W. M., and Sheen, P. J., Heat Transfer and Friction Characteristic of Fin-and-Tube Heat Exchangers, *International Journal of Heat and Mass Transfer*, vol. 43, no. 9, pp. 1651–1659, 2000.

[3] Du, Y. J., and Wang, C. C., An Experimental Study of the Airside Performance of the Superslite Fin-and-Tube Heat Exchangers, *International Journal of Heat and Mass Transfer*, vol. 43, no. 24, pp. 4475–4482, 2000.

[4] Wongwises, S., and Chokeman, Y., Effect of Fin Pitch and Number of Tube Rows on the Air Side Performance of Herringbone Wavy Fin and Tube Heat Exchangers, *Energy Conversion and Management*, vol. 46, no. 13–14, pp. 2216–2231, 2005.

[5] Chokeman, Y., and Wongwises, S., Effect of Fin Pattern on the Air-Side Performance of Herringbone Wavy Fin-and-Tube Heat Exchangers, *Heat and Mass Transfer*, vol. 41, no. 7, pp. 642–650, 2005.

[6] Wen, M. Y., and Ho, C. Y., Heat-Transfer Enhancement in Fin-and-Tube Heat Exchanger With Improved Fin Design, *Applied Thermal Engineering*, vol. 29, no. 5–6, pp. 1050–1057, 2009.

[7] Pirompugd, W., Wang, C. C., and Wongwises, S., Correlations for Wet Surface Ratio of Fin-and-Tube Heat Exchangers, *International Journal of Heat and Mass Transfer*, vol. 53, no. 1–3, pp. 568–573, 2010.

[8] Nuntaphan, A., Kiatsiriroat, T., and Wang, C. C., Air Side Performance at Low Reynolds Number of Cross-Flow Heat Exchanger Using Crimped Spiral Fins, *International Communications in Heat and Mass Transfer*, vol. 32, no. 1–2, pp. 151–165, 2005.

[9] Wongwises, S., and Naphon, P., Heat Transfer Characteristics of a Spiral-Coil, Finned Tube Heat Exchanger Under Dry-Surface Conditions, *Heat Transfer Engineering*, vol. 27, no. 1, pp. 25–34, 2006.

[10] Wongwises, S., and Naphon, P., Thermal Performance of a spiral-Coil Finned Tube Heat Exchanger Under

Downloaded by [Uppsala universitetsbibliotek] at 02:19 19 August 2012

Wet-Surface Conditions, *Journal of Mechanical Science and Technology*, vol. 20, no. 2, pp. 212–226, 2006.
[11] Srisawad, K., and Wongwises, S., Heat Transfer Characteristics of a New Helically Coiled Crimped Spiral Finned Tube Heat Exchanger, *Heat Mass Transfer*, vol. 45, no. 4, pp. 381–391, 2009.
[12] Lee, M., Kang, T., and Kim, Y., Air-Side Heat Transfer Characteristics of Spiral-Type Circular Fin-and-Tube Heat Exchangers, *International Journal of of Refrigeration*, vol. 33, no. 2, pp. 313–320, 2010.
[13] ASHRAE, *ASHRAE Handbook—Fundamentals,* American Society of Heating, Refrigerating and Air-Conditioning Engineers, SI-ed., pp.14–15, Inc., Atlanta, GA, chap. 13, 1993.
[14] Stevens, R. A., Fernandez, J., and Woolf, J. R., Mean-Temperature Difference in One, Two, and Three-Pass Crossflow Heat Exchangers, *ASME Trans.*, vol. 79, pp. 287–297, 1957.
[15] Taborek, J., Charts for Mean Temperature Difference Industrial Heat Exchanger Configuration,in *Heat Exchanger Design Handbook*, ed. Schlunder, Hemisphere, Washington, DC, chap. 1.5, 1983.
[16] ESDU 86018, Effectiveness-NTU Relations for the Design and Performance Evaluation of Two-Stream Heat Exchangers, *Engineering Science Data Unit 86018 with Amendment*, London: ESDU International plc, pp. 92–107, 1991.
[17] Chen, T. D., Conklin, J. C., and Baxter, V. D., Comparison of Analytical and Experimental Effectiveness of Four-Row Plate-Fin-Tube Heat Exchangers With Water R-22 and R-410A, *ASME Winter Annual Meeting*, Anaheim, CA, 1998.
[18] Navarro, H. A., and Cabezas-Gomez, L., A New Approach for Thermal Performance Calculation of Cross-Flow Heat Exchanger, *International Journal of Heat and Mass Transfer*, vol. 48, no. 18, pp. 3880–3888, 2005.
[19] Cabezas-Gomez, L., Navarro, H.A., and Saiz-Jabardo, J. M., Thermal Performance of Multipass Parallel and Counter-Cross-Flow Heat Exchangers, *Journal of Heat Transfer*, vol. 129, no. 3, pp. 282–290, 2007.
[20] Gnielinski, V., New Equation for Heat and Mass Transfer in Turbulent Pipe and Channel Flow, *International Chemical Engineering*, vol. 16, pp. 359–368, 1976.
[21] Gardner, K. A., Efficiency of Extended Surface, *ASME Trans.*, vol. 67 pp. 621–631, 1945.
[22] Kays, W. M., and London, A., *Compact Heat Exchangers, 3rd ed.*, McGraw-Hill, New York, 1984.
[23] Rich, D. G., The Effect of the Number of Tube Rows on Heat Transfer Performance of Smooth Plate Fin-and-Tube Heat, *ASHRAE Trans.*, vol. 81, pp. 307–317, 1975.
[24] Wang, C. C., Chang, Y. J., Hsieh, Y. C., and Lin, Y. T., Sensible Heat and Friction Characteristics of Plate Fin-and-Tube Heat Exchangers Having Plane Fins, *International Journal of Refrigeration*, vol. 19, no. 4, pp. 223–230, 1996.
[25] Wang, C. C., Fu, W. L., and Chang, C. T., Heat Transfer and Friction Characteristics of Typical Wavy Fin-and-Tube Heat Exchangers, *Experimental Thermal and Fluid Science*, vol. 14, no. 2, pp. 174–186, 1997.
[26] Wang, C. C., Chi, K. Y., Chang, Y. J., and Chang, Y. P., An Experimental Study of Heat Transfer and Friction Characteristics of Typical Louver Fin-and-Tube Heat Exchangers, *International Journal of Heat Mass Transfer*, vol. 41, no. 4–5, pp. 817–822, 1998.
[27] Briggs, D. E., and Young, E. H., Convective Heat Transfer and Pressure Drop of Air Flowing Across Triangular Pitch Banks of Finned Tubes, *Chemical Engineering Progress Symp. Ser.*, vol. 59–41, no. 41, pp. 1–10, 1963.
[28] Wang, C. C., and Chang, C. T., Heat and Mass Transfer for Plate Fin-and-Tube Heat Exchangers With and Without Hydrophilic Coating, *International Journal of Heat Mass Transfer*, vol. 41, no. 20, pp. 3109–3120, 1998.

Parinya Pongsoi obtained his B.Eng. and M.Eng. from the Department of Mechanical Engineering, King Mongkut's University of Technology, Thonburi, Thailand. He is now a Ph.D. student at the same institute. His current research interests include the heat transfer performance and flow characteristics of fin-and-tube heat exchangers.

Santi Pikulkajorn is currently a plant manager of Somchai Industrial Co., Ltd., Bangkok, Thailand. He received his B.Eng. in mechanical engineering from King Mongkut's University of Technology, North Bangkok.

Somchai Wongwises is a professor of mechanical engineering at King Mongkut's University of Technology, Thonburi, Bangmod, Thailand. He received his Doktor-Ingenieur (Dr.-Ing.) in mechanical engineering from the University of Hannover, Germany, in 1994. His research interests include two-phase flow, heat transfer enhancement, and thermal system design. He is the head of the Fluid Mechanics, Thermal Engineering and Multiphase Flow Research Laboratory (FUTURE).

Downloaded by [Uppsala universitetsbibliotek] at 02:19 19 August 2012

Provided for non-commercial research and education use.
Not for reproduction, distribution or commercial use.

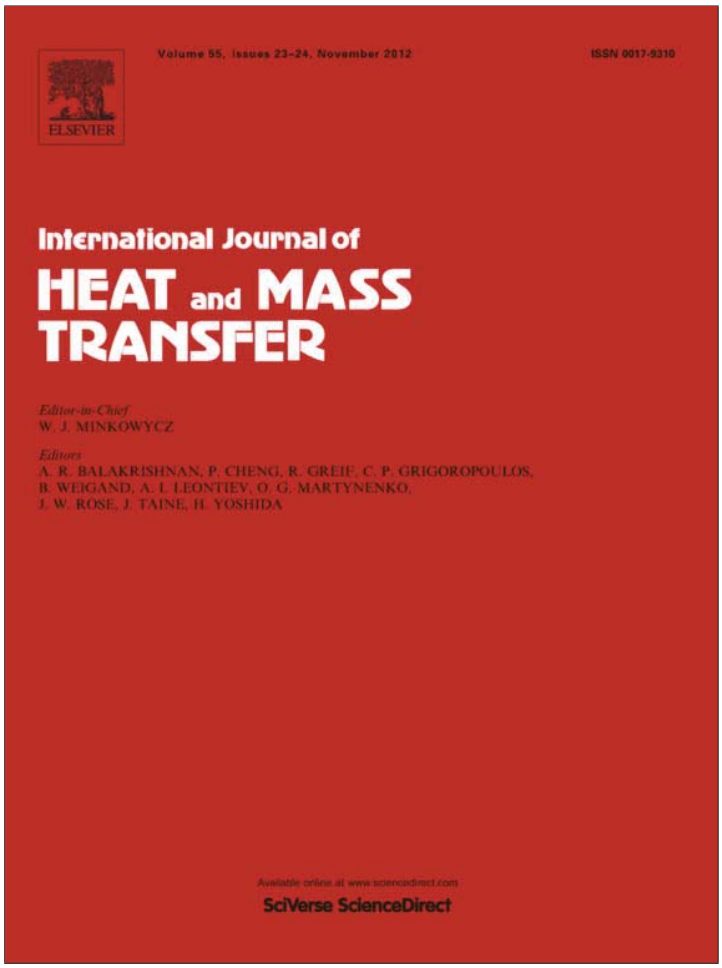

This article appeared in a journal published by Elsevier. The attached copy is furnished to the author for internal non-commercial research and education use, including for instruction at the authors institution and sharing with colleagues.

Other uses, including reproduction and distribution, or selling or licensing copies, or posting to personal, institutional or third party websites are prohibited.

In most cases authors are permitted to post their version of the article (e.g. in Word or Tex form) to their personal website or institutional repository. Authors requiring further information regarding Elsevier's archiving and manuscript policies are encouraged to visit:

http://www.elsevier.com/copyright

Author's personal copy

International Journal of Heat and Mass Transfer 55 (2012) 6555–6566

Contents lists available at SciVerse ScienceDirect

International Journal of Heat and Mass Transfer

journal homepage: www.elsevier.com/locate/ijhmt

Effect of fin pitches on the optimum heat transfer performance of crimped spiral fin-and-tube heat exchangers

Parinya Pongsoi [a], Santi Pikulkajorn [b], Somchai Wongwises [a,c,*]

[a] Fluid Mechanics, Thermal Engineering and Multiphase Flow Research Lab. (FUTURE), Department of Mechanical Engineering, King Mongkut's University of Technology Thonburi, Bangmod, Bangkok 10140, Thailand
[b] Somchai Industry Co., Ltd, Bangkok 10150, Thailand
[c] The Royal Institute of Thailand, Academy of Science, Sanam Suea Pa, Dusit, Bangkok 10300, Thailand

ARTICLE INFO

Article history:
Received 31 December 2011
Received in revised form 18 June 2012
Accepted 20 June 2012
Available online 20 July 2012

Keywords:
Crimped fin
Heat transfer
Heat exchanger
Air–water
Optimum fin pitch

ABSTRACT

This study conducted experiments on the optimized fin pitch for crimped spiral fin-and-tube heat exchangers. The experiments covered a size range of 2.4–6.5 mm, which is the manufacturing limitation for this kind of fin. The water-flow arrangement used in this experiment combined the parallel cross-flow and the counter cross-flow in a two-row configuration. Ambient air was used as the working fluid on the air-side, and hot water was used on the tube-side. The effects of fin pitches on the heat transfer coefficient and pressure drop characteristics were studied. The results clearly showed that the convective heat transfer coefficient (h_o) for a fin pitch of 2.4 mm is relatively low compared with that of other fin pitches with the same air frontal velocity. Using larger fin pitches (i.e., 4.2, 6.2, and 6.5 mm) resulted in negligible differences in the pressure drop. Moreover, this work introduces the parameter of three performances indexes, which can be expressed as the ratio of the desired output to the required input, for optimization purposes. Due to the difference in optimum fin pitch obtained by these performance indexes, an intersection analysis was conducted. The results indicated that the optimum fin pitch is 4.2 mm for this work, which could be valuable for the effective design for industrial thermal-system applications.

© 2012 Elsevier Ltd. All rights reserved.

1. Introduction

The fin-and-tube heat exchanger was designed for thermal systems in many industrial applications involving heat transfer and heating, ventilation, air conditioning, and refrigeration system (HVAC&R) applications that use a forced airflow through a fin-and-tube heat exchanger. Nowadays, the spiral fin-and-tube heat exchanger is the preferred type of heat exchanger for industrial applications. However, the heat transfer rate from the heat exchanger is normally limited by the thermal resistance on the air-side. One way to augment the heat transfer performance of the heat exchanger is to improve its fin geometry, but this method may require more fan power because of the loss associated with the pressure drop.

Many researchers have studied the effects of plate fin geometry—using plain fins, slit fins, wavy fins, louvered fins, compounded fins, circular fins, and conventional spiral fins—on the heat transfer performance and frictional characteristics. On the other hand, the review of the literature indicated that only a few studies indicated the need for research on crimped spiral fin-and-tube heat exchangers [1–7]. The crimped spiral fin features a sine-shaped fin that provides a higher heat transfer rate on the air-side through an increase in the contact surface between the fin base and the tube.

Nuntaphan et al. [1,2] studied the air-side of the crimped spiral fin heat exchanger to analyze the effects of the tubes' diameters, fin spacings, transfer tube pitches, and arrangements, and they proposed a correlation between the heat transfer and friction characteristics in the case of low Reynolds numbers under dry and wet surface conditions. The results showed that the heat transfer coefficient for the dry surface was higher than that for the wet surface. Moreover, heat exchangers using crimped spiral finned tubes were investigated by Srisawad and Wongwises [3], who focused on the air-side performance of helically coiled crimped spiral finned tube heat exchangers in dry surface conditions. Pongsoi et al. [4,5] studied the effects of fin pitch and number of tube rows on the air-side heat transfer characteristics of crimped spiral fin-tube heat exchangers having a multipass parallel and counter cross-flow arrangement under sensible heating conditions at a high Reynolds number, proposed the ε-*NTU* relation equation for this new type of water-flow arrangement, and proposed both heat transfer and friction correlations. Tang et al. [6,7] investigated the air-side heat transfer and friction characteristics of five kinds of fin-and-tube

* Corresponding author at: Fluid Mechanics, Thermal Engineering and Multiphase Flow Research Lab. (FUTURE), Department of Mechanical Engineering, King Mongkut's University of Technology Thonburi, Bangmod, Bangkok 10140, Thailand. Tel.: +66 24709115.
E-mail address: somchai.won@kmutt.ac.th (S. Wongwises).

0017-9310/$ - see front matter © 2012 Elsevier Ltd. All rights reserved.
http://dx.doi.org/10.1016/j.ijheatmasstransfer.2012.06.061

Author's personal copy

Nomenclature

A	area, m^2
A_{min}	minimum free flow area, m^2
A_f	surface area of fin, m^2
A_o	total surface area, m^2
A_p	cross-sectional or profile area of fin, m^2
c_p	specific heat at constant pressure, J/(kg K)
C	heat capacity rate (mc_p), W/K
C^*	capacity rate ratio, dimensionless
C_c	cold-fuid capacity rate, W/K
C_h	hot-fluid capacity rate, W/K
d_f	outside diameter of fin, m
d_i	tube inside diameter, m
d_o	tube outside diameter, m
f	Fanning friction factor, dimensionless
f_p	fin pitch, m
f_t	fin thickness, m
G_c	mass flux of the air based on minimum free flow area, kg/m^2 s
H	height, m
h	heat transfer coefficient, W/(m^2 K)
I_o	modified Bessel function solution of the first kind, order 0
I_1	modified Bessel function solution of the first kind, order 1
k	thermal conductivity, W/(m K)
K_0	modified Bessel function solution of the second kind, order 0
K_1	modified Bessel function solution of the second kind, order 1
L	length, m
m	mass flow rate, kg/s
n	number of tubes in row
N_{row}	number of tube rows
NTU	number of transfer units, dimensionless
P_L	longitudinal tube pitch, m
P_T	transverse tube pitch, m
Pr	Prandtl number, dimensionless
Q	heat transfer rate, W
r_o	radius of tip fin, m
r_i	radius of base fin, m
R	radius function in terms of the radius ratio, dimensionless
Re_{di}	Reynolds number based on tube inside diameter (d_i), dimensionless
Re_{do}	Reynolds number based on tube outside diameter (d_o), dimensionless
T	temperature, °C
U	overall heat transfer coefficient, W/(m^2 K)
V_i	velocity based on tube inside diameter (d_i), m/s
V_{fr}	air frontal velocity, m/s
W_p	fan power, W

Greek symbols

ε	heat exchanger effectiveness
η	fin efficiency
η_o	overall surface effectiveness
ρ	density, kg/m^3
σ	contraction ratio of cross-sectional area
μ	dynamic viscosity of air, Pa s
ϕ	combination of terms, dimensionless
ψ	radius ratio, dimensionless
ΔP	pressure drop, Pa
ζ_1	heat exchanger performance index, W/Pa
ζ_2	system performance index, W/Pa
ζ_3	dimensionless system performance index, dimensionless

Subscripts

1	air-side inlet
2	air-side outlet
a	air
ave	average
b	unfinned base surface
c	multipass counter cross flow or cold fluid
f	fin
fr	frontal ($L \times H$)
h	hot fluid
HX	heat exchanger
i	tube-side
in	inlet
m	mean value
max	maximum
min	minimum
o	air-side
p	multipass parallel cross flow
pc	multipass parallel-and-counter cross flow
Sys	system
t	tube
w	water

heat exchangers crimped spiral fin, plain fin, slit fin, fin with delta-wing longitudinal vortex generators, and mixed fin for which the number of tube rows (N_{row}) was 12 and the diameter of the tubes (d_o) was 18 mm throughout both experimental and numerical investigation. Their results indicated that the crimped spiral fin gave a high pressure drop, but it also provided a higher air-side heat transfer performance than the other types.

According to the literature, several studies have been devoted to the heat transfer and friction characteristics of finned tube heat exchangers under numerous conditions. However, research is needed in the area of the optimal design for fin and tube heat exchangers. Previous researchers [8–10] have extensively observed that the effects of the fin pitch give reliable guidelines for an effective design of the plate and circular fin, in which the other geometric effects, such as fin thickness, longitudinal tube pitch, and transverse tube pitch, show no significance with regard to the optimum fin pitch. Nevertheless, until now, none of the studies in the literature reported on the optimal heat transfer performance of crimped spiral fin-and-tube heat exchangers. Therefore, the purpose of this study is to investigate the optimized fin pitch for a crimped spiral fin-and-tube heat exchanger having a two-row configuration. The fin pitches that were tested covered a size range of 2.4 mm to 6.5 mm, which is the manufacturing limitation for this kind of fin. Finding the optimized fin pitch would be valuable when designing industrial applications in HVAC&R systems, waste heat recovery units (WHRU), and other units and systems.

2. Experimental apparatus

A schematic diagram of the experimental apparatus is shown in Fig. 1. Air and hot water were used as the working fluids. The main

Author's personal copy

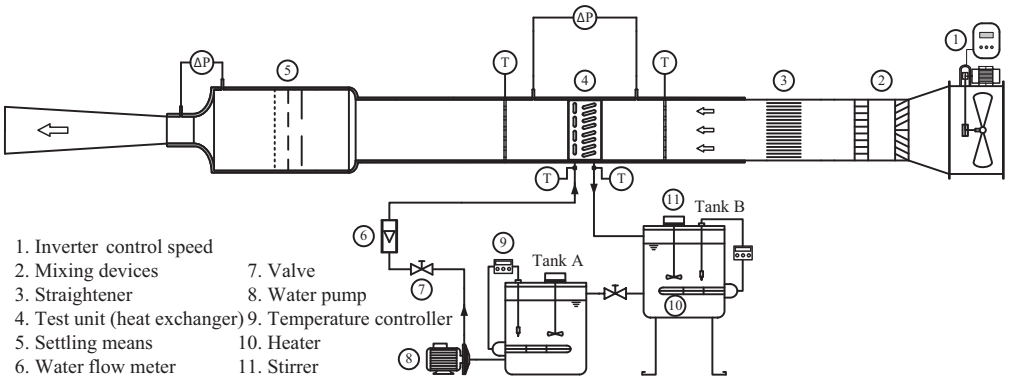

Fig. 1. Schematic diagram of the experimental apparatus.

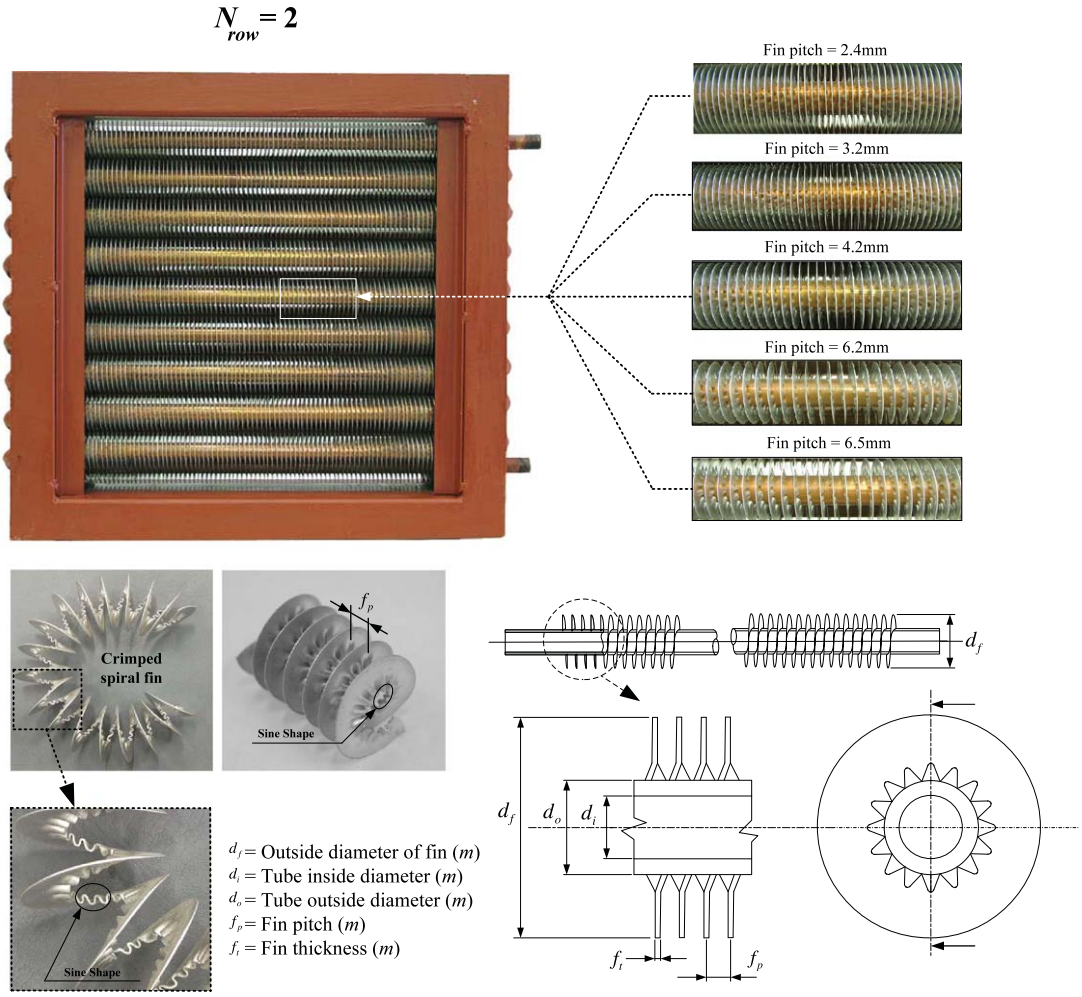

Fig. 2. The photos of the tested crimped spiral fin and tube heat exchangers and schematic diagram of crimped spiral fin.

components of the system were the heat exchanger, water-flow loop, air supply, instrumentation, and data acquisition system.

The present study used a type of fin-and-tube heat exchanger. The copper tubes have a large diameter (about 16 mm), and are very commonly used in ventilator and fan-coil units [11,12]. Moreover, the tubes are also finned with aluminum fins. Photos of the crimped spiral fin pattern are shown in Fig. 2. The water-side circuitry arrangement and detailed dimensions of the tested fin-and-tube heat exchangers are shown in Fig. 3. Finally, the geometric parameters of the heat exchangers are summarized in Table 1.

An open-type wind tunnel was used to push air through the heat exchanger. The connections of the duct were designed so that parts could be changed or repaired quickly and easily. This arrangement operated in a cross-flow with the hot water passing through the heat exchanger. The tunnel was a rectangular air duct fabricated from a 0.43 × 0.48 m steel plate. The duct was insulated with a 16 mm thick Aeroflex standard sheet. The fresh air was drawn into the duct and passed through the mixing device, straightener, and heat exchanger by means of a 2.2 kW axial flow fan. The speed of the fan was adjusted with an inverter.

Author's personal copy

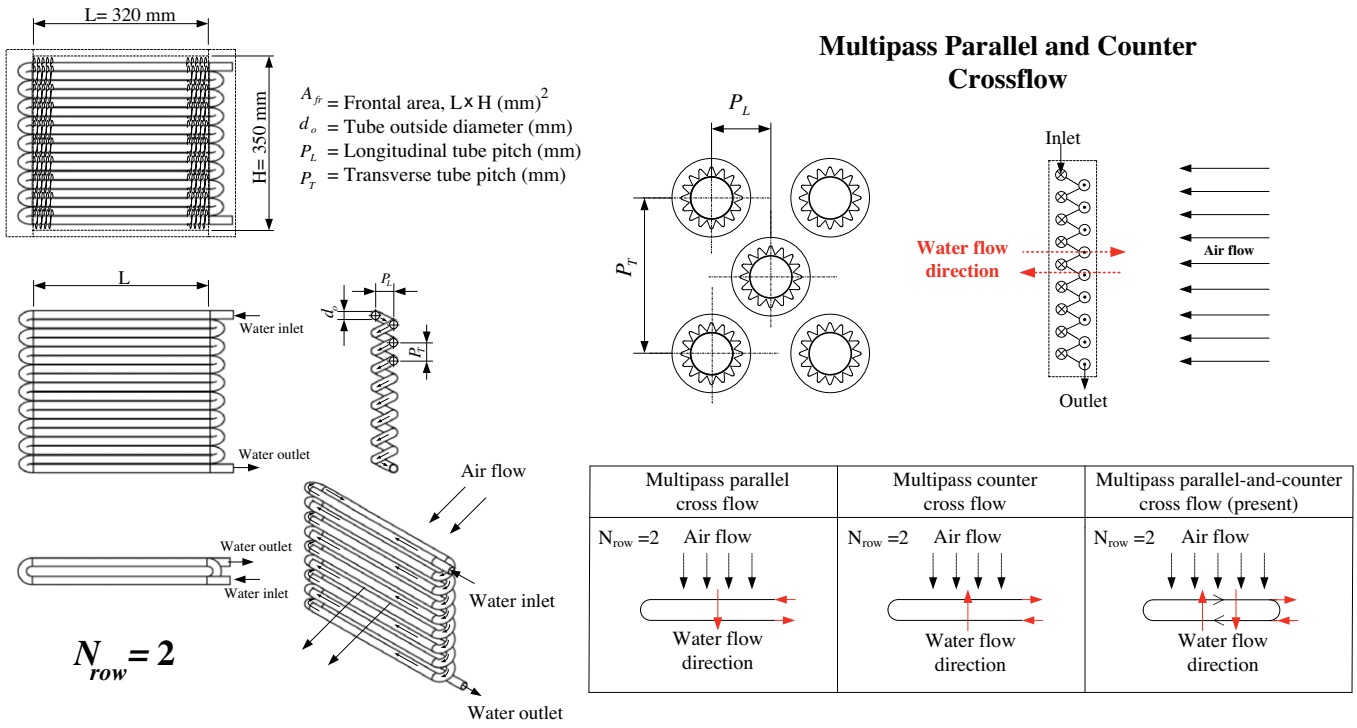

Fig. 3. Geometric details and schematic diagram of the heat exchangers algorithm for multipass parallel cross flow, multipass counter cross flow and multipass parallel-and-counter cross flow (× and • signs indicate that water flows into or out of the paper, respectively).

Table 1
Detailed geometric parameters of the test samples.

No.	Fin type	d_i (mm)	d_o (mm)	d_f (mm)	P_L (mm)	P_T (mm)	f_t (mm)	n_t	N_{row}	f_p (mm)
1–5	Crimped	13.5	16.35	34.8	35	39	0.4	9	2	2.4, 3.2, 4.2, 6.2 and 6.5

Remarks: d_f = outside diameter of fin; d_i = tube inside diameter; d_o = tube outside diameter; f_p = fin pitch; f_t = fin thickness; P_L = longitudinal tube pitch; P_T = transverse tube pitch; n_t = number of tubes in row; N_{row} = number of tube rows.
Notes: Tube layouts of all heat exchangers are staggered layout.

Thermocouple probes were located at the air inlet and outlet sections of the heat exchanger. The temperature was measured with 1 mm diameter probes extending into the duct where the air flowed. The probes were T-type copper-constantan thermocouples grounded to a stainless steel outer sheath. The measuring points were at the positions recommended by the ASHRAE standard [13]. The temperature was monitored and recorded continuously. All temperature-measuring devices were well calibrated in a controlled temperature bath using a standard precision mercury-in-glass thermometer. All sensors were wired directly to terminal control panels mounted on the bench. The air flow rate was detected with a nozzle based on the ISO 5801 standard. The drops in air pressure across the test section and the nozzle were measured with a digital manometer. Four pressure taps were attached on each wall: upstream and downstream taps in the test section and in the nozzle.

To avoid any distortion of the air velocity profile, mixing devices and straighteners were installed in the duct. Air velocity and air velocity fluctuation in the duct were checked with a Constant Temperature Anemometer 90CN10/C10 (CTA, Dantec) that had an automatic probe setup. Stream Ware software was used to set up the anemometer modules, to perform velocity and directional calibrations, and to provide an experimental platform wherein automatic sequences of hardware setup, data acquisitions, and data reductions could be performed. The probe used in this experiment was a wedge-shaped, right-angled film probe 55R33 with a

Table 2
Experimental conditions.

Inlet-air-dry bulb temperature, °C	31.5 ± 0.5
Inlet-air frontal velocity, m/s	2 – 6
Inlet-water temperature, °C	55 – 70
Water flow rate, kg/s	0.2 – 0.233

Table 3
The accuracies of the measurements.

Parameters	Accuracy
Inlet-air dry-bulb temperature, °C	±0.1
Pressure drop, *Pa*	±0.5
Inlet-water temperature, °C	±0.1
Water flow rate, kg/s	±0.4 (±0.02 of full scale)

Table 4
Uncertainties of the derived experimental values.

Parameters	Maximum uncertainties (%)
Air-side heat transfer rate, Q_a	±4.96
Water-side heat transfer rate, Q_w	±3.37
Pressure drop, ΔP	±2.50
Frontal velocity, V_{fr}	±3.30
Air-side heat transfer coefficient, h_o	±8.98

Author's personal copy

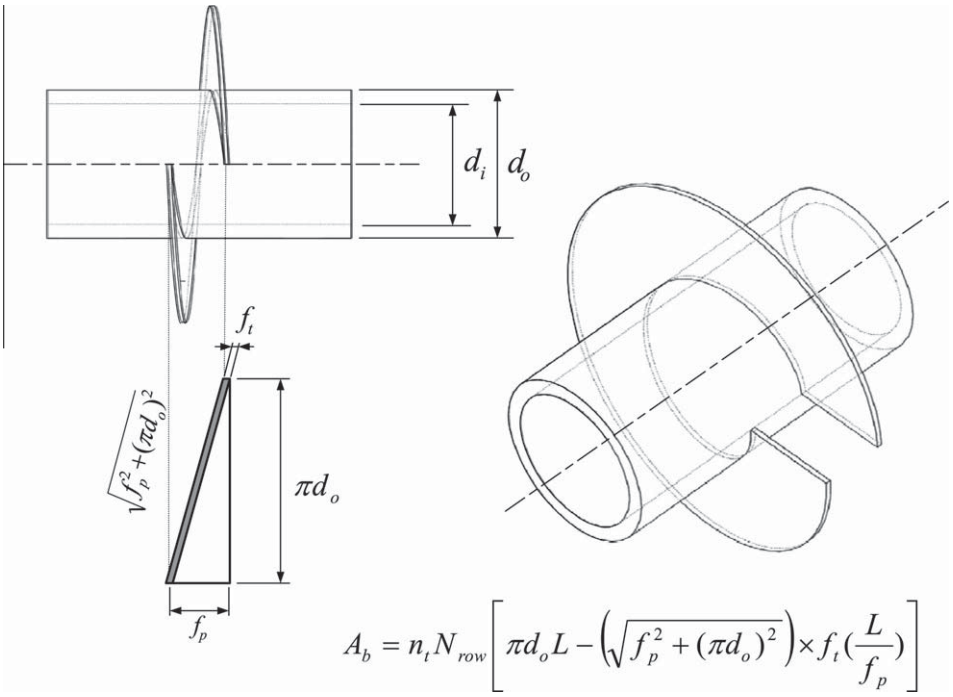

Fig. 4. Details of area of unfinned base surface (A_b) equation.

non-cylindrical sensor in a 1 × 0.2 mm sheath. All signals were registered by a data acquisition system and then averaged over the elapsed time.

The hot-water flow loop consisted of two storage tanks, an 18 kW electric heater, a centrifugal pump, a control unit, and a flow meter with a 0.5 *LPM* resolution (Fig. 1). The purpose of this loop was to transfer heat to the air flowing through the heat exchanger. The temperature of the hot water in the two tanks was measured with T-type copper-constantan thermocouples and was controlled with the temperature controller. After the hot water had been heated to the required temperature, it was pumped out of storage tank (A), delivered to the heat exchanger, and then returned to storage tank (B), which was used to pre-heat the water in order to reduce the temperature difference before entering tank (A). The water temperatures at the inlet and outlet of the heat exchanger were measured with 1 mm diameter probes extending inside the tube where the water flowed. The probes consisted of T-type copper-constantan thermocouples grounded to a stainless steel outer sheath.

In the experiment, at a specific inlet water temperature, the water flow rate was fixed while the air flow rate was increased. The system was allowed to approach a steady state before any data was recorded. After the system reached a steady state, the inlet and outlet temperatures of the air passing across the heat exchanger and the water flow rates were determined. All tested conditions of the heat exchangers are shown in Table 2. It must be noted that for industrial service, the operation velocity is normally much higher, as reported by Xie et al. [11]. Therefore, this study extended the applicable range (V_{fr} up to 6 m s^{-1}). The accuracies of the direct measurement sensors and the uncertainties, which were calculated using the root mean sum square method, are shown in Tables 3 and 4.

3. Data reduction

In order to determine the heat transfer characteristics of the heat exchangers from the data recorded under steady state conditions during each test run, the method of number of transfer units (*ε-NTU*), based on the concept of heat exchanger effectiveness, was applied to determine the *UA* product.

The air-side heat transfer rate is given as:

$$Q_a = m_a c_{P,a} \Delta T_a \tag{1}$$

The water-side heat transfer rate is given as:

$$Q_w = m_w c_{P,w} \Delta T_w \tag{2}$$

The total rate of heat transfer used in the calculation is averaged from the air-side and water-side as follows:

$$Q_{ave} = \frac{|Q_a| + |Q_w|}{2} \tag{3}$$

The overall heat transfer coefficient can be written in terms of the total resistance to heat transfer. This total resistance is the sum of the individual resistances, as follows:

$$\frac{1}{UA} = \frac{1}{h_i A_i} + \frac{ln(d_o/d_i)}{2\pi k_t L} + \frac{1}{\eta_o h_o A_o} \tag{4}$$

The ε-NTU relationships with one fluid mixed and one fluid unmixed in the cross-flow were employed to determine the overall heat transfer coefficient. From Fig. 3, the present mixed circuitry arrangement is a combination of parallel and counter cross-flow. Therefore, the ε-NTU relationships developed by Pongsoi et al. [4] were selected to calculate the heat exchanger effectiveness. This relation combines both the effect of parallel and the counter cross-flow configuration of water-flow arrangement from [14–16], as shown in Eqs. (5)–(7), in order to calculate the overall heat transfer coefficient. However, the multipass parallel and counter cross-flow used in this experiment is a combination of multipass parallel cross-flow and counter cross-flow. It may be suitable to use the average value of those relations shown in Eq. (7). The schematic diagram of the heat exchangers algorithm for multipass parallel cross-flow, multipass counter cross-flow, and multipass parallel and counter cross-flows (Nrow = 2) are shown in Fig. 3. For the present flow configuration, the heat exchanger's

Author's personal copy

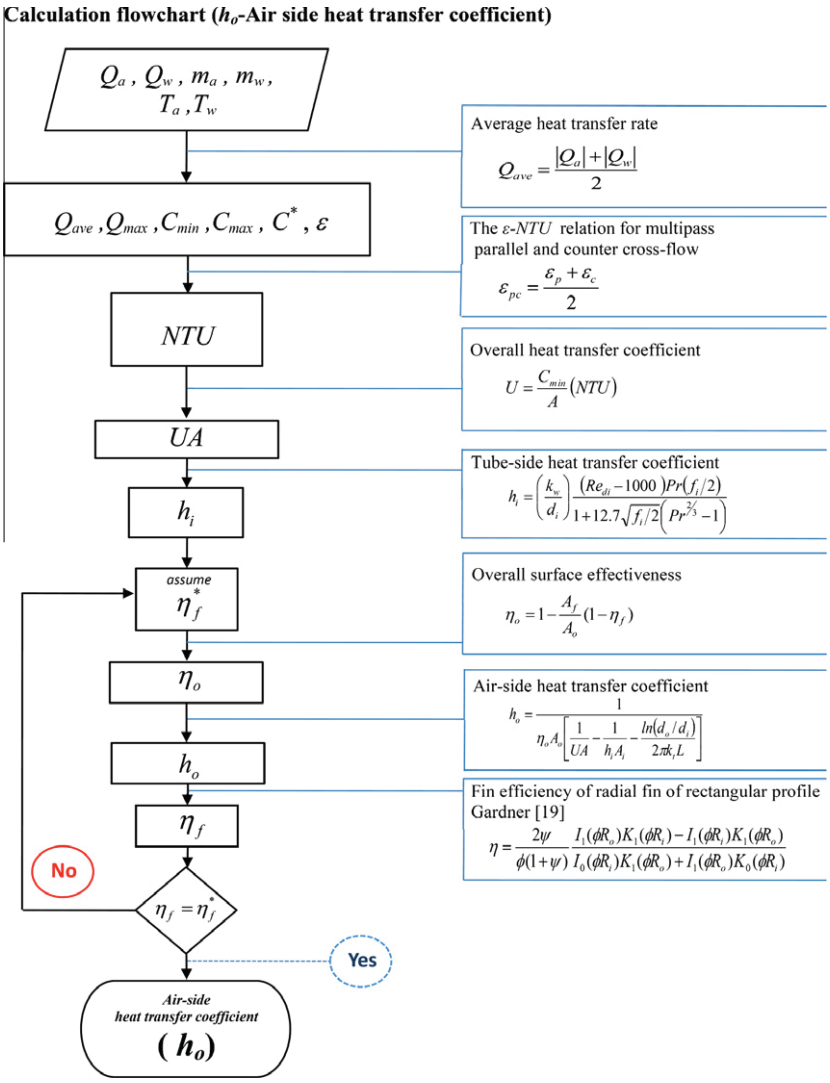

Fig. 5. Flowchart of the data reduction for air-side heat transfer coefficient (h_o).

effectiveness lies between the multipass parallel cross-flow and the counter cross-flow. Note that using inappropriate ε-NTU relationships for complex flow arrangement may lead to an error of up to 10%, as pointed out by Navarro and Cabezas-Gomez [17]. This type of multipass parallel and counter cross-flow arrangement may be an efficient choice for the reverse flow heat exchanger that is employed in recuperative systems in modern industrial complexes.

In this work, the air-side working fluid (air) is defined as fluid A, and the tube-side working fluid (water) is defined as fluid B. It should be noted that the minimum heat capacity rate (Cmin) is on the air-side (fluid A). Therefore, the following relations are applied in the present calculations.

Multipass parallel cross-flow

For (N_{row} = 2):

$$\varepsilon_p = \left(1 - \frac{K}{2}\right)\left(1 - e^{-2K/C_A^*}\right), \quad K = 1 - e^{-NTU_A(C_A^*/2)} \tag{5}$$

Multipass counter cross-flow

For (N_{row} = 2):

$$\varepsilon_c = 1 - \left[\frac{K}{2} + \left(1 - \frac{K}{2}\right)e^{2K/C_A^*}\right]^{-1}, \quad K = 1 - e^{-NTU_A(C_A^*/2)} \tag{6}$$

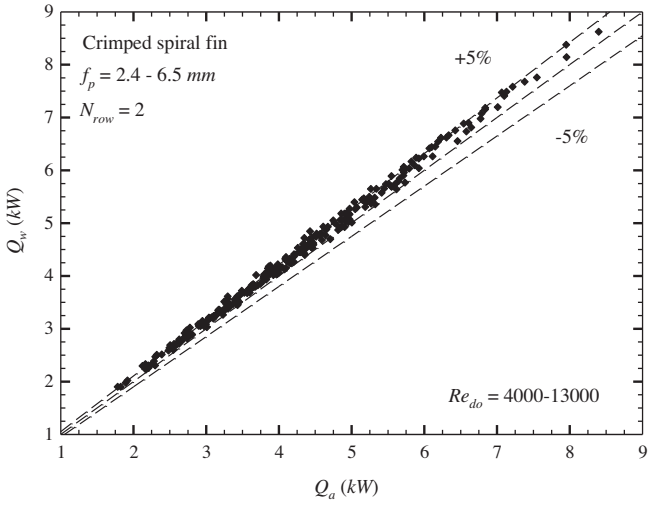

Fig. 6. Energy balance between air and water.

Author's personal copy

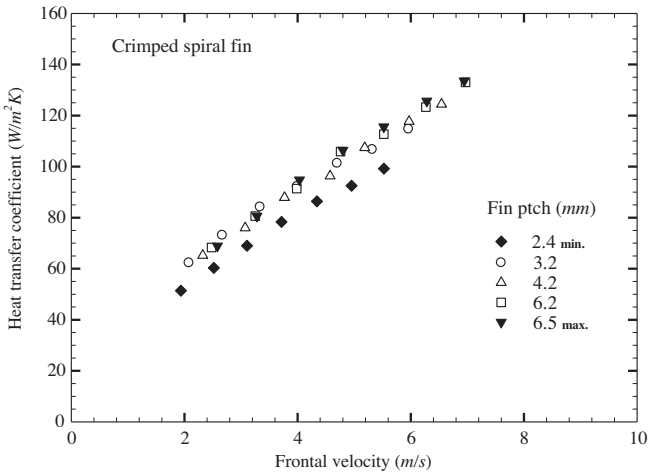

Fig. 7. Effect of fin pitch on the air-side heat transfer coefficient of crimped spiral fin and tube heat exchangers at $T_{w,in}$ = 70 °C and water flow rate of 0.233 kg/s.

where

$$\varepsilon_A = \frac{\varepsilon_p + \varepsilon_c}{2} \tag{7}$$

fluid A is mixed(C_{min}); fluid B is unmixed(C_{max}).

$$\varepsilon_A = \varepsilon_B / C_A^* \tag{8}$$

$$C_A^* = \frac{C_A}{C_B} = \frac{1}{C_B^*} \quad C^* \leqslant 1 \tag{9}$$

$$NTU_A = \frac{NTU_B}{C_A^*} \tag{10}$$

where $C^* = C_{min}/C_{max}$ is equal to C_c/C_h or C_h/C_c, depending on the value of the hot and cold fluid heat capacity rates.

$$C_{min} = C_h; C_h < C_c \tag{11}$$

or

$$C_{min} = C_c; C_c < C_h \tag{12}$$

as

$$Q_{max} = (mc_P)_c(T_{h1} - T_{c1}) \text{ if } C_c < C_h \tag{13}$$

or

$$Q_{max} = (mc_P)_h(T_{h1} - T_{c1}) \text{ if } C_h < C_c \tag{14}$$

$$\varepsilon = \frac{Q_{ave}}{Q_{max}} \tag{15}$$

The UA term in Eq. (4) is calculated by using Eq. (16):

$$UA = C_{min}(NTU) \tag{16}$$

The tube-side heat transfer coefficient (h_i) is evaluated from the semi-empirical correlation of Gnielinski [18]:

$$h_i = \left(\frac{k_w}{d_i}\right) \frac{(Re_{di} - 1000)Pr(f_i/2)}{1 + 12.7\sqrt{f_i/2}\left(Pr^{2/3} - 1\right)} \tag{17}$$

where the friction factor is given by:

$$f_i = (1.58 ln Re_{di} - 3.28)^{-2} \tag{18}$$

where $Re_{di} = \rho V_i d_i/\mu$

The overall surface effectiveness (η_o), which is defined as the ratio of effective heat transfer area to total heat transfer area, can be expressed in terms of fin efficiency (η), fin surface area (A_f), and total surface area (A_o), as follows:

$$\eta_o = 1 - \frac{A_f}{A_o}(1 - \eta) \tag{19}$$

The relationship among the total surface area of the fin (A_o), the surface area of the fin (A_f), and (A_b) equals the area of the unfinned base surface (in Fig. 4). It is determined from Eq. (20):

$$A_b = n_t N_{row}\left[\pi d_o L - \left(\sqrt{f_p^2 + (\pi d_o)^2}\right) \times f_t\left(\frac{L}{f_p}\right)\right] \tag{20}$$

The surface area of fin (A_f) can be estimated by assuming it to be equal to that of the radial fin:

$$A_f = n_t N_{row}\left(\frac{L}{f_p}\right)[0.5\pi d_f^2 - 0.5\pi d_o^2 + \pi d_f f_t] \tag{21}$$

where $A_o = A_f + A_b$

The efficiency of a radial fin with a rectangular profile is determined by the method proposed by Gardner [19]:

$$\eta = \frac{2\psi}{\phi(1+\psi)} \frac{I_1(\phi R_o)K_1(\phi R_i) - I_1(\phi R_i)K_1(\phi R_o)}{I_0(\phi R_i)K_1(\phi R_o) + I_1(\phi R_o)K_0(\phi R_i)} \tag{22}$$

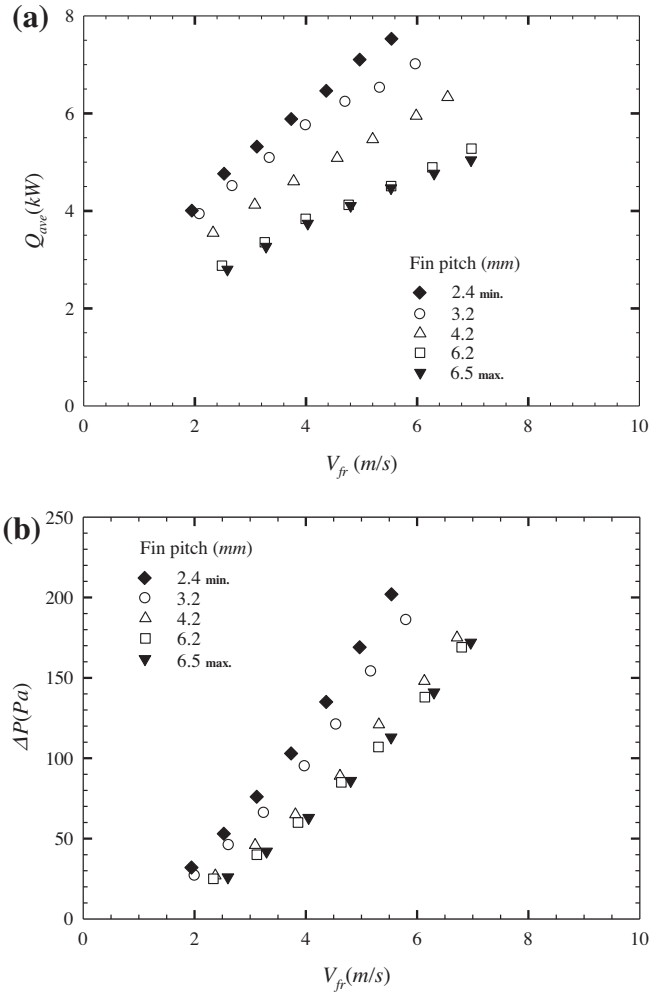

Fig. 8. Effect of fin pitches on (a) the average heat transfer rate and (b) the pressure drop of crimped spiral fin and tube heat exchangers at $T_{w,in}$ = 65 °C and water flow rate of 0.233 kg/s.

Author's personal copy

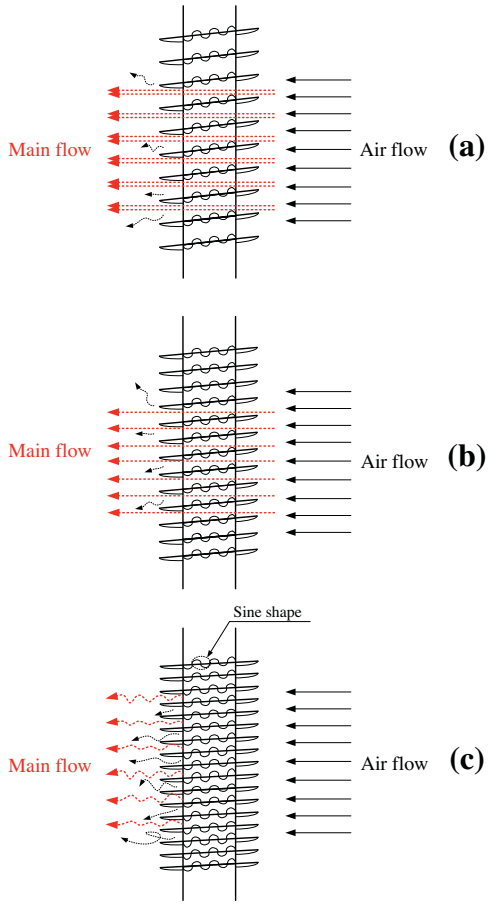

Fig. 9. Schematic showing the flow distribution at fin base of crimped spiral fin (sine shape): (a) f_p = 6.5 and 6.2 mm, (b) f_p = 4.2 mm and (c) f_p = 3.2 and 2.4 mm.

where

$$\phi = (r_o - r_i)^{3/2}\left(\frac{2h_o}{k_f A_p}\right)^{1/2} \tag{23}$$

The air-side heat transfer coefficient (h_o) can then be calculated from Eq. (4). The flow chart with the reduction of the data is shown in Fig. 5.

According to the main purpose of this work, in order to find an optimized fin pitch, the parameter called the performance index must be introduced. In general, the performance index is considered as the ratio of the desired output to the required input. However, there are three performance indexes introduced in this work: the heat exchanger performance index, the system performance index, and the dimensionless system performance index, which can be expressed as below.

The heat exchanger performance index:

$$\zeta_1 = (Q_{ave}/\Delta P)_{HX} \tag{24}$$

which subscript "*HX*" means "heat exchanger".

The system performance index:

$$\zeta_2 = (Q_{ave}/\Delta P)_{Sys} \tag{25}$$

which subscript "*Sys*" means "system".

The dimensionless system performance index:

$$\zeta_3 = (Q_{ave}/W_p)_{Sys} \tag{26}$$

which W_p is fan power.

The pumping (fan) power determined from the equation proposed by Kays and London [20] is given in terms of the fanning friction factor. The equation includes the entrance and exit pressure losses:

$$f = \left(\frac{A_{min}}{A_o}\right)\left(\frac{\rho_m}{\rho_1}\right)\left[\frac{2\Delta P\rho_1}{G_c^2} - (1+\sigma^2)\left(\frac{\rho_1}{\rho_2} - 1\right)\right] \tag{27}$$

where σ is the ratio of minimum free flow area to frontal area, A_o is the total heat transfer area, and A_{min} is the minimum free flow area.

For Eq. (27), if entrance and exit effects are negligible ($\rho_1 = \rho_2$ and $\rho_m = [\rho_1 + \rho_2]/2$), then the friction coefficient can be calculated from

$$f = \frac{A_{min}\rho_m}{A_o}\left[\frac{2\Delta P}{G_c^2}\right] \tag{28}$$

Therefore, the pumping (fan) power is

$$W_p = \frac{G_c A_{min}\Delta P}{\rho_m} \tag{29}$$

The reason for choosing these three performance indexes and how to use them in order to find and optimized the fin pitch will be explained and discussed later in the Results section.

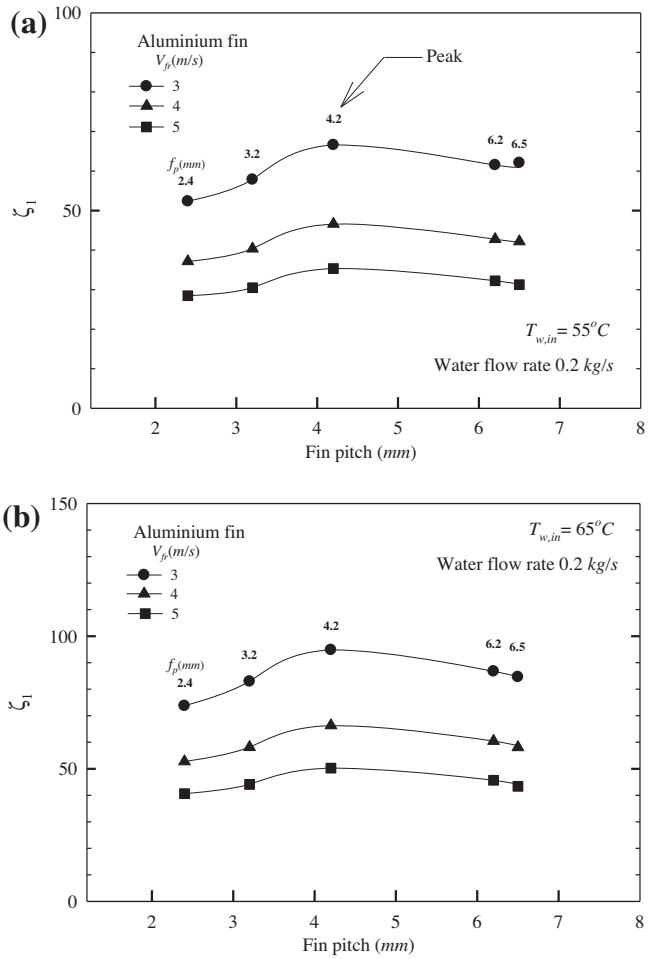

Fig. 10. Effect of fin pitch on the heat exchanger performance index ζ_1 having different inlet-water temperatures (a) 55 °C and (b) 65 °C.

Author's personal copy

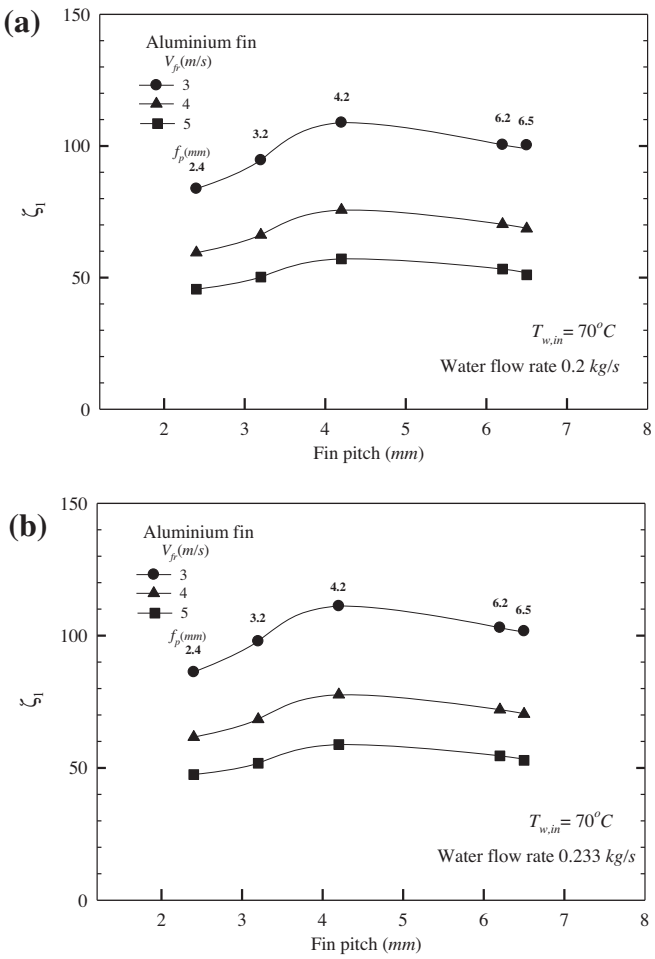

Fig. 11. Effect of fin pitch on the heat exchanger performance index ζ_1 having different water flow rates.

4. Results and discussion

The experimental results of this study are presented based on the energy balances between the air- and water-sides and are used to determine the performance of the crimped spiral fin and tube heat exchangers (Fig. 6). The experiments were conducted following the ANSI/ASHRAE 33 Standards [21] in which the energy unbalance between the air and water of the crimped spiral fin-and-tube heat exchangers, denoting $|Q_a - Q_w|/Q_{ave}$, is less than 0.05. Some experimental data from Pongsoi et al. [4] was also used in this work. The analysis of the heat transfer performance of all the heat exchangers examined are presented in terms of the heat transfer coefficient and pressure drop plotted against the air frontal velocity (V_{fr}). As expected, both the heat transfer and pressure drop increased along with the increasing air frontal velocity. In addition, the experimental results mostly focused on the three performances indexes, ζ_1, ζ_2, and ζ_3, which are important for the analysis of the optimum fin pitch.

Fig. 7 illustrates the effects of fin pitches on the air-side heat transfer coefficient of crimped spiral fin-and-tube heat exchangers having a two-row configuration and fin pitches of 2.4, 3.2, 4.2, 6.2 and 6.5 mm. Test results indicated that the effects of fin pitch on the heat transfer coefficient are very small at 3.2, 4.2, 6.2, and 6.5 mm. In this regard, higher operating velocities promote better mixing and lead to a better heat transfer coefficient, and this phenomenon prevails regardless of a change in the fin pitch. In contrast, for fin pitch 2.4 mm, it can be clearly seen that the heat transfer coefficient lower than other fin pitches, about 11–15% at the same air frontal velocity. This result is similar to that described by Kim and Kim [22] (plate fin or conventional heat exchangers), Mon and Gross [23] (annular fin), and Lee et al. [24] (spiral fin). It is believed to be the result of boundary layer interruption between fin spacing, preventing an increase in heat transfer coefficient. The convection heat transfer coefficient decreases with smaller fin pitches as the boundary layer becomes thicker with a decrease in fin pitch, which can cause easier boundary layer interruption between the fins [24]. However, this phenomenon did not occur at a large fin pitch, as mentioned by Kim and Kim [22].

Fig. 8(a) shows the influence of fin pitches on the average heat transfer rate of crimped spiral fin-and-tube heat exchangers. The average heat transfer rate increases as fin pitch decreases. When f_p decreases from 6.2 mm to 2.4 mm, the average heat transfer rate increases by about <5% (for f_p = 6.2 mm), 27–32% (for f_p = 4.2 mm), 49–55% (for f_p = 3.2 mm), and 65–70% (for f_p = 2.4 mm) to a fin pitch of 6.5 mm over the range of air frontal velocities (2 – 6 m/s). Furthermore, the effects of fin pitch on the average heat transfer rate in case of 6.2 mm and 6.5 mm are negligible. Moreover, Fig. 8(b) shows the effects of fin pitches on the pressure drop of a crimped spiral fin-and-tube heat exchanger. As expected, the pressure drop increases as air frontal velocity increases. Furthermore, using larger fin pitches (i.e., 4.2, 6.2, and 6.5 mm) results in negligible differences in the pressure drop. Over the range of air frontal velocities, it was found that the pressure drops of the f_p = 2.4, 3.2, 4.2, and 6.2 mm are higher than that of the f_p = 6.5 mm by about 78–103%, 52–64%, 11–20% and <8%, respectively. This might be because the main flow at base of the fin can flow along the corrugated channel more effectively compared with smaller fin pitches (i.e., 2.4 mm and 3.2 mm) as illustrated in Fig. 9(a) and (b). On the other hand, the flow distribution at the base of fin (sine shape) in the case of fin pitches of 2.4 mm and 3.2 mm seems to be strongly obstructed by the closer channel of fin pitch as shown in Fig. 9(c), resulting in the highest pressure drop (for f_p = 2.4 mm).

For the optimization of fin pitch, the descriptive analysis is presented for three performances indexes (ζ_1, ζ_2, and ζ_3 These indexes described in this work can be expressed as the ratio of the desired output to the required input, as mention before. However, unlike other thermal systems, the determination of the performance index is too complicated for the heat exchanger. Therefore, in this present work, the performance index will be derived in three terms and will be discussed later in order to determine which one is preferable.

First, the heat exchanger performance index (ζ_1), in which the consideration is a focus only on the heat exchanger section, can be expressed as the ratio of heat absorbed by the air-side to the pressure drop of heat exchanger, which indicates the air flow friction across the heat exchanger. Therefore, (ζ_1) can be described as the performance of the heat exchanger. The effects of fin pitches on the performance index (ζ_1) is shown in Figs. 10 and 11 as having a different inlet-water temperature and a water flow rate, respectively. This figure shows that ζ_1 increases with increasing fin pitch until reaching its maximum value at a fin pitch of 4.2 mm, and then decreases with further increases in the fin pitch. This phenomenon is the same for all air frontal velocity. This might be because by adding fin surface, the flow field is inevitably stabilized, and the contributions of vortices and unstable flow field are also lessened [10]. Moreover, it is commonly known that the pressure drop endures a heat transfer and exhibits a decreasing trend of the heat exchanger performance index with a decreasing fin pitch. The maximum value of ζ_1 means that it is possible to obtain an optimum fin pitch under this criterion when all the other parameters are kept fixed over the range of testing conditions. Actually, using

Author's personal copy

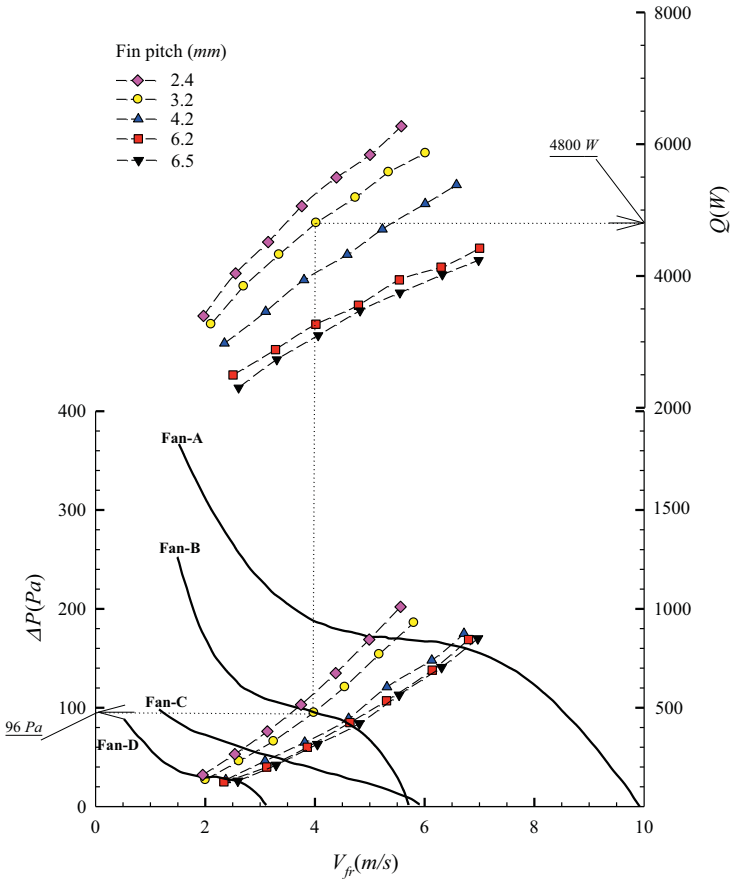

Fig. 12. Axial fan performance curve (P–Q fan curve) with system lines of crimped spiral fin-and-tube heat exchangers having various fin pitches at $T_{w,in}$ = 60 °C and water flow rate of 0.233 kg/s.

a fin pitch higher than 4.2 mm seems to be preferable in terms of production cost because it is cheaper in the sense of having less fin pitch length. However, the value of ζ_1, which is the index to describe the heat exchanger's performance, is relatively lower than that of 4.2 mm. Therefore, it is not recommended to consider only the production cost but also the performance index when designing crimped spiral fin-and-tube heat exchangers.

The next performance index that is derived in this study is the system performance index (ζ_2). Unlike ζ_1, which mainly focuses only in the heat exchanger section, a more advance consideration is developed in order to obtain the performance index that is suitable to describe the whole system, including both the heat exchanger and the pumping fan. Fig. 12 show the axial commercial fan curve fan (P–Q curve) with the system lines of crimped spiral fin-and-tube heat exchangers having various fin pitches. The commercial fan P–Q curve A to D is plotted in Fig. 12, along with the heat exchanger pressure drop, which is referred to as the system line of the heat exchanger. The interception of these two plots could indicate the operating point of heat exchanger. The dashed line in Fig. 12 shows the connection from the operating point to the average heat transfer rate in the case of a fin pitch of 3.2 mm with fan B. The ratio between the average heat transfer rate and the pressure drop at the operating point is introduced as ζ_2. The pressure drop at the operating point obtained for each fin pitch subject to the fan curve is illustrated in Fig. 13(b). Moreover, the obtained average heat transfer rate is also illustrated in Fig. 13(a). In addition, the effect of the fin pitch subject to the actual fan curve on the system performance index is illustrated in Fig. 14. It was found that the system performance index of fin pitches of 2.4, 3.2, and 4.2 mm is similar and significantly higher than those of 6.2 mm and 6.5 mm. The ζ_2 of fin pitch of 2.4, 3.2, and 4.2 mm is generally higher than that of 6.2 mm and 6.5 mm with a maximum discrepancy of about 20% for every fan curve. It is noted that fan A and B is subjected to a high-power fan, and fans C and D are subjected to a low-power fan. The system performance index also decreases with the increasing input power type. The low-power fan gives a higher system performance index than the higher-power one.

Finally, the dimensionless system performance index is introduced. This index is the modification of the system performance index by dividing the average heat transfer rate with pumping (fan) power, which could be expressed as Eq. (30). In the same manner, the dimensionless system performance index could be described as COP for it represents the ratio of the desired heat transfer rate and the provided pumping work. Fig. 15 illustrates the effect of the fin pitch subject to the fan curves on the dimensionless system performance index. Similar to the system performance index, the ζ_3 for a lower-power fan is also greater than that of the higher-power fan. Furthermore, the ζ_3 decreases with increasing fin pitch for all fans. It must be noted that while considering the performance index in term of both ζ_1 and ζ_2, a fin pitch of 4.2 mm seems to be the highest value than that of other cases, illustrating the optimized fin pitch. However, consideration of the performance index in terms of ζ_3 gives an alternate result.

In light of the findings of this study, the value of performance index is validated from the consideration as the ratio of the desired output to the required input, as mentioned above. It can be seen that the fin pitches are key to and directly affect the performance indexes, i.e., the heat exchanger performance index (ζ_1), the system

Author's personal copy

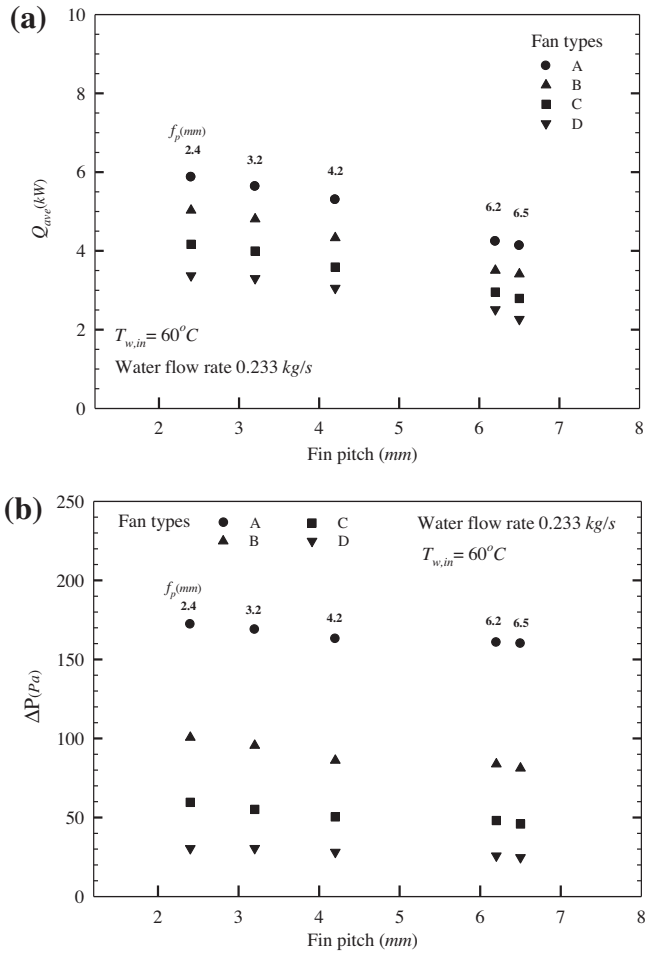

Fig. 13. Effect of fin pitches on (a) the average heat transfer rate and (b) the pressure drop of crimped spiral fin and tube heat exchangers at operating point.

performance index (ζ_2), and the dimensionless system performance index (ζ_3). As the authors have noted, these factors are compared for fin pitches of 2.4, 3.2, 4.2, 6.2, and 6.5 mm in Table 5. It is interesting to note that the fin pitch of 4.2 mm is outstandingly better than other fin pitches. Moreover, as shown in Fig. 16, the results are shown based on the three performance indexes (ζ_1, ζ_2, and ζ_3). This figure can be used to present the optimum fin pitch.

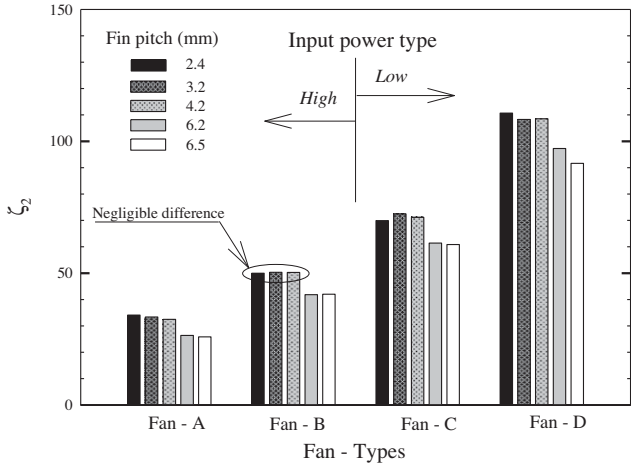

Fig. 14. Effect of fin pitch subjected to fan curve on the performance index ζ_2 at optimum fan operating point ($T_{w,in}$ = 60 °C and water flow rate of 0.233 kg/s).

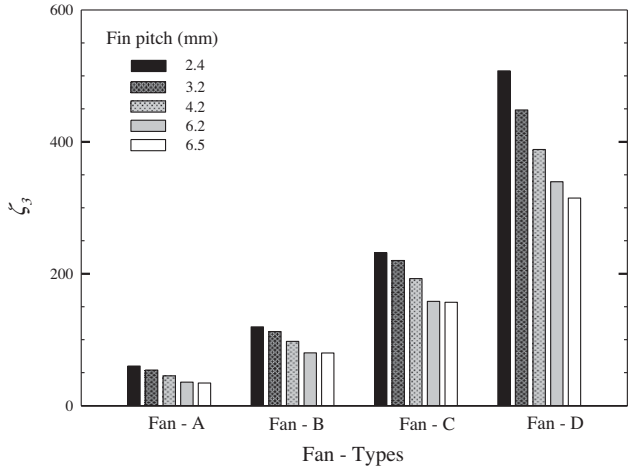

Fig. 15. Effect of fin pitch subjected to pumping (fan) power on the performance index ζ_3 at optimum fan operating point ($T_{w,in}$ = 60 °C and water flow rate of 0.233 kg/s).

Table 5
Characteristics of fin pitch on performances index.

Fin pitches	Heat exchanger performance index (ζ_1)	System performance index (ζ_2)	Dimensionless system performance index (ζ_3)
2.4	Low	High	High
3.2	Low	High	High
4.2*	High*	High*	Intermediate*
6.2	Low	Low	Low
6.5	Low	Low	Low

Note: * Optimum condition.

According to Fig. 16, the intersection area of the three mathematical sets of performance indexes show that the fin pitch of 4.2 mm has good prospects after consideration of each element and of the composition as a whole. Therefore, it is believed that the fin pitch of 4.2 mm is the optimum fin pitch in this study. This report is offered with the expectation that it may be of assistance in designing cost-effective, optimally sized thermal system equipment.

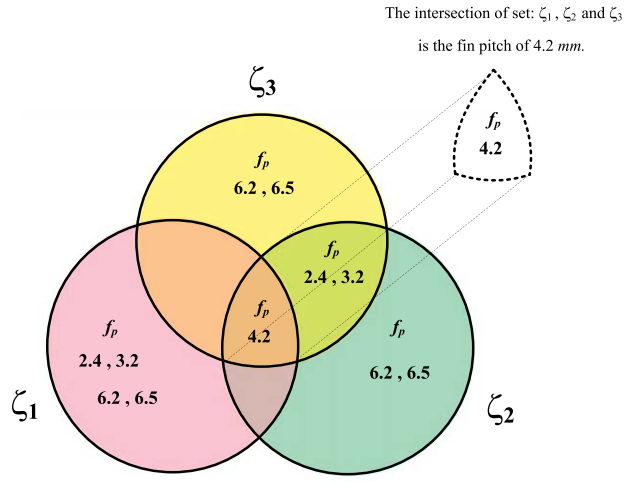

Fig. 16. The intersection of performance index sets defined as the grouping up of the fin pitches.(is the area in the middle of the diagram that represents the intersection point of all two sets and three sets indicating the high and intermediate value of the performance index).

Author's personal copy

5. Conclusion

In this study, an experimental investigation on the optimized fin pitch for crimped spiral fin-and tube-heat exchangers was conducted. The following conclusions based on the tests were obtained:

- It could be clearly seen that the convective heat transfer coefficient (h_o) for a fin pitch of 2.4 mm was relatively low compared to that of the other fin pitches. Furthermore, using larger fin pitches (i.e., 4.2, 6.2, and 6.5 mm) resulted in negligible difference in the pressure drop.
- Three performance indexes are introduced in this work in order to validate the optimum fin pitch. However, the optimum fin pitch obtain by those three are quite different. The heat exchanger performance index (ζ_1) provides the peak value (optimum) at a fin pitch of 4.2 mm, whereas the system performance index (ζ_2) of fin pitches of 2.4, 3.2, and 4.2 mm seem identical. Moreover, the dimensionless system performance index (ζ_3) decreases with increases in the fin pitch.
- Due to the differences in the optimum fin pitch obtained by these performance indexes, the intersection analysis was conducted. The results were that the optimum fin pitch is 4.2 mm (or 6 fins per inch) for this work. Therefore, industrial designers should consider the optimum fin pitch when designing the crimped spiral fin-and-tube heat exchanger.

Acknowledgments

The authors are indebted to the Thailand Research Fund, the Office of the Higher Education Commission and the National Research University Project for supporting this study.

References

[1] A. Nuntaphan, T. Kiatsiriroat, C.C. Wang, Air side performance at low Reynolds number of cross-flow heat exchanger using crimped spiral fins, Int. Commun. Heat Mass Transfer 32 (1–2) (2005) 151–165.
[2] A. Nuntaphan, T. Kiatsiriroat, C.C. Wang, Heat transfer and friction characteristics of crimped spiral finned heat exchangers with dehumidification, Appl. Therm. Eng. 25 (2–3) (2005) 327–340.
[3] K. Srisawad, S. Wongwises, Heat transfer characteristics of a new helically coiled crimped spiral finned tube heat exchanger, Heat Mass Transfer 45 (4) (2009) 381–391.
[4] P. Pongsoi, S. Pikulkajorn, C.C. Wang, S. Wongwises, Effect of fin pitches on the air-side performance of crimped spiral fin-and-tube heat exchangers with a multipass parallel and counter cross-flow configuration, Int. J. Heat Mass Transfer 54 (9–10) (2011) 2234–2240.
[5] P. Pongsoi, S. Pikulkajorn, C.C. Wang, S. Wongwises, Effect of number of tube rows on the air-side performance of crimped spiral fin-and-tube heat exchangers with a multipass parallel and counter cross-flow configuration, International Journal of Heat and Mass Transfer 55 (4) (2012) 1403–1411.
[6] L.H. Tang, G.N. Xie, M. Zeng, M. Lin, Q.W. Wang, A comparative study of fin-and-tube heat exchangers with various fin patterns, ASME Conf. Proc., Heat Transfer Part A and B 4 (2008) 1239–1246.
[7] L.H. Tang, M. Zeng, Q.W. Wang, Experimental and numerical investigation on air-side performance of fin-and-tube heat exchangers with various fin patterns, Exp. Therm. Fluid Sci. 33 (5) (2009) 818–827.
[8] R. Romero-Mendez, M. Sen, K.T. Yang, R. McClain, Effect of fin spacing on convection in a plate fin and tube heat exchanger, Int. J. Heat Mass Transfer 43 (1) (2000) 39–51.
[9] T. Sencic, A. TRP, K. Lenic, Parametric study of operating and geometry characteristics effect on heat transfer in annular finned tube heat exchanger, Eng. Rev. 29 (1) (2009) 25–36.
[10] C.W. Lu, J.M. Huang, W.C. Nien, C.C. Wang, A numerical investigation of the geometric effects on the performance of plate finned-tube heat exchanger, Energ. Convers. Manage. 52 (3) (2011) 1638–1643.
[11] G. Xie, Q. Wang, B. Sunden, Parametric study and multiple correlations on air-side heat transfer and friction characteristics of fin-and-tube heat exchangers with large number of large-diameter tube rows, Appl. Therm. Eng. 29 (1) (2009) 1–16.
[12] Y.C. Liu, S. Wongwises, W.J. Chang, C.C. Wang, Airside performance of fin-and-tube heat exchangers in dehumidifying conditions - Data with larger diameter, Int. J. Heat Mass Transfer 53 (7–8) (2010) 1603–1608.
[13] ASHRAE Handbook Fundamental, American society of heating, Refrigerating and air-conditioning engineers, SI-ed., Inc., Atlanta, chap. 13 (1993) 14–15.
[14] ESDU 86018, Effectiveness-NTU Relations for the design and performance evaluation of two-stream heat exchangers, Engineering science data unit 86018 with amendment, London ESDU International plc, 1991, pp. 92–107.
[15] H.A. Navarro, L. Cabezas-Gomez, A new approach for thermal performance calculation of cross-flow heat exchanger, Int. J. Heat Mass Transfer 48 (2005) 3880–3888.
[16] L. Cabezas-Gomez, H.A. Navarro, J.M. Saiz-Jabardo, Thermal performance of multipass parallel and counter-cross-flow heat exchangers, J. Heat transfer 129 (2007) 282–290.
[17] H.A. Navarro, L. Cabezas-Gomez, Effectiveness-ntu computation with a mathematical model for cross-flow heat exchangers, Braz. J. Chem. Eng. 24 (4) (2007) 509–521.
[18] V. Gnielinski, New eguation for heat and mass transfer in turbulent pipe and channel flow, Int. Chem. Eng. 16 (1976) 359–368.
[19] K.A. Gardner, Efficient of extended surface, ASME Trans. 67 (1945) 621.
[20] W.M. Kays, A. London, Compact Heat Exchangers, third ed., Mcgraw-Hill, New York, 1984.
[21] ANSI/ASHRAE Standard 33-2000, Method of Testing Forced Circulation Air Cooling and Air Heating Coils, 2000.
[22] Y.H. Kim, Y. Kim, Heat transfer characteristics of flate plate finned-tube heat exchangers with large fin pitch, Int. J. Refrig. 28 (6) (2005) 851–858.
[23] M.S. Mon, U. Gross, Numerical study of fin-spacing effects in annular-finned tube heat exchangers, Int. J. Heat Mass Transfer 47 (8–9) (2004) 1953–1964.
[24] M. Lee, T. Kang, Y. Kim, Air-side heat transfer characteristics of spiral-type circular fin- tube heat exchangers, Int. J. of Refrig. 33 (2) (2010) 313–320.

International Communications in Heat and Mass Transfer 39 (2012) 1165–1168

Contents lists available at SciVerse ScienceDirect

International Communications in Heat and Mass Transfer

journal homepage: www.elsevier.com/locate/ichmt

On the thermal cooling of central processing unit of the PCs with vapor chamber ☆

Paisarn Naphon [a,*], Somchai Wongwises [b], Songkran Wiriyasart [a]

[a] Thermo-Fluids and Heat Transfer Enhancement Lab. (TFHT), Department of Mechanical Engineering, Faculty of Engineering, Srinakharinwirot University, 63 Rangsit-Nakhornnayok Rd., Ongkharak, Nakhorn-Nayok, 26120, Thailand

[b] Fluid Mechanics, Thermal Engineering and Multiphase Flow Research Lab. (FUTURE), Department of Mechanical Engineering, King Mongkut's University of Technology Thonburi, 91 Suksawas 48, Bangmod, Bangkok 10140, Thailand

ARTICLE INFO

Available online 20 July 2012

Keywords:
Vapor chamber
Electronics cooling
Central processing unit

ABSTRACT

An experimental investigation on the thermal cooling of vapor chamber for cooling computer processing unit of the personal computer is performed. Two different configurations of the vapor chambers with de-ionized water as working fluid are tested under the real operating conditions of PCs. Parametric studies including different aspect ratios, fill ratios, and operating conditions of PC on the CPU temperature are considered. It was found that the vapor chamber cooling technique has significant effect on the thermal cooling of CPU. Average CPU temperatures obtained from the vapor chamber cooling system are 4.1%, 6.89% lower than those from the conventional cooling system for no load and 90% operating loads, respectively. In additional, this cooling system requires 6.89%, 10.53% lower energy consumption for no load and 90% operating loads, respectively. The results of this study are of technological importance for the efficient design of cooling systems of the personal computers or electronic devices to enhance cooling performance.

© 2012 Elsevier Ltd. All rights reserved.

1. Introduction

Higher performance processor will have larger heat generation. In order to ensure reliable operation, therefore, the PCs or electronics devices must be operated in the specific temperature ranges. For effective cooling the heat must spread to a larger surface area and away from the processor, as there is usually restricted space available in the vicinity of the processor. The best known device for effective heat transfer with lowest thermal resistance is vapor chamber. The heat transfer characteristics of the vapor chamber have been widely studied by researchers. Hsieh et al. [1] analyzed the thermal resistance of vapor chamber heat sink with and without pillar for electronic cooling. Hu and Tang [2] investigated the flow and thermal characteristics of a microphase-change cooling system with a microgroove evaporator. The results indicated that the liquid fill ratio has a significant influence on thermal resistance in the cooling system. Liu et al. [3] investigated startup of a novel two-phase cooling loop. Wang et al. [4] studied the micro-capillary pumped loop system for a cooling high-power device. Xie et al. [5] experimentally investigated a novel high-performance integrated heat pipe–heat sink for high-flux chip cooling. Hsieh et al. [6] examined the spreading thermal resistance of a flat vapor chamber. Vin and Astrain [7] studied the development of a thermoelectric refrigerator with two-phase thermosyphons. Chang et al. [8] experimentally investigated the effects of the evaporation surfaces, fill ratios of working fluid and input heating powers on the thermal performance of the heat pipe cooling system with the thermal resistance model. Chen et al. [9] presented a numerical investigation of a plate-fin heat sink embedded with a vapor chamber, subject to the influence of concentrated heat sources. Zhang et al. [10] numerically and experimentally investigated the flat two-phase thermosyphon. Ma et al. [11] developed an innovative one-side actuating piezoelectric micropump to drive liquid in a cooling system for a laptop. Vasiliev et al. [12] studied the loop heat pipe for cooling of high-power electronic components. Ming et al. [13] experimentally and numerically investigated the grooved vapor chamber. Khandekar et al. [14] investigated the multiple quasi-steady states in a closed loop pulsating heat pipe. Orian et al. [15] predicted the heat transfer coefficients for calculations of various heat and mass transfer processes. Kang et al. [16] experimentally investigated the nanofluids on sintered heat pipe thermal performance. Tsai et al. [17] experimentally investigated the effects of heat source, fill ratio of working fluid, and evaporator surface structure on the thermal performance of the vapor chamber. Wang et al. [18] considered the thermal performance of the vapor chamber for the high-power LEDs. Wong et al. [19] studied a novel vapor chamber with inner groove surface. Wang et al. [20] analyzed the thermal characteristics for board-level high-performance package equipped with vapor chamber. Li et al. [21,22] investigated effects of the width, height and number of fins and of the Reynolds number on the thermal performance and surface temperature distributions of vapor chamber. Harmand et al. [23] presented a theoretical investigation of a flat heat pipe for cooling electronic components. Wang et al. [24] analyzed the pressure-difference phenomenon between the condensing and boiling sections of a heat pipe. Reyes et al. [25]

☆ Communicated by W.J. Minkowycz.

* Corresponding author.
E-mail address: paisarnn@swu.ac.th (P. Naphon).

0735-1933/$ – see front matter © 2012 Elsevier Ltd. All rights reserved.
doi:10.1016/j.icheatmasstransfer.2012.07.013

experimentally and theoretically studied the vapor chamber based heat spreader. Naphon and Wongwises [26] studied the jet nanofluids impingement system for cooling computer processing unit. Attia and El-Assal [27] experimentally investigated of the effects of different working fluids, different charge ratios on the thermal performance of the vapor chamber. Ji et al. [28] studied the vapor chamber performance with sintering the copper foams pieces. Choi et al. [29] studied a new CPU cooler design based on an active cooling heat sink combined with heat pipes.

As mentioned above, the numerous papers presented the study on the heat transfer characteristics of the vapor chamber. However, the trend of the processor performance and heat dissipation increased significantly every year. Heat dissipation increased but in contrary the size of the processor reduced and thus the heat flux is critically high. In 2000, the heat flux is about 10–15 W/cm^2 and could reach over 150 W/cm^2 by year 2012. The purpose of this paper is to study the thermal cooling of central processing unit of personal computers with the vapor chamber. As compared to other cooling devices such as fans, thermoelectric module, liquid pump loop device, the vapor chamber cooling technique has simple structures, has no moving parts and does not use electricity. In addition, selection of the working fluid is based on the operating temperature of the application. For computer application, the operating temperatures are normally between 50 and 100 °C. Effects of operating condition of PC, the fill ratio, and aspect ratio on the CPU temperature and energy consumption are considered.

2. Experimental apparatus and method

The test loop consists of a set of PC, a set of vapor chamber cooling system and data acquisition system. A schematic diagram of the vapor chamber cooling system is shown in Fig. 1. The vapor chamber cooling system consists of the vapor chamber, heat sink unit, and axial fan unit. The details of the vapor chamber are listed as shown in Table 1. The schematic diagram of the vapor chamber unit is shown in Fig. 2. The vapor chamber is fabricated from copper plate which consists of bottom copper plate, wick sheet, sinter column, and top copper plate. The wick sheet and the sinter column are fabricated from the copper powder. The bottom copper plate is the evaporator section that may be mounted on CPU of the PC to absorb the

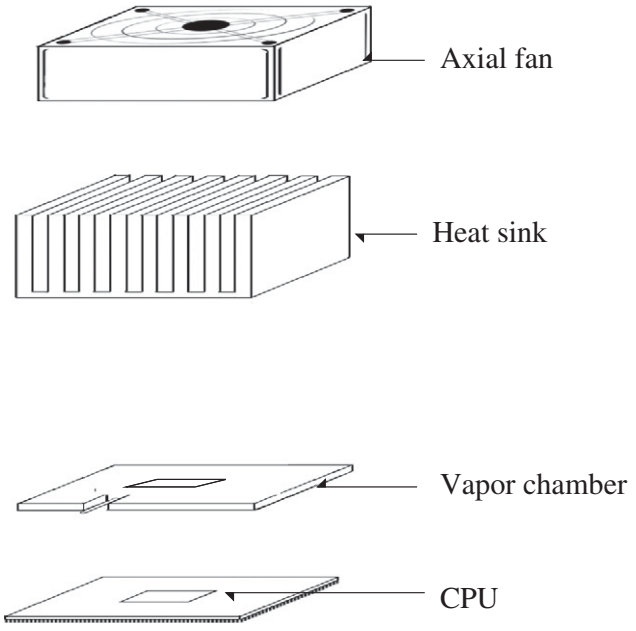

Fig. 1. Schematic diagram of the vapor chamber cooling system.

Table 1
Details of the vapor chambers.

Vapor chamber	Vapor chamber size (mm*mm*mm)	Fill ratio	Copper plate size (mm*mm*mm)
Model A	–	–	60*60*3.8
Model B	32*32*2.2	10%	60*60*3.8
Model C	32*32*2.2	20%	60*60*3.8
Model D	56.8*56.8*2.2	20%	60*60*3.8

generated heat, and the other is the condenser section which heat is transferred to heat sink and air, respectively. In order to minimize thermal resistance between the CPU-vapor chamber, vapor chamber heat sink unit, a thin film of high thermal conductivity grease is applied at their junction interface. There are two vapor chambers with different aspect ratio (CPU surface area to bottom plate surface area) that are tested in the present study. The working fluid (de-ionized water) is evaporated on the heated side and condensed on the cooling side and then returns to the evaporator section under gravity. Type T copper-constantan thermocouples with an accuracy of 0.1% of full scale are employed to measure the temperatures. Four type T copper-constantan thermocouples are applied to measure the vapor chamber temperature. One thermocouple is applied to observe the ambient temperature. A groove within the chamber walls is machined and the high conductivity cement is utilized to embed the thermocouples within the chamber wall. The CPU temperature is measured by two type T copper-constantan thermocouples. All thermocouples are pre-calibrated with dry box temperature calibrator.

Experiments were conducted with various fill ratios, aspect ratios and operating condition of PC. The supplied load into the CPU was adjusted to achieve the desired level by setting the operating conditions of PC: no load and 50% and 90% operating loads. The energy consumption of the PC was measured by the watt-hour meter with an accuracy of 0.2% of full scale. The temperatures at each position and energy consumption were recorded in the period time of 200 min. Data collection was carried out using a data acquisition system (DataTaker).

3. Results and discussion

Initially experiments are performed with the conventional cooling system (copper plate) which forms the basis for comparison of the results with vapor chamber cooling technique. After installing all components, the experiments are performed with different vapor chamber models, different fill ratios and under different operating conditions of personal computer. Fig. 3 shows the variation of the CPU temperature for different operating loads. Model A represents the cooling system in the sensible heat term (copper plate) while others represent the conventional cooling system in the latent heat term (vapor chamber). It can be seen that the CPU temperatures obtained from three vapor chamber models are similar to the one from the conventional cooling system. Model A, which represents the conventional cooling system with copper plate, gives the highest CPU temperature among all the models. This is because the latent heat term has significant effect on the thermal cooling of the CPU. In addition, the CPU temperature rapidly increases as the operating condition load increases. However, this effect becomes relatively less as the operating load >50%.

Fig. 4 shows the variation of the CPU temperature for different models. The total volume of the vapor chamber for the present study is measured to be about 8000 ml. The heat phenomenon by working fluid in the vapor chamber, the working fluid absorbs heat from heat source (CPU) and evaporates in the evaporator (bottom plate). The evaporating fluid moves toward the condenser, and then condenses in the condenser (top plate). For a given operating load and aspect ratio, it can be seen that model C with fill ratio of 20%

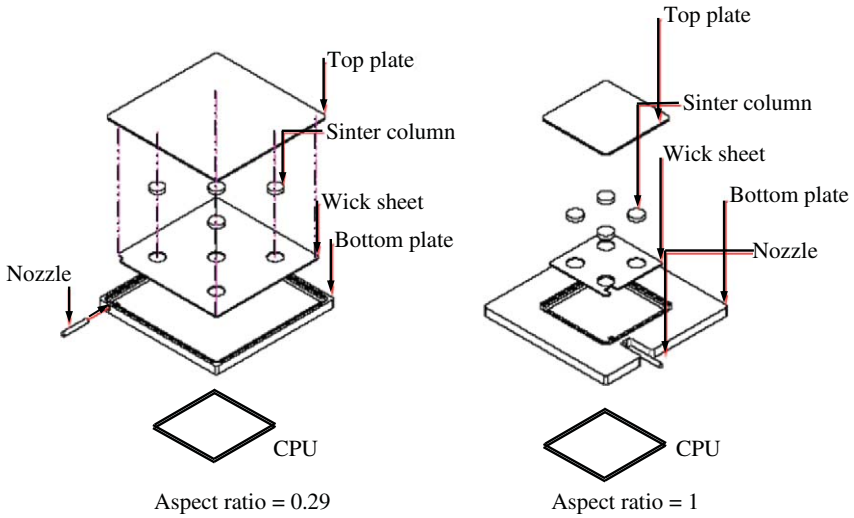

Fig. 2. Schematic diagram of the vapor chamber details.

gives the CPU temperature lower than those from model B with fill ratio of 10%. It may be due to low fill ratio, and the dry out phenomenon might happen. The condensing liquid cannot promptly reflow at this operating load. Therefore, model B gives the CPU temperatures higher than those from model C. In addition, effect of aspect ratio (CPU surface area to bottom plate surface area) on the CPU temperature is also shown in Fig. 4. For model C, there is only the thin liquid film in the heat input region. For model D, however, due to the local boiling and the effect of capillary pressure of the vapor chamber, the liquid film at the heat input region is much thinner than that at the other region (heat input region outside). The thermal resistance of the phase change heat transfer will also increase with the thickness of the liquid film. For a given fill ratio, therefore, model C with an aspect ratio of 1 gives the CPU temperature lower than those from model D with an aspect ratio of 0.29.

The total thermal resistance of the vapor chamber cooling technique is the summation of the contact resistance, the evaporation resistance, the condensation resistance, and the convection resistance. For the same operating condition of PC, the thermal resistance for the CPU with the conventional cooling technique and with the vapor chamber cooling technique is expressed as

$$R_{con} = \frac{T_{CPU,con} - T_{ambient}}{Q} \tag{1}$$

$$R_{vc} = \frac{T_{CPU,vc} - T_{ambient}}{Q} \tag{2}$$

The thermal resistance ratio can be written as

$$\frac{R_{vc}}{R_{con}} = \frac{T_{CPU,vc} - T_{ambient}}{T_{CPU,con} - T_{ambient}} \tag{3}$$

Fig. 5 shows the variation of the thermal resistance ratio for different models and different operating loads. At a lower operating load, the heat is mainly transferred through natural convection. The increasing operating load induces a larger superheat, which activates and intensifies nucleate boiling and consequently leads to higher heat transfer efficiency. Therefore, the thermal resistance at higher operating load condition is higher than those at lower operating load condition. In addition, the thermal resistance with the conventional cooling technique is higher than those with the vapor chamber cooling technique which corresponds to the variation of the CPU temperature as mentioned above.

The CPU temperature and the energy consumption obtained from 20% fill ratio of the vapor chamber cooling system are compared with those from the conventional liquid cooling system for the operating time of 200 min. It can be seen from Table 2 that the CPU

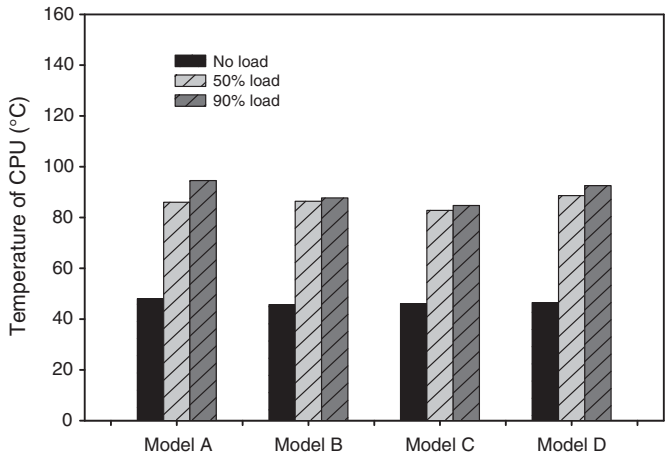

Fig. 3. Variations of CPU temperature for different models of vapor chamber.

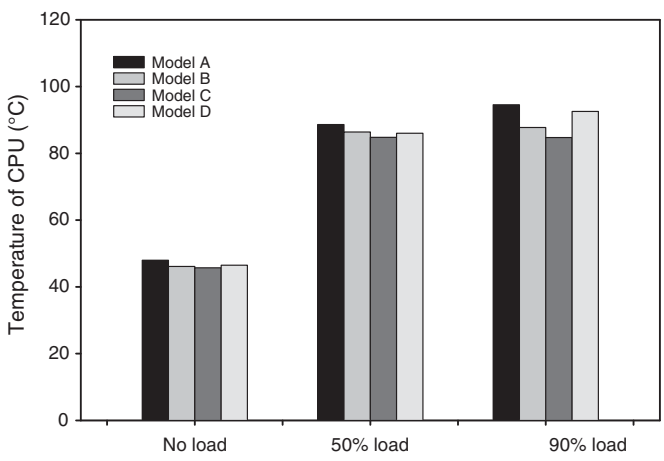

Fig. 4. Variations of CPU temperature for different operating conditions of PC.

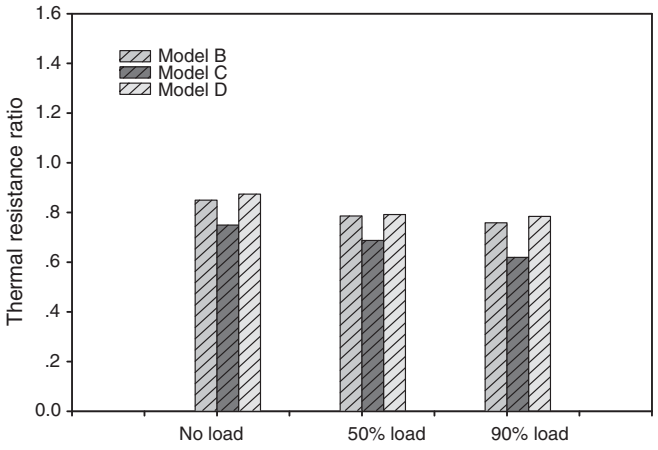

Fig. 5. Variations of thermal resistance ratio for different operating conditions of PC.

temperatures obtained from the vapor chamber cooling system are 4.1%, 6.89% lower than those from the conventional cooling system for no load and 90% operating loads, respectively. In addition, the energy consumption also decreases 6.89%, 10.53% for no load and 90% operating loads, respectively.

4. Conclusions

The space limitation, air cooling limitation and high level of the generated heat are the encountered problems of the cooling system development of the CPU or electronic devices. The vapor chambers have many advantages as compared to other cooling devices such as fans, thermoelectric module, liquid pump loop device: it has simple structures, has no moving parts and does not use electricity. In addition, selection of the working fluid is based on the operating temperature range of the applications. It is found that the CPU temperatures and the energy consumption of the CP obtained from the vapor chamber cooling system are lower than those from the conventional liquid system. The results of this study are expected to lead to guidelines that will allow the design of a cooling system with improved thermal cooling performance for ensuring that these devices are in the specific temperature ranges.

Acknowledgements

The authors would like to express their appreciation to the Excellent Center for Sustainable Engineering (ECSE) of the Srinakharinwirot University (SWU) and the King Mongkut's University of Technology Thonburi (KMUTT) for providing financial support for this study. The authors also wish to acknowledge Fujikura Electronics (Thailand) Ltd. for their assistance in some of the vapor chamber samples.

Table 2
Comparison of the CPU temperature and the energy consumption between the conventional cooling system and 20% fill ratio of the vapor chamber cooling system.

Cooling techniques	CPU temperature (°C)	Energy consumption (W·h)
No load operating condition with the conventional cooling system	47.5	150
No load operating condition with vapor chamber cooling system	45.6	140
Full load operating condition with the conventional cooling system	94.5	300
Full load operating condition with vapor chamber cooling system	88.2	270

References

[1] S.S. Hsieh, R.Y. Lee, J.C. Shyu, S.W. Chen, Analytical solution of thermal resistance of vapor chamber heat sink with and without pillar, Energy Conversion and Management 48 (2007) 2708–2717.
[2] X. Hu, D. Tang, Experimental investigation on flow and thermal characteristics of a microphase-change cooling system with a microgroove evaporator, International Journal of Thermal Sciences 46 (2007) 1163–1171.
[3] J. Liu, N.Q. Pei, K.H. Guo, Z.H. He, T.X. Li, J.M. Gu, Experimental investigation on startup of a novel two-phase cooling loop, Experimental Thermal and Fluid Science 32 (2008) 939–946.
[4] C.T. Wang, T.S. Leu, T.M. Lai, Micro capillary pumped loop system for a cooling high power device, Experimental Thermal and Fluid Science 32 (2008) 1090–1095.
[5] X.L. Xie, Y.L. He, W.Q. Tao, H.W. Yang, An experimental investigation on a novel high-performance integrated heat pipe–heat sink for high-flux chip cooling, Applied Thermal Engineering 28 (2008) 433–439.
[6] S.S. Hsieh, R.Y. Lee, J.C. Shyu, S.W. Chen, Thermal performance of flat vapor chamber heat spreader, Energy Conversion and Management 49 (2008) 1774–1784.
[7] J.G. Vin, D. Astrain, Development of a thermoelectric refrigerator with two-phase thermosyphons and capillary lift, Applied Thermal Engineering 28 (2008) 1514–1521.
[8] Y.W. Chang, C.H. Cheng, J.C. Wang, S.L. Chen, Heat pipe for cooling of electronic equipment, Energy Conversion and Management 49 (2008) 3398–3404.
[9] Y.S. Chen, K.H. Chien, T.C. Hung, C.C. Wang, Y.M. Ferng, B.S. Pei, Numerical simulation of a heat sink embedded with a vapor chamber and calculation of effective thermal conductivity of a vapor chamber, Applied Thermal Engineering 29 (2009) 2655–2664.
[10] M. Zhang, Z. Liu, G. Ma, S. Cheng, Numerical simulation and experimental verification of a flat two-phase thermosyphon, Energy Conversion and Management 50 (2009) 1095–1100.
[11] H.K. Ma, B.R. Chen, J.J. Gao, C.Y. Lin, Development of an OAPCP-micropump liquid cooling system in a laptop, International Communications in Heat and Mass Transfer 36 (2009) 225–232.
[12] L. Vasiliev, D. Lossouarn, C. Romestant, A. Alexandre, Y. Bertin, Y. Piatsiushyk, V. Romanenkov, Loop heat pipe for cooling of high-power electronic components, International Journal of Heat and Mass Transfer 52 (2009) 301–308.
[13] Z. Ming, L. Zhongliang, M. Guoyuan, The experimental and numerical investigation of a grooved vapor chamber, Applied Thermal Engineering 29 (2009) 422–430.
[14] S. Khandekar, A.P. Gautam, P.K. Sharma, Multiple quasi-steady states in a closed loop pulsating heat pipe, International Journal of Thermal Sciences 48 (2009) 535–546.
[15] G. Orian, M. Jelinek, A. Levy, Heat transfer to sub-cooled binary solution in horizontal tube, Applied Thermal Engineering 29 (2009) 661–669.
[16] S.W. Kang, W.C. Wei, S.H. Tsai, C.-C. Huang, Experimental investigation of nanofluids on sintered heat pipe thermal performance, Applied Thermal Engineering 29 (2009) 973–979.
[17] T.E. Tsai, H.H. Wu, C.C. Chang, S.L. Chen, Two-phase closed thermosyphon vapor-chamber system for electronic cooling, International Communications in Heat and Mass Transfer 37 (2010) 484–489.
[18] J.C. Wang, R.T. Wang, T.L. Chang, D.S. Hwang, Development of 30 watt high-power LEDs vapor chamber-based plate, International Journal of Heat and Mass Transfer 53 (2010) 3990–4001.
[19] S.C. Wong, K.C. Hsieh, J.D. Wu, W.L. Han, A novel vapor chamber and its performance, International Journal of Heat and Mass Transfer 53 (2010) 2377–2384.
[20] T.H. Wang, C.C. Lee, Y.S. Lai, Thermal characteristics evaluation for board-level high performance flip-chip package equipped with vapor chamber as heat spreader, Microelectronic Engineering 87 (2010) 2463–2467.
[21] H.Y. Li, M.H. Chiang, C.I. Lee, W.J. Yang, Thermal performance of plate-fin vapor chamber heat sinks, International Communications in Heat and Mass Transfer 37 (2010) 731–738.
[22] H.Y. Li, M.H. Chiang, Effects of shield on thermal-fluid performance of vapor chamber heat sink, International Journal of Heat and Mass Transfer 54 (2011) 1410–1419.
[23] S. Harmand, R. Sonan, M. Fakès, H. Hassan, Transient cooling of electronic components by flat heat pipes, Applied Thermal Engineering 31 (2011) 1877–1885.
[24] R.T. Wang, J.C. Wang, Analyzing the pressure-difference phenomenon between the condensing and boiling sections in a heat pipe cooling system, International Communications in Heat and Mass Transfer 39 (2012) 390–398.
[25] M. Reyes, D. Alonso, J.R. Arias, A. Velazquez, Experimental and theoretical study of a vapour chamber based heat spreader for avionics applications, Applied Thermal Engineering 37 (2012) 51–59.
[26] P. Naphon, S. Wongwises, Experimental study of jet nanofluids impingement system for cooling computer processing unit, Journal of Electronics Cooling and Thermal Control 1 (2012) 1–7.
[27] A.A.A. Attia, B.T.A. El-Assal, Experimental investigation of vapor chamber with different working fluids at different charge ratios, Ain Shams Engineering Journal (in press).
[28] X. Ji, J. Xu, A.M. Abanda, Copper foam based vapor chamber for high heat flux dissipation, Experimental Thermal and Fluid Science 40 (2012) 93–102.
[29] J. Choi, M. Jeong, J. Yoo, M. Seo, A new CPU cooler design based on an active cooling heat sink combined with heat pipes, Applied Thermal Engineering 44 (2012) 50–56.

Send Orders of Reprints at reprints@benthamscience.org

Current Nanoscience, 2012, *8*, 949-969

Forced Convective Heat Transfer of Nanofluids - A Review of the Recent Literature

A.S. Dalkilic[a,*], N. Kayacı[a], A. Celen[a], M. Tabatabaei[a], O. Yıldız[a], W. Daungthongsuk[b] and S. Wongwises[c,d]

[a]*Heat and Thermodynamics Division, Department of Mechanical Engineering, Yildiz Technical University, Yildiz, Istanbul, 34349, Turkey;* [b]*Department of Mechanical Engineering, Faculty of Engineering, South-East Asia University,* [c]*Fluid Mechanics, Thermal Engineering and Multiphase Flow Research Lab. (FUTURE), Department of Mechanical Engineering, Faculty of Engineering, King Mongkut's University of Technology Thonburi, Bangmod, Bangkok, 10140, Thailand;* [d]*The Academy of Science, The Royal Institute of Thailand, Sanam Suea Pa, Dusit, Bangkok 10300, Thailand*

Abstract: The forced convection of fluids has been investigated by numerous researchers, both experimentally and numerically. A good understanding of characteristics of nanofluid flowhas thoroughly been investigated in these studies. Since the nanoparticles behave more like a single-phase fluid than a solid–liquid mixture, it is assumed that nanofluids are ideally suited in the applications as their usage causes little or no penalty in pressure drop. In recent years, many researchers have tried to fill the gaps on this subject in the literature. To meet the demand for improving the performance of heat transfer equipment, re-examination of the individual components is considered to be essential. The addition of the nanoparticles to the base fluid is one of the significant issues for the optimal performance of heat transfer systems. This paper reports on most of the forced convective heat transfer literature occurring both in-tubes and in-channels regarding the use and preparation of nanofluids. The peer reviewed papers published in citation index journals up to 2012 have been selected for review in the paper. Classification of the papers has been performed according to the publication years. The critical information on the theoretical, experimental and numerical works is presented comprehensively for each paper.

Keywords: Nanofluids, ultrafine, effective thermal conductivity, effective viscosity, forced convective heat transfer.

1. INTRODUCTION

Performance of heat transfer equipment can be improved with studies related to a significant increase in heat flux and miniaturization. In many industrial applications such as power generation, microelectronics, heating processes, cooling processes and chemical processes, water, mineral oil and ethylene glycol are used as heat transfer fluid. Effectiveness and high compactness of heat exchangers are obstructed by the lower heat transfer properties of these common fluids as compared to most solids. It is obvious that solid particles having thermal conductivities several hundred times higher than these conventional fluids must be used in the heat transfer applications. To improve thermal conductivity of a fluid, suspension of ultrafine solid particles in the fluid can be acreative idea. Different types of particles (metallic, non-metallic and polymeric) can be added into fluids to form slurries. Due to the fact that sizes of these suspended particles are in the millimeter or even micrometer scale, some serious problems such as the clogging of flow channels, erosion of pipelines and an increase in pressure drop can occur. Moreover, they often suffer from rheological and instability problems. Especially, the particles tend to settle rapidly. For that reason, though the slurries have better thermal conductivities but they are not practical.

Many published articles show that the heat transfer coefficient of nanofluids is much higher than the common-base fluid giving little or no penalty in pressure drop. The main reasons for the heat transfer enhancement of the nanofluids may roughly be listed as follow: the suspended nanoparticles increase the thermal conductivity of the fluids, and the chaotic movement of ultrafine particles increases fluctuation and turbulence of the fluids that accelerates the energy exchange process. Furthermore, that the numerous correlations for single-phase fluid have clearly failed to predict the heat transfer coefficients of nanofluids that might have been caused by the complicated phenomena coexisting in the main flow. However, some sophisticated correlations for predicting the heat transfer performance of nanofluids have been established. At present, the uses of the nanofluids are still in early stages of development. Therefore, urgent theoretical and experimental research works is needed to clearly understand and accurately predict their hydrodynamic and thermal characteristics. Generally, many researchers indicated that nanofluids behave like pure fluids because the suspended particles are ultra-fine. However, at present, no formulated advanced theory exists to explain the behavior of nanofluids by considering them as multi-component materials. Moreover, several attempts have been discussed to determine the physical properties of nanofluids in the literature. They are shown in Table **1** for their dynamic viscosity [1-7] and Table **2** for their thermal conductivity [8-19]. It should be noted that there are some deviations among the results which will be obtained from the correlations in Tables **1** and **2**.

2. EXPERIMENTAL APPROACH

The heat transfer coefficient of the nanofluids can be calculated as follows:

$$Nu_{nf} = \frac{h_{nf} D}{k_{nf}} \tag{1}$$

$$h_{nf} = \frac{q}{T_w - T_f} \tag{2}$$

In the literature, the experimental results usually show that the flow velocity and volume fraction affected the convective heat transfer coefficient of the nanofluids as well as being higher than the base fluid at the same conditions. The Nusselt number of thenanofluid with 2% volume fraction of Cu particles can be 60% higher as compared to water. Moreover, at various volume fractions the Dittus-Boelter equation is not valid for the prediction of the Nusselt number of the nanofluids. According to experimental data, new heat transfer correlations, for the prediction of the heat transfer coefficient of nanofluids flowing in a tube, have been given by Qiang and Yimin [20] in the following forms for laminar and turbulent flows respectively:

$$Nu_{nf} = 0.4328\left(1.0 + 11.285\phi^{0.754} Pe_d^{0.218}\right) \mathrm{Re}_{nf}^{0.333} \mathrm{Pr}_{nf}^{0.4} \tag{3}$$

*Address correspondence to this author at the Heat and Thermodynamics Division, Department of Mechanical Engineering, Yildiz Technical University, Yildiz, Istanbul, 34349, Turkey; Tel: +9 0212 2597070;
Fax: +9 0212 2616659; E-mail: dalkilic@yildiz.edu.tr

1875-6786/12 $58.00+.00 © 2012 Bentham Science Publishers

Table 1. Some Dynamic Viscosity and Specific Heat Correlations of Nanofluids in Recent Literature

Researcher	Correlation
Putra *et al*. [1]	$\mu_{nf}=2.9*10^{-7}*T^2-2*10^{-4}*T+3.4*10^{-2}$ For % 1 $\mu_{nf}=3.4*10^{-7}*T^2-2.3*10^{-4}*T+3.9*10^{-2}$ For % 4
Tang *et al*. [2]	$\mu_{nf}=2.761*10^{-6}*e^{1713/T}$
Tseng and Chen [3]	$\mu_{nf} = \mu_{bf} x\,0,4513 e^{0,6965\phi}$
Chen *et al*. [4]	$\mu_{nf} = \mu_{bf}\left[1+10,6\phi+(10,6\phi)^2\right]$
Nguyen *et al*. [5]	$\mu_{nf} = \mu_{bf} x\,0,904 e^{0,1482\phi}$ $\mu_{nf} = \mu_{bf}(1 + 0,025\phi + 0,015\phi^2)$
Khanafer and Vafai [6]	$\mu_{nf} = \mu_{bf}(1,0538 + 0,1448\phi_p - 3,363x10^{-3} T - 0,0147\phi_p + 6,735x10^{-5} T^2 - 1,337\frac{\phi_p}{T})$
Duanghongsuk and Wongwises [7]	$\mu_{nf} = \mu_{bf}(1,013 + 0,092\phi_p + 0,015\phi_p^2)$

$$Nu_{nf} = 0.0059\left(1.0 + 7.6286\phi^{0.6886} Pe_d^{0.001}\right)\mathrm{Re}_{nf}^{0.9238}\,\mathrm{Pr}_{nf}^{0.4} \quad (4)$$

Where, Nu is the Nusselt number, Pe the Peclet number, Re the Reynolds number, and Pr the Prandtl number.

$$\mathrm{Pe}_d = \frac{u_m d_p}{\alpha_{nf}} \quad (5)$$

$$\mathrm{Re}_{nf} = \frac{u_m D}{\upsilon_{nf}} \quad (6)$$

$$\text{And } \mathrm{Pr}_{nf} = \frac{\upsilon_{nf}}{\alpha_{nf}} \quad (7)$$

To calculate Pe and Pr parameters, the thermal diffusivity of the nanofluid can be defined as follows:

$$\alpha_{nf} = \frac{k_{nf}}{\left(\rho C_p\right)_{nf}} = \frac{k_{nf}}{(1-\phi)\left(\rho C_p\right)_f + \phi\left(\rho C_p\right)_d} \quad (8)$$

In the view of the pressure drop, the results show that the friction factor of the nanofluid being almost equal to those of water under the same flow velocity does not vary with the volume fraction. It means that the usage of the nanofluids does not change required pump power and the single-phase friction factor correlation can be used for more accurate predictions. The friction factor of the nanofluids can be determinedas follows:

$$\lambda_{nf} = \frac{\Delta P_{nf} D}{L}\frac{2g}{u_m^2} \quad (9)$$

Yang *et al*. [21] conducted experiments related to the convective heat transfer coefficient of graphite nanoparticles dispersed in liquid for laminar flow in a horizontal tube heat exchanger. In their study, they used nanoparticles of different sources and focused on an aspect ratio (l/d) of about 0.02 (like a disc), avoiding the addition of large aspect ratio particles into a fluid since it may dramatically increase viscosity compared with the single-phase. In their study, two different nanofluids were used. The experiments were performed for different volume flow rates changing between 62-507 cm^3/min, the heating fluid temperature changing between 50-70 ^oC and the Reynolds number changing between 5-110. The purpose of this study was to define the effect of the volume fraction, fluid temperature, Reynolds number, nanoparticle source and type of base fluid on the convective heat transfer coefficient.

The following calculations are performed to evaluate the heat transfer coefficient of the nanofluids.

The heat transfer rate into the nanofluids is calculated as follows:

$$Q_{nf} = \dot{m} Cp\left(T_{out} - T_{in}\right) \quad (10)$$

The heat transfer rate from the heating fluids is calculated as follows:

$$Q_{hf} = \dot{m}_{hf} Cp_{hf}\left(T_{out} - T_{in}\right)_{hf} \quad (11)$$

The energy balance between the process fluid and the heating fluid was found to be at a difference of about 25%. This is common for small-scale experimental setup equipment.

The heat transfer coefficient of the nanofluids (h_{nf}) can be defined by using overall heat transfer resistance relationship:

$$\frac{1}{U} = \frac{1}{h_{nf}\left(A_i/A_o\right)} + \frac{D_o}{2k}\ln\frac{D_o}{D_i} + \frac{1}{h_o} \quad (12)$$

The overall heat transfer coefficient can then be determined as follows:

$$U = \frac{Q}{A_o \Delta T_{lm}} \quad (13)$$

Table 2. Some Thermal Conductivity Correlations of Nanofluids in Recent Literature

Researcher	Correlation
Yu and Choi [8]	$k_{nf} = k_f * \frac{k_{pe} + 2k_f + 2\phi(k_{pe} - k_f)(1+\beta)^3}{k_{pe} + 2k_f - \phi(k_p - k_f)(1+\beta)^3}$, $\beta = \frac{h}{r}$, $h < 10nm \longrightarrow \beta = 0.1$
Godson *et al*. [9]	$k_{nf} = 0.9692 * \phi + 0.9508$
Prasher *et al*. [10]	$k_{nf} = k_f * \frac{1 + A\phi\, Re^m\, Pr^{0,333} * (1+2\alpha) + 2\phi(1-\alpha)}{(1+2\alpha) - \phi(1-\alpha)}$,$\alpha = \frac{2R_b k_f}{d_p}$, $A = 40000$,$m = 2.5$, $R_b = 0.77 \times 10^{-8}$
Koo and Kleinstreuer [11]	$k_{nf} = k_{MG} + 5 \times 10^4\ \beta\phi\rho_p\, C_p \sqrt{\frac{K_B T}{\rho_p D}}\ f(T,\phi)$, $k_{MG} = k_f * \left(1 + \frac{3\phi\left(\frac{k_p}{k_f} - 1\right)}{\left(\frac{k_p}{k_f} + 2\right) - \phi\left(\frac{k_p}{k_f} - 1\right)}\right)$ $f(T,\phi) = (-6.04\phi + 0.4705) * T + (1722.3\phi - 134.63), \beta = 0.0137(100\phi)^{-0.8229} \rightarrow \phi \le 1\%$
Li and Peterson [12]	$k_{nf} = k_f + k_f(0.764\phi - 0.0187\,(T - 273.15) - 0.462)$ For Al_2O_3 $k_{nf} = k_f + k_f(3.761\phi + 0.0179\,(T - 273.15) - 0.307)$ For CuO
Palm and Roy [136]	Al_2O_3 $\begin{pmatrix} k_{nf} = 0.003352T - 0.3708 & \text{For } \phi = \%1 \\ k_{nf} = 0.004961T - 0.8078 & \text{For } \phi = \%4 \end{pmatrix}$
Nguyen *et al*. [13]	$k_{nf} = k_f\,(4.97\phi^2 + 2.72\phi + 1)$ For Al_2O_3 $k_{nf} = k_f\,(28.905\phi^2 + 2.827\phi + 1)$ For CuO
Bhattacharya *et al*. [14]	$k_{nf} = k_p\phi + (1-\phi)k_f$
Buongiorno [15]	$k_{nf} = k_f\,(1 + 7.47\phi)$
Kim *et al*. [16]	$k_{nf} = 0.65 + 4{,}864 \times 10^{-7} T^3$
Timofeeva *et al*. [17]	$k_{nf} = k_f(1 + 3\phi)$
Chon *et al*. [18]	$k_{nf} = k_f * (1 + 64.7\phi^{0.746}\,(d_f/d_p)^{0.369}(k_p/k_f)^{0.747}\, Re^{1.2321}\, Pr^{0.9955})$ $Pr = \frac{\mu}{\rho_{BF}\alpha}, Re = \frac{\rho_{BF} V d_p}{\mu} = \frac{\rho_{BF} K_B T}{3\pi\mu^2 L_{BF}}, \mu = 2{,}414 \times 10^{-5} \times 10^{\left(\frac{247}{T-140}\right)}$
Murshed *et al*. [19]	$k_{nf} = \frac{k_f * (1 + 0.27\phi^{4/3}\,(\frac{k_p}{k_f} - 1)(1 + \frac{0.52\phi}{1 - \phi^{1/3}}\,(\frac{k_p}{k_f} - 1)}{1 + \phi^{4/3}\,(\frac{k_p}{k_f} - 1)(\frac{0.52}{1 - \phi^{1/3}} + 0.27\phi^{1/3} + 0.27)}$

Monrad and Pelton's equation [22] can be used to estimate the outside heat transfer coefficient, h_o, for turbulent flow in annuli as follows:

$$Nu = 0.020\,Re^{0.8}\,Pr^{1/3}\left(D_2/D_1\right)^{0.53} \tag{14}$$

Subscript 1 and 2 refer to the outer and inner diameter of the annulus, respectively. The equivalent diameter, being represented by D_e, was used instead of the typical diameter (D).

$$D_e = \frac{D_{i,a}^2 - D_o^2}{D_o} \tag{15}$$

By modifying the Seider-Tate equation [23], all of the experimental data can be used to develop a new heat transfer correlation for predicting the heat transfer coefficient of nanofluids flowing laminar in a more convenient form as follows:

$$\Omega = Nu_{nf}\,Pr_{nf}^{-1/3}\left(\frac{L}{D}\right)^{1/3}\left(\frac{\mu_f}{\mu_w}\right)^{-0.14} = a\,Re_{nf}^{b} \tag{16}$$

where a and b are the various constants depending on the experimental conditions.

The Nusselt number and heat transfer coefficient of the nanofluids are calculated by the means of following equations:

$$Nu_{nf,x} = \frac{h_{nf,x} D}{k_{nf}} \tag{17}$$

$$h_{nf,x} = \frac{q}{T_{w,x} - T_{f,x}} \tag{18}$$

The fluid temperature (19)

In the literature, the results showed that Reynolds number and volume fraction are very important parameters for the local heat transfer coefficient. Particularly, the entrance region showed that the use of nanofluids revealed a significant increase in the heat transfer coefficient causing a decrease in the thermal boundary layer thickness and a decrease along the tube length. This behavior indicated that "smart entrance" must be created to improve performance of nanofluids. Furthermore, the Shah correlation for laminar flow and the Dittus-Boelter equation for turbulent flow did not match with the Nusselt number between the experimental results and the calculated values.

Similar to the experimental investigation, many researchers tried to formulate the suitable correlations for the prediction of the thermal conductivity of the nanofluid. Since several challenges such as dispersion, Brownian force, sedimentation and friction force between the fluid and the solid particles may coexist in the main flow it becomes hard to generate any formulated theory for the prediction of the accurate heat transfer behavior of the nanofluid. Nanofluid is considered more like a fluid rather than a liquid-solid mixture by some researchers. There are few articles treating the nanofluid as to have the multiphase feature.

3. LITERATURE REVIEW OF RECENT YEARS

The studies on the use of particles of nanometer dimension were first continuously conducted by a research group at the Argonne National Laboratory approximately a decade ago. Choi [24] was possibly the first researcher who called the fluids with particles of nanometer scale 'nano-fluids'.

Nanofluids have better rheological and stability properties, significantly higher thermal conductivities and no penalty in pressure drop as compared with suspended particles of millimeter-or-micrometer scale.

In recent years, the nanofluid has emerged as an alternative heat transfer fluid for heat transfer applications showing a significant potential for heat transfer improvement. It has been expected to be suitable for the engineering application without severe problems in pipeline and with little or no penalty in pressure drop. According to earlier researches, thermal conductivity has come into the limelight as most studied transport properties of the nanofluid. The convective heat transfer of nanofluids has comparatively been less acclaimed in literature therefore the number of the publications dealing with the convective heat transfer of nanofluids is limited. The most productive research has been continuously carried out by the following studies.

3a. Somestudies of 2012

Alizad *et al*. [25] investigated thermal performance, transient behavior and operational start-up characteristics of flat-shaped heat pipes by using nanofluids. They used three different primary nanofluid of CuO, Al_2O_3, and TiO_2. They benefitted from a comprehensive analytical model having detailed heat transfer characteristics inside the condensation and evaporation sections of the tube. The thermal performance of either the flat-plate or disk-shaped heat pipes was increased by higher concentration of nanoparticles.

Bobbo *et al*. [26] showed some viscosity data for nanofluids. They used water as base fluid and two different primary nanofluids such as single wall carbonnanohorn (SWCNH) and titanium dioxide (TiO_2). They determined viscosity of nanofluids using arhometer experimentally and benefitted from the function of the nanoparticles' mass fraction and the shear rate. Therefore they accounted the possible non-Newtonian behavior for the nanofluid. As a result, different empirical correlations were proposed in their study.

Buschmann [27] studied on ceramic nanofluid's thermal conductivity and heat transfer characteristics. He observed that heat transfer could be increased by using nanofluids in the thermal entrance with test rig. It was revealed that when the thermal conductivity of five different ceramic nano fluids were measured by means of a sophisticated ring gap apparatus the dynamic viscosity was found to be enhanced successfully.

Yang *et al*. [28] enhanced the heat and mass transfer on the ammonia water absorption refrigeration system. They yielded three different nanofluids by inserting the mixture of carbon black with emulsifier OP-10, $ZnFe_2O_4$ with sodium dodecyl benzene sulfonate (SDBS), and Fe_2O_3 with SDBS to the ammonia water solution, respectively. It was found that key parameters for this study werethe content of surfactant and nanoparticles, their interaction, and also the dispersion type that affected the viscosity of ammonia water nanofluid. They correlated mainly two models to predict the viscosity of ammonia water nanofluid.

Colangelo *et al*. [29] intended to observe the diathermic oil based nanofluids being used in many areas such as renewable energy, cogeneration and cooling systems. They used the diathermic oil with CuO, Al_2O_3, ZnO and Cu particles having different shapes and concentrations from 0% to 3.0%. It was found that the heat transfer performance of diathermic oil increased more than that of the water for the same nanoparticle concentrations.

Jamshidi *et al*. [30] investigated the heat transfer rate and pressure drop in helical coils in their study. They assumed that thermophysical properties of nanofluid did not depend on volume fraction and temperature. They utilized from a numerical simulation and Taguchi method to obtain the optimum condition for desired parameter values. Results showed that the use of nanofluids enhanced the thermal-hydraulic performance of helical tube. Although, temperature dependent properties changed with the optimum particle volume fraction, nanofluids were not varied by the optimized shape factor.

Giraldo *et al*. [31] investigated the thermal behavior of a nanofluid loaded with alumina nanoparticles and developed a direct numerical simulation of the flow. They utilized from the boundary element method to solve moving boundary problems. They observed that strong convective currents occurred as a result of the presence of the nanoparticles, which in time increased the total heat flow in the cavity particle concentration. Particle concentration increased the total heat flow influencing both the conductive part of heat transfer and the convective part expectedly.

Özerinç *et al*. [32] studied the application of some empirical correlations of forced convection heat transfer developed for the flow of pure fluids and nanofluids. They compared their results with existing theories in the literature and their model underestimated the heat transfer as a result of the numerical solution pointing that single-phase assumption with temperature-dependent thermal conductivity and thermal dispersion being the certain way of heat transfer enhancement analysis of nanofluids in convective heat transfer.

Yu *et al*. [33] investigated the thermophysical properties and convective heat transfer of Al_2O_3-polyalphaolefin (PAO) nanofluids includingboth the spherical and the rod-like nanoparticles. They determined the viscosity and thermal conductivity of the nanofluids and compared their predictions with several existing theories in the literature. Their results showed that in a convective flow, the shear-induced alignment and specific motion of the particles should be regarded to truly interpret the experimental data of the nanofluids including non-spherical nanoparticles.

Farahani and Kowsary [34] intended to clarify a heat conduction method used for defining the local convective boiling heat transfer coefficient of pure water and copper based nanofluid flowing in a mini channel by utilizing three different concentrations of nanoparticles being 5 mg/L, 10 mg/L and 50 mg/L. They tried to solve the IHCP using sequential specification function method by calculating the space-variable convective heat transfer coefficient. Their results acknowledged two dimensional SFS method to have the optimum experiments for the determination of boiling heat transfer coefficients of pure water and nanofluid flowing in mini channel.

Cimpean and Pop [35] studied on the steady fully developed mixed convection flow of a nanofluid in a channel filled with a porous medium. They used some equations to solve the problem those being non-dimensional and based mainly on the mixed convection parameter, the Péclet number, the inclination angle of the channel to the horizontal and the nanoparticle volume fraction. Their results showed that nanofluid greatly enhanced the heat transfer, even for small additions of nanoparticles in the base water fluid.

Leong *et al.* [36] studied on the flow of nanofluids in shell and tube heat recovery exchangers in a biomass heating plant. They benefited from the literature that included heat exchanger specification, nanofluid properties and mathematical formulations. They found that use of nanofluids augmented the convective and overall heat transfer coefficient as compared to the ethylene glycol or water based fluids shown in Fig. (**1**).

Mahbubul *et al*. [37] investigated different characteristics of viscosity of nanofluids such as nanofluid preparation methods, temperature, particle size and shape, and volume fraction effects. They found that viscosity's augmentation depended on volume concentration, increase and decrease of the temperature rise. They observed that viscosity improved with volume fraction for different concentration of Al_2O_3, TiO_2 as shown in Fig (**2**).

Wenzheng *et al*. [38] studied a Molecular Dynamics simulation on Couette flow of nanofluids and showed the microscopic flow characteristics through visual observation and statistic analysis. They presented the even-distributed liquid argon atoms near solid surfaces of nanoparticles those which might have been appeared as a reform to base liquid had contributed to heat transfer enhancement. Nanoparticles moved rapidly in the shear direction accompanying with motions of rotation and vibration in the other two directions in the process of Couette flow. The motions of nanoparticles were reinforced significantly when the shearing velocity was grown. More enhanced heat transferring in nanofluids obtained by the motions of nanoparticles could disturb the continuity of fluid and strengthen partial flowing around nanoparticles.

3b. Somestudies of 2011

Ahmed *et al*. [39] investigated the characteristics of heat transfer and pressure drop belonging to copper-water nanofluid flow in an isothermally heated corrugated channel. Their model included the equations of continuity, momentum and energy for laminar flow in curvilinear coordinates using the Finite Difference (FD) approach. Reynolds number and nanoparticle volume fraction varied from 100 to 1000 and from 0 to 0.05 in their study, respectively. They studied the effects of using nanofluid on the heat transfer and pressure drop inside the channel. Their results showed that increase in the volume fraction of the nanoparticle and Reynolds number caused both an increase in heat transfer enhancement and a slight increase in pressure drop. They highlighted the effect of Reynolds number for different nanoparticle volume fraction on average Nusselt number enhancement in Fig. (**3**).

Akbarinia *et al*. [40] investigated the heat transfer enhancement at low Reynolds numbers using Al_2O_3-water nanofluid flows in two-dimensional rectangular microchannels. Their results showed that the major enhancement in Nusselt number was not only due to the increase in the nanoparticle concentrations but also due to the increase in the inlet velocity to reach a constant Reynolds number. They reported that constant Reynolds number studies of nanofluids had not sufficient approach to evaluate the heat transfer and the skin friction factor due to the use of nanofluids.

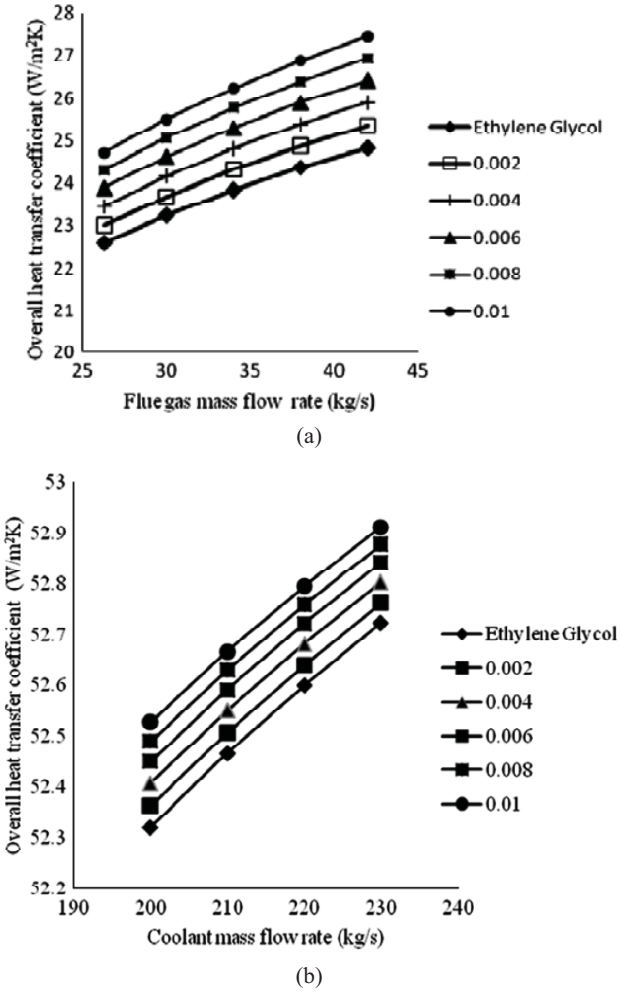

Fig. (1). The effect of flue gas mass flow rate and (**a**) coolant mass flow rate (**b**) on overall heat transfer coefficient [From Leong *et al*. [36], with permission from Elsevier]

In the studies made by Bianco *et al*. [41], turbulent forced convection flow of water-Al_2O_3 nanofluid in a circular tube was calculated numerically depending on a constant and uniform heat flux at the wall. Their study was based on two different approaches: single and two-phase models, with particle diameterequal to 38 nm. It was calculated that convective heat transfer coefficient for nanofluids was greater than that of the base liquid. Their study showed that heat transfer enhancement increased with the particle volume concentration and Reynolds number. Comparisons with correlations in literature were carried out obtaining a very good agreement.

Corcione [42] put forward two empirical correlations and discussed them for predicting the effective thermal conductivity and dynamic viscosity of nanofluids using a high number of experimental data available in the literature. It was observed that at the constant nanoparticle material and the base fluid, the ratio between the thermal conductivities of the nanofluid and the pure base liquid increased by increasing the nanoparticle volume fraction and the temperature, and decreasing the nanoparticle diameter. Moreover, the ratio between the dynamic viscosities of the nanofluid and the

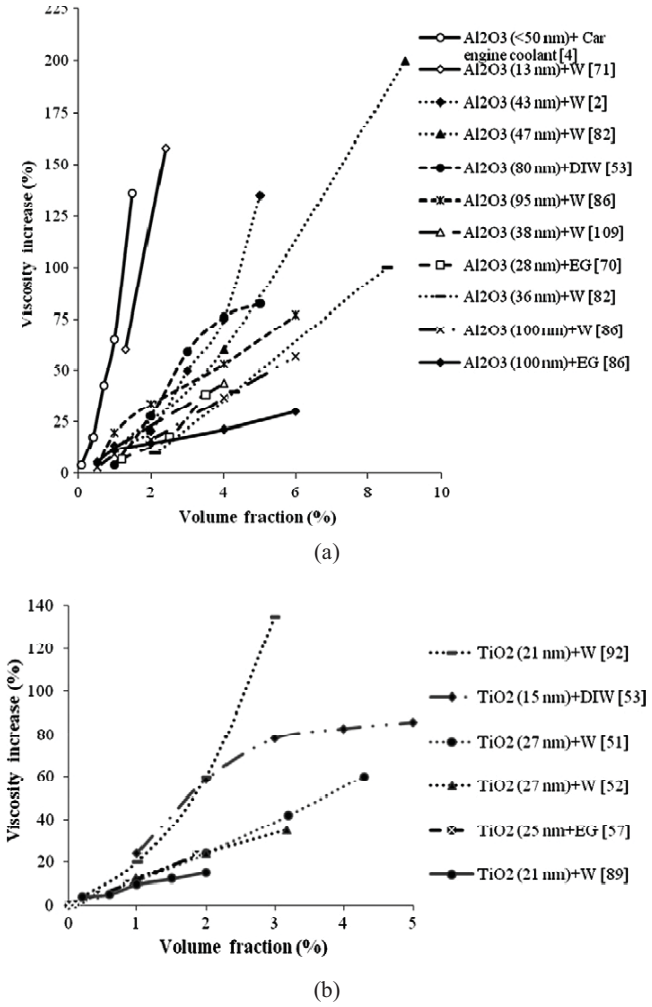

Fig. (2). Viscosity increases with the increase of volume fraction for different concentration of Al_2O_3 (**a**) TiO_2 (**b**) [From Mahbubul *et al*. [37], with permission from Elsevier].

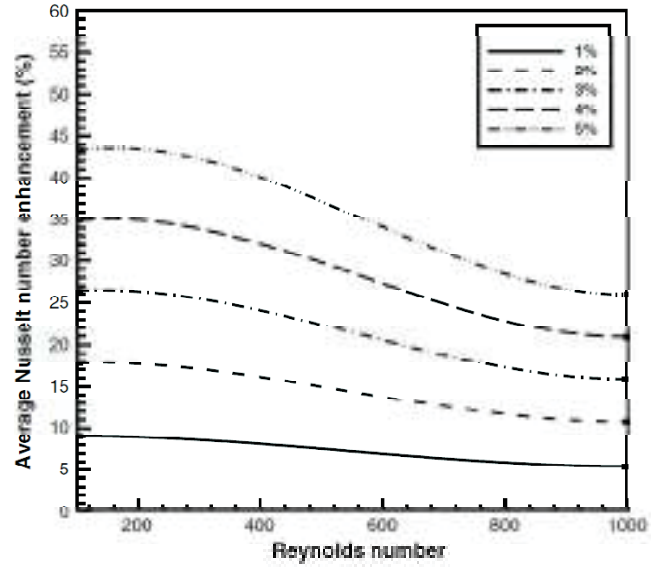

Fig. (3). Average Nusselt number enhancement vs. Reynolds for different nanoparticle volume fractions [From Ahmed *et al*. [39], with permission from Elsevier].

pure base liquid increased with increasing the nanoparticle volume fraction, and decreasing the nanoparticle diameter in the case of those practically being not dependent on temperature.

Firouzfar *et al*. [43] used nanoparticles to investigate the heat transfer mechanisms concerning the thermal conductivity increase, brownian motion, dispersion, and fluctuation of nanoparticles especially near the wall which led an increase in the energy exchange rates and augmented the heat transfer rate between the fluid and the wall of evaporator section. Their experimental results showed that addition of silver nanofluid in methanol led to energy saving around 8.8-31.5% for cooling and 18-100% for reheating the supply air stream in an air conditioning system.

Gherasim *et al*. [44] presented heat transfer enhancement capabilities of coolants using suspended nanoparticles (Al_2O_3 dispersed inwater) inside a confined impinging jet cooling device in their numerical study. A good agreement was found between numerical results and available experimental data. Their study reported heat transfer enhancement being possible in their application using nanofluids. It was observed that the mean Nusselt number increased with increasing particle volume fraction and Reynolds number and also it decreased with increasing in disk spacing. The study deduced that a significant increase in pumping power might impose some limitations on the efficient use of this type of nanofluid in a radial flow configuration.

Hojjat *et al*. [45] experimentally investigated the forced convective heat transfer using dispersing γ-Al_2O_3, CuO, and TiO_2 nanoparticles in an aqueous solution of carboxymethyl cellulose (CMC). Their experimental apparatus included a uniformly heated circular tube under turbulent flow conditions passing through these nanofluids. Their results showed that the local and average heat transfer coefficients of nanofluids were larger than those of the base fluid. A new correlation was therefore proposed for the prediction of the Nusselt number of non-Newtonian nanofluids as a function of the Reynolds and the Prandtl numbers.

Hojjat *et al*. [46], by using γ-Al_2O_3, TiO_2 and CuO nanoparticles in a 0.5 wt% of carboxymethyl cellulose (CMC) aqueous solution calculated thermal conductivity of base fluid and nanofluids with various nanoparticle loadings at different temperatures experimentally. Their results showed that the thermal conductivity varied exponentially with the nanoparticle concentration. In their study, they developed an ANN model for the thermal conductivity as a function of the temperature.

Hojjat *et al*. [47] investigated the forced convection heat transfer of non-Newtonian nanofluids in a circular tube with constant wall temperature condition under turbulent flow conditions of three types of nanofluids (γ-Al_2O_3, TiO_2 and CuO nanoparticles) in the base fluid experimentally. Their base material was the aqueous solution of carboxymethyl cellulose (CMC). Their results showed convective heat transfer coefficient of nanofluids being higher than that of the base fluid.

Huminic and Huminic *et al*. [48] used CuO and TiO_2 nanoparticles with the diameters of 24 nm dispersed in water with volume concentrations of 0.5-3 vol.% as the working fluid in their experiment and investigated three-dimensional analysis on the heat transfer characteristics of double-tube helical heat exchangers using nanofluids under laminar flow conditions. Experimental calculations showed that at 2% CuO nanoparticles in water and same mass flow rate in inner tube and annulus, the heat transfer rate of the nanofluid was found to be approximately 14% greater than that of pure water, while the heat transfer rate of water in the annulus was calculated approximately 19% greater than those nanofluids which were flowing through the inner tube.

Huminic and Huminic [49] studied the heat transfer characteristics of two-phase closed thermosyphon (TPCT) with iron oxide-nanofluids. The TPCT with the de-ionic water and nanofluids (water and nanoparticles) were tested. Effects of TPCT inclination

angle, operating temperature and nanoparticles concentration levels on the heat transfer characteristics of TPCT were investigated. The nanoparticles were found to have a significant effect on the enhancement of heat transfer characteristics of TPCT. The heat transfer characteristics of TPCT of the nanofluids were compared with those of the based fluid. Their experimental results focused on iron oxide-water nanofluid as the working fluid, heat transfer rate, evaporation and condensation heat transfer coefficients and thermal resistances. Different nanoparticle concentration levels in suspension within the two-phase closed thermosyphon, operating temperatures and inclination angles of the heat pipe (30-90°) were experimentally examined and the results were compared with those of pure water.

Jung *et al*. [50] developed binary nanofluids using nanoparticle suspensions to enhance the heat and mass transfer performance of absorption refrigeration cycles. To stabilize the nanoparticles in a strong electrolyte, polymer was used as a steric stabilizer. The effective thermal conductivities of the binary nanofluids with the concentrations of nanoparticle up to 0.1 vol% were measured by means of the transient hot wire method. The study revealed that the dispersion stability of nanofluids was a dominant factor for enhancing the thermal conductivity of binary nanofluids while thermal conductivity was found to be changing with time. It was also observed that thermal conductivity of H_2O/LiBr binary mixture with Al_2O_3 nanoparticles increased with increasing the particle volume concentration and was enhancedat 2.2% at 0.1 vol% concentration conditions.

Khanafer and Vafai [51] came up with a study related with the critical synthesis of the variants within the thermophysical properties of nanofluids. This study showed that it was not clear which analytical model should be used to describe the thermal conductivity of nanofluids. Their results showed that the effective thermal conductivity and viscosity of nanofluids could be estimated using the classical equations at low volume fractions.

Lee *et al.* [52] determined the transmission of electron microscopy and scanning of electron microscope images for characterizing the shape and size of SiC nanoparticles. The dispersion behavior for SiC/deionized water (DIW) nanofluids was investigated under different pH values and characterized with the zeta potential values. The isoelectric point of SiC/DIW nanofluid was determined concerning colloidal stability. Thermal conductivity and viscosity as a function of volume fraction were investigated.

Asirvatham *et al*. [53] performed experiments to investigate the convective heat transfer of nanofluids using silver-water nanofluids under laminar, transition and turbulent flow regimes in a horizontal 4.3 mm inner-diameter tube-in-tube counter-current heat transfer test section. The volume concentration of the nanoparticles was found to be varying from 0.3% to 0.9% in steps of 0.3%. The effects of thermo-physical properties, inlet temperature, volume concentration, and mass flow rate on heat transfer coefficient were investigated. Experiments showed that the suspended nanoparticles remarkably increased the convective heat transfer coefficient, by as much as 28.7% and 69.3% for 0.3% and 0.9% of silver content, respectively. Heat transfer coefficient clearly augmented with an increase in the combination of particle loading and Reynolds number as shown in Fig. (**4**). Based on the experimental results, a correlation was developed to predict the Nusselt number of the silver-water nanofluid, within ±10% deviation band between experimental and predicted values. Predicted and experimental Nusselt numbers were shown in the range of Reynolds number from 800 to 12000, Prandtl number from 4 to 10 and volume concentration from 0 to 2% in Fig. (**5**).

Ebrahimnia-Bajestan [54] presented a numerical investigation on the heat transfer performance and pressure drop of nanofluids flowing through a straight circular pipe during laminar flow regime

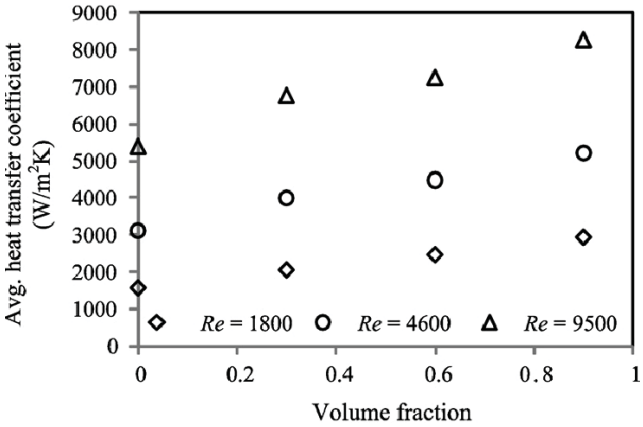

Fig. (4). Heat transfer coefficient increases with volume fraction [From Asirvatham *et al*. [53], with permission from Elsevier].

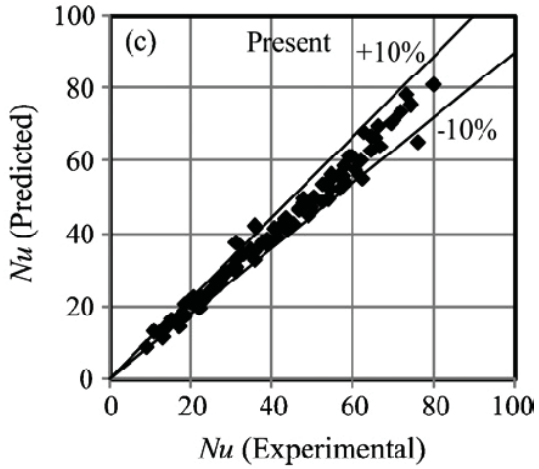

Fig. (5). Variations of Predicted and Experimental Nusselts numbers [From Asirvatham *et al*. [53], with permission from Elsevier].

and constant heat flux boundary condition. Al_2O_3, CuO, carbon nanotube (CNT) and titanate nanotube (TNT) nanoparticles dispersed in water and ethylene glycol/water with particle concentrations ranging between 0 and 6 vol.% were used as working fluids for simulating the heat transfer and flow behaviours of nanofluids. The proposed model was validated with the available experimental data and correlations. The effects of particle concentrations, particle diameter, particles' Brownian motions, Reynolds number, type of the nanoparticles and base fluid on the heat transfer coefficient and pressure drop of nanofluids were determined and discussed in detail. The results indicated that the particle volume concentration, Brownian motion and aspect ratio of nanoparticles increased the heat transfer coefficient while the nanoparticle diameter was found to have an opposite effect on the heat transfer coefficient. They listed temperature increase, pressure drop, and pumping power for different nanofluids flow conditions in Table **3**. Finally, the present study provided some considerations for the appropriate choice of the nanofluids for practical applications.

Raisi *et al*. [55] numerically studied method for both slip and non-slip boundary conditions in the thermal performance of a microchannel, cooled with either pure water or a Cu-water nanofluid on the flow field and heat transfer. They assumed that the microchannel should be partially heated at a constant temperature and cooled by forced convection of a laminar flow at a relatively lower

Table 3. Temperature increase, Pressure drop and Pumping power is listed for different nanofluids flow conditions [Ebrahimnia-Bajestan *et al.* [54], with permission from Elsevier]

Type of working fluids	Re	d_p (nm)	ϕ (vol.%)	ΔT (°C)	ΔP (Pa)	Pump power (W)
Al_2O_3/60% EG/water	1460	20	4	0.56	43240	1.38
60% EG/water	1460	–	–	0.68	26240	0.69
CNT/water	1460	$L_p/d_p > 100$	0.038	0.9	9625	0.16
CuO/water	1460	20	6	1.05	8838	0.12
CuO/water	1460	20	4	1.52	3830	0.04
TNT/water	1460	$d_p = 10$, $L_p = 100$	0.6	1.8	2241	0.017
Al_2O_3/water	1460	100	6	2.05	2020	0.014
Al_2O_3/water	1460	40	6	2.06	2020	0.014
Al_2O_3/water	1460	20	6	2.08	2020	0.014
CuO/water	1460	20	2	2.18	1670	0.011
Al_2O_3/water	1460	40	4	2.39	1416	0.008
Al_2O_3/water	1460	20	4	2.39	1417	0.008
Al_2O_3/water	1460	20	3	2.52	1188	0.007
Water	1620	–	–	2.6	974	0.005
Al_2O_3/water	1460	20	2	2.72	996	0.005
Al_2O_3/water	1460	100	2	2.72	995	0.005
Al_2O_3/water	1460	40	2	2.73	995	0.005
Water	1460	–	–	2.78	869	0.004
Al_2O_3/water	1000	20	4	3.44	936	0.004
Water	1000	–	–	4.08	572	0.002
Al_2O_3/water	500	20	4	6.91	438	0.0009
Water	500	–	–	8.19	266	0.0004

temperature. The effects of pertinent parameters such as Reynolds number, solid volume fraction, and slip velocity coefficient on the thermal performance of the microchannel ewere investigated. The heat transfer rate was significantly affected by the solid volume fraction and slip velocity coefficient at high Reynolds numbers.

Heris *et al*. [56] numerically studied laminar flow-forced convective heat transfer of Al_2O_3/water nanofluid in a triangular duct under constant wall temperature condition. The effects of parameters were investigated such as diameter of nanoparticles, concentration, and Reynolds number on the enhancement of nanofluids heat transfer. By comparing heat transfer between nanofluid and pure fluid it was found that in non-circular ducts the low heat transfer rate was one of the limitations of these systems and use of nanofluid instead of pure fluid because of its potential to increase heat transfer of system could compensate this problem. They obtained that the nanofluid Nusselt number increased with increasing concentration of nanoparticles and decreasing its diameter. Also, the enhancement of the fluid heat transfer became better at high Re in laminar flow with the addition of nanoparticles.

Vincenzo *et al*. [57] numerically studied the developing turbulent forced convection flow of a water-Al_2O_3 nanofluid in a square tube in constant and uniform wall heat flux. The particlesize equal to 38 nm was used in nanofluid flow. The optimal working condition was obtained during an entropy generation analysis for the given geometry under given boundary conditions. A simple analytical procedure was proposed to evaluate the entropy generation and its results were compared with the numerical calculations. The optimal Reynolds number was determined on minimizing entropy generation.

Demir *et al*. [58] numerically investigated forced convection flows of nanofluids consisting of water with TiO_2 and Al_2O_3 nanoparticles in a horizontal tube with constant wall temperature. The horizontal test section was modeled and solved using a CFD program. Palm *et al*.'s correlations were used to determine the nanofluid properties. A single-phase model having two-dimensional equations was employed with either constant or temperature dependent properties to study the hydrodynamics and thermal behaviors of the nanofluid flow. The numerical investigation was performed for a constant particle size of Al_2O_3 as a case study after the validation of its model by means of the experimental data of Duangthongsuk and Wongwises with TiO_2 nanoparticles. The velocity and temperature vectors were presented both in the entrance and fully developed region. The variations in the fluid temperature, local heat transfer coefficient and pressure drop along tube length had been shown in the paper. Effects of nanoparticles concentration and Reynolds number on the wall shear stress, Nusselt number, heat transfer coefficient and pressure drop were highlighted. Numerical results showed the heat transfer enhancement due to presence of the nanoparticles in the fluid concerning the results of the experimental study used for the validation process of the numerical model.

3c. Somestudies of 2010

Nanoparticles of magnetite Fe_3O_4 have been synthesized at various pH values by a method of co-precipitation in Abareshi *et al.* [59]'s study. The characteristic properties of the products were determined by transmission electronic microscopy, Fourier infrared spectroscopy and X-ray diffraction. By using a vibrating sample magnetometer, the magnetic properties of the products were found. According to the obtained results, particles being cubic in shape exhibited super paramagnetic properties at room temperature. Fe_3O_4 nanoparticles were dispersed in water as a base fluid in the presence of a dispersant which was tetramethyl ammonium hydroxide and so the magnetic nanofluids were prepared. As a function of temperature and volume fraction, the thermal conductivity of the nanofluids was measured. The thermal conductivity values of the nanofluids were obtained in terms of volume fraction and temperature. It was found by the results that an increase in the thermal conductivity ratio of the nanofluids resulted in an increase in temperature and volume fraction. As it has been demonstrated in Fig. (**6**), that the thermal conductivity was increased by 11.5% at most at 40°C for the nanofluids having 3 vol% nanoparticles because of the Brownian motion of nanoparticles intensified at high temperatures. Then the experimental results were evaluated and discussed according to the theoretical models.

Under turbulent flow conditions, the measurement of heat transfer characteristics of Gama-Al_2O_3 and TiO_2/water nanofluids was performed in a shell and tube heat exchanger in Farajollahi *et al.* [60]'s study. It was investigated how the heat characteristics were affected by Peclet number, volume concentration of suspended nanoparticles, and particle type. It was evident from the obtained result that when the nanoparticles were added to the base fluid, heat transfer characteristics were significantly enhanced. When the heat transfer behavior of two nanofluid was compared, it was found that at a definite Peclet number, TiO_2/water nanofluid showed greater heat transfer characteristics at its optimum nanoparticle concentration than the heat transfer characteristics of Gama-Al_2O_3/water nanofluid. However, better rate of heat transfer behavior at higher nanoparticle concentrations of Gama-Al_2O_3/water nanofluid was obtained.

By using a CFD approach, under constant wall temperature condition in a circular tube, the laminar convective heat transfer of nanofluids was studied in a numerical way in Fard *et al.* [61]'s study. Single phase and two-phase models were used for the determination of the temperature, flow field, and calculation of heat transfer coefficient. The effects of some important parameters such as nanoparticle sources, nanoparticle volume fraction and nanofluid's Peclet number on heat transfer rate were investigated. The result showed that as the particle concentration increased, heat transfer coefficient also increased. According to their simulation results, it was seen that when their model was compared to the single phase model, better predictions for heat transfer rate were obtained from the two phase approach.

According to Do *et al.* [62]'s study, thermal performance of nanofluids was investigated by testing circular screen mesh of wick heat pipes experimentally. In their study, water-based Al_2O_3 nano-

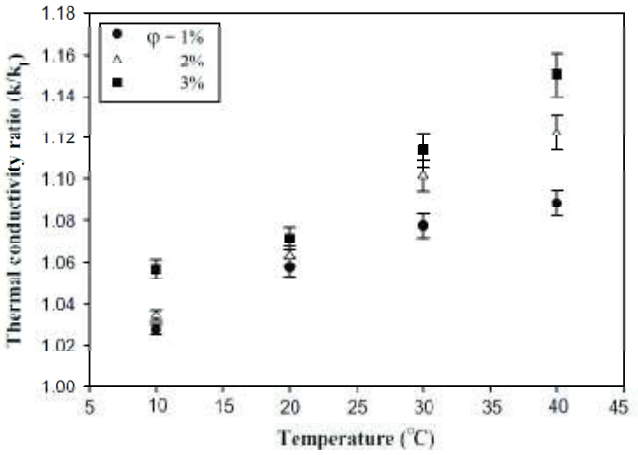

Fig. (6). The effect of temperature at different volume fractions of Fe_3O_4 on the thermal conductivity ratio (k/kf) [From Abareshi *et al.* [59], with permission from Elsevier].

fluids were used by the volume fraction of 1.0 and 3.0 vol.%. According to their study, the use of water based Al_2O_3 nanofluids instead of DI water could accomplish the maximum heat transfer rate of pipe. The thin porous coating layer formed by nanoparticles suspended in nanofluids at wick structures was observed experimentally. It was observed that the coating layer formed by nanoparticles at the evaporator section was the primary mechanism on the enhancement of the thermal performance for the heat pipe due to the fact that the layer could not only extend the evaporation surface with high heat transfer performance but could also improve the surface wettability and capillary wicking performance.

According to Henderson *et al.* [63]'s study, the experiments were performed at low vapor quality (x<20%) with a specific range of mass flux (100<G<400 kg/m^{2}s) for the flow boiling of R-134a and R134a/polyolester mixtures. By using direct dispersion of SiO_2 nanoparticles in R-134a, when compared with pure R-134a, it was observed that the heat transfer coefficient decreased as much as 55%. This degradation was stemmed from, partly, the difficulties in producing a stable dispersion. It was concluded that nanoparticles insignificantly affected the flow pressure drop with the R-134a/POE/CuO nanofluid.

According to Godson *et al.* [64]'s study, the unique features of nanofluids, such as enhancement of heat transfer, improvement in thermal conductivity, increase in surface volume ratio, Brownian motion, thermophoresis, etc. were summarized. Additionally, the recent research in experimental and theoretical studies on forced and free convective heat transfer in nanofluids, their thermophysical properties and applications were summarized. This article identified the challenges and opportunities for future research.

In Kima *et al.* [65]'s study, it was shown that prior studies of pool boiling had demonstrated that nanofluids could improve critical heat flux (CHF) by as much as 200 %. It was observed that heat transfer coefficient increased with the increasing in mass and heat flux during flow boiling. Test section was examined by a confocal microscopy and this technique showed nanoparticle deposition occurring on the boiling surface. The number of micro cavities on the surface, and also the surface wettability were changed by this deposition. In order to estimate the ensuing nucleation site density changes, a simple model was used; however, a successful correlation between the nucleation site density and the heat transfer coefficient could not be obtained.

In Lotfi *et al*. [66]'s study, water and Al_2O_3 nanoparticle mixtures under forced convective condition were studied numerically. Agreeable correlations of computed results were validated. Eulerian model was implemented to observe two phase flow field as a first study in the literature. The two-phase and single phase models were used in the mixture model formulation. According to calculated experimental values, the mixture model was found to be more precise. It should be noted that Nusselt numbers for single-phase model and the two-phase Eulerian model could not be predicted accurately in the study.

In Meibodi *et al*. [67]'s study, modeling of the thermal conductivity of the suspensions was performed by means of the resistance model approach. In this model, Brownian motion, interfacial layer and also a new mechanism were considered. They reported that this model migh be used without any adjustable parameter for estimating the upper and lower limits of nanofluid thermal conductivity. Data of thermal conductivity for CuO nanofluids were acquired experimentally and according to the results, proposed model was found to be consistent with the data. Their model was used to detect the various mechanisms' portions on the thermal conductivity of nanofluids. The results were found to be compatible with the basic knowledge about nanofluids' thermal conductivity mechanism.

According to the theory in Meibodi *et al*. [68]'s study, convective heat transfer coefficient depended on the parameters of velocity and temperature profiles. Within this study, friction factor and convection coefficient were utilized to compare the profiles for both nanofluids and base fluids. To reach this aim, Al_2O_3/water and carbon nanotube/water were preferred. It was demonstrated that the velocity profile of a nanofluid was similar to that of its base fluid. It was suggested that the only responsible variable for unpredictable convective heat transfer coefficient of nanofluids was the alteration of temperature profile for nanofluids.

In Meibodi *et al*. [69]' study, thermal conductivity and stability of carbon nanotube (CNT)/water mixture nanofluid were investigated and an optimum condition for the production and application of nanofluids was also proposed. They revealed a plethora of parameters such as size, shape and source of nanoparticles, surfactants, power of ultrasonic, time of ultrasonication, elapsed time after ultrasonication, pH, temperature, particle concentration and surfactant concentration, which affected this property. It was demonstrated that significant factors on the thermal conductivity and stability were not precisely similar to one another.

Paul *et al*. [70] presented various techniques for the measurement of nanofluid thermal conductivity and developed a unique thermal conductivity measurement device that propped up the thermal comparator principle. The constructional details were elaborated as well. After completing their research they presented some suggestions to enhance the reliability of the measurement of thermal conductivity. Their results indicated that they benefited from the transient hot-wire technique for measuring thermal conductivity.

Paul *et al*. [71] studied on preparation of the nano-gold dispersed water based nanofluid using the chemical reduction method. They described crystallite size, particle size/shape/morphology, and purity of the nanoparticles by benefiting from X-ray diffraction, scanning and transmission electron microscopy and energy dispersion spectroscopy, respectively. It was found that an increase in concentration and a decrease in size of nanoparticles augmented the heat transfer. They observed the maximum enhancement under 48% at 0.00026 vol.% concentration and 21 nm average particle size conditions.

Qu *et al*. [72] analyzed the thermal performance of an oscillating heat pipe (OHP) containing the effects of filling ratios, mass fractions of alumina particles, and power inputs loaded with base water and spherical Al_2O_3 particles of 56 nm in diameter. It was found that the alumina nanofluids enhanced the OHP's thermal performance, with an optimal mass fraction of 0.9 wt.% for maximal heat transfer increase. When the input power was 58.8 W at 70% filling ratio and 0.9% mass fraction, the maximal thermal re-

sistance was decreased by 0.14 °C/W (or 32.5%) in comparison to the pure water.

Rao [73] presented a brief overview of the important scientific disciplines about nanofluids such as stability properties, phase diagram, rheology and applications. He predicted about future development of this area.

Raykar and Singh [74] investigated to estimate the effective thermal conductivity (ETC) of CNT nanofluids by means of a differential effective medium theory together with Brownian motion. Their results showed that augmentation of ETC, correlated with Brownian motion was remarkably greater in dilute nanofluids.

Roberts and Walker [75] studied on the mixture of alumina/water's performance of different volume loadings using a commercially available electronics cooling system. Their results indicated that convective heat transfer increased with the addition of nanoparticles in the commercial cooling system with nanoparticles' volume loadings up to 1.5% by volume. They also observed nanoparticle suspensions from hours to weeks depending on the particle's size.

Rostamani *et al*. [76] numerically investigated the turbulent flow of nanofluids with different volume concentrations of nanoparticles being copper oxide (CuO), alumina (Al_2O_3) and oxide titanium (TiO_2) flowing along two-dimensional duct under constant heat flux condition. They used water as based fluid. It was found that when the volume concentration was increased the wall shear stress and heat transfer rates augmented. As it can be observed in Fig. (**7a**), the wall shear stress increased with increasing volume concentrations for TiO_2-water nanofluid. Also the wall shear stress has been shown for the comparison of three different nanofluids at the Reynolds number of 40,000 and 3% volume concentration in Fig. (**7b**). Nusselt number was affected more from CuO nanoparticles than Al_2O_3 and TiO_2 nanoparticles to get a constant volume concentration and Reynolds number.

Singh *et al*. [77] analyzed entropy generation owing to the flow and heat transfer by using nanofluids theoretically. They used alumina-water nanofluids and mainly three diameters of tube such as a microchannel (0.1 mm), a minichannel (1 mm) and a conventional channel (10 mm) for the sensitivity of entropy. Their results showed that entropy generation behaviour of nanofluids in the microchannel and conventional channel were estimated accurately by the reduced equation with the help of order of magnitude analysis. In conclusion, they reported the existence of an optimum diameter where the entropy generation rate was found to be the minimum for a specific nanofluid during both laminar and turbulent flow.

Sundar and Sharma [78] studied on the measurement of thermal conductivity and viscosity of Al_2O_3 nanofluid via experiments at different volume concentrations and temperatures and verification of them. Researchers inserted a plain tube with twisted tape and tried to obtain the convective heat transfer coefficient and friction factor at various volume concentrations experimentally. According to the results, the heat transfer coefficient and friction factor, which had 0.5% volume concentration of nanofluid and twist ratio of five conditions, increased heat transfer and friction factor 33.51% and 1.096 times respectively in comparison to the base fluid of water.

Vajjha *et al*. [79] developed new correlations for the determination of convective heat transfer and the friction factor. They used nanoparticles of aluminum oxide, copper oxide and silicon dioxide dispersed in 60% ethylene glycol and 40% water by mass. Researchers measured the properties in the fully developed turbulent regime for the mentioned three nanofluids at several particle volumetric concentrations. They calculated the rheological and the thermophysical properties such as viscosity, density, specific heat and thermal conductivity primarily and then utilized form these properties to improve new correlation as a function of these properties and the particle volumetric concentration.

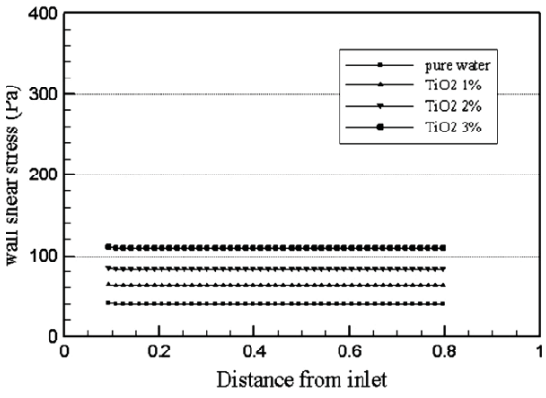

(a)

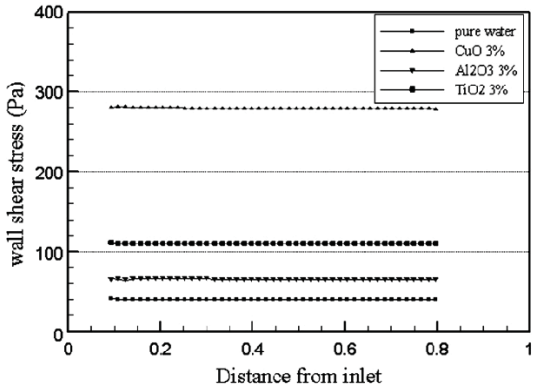

(b)

Fig. (7). Effect of the nanoparticle on wall shear stress (**a**: volume concentration for TiO_2 nanofluid, **b**: Comparison for different nanoparticles at same conditions) [From Rostamani *et al*. [76], with permission from Elsevier].

Vajjha *et al.* [80] analyzed three-dimensional laminar flow and heat transfer with some mixtures containing Al_2O_3 and CuO particles/ethylene glycol and water and also compared these fluids' performance to the base fluid. They developed a new correlation about the determination of viscosity and thermal conductivity of nanofluids as a function of particle volumetric concentration and temperature. It was found that the heat transfer coefficient and the friction factor augmentation increased with the increasing in nanofluids' volumetric concentrations at several Reynolds numbers.

Wei *et al.* [81] investigated the chemical solution method to produce CuS/Cu_2S nanofluids and tried to obtain their thermal conductivity. They mentioned the increase or decrease of the thermal conductivity of nanofluids with proper references.

Wei and Wang [82] presented a microfluidic chemical solution technique, to produce Cu nanofluids. The method changed batch-based macro reactors in the conventional chemical solution method by continuous-flow of microfluidic micro reactors, thus they provided the production of nanofluids with several microstructures. The results showed that Cu nanofluids produced by this technique, had higher stability performance even after more than 100 h.

Yang and Lai [83] benefited from a single-phase approach and focused on creating mathematical model to simulate the forced convection flow of Al_2O_3-water nanofluid in the radial flow cooling system. They indicated that the heat transfer coefficient augmentation depended on increasing of the Reynolds number and the nanoparticle volume fraction, but the pressure drop increase depended more on the increase of particle concentration.

Yu *et al*. [84] investigated preparation of stable ethylene glycol based copper nanofluids via a two-step method. They utilized polyvinyl pyrrolidone as dispersant that could remain stable for a long term. They observed that thermal conductivity significantly increased for the determined nanofluids. The results showed that they achieved 46% increase for the enhancement ratio under 0.5 vol.% at 50 °C conditions. In addition, they suggested 15 min waiting time at least for getting correct thermal conductivities of ethylene glycol based copper nanofluids.

The applied areas and developing process of nanofluids were thoroughly summarized by Wong and Leon [85]'s review paper. Their paper investigated the current and future applications of nanofluids as heat transfer applications (industrial cooling applications, smart fluids, nuclear reactors, extraction of geothermal power and other energy sources), automotive applications (nanofluid coolant, nanofluid in fuel, brake and other vehicular nanofluids), electronic applications (cooling of microchips), biomedical applications (nanodrug delivery, cancer theraupetics, cryopreservation, nanocryosurgery, sensing and imaging) and other applications (nanofluid detergent) generally and also mentioned the increased heat transfer properties by means of nanofluids which made them appropriate for such applications.

Duangthongsuk and Wongwises [86] reported a comparison of the differences between using measured and computed thermophysical properties to describe the heat transfer performance of TiO_2-water nanofluids. In this study, TiO_2 nanoparticles with average diameters of 21 nm and a particle volume fraction of 0.2-1 vol.% were used. The thermal conductivity and viscosity of nanofluids were measured by using transient hot-wire apparatus and a Bohlin rotational rheometer, respectively. The well-known correlations calculating the thermal conductivity and viscosity of nanofluids were used for describing the Nusselt number of nanofluids and were compared with the results from the measured data. The results showed that the use of the models of thermophysical properties for calculating the Nusselt number of nanofluids gave similar results to use of the measured data. Where there was a lack of measured data on thermophysical properties, the most appropriate models for computing the thermal conductivity and viscosity of the nanofluids were the models of Yu and Choi and Wang *et al*., respectively.

Duangthongsuk and Wongwises [87] reported the heat transfer coefficient and friction factor of the TiO_2-water nanofluids flowing in a horizontal double tube counter-flow heat exchanger under turbulent flow conditions, experimentally. TiO_2 nanoparticles with diameters of 21 nm dispersed in water with volume concentrations of 0.2-2 vol.% were used as the test fluid. The results showed that the heat transfer coefficient of nanofluid being higher than that of the base liquid increased with an increase in the Reynolds number and particle concentrations. The heat transfer coefficient of nanofluids was found to be approximately 26% greater than that of pure vol.%, and the results also showed that the heat transfer coefficient of the nanofluids at a volume concentration of 2.0 vol.% was approximately 14% lower than that of base fluids for given conditions. For the pressure drop, the results showed that the pressure drop of nanofluids being slightly higher than that of the base fluid increased with the increasing in volume concentrations. Finally, the new correlations were especially proposed for predicting the Nusselt number and friction factor of the nanofluids.

3d. Somestudies of 2009

Bergman [88] studied laminar, internal forced convection by using nanofluids. The work included the descriptions of nanofluid's specific heat experimentally and explaining their two effects. One of them was about the increased thermal conductivity and the other was about the reduced specific heat of the nanofluid in comparison to its base liquid. To measure heat transfer augmentation, he presented a dimensionless effectiveness number to observe the nanofluid's performance and compared it with base fluid. The results illustrated the use of different nanofluids, that could either increase or decrease thermal performance.

Bianco *et al*. [89] investigated a numerical method in laminar forced convection flow of a water-Al_2O_3 nanofluid in a circular tube used to have a constant and uniform heat flux at the wall. The work was examined with a single and two-phase model by employing either constant or temperature-dependent properties. The size of particles was 100 nm. The maximum difference between single and two-phase models was resulted about 11% in the average heat transfer coefficient. Nanofluids` convective heat transfer coefficient was higher than that of its base liquid. The particle volume concentration increased the heat transfer enhancement but it increased wall shear stress values at the same time. In their study, temperature dependents models had higher heat transfer coefficients and lower shear stresses. They found that the heat transfer always increased with increasing both Reynolds number and shear stress.

He *et al*. [90] studied numerically single phase method and combined it with Euler and Lagrange method on the convective heat transfer of TiO_2 nanofluids those flowing through a straight tube under the laminar flow conditions. They observed the effects of nanoparticles' concentrations, Reynolds number, and various nanoparticle sizes on the flow and the convective heat transfer behavior. It was found that heat transfer of nanofluids increased remarkably in the entrance region. As the numerical results were found to be in good agreement with the experimental data, a reasonable good agreement was accomplished.

Hwang *et al*. [91] quantified the pressure drop and convective heat transfer coefficient of water-based Al_2O_3 nanofluids flowing through a uniformly heated circular tube in the fully developed laminar flow regime. According to the experimental results, they found a good agreement with analytical predictions from the Darcy's equation for single-phase flow for the nanofluid's friction factor. They illustrated the flattening of velocity profile, induced from large gradients in bulk properties such as nanoparticle concentration, thermal conductivity and viscosity in numerical solutions. It was suggested that this flattening of velocity profile had a suitable mechanism for the convective heat transfer coefficient enhancement exceeding the thermal conductivity enhancement.

Jung *et al*. [92] quantitated convective heat transfer coefficient and friction factor of nanofluids in rectangular microchannels. They experimentally studied the effect of the volume fraction of the nanoparticles on the convective heat transfer and fluid flow in microchannels where Aluminum dioxides (Al_2O_3) with diameter of 170 nm nanofluids at different particle volume fractions were flowing. They measured the convective heat transfer coefficient of the Al_2O_3 nanofluid in laminar flow regime that increased up to 32% comparing with the distilled water at a volume fraction of 1.8 volume percent without friction loss. It was established that the measured Nusselt number increased with increasing the Reynolds number in laminar flow regime. The measured Nusselt number was correlated with Reynolds number and Prandtl number by virtue of the thermal conductivity of nanofluids was measured to be less than 0.5. They found that Nusselt number and Friction factor changed various volume fractions of nanoparticles in different dimension of micro-channels as shown in Fig. (**8**).

Kakaç and Pramuanjaroenkij [93] researched literature works on convective heat transfer on the enhancement of heat transfer of nanofluids. The objective of their review study was to compile the significant published articles on the enhancement of the forced convection heat transfer of nanofluids.

Kim *et al*. [94] study showed to examine the effect of nanofluids on convective heat transfer experimentally through a circular straight tube with a constant heat flux condition in the laminar and turbulent flow regime. They studied the effects of thermal conduc tivity and supernatant nanoparticles of the nanofluids on convective heat transfer under differentflow regimes. Thermal conductivity and

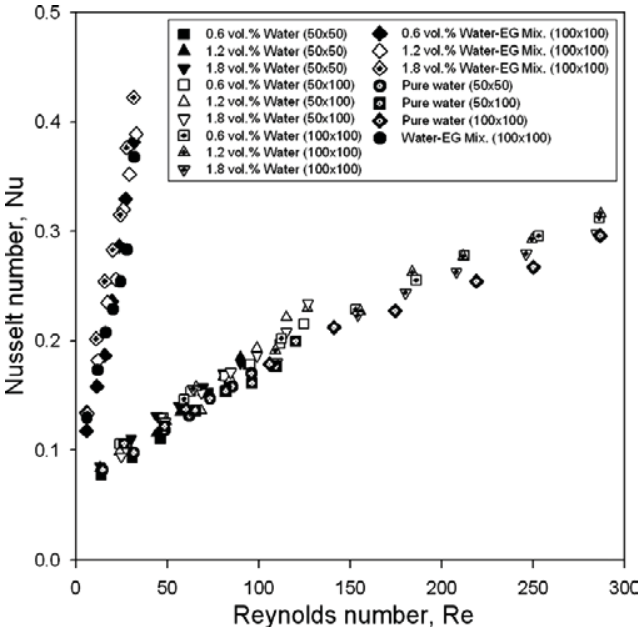

(a)

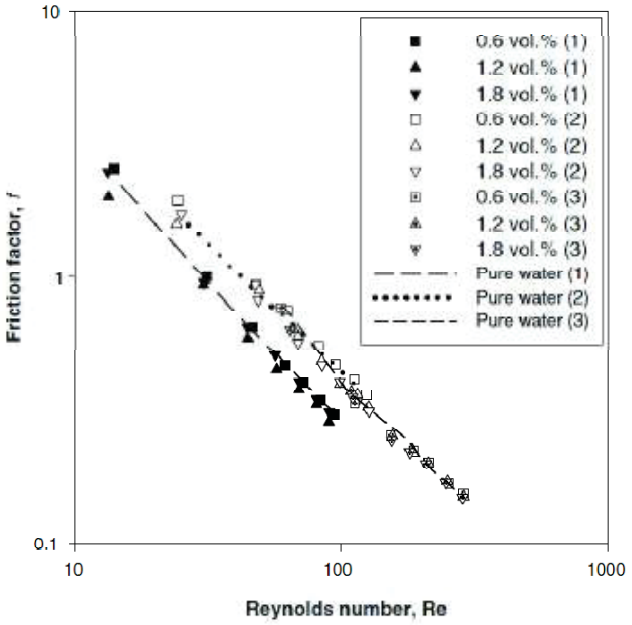

(b)

Fig. (8). Variation of Nusselt number (**a**) and Friction factor (**b**) on Reynolds number in various volume fraction in different dimensions of microchannels of (1)50*50μm^2 (2)50*100 μm^2 (3)100*100 μm^2 [From Jung *et al.*[92], with permission from Elsevier].

convective heat transfer coefficient were increased up to 8% and 20% respectively, in alumina nanofluids including 3 vol% of suspended particles. They reported that the thermal conductivity of nanofluids was similar to that of water, and the convective heat transfer coefficient increased by only 8% in laminar flow in amorphous carbonic nanofluids. It was determined that the augmentation of the convective heat transfer was much greater than that of the thermal conductivity of nanofluids on account of the movements of nanoparticles at the entrance region.

Kulkarni *et al.* [95] investigated measurements of convective heat transfer and viscosity of nanofluids, and estimated how they performed heating buildings in cold regions. They perfromed experimental works using copper oxide, aluminum oxide and silicon dioxide nanofluids, each in an ethylene glycol and water mixture. They obtained some calculations for conventional finned-tube heat exchangers utilizing in buildings in cold regions. The use of nanofluids in heat exchangers decreased volumetric and mass flow rates and resulted in an overall pumping power savings in their study. It was found that the use of nanofluids to heat buildings decreased the size of the heat transfer system and reduced the accompanying pressure loss and the subsequent pumping power. It was observed that the volume concentration increased with the nanofluid viscosity at a specific temperature. Fig. (**9a** and **9b**) indicate the comparison of viscosity and pressure loss of Al_2O_3, CuO, SiO_2 and EG/Water at same particle volumetric concentration.

Mintsa *et al*. [96] researched the effects of particle volume fraction, temperature and particle size to measure the effective thermal conductivity of alumina/water and copper oxide/water nanofluids. Readings at ambient temperature as well as over a relatively large temperature range were performed for different particle volume fractions up to 9%. As a result, they obtained an increase in the effective thermal conductivity with an increase in particle volume fraction and with a decrease in particle size. The relative increase in thermal conductivity was also claimed to be more at high temperatures.

Murshed *et al*. [97] researched a combined static and dynamic mechanisms based on a model for anticipating the effective thermal conductivity of nanofluids. In their study, the model incorporated the effects of particle size, nanolayer, Brownian motion, particle surface chemistry and interaction potential which were about the static and dynamic mechanisms responsible for the enhanced effective thermal conductivity of nanofluids. Also, the model was found to have logically a good agreement with the experimental results of various types of nanofluids

Namburu *et al*. [98] studied a numerical analysis of turbulent flow and heat transfer of three different nanofluids (CuO, Al_2O_3 and SiO_2) in an ethylene glycol and water mixture flowing through a circular tube under constant heat flux condition. They correlated new correlations for viscosity up to 10% volume concentration for these nanofluids as a function of volume concentration and temperature from the experiments. They found out that calculation results had formalized with existing well known correlations. They obtained that nanofluids including smaller diameter nanoparticles had higher viscosity and Nusselt number. They compared the convective heat transfer coefficients of CuO, $Al_2O_3$and SiO_2 nanofluids with each other. They said that Nusselt number improved by 35% for 6% CuO nanofluids over the base fluid at a constant Reynolds number.

Rea *et al*. [99] studied on laminar convective heat transfer and viscous pressure loss of alumina-water and zirconia-water nanofluids in a flow loop with a vertical heated tube. They observed that the heat transfer coefficients of entrance region and fully developed region increased as 17% and 27%, respectively, and for alumina-water nanofluid at 6% vol according to pure water. Furthermore, the zirconia-water nanofluid's heat transfer coefficient increased as 2% in the entrance region and 3% in the fully developed region at 1.32 vol %. They found that the measured pressure loss for the nanofluids was generally much greater than for pure water .It was indicated that the measured nanofluid's heat transfer coefficient and pressure loss were in good agreement with the conventional model predictions of laminar flow.

Pantzali *et al*. [100] studied the efficiency of nanofluids as coolants. Nanoparticles were mixed for testing nanofluid's thermo-

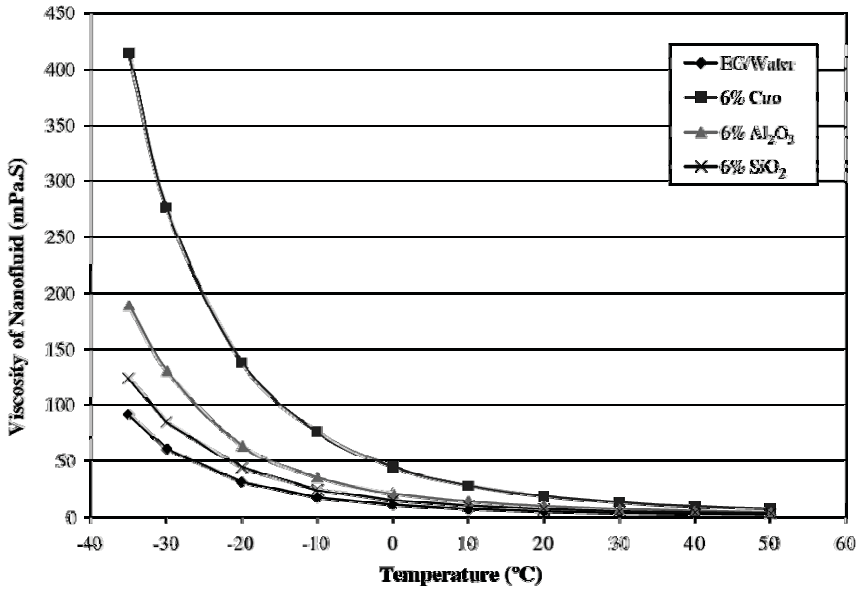

(a)

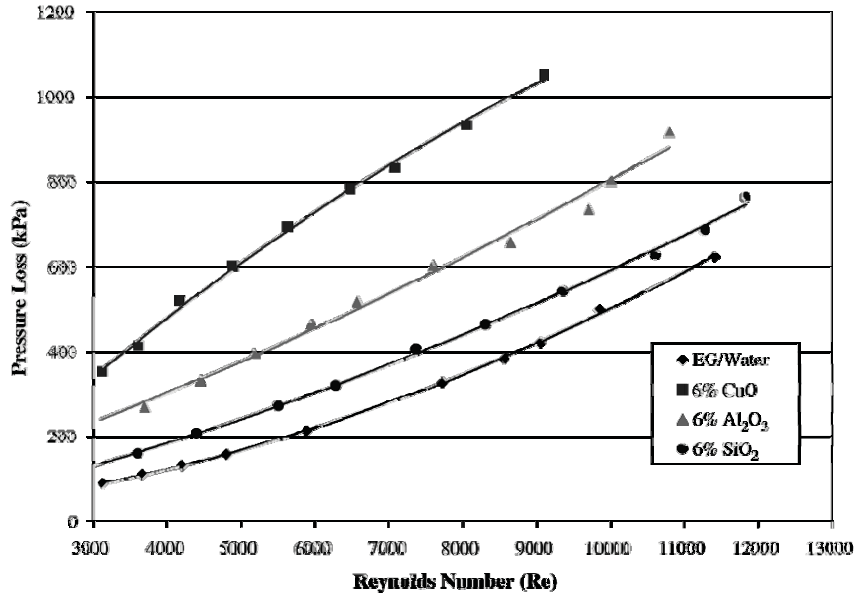

(b)

Fig. (9). The viscosity variation of different nanofluids of same concentration and the base fluid in terms of temperature (**a**) Pressure loss of different nanofluids in terms of conventional glycol/water mixture (**b**) [From D.P. Kulkarni *et al*. [95], with permission from Elsevier].

physical properties. They used a typical nanofluid, namely a 4% CuO suspension in water and investigated nanofluid's performance in a commercial herringbone-type PHE experimentally. They showed the type of flow inside the heat exchanger equipment and also its influence on the efficiency of a nanofluid as coolant. The heat exchanger performance depended on the fluid viscosity due to its significance. They obtained large volumes of required nanofluids and reported that turbulent flow was usually developed in industrial heat exchangers.

Xie and Chen [101] produced homogeneous and stable nanofluids using suspended and well dispersible multi-walled carbon nanotubes (CNTs) into ethylene glycol base fluid. They said that CNT nanofluids improved the thermal conductivity and the enhancement ratios increased with increasing the nanotube loading and their temperature. Their work showed that the straightness ratio, aspect ratio and aggregation had collective effect on the thermal conductivity of CNT nanofluids.

Pantzali *et al*. [102] investigated the effect of the use of a nanofluid in a miniature plate heat exchanger (PHE) with modulated surface both experimentally and numerically. Firstly, they worked on thermophysical properties (i.e., thermal conductivity, heat capacity, viscosity, density and surface tension) of a typical nanofluid (CuO in water, 4% v/v), then the effect of surface modulation on heat transfer augmentation and friction losses were researched by simulating the existing miniature PHE as well as a notional similar PHE with flat plate using a CFD code. Conclusively, they studied the effect of the nanofluid on the PHE performance in comparison to that of a conventional cooling fluid (i.e., water). As a result of

their study, the required nanofluid volumetric flow rate for a given heat duty was found to be lower than that of water causing lower pressure drop. Shortly, they concluded that the use of smaller equipment and less pumping power were required. Since the total volume of the equipment was the main issue, use of the nanofluids seemed to be a promising solution towards designing efficient heat exchanging systems. The only disadvantages were the high price and the possible instability of the nanoparticle suspensions.

Vajjha and Das [103] investigated the determination of the thermal conductivity of three nanofluids comprising aluminum oxide, copper oxide and zinc oxide nanoparticles dispersed in a base fluid of 60:40 (by mass) ethylene glycol and water mixture. According to evaluated particle volumetric concentration being up to 10% and the temperature range of the experiments varied from 298 to 363 K the results indicated an increase in the thermal conductivity of nanofluids compared to the base fluids with an increasing volumetric concentration of nanoparticles parallel with the thermal conductivity that also increased substantially with an increase in temperature. By using their experimental data for comparisons with various existing models to determine thermal conductivity they developed a model that was a refinement of an existing model, that incorporated the classical Maxwell model and the Brownian motion effect to account for the thermal conductivity of nanofluids as a function of temperature, particle volumetric concentration, the properties of nanoparticles, and the base fluid with these experimental data.

Wen *et al*. [104] carried out a critical review of research on heat transfer applications of nanofluids with the aim of identifying the limiting factors so as to boost their development.

Hadjov [105] studied spherical nanoparticles with a conductive interface in the self-consisted scheme for forecasting the thermal conductivity of nanofluids. They adopted a flux jump in the particle-fluid interface opposite to the temperature jump that was assumed in the case of thermal barrier resistance. Upper and lower bounds to the homogenized suspension thermal conductivity were gained by their working to the particle packing.

Ali *et al*. [106] numerically studied two-dimensional turbulent convective heat transfer behavior of alumina nanoparticle dispersed in water flow in a horizontal circular pipe at constant wall temperature. The finite-volume method was employed considering the full range of flow at the entrance length and at the fully developed region. They showed that the shear stress was observed to be increasing at any x station along the pipe as the concentration of nanoparticle increased and achieved its higher value at the beginning of the pipe at the entrance region and then dropped to an asymptotic value at the fully developed region. When the velocity increased, both Nusselt number and the shear stress were observed to be increasing. As a result Reynolds number was observed to decrease as the concentration increased at fixed inlet velocity.

Duangthongsuk and Wongwises [107] reported the thermal conductivity and dynamic viscosity of nanofluids experimentally. TiO_2 nanoparticles dispersed in water with volume concentration of 0.2-2 vol.% were used in their study. A transient hot-wire apparatus was used for measuring the thermal conductivity of nanofluids whereas the Bohlin rotational rheometer (Malvern Instrument) for measuring the viscosity of nanofluids. The data were collected for temperatures ranging from 15 °C to 35 °C. The results showed that the measured viscosity and thermal conductivity of nanofluids increased as the particle concentrations increased and were found to be higher than the values of the base liquids. Furthermore, thermal conductivity of nanofluids increased by increasing nanofluid temperatures and, conversely, the viscosity of nanofluids decreased by increasing temperature of nanofluids. Moreover, the measured thermal conductivity and viscosity of nanofluids were found to be quite different from the predicted values evaluated from the existing correlations and the data reported by other researchers. Finally, new thermophysical correlations were proposed for predicting the thermal conductivity and viscosity of nanofluids.

Duangthongsuk and Wongwises [108] reported an experimental study on the forced convective heat transfer and flow characteristics of a nanofluid consisting of water and 0.2 vol.% TiO_2 nanoparticles. The heat transfer coefficient and friction factor of the TiO_2-water nanofluid flowing in a horizontal double-tube counter flow heat exchanger under turbulent flow conditions were investigated. They utilized Degussa P25 TiO_2 nanoparticles of about 21 nm diameter in their study. The results showed that the convective heat transfer coefficient of nanofluid was found to be slightly higher than that of the base liquid by about 6-11%. The heat transfer coefficient of the nanofluid increased with an increase in the mass flow rate of the hot water and nanofluid, and it also increased with a decrease in the nanofluid temperature, and the temperature of the heating fluid showed no significant effect on the heat transfer coefficient of the nanofluid. It was also noted that the Gnielinski equation failed to predict the heat transfer coefficient of the nanofluid. Finally, the use of the nanofluid presented a little penalty in pressure drop.

3e. Somestudies of 2008

Bi *et al*. [109] studied nanoparticles in the working fluid for observing domestic refrigerator's reliability and performance. They utilized from mineral oil/TiO_2 nanoparticle mixtures such as the lubricant instead of Polyol-ester (POE) oil in the 1,1,1,2-tetrafluoroethane (HFC134a) used in refrigerator. Researchers analyzed that the refrigerator performance regarding the energy consumption and freezing capacity was enhanced with the use of nanoparticles. Their results showed that HFC134a and mineral oil with TiO_2 nanoparticles worked normally and securely in the refrigerator. They also observed that the refrigerator had higher performance than the HFC134a and POE oil system,and the use of nanoparticles with 0.1% mass fraction reduced energy consumption 26.1% compared to the HFC134a and POE oil system.

Hwang *et al*. [110] tested homogeneous dispersion of nanoparticles in nanofluids. They investigated various physical treatment techniques based on two step methods comprising ultrasonic bath, ultrasonic disruptor and high-pressure homogenizer to confirm their versatility for preparing stable nanofluids. They used CB (carbon black) and Ag nanoparticles with the diameter of 330nm to 585nm. Their results indicated that Ag nanoparticle, which was generated by the modified magnetron sputtering system, dispersed homogeneously and sustained its stability in the silicon oil based fluid.

Karthikeyan *et al*. [111] studied on synthesizing of CuO nanoparticles having average diameter of 8 nm by using a simple precipitation technique and observed thermal properties of the suspensions. They utilized from water and ethylene glycol as based fluids and 1 vol.% CuO nanoparticles. Their results showed that thermal conductivity increased with increasing finer particle size and mono dispersity of nanoparticles. They obtained some results from experiments that of thermal conductivity being significantly affected from the nanoparticles size, polydispersity, cluster size and the volume fraction of particles.

Khandekar *et al*. [112] studied on a closed two-phase thermosyphon's overall thermal resistance. They selected pure water and various water based nanofluids (of Al_2O_3, CuO and laponite clay) as working fluids. The results indicated that all these nanofluids had worse thermal performance than pure water. In additionto all nanofluids on copper substrate, having the same average roughness as that of the thermo syphon container pipe was greater than that of pure water.

Lee *et al*. [113] synthesized and characterized aqueous nanofluids including low volume concentrations of Al_2O_3 nanoparticles from 0.01 to 0.3 vol.%. Their results pointed out that those alumina nanoparticles had the highest dispersion and stabilization performance in DI water at 5 h of ultrasonic vibration. They observed that

the temperature increased with decreasing the Al_2O_3-water nano fluids' viscosity. In addition, Al_2O_3-water nano fluids' viscosity indicated a nonlinear correlation with the concentration even in the low volume concentration (from0.01 to 0.3 vol.%.).

Murshed *et al*. [114] searched the existing theories in the literature on thedetermination of nanofluids' properties such as synthesis methods, potential application areas, experimental and analytical studies on the effective thermal conductivity, effective thermal diffsivity, convective heat transfer, and electrokinetic properties and compared them with each other.

Oh *et al*. [115] investigated 3-omega (3 w) method as new application to measure the thermal conductivity of nanofluids and they provided information about it. Their new theoretical model was proposed instead of the transient hot wire method for the determination of thermal conductivity. They tested the effective thermal conductivity of Al_2O_3 nanofluids in DI water and EG at room temperature. Furthermore, thermal response showed interesting effects owing to agglomeration and sedimentation of nanoparticles.

Kang *et al*. [116] studied on measuring the vapor absorption rate and heat transfer rate for falling film flow of binary nanofluids, being tested at the same conditions with pure water, and tried to observe the changes of heat and mass transfer. They used some parameters such as base fluid concentration of LiBr, the concentration of nanoparticles in weight %, and nano-particle constituents. They prepared the mixture of H_2O/LiBr solution with nanoparticles of Fe and Carbon nanotubes (CNT). Their results illustrated that the mass transfer increase was more than the heat transfer augmentationin the binary nanofluids with Fe and CNT and the properties of mass transfer of CNT nanoparticles were better than those of Fe nanoparticles.

Lu and Fan [117] studied on molecular dynamics (MD) simulation method, applicable for a stationary nanofluids of the volume fractions less than 8%. They used this method to simulate nanofluids' thermophysical properties such as thermal conductivity and viscosity. They compared experimental data with numerical results and obtained good results. They found it very useful to estimate some thermal properties of nanofluids. Their results also showed that thermal conductivity and the viscosity of nanofluids depended on the volume fraction and the size of nanoparticles.

Nguyen *et al*. [118] focused on the temperature and particle volume concentration's impact on the dynamic viscosity for the water-Al_2O_3 mixture experimentally. They benefited from piston-type device used as a commercial viscometer for temperatures at room condition. Their results indicated an enhancement on the nanofluid dynamic viscosity in respect with particle volume fraction; however temperature increase showed a negative effect on it.

Chen *et al*. [119] presented the properties of the effective thermal conductivity, their rheological behavior and forced convective heat transfer of the nanofluids. They found that thermal conductivity increased as 3% at 25 °C and 5% at 40 °C for the 2.5 wt.% nanofluid. They observed that nanofluidsincluding spherical titanium nanoparticles had better properties of thermal conductivity and convective heat transfer coefficient. They also suggested new systems to increase the convective heat transfer coefficient.

3f. Somestudies of 2007

Ding *et al*. [120] experimentally studied on the forced convective heat transfer using aqueous and ethylene glycol-based spherical titanium nanofluids, and aqueous-based titanate nanotubes, carbon nanotubes and nano-diamond nanofluids.. They accomplished to formulate these nanofluid's specifications. They indicated that all the formulated nanofluids performed a higher effective thermal conductivity than those predicted by the conventional theories. Apart from the ethylene glycol-based titanium nanofluids, all other nanofluids were observed to be non-Newtonian. They reported that the convective heat transfer coefficient enhancement was substantially higher than the thermal conduction enhancement. However, they indicated deterioration of the convective heat transfer for ethylene glycol-based titanium nanofluids at low Reynolds numbers. They recommended the effective thermal conductivity as to be responsible for the experimental observations.

Zhang *et al*. [121] accomplished to measure the effective thermal conductivity and thermal diffusivity of Au/toluene, Al_2O_3/water, TiO_2/water, CuO/water and CNT/water nanofluids by utilizing from the transient short-hot-wire technique. In their study, the average diameters of Au, Al_2O_3, TiO_2 and CuO spherical particles were 1.65, 20, 40 and 33 nm, respectively. Also the average length and diameter of CNFs were 10 l m and 150 nm, respectively. According to results obtained, the effective thermal conductivities of the nanofluids indicated no abnormal enhancements.

Ko *et al*. [122] published an experimental investigation on the flow characteristics of the aqueous suspensions of carbon nanotubes (CNTs). They tried to measure pressure drop to obtain stable nanotube suspensions by utilizing two methods. They studied the effects of CNT loading and various preparation methods and measured the pressure drops in a horizontal tube and viscosities of nanofluids. They found that the CNT nanofluids prepared by the acid treatment had much smaller viscosity than the ones made with surfactant at the same volume fraction. They indicated that the friction factor of stabilized CNT nanofluids (by adding surfactant) was much greater than that of CNT nanofluids prepared by acid treatment, and nanofluids had greater friction factors than distilled water under laminar flow conditions. It was found that the friction factors of nanofluids were inversely similar to that of the base fluids. As the flow rate improved under turbulent flow conditions,they noticed that nanofluids had low friction factors than pure water flows at definite range of flow rates.

Mansour *et al*. [123] studied the uncertainty impacts regarding with the physical properties of water-Al_2O_3 nanofluid on the determination of the thermohydraulic performance for both laminar and turbulent fully developed forced convection in a tube with uniform wall heat flux. They suggested many experimental data necessary to determine the real potential of nanofluid.

Hong *et al*. [124] firstly reported that the thermal conductivity (TC) and heat transfer of nanofluids could be enhanced by the external magnetic field. The nanofluids contained carbon nanotubes (CNTs) and magnetic-field-sensitive nanoparticles of Fe_2O_3. The sensible explanation for these interesting determinations was that the Fe_2O_3 particles formed aligned chains under applied magnetic field that helped to connect the nanotubes. In that magnetic field, the particles slowly moved and formedlarge clumps of particles, and caused clumping of CNTs, then decreased the TC.

Li and Peterson [125] pointed out the Brownian motion of the nanoparticles in these suspensions as one of the potential contributors to this enhancement and the mechanisms that could contribute considerable discussion and debate to this subject. The mixing effect of the base fluid in the immediate vicinity of the nanoparticles caused by the Brownian motion was examined, modeled and was also compared with the experimental data in the literature. Moreover, simulation results showed the effective thermal conductivity of nanofluids being affected by this mixing effect.

Yoo *et al*. [126] prepared some nanofluids such as T_iO_2, Al_2O_3, F_e, and WO_3compounds in a two-step procedure by dispersing in a base fluid. The transient hot wire method was used for the calculation of thermal conductivity. These nanofluids' thermal conductivities were analyzed and then compared with each other.

Avsec and Oblak [127] proposed a mathematical model for the calculation of thermophysical properties of nanofluids on the basis of statistical nanomechanics. In this study, they indicated two calculation methods to describe the properties such as classical and statistical mechanics. It was reported that the classical mechanics had no insight into the microstructure of the substance. On the other

hand, it calculated the properties of state both on the basis of molecular motions in a space and on the basis of the intermolecular interactions. On the contrary to the classical mechanics, they suggested that the statistical mechanics calculated the thermomechanic properties of state on the basis of intermolecular interactions between particles in the same system of molecules. They illustrated that the systems were composed of a very large number of particles. The results of the analysis were compared with experimental data that indicated a relatively good agreement.

He *et al*. [128] studied different particle (agglomerate) sizes in stable aqueous TiO_2 nanofluids and calculated their static thermal conductivity and rheological behavior. Heat transfer and flow behavior were investigated in a vertical pipe during both laminar and turbulent flow regimes. Thermal conduction was observed to increase with addition of nanoparticles into the base liquid but decreased with increasing particle (agglomerate) size. Increasing particle (agglomerate) size and particle concentration caused to grow the constant viscosity. In both the laminar and turbulent flow regimes, convective heat transfer coefficient increased with increasing nanoparticle concentrations.

Lee and Mudawar [129] experimentally studied water-based nanofluids containing small concentrations of Al_2O_3 in the microchannel cooling. They investigated the high thermal conductivity of nanoparticles in the single-phase heat transfer coefficient, especially for laminar flow. In the entrance region of micro-channels, maximum heat transfer coefficients were obtained. Greater sensitivity to heat flux was caused by higher concentrations.

Wang and Mujumdar [130] reviewed convective heat transfer using suspensions of nanometer-sized solid particles in base liquids. The transport properties and heat transfer characteristics of the suspension were found to be significantly dependable to the suspended nanoparticles.

Trisaksri and Wongwises [131] reviewed the literature on the general heat transfer characteristics of nanofluids. It was found that only a few papers had discussed on the convective heat transfer of nanofluids. The purpose of this article was to review the literature mentioning convective heat transfer of nanofluids, such as the experimental and theoretical investigations.

Daungthongsuk and Wongwises [132] reviewed suspension of ultrafine particles in a conventional base fluid which tremendously enhanced the heat transfer characteristics of the original fluid. They reported that nanofluids were expected to be ideally suited in practical applications as their use incurred little or no penalty in pressure drop because the nanoparticles were ultrafine, therefore, appearing to behave more like a single-phase fluid than a solid-liquid mixture. The purpose of their article was to summarize the published subjects respectively with the investigating forced convective heat transfer of the nanofluids both experimentally and numerically.

3g. Somestudies of 2006

Hwang *et al*. [133] showed the higher effective thermal conductivity of nanofluid consisting of nanoparticles dispersed in base fluid than those dispersed in its pure fluid. They used four kinds of nanofluids such as multiwalled carbon nanotube (MWCNT) in water, CuO in water, SiO_2 in water, and CuO in ethylene glycol. They used transient hot-wire method to measure the thermal conductivities. They reported that the increase in thermal conductivity enhancement of water-based MWCNT nanofluid was 11.3% at a volume fraction of 0.01. According to their results, the thermal conductivities of both particles and the base fluid affected the thermal conductivity enhancement of nanofluids.

Hwang *et al*. [134] used the nanoparticles of multi-walled carbon nanotube (MWCNT), fullerene, copper oxide, silicon dioxide and silver to improve the thermal conductivity and lubrication. DI water, ethylene glycol, oil, silicon oil and poly-a-olefinoil (PAO) were taken as the base fluids. They measured the thermal conductivity and kinematic viscosity to investigate the thermo-physical properties of nanofluids. UV-vis spectrophotometer was used to check the stability estimation of nanofluid. They found that the increase in particle volume fraction displayed a positive effect on the increase in thermal conductivity of nanofluid that increased with increasing particle volume fraction.

Liu *et al*. [135] presented a study on the enhancement of the thermal conductivity of water in the presence of copper (Cu) using the chemical reduction method. They reported that their method was used firstly for the synthesis of nanofluids containing Cu nanoparticles in water. Their results showed that Cu-water nanofluids having low concentration of nanoparticles had higher thermal conductivities than those of the water base fluid without Cu. Beside this, thermal conductivity was improved up to 23.8% for Cu nanoparticles at a volume fraction of 0.001 (0.1 vol.%).

Palm *et al*. [136] investigated the heat transfer enhancement capabilities of coolants' laminar forced convection flow with suspended metallic nanoparticles inside typical radial flow cooling systems. They obtained significant heat transfer enhancement with the use of these fluid/solid particle mixtures. They also indicated the noticeable differences between the use of constant property of nanofluids (temperature independent) and nanofluids with temperature dependent properties.

Heris *et al*. [137] investigated the laminar flow convective heat transfer of nanofluids containing CuO and Al_2O_3 oxide nanoparticles in water through circular tube with constant wall temperature boundary condition. They experimentallyshowed that homogeneous model should be used for the prediction of nanofluids properties concerning the determination of the single phase heat transfer coefficient enhancement. Al_2O_3-water nanofluids were noted to have higher heat transfer enhancement with the increase in the volume fraction.

3h. Somestudies of 2005

Xuan *et al*. [138] determined heat transfer process and flow properties of Cu-water nanofluid flowing inside a channel by using the thermal Lattice Boltzmann model. Because they took into consideration the molecular dynamics and bridged the gap of macroscopic or microscopic challenge of the nanofluids, this method showed a significant advantage. Two existing methods used for application of this method to model the thermal fluid flow problem were the multispeed (MS) and the double-distribution-function (DDF). In this study, double-distribution-function (DDF) was used that led to two separate distribution functions as follows: The temperature was treated as a passive diffusing scalar, that was simulated by a distribution function notdependent on density distribution, respectively. The feature point of the Lattice Boltzmann method was the assumption that the particles mesoscopically located at a series of lattices and their distributions corresponding to the Boltzmann distribution. The viscosity dissipation term in the Lattice Boltzmann equation for energy transport was neglected in order to simulate heat transfer characteristics of the nanofluid. According to numerical results, for 1% volume fraction the Nusselt number of Cu-water nanofluid was calculated 27% higher than that of pure water at the same Reynolds number. Furthermore, random motion of the particles suspended in the fluid could be seen along the main flow direction because of fluctuations of the Nusselt number of the nanofluid.

Liu *et al*. [139] studied thermal conductivity enhancements in ethylene glycol and synthetic engine oil using multiwalled carbon nanotubes (MWNTs). The volume concentration of CNT-ethylene glycol suspensions and synthetic engine oil suspensionswere below 1.0 and 2.0 vol.% respectively. They used a modified transient hot wire method to measure the thermal conductivities of the CNT suspensions and observed significant increase in CNT-ethylene glycol suspensions' thermal conductivities in comparison to the ethylene glycol base fluid without CNT. They noted that CNT–

synthetic engine oil suspensions gave the similar results with CNT-ethylene glycol suspensions. They obtained 12.4% enhancement on thermal conductivity for CNT-ethylene glycol suspensions at a volume fraction of 0.01 (1 vol.%) and 30% enhancement at a volume fraction of 0.02 (2 vol.%) for CNT-synthetic engine oil suspension, thermal conductivity was enhanced by 30% at a volume fraction of 0.02 (2 vol.%). As a result of their analysis, the thermal conductivity ratio of CNT-synthetic engineoil suspension was found to be having a noticeably higher value than that of the CNT-ethylene glycolsuspension.

Maiga *et al*. [140] used two particular geometrical configurations, namely a uniformly heated tube and a system of parallel, coaxial and heated disks to study the laminar forced convection flow of nanofluids numerically. By using the mixtures of water-γAl_2O_3 and Ethylene Glycol-γAl_2O_3they obtained a significant increase in the heat transfer coefficient in the presence of nanoparticles dispersed into the base fluids. They also illustrated that the heat transfer coefficient increased with increasing the particle concentration having severe effects on the wall shear stress that increased considerably with the particle loading. The Ethylene Glycol-γAl_2O_3 nanofluids were found to have a better heat transfer enhancement and adverse effects on the wall shear stress than water-γAl_2O_3.

3i. Somestudies of 2004

Wen and Ding [141] performed experiments in order to calculate the convective heat transfer coefficient of γ-Al_2O_3 nanoparticles suspended in deionized water in a copper tube for laminar flow. Under a constant wall heat flux condition, nanoparticles having 0.6 %, 1.0 %, and 1.6 % concentrations were tested in their study. In the experiments, straight copper tube with 4.5±0.02 mm inner diameter, 6.4±0.05 mm outer diameter and 970 mm length was used as a test section. A flexible silicon rubber having 300W heating capacity was used to maintain a constant heat flux boundary condition. A peristaltic pump was used to deliver a maximum flow rate of 10 l/min. The flow rate was controlled by adjusting rotational speed of the pump. Sodium dodecylbenzene sulfonate (SDBS) was used as a dispersant in order to stabilize the nanoparticles.

Maiga *et al*. [142] reported numerical method and a mathematical formulation for water-γAl_2O_3 and ethylene glycol-γAl_2O_3 to determine the forced convective heat transfer and wall shear stress for the laminar and turbulent regions of water-γAl_2O_3 and ethylene glycol-γAl_2O_3 flowing inside a uniformly heated tube. The solid-liquid mixture was considered as a single-phase, so the slip velocity between the phases was neglected. Moreover, symmetry in flow and the local thermal equilibrium of the mixture were considered. To define heat flux and stresses of the nanofluids for the turbulent flow, the Reynolds-averaged Navier-Stokes equation and κ-ε turbulent model were used. In the numerical simulations, the heated tube having 0.01m diameter and 1.0 m length was used. The conditions of laminar flow were as follows: the Reynolds number was fixed at 250 and the constant heat flux was varied between 10-250 W/m^2. The conditions of turbulent flow were as follows: the constant heat flux was fixed at 500,000 W/m^2 and the Reynolds number was varied in the range of 10,000-50,000.

Roy *et al*. [143] performed a numerical investigation to analyze the heat transfer and wall shear stress for radial laminar flow in a cooling system of water-γAl_2O_3 nanofluids compared with some base fluids such as water, glycol, and oil. All assumptions used in this study being similar to those reported by Maiga *et al*. [142] marked the nanofluid as an incompressible fluid.

Nguyen *et al*. [144] introduced a numerical simulation to determine the efficiency of water-γAl_2O_3 and ethylene glycol-γAl_2O_3 nanofluids for the cooling of a high-heat output microprocessor under laminar forced flow inside a heat sink. The simulation set-up comprised of a 50x50x10 mm rectangular slot having a 3x48 mm fluid flow cross-section. In this article, assumptions were uniform velocity and temperature profile at the inlet section and laminar flow. The contact area for exchange heat was 10x10 mm. The numerical results showed that Reynolds number and the volume fraction were mainly parameters affecting average heat transfer coefficient of nanofluids and ethylene glycol-γAl_2O_3 nanofluid had higher heat transfer coefficient than that of the water-γAl_2O_3 nanofluid.

Ali *et al*. [145] reported the mathematical and numerical formulation to determine heat and mass transfer between air and falling solution film in a cross-flow heat exchanger for the dehumidification and cooling process. Effect of Cu nanoparticles to the heat and mass transfer process were tested by adding them into the solution. In this study, two models from available literature were used. Moreover, the assumptions of this article were laminar and steady state flow. Constant film thickness, thermal properties of the air and the solution were constant except for the thermal conductivity of the solution, gravitational force of the air was neglected for fully developed velocity profile of fluids. According to he results of the study, the dehumidification and cooling process increased with high Cu particle volume fraction, low air Reynolds number, decrease in the channel width, increase in the height and length of the channel. In addition, it was revealed that an increase in Cu volume fraction led to more stability of the solution.

Ali and Vafai [146] suggested the numerical and mathematical formulations in order to analyze the effects of the inclination angel of parallel-and-counter-flow on heat and mass transfer between air and falling desiccant film having Cu nanoparticles suspended. They used the same assumptions in the two approach models as those used in the previous paper such as the simulated conditions used in this study being low and high air Reynolds number for the inclined parallel flow arrangement and low and high air Reynolds number for the inclined counter flow configuration.

Zhu *et al*. [147] developed a method for the preparation of copper nanofluids using the base fluid of ethylene glycol with $CuSO_4 \cdot 5H_2O$ with $NaH_2PO_2 \cdot H_2O$ under microwave irradiation. They investigated the effects of $CuSO_4$concentration with the addition of NaH_2PO_2 and microwave irradiation on the reaction rate and the properties of Cu nanofluids by transmission of electron microscopy, infrared analysis, and sedimentation measurements. They obtained nonagglomerated and stably suspended Cu nanofluids at the end of their analysis.

3j. Somestudies of 2003 and Previous Studies

Li and Xuan [148] and Xuan and Li [149] used an experimental set up in order to determine the convective heat transfer coefficient and friction factor parameters of nanofluids for laminar and turbulent flow in a tube. Deionized water with a dispersion of Cu particles with under 100nm diameter was used in this study. The effect of the nanoparticle concentration on the heat transfer coefficient was determined for different particle volume percentages being 0.3, 0.5, 0.8, 1, 1.5 and 2%. The Reynolds number of the nanofluids varied between 800 and 25,000. The experimental set up was consisted of a test section, a pipeline, a pump, a cooler, a fluid collection and a reservoir tank. A straight brass tube having 800 mm length and 10 mm inner diameter was used and a 3.5 kW electric heater was placed to test section for getting a constant wall heat flux boundary condition. A fatty acid was used to prevent the aggregation of the nanoparticles in the base fluid.

Xuan and Li [149] suggested a method for preparing some nanofluid samples and presented theoretical study of thermal conductivity. The transient hot-wire method was used for measurements in their study. For determining the heat transfer performance of nanofluids flowing in a tube, they proposed a single phase or dispersion model. Cu particles having a diameter of 100 nm were used as nanoparticles where base fluids are water and mineral oil. The particles in the mineral oil and water were stabilized by using oleic acid and laureate salt respectively. For Cu-mineral oil, suspension stabilization time was nearly 1 week and suspension had no sedimentation with a fill of 22 wt%. For Cu-water, suspension with 9

wt% laureate salt, vibrated by an ultrasonic vibrator, the results indicated that the nanoparticles could suspend more 30 h than in stationary state. This behavior implied that particle stability and dispersion were affected by fluid viscosity. Furthermore, this study showed that and Crosser model [150] and Wasp model [151] can be used for predicting thermal conductivity in the absence of a sophisticated formula. According to measurements obtained by using transient hot-wire method, the thermal conductivity was observed to be significantly varied with the volume fraction of the particles. The heat transfer enhancement was evaluated with two different ways the single-phase model and two-phase model. The single phase model assumed that both the liquid and particle phases being in thermal equilibrium were flowing at the same velocity. This model beingsimple required less computation time. The two-phase model provided opportunity to understand functions of liquid phase and solid phase in the heat transfer process but required a long time for computation and a high performance computer.

The purpose of their work aimed to develop a modified single-phase model to determine the heat transfer process of nanofluids flowing in tubes.

Xuan and Roetzel [152] presented two different approaches to define some fundamentals for predicting the convective heat transfer coefficient of nanofluids under the assumption that they behaved like a single-phase liquid rather than a normal solid-liquid mixture. In their study, the effects of thermal dispersion and transport properties of the nanofluid were covered. The first model treated as a single-phase and the other model treated as a multi-phase fluid and dispersed fluid. It was assumed that liquid phase and the particles being in thermal equilibrium state were devoid of slip velocity between them. The nanofluid acted as a common pure liquid. This implied that the all equation of energy continuity, and motion for a single-phase fluid had been applied directly to the nanofluid.

Similar to the Xuan and Li model [153], the Hamilton and Crosser model [150] and Wasp model [151] provided rough results for predicting the thermal conductivity of nanofluid. For a modified conventional approach, known as dispersion model, the slip velocity between the solid-liquid mixture could not be zero because of many factors such as gravity, Brownian force, friction force between the solid-liquid mixture, Brownian diffusion, sedimentation, and dispersion happening simultaneously in the main flow.

Xue [154] presented a model of the effective thermal conductivity for nanofluids, based on Maxwell theory and average polarization theory, considering the interface effect between the solid particles and the base fluid in nanofluids. They found that their theoretical results were in good agreement with the experimental data on the effective thermal conductivity of nanotube/oil nanofluid and Al_2O_3/water nanofluid.

4. CONCLUSIONS

Nanofluid has been classified as a new class of heat transfer fluids engineered by dispersing metallic or non-metallic nanoparticleswith a typical size of less than 100 nm in the conventional heat transfer fluids. Their use remarkably augments the heat transfer potential of the base liquids thus offering an opportunity to the engineers for the development of highly compact and effective heat transfer equipmentfor many industrial applications, nuclear reactors, transportation, electronics as well as biomedicine and food.

Nanofluid is consideredas an innovative heat transfer fluid with superior potential for enhancing the heat transfer performance of conventional fluids. This review presents the recent studies of single phase and two-phase nanofluid flows in tubes and channels and also helps to determine the physical properties of nanofluids chronologically. According to the most recent experimental papers, heat transfer performance of the base fluid can significantly be increased by the suspended nanoparticles since heat transfer coefficient of the nanofluid was found to be larger than that of its base fluid for the same Reynolds number. The volume fraction of nanoparticles increases the heat transfer feature of a nanofluid. Pressure drop and friction factors of nanofluids are also larger than its base fluids. Besides of many attempts made to determine the nanofluids' thermal conductivity and viscosity, being important thermophysical properties no definitive agreements have emerged on these properties. Moreover, there is a lack of studies on the mixture flows of nano particles with the refrigerants as pressurized flows in tubes or channels due to the hardness in the experimental conditions.

CONFLICT OF INTEREST

The authors confirm that this article content has no conflicts of interest.

ACKNOWLEDGEMENTS

The authors would like to thank King Mongkut's University of Technology Thonburi (KMUTT), the Thailand Research Fund, the Office of Higher Education Commission and the National Research University Project for the financial support. Especially, the first author wishes to thank KMUTT for providing him with a Post-doctoral fellowship.

REFERENCES

[1] Putra, N.; Roetzel W.; Das, S. K. Natural convection of nano-fluids. *Int. J. Heat Mass Transfer*., **2003**, *39*, 775-784.

[2] Tang, G.Y.; Yang, C.; Chai, J.C.; Gong, H.Q. Joule heating effect on electroosmotic flow and mass species transport in a microcapillary. *Int. J. Heat and Mass Transfer*., **2004**, *47*, 215-227.

[3] Tseng, W.J.; Chen, C.N. Effect of polymeric dispersant on rheological behavior of nickel–terpineol suspensions. *Mater. Sci. Eng*., **2003**, A *347* (1–2), 145-153.

[4] Chen, H.; Ding, Y.; He, Y.; Tan, C. Rheological behaviour of ethylene glycol based titania nanofluids. *Chem. Phys. Lett.*, **2007**, *444* (4–6), 333-337.

[5] Nguyen, C.; Desgranges, F.; Roy, G.; Galanis, N.; Mare, T.; Boucher, S.; Anguemintsa, H. Temperature and particle-size dependent viscosity data for water-based nanofluids – hysteresis phenomenon. *Int. J. Heat Fluid Flow*., **2007**, *28* (6), 1492-1506.

[6] Khanafer, K.; Vafai, K. A. critical synthesis of thermophysical characteristics of nanofluids. *Int. J. Heat Mass Transfer*, **2011**, *54,* 4410-4428.

[7] Duangthongsuk, W.; Wongwises, S. Measurement of temperature-dependent thermal conductivity and viscosity of TiO2–water nanofluids. *Exp. Therm. Fluid Sci*., **2009**, 33, 706–714.

[8] Yu, W.; Choi, S.U.S. The role of interfacial layers in the enhanced thermal conductivity of nanofluids: a renovated Maxwell model. *J. Nanopart. Res.*, **2003**, *5*, 167-171.

[9] Godson, L.; Raja, B.; Lal, M.D.; Wongwises, S. Experimental investigation on the thermal conductivity and viscosity of silver-deionized water nanofluid. *Exp. Heat Transfer.*, **2010**, *23*, 317-332.

[10] Prasher, R.; Bhattacharya, P.; Phelan, P.E. Thermal conductivity of nanoscale colloidal solutions (nanofluids). *Phys. Rev. Lett.*, **2005**, *94*, 025901-1–025901-4.

[11] Koo J., Kleinstreuer,C. A new thermal conductivity model for nanofluids. *J. Nanopart. Res.*, **2004**, *6*, 577-588.

[12] Li, C.H.; Peterson, G.P. Experimental investigation of temperature and volume fraction variations on the effective thermal conductivity of nanoparticle suspensions (nanofluids). *J. Appl. Phys.*, **2006**, *99*, 084314.

[13] Maiga, S.E.B.; Nguyen, C.T.; Galanis, N.; Roy, G. Heat transfer behaviours of nanofluids in a uniformly heated tube. *Superlattice. Microst.*,**2004**, *35*, 543-557.

[14] Bhattacharya, P.; Saha, S.K.; Yadav, A.; Phelan, P.E.; Prasher, R.S. Brownian dynamics simulation to determine the effective thermal conductivity of nanofluids. *J. Appl. Phys.*, **2004**, *95*, 6492-6494.

[15] Buongiorno, J. Convective transport in nanofluids. *J. Heat Transf.*, **2006**, *128*, 240-251.

[16] Kim, D.; Kwon, Y.; Cho, Y.; Li, C.; Cheong S., Hwang Y., Lee J., Hong D., Moon S., Convective heat transfer characteristics of nanofluids under laminar and turbulent flow conditions. *Curr. Appl. Phys.*, **2009**, *9* (2), 119-123.

[17] Timofeeva, E. V.; Gavrilov, A. N.;McCloskey, J.M.;Tolmachev, Y.V. Thermal conductivity and particle agglomeration in alumina nanofluids: Experiment and Theory. *Phys. Rev. E*, **2007,** *76*, 061203.

[18] Chon, C.H.; Kihm, K.D.; Lee, S.P.; Choi, S.U.S. Empirical correlation finding the role of temperature and particle size for nanofluid (Al2O3) thermal conductivity enhancement. *Appl. Phys. Lett.*, **2005**, *87*.

[19] Murshed, S.M.S.; Leong, K.C.; Yang, C. A model for predicting the effective thermal conductivity of nanoparticles–fluid suspensions, *Int. J. Nanosci*., **2006**, *5,* 23-33.

[20] Qiang, L.; Yimin, X. Convective heat transfer and flow characteristics of Cu-water nanofluid. *Sci. China Ser. E*, **2002**, *45*, 408-416.

[21] Yang, Y.; Zhang, Z.G.; Grulke, E.A.; Anderson, W.B.; Wu, G. Heat Transfer properties of nanoparticle-in-fluid dispersions (Nanofluids) in laminar flow. *Int. J. Heat Mass Transfer*., **2005**, *48*, 1107-1116.

[22] Monrad, C.C; Pelton, J.F. Heat transfer by convection in annular spaces. *Trans. Am. Inst. Chem. Eng.,* **1942**, *38*, 593-611.

[23] Sieder, E.N.; Tate, G.E. Heat transfer and pressure drop of liquids in tubes. *Ind. Eng. Chem.*, **1936**, *28*, 1429-1435.

[24] Choi, U.S. Enhancing thermal conductivity of fluids with nanoparticle. *ASME FED 231*, **1995**, *231*, 99-103.

[25] Alizad, K.; Vafai, K.; Shafahi M. Thermal performance and operational attributes of the startup characteristics of flat-shaped heat pipes using nanofluids. *Int. J. Heat Mass Transfer*, **2012,** *55*, 140-155.

[26] Bobbo, S.; Fedele, L.; Benetti, A.; Colla, L.; Fabrizio, M.; Pagura, C.; Barison, S. Viscosity of water based SWCNH and TiO_2 nanofluids. *Exp. Therm. Fluid Sci.*, **2012,** *36*, 65-71.

[27] Buschmann, M. H.; Thermal conductivity and heat transfer of ceramic nano fluids. *Int. J. Therm. Sci.*, **2011**, Article in Press-Corrected Proof.

[28] Yang, L.; Du, K.; Ding, Y. H.; Cheng, B.; Li, Y. J. Viscosity-prediction models of ammonia water nanofluids based on various dispersion types. *Powder Technol.,* **2012**, *215-216*, 210-218.

[29] Colangelo, G.; Favale E.; Risi A.; Laforgia, D. Results of experimental investigations on the heat conductivity of nanofluids based on diathermic oil for high temperature applications. *Appl. Energy*, **2011**, Article in Press-Corrected Proof..

[30] Jamshidi, N.; Farhadi, M.; Sedighi, K.; Ganji, D. D. Optimization of design parameters for nanofluids flowing inside helical coils. *Int. Commun. Heat Mass Trans.,* **2011***, 39*, 311-317.

[31] Giraldo, M.; Sanin, D.; Flórez, W. F. Heat transfer in nanofluids: A computational evaluation of the effects of particle motion. *Appl. Math. Comput.,* **2011**, Article in Press-Corrected Proof.

[32] S. Özerinç, A .G. Yazıcıoglu, S. Kakaç, Numerical analysis of laminar forced convection with temperature-dependent. *Int. J. Therm. Sci.*, **2011**, Article in Press-Corrected Proof.

[33] Yu, L.; Liu, D.; Botz, F. Laminar convective heat transfer of alumina-polyalphaolefin nanofluids containing spherical and non-spherical nanoparticles. *Exp. Therm. Fluid Sci*., **2011**, *37*, 72-83.

[34] Farahani, S.D.; Kowsary, F. Estimation local convective boiling heat transfer coefficient in mini channel. *Int. Commun. Heat Mass Trans.*, **2011**, *39*, 304-310

[35] Cimpean, D. S.; Pop, I. Fully developed mixed convection flow of a nanofluid through an inclined channel filled with a porous medium. *Int. J. Heat Mass Transfer*, **2012**, *55*, 907-914.

[36] Leong, K.Y.; Saidur, R.; Mahlia, T.M.I.; Yau, Y.H. Modeling of shell and tube heat recovery exchanger operated with nanofluid based coolants. *Int. J. Heat and Mass Transfer*, **2012**, *55*, 808-816.

[37] Mahbubul, I.M.; Saidur, R.; Amalina, M.A. Latest developments on the viscosity of nanofluids. *Int. J. Heat Mass Transfer,* **2012**, *55*, 874-885.

[38] Wenzheng, C.; Minli, B.; Jizu, L.; Xiaojie, Li. On the microscopic flow characteristics of nanofluids by molecular dynamics simulation on Couette Flow. *Open Fuels Energy Sci. J.*, **2012**, *5*, 21-27.

[39] Ahmed, M.A.; Shuaib, N.H.; Yusoff, M.Z.; Al-Falahi A.H. Numerical investigations of flow and heat transfer enhancement in a corrugated channel using nanofluid. *Int. Commun. Heat Mass Trans.,* **2011**, *38*, 1368-1375.

[40] Akbarinia, A.; Abdolzadeh, M.; Laur, R. Critical investigation of heat transfer enhancement using nanofluids in microchannels with slip and non-slip flow regimes. *Appl. Therm. Eng.*, **2011**, *31*, 556-565.

[41] Bianco, V.; Manca, O.; Nardini, S. Numerical investigation on nanofluids turbulent convection heat transfer inside a circular tube. *Int. J. Therm. Sci*., **2011**, *50*, 341-349.

[42] Corcione, M. Empirical correlating equations for predicting the effective thermal conductivity and dynamic viscosity of nanofluids. *Energy Convers. Manage.*, **2011**, *52*, 789-793.

[43] Firouzfar, E.; Soltanieh, M.; Noie, S.H.; Saidi, S.H. Energy saving in HVAC systems using nanofluid. *Appl. Therm. Eng*., **2011**, *31*, 1543-1545.

[44] Gherasim, I.; Roy; G., Nguyen, C.T.; Vo-Ngoc, D. Heat transfer enhancement and pumping power in confined radial flows using nanoparticle suspensions (nanofluids). *Int. J. Therm. Sci.,* **2011**, *50*, 369-377.

[45] Hojjat, M.; Etemad, S.Gh.; Bagheri, R.; Thibault. J. Convective heat transfer of non-Newtonian nanofluids through a uniformly heated circular tube. *Int. J. Therm. Sci.,* **2011**, *50*, 525-531.

[46] Hojjat, M.; Etemad, S.Gh.; Bagheri, R.; Thibault, J. Thermal conductivity of non-Newtonian nanofluids: Experimental data and modeling using neural network. *Int. J. Heat Mass Trans*., **2011**, *54*, 1017-1023.

[47] Hojjat, M.; Etemad, S.Gh.; Bagheri, R.; Thibault. Turbulent forced convection heat transfer of non-Newtonian nanofluids. *Exp. Therm. Fluid Sci.,* **2011***, 35*, 1351-1356.

[48] Huminic, G.; Huminic, A. Heat transfer characteristics in double tube helical heat exchangers using nanofluids. *Int. J. Heat Mass Tran.,* **2011***, 54*, 4280-4287.

[49] Huminic, G.; Huminic, A. Heat transfer characteristics of a two-phase closed thermosyphons using nanofluids. *Exp. Therm. Fluid Sci.,* **2011***, 35,* 550-557.

[50] Jung, J.Y.; Cho, C.; Lee, W.H.; Kang, Y.T. Thermal conductivity measurement and characterization of binary nanofluids. *Int. J. Heat Mass Trans.,* **2011***, 54*, 1728-1733.

[51] Khanafer, K.; Vafai, K. A critical synthesis of thermophysical characteristics of nanofluids. *Int. J. Heat Mass Trans.,* **2011***, 54*, 4410-4428.

[52] Lee, S.W.; Park, S.D.; Kang, S.; Bang, I.C.; Kim, J.H. Investigation of viscosity and thermal conductivity of SiC nanofluids for heat transfer applications. *Int. J. Heat Mass Trans.,* **2011**, *54*, 433-438.

[53] Asirvatham, L.G.; Raja, B.; Lal, D.M.; Wongwises, S., Convective heat transfer of nanofluids with correlations. *Particuology*, **2011**, *9*, 626-631.

[54] Ebrahimnia-Bajestan, E.; Niazmand, H.; Duangthongsuk, W; Wongwises, S. Numerical investigation of effective parameters in convective heat transfer of nanofluids flowing under a laminar flow regime. *Int. J. Heat Mass Trans.,* **2011***, 54*, 4376-4388.

[55] Raisi, A.; Ghasemi, B.; Aminossadati, S. M. A Numerical study on the forced fonvection of laminar nanofluid in a microchannel with both slip and No-slip conditions. *Numer. Heat Tr. A-Appl.*, **2011**, *59*, 114-129.

[56] Heris, S; Z.;Noie, S.H.; Talaii, E.; Sargolzaei, J. Numerical investigation of Al2O3/water nanofluid laminar convective heat transfer through triangular ducts. *Nanoscale Res. Lett.*,**2011**, *6*,1-10.

[57] Vincenzo, B.; Nardini, S.; Manca, O. Enhancement of heat transfer and entropy generation analysis of nanofluids turbulent convection flow in square section tubes. *Nanoscale Res. Lett.,* **2011**, *6*, 1-12.

[58] Demir, H.; Dalkilic, A.S.; Kürekci, N.A.; Wongwises, D. S. Numerical investigation on the single phase forced convection heat transfer characteristics of TiO_2 nanofluids in a double-tube counter flow heat exchanger. *Int. J. Commun. Heat Mass Trans*., **2011**, *38*, 218-228.

[59] Abareshi, M.; Goharshadi, E.; Zebarjad, S.M.; Fadafan, H.K.; Youssefi, A. Fabrication characterization and measurement of thermal conductivity of Fe_3O_4 nanofluids. *J. Magn. Magn.Mater*., **2010**, *322*, 3895-3901.

[60] Farajollahi, B. I; Etemad, S.Gh.; Hojjat, M. Heat transfer of nanofluids in a shell and tube heat exchanger. *Int. J. Heat Mass Trans*., **2010,** *53*, 12-17.

[61] Fard, H. M.; Esfahany, M.N.; Talaie, M.R. Numerical study of convective heat transfer of nanofluids in a circular tube two-phase model versus single-phase model. *Int. J. Commun. Heat Mass Trans*., **2010**, *37*, 91-97.

[62] Do, K.H.; Ha, H.J.; Jang, S.P. Thermal resistance of screen mesh wick heat pipes using the water-based Al_2O_3 nanofluids. *Int. J. Heat Mass Trans*., **2010**, *53*, 5888-5894.

[63] Henderson, K.; Park, Y.G.; Liu, L.; Jacobi, A.M. Flow-boiling heat transfer of R-134a-based nanofluids in a horizontal tube, *Int. J. Heat Mass Trans.*, **2010**, *53*, 944-951.

[64] Godson, L.; Raja, B.; Lal, D.M.; Wongwises, S. Enhancement of heat transfer using nanofluids-An overview. *Renew. Sust. Energ. Rev.*, **2010**, *14*, 629-641.

[65] Kima, S.J.; McKrella, T.; Buongiornoa, J.; Hu, L.W Subcooled flow boiling heat transfer of dilute alumina, zinc oxide, and diamond nanofluids at atmospheric pressure. *Nucl. Eng. Des.*, **2010**, *240*, 1186-1194.

[66] Lotfi, R.; Saboohi, Y.; Rashidi, A.M. Numerical study of forced convective heat transfer of Nanofluids: Comparison of different approaches. *Int. J. Commun. Heat Mass Trans.,* **2010***, 37*, 74-78.

[67] Meibodi, M.E.; Sefti, M.V.; Rashidi, A.M.; Amrollahi, A.; Tabasi, M.; Kalal, H.S. Simple model for thermal conductivity of nanofluids using resistance model approach . *Int. J. Commun. Heat Mass Trans. ,* **2010**, *37*, 555-559.

[68] Meibodi, M.E.; Sefti, M.V.; Rashidi, A.M.; Amrollahi, A.; Tabasi, M.; Kalal, H.S. An estimation for velocity and temperature profiles of nanofluids in fully developed turbulent flow conditions. *Int. J. Commun. Heat Mass Trans.,* **2010**, *37*, 895-900.

[69] Meibodi, M.E.; Sefti, M.V.; Rashidi, A.M.; Amrollahi, A.; Tabasi, M.; Kalal, H.S. The role of different parameters on the stability and thermal conductivity of carbon nanotube/water nanofluids. *Int. J. Commun. Heat Mass Trans.*, **2010***, 37*, 319-323.

[70] Paul, G.; Chopkar, M.; Manna, I.; Das, P.K. Techniques for measuring the thermal conductivity of nanofluids: A review. *Renew. Sust. Energ. Rev.*, **2010**, *14*, 1913-1924.

[71] Paul, G.; Pal, T.; Manna, I. Thermo-physical property measurement of nano-gold dispersed water based nanofluids prepared by chemical precipitation technique. *J. Colloid Interf. Sci.*, **2010**, *349*, 434-437.

[72] Qu, J.; Wu, H.Y.; Cheng, P. Thermal performance of an oscillating heat pipe with Al_2O_3-water nanofluids. *Int. J. Commun. Heat Mass Trans.,* **2010**, *37*, 111-115.

[73] Rao, Y. Nanofluids: Stability, phase diagram, rheology and applications, *Particuology*, **2010**, 549-555.

[74] Raykar, V.S.; Singh, A.K. Dispersibility dependence of thermal conductivity of carbon nanotube based nanofluids. *Phys. Lett. A*, **2010**, *374*, 4618-4621.

[75] Roberts, N.A.; Walker, D.G. Convective performance of nano fluids in commercial electronics cooling systems. *Appl. Therm. Eng.*, **2010**, *30*, 2499-2504.

[76] Rostamani, M.; Hosseinizadeh, S.F.; Gorji, M.; Khodadadi, J.M. Numerical study of turbulent forced convection flow of nano fluids in a long horizontal duct considering variable properties. *Int. J. Commun. Heat Mass Trans*., **2010**, *37*, 1426-1431.

[77] Singh, P.K.; Anoop, K.B.; Sundararajan, T.; Das, S. K. Entropy generation due to flow and heat transfer in nanofluids. *Int. J. Heat Mass Trans*., **2010**, *53*, 4757-4767.

[78] Sundar, L.S. R; Sharma, K.V. Turbulent heat transfer and friction factor of Al_2O_3 Nanofluid in circular tube with twisted tape inserts. *Int. J. Heat Mass Trans*., **2010**, *53*, 1409-1416.

[79] Vajjha, R. S.; Das, D. K.; Kulkarni, D.P. Development of new correlations for convective heat transfer and friction factor in turbulent regime for nanofluids. *Int. J. Heat Mass Trans*., **2010**, *53* 4607-4618.

[80] Vajjha, R.S.; Das, D.K.; Namburu, P. K. Numerical study of fluid dynamic and heat transfer performance of Al_2O_3 and CuO nanofluids in the flat tubes of a radiator. *Int. J. Heat Fluid Fl.*, **2010**, *31*, 613-621.

[81] Wei, X.; Kong, T.; Zhu, H.; Wang, L. CuS/Cu_2S nanofluids: Synthesis and thermal conductivity. *Int. J. Heat Mass Trans*., **2010**, *53*, 1841-1843.

[82] Wei, X.; Wang, L. Synthesis and thermal conductivity of microfluidic copper nanofluids. *Particuology*, **2010**, *8*, 262-271.

[83] Yang, Y.T.; Lai, F.H. Numerical study of heat transfer enhancement with the use of nanofluids in radial flow cooling system. *Int. J. Heat Mass Trans*., **2010**, *53*, 5895-5904.

[84] Yu W., Xie H., Chen L., Li Y. Investigation on the thermal transport properties of ethylene glycol-based nanofluids containing copper nanoparticles. *Powder Technol.*, **2010**, *197*, 218-221.

[85] Wong, K.V.; Leon, O.D. Applications of Nanofluids: Current and Future. *Adv. Mech. Eng*., **2010**, 1-11.

[86] Duangthongsuk, W; Wongwises, S. Comparison of the effects of measured and computed thermophysical properties of nanofluids on heat transfer performance. *Exp. Therm. Fluid Sci.,* **2010**, *34*, 616-624.

[87] Duangthongsuk, W; Wongwises, S. An experimental study on the heat transfer performance and pressure drop of TiO_2-water nanofluids flowing under a turbulent flow regime. *Int. J. Heat Mass Trans*., **2010**, *53*, 334-344.

[88] Bergman, T.L. Effect of reduced specific heats of nanofluids on single phase, laminar internal forced convection. *Int. J. Heat Mass Trans*., **2009**, *52*, 1240-1244.

[89] Bianco, V.; Chiacchio, F.; Manca, O.; Nardini, S. Numerical investigation of nanofluids forced convection in circular tubes. *Appl. Therm. Eng.*, **2009**, *29*, 3632-3642.

[90] He, Y.; Men, Y.; Zhao, Y.; Lu, H.; Ding, Y. Numerical investigation into the convective heat transfer of TiO2 nanofluids flowing through a straight tube under the laminar flow conditions. *Appl. Therm. Eng.,* **2009**, *29*, 1965-1972.

[91] Hwang, K.S.; Jang, S.P.; Choi, S.U.S. Flow and convective heat transfer characteristics of water-based Al2O3 nanofluids in fully developed laminar flow regime. *Int. J. Heat Mass Trans*., **2009**, *52*, 193-199.

[92] Jung, J.Y.; Oh, H.S; Kwak, H.Y. Forced convective heat transfer of nanofluids in microchannels. *Int. J. Heat Mass Trans*., **2009**, *52*, 466-472.

[93] Kakaç S., Pramuanjaroenkij, A., Review of convective heat transfer enhancement with nanofluids. *Int. J. Heat Mass Trans*., **2009**, *52*, 3187-3196.

[94] Kim, D.; Kwon, Y.; Cho, Y.; Li, C.; Cheong, S.; Hwang, Y.; Lee, J.; Hong, D.; Moon S. Convective heat transfer characteristics of nanofluids under laminar and turbulent flow conditions. *Curr. Appl. Phys*., **2009**, *9*, e119-e123.

[95] Kulkarni, D.P.; Das, D.K.; Vajjha, R.S. Application of nanofluids in heating buildings and reducing pollution. *Appl. Energ.*, **2009**, *86*, 2566-2573.

[96] Mintsa, H.A; Roy, G.; Nguyen, C.T.; Doucet, D. New temperature dependent thermal conductivity data for water-based nanofluids. *Int. J. Therm. Sci.*, **2009**, *48*, 363-371.

[97] Murshed, S.M.S.; Leong, K.C.; Yang, C. A combined model for the effective thermal conductivity of nanofluids. *Appl. Therm. Eng.*, **2009**, *29*, 2477-2483.

[98] Namburu, P.K.; Das D. K., Tanguturi, K.M.; Vajjha, R.S. Numerical study of turbulent flow and heat transfer characteristics of nanofluids considering variable properties. *Int. J. Therm. Sci.*, **2009**, *48*, 290-302.

[99] Rea, U.; McKrell, T.; Hu, L.W. Buongiorno J., Laminar convective heat transfer and viscous pressure loss of alumina-water and zirconia-water nanofluids. *Int. J. Heat Mass Trans*., **2009**, *52*, 2042-2048.

[100] Pantzali, M.N.; Mouza, A.A.; Paras, S.V. Investigating the efficacy of nanofluids as coolants in plate heat exchangers (PHE), *Chem. Eng. Sci*., **2009**, *64*, 3290-3300.

[101] Xie, H.; Chen, L. Adjustable thermal conductivity in carbon nanotube nanofluids. *Phys. Lett.*, **2009**, *373*, 1861-1864.

[102] Pantzali, M.N.; Kanaris, A.G.; Antoniadis, K.D.; Mouza, A.A.; Paras, S.V. Effect of nanofluids on the performance of a miniature plate heat exchanger with modulated surface. *Int. J. Heat Fluid Fl.*, **2009**, *30*, 691-699.

[103] Vajjha, R.S.; Das, D. K. Experimental determination of thermal conductivity of three nanofluids and development of new correlations. *Int. J. Heat Mass Trans*., **2009**, *52*, 4675-4682.

[104] Wen D., Lin G., Vafaei S., Zhang K., Review of nanofluids for heat transfer applications. *Particuology,* **2009**, *7*, 141-150.

[105] Hadjov, K.B. Modified self-consisted scheme to predict the thermal conductivity of nanofluids. *Int. J. Therm. Sci.,* **2009**, 48, 2249-2254.

[106] Ali, M.; Zeitoun, O. Nanofluids forced convection heat transfer inside circular tubes. *Int. J. Nanoparticles*, **2009**, *2*, 164-172.

[107] Duangthongsuk, W.; Wongwises, S. Measurement of temperature-dependent thermal conductivity and viscosity of TiO2-water nanofluids.*Exp. Therm. Fluid Sci*., 2009, *33*,706-714.

[108] Duangthongsuk, W.; Wongwises, S. Heat transfer enhancement and pressure drop characteristics of TiO_2-water nanofluid in a double-tube counter flow heat exchanger. *Int. J. Heat Mass Trans*., **2009**, *52*, 2059-2067.

[109] Bi, S.S.; Shi, L.; Zhang, L.L Application of nanoparticles in domestic refrigerators. *Appl. Therm. Eng.*, **2008**, *28*, 1834-1843.

[110] Hwang, Y., Lee, J. K.; Lee, J.K.; Jeong, Y.M.; Cheong, S.; Ahn, Y.C.; Kim, S. H. Production and dispersion stability of nanoparticles in nanofluids. *Powder Technol*., **2008**, *186*, 145-153.

[111] Karthikeyan, N.R.; Philip, J.; Raj, B. Effect of clustering on the thermal conductivity of nanofluids. *Mater. Chem. Phys.,* **2008**, *109*, 50-55.

[112] Khandekar, S.; Joshi, Y.M.; Mehta, B. Thermal performance of closed two-phase thermosyphon using nanofluids. *Int. J. Therm. Sci.,* **2008**, *47*, 659-667.

[113] Lee, J.H; Hwang, K.S.; Jang, S.P; Lee, B.H.; Kim, Ho, J.; Choi, S.U.S. Effective viscosities and thermal conductivities of aqueous nanofluids containing low volume concentrations of Al_2O_3 nanoparticles. *Int. J. Heat Mass Trans*., **2008**, *51*, 2651-2656.

[114] Murshed, S.M.S.; Leong, K.C.; Yang, C. Thermophysical and electrokinetic properties of nanofluids - A critical review. *Appl. Therm. Eng.,* **2008**, *28*, 2109-2125.

[115] Oh, D.W.; Jain, A.; Eaton, J. K.; Goodson, K. E.; Lee, J. S. Thermal conductivity measurement and sedimentation detection of aluminum oxide nanofluids by using the 3 w method. *Int. J. Heat Fluid Fl*., **2008**, *29*, 1456-1461.

[116] Kang, Y.T.; Kim, H. J.; Lee, K.I. Heat and mass transfer enhancement of binary nanofluids for H_2O/LiBr falling film absorption process. *Int. J. Refrig.*,**2008**, *31*, 850-856.

[117] Lu, W.Q.; Fan, Q.M. Study for the particle's scale effect on some thermophysical properties of nanofluids, by a simplified molecular dynamics method. *Eng. Anal. Bound. Elem.*, **2008**, *32*, 282-289.

[118] Nguyen, C.T.; Desgranges, F.; Galanis, N.; Roy, G.; Maré, T.; Boucher, S.; Mintsa, H. A. Viscosity data for Al_2O_3–water nanofluid-hysteresis: is heat transfer enhancement using nanofluids reliable. *Int. J. Therm. Sci.,* **2008**, *47*, 103-111.

[119] Chen, H.; Yang, W.; He, Y.; Ding, Y.; Zhang, L.; Tan, C.; Lapkin, A. A.; Bavykin, D. V. Heat transfer and flow behavior of aqueous suspensions of titanate nanotubes (nanofluids). *Powder Technol.,* **2008**, *183*, 63-72.

[120] Ding, Y.; Chen, H.; He, Y.; Lapkin, A.; Yeganeh, M.; Šiller, L.; Butenko, Y. V. Forced convective heat transfer of nanofluids. *Adv. Powder Technol.*, **2007**, *18*, 813-824.

[121] Zhang, X.; Gu, H.; Fujii, M.; Effective thermal conductivity and thermal diffusivity of nanofluids containing spherical and cylindrical nanoparticles. *Exp. Therm. Fluid Sci.,* **2007**, *31*, 593-599.

[122] Ko, G.H.; Heo, K.; Lee, K.; Kim, D.S.; Kim, C.; Sohn, Y. Choi M., An experimental study on the pressure drop of nanofluids containing carbon nanotubes in a horizontal tube. *Int. J. Heat Mass Trans*., **2007**, *50*, 4749-4753.

[123] Mansour, R.B.; Galanis, N.; Nguyen, C.T. Effect of uncertainties in physical properties on forced convection heat transfer with nanofluids. *Appl. Therm. Eng.*, **2007**, *27*, 240-249.

[124] Hong, H.; Wright, B.; Wensel, J.; Jin, S.; Ye, X.R.; Roy, W. Enhanced thermal conductivity by the magnetic field in heat transfer nanofluids containing carbon nanotube. *Synthetic Met.*, **2007**, *157*, 437-440.

[125] Li, C.H.; Peterson, G.P. Mixing effect on the enhancement of the effective thermal conductivity of nanoparticle suspensions (nanofluids). *Int. J. Heat Mass Trans.*, **2007**, 50, 4668-4677.

[126] Yoo, D.H.; Hong, K.S.; Yang, H.S. Study of thermal conductivity of nanofluids for the application of heat transfer fluids. *Thermochim. Acta*, **2007**, *455*, 66-69.

[127] Avsec, J.; Oblak, M. The calculation of thermal conductivity, viscosity and thermodynamic properties for nanofluids on the basis of statistical nanomechanics. *Int. J. Heat Mass Trans.*, **2007**, *50*, 4331-4341.

[128] He, Y.; Jin, Yi; Chen, H.; Ding, Y.; Cang, D.; Lu, H. Heat transfer and flow behavior of aqueous suspensions of TiO_2 nanoparticles (nanofluids) flowing upward through a vertical pipe. *Int. J. Heat Mass Trans.*, **2007**, *50*, 2272-2281.

[129] Lee, J.; Mudawar, I. Assessment of the effectiveness of nanofluids for single-phase and two-phase heat transfer in micro-channels. *Int. J. Heat Mass Trans.*, **2007**, *50*, 452-463.

[130] Wang, X.Q.; Mujumdar, A.S. Heat transfer characteristics of nanofluids: a review. *Int. J. Therm. Sci.,* **2007***, 46*, 1-19.

[131] Trisaksri, V.; Wongwises S. Critical review of heat transfer characteristics of nanofluids. *Renew. Sust. Ener. Rev.,* **2007***, 11*, 512-523.

[132] Daungthongsuk W.; Wongwises S.; A critical review of convective heat transfer of nanofluids. *Renew. Sust. Ener. Rev.*, **2007**, *11*, 797-817.

[133] Hwang, Y.J.; Ahn, Y.C.; Shin, H.S.; C.G. Lee; G.T. Kim; H.S. Park; J.K. Lee Investigation on characteristics of thermal conductivity enhancement of nanofluids. *Curr. Appl. Phys.*, **2006**, *6*, 1068-1071.

[134] Hwang, Y.; Park, H.S.; Lee, J.K.; Jung, W.H. Thermal conductivity and lubrication characteristics of nanofluids. *Curr. Appl. Phys.*, **2006**, *6* S1, e67-e71.

[135] Liu, M.S.; Lin, M.C.C.; Tsai, C.Y.; Wang, C.C. Enhancement of thermal conductivity with Cu for nanofluids using chemical reduction method. *Int. J. Heat Mass Trans.*, **2006**, *49*, 3028-3033.

[136] Palm, S.J.; Roy, G.; Nguyen, C.T.; Heat transfer enhancement with the use of nanofluids in radial flow cooling systems considering temperature-dependent properties. *Appl. Therm. Eng.*, **2006**, *26*, 2209-2218.

[137] Heris, S. Z.; Etemad, S.G.; Esfahany, M.N. Experimental investigation of oxide nanofluids laminar flow convective heat transfer. *Int. J. Commun. Heat Mass Trans.*, **2006**, *33*, 529-535.

[138] Xuan, Y.; Yu, K.; Li, Q. Investigation on flow and heat transfer of nanofluids by the thermal Lattice Boltzmann model. *Prog. Comput. Fluid Dy.*, **2005**, *5*, 13-19.

[139] Liu, M.S.; Lin, M.C.C.; Huang, I.T. Wang C.C., Enhancement of thermal conductivity with carbon nanotube for nanofluids. *Int. J. Commun. Heat Mass Trans.*, **2005**, *32*, 1202-1210.

[140] Maiga, S.E.B.; Palm, S.J.; Nguyen, C.T.; Roy, G.; Galanis, N. Heat transfer enhancement by using nanofluids in forced convection flows. *Int. J. Heat Fluid Fl.,* **2005**, *26*, 530-546.

[141] Wen, D.; Ding, Y. Experimental investigation into convective heat transfer of nanofluids at the entrance region under laminar flow conditions. *Int. J. Heat Mass Trans.*, **2004**, *47*, 5181-5188.

[142] Maiga, S.E.B.; Nguyen, C.T.; Galanis, N.; Roy, G. Heat transfer behaviours of nanofluids in a uniformly heated tube. *Superlattice. Microst.,* **2004***, 35*, 543-557.

[143] Roy, G.; Nguyen, C.T.; Lajoie, P.R. Numerical investigation of laminar flow and heat transfer in a radial flow cooling system with the use of nanofluids. *Superlattice. Microst.*, **2004**, *35*, 497-511.

[144] Nguyen, C.T.; Roy, G.; Maiga, S.E.B.; Lajoie, P.R. Heat transfer enhancement by using nanofluidsfor cooling of high output microprocessor. *www.electronicscooling.com/html/ 2004_nov_techbrief.html*, **2004**.

[145] Ali, A.; Vafai, K.; Khaled, A.R.A. Analysis of heat and mass transfer between air and falling film in a cross flow Configuration. *Int. J. Heat Mass Trans.*, **2004**, *47*, 743-755.

[146] Ali, A.; Vafai K. An investigation of heat and mass transfer between air and desiccant film in an inclined parallel and counter flow channels. *Int. J. Heat Mass Trans.*, **2004**, *47*, 1745-1760.

[147] Zhu, H.T.; Lin, Y.S.; Yin, Y.S. A novel one-step chemical method for preparation of copper nanofluids. *J. Colloid Interf. Sci.,* **2004**, *277*, 100-103.

[148] Li Q., Xuan Y., Convective heat transfer and flow characteristics of cu-water nanofluid, *Sci. China Ser E*, **2002**, *45*, 408-416.

[149] Xuan Y., Li Q., Investigation on convective heat transfer and flow features of nanofluids. *ASME J. Heat Transfer*, **2003**, *125*, 151-155.

[150] Hamilton R.L., Crosser O.K., Thermal conductivity of heterogeneous two-component systems. *I & EC Fundamentals*, **1962**, *1*, 187-191.

[151] Wasp E.J., Solid-liquid flow slurry pipeline transportation. Trans Tech Publications, **1977**.

[152] Xuan, Y.; Roetzel, W. Conceptions for heat transfer correlation of nanofluids. *Int. J. Heat Mass Trans.*, **2000**, *43*, 3701-3707.

[153] Xuan Y., Li Q., Heat transfer enhancement of nanofluids. *Int. J. Heat Fluid Fl.*, **2000**, *21*, 58-64.

[154] Xue, Q.Z. Model for effective thermal conductivity of nanofluids. *Phys. Lett.*, **2003**, *307*, 313-317.

Received: January 22, 2012 **Revised: April 24, 2012** **Accepted: July 18, 2012**

Send Orders of Reprints at reprints@benthamscience.org

Current Nanoscience, **2012**, *8*, **939-944**

Measurement of Specific Heat of Nanofluids

T. Yiamsawasd[a], A.S. Dalkilic[b] and S. Wongwises[a,c*]

[a]*Fluid Mechanics, Thermal Engineering and Multiphase Flow Research Lab. (FUTURE), Department of Mechanical Engineering, Faculty of Engineering, King Mongkut's University of Technology Thonburi, Bangmod, Bangkok 10140, Thailand;* [b]*Heat and Thermodynamics Division, Department of Mechanical Engineering, Yildiz Technical University (YTU), Yildiz, Besiktas, Istanbul 34349, Turkey;* [c]*The Academy of Science, The Royal Institute of Thailand, Sanam Suea Pa, Dusit, Bangkok 10300, Thailand*

Abstract: This article reports an experiment on specific heat measurement of nanofluids using a calorimeter of the comparison type. The measurement is based on a differential thermal analysis technique. The studied TiO_2 and Al_2O_3 nanoparticles are dispersed in base fluids which are pure water and a mixture of ethylene glycol/water (20/80 wt.%). Concentrations between 0 and 8 vol.% and temperatures are between 15 and 65°C. Results show that the measured specific heat of nanofluids is lower than that of the base liquid decreases as the particle concentrations increases. Furthermore, the specific heat of nanofluids was found to increase with increasing temperatures. When compared with predicted values from existing correlations and data reported by other researchers, measurements are compatible with the prediction from the thermal equilibrium model presented by Xuan and Roetzel. Finally, new correlations are proposed for predicting the specific heat of Al_2O_3 and TiO_2 nanofluids.

Keywords: Specific heat, nanofluids, nano particle, base fluid.

INTRODUCTION

Nanofluids are innovative working fluids gained from dispersing nanometer-sized solid particles in common working fluids. These solid particles with high thermal conductivity are expected to enhance heat transfer with long-term stability in suspensions and minimal effect on pressure drop. The term 'nanofluids' was firstly defined by Choi in 1995 [1] and was widely used since then. Nanofluids are expected to be used in mini- and micro-scaled heat exchangers, such as electrical and electronic appliances and computers. However, their relevant properties should be studied, especially thermal properties. This will be very useful for the effective use of nanofluids and for further analysis and development thereof.

Past studies have shown great interest in nanofluids. Initially, most studies focused on thermal conductivity [1-10], viscosity [6-11], and convective heat transfer [12-17]. Unfortunately, there are only a few studies that are concerned with specific heat. Actually, specific heat is one of the most important basic thermal properties that deserves attention. It can be used to calculate for example, the sensible heat transfer rate, Prandtl numbers and thermal diffusivity for predicting heat transfer performance of heat exchangers. Therefore, specific heat of nanofluids should be studied together with other properties.

Below are recent experimental studies about specific heat of nanofluids.

Namburu *et al.* [11] conducted an experiment to measure specific heat and viscosity of silicon dioxide nanofluids suspended in 60/40 by weight mixture of ethylene glycol/water. Particles sizes of SiO_2 examined were 20, 50 and 100 nm, with concentration range of 0 to 10 vol. %. A specially designed electrical heater calorimeter was used to measure the specific heat of nanofluids. Their experiment showed that specific heat of silicon dioxide nanofluids decreased when concentration increased. At the concentration of 10 vol.%, the specific heat decreased by about 12% when compared to the base fluid.

*Address correspondence to this author at the Fluid Mechanics, Thermal Engineering and Multiphase Flow Research Lab. (FUTURE), Department of Mechanical Engineering, King Mongkut's University of Technology Thonburi, Bangmod, Bangkok 10140, Thailand; Tel: +662-470-9115; Fax: +662-470-9111; E-mail: somchai.won@kmutt.ac.th

Zhou and Ni [18] measured the specific heat of Al_2O_3-water nanofluids with an Al_2O_3 particle size of 45 nm at a temperature of 33°C and a concentration range of 0 to 21.7 vol.%. A differential scanning calorimeter was used for measurement. Their study revealed that when the concentration increased, the specific heat of Al_2O_3-water nanofluids decreased. When compared to the existing correlation, the experimental result was found to be compatible with the prediction from the thermal equilibrium model of Xuan and Roetzel [19], whereas the ideal gas mixtures model of Pak and Cho [5] provided different results.

Vajjha and Das [20] measured the specific heat of 3 types of nanofluids that consisted of Al_2O_3 (44 nm) and ZuO (77 nm) particles suspended in 60/40 % by mass of ethylene glycol-water mixture, and SiO_2 (20 nm) particles suspended in deionized water. A specially designed electrical heating calorimeter was used in a temperature range of 42 to 82°C and a concentration range of 0 to 10 vol.%. Results showed that the specific heat of all 3 types of nanofluids decreased when the concentration increased. On the contrary, the specific heat increased when the temperature increased. However, their results were found to be incompatible with results from the ideal gas mixtures of Pak and Cho and from the thermal equilibrium model of Xaun and Roetzel.

Nelson *et al.* [21] conducted an experiment on thermal properties, as well as flow and forced convection heat transfer characteristics, of exfoliated graphite nanoparticles suspended in polyalphaolfin. The specific heat was measured at the concentration of 0.6 wt.% with a particle diameter of 20 nm and a thickness of 100 nm in a temperature range of 45 to 90°C, using differential scanning calorimeter techniques. They found that the specific heat of nanofluids increased by about 50% when compared to the base fluid and increased with increasing temperature.

Zhou *et al.* [22] measured the specific heat and volumetric heat capacity of CuO-EG nanofluids at a concentration range of 0.1 to 0.6 vol.%. They concluded that when concentration increased, the specific heat of CuO-EG decreased gradually. Volumetric heat capacity was found to change minimally. Their results were compatible with the prediction from the thermal equilibrium model of Xuan and Roetzel, while the ideal gas mixtures model of Pak and Cho could not predict.

Shin and Bernejee [23] measured the specific heat of nanofluids which were used in solar thermal energy storage. Silica nanoparti-

1875-6786/12 $58.00+.00 **© 2012 Bentham Science Publishers**

cles (1 wt.%) suspended in a eutectic of lithium carbonate and potassium carbonate mixture (62/38 % by weight). The silica nanoparticles with an average size of 35 nm were tested in a temperature range of 525 to 555°C using a differential scanning calorimeter. They found that the specific heat of nanofluids increased by about 19–24% when compared with the base fluid. Temperature had little effect on the change of the specific heat of nanofluids used in this experiment.

It can be clearly seen from the study on the nanofluids mentioned above that there are various types of apparatus or measurement techniques used to determine the specific heat of nanofluids and the results obtained from those techniques were also different. Thus, other techniques could be developed to measure the specific heat of nanofluids in order to determine compatibility. To the best of the authors' knowledge, a differential thermal analysis technique has never been found before to be used with nanofluids. In the present study, this technique will be applied to measure the specific heat of nanofluids. The results will be compared with those reported in literature. The correlations for determining the specific heat of nanofluids are also proposed for practical applications.

PREPARATION OF NANOFLUIDS

The preparation of nanofluids is an important step. Generally, there are three methods of nanofluids preparation: pH control, addition of surfactants or dispersants, and use of ultrasonic vibration. The purpose of nanofluids preparation is to suspend nanoparticles stably in base fluids without precipitation of particles in short duration [2].

TiO_2 and Al_2O_3 nanofluids used in the present study were supplied by DEGUSSA Company. The average diameter of the TiO_2 particles is 21 nm and the average diameter of the Al_2O_3 particles is 120 nm. Table **1** shows the density and specific heat of nanoparticles used in the present study determined using Ref. [24] and Ref. [25] for density and specific heat, respectively. Both are suspended in water base fluid with concentrations of 13.8 and 10.6 vol.%. The base fluids used in this research are pure water and ethylene glycol-water mixture at 20/80 wt %. Before the experiment, the nanofluids supplied by the manufacturer were mixed and diluted by adding base fluid to reach the desired concentrations. Then, ultrasonic vibration was used for about 2 hours to create dispersion. Preparation by pH control and addition of surfactants was done discretely by the manufacturer.

Table 1. Properties of Nanoparticles

Nanoparticles	Density (kg/m^3)	Specific heat at 33 °C (kJ/kg K)
TiO_2	4157	0.715
Al_2O_3	3970	0.795

The photograph of TiO_2 nanoparticles taken from the transmission electron microscope (TEM) is shown in Fig. (**1**). The particle size distribution is also shown in Fig. (**2**). Initially, it was found that both nanoparticles have a circular shape, with an average diameter of 21 nm for TiO_2 and of 120 nm for Al_2O_3 which are very similar to the information provided by the manufacturer.

EXPERIMENTAL APPARATUS AND PROCEDURES

In this study, a calorimeter of the comparison type used to measure the specific heat of nanofluids was newly developed. The measurement was based on differential thermal analysis technique as shown in Fig. (**3**). Temperature differences obtained from heating between the reference liquid and the tested nanofluids together with known properties of the reference liquid can be used to determine the specific heat.

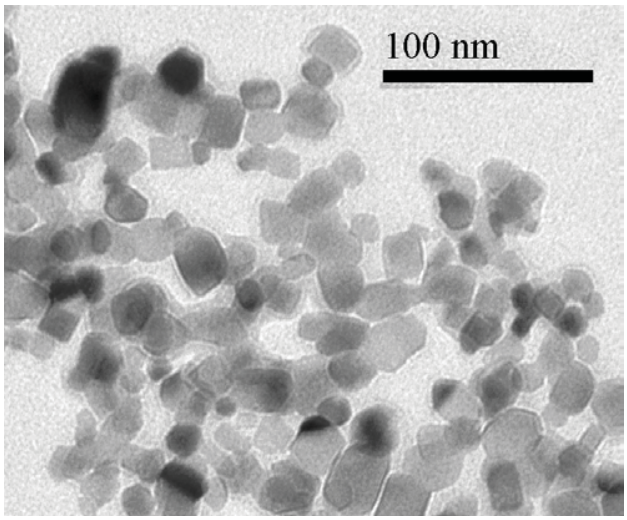

Fig. (1). TEM image of dispersed TiO_2 nanoparticles in water [From Suriyawong and Wongwises [26], with permission from Elsevier].

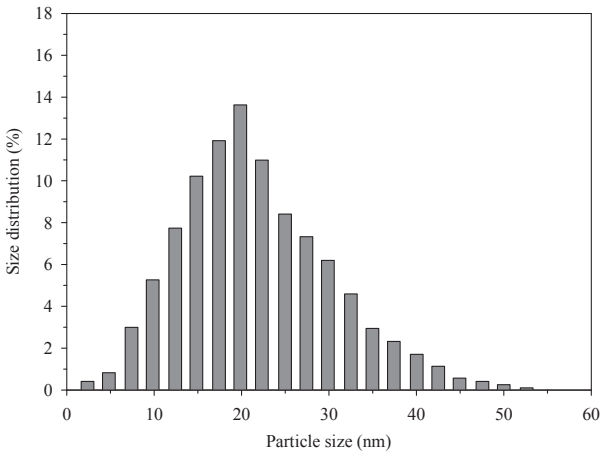

Fig. (2). Size distribution of TiO_2.

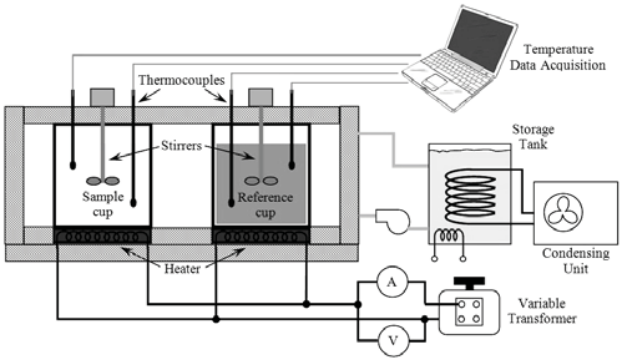

Fig. (3). Schematic diagram of experimental apparatus.

Important components shown in Fig. (**3**) are cups for sample and reference substances that are specially designed in symmetrical sizes. The cups are made from stainless steel with high conductivity

and high sensibility to temperature change. Both cups are placed in temperature control sleeves connected to a hot-cold water tank. Heat for each cup is fed from the bottom of each cup with a 30-watt electrical plate heater. The heater's coils are specially designed to have equal resistance. Heat can be controlled by variable transformers. Each cup has a small propeller with a low speed to create an evenly dispersed temperature and to prevent sedimentation and agglomeration of nanoparticles. The temperatures of both substances are measured with T-type thermocouples installed at the top and the bottom of the cup are recorded precisely via a computerized data logger every 3 seconds.

The experiment began by measuring an equal volume of the prepared nanofluids and reference substances. Both substances were weighed for use in calculation. Next, the substances were put in each cup carefully. The lids of the cups and the temperature control sleeves were then closed. Next, the level of the thermocouples, as well as the level and speed of the propeller, were adjusted and checked. Cooling water was put into the sleeves to adjust the starting temperature of both substances. When the desired starting temperature was reached, the cooling water was poured out of the sleeves and the heater was turned on. The temperature was recorded immediately. The temperature change of the nanofluids and reference substance were observed during the experiment. The experiment was stopped when the final temperature was reached. Both cups were cleaned, along with the other components that came in contact with nanofluids, before repeating the experiment.

Based on the differential thermal analysis, both sample and reference substances received an equal amount of heat. Therefore, specific heat of nanofluids $\left(C_{p,nf}\right)$ could be calculated from

$$Q_{nf} = Q_{ref}$$

$$m_{nf} C_{p,nf} \Delta T_{nf} = m_{ref} C_{p,ref} \Delta T_{ref}$$

$$C_{p,nf} = \frac{m_{ref} C_{p,ref} \Delta T_{ref}}{m_{nf} \Delta T_{nf}} \quad (1)$$

where $C_{p,ref}$ is the specific heat of reference substance; m_{nf} and m_{ref} are the masses of the nanofluids and the reference substances, respectively; and ΔT_{nf} and ΔT_{ref} are the temperature changes during the experiment of the nanofluids and the reference substances, respectively.

RESULTS AND DISCUSSION

Before the experiment, the developed apparatus was calibrated by measuring the specific heat of the water sample and a 20/80 % by weight mixture of ethylene glycol (EG)/water in the temperature range of 15 to 65°C. Results were then compared with the standard values from ASHRAE [27] and were found to be similar. The water sample had a maximum deviation of 1.4% with an average deviation of 1.36%. The EG/water mixture had maximum deviation of 3.21% with average deviation of 2.24%, as shown in Fig. (**4**).

This section discusses the effect of the concentration and temperature on the specific heat of nanofluids with water and mixture of ethylene glycol as base fluids, tested at concentrations of 1, 2, 4, 6 and 8 vol.% in a temperature range of 15 to 65°C. Fig. (**5**(a)) shows that the specific heat of Al_2O_3-water is a function of concentration and temperature. The experimental results indicated that specific heat decreased by about 20% when the concentration increased to 8 vol.%. In terms of temperature, the specific heat increased only slightly when the temperature increased. Fig. (**5**(b)) shows similar results of TiO_2-water. That is, the increasing concentration caused specific heat to decrease by about 5 to 23% at the concentrations of 1 to 8 vol.%. The increasing temperature also caused a slight increase in specific heat.

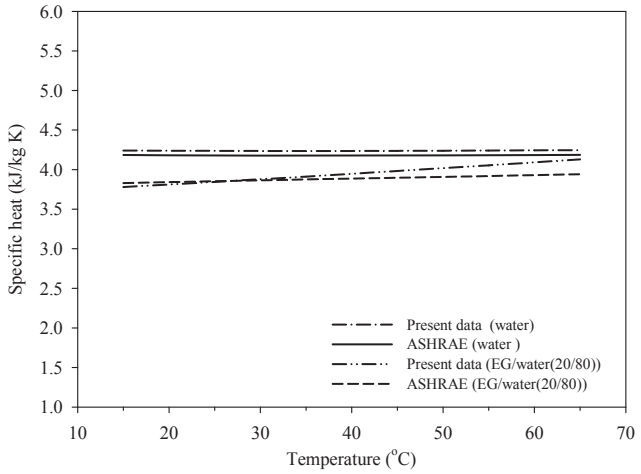

Fig. (4). Comparison of the measured specific heat with reference data.

This research also studied the effect of base fluid on the specific heat of nanofluids. Hence, apart from the water-based nanofluids, the EG/water (20/80)-based fluid was also examined. Al_2O_3-EG/water and TiO_2-EG/water at the concentrations of 1, 2 and 4 vol.% in a temperature range of 15 to 65°C were tested. Figs. (**6**(a) and **6**(b)) show that for both Al_2O_3-EG/water and TiO_2-EG/water the increasing concentrations caused the specific heat to decrease by about 3 to 11% in a concentration range of 1 to 4 vol.%. The specific heat tended to increase when the temperature increased.

From the experimental results of all four types of nanofluids mentioned above, the decrease of the specific heat of nanofluids when the concentration increased could directly result from the fact that the specific heat of nanoparticles mixed is much lower than that of the base fluid. As a result, the overall specific heat of nanofluids decreases. In terms of temperature, the increase of specific heat with the increasing temperature is similar to that of the base fluid. Basically, the specific heat of the base fluids increases when the temperature increases. Different from the base fluids, the specific heat of nanoparticles slightly increases with the increasing temperature. As a result the slope of the experimental lines shown in Figs. (**5** and **6**) are almost the same.

This section compares the experimental results with the prediction from existing models and data obtained from other researches. The widely used models of Pak and Cho [5] assume that nanofluids are homogeneous substances that could be calculated by mixing theory as follows:

$$C_{p,nf} = \phi C_{p,np} + (1-\phi) C_{p,b} \quad (2)$$

where $C_{p,nf}$ is the specific heat of nanofluids; $C_{p,np}$ is the specific heat of nanoparticles; $C_{p,b}$ is the specific heat of the base fluid; and ϕ is the concentration by volume.

Another widely used model of Xuan and Roetzel [19] assumes that the heat transfer process between nanoparticles and the base fluid is thermal equilibrium, as follows:

$$C_{p,nf} = \frac{\phi \rho_{np} C_{p,np} + (1-\phi) \rho_b C_{p,b}}{\phi \rho_{np} + (1-\phi) \rho_b} \quad (3)$$

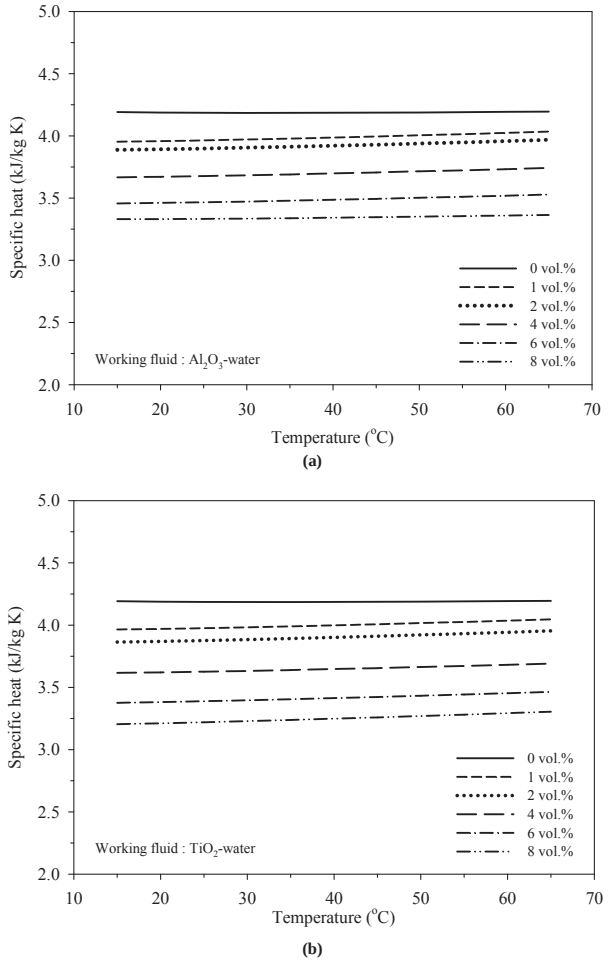

Fig. (5). The specific heat of water-base nanofluids as a function of temperature and volume fraction.

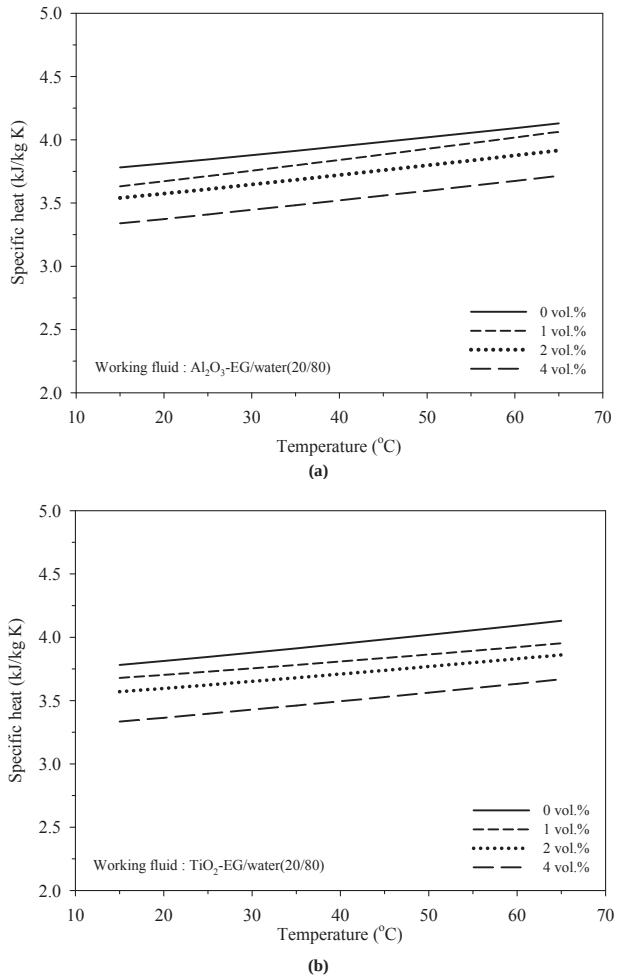

Fig. (6). The specific heat of EG/water (20/80)-base nanofluids as a function of temperature and volume fraction.

where ρ_{np} is the density of the nanoparticles, and ρ_b is the density of the base fluid.

Vajjha and Das [20] also present a correlation developed from the experiment to measure the specific heat of Al_2O_3, ZnO, and SiO_2 nanofluids as follows:

$$C_{p,nf} = \frac{\left((AT) + B(\frac{C_{p,np}}{C_{p,b}}) \right)}{C + \phi} \quad (4)$$

where T is the temperature of the nanofluids, and A, B, and C are coefficients shown in Table **2**.

Table 2. Coefficients in Vajjha and Das Model

Nanoparticle	Coefficients		
	A	**B**	**C**
Al_2O_3	0.0008911	0.5179	0.4250
SiO_2	0.001769	1.1937	0.8021
ZnO	0.0004604	0.9855	0.299

Fig. (**7**(a)) shows the specific heat of Al_2O_3-water nanofluids at various concentrations. Results are similar to those from the model of Xuan and Roetzel. However, the model of Pak and Cho could not be used to predict, particularly at high concentrations. On the other hand, the model of Vajjha and Das gave lower values, particularly at low concentrations. In terms of temperature, the experimental results are also similar to those from the model of Xuan and Roetzel. The model of Pak and Cho gave higher values, whereas the model of Vajjha and Das gave lower values, particularly in the lower temperature ranges, as shown in Fig. (**7**(b)). Similarly, the experimental results of TiO_2-water nanofluids, shown in Figs. (**8**(**a**) and **8**(**b**)), also correspond with the prediction from the model of Xuan and Roetzel, both in terms of concentration and temperature. From all comparisons, it could be said that the sample nanofluids used in this experiment are in a thermal equilibrium during the experiment. Therefore, the specific heat gained from the experiment is similar to the prediction of the thermal equilibrium model presented by Xuan and Roetzel. This could be confirmed with the experiment of Zhon and Ni, who measured Al_2O_3-water nanofluids and obtained similar results to the prediction from the model of Xuan and Roetzel, as shown in Fig. (**7**(a)). Moreover, Zhou *et al*. [21] also concluded from their experiment in measuring the specific heat of CuO-EG nanofluids that the specific heat of CuO-water was also similar to those predicted by the thermal equilibrium model.

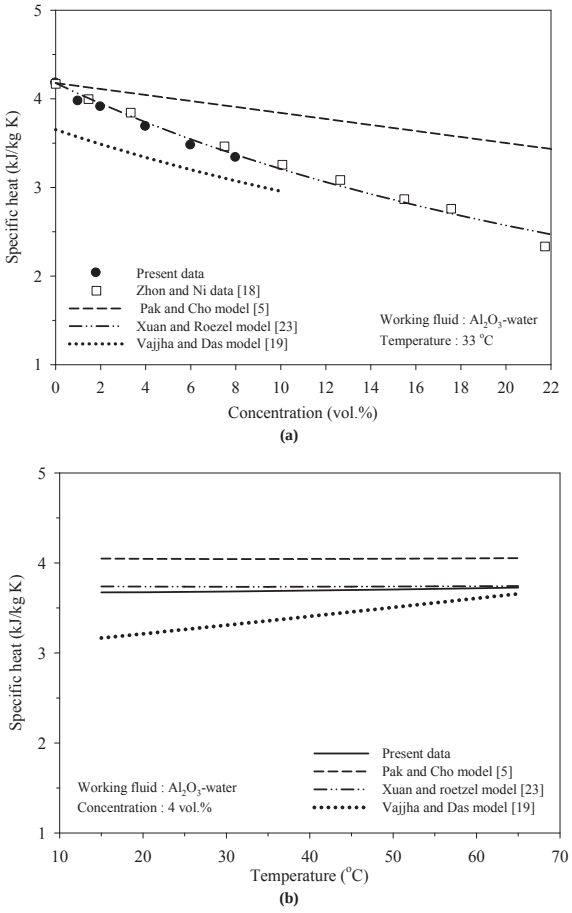

Fig. (7). Comparison of the measured specific heat with those obtained from various researchers.

This research presents a correlation to predict specific heat of Al_2O_3 and TiO_2 nanofluids in a form of specific heat ratio between nanofluids and base fluid $\left(C_{p,nf}/C_{p,b}\right)$ that could be applied to other base fluids. This model considers the effects of temperature, concentration, the specific heat of nanoparticles, and the specific heat of the base fluid as follows:

$$\frac{C_{p,nf}}{C_{p,b}} = A\phi^B T^C \left(\frac{C_{p,np}}{C_{p.b}}\right)^D \quad (5)$$

where A, B, C, and D are the coefficients shown in Table **3**. The model could be used in a temperature range of 15 to 65°C and a concentration range of 1 to 8 vol.%. Fig. (**9**) shows a comparison between experimental specific heat and predictions from the correlation (Eq. (5)). It could be seen that the predicted value is similar to the experimental value at a verifiable and acceptable level.

Table 3. The Coefficients in Presented Correlation for Different Nanofluids

Nanofluid	Coefficients				Max. error	Avg. error
	A	B	C	D		
Al_2O_3	1.249458	-0.05846	0.006467	-0.17236	1.77%	0.79%
TiO_2	1.387402	-0.06425	0.001124	-0.21159	1.82%	0.85%

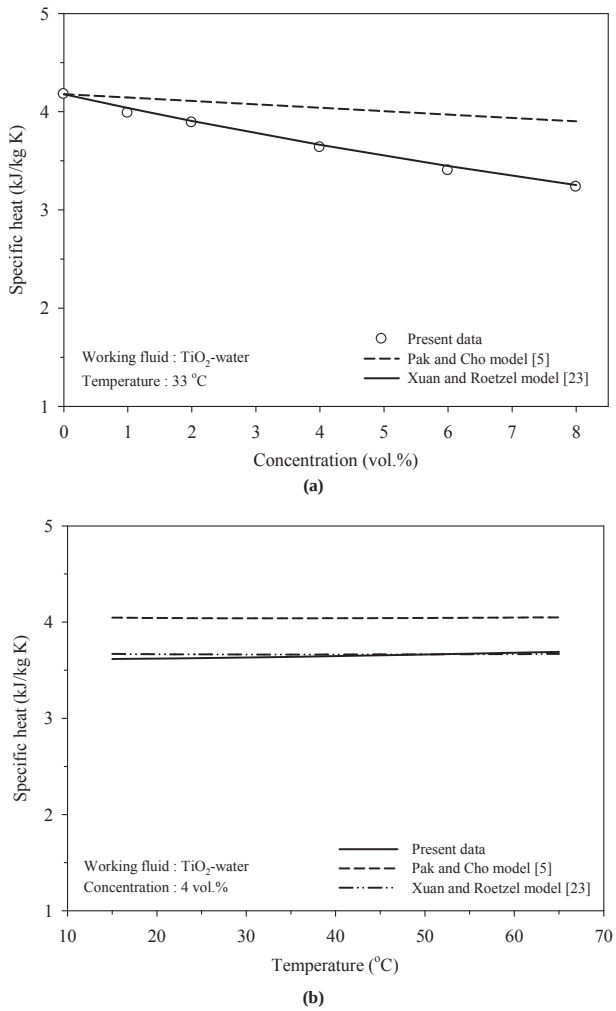

Fig. (8). Comparison of the measured specific heat of TiO_2-water nanofluids with those obtained from various researchers.

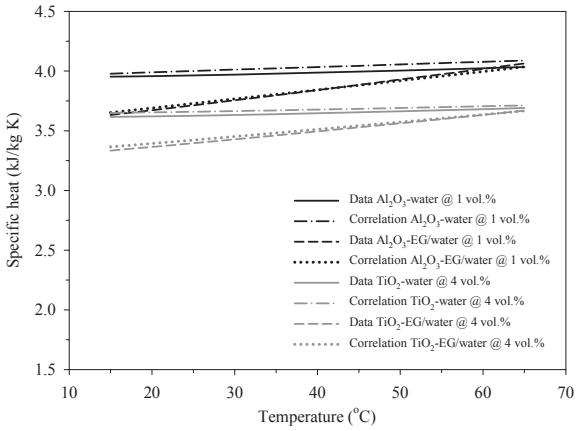

Fig. (9). Comparison of the measured specific heat with the proposed correlations.

CONCLUSIONS

From the calibration of measuring specific heat of water and ethylene glycol, the results are similar to the standard values from

ASHRAE. The developed specific heat measurement apparatus also has an acceptable precision level.

The experimental results indicate that the specific heat of nanofluids is lower than the base fluid and tends to decrease when concentration increases. On the other hand, the increasing temperature causes the specific heat of nanofluids to increase. These experimental results are compatible with the prediction from the thermal equilibrium model of Xuan and Roetzel. This research also presents a newly developed correlation to predict the specific heat of Al_2O_3 and TiO_2 nanofluids.

CONFLICT OF INTEREST

The authors confirm that this article content has no conflicts of interest.

ACKNOWLEDGEMENTS

The present study was supported by the Thailand Research Fund (TRF), the Office of the Higher Education Commission and the National Research University Project whose guidance and assistance are gratefully acknowledged.

REFERENCES

[1] Choi, S.U.S. Enhancing thermal conductivity of fluids with nanoparticles. *ASME FED*, **1995**, *231*, 99-103.

[2] Das, S.K.; Putta, N.; Thiesen, P.; Roetzel, W. Temperature Dependence of Thermal Conductivity Enhancement For Nanofluids. *ASME Trans. J. Heat Transfer*, **2003**, *125*, 567-574.

[3] Eastman, J.A.; Choi, S.U.S.; Li, S.; Yu, W.; Thomson, L.J. Anomalously increased effective thermal conductivities of ethylene glycol-based nanofluids containing copper nanoparticles. *Appl. Phys. Lett*., **2001**, *78*, 718-720.

[4] Wang, X.; Xu, X.; Choi, S.U.S. Thermal Conductivity of Nanoparticles-Fluid Mixture. *J. Thermophys. Heat Transfer*, **1999**, *13*, 474-480.

[5] Pak, B. C.; Cho, Y. I. Hydrodynamic and Heat Transfer Study of Dispersed Fluids with Submicron Metallic Oxide Particles. *Exp. Heat Transfer*, **1998**, *11*, 151-170.

[6] Murshed, S.M.S.; Leong, K.C.; Yang, C. Investigations of Thermal Conductivity and Viscosity of Nanofluids. *Int. J. Therm. Sci.*, **2008**, *47*, 560-568.

[7] Duangthongsuk, W.; Wongwises, S. Measurement of temperature-dependent thermal conductivity and viscosity of TiO_2-water nanofluids. *Exp. Therm. Fluid Sci.*, **2009**, *33*, 706-714.

[8] Yu, W.; Xie, H.; Li, Y.; Chen, L. Experimental investigation on thermal conductivity and viscosity of aluminum nitride nanofluid. *China Particuol.*, **2011**, *9*, 187-191.

[9] Nguyen, C.T.; Desgranges, F.; Roy, G.; Galanis, N.; Mare, T.; Boucher, S.; Mintsa, H.A. Temperature and particle-size dependent viscosity data for water-based nanofluids – Hysteresis phenomenon. *Int. J. Heat Fluid Flow*, **2007**, *28*, 1492-1506.

[10] Masuda, H.; Ebata, A.; Teramae, K.; Hishinuma, N. Alteration of Thermal Conductivity and Viscosity of Liquid by Dispersing Ultra-Fine Particles (Dispersion of Al_2O_3, SiO_2 and TiO_2 Ultra-Fine Particles). *Netsu Bussei (Japan)*, **1993**, *7*, 227-233.

[11] Namburu, P.K.; Kulkarni, D.P.; Dandekar, A.; Das, D.K. Experimental investigation of viscosity and specific heat of silicon dioxide nanofluids. *Micro Nano Lett.*, **2007**, *2*, 67-71.

[12] Yang, Y.; Zhang, Z.G.; Grulke, E.A.; Anderson, W.B.; Wu, G. Heat Transfer Properties of Nanoparticle-in-Fluid Dispersions (Nanofluids) in Laminar Flow. *Int. J. Heat Mass Transfer*, **2005**, *48*, 1107-1116.

[13] Xuan, Y.; Li, Q. Investigation on Convective Heat Transfer and Flow Features of Nanofluids. *ASME J. Heat Transfer*, **2003**, *125*, 151-155.

[14] Nguyen, C.T.; Roy, G.; Gauthier, C.; Galanis, N. Heat Transfer Enhancement Using Al_2O_3-Water Nanofluid for Electronic Liquid Cooling System. *Appl. Therm. Eng.*, **2007**, *28*, 1501-1506.

[15] Heris, S.Z.; Etemad, S.G.; Esfahany, M.N. Experimental Investigation of Oxide Nanofluids Laminar Flow Convective Heat Transfer. *Int. Commun. Heat Mass Transfer*, **2006**, *33*, 529-535.

[16] He, Y.; Jin, Y.; Chen, H.; Ding, Y.; Cang, D.; Lu, H. Heat Transfer and Flow Behavior of Aqueous Suspensions of TiO_2 Nanoparticles (Nanofluids) Flowing Upward Through a Vertical Pipe. *Int. J. Heat Mass Transfer*, **2007**, *50*, 2272-2281.

[17] Duangthongsuk, W.; Wongwises, S. An experimental study on the heat transfer performance and pressure drop of TiO_2-water nanofluids flowing under a turbulent flow regime. *Int. J. Heat Mass Transfer*, **2010**, *53*, 334-344.

[18] Zhou, S.; Ni, R Measurement of the Specific Heat Capacity of Water-Based Al_2O_3 Nanofluid. *Appl. Phys. Lett.*, **2008**, *92*, 093123.

[19] Xuan, Y.; Roezel, W. Conceptions for Heat Transfer Correlations of Nanofluids. *Int. J. Heat Mass Transfer*, **2000**, *43*, 3701-3707.

[20] Vajjha, R.S.; Das, D.K. Specific Heat Measurement of Three Nanofluids and Development of New Correlations. *ASME J. Heat Transfer*, **2009**, *131*, 071601

[21] Nelson, I.C.; Banerjee, D.; Rengasamy, P. Flow Loop Experiments Using Polyalphaolefin Nanofluids. *J. Thermophys. Heat Transfer*, **2009**, *23*, 752-761.

[22] Zhou, L.P.; Wang, B.X.; Peng, X.F.; Du X.Z.; Yang Y.P. Research Article on The Specific Heat Capacity of CuO Nanofluid. *Adv. Mech. Eng.*, **2010**, *2010*, 172085.

[23] Shin, D.; Banerjee, D. Enhanced Specific Heat of Silica Nanofluid. *ASME J. Heat Transfer*, **2011**, *133*, 024501.

[24] Incropera, F.P.; DeWitt, D.P. *Introduction to Heat Transfer*, 3rd ed.; Wiley, New York: **1996**.

[25] Touloukian, Y.S.; Buyco, F.H. In: *Thermophysical Properties of Matter*; Specific Heat Nonmetallic Solids; IFI/Plenum, New York: **1970**; Vol. *5*

[26] Suriyawong, A.; Wongwises, S. Nucleate Pool Boiling Heat Transfer Characteristics of TiO_2-Water Nanofluids at Very Low Concentrations. *Exp. Therm. Fluid Sci.*, **2010**, *34*, 992-999.

[27] ASHRAE, *ASHRAE Handbook: Fundamentals*, American Society of Heating, Refrigerating and Air-Conditioning Engineers Inc., Atlanta, GA, **2005**.

Received: October 22, 2011 **Revised: June 17, 2012** **Accepted: July 11, 2012**

International Journal of Air-Conditioning and Refrigeration
Vol. 20, No. 4 (2012) 1230003 (20 pages)
© World Scientific Publishing Company
DOI: 10.1142/S2010132512300030

World Scientific
www.worldscientific.com

A REVIEW ON THE HEAT-TRANSFER PERFORMANCE AND PRESSURE-DROP CHARACTERISTICS OF VARIOUS ENHANCED TUBES

S. LAOHALERTDECHA*, A. S. DALKILIC† and S. WONGWISES*,‡,§
*Fluid Mechanics, Thermal Engineering and Multiphase Flow Research Lab. (FUTURE)
Department of Mechanical Engineering, Faculty of Engineering
King Mongkut's University of Technology Thonburi (KMUTT) Bangmod
Bangkok, 10140, Thailand
†Heat and Thermodynamics Division, Department of Mechanical Engineering
Yildiz Technical University, Yildiz, Besiktas, Istanbul, 34349, Turkey
‡The Academy of Science, The Royal Institute of Thailand
Sanam Suea Pa, Dusit, Bangkok 10300, Thailand
§somchai.won@kmutt.ac.th

Received 11 May 2012
Revised 28 August 2012
Accepted 3 September 2012
Published 4 December 2012

The enhanced tube is a kind of the passive technique for improving the thermal performance of the heat exchangers with a little increase of the friction penalty. They have stated to use instead of the common smooth tubes for designing of the heat exchangers. The size of these heat exchangers can be reduced considerably by using the enhanced tubes instead of smooth tubes. Normally, they are divided into four groups: the corrugated tube, ribbed tube, grooved tube, and fluted tube. Compared with the common smooth tube, many researchers reported that use of the enhanced tubes dramatically increases the heat-transfer performance, both theoretically and experimentally. Focusing on the advantages of the enhanced tubes, this article summarizes the published studies on the heat-transfer and pressure-drop characteristics of the enhanced tubes, both experimental and quantitative investigations.

Keywords: Enhanced tubes; heat-transfer performance; pressure drop; heat exchanger.

Nomenclature

D : Diameter (m)
e : Corrugation depth (m)
f : Friction factor
G : Mass flux ($\mathrm{kg \cdot m^{-2} \cdot s}$)
h : Heat transfer coefficient ($\mathrm{W \cdot m^{-2} \cdot K}$)
L : Length of the test tube (m)
Nu : Nusselt number
p : Corrugation pitch (m)
Pr : Prandtl number
Re : Reynolds number

§Corresponding author.

t : Corrugation width (m)
x : Quality

Greek Letters

β : Helix angle (degree)

Subscripts

avg : Average
i : Inside
o : Outside

1. Introduction

The surface area of heat exchangers has a directly significant effect on their heat-transfer performance. Improvements to make heat transfer equipment more energy-efficient would need to focus on miniaturization on the one hand and an astronomical increase in heat flux on the other. Normally, heat-transfer enhancement techniques necessarily reduce the thermal resistance in a conventional heat exchanger by promoting a higher convection heat-transfer coefficient in order to minimize the size of the heat exchanger.

In general, enhancement techniques can be divided into two categories — active and passive techniques. The active technique requires external forces such as an electric field or acoustic or surface vibration, whereas the passive technique requires special surface geometries, such as a rough surface, extended surface, or fluid additives. Enhanced heat-transfer surfaces or "enhanced tubes" are one of the passive techniques, in which the surface is modified in such a way as to promote turbulence in the flow field and increase the heat-transfer surface.

These tubes can be employed in many heat exchangers to enhance the heat-transfer performance of both the inside and outside tubes, by mixing and also limiting the fluid boundary layers close to the heat transfer surfaces. Nowadays, enhanced tubes such as spirally corrugated tubes, ribbed tubes, grooved tubes, and fluted corrugated tubes are typically selected to replace conventional smooth tubes in the designs of industrial heat exchangers. They are expected to increase the heat-transfer performance of the heat-transfer equipment with only a very small increase in the pressure-drop penalty.

The heat transfer and pressure drop characteristics of the various refrigerants flowing through different type of the enhanced tubes under condensation process were summarized and reported in Ref. 1. The effects of tube orientation, tube geometry, flow pattern, oil mixture and void fraction on the condensation heat transfer performance and pressure drop were presented.

The purpose of this article is to review the literature mentioning heat-transfer performance and pressure-drop characteristics of the enhanced tubes, both experimental and theoretical studies. Various categories of enhanced tubes will be investigated i.e., corrugated tubes, ribbed tubes, grooved tubes, and fluted tubes. In addition, heat transfer characteristics of a new type of enhanced tube named "Vipertubes" are also presented. Each type is described in detail in the following sections.

2. Corrugated Tubes

This type of tube has a corrugated surface. The overall heat-transfer coefficient has been remarkably improved because of the turbulent flow effect on the inner surface and outer surface of the tube caused by the corrugation. The details of corrugated tubes are shown in Fig. 1. Many experimental investigations have been performed to investigate the effects of corrugation pitch, corrugation depth, and tube diameter on the heat-transfer and pressure-drop characteristics of the corrugated tubes. The heat transfer and flow characteristics of corrugated tubes have been reviewed as described below.

Mimura and Isozaki[2] reported the effect of shapes of corrugated tubes on the experimentally observed heat-transfer and flow characteristics. For heat-transfer experiments, steam is condensed on the

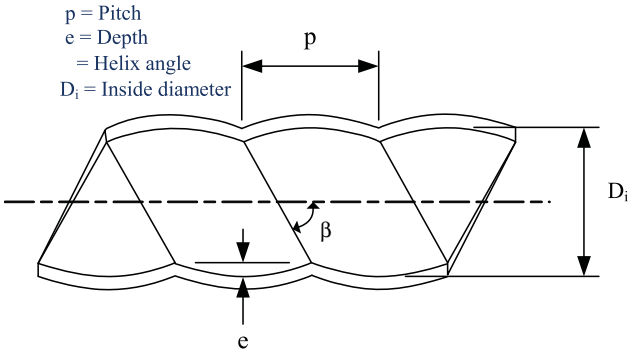

Fig. 1. Schematic diagram of the corrugated tubes.

outside of a horizontally corrugated tube made from 90−10 cupronickel. Similarly, pressure drop is measured under isothermal cold-flow conditions. The results indicated that the heat-transfer coefficient decreased with increasing corrugated pitch. At the ratio of depth to tube diameter of 0.05, the maximum heat-transfer coefficient was obtained. Moreover, the dual-start corrugated tubes gave a slightly higher heat-transfer coefficient than those of the single-start tubes. The friction factor equation was presented by considering the effect of pitch and depth. Finally, the correlation between the tube side heat-transfer coefficient and pressure drop in the corrugated tube was proposed.

Ganeshan and Rao[3] presented an experimental study on the heat-transfer behavior and friction characteristics of hot water flowing through a smooth tube and seven spirally corrugated tubes. The corrugated tubes of one to four helical starts and having constant helix angle of 65° were used as the test sections. They were different geometrical aspect ratios of e/d, p/e and p/d. The experimental data demonstrated that the heat-transfer coefficient of the four-start corrugated tube was larger than the smooth tube by about 100% at a Prandtl number of 4.3. Similarly, at a higher Prandtl number of 109, a 150% increase in the heat transfer coefficient was obtained.

Thien and Khan[4] reported the friction factor of an Oldroyd-type fluid flowing inside a sinusoidally corrugated tube, experimentally and quantitatively. The boundary element method was used to solve the problem and a Deborah number up to 20 was used in their study. The numerical results showed that the friction factor increased with the Deborah number. The results also gave reasonably agreement with the measured data.

Asako *et al.*[5] studied the heat transfer and flow characteristics of corrugated ducts with rounded corners, quantitatively. The results with the rounded corners were compared with the straight duct results. Three assigned corrugation angles and four aspect ratios of corrugated ducts are used as the test section. The simulation conditions were as follows: (1) Reynolds number between 100 and 1000 and (2) a fixed Prandtl number of 0.7. Their results indicated that rounding of the corners led to decreases in both the friction factor and the Nusselt number.

Honda and colleagues[6] investigated heat transfer and flow behaviors of R-11 and R-113 flowing in the annulus of a horizontal double-tube condenser during the condensation process. A corrugated tube with an outside diameter of 19.1 mm and installed with wire fins on the outer surface is used as the inner tube; three smooth tubes with inner diameter of 24.8, 27.2, and 29.9 mm are used as the outer tube. The mass velocity of working fluids were between 50 and $300\,\mathrm{kg}\cdot\mathrm{m}^{-2}\cdot\mathrm{s}$. The Lockhart−Martinelli parameters were used to calculate the frictional pressure gradient and then compared with the measured data. The experimental results showed that the local heat-transfer coefficient was two to 13 times higher than those for horizontal annuli with a smooth and corrugated inner tube. Moreover, the measured data was used to develop the correlation for predicting the local heat-transfer coefficient based on the surface tension controlled flow and the vapor shear controlled-flow model.

Burdette *et al.*[7] presented an upper-convected Maxell (UCM) model for predicting the flow behavior of working fluid flowing through an axisymmetric corrugated tube with a sinusoidally varying cross-section. The explicitly elliptic momentum equation (EEME) was used to solve the problem, and the results showed an agreement with the spectral/finite difference calculations.

Zimparov *et al.*[8] experimentally investigated the heat transfer and frictional pressure drop of a power plant condenser. One smooth tube and 25 spirally corrugated brass tubes were used as the test sections. The corrugated pitch varied from 6.5 to 16.9 mm, the ridge height varied from 0.44 to 1.18 mm, and the spiral angle ranged from 68° to 85°. Performance evaluation criteria were used to estimate the benefit of the spirally corrugated tubes.

Zimparov *et al.*[9] introduced a mixing-length model for predicting the heat-transfer coefficient and the Fanning friction factor of water flowing through a corrugated tube. A Reynolds number between 10^4 and 6×10^4 and a Prandtl number between 2.2 and 3.4 were used as the test conditions.

Gopalan and Ponnalagasamy[10] reported a steady laminar flow of a suspension in a corrugated tube with asymmetric and symmetric wavy wall, numerically. The effects of Reynolds number, Peclet number, wave number and the volume fraction of the particles on the flow were presented. The simulation results indicated that the mixing phenomenon due to secondary flow increased the flow of a relatively large volume fraction of low diffusive particles. In addition, their results also illustrated that

the pressure drop of corrugated tubes is higher than that of the smooth tube and decreased with increases in the diffusive particles.

Hinton and Conklin[11] experimentally studied the condensing heat-transfer and pressure drop characteristics of R-22 and non-azeotropic refrigerant mixture (NARM) of 75 wt.% R-143a and 25 wt.% R-124 flowing through a condenser made from common smooth tubes and then compared with the spirally corrugated tubes. The double-tube counter flow heat exchanger is used as the test section, in which refrigerant flows inside the internal tube and the water circulates in the annulus. Their results showed that the average heat transfer coefficient for the corrugated tube was higher than that for the smooth tube by about 40% for R-22 and 70% for NARM. Similarly, the pressure drop of the corrugated tube working with R-22 and NARM was roughly 23% and 36% larger than that of the smooth tube, respectively.

Chen *et al.*[12] experimentally investigated the heat-transfer and friction characteristics of four-start spirally corrugated tubes. A double-pipe counter flow heat exchanger was used as the test section. In their study, the non-symmetric nature of the corrugation angles along the longitudinal direction was reported. Then, the measured data were compared with the neural network analysis. The differences in heat transfer and friction loss due to effect of the corrugation angles were observed. Moreover, the heat transfer coefficient correlation based on a neural network model was proposed by considering the effect of the corrugation angles.

Dong *et al.*[13] reported the heat transfer and friction characteristics of water and oil flowing through four spirally corrugated tubes under turbulent flow, experimentally. The dimensions of the test tubes are shown in Table 1. The test conditions were conducted for the Reynolds number between 6000 and 93,000 for water and 3200 and 19,000 for oil. Compared with the common smooth tube, the experimental data indicated that the spirally corrugated tubes gave higher heat-transfer coefficient and friction factor by about 30% to 120% and 60% to 160%, respectively, as shown in Fig. 2. Moreover, the increase of e/d has a greater effect on the increase of the friction factor and heat transfer coefficient than the increase of p/d.

Table 1. The dimensions of the corrugated tubes.[13] [From Ref. 13, with permission from Elsevier.]

Number	p (mm)	e (mm)	β (degree)	D_i (mm)	L (mm)
1	10	0.39	78.8	16.04	500
2	10	0.32	78.8	16.12	500
3	10	0.69	82.1	22.82	500
4	12	0.7	79.0	20.08	500

Zimparov[14,15] experimentally investigated the heat-transfer and pressure-drop characteristics of water flow in single-start and three-start spirally corrugated tubes combined with five twisted tape inserts. The effects of height to diameter ratio and relative pitch were presented. The extended performance evaluation criteria equation was used to evaluate the multiplicative effect. At a given condition, the measured data illustrated that the heat-transfer coefficient and friction factor of spirally corrugated tubes combined with twisted tape inserts were higher than those for the conventional smooth tube.

Rainieri and Pagliarini[16] presented experimental study on the convective heat-transfer performance of corrugated wall tubes with axial symmetrical and helical corrugations with various pitch values. The effects of the wall roughness and fluid property variation were determined. Figure 3 presents a photo of the corrugated tubes. The Reynolds number ranged from 90 to 800, and ethylene glycol was used as the working fluid. The experimental data showed that the helical corrugation promoted a significant swirl component. However, an as much significant heat-transfer enhancement was not associated. Moreover, variation of fluid properties with temperature promoted the transition to an unstable flow.

Barba *et al.*[17] reported an experimental study on heat-transfer and pressure-drop characteristics of ethylene glycol flowing through a corrugated tube. The corrugated tube was obtained from a circular SS AISI 304 smooth tube, through a cold mechanical bucking, indenting the smooth tube without abrasion and mass removal as shown in Fig. 4. A Reynolds number ranging from 100 to 800 was tested. In comparison to the smooth tube, their results showed that the Nusselt number of the corrugated tube was significantly increased throughout the test run. However, for pressure drop consideration, the results also showed that using the corrugated tube caused increases in the friction factor by about 1.83 to 2.45. Moreover, the Nusselt number and friction factor correlations were proposed.

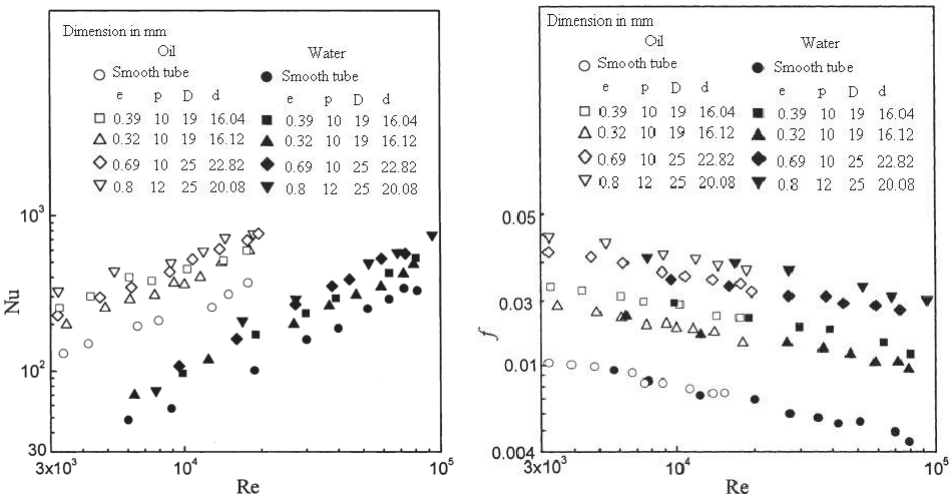

Fig. 2. Nusselt number and friction factor versus Reynolds number.[13] [From Ref. 13, with permission from Elsevier.]

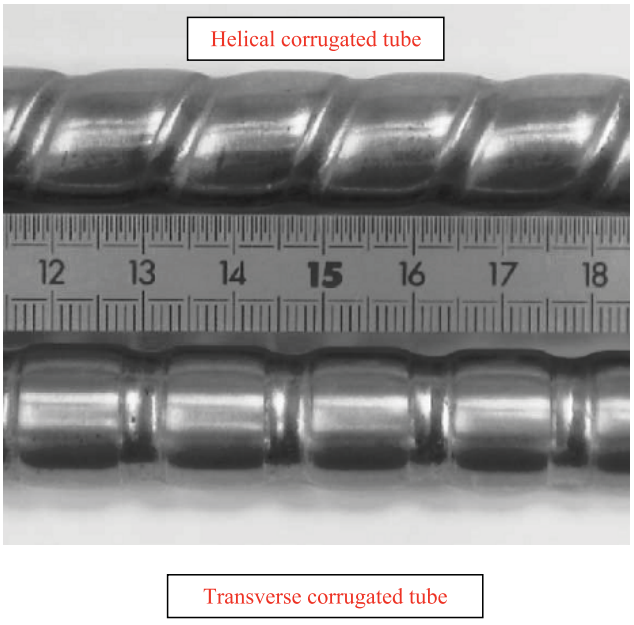

Fig. 3. Helical and transverse corrugated tubes.[16] [From Ref. 16, with permission from Elsevier (color online).]

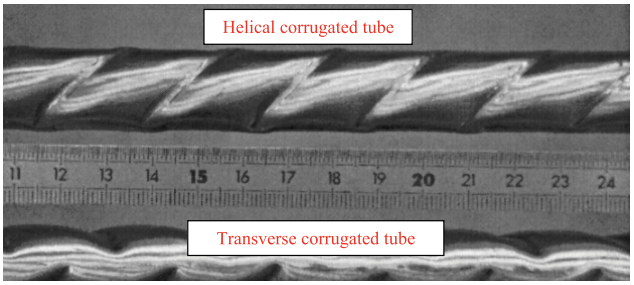

Fig. 4. Helical and transverse corrugated tubes.[17] [From Ref. 17, with permission from Elsevier (color online).]

Vicente and colleagues[18] determined the heat-transfer performance and friction characteristics of water and ethylene glycol flow in 10 corrugated tubes under turbulent flow. In this study, the Prandtl number was in the range of 2.5 to 100. The effect of rib height and spiral pitch was also investigated. Their data indicated that the severity index can be used to identify the effects of roughness on flow behaviors. Moreover, based on the experimental data, the Nusselt number and Fanning friction factor correlations were proposed as function of flow and geometry dimensionless parameters.

Zimparov[18] proposed a simple mathematical model for predicting the friction factor in the case of a spirally corrugated tube combined with a twisted tape insert under a fully developed turbulent flow region. This model was first suggested by Smithberg and Landis. In this study, the flow field was divided into two regions: (1) a helicoidal core flow and (2) a twisting boundary layer flow. Their simulation results demonstrated that the wall roughness had a significant effect on both the axial velocity and tangential velocity, which led to swirl-mixing phenomena. Moreover, their data were compared with 570 experimental data points obtained from the testing of 57 tubes. The results also indicated that the majority of the data falls within $\pm 15\%$ of the proposed model. This means that the proposed model can be used to predict the friction factor in the cases of smooth pipe, smooth pipe with a twisted tape inserts, a corrugated tube, and a corrugated tube combined with twisted tape inserts for turbulent flow regime.

The ongoing work of Zimparov[20] was to present a simple mathematical model created by Smithberg and Landis for predicting the heat-transfer coefficients of a spirally corrugated tube combined with a twisted tape insert in fully developed turbulent flow regime. The effects of both axial and tangential boundary layer were considered. Their results demonstrated that the wall roughness had simultaneous effects on the axial velocity and secondary fluid motion. Similar to the case of friction factor, the proposed model was compared with the 544 measured data obtained from Bergles *et al.*[21] for heat-transfer coefficient. The results showed that the proposed model gave reasonably good agreement with the measured data and deviations of $\pm 15\%$ were obtained.

Vicente *et al.*[18] reported an experimental study on the heat-transfer and pressure-drop characteristics of water and ethylene glycol flowing through corrugated tubes under laminar and transition flow regime. For laminar flow condition, their results indicated that the Nusselt number depended on both the natural convection and the entrance effect, and corrugated tube increases heat-transfer performance by about 30% at high Rayleigh numbers. Similarly, the friction factors in corrugated tubes were 25% larger than those of a smooth tube. Moreover, they reported that roughness of the corrugated tube accelerated the transition to a critical Reynolds number below 1300.

Targanski and Cieslinski[22] studied the evaporation heat-transfer coefficient and pressure drop of pure R407C and R407C/oil mixtures flow in two smooth tubes, corrugated tube and micro-finned tube, experimentally. The dimensions of the test sections are shown in Table 2. The experiments were conducted at saturation temperature of 0°C and mass flux varied between 250 and 500 $\mathrm{kg \cdot m^{-2} \cdot s}$. Their experimental data showed that two enhanced tubes gave a larger heat-transfer coefficient than the smooth tube, as well as a pressure drop. The average heat-transfer coefficient in the micro-finned tube and corrugated tube was up to 50% and 20%, respectively, higher than in the smooth tube. Similarly, pressure drop in the micro-finned tube and corrugated tube was up to 40% and 80%, respectively, higher than in the smooth tube, as shown in Fig. 5. Moreover, compared with pure R407C and R407C/oil mixtures, higher heat-transfer coefficients for pure R407C were obtained.

Table 2. The dimensions of the corrugated tubes[22] (from Ref. 22, with permission from Elsevier).

Number	Tube description	h (mm)	D_i (mm)	L (mm)
1	Smooth	—	8	2000
2	Smooth	—	8.8	2000
3	Corrugated	0.45	8.8	2000
4	Micro-fin	0.2	8.92	2000

Rozzi *et al.*[23] presented an experimental investigation on the convective heat transfer and friction losses in helically corrugated tubes. A shell and tube heat exchanger was used as the test apparatus. Whole milk, cloudy orange juice, apricot, and apple puree were tested under heating and cooling conditions. The experimental data showed that the use of helically corrugated tube had no effect on the heat-transfer performance for a Reynolds number less than 800. For a Reynolds number ranging from 800 to the limit of the transition flow regime, larger heat-transfer coefficients for corrugated tubes were obtained. Moreover, the results indicated that heat-transfer coefficients for corrugated tubes were moderately higher than those for smooth tubes and very high pressure drops were also obtained.

Dalkilic *et al.*[24] showed an experimental comparison of the laminar film condensation heat transfer coefficients of R134a in vertical smooth and micro-fin tubes having inner diameters of 7 mm and lengths of 500 mm at a mass flux of 29 $\mathrm{kg\,m^{-2}\,s^{-1}}$ and the pressures between 0.8 and 0.9 MPa. The original smooth tube heat transfer model was modified by a well-known friction factor to account for the heat transfer enhancement effects due to the presence of micro-fins, shown in Fig. 6(a), on the internal wall surface during annular flow regime conditions. Alterations of the local heat transfer coefficient, and condensation rate along the tube length during downward condensing film were determined. Their results show that the interfacial shear stress is found to have significance for the laminar condensation heat transfer of R134a under the given conditions due to its better predictive performance than the classical solution neglecting the interfacial shear stress effect. A comparison of the convective heat transfer coefficients was done according to the condensing pressures as shown in Fig. 6(b).

In 2010 and 2011, the work of Laohalertdecha and Wongwises[25–29] presented an experimental investigation on the heat-transfer coefficient and pressure-drop characteristics of refrigerant R134a flowing through the corrugated tubes under evaporation and condensation processes. The dimensions of the corrugated tubes are shown in Table 3, while

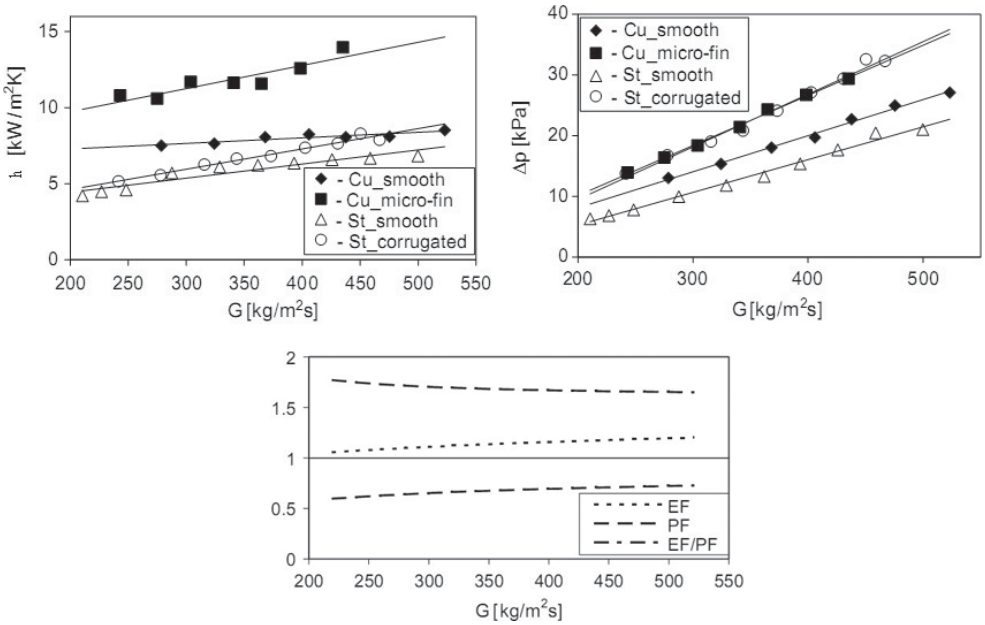

Fig. 5. Average heat transfer coefficient, pressure drop, enhancement factor and penalty factor versus mass flux for R407C.[22] [From Ref. 22, with permission from Elsevier.]

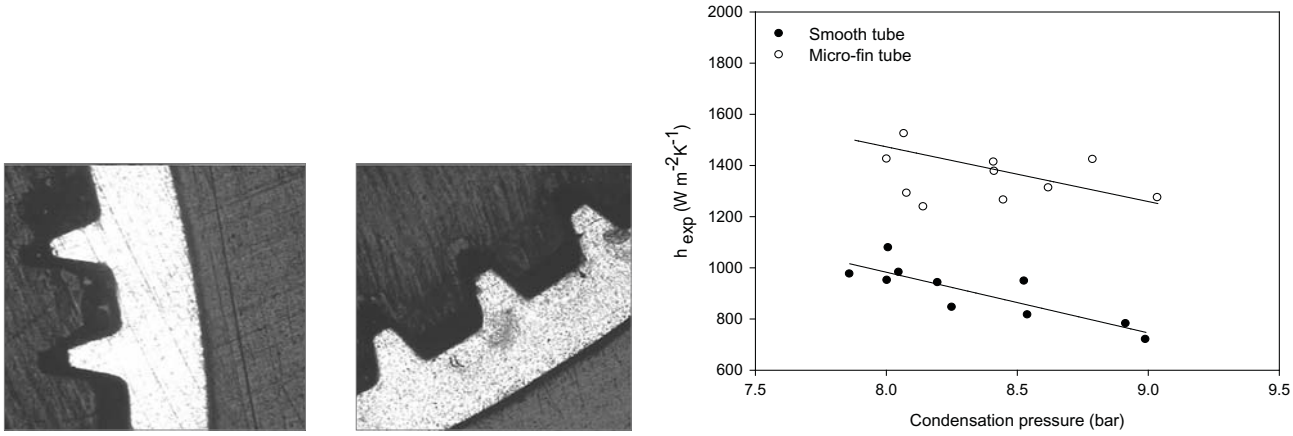

(a) (b)

Fig. 6. Cross-section of the micro-fin tube by electron microscope (100×) (a) and Comparison of average experimental convective heat transfer coefficients of the smooth and micro-fin tubes for the mass flux of 29 kg $m^{-2}s^{-1}$ at pressures of 0.77−0.90 MPa (b)[24] [From Ref. 24, with permission from Turk Isı Bilimi Teknigi Dernegi.]

Table 3. The dimensions of the corrugated tubes.[25−29] [From Refs. 25−27 and 29 with permission from Elsevier and Ref. 28, with permission from ASME.]

Number	p (mm)	e (mm)	β (degree)	β (degree)	D_i (mm)	L (mm)
1	5.08	1	79.47	79.47	8.7	2000
2	5.08	1.25	79.47	79.47	8.7	2000
3	5.08	1.5	79.47	79.47	8.7	2000
4	8.46	1.5	74.20	74.20	8.7	2000
5	6.35	1.5	76.56	76.56	8.7	2000

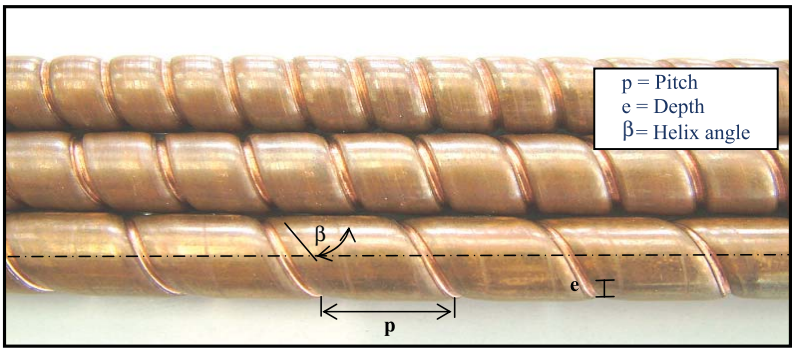

Fig. 7. The photograph of the corrugated tubes.[25–29] [From Refs. 25–29, with permission from Elsevier (color online).]

the photograph of corrugated tubes is displayed in Fig. 7. The tube-in-tube heat exchanger was used as the test section, in which R134a flows inside the corrugated tube and water flows in the annulus. The experimental results demonstrated that the corrugated tube gave higher heat-transfer performance and pressure drop than those of the smooth tube, by about 50% and 70%, respectively. The effect of pitch and depth on the heat-transfer performance and friction characteristics were reported and then compared with the common smooth tube, as illustrated in Fig. 8. Moreover, the new heat transfer and two-phase friction factor correlations were proposed for predicting the Nusselt number and two-phase friction factor for corrugated tubes. Moreover, the two-phase heat transfer coefficient and friction factor correlations were also proposed based on the measured data of R134a flowing through the corrugated tubes under evaporation process.

Aroonrat and Wongwises[30] studied the heat-transfer and friction characteristics of the pure refrigerant HFC-134a during evaporation inside a vertical corrugated tube, experimentally. The double-tube test sections were 0.5 m long with refrigerant flowing in the inner tube and hot water flowing in the annulus. The inner tubes were one smooth tube and two corrugated tubes, which were constructed from smooth copper tube with 8.7 mm inner diameter. The test runs were performed at evaporating temperatures of 10°C, 15°C, and 20°C, heat fluxes of 20, 25, and 30 $kW \cdot m^{-2}$, and mass fluxes of 200, 300, and 400 $kg \cdot m^{-2} \cdot s$. The effects of heat flux, mass flux, and evaporation temperature on the heat-transfer coefficient and two-phase friction factor were also discussed. It was found that the percentage increases of the heat-transfer coefficient and the two-phase friction factor of the corrugated tubes compared with those of the smooth tube are approximately zero to 10% and 70% to 140%, respectively.

Khoeiki *et al.*[31] studied the effect of inclination angle on the heat transfer performance of R134a flows inside a corrugated tube under condensation condition. Inclination angle ranging between −90° and 90°, mass flux varied from 87 to 253 kg/m^2s were tested. The experimental data illustrated that the inclination angle of the test section had a significant effect on the condensation heat transfer coefficient. The highest condensation heat transfer coefficient was obtained at inclination of 30° which was about 140% larger than that at the inclination of −90°. Moreover, a new empirical correlation of the heat-transfer coefficient of R134a flowing inside the corrugated tube with different inclination angles was proposed.

Rainieri *et al.*[32] presented an experimental investigation on the convective heat transfer performance of coiled corrugated tubes for highly viscous fluids such as glycerol and ethylene glycol. The test tube with diameter of 14 mm, curvature ratio of 0.06, corrugation depth of 1 mm, and pitch of 16 mm was used as the test section. The results indicated that the wall curvature could increase the heat transfer performance. Moreover, the wall corrugation had significant effect on the heat transfer performance for only the higher Reynolds number (150–1500).

Garcia *et al.*[33] reported the artificial roughness shape affecting the heat transfer enhancement of corrugated tubes, dimpled tubes and wire coils. The experimental data from their previous works for heat transfer and pressure drop in laminar, transition and turbulent flow regimes were used to compare with the analytical results. The results showed

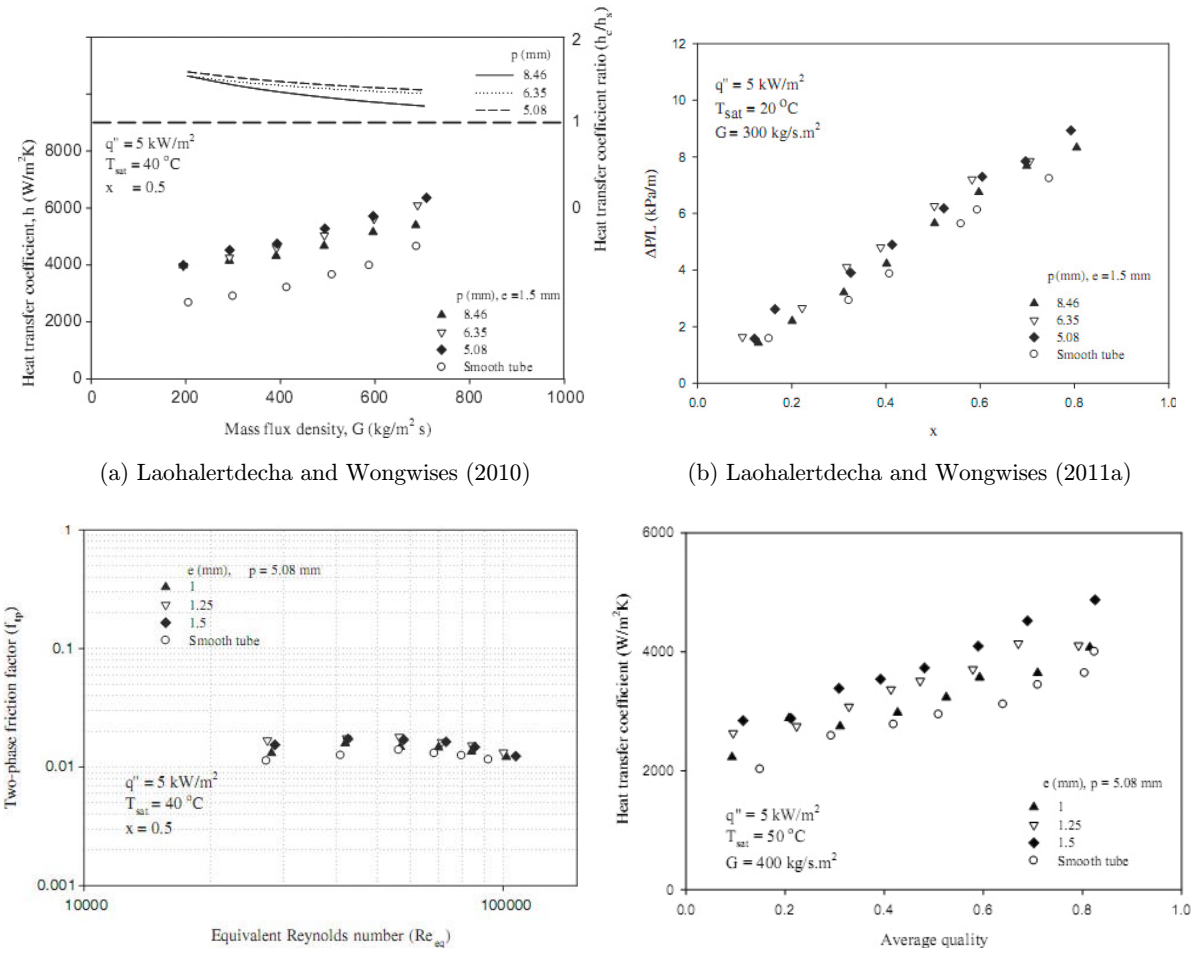

(a) Laohalertdecha and Wongwises (2010)

(b) Laohalertdecha and Wongwises (2011a)

(c) Laohalertdecha and Wongwises (2011b)

(d) Laohalertdecha and Wongwises (2011c)

Fig. 8. The effects of pitch and depth on heat transfer and flow characteristics. [From Refs. 25–28, with permission from Elsevier and ASME.]

that the shape of the artificial roughness had larger effect on the pressure drop than the heat transfer performance. Moreover, they also recommended that the smooth tube should be used for Reynolds number less than 200, wire coil for Reynolds number ranging between 200 and 2000. For Reynolds number larger than 2000, the employment of corrugated and dimpled tubes gave an advantage over the wire coils.

As mentioned above, it is clearly seen that numerous papers are currently available on the single-phase behavior, both experimentally and quantitatively. There are only a few research works that attempt to study the heat-transfer and flow characteristics of the refrigerant two-phase flow. Thus, the research works with respect to the thermal performance and flow characteristics of the refrigerant two-phase flow flowing through fluted tubes with different configurations are required in order to address their performance.

3. Ribbed Tubes

The schematic diagram of an internally finned or ribbed tube is shown in Fig. 9. In an internally finned or ribbed tube, it is difficult to geometrically identify a difference between fin and rib. Normally, both names are assumed to refer to the same geometry. The internal fin or rib geometry is defined by the fin height, the mean fin thickness, pitch of the fin and the apex angle, and the helix angle of the fin. Publications on the heat-transfer and flow characteristics of fluid flow in ribbed tubes are summarized as follows.

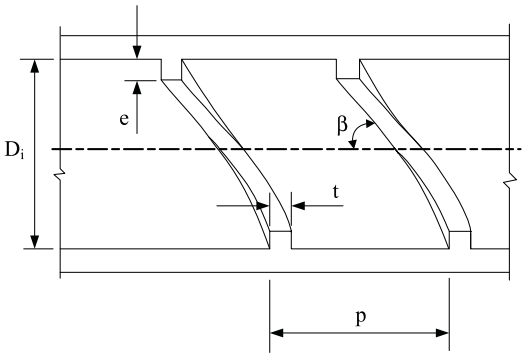

Fig. 9. Schematic diagram of the ribbed tube.

Morris and Rahmat-Asadi[34] conducted an experimental study to investigate the forced convection heat transfer in rotating ribbed tubes. The effect of internal ribs and orthogonal mode rotation on heat transfer was presented. The dimensions of the ribbed tubes are shown in Table 4. Typical three-rib geometries used in turbine rotor blade cooling channels were used as the test tubes. Their experimental data indicated that rotating ribbed tubes increase the heat-transfer performance compared with a common smooth tube as shown in Fig. 10. This behavior is due to the rotation Coriolis-induced secondary flows, which led to the increase in heat-transfer performance on the trailing edge of the tube compared with the leading edge. Finally, the effects of centripetal buoyancy and Coriolis forces were investigated.

Ravigururajan and Bergles[35] use generalized ribbed tube correlations to optimize the thermal performance of heat exchangers based on performance evaluation criteria (PEC). At a given pumping power and surface area, the maximum heat transfer was considered. Similarly, the minimum surface area was taken into account for the case of constant heat load and pumping power. The PEC with their relayed constraint equations were calculated by using a simple iterative procedure. Their simulation results indicated that the Reynolds number and

Table 4. The dimensions of the ribbed tubes.[34] [From Ref. 34, with permission from Elsevier.]

Number	p (mm)	e (mm)	D_i (mm)	L (mm)
1	20	2	10	130
2	15	1.5	10	130
3	10	1	10	130

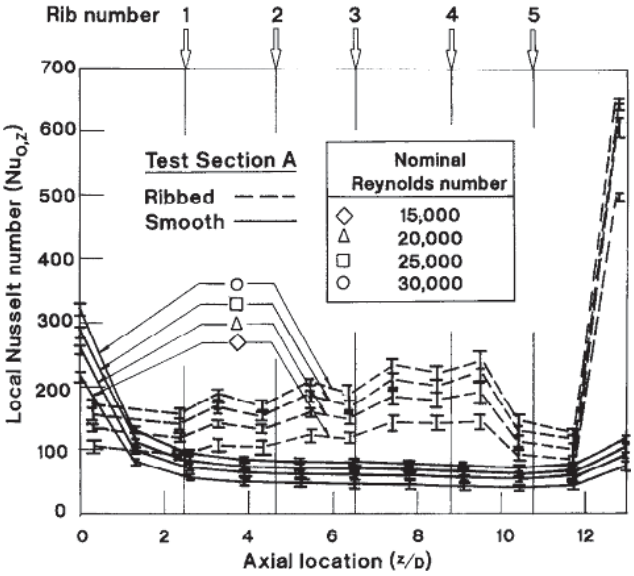

Fig. 10. The effect of ribs on measured local Nusselt number distribution.[34] [From Ref. 34, with permission from Elsevier.]

Prandtl number had a tiny effect on the heat-transfer enhancement. On the contrary, the use of the ribbed tubes can improve the thermal performance, which is useful for designing the enhanced heat exchangers.

Cho and Liu[36] presented an experimental study to investigate the possibility of the electronic anti-fouling (EAF) technique to control precipitation fouling in a spirally ribbed tube used in a common refrigerator. Two new tubes, one with the EAF treatment and another without EAF treatment, were used for testing the fouling tendency of the test tubes. Their measured data showed that the EAF technique could be used to control precipitation fouling that takes place in a spirally ribbed tube.

Chang and Su[37] experimentally investigated the heat-transfer performance of a reciprocating helical tube fitted with full circumferential ribs, which is commonly used in piston designs for a marine diesel engine. The effects of the Reynolds number, Dean number, pulsating number, buoyancy number, and five different reciprocating frequencies on the local heat transfer were tested. The results demonstrated that the presence of Dean vortices caused the increase in local heat-transfer coefficient on the outer surface, even with the agitated flow field caused by ribs under a reciprocating environment. Moreover, the pulsating force and reciprocating buoyancy had also significant effects on the heat-transfer coefficient due to the modified vortex flow

Table 5. The dimensions of the ribbed tubes.[38] [From Ref. 38, with permission from Elsevier.]

Number	p (mm)	e (mm)	D_i (mm)	L (mm)
1	9	0.4–0.6	11.69	1620

structures in the ribbed coils. Finally, an empirical correlation for predicting the heat transfer in the ribbed coils was proposed by considering the effect of pulsating force and reciprocating buoyancy force.

Cheng and Xia[38] presented the critical heat flux (CHF) for water flow in a conventional smooth tube and a four-head spiral internally ribbed tube, experimentally. The test tubes were located in the vertical direction and were heated by an electric power supply. The dimensions of the test tubes are shown in Table 5. The effects of mass flux and pressure on the CHF were investigated. The measured data demonstrated that the increase of wall temperature at which CHF occurs in the spirally internally ribbed tube is less than that of the smooth tube. For both the smooth tube and the spirally internally ribbed tube, fluid enthalpy decreases with the increase of pressure as shown in Fig. 11.

Li and Webb[39] presented long-term cooling tower water fouling data for seven helically ribbed tubes with inner diameter of 15.54 mm, experimentally. The effects of rib starts, helix angle, and height were determined. Based on internal dimensions, there are only two ranges of fouling characteristics, the linear range and nonlinear range. The experimental results showed that the ratio of the enhanced-to-plain tube fouling resistance rose with increases in the product of area indexes and efficiency indexes in the linear range, and the linear relationship fell in a nonlinear range. In addition, the semi-theoretical fouling correlations as a function of the product of area indexes and efficiency indexes and the linear multiple regression correlations as a function of geometric variables and Reynolds number were proposed. These correlations could be used to evaluate the fouling potential of enhanced tubes in actual cooling water situations.

Kim *et al.*[40] experimentally investigated the CHF for flow boiling of R-134a flowing through rifled tubes with four heads and six heads in vertical direction. The test section was shown in Fig. 12. The results were then compared with the data for smooth tube and calculated values from Bowing and Katto correlations. The inner diameters of both the rifled tube and the smooth tube were 17.04 mm. The experimental test runs were conducted at outlet pressure ranging from 13 to 23.9 bar, mass flux ranging from 285 to 1300 $\mathrm{kg \cdot m^{-2} \cdot s}$, and inlet subcooling temperature of five to 40°C. The experimental data showed that the CHF in the rifled tube was approximately 40% to 60% greater than that of the smooth tube and rose with increasing mass flux as well as outlet pressure as shown in Fig. 13.

Naphon and co-workers[41] reported the heat-transfer and pressure-drop characteristics of helical rib tubes, experimentally. The double-tube counter flow heat exchanger was used as the test section, in which hot water flowed inside the test tube and cold water flowed in the annulus. The effects of helical rib height and helical rib pitch were presented. Their results indicated that the heat-transfer coefficient

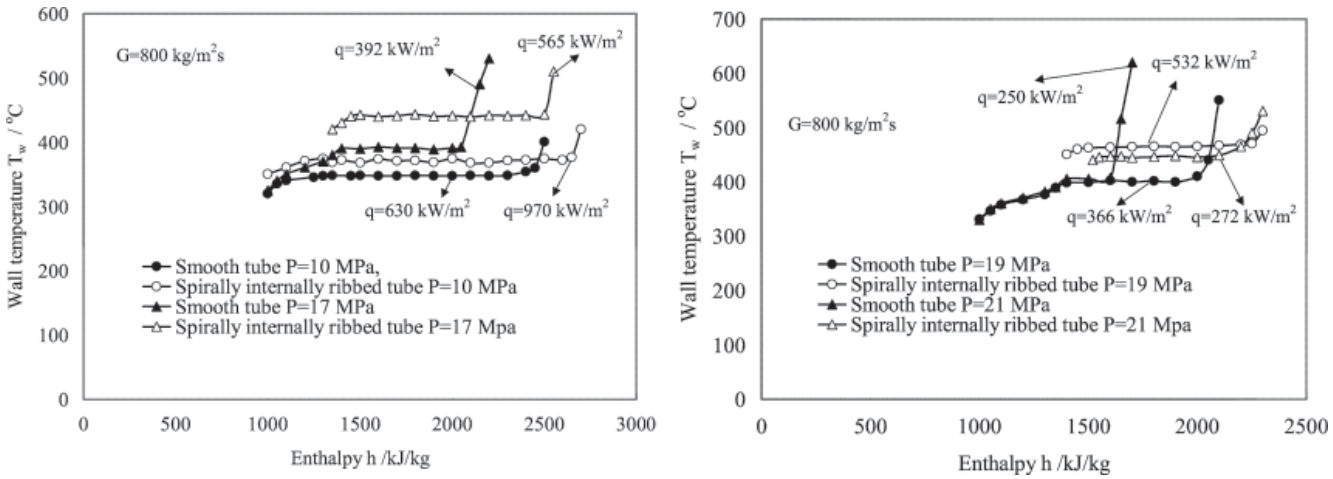

Fig. 11. Variation of wall temperatures with enthalpy.[38] [From Ref. 38, with permission from Elsevier.]

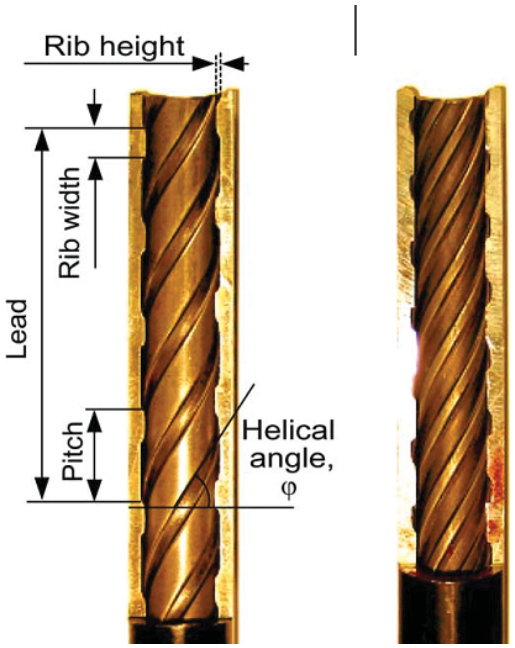

Fig. 12. Cross sectional view of rifled tubes and geometric parameters.[40] [From Ref. 40, with permission from Elsevier (color online).]

and pressure of helical rib tube were significantly higher than that of the smooth tube approximately 10% to 70% and 10% to 280%, respectively. The heat-transfer coefficient rose with increases in the Reynolds number and the helical rib depth, and also rose with decreases in the helical rib pitches. Similarly, the friction factor of the helical ribbed tube rose with an increase in helical rib depth and decreased with increases in the Reynolds number and helical rib pitch. Moreover, they also proposed the heat transfer and friction factor correlation for predicting the Nusselt number and friction characteristics of the helical ribbed tube as a function of helical rib dept and helical rib pitch. The proposed correlations gave good agreement between measured data and calculated values, and the majority of the data fell within $\pm 15\%$ of the proposed equations.

Recently, Ji *et al.*[42] presented an experimental investigation on the heat transfer and friction factor of 16 internal helically ribbed tubes with different geometrical parameters under turbulent flow regime. Reynolds number ranged from 10,000 to 100,000 and Prandtl number varied between 4.98 and 8.22 were tested. A correlation for predicting the average heat transfer coefficient of the ribbed tubes was proposed based on the Gnielinski correlation by replacing the friction factor with the measured friction factor of the internally ribbed tubes. The results indicated that the proposed equation was very appropriate for practical engineering design and gave vary good accuracy.

Similar to the corrugated tubes, a number of researchers reported on the heat-transfer and flow features of ribbed tubes with single-phase flow of

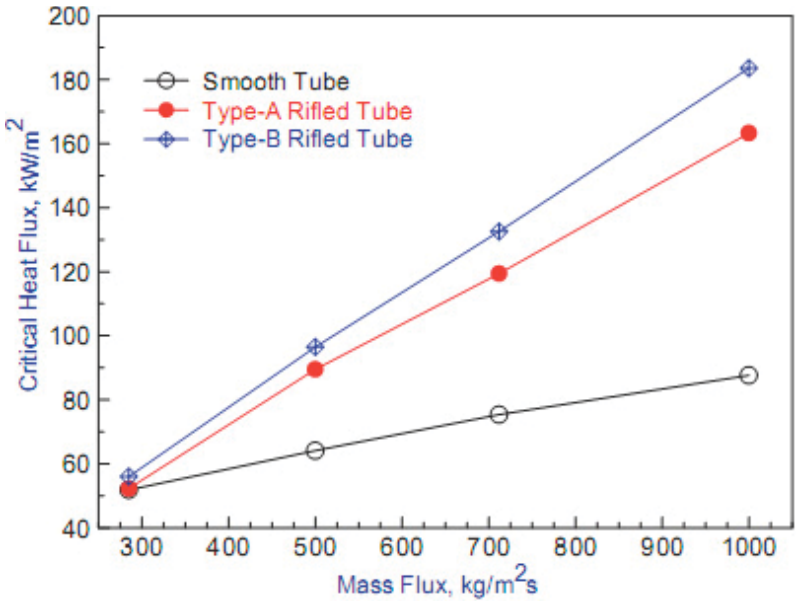

Fig. 13. CHF versus mass flux for one smooth tube and two rifled tubes at 16.5 bar.[40] [From Ref. 40, with permission from Elsevier (color online).]

liquids, both experimentally and quantitatively. Therefore, the two-phase flow data are required to certify the heat transfer and flow characteristics of ribbed tubes.

4. Grooved Tubes

As shown in Fig. 14, internally grooved tubes having an internal surface including many grooves to increase the heat-transfer performance have been used in many applications. The internal surface of an internally grooved tube includes many ribs helically extending along the tube in an axial direction and a groove is formed between each adjacent pair of ribs. Publications on the heat-transfer and flow characteristics of single-phase flow in internally grooved tubes are summarized as follows.

Graham *et al.*[43] presented an experimental study on the heat-transfer and pressure-drop characteristics of R-134a flowing through an axially grooved tube during the condensation process. The measured data were compared with the data for a smooth tube and a common grooved tube with an 18° helix angle. A grooved tube with an inner diameter of 8.91 mm was used as the test section and tested at the mass flux range from 75 to 450 $\mathrm{kg \cdot m^{-2} \cdot s}$. At a mass flux of 75 $\mathrm{kg \cdot m^{-2} \cdot s}$, their results showed that the axially grooved tube gave higher heat-transfer performance than that of a smooth tube smaller than the common grooved tube with an 18° helix angle. In contrast, at a mass flux of 150 $\mathrm{kg \cdot m^{-2} \cdot s}$, the results indicated that the heat-transfer performance of axially grooved tubes was larger than those of both smooth tubes and helically ribbed tubes. For the pressure drop, their data showed that the pressure drops of axially grooved tubes agreed well with those of the helically ribbed tubes.

Herman and Kang[44] presented an experimental study on the unsteady temperature field in the grooved channel with curved vanes (GCV) using holographic interferometry. The heat-transfer performance of GCV was compared with the basic grooved channel (BGC). Their experimental data indicated that addition of the curved vane above the downstream end of the heated block gave higher heat-transfer performance than that of BGC by a factor of approximately 1.5 to 3.5 times. This behavior due to the GCV tube accelerated the flow between the curved vane and the heated block and the large recirculation region in the groove was eliminated. At the Reynolds number of 450, flow transition from steady to oscillatory regime took place. Moreover, their data also showed that the pressure drop for the GCV tube was three to five times greater than those of the BGC tube.

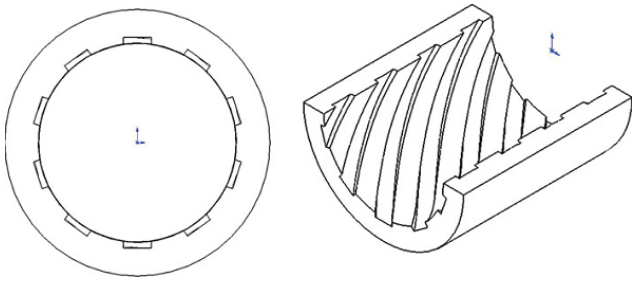

Fig. 14. Schematic diagram of the grooved tube.[51] [From Ref. 51, with permission from Springer.]

Goto *et al.*[45,46] investigated the local condensation and evaporation heat-transfer coefficient of R410A and R22 flow inside the five different kinds of internally grooved tubes placed in the horizontal direction. The test conditions were conducted at a refrigerant mass flow rate ranging from 130 to 400 $\mathrm{kg \cdot m^{-2} \cdot s}$ for both R410A and R22 and the vapor pressures of 2.41 MPa for R410A and 1.53 MPa for R22. The measured data indicated that the local heat-transfer coefficients of the herringbone grooved tube were two times larger than those of the helical tube for both R410A and R22. Moreover, they also proposed the new heat-transfer correlations for predicting the Nusselt number of R410A and R22 flowing in the helical micro-finned tube and herringbone micro-finned tube. Compared with the measured data, good correspondence between the experimental values and the calculated values by the proposed equations were obtained and the majority of the data fell within ± 20% of the proposed equation.

Zhang *et al.*[47] reported the evaporation heat-transfer characteristics of R417A flowing inside horizontal two internally grooved tubes with various geometrical parameters compared with common smooth tube and micro-finned tube correlations, experimentally. The experimental conditions used in their study were summarized as follows: mass flow rate ranged from 176 to 344 $\mathrm{kg \cdot m^{-2} \cdot s}$; heat flux ranged from 11 to 32 $\mathrm{kW \cdot m^{-2}}$; evaporation temperatures ranged from 0°C to 5.5°C; and vapor quality ranged from 0.2 to 1. The effects of the above parameters were presented. The results demonstrated that the evaporation heat-transfer coefficient of R417A was lower than that of the R22 and

significantly smaller in internally grooved tubes than the conventional smooth tube. This means that the heat-transfer enhancement was more effective for pure refrigerant than that for the non-azeotropic refrigerant mixtures. Compared with the calculated values from the existing correlations, the results indicated that the modified Kattan model gave better agreement with the measured data than the standard Kattan model. Moreover, the Koyama and Wellsandt model for micro-finned tubes overestimated the evaporation heat-transfer coefficient, especially for R417A.

Zhang *et al.*[48] presented an experimental investigation on the local heat-transfer coefficient of R417A flowing through internally grooved tubes during the evaporation process, experimentally. Two internally grooved tubes with different geometrical parameters were tested and then compared with the common smooth tube and the existing correlations. Their data showed that the existing micro-finned tube correlations could not be used to predict the local evaporation heat-transfer coefficient of the internally grooved tubes. They also proposed a new correlation based on the modified Kattan model for computing the heat-transfer coefficient of non-azeotropic refrigerant R417A. Compared with the measured data, a deviation of $\pm 30\%$ was obtained for vapor quality less than 0.8.

Bilen *et al.*[49] experimentally studied the heat-transfer and friction characteristics of air flowing inside internally grooved tubes with circular, trapezoidal and rectangular configurations under turbulent flow regime. The geometrical parameters of the grooved tubes are shown in Fig. 15. A Reynolds number ranging from 10,000 to 38,000 was tested. At the highest Reynolds number, the results indicated that the Nusselt number for internally grooved tubes was larger than that for a common smooth tube by about 47% for a rectangular groove, 58% for a trapezoidal groove, and 63% for a circular groove. Moreover, the thermal performance for all internally grooved tubes was shown to be higher than that of a smooth tube — approximately 1.24−1.28 times for a circular groove, 1.22−1.25 times for a trapezoidal groove, and 1.13−1.26 times for a rectangular groove. In addition, the friction factors of all grooved tubes were nearly the same, and the friction factor was independent of the Reynolds number for grooved tubes as shown in Fig. 16.

Bharadwaj *et al.*[50] presented an experimental study on the heat-transfer and pressure-drop characteristics of water flowing through a 75-start spirally grooved tube with twisted tape insert under laminar and turbulent flow regimes. Their results showed that the Nusselt number of the spirally grooved tube without twisted tape insert was 400% and 140% higher than that of a smooth tube for laminar and turbulent flow regime, respectively. Similarly, for the spirally grooved tube with twisted tape insert, maximum heat-transfer enhancements of 600% and 140% were obtained for laminar and

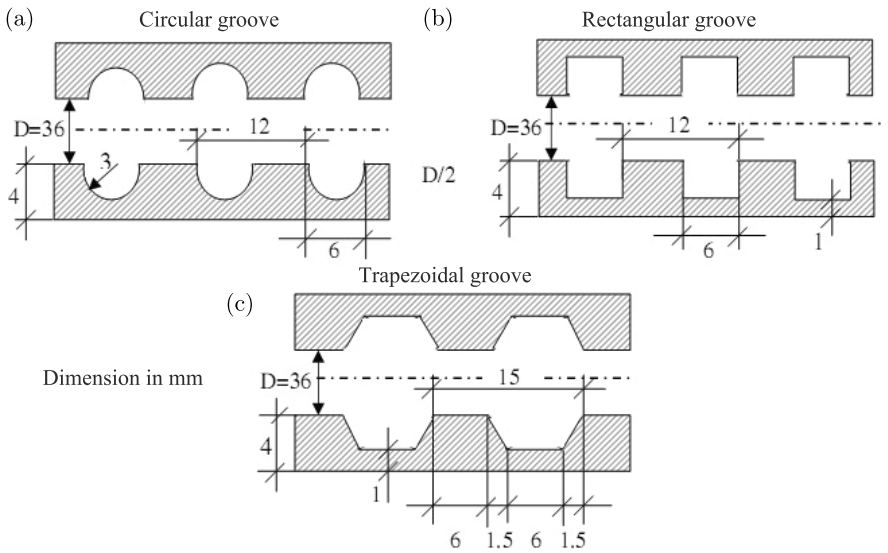

Fig. 15. The geometric shapes of the grooved tubes.[49] [From Ref. 49, with permission from Elsevier.]

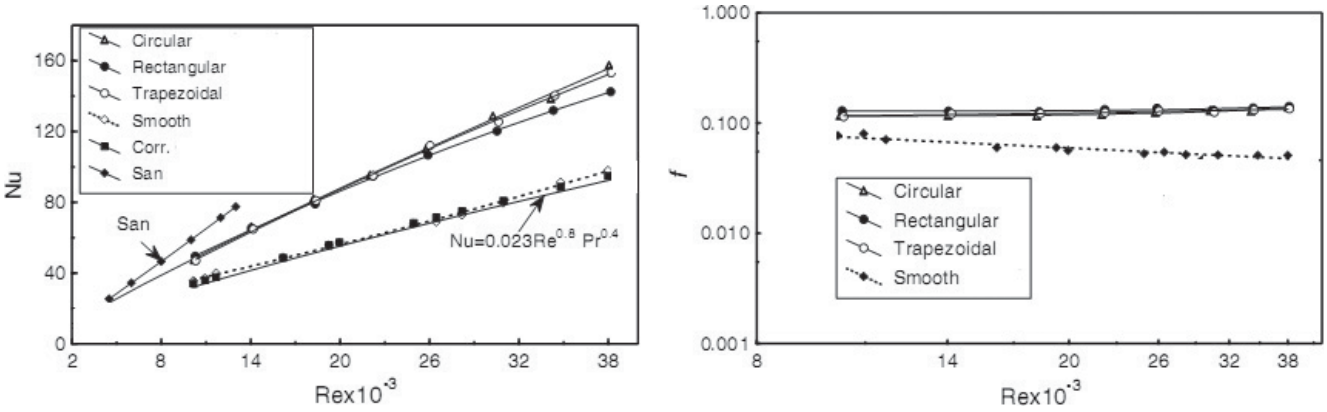

Fig. 16. Variation of the Nusselt number and friction factor with the Reynolds number.[49] [From Ref. 49, with permission from Elsevier (color online).]

turbulent flow regime, respectively. Moreover, the pressure drop of internally grooved tubes was larger than that of the smooth conventional smooth tube.

Wongwises *et al.*[51] reported the evaporation heat-transfer coefficient and pressure drop of R-134a flowing inside internally grooved tubes, experimentally. Four grooved tubes with different configurations made from stainless steel were tested under a condition of constant heat flux. The effects of groove pitch, mass flux, heat flux, and saturation temperature on heat-transfer coefficient and frictional pressure drop were presented. The measured data showed that the grooved tubes gave higher heat-transfer coefficient and frictional pressure drop than those of the common smooth tube.

As mentioned above, many researchers have been focused on the heat-transfer and friction characteristics of two-phase refrigerants flowing through horizontal internally grooved tubes under both evaporation and condensation processes. However, heat-transfer and pressure-drop characteristics of internally grooved tubes in other directions should be studied.

5. Fluted Tubes

From the configuration of the fluted tube, it is evident that they are quite similar to the corrugated tubes. However, from the point view of the authors, there are small differences between the two enhanced tubes. If the ratio of corrugation to cross-sectional area is greater than one, it is a fluted tube; however, if this ratio is less than one, it is a corrugated tube. The published articles describe the heat-transfer enhancements of the fluted tubes as follows.

Aly and Bedrose[52] introduced a theoretical study of heat-transfer performance of stagnant water vapor condensed on both vertical and horizontal spirally fluted tubes. In this study, two regions of fluted tubes, namely the valley and the crest, were separately considered; the condensation process was started on the flute crest and then ran down to the valley by gravity and surface tension. The motion equation and energy balance equation were taken into account to examine the relationships between condensate flow rate and film thickness. Their simulation results indicated that the spirally fluted tube gave five times higher heat-transfer performance than a smooth tube in the case of horizontal direction and about three times higher in the case of vertical direction. Moreover, the calculated Nusselt number from the proposed model coincided well with the experimental results for integral finned tubes and the majority of the data fell within $\pm 20\%$ of the proposed model. Similarly, for vertical tubes, an agreement between the predicted value and the measured data can be seen and the majority of the data fell within $\pm 5\%$ of the proposed model.

Kang *et al.*[53] presented an experimental system to formulate the new flooding correlations for both vertical and horizontal directions as a function of declination angle for a fluted tube with a twisted insert. Figure 17 depicts the sketch of the fluted tube and geometrical parameters. In their study, twisted tubes made from plastic were inserted inside the fluted tube to accelerate the absorption rate in counter-current absorption. Water−ethyl alcohol solution flows downward in the fluted tube, whereas air flows counter-current in an upward direction. For the inclination angle less than 60°, the results

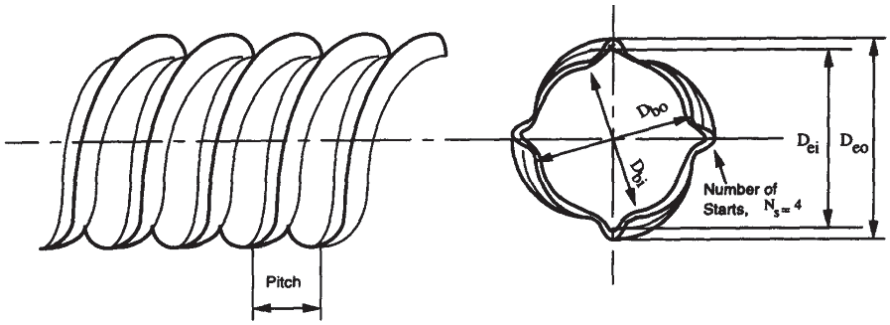

Fig. 17. Schematic diagram of the fluted tube.[53] [From Ref. 53, with permission from Elsevier.]

indicated that flooding was created from the top of the tube. On the contrary, it was initiated from the bottom of the tube for an inclination angle greater than 60°. The position of the twisted insert had no significant effect on the flooding mechanism in the case of a horizontal tube, whereas it had a small effect in the case of a vertical tube. Moreover, for the fluted tube with a twisted insert, the results indicated that the flooding vapor velocity reached a maximum for the inclination angle between 40° and 60° and superficial liquid velocities less than $0.01178\,\mathrm{m}\cdot\mathrm{s}^{-1}$. However, in the case of superficial liquid velocities greater than $0.01178\,\mathrm{m}\cdot\mathrm{s}^{-1}$, the superficial flooding vapor velocity increased with the inclination angle.

Wang and colleagues[54] reported experimental results that illustrated the heat-transfer performance of carbon-steel spirally fluted tubes replacing the conventional copper smooth tubes that corrode easily due to the feed water of boiler. The dimensions of the fluted tubes are shown in Table 6. Compared with the common carbon-steel smooth tube, the experimental results showed that the heat-transfer coefficient of the carbon-steel spirally fluted tube was 10% to 17% higher than that of the smooth tube and it was very close to that of the copper smooth tubes, as shown in Fig. 18.

Qi *et al.*[55] presented an experimental study that evaluated the drag reduction and heat-transfer

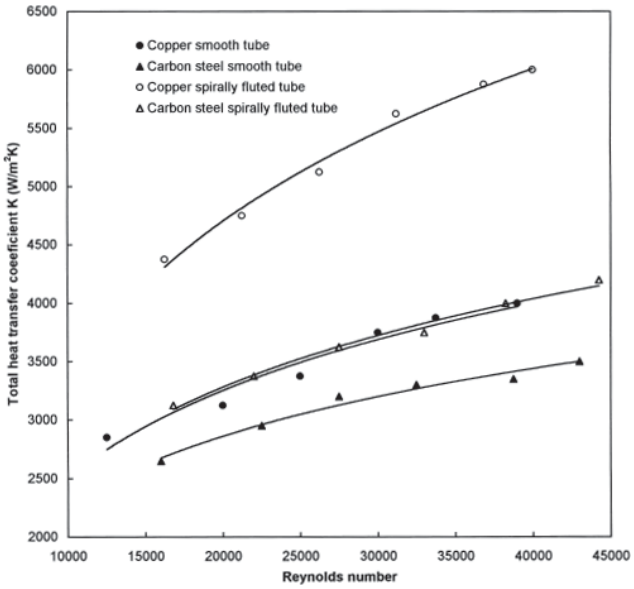

Fig. 18. Heat transfer coefficient versus Reynolds number.[54] [From Ref. 54, with permission from Elsevier.]

enhancement of a fluted tube. Tube-in-tube heat exchanger was used as the test section for cationic surfactant solution Ethoquad T13-50/NaSal (5 mM/8.75 mM) and zwitterionic/anionic reduction surfactant solution SPE98330 (1500 ppm). The results indicated that use of the fluted inner tube increased the heat-transfer coefficient for both surfactant solutions. Moreover, cationic surfactant solution

Table 6. The dimensions of the fluted tubes.[54] [From Ref. 54, with permission from Elsevier.]

Number	Tube description	e (mm)	p (mm)	D_o (mm)	D_i (mm)	β (degree)	L (mm)
1	Copper (Smooth)	—	—	16	13	—	650
2	Carbon steel (Smooth)	—	—	16	13	—	650
3	Copper (Fluted)	0.25	15.6	16	13	40	650
4	Carbon steel (Fluted)	0.25	15.6	16	13	40	650

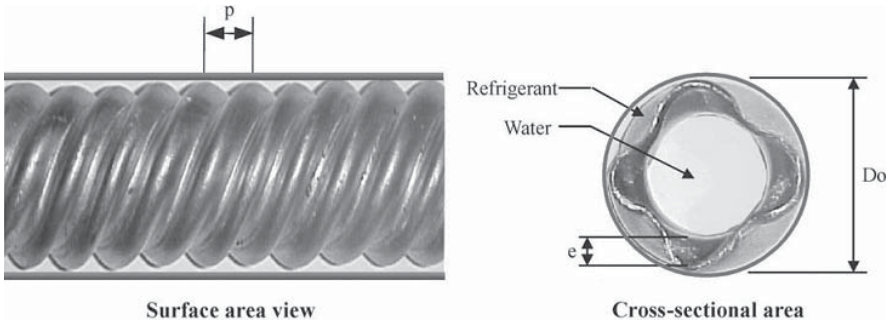

Fig. 19. Photograph of the fluted tube.[56] [From Ref. 56, with permission from Elsevier.]

gave a higher pressure-drop penalty than the zwitterionic/anionic solution.

Rousseau and co-workers[56] presented a mathematical formulation and numerical method to investigate the heat-transfer and pressure-drop characteristics of fluted-tube refrigerant-to-water condensers. Figure 19 shows the photo of the fluted tube. In this model, the surface area was divided into three regions: superheated, two-phase, and subcooled regions, in which all properties of refrigerant and water can be calculated. The proposed model was formulated based on the effectiveness-NTU method. For the water side, the existing empirical correlations for friction factor and heat-transfer coefficient were used. Unfortunately, for the refrigerant side, they reported that there are no available correlations for calculating the friction factor and heat-transfer coefficient of the fluted tube-in-tube condenser. Thus, the existing correlations for smooth tubes, combined with an enhancement ratio based on available correlations for helical coils, as well as an enhancement factor based on empirical data for fluted tube condenser were employed. Data for two commercial fluted tube heat exchangers were used to validate the proposed model. The average difference between the measured and the predicted pressure drop was about 7.27%. Similarly, the difference in the log mean temperature was roughly 4.41%.

As mentioned above, for the fluted tube, a number of researches studied the single-phase heat transfer and flow behaviors for conventional heat transfer fluids. The heat-transfer and pressure-drop characteristics for two-phase flow of refrigerants in the fluted tubes are required for practical applications.

6. Vipertubes

Vipertube is a new type of enhanced tube which produced by Vipertex^{TM} company under ASTM standard. The configuration of the Vipertubes is shown in Fig. 20. Kukulka *et al.*[57] was the first research group who presented the heat-transfer enhancement and fouling characteristics of a series of the Vipertubes. These tubes were made from stainless steel tube (Type 304L) with outer diameter of 1.905 cm and length of 0.9144 m. From their experiment with water, the measured data illustrated that the enhancement ratio of the Vipertubes was

Fig. 20. Photograph of the Vipertube.[57] [From Ref. 57, with permission from Elsevier (color online).]

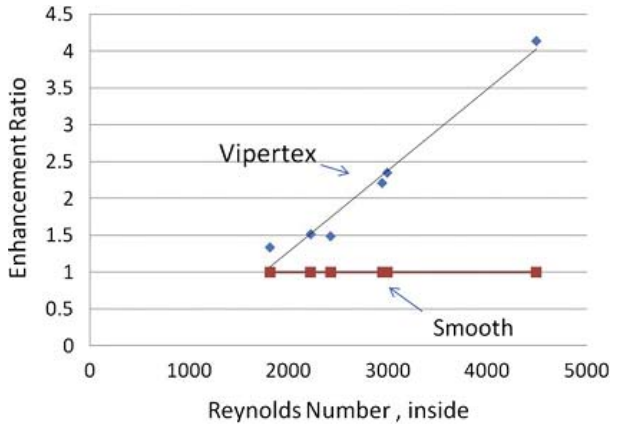

Fig. 21. Heat transfer enhancement ratio versus Reynolds number.[57] [From Ref. 57, with permission from Elsevier (color online).]

varied between 1 and 4, for Reynolds number ranging from 2000 to 5000. This enhancement is due to several factors such as increasing of fluid turbulence, secondary flow, disturbing of the thermal boundary layer and increasing of the heat transfer area. Moreover, the Vipertubes was designed to minimize the effect of fouling. Some results were shown in Fig. 21.

7. Conclusions

As discussed, different types of the enhanced tubes (corrugated tube, ribbed tube, grooved tube and fluted tube) have great potential for heat-transfer enhancement and are highly suited to applications in practical heat-transfer processes. This offers an opportunity for engineers to develop highly compact and effective heat-transfer equipment. Several published articles show that the heat-transfer coefficients of the enhanced tubes are much higher than the conventional smooth tubes and give only marginal drops in pressure. An important reason for the heat-transfer enhancement of the enhanced tubes is the modified rough surface, which causes increases in the turbulence mixing intensity in the flow field, and also by limiting the growth of fluid boundary layers close to the heat transfer surfaces, which leads to increases in heat-transfer performance. Moreover, from the review of the published literature, many researchers reported the heat-transfer performance and pressure-drop characteristics of the enhanced tubes working with single-phase fluids. Only some researchers reported on the use of two-phase flow refrigerants as working fluids for both evaporation and condensation processes. Many researchers suggested that the enhanced tubes have higher potential for replacing the conventional smooth tubes normally used in heat-transfer equipment. This is a great opportunity for researchers to discover new ways for increasing the heat-transfer performance of the enhanced tubes in order to meet high compactness and high heat flux of the heat exchangers. Moreover, new types of enhanced tubes such as Vipertube should be investigated in order to meet highest heat transfer performance and lowest. This is a challenge task of researchers and heat exchanger manufacturer.

Acknowledgments

The authors would like to express their appreciation to the Thailand Research Fund, the Office of the Higher Education Commission and the National Research University Project for providing financial support. Especially, the second author wishes to thank KMUTT for providing him with a Post-doctoral fellowship.

References

1. A. S. Dalkilic and S. Wongwises, Intensive literature review of condensation inside smooth and enhanced tubes, *Int. J. Heat Mass Transfer* **52** (2009) 3409−3426.
2. K. Mimura and A. Isozaki, Heat transfer and pressure drop of corrugated tubes, *Desalination* **22** (2001) 131−139.
3. S. Ganeshan and M. R. Rao, Studies on themohydraulics of single and multi-start spirally corrugated tubes for water and time independent power law fluids, *Int. J. Heat Mass Transfer* **25** (1982) 1013−1022.
4. P. P. Thien and M. M. K. Khan, Flow of an Oldroyd-type fluid through a sinusoidally corrugated tube, *J. Non-Newtonian Fluid Mech.* **24** (1987) 203−220.
5. Y. Asako, H. Nakamura and M. Faghri, Heat transfer and pressure drop characteristics in a corrugated duct with rounded corners, *Int. J. Heat Mass Transfer* **31** (1988) 1237−1245.
6. H. Honda, S. Nozu, Y. Matsuoka, T. Aoyama and H. Nakata, Condensation of R-11 and R-113 in the annuli of horizontal double-tube condensers with an enhanced inner tube, *Exp. Ther. Fluid Sci.* **2** (1989) 173−182.

7. S. R. Burdette, P. J. Coates, R. C. Armstrong and R. A. Brown, Calculations of viscoelastic flow through an axisymmetric corrugated tube using the explicitly elliptic momentum equation formulation (EEME), *J. Non-Newtonian Fluid Mech.* **33** (1989) 1−23.
8. V. Zimparov, N. L. Vulchanov and L. B. Delov, Heat transfer and friction characteristics of spirally corrugated tubes for power plant condensers-1. Experimental investigation and performance evaluation, *Int. J. Heat Mass Transfer* **34** (1991a) 2187−2197.
9. V. Zimparov, N. L. Vulchanov and L. B. Delov, Heat transfer and friction characteristics of spirally corrugated tubes for power plant condensers-2. A mixing-length model for predicting fluid friction and heat transfer, *Int. J. Heat Mass Transfer* **34** (1991b) 2199−2206.
10. N. P. Gopalan and R. Ponnalagasamy, Investigation on laminar flow of a suspension in corrugated straight tubes, *Int. J. Eng. Sci.* **30** (1992) 631−644.
11. D. L. Hinton and J. C. Conklin, Condensation of refrigerants flowing inside smooth and corrugated tubes, *Fourth ASME/JSME Thermal Engineering Joint Conference*, Hawaii, March 1995, pp. 19−24.
12. X. D. Chen, S. K. Nguang and A. E. Bergles, Characterization of the effect of corrugation angles on hydrodynamic and heat transfer performance of four-start spiral tubes, *J. Heat Transfer* **123** (2001) 1149−1158.
13. Y. Dong, L. Huixiong and C. Tingkuan, Pressure drop, heat transfer and performance of single phase turbulent flow in spirally corrugated tubes, *Exp. Therm. Fluid Sci.* **24** (2001) 131−138.
14. V. Zimparov, Enhancement of heat transfer by a combination of three-start spirally corrugated tubes with a twisted tape, *Int. J. Heat Mass Transfer* **44** (2001) 551−574.
15. V. Zimparov, Enhancement of heat transfer by a combination of single-start spirally corrugated tubes with a twisted tape, *Exp. Therm. Fluid Sci.* **25** (2002) 535−546.
16. S. Rainieri and G. Pagliarini, Convective heat transfer to temperature dependent property fluids in the entry region of corrugated tubes, *Int. J. Heat Mass Transfer* **45** (2002) 4525−4536.
17. A. Barba, S. Rainieri and M. Spica, Heat transfer enhancement in a corrugated tube, *Int. Comm. Heat Mass Transfer* **29** (2002) 313−322.
18. P. G. Vicente, A. Garcia and A. Viedma, Mixed convection heat transfer and isothermal pressure drop in corrugated tubes for laminar and transition flow, *Int. Comm. Heat Mass Transfer* **31** (2004a) 651−662.
19. V. Zimparov, Prediction of friction factor and heat transfer coefficients for turbulent flow in corrugated tubes combined with twisted tape inserts. Part 1: Friction factor, *Int. J. Heat Mass Transfer* **47** (2004) 589−599.
20. V. Zimparov, Prediction of friction factor and heat transfer coefficients for turbulent flow in corrugated tubes combined with twisted tape inserts. Part 2: Heat transfer coefficients, *Int. J. Heat Mass Transfer* **47** (2004) 385−393.
21. A. E. Bergles, R. A. Lee and B. B. Mikic, Heat transfer in rough tubes with twisted tape swirl flow, *Trans. ASME, J. Heat Transfer* **91** (1969) 443−445.
22. W. Targanski and J. T. Cieslinski, Evaporation of R407C/Oil mixtures inside corrugated and micro-fin tubes, *Appl. Therm. Eng.* **27** (2007) 2226−2232.
23. S. Rozzi, R. Massini, G. Paciello, G. Pagliarini, S. Raineiri and A. Trifiro, Heat treatment of fluid foods in a shell and tube heat exchanger: Comparison between smooth and helically corrugated wall tubes, *J. Food Eng.* **79** (2007) 249−254.
24. A. S. Dalkiliç, İ. Teke, S. Wongwises, Heat transfer enhancement during downward laminar flow condensation of R134a in vertical smooth and micro-fin tubes, *Isi Bilimi Ve Teknigi Dergisi/Journal of Thermal Science and Technology* **32** (2012) 19v31.
25. S. Laohalertdecha and S. Wongwises, The effects of corrugation pitch on the condensation heat transfer coefficient and pressure drop of R-134a inside horizontal corrugated tube, *Int. J. Heat Mass Transfer* **53** (2010) 2924−2931.
26. S. Laohalertdecha and S. Wongwises, An experimental study into the evaporation heat transfer and flow characteristics of R-134a refrigerant flowing through corrugated tubes, *Int. J. Ref.* **34** (2011a) 280−291.
27. S. Laohalertdecha and S. Wongwises, Condensation heat transfer and flow characteristics of R-134a flowing through corrugated tubes, *Int. J. Heat Mass Transfer* **54** (2011b) 2673−2682.
28. S. Laohalertdecha and S. Wongwises, Effects of pitch and depth on the condensation heat transfer of R-134a flowing through corrugated tubes, *Proc. ASME/JSME 2011 8th Therm. Eng. Con.*, Hawaii, USA (2011c).
29. S. Laohalertdecha, A. S. Dalkilic and S. Wongwises, Correlations for evaporation heat transfer coefficient and two-phase friction factor for R-134a flowing through horizontal corrugated tubes, *Int. J. Heat Mass Transfer* **38** (2011d) 1406−1413.
30. K. Aroonrat and S. Wongwises, Evaporation heat transfer and friction characteristics of R-134a flowing downward in a vertical corrugated tube, *Exp. Therm. Fluid Sci.* **35** (2011) 20−28.
31. D. Khoeiki, M. A. Akhavan-Behabadi and A. Saboonchi, Experimental study on condensation heat transfer of R-134a flow in corrugated tubes with

different inclinations, *Int. Comm. Heat Mass Transfer* **39** (2012) 138−143.
32. S. Rainieri, F. Bozzoli and G. Pagliarini, Experimental investigation on the convective heat transfer in straight and coiled corrugated tubes for highly viscous fluids: Preliminary results, *Int. J. Heat Mass Transfer* **55** (2012) 498−504.
33. A. Garcia, J. P. Solano, P. G. Vicente and A. Viedma, The influence of artificial roughness shape on heat transfer enhancement: Corrugated tubes, dimpled tubes and wire coils, *App. Therm. Eng.* **35** (2012) 196−201.
34. W. D. Morris and W. F. Rahmat-Asadi, Convective heat transfer in rotating ribbed tubes, *Int. J. Heat Mass Transfer* **39** (1996) 2253−2266.
35. T. S. Ravigururajan and A. E. Bergles, Optimization of fin-tube enhancement for large evaporation and condensers, *Energy* **39** (1996) 421−432.
36. Y. I. Cho and R. Liu, Control of fouling in a spirally-ribbed water chilled tube with electronic anti-fouling technology, *Int. J. Heat Mass Transfer* **42** (1999) 3037−3046.
37. S. W. Chang and L. M. Su, Heat transfer of reciprocating helical tube fitted with full circumferential ribs, *Int. J. Heat Mass Transfer* **44** (2001) 3025−3042.
38. L. Cheng and G. Xia, Experimental study of CHF in a vertical spirally internally ribbed tube under the condition of high pressures, *Int. J. Therm. Sci.* **41** (2002) 396−400.
39. W. Li and R. L. Webb, Fouling characteristics of internal helical-rib roughness tubes using low-velocity cooling tower water, *Int. J. Therm. Sci.* **45** (2002) 1685−1691.
40. C. H. Kim, I. C. Bang and S. H. Chang, Critical heat flux performance for flow boiling of R-134a in vertical uniformly heated smooth tube and rifled tubes, *Int. J. Heat Mass Transfer* **48** (2005) 2868−2877.
41. P. Naphon, M. Nuchjapo and J. Kurujareon, Tube side heat transfer coefficient and friction factor characteristics of horizontal tubes with helical rib, *Energ. Convers. Manag.* **47** (2006) 3031−3044.
42. W. T. Ji, D. C. Zhang, Y. L. He and W. Q. Tao, Prediction of fully developed turbulent heat transfer of internal helically ribbed tubes — an extension of gnielinski equation, *Int. J. Heat Mass Transfer* **55** (2012) 1375−1384.
43. D. Graham, J. C. Chato and T. A. Newell, Heat transfer and pressure drop during condensation of refrigerant 134a in an axially grooved tube, *Int. J. Heat Mass Transfer* **42** (1999) 1935−1944.
44. C. Herman and E. Kang, Heat transfer enhancement in a grooved channel with curved vanes, *Int. J. Heat Mass Transfer* **45** (2002) 3741−3757.
45. M. Goto, N. Inoue and N. Ishiwatari, Condensation and evaporation heat transfer of R410A inside internally grooved horizontal tubes, *Int. J. Ref.* **24** (2001) 628−638.
46. M. Goto, N. Inoue and R. Yonemoto, Condensation heat transfer of R410a inside internally grooved horizontal tubes, *Int. J. Ref.* **26** (2003) 410−416.
47. X. Zhang, X. Zhang, Y. Chen and X. Yuan, Heat transfer characteristics for evaporation of R417a flowing inside horizontal smooth and internally grooved tubes, *Energ. Convers. Manag.* **49** (2008) 1731−1739.
48. X. Zhang, C. Ji and X. Yuan, Prediction method for evaporation heat transfer of non-azeotropic refrigerant mixtures flowing inside internally grooved tubes, *Appl. Therm. Eng.* **28** (2008) 1974−1983.
49. K. Bilen, M. Cetin, H. Gul and T. Balta, The investigation of groove geometry effect on heat transfer for internally grooved tubes, *Appl. Therm. Eng.* **29** (2009) 753−761.
50. P. Bharadwaj, A. D. Khondge and A. W. Date, Heat transfer and pressure drop in a spirally grooved tube with twisted tape insert, *Int. J. Heat Mass Transfer* **52** (2009) 1938−1944.
51. S. Wongwises, J. Kaew-On, S. Laohalertdecha, W. Duangthongsuk and K. Sakamatapan, Evaporation Heat Transfer and Flow Characteristics of R-134a Flowing Through Internally Grooved Tubes. Heat Mass Transfer DOI 10.1007/s00231-010-0748-6 (2010).
52. N. H. Aly and S. D. Bedrose, Enhanced film condensation of steam on spirally fluted tubes, *Desalination* **101** (1995) 295−301.
53. Y. T. Kang, R. Stout and R. N. Christensen, The effects of inclination angle on flooding in a helically fluted tube with a twisted insert, *Int. J. Mult. Flow.* **23** (1997) 1111−1129.
54. L. Wang, D. W. Sun, P. Liang, L. Zhuang and Y. Tan, Heat transfer characteristics of carbon steel spirally fluted tube for high pressure preheaters, *Energ. Convers. Manag.* **41** (2000) 993−1005.
55. Y. Qi, Y. Kawaguchi, Z. Lin, M. Ewing, R. N. Christensen and J. L. Zakin, Enhanced heat transfer of drag reducing surfactant solutions with fluted tube-in-tube heat exchanger, *Int. J. Heat Mass Transfer* **44** (2001) 1495−1505.
56. P. G. Rousseau, M. V. Eldik and G. P. Greyvenstein, Detailed simulation of fluted tube water heating condenser, *Int. J. Ref.* **26** (2003) 232−239.
57. P. J. Kukulka, R. Smith and K. G. Fuller, Development and evaluation of enhanced heat transfer tubes, *Appl. Therm. Eng.* **31** (2011) 2141−2145.
58. P. G. Vicente, A. Garcia and A. Viedma, Experimental investigation on heat transfer and frictional characteristics of spirally corrugated tubes in turbulent flow at different Prandtl number, *Int. J. Heat Mass Transfer* **47** (2004b) 671−681.

International Journal of Air-Conditioning and Refrigeration
Vol. 20, No. 4 (2012) 1250019 (11 pages)
© World Scientific Publishing Company
DOI: 10.1142/S2010132512500198

World Scientific
www.worldscientific.com

NUMERICAL AND EXPERIMENTAL INVESTIGATION OF THE FLOW CHARACTERISTICS OF R134a FLOWING THROUGH ADIABATIC HELICAL CAPILLARY TUBES

SUKKARIN CHINGULPITAK[*,‡], JATUPORN KAEW-ON[†,‡] and SOMCHAI WONGWISES[‡,§]

[*]*The Joint Graduate School of Energy and Environment*
King Mongkut's University of Technology Thonburi
Bangmod, Bangkok 10140, Thailand

[†]*Physics Department, Faculty of Science*
Thaksin University, Papayom, Phattalung 93110, Thailand

[‡]*Fluid Mechanics, Thermal Engineering and Multiphase Flow Research Lab. (FUTURE)*
Department of Mechanical Engineering
Faculty of Engineering
King Mongkut's University of Technology Thonburi
Bangmod, Bangkok 10140, Thailand
[§]*somchai.won@kmutt.ac.th*

Received 10 July 2012
Accepted 1 October 2012
Published 14 December 2012

This paper presents numerical and experimental results of the flow characteristics of R134a flowing through adiabatic helical capillary tubes. The local pressure distribution along the length of the capillary tubes is measured at inlet pressures ranging from 10 to 14 bar, mass flow rates from 8 to 20 kg h^{-1}, and degrees of subcooling from 0.5°C to 15°C. The theoretical model is based on conservation of mass, energy and the momentum of the fluids in the capillary tube. The model is divided into three regions: subcooled liquid region, metastable liquid region and equilibrium two-phase region and can be applied for various tube geometries, new alternative refrigerants and critical or noncritical flow conditions. The model is validated by comparing results from the present experimental data with that of the available literature. Based on the comparison results, the model used in the present study provides reasonable agreement with the experimental data.

Keywords: Capillary; expansion valve; R134a; vapor pressure; two-phase flow.

[§]Corresponding author.

Nomenclature

A : Cross-sectional area of capillary tube, m^2
d_i : Capillary tube internal diameter, m
D_C : Coil diameter, m
f : Friction factor
g : Gravitational acceleration, $m\,s^{-2}$
G : Mass flow rate per unit area, $kg\,s^{-1}\,m^{-2}$
h : Specific enthalpy, $J\,kg^{-1}$
k : Entrance loss coefficient
L : Length, m
m : Mass flow rate, $kg\,h^{-1}$
P : Pressure, bar
Re : Reynolds number
s : Specific entropy, $J\,kg^{-1}\,K^{-1}$
T : Temperature, °C
V : Velocity, $m\,s^{-1}$
x : Quality

Greek Letters

ΔT_{sub} : Degree of subcooling, °C
ε : Roughness, m
ν : Specific volume, $m^3\ kg^{-1}$
μ : Dynamic viscosity, $kg\,m^{-1}\ s^{-1}$
ρ : Density, $kg\,m^{-3}$

Subscripts

evap : Evaporator
f : Liquid phase
g : Gas phase
i : Capillary inlet condition
in : Inlet
ml : Metastable liquid
sp : Single-phase
tp : Two-phase
vap : Vaporization

1. Introduction

A capillary tube is an important device in small vapor-compression refrigeration and air conditioning systems used to reduce refrigerant pressure from the condenser to the evaporator. The nominal size of the capillary tube typically ranges between 0.5 and 2.0 mm in diameter and 1−6 m in length. This type of tube is widely used in household refrigerators due to its simplicity, cost-effectiveness, no maintenance requirement, no moving parts and low starting torque. For several decades, the flow characteristics of various refrigerants flowing through capillary tubes have been studied both experimentally and theoretically and primarily for straight capillary tubes. However, in practical applications, household refrigerator systems use a helical capillary tube in order to reduce installation space. To the best of the authors' knowledge, there has been minimal experimental investigation of the differences that might exist for straight and helical tube structures. The available papers regarding numerical and experimental investigations of refrigerant flow in coiled capillary tubes are summarized as follows:

Kim *et al.*[1] presented experimental results of mass flow rate and proposed the mass flow rate correlation based on the Buckingham π theorem. They performed tests at condensing temperatures of 40°C, 45°C and 50°C and subcooling temperature of 1.5°C, 5°C and 10°C. They concluded that the mass flow rates of R22 were lower than those of R407C and R410A by about 4% and 23%, respectively. Moreover, the mass flow rates of the coiled capillary tubes were lower than those of straight capillary tubes, especially at smaller coil diameters. In the case of a 40 mm coil diameter, the mass flow rates of the coiled capillary tubes were approximately 9% lower than those for straight capillary tubes.

Zhou and Zhang[2] theoretically and experimentally investigated the performance of coiled adiabatic capillary tubes and compared the results with straight capillary data for R22. They found that the mass flow rate of a straight capillary tube was approximately 10% more than that of a coiled adiabatic capillary tube with a coil diameter of 40 mm. Moreover, the results showed that the mass flow rate of the refrigerant increased significantly with increases in the coil diameter. However, little change was observed for coil diameters larger than 300 mm.

Valladares[3] presented a numerical simulation describing the flow characteristics of coiled adiabatic capillary tubes based on a finite volume formulation. The numerical model was evaluated for various aspects such as type of fluid (pure substances and mixtures), geometry, metastable regions, critical or noncritical flow conditions and transient behavior. The prediction showed 97.7% agreement of 211 data points evaluated within an error of ± 10%.

Park *et al.*[4] studied the flow characteristics of coiled capillary tubes for R22 and proposed a mass flow rate correlation for coiled capillary tubes. In the same operating conditions, the results showed that the mass flow rates of the coiled capillary tubes decreased by about 5−16% less than those of the straight capillary tubes. The correlation was

developed on the basis of experimental data such as the effects of inlet condition, refrigerant properties and coiled tube geometry. For both straight and coiled capillary tubes, the results showed that the proposed correlation gave reasonable agreement with the experimental data for R22, R407C and R410A.

Mittal *et al.*[5] presented an experimental investigation of coiling effect on the flow characteristics of R407C in an adiabatic helical capillary tube. They observed that the coiling of capillary tubes (coil diameters of 60, 100 and 140 mm) significantly influenced the mass flow rate. From the experimental results, the mass flow rates through the coiled capillary tubes decreased about 5−10% less than those through the straight capillary tubes. In addition, the authors also proposed correlations to predict the mass flow rate of R407C flowing through straight and helical capillary tubes. When compared with experimental data, the majority of the results fell within 10% of their proposed correlation.

Chingulpitak and Wongwises[6] applied a mathematical model to study the flow characteristics of alternative refrigerants in adiabatic helical capillary tube. The model presented is based on conservation of mass, energy and momentum of fluids in the capillary tube. The developed model is validated by comparison with the experimental data from Kim *et al.*[1] for R22, R407C and R410A and Zhou and Zhang for R22.[2,7] The results obtained from the present model show reasonable agreement with the experiment data. Chingulpitak and Wongwises[8,9] studied the effects of various geometries of helical capillary tubes and compared the flow characteristics of refrigerants in straight and helical capillary tubes. The results show that for coil diameters of 40 to 300 mm, the mass flow rate of refrigerants increases rapidly by about 6−7%. For coil diameters between 300 and 600 mm, the increase in mass flow rate of refrigerant is small (about 1−2%). The comparison between the straight and helical capillary tubes showed that the length of the helical capillary tube was 20% shorter than that of the straight capillary tube under the same operating conditions.

Zhou and Zhang[10] studied the inlet pressure fluctuation characteristics of R22 in adiabatic helical and straight capillary tubes. Their results show that the pressure fluctuation for straight capillary tubes is less prominent than for helical ones. In the case of a small coil diameter, the inlet pressure fluctuation is weak. Moreover, the results show that the fluctuation amplitude decreases as the preset inlet pressure increases.

Up to now, as described above, there have been only two works, carried out by Zhou and Zhang[2] and Valladares,[3] dealing with the metastable region in the simulation of refrigerant flow in coil capillary tube. Although some information is currently available, there still remains room to discuss, for example, there are no information regarding local pressure and temperature distributions obtained from either simulation or experiment available yet, the effects of various relevant parameters on flow characteristics also remain unstudied. In this paper, the main concern is to present an experimental and theoretical study for predicting the refrigerant flow characteristics including metastable region in adiabatic helical capillary tubes. R134a which is current widely used but has never been investigated before in helical capillary tube, is studied. The influence of parameters such as inlet pressure, degree of subcooling, capillary tube diameters and coil diameters on local pressure and mass flow rate along the capillary tube length are also investigated. Flashing process behavior and the delay of refrigerant vaporization are also discussed.

2. Experimental Apparatus and Method

A schematic diagram of experimental apparatus is shown in Fig. 1. The main refrigeration system components consist of a compressor, condenser, capillary tube, evaporator and other accessory parts, including the oil separator, liquid receiver, filter/drier, sight glass, subcooler and accumulator. A two-cylinder single stage reciprocating compressor, driven by an electric motor, was used to circulate the refrigerant. The speed of the motor was varied so as to provide a wide range of mass flow rates by means of an inverter. More details of the experimental apparatus are available from Kaew-on *et al.*[11]

The details of the test capillary tube dimensions are presented in Fig. 2. The inlet pressure and inlet temperature were measured at the inlet header. Similarly, the outlet pressure and outlet temperature were obtained from the outlet header. Seven points of the capillary tube were drilled for the installation of pressure taps. Also, seven T-type

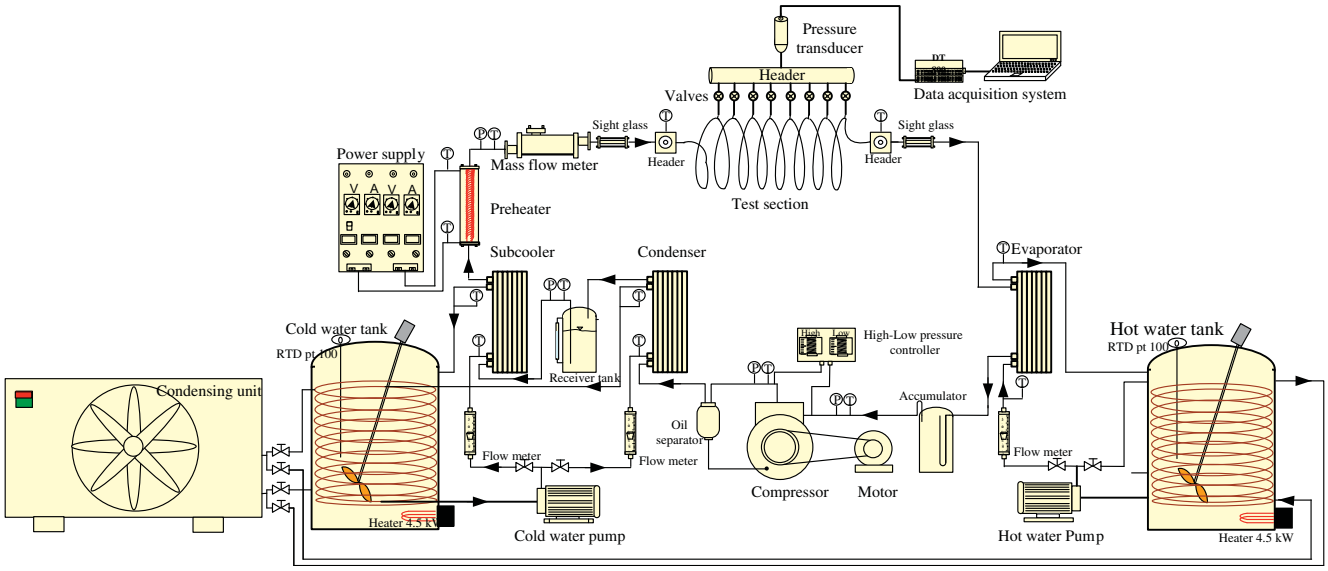

Fig. 1. Schematic diagram of the experimental apparatus.[11]

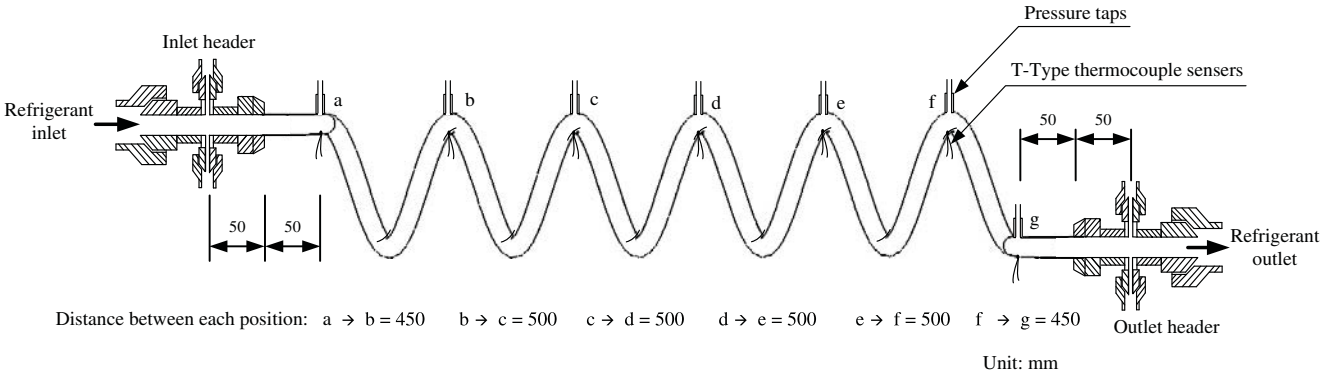

Fig. 2. Schematic diagram of the test section.

thermocouples were installed in the same sections as the pressure taps. The thermocouples were insulated with an Aeroflex standard sheet to reduce the effect of heat transfer on measurement. The range of experimental conditions and the details of test sections are listed in Table 1.

Table 1. The details of test sections and experimental conditions.

Items	Details
Refrigerant	R134a
Capillary diameter, d_i, mm	1.07, 1.27, 1.62
Coil diameter, D_c, mm	25, 50, 100
Capillary length, L, m	3.05
Inlet pressure, P_{in}, bar	10, 12, 14
Degree of subcooling, ΔT_{sub}, °C	0.5−10.5
Mass flow rate, m, kg/h	7−18

3. Mathematical Modeling

In mathematical modeling, the flow characteristics of refrigerant are analyzed by applying the fundamental principles of thermodynamics and fluid mechanics.[6,12] The proposed model assumes that the helical capillary tube is a horizontal capillary tube with constant coil diameter, inner diameter and roughness. Also, the flow inside is considered to be adiabatic, one-dimensional, steady, metastable region and homogeneous two-phase flow. The flow characteristics of refrigerant in a helical capillary tube can be divided into a single-phase flow region,

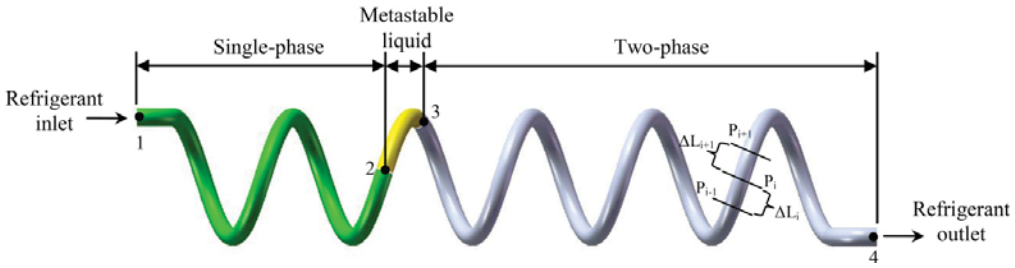

Fig. 3. Schematic diagram of an adiabatic helical capillary tube.

metastable liquid region and a two-phase flow region. The theoretical flow model of refrigerant through the capillary tube is based on the conservation of mass, energy and momentum of fluids in the helical capillary tube. For convenience, the developed model is briefly reviewed.

3.1. *Single-phase flow region*

The single-phase flow region represents the position from the inlet of the capillary tube to the position where the pressure drops to the saturated pressure (points 1 and 2 in Fig. 3). From our previous work,[6] the single-phase length is calculated as follows:

$$L_{\mathrm{sp}} = \frac{d_i}{f_{\mathrm{sp}}}\left[\frac{2}{\rho V^2}(P_1 - P_3) - k - 1\right], \tag{1}$$

where f_{sp} is the single-phase friction factor and k is the entrance loss coefficient (for square edged, $k = 0.5$).

The friction factor of coil capillary tube (f_c) proposed by Mori and Nakayama[13] presented in Eq. (2), is used to calculate the single-phase friction factor.

$$f_c = \frac{C_1(d_i/D_c)^{0.5}}{[\mathrm{Re}(d_i/D_c)^{2.5}]^{1/6}}\left\{1 + \frac{C_2}{[\mathrm{Re}(d_i/D_c)^{2.5}]^{1/6}}\right\}, \tag{2}$$

where

$$\begin{aligned} C_1 &= 1.88411177 \times 10^{-1} + 85.2472168(\varepsilon/d_i) \\ &\quad - 4.63030629 \times 10^{4}(\varepsilon/d_i)^2 \\ &\quad + 1.31570014 \times 10^{7}(\varepsilon/d_i)^3, \\ C_2 &= 6.79778633 \times 10^{-2} + 25.3880380(\varepsilon/d_i) \\ &\quad - 1.06133140 \times 10^{4}(\varepsilon/d_i)^2 \\ &\quad + 2.54555343 \times 10^{6}(\varepsilon/d_i)^3, \end{aligned}$$

and

$$\mathrm{Re} = \frac{\rho V d_i}{\mu}. \tag{3}$$

3.2. *Metastable-liquid flow region*

The metastable phenomenon occurs when the pressure of the liquid approaches the saturation pressure, but the fluid is still in the liquid phase (points 2 and 3 in Fig. 3). The pressure of vaporization (P_{vap}) is calculated using the correlation proposed by Chen *et al.*,[14] as follows;

$$\frac{(P_{\mathrm{sat}} - P_{\mathrm{vap}})\sqrt{kT_{\mathrm{sat}}}}{\sigma^{1.5}} = 0.679\left(\frac{\nu_g}{\nu_g - \nu_l}\right)\mathrm{Re}^{0.914}\left(\frac{\Delta T_{sc}}{T_c}\right)^{-0.208}\left(\frac{d_i}{D'}\right)^{-3.18}, \tag{4}$$

where D' is the reference length $\left(\sqrt{\frac{kT_{\mathrm{sat}}}{\sigma}} \times 10^4\right)$, and k is the Boltzmann constant ($1.380662 \times 10^{-23}\,\mathrm{J\,K^{-1}\,mol^{-1}}$).

According to the recommendation by Zhou and Zhang,[2] the metastable liquid region length is evaluated in the same way as the single-phase region.

3.3. *Two-phase flow region*

The flow in this region is assumed to be homogeneous flow. The fundamental equations used for this section are conservation of mass, energy and momentum. The following equations are based on the control volume considerations in the two-phase region. Also, calculation of the two-phase length can be followed from our previous model.[6]

$$dL = \frac{2d_i}{f_{\mathrm{tp}}}\left[-\frac{\rho dP}{\rho V^2} + \frac{d\rho}{\rho}\right]. \tag{5}$$

The two-phase friction factor can be calculated using Eq. (2), in the same way as the single-phase region, where the Reynolds number in the two-phase region is determined by

$$\mathrm{Re}_{\mathrm{tp}} = \frac{Vd_i}{\mu_{\mathrm{tp}}\nu_{\mathrm{tp}}}\,, \tag{6}$$

where

$$V = G\nu_{\mathrm{tp}} = G\big(x\nu_g + (1-x)\nu_f\big)\,. \tag{7}$$

The two-phase dynamic viscosity correlation proposed by McAdams *et al.*[15] is presented as follows:

$$\frac{1}{\mu_{\mathrm{tp}}} = \frac{x}{\mu_g} + \frac{1-x}{\mu_f}\,. \tag{8}$$

4. Solution Methodology

The solution methodology used in the present stydy is modified from Wongwises and Pirompak,[12] Bansal and Rupasingh.[16]

For the two-phase region, as shown in Fig. 3, the capillary tube between points 3 and 4 can be divided into numerous sections. Since P_3 is known (the pressure of vaporization, P_{vap}), the pressure in any section, i, can be expressed as

$$P_i = P_3 - i\Delta P\,. \tag{9}$$

The entropy of each section can be calculated from

$$s_i = s_{if}(1-x) + s_{ig}\,x\,. \tag{10}$$

The calculation is done section by section along the capillary tube until the entropy reaches its maximum value. At this point, the fluid velocity is equal to the local speed of sound and the flow is choked. The pressure of the element, where the entropy has the maximum value, $(P_i)_{s\,\max}$, is then compared to the evaporator pressure, P_{evap}, as follows:

if $P_{i,s\max} > P_{\mathrm{evap}}$ then $P_4 = P_{i,s\max}$ and if $P_{i,s\max} < P_{\mathrm{evap}}$ then $P_4 = P_{\mathrm{evap}}$.

Thus, from Eq. (5) the two-phase length (L_{tp}) can be expressed as follows:

$$L_{\mathrm{tp}} = d_i\left[\frac{-2}{G^2}\int_{P_3}^{P_{s\max}}\frac{\rho}{f_{\mathrm{tp}}}dp + 2\int_{P_3}^{P_{s\max}}\frac{d\rho}{\rho f_{\mathrm{tp}}}\right]. \tag{11}$$

Finally, the total length of the capillary tube is a summation of the single-phase, metastable liquid region and two-phase lengths, which is defined as follows:

$$L_{\mathrm{total}} = L_{\mathrm{sp}} + L_{\mathrm{ml}} + L_{\mathrm{tp}}\,. \tag{12}$$

All refrigerant properties are taken from the REFPROP version 6.01 computer program,[17] and are developed in the pressure function.

5. Results and Discussion

5.1. *Mathematical model verification*

To validate the present model, comparison is made with the available experimental data from Ref. 7. As shown in Fig. 4, a comparison between the present numerical result and experimental data from Ref. 7 for R22 was used to validate the temperature distribution along the capillary tube length. In the subcooled liquid region, the temperature remains nearly constant along the tube, while rapidly decreasing after the refrigerant flashes. This is due to the delay of vaporization. However, the actual point of inception of vaporization did not occur at the end of the subcooled liquid region. The result shows that the calculated tube length of R22 deviates from the experimental results. However, the results also indicate that the tendency of temperature distribution along the capillary tube length obtained from the present model shows reasonable agreement with previous data.

5.2. *Comparison of the present model and the Chingulpitak and Wongwises model*[6]

Figure 5 shows the comparison of simulation results of our previous model[6] with the present model. It is

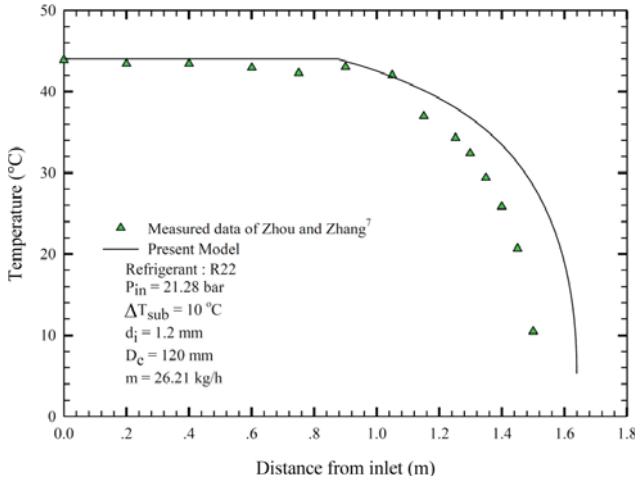

Fig. 4. Comparison of present numerical results with experimental data.

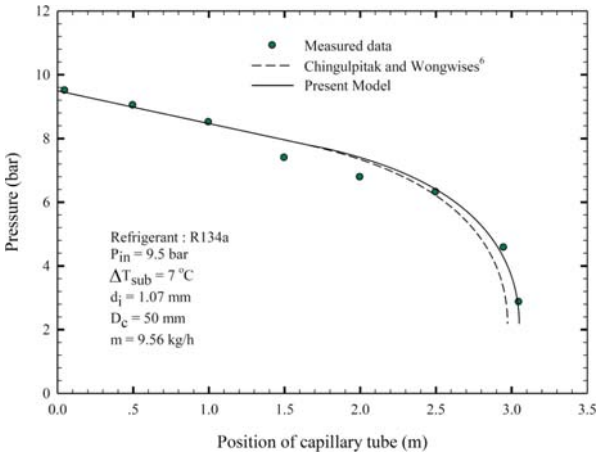

(a)

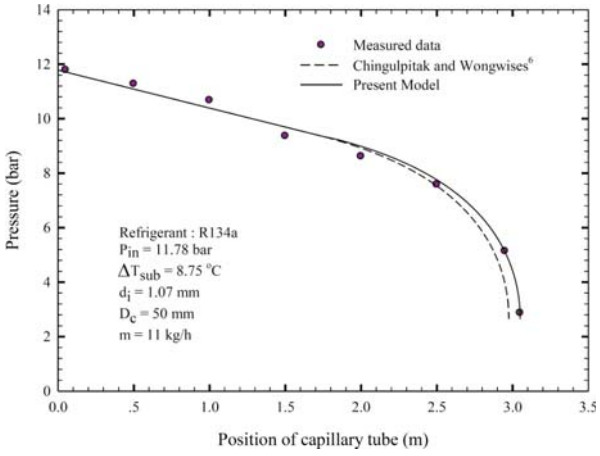

(b)

Fig. 5. Comparison of the present model and nonmetastable region model proposed by Chingulpitak and Wongwises[6] with experimental data.

clear that the pressure distribution along the helical capillary tube obtained from the present model gives a better prediction than those of our previous model.[6] This is due to the fact that the previous model was developed excluding a metastable liquid region. The metastable phenomenon is an effect on increasing the capillary tube's length in the single-phase region.

5.3. *Pressure distributions*

5.3.1. *Effect of inlet pressure on pressure distribution*

The variations of refrigerant pressure along the capillary tube at different inlet pressures are depicted in Fig. 6. It is apparent that the pressure drop of

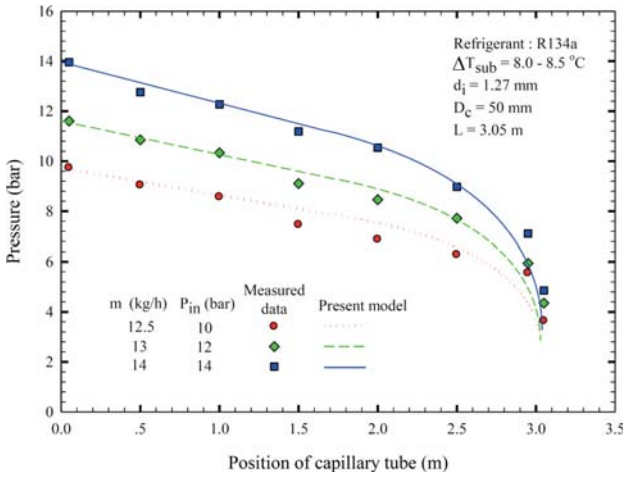

Fig. 6. Effect of inlet pressure on the pressure distribution along the capillary tube length.

refrigerant increases as the inlet pressure increases. The enlargement of inlet pressure led to an increased difference between inlet and outlet pressure, resulting in an increase of refrigerant mass flow rate and velocity. Therefore, the frictional and accelerational pressure drop inside the capillary tube increased.

5.3.2. *Effect of coil and inner diameters on pressure distribution*

The effects of coil and inner diameters on pressure distribution are presented in Fig. 7. In Fig. 7(a), the results show that decreases in pressure for all conditions have similar profiles. Thus, it can be concluded that coil diameter has no significant effect on pressure distribution in the range of the present study. However, in terms of inner diameter, the pressure drop along the capillary tube decreased with increasing capillary tube diameter, as shown in Fig. 7(b).

5.3.3. *Effect of degree of subcooling on pressure distribution*

At the same inlet pressure and dimensions of capillary tube, the effect of degree of subcooling on pressure distribution along the capillary tube is presented in Fig. 8. It is evident from this data that the single-phase length increases with increasing subcooling temperature. In the subcooled liquid region, the pressure drop remains nearly constant along the tube, while it decreases rapidly after the refrigerant flashes.

From the comparison results, the present model gives a good tendency of pressure distribution along

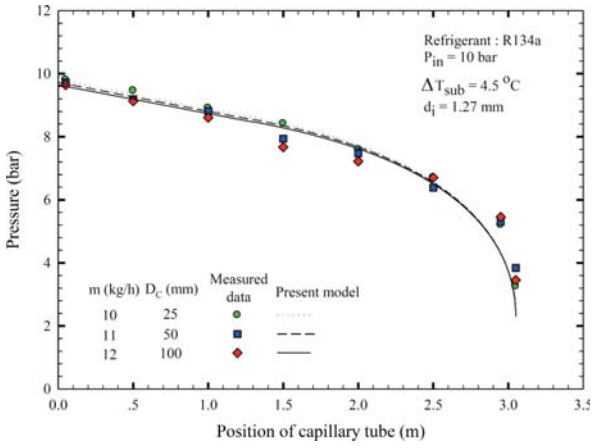

(a)

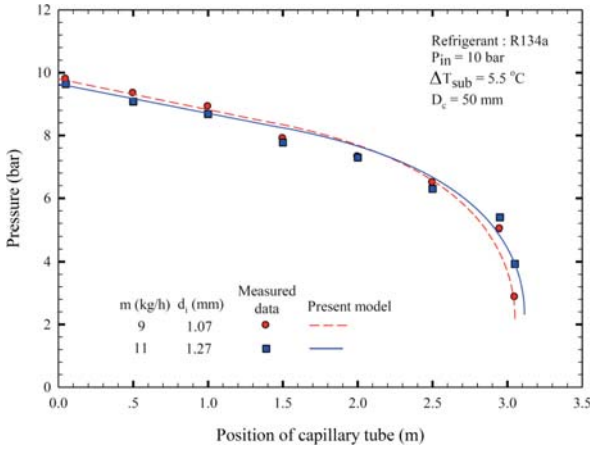

(b)

Fig. 7. Effect of the relevant parameters on pressure distribution of the R134a through the capillary tubes (a) effect of coil diameters and (b) effect of inner diameters.

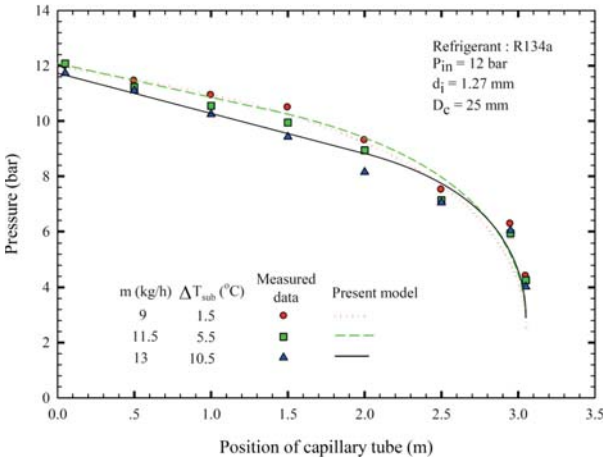

Fig. 8. Effect of degree of subcooling on pressure distribution of the R134a through the capillary tube.

the tube's length compared with experimental data. The present model can be used to predict the flow characteristics of R134a flowing through adiabatic helical capillary tube.

5.4. *The mass flow rate*

5.4.1. *Effect of inlet pressure on mass flow rate*

In Fig. 9(a), the variation of mass flow rates for capillary inlet pressures of 10 and 12 bar with varying degrees of subcooling is presented. The results show that for a given capillary diameter, the mass flow rate increased with an increase of inlet pressure. At higher inlet pressures, the driving force was also higher and resulted in an increase of mass flow rate. Moreover, the comparison of the predicted mass flow rates with the measured data at inlet pressure 10 and 12 bar shows that the present model gives a mean absolute error of 2.1% and 4.1%, respectively.

5.4.2. *Effect of coil diameters on mass flow rate*

As shown in Fig. 9(b), the variation of mass flow rates with coil diameters of 50 and 100 mm is presented. Here, the refrigerant mass flow rate increased with an increase in coil diameter. At 4.5°C of subcooling, the refrigerant mass flow rate of the helical capillary tube from coil diameters of 50 to 100 mm, increased by 9%. Comparison of mass flow rates obtained from the present model with the measured data at coil diameter 50 and 100 mm shows that the present model gives a mean absolute error of 5.9% and 2.1%, respectively.

5.4.3. *Effect of degree of subcooling and inner diameter on mass flow rate*

Figure 9(c) shows mass flow rates and degrees of subcooling for capillary tube diameters of 1.07 and 1.27 mm, inlet pressure of 10 bar and coil diameter of 50 mm. The results show that the mass flow rate increased with increasing degree of subcooling. This phenomenon can be explained by the fact that the increase in mass flow rate was a result of increased liquid length for high inlet subcooling. Moreover, the results also indicate that the effect of capillary tube diameter on the refrigerant mass flow rate is clear and significant. The results show that the mass flow

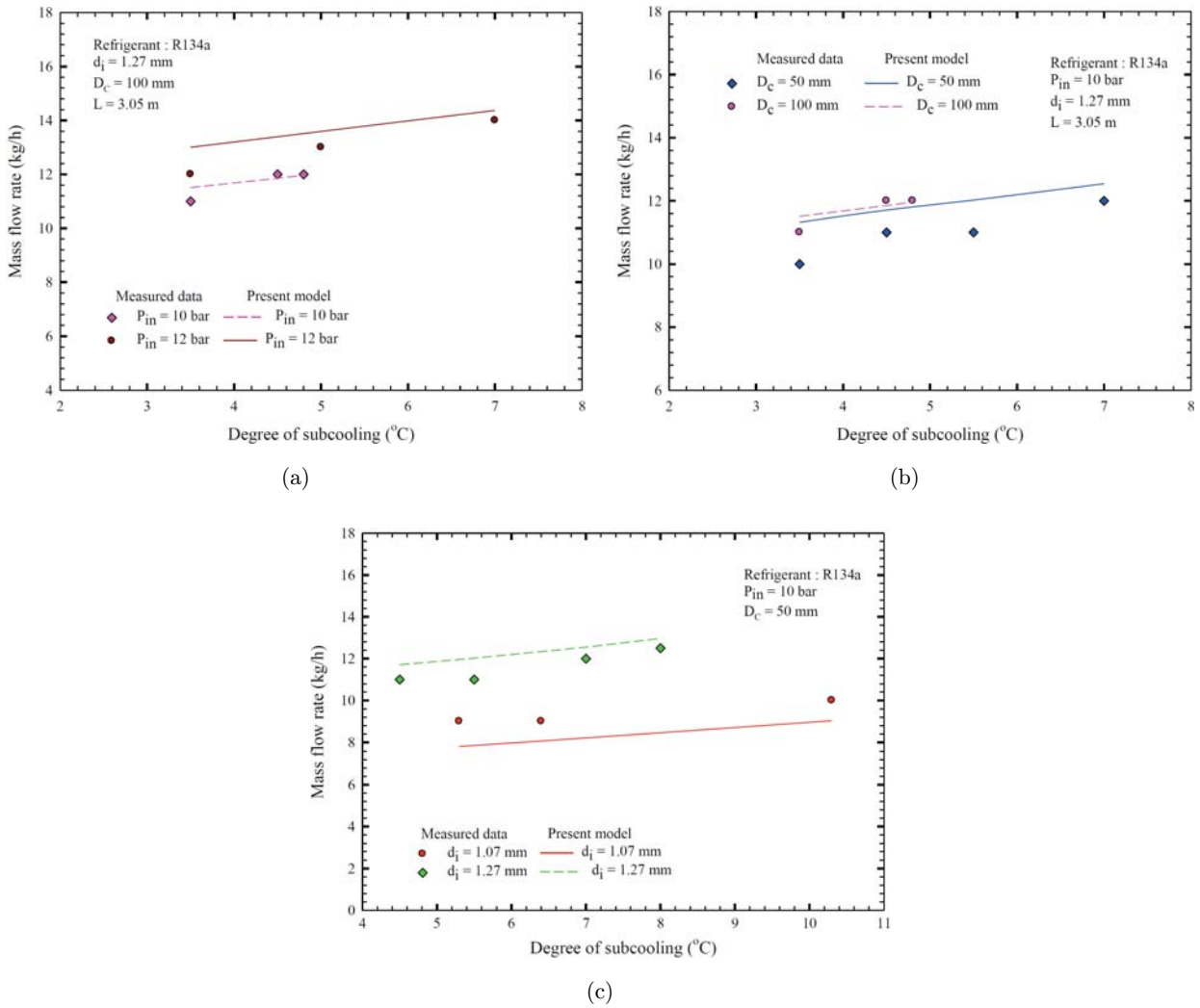

Fig. 9. Effect of the relevant parameter on the mass flow rate of the R134a through the capillary tubes (a) effect of inlet pressure, (b) effect of coil diameter and (c) effect of degree of subcooling and capillary tube diameter.

rates dramatically increased with an increase in capillary tube diameter.

5.5. *Effect of the choked flow condition on pressure distribution and total capillary tube length*

As shown in Fig. 10, with an inner diameter of 1.62 mm, the pressure distribution along capillary tube length of the present model with a mass flow rate 18.1 kg h^{-1} fits very well with the measured data, although the numerical result gives the total capillary tube length longer than that of the measured data by about 11.14%. On the other hand, a mass flow rate of 19.1 kg h^{-1} gives the best result for the total capillary tube length but this mass flow

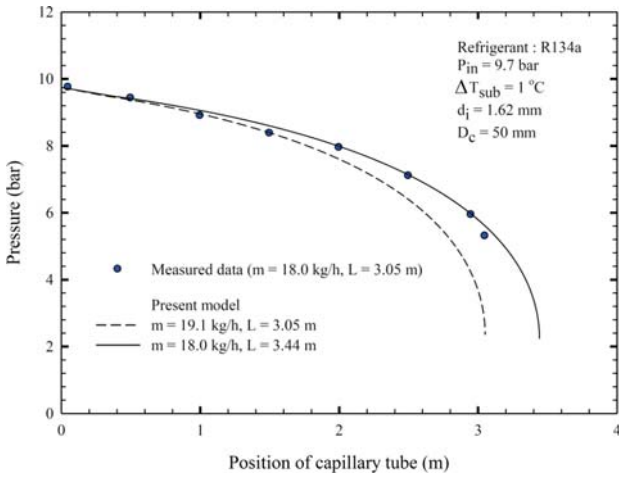

Fig. 10. Comparison of measured pressure distribution with present numerical results at different mass flow rate.

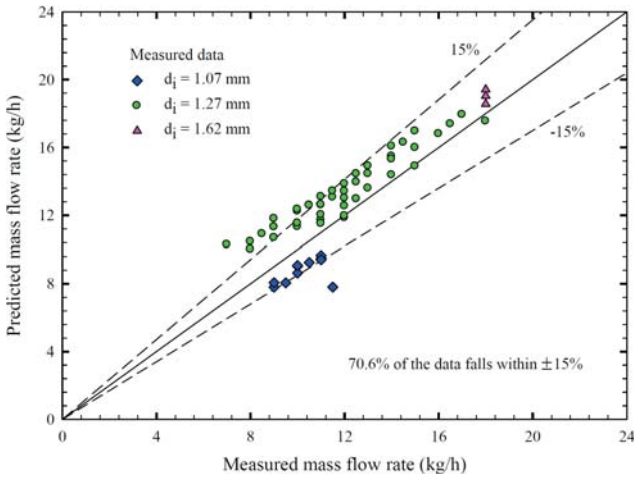

Fig. 11. Comparison of mass flow rate obtained from the present model with measured data for R134a.

rate failed with the tendency of pressure distribution inside the helical capillary tube. This is due to the fact that the present model is limited at the choked flow condition for any computation. Therefore, the pressure profile of refrigerant in the capillary tube should be considered for accuracy of the comparison between the simulation and experiment results. In addition, considering the pressure distribution at any position along capillary tube length is one of the main purposes of the present experiment.

In Fig. 11, the comparison of the predicted mass flow rates with all of the present measured data for R134a shows that 70.6% of the 58 data points are within $\pm 15\%$.

6. Conclusion

In this study, the flow characteristics of R134a flowing through adiabatic helical capillary tubes were theoretically and experimentally investigated. From the measured mass flow rate data, the capillary tube diameter has a more significant effect on mass flow rate than the other variables. For example, at 5.5°C of subcooling, as the capillary tube diameter increased from 1.07 mm to 1.27 mm, the refrigerant mass flow rate increased by 22.2%. Similarly, at 4.5°C of subcooling, the refrigerant mass flow rate of the helical capillary tube from coil diameters of 50 mm to 100 mm increased by 9%. In terms of the theoretical study, the present model was validated by comparing its results with the experimental data. The comparison results show that the proposed model, including metastable liquid region, can be used to predict the flow characteristics of R134a flowing through an adiabatic helical capillary tube, and specifically, local pressure distribution along the tube's length.

Acknowledgments

The authors are indebted to the Thailand Research Fund, the Office of the Higher Education Commission and the National Research University Project for supporting this study.

References

1. S. G. Kim, M. S. Kim and S. T. Ro, Experimental investigation of the performance of R22 R407C and R410A in several capillary tubes for air-conditioners, *Int. J. Ref.* **25** (2002) 521−531.
2. G. Zhou and Y. Zhang, Numerical and experimental investigations on the performance of coiled adiabatic capillary tubes, *Appl. Therm. Eng.* **26** (2006) 1106−1114.
3. O. G. Valladares, Numerical simulation and experimental validation of coiled adiabatic capillary tubes, *Appl. Therm. Eng.* **27** (2007) 1062−1071.
4. C. Park, S. Lee, H. Kang and Y. Kim, Experimentation and modeling of refrigerant flow through coiled capillary tubes, *Int. J. Ref.* **30** (2007) 1168−1175.
5. M. K. Mittal, R. Kumar and A. Gupta, An experimental study of the flow of R-407C in an adiabatic helical capillary tube, *Int. J. Ref.* **33** (2010) 840−847.
6. S. Chingulpitak and S. Wongwises, Two-phase flow model of refrigerants flowing through helically coiled capillary tubes, *Appl. Therm. Eng.* **30** (2010) 1927−1936.
7. G. Zhou and Y. Zhang, Experimental investigation on hysteresis effect of refrigerant flowing through a coiled adiabatic capillary tube, *Energy Convers. Manage.* **47** (2006) 3084−3093.
8. S. Chingulpitak and S. Wongwises, Effects of coil diameter and pitch on the flow characteristics of alternative refrigerants flowing through adiabatic helical capillary tubes, *Int. Commun. Heat Mass Transfer* **37** (2010) 1305−1311.
9. S. Chingulpitak and S. Wongwises, A comparison of flow characteristics of refrigerants flowing through adiabatic straight and helical capillary tubes, *Int. Commun. Heat Mass Transfer* **38** (2011) 398−404.
10. G. Zhou and Y. Zhang, Inlet pressure fluctuation characteristics of coiled adiabatic capillary tubes, *Appl. Therm. Eng.* **33–34** (2012) 183−189.

11. J. Kaew-on, K. Nilpuang, S. Chingulpitak and S. Wongwises, Experimental investigation of R134A flowing through adiabatic helically coiled capillary tubes, *Int. J. Air-conditioning Ref.* **20** (2012) 1−11.
12. S. Wongwises and W. Pirompak, Flow characteristics of pure refrigerants and refrigerant mixtures in adiabatic capillary tubes, *Appl. Therm. Eng.* **21** (2001) 845−861.
13. Y. Mori and W. Nakayama, Study on forced convective heat transfer in curved pipes (2nd, report turbulent region), *Int. J. Heat Mass Transfer* **10** (1967) 37−59.
14. Z. H. Chen, R. Y. Li, S. Lin and Z. Y. Chen, A correlation for metastable flow of refrigerant 12 through capillary tubes, *ASHRAE Trans.* **96** (1990) 550−554.
15. W. H. McAdams, W. K. Wood and R. L. Bryan, Vaporization inside horizontal tubes. II, Benzence-oil mixture, *Trans. ASME* **64** (1942) 193.
16. P. K. Bansal and A.S. Rupasinghe, A homegeneous model for adiabatic capillary tubes, *Appl. Therm. Eng.* **18** (1998) 207−219.
17. M. O. McLinden, S. A. Klein and E. W. Lemmon, REFPROP — thermodynamic and transport properties of refrigerants and refrigerant mixtures, NIST Standard Reference Database — version 6.01 (1998).

Provided for non-commercial research and education use.
Not for reproduction, distribution or commercial use.

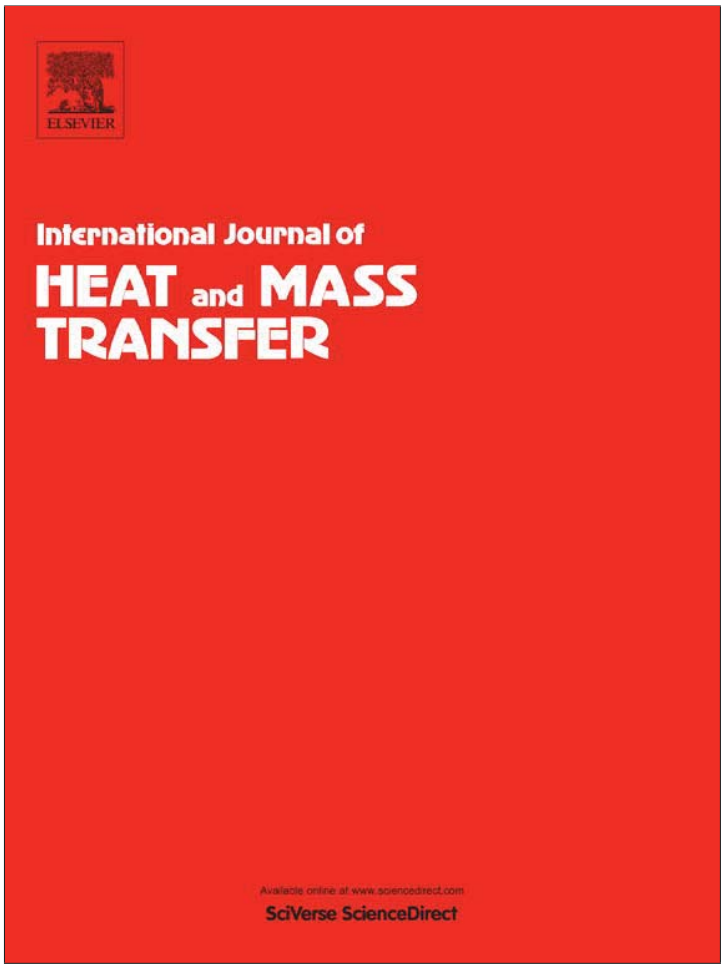

(This is a sample cover image for this issue. The actual cover is not yet available at this time.)

This article appeared in a journal published by Elsevier. The attached copy is furnished to the author for internal non-commercial research and education use, including for instruction at the authors institution and sharing with colleagues.

Other uses, including reproduction and distribution, or selling or licensing copies, or posting to personal, institutional or third party websites are prohibited.

In most cases authors are permitted to post their version of the article (e.g. in Word or Tex form) to their personal website or institutional repository. Authors requiring further information regarding Elsevier's archiving and manuscript policies are encouraged to visit:

http://www.elsevier.com/copyright

Author's personal copy

International Journal of Heat and Mass Transfer 57 (2013) 582–594

Contents lists available at SciVerse ScienceDirect

International Journal of Heat and Mass Transfer

journal homepage: www.elsevier.com/locate/ijhmt

A review of the applications of nanofluids in solar energy

Omid Mahian [a], Ali Kianifar [a], Soteris A. Kalogirou [b], Ioan Pop [c,*], Somchai Wongwises [d,e]

[a] Department of Mechanical Engineering, Engineering Faculty, Ferdowsi University of Mashhad, Mashhad, Iran
[b] Department of Mechanical Engineering and Materials Science and Engineering, Cyprus University of Technology, Cyprus
[c] Department of Mathematics, Babeş-Bolyai University, 400084 Cluj-Napoca, CP 325, Romania
[d] Fluid Mechanics, Thermal Engineering and Multiphase Flow Research Lab. (FUTURE), Department of Mechanical Engineering, Faculty of Engineering, King Mongkut's University of Technology Thonburi, Bangmod, Bangkok 10140, Thailand
[e] The Academy of Science, The Royal Institute of Thailand, Sanam Suea Pa, Dusit, Bangkok 10300, Thailand

ARTICLE INFO

Article history:
Received 27 May 2012
Received in revised form 26 August 2012
Accepted 11 October 2012

Keywords:
Nanofluids
Solar energy
Efficiency
Economic and environmental considerations
Challenges

ABSTRACT

Utilizing nanofluids as an advanced kind of liquid mixture with a small concentration of nanometer-sized solid particles in suspension is a relatively new field, which is less than two decades old. The aim of this review paper is the investigation of the nanofluids' applications in solar thermal engineering systems. The shortage of fossil fuels and environmental considerations motivated the researchers to use alternative energy sources such as solar energy. Therefore, it is essential to enhance the efficiency and performance of the solar thermal systems. Nearly all of the former works conducted on the applications of nanofluids in solar energy is regarding their applications in collectors and solar water heaters. Therefore, a major part of this review paper allocated to the effects of nanofluids on the performance of solar collectors and solar water heaters from the efficiency, economic and environmental considerations viewpoints. In addition, some reported works on the applications of nanofluids in thermal energy storage, solar cells, and solar stills are reviewed. Subsequently, some suggestions are made to use the nanofluids in different solar thermal systems such as photovoltaic/thermal systems, solar ponds, solar thermoelectric cells, and so on. Finally, the challenges of using nanofluids in solar energy devices are discussed.

© 2012 Elsevier Ltd. All rights reserved.

Contents

1. Introduction . . . 583
2. Applications of nanofluids in solar energy . . . 583
 2.1. Collectors and solar water heaters . . . 583
  2.1.1. Efficiency of nanofluid-based solar collectors . . . 584
  2.1.2. Economic and environment considerations . . . 588
 2.2. Other applications . . . 588
  2.2.1. Thermal energy storage . . . 588
  2.2.2. Solar cells . . . 589
  2.2.3. Solar stills . . . 589
3. Future work . . . 589
 3.1. Parabolic trough systems . . . 590
 3.2. Photovoltaic/thermal systems . . . 590
 3.3. Solar thermoelectric cells . . . 590
 3.4. Solar ponds . . . 591
 3.5. Other possibilities . . . 591
4. Challenges . . . 591
 4.1. High cost . . . 591
 4.2. Instability and agglomerating . . . 592
 4.3. Pumping power and pressure drop . . . 592
 4.4. Erosion and corrosion of components . . . 592

* Corresponding author. Tel.: +40 264405300; fax: +40 264591906.
E-mail address: popm.ioan@yahoo.co.uk (I. Pop).

0017-9310/$ - see front matter © 2012 Elsevier Ltd. All rights reserved.
http://dx.doi.org/10.1016/j.ijheatmasstransfer.2012.10.037

Author's personal copy

5. Conclusion . . . 592
Acknowledgments . . . 592
References . . . 592

1. Introduction

Common fluids such as water, ethylene glycol, and heat transfer oil play an important role in many industrial processes such as power generation, heating or cooling processes, chemical processes, and microelectronics. However, these fluids have relatively low thermal conductivity and thus cannot reach high heat exchange rates in thermal engineering devices. A way to overcome this barrier is using ultra fine solid particles suspended in common fluids to improve their thermal conductivity. The suspension of nano-sized particles (1–100 nm) in a conventional base fluid is called a nanofluid. Choi first used the term "nanofluid" in 1995 [1]. Nanofluids, compared to suspensions with particles of millimeter-or-micrometer size, show better stability, rheological properties, and considerably higher thermal conductivities.

In recent years, many researchers have investigated the effects of nanofluids on the enhancement of heat transfer in thermal engineering devices, both experimentally and theoretically. Researchers have also applied a variety of preparation methods, characteristics, and different models used for the calculation of thermophysical properties of nanofluids (i.e., thermal conductivity, viscosity, density, specific heat capacity) [2–9]. Some investigators have also summarized the effects of nanofluids on flow and heat transfer in natural and forced convection in different systems [10–13]. The enhanced thermal behavior of nanofluids could provide a basis for an enormous innovation for heat transfer intensification, which is of major importance to a number of industrial sectors including transportation, power generation, micromanufacturing, thermal therapy for cancer treatment, chemical and metallurgical sectors, as well as heating, cooling, ventilation and air-conditioning. Nanofluids are also important for the production of nanostructured materials for the engineering of complex fluids as well as for cleaning oil from surfaces due to their excellent wetting and spreading behavior (Ding et al. [14]). Another application of the nanofluid flow is in the delivery of nano-drug as suggested by Kleinstreuer et al. [15].

Saidur et al. [16] reviewed the potential of nanofluids in the improvement of heat transfer in refrigeration systems. The authors concluded that more studies are required to find the reasons behind the considerable improvements in heat transfer whereas an insignificant increase in pressure occurs. Thomas and Sobhan [17] presented experimental studies on nanofluids, with emphasis on the techniques of measuring the effective thermal conductivity. Escher et al. [18] investigated the applications of nanofluids in cooling electronics. Recently, applications of computer simulations and computational fluid dynamics (CFD) used to model systems employing nanofluids were reviewed and analyzed by Abouali and Ahmadi [19] and Kamyar et al. [20]. Ahn and Kim [21] also published a review on the critical heat flux of nanofluids for both convective flow boiling and pool boiling applications. In another publication, Saidur et al. [22] reviewed the general applications of nanofluids in some fields such as cooling of electronics, heat exchangers, medical applications, fuel cells, nuclear reactors, and many more. They also mentioned briefly the applications of nanofluids in solar water heaters. They investigated challenges in using nanofluids, including an increased pressure drop and pumping power, long-term stability of nanoparticles dispersion, and the high cost of nanofluids.

In recent years, the use of solar energy has had a remarkable edge. The perceived shortage of fossil fuels as well as environmental considerations will constrain the use of fossil fuels in the future. Therefore, researchers are motivated to find alternative sources of energy. This has become even more popular as the price of fossil fuels continues to rise. The earth receives in just about 1 h more energy from the sun than that consumed by the entire world for 1 year. Most solar energy applications are financially viable while small systems for individual use require just a few kilowatts of power [23,24]. It is important to apply solar energy to a wide range of applications and provide solutions through the modification of the energy proportion, improving energy stability, increasing energy sustainability, and enhancing system efficiency [25]. This paper presents a review of former studies on the application of nanofluids in solar thermal engineering systems. The former works on applications of nanofluids in solar energy are mainly related to their applications in collectors. Therefore, this review mainly investigates the effects of nanofluids on the efficiency improvement of solar collectors as well as on economic and environmental considerations regarding the usage of these systems. Other applications of nanofluids in thermal energy storage, solar cells, and solar stills are also reviewed. Some suggestions also are made for future works in this field. In addition, the existing challenges of using nanofluids in solar energy applications are discussed. Finally, the authors wish to mention that in contrast with the comprehensive references on nanofluids mentioned above much less is known about the application of nanofluids in solar energy applications. It should be reiterated here that, as this is the first systematic review paper on this subject, it is desirable to provide as complete details as possible. However, in an attempt to reduce the overall length of the paper, without compromising the technical quality, only some very important questions for problems of practical applications have been briefly described.

2. Applications of nanofluids in solar energy

Initially, the application of nanofluids in collectors and water heaters are investigated from the efficiency, economic, and environmental aspects. Some studies conducted on thermal conductivity and optical properties of nanofluids are also briefly reviewed, because these parameters can determine the capability of nanofluids to enhance the performance of solar systems.

2.1. Collectors and solar water heaters

Solar collectors are particular kind of heat exchangers that transform solar radiation energy into internal energy of the transport medium. These devices absorb the incoming solar radiation, convert it into heat, and transfer the heat to a fluid (usually air, water, or oil) flowing through the collector. The energy collected is carried from the working fluid, either directly to the hot water or space conditioning equipment or to a thermal energy storage tank, from which it can be drawn for use at night or on cloudy days [26]. Solar water heaters are the most popular devices in the field of solar energy. As mentioned in the introduction, the nanofluid-based solar collectors are investigated in two aspects. In the first, these devices are studied from the efficiency viewpoint, and in the second, from economic and environmental viewpoints.

Author's personal copy

2.1.1. Efficiency of nanofluid-based solar collectors

Tyagi et al. [27] investigated theoretically the effects of different parameters on the efficiency of a low-temperature nanofluid-based direct absorption solar collector (DAC) where the working fluid is a mixture of water and aluminum nanoparticles. A schematic of the direct absorption collector is shown in Fig. 1. The upper side of this collector is covered by a glass while the lower side is well insulated, so it is adiabatic. The efficiency of the collector is obtained by the following equation:

$$\eta = \frac{useful\ gain}{available\ energy} = \frac{\dot{m}c_p(\overline{T}_{out} - \overline{T}_{in})}{AG_T} \quad (1)$$

where $\dot{m}$ is the mass flow rate of the fluid flowing through the collector; c_p is the specific heat; and $\overline{T}_{in}$ and $\overline{T}_{out}$ are the mean fluid inlet and outlet temperatures, respectively. A is the cover area of the collector, and G_T is the solar flux incident on the solar collector. In the analysis, they assumed that the values of $\overline{T}_{in}$, G_T, and $\dot{m}$ to be 35 °C, 1000 W/m^2, and 1.2 kg/s, respectively.

Tyagi et al. [27] plotted the variation of collector efficiency as a function of the particle volume fraction (%), where the volume fraction varies from 0.1% to 5% (see Fig. 2). Their results showed that by adding nanoparticles to the working fluid, the efficiency increases remarkably for low values of volume fraction of nanoparticles. They attributed the increase of collector efficiency to the increase in attenuation of sunlight passing through the collector due to the nanoparticles addition that leads to the increase of collector efficiency. However, for a volume fraction higher than 2%, the efficiency remains nearly constant, so adding more nanoparticles is not beneficial. Tyagi et al. [27] also investigated the effects of nanoparticles size on the collector efficiency where the volume fraction is equal to 0.8%. The results revealed that the efficiency increases slightly with an increase in the size of nanoparticles (see Fig. 3).

Otanicar et al. [28] investigated both experimentally and numerically the effects of different nanofluids (carbon nanotubes, graphite, and silver) on the performance of a micro scale direct absorption solar collector (DASC). The schematic of the experimental set up showing also the dimensions of the collector is presented in Fig. 4. Fig. 5 shows the variation of collector efficiency with volume fraction for different materials, estimated using Eq. (1). The DASC data are compared to a conventional collector configuration where the solar energy is absorbed on a black plate surface. As

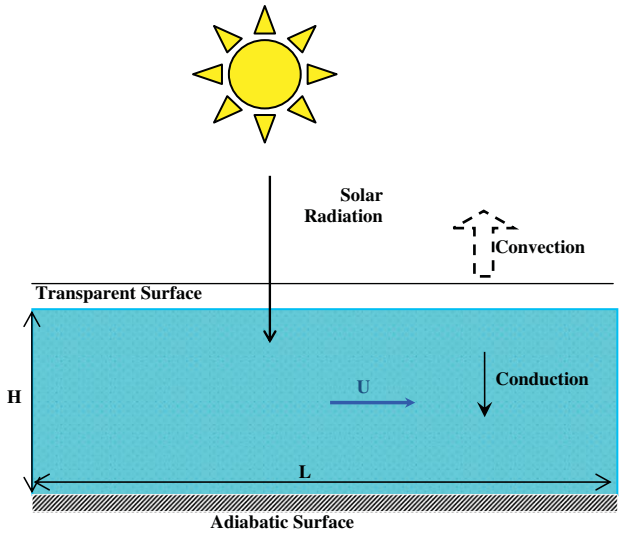

Fig. 1. Schematic of the nanofluid-based direct absorption solar collector (Reprinted from Tyagi et al. [27], with permission from ASME).

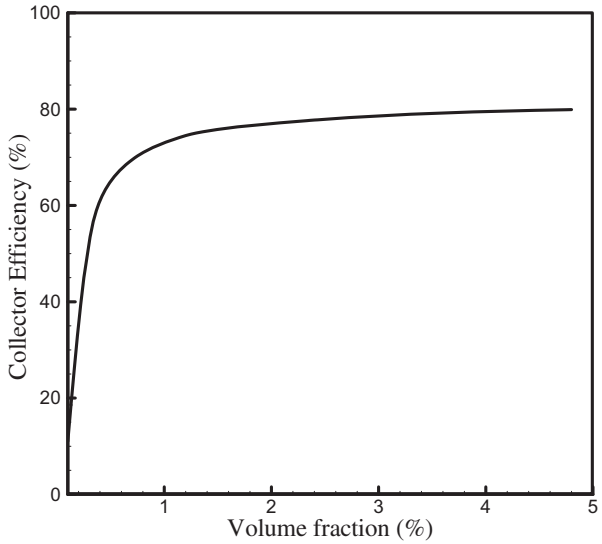

Fig. 2. Effect of particle volume fraction on collector efficiency (Reprinted from Tyagi et al. [27], with permission from ASME).

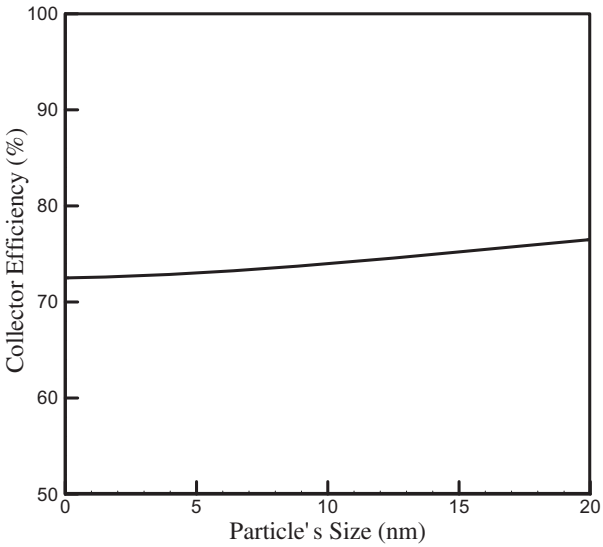

Fig. 3. Effect of nanoparticles size on collector efficiency (Reprinted from Tyagi et al. [27], with permission from ASME).

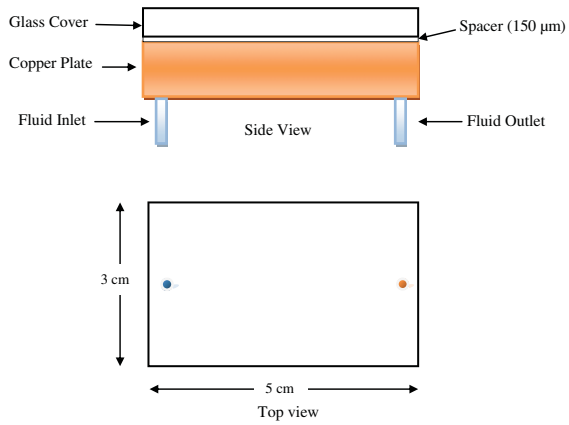

Fig. 4. Experimental schematic of the microsolar thermal collector (Reprinted with permission from Otanicar et al. [28]. Copyright 2010, American Institute of Physics).

Author's personal copy

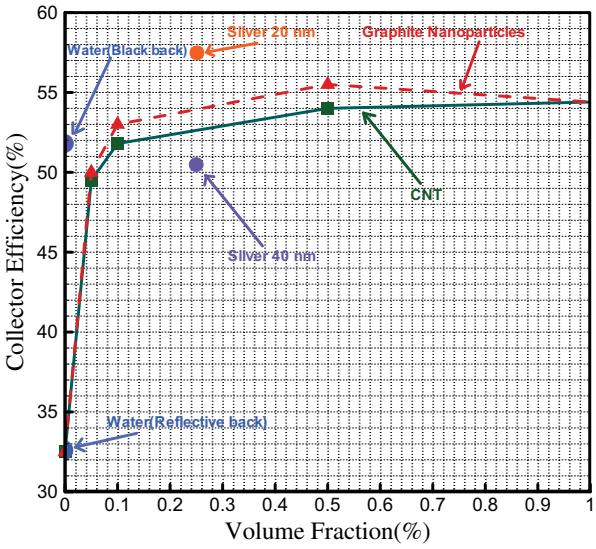

Fig. 5. Experimental microsolar thermal collector: steady-state collector efficiency (Reprinted with permission from Otanicar et al. [28]. Copyright 2010, American Institute of Physics).

shown, adding small quantities of nanoparticles leads to the remarkable enhancement of the efficiency until a volume fraction of approximately 0.5%. After a volume fraction of 0.5%, the efficiency begins to level off and even decrease slightly with increasing volume fraction. The authors attributed this reduction to the high increase of the fluid absorption at high particle loadings. The main difference in the steady-state efficiency between nanofluids occurs in silver particles when the size of the particles is between 20 and 40 nm. When halving the size from 40 to 20 nm, a 6% efficiency increase is found. The effect of particle size on efficiency is shown in Fig. 6 for silver nanoparticles. Unlike the results obtained by Tyagi et al. [27], with increase in size of nanoparticles, the efficiency of the collector decreases.

Taylor et al. [29] compared a nanofluid-based concentrating solar thermal system with a conventional one. Their results show that the use of a nanofluid in the receiver can improve the

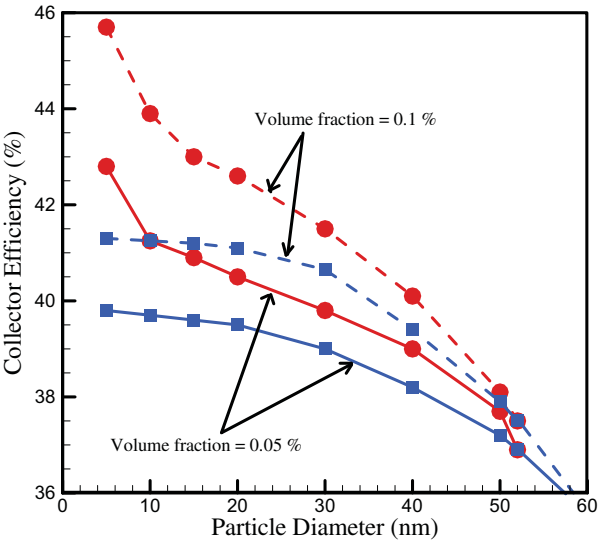

Fig. 6. Collector efficiency as a function of silver nanoparticle diameter (squares: bulk properties; circles: size-dependent properties and volume fraction (Reprinted with permission from Otanicar et al. [28]. Copyright 2010, American Institute of Physics).

efficiency by 10%. They also concluded that for 10–100 MWe power plants, using graphite/therminol VP-1 nanofluid with volume fractions approximately to 0.001% or less could be beneficial. The authors estimated that combining a nanofluid receiver with a solar thermal power tower with the capacity of 100 MWe operating in a solar resource like Tucson, Arizona, could generate $3.5 million more per year. Taylor et al. [29] considered two notional designs of potential nanofluid receivers, designated as A and B, as shown in Fig. 7.

He et al. [30] investigated the light-heat conversion characteristics of two nanofluids, water–TiO_2 and water–carbon nanotube (CNT), in a vacuum tube solar collector under sunny and cloudy weather conditions. The experimental results show a very good light heat conversion characteristic of the CNT–H_2O nanofluid with the weight concentration of 0.5%. Because of the better light-heat conversion characteristics of the CNT–H_2O nanofluid compared to the TiO_2–H_2O nanofluid, the temperature of the CNT–H_2O nanofluid is higher than that of the TiO_2–H_2O one. This means that the CNT–H_2O nanofluid is more suitable than the TiO_2–H_2O to be utilized in a vacuum tube solar collector.

Li et al. [31] studied the effects of three different nanofluids, Al_2O_3/water, ZnO/water, and MgO/water, on the performance of a tubular solar collector. Their results show that ZnO–H_2O nanofluid with 0.2% volume concentration is the best selection for the collector. Taylor et al. [32] investigated the optical property characterization of graphite, silver, copper, gold, and aluminum nanoparticles in water and VP1 as the based fluids to determine their potential to be used in direct absorption solar collectors. They revealed that over 95% of incoming sunlight can be absorbed (in a nanofluid thickness $\geqslant$10 cm) with very low nanoparticle volume fractions (less than 1×10^{-5}, or 10 ppm).

Khullar et al. [33] investigated theoretically a nanofluid-based concentrating parabolic solar collector (NCPSC) and compared the results obtained with the experimental results of conventional concentrating parabolic solar collectors operating under similar conditions. They used Aluminum nanoparticles with 0.05 vol.% suspended in Therminol VP-1 as the base fluid for the analysis. Fig. 8 shows the schematic of the nanofluid-based concentrating parabolic solar collector (NCPSC) that they considered in their work. They found that the thermal efficiency of NCPSC compared to a conventional parabolic solar collector is about 5–10% higher under the same weather conditions (see Fig. 9).

Yousefi et al. [34] experimentally investigated the effects of Al_2O_3/water nanofluid on the efficiency of a flat-plate solar collector. They examined the effects of two different weight fractions of the nanofluid, including 0.2% and 0.4%, where the diameter of particles was 15 nm. In addition, they studied the effects on efficiency of Triton X-100 used as a surfactant. The photograph and specifications of the flat-plate collector tested are presented in Fig. 10 and Table 1, respectively.

Yousefi et al. [34] conducted the experiments using a schematic setup shown in Fig. 11. Their findings are as follows:

1. The efficiency of the solar collector with 0.2% weight fraction (wt.) nanofluid is greater than that with water by 28.3% (see Fig. 12).
2. For a wide range of the reduced temperature parameter $(T_i - T_a)/G_T$, the efficiency of collector with 0.2% wt.% nanofluid is higher compared to 0.4 wt.% (see Fig. 12).
3. Using surfactant leads to a 15.63% enhancement of the efficiency.

Later, Yousefi et al. [35], using the same experimental setup as in their previous work [34], examined the effects of water–Multi wall carbon nanotubes (MWCNT) – Water nanofluid on the efficiency of the flat plate collector. They observed that:

Author's personal copy

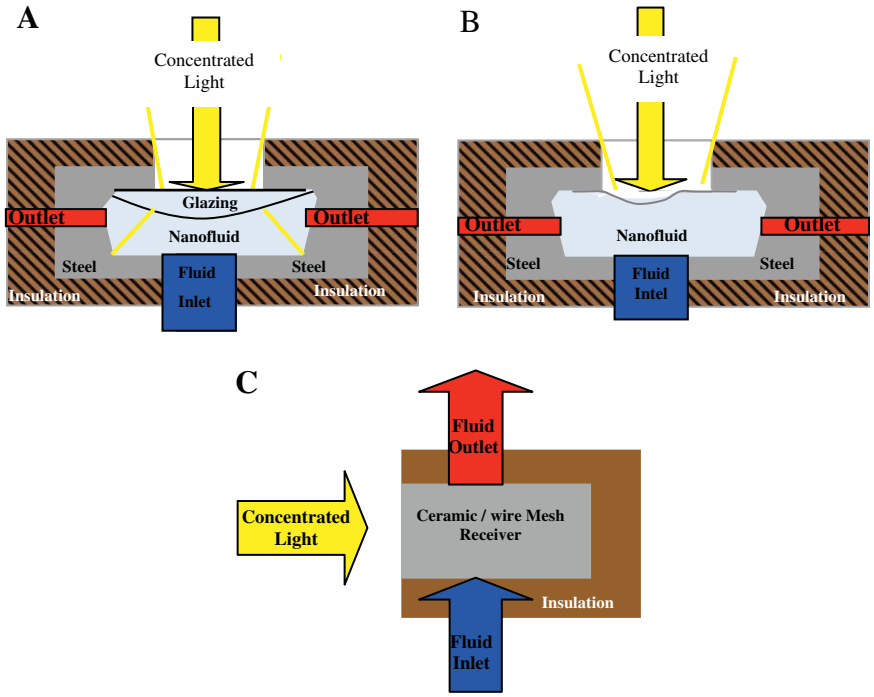

Fig. 7. (a) Conceptual design of a nanofluid concentrating collector with glazing. (b) Conceptual design of a nanofluid concentrating collector without glazing. (c) Conceptual drawing of a conventional power tower solid surface absorber (Reprinted with permission from Taylor et al. [29]. Copyright 2011, American Institute of Physics).

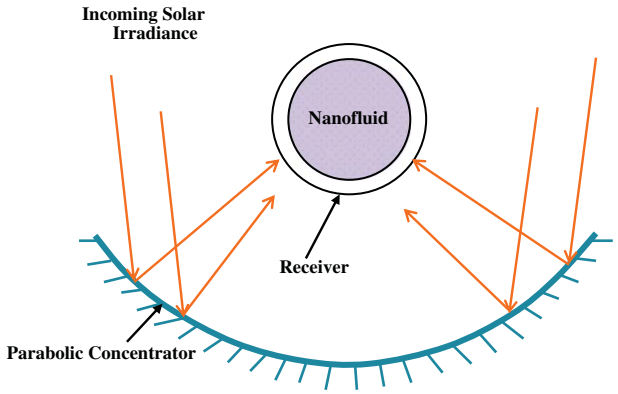

Fig. 8. Schematic of nanofluid-based concentrated parabolic solar collector (NCPSC) (Reprinted from Khullar et al. [33], with permission from ASME).

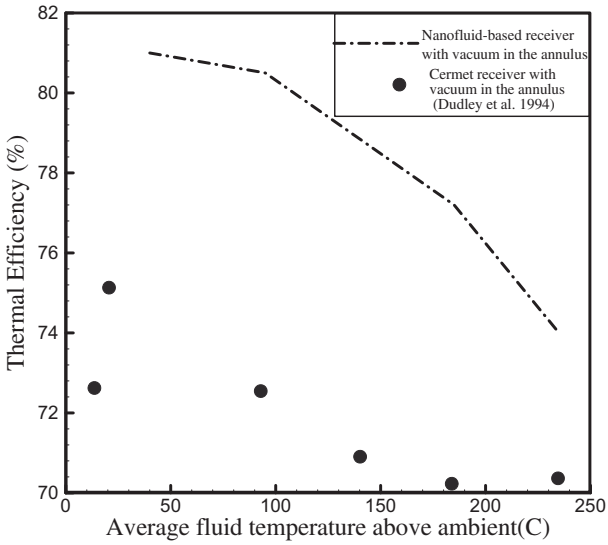

Fig. 9. Comparison of thermal efficiency as a function of average fluid temperature above ambient for NCPSC with conventional linear parabolic solar collector (Reprinted from Khullar et al. [33], with permission from ASME).

1. The efficiency of the collector by using of MWCNT–water nanofluid without surfactant is remarkably increased for 0.4 wt.% nanofluid, whereas with 0.2 wt.% the efficiency reduces compared to water as the working fluid.
2. For 0.2 wt.% nanofluid, using surfactant increases the efficiency of the collector compared to water.

In another study, Yousefi et al. [36], investigated the effects of pH variation of the MWCNT–water nanofluid on the efficiency of the flat plate collector. They used 0.2 wt.% MWCNT with various pH values −3.5, 6.5, and 9.5 – and Triton X-100 as an additive. They found that a bigger difference between the pH of nanofluid and pH of isoelectric point leads to higher efficiency. The isoelectric point is the point at which the molecules carry no electrical charge. For MWCNT, the pH of the isoelectric point is 7.4. The effects of pH variation of H_2O–MWCNT nanofluid on the efficiency of the flat plate collector are presented in Fig. 13.

In the following, some previous works are reviewed in which the potential of nanofluids for use in solar energy system is performed through the study of optical properties and thermal conductivity of nanofluids. Link and El-Sayed [37] reviewed the optical properties of gold nanoparticles. Particularly, they studied the shape and size dependence of radiative, and photothermal properties of gold nanocrystals. Khlebtsov et al. [38] investigated the effects of the size, shape, and structure of gold and silver nanoparticles on the optical properties of the nanofluids and perceived that the shape and size of the nanoparticle have great effect on the optical properties of a nanofluid. Sani et al. [39] reported the

Author's personal copy

Fig. 10. Flat-plate collector used by Yousefi et al. (Reprinted from Yousefi et al. [34], with permission from Elsevier).

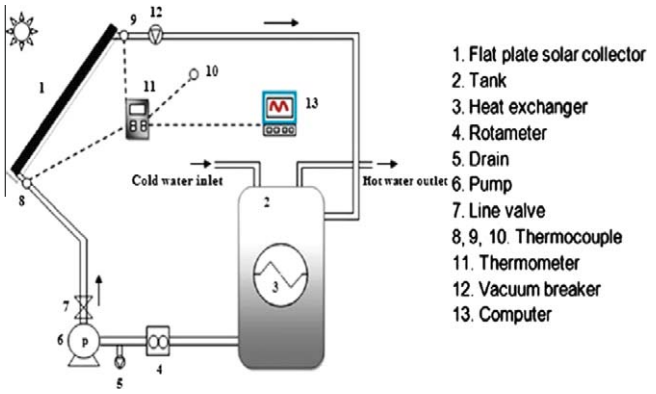

Fig. 11. Schematic of the experiment used by Yousefi et al. (Reprinted from Yousefi et al. [34], with permission from Elsevier).

Table 1
The specifications of the flat-plate collector (Reprinted from Yousefi et al. [34], with permission from Elsevier).

Specification	Dimension/value	Unit
Occupied area	200 × 94 × 9.5	cm
Absorption area	1.51	m^2
Weight	38.5	kg
Frame (Al6063 extruded)	–	–
Glass (float)	$t = 4$	mm
Header pipe (Cu)	Ø22, $t = 0.9$	mm
Connector riser pipe to absorber sheet (Cu)	Ø10, $t = 0.9$	mm
Absorption sheet:	–	–
Thermal emission:	7	%
Solar absorption:	96.2	%
Coating method:	Vacuum magnetron sputtering	–

optical characterization of a new fluid consisting of single-wall carbon nanohorns and ethylene glycol for solar energy applications. They concluded that carbon nanohorns could enhance remarkably the sunlight absorption with respect to pure base-fluid. The results obtained are compared with those obtained for fluids suspending more conventional carbon forms, i.e., carbon-black particles. They found that nanohorn spectral features are considerably more favorable than those of amorphous carbon for a specific application. This result shows that using carbon nanohorn-based nanofluids in thermal solar devices leads to the enhancement of efficiency and compactness in the systems. Mercatelli et al. [40,41] investigated the potential of single-wall carbon nanohorns nanoparticles with two different base fluids including water and glycol. Their measurements showed that these nanofluids are very suitable for direct absorption solar devices because only about 5% of the total extinction is scattered by SWCNH particles. In another work, Mercatelli et al. [42] applied a simple spectrophotometric to estimate the spectral scattering albedo of SWCNHs/water nanofluid. Recently, Saidur et al. [43] investigated the potential of Aluminum/water nanofluid to use in direct absorption solar collectors. They concluded that Aluminum/water nanofluid with 1% volume fraction improves considerably the solar absorption so that it is a fine solution for a direct solar collector. To use of the nanofluid they suggested, although the particle size has no effect on the extinction coefficient of nanofluid, in order to have Rayleigh scattering the size of nanoparticles should be less than 20 nm. They also found that the extinction coefficient varies linearly with volume fraction. Lenert and Wang [44] and Lenert [45] presented a combined theoretical and experimental work to optimize the efficiency of liquid-based solar receivers seeded with carbon-coated absorbing nanoparticles. They concluded that the efficiency of nanofluid volumetric receivers increases with increasing solar concentration and nanofluid height. Colangelo et al. [46] measured the thermal conductivities of CuO, Al_2O_3, ZnO and Cu with different shapes and volume fraction by 3%, where water and diathermic oil are as the base fluids, to evaluate their potential to use for high temperature applications such as in solar collectors. They found that the thermal conductivity enhancement of the nanofluids with diathermic oil is higher than that with water, with the same nanoparticles and at the same conditions. They also concluded that the thermal conductivity is reduced with increasing the size of particles. Kameya and Hanamura [47] found experimentally that the solar radiation absorption for the nanofluid of Ni/alkyl naphthalene with 0.1% volume fraction is much higher than the base fluid. Gan and Qiao [48] investigated the optical properties of ethanol-based nanofluids containing multiwalled carbon nanotubes (MWCNTs), carbon and aluminum nanoparticles. They concluded that MWCNTs leads to more absorption than aluminum and carbon nanoparticles. Finally, Gan and Qiao [49] found that for ethanol-based nanofluids, the radiation absorption for nanofluids

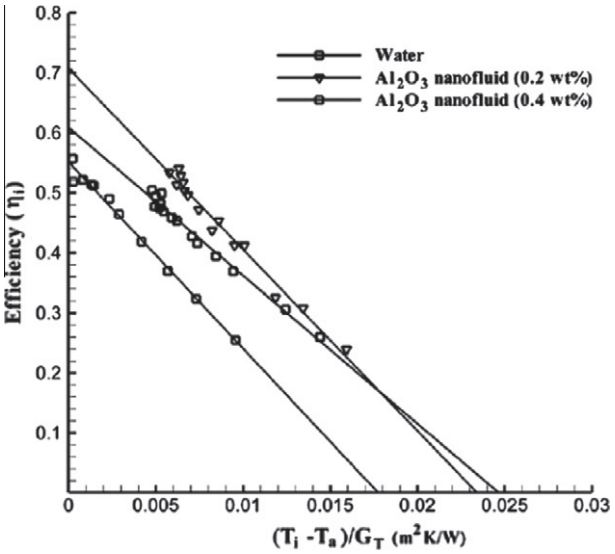

Fig. 12. The efficiencies of solar collectors for Al_2O_3 nanofluid without surfactant and for water (Reprinted from Yousefi et al. [34], with permission from Elsevier).

Author's personal copy

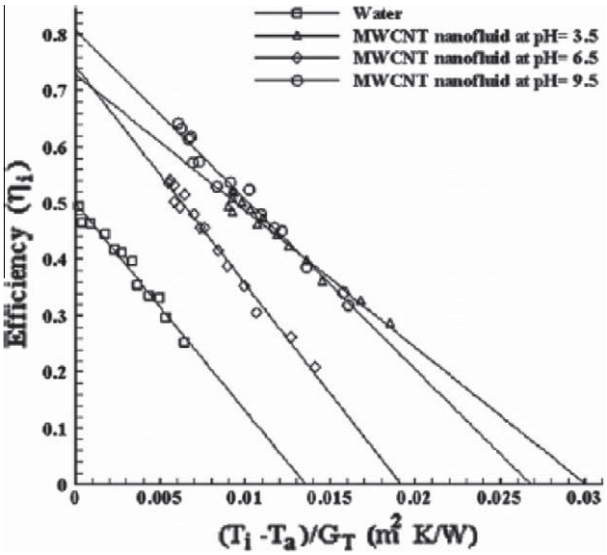

Fig. 13. The efficiency of the flat-plate solar collector with MWCNT nanofluid as a base fluid at three pH values compared water at a 0.0333 kg/s mass flow rate (Reprinted from Yousefi et al. [36], with permission from Elsevier).

containing Al_2O_3 nanoparticles is higher than nanofluids containing aluminum nanoparticles.

2.1.2. Economic and environment considerations

An accepted way to determine the economic and environmental impacts of a product is life cycle assessment [50]. This section presents the economic and environment considerations of nanofluid-based collectors. Otanicar and Golden [50] compared the environmental and economic aspects of using a conventional solar collector against a nanofluid based collector located in Phoenix, Arizona. The economic analysis shows that the capital cost and maintenance costs of the nanofluid-based solar collector compared to the conventional one are $120 and $20 higher, respectively (see Table 2). However, because of the higher efficiency and annual solar fraction of the nanofluid-based solar collector, the fuel cost savings per year, for both electricity and natural gas, is greater than that of the conventional solar collector. Moreover, due to the high cost of nanofluids compared the conventional collector, the payback period for a nanofluid-based collector is longer, but at the end of its useful life, it has the same life cycle savings as a conventional collector.

Embodied energy for both solar collectors, including conventional and nanofluid-based collectors, are compared in Table 3. The embodied energy for the nanofluid-based collector is about 9% lower. Additionally, from an environmental point of view, as shown in Table 4, the manufacturing of the nanofluid-based solar collector leads to 34 kg fewer CO_2 emissions while during its operation it saves 50 kg year when compared to the conventional solar collector. The magnitudes of other emissions including SO_x and NO_x are very small, so the differences are not considerable. Over the 15-year expected lifetime of the solar collectors, the nanofluid-based solar collector would offset more than 740 kg of CO_2 in comparison to a conventional collector. The authors concluded that more than one million metric tons of CO_2 could be offset per year if the usage of nanofluid-based solar collector systems for hot water heating increases by 50% in Phoenix, Arizona.

Khullar and Tyagi [51] examined the potential of the nanofluid-based concentrating solar water heating system (NCSWHS) as an alternative for systems based on fossil fuels. Using NCSWHS leads to annual electricity and liquefied petroleum gas (LPG) savings of approximately 1716 kWh/household/year and 206 kg/household /year, respectively, which produces significant economic benefits. In addition, they concluded that based on the annual estimation, CO_2 emissions are reduced by about 2.2×10^3 kg of CO_2/household/year. The use of nanofluid-based collectors is beneficial to reduce the environment problems. Table 5 summarizes the most important results obtained from the former works concerning the application or potential of nanofluids to use in solar collectors.

2.2. Other applications

In this section, other applications of nanofluids in solar energy systems including their applications in thermal energy storage materials, solar cells, and solar stills are reviewed. It should be noted that the reported works in this field are very scarce.

2.2.1. Thermal energy storage

Typical solar thermal-energy storage facilities require the storage medium to have high heat capacity and thermal conductivity. However, few materials are available with these properties and applicable in high temperatures. Recently, Shin and Banerjee [52] reported the anomalous enhancement of specific heat capacity of high-temperature nanofluids. They found that Alkali metal chloride salt eutectics when is doped with silica nanoparticles at 1% mass concentration increases the specific heat capacity of the nanofluid by 14.5%, so that this material can be a suitable one to use in solar thermal-energy storage facilities. One of techniques of storing solar energy is the application of PCMs. Among lots of PCMs available, paraffin is the most suitable due to its desirable characteristics, including large latent heat capacity, negligible super cooling and low cost. However, the inherent low thermal conductivity (0.21–0.24 W/mK) strongly prevents possible applications [53]. Wua et al. [53] numerically investigated the melting processes of Cu/paraffin nanofluids PCMs. Their results revealed that with 1 wt.% Cu/paraffin, the melting time can be saved by 13.1%. Therefore, they concluded that adding nanoparticles is an efficient technique to enhance the heat transfer in latent heat thermal energy storage system.

Table 2
Economic comparisons for conventional and nanofluid-based solar collectors (Reprinted with permission from Otanicar and Golden [50]. Copyright (2009) American Chemical Society).

Parameter	Conventional solar collector {$}	Nanofluid solar collector {$}
Independent costs	200.00	200.00
Area based costs	397.80	327.80
Nanoparticles		188.79
Total capital (one time cost)	597.80	716.59
Total maintenance (for 15 year life)	96.23	115.35
Total costs	694.03	831.94
Electricity cost saving per year	270.13	278.95
Years until electricity savings = costs	2.57	2.98
Natural gas cost saving per year	80.37	83.02
Years until natural gas savings = costs	8.64	10.02
Electricity price		
November_March (per kWh)	0.08	0.08
May_October (per kWh)	0.09	0.09
Daily service charge	0.25	0.25
Gas price		
Rate (per therm)	0.74	0.74
Monthly service charge	9.70	9.70

Author's personal copy

Table 3
Embodied energy comparisons for conventional and nanofluid-based solar collectors (Reprinted with permission from Otanicar and Golden [50]. Copyright (2009) American Chemical Society).

Description	Embodied energy index (MJ/kg)	Conventional solar collector		Nanofluid-based solar collector	
		Mass (kg)	Embodied energy content (MJ)	Mass (kg)	Embodied energy (MJ)
Insulation					
Polyester	53.7	1.74	93.22	1.74	93.22
Fiberglass	30.3	3.26	98.75	3.26	98.75
Glass	15.9	14.20	225.76	28.40	451.52
Copper pipe					
Collector	70.6	4.97	350.72	0.00	0.00
Manifold	70.6	3.48	245.57	3.48	245.57
Aluminum extrusion	201.0	0.56	111.58	0.56	111.58
Aluminum backplate	199.0	2.12	421.75	2.12	421.75
Steel backplate	34.8	0.00	0.00	5.97	207.65
Sealant	87.0	0.70	60.90	0.70	60.90
Black paint	90.4	0.30	27.12	0.30	27.12
Casing paint	90.4	0.90	81.36	0.90	81.36
Screws	34.8	0.00	0.04	0.00	0.04
Copper absorber	70.6	4.05	285.80	0.00	0.00
Nanoparticles	246.8	0.00	0.00	0.06	15.55
Thermal fluid	17.0	5.84	99.28	5.84	99.28
Conversion rate (27%)			567.50		516.86
Total		42.10	2669.34	53.32	2431.14

Table 4
Embodied energy emissions and consumer phase operational energy (Reprinted with permission from Otanicar and Golden [50]. Copyright (2009) American Chemical Society).

Emissions	Pollution from collector embodied energy		Saving of solar energy	
	Conventional (kg)	Nanofluid-based (kg)	Conventional (kg/year)	Nanofluid-based (kg/year)
Carbon dioxide (CO_2)	599.77	564.94	1500.89	1550.33
Sulfur oxides (SO_x)	0.51	0.48	0.83	0.85
Nitrogen oxides (NO_x)	0.84	0.79	1.53	1.58

2.2.2. Solar cells

Cooling of solar cells can improve the efficiency of such solar devices. Nanofluids can be used as a solution to cool the solar cells. Elmir et al. [54] simulated the cooling of a silicon solar cell using the finite element method. They considered the solar panel as an inclined cavity (with a slope of 30°) and solved the equations in Cartesian coordinate system. They used Al_2O_3/water nanofluid for their analysis, where the thermal conductivity and viscosity of the nanofluid are estimated using the models of Wasp [55] and Brinkman [56], respectively. As seen in Fig. 14, they concluded that using nanofluids leads to the increase of the average Nusselt number, and, hence, the rate of cooling increases with increases in volume fraction. Of course, it should be noted that the thermophysical properties, which are used in this study, are old and they do not predict the thermal conductivity and viscosity of nanofluids correctly. Therefore, it is suggested that in the future works, temperature-dependent models, or at least newer temperature-independent models are used to calculate the thermophysical properties of nanofluids. For example, to calculate the viscosity of nanofluids, the models and relation presented by Maiga et al. [57], Buongiorno [58], Nguyen et al. [59], Koo and Kleinstreuer [60], and Duangthongsuk and Wongwises [61] can be used. To estimate the thermal conductivity of nanofluids, the relations presented by Maiga et al. [57], Xuan et al. [62], Jang and Choi [63], Koo and Kleinstreuer [64], Chon et al. [65], Duangthongsuk and Wongwises [61] and Yiamsawasd et al. [66] can be applied.

2.2.3. Solar stills

Potable water demand is increasing due to rapid population increase and due to uncontrolled pollution of freshwater resources. According to the World Health Organization, nearly 2.8 billion people (approximately 40% of the world population) currently have no access to safe drinking water, and water-borne diseases account for 90% of all infectious diseases in the developing world [67]. In arid remote regions in the world, the provision of fresh water is more critical. In these regions, solar desalination systems can solve part of the problem where solar energy is available. Solar stills can be used to avoid the greenhouse gas emissions from the production of fresh water [68]. Many researches have carried out research on solar stills, and different methods are applied to improve their productivity. Recently, Gnanadason et al. [69] reported that using nanofluids in a solar still can increase its productivity. The schematic of their experimental set-up is shown in Fig. 15. They investigated the effects of adding carbon nanotubes (CNTs) to the water inside a single basin solar still. Their results revealed that adding nanofluids increases the efficiency by 50%. Nevertheless, they have not mentioned the amount of nanofluid added to the water inside the solar still. Regarding the addition of nanofluids to the solar still, the economic viability should be considered. In literature, some works reported that adding dyes to solar stills could improve the efficiency. For instance, Nijmeh et al. [70] concluded that adding violet dye to the water inside the solar still increases the efficiency by 29%, which is considerable. On the other hand, it is evident that nanofluids (especially CNTs) compared to dyes are more expensive, hence this may be a challenge on using nanofluids in solar stills, because in this type of use of nanofluids in solar stills the nanofluids have no flow in a closed loop so that they could be recovered.

3. Future work

The above review shows that the application of nanofluids in solar energy applications is still in its infancy. Nanofluids can be used in many fields of solar energy. Here, some suggestions are presented for future work in the area. The authors hope that these

Author's personal copy

Table 5
Summary of former works on the application or potential of nanofluids to use in solar collectors.

Author(s) and type of study	Collector type	Nanofluid type and nanoparticle size	Results
Tyagi et al. [27] (Theoretically)	Non-concentrating direct absorption	Aluminum/water (0–20 nm)	–Efficiency remarkably increases for volume fraction less than 2% –Efficiency remains nearly constant for volume fraction higher than 2% –Efficiency increases slightly with an increase in the size of nanoparticles
Otanicar et al. [28] (Theoretically and experimentally)	Non-concentrating micro scale direct absorption	Graphite/water (30 nm) silver/water (20 and 40 nm) carbon nanotube/water (6–20 nm diameter, 1000–5000 nm length)	–Efficiency considerably increases for volume fractions less than 0.5% –Efficiency for volume fractions higher than 0.5% may even decrease –Efficiency increases by 6%, with decreasing the nanoparticle size in Silver/Water nanofluid
Taylor et al. [29] (Theoretically and experimentally)	Concentrating direct absorption	Graphite/therminol VP-1 aluminum/therminol VP-1 silver/therminol VP-1 copper/therminol VP-1 (10–100 nm)	–Efficiency increases up to 10% by using a nanofluid in the receiver –Using graphite/therminol VP-1 nanofluid with volume fractions less than 0.001% is beneficial for 10–100 MWe power plants
He et al. [30] (Experimentally)	Vacuum tube	TiO_2/water (5–10 nm) CNT/water (10–50 nm diameter, 100–1000 nm length)	–CNT/water nanofluid is more suitable than the TiO_2/water to be used in a vacuum tube solar collector
Li et al. [31] (Experimentally)	Tubular	Al_2O_3/water ZnO/water MgO/water(size < 20 nm)	–ZnO/water nanofluid with 0.2% volume concentration is the best selection for the collector
Taylor et al. [32] (Theoretically and experimentally)	Direct absorption	Graphite/water and graphite/VP1 aluminum/water and aluminum/VP1 copper/water and copper/VP1 silver/water and silver/VP1 gold/water and silver/VP1	–Over 95% of incoming sunlight can be absorbed for nanofluid thickness $\geqslant$ 10 and nanoparticle volume fractions less than 1×10^{-5}
Khullar et al. [33] (Theoretically)	Concentrating Parabolic	Aluminum/therminol VP-1 (5 nm)	–Thermal efficiency of nanofluid concentrating parabolic collectors compared to a conventional parabolic solar collector is about 5–10% higher
Yousefi et al. [34] (Experimental)	Flat plate	Al_2O_3/water (15 nm) Triton X-100 is used as a surfactant	–Efficiency of the solar collector with 0.2% weight fraction (wt) nanofluid is higher than that with water by 28.3%. –Efficiency increases by15.63% using the surfactant
Yousefi et al. [35] (Experimental)	Flat plate	Water-Multi wall carbon nanotubes (MWCNT)/water (10–30 nm) Triton X-100 is used as a surfactant	–Efficiency of the collector increases remarkably for 0.4 wt.% nanofluid, whereas with 0.2 wt.% the efficiency reduces compared to water –For 0.2 wt.% nanofluid, using surfactant increases the efficiency of the collector compared to water
Yousefi et al. [36] (Experimental)	Flat plate	Water-Multi wall carbon nanotubes (MWCNT)/water with various pH values: 3.5, 6.5, and 9.5 Triton X-100 is used as a surfactant	–A bigger difference between the pH of nanofluid and pH of isoelectric point leads to higher efficiency
Otanicar and Golden [50] (Theoretical)	Direct absorption	Graphite/water and propylene glycol	–Using a nanofluid-based solar collector leads to fewer CO_2 emissions compared to the conventional solar collector
Khullar and Tyagi [51] (Theoretical)	Concentrating direct absorption	Aluminum/water	–Using this type of collector leads to fewer CO_2 emissions by 2.2×10^3 kg in 1 year

proposals will be helpful for the development on the use of nanofluids in the solar thermal devices.

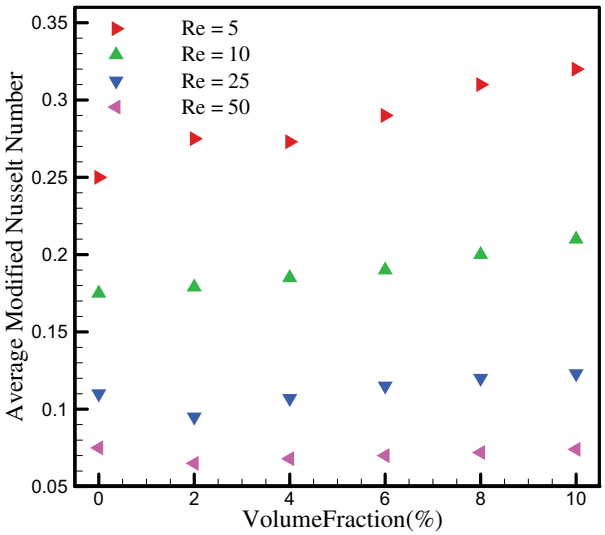

Fig. 14. Effects of volume fraction on Nusselt number for cooling a solar cell (Reprinted from Elmir et al. [54], with permission from Elsevier).

3.1. Parabolic trough systems

As mentioned, only a theoretical work has been done on parabolic trough collectors, therefore some experimental studies can be performed on the effects of nanofluids on the efficiency of parabolic trough systems.

3.2. Photovoltaic/thermal systems

A photovoltaic/thermal (PV/T) system is a hybrid structure that converts part of the sun's radiation to electricity and part to thermal energy [71]. One can investigate experimentally the effects of using different nanofluids on the cooling rate, and, hence, the efficiency of the PV/T systems. In this area, the effects of different volume fractions, nanoparticle size on the efficiency of the system can be studied. A review of the literature shows that many researches have been carried out on the potential of nanofluids for cooling of different thermal systems such as electronic devices [72–74], automobile radiator [75], and micro channel heat sinks [76]. Therefore, using nanofluids to cool the PV/T system may be reasonable.

3.3. Solar thermoelectric cells

In recent years, interest in the development of solar thermoelectric systems has been considerably increased [77]. The

Author's personal copy

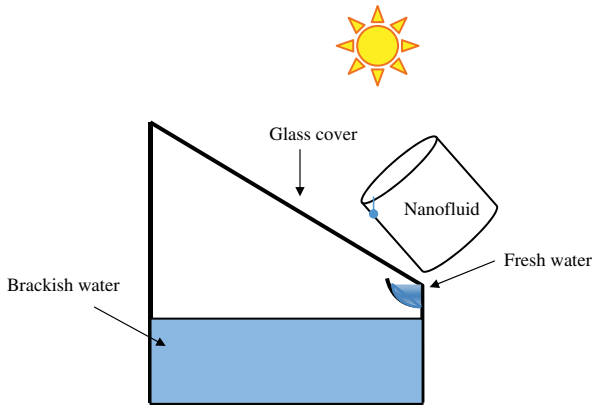

Fig. 15. Schematic of the experimental set up used by Gnanadason et al. [69].

thermoelectric cells can be used to convert the solar energy to electricity due to the temperature difference between two hot and cold surfaces. A greater temperature difference between the hot and cold surfaces of the thermoelectric cell leads to a bigger electricity production. The authors would like to suggest an experimental set-up to investigate the effects of nanofluids on the performance of such systems. Fig. 16 shows the schematic of the set-up, which is a development of the work done by Fan et al. [77]. In this work, a dish concentrates the solar radiation on the thermoelectric cells installed on the focal point of the dish. In this way the effects of different nanofluids with various mass flow rates on the efficiency of the solar thermoelectric cell can be studied.

3.4. Solar ponds

Salinity gradient solar ponds are great bodies of water between 2–5 m deep, which could collect solar radiation and store it in the form of heat [78,79].

Heat can be extracted from the solar ponds and has been used for industrial process heating, space heating, and power generation. In all these applications heat is extracted from the bottom of the solar pond which is at a temperature of about 50–60 °C higher than the top surface of the solar pond [80,81]. Concerning the application of nanofluids in solar ponds an experimental set up is proposed in Fig. 17. As seen, a nanofluid flows through a heat exchanger mounted at the bottom of the solar pond to absorb the heat. It expects that nanofluids could enhance the rate of heat removal from the bottom of the solar pond.

3.5. Other possibilities

The above suggestions are only a few of the possible applications relating to the use of nanofluids in solar energy. Besides the above ideas, nanofluids also can be used in solar cooling systems, solar absorption refrigeration systems, and a combination of different solar devices. Here, for instance, the authors would like to suggest some Refs. [82–86], in which there is a potential to use a nanofluid as the working fluid. In addition, in numerical studies such as the simulation of solar cell cooling, which it is mentioned in Section 2.2.2, new models can be used to calculate the thermophysical properties. Additionally, the nanofluid can be considered as a two-phase mixture [87].

4. Challenges

The possible challenges for the application of nanofluids in solar thermal devices are mentioned briefly in the following sections.

4.1. High cost

The first possible challenge in the use of nanofluids in solar thermal devices is the high cost of nanofluids because of difficulties in production. The high cost of nanofluids to use in thermal engineering systems such as heat exchangers is emphasized as a disadvantage in some works [88,89].

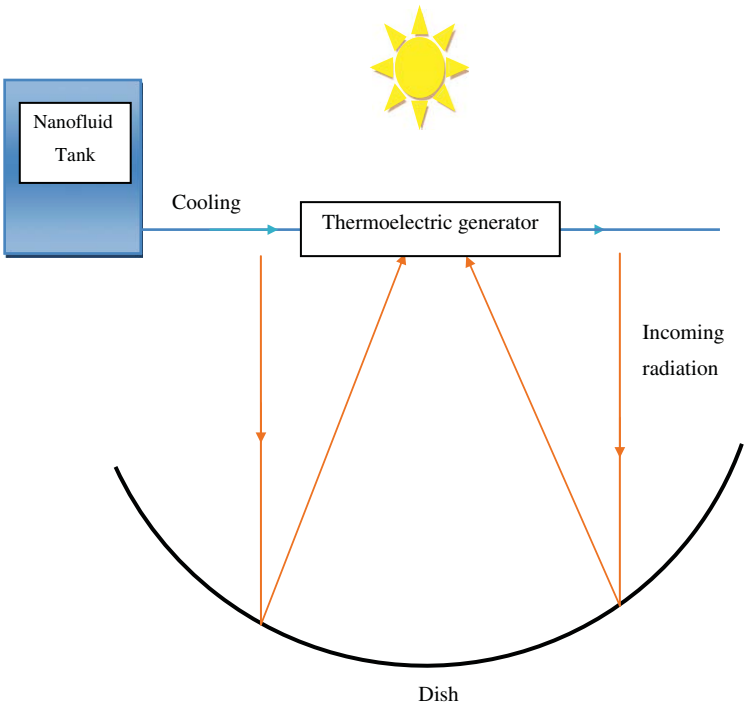

Fig. 16. The experimental set-up proposed for using nanofluids in thermoelectric cells.

Author's personal copy

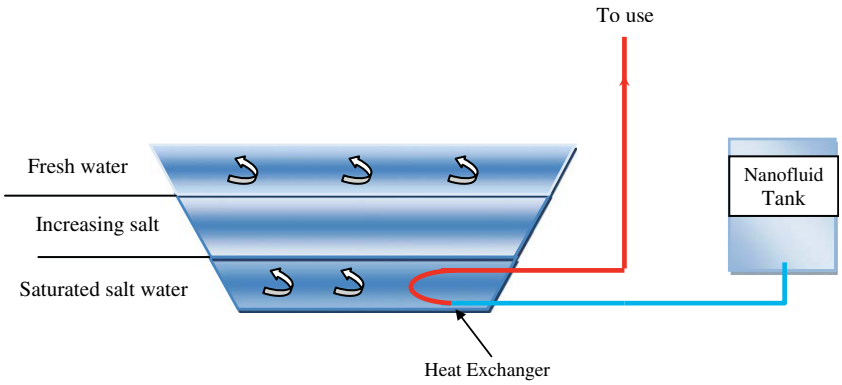

Fig. 17. The experimental set-up proposed for using nanofluids in solar ponds.

4.2. Instability and agglomerating

Instability and agglomerating of the nanoparticles is another problem. Therefore, using nanofluids in solar systems with natural circulation (such as thermosiphons) where there is no pump to circulate the fluid, is not reasonable. It should be also noted that for high temperature gradients the agglomeration of nanoparticles seems to be more serious [90]. Therefore, exact investigations are needed for an appropriate selection of a nanofluid for applications in high temperatures.

4.3. Pumping power and pressure drop

Using a nanofluid with higher viscosity compared to the base fluid leads to the increase of pressure drop and consequently the increases in the required power for pumping. For example, Duangthongsuk and Wongwises [91] found during their experiments that the pressure drop under a turbulent regime increases with an increase in volume fraction of TiO_2/water nanofluid. In another experimental research, Razi et al. [92] also concluded that using CuO/oil nanofluid increases the pressure drop under a laminar regime.

4.4. Erosion and corrosion of components

Existing of nanoparticles in nanofluid may lead to corrosion and erosion of thermal devices in a long time. Celata et al. [93] recently investigated the effects of nanofluid flow effects on erosion and corrosion of metal surfaces. They conducted their experiments for TiO_2, Al_2O_3, SiC, ZrO_2 nanoparticles with water as the base fluid where the nanofluids flow in pipes with three different materials, i.e., aluminum, copper and stainless. They concluded that the nanofluids have no effect on the erosion of the stainless pipe, while the aluminum pipe has highest erosion. They also found that ZrO_2 and TiO_2 nanoparticles lead to highest erosion while SiC nanoparticles results in lowest erosion.

5. Conclusion

Nanofluids are advanced fluids containing nano-sized particles that have emerged during the last two decades. Nanofluids are used to improve system performance in many thermal engineering systems. This paper presented a review of the applications of nanofluids in solar thermal engineering. The experimental and numerical studies for solar collectors showed that in some cases, the efficiency could increase remarkably by using nanofluids. Of course, it is found that using a nanofluid with higher volume fraction always is not the best option (Yousefi et al. [34]). Therefore, it is suggested that the nanofluids in different volume fractions should be tested to find the optimum volume fraction. It is also seen that the available theoretical works give different results on the effects of particle size on the efficiency of the collectors (see Refs. [27,28]). It is worth to carry out an experimental work on the effect of particle size on the collector efficiency. It is also concluded that some factors such as adding surfactant to nanofluid and a suitable selection of the pH of nanofluid are effective in the collector efficiency. From the economic and environmental point of view, the previous studies showed that using nanofluids in collectors leads to a reduction in CO_2 emissions and annual electricity and fuel savings. Some other reported works of applications of nanofluids in solar cells, solar thermal energy storage, and solar stills are also reviewed. It is also stressed that for the numerical study of solar systems (for example cooling of solar cells), it is better to use the new thermophysical (temperature-dependent) models and two phase mixture models for the nanofluid to have a more exact prediction of the system performance. This review reveals that the application of nanofluids in solar energy is yet in its infancy. Therefore, some proposals are presented to develop the use of nanofluids in different solar systems such as solar ponds, solar thermoelectric cells, and so on. Finally, the most important challenges on the use of nanofluids in solar systems including high costs of production, instability and agglomeration problems, increased pumping power and erosion are mentioned. These challenges may be reduced with the development of nanotechnology in the future.

Acknowledgments

The fifth author wishes to thank the Thailand Research Fund, and the National Research University Project for support for his study. Also, the valuable help of Prof. Akbarzadeh and Dr. Singh from RMIT University, Australia, and Dr. Tyagi from the School of Mechanical, Materials and Energy Engineering, Indian Institute of Technology Ropar, India is appreciated.

References

[1] U.S. Choi, Enhancing thermal conductivity of fluids with nanoparticles, ASME FED 231 (1995) 99–103.
[2] Y. Li, J. Zhou, S. Tung, E. Schneider, S. Xi, A review on development of nanofluid preparation and characterization, Powder Technol. 196 (2009) 89–101.
[3] J.H. Lee, S.H. Lee, C.J. Choi, S.P. Jang, S.U.S. Choi, A review of thermal conductivity data, mechanics and models for nanofluids, Int. J. Micro–Nano Scale Transport 1 (2010) 269–322.
[4] A. Ghadimi, R. Saidur, H.S.C. Metselaar, A review of nanofluid stability properties and characterization in stationary conditions, Int. J. Heat Mass Transfer 54 (2011) 4051–4068.

Author's personal copy

[5] G. Ramesh, N.K. Prabhu, Review of thermo-physical properties, wetting and heat transfer characteristics of nanofluids and their applicability in industrial quench heat treatment, Nanoscale Res. Lett. 6 (2011) 334.
[6] K. Khanafer, K. Vafai, A critical synthesis of thermophysical characteristics of nanofluids, Int. J. Heat Mass Transfer 54 (2011) 4410–4428.
[7] J. Fan, L. Wang, Review of heat conduction in nanofluids, ASME J. Heat Transfer 133 (2011) 040801.
[8] R.S. Vajjha, D.K. Das, A review and analysis on influence of temperature and concentration of nanofluids on thermophysical properties, heat transfer and pumping power, Int. J. Heat Mass Transfer (2012), http://dx.doi.org/10.1016/j.ijheatmasstransfer.2012.03.048.
[9] V. Trisaksri, S. Wongwises, Critical review of heat transfer characteristics of nanofluids, Renew. Sustain. Energy Rev. 11 (2007) 512–523.
[10] W. Daungthongsuk, S. Wongwises, A critical review of convective heat transfer of nanofluids, Renew. Sustain. Energy Rev. 11 (2007) 797–817.
[11] S. Kakaç, Pramuanjaroenkij, Review of convective heat transfer enhancement with nanofluids, Int. J. Heat Mass Transfer 52 (2009) 3187–3196.
[12] L. Godson, B. Raja, D. Mohan, S. Wongwises, Enhancement of heat transfer using nanofluids – An overview, Renew. Sustain. Energy Rev. (2009), http://dx.doi.org/10.1016/j.rser.2009.10.004.
[13] J. Sarkar, A critical review on convective heat transfer correlations of nanofluids, Renew. Sustain. Energy Rev. 11 (2011) 3271–3277.
[14] Y. Ding, H. Chen, L. Wang, C.-Y. Yang, Y. He, W. Yang, W.P. Lee, L. Zhang, R. Huo, Heat transfer intensification using nanofluids, Kona, Nr. 25 (2007) 23–38.
[15] C. Kleinstreuer, J. Li, J. Koo, Microfluidics of nano-drug delivery, Int. J. Heat Mass Transfer 51 (2008) 5590–5597.
[16] R. Saidur, S.N. Kazi, M.S. Hossain, M.M. Rahman, H.A. Mohammed, A review on the performance of nanoparticles suspended with refrigerants and lubricating oils in refrigeration systems, Renew. Sustain. Energy Rev. 15 (2011) 310–323.
[17] S. Thomas, C. Sobhan, A review of experimental investigations on thermal phenomena in nanofluids, Nanoscale Res. Lett. 6 (2011) 377.
[18] W. Escher, T. Brunschwiler, N. Shalkevich, A. Shalkevich, T. Burgi, B. Michel, D. Poulikakos, On the cooling of electronics with nanofluids, ASME J. Heat Transfer 133 (2011) 051401.
[19] O. Abouali, G. Ahmadi, Computer simulations of natural convection of single phase nanofluids in simple enclosures: a critical review, Appl. Therm. Eng. 36 (2012) 1–13.
[20] A. Kamyar, R. Saidur, M. Hasanuzzaman, Application of computational fluid dynamics (CFD) for nanofluids, Int. J. Heat Mass Transfer (2012), http://dx.doi.org/10.1016/j.ijheatmasstransfer.2012.03.052.
[21] H.S. Ahn, M.H. Kim, A review on critical heat flux enhancement with nanofluids and surface modification, ASME J. Heat Transfer 134 (2012) 024001.
[22] R. Saidur, K.Y. Leong, H.A. Mohammad, A review on applications and challenges of nanofluids, Renew. Sustain. Energy Rev. 15 (2011) 1646–1668.
[23] M. Thirugnanasambandam, S. Iniyan, R. Goic, A review of solar thermal technologies, Renew. Sustain. Energy Rev. 14 (2010) 312–322.
[24] A. Sharma, A comprehensive study of solar power in India and World, Renew. Sustain. Energy Rev. 15 (2011) 1767–1776.
[25] S. Mekhilef, R. Saidur, A. Safari, A review on solar energy use in industries, Renew. Sustain. Energy Rev. 15 (2011) 1777–1790.
[26] S.A. Kalogirou, Solar Energy Engineering: Processes and Systems, Elsevier, Oxford, 2009.
[27] H. Tyagi, P. Phelan, R. Prasher, Predicted efficiency of a low-temperature nanofluid – based direct absorption solar collector, J. Solar Energy Eng. 131 (2009) 041004.
[28] T.P. Otanicar, P.E. Phelan, R.S. Prasher, G. Rosengarten, R.A. Taylor, Nanofluid-based direct absorption solar collector, J. Renew. Sustain. Energy 2 (2010) 033102.
[29] R.A. Taylor, P.E. Phelan, T.P. Otanicar, C.A. Walker, M. Nguyen, S. Trimble, R. Prasher, Applicability of nanofluids in high flux solar collectors, J. Renew. Sustain. Energy 3 (2011) 023104.
[30] Y. He, S. Wang, J. Ma, F. Tian, Y. Ren, Experimental study on the light-heat conversion characteristics of nanofluids, Nanosci. Nanotechnol. Lett. 3 (2011) 494–496.
[31] Y. Li, H. Xie, W. Yu, J. Li, Investigation on heat transfer performances of nanofluids in solar collector, Mater. Sci. Forum 694 (2011) 33–36.
[32] R.A. Taylor, P.E. Phelan, T.P. Otanicar, R. Adrian, R.P. Prasher, Nanofluid optical property characterization: towards efficient direct absorption solar collectors, Nanoscale Res. Lett. 6 (2011) 225.
[33] V. Khullar, H. Tyagi, P.E. Phelan, T.P. Otanicar, H. Singh, R.A. Taylor, Solar energy harvesting using nanofluids-based concentrating solar collector, in: Proceedings of MNHMT2012 3rd Micro/Nanoscale Heat & Mass Transfer International Conference on March 3–6, Atlanta, Georgia, USA, 2012.
[34] T. Yousefi, F. Veysi, E. Shojaeizadeh, S. Zinadini, An experimental investigation on the effect of Al_2O_3–H_2O nanofluid on the efficiency of flat-plate solar collectors, Renew. Energy 39 (2012) 293–298.
[35] T. Yousefi, F. Veysi, E. Shojaeizadeh, S. Zinadini, An experimental investigation on the effect of MWCNT–H_2O nanofluid on the efficiency of flat-plate solar collector, Exp. Therm. Fluid Sci. 39 (2012) 207–212.
[36] T. Yousefi, F. Veysi, E. Shojaeizadeh, S. Zinadini, An experimental investigation on the effect of pH variation of MWCNT–H2O nanofluid on the efficiency of a flat-plate solar collector, Solar Energy 86 (2012) 771–779.
[37] S. Link, M.A. El-Sayed, Shape and size dependence of radiative, non-radiative and photothermal properties of gold nanocrystals, Int. Rev. Phys. Chem. 19 (2000) 409–453.
[38] N. Khlebtsov, L. Trachuk, A. Mel'nikov, The effect of the size, shape, and structure of metal nanoparticles on the dependence of their optical properties on the refractive index of a disperse medium, Optics Spectrosc. 98 (1) (2005) 77–83.
[39] E. Sani, L. Mercatelli, S. Barison, C. Pagura, F. Agresti, L. Colla, P. Sansoni, Potential of carbon nanohorn-based suspensions for solar thermal collectors, Solar Energy Mater. Solar Cells 95 (2011) 2994–3000.
[40] L. Mercatelli, E. Sani, G. Zaccanti, F. Martelli, D.P. Ninni, S. Barison, C. Pagura, F. Agresti, D. Jafrancesco, Absorption and scattering properties of carbon nanohorn-based nanofluid for direct sunlight absorbers, Nanoscale Res. Lett. 6 (1) (2011) 282.
[41] L. Mercatelli, E. Sani, D. Fontani, G. Zaccanti, F. Martelli, D.P. Ninni, Scattering and absorption properties of carbon nanohorn-based nanofluids for solar energy applications, J. Euro. Optical Soc. 6 (2011) 11025.
[42] L. Mercatelli, E. Sani, A. Giannini, D.P. Ninni, F. Martelli, G. Zaccanti, Carbon nanohorn-based nanofluids: characterization of the spectral scattering albedo, Nanoscale Res. Lett. 7 (2012) 96.
[43] R. Saidur, T.C. Meng, Z. Said, M. Hasanuzzaman, A. Kamyar, Evaluation of the effect of nanofluid-based absorbers on direct solar collector, Int. J. Heat Mass Transfer 55 (2012) 589–5907.
[44] A. Lenert, E.N. Wang, Optimization of nanofluid volumetric receivers for solar thermal energy conversion, Solar Energy (2011).
[45] A. Lenert, Nanofluid-based receivers for high-temperature, high-flux direct solar collectors. M.Sc. Thesis, Massachusetts Institute of Technology, 2010.
[46] G. Colangelo, E. Favale, A. de Risi, D. Laforgia, Results of experimental investigations on the heat conductivity of nanofluids based on diathermic oil for high temperature applications, Appl. Energy 97 (2012) 828–833.
[47] Y. Kameya, K. Hanamura, Enhancement of solar radiation absorption using nanoparticle suspension, Solar Energy 85 (2011) 299–307.
[48] Y. Gan, L. Qiao, Optical properties and radiation-enhanced evaporation of nanofluid fuels containing carbon-based nanostructures, Energy Fuels 26 (2012) 4224–4230.
[49] Y. Gan, L. Qiao, Radiation-enhanced evaporation of ethanol fuel containing suspended metal nanoparticles, Int. J. Heat Mass Transfer 55 (2012) 5777–5782.
[50] T.P. Otanicar, J. Golden, Comparative environmental and economic analysis of conventional and nanofluid solar hot water technologies, Environ. Sci. Technol. 43 (2009) 6082–6087.
[51] V. Khullar, H. Tyagi, A study on environmental impact of nanofluid based concentrating solar water heating system, Int. J. Environ. Studies 69 (2012) 220–232.
[52] D. Shin, D. Banerjee, Enhancement of specific heat capacity of high-temperature silica-nanofluids synthesized in alkali chloride salt eutectics for solar thermal-energy storage applications, Int. J. Heat Mass Transfer 54 (2011) 1064–1070.
[53] S. Wua, H. Wanga, S. Xiaoa, D. Zhub, Numerical simulation on thermal energy storage behavior of Cu/paraffin nanofluids PCMs, Energy Procedia 31 (2012) 240–244.
[54] M. Elmir, R. Mehdaoui, A. Mojtabi, Numerical simulation of cooling a solar cell by forced convection in the presence of a nanofluid, Energy Procedia 18 (2012) 594–603.
[55] F.J. Wasp, Solid–Liquid Slurry Pipeline Transportation, Trans. Tech, Berlin, 1977.
[56] H.C. Brinkman, The viscosity of concentrated suspensions and solutions, J. Chem. Phys. 20 (1952) 571.
[57] S. Maiga, S.J. Palm, C.T. Nguyen, G. Roy, N. Galanis, Heat transfer enhancement by using nanofluids in forced convection flows, Int. J. Heat Fluid Flow 26 (2005) 530–546.
[58] J. Buongiorno, Convective transport in nanofluids, ASME J. Heat Transfer 128 (2006) 240–250.
[59] C.T. Nguyen, F. Desgranges, G. Roy, N. Galanis, T. Maŕe, S. Boucher, H.A. Mintsa, Temperature and particle-size dependent viscosity data for waterbased nanofluids– hysteresis phenomenon, Int. J. Heat Fluid Flow 28 (2007) 1492–1506.
[60] J. Koo, C. Kleinstreuer, Laminar nanofluid flow in microheat-sinks, Int. J. Heat Mass Transfer 48 (2005) 2652–2661.
[61] W. Duangthongsuk, S. Wongwises, Measurement of temperature-dependent thermal conductivity and viscosity of TiO2–water nanofluids, Exp. Therm. Fluid Sci. 33 (2009) 706–714.
[62] Y. Xuan, Q. Li, W. Hu, Aggregation structure and thermal conductivity of nanofluids, AIChE J. 49 (2003) 1038–1043.
[63] S.P. Jang, S.U.S. Choi, Role of Brownian motion in the enhanced thermal conductivity of nanofluids, Appl. Phys. Lett. 84 (2004) 4316–4318.
[64] J. Koo, C. Kleinstreuer, A new thermal conductivity model for nanofluids, J. Nanopart. Res. 6 (2004) 577–588.
[65] C.H. Chon, K.D. Kihm, S.P. Lee, S.U.S. Choi, Empirical correlation finding the role of temperature and particle size for nanofluid (Al_2O_3) thermal conductivity enhancement, Appl. Phys. Lett. 87 (2005) 153107.
[66] T. Yiamsawasd, A. Dalkilic, S. Wongwises, Measurement of the thermal conductivity of titania and alumina nanofluids, Thermochim. Acta 545 (2012) 48–56.
[67] O. Mahian, A. Kianifar, Mathematical modeling and experimental study of a solar distillation system, Proc. Inst. Mech. Eng., Part C J. Mech. Eng. Sci. 225 (2011) 1203–1212.
[68] A. Kianifar, S. Zeinali Heris, O. Mahian, Exergy and economic analysis of a pyramid shaped solar water purification system: active and passive cases, Energy 38 (2012) 31–36.

Author's personal copy

[69] M.K. Gnanadason, P.S. Kumar, S. Rajakumar, M.H.S. Yousuf, Effect of nanofluids in a vacuum single basin solar still, I.J.AERS 1 (2011) 171–177.
[70] S. Nijmeh, S. Odeh, B. Akash, Experimental and theoretical study of a single-basin solar still in Jordan, Int. Commun. Heat Mass Transfer 32 (2005) 565–572.
[71] A. Bouzoukas, New approaches for cooling photovoltaic/thermal (PV/T) systems, Ph.D Thesis, University of Nottingham, 2008.
[72] C.T. Nguyen, G. Roy, C. Gauthier, N. Galanis, Heat transfer enhancement using Al_2O_3–water nanofluid for an electronic liquid cooling system, Appl. Therm. Eng. 27 (2007) 1501–1506.
[73] M. Elmir, R. Mehdaoui, A. Mojtabi, A vertical magneto-convection in square cavity containing Al_2O_3/water nanofluid: cooling of electronic compounds, Energy Procedia 18 (2012) 724–732.
[74] A. Ijam, R. Saidur, Nanofluid as a coolant for electronic devices (cooling of electronic devices, Appl. Therm. Eng. 32 (2012) 76–82.
[75] S.M. Peyghambarzadeh, S.H. Hashemabadi, M. Seifi Jamnani, S.M. Hoseini, Improving the cooling performance of automobile radiator with Al_2O_3/water nanofluid, Appl. Therm. Eng. 31 (2011) 1833–1838.
[76] T. Hung, W. Yan, Enhancement of thermal performance in double-layered microchannel heat sink with nanofluids, Int. J. Heat Mass Transfer 55 (2012) 3225–3238.
[77] H. Fan, R. Singh, A. Akbarzadeh, Electric power generation from thermoelectric cells using a solar dish concentrator, J. Electron. Mater. 40 (2011). pages !.
[78] H. Tabor, Z. Weinberger, Nonconvecting solar ponds, in: J.F. Kreider, F. Kreith (Eds.), Solar Energy Handbook, McGraw-Hill, New York, 1980.
[79] J. Hull, C.E. Nielsen, P. Golding, Salinity Gradient Solar Ponds, CRC Press, Boca Raton, FL, 1989.
[80] J. Andrews, A. Akbarzadeh, Enhancing the thermal efficiency of solarponds by extracting heat from the gradient layer, Solar Energy 78 (2005) 704–716.
[81] R. Singh, S. Tundee, A. Akbarzadeh, Electric power generation from solar pond using combined thermosyphon and thermoelectric modules, Solar Energy 85 (2011) 371–378.
[82] M. Ozgoren, M. Bilgili, O. Babayigit, Hourly performance prediction of ammoniaewater solar absorption refrigeration, Appl. Therm. Eng. 40 (2012) 80–90.
[83] M. Balghouthi, M.H. Chahbani, A. Guizani, Investigation of a solar cooling installation in Tunisia, Appl. Energy 98 (2012) 138–148.
[84] T.S. Ge, Y.J. Dai, Y. Li, R.Z. Wang, Simulation investigation on solar powered desiccant coated heat exchanger cooling system, Appl. Energy 93 (2012) 532–540.
[85] Z.S. Lu, R.Z. Wang, Z.Z. Xia, X.R. Lu, C.B. Yang, Y.C. Ma, G.B. Ma, Study of a novel solar adsorption cooling system and a solar absorption cooling system with new CPC collectors, Renew. Energy 50 (2013) 299–306.
[86] Y.J. Dai, R.Z. Wang, L. Ni, Experimental investigation and analysis on a thermoelectric refrigerator driven by solar cells, Solar Energy Mater. Solar Cells 77 (2003) 377–391.
[87] M. Alinia, D.D. Ganji, M. Gorji-Bandpy, Numerical study of mixed convection in an inclined two sided lid driven cavity filled with nanofluid using two-phase mixture mode, Int. Commun. Heat Mass Transfer 38 (2011) 1428–1435.
[88] M.N. Pantzali, A.A. Mouza, S.V. Paras, Investigating the efficacy of nanofluids as coolants in plate heat exchangers (PHE), Chem. Eng. Sci. 64 (2009) 3290–3300.
[89] J. Lee, I. Mudawar, Assessment of the effectiveness of nanofluids for singlephase and two-phase heat transfer in micro-channels, Int. J. Heat Mass Transfer 50 (2007) 452–463.
[90] R.A. Taylor, P.E. Phelan, R.J. Adrian, A. Gunawan, T.P. Otanicar, Characterization of light-induced, volumetric steam generation in nanofluids, Int. J. Therm. Sci. 56 (2012) 1–11.
[91] W. Duangthongsuk, S. Wongwises, An experimental study on the heat transfer performance and pressure drop of TiO_2–water nanofluids flowing under a turbulent flow regime, Int. J. Heat Mass Transfer 53 (2010) 334–344.
[92] P. Razi, M.A. Akhavan-Behabadi, M. Saeedinia, Pressure drop and thermal characteristics of CuO-base oil nanofluid laminar flow in flattened tubes under constant heat flux, Int. Commun. Heat Mass Transfer 38 (2011) 964–971.
[93] G.P. Celata, F.D. Annibale, A. Mariani, Nanofluid Flow Effects on metal surfaces, Energia Ambiente e Innovazione 4–5 (2011) 94–98.

Provided for non-commercial research and education use.
Not for reproduction, distribution or commercial use.

This article appeared in a journal published by Elsevier. The attached copy is furnished to the author for internal non-commercial research and education use, including for instruction at the authors institution and sharing with colleagues.

Other uses, including reproduction and distribution, or selling or licensing copies, or posting to personal, institutional or third party websites are prohibited.

In most cases authors are permitted to post their version of the article (e.g. in Word or Tex form) to their personal website or institutional repository. Authors requiring further information regarding Elsevier's archiving and manuscript policies are encouraged to visit:

http://www.elsevier.com/copyright

Author's personal copy

Experimental Thermal and Fluid Science 45 (2013) 8–15

Contents lists available at SciVerse ScienceDirect

Experimental Thermal and Fluid Science

journal homepage: www.elsevier.com/locate/etfs

An experimental investigation of the heat transfer and pressure drop characteristics of a circular tube fitted with rotating turbine-type swirl generators

Weerapun Duangthongsuk [a,b], Somchai Wongwises [b,c,*]

[a] Department of Mechanical Engineering, South-East Asia University, Bangkok, Thailand
[b] Fluid Mechanics, Thermal Engineering and Multiphase Flow Research Lab. (FUTURE), Department of Mechanical Engineering, Faculty of Engineering, King Mongkut's University of Technology Thonburi, Bangmod, Bangkok 10140, Thailand
[c] The Academy of Science, The Royal Institute of Thailand, Sanam Suea Pa, Dusit, Bangkok 10300, Thailand

ARTICLE INFO

Article history:
Received 17 March 2012
Received in revised form 6 July 2012
Accepted 9 September 2012
Available online 2 November 2012

Keywords:
Heat transfer coefficient
Pressure drop
Swirl generator
Passive technique

ABSTRACT

Heat transfer enhancement and flow behaviors in horizontal circular tubes installed with five rotating turbine-type swirl generators (RTSG) are presented experimentally. This type of RTSG is an innovative design that has not been seen in the previous research. Deionized water is used as a working fluid and flows through the test section under turbulent flow conditions. A smooth, stainless steel tube 9.2 mm in ID, 0.4 mm in thickness, and 2.3 m in length is used as the test section. RTSG made from aluminum, with a twisted angle of 60° and a length of 2 cm, are located at 0.46 m equally distant along the test section. When fluid flows through the RTSG, continuously free rotations are observed, and swirl flow after RTSG is created. A DC power supply is used to supply heat load to the test section. Compared with a common, plain tube (without rotating swirl devices), the experimental results indicate that the local heat transfer coefficient of the tube with RTSG inserts is higher than that of the common, plain tube, and they increase when the working fluid flows through the RTSG. Similarly, the wall temperatures of the tube with RTSG inserts are lower than those of the common tube. However, the pressure drop of the tube fitted with RTSG is significantly greater than that of the common, plain tube.

© 2012 Elsevier Inc. All rights reserved.

1. Introduction

Heat transfer enhancement techniques are ways to increase heat transfer performance and minimize the size and cost of heat exchangers. A variety of approaches is concluded by Goldstein et al. [1]. Normally, there are two heat transfer enhancement techniques. The first is a passive technique, and the other is an active technique. The passive technique requires special surface geometries, such as a rough surface, an extended surface, fluid additives, displaced insert devices, or swirl flow devices, whereas the active technique requires external forces, such as an electrical field, stirring of the fluid, fluid and surface vibration, or jet impingement. Focusing on passive techniques, displaced insert devices or swirl flow devices can be equipped inside and outside of the tubes to generate swirl flow, thereby reducing the thermal boundary layer thickness, which leads to an increase in heat transfer performance. However, the addition of some devices into the main flow can cause an increase in the natural pressure drop. A significant increase in heat transfer performance and reduction of the pressure drop to the minimum value are the most suitable ways to improve the heat transfer performance of heat exchangers. As a result, a number of researchers have tried to investigate the heat transfer performance and flow characteristics of conventional tubes with the insertion of swirl flow devices. Several existing articles describing these attempts follow.

Garcia et al. [2] reported on an experimental investigation of heat transfer enhancement of a circular tube with different helical-wire-coil inserts. Water and water-propylene glycol were used as working fluids, along with flowing under laminar, transition, and turbulent flow regimes. Under turbulent flow conditions, their results showed that heat transfer performance and the pressure of wire coils were four times and nine times higher, respectively, than those for plain tubes. However, at a low Reynolds number, the wire coils behaved like smooth tubes. Under transition flow conditions, the heat transfer rate of the wire coils was 200% higher than that of the smooth tube, without a decrease in pumping power. Correlations for predicting the Fanning friction factor and Nusselt number were also proposed.

Tandiroglu [3] reported on the effect of flow geometry parameters on transient forced convective heat transfer of an experimental round tube with baffle inserts. Air was used as a working fluid, and flowing took place under constant heat flux and turbulent flow regimes. Time-averaged Nusselt number and time-averaged pressure drop correlations were also proposed.

* Corresponding author at: Fluid Mechanics, Thermal Engineering and Multiphase Flow Research Lab. (FUTURE), Department of Mechanical Engineering, King Mongkut's University of Technology Thonburi, Bangmod, Bangkok 10140, Thailand.
E-mail address: somchai.won@kmutt.ac.th (S. Wongwises).

0894-1777/$ - see front matter © 2012 Elsevier Inc. All rights reserved.
http://dx.doi.org/10.1016/j.expthermflusci.2012.09.009

Author's personal copy

Nomenclature

A	area, m^2
C_p	specific heat, J/kg K
D	diameter, m
f	friction factor
h	heat transfer coefficient, W/m^2 K
I	electric current (A)
k	thermal conductivity, W/m K
L	length of the test tube, m
$\dot{m}$	mass flow rate, kg/s
Nu	Nusselt number
Pr	Prandtl number
ΔP	Pressure drop, Pa
Q	heat transfer rate, W
Re	Reynolds number
T	temperature, °C
u	velocity, m/s
V	electric voltage, V

Greek symbols

ε	roughness, m
ρ	density, kg/m^3
μ	viscosity, kg/ms

Subscript

ave	average
elec	electric
f	fluid
in	inlet
m	mean
out	outlet
s	surface
w	tube wall
x	local distance

Sivashanmugam and Suresh [4] experimentally investigated the heat transfer performance and friction factor of a round tube fitted with a full-length helical screw element with different twist ratios and spacer lengths. Their data indicated that the helical screw inserts with spacers provided higher heat transfer enhancement than those in the round tube only under turbulent flow conditions, and less of a reduction in pumping power was observed. Moreover, the empirical equations for Nusselt number and friction factor were performed.

Chang et al. [5] reported on an experimental study on the local heat transfer coefficient and pressure drop characteristics of a circular tube with a broken twisted tape insert. The data showed that the use of the broken twisted tape insert could increase the heat transfer coefficient and friction factor. Finally, the local Nusselt number and Fanning friction factor correlations for the tube fitted with broken twisted tape were presented.

Garcia et al. [6] reported on the heat transfer performance and pressure drop characteristics of an experimental smooth tube with three different wire coils inserts. The test fluids flowed under laminar and transition conditions. Their results indicated that the use of wire coils did not increase the heat transfer performance at a Reynolds number less than 200. However, at a Reynolds number ranging between 200 and 1000, the heat transfer coefficients of the wire coil inserts were much larger than those of the conventional smooth tube. At a Reynolds number of 1000, eight times the heat transfer coefficient over the smooth tube was obtained.

Kurtbas et al. [7] investigated the effects of propeller-type turbulators fitted into a circular tube on the entropy generation rate and exergy loss rate. The experimental data indicated that the Nusselt number and exergy loss rate of a round tube with propeller-type turbulator inserts were higher than those of a smooth tube.

Sarac and Bali [8] reported on an experimental investigation into the heat transfer and pressure drop characteristics of a circular tube fitted with a decaying swirl flow. Their data showed that a round tube with decaying swirl flow inserts provided higher heat transfer performance than a smooth tube by approximately 18.1–163%.

Gul and Evin [9] reported on an experimental investigation of the heat transfer and friction characteristics under decaying turbulent swirl flow conditions generated by a short helical tape fitted at the entrance of the test section. Their measured data demonstrated that the use of helical tape inserted into the tube led to a significant increase in the heat transfer rate, compared with a circular tube. Moreover, the number of helical channels and the helical angle had no significant effects on heat transfer performance.

Akhavan-Behabadi et al. [10] carried out an experimental study on the heat transfer enhancement and pressure drop characteristics due to twisted tape inserts in a horizontal evaporator of R-134a. The experiments were carried out for four tubes with different twist ratios and refrigerant mass flux.

Kurtbas et al. [11] experimentally investigated the heat transfer performance and pressure drop characteristics of a circular tube fitted with a conical injector-type swirl generator (CITSG). The results demonstrated that the heat transfer enhancement ratio of CITSG decreased with increasing Reynolds number. The director angle and the director diameter and width decreased with increasing CITSG angle.

Akhavan-Behabadi et al. [12] studied the heat transfer coefficient and pressure drop of a round tube with coiled wire inserts during the heating of engine oil. The results showed that the use of coiled wire inserted into the round tube provided higher heat transfer augmentation than the plain tube, by approximately 2.2–3.2 times, and there was an increase in the friction factor. Heat transfer correlations for coiled wire inserts were proposed.

Khali et al. [13] experimentally studied the heat transfer and pressure drop characteristics of turbulent swirling air flow through a sudden expansion pipe. Their data showed that the sudden expansion pipe with a swirl generator inserts remarkably 40% increased the heat transfer performance of the tested pipe. Moreover, the Nusselt number and friction factor correlations for swirl flow were proposed.

In the last year, Zohir et al. [14] examined the heat transfer enhancement and pressure drop characteristics of a sudden expansion pipe experimentally implanted with a propeller-type swirl generator and a spiral spring for turbulent air flow. The measured data showed that the tube with the propeller inserts provided a higher heat transfer rate and a larger pressure drop than the plain tube, by roughly 1.69 times and 1.5 times, respectively. The Nusselt number correlations for propeller inserts were also presented.

Ibrahim [15] presented an experimental investigation on the heat transfer and friction factor characteristics of flat tubes with full-length helical screw-tape inserts. The results indicated that the Nusselt number and friction factor of a flat tube decreased with increasing spacer length, as did the twist ratio. The Nusselt number and friction factor correlations were also presented.

Patil and Babu [16] experimentally studied the heat transfer and pressure drop characteristics of a double-pipe counter flow

Author's personal copy

heat exchanger fitted with full-length twisted tape and full-length screw tape inserts. Their data indicated that the Nusselt number of the screw tape and twisted tape inserts was higher than that of the plain tube, by approximately 5.3 and 2.85 times, respectively. Similarly, the friction factor of the screw tape and twisted tape inserts was found to be 14 and 7.7 times, respectively, that of the plain duct.

As mentioned above, it has been seen that the use of some devices inserted in plain tubes resulted in better heat transfer performance than with a common plain tube. These devices also generate higher pressure drops than that of plain tubes, by roughly four to five times, due to their being fixed or their not freely rotating. Only the research of Kurtbas et al. [7], and Zohir et al. [14] has been concerned with freely rotating swirl devices. However, the sizes of their test tubes have varied from 40 to 100 mm, which are rather large and the fluid used in their studies are air. This research aimed to investigate the heat transfer performance and pressure drop characteristics of a small, round tube (ID = 9.2 mm) fitted with rotating turbine-type swirl generators (RTSGs) at five positions along the test section. These types of RTSG inserts are new designs that have never been seen before in the available literature. Five RTSG with twist angles of 60° were made from aluminum. The length of each RTSG was 2 cm, with thickness of 0.5 mm and diameter of 6.6 mm, and each RTSG had four blades. When the working fluid flowed through the RTSG, continuously free rotation took place, and swirl flow after each RTSG was created. They were expected to improve the heat transfer performance and result in a small decrease in pressure drop. The experimental data for the RTSG inserts were compared with conventional plain tubes.

2. Experimental apparatus and procedures

The experimental apparatus used in this research is shown schematically in Fig. 1. It mainly consisted of two test sections: the first section was the common plain tube, and the other was the tube with RTSG inserts. Moreover, it consisted of two cooling tanks, a pump with a speed controller, and a rotameter. De-ionized water was used as the working fluid flowing under constant heat flux and turbulent flow conditions. The test section was made from stainless steel and was 2.3 m in length, 10 mm in outer diameter, and 0.4 mm in thickness. For the test section with RTSG inserts, five RTSG were mounted at x/L of 0.0, 0.2, 0.4, 0.6 and 0.8, respectively. RTSG with twist angles of 60° were made from aluminum material with 2 cm in length, 0.5 mm thickness, and 6.6 mm in outer diameter, and each RTSG had four blades. Each RTSG was installed inside the transparency tube for observation of the rotation of the RTSG. When the fluid was forced through the RTSG, continuously free rotation was observed, and swirl flow was produced after the RTSG. The detail of the RTSG is shown in Fig. 2. To measure the pressure drop and the bulk temperature of the de-ionization, the differential pressure transmitter and a T-type thermocouple were mounted at both ends of the test section. Similarly, 10 T-type thermocouples were mounted at different longitudinal positions on the outer surface to measure the wall temperature along the test tube. For the thermocouple fixations at the outer wall of the test section, the thermal insulation tape was used to bind the thermocouple end around the tube. The positions of the wall temperature measurements and the RTSG locations are depicted in Fig. 3. A DC power supply was used to supply the heat load to the test section. Cooling tank No. 1, with a 3.52 kW cooling capacity, a 4 kW electric heater, and an RTD with a temperature controller were used to keep the water temperature constant at a desired value. Similarly, cooling tank No. 2, with an 5.28 kW cooling capacity, and an RTD with a temperature controller was used to cool the water temperature leaving from the test section to the setting temperature of tank No. 1. The water flow rate was measured by a rotameter and was controlled by adjusting the rotation speed of the pump. Finally, in order to minimize the

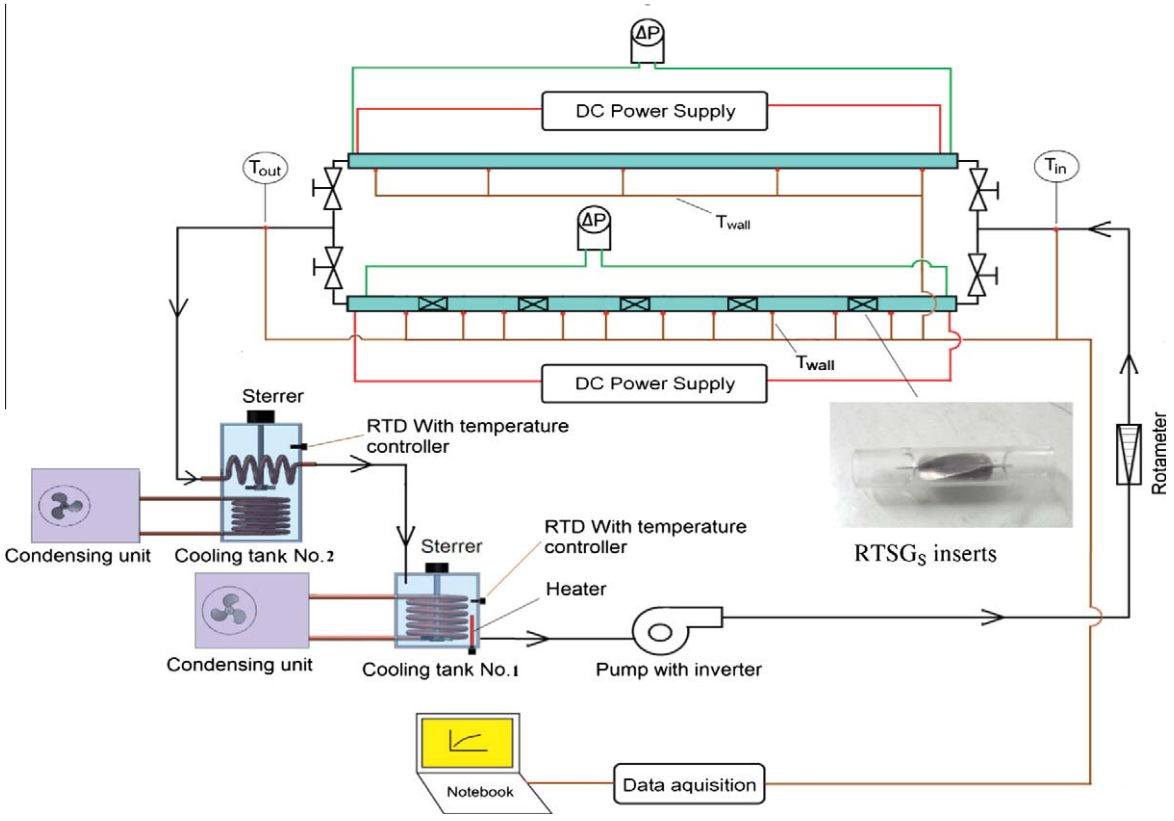

Fig. 1. Schematic diagram of the experimental apparatus used in the present study.

Author's personal copy

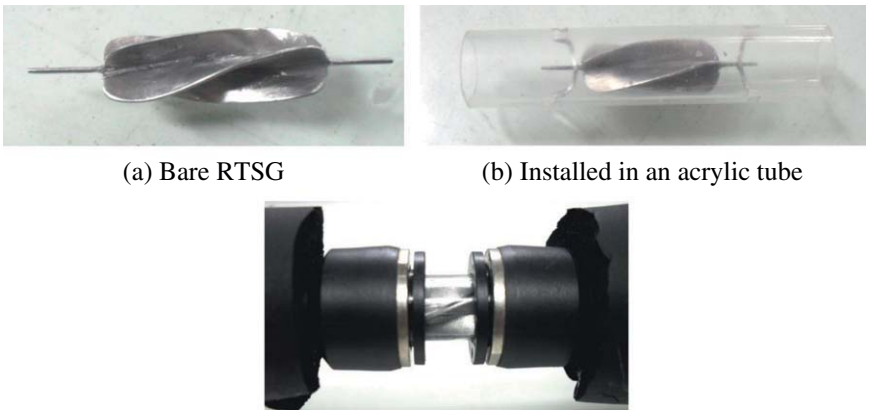

(a) Bare RTSG (b) Installed in an acrylic tube

(c) After fitting in the experimental system

Fig. 2. Configuration of the RTSG used in this study.

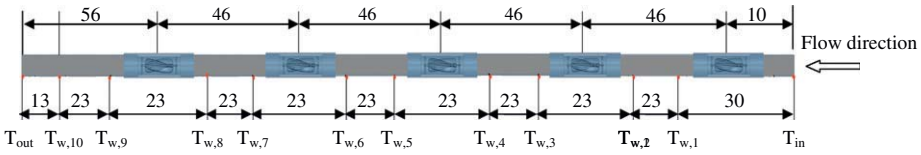

Fig. 3. Position of the wall temperature measurement and the $RTSG_S$ insert (Unit: cm).

Table 1
The dimensions of the test section and testing conditions used in the present study.

Parameter	Quantity
1. Tube length (m)	2.3
2. Outside diameter (mm)	10
3. Tube thickness (mm)	0.4
4. Inlet fluid temperature (°C)	15
5. Wall heat flux (kW/m^2)	15
6. Reynolds number	4500–9500
7. Volume flow rate (LPM)	2–4

heat loss along the test section, the elastomer type insulator with thickness of 20 mm and thermal conductivity of 0.04 W/mK was used to insulate the outer surface of the tube. The dimensions of the test tube and operating conditions are shown in Table 1.

In the present study, the differential pressure transmitter was calibrated using an air-operated dead weight tester. The uncertainty of the pressure measurement was ±0.030 kPa. All of the temperature-measuring devices were well calibrated in a controlled temperature bath, using standard precision mercury glass thermometers. The uncertainty of the temperature measurements as recorded by the data acquisition system was ±0.1 °C. The rotameter was specially calibrated by the manufacturer, and its accuracy was ±7% of full scale. In the present study, the root mean sum square method was used to estimate the uncertainty of the measured data. Therefore, the uncertainty of the measured heat transfer coefficient was approximately 5%.

The experiments were conducted with various flow rates of water. A Reynolds number ranging between 4500 and 9500 was employed. Heat flux was kept at 15 kW/m^2. The inlet water temperature was kept at 15 °C. During each experiment, the heat transferred from the test section was kept at a desired value by adjusting the voltage regulator. The system was allowed to approach a steady state before any data were recorded. After stabilization, the wall temperatures and the inlet and outlet temperatures of the water and the pressure drop across the test section and flow rates of water were all recorded.

3. Data reduction

The accuracy and reliability of the experimental system were tested before measuring the convective heat transfer coefficient and the pressure drop of the round tube fitted with RTSG. Thus, a plain circular tube was tested. The experimental results of the convective heat transfer coefficient and pressure drop were compared with the predicted values obtained from Gnielinski's equation and Colebrook's equation, respectively, which are defined as follows.

The Gnielinski equation [17] is defined as:

$$Nu = \frac{(f/8)(\mathrm{Re}-1000)\mathrm{Pr}}{1+12.7(f/8)^{0.5}(\mathrm{Pr}^{2/3}-1)}, \quad (1)$$

where Nu is the Nusselt number, Re is the Reynolds number, Pr is the Prandtl number, and f is the friction factor.

The Colebrook equation [18] is defined as:

$$\frac{1}{\sqrt{f}} = -2.0\log\left(\frac{\varepsilon/D}{3.7}+\frac{2.51}{\mathrm{Re}\sqrt{f}}\right), \quad (2)$$

The pressure drop across the test section is defined as:

$$\Delta P = f\frac{Lu_m^2}{2D}g, \quad (3)$$

where ΔP is the measured pressure drop, L is the length of the tube, D is the inner diameter of the tube, and u_m is the mean velocity of fluid.

Then, the heat transfer performance of RTSG could be computed from the following equation.

The heat supplied to the test section can be calculated from:

$$Q_{elec} = VI, \quad (4)$$

The heat transfer rate into the fluid was computed from:

$$Q_f = \dot{m}Cp(T_{out}-T_{in}), \quad (5)$$

Author's personal copy

The average heat transfer rate was described as follows:

$$Q_{ave} = \frac{Q_{elec} + Q_f}{2}, \tag{6}$$

where Q_{elec} and Q_f are the heat transfer rate of electric power and the fluid, respectively, Q_{ave} is the average heat transfer rate, V is the electric voltage, I is the electric current, $\dot{m}$ is the mass flow rate of the fluid, Cp is the specific heat, and T_m and T_{out} are the temperature of the water at the inlet and exit, respectively, of the test section. However, the difference between electric power input and energy absorbed by working fluids is approximately less than 2.0%.

The local heat transfer coefficient and the local Nusselt number are evaluated from the following equations:

$$h_x = \frac{q}{(T_w - T_f)_x}, \tag{7}$$

$$Nu_x = \frac{h_x D}{k}, \tag{8}$$

The bulk fluid temperature along the test section is calculated from:

$$T_{f,2} = T_{f,1} + \frac{q\pi Dx}{\dot{m}C_P}, \tag{9}$$

where h_x is the local heat transfer coefficient, T_{wall} is the average wall temperature of the tube, q is the wall heat flux, T_f is the bulk temperature of the fluid at each section, x is the length of the each section, Nu_x is the local Nusselt number, A_S is the surface area of the test tube, and k is the thermal conductivity of the fluid.

The average heat transfer coefficient (h_{ave}) can be computed by using the following equation:

$$h_{ave} = \frac{1}{L}\int_{x_1}^{x_2} h_x dx = \frac{1}{L}\sum_{i=1}^{n}\frac{1}{2}(h_{x,i} + h_{x,i+1})x_i, . \tag{10}$$

Moreover, the Reynolds number can be calculated by using the following equation:

$$\mathrm{Re} = \frac{\rho u_m D}{\mu}, \tag{11}$$

where ρ is the density, and μ is the viscosity of the fluids.

Similarly, the Prandtl number is defined as:

$$\mathrm{Pr} = \frac{\mu Cp}{k}. \tag{12}$$

For cases of pressure drop, the measured pressure drops of RTSG were compared with the conventional plain tube.

4. Results and discussion

As shown in Figs. 4 and 5, an agreement between the experimental results and the calculated values for the common, plain tube could be seen.

Fig. 6a and b shows the variation of the wall temperature along the test section for the common, plain tube and the RTSG inserts, respectively. For common plain tube, the results showed that the wall temperature increased with the increasing distance of the test section. This result was due to the heat from the electric power continuously transmitted to the test section, which resulted in an increase of the wall temperature. However, for the case of the RTSG inserts, abnormal behavior was obtained. As shown in Fig. 6b, the wall temperature of the test tube decreased after the fluid flowed past the RTSG. This result might due to fluid swirl flow freely rotating after each RTSG, which led to higher heat transfer rate from the tube wall. Thus, the lower wall temperature after the RTSG was obtained.

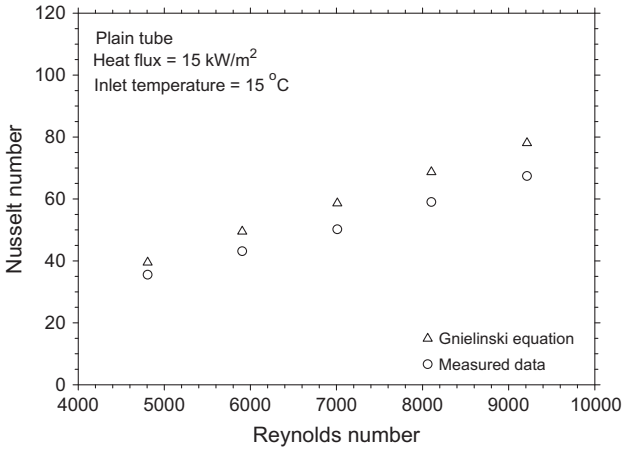

Fig. 4. Comparison between the measured Nusselt number and that calculated from Gnielinski equation.

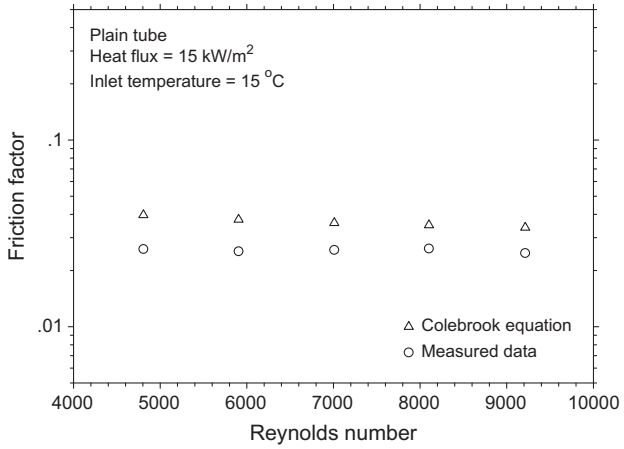

Fig. 5. Comparison between the measured friction factor and that calculated from Colebrook equation.

Fig. 7 shows the comparisons between the local wall temperatures obtained from the common, plain tube and those obtained from the RTSG inserts. The results showed that the wall temperature of the RTSG inserts was lower than that of the common, round tube. This result means that the use of RTSG inserted inside the round tube provide better thermal performance than the conventional plain tube.

Similarly, the variation of the water temperatures along the test tube for the common round tube and the tube fitted with $RTSG_S$ was shown in Fig. 8a and b, respectively. The data indicated that the water temperature along the test section increases with increasing the tube length and varied linearly with the length of the test section. This result was caused from heat supplied to the test tube continuously transferring to the fluid, which led to increase in the water temperature.

Comparison of the water temperature along the test section between common plain tube and RTSG inserts was shown in Fig. 9. The results showed that the tube with RTSG inserts gave lower water temperature than those of the common plain tube. This behavior caused from use of the RTSG inserted into the common tube led to decrease in the wall temperature which resulted decrease in the water temperature at the same time which described in Fig. 7.

Fig. 10a and b shows the variation in the local heat transfer coefficient along the test tube as a function of the volume flow

Author's personal copy

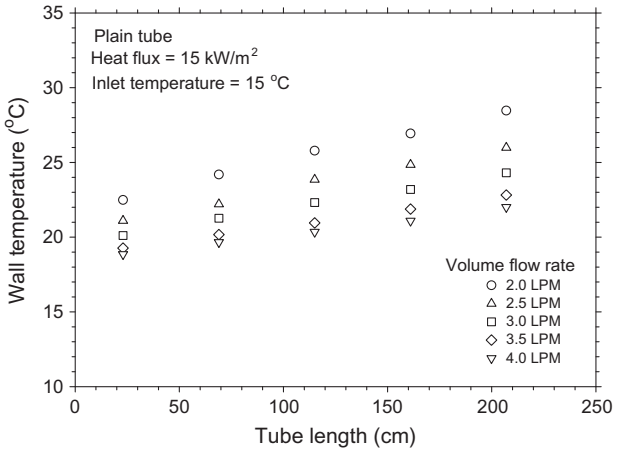

(a) For the common plain tube

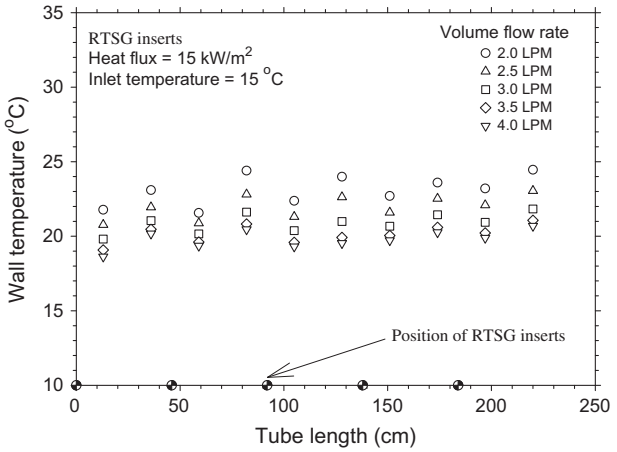

(b) For RTSG inserts

Fig. 6. Variation of the wall temperatures along the test section.

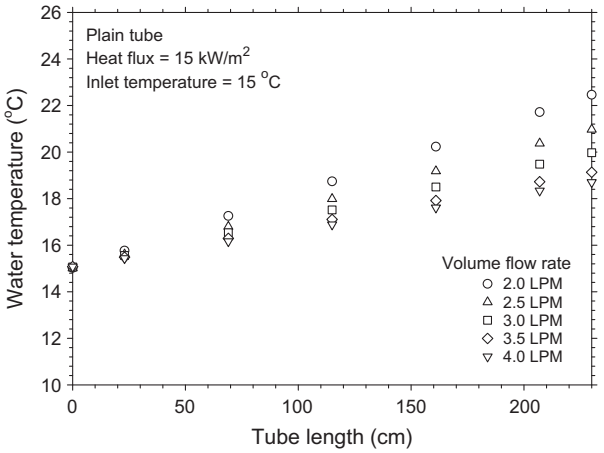

(a) For the common plain tube

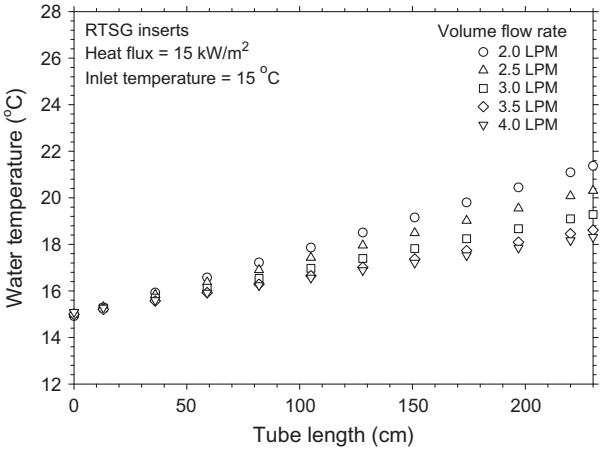

(b) For RTSG inserts

Fig. 8. Variation of the water temperatures along the test section.

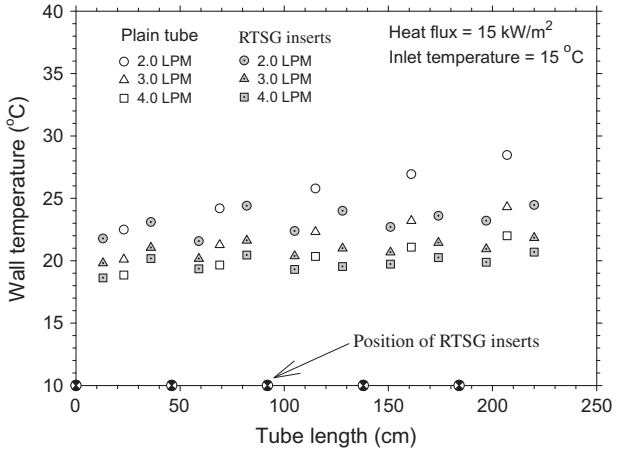

Fig. 7. Comparison of the wall temperature along the test section between the plain tube and the tube fitted with RTSG.

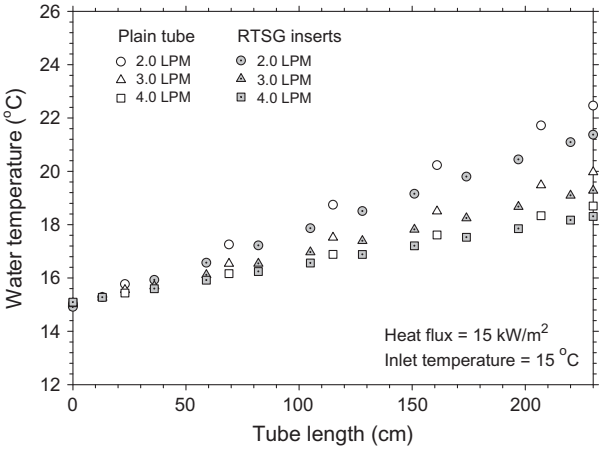

Fig. 9. Comparison of the water temperature along the test section between the plain tube and the RTSG inserts.

rates for the common, plain tube and the RTSG inserts, respectively. For the common, plain tube, the results indicated that the local heat transfer coefficient increased with the increasing volume flow rate and remained constant along the tube length. However, for the case of RTSG inserts, abnormal heat transfer behavior could be clearly seen. From the measured data, it was seen that the heat transfer coefficient of the round tube fitted with RTSG increased with increasing tube length. Moreover, focusing on the position behind the RTSG, a significantly higher heat transfer coefficient is obtained. This result was due to the swirling flow after the RTSG, creating higher heat transfer performance.

Author's personal copy

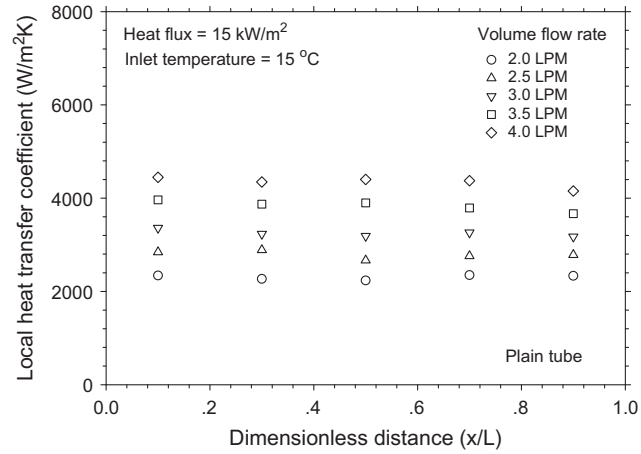

(a) For the common plain tube

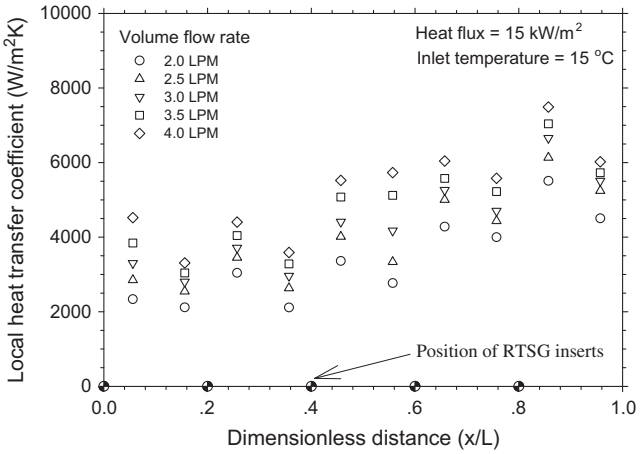

(b) For RTSG inserts

Fig. 10. Local heat transfer coefficient along the test section at different volume flow rates.

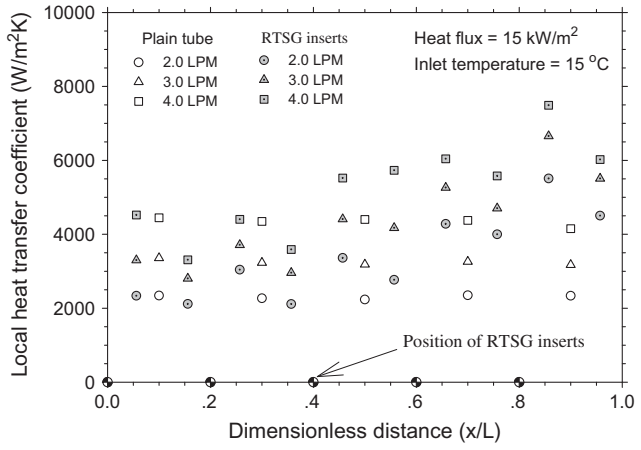

Fig. 11. Comparison of the local heat transfer coefficient between the plain tube and the RTSG inserts.

Fig. 11 also shows comparisons between the local heat transfer coefficients obtained from the common, plain tube and those obtained from the tube fitted with RTSG. The results indicated that the use of RTSG inserted inside a common, round tube provided

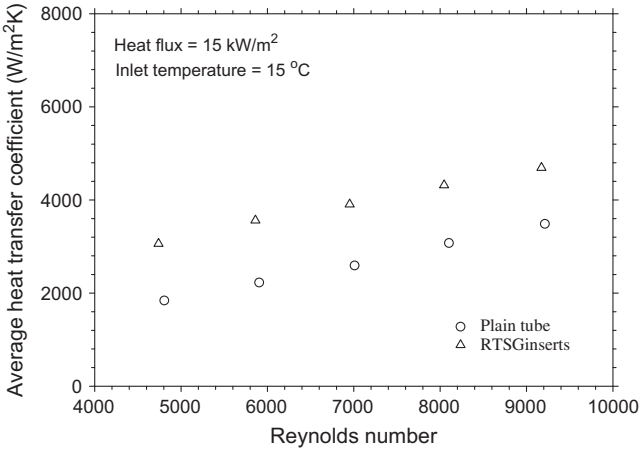

Fig. 12. Comparison of the average heat transfer coefficient between the plain tube and the RTSG inserts.

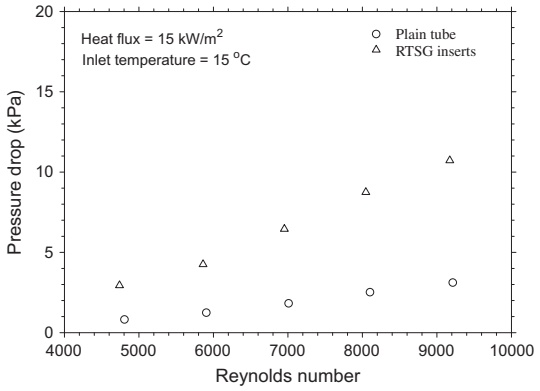

Fig. 13. Comparison of the pressure drop obtained from the common, plain tube and that of the RTSG inserts.

significantly higher heat transfer performance than the plain tube. The results were described in the above sub-section.

Similarly, a comparison of the average heat transfer coefficient between the common, plain tube and the RTSG inserts, as a function of the Reynolds number, is shown in Fig. 12. The measured results showed that the average heat transfer coefficient of the RTSG inserts was approximately 35–37% higher than that of the plain tube and increases with increasing Reynolds number. The reason for this was given in the preceding section. This result was due to the fact that the swirl flow was created after the RTSG in which led to enhance the heat transfer performance.

The pressure drops of the common plain, tube and the tube fitted with RTSG are shown in Fig. 13. The results show that the pressure drop of the RTSG inserts was larger than that of the plain tube by roughly 2.5 times. However, this value was still smaller than in the previous work of other researchers. This behavior, due to a freely rotating device, was used in the present study. Moreover, different distances (short-length tabulators) of RTSG were installed in the round tube, and its configuration could not resist the flow as could a propeller.

5. Conclusions

The heat transfer enhancement and pressure drop characteristics of a plain tube fitted with a rotating turbine-type swirl generator (RTSG) were experimentally investigated. This type of RTSG is

Author's personal copy

an innovative design that has not been seen in the previous research. The measured data for RTSG inserts were compared with the data for the common, plain tube. Important conclusions have been obtained and summarized as follows:

- The tube with RTSG inserts creates abnormal behaviors of the local heat transfer coefficients which increase after the flow passes the RTSG;
- the use of RTSG inserted into the round tube at different locations provided a significantly higher average heat transfer coefficient than that of the common, plain tube by roughly 35%;
- the wall temperatures and water temperature of the round tube with RTSG inserts were lower than those of the common, plain tube, and they significantly decreased after the fluid flowed past the RTSG; and
- the pressure drops of the tube with RTSG inserted were higher than those of the conventional, plain tube by approximately 2.5 times. However, this value was less than that seen in the previous literature, due to the freely rotating device used in the present study.

Acknowledgments

The authors would like to express their appreciation to the Office of Research, South-East Asia University, the Thailand Research Fund, the Office of the Higher Education Commission and the National Research University Project for providing financial support. The authors also wish to thank Mr. Arnont Kamlangsuea and Mr. Theindham Kaenak for their help during our study.

References

[1] R.J. Goldstein, W.E. Ibele, S.V. Patankar, T.W. Simon, T.H. Kuehn, P.J. Strykowski, K.K. Tamma, J.V.R. Heberlein, J.H. Davidson, J. Bischof, F.A. Kulacki, U. Kortshagen, S. Garrick, V. Srinivasan, Heat transfer—A review of 2003 literature, International Journal of Heat and Mass Transfer 49 (2006) 451–534.
[2] A. Garcia, P.G. Vicente, A. Viedma, Experimental study of heat transfer enhancement with wire coil inserts in laminar-transition-turbulent regimes at different Prandtl numbers, International Journal of Heat and Mass Transfer 48 (2005) 4640–4651.
[3] A. Tandiroglu, Effect of flow geometry parameters on transient heat transfer for turbulent flow in a circular tube with baffle inserts, International Journal of Heat and Mass Transfer 49 (2006) 1559–1567.
[4] P. Sivashanmugam, S. Suresh, Experimental studies on heat transfer and friction factor characteristics of turbulent flow through a circular tube fitted with regularly spaced helical screw-tape inserts, Applied Thermal Engineering 27 (2007) 1311–1319.
[5] S.W. Chang, T.L. Yang, J.S. Liou, Heat transfer and pressure drop in tube with broken twisted tape insert, Experimental Thermal and Fluid Science 32 (2007) 489–501.
[6] A. Garcia, J.P. Solano, P.G. Vicente, A. Viedma, Enhancement of laminar and transitional flow heat transfer in tubes by means of wire coil inserts, International Journal of Heat and Mass Transfer 50 (2007) 3176–3189.
[7] I. Kurtbas, A. Durmus, H. Eren, E. Turgut, Effect of propeller type swirl generators on the entropy generation and efficiency of heat exchangers, International Journal of Thermal Sciences 46 (2007) 300–307.
[8] B.A. Sarac, T. Bali, An experimental study on heat transfer and pressure drop characteristics of decaying swirl flow through a circular pipe with a vortex generator, Experimental Thermal and Fluid Science 32 (2007) 158–165.
[9] H. Gul, D. Evin, Heat transfer enhancement in circular tubes using helical swirl generator insert at the entrance, International Journal of Thermal Sciences 46 (2007) 1297–1303.
[10] M.A. Akhavan-Behabadi, R. Kumar, A. Mohammadpour, M. Jamali-Asthiani, Effect of twisted tape insert on heat transfer and pressure drop in horizontal evaporators for the flow of R-134a, International Journal of Refrigeration 32 (2009) 922–930.
[11] I. Kurtbas, F. Gulcimen, A. Akbulut, D. Buran, Heat transfer augmentation by swirl generators inserted into a tube with constant heat flux, International Communications in Heat and Mass Transfer 36 (2009) 865–871.
[12] M.A. Akhavan-Behabadi, R. Kumar, M.R. Salimpour, R. Azimi, Pressure drop and heat transfer augmentation due to coiled wire inserts during laminar flow of oil inside a horizontal tube, International Journal of Thermal Sciences 49 (2010) 373–379.
[13] A. Khali, A.E. Zohir, A.M. Farid, Heat transfer characteristics and friction of turbulent swirling air flow through abrupt expansion, American Journal of Scientific and Industrial Research 1 (2) (2010) 364–374.
[14] A.E. Zohir, A.A. Abdel Aziz, M.A. Habib, Heat transfer characteristics in a sudden expansion pipe equipped with swirl generators, International Journal of Heat and Fluid Flow 32 (2011) 352–361.
[15] E.Z. Ibrahim, Augmentation of laminar flow and heat transfer in flat tubes by means of helical screw-tape inserts, Energy Conversion and Management 52 (2011) 250–257.
[16] S.V. Patil, P.V. Vijay Babu, Performance comparison of twisted tape inserts in square duct, in: Proceedings of the International Conference on Advanced Science, Engineering and Information Technology (Malaysia), 2011, pp. 50–55.
[17] V. Gnielinski, New equations for heat and mass transfer in turbulent pipe and channel flow, International Chemical Engineering 16 (1976) 359–368.
[18] C.F. Colebrook, Turbulent flow in pipes, with particular reference to the transition between the smooth and rough pipe laws, Journal of the Institution of Civil Engineers, London 11 (1939) 133–156.

International Communications in Heat and Mass Transfer 40 (2013) 32–35

Contents lists available at SciVerse ScienceDirect

International Communications in Heat and Mass Transfer

journal homepage: www.elsevier.com/locate/ichmt

Application of two-phase vapor chamber technique for hard disk drive cooling of PCs ☆

P. Naphon [a,*], S. Wongwises [b], S. Wiriyasart [a]

[a] Thermo-Fluids and Heat Transfer Enhancement Lab. (TFHT), Department of Mechanical Engineering, Faculty of Engineering, Srinakharinwirot University, 63 Rangsit-Nakhornnayok Rd., Ongkharak, Nakhorn-Nayok, 26120, Thailand

[b] Fluid Mechanics, Thermal Engineering and Multiphase Flow Research Lab. (FUTURE), Department of Mechanical Engineering, King Mongkut's University of Technology Thonburi, 91 Suksawas 48, Bangmod, Bangkok 10140, Thailand

ARTICLE INFO

Available online 22 October 2012

Keywords:
Vapor chamber
Electronics cooling
Hard disk drive

ABSTRACT

The internal mechanism of the hard disk drive is seriously damaged if it is subjected to forces outside the environmental specifications. The results of the investigation on the thermal cooling of vapor chamber for cooling hard disk drive of the personal computer are presented. It was found that the vapor chamber cooling technique has a significant effect on the thermal cooling of a hard disk drive. The average hard disk drive temperature with the vapor chamber cooling system is 15.21%, which is lower than those without the vapor chamber cooling system. The results of this study are of technological importance for the efficient design of cooling systems of personal computers or electronic devices to enhance cooling performance.

© 2012 Elsevier Ltd. All rights reserved.

1. Introduction

In recent years, the generated heat of PCs or electronic devices has been increasing along with the enhancement of CPU performance, memory capacity, and other devices. Therefore, the cooling system cools not only the CPU, but also others devices such as the HDD. In order to ensure the specified lifetime guarantee, most HDD suppliers do not allow the case temperature of the HDD to exceed 60 °C. For effective cooling the heat must spread to a larger surface area and away from those devices, as there is usually restricted space available. The heat transfer characteristics of the vapor chamber have been widely studied by researchers. Liu et al. [1] investigated on the startup of a novel two-phase cooling loop. Wang et al. [2] studied on the micro capillary pumped loop system for cooling high power devices. Xie et al. [3] experimentally investigated on a novel high-performance integrated heat pipe–heat sink for high-flux chip cooling. Hsieh et al. [4] examined the spreading thermal resistance of a flat vapor chamber. Vin and Astrain [5] studied on the development of a thermoelectric refrigerator with two-phase thermosyphons. Chang et al. [6] experimentally investigated the effects of the evaporation surfaces, fill ratios of working fluid and input heating powers on the thermal performance of the heat pipe cooling system with the thermal resistance model. Chen et al. [7] presented a numerical investigation of a plate-fin heat sink embedded with a vapor chamber, subject to the influence of concentrated heat sources. Zhang et al. [8] numerically and experimentally investigated on the flat two-phase thermosyphon. Vasiliev et al. [9] studied on the loop heat pipe for cooling of high-power electronic components. Ming et al. [10] experimentally and numerically investigated on the grooved vapor chamber. Tsai et al. [11] experimentally investigated on the effects of heat source, fill ratio of working fluid, and evaporator surface structure on the thermal performance of the vapor chamber. Wang et al. [12] considered the thermal performance of the vapor chamber for high-power LEDs. Wong et al. [13] studied on a novel vapor chamber with an inner groove surface. Wang et al. [14] analyzed the thermal characteristics for a board-level high performance package equipped with a vapor chamber. Li et al. [15,16] investigated the effects of the width, height and number of fins on the thermal performance of the vapor chamber. Reyes et al. [17] experimentally and theoretically studied on the vapor chamber based heat spreader. Attia et al. [18] experimentally investigated the effects of different working fluids, and different charge ratios on the thermal performance of the vapor chamber. Ji et al. [19] studied on the vapor chamber performance with sintering of the copper foam pieces. Choi et al. [20] studied a new CPU cooler design based on an active cooling heat sink combined with heat pipes.

As mentioned above, the numerous papers present studies on the heat transfer characteristics of the vapor chamber for cooling electronics devices. However, there are no researches present for the study on the thermal cooling of the hard disk drive (HDD). Therefore, the purpose of this paper is to study the thermal cooling of hard disk drives of personal computers with the vapor chamber. For computer applications, the operating temperatures are normally between 50 and 100 °C. Effects of the operating condition of a PC, and the fill ratio on the hard disk drive temperature are considered.

2. Experimental apparatus and method

The test loop consists of a set of PCs, and a set of vapor chamber cooling system and data acquisition system. A schematic diagram of

☆ Communicated by W.J. Minkowycz.

* Corresponding author.
E-mail address: paisarnn@swu.ac.th (P. Naphon).

0735-1933/$ – see front matter © 2012 Elsevier Ltd. All rights reserved.
http://dx.doi.org/10.1016/j.icheatmasstransfer.2012.10.014

the vapor chamber cooling system is shown in Fig. 1. The vapor chamber cooling system consists of the vapor chamber, the heat sink unit, and the axial fan unit. The vapor chamber is fabricated from a copper plate which consists of a bottom copper plate, a wick sheet, a sinter column, and a top copper plate. The wick sheet and the sinter column are fabricated from the copper powder. The bottom copper plate is the evaporator section that may be mounted on the hard disk drive of the PC to absorb the generated heat, and the other is the condenser section in which heat is transferred to the heat sink and air, respectively. In order to minimize thermal resistance between the HDD-vapor chamber and vapor chamber-heat sink unit, a thin film of high thermal conductivity grease is applied at their junction interface. The working fluid (de-ionized water) is evaporated on the heated side and condensed on the cooling side and then returns to the evaporator section under gravity. Type T copper-constantan thermocouples with an accuracy of 0.1% of full scale are employed to measure the temperatures. Four type T copper-constantan thermocouples are applied to measure the vapor chamber temperature (T_{vc}). Two thermocouples are applied to observe the air temperature in the computer case (T_{case}). A groove within the chamber walls is machined and the high conductivity cement is utilized to embed the thermocouples within the chamber wall. The hard disk drive temperature is measured by four type-T copper-constantan thermocouples (T_{hdd}). All thermocouples are pre-calibrated with a dry box temperature calibrator.

Experiments were conducted with various fill ratios and operating conditions of the PC. The supplied load into the hard disk drive was adjusted to achieve the desired level by setting the operating conditions of the hard disk drive: no load, 50%, and 100% operating loads. The temperatures at each position were recorded in a time period of 200 min. Data collection was carried out using a data acquisition system.

3. Results and discussion

The hard disk drive, with a 5.5-in. size, and two rotating disks with a nominal speed of 15,000 rpm, is tested in the present study. The hard disk drive was supported with insulation blocks under each corner.

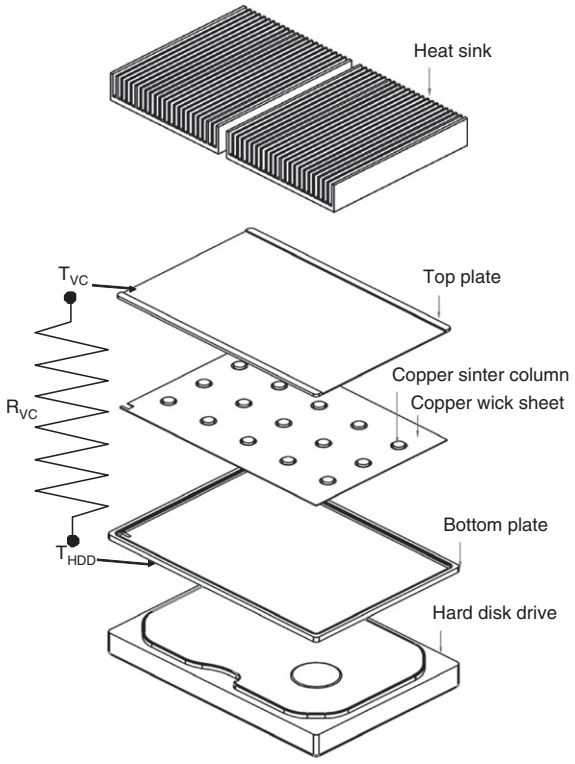

Fig. 1. Schematic diagram of the vapor chamber cooling system.

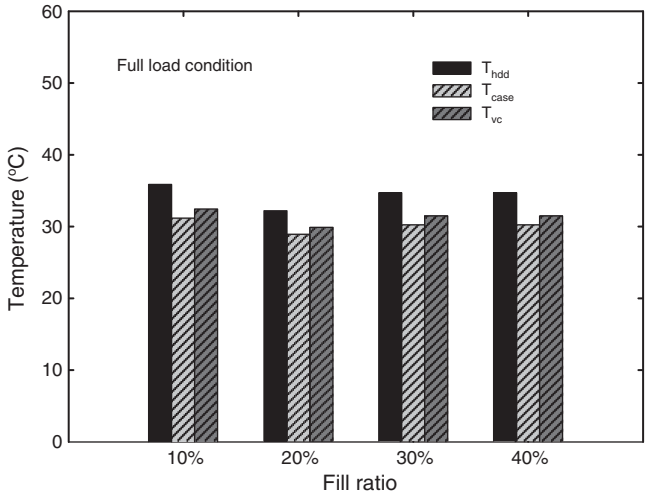

Fig. 2. Variation of HDD, vapor chamber and air temperatures for different fill ratios.

Both the top and bottom surfaces of the hard disk drive were exposed to the quiescent environment of the laboratory room with constant temperature of 26 °C. Initially experiments are performed without the vapor chamber cooling system which forms the basis for comparison of the results with the vapor chamber cooling technique. In order to ensure long life and reliable operations, hard disk drives are all designed to function only in specific temperature ranges. Fig. 2 shows the variation of the temperature of the HDD, vapor chamber and air in the computer temperatures for the different of fill ratios of the working fluid. For all fill ratios of the working fluid, it can be seen that the HDD temperatures are higher than those of the vapor chamber and air on the computer temperature. The full load operation of the HDD can be done by setting the writing data into both partitions of the HDD.

Fig. 3 shows the variation of the hard disk drive temperature for different fill ratios of the working fluid. It can be seen the HDD without the vapor chamber the cooling system gives a temperature higher than those with the vapor chamber cooling system. The values of the heat input to the system by various components depend on the operating condition of the hard disk drive. In general, the heat within the hard disk drive operation is mainly generated by the spindle motor, voice coil motor, magnetic read/write head sensor, and windage loss. Therefore, the HDD temperatures without the operating load are lower than those with the operating load. At a lower operating load, however, the heat is mainly transferred through natural

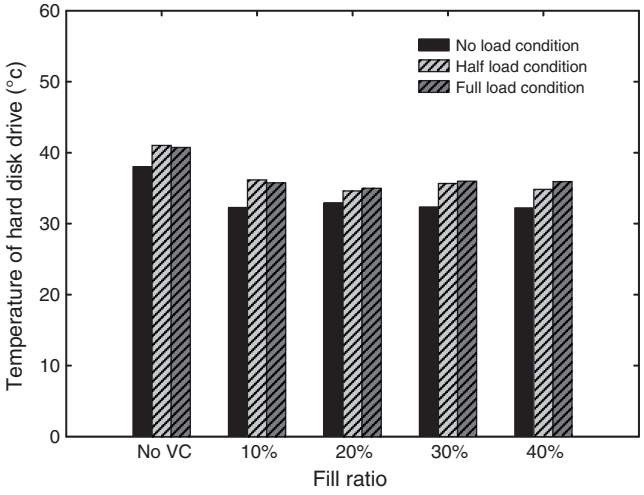

Fig. 3. Variation of HDD temperatures for different fill ratios.

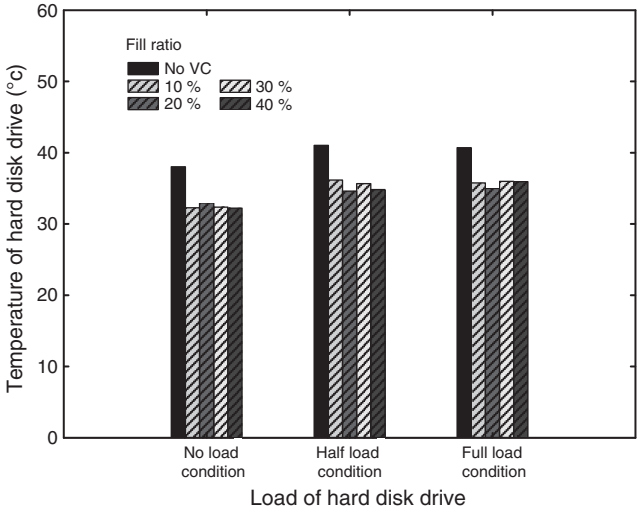

Fig. 4. Variation of HDD temperatures for different operating conditions of HDD.

convection. The increasing operating load induces a larger superheat, which activates and intensifies nucleate boiling and consequently leads to higher heat transfer efficiency. Therefore, a higher operating load of the hard disk drive has a slight effect on the hard disk drive temperature.

Fig. 4 shows the variation of hard disk drive temperature for different operating conditions of HDD. For a given operating load, it can be seen that the HDD temperatures of the HDD with the vapor chamber cooling system are lower than those without the vapor chamber cooling system. In addition, the hard disk drive with a fill ratio of 20% gives the lowest HDD temperature among the other fill ratios. It may be due to the low fill ratio that the dry out phenomenon might happen. The condensing liquid cannot promptly reflow at this operating load. For a higher fill ratio, there is a thin liquid film in the heat input region. The thermal resistance of the phase change heat transfer will also increase with the thickness of the liquid film. Therefore, the vapor chamber with a 20% fill ratio of the vapor chamber gives the lowest HDD temperature among the other fill ratios.

Fig. 5 shows the variation of vapor chamber temperature for different operating conditions of HDD. The average vapor chamber temperature is obtained from the top plate temperature and the bottom plate temperature of the vapor chamber. It can be seen that the fill

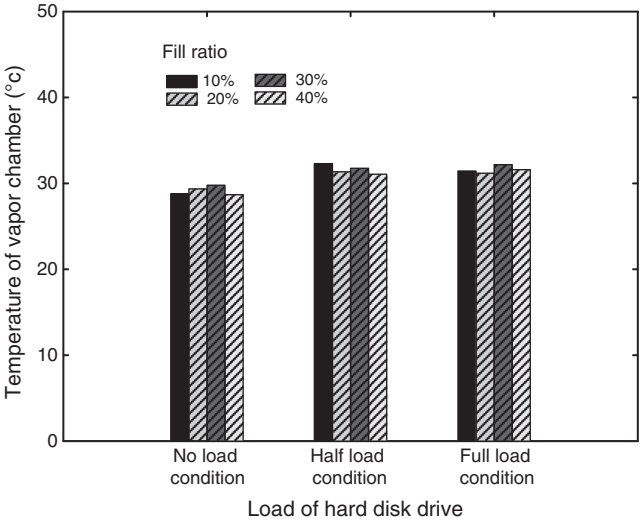

Fig. 5. Variation of vapor chamber temperatures for different operating conditions of HDD.

Table 1
Comparison of the energy consumption and hard disk drive temperature between the hard disk drive with and without vapor chamber cooling system.

Hard disk condition	Energy consumption	Hard disk drive temperature (°C)
HDD with 20% fill ratio for no load condition	+28.57%	−14.16%
HDD with 20% fill ratio for full load condition	+14.81%	−16.21%

ratio of the working fluid has a significant effect on the vapor chamber temperature. The heat phenomenon by the working fluid in the vapor chamber shows how the working fluid absorbs heat from heat source (HDD) and evaporates in the evaporator (bottom plate). The evaporating fluid moves toward the condenser, and then condenses in the condenser (top plate).

The HDD temperature and the energy consumption obtained from the HDD with the vapor chamber cooling system are compared with those without the vapor chamber cooling system. As seen in Table 1, the plus symbol represents the higher values while the minus symbol is represents the lower values as compared with those without the vapor chamber cooling system. It can be seen that the HDD temperatures obtained from the HDD with vapor chamber cooling system are lower than those without vapor chamber cooling system and with the same explanation as mentioned above. However, the energy consumption also increases.

4. Conclusions

Temperature is often quoted as the most important environmental factor affecting hard disk drive reliability. However, the space limitation and air cooling limitation are the encountered problems of the cooling system development of the hard disk drive or electronic devices. The vapor chambers have many advantages as compared to other cooling devices such as fans, thermoelectric modules, and liquid pump loop devices, which are that it has a simple structure, no moving parts and does not use electricity. In addition, selection of the working fluid is based on the operating temperature range of the applications. It is found that the HDD with the vapor chamber cooling system gives HDD temperatures lower than those without the vapor chamber cooling system.

Acknowledgments

The authors would like to express their appreciation to the Excellent Center for Sustainable Engineering (ECSE) of the Srinakharinwirot University (SWU) and the King Mongkut's University of Technology Thonburi (KMUTT) for providing financial support for this study. The authors also wish to acknowledge Fujikura Electronics (Thailand) Ltd. for their assistance in some of the vapor chamber samples.

References

[1] J. Liu, N.Q. Pei, K.H. Guo, Z.H. He, T.X. Li, J.M. Gu, Experimental investigation on startup of a novel two-phase cooling loop, Experimental Thermal and Fluid Science 32 (2008) 939–946.
[2] C.T. Wang, T.S. Leu, T.M. Lai, Micro capillary pumped loop system for a cooling high power device, Experimental Thermal and Fluid Science 32 (2008) 1090–1095.
[3] X.L. Xie, Y.L. He, W.Q. Tao, H.W. Yang, An experimental investigation on a novel high-performance integrated heat pipe–heat sink for high-flux chip cooling, Applied Thermal Engineering 28 (2008) 433–439.
[4] S.S. Hsieh, R.Y. Lee, J.C. Shyu, S.W. Chen, Thermal performance of flat vapor chamber heat spreader, Energy Conversion and Management 49 (2008) 1774–1784.
[5] J.G. Vin, D. Astrain, Development of a thermoelectric refrigerator with two-phase thermosyphons and capillary lift, Applied Thermal Engineering 28 (2008) 1514–1521.
[6] Y.W. Chang, C.H. Cheng, J.C. Wang, S.L. Chen, Heat pipe for cooling of electronic equipment, Energy Conversion and Management 49 (2008) 3398–3404.
[7] Y.S. Chen, K.H. Chien, T.C. Hung, C.C. Wang, Y.M. Ferng, B.S. Pei, Numerical simulation of a heat sink embedded with a vapor chamber and calculation of effective

thermal conductivity of a vapor chamber, Applied Thermal Engineering 29 (2009) 2655–2664.
[8] M. Zhang, Z. Liu, G. Ma, S. Cheng, Numerical simulation and experimental verification of a flat two-phase thermosyphon, Energy Conversion and Management 50 (2009) 1095–1100.
[9] L. Vasiliev, D. Lossouarn, C. Romestant, A. Alexandre, Y. Bertin, Y. Piatsiushyk, V. Romanenkov, Loop heat pipe for cooling of high-power electronic components, International Journal of Heat and Mass Transfer 52 (2009) 301–308.
[10] Z. Ming, L. Zhongliang, M. Guoyuan, The experimental and numerical investigation of a grooved vapor chamber, Applied Thermal Engineering 29 (2009) 422–430.
[11] T.E. Tsai, H.H. Wu, C.C. Chang, S.L. Chen, Two-phase closed thermosyphon vapor-chamber system for electronic cooling, International Communications in Heat and Mass Transfer 37 (2010) 484–489.
[12] J.C. Wang, R.T. Wang, T.L. Chang, D.S. Hwang, Development of 30 Watt high-power LEDs vapor chamber-based plate, International Journal of Heat and Mass Transfer 53 (2010) 3990–4001.
[13] S.C. Wong, K.C. Hsieh, J.D. Wu, W.L. Han, A novel vapor chamber and its performance, International Journal of Heat and Mass Transfer 53 (2010) 2377–2384.
[14] T.H. Wang, C.C. Lee, Y.S. Lai, Thermal characteristics evaluation for board-level high performance flip-chip package equipped with vapor chamber as heat spreader, Microelectronic Engineering 87 (2010) 2463–2467.
[15] H.Y. Li, M.H. Chiang, C.I. Lee, W.J. Yang, Thermal performance of plate-fin vapor chamber heat sinks, International Communications in Heat and Mass Transfer 37 (2010) 731–738.
[16] H.Y. Li, M.H. Chiang, Effects of shield on thermal-fluid performance of vapor chamber heat sink, International Journal of Heat and Mass Transfer 54 (2011) 1410–1419.
[17] M. Reyes, D. Alonso, J.R. Arias, A. Velazquez, Experimental and theoretical study of a vapour chamber based heat spreader for avionics applications, Applied Thermal Engineering 37 (2012) 51–59.
[18] A.A.A. Attia, B.T.A. El-Assal, Experimental investigation of vapor chamber with different working fluids at different charge ratios, Ain Shams Engineering Journal, 2 (2012) 289–297.
[19] X. Ji, J. Xu, A.M. Abanda, Copper foam based vapor chamber for high heat flux dissipation, Experimental Thermal and Fluid Science 40 (2012) 93–102.
[20] J. Choi, M. Jeong, J. Yoo, M. Seo, A new CPU cooler design based on an active cooling heat sink combined with heat pipes, Applied Thermal Engineering 44 (2012) 50–56.

Provided for non-commercial research and education use.
Not for reproduction, distribution or commercial use.

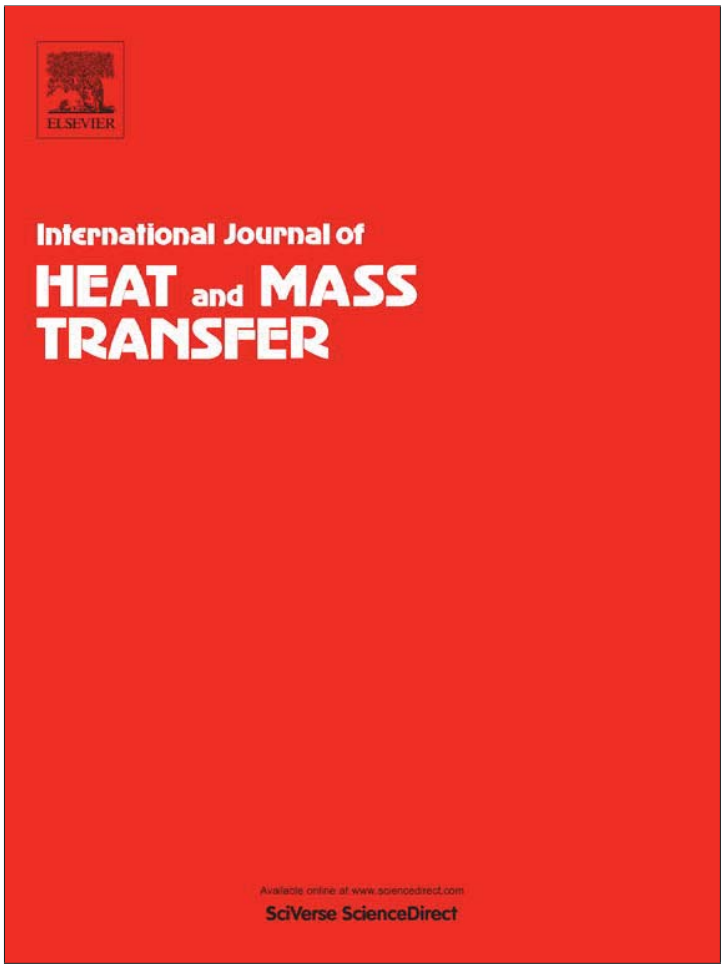

(This is a sample cover image for this issue. The actual cover is not yet available at this time.)

This article appeared in a journal published by Elsevier. The attached copy is furnished to the author for internal non-commercial research and education use, including for instruction at the authors institution and sharing with colleagues.

Other uses, including reproduction and distribution, or selling or licensing copies, or posting to personal, institutional or third party websites are prohibited.

In most cases authors are permitted to post their version of the article (e.g. in Word or Tex form) to their personal website or institutional repository. Authors requiring further information regarding Elsevier's archiving and manuscript policies are encouraged to visit:

http://www.elsevier.com/copyright

Author's personal copy

International Journal of Heat and Mass Transfer 59 (2013) 75–82

Contents lists available at SciVerse ScienceDirect

International Journal of Heat and Mass Transfer

journal homepage: www.elsevier.com/locate/ijhmt

Effect of fin pitches on the air-side performance of L-footed spiral fin-and-tube heat exchangers

Parinya Pongsoi [a], Patcharapit Promoppatum [a], Santi Pikulkajorn [b], Somchai Wongwises [a,c,*]

[a] Fluid Mechanics, Thermal Engineering and Multiphase Flow Research Lab (FUTURE), Department of Mechanical Engineering, Faculty of Engineering, King Mongkut's University of Technology Thonburi, Bangmod, Bangkok 10140, Thailand
[b] Somchai Industry Co., Ltd., Bangkok 10150, Thailand
[c] The Academy of Science, The Royal Institute of Thailand, Sanam Suea Pa, Dusit, Bangkok 10300, Thailand

ARTICLE INFO

Article history:
Received 24 August 2012
Received in revised form 15 November 2012
Accepted 21 November 2012

Keywords:
L-footed fin
Heat transfer
Heat exchanger
Air–water
Extended surface

ABSTRACT

The purpose of this experimental investigation is to investigate the effects of fin pitch (i.e., f_p of 2.4, 3.2, and 4.2 mm) on the air-side heat transfer performance and frictional characteristics of L-footed spiral fin-and-tube heat exchangers at high Reynolds numbers (Re_{dc}) of 4000–15,000. A determinant of the parallel cross-flow and the counter cross-flow is the flow arrangement of the test heat exchangers. Ambient air and hot water are used as a working fluid on the air- and the tube-side, respectively. The results indicate that the air-side heat transfer coefficient and Colburn factor are independent of fin pitch. However, fin pitch does have an influential effect on the average heat transfer rate, pressure drop, and friction factor. In terms of industrial applications, the correlation of the Colburn factor and friction factor are proposed for practical applications.

© 2012 Elsevier Ltd. All rights reserved.

1. Introduction

The heat exchangers are used in two main methods of heat transfer (convection and conduction modes). Many types of heat exchangers are used in industrial applications, such as intercoolers, boilers, economizers, air and liquid pre-heaters, evaporating and condensing heat exchangers, etc. Fin and tube heat exchangers are among the more favored types of heat exchangers. This kind of heat exchanger is designed for enhancing heat transfer performance. This enhancement is very important for thermo-economic analysis. Moreover, this heat transfer enhancement is normally limited by the thermal resistance on the heat exchanger's air-side. Arguably, fin configuration improvement is one of the most effective ways to augment the heat transfer rate on heat exchangers' air-side.

Over the years, the spiral fin has been studied by a number of researchers. Some examples related to this subject can be found in [1–13].

Nuntaphan et al. [1] tested crimped spiral fin-and-tube heat exchangers to analyze the effect of tube arrangement, transverse tube pitch, fin pacing, tube diameter, and they proposed heat transfer and friction characteristics correlations under wet conditions at low Reynolds numbers. Wongwises and Naphon [2,3] studied the heat transfer characteristics and the performance of a spirally coiled finned tube heat exchanger under dry-surface and wet surface conditions. Moreover, they tested heat exchangers that rely on a crimped spiral finned tube. Then, Srisawad and Wongwises [4] tested the helically coiled crimped spiral finned tube heat exchanger, aiming on the heat transfer performance in dry-surface conditions. Pongsoi et al. [5–7] studied the effect of number of tube rows and fin pitches on the air-side heat transfer characteristics and the optimized fin pitch of crimped spiral fin-tube heat exchangers having multipass parallel and counter cross-flow under sensible heating conditions and purpose the ε-*NTU* relation equation for this new water flow arrangement. In addition, the correlation of Colburn factor (j) and friction factor (f) of crimped spiral fin-and-tube heat exchangers at high Reynolds number were proposed in this study. Hamakawa et al. [8] investigated the flow around the fin and vortex shedding from the fin tube by using smoke wire technique. According to results, the spiral fin seemed to have more heat transfer over the conventional circular fin by the influence of downstream rotational vortices. Lee et al. [9,10] studied the air-side heat transfer characteristics of spiral-type circular fin-tube heat exchangers under frosting and non-frosting conditions. They measured these characteristics by varying the fin pitches, the number of tube rows and the fin alignments. Kawaguchi et al. [11] studied the effects of fin pitches on the serrated finned tube bank on

* Corresponding author at: Fluid Mechanics, Thermal Engineering and Multiphase Flow Research Lab (FUTURE), Department of Mechanical Engineering, Faculty of Engineering, King Mongkut's University of Technology Thonburi, Bangmod, Bangkok 10140, Thailand. Tel.: +66 24709115.
E-mail address: somchai.won@kmutt.ac.th (S. Wongwises).

0017-9310/$ - see front matter © 2012 Elsevier Ltd. All rights reserved.
http://dx.doi.org/10.1016/j.ijheatmasstransfer.2012.11.071

Author's personal copy

Nomenclature

A	area, m^2
A_{min}	minimum free flow area, m^2
A_o	total surface area, m^2
A_p	cross-sectional or profile area of fin, m^2
Al	aluminum
c_P	specific heat at constant pressure, J/(kg K)
d_c	fin collar outside diameter, m
d_f	fin outside diameter, m
d_i	tube inside diameter, m
d_o	tube outside diameter, m
f	Fanning friction factor, dimensionless
f_p	fin pitch, m
f_t	fin thickness, m
G_c	mass flux of the air based on minimum free flow area, kg/m^2 s
H	height, m
h	heat transfer coefficient, $W/(m^2 K)$
I_0	modified Bessel function solution of the first kind, order 0
I_1	modified Bessel function solution of the first kind, order 1
j	Colburn factor, dimensionless
k	thermal conductivity, W/(m K)
K_0	modified Bessel function solution of the second kind, order 0
K_1	modified Bessel function solution of the second kind, order 1
L	length, m
m	mass flow rate, kg/s
M	data point
n_t	number of tubes in row
N_{row}	number of tube rows
NTU	number of transfer units, dimensionless
Nu	Nusselt number, dimensionless
P_L	longitudinal tube pitch, m
P_T	transverse tube pitch, m
Pr	Prandtl number, dimensionless
Q	heat transfer rate, W
r_o	radius of tip fin, m
r_i	radius of base fin, m
R	radius function in terms of the radius ratio, dimensionless
Re_{dc}	Reynolds number based on fin collar outside diameter (d_c)
T	temperature, °C
U	overall heat transfer coefficient, $W/(m^2 K)$
V_{fr}	air frontal velocity, m/s
V_{max}	maximum velocity across heat exchanger, m/s

Greek symbols

ε	heat exchanger effectiveness
η	fin efficiency
η_o	overall surface effectiveness
ρ	density, kg/m^3
σ	contraction ratio of cross-sectional area
μ	dynamic viscosity of air, Pa s
ϕ	combination of terms, dimensionless;
ψ	radius ratio
ΔP	pressure drop, Pa

Subscripts

1	air-side inlet
2	air-side outlet
a	air
ave	average
corr	correlation
c	multipass counter cross flow or cold fluid
exp	experiment
f	fin
h	hot fluid
i	tube-side
m	mean value
max	maximum
o	air-side
p	multipass parallel cross flow
pc	multipass parallel-and-counter cross flow
t	tube
w	water

the pressure drop characteristics for higher improvement of heat transfer than circular spiral finned tube. Næss [12] investigated the effects of tube layout and fin geometry on the heat transfer and pressure drop performance of serrated fin and tube heat exchangers. Moreover, Lemouedda et al. [13] studied the optimization of fin serration, fin twisting and the number of segments by numerical calculations for serrated spiral fin-and-tube heat exchangers.

The L-footed spiral fin is one of several types of fin configurations. The base of the fin has an L-shape, which provides a large contact area, ensuring a good path for heat transfer from the tube surface to the fin. The spiral fin seems to have a greater heat transfer coefficient than the conventional circular fin. The L-footed spiral fin-and-tube heat exchanger may be suitable for industrial processes that present a high risk of tube corrosion. Despite its importance in many applications, the air-side performance of L-footed spiral fin-and-tube heat exchangers has received little attention in the literature. To the best of our knowledge, Pongsoi et al. [14] is the only work dealing with this issue. In the present study, the primary concern is to study the heat transfer performance and frictional characteristics of L-footed spiral fin-and-tube heat exchangers at high Reynolds numbers in industrial applications. The effect of fin pitch on the performance of the L-footed spiral fin and tube heat exchangers, which have not yet appeared in the available literature, are presented.

2. Data reduction

In this experimental work, air and hot water were used as working fluids. The main components of the system were the heat exchanger, water flow loop, air supply, and the instrumentation and data acquisition system. In addition, detailed descriptions of the essential components are available from Pongsoi et al. [7].

The test samples are a type of fin-and-tube cross-flow heat exchanger. The copper tube is finned with an aluminum fin. Fig. 1 details the water-side circuit and the dimensions of the tested fin-and-tube heat exchangers. Additionally, the schematic diagram of the heat exchangers algorithm for multi-pass parallel cross-flow, multi-pass counter cross-flow, and multi-pass parallel and counter cross-flows ($N_{row} = 2$) are shown in the previous figure. For the present flow configuration, the heat exchanger's effectiveness lies between the multi-pass parallel cross-flow and the counter cross-flow. Finally, the geometric parameters of the heat exchangers are

Author's personal copy

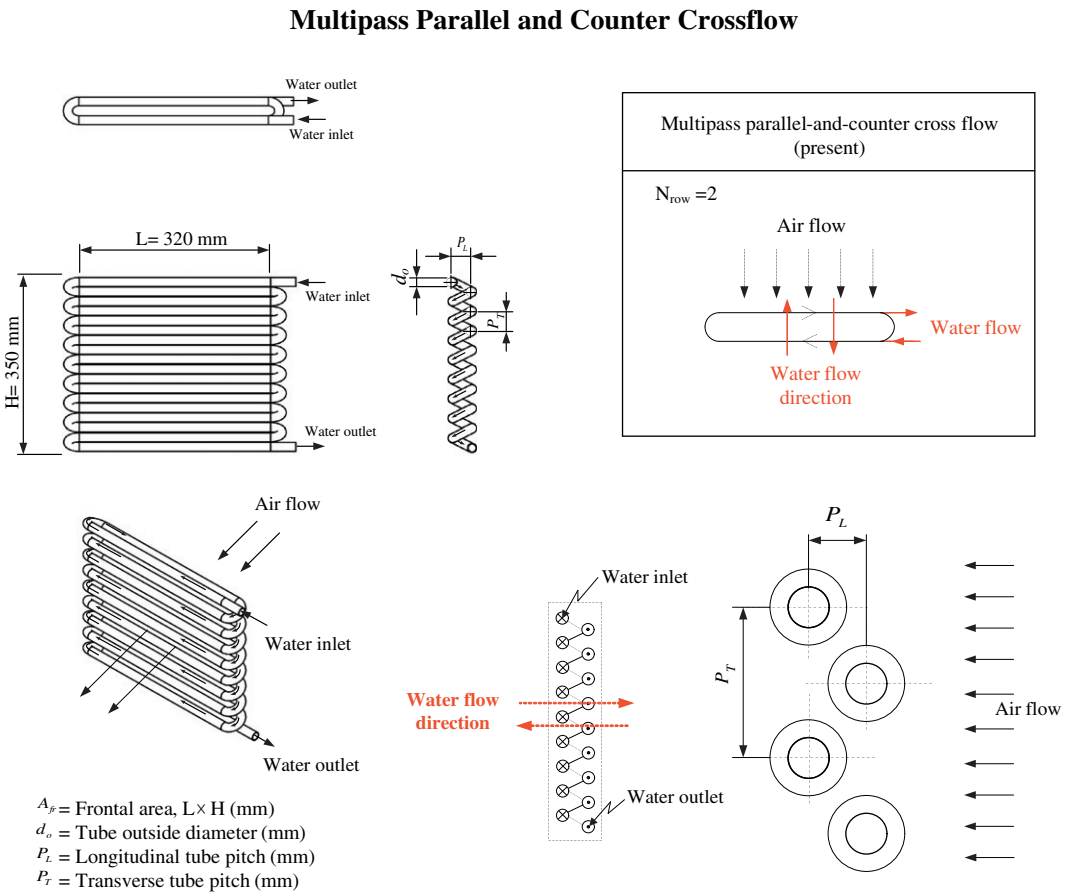

Fig. 1. Geometric details and schematic diagram of the heat exchangers algorithm for multipass parallel cross flow, multipass counter cross flow and multipass parallel-and-counter cross flow (× and ● signs indicate that water flows into or out of the paper, respectively).

Table 1
Detailed geometric parameters of the test samples.

No.	Fin type	d_i (mm)	d_c (mm)	d_f (mm)	P_L (mm)	P_T (mm)	f_t (mm)	n_t	N_{row}	Fin material	f_p (mm)
1	L-footed	13.5	16.85	34.8	35	39	0.25	9	2	Al	**2.4**
2	L-footed	13.5	16.85	34.8	35	39	0.25	9	2	Al	**3.2**
3	L-footed	13.5	16.85	34.8	35	39	0.25	9	2	Al	**4.2**

Remarks: d_f = Outside diameter of fin; d_i = Tube inside diameter; d_c = fin collar outside diameter; f_p = Fin pitch; f_t = Fin thickness; P_L = Longitudinal tube pitch; P_T = Transverse tube pitch; n_t = number of tubes in row; N_{row} = number of tube rows.
Notes: Tube layouts of all heat exchangers are staggered layout and all test sections have a tube outside diameter (d_o) of 16.35 mm.

summarized in Table 1, while the photographs and schematic diagram of L-footed spiral finned tube are shown in Fig. 2.

In the experiment, at a specific inlet water temperature, the water flow rate was fixed while the air flow rate was increased. The system was allowed to approach a steady state before any data was recorded under the experimental conditions shown in Table 2. After the system reached a steady state, the inlet and outlet temperatures of the air passing across the heat exchanger and the water flow rates were determined.

The overall heat transfer coefficient can be written in terms of the total resistance to heat transfer. This total resistance is the sum of the individual resistance values, as follows:

$$\frac{1}{UA} = \frac{1}{h_i A_i} + \frac{ln(d_o/d_i)}{2\pi k_t L} + \frac{ln(d_c/d_o)}{2\pi k_f L} + \frac{1}{\eta_o h_o A_o} \tag{1}$$

The multipass parallel and counter cross-flow used in this experiment is a combination of multipass parallel cross-flow and counter cross-flow. It may be suitable to use the average value of the heat exchanger effectiveness relations shown in Eq. (4). The air-side working fluid and the tube-side working fluid (water) are defined as fluid *A* and fluid B, respectively. It should be noted that the minimum heat capacity rate (C_{min}) is on the air-side (Fluid *A*). Therefore, the following relations are applied in the present calculation.

Multipass parallel cross-flow

For (N_{row} = 2);

$$\varepsilon_p = \left(1 - \frac{K}{2}\right)\left(1 - e^{-2K/C_A^*}\right), \quad K = 1 - e^{-NTU_A(C_A^*/2)} \tag{2}$$

Multipass counter cross-flow

For (N_{row} = 2);

$$\varepsilon_c = 1 - \left[\frac{K}{2} + \left(1 - \frac{K}{2}\right)e^{2K/C_A^*}\right]^{-1}, \quad K = 1 - e^{-NTU_A(C_A^*/2)} \tag{3}$$

where

$$\varepsilon_A = \frac{\varepsilon_p + \varepsilon_c}{2} \tag{4}$$

Author's personal copy

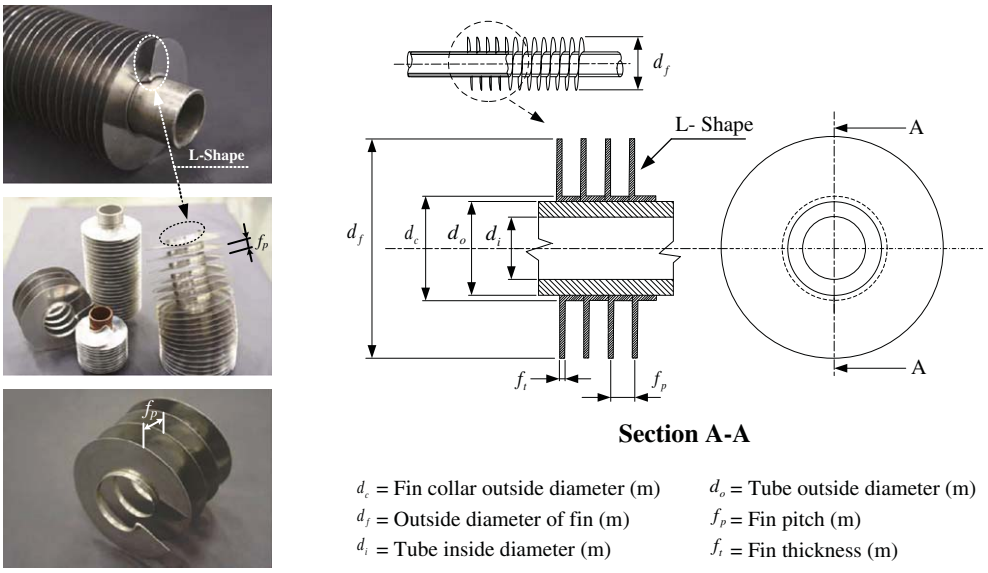

Fig. 2. Photographs and schematic diagram of L-footed spiral finned tube.

Table 2
Experimental conditions.

Inlet-air-dry bulb temperature, °C	31.5 ± 0.5
Inlet-air frontal velocity, m/s	2–8 or Re_{dc} (4000–15000)
Inlet-water temperature, °C	55–70
Water flow rate, LPM	12–14 or (0.2–0.233 kg/s)

Fluid A is mixed (C_{min}); Fluid B is unmixed (C_{max}).

$$\varepsilon_A = \varepsilon_B / C_A^* \tag{5}$$

$$C_A^* = \frac{C_A}{C_B} = \frac{1}{C_B^*}; \quad C^* \leqslant 1 \tag{6}$$

$$NTU_A = \frac{NTU_B}{C_A^*} \tag{7}$$

where $C^* = C_{min}/C_{max}$ is equal to C_c/C_h or C_h/C_c, depending on the value of the hot and cold fluid heat capacity rates.

$$C_{min} = C_h; \quad C_h < C_c \tag{8}$$

or

$$C_{min} = C_c; \quad C_c < C_h \tag{9}$$

as

$$Q_{max} = (mc_P)_c (T_{h1} - T_{c1}) \text{ if } C_c < C_h \tag{10}$$

or

$$Q_{max} = (mc_P)_h (T_{h1} - T_{c1}) \text{ if } C_h < C_c \tag{11}$$

$$\varepsilon = \frac{Q_{ave}}{Q_{max}} \tag{12}$$

The UA term in Eq. (1) is calculated by using Eq. (13):

$$UA = C_{min}(NTU) \tag{13}$$

The efficiency of a radial fin with a rectangular profile is determined by Gardner's [15] proposed method:

$$\eta = \frac{2\psi}{\phi(1+\psi)} \frac{I_1(\phi R_o)K_1(\phi R_i) - I_1(\phi R_i)K_1(\phi R_o)}{I_0(\phi R_i)K_1(\phi R_o) + I_1(\phi R_o)K_0(\phi R_i)} \tag{14}$$

where

$$\phi = (r_o - r_i)^{3/2} \left(\frac{2h_o}{k_f A_p}\right)^{1/2} \tag{15}$$

and where A_p is the area in the profile of the fin, as shown in Fig. 8:

$$A_p = f_t(r_o - r_i) \tag{16}$$

The parameters R_o, R_i are given in terms of the radius ratio (ψ):

$$R_o = \frac{1}{1-\psi} \tag{17}$$

and

$$R_i = \frac{\psi}{1-\psi} \tag{18}$$

where

$$\psi = \frac{r_i}{r_o} \tag{19}$$

The tube-side heat transfer coefficient (h_i) is calculated from the semi-empirical correlation of Gnielinski [16]:

$$h_i = \left(\frac{k_w}{d_i}\right) \frac{(Re_{di} - 1000)Pr(f_i/2)}{1 + 12.7\sqrt{f_i/2}\left(Pr^{2/3} - 1\right)} \tag{20}$$

where the friction factor is given by:

$$f_i = (1.58 \ln Re_{di} - 3.28)^{-2} \tag{21}$$

where $Re_{di} = \rho V d_i/\mu$.

The air-side heat transfer coefficient (h_o) can then be calculated from Eq. (1).

The heat transfer characteristics of the heat exchanger are presented in terms of non-dimensional groups:

$$Re_{dc} = \frac{\rho_a V_{max} d_c}{\mu} \tag{22}$$

$$j = \frac{Nu}{Re_{dc} Pr^{1/3}} = \frac{h_o}{\rho_a V_{max} c_P} (Pr)^{2/3} \tag{23}$$

The flow characteristics determined from the equation proposed by Kays and London [17] are given in terms of the fanning friction factor. The equation includes the entrance and exit pressure losses:

$$f = \left(\frac{A_{min}}{A_o}\right)\left(\frac{\rho_m}{\rho_1}\right)\left[\frac{2\Delta P \rho_1}{G_c^2} - (1+\sigma^2)\left(\frac{\rho_1}{\rho_2} - 1\right)\right] \tag{24}$$

Author's personal copy

where σ is the ratio of minimum free flow area to frontal area, A_o is the total heat transfer area, and A_{min} is the minimum free flow area.

The uncertainties are calculated from the root mean sum square method. The maximum uncertainties are 11% for the j-factor and 10% for the f-factor. The highest uncertainties were associated with the lowest Reynolds numbers.

3. Results and discussion

The primary analysis of the experimental data involved the energy balance between air and water. The energy balance related to systems, which investigated both heat transfer rates. The energy balance between the air and water associated with the L-footed spiral fin-and-tube heat exchangers had relative errors less than 5% (or $|Q_a - Q_w|/Q_{ave} < 0.05$). In addition, it is found that the ranges of the fin efficiency (η) and the heat exchanger effectiveness (ε) are 0.87–0.94 and 0.14–0.36, respectively. The air-side heat transfer and friction characteristics of all heat exchangers were examined in this experiment, which were presented in terms of the average heat transfer rate (Q_{ave}), air-side heat transfer coefficient (h_o), and pressure drop (ΔP) with air frontal velocity (V_{fr}). Moreover, the terms of a dimensionless number included the Colburn factor (j)

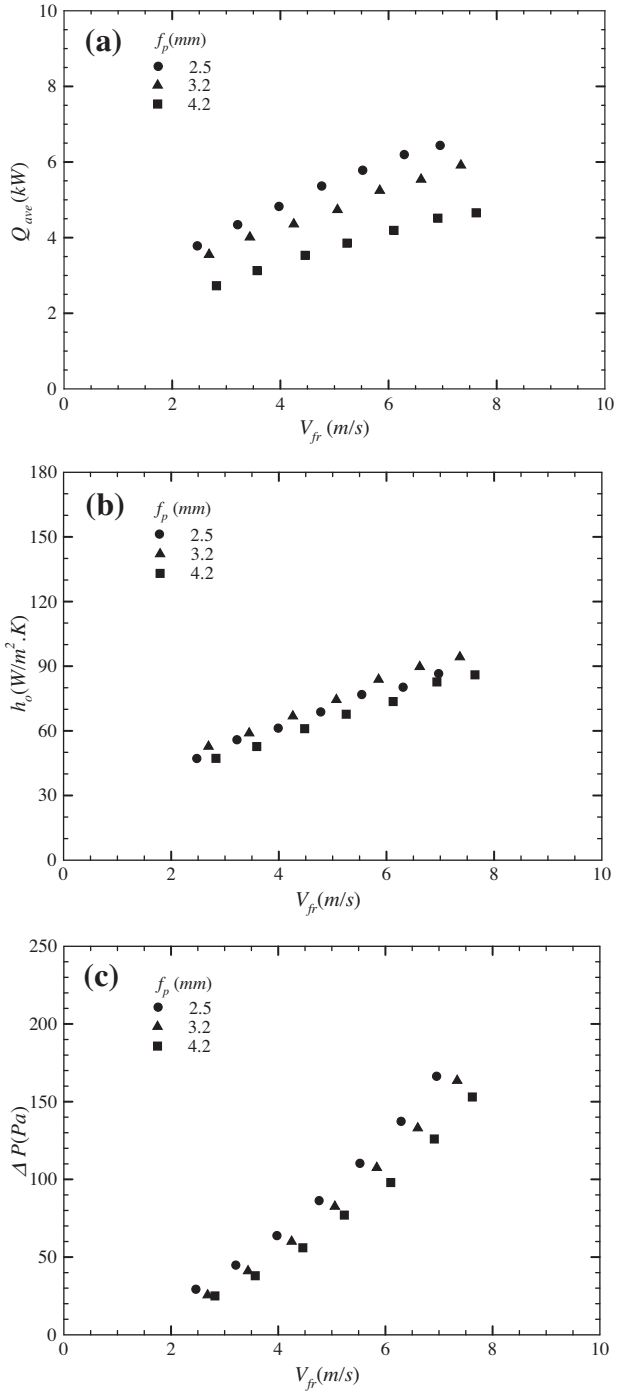

Fig. 3. Effect of fin pitches on the average heat transfer rate (a), heat transfer coefficient (b) and pressure drop (c) of L-footed spiral fin and tube heat exchangers. ($T_{w,in}$ = 65 °C/$m_{w,in}$ = 0.2 kg/s).

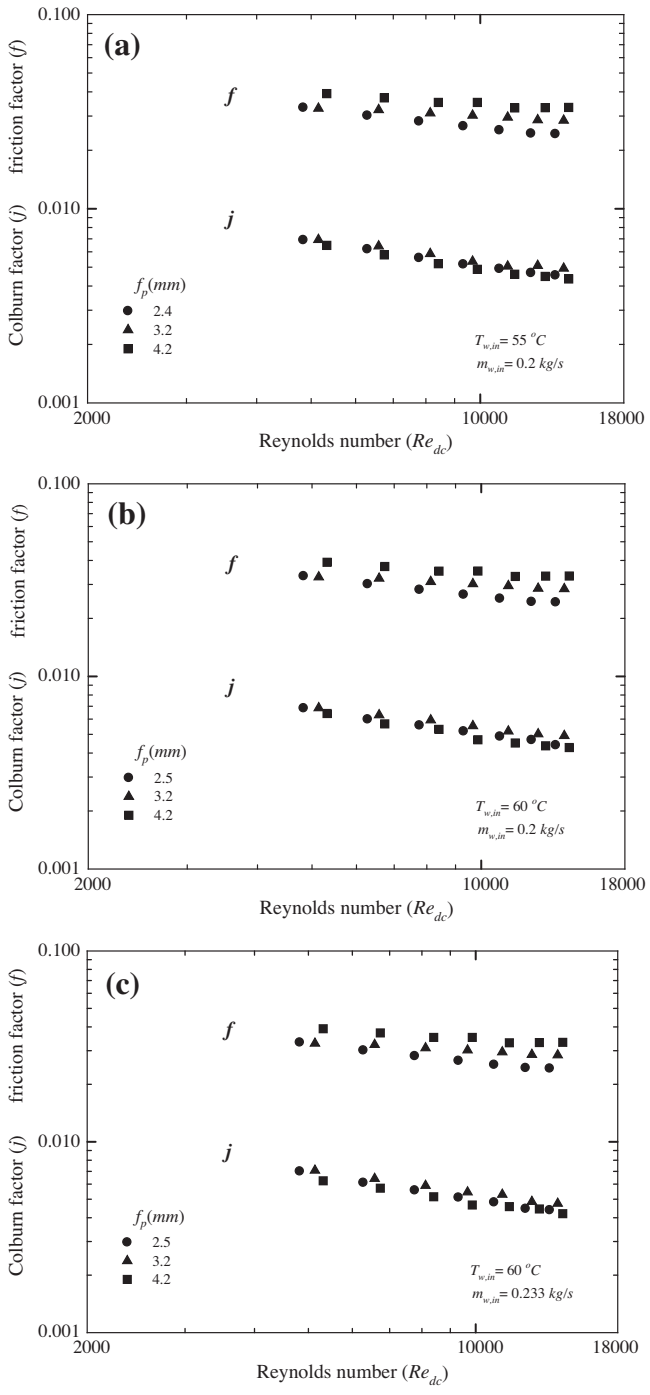

Fig. 4. Effect of fin pitches on the Colburn factor and friction factor at $T_{w,in}$ = 55 °C/$m_{w,i}$ = 0.2 kg/s (a), $T_{w,in}$ = 60 °C/$m_{w,in}$ = 0.2 kg/s (b) and $T_{w,in}$ = 60 °C/$m_{w,in}$ = 0.233 kg/s (c).

Author's personal copy

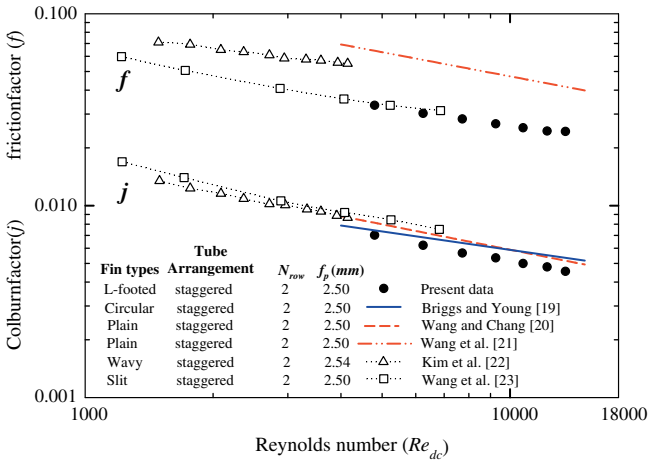

Fig. 5. Comparison of Colburn factor and friction factor between present data with correlational and experimental data of several fin types.

and friction factor (f) plotted against Re_{dc}, which was the Reynolds number based on the fin collar's outside diameter ($d_o + 2f_t$).

Fig. 3 shows the effect of the fin pitches on the average heat transfer rate, air-side heat transfer coefficient, and pressure drop for an aluminum fin with an outside fin collar diameter of 16.85 mm and outside fin diameter of 34.8 mm. This study has extended the fin pitches of 2.4, 3.2, and 4.2 mm. The results show that the average heat transfer rate, air-side heat transfer coefficient, and pressure drop increase with increasing air frontal velocity. Fig. 3(a) depicts the effect of fin pitches on average heat transfer rate. It was found that the average heat transfer rate of $f_p = 2.4$ and 3.2 mm are higher than that for $f_p = 4.2$ mm by about 37% and 26%, respectively, over the range of air frontal velocities. This is be because the surface heat transfer area of the smaller fin pitch is generally higher than that of larger ones which leads to the increasing of the average heat transfer rate.

However, Fig. 3(b) shows that the fin pitches had an insignificant effect on the air-side heat transfer coefficient. The present data correspond with Pongsoi et al. [5], who studied the effect of fin pitch on the air-side performance of the crimped spiral fin. Furthermore, as illustrated in Fig. 3(c), when f_p decreases from 4.2 to 2.4 mm, the pressure drop increases by about 18% (for $f_p = 3.2$) and 38% (for $f_p = 2.4$). The reason for this is increasing pressure blocking the flow area due to decreasing fin pitch.

The examination on the effect of fin pitch in the dimensionless terms is shown in Fig. 4. As expected, both the Colburn factor (j) and the friction factor (f) decrease with increasing Reynolds number over the range of operating conditions. The result shows that the fin pitch has a negligible effect on the Colburn factor (j), which is supported by findings in other research [5,6,18]. This phenomenon occurs because the high Reynolds number accentuates the good mixing, leading to better heat transfer performance, regardless of fin pitch changes.

In terms of the friction factor, it is clear that at Reynolds numbers greater than 6000, fin pitch has a significant effect (i.e., the friction factor is higher for a larger fin pitch than for a smaller fin pitch). According to Eq. (24), the ratio of minimum free-flow area and the total heat transfer area (A_{min}/A_o) and mass flux of air (G_c) showed that A_o significantly increases as fin pitch is changed from 4.2 to 3.2 or 2.4 mm. Conversely, the reduction of A_{min} is comparatively small. For these reasons, the friction factor signals a detectable rise for greater fin pitch. In summary, a large fin pitch increases the ratio of minimum free-flow area and the total heat transfer area (A_{min}/A_o), but decreases mass flux of the air (G_c). A low value of G_c will make the friction factor higher. It should be noted that the dynamic effects (A_{min}/A_o and G_c) have a more pronounced effect upon the friction factor than the air-side pressure drop (ΔP). Nevertheless, the effect of fin pitch on the friction factor tends to vanish at Reynolds numbers less than about 6000.

Initial validation comparison for the air-side heat transfer and flow characteristics of the performance of an L-footed spiral fin contrast with the performance of several plate fin types (circular [19], plain [20,21], wavy [22], and slit [23] fin) at high Reynolds numbers, as shown in Fig. 5. It was found that the present data and other fin types produce similar trends and slopes of the Colburn factor, which decrease with an increasing Reynolds number. However,

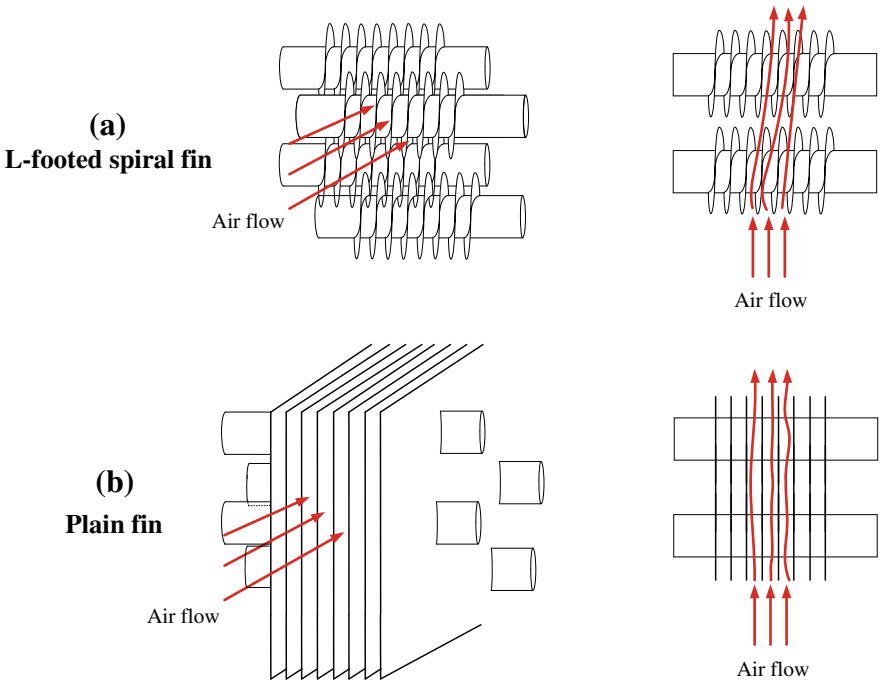

Fig. 6. Schematic showing the flow distribution (a) L-footed spiral fin (b) plain fin.

Author's personal copy

significant difference existed between an L-footed fin and plain fin on the friction factor. The authors found that the friction factor of L-footed spiral fins is about 80–90% different from the plain fin (conventional heat exchanger). As demonstrated in Fig. 6, the plain fin experiences single flow though channels. Therefore, this phenomenon might occur from the geometry of the plain fin that leads to contact surface friction greater than that of L-footed spiral fins.

Finally, empirical correlations for the Colburn factor (j) and the friction factor (f) are proposed in this study which parallel actual industrial applications operated at high Reynolds numbers. It must be noted that fin pitches have a negligible influence on the Colburn factor, as mentioned above. Thus, the fin pitch is not included in the Colburn factor correlation. The present data is correlated as suggested by Pongsoi et al. [6] in the form of $j = aRe_{dc}^{b}$ and $f = aRe_{dc}^{b}\left(\frac{f_p}{d_c}\right)^{c}$, where a, b, and c are the empirical constants obtained from least-square fitting of the experimental data. According to the data analysis, friction factor correlation was also associated with fin pitch. Therefore, the present correlation for f factor is modified by including the dimensionless fin pitch (f_p) normalized by the tube's outside diameter (d_c). The computable correlations for the Colburn and friction factors were suggested according to the form:

$$j_{corr} = 0.2150Re_{dc}^{-0.4059} \tag{25}$$

$$f_{corr} = 0.4852Re_{dc}^{-0.2156}\left(\frac{f_p}{d_c}\right)^{0.4771} \tag{26}$$

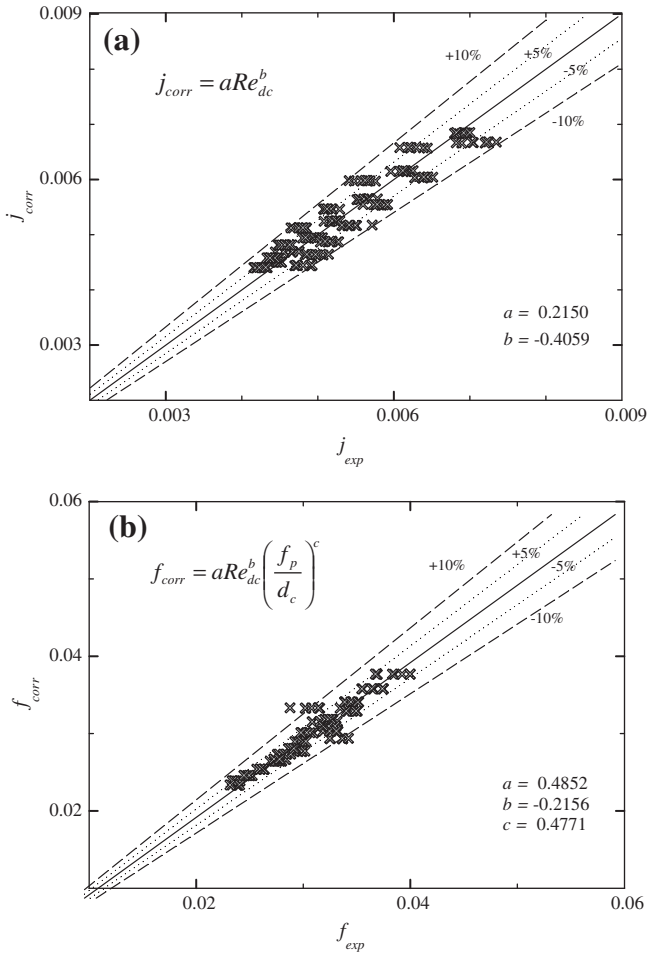

Fig. 7. Comparison of the proposed correlations with experimental data: (a) Colburn factor and (b) friction factor.

$$\text{Mean deviations} = \frac{1}{M}\left[\sum_{1}^{M}\frac{|\Phi_{corr} - \Phi_{exp}|}{\Phi_{exp}}\right] \times 100\% \tag{27}$$

Fig. 7 shows the comparison of the proposed correlations with experimental data. The correlation Eqs. (25) and (26) describe 100% and 95% of the j and f factors, respectively, to be within ±10%. The proposed heat transfer and friction correlations have mean deviations in Eq. (27) of 4.29% and 2.12%, respectively. However, these correlations can be used not only for parallel-and-counter cross-flow types of water flow arrangements, but also used for parallel cross-flow, counter cross-flow, and pure cross-flow.

4. Conclusions

This research determined the extent of the probable effect of fin pitch on the heat transfer performance of L-footed spiral fin-and-tube heat exchangers. Total test sections have a fin thickness of 0.25 mm, outside fin diameter (d_f) of 34.8 mm, two tube rows (N_{row}) and various fin pitches from 2.4, 3.2, and 4.2 mm (i.e., 10, 8, and 6 fpi, respectively), which are the manufacturing limitations for this kind of fin. The test samples were multi-pass parallel-and-counter cross-flows arrangement under sensible heating conditions and examined at a high Reynolds number (4000–15,000) based on the fin collar's outside diameter. In summary, the following major conclusions emerged from this study:

- It was confirmed that the average heat transfer rate, air-side heat transfer coefficient, and pressure drop increase with increasing Reynolds numbers. In addition, the effect of fin pitch on average heat transfer rate and pressure drop were considered significant. On the contrary, results suggest that the air-side heat transfer coefficient is independent of fin pitch.
- Fin pitch has no significant effect on the Colburn factor (j factor) at high Reynolds numbers (4000–15,000).
- The effect of fin pitch on the friction factor is negligible at Reynolds numbers lower than 6000. In other words, a detectable increment in friction factor is found for greater fin pitch when the Reynolds number is more than 6000.
- A correlation is proposed for the Colburn factor (j) and friction factor (f) for L-footed spiral fin-and-tube heat exchangers at high Reynolds number. The mean deviations of the proposed Colburn and friction factors correlations are 4.29% and 2.12%, respectively.
- The authors hope that future research will use this study as a foundation for enhancing our understanding of the effect of fin pitch on L-footed spiral fin-and-tube heat exchangers.

Acknowledgments

The authors are indebted to the Thailand Research Fund, the Office of the Higher Education Commission and the National Research University Project for supporting this study.

References

[1] A. Nuntaphan, T. Kiatsiriroat, C.C. Wang, Heat transfer and friction characteristics of crimped spiral finned heat exchangers with dehumidification, Appl. Therm. Eng. 25 (2005) 327–340.
[2] S. Wongwises, P. Naphon, Heat transfer characteristics of a spiral-coil, finned tube heat exchanger under dry-surface conditions, Heat Transfer Eng. 27 (1) (2006) 25–34.
[3] S. Wongwises, P. Naphon, Thermal performance of a spiral-coil finned tube heat exchanger under wet-surface conditions, J. Mech. Sci. Technol. 20 (2) (2006) 212–226.
[4] K. Srisawad, S. Wongwises, Heat transfer characteristics of a new helically coiled crimped spiral finned tube heat exchanger, Heat Mass Transfer 45 (4) (2009) 381–391.

Author's personal copy

[5] P. Pongsoi, S. Pikulkajorn, C.C. Wang, S. Wongwises, Effect of fin pitches on the air-side performance of crimped spiral fin-and-tube heat exchangers with a multipass parallel and counter cross-flow configuration, Int. J. Heat Mass Transfer 54 (9–10) (2011) 2234–2240.
[6] P. Pongsoi, S. Pikulkajorn, C.C. Wang, S. Wongwises, Effect of number of tube rows on the air-side performance of crimped spiral fin-and-tube heat exchangers with a multipass parallel and counter cross-flow configuration, Int. J. Heat Mass Transfer 55 (4) (2012) 1403–1411.
[7] P. Pongsoi, S. Pikulkajorn, S. Wongwises, Effect of fin pitches on the optimum heat transfer performance of crimped spiral fin-and-tube heat exchangers, Int. J. Heat Mass Transfer 55 (23–24) (2012) 6555–6566.
[8] H. Hamakawa, K. Nakashima, T. Kudo, E. Nishida, T. Fukano, Vortex shedding from a circular cylinder with spiral fin, J. Fluid Sci. Technol. 3 (6) (2008) 787–795.
[9] M. Lee, T. Kang, Y. Kim, Air-side heat transfer characteristics of spiral-type circular fin-and-tube heat exchangers, Int. J. Refrig. 33 (2) (2010) 313–320.
[10] M. Lee, T. Kang, Y. Joo, Y. Kim, Heat transfer characteristics of spirally-coiled circular fin-tube heat exchangers operating under frosting conditions, Int. J. Refrig. 34 (1) (2011) 328–336.
[11] K. Kawaguchi, K. Okui, Y. Asai, Y. Hasegawa, Effects of serrated fin and fin pitch on pressure drop of the finned tube banks, Turbomachinery 32 (2004) 551–559.
[12] E. Næss, Experimental investigation of heat transfer and pressure drop in serrated-fin tube bundles with staggered tube layouts, Appl. Therm. Eng. 30 (2010) 1531–1537.
[13] A. Lemouedda, A. Schmid, E. Franz, M. Breuer, A. Delgado, Numerical investigations for the optimization of serrated finned-tube heat exchangers, Appl. Therm. Eng. 31 (2011) 1393–1401.
[14] P. Pongsoi, S. Pikulkajorn, S. Wongwises, Experimental study on the air-side performance of a multipass parallel and counter cross-flow L-footed spiral fin-and-tube heat exchanger, Heat Transfer Eng. 33 (15) (2012) 1251–1263.
[15] K.A. Gardner, Efficient of extended surface, ASME Trans. 67 (1945) 621.
[16] V. Gnielinski, New equation for heat and mass transfer in turbulent pipe and channel flow, Int. Chem. Eng. 16 (1976) 359–368.
[17] W.M. Kays, A. London, Compact Heat Exchangers, third ed., Mcgraw-Hill, New York, 1984.
[18] S. Wongwises, Y. Chokeman, Effect of fin pitch and number of tube rows on the air side performance of herringbone wavy fin and tube heat exchangers, Energy Convers. Manage. 46 (2005) 2216–2231.
[19] D.E. Briggs, E.H. Young, Convective heat transfer and pressure drop of air flowing across triangular pitch banks of finned tubes, Chem. Eng. Prog. Symp. Ser. 59 (41) (1963) 1–10.
[20] C.C. Wang, C.-T. Chang, Heat and mass transfer for plate fin-and-tube heat exchangers with and without hydrophilic coating, Int. J. Heat Mass Transfer 41 (1998) 3109–3120.
[21] C.C. Wang, Y.J. Chang, Y.C. Hsieh, Y.T. Lin, Sensible heat and friction characteristics of plate fin-and-tube heat exchangers having plane fins, Int. J. Refrig. 19 (4) (1996) 223–230.
[22] N.H. Kim, J.H. Ham, J.P. Cho, Experimental investigation on the airside performance of fin-and-tube heat exchangers having herringbone wave fins and proposal of a new heat transfer and pressure drop correlation, J. Mech. Sci. Technol. 22 (2008) 545–555.
[23] C.C. Wang, W.H. Tao, C.J. Chang, An investigation of the airside performance of the slit fin-and-tube heat exchangers, Int. J. Refrig. 22 (1999) 595–603.

This article was downloaded by: [S. Wongwises]
On: 16 January 2013, At: 20:32
Publisher: Taylor & Francis
Informa Ltd Registered in England and Wales Registered Number: 1072954 Registered office: Mortimer House, 37-41 Mortimer Street, London W1T 3JH, UK

Experimental Heat Transfer: A Journal of Thermal Energy Generation, Transport, Storage, and Conversion

Publication details, including instructions for authors and subscription information:
http://www.tandfonline.com/loi/ueht20

Experimental Study on Evaporative Heat Transfer and Pressure Drop of R-134a Flowing Downward Through Vertical Corrugated Tubes with Different Corrugation Pitches

K. Aroonrat [a] , A. S. Dalkilic [b] & S. Wongwises [a c]

[a] Fluid Mechanics, Thermal Engineering and Multiphase Flow Research Lab (FUTURE), Department of Mechanical Engineering, Faculty of Engineering, King Mongkut's University of Technology Thonburi, Bangmod, Bangkok, Thailand

[b] Heat and Thermodynamics Division, Department of Mechanical Engineering, Yildiz Technical University (YTU), Yildiz, Besiktas, Istanbul, Turkey

[c] The Academy of Science, The Royal Institute of Thailand, Sanam Suea Pa, Dusit, Bangkok, Thailand

To cite this article: K. Aroonrat , A. S. Dalkilic & S. Wongwises (2013): Experimental Study on Evaporative Heat Transfer and Pressure Drop of R-134a Flowing Downward Through Vertical Corrugated Tubes with Different Corrugation Pitches, Experimental Heat Transfer: A Journal of Thermal Energy Generation, Transport, Storage, and Conversion, 26:1, 41-63

To link to this article: http://dx.doi.org/10.1080/08916152.2011.631080

PLEASE SCROLL DOWN FOR ARTICLE

Full terms and conditions of use: http://www.tandfonline.com/page/terms-and-conditions

This article may be used for research, teaching, and private study purposes. Any substantial or systematic reproduction, redistribution, reselling, loan, sub-licensing, systematic supply, or distribution in any form to anyone is expressly forbidden.

The publisher does not give any warranty express or implied or make any representation that the contents will be complete or accurate or up to date. The accuracy of any instructions, formulae, and drug doses should be independently verified with primary sources. The publisher shall not be liable for any loss, actions, claims, proceedings,

demand, or costs or damages whatsoever or howsoever caused arising directly or indirectly in connection with or arising out of the use of this material.

Downloaded by [S. Wongwises] at 20:32 16 January 2013

Experimental Heat Transfer, 26:41–63, 2013
Copyright © Taylor & Francis Group, LLC
ISSN: 0891-6152 print/1521-0480 online
DOI: 10.1080/08916152.2011.631080

Downloaded by [S. Wongwises] at 20:32 16 January 2013

EXPERIMENTAL STUDY ON EVAPORATIVE HEAT TRANSFER AND PRESSURE DROP OF R-134a FLOWING DOWNWARD THROUGH VERTICAL CORRUGATED TUBES WITH DIFFERENT CORRUGATION PITCHES

K. Aroonrat,[1] A. S. Dalkilic,[2] and S. Wongwises[1,3]

[1]Fluid Mechanics, Thermal Engineering and Multiphase Flow Research Lab (FUTURE), Department of Mechanical Engineering, Faculty of Engineering, King Mongkut's University of Technology Thonburi, Bangmod, Bangkok, Thailand

[2]Heat and Thermodynamics Division, Department of Mechanical Engineering, Yildiz Technical University (YTU), Yildiz, Besiktas, Istanbul, Turkey

[3]The Academy of Science, The Royal Institute of Thailand, Sanam Suea Pa, Dusit, Bangkok, Thailand

This study reports an experimental investigation of evaporative heat transfer and pressure drop of R-134a flowing downward inside vertical corrugated tubes with different corrugation pitches. The double tube test section is 0.5 m long with refrigerant flowing in the inner tube and hot water flowing in the annulus. The inner tubes are comprised of one smooth tube and three corrugated tubes with different corrugation pitches of 6.35, 8.46, and 12.7 mm. The test runs are performed at evaporating temperatures of 10°C, 15°C, and 20°C; heat fluxes of 20, 25, and 30 kW/m^2; and mass fluxes of 200, 300, and 400 kg/m^{2}s. The experimental data obtained from the smooth tube are plotted with flow pattern map for vertical flow. Comparisons between smooth and corrugated tubes on the heat transfer and pressure drop are also discussed. It is observed that the heat transfer coefficient and frictional pressure drop obtained from the corrugated tubes are higher than those from the smooth tube. Furthermore, the heat transfer coefficient and frictional pressure drop increase as the corrugation pitch decreases. The maximum heat transfer enhancement factor and penalty factor are up to 1.22 and 4.0, respectively.

Keywords vertical, evaporative, heat transfer, pressure drop, corrugated tube

INTRODUCTION

Heat exchangers are devices used to implement the exchange of heat between two fluids that are at different temperatures and separated by a solid wall. They are commonly used in a wide range of applications, such as refrigeration and air-conditioning systems, power plants, and the chemical process industry. The aim in designing a heat exchanger is to reduce the heat transfer surface area required for a given application and thus reduce the heat exchanger size and material cost or to increase the heat

Received 6 September 2011; accepted 13 September 2011.

Address correspondence to S. Wongwises, Department of Mechanical Engineering, Faculty of Engineering, King Mongkut's University of Technology Thonburi, 126 Pracha-utid Road, Bangmod, Bangkok 10140, Thailand. E-mail: somchai.won@kmutt.ac.th

NOMENCLATURE

A	surface area of the test section (m^2)
c_p	specific heat at constant pressure (J/kg K)
d	tube diameter (m)
e	depth of corrugation (mm)
f	friction factor
g	gravitational acceleration (m/s^2)
G	mass flux (kg/m^2s)
h	heat transfer coefficient (W/m^2K)
i	specific enthalpy (J/kg)
i_{fg}	specific enthalpy of vaporization (J/kg)
J_g	superficial gas velocity, Gx/ρ_g (m/s)
J_l	superficial liquid velocity, $G(1-x)/\rho_l$ (m/s)
k	thermal conductivity (W/m K)
m	mass flow rate (kg/s)
p	pitch of corrugation (mm)
P	pressure (Pa)
Q	heat transfer rate (W)
q''	heat flux (kW/m^2)
Re	Reynolds number
T	temperature (°C)
x	vapor quality
z	axial coordinate (m)

Greek Symbols

α	void fraction
ΔP	pressure drop (Pa/m)
θ	helix angle (°)
μ	dynamic viscosity (kg/m s)
ρ	density (kg/m^3)

Subscripts

avg	average
eq	equivalent
F	frictional term
g	gas/vapor
G	gravitational term
i	inside
in	inlet
l	liquid
M	momentum term
o	outside
out	outlet
ph	pre-heater
ref	refrigerant
sat	saturation
tp	two-phase
TS	test section
w	water
wi	inner wall

Downloaded by [S. Wongwises] at 20:32 16 January 2013

exchanger effectiveness for a given surface area. In recent years, many researchers use the heat transfer enhancement techniques to improve the performance of the heat exchanger. In general, heat transfer enhancement techniques can be categorized as active and passive methods. Active methods are those that use the addition of external power—such as electric field, mechanical vibration, and injection—to facilitate the desired flow modification and concomitant improvement in the rate of heat transfer. Passive methods employ special surface geometries, such as rough surfaces, extended surfaces, and swirl flow devices. Rough surfaces are utilized in many configurations to promote turbulence rather than increase the heat transfer area. A corrugated tube has corrugation on the surface to increase the heat transfer coefficient by mixing the flow boundary layer and increasing the turbulence level of fluid flow.

In past decades, many researchers have thoroughly analyzed the heat transfer and flow characteristics of refrigerants in a horizontal smooth tube. Heat transfer enhancement of refrigerant using horizontal enhanced tubes has been the subject of some research, for example, Thors and Bogart [1]. However, there are not many investigations concerning the heat transfer and pressure drop of refrigerant in vertical tubes. Several experimental studies have been performed on condensation heat transfer and flow characteristics of refrigerant in vertical tube (Briggs et al. [2], Ma et al. [3], and Dalkilic et al. [4–8]). Publications on boiling heat transfer and flow characteristics of refrigerant flow in vertical tubes are summarized as follows.

Downloaded by [S. Wongwises] at 20:32 16 January 2013

Shah [9] proposed equations to fit his chart correlation, used for the estimation of heat transfer coefficients during saturated boiling of water, R-11, R-12, R-22, R-113, and cyclohexanein tubes and annuli. The correlation was shown to be applicable to both horizontal and vertical tubes. Gungor and Winterton [10] presented a new general correlation for forced-convection boiling that has been developed with a large data bank. This data bank consists of more than 4,300 data points for water, refrigerants, and ethylene glycol, covering 7 fluids and 28 authors, mostly for saturated boiling in vertical and horizontal tubes. Kandlikar [11] proposed the correlation for predicting saturated flow boiling heat transfer coefficients inside horizontal and vertical tubes. The correlation has been developed with 5,246 data points for water, refrigerants, and cryogenic fluids from 24 experimental investigations. Lee and Chang [12] investigated the heat transfer characteristics in the post-dryout region for the boiling of up-flow of R-134a in vertical smooth tubes and rifled tubes. Aroonrat and Wongwises [13] investigated the heat transfer and friction characteristics of pure refrigerant R-134a during evaporation inside vertical corrugated tubes. One smooth tube and two corrugated tubes were tested.

Among the above-described works, most experimental investigations focused on the heat transfer and flow characteristics of refrigerant flow inside vertical smooth tubes. There have been some works dealing with the flow in vertical enhanced tubes. In addition, there has been only one work—Aroonrat and Wongwises [13]—concerning the heat transfer and flow characteristics of R-134a during downward evaporation inside vertical corrugated tubes. Although some information is currently available, there still remains room for further research. In particular, the effects of corrugation pitch on the evaporative heat transfer and pressure drop characteristics of R-134a flow through vertical corrugated tubes remain unstudied. As a consequence, the objective of this current work is to study the effect of corrugation pitch on the evaporative heat transfer and pressure drop characteristics of R-134a flowing downward through vertical corrugated tubes. This article presents experimental data that have never been seen before on heat transfer and pressure drop.

EXPERIMENTAL APPARATUS AND METHOD

Figure 1 shows a schematic diagram of the test apparatus. The refrigerant loop consists of a pre-heating loop, test section, heating loop, and chilling loop. The refrigerant is forced by a gear pump controlled by an inverter. The refrigerant then passes through a filter/dryer, a refrigerant flow meter, a pre-heater, and a sight glass, and then enters the test section. The pre-heater controls the inlet quality before entering the test section; it consists of a spiral counter-flow tube-in-tube heat exchanger that is designed to supply heat to prepare an inlet quality for the vaporization of the refrigerant. Leaving the test section, the refrigerant vapor then condenses inside a sub-cooler and is collected in a receiver. After exiting the chilling loop, the refrigerant returns from a two-phase refrigerant to a sub-cooled state. Finally, the refrigerant returns to the refrigerant pump, completing the cycle.

Details of the test section are shown schematically in Figure 2. The test section is a vertical counter-flow double-tube heat exchanger with refrigerant flowing downward in the inner tube and heating water flowing upward in the annulus. Four different inner copper tubes, which are one smooth tube and three corrugated tubes having different corrugation pitches, are tested. The inner diameter and outer diameter of the inner tube

Downloaded by [S. Wongwises] at 20:32 16 January 2013

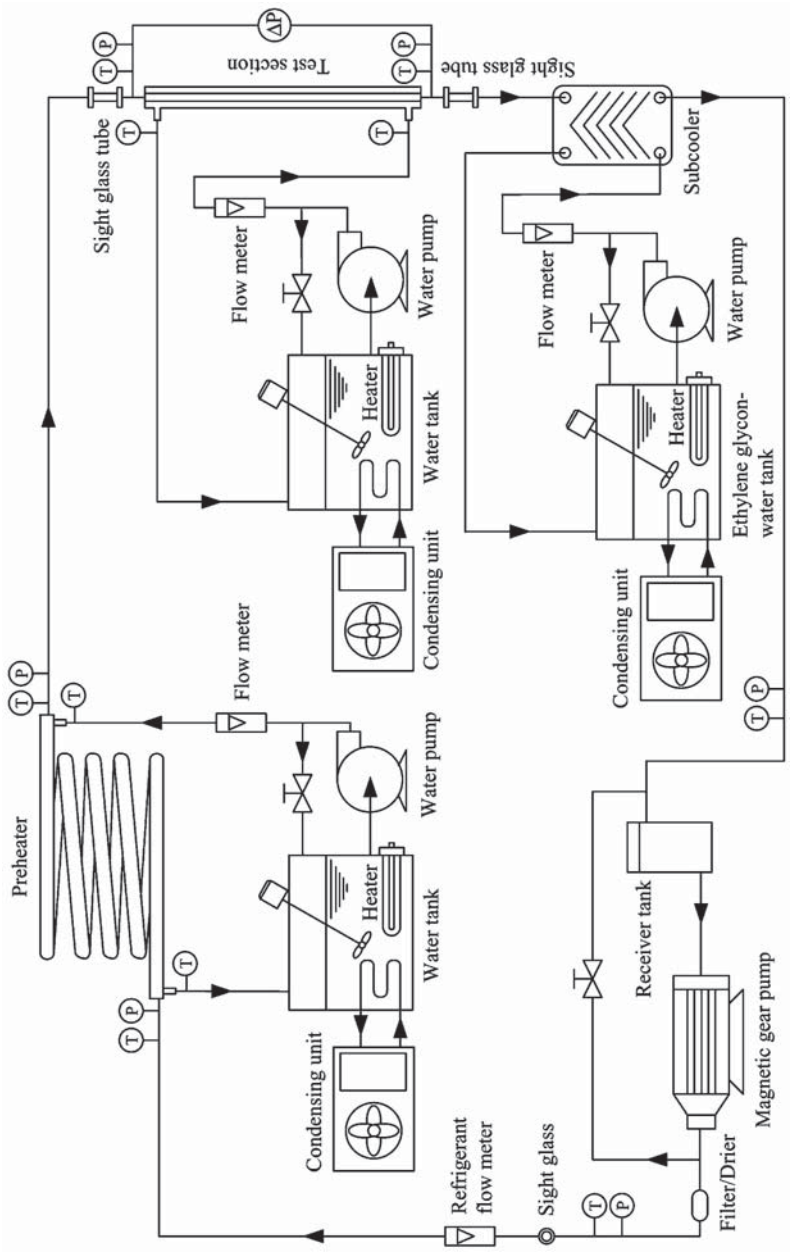

Figure 1. Schematic diagram of the experimental apparatus.

Downloaded by [S. Wongwises] at 20:32 16 January 2013

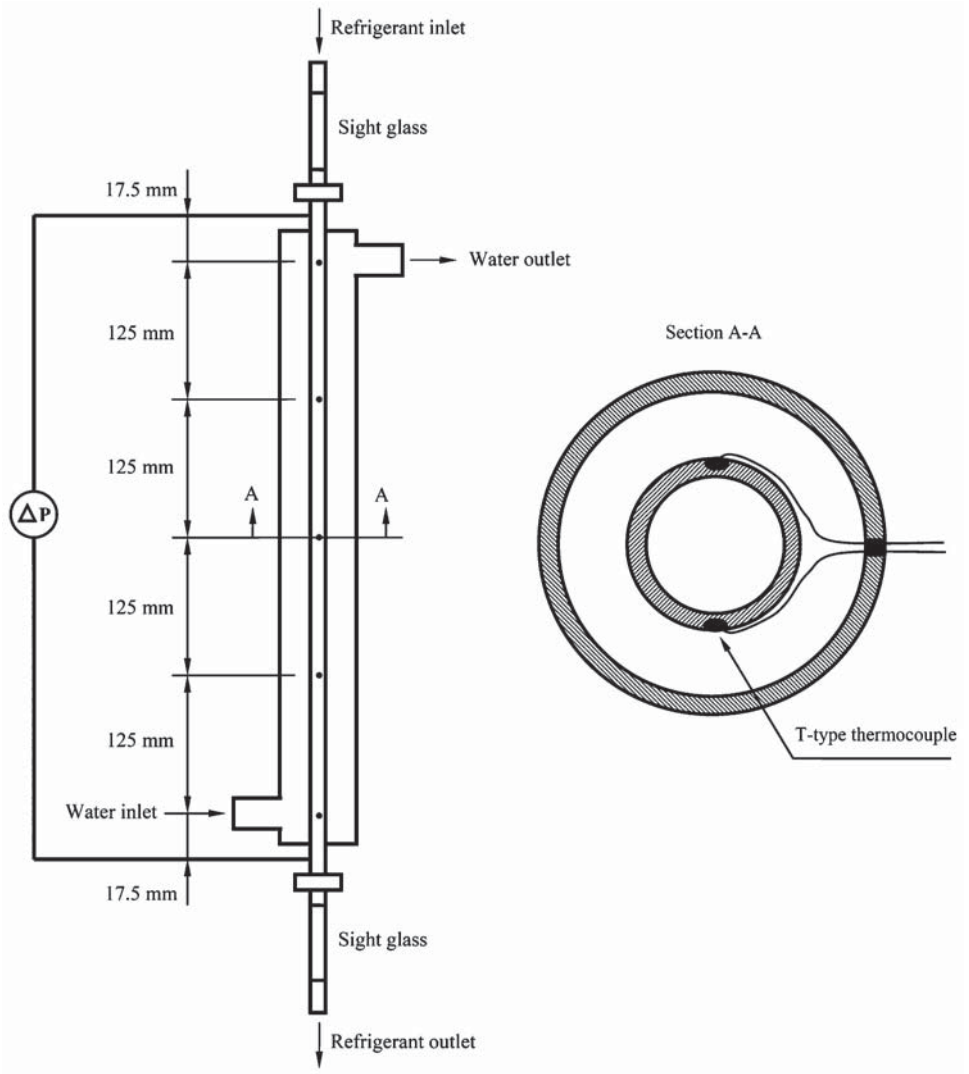

Figure 2. Schematic diagram of the test section.

are 8.7 and 9.52 mm, respectively. The length of the test section is 500 mm. Figure 3 shows the sketch and the actual photograph of the corrugated tube. The dimensions of the test section are listed in Table 1. T-type thermocouples are installed at the inlet and outlet of the test section to measure the saturation temperature of the refrigerant. Similarly, the differential pressure transducer is installed to measure the pressure drop across the test section. The length between the pressure taps is 850 mm. There are ten thermocouples located at five positions along the test section; all of the wall thermocouples are affixed with special glue having low thermal conductivity. The test section is well insulated with a proper material to minimize the heat loss. All of the thermocouples are well calibrated

Downloaded by [S. Wongwises] at 20:32 16 January 2013

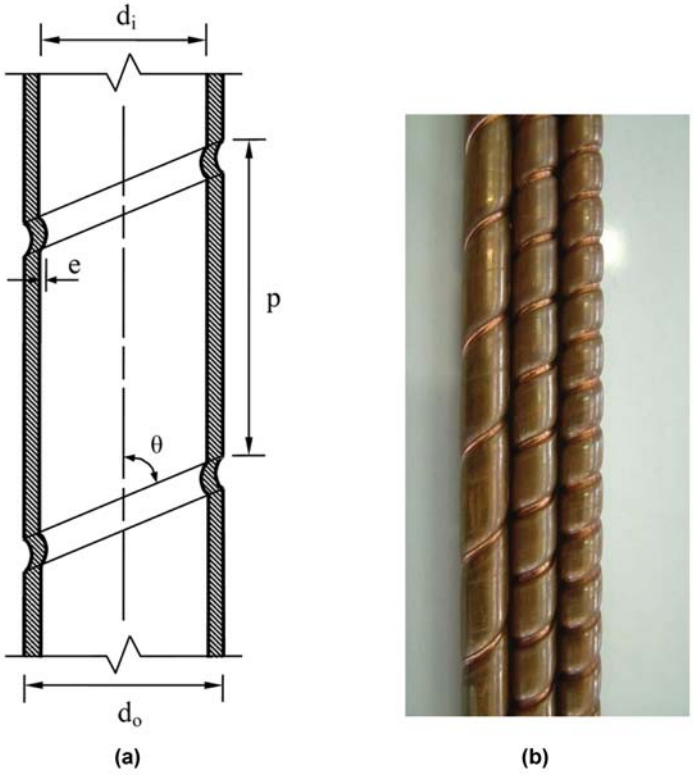

Figure 3. Corrugated tube: (a) sketch and (b) actual photograph. (color figure available online)

by standard thermometers with a precision of 0.1°C. The refrigerant flow meter is a variable area type and is specially calibrated in the range of 0.2–3.4 liters per minute (LPM) for R-134a by the manufacturer, as is the differential pressure transducer.

In the experiments, the inlet quality of the test section is varied by small increments. The imposed heat flux, mass flux, and saturation temperature are kept constant at the

Table 1. Dimensions of the test sections

Parameters	Smooth tube	Corrugated tube		
		Corrugation pitch 1	Corrugation pitch 2	Corrugation pitch 3
Outer diameter (mm)	9.52	9.52	9.52	9.52
Inner diameter (mm)	8.7	8.7	8.7	8.7
Length of test section (mm)	500	500	500	500
Inside tube area (mm^2)	13,665.9	15,362.2	15,951.1	16,582.8
Corrugation pitch (mm)	—	12.7	8.46	6.35
Corrugation depth (mm)	—	1	1	1
Helix angle (°)	—	53.875	64.07	69.95

Table 2. Experimental conditions

Controlled variable	Evaporation
Mass flux (kg/m^{2}s)	200, 300, 400
Heat flux (kW/m^2)	20, 25, 30
Saturation temperature (°C)	10, 15, 20
Tested tube material	Copper
Refrigerant	R-134a
Average vapor quality	0.2–0.8

desired values. The system is allowed to approach a steady state before any data are recorded. During experiments, the temperature and pressure are continuously recorded along the test section by the data acquisition system. The range of experimental conditions tested in this study is listed in Table 2. The uncertainties of measured quantities and calculated parameters calculated from the root mean sum square method are shown in Table 3.

Downloaded by [S. Wongwises] at 20:32 16 January 2013

DATA REDUCTION

The following calculation is employed to determine the vapor quality of the refrigerant entering and exiting the test section, heat transfer coefficient, and two-phase friction factor from the data recorded during each test run at steady-state conditions.

The Inlet Vapor Quality of the Test Section ($x_{TS,in}$)

The inlet vapor quality of the test section ($x_{TS,in}$) can be defined as

$$x_{TS,in} = \frac{i_{TS,in} - i_{lT_{TS,in}}}{i_{fgT_{TS,in}}}, \tag{1}$$

where $i_{lT_{TS,in}}$ and $i_{fgT_{TS,in}}$ are the enthalpy of the saturated liquid and the enthalpy of vaporization, respectively, based on the temperature at the test section inlet; $i_{TS,in}$ is

Table 3. Uncertainties of measured quantities and calculated parameters

Parameter	Uncertainty
Temperature, T	± 0.1
Frictional pressure drop, ΔP_F	± 10 %
Mass flow rate of refrigerant, m_{ref}	± 2% Full scale
Heat transfer rate of test section, Q_{TS}	± 15 %
Heat transfer rate of pre-heater, Q_{ph}	± 10 %
Average heat transfer coefficient, h_{avg}	± 15 %
Two-phase friction factor, f_{tp}	± 13 %
Average quality, x_{avg}	± 8 %
Equivalent Reynolds number, Re_{eq}	± 6 %

the enthalpy of refrigerant at the test section inlet, which is calculated by the following equation:

$$i_{TS,in} = i_{ph,in} + \frac{Q_{ph}}{m_{ref}}, \tag{2}$$

where $i_{ph,in}$ is the inlet enthalpy of the liquid refrigerant before entering the pre-heater, m_{ref} is the mass flow rate of the refrigerant, and Q_{ph} is the heat transfer rate in the pre-heater:

$$Q_{ph} = m_{w,ph} c_{p,w} (T_{w,in} - T_{w,out})_{ph}, \tag{3}$$

with $m_{w,ph}$ as the mass flow rate of water entering the pre-heater.

Downloaded by [S. Wongwises] at 20:32 16 January 2013

The Outlet Vapor Quality of the Test Section ($x_{TS,out}$)

The outlet vapor quality of the test section ($x_{TS,out}$) can be defined as

$$x_{TS,out} = \frac{i_{TS,out} - i_{lT_{TS,out}}}{i_{fgT_{TS,out}}}, \tag{4}$$

where $i_{TS,out}$ is the refrigerant enthalpy at the test section outlet, $i_{lT_{TS,out}}$ is the enthalpy of the saturated liquid based on the temperature at the test section outlet, and $i_{fgT_{TS,out}}$ is the enthalpy of vaporization based on the temperature at the test section outlet. As a consequence, the outlet enthalpy of the refrigerant flow is calculated as

$$i_{TS,out} = i_{TS,in} + \frac{Q_{TS}}{m_{ref}}, \tag{5}$$

where the heat transfer rate Q_{TS} in the test section is obtained from

$$Q_{TS} = m_{w,TS} c_{p,w} (T_{w,in} - T_{w,out})_{TS}, \tag{6}$$

where $m_{w,TS}$ is the mass flow rate of the water entering the test section, and $(T_{w,in} - T_{w,out})_{TS}$ is the difference in water temperature between the outlet and inlet positions.

Average Heat Transfer Coefficient (h_{avg})

The average heat transfer coefficient (h_{avg}) can be calculated using the following equation:

$$h_{avg} = \frac{Q_{TS}}{A_i (T_{i,avg,wi} - T_{avg,sat})}, \tag{7}$$

where $T_{avg,sat}$ is the average temperature of the refrigerant at the test section inlet and outlet, $T_{i,avg,wi}$ is the average temperature of the inner wall, and A_i is the inside surface area of the test section.

Downloaded by [S. Wongwises] at 20:32 16 January 2013

Nusselt Number (Nu)

The Nusselt number is calculated as follows:

$$\mathrm{Nu} = \frac{h_{avg} d_i}{k_l}, \tag{8}$$

where k_l is thermal conductivity of liquid refrigerant.

Two-Phase Friction Factor (f_{tp})

The total pressure gradient is the sum of three contributions: the gravitational pressure gradient, the momentum pressure gradient, and the frictional pressure gradient, as follows:

$$\left(\frac{dP}{dz}\right)_T = \left(\frac{dP}{dz}\right)_F + \left(\frac{dP}{dz}\right)_G + \left(\frac{dP}{dz}\right)_M. \tag{9}$$

Pressure drop due to gravity can be determined from

$$\left(\frac{dP}{dz}\right)_G = -g\left[(1-\alpha)\rho_l + \alpha\rho_g\right], \tag{10}$$

where the void fraction α can be determined from the Zivi correlation [14], as follows:

$$\alpha = \frac{1}{1 + \dfrac{(1-x)}{x}\left(\dfrac{\rho_g}{\rho_l}\right)^{2/3}}. \tag{11}$$

The momentum pressure gradient can be defined as follows:

$$\left(\frac{dP}{dz}\right)_M = G^2 \frac{d}{dz}\left[\frac{(1-x)^2}{\rho_l(1-\alpha)} + \frac{x^2}{\rho_g \alpha}\right]. \tag{12}$$

The two-phase frictional pressure gradient can be obtained by subtracting the gravitational and momentum terms from the total measured pressure drop, as follows:

$$\left(\frac{dP}{dz}\right)_F = \left(\frac{dP}{dz}\right)_T - \left(\frac{dP}{dz}\right)_G - \left(\frac{dP}{dz}\right)_M. \tag{13}$$

The two-phase friction factor is calculated by the following equation based on the equivalent Reynolds number:

$$f_{tp} = \left(\frac{dP}{dz}\right)_F \frac{\rho_l d_i^3}{2\,\mathrm{Re}_{eq}^2\,\mu_l^2}, \tag{14}$$

where the equivalent Reynolds number is determined from

$$\mathrm{Re}_{eq} = \frac{G_{eq} d_i}{\mu_l}, \tag{15}$$

and equivalent mass flux is defined as

$$G_{eq} = G\left[(1-x) + x\sqrt{\frac{\rho_l}{\rho_g}}\right]. \tag{16}$$

RESULTS AND DISCUSSION

The present study is performed to investigate the effect of corrugation pitch on the heat transfer coefficient and pressure drop of R-134a during evaporation inside vertical corrugated tubes. The experimental data obtained from this work are not from the dry-out region. Before measuring the two-phase heat transfer coefficient and pressure drop during evaporation of refrigerant in the test section, the experimental results obtained from the smooth tube are checked by sight glass at the inlet and outlet of the test section, and they are also checked with the flow pattern maps for vertical flow. Figures 4–6 show the flow pattern map of Hewitt and Roberts [15], Taitel et al. [16], and Mishima and Ishii [17] with the plotted experimental data of the current study, respectively. They are observed that more than 90% of the data points locate in the region of annular flow regime.

Heat Transfer Coefficient

The experimental data obtained from the smooth tube are validated by comparing the present heat transfer coefficient data with the correlations for vertical flow proposed by Shah [9], Gungor and Winterton [10], Kandlikar [11], Wright [18], Schrock and

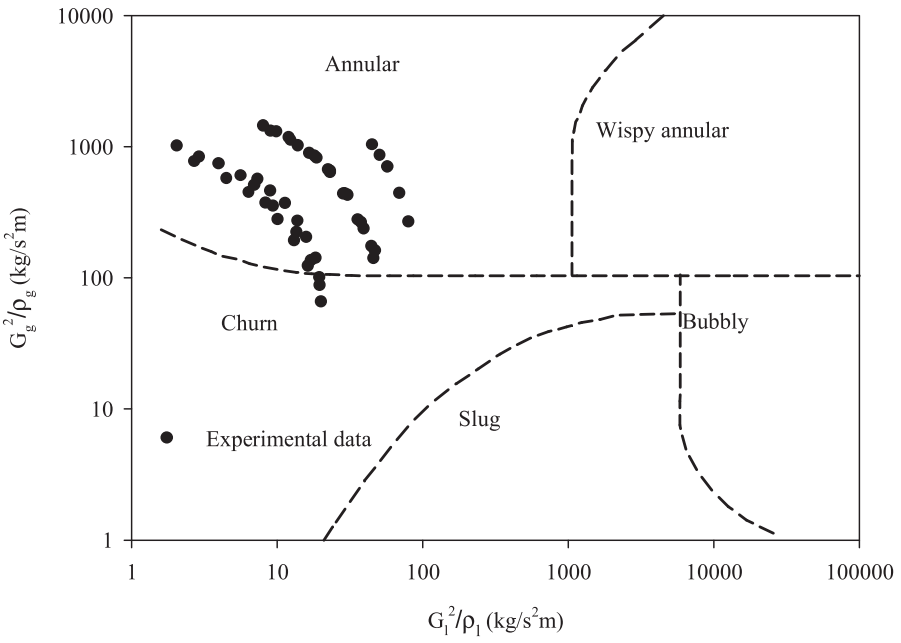

Figure 4. Flow pattern identification of the experimental data by means of Hewitt and Roberts [15] flow regime map.

Downloaded by [S. Wongwises] at 20:32 16 January 2013

Downloaded by [S. Wongwises] at 20:32 16 January 2013

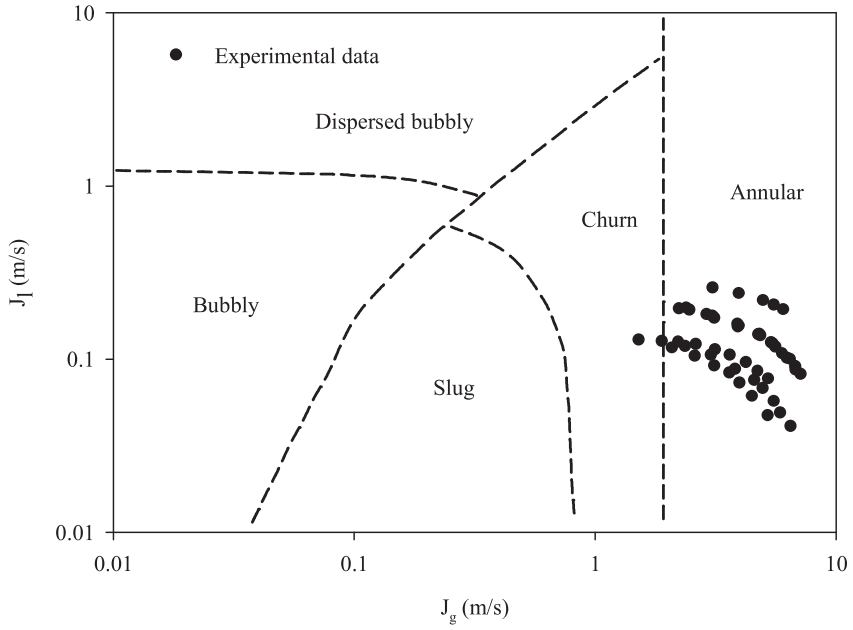

Figure 5. Flow pattern identification of the experimental data by means of Taitel et al. [16] flow regime map.

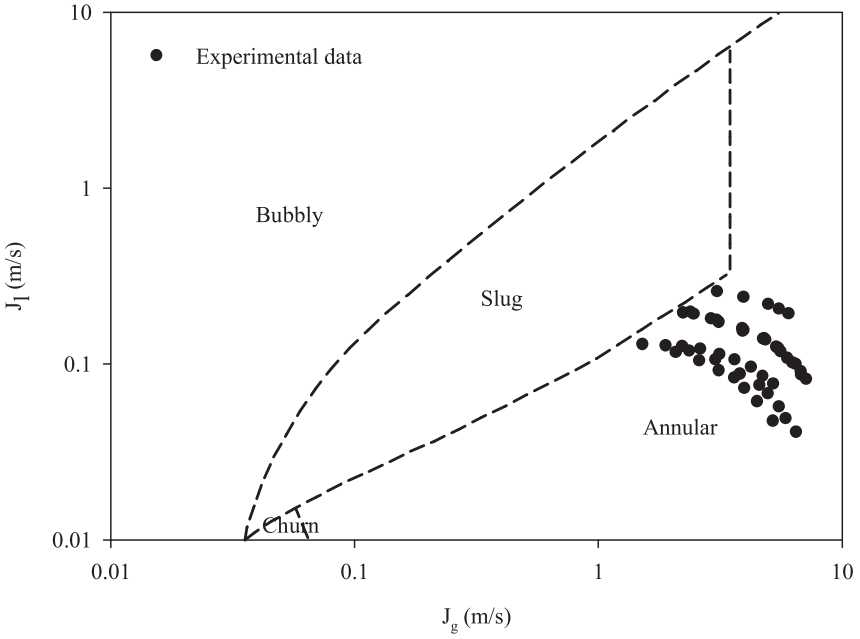

Figure 6. Flow pattern identification of the experimental data by means of Mishima and Ishii [17] flow regime map.

Grossman [19], and Pujol and Stenning [20], as shown in Figure 7. It is observed that almost all of data correlate within the deviation of ± 30%.

Figure 8 shows the relationship between average heat transfer coefficient and average quality in the smooth tube and corrugated tube having different corrugation pitches of 6.35, 8.46, and 12.7 mm at heat flux of 20 kW/m^2, saturation temperature of 20°C, and mass fluxes of 200 kg/m^{2}s. It can be observed that higher average vapor quality results in a higher average heat transfer coefficient. This occurs because at high vapor quality, the velocity of the vapor flow is high, resulting in high shear stress at the interface between the vapor and liquid film. The increasing shear stress causes more entrainment of droplets, making the liquid film thinner. As a result, thermal resistance is decreased. In addition, during evaporation, the liquid film boils and turns to vapor, which, in turn, increases the velocity of two-phase flow. For these reasons, the average heat transfer coefficient tends to increase as the average vapor quality increases.

Figure 9 shows the variation of the average heat transfer coefficient as a function of the mass flux at the heat flux of 20 kW/m^2, the average vapor quality of 0.35, and the saturation temperature of 20°C. It is observed that the average heat transfer coefficient increases with increasing mass flux. This occurs because the velocity of the vapor and liquid film increase as the mass flux increases, and therefore, the average heat transfer coefficient also increases.

As seen from these figures, the heat transfer coefficients obtained from the corrugated tubes are higher than those from the smooth tube. This can be explained by the fact that the corrugated surface promotes more turbulence by increasing the mixing of the refrigerant flow. Further, it is speculated that the rotational flow produced by the

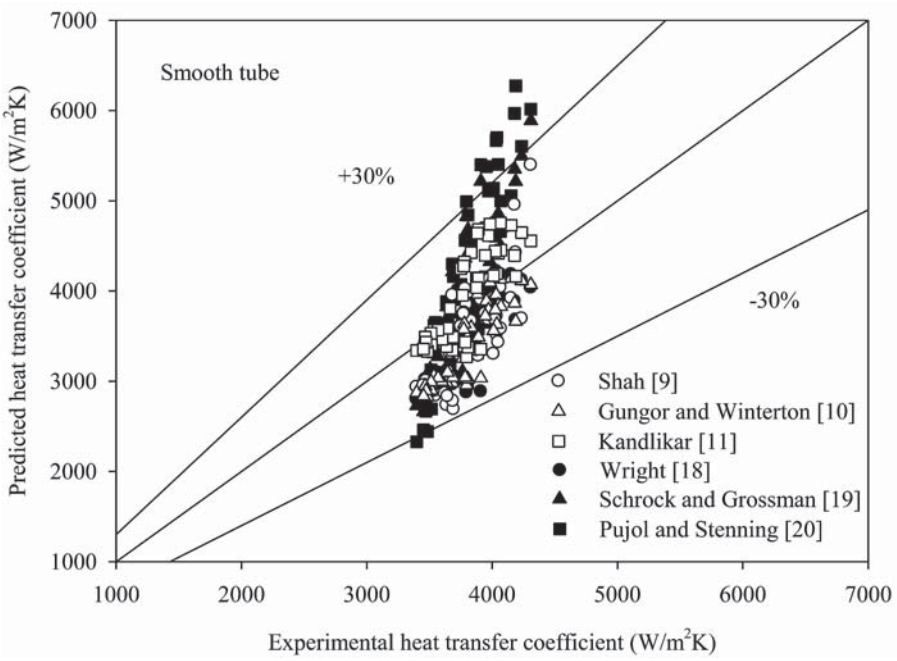

Figure 7. Comparison of experimental heat transfer coefficient data with existing correlations.

Downloaded by [S. Wongwises] at 20:32 16 January 2013

Downloaded by [S. Wongwises] at 20:32 16 January 2013

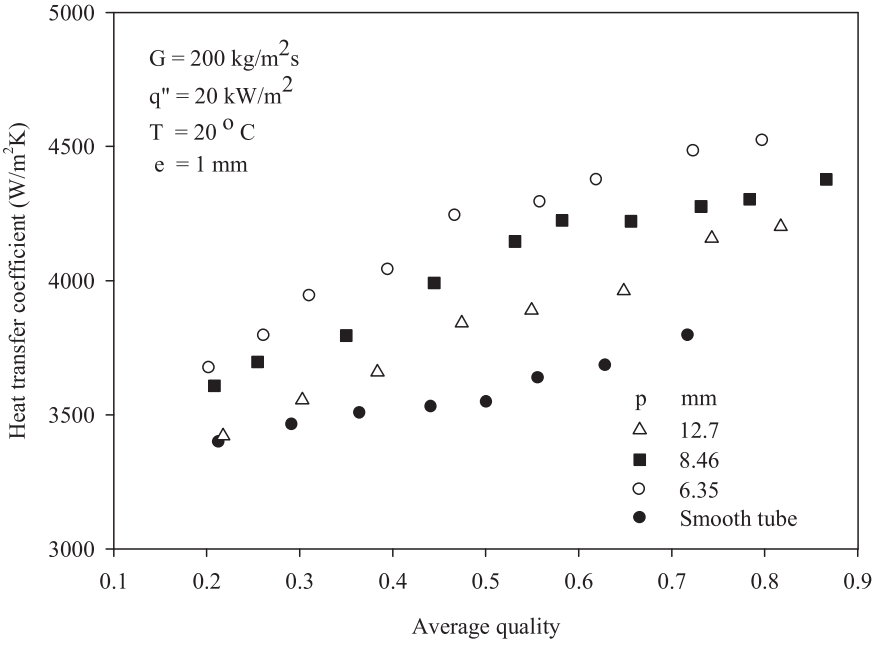

Figure 8. Average heat transfer coefficient as a function of average quality for $G = 200$ kg/m^{2}s, $q'' = 20$ kW/m^2, and $T = 20°$C.

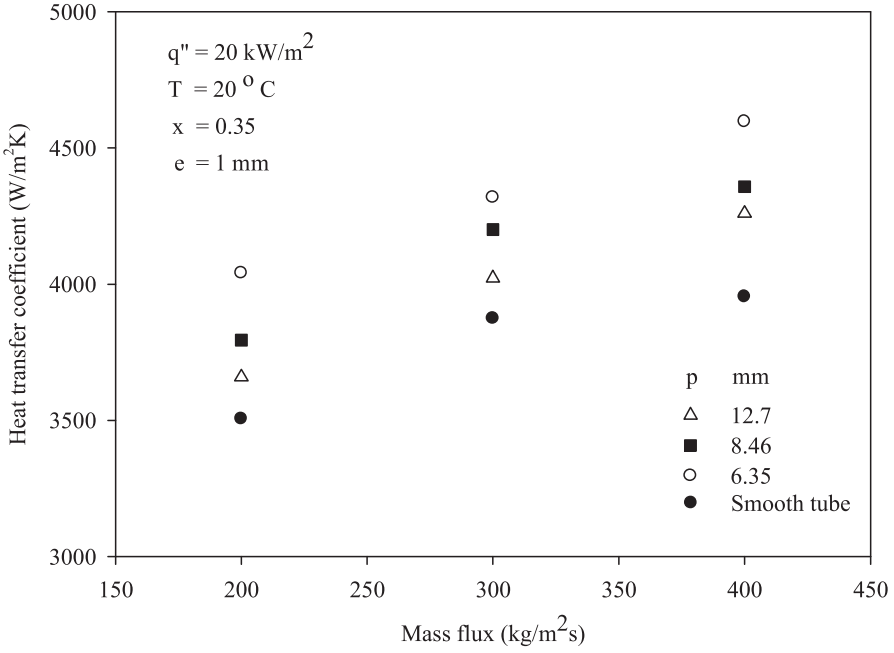

Figure 9. Average heat transfer coefficient as a function of mass flux for $x = 0.35$, $q'' = 20$ kW/m^2, and $T = 20°$C.

corrugation causes the liquid film to become thinner as a result of enhancing heat transfer. Moreover, the heat transfer coefficient increases with the decrease of corrugation pitch. This occurs because the tube with lower corrugation pitch produces more turbulence of the fluid flow and increases the heat transfer area. Hence, the highest heat transfer coefficient is achieved by the tube with the lowest corrugation pitch. The maximum heat transfer enhancement is obtained up to 22% for a pitch of 6.35 mm, 16% for a pitch of 8.46 mm, and 11% for a pitch of 12.7 mm in comparison with the smooth tube at the mass flux of 200 kg/m^{2}s, the heat flux of 20 kW/m^2, and the saturation temperature of 20°C.

The heat transfer enhancement factors as a function of vapor quality are shown in Figures 10 and 11, defined as the ratio of the heat transfer coefficient for a corrugated tube to that of a comparable smooth tube. The heat transfer enhancement factor is calculated by a linear regression analysis using a least-squares method to determine the best-fitting straight line. It is found that the heat transfer enhancement factor increases as the average vapor quality increases. This can be explained by the effect of corrugation on the heat transfer coefficient, which is weak in low vapor quality region but becomes stronger at high vapor quality. At low vapor quality, the liquid film thickness is higher than that at high vapor quality, and, as a result, the turbulence effects produced by the corrugation depth are reduced. When the liquid film thickness is close to the corrugation depth, the periodic liquid wave caused by corrugation pitch produces an unstable liquid flow, which maximizes thermal efficiency and turbulent effects [21]. The heat transfer enhancement factor varies from 1.09 to 1.22 for a pitch of 6.35 mm, 1.06 to 1.16 for a pitch of

Downloaded by [S. Wongwises] at 20:32 16 January 2013

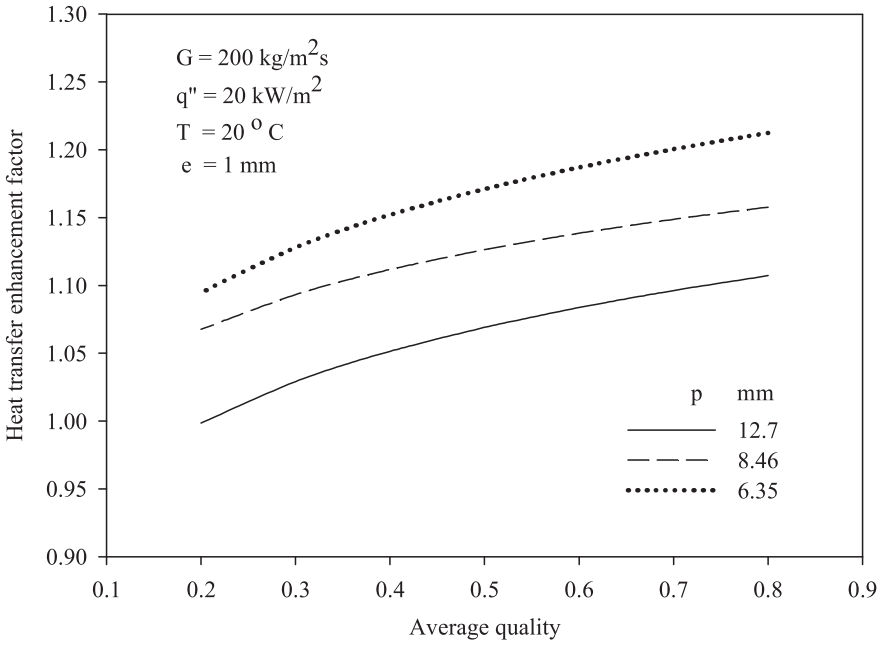

Figure 10. Heat transfer enhancement factors as a function of average quality for $G = 200$ kg/m^{2}s, $q'' = 20$ kW/m^2, and $T = 20$°C.

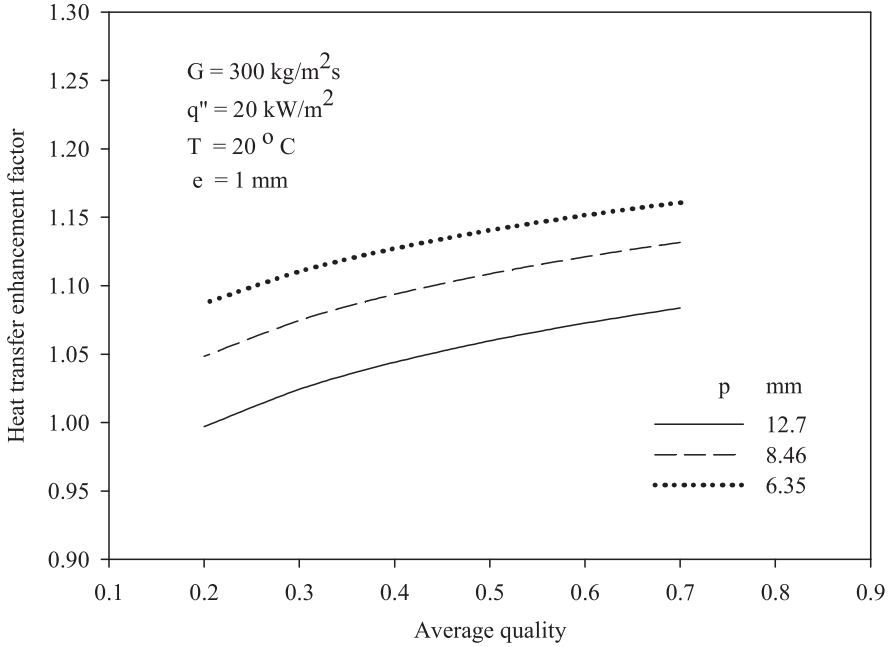

Figure 11. Heat transfer enhancement factors as a function of average quality for $G = 300$ kg/m^{2}s, $q'' = 20$ kW/m^2, and $T = 20$°C.

8.46 mm, and 1.00 to 1.11 for a pitch of 12.7 mm at the mass flux of 200 kg/m^{2}s, heat flux of 20 kW/m^2, and saturation temperature of 20°C.

Figure 12 shows a comparison of the experimental data for the corrugated tube with the proposed correlations. The correlation is expressed as a function of Nusselt number, equivalent Reynolds number, corrugation pitch, and inside diameter as follows:

$$\mathrm{Nu} = 35.948\,\mathrm{Re}_{eq}^{0.237}\left(\frac{p}{d_i}\right)^{-0.114}. \tag{17}$$

As shown in Figure 12, the results show that more than 95% of data fall within a deviation of ± 5%.

Pressure Drop

Figure 13 compares the frictional pressure drop for the smooth tube with the correlations from literature. The correlations proposed by Lockhart and Martinelli [22] and Chisholm [23] are in agreement with the present data within 30%. About 70% of the data are captured within 30% by Laohalertdecha et al.'s [24] correlation, while the Friedel [25], and Quibén and Thome [26] correlations underestimate the data by more than 30%.

The variation of the frictional pressure drop with average quality in smooth and corrugated tubes is illustrated in Figure 14. The frictional pressure drop increases with increasing vapor quality. This occurs because at higher vapor quality, the higher velocity

Downloaded by [S. Wongwises] at 20:32 16 January 2013

Downloaded by [S. Wongwises] at 20:32 16 January 2013

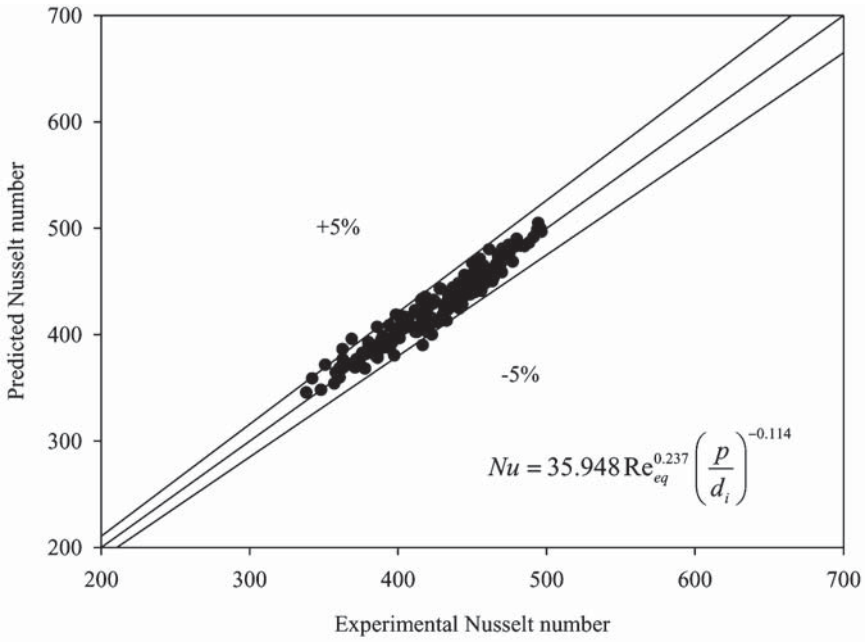

Figure 12. Predicted Nusselt number using the proposed correlation versus the experimental data.

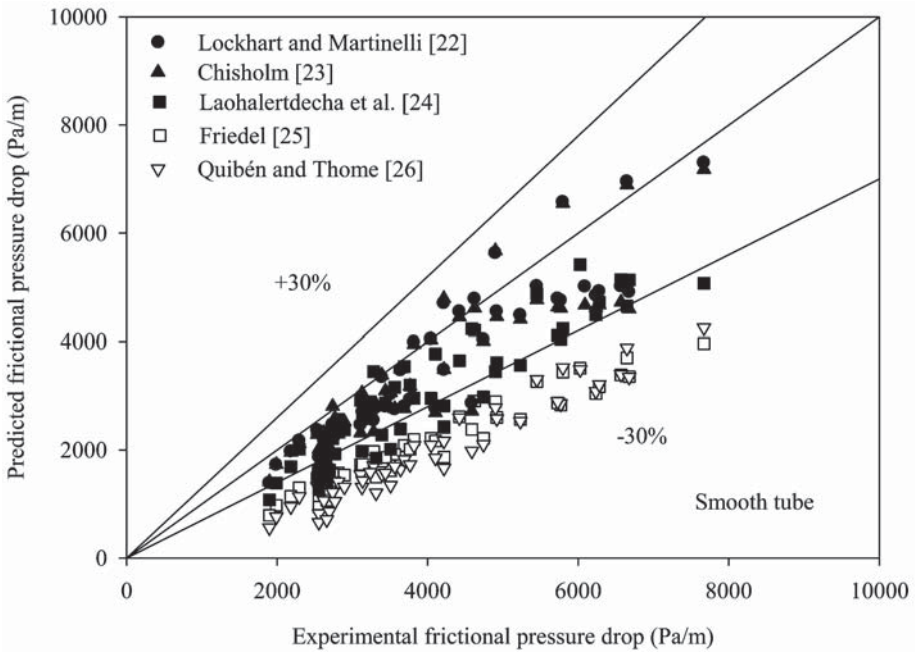

Figure 13. Comparison of experimental frictional pressure drop data with existing correlations.

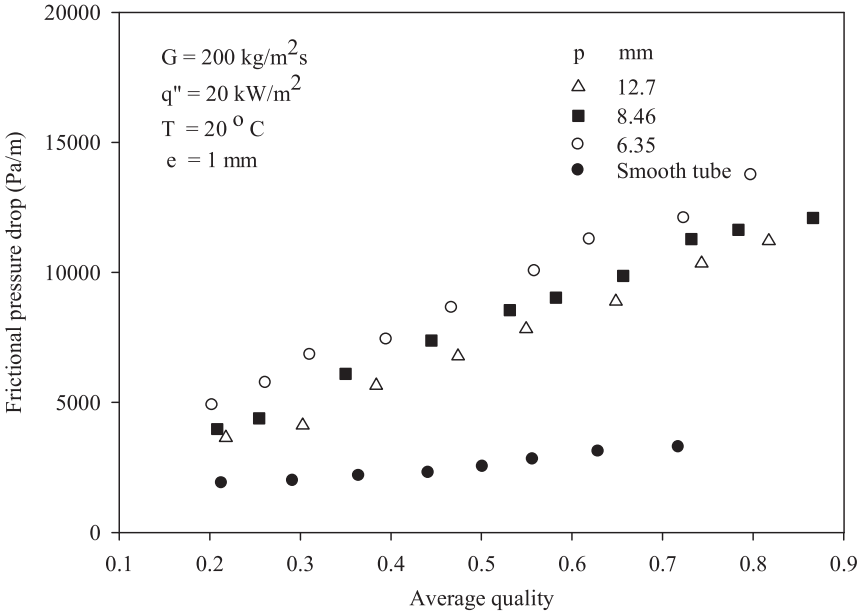

Figure 14. Frictional pressure drop as a function of average quality for $G = 200$ kg/m^{2}s, $q'' = 20$ kW/m^2, and $T = 20°$C.

of vapor flow causes more shear stress at the interface of the vapor and liquid film. Moreover, the secondary flow that becomes stronger at higher vapor velocity will produce more entrainment and redeposition of droplets, causing more flow turbulence.

Figure 15 illustrates the variation of the frictional pressure drop as a function of the saturation temperature at the heat flux of 20 kW/m^2, average vapor quality of 0.45, and mass flux of 200 kg/m^{2}s. The frictional pressure drop decreases significantly as the evaporating temperature increases. This is because when the evaporating temperature increases, the viscosity of liquid film decreases, resulting in lower flow resistance. Consequently, the frictional pressure drop decreases as the evaporating temperature increases.

As shown in Figures 14 and 15, the frictional pressure drops for the corrugated tubes are higher than those for the smooth tube. This is due to the pressure-drop augmentation in corrugated tubes that is produced by (1) drag forces exerted on the flow field by the corrugation, (2) flow blockage due to area reduction, (3) turbulence augmentation, and (4) rotational flow produced by the corrugation [27]. The figures also show the effect of the corrugation pitch at constant corrugation depth of 1 mm on the frictional pressure drop. These plots show that the higher frictional pressure drop is obtained from the tube with lower corrugation pitch; lower corrugation pitch results in increased corrugation surface, more turbulence of the fluid flow, and more pressure loss. The maximum value of frictional pressure drop is obtained from the tube having a corrugation pitch of 6.35 mm up to 300% in comparison with the smooth tube at the mass flux of 200 kg/m^{2}s, heat flux of 20 kW/m^2, and saturation temperature of 20°C.

The relationship between the two-phase friction factor and the equivalent Reynolds number is demonstrated in Figure 16. The two-phase friction factor decreases with

Downloaded by [S. Wongwises] at 20:32 16 January 2013

Downloaded by [S. Wongwises] at 20:32 16 January 2013

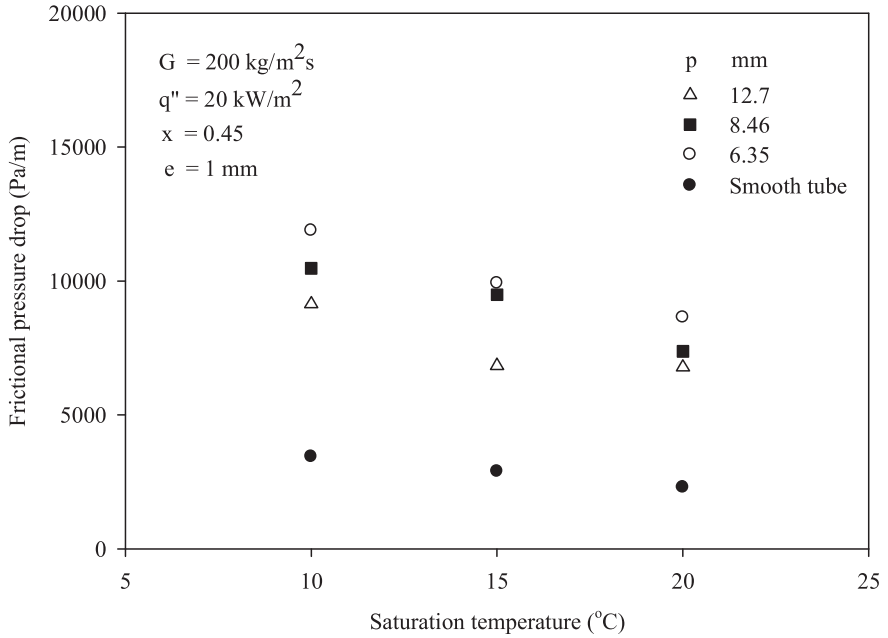

Figure 15. Frictional pressure drop as a function of saturation temperature for $G = 200$ kg/m^{2}s, $q'' = 20$ kW/m^2, and $x = 0.45$.

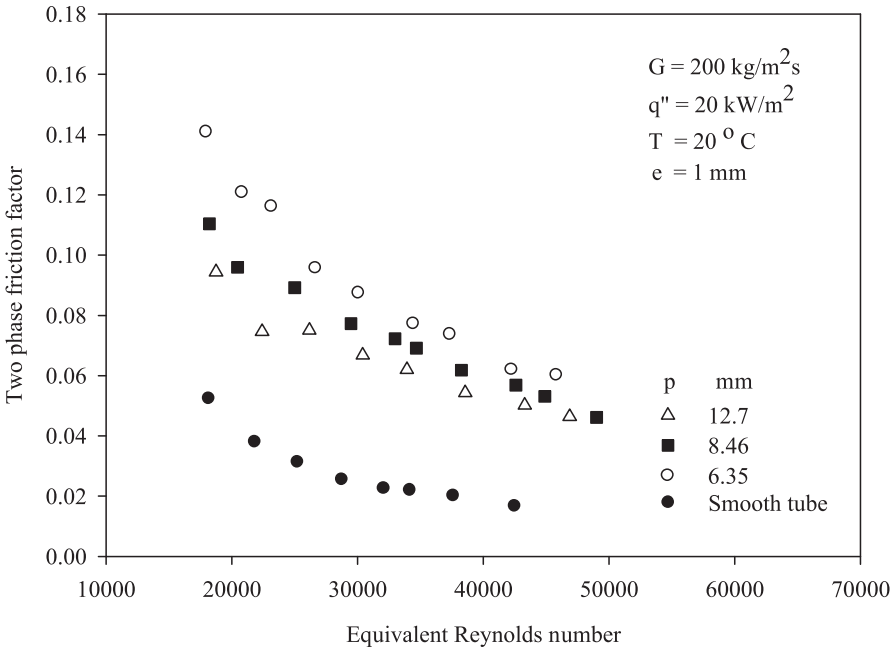

Figure 16. Two-phase friction factor as a function of equivalent Reynolds number for $G = 200$ kg/m^{2}s, $q'' = 20$ kW/m^2, and $T = 20$°C.

increasing equivalent Reynolds number. This is because both the frictional pressure drop and equivalent Reynolds number increase with increasing vapor quality. According to Eq. (14), the equivalent Reynolds number dominates the two-phase friction factor. Therefore, the increase in average quality causes the two-phase friction factor to decrease. Figure 16 also shows that the two-phase friction factor for the corrugated tubes is higher than that for the smooth tube. In addition, the two-phase friction factor tends to increase as the corrugation pitch decreases. The reason for this is similar to the above-mentioned explanation concerning the frictional pressure drop.

Figures 17 and 18 illustrate the variation of the penalty factor with the average vapor quality. The penalty factor is defined as the ratio of the frictional pressure drop for a corrugated tube to that of a comparable smooth tube. The penalty factor increases with a rise of the average vapor quality. This is because the turbulence effects produced by corrugation depth are strong at high vapor quality as a result of more pressure loss. The penalty factor ranges from 2.8 to 4.0 for a pitch of 6.35 mm, 2.2 to 3.5 for a pitch of 8.46 mm, and 1.8 to 3.2 for a pitch of 12.7 mm at the mass flux of 200 kg/m^{2}s, heat flux of 20 kW/m^2, and saturation temperature of 20°C.

Figure 19 shows the experimental two-phase friction factor plotted against predicted two-phase friction factor obtained from Eq. (18). It is found that about 90% of the data fall within a deviation of ± 15%:

$$f_{tp} = 37.337\,\mathrm{Re}_{eq}^{-0.594}\left(\frac{p}{d_i}\right)^{-0.301} . \tag{18}$$

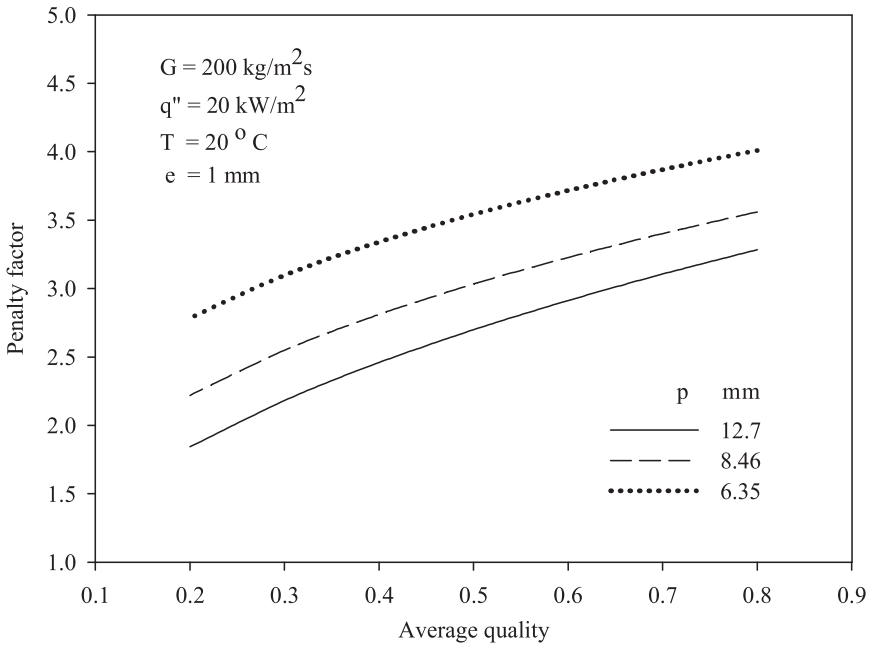

Figure 17. Penalty factors as a function of average quality for $G = 200$ kg/m^{2}s, $q'' = 20$ kW/m^2, and $T = 20$°C.

Downloaded by [S. Wongwises] at 20:32 16 January 2013

Downloaded by [S. Wongwises] at 20:32 16 January 2013

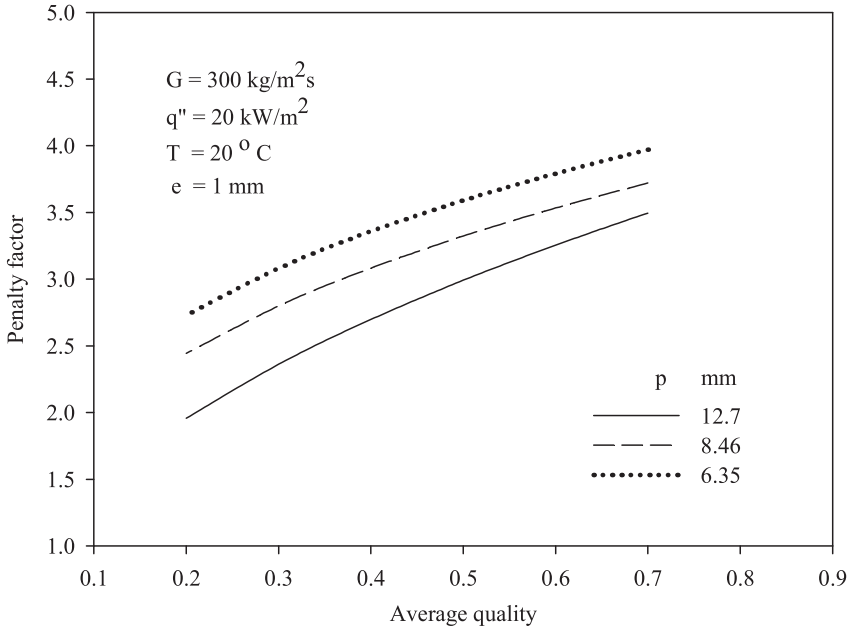

Figure 18. Penalty factors as a function of average quality for $G = 300$ kg/m^{2}s, $q'' = 20$ kW/m^2, and $T = 20$°C.

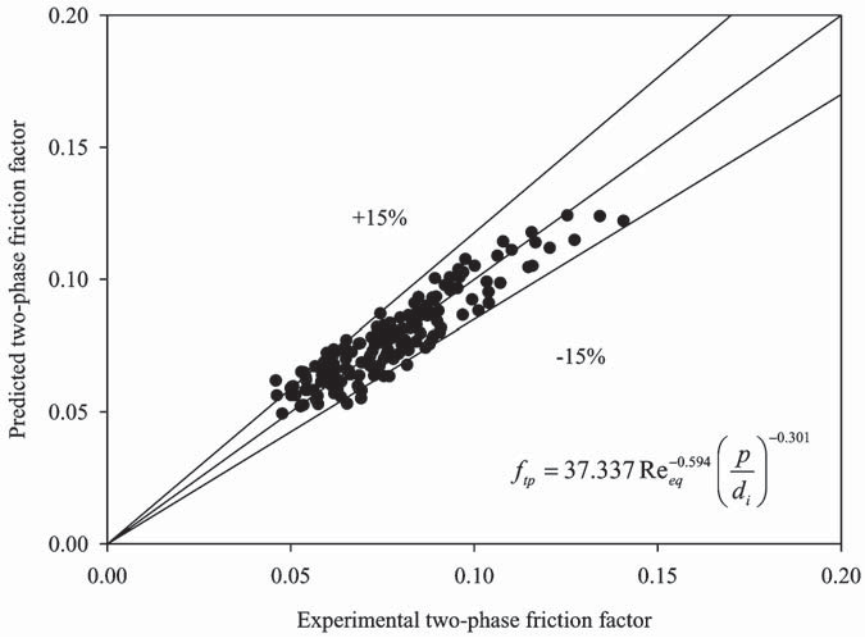

Figure 19. Predicted two-phase friction factor using the proposed correlation versus the experimental data.

CONCLUSION

This study is conducted to investigate the evaporative heat transfer and pressure drop characteristics of R-134a flow through vertical smooth and corrugated tubes with different corrugation pitches. The conclusions follow.

1. The experimental data obtained from the smooth tube are plotted with a flow pattern map for vertical flow proposed by Hewitt and Roberts [15], Taitel et al. [16], and Mishima and Ishii [17]. It is observed that more than 90% of the data points locate in the region of annular flow regime.
2. The heat transfer coefficient tends to increase with increasing average vapor quality and mass flux. The heat transfer coefficient obtained from the corrugated tube is higher than that from the smooth tube. Moreover, the heat transfer coefficient increases with the decrease of corrugation pitch.
3. The frictional pressure drop increases with increasing vapor quality, while it decreases significantly as the evaporating temperature increases. The two-phase friction factor decreases with increasing equivalent Reynolds number. The frictional pressure drops for the corrugated tube is higher than that for the smooth tube. In addition, the higher frictional pressure drop is obtained from the tube with lower corrugation pitch.
4. The heat transfer enhancement factor and penalty factor increase with a rise of the average vapor quality. The heat transfer enhancement factor varies from 1.09 to 1.22, 1.06 to 1.16, and 1.00 to 1.11, while the penalty factor ranges from 2.8 to 4.0, 2.2 to 3.5, and 1.8 to 3.2 for a pitch of 6.35 mm, 8.46 mm, and 12.7 mm, respectively.

Downloaded by [S. Wongwises] at 20:32 16 January 2013

ACKNOWLEDGMENTS

The present study was supported financially by the Thailand Research Fund and the National Research University Project, whose guidance and assistance are gratefully acknowledged.

REFERENCES

1. P. Thors and J. Bogart, In Tube Evaporation of HCFC-22 with Enhanced Tubes, *J. Enhanced Heat Transf.*, vol. 1, pp. 365–377, 1994.
2. A. Briggs, C. Kelemenis, and J. W. Rose, Condensation of CFC-113 with Downflow in Vertical Internally Enhanced Tubes, *Proceedings of 11th IHTC*, Keongju, Korea, pp. 23–28, August 23–28, 1998.
3. X. Ma, A. Briggs, and J. W. Rose, Heat Transfer and Pressure Drop Characteristics for Condensation of R113 in a Vertical Micro-Finned Tube with Wire Insert, *Int. Commun. Heat Mass Transf.*, vol. 31, pp. 619–627, 2004.
4. A. S. Dalkilic, S. Laohalertdecha, and S. Wongwises, Two-Phase Friction Factor in Vertical Downward Flow in High Mass Flux Region of Refrigerant HFC-134a During Condensation, *Int. Commun. Heat Mass Transf.*, vol. 35, pp. 1147–1152, 2008.

5. A. S. Dalkilic, S. Laohalertdecha, and S. Wongwises, Effect of Void Fraction Models on the Two-Phase Friction Factor of R134a During Condensation in Vertical Downward Flow in a Smooth Tube, *Int. Commun. Heat Mass Transf.*, vol. 35, pp. 921–927, 2008.
6. A. S. Dalkilic, S. Laohalertdecha, and S. Wongwises, Effect of Void Fraction Models on the Film Thickness of R134a During Downward Condensation in a Vertical Smooth Tube, *Int. Commun. Heat Mass Transf.*, Vol. 36, pp. 172–179, 2009.
7. A. S. Dalkilic, S. Laohalertdecha, and S. Wongwises, Experimental Investigation of Heat Transfer Coefficient of R134a During Condensation in Vertical Downward Flow at High Mass Flux in a Smooth Tube, *Int. Commun. Heat Mass Transf.*, vol. 36, pp. 1036–1043, 2009.
8. A. S. Dalkilic, S. Yildiz, and S. Wongwises, Experimental Investigation of Convective Heat Transfer Coefficient During Downward Laminar Flow Condensation of R134a in a Vertical Smooth Tube, *Int. J. Heat Mass Transf.*, vol. 52, pp. 142–150, 2009.
9. M. M. Shah, Chart Correlation for Saturated Boiling Heat Transfer Equation and Further Study, *ASHRAE Trans.*, vol. 88, pp. 185–196, 1982.
10. K.E. Gungor and R. H. S. Winterton, A General Correlation for Flow Boiling in Tubes and Annuli, *Int. J. Heat Mass Transf.*, vol. 29, pp. 351–358, 1986.
11. S. G. Kandlikar, A General Correlation for Saturated Two-Phase Flow Boiling Heat Transfer Inside Horizontal and Vertical Tubes, *ASME J. Heat Transf.*, vol. 112, pp. 219–228, 1990.
12. S. K. Lee and S. H. Chang, Experimental Study of Post-Dryout with R-134a Upward Flow in Smooth Tube and Rifled Tubes, *Int. J. Heat Mass Transf.*, vol. 51, pp. 3153–3163, 2008.
13. K. Aroonrat and S. Wongwises, Evaporation Heat Transfer and Friction Characteristics of R-134a Flowing Downward in a Vertical Corrugated Tube, *Exp. Thermal Fluid Sci.*, vol. 35, pp. 20–28, 2011.
14. S. M. Zivi, Estimation of Steady-State Steam Void-Fraction by Means of the Principle of Minimum Entropy Production, *ASME J. Heat Transf.*, vol. 86, pp. 247–252, 1975.
15. G. F. Hewitt and D. N. Roberts, *Studies of Two-Phase Flow Patterns by Simultaneous X-Ray and Flash Photography*, AERE-M 2159, Her Majesty's Stationery Office, London, 1969.
16. Y. Taitel, D. Barnea, and A. E. Dukler, Modelling Flow Pattern Transitions for Steady Upward Gas-Liquid Flow in Vertical Tubes, *AIChE J.*, vol. 26, pp. 345–354, 1980.
17. K. Mishima and M. Ishii, Flow Regime Transition Criteria for Upward Two-Phase Flow in Vertical Tubes, *Int. J. Heat Mass Transf.*, vol. 27, pp.723–737, 1984.
18. R. M. Wright, *Down Flow Forced Convection Boiling of Water in Uniformly Heated Tubes*, UCRL-9744, University of California, Berkeley, CA, 1961.
19. V. E. Schrock and L. M. Grossman, Forced Convection Boiling in Tubes, *Nuclear Sci. Eng.*, vol. 12, pp. 474–481, 1962.
20. L. Pujol and A. H. Stenning, Effects of Flow Directions on the Boiling Heat Transfer Coefficients in Vertical Tubes, in E. R. Rhodes and D. S. Scott (Eds.), *Co-Current Gas-Liquid Flow*, Plenum Press, New York, pp. 401–453, 1969.
21. R. Yun, Y. Kim, K. Seo, and H. Y. Kim, A Generalized Correlation for Evaporation Heat Transfer of Refrigerants in Micro-Fin Tubes, *Int. J. Heat Mass Transf.*, vol. 45, pp. 2003–2010, 2002.
22. R. W. Lockhart and R. C. Martinelli, Proposed Correlation of Data for Isothermal Two-Phase Two Component Flow in Pipes, *Chem. Eng. Progress*, vol. 45, pp. 39–48, 1949.
23. D. Chisholm, Pressure Gradients Due to Friction During the Flow of Evaporating Two-Phase Mixtures in Smooth Tubes and Channels, *Int. J. Heat Mass Transf.*, vol. 16, pp. 347–358, 1973.
24. S. Laohalertdecha, A. S. Dalkilic and S. Wongwises, Correlations for Evaporation Heat Transfer Coefficient and Two-Phase Friction Factor for R-134a Flowing Through Horizontal Corrugated Tubes, *Int. Commun. Heat Mass Transf.*, vol. 38, pp. 1406–1413, 2011.

Downloaded by [S. Wongwises] at 20:32 16 January 2013

25. L. Friedel, Improved Friction Pressure Drop Correlations for Horizontal and Vertical Two-Phase Pipe Flow, Paper E2, *The European Two-Phase Flow Group Meeting*, Ispra, Italy, June 5–8, 1979.
26. J. M. Quibén and J. R. Thome, Flow Pattern Based Two-Phase Frictional Pressure Drop Model for Horizontal Tubes, Part II: New Phenomenological Model, *Int. J. Heat Fluid Flow*, vol. 28, pp. 1060–1072, 2007.
27. P. G. Vicente, A. Garcia, and A. Viedma, Experimental Investigation on Heat Transfer and Friction Factor Characteristics of Spirally Corrugated Tubes in Turbulent Flow at Different Prandtl Number, *Int. J. Heat Mass Transf.*, vol. 47, pp. 671–681, 2004.

Downloaded by [S. Wongwises] at 20:32 16 January 2013

Technical Note

Performance of Two-Stage Upflow Anaerobic Sludge Blanket Reactor Treating Wastewater from Latex-Processing Factory

S. Phoolphundh[1]; K. Hathaisamit[2]; and S. Wongwises[3]

Abstract: In this study, a relatively high-rate treatment (hydraulic retention time ≤2.5 days) of latex-processing wastewater was achieved in a two-stage upflow anaerobic sludge blanket reactor. A maximum acid production rate of 1.8 $g\,L^{-1}\,d^{-1}$ acetic acid was obtained when the acidogenic reactor was operated over a hydraulic retention time (HRT) of 4 hr. Total chemical oxygen demand (COD) and sulfate removal efficiencies of the system were 51.6 and 75.9%, respectively, when the methanogenic reactor was operated over an HRT of 24 h. The specific acidogenic activity of granular sludge in the acidogenic and methanogenic reactor varied between 1.33–2.02 g COD g volatile suspended solids $(VSS)^{-1}\,d^{-1}$, and the specific methanogenic activity ranged from 0.0078 to 0.0138 $g\,COD\text{-}CH_4\,g\,VSS^{-1}\,d^{-1}$. Microbial diversity monitoring using the denaturing gradient gel electrophoresis technique revealed that there was more sulfate-reducing bacteria in both reactors than *archea* bacteria. **DOI: 10.1061/(ASCE)EE.1943-7870.0000604.** © *2013 American Society of Civil Engineers.*

CE Database subject headings: Reactors; Wastewater management; Sludge.

Author keywords: Acidogenic reactor; Latex-processing wastewater; Methanogenic reactor; Sulfate reduction; Two-stage upflow anaerobic sludge blanket system.

Downloaded from ascelibrary.org by Kasetsart University on 01/10/13. Copyright ASCE. For personal use only; all rights reserved.

Introduction

Thailand is the leading natural rubber producer in the world. According to a report from the Thailand Office of Agricultural Economics (2009), there are approximately 27,200 square kilometres of rubber tree plantations in Thailand, 75% of which are located in the southern region. Latex concentrate, which is produced by centrifugation of rubber latex (sap), is generally used as a raw material for an enormous variety of products, e.g., sheet rubber, gloves, and tires. Wastewater from concentrated latex factories is a significant source of pollution because of its high organic content and sulphate concentration. Rubber latex wastewater is widely treated by an anaerobic process. A major problem associated with the anaerobic treatment of sulfate-rich wastewater is the production of sulfide by sulphate-reducing bacteria (SRB), which may lead to process failure. One of the strategies to accomplish the successful treatment of sulfate-containing wastewater is the separation of sulfide production and methanogenesis through a two-stage anaerobic digestion process (Lens et al. 1998). The resulting sulfide will be removed during the first stage (acidification) via stripping that can easily occur as a result of the low pH (approximately 5.0–6.5) in the reactor. This reduces the toxicity of sulfide to methane-producing bacteria (MPB) and acetogenic bacteria (AB) in the second stage (methanogenesis). This study attempted to determine the effect of hydraulic retention time (HRT) in an acidogenic reactor and methanogenic reactor on volatile fatty acid (VFA) production, chemical oxygen demand (COD) removal, sulfate reduction, and biogas production, to evaluate the performance of a two-stage upflow anaerobic sludge blanket (UASB) reactor on treating wastewater from a concentrated latex-processing factory.

Materials and Methods

Experimental Setup and Operation

A laboratory-scale two-stage UASB system, consisting of an acidogenic (A) reactor and a methanogenic reactor (M), was used in this study. The working volume of the A and M reactors was 2.9 and 4.1 L, with an inner diameter of 5 cm and a height of 96 and 120 cm, respectively. Fig. 1 is a schematic diagram of the two-stage UASB system. Both reactors were separated by an effluent tank that received the effluent from the A reactor and provided the feed for the M reactor. A water displacement-type gas meter was connected to the M reactor to measure the volume of produced biogas. One-third of each reactor was inoculated with granular sludge from a full-scale UASB reactor belonging to a beverage company (Sermsuk Co., Ltd., Pathumthani province, Thailand). The concentration of total suspended solids (TSS) and volatile suspended solids (VSS) of the seed sludge were 39 and 36 g/L, respectively. The latex-processing wastewater used in this study was taken from the first anaerobic pond at the wastewater treatment plant of Srithepthai Latex Co., Ltd. (Rayong province, Thailand), and was stored at 4°C before use. The characteristics of this latex-processing wastewater are shown in Table 1.

During the start-up period, seed sludge in both reactors was acclimatized by continuously fed with diluted latex-processing wastewater

[1]Dept. of Microbiology, Faculty of Science, King Mongkut's Univ. of Technology Thonburi, 126 Prachauthid Rd., Thungkru, Bangkok 10140, Thailand (corresponding author). E-mail: sivawan.pho@kmutt.ac.th

[2]Environmental Science, Faculty of Science and Technology, Bansomdejchaopraya Rajabhat Univ., Isaraphab Rd., Dhonburi, Bangkok 10600, Thailand.

[3]Dept. of Mechanical Engineering, Faculty of Engineering, King Mongkut's Univ. of Technology Thonburi, 126 Prachauthid Rd., Thungkru, Bangkok 10140, Thailand.

Note. This manuscript was submitted on September 21, 2011; approved on June 11, 2012; published online on August 3, 2012. Discussion period open until June 1, 2013; separate discussions must be submitted for individual papers. This technical note is part of the ***Journal of Environmental Engineering***, Vol. 139, No. 1, January 1, 2013. © ASCE, ISSN 0733-9372/2013/1-141-146/$25.00.

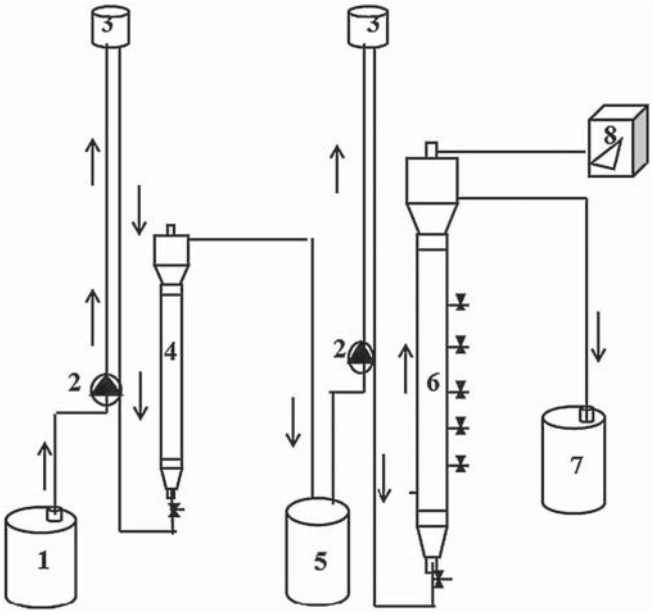

Fig. 1. Schematic diagram of two-stage UASB system: (1) influent tank, (2) feed pump, (3) control level tank, (4) acidogenic reactor, (5) effluent tank 1, (6) methanogenic reactor, (7) effluent tank 2, (8) gas meter

Table 1. Characteristics of Latex-Processing Wastewater in the First Anaerobic Pond of Srithepthai Latex Co., Ltd.

Parameters	Units	Value
pH	—	4.8–7.1
COD	mg/L	5,240–12,450
Sulfate	mg/L as SO_4^{-2}	1,889–4,210
Ammonia-N	mg/L as N	523–1,435
TKN	mg/L as N	816–1,970
Phosphate	mg/L as P	80–164
SS	mg/L	840–1,125
VSS	mg/L	670–924

(30% of the designated concentration, ≅6,000 mg COD/L) and the reactors were operated at HRT of 24 h. A stepwise increase of influent COD concentration from 30 to 50, 70, and 100% was conducted when ≥70% of COD removal efficiency at each dilution was attained. Tap water was used to prepare diluted wastewater and sodium bicarbonate solution was added to increase the pH of wastewater to neutral values (6.5–7.2). After the acclimation period, the pH and COD concentration of the influent were controlled at 5.5–6.0 and 6,000 mg/L, respectively. In Phase I of the experiment, the A reactor was first operated at HRT of 8 h and then was stepwise decreased to 6 and 4 h, respectively, while the M reactor was operated at HRT of 18 h. The steady state of each HRT was defined by the constant effluent COD and VFA concentrations. The HRT that permitted the highest VFA production rate will be used as the HRT for the A reactor of the two-stage UASB system in Phase II of the experiment. The HRT of the M reactor will be varied from 24, 32, and 56 h to maintain the HRT of the system at 28, 36, and 60 h, respectively.

Analysis

The measurement of COD, Total Kjeldahl Nitrogen (TKN), SO_4^{2-}, TSS, VSS, pH, and alkalinity in influent and effluent samples from both reactors was performed according to the *Standard Methods for Examination of Water and Wastewater* [American Public Health Association (APHA) 1992]. The VFA was determined by both direct titration and the use of a gas chromatograph (PerkinElmer, Auto System XL) equipped with a flame ionization detector (FID) and capillary column (Aquawax). The temperatures of the column, the injection port and the FID detector were 120, 180, and 250°C, respectively. The contents of CH_4 and CO_2 in the biogas was analyzed by another gas chromatograph (Shimadzu, GC-148) equipped with a thermal conductivity detector and a stainless-steel column (Porapak Q). The temperatures of the column, the injection port, and the detector were 45, 100, and 120°C, respectively. At the end of each HRT, sludge was taken from the A and M reactors to assess the specific acidogenic activity (SAA) and specific methanogenic activity (SMA) in a 120-mL serum bottle using glucose and acetic acid, respectively, as substrate (Soto et al. 1993). The external structure of the granular sludge from both reactors was examined using the JEOL scanning electron microscope (SEM), with the granules prepared according to Kalyuzhnyi et al. (1996). Sample sludge for DNA extraction was taken from the A and M reactors when each steady state was reached, and was stored in a refrigerator before use. Polymerase chain reaction-denaturing gel gradient electrophoresis (PCR-DGGE) was performed according to a previously published method (O-Thong et al. 2007).

Results and Discussion

Effect of HRT on Acidification in the UASB Reactor

Acidification and VFAs

The suitable HRT of A reactors in the two-stage anaerobic digestion process treating wastewater with a high COD concentration has been reported in the range of 6–24 h (Chathanee 1988). In the present study, it was found that the VFA concentration in the effluent decreased with the increasing HRT (Fig. 2) when the UASB reactors were operated at HRTs of 8 and 18 h. Because effluent VFA concentration is the sum of VFA production during acidification of the substrate and bacterial VFA degradation, this result indicated that the degradation of VFA in the reactor exceeded its production. Therefore, the HRTs of the experimental UASB reactors were lowered to 4 and 6 h in an attempt to achieve a high VFA concentration (especially of acetic acid) in the A reactor. The effluent VFA concentrations were found to be 8.9 and 2.67%, respectively, higher than those in the influent (Fig. 2). The concentration of each VFA, as determined by gas chromatography (data not shown), revealed that the acetic acid concentration in the

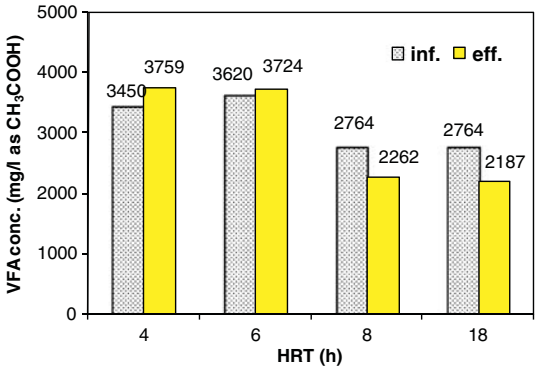

Fig. 2. VFA concentration in the influent and effluent at each HRT of the UASB reactor under acidogenic conditions

J. Environ. Eng. 2013.139:141-146.

Downloaded from ascelibrary.org by Kasetsart University on 01/10/13. Copyright ASCE. For personal use only; all rights reserved.

effluent (1,783–2,907 mg/L) at each HRT was higher than the concentrations of propionic and butyric acids. This will be of benefit to the MPB in the second stage, because MPB can use acetic acid, formic acid, H_2, methanol, and methylamine as a substrate, but not VFAs that have a C atom > 2, e.g., propionic acid or butyric acid (Speece 1995). Butyrate is easily degraded to acetate by butyrate-oxidizing bacteria [Eq. (1)], whereas the degradation of propionate to acetate is thermodynamically infeasible unless the by-product, hydrogen, is removed by the hydrogen-consuming bacteria (Shin et al. 2001). However, the SRB are able to grow with a variety of organic carbon and sulfur compounds, including propionate [Eq. (2)]:

$$2\,\text{butyrate} + 4\,H_2O \longrightarrow 4\,\text{acetate} + H^+ + 4\,H_2 \quad (1)$$

$$4\,\text{propionate} + 3SO_4^{2-} \longrightarrow 4\,\text{acetate} + 4HCO_3^- + 3HS^- + H^+ \quad (2)$$

The reduction of propionic acid in the effluent, even for the short HRTs (4 and 6 h) observed in this study, may be attributable to the cooperation between propionate-degrading bacteria, hydrogen-consuming bacteria, and the activity of the SRB in the reactor.

COD removal and Sulfate Reduction

Generally, organic matter in sulfate-rich wastewater will be removed via sulfate reduction and methanogenesis in an anaerobic bioreactor (Hulshoff Pol et al. 1998). The SRBs obtain the energy for growth through oxidation of the organic substrate, and use sulfate as the terminal electron acceptor. The experimental results illustrate that COD and sulfate removal efficiency increased with the increasing HRT, in that 16–55% of COD and 23–35% of sulfate were removed (Fig. 3). The MPB and SRB were reported to be very competitive for substrate at a COD/SO_4^{2-} ratio of between 1.7 and 2.7, but which one will be dominant depends on the experimental conditions (Hao et al. 1996). Considering the COD/SO_4^{2-} ratio of this study (2.12–2.97) and the operating conditions of the reactor (pH 5.5, short HRT), which were not conducive to the optimal function of the MPB, it can be assumed that the reduction of COD concentration at each HRT was more because of the activity of the SRB than that of the MPB. The COD demand for SRB is in the range of 0.7 to 1.5 g $COD/g\,SO_4^{2-}$, depending on the C-source used as substrate (Hao et al. 1996). The increasing of alkalinity and pH (pH 7–8) in the effluent was observed although the influent pH was controlled at between pH 5.4–5.9. This may due to the degradation of protein and ammonia in latex-processing wastewater by the hydrolytic bacteria, which leads to the formation of NH_4HCO_3 [Eqs. (3) and (4)]. Moreover, the alkalinity could come from HCO_3^- alkalinity, HS^- alkalinity, and volatile acid alkalinity, which occur from sulfate reduction [Eqs. (5) and (6)]:

$$\text{Org-N} + H_2O \longrightarrow NH_3 + CO_2 \quad (3)$$

$$NH_3 + CO_2 + H_2O \longrightarrow NH_4HCO_3 \quad (4)$$

$$SO_4^{2-} + \text{organic matter} \xrightarrow{\text{SRB}} HS^- + H_2O + HCO_3^- \quad (5)$$

$$CH_3COO^- + SO_4^{2-} \xrightarrow{\text{SRB}} 2HCO_3^- + HS^- \quad (6)$$

Considering all the results, the suitable HRT for the acidification stage was 4 h, because a high degree of acidification and acetic acid concentration was achieved at this HRT. Although the COD removal efficiency at this HRT was rather low (<20%), the sulfate reduction efficiency was at the same level as it had been over HRTs of 6 and 8 h (Fig. 3). Moreover, effluent pH (6.5–7.5) and alkalinity

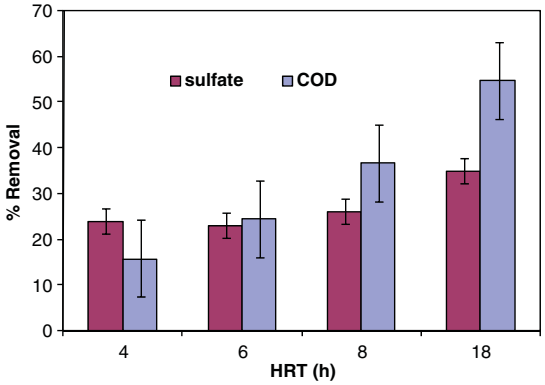

Fig. 3. COD and sulfate removal efficiency at each HRT of the UASB reactor under acidogenic conditions

at HRT of 4 h were optimal for the MPB; therefore, the effluent from the aforementioned conditions could feed directly to the methanogenic reactor without any alkaline addition.

Performance of the Two-stage UASB Reactor Treating Latex-Processing Wastewater

COD and Sulfate Removal Efficiency

The A reactor in the two-stage UASB system was constantly operated over an HRT of 4 h, while the HRTs of the M reactor were varied at 24, 32, and 56 h, respectively. The performance of the two-stage UASB system for each HRT, treating wastewater from a latex-processing factory, is shown in Table 2. The COD removal efficiency of the system was found to increase with the increasing HRT, in which 87.3% of COD was removed for HRT of 60 h [Fig. 4(a)]. A significantly decreased SS concentration was also observed after each stage of treatment. Suspended solids in the latex-processing wastewater are primarily rubber particles, which occur from the skim crepe recovery by adding H_2SO_4 to the skim latex. The decrease of SS concentration was presumably due to the degradation of the rubber particles, which resulted in the formation of rubber scum. It was noticed that most of the COD removal took place in the M reactor; however, the methane content of the biogas could be analyzed only at HRT of 28 h. It was found that the gas outlet in the gas-liquid-solid separator (GSS) of the methanogenic reactor was covered with a lot of rubber scum, which led to the loss of biogas with the effluent. The decrease in the VFA content was also consistent with the increase in efficiency of COD removal.

An increase in sulfate removal efficiency from 71 to 83% was observed when the HRT of the system increased from 28 to 36 h [Fig. 4(b)]. Corresponding to the COD removal, most of the sulfate reduction at those HRTs occurred in the M reactor. It can be presumed that the SRB shared contribution with MPB on COD removal in the M reactor, despite the presence of favorable conditions for the MPB in the reactor. Such results were not surprising, because in the anaerobic treatment of wastewater in the presence of sulfate, hydrogenotrophic SRB (HSRB) has a higher growth rate, substrate affinity, and cell yield than hydrogenotrophic MPB (HMPB) (Oude Elferink et al. 1994; Colleran et al. 1995). Acetate-utilizing SRB (ASRB) has a thermodynamic and kinetic advantage over acetate-utilizing MPB (AMPB) in its competition for acetate (Widdel 1988). In contrast to the COD removal, a remarkably low sulfate-reduction efficiency of only 17% was observed in the M reactor, operating for HRT of 56 h. A lower sulfate concentration in the A reactor (901 mg/L), which resulted in a

J. Environ. Eng. 2013.139:141-146.

Downloaded from ascelibrary.org by Kasetsart University on 01/10/13. Copyright ASCE. For personal use only; all rights reserved.

Downloaded from ascelibrary.org by Kasetsart University on 01/10/13. Copyright ASCE. For personal use only; all rights reserved.

Table 2. Performance of the Two-Stage UASB Reactor Treating Latex-Processing Wastewater at Each HRT

	HRT 28 h			HRT 36 h			HRT 60 h		
Parameters[a]	Influent	Acid tank (4 h)	Methane tank (24 h)	Influent	Acid tank (4 h)	Methane tank (32 h)	Influent	Acid tank (4 h)	Methane tank (56 h)
pH	5.41 ± 0.21	7.01 ± 0.3	8.00 ± 0.17	5.84 ± 0.22	7.83 ± 0.51	8.56 ± 0.13	6.2 ± 0.52	8.3 ± 0.24	8.9 ± 0.13
COD	$6,394 \pm 380$	$5,460 \pm 449$	$3,093 \pm 461$	$6,660 \pm 817$	$5,230 \pm 596$	$2,140 \pm 499$	$5,821 \pm 452$	$3,887 \pm 373$	742 ± 181
VFA	$3,450 \pm 329$	$3,759 \pm 314$	$2,297 \pm 236$	$3,385 \pm 932$	$3,261 \pm 1,081$	$1,260 \pm 763$	$2,631 \pm 567$	$2,217 \pm 228$	239 ± 74
Acetic acid	1,346	2,664	1,251	1,693	2,392	1,496	1,740	1,820	53
Propionic acid	1,032	309	n.d.[b]	1,062	284	40	878	141	n.d.[b]
Butyric acid	126	11	n.d.[b]	75	50	n.d.[b]	18	n.d.[b]	n.d.[b]
Alkalinity	$2,220 \pm 80$	$2,848 \pm 206$	$4,120 \pm 460$	$2,495 \pm 699$	$2,903 \pm 900$	$3,768 \pm 1470$	$2,249 \pm 609$	$2,971 \pm 249$	$2,943 \pm 286$
Sulfate	$2,987 \pm 257$	$2,270 \pm 82$	859 ± 302	$2,938 \pm 999$	$2,037 \pm 622$	506 ± 333	$1,767 \pm 333$	901 ± 185	807 ± 183
Sulfide	—	38 ± 15	132 ± 39	—	77 ± 28	139 ± 28	—	142 ± 25	56 ± 11
SS	955 ± 320	531 ± 304	252 ± 116	926 ± 157	344 ± 57	94 ± 16	742 ± 122	349 ± 98	66 ± 26
CH_4 (%)	—	7.14	48.98	—	n.a.[c]	n.a.[c]	—	n.a.[c]	n.a.[c]
CO_2 (%)	—	2.41	3	—	n.a.[c]	n.a.[c]	—	n.a.[c]	n.a.[c]

[a]The units of all parameters are mg/L, except pH, CH_4, CO_2.
[b]Not detected.
[c]Could not analyzed (because GSS was blocked by rubber scum).

Fig. 4. Removal efficiency of the two-stage UASB reactor at each HRT: (a) COD removal efficiency; (b) sulfate removal efficiency

COD/SO_4^{2-} ratio of 4.31, might be the reason for the low sulfate reduction efficiency, because MPB outcompeted SRB for available electron donors when the COD/SO_4^{2-} ratio of the wastewater was greater than 2.7 (Hao et al. 1996). Thus, it can be presumed that the degradation of COD in the M reactor operating at HRT of 56 h was primarily due to MPB.

Nevertheless, relatively low methane content in the biogas and low SMA were detected. Visser et al. (1996) found that sludge granules were 50% inhibited at H_2S concentrations of 250 and 90 mg L^{-1} at pH values of 6.4–7.2 and 7.8–8.0, respectively. The methane production of MPB was thought to be inhibited by sulfide toxicity, because the sulfide concentration in the effluent from the acidogenic reactor was 142 mg L^{-1} (Table 2). Moreover, it was noticeable that both the COD removal and sulfate reduction efficiency of the A reactor, even when it operated constantly for HRT of 4 h, increased as the HRT of the system increased from 28 to 36 and 60 h. This might be explained by two reasons: (1) the acclimation of microorganisms to the latex-processing wastewater; and (2) a rapid increase of SRB and acidogenic bacteria in the reactor, because the maximum specific growth rates (μ_{max}) of SRB and acidogenic bacteria were 0.85–2.0 and 0.05–7.2 day^{-1}, respectively (Speece 1995).

The COD removal efficiency of the two-stage UASB system in this study was compared to that of the anaerobic hybrid reactor (one stage) that treated latex-processing wastewater from the same source (Wongkittiwimol 2000). The average COD removal efficiencies when the anaerobic hybrid reactor was operated at HRTs of 36, 60, 96, and 144 h were 41, 59, 81, and 84%, respectively. It was found that the two-stage UASB system had higher removal efficiency than the anaerobic hybrid reactor for the same HRT. For example, a COD removal efficiency of 87.3% could be achieved by the two-stage UASB system at an HRT of 60 h, whereas the same level of efficiency was attained only when the anaerobic hybrid reactor was operated under HRT longer than

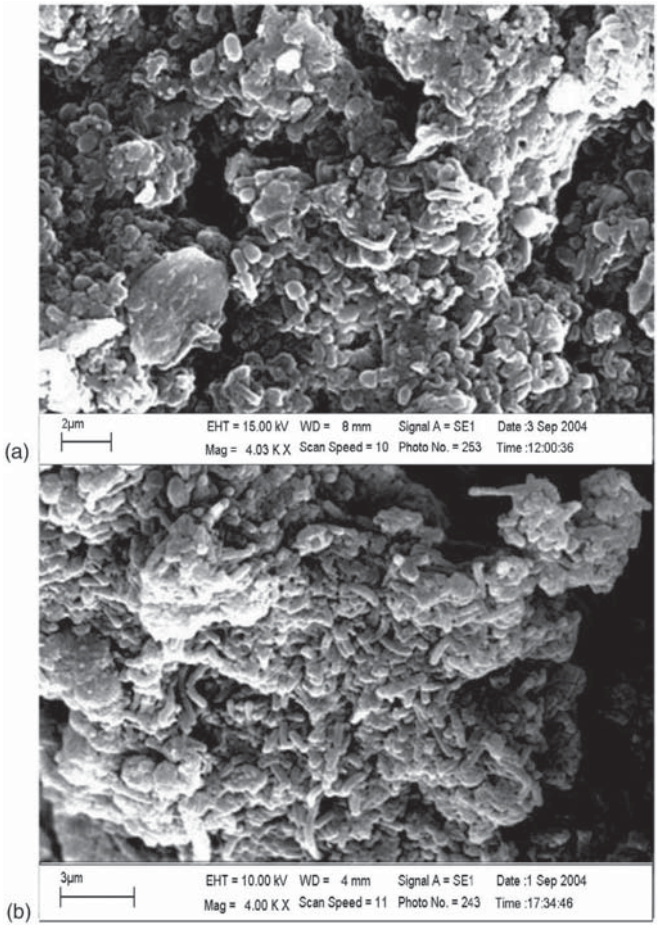

Fig. 5. Scanning electron micrograph of the surface of sludge from: (a) A reactor; (b) M reactor

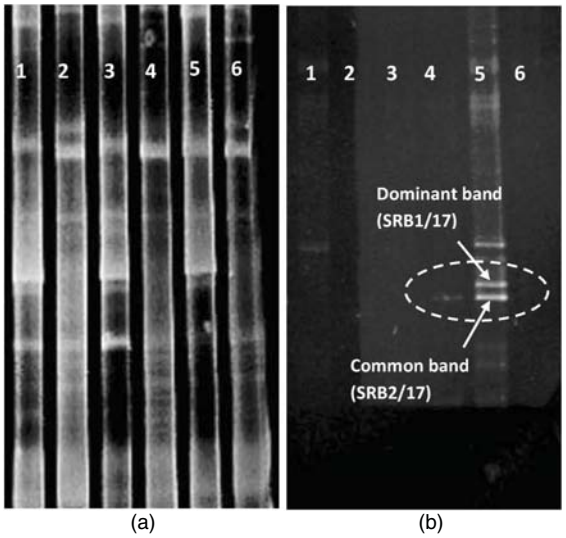

Fig. 6. DGGE profiles of 16S rRNA genes in sludge from the A reactor (columns 1, 3, 5: HRT 4 h) and the M reactor (column 2: HRT 24 h; column 4: HRT 32 h; column 6: HRT 56 h): (a) *archae* bacteria (571 bps); (b) sulfate reducing bacteria (522 bps)

4 days (96 h). This highlights the advantages of the two-stage UASB system, in which the accumulation of VFA and the interference or inhibition of the SRB in relation to the MPB could be reduced in the first stage of the system.

Sludge Morphology and Sludge Activity

The morphology of the sludge from both the acidogenic and the methanogenic reactor, as examined by SEM, revealed that the surfaces of most granules were covered by rubber polymer. A heterogeneous population of rod and filament bacteria was found on the surfaces of both types of sludge. Acidogenic granules predominantly consisted of short-rod bacteria [Fig. 5(a)], whereas networks of long multicellular filaments appeared to colonize the surface of the methanogenic sludge [Fig. 5(b)].

The SAA of sludge from the A reactor was between 1.705–1.835 g COD g VSS^{-1} d^{-1}, and the SAA of the M sludge was slightly broader (1.326–2.024 g COD g VSS^{-1} d^{-1}). Compared to the maximum acidogenic activity in pure cultures and in mixed cultures from anaerobic reactors in the literature (Henze and Harremoes 1983; Soto et al. 1993), the SAA of the tested sludge was 5–10 times lower. Unexpectedly low SMA in the range of 0.0078 to 0.0138 g COD-CH_4 g VSS^{-1} d^{-1}, accompanied by methane content of 25–36% in the biogas, was obtained from the acidogenic and the methanogenic sludge. It was hypothesized that the MPB in the UASB reactor, particularly the M reactor, were eliminated or inhibited by the other bacteria. The monitoring of the microbial community, using a denaturing gradient gel electrophoresis (DGGE) technique, revealed that MPB could still be detected in both the A and M reactors (Fig. 6), but were dominated by the SRB. This was clearly observed in the acidogenic sludge when the system was operated at HRT of 36 h. The ability of SRB to use several intermediates of the anaerobic process (e.g., propionate, butyrate, and acetate) as energy sources in the presence of sulfate, coupled with their high substrate affinity (Hao et al. 1996), were supposed to be the reasons for the overwhelming numbers of SRB in the M reactor. This assumption was confirmed by the SAA of the sludge from the M reactor, which was at the same level as the sludge from the A reactor, and by the high sulfate-reduction efficiency concomitant with the COD removal in the methanogenic reactor at HRTs of 28 and 36 h (Fig. 4).

Conclusions

Latex-processing wastewater was successfully treated in a two-stage UASB reactor. Maximum COD removal efficiency of 87% was achieved at HRT of 60 h and 83% sulfate reduction efficiency was observed at HRT of 36 h. Most of the COD removal was attributable to SRB rather than MPB. Not much difference was observed between the SAA of the acidogenic and methanogenic sludge, which indicates the existence of acetogenic, methanogenic, and sulfate-reducing bacteria in the methanogenic reactor. Microbial community monitoring by the DGGE technique confirmed the domination of SRB in both reactors.

Acknowledgments

The authors would like to express their acknowledgement to the Thailand Research Fund, the Office of the Higher Education Commission and the National Research University Project for the financial support. A grateful thank is also for Dr. Srisuda Dhamwichukorn for her helping hand in PCR-DGGE analysis and the Department of Microbiology, King Mongkut's University of Technology Thonburi for providing the facilities for this study.

J. Environ. Eng. 2013.139:141-146.

Downloaded from ascelibrary.org by Kasetsart University on 01/10/13. Copyright ASCE. For personal use only; all rights reserved.

References

American Public Health Association (APHA). (1992). *Standard methods for the examination of water and wastewater*, 18th ed., APHA/American Water Works Association/Water Environment Federation, Washington DC.

Chathanee, C. (1988). "Tapioca wastewater treatment by two-stage anaerobic digestion process." Master's thesis, Biotechnology, Chulalongkorn Univ., Bangkok, Thailand, 35–46 (in Thai).

Colleran, E., Finnegan, S., and Lens, P. (1995). "Anaerobic treatment of sulphate-containing waste streams." *Antonie Leeuwenhoek*, 67(1), 29–46.

Hao, O. J., Chen, J. M., Huang, L., and Buglass, R. L. (1996). "Sulfate-reducing bacteria." *Crit. Rev. Env. Sci. Technol.*, 26(2), 155–187.

Henze, M., and Harremoes, P. (1983). "Anaerobic treatment of wastewater in fixed film reactors—A literature review." *Water Sci. Technol.*, 15, 1–101.

Hulshoff Pol, L. W., Lens, P. N. L., Stams, A. J. M., and Lettinga, G. (1998). "Anaerobic treatment of sulphate-rich wastewaters." *Biodegradation*, 9(3–4), 213–224.

Kalyuzhnyi, S. V., et al. (1996). "Organic removal and microbiological features of UASB-reactor under various organic loading rates." *Bioresour. Technol.*, 55(1), 47–54.

Lens, P. N. L., Visser, A., Janssen, A. J. H., Hulshoff Pol, L. W., and Lettinga, G. (1998). "Biotechnological treatment of sulfate-rich wastewaters." *Crit. Rev. Env. Sci. Tech.*, 28(1), 41–88.

O-Thong, S., Prasertsan, P., Intrasungkha, N., Dhamwichukorn, S., and Birkeland, N. (2007). "Improvement of biohydrogen production and treatment efficiency on palm oil mill effluent with nutrient supplementation at thermophilic condition using an anaerobic sequencing batch reactor." *Enzyme Microb. Technol.*, 41(5), 583–590.

Oude Elferink, S. J. W. H., Visser, A., Hulshoff Pol, L. W., and Stams, A. J. M. (1994). "Sulfate reduction in methanogenic bioreactors." *FEMS Microb. Rev.*, 15(2–3), 119–136.

Shin, H. S., Han, S. K., Song, Y. C., and Lee, C. Y. (2001). "Performance of UASB reactor treating leachate from acidogenic fermenter in the two-phase anaerobic digestion of food waste." *Water Res.*, 35(14), 3441–3447.

Soto, M., Mendez, R., and Lema, J. M. (1993). "Methanogenic and non-methanogenic activity tests: Theoretical basis and experimental set up." *Water Res.*, 27(8), 1361–1376.

Speece, R. E. (1995). *Anaerobic biotechnology for industrial wastewater*, Archae Press, Nashville, TN.

Thailand Office of Agricultural Economics. (2009). ⟨http://www.oae.go.th/download/prcai/Rubber09.xls⟩ (Jun. 27, 2011).

Visser, A., Hulshoff Pol, L. W., and Lettinga, G. (1996). "Competition of methanogenic and sulfidogenic bacteria." *Water Sci. Technol.*, 33(3), 99–110.

Widdel, F. (1988). "Microbiology and ecology of sulfate- and sulphur reducing bacteria." *Biology of anaerobic microorganisms*, A. J. B. Zehnder, ed., Wiley, New York, 469–586.

Wongkittiwimol, A. (2000). "Treatment of concentrated latex wastewater in the anaerobic hybrid reactor." Master's thesis, Faculty of Engineering, King Mongkut's Univ. of Technology Thonburi, Bangkok, Thailand.

Downloaded from ascelibrary.org by Kasetsart University on 01/10/13. Copyright ASCE. For personal use only; all rights reserved.

J. Environ. Eng. 2013.139:141-146.

Send Orders of Reprints at bspsaif@emirates.net.ae

56 *Current Nanoscience,* **2013,** *9,* **56-60**

Pool-Boiling Heat Transfer Characteristics of Al_2O_3-Water Nanofluids on a Horizontal Cylindrical Heating Surface

Weerapun Duangthongsuk[a,b], Taklaew Yiamsawasd[a], Ahmet Selim Dalkilic[c] and Somchai Wongwises[a,d*]

[a]*Fluid Mechanics, Thermal Engineering and Multiphase Flow Research Lab. (FUTURE), Department of Mechanical Engineering, Faculty of Engineering, King Mongkut's University of Technology Thonburi, Bangmod, Bangkok 10140, Thailand;* [b]*Department of Mechanical Engineering, South-East Asia University, Bangkok, Thailand;* [c]*Heat and Thermodynamics Division, Department of Mechanical Engineering, Yildiz Technical University (YTU), Yildiz, Besiktas, Istanbul 34349, Turkey;* [d]*The Academy of Science, The Royal Institute of Thailand, SanamSueaPa, Dusit, Bangkok 10300, Thailand*

Abstract: This research involved conducting an experiment on pool boiling characteristics of Al_2O_3–water nanofluid. The experimental concentration ranged between 0.00005 and 0.03 %vol. The pressure used was at 1 and 2 atm. The boiling surface was a horizontal copper cylinder with a diameter of 28.5 mm, a length of 90 mm, and surface roughness of 3.14 μm. The main purpose of this research was to study the effect of the nanofluid's concentration and pressure on the heat transfer coefficient and on heat flux, by comparing with water. Calibration of the experimental apparatus with water revealed that the experimental results corresponded to the prediction by Rohsenow's equation. Results from the experiment on pool boiling of nanofluids indicated that the heat transfer coefficient of Al_2O_3–water nanofluid was lower than that of water and tended to decrease when the concentration was higher.

Keywords: Pool boiling, nanofluid, heat transfer coefficient, particle concentration.

1. INTRODUCTION

Heat exchangers are important energy devices commonly found in various industries. They include steamers, heat ventilators in mechanical or electronic devices, coolers, air-conditioners, and other types of devices. At present, the world is facing energy problems. Therefore, many researchers are interested in design and development of devices that use energy more efficiently, including heat exchangers. Working fluids used with heat exchangers include both phase-change (between liquid and vapor) and non phase-change types. The phase-change type produces better heat transfer, compared with the non-phase change type. Pool-boiling heat transfer is one of the mechanisms that occur in heat exchangers. Examples of pool-boiling heat exchangers are heat pipes in heat exchanger units of processors in mobile computers or military communication devices, and fire-tube steamers in industrial factories. Development of pool-boiling heat exchangers maybe carried out in two parts: 1) development of the heating surface and 2) development of the working substance used in the system. The first and most widely used for nucleate pool boiling was developed by Rohsenow [1]. The effects of the surface were taken into account in the correlation. The development of a working substance used in pool-boiling heat exchangers has been carried out in many ways. At present, one of the methods that many researchers are interested in is the addition of solid nanoparticles with high conductivity into base fluids in order to increase thermal conductivity of working fluids. Choi [2] termed the fluids obtained from the addition of solid nanoparticles into abase fluid as "Nanofluid." Regarding the use of nanofluids in forced heat transfer, many researchers have reported increases in the heat transfer coefficient by about 7% to 40% [3-10]. This is because nanofluids have higher conductivity than base fluids. However, only a few studies have used nanofluids with pool-boiling heat transfer, and their results are still inconsistent. Studies concerning specific characteristics of pool boiling of nanofluids in the past decade are summarized here.

*Address correspondence to this author at the Fluid Mechanics, Thermal Engineering and Multiphase Flow Research Lab. (FUTURE), Department of Mechanical Engineering, Faculty of Engineering, King Mongkut's University of Technology Thonburi, Bangmod, Bangkok 10140, Thailand;
Tel: +662-470-9115; Fax: +662-470-9111;
E-mail: somchai.won@kmutt.ac.th

Das *et al*. [11] studied specific characteristics of pool-boiling heat transfer of nanofluids by adding 58.4 mm Al_2O_3 particles to Al_2O_3–water nanofluid at a concentration of 0.1–4 vol.%. The heating surface was a horizontal tube with a diameter of 20 mm and surface roughness of 0.4 to 1.15 μm. Their experimental results showed that the pool boiling heat transfer performance was increased when level of surface roughness increased. However, when the concentration of the nanofluid was increased, the specific characteristics of the heat transfer decreased.

You *et al*. [12] studied the increase incritical heat flux caused by pool boiling of an Al_2O_3–water nanofluid with concentrations of 0.001–0.05 g/l. The heating surface was a horizontal 10x10 mm^2 square copper plate. During the experiment, pressure and temperature were fixed at 2.89 psi and 60°C, respectively. Their results showed that the critical heat flux of the nanofluid was higher than that of water and that it also increased with the increase of the nanofluid's concentration. They found that the critical heat flux increased by 200% at a concentration of 0.05 g/l.

Li *et al*. [13] studied pool-boiling heat transfer characteristics under atmospheric-pressured subcooled boiling of 25 mm silicon dioxide nanoparticles suspended in water at concentrations of 0.05–0.5 wt.%. The heating surface was platinum wire with a diameter of 0.1mm. They found that the pool-boiling heat transfer of SiO_2–water nanofluid was higher than that of water that it varied with the nanofluid's concentration level. In addition, they found that the critical heat flux also increased when the concentration increased.

Vassallo *et al*. [14] studied the pool-boiling heat transfer characteristics of a SiO_2–water nanofluid with Si-deionized size of 15 nm, 50 nm, and 3 μm, and with concentration levels of 0.5–9 vol.%. The heating surface was nickel-chromium wire with a diameter of 0.4 mm and a length of 75 mm. The experiment at atmospheric pressure showed that the critical heat flux of the nanofluid was higher than that of the base fluid, and that it increased when concentration levels of the particles increased.

Bang and Chang [15] studied specific characteristics of nucleate pool-boiling heat transfer of an Al_2O_3–water nanofluid with particle size of 47 nm and concentration levels of 0.5–4 vol.%. The heating surface consisted of 4×100 mm^2 rectangular copper plates placed both horizontally and vertically. Their results showed that increases in the nanofluid's concentration lowered the pool-boiling heat

1875-6786/13 $58.00+.00 © 2013 Bentham Science Publishers

transfer coefficient. However, the critical heat flux was higher than that of water. Analysis from photography revealed that at heat flux higher than 100 kW/m^2, the boiling pattern of the nanofluid was less vigorous than water. They also found that the horizontal heating surface produced higher heat flux than the vertical one.

Kim *et al*. [16] studied the critical heat flux of pool-boiling nanofluids at atmospheric pressure. The 85 nm TiO_2 particles were suspended in water at concentration levels of 0.00001–0.1 vol.%. The heating surface was 0.2 mm nickel-chromium wire. The effect of a heating surface covered with nanoparticles was also studied. They found that the critical heat flux of the nanofluid was higher than that of the base fluid and that the critical heat flux increased when the heating surface was covered with nanoparticles.

Nguyen *et al*. [17] studied specific characteristics of pool-boiling heat transfer of an Al_2O_3–distilledwater nanofluid at atmospheric pressure. The particle size was 47 nm and the concentration level was 0.5–2 vol.%. The heating surface was a horizontal 24 mm-diameter chromium-coated copper disc. Their results showed that when the nanofluid's concentration increased, its pool-boiling heat transfer capacity decreased, compared to water.

Kim *et al*. [18] studied the pool-boiling heat transfer of three-types of nanofluids: Al_2O_3, ZrO_2 and SiO_2 particles suspended in water at concentrations of 0.001–0.1 vol.%. Two types of heating surfaces were used: stainless steel wire with a diameter of 0.381mm and a length of 120mm, and a horizontal 5x45mm^2 plate. The experiment was carried out at atmospheric pressure. The researchers found that the critical heat flux increased with the increase of concentration and heat transfer coefficient was higher than that of water. For all nanofluids, the enhancement of critical heat flux (CHF) is obtained, up to 52% for alumina nanofluids, up to 75% for zirconia nanofluids and up to 80% for silica nanofluids.

Kiu *et al*. [19] studied pool-boiling heat transfer of nanofluids with 50nm CuO and 35 nm SiO_2 particles, each suspended in water and in ethyl alcohol with concentrations of 0.5 wt.%. The heating surface was a horizontal 20mm-diameter copper disc. Their results showed that the critical heat flux of nanofluids was higher than that of the base fluids.

Golubovic *et al*. [20] studied the effect of concentration levels on the critical heat flux of BiO_2–water and Al_2O_3–water nanofluids at a concentration range of 0.0005714–0.0064615 g/l. The heating surface was nickel-chromium wire with a diameter of 0.64 mm and a length of 50 mm, applied at atmospheric pressure. They found that the critical heat flux varied as concentration levels increased, and that it was overall higher than that of water. The CHF was increased by 50% when Al_2O_3 nanoparticles were suspended in pure distilled water and by 33% when BiO particles were suspended.

Trisaksri and Wongwises [21] studied the specific characteristics of pool-boiling heat transfer of a nanofluid with 21nm-diameter TiO_2 nanoparticles suspended in R141b refrigerant at concentrations of 0.01–0.05 vol.%. The heating surface was a horizontal cylinder with a diameter of 28.5 mm and length of 90mm,appliedat pressure levels of 200 to 500 kPa. The researchers concluded that the pool-boiling heat transfer coefficient decreased when the nanofluid's concentration increased, but it increased with increases in the pressure level.

Suriyawong and Wongwises [22] studied pool-boiling heat transfer characteristics of a TiO2–water nanofluid at very low concentration levels (0.00005–0.01 vol.%). The heating surface was made from copper and aluminum, with roughness of 0.2 and 4 μm, applied at atmospheric pressure. In the case of the copper surface, it was found that at concentrations of 0.00005–0.0001 vol.%, the heat transfer coefficient was higher than that of the base fluid. On the other hand, at concentrations higher than 0.0001 vol.%, the heat transfer coefficient was lower than that of the base fluid. In the case of the aluminum surface, the heat transfer coefficient was found to be lower than that of the base fluid at every concentration level. Regarding roughness, a surface roughness of 0.2μm produced a higher heat transfer than roughness of 4μm.

Cieslinski and Kaczmarczyk [23] studied pool-boiling heat transfer of Al_2O_3–water and Cu–water nanofluids at concentrations of 0.01%, 0.1% and 1% by weight. The heating surface was a horizontal smooth-surfaced tube made from copper and stainless steel with a diameter of 10 mm. The effects of concentration level and of surface material on heat transfer characteristics were studied at atmospheric pressure. They found that the concentration level had very little effect on the boiling heat transfer coefficient of Al_2O_3–water and Cu–water nanofluids on the copper heating surface. Additionally, the type of surface material used seemed to have no effect on boiling heat transfer of Cu–water at a concentration of 0.1 wt.%. However, at other concentration levels of both Al_2O_3–water and Cu–water, the boiling heat transfer coefficient on the stainless steel tube was higher than that onthe copper tube at the same heat flux.

From the above review of the literature, there are seemingly very few studies concerning the specific characteristics of pool-boiling heat transfer of nanofluids, and their results are inconsistent. Some researchers reported that the heat transfer coefficient varied with the concentration level of the nanofluid [12-14, 16, 18- 20], while some reported an inverse variation with concentration levels [11, 15, 17, 21, 22]. Every experiment was conducted at atmospheric pressure, except the experiment by Trisaksri and Wongwises [21], who also observed the effects of pressure. Thus, the researchers in the current study aimed to conduct additional experiments on pool-boiling heat transfer in order to clarify the inconsistent results mentioned above. This research uses a nanofluid with $A1_2O_3$ nanoparticles suspended in water at concentrations of 0.00005–0.03 vol.% and at pressure levels of 1 and 2 atm. The heating surface used is a horizontal copper cylinder.

2. PREPARATION OF THE NANOFLUID

The Al_2O_3–water nanofluidused in this study is a product supplied by DEGUSSA Company Limited (Thailand) under the code of AeroDisp. W630. The 120nm-diameter Al_2O_3 particles are suspended in water at a concentration of 30 wt.%. In order to study the effect of the concentration level, the fluidis diluted by addition of base water to obtain concentration levels of 0.00005, 0.0001, 0.005 and 0.03 vol.%. To attaineven dispersion of particles in the base fluid, an ultrasonic vibrator is used for sonication for 2 hours before every experiment. The preparation of the nanofluid with pH-control and the addition of surfactants were accomplished by the manufacturer without revealing information about the process.

3. EXPERIMENTAL APPARATUS AND PROCEDURES

The experimental apparatus includes a pressure vessel, a water-cooling unit, a boiling heating surface, and a DC power supply, as shown in Fig. (**1**).

The pressure vessel containing the nanofluid used in the experiment is made from stainless steel with a diameter of 10 cm, a height of 30 cm, and a thickness of 1 cm. Its outer surface is coated with insulator to prevent heat loss. A cooling coil and a pressure gauge are installed on top of the vessel to control the pressure level and to condense the upward flow of vapors into liquid, in order to maintain a stable concentration throughout the experiment. The control is done by adjusting the flow rate of cold water pumped from the cooling unit. A T-type thermocouple is also installed on top of the vessel to measure the temperature of the fluid mass.

The heating surface, as shown in Fig. (**2**), consists of a 2-kilowatt heater stick buried inside the copper cylinder (28.5 mm diameter and 90 mm length). Both ends of the copper cylinder are covered with insulators to force heat from the heater to the heating surface on its side only (radially). Four sets of T-type thermocouple are installed along the length at even intervals to measure surface

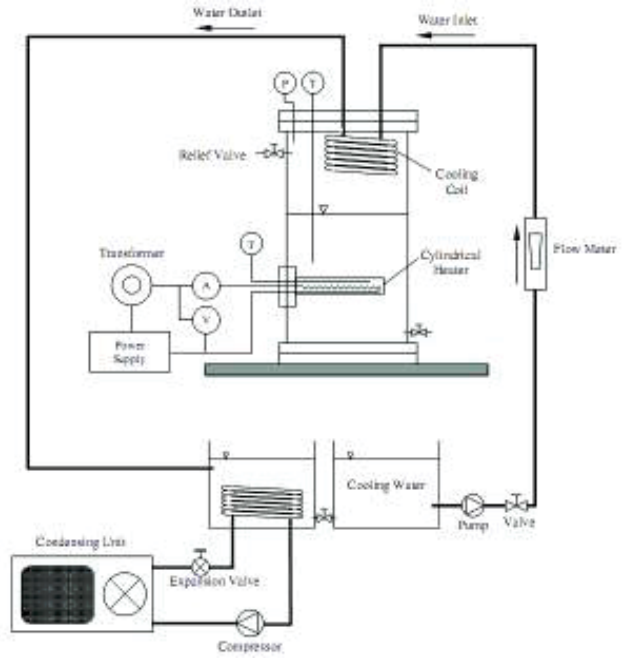

Fig. (1). Schematic diagram of experimental apparatus [Trisaksri and Wongwises [21], with permission from Elsevier].

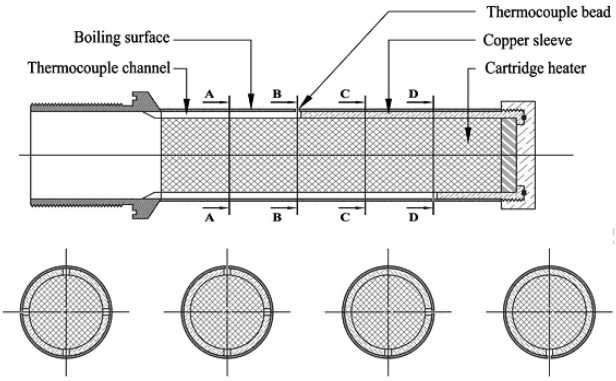

Fig. (2). Cross-sectional view of the heating surface [Trisaksri and Wongwises [21], with permission from Elsevier].

temperature of the tested unit. Each set is placed at an angle of 90 degrees radially. The thermocouples are specially designed so that only the small temperature gauge head is fixed directly onto the outer heating surface, while other signal wires are concealed inside to prevent interference on the heating surface and movement of vapor bubbles during the boiling process.

4. DATA REDUCTION

The heat transfer coefficient and the heat flux of pool boiling may be calculated with the following equations.

The heat flux q (W/m^2) maybe calculated with Eq. (1).

$$q = \frac{IV}{A} \tag{1}$$

where I is electrical current(Amp), V is voltage(Volt), and A is heating surface(m^2).

The average heat transfer coefficient of pool boiling, $h_b(W/m^2K)$ maybe calculated with Eq. (2).

$$h_b = \frac{q}{T_h - T_{sat}} \tag{2}$$

where T_{sat} is the saturated temperature of working fluids (^oC)and T_h is the average temperature of the heating surface, which maybe calculated with Eq. (3).

$$T_h = \frac{T_{h,top} + 2T_{h,side} + T_{h,bottom}}{4} \tag{3}$$

where $T_{h,top}$, $T_{h,side}$ and $T_{h,bottom}$ are temperatures at each location as shown in Fig. (**2**).

The uncertainties of the heat flux, heating surface temperature and heat transfer coefficient are ±2.92%, ±2.39% and ±5.89%, respectively.

Regarding calibration of the experimented apparatus, Rohsenow's equation [1] is used with water as the working fluid, as follows:

$$q = \mu_l h_{fg} \left[\frac{g(\rho_l - \rho_v)}{\sigma} \right]^{0.5} \left[\frac{C_p (T_h - T_{sat})}{C_{sf} h_{fg} \Pr_l^n} \right]^3 \tag{4}$$

where μ is viscosity of fluid, ρ is density of fluid, σ is surface tension of fluid, C_p is specific heat, h_{fg} is latent heat, Pr is Prandtl number, and C_{sf} and n are constants between heating surface and fluid. In the case of the copper surface and water, the constants are 0.031 and 1.0, respectively. The subscripts l and v represent the liquid phase and vapor phase, respectively.

5. RESULTS AND DISCUSSION

Before the experiment on boiling of the nanofluid, the invented apparatus was calibrated to confirm its accuracy by testing with water. The test results were compared with calculations from Rohsenow's equation [1] and data from the experiments of other researchers, as shown in Fig. (**3**). The calibration results confirmed that data gained from the invented apparatus were consistent with calculations from Rohsenow' sequation and with measurements by other researchers.

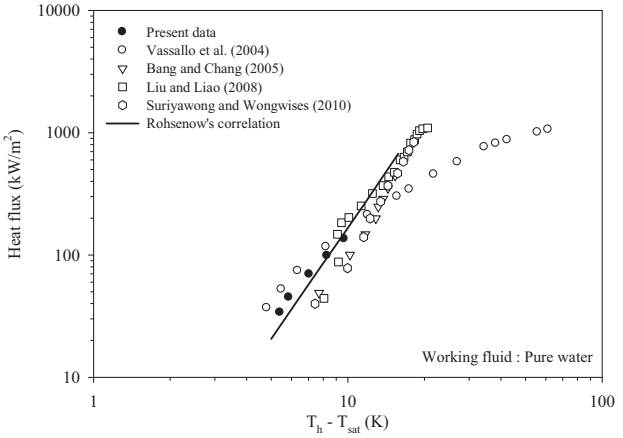

Fig. (3). Comparison of present data with Rohsenow's correlation and various researchers.

Fig. (**4**) shows boiling curves ofAl_2O_3–water nanofluidat various concentration levels. At the same heat flux, the boiling curves tend to move in a direction to the right when concentration levels of nanoparticles increased or when differences in temperature between the heating surface and the fluid increased. It could be said that the

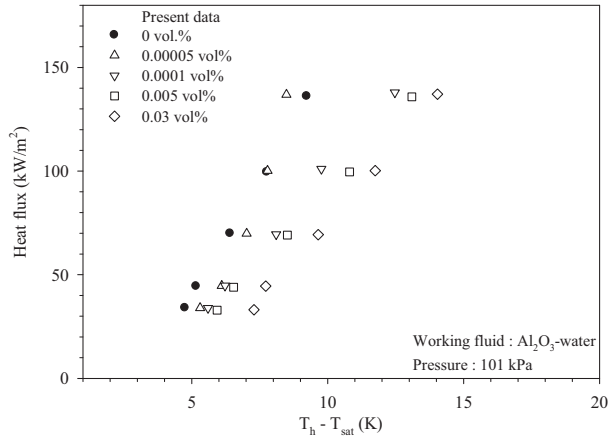

Fig. (4). Boiling curves for Al_2O_3-water nanofluid at 101 kPa.

onset of nucleate boiling is slower. That is, the heat transfer coefficient is lower than the water base fluid and decreases when the concentration increases, as clearly evident in Fig. (**5**). However, at a concentration of 0.00005 vol.%, it was found that at high heat flux, the heat transfer tended to be higher than that of the base fluid. Regarding heat flux, it was found that at the same concentration level, the heat transfer coefficient varied with heat flux in both water and nanofluidat every concentration level.

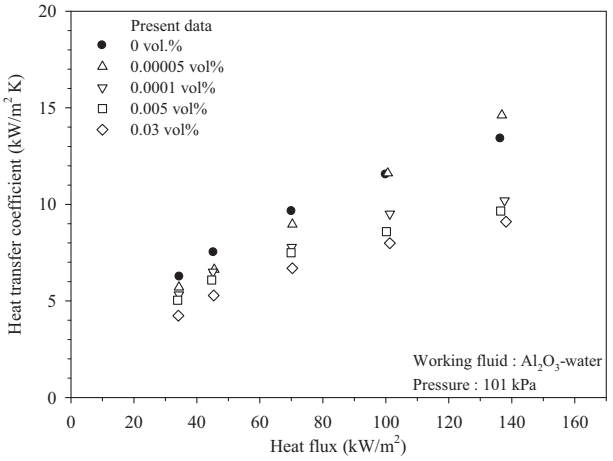

Fig. (5). Boiling heat transfer coefficient for Al_2O_3-water nanofluid at 101 kPa.

The results of the experiment on the pool-boiling heat transfer of an Al_2O_3–water nanofluid were compared with those of other studies, as shown in Fig. (**6**). Correspondence was found with the studies by Das *et al*. [11] and by Cieslinski and Kaczmarczyk [23]. Both of those studies used a horizontal copper cylinder boiling surface similar to that used in this research. It can be seen in the figure that when the concentration increases, the boiling curves tend to move in a direction to the right. In other words, the heat transfer coefficient tends to decrease and is lower than the base fluid. This could be clearly seen in Fig. (**7**), where the experimental results are presented in terms of heat transfer enhancement, which is a ratio between heat the transfer coefficient of nanofluid and the heat transfer coefficient of the base fluid. This figure also shows that at a low concentration level of 0.00005 vol.%, the heat transfer coefficientis higher than that of the base fluid. This is consistent with Suriyawong and Wongwises [22], who found that heat transfer

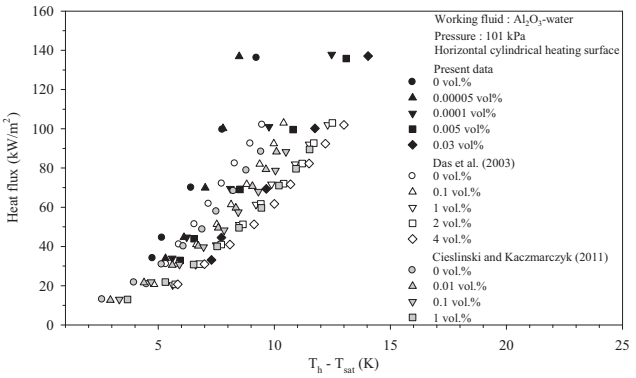

Fig. (6). Comparison of experimental boiling curves with those reported by various researchers.

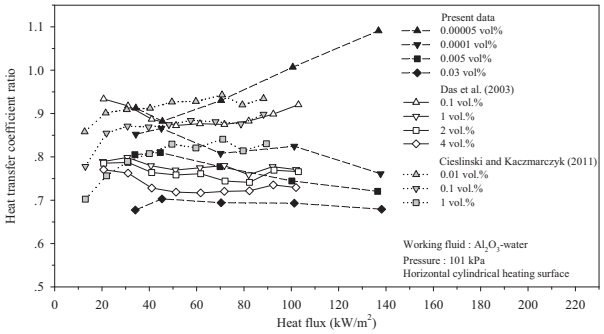

Fig. (7). Comparison of experimental pool boilingheat transfer enhancement with those reported by various researchers.

coefficient of TiO_2-water nanofluid was higher than the base fluid at low concentration levels (between 0.00005 to 0.01 vol.%), but decreased at high concentration level.

Fig. (**8**) shows the effect of pressure on the boiling curve of Al_2O_3–water nanofluid at a concentration of 0.00005 vol.%. The experiment reveals that when the pressure of a fluid increases, the boiling curvetends to move in the left direction, which means that the heat transfer coefficient is higher. Fig. (**9**) shows consistency with the study of Trisaksri and Wongwises [21] who found that the heat transfer coefficient of TiO_2–R141b decreased when the pressure decreased.

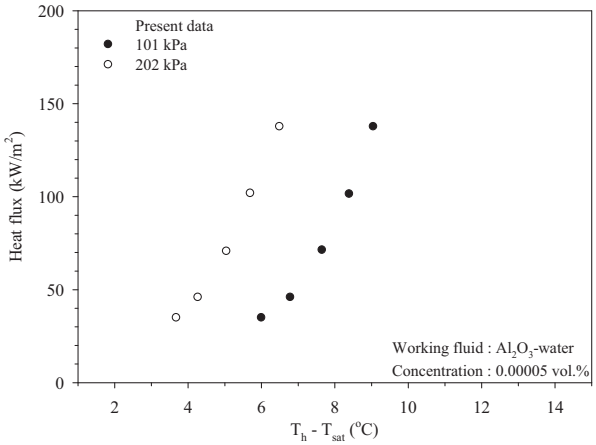

Fig. (8). Variation of boiling curves of nanofluid with pressures.

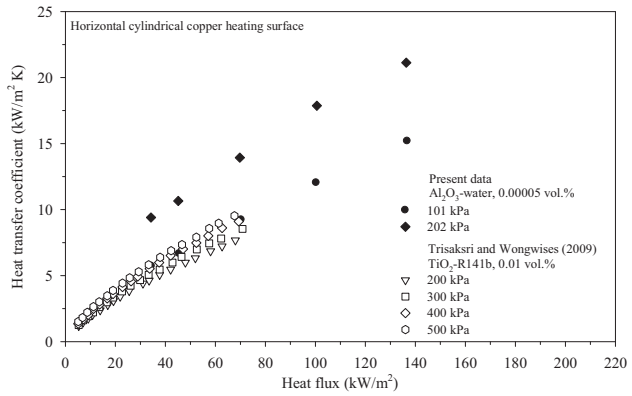

Fig. (9). Variation of heat transfer coefficient with heat flux at different pressures.

The fact that pool-boiling heat transfer coefficient of nanofluid used in this experiment is lower than the water base fluid and decreases when the concentration increases could occur because nanoparticles cover or clog up tiny pores on the heating surface and reduce nucleation site. Normally, these tiny pores produce nucleate bubbles which flow upward and help with circulation and turbulence of fluid that lead to better heat transfer. Moreover, the cover of nanoparticles on heating surface also increases thermal resistance which decreases its heat transfer coefficient.

6. CONCLUSIONS

This research studies pool-boiling heat transfer characteristics of Al_2O_3–water nanofluid with the concentration of 0.00005, 0.0001, 0.005 and 0.03 vol.% at the pressure levels of 1 and 2 atm. The heating surface used is a horizontal copper cylinder. The results from the experiment could be concluded as follows:

- The use ofAl_2O_3–water nanofluid does not help in increasing pool-boiling heat transfer coefficient when compared to water. It also decreases when the concentration increases.
- The heat transfer coefficient decreases when the pressure level decreases.

CONFLICT OF INTEREST

The authors confirm that this article content has no conflicts of interest.

ACKNOWLEDGEMENTS

The authors would like to express their appreciation to the Thailand Research Fund, the Office of the Higher Education Commission and the National Research University Project for providing financial support. The authors also thank Mr. Prawitt Kerdpermdee, Mr. Pumpat Jaturapattanapum and Mr. Theanthum Kaenak for their help in the experimental works.

REFERENCES

[1] Rohsenow, W.M. A method of correlation heat transfer data for surface boiling liquids. *ASME Transaction*, **1952**, *77,* 969.

[2] Choi, S.U.S. Enhancing thermal conductivity of fluids with nanoparticle. *ASME FED*, **1995**, *231*, 99-103.

[3] Duangthongsuk, W.; Wongwises, S. A critical review of convective heat transfer of nanofluids. *Renew. Sustain. Energy Rev.*, **2007**, *11*, 797-817.

[4] Pak, B. C.; Cho, Y. I. Hydrodynamic and heat transfer study of dispersed fluids with submicron metallic oxide particles. *Exp. Heat Transfer*, **1998**, *11*, 151-170.

[5] Xuan, Y.; Li, Q. Investigation on convective heat transfer and flow features of nanofluids. *ASME J. Heat Transfer*, **2003**, *125*, 151.

[6] Wen, D.; Ding, Y. Experimental investigation into convective heat transfer of nanofluids at the entrance region under laminar flow conditions. *Int. J. Heat Mass Transfer*, **2004**, *47*, 5181.

[7] He, Y.; Jin, Y.; Chen, H.; Ding, Y.; Cang, D.; Lu, H. Heat transfer and flow behavior of aqueous suspensions of TiO_2 nanoparticles (nanofluids) flowing upward through a vertical pipe. *Int. J. Heat Mass Transfer*, **2007**, *50*, 2272.

[8] Duangthongsuk, W.; Wongwises, S. Effect of thermophysical properties models on the prediction of the convective heat transfer coefficient for low concentration nanofluid. *Int. Commun. Heat Mass Transfer*, **2008**, *35*, 1320.

[9] Duangthongsuk, W.; Wongwises, S. Heat transfer enhancement and pressure drop characteristics of TiO_2-water nanofluid in a double-tube counter flow heat exchanger. *Int. J. Heat Mass Transfer*, **2009**, *52*, 2059.

[10] Duangthongsuk, W.; Wongwises, S. An experimental study on the heat transfer performance and pressure drop of TiO_2-water nanofluids flowing under a turbulent flow regime. *Int. J. Heat Mass Transfer*, **2010**, *53*, 334-344.

[11] Das, S.K.; Putra, N.; Roetzel, W. Pool boiling characteristics of nanofluids. *Int. J. Heat Mass Transfer*, **2003**, *46*, 851-862.

[12] You, S.M.; Kim, J.H.; Kim, K.H. Effect of nanoparticles on critical heat flux of water in pool boiling heat transfer. *Appl. Phys. Lett.*, **2003**, *83*, 3374-3376.

[13] Li, C.H.; Wang, B.X.; Peng, X.F. On the pool boiling of subcoolednano-particle suspensions. *paper presented in the 6th International Symposium on Heat Transfer*, Beijing, China, **2004**.

[14] Vassallo, P.; Kumar, R.; Amico, S.D. Pool boiling heat transfer experiments in silica–water nanofluids. *Int. J. Heat Mass Transfer*, **2004**, *47*, 407-411.

[15] Bang, I.C.; Chang, S.H. Boiling heat transfer performance and phenomena of Al_2O_3-water nanofluids from a plain surface in a pool. *Int. J. Heat Mass Transfer*, **2005**, *48*, 2407-2419.

[16] Kim, H.; Kim, J.; Kim, M. Experimental study on characteristics of water-TiO_2 nanofluids. *Nucl. Eng. Technol.*, **2006**, *38*, 61-68.

[17] Nguyen, C.T.; Galanis, N.; Roy, G.; Divoux, S.; Gillbert, D. Pool boiling characteristics of water-Al_2O_3 nanofluid, *paper presented in the 13th International Heat transfer conference*, Sydney, Australia, **2006**.

[18] Kim, S.J.; Bang, I.C.; Buongiorno, J.; Hu, L.W. Surface wettability change during pool boiling of nanofluids and its effect on critical heat flux. *Int. J. Heat Mass Transfer*, **2007**, *50*, 4105-4116.

[19] Liu, Z.; Liao, L. Sorption and agglutination phenomenon of nanofluids on a plain heating surface during pool boiling. *Int. J. Heat Mass Transfer*, **2008**, *51*, 2593-2602.

[20] Golubovic, M.N.; Madhawa, H.D.; Hettiarachchi, M.; Worek, W.M.; Minkowycz, W.J. Nanofluids and critical heat flux, experimental and analytical study. *Appl. Therm. Eng.*, **2009**, *29*, 1281-1288.

[21] Trisaksri, V.; Wongwises, S. Nucleate pool boiling heat transfer of TiO_2-R141b nanofluids. *Int. J. Heat Mass Transfer*, **2009**, *52*, 1582-1588.

[22] Suriyawong, S.; Wongwises, S. Nucleate pool boiling heat transfer characteristics of TiO_2-waternanofluids at very low concentrations. *Exp. Therm. Fluid Sci.*, **2010**, *34*, 992-999.

[23] Cieslinski, J.T.; Kaczmarczyk, T.Z. Pool boiling of water-Al_2O_3 and water-Cu nanofluids on horizontal smooth tubes. *Nanoscale Res. Lett.*, **2011**, *6*, 1-9.

Received: April 2, 2012 **Revised: September 13, 2012** **Accepted: October 14, 2012**

Send Orders of Reprints at bspsaif@emirates.net.ae

Current Nanoscience, 2013, *9*, 61-80

Determination of the Single-Phase Forced Convection Heat Transfer Characteristics of TiO_2Nanofluids Flowing in Smooth and Micro-Fin Tubes by Means of CFD and ANN Analyses

N. Kayaci[1], M. Balcilar[2], M. Tabatabaei[1], A. Celen[1], O. Yıldız[3], A.S. Dalkilic*,[1] and S. Wongwises[4]

[1]*Heat and Thermodynamics Division, Department of Mechanical Engineering,Yildiz Technical University (YTU), Yildiz, Besiktas, Istanbul 34349, Turkey;* [2]*Computer Engineering Departmant, Yildiz Technical University (YTU), Davutpasa, Esenler, Istanbul 34220, Turkey;* [3]*Department of Mechanical Engineering, Kocaeli University, Umuttepe Campus, Kocaeli, 41380, Turkey;* [4]*Fluid Mechanics, Thermal Engineering and Multiphase Flow Research Lab. (FUTURE), Department of Mechanical Engineering, Faculty of Engineering, King Mongkut's University of Technology Thonburi (KMUTT), Bangmod, Bangkok 10140, Thailand*

Abstract: A numerical study including a validation process with experimental data was performed on the forced convection flows of nanofluids; the object of study was water containing TiO_2 nanoparticles in smooth and micro-fin tubes at a constant wall temperature. Constant heat flux and temperature-dependent properties were used to determine the hydrodynamics and thermal behaviors of the nanofluid flow;a single-phase numerical model was used to solve two-dimensional equations by means of a CFD program for the water flow, contained in a smooth tube and in various micro-fin tubes having various helix angles (0^o, 18^o). An extensive literature review on the determination of the physical properties (k, μ, ρ, Cp) of nanofluids is given in this paper. Multilayer Perceptron (MLP), one of theartificial neural network (ANN) methods, was used to determine the most agreeable physical propertiesof TiO_2 nanofluids among correlations. The inputs ofthe ANN analyses were the correlations of physical properties, the average temperature and velocity of water in the test tubes, and the nanoparticle concentrations, while the outputs were shear stress, friction factor, heat flux, convective heat transfer coefficient, and pressure drop. After obtaining the best combination of physical properties of TiO_2 nanofluids from the ANN analyses, the numerical model was validated by means of a CFD program,with the experimental smooth tube data as a case study; it was also validatedas a simulation studyfor several micro-fin tubes through a CFD program. This paper shows temperature, pressure, and velocity distributions in the investigated tubes; in addition, average and local experimental, theoretical, and numerical values in the smooth and micro-fin tubes are compared with oneanother in terms of friction factors, shear stresses, convective heat transfer coefficients, and pressure drops, according to various nanoparticle concentrations.

Keywords: Heat transfer coefficient, Pressure drop, ANN, Nanofluid, Single-phase flow, CFD.

1. INTRODUCTION

Thermal conductivity is an important parameter that expresses the heat transfer performance of a heat transfer fluid. Due to their low thermal conductivity, conventional heat transfer fluids (e.g. water, oil, ethylene glycol mixtures) restrict the enhancement of performance and compactness in heat exchangers used in the electronic, automotive, and aerospace industries. One solution for improving the thermal conductivity of a fluid is to suspend small solid particles in the fluid. Since the thermal conductivity of solid metals is higher than that of fluids, the suspended particles are expected to be able to increase thermal conductivity and heat transfer performance. Experimental studies on the thermal conductivity of nanofluids have been performed by many researchers. Slurries are formed by adding metallic, non-metallic and polymeric particles to fluids. Due to the large size of these suspended particles (on the millimeter scale), problems such as abrasion and clogging can occur. For this reason, such large particles cannot offer a workable solution for heat transfer enhancement. Recently, progress in manufacturing technologies has made possible the production of particles on the nanometer scale (i.e., particle diametersranging from 10 to 100 nm). These smaller-sized particles allow uniform and stable suspensions to form; thus, nanofluidsprovide higher heat transfer enhancement than do existing techniques. The first continuous studies on the use of particles of nanometer dimension were conducted by a research group at the Argonne National Laboratory approximately a decade ago. Choi [1] was likely the first researcher who called the fluids with nanometer particles 'nano-fluids'. The term 'nanofluid' thus refers to a two-phase mixture usually composed of a continuous liquid phase and of dispersed nanoparticles in suspension.

Xuan and Li [2] stated that nanofluids are easily fluidized and can almostbe considered a fluid due to their tiny particle size, despite their character as atwo-phase mixture. For this reason, nanofluid flow can be treated as a single-phase flow. Maxwell [3] assumed that the fluid phase and the particles are in thermal equilibrium and move at the same velocity under certain conditions,given the ultra-fine and lowvolume fraction of the solid particles. Advantages of a single-phase flow include its simplicity and its lowerrequired computational time. It should be emphasizedthat physical properties of nanofluids have a strong impact on experimental, numerical, and theoretical solutions. The most well-known nanoparticles are Al_2O_3, CuO, TiO_2, each of which is used, together with the base fluids of water and ethylene glycol, in the experimental work of many researchers. Across the range ofparticle sizes and types of base fluids, the enhancement of thermal conductivity has beenachievedunder all experimental conditions with these nanoparticles.

The following paragraph summarizes some of the recent studies presented by researchers on the flow of nanofluids. The review paper of Daungthongsuk and Wongwises [4] summarized published resultson the forced convective heat transfer of nanofluids inboth experimental and numerical investigation. Daungthongsuk and Wongwises [5] reported that the thermal conductivity of nanofluids increased with increasing nanofluid temperatures and, conversely, that the viscosity of nanofluids decreased with increasing nanofluid temperatures. Duangthongsuk and Wongwises [6] studied the differences between using measured and computed thermophysical

*Address correspondence to this author at the Heat and Thermodynamics Division, Department of Mechanical Engineering, Yildiz Technical University (YTU), Yildiz, Besiktas, Istanbul 34349, Turkey; Tel: +9 0212 3832819; Fax: +9 0212 2616659; E-mail: dalkilic@yildiz.edu.tr

1875-6786/13 $58.00+.00 © 2013 Bentham Science Publishers

properties to describe the heat transfer performance of TiO_2-water nanofluids; they concluded that measuring the thermophysical properties of nanofluids is an important way to address the transport behavior of nanofluids.Duangthongsuk and Wongwises [7] also conducted an experimental study on the heat transfer performance and pressure drop results of TiO_2-water nanofluids under a turbulent flow regimen. Their results indicated that the dispersion of nanoparticles into the base liquid increases the thermal conductivity and viscosity of the nanofluids, and that this augmentation increases with increasing particle concentrations. Daungthongsuk and Wongwises [8] further reported their study on the forced convective heat transfer and flow characteristics of a nanofluid consisting of water and 0.2vol.%TiO_2 nanoparticles. According to their results, the heat transfer coefficient of the nanofluid increases with an increase in the mass flow rate of the hot water and nanofluid; increases with a decrease in the nanofluid temperature; and does not significantly respond to the temperature of the heating fluid. Duangthongsuk and Wongwises [9] also studied the role of thermophysical properties models in the prediction of convective heat transfer coefficientsin low concentration nanofluids. They reported that precise values for thermal and physical properties such as specific heat, viscosity, and thermal conductivity are required in order to study the heat transfer behavior of the nanofluids. Daungthongsuk *et al*. [10] presented an experimental study on the heat transfer and pressure drop characteristics of Al_2O_3-water nanofluids flowing through a microchannel heat sink (MCHS). The study investigated the effects of the Reynolds number and of particle concentrations on the heat transfer and flow behavior of the nanofluids. Results indicatedan increase in the heat transfer performance of MCHS both with an increase in the Reynolds number and with an increase in particle concentration. Suriyawong and Wongwises [11] studied the nucleate pool-boiling heat transfer of TiO_2-water nanofluids experimentally. Nanofluids with varying concentrations of 0.00005, 0.0001, 0.0005, 0.005, and 0.01vol.% were employed in their study. The experiments explored the effects of nanofluid concentrations and of the heating and roughnessof the surface material on the nucleate pool-boiling characteristics and on the heat transfer coefficient under ambient pressure. In the case ofaheated copper surface tested at a concentration of 0.0001vol.%, results showed a higher nucleate pool-boiling heat transfer coefficient than was obtained with the base fluid. Trisaksri and Wongwises [12] investigated the nucleate pool-boiling heat transfer of a refrigerant-basednanofluid at different nanoparticle concentrations and pressures. TiO_2 nanoparticles were mixed with the refrigerant HCFC 141b at 0.01, 0.03 and 0.05vol.%, and pool-boiling experiments on nanofluids were compared tofindings on the base refrigerant. Results indicated that the nucleate pool-boiling heat transfer deteriorated with increasing particle concentrations, especially at high heat fluxes.

This paragraph summarizes some of the recent studies presented on the CFD analyses of in-tube flows. Dalkilic *et al*. [13-14] presented theoretical flow models for homogeneous and separated flows applied to in-tube condensation to predict the pressure drop characteristics of R134a. Numerical analyses were performed by means of a CFD program to determine average and local homogeneous wall shear stresses and friction factors [15]. Refrigerant-side total pressure drops, frictional pressure drops, friction factors, and wall shear stresses were determined within a ±30% error band. Demir *et al*. [16] numerically investigated laminar and turbulent forced convection flows of a nanofluid consisting of water and Al_2O_3 particles in a horizontal smooth tube with constant wall temperature. Their CFD15 results demonstrated a heat transfer enhancement due to the presence of the nanoparticles in the fluid. Demir *et al*. [17] studied numerically the single-phase forced convection heat transfer characteristics of TiO_2 nanofluids in a double-tube counter-flow heat exchanger. In their paper, they used Palm *et al*.'s [18] correlations to determine the thermophysical properties of the nanofluids. Their CFD [15] results indicateda heat transfer enhancement due to the presence of the nanoparticles in the fluid,agreeing with the results of the experimental study used in the validation process for the numerical model. Agra *et al*. [19] investigated the heat transfer and pressure drop characteristics of smooth, corrugated, and helically finned tubes by using Fluent CFD software [15] and Gambit software [15] to plot and mesh models of the test tubes. The problem under investigation was a two-dimensional (axisymmetric), steady forced turbulent convection flow of water flowing inside straight and enhanced circular tubes. Their paper compared numerical results with experimental data and with the Blasius equation. It was seen that the Fluent CFD [15] program predicted the experimental data more accurately than did the Blasius equation.

The following paragraph summarizes some of the recent studies presented on the artificial intelligence analyses of in-tube flows. Balcilar *et al*. [20] used computational numerical methods such as artificial neural networks (ANNs) to determine the compatibility of the most suitable coefficients of the correlations with the majority of experimental data; Balcilar *et al*. [21] and Bolat *et al*. [22] studied heat transfer characteristics in their analyses by means of ANNs. The inputs of the ANNs are the measured values of test sections such as mass flux, heat flux, temperature differences between the tube wall and the saturation temperature, and average vapor quality, while the outputs are the experimental condensation heat transfer coefficient and the pressure drop measured in the analysis. Balcilar *et al*. [23-24] investigated the nucleate pool-boiling heat transfer characteristics of TiO_2 nanofluids to determine the effects of the important parameterson the heat transfer coefficient, and also to formreliable empirical correlations based on the neural network analysis. Balcilar *et al*. [25] predicted the condensation and evaporation pressure drops of R32, R125, R410A, R134a, R22, R502, R507a, R32/R134a (25/75 by wt%), R407C, and R12, flowing inside various horizontal smooth and micro-fin tubes, by means of the numerical techniques of ANNs and of non-linear least squares (NLS). Total pressure drops within in-tube condensation and in-tube evaporation tests were modeled using the ANN method of multi-layer perceptron (MLP) with a 12-40-1 architecture. In light of cross-validation tests of 1485 evaporation and condensation data points,the average error rate of this method was 7.085%.

For some time now, many studies have concentrated on proposing a model to predict the heat transfer enhancement of nanofluids. It should be noted, however, that there has not yet been a paper on the investigation of the proper physical properties of nanofluids by ANN analyses. In the remainder of this paper, the most agreeable physical properties (k, μ, ρ, c_p) of nanofluids will be analyzed through experimental data, making use ofnearly all correlations in the current literature. To this end, two ANN models with different input values were developed using experimental results to determine the most suitable physical properties among these correlations. Smooth and micro-fin tubes were drawn in SOLIDWORKS [26] software and then imported into ANSYS Fluent [27] software for CFD analysis. Prior to thesimulation of the micro-fin tubes in the CFD program, the smooth-tube model was validated using the agreeable physical properties obtained from ANN analyses and experimental data from the forced convection of TiO_2nanofluids, which were calculated and measured for heat transfer coefficients and pressure drops. Temperature distributions, pressure and velocity of the inner surface and of the fluids at the inlet and outlet sections of the tube, friction factors, wall shear stresses, pumping powers and particle concentrations, local heat transfer coefficients, and pressure drops along the tubes were also obtained from the numerical study for smooth and micro-fin tubes. Last of all,this paper demonstrates a heat transfer enhancement and an increase in pressure drop and pumping power due to the presence of the nanofluids and the micro-fin tubes.

2. SAMPLE PREPARATION

In the present study, nanofluids provided by a commercial source (DEGUSSA, VP Disp. W740x) were used as working fluid. The fluid mixture was composed of TiO_2 nanoparticles with an average diameter of 21 nm dispersed in water. The original particle concentration was 40 wt.%. In order to produce other required particle volume fractions, dilution with water and stirring action were employed. An ultrasonic vibrator was used to sonicate the solution continuously for about 2 h in order to break down the agglomeration of the nanoparticles. The desired volume concentrations used in this study were 0.2%, 0.6%, and 1.0%, with pH values of 7.5, 7.1, and 7.0, respectively. From these pH values it can be seen that the solution chemistry of nanofluids is nearly neutral. A transmission electron microscope (TEM) was used to approximate the size of the primary nanoparticles. As Fig. (**1**) shows, it is clear that the primary size of the nanoparticles was approximately spherical, with an average diameter of around 21 nm.

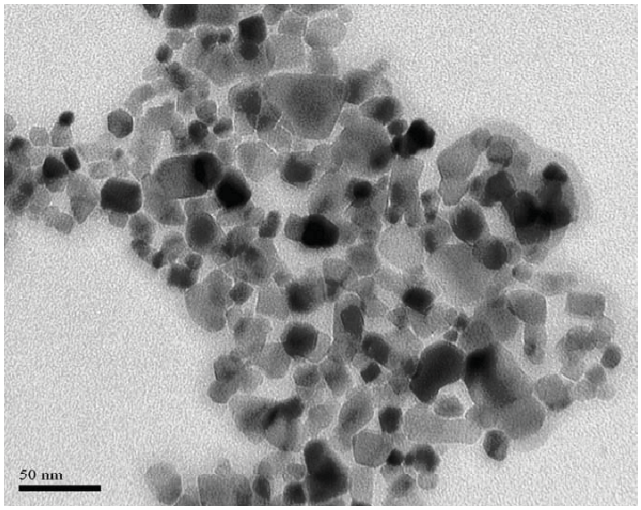

Fig. (1). TEM image of dispersed TiO_2 nanoparticles in water [From Duangthongsuk and Wongwises [6], with permission from Elsevier].

3. EXPERIMENTAL APPARATUS

The experimental system used in the present study is shown schematically in Fig. (**2a**). It consisted mainly of a test section, two receiver tanks, a magnetic gear pump, a hot water pump, a cooler tank, a hot water tank, and a collection tank. The test section was a 1.5 m long counter-flow horizontal double-tube heat exchanger with nanofluid flowing inside the tube and hot water flowing in the annular. The inner tube was made from smooth copper tubing with a 9.53 mm outer diameter and a 0.7 mm thickness, while the outer tube was made from PVC tubing and has a 33.9 mm outer diameter and a 3 mm thickness. The test section was thermally isolated from its upstream and downstream sections by plastic tubes in order to reduce the heat loss along the axial direction. The differential pressure transmitter and the T-type thermocouple were mounted at both ends of the test section to measure the nanofluid's pressure drop and bulk temperature,respectively. Thermocouples were mounted in sets of three, equally spaced around the tube circumference, at different longitudinal positions along the surface of the inner tube wall. The inlet and exit temperatures of the hot water were measured using T-type thermocouples inserted directly into the flow. The 60 L receiver tanks,made of stainless steel, stored the nanofluid and hot water leaving the test section. The cooler tank had a 4.2 kW cooling capacity, and a thermostat was used to keep the nanofluid temperature constant. As with the cooler tank, a 3 kW electric heater with a thermostat was installed to keep the temperature of the hot water constant. The nanofluid flow rate was controlled by adjusting the rotation speed of the magnetic gear pump. The hot water flow rate was measured by a rotameter, while the nanofluid flow rate wascalculated from the exact time required for the entire mass of nanofluid to be discharged. For each pump speed, five measurements were taken. Averagesare given for all data in the present study.

A portable programmable calibrator was used to calibrate all T-type thermocouples, with a maximum precision of 0.1 °C. The nanofluid mass flow rates were determined by electronic balance, with an uncertainty of ±0.0006 kg. Maximum uncertainty of the nanofluid mass flow rate was evaluated at 2.2%; this was taken into account in calculating the uncertainty of the Nusselt number.

The uncertainty of the hot water mass flow rate was evaluated $\pm$7% (full scale). As noted above, the uncertainty of the measured Nusselt number can readily be seen to depend on measurements of temperature, nanofluid flow rate, and hot water flow rate. The uncertainty of the measured Nusselt number was evaluated using the root mean sum square method, and was found to be 5%.

During the test run, wall temperatures of the test section, mass flow rates of the hot water and nanofluid, and the inlet and exit temperatures of the hot water and nanofluid were measured.

A view of the geometrical parameters of the micro-fin tubes is given in Fig. (**2b**). The dimensional parameters of the investigated tubes are given in Table **4**.

4. DATA REDUCTION

4.1. Thermal and Physical Properties of Nanofluids

The determination of nanofluid properties is known to be a widespread pursuit in current research. Some correlations have been developed toward this end by Williams *et al*. [28]. The measurement of physical properties has been undertaken by several researchers within the literature,including Rea *et al*. [29] and Duangthongsuk and Wongwises [7].

Tables **1**, **2**, and **3** provide a summary of the current literature on almost all empiricalcorrelations for nanofluid dynamic viscosity [30-53], thermal conductivity [3, 18, 54-68], and specific heat capacity at constant pressure [3, 54, 69-70], respectively.

It should be noted that the density of the nanofluid was calculated from Pak and Cho's [48] correlation, as follows:

$$\rho_{nf} = \rho_s.\phi + (1-\phi).\rho_w \tag{1}$$

4.2. Governing Dimensionless Numbers, Heat Flux, the Heat Transfer Coefficient, and the Nusselt Number

As test fluid flows through ducts, the heat transfer surface surrounds and guides the stream, and the convection process is said to be internal. The velocity distribution in a duct has two distinct regions in laminar flow: first, the entrance region, where the walls are lined by successive boundary layers, and second, farther downstream, the fully developed region, where longitudinal velocity is independent of position along the duct. It is assumed that duct geometry does not change with longitudinal position. The flow through a straight duct ceases to be laminar when the Reynolds number (Re) exceeds approximately 2300, and the turbulent flow becomes fully developed hydrodynamically and thermally after a relatively short entrance distance [71].

The Reynolds number (Re) and the Prandtl number are used in theoretical analysis [18]; the particle volume fraction (φ) and the ratios k_p/k_{bf} and Cp_p/Cp_{bf} are used to characterize the problem, and can be calculated as follows:

$$\mathrm{Re} = \frac{2Q}{\pi d\nu} \tag{2}$$

$$\mathrm{Pr} = \frac{C_p\mu}{k} \tag{3}$$

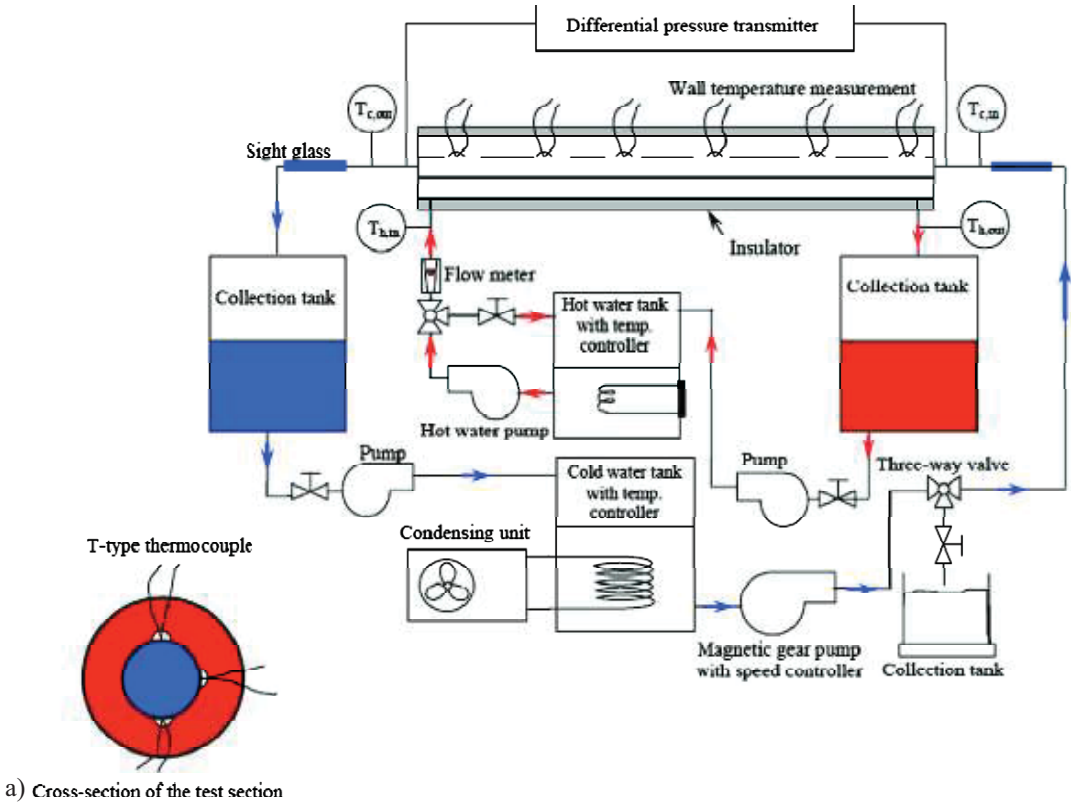

Fig. (2). Schematic diagram of the experimental apparatus (**a**) [From Duangthongsuk and Wongwises [6], with permission from Elsevier] and view of geometrical parameters of micro-fin tubes (**b**).

In the fully developed region, the friction factor is defined as in the laminar flow:

$$f = \frac{64}{\mathrm{Re}} \tag{4}$$

Petukhov [72] discovered a formula for the friction factor in turbulent flow, as follows:

$$f = (0.970 \ln \mathrm{Re} - 1.64)^{-2} \tag{5}$$

By using the Darcy friction factor, wall shear stress can be calculated as below:

$$\tau = \frac{f \rho V_{avg}^2}{8} \tag{6}$$

Table 1. Some Dynamic Viscosity Correlations of Nanofluids in Literature

Researcher	Correlation
(1) Einstein [30]	$\mu_{eff} = (1 + 2.5\varphi)\mu_f$
(2) Brinkman [31]	$\mu_{eff} = \mu_{bf}(1 - \varphi)^{2.5}$
(3) Batchelor [32]	$\mu_{eff} = (1 + \eta\varphi + k_H\varphi^2)\mu_f = (1 + 2.5\varphi + 6.2\varphi^2)\mu_f$
(4) Graham [33]	$\mu_{eff} = (1 + 2.5\varphi)\mu_f + \left[\frac{4.5}{(h/r_p)(2+h/r_p)(1+h/r_p)^2}\right]\mu_f$
(5) Kitano *et al*. [34]	$\mu_{eff} = \mu_{bf}\left[1-(\varphi-\varphi_m)\right]^{-2}$
(6) Bicerano *et al*. [35]	$\mu_{nf} = \mu_{bf}\left[1+\eta\phi+k_H\phi^2)\right]$
(7) Wang *et al*. [36]	$\mu_{nf} = \mu_{bf}\left[1+7,3\phi+123\phi^2\right]$
(8) Tseng and Chen [37]	$\mu_{nf} = \mu_{bf}\,0,4513e^{0,6965\phi}$
(9) Chen *et al*. [38]	$\mu_{nf} = \mu_{bf}\left[1+10,6\phi+(10,6\phi)^2\right]$
(10)-(11) Nguyen *et al*. [39]	$\mu_{nf} = \mu_{bf}\,0,904e^{0,1482\phi}$ $\mu_{nf} = \mu_{bf}(1 + 0,025\phi + 0,015\phi^2)$
(12) Khanafer and Vafai [40]	$\mu_{nf} = \mu_{bf}(1,0538 + 0,1448\phi - 3,363x10^{-3}T - 0,0147\phi + 6,735x10^{-5}T^2 - 1,337\frac{\phi}{T})$
(13) Duanghongsuk and Wongwises [5]	$\mu_{nf} = \mu_{bf}(1,013 + 0,092\phi + 0,015\phi^2)$
(14) Vand [41]	$\mu_{nf}=\mu_{bf}e^{2.5\phi+2.7\phi^2/(1-0.609\phi)}$
(15) Mooney [42]	$\mu_{nf} = \mu_{bf}e^{(\frac{2.5*\phi_m*\phi}{1-\phi})}$
(16)-(17) Krieger [43-44]	$\mu_{nf} = \mu_{bf}(\frac{\phi_m}{1-\phi})^a$ $\mu_{nf} = \mu_{bf}(\frac{\phi_m}{1-\phi})^{1.82}$
(18) Frankel and Acrivos [45]	$\mu_{nf} = \mu_{bf}1.125(\frac{\phi}{\phi_m})^{1/3}/(1-(\frac{\phi}{\phi_m})^{1/3})$
(19) Miler *et al*. [46]	$\mu_{nf} = \mu_{bf}(537.42\phi - 0.188)$
(20) Chow [47]	$\mu_{nf} = \mu_{bf} * (e^{\frac{2.5*\phi}{1-\phi}}) + (A*\phi^2)/(1 - A*\phi^2*\phi_m)$
(21) Pak and Cho [48]	$\mu_{nf} = \mu_{bf}(108.2\phi^2 + 5.45\phi + 1)$

(Table 1) Contd….

Researcher	Correlation
(22) Liu [49]	$\mu_{nf} = \mu_{bf}((\frac{1-\phi}{\phi_m})^2 + (\frac{k_1 - 2}{\phi_m})\phi + (\frac{k_2 - 6}{\phi_m^2})\phi^2)$
(23)-(24) Wang *et al*. [50]	$\mu_{nf} = \mu_{bf}(123\phi^2 + 7.3\phi + 1)$ $\mu_{nf} = \mu_{bf}(306\phi^2 - 0.19\phi + 1)$
(25) Davalos *et al*. [51]	$\mu_{nf} = \mu_{bf}(6.17\phi^2 + 2.5\phi + 1)$
(26)-(27) Putra *et al*. [52]	$\mu_{nf} = 2.9x10^{-7}xT^2 - 2x10^{-4}xT + 3.4x10^{-2}$ for %1 $\mu_{nf} = 3.4x10^{-7}xT^2 - 2.3x10^{-4}xT + 3.9x10^{-2}$ for %4
(28) Tang *et al*. [53]	$\mu_{nf} = 2.761x10^{-6}xe^{1713/T}$

Table 2. Some Thermal Conductivity Correlations of Nanofluids in Literature

Researcher	Correlation
(1) Maxwell [3]	$k_{nf}=k_f * \frac{k_p+2k_f+2\phi(k_p-k_f)}{k_p+2k_f-\phi(k_p-k_f)}$
(2) Hamilton and Crosser [54]	$k_{nf}=k_f * \frac{k_p+(n-1)k_f-(n-1)\phi(k_f-k_p)}{k_p+(n-1)k_f+\phi(k_f-k_p)}, n=\frac{3}{\Psi}, \Psi=\frac{\phi\rho_f}{\rho_p+\phi\rho_f-\phi\rho_p}$
(3) Hui *et al*. [55]	$k_{nf}=\frac{1}{4}[(3\phi-1)k_p+(2-3\phi)k_f]+\frac{k_p}{4}\sqrt{\Delta},$ $\Delta=(3\phi-1)^2(\frac{k_p}{k_f})^2+(2-3\phi)^2+2(2+9\phi-9\phi^2)(\frac{k_p}{k_f})$
(4) Xuan and Li [56]	$k_{nf}=k_f \frac{k_p+2k_f-2\phi(k_f-k_p)}{k_p+2k_f+\phi(k_f-k_p)}$
(5) Yu and Choi [57]	$k_{nf}=k_f * \frac{k_{pe}+2k_f+2\phi(k_{pe}-k_f)(1+\beta)^3}{k_{pe}+2k_f-\phi(k_p-k_f)(1+\beta)^3}$, $\beta=\frac{h}{r}$, h<10nm,β=0.1
(6) Godson *et al*. [58]	$k_{nf} = 0.9692\phi + 0.9508$
(7) Prasher *et al*. [59]	$k_{nf}=k_f \frac{1+A\phi\ Re^m\ Pr^{0,333}*(1+2\alpha)+2\phi(1-\alpha)}{(1+2\alpha)-\phi(1-\alpha)}$, $\alpha=\frac{2R_bk_f}{d_p}$, A=40000 ,m=2.5 , $R_b=0.77.10^{-8}$
(8) Koo and Kleinstreuer [60]	$k_{nf}=k_{MG}+5\times10^4\ \beta\phi\rho_p\ C_p\sqrt{\frac{K_B\ T}{\rho_p D}}\ f(T,\phi)$, $k_{MG}=k_f\left(1+\frac{3\phi\left(\frac{k_p}{k_f}-1\right)}{\left(\frac{k_p}{k_f}+2\right)-\phi\left(\frac{k_p}{k_f}-1\right)}\right)$ $f(T,\phi)=(-6.04\phi+0.4705).T+(1722.3\phi-134.63), \beta=0.0137(100\phi)^{-0.8229} \rightarrow \phi\le 1\%$
(9)-(10) Li and Peterson [61]	$k_{nf}=k_f+k_f(0.764\phi-0.0187\ (T-273.15)-0.462)$ For Al_2O_3 $k_{nf}=k_f+k_f(3.761\phi+0.0179\ (T-273.15)-0.307)$ For CuO
(11)-(12) Palm [18]	Al_2O_3 $\left(\begin{array}{l} k_{nf}=0.003352T-0.3708 \text{ For } \phi=\%1 \\ k_{nf}=0.004961T-0.8078 \text{ For } \phi=\%4 \end{array}\right)$
(13)-(14) Maiga *et al*. [62]	$k_{nf}=k_f(4.97\phi^2+2.72\phi+1)$ For Al_2O_3 $k_{nf}=k_f(28.905\phi^2+2.827\phi+1)$ For CuO

(Table 2) Contd….

Researcher	Correlation
(15) Bhattacharya *et al*. [63]	$k_{nf}=k_p\phi+(1-\phi)k_f$
(16) Buongiorno [64]	$k_{nf}=k_f\ (1+7.47\phi)$
(17) Kim *et al*. [65]	$k_{nf}=0.65+4{,}864\times10^{-7}T^3$
(18) Timofeeva *et al*. [66]	$k_{nf}=k_f(1+3\phi)$
(19) Chon *et al*. [67]	$k_{nf}=k_f\ .(1+64.7\phi^{0.746}\ (d_f/d_p\ )^{0.369}(k_p/k_f)^{0.747}Re^{1.2321}\ Pr^{0.9955})$ $Pr=\frac{\mu}{\rho_{BF}\alpha},Re=\frac{\rho_{BF}Vd_p}{\mu}=\frac{\rho_{BF}K_BT}{3\pi\mu^2L_{BF}},\mu=2.414\times10^{-5}\times10^{(\frac{247}{T-140})}$
(20) Murshed *et al*. [68]	$k_{nf}=\frac{k_f(1+0.27\phi^{4/3}\ (\frac{k_p}{k_f}-1)(1+\frac{0.52\phi}{1-\phi^{1/3}}\ (\frac{k_p}{k_f}-1)}{1+\phi^{4/3}\ (\frac{k_p}{k_f}-1)(\frac{0.52}{1-\phi^{1/3}}+0.27\phi^{1/3}+0.27)}$

Table 3. Some Specific Heat Capacity Correlations of Nanofluids in Literature

Researcher	Correlation
(1) Maxwell [3]	$Cp_{nf}=(1-\varphi)Cp_{nf}(1+2.5\varphi_p)\mu_f$
(2) Hamilton and Crosser [54]	$Cp_{nf}=\frac{\phi.\rho_s.Cp_s+(1-\phi).\rho_w.Cp_w}{\rho_{nf}}$
(3) Yang *et al*. [69]	$\frac{Cp_{eff}}{Cp_f}=(1-\phi)+\phi\frac{Cp_n}{Cp_f}$
(4) Yu *et al*. [70]	$Cp_{nf}=\frac{\varphi(p_s)Cp_s+(1-\varphi).(\rho.c_p)}{\varphi\rho_p+(1-\varphi).\rho_{bf}}$

Because of viscous effects, pressure loss occurs, and is expressed for all types of fullydeveloped internal flows as follows:

$$\Delta P_L=f\frac{L}{D}\frac{\rho V_{avg}^2}{2} \quad (7)$$

When a pressure drop occurs, the pumping power required to overcome flow resistance can be determined as follows:

$$W_P=\dot{Q}.\Delta P \quad (8)$$

Heat flux in the test section is determined as follows:

$$q"=\frac{m_wC_{p,w}(T_i-T_o)}{\pi dL} \quad (9)$$

The heat transfer coefficient of the base fluid and the nanofluid can be calculated as follows:

$$h=\frac{q"}{(T_w-T_{f,m})} \quad (10)$$

The Nusselt numberfor the base fluid and the nanofluid can be calculated as follows:

$$Nu=\frac{hd}{k} \quad (11)$$

4.3. Numerical method - CFD Approach

The ANSYS Fluent program [15] is commonly used software in CFD analysis, and a detailed description of its mathematical models can be found in the Fluent User's Guide. The program uses a technique based on control volume theory to convert governing equations into algebraic equations so that they can be solved numerically, providing a significant research solution [27]. The control volume technique works by integrating the governing equations for each control volume, and then by discretizing the equations that conserve each quantity based on the control volume.

Classic single-phase conservation equations found a solution in the control volume approach, since governing equations could be given numerical solutions after being converted into a set of algebraic equations. This addressed some of the entailments of governing equations, including convection terms, diffusion terms, and other quantities, which were not properly addressed in a second-order upwind scheme. All scalar values and velocity components are calculated at the center of control volume interfaces, where grid

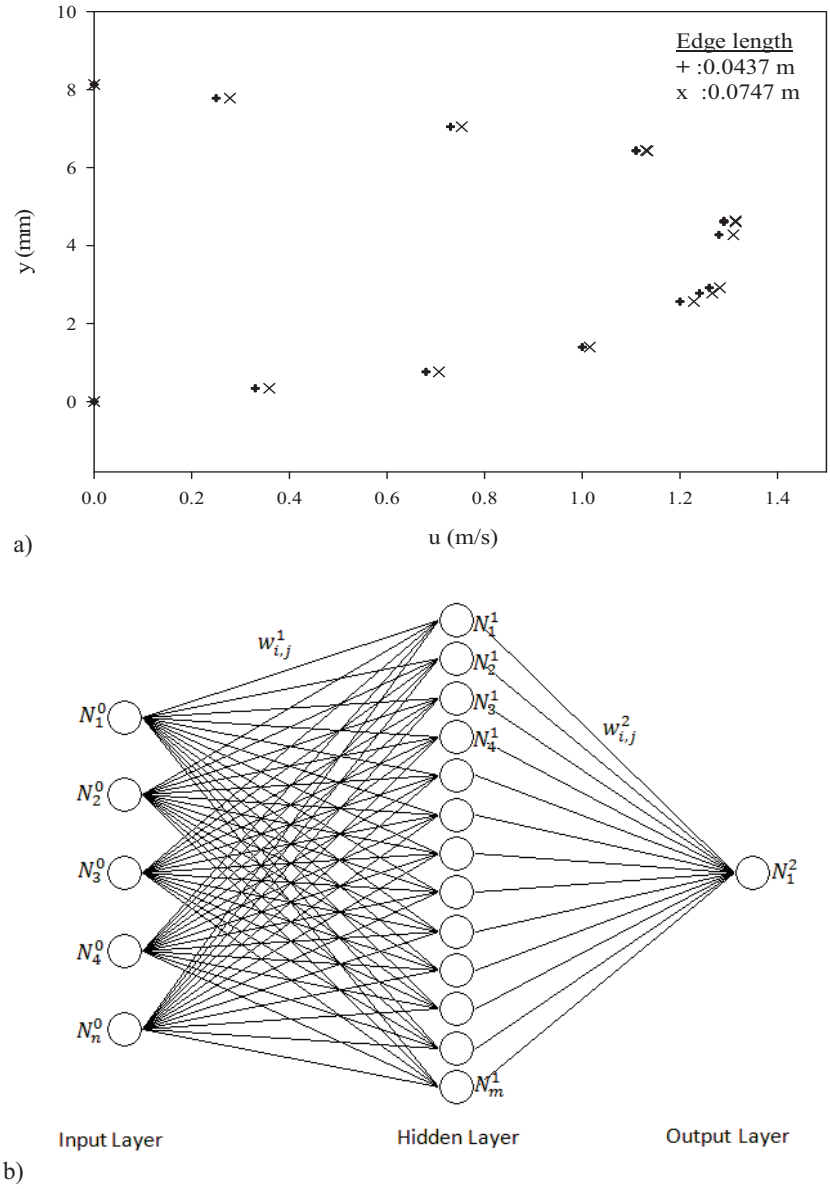

Fig. (3). Achieving the grid independency for velocity profiles at Re=8895.2 (**a**) and schematic representation of MLP (**b**) for the numerical part of the study.

schemes are used extensively. The Semi-Implicit Method for Pressure Linked Equations (SIMPLE) was used to pair pressure and velocity. A point-implicit (Gauss-Seidel) linear equation solver, in conjunction with an algebraic multigrid method, was employed in the Fluent CFD program [15] to solve the linear systems resulting from discretization schemes. k-ε turbulence models were chosen in the viscous model. Residuals were thoroughly monitored during the iterative process, and all solutions were considered to have converged when the residuals for each governing equation fell below 10^{-6}. Boundary conditions were defined for the velocity inlet at the pipe inlet and for the pressure outlet at the pipe exit; turbulence intensity and hydraulic diameter were defined for the turbulence parameters. Constant heat flux was applied to the pipe surface. To show grid-independent solutions, two different edge lengths were used in the tetrahedrons grid type for Re=8895.2. Fig. (**3a**) shows the velocity profile distributions of the two, which are nearly identical.

4.4. Numerical Method- ANN Approach

An artificial neural network (ANN) is an information-processing system that has certain performance characteristics in common with biological neural networks. Artificial neural networks have been developed as generalizations of mathematical models of human cognition or neural biology, based on the assumptions as follows [73].

- Information processing occurs at many simple elements called neurons
- Signals are passed between neurons over connection links
- Each connection link has an associated weight, which, in a typical neural net, multiplies the signal transmitted
- Each neuron applies an activation function (usually non-linear) to its net input (sum of weighted input signals) to determine its output signal.

The ANN is the most widely used model, and is able to find linear and non-linear relationships between input and output patterns. To find a relationship between input and output sets, well-known training sets are first used to generalize concerning a relationship. Once a generalization is made, the ANN tries to predict the outputs of a new test set. The performance metrics of the ANN are measured by the quality of its test set predictions. There are many types of ANN in function approximation literature, including the Multi-Layer Perceptron (MLP), the Radial Basis Functions Networks (RBFN), the Generalized Regression Neural Network (GRNN), and the decision-making system based on human 'fuzzy logic', the ANN Artificial Neural Fuzzy Inference System (ANFIS).

4.4.1. Multi-layer Perceptron

A multilayer perceptron (MLP) is a feedforward artificial neural network model that maps sets of input data onto a set of appropriate output. An MLP consists of multiple layers of nodes in a directed graph, with each layer fully connected to the next one. Except for the input nodes, each node is a with a nonlinear activation function. MLP utilizes a supervised learning technique called back propagation for training the network [74-75].

The MLP consists of three different layers, the input layer, the hidden layer, and the output layer. The input layer's neuron number and the output layer's neuron number are equal to the dimensions of the input variables and output variables, respectively. The number of the hidden layer and the number of any hidden layer's neuron may be manipulated at will; if the number of the hidden layer and any hidden layer's neuron increases, then the non-linear feature of the model will increase as well. A schematic representation of the MLP model is shown in Fig. (**3b**).

Let Nbe the number of input parameters used for the estimation of displacement, and M the neuron number in the hidden layer;let the inputs of the MLP (0^{th} layer outputs) be shown as $\left\{N_1^0, N_2^0, ...N_n^0\right\}$, the output values of the hidden layer (1^{st} layer outputs) as $\left\{N_1^1, N_2^1, ...N_m^1\right\}$, the output values of the output layer (2^{nd} layer outputs, predicted value) as N_1^2, the connection weight of the i^{th} neuron of the input layer to the j^{th} neuron of the hidden layer as $w_{i,j}^1$, the j^{th} neuron of the l^{st} layer's bias value as b_j^l, andthe l^{st} layer's transfer function as f_l ;the j^{th} neuron of the l^{st} layer's output is then calculated as in Eq. (12):

$$N_j^l = f_l\left(b_j^l + \sum_i N_i^{l-1}.w_{i,j}^l\right) \tag{12}$$

In the literature, there are many different kinds of transfer functions,including purelin, tansig, logsig, and so on. If the training output set is shown by D, then the error function of the prediction is calculated as in Eq. (13):

$$J = \frac{1}{2}\sum\left(N^{out} - D\right)^2 \tag{13}$$

The optimization method appliedin Eq. (12) in order to find the w and b values, and to yield a minimum value of J, is called the MLP learning algorithm. The mean of training calculates optimal w and b values by way of the training set. The Gradient Descent, Gradient Descent with Momentum, Conjugate Gradient, Quasi-Newton, and Levenberg-Marquardt methods are well-known learning algorithmswithin the literature.

4.4.2. Validation and Performance Metrics

Validation is a supervised learning method using data points obtained from experiments, and must be performed in order to gauge the success of learning algorithms. The most well-known validation methods are the hold-out, the k-fold cross, and the leave-one-out cross-validation methods.

In the k-fold cross-validation method, n number data obtained from experimentationare divided randomly into k number sets,each data cluster having equal elements and each being numbered from 1 to k.

$$\upsilon_i \in \{1,2,..k\} \qquad i=1..n \tag{14}$$

Data whose υ_i values are equal to 1 are first placed in the test set, while data whose υ_i values are different from 1 are placed in the training set. The suggested method is then to train using the training set and to examine using the test set. The researcher's next step is to send data with a υ_i value of 2 to the test set and data with υ_i values different from 2 to the training set. The method is repeated once again with a new training set and a new testing set, and the process continues until all folds are tested [76].

To determine the most appropriate inputs for this process, the mean squared error (MSE) and the coefficient of correlation determination (R) metrics are used as performance criteria for the validation sets. If n is the number of experimental data, y is the value of the experiment, and $\hat{y}$ is the prediction of the MLP, then the formulations of MSE and R are shown in Eq. (15) and Eq. (16), respectively.

$$mse = \frac{1}{n}\sum_{i=1}^{n}\left(y_i - \hat{y}_i\right)^2 \tag{15}$$

$$R = \frac{n.\sum(y.\hat{y}) - \sum(\hat{y}).\sum(y)}{\sqrt{\left(n.\sum y^2 - \left(\sum y\right)^2\right).\left(n.\sum \hat{y}^2 - \left(\sum \hat{y}\right)^2\right)}} \tag{16}$$

4.4.3. Application of Multi-Layer Perceptron

To simulate the behavior of liquids flowing inside a pipe, CFD software processes 7 different inputs: the physical properties of nanofluids (k,μ,C_p,ρ),volume fraction, and the average temperature and velocity of the water. This simulation produces the outputs $h,\tau,\Delta P$, and Q. These outputs are maximally compatible with the experimental data, defined in the literature in terms of 20 different thermal conductivity correlations, 28 different dynamic viscosity correlations, and 4 different specific correlations of heat at constant pressure. To determine which combination of these correlations should be used, all of the possibilities can be tested individually. So many options can so prolong the simulation process as to make it infeasible; if the MLP model can simulate CFD software, however, finding relationships between the inputs and outputs of the CFD software within acceptable limits, the MLP model can be used instead of CFD software to determine the best input combination.

Because the CFD software requires 7 inputs and produces 4 outputs, the MLP requires 7 input neurons and 4 output neurons. In practice, the selected architecture of MLP has only 1 hidden layer with 5 neurons, as shown in Fig. (**3b**).; the MLP also has an available 7-5-4 architecture. The back-propogation model can be used, along with the Levenberg-Marquardt methods,as a learning algorithm. The transfer functions of the hidden layer (1st layer) and the output layer (2nd layer) are tansig and purelin, respectively, shown in Eq. (17):

$$f(x) = \frac{2}{1+e^{-2x}} - 1 \qquad f(x) = x \tag{17}$$

The validation process was performed by the 2-fold cross-validation method, using data groups according to test results and R criteria.

5. RESULTS AND DISCUSSION

The commercial software package ANSYS Fluent [27] was employed in the numerical study. Investigated tubes were plotted in the SolidWorks program [26], and were imported to ANSYS Geometry as shown in Fig. (**4a**) and Fig. (**4b**). After the investigated tubes were imported to ANSYS Geometry, they were forwarded for meshing in the ANSYS Meshing program. The mesh influences the accuracy, convergence, and speed of the solution. Furthermore, the time required to create a mesh model often represents a significant portion of the time required to acquire results from the solutions; this means that the better and more automated the meshing tools, the better the solution. The mesh performed for the investigated tubes is shown in Fig. (**4c**) and Fig. (**4d**).

Two different ANN models were developed to determine the best combination of physical properties for the TiO_2 nanofluid. The inputs of the ANN model 1 analyses were the correlations of physical properties, the average temperature and velocity of water in the test tube, and the nanoparticle concentration, while the outputs of the analyses were shear stress, friction factor, heat flux, convective heat transfer coefficient, and pressure drop. The inputs of the ANN model 2 analyses were the correlations of physical properties and the inlet and outlet temperature and velocity of the water in the test tube, while the outputs were the convective heat transfer coefficient and the pressure drop. The success of the ANN models are represented in Table **5**. The changes inthe numerical and experimental results ofthe ANN models are shown in Figs. (**5a** and **5b**) and (Figs. **6a** and **6b**). All results seemed to be successful within the ±5% deviation band. The most substantiated correlations were obtained from the ANN 1 model for the physical properties (k, μ, Cp) of nanofluids. They are given below:

$$k_{nf}=k_p\phi+(1-\phi)k_f \quad (18)$$

$$\mu_{nf}=\mu_{bf}(306\phi^2-0.19\phi+1) \quad (19)$$

$$Cp_{nf}=(1-\phi)Cp_{nf}(1+2.5\phi_p)\mu_f \quad (20)$$

These equations were obtained from ANN results; Eq. (18) is the thermal conductivity correlation of Bhattacharya *et al*. [63], numbered 15 in Table **2**; Eq. (19) is the viscosity correlation of Wang *et al*. [50], numbered 24 in Table **1**; and Eq. (20) is the heat capacity correlation of Maxwell [3], numbered 1 in Table **3**.

The validation process for numerical models is performed by means of the experimental data [6], as shown in Fig. (**7**) regarding heat transfer characteristics. Fig. (**7**) clearly demonstrates that the numerical model of ANSYS Fluent [27] is in substantialagreement with experimental values [6] in the calculation of the heat transfer coefficient (within a ±25% range) and of the pressure drop (within a ±10% range) for the in-tube single-phase flow of pure water and nanofluid with TiO_2 volume concentrations of 0.2, 0.6, and 1%. Table **6** further shows error rates of less than 1.56% and 2.02% between experimental and numerical temperatures at the outlet section and at the surface, respectively. It should be noted that experimental and numerical studies are conducted for Re numbers between 4516 and 15681 and for surface heat fluxes between 7233 and 13340 W m^{-2}.

The velocity of the fluid in contact with the pipe wall is essentially zero, and it increases with increasing distance from the wall. The velocity profile depends upon the surface condition of the pipe wall;a smoother wall results in a more uniform velocity profile than does a rough pipe wall. The pressure of the fluid in contact with the pipe wall is likewise small, and likewise increases with increasing distance from the wall. The pressure of the fluid has its maximum value at the entrance of pipe and decreases with increasing distance from the entrance. The temperature of the fluid has its maximum value on the wall, since a constant heat flux is applied to the pipe surface. The temperature of the fluid has its minimum value at the entrance of pipe and increases with increasing distance fromthe entrance, due to the constant heat flux. The ANSYS Fluent CFD [27] program was used in numerical analyses to develop velocity, pressure, and temperature profiles at various locations, and was applied to φ=1% to the smooth tube (Fig. **8**), to the micro-fin tube with a helix angle of 0º (Fig. **9**), and to the micro-fin tube with a helix angle of 18º (Fig. **10**).

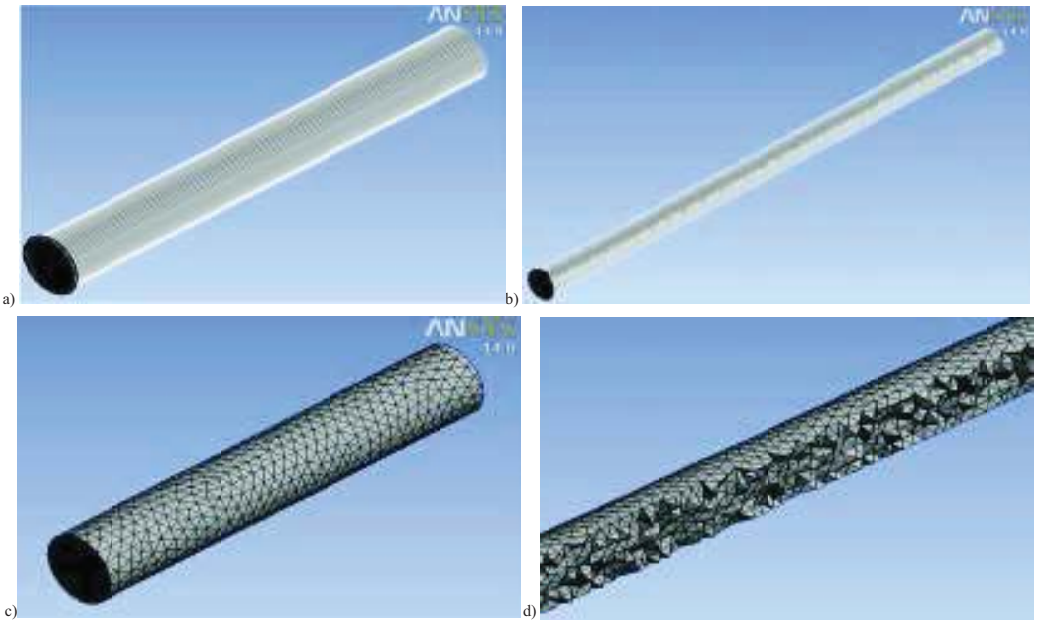

Fig. (4). Views of different helix angles of micro-fin tubes 0º (**a**), 18º (**b**), and views of meshing (**c**) and detailes of meshing (d) for smooth tube.

Table 4. Geometrical Parameters of the Investigated Tubes

Tubes	Smooth	Micro-fin 1	Micro-fin 2
a(°)	-	0	18
Θ(°)	-	36	36
e (mm)	-	0.435	0.435
p (mm)	-	0.378	0.378
n_f	-	60	60
s (mm)	-	0.293	0.293
di (mm)	8.13	8.13	8.13
do (mm)	9.13	9.13	9.13
L (m)	1.5	1.5	1.5
A (mm^2)	38311.7	92180.86	96210

Table 5. The Best Inputs Obtained from ANN Analyses and Numbered in Tables 1-2-3

k ($W\ m^{-1}K^{-1}$)	μ ($kg\ m^{-1}s^{-1}$)	c_p ($J\ kg^{-1}K^{-1}$)	R^2
12	24	1	0.967465
10	10	2	0.963421
6	7	2	0.961502
12	11	2	0.960374
13	8	1	0.958547
16	9	2	0.958514
14	27	2	0.958276
5	3	2	0.957927
11	11	3	0.957073
1	7	2	0.956864

a-) considering the determination of shear stress, friction factor, heat flux, convective heat transfer coefficient and pressure drop as outputs (ANN model 1)

k ($W\ m^{-1}K^{-1}$)	μ ($kg\ m^{-1}s^{-1}$)	c_p ($J\ kg^{-1}K^{-1}$)	R^2
18	2	2	0.99290234
6	21	2	0.99105436
11	1	4	0.99006633
15	1	2	0.98885878
6	1	1	0.98860543
19	26	3	0.9881786
7	12	1	0.98806904
8	28	2	0.98798953
6	7	2	0.98795459
16	2	4	0.98774095

b-) considering the determination of pressure drop and convective heat transfer coefficient as outputs (ANN model 2)

Table 6. Comparison of Experimental and Numerical Temperatures at Outlet Section and at Surface Using Pure Water with 0.2%, 0.6% and 1% TiO_2 Particles Data [4]

Concentration (%)	$T_{o,exp}$(°C)	$T_{o,num}$(°C)	Error Rate (%)	$T_{s,exp}$(°C)	$T_{s,num}$(°C)	Error Rate (%)
Pure water	26.6	26.9	1.26	27.4	27.8	1.45
0.2 %	27.0	27.4	1.52	27.85	28.4	1.97
0.6 %	27.2	27.6	1.56	28.13	28.7	2.02
1 %	27.0	27.4	1.45	27.75	28.2	1.62

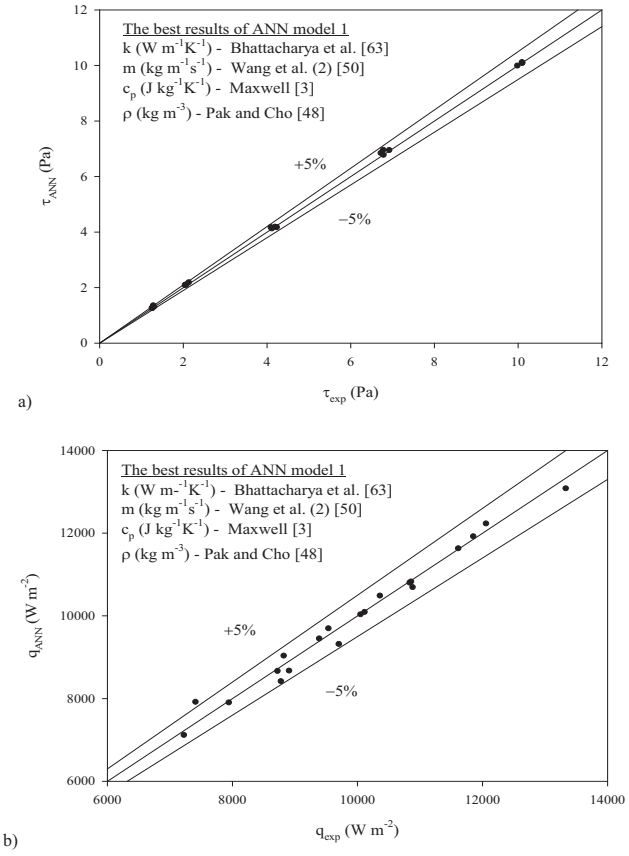

Fig. (5). The best results of ANN model 1 regarding with the shear stress (**a**) and heat flux (**b**).

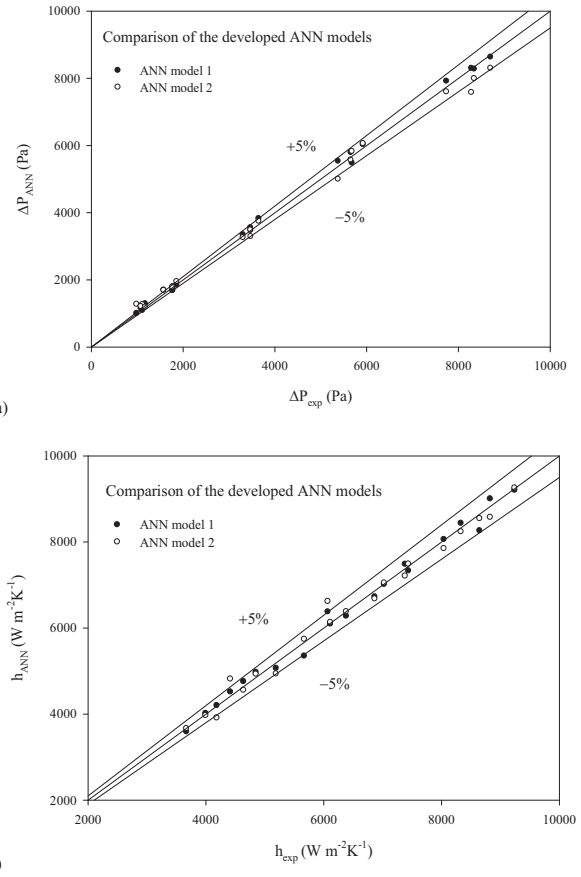

Fig. (6). Comparison of the developed ANN models regarding with the pressure drop (**a**) and convective heat transfer coefficient (**b**).

The variation in the local heat transfer coefficients along the pipe length for the flow of pure water, and for the nanofluids with different particle weight concentrations inside the smooth tube, are shown in Fig. (**11a**). This figure indicates that the additionof solid nanoparticles to the pure water did in fact lead to an increase in the local heat transfer coefficient for the flow inside the smooth tube. As has been shown before, the addition of nanoparticles improves the thermal conductivity of the base fluid. The convective heat transfer enhancement from the nanofluid may be due to an increase in thermal conductivity or to the random movement and dispersion of nanoparticles in the nanofluid. Disordered movements of the solid particles in the flow will alsoupset the thermal boundary layer formation on the tube wall surface, causing the development of the thermal boundary layer to lag and higher heat transfer coefficientsto obtain at the thermal entrance region. Here too, it appears that adding nanoparticles will improve the local heat transfer coefficient in a fluid flow. At higher weight concentrations of nanofluids, both the thermal conductivity of the TiO_2-water mixture and the disturbance effect of the solid nanoparticles will increase; nanofluids with higher weight concentrations will therefore haveeven higher convective heat transfer coefficients.

Fig. (**11b**) further demonstrates that nanofluids display better heat transfer performance when they flow inside micro-fin tubes with helix angles of 0º and 18º than when they flow insidesmooth tubes. The results clearly indicate that the highest heat transfer coefficientswere obtained for micro-fin tubeswith a helix angle of 18º and a volume concentration of 1%; these results are compatible withother current findings in the literature. (Fig. **11c**), furthermore, compares heat transfer coefficients between smooth and micro-fin tubes, and shows that the heat transfer coefficients of micro-fin tubeswith a helix angle of 18º are higher those of than micro-fin tubeswith a helix angle of 0º at nearly the same Reynolds numbers,

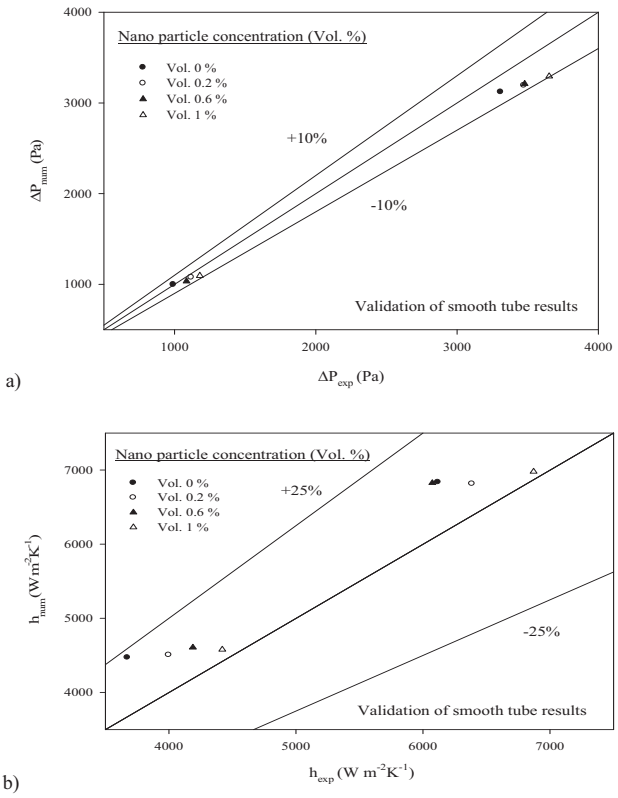

Fig. (7). Comparison of experimental and numerical pressure drops (**a**) and heat transfer coefficients (**b**) and using pure water with 0.2%, 0.6% and 1% TiO_2 particles data [6].

heat flux, and volume concentrations along the pipe. Similarly, the heat transfer coefficients of micro-fin tubes with a helix angle of 0º are higher than those of the smooth tubes.

Fig. (**12a**) shows a remarkable increase in the pressure drop of nanofluids with 0.2, 0.6, and 1 wt.% particle concentrations compared to pure water when flowing inside smooth and micro-fin tubes. This trend tends to continue for nanofluids at higher weight fractions. This is due to the fact that suspending solid particles in a fluid generally increases dynamic viscosity relative to the base fluid. Since viscosity stands in direct relation to pressure drop, the higher viscosity naturally leads to an increased pressure drop. Experimental results show that the pressure drop of micro-fin tubes with a helix angle of 18º is higher than that of micro-fin tubes with a helix angle of 0º. Moreover, the pressure drop of micro-fin tubes with a helix angle of 0º is higher than that of the smooth tubes. More exactly, the pressure drop of micro-fin tubes with a helix angle of 18º is 21.5% higher than that of smooth tubes, and the pressure drop of micro-fin tubes with a helix angle of 0º is 15.5% higher than that of smooth tubes at φ=1%.

From Fig. (**12b**), it is evident that the friction factor increases with increasing concentrations of nanoparticles because of the rise in working fluid viscosity. As was previously observed, nanofluids in smooth tubes with concentrations of 0.2%, 0.6%, and 1% provide friction factors higher than those of base fluids by 1.5, 5.1, and 5.8%, respectively. Similarly, nanofluids in micro-fin tubes with a helix angle of 18º, and with concentrations of 0.2%, 0.6%, and 1%, provide friction factors higher than those of base fluids by around 0.33%, 2.2% and 3.2%, respectively. It can be observed from Fig. (**12c**) that wall shear stress increases with the increasing volume concentration of the nanoparticles; the Reynolds number of the flow also increases as the inclusion of nanoparticles raises the viscosity of the mixture.

As the numbers indicate, nanofluids in smooth tubes with concentrations of 0.2%, 0.6%, and 1% induced a wall shear stress higher than that of the base fluid by around 2.2, 2.7% and 5.2%, respectively. Likewise, nanofluids in micro-fin tubes with a helix angle of 18º, and with concentrations of 0.2%, 0.6% and 1%, induced a wall shear stress higher than that of the base fluid by around 1%, 1.2%, and 4.2%, respectively. According to Fig. (**12c**), the wall shear stress of micro-fin tubes with a helix angle of 18º is 21.1% higher than that of smooth tubes, and the wall shear stress of micro-fin tubes with a helix angle of 0º is 3.77% higher at φ=0.6 % than that of smooth tubes. Fig. (**12d**) shows, finally, a remarkable increase in pumping power due to the increase in the pressure drop of the nanofluid in a large cross-section of the micro-fin tubes. The results show that the pumping power of micro-fin tubes with a helix angle of 18º is higher than that of micro-fin tubes with a helix angle of 0º; similarly, the pumping power of micro-fin tubes with a helix angle of 0º is higher than that of smooth tubes. In all, the characteristics of in the sub-figures of Fig. (**12**) are found to be compatible with other current findings in the literature.

6. CONCLUSION

This study investigated the heat transfer characteristics of pure water and of a water-TiO_2 mixture flowing inside smooth tubes, as a validation study, and inside micro-fin tubes, as a simulation study, with various volume concentrations investigated for forced flow conditions using two- dimensional governing equations. The conclusions of this study can be outlined as follows:

- The heat transfer coefficient was slightly increased with increasing nanofluid volume concentration.
- Micro-fin tubes with helix angles of 0° and 18° enhanced the heat transfer coefficient significantly under the same flow conditions, yielding at φ=1% mean heat transfer coefficients higher than those of smooth tubes by 23.5% and 32.5%, respectively.
- Compared to micro-fin tubes with a helix angle of 0°, the mean heat transfer coefficient and pressure drop of micro-fin tubes with a helix angle of 18° increased at φ=1% by 11.8% and 7.55%, respectively.
- Nanofluids with concentrations of 0.2%, 0.6%, and 1% in micro-fin tubes with a helix angle of 18º yielded friction factors higher than those of the base fluid by approximately 0.33%, 2.2%, and 3.2%, respectively.
- The wall shear stress of micro-fin tubeswith a helix angle of 18º was 21.1% higher at φ=0.6% than those of smooth tubes, and the wall shear stress of micro-fin tubeswith a helix angle of 0º was 3.77% higher than that of smooth tubes.
- The pumping power of micro-fin tubeswith a helix angle of 18º was 68.8% higher at φ=1% than that of smooth tubes and 11.5% higher than that of micro-fin tubeswith a helix angle of 0º.
- Nanofluids at higher volume concentrations showed both higher heat transfer enhancement and higher pressure drop. Therefore, judicious decisions should be taken to select a nanofluid that will balance the heat transfer enhancement and the pressure drop penalty.

As this study has also found, the proven tools of computational fluid dynamics (CFD) will make it feasible for researchers to analyze different geometrical configurations and various nanofluids without needing to perform additional experimental studies, once they have performed their validation process on the experimental data.

a)

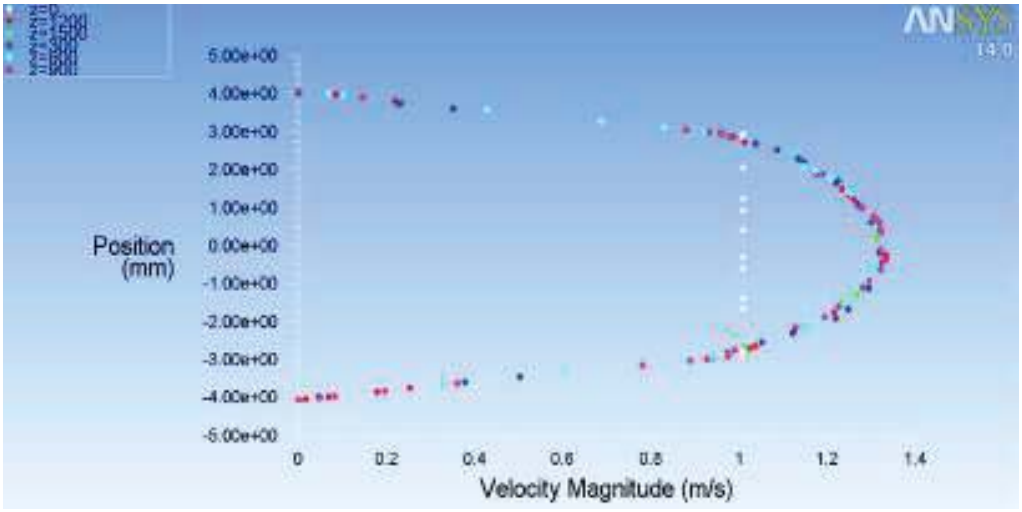

b)

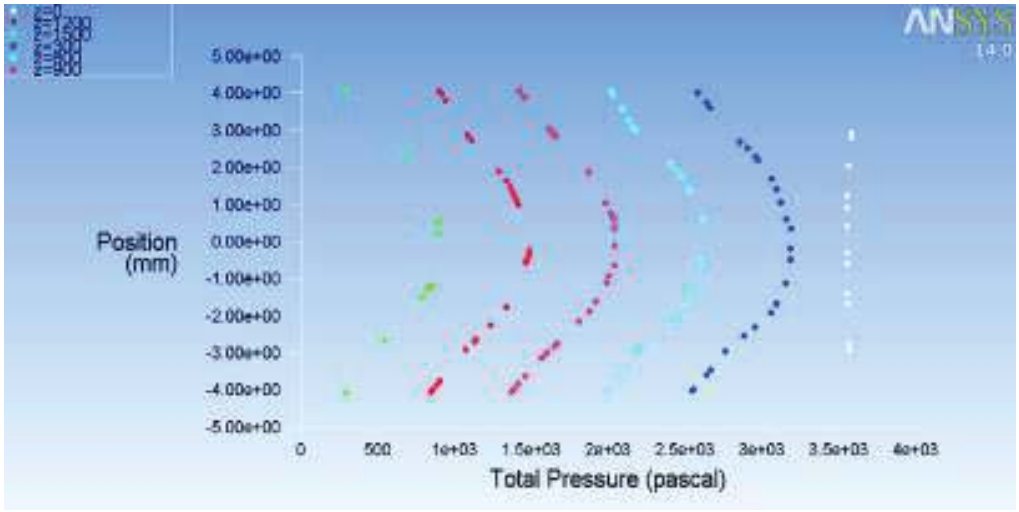

c)

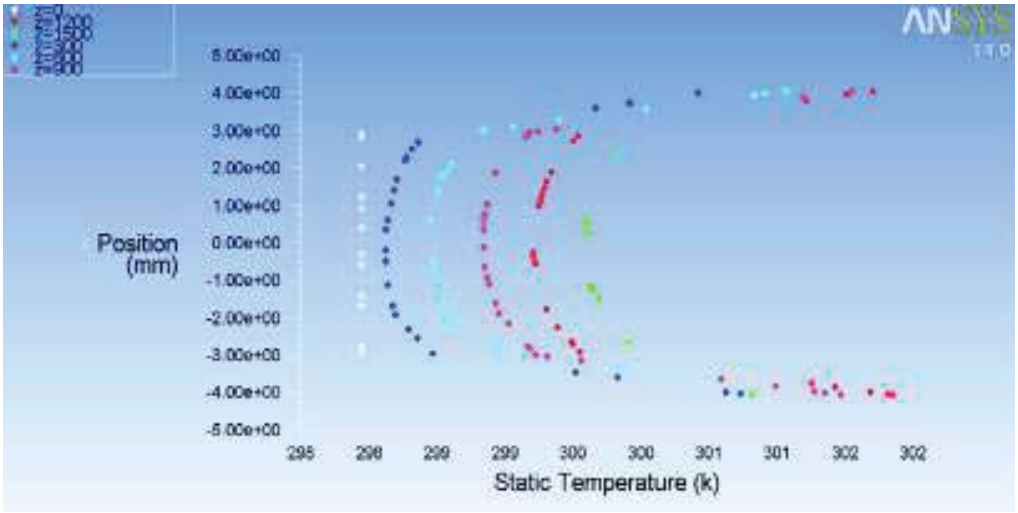

Fig. (8). Velocity profile (**a**), pressure profile (**b**) and temperature profile (**c**) at various locations in smooth tube.

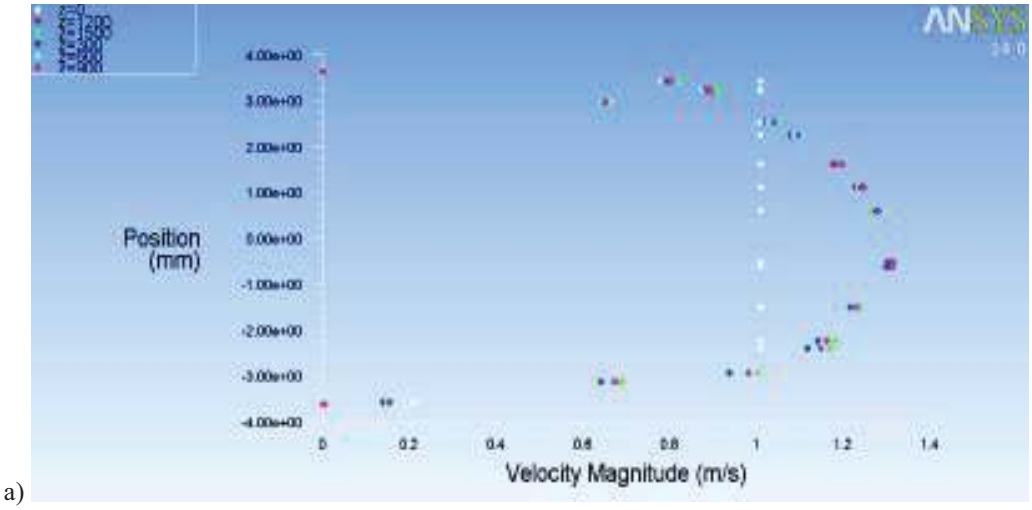

a)

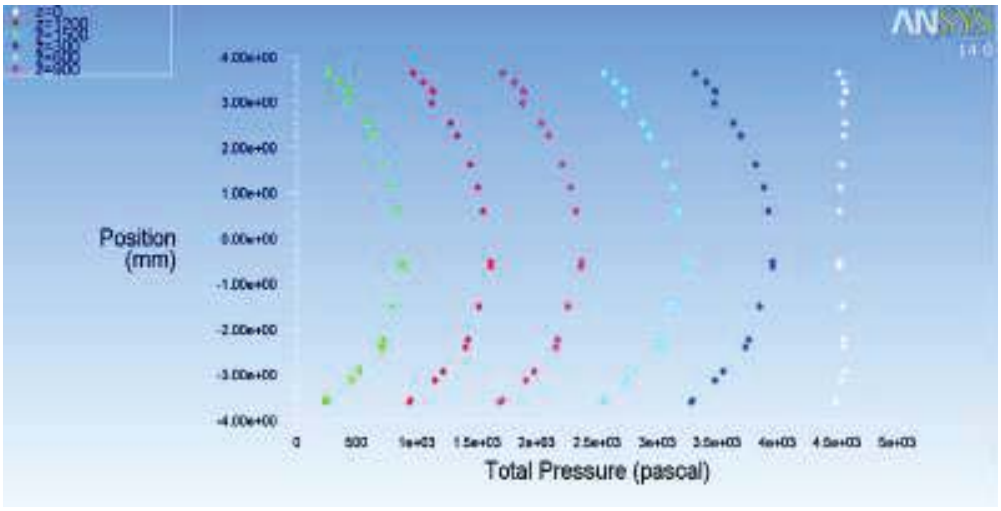

b)

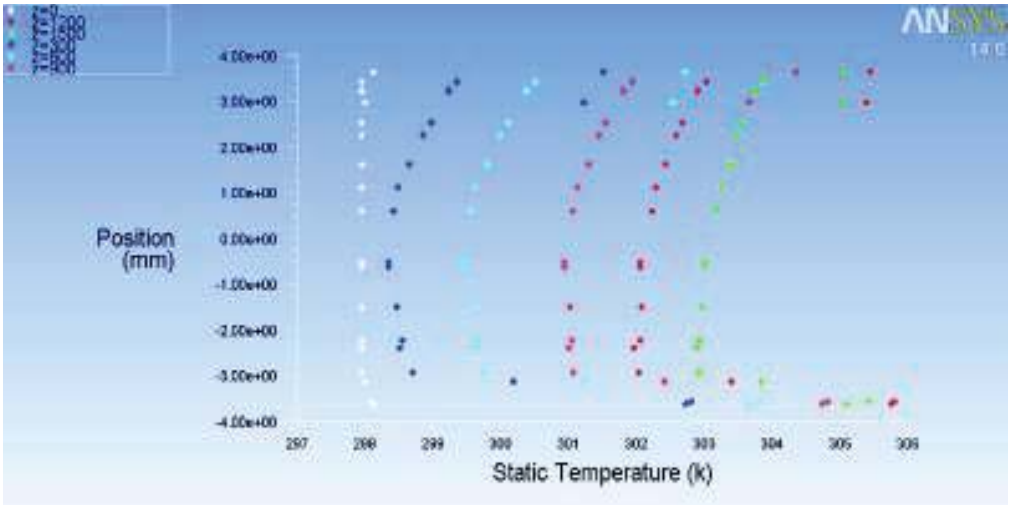

c)

Fig. (9). Velocity profile (**a**), pressure profile (**b**) and temperature profile (**c**) at various locations in micro-fin tube having helix angle 0º.

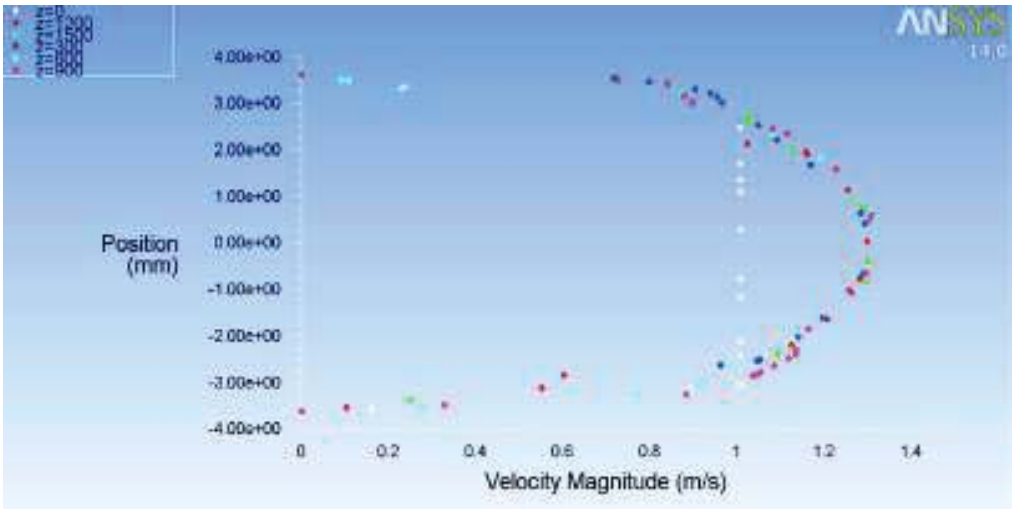

a)

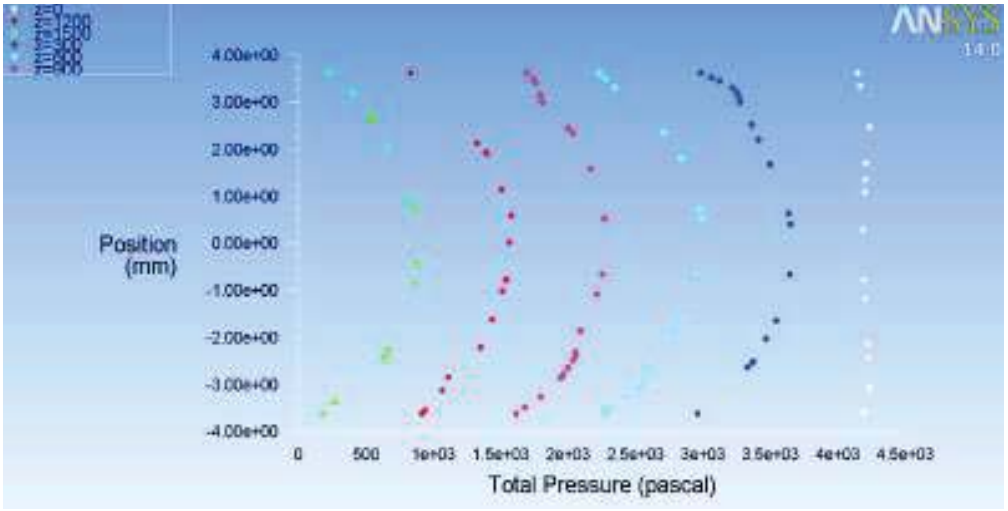

b)

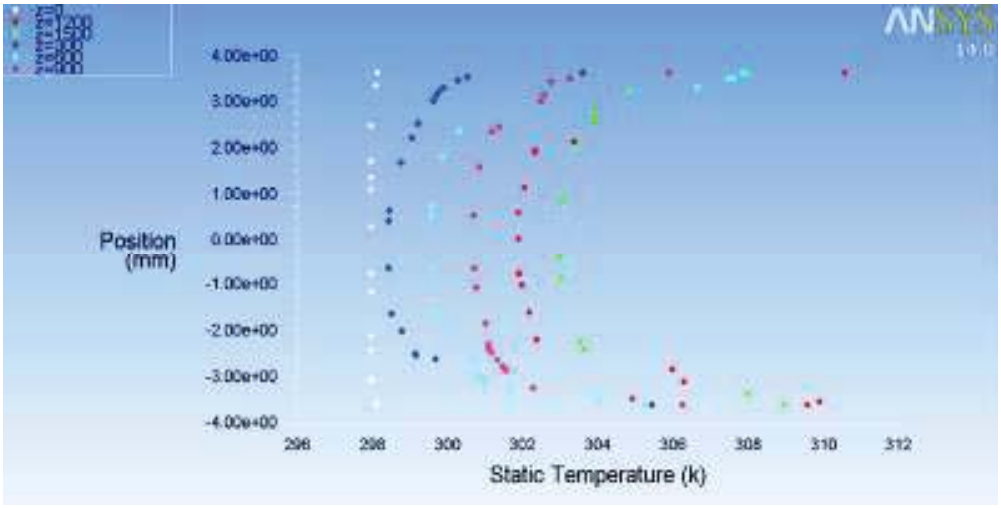

c)

Fig. (10). Velocity profile (**a**), pressure profile (**b**) and temperature profile (**c**) at various locations in micro-fin tube having helix angle 18º.

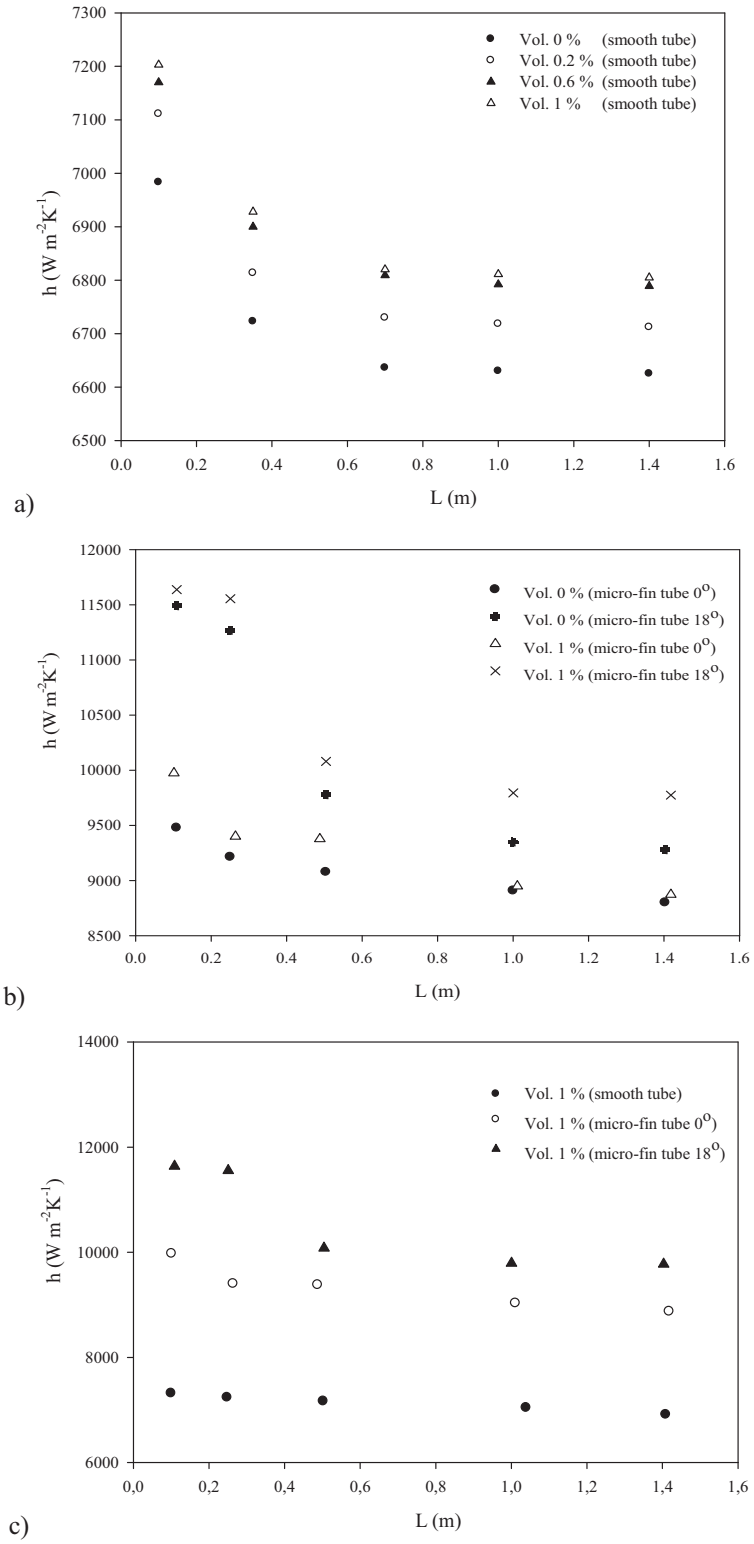

Fig. (11). Variations in heat transfer coefficient of smooth tube (**a**), micro-fin tubes (**b**) and smooth-micro-fin tubes (**c**) on volume concentration along the tube length.

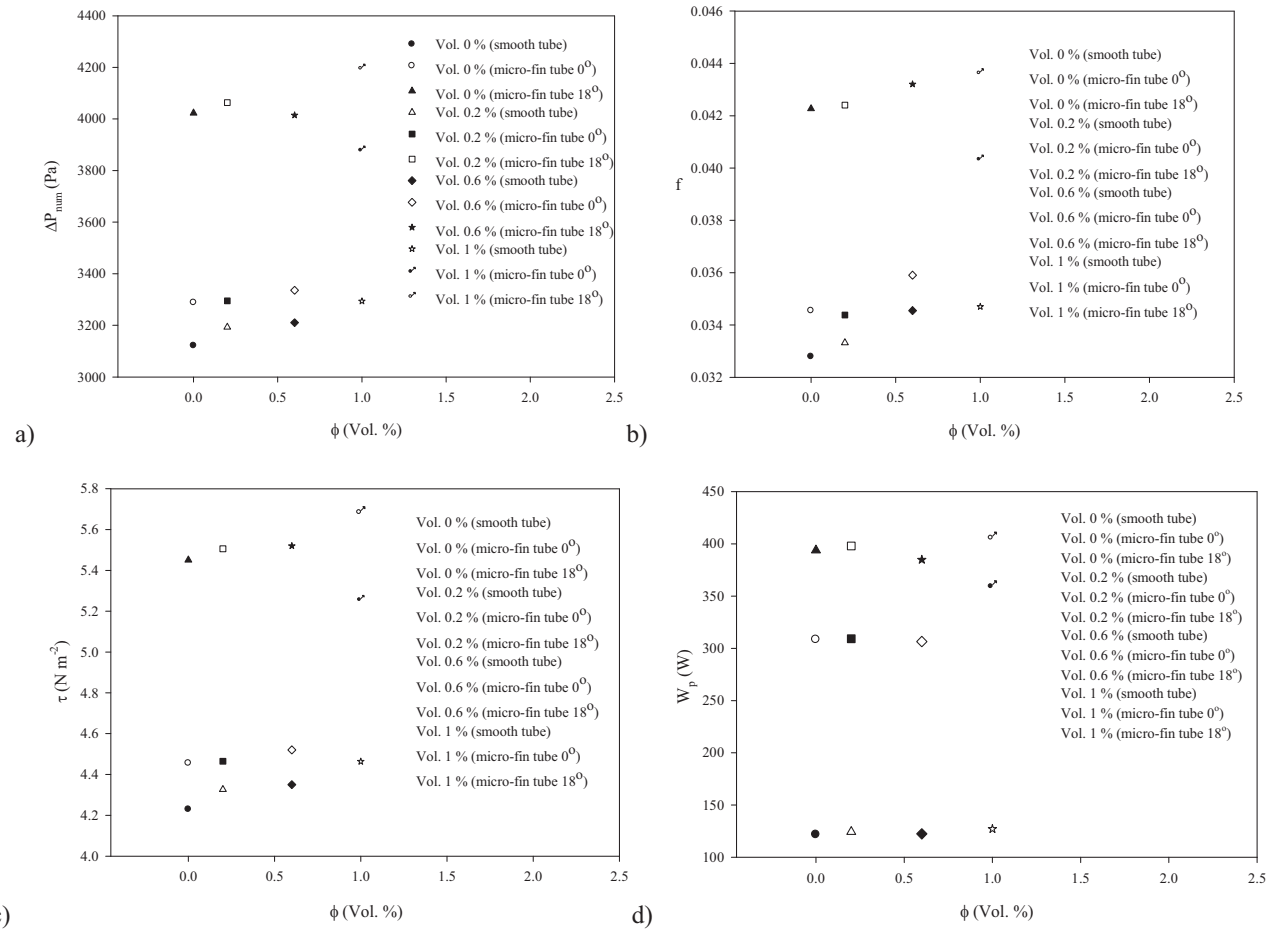

Fig. (12). Variations in pressure drop (**a**), friction factor (**b**), wall shear stress (**c**) and pumping power (**d**) of smooth tube and micro-fin tubes on different volume.

CONFLICT OF INTEREST

The authors confirm that this article content has no conflicts of interest.

ACKNOWLEDGEMENTS

The authors would like to express their appreciation to the Thailand Research Fund (TRF) and The National Research University Project for providing financial support for this study. Especially, the First author wishes to thank KMUTT for providing him with a Postdoctoral fellowship. The authors also wish to thank DEGUSSA AG, Germany for the valuable donation of the nanoparticles used in the present study. This research has been supported by Yıldız Technical University Scientific Research Projects Coordination Department. Project Number: 29-06-01-01.

NOMENCLATURE

Cp	=	Specific heat [J $kg^{-1}K^{-1}$]
d	=	Internal tube diameter [m]
h	=	Heat transfer coefficient [W $m^{-2}K^{-1}$]
k	=	Thermal conductivity [W $m^{-1}K^{-1}$]
k_H	=	Huggins coefficient.
L	=	Length of test tube [m]
m	=	Mass flow rate [kg s^{-1}],
Nu	=	Nusselt number
ΔP	=	Pressure drop [Pa]
Pr	=	Prandtl number
Re	=	Reynolds number
Q	=	Heat transfer rate [W]
q"	=	Heat flux [W m^{-2}]
T	=	Temperature [°C]
μ	=	Dynamic viscosity [Pa.s]
ρ	=	Density [kg m^{-3}]
τ	=	Shear stress [N m^{-2}]
φ	=	Volume fraction [%]
$φ_m$	=	maximum particle packing fraction
ν	=	Kinematic viscosity [m^2 s^{-1}]
m	=	Mass [kg]
f	=	Friction factor
W	=	Work [J]
P	=	Pressure [Pa]
A	=	Area [m^2]
u	=	Average velocity [m/s]
n	=	Number of fins

e = Height of fin [m]
p = Distance between micro-fins [m]
Q = Flow rate

SUBSCRIPTS

avg = Average
bf = Base fluid
nf = Nano fluid
exp = Experimental
ext = External
f = Fluid
h = Hot
i = Inlet
m = Mean
nf = Nanofluid
num = Numerical
p = Particle
r = Radius of particle
s = Surface
o = Outlet
w = Water

REFERENCES

[1] Choi, U.S. Enhancing thermal conductivity of fluids with nanoparticles. *ASME FED,* **1995**, *66*, 99-103.

[2] Xuan, Y.; Li, Q. Heat transfer enhancement of nanofluids. *Int. J. Heat Fluid Fl.*, **2000**, *21*, 58-64.

[3] Maxwell, J.C. *Electricity and Magnetism*.; Clarendon Press: Oxford UK, **1873**.

[4] Daungthongsuk, W.; Wongwises, S. A critical review of convective heat transfer of nanofluids. *Renew. Sustain. Energy Rev.,* **2007**, *11*, 797-817.

[5] Duangthongsuk, W.; Wongwises, S.Measurement of temperature-dependent thermal conductivity and viscosity of TiO_2-water nanofluids. *Exp. Therm. Fluid Sci.*, **2009**, *32*, 706-714.

[6] Duangthongsuk, W.; Wongwises, S. Comparison of the effects of measured and computed thermophysical properties of nanofluids on heat transfer performance. *Exp. Therm. Fluid Sci.*, **2010**, *34*, 616-624.

[7] Duangthongsuk, W.; Wongwises, S. An experimental study on the heat transfer performance and pressure drop of TiO_2-water nanofluids flowing under a turbulent flow regime. *Int. J. Heat Mass Trans.,* **2010**, *53*, 334-344.

[8] Duangthongsuk, W.; Wongwises, S. Heat transfer enhancement and pressure drop characteristics of TiO2-water nanofluid in a double-tube counter flow heat exchanger. *Int. J. Heat Mass Tran.*, **2009**, *52*, 2059-2067.

[9] Duangthongsuk, W.; Wongwises, S. Effect of thermophysical properties models on the predicting of the convective heat transfer coefficient for low concentration nanofluid. *Int. Commun. Heat Mass.,* **2008**, *35*, 1320-1326.

[10] Duangthongsuk, W.; Dalkilic, A.S.; Wongwises, S. Convective heat transfer of Al2O3-water nanofluids in a microchannel heat sink. *Curr. Nanosci.,* **2012**, *8,* 317-322.

[11] Suriyawong, A.; Wongwises, S., Nucleate pool boiling heat transfer characteristics of TiO_2-water nanofluids at very low concentrations. *Exp. Therm. Fluid Sci.*, **2010**, *34*, 992-999.

[12] Trisaksri, V.; Wongwises, S. Nucleate pool boiling heat transfer of TiO2–R141b nanofluids. *Int. J. Heat Mass Trans.*, **2009**, *52*, 1582-1588.

[13] Dalkilic, A.S.; Kürekci, N.A.; Wongwises, S. Effect of void fraction and friction factor models on the prediction of pressure drop of R134a during downward condensation in a vertical tube. *Heat Mass Transfer*., **2012**, *48*, 123-139.

[14] Dalkilic, A.S.; Kürekci, N.A.; Wongwises , S. Prediction of two-phase friction factor of refrigerants inside a horizontal tube using CFD analysis for the homogeneous condensation flow.*ASME-JSME-KSME Joint Fluids Engineering Conference, ASME-JSME-KSME.*, **2011**, *July 24-29*, Japan.

[15] Fluent release 6.2.16, Fluent Incorporated, **2005.**

[16] Demir, H.; Dalkilic, A.S.; Kurekci , N.A.; Kelesoglu, B.; Wongwises, S. A numerical investigation of nanofluids forced convection flow in a horizontal smooth tube. *Int. Heat Transfer Con.* ASME. , **2010**, *August 8-13*, USA.

[17] Demir, H.; Dalkilic, A.S.; Kurekci , N.A.; Kelesoglu, B.; Wongwises, S., Numerical investigation on the single phase forced convection heat transfer characteristics of TiO_2nanofluids in a double-tube counter flow heat exchanger. *Int. Commun. Heat Mass.,* **2011**, *38*, 218-228.

[18] Palm, S.J.; Roy, G.; Nguyen, C.T. Heat transfer enhancement with the use of nanofluids in radial flow cooling systems considering temperature-dependent properties. *Appl. Therm. Eng.*, **2006**, *26*, 2209-2218.

[19] Ağra, Ö.; Demir, H.; Atayılmaz, Ş.Ö.; Kantaş, F.; Dalkılıç, A.S. Numerical investigation of heat transfer and pressure drop in enhanced tubes. *Int. Commun. Heat Mass.,* **2011**, *38*, 1384-1391.

[20] Balcılar, M.; Dalkılıç, A.S.; Bolat, B.; Wongwises, S. Investigation of empirical correlations on the determination of condensation heat transfer characteristics during downward annular flow of R134a inside a vertical smooth tube using artificial intelligence algorithms. *J. Mec. Sci. Technol.,* **2011**, *25*, 2683-2701.

[21] Bolat, B.; Balcilar , M.; Dalkilic, A.S.; Wongwises, S. Optimization of the relationship between the two-phase friction factor and Reynolds equivalent number model by the means of Genetic Algorithm. *ASME/JSME 8th Thermal Engineering Joint Conference. ASME.,* **2011**, *March 13-17*, Hawaii.

[22] Balcilar, M.; Dalkilic, A.S.; Wongwises S. Artificial neural network (ANN) techniques for the determination of condensation heat transfer characteristics during downward annular flow of R134a inside a vertical smooth tube.*Int. Commun. Heat Mass.,* **2011**, *38*, 75-84.

[23] Balcilar, M.; Dalkilic, A.S.; Wongwises S. Determination of condensation heat transfer characteristics of R134a by means of artificial intelligence method. *International Mechanical Engineering Congress and Exposition, ASME*., **2010,** *November 12-18*, USA.

[24] Balcilar, M.; Dalkilic, A.S.; Suriyawong, A.; Yiamsawas , T.; Wongwises, S. Investigation of pool boiling of nanofluids using artificial neural networks and correlation development techniques. *Int. Commun. Heat Mass.,* **2012**, *39*, 424-431.

[25] Balcilar, M.; Dalkilic, A.S.; Agra, O.; Atayilmaz, S.O.; Wongwises, S. A correlation development study on the prediction of pressure drop during condensation and evaporation of various refrigerants in horizontal smooth and micro-fin tubes. *Int. Commun. Heat Mass.,* **2012**, *39*, 937-944.

[26] SolidWorks, SolidWorks Corporation, 300 Baker Avenue, Concord, MA 01742. Available from: http://www.solidworks.com/.

[27] ANSYS Fluent, ANSYS Inc., 10 Cavendish Court Lebanon, NH 03766 Available from: http://www.ansys.com/.

[28] Williams, W.C.; Buongiorno, J.; Hu, L.W. Experimental investigation of turbulent convective heat transfer and pressure loss of alumina/water and zirconia/water nanoparticle colloids (nanofluids) in horizontal tubes. *J. Heat Transf*., **2008**, *130*, 042412.

[29] Rea, U.; McKrell, T.; Hu, L.; Buongiorno, J. Laminar convective heat transfer and viscous pressure loss of alumina-water and zirconia-water nanofluids.*Int. J. Heat Mass Tran.,* **2009**, 52, 2042-2048.

[30] Einstein, A. Eineneuebestimmung der moleküldimensionen.*Ann Phys-Newyork***., 1906**, *324*, 289-306.

[31] Brinkman, H. The viscosity of concentrated suspensions and solutions.*J. Chem. Phys.*, **1952**, *20*, 571-581.

[32] Batchelor, G. The effect of brownian motion on the bulk stress in a suspension of spherical particles.*J. Fluid Mech.,* **1977**, *83*, 97-117.

[33] Graham, A.L. On the viscosity of suspensions of solid spheres.*J. ApplSci Res*., **1981**, *37*, 275-286.

[34] Kitano, T.; Kataoka, T.; Shirota, T. An empirical equation of the relative viscosity of polymer melts filled with various inorganic fillers. *The Journal RheologicaActa*., **1981** , *20*, 207-209.

[35] Bicerano, J.; Douglas, J.F.; Brune, D.A. Model for the viscosity of particle dispersions. *J. Macromol Sci-Rev. M.,* **1999**, *39*, 561-642.

[36] Wang, X.; Xu, X.; Choi, S.U.S. Thermal conductivity of nanoparticle–fluid mixture. *J.Thermophys Heat Tr.*, **1999**, *13*, 474-480.

[37] Tseng, W.J.; Chen, C.N. Effect of polymeric dispersant on rheological behavior of nickel-terpineol suspensions.*Mat. Sci. Eng.A-Struct*, **2003**, *347*, 145-153.

[38] Chen, H.; Ding, Y.; He, Y.; Tan, C. Rheological behaviour of ethylene glycol based titanianofluids. *Chem. Phys. Lett.*, **2007**, *444*, 333-337.

[39] Nguyen, C.; Desgranges, F.; Roy, G.; Galanis, N.; Mare, T.; Boucher, S.; Anguemintsa, H. Temperature and particle-size dependent viscosity data for water-based nanofluids-hysteresis phenomenon. *Int. J. Heat Fluid Fl.*, **2007**, *28*, 1492-1506.

[40] Khanafer, K.; Vafai, K. A critical synthesis of thermophysical characteristics of nanofluids.*Int. J. Heat Mass Tran.*, **2011**, *54*, 4410-4428.

[41] Vand , V. Viscosity of solutions and suspensions I. Theory, *J. Phys. Colloid Chem.*, **1948**, *52*, 277-299.

[42] Mooney, M. The viscosity of a concentrated suspension of spherical particles. *J. Coll. Sci. Imp. U. Tok***., 1951**, 6-8.

[43] Krieger , I. M.; Dougherty, T. J. A mechanism for non-newtonian flow in suspensions of rigid spheres. *J. Rheol.*, **1959**, *3*, 137-152.
[44] Krieger, I.M. Rheology of monodisperse lattices., *Adv. Colloid Interfac.*, **1972**, *3*, 111-136.
[45] Frankel, N.A.; Acrivos, A. On the viscosity of a concentrated suspension of solid spheres. *Chem. Eng. Sci.*, **1967**, *22*, 847-853.
[46] Miller, A.; Gidaspow, D.; Dense, D. Vertical gas-solid flow in a pipe. *AIChE journal*, **1992**, *38*, 1801-1815.
[47] Chow , T.S. Viscosities of concentrated dispersions.*Phys. Rev. E.*, 1993, *48*, 1977-1983.
[48] Pak, B.C.; Cho, Y.I. Hydrodynamic and heat transfer study of dispersed fluids with submicron metallic oxide particles.*Exp. Heat Transfer.*, **1998**, *11*, 151-170.
[49] Liu, S. Particle dispersion for suspension flow. *Chem. Eng. Sci.*, **1999**, *54*, 873-891.
[50] Wang, X.; Xu, X. Choi S.U.S., Thermal conductivity of nanoparticle-fluid mixture, *J. Thermophys. Heat Tr.*, **1999**, *13*, 474-480.
[51] Davalos, L.A.; Orozco, L.A.; Castillo, L.F. Del. Hydrodynamic behavior of suspensions of polar particles. *Encycl. Surf. Colloid Sci.*, **2002**, *4*, 2375-2396.
[52] Putra, N.; Roetzel, W.; Das, S.K. Natural convection of nano-fluids.*Heat Mass Transfer*., **2003**, *39*, 775-784.
[53] Tang, G.Y.; Yang, C.; Chai, J.C.Gong, H.Q. Joule heating effect on electroosmotic flow and mass species transport in a microcapillary. *Int. J. Heat Mass Trans.*, **2004**, *47*, 215-227.
[54] Hamilton, R.L.; Crosser , O.K. Thermal conductivity of heterogeneous two component systems.*Ind. Eng. Chem.*, **1962**, *1*, 187-191.
[55] Hui , P.M.; Zhang, X.; Markworth , A.J.; Stroud, D. Thermal conductivity of graded composites: numerical simulations and an effective medium approximation. *J. Mater. Sci.*, **1999**, *34*, 5497-5503.
[56] Xuan, Y.; Li , Q. Heat transfer enhancement of nanofluids.*Int. J. Heat Fluid Fl.*, **2000**, 21, 58-64.
[57] Yu, W.; Choi, S.U.S. The role of interfacial layers in the enhanced thermal conductivity of nanofluids: a renovated Maxwell model. *J. Nanopart. Res.*, **2003**, *5*, 167-171.
[58] Godson, L.; Raja, B.; Mohan, D. Lal; Wongwises, S. Experimental investigation on the thermal conductivity and viscosity of silver-deionized water nanofluid. *Exp. Heat Transfer.*, **2010**, *23*, 317-332.
[59] Prasher, R.; Bhattacharya, P.; Phelan, P.E. Thermal conductivity of nanoscale colloidal solutions (nanofluids). *Phys. Rev. Lett.*, **2005**, *94*, 025901-1–025901-4.
[60] Koo, J.; Kleinstreuer, C. A new thermal conductivity model for nanofluids. *J. Nanopart. Re.,* **2004**, *6,* 577-588.
[61] Li, C.H.; Peterson, G.P. Experimental investigation of temperature and volume fraction variations on the effective thermal conductivity of nanoparticle suspensions (nanofluids). *J. Appl. Phys.*, **2006**, 99-084314.
[62] Maiga, S.E.B.; Nguyen, C.T.; Galanis, N.; Roy, G. Heat transfer behaviours of nanofluids in a uniformly heated tube. *Superlattice Microst.*, **2004**, *35*, 543-557.
[63] Bhattacharya, P.; Saha, S.K.; Yadav, A.; Phelan, P.E.; Prasher, R.S. Brownian dynamics simulation to determine the effective thermal conductivity of nanofluids. *J. Appl. Phys.,* **2004**, *95*, 6492-6494.
[64] Buongiorno, J. Convective transport in nanofluids. *J. Heat Transf.*, **2006**, *128*, 240-251.
[65] Kim, D.; Kwon, Y.; Cho, Y.; Li, C.; Cheong, S.; Hwang, Y.; Lee, J.; Hong, D.; Moon, S. Convective heat transfer characteristics of nanofluids under laminar and turbulent flow conditions.*Curr. Appl. Phys.*, **2009**, *9 (2)*, 119-123.
[66] Elena, V.; Timofeeva, V.; Gavrilov, N.A.; McCloskey, J.M.; Tolmachev, Y.V. Thermal conductivity and particle agglomeration in alumina nanofluids: Experiment and Theory. *Phys. Rev. E.*, **2007,** *76*, 061203.
[67] Chon, C.H.; Kihm, K.D.; Lee, S.P.; Choi, S.U.S. Empirical correlation finding the role of temperature and particle size for nanofluid (Al_2O_3) thermal conductivity enhancement. *Appl. Phys. Lett.*, **2005**, 87.
[68] Murshed, S.M.S.; Leong, K.C.; Yang, C. A. model for predicting the effective thermal conductivity of nanoparticles–fluid suspensions. *Int. J. Nanosci.*, **2006**, *5*, 23-33.
[69] Yang, Y.; Zhang, Z.G.; Grulke, E.A.; Anderson, W.B.; Wu, G. Heat transfer properties of nanoparticle-in-fluid dispersions (nanofluids) in laminar flow.*Int. J. Heat Mass Trans.,* **2005**, 1107-1116
[70] Yu , W.; France, D.M.; Routbort, J.L.; SUS., Choi., Review and comparison of nanofluid thermal conductivity and heat transfer enhancements. *Heat Transfer Eng.*, **2008**, *29 5*, 432-460.
[71] Bejan, A.; Tsatsaronics, G.; Moran, M. Thermal design and optimization, Wiley-Interscience Publication:**1996**.
[72] Petukhov, B. S. Heat transfer and friction in turbulent referred to in handbook of single-phase convective pipe flow with variable physical properties. In Heat Transfer, ed. T. F. Irvine and J. P.New York: Wiley Interscience, 1987. Hartnett, Vol. 6, Academic Press:New York, **1970.**
[73] Fausett, L., *Fundamentals of Neural Networks, Architectures, Algorithms, and Application; Prentice-HallInc. Press*, **1994**.
[74] Rosenblatt , F., *Principles of Neurodynamics: Perceptrons and the Theory of BrainMechanisms*; Washington DC: Spartan Books, **1961**.
[75] Rumelhart D.E., G. E., Hinton, R.J., Williams, *Learning internal representations by error propagation.In D. E. Rumelhart& J. L. McClelland (Eds.), Parallel Distributed Processing1*, **1986**, pp. 318-362.
[76] Alpaydin, E.*Introduction to Machine Learning*, (T. Dietterich, C. Bishop, D. Heckerman, M. Jordan, & M. Kearns, Eds.) Machine Learning , **2004**, *56*, pp.387-99.

Received: August 22, 2012 **Revised: October 16, 2012** **Accepted: October 25, 2012**

Provided for non-commercial research and education use.
Not for reproduction, distribution or commercial use.

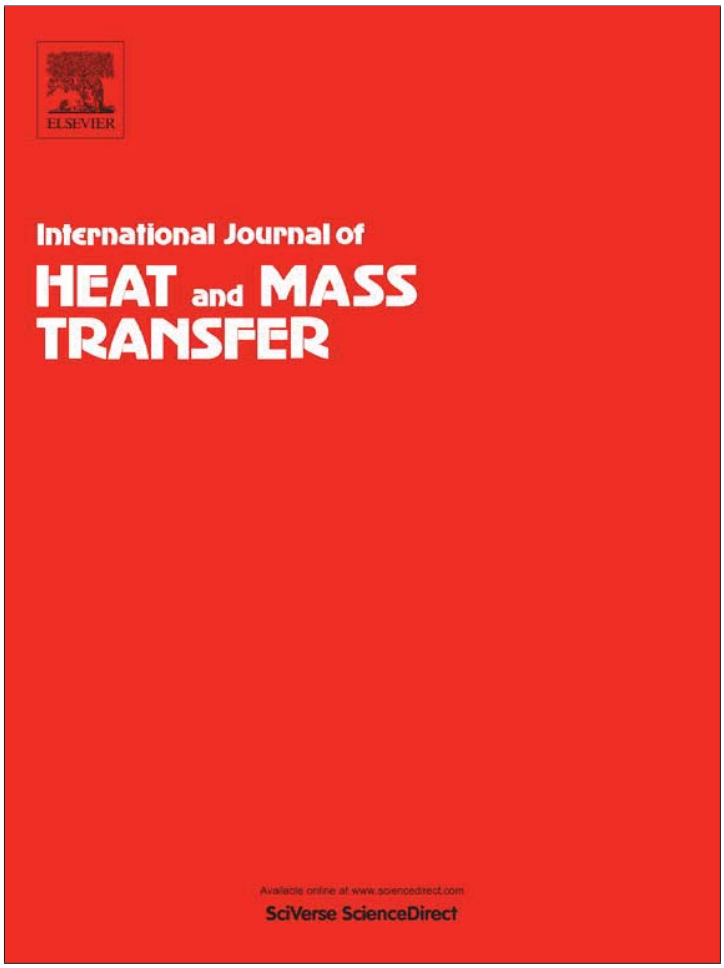

(This is a sample cover image for this issue. The actual cover is not yet available at this time.)

This article appeared in a journal published by Elsevier. The attached copy is furnished to the author for internal non-commercial research and education use, including for instruction at the authors institution and sharing with colleagues.

Other uses, including reproduction and distribution, or selling or licensing copies, or posting to personal, institutional or third party websites are prohibited.

In most cases authors are permitted to post their version of the article (e.g. in Word or Tex form) to their personal website or institutional repository. Authors requiring further information regarding Elsevier's archiving and manuscript policies are encouraged to visit:

http://www.elsevier.com/copyright

Author's personal copy

International Journal of Heat and Mass Transfer 60 (2013) 201–209

Contents lists available at SciVerse ScienceDirect

International Journal of Heat and Mass Transfer

journal homepage: www.elsevier.com/locate/ijhmt

Heat transfer performance of screen mesh wick heat pipes using silver–water nanofluid

Lazarus Godson Asirvatham [a,*], Rajesh Nimmagadda [a], Somchai Wongwises [b,c]

[a] Department of Mechanical Engineering, Karunya University, Coimbatore 641 114, Tamil Nadu, India
[b] Fluid Mechanics, Thermal Engineering and Multiphase Flow Research Lab (FUTURE), Department of Mechanical Engineering, Faculty of Engineering, King Mongkut's University of Technology Thonburi,126 Bangmod, Tongkru, Bangkok 10140, Thailand
[c] The Academy of Science, The Royal Institute of Thailand, Sanam Suea Pa, Dusit, Bangkok 10300, Thailand

ARTICLE INFO

Article history:
Received 3 May 2012
Received in revised form 6 November 2012
Accepted 10 November 2012

Keywords:
Silver
De-ionized water
Nanofluid
Thermal resistance
Evaporation and condensation heat transfer coefficients
Dry-out condition

ABSTRACT

This study presents the improvement in heat transfer performance of a heat pipe using silver nanoparticles dispersed in DI (De-Ionized) water. The nanoparticles suspended in conventional fluids have superior heat transfer capability due to improved thermal conductivity. The heat pipes are tested for heat inputs ranging from 20 W to 100 W in five steps, which is suitable for removing heat from power transistors in electronics and processors in computers. The effect of various operational limits and test parameters such as heat inputs, volume fraction, vapour temperature on the thermal resistance, evaporation and condensation heat transfer coefficients, are experimentally investigated. The tested silver nanoparticles volume concentration ranged from 0.003% to 0.009% with average nanoparticle diameter of 58.35 nm. The experimental results are evaluated in terms of performance metrics by direct measurement of vapour temperatures in the centre core of heat pipe. A substantial reduction in thermal resistance of 76.2% is observed for 0.009 vol.% concentration of silver nanoparticles. Further an enhancement in the evaporation heat transfer coefficient of 52.7% is observed for the same concentration. The use of nanoparticles enhances the operating range of heat pipe by 21% compared with that of DI water.

© 2012 Elsevier Ltd. All rights reserved.

1. Introduction

Heat pipes and their applications in thermal management have been studied for decades. They constitute an efficient compact tool to dissipate substantial amount of heat from various engineering systems including electronics cooling [1,2] like computers, laptop notebooks etc. In fact, virtually every notebook computer manufactured today uses at least one heat pipe assembly, typically designed to carry 30 W of power. The results of reports from various researchers [3] concludes that the conventional working fluids such as DI water, methanol etc. in heat pipes possess limited heat transport capabilities which arises due to working fluid transport properties. To overcome these limitations, the thermo physical properties of working fluid have to be improved. An innovative way to enhance liquid thermal conductivity is the dispersion of highly conductive solid nanoparticles within the base fluid. This new generation of conductive fluids with nanoparticles is referred to as nanofluid [4,5]. Taehyun Cho et al. [6] investigated thermal conductivity of fluids suspended with silver nanoparticles. The observation concludes an improvement in thermal conductivity by 10%, 16% and 18% for respective concentrations of 1000, 5000 and 10000 ppm.

Das et al. [7] investigated the increase in thermal conductivity with temperature and volume fraction for Al_2O_3 and CuO nanoparticles dispersed in water. The increase in effective thermal conductivity of nanofluids between 20 and 40 °C is found to be 15% for each type nanofluid. It was observed that in comparison with distilled water, the addition of nanoparticles gives a better enhancement with temperature for low volume fraction of particles. Terekhov et al. [8] reviewed experimental and theoretical results on heat transfer mechanism in nanofluids and concluded significant divergences in data of different researchers and possible reasons for this divergence. Lee et al. [9] used transient hot wire method to measure thermal conductivities of oxide nanofluids. The results shows that nanofluids have higher thermal conductivity than base fluid and the enhancement observed is 5%–60% increment in thermal conductivity for volume fraction ranging from 0.1% to 5%. Paisarn Naphon et al. [10] experimentally investigated titanium nanofluids on heat pipe thermal efficiency. The heat pipes with the de-ionic water, alcohol, and nanofluids (alcohol and nanoparticles) are tested. The titanium nanoparticles with diameter of 21 nm are used in the present study. Effects of percentage charge amount of working fluid, heat pipe tilt angle and percentage

* Corresponding author. Tel.: +91 422 2614430; fax: +91 422 2615615.
E-mail addresses: godson@karunya.edu, godasir@yahoo.co.in (L.G. Asirvatham), rajesh.mech335@gmail.com (R. Nimmagadda), somchai.won@kmutt.ac.th (S. Wongwises).

0017-9310/$ - see front matter © 2012 Elsevier Ltd. All rights reserved.
http://dx.doi.org/10.1016/j.ijheatmasstransfer.2012.11.037

Author's personal copy

Nomenclature

A	surface area (m^2)
C_p	specific heat (J/kg K)
d	outer diameter (m)
h	heat transfer coefficient (W/m^2 K)
K	thermal conductivity (W/m K)
L	length (m)
m	mass flow rate (kg/s)
Q	heat load (W)
q	heat flux (kW/m^2)
R	thermal resistance (°C/W)
ΔT	temperature difference (°C)
$\overline{T}$	average temperature (°C)
U	uncertainty

Subscript

A	adiabatic
C	condenser
CT	condenser temperature
CW	cooling water
c/s	cross-sectional
E	evaporator
EC	evaporator and condenser
ET	evaporator temperature
eff	effective
H.P	heat pipe
Inlet	inlet to condenser
nf	nanofluid
p	particle
Surf	surface
Vap	vapour
vs	vapour and surface
w	water

Greek Symbols

φ	volume fraction
ρ	density (kg/m^3)
μ	dynamic viscosity (kg/m-s)
Δ	increment

nanoparticles volume concentrations on the thermal efficiency of heat pipe are considered. For the heat pipe with 0.10% nanoparticles volume concentration, the thermal efficiency is 10.60% higher than that with the base fluid.

Riehl [11] has observed that a higher heat transfer coefficient can be seen when using nanoparticles in water under low heat input conditions. Tsaia et al. [12] investigated the influence of particle size on the heat pipe thermal performance. The study is based on the structural characteristics of gold nanoparticles of various sizes dispersed in aqueous solution on heat pipe thermal resistance. The thermal resistance of heat pipe ranges from 0.17 to 0.215 °C/W with different nanoparticle solutions. Furthermore, the thermal resistance of the heat pipes with nanoparticle solution is lower than that with DI water. Shafahi et al. [3] used a two-dimensional analysis to study the thermal performance of a cylindrical heat pipe using Al_2O_3, CuO, and TiO_2 nanoparticles suspended in water as the working fluid. The existence of optimum mass concentration to improve heat transfer performance is obtained as 5%, 15% and 7% for Al_2O_3, CuO, and TiO_2 respectively. It was found that smaller nanoparticles with particle diameter of 10 nm have a more pronounced effect on the temperature gradient along the heat pipe when compared to 40 nm. Kang et al. [13] used dilute dispersion of silver nano particles in pure water as working fluid in a circular heat pipe. The diameters of the nano particles used are 10 and 35 nm, respectively. The results showed that the nanofluid as working fluid in heat pipe can transport heat up to 70 W and is higher than pure water by about 20 W. Do et al. [14] investigated the effect of water-based Al_2O_3 nanofluids on the thermal performance of circular screen mesh wick heat pipes. The volume fraction of the nanoparticles used are 1 and 3 vol.%. It is found that the thermal resistance at the evaporator-adiabatic section decreases by 40% when using nanofluid with volume fraction of 3.0 vol.%. It is also shown that the use of water based Al_2O_3 nanofluids enhances the maximum heat transport rate of heat pipes. Do and Jang [15] evaluated the thermal performance of a heat pipe with rectangular grooved wick using water-based Al_2O_3 nanofluid. They found that the thin porous coating layer formed by nanoparticles is the key effect for higher heat transfer. The results showed the feasibility of enhancing the thermal performance up to 100% although water-based Al_2O_3 nanofluids with the concentration less than 1.0% is used as working fluid.

Yang et al. [16] carried out an experiment to study the heat transfer performance of a horizontal micro-grooved heat pipe using CuO–water nanofluids. Mass concentration of CuO nanoparticles ranging from 0.5 to 2.0 wt.% having the average diameter of 50 nm and the operating pressure varying from 7.45, 12.38 and 19.97 kPa, are respectively used. The experimental results showed that the CuO–water nanofluids can improve the thermal performance of the heat pipe at optimum mass concentration of 1 wt.%. Under an operating pressure of 7.45 kPa, the heat transfer coefficients of the evaporator can be averagely enhanced by 46% and the CHF (critical heat flux) can be maximally enhanced by 30% compared with those of the heat pipe using DI water. Guo-Shan Wang et al. [17] have carried out an experimental study on thermal performance of a cylindrical miniature grooved heat pipe using aqueous CuO nanofluids for two different operating conditions. One was the steady operating processes with constant cooling conditions and the other was the unsteady start up processes with constant cooling conditions. The start up characteristics of the heat pipe using nanofluids was especially compared with that of the heat pipe using water. The experimental results are useful for designing miniature grooved heat pipes using nano-fluids as the working liquid. It was found that the thermal performance of the heat pipe had a remarkable increase by adding CuO nanoparticles into the base liquid. For unsteady start-up process, substituting the nanofluid for water as the working fluid, cannot only improve the thermal performance, but also reduce significantly the start-up time. The total heat resistance was reduced by 50% and heat removal capacity increases by 40% for nanofluid based heat pipe when compared with that of heat pipe using water. Park et al. [18] and Shung-Wen Kang et al. [19] also observed in another study that silver nanofluid grooved heat pipe thermal performance was higher than that for a conventional grooved heat pipe with water as working fluid.

It is found from the above mentioned literature [10,12,13] that all the researchers have observed an enhancement in the thermal performance of heat pipes using nanofluids. It is also observed that most of the previous investigations have been performed with high concentrations of metal oxide nanoparticles [3,14–16]; and very little amount of work has been carried out with the use of pure metal nanoparticles in predicting the thermal performance of heat pipes. It is also reported that use of high concentration

Author's personal copy

nanoparticles will block the wick due to the deposited nanoparticles and causes more resistance on the returning fluid to reach from condenser to evaporator. This eventually results in early evaporator dry out and causes heat pipe failure. Moreover, the earlier experiments have been performed by measuring only the wall temperature to evaluate the heat transfer performance of heat pipes. Interestingly, it is observed from the present study that there exist 5.8 °C difference between the wall and vapour temperatures measured at the core of the evaporator. Hence, there is a need to analyze the performance of heat pipes by considering the effect of the temperature difference between the wall and the vapour core which have never before appeared in the open literature. Therefore, the present study aims to experimentally analyze the thermal performance of heat pipe using low volume concentration (0.003%, 0.006% and 0.009%) of pure metal (silver) nanoparticles by measuring both the vapour and wall temperatures at the same time in all the three regions. The effect of heat load on the quantities such as thermal resistance, axial temperature distribution, evaporation, condensation heat transfer coefficients, effective thermal conductivity etc. are experimentally analyzed on the basis of vapour core and wall temperatures are discussed and presented.

2. Experimentation

2.1. Experimental setup

The schematic layout of test facility to measure the effect of nanoparticle concentration on the performance of heat pipe is shown in Fig. 1. The test section is made up of copper with outer diameter and length as 10 and 180 mm, respectively. The wall thickness, lengths of evaporator section, adiabatic section and condenser section of the heat pipes are 0.5, 50, 50 and 80 mm, respectively. Two layers of copper wick with a wire diameter of 0.105 mm and mesh number 100/inch is wrapped inside the heat pipe. 30% of the total volume of the heat pipe is charged with working fluid to completely saturate the wick. The condenser section of the het pipe was inserted horizontally into a cooling chamber made up of acrylic material. The test set up also consists of a pump and flow meter (with an uncertainty of ±10 ml) to circulate cooling water at a constant flow rate of 260 ml per minute through the condenser section. A constant temperature chilled water bath is used to maintain the inlet temperature of the circulating cooling water at 24 °C for all the test sections at various heat loads to obtain performance accuracy. The temperatures of the cooling water circulating through the condenser section are recorded by using two T-type thermocouples fixed at inlet and outlet of the condenser. A total of eight thermo couple sensors with T-type thermocouples of uncertainty ±0.5 °C are fixed along the test section include two in evaporator, three in adiabatic and three in condenser section, respectively. These sensors will directly measure the vapour temperature which is passing through the centre core of the heat pipe from evaporator section to condenser section. The evaporator and condenser surface temperatures are measured by fixing four T-type thermocouples two on each section.

The heat input to the heat pipe is applied using a digital wattmeter (with an uncertainty of ±0.5 W) connected to an electric heater wounded on the evaporator section. A 220 V A.C supply is used to energize the heater. The evaporator and adiabatic sections of the heat pipe are completely insulated using glass wool to minimize the heat loss. The temperature readings of the test section are recorded by connecting thermo couples to data logger [Model-(DA 100-13-1F), Yokogawa-N 200]. The entire data acquisition system is monitored and controlled by using a P.C.

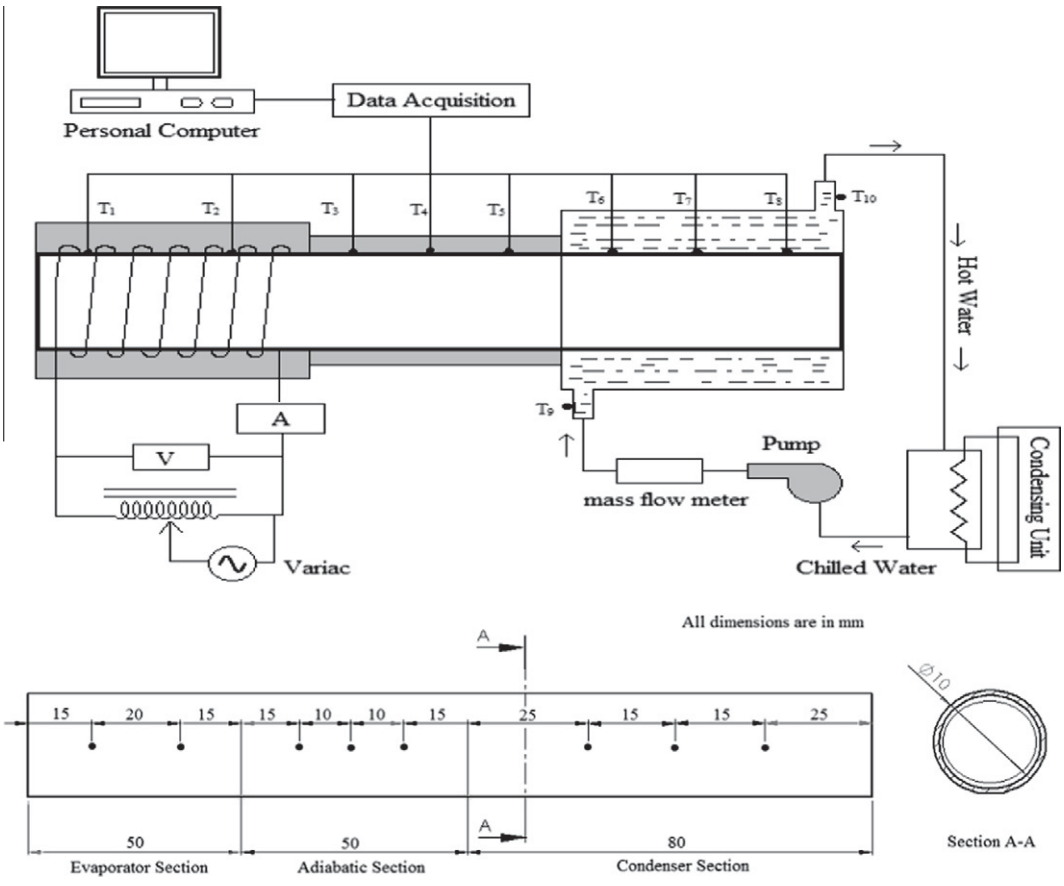

Fig. 1. Schematic diagram of the experimental apparatus.

Author's personal copy

2.2. Experimental procedure

2.2.1. Nanofluid preparation

The nanoparticles used in the present study is silver (manufactured by Sigma Aldrich; The Product Number - 576832, Silver nano-powder, <100 nm, 99.5% metals). A two step method is used to prepare silver–water nanofluid. The nanoparticles are mixed directly with De-ionized water without addition of any surfactant. The nanofluids are sonicated well for about 1 h in an ultra sonicator at sound frequencies of 50–60 kHz to ensure uniform and stable dispersion of nanoparticles in base fluid. The silver nanoparticles are further characterized by using scanning electron microscope (SEM) and particle size analyzer to study the size distribution and morphology. Fig. 2 shows the SEM image of 0.009 vol.% concentration of silver nanoparticles taken at 45,000X magnification. The size of the nanoparticles is marked in the SEM image. It is found that the size of the silver nanoparticles vary from 51 nm to 67 nm in some places. It is clearly seen that the nanoparticles are well dispersed with certain level of agglomeration. It is also observed that the size of the agglomerated nanoparticles exceed 100 nm in some places. Hence, the agglomerated nanoparticles are finely grinded in a ball grinder before adding to base fluid for sonication. Similarly, the size of the silver nanoparticles is measured using the particle size analyzer and shown in Fig. 3. It is clearly observed from the figure that the majority of the nanoparticles have the average size of 110–120 nm with an intensity of 13% and it is also seen from the peak that 10% of the nanoparticles have the size varying between 40 and 60 nm with 1.5% intensity. This justifies the average size of the silver nanoparticles used for the present study.

2.2.2. Experimental test

The experiments are conducted using four identical heat pipes in horizontal orientation which are fabricated as per mentioned dimensions. One of the heat pipes is filled with De-ionized water and remaining three heat pipes are filled with three different concentrations of silver–water nanofluid. The tests on all the four heat pipes are conducted under identical operating conditions such as constant flow rate and inlet temperature of the cooling water circulating through the condenser section. The power supply was turned on and the heater was energized with a heat load of 20 W. The steady state vapour temperature reading as well as surface temperature reading is recorded using data acquisition system. The input heat load is incremented gradually in equal steps from 20 W to beyond 100 W until dry out condition is reached.

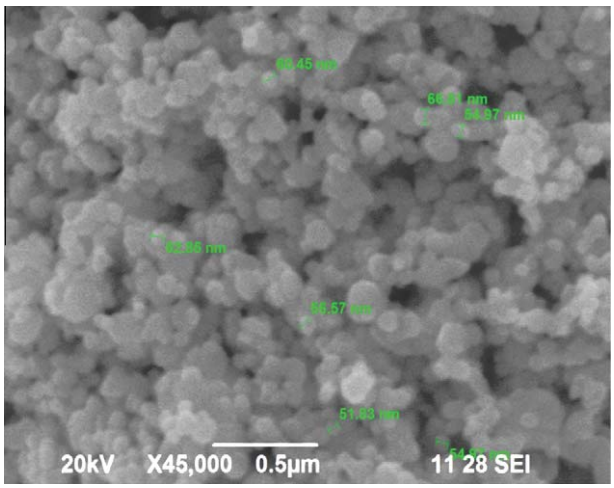

Fig. 2. SEM image of 0.009 vol.% concentration of silver nanoparticles.

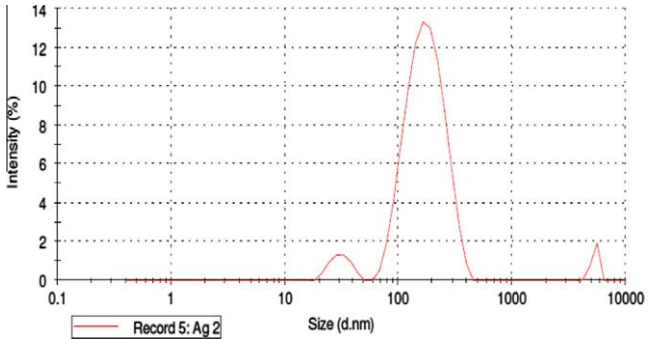

Fig. 3. Size distribution by intensity of the silver nanoparticles.

The heat input at which dry out condition is observed is assumed as maximum heat transport capability of heat pipe. At this condition the vapour temperature difference between evaporator and condenser abruptly increases.

2.3. Thermo physical properties of nanofluid

The thermo-physical properties of silver water nanofluid are calculated as follows.

The density is calculated from Pak and Cho [21] using the following equation:

$$\rho_{nf} = \varphi\rho_p + (1-\varphi)\rho_w \tag{1}$$

The specific heat is calculated from Xuan and Roetzel [22] as follows:

$$(\rho C_p)_{nf} = \varphi(\rho C_p)_p + (1-\varphi)(\rho C_p)_w \tag{2}$$

where $(\rho C_p)_{nf}$ is the heat capacity of the nanofluid, $(\rho C_p)_p$ is the heat capacity of the nanoparticles and $(\rho C_p)_w$ is the heat capacity of the base fluid.

The other properties such as viscosity and thermal conductivity are measured using the following equations proposed by the present authors. The detailed measurement techniques and procedure are given elsewhere [23] in a published literature for reference

$$\frac{\mu_{nf}}{\mu_w} = (1.005 + 0.497\varphi - 0.1149\varphi^2) \tag{3}$$

$$\frac{K_{nf}}{K_W} = (0.9692\varphi + 0.9508) \tag{4}$$

2.4. Data reduction

$$R_{H,P} = \frac{\overline{T}_{E,Vap} - \overline{T}_{C,Vap}}{Q} \tag{5}$$

The thermal resistance of heat pipe ($R_{H,P}$) is defined as the ratio of vapour temperature difference measured between evaporator and condenser ($\overline{T}_{E,Vap} - \overline{T}_{C,Vap}$) to the applied heat load (Q)

$$h_C = \frac{Q}{A_C \Delta T_C} \quad \text{where } A_C = \pi d_C L_C, \quad \Delta T_C = \overline{T}_{C,Vap} - \overline{T}_{C,Surf} \tag{6}$$

The condenser heat transfer coefficient (h_C) is defined as the ratio of heat load (Q) to the product of condenser surface area (A_C) and the temperature difference (ΔT_C) between vapour ($\overline{T}_{C,Vap}$) and surface ($\overline{T}_{C,Surf}$) in the condenser region. In the condenser region the vapour temperature ($\overline{T}_{C,Vap}$) is higher than the surface temperature ($\overline{T}_{C,Surf}$) due to heat rejection

Author's personal copy

$$h_E = \frac{Q}{A_E \Delta T_E} \quad \text{where } A_E = \pi d_E L_E, \quad \Delta T_E = \overline{T}_{E,Surf} - \overline{T}_{E,Vap} \tag{7}$$

The evaporator heat transfer coefficient (h_E) is defined as the ratio of applied heat load (Q) to the product of evaporator surface area (A_E) and the temperature difference (ΔT_E) between surface ($\overline{T}_{E,Surf}$) and vapour ($\overline{T}_{E,Vap}$) in the evaporator region. In the evaporator region the surface temperature ($\overline{T}_{E,Surf}$) is higher than the vapour temperature ($\overline{T}_{E,Vap}$) due to heat addition

$$K_{eff} = \frac{1}{A_{c/s,H,P} R_{H,P}} \quad \text{where } A_{c/s,H,P} = \frac{\pi}{4} d^2 \tag{8}$$

The effective thermal conductivity of heat pipe is defined as the inverse of product of cross sectional area of the heat pipe ($A_{c/s,H,P}$) and the thermal resistance of heat pipe ($R_{H,P}$).

2.4.1. Uncertainty analysis of measured parameters

$$\frac{\Delta Q}{Q} = \left[\left(\frac{\Delta V}{V}\right)^2 + \left(\frac{\Delta I}{I}\right)^2 + \left(\frac{\Delta L_E}{L_E}\right)^2 + \left(\frac{\Delta d_E}{d_E}\right)^2 \right]^{1/2} \tag{9}$$

Uncertainty in heat flux is calculated using Eq. (9). It is calculated based on the uncertainties in the applied voltage (ΔV), applied current (ΔI) to the heater coil. It also includes the uncertainties in the measured length (ΔL_E) and diameter (Δd_E) of the evaporator region over which heater coil is wrapped. The least count of the vernier calipers used to measure this length and diameter is taken as the uncertainty value

$$\frac{\Delta R}{R} = \left[\left(\frac{\Delta Q}{Q}\right)^2 + \left(\frac{\Delta(\Delta T)}{\Delta T_{EC}}\right)^2 \right]^{1/2} \tag{10}$$

Uncertainty in calculated thermal resistance is done using the Eq. (10). It depends on uncertainty in heat applied (ΔQ) and uncertainty in the measured temperature difference between evaporator and condenser ($\Delta(\Delta T)$). The actual temperature difference measured is found to be (ΔT_{EC})

$$\frac{\Delta h}{h} = \left[\left(\frac{UQ}{Q}\right)^2 + \left(\frac{U\Delta T}{\Delta T_{VS}}\right)^2 \right]^{1/2} \tag{11}$$

Uncertainty in the calculated heat transfer coefficient is made using Eq. (11). The calculation is done by taking into consideration all the uncertainties in the parameters on which heat transfer coefficient depends. The various uncertainties on which this heat transfer coefficient depends are uncertainty in the applied heat load (UQ) and uncertainty in the measured temperature difference between surface and vapour ($U\Delta T$). All these calculations are done to eliminate the experimental errors and the obtained results are taken from a standardized experimental test facility. The maximum uncertainties in thermal resistance and heat transfer coefficient are found to be 5.57% and 6.64%.

3. Results and discussion

The experiments are conducted for various heat loads (20, 40, 60, 80, 100 W) with heat pipes kept in horizontal position. The vapour temperatures as well as the surface temperature readings are recorded using thermocouples connected to a data acquisition system. The experimental results are compared between base fluid and nanofluid for all the concentrations and the enhancement in heat transfer performance with respect to concentration, heat load, thermo physical properties etc. are discussed in the following sub sections. Many day-to-day experiments have been conducted with the base fluid to check the repeatability in the experimental readings and found that the deviation between day1 and day2 reading is found to be less than 1.4%. The operating conditions of all the heat pipes such as evaporator heat load, cooling water inlet temperature and circulation rate are maintained constant for effective comparison of the results. Table 1 gives the experimental conditions chosen for the present study.

Table 1
Experimental conditions.

Working fluid charged (ml)	Q (W)	m_{CW} (kg/s)	$T_{CW,Inlet}$ (°C)
3.5	20	4.3333×10^{-3}	24
	40	4.3333×10^{-3}	24
	60	4.3333×10^{-3}	24
	80	4.3333×10^{-3}	24
	100	4.3333×10^{-3}	24

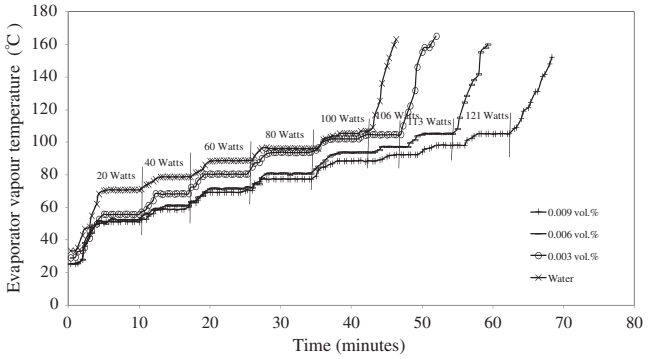

Fig. 4. Vapour temperature in the evaporator with respect to time in minutes.

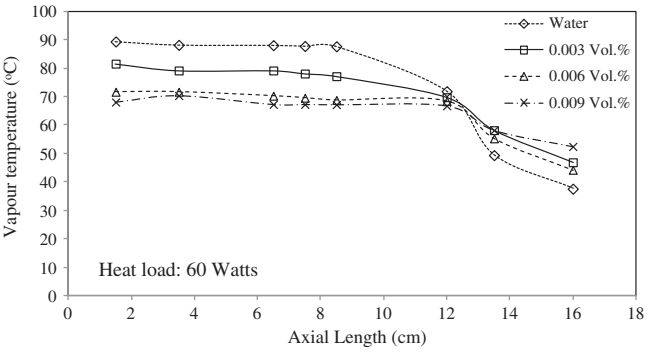

Fig. 5. Vapour temperature distribution with respect to axial length.

The vapour temperature in the evaporator section as a function of time for various heat loads and concentrations are shown in Fig. 4. It is observed that the steady state has been attained approximately after 15–20 min. The steady state temperature reading is taken for the analysis and data reduction. The dry out condition is observed beyond 100 W for heat pipes with DI water as working fluid. The vapour temperature reading decreases with the increase in concentration of nanofluid. This drop in temperature increases the operating range of heat pipe beyond 100 W, with nanofluid. It is also seen that for 0.003 and 0.006 vol.%, dry out is observed near 106 and 113 W. Whereas for heat pipe with 0.009 vol.% the dry out appears beyond 121 W. This shows that an increment of 21% in heat transfer capability is observed by using nanofluid as working fluid in heat pipe. The vapour temperature distribution along the axial length of the heat pipe for heat load of 60 W is shown in Fig. 5. It is clearly seen that a reduction in vapour temperature is observed by using nanofluids due to high thermal

Author's personal copy

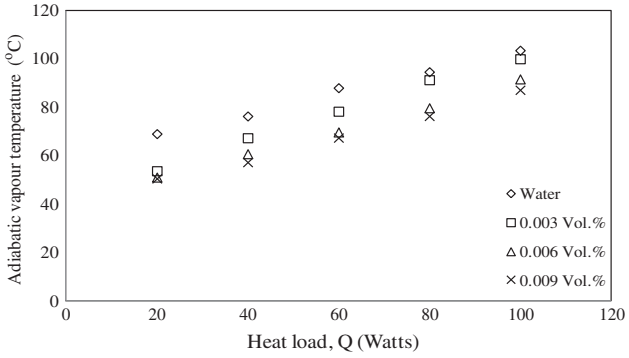

Fig. 6. Variation in adiabatic vapour temperature as a function of heat load.

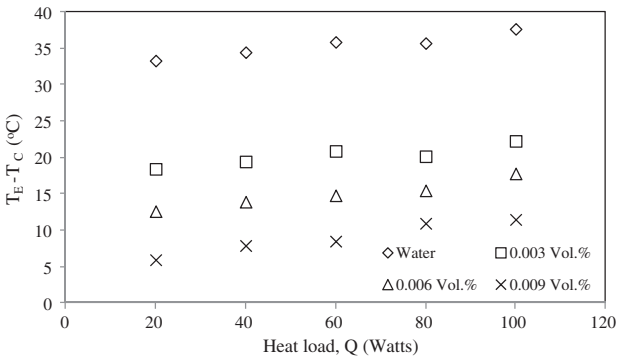

Fig. 8. Evaporator and condenser vapour temperature difference as a function of heat load.

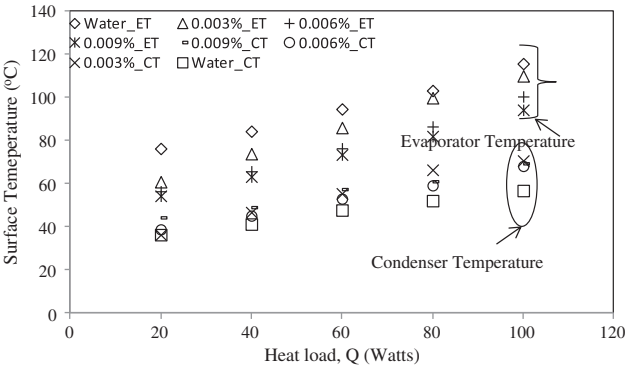

Fig. 7. Evaporator and condenser surface temperature as a function of heat load.

conductivity of silver nanoparticles. This reduces the vapour temperature inside the heat pipe. 19.5 °C temperature difference is observed in the evaporator for maximum concentration of the heat pipe when compared with DI water. Subsequent slight drop in vapour temperature is also observed in condenser section for a constant cooling water flow rate at constant inlet temperature. A slight drop of 1–2 °C is observed between evaporator and adiabatic chamber due to losses. The low vapour temperature for constant heat input indicates that an increment in the operating range of the heat load when compared with that of base fluid heat load.

The adiabatic vapour temperature as a function of heat load is shown in Fig. 6. It is observed from the figure that the adiabatic vapour temperature which is also called as operating temperature of heat pipe increases as heat load on the evaporator section increases and decreases as volume concentration of nanoparticles in base fluid increases. The reduction in this temperature indicates an effective heat transfer capability due to addition of additives in base fluid. 21.54% reduction is observed in case of heat pipe operating with 0.009 vol.% concentration. This increases the operating range of the heat pipe beyond 100 W which is the maximum heat load in the case of water based heat pipe. Similarly a reduction of 9.49% and 18.25% is observed respectively for 0.003 and 0.006 vol.% concentration when compared to heat pipe operating with water. The surface temperatures of evaporator and condenser with respect to various heat loads are shown in Fig. 7. The evaporator surface temperature increases with increment in heat load and decreases with increment in volume concentration of nanoparticles. This reduction in surface temperature enhances and aids faster cooling rate of the heat dissipating components. It is found that for the maximum volume concentration of 0.009%, the decrement in the evaporator surface temperature is 21 °C for input heat load of 60 W. Similarly the evaporator surface temperatures of heat pipes with volume concentration of 0.003% and 0.006% is reduced by 8.6 and 18.2 °C when compared to heat pipe with DI water. The lowering of the evaporator surface temperature with the increase in the volume concentration of nanoparticles permits the heat pipe with additional heat flow rate before reaching dry out condition. It is also found that the increase in volume concentration of nanoparticles in base fluid increases the condenser surface temperature due to effective heat rejection in condenser section.

The temperature difference between evaporator and condenser as a function of heat load is shown in Fig. 8. It is observed that the temperature difference between evaporator and condenser gradually decreases with respect to the increase in the concentration level of nano particles for a given heat load. It is found that for a constant temperature difference between evaporator and condenser the use of nanofluid allows the heat pipe to operate under larger heat loads. It is also seen that the temperature difference reduces by 72.57%, 56.39% and 42% respectively for 0.009, 0.006 and 0.003 vol.% of silver water nanofluid when compared to heat pipe operating with DI water. This reduction in temperature difference enhances an increment in heat transport capability of heat pipe. The reason for this is that the nanoparticles suspended in water forms a porous coating in the evaporator region. This increases the surface roughness and cause enhancement in the bubble formation, growth and collapse. The porous coating formed on the screen mesh wick eventually increases the evaporator heating surface and leads to high heat transfer. It also increases the pumping capability of the wick. Researchers like Kim et al. [24] and Yang et al. [16] indicated that the formation of coating layer by nanoparticles reduces the contact angle and increases the surface wettability and surface roughness. It is observed that the porous coating layer formed on the wick surface reduces the evaporator vapour temperature by increasing the evaporator heating surface. It also increases the wick capillary pumping ability and eventually induces liquid suction due to capillary wicking into the evaporator region, which enhances the maximum heat transport rate This eventually reduces the vapour temperature difference between evaporator and condenser.

The thermal resistances of the heat pipes are calculated based on the vapour temperatures to quantitatively evaluate the thermal performance of heat pipes using silver–water nanofluids. As shown in Fig. 9 the thermal resistances of heat pipes using both the base fluid and nanofluids are high at low heat loads as thick liquid film resides in the evaporator section. However the thermal resistance decreases rapidly as heat load increases. This reduction in thermal resistance of heat pipes using silver–water nanofluid is more when compared with that of the heat pipe operating with DI water. 40% reduction in thermal resistance is observed for 0.003 vol.% silver nanofluid when compared with that of DI water. It is also observed

Author's personal copy

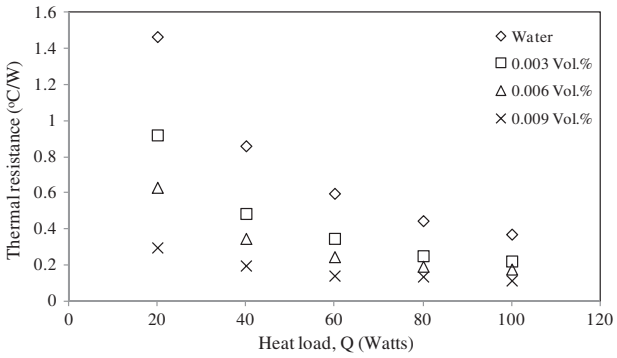

Fig. 9. Variation in thermal resistance as a function of heat load.

that this reduction in thermal resistance gradually increases as concentration of nanoparticles in base fluid increases. However for the maximum concentration of 0.009 vol.% of silver nanofluid, 76% reduction in thermal resistance is observed when compared with DI water. The thin porous coating layer formed by nanoparticles, not only improve the maximum heat transport rate but also significantly reduce the thermal resistance of the heat pipe using nanofluids is considered to be the main reason for the decrease in the thermal resistance of the heat pipe. Similar results have also been observed by Do et al. [14].

In order to check formation of the porous coating layer by addition of silver nanoparticles in the screen mesh wick surface of the evaporator region, a SEM image has been taken with the plain wick and the one with the addition of nanoparticles after conducting the experiments. The Fig. 10(a), shows the SEM image of the plain screen mesh wick surface without adding the nanoparticles. It is observed from the figure that the walls of the wick surface are found to be smooth and does have any pores or coating. However, the Fig. 10(b) shows the SEM image of the screen mesh wick surface with 0.009 vol.% of silver–water nanofluids. It clearly seen from the figure that there exists the porous coating layer which is formed by silver nanoparticles on the wick surface. This observation shows evidence for the formation of the thin porous coating layer at screen mesh wick of the evaporation region. The coating layer on the mesh wick surface provides an additional evaporating surface where high heat transfer rates occur. This drastically reduces the thermal resistance of the mesh wicked heat pipe and increases the capillary pumping ability to pull the liquid to the mesh wick surface. This leads to the enhancement in the heat transport rate of the of the heat pipe when using the silver–water nanofluid. The effective thermal conductivity of heat pipes with respect to various heat loads is shown in Fig. 11. It is clearly seen that the effective thermal conductivity of heat pipe increases with respect to heat load and concentration. The enhancement observed is 73.5% for 0.009 vol.% concentration of silver–water nanofluid. This concludes effective heat transfer is possible through the heat pipes employed with nanofluids. Similarly the heat pipes operating with 0.003 and 0.006 vol.% gives 42.4% and 56.8% increment in conductivity when compared with water based heat pipe.

The evaporation heat transfer coefficient as a function of heat flux is shown in Fig. 12. It is found that the evaporation heat transfer coefficients of heat pipe with silver–water nanofluid is higher when compared with that of the heat pipe with DI water for the same heat flux. The increment in nanoparticles volume concentration in base

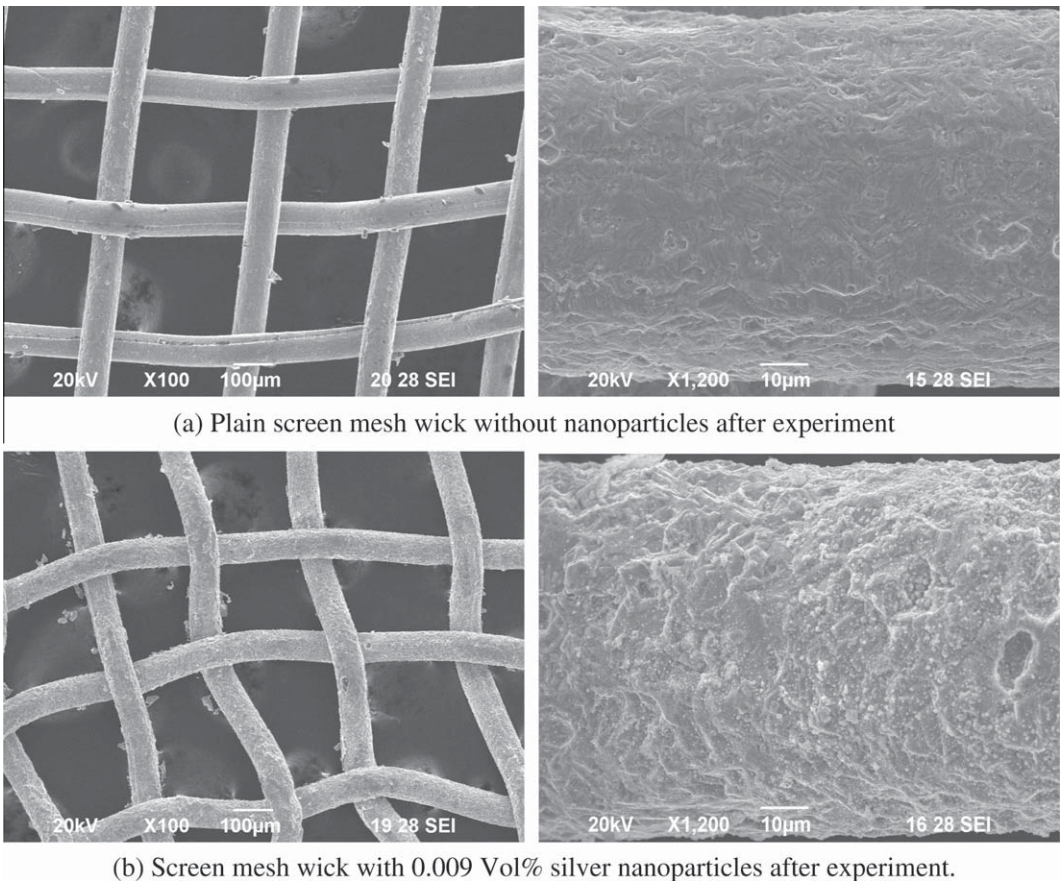

Fig. 10. SEM image of the screen mesh wick surface (a) plain screen mesh wick without nanoparticles after experiment; (b) Screen mesh wick with 0.009 vol.% silver nanoparticles after experiment.

Author's personal copy

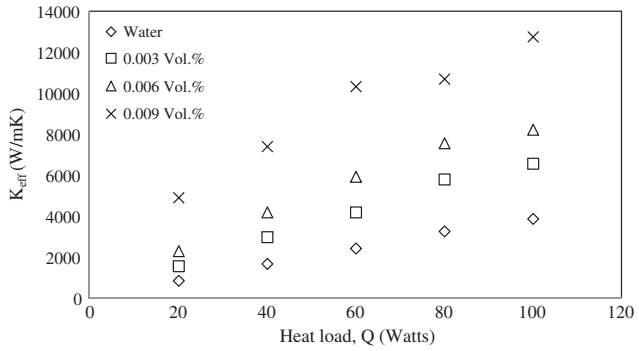

Fig. 11. Effective thermal conductivity of heat pipe as a function of heat load.

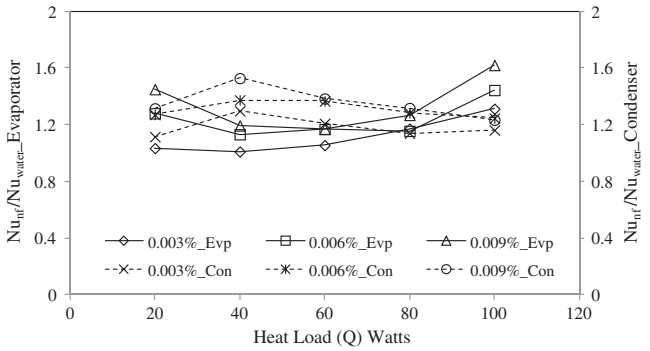

Fig. 13. Nusselt number ratio of evaporator and condenser as a function of heat load.

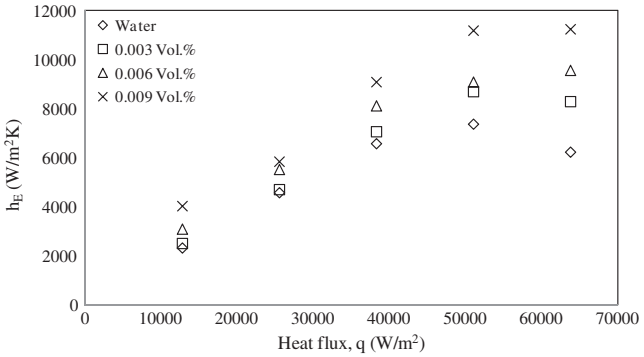

Fig. 12. Evaporation heat transfer coefficient with respect to the heat flux.

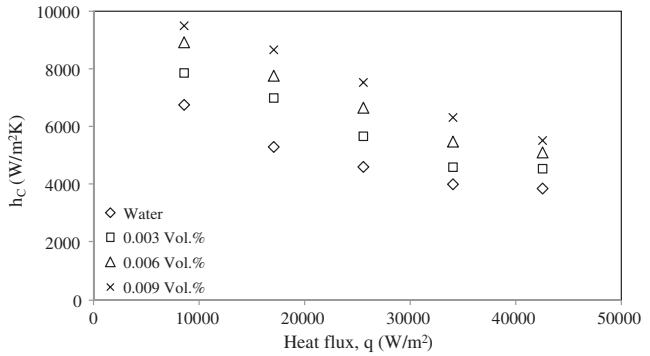

Fig. 14. Condensation heat transfer coefficient with respect to the heat flux.

fluid increases the evaporation heat transfer coefficient. For 0.009 vol.%, concentration an increment of 52.7% in evaporation heat transfer coefficient is observed experimentally when compared to heat pipe with DI water. It is mainly due to less temperature difference between the evaporator surface and vapour core. This concludes that the effective heat transfer is possible through heat pipes employed with nanofluids as working fluid. It is also found and clearly observed from Fig. 12 that the evaporation heat transfer coefficient of DI water based heat pipe decreases as the heat flux increases beyond 50 kW/m^2 due to reaching out of partial dry out condition. The reason for this is that the evaporator region is completely filled with vapour, since the optimum heat transport capacity of heat pipe is reached near 100 W; the heat pipe tends to move closer to the dry-out condition. Due to this partial dry out condition the temperature difference between evaporator surface and vapour increases and tends the heat transfer coefficient to decrease. However, for heat pipes with silver water nanofluid, the evaporation heat transfer coefficient still increases beyond the heat flux of 50 kW/m^2 because of higher heat transport capability employed with the presence of nanoparticles. From the observed results it is significantly seen that the presence of nanoparticles decreases the wall and the vapour temperatures which in turn increases the operating range of the pipe to higher heat flux when compared with that of the DI water.

The Nusselt number ratio of evaporator and condenser drawn respectively in the primary and secondary axis against heat load is shown in Fig. 13. It is observed that the Nusselt number ratio of both evaporator and condenser increases with the increase in the volume concentration of silver nanoparticles. At higher heat load the Nusselt number ratio for evaporator is found to be higher when compared with that of condenser Nusselt number ratio. As Nusselt number is a dimensionless parameter which depends on heat transfer coefficient, thermal conductivity of working fluid and characteristic length. It is found that at low heat load say for example (40 W) the Nusselt number ratio of condenser is more when compared with that of the evaporator. The reason is that the temperature difference (ΔT) between the wall surface and vapour core in the evaporator is high at low heat load and the temperature difference between the vapour core and the wall surface is less in the condenser section. This increases the heat transfer coefficient in the condenser which is directly proportional to the Nusselt number ratio at low heat loads and the inverse effect is found in the case of evaporator.

The condensation heat transfer coefficient as a function of heat flux is shown in Fig. 14. It is found that at low heat flux say for example (12 kW/m^2) the condensation heat transfer coefficient is more when compared with that of the evaporation heat transfer coefficient. The reason is that the temperature difference (ΔT) between the wall surface and vapour core in the evaporator is high at low heat flux and the temperature difference between the vapour core and the wall surface is less in the condenser section. Also the surface area of the condenser is more than the evaporator; since the length is 1.5 times the length of the evaporator section. As the heat flux increases the (ΔT) in evaporator decreases due to the formation of large number of small nucleation sites by the nanoparticle layer deposited on the heating surface. This eventually increases the evaporation heat transfer coefficient. However in condenser the (ΔT) increases with respect to heat flux, which results in a decrement in the condensation heat transfer coefficient. A similar trend of results has also been observed and reported in the published literature by Liu et al. [20]. Meantime, on an average the enhancement of the condensation heat transfer coefficient is also quite similar to that of the evaporation heat transfer coefficient for the same nanofluid. On the other hand, the condensation heat transfer coefficient curves has the similar trend for both water

Author's personal copy

and nanofluids at the present operating pressure, that describes actually a heat transfer characteristic of the convective condensation. The mode of heat transfer in evaporator and condenser is convective. The main reasons for the enhancement of heat transfer effect of nanofluid based heat pipes are:

1. The highly conductive nanoparticles in base fluid will increase the effective thermal conductivity of nanofluid.
2. During heat pipe operation, the working fluid travels through the porous wick and the nanoparticles present in it forms a coating layer on the wick and on the heating surface. This enhances the heat transfer effect of heat pipe.
3. The random motion (Brownian motion) of nanoparticles in base fluid causes the particles to collide with each other and with particles of DI water. This will enhance the heat transfer effect by convection. This Brownian motion is significant at higher temperatures.

4. Conclusion

The heat transfer performance of heat pipe using silver–water nanofluid with volume concentrations of 0.003%, 0.006% and 0.009% is experimentally investigated. It is clearly seen that by using silver–water nanofluid, the operating range of heat pipe increases beyond 100 W which is the maximum heat transport range for DI water based heat pipe. The dry out condition is observed near 106, 113 and 121 W respectively for 0.003, 0.006 and 0.009 vol.% concentrations. It is also observed that the thermal resistance of heat pipe decreases with the use of silver–water nanofluid, which in turn increases the effective thermal conductivity by 42.4%, 56.8% and 73.5% respectively for 0.003, 0.006, 0.009 vol.% concentrations. It is also observed that the evaporation and condensation heat transfer coefficients increases with the increases in the concentration of silver nanoparticles. Similarly, the difference between evaporator wall temperature and vapour temperature near a heat load of 60 W is observed to be 5.8, 5.4, 4.7 and 4.2 °C respectively for DI water, 0.003, 0.006 and 0.009 vol.% concentrations of the silver nanoparticles indicating the improved performance of heat pipes.

Acknowledgements

The authors would like to thank Mr. Seelan, Mr. P. Augustine and Mr. Jeyakumar of Karunya University for helping in the fabrication of the experimental test facility. The third author would like to thank the Thailand Research Fund for the supporting.

References

[1] Mariya Ivanova, Yvan Avenas, Christian Schaeffer, Jean-Bernard Dezord, Juergen Schulz-Harder, Heat pipe integrated in direct bonded copper (DBC) technology for cooling of power electronics packaging, IEEE Trans. Power Electron. 21 (6) (2006) 1541–1547.

[2] R. Sonan, S. Harmand, J. Pelle, D. Leger, M. Fakès, Transient thermal and hydrodynamic model of flat heat pipe for the cooling of electronics components, Int. J. Heat Mass Transfer 51 (25–26) (2008) 6006–6017.

[3] Maryam Shafai, Vincenzo Bianco, Kambiz Vafai, Oronzio Manca, An investigation of the thermal performance of cylindrical heat pipes using nanofluids, Int. J. Heat Mass Transfer 53 (2010) 376–383.

[4] S.U.S. Choi, Enhancing thermal conductivity of fluids with nanoparticles, ASME FED 231 (1995) 99–105.

[5] S. Kakac, A. Pramuanjaroenkij, Review of convective heat transfer enhancement with nanofluids, Int. J. Heat Mass Transfer 52 (2009) 3187–3196.

[6] Taehyun cho, Ilhyun Baek, Jonghee Lee, Sangdo Park, Preparation of nanofluids containing suspended silver particles for enhancing fluid thermal conductivity of fluids, J. Ind. Eng. Chem. 11 (3) (2005) 400–406.

[7] S.K. Das, N. Putra, P. Thiesen, W. Roetzel, Temperature dependence of thermal conductivity enhancement for nanofluids, J. Heat Transfer 125 (2003) 567–574.

[8] V.I. Terekhov, S.V. Kalinina, V.V. Lemanov, The mechanism of heat transfer in nanofluids, state of the art (review). Part 1. Synthesis and properties of nanofluids, Thermophys. Aeromech. 17 (1) (2010).

[9] S. Lee, S.U.S. Choi, S. Li, J.A. Eastman, Measuring thermal conductivity of fluids containing oxide nanoparticles, J. Heat Transfer 121 (1999) 280–289.

[10] Paisarn Naphon, Pichai Assadamongkol, Teerapong Borirak, Experimental investigation of titanium nanofluids on the heat pipe thermal efficiency, Int. Commun. Heat Mass Transfer 35 (10) (2008) 1316–1319.

[11] R.R. Riehl, Analysis of loop heat pipe behavior using nanofluid, in: Heat Powered Cycles International Conference (HPC), New Castle, UK, 2006, Paper: 06102.

[12] C.Y. Tsaia, H.T. Chiena, P.P. Dingb, B. Chanc, T.Y. Luhd, P.H. Chena, Effect of structural character of gold nanoparticles in nanofluid on heat pipe thermal performance, Mater. Lett. 58 (2004) 1461–1465, http://dx.doi.org/10.1016/j.matlet.2003.10.009.

[13] S. Kang, W. Wei, S. Tsai, C. Huang, Experimental investigation of nanofluids on sintered heat pipe thermal performance, Appl. Therm. Eng. 29 (5–6) (2009) 973–979.

[14] K. Do, H. Ha, S. Jang, Thermal resistance of screen mesh wick heat pipes using the water-based Al_2O_3 nanofluids, Int. J. Heat Mass Transfer 53 (25–26) (2010) 5888–5894.

[15] K.H. Do, S.P. Jang, Effect of nanofluids on the thermal performance of a flat micro heat pipe with a rectangular grooved wick, Int. J. Heat Mass Transfer 53 (9–10) (2010) 2183–2192.

[16] X.F. Yang, Z. Liu, J. Zhao, Heat transfer performance of a horizontal micro grooved heat pipe using CuO nanofluid, J. Micromech. Microeng. 18 (3) (2008) 035038.

[17] Guo-Shan Wang, Bin Song, Zhen-Hua Liu, Operation characteristics of cylindrical miniature grooved heat pipe using aqueous CuO nanofluids, Exp. Therm. Fluid Sci. 34 (8) (2010) 1415–1421.

[18] K.H. Park, W.H. Lee, K.W. Lee, I.H. Baek, S.H. Rhi, D.R. Shin, Study on the operating characteristics in small size heat pipe using nanofluids, in: Proceedings of the Third IASME/WSEAS International Conference on Heat Transfer, Thermal Engineering and Environment, Corfu Greece, August 20–25 (2005) pp. 106–109.

[19] Shung-Wen Kang, Wei-Chiang Wei, Sheng-Hong Tsai, Shih-Yu Yang, Experimental investigation of silver nanofluid on heat pipe thermal performance, Appl. Therm. Eng. 26 (17–18) (2006) 2377–2382.

[20] Zhen-Hua Liu, Yuan-Yang Li, Ran Bao, Compositive effect of nanoparticle parameter on thermal performance of cylindrical micro-grooved heat pipe using nanofluids, Int. J. Therm. Sci. 50 (2011) 558–568.

[21] Bock Choon Pak, I. Young Cho, Hydrodynamic and heat transfer study of dispersed fluids with sub-micron metallic oxide particles, Exp. Heat Transfer 11 (2) (1998) 151–170.

[22] Yimin Xuan, Wilfried Roetzel, Conceptions for heat transfer correlation of nanofluids, Int. J. Heat Mass Transfer 43 (19) (2000) 3701–3707.

[23] L. Godson, B. Raja, D. Mohan lal, S. Wongwises, Experimental investigation of thermal conductivity and viscosity of silver-deionized water nanofluid, Exp. Heat Transfer 23 (4) (2010) 317–332.

[24] H.D. Kim, J. Kim, M.H. Kim, Experimental studies on CHF characteristics of nanofluids at pool boiling, Int. J. Multiphase Flow 33 (2007) 691–706.

JOURNAL OF THERMOPHYSICS AND HEAT TRANSFER
Vol. 27, No. 1, January–March 2013

Entropy Generation Between Two Rotating Cylinders with Magnetohydrodynamic Flow Using Nanofluids

Omid Mahian*
Islamic Azad University, 91735 Mashhad, Iran
Shohel Mahmud†
University of Guelph, Guelph, Ontario N1G 2W1, Canada
and
Somchai Wongwises‡
King Mongkut's University of Technology Thonburi, Bangmod, Bangkok 10140, Thailand

DOI: 10.2514/1.T3908

The flow between two cylinders where one or both of the cylinders rotate has many practical applications such as swirl nozzles, rotating electrical machines, rotating disks, standard commercial rhymesters, and chemical and mechanical mixing equipment. In this paper, the effect of using TiO_2-water nanofluid ($\phi \leq 2\%$) on entropy generation between two corotating cylinders in the presence of magnetohydrodynamic flow is investigated. An analytical approach is applied to solve the simplified governing equations in the cylindrical coordinate system. To calculate the thermal conductivity and viscosity of the nanofluid, two correlations, which are based on the experimental data, are used. The velocity field is obtained as modified Bessel functions, and then, using the expansions of these Bessel functions with three terms, the temperature field and, subsequently, the entropy generation rate are estimated. The results are presented for various parameters, including the entropy generation number (N_S), Bejan number (Be), Hartmann number (M), Brinkman number (Br), and a group parameter ($\frac{\Omega}{Br}$). From the results, it is concluded that, at low Brinkman numbers (depending on the value of $\frac{\Omega}{Br_f}$), the average entropy generation number $(N_S)_{ave}$ decreases with the increase in nanoparticle volume fraction.

Downloaded by UNIVERSITY OF WATERLOO on February 10, 2013 | http://arc.aiaa.org | DOI: 10.2514/1.T3908

Nomenclature

Be	=	Bejan number
Br	=	Brinkman number
B_0	=	constant magnetic flux density
C_p	=	specific heat
E	=	electric field
Ec	=	Eckert number
J	=	electric current
k	=	thermal conductivity
M	=	Hartmann number
N_F	=	entropy generation number, fluid friction
N_H	=	entropy generation number, heat transfer
N_m	=	entropy generation number, magnetohydrodynamic flow
N_S	=	entropy generation number, total
$N_{S,a}$	=	augmentation entropy generation number
Pr	=	Prandtl number
Q	=	electric charge density
R	=	dimensionless radius
r	=	radius
$\dot{S}'''_{\text{gen}}$	=	entropy generation rate
T	=	temperature
u	=	peripheral velocity
$\boldsymbol{V}$	=	velocity vector
α	=	thermal diffusivity
Γn	=	constants of integration, $n = 1 \times$ to $\times$ 12
θ	=	dimensionless temperature
λ	=	velocity ratio
μ	=	dynamic viscosity
Π	=	radius ratio
ρ	=	density
ϕ	=	volume fraction of nanoparticles
Ω	=	dimensionless temperature difference
ω	=	angular velocity
$\forall$	=	volume

Subscripts

ave	=	average (overall value)
f	=	base fluid
nf	=	nanofluid
0	=	value at the inner cylinder
1	=	value at the outer cylinder

Received 27 February 2012; revision received 29 May 2012; accepted for publication 31 May 2012; published online 29 November 2012. Copyright © 2012 by the American Institute of Aeronautics and Astronautics, Inc. All rights reserved. Copies of this paper may be made for personal or internal use, on condition that the copier pay the $10.00 per-copy fee to the Copyright Clearance Center, Inc., 222 Rosewood Drive, Danvers, MA 01923; include the code 1533-6808/12 and $10.00 in correspondence with the CCC.

*Graduate Student, Young Researcher's Club, Mashhad Branch; omid.mahian@gmail.com (Corresponding Author).
†Assistant Professor, School of Engineering.
‡Professor, Fluid Mechanics, Thermal Engineering, and Multiphase Flow Research Laboratory (FUTURE), Department of Mechanical Engineering, Faculty of Engineering.

I. Introduction

IN THE last three decades, many studies have been conducted on the analysis of the second law of thermodynamics with the aim of entropy generation minimization to improve the performance of thermal engineering systems. Bejan [1,2] investigated the different effective factors behind entropy generation in heat transfer engineering, in which the destruction of useful energy (exergy) of a system occurs through entropy generation. Recently, Naterer and Camberos [3] presented past analytical methods of entropy generation minimization to numerical simulations involving more complex configurations and experimental measurement techniques. Of course, it should be noted that some researchers during the analysis of heat exchangers concluded that the minimum entropy generation is not always related to the optimal performance. Therefore, the parameter of heat exchanger effectiveness should be considered to examine the real performance of heat exchanges for avoiding the entropy generation paradox [4–7].

In recent years, various methods have been used to improve the performance of thermal engineering systems. One of these methods is using a nanofluid as the working fluid in heat transfer devices.

Downloaded by UNIVERSITY OF WATERLOO on February 10, 2013 | http://arc.aiaa.org | DOI: 10.2514/1.T3908

Nanofluid is the name given to a fluid in which nanometer-sized particles (1–100 nm) are suspended [8]. The enhancement of heat transfer using nanofluids is a relatively new field within the past decade. Currently, research groups worldwide are focusing on the properties of various nanofluids and their applications in different thermal engineering systems and devices [9]. For more recent studies on nanofluids, readers can refer to some research articles and review papers in which various models to calculate the thermophysical properties of nanofluids and their applications are reviewed [10–14]. Relatively little information is currently available on the effects of flow and heat transfer of nanofluids on entropy generation.

Here, the main studies concerning the second-law analysis of the flow and heat transfer of nanofluids are presented. Singh et al. [15] conducted an analytical analysis of entropy generation due to the flow and heat transfer of water-alumina nanofluids in different regimes within channels (with different sizes), including microchannels, minichannels, and conventional channels. Their results indicated that there is an optimum channel type in which entropy generation is minimized. They also found that using a water-alumina nanofluid with high viscosity in microchannels with laminar flow, as well as in minichannels and conventional channels with turbulent flow, is not beneficial. Li and Kleinstreuer [16] numerically investigated entropy generation due to the steady laminar flow of pure water and water-CuO nanofluids in trapezoidal microchannels. They determined that using nanofluids with very low particle loading reduces entropy generation at low Reynolds numbers. Feng and Kleinstreuer [17] considered the flow of an alumina-water nanofluid with heat transfer in a parallel disk system. They found that the total entropy generation rate decreases with an increase in the volume fraction of nanofluid.

Moghaddami et al. [18] analytically studied entropy generation due to water-Al_2O_3 and ethylene gylcol-Al_2O_3 nanofluid flow inside a circular pipe with constant heat flux for both laminar and turbulent regimes. Their results revealed that adding a volume fraction of nanofluids is effective only when irreversibility caused by heat transfer is dominant. Concerning the turbulent flow of water-Al_2O_3 nanofluid, they concluded that adding nanoparticles only for Reynolds numbers smaller than 40,000 decreases entropy generation, whereas for Reynolds numbers bigger than 80,000, entropy generation becomes higher in magnitude. Shahi et al. [19] studied numerically entropy generation due to the natural convection cooling of a heat source within a cavity filled by water-Cu nanofluid, in which the heat source can be mounted at different positions on the walls of the cavity. They investigated the effects of the Rayleigh number, nanoparticle concentration, and the position of the heat source on entropy generation. Esmaeilpour and Abdollahzadeh [20] investigated entropy generation numerically due to the natural convection of Cu-water nanofluids with a volume fraction from 0 to 10% inside a two-dimensional wavy enclosure. Their results showed that, with the addition of nanoparticles to a base fluid, the entropy generation rate decreases. Bianco et al. [21] presented a numerical analysis of the turbulent forced-convection flow of water-Al_2O_3 nanofluids inside a square tube with constant and uniform wall heat flux. They determined analytically the optimum Reynolds number at which entropy production becomes smallest. Recently, Falahat and Vosough [22] investigated entropy generation through a coiled tube heat exchanger with uniform wall heat flux conditions in both laminar and turbulent regimes using water-Al_2O_3 nanofluid. They obtained the optimum conditions based on the entropy generation sense for both laminar and turbulent regimes.

A review of the literature shows that there is no analytical report concerning the effect of using nanofluids on entropy generation between two concentric rotating cylinders in the presence of magnetohydrodynamic (MHD) flow. The flow between two cylinders where one or both of the cylinders rotate has many practical applications, such as swirl nozzles, rotating electrical machines, rotating disks, standard commercial rhymesters, and chemical and mechanical mixing equipment. In addition, the flow and heat transfer in annuli, where the outer cylinder rotates and the inner one is stationary, is an important research subject in many engineering applications, such as in the petroleum, food, and automobile industries [23,24].

Yilbas [23] conducted an entropy generation analysis for a rotating outer cylinder and differentially heated isothermal boundary condition assuming a linear velocity distribution in the annuli. Mahmud and Fraser [24,25] investigated entropy generation inside the cylindrical annular space with different boundary conditions. They simplified and solved governing equations in cylindrical coordinates to obtain analytical expressions for dimensionless entropy generation and the Bejan number as a function of the parameters involved in the problem. In another work, Mirzazadeh et al. [26] focused on entropy generation induced by the flow of a nonlinear viscoelastic fluid between concentric rotating cylinders.

Using an external magnetic field is of significant importance in many industrial applications, particularly as a control mechanism in material manufacturing [27]. In addition, the study of flow and heat transfer in a closed cavity or a channel in the presence of a magnetic field is important because of engineering applications such as the cooling of nuclear reactors, MHD micropumps, electronic packages, and microelectronic devices. In the past decade, the study of MHD flow and its effect on entropy generation in related systems has received extensive attention because of its importance in industry, as mentioned previously. Some works that investigated the effect of MHD flow on entropy generation for various flows and geometries are mentioned.

Salas et al. [28] analyzed the second law for MHD induction devices such as electromagnetic pumps and electrical generators. Ibanez et al. [29] optimized the operation conditions for an alternate MHD generator based on the global entropy generation rate. Mahmud et al. [30] studied the effect of a transverse magnetic field on entropy generation inside a vertical channel made of two parallel plates by considering mixed convection inside the channel. Later, Tasnim et al. [31] considered the same problem for porous media. Mahmud and Fraser [32] investigated the second law analytically for a mixed convection–radiation interaction in a vertical porous channel in the presence of MHD flow. Mahmud and Fraser [33] examined the problem of entropy generation in a fluid-saturated porous cavity for laminar natural convection heat transfer where the magnetic field is assumed to act along the direction of the force of gravity.

Ibanez and Cuevas [34] applied the approach of entropy generation minimization by considering joule dissipation, heat conduction, and viscosity to optimize the MHD flow between two infinite parallel walls with limited electrical conductivity. Mahmud and Fraser [35] presented a general relation for entropy generation for a single-plate thermoacoustic system that was exposed to a transverse magnetic field. Ibanez and Cuevas [36] considered a stationary buoyant MHD flow of a liquid metal immersed in a magnetic field through a vertical rectangular duct with thin conducting or insulating walls.

Arikoglu et al. [37] investigated the effect of slip and joule dissipation on entropy generation in a single rotating disk in the presence of MHD flow by a seminumerical analytical solution method, in which the magnetic field is constant and acts only in the axial direction. In addition, the effect of a magnetic field on entropy generation in a microchannel was investigated by Ibanez and Cuevas [38].

As mentioned, the aim of this study is to investigate the effect of using nanofluids on entropy generation between two rotating cylinders in the presence of MHD flow. The governing equations in cylindrical coordinates are simplified and analytically solved using isothermal boundary conditions to obtain the average entropy generation in the annulus.

II. Description of the Problem

The geometry of the cylindrical annulus considered is indicated in Fig. 1. A Newtonian nanofluid fills the gap between the inner and outer cylinders, which are of radii r_0 and r_1 and with constant surface temperatures of T_0 and T_1, respectively. The inner and outer cylinders can rotate with constant angular velocities of ω_0 and ω_1, respectively. A magnetic field (B_0) constantly acts in parallel to the axial direction

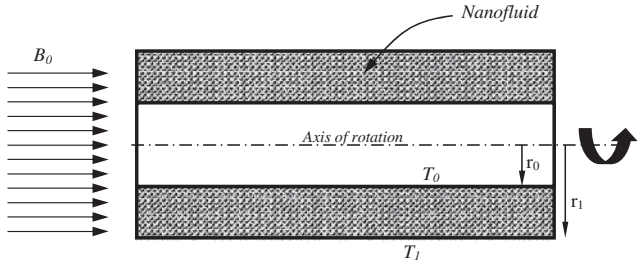

Fig. 1 Schematic diagram of the problem under consideration.

of the cylinders while the flow between the cylinders is laminar and steady.

It is assumed that the fluid and nanoparticles are in thermal equilibrium and that no slip occurs between them. It should be remarked that, in practical situations, most nanofluids used for enhancement of heat transfer are made up of very fine particles, normally less than 40 nm. Hence, the nanofluids can be considered to behave like a conventional, homogeneous, single-phase fluid [39]. Also, the thermophysical properties of the nanofluid are assumed to be constant. In the present work, TiO_2-water nanofluid is considered in the analysis.

III. Problem Formulation and Analysis

A. First Law Analysis

With the assumption of no relative axial motion between the cylinders and ignoring the radial velocity component compared to the tangential one, the momentum equation in cylindrical coordinates is simplified as follows:

$$\left(\frac{\partial^2 u_\theta}{\partial r2}+\frac{1}{r}\frac{\partial u_\theta}{\partial r}-\frac{u_\theta}{r^2}\right)-\frac{\sigma B_0^2}{\mu_{\rm nf}}u_\theta=0 \tag{1}$$

where u_θ is the tangential velocity component and σ is the fluid's electrical conductivity. The energy equation disregarding the convection term becomes (see Jiji [40] for details)

$$\frac{k_{\rm nf}}{r}\frac{\partial}{\partial r}\left(r\frac{\partial T}{\partial r}\right)=-\mu_{\rm nf}\left(\frac{\partial u_\theta}{\partial r}-\frac{u_\theta}{r}\right)^2 \tag{2}$$

The boundary conditions for the momentum and energy equations are as follows:

$$\begin{aligned} &r=r_0\colon\ u_\theta=u_0=r_0\omega_0 \quad \text{and} \quad T=T_0\\ &r=r_1\colon\ u_\theta=u_1=r_1\omega_1 \quad \text{and} \quad T=T_1 \end{aligned} \tag{3}$$

To calculate the thermal conductivity ($k_{\rm nf}$) and viscosity ($\mu_{\rm nf}$) of the nanofluid, the Duangthongsuk and Wongwises equations [41], which are based on experimental results, are considered as follows:

$$\frac{k_{\rm nf}}{k_f}=1.0204+0.0249\phi \tag{4}$$

$$\frac{\mu_{\rm nf}}{\mu_f}=1.013+0.092\phi-0.015\phi^2 \tag{5}$$

In the previous relation, ϕ is the volume fraction of nanoparticles, and k_f and μ_f are the thermal conductivity and viscosity of the base fluid, respectively. It should be stated that Eqs. (4) and (5) are valid for 0.2–2 vol % of TiO_2-water nanofluid. These relations are obtained for 25° C, but in this work, the properties of nanofluids are assumed to be independent of temperature.

Using the following dimensionless parameters and considering the outer cylinder as the reference,

$$\begin{aligned} &R=\frac{r}{r_1},\quad U=\frac{u_\theta}{r_1\omega_1},\quad \theta=\frac{T-T_1}{T_0-T_1},\quad \Pi=\frac{r_0}{r_1},\\ &\lambda=\frac{\omega_0}{\omega_1}\quad Pr_f=\frac{\mu_f C_{p,f}}{k_f},\quad Ec_f=\frac{(r_1\omega_1)^2}{C_{p,f}\Delta T},\quad M^2=\frac{\sigma B_0^2}{\mu_f}r_1^2 \end{aligned} \tag{6}$$

The governing equations in dimensionless form can be expressed as follows: Momentum equation:

$$\begin{aligned} &R^2\frac{\partial^2 U}{\partial R^2}+R\frac{\partial U}{\partial R}-\left[1+\left(\frac{\mu_f}{\mu_{\rm nf}}\right)M^2R^2\right]U=0 R=\Pi\colon\ U=\Pi\lambda\\ &R=1\colon\ U=1 \end{aligned} \tag{7}$$

Energy equation:

$$\begin{aligned} &\frac{1}{R}\frac{\partial}{\partial R}\left(R\frac{\partial\theta}{\partial R}\right)=-Ec_f Pr_f\left(\frac{\mu_{\rm nf}}{\mu_f}\right)\left(\frac{k_f}{k_{\rm nf}}\right)\left(\frac{\partial U}{\partial R}-\frac{U}{R}\right)^2\ R=\Pi\colon\ \theta=1\\ &R=1\colon\ \theta=0 \end{aligned} \tag{8}$$

where M is the Hartmann number, Ec_f is the Eckert number, and Pr_f is the Prandtl number. By noting that the multiplication of $(\mu_f/\mu_{\rm nf})$ by M^2 is a positive quantity, and then by considering $H^2=(\mu_f/\mu_{\rm nf})M^2$, the solution of the momentum equation is obtained as follows:

$$U(R)=\Gamma_1 I_1(HR)+\Gamma_2 K_1(HR) \tag{9}$$

where $I_1(HR)$ is known as the modified Bessel function of the first kind, of order 1, and $K_1(HR)$ as the modified Bessel function of the second kind, of order 1. The constants of integration Γ_1 and Γ_2 can be calculated while applying the boundary conditions; therefore, the constants are obtained as follows:

$$\begin{aligned} \Gamma_1&=\frac{\Pi\lambda K_1(H)-K_1(H\Pi)}{I_1(H\Pi)K_1(H)-K_1(H\Pi)I_1(H)}\\ \Gamma_2&=\frac{\Pi\lambda I_1(H)-I_1(H\Pi)}{K_1(H\Pi)I_1(H)-I_1(H\Pi)K_1(H)} \end{aligned} \tag{10}$$

To find the temperature field from Eq. (8), the expansions of the Bessel functions $I_1(HR)$ and $K_1(HR)$, with three terms, are used as follows:

$$\begin{aligned} I_1(HR)&\cong\frac{1}{2}HR+\frac{(HR)^3}{16}+\frac{(HR)^5}{384}\\ K_1(HR)&\cong\frac{1}{HR}+\left[\frac{1}{2}\ln\left(\frac{HR}{2}\right)-\frac{1}{4}(-2\gamma+1)\right](HR)\\ &\quad+\left[\frac{1}{16}\ln\left(\frac{HR}{2}\right)-\frac{1}{32}\left(\frac{5}{2}-2\gamma\right)\right](HR)^3 \end{aligned} \tag{11}$$

in which

$$\gamma\approx 0.57722\ldots$$

By substituting the values of $I_1(HR)$ and $K_1(HR)$ for the expansions in the velocity distribution equation [Eq. (9)], and using the new velocity distribution in Eq. (8), the temperature gradient that is required in the entropy generation analysis is given as follows:

Downloaded by UNIVERSITY OF WATERLOO on February 10, 2013 | http://arc.aiaa.org | DOI: 10.2514/1.T3908

$$\frac{\partial\theta}{\partial R}=\frac{\Gamma_3}{R}+\left(\frac{\mu_{\rm nf}}{\mu_f}\right)\left(\frac{k_f}{k_{\rm nf}}\right)\frac{Br_f}{R}\times\left[\begin{array}{l}2\Gamma_2^2\ \ln\left(\frac{HR}{2}\right)+\frac{2\Gamma_2^2}{H^2R^2}+\Gamma_5(HR)^6\ \ln\left(\frac{HR}{2}\right)\\+\Gamma_6(HR)^6-\frac{1}{384}\Gamma_2^2(HR)^6\left[\ln\left(\frac{HR}{2}\right)\right]^2\\+\Gamma_7(HR)^2+\Gamma_8(HR)^4-\frac{1}{32}\Gamma_2^2(HR)^4\ \ln\left(\frac{HR}{2}\right)\\+\Gamma_9(HR)^8-\frac{1}{3072}\Gamma_1\Gamma_2(HR)^8\ \ln\left(\frac{HR}{2}\right)-\frac{1}{92{,}160}(HR)^{10}\Gamma_1^2\end{array}\right]\tag{12}$$

In this equation, Br_f is the Brinkman number that is the multiplication of Ec_f by Pr_f. Also, Γ_3 is the constant of integration and the constants Γ_5 to Γ_9 are in terms of Γ_1, Γ_2, and γ as follows:

$$\begin{aligned}\Gamma_5&=\frac{11}{2304}\Gamma_2^2-\frac{1}{192}\Gamma_1\Gamma_2-\frac{1}{192}\Gamma_2^2\gamma\\\Gamma_6&=\frac{11}{2304}\Gamma_2^2\gamma+\frac{7}{2304}\Gamma_1\Gamma_2-\frac{1}{384}\Gamma_2^2\gamma^2-\frac{1}{384}\Gamma_1^2\\&\quad-\frac{125}{55,296}\Gamma_2^2-\frac{1}{192}\Gamma_1\Gamma_2\gamma\\\Gamma_7&=\frac{1}{4}\Gamma_2^2\gamma-\frac{7}{16}\Gamma_2^2+\frac{1}{4}\Gamma_1\Gamma_2\\\Gamma_8&=\frac{1}{32}\Gamma_2^2-\frac{1}{32}\Gamma_2^2\gamma-\frac{1}{48}\Gamma_1\Gamma_2\\\Gamma_9&=\frac{7}{24,576}\Gamma_1\Gamma_2-\frac{1}{3072}\Gamma_1\Gamma_2\gamma-\frac{1}{3072}\Gamma_1^2\end{aligned}$$

Therefore, the temperature field is given by integrating Eq. (12) as follows:

$$\theta=\Gamma_4+\Gamma_3\ \ln(R)\quad+\left(\frac{\mu_{\rm nf}}{\mu_f}\right)\left(\frac{k_f}{k_{\rm nf}}\right)Br_f\left\{\begin{array}{l}\Gamma_{10}(HR)^6+\Gamma_{11}(HR)^8+\Gamma_{12}(HR)^4+\frac{1}{2}\Gamma_7(HR)^2-\frac{1}{921{,}600}\Gamma_1^2(HR)^{10}\\+\Gamma_2^2\left[\ln\left(\frac{HR}{2}\right)\right]^2-\frac{\Gamma_2^2}{(HR)^2}+\frac{1}{6}\Gamma_5\ \ln\left(\frac{HR}{2}\right)(HR)^6-\frac{1}{2304}\Gamma_2^2\left[\ln\left(\frac{HR}{2}\right)\right]^2(HR)^6\\+\frac{1}{6912}\Gamma_2^2\ \ln\left(\frac{HR}{2}\right)(HR)^6-\frac{1}{128}\Gamma_2^2\ \ln\left(\frac{HR}{2}\right)(HR)^4-\frac{1}{24{,}576}\Gamma_1\Gamma_2\ \ln\left(\frac{HR}{2}\right)(HR)^8\end{array}\right\}\tag{13}$$

The constants of integration Γ_3 and Γ_4 will be readily obtained using isothermal boundary conditions. To conserve space, the expressions for Γ_3 and Γ_4 are not presented here due to length constraints. Constants Γ_{10}, Γ_{11}, and Γ_{12} are given as follows:

$$\Gamma_{10}=-\frac{1}{36}\Gamma_5+\frac{1}{6}\Gamma_6-\frac{1}{41,472}\Gamma_2^2\quad\Gamma_{11}=\frac{1}{8}\Gamma_9+\frac{1}{196,608}\Gamma_1\Gamma_2$$
$$\Gamma_{12}=\frac{1}{4}\Gamma_8+\frac{1}{512}\Gamma_2^2$$

B. Entropy Generation Analysis

In the presence of a magnetic field, the local volumetric entropy generation rate can be expressed as follows (see [37] with a similar analysis):

$$\dot{S}'''_{\rm gen}=\frac{k_{\rm nf}}{T_1^2}[\nabla T]^2+\frac{\mu_{\rm nf}}{T_1}\phi+\frac{1}{T_1}[(J-QV)(E+V\times B)]\tag{14}$$

where

$$J=\sigma(E+V\times B)\tag{15}$$

In Eq. (14), ϕ is viscous dissipation, J is the electric current, Q is the electric charge density, V is the velocity vector, E is the electric field, and B is the magnetic induction. Assuming that QV is negligible compared with J, and disregarding E in comparison with $V\times B$, the entropy production rate [Eq. (14)] decreases in this case to

$$\dot{S}'''_{\rm gen}=\frac{k_{\rm nf}}{T_1^2}\left(\frac{\partial T}{\partial r}\right)^2+\frac{\mu_{\rm nf}}{T_1}\left[r\frac{\partial}{\partial r}\left(\frac{u}{r}\right)\right]^2+\frac{\sigma B_0^2}{T_1}u^2\tag{16}$$

Equation (16) shows that entropy generation is due to three effects: a conductive effect ($k_{\rm nf}$), a viscous effect ($\mu_{\rm nf}$), and a magnetic effect (B_0). Defining N_S as the entropy generation number, the dimensionless form of Eq. (16) can be expressed as follows:

$$\begin{aligned}N_S&=\frac{\dot{S}'''_{\rm gen}}{\left(\frac{\mu_{\rm nf}\omega_1^2}{T_1}\right)}=\frac{\Omega}{Br_f}\left(\frac{k_{\rm nf}}{k_f}\right)\left(\frac{\mu_f}{\mu_{\rm nf}}\right)\left(\frac{\partial\theta}{\partial R}\right)^2+\left(R\frac{\partial}{\partial R}\left(\frac{U}{R}\right)\right)^2+H^2U^2\\&=N_H+N_F+N_M\end{aligned}\tag{17}$$

where Ω is the dimensionless temperature difference, which equals $\Delta T/T_1$. On the right side of Eq. (17), the first term ($=N_H$) is the local entropy generation due to heat transfer irreversibility, the second term ($=N_F$) is the local entropy generation due to fluid friction irreversibility, and the last term ($=N_M$) is the local entropy generation due to the magnetic field. To calculate the entropy generation number N_S in Eq. (17), the terms N_F and N_M are determined directly by using Eq. (9) without any approximation, unlike the term N_H, in which the temperature gradient is obtained using approximation.

To evaluate the irreversibility distribution, the parameter Be (Bejan number), which is the ratio of entropy generation due to heat transfer to the overall entropy generation [42], is defined as follows:

$$Be=\frac{N_H}{N_H+N_F+N_M}\tag{18}$$

The Bejan number varies from 0 to 1. Subsequently, $Be=0$ reveals that the irreversibility due to fluid friction and magnetic field dominates, whereas $Be=1$ indicates that the irreversibility due to heat transfer is dominant. It is obvious that $Be=0.5$ is the case in which the irreversibility due to heat transfer is equal to fluid friction and magnetic field contributions in the entropy production.

The volumetric averaged entropy generation rate, $(N_S)_{\rm ave}$, can be obtained using Eq. (17) as follows:

$$(N_S)_{\rm ave}=\frac{1}{\forall}\int_{\forall}N_S\,{\rm d}\forall=\frac{2}{(1-\Pi^2)}\int N_SR\,{\rm d}R\tag{19}$$

or

$$(N_S)_{\rm ave}=\frac{2}{(1-\Pi^2)}\int(N_H+N_F+N_M)R\,{\rm d}R\tag{20}$$

From this relation, it is possible to evaluate the contributions of heat transfer, fluid friction, and the magnetic field in the averaged entropy

Downloaded by UNIVERSITY OF WATERLOO on February 10, 2013 | http://arc.aiaa.org | DOI: 10.2514/1.T3908

Downloaded by UNIVERSITY OF WATERLOO on February 10, 2013 | http://arc.aiaa.org | DOI: 10.2514/1.T3908

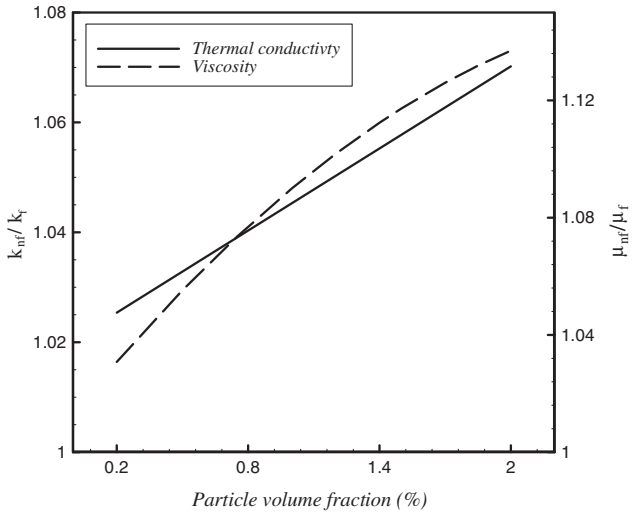

Fig. 2 Variations of the thermal conductivity and viscosity ratios with particle volume fraction.

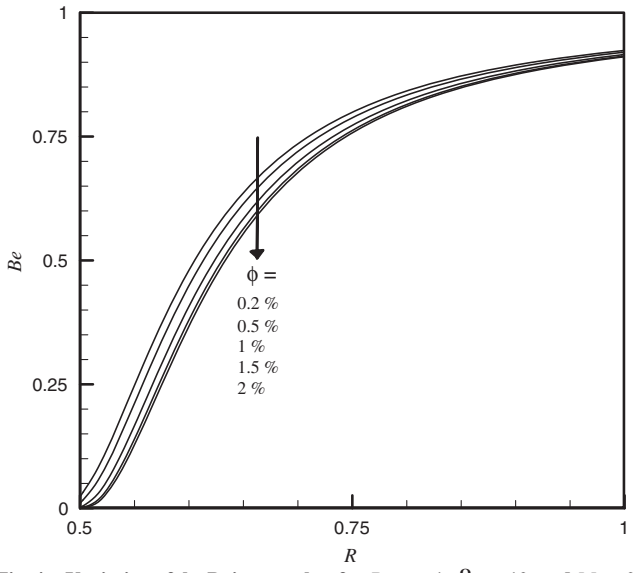

Fig. 4 Variation of the Bejan number for $Br_f = 1$, $\frac{\Omega}{Br_f} = 10$, and $M = 0$ at different nanoparticle volume fractions.

generation. It should be noted that, in practical applications, the inner cylinder is assumed at rest, and therefore the velocity ratio ($\lambda = \frac{\omega_0}{\omega_1}$) becomes zero. It is also assumed that the radius ratio ($\Pi = \frac{r_0}{r_1}$) is equal to 0.5.

IV. Results and Discussion

Figure 2 shows the variations of the thermal conductivity ratio ($\frac{k_{nf}}{k_f}$) and the viscosity ratio ($\frac{\mu_{nf}}{\mu_f}$) of the nanofluid with the particle volume fraction for TiO_2-water nanofluid. It was observed that, as the particle volume fraction increased up to 2 vol %, the thermal conductivity and viscosity increased by ~7 and ~14%, respectively.

The variation of the entropy generation number (N_S) with radial distance (R) is shown in Fig. 3 for $Br_f = 1$, $\frac{\Omega}{Br_f} = 10$, $M = 0$, and volume fraction (ϕ) from 0.2 to 2%. The figure reveals that the temperature and velocity gradients are highest on the inner cylinder, whereas the minimum gradients occur on the outer cylinder. As shown, with the increase in volume fraction, the entropy generation number falls in the gap due to the decreasing temperature gradients in the annulus. In this case, the temperature gradients decrease, because with an increase in the volume fraction the effective thermal conductivity increases. Consequently, the thermal conductance in the gap enhances, and the irreversibility due to heat transfer decreases. It also is seen that the decreasing tendency in the entropy generation number is more obvious between $\phi = 0.5\%$ to $\phi = 1\%$ compared with $\phi = 1.5\%$ to $\phi = 2\%$. This is because the effects of viscosity and fluid friction are higher at high volume fractions than at low volume fractions; therefore, the decreases in entropy generation decrease.

The variation of the Bejan number with radial distance is displayed in Fig. 4 for the same conditions of Fig. 3. As shown in Fig. 4, the Bejan number falls in the annulus in response to an increase in the particle volume fraction. This phenomenon can be described by considering the definition of the Bejan number in Eq. (18). When the particle volume fraction increases, the effective viscosity in the annulus increases; hence, the irreversibility due to fluid friction (N_F) increases. Thus, Be decreases with an increase in N_F, because N_F is in the denominator of Eq. (18). On the other hand, increasing the volume fraction leads to the increase of effective thermal conductivity; hence, the irreversibility due to heat transfer (N_H) decreases. Therefore, the Bejan number decreases due to the increase in nanoparticle loading, and the Bejan number is maximized on the

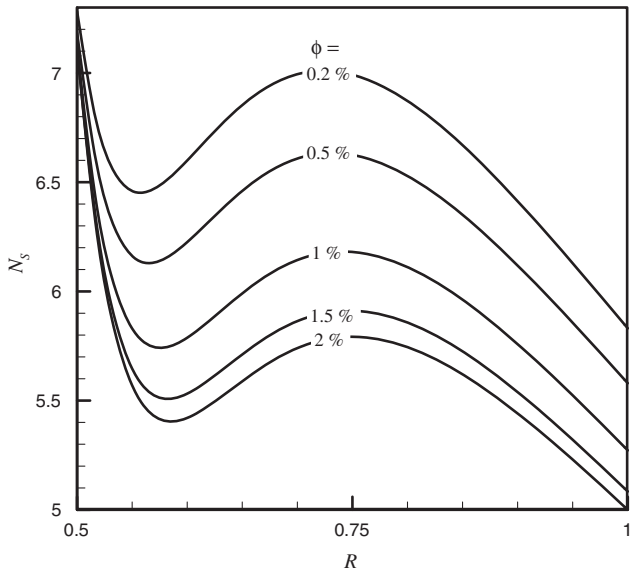

Fig. 3 Variation of the entropy generation number for $Br_f = 1$, $\frac{\Omega}{Br_f} = 10$, and $M = 0$ at different nanoparticle volume fractions.

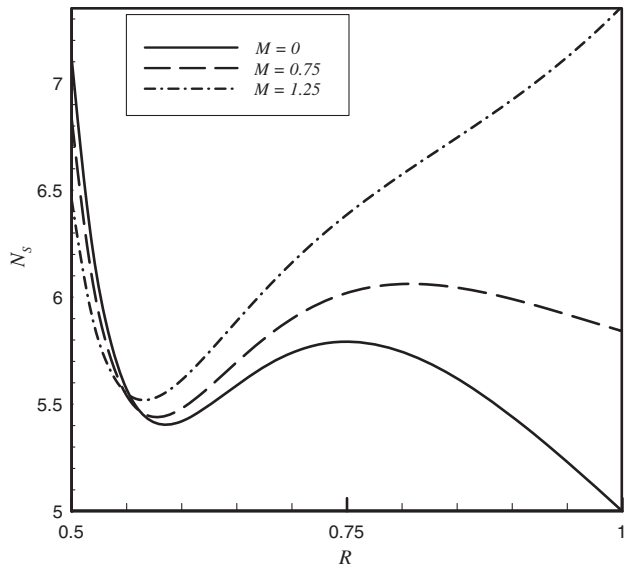

Fig. 5 Variation of the entropy generation number for $Br_f = 1$, $\frac{\Omega}{Br_f} = 10$, $\phi = 2\%$, and different values of the Hartmann number.

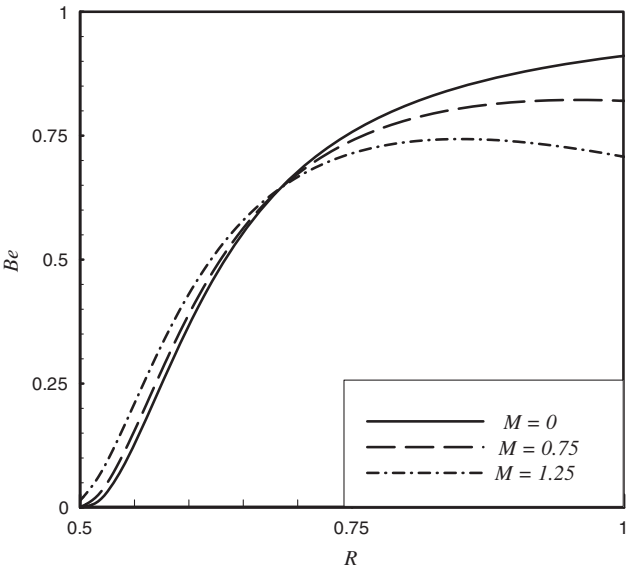

Fig. 6 Variation of the Bejan number for $Br_f = 1$, $\frac{\Omega}{Br_f} = 10$, $\phi = 2\%$, and different values of the Hartmann number.

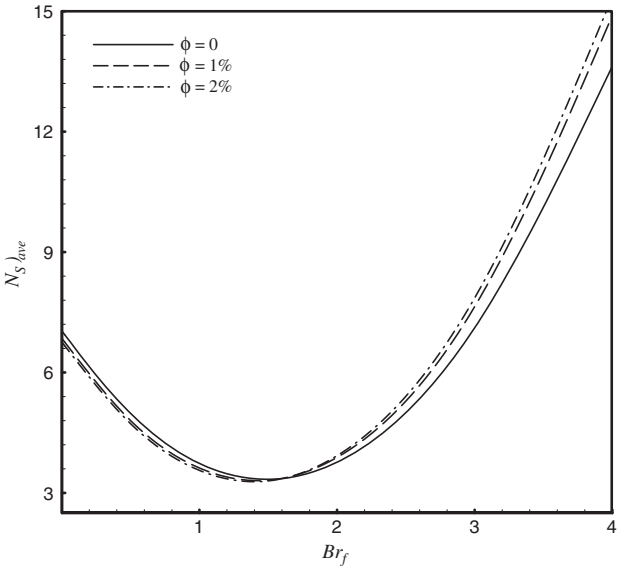

Fig. 8 Effect of nanoparticle loading on the average entropy generation number at different Brinkman numbers for $\frac{\Omega}{Br_f} = 1$.

outer cylinder. This indicates that in regions near the outer cylinder, the contribution of heat transfer to entropy generation is greater than in other regions.

The variation of the entropy generation number with radial distance is indicated in Fig. 5 for $Br_f = 1$, $\frac{\Omega}{Br_f} = 10$, $\phi = 2\%$, and three different values of the Hartmann number. It was found that the entropy generation number in the vicinity of the inner cylinder decreased a little with an increase in the Hartmann number from 0 to 1.25, whereas, with movement toward the outer cylinder, the entropy generation number increased with the increasing intensity of the magnetic field. In other words, as the Hartmann number increases, the gradients near the outer cylinder increase. In this case, an enhanced magnetic field leads to a decrease in the fluid velocity, and consequently, the boundary layer thickness in the annulus decreases. This leads to the increases in the velocity gradients.

Figure 6 shows the variation of the Bejan number with radial distance for the same conditions of Fig. 5. It was observed that an increase in the Hartmann number decreased the contribution of heat transfer in entropy generation near the outer cylinder; thus, Be decreased. In addition, it was found that because high values of shear stresses and high viscous dissipations are dominant near the inner cylinder, the Bejan number tends toward zero.

In this section, the effect of different parameters on average entropy generation is investigated. The effect of particle loading on the average entropy generation number at different Brinkman numbers from 0.001 to 4 is illustrated in Fig. 7 for $\frac{\Omega}{Br_f} = 0.1$ and $M = 1$. For $Br_f \leq 2.7$, the average entropy generation number decreased with an increase in ϕ; for $Br_f > 2.7$, $(N_S)_{\text{ave}}$ increases with the nanoparticle loading. The Brinkman number determines the relative significance between dissipation effects and fluid conduction effects (see White [43]). At high Brinkman numbers, the dissipation effects dominate conduction effects; hence, an increase in particle volume fraction is more effective in the irreversibility due to fluid friction, and consequently the average entropy generation increases. It also is shown that there is an optimum Brinkman number at which the average entropy generation is minimized. This optimum point can be obtained readily by the following relation:

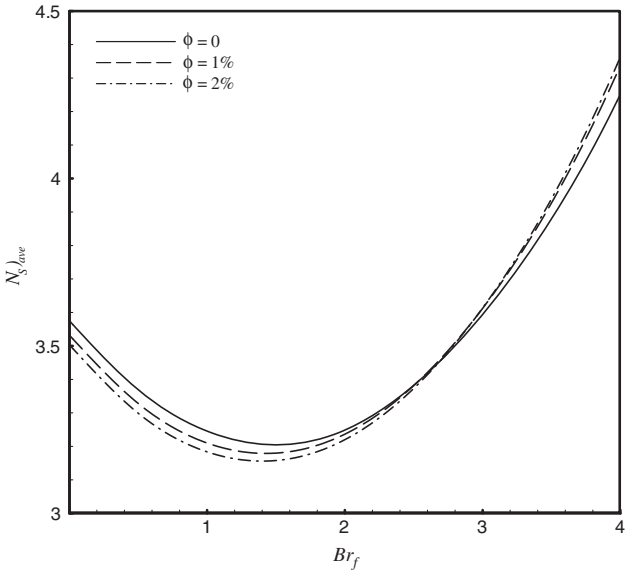

Fig. 7 Effect of nanoparticle loading on the average entropy generation number at different Brinkman numbers for $\frac{\Omega}{Br_f} = 0.1$.

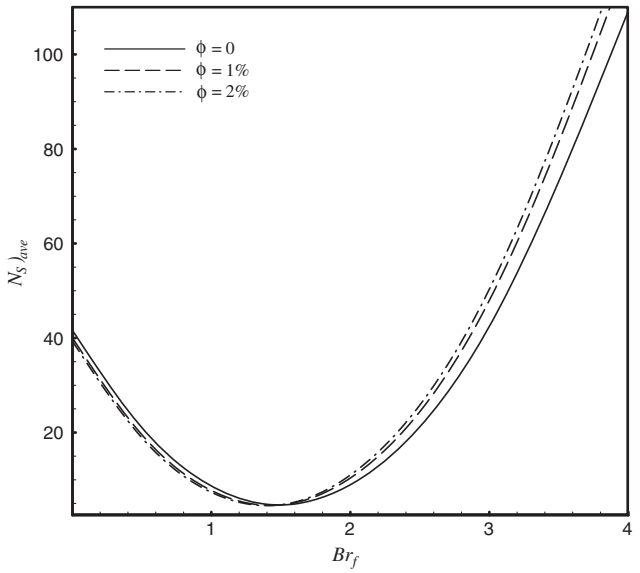

Fig. 9 Effect of nanoparticle loading on the average entropy generation number at different Brinkman numbers for $\frac{\Omega}{Br_f} = 10$.

Downloaded by UNIVERSITY OF WATERLOO on February 10, 2013 | http://arc.aiaa.org | DOI: 10.2514/1.T3908

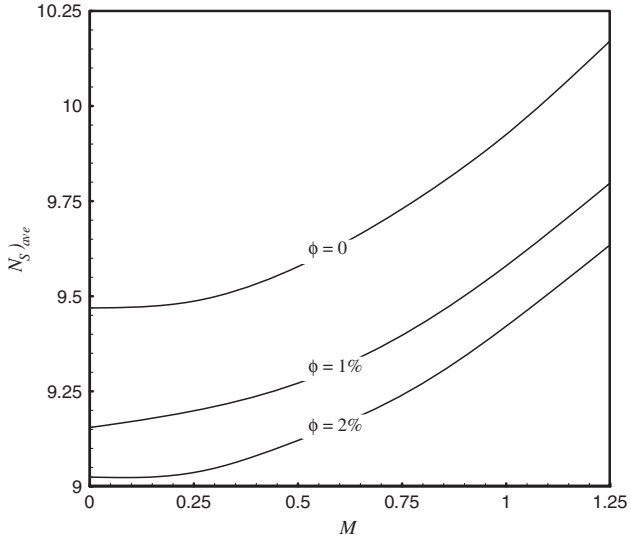

Fig. 10 Variation of the average entropy generation number with the Hartmann number for $Br_f = 0.1$ and $\frac{\Omega}{Br_f} = 2$.

$$\frac{(\partial N_S)_{\text{ave}}}{\partial Br_f} = 0 \quad \text{or} \quad \frac{\partial(\int_{0.5}^{1} N_S R\, \mathrm{d}R)}{\partial Br_f} = 0 \tag{21}$$

The optimum Brinkman number is approximately equal to 1.5.

Figures 8 and 9 present the variation of $(N_S)_{\text{ave}}$ with the Brinkman number for $M = 1$, $\frac{\Omega}{Br_f} = 1$, and $\frac{\Omega}{Br_f} = 10$. In these two cases, as in the previous case, the optimum Brinkman number at which entropy generation is minimized is approximately 1.5. However, unlike the previous case, the range of the Brinkman number at which increasing ϕ results in decreasing$(N_S)_{\text{ave}}$ decreases from 2.7 to 1.5. With increasing $\frac{\Omega}{Br_f}$, the average entropy generation increases, as expected.

The results of Figs. 7–9 have significance for industrial applications as follows. When the Brinkman number is small and the outer cylinder rotates at low speed, the addition of nanoparticles leads to a reduction in entropy generation of the system. By contrast, the addition of nanoparticles is not recommended when the outer cylinder rotates at high speeds.

The variation of the average entropy generation number with the Hartmann number is presented in Fig. 10 for $Br_f = 0.1$ and $\frac{\Omega}{Br_f} = 2$. As mentioned in the previous section, the average entropy generation decreases for Brinkman numbers of less than 1.5 with an increase in the nanoparticle volume fraction. This fact also is shown in Fig. 10. The decreasing tendency in entropy generation is more obvious between $\phi = 0$ and $\phi = 1\%$, because the viscous dissipation effects are smaller at lower particle volume fractions. Hence, the addition of nanoparticles leads to more reduction in entropy generation.

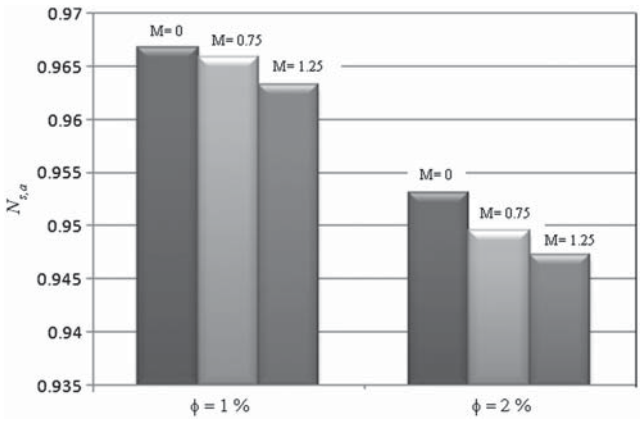

Fig. 11 Augmentation entropy generation number for $Br_f = 0.1$ and $\frac{\Omega}{Br_f} = 2$.

It also is shown in the figure that, with the augmentation of the magnetic field, the average entropy generation increases. The presence of the magnetic field makes a resistive force similar to the drag force, which acts in the opposite direction of fluid movement. This reduces the fluid velocity, leads to the increase in viscous dissipation, and results in more internal heating of the working fluid. Consequently, there is an increase of the entropy generation. As shown, the profiles of $(N_S)_{\text{ave}}$ for different values of ϕ are parallel and regular.

The proper effect of the augmentation method (here, adding nanoparticles) on the thermodynamic performance of the thermal system can be appraised by comparing the irreversibility before and after using the augmentation method. For this purpose, the augmentation entropy generation number is defined as follows [22]:

$$N_{S,a} = \frac{N_S}{N_{S,0}} \tag{22}$$

where $N_{S,0}$ indicates the degree of irreversibility when the volume fraction is zero (distilled water). According to Eq. (22), adding nanoparticles is advantageous with respect to the second law of thermodynamics when $N_{S,a}$ values are less than 1. Figure 11 presents the variation of augmentation entropy generation number at different Hartmann numbers and volume fractions (1 and 2%) for the conditions of Fig. 10. The figure shows that the augmentation entropy generation decreases with an increase in volume fraction and the Hartmann number. Therefore, for this case, the following suggestion can be given. With respect to the second law of thermodynamics, adding nanoparticles to the working base fluid is more justifiable with increasing intensity of magnetic field than in the case in which the magnetic field is poor.

V. Conclusions

An analytical analysis of the second law of thermodynamics is presented to investigate the effect of using TiO_2-water nanofluid (up to 2 vol %) on entropy generation between two rotating cylinders in the presence of magnetohydrodynamic flow. The governing equations in a cylindrical coordinate system are simplified and solved to obtain analytical expressions for the velocity and temperature fields and, consequently, the entropy generation rate. To calculate the thermophysical properties of the nanofluid, including thermal conductivity and viscosity, the Duangthongsuk and Wongwises models, which are based on experimental data, have been used. The results for the local entropy generation analysis reveal that entropy generation is highest near the inner cylinder due to the maximum gradients of velocity and temperature. In addition, with an increase in the Hartmann number (magnetic field), entropy generation in the vicinity of the inner cylinder decreases, whereas in other regions, the entropy generation number is raised. The results show that, at low Brinkman numbers (depending on the value of $\frac{\Omega}{Br_f}$), the average entropy generation number decreases with the addition of nanoparticle volume fraction. It also was found that the increase in the Hartmann number results in an increase in the average entropy generation number. Hence, with respect to the second law of thermodynamics, using nanofluids for the flow between two rotating cylinders in the presence of a magnetohydrodynamic field is suggested only at low Brinkman numbers.

Acknowledgments

The third author would like to thank the Thailand Research Fund and the National Research University Project for support.

References

[1] Bejan, A., "Second-Law Analysis in Heat Transfer and Thermal Design," *Advances in Heat Transfer*, Vol. 15, 1982, pp. 1–58. doi:10.1016/S0065-2717(08)70172-2

[2] Bejan, A., *Entropy Generation Minimization*, CRC Press, Boca Raton, FL, 1996.

Downloaded by UNIVERSITY OF WATERLOO on February 10, 2013 | http://arc.aiaa.org | DOI: 10.2514/1.T3908

[3] Naterer, G. F., and Camberos, J. A., *Entropy Based Analysis and Design of Fluids Engineering Systems*, CRC Press, Boca Raton, FL, 2008.
[4] Shah, R. K., and Skiepko, T., "Entropy Generation Extrema and their Relationship with Heat Exchanger Effectiveness—Number of Transfer Unit Behavior for Complex Flow Arrangements," *Journal of Heat Transfer*, Vol. 126, No. 6, 2004, pp. 994–1002. doi:10.1115/1.1846694
[5] Guo, Z. Y., Liu, X. B., Tao, W. Q., and Shah, R. K., "Effectiveness–Thermal Resistance Method for Heat Exchanger Design and Analysis," *International Journal of Heat and Mass Transfer*, Vol. 53, Nos. 13–14, 2010, pp. 2877–2884. doi:10.1016/j.ijheatmasstransfer.2010.02.008
[6] Guo, J., and Xu, M., "The Application of Entransy Dissipation Theory in Optimization Design of Heat Exchanger," *Applied Thermal Engineering*, Vol. 36, 2012, pp. 227–235. doi:10.1016/j.applthermaleng.2011.12.043
[7] Cheng, X., and Liang, X., "Computation of Effectiveness of Two-Stream Heat Exchanger Networks Based on Concepts of Entropy Generation, Entransy Dissipation and Entransy-Dissipation-Based Thermal Resistance," *Energy Conversion and Management*, Vol. 58, 2012, pp. 163–170. doi:10.1016/j.enconman.2012.01.016
[8] Yu, W., France, D. M., Routbort, J. L., and Choi, S. U. S., "Review and Comparison of Nanofluid Thermal Conductivity and Heat Transfer Enhancements," *Heat Transfer Engineering*, Vol. 29, No. 5, 2008, pp. 432–460. doi:10.1080/01457630701850851
[9] Yu, W., France, D. M., Smith, D. S., Singh, D., Timofeeva, E. V., and Routbort, J. L., "Heat Transfer to a Silicon Carbide/Water Nanofluid," *International Journal of Heat and Mass Transfer*, Vol. 52, Nos. 15–16, 2009, pp. 3606–3612. doi:10.1016/j.ijheatmasstransfer.2009.02.036
[10] Trisaksri, V., and Wongwises, S., "Critical Review of Heat Transfer Characteristics of Nanofluids," *Renewable and Sustainable Energy Reviews*, Vol. 11, No. 3, 2007, pp. 512–523. doi:10.1016/j.rser.2005.06.005
[11] Duangthongsuk, W., and Wongwises, S., "A Critical Review of Convective Heat Transfer of Nanofluids," *Renewable and Sustainable Energy Reviews*, Vol. 11, No. 5, 2007, pp. 797–817. doi:10.1016/j.rser.2005.06.005
[12] Godson, L., Raja, B., Mohan Lal, D., and Wongwises, S., "Enhancement of Heat Transfer Using Nanofluids—An Overview," *Renewable and Sustainable Energy Reviews*, Vol. 14, No. 2, 2009, pp. 629–641. doi:10.1016/j.rser.2009.10.004
[13] Saidur, R., Leong, K. Y., and Mohammad, H. A., "A Review on Applications and Challenges of Nanofluids," *Renewable and Sustainable Energy Reviews*, Vol. 15, No. 3, 2011, pp. 1646–1668. doi:10.1016/j.rser.2010.11.035
[14] Khanafer, K., and Vafai, K., "A Critical Synthesis of Thermophysical Characteristics of Nanofluids," *International Journal of Heat and Mass Transfer*, Vol. 54, Nos. 19–20, 2011, pp. 4410–4428. doi:10.1016/j.ijheatmasstransfer.2011.04.048
[15] Singh, P. K., Anoop, K. B., Sundararajan, T., and Das, S. K., "Entropy Generation Due to Flow and Heat Transfer in Nanofluids," *International Journal of Heat and Mass Transfer*, Vol. 53, Nos. 21–22, 2010, pp. 4757–4767. doi:010.1016/j.ijheatmasstransfer.2010.06.016
[16] Li, J., and Kleinstreuer, C., "Entropy Generation Analysis for Nanofluid Flow in Microchannels," *Journal of Heat Transfer*, Paper 122401, Vol. 132, No. 12, 2010
[17] Feng, Y., and Kleinstreuer, C., "Nanofluid Convective Heat Transfer in a Parallel-Disk System," *International Journal of Heat and Mass Transfer*, Vol. 53, No. 21–22, 2010, pp. 4619–4628. doi:10.1016/j.ijheatmasstransfer.2010.06.031
[18] Moghaddami, M., Mohammadzade, A., and Varzane Esfehani, S. A., "Second Law Analysis of Nanofluid Flow," *Energy Conversion and Management*, Vol. 52, No. 2, 2011, pp. 1397–1405. doi:10.1016/j.enconman.2010.10.002
[19] Shahi, M., Mahmoudi, A. H., and Raouf, A. H., "Entropy Generation Due to Natural Convection Cooling of a Nanofluid," *International Communications in Heat and Mass Transfer*, Vol. 38, No. 7, 2011, pp. 972–983. doi:10.1016/j.icheatmasstransfer.2011.04.008
[20] Esmaeilpour, M., and Abdollahzadeh, M., "Free Convection and Entropy Generation of Nanofluid Inside an Enclosure with Different Patterns of Vertical Wavy Walls," *International Journal of Thermal Sciences*, Vol. 52, 2012, pp. 127–136. doi:10.1016/j.ijthermalsci.2011.08.019
[21] Bianco, V., Nardini, S., and Manca, O., "Enhancement of Heat Transfer and Entropy Generation Analysis of Nanofluids Turbulent Convection Flow in Square Section Tubes," *Nanoscale Research Letters*, Vol. 6, 2011, p. 252. doi:10.1186/1556-276X-6-252
[22] Falahat, A., and Vosough, A., "Effect of Nanofluid on Entropy Generation and Pumping Power in Coiled Tube," *Journal of Thermophysics and Heat Transfer*, Vol. 26, No. 1, 2012, pp. 141–146. doi:10.2514/1.T3771
[23] Yilbas, B. S., "Entropy Analysis of Concentric Annuli with Rotating Outer Cylinder," *International Journal of Exergy*, Vol. 1, No. 1, 2001, pp. 60–66. doi:10.1016/S1164-0235(01)00011-5
[24] Mahmud, S., and Fraser, R. A., "Second Law Analysis of Heat Transfer and Fluid Flow Inside a Cylindrical Annular Space," *International Journal of Exergy*, Vol. 2, No. 4, 2002, pp. 322–329. doi:10.1016/S1164-0235(02)00078-X
[25] Mahmud, S., and Fraser, R. A., "Analysis of Entropy Generation Inside Concentric Cylindrical Annuli with Relative Rotation," *International Journal of Thermal Sciences*, Vol. 42, No. 5, 2003, pp. 513–521. doi:10.1016/S1290-0729(02)00051-0
[26] Mirzazadeh, M., Shafaei, A., and Rashidi, F., "Entropy Analysis for Non-Linear Viscoelastic Fluid in Concentric Rotating Cylinders," *International Journal of Thermal Sciences*, Vol. 47, No. 12, 2008, pp. 1701–1711. doi:10.1016/j.ijthermalsci.2007.11.002
[27] Jery, A. E., Hidouri, N., Magherbi, M., and Brahim, A. B., "Effect of an External Oriented Magnetic Field on Entropy Generation in Natural Convection," *Entropy*, Vol. 12, No. 6, 2010, pp. 1391–1417. doi:10.3390/e12061391
[28] Salas, H., Cuevas, S., and Haro, M. L., "Entropy Generation Analysis of Magnetohydrodynamic Induction Devices," *Journal of Physics D: Applied Physics*, Vol. 32, No. 20, 1999, pp. 2605–2608. doi:10.1088/0022-3727/32/20/304
[29] Ibanez, G., Cuevas, S., and Haro, M. L., "Optimization Analysis of an Alternate Magnetohydrodynamic Generator," *Energy Conversion and Management*, Vol. 43, No. 14, 2002, pp. 1757–1771. doi:10.1016/S0196-8904(01)00133-9
[30] Mahmud, S., Tasnim, S. H., and Mamun, M. A. H., "Thermodynamic Analysis of Mixed Convection in a Channel with Transverse Hydromagnetic Effect," *International Journal of Thermal Science*, Vol. 42, No. 8, 2003, pp. 731–740. doi:10.1016/S1290-0729(03)00040-1
[31] Tasnim, S. H., Mahmud, S., and Mamun, M. A. H., "Entropy Generation in a Porous Channel with Hydromagnetic Effect," *Energy*, Vol. 2, No. 4, 2002, pp. 300–308. doi:10.1016/S1164-0235(02)00065-1
[32] Mahmud, S., and Fraser, R. A., "Mixed Convection-Radiation Interaction in a Vertical Porous Channel: Entropy Generation," *Energy*, Vol. 28, No. 15, 2003, pp. 1557–1577. doi:10.1016/S0360-5442(03)00154-3
[33] Mahmud, S., and Fraser, R. A., "Magnetohydrodynamic Free Convection and Entropy Generation in a Square Porous Cavity," *International Journal of Heat and Mass Transfer*, Vol. 47, Nos. 14–16, 2004, pp. 3245–3256. doi:10.1016/j.ijheatmasstransfer.2004.02.005
[34] Ibanez, G., and Cuevas, S., "Optimum Wall Conductance Ratio in Magnetoconvective Flow in a Long Vertical Rectangular Duct," *International Journal of Thermal Science*, Vol. 47, No. 8, 2008, pp. 1012–1019. doi:10.1016/j.ijthermalsci.2007.09.003
[35] Mahmud, S., and Fraser, R. A., "The Thermoacoustic Irreversibility for a Single-Plate Thermoacoustic System," *International Journal of Heat and Mass Transfer*, Vol. 49, Nos. 19–20, 2006, pp. 3448–3461. doi:10.1016/j.ijheatmasstransfer.2006.02.051
[36] Ibanez, G., and Cuevas, S., "Optimum Wall Conductance Ratio in Magnetoconvective Flow in a Long Vertical Rectangular Duct," *International Journal of Thermal Science*, Vol. 47, No. 8, 2008, pp. 1012–1019. doi:10.1016/j.ijthermalsci.2007.09.003
[37] Arikoglu, A., Ozkol, I., and Komurgoz, G., "Effect of Slip on Entropy Generation in a Single Rotating Disk in MHD Flow," *Applied Energy*, Vol. 85, No. 12, 2008, pp. 1225–1236. doi:10.1016/j.apenergy.2008.03.004
[38] Ibanez, G., and Cuevas, S., "Entropy Generation Minimization of a MHD (Magnetohydrodynamic) Flow in a Microchannel," *Energy*, Vol. 35, No. 10, 2010, pp. 4149–4155. doi:10.1016/j.energy.2010.06.035

Downloaded by UNIVERSITY OF WATERLOO on February 10, 2013 | http://arc.aiaa.org | DOI: 10.2514/1.T3908

[39] Mansour, R. B., Galanis, N., and Nguyen, C. T., "Effect of Uncertainties in Physical Properties on Forced Convection Heat Transfer with Nanofluids," *Applied Thermal Engineering*, Vol. 27, No. 1, 2007, pp. 240–249. doi:10.1016/j.applthermaleng.2006.04.011
[40] Jiji, L. M., *Heat Convection*, Springer-Verlag, Berlin, 2006.
[41] Duangthongsuk, W., and Wongwises, S., "Measurement of Temperature-Dependent Thermal Conductivity and Viscosity of TiO_2 Water Nanofluids," *Experimental Thermal and Fluid Science*, Vol. 33, No. 4, 2009, pp. 706–714. doi:10.1016/j.expthermflusci.2009.01.005
[42] Paoletti, S., Rispoli, F., and Sciubba, E., "Calculation of Exergetic Losses in Compact Heat Exchanger Passages," *American Society of Mechanical Engineers, Advanced Energy Systems Division*, Vol. 10, No. 2, 1980, pp. 21–29.
[43] White, F. M., *Viscous Fluid Flow*, McGraw–Hill, New York, 1974.

Downloaded by UNIVERSITY OF WATERLOO on February 10, 2013 | http://arc.aiaa.org | DOI: 10.2514/1.T3908

HVAC&R Research (2013) **19**, 159–174
Copyright © 2013 ASHRAE.
ISSN: 1078-9669 print / 1938-5587 online
DOI: 10.1080/10789669.2012.751812

Taylor & Francis
Taylor & Francis Group

Numerical simulation of refrigerants flowing through short-tube orifices during flashing process

KITTI NILPUENG[1,2] and SOMCHAI WONGWISES[2,3,*]

[1]*Department of Mechanical Engineering, South East Asia University, Bangkok 10160, Thailand*
[2]*Fluid Mechanics, Thermal Engineering and Multiphase Flow Research Lab (FUTURE), Department of Mechanical Engineering, Faculty of Engineering, King Mongkut's University of Technology Thonburi, Bangmod, Bangkok 10140, Thailand*
[3]*The Academy of Science, The Royal Institute of Thailand, Sanam Suea Pa, Dusit, Bangkok 10300, Thailand*

A numerical simulation for calculating the flashing flow characteristics of refrigerants inside short-tube orifices is presented. The refrigerant flow behaviors along short-tube orifices are separated into three sections: subcooled liquid region, metastable liquid region, and two-phase region. Annular two-phase flow pattern is developed from the mass, energy, and momentum equation. The present simulation is corroborated by comparison with the experimental data. The selection charts are also presented to estimate the refrigerant mass flow rate along short-tube orifices in practical applications.

Introduction

Expansion device is one of four main parts of refrigeration system. The functions are two-fold: (1) to reduce the refrigerant pressure from high pressure in condenser to low pressure in evaporator and (2) to control the refrigerant flow rate from the condenser to the evaporator. Short-tube orifice is a constant-restriction type of expansion device commonly used in domestic and automobile air conditioners. It is a short and narrow tube with length-to-diameter ratio of 3–20 and lengths of 10–13 mm (0.394–0.512 in.) for domestic air conditioners. Length-to-diameter ratio and diameter of short-tube orifices are 21–35 mm (0.827–1.378 in.) and 1–2 mm (0.039–0.079 in.) for automobile air conditioners (ASHRAE 1998). The benefits of using short-tube orifices are low starting torque of the compressor, high reliability, low cost, and simplicity. However, it is found that to obtain the optimum air conditioner performance, the refrigerant flow inside the short-tube orifice should be choked. Moreover, after the size of a short-tube orifice is selected to install into an air-conditioning system, it will be suitable for only one design condition. This means that the refrigerant flow rate and pressure drop cannot be satisfied under different operating conditions. Therefore, a design tool for estimating the refrigerant mass flow rate along the short-tube orifice at a given operating condition is very necessary.

During the past decades, the numerical analysis on the refrigerant flashing flow through short-tube orifices has been reported in the publications. It is separated into two classifications: semi-empirical models and theoretical models. Semi-empirical models are generated in the form of simple equations with the correction factor created from experimental data. It was found that a single-phase orifice equation (ASME 1971) has been proposed by most previous researchers as follows:

$$\dot{m} = CA\sqrt{\frac{2\rho(P_{up} - P_{down})}{(1-\beta^4)}}. \tag{1}$$

As shown in Equation 1, it was found that the mass flow rate was a function of downstream pressure (P_{down}), upstream pressure (P_{up}), short-tube orifice flow area (A), upstream density (ρ), and the orifice diameter-to-tube diameter ratio (β). The correction factor, which was combined in the single-phase orifice equation, was presented into two forms: orifice constant correlation (C) and downstream pressure correlation. The first one was dependent on the difference of upstream pressure and downstream pressure, downstream vapor quality, ratio of length to diameter, and degree of subcooling (Mei 1982; Pasqua 1953; Tu et al. 2006). The other one was dependent on the ratio of length to diameter, upstream temperature, downstream pressure, and upstream pressure (Aaron and Domanski 1990; Kim 1993; Kim et al. 2002; Liu et al. 2004). A generalized mass flow rate correlation of alternative refrigerant through short-tube orifices was proposed in few publications (Choi et al. 2004). The correlation in power law form, which was included with dimensionless parameters, was generated and proposed. Buckingham Pi theorem was used to create the dimensionless parameters.

Although the semi-empirical models can be used to calculate the refrigerant mass flow rate through short-tube orifices, they cannot be used to indicate the physical meaning of refrigerant flow mechanism; the accuracy of the models are valid only over the testing conditions. Therefore, theoretical

Received June 14, 2012; accepted November 9, 2012
Kitti Nilpueng, D.Eng, is lecturer and researcher. **Somchai Wongwises, PhD, Dr-Ing**, is professor.
*Corresponding author e-mail: somchai.won@kmutt.ac.th

models have been proposed to simulate the characteristic of refrigerant through short-tube orifice by some researchers. Eight critical flow models were compared with the experimental data of HCFC-22 and HFC-134a by Kim and O'Neal (1995). These models were divided into three classes: homogeneous equilibrium models (HEMs), nonhomogeneous equilibrium models (NEMs), and homogeneous frozen models (HFMs). A comparison between the experimental data and calculated results of models showed that the HFM gave the best agreement except at outlet qualities below 0.06. A nonequilibrium two-fluid model, which consisted of mass, momentum, and energy equations for each phase, was represented for predicting the refrigerant flow behavior through short-tube orifices by Yang and Zhang (2005). Based on the measured mass flow rates of HFC-134a, CFC-12, HCFC-22, HFC-410A, and HFC-407C, it was found that the two-fluid model gave an acceptable prediction with a deviation of $\pm 20\%$. However, in the case of supercritical carbon dioxide (CO_2), Zhang and Yang (2005) reported that the difference of interphase temperature and velocity in two-phase region between gas and liquid were small. Therefore, the nonhomogeneous and nonequilibrium flow behavior inside the short-tube orifice was insignificant. They also concluded that the accuracy of the two-fluid model was similar to that of the HEM. The fluid-dynamic flow characteristic of CO_2 through short-tube orifices was simulated by Garcia-Valladares (2006). He developed the governing equations from the continuity equation, energy equation, entropy equation, and momentum equation. The simulation has been solved by a finite volume formulation. The numerical results showed good acceptance with the measured results.

As mentioned above, it is observed that the theoretical model is more attractive than the semi-empirical model because it can show the physical meaning of the refrigerant along the short-tube orifice. However, the theoretical model is rather difficult to solve when it includes the complicated equations and correlations. As a result, only a few research works have been reported and it is still not clear which one is the best.

The objective of this research work is to develop the numerical model for estimating the flashing flow of refrigerant along the short-tube orifice. The assumptions of metastable liquid flow and annular flow pattern in a two-phase section are applied in this model. The numerical results of refrigerant flow rate and distribution of pressure inside a short tube orifice are verified with the experimental data. Moreover, the short-tube orifice selection charts are presented to estimate the refrigerant mass flow rate along short-tube orifices in practical applications.

Mathematical modeling

The refrigerant flow behavior inside a short-tube orifice is shown diagrammatically in Figure 1. It is separated into three sections: subcooled liquid region, metastable liquid region, and two-phase region. To simulate the refrigerant flow behavior along the short-tube orifice, a present model is developed from the mass, energy, and momentum equation with the following assumptions:

- one dimensional steady flow;
- adiabatic flow; and
- the short-tube orifice diameter and surface roughness is constant.

Subcooled liquid region

As shown in Figure 1, the steady flow energy equation for subcooled liquid region (points 1–3) can be expressed as:

$$\frac{P_1}{\rho_1 g} + \frac{V_1^2}{2g} + z_1 = \frac{P_3}{\rho_3 g} + \frac{V_3^2}{2g} + z_3 + h_L. \tag{2}$$

For an incompressible fluid ($\rho_2 \cong \rho_3 = \rho_L$), the continuity equation is written as:

$$\dot{m} = \rho_2 V_2 A = \rho_3 V_3 A = \rho V A, \tag{3}$$

where h_L is the head loss due to the sudden contraction and friction of the tube wall. It is determined by the following equation:

$$h_L = k\frac{V^2}{2g} + f_{sp}\frac{L}{D}\frac{V^2}{2g}, \tag{4}$$

where k is the entrance loss coefficient and f_{sp} is the friction factor for single-phase flow. It is calculated from the Colebrook

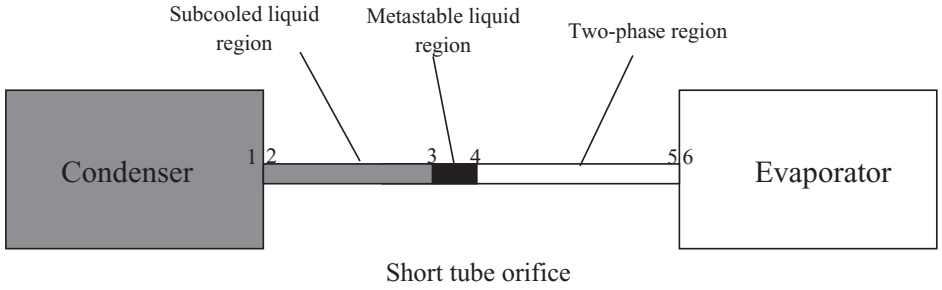

Fig. 1. Schematic diagram a short-tube orifice (color figure available online).

formula as follows:

$$\frac{1}{\sqrt{f_{sp}}} = 1.14 - 2\log\left[\frac{\varepsilon}{D} + \frac{9.3}{\mathrm{Re}\sqrt{f_{sp}}}\right], \quad (5)$$

where

$$\mathrm{Re} = \rho V D/\mu. \quad (6)$$

For a horizontal short-tube orifice ($z_2 = z_3$), substituting Equation 4 into Equation 2, the subcooled liquid length can be estimated from:

$$L_{sub} = \left[(P_1 - P_3)\frac{2}{\rho V^2} - (k+1)\right]\frac{D}{f_{sp}}, \quad (7)$$

where P_3 is the saturation pressure corresponding to the upstream temperature.

Metastable liquid region

The experimental data from prior studies (Kim 1993; Nilpueng and Wongwises 2009) show that even the pressure was decreased lower than the saturation pressure; the refrigerant inside the short-tube orifice was liquid. This indicates that the inception of vaporization is delayed. This flow phenomenon is defined as metastable liquid flow. Considering the length of the metastable liquid region (points 3–4) in Figure 1, it can be calculated based on the steady flow energy equation as follows:

$$L_{mt} = \left[\frac{2}{\rho V^2}(P_3 - P_4)\right]\frac{D}{f_{sp}}, \quad (8)$$

where P_4 is the actual pressure of vaporization. In this model, two empirical correlations of actual pressure of vaporization (P_υ) are applied as follows:

- *Chen et al. correlation* (Chen et al. 1990):
  The Chen et al. correlation was developed based on the flow of R12 through capillary tubes for predicting the actual pressure of vaporization. In this study, it is applied as follows:

$$\frac{(P_s - P_\upsilon)\sqrt{kT_s}}{\sigma^{3/2}} = 0.679\left(\frac{\upsilon_G}{\upsilon_G - \upsilon_L}\right)\mathrm{Re}^{0.914} \times \left(\frac{\Delta T_{sub}}{T_c}\right)^{-0.208}\left(\frac{D}{D'}\right)^{-3.18}, \quad (9)$$

  where D' is the reference length ($\sqrt{kT_s/\sigma}\times 10^4$), T_c is the refrigerant critical temperature, and k is the Boltzman constant (1.380662×10^{-23}). The thermodynamic properties are determined at saturation condition.
- *Lackme correlation* (Lackme 1979):

$$P_\upsilon = k_1 P_s, \quad (10)$$

  where the average value of k_1 ($k_1 = 0.93$) is applied in this study.

Two-phase region

The model is developed from the separated flow model presented by Collier and Thome (1996). The flow pattern of the vapor core is covered by the liquid film (annular flow) is applied in this model (Wongwises and Suchatawat 2002). The governing equations of annular flow are developed from the mass, energy, and momentum equation. The continuity equation for two-phase flow is presented in the following relationship:

$$\frac{d\dot{m}_L}{dz} + \frac{d\dot{m}_G}{dz} = \frac{d\dot{m}}{dz} = 0. \quad (11)$$

The momentum equation for each phase can be expressed as:

$$\frac{d(\dot{m}_L V_L)}{dz} = -\tau_{Lw}C_{Lw} + \tau_i C_i - A_L\frac{dP}{dz} + V_L\frac{d\dot{m}_L}{dz}, \quad (12)$$

$$\frac{d(\dot{m}_G V_G)}{dz} = -\tau_i C_i - A_G\frac{dP}{dz} + V_G\frac{d\dot{m}_G}{dz}. \quad (13)$$

The momentum transfer between liquid and vapor is:

$$\tau_i C_i + V_L\frac{d\dot{m}_L}{dz} - \tau_i C_i + V_G\frac{d\dot{m}_G}{dz} = 0. \quad (14)$$

Combining Equations 12 and 13 by using the relation of the momentum transfer between liquid and vapor (Equation 14), the following is obtained:

$$\frac{d(\dot{m}_L V_L + \dot{m}_G V_G)}{dz} = -\tau_{Lw}C_{Lw} - (A_L + A_G)\frac{dP}{dz}. \quad (15)$$

If Equation 15 is rearranged with the following basic relationships:

$$G = \frac{\dot{m}}{A} = \rho V = \frac{V}{\upsilon}, \quad \dot{m}_G = GAx, \dot{m}_L = GA(1-x),$$
$$\alpha = \frac{A_G}{A}, (1-\alpha) = \frac{A_L}{A}, \quad V_G = \frac{Gx}{\rho_G\alpha}, V_L = \frac{G(1-x)}{\rho_L(1-\alpha)},$$

then it can be written as:

$$-\left(\frac{dP}{dz}\right) = \frac{\tau_{Lw}C_{Lw}}{A} + G^2\frac{d}{dz}\left[\frac{x^2\upsilon_G}{\alpha} + \frac{(1-x)^2\upsilon_L}{(1-\alpha)}\right]. \quad (16)$$

The two-phase frictional pressure gradient is calculated by using the Lockhart Martinelli correlation as follows:

$$\left(\frac{dP_F}{dz}\right)_{TP} = \frac{\tau_{Lw}C_{Lw}}{A} = \phi_L^2\left(\frac{dP_F}{dz}\right)_L. \quad (17)$$

The two-phase multiplier is:

$$\phi_L^2 = 1 + \frac{C}{X} + \frac{1}{X^2}. \quad (18)$$

The value of constant C depends on the flow condition of the gas and liquid phase. It is varied from 5 to 20. The Martinelli parameter can be expressed as:

$$X^2 = \frac{(dP_F/dz)_L}{(dP_F/dz)_G}, \tag{19}$$

when

$$\left(\frac{dP_F}{dz}\right)_L = \frac{2f_L G_L^2}{\rho_L D}, \tag{20}$$

$$\left(\frac{dP_F}{dz}\right)_G = \frac{2f_G G_G^2}{\rho_G D}. \tag{21}$$

The void fraction is expressed in the following equation:

$$\alpha = \frac{x\upsilon_G}{(1-x)\upsilon_L S + x\upsilon_G}. \tag{22}$$

In this equation, three empirical correlations of slip ratio, which are used to indicate the difference between liquid and vapor velocities, are considered as follows:

- *Chisholm correlation* (Chisholm 1973):

$$S = \left[1 - x\left(1 - \frac{\rho_L}{\rho_G}\right)\right]^{1/2}. \tag{23}$$

- *Miropolskiy et al.* correlation (Miropolskiy et al. 1970):

$$S = 1 - \frac{13.5(1 - P/P_c)}{Fr_L^{5/12}\mathrm{Re}_L^{1/6}}, \tag{24}$$

where

$$Fr_L = G^2\upsilon_L^2/gD \quad \text{and} \quad \mathrm{Re}_L = GD/\mu_L.$$

- *Zivi correlation* (Zivi 1964):

$$S = \left(\frac{\rho_L}{\rho_G}\right)^{1/3}. \tag{25}$$

As shown in Equation 16, the accelerational pressure gradient, which is the last term of the equation, can be expanded as:

$$\begin{aligned}\frac{\mathrm{d}}{\mathrm{d}z}\left[\frac{x^2\upsilon_\mathrm{G}}{\alpha} + \frac{(1-x)^2\upsilon_\mathrm{L}}{(1-\alpha)}\right] &= \frac{\mathrm{d}x}{\mathrm{d}z}\left\{\left[\frac{2x\upsilon_\mathrm{G}}{\alpha} - \frac{2(1-x)\upsilon_\mathrm{L}}{(1-\alpha)}\right]\right.\\ &\left.+\left(\frac{\partial\alpha}{\partial x}\right)_P\left[\frac{(1-x)^2\upsilon_\mathrm{L}}{(1-\alpha)^2} - \frac{x^2\upsilon_\mathrm{G}}{\alpha^2}\right]\right\}\\ &+\frac{\mathrm{d}P}{\mathrm{d}z}\left\{\left[\frac{x^2}{\alpha}\frac{\mathrm{d}\upsilon_\mathrm{G}}{\mathrm{d}P} + \frac{(1-x)^2}{(1-\alpha)}\frac{\mathrm{d}\upsilon_\mathrm{L}}{\mathrm{d}z}\right]\right\}\\ &+\left(\frac{\partial\alpha}{\partial P}\right)_x\left[\frac{(1-x)^2\upsilon_\mathrm{L}}{(1-\alpha)^2} - \frac{x^2\upsilon_\mathrm{G}}{\alpha^2}\right].\end{aligned} \tag{26}$$

Therefore, Equation 16 can be expressed as:

$$A_1\left(-\frac{\mathrm{d}P}{\mathrm{d}z}\right) - A_2\left(\frac{\mathrm{d}x}{\mathrm{d}z}\right) = B_1, \tag{27}$$

where

$$\begin{aligned}A_1 &= 1 + G^2\left\{\left[\frac{x^2}{\alpha}\frac{\mathrm{d}\upsilon_\mathrm{G}}{\mathrm{d}P} + \frac{(1-x)^2}{(1-\alpha)}\frac{\mathrm{d}\upsilon_\mathrm{L}}{\mathrm{d}z}\right]\right.\\ &\left.+\left(\frac{\partial\alpha}{\partial P}\right)_x\left[\frac{(1-x)^2\upsilon_\mathrm{L}}{(1-\alpha)^2} - \frac{x^2\upsilon_\mathrm{G}}{\alpha^2}\right]\right\},\\ A_2 &= G^2\left\{\left[\frac{2x\upsilon_\mathrm{G}}{\alpha} - \frac{2(1-x)\upsilon_\mathrm{L}}{(1-\alpha)}\right]\right.\\ &\left.+\left(\frac{\partial\alpha}{\partial x}\right)_P\left[\frac{(1-x)^2\upsilon_\mathrm{L}}{(1-\alpha)^2} - \frac{x^2\upsilon_\mathrm{G}}{x^2}\right]\right\},\\ B_1 &= \frac{\tau_{Lw}C_{Lw}}{A}.\end{aligned}$$

Based on the assumptions of adiabatic flow, steady state steady flow, no energy transfer by work, and horizontal short-tube orifice, the liquid and vapor energy equations are expressed as:

$$\begin{aligned}\frac{d}{dz}\left[\dot{m}_L\left(h_L + \frac{V_L^2}{2}\right)\right] &= -q''_{Lw}C_{Lw} + q''_i C_i + \tau_i V_i C_i\\ &+\left(h_L + \frac{V_L^2}{2}\right)\frac{d\dot{m}_L}{dz},\end{aligned} \tag{28}$$

$$\begin{aligned}\frac{d}{dz}\left[\dot{m}_G\left(h_G + \frac{V_G^2}{2}\right)\right] &= -q''_i C_i - \tau_i V_i C_i\\ &+\left(h_G + \frac{V_G^2}{2}\right)\frac{d\dot{m}_G}{dz}.\end{aligned} \tag{29}$$

At the interface between liquid and vapor, the conservation of energy is written as:

$$\begin{aligned}q''_i C_i + \tau_i V_i C_i + \left(h_L + \frac{V_L^2}{2}\right)\frac{d\dot{m}_L}{dz} - q_i C_i - \tau_i V_i C_i\\ +\left(h_G + \frac{V_G^2}{2}\right)\frac{d\dot{m}_G}{dz} = 0.\end{aligned} \tag{30}$$

Combining Equations 28 and 29 with using the relationship of energy at the interfacial (Equation 30), the following is obtained:

$$\frac{d}{dz}(\dot{m}_G h_G + \dot{m}_L h_L) + \frac{d}{dz}\left[\dot{m}_G\frac{V_G^2}{2} + \dot{m}_L\frac{V_L^2}{2}\right] = -q''_{Lw}C_{Lw}. \tag{31}$$

In this work, the energy transfer by heat from the tube wall to liquid film is neglected ($q''_{Lw} \approx 0$). This is because the axial conduction along the wall is very slight (Chisholm 1973).

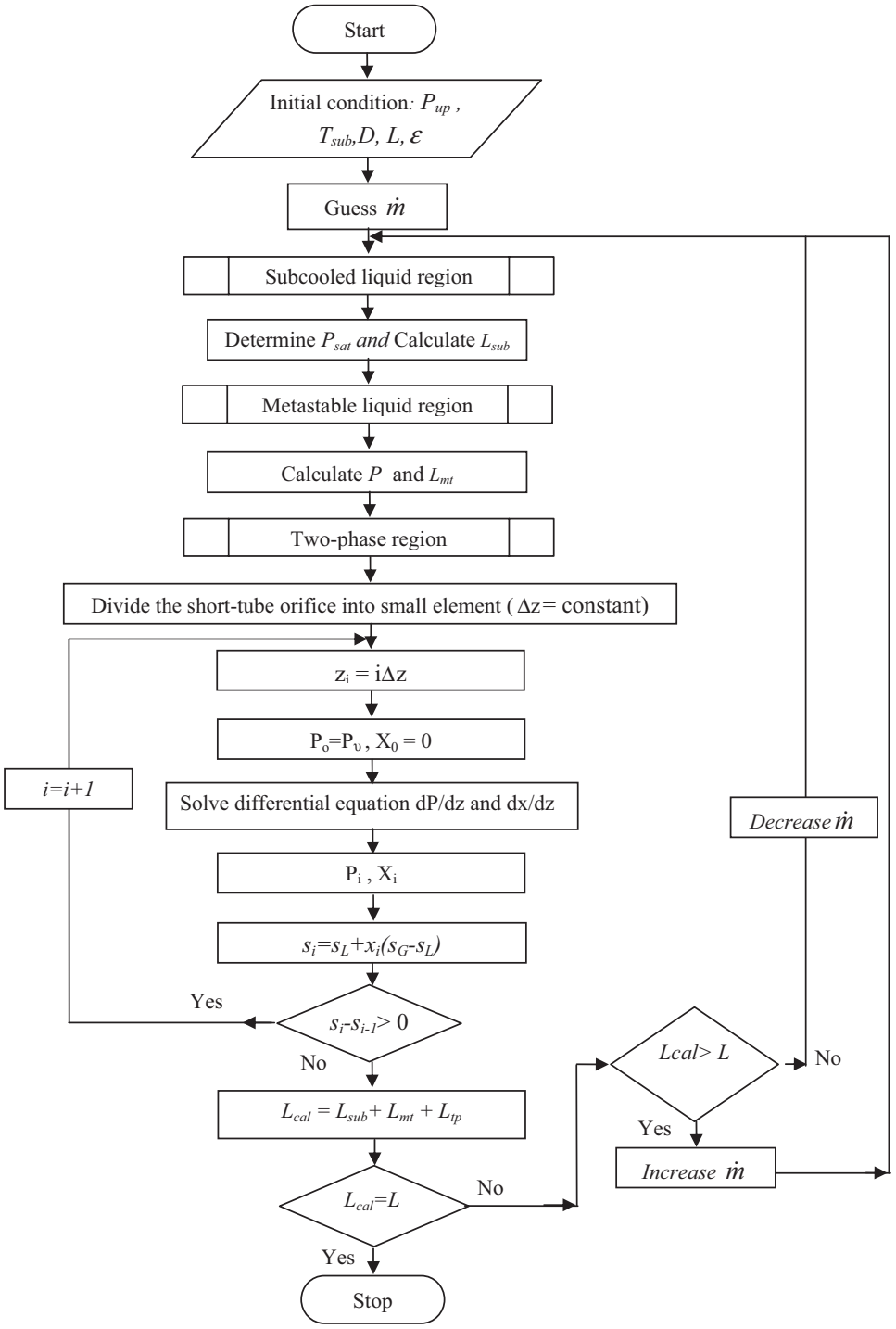

Fig. 2. Flow chart for calculating the critical mass flow rate inside short-tube orifice.

Substituting the basic two-phase relationship into Equation or 31, it can be expressed as:

$$\frac{d}{dz}\left[(GAx)h_G + GA(1-x)\,h_L\right] + \frac{1}{2}\frac{d}{dz}\left[GAx\,V_G^2 + GA(1-x)\,V_L^2\right] = 0 \qquad (32)$$

$$x\frac{dh_G}{dz} + h_G\frac{dx}{dz} + (1-x)\frac{dh_L}{dz} - h_L\frac{dx}{dz} + \frac{1}{2}\left[2xV_G\frac{dV_G}{dz} + V_G^2\frac{dx}{dz} + 2(1-x)V_L\frac{dV_L}{dz} - V_L^2\frac{dx}{dz}\right] = 0, \qquad (33)$$

Table 1. Testing conditions of the experimental data.

Refrigerant	Short-tube orifice diameter (mm)	Short-tube orifice diameter (in.)	Short-tube orifice length (mm)	Short-tube orifice length (in.)	Upstream pressure (kPa)	Upstream pressure (psi)	Degree of subcooling (°C)	Degree of subcooling (°F)	Downstream pressure (kPa)	Downstream pressure (psi)
HFC-134a										
• Kim (1993)	1.097–1.731	0.043–0.068	9.48–24.47	0.037–0.963	890–1459	129.1–211.6	2.8–13.9	5.04–25.02	310–483	44.9–70.1
• Singh et al. (2001)	1.22–1.71	0.048–0.067	13.1–38.4	0.515–1.512	1020–2140	147.9–310.4	0.6–24.5	1.08–44.1	3.4–5.2	49.3–75.4
• Nilpueng and Wongwises (2009)	0.961–1.2	0.037–0.047	10–20	0.394–0.787	900–1300	130.5–188.6	1–12	1.8–21.6	300–400	43.5–58.0
HFC-407C										
• Payne and O'Neal (1998)	1.097–1.94	0.043–0.076	12.68–25.39	0.499–0.999	1526–2273	221.3–329.6	0.28–11.28	0.50–20.3	630–770	91.4–111.7
HFC-410A										
• Payne and O'Neal (1999)	1.097–1.983	0.043–0.078	12.67–25.57	0.498–1.01	2130–3179	308.9–461.1	0.479–11.18	0.862–20.12	800–1100	116.0–159.5
• Kim et al. (2005)	1.097–1.799	0.043–0.071	12.7	0.5	2349–2617	340.7–379.6	1.792–11.03	3.225–19.85	772–1274	111.9–184.8

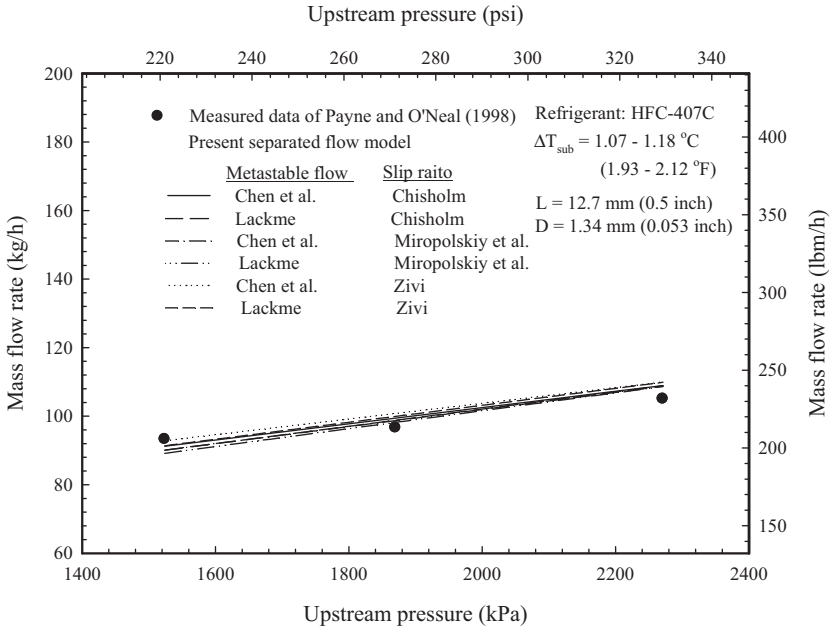

Fig. 3. Comparison of the numerical results with the measured mass flow rate at different upstream pressure.

where

$$\frac{dV_G}{dz} = G\left[\frac{x}{\alpha}\frac{d\upsilon_G}{dP}\frac{dP}{dz} + \frac{\upsilon_G}{\alpha}\frac{dx}{dz} - \frac{x\upsilon_G}{\alpha^2}\left(\left(\frac{\partial\alpha}{\partial P}\right)_x\frac{dP}{dz} + \left(\frac{\partial\alpha}{\partial x}\right)_p\frac{dx}{dz}\right)\right] \tag{34}$$

and

$$\frac{dV_L}{dz} = G\left\{\frac{1}{(1-\alpha)}\left[(1-x)\frac{d\upsilon_L}{dP}\frac{dP}{dz} - \upsilon_L\frac{dx}{dz}\right] + \frac{(1-x)\upsilon_L}{(1-\alpha)^2}\left[\left(\frac{\partial\alpha}{\partial P}\right)_x\frac{dP}{dz} + \left(\frac{\partial\alpha}{\partial x}\right)_p\frac{dx}{dz}\right]\right\}. \tag{35}$$

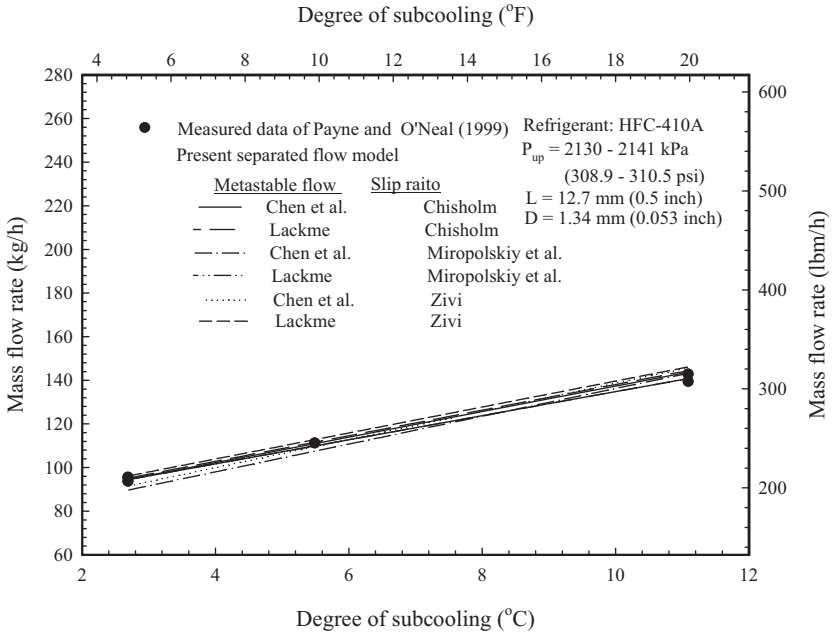

Fig. 4. Comparison of the numerical results with the measured mass flow rate at different degree of subcooling.

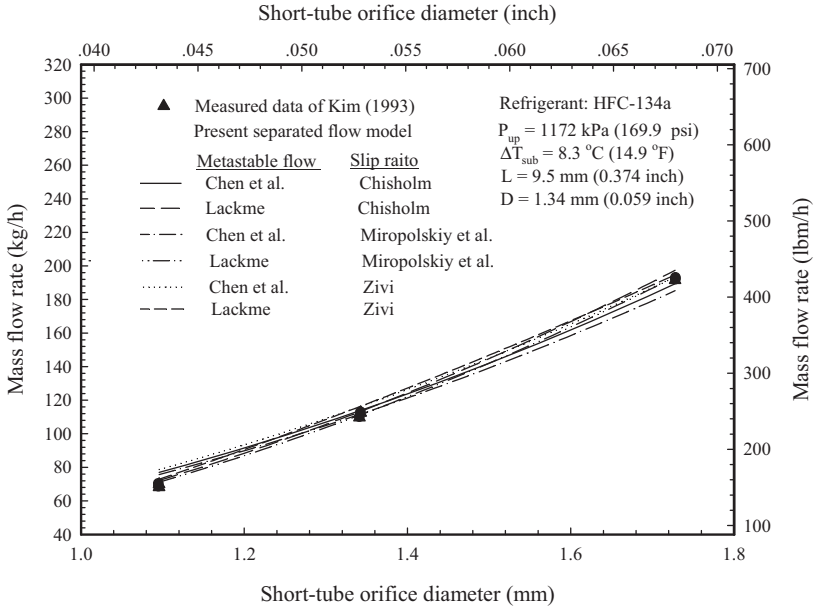

Fig. 5. Comparison of the numerical results with the measured mass flow rate at different short-tube orifice diameter.

Substituting Equations 34 and 35 into Equation 33 gives the following:

$$
\begin{aligned}
&(h_G - h_L)\frac{dx}{dz} + x\frac{dh_G}{dP}\frac{dP}{dz} + (1-x)\frac{dh_L}{dP}\frac{dP}{dz} + Gx\left(\frac{Gx\upsilon_G}{\alpha}\right)\\
&\times\left[\frac{x}{\alpha}\frac{d\upsilon_G}{dP}\frac{dP}{dz} + \frac{\upsilon_G}{\alpha}\frac{dx}{dz} - \frac{x\upsilon_G}{\alpha^2}\left(\left(\frac{\partial\alpha}{\partial P}\right)_x\frac{dP}{dz}\right.\right.\\
&\left.\left.+\left(\frac{\partial\alpha}{dx}\right)_p\frac{dx}{dz}\right)\right] + \frac{1}{2}\left[\frac{Gx\upsilon_G}{\alpha}\right]^2\frac{dx}{dz} + (1-x)G\\
&\times\left[\frac{G(1-x)\upsilon_L}{1-\alpha}\right]\left\{\frac{(1-x)}{(1-\alpha)}\frac{d\upsilon_L}{dP}\frac{dP}{dz} - \frac{\upsilon_L}{1-\alpha}\frac{dx}{dz}\right.\\
&\left.+\frac{(1-x)\upsilon_L}{(1-\alpha)^2}\left[\left(\frac{\partial\alpha}{\partial P}\right)_x\frac{dP}{dz} + \left(\frac{\partial\alpha}{\partial x}\right)_p\frac{dx}{dz}\right]\right\}\\
&-\frac{1}{2}\left[\frac{G(1-x)\upsilon_L}{1-\alpha}\right]^2\frac{dx}{dz} = 0. \qquad (36)
\end{aligned}
$$

Therefore, Equation 36 can be written as:

$$A_3\left(-\frac{dP}{dz}\right) - A_4\left(\frac{dx}{dz}\right) = B_2, \qquad (37)$$

where

$$
\begin{aligned}
A_3 &= \left\{x\frac{dh_G}{dP} + (1-x)\frac{dh_L}{dP} + \frac{G^2x^3\upsilon_G}{\alpha^2}\frac{d\upsilon_G}{dP}\right.\\
&\quad + \frac{G^2(1-x)^3\upsilon_L}{(1-\alpha)^2}\frac{d\upsilon_L}{dP}\\
&\quad \left. - \left[\frac{G^2x^3\upsilon_G^2}{\alpha^3} - \frac{G^2(1-x)^3\upsilon_L^2}{(1-\alpha)^3}\right]\left(\frac{\partial\alpha}{\partial P}\right)_x\right\},\\
A_4 &= \left\{(h_G - h_L) + \frac{3}{2}\frac{G^2x^2\upsilon_G^2}{\alpha^2} - \frac{3}{2}\frac{G^2(1-x)^2\upsilon_L^2}{(1-\alpha)^2}\right.\\
&\quad \left. - \left[\frac{G^2x^3\upsilon_G^2}{\alpha^3} - \frac{G^2(1-x)^3\upsilon_L^2}{(1-\alpha)^3}\right]\left(\frac{\partial\alpha}{\partial x}\right)_P\right\}, \quad B_2 = 0.
\end{aligned}
$$

Table 2. Mean absolute deviations between measured and calculated mass flow rate with different correlations.

	Actual pressure of vaporization correlation	Slip ratio correlation	HFC-134a (%)	HFC-407C (%)	HFC-410A (%)
1.	Chen et al.	Chisholm	8.32	12.94	16.67
2.	Chen et al.	Miropolskiy et al.	8.89	12.45	16.16
3.	Chen et al.	Zivi	9.13	14.10	17.68
4.	Lackme	Chisholm	9.03	12.20	15.43
5.	Lackme	Miropolskiy et al.	9.02	11.74	14.83
6.	Lackme	Zivi	9.08	13.19	16.41

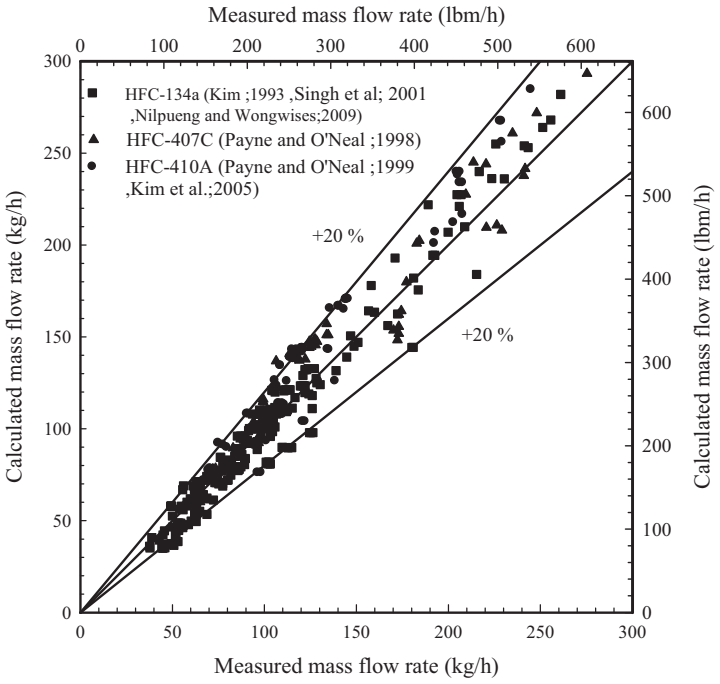

Fig. 6. Measured mass flow rateversus calculated massflow rate obtained from present model with Lackme (1979) and Miropolskiy et al. (1970) correlation.

According to Equations 27 and 37, the system of differential and equations is solved by the following equations:

$$-\frac{dP}{dz} = \frac{A_4 B_1 - A_2 B_2}{A_1 A_4 - A_2 A_3} \tag{38}$$

$$\frac{dx}{dz} = \frac{A_3 B_1 - A_1 B_2}{A_1 A_4 - A_2 A_3}. \tag{39}$$

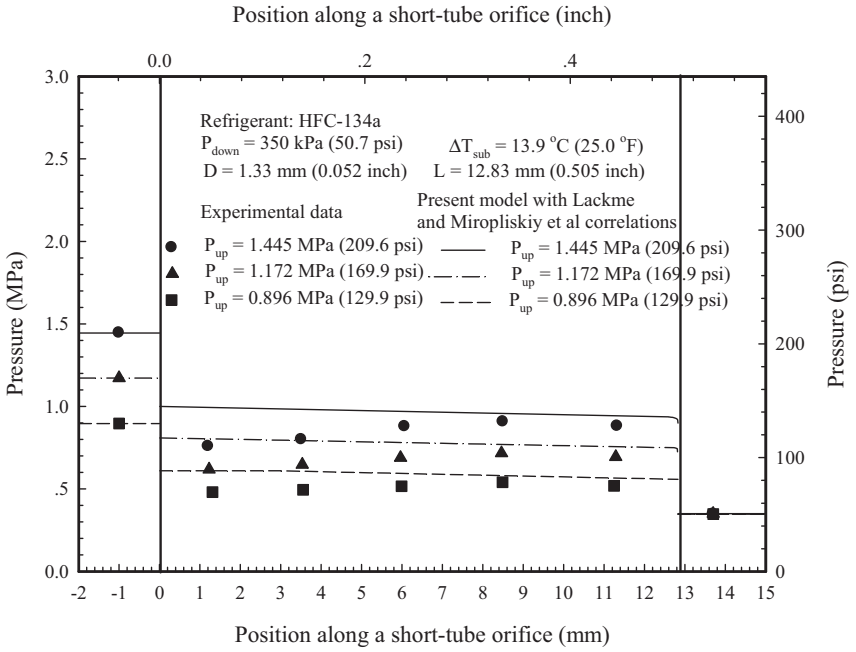

Fig. 7. Comparison of measured pressure distribution with numerical results at different upstream pressure.

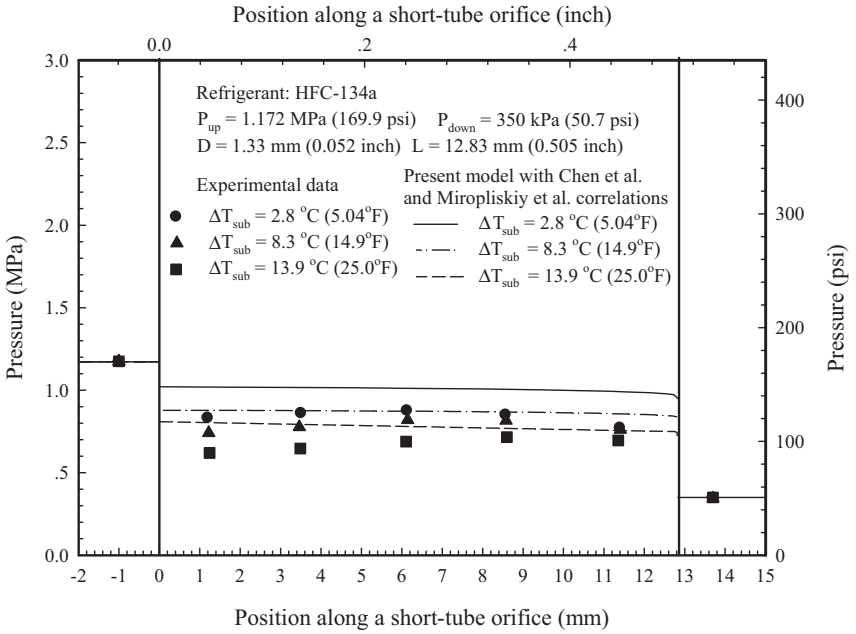

Fig. 8. Comparison of measured pressure distribution with numerical results at different degree of subcooling.

Solution method

The calculation procedure of the mass flow rate inside the short-tube orifice is presented by using the flow chart as shown in Figure 2. The thermodynamic properties and initial conditions, including upstream pressure, diameter, length, and degree of subcooling are specified. The thermodynamic properties of refrigerants are computed as a function of the pressure by using REFPROP (McLinden et al. 1998). As described above, the refrigerant flow behavior inside the short-tube orifice is separated into three sections, subcooled liquid region, metastable liquid region, and two-phase region. The surface roughness of drawn brass ($\varepsilon = 0.0000015$ m [0.0000049 ft.]) is assumed and used for Equation 5. To calculate the subcooled liquid length, the saturation pressure corresponding to the inlet temperature and friction factor obtained from the Colebrook equation are determined and applied into Equation 7. Similarly, the metastable liquid length is calculated by using Equation 8 with the correlation of actual pressure of vaporization. In this study, two correlations of actual vapor pressure obtained from Lackme (1979) and Chen et al. (1990) are considered. In the case of a two-phase region, short-tube orifice length is separated into numerous sections. The refrigerant pressure, which is calculated at the ending of the metastable liquid flow, is the initial condition of two-phase flow region. The fourth-order Runge-Kutta method is used to solve the system of differential equations, which are presented by Equations 38 and 39. The computation of each section is run until the choked flow phenomenon is appeared. Under choked flow condition, the refrigerant velocity reaches sonic speed and the entropy at the exit plane is equal to the maximum value. To verify the appearance of choked flow, the entropy increment at the exit plane of tube is inspected. That is, the choked flow occurs as the entropy increment is negative. The entropy of two-phase flow of each section can be estimated by:

$$s_i = s_L(1 - x_i) + s_G x_i. \tag{40}$$

After the choked flow appears, the length of the two-phase region can be calculated by:

$$L_{tp} = \Delta z n, \tag{41}$$

where n is number of sections. Therefore, the calculated length is the summation of lengths in the subcooled liquid region, metastable liquid region and two-phase flow:

$$L_{cal} = L_{sub} + L_{mt} + L_{tp}. \tag{42}$$

To obtain the critical mass flow rate under a given short-tube orifice length, the iteration procedure is done until the calculated length (L_{cal}) and the actual length are equal. That is, as the calculated length is higher than the actual length, the mass flow rate is increased. Conversely, the mass flow rate decreases when the calculated length is less than the actual length.

Results and discussion

To confirm the accuracy of the present model, the numerical results of mass flow rate and distribution of pressure inside the short-tube orifice are compared with the experimental data under choked flow conditions. The present model with three correlations of slip ratio (Chisholm 1973; Miropolskiy et al. 1970; Zivi 1964) and two correlations of actual pressure of vaporization (Chen 1990; Lackme 1979) are proved. The experimental data, which are used to validate the numerical results,

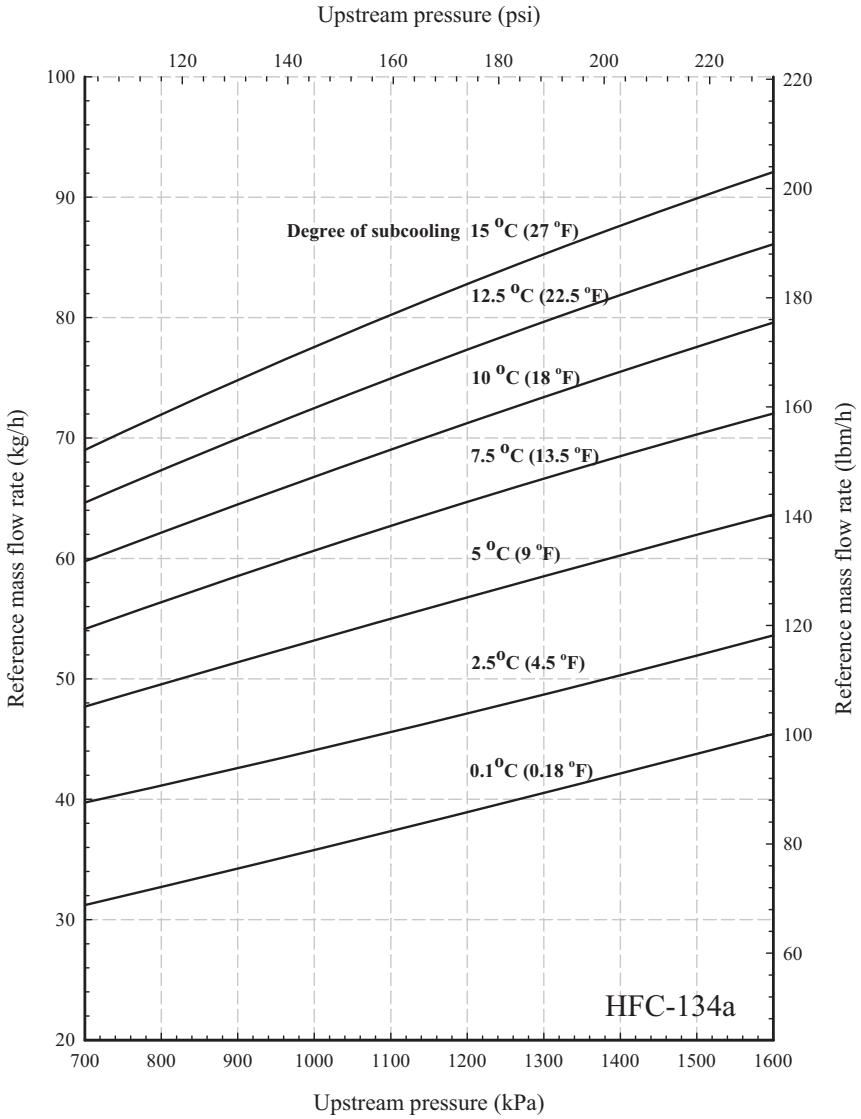

Fig. 9. Short-tube orifice selection chart generated from the present model for HFC-134a ($D = 1.1$ mm (0.043 in.) and $L = 12.7$ mm (0.5 in.)).

include 279 data points for HFC-134a (Kim 1993; Nilpueng and Wongwises 2009; Singh et al. 2001), 122 data points for HFC-407C (Payne and O'Neal 1998), and 95 data points for HFC-410A (Payne and O'Neal 1999; Kim et al. 2005). The testing conditions of experimental data are listed in Table 1.

The comparisons between the experimental and calculated mass flow rate at different upstream pressures are presented in Figure 3. It is found that the calculated results show good agreement with the experimental data, especially, the model with correlations of Lackme (1979) and Miropolskiy et al. (1970), which gives the MAD (mean absolute deviation) of 4.78%. It is also clear that the mass flow rate obtained from the present model increases in direct proportion as the upstream pressure is increased. This is because, based on the numerical results, the difference of pressure across the short-tube orifice is increased as the upstream pressure increases. This leads to an increase of mass flow rate. On the other hand, it is also observed that the upstream density is decreased when the upstream pressure is increased which results in the decrease of mass flow rate. However, the influence of the difference of pressure across the short-tube orifice dominates the influence of refrigerant density, which results in an increase of the refrigerant flow rate. In addition, based on the calculations in the present model, it is found that the prediction of underpressure (*Ps* - *Pv*) obtained from Lackme correlation is higher than that obtained from Chen correlation, about 42.5%.

Figure 4 shows the effect of degree of subcooling on the mass flow rate by comparing the experimental data with the numerical results. The tendency of calculated mass flow rate and experimental results is consistent. The prediction of the present model using Chen et al. (1990) and Miropolskiy et al. (1970) correlations gives the smallest mean absolute deviation (MAD), which is 1.32%. The numerical results indicate that the mass flow rate proportionally enhanced when the degree

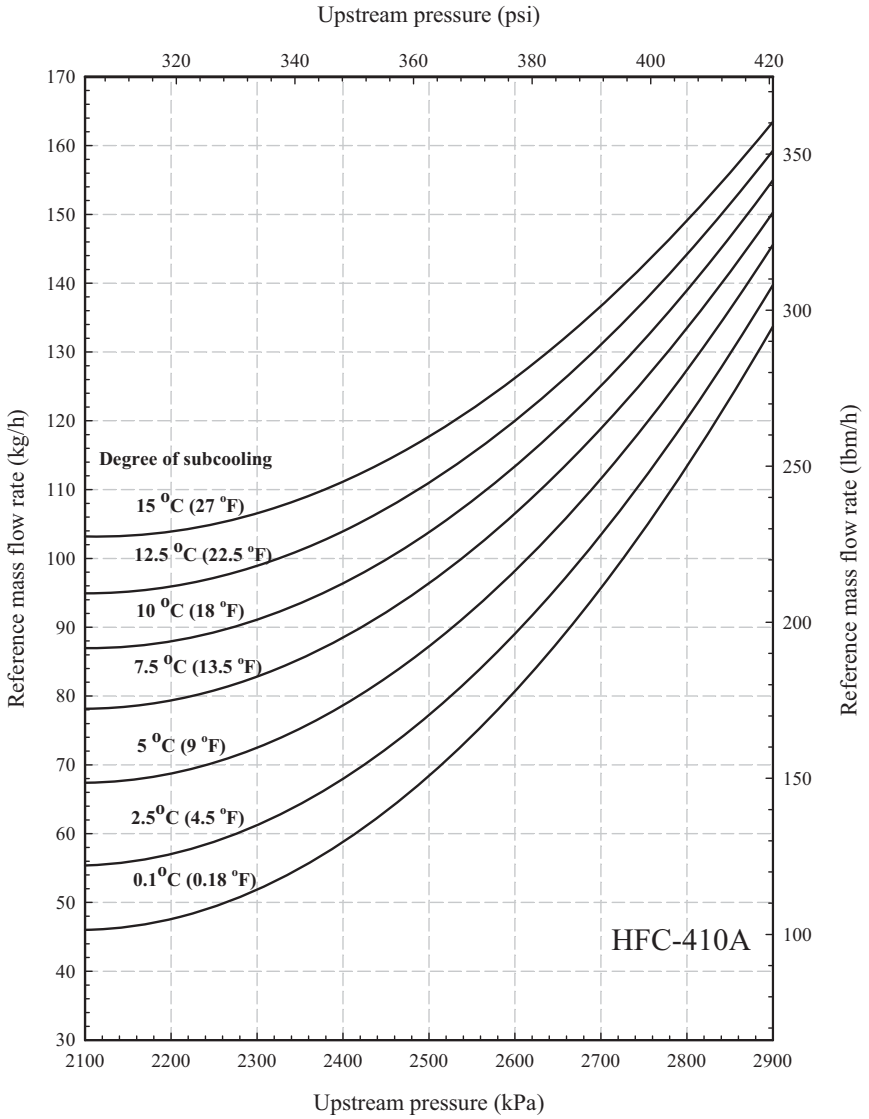

Fig. 10. Short-tube orifice selection chart generated from thepresent model for HFC-410A ($D = 1.1$ mm (0.043 in.) and $L = 12.7$ mm (0.5 in.)).

of subcooling increased. This is because the increase of degree of subcooling results in an increase of upstream density and the difference of pressure across the short-tube orifice, which results in an increase of mass flow rate.

The influence of short-tube orifice diameter on the mass flow rate is presented in Figure 5. It is found that the mass flow rate is strongly increased by enlarging short-tube orifice diameter. This is because the increase of diameter results in an increase of cross-sectional flow area. All of the calculated results give acceptable predictions compared with the measured data. However, the proposed model with Chen et al. (1990) and Miropolskiy et al. (1970) correlation shows the best prediction with MAD of 4.52%.

As mentioned above, the tendency of numerical results is estimated and compared with the experimental data at different sizes of short-tube orifice and working conditions. However, to verify the accuracy of the model at the same condition, the MAD between the numerical results and all experimental data is also examined. Based on the 496 data points of experimental results of HFC-134a, HFC-407C, and HFC-410A, the MAD of mass flow rate are estimated as showed in Table 2. It is found that the present model with Chen et al. (1990) and Chisholm (1973) gives the best prediction for HFC-134a, whereas the present model with Lackme (1979) and Miropolskiy et al. (1970) gives the best prediction for HFC-407C and HFC-410A. However, for all refrigerant types, the present model with the correlations of Lackme (1979) and Miropolskiy et al. (1970) shows the best calculation with MAD of 11.86%. In addition, the calculated results from the model with Lackme (1979) and Miropolskiy et al. (1970) correlations is compared with the measured mass flow rate (Figure 6). It is found that the present model can describe 98.2% of mass flow rate within

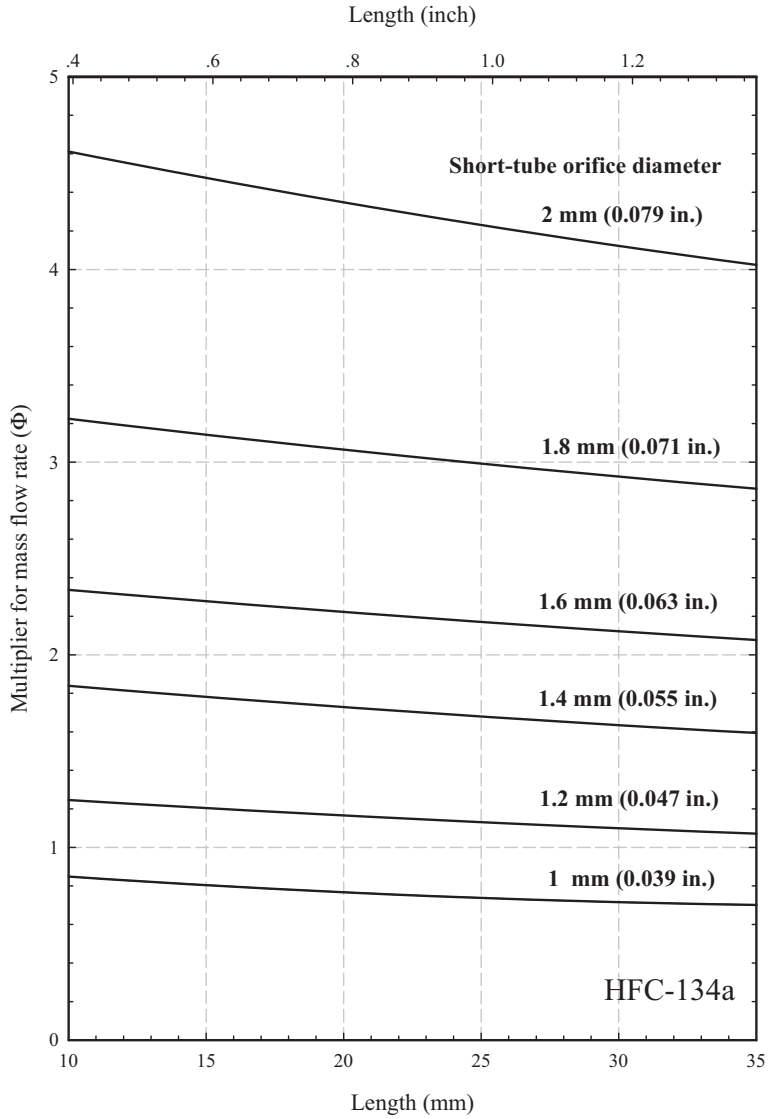

Fig. 11. Multiplier for mass flow rate to be applied to Figure 9 for other diameter and lengths of short-tube orifice.

±20%. Comparing the accuracy of this model with the two-fluid model (Yang and Zhang 2005), it is found that, for the two-fluid model, the relative deviations of 94% data are within 20%. This indicates that the relative deviation obtained from both models is similar. However, it can be noted that the two-fluid model is rather complicated when it is included with the six governing equations.

Figure 7 depicts the relationship between the pressure distribution and upstream pressure obtained from experimental data and the present model with the correlation of Lackme (1979) and Miropolskiy et al. (1970). The average of pressure distribution along the short-tube orifice is enhanced with increasing the upstream pressure. It is also discovered that the pressure decreases suddenly at the inlet, while it slightly increases over a short length and gradually decreases thereafter inside the short-tube orifice. This phenomenon indicates that the vena contracta occur inside the short tube- orifice. The reasons for the variation of pressure inside the short-tube are due to the increase of flow area after the vena contracta, and wall shear stress. In the model, the equation of head loss at the inlet section indicates the loss of flow due to sudden contraction after the refrigerant flow past the inlet section. However, the model does not include the flow behavior at the vena contracta. As a consequence, the variation of pressure obtained from numerical model is inconsistent with experimental results at the vena contracta, whereas it agrees with experimental results after the vena contracta. The large pressure drop at the outlet section can be explained by choked flow phenomenon. Under the choked flow condition, the pressure at the exit plane reaches the infinity value. In addition, the numerical results give an average overestimation of 9.54%. It is also found that the calculated mass flow rate shows good agreement with the experimental data with a MAD of 3.12%.

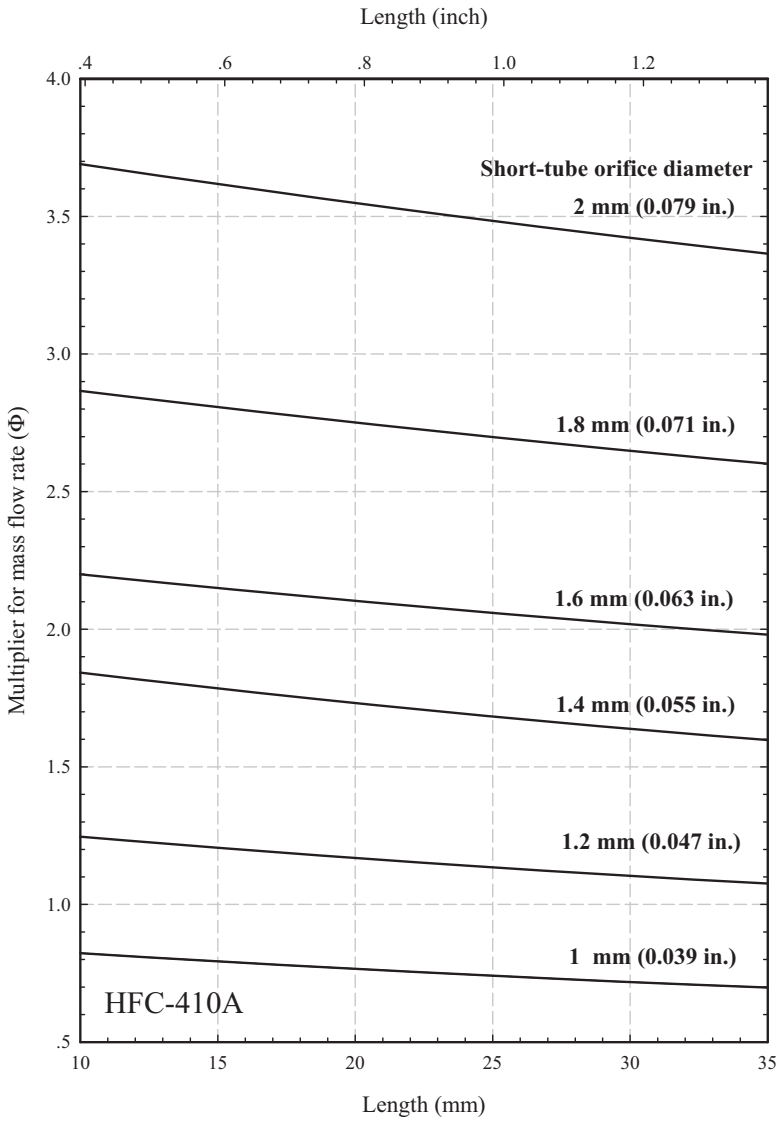

Fig. 12. Multiplier for mass flow rate to be applied to Figure 10 for other diameter and lengths of short-tube orifice.

The comparison of pressure distribution inside the short-tube orifice obtained from numerical and experimental results at different degrees of subcooling are shown in Figure 8. The present model gives an average over-prediction of 11.98%. It can be seen that the increase of degree of subcooling results in the decrease of average pressure along the short-tube orifice. This is due to, based on the numerical calculation, the difference of upstream and critical pressure, and upstream density is increased as the degree of sub-cooling is increased. These effects result in an increase of the refrigerant velocity. Therefore, the average refrigerant pressure along the short-tube orifice decreases. In addition, the predicted mass flow rate agrees well with the experimental data and gives the MAD of 2.64%.

In order to utilize the present numerical model in practical applications, the selection charts, which are generated for various condenser pressures and degree of sub-cooling at given short-tube orifice diameters and lengths, are presented for HFC-134a and HFC-410A. The proposed charts are similar to the rating chart for flow through capillary tube developed by ASHRAE (1998). For a short-tube orifice having a diameter of 1.1 mm (0.043 in.) and a length of 12.7 mm (0.5 in.), the mass flow rate can be estimated directly from selection charts (Figures 9 and 10) by specifying the condenser pressures and degree of subcooling. However, under the different size of diameter and length, the multiplier obtained from correction charts is required (Figures 11 and 12). Based on the proposed selection charts, the MAD of the mass flow rate is 9.48% and 16.04% for HFC-134a and HFC-410A, respectively.

Conclusion

The numerical simulation for calculating the flashing flow of refrigerant along the short-tube orifices is presented. The

precision of the present model is verified with 496 data points of experimental results of HFC-134a, HFC-407C, and HFC-410A. The results show that the calculated mass flow rate and pressure distribution through the short-tube orifice give reasonable agreement with the experimental data. The proposed model with the correlation of Lackme (1979) and Miropolskiy et al. (1970) shows the best prediction with MAD of 11.86%. This implied that the proposed model with appropriate correlations of slip ratio and actual vapor pressure can be used to calculate the refrigerant flow characteristic inside the short-tube orifice. Moreover, based on the present model with Lackme (1979) and Miropolskiy et al. (1970) correlations, the selection charts are also proposed to calculate the refrigerant mass flow rate along short-tube orifices.

Acknowledgments

The present study is supported by the Thailand Research Fund, the Office of the Higher Education Commission, and the National Research University Project whose guidance and assistance are gratefully acknowledged.

Nomenclature

A = cross section area of tube, m^2 (ft^2)
C = circumference of tube, m (ft)
D = diameter of tube, m (ft)
f = friction factor
g = gravitational acceleration, m/s^2 (ft/s^2)
G = mass flux, kg/m^2 s (lbm/ft^2 s)
h = specific enthalpy, J/kg (Btu/lbm)
L = length, m (lbm)
$\dot{m}$ = mass flow rate, kg/s (lbm/s)
P = pressure, Pa (psi)
q'' = heat flux, W/m^2 (Btu/lbm^2 h)
Re = Reynolds number
S = slip ratio
s = specific entropy, J/kg K (Btu/lbm ^oR)
T = temperature, K (^oR)
V = velocity, m/s (ft/s)
x = vapor quality
z = horizontal position, m (ft)

Greek symbols

α = void fraction
ε = wall roughness, m (ft)
μ = dynamic viscosity, kg/m s (lb s/ft^2)
ρ = density, kg/m^3 (lbm/ft^3)
σ = surface tension, N/m (lb/ft)
τ = shear stress, N/m^2 (lb/ft^2)
υ = specific volume, m^3/kg (ft^3/lbm)

Subscripts

G = vapor phase
L = liquid phase
in = inlet condition
i = liquid-vapor interface
Lw = liquid-wall interface
mt = metastable region
s = saturated condition
sp = single-phase
sub = subcooling
tp = two-phase
v = vaporization

References

Aaron, A.A.20, and P.A. Domanski. 1990. Experimentation analysis and correlation of refrigerant-22 flow through short tube restrictors. *ASHRAE Transactions* 96:729–42.

ASHRAE. 1998. *ASHRAE Handbook*—Refrigeration, chap. 45. Atlanta, GA: ASHRAE.

ASME. 1971. *Fluid Meters—Their Theory and Application*. New York: American Society of Mechanical Engineers.

Chen, Z.H., R.Y. Li, S.Lin, and Z.Y. Chen. 1990. A correlation for metastable flow of refrigerant 12 through capillary tubes. *ASHRAE Transactions* 96:550–4.

Chisholm, D. 1973. Pressure gradient due to friction during the flow of evaporating two-phase mixture in smooth tube and channel. *International Journal of Heat and Mass Transfer* 16:347–58.

Choi, J., J.T. Chung, and Y. Kim. 2004. A generalized correlation for two-phase flow of alternative refrigerants through short tube orifices. *International Journal of Refrigeration* 27:393–400.

Collier, J.G., and J.R. Thome. 1996. *Convective Boiling and Condensation, 3rd ed.* Oxford University Press, New York.

Garcia-Valladares, O. 2006. Numerical simulation of trans-critical carbon dioxide (R744) flow through short tube orifices. *Applied Thermal Engineering* 144–51.

Kim, Y. 1993. Two-phase flow of HFC134a and HCFC22 through short tube orifices. Ph.D. Thesis, Texas A&M University, College Station, TX.

Kim, Y., and D.L. O'Neal. 1995. A comparison of critical flow models for estimating two-phase flow of HCFC22 and HFC134a through short tube orifices. *International Journal of Refrigeration* 18:447–55.

Kim, Y.C., W.V. Payne, D.L. O'Neal, and M. Farzad. 2002. Refrigerant flow through flexible short tube orifices. *HVAC&Research* 8:179–90.

Kim, Y., V. Payne, J. Choi, and P. Domanski. 2005. Mass flow of R410A through short tube working near the critical point. *International Journal of Refrigeration* 28:547–53.

Lackme, C. 1979. Incompleteness of the flashing of supersaturated liquid and sonic ejection of the produced phases. *International Journal of Multiphase Flow* 5:131–41.

Liu, J.P., Y.M. Niu, J.P. Chen, Z.J. Chen, and X. Feng. 2004. Experimental and correlation of R744 two-phase flow through short tubes. *Experimental Thermal and Fluid Science* 28:565–73.

McLinden, M.O., S.A. Klein, and E.W. Lemmon. 1998. REFPROP-thermodynamic and transport properties of refrigerant and refrigerant mixtures. NIST Standard Reference Database, Version 6.01.

Mei, V.C. 1982. Short-tube refrigerant flow restrictors. *ASHRAE Transactions* 88:157–69.

Miropolskiy, Z.L., R.I. Shneyerova, and A.I. Karamysheva. 1970. Vapour void fraction in steam fluid mixture flowing in heated and unheated channels. *International Heat Transfer Conference, Paris, France, August 31–September 5,* paper B4.75.

Nilpueng, K., and S. Wongwises. 2009. Experimental investigation of two-phase flow characteristics of HFC-134a through short-tube orifices. *International Journal of Refrigeration* 32:854–64.

Pasqua, P.F. 1953. Metastable flow of Freon-12. *Refrigeration Engineering* 61:1084–8.

Payne, W.V., and D.L. O'Neal. 1998. Mass flow characteristics of R407C through short-tube orifices. *ASHRAE Transactions* 104:197–209.

Payne, W.V., and D.L. O'Neal. 1999. Multiphase flow of refrigerant 410A through short tube orifices. *ASHRAE Transactions* 105: 66–74.

Singh, G.M., P.S. Hrnjak, and C.W. Bullard. 2001. Flow of refrigerant R134a through orifice tubes. *HVAC&R Research* 7: 245–62.

Tu, X., P.S. Hrnjak, and C.W. Bullard. 2006. Refrigerant 134a liquid flow through micro-scale short tube orifices with/without phase change. *Experimental Thermal and Fluid Science* 30:253–62.

Wongwises, S., and M. Suchatawat. 2002. A simulation for predicting the refrigerant flow characteristics including metastable region in adiabatic capillary tubes. *International Journal of Energy Research* 27:93–109.

Yang, L., and C.-L. Zhang. 2005. Two-fluid model of refrigerant two-phase flow through short tube orifice. *International Journal of Refrigeration* 28:419–27.

Zhang, C-L., and L. Yang. 2005. Modeling of supercritical CO_2 flow through short tube orifice. *Journal of Fluid Engineering, Transactions of ASME* 127:1194–8.

Zivi, S.M. 1964. Estimation of steady-state steam void fraction by means of the principle of minimum entropy production. *ASME Journal of Heat Transfer* 86:247–52.